CHARGED PARTICLES IN ONCOLOGY

EDITED BY: Marco Durante, Francis A. Cucinotta and Jay S. Loeffler

PUBLISHED IN: Frontiers in Oncology

frontiers Research Topics

Frontiers Copyright Statement

© Copyright 2007-2018 Frontiers Media SA. All rights reserved.

All content included on this site, such as text, graphics, logos, button icons, images, video/audio clips, downloads, data compilations and software, is the property of or is licensed to Frontiers Media SA ("Frontiers") or its licensees and/or subcontractors. The copyright in the text of individual articles is the property of their respective authors, subject to a license granted to Frontiers.

The compilation of articles constituting this e-book, wherever published, as well as the compilation of all other content on this site, is the exclusive property of Frontiers. For the conditions for downloading and copying of e-books from Frontiers' website, please see the Terms for Website Use. If purchasing Frontiers e-books from other websites or sources, the conditions of the website concerned apply.

Images and graphics not forming part of user-contributed materials may not be downloaded or copied without permission.

Individual articles may be downloaded and reproduced in accordance with the principles of the CC-BY licence subject to any copyright or other notices. They may not be re-sold as an e-book.

As author or other contributor you grant a CC-BY licence to others to reproduce your articles, including any graphics and third-party materials supplied by you, in accordance with the Conditions for Website Use and subject to any copyright notices which you include in connection with your articles and materials.

All copyright, and all rights therein, are protected by national and international copyright laws.

The above represents a summary only. For the full conditions see the Conditions for Authors and the Conditions for Website Use.

ISSN 1664-8714
ISBN 978-2-88945-391-7
DOI 10.3389/978-2-88945-391-7

About Frontiers

Frontiers is more than just an open-access publisher of scholarly articles: it is a pioneering approach to the world of academia, radically improving the way scholarly research is managed. The grand vision of Frontiers is a world where all people have an equal opportunity to seek, share and generate knowledge. Frontiers provides immediate and permanent online open access to all its publications, but this alone is not enough to realize our grand goals.

Frontiers Journal Series

The Frontiers Journal Series is a multi-tier and interdisciplinary set of open-access, online journals, promising a paradigm shift from the current review, selection and dissemination processes in academic publishing. All Frontiers journals are driven by researchers for researchers; therefore, they constitute a service to the scholarly community. At the same time, the Frontiers Journal Series operates on a revolutionary invention, the tiered publishing system, initially addressing specific communities of scholars, and gradually climbing up to broader public understanding, thus serving the interests of the lay society, too.

Dedication to quality

Each Frontiers article is a landmark of the highest quality, thanks to genuinely collaborative interactions between authors and review editors, who include some of the world's best academicians. Research must be certified by peers before entering a stream of knowledge that may eventually reach the public - and shape society; therefore, Frontiers only applies the most rigorous and unbiased reviews.

Frontiers revolutionizes research publishing by freely delivering the most outstanding research, evaluated with no bias from both the academic and social point of view.

By applying the most advanced information technologies, Frontiers is catapulting scholarly publishing into a new generation.

What are Frontiers Research Topics?

Frontiers Research Topics are very popular trademarks of the Frontiers Journals Series: they are collections of at least ten articles, all centered on a particular subject. With their unique mix of varied contributions from Original Research to Review Articles, Frontiers Research Topics unify the most influential researchers, the latest key findings and historical advances in a hot research area! Find out more on how to host your own Frontiers Research Topic or contribute to one as an author by contacting the Frontiers Editorial Office: **researchtopics@frontiersin.org**

CHARGED PARTICLES IN ONCOLOGY

Topic Editors:
Marco Durante, TIFPA-INFN, Trento, Italy
Francis A. Cucinotta, University of Nevada, Las Vegas, United States
Jay S. Loeffler, Harvard Medical School, United States

Image: Rick Partington/Shutterstock.com

High-energy charged particles represent a cutting-edge technique in radiation oncology. Protons and carbon ions are used in several centers all over the world for the treatment of different solid tumors. Typical indications are ocular malignancies, tumors of the base of the skull, hepatocellular carcinomas and various sarcomas. The physical characteristics of the charged particles (Bragg peak) allow sparing of much more normal tissues than it is possible using conventional X-rays, and for this reason all pediatric tumors are considered eligible for protontherapy. Ions heavier than protons also display special radiobiological characteristics, which make them effective against radioresistant and hypoxic tumors.

On the other hand, protons and ions with high charge (Z) and energy (HZE particles) represent a major risk for human space exploration. The main late effect of radiation exposure is cancer induction, and at the moment the dose limits for astronauts are based on cancer mortality risk. The Mars Science Laboratory (MSL) measured the dose on the route to Mars and on the planet's surface, suggesting that a human exploration missions will exceed the radiation risk limits. Notwithstanding many studies on carcinogenesis induced by protons and heavy ions, the risk uncertainty remains very high.

In this research topic we aim at gathering the experiences and opinions of scientists dealing with high-energy charged particles either for cancer treatment or for space radiation protection. Clinical results with protons and heavy ions, as well as research in medical physics and pre-clinical radiobiology are reported. In addition, ground-based and spaceflight studies on the effects of space radiation are included in this book. Particularly relevant for space studies are the clinical results on normal tissue complications and second cancers.

The eBook nicely demonstrates that particle therapy in oncology and protection of astronauts from space radiation share many common topics, and can learn from each other.

Citation: Durante, M., Cucinotta, F. A., Loeffler, J. S., eds. (2018). Charged Particles in Oncology. Lausanne: Frontiers Media. doi: 10.3389/978-2-88945-391-7

Table of Contents

10 ***Editorial: Charged Particles in Oncology***
Marco Durante, Francis A. Cucinotta and Jay S. Loeffler

Chapter 1 – Particle Radiobiology

Section 1.1 DNA Repair

13 ***Efficient Rejoining of DNA Double-Strand Breaks despite Increased Cell-Killing Effectiveness following Spread-Out Bragg Peak Carbon-Ion Irradiation***
Nicole B. Averbeck, Jana Topsch, Michael Scholz, Wilma Kraft-Weyrather, Marco Durante and Gisela Taucher-Scholz

21 ***DNA Damage Response Proteins and Oxygen Modulate Prostaglandin E_2 Growth Factor Release in Response to Low and High LET Ionizing Radiation***
Christopher P. Allen, Walter Tinganelli, Neelam Sharma, Jingyi Nie, Cory Sicard, Francesco Natale, Maurice King III, Steven B. Keysar, Antonio Jimeno, Yoshiya Furusawa, Ryuichi Okayasu, Akira Fujimori, Marco Durante and Jac A. Nickoloff

35 ***Higher Initial DNA Damage and Persistent Cell Cycle Arrest after Carbon Ion Irradiation Compared to X-irradiation in Prostate and Colon Cancer Cells***
Annelies Suetens, Katrien Konings, Marjan Moreels, Roel Quintens, Mieke Verslegers, Els Soors, Kevin Tabury, Vincent Grégoire and Sarah Baatout

45 ***Impact of Charged Particle Exposure on Homologous DNA Double-Strand Break Repair in Human Blood-Derived Cells***
Melanie Rall, Daniela Kraft, Meta Volcic, Aljona Cucu, Elena Nasonova, Gisela Taucher-Scholz, Halvard Bönig, Lisa Wiesmüller and Claudia Fournier

56 ***Induction of Chronic Inflammation and Altered Levels of DNA Hydroxymethylation in Somatic and Germinal Tissues of CBA/CaJ Mice Exposed to ^{48}Ti Ions***
Kanokporn Noy Rithidech, Witawat Jangiam, Montree Tungjai, Chris Gordon, Louise Honikel and Elbert B. Whorton

67 ***Novel Biological Approaches for Testing the Contributions of Single DSBs and DSB Clusters to the Biological Effects of High LET Radiation***
Veronika Mladenova, Emil Mladenov and George Iliakis

79 ***Short DNA Fragments Are a Hallmark of Heavy Charged-Particle Irradiation and May Underlie Their Greater Therapeutic Efficacy***
Dalong Pang, Sergey Chasovskikh, James E. Rodgers and Anatoly Dritschilo

Section 1.2 Chromosomal Aberrations

88 ***Biological Effectiveness of Accelerated Protons for Chromosome Exchanges***
Kerry A. George, Megumi Hada and Francis A. Cucinotta

95 ***Three-Color Chromosome Painting as Seen through the Eyes of mFISH: Another Look at Radiation-Induced Exchanges and Their Conversion to Whole-Genome Equivalency***

Bradford D. Loucas, Igor Shuryak and Michael N. Cornforth

Section 1.3 Cell Radiobiology

109 ***Correlation of Particle Traversals with Clonogenic Survival Using Cell-Fluorescent Ion Track Hybrid Detector***

Ivana Dokic, Martin Niklas, Ferdinand Zimmermann, Andrea Mairani, Philipp Seidel, Damir Krunic, Oliver Jäkel, Jürgen Debus, Steffen Greilich and Amir Abdollahi

116 ***Differential Superiority of Heavy Charged-Particle Irradiation to X-Rays: Studies on Biological Effectiveness and Side Effect Mechanisms in Multicellular Tumor and Normal Tissue Models***

Stefan Walenta and Wolfgang Mueller-Klieser

128 ***Effects of Charged Particles on Human Tumor Cells***

Kathryn D. Held, Hidemasa Kawamura, Takuya Kaminuma, Athena Evalour S. Paz, Yukari Yoshida, Qi Liu, Henning Willers and Akihisa Takahashi

147 ***Exposure to Carbon Ions Triggers Proinflammatory Signals and Changes in Homeostasis and Epidermal Tissue Organization to a Similar Extent as Photons***

Palma Simoniello, Julia Wiedemann, Joana Zink, Eva Thoennes, Maike Stange, Paul G. Layer, Maximilian Kovacs, Maurizio Podda, Marco Durante and Claudia Fournier

160 ***The Effect of X-Ray and Heavy Ions Radiations on Chemotherapy Refractory Tumor Cells***

Zhan Yu, Carola Hartel, Diana Pignalosa, Wilma Kraft-Weyrather, Guo-Liang Jiang, David Diaz-Carballo and Marco Durante

169 ***The Influence of C-Ions and X-rays on Human Umbilical Vein Endothelial Cells***

Alexander Helm, Ryonfa Lee, Marco Durante and Sylvia Ritter

179 ***Transcription Factors in the Cellular Response to Charged Particle Exposure***

Christine E. Hellweg, Luis F. Spitta, Bernd Henschenmacher, Sebastian Diegeler and Christa Baumstark-Khan

199 ***Translational Research to Improve the Efficacy of Carbon Ion Radiotherapy: Experience of Gunma University***

Takahiro Oike, Hiro Sato, Shin-ei Noda and Takashi Nakano

Section 1.4 Carcinogenesis

209 ***Comparison of Individual Radiosensitivity to γ-Rays and Carbon Ions***

Grace Shim, Marie Delna Normil, Isabelle Testard, William M. Hempel, Michelle Ricoul and Laure Sabatier

218 ***Decreased RXRα is Associated with Increased β-Catenin/TCF4 in ^{56}Fe-Induced Intestinal Tumors***

Shubhankar Suman, Santosh Kumar, Albert J. Fornace Jr. and Kamal Datta

225 ***HZE Radiation Non-Targeted Effects on the Microenvironment That Mediate Mammary Carcinogenesis***

Mary Helen Barcellos-Hoff and Jian-Hua Mao

235 ***Ionizing Particle Radiation as a Modulator of Endogenous Bone Marrow Cell Reprogramming: Implications for Hematological Cancers***

Sujatha Muralidharan, Sharath P. Sasi, Maria A. Zuriaga, Karen K. Hirschi, Christopher D. Porada, Matthew A. Coleman, Kenneth X. Walsh, Xinhua Yan and David A. Goukassian

244 ***Corrigendum: Ionizing Particle Radiation as a Modulator of Endogenous Bone Marrow Cell Reprogramming: Implications for Hematological Cancers***

Sujatha Muralidharan, Sharath P. Sasi, Maria A. Zuriaga, Karen K. Hirschi, Christopher D. Porada, Matthew A. Coleman, Kenneth X. Walsh, Xinhua Yan and David A. Goukassian

246 ***Radiation-Induced Reprogramming of Pre-Senescent Mammary Epithelial Cells Enriches Putative $CD44^{+}/CD24^{-/low}$ Stem Cell Phenotype***

Xuefeng Gao, Brock J. Sishc, Christopher B. Nelson, Philip Hahnfeldt, Susan M. Bailey and Lynn Hlatky

255 ***Telomeres and Telomerase in the Radiation Response: Implications for Instability, Reprograming, and Carcinogenesis***

Brock J. Sishc, Christopher B. Nelson, Miles J. McKenna, Christine L. R. Battaglia, Andrea Herndon, Rupa Idate, Howard L. Liber and Susan M. Bailey

Chapter 2 – Particle Therapy

Section 2.1 Medical Physics

274 ***Range Verification Methods in Particle Therapy: Underlying Physics and Monte Carlo Modeling***

Aafke Christine Kraan

301 ***Experimental Comparison of Knife-Edge and Multi-Parallel Slit Collimators for Prompt Gamma Imaging of Proton Pencil Beams***

Julien Smeets, Frauke Roellinghoff, Guillaume Janssens, Irene Perali, Andrea Celani, Carlo Fiorini, Nicolas Freud, Etienne Testa and Damien Prieels

309 ***Compton Camera and Prompt Gamma Ray Timing: Two Methods for In Vivo Range Assessment in Proton Therapy***

Fernando Hueso-González, Fine Fiedler, Christian Golnik, Thomas Kormoll, Guntram Pausch, Johannes Petzoldt, Katja E. Römer and Wolfgang Enghardt

322 ***First Images of a Three-Layer Compton Telescope Prototype for Treatment Monitoring in Hadron Therapy***

Gabriela Llosá, Marco Trovato, John Barrio, Ane Etxebeste, Enrique Muñoz, Carlos Lacasta, Josep F. Oliver, Magdalena Rafecas, Carles Solaz and Paola Solevi

328 ***Assessment of Geant4 Prompt-Gamma Emission Yields in the Context of Proton Therapy Monitoring***

Marco Pinto, Denis Dauvergne, Nicolas Freud, Jochen Krimmer, Jean M. Létang and Etienne Testa

335 ***The FLUKA Code: An Accurate Simulation Tool for Particle Therapy***

Giuseppe Battistoni, Julia Bauer, Till T. Boehlen, Francesco Cerutti, Mary P. W. Chin, Ricardo Dos Santos Augusto, Alfredo Ferrari, Pablo G. Ortega, Wioletta Kozłowska, Giuseppe Magro, Andrea Mairani, Katia Parodi, Paola R. Sala, Philippe Schoofs, Thomas Tessonnier and Vasilis Vlachoudis

359 ***Comparative Characterization Study of a $LaBr_3$(Ce)Scintillation Crystal in Two Surface Wrapping Scenarios: Absorptive and Reflective***

Saad Aldawood, Ines Castelhano, Roman Gernhäuser, Hugh Van Der Kolff, Christian Lang, Silvia Liprandi, Rudolf Lutter, Ludwig Maier, Tim Marinšek, Dennis R. Schaart, Katia Parodi and Peter G. Thirolf

368 ***Fast Pencil Beam Dose Calculation for Proton Therapy Using a Double-Gaussian Beam Model***

Joakim da Silva, Richard Ansorge and Rajesh Jena

379 ***First Steps Toward Ultrasound-Based Motion Compensation for Imaging and Therapy: Calibration with an Optical System and 4D PET Imaging***

Julia Schwaab, Christopher Kurz, Cristina Sarti, André Bongers, Frédéric Schoenahl, Christoph Bert, Jürgen Debus, Katia Parodi and Jürgen Walter Jenne

389 ***Monitoring of Hadrontherapy Treatments by Means of Charged Particle Detection***

Silvia Muraro, Giuseppe Battistoni, Francesco Collamati, Erika De Lucia, Riccardo Faccini, Fernando Ferroni, Salvatore Fiore, Paola Frallicciardi, Michela Marafini, Ilaria Mattei, Silvio Morganti, Riccardo Paramatti, Luca Piersanti, Davide Pinci, Antoni Rucinski, Andrea Russomando, Alessio Sarti, Adalberto Sciubba, Elena Solfaroli-Camillocci, Marco Toppi, Giacomo Traini, Cecilia Voena and Vincenzo Patera

406 ***Monte Carlo Calculations Supporting Patient Plan Verification in Proton Therapy***

Thiago V. M. Lima, Manjit Dosanjh, Alfredo Ferrari, Silvia Molineli, Mario Ciocca and Andrea Mairani

414 ***Phase Space Generation for Proton and Carbon Ion Beams for External Users' Applications at the Heidelberg Ion Therapy Center***

Thomas Tessonnier, Tiago Marcelos, Andrea Mairani, Stephan Brons and Katia Parodi

429 ***Treatment Parameters Optimization to Compensate for Interfractional Anatomy Variability and Intrafractional Tumor Motion***

Romain Brevet, Daniel Richter, Christian Graeff, Marco Durante and Christoph Bert

440 ***Introduction to the EC's Marie Curie Initial Training Network Project: The European Training Network in Digital Medical Imaging for Radiotherapy (ENTERVISION)***

Manjit Dosanjh, Manuela Cirilli and Sparsh Navin

447 ***Medical Applications at CERN and the ENLIGHT Network***

Manjit Dosanjh, Manuela Cirilli, Steve Myers and Sparsh Navin

Section 2.2 Biophysical Models

455 ***A Simpler Energy Transfer Efficiency Model to Predict Relative Biological Effect for Protons and Heavier Ions***

Bleddyn Jones

464 ***Corrigendum: A Simpler Energy Transfer Efficiency Model to Predict Relative Biological Effect for Protons and Heavier Ions***

Bleddyn Jones

465 ***Calculating Variations in Biological Effectiveness for a 62 MeV Proton Beam***

Mario Pietro Carante and Francesca Ballarini

475 ***Modeling Combined Chemotherapy and Particle Therapy for Locally Advanced Pancreatic Cancer***

Marco Durante, Francesco Tommasino and Shigeru Yamada

Section 2.3 Clinical Results

487 ***Paving the Road for Modern Particle Therapy – What Can We Learn from the Experience Gained with Fast Neutron Therapy in Munich?***

Hanno M. Specht, Teresa Neff, Waltraud Reuschel, Franz M. Wagner, Severin Kampfer, Jan J. Wilkens, Winfried Petry and Stephanie E. Combs

494 ***Increase in Tumor Control and Normal Tissue Complication Probabilities in Advanced Head-and-Neck Cancer for Dose-Escalated Intensity-Modulated Photon and Proton Therapy***

Annika Jakobi, Armin Lühr, Kristin Stützer, Anna Bandurska-Luque, Steffen Löck, Mechthild Krause, Michael Baumann, Rosalind Perrin and Christian Richter

503 ***Protons, Photons, and the Prostate – Is There Emerging Evidence in the Ongoing Discussion on Particle Therapy for the Treatment of Prostate Cancer?***

Kilian C. Schiller, Gregor Habl and Stephanie E. Combs

510 ***The Emerging Role of Carbon-Ion Radiotherapy***

Daniel K. Ebner and Tadashi Kamada

516 ***The Role of Hypofractionated Radiation Therapy with Photons, Protons, and Heavy Ions for Treating Extracranial Lesions***

Aaron Michael Laine, Arnold Pompos, Robert Timmerman, Steve Jiang, Michael D. Story, David Pistenmaa and Hak Choy

Section 2.4 Late Effects

530 ***A Review of Radiotherapy-Induced Late Effects Research after Advanced Technology Treatments***

Wayne D. Newhauser, Amy Berrington de Gonzalez, Reinhard Schulte and Choonsik Lee

541 ***Secondary Malignancy Risk Following Proton Radiation Therapy***

Bree R. Eaton, Shannon M. MacDonald, Torunn I. Yock and Nancy J. Tarbell

547 ***The Impact of Neutrons in Clinical Proton Therapy***

Uwe Schneider and Roger Hälg

Section 2.5 New Techniques

552 ***Applications of High-Throughput Clonogenic Survival Assays in High-LET Particle Microbeams***

Antonios Georgantzoglou, Michael J. Merchant, Jonathan C. G. Jeynes, Natalie Mayhead, Natasha Punia, Rachel E. Butler and Rajesh Jena

561 ***Charged Particle Therapy with Mini-Segmented Beams***

F. Avraham Dilmanian, John G. Eley, Adam Rusek and Sunil Krishnan

569 ***Clinical and Research Activities at the CATANA Facility of INFN-LNS: From the Conventional Hadrontherapy to the Laser-Driven Approach***

Giuseppe A. P. Cirrone, Giacomo Cuttone, Luigi Raffaele, Vincenzo Salamone, Teresio Avitabile, Giuseppe Privitera, Corrado Spatola, Antonio G. Amico, Giuseppina Larosa, Renata Leanza, Daniele Margarone, Giuliana Milluzzo, Valeria Patti, Giada Petringa, Francesco Romano, Andrea Russo, Antonio Russo, Maria G. Sabini, Francesco Schillaci, Valentina Scuderi and Lucia M. Valastro

Chapter 3 – Space Radiation Protection

582 ***Evaluation of Superconducting Magnet Shield Configurations for Long Duration Manned Space Missions***

Filippo Ambroglini, Roberto Battiston and William J. Burger

603 ***Issues for Simulation of Galactic Cosmic Ray Exposures for Radiobiological Research at Ground-Based Accelerators***

Myung-Hee Y. Kim, Adam Rusek and Francis A. Cucinotta

617 ***Personalized Cancer Risk Assessments for Space Radiation Exposures***

Paul A. Locke and Michael M. Weil

626 ***Radiation Measurements Performed with Active Detectors Relevant for Human Space Exploration***

Livio Narici, Thomas Berger, Daniel Matthiä and Günther Reitz

636 ***The Role of Nuclear Fragmentation in Particle Therapy and Space Radiation Protection***

Cary Zeitlin and Chiara La Tessa

frontiers in Oncology

EDITORIAL
published: 08 December 2017
doi: 10.3389/fonc.2017.00301

Editorial: Charged Particles in Oncology

Marco Durante[1], Francis A. Cucinotta[2] and Jay S. Loeffler[3]*

[1] Trento Institute for Fundamental Physics and Applications (TIFPA), National Institute of Nuclear Physics (INFN), University of Trento, Rome, Italy, [2] University of Nevada, Las Vegas, NV, United States, [3] Massachusetts General Hospital, Harvard Medical School, Boston, MA, United States

Keywords: radiotherapy, particle therapy, proton therapy, carbon ions, space radiation

Editorial on the Research Topic

Charged Particles in Oncology

High-energy charged particles represent a cutting-edge technique in radiation oncology (1). Protons and carbon ions are used in several centers all over the world for the treatment of different solid tumors. Typical indications are ocular malignancies, tumors of the base of the skull, hepatocellular carcinomas, and various sarcomas (2). The physical characteristics of the charged particles (Bragg peak) allow sparing of much more normal tissues than it is possible using conventional X-rays (3), and for this reason, all pediatric tumors are considered eligible for proton therapy (4). Ions heavier than protons also display special radiobiological characteristics, which make them effective against radioresistant and hypoxic tumors (5).

Protons and ions with high charge (Z) and energy (HZE particles) represent a major risk for human space exploration (6, 7). The main late effect of radiation exposure is cancer induction (8), and at the moment the dose limits for astronauts are based on lifetime cancer mortality risk (9, 10). The Mars Science Laboratory measured the dose on the route to Mars (11) and on the planet's surface (12), supporting predictions that a human exploration mission to Mars will exceed the radiation risk limits (7, 13). Notwithstanding many studies on carcinogenesis induced by protons and heavy ions, the risk uncertainty remains high with important risk assessment questions to non-targeted effects (13) and the "quality" of HZE particle-induced tumors compared to spontaneous and photon-induced tumors (8).

In this research topic, we invited scientists studying high-energy charged particles either for cancer treatment or for space radiation protection. We believe that space radiation protection and particle therapy share many common problems, and this research topic can be an inspiration to find applications and answers from fields that are apparently far away. Physics, biology, and medical contributions in this field will be found in the volume, owing to the fact that the field of charged particles in oncology is highly interdisciplinary.

The research topics accepted 59 articles including a total of 351 authors, demonstrating the high interest in this field. It is in the top five most viewed research topics of this journal. The articles can be divided into the following topics.

PHYSICS

A number of contributions deal with medical physics in particle therapy. Articles with most views are the reviews of range verification methods in particle therapy by Aafke Kraan and of the FLUKA Monte Carlo code. FLUKA is widely used at CERN but, from high-energy physics uses, has found several applications both in particle therapy and space radiation simulations. Cary Zeitlin and Chiara La Tessa describe the role of nuclear fragmentation in particle therapy and space radiation

OPEN ACCESS

Edited and Reviewed by:
Timothy James Kinsella, Warren Alpert Medical School of Brown University, United States

****Correspondence:***
Marco Durante
marco.durante@tifpa.infn.it

Specialty section:
This article was submitted to Radiation Oncology, a section of the journal Frontiers in Oncology

Received: *14 November 2017*
Accepted: *23 November 2017*
Published: *08 December 2017*

Citation:
Durante M, Cucinotta FA and Loeffler JS (2017) Editorial: Charged Particles in Oncology. Front. Oncol. 7:301. doi: 10.3389/fonc.2017.00301

shielding. A highly viewed article by Kim et al. details how nuclear fragmentation can be exploited to simulate the full galactic cosmic ray spectra using a few particle beams with applications in biological countermeasure and radiation shielding studies. Six articles deal with experimental methods for range verification in particle therapy, using prompt γ-rays, secondary charged particles, 4D-PET, or ultrasounds. For space radiation protection, the use of active detectors for personal dosimetry is described, and potential applications of superconducting magnets for active shielding are reported from the SR2S European project.

BIOLOGY

Several articles deal with experimental radiobiology and carcinogenesis induced by high-energy charged particles. In a highly viewed article, Sishc et al. discuss the role of telomeres in radiation-induced carcinogenesis. Cellular effects of charged particles in comparison to X-rays are reported in tumor cells and in normal human endothelial cells. Chromosome aberrations and DNA damage response pathways are the main topic of five different articles. Specific molecular pathways following exposure to charged particles are also described in various articles, e.g., transcription factors, prostaglandin ("Phoenix rising" effect), bone marrow and mammary cell reprogramming, β-catenin, proinflammatory signals.

MEDICINE

Twelve manuscripts report clinical results of particle therapy. Schiller et al. review the results of particle therapy in prostate cancer, while two articles summarize the Japanese experience with carbon ion therapy in Chiba and Gunma. The articles on second cancers and late effects after proton therapy are important examples of the bridge between therapy and space: the results are, in fact, also very important for the assessment of late effects caused by cosmic rays in crews of long-term space missions. Lane et al. describe results with X-rays using hypofractionation, and how high dose/fractionation can be beneficial using protons and heavy ions. Modeling clinical results is described in other articles, dealing with RBE in proton therapy and combination of particle therapy and chemotherapy. An interesting article from Specht et al. collects the data on fast neutron therapy and indicates what can be learned form that experience in charged particle therapy. Fast neutrons are an important risk factor for space missions, too.

FACILITIES AND NETWORKS

Finally, a few articles are dedicated to the analysis of facilities for ground-based space research and preclinical radiobiology, mini-beams in therapy, and networks and educational activities in particle therapy.

The high number of articles submitted, and their excellent quality, indicates that the topic is considered of great interest for researchers in many different fields. Looking at the overall picture, it is clear that space radiation protection and particle therapy share many common research problems (14) and can learn from each other. Differences are also clear: space radiation protection conditions are whole body, low-dose rate for a specialized group of highly skilled workers; radiotherapy is characterized by partial body, high-dose, fractionated exposures of cancer patients. Nevertheless, many research topics are similar: late effects (see Newhauser et al. in this issue), including cancer (see articles by Locke and Weil and Eaton et al. in this issue) and tissue degenerative effects such as cardiovascular (15) and CNS (16); individual radiosensitivity (see the article by Shim et al. in this article); particle and neutron dosimetry (see Schneider and Hälg in this issue) and microdosimetry (17); transport calculations with Monte Carlo (Lima et al. in this issue) and analytical codes; radioprotectors; and non-targeted effects (see the article by Barcellos-Hoff and Mao in this issue). They also share common platforms for research. We hope that this ebook will be useful for researchers working on charged particles in looking for answers to the many questions that these two topics, only apparently far away, share.

AUTHOR CONTRIBUTIONS

All authors contributed equally to this editorial.

REFERENCES

1. Bortfeld TR, Loeffler JS. Three ways to make proton therapy affordable. *Nature* (2017) 549(7673):451–3. doi:10.1038/549451a
2. Durante M, Orecchia R, Loeffler JS. Charged-particle therapy in cancer: clinical uses and future perspectives. *Nat Rev Clin Oncol* (2017) 14(8):483–95. doi:10.1038/nrclinonc.2017.30
3. Durante M, Paganetti H. Nuclear physics in particle therapy: a review. *Rep Prog Phys* (2016) 79:96702. doi:10.1088/0034-4885/79/9/096702
4. Yock TI, Yeap BY, Ebb DH, Weyman E, Eaton BR, Sherry NA, et al. Long-term toxic effects of proton radiotherapy for paediatric medulloblastoma: a phase 2 single-arm study. *Lancet Oncol* (2016) 17(3):287–98. doi:10.1016/S1470-2045(15)00167-9
5. Kamada T, Tsujii H, Blakely EA, Debus J, De Neve W, Durante M, et al. Carbon ion radiotherapy in Japan: an assessment of 20 years of clinical experience. *Lancet Oncol* (2015) 16(2):e93–100. doi:10.1016/S1470-2045(14)70412-7
6. Durante M, Cucinotta FA. Physical basis of radiation protection in space travel. *Rev Mod Phys* (2011) 83(4):1245. doi:10.1103/RevModPhys.83.1245
7. Cucinotta FA, Kim MY, Chappell LJ, Huff JL. How safe is safe enough? Radiation protection for a human mission to Mars. *PLoS One* (2013) 8(10):e74988. doi:10.1371/journal.pone.0074988
8. Durante M, Cucinotta FA. Heavy ion carcinogenesis and human space exploration. *Nat Rev Cancer* (2008) 8(6):465–72. doi:10.1038/nrc2391
9. Cucinotta FA. Space radiation risks for astronauts on multiple international space station missions. *PLoS One* (2014) 9(4):e96099. doi:10.1371/journal.pone.0096099
10. McKenna-Lawlor S, Bhardwajb A, Ferraric F, Kuznetsovd N, Lale AK, Lif Y, et al. Feasibility study of astronaut standardized career dose limits in LEO and the outlook for BLEO. *Acta Astronaut* (2014) 104(2):565–73. doi:10.1016/j.actaastro.2014.07.011
11. Zeitlin C, Hassler DM, Cucinotta FA, Ehresmann B, Wimmer-Schweingruber RF, Brinza DE, et al. Measurements of energetic particle radiation in transit to Mars on the Mars Science Laboratory. *Science* (2013) 340(6136):1080–4. doi:10.1126/science.1235989
12. Hassler DM, Zeitlin C, Wimmer-Schweingruber RF, Ehresmann B, Rafkin S, Eigenbrode JL, et al. Mars' surface radiation environment measured with

the Mars Science Laboratory's curiosity rover. *Science* (2014) 343(6169): 1244797. doi:10.1126/science.1244797
13. Cucinotta FA, Cacao E. Non-targeted effects models predict significantly higher Mars mission cancer risk than targeted effects model. *Sci Rep* (2017) 7(1):1832. doi:10.1038/s41598-017-02087-3
14. Durante M, Eighth Warren K. Sinclair keynote address: heavy ions in therapy and space: benefits and risks. *Health Phys* (2012) 103(5):532–9. doi:10.1097/HP.0b013e318264b4b6
15. Hughson RL, Helm A, Durante M. Heart in space: effect of the extraterrestrial environment on the cardiovascular system. *Nat Rev Cardiol* (2017). doi:10.1038/nrcardio.2017.157
16. Cucinotta FA, Alp M, Sulzman FM, Wang M. Space radiation risks to the central nervous system. *Life Sci Space Res* (2014) 2:54–69. doi:10.1016/j.lssr.2014.06.003
17. Wambersie A, Menzel H, Guelette J, Pihet P. Fifteen symposia on microdosimetry: implications for modern particle-beam cancer radiotherapy. *Radiat Prot Dosimetry* (2015) 166(1–4):328–33. doi:10.1093/rpd/ncv304

Conflict of Interest Statement: The authors declare that the research was conducted in the absence of any commercial or financial relationships that could be construed as a potential conflict of interest.

Copyright © 2017 Durante, Cucinotta and Loeffler. This is an open-access article distributed under the terms of the Creative Commons Attribution License (CC BY). The use, distribution or reproduction in other forums is permitted, provided the original author(s) or licensor are credited and that the original publication in this journal is cited, in accordance with accepted academic practice. No use, distribution or reproduction is permitted which does not comply with these terms.

frontiers in Oncology

ORIGINAL RESEARCH
published: 12 February 2016
doi: 10.3389/fonc.2016.00028

Efficient Rejoining of DNA Double-Strand Breaks despite Increased Cell-Killing Effectiveness following Spread-Out Bragg Peak Carbon-Ion Irradiation

Nicole B. Averbeck[1], Jana Topsch[1†], Michael Scholz[1], Wilma Kraft-Weyrather[1], Marco Durante[1,2] and Gisela Taucher-Scholz[1,2]*

[1] Department of Biophysics, GSI Helmholtzzentrum für Schwerionenforschung GmbH, Darmstadt, Germany, [2] Technische Universität Darmstadt, Darmstadt, Germany

Radiotherapy of solid tumors with charged particles holds several advantages in comparison to photon therapy; among them conformal dose distribution in the tumor, improved sparing of tumor-surrounding healthy tissue, and an increased relative biological effectiveness (RBE) in the tumor target volume in the case of ions heavier than protons. A crucial factor of the biological effects is DNA damage, of which DNA double-strand breaks (DSBs) are the most deleterious. The reparability of these lesions determines the cell survival after irradiation and thus the RBE. Interestingly, using phosphorylated H2AX as a DSB marker, our data in human fibroblasts revealed that after therapy-relevant spread-out Bragg peak irradiation with carbon ions DSBs are very efficiently rejoined, despite an increased RBE for cell survival. This suggests that misrepair plays an important role in the increased RBE of heavy-ion radiation. Possible sources of erroneous repair will be discussed.

Keywords: heavy ions, carbon-ion radiotherapy, DSB complexity, DSB repair, error-prone DNA repair, RBE

OPEN ACCESS

Edited by:
Joel S. Greenberger, University of Pittsburgh Medical Center-Shadyside, USA

Reviewed by:
Michael Wayne Epperly, University of Pittsburgh Cancer Institute, USA
Bevin P. Engelward, Massachusetts Institute of Technology, USA

****Correspondence:***
Nicole B. Averbeck
n.averbeck@gsi.de

†Present address:
Jana Topsch, Interdisziplinäres Zentrum Klinische Studien (IZKS), Universitätsmedizin der Johannes Gutenberg-Universität Mainz, Mainz, Germany

Specialty section:
This article was submitted to Radiation Oncology, a section of the journal Frontiers in Oncology

Received: *19 August 2015*
Accepted: *25 January 2016*
Published: *12 February 2016*

Citation:
Averbeck NB, Topsch J, Scholz M, Kraft-Weyrather W, Durante M and Taucher-Scholz G (2016) Efficient Rejoining of DNA Double-Strand Breaks despite Increased Cell-Killing Effectiveness following Spread-Out Bragg Peak Carbon-Ion Irradiation. Front. Oncol. 6:28. doi: 10.3389/fonc.2016.00028

INTRODUCTION

Radiotherapy is an indispensable tool for treating solid tumors (1). Advances in conventional radiation therapy with photons and especially new approaches using charged particles have led to an improved physical delivery of dose in radiation therapy (2–4). Irradiation with accelerated ions heavier than protons, namely carbon ions, has additional advantage as it is characterized by an increased relative biological effectiveness (RBE) in the targeted tumor volume (4). This allows the irradiation of deep-seated tumors, minimizing at the same time the dose to normal tissue or in organs at risk (2). Accelerated ions of a linear energy transfer (LET) of >10 keV/μm are considered high-LET radiation. Due to their characteristic energy deposition within a confined volume, they cause DNA damage of greater complexity (5–7). A special feature of this densely ionizing radiation is the induction of clustered lesions – two or more DNA lesions within one or two helix turns (8) – comprising double-strand breaks (DSBs) in close proximity that are more difficult to repair (9, 10). An additional level of complexity arises due to the localized microscopic energy deposition occurring along the particle track when traversing nuclear chromatin. At different size scales, from

the nucleosome to chromatin fiber loops, the induction of spatially correlated DSBs within chromatin subunits can increase the severity of the induced lesions (11, 12), resulting in a decreased probability of DSB repair (13). Damage clustering at different levels is thus a crucial factor for the enhanced biological effects of radiotherapeutical heavy-ion irradiation and was shown earlier (14, 15).

Several studies have analyzed the repair capacity of heavy ion radiation-induced DSBs with different kinds of methods (13, 16–20). All studies revealed that with increasing LET repair slows down and the number of DSBs remaining unrepaired increases. Furthermore, chromosome studies applying premature chromosome condensation (PCC) on cells exposed to radiation of different LET agree with these data; with increasing LET, the fraction of excess PCC fragments increases and correspondingly the unrejoined breaks (21–25). In addition, high-LET radiation is also more effective in inducing mutations and chromosome aberrations, especially of the complex type, i.e., involving at least two or more chromosomes, which indicates misrepair of DSBs (26–30). Likely sources for misrepair are the close proximity of the breaks, which could facilitate the ligation of wrong break ends and the choice of the DSB-repair pathway (7, 31). The latter is supported by our findings that repair of carbon ion-induced DSBs is dependent on resection (32), a process that clearly influences the repair pathway choice (33). Thus, the increased RBE of high-LET radiation is presumably based on an increased number of unrejoined and misrepaired DSBs.

In carbon-ion radiotherapy the target volume is typically irradiated with ions from opposing fields. Beams with different ion energies are superimposed, resulting in a spread-out Bragg peak (SOBP) with the desired homogeneous distribution of dose (4). Consequently, the cells within the SOBP are exposed to a wide spectrum of carbon ions with different individual energies and LET. Due to this mixed radiation field, DNA damage of different complexity is expected to occur, from rather simple lesions induced by high-energy ions to very complex damage induced by low-energy ions. The DNA damage of different quality will likely influence the efficiency of cell killing and thus the RBE.

Earlier survival studies have shown that the RBE depends on the capacity to repair the induced DNA damage (14, 15). These and most of the above mentioned research, which revealed an increased number of unrejoined DSBs in repair studies and misrepaired DSBs in cytogenetic analyses, was performed using mainly monoenergetic ions or hamster cells (13, 16–20, 26–29). Aimed at a better understanding of the relationship between DSB repair and the RBE of therapeutic carbon-ion irradiation, we examined the effect of radiation quality on the survival of human fibroblasts and DSB repair.

RESULTS

Within this study, we used normal human fibroblasts to first examine the systematics of survival depending on the changing radiation quality along the penetration path of carbon ions. Furthermore, we compared the repair of DSBs after exposure to the different radiation qualities in the carbon-ion entrance channel (EC) and SOBP, where the target tumor volume would be seated. The confluent fibroblast cells analyzed in this study preclude the interference of cell cycle changes and are thus especially suitable for reliable repair measurements using phosphorylated H2AX (γH2AX) as a marker for DSBs (34).

Cell Survival in Dependence of the Penetration Depth of Carbon Ions

To study cell survival along the carbon-ion EC and SOBP, we applied an experimental setup that allows irradiating cells at different positions within a polyacrylic tank previously described (35) (**Figure 1A**). Following the one-field irradiation with a 4-cm SOBP of carbon ions in a water-equivalent depth of 6–10 cm, the survival data obtained for confluent, human fibroblasts show the expected depth profile with higher survival levels in the EC and a decline of cell survival in the target SOBP region, yielding a region with clearly reduced cell survival compared to the EC (**Figure 1C**). The increase of the RBE with penetration depth – represented by the ratio of the two depth-dose curves in **Figure 1B** – becomes obvious from the fact that despite the reduction of absorbed dose toward the distal end of the SOBP the biological effect still increases, i.e., the survival drops within the SOBP. The RBE reaches a value of 2.3 at the distal edge, whereas in the EC, it is approximately 1.1.

These data have been also used to validate the local effect model (LEM) that has been developed for biological optimization in treatment planning (35). Very good agreement is found between the model prediction and the experimental data both in the EC and in the target region.

Repair Kinetics of DSBs Induced in the Carbon-Ion EC and SOBP

Aimed at mimicking a therapy-like configuration, we studied the DSB-repair capacity of confluent (G0/G1-phase) human fibroblasts upon a two-field SOBP carbon-ion irradiation. The irradiation from two opposing sides, typical for patient treatment, has the advantage of compensating for the variations in LET and RBE gradients observed in **Figure 1**. The applied physical dose within the SOBP was 2 Gy according to a typical therapeutic fraction; the corresponding EC dose was 0.6 Gy. We adapted the previously described experimental setup (**Figure 1A**) placing cells grown on coverslips (to allow DSB microscopy analysis; see below) at positions equivalent to those in the EC and the SOBP (**Figure 2A**). The irradiation geometry was verified by the measured clonogenic cell survival. The experimental data showing clearly lower survival in the SOBP compared to the EC (**Figure 2B**, circles) agree very well with the calculated survival from the LEM (**Figure 2B**, line). In this case, it has been taken into account that cells growing on glass typically show a higher sensitivity as compared to cells grown on plastic material (36). Subsequently, this setup was used to measure the repair of DSBs induced in the EC and SOBP. We first directly compared the repair of DSBs induced by 0.6 Gy carbon ions in the EC with that after the same dose of X-rays (**Figure 3A**) using immunofluorescence microscopy to detect the DSB marker γH2AX (34). This method had proven most appropriate at the dose applied here and represents a suitable DSB-repair assay in G0/G1-phase cells

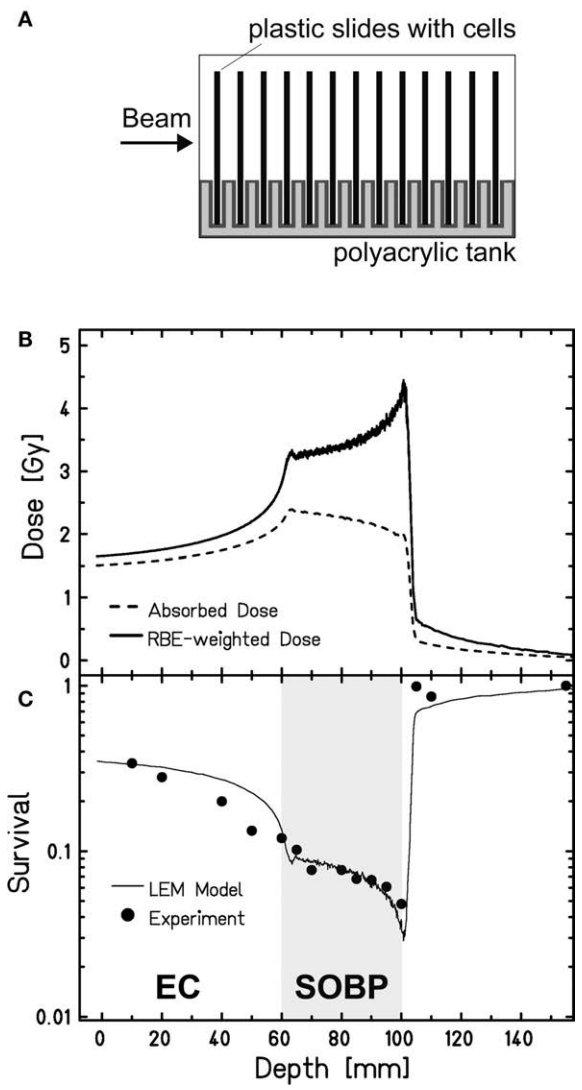

FIGURE 1 | Survival of human fibroblasts upon a one-field carbon-ion irradiation along the beam penetration path. **(A)** Experimental setup for a one-field irradiation. Confluent, human fibroblasts (AG1522D) grown on slides were placed perpendicular to the beam direction in a medium filled tank at different positions from the beam entrance side, as described earlier (35). The irradiation at the heavy-ion synchrotron (SIS), GSI Darmstadt, was done with a 4-cm SOBP in a water-equivalent depth of 6–10 cm (LET: 45 keV/μm at the proximal edge, 150 keV/μm at the distal edge). **(B)** Depth-dose distribution of the absorbed dose (dashed line) and the RBE-weighted dose (LEM calculated; solid line) of the carbon ions. **(C)** Measured (circles; $n = 1$) and calculated (line; LEM) clonogenic cell survival of human fibroblasts along the beam axes.

(34). The repair of DSBs for both types of irradiation was similar and mostly completed within 12 h, as determined by γH2AX-foci loss. This agrees well with earlier findings on DSB rejoining along the irradiation axis of therapy-relevant carbon ions or X-rays (16). By contrast, following irradiation with a comparable dose (0.8 Gy) of high LET (168 keV/μm), low-energy (9.9 MeV/u on target) carbon ions, which correspond to stopping ions in the SOBP, a significant fraction of γH2AX foci is still remaining 24 h post exposure (**Figure 3A**). These results emphasize the impact of radiation quality on DSB repair and show that repair of clustered DSBs is impaired, which is in line with earlier findings (18–20, 37). It should be noted, however, that despite irradiation with the beam almost parallel to the cell monolayer enabling improved foci counting along the ion tracks, γH2AX foci induced by these densely ionizing ions may not represent individual DSBs (38–41).

We next applied the two-field carbon-ion irradiation to measure the repair of DSBs induced in the center of an SOBP at a dose of 2 Gy. In order to avoid inconsistencies in foci counting due to overlapping foci at the higher dose and LET (41, 44, 45), flow cytometry was used to quantify the global γH2AX signal. This method is suggested to give an enhanced resolution in measuring DSB damage induced by high-LET high-energy ion irradiation compared to γH2AX-foci counting (20, 46). The γH2AX signal was measured up to 65 h post exposure and the DSB-repair data for irradiation in the SOBP are compared with the corresponding γH2AX values obtained after exposure of the cells to the same dose (2 Gy) of ions in the EC (**Figure 3B**). As expected, DSBs induced within the EC are mostly repaired within 12 h, similar to the result obtained by the γH2AX-foci assay upon irradiation with 0.6 Gy. Interestingly, also the cells placed in the SOBP region repaired the carbon ion-induced DSBs very efficiently to the same extent as in the EC. Although the decay of the γH2AX signal appeared to be slightly slower up to 24 h post SOBP irradiation, it declined similar to the EC almost to control values within 48 h.

DISCUSSION

Here, we aimed at clarifying the relationship between DSB repair and RBE of therapeutic carbon-ion irradiation. We confirmed that the repair capacity represents an important factor in this relationship, and our data further suggest that the quality of the repair also affects the RBE.

Efficiency of Cell Killing and DSB Rejoining along the Penetration Path of Carbon Ions

The survival data of the G0/G1-phase human fibroblasts and the calculated RBE in the EC and the SOBP demonstrate that the RBE is highest in the SOBP. This is in accordance with data obtained with hamster cells in a similar setup (35). Interestingly, the smallest survival and highest RBE are observed within the SOBP where the ion energy is smallest, at the very distal edge. Our repair data on ion irradiation of this quality, i.e., high LET, low-energy carbon ions (9.9 keV/u on target) in **Figure 3A**, show impaired repair of DSBs. Thus, the decreased survival at the distal edge of a one-field SOBP irradiation corresponds well with the decreased repair capacity we observed for low-energy ions and as it was seen earlier (16, 19). The notion that the decreased DSB-repair capacity is responsible for the decreased survival upon low-energy carbon-ion irradiation is further supported by earlier data on survival of confluent, human fibroblasts upon fractionated and non-fractionated irradiation with low-energy carbon ions (11 MeV/u, 153.5 keV/μm); fractionating the dose with

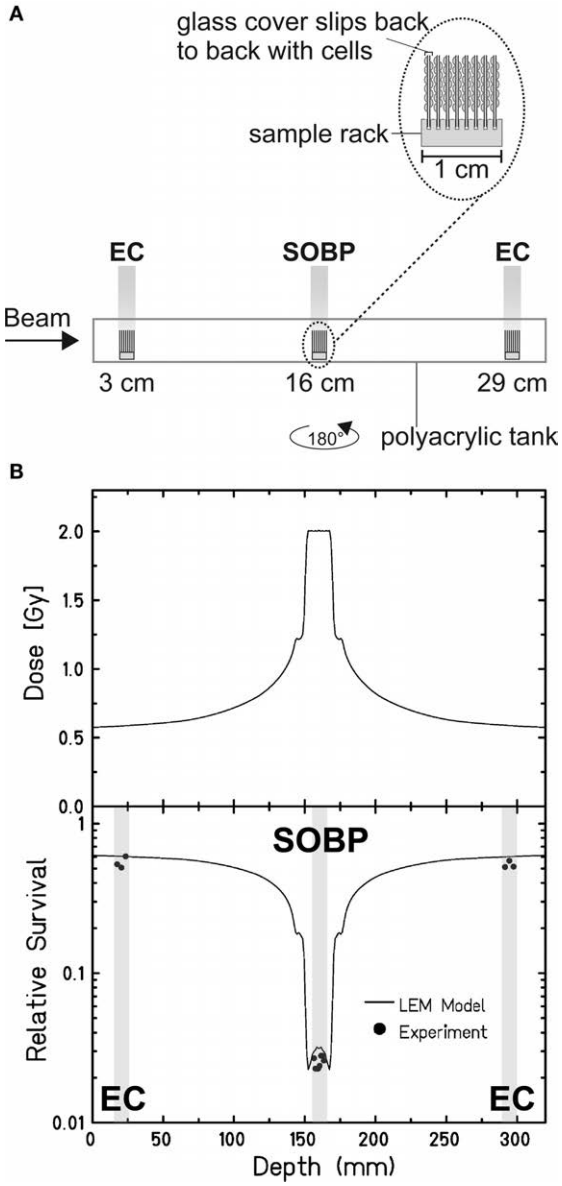

FIGURE 2 | **Verification of the experimental setup to mimic therapy-like carbon-ion irradiation**. **(A)** Experimental setup for a two-field irradiation. Confluent, human fibroblasts (AG1522D) were exposed at different positions from the beam entrance side within a medium filled tank. At the SIS, GSI Darmstadt, the two-field configuration typical for patient irradiation was simulated by irradiating the tank from both sides with a horizontal turn of 180°. The irradiation was done with an SOBP of 2.4 cm at a water-equivalent depth of 16 cm. The dose in the SOBP was 2 Gy (dose-averaged LET: 70–85 keV/μm). Samples in the EC region were irradiated with a corresponding dose of 0.6 Gy (dose-averaged LET: 13 keV/μm). **(B)** Top: distribution of the absorbed dose upon two-sided therapy-like irradiation. Bottom: corresponding calculated (line; LEM) and measured (circles; $n = 1$) cell survival. The gray boxes indicate the position of the samples during irradiation.

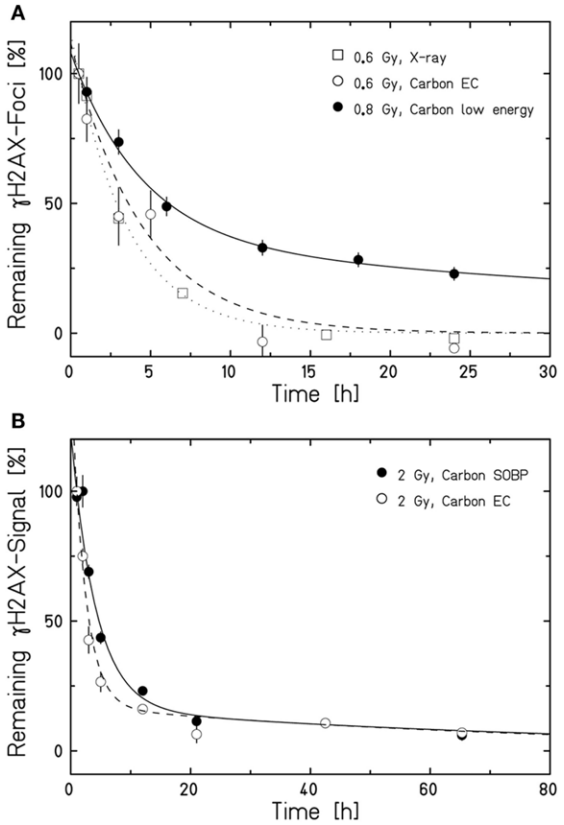

FIGURE 3 | **Human fibroblasts repair DSBs induced by therapy-like carbon-ion irradiation**. DSB-repair kinetics of confluent (G0/G1-phase) human AG1522 fibroblasts was measured after exposure to different radiation qualities. The average γH2AX-foci number **(A)** or γH2AX signal **(B)** of mock irradiated cells was subtracted from all data measured after irradiation. The curves are a guide to the eye obtained by exponential fits after normalization to the initial or extrapolated γH2AX values at 30 min **(A)** or 1 h **(B)** post irradiation. Data points represent the average of 2–4 experiments ± SEM [exception: low-energy carbon-ion irradiation in **(A)**; $n = 1 \pm$ SEM foci number/nucleus, at least 100 cells were analyzed]. **(A)** Kinetics after irradiation with 0.6 Gy X-rays, 0.6 Gy carbon ions in the EC (for irradiation conditions see **Figure 2A**), or 0.8 Gy low-energy carbon ions almost parallel to the cell monolayer (9.9 MeV/u on target; 168 keV/μm). DSBs were revealed by a γH2AX-foci analysis after γH2AX immunostaining performed as described in Meyer et al. (42). **(B)** Comparison of the DSB-repair capacity in human fibroblasts after 2 Gy carbon-ion irradiation in the EC or SOBP (for irradiation conditions see **Figure 2A**). The global immunofluorescent γH2AX signal was analyzed by flow cytometry according to Tommasino et al. (43).

a 24 h interval between fractions did not improve the survival indicating that the capacity to repair the induced DNA damage is very low (14).

The survival data and repair kinetics of cells irradiated within the EC (**Figures 2** and **3**) show that the cells can cope well with this irradiation. DSB rejoining is complete and its kinetics comparable to the rejoining kinetics of X-ray-induced DSBs (**Figure 3A**). This suggests that the repair is successful and hence ensures survival. This conclusion is supported by earlier work with the same cell system. This work revealed an RBE_{10} of 1.2 ± 0.3 for high-energy carbon ions (266 keV/u; 13.7 keV/μm) (14), which are in the range of carbon ions within the EC in the here presented experiment. In addition, Wang et al. showed clearly increased survival for both radiation qualities upon fractionated irradiation, which

further corroborates that DNA damage in the EC can be effectively repaired (14).

Our data in **Figure 2** revealed that the survival within the SOBP is smallest, yet DSBs induced within this region are repaired only slightly slower than DSBs induced within the EC (**Figure 3B**). This result is most likely based on the mixed energy and LET of the ions within this region. The fraction of low-energy ions is small, and this is mirrored in the repair capacity. Similar results were obtained with one-field SOBP–carbon-ion irradiation (50 keV/μm dose-averaged LET) of non-synchronized hamster cells (47). Nonetheless, although the DSBs induced in the SOBP are repaired the RBE of therapy-relevant carbon-ion irradiation is increased [see above and Ref. (48)]. This leads to the assumption that misrepair plays a non-negligible role in the increased RBE. The proximity of the DSBs within clusters may enhance the probability of misrejoining. In addition, the pathway choice has an important impact on the accuracy of the DNA repair, and hence, will be discussed in greater detail. **Figure 4** summarizes known and proposed repair activities at complex, ion-induced DSBs.

Repair Pathways of Complex DSBs

The observation that DSBs induced in G0/G1-phase human fibroblasts within the SOBP are repaired slightly slower than DSBs induced within the EC (**Figure 3B**) suggests that DNA-repair pathways involving different types of end processing might be used. This is supported by earlier findings showing that with increasing LET an increasing number of resected DSBs is found. This occurs independent of the cell cycle phase (32, 49, 50) and is important for DSB repair (32). Notably, DSB repair involving resected ends represents a potential source of erroneous repair (33). The observed resection is dependent on MRE11, CtIP, and EXO1 (32, 49, 50). In addition, break-end processing by Artemis may take also place as this nuclease was shown to be important for the survival upon ion irradiation (9, 51) and was suggested to be involved in the repair of α particle-induced DSBs (52).

Which pathways repair DSBs induced by therapy-relevant carbon ions is still under investigation. Based on data on X-ray and carbon-ion irradiated human G2-phase cells, it was proposed that classical non-homologous end joining (c-NHEJ) will make an initial attempt to repair the DSBs (37, 53). This hypothesis is supported by data on proliferating hamster cells irradiated with SOBP–carbon ions, which show that c-NHEJ is vital to repair the induced DSBs (47). The choice of this pathway is supported by the findings that the repair of high-LET iron-ion (150 keV/μm) and α-particle (130 ± 10 keV/μm)-induced DSBs require DNA-PKcs, an important component of c-NHEJ (54). In addition, recruitment of GFP-tagged Ku80, a further important component of c-NHEJ, to DSBs induced by single gold ions was observed in living murine cells (55). If due to DNA fragmentation generated by ion irradiation the Ku complex cannot form fast enough (56), c-NHEJ may fail to proceed quickly. Then, resection of ion-induced DSBs by MRE11, CtIP, and EXO1 and break-end processing by Artemis may occur (32, 49, 50, 57). It is conceivable that Artemis in its function as endonuclease trims the resected

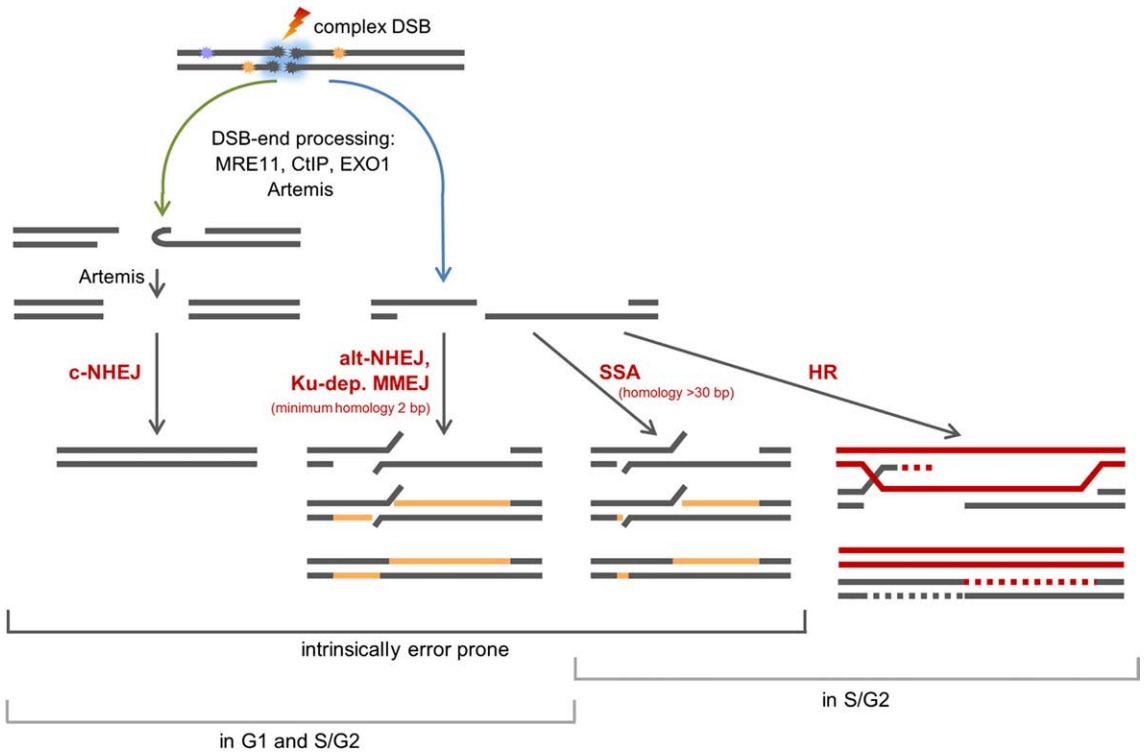

FIGURE 4 | Scheme of the repair of complex, carbon ion-induced DSBs. DSBs that cannot be rapidly repaired by c-NHEJ will undergo break-end resection by MRE11, CtIP, EXO1, and break-end processing by Artemis. Blue arrow: resected DSBs can be repaired by alt-NHEJ, a potentially Ku-dependent MMEJ, SSA, or HR. The latter two pathways operate in S- and G2-phase only. Green arrow: Artemis may make resected DSB ends available for c-NHEJ.

DSB ends – either by opening hairpins that form from single-stranded stretches or by trimming off single-stranded areas (58, 59) – to make the break ends available for the c-NHEJ repair machinery (45, 52). DSBs with single-stranded overhangs will be channeled into homology-mediated repair. In G2-phase cells, this might be single strand annealing (SSA), but it mainly represents homologous recombination (HR) as was shown upon irradiation with carbon or iron ions (37, 47, 60). The fate of resected DSBs in G1-phase cells is mainly unknown. They are not repaired by HR (32, 60). c-NHEJ factors are discussed to be involved in a repair option involving a Ku-dependent microhomology-mediated end joining (MMEJ) pathway in G1-phase cells (45, 61). However, c-NHEJ itself is considered to be unable to repair DSB break ends with long single-stranded overhangs (33). Ku- and LIG4-independent alternative (alt)-NHEJ represents a further repair choice for G1-phase DSBs with long single-stranded overhangs (62, 63), since it frequently involves CtIP- and MRE11-dependent break resection and microhomologies for ligation (64–69). Although it was described to operate only if Ku is absent (70, 71), it was proposed to operate in repair proficient cells if c-NHEJ fails locally (7). The choice of microhomology-mediated pathways is supported by the fact that ion-induced, rejoined DSBs are often characterized by deletions and flanking microhomologies (72). It should be noted that besides HR all repair pathways using processed break ends are inherently erroneous.

An increased use of error-prone repair and the close proximity of the breaks, which could facilitate the ligation of wrong break ends, represent likely reasons for the increased mutation and chromosome-aberration rate seen in cells treated with high-LET radiation (72). Considering our here presented data, we propose that misrepair and thus mutations and aberrations play a non-negligible role in the increased RBE for cell killing of therapy-relevant carbon radiation.

MATERIALS AND METHODS

Cells, Cell Culture, and Survival Assay

Normal human foreskin fibroblasts AG1522 (Coriell Cell Repository, Camden, NJ, USA; passage 11–15) were cultured in EMEM with EBSS salts, 15% FCS, 2 mM L-glutamine, and 1% penicillin/streptomycin at 37°C, 5% CO_2. To obtain confluent cultures enriched in G1 cells, 10^4 cells/cm^2 were seeded and used for experiments 10 days later. For the survival assays, the clonogenic survival was determined, as described earlier (14). For the survival data in **Figure 1**, cells were cultivated on polystyrene slides (35). For the repair kinetics and the associated survival data, cells were cultivated on glass cover slips (ø 30 mm or 24 mm × 24 mm).

Irradiation

Cells were irradiated with X-rays (250 keV, 16 mA; X-ray tube IV320-13, Seifert, Germany) or carbon ions at the GSI Helmholtz Center for Heavy Ion Research (Darmstadt, Germany). Irradiations with low-energy carbon ions were performed at the UNILAC beam line (11.4 MeV/u primary energy, 9.9 MeV/u on target, LET 168 keV/μm) and with high-energy carbon ions at the heavy-ion synchrotron (SIS) using active energy variation and raster scanning (48). Since the selection of ions available is limited some data are from single experiments only. For the survival data in **Figure 1**, cells were irradiated in a medium filled polyacrylic tank (35) (**Figure 1A**). The one-field carbon-ion irradiation was done with a 4-cm SOBP in a water-equivalent depth of 6–10 cm (LET: 45 keV/μm at the proximal edge, 150 keV/μm at the distal edge). For the repair kinetics and corresponding survival data, cells were exposed at different positions within a medium filled polyacrylic tank (**Figure 2A**). Cells seeded on glass cover slips were positioned approximately 3, 16, and 29 cm from the beam entrance side. To simulate the two-field configuration typical for patient irradiation, the tank was first irradiated from one side and after turning it horizontally by 180°, it was irradiated from the other side with the same dose distribution. An SOBP with a width of 2.4 cm at a water-equivalent depth of 16 cm was applied. The dose in the SOBP was 2 Gy and the dose-averaged LET values were about 70 and 85 keV/μm in the center and at the edges of the SOBP, respectively. Samples for SOBP irradiation were placed in the middle of the SOPB to minimize the influence of variations in positioning. Samples in the EC region were irradiated at a depth of a few millimeter, corresponding to a dose-averaged LET of 13 keV/μm and a dose of 0.6 Gy.

Model Calculations

Model calculations were performed using the LEM, as described by Elsässer et al. (35). The model allows predicting the effects of ion radiation based on the localized, microscopic energy deposition pattern of particle tracks in combination with the knowledge of the photon dose–response curve for the endpoint under consideration. The corresponding parameters of the photon cell survival curve were $\alpha = 0.54$ Gy^{-1}, $\beta = 0.062$ Gy^{-2}, and $D_t = 13.5$ Gy, where D_t characterizes the transition from a curvilinear shape at low and intermediate doses to a linear shape at high doses [for details see, e.g., Ref. (73)]. The dose–response of AG1522D cells on glass cover slips was estimated by scaling the dose values by a factor of 1.3 according to the information given in Furre et al. (36).

Immunostaining

For the γH2AX-foci analyses, DSBs were visualized by γH2AX immunostaining performed, as described in Meyer et al. (42). The global immunofluorescent γH2AX signal was analyzed by flow cytometry according to Tommasino et al. (43).

AUTHOR CONTRIBUTIONS

GTS designed research; WKW and JT performed research; NBA, WKW, MS, and JT analyzed data; and NBA, MD, MS, and GTS wrote the paper. All authors approved the work for publication.

ACKNOWLEDGMENTS

We thank M. Herrlitz and B. Meyer for irradiation and γH2AX-foci counting using X-rays and monoenergetic carbon ions, respectively, and Y. Schweinfurth for carbon-ion irradiation in the EC and γH2AX-foci analysis with Image-Pro Plus (Media Cybernetics, USA) as well as for the survival data in **Figure 2**. This project was partially funded by the German Federal Ministry of Education and Research (grant number 02NUK001A).

REFERENCES

1. Loeffler JS, Durante M. Charged particle therapy – optimization, challenges and future directions. *Nat Rev Clin Oncol* (2013) **10**(7):411–24. doi:10.1038/nrclinonc.2013.79
2. Durante M, Loeffler JS. Charged particles in radiation oncology. *Nat Rev Clin Oncol* (2010) **7**(1):37–43. doi:10.1038/nrclinonc.2009.183
3. Schulz-Ertner D, Tsujii H. Particle radiation therapy using proton and heavier ion beams. *J Clin Oncol* (2007) **25**(8):953–64. doi:10.1200/JCO.2006.09.7816
4. Schardt D, Elsässer T, Schulz-Ertner D. Heavy-ion tumor therapy: physical and radiobiological benefits. *Rev Mod Phys* (2010) **82**(1):383–425. doi:10.1103/RevModPhys.82.383
5. Kramer M, Kraft G. Track structure and DNA damage. *Adv Space Res* (1994) **14**(10):151–9. doi:10.1016/0273-1177(94)90465-0
6. Nikjoo H, O'Neill P, Wilson WE, Goodhead DT. Computational approach for determining the spectrum of DNA damage induced by ionizing radiation. *Radiat Res* (2001) **156**(5 Pt 2):577–83. doi:10.1667/0033-7587(2001)156[0577:CAFDTS]2.0.CO;2
7. Schipler A, Iliakis G. DNA double-strand-break complexity levels and their possible contributions to the probability for error-prone processing and repair pathway choice. *Nucleic Acids Res* (2013) **41**(16):7589–605. doi:10.1093/nar/gkt556
8. Sage E, Harrison L. Clustered DNA lesion repair in eukaryotes: relevance to mutagenesis and cell survival. *Mutat Res* (2011) **711**(1–2):123–33. doi:10.1016/j.mrfmmm.2010.12.010
9. Asaithamby A, Chen DJ. Mechanism of cluster DNA damage repair in response to high-atomic number and energy particles radiation. *Mutat Res* (2011) **711**(1–2):87–99. doi:10.1016/j.mrfmmm.2010.11.002
10. Lorat Y, Brunner CU, Schanz S, Jakob B, Taucher-Scholz G, Rube CE. Nanoscale analysis of clustered DNA damage after high-LET irradiation by quantitative electron microscopy – the heavy burden to repair. *DNA Repair (Amst)* (2015) **28**:93–106. doi:10.1016/j.dnarep.2015.01.007
11. Rydberg B. Radiation-induced DNA damage and chromatin structure. *Acta Oncol* (2001) **40**(6):682–5. doi:10.1080/02841860152619070
12. Friedrich T, Scholz U, Elsasser T, Durante M, Scholz M. Calculation of the biological effects of ion beams based on the microscopic spatial damage distribution pattern. *Int J Radiat Biol* (2012) **88**(1–2):103–7. doi:10.3109/09553002.2011.611213
13. Tommasino F, Friedrich T, Scholz U, Taucher-Scholz G, Durante M, Scholz M. A DNA double-strand break kinetic rejoining model based on the local effect model. *Radiat Res* (2013) **180**(5):524–38. doi:10.1667/RR13389.1
14. Wang J, Li R, Guo C, Fournier C, K-Weyrather W. The influence of fractionation on cell survival and premature differentiation after carbon ion irradiation. *J Radiat Res* (2008) **49**(4):391–8. doi:10.1269/jrr.08012
15. Weyrather WK, Ritter S, Scholz M, Kraft G. RBE for carbon track-segment irradiation in cell lines of differing repair capacity. *Int J Radiat Biol* (1999) **75**(11):1357–64. doi:10.1080/095530099139232
16. Heilmann J, Taucher-Scholz G, Haberer T, Scholz M, Kraft G. Measurement of intracellular DNA double-strand break induction and rejoining along the track of carbon and neon particle beams in water. *Int J Radiat Oncol Biol Phys* (1996) **34**(3):599–608. doi:10.1016/0360-3016(95)02112-4
17. Hoglund H, Stenerlow B. Induction and rejoining of DNA double-strand breaks in normal human skin fibroblasts after exposure to radiation of different linear energy transfer: possible roles of track structure and chromatin organization. *Radiat Res* (2001) **155**(6):818–25. doi:10.1667/0033-7587(2001)155[0818:IARODD]2.0.CO;2
18. Asaithamby A, Uematsu N, Chatterjee A, Story MD, Burma S, Chen DJ. Repair of HZE-particle-induced DNA double-strand breaks in normal human fibroblasts. *Radiat Res* (2008) **169**(4):437–46. doi:10.1667/RR1165.1
19. Schmid TE, Dollinger G, Beisker W, Hable V, Greubel C, Auer S, et al. Differences in the kinetics of gamma-H2AX fluorescence decay after exposure to low and high LET radiation. *Int J Radiat Biol* (2010) **86**(8):682–91. doi:10.3109/09553001003734543
20. Whalen MK, Gurai SK, Zahed-Kargaran H, Pluth JM. Specific ATM-mediated phosphorylation dependent on radiation quality. *Radiat Res* (2008) **170**(3):353–64. doi:10.1667/RR1354.1
21. Wu H, Furusawa Y, George K, Kawata T, Cucinotta FA. Analysis of unrejoined chromosomal breakage in human fibroblast cells exposed to low- and high-LET radiation. *J Radiat Res* (2002) **43**(Suppl):S181–5. doi:10.1269/jrr.43.S181
22. Kawata T, Durante M, George K, Furusawa Y, Gotoh E, Takai N, et al. Kinetics of chromatid break repair in G2-human fibroblasts exposed to low- and high-LET radiations. *Phys Med* (2001) **17**(Suppl 1):226–8.
23. Kawata T, Durante M, Furusawa Y, George K, Ito H, Wu H, et al. Rejoining of isochromatid breaks induced by heavy ions in G2-phase normal human fibroblasts. *Radiat Res* (2001) **156**(5 Pt 2):598–602. doi:10.1667/0033-7587(2001)156[0598:ROIBIB]2.0.CO;2
24. Nasonova E, Ritter S. Cytogenetic effects of densely ionising radiation in human lymphocytes: impact of cell cycle delays. *Cytogenet Genome Res* (2004) **104**(1–4):216–20. doi:10.1159/000077492
25. Deperas-Standylo J, Lee R, Nasonova E, Ritter S, Gudowska-Nowak E. Production and distribution of aberrations in resting or cycling human lymphocytes following Fe-ion or Cr-ion irradiation: emphasis on single track effects. *Adv Space Res* (2012) **50**(5):584–97. doi:10.1016/j.asr.2012.05.007
26. Kawata T, Ito H, George K, Wu H, Cucinotta FA. Chromosome aberrations induced by high-LET radiations. *Biol Sci Space* (2004) **18**(4):216–23. doi:10.2187/bss.18.216
27. Durante M, Bedford JS, Chen DJ, Conrad S, Cornforth MN, Natarajan AT, et al. From DNA damage to chromosome aberrations: joining the break. *Mutat Res* (2013) **756**(1–2):5–13. doi:10.1016/j.mrgentox.2013.05.014
28. Hill MA. Fishing for radiation quality: chromosome aberrations and the role of radiation track structure. *Radiat Prot Dosimetry* (2015) **166**(1–4):295–301. doi:10.1093/rpd/ncv151
29. Yatagai F. Mutations induced by heavy charged particles. *Biol Sci Space* (2004) **18**(4):224–34. doi:10.2187/bss.18.224
30. Blakely EA, Kronenberg A. Heavy-ion radiobiology: new approaches to delineate mechanisms underlying enhanced biological effectiveness. *Radiat Res* (1998) **150**(5 Suppl):S126–45. doi:10.2307/3579815
31. Mladenov E, Iliakis G. Induction and repair of DNA double strand breaks: the increasing spectrum of non-homologous end joining pathways. *Mutat Res* (2011) **711**(1–2):61–72. doi:10.1016/j.mrfmmm.2011.02.005
32. Averbeck NB, Ringel O, Herrlitz M, Jakob B, Durante M, Taucher-Scholz G. DNA end resection is needed for the repair of complex lesions in G1-phase human cells. *Cell Cycle* (2014) **13**(16):2509–16. doi:10.4161/15384101.2015.941743
33. Grabarz A, Barascu A, Guirouilh-Barbat J, Lopez BS. Initiation of DNA double strand break repair: signaling and single-stranded resection dictate the choice between homologous recombination, non-homologous end-joining and alternative end-joining. *Am J Cancer Res* (2012) **2**(3):249–68.
34. Lobrich M, Shibata A, Beucher A, Fisher A, Ensminger M, Goodarzi AA, et al. gammaH2AX foci analysis for monitoring DNA double-strand break repair: strengths, limitations and optimization. *Cell Cycle* (2010) **9**(4):662–9. doi:10.4161/cc.9.4.10764
35. Elsässer T, Weyrather WK, Friedrich T, Durante M, Iancu G, Kramer M, et al. Quantification of the relative biological effectiveness for ion beam radiotherapy: direct experimental comparison of proton and carbon ion beams and a novel approach for treatment planning. *Int J Radiat Oncol Biol Phys* (2010) **78**(4):1177–83. doi:10.1016/j.ijrobp.2010.05.014
36. Furre T, Bergstrand ES, Pedersen E, Koritzinsky M, Olsen DR, Hole EO, et al. Measurement of dose rate at the interface of cell culture medium and glass dishes by means of ESR dosimetry using thin films of alanine. *Radiat Res* (1999) **152**(1):76–82. doi:10.2307/3580052
37. Shibata A, Conrad S, Birraux J, Geuting V, Barton O, Ismail A, et al. Factors determining DNA double-strand break repair pathway choice in G2 phase. *EMBO J* (2011) **30**(6):1079–92. doi:10.1038/emboj.2011.27
38. Antonelli F, Campa A, Esposito G, Giardullo P, Belli M, Dini V, et al. Induction and repair of DNA DSB as revealed by H2AX phosphorylation foci in human fibroblasts exposed to low- and high-LET radiation: relationship with early and delayed reproductive cell death. *Radiat Res* (2015) **183**(4):417–31. doi:10.1667/RR13855.1
39. Desai N, Davis E, O'Neill P, Durante M, Cucinotta FA, Wu H. Immunofluorescence detection of clustered gamma-H2AX foci induced by HZE-particle radiation. *Radiat Res* (2005) **164**(4 Pt 2):518–22. doi:10.1667/RR3431.1
40. Jakob B, Scholz M, Taucher-Scholz G. Biological imaging of heavy charged-particle tracks. *Radiat Res* (2003) **159**(5):676–84. doi:10.1667/0033-7587(2003)159[0676:BIOHCT]2.0.CO;2

41. Jakob B, Splinter J, Taucher-Scholz G. Positional stability of damaged chromatin domains along radiation tracks in mammalian cells. *Radiat Res* (2009) **171**(4):405–18. doi:10.1667/RR1520.1
42. Meyer B, Voss KO, Tobias F, Jakob B, Durante M, Taucher-Scholz G. Clustered DNA damage induces pan-nuclear H2AX phosphorylation mediated by ATM and DNA-PK. *Nucleic Acids Res* (2013) **41**(12):6109–18. doi:10.1093/nar/gkt304
43. Tommasino F, Friedrich T, Jakob B, Meyer B, Durante M, Scholz M. Induction and processing of the radiation-induced gamma-H2AX signal and its link to the underlying pattern of DSB: a combined experimental and modelling study. *PLoS One* (2015) **10**(6):e0129416. doi:10.1371/journal.pone.0129416
44. Costes SV, Chiolo I, Pluth JM, Barcellos-Hoff MH, Jakob B. Spatiotemporal characterization of ionizing radiation induced DNA damage foci and their relation to chromatin organization. *Mutat Res* (2010) **704**(1–3):78–87. doi:10.1016/j.mrrev.2009.12.006
45. Goodarzi AA, Jeggo PA. The repair and signaling responses to DNA double-strand breaks. *Adv Genet* (2013) **82**:1–45. doi:10.1016/B978-0-12-407676-1.00001-9
46. Sridharan DM, Chappell LJ, Whalen MK, Cucinotta FA, Pluth JM. Defining the biological effectiveness of components of high-LET track structure. *Radiat Res* (2015) **184**(1):105–19. doi:10.1667/RR13684.1
47. Gerelchuluun A, Manabe E, Ishikawa T, Sun L, Itoh K, Sakae T, et al. The major DNA repair pathway after both proton and carbon-ion radiation is NHEJ, but the HR pathway is more relevant in carbon ions. *Radiat Res* (2015) **183**(3):345–56. doi:10.1667/RR13904.1
48. Weyrather WK, Debus J. Particle beams for cancer therapy. *Clin Oncol* (2003) **15**(1):S23–8. doi:10.1053/clon.2002.0185
49. Barton O, Naumann SC, Diemer-Biehs R, Kunzel J, Steinlage M, Conrad S, et al. Polo-like kinase 3 regulates CtIP during DNA double-strand break repair in G1. *J Cell Biol* (2014) **206**(7):877–94. doi:10.1083/jcb.201401146
50. Yajima H, Fujisawa H, Nakajima NI, Hirakawa H, Jeggo PA, Okayasu R, et al. The complexity of DNA double strand breaks is a critical factor enhancing end-resection. *DNA Repair (Amst)* (2013) **12**(11):936–46. doi:10.1016/j.dnarep.2013.08.009
51. Sridharan DM, Whalen MK, Almendrala D, Cucinotta FA, Kawahara M, Yannone SM, et al. Increased Artemis levels confer radioresistance to both high and low LET radiation exposures. *Radiat Oncol* (2012) **7**:96. doi:10.1186/1748-717X-7-96
52. Riballo E, Kuhne M, Rief N, Doherty A, Smith GC, Recio MJ, et al. A pathway of double-strand break rejoining dependent upon ATM, Artemis, and proteins locating to gamma-H2AX foci. *Mol Cell* (2004) **16**(5):715–24. doi:10.1016/j.molcel.2004.10.029
53. Jeggo PA, Geuting V, Lobrich M. The role of homologous recombination in radiation-induced double-strand break repair. *Radiother Oncol* (2011) **101**(1):7–12. doi:10.1016/j.radonc.2011.06.019
54. Anderson JA, Harper JV, Cucinotta FA, O'Neill P. Participation of DNA-PKcs in DSB repair after exposure to high- and low-LET radiation. *Radiat Res* (2010) **174**(2):195–205. doi:10.1667/RR2071.1
55. Merk B, Voss KO, Müller I, Fischer BE, Jakob B, Taucher-Scholz G, et al. Photobleaching setup for the biological end-station of the darmstadt heavy-ion microprobe. *Nucl Instrum Methods Phys Res B* (2013) **306**(0):81–4. doi:10.1016/j.nimb.2012.11.043
56. Wang H, Wang X, Zhang P, Wang Y. The Ku-dependent non-homologous end-joining but not other repair pathway is inhibited by high linear energy transfer ionizing radiation. *DNA Repair (Amst)* (2008) **7**(5):725–33. doi:10.1016/j.dnarep.2008.01.010
57. Moscariello M, Wieloch R, Kurosawa A, Li F, Adachi N, Mladenov E, et al. Role for Artemis nuclease in the repair of radiation-induced DNA double strand breaks by alternative end joining. *DNA Repair (Amst)* (2015) **31**:29–40. doi:10.1016/j.dnarep.2015.04.004
58. Gu J, Li S, Zhang X, Wang LC, Niewolik D, Schwarz K, et al. DNA-PKcs regulates a single-stranded DNA endonuclease activity of Artemis. *DNA Repair (Amst)* (2010) **9**(4):429–37. doi:10.1016/j.dnarep.2010.01.001
59. Ma Y, Pannicke U, Schwarz K, Lieber MR. hairpin opening and overhang processing by an Artemis/DNA-dependent protein kinase complex in nonhomologous end joining and V(D)J recombination. *Cell* (2002) **108**(6):781–94. doi:10.1016/S0092-8674(02)00671-2
60. Zafar F, Seidler SB, Kronenberg A, Schild D, Wiese C. Homologous recombination contributes to the repair of DNA double-strand breaks induced by high-energy iron ions. *Radiat Res* (2010) **173**(1):27–39. doi:10.1667/RR1910.1
61. Katsura Y, Sasaki S, Sato M, Yamaoka K, Suzukawa K, Nagasawa T, et al. Involvement of Ku80 in microhomology-mediated end joining for DNA double-strand breaks in vivo. *DNA Repair (Amst)* (2007) **6**(5):639–48. doi:10.1016/j.dnarep.2006.12.002
62. Iliakis G. Backup pathways of NHEJ in cells of higher eukaryotes: cell cycle dependence. *Radiother Oncol* (2009) **92**(3):310–5. doi:10.1016/j.radonc.2009.06.024
63. Mansour WY, Rhein T, Dahm-Daphi J. The alternative end-joining pathway for repair of DNA double-strand breaks requires PARP1 but is not dependent upon microhomologies. *Nucleic Acids Res* (2010) **38**(18):6065–77. doi:10.1093/nar/gkq387
64. Rahal EA, Henricksen LA, Li Y, Williams RS, Tainer JA, Dixon K. ATM regulates Mre11-dependent DNA end-degradation and microhomology-mediated end joining. *Cell Cycle* (2010) **9**(14):2866–77. doi:10.4161/cc.9.14.12363
65. Rass E, Grabarz A, Plo I, Gautier J, Bertrand P, Lopez BS. Role of Mre11 in chromosomal nonhomologous end joining in mammalian cells. *Nat Struct Mol Biol* (2009) **16**(8):819–24. doi:10.1038/nsmb.1641
66. Xie A, Kwok A, Scully R. Role of mammalian Mre11 in classical and alternative nonhomologous end joining. *Nat Struct Mol Biol* (2009) **16**(8):814–8. doi:10.1038/nsmb.1640
67. Bennardo N, Cheng A, Huang N, Stark JM. Alternative-NHEJ is a mechanistically distinct pathway of mammalian chromosome break repair. *PLoS Genet* (2008) **4**(6):e1000110. doi:10.1371/journal.pgen.1000110
68. Zhang Y, Jasin M. An essential role for CtIP in chromosomal translocation formation through an alternative end-joining pathway. *Nat Struct Mol Biol* (2011) **18**(1):80–4. doi:10.1038/nsmb.1940
69. Truong LN, Li Y, Shi LZ, Hwang PY, He J, Wang H, et al. Microhomology-mediated end joining and homologous recombination share the initial end resection step to repair DNA double-strand breaks in mammalian cells. *Proc Natl Acad Sci U S A* (2013) **110**(19):7720–5. doi:10.1073/pnas.1213431110
70. Fattah F, Lee EH, Weisensel N, Wang Y, Lichter N, Hendrickson EA. Ku regulates the non-homologous end joining pathway choice of DNA double-strand break repair in human somatic cells. *PLoS Genet* (2010) **6**(2):e1000855. doi:10.1371/journal.pgen.1000855
71. Wang M, Wu W, Rosidi B, Zhang L, Wang H, Iliakis G. PARP-1 and Ku compete for repair of DNA double strand breaks by distinct NHEJ pathways. *Nucleic Acids Res* (2006) **34**(21):6170–82. doi:10.1093/nar/gkl840
72. Singleton BK, Griffin CS, Thacker J. Clustered DNA damage leads to complex genetic changes in irradiated human cells. *Cancer Res* (2002) **62**(21):6263–9.
73. Elsasser T, Scholz M. Cluster effects within the local effect model. *Radiat Res* (2007) **167**(3):319–29. doi:10.1667/RR0467.1

Conflict of Interest Statement: The authors declare that the research was conducted in the absence of any commercial or financial relationships that could be construed as a potential conflict of interest.

Copyright © 2016 Averbeck, Topsch, Scholz, Kraft-Weyrather, Durante and Taucher-Scholz. This is an open-access article distributed under the terms of the Creative Commons Attribution License (CC BY). The use, distribution or reproduction in other forums is permitted, provided the original author(s) or licensor are credited and that the original publication in this journal is cited, in accordance with accepted academic practice. No use, distribution or reproduction is permitted which does not comply with these terms.

frontiers in Oncology

ORIGINAL RESEARCH
published: 07 December 2015
doi: 10.3389/fonc.2015.00260

DNA Damage Response Proteins and Oxygen Modulate Prostaglandin E_2 Growth Factor Release in Response to Low and High LET Ionizing Radiation

*Christopher P. Allen[1], Walter Tinganelli[2,3], Neelam Sharma[1], Jingyi Nie[1], Cory Sicard[1], Francesco Natale[2], Maurice King III[1], Steven B. Keysar[4], Antonio Jimeno[4], Yoshiya Furusawa[3,5], Ryuichi Okayasu[6], Akira Fujimori[6], Marco Durante[2] and Jac A. Nickoloff[1]**

[1] Department of Environmental and Radiological Health Sciences, Colorado State University, Fort Collins, CO, USA, [2] GSI Helmholtzzentrum für Schwerionenforschung GmbH, Darmstadt, Germany, [3] Research Development and Support Center, National Institute of Radiological Sciences, Chiba, Japan, [4] Division of Medical Oncology, University of Colorado School of Medicine, Aurora, CO, USA, [5] Research Center for Radiation Protection, National Institute of Radiological Sciences, Chiba, Japan, [6] Research Center for Charged Particle Therapy, National Institute of Radiological Sciences, Chiba, Japan

OPEN ACCESS

Edited by:
Anatoly Dritschilo,
Georgetown University School of Medicine, USA

Reviewed by:
Kevin Prise,
Queen's University Belfast, UK
Chuan-Yuan Li,
Duke University, USA

***Correspondence:**
Jac A. Nickoloff
j.nickoloff@colostate.edu

Specialty section:
This article was submitted to Radiation Oncology, a section of the journal Frontiers in Oncology

Received: 02 October 2015
Accepted: 09 November 2015
Published: 07 December 2015

Citation:
Allen CP, Tinganelli W, Sharma N, Nie J, Sicard C, Natale F, King M III, Keysar SB, Jimeno A, Furusawa Y, Okayasu R, Fujimori A, Durante M and Nickoloff JA (2015) DNA Damage Response Proteins and Oxygen Modulate Prostaglandin E_2 Growth Factor Release in Response to Low and High LET Ionizing Radiation. Front. Oncol. 5:260. doi: 10.3389/fonc.2015.00260

Common cancer therapies employ chemicals or radiation that damage DNA. Cancer and normal cells respond to DNA damage by activating complex networks of DNA damage sensor, signal transducer, and effector proteins that arrest cell cycle progression, and repair damaged DNA. If damage is severe enough, the DNA damage response (DDR) triggers programed cell death by apoptosis or other pathways. Caspase 3 is a protease that is activated upon damage and triggers apoptosis, and production of prostaglandin E_2 (PGE_2), a potent growth factor that can enhance growth of surviving cancer cells leading to accelerated tumor repopulation. Thus, dying tumor cells can promote growth of surviving tumor cells, a pathway aptly named Phoenix Rising. In the present study, we surveyed Phoenix Rising responses in a variety of normal and established cancer cell lines, and in cancer cell lines freshly derived from patients. We demonstrate that IR induces a Phoenix Rising response in many, but not all cell lines, and that PGE_2 production generally correlates with enhanced growth of cells that survive irradiation, and of unirradiated cells co-cultured with irradiated cells. We show that PGE_2 production is stimulated by low and high LET ionizing radiation, and can be enhanced or suppressed by inhibitors of key DDR proteins. PGE_2 is produced downstream of caspase 3 and the cyclooxygenases COX1 and COX2, and we show that the pan COX1–2 inhibitor indomethacin blocks IR-induced PGE_2 production in the presence or absence of DDR inhibitors. COX1–2 require oxygen for catalytic activity, and we further show that PGE_2 production is markedly suppressed in cells cultured under low (1%) oxygen concentration. Thus, Phoenix Rising is most likely to cause repopulation of tumors with relatively high oxygen, but not in hypoxic tumors. This survey lays a foundation for future studies to further define tumor responses to radiation and inhibitors of the DDR and Phoenix Rising to enhance the efficacy of radiotherapy with the ultimate goal of precision medicine informed by deep understanding of specific tumor responses to radiation and adjunct chemotherapy targeting key factors in the DDR and Phoenix Rising pathways.

Keywords: radiotherapy, DNA damage response, growth factor, apoptosis, caspase

INTRODUCTION

The majority of cancer patients receive radiotherapy (RT), and virtually all cancer treatments employ chemical or physical genotoxins that directly damage DNA, or inhibit DNA metabolism (such as topoisomerase inhibitors). DNA damage activates DNA damage response (DDR) pathways, but the specific DDR pathways activated, the degree of activation, and cell fate depend on many factors, including the amount and type of damage, as well as the genetic and environmental state of the cell (cell type, cell cycle phase, normal vs. tumor, hypoxic vs. normoxic, etc). Low and high LET IR yield different dose distributions in tissue and induce different types of damage, and may, thus, differentially activate DDR pathways. Solid tumors are genetically heterogeneous, which contributes to therapeutic resistance (1), and it is difficult to achieve 100% elimination of tumor cells while minimizing normal tissue toxicity. Rare surviving tumor cells, thus, pose a risk of tumor repopulation. A long recognized problem is that following RT, tumors may be rapidly repopulated, a phenomenon termed "accelerated tumor repopulation." The Li lab identified a paracrine growth factor signaling pathway that contributes to accelerated repopulation called "Phoenix Rising" (2–4). This pathway is initiated when lethally irradiated tumor cells activate caspase 3/7 (a key step in caspase-dependent apoptosis), leading to production of prostaglandin E^2 (PGE^2), a potent growth factor (**Figure 1A**). Thus, dying cells trigger growth of neighboring viable cells, a process akin to wound healing. PGE_2 produced via Phoenix Rising stimulates cell growth in culture and tumor repopulation in mice (2). Given the high radiation doses required to kill high fractions of tumor cells, the rare surviving cells are likely to experience significant DNA damage, and rapid proliferation of such cells is expected to enhance mutagenesis and may drive tumor progression toward a more aggressive metastatic state. There is accumulating evidence that PGE_2/Phoenix Rising is clinically relevant. Patients with head and neck squamous cell carcinoma or breast cancers that express caspase 3 show reduced survival (2), PGE_2 promotes renal carcinoma cell invasion that may contribute to metastasis (5), and recent studies indicate that blocking PGE_2 production with cyclooxygenase inhibitors improves outcomes in bladder and breast cancer patients treated with chemotherapy or RT (6, 7).

The DDR comprises complex networks of DNA repair and DNA damage signaling (checkpoint) pathways that control cell fate in response to DNA damage; a simplified view of DDR responses to ionizing radiation is shown in **Figure 1B**. The most fundamental cell fate decision is survival vs. death. Central to the DDR are protein kinases, including upstream PI3-like kinases ATM, ATR, and DNA-PKcs, that converge on downstream checkpoint kinases Chk1 and Chk2 (8). When cells experience limited damage, these factors promote cell survival and suppress cancer by effecting cell cycle arrest, stimulating repair, and promoting genome stability. Above a certain DNA damage threshold, these pathways promote senescence or programed cell death by apoptosis, necrosis, or autophagy (9, 10). Thus, DDR pathways are not "on or off" but show graded responses depending on the level of damage, and DDR thresholds are known to be genetically regulated (11, 12), and may vary for each checkpoint (13). There is substantial crosstalk among checkpoint and DNA repair pathways (14–22), and a major goal in the field is to identify synthetic (genetic) lethal interactions to exploit in cancer therapy (23).

There is considerable interest in targeting DDR proteins to augment therapeutic responses to chemotherapy and/or RT (24–26), for example, by sensitizing tumor cells to DNA damage. A common goal in cancer therapy is to kill tumor cells by inducing apoptosis. However, increasing caspase 3-dependent apoptosis may be a double-edged sword, leading initially to increased tumor killing, but accompanied by increased PGE_2 secretion and subsequent growth stimulation of rare surviving tumor cells. The present study was designed to determine whether modulating the DDR (by chemical inhibition of DNA-PKcs, ATM, or Chk1) influences Phoenix Rising in a variety of normal or tumor cells following exposure to low and high LET IR. Phoenix Rising can be blocked at many steps along the pathway from caspase-3 cleavage, to PGE_2 production/receptor binding (2, 27), and we tested whether chemical inhibition of COX1 and COX2 (COX1–2) blocked PGE_2 production. Certain tumors are hypoxic, and because oxygen is a necessary co-factor for COX1–2 activity, we also tested whether PGE_2 production differed under normoxic vs. hypoxic conditions. We show that PGE_2 production, and proliferation of co-cultured unirradiated cells vary widely among cell lines. In some cell lines, we observed enhanced PGE_2 production with inhibition of DNA-PKcs, suppression by inhibition of ATM, and both COX1–2 inhibition and hypoxia robustly suppressed PGE_2 production. In general, PGE_2 production did not affect short-term growth of irradiated cells (up to 48 h post IR), but PGE_2 levels correlated with growth of co-cultured, unirradiated cells in longer-term growth assays. Interestingly, both oxygen concentration and LET alter PGE_2 production. Together, these findings suggest that RT of certain tumor types may be enhanced by specific combinations of DDR and/or COX1–2 inhibitors that enhance tumor cell killing and mitigate accelerated tumor repopulation.

MATERIALS AND METHODS

Cell Culture and Chemical Inhibitors

Human cell lines HeLa, HT1080, HCT116, MCF7, BJ1hTERT, and HFL3, and mouse melanoma D17 cells, were cultured in Dulbecco's minimal essential medium (DMEM, Gibco) with 10% fetal bovine serum (Sigma or Atlas Biologicals), 100 IU/mL penicillin, 100 μg/mL streptomycin, 2.5 μg/mL amphotericin B (antibiotic/antimycotic, LifeTechnologies), 1 mM sodium pyruvate (Gibco) and incubated at 37°C with 5% CO_2 in air. For the hypoxia experiments, HeLa cells were maintained in a hypoxic incubator in the same media and growth conditions except that the oxygen concentration was limited to 1%. Primary head and neck tumor [patient-derived xenograft (PDX)] cell lines CUHN013, CUHN036 (28), CUHN065, and CUHN067 were cultured in Rhesus Monkey Kidney, *Mucaca mulatta* (RM_K)

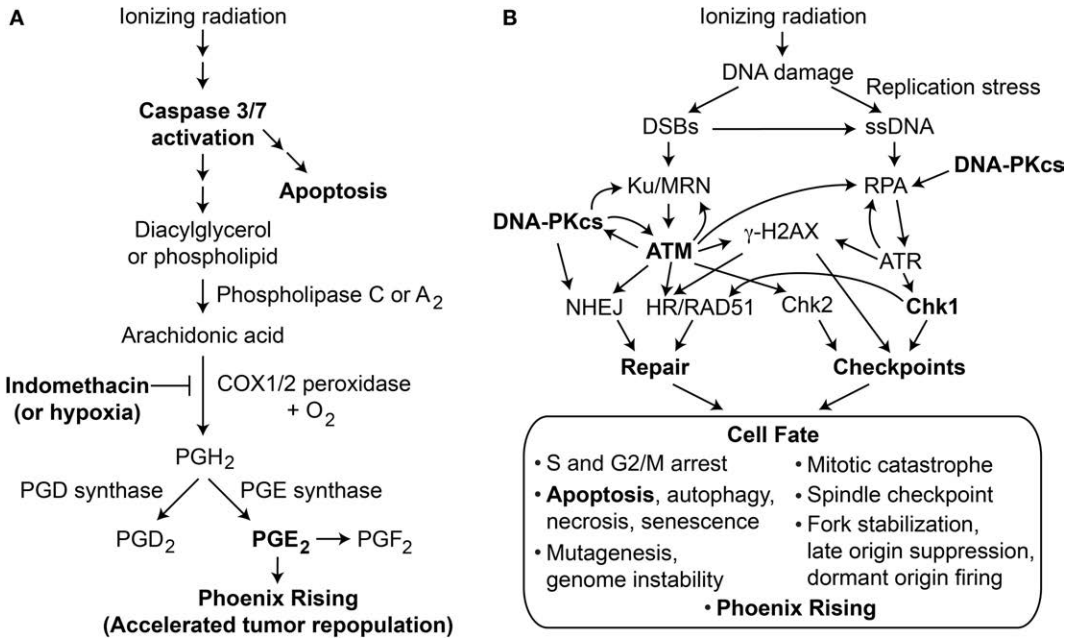

FIGURE 1 | (A) Phoenix Rising pathway of accelerated tumor repopulation. The cascade is initiated by cleavage and activation of caspase 3, which also promotes programed cell death by apoptosis. Activated caspase 3 cleaves and activates phospholipase 2 that hydrolyzes fatty acid phospholipid bonds, releasing arachidonic acid and lysophospholipids. Arachidonic acid is converted to PGH_2 by COX1 and COX2 peroxidases in the presence of oxygen; this step can be blocked by COX1–COX2 inhibitor indomethacin or hypoxia. Prostaglandin synthases generate the family of prostanoids, including PGD_2, PGE_2, and PGF_2. PGE_2 (and possibly other PGs) excreted from dying cells promote growth of surviving cells, accelerating tumor repopulation. **(B)** The DDR regulates cell fate after radiation damage. Proteins involved in DNA repair and damage checkpoint pathways crosstalk with programed cell death pathways to determine a variety of short- and long-term cell fates. Phoenix Rising and the DDR are linked through apoptosis and possibly other processes.

primary cell line media consisting of DMEM:F12 (3:1) with 10% FBS, insulin (5 μg/mL), hEGF (10 ng/mL), hydrocortisone (0.4 μg/mL), transferrin (5 μg/mL), penicillin (200 units/mL), and streptomycin (200 μg/mL).

Inhibitors of ATM (KU55933), Chk1 (UCN-01) DNA-PKcs (NU7026), and COX1–2 [indomethacin (Indo)] were purchased from Tocris Bioscience or Sigma and stored in powdered form at −20 or 4°C (NU7026). All compounds were freshly solubilized in DMSO to 100× working concentrations immediately prior to addition to cell cultures. Master mixes containing 1× final concentration of inhibitors in fresh media were prepared and added to wells pre- and post-irradiation. Final inhibitor concentrations were: 10 μM for ATMi, DNA-PKi, and COX1–2i, and 100 nM for Chk1i.

Human-Derived Head and Neck Squamous Cell Carcinoma Cell Lines

Head and neck squamous cell carcinoma patients were consented at the University of Colorado Hospital in accordance with the protocol approved by the Colorado Multiple Institutional Review Board (COMIRB #: 08-0552). CUHN013, CUHN065, and CUHN067 cell lines were derived directly from fresh patient post-surgical tumor tissue. Due to minimal tissue procured, the CUHN036 cell line required expansion and was, therefore, derived from PDX tumors. Tumor tissue was processed into ~2 mm × 2 mm × 2 mm pieces using a scalpel and forceps and two to three pieces were placed in wells of cell culture grade six-well dishes without media. Uncovered plates were placed in the back of a cell culture hood and tumor pieces were allowed to dry/adhere to the plate for 15 min, then 2 mL of RM_K media was added to each well. Fresh media was added to tumor slices twice per week.

Outgrowing cells were characterized by flow cytometry (Cyan-ADP, Beckman Coulter) to confirm the presence of epithelial cancer cells (anti-CD44-APC, anti-EPCAM-FITC, anti-EGFR-PE) within the cancer-associated fibroblast cells (anti-mouse H2kd-PerCP–Cy5.5 for PDX tissue). Once cell populations had expanded sufficiently (~10^7 cells), cells were sorted (MoFlo-XDP, Beckman Coulter) twice in succession using the above combination of cell surface markers to eliminate contaminating fibroblasts. To confirm the origin of resulting cell lines, we conducted short tandem repeat (STR) analysis comparing sorted cells to the originating patient tissue. Finally, tumors generated in immune-compromised nude mice from these human-derived cell lines recapitulated the morphology and histology of the original patient or PDX tumors.

PGE_2 Detection by ELISA

Cells (10,000–20,000) were seeded into individual wells of 96-well microtiter dishes and incubated overnight using two to three replicate wells per treatment group. The dishes were irradiated with 10 Gy γ-rays (CSU, ^{137}Cs source), or 3 or 10 Gy X-rays

(NIRS) low LET IR. The cells were treated with either DDR or COX-1/COX-2 inhibitors 12–16 h prior to IR and the inhibitors were present in the media during and after IR. PGE_2 concentrations in growth media were measured at 0, 24, and 48 h after IR using a PGE_2 Parameter ELISA kit (R & D Systems) according to the manufacturer's directions. PGE_2 standard concentration curves (Figure S1 in Supplementary Material) were derived from dilutions of pure PGE_2 (R & D Systems) and fit to asymmetric 5-parameter logistic non-linear regressions using Prism software (Graphpad).

Cell Proliferation Assay

Cell proliferation was measured using sulforhodamine B (SRB) assays (29) performed on cells adhering to PGE_2 assay plates, since PGE_2 assays required only the growth media, and SRB assays required only adherent cells. Optical densities were measured at 560 nm wavelength in a 96-well microtiter plate reader and baseline readings for controls (empty wells and media only wells) were subtracted to yield final O.D. values. The resultant data were processed using Excel and Prism software.

PGE_2 Detection by Liquid Chromatography-Tandem Mass Spectrometry

BJ1hTERT or HT1080 cells (300,000) were seeded into T-25 flasks, incubated overnight and pretreated with DDR inhibitors as above. Supernatants from non-irradiated samples and samples irradiated with 3 Gy high LET (70 keV/μm) carbon ion IR were collected 48 h post irradiation and stabilized by the addition of 0.1% (v/v) butylated hydroxytoluene. The samples were immediately frozen, stored, and shipped to the CSU Center for Environmental Medicine Analytical Laboratory for liquid chromatography-tandem mass spectrometry (LC-MS/MS) analysis using methods developed to detect PGD_2, PGE_2, and PGF_2 (manuscript in preparation).

PGE_2 Detection After Low or High LET IR Under Normoxic or Hypoxic Conditions

HeLa cells were maintained in either normoxic (ambient) or 1% oxygen concentrations for 72 h after irradiation with low LET X-ray, either of two moderately high LET carbon ion beams (290 MeV/nucleon monoenergetic beam at 30 keV/μm, or 290 MeV/nucleon monoenergetic beam at 70 keV/μm), or a higher LET silicon ion beam (135 or 490 MeV/nucleon monoenergetic beam at 300 keV/μm). PGE_2 in the supernatant media was detected by ELISA. Normoxic and hypoxic cells that did not receive IR served as controls. Pretreatment with 10 μM COX-1/COX-2 inhibitor (Indo) was the same as described above.

Functional Assay for IR-Induced, PGE_2-Stimulated Growth of Co-cultured, Unirradiated Cells

Twenty-four hours prior to IR, 30,000 (no IR) or 100,000 (to be irradiated) HeLa cells were seeded into wells of six-well plates and incubated at 37°C in 5% CO_2 air. Additionally, 1,000 or 1,500 HeLa cells were seeded into ThinCert transwell inserts with 1 μm pores (Greiner), placed into 10 cm dishes and incubated at 37°C in 5% CO_2 in air. Once cells had attached, transwells were transferred into their corresponding wells. Control wells were prepared with equal numbers of cells in the transwells but no cells below. Twelve hours prior to IR, cells were treated with DDR inhibitors and/or Indo as above. Six-centimeter spread out Bragg Peak (SOBP) beams of moderately high LET carbon ions (290 MeV/nucleon, dose average LET of 50 keV/μm at the center of the SOBP) were generated at the Heavy Ion Medical Accelerator (HIMAC) facility of the National Institute of Radiological Sciences (NIRS), Chiba, Japan. The transwells for the irradiated plates were transferred to six-well holding plates immediately preceding irradiation and the media in the remaining wells was aspirated. Vertically oriented plates containing the cells were irradiated with 4 Gy carbon ion IR. Following irradiation, fresh media containing DDR inhibitor was added to the wells and the transwells, and the transwells were returned to their previous position. For the no IR controls, the media (in wells and transwells) was aspirated and fresh media containing DDR inhibitor was added and dishes were incubated for 3–6 days. On day 3 or day 6 post-irradiation, PGE_2 concentrations in transwell media was analyzed by ELISA. On day 7, sufficient media was added to transwells to allow cell growth for two more days, and on day 9 post-irradiation, transwell cells were trypsinized, and resuspended in 500–1000 μL of PBS and counted using a Coulter Counter or Scepter cell counting device (EMD Millipore).

Analysis of Apoptosis by Caspase 3/7 Cleavage and Annexin V Assays

Duplicate dishes were prepared for apoptosis assays as follows. Twenty-four hours prior to IR, 60,000 (no IR control) or 250,000 (to be irradiated), HeLa cells were seeded into wells of six-well plates and incubated at 37°C in 5% CO_2 in air. Twelve hours prior to IR, cells were treated with DDR and/or COX-1/COX-2 inhibitors and irradiated in parallel as described in the previous section. Following irradiation cells were incubated for 72 h and subsequently assayed by flow cytometry for two apoptosis endpoints. Caspase 3/7 cleavage/activation was monitored by cleavage of a DEVD peptide substrate conjugated to Alexafluor 488 (Cell Event 3/7 Caspase Green Reagent, Life Technologies) as follows. Cells from non-irradiated and irradiated treatment groups were trypsinized, harvested, and combined with supernatants from each well (containing potential apoptotic cells), centrifuged at 1200 rpm for 5 min, and the media was removed by aspiration. Cells were suspended in 500 μL of fresh media containing 1 μL Cell Event reagent (4 μM final concentration) and incubated at 37°C in 5% CO_2 in air for 15 min, then 500 uL of PBS was added to each sample and cells were analyzed on a BD FACSCaliber flow cytometer using 488 nm excitation and collecting fluorescent emissions with a 530/30 filter set. Gates were set using unstained and no treatment/no IR cells as negative control populations. Data represent the percent caspase-positive cells among 10,000 cells analyzed per sample. Data were acquired with CellQuest (Becton Dickinson) software, and analyzed using FloJo (Version 7.6.5, Tree Star Inc.) and Prism (Version 5.04, GraphPad) software.

Annexin V (AV) is a Ca^{2+}-dependent phospholipid binding protein that binds with high affinity to phosphatidyl serine residues that have translocated to the outer leaflet of the plasma membrane as a result of upstream apoptotic signaling, representing an early marker of apoptosis. Propidium iodide (PI) is a cell impermeant DNA binding dye that will penetrate into cells with compromised (leaky) membranes indicative of cellular necrosis, representing late-stage apoptosis. It is possible to discriminate the early (AV only), middle (AV and PI double positive), and late (PI-positive only) stages of cell death by co-staining with AV and PI. Approximately 5×10^5 cells (and supernatants containing potential apoptotic cells) were harvested from wells processed as above to generate cell pellets which were washed once in cold PBS, harvested by centrifugation, and suspended in 500 μL annexin binding buffer (10 mM HEPES, 140 mM NaCl, 2.5 mM $CaCl_2$, pH 7.4) yielding cell concentrations of approximately 1×10^6 cells/mL. Three microliters of Annexin V, Alexa Fluor 488® conjugate (Life Technologies) and 150 μL of annexin binding buffer were aliquoted to flow cytometry tubes, and 150 μL of cell suspensions were added, samples were mixed, incubated at room temperature for 15 min, and an additional 300 μL of annexin binding buffer was added, samples were mixed, stored on ice, and analyzed on a BD FACSCaliber flow cytometer using 488 nm excitation and collecting fluorescent emissions for FL1 and FL2 parameters using 530/30 and 585/42 filter sets, respectively. Compensation was established using the single-stained samples for the +IR treatment group and quadrant gating was established to identify AV^-/PI^- (apoptosis negative), AV^+/PI^- (early apoptotic), AV^+/PI^+ (middle apoptotic), and AV^-/PI^+ (late apoptotic/necrotic) populations. Data represent the percentage of cells in each quadrant from 5,000–10,000 cells collected per sample, using data acquisition and analysis software as above.

Clonogenic Cell Survival Assay

T25 flasks were seeded to ~20% confluence with cell lines to be tested, and incubated overnight. Cells were pretreated with DDR inhibitors at least 12 h prior to exposure to low or high LET IR. Cells were irradiated at ~50% confluence and allowed to recover for 30 min before they were trypsinized, harvested, suspended in fresh media, and counted using a Coulter Counter. Appropriate numbers of cells to yield ~100 colonies per 6 cm dish were suspended in fresh medium and distributed to three replicate dishes per treatment group. Forty-eight hours post irradiation, the media was aspirated and replaced with fresh media without drug. The cells were incubated for 8–11 days to allow colonies to develop. The dishes were stained with 0.5% (w/v) crystal violet in 70% methanol solution and the colonies were counted. Survival fractions were calculated and plotted using Excel and Prism software. We derived *p*-values for statistical analysis by using student's *t*-tests.

RESULTS

PGE_2 Production and Cell Viability After IR Vary Among Cell Types and Are Regulated by the DDR

The goals of this study were to determine whether DDR inhibitors and/or oxygen alter PGE_2 production and cell growth of irradiated cells in response to low and high LET ionizing radiation. We initially surveyed PGE_2 production in five cancer cell lines (HT1080 fibrosarcoma, HCT116 colorectal carcinoma, MCF7 breast adenocarcinoma, HeLa cervical adenocarcinoma, and B16 mouse melanoma) and two normal cell lines (BJ1hTERT, hTERT-immortalized human foreskin fibroblasts, and HFL3 spontaneously immortalized human fetal lung cells) following exposure to low LET γ-rays or X-rays. In the absence of DDR inhibitors, PGE_2 levels increased several fold 24 or 48 h after 10 Gy γ-rays with most cell lines, with statistically significant differences in MCF7 and BJ1hTERT, and trending toward significance in HT1080 ($p = 0.06$); HCT116 showed an approximately eightfold increase at 48 h, but significance could not be calculated because only a single determination was made at this time point (**Figure 2A**). In parallel with the PGE_2 assays, we measured cell survival/proliferation by SRB assay and found significant increases in cell number 48 h after IR in HT1080 and BJ1hTERT, but not HCT116 nor MCF7 (**Figure 2A**). PGE_2 effects on growth were previously observed at later times after IR (>5 days) (2) so the absence of a consistent early growth effect is not surprising. These PGE_2 effects were observed at IR doses of 3–10 Gy, higher than the 2 Gy doses typically used in fractionated photon RT, but well within the range of doses used in hypofractionated stereotactic body RT. PGE_2 production is likely proportional to levels of caspase activation (and apoptosis), but more studies are required to determine whether PGE_2 production follows a standard dose–response or displays threshold effects. These data demonstrate that basal and IR-induced PGE_2 levels, and early effects on survival/proliferation, vary among cell types.

DNA damage response inhibitors affected IR-induced PGE_2 production that again varied among cell types. In control experiments, we confirmed that inhibitors of DNA-PK, ATM, and Chk1 reduced clonogenic survival (Figure S2 in Supplementary Material and data not shown). DNA-PKi slightly increased PGE_2 production in HT1080 cells 48 h after IR, but the difference was not significant, and DNA-PKi had no effect on PGE_2 production in HCT116, MCF7, or BJ1hTERT cells (**Figure 2A**). ATMi suppressed PGE_2 levels in HT1080 cells 48 h post IR by ~1.5-fold, but ATMi did not affect PGE_2 in other cell types. Chk1i significantly enhanced PGE_2 production in HCT116, but other cell types showed no Chk1i effects. At 48 h after IR, ATMi dramatically decreased cell number (by ~20-fold) of both HT1080 and BJ1hTERT cells, whereas HCT116 and MCF7 cells were not affected. Because the SRB assay provides an estimate of survival/proliferation based on the amount of protein in attached cells (29), the sharp decrease in the number of attached HT1080 and BJ1hTERT cells with ATMi reflects massive cell death/detachment in response to the combined IR + ATMi treatment. Note that in both HT1080 and BJ1hTERT cells ATMi sharply reduced PGE_2, but only HT1080 showed reduced cell numbers, suggesting that PGE_2 is reduced by distinct mechanisms in these cell lines, with death and detachment preceding PGE_2 production in HT1080, but not BJ1hTERT.

Prostaglandin E_2 production depends on COX1–2 (**Figure 1A**) that can be inhibited with Indo. We next measured PGE_2 and cell survival/proliferation with HeLa, B16, BJ1hTERT, and HFL3 cells 48 h after 3 or 10 Gy doses of X-rays in presence or absence of Indo

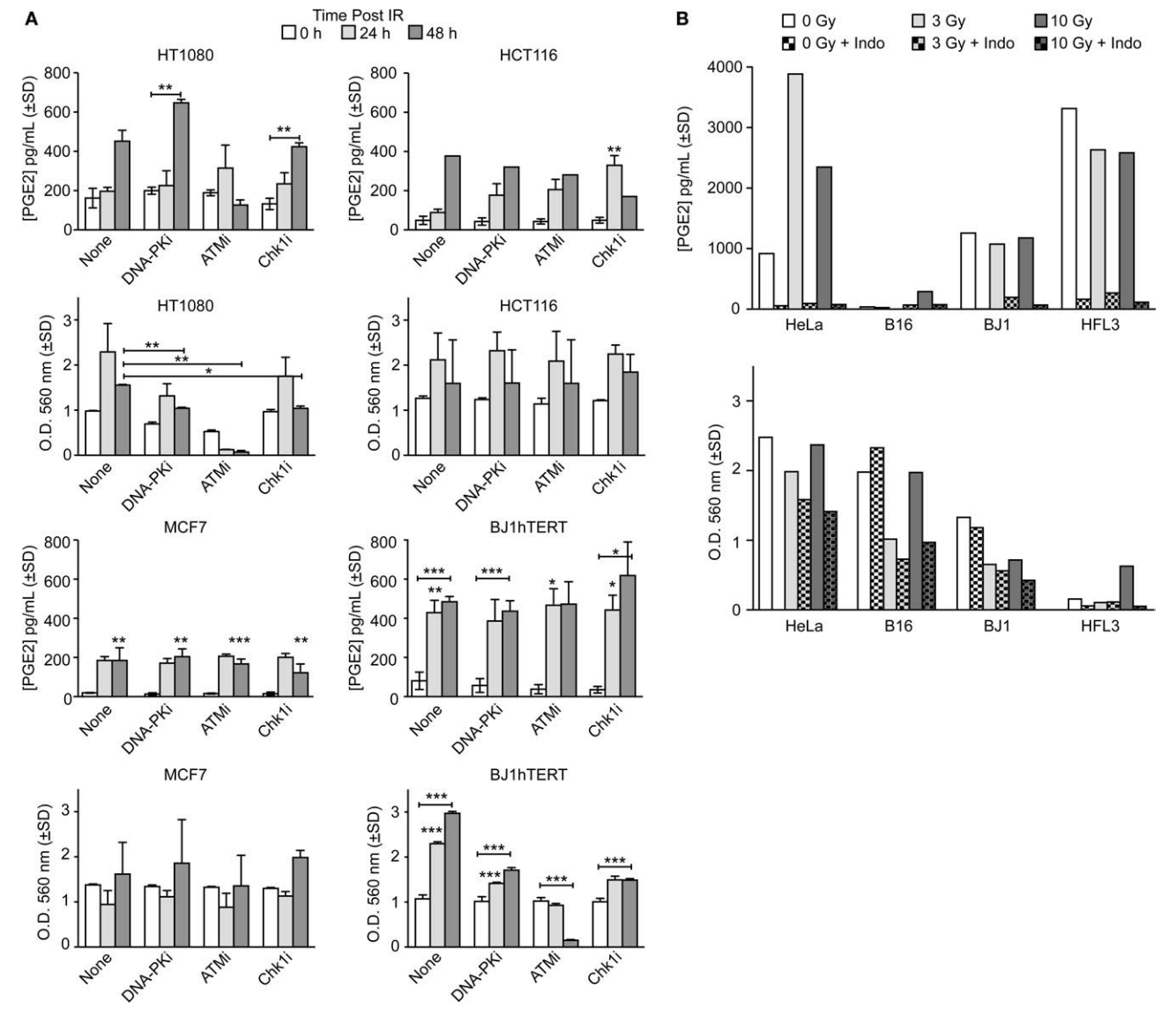

FIGURE 2 | PGE_2 production and short-term cell viability/proliferation in response to γ-rays or X-rays in the presence or absence of DDR or COX inhibitors. PGE_2 and cell growth were measured by ELISA and SRB assay in response to **(A)** 10 Gy γ-rays or **(B)** 3 or 10 Gy X-rays in the presence or absence of indomethacin (Indo). Data are averages ±SD for two to four replicates per treatment group **(A)** or single determinations **(B)**. In this and all subsequent figures, statistical significance was determined by *t*-tests, * indicates $p < 0.05$, ** $p < 0.01$, *** $p < 0.001$.

(**Figure 2B**). With HeLa cells, PGE_2 levels increased approximately fourfold with an X-ray dose of 3 Gy, and approximately twofold with 10 Gy. B16 cells produced very little PGE_2 without IR or with a 3 Gy X-ray dose, but PGE_2 increased eightfold at 10 Gy. HFL3 and BJ1hTERT cells had high basal levels of PGE_2 that did not change substantially in response to X-rays. Uniformly, Indo dramatically suppressed PGE_2 levels (>20-fold), including basal and X-ray induced levels in both cancer and normal cells (**Figure 2B**). These data concur with numerous studies showing that inflammatory prostaglandin production can be mitigated by COX1–2 inhibitors (30). The variable basal levels of PGE_2 among cell lines may reflect differential expression or activation of PGE_2 pathway proteins, including caspase 3, which may be activated when rapidly growing cells reach confluence and deplete growth media. There was a general trend toward decreased cell growth with increased IR dose. HeLa cells showed both stronger PGE_2 induction with X-rays, and greater radioresistance than the other cell lines. Note that HFL3 cells showed poor viability/proliferation after IR, and high basal PGE_2 levels, yet PGE_2 was not induced with IR in these cells. These features may be specific to HFL3 cells or perhaps reflect general properties of fetal cells.

To determine if low and high LET IR produce similar PGE_2 responses, absolute PGE_2 levels in media from HT1080 and BJ1hTERT cultures were determined by LC-MS/MS in response to 3 Gy high LET (70 keV/μm) carbon ions (**Figure 3**). This alternate PGE_2 assay helped us validate and expand on findings

from the ELISA assay. In the absence of DDR inhibitors, HT1080 cells showed robust PGE_2 induction with carbon ions, similar to the effect of low LET IR, and BJ1hTERT cells were unresponsive to both low and high LET IR (**Figures 2** and **3**). These results indicate that PGE_2 production is stimulated by both low and high LET IR in a cell-type-dependent manner. The variation in absolute basal levels of PGE_2 in BJ1hTERT cells measured by LC-MS/MS and ELISA may reflect different sensitivities of ELISA and LC-MS/MS assays.

Inhibition of DNA-PK and ATM decreased carbon ion-induction of PGE_2 in HT1080 cells. The decrease in PGE_2 with DNA-PKi after high LET contrasts with that seen with γ-rays. This difference in DNA-PKi effects with low and high LET IR could reflect DNA-PK's dual role in damage signaling and DSB repair by NHEJ (**Figure 1B**), in particular, the shift from NHEJ-dominant repair of low LET IR damage to HR-dominant repair of high LET damage (31–33). By contrast, Chk1 inhibition markedly increased PGE_2 in BJ1hTERT cells, with or without IR. The Chk1i effect in the absence of IR suggests that the cytotoxicity of Chk1i alone is sufficient to trigger Phoenix Rising. This Chk1i effect may reflect aberrant signaling to the p53-directed apoptotic cascade culminating in PGE_2 production, since p53 is stabilized by Chk1 phosphorylation of several sites after DNA damage (34). Together the results indicate that PGE_2 production following low or high LET IR can be enhanced or suppressed by inhibition of different pathways in the DDR network.

IR-Induced PGE_2 Stimulates Proliferation of Co-Cultured, Unirradiated Cells that can be Modulated by DDR and COX1–2 Inhibitors

A transwell multiple-endpoint assay system was used to examine the effects of low and high LET IR on co-cultured irradiated and unirradiated cells (**Figure 4A**). The pore size of the transwell membranes allows free diffusion of small molecules, but cell migration is blocked. This system allows simultaneous analysis of

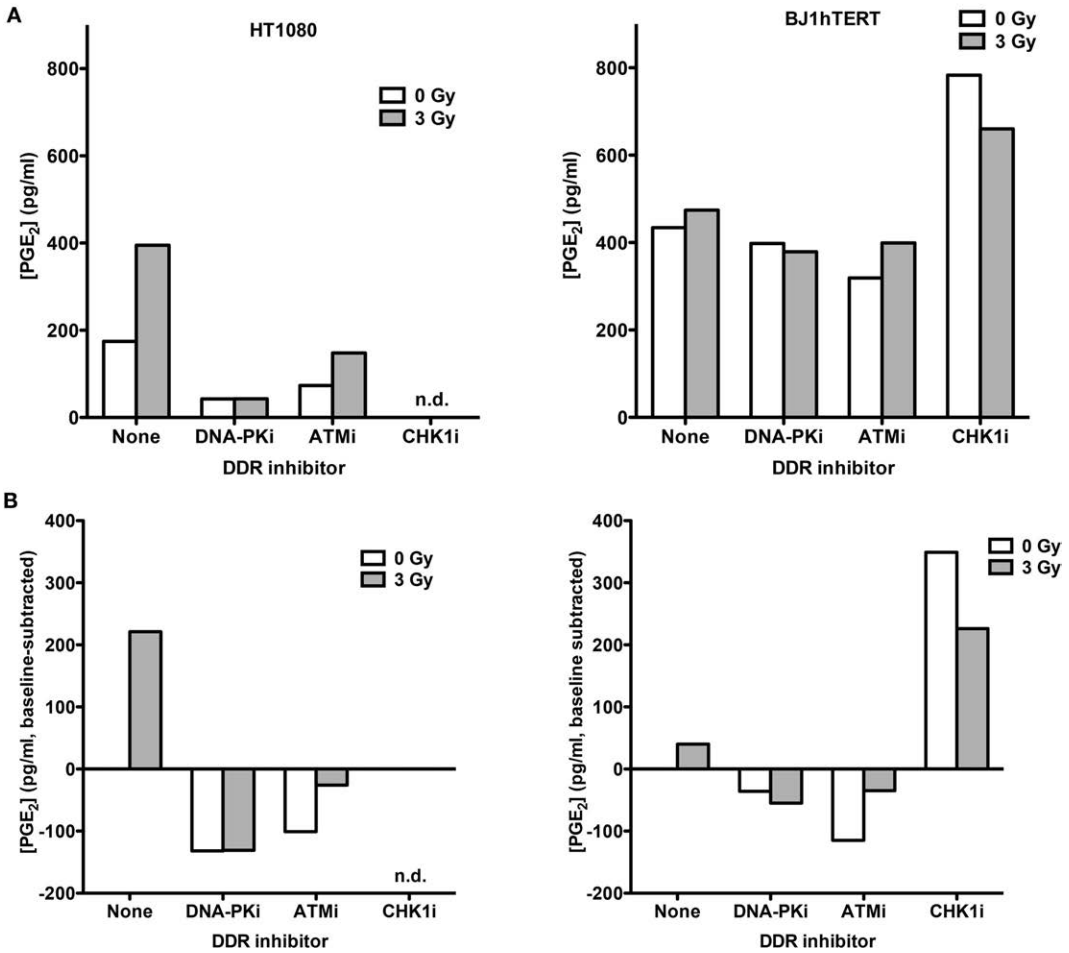

FIGURE 3 | PGE_2 production in response to high LET IR ± DDRi. LC-MS/MS was used to quantify PGE_2 levels in supernatants from HT1080 and BJ1hTERT cultures after irradiation with 3 Gy carbon ions (70 keV/μm). **(A)** Absolute PGE_2 levels. **(B)** PGE_2 levels were derived by subtracting the baseline values (no IR, no drug); n.d., not determined.

PGE_2 production, apoptosis, and cell growth as a key functional endpoint. We assessed the effects of radiation quality, DDR and COX1–2 inhibitors, and oxygen concentration on these endpoints. We chose HeLa cells for these studies because the cell line survey showed that HeLa cells have low basal PGE_2 levels, and relatively robust PGE_2 production after IR that is blocked by cyclooxygenase inhibition. A preliminary test of cell proliferation of unirradiated co-cultured cells 7 days after "feeder" cells received 10 Gy γ-rays showed a 2.7-fold increase in growth compared to control with mock-irradiated feeder cells, and that COX1–2i suppressed this growth (**Figure 4B**). This result is similar to a prior report in which luciferase-expressing cancer cell growth was enhanced two- to fivefold when in direct contact with irradiated feeder cells (2). The transwell system eliminates any influence of cell-to-cell contact, measuring only the growth effects of diffusible factors through the transwell membrane.

To investigate whether high LET IR would elicit similar growth effects on co-cultured unirradiated cells, we used the transwell system to monitor PGE_2 production and cell growth in response to 70 keV/μm carbon ions. We also tested whether DDR inhibitors and/or the COX1–2 inhibitor Indo would modulate growth stimulation. PGE_2 production and growth of unirradiated HeLa cells was measured 6 days after IR. PGE_2 levels increased >20-fold in response to IR in the absence of inhibitors (**Figure 5A**), similar to the increase seen with X-rays (**Figure 2B**). Both DNA-PKi and ATMi significantly decreased IR-induced PGE_2 levels (approximately fourfold), and these were further reduced by approximately twofold by Indo (**Figure 5A**), although the latter differences were not statistically significant. Growth of unirradiated co-cultured HeLa cells was also monitored 6 days after IR. At this time point, moderate effects on growth were observed in the absence of DDR inhibitors, DNA-PKi increased growth but ATMi had no effect (**Figure 5B**). The increased growth with DNA-PKi does not appear to correlate with the lower PGE_2 level, but we note that PGE_2 levels were approximately twofold higher with DNA-PKi than untreated cells 3 days after IR (data not shown); the growth stimulation seen 6 days after IR may reflect this early burst of PGE_2, and the higher PGE_2 levels without DNA-PKi 6 days after IR would enhance growth at later times. The increased growth with DNA-PKi relative to untreated cells was dependent on feeder cells; no growth stimulation occurred without feeder cells (**Figure 5C**). As expected, blocking PGE_2 production with Indo (**Figure 5A**) also blocked growth stimulation (**Figures 5A,B**). As noted above, inhibiting DNA-PKcs or ATM radiosensitized cells (Figure S2 in Supplementary Material); thus, the differences in PGE_2 and growth effects with DNA-PKi and ATMi cannot be traced to differential degrees of cell killing, suggesting that inhibition of different DDR pathways can differentially affect Phoenix Rising and death pathway choice.

The transwell assay system is versatile in that in addition to PGE_2 and growth, simultaneous measures of apoptotic stages can be determined with the same cultures, including early apoptosis (caspase cleavage, detected with a cell-permeable caspase 3/7 DEVD peptide conjugated to a quenched fluorophore, which becomes fluorescent upon peptide cleavage), mid-apoptosis (Annexin V staining), and late apoptosis (revealed as gross membrane changes with propidium iodide staining). These endpoints were measured 3 and 6 days after high LET IR by flow

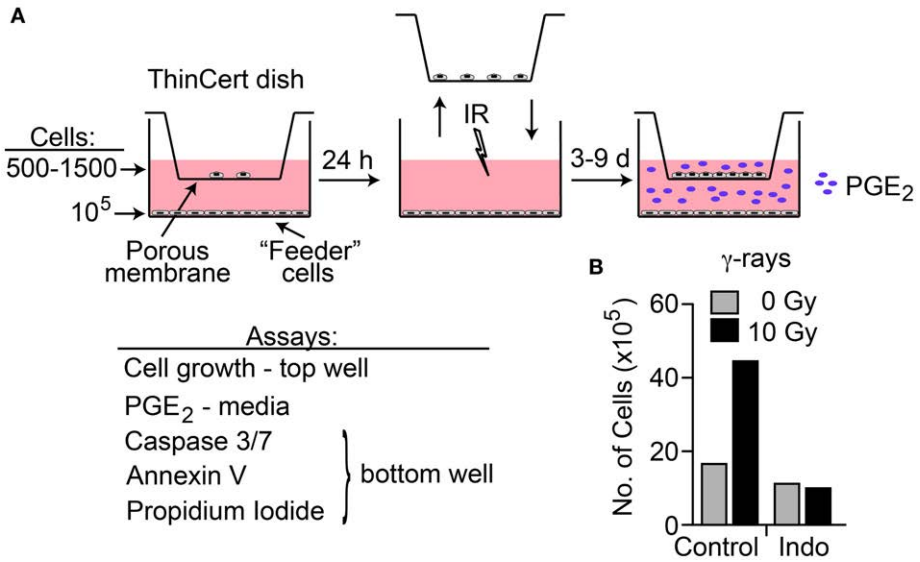

FIGURE 4 | (A) Transwell multiple-endpoint assay system. Cells were seeded into the top (500–1,500 cells) and bottom (feeder, 100,000 cells) sections of the transwell system and incubated for 24 h. The top section was transferred to a separate dish while the bottom section was irradiated, and then replaced. PGE_2 was measured in the media 3 and 6 days after IR; growth of unirradiated cells was determined 7–9 days after IR. Apoptotic endpoints (caspase 3/7 activation, Annexin V, and membrane changes by propidium iodide staining) were measured at 3, 6, or 9 days post IR in irradiated feeder cells. When used, DDR or cyclooxygenase inhibitors were present during the entire experiment. **(B)** HeLa cells assayed for growth stimulation using the transwell assay system after irradiation with 10 Gy low LET γ-rays. Indomethacin (Indo) inhibits COX1–2 and suppresses PGE_2 production.

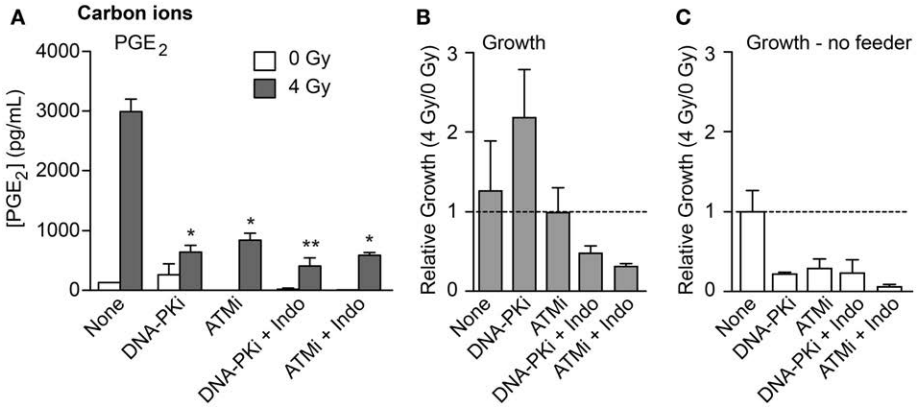

FIGURE 5 | PGE_2 production and stimulated proliferation of unirradiated HeLa cells in response to high LET carbon ions. **(A)** ELISA measurements from media in transwells containing HeLa cells 6 days after 0 or 4 Gy carbon ion irradiation. **(B)** Relative growth of unirradiated cells in transwells with or without DDR inhibitors or indomethacin, 6 days after irradiation of feeder cells. **(C)** As in **(B)** but without feeder cells. Data are averages (±SEM) for two determinations per condition.

cytometry (**Figure 6**). Minimal caspase activation was detected in unirradiated controls, and ~30% of cells activated caspase 3 and 6 days after IR. DDRi and Indo moderately suppressed caspase activation at both time points. Caspase is activated upstream of arachidonic acid that is processed by the Indo target, COX1–2, in the Phoenix Rising pathway (**Figure 1A**). This raises the possibility of a caspase–COX1–2 feedback loop, although the present experiments cannot rule out off target effects of Indo. Strikingly, ATMi appeared to completely block progression to later apoptotic stages; to a lesser extent DNA-PKi and Indo also suppressed progression to later apoptotic stages. Since ATMi is a strong radiosensitizer, the lack of progression to late apoptosis indicates that cells are shunted to one or more alternative death or senescence pathways.

Robust Phoenix Rising Responses in Cell Lines Derived From Fresh Tumor Tissue

Cell lines freshly derived from patient tumor tissue have emerged as important models for cancer cell biology studies (28, 35–37). We chose HNSCC-derived cell lines because head and neck cancers are treated with low and high LET RT. Low passage tumor cell lines were tested within 3 months of culture expansion. Two cell lines, CUHN036 and CUHN065, senesced or grew too slowly to study. Two others, CUHN013 and CUHN067, were reproductively robust and viable throughout the course of the experiments. CUHN013 is from a moderately focally keratinizing submental mass tumor. CUHN067 is from a base of tongue tumor that displayed extensive perineural invasion. Radiosensitivity was evaluated by clonogenic survival after X-rays or a clinical, 6 cm SOBP, high LET (~50 keV/μm) carbon ion beam. CUHN013 was more radiosensitive than CUHN067 to both X-rays and carbon ions, and both cell lines showed typical carbon ion RBEs of ~2–3 (Figure S3B in Supplementary Material).

Doses of 4 Gy SOBP carbon ions significantly increased caspase 3/7 activation compared to mock-irradiated controls, and DDRi and Indo had little effect on this endpoint (**Figure 7A**). These results demonstrated that the initiating event of Phoenix Rising was functioning in these clinically relevant models. As with HeLa, in transwell experiments the CUHN cell lines showed moderate to strong growth stimulation of unirradiated cells that was dependent on irradiated feeder cells (**Figures 7B–E**). Neither CUHN cell line showed significant alterations in growth with DDRi or Indo. These early (caspase activation), late (growth stimulation, suppressible with Indo) Phoenix Rising markers indicate that Phoenix Rising is functioning in CUHN067. By contrast, CUHN013 displayed the early caspase marker and modest, but statistically significant ($p < 0.01$) growth stimulation, but Indo failed to suppress this growth, suggesting a late-stage defect. The distinct phenotypes of the two CUHN cell lines, in radiosensitivity and growth responses with or without inhibition of DNA-PK or COX1–2, highlight the challenges associated with targeting DDR and Phoenix Rising pathways for precision medicine.

Oxygen Concentration and LET Attenuate PGE_2 Production After Exposure to Carbon or Silicon Ion Beams

COX1 and COX2 require sufficient oxygen to function efficiently. A number of tumor types are naturally hypoxic and/or have hypoxic regions. We tested the hypothesis that hypoxic cells will produce less PGE_2 after IR than normoxic cells due to impaired COX1–2 function (**Figure 1A**). HeLa cells were incubated under normal conditions (5% CO_2 in air, ~20% oxygen), or hypoxic conditions (1% oxygen) for 72 h after IR and PGE_2 production was determined by ELISA. Normoxic and hypoxic cultures that did not receive IR served as controls. As above, 10 Gy X-irradiation increased PGE_2 production by ~20-fold under normoxic conditions, but this was significantly reduced (to less than fivefold) under hypoxic conditions (**Figure 8**). Oxygen concentration had no effect on PGE_2 levels without IR. We next tested the effects of oxygen on particle radiation at three LET values, 30 keV/μm carbon ion, 70 keV/μm carbon ion, and 300 keV/μm silicon ions.

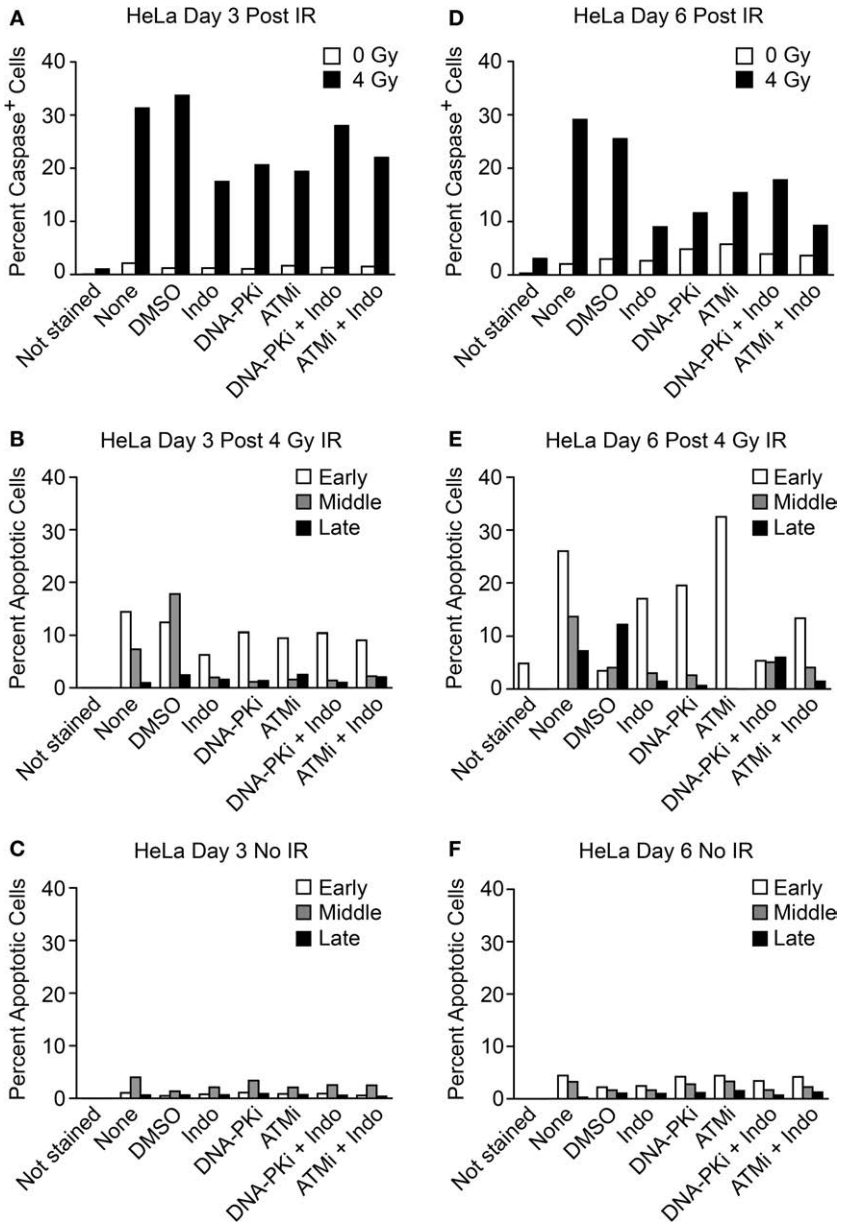

FIGURE 6 | Flow cytometric analysis of apoptotic phenotypes of feeder cells (from Figure 5) irradiated with high LET carbon ion IR. Duplicate plates were irradiated in parallel for assays 3 days post IR. Feeder cells co-cultured with transwell inserts were assayed 6 days post IR. Each sample was split at the time of harvest for two assay endpoints. Caspase cleavage and activation was assayed in live cells **(A)** 3 or **(D)** 6 days post IR using a fluorescent caspase 3/7 peptide fragment. Annexin V/propidium iodide co-staining of fixed cells discriminates between early, mid, or late apoptotic stages and was assayed **(B)** 3 or **(E)** 6 days post IR. No IR controls for the annexin V/PI assay **(C)** 3 or **(F)** 6 days post IR; ~10,000 cells were interrogated per determination. Unstained cells served as negative controls.

In all cases, hypoxia markedly reduced PGE_2 production, and with 30 or 70 keV/μm carbon ions, treatment with Indo further reduced PGE_2 production, in both normoxic and hypoxic treatment groups (**Figure 8**). Interestingly, 70 keV/μm carbon ions consistently caused approximately two- to threefold greater induction of PGE_2 than 30 keV/μm carbon ions under normoxic or hypoxic conditions, and in the presence or absence of Indo. While this suggests an LET dependence for PGE_2 production, this is questionable given that PGE_2 induction was greatest with low LET X-rays, and that the highest LET radiation (300 keV/μm silicon ions) induced PGE_2 no more than 70 keV/μm carbon ions; this parallels earlier findings that RBE peaks at 150–200 keV/μm. Further studies are required to determine whether LET dependence follows a complex pattern (e.g., plateaus above a certain LET), and whether there are signaling differences with photons vs. particle radiation that account for the high level of PGE_2

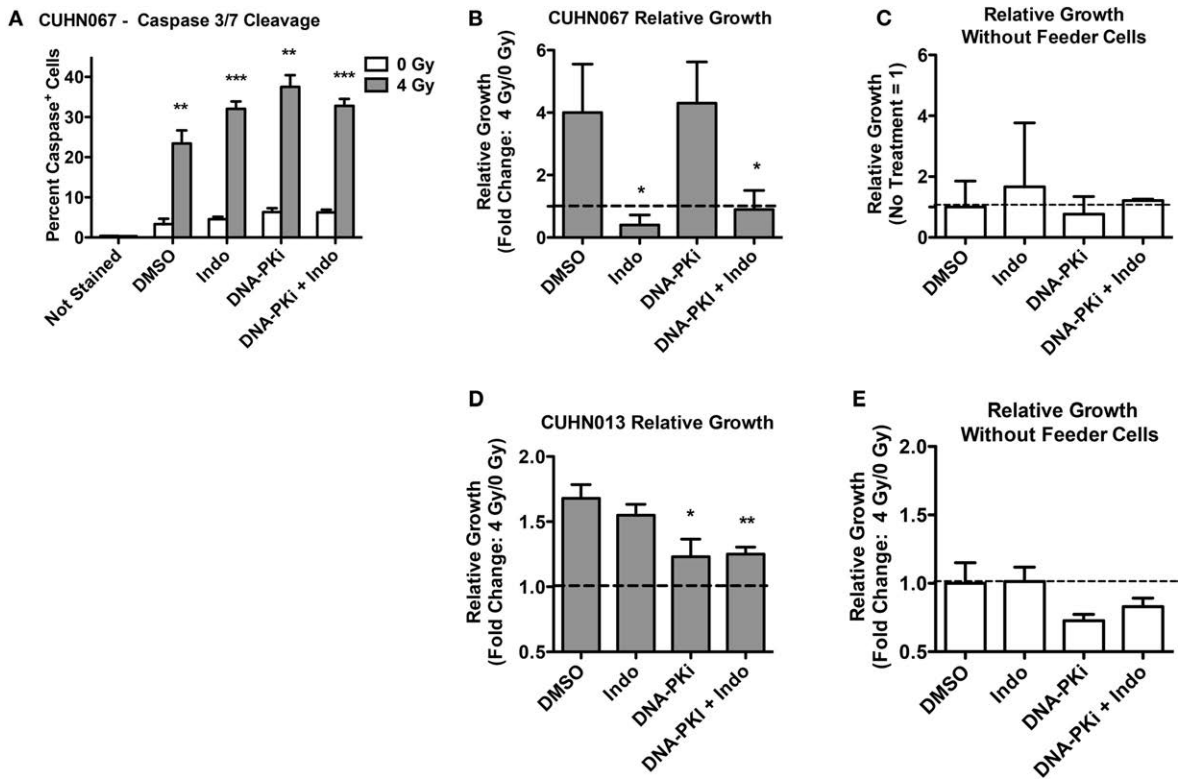

FIGURE 7 | Caspase activation and relative growth in two HNSCC cell lines after exposure to 4 Gy high LET IR. **(A)** Caspase cleavage and activation was assayed in live cells 48 h post IR. **(B,D)** Relative growth of primary tumor cells from transwells 6 days post IR with or **(C,E)** without irradiated feeder cells. Data represent the averages and SDs for three replicate measurements per determination.

induction with X-rays. Our results clearly indicate that, regardless of radiation quality, PGE_2 production is very sensitive to oxygen concentration. Thus, hypoxic tumor regions are unlikely to contribute to tumor repopulation via Phoenix Rising.

DISCUSSION

The Phoenix Rising pathway correlates with tumor repopulation *in vitro* and *in vivo* (27, 38, 39). The present study revealed several important features of IR-induced PGE_2 responses of normal and cancer cells. IR-induced, caspase 3-dependent, PGE_2 production (whether associated with apoptosis or other death pathways), is a common response of irradiated tumor cells, and some normal cells. PGE_2 levels generally enhanced growth of neighboring viable cells. Such growth, if unchecked, could spawn cells with high mutation rates, through replication of damaged genomes, as well as by an alternative mechanism activated in cells with moderately active caspase 3, that induces genome instability and carcinogenesis (40). Such small- and large-scale genetic change can drive rapid evolution of tumors, converting a local problem into lethal metastases.

Here, we focused on PGE_2 production, cell viability, and proliferation of irradiated and unirradiated cells in response to signaling factor(s) from co-cultured irradiated, apoptotic "feeder" cells; the modulation of these responses by DDR and COX1–2 inhibition and by varying oxygen concentration; and the effects of radiation quality. Interconnected DDR and growth pathways coordinate responses radiation and chemotherapy-induced DNA injury and conspire with programed cell death pathways to determine cell fate (**Figure 1B**). In this study, we found that PGE_2 production and growth responses varied among cancer and normal cell lines, including cell lines freshly derived from patient tumors.

Although DDR inhibition enhanced radiosensitivity (Figure S2 in Supplementary Material), this did not correlate with a single pattern (increase or decrease) in PGE_2 production. Inherent radiosensitivity, and DDRi effects on radiosensitivity, varies widely among different cell types (4, 41) as observed here (Figures S2 and S3 in Supplementary Material). In general, the effects of radiation on the various endpoints (caspase activation, PGE_2 production, growth) were consistent across all radiation types tested. This suggests that targeting PGE_2-driven accelerated tumor repopulation may be an effective adjunct to both photon and particle radiotherapies. A fairly common response of ATMi and DNA-PKi was suppression of PGE2 production. A plausible explanation for this effect stems from the observations that ATM and DNA-PK activate the NFκB transcription factor in response to IR and other genotoxins (42–45), and COX-2, the upstream regulator of PGE2, is one of many NFκB targets (46). Because of the extensive crosstalk between DDR and growth factor networks, considerably more effort is required to define the multitude of

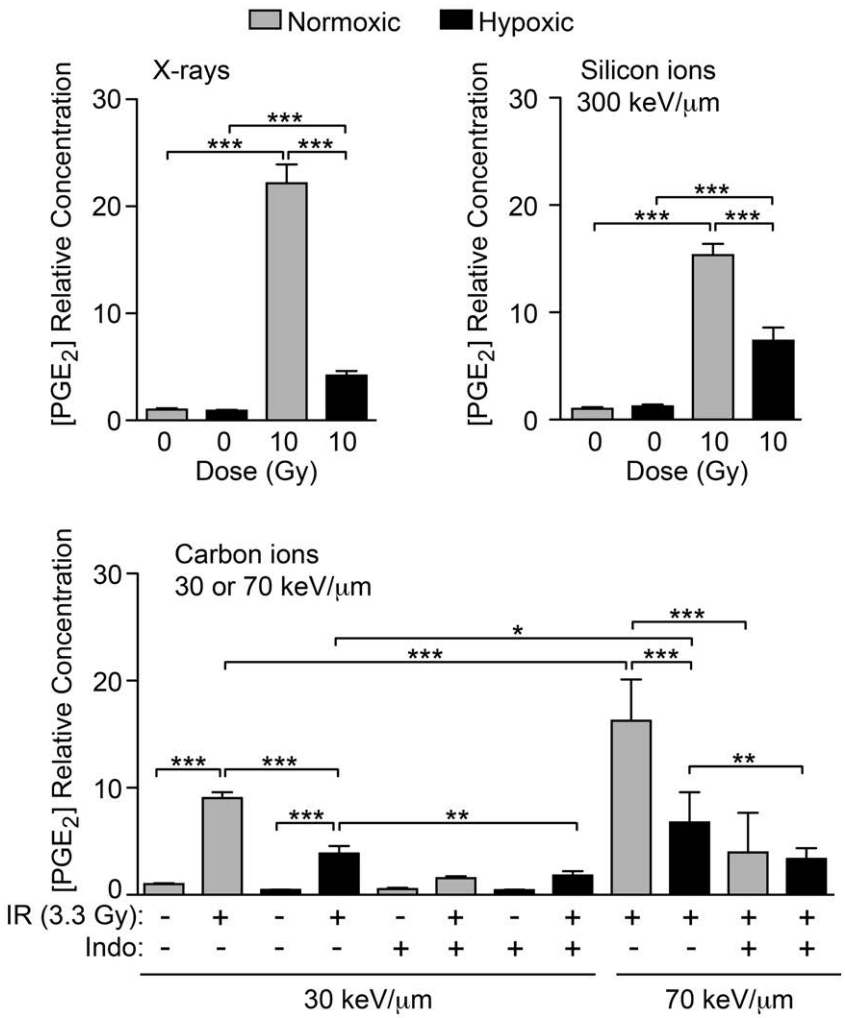

FIGURE 8 | IR-induced PGE2 production is suppressed by hypoxia. PGE_2 levels were determined by ELISA 3 days after X-ray, silicon ion, or carbon ion radiation at indicated LET and doses. Cells were incubated under normoxic, or hypoxic (1% O2) conditions. Data represent the averages and SDs for nine replicate measurements per determination.

tumor type responses to genetic and chemotherapeutic manipulation of DDR/growth regulatory factors. Phenotypic patterns emerging from such studies will guide mechanistic understanding of these various pathways, and may lead to rapid, inexpensive screening tools that will inform RT practice.

One facet that is consistent throughout our study and several others (2, 27, 47) is caspase activation and PGE_2 production. This is important because caspase status in tumors correlates with patient survival: patients with caspase 3-positive tumors do not survive as long as those with caspase 3-negaitve tumors (2, 48, 49). In addition, a recent study showed that low doses of radiation cause partial caspase 3 activation that leads to genome instability *in vitro* and *in vivo* through the generation of persistent DNA strand breaks (40). Another recent study demonstrated that caspase 3 defects created by shRNA, dominant negative gene expression, or gene deletion suppressed tumor growth *in vitro* and *in vivo* (47). Together, these findings implicate caspase 3 as a promising target to improve chemotherapy or RT outcomes.

COX1 and COX2 are also promising targets to enhance cancer therapy. The present study and others (2, 40, 47, 50) demonstrate that PGE_2 production and stimulated growth can be effectively suppressed by Indo and other COX1 and COX2 inhibitors. Non-steroidal anti-inflammatory compounds (NSAIDS) effectively target cyclooxygenase enzymes and are generally safe. Our study focused on Indo, a pan-COX1–2 inhibitor; other well-characterized examples are Naproxen and Ibuprofen, which are widely used and well tolerated. Selective COX2 inhibitors, such as Celecoxib, have been marketed but many have been withdrawn due to increased risk of myocardial infarction; it is possible that such risk is minimal for short-term courses during cancer therapy. A body of literature is beginning to emerge that describes tests of cyclooxygenase inhibitors in combination with RT or chemotherapy. In one study, Celecoxib delivered between rounds

of gemcitabine and cisplatin substantially suppressed bladder urothelial carcinoma xenograft regrowth, and enhanced the chemotherapeutic response in xenografts from a chemoresistant patient (7). An earlier study of LNCaP-COX2 mouse xenografts showed that topical application of the NSAID Diclofenac significantly reduced tumor growth in combination with 3 Gy IR (51).

Finally, we demonstrate that PGE_2 production in response to IR is highly sensitive to oxygen concentration, including low and high LET radiation. Hypoxic regions of tumors are typically resistant to low LET IR. By contrast, high LET IR has a minimal oxygen enhancement ratio and, therefore, has greater efficacy than photons against these hypoxic regions (52). PGE_2-stimulated tumor repopulation may not be a critical issue to consider during treatment planning for hypoxic regions of tumors. We stand at a new frontier on the path toward personalized precision medicine. As basic scientists and clinicians look to improve the efficacy and safety of cancer treatment in the future, it will be important to develop techniques for rapid, accurate detection of Phoenix Rising biomarkers to personalize patient care. Preventing accelerated tumor repopulation during RT and chemotherapy will improve local control and reduce the likelihood that early stage cancer will progress to more dangerous invasive and metastatic stages.

AUTHOR CONTRIBUTIONS

CA, WT, NS, YF, RO, AF, MD, and JN conceived and designed experiments; CA, WT, NS, CS, FN, MK, and AF conducted experiments; CA, WT, NS, FN, MK, AF, MD, and JN participated in data analysis; CA, WT, SK, AJ, and JN wrote the manuscript; all authors participated in critical revision.

ACKNOWLEDGMENTS

We thank Greg Dooley of Colorado State University Center for Environmental Medicine Analytical Toxicology Laboratory, for assay development and technical assistance with the LC-MS/MS analysis, and the Japan National Institute of Radiological Sciences for generous provision of heavy ion beam time.

FUNDING

This work was supported by funding from the Japan National Institute of Radiological Sciences International Open Laboratory, NIH grant R01 GM084020 to JN and CA; R01 CA149456 to AJ; JSPS KAKENHI grants #24249067 and #23390301 and National Cancer Center Research and Development Funds (H23-A-43) to RO; and Research Projects with Heavy Ions at NIRS-HIMAC (18B468, 21B468, 12J468) to YF.

SUPPLEMENTARY MATERIAL

The Supplementary Material for this article can be found online at http://journal.frontiersin.org/article/10.3389/fonc.2015.00260

REFERENCES

1. Calderwood SK. Tumor heterogeneity, clonal evolution, and therapy resistance: an opportunity for multitargeting therapy. *Discov Med* (2013) **15**(82):188–94.
2. Huang Q, Li F, Liu X, Li W, Shi W, Liu F-F, et al. Caspase-mediated paracrine signaling from dying cells potently stimulate tumor cell repopulation during cancer radiotherapy. *Nat Med* (2011) **17**:860–6. doi:10.1038/nm.2385
3. Ng WL, Huang Q, Liu X, Zimmerman M, Li F, Li CY. Molecular mechanisms involved in tumor repopulation after radiotherapy. *Transl Cancer Res* (2013) **2**(5):442–8. doi:10.3978/j.issn.2218-676X.2013.10.03
4. Zimmerman MA, Huang Q, Li F, Liu X, Li CY. Cell death-stimulated cell proliferation: a tissue regeneration mechanism usurped by tumors during radiotherapy. *Semin Radiat Oncol* (2013) **23**(4):288–95. doi:10.1016/j.semradonc.2013.05.003
5. Li Z, Zhang Y, Kim WJ, Daaka Y. PGE2 promotes renal carcinoma cell invasion through activated RalA. *Oncogene* (2013) **32**(11):1408–15. doi:10.1038/onc.2012.161
6. Generali D, Buffa FM, Deb S, Cummings M, Reid LE, Taylor M, et al. COX-2 expression is predictive for early relapse and aromatase inhibitor resistance in patients with ductal carcinoma in situ of the breast, and is a target for treatment. *Br J Cancer* (2014) **111**(1):46–54. doi:10.1038/bjc.2014.236
7. Kurtova AV, Xiao J, Mo Q, Pazhanisamy S, Krasnow R, Lerner SP, et al. Blocking PGE2-induced tumour repopulation abrogates bladder cancer chemoresistance. *Nature* (2015) **517**(7533):209–13. doi:10.1038/nature14034
8. Stracker TH, Usui T, Petrini JH. Taking the time to make important decisions: the checkpoint effector kinases Chk1 and Chk2 and the DNA damage response. *DNA Repair* (2009) **8**(9):1047–54. doi:10.1016/j.dnarep.2009.04.012
9. Ciccia A, Elledge SJ. The DNA damage response: making it safe to play with knives. *Mol Cell* (2010) **40**(2):179–204. doi:10.1016/j.molcel.2010.09.019
10. Reinhardt HC, Yaffe MB. Kinases that control the cell cycle in response to DNA damage: Chk1, Chk2, and MK2. *Curr Opin Cell Biol* (2009) **21**(2):245–55. doi:10.1016/j.ceb.2009.01.018
11. Putnam CD, Jaehnig EJ, Kolodner RD. Perspectives on the DNA damage and replication checkpoint responses in *Saccharomyces cerevisiae*. *DNA Repair* (2009) **8**(9):974–82. doi:10.1016/j.dnarep.2009.04.021
12. Peng A, Lewellyn AL, Schiemann WP, Maller JL. Repo-man controls a protein phosphatase 1-dependent threshold for DNA damage checkpoint activation. *Curr Biol* (2010) **20**(5):387–96. doi:10.1016/j.cub.2010.01.020
13. Fernet M, Megnin-Chanet F, Hall J, Favaudon V. Control of the G2/M checkpoints after exposure to low doses of ionising radiation: implications for hyper-radiosensitivity. *DNA Repair* (2010) **9**(1):48–57. doi:10.1016/j.dnarep.2009.10.006
14. Allen C, Ashley AK, Hromas R, Nickoloff JA. More forks on the road to replication stress recovery. *J Mol Cell Biol* (2011) **3**:4–12. doi:10.1093/jmcb/mjq049
15. Kastan MB, Lim DS, Kim ST, Yang D. ATM – a key determinant of multiple cellular responses to irradiation. *Acta Oncol* (2001) **40**(6):686–8. doi:10.1080/02841860152619089
16. Kitagawa R, Bakkenist CJ, McKinnon PJ, Kastan MB. Phosphorylation of SMC1 is a critical downstream event in the ATM-NBS1-BRCA1 pathway. *Genes Dev* (2004) **18**(12):1423–38. doi:10.1101/gad.1200304
17. Baskaran R, Wood LD, Whitaker LL, Canman CE, Morgan SE, Xu Y, et al. Ataxia telangiectasia mutant protein activates c-Abl tyrosine kinase in response to ionizing radiation. *Nature* (1997) **387**(6632):516–9. doi:10.1038/387516a0
18. Burma S, Chen BP, Murphy M, Kurimasa A, Chen DJ. ATM phosphorylates histone H2AX in response to DNA double-strand breaks. *J Biol Chem* (2001) **276**(45):42462–7. doi:10.1074/jbc.C100466200
19. Chen BP, Uematsu N, Kobayashi J, Lerenthal Y, Krempler A, Yajima H, et al. Ataxia telangiectasia mutated (ATM) is essential for DNA-PKcs phosphorylations at the Thr-2609 cluster upon DNA double strand break. *J Biol Chem* (2007) **282**(9):6582–7. doi:10.1074/jbc.M611605200
20. Shrivastav M, Miller CA, De Haro LP, Durant ST, Chen BP, Chen DJ, et al. DNA-PKcs and ATM co-regulate DNA double-strand break repair. *DNA Repair* (2009) **8**(8):920–9. doi:10.1016/j.dnarep.2009.05.006
21. Yajima H, Lee K-J, Chen BPC. ATR-dependent DNA-PKcs phosphorylation in response to UV-induced replication stress. *Mol Cell Biol* (2006) **26**:7520–8.

22. Matsuoka S, Ballif BA, Smogorzewska A, McDonald ER III, Hurov KE, Luo J, et al. ATM and ATR substrate analysis reveals extensive protein networks responsive to DNA damage. *Science* (2007) **316**(5828):1160–6. doi:10.1126/science.1140321
23. Shaheen M, Allen C, Nickoloff JA, Hromas R. Synthetic lethality: exploiting the addiction of cancer to DNA repair. *Blood* (2011) **117**:6074–82. doi:10.1182/blood-2011-01-313734
24. Kelley MR, Logsdon D, Fishel ML. Targeting DNA repair pathways for cancer treatment: what's new? *Future Oncol* (2014) **10**(7):1215–37. doi:10.2217/fon.14.60
25. Hosoya N, Miyagawa K. Targeting DNA damage response in cancer therapy. *Cancer Sci* (2014) **105**(4):370–88. doi:10.1111/cas.12366
26. Basu B, Yap TA, Molife LR, de Bono JS. Targeting the DNA damage response in oncology: past, present and future perspectives. *Curr Opin Oncol* (2012) **24**(3):316–24. doi:10.1097/CCO.0b013e32835280c6
27. Li F, Huang Q, Chen J, Peng Y, Roop DR, Bedford JS, et al. Apoptotic cells activate the "phoenix rising" pathway to promote wound healing and tissue regeneration. *Sci Signal* (2010) **3**(110):ra13. doi:10.1126/scisignal.2000634
28. Keysar SB, Astling DP, Andersona RT, Vogler BW, Bowles DW, Morton JJ, et al. A patient tumor transplant model of squamous cell cancer identifies PI3K inhibitors as candidate therapeutics in defined molecular bins. *Mol Oncol* (2013) **7**(4):776–90. doi:10.1016/j.molonc.2013.03.004
29. Skehan P, Storeng R, Scudiero D, Monks A, McMahon J, Vistica D, et al. New colorimetric cytotoxicity assay for anticancer-drug screening. *J Natl Cancer Inst* (1990) **82**(13):1107–12. doi:10.1093/jnci/82.13.1107
30. Hawkey CJ. COX-1 and COX-2 inhibitors. *Best Pract Res Clin Gastroenterol* (2001) **15**(5):801–20. doi:10.1053/bega.2001.0236
31. Okayasu R, Okada M, Okabe A, Noguchi M, Takakura K, Takahashi S. Repair of DNA damage induced by accelerated heavy ions in mammalian cells proficient and deficient in the non-homologous end-joining pathway. *Radiat Res* (2006) **165**(1):59–67. doi:10.1667/RR3489.1
32. Hirakawa H, Fujisawa H, Masaoka A, Noguchi M, Hirayama R, Takahashi M, et al. The combination of Hsp90 inhibitor 17AAG and heavy-ion irradiation provides effective tumor control in human lung cancer cells. *Cancer Med* (2015) **4**:426–36. doi:10.1002/cam4.377
33. Wang H, Wang Y. Heavier ions with a different linear energy transfer spectrum kill more cells due to similar interference with the Ku-dependent DNA repair pathway. *Radiat Res* (2014) **182**(4):458–61. doi:10.1667/RR13857.1
34. Shieh SY, Ahn J, Tamai K, Taya Y, Prives C. The human homologs of checkpoint kinases Chk1 and Cds1 (Chk2) phosphorylate p53 at multiple DNA damage-inducible sites. *Genes Dev* (2000) **14**(3):289–300. doi:10.1101/gad.14.3.289
35. Anderson RT, Keysar SB, Bowles DW, Glogowska MJ, Astling DP, Morton JJ, et al. The dual pathway inhibitor rigosertib is effective in direct patient tumor xenografts of head and neck squamous cell carcinomas. *Mol Cancer Ther* (2013) **12**(10):1994–2005. doi:10.1158/1535-7163.MCT-13-0206
36. Jimeno A, Weiss GJ, Miller WH, Gettinger S, Eigl BJC, Chang ALS, et al. Phase I study of the hedgehog pathway inhibitor IPI-926 in adult patients with solid tumors. *Clin Cancer Res* (2013) **19**(10):2766–74. doi:10.1158/1078-0432.CCR-12-3654
37. Keysar SB, Le PN, Anderson RT, Morton JJ, Bowles DW, Paylor JJ, et al. Hedgehog signaling alters reliance on EGF receptor signaling and mediates anti-EGFR therapeutic resistance in head and neck cancer. *Cancer Res* (2013) **73**(11):3381–92. doi:10.1158/0008-5472.CAN-12-4047
38. Connell PP, Weichselbaum RR. A downside to apoptosis in cancer therapy? *Nat Med* (2011) **17**(7):780–2. doi:10.1038/nm0711-780
39. Labi V, Erlacher M. How cell death shapes cancer. *Cell Death Dis* (2015) **6**(3):e1675. doi:10.1038/cddis.2015.20
40. Liu X, He Y, Li F, Huang Q, Kato TA, Hall RP, et al. Caspase-3 promotes genetic instability and carcinogenesis. *Mol Cell* (2015) **58**(2):284–96. doi:10.1016/j.molcel.2015.03.003
41. Rich T, Allen RL, Wyllie AH. Defying death after DNA damage. *Nature* (2000) **407**(6805):777–83. doi:10.1038/35037717
42. McCool KW, Miyamoto S. DNA damage-dependent NF-kappaB activation: NEMO turns nuclear signaling inside out. *Immunol Rev* (2012) **246**(1):311–26. doi:10.1111/j.1600-065X.2012.01101.x
43. Dent P, Yacoub A, Contessa J, Caron R, Amorino G, Valerie K, et al. Stress and radiation-induced activation of multiple intracellular signaling pathways. *Radiat Res* (2003) **159**(3):283–300. doi:10.1667/0033-7587(2003)159[0283:SARIAO]2.0.CO;2
44. Basu S, Rosenberg KR, Youmell M, Price BD. The DNA-dependent protein kinase participates in the activation of NFkB following DNA damage. *Biochem Biophys Res Commun* (1998) **247**:79–83. doi:10.1006/bbrc.1998.8741
45. Sabatel H, Pirlot C, Piette J, Habraken Y. Importance of PIKKs in NF-kappaB activation by genotoxic stress. *Biochem Pharmacol* (2011) **82**(10):1371–83. doi:10.1016/j.bcp.2011.07.105
46. Tsatsanis C, Androulidaki A, Venihaki M, Margioris AN. Signalling networks regulating cyclooxygenase-2. *Int J Biochem Cell Biol* (2006) **38**(10):1654–61. doi:10.1016/j.biocel.2006.03.021
47. Donato AL, Huang Q, Liu X, Li F, Zimmerman MA, Li CY. Caspase 3 promotes surviving melanoma tumor cell growth after cytotoxic therapy. *J Invest Dermatol* (2014) **134**(6):1686–92. doi:10.1038/jid.2014.18
48. Zhang Z, Wang M, Zhou L, Feng X, Cheng J, Yu Y, et al. Increased HMGB1 and cleaved caspase-3 stimulate the proliferation of tumor cells and are correlated with the poor prognosis in colorectal cancer. *J Exp Clin Cancer Res* (2015) **34**:51. doi:10.1186/s13046-015-0166-1
49. Hu Q, Peng J, Liu W, He X, Cui L, Chen X, et al. Elevated cleaved caspase-3 is associated with shortened overall survival in several cancer types. *Int J Clin Exp Pathol* (2014) **7**(8):5057–70.
50. Yang J, Yue JB, Liu J, Sun XD, Hu XD, Sun JJ, et al. Effect of celecoxib on inhibiting tumor repopulation during radiotherapy in human FaDu squamous cell carcinoma. *Contemp Oncol (Pozn)* (2014) **18**(4):260–7. doi:10.5114/wo.2014.43932
51. Inoue T, Anai S, Onishi S, Miyake M, Tanaka N, Hirayama A, et al. Inhibition of COX-2 expression by topical diclofenac enhanced radiation sensitivity via enhancement of TRAIL in human prostate adenocarcinoma xenograft model. *BMC Urol* (2013) **13**:1. doi:10.1186/1471-2490-13-1
52. Allen CP, Borak TB, Tsujii H, Nickoloff JA. Heavy charged particle radiobiology: using enhanced biological effectiveness and improved beam focusing to advance cancer therapy. *Mutat Res* (2011) **711**:150–7. doi:10.1016/j.mrfmmm.2011.02.012

Conflict of Interest Statement: The authors declare that the research was conducted in the absence of any commercial or financial relationships that could be construed as a potential conflict of interest.

Copyright © 2015 Allen, Tinganelli, Sharma, Nie, Sicard, Natale, King, Keysar, Jimeno, Furusawa, Okayasu, Fujimori, Durante and Nickoloff. This is an open-access article distributed under the terms of the Creative Commons Attribution License (CC BY). The use, distribution or reproduction in other forums is permitted, provided the original author(s) or licensor are credited and that the original publication in this journal is cited, in accordance with accepted academic practice. No use, distribution or reproduction is permitted which does not comply with these terms.

frontiers in Oncology

ORIGINAL RESEARCH
published: 13 April 2016
doi: 10.3389/fonc.2016.00087

Higher Initial DNA Damage and Persistent Cell Cycle Arrest after Carbon Ion Irradiation Compared to X-irradiation in Prostate and Colon Cancer Cells

Annelies Suetens[1,2†], Katrien Konings[1,3†], Marjan Moreels[1], Roel Quintens[1], Mieke Verslegers[1], Els Soors[1], Kevin Tabury[1], Vincent Grégoire[3] and Sarah Baatout[1]*

[1] Expert Group for Molecular and Cellular Biology, Radiobiology Unit, Belgian Nuclear Research Centre (SCK•CEN), Institute for Environment, Health and Safety, Mol, Belgium, [2] Radiation Oncology Department, Center for Molecular Imaging, Radiotherapy and Oncology, Institut de Recherche Expérimentale et Clinique (IREC), Université Catholique de Louvain (UCL), Bruxelles, Belgium, [3] Laboratory of Experimental Radiotherapy, Department of Oncology, KU Leuven, Leuven, Belgium

The use of charged-particle beams, such as carbon ions, is becoming a more and more attractive treatment option for cancer therapy. Given the precise absorbed dose-localization and an increased biological effectiveness, this form of therapy is much more advantageous compared to conventional radiotherapy, and is currently being used for treatment of specific cancer types. The high ballistic accuracy of particle beams deposits the maximal dose to the tumor, while damage to the surrounding healthy tissue is limited. In order to better understand the underlying mechanisms responsible for the increased biological effectiveness, we investigated the DNA damage and repair kinetics and cell cycle progression in two p53 mutant cell lines, more specifically a prostate (PC3) and colon (Caco-2) cancer cell line, after exposure to different radiation qualities. Cells were irradiated with various absorbed doses (0, 0.5, and 2 Gy) of accelerated ^{13}C-ions at the Grand Accélérateur National d'Ions Lourds facility (Caen, France) or with X-rays (0, 0.1, 0.5, 1, 2, and 5 Gy). Microscopic analysis of DNA double-strand breaks showed dose-dependent increases in γ-H2AX foci numbers and foci occupancy after exposure to both types of irradiation, in both cell lines. However, 24 h after exposure, residual damage was more pronounced after lower doses of carbon ion irradiation compared to X-irradiation. Flow cytometric analysis showed that carbon ion irradiation induced a permanent G2/M arrest in PC3 cells at lower doses (2 Gy) compared to X-rays (5 Gy), while in Caco-2 cells the G2/M arrest was transient after irradiation with X-rays (2 and 5 Gy) but persistent after exposure to carbon ions (2 Gy).

Keywords: carbon ion irradiation, PC3, Caco-2, cell cycle progression, DNA double-strand break damage and repair

OPEN ACCESS

Edited by:
Marco Durante, GSI, Germany

Reviewed by:
Christine Elisabeth Hellweg, German Aerospace Center (DLR), Germany
Yoshiya Furusawa, National Institute of Radiological Science, Japan

***Correspondence:**
Marjan Moreels
marjan.moreels@sckcen.be

†Annelies Suetens and Katrien Konings shared first authorship and contributed equally to this work.

Specialty section:
This article was submitted to Radiation Oncology, a section of the journal Frontiers in Oncology

Received: *20 January 2016*
Accepted: *28 March 2016*
Published: *13 April 2016*

Citation:
Suetens A, Konings K, Moreels M, Quintens R, Verslegers M, Soors E, Tabury K, Grégoire V and Baatout S (2016) Higher Initial DNA Damage and Persistent Cell Cycle Arrest after Carbon Ion Irradiation Compared to X-irradiation in Prostate and Colon Cancer Cells. Front. Oncol. 6:87. doi: 10.3389/fonc.2016.00087

INTRODUCTION

Over the past decades, an increase in the use of hadrontherapy has been observed (1). Hadrontherapy uses accelerated particles, such as protons or carbon ions, thereby offering a ballistic advantage during treatment. The inverted depth–dose profile and a sharp dose fall-off result in a precise dose-localization called Bragg peak (2). As such, a very specific energy deposition is focused on the tumor, while the surrounding healthy tissue is spared to a maximum. When carbon ions are used, the high-linear energy transfer (LET) also offers biological advantages compared to X-irradiation (3). From a physical point of view, low-LET photon irradiation deposits its energy in a disperse manner. This homogeneous distribution of energy in the irradiation field strongly relies on secondary ionizations (by the formation of reactive oxygen species) in the cell that will indirectly induce DNA damage homogeneously. By contrast, with particle irradiation, energy is not released in a disperse manner but rather along the track of the beam. Therefore, damage is more straightforward along the track that induces more complex and clustered DNA damage via a direct mechanism (4, 5). In view of therapeutic measures, the induction of DNA damage and specifically the double-strand break (DSB) is seen as the most prominent target in order to destroy cancer cells (6). Since DNA damage induced by high-LET radiation is more complex compared to low-LET irradiation, the relative biological effectiveness (RBE) of particle beams will be higher compared to X-rays (6). In this regard, it has been shown that hadrontherapy with carbon ions is more cytotoxic due to the higher RBE compared to photon irradiation (7, 8). However, the specific impact of carbon ion irradiation on cell cycle changes and comparison with X-irradiation in PC3 and Caco-2 cancer cells has not been investigated so far.

When DNA damage is induced, DSBs are detected in the cell by sensing molecules, such as DNA-dependent protein kinases (DNA-PK) or Ku70, which activate a signaling cascade by phosphorylating the histone H2AX (γ-H2AX) (9, 10). Another sensing molecule that is activated after DNA damage is p53, also known as the guardian of the genome (11). Repair enzymes will be attracted to the damaged site and the cell will go into cell cycle arrest to allow time for repair. It is well known that the number of γ-H2AX foci is proportional to the amount of DSBs (12–14). By immunofluorescent staining of the γ-H2AX foci, quantitative and qualitative evaluation of the damage can be performed. A previous *in vitro* study investigating the differential effect of high- and low-LET radiation has shown that the initial formation (as early as 15 min) of γ-H2AX foci is similar for equal doses of different beam qualities (15). However, repair kinetics (investigated at later time points) have shown a delayed or less successful repair of DSBs after high-LET radiation (16, 17). Therefore, particle irradiation can be effective in inducing cell death even in highly radioresistant cells (18). One of the factors that plays a major role in determining radiosensitivity is p53. Mutations or deletions in the p53 gene can lead to the radioresistance of cancer cells to conventional radiotherapy (19–22). By contrast, previous studies with high-LET radiation have shown that this type of radiation can induce apoptosis effectively regardless of p53 gene status (7, 23).

In vitro studies comparing the effect of particle or photon irradiation have shown a more pronounced cell cycle arrest induced by particles (24, 25). Furthermore, it has been shown that cells are more sensitive to the induction of DSBs by X-irradiation during the G2/M-phase of the cell cycle (26). Contrarily, the radiation sensitivity of cancer cells irradiated with particles is less, but not entirely, dependent on the cell cycle stage (27). Thus, particle beam therapy is more suitable to damage a heterogeneous tumor population, consisting of cells in different cell cycle stages (24).

We previously investigated the transcriptional response of PC3 and Caco-2 cells after X- and carbon ion irradiation, in which we observed more pronounced changes in gene expression after carbon ion irradiation. Genome-wide analysis in PC3 cells showed that gene sets involved in cell cycle regulation and, interestingly, also in motility processes were found to be modulated, especially after carbon ion irradiation (28). In a next step, we further investigated the changes of genes involved in motility processes. Our results showed that the magnitude of expression of these genes was time- and dose-dependent for both PC3 and Caco-2 cells, although a cell-type-specific response to X- and carbon ion irradiation was observed (29). With regard to the changes in cell cycle-related gene sets, we further aimed to investigate the acute cellular responses induced by different radiation qualities. Therefore, in this study, we examined both DNA repair kinetics and cell cycle progression in PC3 and Caco-2 cells in response to carbon ion or X-irradiation. Cells were irradiated with different doses ranging from 0.1 up to 5 Gy depending on the type of radiation. DNA damage and repair kinetics were analyzed up to 24 h after irradiation and cell cycle progression up to 72 h after irradiation. Further elucidation of the effect of different beam qualities on different cancer cell lines will contribute to a better understanding of which therapy would be most suited for these types of cancers.

MATERIALS AND METHODS

Cell Culture

Human prostate adenocarcinoma cells (PC3; ATCC® CRL-1435™) and colorectal adenocarcinoma cells (Caco-2; ATCC® HTB-37™) were obtained from the American Type Culture Collection (ATCC, Molsheim Cedex, France). PC3 cells were cultured in Kaighn's Modification of Ham's F-12 Medium (F-12K) (ATCC) supplemented with 10% fetal bovine serum (FBS) (GIBCO, Life Technologies, Ghent, Belgium), as specifically recommended by ATCC. Caco-2 cells were cultured in Dulbecco's Modified Eagle medium (DMEM) (GIBCO) supplemented with 10% FBS and 1% non-essential amino acids (GIBCO). Cell cultures were maintained in a humidified incubator (37°C; 5% CO_2). For all irradiation experiments, the same passage number of cells was used. Cell doubling time was 26 and 20 h for PC3 and Caco-2 cells, respectively (data not shown). Cell cultures were regularly tested for mycoplasma contamination (DSMZ, Braunschweig, Germany).

X-irradiation

X-irradiation experiments were performed at the irradiation facility available at SCK•CEN (Mol, Belgium). Medium was replaced

prior to irradiation in a horizontal position. Cells were exposed to different doses of X-rays (0, 0.1, 0.5, 1, 2, and 5 Gy) using a Pantak HF420 RX machine (250 kV, 15 mA, 1.2 mm Aluminum equivalent, 1 mm Cu-filtered X-rays, and a calculated dose rate of 0.25 Gy/min). The beam quality of H-250 (as recommended by ISO 4037-1) was used. This beam quality was created using a tube voltage of 250 kV and 1 mm Cu additional filtration. The secondary standard for X-rays is the NE2571 0.6 cc ionization chamber SN309 connected to Keithley 6517B SN1335646 electrometer. The calibration of this chamber in terms of air Kerma (K_{air}), for H-250 beam quality, was done in 2013 at the primary standard laboratory PTB, Germany. The reference quantity is K_{air} in one point, taken as the reference position of the irradiated sample, which typically is its center. No correction is done for the extended volume and self-absorption of the sample itself and such effect is not included in the uncertainties budget either. The irradiation is based on the ISO 4037 standard. All uncertainties are the expanded uncertainties for $k = 2$ (confidence level 95%). The dose rate was measured for each distance, by using repeatedly the same distance, one relies on stability from 1 day to another and, therefore, only periodic checks of beam stability are performed at the irradiation facility.

Carbon Ion Irradiation

For our experiment, we were assigned ^{13}C beam time at the Grand Accélérateur National d'Ions Lourds (GANIL) (Caen, France). Cells were transported by car in a transportable incubator at 37°C to GANIL. For all assays, 10^5 cells were plated in 12.5 cm^2-tissue culture flasks (Falcon; VWR; Leuven, Belgium) 3 days before transport, during which all culture flasks were completely filled with medium. After arrival, medium was changed, and cells were placed overnight in a humidified incubator. Before the irradiation, culture flasks were completely filled with medium to allow irradiation in a vertical position, perpendicular to a horizontal carbon ion beam. The cells were irradiated with a ^{13}C beam with an initial energy of 75 MeV/u (LET = 33.7 keV/μm). The applied doses were 0, 0.5, 1, and 2 Gy. Carbon ion dosimetry was performed as previously described (28, 30). The RBE of carbon ions at 10% survival was 1.67 for PC3 cells and 1.83 for Caco-2 cells (29).

Immunocytochemistry for γ-H2AX

For X-irradiation experiments, cells were plated on coverslips at a density of 20,000 cells/well and grown for 2 days. Due to practical reasons, samples were irradiated in T12.5 flasks for the carbon ion irradiation (vertical position). Irradiation with both radiation qualities was then performed with a series of doses as mentioned before. At various time points after irradiation (30 min, 1, 2, 4, 8, and 24 h), cells were fixed in 4% paraformaldehyde (Merck KGaA, Darmstadt, Germany) for at least 20 min at 4°C. Afterwards, cells were washed with PBS and permeabilized in 0.25% Triton (Sigma-Aldrich Co.) in PBS for 3 min. Subsequently, cells were probed with mouse anti-γ-H2AX antibody (ab26350, Abcam, Cambridge, UK) (1:300 dilution) and incubated overnight at 4°C. Next, the cells were washed with PBS and stained with Alexa Fluor 488 goat anti-mouse (H + L)-labeled antibody (A11001, Invitrogen, Life technologies) (1:300 dilution) for 2 h at room temperature. All antibody dilutions were prepared in 3% bovine serum albumin (BSA). Following this, three washing steps were performed with PBS after which a cover glass was mounted on the samples with Vectashield containing 4′,6-diamidino-2-phenylindole (DAPI) (Vector Laboratories, Brussels, Belgium).

Automated Fluorescence Microscopy and Image Analysis

Images were acquired with a Nikon Eclipse Ti (automated inverted wide-field epifluorescence microscope) equipped with a 40× magnification (Plan Fluor, numerical aperture 1.3) oil objective and a Nikon TE2000-E camera controlled by the NIS Elements software. The images were taken in the same orientation as the irradiation was performed, i.e., the viewer position was perpendicular to the cellular plane. Per condition a mosaic of 25 fields was acquired with a lateral spacing of 190 μm between fields (corresponding to the size of the field of view) and each field was acquired as a z-stack of nine planes axially separated by 1 μm. Images were analyzed with Fiji software (31) using the InSCyDe-02 toolbox. The software allowed to analyze each nucleus based on the DAPI signal. Within each nucleus, pixel size and intensity emitted from the Alexa 488 fluorochrome were analyzed after which the γ-H2AX foci number per nucleus and the foci occupancy are determined in a fully automatic manner. These data were then used to count the radiation-induced damage, i.e., subtract the damage of control cells from irradiated cells. As mentioned before, for carbon ion irradiation experiments, cells were seeded in T12.5 flasks (plastic surface) since these samples were irradiated in a vertical position. X-irradiated samples were seeded on glass cover slips for γ-H2AX. As a result, image quality was less good for carbon ion samples, and as a consequence Fiji software was unable to correctly count the number of spots in each nucleus for the carbon ion-irradiated samples. Therefore, we decided to count the spots manually for the carbon ion samples. At least 170 and 100 nuclei were analyzed per sample for X-ray and carbon ion irradiation, respectively.

Cell Cycle Analysis

Cells were collected at 24, 48, and 72 h after irradiation by use of trypsinization. In addition, supernatants and PBS used during wash steps were kept as well to ensure the collection of both adherent and detached cells. After collection, samples were fixed in a cold 80% EtOH solution at 4°C for at least 1 h. Fixed samples obtained in GANIL were transported back to SCK•CEN for further processing. Next, samples were washed with PBS and stained with a 500 μl propidium iodide (PI) solution (50 μg/ml PI + 1% RNase A) (Sigma-Aldrich Co. LLC; Bornem; Belgium) for 50 min at 37°C. Samples were measured immediately afterwards by flow cytometry (Accuri C6 system; BD Biosciences, Erembodegem, Belgium). PI fluorescence of a minimum of 10,000 cells was measured. Cells in G0/G1, S, and G2/M-phase were determined after filtering for doublets and aggregates. Doublets were filtered based on a FSC-A vs. FSC-H dot plot with Accuri C6 software. In addition, sub G1 cells were identified as cells with a DNA content of between half the mean value of G1 phase and the minimum

value of G1 phase. Based on the histogram, we determined the peak of G1, on which the settings were placed in such a way that 90% falls within the peak. The peak of G2 needs to be 2 × G1 and also for this the settings were placed in such a way that 90% falls within the peak. Everything in-between was seen as S-phase. Everything in-between 0.5 × G1 and the beginning of G1 phase was the sub G1 peak. Re-analysis of samples was performed with ModFit LT software (Verity Software House, Topsham, ME, USA). Representative histograms are visualized in **Figure 1**.

Statistical Analysis

Cell cycle data were analyzed by two-way analysis of variance (ANOVA) with dose and time point as independent variables. Analysis of γ-H2AX foci count data was performed using Kruskal–Wallis and *post hoc* Dunn's multiple comparison tests. All analyses were performed using GraphPad Prism 5.00 software. For all tests, a value of $p < 0.05$ was considered statistically significant.

RESULTS

DNA Damage and Repair Kinetics

DNA DSBs were visualized by immunofluorescent staining for γ-H2AX foci that were analyzed at various time points (30 min, 1, 2, 4, 8, and 24 h) after irradiation. Representative images of the γ-H2AX foci for both PC3 and Caco-2 are shown in **Figure 2**. We counted both the number of radiation-induced foci, as a measure of DSBs, and the foci occupancy because H2AX phosphorylation as well as the size of foci differs throughout the cell cycle (32). Upon irradiation, a clear dose-dependent induction in the number and nuclear occupancy of foci was observed. A significant dose-dependent increase in foci number was detected after X-irradiation in PC3 cells as early as 30 min after irradiation (**Figure 3A**). Increased foci numbers induced by irradiation were associated with a higher percentage of the area of the nucleus covered by foci as seen in the elevated foci occupancy (**Figure 3B**). A follow-up of foci number and foci occupancy over time evidenced time-dependent repair of foci (**Figures 3A,B**). Maximum foci numbers were detected 1 h after X-irradiation (**Figure 3A**), after which repair seems to have initiated. Interestingly, most γ-H2AX foci were repaired 24 h after X-irradiation with doses up to 0.5 Gy, while residual foci were still visible after exposure to higher X-ray doses (**Figures 3A,B**). For carbon ion irradiation, the number of foci was still significantly elevated at 24 h after irradiation after all doses in PC3 cells (**Figure 3C**). Maximum foci numbers were detected 1 h after irradiation with carbon ions. A similar trend was observed for the foci occupancy in PC3 cells (**Figure 3D**).

Similar results were observed for the Caco-2 cells. More specifically, a dose-dependent increase in foci number was observed as early as 30 min after X-irradiation (**Figure 4A**). This increase was accompanied by an increase in foci occupancy (**Figure 4B**). Maximum foci numbers were observed at 1 to 2 h after X-irradiation after which a time-dependent repair was evidenced (**Figure 4A**). For the Caco-2 cells, 24 h after X-irradiation residual foci were still present for doses up to 1 Gy (**Figure 4A**).

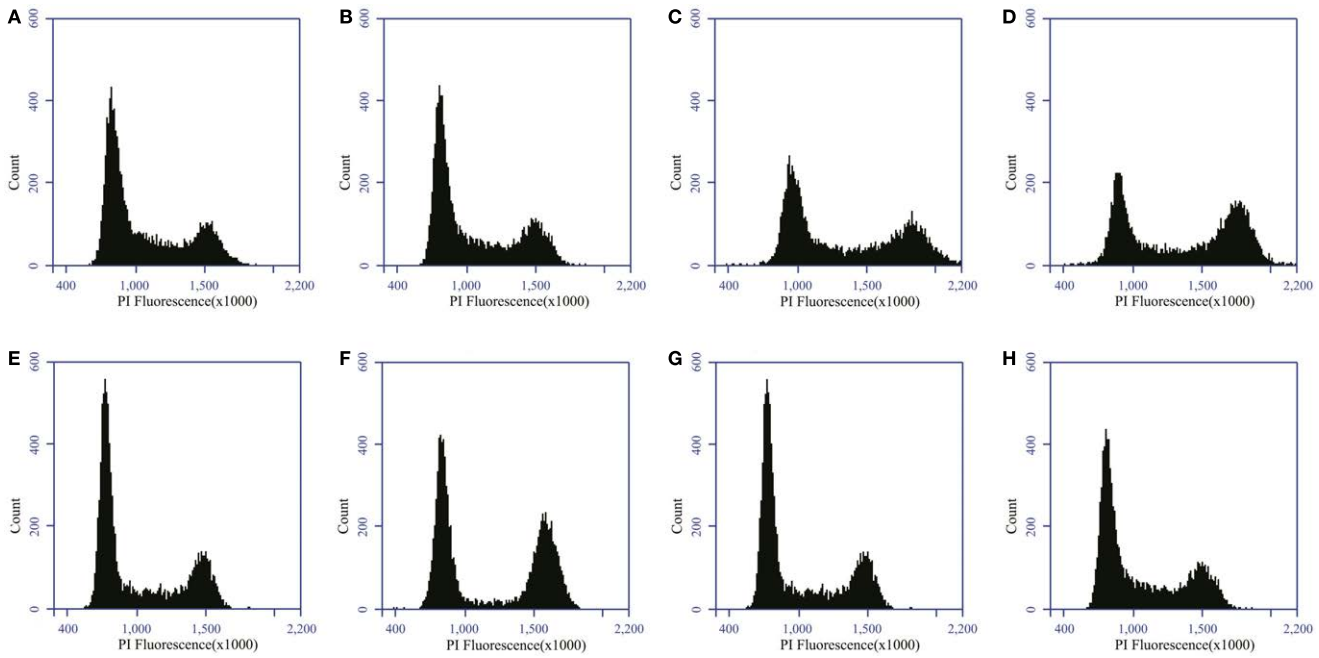

FIGURE 1 | **Distribution of PC3 and Caco-2 cells in the different phases of the cell cycle**. Distribution of PC3 cells in the cell cycle for control **(A)** and 2 Gy X-ray irradiated **(B)** samples 24 h after irradiation. Distribution of Caco-2 cells in the cell cycle for control **(C)** and 2 Gy X-ray-irradiated **(D)** samples 24 h after irradiation. Distribution of PC3 cells in the cell cycle for control **(E)** and 2 Gy carbon ion-irradiated **(F)** samples 24 h after irradiation. Distribution of Caco-2 cells in the cell cycle for control **(G)** and 2 Gy carbon ion-irradiated **(H)** samples 24 h after irradiation.

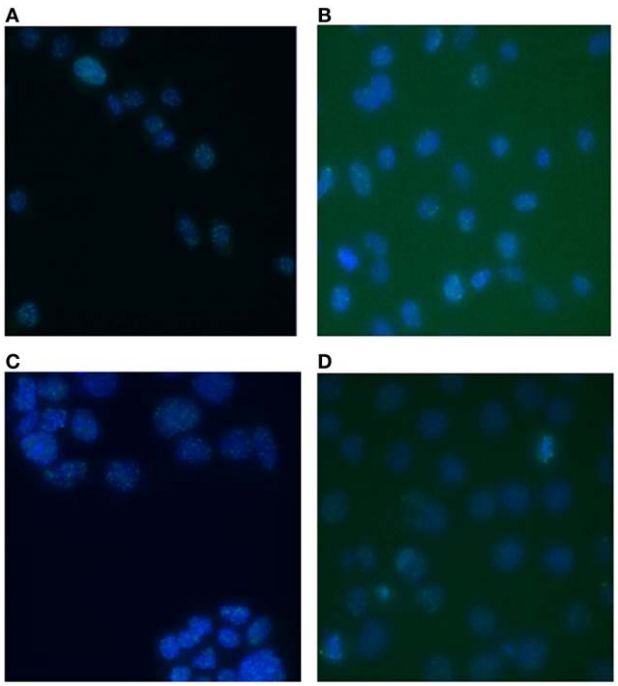

FIGURE 2 | γ-H2AX foci in PC3 and Caco-2 cells after irradiation with X-rays or carbon ions. Representative images of γ-H2AX foci in PC3 cells 1 h after 2 Gy X-irradiation **(A)** and 1 h after 2 Gy carbon ion irradiation **(B)**. Representative images of γ-H2AX foci in Caco-2 cells 1 h after 2 Gy X-irradiation **(C)** and 1 h after 2 Gy carbon ion irradiation **(D)**. Images were acquired with a Nikon Eclipse Ti (automated inverted wide-field epifluorescence microscope) equipped with a 40× magnification (Plan Fluor, numerical aperture 1.3) oil objective and a Nikon TE2000-E camera controlled by the NIS Elements software.

Similar observations were made for carbon ion-irradiated Caco-2 cells, where significantly elevated foci number were still observed 24 h after irradiation for all doses (**Figure 4C**). Maximum foci numbers were already detected 30 min after irradiation with carbon ions. Foci occupancy was also significantly elevated 24 h after 0.5 and 2 Gy of carbon ion irradiation in Caco-2 cells (**Figure 4D**).

For carbon ion experiments, we additionally correlated the number of γ-H2AX foci with the number of ion traversals (**Table 1**). This was calculated by dividing the nuclear area of the cells (PC3 or Caco-2) by the fluence (different for each dose). The higher the number of ions passing the cell nucleus, the higher the number of foci that we counted after carbon ion irradiation. In addition, the (slightly) higher number of ions that pass the cell nucleus for Caco-2 cells compared to PC3 cells correlates with the higher number of foci that were counted in Caco-2 cells compared to PC3 cells 30 min after carbon ion irradiation.

Cell Cycle Analysis

Radiation-induced cell cycle changes were analyzed by flow cytometry at 24, 48, and 72 h after X- and carbon ion irradiation using PI staining. Representative histograms are shown in **Figure 1** for both PC3 and Caco-2 cells.

In PC3 cells, 5 Gy of X-irradiation resulted in an increase of the percentage of cells in G2 phase (~10%) at all time points at the expense of G1 cells (**Figure 5A**), suggestive of a persistent G2/M arrest. Lower doses of X-rays did not affect the cell cycle of PC3 cells. On the other hand, carbon ion irradiation of PC3 cells resulted in a significant increase of cells in G2/M-phase, 24 h after 2 Gy and 48 and 72 h after both 1 and 2 Gy (**Figure 5B**). This was combined with a decrease in cells in G1 phase at all time points both at 1 and 2 Gy. After 1 Gy carbon ion irradiation, significant changes in the fraction of S-phase cells were found after 24 and 48 h.

In Caco-2 cells, a dose of 2 and 5 Gy of X-rays increased the number of cells in G2/M-phase, although only transiently (**Figure 5C**). This was combined with a decrease in the number of cells in G1 for both doses and a decrease in cells in S-phase for 5-Gy X-irradiation. After 48 and 72 h, the G2/M arrest was resolved in Caco-2 cells irradiated with X-rays. However, a small but significant decrease (almost 4%) in G1 phase cells was found at 72 h after 5-Gy X-irradiation. Irradiation of Caco-2 cells with 2 Gy of carbon ions resulted in a persistent G2/M arrest, accompanied by a decrease of cells in G1 phase (**Figure 5D**). At the earliest time point, this could also be observed after 1 Gy carbon ion irradiation.

DISCUSSION

From a physical point of view, the rationale for the use of particle irradiation in cancer therapy has been clear for a very long time. Along with the positive patient responses observed in clinical trials using particle therapy, it has been of increasing interest to understand and unravel the underlying biological mechanisms and pathways involved by means of *in vitro* studies. Important differences between both radiation qualities in DNA damage and subsequent cell cycle arrest have been indicated (33), which explain the higher RBE induced by particle radiation. In this study, we investigated changes in DNA damage and repair kinetics of PC3 and Caco-2 cell lines exposed to carbon ion or X-irradiation. In addition, cell cycle stages in both cell lines were analyzed. We observed an increase in γ-H2AX foci number and foci occupancy after X-irradiation with some interesting differences between both cell lines. The initial induction of γ-H2AX was similar for both cell lines although foci occupancy was higher in PC3 cells than in Caco-2 cells after exposure to X-rays. One explanation for this could be the difference in radiosensitivity between both cell lines, as we previously observed (29). Exposure to carbon ions resulted in a higher initial induction of γ-H2AX foci for Caco-2 cells compared to PC3 cells. In samples exposed to X-rays relatively less residual damage after 24 h was observed in Caco-2 cells compared to PC3 cells (mean foci count after 5 Gy was 25 foci after 30 min and 20 foci after 24 h in PC3 cells, and 26 foci after 30 min and 8 foci after 24 h in Caco-2 cells). This lower residual damage observed in Caco-2 cells after X-irradiation can also be linked to a higher surviving fraction of Caco-2 cells compared to PC3 cells as we observed previously (29).

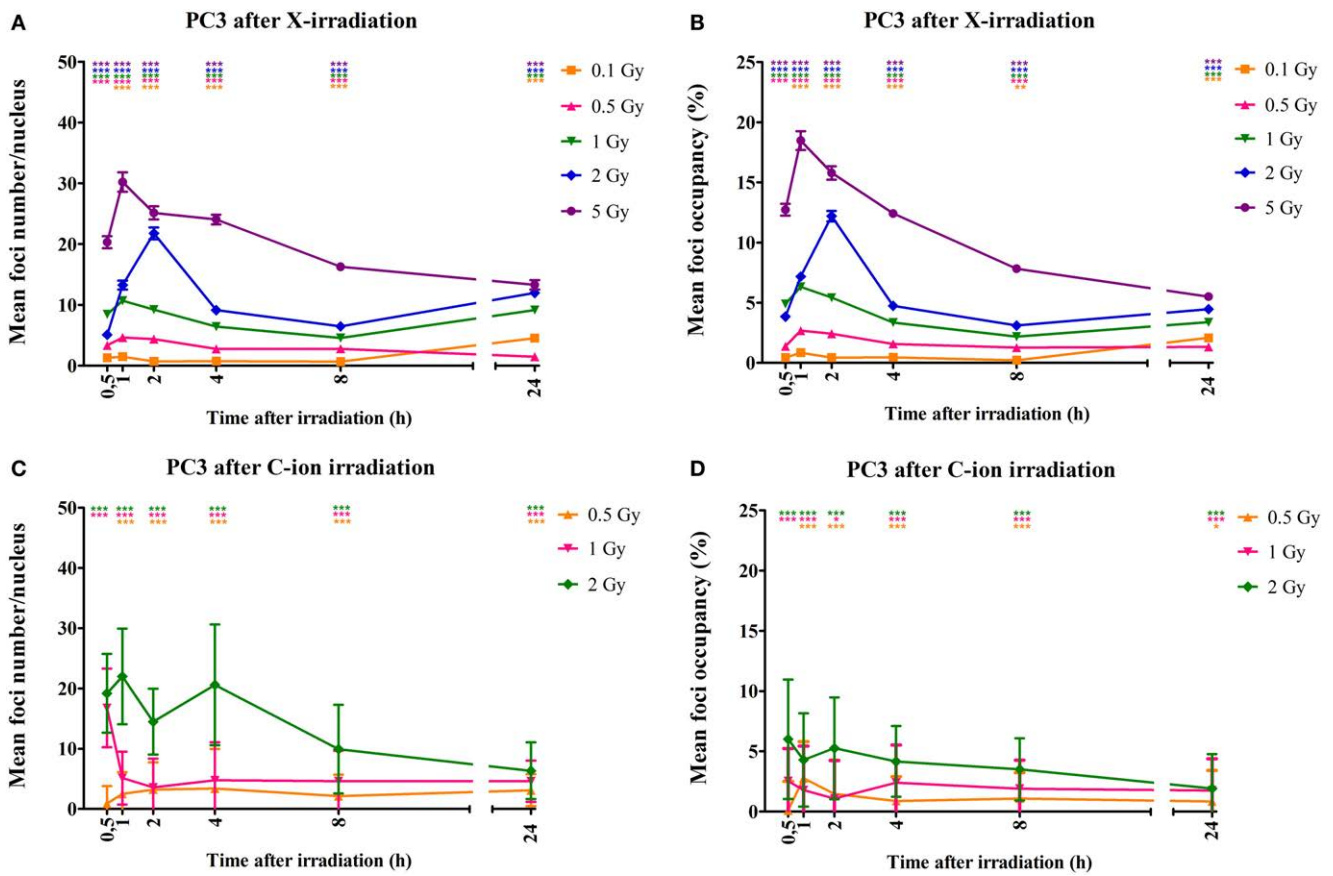

FIGURE 3 | **Quantification of γ-H2AX foci number and occupancy in X- and carbon ion-irradiated PC3 cells**. Dots representing mean γ-H2AX foci number per nucleus vs. time **(A)** and mean foci occupancy per nucleus vs. time **(B)** after X-irradiation in PC3 cells. Dots representing mean γ-H2AX foci number per nucleus vs. time **(C)** and mean foci occupancy per nucleus vs. time **(D)** after exposure to carbon ions. Fiji software was used to count the number of nuclei and foci occupancy in each nucleus. The number of foci in non-irradiated cells was subtracted from that of irradiated cells for each dose and time point. For X-rays, the error bars represent the SEM of three independent experiments; for carbon ion data, the error bars represent STDEV of the experiment. Statistical Kruskal–Wallis analysis with Dunn's multiple comparison tests were performed in GraphPad with $^{*}p < 0.05$ (vs. control cells), $^{**}p < 0.01$ (vs. control cells), and $^{***}p < 0.001$ (vs. control cells).

We found no reports on γ-H2AX analysis of irradiated Caco-2 cells and only one for PC3 cells (34). They irradiated confluent PC3 cells with 2 Gy X-rays and visualized γ-H2AX foci after 30 min and 24 h. After 30 min, 10 foci were observed after 2 Gy of X-rays, compared to 5 foci in our PC3 cells. However 24 h after exposure we found a higher residual number of γ-H2AX foci in the PC3 cells (i.e., 7 foci observed by van Oorschot vs. 12 foci observed in our study). One explanation for this could be the different set-up of the experiment; more specifically van Oorschot et al. used a dose rate of 3 Gy/min, whereas we used a dose rate of 0.25 Gy/min. Another explanation could be a difference in the confluence of the irradiated cells, which could synchronize the cells in a certain phase making the cells more or less resistant to the effect of (X-ray) irradiation.

Our data showed that 30 min after exposure to carbon ions, a higher number of foci were induced at a therapeutic dose of 2 Gy compared to X-rays. More specifically, in PC3 cells, we observed five radiation-induced foci after irradiation with 2 Gy of X-rays compared to 19 foci after an equal dose of carbon ions. For Caco-2 cells, the number of radiation-induced foci after 2 Gy of X-rays and carbon ions was 8 and 30, respectively. This is in contrast to a study by Ghosh et al. (15) in which A549 cells were irradiated with γ-rays (1, 2, or 3 Gy) or ^{12}C ions (1 Gy, 5.2 MeV/u; LET = 290 keV/μm). They observed that equal doses of both radiation qualities induced similar numbers of foci 15 min after irradiation.

A closer look at the residual foci number (at 24 h) after 2 Gy irradiations shows that less foci are detected in carbon ion-irradiated PC3 samples compared to X-ray samples (i.e., increase of 6 foci after carbon ion irradiation; increase of 12 foci after X-rays;). However, we should note that samples exposed to carbon ions were irradiated in a vertical position, perpendicular to the irradiation beam. Since carbon ion irradiation is expected to induce more complex damage along the ionization tracks, more foci would be present behind one another along the *Z*-axis. This could explain why although less foci are counted in general and less are present after 24 h, the residual damage could still be more complex, which, in turn, explains the persistent G2/M arrest we observed after both 1 and 2 Gy carbon ion irradiation.

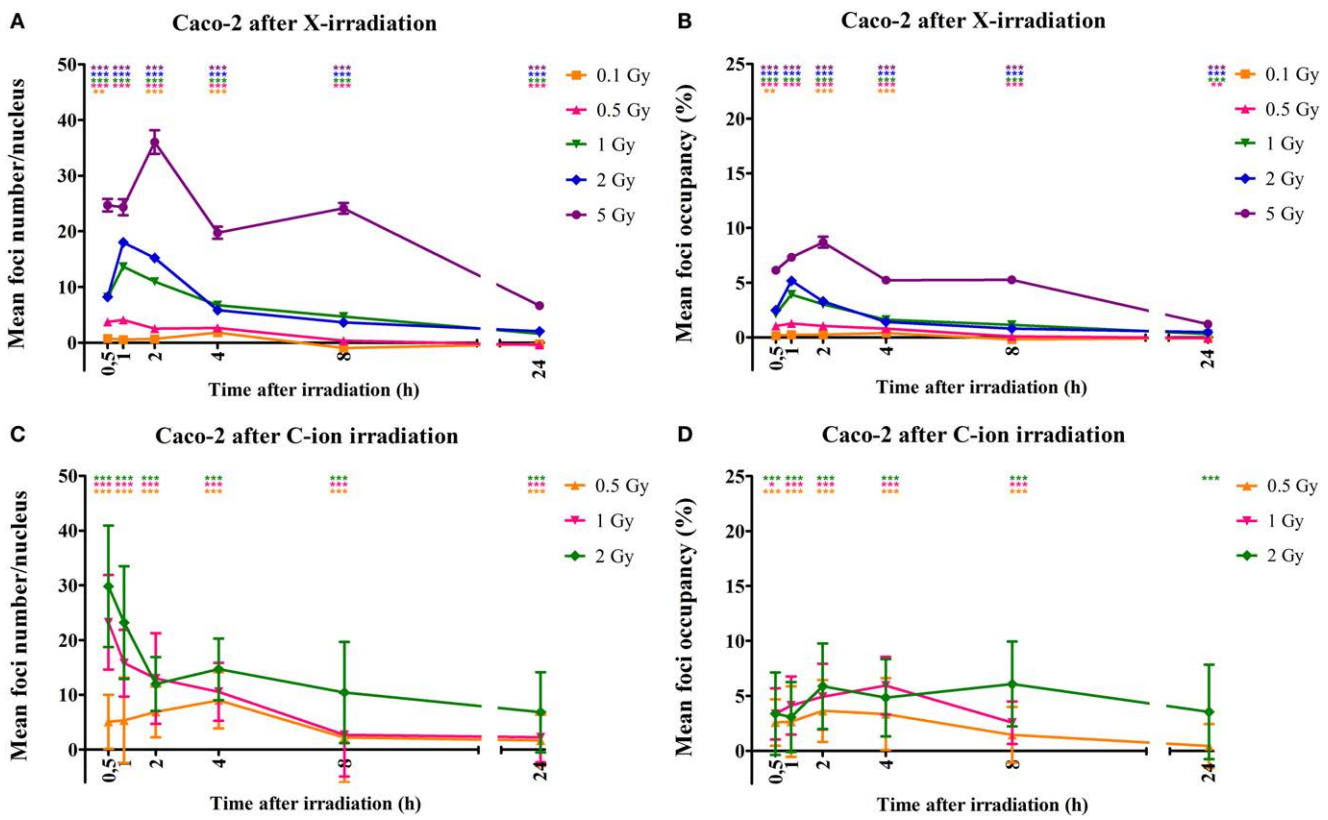

FIGURE 4 | Quantification of γ-H2AX foci number and occupancy in X- and carbon ion-irradiated Caco-2 cells. Dots representing mean γ-H2AX foci number per nucleus vs. time **(A)** and mean foci occupancy per nucleus vs. time **(B)** after X-irradiation in Caco-2 cells. Dots representing mean γ-H2AX foci number per nucleus vs. time **(C)** and mean foci occupancy per nucleus vs. time **(D)** after exposure to carbon ions. Fiji software was used to count the number of nuclei and foci occupancy in each nucleus. For X-rays, the error bars represent the SEM of three independent experiments; for carbon ion data, the error bars represent STDEV of the experiment. Statistical Kruskal–Wallis analysis with Dunn's multiple comparison tests were performed in GraphPad with $^{**}p < 0.01$ (vs. control cells), $^{***}p < 0.001$ (vs. control cells).

TABLE 1 | Ion traversals per cell nucleus were calculated for PC3 and Caco-2 and compared to the results of γ-H2AX foci 30 min after carbon ion exposure.

	PC3		Caco-2	
	Number of traversals calculated	Number of foci counted after 30 min	Number of traversals calculated	Number of foci counted after 30 min
0.5 Gy	12.5	0.9	15.9	5.1
1 Gy	25.1	16.7	31.7	23.2
2 Gy	49.9	19.2	63.1	29.8

The number of traversals was calculated by dividing the nuclear area of the cells (PC3 or Caco-2) by the fluence (different for each dose). Nuclear area for PC3 cells was on average 134.7 μm and for Caco-2 cells 170.5 μm.

Additionally, because we analyzed the foci in the same direction as the position of the irradiation beam, it is possible that spots overlapped, causing the foci number to be lower than expected (35). Similar observations were made by a study of Rall et al. in which human blood-derived cells were irradiated with 2 Gy of high-LET irradiation (iron ions, LET = 155 keV/μm). Because of the higher RBE of iron ions, a higher induction of γ-H2AX foci for iron ion-irradiated samples compared to the X-ray irradiated samples was expected, but not observed. The authors hypothesized that the formation of γ-H2AX foci along the beam track has a limited resolution, leading to lower foci numbers (12, 36, 37). In Caco-2 cells, however, we measured lower levels of residual γ-H2AX foci after 24 h in X-irradiated samples compared to carbon ions (i.e., increase of 2 foci after 2 Gy X-rays; increase of 7 foci after 2 Gy carbon ion irradiation). Also here, damage is expected to be more complex and could, therefore, be responsible for the persistent G2/M arrest induced by carbon ions, which was not observed after X-irradiation.

As could be expected, carbon ion irradiation was more potent in inducing cell cycle arrest as compared to equal doses of X-ray irradiation. A persistent G2/M arrest was observed in PC3 cells, already after a dose of 1 Gy of carbon ions. By contrast, only a dose of 5 Gy X-rays was able to induce a persistent cell cycle arrest in PC3 cells (up to 72 h post irradiation). For Caco-2 cells, 2 Gy carbon ion irradiation was capable of inducing a persistent G2/M arrest, whereas after X-radiation Caco-2 cells seemed to escape from the G2/M arrest 48 h after irradiation. These differences indicate the potency of particle radiation to induce more severe

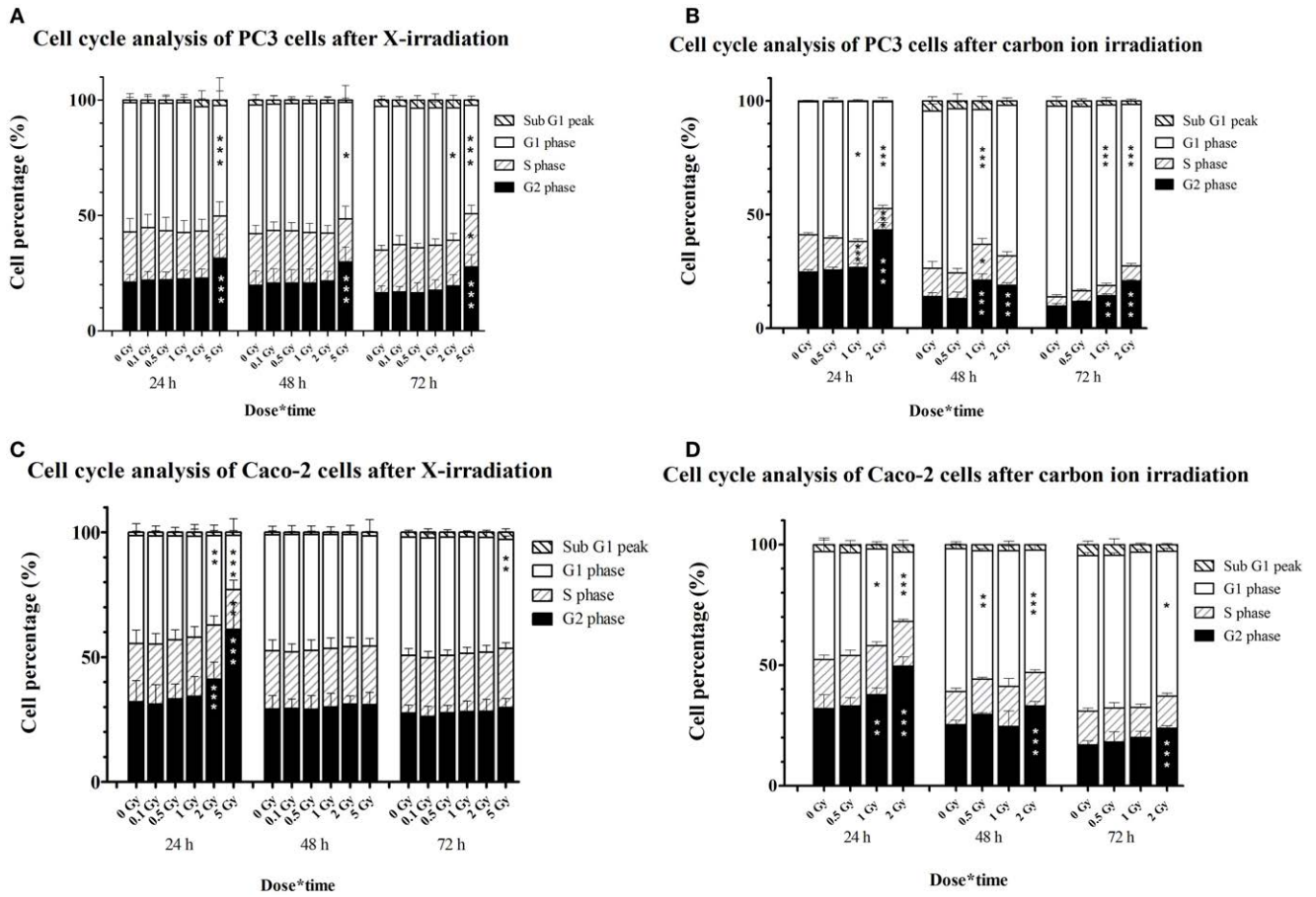

FIGURE 5 | Cell cycle distribution of irradiated PC3 and Caco-2 cells assessed by PI staining and flow cytometry. Stacked graphs representing percentages of cells per cell cycle phase in PC3 cells irradiated with X-rays **(A)** or carbon ions **(B)** and in Caco-2 cells irradiated with X-rays **(C)** or carbon ions **(D)**. Bars represent an average of three experiments for X-irradiated samples and one experiment for the carbon ion-irradiated samples. Statistical two-way ANOVA with Bonferroni *post hoc* test was performed in GraphPad Prism with $^{*}p < 0.05$ (vs. control cells), $^{**}p < 0.01$, and $^{***}p < 0.001$ (vs. control cells).

damage that can lead to (persistent) cell cycle arrest. In Caco-2 cells, a transient G2/M arrest was observed after X-irradiation; whereas in PC3 cells, this arrest persisted until 72 h after exposure. These different results could be explained by the lower residual DNA damage that we observed after 24 h in Caco-2 cells compared to PC3 cells. Another explanation could be the difference in doubling time between both cell lines, where PC3 cells have a higher doubling time compared to Caco-2 cells.

To our knowledge, no previous studies investigated the effect of particle irradiation on cell cycle progression of Caco-2 cells, while only one study investigated cell cycle changes in PC3 cells after proton irradiation (38). In their study, cells were exposed to 10, 20, or 40 Gy of either photon or proton irradiation. With regard to cell cycle changes, they observed a less pronounced and delayed G2/M arrest after photons compared to proton irradiation. This is consistent with our and previously published results comparing various cell lines irradiated with different beam qualities (25, 39–42). However, most of these studies only focused on cell cycle changes up to 24 h post irradiation. We analyzed as far as 72 h after irradiation and found that, compared to X-rays, a lower equal dose of carbon ions was sufficient to induce a permanent G2/M arrest in PC3 cells. For Caco-2 cells however, a qualitative difference in cell cycle arrest was observed. To this regard, we demonstrated that a lower dose of carbon ion particles was capable of inducing a persistent arrest that was not present after X-rays.

Differences in repair kinetics between X- and carbon ion irradiation, as we observed here, might be an indication of activation of different DNA repair pathways due to differences in the complexity of the DNA damage (37, 43, 44). In this context, it is also important to note that the genetic background of the tumor will influence the effectiveness of radiotherapy. The cell lines we used in this study do not express p53, as described in the literature (45–48) and this lack of p53 expression was confirmed for both our cell lines (data not shown). As mentioned before, p53 is normally activated in response to DNA damage and induces cell cycle arrest. Since p53 can control both G2/M and G1 cell cycle check points (49, 50), our data suggest that, at higher doses of X-rays, p53-independent

mechanisms are responsible for the observed G2/M arrest. This may partly explain the radioresistance of both cell lines to X-ray therapy. Previous studies have shown that carbon ion-induced cell killing is independent of the p53 status (7, 51–53). On the other hand, the repair of γ-H2AX foci, which can be observed 24 h after exposure, also indicates that p53-independent repair mechanisms are still active within these cell lines. Importantly, our observation that the threshold for p53-independent cell cycle arrest is reached after exposure to lower doses of carbon ion irradiation, while DNA damage repair is less efficient, suggests that carbon ion radiotherapy could be more appropriate to treat radioresistant tumors with a mutated p53 status.

CONCLUSION

In the present study, we investigated the acute cellular responses after carbon ion and X-ray exposure in two p53-defective cancer cell lines. First, our results indicate that a higher amount of initial DNA damage is induced by carbon ion irradiation compared to X-irradiation, even when lower doses are used. In addition, repair kinetics of γ-H2AX foci of Caco-2 cells showed relatively more residual DNA damage at 24 h after carbon ion irradiation compared to X-irradiation. Second, cell cycle progression assays demonstrated a persistent cell cycle arrest of PC3 cells, which was induced by lower equal doses of carbon ion compared to X-irradiation. In Caco-2 cells, a persistent arrest was induced by carbon ions but not by X-irradiation. Further research is needed to better understand how different radiation qualities influence acute cellular responses, which are in part responsible for the increased biological effectiveness of particle beam irradiation.

AUTHOR CONTRIBUTIONS

AS performed experiments both at SCK•CEN and GANIL. KK performed experiments at SCK•CEN. MM designed the experimental set-up and performed experiments at GANIL. VG contributed to the design of the work. SB contributed to the design of the work, as well as with interpretation of obtained data. All co-authors critically reviewed and approved the final version to be submitted to this Journal.

ACKNOWLEDGMENTS

We would like to thank the iPAC committee of the Grand Accélérateur National d'Ions Lourds (GANIL, Caen, France) for the carbon ion beam time granted (P911-H) and the staff of the LARIA, CIRIL (GANIL) for allowing us access to and use of their facility. We also thank Bart Marlein and Ludo Melis for their continued assistance during the X-irradiations at SCK•CEN. We thank Winnok de Vos for the InSCyDe-02 toolbox used in Fiji. We are grateful to Vanessa Bol, Stefaan Vynckier and Pierre Scalliet (UCL) for their guidance in dosimetry and feedback on the experimental design.

FUNDING

This work was partly supported by the Federal Public Service in the context of the feasibility study "Application of hadrontherapy in Belgium," which is part of action 30 of the Belgian cancer plan (CO-90-2088-01), the ESA/BELSPO/Prodex IMPULSE contract (CO-90-11-2801-03). KK is a recipient of a SCK•CEN-KUL PhD grant, and AS is a recipient of a SCK•CEN-UCL PhD grant.

REFERENCES

1. Degiovanni A, Amaldi U. History of hadron therapy accelerators. *Phys Med* (2015) **31**:322–32. doi:10.1016/j.ejmp.2015.03.002
2. Karger CP, Jakel O. Current status and new developments in ion therapy. *Strahlenther Onkol* (2007) **183**:295–300. doi:10.1007/s00066-007-1645-x
3. Kramer M, Weyrather WK, Scholz M. The increased biological effectiveness of heavy charged particles: from radiobiology to treatment planning. *Technol Cancer Res Treat* (2003) **2**:427–36. doi:10.1177/153303460300200507
4. Asaithamby A, Uematsu N, Chatterjee A, Story MD, Burma S, Chen DJ. Repair of HZE-particle-induced DNA double-strand breaks in normal human fibroblasts. *Radiat Res* (2008) **169**:437–46. doi:10.1667/RR1165.1
5. Hada M, Georgakilas AG. Formation of clustered DNA damage after high-LET irradiation: a review. *J Radiat Res* (2008) **49**:203–10. doi:10.1269/jrr.07123
6. Ward JF. The complexity of DNA damage: relevance to biological consequences. *Int J Radiat Biol* (1994) **66**:427–32. doi:10.1080/09553009414551401
7. Iwadate Y, Mizoe J, Osaka Y, Yamaura A, Tsujii H. High linear energy transfer carbon radiation effectively kills cultured glioma cells with either mutant or wild-type p53. *Int J Radiat Oncol Biol Phys* (2001) **50**:803–8. doi:10.1016/S0360-3016(01)01514-0
8. Wada S, Kobayashi Y, Funayama T, Natsuhori M, Ito N, Yamamoto K. Detection of DNA damage in individual cells induced by heavy-ion irradiation with an non-denaturing comet assay. *J Radiat Res* (2002) **43**(Suppl):S153–6. doi:10.1269/jrr.43.S153
9. Kinner A, Wu W, Staudt C, Iliakis G. Gamma-H2AX in recognition and signaling of DNA double-strand breaks in the context of chromatin. *Nucleic Acids Res* (2008) **36**:5678–94. doi:10.1093/nar/gkn550
10. Rogakou EP, Pilch DR, Orr AH, Ivanova VS, Bonner WM. DNA double-stranded breaks induce histone H2AX phosphorylation on serine 139. *J Biol Chem* (1998) **273**:5858–68. doi:10.1074/jbc.273.10.5858
11. Kastan MB, Onyekwere O, Sidransky D, Vogelstein B, Craig RW. Participation of p53 protein in the cellular response to DNA damage. *Cancer Res* (1991) **51**:6304–11.
12. Costes SV, Boissiere A, Ravani S, Romano R, Parvin B, Barcellos-Hoff MH. Imaging features that discriminate between foci induced by high- and low-LET radiation in human fibroblasts. *Radiat Res* (2006) **165**:505–15. doi:10.1667/RR3538.1
13. Rothkamm K, Lobrich M. Evidence for a lack of DNA double-strand break repair in human cells exposed to very low x-ray doses. *Proc Natl Acad Sci U S A* (2003) **100**:5057–62. doi:10.1073/pnas.0830918100
14. Sedelnikova OA, Rogakou EP, Panyutin IG, Bonner WM. Quantitative detection of (125)IdU-induced DNA double-strand breaks with gamma-H2AX antibody. *Radiat Res* (2002) **158**:486–92. doi:10.1667/0033-7587(2002)158[0486:QDOIID]2.0.CO;2
15. Ghosh S, Narang H, Sarma A, Krishna M. DNA damage response signaling in lung adenocarcinoma A549 cells following gamma and carbon beam irradiation. *Mutat Res* (2011) **716**:10–9. doi:10.1016/j.mrfmmm.2011.07.015
16. Autsavapromporn N, Suzuki M, Plante I, Liu C, Uchihori Y, Hei TK, et al. Participation of gap junction communication in potentially lethal damage repair and DNA damage in human fibroblasts exposed to low- or high-LET radiation. *Mutat Res* (2013) **756**:78–85. doi:10.1016/j.mrgentox.2013.07.001
17. Rydberg B, Cooper B, Cooper PK, Holley WR, Chatterjee A. Dose-dependent misrejoining of radiation-induced DNA double-strand breaks in human fibroblasts: experimental and theoretical study for high- and low-LET radiation. *Radiat Res* (2005) **163**:526–34. doi:10.1667/RR3346

18. Hofman-Huther H, Scholz M, Rave-Frank M, Virsik-Kopp P. Induction of reproductive cell death and chromosome aberrations in radioresistant tumour cells by carbon ions. *Int J Radiat Biol* (2004) **80**:423–35. doi:10.1080/09553000410001702319
19. Fan S, el-Deiry WS, Bae I, Freeman J, Jondle D, Bhatia K, et al. p53 gene mutations are associated with decreased sensitivity of human lymphoma cells to DNA damaging agents. *Cancer Res* (1994) **54**:5824–30.
20. McIlwrath AJ, Vasey PA, Ross GM, Brown R. Cell cycle arrests and radiosensitivity of human tumor cell lines: dependence on wild-type p53 for radiosensitivity. *Cancer Res* (1994) **54**:3718–22.
21. O'Connor PM, Jackman J, Jondle D, Bhatia K, Magrath I, Kohn KW. Role of the p53 tumor suppressor gene in cell cycle arrest and radiosensitivity of Burkitt's lymphoma cell lines. *Cancer Res* (1993) **53**:4776–80.
22. Ribeiro JC, Barnetson AR, Fisher RJ, Mameghan H, Russell PJ. Relationship between radiation response and p53 status in human bladder cancer cells. *Int J Radiat Biol* (1997) **72**:11–20. doi:10.1080/095530097143491
23. Mori E, Takahashi A, Yamakawa N, Kirita T, Ohnishi T. High LET heavy ion radiation induces p53-independent apoptosis. *J Radiat Res* (2009) **50**:37–42. doi:10.1269/jrr.08075
24. Fournier C, Taucher-Scholz G. Radiation induced cell cycle arrest: an overview of specific effects following high-LET exposure. *Radiother Oncol* (2004) **73**(Suppl 2):S119–22. doi:10.1016/S0167-8140(04)80031-8
25. Hu Y, Hellweg CE, Baumstark-Khan C, Reitz G, Lau P. Cell cycle delay in murine pre-osteoblasts is more pronounced after exposure to high-LET compared to low-LET radiation. *Radiat Environ Biophys* (2014) **53**:73–81. doi:10.1007/s00411-013-0499-0
26. Sinclair WK. Cyclic x-ray responses in mammalian cells in vitro. *Radiat Res* (1968) **33**:620–43. doi:10.2307/3572419
27. Linz U, editor. Ion beam therapy fundamentals, technology, clinical applications. *Biological and Medical Physics, Biomedical Engineering*. Berlin, Heidelberg: Springer-Verlag (2012). XXXV, 729 p.
28. Suetens A, Moreels M, Quintens R, Chiriotti S, Tabury K, Michaux A, et al. Carbon ion irradiation of the human prostate cancer cell line PC3: a whole genome microarray study. *Int J Oncol* (2014) **44**:1056–72. doi:10.3892/ijo.2014.2287
29. Suetens A, Moreels M, Quintens R, Soors E, Buset J, Chiriotti S, et al. Dose- and time-dependent gene expression alterations in prostate and colon cancer cells after in vitro exposure to carbon ion and X-irradiation. *J Radiat Res* (2015) **56**:11–21. doi:10.1093/jrr/rru070
30. Durantel F, Balanzat E, Cassimi A, Chevalier F, Ngono-Ravache Y, Madi T, et al. Dosimetry for radiobiology experiments at GANIL. *Nucl Instrum Methods Phys Res A* (2016) **816**:70–7. doi:10.1016/j.nima.2016.01.052
31. Schindelin J, Arganda-Carreras I, Frise E, Kaynig V, Longair M, Pietzsch T, et al. Fiji: an open-source platform for biological-image analysis. *Nat Methods* (2012) **9**:676–82. doi:10.1038/nmeth.2019
32. Dieriks B, De Vos WH, Derradji H, Baatout S, Van Oostveldt P. Medium-mediated DNA repair response after ionizing radiation is correlated with the increase of specific cytokines in human fibroblasts. *Mutat Res* (2010) **687**:40–8. doi:10.1016/j.mrfmmm.2010.01.011
33. Castro JR. Results of heavy ion radiotherapy. *Radiat Environ Biophys* (1995) **34**:45–8. doi:10.1007/BF01210545
34. van Oorschot B, Hovingh SE, Rodermond H, Guclu A, Losekoot N, Geldof AA, et al. Decay of gamma-H2AX foci correlates with potentially lethal damage repair in prostate cancer cells. *Oncol Rep* (2013) **29**:2175–80. doi:10.3892/or.2013.2364
35. Nakajima NI, Brunton H, Watanabe R, Shrikhande A, Hirayama R, Matsufuji N, et al. Visualisation of gammaH2AX foci caused by heavy ion particle traversal; distinction between core track versus non-track damage. *PLoS One* (2013) **8**:e70107. doi:10.1371/journal.pone.0070107
36. Jakob B, Scholz M, Taucher-Scholz G. Biological imaging of heavy charged-particle tracks. *Radiat Res* (2003) **159**:676–84. doi:10.1667/0033-7587(2003)159[0676:BIOHCT]2.0.CO;2
37. Rall M, Kraft D, Volcic M, Cucu A, Nasonova E, Taucher-Scholz G, et al. Impact of charged particle exposure on homologous DNA double-strand break repair in human blood-derived cells. *Front Oncol* (2015) **5**:250. doi:10.3389/fonc.2015.00250
38. Di Pietro C, Piro S, Tabbi G, Ragusa M, Di Pietro V, Zimmitti V, et al. Cellular and molecular effects of protons: apoptosis induction and potential implications for cancer therapy. *Apoptosis* (2006) **11**:57–66. doi:10.1007/s10495-005-3346-1
39. Fokas E, Kraft G, An H, Engenhart-Cabillic R. Ion beam radiobiology and cancer: time to update ourselves. *Biochim Biophys Acta* (2009) **1796**:216–29. doi:10.1016/j.bbcan.2009.07.005
40. Ghorai A, Bhattacharyya NP, Sarma A, Ghosh U. Radiosensitivity and induction of apoptosis by high LET carbon ion beam and low LET gamma radiation: a comparative study. *Scientifica (Cairo)* (2014) **2014**:438030. doi:10.1155/2014/438030
41. Hamada N, Hara T, Omura-Minamisawa M, Funayama T, Sakashita T, Sora S, et al. Energetic heavy ions overcome tumor radioresistance caused by overexpression of Bcl-2. *Radiother Oncol* (2008) **89**:231–6. doi:10.1016/j.radonc.2008.02.013
42. Lucke-Huhle C, Blakely EA, Chang PY, Tobias CA. Drastic G2 arrest in mammalian cells after irradiation with heavy-ion beams. *Radiat Res* (1979) **79**:97–112. doi:10.2307/3575025
43. Gerelchuluun A, Manabe E, Ishikawa T, Sun L, Itoh K, Sakae T, et al. The major DNA repair pathway after both proton and carbon-ion radiation is NHEJ, but the HR pathway is more relevant in carbon ions. *Radiat Res* (2015) **183**:345–56. doi:10.1667/RR13904.1
44. Zafar F, Seidler SB, Kronenberg A, Schild D, Wiese C. Homologous recombination contributes to the repair of DNA double-strand breaks induced by high-energy iron ions. *Radiat Res* (2010) **173**:27–39. doi:10.1667/RR1910.1
45. Aryankalayil MJ, Makinde AY, Gameiro SR, Hodge JW, Rivera-Solis PP, Palayoor ST, et al. Defining molecular signature of pro-immunogenic radiotherapy targets in human prostate cancer cells. *Radiat Res* (2014) **182**:139–48. doi:10.1667/RR13731.1
46. Isaacs WB, Carter BS, Ewing CM. Wild-type p53 suppresses growth of human prostate cancer cells containing mutant p53 alleles. *Cancer Res* (1991) **51**:4716–20.
47. Liu Y, Bodmer WF. Analysis of P53 mutations and their expression in 56 colorectal cancer cell lines. *Proc Natl Acad Sci U S A* (2006) **103**:976–81. doi:10.1073/pnas.0510146103
48. Wang W, Heideman L, Chung CS, Pelling JC, Koehler KJ, Birt DF. Cell-cycle arrest at G2/M and growth inhibition by apigenin in human colon carcinoma cell lines. *Mol Carcinog* (2000) **28**:102–10. doi:10.1002/1098-2744(200006)28:2<102::AID-MC6>3.3.CO;2-U
49. Agarwal ML, Agarwal A, Taylor WR, Stark GR. p53 controls both the G2/M and the G1 cell cycle checkpoints and mediates reversible growth arrest in human fibroblasts. *Proc Natl Acad Sci U S A* (1995) **92**:8493–7. doi:10.1073/pnas.92.18.8493
50. Nayak B, Krishnegowda N, Galindo C, Meltz M, Swanson G. Synergistic effect between curcumin (diferuloylmethane) and radiation on clonogenic cell death independent of p53 in prostate cancer cells. *J Cancer Sci Ther* (2010) **2**:171–81. doi:10.4172/1948-5956.1000046
51. Amornwichet N, Oike T, Shibata A, Ogiwara H, Tsuchiya N, Yamauchi M, et al. Carbon-ion beam irradiation kills X-ray-resistant p53-null cancer cells by inducing mitotic catastrophe. *PLoS One* (2014) **9**:e115121. doi:10.1371/journal.pone.0115121
52. Takahashi A, Matsumoto H, Furusawa Y, Ohnishi K, Ishioka N, Ohnishi T. Apoptosis induced by high-LET radiations is not affected by cellular p53 gene status. *Int J Radiat Biol* (2005) **81**:581–6. doi:10.1080/09553000500280484
53. Takahashi T, Fukawa T, Hirayama R, Yoshida Y, Musha A, Furusawa Y, et al. In vitro interaction of high-LET heavy-ion irradiation and chemotherapeutic agents in two cell lines with different radiosensitivities and different p53 status. *Anticancer Res* (2010) **30**:1961–7.

Conflict of Interest Statement: The authors declare that the research was conducted in the absence of any commercial or financial relationships that could be construed as a potential conflict of interest.

Copyright © 2016 Suetens, Konings, Moreels, Quintens, Verslegers, Soors, Tabury, Grégoire and Baatout. This is an open-access article distributed under the terms of the Creative Commons Attribution License (CC BY). The use, distribution or reproduction in other forums is permitted, provided the original author(s) or licensor are credited and that the original publication in this journal is cited, in accordance with accepted academic practice. No use, distribution or reproduction is permitted which does not comply with these terms.

frontiers in Oncology

ORIGINAL RESEARCH
published: 11 November 2015
doi: 10.3389/fonc.2015.00250

Impact of Charged Particle Exposure on Homologous DNA Double-Strand Break Repair in Human Blood-Derived Cells

Melanie Rall[1†], Daniela Kraft[2†], Meta Volcic[1], Aljona Cucu[2], Elena Nasonova[2‡], Gisela Taucher-Scholz[2], Halvard Bönig[3], Lisa Wiesmüller[1†] and Claudia Fournier[2†*]*

[1] Department of Obstetrics and Gynaecology, Ulm University, Ulm, Germany, [2] Department of Biophysics, GSI Helmholtz Center for Heavy Ion Research, Darmstadt, Germany, [3] German Red Cross Blood Service Baden-Wuerttemberg – Hessen, Institute for Transfusion Medicine and Immunohematology, Johann Wolfgang Goethe-University Hospital, Frankfurt, Germany

Ionizing radiation generates DNA double-strand breaks (DSB) which, unless faithfully repaired, can generate chromosomal rearrangements in hematopoietic stem and/or progenitor cells (HSPC), potentially priming the cells towards a leukemic phenotype. Using an enhanced green fluorescent protein (EGFP)-based reporter system, we recently identified differences in the removal of enzyme-mediated DSB in human HSPC versus mature peripheral blood lymphocytes (PBL), particularly regarding homologous DSB repair (HR). Assessment of chromosomal breaks via premature chromosome condensation or γH2AX foci indicated similar efficiency and kinetics of radiation-induced DSB formation and rejoining in PBL and HSPC. Prolonged persistence of chromosomal breaks was observed for higher LET charged particles which are known to induce more complex DNA damage compared to X-rays. Consistent with HR deficiency in HSPC observed in our previous study, we noticed here pronounced focal accumulation of 53BP1 after X-ray and carbon ion exposure (intermediate LET) in HSPC versus PBL. For higher LET, 53BP1 foci kinetics was similarly delayed in PBL and HSPC suggesting similar failure to repair complex DNA damage. Data obtained with plasmid reporter systems revealed a dose- and LET-dependent HR increase after X-ray, carbon ion and higher LET exposure, particularly in HR-proficient immortalized and primary lymphocytes, confirming preferential use of conservative HR in PBL for intermediate LET damage repair. HR measured adjacent to the leukemia-associated *MLL* breakpoint cluster sequence in reporter lines revealed dose dependency of potentially leukemogenic rearrangements underscoring the risk of leukemia-induction by radiation treatment.

Keywords: breakpoint cluster region, charged particles, chromosomal breaks, radiation damage response, DNA double-strand break repair, hematopoietic stem and progenitor cells, radiation-induced leukemia

OPEN ACCESS

Edited by:
Francis A. Cucinotta, University of Nevada Las Vegas, USA

Reviewed by:
Kevin Du, NYU Langone Medical Center, USA
Kerry George, Wyle Science, Technology and Engineering Group, USA
Michael Cornforth, University of Texas Medical Branch, USA

***Correspondence:**
Lisa Wiesmüller
lisa.wiesmueller@uni-ulm.de;
Claudia Fournier
c.fournier@gsi.de

†Shared co-authorship; these authors contributed equally to this work.

***‡Present Address:**
Elena Nasonova
Joint Institute for Nuclear Research, Dubna, Russia

Specialty section:
This article was submitted to Radiation Oncology, a section of the journal Frontiers in Oncology

Received: *27 August 2015*
Accepted: *26 October 2015*
Published: *11 November 2015*

Citation:
Rall M, Kraft D, Volcic M, Cucu A, Nasonova E, Taucher-Scholz G, Bönig H, Wiesmüller L and Fournier C (2015) Impact of Charged Particle Exposure on Homologous DNA Double-Strand Break Repair in Human Blood-Derived Cells. Front. Oncol. 5:250. doi: 10.3389/fonc.2015.00250

INTRODUCTION

Radiation exposure increases the risk for acute myeloid leukemia (AML), as observed in atomic bomb survivors (1), occupational radiation workers (2, 3), and cancer survivors treated with radiotherapy (4). This is important especially in light of the increasing use of charged particles in cancer therapy (5, 6). Furthermore, a long-term leukemia risk for astronauts exposed to protons and high-energy charged particles during extended space travel is expected (7–9). As for all of these radiation scenarios densely ionizing radiation, such as charged particles or neutrons, contribute to the delivered dose, we need to understand whether densely ionizing radiation and photons differ in their impact on AML development.

Densely ionizing charged particles differ from sparsely ionizing photons in both physical characteristics and biological effectiveness (10). The greater effectiveness of densely ionizing charged particles is reflected in the severity of DNA lesions, which manifests both at the nanometer and the micrometer scale: DNA lesions are more complex and hence, more difficult to repair, as well as the complexity of chromosomal aberrations is higher (11, 12). In consequence, the number of unrepaired or misrepaired lesions and their transmission to the affected cell's progeny, considered to be the basis for cancer induction, is greater for charged particles than for photons.

In the context of radiation exposure, induction of hematological malignancies, in particular of AML, was discussed to originate from error-prone repair of radiation-induced double-strand breaks (DSB) causing chromosomal rearrangements (13–16). Especially precarious targets for leukemic transformation are hematopoietic stem and/or progenitor cells (HSPC). HSPC are long-lived, self-renewed, and give rise to all types of mature blood cells and therefore are an ideal model system to study consequences of radiation exposure and the fate changes associated there with. On the other hand, mature peripheral blood lymphocytes (PBL) represent an extensively studied system in which cytogenetic damage has been established as a reliable biomarker of radiation late effects (17–19).

In our previous work, we studied the repair of DSB induced by photon radiation in the hematopoietic system (20, 21). We comparatively analyzed the capacity and quality of DSB repair in cycling human HSPC and PBL cultures mimicking exit from quiescence in response to stress conditions, such as infection or irradiation (22). Even though γH2AX signals and cytogenetic analysis suggested quantitatively similar DSB formation and removal after irradiation, we found substantial qualitative differences in DNA damage responses, i.e., differential use of DNA repair pathways. To dissect DSB repair mechanisms, we used our fluorescence-based assay system for extrachromosomal DSB repair (23), which has proven a valuable tool in various cell types including lymphoblastoid cell lines (LCL) derived from patients with genomic instability syndromes (24–26). Using this system, recombination of DSB can be detected after I-*Sce*I-endonuclease-mediated cleavage, but also independently of targeted cleavage by I-*Sce*I after various carcinogenic treatments including ionizing radiation (27–29). Application of this enhanced green fluorescent protein (EGFP)-based reporter system revealed a relative preference of error-prone non-homologous end joining (NHEJ), such as microhomology-mediated end joining (MMEJ) and single-strand annealing (SSA) in HSPC, as opposed to conservative NHEJ and high-fidelity homologous DSB repair (HR) in PBL. Furthermore, differential recruitment of repair proteins suggested a delay in the progress of the repair steps toward HR. We could identify differential NF-κB signaling as a critical molecular component underlying the observed differences: while in PBL, active NF-κB promotes HR and prevents compensatory accumulation of radiation-induced 53BP1 foci, in HSPCs, significantly reduced NF-κB activity and hence NF-κB target genes impedes accurate DSB repair.

To assess the effect of different radiation qualities in this study, we used the substrates HR-EGFP/3′EGFP or HR-EGFP/5′EGFP which detect both conservative and non-conservative HR or solely conservative HR, respectively, i.e., the very repair pathways which markedly differ in HSPC compared to PBL (20). Since radiation not only causes clean DSB but also generates base damage, single-strand breaks and complex DSB (12, 30), recombinative rearrangements, as monitored in our assay system, are ideal readouts to sense all these types of DNA lesions (29). The usage of differentially designed repair substrate plasmids allows discrimination between different repair mechanisms and repair qualities which is of major interest with regard to the repair of complex DNA lesions, such as are induced by charged particle radiation (11, 18, 31).

A refined repair assay variant integrates a highly fragile region within the mixed lineage leukemia breakpoint cluster region (*MLL*bcr), where cancer treatment-induced translocation sites predisposing to secondary leukemia have been found to cluster (29, 32, 33). Rearrangements involving the *MLL* gene are found in ~40% of therapy-related acute leukemias (33). Both chemotherapy and radiotherapy increase the risk factor for secondary malignancies of the hematopoietic system (34). Moreover, *MLL* rearrangements were identified after radiation exposure following the Chernobyl accident (35). Our own published data confirm preferential *MLL*bcr breakage compared to other sequences within the genome by γ-rays in both human HSPC and human PBL (20). In the current study, *MLL*bcr-based reporter cell lines were employed for the detection of radiation-induced chromosomal rearrangements. To this end, a 0.4 kb fragment of the *MLL*bcr sequence was introduced between the differentially mutated *EGFP* genes in the HR-EGFP/3′EGFP substrate. *MLL*bcr-based reporter cell clones were generated by stably integrating the substrate into the genome of the human myeloid leukemia cell line K562 and the human LCL WTK1 (29). The resulting K562(HR-EGFP/3′EFP-MLL) and WTK1(HR-EGFP/3′EFP-MLL) reporter cell lines represent more sensitive systems to study genotoxic treatment-induced (and thus likely also radiation-inducible) rearrangements.

The work presented here focuses on the impact of high LET compared to photon exposure on the induction and removal of DNA damage in immature and mature hematopoietic cells. Extra- and intrachromosomal reporter systems as described above were applied to compare maturity-dependent HR pathway usage and to analyze leukemia-associated rearrangements in reporter cell lines as a function of radiation quality.

MATERIALS AND METHODS

Primary Cells

Hematopoietic stem and/or progenitor cells and PBL were isolated from peripheral blood samples of healthy donors, provided by one of us (HB). Donors provided written informed consent. The study was approved by the local advisory boards (approvals #329/10; #157/10; and #155/13). Donor treatment was performed with 10 μg/kg G-CSF per day for five consecutive days as described (36). HSPC were enriched by immuno-magnetically isolating $CD34^+$ cells (MicroBead Kit, Miltenyi Biotech, Bergisch Gladbach, Germany) from G-CSF-mobilized donor blood as described (31). PBL were isolated from healthy donor buffy coats by Ficoll density-gradient centrifugation as described in Ref. (26).

Quiescent (G_0-phase) HSPC and PBL were recruited into cell cycle prior to irradiation experiments by culturing in expansion media for 72 h at 37°C in a humidified atmosphere (95%). HSPC were kept in serum-free StemSpan SFEM medium supplemented with 100 ng/ml Flt-3 ligand (Flt3L), 100 ng/ml stem cell factor (SCF), 20 ng/ml Interleukin-3 (IL3), and 20 ng/ml Interleukin-6 (IL6) (Cytokine Cocktail CC100, both from StemCell Technologies Inc., Cologne, Germany). PBL were cultured in RPMI 1640 medium supplemented with 20% fetal calf serum (FCS), 3 mM L-glutamine, and 2% phytohemagglutinin (PHA) (components from Biochrom AG, Berlin, Germany).

Cell Lines

In parallel to primary cells and as internal standards, we used the LCL 416MI and TK6, cultured in RPMI 1640 medium supplemented with 10% FBS, 1% penicillin/streptomycin, and 1% L-glutamine, as described before (25).

The human myeloid leukemia cell line K562(HR-EGFP/3′EFP-MLL) and the human B-LCL WTK1(HR-EGFP/3′EFP-MLL) were grown in suspension culture in RPMI 1640 medium supplemented with 10 and 12% FCS, respectively, and 100 U/ml penicillin and 100 μg/ml streptomycin (all reagents from Biochrom AG).

Irradiation with Photons and Heavy Ions

Actively cycling cells were exposed to X-rays (16 mA, 250 kV, Seifert Isovolt DSI X-ray tube) or to γ rays (gamma irradiator, GSR D1, Gamma-Service Medical GmbH). Exposure of cells to heavy ions was performed at the heavy ion synchrotron ("Schwerionensynchroton," SIS, GSI Helmholtzzentrum für Schwerionenforschung GmbH, Darmstadt, Germany).

At the time of photon exposure, cells were kept in medium in 5 ml tubes or 24-well plates with a dose rate of ~1 Gy/min. For heavy ion irradiation, the exposure with a monoenergetic beam or spread-out Bragg peak (SOBP) was performed, as described in Ref. (31). The parameters of the radiation exposure for the heavy ions used in this study are listed in **Table 1**.

Premature Chromosome Condensation

At different time points after irradiation (0–9 h) radiation-induced breaks were measured in G_2-phase cells by premature chromosome condensation (PCC) technique, as described elsewhere (38). Briefly, PCC was chemically induced by Calyculin A. Samples were processed as for metaphase analysis and stained with Giemsa, as described in Becker et al. (31). At least 50 G_2-phase cells were analyzed per data point. In G_2-phase cells, the total number of breaks was counted; chromatid and isochromatid breaks were scored as one and two breaks, respectively. In the following, we refer to the sum of both as "chromatid breaks." A minor number of exchanges (≤5% of the breaks and comparable for both cell types), which appeared some hours after exposure, were scored as two breaks. The type of exchanges and the low fraction are comparable to previously reported ones (38).

Quantitative Immunofluorescence Microscopy

At different time points after irradiation (1–24 h), cells were spun on cover slips, fixed with 3.7% PFA and permeabilized with 0.5% Triton followed by washing and blocking steps with PBS and 5% goat serum in PBS. Cells on cover slips were immunostained with primary antibodies anti-γH2AX (Ser139, clone JBW301, Millipore), anti-53BP1 rabbit NB100-304 (Novus Biologicals, Littleton, CO, USA) and with Alexa Fluo®555-conjugated secondary antibodies (Invitrogen). Nuclear counter staining was performed with DAPI and cover slips were mounted with VectaShield mounting media (Vector Labs, Burlingame, CA, USA). Immunofluorescence signals were visualized by an Olympus BX51 epifluorescence microscope equipped with an Olympus XC10 camera and acquired images automatically analyzed by CellF2.5_analysis software including the mFIP software (Olympus Soft Imaging System, Münster, Germany) or by Keyence BZ-II Analyzer software (Keyence, Neu-Isenburg, Germany).

DSB Repair by HR in HSPC and PBL

Pathway-specific DSB repair analysis in HSPC and PBL was performed as described in Ref. (23, 26, 39). Briefly, actively cycling cells were transiently nucleofected with the DSB repair substrate HR-EGFP/5′EGFP (long homologies), detecting conservative HR, according to an Amaxa® protocol (Human B Cell Nucleofector Kit; Human $CD34^+$ Cell Nucleofector Kit; Lonza, Cologne, Germany) via electroporation (Bio-Rad Laboratories, Hercules, CA, USA). While DSB formation within the substrate is usually induced by co-nucleofection of the I-*Sce*I meganuclease expression plasmid pCMV-I-SceI, in the present study, the nucleofection mixture did not contain the expression plasmid. Instead, DSB were induced by exposing the cells 2–4 h after nucleofection to X-rays or heavy ions (carbon and calcium ions).

The assay monitors reconstitution of wild-type EGFP, so that EGFP-positive cells were quantified 24 h post-irradiation by the diagonal gating method in the FL1/FL2 dot plot (FACS Calibur® FACScan, Becton Dickinson, Heidelberg, Germany), as described in Ref. (40). All nucleofections were performed in triplicates. The transfection controls additionally contained pBS filler plasmid (pBlueScriptII KS, Stratagene, Heidelberg, Germany) and wild-type EGFP expression plasmid for normalization of repair frequencies.

TABLE 1 | Parameters for the heavy ions used.

Ion	Energy (MeV/u)	LET (keV/μm)	Track radius (μm)[a]	Dose	Fluence[b] (particles/cm^2)	Hits per nucleus[c]
Nitrogen	130	40–65	243	2 Gy	2.4×10^7	14 (HSPC) 12 (PBL)
Carbon	114–158	60–85	262	2 Gy	1.72×10^7	10 (HSPC) 9 (PBL)
Titanium	1000	150	310	2 Gy	8.3×10^6	5 (HSPC) 4 (PBL)
Iron	1000	155	328	2 Gy	8.1×10^6	5 (HSPC) 4 (PBL)
Calcium	200	180	505	2 Gy	7×10^6	4 (HSPC) 3,5 (PBL)

[a]*The maximum range of delta electrons/track radius was calculated according to Ref. (37): R_{max} (μm) = 0.062 × E (MeV/u)$^{1.7}$.*

[b]*The fluence was calculated according to the formula:* $D[Gy] = 1.6 \times 10^{-9} \times L_\Delta \left[\frac{keV}{\mu m}\right] \times \varphi \left[\frac{1}{cm^2}\right]$.

If SOBP irradiation was performed, the fluence of particles mostly contributing to dose deposition was calculated from the mean of the dose averaged LET.

[c]*The hits per nucleus were calculated based on the geometric cross section, i.e., area of the cell nuclei (HSPC: 60 μm^2; PBL: 50 μm^2) and the fluence.*

Cell Lines (K562 and WTK1) with Stably Integrated *MLL*bcr Repair Substrate

Clones containing a single stably integrated copy of HR-EGFP/3′EGFP-MLL repair substrate were established from K562 and WTK1 cell lines, as described in detail in Ref. (29, 41). Briefly, cells were stably transfected with the *Xmn*I-linearized recombination vector pHR-EGFP/3′EGFP-MLLbcr.fwd. This DNA recombination substrate contains a 0.4-kb sequence of the genomic breakpoint cluster region (bcr) from the human *MLL* gene, which undergoes carcinogenic rearrangements in response to genotoxic treatment (42, 43). The cells were irradiated with X-rays or carbon ions. The reconstitution of wild-type EGFP (via conservative HR and SSA) was measured 24–48 h post-irradiation, as described in the previous section (see DSB Repair by HR in HSPC and PBL).

RESULTS

Induction, Rejoining, and Manifestation of Radiation-Induced Chromatid Breaks

Induction and rejoining of radiation-induced breaks in PBL and HSPC were investigated with the PCC technique. Following *ex vivo* cultivation for 72 h, cells were irradiated with X-rays or charged particles (nitrogen, carbon, titanium, and calcium) in the LET range 45–180 keV/μm.

Regarding the induction level, it has to be taken into account that the number of chromatid breaks at 0 h (referred to as "initial breaks") corresponds to the number of chromatid breaks detectable 5–15 min after exposure during which Calyculin A reaches the cells and prevents further repair. As shown in Figure S1 in Supplementary Material, the number of initial chromatid breaks increased in a linear dose-dependent fashion for both PBL and HSPC and also depended on radiation quality. For both cell types, the yield of chromatid breaks was similar. At the same physical dose (2 Gy), around 60–70 versus 40 chromatid breaks after irradiation with the different ions versus after X-ray exposure were measured in G_2-phase cells, respectively.

Rejoining of radiation-induced chromatid breaks was observed for 9 h after exposure (**Figure 1**). The number of chromatid breaks decreased with culture time with similar kinetics in both cell types. For X-ray irradiation, 1–2 h after irradiation more than half of the initial chromatid breaks had already been repaired. The time course of rejoining was similar for carbon ions (intermediate LET, 60–85 keV/μm, assessed in PBL) (**Figure 1A**), although the level of initial damage was higher compared to photons. However, following high LET exposure (calcium and titanium ions, 180 and 150 keV/μm, respectively), rejoining of chromatid breaks was slower. A major difference between the repair kinetics following exposure to X-rays and ions was that the number of chromatid breaks dropped to the level of controls, i.e., rejoining was finished almost completely within 9 h after irradiation (10% residual chromatid breaks, **Figures 1A,B**). In contrast, following irradiation with carbon ions a significant fraction of breaks remained unrejoined (23% residual chromatid breaks in PBL, **Figure 1A**), and after high LET calcium and titanium exposure, the level of residual damage was even higher (40–48% residual chromatid breaks, **Figures 1A,B**).

Immunofluorescence Analysis of DSB Processing

To monitor DSB processing in response to treatment with ionizing radiation, we performed quantitative immunofluorescence microscopy of discrete nuclear foci, indicative of DNA lesions and in time course experiments of the accumulation and their removal (44). As shown in **Figure 2**, we measured γH2AX and 53BP1 foci in PBL and HSPC up to 24 h after radiation exposure with 2 Gy of X-rays, carbon (60–85 keV/μm), and iron ions (155 keV/μm). The different data sets were normalized to maximum foci values reached after X-ray irradiation to facilitate comparison with our recently published results (20). Using γH2AX as a DSB marker, formation and disappearance of foci was similar in both cell types for X-rays (**Figure 2A**), in agreement with our previous observations (20). Similar γH2AX curves for both cell types were also obtained following high LET iron ion exposure, but approximately threefold elevated levels

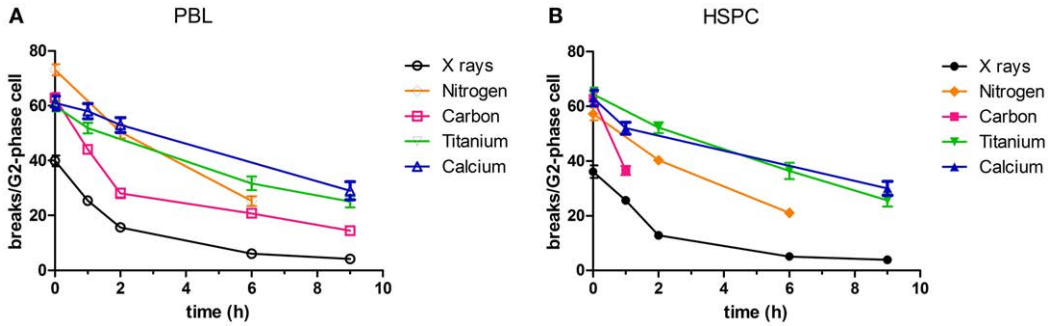

FIGURE 1 | Rejoining of radiation-induced chromatid breaks. PBL and HSPC were stimulated for 72 h prior to irradiation with a dose of 2 Gy X-rays or charged particles. After irradiation, the cells were cultivated during the indicated periods of time. Charged particle exposure: nitrogen (45–65 keV/μm), carbon (60–85 keV/μm), titanium (150 keV/μm), or calcium (180 keV/μm). Premature chromosome condensation (PCC) was induced by Calyculin A. Slides were stained with Giemsa and at least 50 G_2-phase cells were scored per data point. Numbers of independent experiments were for X-rays: $n = 3$; nitrogen, carbon, titanium, and calcium: $n = 1$. Mean values and SEM are indicated. For X-rays, SEM was calculated from mean values derived from independent experiments. For nitrogen, carbon, titanium, and calcium, SEM was calculated from values attributed to individual nuclei (>50). Connecting lines serve to guide the eye. Data for X-ray exposure are plotted from Kraft et al. (20). **(A)** PBL and **(B)** HSPC.

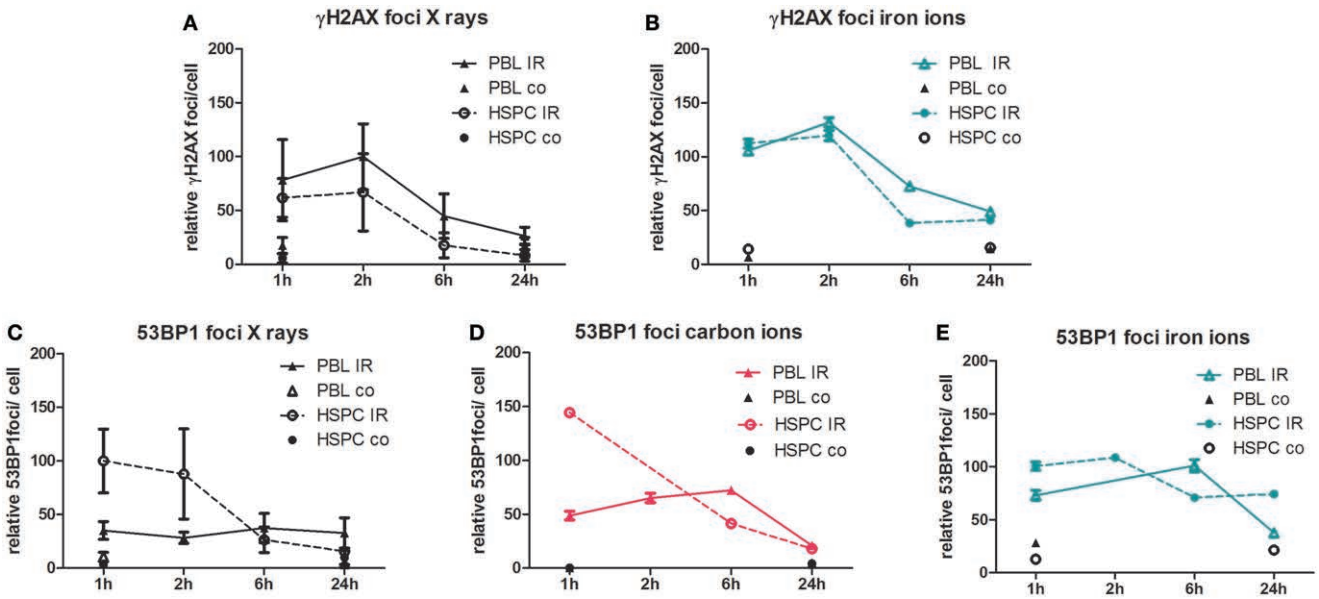

FIGURE 2 | Immunofluorescence analysis of DSB induction and repair after irradiation. PBL and HSPC were stimulated for 72 h prior to irradiation without (co) or with (IR) a dose of 2 Gy of **(A,C)** X-rays, **(D)** carbon ions (60–85 keV/μm), or **(B,E)** iron ions (155 keV/μm). After irradiation, the cells were re-cultivated, fixed at the indicated time points, and immunolabeled for detection of **(A,B)** γH2AX or **(C–E)** 53BP1. Foci were scored by automated quantification from ~250 nuclei at each time point. Each number of foci per cell was normalized to the maximum mean value from the X-ray exposure time course data from the same experimental day. The 100% relative foci represent the following mean scores after X-ray exposure for γH2AX: 8 foci/cell (PBL/2 h) and 53BP1: 8 foci/cell (HSPC/1 h). Mean normalized values attributed to individual nuclei are shown with SEM (number of independent experiments for X-rays, PBL: $n = 5$; HSPC: $n = 4$; and heavy ions PBL and HSPC: $n = 1$).

of persisting DNA damage were detectable 24 h post-iron ion versus X-ray exposure (**Figure 2B**). Recently, we reported more pronounced accumulation of X-ray-induced nuclear 53BP1 foci in HSPC relative to PBL (20), which was confirmed here for X-ray and newly demonstrated for carbon ion exposure with intermediate LET (**Figures 2C,D**). However, with high LET iron ions, this striking difference between 53BP1 foci peak levels in HSPC and PBL disappeared (**Figure 2E**), mostly due to an increase of 53BP1 foci numbers in PBL 1 h post-irradiation with iron ions versus X-ray (**Figures 2C,E**). Concomitantly, the level of persisting 53BP1 foci 24 h post-irradiation was fivefold greater in HSPC following iron ion compared with X-ray exposure

resulting in aggregate in very similar 53BP1 foci numbers 1–24 h post-irradiation. We obtained similar results as for iron ions with cells irradiated with high LET calcium ions (180 keV/μm, Figure S2 in Supplementary Material), i.e., 53BP1 foci curves for PBL and HSPC were comparable and the level of 53BP1 foci diminished only slightly over the time.

Extrachromosomal DSB Repair Analysis Using Plasmid Reporter Systems

In order to detect HR after exposure to X-rays and charged particles in PBL and HSPC, we used the EGFP-based plasmid reporter system described elsewhere (20, 23). In difference from our previous analyses engaging I-*Sce*I meganuclease for targeted cleavage, we tested if DSB formation within the substrate and subsequent repair can be induced by ionizing radiation. For this purpose, we transfected first the LCL 416MI and TK6 (25) either with the substrate HR-EGFP/3′EGFP (which supports both conservative and non-conservative HR) or HR-EGFP/5′EGFP (which detects conservative HR only), as these repair mechanisms were previously shown to be differentially active in PBL and HSPC (20). As demonstrated in **Figure 3**, in all LCL, exposure to photons (2 and 5 Gy) induced a significant dose-dependent HR increase. A dose-dependent effect was only detectable for the substrate HR-EGFP/5′EGFP, whereas for substrate HR-EGFP/3′EGFP, a general increase was observed (data not shown).

Based on these results, we investigated HR focusing on substrate HR-EGFP/5′EGFP in PBL and HSPC after photon or charged particle exposure by applying doses of 2 and 5 Gy (**Figure 4**). We observed a twofold higher 5 Gy radiation-induced HR frequency in PBL versus HSPC (0.2×10^{-2} versus 0.1×10^{-2}), consistent with previous results for enzymatic cleavage (20). Interestingly, as can be seen in **Figure 4A**, X-ray irradiation led to relative increases in HR frequencies particularly in PBL even though in contrast to the LCL data (**Figure 3**), not reaching statistical significance with the limited number of experiments performed. Comparing radiation qualities at a single physical dose (2 Gy) revealed moderately, albeit statistically not significantly increased HR frequencies with higher LET (intermediate carbon ions and high LET calcium ions) (**Figure 4B**). Reminiscent of 53BP1 foci data, differences between HR frequencies were smaller in PBL and HSPC after calcium compared with carbon ion exposure.

In order to rule out that HR frequencies were influenced by potentially confounding factors in PBL and HSPC, the fraction of apoptotic cells and the cell cycle distribution were determined for X-ray and 60–85 keV/μm carbon ion exposures (Figure S3 in Supplementary Material). These radiation treatments increased the fraction of apoptotic cells (Figure S3A in Supplementary Material) and G_2-phase cells (Figure S3B in Supplementary Material) in PBL and HSPC to a similar extent excluding a major role in cell type-specific HR activities.

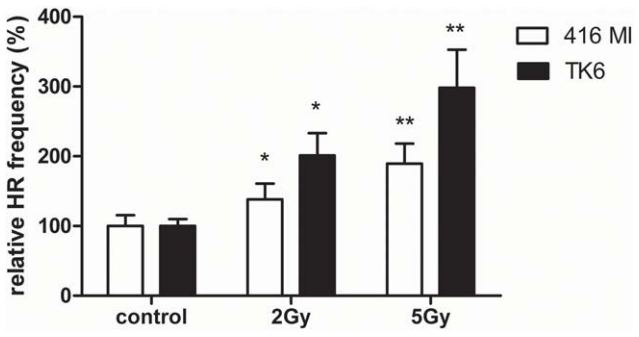

FIGURE 3 | Extrachromosomal DSB repair analysis in LCL following photon exposure. The LCL 416MI and TK6 were transfected with HR-EGFP/5′EGFP, a DSB repair substrate which supports HR. Irradiation was performed with 2 or 5 Gy of photons (γ or X-rays). After subsequent incubation for 24–48 h, the fraction of EGFP-positive cells was quantified by flow cytometric measurement. Data were normalized to the non-irradiated control each. Mean values and SEM were calculated (416MI: $n = 9$–15 and TK6: $n = 15$–18). Statistically significant of differences between non-irradiated control and irradiated cells were calculated with the Wilcoxon matched-pairs signed rank test with $^{*}p < 0.05$ and $^{**}p < 0.01$.

Radiation-Induced Intrachromosomal Recombination at the *MLL*bcr Sequence

The observed differences in extrachromosomal HR when comparing radiation qualities or cell types were mostly not statistically significant, which can be explained by the low probability of inducing a DSB in the target sequence of the reporter plasmid. The fraction of cells with one DSB was estimated at around 0.3%, taking into account the transfection efficiency, copy numbers, the size of the target sequence, and the estimated number of DSB per gray. As the fraction of cells with DSB is small and not all DSB are repaired by HR, we pursued an additional experimental strategy, using leukemia K562(HR-EGFP/3′EFP-MLL) and lymphoblastoid WTK1(HR-EGFP/3′EFP-MLL) cell lines (29) stably transfected with plasmid reporter comprising the highly fragile *MLL*bcr sequence (33). Exposure to different doses of X-rays or charged particles was performed. Highest doses (10 and 15 Gy X-rays, 5 Gy carbon and calcium ions) were excluded from the analyses because of associated cytotoxic effects as indicated by apoptosis-induction from sub G_1 analysis (data not shown).

Results from recombination measurements 24 and 48 h post-irradiation, indicating intrachromosomal rearrangements adjacent to the *MLL*bcr sequence, are shown in **Figure 5**. In general, radiation-induced stimulation of intrachromosomal HR was detectable in both cell lines (**Figures 5A,B**). Thus, we observed increased HR frequencies at least 48 h after X-ray exposure, except for one data point [0.5 Gy X-rays; WTK1(HR-EGFP/3′EFP-MLL)], displaying dose dependency and reaching statistical significance for 5 Gy in WTK1(HR-EGFP/3′EFP-MLL) cells. When comparing the same physical dose of 2 Gy in K562(HR-EGFP/3′EFP-MLL) cells applying X-ray versus ion exposure (**Figure 5C**), for carbon ions, more pronounced HR stimulation was observed after 48 h and for calcium, a trend toward enhancement was detectable after 24 h (48 h was not assessed). These data suggest that stably integrated *MLL*bcr sequences in a cell-based reporter assay can be useful for assessment of biological radiation effects.

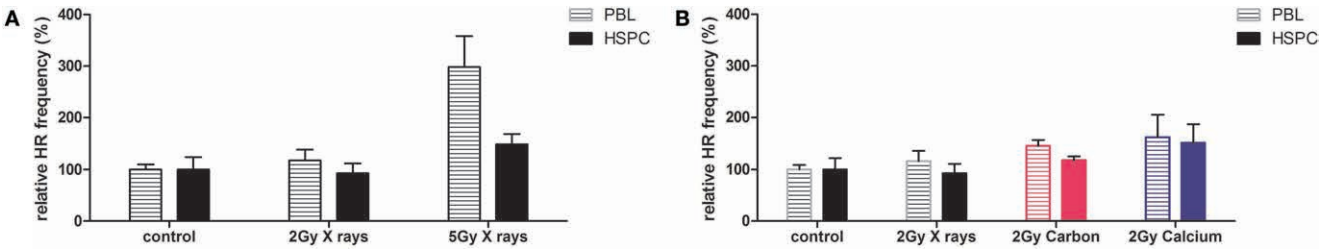

FIGURE 4 | Extrachromosomal DSB repair analysis in PBL and HSPC after irradiation with X-rays or charged particles. PBL and HSPC were cultivated for 72 h, transfected with the DSB repair substrate HR-EGFP/5′EGFP which supports HR prior to irradiation with 2 or 5 Gy of **(A)** X-rays or **(B)** X-rays and charged particles (carbon ions, 60–85 keV/μm and calcium ions, 180 keV/μm). After incubation for 24 h, the fraction of EGFP-positive cells was quantified. HR data were individually normalized to the non-irradiated control representing 100% (PBL: 0.043×10^{-2} and HSPC: 0.048×10^{-2}). Mean values and SEM are indicated (X-rays: $n = 3$ from one to three independent experiments, and carbon and calcium ions: $n = 3$ from one experiment). Mean values for non-irradiated controls and irradiated cells were compared with the Wilcoxon matched-pairs signed rank test; however, none of the differences reached statistical significance with $^*p < 0.05$.

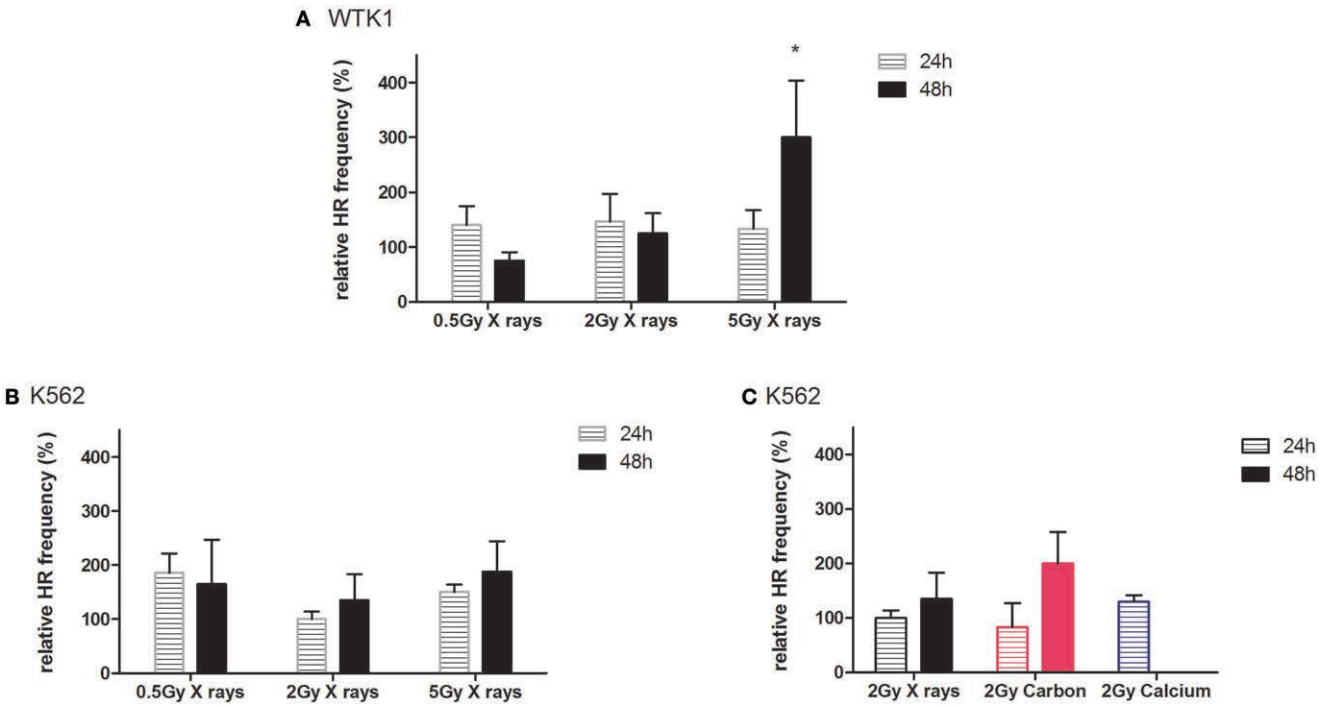

FIGURE 5 | Intrachromosomal DSB repair in WTK1(HR-EGFP/3′EFP-MLL) and K562(HR-EGFP/3′EFP-MLL) cells after irradiation. Stably transfected WTK1(HR-EGFP/3′EFP-MLL) and K562(HR-EGFP/3′EFP-MLL) reporter cells were irradiated with **(A,B)** X-rays or **(C)** X-rays and charged particles (carbon ions, 60–85 keV/μm and calcium ions, 180 keV/μm). Radiation-induced breakage in the *MLL*bcr sequence within the chromosomally integrated HR reporter (HR-EGFP/3′EGFP-MLL) initiated HR events. After subsequent incubation for 24 or 48 h, EGFP-positive viable cells were analyzed within the total cell population by flow cytometric measurement. HR measurements were individually normalized to the unirradiated control representing 100%. Mean values and SEM are indicated (X-rays, WTK1 cells: $n = 12$ from four independent experiments; X-rays, K562 cells: $n = 18$ from six independent experiments; exposure to calcium and carbon ions: $n = 3$ from one independent experiment). Values for non-irradiated control and irradiated cells were compared with the Wilcoxon matched-pairs signed rank test with $^*p < 0.05$.

DISCUSSION

Development of AML can be induced by ionizing radiation exposure (2, 3) and is contingent on the induction of specific chromosomal rearrangements and instability (45–47). For some time, we have known that chromosomal aberrations are mainly the result of DSB, which remain unrepaired or are not correctly repaired (48, 49). The frequency of misrepair depends on the type of damage, which can be simple or complex, and on the fidelity of the repair pathway chosen by the damaged cells.

The induction of complex DNA lesions is characteristic of ionizing irradiation; DNA and chromosomal damage induced by

heavy ion irradiation is of higher complexity than photon induced damage due to the densely ionizing events occurring along the track of heavy ions. This leads to the occurrence of clustered lesions, i.e., closely spaced single-strand breaks or DSB that are frequently associated with additional types of lesions (50). These clustered lesions are difficult to repair and the level of unrepaired, persisting damage increases with ionizing density. Unrepaired lesions remain detectable as chromosome breakage (12), i.e., for terminal deletions, or lead to complex exchanges involving more than three chromosome breaks and multiple chromosomes (51, 52). Incorrect repair after high LET irradiation can cause point mutations (53) or enhance formation of intra- and interchromosomal exchanges (54–57). If the aberrations are lethal, these result in cell death or reduced clonogenic survival (58).

In our current study, we show a dose-dependent induction of chromatid breaks by X-ray irradiation (Figure S1 in Supplementary Material), and a more pronounced break induction and incomplete rejoining in response to high LET radiation qualities in PBL. We irradiated with five different ions (nitrogen, carbon, calcium, titanium, and iron ions) covering a LET range from 45 to 180 keV/μm (**Figure 1A**; Figure S1A in Supplementary Material). The level of residual damage at 9 h increased with LET, indicating a larger fraction of initial chromatid breaks refractory to rejoining after high LET compared to photon irradiation. This is in accordance with studies performed in different cell types (PBL, fibroblasts, epithelial cells) measuring residual chromosomal damage in mitotic or interphase cells (38, 52, 59–61). Of note, when comparing our results to reported data, one has to take into account that the absolute number of breaks depends on the protocol used for PCC technique (fusion with mitotic cells or Calyculin induced chromosome condensation) (62), the cell type (63), and the cell cycle stage of the irradiated and analyzed cells.

Up to now, rejoining of DSB in terms of chromosomal breaks by PCC has not been investigated for hematopoietic progenitor cells, i.e., HSPC. We demonstrate here similar, dose-dependent induction of chromatid breaks as for PBL and similarly decelerated rejoining after high LET exposure (**Figure 1B**; Figure S1B in Supplementary Material). Cytogenetic changes are considered a valid biomarker for cancer risk assessment (64), and have as such mostly been investigated in PBL isolated from blood of exposed individuals. The observed equivalent induction and repair of chromatid breaks in PBL and HSPC provides useful information because the cell of origin of leukemia is believed to be a transformed HSPC (65) and PBL are a commonly used model for assessment of chromosomal breakage and rejoining.

In good agreement with the cytogenetic data, using phosphorylation of H2AX as a DSB marker, we show that formation and removal of γH2AX foci is similar in both cell types for low and high LET radiation qualities (X-rays, iron ions). Based on the observed enhanced biological efficiency of titanium ions for the induction of chromatid breaks (**Figure 1B**), a higher induction of γH2AX foci by iron ions compared to photons might have been expected but was not observed (**Figures 2A,B**). We posit that this was most likely due to the limited resolution of γH2AX foci formed along a particle track (66, 67), although it is difficult to assess to what extent irradiation geometry would impact the irradiation of suspension cells.

As observed in the cytogenetic analyses, we also measured a higher level of persisting DNA damage after exposure to high LET iron ions compared to X-ray (**Figures 2A,B**). This characteristic of the high LET response, i.e., enhanced levels of γH2AX foci persisting after 24 h, was previously reported mainly in human fibroblasts, epithelial cells, and organotypic cultures (12, 68–72), while data for HSPC were not available.

Having identified an NF-κB-mediated decrease of HR in HSPC versus PBL in our preceding work (20), we assessed how this pathway is affected by radiation and damage quality in the different cell types. Using an EGFP-based reporter plasmid without expression of the cleaving enzyme, we found that extrachromosomal HR frequencies increased in immortalized lymphocytes (LCL 416MI and TK6) with X-ray dose (**Figure 3**). Consistent with previous results from enzyme-mediated cleavage, HR frequencies increased in X-ray-treated PBL and, less so, in HSPC (**Figure 4**). Interestingly, the difference between PBL and HSPC, best observed for 5 Gy X-ray, was not detectable for high LET calcium ions at 2 Gy despite a trend toward HR stimulation by 2 Gy heavy ion versus 2 Gy X-ray exposure.

Higher HR frequencies in PBL after irradiation were indeed expected from the previously obtained results for enzyme mediated cleavage. Comparing the same physical dose of 2 Gy X-ray and heavy ion irradiation, we further noticed a trend toward HR stimulation by heavy ion versus X-ray exposure. Interestingly, the difference between PBL and HSPC observed best for 5 Gy X-ray (**Figure 4A**) was no longer visible for high LET calcium ions (**Figure 4B**). This observation is likely not attributable to differences in cell cycle distribution between PBL and HSPC, because of a comparable radiation-induced cell cycle delay in G_2 phase (Figure S3B in Supplementary Material).

In addition, we recently reported that the more pronounced formation of 53BP1 foci after X-ray-induced DSB in HSPC was a consequence of reduced NF-κB activity (20). Compromised NF-κB-mediated BRCA1-CtIP activation (73) can explain the observed relative shift to error-prone repair pathways in HSPC, possibly under participation of EXO1 nuclease as a resection factor (74, 75). This might also be relevant for particle radiation-induced DSB because we similarly found accumulation of 53BP1 foci after X-ray and carbon ion exposure (intermediate LET) of HSPC. However, this difference between immature and mature cells was lost after higher LET exposure (**Figure 2E**), consistent with similar HR frequencies after calcium ion irradiation (**Figure 4B**). Neutralization of the differences in 53BP1 foci numbers between PBL and HSPC was mostly due to elevated 53BP1 signals in PBL, suggesting incomplete HR repair of higher LET damage not only in HSPC but also in PBL. Results using LCL with stably integrated *MLL*bcr sequences further supported the impression of a dose and LET-dependent increase in HR frequencies (**Figure 5**). Even though further experiments are needed to generate a robust assay system to monitor the effects of different radiation qualities, our results provided clues for future directions (e.g., lentivirus-based integration of the reporter into primary cells of the hematopoietic system). Moreover, it underscored the detrimental potential of radiation-induced breaks to induce AML-related genome rearrangements at the *MLL*bcr in particular. Notably, HR was identified as a DNA repair pathway involved in *MLL*bcr rearrangements

in response to replication stress, which can be induced in HSPC by stimuli, such as infection or irradiation (33).

Similarly, elevated 53BP1 damage levels and HR frequencies induced by high LET in PBL and HSPC match the concept that heavy ion-induced complex DSBs are predominantly repaired by HR and thus may exhaust the cellular HR machinery in both cell types (76). Conservative HR is limited to S/G_2-phase cells (77–79) representing 40–60% of the primary cell populations in our study (Figure S3B in Supplementary Material). Other resection-dependent pathways, which are error-prone, have been suggested to contribute to the repair of complex damage (80). However, errors in repair can lead to chromosomal aberrations, in particular translocations (81, 82). Consistent with error-prone pathway usage in HSPC (20, 21), HSPC show a higher level of translocations compared to PBL at moderately enhanced LET (21, 31, 83). An additional explanation for similar HR frequencies in PBL and HSPC after high LET versus X-ray and carbon ion exposure could be earlier activation of NF-κB with increasing LET (84), which could compensate for the low intrinsic NF-κB activity in HSPC. In addition, activation of ATM, a prerequisite for NF-κB signaling, is also more pronounced with increasing LET (67).

Taken together, we could show that overall removal of radiation-induced DNA damage and chromosomal breaks is comparable for mature and immature cells of the hematopoietic system (PBL and HSPC). However, exposure to low and moderate LET reveals higher conservative HR in PBL versus HSPC, consistent with increased usage of low fidelity pathways during repair of enzyme-mediated DSB by HSPC. However, after exposure to high LET HR frequencies of PBL and HSPC are comparable, underlining the importance of HR for the repair of complex DNA damage for the outcome of the damaged cells (85, 86).

ACKNOWLEDGMENTS

We would like to thank P. Partscht, Darmstadt, L. Bauer Darmstadt, and Andreea I. Stahl, Ulm, for dedicated help in the experiments. We also thank Michael Scholz and Thomas Friedrich and the dosimetry team for excellent technical support during the experimental runs. Furthermore, we are grateful to Marco Durante for his continuous support.

FUNDING

This work was partly supported by the German Ministry of Economy (BMWi), grant no. 50WB1225; A0-10 IBER from Federal Ministry of Economics and Technology provided by ESA, German Aerospace Center; grant no. 02NUK017A (GREWIS) from German Federal Ministry of Research and Education; German Research Foundation (DFG, PA3 in Research Training Group 1789 "Cellular and Molecular Mechanisms in aging," CEMMA). MR is a member of the International Graduate School in Molecular Medicine Ulm. AC is a member of DFG-funded Graduate College 1657 and the Helmholtz Graduate School for Hadron and Ion Research. HB is a member of the LOEWE Cell and Gene Therapy Frankfurt faculty funded by Hessian Ministry of Higher Education, Research and the Arts ref. no.: III L 4-518/17.004 (2010). The authors thank the Helmholtz Association for funding of this work through Helmholtz-Portfolio Topic "Technology and Medicine."

SUPPLEMENTARY MATERIAL

The Supplementary Material for this article can be found online at http://journal.frontiersin.org/article/10.3389/fonc.2015.00250

REFERENCES

1. Hsu W-L, Preston DL, Soda M, Sugiyama H, Funamoto S, Kodama K, et al. The incidence of leukemia, lymphoma and multiple myeloma among atomic bomb survivors: 1950-2001. *Radiat Res* (2013) **179**(3):361–82.
2. Muirhead CR, O'Hagan JA, Haylock RGE, Phillipson MA, Willcock T, Berridge GLC, et al. Mortality and cancer incidence following occupational radiation exposure: third analysis of the national registry for radiation workers. *Br J Cancer* (2009) **100**(1):206–12. doi:10.1038/sj.bjc.6604825
3. Linet MS, Kim KP, Miller DL, Kleinerman RA, Simon SL, Berrington de Gonzalez A. Historical review of occupational exposures and cancer risks in medical radiation workers. *Radiat Res* (2010) **174**(6):793–808. doi:10.1667/RR2014.1
4. Newhauser WD, Durante M. Assessing the risk of second malignancies after modern radiotherapy. *Nat Rev Cancer* (2011) **11**(6):438–48. doi:10.1038/nrc3069
5. Schulz-Ertner D, Tsujii H. Particle radiation therapy using proton and heavier ion beams. *J Clin Oncol* (2007) **25**(8):953–64. doi:10.1200/JCO.2006.09.7816
6. Durante M. New challenges in high-energy particle radiobiology. *Br J Radiol* (2014) **87**(1035):20130626. doi:10.1259/bjr.20130626
7. Cucinotta FA, Durante M. Cancer risk from exposure to galactic cosmic rays: implications for space exploration by human beings. *Lancet Oncol* (2006) **7**(5):431–5. doi:10.1016/S1470-2045(06)70695-7
8. Durante M, Cucinotta FA. Heavy ion carcinogenesis and human space exploration. *Nat Rev Cancer* (2008) **8**(6):465–72. doi:10.1038/nrc2391
9. Barcellos-Hoff MH, Blakely EA, Burma S, Fornace AJ, Gerson S, Hlatky L, et al. Concepts and challenges in cancer risk prediction for the space radiation environment. *Life Sci Space Res* (2015) **6**:92–103. doi:10.1016/j.lssr.2015.07.006
10. Durante M, Loeffler JS. Charged particles in radiation oncology. *Nat Rev Clin Oncol* (2010) **7**(1):37–43. doi:10.1038/nrclinonc.2009.183
11. Anderson RM, Stevens DL, Sumption ND, Townsend KMS, Goodhead DT, Hill MA. Effect of linear energy transfer (LET) on the complexity of alpha-particle-induced chromosome aberrations in human CD34+ cells. *Radiat Res* (2007) **167**(5):541–50. doi:10.1667/RR0813.1
12. Asaithamby A, Hu B, Chen DJ. Unrepaired clustered DNA lesions induce chromosome breakage in human cells. *Proc Natl Acad Sci U S A* (2011) **108**(20):8293–8. doi:10.1073/pnas.1016045108
13. Pedersen-Bjergaard J, Christiansen DH, Desta F, Andersen MK. Alternative genetic pathways and cooperating genetic abnormalities in the pathogenesis of therapy-related myelodysplasia and acute myeloid leukemia. *Leukemia* (2006) **20**(11):1943–9. doi:10.1038/sj.leu.2404381
14. Francis R, Richardson C. Multipotent hematopoietic cells susceptible to alternative double-strand break repair pathways that promote genome rearrangements. *Genes Dev* (2007) **21**(9):1064–74. doi:10.1101/gad.1522807
15. Mohrin M, Bourke E, Alexander D, Warr MR, Barry-Holson K, Le Beau MM, et al. Hematopoietic stem cell quiescence promotes error-prone DNA repair and mutagenesis. *Cell Stem Cell* (2010) **7**(2):174–85. doi:10.1016/j.stem.2010.06.014
16. Zhang L, Wang SA. A focused review of hematopoietic neoplasms occurring in the therapy-related setting. *Int J Clin Exp Pathol* (2014) **7**(7):3512–23.
17. IAEA. *Cytogenetic Analysis for Radiation Dose Assessment a Manual [Internet]* (2015) [cited 2015 Aug 23]. Available from: http://www-pub.iaea.org/books/IAEABooks/6303/Cytogenetic-Analysis-for-Radiation-Dose-Assessment-A-Manual
18. Durante M, Bonassi S, George K, Cucinotta FA. Risk estimation based on chromosomal aberrations induced by radiation. *Radiat Res* (2001) **156**(5 Pt 2):662–7. doi:10.1667/0033-7587(2001)156[0662:REBOCA]2.0.CO;2

19. Tucker JD. Low-dose ionizing radiation and chromosome translocations: a review of the major considerations for human biological dosimetry. *Mutat Res* (2008) **659**(3):211–20. doi:10.1016/j.mrrev.2008.04.001
20. Kraft D, Rall M, Volcic M, Metzler E, Groo A, Stahl A, et al. NF-κB-dependent DNA damage-signaling differentially regulates DNA double-strand break repair mechanisms in immature and mature human hematopoietic cells. *Leukemia* (2015) **29**(7):1543–54. doi:10.1038/leu.2015.28
21. Kraft D, Ritter S, Durante M, Seifried E, Fournier C, Tonn T. Transmission of clonal chromosomal abnormalities in human hematopoietic stem and progenitor cells surviving radiation exposure. *Mutat Res* (2015) **777**:43–51. doi:10.1016/j.mrfmmm.2015.04.007
22. Walter D, Lier A, Geiselhart A, Thalheimer FB, Huntscha S, Sobotta MC, et al. Exit from dormancy provokes DNA-damage-induced attrition in haematopoietic stem cells. *Nature* (2015) **520**(7548):549–52. doi:10.1038/nature14131
23. Akyüz N, Boehden GS, Süsse S, Rimek A, Preuss U, Scheidtmann K-H, et al. DNA substrate dependence of p53-mediated regulation of double-strand break repair. *Mol Cell Biol* (2002) **22**(17):6306–17. doi:10.1128/MCB.22.17.6306-6317.2002
24. Keimling M, Kaur J, Bagadi SAR, Kreienberg R, Wiesmüller L, Ralhan R. A sensitive test for the detection of specific DSB repair defects in primary cells from breast cancer specimens. *Int J Cancer* (2008) **123**(3):730–6. doi:10.1002/ijc.23551
25. Keimling M, Volcic M, Csernok A, Wieland B, Dörk T, Wiesmüller L. Functional characterization connects individual patient mutations in ataxia telangiectasia mutated (ATM) with dysfunction of specific DNA double-strand break-repair signaling pathways. *FASEB J* (2011) **25**(11):3849–60. doi:10.1096/fj.11-185546
26. Keimling M, Deniz M, Varga D, Stahl A, Schrezenmeier H, Kreienberg R, et al. The power of DNA double-strand break (DSB) repair testing to predict breast cancer susceptibility. *FASEB J* (2012) **26**(5):2094–104. doi:10.1096/fj.11-200790
27. Akyüz N, Wiesmüller L. Proof of principle: detection of genotoxicity by a fluorescence-based recombination test in mammalian cells. *ALTEX* (2003) **20**(2):77–84.
28. Siehler SY, Schrauder M, Gerischer U, Cantor S, Marra G, Wiesmüller L. Human MutL-complexes monitor homologous recombination independently of mismatch repair. *DNA Repair* (2009) **8**(2):242–52. doi:10.1016/j.dnarep.2008.10.011
29. Ireno IC, Baumann C, Stöber R, Hengstler JG, Wiesmüller L. Fluorescence-based recombination assay for sensitive and specific detection of genotoxic carcinogens in human cells. *Arch Toxicol* (2014) **88**(5):1141–59. doi:10.1007/s00204-014-1229-3
30. Fernández JL, Vázquez-Gundín F, Rivero MT, Genescá A, Gosálvez J, Goyanes V. DBD-fish on neutral comets: simultaneous analysis of DNA single- and double-strand breaks in individual cells. *Exp Cell Res* (2001) **270**(1):102–9. doi:10.1006/excr.2001.5328
31. Becker D, Elsässer T, Tonn T, Seifried E, Durante M, Ritter S, et al. Response of human hematopoietic stem and progenitor cells to energetic carbon ions. *Int J Radiat Biol* (2009) **85**(11):1051–9. doi:10.3109/09553000903232850
32. Boehden GS, Restle A, Marschalek R, Stocking C, Wiesmüller L. Recombination at chromosomal sequences involved in leukaemogenic rearrangements is differentially regulated by p53. *Carcinogenesis* (2004) **25**(8):1305–13. doi:10.1093/carcin/bgh092
33. Gole B, Wiesmüller L. Leukemogenic rearrangements at the mixed lineage leukemia gene (MLL)-multiple rather than a single mechanism. *Front Cell Dev Biol* (2015) **3**:41. doi:10.3389/fcell.2015.00041
34. Allan JM, Travis LB. Mechanisms of therapy-related carcinogenesis. *Nat Rev Cancer* (2005) **5**(12):943–55. doi:10.1038/nrc1749
35. Klymenko SV, Bink K, Trott KR, Bebeshko VG, Bazyka DA, Dmytrenko IV, et al. MLL gene alterations in radiation-associated acute myeloid leukemia. *Exp Oncol* (2005) **27**(1):71–5.
36. Mueller MM, Bialleck H, Bomke B, Brauninger S, Varga C, Seidl C, et al. Safety and efficacy of healthy volunteer stem cell mobilization with filgrastim G-CSF and mobilized stem cell apheresis: results of a prospective longitudinal 5-year follow-up study. *Vox Sang* (2013) **104**(1):46–54. doi:10.1111/j.1423-0410.2012.01632.x
37. Kiefer J, Straaten H. A model of ion track structure based on classical collision dynamics. *Phys Med Biol* (1986) **31**(11):1201–9. doi:10.1088/0031-9155/31/11/002
38. Kawata T, Gotoh E, Durante M, Wu H, George K, Furusawa Y, et al. High-LET radiation-induced aberrations in prematurely condensed G2 chromosomes of human fibroblasts. *Int J Radiat Biol* (2000) **76**(7):929–37. doi:10.1080/09553000050050945
39. Bennardo N, Cheng A, Huang N, Stark JM. Alternative-NHEJ is a mechanistically distinct pathway of mammalian chromosome break repair. *PLoS Genet* (2008) **4**(6):e1000110. doi:10.1371/journal.pgen.1000110
40. Böhringer M, Wiesmüller L. Fluorescence-based quantification of pathway-specific DNA double-strand break repair activities: a powerful method for the analysis of genome destabilizing mechanisms. *Subcell Biochem* (2010) **50**:297–306. doi:10.1007/978-90-481-3471-7_15
41. Restle A, Färber M, Baumann C, Böhringer M, Scheidtmann KH, Müller-Tidow C, et al. Dissecting the role of p53 phosphorylation in homologous recombination provides new clues for gain-of-function mutants. *Nucleic Acids Res* (2008) **36**(16):5362–75. doi:10.1093/nar/gkn503
42. Mirault M-E, Boucher P, Tremblay A. Nucleotide-resolution mapping of topoisomerase-mediated and apoptotic DNA strand scissions at or near an MLL translocation hotspot. *Am J Hum Genet* (2006) **79**(5):779–91. doi:10.1086/507791
43. Meyer C, Hofmann J, Burmeister T, Gröger D, Park TS, Emerenciano M, et al. The MLL recombinome of acute leukemias in 2013. *Leukemia* (2013) **27**(11):2165–76. doi:10.1038/leu.2013.135
44. Löbrich M, Rief N, Kühne M, Heckmann M, Fleckenstein J, Rübe C, et al. In vivo formation and repair of DNA double-strand breaks after computed tomography examinations. *Proc Natl Acad Sci U S A* (2005) **102**(25):8984–9. doi:10.1073/pnas.0501895102
45. Mitelman Database. *Mitelman Database of Chromosome Aberrations and Gene Fusions in Cancer [Internet]* (2015) [cited 2015 Aug 23]. Available from: http://cgap.nci.nih.gov/Chromosomes/Mitelman
46. Rassool FV, Gaymes TJ, Omidvar N, Brady N, Beurlet S, Pla M, et al. Reactive oxygen species, DNA damage, and error-prone repair: a model for genomic instability with progression in myeloid leukemia? *Cancer Res* (2007) **67**(18):8762–71. doi:10.1158/0008-5472.CAN-06-4807
47. Negrini S, Gorgoulis VG, Halazonetis TD. Genomic instability – an evolving hallmark of cancer. *Nat Rev Mol Cell Biol* (2010) **11**(3):220–8. doi:10.1038/nrm2858
48. Bender MA, Griggs HG, Bedford JS. Mechanisms of chromosomal aberration production. 3. Chemicals and ionizing radiation. *Mutat Res* (1974) **23**(2):197–212. doi:10.1016/0027-5107(74)90140-7
49. Obe G, Pfeiffer P, Savage JRK, Johannes C, Goedecke W, Jeppesen P, et al. Chromosomal aberrations: formation, identification and distribution. *Mutat Res* (2002) **504**(1–2):17–36. doi:10.1016/S0027-5107(02)00076-3
50. Asaithamby A, Chen DJ. Mechanism of cluster DNA damage repair in response to high-atomic number and energy particles radiation. *Mutat Res* (2011) **711**(1–2):87–99. doi:10.1016/j.mrfmmm.2010.11.002
51. Savage JR, Simpson PJ. FISH "painting" patterns resulting from complex exchanges. *Mutat Res* (1994) **312**(1):51–60. doi:10.1016/0165-1161(94)90008-6
52. Loucas BD, Durante M, Bailey SM, Cornforth MN. Chromosome damage in human cells by γ rays, α particles and heavy ions: track interactions in basic dose-response relationships. *Radiat Res* (2013) **179**(1):9–20. doi:10.1667/RR3089.1
53. Hall EJ, Hei TK. Genomic instability and bystander effects induced by high-LET radiation. *Oncogene* (2003) **22**(45):7034–42. doi:10.1038/sj.onc.1206900
54. Lee R, Sommer S, Hartel C, Nasonova E, Durante M, Ritter S. Complex exchanges are responsible for the increased effectiveness of C-ions compared to X-rays at the first post-irradiation mitosis. *Mutat Res* (2010) **701**(1):52–9. doi:10.1016/j.mrgentox.2010.03.004
55. Ritter S, Durante M. Heavy-ion induced chromosomal aberrations: a review. *Mutat Res* (2010) **701**(1):38–46. doi:10.1016/j.mrgentox.2010.04.007
56. Durante M, Bedford JS, Chen DJ, Conrad S, Cornforth MN, Natarajan AT, et al. From DNA damage to chromosome aberrations: joining the break. *Mutat Res* (2013) **756**(1–2):5–13. doi:10.1016/j.mrgentox.2013.05.014
57. Ray FA, Robinson E, McKenna M, Hada M, George K, Cucinotta F, et al. Directional genomic hybridization: inversions as a potential biodosimeter for retrospective radiation exposure. *Radiat Environ Biophys* (2014) **53**(2):255–63. doi:10.1007/s00411-014-0513-1
58. Franken NAP, Oei AL, Kok HP, Rodermond HM, Sminia P, Crezee J, et al. Cell survival and radiosensitisation: modulation of the linear and quadratic

parameters of the LQ model (review). *Int J Oncol* (2013) **42**(5):1501–15. doi:10.3892/ijo.2013.1857
59. Nasonova E, Ritter S. Cytogenetic effects of densely ionising radiation in human lymphocytes: impact of cell cycle delays. *Cytogenet Genome Res* (2004) **104**(1–4):216–20. doi:10.1159/000077492
60. Hada M, Cucinotta FA, Gonda SR, Wu H. mBAND analysis of chromosomal aberrations in human epithelial cells exposed to low- and high-LET radiation. *Radiat Res* (2007) **168**(1):98–105. doi:10.1667/RR0759.1
61. Okayasu R. Repair of DNA damage induced by accelerated heavy ions – a mini review. *Int J Cancer* (2012) **130**(5):991–1000. doi:10.1002/ijc.26445
62. Deperas-Standylo J, Lee R, Nasonova E, Ritter S, Gudowska-Nowak E. Production and distribution of aberrations in resting or cycling human lymphocytes following Fe-ion or Cr-ion irradiation: emphasis on single track effects. *Adv Space Res* (2012) **50**(5):584–97. doi:10.1016/j.asr.2012.05.007
63. Themis M, Garimberti E, Hill MA, Anderson RM. Reduced chromosome aberration complexity in normal human bronchial epithelial cells exposed to low-LET γ-rays and high-LET α-particles. *Int J Radiat Biol* (2013) **89**(11):934–43. doi:10.3109/09553002.2013.805889
64. Bonassi S, Norppa H, Ceppi M, Strömberg U, Vermeulen R, Znaor A, et al. Chromosomal aberration frequency in lymphocytes predicts the risk of cancer: results from a pooled cohort study of 22 358 subjects in 11 countries. *Carcinogenesis* (2008) **29**(6):1178–83. doi:10.1093/carcin/bgn075
65. Brendel C, Neubauer A. Characteristics and analysis of normal and leukemic stem cells: current concepts and future directions. *Leukemia* (2000) **14**(10):1711–7. doi:10.1038/sj.leu.2401907
66. Jakob B, Scholz M, Taucher-Scholz G. Biological imaging of heavy charged-particle tracks. *Radiat Res* (2003) **159**(5):676–84. doi:10.1667/0033-7587(2003)159[0676:BIOHCT]2.0.CO;2
67. Costes SV, Boissière A, Ravani S, Romano R, Parvin B, Barcellos-Hoff MH. Imaging features that discriminate between foci induced by high- and low-LET radiation in human fibroblasts. *Radiat Res* (2006) **165**(5):505–15. doi:10.1667/RR3538.1
68. Asaithamby A, Uematsu N, Chatterjee A, Story MD, Burma S, Chen DJ. Repair of HZE-particle-induced DNA double-strand breaks in normal human fibroblasts. *Radiat Res* (2008) **169**(4):437–46. doi:10.1667/RR1165.1
69. Asaithamby A, Hu B, Delgado O, Ding L-H, Story MD, Minna JD, et al. Irreparable complex DNA double-strand breaks induce chromosome breakage in organotypic three-dimensional human lung epithelial cell culture. *Nucleic Acids Res* (2011) **39**(13):5474–88. doi:10.1093/nar/gkr149
70. Groesser T, Chang H, Fontenay G, Chen J, Costes SV, Helen Barcellos-Hoff M, et al. Persistence of γ-H2AX and 53BP1 foci in proliferating and non-proliferating human mammary epithelial cells after exposure to γ-rays or iron ions. *Int J Radiat Biol* (2011) **87**(7):696–710. doi:10.3109/09553002.2010.549535
71. Saha J, Wilson P, Thieberger P, Lowenstein D, Wang M, Cucinotta FA. Biological characterization of low-energy ions with high-energy deposition on human cells. *Radiat Res* (2014) **182**(3):282–91. doi:10.1667/RR13747.1
72. Sridharan DM, Chappell LJ, Whalen MK, Cucinotta FA, Pluth JM. Defining the biological effectiveness of components of high-LET track structure. *Radiat Res* (2015) **184**(1):105–19. doi:10.1667/RR13684.1
73. Volcic M, Karl S, Baumann B, Salles D, Daniel P, Fulda S, et al. NF-κB regulates DNA double-strand break repair in conjunction with BRCA1-CtIP complexes. *Nucleic Acids Res* (2012) **40**(1):181–95. doi:10.1093/nar/gkr687
74. Tomimatsu N, Mukherjee B, Deland K, Kurimasa A, Bolderson E, Khanna KK, et al. Exo1 plays a major role in DNA end resection in humans and influences double-strand break repair and damage signaling decisions. *DNA Repair* (2012) **11**(4):441–8. doi:10.1016/j.dnarep.2012.01.006
75. Desai A, Gerson S. Exo1 independent DNA mismatch repair involves multiple compensatory nucleases. *DNA Repair* (2014) **21**:55–64. doi:10.1016/j.dnarep.2014.06.005
76. Shibata A, Conrad S, Birraux J, Geuting V, Barton O, Ismail A, et al. Factors determining DNA double-strand break repair pathway choice in G2 phase. *EMBO J* (2011) **30**(6):1079–92. doi:10.1038/emboj.2011.27
77. Tamulevicius P, Wang M, Iliakis G. Homology-directed repair is required for the development of radioresistance during S phase: interplay between double-strand break repair and checkpoint response. *Radiat Res* (2007) **167**(1):1–11. doi:10.1667/RR0751.1
78. Daley JM, Sung P. 53BP1, BRCA1, and the choice between recombination and end joining at DNA double-strand breaks. *Mol Cell Biol* (2014) **34**(8):1380–8. doi:10.1128/MCB.01639-13
79. Mjelle R, Hegre SA, Aas PA, Slupphaug G, Drabløs F, Saetrom P, et al. Cell cycle regulation of human DNA repair and chromatin remodeling genes. *DNA Repair* (2015) **30**:53–67. doi:10.1016/j.dnarep.2015.03.007
80. Averbeck NB, Ringel O, Herrlitz M, Jakob B, Durante M, Taucher-Scholz G. DNA end resection is needed for the repair of complex lesions in G1-phase human cells. *Cell Cycle* (2014) **13**(16):2509–16. doi:10.4161/15384101.2015.941743
81. Hlatky L, Sachs RK, Vazquez M, Cornforth MN. Radiation-induced chromosome aberrations: insights gained from biophysical modeling. *Bioessays* (2002) **24**(8):714–23. doi:10.1002/bies.10126
82. Roukos V, Misteli T. The biogenesis of chromosome translocations. *Nat Cell Biol* (2014) **16**(4):293–300. doi:10.1038/ncb2941
83. Hartel C, Nikoghosyan A, Durante M, Sommer S, Nasonova E, Fournier C, et al. Chromosomal aberrations in peripheral blood lymphocytes of prostate cancer patients treated with IMRT and carbon ions. *Radiother Oncol* (2010) **95**(1):73–8. doi:10.1016/j.radonc.2009.08.031
84. Hellweg CE, Baumstark-Khan C, Schmitz C, Lau P, Meier MM, Testard I, et al. Carbon-ion-induced activation of the NF-κB pathway. *Radiat Res* (2011) **175**(4):424–31. doi:10.1667/RR2423.1
85. Zafar F, Seidler SB, Kronenberg A, Schild D, Wiese C. Homologous recombination contributes to the repair of DNA double-strand breaks induced by high-energy iron ions. *Radiat Res* (2010) **173**(1):27–39. doi:10.1667/RR1910.1
86. Gerelchuluun A, Manabe E, Ishikawa T, Sun L, Itoh K, Sakae T, et al. The major DNA repair pathway after both proton and carbon-ion radiation is NHEJ, but the HR pathway is more relevant in carbon ions. *Radiat Res* (2015) **183**(3):345–56. doi:10.1667/RR13904.1

Conflict of Interest Statement: Lisa Wiesmüller is an inventor of a patent on a test system for determining genotoxicities, which is owned by Lisa Wiesmüller. The remaining authors do not have any conflict of interest to declare.

Copyright © 2015 Rall, Kraft, Volcic, Cucu, Nasonova, Taucher-Scholz, Bönig, Wiesmüller and Fournier. This is an open-access article distributed under the terms of the Creative Commons Attribution License (CC BY). The use, distribution or reproduction in other forums is permitted, provided the original author(s) or licensor are credited and that the original publication in this journal is cited, in accordance with accepted academic practice. No use, distribution or reproduction is permitted which does not comply with these terms.

frontiers in Oncology

ORIGINAL RESEARCH
published: 27 June 2016
doi: 10.3389/fonc.2016.00155

Induction of Chronic Inflammation and Altered Levels of DNA Hydroxymethylation in Somatic and Germinal Tissues of CBA/CaJ Mice Exposed to ^{48}Ti Ions

Kanokporn Noy Rithidech[1], Witawat Jangiam[1,2], Montree Tungjai[1,3], Chris Gordon[1], Louise Honikel[1] and Elbert B. Whorton[4]*

[1] Department of Pathology, Stony Brook University, Stony Brook, NY, USA, [2] Department of Chemical Engineering, Faculty of Engineering, Burapha University, Chonburi, Thailand, [3] Department of Radiologic Technology, Faculty of Associated Medical Sciences, Center of Excellence for Molecular Imaging, Chiang Mai University, Chiang Mai, Thailand, [4] StatCom, Galveston, TX, USA

OPEN ACCESS

Edited by:
Marco Durante,
University of Trento, Italy

Reviewed by:
Nicole Averbeck,
GSI Helmholtzzentrum für Schwerionenforschung, Germany
Paula Vertino,
Emory University, USA

***Correspondence:**
Kanokporn Noy Rithidech
kanokporn.rithidech@stonybrookmedicine.edu

Specialty section:
This article was submitted to Radiation Oncology, a section of the journal Frontiers in Oncology

Received: 28 October 2015
Accepted: 10 June 2016
Published: 27 June 2016

Citation:
Rithidech KN, Jangiam W, Tungjai M, Gordon C, Honikel L and Whorton EB (2016) Induction of Chronic Inflammation and Altered Levels of DNA Hydroxymethylation in Somatic and Germinal Tissues of CBA/CaJ Mice Exposed to ^{48}Ti Ions. Front. Oncol. 6:155. doi: 10.3389/fonc.2016.00155

Although the lung is one of the target organs at risk for cancer induction from exposure to heavy ions found in space, information is insufficient on cellular/molecular responses linked to increased cancer risk. Knowledge of such events may aid in the development of new preventive measures. Furthermore, although it is known that germinal cells are sensitive to X- or γ-rays, there is little information on the effects of heavy ions on germinal cells. Our goal was to investigate *in vivo* effects of 1 GeV/n ^{48}Ti ions (one of the important heavy ions found in the space environment) on somatic (lung) and germinal (testis) tissues collected at various times after a whole body irradiation of CBA/CaJ mice (0, 0.1, 0.25, or 0.5 Gy, delivered at 1 cGy/min). We hypothesized that ^{48}Ti-ion-exposure induced damage in both tissues. Lung tissue was collected from each mouse from each treatment group at 1 week, 1 month, and 6 months postirradiation. For the testis, we collected samples at 6 months postirradiation. Hence, only late-occurring effects of ^{48}Ti ions in the testis were studied. There were five mice per treatment group at each harvest time. We investigated inflammatory responses after exposure to ^{48}Ti ions by measuring the levels of activated nuclear factor kappa B and selected pro-inflammatory cytokines in both tissues of the same mouse. These measurements were coupled with the quantitation of the levels of global 5-methylcytosine (5mC) and 5-hydroxymethylcytosine (5hmC). Our data clearly showed the induction of chronic inflammation in both tissues of exposed mice. A dose-dependent reduction in global 5hmC was found in the lung at all time-points and in testes collected at 6 months postirradiation. In contrast, significant increases in global 5mC were found only in lung and testes collected at 6 months postirradiation from mice exposed to 0.5 Gy of 1 GeV/n ^{48}Ti ions. Overall, our data showed that ^{48}Ti ions may create health risks in both lung and testicular tissues.

Keywords: titanium ions, chronic inflammation, NF-κB, pro-inflammatory cytokines, lung, testes, 5-methylcytosine, 5-hydroxymethylcytosine

INTRODUCTION

Spaceflight results in unavoidable exposure of astronauts to space radiation (such as heavy ions and energetic protons) that may create potential risks for late-occurring injuries in both somatic and germinal cells/tissues. To protect astronauts, we must improve our understanding of changes at the cellular and molecular levels that are linked to increasing astronaut health risks and are valuable in developing countermeasures. In order to obtain reliable information about radiation-induced detrimental health effects, the data must be obtained using appropriate *in vivo* systems because *in vitro* systems cannot faithfully mimic the complex *in vivo* situation (1). Hence, appropriate whole-animal systems are critically important surrogates for assessment of health risks associated with exposure to space radiation.

The aim of this study was to improve our knowledge of *in vivo* biological effects of a whole body exposure to 1 GeV/n ^{48}Ti ions (one of the important types of heavy ions found in the space environment). We used the CBA/CaJ mouse as an experimental model to study the effects of 1 GeV/n ^{48}Ti ions on the lung (representing somatic tissue) and the testis (representing germinal tissue) of the same mouse, employing the inflammatory responses and DNA methylation endpoints. These two endpoints have not been used to evaluate the biological effects of 1 GeV/n ^{48}Ti ions in somatic and germinal cells of the same mouse, setting our approach apart from the existing reports.

It is known that the lung is a highly radiosensitive organ (2–4) and that impairment of the immune function in the lung is one of the major concerns after exposure to low LET radiation (4–7). It also has been suggested that the lung is one of the target organs at risk for cancer induction from exposure to heavy ions found in space (8). However, very little is known about the responses of the lung to space radiation. Recently, it was found that 350 MeV/n ^{28}Silicon (^{28}Si) or ^{56}Iron (^{56}Fe) ions, which are also important heavy ions found in the space environment, induced both histological and functional injuries in the lungs of exposed C3H/HeNCrl mice (9). Furthermore, it was reported that 1 GeV/n ^{56}Fe ions induced lung cancer in transgenic mice (the Kras^{LA1} mice) engineered to be susceptible to lung cancer (10, 11).

With respect to testes, deleterious effects (e.g., DNA double-strand breaks, cytogenetic effects, and mutagenesis) of X or γ rays on spermatogenesis were reported several decades ago (12–19). It is known that the testis is one of the most radiosensitive organs (20) and is more sensitive to radiation exposure than female germ cells (21). Thus, male-mediated reproductive and developmental toxicology has been a concern for decades in atomic bomb survivors and in the Sellafield nuclear plant workers (22). However, very little is known about the effects of heavy ions on testes. It was found that exposure to 2.0–8.07 Gy of 0.35 GeV/n ^{12}Carbon (^{12}C) ions (LET = 13 keV/μm) or to 0.3–2.0 Gy of 1 GeV/n ^{56}Fe ions (LET = 147 keV/μm) did not increase mutation rates (assayed by the specific locus and the dominant lethal tests in Medaka fish), as compared to those exposed to 250 kVp X rays, a reference radiation (22). However, prenatal irradiation of pregnant rats to 0.1–2.0 Gy of 0.3 GeV/n ^{12}C or to 0.1–0.5 Gy of 0.4 MeV/n ^{20}Neon (^{20}Ne) ions (LET = 30 keV/μm) caused abnormal testicular development and breeding activity of male offspring (23). Further, an increased level of interleukin-1β, lower number of sperms, and an abnormal tubular architecture were found in testes of C57BL/6 mice flown with the Space Shuttle Discovery for 114 days, in relation to that of the corresponding sham controls (with no spaceflight) (24). Of note, it is known that the space environment is complex. Several factors (e.g., radiation, microgravity, and reactivation of herpes virus infection) may have contributed to such changes. Hence, to reduce the uncertainties in the assessment of health risks of space radiation, further ground-based studies are required to help improve our understanding of the effects of heavy ions on germinal cells and somatic cells as well.

Currently, there is no information on the *in vivo* effects of 1 GeV/n ^{48}Ti ions to the lung and the testes. Based upon the existing, but limited, information on responses to 1 GeV/n ^{48}Ti ions (25–27), we hypothesized that 1 GeV/n ^{48}Ti ions induced damage to these two tissues of exposed mice. To address this hypothesis, we used two biological endpoints to evaluate the effects of 1 GeV/n ^{48}Ti ions on lung and testicular tissues of the same mouse. These endpoints were inflammatory responses and global DNA methylation, including both 5-methylcytosine (5mC) and 5-hydroxymethylcytosine (5hmC). These two biological endpoints were chosen for analyses because they are highly relevant surrogate biomarkers for assessing health risks, but they have not previously been assessed following *in vivo* exposure to 1 GeV/n ^{48}Ti ions. Importantly, the induction of chronic inflammation has been reported in studies of astronauts' blood samples (28–30).

There has been increasing evidence of space-radiation-induced acute and chronic inflammation (26, 31–35), and radiation-induced aberrant DNA methylation at the global (26, 36) or specific locus levels (37–41). For the inflammatory responses, in this report, we chose to study the nuclear-factor kappa B (NF-κB) pathway because NF-κB is a key transcription factor playing a pivotal role in inflammatory responses to oxidative stress induced by several stimuli, including radiation (42). Although NF-κB is a member of the ubiquitously expressed family of the Rel-related transcription factors (43), only the activation of NF-κB/p65 was the focus of our study and referred to as NF-κB throughout the article. It also has been well recognized that NF-κB is a key transcription factor known to be part of a common network between inflammation and cancer (44–46), and that there is a close association between inflammation and cancer (44, 47–54). In addition, chronic inflammation in male germinal cells has been linked to male infertility (55–57). In addition to the levels of activated NF-κB, we measured the expression, at the protein levels, of selected NF-κB-regulated pro-inflammatory cytokines, i.e., tumor necrosis factor alpha (TNF-α), interleukin-1 beta (IL-1β), and interleukin 6 (IL-6). This is because their increased levels have been found in the liver (26) of the same exposed mice included in this present study. Furthermore, the expression of these proteins (at the gene level) was elevated in human mononuclear cells obtained from healthy adult individuals who lived near the Chernobyl Nuclear Power Plant and were chronically exposed to low-dose radiation ranging from 0.18 to 49 mSv (58).

Relating to DNA methylation, it has been well recognized that it is one of the key epigenetic events that plays a critical role in carcinogenesis, both initiation and promotion, in somatic and

germinal cells (59, 60), and other untoward health outcomes (14) including male-mediated developmental toxicology (61), male infertility (62–64), and transgeneration effects (65, 66). Furthermore, a high level of 5mC (hypermethylation) has been linked to gene silencing (59, 67); while a reduction in global levels of 5hmC has been associated with cancer development (68). Since inflammatory responses and DNA methylation were analyzed in the lung and the testes of the same mouse, it is possible to investigate the differential sensitivity of these two tissues in the same mouse.

MATERIALS AND METHODS

Animals

The CBA/CaJ mice included in this study were the same cohort that were used to investigate the effects of 1 GeV/n ^{48}Ti ions on the liver previously reported (26), where the description of the CBA/CaJ mice, ^{48}Ti-irradiation, and animal husbandry were presented. The experimental design of the study was approved by both the Brookhaven National Laboratory (BNL) and the Stony Brook University (SBU) Institutional Animal Care and Use Committee (IACUC). Of note, the CBA/CaJ mouse is known to be sensitive to the development of radiation-induced myeloid leukemia (ML) (69–76), liver cancer (hepatocellular carcinoma or HCC) (70, 75), and lung cancer (70).

Irradiation of Mice

Figure 1 is a diagram of the experimental design. Mice were exposed, whole-body, to average total-body doses of 0, 0.1, 0.25, or 0.5 Gy of 1 GeV/n ^{48}Ti ions, delivered at a dose rate of 0.01 Gy/min by a 20 cm × 20 cm beam. Mice included in the sham-control group (i.e., those that were exposed to 0 Gy) were age-matched to exposed mice. Therefore, the age of mice in each treatment group would be similar at each sacrifice time. The exposure of mice was done at the National Aeronautics and Space Administration (NASA) Research Laboratory (NSRL) located at BNL. Details of the NSRL facility and irradiation procedure were previously provided (26, 34, 35, 77). We designated the first day after irradiation as day 1 after exposure. Mice were transported to the animal facility of SBU in a climate-controlled vehicle within 2 days postirradiation. Similar to the animal facility located in BNL, the animal facility of SBU, where sample collections were performed, is also approved by the Association for Assessment and Accreditation of Laboratory Animal Care (AAALAC), with the same light cycle (12 h light/12 h dark), temperature (21 ± 2°C), 10–15 hourly cycles of fresh air, and relative humidity (50 ± 10%).

Collection of the Lung and Testis

For the lung, groups of mice were used for sampling at 1 week, 1 month, and 6 months following the exposure to 1 GeV/n ^{48}Ti ions. In contrast, the collection of the testis was done at 6 months postexposure only. Hence, at 6 months postirradiation, the lung and the testis were collected from the same mouse. The rational for choosing only one harvest time for the testis was because our goal was to study the effects of ^{48}Ti ions on the stem-cell compartment of spermatogenesis. It is known that spermatogenesis is a complex biological process involving the transformation of spermatogonial stem cells (types A and B) into primary and secondary spermatocytes, round spermatids, and, eventually, spermatozoa over an extended period of time within seminiferous tubules of the testis (60, 65, 78). The duration of mouse spermatogenesis from the primitive type A_{single} spermatogonial stem cells (SSCs) to mature sperms (spermatozoa) is about 52 days, but 35 days from differentiated spermatogonia to mature sperms (62, 79). Hence, the results obtained from the analyses of the testes collected at 6 months postirradiation reflect the effects of radiation on type A_{single} SSCs.

From each treatment group, we collected the tissues from each mouse (five mice per dose of ^{48}Ti ions). Briefly, the lung and testicular tissues were removed, rinsed three times with 1 mL phosphate buffered saline (PBS) each time to remove external contamination (i.e., blood), snap frozen in liquid nitrogen, and stored in a −80°C freezer until needed for protein extraction and further analyses. After thawing, the total lung tissue was homogenized using a Bullet Blender Homogenizer (Next Advance Inc., Averill Park, NY, USA). Likewise, after thawing, the epididymis was removed from each testis to obtain seminiferous tubules, which were homogenized for use in protein extraction. The protocols for protein extraction from the lung and the testis suggested by the manufacturer were followed. Then, the cell lysates from each tissue of each mouse were divided into two fractions, i.e., fractions A and B. Fraction A of the tissue lysate was used to extract proteins from nuclear and cytosolic samples using the method we previously described (26, 34, 35, 80, 81). The total protein obtained from the nuclear portion of the lysate suspension of the lung or the testis was used for measuring the levels of NF-κB, while the total protein obtained from the cytosolic portion was used for the measurements of NF-κB-regulated pro-inflammatory cytokines, i.e., TNF-α, IL-1β, and IL-6. Protein contents in the cytosolic portion and the nuclear portion of the lung or the testis were measured by the Bradford assay using a BioPhotometer (Eppendorf, Inc., Westbury, NY, USA). Fraction B of the tissue lysate was used to isolate DNA for the measurements of global 5mC and global 5hmC.

Measurement of Activated Nuclear Factor-Kappa B

As with our previous work (26, 34, 35, 81), we used the enzyme-linked immunosorbent assay (ELISA) NF-κB kits from Active Motif North America, Inc. for measuring the levels of activated NF-κB in the nuclear portions obtained from the lung and testis lysates. The assay was performed in duplicate wells for each lung or testis sample of each treatment group. The mean value of activated NF-κB levels for the tissue of each mouse was obtained and reported. Then, the mean value of ten measurements from five mice and the SE for each treatment group were obtained.

Measurement of NF-κB-Regulated Pro-Inflammatory Cytokines, Including Tumor Necrosis Factor-α, Interleukin-1β, and Interleukin-6

Coupled with the levels of activated NF-κB, we measured the expression (at the protein levels) of NF-κB-regulated pro-inflammatory

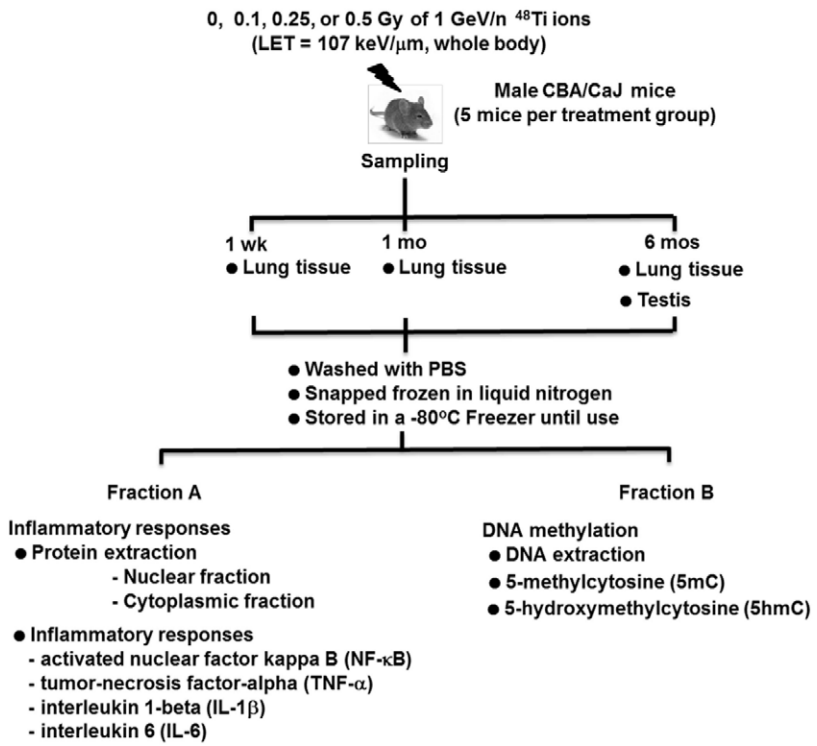

FIGURE 1 | **Diagram of the experimental design**.

cytokines, i.e., TNF-α, IL-1β, and IL-6. The rational for studying these pro-inflammatory cytokines has been presented in the Section "Introduction." We applied the methods routinely used in our laboratory for measuring the expression levels of these selected cytokines in lung or testicular cell suspensions (the cytosolic portions) using the specific ELISA kits for TNF-α, IL-1β, and IL-6 from Biosource (Invitrogen, Carlsbad, CA, USA) (26, 34, 35, 82). The mean value and SE of each cytokine for each treatment group were calculated from the means of five mice.

Measurement of Global 5-Methylcytosine and 5-Hydroxymethylcytosine

The methods for DNA isolation from mouse tissues have previously been presented (26, 36). Commercially available ELISA kits for the detection of global 5mC and 5hmC (Zymo Research, Inc., Irvine, CA, USA) were used to measure the percentage of global 5mC and 5hmC in the DNA samples isolated from lung or testicular tissues. The levels of global 5mC and 5hmC were measured using a microplate spectrophotometer (Molecular Devices) at 405 nm. The % 5mC and % 5hmC was calculated from a standard curve generated using the control DNA set provided by the manufacturer. The measurements of 5mC and 5hmC in the DNA sample from each tissue of each mouse were done in duplicate (using 200 ng of DNA per well). Then, the mean value of global 5mC and global 5hmC for each mouse were obtained. Finally, the mean value of ten measurements and SE of global 5mC and global 5hmC for each treatment group were calculated from the means of five mice.

Statistical Analyses

We expressed levels of each biological endpoint as mean ± SE. For each tissue, the mean value for each assay of each mouse was used as a single datum point for statistical analyses. At each harvest time, an ANOVA method appropriate for a one-factor experiment (i.e., dose of 1 GeV/n ^{48}Ti ions) was used to assess the significance of the radiation dose. Further, the Student's *t*-test was used, independently, to evaluate statistical differences in the mean values between each exposed group and the corresponding sham-control group. A *P*-value of ≤ 0.05 was considered as statistically significant.

RESULTS

Figures 2–**7** show the effects of various doses of 1 GeV/n ^{48}Ti ions on the lung and testicular tissues of exposed CBA/CaJ mice. *P* values (Student's *t*-test) shown in each figure indicate statistically significant levels between exposed and sham-control groups. **Tables 1** and **2** show the results of the ANOVA for the lung and testicular tissues, respectively.

Activated Nuclear Factor-Kappa B

There were dose-dependent increases in the levels of activated NF-κB in lung tissues from all exposed groups (ANOVA,

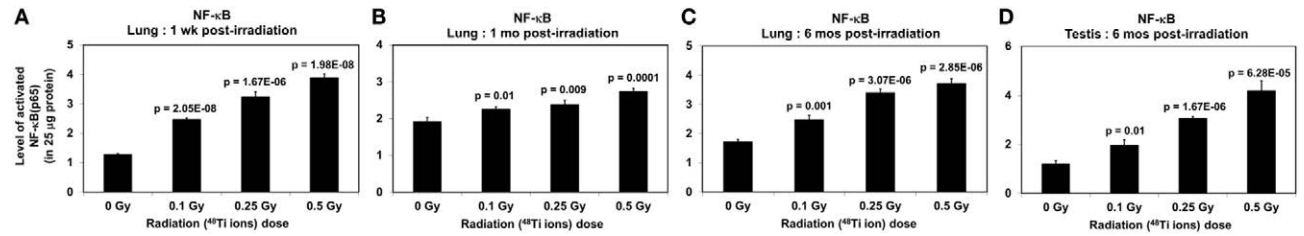

FIGURE 2 | Levels of activated NF-κB (±SE) in lung tissues collected at 1 week (A), 1 month (B), 6 months (C), and in testicular tissues collected at 6 months (D) from CBA/CaJ mice after a whole body exposure to various doses of 1 GeV/n ^{48}Ti ions. *P* values (Student's *t*-test) indicate significant differences in the levels of NF-κB between exposed and corresponding sham control groups.

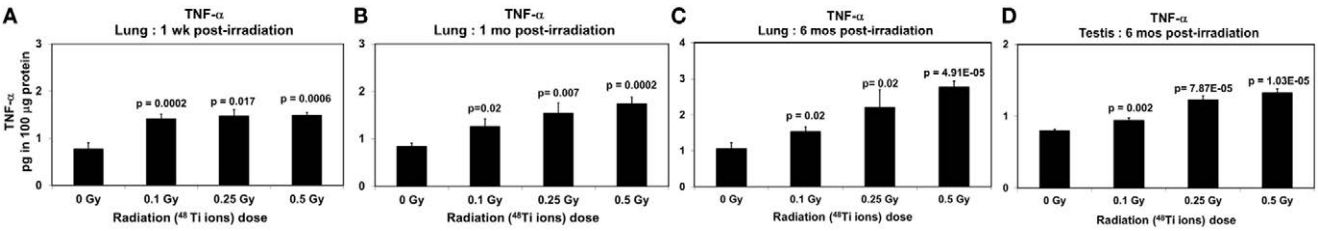

FIGURE 3 | Levels of TNF-α (±SE) in lung tissues collected at 1 week (A), 1 month (B), 6 months (C), and in testicular tissues collected at 6 months (D) from CBA/CaJ mice after a whole body exposure to various doses of 1 GeV/n ^{48}Ti ions. *P* values (Student's *t*-test) indicate significant differences in the levels of TNF-α between exposed and corresponding sham control groups.

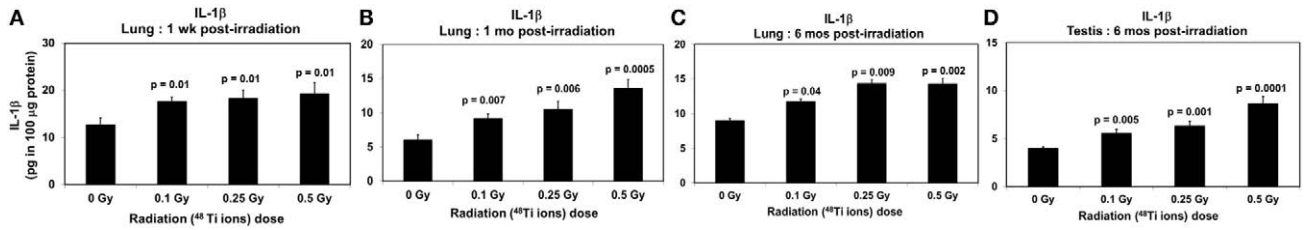

FIGURE 4 | Levels of IL-1β (±SE) in lung tissues collected at 1 week (A), 1 month (B), 6 months (C), and in testicular tissues collected at 6 months (D) from CBA/CaJ mice after a whole body exposure to various doses of 1 GeV/n ^{48}Ti ions. *P* values (Student's *t*-test) indicate significant differences in the levels of IL-1β between exposed and corresponding sham control groups.

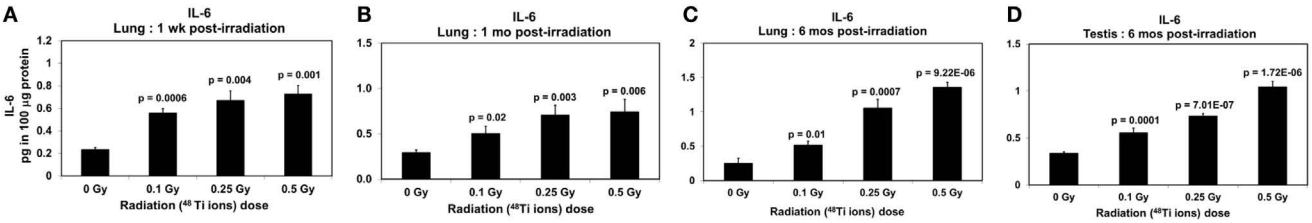

FIGURE 5 | Levels of IL-6 (±SE) in lung tissues collected at 1 week (A), 1 month (B), 6 months (C), and in testicular tissues collected at 6 months (D) from CBA/CaJ mice after a whole body exposure to various doses of 1 GeV/n ^{48}Ti ions. *P* values (Student's *t*-test) indicate significant differences in the levels of IL-6 between exposed and corresponding sham control groups.

$P < 0.01$), regardless of the harvest time (**Figures 2A–C**). Of note, there is a fluctuation in the levels of activated NF-κB in lung tissues collected from sham control mice (in particular in those collected at 1 month postirradiation). However, the factors contributing to this temporal change are unknown. We also detected a dose-dependent increase in the levels of activated NF-κB in the testicular tissues (ANOVA, $P < 0.01$) at 6 months postirradiation (as shown in **Figure 2D**).

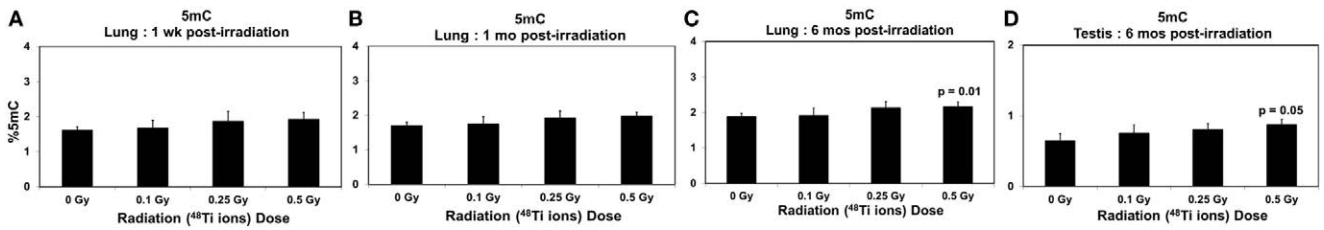

FIGURE 6 | Levels of 5mC (±SE) in lung tissues collected at 1 week (A), 1 month (B), 6 months (C), and in testicular tissues collected at 6 months (D) from CBA/CaJ mice after a whole body exposure to various doses of 1 GeV/n ^{48}Ti ions. *P* values (Student's *t*-test) indicate significant differences in the levels of 5mC between exposed and corresponding sham control groups.

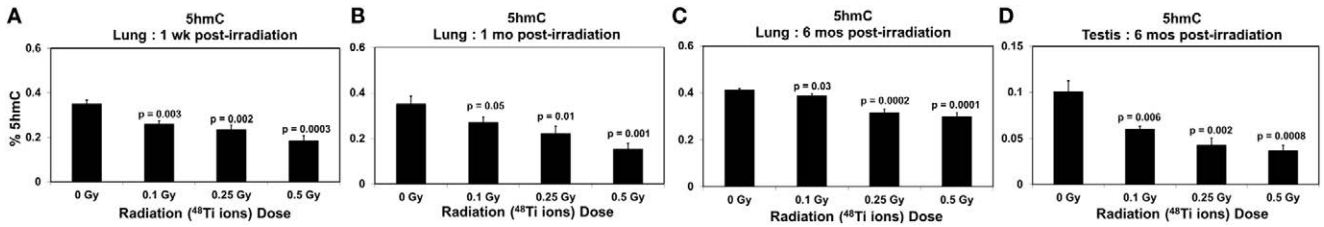

FIGURE 7 | Levels of 5hmC (±SE) in lung tissues collected at 1 week (A), 1 month (B), 6 months (C), and in testicular tissues collected at 6 months (D) from CBA/CaJ mice after a whole body exposure to various doses of 1 GeV/n ^{48}Ti ions. *P* values (Student's *t*-test) indicate significant differences in the levels of 5hmC between exposed and corresponding sham control groups.

Tumor Necrosis Factor-α

Similar to the levels of activated NF-κB, there were dose-dependent increases in the level of TNF-α in lung tissues collected at all time-points (ANOVA, $P < 0.01$), as shown in **Figures 3A–C**. Likewise, at 6 months postirradiation, a dose-dependent increase (ANOVA, $P < 0.01$) in the levels of IL-6 was found in testicular tissues collected at 6 months postirradiation (**Figure 3D**).

Interleukin-1β and Interleukin-6

Clearly, dose-dependent increases in the levels of IL-1β (**Figures 4A–C**) and IL-6 (**Figures 5A–C**) were observed in lung tissues collected at 1 week, 1 month, and 6 months postirradiation (ANOVA, $P < 0.01$), respectively. Of note, similar to activated NF-κB, there was a fluctuation in the levels of IL-1β in lung tissues of sham control mice, in particular in those collected at 1 month postirradiation. The cause of such fluctuation remains unidentified. Likewise, dose-dependent increases in the levels of IL-1β (**Figure 4D**) and IL-6 (**Figure 5D**) in testicular tissues collected at 6 months postirradiation (ANOVA, $P < 0.01$) were evident.

5-Methylcytosine and 5-Hydroxymethylcytosine

Figures 6A–C show the effects of ^{48}Ti ions on the levels of global 5mC in lung tissues of exposed mice. There was a trend of increased levels of global 5mC in the lung tissues of exposed mice, in relation to those of the corresponding sham controls. However, such increases were not statistically different, except in the lung tissues collected at 6 months from mice exposed to the highest dose of 1 GeV/n ^{48}Ti ions. A similar finding was found in testicular tissues collected at 6 months postirradiation (**Figure 6D**).

In contrast, **Figures 7A–C** show significant dose-dependent decreases in the levels of 5hmC in the lungs of exposed mice (ANOVA, $P < 0.05$) at 1 week, 1 month, and 6 months, respectively. The decreases in 5hmC levels in lung tissues of exposed mice relative to the corresponding sham controls were: 1.33-, 1.48-, and 1.88-fold at 1 week postirradiation; 1.29-, 1.58-, and 2.29-fold at 1 month postirradiation; 1.06-, 1.30-, and 1.38-fold at 6 months postirradiation. Likewise, there was a dose-dependent reduction in the levels of global 5hmC in testicular tissues collected at 6 months postirradiation as shown in **Figure 7D**.

DISCUSSION

Our data are the first to report the presence of chronic inflammation and altered levels of global 5hmC in the lung and testicular tissues of CBA/CaJ mice after a whole body exposure to 1 GeV/n ^{48}Ti ions at low doses and a low dose-rate relevant to what is found in space, i.e., 0.1–0.5 Gy (delivered at 0.01 Gy/min). Our data also indicated that only 0.5 Gy (the highest dose used in our study) of 1 GeV/n ^{48}Ti ions induced significant increases in the levels of global 5mC in both tissues of the same mouse. The magnitude of the effects of ^{48}Ti ions on each tissue is similar. Since these two endpoints were detected in both tissues of the same mouse, it is plausible to speculate that there is a connection between chronic inflammation and altered DNA methylation. The information obtained from our study is important because these two *in vivo* endpoints are the hallmarks of cancer (52, 53, 68) and several

TABLE 1 | Analysis of variance results for lung tissues collected at 1 week, 1 month, and 6 months postirradiation, respectively (SS, sum of squares; df, degree of freedom; MS, mean of squares; *F*, *F*-statistic).

1 Week postirradiation						1 Month week postirradiation						6 Months postirradiation					
Source of variation	**SS**	**df**	**MS**	**F**	***P*-value**	***Source of variation***	**SS**	**df**	**MS**	**F**	***P*-value**	***Source of variation***	**SS**	**df**	**MS**	**F**	***P*-value**
NF-κB																	
Between groups	18.95	3	6.32	102.1	1E-10	Between groups	1.74	3	0.58	12.6	0.0001	Between groups	12.44	3	4.15	43.86	6E-08
Within groups	0.99	16	0.06			Within groups	0.74	16	0.05			Within groups	1.51	16	0.09		
Total	19.94	19				Total	2.48	19				Total	13.95	19			
TNF-α																	
Between groups	1.78	3	0.59	5.25	0.01	Between groups	2.27	3	0.76	6.31	0.0049	Between groups	8.55	3	2.85	7.15	0.002
Within groups	1.81	16	0.11			Within groups	1.92	16	0.12			Within groups	6.37	16	0.40		
Total	3.59	19				Total	4.19	19				Total	14.92	19			
IL-1β																	
Between groups	128.91	3	42.97	2.86	0.04	Between groups	144.64	3	48.21	9.67	0.0007	Between groups	62.52	3	20.84	6.86	0.003
Within groups	240.68	16	15.04			Within groups	79.74	16	4.98			Within groups	48.58	16	3.04		
Total	369.59	19				Total	224.38	19				Total	111.09	19			
IL-6																	
Between groups	0.51	3	0.17	7.62	0.0029	Between groups	0.64	3	0.21	4.37	0.02	Between groups	3.50	3	1.17	29.49	2E-06
Within groups	0.31	16	0.02			Within groups	0.78	16	0.05			Within groups	0.59	16	0.04		
Total	0.82	19				Total	1.43	19				Total	111.09	19			
5mC																	
Between groups	0.34	3	0.11	0.49	0.68	Between groups	0.26	3	0.09	0.39	0.76	Between groups	0.61	3	0.20	1.65	0.22
Within groups	3.64	16	0.23			Within groups	3.61	16	0.23			Within groups	1.99	16	0.12		
Total	3.98	19				Total	3.87	19				Total	2.61	19			
5hmC																	
Between groups	0.07	3	0.02	11.38	0.0003	Between groups	0.05	3	0.02	7.29	0.003	Between groups	0.05	3	0.02	16.15	4E-05
Within groups	0.03	16	0.002			Within groups	0.01	16	0.0050			Within groups	0.01	16	0.0009		
Total	0.1	19				Total	0.06	19				Total	0.06	19			

types of male germ-cell disturbance (55–57, 62, 63, 83, 84). Hence, our findings provide an important foundation for future studies in which an association between molecular changes and the histopathological, pathological and/or functional damage in the lung and the testes, including the incidence of lung or testicular cancer, can be achieved. Of note, in future studies, it is important to measure the levels of activated NF-κB and related pro-inflammatory cytokines not only in tissues but also in plasma obtained from the same mice. The obtained information will help to determine whether there is a correlation between chronic inflammation in tissues and the levels of circulating cytokines, which should have clinical implications.

The approach we used in this study has allowed the investigation of the kinetics of effects of 1 GeV/n ^{48}Ti ions on the lung, not only as a function of radiation dose but also time after exposure, since lung tissues were collected at various times up to 6 months postirradiation. We observed dose- and time-dependent increases in the levels of activated NF-κB and expression of NF-κB-related pro-inflammatory cytokines (i.e., TNF-α, IL-1β, and IL-6). Our data indicate that ^{48}Ti-ion-exposure induces disturbances of cytokine production, reflecting chronic inflammation and an impairment of the immune system. Relating to the kinetics of the levels of global 5mC and 5hmC in the lung, our data indicated no significant change in the levels of global 5mC, except a significant increase in lung tissues collected at 6 months postirradiation from mice exposed to 0.5 Gy of ^{48}Ti ions. In contrast, there were significant dose-dependent decreases in the levels of global 5hmC at all harvest time-points. Such findings were similar to those detected in the liver collected from the same mouse previously reported (26). Hence, our data suggest that the loss of global

TABLE 2 | Analysis of variance results for testicular tissues collected at 6 months postirradiation (SS, sum of squares; df, degree of freedom; MS, mean of squares; *F*, *F*-statistic).

Source of variation	SS	df	MS	*F*	*P*-value
NF-kB					
Between groups	25.70	3	8.57	27.39	1.5379E-06
Within groups	5.00	16	0.31		
Total	30.70	19			
TNF-α					
Between groups	0.91	3	0.30	29.46	9.4514E-07
Within groups	0.16	16	0.01		
Total	1.07	19			
IL1-β					
Between groups	56.46	3	18.82	14.45	8.1361E-05
Within groups	20.85	16	1.30		
Total	77.31	19			
IL-6					
Between groups	1.34	3	0.45	49.31	2.6281E-08
Within groups	0.14	16	0.01		
Total	1.48	19			
5mC					
Between groups	0.16	3	0.05	1.19	0.35
Within groups	0.72	16	0.05		
Total	0.88	19			
5hmC					
Between groups	0.01	3	0.0042	12.88	0.0001
Within groups	0.01	16	0.0003		
Total	0.02	19			

5hmC is a significant response to ^{48}Ti-ion-irradiation, regardless of tissue type. It also is reasonable to hypothesize that chronic inflammation enhances radiation-induced loss of global 5hmC and *vice versa*.

Our study is the first to report the levels of global 5hmC in the lung of mice exposed to radiation. Of note, the focus of previous studies on the effects of radiation, both low and high LET, has been on specific loci of 5mC (38, 39, 41, 85–88). We included the levels of global 5hmC because it is currently recognized that a reduction in global 5hmC is a biomarker for cancer (68). Taken together, our data suggest that a reduction in the level of global 5hmC may be a better hallmark of radiation exposure than an increased level of global 5mC. In the future, it will be important to conduct studies to determine the genome-wide profiling of 5hmC/5mC to reveal the affected regions of the genome so that, in turn, the identification of affected genes will be possible.

Regarding the testes collected at 6 months from the same mouse from which the lung tissue was collected for our study, the data clearly showed that there were dose-dependent increases in the levels of activated NF-κB and expression of NF-κB-regulated pro-inflammatory cytokines (i.e., TNF-α, IL-1β, and IL-6). These findings represent the effects of 1 GeV/n ^{48}Ti ions on the primitive type of spermatogonial stem cells (SSCs), i.e., type A_{single} SSCs. The induced damage arising from exposed SSCs is highly relevant for genetic risk assessment since SSCs are capable of self-renewal and differentiation into spermatocytes and mature sperm. Hence, any induced damage in the SSC compartment, if not repaired, will be carried onto the next generation and will adversely impact self-renewal, proliferation, and differentiation. In contrast, the damage that is induced in other male germ cell stages (e.g., spermatocytes, where cell divisions, both in meiosis and mitosis, take place) will affect progenies that are conceived shortly after irradiation. Our new data are important because it has been well recognized that SSCs are responsible for long-term effects of radiation on fertility (15, 89). Further, it was suggested that inflammation in SSCs leads to failure of testicular androgen and sperm production, resulting in infertility (90), and testicular cancer (91). Thus, exposure to 1 GeV/n ^{48}Ti ions may lead to health risks associated with the male reproductive system. At 6 months postirradiation, the effects of 1 GeV/n ^{48}Ti ions on levels of global 5mC and 5hmC in the testes of exposed mice are similar to those found in the lung of the same mouse. As mentioned previously, altered DNA methylation plays an important role in male infertility (62–64), germ cell tumors (59, 60), and transgeneration effects (65, 78). Hence, our data provide critical information for conducting further studies to investigate the potential induction of these untoward outcomes on male germinal cells from exposure to 1 GeV/n ^{48}Ti ions.

In summary, our results provide new information on *in vivo* biological responses to ^{48}Ti ions. Our new data show that 1 GeV/n ^{48}Ti ions (at doses ranging from 0.1 to 0.5 Gy, delivered at 0.01 Gy/min) can induce chronic inflammation, and a persistence of altered DNA methylation (at the global level) in lung and testicular tissues of exposed CBA/CaJ mice. Importantly, our findings provide an important foundation for further investigations on the genes/proteins involved in ^{48}Ti-ion-induced chronic inflammation and altered DNA methylation. Knowing such detailed molecular markers for health risks from exposure to heavy ions would not only greatly improve radiation protection guidance for astronauts (or cancer patients receiving heavy-ion radiation therapy) but would also provide significantly valuable insight for developing biological countermeasures.

AUTHOR CONTRIBUTIONS

KR was responsible for the study concept and design; critical revision of the manuscript for important intellectual content. WJ was responsible for acquisition of the data. MT was responsible for acquisition of the data. CG was responsible for acquisition of the data. LH was responsible for acquisition of the data. EW was responsible for statistical analyses and critical revision of the manuscript for important intellectual content.

ACKNOWLEDGMENTS

This research was supported in part by the National Aeronautics and Space Administration (NASA) Grant # NNX11AK91G and the Department of Pathology, Stony Brook University, Stony Brook, NY, USA. We thank Dr. Peter Guida and his team for logistic support, MaryAnn Petry and her staff at Brookhaven Laboratory Animal Facilities (BLAF) for their assistance in animal handling. We also thank Drs. Adam Rusek and Michael Sivertz for dosimetry support.

REFERENCES

1. Nestor C, Ottaviano R, Reinhardt D, Cruickshanks H, Mjoseng H, McPherson R, et al. Rapid reprogramming of epigenetic and transcriptional profiles in mammalian culture systems. *Genome Biol* (2015) 16(1):11. doi:10.1186/s13059-014-0576-y
2. Coggle JE, Lambert BE, Moores SR. Radiation effects in the lung. *Environ Health Perspect* (1986) 70:261–91. doi:10.1289/ehp.8670261
3. Marks LB, Yu X, Vujaskovic Z, Small W, Folz R, Anscher MS. Radiation-induced lung injury. *Semin Radiat Oncol* (2003) 13(3):333–45. doi:10.1016/S1053-4296(03)00034-1
4. Hill RP. Radiation effects on the respiratory system. *Br J Radiol* (2005) 27(Suppl 1):75–81. doi:10.1259/bjr/34124307
5. Finkelstein JN, Johnston CJ, Baggs R, Rubin P. Early alterations in extracellular matrix and transforming growth factor [beta] gene expression in mouse lung indicative of late radiation fibrosis. *Int J Radiat Oncol Biol Phys* (1994) 28(3):621–31. doi:10.1016/0360-3016(94)90187-2
6. Hong JH, Chiang CS, Tsao CY, Lin PY, McBride WH, Wu CJ. Rapid induction of cytokine gene expression in the lung after single and fractionated doses of radiation. *Int J Radiat Biol* (1999) 75(11):1421–7. doi:10.1080/095530099139287
7. Rübe CE, Wilfert F, Palm J, König J, Burdak-Rothkamm S, Liu L, et al. Irradiation induces a biphasic expression of pro-inflammatory cytokines in the lung. *Strahlenther Onkol* (2004) 180(7):442–8. doi:10.1007/s00066-004-1265-7
8. Cucinotta FA. Space radiation risks for astronauts on multiple international space station missions. *PLoS One* (2014) 9(4):e96099. doi:10.1371/journal.pone.0096099
9. Christofidou-Solomidou M, Pietrofesa RA, Arguiri E, Schweitzer KS, Berdyshev EV, McCarthy M, et al. Space radiation-associated lung injury in a murine model. *Amer J Physiol Lung Cell Mol Physiol* (2015) 308(5):L416–28. doi:10.1152/ajplung.00260.2014
10. Shay JW, Cucinotta FA, Sulzman FM, Coleman CN, Minna JD. From mice and men to earth and space: joint NASA-NCI workshop on lung cancer risk resulting from space and terrestrial radiation. *Cancer Res* (2011) 71(22):6926–9. doi:10.1158/0008-5472.CAN-11-2546
11. Kim SB, Kaisani A, Shay JW. Risk assessment of space radiation-induced invasive cancer in mouse models of lung and colorectal cancer. *J Radiat Res* (2014) 55(Suppl 1):i46–7. doi:10.1093/jrr/rrt149
12. van Buul PP. Dose-response relationship for radiation-induced translocations in somatic and germ cells of mice. *Mutat Res* (1977) 45(1):61–8. doi:10.1016/0027-5107(77)90043-4
13. Vaiserman AM, Mekhova LV, Koshel NM, Voitenko VP. Cancer incidence and mortality after low-dosage radiation exposure: epidemiological aspects. *Biophysics* (2011) 56(2):371–80. doi:10.1134/S000635091102031X
14. Vaiserman AM. Epigenetic programming by early-life stress: evidence from human populations. *Dev Dyn* (2015) 244(3):254–65. doi:10.1002/dvdy.24211
15. Hacker-Klom U. Long term effects of ionizing radiation on mouse spermatogenesis. *Acta Radiol Oncol* (1985) 24(4):363–7. doi:10.3109/02841868509136066
16. Hamer G, Roepers-Gajadien HL, van Duyn-Goedhart A, Gademan IS, Kal HB, van Buul PPW, et al. DNA double-strand breaks and γ-H2AX signaling in the testis. *Biol Reprod* (2003) 68(2):628–34. doi:10.1095/biolreprod.102.008672
17. Cordelli E, Eleuteri P, Grollino MG, Benassi B, Blandino G, Bartoleschi C, et al. Direct and delayed X-ray-induced DNA damage in male mouse germ cells. *Environ Mol Mutagen* (2012) 53(6):429–39. doi:10.1002/em.21703
18. Spalding JF, Wellnitz JM, Schweitzer WH. Effects of rapid massive doses of gamma-rays on the testes and germ cells of the rat. *Radiat Res* (1957) 7(1):65–70. doi:10.2307/3570555
19. Generoso WM, Cain KT, Cacheiro NL, Cornett CV, Gossle DG. Response of mouse spermatogonial stem cells to X-ray induction of heritable reciprocal translocations. *Mutat Res* (1984) 126(2):177–87. doi:10.1016/0027-5107(84)90060-5
20. Ory C, Ugolin N, Hofman P, Schlumberger M, Likhtarev IA, Chevillard S. Comparison of transcriptomic signature of post-chernobyl and postradiotherapy thyroid tumors. *Thyroid* (2013) 23(11):1390–400. doi:10.1089/thy.2012.0318
21. Hall EJ, editor. *Radiobiology for the Radiologist*. 2000 ed. Philadelphia: Lippincott Williams & Wilkins (2000).
22. Shimada A, Shima A, Nojima K, Seino Y, Setlow RB. Germ cell mutagenesis in medaka fish after exposures to high-energy cosmic ray nuclei: a human model. *Proc Natl Acad Sci U S A* (2005) 102(17):6063–7. doi:10.1073/pnas.0500895102
23. Verdelli C, Forno I, Vaira V, Corbetta S. Epigenetic alterations in human parathyroid tumors. *Endocrine* (2015) 49(2):324–32. doi:10.1007/s12020-015-0555-4
24. Masini MA, Albi E, Barmo C, Bonfiglio T, Bruni L, Canesi L, et al. The impact of long-term exposure to space environment on adult mammalian organisms: a study on mouse thyroid and testis. *PLoS One* (2012) 7(4):e35418. doi:10.1371/journal.pone.0035418
25. Jain MR, Li M, Chen W, Liu T, de Toledo SM, Pandey BN, et al. In vivo space radiation-induced non-targeted responses: late effects on molecular signaling in mitochondria. *Curr Mol Pharmacol* (2011) 4(2):106–14. doi:10.2174/1874467211104020106
26. Jangiam W, Tungjai M, Rithidech K. Induction of chronic oxidative stress, chronic inflammation and aberrant patterns of DNA methylation in the liver of titanium-exposed CBA/CaJ mice. *Int J Radiat Biol* (2015) 91(5):389–98. doi:10.3109/09553002.2015.1001882
27. Rabin BM, Shukitt-Hale B, Joseph JA, Carrihill-Knoll KL, Carey AN, Cheng V. Relative effectiveness of different particles and energies in disrupting behavioral performance. *Radiat Environ Biophys* (2007) 46(2):173–7. doi:10.1007/s00411-006-0071-2
28. Crucian BE, Stowe RP, Pierson DL, Sams CF. Immune system dysregulation following short- vs long-duration spaceflight. *Aviat Space Environ Med* (2008) 79(9):835–43. doi:10.3357/ASEM.2276.2008
29. Sonnenfeld G, Shearer W. Immune function during space flight. *Nutrition* (2002) 18(10):899–903. doi:10.1016/S0899-9007(02)00903-6
30. Crucian B, Stowe RP, Mehta S, Quiriarte H, Pierson D, Sams C. Alterations in adaptive immunity persist during long-duration spaceflight. *NPJ Microgravity* (2015) 1:15013. doi:10.1038/npjmgrav.2015.13
31. Gridley DS, Miller GM, Pecaut MJ. Radiation and primary response to lipopolysaccharide: bone marrow-derived cells and susceptible organs. *In Vivo* (2007) 21(3):453–61.
32. Gridley DS, Pecaut MJ, Nelson GA. Total-body irradiation with high-LET particles: acute and chronic effects on the immune system. *Amer J Physiol Regul Integr Comp Physiol* (2002) 282(3):R677–88. doi:10.1152/ajpregu.00435.2001
33. Gridley DS, Rizvi A, Makinde AY, Luo-Owen X, Mao XW, Tian J, et al. Space-relevant radiation modifies cytokine profiles, signaling proteins and Foxp3+ T cells. *Int J Radiat Biol* (2013) 89(1):26–35. doi:10.3109/09553002.2012.715792
34. Rithidech K, Reungpatthanaphong P, Honikel L, Rusek A, Simon S. Dose-rate effects of protons on in vivo activation of nuclear factor-kappa B and cytokines in mouse bone marrow cells. *Radiat Environ Biophys* (2010) 49:405–19. doi:10.1007/s00411-010-0295-z
35. Tungjai M, Whorton E, Rithidech K. Persistence of apoptosis and inflammatory responses in the heart and bone marrow of mice following whole-body exposure to ^{28}Silicon (^{28}Si) ions. *Radiat Environ Biophys* (2013) 52(3):339–50. doi:10.1007/s00411-013-0479-4
36. Rithidech KN, Honikle LM, Reungpathanaphong P, Tungjai M, Jangiam W, Whorton EB. Late-occurring chromosome aberrations and global DNA methylation in hematopoietic stem/progenitor cells of CBA/CaJ mice exposed to silicon (28Si) ions. *Mutat Res* (2015) 781:22–31. doi:10.1016/j.mrfmmm.2015.09.001
37. Götze S, Schumacher EC, Kordes C, Häussinger D. Epigenetic changes during hepatic stellate cell activation. *PLoS One* (2015) 10(6):e0128745. doi:10.1371/journal.pone.0128745
38. Lima F, Ding D, Goetz W, Yang AJ, Baulch JE. High LET ^{56}Fe ion irradiation induces tissue-specific changes in DNA methylation in the mouse. *Environ Mol Mutagen* (2014) 55(3):266–77. doi:10.1002/em.21832
39. Nzabarushimana E, Miousse IR, Shao L, Chang J, Allen AR, Turner J, et al. Long-term epigenetic effects of exposure to low doses of ^{56}Fe in the mouse lung. *J Radiat Res* (2014) 55(4):823–8. doi:10.1093/jrr/rru010
40. Aypar U, Morgan WF, Baulch JE. Radiation-induced epigenetic alterations after low and high LET irradiations. *Mutat Res* (2011) 707(1–2):24–33. doi:10.1016/j.mrfmmm.2010.12.003
41. Miousse IR, Shao L, Chang J, Feng W, Wang Y, Allen AR, et al. Exposure to low-dose ^{56}Fe-ion radiation induces long-term epigenetic alterations in mouse

bone marrow hematopoietic progenitor and stem cells. *Radiat Res* (2014) 182(1):92–101. doi:10.1667/RR13580.1
42. Li N, Karin M. Is NF-kappa B the sensor of oxidative stress? *FASEB J* (1999) 13(10):1137–43.
43. Verma IM, Stevenson JK, Schwarz EM, Van Antwerp D, Miyamoto S. Rel/NF-kappa B/I kappa B family: intimate tales of association and dissociation. *Genes Develop* (1995) 9(22):2723–35. doi:10.1101/gad.9.22.2723
44. Karin M, Greten FR. NF-[kappa]B: linking inflammation and immunity to cancer development and progression. *Nat Rev Immunol* (2005) 5(10):749–59. doi:10.1038/nri1703
45. Pikarsky E, Porat RM, Stein I, Abramovitch R, Amit S, Kasem S, et al. NF-[kappa]B functions as a tumour promoter in inflammation-associated cancer. *Nature* (2004) 431(7007):461–6. doi:10.1038/nature02924
46. Dolcet X, Llobet D, Pallares J, Matias-Guiu X. NF-kB in development and progression of human cancer. *Virchows Archiv* (2005) 446(5):475–82. doi:10.1007/s00428-005-1264-9
47. Coussens LM, Werb Z. Inflammation and cancer. *Nature* (2002) 420(6917):860–7. doi:10.1038/nature01322
48. Takahashi H, Ogata H, Nishigaki R, Broide DH, Karin M. Tobacco smoke promotes lung tumorigenesis by triggering IKK[beta]- and JNK1-dependent inflammation. *Cancer Cell* (2010) 17(1):89–97. doi:10.1016/j.ccr.2009.12.008
49. Grivennikov SI, Greten FR, Karin M. Immunity, inflammation, and cancer. *Cell* (2010) 140(6):883–99. doi:10.1016/j.cell.2010.01.025
50. Schetter AJ, Heegaard NHH, Harris CC. Inflammation and cancer: interweaving microRNA, free radical, cytokine and p53 pathways. *Carcinogenesis* (2010) 31(1):37–49. doi:10.1093/carcin/bgp272
51. Li Q, Withoff S, Verma IM. Inflammation-associated cancer: NF-[kappa]B is the lynchpin. *Trends Immunol* (2005) 26(6):318–25. doi:10.1016/j.it.2005.04.003
52. Colotta F, Allavena P, Sica A, Garlanda C, Mantovani A. Cancer-related inflammation, the seventh hallmark of cancer: links to genetic instability. *Carcinogenesis* (2009) 30(7):1073–81. doi:10.1093/carcin/bgp127
53. Hanahan D, Weinberg Robert A. Hallmarks of cancer: the next generation. *Cell* (2011) 144(5):646–74. doi:10.1016/j.cell.2011.02.013
54. Lee JM, Yanagawa J, Peebles KA, Sharma S, Mao JT, Dubinett SM. Inflammation in lung carcinogenesis: new targets for lung cancer chemoprevention and treatment. *Crit Rev Oncol Hematol* (2008) 66(3):208–17. doi:10.1016/j.critrevonc.2008.01.004
55. Eggert-Kruse W, Boit R, Rohr G, Aufenanger J, Hund M, Strowitzki T. Relationship of seminal plasma interleukin (IL)-8 and IL-6 with semen quality. *Hum Reprod* (2001) 16(3):517–28. doi:10.1093/humrep/16.3.517
56. Haidl F, Haidl G, Oltermann I, Allam JP. Seminal parameters of chronic male genital inflammation are associated with disturbed sperm DNA integrity. *Andrologia* (2015) 47(4):464–9. doi:10.1111/and.12408
57. Schuppe HC, Meinhardt A, Allam JP, Bergmann M, Weidner W, Haidl G. Chronic orchitis: a neglected cause of male infertility? *Andrologia* (2008) 40(2):84–91. doi:10.1111/j.1439-0272.2008.00837.x
58. Albanese J, Martens K, Karkanitsa LV, Schreyer SK, Dainiak N. Multivariate analysis of low-dose radiation-associated changes in cytokine gene expression profiles using microarray technology. *Exp Hematol* (2007) 35(4 Suppl 1): 47–54. doi:10.1016/j.exphem.2007.01.012
59. Feinberg AP, Ohlsson R, Henikoff S. The epigenetic progenitor origin of human cancer. *Nat Rev Genet* (2006) 7(1):21–33. doi:10.1038/nrg1748
60. Rijlaarsdam MA, Tax DMJ, Gillis AJM, Dorssers LCJ, Koestler DC, de Ridder J, et al. Genome wide DNA methylation profiles provide clues to the origin and pathogenesis of germ cell tumors. *PLoS One* (2015) 10(4):e0122146. doi:10.1371/journal.pone.0122146
61. Anderson D, Schmid TE, Baumgartner A. Male-mediated developmental toxicity. *Asian J Androl* (2014) 16(1):81–8. doi:10.4103/1008-682X.122342
62. Cisneros FJ. DNA methylation and male infertility. *Front Biosci* (2004) 1(9):1189–200. doi:10.2741/1332
63. Rajender S, Avery K, Agarwal A. Epigenetics, spermatogenesis and male infertility. *Mutat Res* (2011) 727(3):62–71. doi:10.1016/j.mrrev.2011.04.002
64. Wang X-X, Sun B-F, Jiao J, Chong Z-C, Chen Y-S, Wang X-L, et al. Genome-wide 5-hydroxymethylcytosine modification pattern is a novel epigenetic feature of globozoospermia. *Oncotarget* (2015) 6(9):6535–43. doi:10.18632/oncotarget.3163
65. Soubry A, Hoyo C, Jirtle RL, Murphy SK. A paternal environmental legacy: evidence for epigenetic inheritance through the male germ line. *Bioessays* (2014) 36(4):359–71. doi:10.1002/bies.201300113
66. Siklenka K, Erkek S, Godmann M, Lambrot R, McGraw S, Lafleur C, et al. Disruption of histone methylation in developing sperm impairs offspring health transgenerationally. *Science* (2015) 350(6261):aab2006. doi:10.1126/science.aab2006
67. Bird A. DNA methylation patterns and epigenetic memory. *Genes Dev* (2002) 16:6–12. doi:10.1101/gad.947102
68. Pfeifer G, Kadam S, Jin S-G. 5-Hydroxymethylcytosine and its potential roles in development and cancer. *Epigenet Chromatin* (2013) 6(1):631–41. doi:10.1186/1756-8935-6-10
69. Bouffler SD, Breckon G, Cox R. Chromosomal mechanisms in murine radiation acute myeloid leukaemogenesis. *Carcinogenesis* (1996) 17(4):655–9. doi:10.1093/carcin/17.4.655
70. Cronkite EP, Bond VP. *Radiation Leukemic-Prediction of Low Dose Effects*. Upton: NCI Report, Contract Y01-CO 10712 (1988).
71. Peng Y, Brown N, Finnon R, Warner CL, Liu X, Genik PC, et al. Radiation leukemogenesis in mice: loss of PU.1 on chromosome 2 in CBA and C57BL/6 mice after irradiation with 1 GeV/nucleon ^{56}Fe ions, X rays or γ rays. Part I. Experimental observations. *Radiat Res* (2009) 171(4):474–83. doi:10.1667/RR1547.1
72. Rithidech K, Bond VP, Cronkite EP, Thompson MH, Bullis JE. Hypermutability of mouse chromosome 2 during the development of x-ray-induced murine myeloid leukemia. *Proc Natl Acad Sci U S A* (1995) 92(4):1152–6. doi:10.1073/pnas.92.4.1152
73. Rithidech K, Dunn JJ, Roe BA, Gordon CR, Cronkite EP. Evidence for two commonly deleted regions on mouse chromosome 2 in gamma ray-induced acute myeloid leukemic cells. *Exp Hematol* (2002) 30(6):564–70. doi:10.1016/S0301-472X(02)00799-3
74. Rithidech KN, Cronkite EP, Bond VP. Advantages of the CBA mouse in leukemogenesis research. *Blood Cells Mol Dis* (1999) 25(1):38–45. doi:10.1006/bcmd.1999.0225
75. Weil MM, Bedford JS, Bielefeldt-Ohmann H, Ray FA, Genik PC, Ehrhart EJ, et al. Incidence of acute myeloid leukemia and hepatocellular carcinoma in mice irradiated with 1 GeV/nucleon ^{56}Fe ions. *Radiat Res* (2009) 172(2):213–9. doi:10.1667/RR1648.1
76. Verbiest T, Bouffler S, Nutt SL, Badie C. PU.1 downregulation in murine radiation-induced acute myeloid leukaemia (AML): from molecular mechanism to human AML. *Carcinogenesis* (2015) 36(4):413–9. doi:10.1093/carcin/bgv016
77. Rithidech KN, Honikel LM, Reungpatthanaphong P, Tungjai M, Golightly M, Whorton EB. Effects of 100 MeV protons delivered at 0.5 or 1 cGy/min on the in vivo induction of early and delayed chromosomal damage. *Mutat Res* (2013) 756(1–2):127–40. doi:10.1016/j.mrgentox.2013.06.001
78. Kanherkar RR, Bhatia-Dey N, Csoka AB. Epigenetics across the human lifespan. *Front Cell Dev Biol* (2014) 2:49. doi:10.3389/fcell.2014.00049
79. Baulch JE, Aypar U, Waters KM, Yang AJ, Morgan WF. Genetic and epigenetic changes in chromosomally stable and unstable progeny of irradiated cells. *PLoS One* (2014) 9(9):e107722. doi:10.1371/journal.pone.0107722
80. Rithidech K, Tungjai M, Arbab E, Simon SR. Activation of NF-kappa B in bone marrow cells of BALB/cJ mice following exposure in vivo to low doses of 137Cs gamma rays. *Radiat Environ Biophys* (2005) 44(2):139–43. doi:10.1007/s00411-005-0004-5
81. Rithidech KN, Tungjai M, Reungpatthanaphong P, Honikel L, Simon SR. Attenuation of oxidative damage and inflammatory responses by apigenin given to mice after irradiation. *Mutat Res* (2012) 749(1–2):29–38. doi:10.1016/j.mrgentox.2012.08.001
82. Rithidech K, Tungjai M, Reungpatthanaphong P, Honikel L, Sanford SR. Attenuation of oxidative damage and inflammatory responses by apigenin given to mice after irradiation. *Mutat Res* (2012) 749(1–2):29–38. doi:10.1016/j.mrgentox.2012.08.001
83. Curley JP, Mashoodh R, Champagne FA. Epigenetics and the origins of paternal effects. *Horm Behav* (2011) 59(3):306–14. doi:10.1016/j.yhbeh.2010.06.018
84. Aston KI, Uren PJ, Jenkins TG, Horsager A, Cairns BR, Smith AD, et al. Aberrant sperm DNA methylation predicts male fertility status and embryo quality. *Fertil Steril* (2015) 104(6):1388–97.e5. doi:10.1016/j.fertnstert.2015.08.019

85. Goetz W, Morgan MNM, Baulch JE. The effect of radiation quality on genomic DNA methylation profiles in irradiated human cell lines. *Radiat Res* (2011) 175(5):575–87. doi:10.1667/RR2390.1
86. Koturbash I, Pogribny I, Kovalchuk O. Stable loss of global DNA methylation in the radiation-target tissue – a possible mechanism contributing to radiation carcinogenesis? *Biochem Biophys Res Commun* (2005) 337(2):526–33. doi:10.1016/j.bbrc.2005.09.084
87. Kovalchuk O, Burke P, Besplug J, Slovack M, Filkowski J, Pogribny I. Methylation changes in muscle and liver tissues of male and female mice exposed to acute and chronic low-dose X-ray-irradiation. *Mutat Res* (2004) 548(1–2):75–84. doi:10.1016/j.mrfmmm.2003.12.016
88. Pogribny I, Raiche J, Slovack M, Kovalchuk O. Dose-dependence, sex- and tissue-specificity, and persistence of radiation-induced genomic DNA methylation changes. *Biochem Biophys Res Commun* (2004) 320(4):1253–61. doi:10.1016/j.bbrc.2004.06.081
89. Meistrich ML. Effects of chemotherapy and radiotherapy on spermatogenesis in humans. *Fertil Steril* (2013) 100(5):1180–6. doi:10.1016/j.fertnstert.2013.08.010
90. Hedger MP. Toll-like receptors and signalling in spermatogenesis and testicular responses to inflammation – a perspective. *J Reprod Immunol* (2011) 88(2):130–41. doi:10.1016/j.jri.2011.01.010
91. Singh SR, Burnicka-Turek O, Chauhan C, Hou SX. Spermatogonial stem cells, infertility and testicular cancer. *J Cell Mol Med* (2011) 15(3):468–83. doi:10.1111/j.1582-4934.2010.01242.x

Conflict of Interest Statement: The authors declare that the research was conducted in the absence of any commercial or financial relationships that could be construed as a potential conflict of interest.

Copyright © 2016 Rithidech, Jangiam, Tungjai, Gordon, Honikel and Whorton. This is an open-access article distributed under the terms of the Creative Commons Attribution License (CC BY). The use, distribution or reproduction in other forums is permitted, provided the original author(s) or licensor are credited and that the original publication in this journal is cited, in accordance with accepted academic practice. No use, distribution or reproduction is permitted which does not comply with these terms.

frontiers in Oncology

REVIEW
published: 28 June 2016
doi: 10.3389/fonc.2016.00163

Novel Biological Approaches for Testing the Contributions of Single DSBs and DSB Clusters to the Biological Effects of High LET Radiation

*Veronika Mladenova, Emil Mladenov and George Iliakis**

Institute of Medical Radiation Biology, University of Duisburg-Essen Medical School, Essen, Germany

The adverse biological effects of ionizing radiation (IR) are commonly attributed to the generation of DNA double-strand breaks (DSBs). IR-induced DSBs are generated by clusters of ionizations, bear damaged terminal nucleotides, and frequently comprise base damages and single-strand breaks in the vicinity generating a unique DNA damage-clustering effect that increases DSB "complexity." The number of ionizations in clusters of different radiation modalities increases with increasing linear energy transfer (LET), and is thought to determine the long-known LET-dependence of the relative biological effectiveness (RBE). Multiple ionizations may also lead to the formation of DSB clusters, comprising two or more DSBs that destabilize chromatin further and compromise overall processing. DSB complexity and DSB-cluster formation are increasingly considered in the development of mathematical models of radiation action, which are then "tested" by fitting available experimental data. Despite a plethora of such mathematical models the ultimate goal, i.e., the *"a priori"* prediction of the radiation effect, has not yet been achieved. The difficulty partly arises from unsurmountable difficulties in testing the fundamental assumptions of such mathematical models in defined biological model systems capable of providing conclusive answers. Recently, revolutionary advances in methods allowing the generation of enzymatic DSBs at random or in well-defined locations in the genome, generate unique testing opportunities for several key assumptions frequently fed into mathematical modeling – including the role of DSB clusters in the overall effect. Here, we review the problematic of DSB-cluster formation in radiation action and present novel biological technologies that promise to revolutionize the way we address the biological consequences of such lesions. We describe new ways of exploiting the I-*Sce*I endonuclease to generate DSB-clusters at random locations in the genome and describe the possible utility of Zn-finger nucleases and of TALENs in generating DSBs at defined genomic locations. Finally, we describe ways to harness the revolution of CRISPR/Cas9 technology to advance our understanding of the biological effects of DSBs. Collectively, these approaches promise to improve the focus of mathematical modeling of radiation action by providing testing opportunities for key assumptions on the underlying biology. They are also likely to further strengthen interactions between experimental radiation biologists and mathematical modelers.

Keywords: radiation effects, high-LET, RBE, DSB clusters, DSB repair, I-*Sce*I, CRISPR/Cas9

OPEN ACCESS

Edited by:
Francis A. Cucinotta, University of Nevada Las Vegas, USA

Reviewed by:
Janice Marie Pluth, Lawrence Berkeley National Laboratory, USA
Asaithamby Aroumougame, UT Southwestern Medical Center, USA

***Correspondence:**
George Iliakis
georg.iliakis@uk-essen.de

Specialty section:
This article was submitted to Radiation Oncology, a section of the journal Frontiers in Oncology

Received: *22 March 2016*
Accepted: *15 June 2016*
Published: *28 June 2016*

Citation:
Mladenova V, Mladenov E and Iliakis G (2016) Novel Biological Approaches for Testing the Contributions of Single DSBs and DSB Clusters to the Biological Effects of High LET Radiation. Front. Oncol. 6:163. doi: 10.3389/fonc.2016.00163

INTRODUCTION

All living organisms are continuously exposed to background ionizing radiation (IR) deriving from space, solar activity, or emitted by certain minerals and soils. Although it is generally accepted that IR "*per se*" can be harmful, IR is nevertheless extensively used for diagnostic purposes and in cancer therapy. Therefore, it is of a great importance to investigate and rationalize the mechanisms of IR action on living organisms, as this will directly help to maximize human radiation protection and to optimize approaches to cancer treatment.

Ionizing radiation generates a broad spectrum of DNA damages, encompassing single-strand breaks (SSB), a variety of oxidative base lesions, DNA–DNA crosslinks as well as DNA–Protein crosslinks, and double-strand breaks (DSBs) (1, 2). However, from the variety of lesions induced by IR, the DSB elicits most of the documented detrimental effects (3, 4), including genomic rearrangements, chromosome aberrations, cell death, genetic mutations, and cancer (5–8).

It has long been known that different IR modalities generate markedly different biological responses although they generate in principle the same basic lesions described above. Thus, α-particles, neutrons, or high-charge and energy particles (HZE ions) are significantly more effective in killing cells than high-energy electrons or protons, γ-rays, or X-rays (9, 10). This increased efficacy, typically described by the higher relative biological effectiveness (RBE), depends on the linear energy transfer (LET) of the radiation modality – which for charged particles is the energy absorbed per unit particle track-length, expressed as kiloelectron-volts/micrometer. Typically, RBE increases with increasing LET of radiation up to a maximum and declines subsequently (11–14).

In the recent years, charged particles such as carbon ions are increasingly considered as main modality for cancer radiotherapy and inflammation treatment in an effort to harness in a targeted manner their higher LET (15–18).

COMPLEXITY OF IR INDUCED DSBs: THE ROLE OF LET

Bacteria harness the severity of DSB as a lesion to protect themselves from foreign DNA. A family of enzymes, known as restriction endonucleases (RE), recognize and cut specific DNA sequences generating DSBs with blunt or staggered ends. During this process, nucleotides are not altered and the phosphodiester bond retains the 5′-phosphate and 3′-OH groups at each DNA strand. As a result, processing and removal of the DSB by simple ligation is in principle possible. RE-generated DSBs have been used to model IR-induced DSBs (see below) (19, 20) and found to have reparability that depends on the type of ends generated (21–23).

The approach to model DSBs using nucleases gained ground with the introduction of I-*Sce*I homing endonuclease, whose 18-bp long recognition sequence (5′-TAGGGATAA/CAGGGTAAT-3′) is not present in the mammalian genome. The I-*Sce*I recognition sequence can nevertheless be inserted into a mammalian genome according to a pre-conceived design using molecular biology approaches (24–27). I-*Sce*I recognition sequences artificially introduced in a genome can be cut to generate DSBs by expressing constitutive or inducible forms of the endonuclease (28, 29). The biological consequences of these DSBs can then be analyzed using molecular biology approaches. The strength of the method lies in the fact that DSBs are generated at defined locations in the genome, and that combination with appropriately constructed reporters allows analysis of the underlying processing mechanisms.

When DSBs are induced by IR *via* oxidation reactions – either direct loss of an electron or attack from an $^{\cdot}OH$ produced from the radiolysis of water – they frequently comprise ends with a 3′-damaged sugar in the form of phosphoglycolate and a 5′-OH groups (30–33). Such ends prevent direct DNA ligation and necessitate end-processing during repair (34). Moreover, the adverse biological effects of X-rays or γ-rays are thought to derive from DSBs generated within ionization clusters (35, 36), and not by the coincidence of independently generated ionizations on opposite DNA strands. Indeed, track-structure calculations using computational approaches (37–39) show that secondary electrons, at the end of their tracks generate clusters of ionizations, i.e., multiple ionizations confined in a small volume.

Despite the generation of ionization clusters at the ends of low-energy electron tracks, X-rays and γ-rays still deposit 50–70% of their energy in well-separated ionization events that generate a relatively even ionization pattern within the cell (35, 36). Consequently, X-rays and γ-rays are considered low-LET forms of IR. On the other hand, charged particles (e.g., α-particles or carbon ions) are considered as high-LET forms of radiation because they ionize along their tracks at a higher rate than the electrons generated by X-rays (40).

This increased clustering of ionizations generates DNA damage that is more complex than that induced by low-LET radiations, in the sense that it comprises more DNA lesions within one or two turns of the DNA helix (33). It constitutes what is sometimes called clustered damage sites (CDS) or multiply damaged sites (MDS) (41, 42). While MDS are generated by low-LET radiation such as X-rays, they occur more frequently after exposure to high-LET radiations and are implicated in their enhanced biological effects.

Indeed, about 30% of DSBs contain additional lesions following exposure to low-energy electrons; notably, this fraction increases up to 70% at the same dose of α-particles. In addition, the ratio of the number of SSBs to DSBs decreases from 22.8 for ^{60}Co γ-rays to 3.4 for 50 MeV ^{12}C-ions (39, 43). Since these shifts in the spectrum of lesions do not increase the yields of DSBs in a manner corresponding to the increased killing after exposure to high- versus low-LET radiation, it can be inferred that increased clustering of DNA damage is an important determinant of the biological effect (see also below) (44).

Complexity at a DSB may compromise repair through the simultaneous recruitment of multiple repair-pathway-factors (e.g., from one of the DSB repair pathways together with factors of BER) to close-by lesions in the DNA. Moreover, it may even generate a DSB indirectly when in a complexly damaged DNA, individual lesions in the two strands are processed independently (6, 43, 45, 46). There is evidence that this form of clustered DNA damage outnumbers direct DSBs after exposure to low-LET radiation by nearly 4:1. Similarly, delayed formation of DSBs can

occur from the chemical evolution in cells of thermally unstable lesions, which initially do not break the DNA, but which do so minutes after irradiation as they become chemically modified in the cellular milieu (47–52). DSB repair models considering DSB complexity have been also developed to describe radiation effects and DSB repair kinetics throughout the cell cycle (53).

It is thus evident that IR-induced DSBs are the products of ionization clusters that generate clustered DNA damage, which can present in different forms of complexity including modified ends, presence of other lesions in the vicinity of the break, as well lesions that generate DSBs only after enzymatic or chemical processing. Since the size of ionization clusters that generate complex DSBs increases with increasing LET, it is plausible to consider this form of DNA damage complexity as a relevant determinant of the increased effectiveness of high-LET radiation.

HIGHER ORDER OF DNA DAMAGE COMPLEXITY: DSB CLUSTERS

An additional level of DSB complexity is generated by clusters of DSBs (33, 54). This form of DNA damage severely undermines local chromatin stability and thus overall processing in a chromatin-location and composition-dependent manner. DSB clustering as a cause of irreversible radiation effects has been considered by several investigators [see Ref. (39) for a review]. Thus, Bryant and his group developed a non-ionic neutral filter elution assay to generate histone-depleted nuclear structures retaining higher order nuclear matrix organization, and used it to measure DNA fragment loss from two or more DSBs within a single-looped chromatin domain (55–57). They proposed that the spatial distribution of DSBs in higher order chromatin loops affects their reparability, and that misrepair involves DNA fragment-loss at such DSB clusters.

Holley and Chatterjee also considered DSB clusters as a particularly consequential form of radiation damage particularly for high-LET radiations (58). In their calculations, they found fragmentation peaks at 85 bp and then again at multiples of 1000 bp, which they interpreted as reflecting aspects of chromatin structure. Notably, such fragments could indeed be detected by pulsed-field gel electrophoresis in irradiated cells (59, 60) and have also been postulated using alternative modeling approaches (14, 39, 61, 62).

Atomic force microscopy imaging shows clustered DSBs and formation of short DNA fragments – even when irradiating "naked" DNA (63). Small (<30 bp) DNA fragments generated from clustered DSBs have also been propose to compromise Ku function (64). Further work shows that DNA–PK, a complex between the Ku and DNA–PKcs, is also inhibited by short (14–20 bp) DNA fragments (63).

The contribution of DSB clusters to the adverse effects of IR has been the focus of extensive mathematical modeling (39). Ostashevsky developed a model according to which DSB clusters generate small DNA fragments, which can be lost from the chromatin context, thus compromising repair of the constituent DSBs (65, 66). A more specialized induction of DSB clusters within chromatin loops, similar to that considered by Bryant, has been used to develop alternative mathematical models (39, 61, 62, 67, 68). In addition, Scholz and his group (69–71) use an extension of the Giant LOop Binary LEsion (GLOBLE) model (72) and classify DNA lesions with respect to their distribution in giant chromatin loops as single DSBs or DSB clusters (~2 Mbp in size) (73–75). These assumptions generally allow successful fitting of cell survival data (76, 77), including fluctuations of radiosensitivity throughout the cell cycle (72).

Mathematical models to analyze DSB repair kinetics based on DSB complexity have been also recently developed (78). In the synapsis formation (SF) model, the rejoining of complex DSBs is not simulated as a first order event (break filling/joining). Rather the rejoining of complex DSBs is assumed to be realized through SF, similar to a second-order reaction between DNA ends. This approach allows DNA ends to be clearly defined before the SF, which is essential for predicting higher number of chromosomal aberrations after high- as compared to low-LET radiation.

Notably, the generation of DSB clusters represents a form of chromothripsis, defined as chromosome shattering and subsequent incorrect rejoining that underpins carcinogenesis (79–82).

The satisfactory fitting of experimental data achieved under these assumptions points to the biological relevance of DSB clusters as a level of DNA damage complexity that likely explains the increased biological efficacy of high LET radiation.

MATHEMATICAL MODELING OF RADIATION ACTION WILL BENEFIT FROM MOLECULAR BIOLOGY APPROACHES DIRECTLY TESTING THEIR BASIC ASSUMPTIONS

Collectively, the above outline shows how the physical clustering of ionizations generates DSBs of different complexity, as well as DSB-clusters, and places these forms of DNA damage to the center of responses elicited by radiation modalities of different LET. The recognition that discontinuities in the genome may be caused by DSBs of widely different complexity, immediately implies different biological consequences.

Information on the molecular underpinnings of the responses elicited by genomic breaks of different complexity is scarce despite the central contribution widely attributed to this parameter in the overall radiation effect. As a result, DNA damage complexity is typically only mathematically "modeled" in radiation response formalisms, without direct knowledge of the biological effects of each complexity level. As a consequence, quality of fitting is the only way for testing the validity of the basic assumptions on which these models rest. Yet, this approach is not satisfactory due to the large spectrum of DNA damages induced by IR and their dependence on LET that increases the number of parameters required for complete mathematical modeling.

Furthermore, IR-dependent DSB induction by nature precludes mechanistic molecular biology experiments on the molecular processing of *individual* lesions, as irradiated cells sustain DSBs in a stochastic manner at different numbers and severity that are randomly distributed throughout the genome. As a result, analysis of effects is only possible by theoretical modeling (39).

The above difficulties and shortcomings suggest that the field will benefit from molecular biology approaches allowing induction and processing analysis for specific forms of DSBs generated at specific locations in the genome. With such model-DSBs, the probability associated with each form to be processed correctly or incorrectly by each of the available repair pathways can be estimated. This information may subsequently be fed as a defined constant in mathematical models, reducing thus the number of free parameters and increasing the predictive power of the model. In the following sections, we describe such biological approaches and explain strengths and limitations.

ENDONUCLEASE-INDUCED DSBs: THE SIMPLEST FORM

Almost a decade ago, a fundamentally new approach for analyzing the effects of DSBs in living cells was introduced using rare cutting homing endonucleases. The most widely used member of this family of enzymes is the *Saccharomyces cerevisiae* I-*Sce*I endonuclease. As already mentioned, I-*Sce*I recognizes a unique 18-bp long DNA sequence (**Figure 1A**), which is absent from the human and mouse genomes. Thus, in order for I-*Sce*I to generate a DSB in these genomes, its recognition sequence must first be inserted using molecular biology approaches. Subsequent expression of I-*Sce*I will generate a DSB, specifically at the site of integration of the recognition sequence, which can be preselected or random (83, 84). Expression of I-*Sce*I must be transient and can be mediated by transient transfection of constitutively expressing vectors, or by the proper activation of an inducible enzyme.

In the most typical application of this model system, the I-*Sce*I recognition sequence is combined in a construct including a reporter gene [e.g., neomycin or in recent reporter assays, green fluorescence protein (GFP)] and located to interrupt its expression. Restoration of reporter expression serves as readout for the operation of a particular repair pathway in the processing of the DSB. These reporter constructs are in their majority integrated in the genome and are appropriately designed to evaluate repair efficiency through homologous recombination repair (HRR), classical non-homologous end joining (c-NHEJ), alternative end joining (alt-EJ), or single-strand annealing (SSA). Thus, analysis of DSB processing by a specific DSB repair pathway requires the construction of the appropriate vector and its integration into the genome.

In initial studies, I-*Sce*I was utilized to induce a DSB between two inactive *neomycin (neo)* direct repeat genes integrated into the genome of CHO cells, processing of which by homologous recombination generated a functional *neo* gene (86, 89) (**Figure 1B**). In these constructs, the fist *neo* allele is inactivated by the I-*Sce*I recognition sequence. The second *neo* allele is promoterless or truncated and may carry silent single-base substitutions that create restriction sites useful in product characterization through restriction fragment length polymorphism analysis. In the native state of this construct, *neo* is not expressed, and cells are sensitive to neomycin. However, after I-*Sce*I-mediated DSB induction, gene conversion may generate a functional *neo* gene and thus also neomycin-resistant clones. Such events are considered to reflect successful processing of the DSB by HRR.

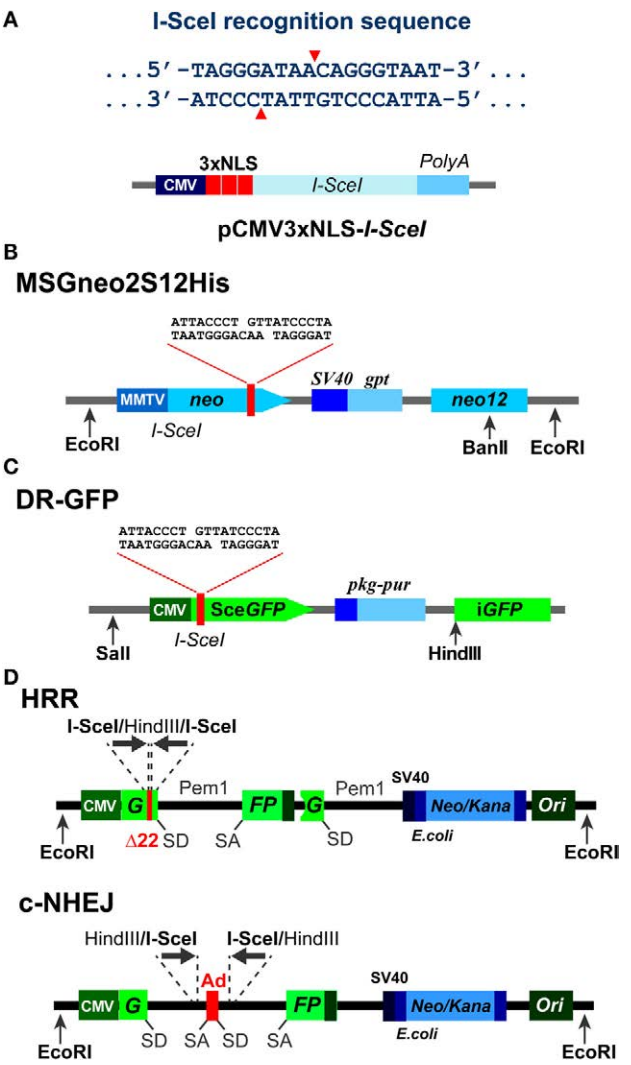

FIGURE 1 | Background information on I-*Sce*I based constructs. (A) Top: recognition sequence of I-*Sce*I endonuclease. Note the generation of 3′ 4-bp overhangs. Bottom: domain structure of an expression vector, pCMV3xnls-I-*Sce*I, used frequently in transient transfection experiments to express I-*Sce*I (85). Note the three NLS sites that ensure the nuclear localization of the expressed enzyme. **(B)** Schematic representation of the MSGneo2S12His neomycin reporter vector developed to specifically analyze repair of the I-*Sce*I DSB by HRR (86). **(C)** Schematic representation of the DR-GFP vector developed to specifically analyze repair of the I-*Sce*I DSB by HRR (87). The GFP signal allows analysis by flow cytometry 1–3 days after transfection. **(D)** Schematic representation of reporter constructs utilizing the Pem1 intron and the Ad2 exon elements, and specifically developed to analyze repair of the I-*Sce*I-DSB by HRR and c-NHEJ, respectively (88).

More recently, DR-GFP reporter systems based on two directly repeated copies of the gene encoding GFP have been developed in the laboratory of Dr. Jasin (87) (**Figure 1C**) and find in different forms wide application in the field. In this system, gene

conversion events result in expression of GFP, which can be quantitated by flow cytometry. The two mutated GFP genes are oriented as direct repeats and are separated by a puromycin *N*-acetyltransferase gene, which allows selection for cells carrying the construct. Distinct advantage of this version of the assay is that results are typically available 1–3 days after transfection of the I-*Sce*I expression plasmid. Analysis of neomycin resistance, on the other hand, requires 1–2 weeks.

The DR-GFP reporter system has been successfully adapted to human cells, resulting in generation of U2OS–DR-GFP cells (90) (**Figure 2A**). Similar to the previously described system, one of the GFP genes in DR-GFP, SceGFP, is mutated by the insertion of the I-*Sce*I recognition site, while the second, internal GFP fragment, iGFP, located 821 bp downstream from SceGFP, has lost its active promotor element.

All reporter systems described above are designed to determine the activity of HRR in the processing of a single DSB induced by I-*Sce*I endonuclease. In addition to the above systems, a set of GFP-based fluorescent reporter constructs has been generated by Gorbunova et al. (88, 91) (**Figure 1D**), allowing analysis of NHEJ and HRR. These constructs are also based on artificially engineered GFP genes containing I-*Sce*I recognition sites for the induction of a DSB. In their native state, the integrated constructs do not express GFP as a result of an N-terminal truncation

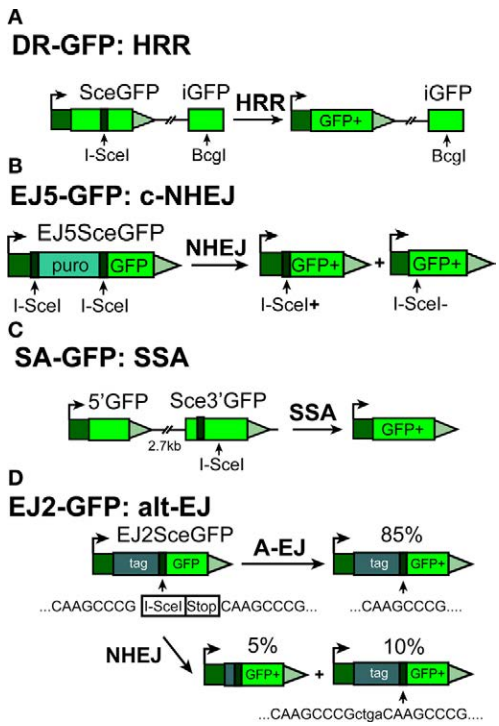

FIGURE 2 | Outline of reporter constructs developed in the laboratory of Dr. J. Stark (90) to analyze efficiency of I-*Sce*I-DSB-processing by different DSB repair pathways in human cells. **(A)** DR-GFP construct for analyzing HRR. **(B)** EJ5-GFP for analyzing c-NHEJ **(C)** SA-GFP construct for analyzing single-strand annealing (SSA) and **(D)** EJ2-GFP construct for analyzing alt-EJ.

and mutations in the duplicated gene (in the case of the HRR construct), or by the integration within the GFP gene of an exon (Ad) flanked by the Pem1 intron elements (in case of the NHEJ construct). Here again, successful repair of the I-*Sce*I-induced DSB by NHEJ or HRR will restore the GFP gene, an event that is quantitated by flow cytometry.

Green fluorescence protein-based reporter substrates are now also available to specifically assess c-NHEJ, SSA, or alt-EJ (29, 90, 92, 93). Most of these constructs rely on the principles described above, but include elements allowing analysis of a specific DSB repair pathway (**Figures 2A–D**).

As already mentioned, use of I-*Sce*I as DSB inducer requires integration of its recognition sequence in the genome of human, mouse, or hamster cells. During the last few years, alternative approaches have been developed using endonucleases for which recognition sequences are present in the genome. One of these systems utilizes the I-*Ppo*I endonuclease, a member of a His–Cys box family of homing endonucleases isolated from the myxomycetous *Physarum polycephalum* (94), to induce multiple DSBs in the human genome (95–97).

I-*Ppo*I is a relatively small enzyme (18–20 kDa), operating as a homodimer, which in its natural host functions to cleave the highly conserved 15-bp ribosomal DNA homing sites (**Figure 3A**) to generate target intron transposition or "homing" (98). Expression of I-*Ppo*I in human cells causes cleavage of approximately 10% of the identified I-*Ppo*I genomic target sites (200–300 per genome) (95), generating 20–30 DSBs per cell, equivalent to the number of DSBs introduced by 1 Gy of X-rays. For increased versatility, a system has been developed using an I-*Ppo*I fused to a mutant estrogen receptor hormone-binding domain. The fusion protein stays constitutively in the cytoplasm unable to generate DSBs. Translocation into the nucleus can be mediated by incubation with 4-hydroxytamoxifen (4-OHT) (99–101), allowing thus the regulated induction of DSBs.

This system allows characterization of several features of the DSB response in human cells and has certain advantages over I-*Sce*I-based systems. First, I-*Ppo*I sites are present at well-known locations in the genome, which obviates their artificial introduction. Second, evolutionary conservation of the endogenous I-*Ppo*I sites permits DSBs to be introduced and assays to be performed in virtually any eukaryotic cell line. Third, as I-*Ppo*I induces multiple DSBs in the genome, full activation of the DNA damage response ensues, which allows analyses that go beyond repair pathway utilization.

An elegant assay along similar lines has also been proposed by Aymard et al. (103). These investigators developed a cellular system harboring a stable integration of a gene expressing the rare-cutting *Asi*SI restriction nuclease, which targets an 8-bp double-stranded DNA sequence (**Figure 3A**) and cleaves between the T and C to generate a 2-bases, 3′ overhanging ends (25, 104, 105). The genome-integrated *Asi*SI endonuclease in this model system is also fused to a modified estrogen-receptor ligand-binding domain. Thus, treatment of cells with 4-OHT triggers nuclear localization of the *Asi*SI enzyme and the rapid induction of approximately 150 sequence-specific DSBs dispersed across the genome (25, 104). This system provides a unique opportunity to simultaneously study, at a molecular level, repair events that

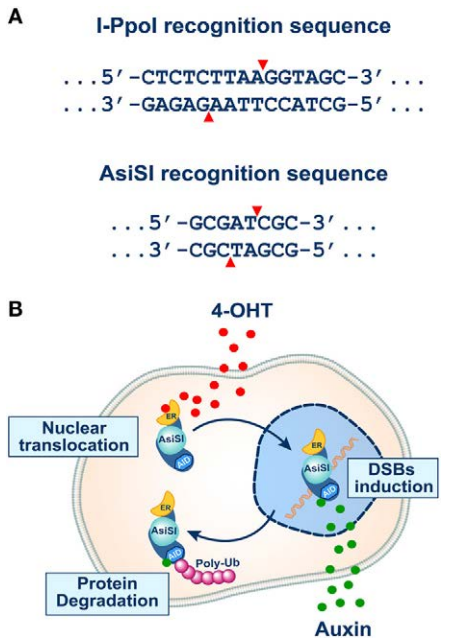

FIGURE 3 | **(A)** Recognition sequences of I-*Ppo*I (top) and *Asi*SI (bottom) endonucleases (see text for details). Note that both endonucleases generate 3′ overhangs. **(B)** The inducible system of *Asi*SI endonuclease developed in the laboratory of Dr. Legube (102). The DIvA cell line expresses a form of the *Asi*SI endonuclease fused to estrogen receptor (ER) and the auxin-inducible degron (AID). The enzyme sequesters under normal conditions in the cytoplasm unable to reach the nucleus and thus to induce DSBs. Administration of tamoxifen (4-OHT) causes efficient translocation of the enzyme to the cell nucleus and the induction of DSBs (top part of the schematic). In this system, the endonuclease activity of *Asi*SI can be rapidly turned off by removing 4-OHT and administering auxin that activates the degron element and causes ubiquitin-mediated degradation of the enzyme (bottom part of the schematic).

transpire at many different DSBs located within various known chromatin locations (103).

Furthermore, as the *Asi*SI cleavage-sites are known, it is possible to use chromatin immunoprecipitation (ChIP) to directly monitor recruitment of repair factors onto damaged chromatin (103). Using this approach, it could be demonstrated that DSBs induced across the genome are not repaired by the same DSB repair pathway, and that transcriptionally active, H3K36me3 enriched, chromatin is preferentially repaired by homologous recombination, thereby pointing out a critical role of pre-existing chromatin state as determinant of DSB repair pathway selection (103).

As with the I-*Sce*I and I-*Ppo*I systems, the *Asi*SI system does not allow analysis of DSB repair kinetics because the enzyme remains present in the nucleus for prolonged periods of time and can cut repeatedly. To reduce this limitation, the same group added an auxin-inducible degron (AID) to *Asi*SI-ER fusion nuclease, thus allowing fast and efficient degradation upon auxin addition (102, 106) (**Figure 3B**). A similar improvement has also been successfully introduced in the I-*Sce*I system and was coupled with an extension allowing parallel analysis of HRR and alt-EJ (29).

Zn-F NUCLEASES AND TALENs: TOOLS FOR SITE-SPECIFIC DSB GENERATION

Before the discovery of the CRISPR/Cas9 system that rapidly overtakes all previous systems (see below), significant effort and investment in resources was placed in two families of site-specific nucleases: the zinc-finger nucleases (ZFNs) and the transcription activator-like effector nucleases (TALENs). Both families of engineered proteins have a chimeric design with a common nuclease domain and a DNA-binding domain (**Figure 4**). In both families, DSB formation is mainly catalyzed by FOK1 endonuclease (107, 108) that generates, depending on the design, cohesive, or blunt DNA ends without sequence specificity (**Figure 4**). Yet, the concepts underlying the DNA-binding characteristics of ZFNs and TALENs are distinct and responsible for their inherent strengths and limitations. Their versatility arises from the ability to customize through molecular biology approaches their DNA-binding domains in ways that allow the recognition of virtually any DNA sequence.

The Cys2–His2 zinc-finger domain is among the most common types of DNA-binding motifs in eukaryotes operating in a widely different array of DNA sequences. It actually represents the second most frequently encoded protein domain in the human genome. The ZFN technology harnesses this biological evolution. An individual zinc-finger consists of approximately 30 amino acids in a conserved ββa (beta-sheet, beta-sheet, and alpha-helix) motif configuration. Each zinc-finger domain contacts 3 or 4 bp in the major groove of the DNA (108). In this technology, different zinc-finger motifs are combined to generate ZFNs that recognize the desired sequence 9 bp left and right from the target region (**Figure 4A**). The two components of the ZFN cut the corresponding DNA strands using FOK1, which is attached to the C-terminus of the ZFN modules (**Figure 4A**). Moreover, the cleavage domain requires the 5′ edge of each binding site to be separated by a 5–7 bp spacer region (**Figure 4A**).

Despite distinct strengths, the construction of ZFNs is complex requiring extensive know-how; it is very time consuming and shows limited flexibility in terms of engineering proteins recognizing any DNA sequence. As a result, their utilization, even before the advent of the CRIPSR/Cas9 system, had given way to the much more flexible TALENS.

TALENs contain TALE repeats of about 33–35 amino acids that recognize a *single* base pair *via* two hypervariable residues (repeat-variable di-residues, RVDs) (108). Combined TALE repeats can recognize a specific DNA target site of about 17 bp in length (**Figure 4B**). As a result of this unique property, TALENs can be easily and flexibly engineered to recognize DNA sequences of arbitrarily chosen lengths and compositions. For the application of TALENs discussed here, the number and location of the induced DSBs will depend on the frequency and the location in the genome of the selected sequence used to design the nuclease (109, 110). Thus, sequences can be selected and TALENs designed inducing in the genome a single DSB or multiple DSBs in variable configurations, depending on the specific question addressed.

The TALEN technology is powerful and flexible, and engineering of a site specific TALEN can be accelerated by "off-the-shelf"

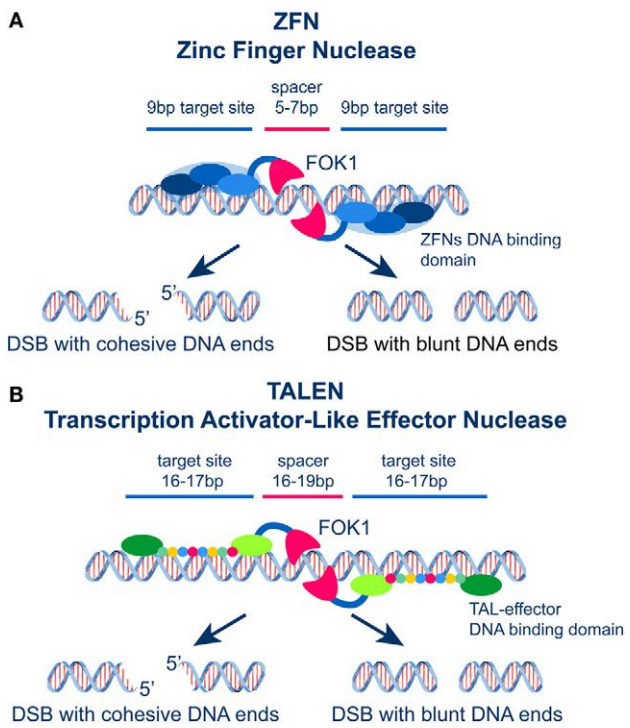

FIGURE 4 | **(A)** Schematic representation of ZFNs showing the DNA binding and the FOK1 nuclease domains. Two zinc fingers bind left and right the site of DSB generation and localize the activity of FOK1 in a DNA molecule. The DNA binding domains are frequently designed to recognize a 9 bp target sequence. The FOK1 nuclease cuts the DNA strand 5–7 bp 3′ of the target site. Depending on the design of the target sites, expression of a ZNF nuclease will result in the formation of cohesive or blunt DNA ends. **(B)** Schematic representation of TALENs showing the DNA binding and the FOK1 nuclease domains. Targeting sites and spacer regions are indicated. Here again, cohesive or blunt ends are generated at the DSB depending on the selection of the recognition sites left and right the DSB.

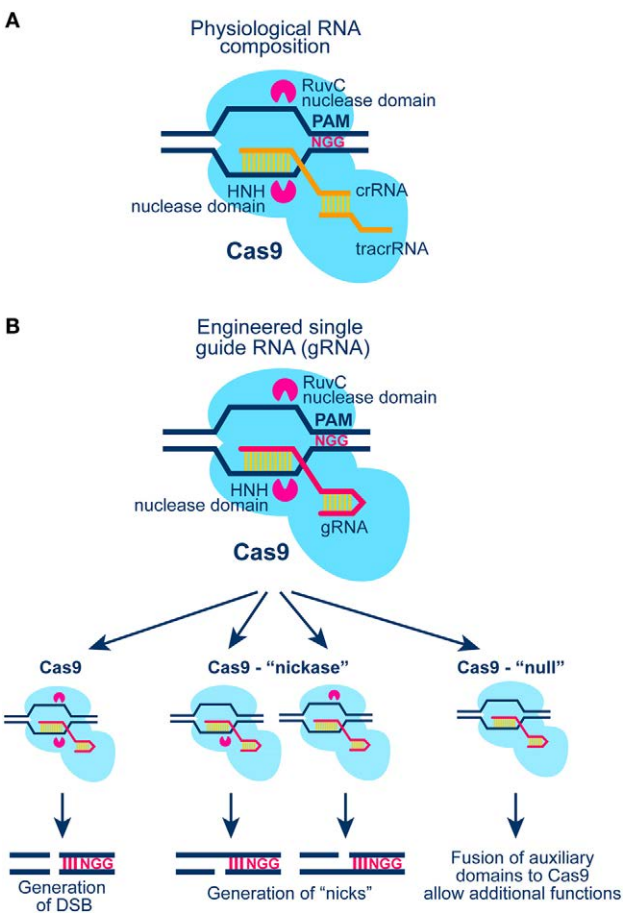

FIGURE 5 | **(A)** Schematic representation of the CRISPR/Cas9 system in *S. Pyogenes* (see text for details). Cas9 generates blunt ends by cutting 3 bp downstream the PAM region of the target DNA molecule. **(B)** Schematic representation of Cas9 activation with a chimeric gRNA combining crRNA and tracrRNA (see A; see also text for more details). Cas9 nuclease harbors two nuclease domains: HNH and RuvC-like; mutation of one or both of these nuclease domains results in Cas9 enzymes with "nickase" properties, or with null nuclease activity. The latter form of Cas9 can be tethered to other proteins for gain-of-function DNA sequence-specific operations.

components that are combined to generate a functional protein within 1–2 weeks. Although the second generation of TALEN technology further improves on the distinct advantages of the approach, the work required to generate and test a single site specific TALEN nuclease is still considerable (111). As a result, this technology is also rapidly losing ground to CRIPR/Cas9 technology.

THE CRISPR/Cas9 SYSTEM: GREAT VERSATILITY, SHORT LEARNING CURVE

The CRISPR/Cas9 system with all its applications and potential is arguably the most rapidly expanding and evolving field in modern biology (**Figure 5**). From the initial discovery of the system as part of bacteria immunity to its modification for sequence specific genome editing, the technology has gone through a series of revolutionary developments that have been extensively reviewed (112–114). Relevant for the present outline is the potential of the system to generate a DSB anywhere in the genome by targeting at the specific location the Cas9 nuclease. Cas9 cuts the DNA as shown in **Figure 5** to generate blunt DNA ends, guided by a partially complementary RNA molecule (gRNA). In its current stage of development, gRNA carries in addition to the sequence required for the proper targeting of Cas9 to the DNA molecule also a sequence for its activation.

Originally, Clustered Regularly Interspaced Short Palindromic Repeats (CRISPR) were found in the genome of *Escherichia coli*, but their function remained unknown until recently, when it was shown that these genetic elements are essential for the development of resistance against bacteriophages (115). Moreover, the CRISPR-associated protein 9 (Cas9) was described as a RNA-guided DNA endonuclease associated with the CRISPR-adaptive "immune" system in *Streptococcus pyogenes* (115, 116).

Three types of CRISPR systems have been identified thus far; from these forms type II is the most widely studied and the

most relevant to the present outline. In type II CRISPR system, invading DNA is nucleolytically processed into small fragments (approximately 20 bp) that are incorporated into the CRISPR locus. This locus is transcribed, and transcripts are then processed to generate small CRISPR-RNAs (crRNA), which together with a trans-activating-CRISPR-RNA (tracrRNA) guide Cas9 to digest invading DNA upon repeat encounter (**Figure 5A**).

An important element of Cas9 activation is the Protospacer Adjacent Motif (PAM) at the target DNA sequence, which is essential for interactions between Cas9 and DNA (**Figure 5A**). Early work revealed that all three components (Cas9 protein, mature crRNA and tracrRNA) are required for efficient recruitment to and digestion of the target DNA sequence. A major development in the field was the recognition that crRNA and tracrRNA can be combined to generate a single guide RNA (gRNA) that enables all operations required for the targeted function of Cas9 (**Figure 5B**). This development greatly simplified the evolution of a large array of applications and forms the basis of the applications described here.

The number of applications utilizing CRISPR/Cas9-related genome editing/manipulation approaches is increasing exponentially with time. The technology is also very powerful for studies on the effects of single DSBs and DSB clusters in the mammalian genome (117, 118). Thus, existing CRISPR/Cas9 systems (116, 119) can be combined with appropriately designed gRNAs with the aim of inducing single DSBs or DSB clusters of different complexity within exons or introns of selected genes and study consequences in cell survival, genome integrity, DSB-response, or gene function. **Figures 6A,B** show as an example possible site selections for DSB induction within the HPRT gene, since it has been extensively used in the past to study IR-induced mutation induction (120, 121). Here, single DSBs and DSB clusters are induced at selected locations throughout the gene and at various constellations by combining different gRNAs (**Figure 6**).

The CRISPR/Cas9 technology is extremely powerful and promises to revolutionize the field by virtue of its ability to generate DSBs with great ease at any location of a known genome. In addition, mutated forms of Cas9 can be introduced in which one or both endonuclease domains are inactivated, thus generating enzymes with "nickase" or "null" activity (**Figure 5B**). Combination of Cas9 "nickase" with other systems of DSB generation, including the I-*Sce*I system described below, will allow testing of the biological consequences of a single-strand break in the vicinity of a DSB (complex DSB). Finally, fusions between a non-functional Cas9 enzyme and protein domains generating additional forms of DNA damage will further expand the spectrum of experiments investigating DSB complexity as a parameter in biological responses (**Figure 5B**). As with the I-*Sce*I, I-*Ppo*I, and the *Asi*SI systems, Cas9 will also generate repeated DSBs in the genome and its prolonged presence in the cell nucleus precludes analysis of DSB repair kinetics.

The fact that the generation of each DSB using the CRISPR/Cas9 technology requires individual gRNAs restricts somewhat its application for generating multiple DSBs, which at times may be a desirable outcome (see next session). This is because the generation of multiple single DSBs or DSB clusters at different genomic locations will require a number of gRNAs. This problem

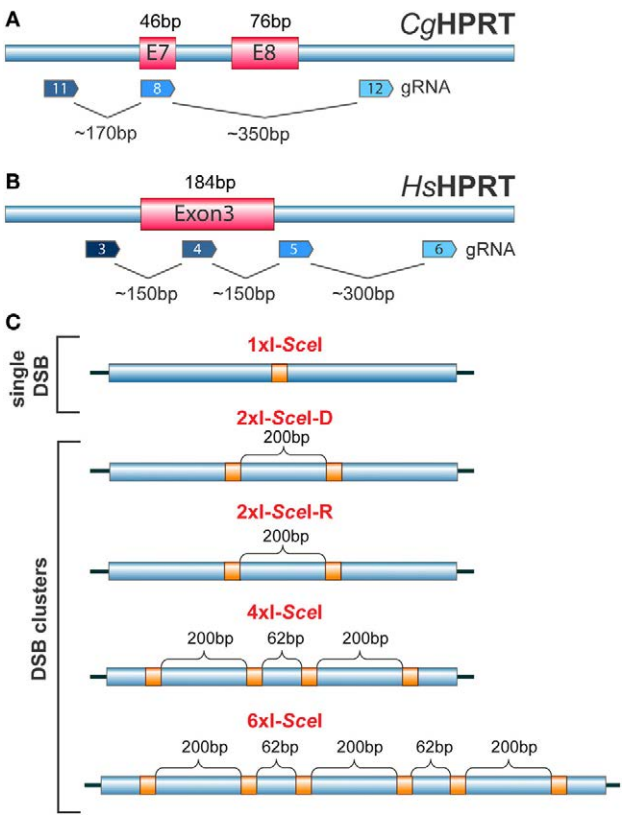

FIGURE 6 | **(A)** Organization of the HPRT gene in the Chinese hamster *C. griseous* (*Cg*) near exons 7 and 8. Possible recognition sites of gRNAs allowing the generation of DSBs at different locations within exons and introns are indicated. **(B)** Exon 3 of the HPRT gene in *H. sapiens* (*Hs*). Possible recognition sites for gRNAs allowing the generation of single DSBs or DSB clusters within exons and introns are indicated. **(C)** Constructs carrying different combinations of I-*Sce*I sites engineered at different distances to model DSB clusters of increasing complexity. The schematic shows I-*Sce*I constructs that would generate upon integration in the genome of a cell, single DSBs, DSB pairs, DSB quadruplets or a cluster of six DSBs. The distances shown are arbitrary and chosen only for illustration purposes.

may be partly overcome by designing gRNAs, which recognize sequences in the genome that are repeated several times – excluding of course highly repeated DNA sequences. For example, many proteins contain common functional domains, encoded by similar if not identical DNA sequences, which could be targeted at once using a single gRNA molecule. An alternative solution for this limitation is offered by the model system described in the following section.

I-*Sce*I-BASED MODELS OF DSB CLUSTERING

We conclude this overview by outlining a recently introduced I-*Sce*I-based model system, complementary to the system outlined in the previous section using the CRISPR/Cas9 technology that allows direct analysis of assumptions regarding the biological effects of multiple single DSBs and DSB clusters (54). The model

system utilizes transposon technology (122) to generate clonal cell lines with multiple genomic integrations of constructs carrying I-*Sce*I restriction sites at arrangements selected depending on the specific question addressed (**Figure 6C**). Cleavage of these sites by transient or conditional expression of I-*Sce*I to generate single DSBs or DSB clusters at different numbers (typically 1–15) and constellations allow analysis of the biological consequences at different endpoints. First results obtained using this model system (54) indicate that DSB clusters compromise c-NHEJ and possibly HRR, leaving alt-EJ as last resort in DSB processing.

Application of the same technology to mutant cell lines with defects in different aspects of DSB repair will allow extensive analysis of the DSB repair pathways handling this form of damage (4, 123, 124).

CONCLUDING REMARKS

It is evident from the above outline that numerous novel technologies are available that promise to revive and revolutionize the ways we address fundamental questions of radiation damage and the associated radiation responses. These technologies allow the testing in well-defined systems of key hypotheses of mathematical models of radiation action, and the generation of data that may help to reduce their free variables. Such systems will be particularly useful in the analysis and characterization of the role of single DSBs and DSB cluster formation in the biological responses of high LET radiation.

The system utilizing the I-*Sce*I meganuclease to generate single DSBs and DSB clusters at random locations in the genome will extend the successful application this enzyme saw during the past 15 years to new questions relevant to DNA damage response. Zn-finger nucleases and TALENs will perhaps remain useful in addressing related questions at specific settings. Certainly, the most promising technology is the one utilizing the CRISPR/Cas9 system to introduce DSBs at pre-selected locations in the unmodified genome, with a pre-defined constellation.

One aspect with all systems of enzymatic DSB generation that needs to be considered in comparisons with the effects of IR concerns the specifics of DSB induction. Thus, IR by virtue of its well defined and typically short exposure times induces DSBs through non-recurring, distinct energy deposition events; DSBs induced in this way are subsequently processed and terminally removed from the genome. Nucleases, on the other hand, through their prolonged presence after expression or activation in the cell nucleus, will generate cycles in which initial DSB induction and subsequent processing will be followed by additional cutting and processing cycles, which will in principle continue until repeat processing mutates the nuclease recognition sequence, or until enzyme expression or activity subside. Since both "solutions" require a relatively long window of time, which is also likely to be different for each individual DSB, they generate a condition of chronic assault to the DNA generating "chronic" DSBs. Such chronic DSBs may induce responses with facets not present to those generated by the single events of IR, and which may engage distinct processing mechanisms that change the ultimate outcome. Additional problems may arise from off-target effects, variable on-target cutting frequencies, and the induction of a single form of DSB these systems allow.

Despite these inherent limitations, the approaches described above promise to enrich our knowledge of the biological responses to DSBs, to improve the focus on this form of DNA damage, and to enhance the power and utility of mathematical modeling by generating first principles that can be used as starting points. Last but not least, they are likely to strengthen interactions between experimental radiation biologists and mathematical modelers.

AUTHOR CONTRIBUTIONS

VM and EM wrote the manuscript and participated in preparation of the figures. GI generated the main outline of the article and wrote the manuscript.

FUNDING

Work supported by grants from BMBF (02NUK043B –COLLAR) and the DFG (GRK1739).

REFERENCES

1. Goodhead DT, Thacker J, Cox R. Effects of radiations of different qualities on cells: molecular mechanisms of damage and repair. *Int J Radiat Biol* (1993) 63:543–56. doi:10.1080/09553009314450721
2. Prise KM, Ahnström G, Belli M, Carlsson J, Frankenberg D, Kiefer J, et al. A review of dsb induction data for varying quality radiations. *Int J Radiat Biol* (1998) 74:173–84. doi:10.1080/095530098141564
3. Kinner A, Wu W, Staudt C, Iliakis G. γ-H2AX in recognition and signaling of DNA double-strand breaks in the context of chromatin. *Nucleic Acids Res* (2008) 36:5678–94. doi:10.1093/nar/gkn550
4. Mladenov E, Iliakis G. Induction and repair of DNA double strand breaks: the increasing spectrum of non-homologous end joining pathways. *Mutat Res* (2011) 711:61–72. doi:10.1016/j.mrfmmm.2011.02.005
5. Bryant PE, Riches AC, Terry SYA. Mechanisms of the formation of radiation-induced chromosomal aberrations. *Mutat Res* (2010) 701:23–6. doi:10.1016/j.mrgentox.2010.03.016
6. Sage E, Harrison L. Clustered DNA lesion repair in eukaryotes: relevance to mutagenesis and cell survival. *Mutat Res* (2011) 711:123–33. doi:10.1016/j.mrfmmm.2010.12.010
7. Byrne M, Wray J, Reinert B, Wu Y, Nickoloff J, Lee S-H, et al. Mechanisms of oncogenic chromosomal translocations. *Ann N Y Acad Sci* (2014) 1310:89–97. doi:10.1111/nyas.12370
8. Soni A, Siemann M, Pantelias GE, Iliakis G. Marked contribution of alternative end-joining to chromosome-translocation-formation by stochastically induced DNA double-strand-breaks in G(2)-phase human cells. *Mutat Res* (2015) 793:2–8. doi:10.1016/j.mrgentox.2015.07.002
9. Barendsen GW. Responses of cultured cells, tumours, and normal tissues to radiations of different linear energy transfer. *Curr Top Radiat Res* (1968) 4:293–356.
10. Bertsche U, Iliakis G, Kraft G. Inactivation of Ehrlich ascites tumor cells by heavy ions. *Radiat Res* (1983) 95:57–67. doi:10.2307/3576071
11. Bedford JS, Goodhead DT. Breakage of human interphase chromosomes by alpha particles and X-rays. *Int J Radiat Biol* (1989) 55(2):211–6. doi:10.1080/09553008914550261
12. Hall EJ, Giaccia AJ. *Radiobiology for the Radiologist*. Philadelphia, Baltimore, New York, London, Buenos Aires, Hong Kong, Sydney, Tokyo: Lippincott Williams & Wilkins (2006).
13. Franken N, Ten Cate R, Krawczyk P, Stap J, Haveman J, Aten J, et al. Comparison of RBE values of high- LET α-particles for the induction of

DNA-DSBs, chromosome aberrations and cell reproductive death. *Radiat Oncol* (2011) 6:64. doi:10.1186/1748-717X-6-64
14. Li Y, Qian H, Wang Y, Cucinotta FA. A stochastic model of DNA fragments rejoining. *PLoS One* (2012) 7:e44293. doi:10.1371/journal.pone.0044293
15. Brenner DJ, Doll R, Goodhead DT, Hall EJ, Land CE, Little JB, et al. Cancer risks attributable to low doses of ionizing radiation: assessing what we really know. *Proc Natl Acad Sci USA* (2003) 100:13761–6. doi:10.1073/pnas.2235592100
16. Durante M, Cucinotta FA. Heavy ion carcinogenesis and human space exploration. *Nat Rev Cancer* (2008) 8:465–72. doi:10.1038/nrc2391
17. Durante M, Loeffler JS. Charged particles in radiation oncology. *Nat Rev Clin Oncol* (2010) 7:37–43. doi:10.1038/nrclinonc.2009.183
18. Loeffler JS, Durante M. Charged particle therapy – optimization, challenges and future directions. *Nat Rev Clin Oncol* (2013) 10:411–24. doi:10.1038/nrclinonc.2013.79
19. Obe G, Winkel E-U. The chromosome-breaking activity of the restriction endonuclease Alu I in CHO cells is independent of the S-phase of the cell cycle. *Mutat Res* (1985) 152:25–9. doi:10.1016/0027-5107(85)90042-9
20. Bryant PE, Johnston PJ. Restriction-endonuclease-induced DNA double-strand breaks and chromosomal aberrations in mammalian cells. *Mutat Res* (1993) 299:289–96. doi:10.1016/0165-1218(93)90105-M
21. Pfeiffer P, Feldmann E, Odersky A, Kuhfittig-Kulle S, Goedecke W. Analysis of double-strand break repair by non-homologous DNA end joining in cell-free extracts from mammalian cells. *Methods Mol Biol* (2005) 291:351–71. doi:10.1007/978-1-62703-739-6_39
22. Van Gent DC, Van Der Burg M. Non-homologous end-joining, a sticky affair. *Oncogene* (2007) 26:7731–40. doi:10.1038/sj.onc.1210871
23. Lieber MR. The mechanism of double-strand DNA break repair by the nonhomologous DNA end-joining pathway. *Annu Rev Biochem* (2010) 79:1.1–1.31. doi:10.1146/annurev.biochem.052308.093131
24. Jasin M. Genetic manipulation of genomes with rare-cutting endonucleases. *Trends Genet* (1996) 12:224–8. doi:10.1016/0168-9525(96)10019-6
25. Iacovoni JS, Caron P, Lassadi I, Nicolas E, Massip L, Trouche D, et al. High-resolution profiling of γH2AX around DNA double strand breaks in the mammalian genome. *EMBO J* (2010) 29:1446–57. doi:10.1038/emboj.2010.38
26. Fenina M, Simon-Chazottes D, Vandormael-Pournin S, Soueid J, Langa F, Cohen-Tannoudji M, et al. I-*Sce*I-mediated double-strand break does not increase the frequency of homologous recombination at the *Dct* locus in mouse embryonic stem cells. *PLoS One* (2012) 7:e39895. doi:10.1371/journal.pone.0039895
27. Gunn A, Stark JM. I-*Sce*I-based assays to examine distinct repair outcomes of mammalian chromosomal double strand-breaks. *Methods Mol Biol* (2012) 920:379–91. doi:10.1007/978-1-61779-998-3_27
28. Soutoglou E, Misteli T. Activation of the cellular DNA damage response in the absence of DNA lesions. *Science* (2008) 320:1507–10. doi:10.1126/science.1159051
29. Bindra RS, Goglia AG, Jasin M, Powell SN. Development of an assay to measure mutagenic non-homologous end-joining repair activity in mammalian cells. *Nucleic Acids Res* (2013) 41:e115. doi:10.1093/nar/gkt255
30. Henner WD, Grunberg SM, Haseltine WA. Sites and structure of γ radiation-induced DNA strand breaks. *J Biol Chem* (1982) 257:11750–4.
31. Henner WD, Rodriguez LO, Hecht SM, Haseltine WA. Gamma-ray Induced deoxyribonucleic acid strand breaks. *J Biol Chem* (1983) 258:711–3.
32. Von Sonntag C. *Free-Radical-Induced DNA Damage and Its Repair*. Berlin, Heidelberg: Springer (2006).
33. Schipler A, Iliakis G. DNA double-strand-break complexity levels and their possible contributions to the probability for error-prone processing and repair pathway choice. *Nucleic Acids Res* (2013) 41:7589–605. doi:10.1093/nar/gkt556
34. Weinfeld M, Mani RS, Abdou I, Aceytuno RD, Glover JNM. Tidying up loose ends: the role of polynucleotide kinase/phosphatase in DNA strand break repair. *Trends Biochem Sci* (2011) 36:262–71. doi:10.1016/j.tibs.2011.01.006
35. Ward JF. DNA damage produced by ionizing radiation in mammalian cells: identities, mechanisms of formation, and reparability. *Prog Nucl Acid Res* (1988) 35:95–125. doi:10.1016/S0079-6603(08)60611-X
36. Goodhead DT, Nikjoo H. Track structure analysis of ultrasoft X-rays compared to high- and low-LET radiations. *Int J Radiat Biol* (1989) 55:513–29. doi:10.1080/09553008914550571
37. Paretzke HG. Radiation track structure theory. In: Freeman GR, editor. *Kinetics of Nonhomogeneous Processes*. New York City, NY: John Wiley & Sons, Inc (1987). p. 89–170.
38. Friedland W, Jacob P, Kundrá TP. Stochastic simulation of DNA double-strand break repair by non-homologous end joining based on track structure calculations. *Radiat Res* (2010) 173:677–88. doi:10.1667/RR1965.1
39. Friedland W, Dingfelder M, Kundrát P, Jacob P. Track structures, DNA targets and radiation effects in the biophysical Monte Carlo simulation code PARTRAC. *Mutat Res* (2011) 711:28–40. doi:10.1016/j.mrfmmm.2011.01.003
40. Allen C, Borak TB, Tsujii H, Nickoloff JA. Heavy charged particle radiobiology: using enhanced biological effectiveness and improved beam focusing to advance cancer therapy. *Mutat Res* (2011) 711:150–7. doi:10.1016/j.mrfmmm.2011.02.012
41. Ward JF. Biochemistry of DNA lesions. *Radiat Res* (1985) 104:S103–11. doi:10.2307/3576637
42. Ward JF, Evans JW, Limoli CL, Calabro-Jones PM. Radiation and hydrogen peroxide induced free radical damage to DNA. *Br J Cancer* (1987) 55:105–12.
43. Georgakilas AG, O'neill P, Stewart RD. Induction and repair of clustered DNA lesions: what do we know so far? *Radiat Res* (2013) 180:100–9. doi:10.1667/RR3041.1
44. Goodhead DT. Initial events in the cellular effects of ionizing radiations: clustered damage in DNA. *Int J Radiat Biol* (1994) 65:7–17. doi:10.1080/09553009414550021
45. Eccles LJ, O'neill P, Lomax ME. Delayed repair of radiation induced clustered DNA damage: friend or foe? *Mutat Res* (2011) 711:134–41. doi:10.1016/j.mrfmmm.2010.11.003
46. Wilson DM 3rd, Kim D, Berquist BR, Sigurdson AJ. Variation in base excision repair capacity. *Mutat Res* (2011) 711:100–12. doi:10.1016/j.mrfmmm.2010.12.004
47. Singh SK, Wu W, Wu W, Wang M, Iliakis G. Extensive repair of DNA double-strand breaks in cells deficient in the DNA-PK dependent pathway of NHEJ after exclusion of heat-labile sites. *Radiat Res* (2009) 172:152–64. doi:10.1667/RR1745.1
48. Singh SK, Wang M, Staudt C, Iliakis G. Post-irradiation chemical processing of DNA damage generates double-strand breaks in cells already engaged in repair. *Nucleic Acids Res* (2011) 39:8416–29. doi:10.1093/nar/gkr463
49. Singh SK, Wu W, Stuschke M, Bockisch A, Iliakis G. Reduced contribution of thermally-labile sugar lesions to DNA double-strand break formation after exposure to neutrons. *Radiat Res* (2012) 178:581–90. doi:10.1667/RR2996.1
50. Singh SK, Bencsik-Theilen A, Mladenov E, Jakob B, Taucher-Scholz G, Iliakis G. Reduced contribution of thermally labile sugar lesions to DNA double strand break formation after exposure to heavy ions. *Radiat Oncol* (2013) 8:77. doi:10.1186/1748-717X-8-77
51. Cheng Y, Li F, Mladenov E, Iliakis G. The yield of DNA double strand breaks determined after exclusion of those forming from heat-labile lesions predicts tumor cell radiosensitivity to killing. *Radiother Oncol* (2015) 116:366–73. doi:10.1016/j.radonc.2015.08.004
52. Li F, Cheng Y, Iliakis G. The contribution of thermally labile sugar lesions to DNA double-strand break formation in cells grown in the presence of BrdU. *Int J Radiat Biol* (2015) 91:312–20. doi:10.3109/09553002.2014.996260
53. Taleei R, Nikjoo H. Biochemical DSB-repair model for mammalian cells in G1 and early S phases of the cell cycle. *Mutat Res* (2013) 756:206–12. doi:10.1016/j.mrgentox.2013.06.004
54. Schipler A, Mladenova V, Soni A, Nikolov V, Saha J, Mladenov E, et al. Chromosome thripsis by DNA double strand break clusters causes enhanced cell lethality, chromosomal translocations and 53BP1-recruitment. *Nucleic Acids Res* (2016). doi:10.1093/nar/gkw487
55. Johnston PJ, Bryant PE. A component of DNA double-strand break repair is dependent on the spatial orientation of the lesions within the higher-order structures of chromatin. *Int J Radiat Biol* (1994) 66:531–6. doi:10.1080/09553009414551571
56. Johnston PJ, Olive PL, Bryant PE. Higher-order chromatin structure-dependent repair of DNA double-strand breaks: modeling the elution of DNA from nucleoids. *Radiat Res* (1997) 148:561–7. doi:10.2307/3579731
57. Johnston PJ, Macphail SH, Banáth JP, Olive PL. Higher-order chromatin structure-dependent repair of DNA double-strand breaks: factors affecting elution of DNA from nucleoids. *Radiat Res* (1998) 149:533–42. doi:10.2307/3579785

58. Holley WR, Chatterjee A. Clusters of DNA damage induced by ionizing radiation: formation of short DNA fragments. 1. Theoretical modeling. *Radiat Res* (1996) 145:188–99. doi:10.2307/3579174
59. Löbrich M, Cooper PK, Rydberg B. Non-random distrubution of DNA double-strand breaks induced by particle irradiation. *Int J Radiat Biol* (1996) 70:493–503. doi:10.1080/095530096144680
60. Rydberg B. Clusters of DNA damage induced by ionizing radiation: formation of short DNA fragments. 11. Experimental detection. *Radiat Res* (1996) 145:200–9. doi:10.2307/3579175
61. Friedland W, Jacob P, Paretzke HG, Stork T. Monte carlo simulation of the production of short DNA fragments by low-linear energy transfer radiation using higher-order DNA models. *Radiat Res* (1998) 150:170–82. doi:10.2307/3579852
62. Friedland W, Dingfelder M, Jacob P, Paretzke HG. Calculated DNA double-strand break and fragmentation yields after irradiation with He ions. *Radiat Phys Chem* (2005) 72:279–86. doi:10.1016/j.radphyschem.2004.05.053
63. Pang D, Winters TA, Jung M, Purkayastha S, Cavalli LR, Chasovkikh S, et al. Radiation-generated short DNA fragments may perturb non-homologous end-joining and induce genomic instability. *J Radiat Res* (2011) 52:309–19. doi:10.1269/jrr.10147
64. Wang H, Zhang X, Wang P, Yu X, Essers J, Chen D, et al. Characteristics of DNA-binding proteins determine the biological sensitivity to high-linear energy transfer radiation. *Nucleic Acids Res* (2010) 38:3245–51. doi:10.1093/nar/gkq069
65. Ostashevsky JY. A model relating cell survival to DNA fragment loss and unrepaired double-strand breaks. *Radiat Res* (1989) 118:437–66. doi:10.2307/3577405
66. Ostashevsky JY. Higher-order structure of interphase chromosomes and radiation-induced chromosomal exchange aberrations. *Int J Radiat Biol* (2000) 76:1179–87. doi:10.1080/09553000050134410
67. Friedland W, Jacob P, Bernhardt P, Paretzke HG, Dingfelder M. Simulation of DNA damage after proton irradiation. *Radiat Res* (2003) 159:401–10. doi:10.1667/0033-7587(2003)159[0401:SODDAP]2.0.CO;2
68. Ponomarev AL, Cucinotta FA. Chromatin loops are responsible for higher counts of small DNA fragments induced by high-LET radiation, while chromosomal domains do not affect the fragment sizes. *Int J Radiat Biol* (2006) 82:293–305. doi:10.1080/09553000600637716
69. Elsässer T, Brons S, Psonka K, Scholz M, Gudowska-Nowak E, Taucher-Scholz G. Biophysical modeling of fragment length distributions of DNA plasmids after X and heavy-ion irradiation analyzed by atomic force microscopy. *Radiat Res* (2008) 169:649–59. doi:10.1667/RR1028.1
70. Friedrich T, Durante M, Scholz M. Modeling cell survival after photon irradiation based on double-strand break clustering in megabase pair chromatin loops. *Radiat Res* (2012) 178:385–94. doi:10.1667/RR2964.1
71. Friedrich T, Scholz U, Elsässer T, Durante M, Scholz M. Calculation of the biological effects of ion beams based on the microscopic spatial damage distribution pattern. *Int J Radiat Biol* (2012) 88:103–7. doi:10.3109/09553002.2011.611213
72. Hufnagl A, Herr L, Friedrich T, Durante M, Taucher-Scholz G, Scholz M. The link between cell-cycle dependent radiosensitivity and repair pathways: a model based on the local, sister-chromatid conformation dependent switch between NHEJ and HR. *DNA Repair* (2015) 27:28–39. doi:10.1016/j.dnarep.2015.01.002
73. Sachs RK, Van Den Engh G, Trask B, Yokota H, Hearst JE. A random-walk/giant-loop model for interphase chromosomes. *Proc Natl Acad Sci USA* (1995) 92:2710–4. doi:10.1073/pnas.92.7.2710
74. Ostashevsky J. A polymer model for the structural organization of chromatin loops and minibands in interphase chromosomes. *Mol Biol Cell* (1998) 9:3031–40. doi:10.1091/mbc.9.11.3031
75. Gauter B, Zlobinskaya O, Weber K-J. Rejoining of radiation-induced DNA double-strand breaks: pulsed-field electrophoresis analysis of fragment size distributions after incubation for repair. *Radiat Res* (2002) 157:721–33. doi:10.1667/0033-7587(2002)157[0721:RORIDD]2.0.CO;2
76. Menegakis A, Yaromina A, Eicheler W, Dörfler A, Beuthien-Baumann B, Thames HD, et al. Prediction of clonogenic cell survival curves based on the number of residual DNA double strand breaks measured by γH2AX staining. *Int J Radiat Biol* (2009) 85:1032–41. doi:10.3109/09553000903242149
77. Koch U, Höhne K, Von Neubeck C, Thames HD, Yaromina A, Dahm-Daphi J, et al. Residual γH2AX foci predict local tumour control after radiotherapy. *Radiother Oncol* (2013) 108:434–9. doi:10.1016/j.radonc.2013.06.022
78. Li Y, Reynolds P, O'neill P, Cucinotta FA. Modeling damage complexity-dependent non-homologous end-joining repair pathway. *PLoS One* (2014) 9:e85816. doi:10.1371/journal.pone.0085816
79. Stephens PJ, Greenman CD, Fu B, Yang F, Rignell GR, Mudie LJ, et al. Massive genomic rearrangement acquired in a single catastrophic event during cancer development. *Cell* (2011) 144:27–40. doi:10.1016/j.cell.2010.11.055
80. Forment JV, Kaidi A, Jackson SP. Chromothripsis and cancer: causes and consequences of chromosome shattering. *Nat Rev Cancer* (2012) 12:663–70. doi:10.1038/nrc3352
81. Kloosterman WP, Tavakoli-Yaraki M, Van Roosmalen MJ, Van Binsbergen E, Renkens I, Duran K, et al. Constitutional chromothripsis rearrangements involve clustered double-stranded DNA breaks and nonhomologous repair mechanisms. *Cell Rep* (2012) 1:648–55. doi:10.1016/j.celrep.2012.05.009
82. Molenaar JJ, Koster J, Zwijnenburg DA, Van Sluis P, Valentijn LJ, Van Der Ploeg I, et al. Sequencing of neuroblastoma identifies chromothripsis and defects in neuritogenesis genes. *Nature* (2012) 483:589–93. doi:10.1038/nature10910
83. Rouet P, Smih F, Jasin M. Expression of a site-specific endonuclease stimulates homologous recombination in mammalian cells. *Proc Natl Acad Sci USA* (1994) 91:6064–8. doi:10.1073/pnas.91.13.6064
84. Richardson C, Jasin M. Frequent chromosomal translocations induced by DNA double-strand breaks. *Nature* (2000) 405:697–700. doi:10.1038/35015097
85. Liang F, Han M, Romanienko PJ, Jasin M. Homology-directed repair is a major double-strand break repair pathway in mammalian cells. *Proc Natl Acad Sci USA* (1998) 95:5172–7. doi:10.1073/pnas.95.9.5172
86. Taghian DG, Nickoloff JA. Chromosomal double-strand breaks induce gene conversion at high frequency in mammalian cells. *Mol Cell Biol* (1997) 17:6386–93. doi:10.1128/MCB.17.11.6386
87. Pierce AJ, Johnson RD, Thompson LH, Jasin M. XRCC3 promotes homology-directed repair of DNA damage in mammalian cells. *Genes Dev* (1999) 13:2633–8. doi:10.1101/gad.13.20.2633
88. Mao Z, Bozzella M, Seluanov A, Gorbunova V. Comparison of nonhomologous end joining and homologous recombination in human cells. *DNA Repair* (2008) 7:1765–71. doi:10.1016/j.dnarep.2008.06.018
89. Johnson RD, Liu N, Jasin M. Mammalian XRCC2 promotes the repair of DNA double-strand breaks by homologous recombination. *Nature* (1999) 401:397–9. doi:10.1038/43932
90. Bennardo N, Cheng A, Huang N, Stark JM. Alternative-NHEJ is a mechanistically distinct pathway of mammalian chromosome break repair. *PLoS Genet* (2008) 4:e1000110. doi:10.1371/journal.pgen.1000110
91. Mao Z, Seluanov A, Jiang Y, Gorbunova V. TRF2 is required for repair of nontelomeric DNA double-strand breaks by homologous recombination. *Proc Natl Acad Sci USA* (2007) 104:13068–73. doi:10.1073/pnas.0702410104
92. Mansour WY, Rhein T, Dahm-Daphi J. The alternative end-joining pathway for repair of DNA double-strand breaks requires PARP1 but is not dependent upon microhomologies. *Nucleic Acids Res* (2010) 38:6065–77. doi:10.1093/nar/gkq387
93. Gomez-Cabello D, Jimeno S, Fernández-Ávila MJ, Huertas P. New tools to study DNA double-strand break repair pathway choice. *PLoS One* (2013) 8:e77206. doi:10.1371/journal.pone.0077206
94. Muscarella DE, Ellison EL, Ruoff BM, Vogt VM. Characterization of I-Ppo, an intron-encoded endonuclease that mediates homing of a group I intron in the ribosomal DNA of Physarum polycephalum. *Mol Cell Biol* (1990) 10:3386–96. doi:10.1128/MCB.10.7.3386
95. Monnat RJ Jr, Hackmann AFM, Cantrell MA. Generation of highly site-specific DNA double-strand breaks in human cells by the homing endonucleases I-PpoI and I-CreI. *Biochem Biophys Res Commun* (1999) 255:88–93. doi:10.1006/bbrc.1999.0152
96. Berkovich E, Monnat RJ Jr, Kastan MB. Roles of ATM and NBS1 in chromatin structure modulation and DNA double-strand break repair. *Nat Cell Biol* (2007) 9:683–90. doi:10.1038/ncb1599
97. Berkovich E, Monnat RJ Jr, Kastan MB. Assessment of protein dynamics and DNA repair following generation of DNA double-strand breaks at defined genomic sites. *Nat Protoc* (2008) 3:915–22. doi:10.1038/nprot.2008.54

98. Belfort M, Roberts RJ. Homing endonucleases: keeping the house in order. *Nucleic Acids Res* (1997) 25:3379–88. doi:10.1093/nar/25.17.3379
99. Vigo E, Müller H, Prosperini E, Hateboer G, Cartwright P, Moroni MC, et al. CDC25A phosphatase is a target of E2F and is required for efficient E2F-induced S phase. *Mol Cell Biol* (1999) 19:6379–95. doi:10.1128/MCB.19.9.6379
100. Berkovich E, Lamed Y, Ginsberg D. E2F and Ras synergize in transcriptionally activating p14ARF expression. *Cell Cycle* (2003) 2:127–34. doi:10.4161/cc.2.2.293
101. Goldstein M, Derheimer FA, Tait-Mulder J, Kastan MB. Nucleolin mediates nucleosome disruption critical for DNA double-strand break repair. *Proc Natl Acad Sci USA* (2013) 110:16874–9. doi:10.1073/pnas.1306160110
102. Caron P, Choudjaye J, Clouaire T, Bugler B, Daburon V, Aguirrebengoa M, et al. Non-redundant functions of ATM and DNA-PKcs in response to DNA double-strand breaks. *Cell Rep* (2015) 13:1598–609. doi:10.1016/j.celrep.2015.10.024
103. Aymard F, Bugler B, Schmidt CK, Guillou E, Caron P, Briois S, et al. Transcriptionally active chromatin recruits homologous recombination at DNA double-strand breaks. *Nat Struct Mol Biol* (2014) 21:366–74. doi:10.1038/nsmb.2796
104. Massip L, Caron P, Iacovoni JS, Trouche D, Legube G. Deciphering the chromatin landscape induced around DNA double strand breaks. *Cell Cycle* (2010) 9:2963–72. doi:10.4161/cc.9.15.12412
105. Caron P, Aymard F, Iacovoni JS, Briois S, Canitrot Y, Bugler B, et al. Cohesin protects genes against γH2AX induced by DNA double-strand breaks. *PLoS Genet* (2012) 8:e1002460. doi:10.1371/journal.pgen.1002460
106. Nishimura K, Fukagawa T, Takisawa H, Kakimoto T, Kanemaki M. An auxin-based degron system for the rapid depletion of proteins in nonplant cells. *Nat Methods* (2009) 6:917–22. doi:10.1038/nmeth.1401
107. Wood AJ, Lo T-W, Zeitler B, Pickle CS, Ralston EJ, Lee AH, et al. Targeted genome editing across species using ZFNs and TALENs. *Science* (2011) 333:307. doi:10.1126/science.1207773
108. Gaj T, Gersbach CA, Barbas Iii CF. ZFN, TALEN, and CRISPR/Cas-based methods for genome engineering. *Trends Biotechnol* (2013) 31:397–405. doi:10.1016/j.tibtech.2013.04.004
109. Ghezraoui H, Piganeau M, Renouf B, Renaud J-B, Sallmyr A, Ruis B, et al. Chromosomal translocations in human cells are generated by canonical nonhomologous end-joining. *Mol Cell* (2014) 55:829–42. doi:10.1016/j.molcel.2014.08.002
110. Nakade S, Tsubota T, Sakane Y, Kume S, Sakamoto N, Obara M, et al. Microhomology-mediated end-joining-dependent integration of donor DNA in cells and animals using TALENs and CRISPR/Cas9. *Nat Commun* (2014) 5:5560. doi:10.1038/ncomms6560
111. Sun N, Bao Z, Xiong X, Zhao H. SunnyTALEN: a second-generation TALEN system for human genome editing. *Biotechnol Bioeng* (2014) 111(4):683–91. doi:10.1002/bit.25154
112. Doudna JA, Charpentier E. The new frontier of genome engineering with CRISPR-Cas9. *Science* (2014) 346:1077. doi:10.1126/science.1258096
113. Sanchez-Rivera FJ, Jacks T. Applications of the CRISPR-Cas9 system in cancer biology. *Nat Rev Cancer* (2015) 15:387–95. doi:10.1038/nrc3950
114. Shalem O, Sanjana NE, Zhang F. High-throughput functional genomics using CRISPR-Cas9. *Nat Rev Genet* (2015) 16:299–311. doi:10.1038/nrg3899
115. Marraffini LA. CRISPR-Cas immunity in prokaryotes. *Nature* (2015) 526:55–61. doi:10.1038/nature15386
116. Mali P, Yang L, Esvelt KM, Aach J, Guell M, Dicarlo JE, et al. RNA-Guided Human Genome Engineering via Cas9. *Science* (2013) 339:823–6. doi:10.1126/science.1232033
117. Maddalo D, Manchado E, Concepcion CP, Bonetti C, Vidigal JA, Han Y-C, et al. In vivo engineering of oncogenic chromosomal rearrangements with the CRISPR/Cas9 system. *Nature* (2014) 516:423–7. doi:10.1038/nature13902
118. Li Y, Park AI, Mou H, Colpan C, Bizhanova A, Akama-Garren E, et al. A versatile reporter system for CRISPR-mediated chromosomal rearrangements. *Genome Biol* (2015) 16:111. doi:10.1186/s13059-015-0680-7
119. Mali P, Esvelt KM, Church GM. Cas9 as a versatile tool for engineering biology. *Nat Methods* (2013) 10:957–63. doi:10.1038/nmeth.2649
120. Iliakis G. The influence of conditions affecting repair and expression of potentially lethal damage on the induction of 6-thioguanine resistance after exposure of mammalian cells to x-rays. *Mutat Res* (1984) 126:215–25. doi:10.1016/0027-5107(84)90063-0
121. Thacker J. The molecular nature of mutations in cultured mammalian cells: a review. *Mutat Res* (1985) 159:431–42. doi:10.1016/0027-5107(85)90140-X
122. Hyland KA, Olson ER, Clark KJ, Aronovich EL, Hackett PB, Blazar BR, et al. *Sleeping Beauty*-mediated correction of Fanconi anemia type C. *J Gene Med* (2011) 13:462–9. doi:10.1002/jgm.1589
123. Mladenov E, Magin S, Soni A, Iliakis G. DNA double-strand break repair as determinant of cellular radiosensitivity to killing and target in radiation therapy. *Front Oncol* (2013) 3:113. doi:10.3389/fonc.2013.00113
124. Iliakis G, Murmann T, Soni A. Alternative end-joining repair pathways are the ultimate backup for abrogated classical non-homologous end-joining and homologous recombination repair: implications for the formation of chromosome translocations. *Mutat Res* (2015) 793:166–75. doi:10.1016/j.mrgentox.2015.07.001

Conflict of Interest Statement: The authors declare that the research was conducted in the absence of any commercial or financial relationships that could be construed as a potential conflict of interest.

Copyright © 2016 Mladenova, Mladenov and Iliakis. This is an open-access article distributed under the terms of the Creative Commons Attribution License (CC BY). The use, distribution or reproduction in other forums is permitted, provided the original author(s) or licensor are credited and that the original publication in this journal is cited, in accordance with accepted academic practice. No use, distribution or reproduction is permitted which does not comply with these terms.

frontiers in Oncology

ORIGINAL RESEARCH
published: 10 June 2016
doi: 10.3389/fonc.2016.00130

Short DNA Fragments Are a Hallmark of Heavy Charged-Particle Irradiation and May Underlie Their Greater Therapeutic Efficacy

Dalong Pang[1], Sergey Chasovskikh[1], James E. Rodgers[2] and Anatoly Dritschilo[1]*

[1] Radiation Medicine, Georgetown University Medical Center, Washington, DC, USA, [2] Radiation Oncology, Medstar Franklin Square Medical Center, Rosedale, MD, USA

Growing interest in proton and heavy ion therapy has reinvigorated research into the fundamental biological mechanisms underlying the therapeutic efficacy of charged-particle radiation. To improve our understanding of the greater biological effectiveness of high-LET radiations, we have investigated DNA double-strand breaks (DSBs) following exposure of plasmid DNA to low-LET Co-60 gamma photon and electron irradiation and to high-LET Beryllium and Argon ions with atomic force microscopy. The sizes of DNA fragments following radiation exposure were individually measured to construct fragment size distributions from which the DSB per DNA molecule and DSB spatial distributions were derived. We report that heavy charged particles induce a significantly larger proportion of short DNA fragments in irradiated DNA molecules, reflecting densely and clustered damage patterns of high-LET energy depositions. We attribute the enhanced short DNA fragmentation following high-LET radiations as an important determinant of the observed, enhanced biological effectiveness of high-LET irradiations.

Keywords: short DNA fragments, radiation, AFM, low-LET, charged particle

OPEN ACCESS

Edited by:
Francis A. Cucinotta,
University of Nevada Las Vegas, USA

Reviewed by:
Megumi Hada,
Prairie View A&M University, USA
Maria Antonella Tabocchini,
Istituto Superiore di Sanità, Italy

****Correspondence:***
Dalong Pang
dalong.pang@gunet.georgetown.edu

Specialty section:
This article was submitted to Radiation Oncology, a section of the journal Frontiers in Oncology

Received: *01 March 2016*
Accepted: *16 May 2016*
Published: *10 June 2016*

Citation:
Pang D, Chasovskikh S, Rodgers JE and Dritschilo A (2016) Short DNA Fragments Are a Hallmark of Heavy Charged-Particle Irradiation and May Underlie Their Greater Therapeutic Efficacy. Front. Oncol. 6:130. doi: 10.3389/fonc.2016.00130

INTRODUCTION

DNA is the critical target of ionizing radiation-induced cellular damage, and DNA double-strand breaks (DSBs) are the most lethal of more than 100 various DNA lesions induced by ionizing radiation (1–3). Biological observations implicate DNA DSBs resulting from high-LET radiation in cell death and carcinogenesis to a greater extent than that observed following low-LET radiations (4–6). Mechanisms underlying such observations have focused on dense and complex ionization events resulting in clustered DNA DSBs that are more difficult to repair (7, 8).

Established methods for measurements of DSBs include sucrose gradient sedimentation (9), neutral filter elusion (10), continuous or pulsed-field gel electrophoresis (PFGE) (11–13), the comet assay (14, 15), and, more recently, the γ-H2AX foci quantification (16, 17). DSBs induced in cellular environment and in denatured DNA have been determined (18–23); however, measured DSBs following high-LET radiations were reported equal to or only marginally greater than that observed following low-LET radiations (6, 24, 25). This is in contradiction to the observed greater relative biological effectiveness (RBE) by several fold for cell survival following high-LET radiation exposures (26, 27). However, a better correlation between RBE survival and DSB induction was found with assays of unrepaired DSBs (28–31).

This apparent discrepancy between RBE for cell survival as compared to DSB induction contradicted the accepted thesis of DSB as the primary lesion for cell killing. Subsequently, detailed examination of the techniques used for DSB measurements has revealed that they were reliable only for DNA fragments in the kilobase-pair region and possible shorter DNA fragments were potentially unaccounted for (32–34).

In addition to experimental investigation of DSB induction by ionizing radiation, theoretical modeling employing individual particle track structures has also been pursued (35–38). Ionizing events by individual particles based on established physics principles have shown that heavy charged-particle radiations produce a much greater clustered energy depositions (within a few base pairs) imparting sufficient energy to generate free radicals, which can lead to DNA DSBs or directly cause DSBs when occurring on the opposite strand within a certain distance (39–41). Such Monte Carlo simulations have revealed induction of short DNA fragments less than a few hundred base pairs by both low- and high-LET radiations, which were not quantified in experimental measurements (41, 42).

As a single molecule imaging instrument, the atomic force microscopy (AFM) offers the resolution to image individual atoms of solid state materials and nanometer resolution to visualize biological molecules, e.g., DNA molecules (43–46). Unlike Electron Microscopy or Scanning Tunneling Microscopy, AFM requires minimum sample preparation, reducing or eliminating potential distortions attributable to sample preparation (47, 48). In addition, its ability to measure biomolecules in aqueous solutions, similar to the native environment, offers the possibility for examining *in vitro* behaviors and interactions of biomolecules of interest (49–51).

We have previously reported the presence of short DNA fragments in neutron irradiated plasmid DNA, reflecting the high-LET energy deposition of neutrons (52). Here, we address the effectiveness of high-LET charged-particle irradiation in producing short DNA fragments in plasmid DNA. Use of plasmid DNA molecules as the targets allows for high-resolution imaging and easy identification of DNA fragmentation in sizes of a few to a few hundred nanometers in lengths. We investigated DNA fragmentation following radiations of the low-LET Co-60 photon and electron, and the high-LET Beryllium and Argon ions.

MATERIALS AND METHODS

DNA Samples

Plasmid DNA (pUC19, 2686 bp in length) was purchased from New England Biolab at a concentration of 1000 μg/ml in HEPES buffer (Beverley, MA, USA). The samples were diluted to a concentration of 5 μg/ml in buffer containing 10 mM HEPES and 1 mM $MgCl_2$ and aliquoted into vials containing 250 μl DNA solution each.

Irradiation

Irradiation of the aliquots of DNA solutions was performed at the following sites.

Electron irradiations were performed at the Georgetown University Medical Center in Washington, DC, USA on a medical linear accelerator with 6 MV energy (Varian 2100 C/D, Varian, Palo Alto, CA, USA) to doses of 1000–8000 Gy in 1000 Gy increment. The dose was calibrated using a NIST traceable ionization chamber.

Co-60 photon irradiations were performed at Neutron Products in Dickerson, MD, USA using an industrial Co-60 irradiator at a dose rate of 20 kGy/h in the same dose range as that for electrons.

Beryllium ion irradiations were performed at the Oak Ridge National Laboratory in Oak Ridge, TN, USA. The energy of the Beryllium particle beam was 100 MeV/n, and the LET was 11.6 keV/μm. The doses delivered ranged from 3 to 12 kGy, calculated as the product of the particle fluence rate and the LET of the ion multiplied by the time the beam was on.

Argon ion irradiations were performed on the HIMAC charged-particle accelerator at the National Institute of Radiological Science in Chiba, Japan. The energy of the Argon ion beam was 390 MeV/n, and the LET was 99.5 keV/μm. The doses delivered were 3–12 kGy, using a similar way for dose determination as that for Beryllium irradiation.

As a control, a set of three un-irradiated DNA samples was prepared for each experiment.

AFM Imaging

A Bruker Nano Scope IIIa AFM (Bruker, Santa Barbara, CA, USA) was used for DNA imaging in tapping mode in air. The AFM cantilevers were commercially available from Bruker with a tip radius of approximately 10 nm. Sample preparation for imaging consisted of deposition of 2 μl of the DNA solution on freshly cleaved mica surface, followed by a gentle rinse with 1 ml of distilled water and subsequent drying in the gentle flow of Nitrogen gas. The Scanning frequency was 1 Hz and typical scanning size was 2 μm × 2 μm.

The sizes of the DNA fragments in each image were measured individually using the NanoScope IIIa software. Over a thousand DNA fragments were measured for each irradiated DNA sample to ensure a statistical uncertainty of <5%. Fragment size distribution profiles relating the numbers of DNA fragments to their sizes were constructed. The average numbers of DSBs per DNA, per broken DNA, and DSB distributions as a function of spatial distance were derived from the constructed size distribution profiles. For details on the technique and data analysis, the reader is referred to our previous paper (52).

RESULTS

Figures 1A–E show representative AFM images of the plasmid DNA of un-irradiated controls and following irradiation by Co-60 photon, electron, Beryllium, and Argon ions to doses of 6 kGy. As shown in **Figure 1A**, the majority of the control DNA molecules were in relaxed circular conformation with occasional super coiling of one or two twists. In **Figures 1B,C**, the amount of DNA fragmentation and sizes appear similar, demonstrating similar physical characteristics of low-LET energy deposition patterns following Co-60 photon and electron irradiations.

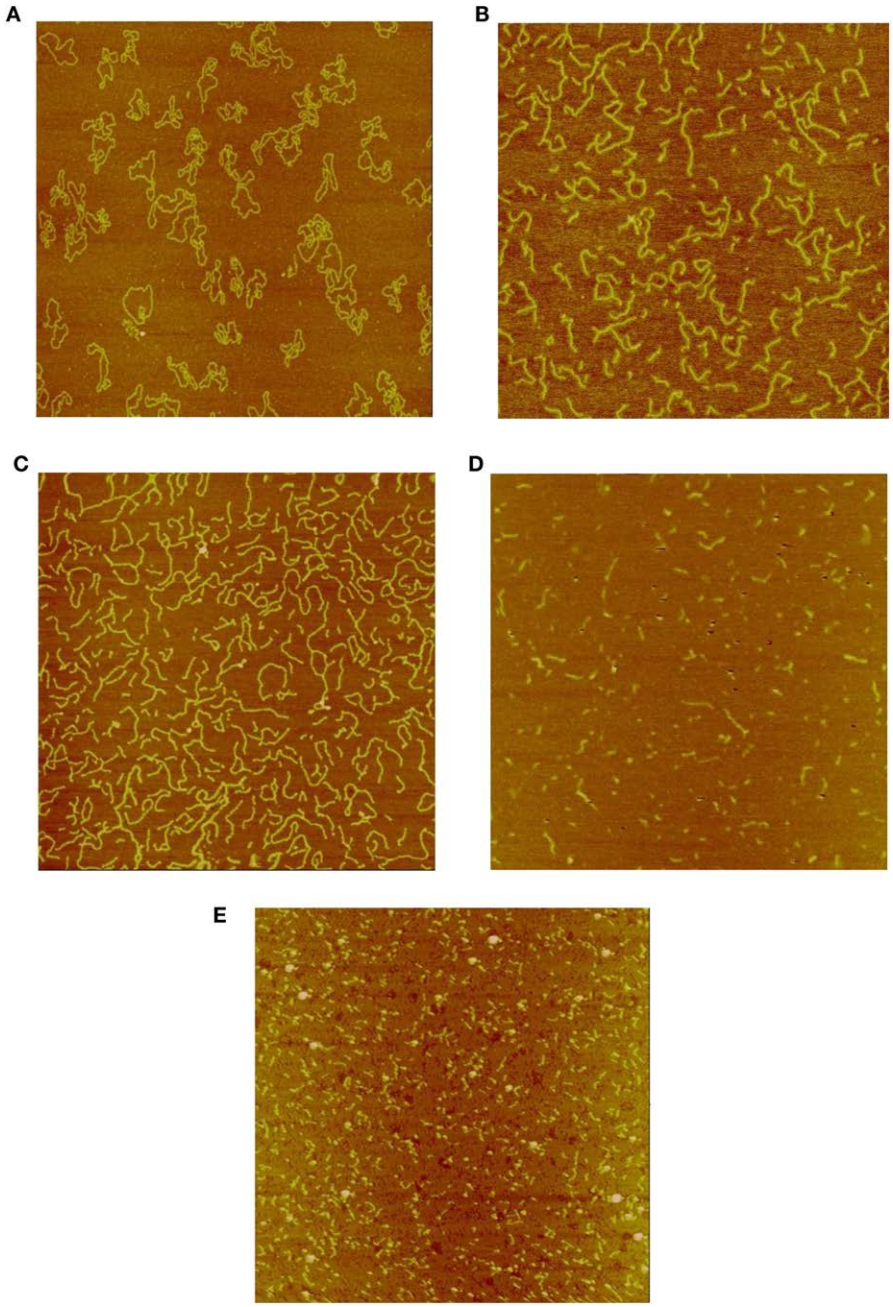

FIGURE 1 | **(A)** Sample image of un-irradiated pUC19 plasmid DNA. The size of the image is 2 μm × 2 μm, as that for the rest of the images. **(B)** Sample image of Co-60 photon irradiated pUC19 plasmid DNA. The radiation dose is 6 kGy. **(C)** Sample image of electron irradiated pUC19 plasmid DNA. The radiation dose is 6 kGy. **(D)** Sample image of Beryllium ion irradiated pUC19 plasmid DNA. The radiation dose is 6 kGy. **(E)** Sample image of Argon ion irradiated pUC19 plasmid DNA. The radiation dose is 6 kGy.

Examination of **Figures 1D,E** shows that DNA fragmentation is markedly greater than that shown in **Figures 1B,C**. Furthermore, the average sizes of DNA fragments are shorter, demonstrating the enhanced capability of the high-LET Beryllium and Argon ions to fragment DNA to a much greater extent.

Figures 2A–E show the corresponding reconstructed DNA fragment size distributions based on individually measured DNA fragment sizes for each irradiated samples. The size of the original, un-fragmented pUC19 plasmid DNA is 850 nm and is evenly divided into 50 nm bins in the range of 0–850 nm. Size profile of the un-irradiated DNA was marked by a near 100% uni-spike at the 850 nm bin, represented by the unbroken and occasional DNA molecules with one break only. Mirroring images shown in **Figures 1B,C**, the DNA fragment size distributions

in **Figures 2B,C** are essentially identical, and approximating an exponential distribution as a function of the fragment sizes. However, the size distributions shown in **Figures 2D,E** are quite different from that in **Figures 2B,C**, marked by pronounced spikes of fragments in the shortest bin of 50 nm. This demonstrates a much enhanced induction of short DNA fragments by the Beryllium and Argon ions. Size distributions in bins longer than 50 nm follow a similar exponential-like distribution as that in **Figures 2B,C**, but at a more accelerated drop off with increasing fragment size.

Based on the measured DNA fragment sizes, the average numbers of DNA DSB per DNA molecule are derived for DNA molecules including both fragmented and intact DNA. In addition, DSBs per DNA for fragmented DNA molecules only are also derived to further illustrate the DNA fragmentation capability by different types of radiation. Derivation of these quantities is based on the following considerations. If a plasmid DNA contains only one DSB, it becomes linearized as a single linear DNA fragment of the original length of 850 nm; if it contains two DSBs, a plasmid is broken into two pieces and the combined lengths of the two fragments add up to the original DNA length and this pattern holds for DNA containing N DSBs. Therefore, the number of fragments equals the number of DSBs, and consequently, the number of DSBs per DNA molecule simply equals to the number of fragments divided by the total number of DNA molecules from which the fragments are originated, which can be calculated as the sum of all the fragment lengths divided by the length of an intact DNA.

In addition to the average number of DSB per DNA, which provides a general indication of the DNA breaking capability by ionizing radiation, information on the spatial correlation of the DSBs on a DNA molecule can be further derived from the size distributions. As an illustrative example, we calculate the number of DSBs distributed within a distance of 50 nm on a DNA

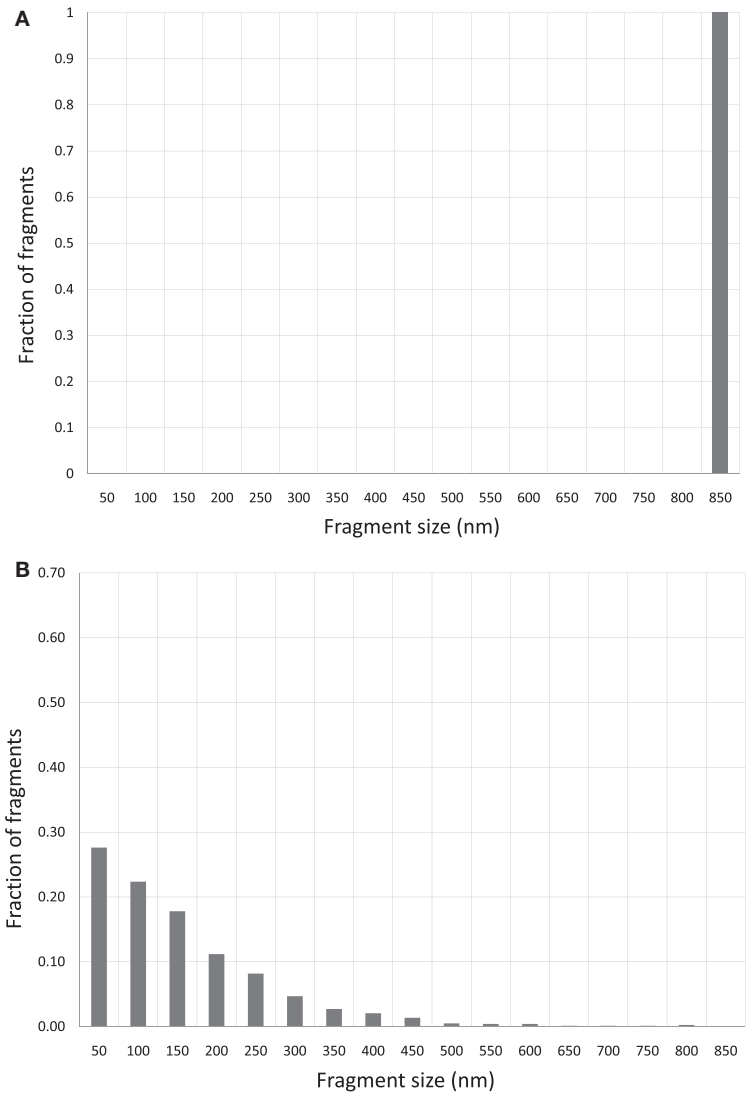

FIGURE 2 | **Continued**

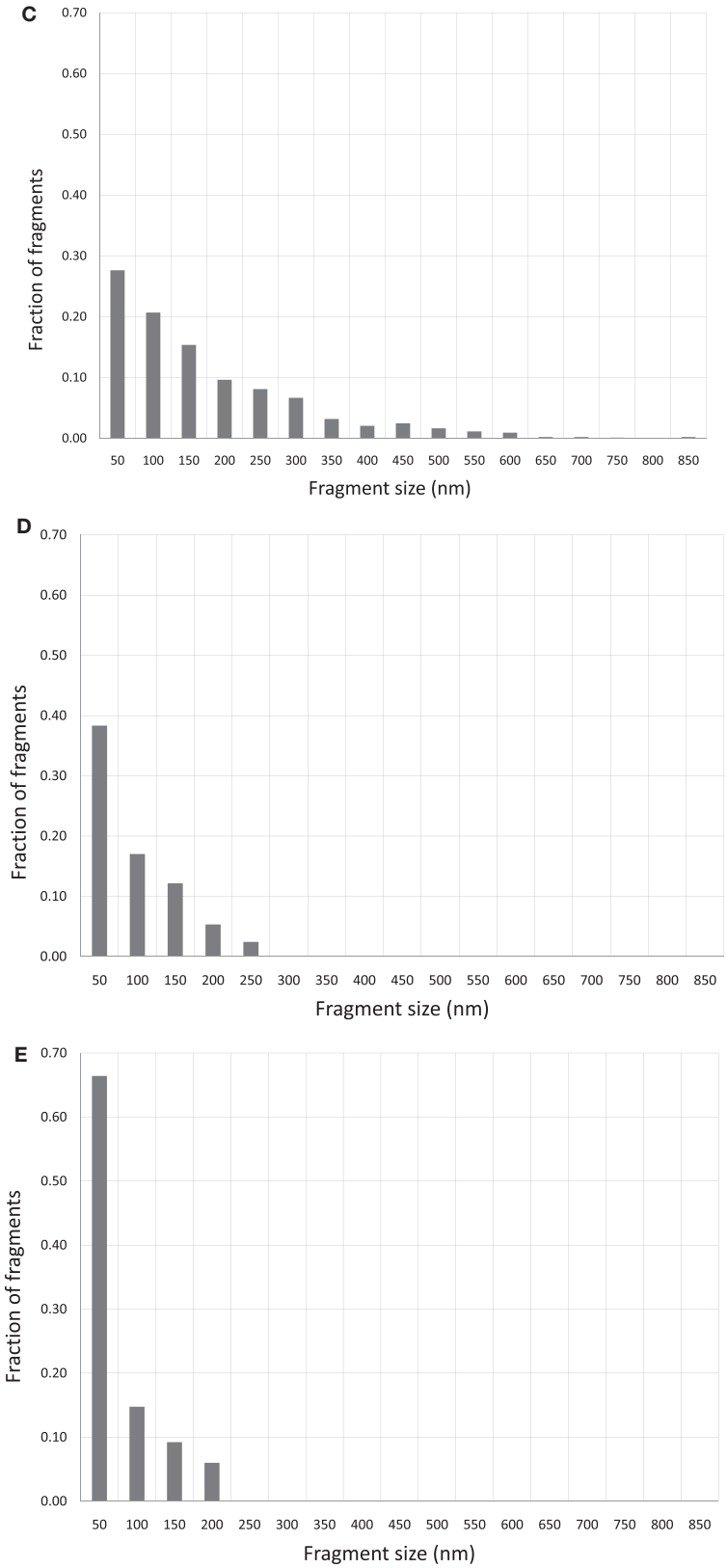

FIGURE 2 | **(A)** DNA fragment size distribution of un-irradiated pUC19 plasmid DNA. **(B)** DNA fragment size distribution of 6 kGy Co-60 photon irradiated DNA. **(C)** DNA fragment size distribution of 6 kGy electron irradiated DNA. **(D)** DNA fragment size distribution of 6 kGy Beryllium ion irradiated DNA. **(E)** DNA fragment size distribution of 6 kGy Argon ion irradiated DNA.

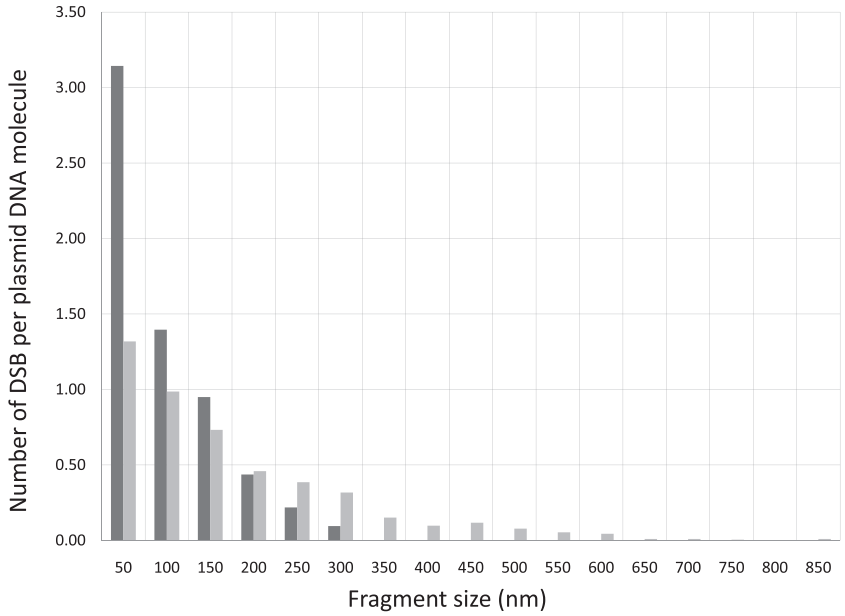

FIGURE 3 | **DSB spatial distribution on a pUC19 plasmid DNA molecule induced by Beryllium ion and electron irradiation to a dose of 6 kGy**.

TABLE 1 | Measured DSB per DNA molecule and corresponding RBE for radiations investigated in this and a previous report (52).

Radiation	DSB/DNA	STD	RBE	STD	LET (keV/um)
Electron	4.77	0.4	0.82	0.08	0.2
Co-60	5.83	0.33	1.00	0.08	0.2
Neutron	7.36	0.78	1.26	0.15	55
Be	6.24	0.71	1.07	0.14	11.6
Argon	26.09	5.69	4.48	1.01	99.5

The comparison was made for the radiation dose of 6 kGy. RBE was calculated with Co-60 as the reference. The LET value for neutron is the average LET of the recoil protons generated by the primary neutrons, and the LET for Co-60 photon is the average LET of the secondary electrons produced by the primary photon through Compton effects.

molecule. This is derived by counting the number of fragments in the length interval from 0 to 50 nm, which is then divided by the total number of DNA molecules as determined in the previous paragraph. This calculation can be extended to determine DSBs distributed in other longer length intervals. By this information, we obtain a clear indication of whether DSBS are distributed in a confined small spatial region or more spread out on a DNA molecule. Correlation of this DSB distribution pattern with the type of radiation provides a simple measure for the assessment of ionization clustering. In **Figure 3**, we construct the number of DSBs per DNA for electron and Beryllium irradiated DNA samples to a dose of 6 kGy in relation to the fragment sizes to demonstrate the DSB spatial distribution on a DNA molecule. Clearly, Beryllium ions induce more dense and localized DSBs, whereas electrons generate more uniformly distributed DSBs on a DNA molecule, demonstrating the high degree of DNA damage clustering by high-LET irradiations.

We further calculated the RBE for DSB induction as a function of radiation quality. The RBE calculated in this report is defined as the ratio of the number of DSBs per unit DNA molecule of a given type of radiation to that by Co-60 photon. **Table 1** gives the DSB per DNA molecule for the radiations investigated and the corresponding RBEs determined at 6 kGy. For comparison purposes, we also have included the RBE for neutron studied in a previous publication (52).

DISCUSSION

In this report, we employ AFM for the measurement of DNA fragmentation by the charged particles of Beryllium and Argon in comparison to that by the low-LET photon and electron to demonstrate the enhanced DNA fragmentation capability of high-LET radiations. As shown in the AFM images, short DNA fragments are produced after plasmid DNA exposure to both low- and high-LET radiations. However, the relative amounts of short DNA fragments are substantially greater after high-LET irradiations, with Beryllium and Argon ions, demonstrating a prevalence of clustered DNA DSBs produced by high-LET radiations not previously quantified due to limitations in the conventional biological techniques.

As discussed in the Section "Introduction," the RBE for cell killing reported in the literature are generally a few fold higher for high-LET radiations (4, 5), but the DSB induction as measured using gel electrophoresis or other biological techniques are approximately unity or only slightly higher (25), presenting a contradiction to the fundamental concept of lethality of DSBs. Using Monte Carlo modeling of radiation-induced DNA damage, the groups led by Paretzke and Goodhead have reported clustered DNA lesions after exposure of modeled DNA molecules to high-LET radiations (38, 41, 53, 54). Campa and coauthors have further calculated the frequency of short DNA fragments generation by high energy protons and ions (42). The

prominence of short DNA fragments induced by high-LET radiations presented in this and our previous publications, as well as reports by other investigators, provide experimental validation of the model-predicted short DNA fragments (52, 55, 56). It is apparent that short DNA fragments were undetected by techniques exploiting the migratory property of DNA fragments in gels, leaving accounted the DSBs corresponding to short DNA fragments, in particular, DSBs induced by high-LET radiations. It appears likely that with short DNA fragments included, the DSB induction by high-LET radiations should correlate better to RBE for cell survival.

To evaluate the capacity for DNA strand breakage by radiations of different quality, we calculated the RBE for DSB induction by the radiations investigated in this report together with that by neutrons for which the DNA fragment size distributions have been reported before (52). As shown in **Table 1**, the RBE increases as the LET of radiation increases, demonstrating the greater capacity of DNA damage by high-LET radiations. The ability of AFM to image short DNA fragments has permitted measurement of DSBs produced in close proximity resulting from clustered DSBs by high-LET radiations, and therefore offers a sensitive technique to quantify clustered DSBs not easily measurable using conventional biological methods.

In a previous report, we investigated the biological significance of short DNA fragments in DNA damage and repair and their potentially important roles in cell survival and carcinogenesis (57). We evaluated DNA binding and rejoining by Ku and DNA-PK, two major DNA repair proteins involved in the non-homologous end-joining (NHEJ) pathway and confirmed reports by other investigators on the minimum DNA length requirements for protein binding and activation (58, 59). When DNA fragments are short, the challenge to rejoin and repair them by the cell's repair mechanisms becomes greater. Furthermore, the presence of un-rejoined and repaired short DNA fragments in cells can trigger genomic instability, leading to mutation or cell death by way of apoptosis (57, 60). Compared to longer DNA fragments, which are more frequently produced by low-LET radiations, short DNA fragments present a more lethal challenge to cellular repair mechanisms and survivability after exposure to high-LET radiations.

The fragment size distribution data for Co-60 photon and Argon ion at 10 kGy presented in this paper were for illustrative purpose only to show the greater capacity of high-LET radiations in generating short fragments. That data, as well as the data at 6 kGy presented in this report, are a subset of the range explored in our experiments. Naturally, it would be desirable to construct a complete dose–response for DSB induction for all the doses and radiation types investigated. However, contamination of certain samples has precluded AFM image acquisition of sufficient quality for more extensive analysis as we performed in our previous study of neutron and electron irradiations (55). Nonetheless, the DSB data at 6 kGy clearly show a radiation quality dependence of RBE for DSB induction.

The RBE for DSB induction has been measured for both cells and in aqueous solutions. Prise et al. summarized the DSB induction data for radiations of varying quality for various cell line (25). It was shown that the RBE generally remained approximately close to 1 for a wide range of LET values from 10.9 to 998 keV/μm. In a subsequent report, Prise et al. presented additional DSB induction data for a few additional ions in the LET range of 40–225 keV/μm obtained with the PFGE either using the fraction of activity released (FAR) or fragmentation method and showed a substantial difference in RBE values obtained with these two techniques (61). Again, the RBE values obtained with the FAR method remained close to 1 or less, but varied from 1.1 to 1.5 when measured using the fragmentation method. They concluded that the fragmentation method permitted quantification of shorter DNA fragments that were not measured with the FAR method and thus resulted in increased DSB collection.

The RBE values determined in this report were based on AFM measurement of individual DNA fragments induced in aqueous solution that were orders of magnitude shorter than what measured using the gel electrophoresis fragmentation method. The much larger RBE values obtained here reflect a much enhanced capability of AFM to measure short DNA fragments. It is, however, difficult to make a direct comparison of these RBE values to what Prise and coauthors have summarized, as our DNA model system is plasmid DNA in aqueous solution, while that in Prise's report were DNA in cellular environments. The different DNA configuration and the substantially greater scavenging capacity of cells influence greatly the induction of DSB. Nevertheless, the techniques employed for DSB measurement have much greater impact on the accuracy of RBE values determined.

Therapeutic application of proton and heavy charged-particle irradiation has been gaining increasing acceptance, recognition, and popularity in the radiation oncology community worldwide (62–64). Heavy charged particles possess highly desired dosimetric advantages over photon or electron irradiations, exemplified by their finite range in tissue and Bragg peak in energy deposition (65). Furthermore, the biological advantage, as represented by their greater RBE for cell survival, adds another important dimension to the medical application of charged-particle irradiation. As presented in this and previous studies, heavy charged-particle radiations produce significantly more short DNA fragments than do low-LET radiations. We propose that the greater RBE of high-LET radiations is a result of the increased production of short DNA fragments by high-LET radiations.

CONCLUSION

Atomic force microscopy imaging of plasmid DNA molecules as the DNA targets of irradiation demonstrates that heavy charged particles induce a significantly greater proportion of short DNA fragments than observed following low-LET irradiations. The increased short DNA fragment generation is attributed to clustered DNA DSB generation following high-LET irradiations. The increased short DNA fragment production may be a critical factor underlying the greater biological effectiveness of heavy charged-particle radiation.

AUTHOR CONTRIBUTIONS

DP designed, performed the experiments, data analyses, and wrote the manuscript; SC performed AFM imaging of the DNA

samples; JR participated in electron and Co-60 irradiation experiments and reviewed the manuscript; AD participated in design of the experiments, reviewed, and edited the manuscript.

ACKNOWLEDGMENTS

The authors gratefully acknowledge the important contributions made by Barry L. Berman and Seldon Datz in arranging and participating in the irradiations performed at Oak Ridge National Laboratory and at HIMAC in Chiba, Japan. The authors are saddened that both Professors Berman and Datz have since passed away. The authors also gratefully acknowledge the technical and scientific staff at Oak Ridge and Chiba for their expertise in assisting performance of the irradiation experiments. Finally, the authors acknowledge the numerous hours Max Goldberg, a high school intern from Witmann High School in Bethesda, MD, USA, had spent on measuring the DNA fragment sizes.

REFERENCES

1. Curtis SB. Lethal and potentially lethal lesions induced by radiation – a unified repair model. *Radiat Res* (1986) 106(2):252–70. doi:10.2307/3576798
2. Frankenberg D, Frankenberg-Schwager M, Blöcher D, Harbich R. Evidence for DNA double-strand breaks as the critical lesions in yeast cells irradiated with sparsely or densely ionizing radiation under oxic or anoxic conditions. *Radiat Res* (1981) 88(3):524–32. doi:10.2307/3575641
3. Radford IR. The level of induced DNA double-strand breakage correlates with cell killing after X-irradiation. *Int J Radiat Biol Relat Stud Phys Chem Med* (1985) 48(1):45–54. doi:10.1080/09553008514551051
4. Barendsen G. RBE-LET relationships for different types of lethal radiation damage in mammalian cells: comparison with DNA DSB and an interpretation of differences in radiosensitivity. *Int J Radiat Biol* (1994) 66(5):433–6. doi:10.1080/09553009414551411
5. Blakely EA. Cell inactivation by heavy charged particles. *Radiat Environ Biophys* (1992) 31(3):181–96. doi:10.1007/BF01214826
6. Weber K, Flentje M. Lethality of heavy ion-induced DNA double-strand breaks in mammalian cells. *Int J Radiat Biol* (1993) 64(2):169–78. doi:10.1080/09553009314551261
7. Ward JF. The complexity of DNA damage: relevance to biological consequences. *Int J Radiat Biol* (1994) 66(5):427–32. doi:10.1080/09553009414551401
8. Prise KM, Folkard M, Newman HC, Michael BD. Effect of radiation quality on lesion complexity in cellular DNA. *Int J Radiat Biol* (1994) 66(5):537–42. doi:10.1080/09553009414551581
9. Martin RG, Ames BN. A method for determining the sedimentation behavior of enzymes: application to protein mixtures. *J Biol Chem* (1961) 236(5):1372–9.
10. Bradley MO, Kohn KW. X-ray induced DNA double strand break production and repair in mammalian cells as measured by neutral filter elution. *Nucleic Acids Res* (1979) 7(3):793–804. doi:10.1093/nar/7.3.793
11. Schwartz DC, Cantor CR. Separation of yeast chromosome-sized DNAs by pulsed field gradient gel electrophoresis. *Cell* (1984) 37(1):67–75. doi:10.1016/0092-8674(84)90301-5
12. Olive PL, Wlodek D, Banáth JP. DNA double-strand breaks measured in individual cells subjected to gel electrophoresis. *Cancer Res* (1991) 51(17):4671–6.
13. Smith CL, Klco SR, Cantor CR. Pulsed-field gel electrophoresis and the technology of large DNA molecules. In: Davies K, editor. *Genome Analysis: A Practical Approach*. Oxford, England: IRL Press (1988). p. 41–72.
14. Fairbairn DW, Olive PL, O'Neill KL. The comet assay: a comprehensive review. *Mutat Res* (1995) 339(1):37–59. doi:10.1016/0165-1110(94)00013-3
15. Collins AR. The comet assay for DNA damage and repair. *Mol Biotechnol* (2004) 26(3):249–61. doi:10.1385/MB:26:3:249
16. Pilch DR, Sedelnikova OA, Redon C, Celeste A, Nussenzweig A, Bonner WM. Characteristics of γ-H2AX foci at DNA double-strand breaks sites. *Biochem Cell Biol* (2003) 81(3):123–9. doi:10.1139/o03-042
17. Sedelnikova OA, Rogakou EP, Panyutin IG, Bonner WM. Quantitative detection of 125IdU-induced DNA double-strand breaks with γ-H2AX antibody. *Radiat Res* (2002) 158(4):486–92. doi:10.1667/0033-7587(2002)158[0486:QDOIID]2.0.CO;2
18. Kraxenberger F, Weber KJ, Friedl AA, Eckardt-Schupp F, Flentje M, Quicken P, et al. DNA double-strand breaks in mammalian cells exposed to Á-rays and very heavy ions. *Radiat Environ Biophys* (1998) 37(2):107–15. doi:10.1007/s004110050102
19. Ikpeme S, Löbrich M, Akpa T, Schneider E, Kiefer J. Heavy ion-induced DNA double-strand breaks with yeast as a model system. *Radiat Environ Biophys* (1995) 34(2):95–9. doi:10.1007/BF01275213
20. Obe G, Johannes C, Schulte-Frohlinde D. DNA double-strand breaks induced by sparsely ionizing radiation and endonucleases as critical lesions foe cell death, chromosomal aberrations, mutations and oncogenic transformation. *Mutagenesis* (1992) 7(1):3–12. doi:10.1093/mutage/7.1.3
21. Schulte-Frohlinde D. Biological consequences of strand breaks in plasmid and viral DNA. *Br J Cancer Suppl* (1987) 8:129.
22. Siddiqi MA, Bothe E. Single-and double-strand break formation in DNA irradiated in aqueous solution: dependence on dose and OH radical scavenger concentration. *Radiat Res* (1987) 112(3):449–63. doi:10.2307/3577098
23. Spotheim-Maurizot M, Charlier M, Sabattier R. DNA radiolysis by fast neutrons. *Int J Radiat Biol* (1990) 57(2):301–13. doi:10.1080/09553009014552421
24. Sutherland BM, Bennett PV, Sidorkina O, Laval J. Clustered DNA damages induced in isolated DNA and in human cells by low doses of ionizing radiation. *Proc Natl Acad Sci U S A* (2000) 97(1):103–8. doi:10.1073/pnas.97.1.103
25. Prise K, Ahnström G, Belli M, Carlsson J, Frankenberg D, Kiefer J, et al. A review of DSB induction data for varying quality radiations. *Int J Radiat Biol* (1998) 74(2):173–84. doi:10.1080/095530098141564
26. Prise KM, Davies S, Michael BD. The relationship between radiation-induced DNA double-strand breaks and cell kill in hamster V79 fibroblasts irradiated with 250 kVp X-rays, 2· 3 MeV neutrons or 238Pu α-particles. *Int J Radiat Biol Relat Stud Phys Chem Med* (1987) 52(6):893–902. doi:10.1080/09553008714552481
27. Barendsen G. The relationships between RBE and LET for different types of lethal damage in mammalian cells: biophysical and molecular mechanisms. *Radiat Res* (1994) 139(3):257–70. doi:10.2307/3578823
28. Blöcher D. DNA double-strand break repair determines the RBE of α-particles. *Int J Radiat Biol* (1988) 54(5):761–71. doi:10.1080/09553008814552201
29. Frankenberg D, Frankenberg-Schwager M, Harbich R. Interpretation of the shape of survival curves in terms of induction and repair/misrepair of DNA double-strand breaks. *Br J Cancer Suppl* (1984) 6:233.
30. Frankenberg-Schwager M. Induction, repair and biological relevance of radiation-induced DNA lesions in eukaryotic cells. *Radiat Environ Biophys* (1990) 29(4):273–92. doi:10.1007/BF01210408
31. Frankenberg-Schwager M, Frankenberg D, Harbich R. Repair of DNA double-strand breaks as a determinant of RBE of alpha particles. *Br J Cancer Suppl* (1984) 6:169.
32. Hada M, Georgakilas AG. Formation of clustered DNA damage after high-LET irradiation: a review. *J Radiat Res* (2008) 49(3):203–10. doi:10.1269/jrr.07123
33. Holley WR, Chatterjee A. Clusters of DNA damage induced by ionizing radiation: formation of short DNA fragments. I. Theoretical modeling. *Radiat Res* (1996) 145(2):188–99. doi:10.2307/3579174
34. Löbrich PC, Cooper PK, Rydberg MB. Non-random distribution of DNA double-strand breaks induced by particle irradiation. *Int J Radiat Biol* (1996) 70(5):493–503. doi:10.1080/095530096144680
35. Friedland W, Dingfelder M, Kundrát P, Jacob P. Track structures, DNA targets and radiation effects in the biophysical Monte Carlo simulation code PARTRAC. *Mutat Res* (2011) 711(1):28–40. doi:10.1016/j.mrfmmm.2011.01.003
36. Friedland W, Jacob P, Paretzke HG, Merzagora M, Ottolenghi A. Simulation of DNA fragment distributions after irradiation with photons. *Radiat Environ Biophys* (1999) 38(1):39–47. doi:10.1007/s004110050136
37. Goodhead D. Molecular and cell models of biological effects of heavy ion radiation. *Radiat Environ Biophys* (1995) 34(2):67–72. doi:10.1007/BF01275208
38. Goodhead DT. Initial events in the cellular effects of ionizing radiations: clustered damage in DNA. *Int J Radiat Biol* (1994) 65(1):7–17. doi:10.1080/09553009414550021

39. Nikjoo H, O'Neill P, Terrissol M, Goodhead DT. Quantitative modelling of DNA damage using Monte Carlo track structure method. *Radiat Environ Biophys* (1999) 38(1):31–8. doi:10.1007/s004110050135
40. Semenenko V, Stewart R. Fast Monte Carlo simulation of DNA damage formed by electrons and light ions. *Phys Med Biol* (2006) 51(7):1693. doi:10.1088/0031-9155/51/7/004
41. Friedland W, Jacob P, Paretzke HG, Stork T. Monte Carlo simulation of the production of short DNA fragments by low-linear energy transfer radiation using higher-order DNA models. *Radiat Res* (1998) 150(2):170–82. doi:10.2307/3579852
42. Campa A, Ballarini F, Belli M, Cherubini R, Dini V, Esposito G, et al. DNA DSB induced in human cells by charged particles and gamma rays: experimental results and theoretical approaches. *Int J Radiat Biol* (2005) 81(11):841–54. doi:10.1080/09553000500530888
43. Binnig G, Quate CF, Gerber C. Atomic force microscope. *Phys Rev Lett* (1986) 56(9):930. doi:10.1103/PhysRevLett.56.930
44. Hansma HG, Vesenka J, Siegerist C, Kelderman G, Morrett H, Sinsheimer RL, et al. Reproducible imaging and dissection of plasmid DNA under liquid with the atomic force microscope. *Science* (1992) 256(5060):1180–4. doi:10.1126/science.256.5060.1180
45. Lyubchenko YL, Shlyakhtenko LS. AFM for analysis of structure and dynamics of DNA and protein-DNA complexes. *Methods* (2009) 47(3):206–13. doi:10.1016/j.ymeth.2008.09.002
46. Binnig G, Gerber CH, Stoll E, Albrecht TR, Quate CF. Atomic resolution with atomic force microscope. *EPL Europhys Lett* (1987) 3(12):1281. doi:10.1209/0295-5075/3/12/006
47. Williams DB, Carter CB. *The Transmission Electron Microscope*. New York: Springer (1996).
48. Tersoff J, Hamann D. *Theory of the Scanning Tunneling Microscope, in Scanning Tunneling Microscopy*. Netherlands: Springer (1985). p. 59–67.
49. Drake B, Prater CB, Weisenhorn AL, Gould SA, Albrecht TR, Quate CF, et al. Imaging crystals, polymers, and processes in water with the atomic force microscope. *Science* (1989) 243(4898):1586–9. doi:10.1126/science.2928794
50. Hansma HG, Bezanilla M, Zenhausern F, Adrian M, Sinsheimer RL. Atomic force microscopy of DNA in aqueous solutions. *Nucleic Acids Res* (1993) 21(3):505–12. doi:10.1093/nar/21.3.505
51. Hinterdorfer P, Baumgartner W, Gruber HJ, Schilcher K, Schindler H. Detection and localization of individual antibody-antigen recognition events by atomic force microscopy. *Proc Natl Acad Sci U S A* (1996) 93(8):3477–81. doi:10.1073/pnas.93.8.3477
52. Pang D, Berman BL, Chasovskikh S, Rodgers JE, Dritschilo A. Investigation of neutron-induced damage in DNA by atomic force microscopy: experimental evidence of clustered DNA lesions. *Radiat Res* (1998) 150(6):612–8. doi:10.2307/3579883
53. Ottolenghi A, Merzagora M, Tallone L, Durante M, Paretzke HG, Wilson WE. The quality of DNA double-strand breaks: a Monte Carlo simulation of the end-structure of strand breaks produced by protons and alpha particles. *Radiat Environ Biophys* (1995) 34(4):239–44. doi:10.1007/BF01209749
54. Goodhead DT. Mechanisms for the biological effectiveness of high-LET radiations. *J Radiat Res* (1999) 40(Suppl):S1–13. doi:10.1269/jrr.40.S1
55. Pang D, Rodgers JE, Berman BL, Chasovskikh S, Dritschilo A. Spatial distribution of radiation-induced double-strand breaks in plasmid DNA as resolved by atomic force microscopy. *Radiat Res* (2005) 164(6):755–65. doi:10.1667/RR3425.1
56. Psonka K, Gudowska-Nowaka E, Bronsb S, Elsässerb TH, Heissb M, Taucher-Scholz G. Ionizing radiation-induced fragmentation of plasmid DNA – atomic force microscopy and biophysical modeling. *Adv Space Res* (2007) 39(6):1043–9. doi:10.1016/j.asr.2007.02.089
57. Pang D, Winters TA, Jung M, Purkayastha S, Cavalli LR, Chasovkikh S, et al. Radiation-generated short DNA fragments may perturb non-homologous end-joining and induce genomic instability. *J Radiat Res* (2011) 52(3):309–19. doi:10.1269/jrr.10147
58. Ma Y, Lieber MR. DNA length-dependent cooperative interactions in the binding of Ku to DNA. *Biochemistry* (2001) 40(32):9638–46. doi:10.1021/bi010932v
59. Blier PR, Griffith AJ, Craft J, Hardin JA. Binding of Ku protein to DNA. Measurement of affinity for ends and demonstration of binding to nicks. *J Biol Chem* (1993) 268(10):7594–601.
60. Wang H, Wang X, Zhang P, Wang Y. The Ku-dependent non-homologous end-joining but not other repair pathway is inhibited by high linear energy transfer ionizing radiation. *DNA Repair* (2008) 7(5):725–33. doi:10.1016/j.dnarep.2008.01.010
61. Prise KM, Pinto M, Newman HC, Michael BD. A review of studies of ionizing radiation-induced double-strand break clustering. *Radiat Res* (2001) 156(5):572–6. doi:10.1667/0033-7587(2001)156[0572:AROSOI]2.0.CO;2
62. Levin WP, Kooy H, Loeffler JS, DeLaney TF. Proton beam therapy. *Br J Cancer* (2005) 93(8):849–54. doi:10.1038/sj.bjc.6602754
63. Hug EB, Loredo LN, Slater JD, DeVries A, Grove RI, Schaefer RA, et al. Proton radiation therapy for chordomas and chondrosarcomas of the skull base. *J Neurosurg* (1999) 91(3):432–9. doi:10.3171/jns.1999.91.3.0432
64. Schulz-Ertner D, Tsujii H. Particle radiation therapy using proton and heavier ion beams. *J Clin Oncol* (2007) 25(8):953–64. doi:10.1200/JCO.2006.09.7816
65. Kjellberg RN, Hanamura T, Davis KR, Lyons SL, Adams RD. Bragg-peak proton-beam therapy for arteriovenous malformations of the brain. *N Engl J Med* (1983) 309(5):269–74. doi:10.1056/NEJM198308043090503

Conflict of Interest Statement: The authors declare that the research was conducted in the absence of any commercial or financial relationships that could be construed as a potential conflict of interest.

Copyright © 2016 Pang, Chasovskikh, Rodgers and Dritschilo. This is an open-access article distributed under the terms of the Creative Commons Attribution License (CC BY). The use, distribution or reproduction in other forums is permitted, provided the original author(s) or licensor are credited and that the original publication in this journal is cited, in accordance with accepted academic practice. No use, distribution or reproduction is permitted which does not comply with these terms.

frontiers in Oncology

ORIGINAL RESEARCH
published: 19 October 2015
doi: 10.3389/fonc.2015.00226

Biological effectiveness of accelerated protons for chromosome exchanges

Kerry A. George[1], Megumi Hada[1] and Francis A. Cucinotta[2]*

[1] Wyle Science, Technology and Engineering Group, Houston, TX, USA, [2] University of Nevada Las Vegas, Las Vegas, NV, USA

We have investigated chromosome exchanges induced in human cells by seven different energies of protons (5–2500 MeV) with LET values ranging from 0.2 to 8 keV/μm. Human lymphocytes were irradiated *in vitro* and chromosome damage was assessed using three-color fluorescence *in situ* hybridization chromosome painting in chemically condensed chromosomes collected during the first cell division post irradiation. The relative biological effectiveness (RBE) was calculated from the initial slope of the dose–response curve for chromosome exchanges with respect to low dose and low dose-rate γ-rays (denoted as $RBE_{max)}$, and relative to acute doses of γ-rays (denoted as $RBE_{\gamma Acute)}$. The linear dose–response term was similar for all energies of protons, suggesting that the decrease in LET with increasing proton energy was balanced by the increase in dose from the production of nuclear secondaries. Secondary particles increase slowly above energies of a few hundred megaelectronvolts. Additional studies of 50 g/cm^2 aluminum shielded high-energy proton beams showed minor differences compared to the unshielded protons and lower RBE values found for shielded in comparison to unshielded beams of 2 or 2.5 GeV. All energies of protons produced a much higher percentage of complex-type chromosome exchanges when compared to acute doses of γ-rays. The implications of these results for space radiation protection and proton therapy are discussed.

Keywords: chromosomal aberrations, biomarkers, protons, proton therapy, space radiation

OPEN ACCESS

Edited by:
Marco Durante, GSI, Germany

Reviewed by:
Michael Wayne Epperly, University of Pittsburgh Cancer Institute, USA
Michael Cornforth, University of Texas Medical Branch, USA

****Correspondence:***
Kerry A. George
kerry.a.george@nasa.gov

Specialty section:
This article was submitted to Radiation Oncology, a section of the journal Frontiers in Oncology

Received: *24 June 2015*
Accepted: *30 September 2015*
Published: *19 October 2015*

Citation:
George KA, Hada M and Cucinotta FA (2015) Biological effectiveness of accelerated protons for chromosome exchanges. Front. Oncol. 5:226. doi: 10.3389/fonc.2015.00226

INTRODUCTION

The study of the biological effectiveness of accelerated proton exposures is of interest for clinical treatment plans and for assessing normal tissue damage from protons of various energies that are generated outside of the Bragg peak during proton therapy (1–4). Protons are also a concern for space radiation exposures to astronauts because the space radiation flux is predominantly energetic protons or secondary protons produced in nuclear interactions (5–7). Although evidence now indicates that relative biological effectiveness (RBE) varies considerably along the proton depth-dose distribution, RBE modeling in treatment planning still involves significant uncertainties and, consequently, clinical proton therapy is usually based on the use of a generic RBE of 1.1 (4). Further experimental data are required before a consensus can be reached on weighting factors across the depth-dose profile and for different tissue effects.

Experimental studies have shown that the RBE of protons varies with biological endpoint, tissue type, dose, and energy of the protons. RBE values calculated by cell killing and mutation induction indicate that low energy protons are significantly higher than unity and values are LET dependent (8). Published data on chromosome damage have indicated that RBEs or RBE_{max} values for protons of energies above 10 MeV vary from <1 to about 2 in comparison to X-rays or γ-rays, whereas lower energy protons (<10 MeV) were significantly higher than unity and the values were LET dependent (9–11). RBEs for tumor induction were close to 1 in several studies (12, 13), and as high as 2 for Harderian gland tumors (14) and for rat mammary carcinomas (15) that were induced by 250 MeV protons. The choice of reference radiation can complicate the analysis of RBE because differences have been found for X-rays and γ-rays (16), and variability has been reported for low doses of photons and protons. In addition, high-energy protons induce nuclear spallation and other interactions that produce secondary protons, neutrons, and heavy ion fragments. Nuclear interaction cross sections generally increase with the energy of the protons (3), and the secondary particles typically have higher LET values that can increase RBE.

In the present study, we considered the induction of simple and complex-type chromosome exchanges in normal human lymphocytes. Chromosome exchanges, especially translocations, are positively correlated with many cancers, and are therefore a potential biomarker of cancer risk associated with radiation exposure (17–19). In addition, RBE factors for chromosome aberrations are similar to RBEs observed for induction of solid tumors in mice (16, 20, 21). Therefore, chromosome exchanges are a useful biomarker for cancer risk and can be compared with other biomarkers in the absence of human data for galactic cosmic rays (GCR). In earlier work (22), we considered the effects of 250 MeV protons at different dose-rates. Here, we consider several proton energies from 5 to 2500 MeV with additional studies on the effects of heavy aluminum and polyethylene shielding for the high-energy proton exposures.

MATERIALS AND METHODS

These studies were conducted in accordance with accepted ethical and humane practices, and were approved by the appropriate institutional and/or governmental committee(s) and/or organization(s).

Irradiation

Whole blood was collected from healthy volunteers and was irradiated with accelerated protons using the NASA Space Radiation Laboratory (NSRL) facility at Brookhaven National Laboratory (BNL). The same volunteer donated the blood samples for each experiment. All samples were exposed in the plateau portion of the Bragg curves and dose rates were between 0.2 and 0.5 Gy/min, depending on the dose delivered. Doses were measured at the target using ionization chambers. Samples were exposed at room temperature. Each sample received at least three pulses and no exposure lasted more than 10 min. The beam uniformity was checked using a digital beam imager and dose did not vary more than 5% over the target area. For the 2.5 and 2 GeV protons exposures, the target areas was shielded, respectively, with 50 g/cm^2 of aluminum and 50 g/cm^2 of aluminum plus 10 cm of polyethylene. At these proton energies, the dose increases as the protons pass through the shielding due to secondary radiation, and doses were normalized using BNL dosimetry to generate the same total dose to the sample as the unshielded studies.

Cell Culture

Immediately after exposure, whole-blood cultures in RPMI 1640 medium (Gibco BRL) supplemented with 20% calf serum and 1% phytohemagglutinin (Gibco, BRL) were incubated at 37°C for 48–50 h. Chemically induced PPC were collected using the method described by Durante et al. (23), which results in well-condensed chromosomes from cells in G2 and metaphase. Briefly, 50 nM calyculin A (Wako Chemicals) was added to the growth medium for the last 30 min of the incubation. Cells were then treated with hypotonic KCl (0.075M) for 15 min at 37°C and fixed in methanol:acetic acid (3:1). A 0.5 ml volume of blood from each sample was cultured with 10 μm bromodeoxyuridine (BrdU), and a differential replication staining procedure was completed on chromosomes from these samples by incubating slides in 0.5 mg/ml of Hoechst during exposure to black light (General Electric 15T8/BL bulb). Chromosomes were stained with Giemsa to visualized replication rounds, revealing the percentage of cells in first mitosis was >95% for all samples analyzed.

Fluorescence *In situ* Hybridization

Chromosomes were dropped onto clean microscope slides and hybridized *in situ* with a combination of fluorescence whole-chromosome probes for chromosomes 1, 2, and 4, or chromosome 1, 2, and 5 (Rainbow Scientific) using the procedures recommended by the manufacturer. Chromosome 1 was painted with a Texas red fluorophore, chromosome 2 was painted with FTIC, and chromosome 4 (or 5) was painted with a 1:1 combination of Texas Red and FITC that appeared yellow under the triple-band-pass filter set. Unlabeled chromosomes were always counterstained with 4′,6-diamidino-2-phenylindole (DAPI).

Chromosome Analysis

Chromosomes were analyzed on a Zeiss Axioplan fluorescence microscope. The images of all damaged cells were captured electronically using a Sensys charge-coupled device (CCD) camera (Photometrics Ltd., AZ, USA) and the Cytovision computer software. The number of cells analyzed for each sample varied, exact numbers are listed in **Table 1**. All slides analyzed in this study were coded and scored blind. Complex exchanges were scored when it was determined that an exchange involved a minimum of three breaks in two or more chromosomes (24). An exchange was defined as simple if it appeared to involve two breaks in two chromosomes, that is, dicentrics and translocations. Incomplete translocations and incomplete dicentrics were included in the category of simple exchanges, assuming that in most cases the reciprocal fragments were below the level of detection (25). Each type of exchange – dicentrics, apparently simple reciprocal exchanges, incompletes, or complex exchanges – was counted as one exchange, and values for total exchanges were derived by

TABLE 1 | Dose–response data for chromosome aberrations per 100 cells induced by 5 different energies of protons measured in first post irradiation chemically induced PCC.

Dose (Gy)	Cells scored	Simple exchanges	Complex exchanges
E = 5 MeV			
0.10	1018	2.3 ± 0.7	0 ± 0
0.20	1044	1.2 ± 0.9	0.7 ± 0.4
0.40	909	6.8 ± 1.6	1.1 ± 0.6
0.70	869	8.0 ± 1.7	2.1 ± 0.8
1.00	634	14.9 ± 2.6	4.3 ± 1.3
E = 120 MeV[a]			
0.15	1188	1.5 ± 0.6	0.4 ± 0.3
0.30	1437	2.1 ± 0.6	1.0 ± 0.4
0.50	1369	3.6 ± 0.8	2.7 ± 0.7
0.75	1136	6.1 ± 1.2	2.4 ± 0.7
1.00	825	13.8 ± 2.0	3.6 ± 1.0
1.50	357	31.2 ± 4.7	11.1 ± 2.8
2.00	203	61.0 ± 8.6	34.2 ± 6.5
E = 250 MeV			
0.25	491	1.9 ± 1.8	3.1 ± 1.3
0.50	536	2.8 ± 1.8	5.3 ± 1.6
0.80	427	5.2 ± 2.3	3.6 ± 1.5
1.20	563	7.6 ± 2.3	5.5 ± 1.6
2.00	325	29.4 ± 5.1	11.1 ± 3.0
E = 800 MeV			
0.25	330	0 ± 1.1	2.3 ± 1.4
0.50	609	0 ± 0.8	0.4 ± 0.4
0.80	655	13.8 ± 2.6	5.1 ± 1.4
1.20	561	14.0 ± 2.9	6.0 ± 1.7
2.00	263	35.2 ± 6.2	7.8 ± 2.8
E = 1000 MeV			
0.20	231	3.0 ± 2.2	0 ± 0
1.20	321	13.0 ± 3.7	4.3 ± 2.2
3.00	134	87.9 ± 15.1	38.8 ± 10.0
E = 2000 MeV			
0.25	330	0.7 ± 1.3	0.8 ± 0.8
0.50	284	9.7 ± 3.2	6.1 ± 2.3
0.80	378	13.5 ± 3.1	3.3 ± 1.5
1.20	538	9.9 ± 2.3	7.4 ± 1.8
2.00	243	46.3 ± 7.0	15.3 ± 4.0
E = 2500 MeV			
0.20	1342	1.4 ± 0.5	0.8 ± 0.4
0.40	1127	3.4 ± 0.9	2.1 ± 0.7
0.60	1635	7.6 ± 1.1	2.6 ± 0.6
0.80	218	7.1 ± 2.9	4.7 ± 2.4
1.20	304	24.7 ± 4.6	4.3 ± 1.9

Data represent whole-genome equivalent values with background subtracted.[a]*150 MeV protons with 5 cm polyethylene shielding leading to residual energy of 120 MeV.*

adding the yields. When two or more painted chromosomes were damaged, each was scored separately.

Statistical Analysis

The frequency of chromosomal aberrations in the painted chromosomes was evaluated as the ratio between aberrations scored and total cells analyzed. Several studies have indicated that the distribution of radiation damage among chromosomes is random, and the yield of exchanges measured within the first division after exposure is proportional to the DNA content of the chromosome analyzed, with some fluctuation of data (26). Therefore, the frequencies of exchanges in individual chromosomes can be extrapolated to whole-genome equivalents using a modified version of the Lucas et al. (27) formula, $Fp = 2.05[fp(1-fp) + fp1fp2 + fp1fp3 + fp2fp3]FG$. Fp is the combined frequency of exchanges in all painted chromosomes, fp is the fraction of the whole genome comprised of the painted chromosomes, fp1, fp2, and fp3 are the fractions of the genome for each individual chromosome, and FG is the whole-genome aberration frequency. Using this formula, the genomic frequency for a male donor was estimated as 2.48 times that detected in chromosomes 1, 2, and 4.

Standard errors for aberration frequencies were calculated assuming Poisson statistics. Error bars in each figure represent SEs of the mean values. The data were modeled assuming binomial errors per number of chromosomes analyzed with the frequencies of aberrations of various types extrapolated to whole-genome equivalents as described above.

A weighted linear-quadratic (LQ) or linear (L) regression model was used to fit dose–responses for each proton energy, and the γ-ray dose–responses. Using the maximum likelihood method, the linear and quadratic coefficients α and β in

$$Y = Y_0 + \alpha D + \beta D^2$$

were found for simple, complex, and total exchanges. Estimates of RBE were made from the α-coefficient from the acute response (21), denoted as $RBE_{\gamma Acute}$, and from the ratio of initial slopes for γ-rays using our previous data (28–30) of low dose and low dose-rate irradiation, denoted as RBE_{max}. For estimating a low dose and low dose-rate γ-ray component, we combined the data from our previous analysis of 0.1 Gy/h with additional data at low doses (<0.5 Gy) from the same volunteer used for the proton experiments. For complex exchanges, the low dose and dose-rate γ-rays, complex exchanges were rare and RBE_{max} estimates could not be made.

RESULTS

Tables 1 and **2** list the dose–response data for simple and complex-type chromosome exchanges for each energy of protons, and are represented as whole-genome equivalent values with background subtracted. The data, plotted in **Figure 1**, show a high degree of similarity in the dose–response for simple and complex exchanges for all proton energies considered. A weighted regression model based on the experimental errors was used to estimate α and β values with SEs for a linear-quadratic dose–response fit to the data for γ-rays and each proton energy. **Tables 3–5** show results of this analysis for total exchanges, simple exchanges, and complex exchanges respectively. Comparison of the α values for acute and low dose rate (LDR) γ-rays fits indicates a dose-rate modifier factor of 1.83 and 1.74 for total exchanges and simple exchanges, respectively.

The linear (α) coefficients from the dose–response data (**Tables 3–5**) are similar for all energies as determined by either the LQ or L weighted regression models. The α values produced from the LQ models resulted in somewhat larger SD compared to fits from the linear weighted regression model (results not shown). RBE values for simple exchanges were slightly less or more than unity using the $RBE_{\gamma Acute}$ and RBE max models, respectively.

However, a much higher frequency of complex exchanges was observed for each proton beam compared to γ-rays resulting in RBEs for complex exchanges varied from 2.1 to 4.1, and this led to a modest increase the RBEs for total exchanges. A trend toward increasing RBE_{max} values for proton energies of 1 GeV and higher was found for simple and total exchanges.

TABLE 2 | Dose–response data for chromosome exchanges per 100 cells induced by 2 and 2.5 GeV protons with and without shielding and measured in first post irradiation chemically induced PCC.

Dose (Gy)	Cells scored	Simple exchanges	Complex exchanges
E = 2000 MeV, no shielding			
0.25	330	0.7 ± 1.3	0.8 ± 0.8
0.50	284	9.7 ± 3.2	6.1 ± 2.3
0.80	378	13.5 ± 3.1	3.3 ± 1.5
1.20	538	9.9 ± 2.3	7.4 ± 1.8
2.00	243	46.3 ± 7.0	15.3 ± 4.0
E = 2000 MeV, 50 g/cm² Aluminum + 10 cm polyethylene			
0.25	401	1.3 ± 0.9	0.6 ± 0.6
0.5	1029	4.8 ± 1.1	2.0 ± 0.7
0.8	940	7.7 ± 1.5	1.6 ± 0.7
1.2	709	15.2 ± 2.4	4.4 ± 1.3
2.0	456	28.7 ± 4.0	3.0 ± 1.5
E = 2500 MeV, no shielding			
0.20	1342	1.4 ± 0.5	0.8 ± 0.4
0.40	1127	3.4 ± 0.9	2.1 ± 0.7
0.60	1635	7.6 ± 1.1	2.6 ± 0.6
0.80	218	7.1 ± 2.9	4.7 ± 2.4
1.20	304	24.7 ± 4.6	4.3 ± 1.9
E = 2500 MeV, 50 g/cm² aluminum			
0.20	485	1.1 ± 0.8	0.5 ± 0.5
0.40	696	2.2 ± 0.9	0.7 ± 0.5
0.60	629	9.0 ± 1.9	2.5 ± 1.0
0.80	729	8.8 ± 1.8	3.5 ± 1.1
1.2	551	19.1 ± 3.0	9.3 ± 2.1

Dose was measured at the target area for both shielded and unshielded exposures. Data represent whole-genome equivalent values with background subtracted.

Data for the yield of chromosome exchanges in the shielded samples are listed in **Table 2** where values are represented as whole-genome equivalent with background subtracted. The 2.5 GeV protons were shielded with 50 g/cm² of aluminum, and the 2 GeV protons were shielded with 50 g/cm² of aluminum plus 10 cm polyethylene. The doses represent the values measures at the target. A comparison of shielded and unshielded data shown in **Figure 2** indicates similar dose–responses for the shielded and unshielded high-energy proton beams. However, RBE_{max} values were reduced with shielding. For example, RBE values for total exchanges induced

TABLE 3 | Results for parameter estimates of linear-quadratic dose–response model for total exchanges, and relative biological effectiveness (RBE) factors for protons of different energies compared to acute, or low dose or low dose-rate γ-rays.

Radiation type	α (Gy⁻¹)	β (Gy⁻²)	$RBE_{\gamma Acute}$	RBE_{max}
γ-Rays acute	0.176 ± 0.018	0.119 ± 0.038	–	–
γ-Rays LD	0.096 ± 0.01	–	–	–
Proton, 5 MeV	0.171 ± 0.018	0.043 ± 0.065	0.98 ± 0.11	1.78 ± 0.19
Proton, 120 MeV[a]	0.156 ± 0.016	0.167 ± 0.039	0.89 ± 0.09	1.62 ± 0.16
Proton, 250 MeV	0.144 ± 0.017	0.05 ± 0.032	0.82 ± 0.1	1.5 ± 0.18
Proton, 800 MeV	0.153 ± 0.036	0.114 ± 0.064	0.87 ± 0.21	1.59 ± 0.38
Proton, 1000 MeV	0.219 ± 0.037	0.12 ± 0.043	1.25 ± 0.21	2.27 ± 0.38
Proton, 2000 MeV	0.201 ± 0.033	0.093 ± 0.067	1.15 ± 0.19	2.09 ± 0.34
Proton, 2500 MeV	0.184 ± 0.006	0.105 ± 0.01	1.05 ± 0.05	1.91 ± 0.07

[a]150 MeV protons with 5 cm polyethylene shielding leading to residual energy of 120 MeV.

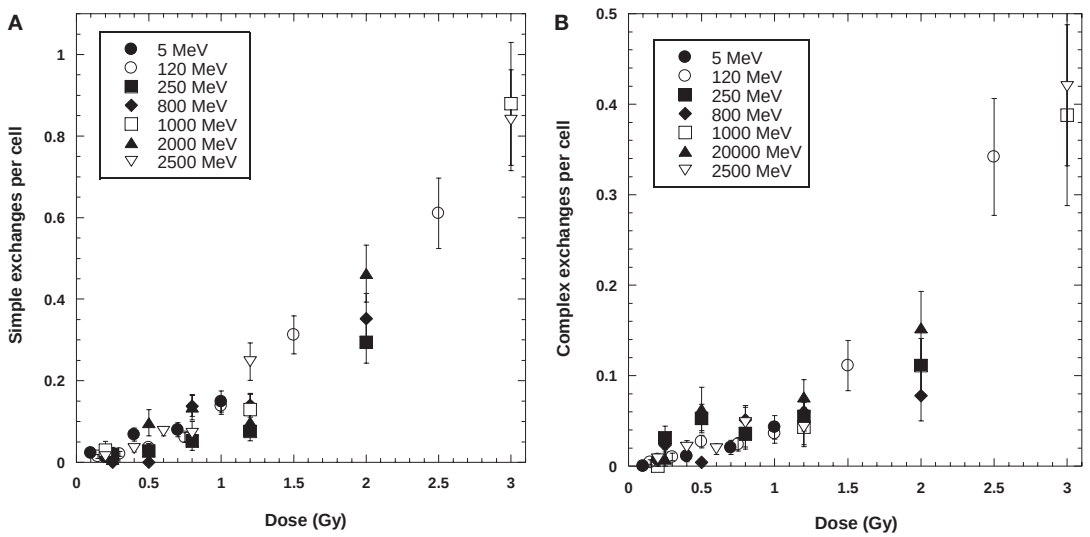

FIGURE 1 | Dose response curves for simple (A) and complex (B) chromosome exchanges induced by each ion. Error bars indicate SEMs and background values have been subtracted for all data.

by unshielded and shielded 2 GeV protons were 2.09 ± 0.34 and 1.26 ± 0.11, respectively, and values were 1.91 ± 0.67 and 1.53 ± 0.14 for unshielded and shielded 2.5 GeV protons, respectively.

DISCUSSION

The similarity in frequency of simple and complex exchanges over a wide range of proton energies found in our experiments suggests that decreases in LET with increasing proton energy is balanced by the increase in doses from secondary radiation, most notably secondary protons and neutrons (3, 31, 32). When the proton LET decreases from about 5 keV/μm at 5 MeV to 0.24 keV/μm at the highest energy of 2.5 GeV, there is concomitant increase in the contribution from nuclear secondaries and their contribution to the biological action cross section (3). Details of the beam characteristics for the shielded and unshielded protons used in our study are given in **Table 6**. Neutrons are produced in the absorbers or tissue equivalent materials through nuclear reactions by protons and other charged particles. Low energy neutrons (<5 MeV) are known to have large RBEs for different types of biological damage, including late effects (16). For our unshielded proton experiments, neutrons produced by the small amount of absorbing material present in the NSRL beam-line and biological samples themselves are largely high energy and unlikely to have slowed down to the more biologically effective neutron energies (<5 MeV). However, our experiments comparing shielding to unshielded protons at high energies led to similar yields of chromosome exchanges per unit dose. This is consistent with previous radiobiology studies

TABLE 4 | Results for parameter estimates of linear-quadratic dose–response model for simple exchanges, and relative biological effectiveness (RBE) factors for protons of different energies compared to acute or low dose or low dose-rate γ-rays.

Radiation type	α (Gy^{-1})	β (Gy^{-2})	$RBE_{\gamma Acute}$	RBE_{max}
γ-Rays acute	0.157 ± 0.013	0.092 ± 0.027	–	–
γ-Rays LD	0.09 ± 0.004	–	–	–
Proton, 5 MeV	0.132 ± 0.016	0.031 ± 0.057	0.84 ± 0.1	1.5 ± 0.18
Proton, 120 MeV[a]	0.121 ± 0.015	0.137 ± 0.036	0.77 ± 0.1	1.36 ± 0.17
Proton, 250 MeV	0.088 ± 0.009	0.064 ± 0.017	0.56 ± 0.06	1.0 ± 0.1
Proton, 800 MeV	0.116 ± 0.028	0.104 ± 0.049	0.73 ± 0.18	1.3 ± 0.31
Proton, 1000 MeV	0.159 ± 0.02	0.081 ± 0.023	1.01 ± 0.13	1.79 ± 0.23
Proton, 2000 MeV	0.132 ± 0.028	0.071 ± 0.058	0.84 ± 0.19	1.49 ± 0.31
Proton, 2500 MeV	0.119 ± 0.01	0.077 ± 0.015	0.76 ± 0.07	1.35 ± 0.11

[a]150 MeV proton beam with 5 cm polyethylene shielding leading to residual energy of 120 MeV.

TABLE 5 | Results for parameter estimates of linear-quadratic dose–response model for complex exchanges, and relative biological effectiveness (RBE) factors for protons of different energies compared to acute γ-rays.

Radiation type	α (Gy^{-1})	β (Gy^{-2})	$RBE_{\gamma Acute}$
γ-Rays acute	0.015 ± 0.005	0.025 ± 0.014	–
Proton, 5 MeV	0.039 ± 0.004	0.006 ± 0.017	2.56 ± 0.85
Proton, 120 MeV[a]	0.032 ± 0.0043	0.024 ± 0.01	2.1 ± 0.28
Proton, 250 MeV	0.055 ± 0.009	0.03 ± 0.017	3.59 ± 1.3
Proton, 800 MeV	0.029 ± 0.010	0.02 ± 0.017	1.92 ± 0.87
Proton, 1000 MeV	0.06 ± 0.016	0.046 ± 0.022	3.96 ± 1.64
Proton, 2000 MeV	0.063 ± 0.009	0.028 ± 0.017	4.12 ± 1.41
Proton, 2500 MeV	0.058 ± 0.006	0.026 ± 0.01	3.81 ± 1.26

RBE_{max} was not determined because low dose-rate γ-rays have very low induction of complex exchanges.
[a]150 MeV proton beam with 5 cm polyethylene shielding leading to residual energy at samples of 120 MeV.

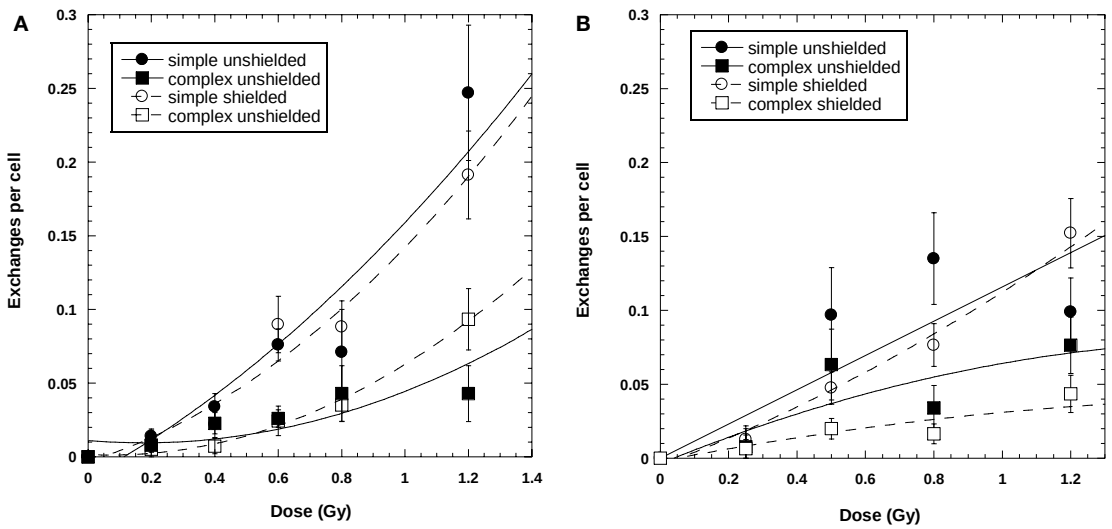

FIGURE 2 | Dose–response curves for chromosome exchanges induced by 2500 MeV protons (A) and 2000 MeV/μ protons (B). The 2000-MeV exposures were shielded with a combination of 50 g/cm² aluminum and 10 cm polyethylene. The 2500-MeV exposure were shielded with 50 g/cm² aluminum only. Error bars indicate SEMs and background values have been subtracted for all data points. Curve fit is extrapolated to the axis.

TABLE 6 | Details of protons shielding characteristics.

Energy at beam entrance (MeV)	Shielding	Energy of beam at target (MeV)	LET (keV/μm)	Percentage of dose from secondaries
5	None	–	7.80	–
120	5 cm polyethylene	42	0.64	6.4
250	None	220	0.43	17.4
800	None	770	0.24	33.1
1000	None	970	0.22	36.5
2000	None	1924	0.21	42.6
	50 g/cm^2 aluminum + 10 cm polyethylene	1624	0.21	80.0
2500	None	2470	0.21	43.7
	50 g/cm^2 aluminum	2241	0.21	78.4

Shielding from booster window, ion chambers, and binary filter contribute 1.2 g/cm^2 of aluminum equivalent shielding to all exposures (shielded or unshielded).
LET reflects values for the beam only and does not include the effect of secondary particles.

with high-energy proton beams using very thick absorbers (33) and suggests that neutrons are ineffective in producing biological damage at high energy (>100 MeV). This observation is readily predicted by the mean-free path of neutrons which is generally >10 g/cm^2 for materials of interest. Because the nuclear absorption cross sections are similar, secondary particles and target fragmentation spectrum produced by protons and neutrons are nearly identical for energies above a few hundred megaelectron-volts. Thus, high-energy protons are biologically more effective than neutrons of the same energy per unit fluence because of the proton charge state, while high-energy neutrons will have higher effectiveness per unit dose.

The NSRL beam-line and the sample holders provide a minimum of 1.2 g/cm^2 of aluminum equivalent shielding. The additional shielding used in our experiments had a minor influence on the biological effectiveness when comparing unshielded high-energy proton beams because the secondary radiation produced behind the shielding will be of similar biological effectiveness as the primary beam, while similar numbers of low energy target fragments of high-LET produced for both the primary and secondary protons and neutrons will be produced for the shielded and unshielded beams.

The α values for acute and LDR γ-rays fits indicate a dose-rate modification factor of 1.83 and 1.74 for total exchanges and simple exchanges, respectively. These values are similar to those reported for dose-rate reduction factors found by Peng et al. (34), dose and dose-rate reduction effectiveness factors (DDREF) for tumor induction in mice (21), and larger than values reported for solid tumors in the atomic bomb survivors where a DDREF of 1.3 is estimated in the BEIR VII report (35).

In the present study, we used three-color combinations of fluorescence in situ hybridization (FISH) chromosome painting probes (chromosomes 1, 2, and 4, or 1, 2, and 5) to analyze our data. Presumably complex exchanges would be underestimated with this method due to the presence of some pseudosimple-type exchanges [that is, complex patterns that are indistinguishable from those created by simple reciprocal exchanges (36)]. Although the true complexity of exchanges can be determined only by analysis of all chromosomes, a significant number of chromosome exchanges found for all proton energies in this study were determined to be complex, which were significantly increased compared to acute or low dose-rate γ-rays.

In conclusion, our study of the proton energy dependence of chromosome exchanges in human lymphocytes suggests that biological effects are similar over a wide range of proton energies (5–2500 MeV) with RBE values for total exchanges are close to unity when measured against acute γ rays, and approach 2 when measured against low dose rate γ rays due to the increased number of complex exchanges at all proton energies compared to γ-rays.

ACKNOWLEDGMENTS

The authors are grateful to the staff of the Brookhaven National Laboratory for supporting the accelerator studies. Financial support for his work was provided by National Aeronautics and Space Administration's Space Radiation Program Element (NASA contract number NAS9-02078).

REFERENCES

1. Terasawa T, Dvorak T, Ip S, Raman G, Lau J, Trikalinos TA. Systematic review: charged-particle radiation therapy for cancer. *Ann Intern Med* (2009) **151**(8):556–65. doi:10.7326/0003-4819-151-8-200910200-00145
2. Shulz-Ertner D, Tsujii H. Particle radiation therapy using proton and heavier ion beams. *J Clini Oncol* (2007) **25**:953–64. doi:10.1200/JCO.2006.09.7816
3. Cucinotta FA, Katz R, Wilson JW, Townsend LW, Shinn JL, Hajnal F. Biological effectiveness of high-energy protons: target fragmentation. *Radiat Res* (1991) **127**:130–7. doi:10.2307/3577956
4. Wouters BG, Skarsgard LD, Gerweck LE, Carabe-Fernandez A, Wong M, Durand RE, et al. Radiobiological intercomparison of the 160 MeV and 230 MeV proton therapy beams at the Harvard Cyclotron Laboratory and at Massachusetts General Hospital. *Radiat Res* (2015) **183**:174–87. doi:10.1667/RR13795.1
5. Cucinotta FA, Durante M. Cancer risk from exposure to galactic cosmic rays: implications for space exploration by human beings. *Lancet Oncol* (2006) **7**:431–5. doi:10.1016/S1470-2045(06)70695-7
6. Durante M, Cucinotta FA. Heavy ion carcinogenesis and human space exploration. *Nat Rev Cancer* (2008) **8**:465–72. doi:10.1038/nrc2391
7. NCRP. *Recommendations of Dose Limits for Low Earth Orbit*. Bethesda, MD: National Council on Radiation Protection and Measurements. NCRP Report 132 (2000).
8. Belli M, Cera F, Cherubini R, Haque AMI, Ianzini F, Moschini G, et al. Inactivation and mutation induction In V79 cells by low energy protons: re-evaluation of the results at the LNL facility. *Int J Radiat Biol* (1993) **63**:331–7. doi:10.1080/09553009314550441
9. Edwards AA, Lloyd DC, Prosser JS, Finnon P, Moquet JE. Chromosome aberrations induced by 8.7 MeV protons and 23.5 helium-3 ions. *Int J Radiat Biol* (1986) **50**:137–45. doi:10.1080/09553008614550511
10. Edwards AA, Llyod DC, Prosser JS. The induction of chromosome aberrations in human lymphocytes by accelerated particles. *Radiat Prot Dosimetry* (1985) **13**:205–9.
11. Schmid E, Roos H, Rumple G, Bauchinger M. Chromosome aberration frequencies in human lymphocytes irradiated in a multi-layer array by protons with different LET. *Int J Radiat Biol* (1998) **72**(6):661–5. doi:10.1080/095530097142816

12. Clapp NK, Darden EB Jr, Jernigan MC. Relative effects of whole-body sublethal doses of 60-MeV protons and 300-kVp X-rays on disease incidence in RF mice. *Radiat Res* (1974) **57**:158–86. doi:10.2307/3573764
13. Weil MM, Ray FA, Genik PC, Yu Y, McCarthy M, Fallgren CM, et al. Effects of ^{28}Si ions, ^{56}Fe ions, and protons on the induction of murine acute myeloid leukemia and hepatocellular carcinoma. *PLoS One* (2014) **9**(8):e104819. doi:10.1371/journal.pone.0104819
14. Alpen EL, Powers-Risius P, Curtis SB, DeGuzman R. Tumorigenic potential of high-Z, high-LET charged particle radiations. *Radiat Res* (1993) **88**:132–43. doi:10.2307/3575758
15. Dicello JF, Christian A, Cucinotta FA, Gridley DS, Kathirithhamby R, Mann J, et al. *In vivo* mammary tumorigenesis in the Sprague-Dawley rat and microdosimetric correlates. *Phys Med Biol* (2004) **49**:3817–30. doi:10.1088/0031-9155/49/16/024
16. ICRP. *Relative Biological Effectiveness (RBE), Quality Factor (Q), and Radiation Weighting Factor (w_R)*. Pergamon: International Commission on Radiation Protection (2003). ICRP Publication 103.
17. George K, Durante M, Wu H, Willingham V, Badhwar G, Cucinotta FA. Chromosome aberrations in the blood lymphocytes of astronauts after space flight. *Radiat Res* (2001) **156**:731–8. doi:10.1667/0033-7587(2001)156[0731:CAITBL]2.0.CO;2
18. Bonassi S, Norppa H, Ceppi M, Strömberg U, Vermeulen R, Znaor A, et al. Chromosomal aberration frequency in lymphocytes predicts the risk of cancer: results from a pooled cohort study of 22 358 subjects in 11 countries. *Carcinogenesis* (2008) **29**:1178–83. doi:10.1093/carcin/bgn075
19. ICRP – International Commission on Radiological Protection. Assessment of radiation exposure of astronauts in space. ICRP Publication 123. *Ann ICRP* (2013) **42**(4):1–139. doi:10.1016/j.icrp.2013.05.004
20. Cucinotta FA, Kim MY, Chappell L. *Space Radiation Cancer Risk Projections and Uncertainties – 2012*. NASA TP 2013-217375 (2013). Available from: http://www.sti.nasa.gov
21. Cucinotta FAA. New approach to reduce uncertainties in space radiation cancer risk predictions. *PLoS One* (2015) **10**(3):e0120717. doi:10.1371/journal.pone.0120717
22. George K, Willingham V, Wu H, Gridley D, Nelson G, Cucinotta FA. Chromosome aberrations in human lymphocytes induced by 250 MeV protons: effects of dose, dose rate and shielding. *Adv Space Res* (2002) **30**:891–9. doi:10.1016/S0273-1177(02)00406-4
23. Durante M, Furusawa Y, Majima H, Kawata T, Gotoh E. Association between G2-phase block and repair of radiation-induced chromosome fragments in human lymphocytes. *Radiat Res* (1999) **151**:670–6. doi:10.2307/3580205
24. Savage RK, Simpson PJ. On scoring of FISH-"painted" chromosome-type exchange aberrations. *Mutat Res* (1994) **307**:345–53. doi:10.1016/0027-5107(94)90308-5
25. Wu H, George K, Yang TC. Estimate of true incomplete exchanges using fluorescence in situ hybridization with telomere probes. *Int J Radiat Biol* (1998) **73**:521–7. doi:10.1080/095530098142068
26. Luomahaara S, Lindholm C, Mustonen R, Salomaa S. Distribution of radiation-induced exchange aberrations in human chromosomes 1, 2 and 4. *Int J Radiat Biol* (1999) **75**:1551–6. doi:10.1080/095530099139151
27. Lucas JN, Poggensee M, Straume T. The persistence of chromosome translocations in a radiation worker accidentally exposed to tritium. *Cytogenet Cell Genet* (1992) **60**:255–6. doi:10.1159/000133353
28. George K, Wu H, Willingham V, Furusawa Y, Kawata T, Cucinotta FA. High- and low-LET induced chromosome damage in human lymphocytes; a time course of aberrations in metaphase and interphase. *Int J Radiat Biol* (2001) **77**:175–83. doi:10.1080/0955300001003760
29. George K, Cucinotta FA. The influence of shielding on the biological effectiveness of accelerated particles for the induction of chromosome damage. *Adv Space Res* (2007) **39**:1076–81. doi:10.1016/j.asr.2007.01.004
30. George K, Durante M, Willingham V, Wu H, Yang TC, Cucinotta FA. Biological effectiveness of accelerated particles for the induction of chromosome damage measured in metaphase and interphase in human lymphocytes. *Radiat Res* (2003) **160**:425–35. doi:10.1667/RR3064
31. Tripathi RK, Cucinotta FA, Wilson JW. Accurate universal parameterization of absorption cross sections III – light systems. *Nucl Instrum Methods Phy Res B* (1999) **155**:349–56. doi:10.1016/S0168-583X(99)00479-6
32. Wilson JW, Cucinotta FA, Shinn JL, Townsend LW. *Target Fragmentation in Radiobiology*. Washington, DC (1993). NASA TM-1993-4408. Available from: http://www.sti.nasa.gov
33. Bertucci A, Durante M, Gialanella G, Grossi G, Manti L, Pugliese M, et al. Shielding of relativistic protons. *Radiat Environ Biophys* (2007) **46**:107–12. doi:10.1007/s00411-006-0088-6
34. Peng Y, Hatsumi N, Warner C, Bedford JS. Genetic susceptibility: radiation effects relevant to space travel. *Health Phys* (2012) **103**:607–20. doi:10.1097/HP.0b013e31826945b9
35. BEIR VII. *Health Risks from Exposure to Low Levels of Ionizing Radiation. National Academy of Sciences Committee on the Biological Effects of Radiation*. Washington, DC: National Academy of Sciences Press (2006).
36. Simpson PJ, Papworth DG, Savage JP. X-ray-induced simple, pseudosimple and complex exchanges involving two distinctly painted chromosomes. *Int J Radiat Biol* (1999) **75**:11–8. doi:10.1080/095530099140753

Conflict of Interest Statement: The authors declare that the research was conducted in the absence of any commercial or financial relationships that could be construed as a potential conflict of interest.

Copyright © 2015 George, Hada and Cucinotta. This is an open-access article distributed under the terms of the Creative Commons Attribution License (CC BY). The use, distribution or reproduction in other forums is permitted, provided the original author(s) or licensor are credited and that the original publication in this journal is cited, in accordance with accepted academic practice. No use, distribution or reproduction is permitted which does not comply with these terms.

frontiers in Oncology

ORIGINAL RESEARCH
published: 15 March 2016
doi: 10.3389/fonc.2016.00052

Three-Color Chromosome Painting as Seen through the Eyes of mFISH: Another Look at Radiation-Induced Exchanges and Their Conversion to Whole-Genome Equivalency

Bradford D. Loucas[1], Igor Shuryak[2] and Michael N. Cornforth[1]*

[1] *Department of Radiation Oncology, University of Texas Medical Branch, Galveston, TX, USA,* [2] *Center for Radiological Research, Columbia University, New York, NY, USA*

Whole-chromosome painting (WCP) typically involves the fluorescent staining of a small number of chromosomes. Consequently, it is capable of detecting only a fraction of exchanges that occur among the full complement of chromosomes in a genome. Mathematical corrections are commonly applied to WCP data in order to extrapolate the frequency of exchanges occurring in the entire genome [whole-genome equivalency (WGE)]. However, the reliability of WCP to WGE extrapolations depends on underlying assumptions whose conditions are seldom met in actual experimental situations, in particular the presumed absence of complex exchanges. Using multi-fluor fluorescence in situ hybridization (mFISH), we analyzed the induction of simple exchanges produced by graded doses of ^{137}Cs gamma rays (0–4 Gy), and also 1.1 GeV ^{56}Fe ions (0–1.5 Gy). In order to represent cytogenetic damage *as it would have appeared to the observer* following standard three-color WCP, all mFISH information pertaining to exchanges that did not specifically involve chromosomes 1, 2, or 4 was ignored. This allowed us to reconstruct dose–responses for three-color *apparently simple* (AS) exchanges. Using extrapolation methods similar to those derived elsewhere, these were expressed in terms of WGE for comparison to mFISH data. Based on AS events, the extrapolated frequencies systematically overestimated those actually observed by mFISH. For gamma rays, these errors were practically independent of dose. When constrained to a relatively narrow range of doses, the WGE corrections applied to both ^{56}Fe and gamma rays predicted genome-equivalent damage with a level of accuracy likely sufficient for most applications. However, the apparent accuracy associated with WCP to WGE corrections is both fortuitous and misleading. This is because (in normal practice) such corrections can only be applied to AS exchanges, which are known to include complex aberrations in the form of pseudosimple exchanges. When WCP to WGE corrections are applied to *true simple exchanges*, the results are less than satisfactory, leading to extrapolated values that *underestimate* the true WGE response by unacceptably large margins. Likely explanations for these results are discussed, as well as their implications for radiation protection. Thus, in seeming contradiction to notion that complex aberrations be avoided altogether in WGE corrections – and in violation of assumptions upon which these corrections are based – their inadvertent inclusion in three-color WCP data is *actually required* in order for them to yield even marginally acceptable results.

Keywords: chromosome painting, mFISH, radiation biomarkers

OPEN ACCESS

Edited by:
Marco Durante,
GSI, Germany

Reviewed by:
Rainer K. Sachs,
University of California Berkeley, USA
Rhona M. Anderson,
Brunel University, UK

****Correspondence:***
Michael N. Cornforth
mcornfor@utmb.edu

Specialty section:
This article was submitted to Radiation Oncology, a section of the journal Frontiers in Oncology

Received: *31 December 2015*
Accepted: *22 February 2016*
Published: *15 March 2016*

Citation:
Loucas BD, Shuryak I and Cornforth MN (2016) Three-Color Chromosome Painting as Seen through the Eyes of mFISH: Another Look at Radiation-Induced Exchanges and Their Conversion to Whole-Genome Equivalency. Front. Oncol. 6:52. doi: 10.3389/fonc.2016.00052

INTRODUCTION

Whole-chromosome painting (WCP) involves the labeling of a few select chromosomes of the genome, thereby producing discrete changes in fluorescent color patterns that accompany the junctions of exchange breakpoints. These include junctions between the painted and unpainted chromosomes, and between the painted chromosomes themselves.

Whole-chromosome painting data can be extrapolated in order to approximate the total number of exchanges that *would have been detected* if all homologous chromosome pairs *would have been painted* a unique color, as in the combinatorial painting technologies of multi-fluor fluorescence *in situ* hybridization (mFISH) (1) or spectral karyotyping (SKY) (2). Converting WCP data to that of whole-genome equivalency (WGE) provided by mFISH or SKY makes use of relationships similar to that developed by Lucas and colleagues (3). These consider exchanges between painted and unpainted (counterstained) chromosomes, adjusting for unseen exchanges presumed to have occurred between unpainted chromosomes. After three-color WCP was introduced, subsequent refinements were made to accommodate exchanges occurring among the individually painted chromosomes as well (4, 5).

There are two central assumptions common to these mathematical extrapolations. First, that exchange breakpoints are produced *randomly* throughout the genome, in direct proportion to the size of chromosomes participating in an exchange. Second, these corrections (extrapolations) are derived solely in consideration of simple reciprocal interchange events (dicentrics and translocations). Complex exchanges, which involve rejoining among multiple chromosomes, are ignored. For that reason, corrections are usually restricted to data associated with low to moderate doses of X- or gamma rays, where the incidence of complex exchanges is assumed to be minimal. Earlier work provided support for the soundness of the basic approach and whole-genome corrections soon became routinely applied to WCP (3, 6–8) data. However, papers began to appear shortly thereafter questioning the first of the aforementioned assumptions (9–11).

More recently, and with basic intent similar to ours, Braselmann and colleagues compared genome-corrected three-color WCP data with experimental data derived independently using mFISH and SKY (4). When applied to three-color WCP data, they found that modification to the original Lucas formula (3) produced results comparable to that of mFISH or SKY. Attached to this conclusion, however, was a cautionary note about the influence of pseudosimple exchanges – aberrations that appear to be simple pairwise interchanges by WCP, but that are actually complex, involving three or more exchange breakpoints distributed among multiple chromosomes (12–14).

In this paper, we reconsider the issue in detail by comparing 24-color mFISH data to 3-color data retrospectively extracted from mFISH images. This method was used to assess the accuracy with which a commonly used mathematical formalism can be applied 3-color WCP data in order to extrapolate full 24-color genome equivalency for simple chromosome interchanges. It involves experimental conditions under which WCP extrapolations are ostensibly valid, such as low to moderate doses of gamma rays. Unlike previous reports, however, it also includes situations where the validity of such extrapolation is dubious: higher doses of gamma rays and exposure to heavy ions, both of which are well known to favor the production of complex exchanges (5, 15–22).

MATERIALS AND METHODS

Irradiations and Culture Conditions

Methods pertaining to the exposure of lymphocytes to gamma rays have been detailed elsewhere (22, 23). Whole venous blood from two healthy consenting male volunteers was exposed to graded doses of ^{137}Cs γ-rays at a rate of 1.3 Gy/min using a J.L. Shepherd Mark I cesium irradiator located at the University of Texas Medical Branch (UTMB), following procedures approved by UTMB's Institutional Review Board (IRB). 0.4 ml aliquots of blood were cultured in RPMI-1640 (Gibco) medium containing 0.1 ml phytothemagglutinin (PHA; Murix, Dartford, UK) and supplemented with 15% fetal bovine serum. Colcemid (GIBCO), to a final concentration of 0.1 μg/ml, was added 45 h later, and cultures were harvested for metaphase analysis at 48 h.

Heavy ion irradiations took place at Brookhaven National Laboratory (BNL; Upton, NY, USA) within the NASA Space Radiation Laboratory (NSRL). Procedures followed those of BNL's IRB. Whole blood was suspended in RPMI-1640 medium, supplemented with 20% fetal bovine serum. From this suspension, approximately 2×10^6 cells were loaded into custom-made Lucite holders and irradiated at room temperature with graded doses of 1.1 GeV/amu ^{56}Fe ions. The dose average LET of this beam was 147 keV/μm. Immediately after exposure, lymphocytes were aspirated from the holder and transferred into 25 cm^2 tissue culture flasks containing 10 ml of RPMI-1640 medium supplemented with 1% phytohemagglutinin (PHA; Gibco). Cultures were incubated at 37°C for 46 h before Colcemid (Gibco) was added (0.2 μg/ml final concentration) 2 h prior to the harvest of mitotic cells. Calyculin-A (50 nM final concentration) was added to Colcemid-blocked cultures to induce premature chromosome condensation (PCC) in G_2-phase cells (24). As a result, mitotic figures contained a mixture of metaphase chromosomes and G_2-phase PCC. Cells were fixed in a 3:1 mixture of methanol to acetic acid and transported to the University of Texas Medical Branch at Galveston for further processing and subsequent analysis.

mFISH Hybridization and Image Capture

Following fixation in methanol/acetic acid, lymphocytes were spread onto glass microscope slides by standard cytogenetic procedures. Slides were then treated with acetone, RNase A, and proteinase K before another fixation in 3.7% formaldehyde. Slides were dehydrated through an ethanol series (70, 85, and 100%) and air dried. In order to denature chromosomal DNA, they were next incubated in 70% formamide (72°C) in 2× SSC (0.3 M NaCl, 0.03 M sodium citrate) for 2 min. After dehydration through another ethanol series, 10 μl of denatured (10 min at 72°C) SpectraVision 24-color mFISH Assay probe (Vysis) was applied to each slide. Slides were covered with a 22 mm × 22 mm glass cover slip,

sealed into position with rubber cement. Samples were allowed to hybridize for 48 h in a 37°C incubator. Following hybridization, cover slips were removed and the slides were washed for 2 min in 0.4× SSC containing IGEPAL (0.3%) non-ionic detergent at 72°C. This was followed by a 30-s wash in 2× SSC (0.1% IGEPAL) at room temperature.

Prior to image capture, 15 µl of DAPI (0.14 µg/ml) dissolved in anti-fade mounting medium (Vectashield; Vector Laboratories) was applied to each slide and covered with a 24 mm × 40 mm cover slip. Images of chromosome spreads were captured using a Zeiss Axiophot epifluorescence microscope interfaced with a SensSys black-and-white CCD camera. Karyotypes were constructed from good-quality chromosome spreads using PowerGene image analysis software (23).

24-Color Analysis

We conducted a retrospective examination of a large 24-color mFISH data base that contained detailed information on aberrations produced in human cells by graded doses radiations of different ionization densities (22, 23). Metaphase cells were analyzed by procedures previously established (23). Briefly, mPAINT descriptors were assigned to chromosomes involved in each rearrangement. Next, each rearrangement was brought to "pattern closure" by grouping elements in the most conservative way possible, minimizing the number of breakpoints required to reconstruct the exchange (25). Reciprocal pairwise rejoinings between one chromosome (rings and interstitial deletions) or two chromosomes (translocations and dicentrics) were scored as simple exchanges. Exchanges involving three or more breakpoints were regarded as complex. This classification was also applied to incomplete exchanges where one or more elements failed to rejoin, as well as the so-called "one-way" exchanges where one or more translocated segments appeared to be missing, presumably because they were too small to be resolved by chromosome painting. The large majority of one-way staining patterns are known to be complete exchanges (26). And since we lacked the ability to simultaneously visualize telomere signals in mFISH preparations, such rearrangements were treated as being complete for the purpose of achieving pattern closure.

Retrospective Three-Color Analysis

We focused on chromosomes 1, 2, and 4, since this represents one of the more commonly used three-color painting schemes. On a cell-by-cell basis, we stripped from the full 24-color mFISH profile all information concerning exchanges *except* that pertaining to the three painted chromosomes. In other words, from a full 24-color karyotype, we imagined what the microscopist *would have observed* if, instead of mFISH, three-color WCP had been applied to the samples. From this information, we used a mathematical correction of the form described by Braselmann et al. (4) to scale WCP data back to full genome equivalency originally provided by mFISH. The correction we used applies only to simple reciprocal interchanges involving exactly two chromosomes (translocations and dicentrics). Neither mFISH nor WCP analysis specifically considered intrachanges: rings, interstitial deletions, inversions; nor were terminal deletions considered. To be clear then, the term "exchange" (as used hereafter) refers only to interchanges. One-way exchanges were handled in a manner similar to that for mFISH.

Extraction of Three-Color Data from mFISH Images

Figure 1 depicts the process used in rendering 24-color mFISH images in order to produce 3-color WCP data. It is also meant to illustrate some of the problems inherent to WCP for aberration analysis. The figure shows various staining protocols applied to a metaphase cell that had previously been exposed in G_0 phase to 4 Gy of ^{137}Cs gamma rays. The cell is replete with various chromosome rearrangements whose complexity becomes increasingly apparent as different chromosomes are painted. Panels A, B, and C derive from an mFISH image that was rendered to exclude painting information from all chromosomes *except* chromosomes 1, 2, and 1 + 2 + 4, respectively.

Figure 1A is of a cell probed for chromosome 1 that contains an apparently simple (AS) translocation between chromosome 1 and an anonymous blue (DAPI-counterstained) chromosome. The cell also contains an AS dicentric involving the other homolog of chromosome 1. [In this case, the accompanying compound acentric fragment shows a "one-way" staining pattern, and is therefore assumed joined with a submicroscopic counterstained segment (26–29)]. **Figure 1B** shows the same cell, as it would appear if probed for chromosome 2 instead. Here, an AS translocation has occurred. **Figure 1C** simulates the three-color painting patterns of the same cell that derive from mFISH data, rendered so as to include data for chromosomes 1, 2, and 4 simultaneously. The full extent of complexity is revealed by mFISH in **Figure 1D**. Actually, the cell in question is shown to harbor three rearrangements. It contains a simple dicentric between chromosome 1 and the X (red arrows). This exchange would be correctly identified given the staining patterns shown in **Figures 1A,C**. Judging by staining patterns of **Figure 1A**, it also contains a simple translocation involving the homologous chromosome 1. In reality, the exchange is pseudosimple. mFISH reveals the chromosome to be part of a large complex exchange involving five other chromosomes marked by white arrows. Likewise, the AS translocation involving chromosome 2 is also pseudosimple, since mFISH shows it to be part of the same large complex exchange (white arrows).

The three-color rendering shown in **Figures 1C** represents the type of WCP data to which the CF corrections of equation (8) (shown below) were applied in order to calculate WGE. In this particular cell, three-color painting was able to detect the occurrence of the complex exchange. However, from the three-color staining pattern alone, one may conclude only that the complex involved a minimum of three chromosomes: 1, 2, and an anonymous third DAPI-stained chromosome, when six chromosomes were actually involved (**Figure 1D**). In fact, there are many instances where three-color painting fails to detect the occurrence of complex exchanges altogether. The misidentification of complex exchanges as being simple is of concern to mathematical extrapolations applied to three-color data, because it violates a central assumption that only simple exchanges be considered, a point made repeatedly in this paper.

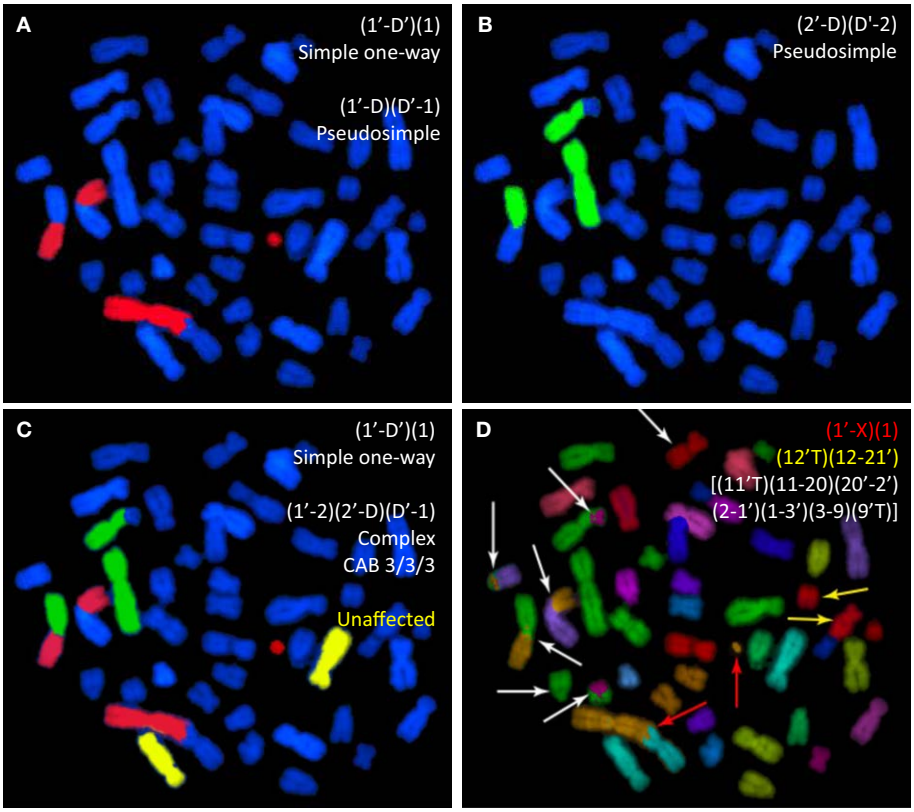

FIGURE 1 | Whole-chromosome paints applied to a human metaphase spread from a cell previously exposed to gamma rays. The same spread is shown following WCP applied to chromosomes 1 and 2 [**(A,B)**, respectively]. **(C)** The same spread following simultaneous painting with the same two probes. In **(D)**, mFISH reveals the full extent of exchange complexity. mPAINT nomenclature is used to describe the various visible rearrangements (25).

Extrapolation to Whole-Genome Equivalency

Over the years, various modifications to the original Lucas formula (3) have been used to estimate the fraction of total interchanges visible by WCP. The extrapolation we used follows closely that of Braselmann and colleagues (4). It considers exchanges between painted and unpainted (counterstained) chromosomes, as well as exchanges taking place among the uniquely painted chromosomes. It also makes provisions for the fact that dicentrics involving homologous chromosomes are detectable by mFISH, whereas translocations are not. Values for the genomic content of chromosomes used in the following derivation are from Mendelsohn et al. (30) as cited by Morton (31). Its derivation, as applied to our particular experimental system, is as follows.

Let f_p represent the fractional sum of the genome covered by the individual chromosomes 1, 2, and 4, where $f_1 = 0.0821$; $f_2 = 0.0804$; $f_4 = 0.0635$

$$f_p = (f_1 + f_2 + f_4) = 0.226. \quad (1)$$

The unpainted (DAPI-counterstained) fraction then becomes

$$(1 - f_p) = 0.774 \quad (2)$$

For WCP, the frequency of visible interchanges in the genome that can occur between painted and unpainted chromosomes (F_P) is given by the cross product of the binomial expansion $(p+q)^2 = p^2 + 2pq + q^2$ – namely 2pq – where $p = (f_p)$ *and* $q = 1-(f_p)$. Substituting values in Eq. (2) gives the following expression.

$$F_P = 2pq = 2f_p\,(1 - f_p) = 0.350 \quad (3)$$

If, as is the case here, the individual painted chromosomes can be distinguished from one another, then Eq. (3) can be expanded to include exchanges that now become visible among the three possible pairs of uniquely colored chromosomes (4, 32).

$$F_P = 2\,[f_p\,(1 - f_p) + f_1 f_2 + f_1 f_4 + f_2 f_4] = 0.384 \quad (4)$$

Thus, three-color WCP is theoretically capable of detecting 38.4% of the interchanges occurring throughout the whole genome. However, in the context of this paper, three-color WCP frequencies are to be compared to those detected by mFISH and it should be recognized that the latter is not capable of detecting all interchanges. The frequency of all mFISH-detectable interchanges (F_{mFISH}), including translocations and dicentrics, is proportional to the sum of all products (f_i) x (f_j) representing the fractional DNA content of chromosomes i and j. But because mFISH cannot reliably detect events that occur between homologous chromosomes, an additional stipulation is that $i \neq j$. For a human karyotype containing 23 individually identifiable

types of chromosomes, this can be represented by the following expression (4).

$$F_{mFISH} = 1 - \sum_{i=1}^{23} f_i^2 = 0.948 \quad (5)$$

The numerical value resulting from Eq. (5) is essentially a constant for a given diploid species. We note that our calculated value of 0.948 (for human males) is virtually identical to the number 0.949 reported by Braselmann et al. for females (4).

A final point to consider is that mFISH typically allows for the detection of asymmetrical exchanges (dicentrics) involving homologous chromosomes, but not their symmetrical counterpart (translocations). In that sense, Eq. (5) "overcorrects" for undetectable exchanges between homologs. If we make the usual assumption that symmetrical and asymmetrical exchanges, as measured by mFISH, occur with approximately equal frequency (23), then half the deviation from unity shown in Eq. (5) no longer applies. Thus, the true frequency of interchanges visible by mFISH – to include dicentrics between homologs (but not translocations) – is given by Eq. (6).

$$F_{mFISH} = 0.948 + \left(\frac{1 - 0.948}{2}\right) = 0.974 \quad (6)$$

In order to calculate the detection efficiency of WCP, we compare this value to the theoretical frequency of interchanges detectable by three-color FISH, F_P of Eq. (4). As compared to the frequency of interchanges visible by 24-color mFISH, the WGE for such detection by three-color WCP becomes:

$$\begin{aligned} F_{mFISH}^{3\ color} &= \left(\frac{2}{0.974}\right)[f_p(1-f_p) + f_1 f_2 + f_1 f_4 + f_2 f_4] \\ &= 2.053\,[f_p(1-f_p) + f_1 f_2 + f_1 f_4 + f_2 f_4] = 0.394 \quad (7) \end{aligned}$$

Thus, by covering 23% of the genome [Eq. (1)], three-color FISH is capable of detecting 39% of the interchanges seen by mFISH. In theory, three-color WCP frequencies can be multiplied by the following correction factor *CF* in order to achieve full 24-color mFISH equivalency.

$$\begin{aligned} F_{WCP} \times CF &= F_{mFISH} \\ CF &= \frac{1}{0.394} = 2.54 \quad (8) \end{aligned}$$

This value differs from the CF of 2.9 reported by Braselmann and colleagues, mainly because the three chromosomes we have chosen to analyze (1, 2, and 4) constitute a larger proportion of the genome than the chromosome 1–4–12 triplet used by these authors. Hereafter, the derivation of Eq. (8) will be referred to the CF *derived from first principles*.

Dose Dependency

As discussed later, correction factors derived from Eq. (8) are of limited value if they display dose dependency. In other words, the transformation of three-color data to WGE is based on the tacit assumption that the two dose–responses can be scaled to match each other (made superimposable) *over a range of doses* through use of a single multiplier, i.e., the constant CF of Eq. (8). It should be intuitively obvious that this is not possible unless certain conditions are met, foremost is that the two dose–responses share the same functional form – a comparison of two linear dose responses would be a trivial example here. However, this alone is insufficient for the general case, as demonstrated for the familiar linear-quadratic formalism of Eq. (9) below. It will be used to describe each of the underlying dose–responses considered in this paper. Let $F_{(D)}$ represent the dose-dependent frequency for simple exchanges, as given by the second-order polynomial where α, $\beta \geq 0$.

$$F_{1(D)} = \alpha_1 D + \beta_1 D^2 \quad (9)$$

Assume that Eq. (9) represents exchanges as measured by mFISH, and that a similar expression $F_{2(D)}$ describes the dose–response as measured by three-color WCP.

$$F_{2(D)} = \alpha_2 D + \beta_2 D^2 \quad (10)$$

The ratio of Eqs. (9) and (10) defines CF as a function of D, which hereafter is referred to as the *empirically derived* CF.

$$CF = \frac{F_{1(D)}}{F_{2(D)}} = \frac{\alpha_1 D + \beta_1 D^2}{\alpha_2 D + \beta_2 D^2} \quad (11)$$

If we let the proportionality constant (k) hold the place of CF, then

$$\alpha_1 D + \beta_1 D^2 = k\left(\alpha_2 D + \beta_2 D^2\right). \quad (12)$$

Equivalently,

$$D(\alpha_1 - k\alpha_2) + D^2(\beta_1 - k\beta_2) = 0. \quad (13)$$

For our purposes, corrections must be applicable over a *range of doses* (interval of D). It follows that if either of the polynomial coefficients in Eq. (13) is non-zero, then the equation is either linear or quadratic, and can therefore have at most two solutions. Therefore Eq. (13) cannot hold over an interval of dose with k fixed unless both its coefficients are 0. In this case, the following relationships are satisfied which, as required, are invariant of dose:

$$\begin{aligned} \alpha_1 &= k\alpha_2 \\ \beta_1 &= k\beta_2 \quad (14) \end{aligned}$$

It then follows that

$$\frac{\alpha_1}{\beta_1} = \frac{\alpha_2}{\beta_2}. \quad (15)$$

Thus, formally speaking, the concept of a single CF can be applied to a pair of second-order polynomials only when α/β ratios of the two are equal. In principle, the validity of Eq. (15) can be used to ascertain the appropriateness of using a single CF to convert a three-color WCP data set to full genome equivalency. In practice, we found that designing a statistical test for this purpose to be problematic, largely because AS and TR frequencies are actually subsets mFISH data and, therefore, cannot be considered independent measurements. Thus, whereas testing the identity of ratios in Eq. (15) is conceptually sound (and useful in the discussion that follows) an alternative statistical approach was required to ascertain dose dependency. We used the approach described below, which models the *proportions* of AS interchanges among all interchanges (pAS = AS/mFISH) and true simple (TR) exchanges among AS exchanges (pTR = TR/AS).

Statistical Analysis

If pAS is constant and independent of radiation dose, then a multiplicative CF can be used to predict the total number of simple exchanges (interchanges) in all chromosomes (mFISH) based on the number of AS exchanges in chromosomes 1, 2, and 4. The same applies to pTR. Alternatively, if either pAS or pTR depend on dose, their dose responses will have slopes statistically different from 0.

We used logistic regression to model the potential dose dependences of pAS and pTR. Using matrix notation, the model structure is summarized as follows, where $\text{logit}(x) = 1/[1 + \exp(-x)]$:

$$\text{logit}\ (o)\ =\ \varphi \times\ V\ +\ \varepsilon \tag{16}$$

Here, $\boldsymbol{o}$ is a vector of outcome variables: predicted pAS and pTR. $\boldsymbol{V}$ is a vector of radiation doses, φ is a vector of regression coefficients, and ε is a vector of errors.

Three types of radiation dose dependences for pAS and pTR were assessed using this approach:

(a) a dose–response with intercept (the predicted value of pAS or pTR at zero dose) and slope (the predicted rate of change of pAS or pTR per unit dose), with quasi-binomial error distribution;
(b) intercept plus slope with a binomial error distribution; and
(c) intercept only (with slope effectively set to 0 and not counted as an adjustable parameter) having a binomial error distribution. We performed these analyses separately on γ-ray and Fe ion data. Model fitting was performed using R software (version 3.2.0).

According to the binomial distribution, the variance is not an independent parameter, whereas the quasi-binomial option allows the variance to be adjustable (33). Consequently, comparison of binomial and quasi-binomial model fits to the same data (i.e., options a and b), using the X^2 (Chi-squared) test on residual deviances, provides information on whether or not there is evidence of "overdispersion" in the data – in other words, whether or not the variance of the data is larger than what would be expected from the binomial distribution.

Comparison of the slope plus intercept versus intercept-only models (i.e., options b and c) on the same data provides information on whether or not the data are consistent with being represented by a constant dose-independent term (intercept-only), or if there is evidence for dose dependence (slope). This assessment was performed using the sample-size corrected Akaike information criterion (AICc). AICc is an information theoretic criterion that quantifies relative support from the data for the compared models, taking into account the sample size (number of data points) and the number of adjustable parameters in each model.

Goodness of fit (GOF) was assessed for the models under the assumption that the residual deviance follows the X^2 distribution. The null hypothesis was that the model provides an adequate fit to the data, and small p-values were interpreted to mean that the null hypothesis has poor support.

RESULTS

There are two separate issues to consider when determining how well multiplicative correction factors predict the mFISH dose–responses from three-color data. The overarching first issue is whether such a multiplicative factor *even exits* that can bring three-color data into registry with mFISH data over a range of relevant doses. Obviously, this necessitates that CFs not exhibit dose dependency. That is, assuming a linear-quadratic model for the dose responses that Eq. (15) is not violated.

The analysis of frequencies of AS and TR, as function of dose for both types of radiation (γ-rays and Fe ions) is shown in **Figure 2**, which derives from data shown in **Table 1**. For the densely ionizing Fe ions, there was no evidence for dose dependence for the proportion of AS exchanges among all exchanges (pAS), or for the proportion of TR exchanges among AS ones (pTR). This conclusion was reinforced by the finding that AICc for the intercept-only dose–response model was lower (suggesting higher support from the data), than the AICc for the intercept plus slope model. The best-fit values for pAS and pTR at all doses were 0.420 (95% CI: 0.365, 0.477) and 0.593 (0.505, 0.677), respectively. For sparsely ionizing γ-rays, pAS was also consistent with dose-independence with a best-fit value of 0.426 (0.382, 0.471).

However, the pattern was altogether different for TR exchanges. The γ-ray-induced pTR decreased with dose with a best-fit logistic slope coefficient of −0.3416 (SE: 0.1806, $p = 0.0585$) Gy^{-1}. Although the p-value for this coefficient was marginally higher than the commonly used significance threshold of 0.05, the intercept and slope model had higher support (by 1.87 AICc units) than the intercept-only model. This favors a response model containing a slope parameter over the intercept-only model having no dose dependence: the strength of evidence for the first model over the second is $\exp(1.87/2) = 2.54$. In other words, although the strength of statistical evidence falls short of being overwhelming, the data suggest that pTR decreases with radiation dose for γ-rays (**Figure 2**).

From a dose-dependency standpoint, these results show that the response for AS exchange frequencies for gamma rays and ^{56}Fe ions are *theoretically* capable of being transformed to match that from mFISH data using a simple multiplicative CF; the same for TR exchanges induced by iron ions. Unfortunately, the same cannot be said for TR exchanges produced by gamma rays, due to the aforementioned dose dependency.

Findings concerning dose dependency, however, say nothing about the inherent accuracy of the transformation constant itself, which depends entirely on the assumptions underlying the derivation of Eq. (8). This is the second issue that determines how well a particular CF applied to three-color data predict genome-equivalent frequencies. **Figures 3** and **4** are introduced to help visualize the added influence this aspect brings to whole-genome correction. The figures are not intended to imply any sort of rigorous statistical analysis, but to illustrate the overall effect of applying CFs to both AS and TR exchanges. Here, we performed least-squares regression on the data using the linear-quadratic dose–response model [Eqs. (9) and (10)]. The parameters derived from this procedure (**Table 1**) were used to generate the dose–responses for simple exchanges shown in **Figures 3** and **4**. The response in lymphocytes exposed to gamma rays is shown in **Figure 3**. The uppermost solid curve shows a regression to

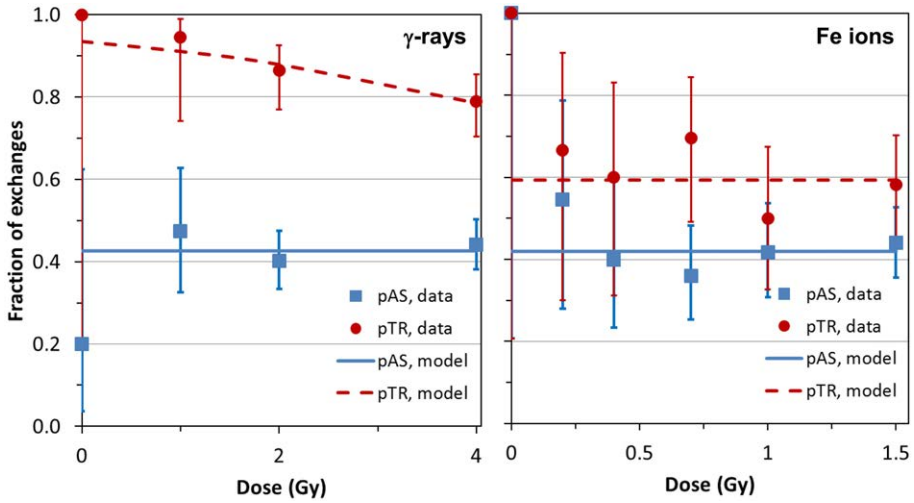

FIGURE 2 | Data (symbols) and model predictions (curves) for the proportion of apparently simple exchanges among all exchanges (pAS) and for the proportion of true simple exchanges among apparently simple exchanges (pTR). Error bars represent 95% confidence intervals (CIs) from the binomial distribution. Details are described in the main text.

TABLE 1 | Chromosome exchange data and fit parameters.

IR	Dose (Gy)	No. Cells	[a]AS (3-color)	[b]True (3-color)	[c]mFISH (24-color)	pAS = AS/mFISH	pTR = True/AS
^{137}Cs γ-rays	0.0	365	1	1	5	0.200 (0.036, 0.624)[f]	1.000 (0.207, 1.000)
	1.0	238	18	17	38	0.474 (0.325, 0.627)	0.944 (0.742, 0.990)
	2.0	342	74	64	184	0.402 (0.334, 0.474)	0.865 (0.769, 0.925)
	4.0	179	109	86	247	0.441 (0.381, 0.504)	0.789 (0.703, 0.855)
	Σ	1124	202	168	474		
Parameters		[d]α	0.05 ± 0.01	0.06 ± 0.01	0.13 ± 0.05		
		[e]β	0.03 ± 0.00	0.02 ± 0.00	0.06 ± 0.02		
		α/β	2.20 ± 0.01	3.89 ± 0.01	2.27 ± 0.05		
1.1 GeV ^{56}Fe Ions	0.0	98	1	1	1	1.000 (0.207, 1.000)	1.000 (0.207, 1.000)
	0.2	191	6	4	11	0.545 (0.280, 0.787)	0.667 (0.300, 0.903)
	0.4	179	10	6	25	0.400 (0.234, 0.593)	0.600 (0.313, 0.832)
	0.7	197	23	16	64	0.359 (0.253, 0.482)	0.696 (0.491, 0.844)
	1.0	189	28	14	67	0.418 (0.307, 0.537)	0.500 (0.326, 0.674)
	1.5	218	55	32	125	0.440 (0.356, 0.528)	0.582 (0.450, 0.703)
	Σ	1072	123	73	293		
Parameters		α	0.14 ± 0.03	0.09 ± 0.03	0.36 ± 0.07		
		β	0.02 ± 0.03	0.00 ± 0.03	0.02 ± 0.06		
		α/β	9.53 ± 0.43	105 ± 82.4	17.6 ± 3.16		

[a]Apparently simple exchanges; chromosomes 1/2/4; [b]True simple exchanges; chromosomes 1/2/4; [c]True simple exchanges; all chromosomes, mFISH; [d,e]Linear and quadratic coefficients; $Y = \alpha D + \beta D^2$; [f]Parentheses indicate 95% confidence intervals (CIs).

the data (filled circles) for all simple reciprocal exchanges measured by mFISH. These are truly simple exchanges and represent WGE of Eq. (9) having the fitted parameters shown in the table. The open symbols of the figure represent three-color data that was extracted from this dose–response. Open circles show the response for simple exchanges as they would appear to the observer using three-color WCP; see Eq. (10). These are labeled "AS" because (as revealed by mFISH) they are partly comprised of pseudosimple exchanges.

The CF of Eq. (8) was applied to the (extracted) AS data in order to convert them to WGE (i.e., mFISH frequencies). The resultant dose–responses are shown by the two dashed-line curves of the figure. Since pseudosimple exchanges are (by definition) hidden to three-color analysis, CFs can only be applied to AS exchanges during actual three-color painting. The resulting AS to WGE extrapolation (long-dashed curve) is symbolized by the vertical arrowed bracket of the figure labeled "apparent." As shown in the figure, the extrapolated genome-equivalent dose–response based on three-color WCP systematically *overestimates* the total frequency of simple exchanges measured by mFISH. Nevertheless, as a first approximation for gamma rays, WGE corrections produce results whose accuracy is probably adequate for many purposes, even if only marginally so at higher doses.

A noteworthy aspect of our retrospective analysis is that it also allows the extraction of TR exchanges from the three-color data, as shown by the triangles of the lowermost curve. This represents the

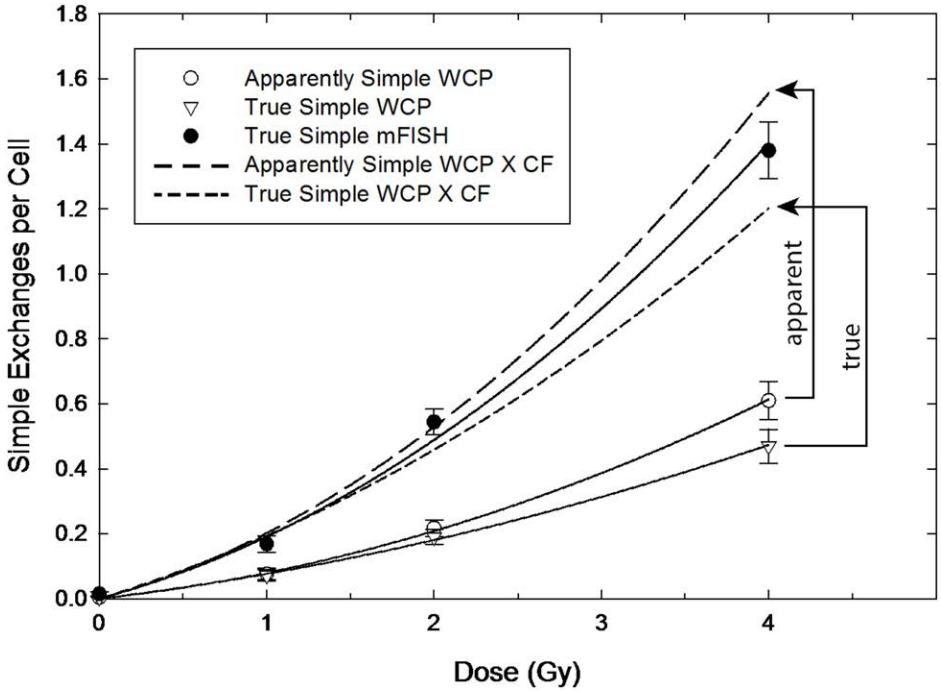

FIGURE 3 | Gamma ray dose–responses for apparently simple (AS) and true simple (TR) exchanges (open circle and triangle symbols, respectively) as reconstructed from mFISH data. Arrowed brackets show the predicted dose responses following the application of the CF from Equation (8), which can be compared to the actual whole-genome frequencies for simple exchanges measured by mFISH (solid circles).

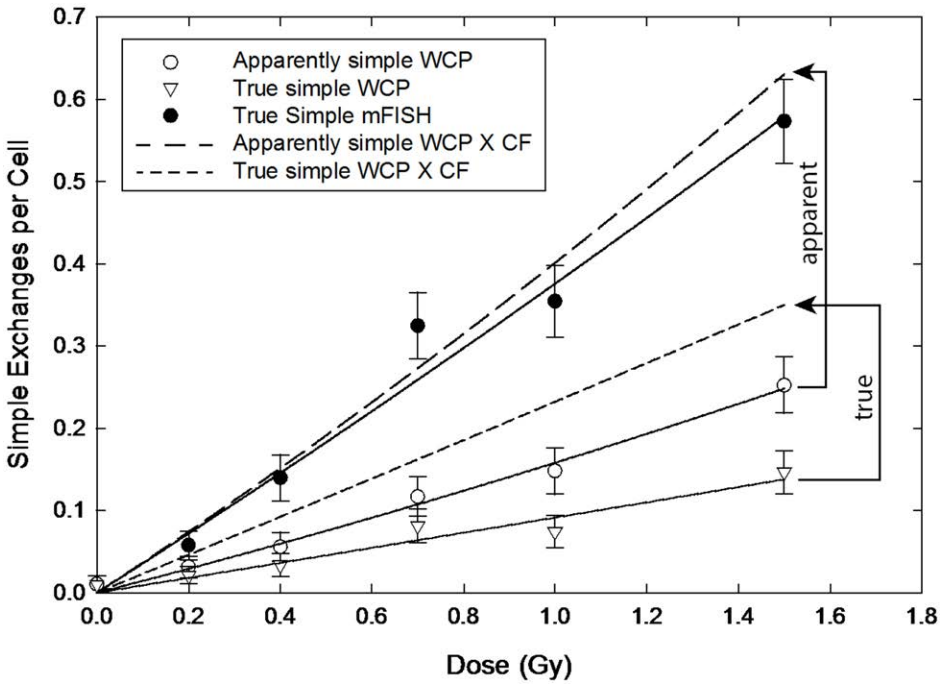

FIGURE 4 | Dose–responses for apparently simple (AS) and true simple (TR) exchanges (open circle and triangle symbols, respectively) following exposure to ^{56}Fe ions. Arrowed brackets project the dose–responses following the application of the CF from Equation (8). Solid circles are actual whole-genome frequencies for simple exchanges, as measured by mFISH.

dose–response for TR exchanges involving the three painted chromosomes, whose associated fit parameters appear in **Table 1**.The result of corrections applied to TR *exchanges* is symbolized by the vertical bracket of the figure labeled "true"; it is associated with the dose–response shown by the short-dashed curve. It should be noted that, in this case, extrapolation *underestimates* the frequencies of the mFISH dose–response.

The difference between CFs applied to AS versus TR exchanges is magnified when we consider exposure to 1.1 MeV ^{56}Fe ions, as shown in **Figure 4**. The solid symbols represent full genome equivalence for TR exchanges (mFISH). The open circles and triangles are for AS and TR exchanges, respectively, and represent 3-color data rendered from 24-color mFISH images. As with gamma rays, CFs applied to AS exchanges produced rather good results, although they tended to overestimate the mFISH response. However, the same corrections applied to TRs *grossly underestimated* WGE across the full range of doses examined.

The situation is graphically represented in **Figure 5**, which compares the results of actual (empirically derived) CFs of Eq. (11) to those derived from first principles of Eq. (8), as expressed by the following Eq. (17).

$$\%\,Deviation = \left[\frac{CF\,(\alpha_{3\ color} + \beta_{3\ color}D)}{\alpha_{mFISH} + \beta_{mFISH}D} - 1\right] \times 100 \qquad (17)$$

The figure shows errors associated with CFs as a function of dose applied to both AS and TR exchanges. The upper portion of the **Figure 4** shows deviations as applied to AS exchanges. The errors are positive for both radiation types, meaning that the CF of Eq. (8) *over estimates* the WGE mFISH response. For gamma rays, the deviations are relatively small (~10%) and (as we have shown statistically) are practically invariant of dose. Plotted this way, errors for ^{56}Fe ions increase with dose, although as shown in a previous section, this increase could not be validated on the basis of our statistical tests. Rather unexpectedly, errors are practically nil at doses approaching 0, before climbing to about 8% at the highest dose of 1.5 Gy. When extrapolated beyond this dose (extended dashed curve) errors continue to rise in a near-linear fashion, crossing that for gamma rays at ~1.8 Gy, the significance of which is discussed in the following section.

The lower portion of the **Figure 5** refers to corrections applied to TR exchanges. Here, extrapolation to WGE badly *underestimates* the true frequency for both types of radiation, as indicated by negative percentage values shown in the figure.

For gamma rays, the (absolute) errors associated with lower doses exceed 50%. Consistent with our statistical analysis, errors decrease sharply with dose, but even at 4 Gy, values are still some 30% lower than those measured by mFISH. Although unsubstantiated by our statistical tests, for ^{56}Fe ions there is a seemingly linear increase in relative error with dose, from about 35% at doses approaching 0, to roughly 40% at 1.5 Gy, the highest dose used in these experiments. The response extrapolated to 4 Gy is shown by the dotted line, based on fitted parameters of **Table 1**.

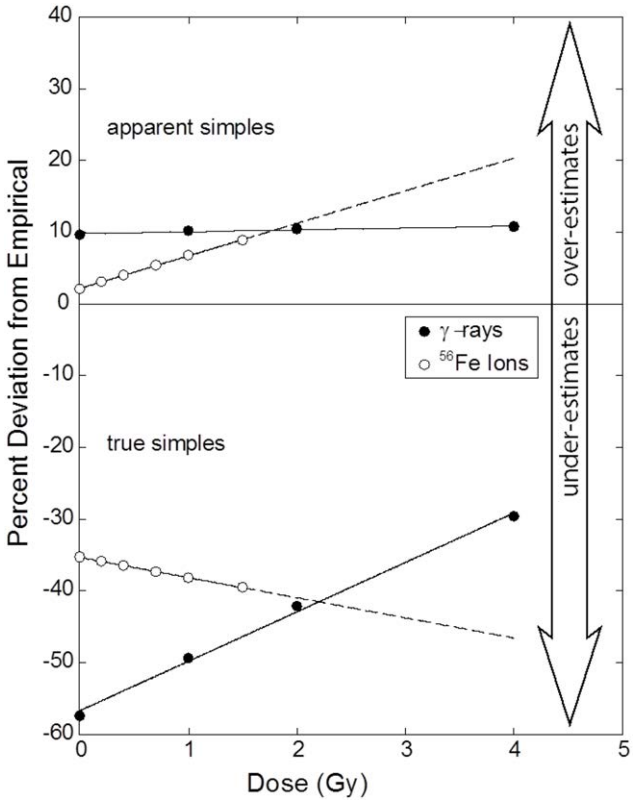

FIGURE 5 | Percentage errors as a function of dose that result from the application of the CF to AS (upper panel) and TR exchanges (lower panel) for gamma rays and iron ions. Symbols mark dose points where raw data (**Table 1**) was collected and whose ordinate values derive from Eq. (17). Errors for AS exchanges induced by gamma rays are invariant of dose. Dose dependency is apparent for the three remaining responses, a result statistically supported for TR exchanges induced by gamma rays. A perfect correction would be represented by a flat dose–response that is centered on 0%. See text for full explanation.

DISCUSSION

We feel compelled to point out – after attending to various tedious details specific to our experimental system – that the 2.053 constant appearing in Eq. (7) is practically identical to the 2.05 value originally published by Lucas et al. (3). Actually, we find it amusing that ignoring all such adjustments made subsequent to Eq. (4) leads to a mere 2.5% error by comparison to Eq. (7), which is small compared to the errors shown in **Figure 5**, and which we imagine would be sufficiently accurate for most experimental purposes.

Clearly, mFISH is capable of providing more cytogenetic information than three-color WCP, including the ability to distinguish TR exchanges from psuedosimples. It is also considerably more demanding of resources and, in many cases, yields data superfluous to the investigator. Presupposing that the two approaches produce quantitatively comparable results, WCP would be the method of choice in instances where less detailed information is an acceptable compromise given its lower expense, rapidity of data acquisition, and ease of analysis.

Regarding the study of whole-genome corrections, there are a couple of points in favor of our retrospective mFISH approach. Unlike earlier studies that sought to establish correlations between mFISH and multi-color data, we establish a proper *correspondence*. In other words, for each and every "three-color cell," there is a corresponding cell for which 24-color data are obtained. Most WCP studies are vexed by the very prospect of pseudosimple exchanges. For that reason, they are limited to experimental doses and radiation types for which one can reasonably assume the frequency of complex aberrations is minimal, namely low doses of sparsely ionizing radiation. The ability to cull psuedosimples from AS exchanges allows us to analyze full dose–response relationships for TR exchanges, irrespective of dose and radiation quality. Later in this section, we consider the theoretical implications of WGE corrections applied to TR exchanges (TR). But first we discuss the more practical aspects of WGE corrections, which involve their application to AS exchanges.

Apparently Simple Exchanges

As routinely practiced, WCP to WGE corrections are confined to AS events, simply because WCP is incapable of distinguishing TRs from pseudosimple exchanges. Looking to **Figure 3**, we find basic agreement with conclusions of Braselmann (4) and others (3, 7, 8) that biophysically based corrections do a reasonably good job of predicting WGE for gamma rays. Applying a multiplicative CF of Eq. (8) to three-color data overestimates mFISH frequencies for simple exchanges, but only by about 10%. Equally important is that the 10% error is essentially constant over the dose interval examined. This is a direct consequence of α/β ratios for mFISH and AS dose–responses being equal, and is reflected in the flat dose–response shown in the leftmost panel (blue-coded data) of **Figure 2**, and the upper panel of **Figure 5** for gamma rays. Thus, reducing the CF of 2.54 in Eq. (8) by 10% would lead to a near perfect match across the full range of doses examined for AS versus mFISH dose–responses shown in **Figure 3**.

Although not detected with confidence by our statistical methods (**Figure 2**), α/β ratios for ^{56}Fe ions (WCP data versus that of mFISH) are probably not precisely equivalent. This would explain the apparent sloped dose–response shown in the upper panel of **Figure 5**. If true, then there is no interval of dose over which Eq. (11) is stable enough to be represented by a constant. That being said, the Figure shows that the errors are not large. Across the range of ^{56}Fe ion doses studied, they deviate from the empirically derived CF by less than 10%, and actually *diminish* with dose. Said differently, we suspect that Eq. (15) has been violated by some small degree, but as a practical matter, this produces a CF that would be deemed acceptable for many purposes. At first glance, these results seem counterintuitive, since high LET radiations are known to produce copious quantities of complex aberrations that are cryptically embedded in the AS data as pseudosimples. However, they are entirely consistent with the interpretation that, to a first approximation, all effects from high LET radiation are "intra-track." Consequently, there would be the same fixed fraction of aberrations (of any kind, including complex exchanges) per unit dose of Fe ions.

Chromosome aberrations are a viable surrogate endpoint for mutations and cancer, and have long been the *de facto* "gold standard" for biodosimetry (34). WCP to WGE corrections, therefore, have implications for radiation protection, where concerns over the biological effects of very low doses are paramount. At issue is the concept of relative biological effectiveness (RBE), which for the present work, involves a comparison between the effects of gamma rays and heavy ions. Here, WCP finds a place because of cost and sample throughput considerations related to the need to score many cells.

As shown graphically in **Figure 5**, it is debatable whether a common CF can be assigned to *both types* of radiation that is valid over a range of doses. It was previously mentioned that the upper portion of the Figure shows that AS errors for both radiations intersect at about 2 Gy. A common CF is valid for both radiations only at this dose, which is far too large to be of practical use as regards issues of radiation risk. At more relevant lower doses, the two curves diverge sharply. This significantly complicates RBE calculations, which are made on the basis of the ratio of doses for a given isoeffect. For RBEs other than unity, the isoeffective doses will differ, meaning that separate CFs would need to be applied to each type of radiation. Moreover, in the case of 1.1 GeV ^{56}Fe ions used in these studies, CFs will also change depending on the chosen level of isoeffect. That said, and as a practical matter, **Figure 4** indicates these errors are capable of altering RBE values for ^{56}Fe ions by about 8% at very low doses. Whereas these errors do not seem particularly large in an experimental setting, in the context of RBE-related radiation protection issues, they probably should not be ignored.

True Simple Exchanges

The remaining discussion focuses on TR exchanges. Recall that the presence of complex aberrations – in this case, taking the form of pseudosimple exchanges in AS data – is specifically ignored during the derivation of Eq. (8), and only simple pairwise exchanges are considered. So, in theory, one would imagine that CFs applied to TR exchanges would produce better results than CFs applied to AS exchanges. As we have seen, the opposite is true. Errors of mFISH predictions based on TR show a pronounced dose dependency for γ-rays (**Figure 2**), and underestimates of WGE for both radiation types occur (**Figures 3** and **4**). From a predictive standpoint, the errors for ^{56}Fe ions are severe enough to render such extrapolation practically useless. Ironically then, after culling pseudosimples from the data – thus satisfying a principle assumption underlying the derivation of Eq. (8) – the resulting predictions were much poorer than if CFs were applied to AS exchanges. Said differently, our data show that the "contaminating" influence of pseudo simple exchanges actually serves to *improve* the predictive ability of WGE corrections. So, to the extent that WGE corrections are considered sufficiently accurate, they owe this accuracy to the very presence of complex aberrations! While this result may be reassuring from a practical standpoint, from theoretical perspective it is disconcerting, because it implies either that the basic approach underpinning WCP-to-WGE conversion is fundamentally flawed, or that a violation of some primary assumption has taken place.

The Discrepancy for True Simples

The derivation of Eq. (8) makes the assumption of *random* pairwise interactions between primary radiogenic breaks leading to interchanges. In that case, variance/mean ratios of unity should result, consistent with the expectations of a Poisson distribution (35, 36). The total counts of chromosomal exchanges in the genome (mFISH), as well as subsets of these data – AS and TR exchanges – showed no clear evidence of overdispersion. For both γ-rays and Fe ions, the dispersion parameter in quasi-binomial fits was always in the range of 0.58–1.19, close to unity. The X^2 test for residual deviances, which compares the fits of dose–response models with binomial and quasi-binomial errors, produced *p*-values of 0.43–0.88, also suggesting no overdispersion. These results are largely consistent with the analysis of the raw data to which the U-test (36) was also applied to check σ^2/Y ratios for overdispersion (data not shown). By applying this latter criterion to the data for gamma rays, we found no evidence that the distribution of TR or AS exchanges deviated from that of the Poisson. For the high LET ^{56}Fe ions, significant over dispersion was detected by the U-test, but only for one of the five doses examined. From this, we conclude that systematic deviation from randomness in the distribution of exchanges per cell is not the principle cause for the failure of Eq. (8) to predict the outcomes of TR exchanges measured by mFISH.

We think a more likely explanation for the large discrepancy involves the remaining fundamental assumption attached to the derivation of Eq. (8), namely that the probability of an exchange between two chromosomes is a product of their proportional genomic content. [We hasten to make a minor point here that, strictly speaking, it is probably more accurate to consider the length of interphase chromosome arms, or chromatin fibers (the chromonema) of individual chromosomes in such interactions (37), rather than gross DNA content, although the two parameters are sufficiently related (38) that they can probably be used interchangeably in the present context.]

During interphase, it is now well established that chromosomes occupy rather distinct globular domains (39–41), which, it is reasonable to assume, severely limit the opportunity for the interaction of radiogenic breaks between different chromosomes. Consequently, models have been developed that consider interchanges constrained to boundary regions where two chromosomes abut (42), in which case interchanges would be proportional to the product of domain surface areas. For chromosome domains of spherical shape, exchange frequencies would, therefore, be proportional to [DNA content] $^{2/3}$ (43). For spherical domains of radii *r*, the ratio of volume to surface area varies as *r*/3. Consequently, by comparison to models based on volume, predictions based on DNA content tend to systematically overestimate exchange frequencies involving larger chromosomes (9, 44, 45). Unfortunately, this leads to a further lowering of predicted frequencies for exchanges involving the large-sized chromosomes examined here – the opposite of what is needed to bring three-color data in line with that of mFISH for TRs (**Figure 5**; lower panel). The problem is further exacerbated when one considers that chromosome domains are not actually spherical, but globular instead, because for any irregular volume the surface-to-volume ratio is larger than that of a sphere, or for that matter, any platonic solid.

One should appreciate that simple pairwise exchanges do not form in a vacuum, meaning their formation is always in potential competition with the formation of complex exchanges. Said another way, simple and complex exchanges often compete for the same radiogenic breaks. Consider a constellation of four such *proximate* breaks, defined as breaks that – by virtue of being close in time and space – are capable of freely interacting (rejoining) with one another. An obvious rejoining possibility is that the four breaks rejoin in such a way as to give two simple exchanges. But, should any other misrejoining possibility occur, a complex exchange will result, simultaneously negating the possibility of simple pairwise exchange. Crudely put, the formation of complex exchanges can be envisioned to "steal away" breaks that would otherwise be destined to become involved in forming simple exchanges (46). In this sense, complex exchanges form *at the expense* of simple exchanges, a process that is bound to be dose dependent, since it is strongly influenced by lesion density. To our knowledge, no one has formally modeled this scenario, but it most assuredly would have the overall effect of depressing the expected yields of simple exchanges.

Other explanations for our results involve the higher order organization of the mammalian cell genome (i.e., beyond that of the 30 nm chromatin fiber). Since this remains as one of the least understood aspects of cell biology, a fair amount of speculation is unavoidable. Until now, we have assumed random interaction between radiogenic breaks – either those contained within interphase chromosome domains, or those associated with their surface areas. In fact, the radial distribution of chromosomes in the nucleus is often not random, and differs among cell type and stage of cellular differentiation (47). There is some evidence that larger human chromosomes tend to be located near the periphery of the nucleus. If true, then larger chromosomes would share a proportion of their surface area with the outside nuclear boundary – regions that presumably would be unavailable for interaction with that of more interior domains (48, 49). Such is the case for chromosome 1, at least in fibroblasts (50, 51), although there is also evidence to the contrary for lymphocytes (52, 53). Such a relationship (in principle) would necessitate a higher correction factor be applied exchanges involving the large-sized chromosomes used in this study, which would have the effect of reducing CF errors shown in **Figure 5** for TRs.

The assumption of random breakage also implies a more-or-less uniform breakage per unit length of DNA or chromatin. While this is probably true for the initial radiogenic lesions (i.e., DNA double-strand breaks), there is evidence that exchanges themselves occur preferentially in G-light bands (54, 55) or at the interface between light and dark bands (56). These regions, particularly T-bands (a subset of G-light bands) have a much higher than average gene density (57). As long as these "sensitive" regions are randomly distributed among various chromosomes, this should not materially affect the underlying assumptions relating to Eq. (8). However, certain chromosomes are known to be gene-rich, on average, a case in point being chromosome 19 (41) which, perhaps not by coincidence, is thought to occupy an interior position within the nucleus (58). By this argument, gene-rich chromosomes may be subject to increased exchange involvement compared to chromosomes with lower gene density.

Additionally, if one equates gene density with transcriptional activity, then the DNA of such regions would presumably have a more "open" or diffuse structure (59, 60), and consequently be less dense in terms DNA content/surface area. In this way, increased transcription associated with gene-rich regions (or whole chromosomes) may have the secondary effect of lowering the physical density of DNA per unit volume. The opposite would be true of more gene-poor chromosomes. With respect to interactions based on surface area, larger chromosomes would then require larger CFs to compensate, again mitigating CF discrepancies shown in **Figure 5**. These ideas represent little more than a speculative attempt to explain our findings. Whether or not they help to resolve the thorny issue of dose dependency of CFs associated with violation of Eq. (15) remains to be seen.

CONCLUSION

The good news – at least from a utilitarian perspective – is that for the purpose of converting WCP data to WGE, CFs work reasonably well across the range of doses to which they are usually applied. The less welcome news is the large discrepancy between WGE-corrected TR exchange frequencies compared to those detected by mFISH, which implies problems with the biophysical underpinnings upon which the derivation CFs rely. We imagine that the fundamental assumptions underlying Eq. (8) are overly simplistic, failing to account for structural features of chromatin, and its dynamic interactions within the interphase nucleus. Sophisticated methods are being applied to this area of study that, in principle, can provide the investigator a "snapshot" into physical relationships that exist between interphase chromosomes (61, 62), but these fall short in addressing any potential time-dependent dynamic interactions. We have known, for the better part of a century, that initial radiogenic breaks in chromosomes need to be both spatially and temporally close for exchanges to occur (63). And yet, there are almost certainly aspects of this relationship that we do not fully understand. A phrase used often by the preeminent cytogeneticist J.R.K Savage seems an appropriate closing note: "Everything is more complex than it appears at first sight."

AUTHOR CONTRIBUTIONS

BL conducted the experiments and helped analyze the data. IS provided critical statistical support and helped edit the manuscript. MC conceived of the experiment, provided financial support, and wrote most of the paper.

ACKNOWLEDGMENTS

The authors gratefully acknowledge assistance provided by Drs. Daniel Cornforth for the proof related to Equation (15), and Dudley Goodhead for valuable theoretical discussion. This work was supported by the following grants from NASA: NNX15AG74G (MC) and NNX14AC76G (BL).

REFERENCES

1. Speicher MR, Ballard SG, Ward DC. Karyotyping human chromosomes by combinatorial multi-fluor fish. *Nat Genet* (1996) **12**:368–75. doi:10.1038/ng0496-368
2. Schrock E, du Manoir S, Veldman T, Schoell B, Wienberg J, Ferguson-Smith MA, et al. Multicolor spectral karyotyping of human chromosomes. *Science* (1996) **273**:494–7. doi:10.1126/science.273.5274.494
3. Lucas JN, Awa A, Straume T, Poggensee M, Kodama Y, Nakano M, et al. Rapid translocation frequency analysis in humans decades after exposure to ionizing radiation. *Int J Radiat Biol* (1992) **62**:53–63. doi:10.1080/09553009214551821
4. Braselmann H, Kulka U, Baumgartner A, Eder C, Muller I, Figel M, et al. Sky and fish analysis of radiation-induced chromosome aberrations: a comparison of whole and partial genome analysis. *Mutat Res* (2005) **578**:124–33. doi:10.1016/j.mrfmmm.2005.04.006
5. George KA, Hada M, Jackson LJ, Elliott T, Kawata T, Pluth JM, et al. Dose response of gamma rays and iron nuclei for induction of chromosomal aberrations in normal and repair-deficient cell lines. *Radiat Res* (2009) **171**:752–63. doi:10.1667/RR1680.1
6. Tucker JD, Ramsey MJ, Lee DA, Minkler JL. Validation of chromosome painting as a biodosimeter in human peripheral lymphocytes following acute exposure to ionizing radiation in vitro. *Int J Radiat Biol* (1993) **64**:27–37. doi:10.1080/09553009314551081
7. Nakano M, Nakashima E, Pawel DJ, Kodama Y, Awa A. Frequency of reciprocal translocations and dicentrics induced in human blood lymphocytes by x-irradiation as determined by fluorescence in situ hybridization. *Int J Radiat Biol* (1993) **64**:565–9. doi:10.1080/09553009314551781
8. Finnon P, Lloyd DC, Edwards AA. Fluorescence in situ hybridization detection of chromosomal aberrations in human lymphocytes: applicability to biological dosimetry. *Int J Radiat Biol* (1995) **68**:429–35. doi:10.1080/09553009514551391
9. Knehr S, Zitzelsberger H, Braselmann H, Bauchinger M. Analysis for DNA-proportional distribution of radiation-induced chromosome aberrations in various triple combinations of human chromosomes using fluorescence in situ hybridization. *Int J Radiat Biol* (1994) **65**:683–90. doi:10.1080/09553009414550801
10. Knehr S, Zitzelsberger H, Braselmann H, Nahrstedt U, Bauchinger M. Chromosome analysis by fluorescence in situ hybridization: further indications for a non-DNA-proportional involvement of single chromosomes in radiation-induced structural aberrations. *Int J Radiat Biol* (1996) **70**:385–92. doi:10.1080/095530096144851
11. Barquinero JF, Knehr S, Braselmann H, Figel M, Bauchinger M. DNA-proportional distribution of radiation-induced chromosome aberrations analysed by fluorescence in situ hybridization painting of all chromosomes of a human female karyotype. *Int J Radiat Biol* (1998) **74**:315–23. doi:10.1080/095530098141456
12. Brown JM, Evans JW, Kovacs MS. Mechanism of chromosome exchange formation in human fibroblasts: insights from "chromosome painting". *Environ Mol Mutagen* (1993) **22**:218–24. doi:10.1002/em.2850220407
13. Simpson PJ, Savage JR. Detecting 'hidden' exchange events within x-ray-induced aberrations using multicolour chromosome paints. *Chromosome Res* (1995) **3**:69–72. doi:10.1007/BF00711165
14. Simpson PJ, Papworth DG, Savage JRK. X-ray-induced simple, pseudosimple and complex exchanges involving two distinctly painted chromosomes. *Int J Radiat Biol* (1999) **75**:11–8. doi:10.1080/095530099140753
15. Griffin CS, Marsden SJ, Stevens DL, Simpson P, Savage JR. Frequencies of complex chromosome exchange aberrations induced by 238pu alpha-particles and detected by fluorescence in situ hybridization using single chromosome-specific probes. *Int J Radiat Biol* (1995) **67**:431–9. doi:10.1080/09553009514550491
16. Griffin CS, Stevens DL, Savage JR. Ultrasoft 1.5 kev aluminum k x rays are efficient producers of complex chromosome exchange aberrations as revealed by fluorescence in situ hybridization. *Radiat Res* (1996) **146**:144–50. doi:10.2307/3579586
17. Anderson RM, Marsden SJ, Wright EG, Kadhim MA, Goodhead DT, Griffin CS. Complex chromosome aberrations in peripheral blood lymphocytes as a potential biomarker of exposure to high-let alpha-particles. *Int J Radiat Biol* (2000) **76**:31–42. doi:10.1080/095530000138989

18. George K, Wu H, Willingham V, Furusawa Y, Kawata T, Cucinotta FA. High- and low-let induced chromosome damage in human lymphocytes: a time-course of aberrations in metaphase and interphase. *Int J Radiat Biol* (2001) **77**:175–83. doi:10.1080/0955300001003760
19. Anderson RM, Stevens DL, Goodhead DT. M-fish analysis shows that complex chromosome aberrations induced by alpha-particle tracks are cumulative products of localized rearrangements. *Proc Natl Acad Sci U S A* (2002) **99**:12167–72. doi:10.1073/pnas.182426799
20. Durante M, Ando K, Furusawa Y, Obe G, George K, Cucinotta FA. Complex chromosomal rearrangements induced in vivo by heavy ions. *Cytogenet Genome Res* (2004) **104**:240–4. doi:10.1159/000077497
21. Cornforth MN. Perspectives on the formation of radiation-induced exchange aberrations. *DNA Repair* (2006) **5**:1182–91. doi:10.1016/j.dnarep.2006.05.008
22. Loucas BD, Durante M, Bailey SM, Cornforth MN. Chromosome damage in human cells by rays, particles and heavy ions: track interactions in basic dose-response relationships. *Radiat Res* (2013) **179**:9–20. doi:10.1667/RR3089.1
23. Loucas BD, Cornforth MN. Complex chromosome exchanges induced by gamma rays in human lymphocytes: an mFISH study. *Radiat Res* (2001) **155**:660–71. doi:10.1667/0033-7587(2001)155[0660:CCEIBG]2.0.CO;2
24. Durante M, Furusawa Y, Gotoh E. A simple method for simultaneous interphase-metaphase chromosome analysis in biodosimetry. *Int J Radiat Biol* (1998) **74**:457–62. doi:10.1080/095530098141320
25. Cornforth MN. Analyzing radiation-induced complex chromosome rearrangements by combinatorial painting. *Radiat Res* (2001) **155**:643–59. doi:10.1667/0033-7587(2001)155[0643:ARICCR]2.0.CO;2
26. Wu H, George K, Yang TC. Estimate of true incomplete exchanges using fluorescence in situ hybridization with telomere probes. *Int J Radiat Biol* (1998) **73**:521–7. doi:10.1080/095530098142068
27. Kodama Y, Nakano M, Ohtaki K, Delongchamp R, Awa AA, Nakamura N. Estimation of minimal size of translocated chromosome segments detectable by fluorescence in situ hybridization. *Int J Radiat Biol* (1997) **71**:35–9. doi:10.1080/095530097144391
28. Boei JJ, Vermeulen S, Fomina J, Natarajan AT. Detection of incomplete exchanges and interstitial fragments in x-irradiated human lymphocytes using a telomeric pna probe. *Int J Radiat Biol* (1998) **73**:599–603. doi:10.1080/095530098141843
29. Fomina J, Darroudi F, Boei JJ, Natarajan AT. Discrimination between complete and incomplete chromosome exchanges in x-irradiated human lymphocytes using fish with pan-centromeric and chromosome specific DNA probes in combination with telomeric pna probe. *Int J Radiat Biol* (2000) **76**:807–13. doi:10.1080/09553000050028968
30. Mayall BH, Carrano AV, Moore DH II, Ashworth LK, Bennett DE, Mendelsohn ML. The DNA-based human karyotype. *Cytometry* (1984) **5**:376–85. doi:10.1002/cyto.990050414
31. Morton NE. Parameters of the human genome. *Proc Natl Acad Sci U S A* (1991) **88**:7474–6. doi:10.1073/pnas.88.17.7474
32. George KA, Hada M, Chappell L, Cucinotta FA. Biological effectiveness of accelerated particles for the induction of chromosome damage: track structure effects. *Radiat Res* (2013) **180**:25–33. doi:10.1667/RR3291.1
33. Agresti A, Coull BA. Approximate is better than "exact" for interval estimation of binomial proportions. *Am Stat* (1998) **52**:119–26. doi:10.2307/2685469
34. Pernot E, Hall J, Baatout S, Benotmane MA, Blanchardon E, Bouffler S, et al. Ionizing radiation biomarkers for potential use in epidemiological studies. *Mutat Res* (2012) **751**:258–86. doi:10.1016/j.mrrev.2012.05.003
35. Virsik RP, Harder D. Statistical interpretation of the overdispersed distribution of radiation-induced dicentric chromosome aberrations at high let. *Radiat Res* (1981) **85**:13–23. doi:10.2307/3575434
36. Edwards AA, Lloyd DC, Purrott RJ. Radiation induced chromosome aberrations and the poisson distribution. *Radiat Environ Biophys* (1979) **16**:89–100. doi:10.1007/BF01323216
37. Savage JRK, Papworth DG. Frequency and distribution studies of asymmetrical versus symmetrical chromosome aberrations. *Mutat Res* (1982) **95**:7–18. doi:10.1016/0027-5107(82)90062-8
38. Korenberg JR, Engels WR. Base ratio, DNA content, and quinacrine-brightness of human chromosomes. *Proc Natl Acad Sci U S A* (1978) **75**:3382–6. doi:10.1073/pnas.75.7.3382
39. Pinkel D, Landegent J, Collins C, Fuscoe J, Segraves R, Lucas J, et al. Fluorescence in situ hybridization with human chromosome-specific libraries: detection of trisomy 21 and translocations of chromosome 4. *Proc Natl Acad Sci U S A* (1988) **85**:9138–42. doi:10.1073/pnas.85.23.9138
40. Cremer T, Kreth G, Koester H, Fink RH, Heintzmann R, Cremer M, et al. Chromosome territories, interchromatin domain compartment, and nuclear matrix: an integrated view of the functional nuclear architecture. *Crit Rev Eukaryot Gene Expr* (2000) **10**:179–212. doi:10.1615/CritRevEukarGeneExpr.v10.i2.60
41. Cremer T, Cremer C. Chromosome territories, nuclear architecture and gene regulation in mammalian cells. *Nat Revs Genet* (2001) **2**:292–301. doi:10.1038/35066075
42. Savage JR, Papworth DG. The relationship of radiation-induced dicentric yield to chromosome arm number. *Mutat Res* (1973) **19**:139–43. doi:10.1016/0027-5107(73)90122-X
43. Cigarran S, Barrios L, Barquinero JF, Caballin MR, Ribas M, Egozcue J. Relationship between the DNA content of human chromosomes and their involvement in radiation-induced structural aberrations, analysed by painting. *Int J Radiat Biol* (1998) **74**:449–55. doi:10.1080/095530098141311
44. Wu H, Durante M, Lucas JN. Relationship between radiation-induced aberrations in individual chromosomes and their DNA content: effects of interaction distance. *Int J Radiat Biol* (2001) **77**:781–6. doi:10.1080/09553000110050227
45. Cornforth MN, Greulich-Bode KM, Loucas BD, Arsuaga J, Vazquez M, Sachs RK, et al. Chromosomes are predominantly located randomly with respect to each other in interphase human cells. *J Cell Biol* (2002) **159**:237–44. doi:10.1083/jcb.200206009
46. Loucas BD, Eberle R, Bailey SM, Cornforth MN. Influence of dose rate on the induction of simple and complex chromosome exchanges by gamma rays. *Radiat Res* (2004) **162**:339–49. doi:10.1667/RR3245
47. Bridger JM, Arican-Gotkas HD, Foster HA, Godwin LS, Harvey A, Kill IR, et al. The non-random repositioning of whole chromosomes and individual gene loci in interphase nuclei and its relevance in disease, infection, aging, and cancer. *Adv Exp Med Biol* (2014) **773**:263–79. doi:10.1007/978-1-4899-8032-8_12
48. Foster HA, Estrada-Girona G, Themis M, Garimberti E, Hill MA, Bridger JM, et al. Relative proximity of chromosome territories influences chromosome exchange partners in radiation-induced chromosome rearrangements in primary human bronchial epithelial cells. *Mutat Res* (2013) **756**:66–77. doi:10.1016/j.mrgentox.2013.06.003
49. Themis M, Garimberti E, Hill MA, Anderson RM. Reduced chromosome aberration complexity in normal human bronchial epithelial cells exposed to low-let gamma-rays and high-let alpha-particles. *Int J Radiat Biol* (2013) **89**:934–43. doi:10.3109/09553002.2013.805889
50. Sun HB, Shen J, Yokota H. Size-dependent positioning of human chromosomes in interphase nuclei. *Biophys J* (2000) **79**:184–90. doi:10.1016/S0006-3495(00)76282-5
51. Zeitz MJ, Mukherjee L, Bhattacharya S, Xu J, Berezney R. A probabilistic model for the arrangement of a subset of human chromosome territories in wi38 human fibroblasts. *J Cell Physiol* (2009) **221**:120–9. doi:10.1002/jcp.21842
52. Boyle S, Gilchrist S, Bridger JM, Mahy NL, Ellis JA, Bickmore WA. The spatial organization of human chromosomes within the nuclei of normal and emerin-mutant cells. *Hum Mol Genet* (2001) **10**:211–9. doi:10.1093/hmg/10.3.211
53. Ioannou D, Kandukuri L, Quadri A, Becerra V, Simpson JL, Tempest HG. Spatial positioning of all 24 chromosomes in the lymphocytes of six subjects: evidence of reproducible positioning and spatial repositioning following DNA damage with hydrogen peroxide and ultraviolet b. *PLoS One* (2015) **10**:e0118886. doi:10.1371/journal.pone.0118886
54. Holmberg M, Jonasson J. Preferential location of x-ray induced chromosome breakage in the r-bands of human chromosomes. *Hereditas* (1973) **74**:57–67. doi:10.1111/j.1601-5223.1973.tb01104.x
55. Holmberg M, Carrano AV. Neutron induced break-points in human chromosomes have a similar location as x-ray induced break-points. *Hereditas* (1978) **89**:183–7. doi:10.1111/j.1601-5223.1978.tb01274.x
56. Buckton KE. Identification with g and r banding of the position of breakage points induced in human chromosomes by in vitro x-irradiation. *Int J Radiat Biol Relat Stud Phys Chem Med* (1976) **29**:475–88. doi:10.1080/09553007614550571
57. Craig JM, Bickmore WA. The distribution of cpg islands in mammalian chromosomes. [erratum appears in nat genet 1994 Aug;7(4):551]. *Nat Genet* (1994) **7**:376–82. doi:10.1038/ng0794-376

58. Croft JA, Bridger JM, Boyle S, Perry P, Teague P, Bickmore WA. Differences in the localization and morphology of chromosomes in the human nucleus. *J Cell Biol* (1999) **145**:1119–31. doi:10.1083/jcb.145.6.1119
59. Franke WW, Scheer U, Trendelenburg M, Zentgraf H, Spring H. Morphology of transcriptionally active chromatin. *Cold Spring Harb Symp Quant Biol* (1978) **42**:755–72. doi:10.1101/SQB.1978.042.01.076
60. Paul J, Zollner EJ, Gilmour RS, Birnie GD. Properties of transcriptionally active chromatin. *Cold Spring Harb Symp Quant Biol* (1978) **42**(Pt 1):597–603. doi:10.1101/SQB.1978.042.01.062
61. Gondor A, Ohlsson R. Chromosome crosstalk in three dimensions. *Nature* (2009) **461**:212–7. doi:10.1038/nature08453
62. Arsuaga J, Jayasinghe RG, Scharein RG, Segal MR, Stolz R, Vazquez M. Current theoretical models fail to predict the topological complexity of the human genome. *Front Mol Biosci* (2015) **2**:48. doi:10.3389/fmolb.2015.00048
63. Lea DE. *Actions of Radiations on Living Cells*. London: Cambridge University Press (1946).

Conflict of Interest Statement: The authors declare that the research was conducted in the absence of any commercial or financial relationships that could be construed as a potential conflict of interest.

Copyright © 2016 Loucas, Shuryak and Cornforth. This is an open-access article distributed under the terms of the Creative Commons Attribution License (CC BY). The use, distribution or reproduction in other forums is permitted, provided the original author(s) or licensor are credited and that the original publication in this journal is cited, in accordance with accepted academic practice. No use, distribution or reproduction is permitted which does not comply with these terms.

frontiers in Oncology

ORIGINAL RESEARCH
published: 07 December 2015
doi: 10.3389/fonc.2015.00275

Correlation of Particle Traversals with Clonogenic Survival Using Cell-Fluorescent Ion Track Hybrid Detector

Ivana Dokic[1,2,3], Martin Niklas[1,2,3], Ferdinand Zimmermann[1,2,3], Andrea Mairani[2,4], Philipp Seidel[1,2,3], Damir Krunic[5], Oliver Jäkel[2,3,6], Jürgen Debus[1,2,3], Steffen Greilich[3,6] and Amir Abdollahi[1,2,3]**

[1] German Cancer Consortium, Translational Radiation Oncology, National Center for Tumor Diseases, German Cancer Research Center, Heidelberg University Medical School, Heidelberg, Germany, [2] Heidelberg Ion Therapy Center, Heidelberg, Germany, [3] Heidelberg Institute of Radiation Oncology, National Center for Radiation Research in Oncology, Heidelberg, Germany, [4] National Center for Oncological Hadrontherapy, Pavia, Italy, [5] Light Microscopy Facility, German Cancer Research Center, Heidelberg, Germany, [6] Division of Medical Physics in Radiation Oncology, German Cancer Research Center, Heidelberg, Germany

OPEN ACCESS

Edited by:
Marco Durante,
GSI, Germany

Reviewed by:
M. Christine Hollander,
National Institutes of Health, USA
Lorenzo Manti,
University of Naples Federico II, Italy

***Correspondence:**
Ivana Dokic
i.dokic@dkfz.de;
Amir Abdollahi
a.amir@dkfz.de

Specialty section:
This article was submitted to Radiation Oncology, a section of the journal Frontiers in Oncology

Received: 30 September 2015
Accepted: 23 November 2015
Published: 07 December 2015

Citation:
Dokic I, Niklas M, Zimmermann F, Mairani A, Seidel P, Krunic D, Jäkel O, Debus J, Greilich S and Abdollahi A (2015) Correlation of Particle Traversals with Clonogenic Survival Using Cell-Fluorescent Ion Track Hybrid Detector. Front. Oncol. 5:275. doi: 10.3389/fonc.2015.00275

Development of novel approaches linking the physical characteristics of particles with biological responses are of high relevance for the field of particle therapy. In radiobiology, the clonogenic survival of cells is considered the gold standard assay for the assessment of cellular sensitivity to ionizing radiation. Toward further development of next generation biodosimeters in particle therapy, cell-fluorescent ion track hybrid detector (Cell-FIT-HD) was recently engineered by our group and successfully employed to study physical particle track information in correlation with irradiation-induced DNA damage in cell nuclei. In this work, we investigated the feasibility of Cell-FIT-HD as a tool to study the effects of clinical beams on cellular clonogenic survival. Tumor cells were grown on the fluorescent nuclear track detector as cell culture, mimicking the standard procedures for clonogenic assay. Cell-FIT-HD was used to detect the spatial distribution of particle tracks within colony-initiating cells. The physical data were associated with radiation-induced foci as surrogates for DNA double-strand breaks, the hallmark of radiation-induced cell lethality. Long-term cell fate was monitored to determine the ability of cells to form colonies. We report the first successful detection of particle traversal within colony-initiating cells at subcellular resolution using Cell-FIT-HD.

Keywords: clonogenic survival, fluorescent nuclear track detector, carbon ion irradiation, 53BP1, DNA damage foci

INTRODUCTION

Radiotherapy with protons and heavier ions has become a swiftly growing field, and it is becoming an integrative part of therapy of solid tumors, due to its high success rate in treating certain tumors (1). Nevertheless, intracellular molecular events caused by interactions between the charged particles and cellular structures are not yet well understood. Development of novel approaches that will facilitate deciphering those processes is of high relevance for the field.

Recently, a cell-fluorescent ion track hybrid detector (Cell-FIT-HD) was engineered by our group. It provides information on spatial correlation between single ion traversals and the events within a cell (2, 3). Cell-FIT-HD technology is based on growing a cellular monolayer (biological compartment) on a surface of a fluorescent nuclear track detector [FNTD; physical compartment (4)]. Due to its unique design, Cell-FIT-HD enables simultaneous investigation of microscopic beam parameters and their effect on various cellular structures and biological processes, using confocal laser scanning microscope (5).

In this work, we investigated the feasibility of Cell-FIT-HD for colony formation analysis. Colony formation assay (also called clonogenic assay), developed in 1950s (6), is the most reliable and relevant method for studying the efficacy of the radiation treatment *in vitro*. It has been named "gold standard" in radiation research as it combines contribution of all types of cell death, as well as ability of surviving cells' to indefinitely proliferate and form colonies (7, 8). For particle therapy planning, clonogenic survival data are of utmost importance for studying radiobiological effectiveness (RBE) and they continue to be used as the main biological experimental outcome for testing biophysical models for predicting tumor response to irradiation (9). Colony formation and cellular clonogenic survival after irradiation are highly depend on radiation potential to induce complex, difficult to repair, DNA damage [such as DNA double-strand breaks (DSB)] (10). Commonly used molecular surrogate for detecting DNA damage and DNA DSB is p53 binding protein 1 (53BP1), which localizes at the sites of DSB and forms nuclear radiation-induced foci (RIF) (11, 12). In irradiated cells, on DNA DSB sites, 53BP1 foci colocalize with Serine 139 phosphorylated histone H2AX foci (γ-H2AX) flanking a larger area around a DSB and hence considered another sensitive marker for DNA DSB damage (13, 14).

Combination of Cell-FIT-HD technology, clonogenic assay, and RIF detection should provide a platform for simultaneous analysis of microscopic beam parameters, particle effects on RIF formation and the ability of cells to form colonies as a function of particle number, quality, and spatial distribution.

MATERIALS AND METHODS

Cell Culture

Cell lines used in this study were murine (Balb/c) renal adenocarcinoma cells (RENCA) and human alveolar adenocarcinoma cell line (A549), obtained from ATCC. RENCA were cultured in RPMI-1640 Medium (Gibco) supplemented with 10% fetal bovine serum (FBS, Gibco), non-essential amino acids (0.1 mM, Sigma), sodium pyruvate (1 mM, Sigma), and L-glutamine (2 mM, Sigma). A549 cells were cultured in Dulbecco's Modified Eagle Medium (DMEM, ATCC) supplemented with 10% heat-inactivated FBS (Millipore), 2 mM glutamine, and 1% penicillin/streptomycin (complete DMEM).

Cells Transduction and Immune Staining

A549 cells were transduced using a retroviral construct containing mCherry-53BP1-2 pLPC-Puro [Addgene plasmid # 19836; (15)]. Retrovirus production and cells transduction with mCherry-53BP1 construct were carried out, as previously described (15). Retrovirus production was performed using Retro-X Universal Packaging System (Clontech), according to manufacturer's instructions. Transduction was conducted by the incubation of cells and viral particles in a complete medium containing 8 μg/ml Polybrene (Sigma) at 37°C, 5% CO_2. Selection of transduced cells was performed using 2 μg/ml of Puromycin (Gibco). A549 cells expressing mCherry-53BP1 were cultured in complete DMEM containing 0.4 μg/ml of Puromycin (Gibco). All cells were incubated at 37°C at 5% CO_2 atmosphere. A549 cells expressing mCherry-53BP1 construct were counterstained for γ-H2AX marker as described (16). Fixed (4% paraformaldehyde, for 10 min) and permeabilized (0.1% Triton-X for 10 min) cells were labeled using primary anti-γ-H2AX antibody (1:100, Cell Biolabs) and secondary Alexa Fluor 488-conjugated donkey anti-mouse antibody (Molecular Probes).

Colony-Forming Cell Assay and Irradiation

For preparation of colony-forming cell assay using FNTD as a substrate (Cell-FIT-HD), FNTDs were first washed in an ultrasonic bath (Bandelin Sonorex) for 15 min at room temperature (RT). FNTDs were then placed in 70% ethanol overnight at RT. FNTDs were thoroughly washed in PBS, before used for cell culture.

Standard clonogenic assay (8) was performed using RENCA cells in six-well cell culture plates (200 cells/well). After attachment, cells were irradiated with ^{12}C ion beam at Heidelberg Ion-Beam Therapy Center (HIT). Cells were positioned in the middle of a 1-cm widespread out Bragg peak (SOBP, 1 Gy) centered at approximately 3.5 cm water-equivalent depth, mimicking the clinical-like settings. Dose averaged linear energy transfer (LET) was 95 keV/μm. Non-irradiated cells were used as control. After colonies were formed, cells were fixed with 75% methanol and 25% acetic acid for 10 min at RT and stained with 0.1% crystal violet for 15 min.

Standard clonogenic assay was modified for studying the colony formation on FNTDs. Forty microliters of growth medium drop containing 50 cells were placed on the polished surface of the FNTD. The growth area was approximately 4 mm × 8 mm. For studying the ability of cells to grow on FNTD surface and form colonies, FNTDs containing cells (Cell-FIT-HD) were either irradiated as described above, or left without irradiation (control) and incubated for 7 days. After colony formation, cells were fixed and stained as in standard clonogenic assay (as above). FNTDs containing colonies were scanned (EPSON Scan). All obtained images were corrected for brightness and contrast by ImageJ (http://rsb.info.nih.gov/ij/) using the same image processing settings.

To correlate colony forming ability of a single cell and microscopic ion beam parameters, mCherry-53BP1 A549 cells were allowed to attach (100 cells/FNTD for control and 200 cells/FNTD for irradiated sample) at 37°C at 5% CO_2 for at least 8 h prior to irradiation. Cell-FIT-HD was irradiated perpendicularly with respect to the incident ^{12}C ion beam, as described above.

Approximately 30 min post-irradiation ($t = 30$ min), the entire area of the Cell-FIT-HD was imaged by widefield microscopy

(see below). After the initial imaging, Cell-FIT-HD was placed in the incubator (37°C at 5% CO_2 atmosphere) for 7 days to allow colony formation on the polished surface of the FNTD. The ability of colony formation with/without irradiation after 7 days ($t = 7$ days) was assessed by additional imaging of Cell-FIT-HD by widefield microscopy.

Read-Out of Cell-FIT-HD

The read-outs of the physical compartment (FNTD) and of the biological compartment (single cells or colonies) of Cell-FIT-HD were uncoupled. 53BP1 (mCherry signal) and γ-H2AX (Alexa Fluor 488) in **Figure 2** were imaged by Zeiss LSM710, Confocor 3 confocal laser scanning microscope, as previously described (3), at 30 min post-irradiation.

Initial cell attachment and colonies were imaged by the inverted widefield microscope Cell Observer (Carl Zeiss AG). To record the initial cell attachment, an overview scan of the entire cell attachment area (polished surface of the FNTD) was performed. Image stacks of regions of interests (ROIs) containing single cells were subsequently recorded. The stacks contained 41 and 45 image planes (each separated by 2 μm) for the imaging at $t = 30$ min, and at $t = 7$ days, respectively. The entire depth of the cell layer was covered. For each imaging plane, the bright field (BF) as well as the mCherry fluorescent channel (mPlum filter set) was recorded. After recording the overview scan, single ROI was subsequently imaged to allow for visualization of 53BP1 foci formation in individual cell nuclei of the colony. ROIs were chosen to match approximately the positions of time point 0. Individual tiles of the overview scan were corrected for shading and stitched using the ZEN software. The cells were washed away from FNTDs after the last widefield microscopy read-out. ROIs in the FNTD were then imaged by the Zeiss LSM710, Confocor 3 confocal laser scanning microscope. The imaging parameters were adjusted to gain optimal read-outs for the primary particles (5). The frequency distribution of fluorescence intensity of the ion tracks was assessed as a proxy for the LET spectrum. There are two distinct peaks that can be attributed to the primary carbon ions and the lighter fragments, respectively. A threshold was set to separate between the two species. Obviously, some heavier fragments might be considered as primaries, what, however, does not affect the generality of the results of this study. For each position, a z-stack of 35 imaging planes was recorded by 633 nm HeNe laser line (17). T-PMT detection was recorded in parallel. For widefield and for confocal imaging uncoated glass bottom, culture dishes (MatTek Corp.) were used.

Registration of Biological and Physical Beam Data

Widefield (biological compartment) and confocal images (physical compartment) were registered employing point mapping to correlate cellular response to microscopic ion beam parameters spatially at time point 0. To this end, non-fluorescent Al–Al spinel cubical inclusions in the Al2O3:C, Mg crystal – both visible in the T-PMT and the BF channel – were used as point pairs. At least four point pairs were used yielding an accuracy of the projective registration smaller than 0.3 μm, i.e., on a sub-pixel scale. The same registration procedure was performed when projecting the nuclei positions at time point 0 into the cell layer at time point 7 days post-irradiation. It was ensured that the fluorescence (mCherry) and the brightfield channels of the widefield microscopy were spatially aligned.

Ion-Hit Statistics

Due to perpendicular irradiation setup, all track spot centers at $z = -3$ μm (measuring from the FNTD surface, $z = 0$ μm) were projected onto the maximum intensity projection (MIP) of the 53BP1 mCherry signal of the cell layer. Positions of single ion traversals were assessed by using an in-house developed thresholding algorithm. To determine intranuclear ion hits, the positions of the track spot center (rounded to pixel values) were projected onto the nuclei mask of the MIP of the 53BP1 mCherry signal. Trajectory reconstruction and angle assessment confirmed the validity of perpendicular extrapolation (3, 5). In the imaging plane at approximately $z = -3$ μm each track spot was masked and the maximum intensity value assessed. The maximum intensity value was converted into count-rate and was corrected for non-linearity in APD detection (18).

RESULTS

Colony Formation on FNTD

To study the feasibility of a FNTD's surface for colony formation, murine renal adenocarcinoma cells (RENCA) were used. As shown in **Figure 1A**, the cells were able to attach and form

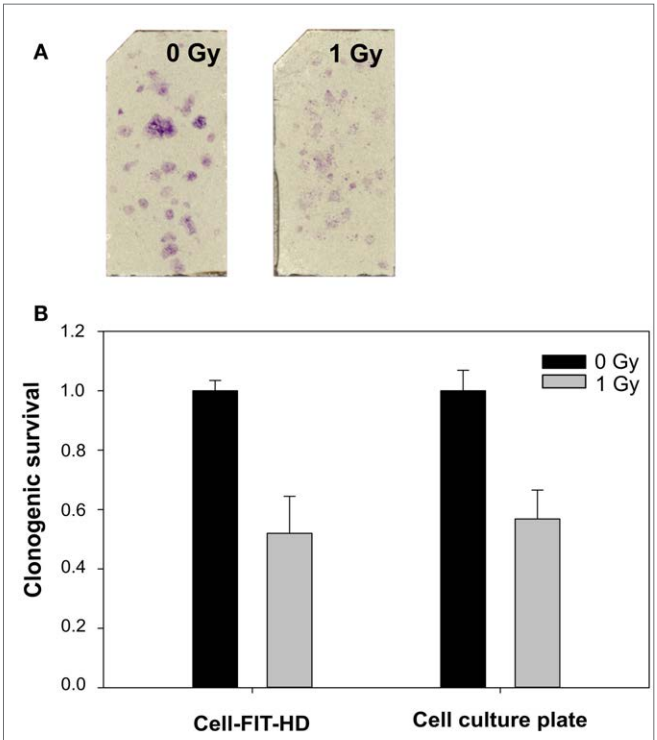

FIGURE 1 | Example of colony formation on FNTDs. **(A)** Spots on FNTD surface: crystal violet staining of cell colonies. Brightness/contrast was adjusted for better visualization. **(B)** Comparison of clonogenic survival on FNTDs and in culture flasks. Means and SDs of triplicates are shown.

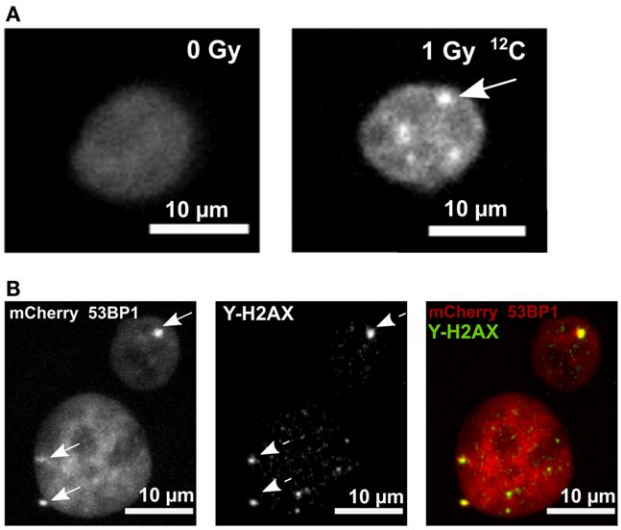

FIGURE 2 | mCherry 53BP1 and γ-H2AX signal in cell nuclei of A549 cells. **(A)** Pan-nuclear expression of 53BP1-mCherry fusion protein in a control sample (panel left). Irradiated (1 Gy ^{12}C) nucleus showing accumulation of 53BP1-mCherry signal (53BP1 foci, arrow). **(B)** mCherry-53BP1 signal (left panel, arrows point to 53BP1 foci), γ-H2AX signal (middle panel; dashed arrows point to γ-H2AX foci) in irradiated mCherry-53BP1 cells. Colocalization of 53BP1 and γ-H2AX foci (panel right). Sum of intensities of *Z*-stack slices is shown. Brightness and contrast were adjusted for better visualization.

colonies on FNTD surface. The mean plating efficacy and SD on FNTD surface was 33 ± 1.2%, whereas in a six-well plate it was 37 ± 6%. The results for colony formation and clonogenic survival on FNTDs correspond to those obtained using the standard clonogenic assay in cell culture dishes (**Figure 1B**).

To investigate colony formation on FNTDs, on a microscopic level, as well as DNA damage foci formation, we utilized human A549 cells expressing mCherry-53BP1 fusion protein. A549 cell line was selected because of its low level of background foci (2). The stable expression of the fluorescent fusion protein, localized in cell nuclei, provided homogeneous pan-nuclear staining, which enabled microscopic imaging of cellular nuclei, as well as individual foci formation after irradiation (**Figure 2A**). 53BP1 signal in irradiated cells colocalizes with γ-H2AX signal, which confirms the fact that 53BP1 accumulates at the DNA DSB sites (**Figure 2B**).

In order to localize colony-initiating cell within a respective colony, the whole surface of Cell-FIT-HD was imaged at early ($t = 30$ min; red pseudocolor) and late ($t = 7$ days; green pseudocolor) time point, and the images were overlaid (**Figure 3**). At the seventh day post-irradiation, A549 cells formed dense colonies. This stands particularly true in case of control samples, where most of the cells were able to produce colonies (**Figure 3A**). Irradiated cells showed lower capability for clonogenic growth when compared to the control cells. They produced smaller colonies in comparison to a control sample, and many cells were not dividing (**Figure 3B**).

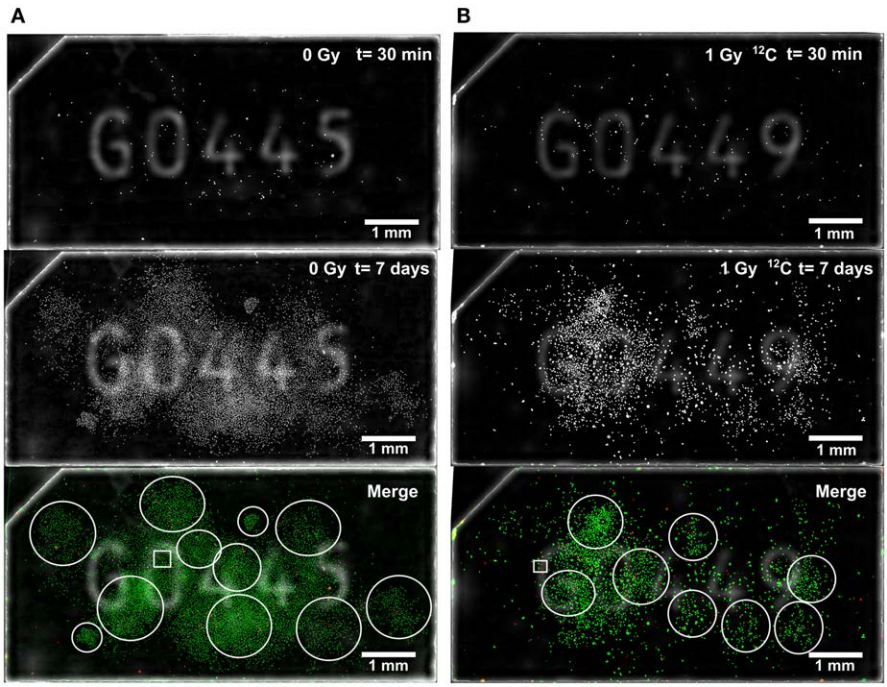

FIGURE 3 | Microscopic visualization of Cell-FIT-HD. **(A)** Control sample (mock irradiation) and **(B)** irradiated sample (1Gy ^{12}C-irradiation). FNTD surface was imaged at two time points: 30 min post irradiation ($t = 30$ min) and at 7 days ($t = 7$ days) post-irradiation. Early and late image orientations as well as brightness and contrast were adjusted and images were merged. Pan-nuclear mCherry-53BP1 signal was shown in red pseudocolor for $t = 30$ min, and in green pseudocolor for $t = 7$ days. White empty circles were used to mark different colonies. White empty squares indicate ROIs used for **Figure 4**. Numbers seen on FNTDs' surface are identification numbers engraved in each FNTD.

Even though cells can migrate on the surface during the colony formation time, it was assumed that the colony-initiating cell retained its position within the respective colony region. In the previous experiments, we observed that A549 cells can migrate up to 1 μm within 30 min in different directions, and these motion patterns of A549 cells would not be sufficient for a colony-initiating cell to leave the colony regions, especially in the case of larger colonies. Continuous live imaging of a colony formation was impossible due to the cytotoxicity induced by the long-term imaging settings.

Irradiation-Induced Foci and Ion Hits

To demonstrate the feasibility of a Cell-FIT-HD for analyzing ion traversals together with the irradiation-induced foci formation in a single cell, and investigate cell's fate in regards to colony formation, ROIs were selected in both control and irradiated Cell-FIT-HD. For the control sample, ROI containing three cells (at the early time point) was selected. These cells divided multiple times forming a large colony (**Figure 4A**). Initial positions of the colony-initiating cells' nuclei are marked by green closed lines (**Figure 4A**). At the seventh day post-irradiation, in case of irradiated samples, we analyzed the ROI containing cells that were not capable of colony formation (**Figure 4B**, right panel). Even though those cells did not form colonies, additional cells were found in their close proximity. This could imply either cell migration, or a single division of a cell (**Figure 4B**, top right panel). For the same ROI, we extracted the particle beam information from a physical compartment (FNTD) of a Cell-FIT-HD to visualize ion tracks. Within selected ROI, two nuclei showed large 53BP1 foci formation. Respective ion track spots were assigned to these irradiation-induced 53BP1 foci based on the closest proximity (orange circles, **Figure 4B**, left panel). These track spots were induced by primary-like carbon ions, since the imaging parameters were adjusted to detect primarily carbon ions. However, secondary high LET fragments can be in principle also included. Fast protons of low LET were not visualized. The ion beam fluency assessed was approximately 7.0×10^6 particles/cm^2.

DISCUSSION

Colony formation assay is a quantitative, macroscopic assay, which represents the standard for studying cell's sensitivity to irradiation (8). It provides valuable information on the outcome

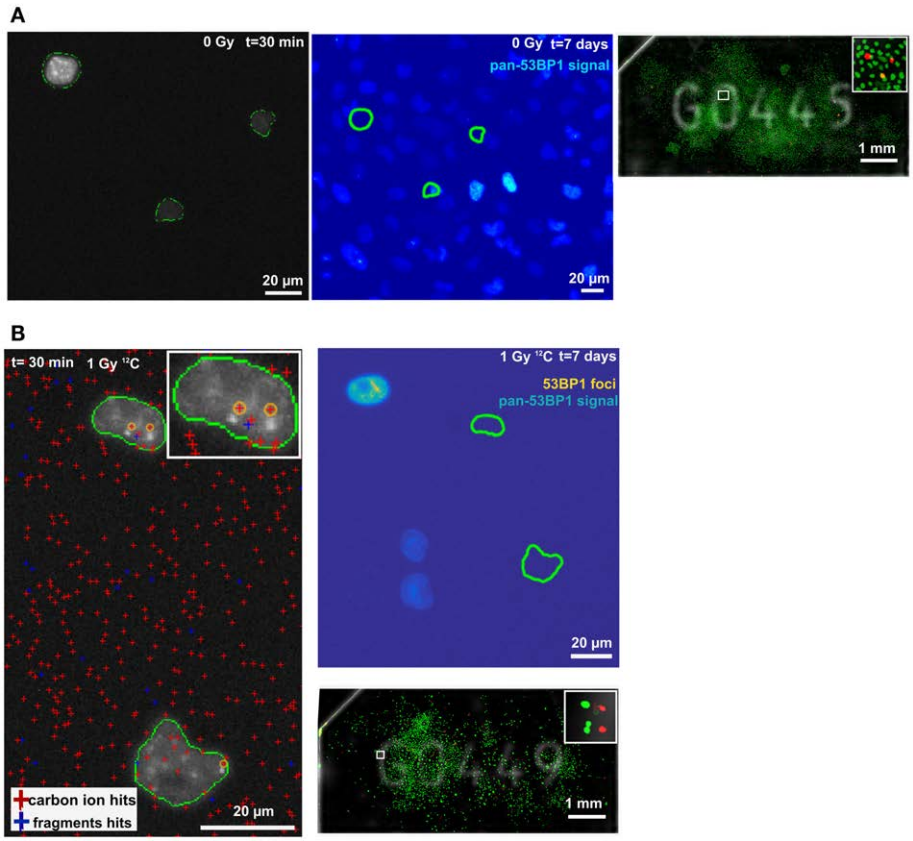

FIGURE 4 | Maximum intensity projections of 53BP1-mCherry signal and ion hits. **(A)** Control sample at t = 30 min (panel left) and t = 7 days (large colony formation; middle panel). Position of selected ROI on FNTD (white empty square). Insert: magnification of selected ROI (panel right). **(B)** Irradiated sample at t = 30 min (panel left). The cross sectional area of the nuclei at t = 30 min is encircled in green. The bright spots in the nuclei are 53BP1-mCherry foci most probably induced by carbon ions (highlighted by yellow circles, closest proximity). The positions of ion traversals and fragments are indicated by the red and blue crosses, respectively. Insert: magnification of the upper nucleus. Upper right panel shows the irradiated nuclei at t = 7 days, and no colony formation. Dense aggregation of 53BP1 signal is marked in yellow. The position of the nuclei at t = 30 min is labeled by green lines. The positions were registered to t = 7 days using the unique spinel fingerprint of spinels in the FNTD. Position of selected ROI on FNTD (white empty square). Insert: magnification of selected ROI (bottom right).

of a large cell population upon the irradiation. However, this assay does not provide an insight on a single cell fate within a population, and why certain cells within a population will stop dividing and eventually die, whereas the other ones will still be capable of clonogenic growth. It can be hypothesized that certain cells within a population accumulate lethal level of irradiation-induced damage, and lose capability to divide and form colonies, whereas the other cells remain unaffected. The unaffected cells might have higher DNA damage repair potential or may be "missed" by the irradiation particles (19, 20). The first step for addressing these questions is to develop a platform that provides direct information about spatial distribution of irradiation particles and correlates it at a single cell level with the clonogenic capacity. For that purpose, we adapted the conventional approach for colony formation assay and combined it with the usage of FNTDs (Cell-FIT-HD). This approach enables simultaneous analysis of the microscopic beam parameters together with the events in colonies, single cells, and at sub-cellular level. We were able to show that single cells can attach and grow as colonies on FNTD surface. The size of a surface area of a FNTD (4 mm × 8 mm) is not optimal for clonogenic growth, resulting in many overlapping colonies, and therefore the current design of the Cell-FIT-HD is not suitable for performing large-scale quantitative clonogenic assay. This might be restricted to certain cell types, such as the RENCA, where circumscribed colonies could be detected at an early phase of colony formation. Further studies are needed to find the optimal constraints for colony forming cell lines/primary cells in the Cell-FIT-HD setting. Nevertheless, our primary purpose was the application for analyzing single colonies, single cells, subcellular structures, and microscopic beam parameters, which was successfully demonstrated.

The current work represents a proof of principle study for correlation of particle traversal with long-term colony formation using Cell-FIT-HD. The entire workflow is established and builds a solid foundation for further improvements toward population level quantitative analysis. Further application of Cell-FIT-HD may provide necessary information for dissecting underlying mechanisms for colony formation of irradiated cells, which is important for studying time-dependent repair capability analyzing eventually correlation between fast and slow repair and the complexity of the induced damage, as well as bystander effect.

AUTHOR CONTRIBUTIONS

ID, MN, FZ, AM, PS, and DK performed experimental design, acquisition, analysis, and interpretation of the results. They participated in manuscript writing, revision, and approval of the final version for submission and publishing. ID, MN, OJ, SG, JD, and AA participated in the conception and design of the work, as well as interpretation of the data. They participated in manuscript writing, revision, and approval of the final version for submission and publishing. All authors agree to be accountable for all aspects of the work in ensuring that questions related to the accuracy or integrity of any part of the work are appropriately investigated and resolved.

FUNDING

This work was supported by German Research Council (DFG-KFO214), Deutsche Krebshilfe (Max-Eder 108876), Heidelberg School of Oncology Stipend (to MN) and intramural grants from National Center for Tumor diseases (NCT/DKFZ-DKTK, Heidelberg, Germany).

REFERENCES

1. Loeffler JS, Durante M. Charged particle therapy – optimization, challenges and future directions. *Nat Rev Clin Oncol* (2013) **10**:411–24. doi:10.1038/nrclinonc.2013.79
2. Niklas M, Abdollahi A, Akselrod MS, Debus J, Jakel O, Greilich S. Subcellular spatial correlation of particle traversal and biological response in clinical ion beams. *Int J Radiat Oncol Biol Phys* (2013) **87**:1141–7. doi:10.1016/j.ijrobp.2013.08.043
3. Niklas M, Greilich S, Melzig C, Akselrod MS, Debus J, Jakel O, et al. Engineering cell-fluorescent ion track hybrid detectors. *Radiat Oncol* (2013) **8**:141. doi:10.1186/1748-717X-8-141
4. Akselrod MS, Sykora GJ. Fluorescent nuclear track detector technology – a new way to do passive solid state dosimetry. *Radiat Meas* (2011) **46**:1671–9. doi:10.1016/j.radmeas.2011.06.018
5. Greilich S, Osinga JM, Niklas M, Lauer FM, Klimpki G, Bestvater F, et al. Fluorescent nuclear track detectors as a tool for ion-beam therapy research. *Radiat Meas* (2013) **56**:267–72. doi:10.1016/j.radmeas.2013.01.033
6. Puck TT, Marcus PI. Action of x-rays on mammalian cells. *J Exp Med* (1956) **103**:653–66. doi:10.1084/jem.103.5.653
7. Brown JM, Attardi LD. The role of apoptosis in cancer development and treatment response. *Nat Rev Cancer* (2005) **5**:231–7. doi:10.1038/nrc1560
8. Franken NA, Rodermond HM, Stap J, Haveman J, Van Bree C. Clonogenic assay of cells in vitro. *Nat Protoc* (2006) **1**:2315–9. doi:10.1038/nprot.2006.339
9. Friedrich T, Scholz U, Elsasser T, Durante M, Scholz M. Systematic analysis of RBE and related quantities using a database of cell survival experiments with ion beam irradiation. *J Radiat Res* (2013) **54**:494–514. doi:10.1093/jrr/rrs114
10. Khanna KK, Jackson SP. DNA double-strand breaks: signaling, repair and the cancer connection. *Nat Genet* (2001) **27**:247–54. doi:10.1038/85798
11. Noon AT, Goodarzi AA. 53BP1-mediated DNA double strand break repair: insert bad pun here. *DNA Repair (Amst)* (2011) **10**:1071–6. doi:10.1016/j.dnarep.2011.07.012
12. Markova E, Vasilyev S, Belyaev I. 53BP1 foci as a marker of tumor cell radiosensitivity. *Neoplasma* (2015) **62**:770–6. doi:10.4149/neo_2015_092
13. Ward IM, Minn K, Jorda KG, Chen J. Accumulation of checkpoint protein 53BP1 at DNA breaks involves its binding to phosphorylated histone H2AX. *J Biol Chem* (2003) **278**:19579–82. doi:10.1074/jbc.C300117200
14. Sharma A, Singh K, Almasan A. Histone H2AX phosphorylation: a marker for DNA damage. *Methods Mol Biol* (2012) **920**:613–26. doi:10.1007/978-1-61779-998-3_40
15. Dimitrova N, Chen YCM, Spector DL, De Lange T. 53BP1 promotes non-homologous end joining of telomeres by increasing chromatin mobility. *Nature* (2008) **456**:524–U551. doi:10.1038/nature07433
16. Dokic I, Mairani A, Brons S, Schoell B, Jauch A, Krunic D, et al. High resistance to X-rays and therapeutic carbon ions in glioblastoma cells bearing dysfunctional ATM associates with intrinsic chromosomal instability. *Int J Radiat Biol* (2015) **91**:157–65. doi:10.3109/09553002.2014.937511
17. Niklas M, Bartz JA, Akselrod MS, Abollahi A, Jokel J, Greilich S. Ion track reconstruction in 3D using alumina-based fluorescent nuclear track

detectors. *Phys Med Biol* (2013) **58**:N251–66. doi:10.1088/0031-9155/58/18/N251

18. Niklas M, Melzig C, Abdollahi A, Bartz J, Akselrod MS, Debus J, et al. Spatial correlation between traversal and cellular response in ion radiotherapy – towards single track spectroscopy. *Radiat Meas* (2013) **56**:285–9. doi:10.1016/j.radmeas.2013.01.060
19. Haynes RH, Eckardt F, Kunz BA. The DNA damage-repair hypothesis in radiation biology: comparison with classical hit theory. *Br J Cancer Suppl* (1984) **6**:81–90.
20. Schaue D, McBride WH. Counteracting tumor radioresistance by targeting DNA repair. *Mol Cancer Ther* (2005) **4**:1548–50. doi:10.1158/1535-7163.MCT-05-CO1

Conflict of Interest Statement: The authors declare that the research was conducted in the absence of any commercial or financial relationships that could be construed as a potential conflict of interest.

Copyright © 2015 Dokic, Niklas, Zimmermann, Mairani, Seidel, Krunic, Jäkel, Debus, Greilich and Abdollahi. This is an open-access article distributed under the terms of the Creative Commons Attribution License (CC BY). The use, distribution or reproduction in other forums is permitted, provided the original author(s) or licensor are credited and that the original publication in this journal is cited, in accordance with accepted academic practice. No use, distribution or reproduction is permitted which does not comply with these terms.

frontiers in Oncology

REVIEW
published: 25 February 2016
doi: 10.3389/fonc.2016.00030

Differential Superiority of Heavy Charged-Particle Irradiation to X-Rays: Studies on Biological Effectiveness and Side Effect Mechanisms in Multicellular Tumor and Normal Tissue Models

*Stefan Walenta and Wolfgang Mueller-Klieser**

Institute of Pathophysiology, University Medical Center, University of Mainz, Mainz, Germany

This review is focused on the radiobiology of carbon ions compared to X-rays using multicellular models of tumors and normal mucosa. The first part summarizes basic radiobiological effects, as observed in cancer cells. The second, more clinically oriented part of the review, deals with radiation-induced cell migration and mucositis. Multicellular spheroids from V79 hamster cells were irradiated with X-rays or carbon ions under ambient or restricted oxygen supply conditions. Reliable oxygen enhancement ratios could be derived to be 2.9, 2.8, and 1.4 for irradiation with photons, $^{12}C^{+6}$ in the plateau region, and $^{12}C^{+6}$ in the Bragg peak, respectively. Similarly, a relative biological effectiveness of 4.3 and 2.1 for ambient pO_2 and hypoxia was obtained, respectively. The high effectiveness of carbon ions was reflected by an enhanced accumulation of cells in G_2/M and a dose-dependent massive induction of apoptosis. These data clearly show that heavy charged particles are more efficient in sterilizing tumor cells than conventional irradiation even under hypoxic conditions. Clinically relevant doses (3 Gy) of X-rays induced an increase in migratory activity of U87 but not of LN229 or HCT116 tumor cells. Such an increase in cell motility following irradiation *in situ* could be the source of recurrence. In contrast, carbon ion treatment was associated with a dose-dependent decrease in migration with all cell lines and under all conditions investigated. The radiation-induced loss of cell motility was correlated, in most cases, with corresponding changes in β_1 integrin expression. The photon-induced increase in cell migration was paralleled by an elevated phosphorylation status of the epidermal growth factor receptor and AKT-ERK1/2 pathway. Such a hyperphosphorylation did not occur during $^{12}C^{+6}$ irradiation under all conditions registered. Comparing the gene toxicity of X-rays with that of particles using the γH2AX technique in organotypic cultures of the oral mucosa, the superior effectiveness of heavy ions was confirmed by a twofold higher number of foci per nucleus. However, proinflammatory signs were similar for both treatment modalities, e.g., the activation of NFκB and the release of IL6 and IL8. The presence of peripheral blood mononuclear cell increased the radiation-induced release of the proinflammatory cytokines by factors of

OPEN ACCESS

Edited by:
Marco Durante,
GSI, Germany

Reviewed by:
Simeng Suy,
Georgetown University Hospital, USA
Felicitas Merz,
GSI, Germany

***Correspondence:**
Wolfgang Mueller-Klieser
mue-kli@uni-mainz.de

Specialty section:
This article was submitted to Radiation Oncology, a section of the journal Frontiers in Oncology

Received: *24 August 2015*
Accepted: *28 January 2016*
Published: *25 February 2016*

Citation:
Walenta S and Mueller-Klieser W (2016) Differential Superiority of Heavy Charged-Particle Irradiation to X-Rays: Studies on Biological Effectiveness and Side Effect Mechanisms in Multicellular Tumor and Normal Tissue Models. Front. Oncol. 6:30. doi: 10.3389/fonc.2016.00030

2–3. Carbon ions are part of the cosmic radiation. Long-term exposure to such particles during extended space flights, as planned by international space agencies, may thus impose a medical and safety risk on the astronauts by a potential induction of mucositis. In summary, particle irradiation is superior to gamma-rays due to a higher radiobiological effectiveness, a reduced hypoxia-induced radioresistance, a multicellular radiosensitization, and the absence of a radiation-induced cell motility. However, the potential of inducing mucositis is similar for both radiation types.

Keywords: radiobiology, particle irradiation, oxygen enhancement ratio, relative biological effectiveness, organotypic tumor and mucosa cultures, mucositis, cell migration

INTRODUCTION

This article summarizes data which we have acquired in close collaboration with a number of scientists at the Gesellschaft fuer Schwerionenforschung (GSI) Darmstadt, Germany, for more than one decade. At the beginning of this collaboration, little was known about the basic radiobiology of particle irradiation, although there was emerging evidence already at that time for the usefulness of a carbon ion radiotherapy in clinical oncology (1). Consequently, the ultimate goal of the interactive work at the GSI accelerator was to augment our knowledge on biological effects of heavy charged particles in malignant tumors and in healthy tissue in comparison to the effect of conventional X-rays under equivalent conditions.

In most of the experiments, a carbon-12 ($^{12}C^{6+}$) beam was applied in the scanning mode either in the extended Bragg peak or in the plateau region at 227 MeV/nucleon. Conventional X-rays served as a reference, and X-ray equivalent doses were derived for heavy charged particle irradiation. Since beam-time is highly cost-intensive and since there is a pronounced competition among scientists for the acquisition of beam-time, design and performance of experiments with heavy charged particles are subjected to practical limitations by the restricted availability of the particle beam. This reduces the number of experiments within a given time frame and consequently restricts statistical corroboration of findings by multiple approaches. This has to be kept in mind, when data from particle irradiation are compared with those from other assays.

All irradiation experiments were carried out on cultured cells using various tumor and normal cell models. Besides conventional single cell cultures, complex three-dimensional (3D) cell cultures were used; these included organotypic cultures of the human oral mucosa with or without immune cells, planar cell multilayers of WiDr colon adenocarcinoma cells or of SiHa cervix carcinoma cells, and multicellular spheroids (MCS) from V79 cells. With a few exceptions, irradiation was routinely performed under standardized cell culture conditions at 37°C and ambient (20% O_2) or reduced (pO_2 close to 0 mmHg) oxygen supply conditions.

"Classical" radiobiological endpoints, such as clonogenic cell survival, spheroid volume growth, or cell cycle effects as a function of radiation dose, were used to quantify the efficiency of particle versus conventional radiation. Furthermore, the relative biological effectiveness (RBE) and the oxygen enhancement ratio (OER) for the two radiation modalities were derived. One specific endpoint was cell migration and motility in 2D and 3D conditions under the impact of irradiation. The gene toxicity of both radiation types in normal tissue was quantified using the γH2AX technique in organotypic mucosa cultures. In this multicellular model, assays for early events of a radiation-induced mucositis, such as activation of the transcription factor NFκB or release of cytokines IL6 and IL8, were applied. The cocultivation of the mucosa model with human peripheral blood mononuclear cells (PBMCs) revealed a significant role of immune cells in the emergence of radiation-related mucositis.

Following the introduction, the experimental part of this review article is subdivided into three major chapters. The first chapter deals with our data related to the basic radiobiology of carbon ion irradiation compared to that of conventional gamma-radiation. This includes the relative biological effectiveness, the oxygen effect, and the multicellular radioresistance. The second chapter is focused on our findings regarding clinical aspects of undesirable side effects of the two radiation types considered. These aspects refer to radiation-induced cell motility and to radiation-associated mucositis. The third chapter of this review links our own data to findings from the literature. For many years, radiobiological studies on heavy charged particles have remained sparse, but very recently, there is a tremendous increase in the number of reports on radiobiology of heavy ions, on their clinical use, as well as on a combination of their radiobiological and clinical aspects. Consequently, the intention of the third chapter of this review is by no means to give a comprehensive review of the literature on particle irradiation, but rather to present a selection of very recent reports that are closely related to the data presented here. The final paragraph of this review presents a brief resume of the article.

BASIC RADIOBIOLOGY OF HEAVY CHARGED PARTICLES

RBE and OER Values for Carbon Ion Irradiation of Multicellular V79 Spheroids

Ever since the pioneering work of Robert Sutherland and colleagues (2), reviewed in Ref. (3), MCS represent classical 3D cell models in radiation research. Based on a sabbatical in Sutherland's laboratory (4) and on the pioneer's personal assistance as a Humboldt awardee at the University of Mainz (5), one of us set up a state-of-the-art spheroid laboratory at our research institute.

Within the frame of a number of different research projects, we collected a large amount of data on 3D versus 2D growth characteristics, on 3D interaction between tumor and immune cells, or on tumor microenvironment with regard to hypoxia, hypoglycemia, acidosis, and other factors (6).

Occasionally, these data sparked the interest of scientists at the GSI in using our expertise with the spheroid technology for the exploration of heavy charged particle radiobiology. Spheroids from immortalized and tumorigenic V79 hamster cells have been frequently used in radiobiological investigations, and we decided to initiate our studies on heavy ion radiobiology with this spheroid type having an abundance of comparative data from X-ray experiments.

Multicellular spheroids from V79 cells with 200 μm in diameter were irradiated with X-rays or carbon $^{12}C^{6+}$ ions under elevated, ambient, or restricted oxygen supply conditions. From previous microelectrode measurements, the oxygen tension distribution within the MCS as a function of the external oxygen tension was known, which made it possible to exactly relate the local oxygen to the radiation effects. For reasons of simplicity, average numbers for the environmental oxygen tension (pO_2) in mm Hg are given for characterizing the experimental conditions. **Figure 1** shows clonogenic cell survival curves for V79 MCS irradiated with X-rays (**Figure 1A**) in environmental pO_2 values of 144 mmHg (circles), 35 mmHg (squares), and 0 mmHg (diamonds) or irradiated with $^{12}C^{6+}$ ions in the extended Bragg peak (**Figure 1B**) in environmental pO_2 values of 690 mmHg (circles) and 0 mmHg (diamonds). It is obvious that (i) survival curves after particle irradiation are close to being linear with almost no shoulder compared to the X-ray data and (ii) the oxygen effect is much less pronounced with particle compared to photon irradiation. Survival curves of V79 single cells were almost identical with that of V79 spheroids with no indication of a multicellular resistance or contact effect (data not shown). Irradiation of V79 MCS with carbon ions in the plateau region (227 MeV/nucleon $^{12}C^{6+}$) in the same oxygen atmospheres as used with X-ray treatment produced survival curves that were almost identical with those from photon irradiation (data not shown).

The survival curves of V79 MCS displayed in **Figure 1** were fitted with the linear quadratic model. This was used for deriving reliable OER and relative biological effectiveness (RBE values). OER values at several survival levels *S* (=37, 10, 1, and 0.1%) were calculated as the ratio of doses to achieve a given survival under hypoxia compared to normoxia. Averages were derived from the individual values, which varied with *S* by around 5%. A corresponding procedure was used for the derivation of RBE, which was defined as the ratio of X-ray dose to that of particle radiation to reach a given *S*. These data are compiled in **Table 1**. Besides the very low OER value of 1.40 for particle irradiation, the RBE value of heavy charged particles is remarkably high at 4.31. Further details on the data evaluation were published earlier (7).

Furthermore, the high effectiveness of heavy charged particles in the extended Bragg peak compared to conventional radiation was reflected by a massive, dose-dependent induction of apoptosis [quantified by the TUNEL assay (7)], as shown in **Figure 2**. Although a respective curve for the extended Bragg peak induction of apoptosis under ambient oxygen conditions could not be assessed in this set of experiments for technical reasons, explorative data were indicative of an absence of an oxygen effect with regard to apoptotic cell kill [for further details, see Ref. (7)]. All data obtained in this spheroid study clearly show that heavy charged particles are more efficient in sterilizing tumor cells than conventional irradiation even under hypoxic conditions.

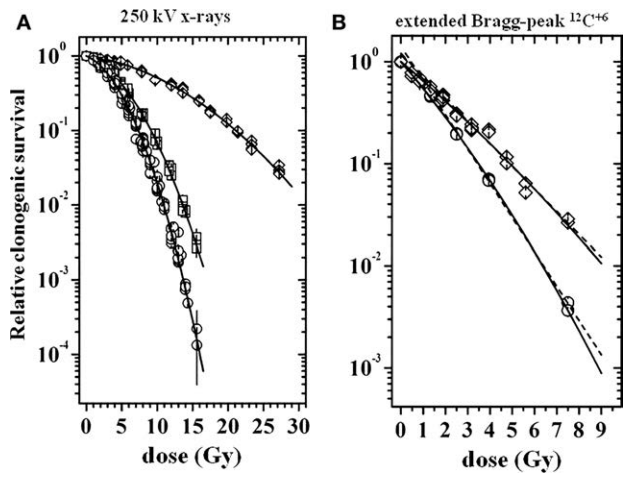

FIGURE 1 | Relative clonogenic survival of cells from V79 MCS as a function of dose [modified according to Ref. (7)]. (A) Following X-ray irradiation at external pO_2 values of 144 mmHg (circles), 35 mmHg (squares), and 0 mmHg (diamonds), **(B)** following $^{12}C^{6+}$ irradiation in the extended Bragg peak at external pO_2 values of 690 mmHg (circles) and 0 mmHg (diamonds); dose values represent X-ray equivalent dose.

Unexpected Multicellular Radiosensitization in Human Colon Adenocarcinoma-Derived Multilayer Cells

Planar cell multilayers in comparison with monolayer cultures of WiDr and SiHa human colon adenocarcinoma-derived cells were used for investigations on the role of cell cycle effects in the treatment with photon or particle irradiation. Development of a special cryostat sectioning technique made it possible to assess histology and growth characteristics of the planar 3D model (8). This is exemplified by **Figure 3**, with **Figure 3A** displaying cryostat sections that were cut perpendicular to the multilayer

TABLE 1 | Oxygen enhancement ratio (OER) and relative biological effectiveness (RBE) values derived from the clonogenic survival curves shown in Figure 1 after irradiation in atmospheres with a pO_2 of 690 mmHg or 145 mmHg (aerobic) or 0 mmHg (hypoxic).

Radiation type	OER	RBE	
		Aerobic	Hypoxic
X-rays	2.87	1.00	1.00
Ext. Bragg peak	1.40	2.11	4.31

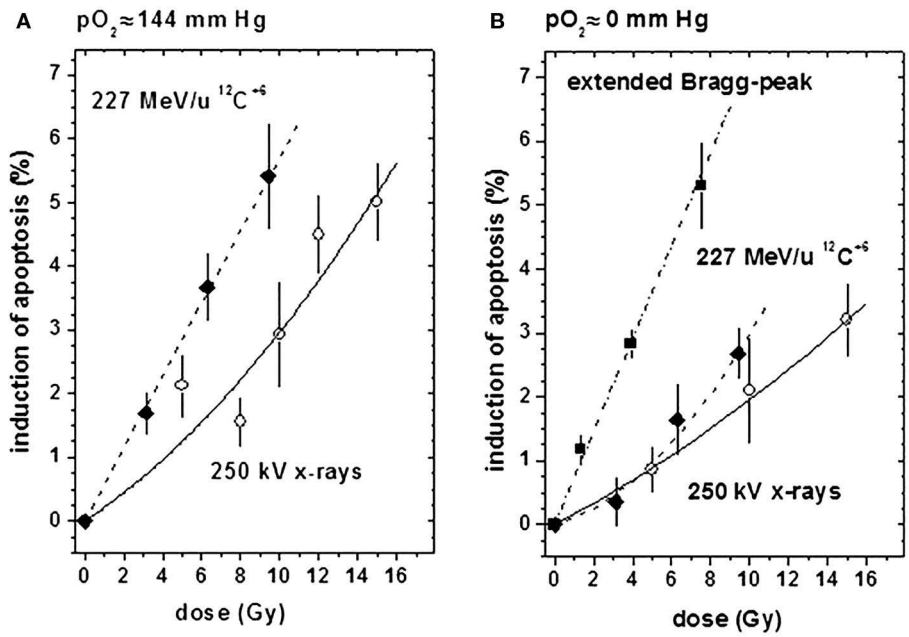

FIGURE 2 | Induction of apoptosis (relative to untreated controls) by X-ray (open circles) or $^{12}C^{6+}$ irradiation in the plateau region (filled diamonds) or in the extended Bragg peak (filled squares) under ambient or hypoxic oxygen supply conditions [modified according to Ref. (7)]. (A) At an external pO_2 of 144 mm Hg and **(B)** at an external pO_2 of 0 mm Hg.

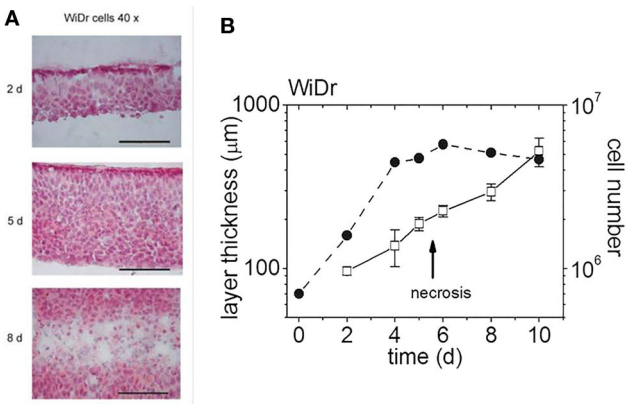

FIGURE 3 | Multilayers of WiDr cells at various days in culture [modified according to Ref. (7, 8)]. (A) H&E-stained cryosections of multilayers on three different days (d) in culture (scale bar: 100 μm), **(B)** multilayer thickness and cell content as a function of days in culture (the arrow indicates the emergence of a central necrotic layer).

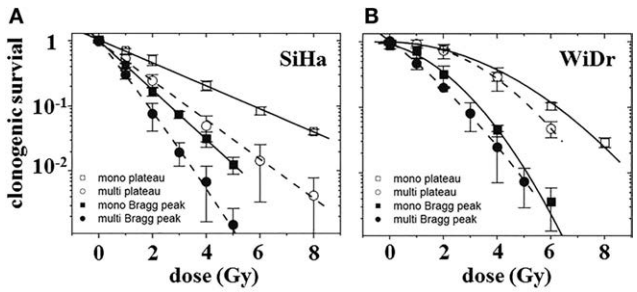

FIGURE 4 | Clonogenic survival of cells in monolayer (squares) or multilayer (circles) culture as a function of dose after carbon-ion irradiation in the plateau region (370 MeV/nucleon; open symbols) or in the extended Bragg peak [closed symbols; modified according to Ref. (8)]. (A) SiHa cells (n = 4) and **(B)** WiDr cells (n = 2–3).

plane at three different times of growth for both cell lines considered. **Figure 3B** shows the multilayer thickness and viable cell content as a function of time in culture. Obviously, the total layer thickness is expanding continuously after the emergence and expansion of a central necrotic layer, whereas the total number of viable cells is stagnating. As such, planar cellular multilayers grow in a way, which is very similar to that of MCS despite the different diffusion geometries.

Unexpectedly, there was a multicellular radiosensitization of multi- versus monolayers under all treatments considered, as demonstrated by standardized clonogenic survival curves for $^{12}C^{6+}$ ion irradiation in the plateau region and the Bragg peak (**Figure 4**). This is in contrast to the generally detected multicellular radioresistance. The phenomenon was attributable, at least in parts, to a difference in the proportion of cells in the G_0/G_1 phase between the two culture types used. Furthermore, **Figure 4** illustrates cell line-dependent differences in the type of cell survival curves: whereas WiDr cells exhibit "classical" shoulder curves except for Bragg peak particle irradiation, SiHa cell survival curves are very close to linearity with all treatments considered.

This difference may indicate a different extent of DNA repair in these two cell lines due to either a different intensity/quality of DNA damage or different repair capacities.

Flow cytometric studies showed that X-rays induced a G_2/M arrest, which was considerably prolonged in multi- compared to monolayers (**Figure 5A**). After Bragg peak irradiation of monolayers, the arrest time was increased compared to X-rays by 12–24 h, and more cells were arrested than with X-rays (**Figures 5A,B**). However, in multilayers, both radiation modalities lead to similar growth arrests (see **Figures 5A,B**).

In essence, our data obtained in the multilayer project contribute to accumulating results in the literature regarding differences in biological properties and molecular mechanisms between 2D and 3D culture systems. Under many aspects, 3D planar cellular multilayers and 3D spherical cellular aggregates share common properties and behave in similar ways. On the other hand, multilayers tend to show a small but reproducible multicellular radiosensitization, whereas most spheroids exhibit a multicellular resistance. It is worth noting that this effect is even more pronounced with heavy charged particles than with photons [for further details on planar multilayers, see Ref. (8)].

CLINICAL ASPECTS OF POTENTIAL SIDE EFFECTS OF HEAVY CHARGED PARTICLE IRRADIATION

Differential Effects of Radiation on Cell Migration Depending on Radiation Type and Cell Line

When we initiated this project, there was an ongoing controversy within the science community about radiation-related modulation of tumor cell migration, mainly with regard to irradiation of glioblastomas (GBMs). The cellular motility of certain tumor cell lines is enhanced under *in vitro* conditions by sublethal doses of photon irradiation, as we and others have previously reported (9–11). In contrast, several other studies demonstrated that either similar sublethal or slightly higher doses impair GBM cell migration and invasion (12) or fail to modify these cell functions (13). The clarification of the respective controversy is clinically highly relevant: if therapeutic irradiation would enhance cell motility, tumor cells may leave the therapeutic field without receiving a cytotoxic dose and may thus be a source of recurrence. Some recent data were suggestive of heavy charged particle irradiation to consistently reduce the migratory potential of tumor cells, but the respective study was lacking parallel evaluation of radiation-induced cell killing (14).

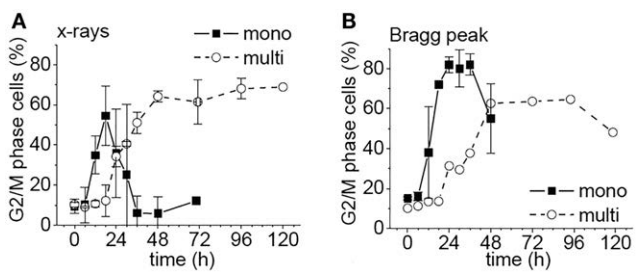

FIGURE 5 | Percentage of WiDr cells from mono- or multilayers in G_2/M phase as a function of time after irradiation [modified according to Ref. (8)] with (A) X-rays and (B) carbon ions.

Recent therapeutic strategies target the epidermal growth factor receptor (EGFR), which is overexpressed in about 40–50% of GBMs (15). There is evidence in the literature for such anti-EGFR therapeutics to improve the efficacy of conventional radiotherapy (16). EGFR is a member of the cell-surface receptor family ErbB and functions as an oncogene. Activation of EGFR by binding of its specific ligands, including epidermal growth factor (EGF), leads to dimerization of the receptor and subsequently to autophosphorylation of its tyrosine-kinase domain. Following activation, the EGFR kinase stimulates a number of cellular signaling cascades, such as the phosphatidylinositol-3-kinase (PI3K)/AKT or the mitogen-activated protein kinase (MAPK) pathway (17). Thereby, numerous cellular responses are precisely regulated, such as proliferation, cell survival, and cell migration. EGF-induced EGFR activation has been shown to promote tumor cell migration (18). In addition to auto- and paracrine stimulation, it remains to be clarified whether therapies, such as radiotherapy, induce EGFR activation and pro-proliferative signaling directly or indirectly *via* production of radicals. Before starting our research in this field, no data existed with respect to EGFR activation by heavy charged particle irradiation.

Considering this background information, we initiated investigations on the impact of carbon ion irradiation on GBM cell motility and EGFR-related cell signaling *in vitro*. Most cell migration data were generated in "classical" Boyden (or transwell) chamber assays. Core proteins and phospho-proteins were analyzed with Western Blotting.

Investigations on U87 and LN229 glioma cells (with overexpression of $EGFR^{++}$) showed that the migratory response of cancer cells to radiation is dependent on radiation dose, as well as on cell and radiation type. Clinically relevant doses (2 or 3 Gy) of X-rays induced a small, but consistent and significant, increase in migratory activity of U87, but not of LN229, as illustrated in **Figure 6A**. $^{12}C^{6+}$ ion treatment was associated with a dose-dependent decrease in migration with all cell lines and under all conditions investigated (**Figure 6B**). The radiation-induced loss of cell motility was correlated, in most cases, with corresponding changes in β_1 integrin expression (9, 14). The photon-induced increase in cell migration in U87 glioma cells was paralleled by an elevated phosphorylation status of the EGFR and AKT–ERK1/2 pathway (see **Figures 7** and **8**). Such a hyperphosphorylation did not occur during $^{12}C^{6+}$ irradiation under all conditions registered (see **Figures 7** and **8**). Using a 3D collagen type I invasion and migration model, glioma cell migration remained unaffected by irradiation with either photon or particles, despite the induction of massive gene toxicity as determined by the γH2AX technique (13).

On the one hand, with a few exceptions, our *in vitro* findings on the interrelationship between irradiation and tumor cell migration are in accordance with data from the literature (14, 20, 21). On the other hand, *in vivo* studies are warranted for the evaluation of the clinical significance of this issue.

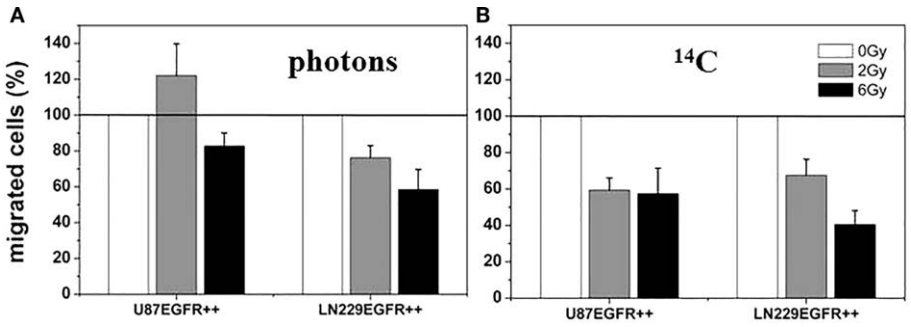

FIGURE 6 | Relative cell migration 24 h after photon and ^{12}C heavy ion irradiation. U87 EGFR^{++} and LN229 EGFR^{++} were irradiated with single doses of 2 and 6 Gy of photon radiation, respectively **(A)** and ^{12}C heavy ions **(B)** and migrated cells were counted after Boyden Chamber assay. The relative mean numbers of migrated cells ± SD of at least three independent experiments are plotted with the migration of untreated cells set to 100%. All differences between treated and untreated cells are significant ($p < 0.05$, *t*-test). There was no significant change in cell viability under all conditions investigated (data not shown) [modified according to Ref. (19)].

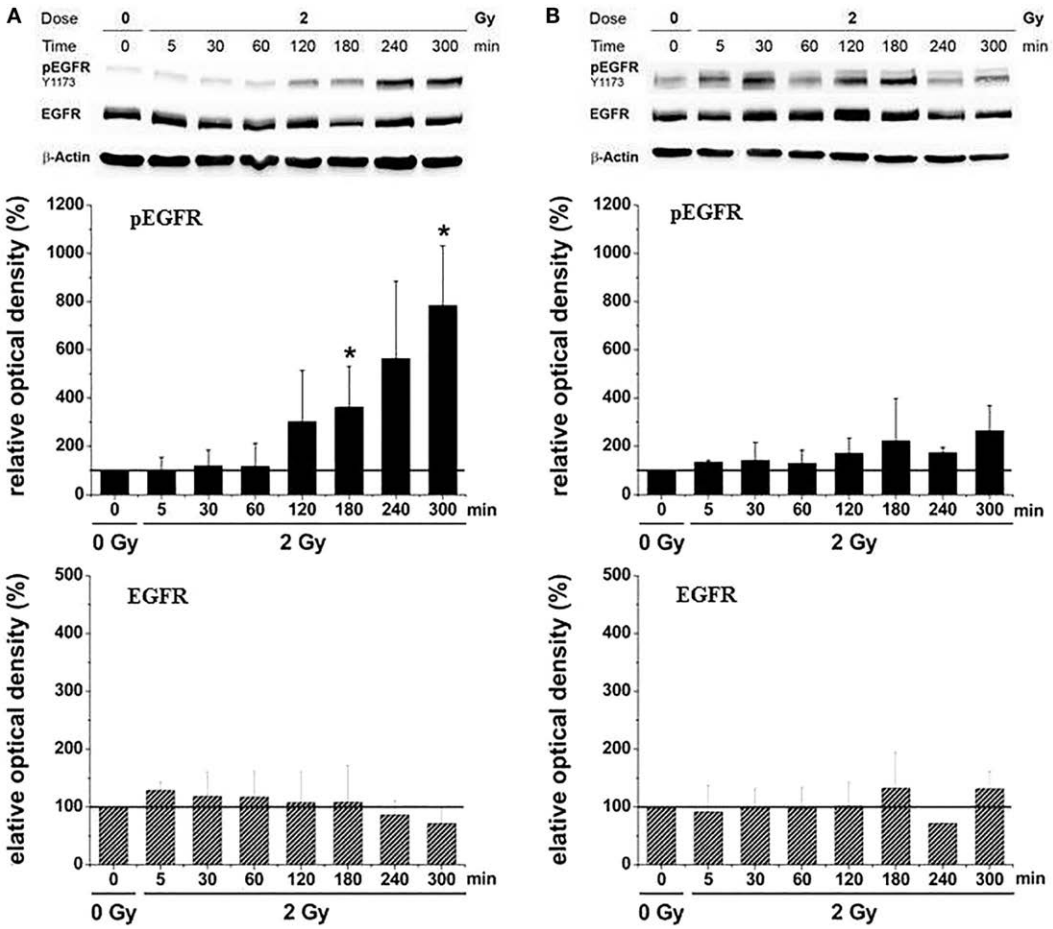

FIGURE 7 | Relative EGFR-phosphorylation (pEGFR) and total EGFR-protein (EGFR) in U87 glioma cells as a function of time after irradiation with 2 Gy [modified according to Ref. (19)] applying (A) X-rays and (B) carbon ions.

Four major conclusions were derived from the *in vitro* migration studies on glioma cells: (i) the impact of radiation on glioma cell migration depends on the migration assay used with both X-rays and carbon ions; (ii) under certain conditions and in a few glioma cell lines, clinically relevant doses of photons but not particles consistently increases cell migration; (iii) under a wide

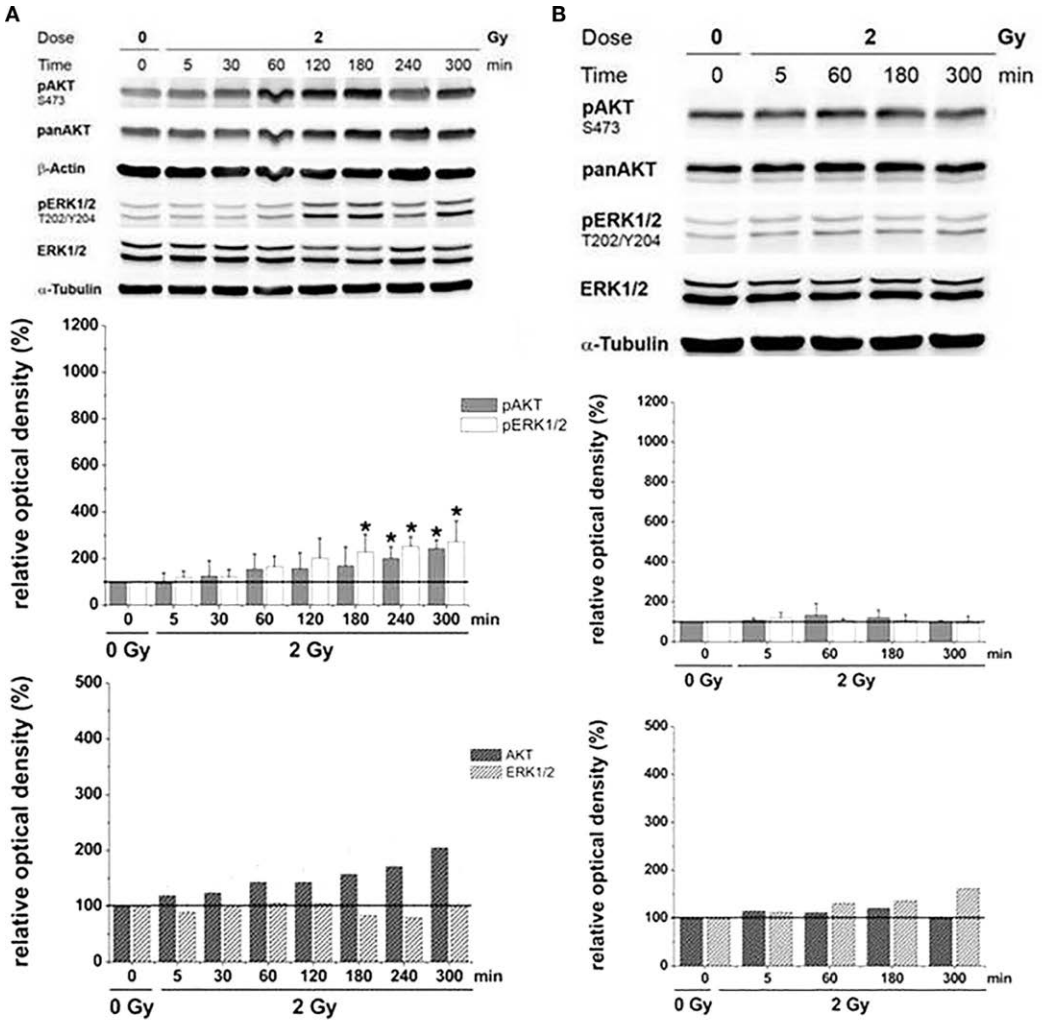

FIGURE 8 | **Relative AKT/ERK-phosphorylation (pAKT/pERK) and total AKT/ERK-protein (AKT/ERK) in U87 glioma cells as a function of time after irradiation with 2 Gy [modified according to Ref. (19)] applying (A) X-rays and (B) carbon ions**.

spectrum of conditions, glioma cell migration *in vitro* was either unaffected or reduced by $^{12}C^{6+}$ irradiation; and (iv) this differential between photon and particle irradiation may contribute to a higher efficiency of a local carbon ion treatment compared to X-rays with regard to tumor recurrence.

Studies on Early Events in Radiation-Induced Mucositis Using Organotypic Cultures of the Oral Mucosa Including Immune Cells

Oral mucositis is a frequent complication of standardized radiotherapy in the clinic. There is an abundance of literature regarding preclinical and clinical research in this field, as reviewed recently, among others, by Mallick and colleagues (22). Much less is known, in this regard, about the side effects of particle irradiation, although the induction of mucositis by carbon ions has been clearly documented in patients already in 2002 (23). Although the number of centers for treatment with heavy charged particle is still undesirably low, the successful application of this technology in radiation oncology for the past two decades confers clinical relevance to particle treatment-associated mucositis (24).

A relatively novel aspect of radiation-associated mucositis results from the ambitious plans of several space agencies, in particular of the NASA and the ESA, for manned missions to the Mars. During such a mission which would last around 3 years, astronauts would be chronically exposed to cosmic radiation due to the absence of a protecting magnetic field. Space radiation consists of protons (87%), α-particles (12%), and heavy ions (1%) in solar particle events and galactic cosmic rays (25). In particular, highly ionizing heavy ions can be hardly shielded exposing the crew members to a serious medical safety risk (26), since the probability of getting a hit by heavy charged particles increases with time in space. It is obvious that the occurrence of oral or intestinal mucositis during a prolonged space flight would lead to hazardous situations.

Oral mucositis as a result of X-ray exposure has been studied in numerous animal models, the advantages and limitations of which have been reviewed recently by Viet and co-workers (27). One major cutback of animal models that has been reported earlier is their unsuitability for the assessment of early molecular and pathophysiological events following irradiation (28).

Based on this background knowledge, we initiated a project, which was supported mainly by the GSI Darmstadt and the ESA, with investigations on early inflammatory events induced by heavy charged particle irradiation in organotypic cultures of the human oral mucosa. We re-activated a 3D culture model, previously established in our laboratory (29). The artificial mucosa, which was cultured at the liquid–gas interface, consisted of immortalized human gingival keratinocytes (IHGK) and immortalized human dermal fibroblasts (HH4ded), grown with or without PBMCs. The organotypic mucosa culture exhibited many features of the human oral mucosa, such as the formation of a basal membrane, a papillary shape of the epithelium-connective tissue boundary, or the differentiation status of the keratinocytes with regard to expression of keratins. A special technology was designed making it possible to irradiate the 3D cultures in the extended Bragg peak of the heavy ion beam including an appropriate dosimetry. Further details are described in Ref. (30).

Comparing the gene toxicity of X-rays with that of particles using the γH2AX technique, the superior effectiveness of heavy ions was confirmed by a roughly twofold higher number of foci per nucleus 4 and 48 h after treatment. This is shown in **Figure 9** for X-rays (**Figure 9A**) and $^{12}C^{6+}$ irradiation (**Figure 9B**).

Proinflammatory signs were quantitatively similar for both treatment modalities. For example, confocal microscopy made it possible to quantify the activation of NFκB by the assessment of the nuclear location of NFκB p50. The corresponding results are depicted in **Figures 10A,B** for photons and particles, respectively. The release rates of the proinflammatory cytokines IL6 and IL8 from the organotypic cultures into the culture medium was registered using commercial ELISA assays [further details in Ref. (30)]. **Figure 11** demonstrates a consistent and significant elevation of the release of both cytokines upon irradiation for both photons (**Figures 11A,B**) and particles (**Figures 11C,D**), albeit in the absence of a consistent dose dependency. **Figures 12A,B** illustrate for X-rays and carbon ions, respectively, that the addition of PBMC increases the radiation-induced release of IL6 and IL8 by factors of 2–3.

DISCUSSION AND RESUME

Data from the Literature

The very recent literature on heavy charged particle research clearly emphasizes the advantages of particle versus X-ray irradiation in a meanwhile broad spectrum of tumor entities as shown in a large number of patients mainly in Japan (more than 8,000 patients) and Germany (31, 32). Whereas different ions, such as carbon, helium, or protons (33), may be used in different treatment scenarios, carbon and helium appear to be superior to protons in the majority of cases (34). One review lately points out the importance of combining radiobiological and clinical research with carbon ion therapy (35–37). There is a common optimism among these authors with regard to further spread of charged particle treatment facilities world-wide (31, 32, 34, 38). Besides these clinical aspects, the already-mentioned significance of charged particle radiobiology for long-term exposition to space radiation during extended space flights has been detailed explicitly by an international consortium of experts in a recent article (39).

Several actual reports on cell and animal studies using carbon ions present RBE values, which are in a fairly good agreement with our data from multicell spheroid studies (35, 40, 41). At the same time, data are presented that show a multitude of parameters to impact on RBE values, such as radiation dose, linear energy transfer (LET), and the model used for the derivation of RBE

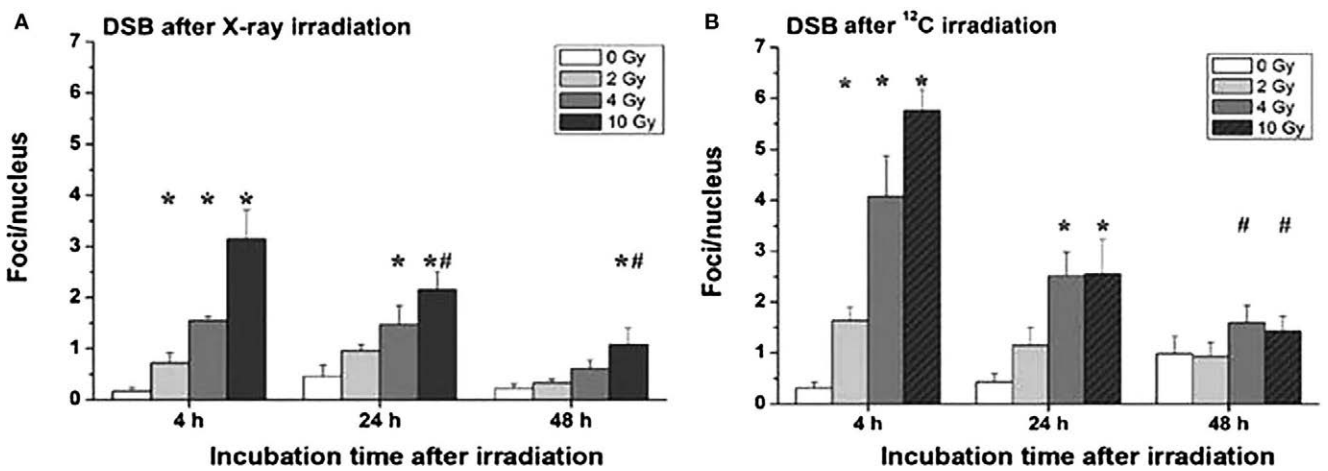

FIGURE 9 | Double-strand breaks (DSB) in organotypic cultures of oral mucosa, determined by evaluation of γH2AX stainings in immune fluorescence microscopy, as a function of radiation dose and time after radiation [modified according to Ref. (19)] applying (A) X-rays and (B) carbon ions.

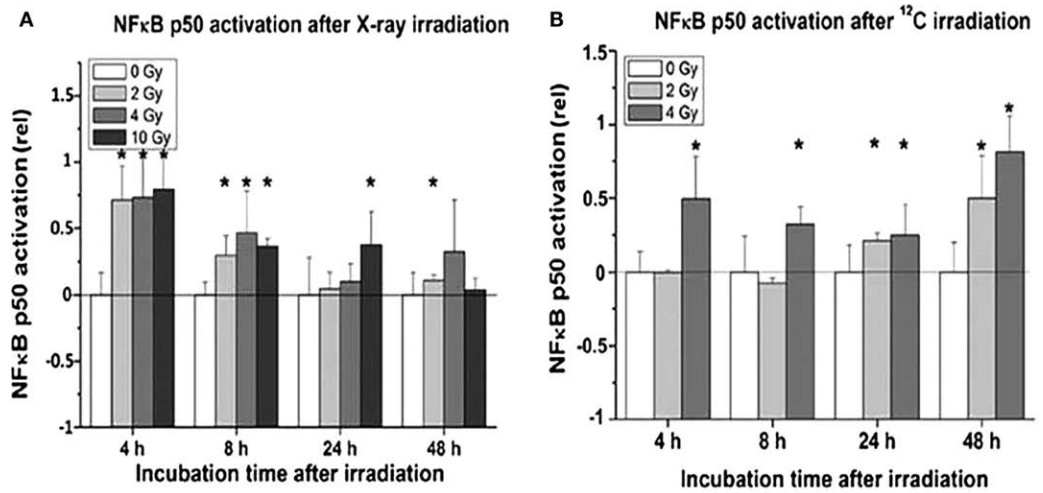

FIGURE 10 | **Activation of NFκB in organotypic cultures of oral mucosa, determined by evaluation of nuclear translocation of NFκB p50 stainings in immune fluorescence confocal microscopy, as a function of radiation dose and time after radiation [modified according to Ref. (19)] applying (A) X-rays and (B) carbon ions**.

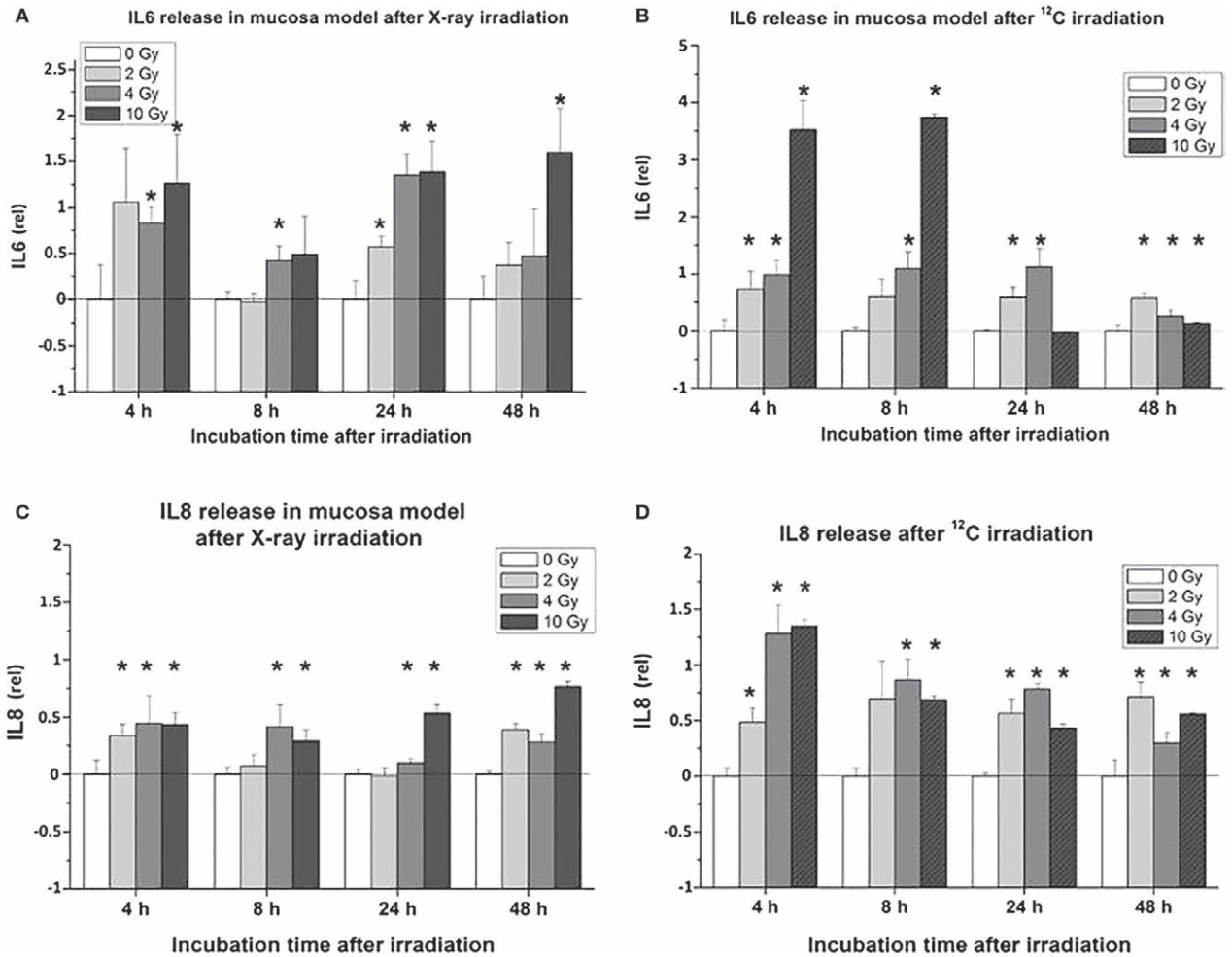

FIGURE 11 | **Cytokine release [IL6: (A,B); IL8: (C,D)] in organotypic cultures of oral mucosa, determined by commercial ELISA test, as a function of radiation dose and time after radiation [modified according to Ref. (19)] applying (A,C) X-rays and (B,D) carbon ions**.

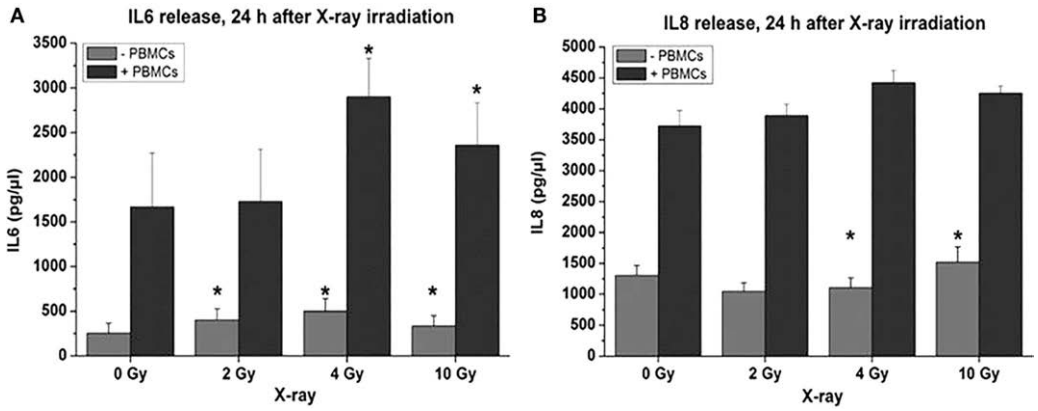

FIGURE 12 | Cytokine release following X-ray treatment of organotypic cultures of oral mucosa, determined by commercial ELISA test, as a function of radiation dose and time after radiation with or without coculturing of peripheral blood mononuclear cells [PBMCs; modified according to Ref. (19)]. (A) IL6 and **(B)** IL8.

(35, 37). Taking this into account, the derivation of RBE values for clinical dosimetry is still a matter of debate (37). In a recent simulation study on hypoxia in clinical tumors treated with carbon ions, OER were found that corresponded well to our data from MCS (42). The authors also point to the existence of a non-negligible oxygen effect that can influence the outcome of carbon ion therapy at low LET in the spread-out Bragg peak. A recent investigation using a carbon ion beam or X-rays for irradiating neuro-spheres of human GBM cells documents the occurrence of a multicellular resistance that was much less pronounced – but still detectable – with particle radiation compared to photons (43). As many studies with X-rays before, this investigation demonstrates a multicellular radioresistance, eventually termed contact effect, to exist for carbon ions as well. This is in contrast to the multicellular radiosensitization, which we have shown for charged particle irradiation of planar tumor cell multilayers compared to corresponding single cells [(8); see above].

There are two recent reports confirming our observation on charged particle effects on cell migration and related signaling pathways. Simon et al. (44) were able to show that migration of meningioma cells was promoted by photon but not by carbon ion irradiation. Our results on an increased cell migration associated with an elevated phosphorylation status of the EGFR and AKT–ERK1/2 pathway following X-ray but not carbon irradiation was partially confirmed by corresponding findings of Jin and colleagues (45). These data are in accordance with previous observations regarding the inhibitory influence of heavy charged particle irradiation on tumor cell migration and formation of metastasis (21, 46). Recent reviews, such as the article by Fujita (47), mirror a still ongoing and partially controversial debate with regard to the impact of radiation on cancer cell motility, invasiveness, and metastatic potential. Interestingly, a recent experimental study using carbon ion irradiation in a rat prostate carcinoma has demonstrated an increase in the metastatic rate upon treatment (48).

As a brief resume, the experimental therapeutics part of the data compiled clearly demonstrates the efficiency of $^{12}C^{6+}$ irradiation to be consistently higher than that of conventional X-rays; this is mirrored by RBE values for particles versus photons of >1.0 and up to 4.3 under hypoxic conditions. Since hypoxia occurs in 50–60% of all human solid tumors (49), it is of high clinical relevance that $^{12}C^{6+}$ irradiation is much more efficient than conventional radiation under these conditions. Whereas OER values are close to 3 for X-rays, an OER value of 1.4 was derived for carbon ions. Here, multicellular tumor spheroids proved themselves as useful models for quantitative studies on the radiobiology of heavy charged particles. In the experimental inflammation part of the data compilation, organotypic cultures of the oral mucosa were shown to be useful for investigations on immediate and early inflammatory events, i.e., within a few hours up to 2 days following $^{12}C^{6+}$ radiation treatment. Besides the quantification of gene toxicity and proinflammatory cytokine release, the consistent, immediate, and early, as well as dose-dependent activation of NFκB by $^{12}C^{6+}$ irradiation of oral mucosa cultures is one of the core results of this part of the studies.

AUTHOR CONTRIBUTIONS

Both the authors listed have made substantial, direct, and intellectual contribution to the work and approved it for publication.

ACKNOWLEDGMENTS

Special thanks are given to Nicole Averbeck, Gerhard Kraft, Michael Scholz, and Gisela Taucher-Scholz at the GSI Darmstadt and to Nils Cordes at Oncoray, University of Dresden, for many helpful discussions and for their professional support of the projects.

FUNDING

This work was supported by the Gesellschaft für Schwerionenforschung (GSI) Darmstadt, Germany, the European Space Agency (ESA)/German Aerospace Center (DLR)/Federal Ministry of Economics and Technology (BMWi): 50 WB 0926 and by the Deutsche Forschungsgemeinschaft (DFG; MU 576/17-1).

REFERENCES

1. Schulz-Ertner D, Nikoghosyan A, Didinger B, Debus J. Carbon ion radiation therapy for chordomas and low grade chondrosarcomas – current status of the clinical trials at GSI. *Radiother Oncol* (2004) **73**(Suppl 2):S53–6. doi:10.1016/S0167-8140(04)80014-8
2. Sutherland RM, McCredie JA, Inch WR. Growth of multicell spheroids in tissue culture as a model of nodular carcinomas. *J Natl Cancer Inst* (1971) **46**(1):113–20.
3. Sutherland RM. Cell and environment interactions in tumor microregions: the multicell spheroid model. *Science* (1988) **240**(4849):177–84. doi:10.1126/science.2451290
4. Mueller-Klieser WF, Sutherland RM. Influence of convection in the growth medium on oxygen tensions in multicellular tumor spheroids. *Cancer Res* (1982) **42**(1):237–42.
5. Sutherland RM, Sordat B, Bamat J, Gabbert H, Bourrat B, Mueller-Klieser W. Oxygenation and differentiation in multicellular spheroids of human colon carcinoma. *Cancer Res* (1986) **46**(10):5320–9.
6. Hirschhaeuser F, Menne H, Dittfeld C, West J, Mueller-Klieser W, Kunz-Schughart LA. Multicellular tumor spheroids: an underestimated tool is catching up again. *J Biotechnol* (2010) **148**(1):3–15. doi:10.1016/j.jbiotec.2010.01.012
7. Staab A, Zukowski D, Walenta S, Scholz M, Mueller-Klieser W. Response of Chinese hamster v79 multicellular spheroids exposed to high-energy carbon ions. *Radiat Res* (2004) **161**(2):219–27. doi:10.1667/RR3113
8. Topsch J, Scholz M, Mueller-Klieser W. Radiobiological characterization of human tumor cell multilayers after conventional and particle irradiation. *Radiat Res* (2007) **167**(6):645–54. doi:10.1667/RR0775.1
9. Goetze K, Scholz M, Taucher-Scholz G, Mueller-Klieser W. The impact of conventional and heavy ion irradiation on tumor cell migration in vitro. *Int J Radiat Biol* (2007) **83**(11–12):889–96. doi:10.1080/09553000701753826
10. Rieken S, Habermehl D, Mohr A, Wuerth L, Lindel K, Weber K, et al. Targeting alphanubeta3 and alphanubeta5 inhibits photon-induced hypermigration of malignant glioma cells. *Radiat Oncol* (2011) **6**:132. doi:10.1186/1748-717X-6-132
11. Wild-Bode C, Weller M, Rimner A, Dichgans J, Wick W. Sublethal irradiation promotes migration and invasiveness of glioma cells: implications for radiotherapy of human glioblastoma. *Cancer Res* (2001) **61**(6):2744–50.
12. Cordes N, Hansmeier B, Beinke C, Meineke V, van Beuningen D. Irradiation differentially affects substratum-dependent survival, adhesion, and invasion of glioblastoma cell lines. *Br J Cancer* (2003) **89**(11):2122–32. doi:10.1038/sj.bjc.6601429
13. Eke I, Storch K, Kastner I, Vehlow A, Faethe C, Mueller-Klieser W, et al. Three-dimensional invasion of human glioblastoma cells remains unchanged by X-ray and carbon ion irradiation in vitro. *Int J Radiat Oncol Biol Phys* (2012) **84**(4):e515–23. doi:10.1016/j.ijrobp.2012.06.012
14. Rieken S, Habermehl D, Wuerth L, Brons S, Mohr A, Lindel K, et al. Carbon ion irradiation inhibits glioma cell migration through downregulation of integrin expression. *Int J Radiat Oncol Biol Phys* (2012) **83**(1):394–9. doi:10.1016/j.ijrobp.2011.06.2004
15. Schlegel J, Stumm G, Brandle K, Merdes A, Mechtersheimer G, Hynes NE, et al. Amplification and differential expression of members of the erbB-gene family in human glioblastoma. *J Neurooncol* (1994) **22**(3):201–7. doi:10.1007/BF01052920
16. Nieder C, Pawinski A, Dalhaug A, Andratschke N. A review of clinical trials of cetuximab combined with radiotherapy for non-small cell lung cancer. *Radiat Oncol* (2012) **7**(1):3. doi:10.1186/1748-717X-7-3
17. Eppenberger U, Mueller H. Growth factor receptors and their ligands. *J Neurooncol* (1994) **22**(3):249–54. doi:10.1007/BF01052929
18. Dittmar T, Husemann A, Schewe Y, Nofer JR, Niggemann B, Zanker KS, et al. Induction of cancer cell migration by epidermal growth factor is initiated by specific phosphorylation of tyrosine 1248 of c-erbB-2 receptor via EGFR. *FASEB J* (2002) **16**(13):1823–5. doi:10.1096/fj.02-0096fje
19. Stahler C, Roth J, Cordes N, Taucher-Scholz G, Mueller-Klieser W. Impact of carbon ion irradiation on epidermal growth factor receptor signaling and glioma cell migration in comparison to conventional photon irradiation. *Int J Radiat Biol* (2013) **89**(6):454–61. doi:10.3109/09553002.2013.766769
20. Mukherjee B, McEllin B, Camacho CV, Tomimatsu N, Sirasanagandala S, Nannepaga S, et al. EGFRvIII and DNA double-strand break repair: a molecular mechanism for radioresistance in glioblastoma. *Cancer Res* (2009) **69**(10):4252–9. doi:10.1158/0008-5472.CAN-08-4853
21. Ogata T, Teshima T, Inaoka M, Minami K, Tsuchiya T, Isono M, et al. Carbon ion irradiation suppresses metastatic potential of human non-small cell lung cancer A549 cells through the phosphatidylinositol-3-kinase/Akt signaling pathway. *J Radiat Res* (2011) **52**(3):374–9. doi:10.1269/jrr.10102
22. Mallick S, Benson R, Rath GK. Radiation induced oral mucositis: a review of current literature on prevention and management. *Eur Arch Otorhinolaryngol* (2015). doi:10.1007/s00405-015-3694-6
23. Schulz-Ertner D, Haberer T, Scholz M, Thilmann C, Wenz F, Jakel O, et al. Acute radiation-induced toxicity of heavy ion radiotherapy delivered with intensity modulated pencil beam scanning in patients with base of skull tumors. *Radiother Oncol* (2002) **64**(2):189–95. doi:10.1016/S0167-8140(02)00153-6
24. Loeffler JS, Durante M. Charged particle therapy – optimization, challenges and future directions. *Nat Rev Clin Oncol* (2013) **10**(7):411–24. doi:10.1038/nrclinonc.2013.79
25. Maalouf M, Durante M, Foray N. Biological effects of space radiation on human cells: history, advances and outcomes. *J Radiat Res* (2011) **52**(2):126–46. doi:10.1269/jrr.10128
26. Durante M, Cucinotta FA. Heavy ion carcinogenesis and human space exploration. *Nat Rev Cancer* (2008) **8**(6):465–72. doi:10.1038/nrc2391
27. Viet CT, Corby PM, Akinwande A, Schmidt BL. Review of preclinical studies on treatment of mucositis and associated pain. *J Dent Res* (2014) **93**(9):868–75. doi:10.1177/0022034514540174
28. Yeoh A, Gibson R, Yeoh E, Bowen J, Stringer A, Giam K, et al. Radiation therapy-induced mucositis: relationships between fractionated radiation, NF-kappaB, COX-1, and COX-2. *Cancer Treat Rev* (2006) **32**(8):645–51. doi:10.1016/j.ctrv.2006.08.005
29. Kunz-Schughart LA, Mueller-Klieser W. Three-dimensional culture. 3rd ed. In: Masters JRW, editor. *Animal Cell Culture: A Practical Approach*. Oxford; New York; Tokyo: IRL Press at Oxford University Press (2000). p. 123–48.
30. Tschachojan V, Schroer H, Averbeck N, Mueller-Klieser W. Carbon ions and X rays induce proinflammatory effects in 3D oral mucosa models with and without PBMCs. *Oncol Rep* (2014) **32**(5):1820–8. doi:10.3892/or.2014.3441
31. Kamada T, Tsujii H, Blakely EA, Debus J, De NW, Durante M, et al. Carbon ion radiotherapy in Japan: an assessment of 20 years of clinical experience. *Lancet Oncol* (2015) **16**(2):e93–100. doi:10.1016/S1470-2045(14)70412-7
32. Marx V. Cancer treatment: sharp shooters. *Nature* (2014) **508**(7494):133–8. doi:10.1038/508133a
33. Tommasino F, Durante M. Proton radiobiology. *Cancers (Basel)* (2015) **7**(1):353–81. doi:10.3390/cancers7010353
34. Grun R, Friedrich T, Kramer M, Zink K, Durante M, Engenhart-Cabillic R, et al. Assessment of potential advantages of relevant ions for particle therapy: a model based study. *Med Phys* (2015) **42**(2):1037–47. doi:10.1118/1.4905374
35. Saager M, Glowa C, Peschke P, Brons S, Grun R, Scholz M, et al. Split dose carbon ion irradiation of the rat spinal cord: dependence of the relative biological effectiveness on dose and linear energy transfer. *Radiother Oncol* (2015) **117**(2):358–63. doi:10.1016/j.radonc.2015.07.006
36. Schlaff CD, Krauze A, Belard A, O'Connell JJ, Camphausen KA. Bringing the heavy: carbon ion therapy in the radiobiological and clinical context. *Radiat Oncol* (2014) **9**(1):88. doi:10.1186/1748-717X-9-88
37. Steinstrater O, Scholz U, Friedrich T, Kramer M, Grun R, Durante M, et al. Integration of a model-independent interface for RBE predictions in a treatment planning system for active particle beam scanning. *Phys Med Biol* (2015) **60**(17):6811–31. doi:10.1088/0031-9155/60/17/6811
38. Tomlinson DC, Baldo O, Harnden P, Knowles MA. FGFR3 protein expression and its relationship to mutation status and prognostic variables in bladder cancer. *J Pathol* (2007) **213**(1):91–8. doi:10.1002/path.2207
39. Barcellos-Hoff MH, Blakely EA, Burma S, Fornace AJ Jr, Gerson S, Hlatky L, et al. Concepts and challenges in cancer risk prediction for the space radiation environment. *Life Sci Space Res (Amst)* (2015) **6**:92–103. doi:10.1016/j.lssr.2015.07.006

40. Ferrandon S, Magne N, Battiston-Montagne P, Hau-Desbat NH, Diaz O, Beuve M, et al. Cellular and molecular portrait of eleven human glioblastoma cell lines under photon and carbon ion irradiation. *Cancer Lett* (2015) **360**(1):10–6. doi:10.1016/j.canlet.2015.01.025
41. Sorensen BS, Horsman MR, Alsner J, Overgaard J, Durante M, Scholz M, et al. Relative biological effectiveness of carbon ions for tumor control, acute skin damage and late radiation-induced fibrosis in a mouse model. *Acta Oncol* (2015) **54**(9):1623–30. doi:10.3109/0284186X.2015.1069890
42. Antonovic L, Lindblom E, Dasu A, Bassler N, Furusawa Y, Toma-Dasu I. Clinical oxygen enhancement ratio of tumors in carbon ion radiotherapy: the influence of local oxygenation changes. *J Radiat Res* (2014) **55**(5):902–11. doi:10.1093/jrr/rru020
43. Takahashi M, Hirakawa H, Yajima H, Izumi-Nakajima N, Okayasu R, Fujimori A. Carbon ion beam is more effective to induce cell death in sphere-type A172 human glioblastoma cells compared with X-rays. *Int J Radiat Biol* (2014) **90**(12):1125–32. doi:10.3109/09553002.2014.927933
44. Simon F, Dittmar JO, Brons S, Orschiedt L, Urbschat S, Weber KJ, et al. Integrin-based meningioma cell migration is promoted by photon but not by carbon-ion irradiation. *Strahlenther Onkol* (2015) **191**(4):347–55. doi:10.1007/s00066-014-0778-y
45. Jin X, Li F, Zheng X, Liu Y, Hirayama R, Liu X, et al. Carbon ions induce autophagy effectively through stimulating the unfolded protein response and subsequent inhibiting Akt phosphorylation in tumor cells. *Sci Rep* (2015) **5**:13815. doi:10.1038/srep13815
46. Ogata T, Teshima T, Kagawa K, Hishikawa Y, Takahashi Y, Kawaguchi A, et al. Particle irradiation suppresses metastatic potential of cancer cells. *Cancer Res* (2005) **65**(1):113–20.
47. Fujita M, Yamada S, Imai T. Irradiation induces diverse changes in invasive potential in cancer lines. *Semin Cancer Biol* (2015) **35**:45–52. doi:10.1016/j.semcancer.2015.09.003
48. Karger CP, Scholz M, Huber PE, Debus J, Peschke P. Photon and carbon ion irradiation of a rat prostate carcinoma: does a higher fraction number increase the metastatic rate? *Radiat Res* (2014) **181**(6):623–8. doi:10.1667/RR13611.1
49. Harrison L, Blackwell K. Hypoxia and anemia: factors in decreased sensitivity to radiation therapy and chemotherapy? *Oncologist* (2004) **9**(Suppl 5):31–40. doi:10.1634/theoncologist.9-90005-31

Conflict of Interest Statement: The authors declare that the research was conducted in the absence of any commercial or financial relationships that could be construed as a potential conflict of interest.

Copyright © 2016 Walenta and Mueller-Klieser. This is an open-access article distributed under the terms of the Creative Commons Attribution License (CC BY). The use, distribution or reproduction in other forums is permitted, provided the original author(s) or licensor are credited and that the original publication in this journal is cited, in accordance with accepted academic practice. No use, distribution or reproduction is permitted which does not comply with these terms.

frontiers in Oncology

REVIEW
published: 12 February 2016
doi: 10.3389/fonc.2016.00023

Effects of Charged Particles on Human Tumor Cells

Kathryn D. Held[1], Hidemasa Kawamura[2,3], Takuya Kaminuma[1,2,3], Athena Evalour S. Paz[2], Yukari Yoshida[2], Qi Liu[1], Henning Willers[1] and Akihisa Takahashi[2]*

[1] Department of Radiation Oncology, Massachusetts General Hospital, Harvard Medical School, Boston, MA, USA, [2] Gunma University Heavy Ion Medical Center, Gunma, Japan, [3] Department of Radiation Oncology, Gunma University Graduate School of Medicine, Gunma, Japan

The use of charged particle therapy in cancer treatment is growing rapidly, in large part because the exquisite dose localization of charged particles allows for higher radiation doses to be given to tumor tissue while normal tissues are exposed to lower doses and decreased volumes of normal tissues are irradiated. In addition, charged particles heavier than protons have substantial potential clinical advantages because of their additional biological effects, including greater cell killing effectiveness, decreased radiation resistance of hypoxic cells in tumors, and reduced cell cycle dependence of radiation response. These biological advantages depend on many factors, such as endpoint, cell or tissue type, dose, dose rate or fractionation, charged particle type and energy, and oxygen concentration. This review summarizes the unique biological advantages of charged particle therapy and highlights recent research and areas of particular research needs, such as quantification of relative biological effectiveness (RBE) for various tumor types and radiation qualities, role of genetic background of tumor cells in determining response to charged particles, sensitivity of cancer stem-like cells to charged particles, role of charged particles in tumors with hypoxic fractions, and importance of fractionation, including use of hypofractionation, with charged particles.

Keywords: charged particles, proton therapy, carbon-ion therapy, relative biological effectiveness, clustered DNA damage, cancer stem cells, hypoxic radioresistance, altered fractionation

OPEN ACCESS

Edited by:
Marco Durante,
GSI Helmholtz Centre for Heavy Ion Research, Germany

Reviewed by:
Kevin Prise,
Queen's University Belfast, UK
Thomas Friedrich,
GSI Helmholtz Centre for Heavy Ion Research Darmstadt, Germany

****Correspondence:***
Kathryn D. Held
kheld@mgh.harvard.edu

Specialty section:
This article was submitted to Radiation Oncology, a section of the journal Frontiers in Oncology

Received: *23 October 2015*
Accepted: *21 January 2016*
Published: *12 February 2016*

Citation:
Held KD, Kawamura H, Kaminuma T, Paz AES, Yoshida Y, Liu Q, Willers H and Takahashi A (2016) Effects of Charged Particles on Human Tumor Cells. Front. Oncol. 6:23. doi: 10.3389/fonc.2016.00023

INTRODUCTION

Radiation therapy is a mainstay of cancer treatment, being a common and effective therapy for both curative and palliative treatment of cancer patients. In the last few decades, there has been increasing use of charged particles in radiation therapy. Protons were first proposed for use in cancer therapy by Robert R. Wilson (1), and the number of patients treated with protons has increased dramatically in recent years to a total of over 100,000 patients now treated worldwide (http://www.ptcog.ch/index.php/facilities-in-operation). Radiation treatment of cancer with helium ions began at Berkeley in the late 1950s and was expanded to heavier ions in the 1970s [see a review of the history of charged particles by Skarsgard (2)]. Much of the emphasis has been on carbon ions, with most patients treated in Japan and now totaling over 10,000 patients treated worldwide. The major clinical advantage of protons and heavier charged particles, such as carbon, comes from physics: the Bragg curve provides excellent radiation dose distributions [see reviews in Ref. (3, 4)]. In addition, heavier ions, e.g., carbon, offer the potential of additional biological gains such as increased relative biological effectiveness (RBE) and decreased oxygen enhancement ratio (OER) due to their higher

linear energy transfer (LET) in the Bragg peak region, where the tumor is located [reviewed, e.g., in Ref. (3, 5, 6)].

Despite the often-made assumption that the RBE for tumor cells is higher than that for normal cells irradiated under identical conditions, there is only a limited amount of experimental *in vitro* data that support that assertion (3). However, there have been interesting recent research findings on the differential DNA repair pathways of cancer cells after particle versus photon irradiation, new studies on the effects of charged particles on cancer stem cells, and increasing questions about different responses of tumor and normal cells to hypofractionation, especially with charged particle irradiations, suggest that there may be novel ways to take advantage of differences in characteristics of tumor cells from normal cells to improve or better tailor the use of charged particles in cancer therapy. This review will discuss these issues, with emphasis on data on responses of human tumor cells, largely based on *in vitro* findings. As discussed in more detail below, RBE is a complex quantity, depending on physical parameters, such as particle type and energy, dose and LET, and biological parameters, including cell/tissue type, cell cycle phase, oxygen level, and endpoint. *In vitro* assays have limitations compared to *in vivo* studies and the clinical situation due to lack of 3D architecture and microenvironmental context, including interactions among various cell types, vasculature, and immune system influences. Nevertheless, for studies of RBE, *in vitro* assays are critical for systematic testing and characterization of effects of various ions, elucidation of DNA damage pathways, and the importance of DNA repair processes and other genetic factors. Furthermore, *in vitro* studies provide experimental tests for validation of biophysical models, e.g., the local effects model (LEM), prior to clinical application (7), and yield insight on systematic variations in RBE relevant to clinical use (8, 9).

In this review, we start with brief overview sections on the unique biological advantages of charged particle therapy and DNA damage responses that may be important for particle therapy. That introduction is followed by consideration of recent findings on RBEs in human tumor cells, including discussion of the possible roles of genetic factors on RBE, then discussions of new findings on cancer stem cells, hypoxia, and fractionation. In particular, we stress approaches to use the increasing knowledge of the properties of tumors and tumor cells to better advantage when using charged particles in cancer therapy.

AN OVERVIEW OF THE UNIQUE BIOLOGICAL ADVANTAGES OF CHARGED PARTICLE THERAPY

A number of reviews [e.g., in Ref. (3–5)] have discussed the substantial dose distribution advantages of charged particles where, as a result of the Bragg peak, normal tissues can be spared by limiting dose to them, while maximum dose is deposited in the tumor. Heavier ions, such as carbon, have an additional dose distribution advantage over protons because of their reduced lateral scattering compared to protons. However, the major potential advantage of heavier ions in tumor irradiations is their enhanced biological effects, which include increased cell killing, decreased protection by hypoxia, decreased effect of fractionation, and decreased cell cycle dependence. The biological effectiveness of cell killing by higher LET radiations is usually quantified by use of RBE, the ratio of the dose of low-LET radiation (usually X-rays or gamma-rays) to dose of high-LET radiation (e.g., charged particle) for the same biological effect. Many *in vitro* studies over the years have shown the bell-shaped dependence of RBE for cell killing on LET (6, 10–12) wherein RBE increases with LET to a maximum at about 30–150 keV/μm, then decreases at higher LET. The LET value at which the RBE is maximal depends on the individual ion species, with the peak at higher LET with increasing atomic number of the ions (2). Furthermore, it has also long been recognized that there is great variation in the absolute values of RBE because RBE depends on numerous factors, including particle type and energy, cell type, experimental endpoint, cell cycle phase, dose and dose rate, oxygenation status, culture conditions, etc. (6, 7, 11).

The increased biological effectiveness of radiations with increasing LET lies in the physical dose distribution of the energy of the particles on the micro, and even nano, scale as they traverse matter, the clustering of DNA damages that results from the particle tracks and the increased difficulty cells have in accurately repairing the clustered damage (13–16). As energetic charged particles traverse matter, e.g., cells and tissues of organisms, their electronic interactions with atoms and molecules, mostly through inelastic collisions with atomic electrons, create a path, or track of ionizations before they run out of energy at a finite range, the Bragg peak. The tracks of heavy charged particles are fairly straight, but the electrons ejected from atoms along the track, being much lighter, follow paths that are quite tortuous, with their ranges depend on the energy they acquired when ejected. LET is a measure of the energy imparted to matter by the passage of an ionizing particle. Along the path of a charged particle, the three-dimensional distribution of energy depositions, which cause ionizations and excitations, is called the track structure. For low-LET sparsely ionizing radiations, there are relatively long distances between the energy depositions except at track ends, but with increasing LET, the ionizations along the track become denser and there is lateral spread of the track due to delta-ray electrons, the spectrum of which is determined by the velocity of the heavy charged particle.

If the ionizations from radiation were randomly distributed in cells, the consequences of those energy depositions would likely be minimal, but the non-randomness of the energy depositions accounts for the increased effectiveness of ionizing radiation (14, 17, 18). The clustering of ionizations along radiation tracks occurs on the same scale as the diameter of a DNA molecule and nucleosomes such that if a track traverses DNA it can effectively create clustered DNA damages, such as double-strand breaks (DSBs), clusters of two or more base damages, or clusters of single-strand breaks with base damages. As LET of radiation increases, the clustering becomes more complex, creating, for example, a complex DSB where the break is associated with additional damages, such as base changes or single-strand breaks. Both the proportion and degree of complexity increase with high-LET radiations (19). A number of studies have shown that the complex DNA damages produced by high-LET radiations are repaired less rapidly, less accurately, and less completely than damages from low-LET

photons [reviewed recently in Ref. (20, 21)]. Additionally, it is important to bear in mind that track structure has biological relevance not only at the level of DNA damage but also at higher levels of chromatin organization (17): a single high-LET particle track passing through a cell nucleus may cause correlated damages through chromatin structures, such as chromatin fibers, or in adjacent chromosome territories *via* a string of DSBs along its path, and these correlated damages may result in complex chromosome aberrations. Altogether, the net effect is that complex DNA damages resulting from the greater clustering of ionizations with increasing LET of radiation increases the production of all chromosome aberrations, simple as well as complex.

The increased DNA damage complexity and decreased repair accuracy with radiations of increasing LET not only cause increased cell killing but also result in decreased cell cycle dependence of that killing and play a factor in the decrease in OER. Cells exposed to low-LET radiation show increased resistance when irradiated in late S-phase and increased sensitivity when irradiated in M-phase (22). This fluctuation through the cell cycle decreases with higher LET radiations. However, since in many tumors, the majority of cells are not in the radiation-resistant phases, this effect on treatment outcome in irradiated tumors is likely to be modest (3). The importance of the decreased OER with high LET is discussed below.

Although there has been increasing interest in recent years in the so-called "non-targeted" effects of radiation, including bystander effects and genomic instability in progeny of irradiated cells [for recent reviews, see Ref. (23, 24)], it remains far from clear whether non-targeted effects are similar or different after irradiation with photons versus charged particles (25–27). Furthermore, the role of non-targeted effects or intercellular signaling in response of tumors to radiation remains under investigation (28, 29), with very little work having been done with charged particles. This review is limited to discussion of targeted effects of charge particles.

OVERVIEW OF DNA DAMAGE RESPONSES RELEVANT TO CHARGED PARTICLE BIOLOGY

Central to any consideration of the effects of charged particles on cells and tissues must be DNA damage response processes. Cells have two main pathways for the repair of radiation-induced DSBs: non-homologous end-joining (NHEJ) and homologous recombination (HR) (30–32). NHEJ is active throughout the cell cycle and is responsible for the repair of most DSBs in cells. NHEJ involves the initial binding of the Ku70/Ku80 heterodimer, recruitment of DNA–PKcs and eventual ligation of the DNA ends by XRCC4–DNA Ligase IV. However, NHEJ is an error-prone repair, and the quality of its repair processes can decrease with increasing levels of DNA damage. HR is active primarily during the S/G2 phases of the cell cycle, when a homologous DNA region is available, and generally results in the preservation of the original DNA sequence. HR involves DSB recognition by the MRN complex (Mre11, Rad50, Nbs1), 3′–5′ DNA resection, DNA stabilization by replication protein A (RPA), Rad51-mediated formation of Holliday junctions, and ultimately resolution of the Holliday junction (31, 33). HR is also involved in the repair and restart of collapsed DNA replication forks (34). At the forks, the BRCA1/2-dependent HR pathway converges with the Fanconi anemia (FA) pathway to resolve the damage (35). It has been suggested that unrepaired clustered DNA damages that collide with replication forks in cells in S-phase require HR for DNA repair and replication restart (36, 37).

It also has been reported that the end-resection activity in cells in the G_1 phase may promote micro-homology-mediated end joining (MMEJ) to repair DSBs that cannot be repaired efficiently by NHEJ (38). However, it is unknown how much the activation of HR and MMEJ pathways contribute to escaping cell death in high-LET-irradiated cells. Recently, we showed that targeting and suppressing NHEJ repair yields a high radiosensitivity in cells exposed to carbon-ion beams when compared to the suppression of HR repair (39).

RBEs OF CHARGED PARTICLES IN HUMAN TUMOR CELLS

Experimental studies to determine RBEs have been conducted for many years, with the majority using clonogenic cell survival as the endpoint. It has been felt that lack of clonogenicity is a highly relevant indicator of the efficacy of radiation and its modification because eradication of tumor cells is needed to cure tumors (22). In fact, the shape of curves of tumor control probability, as detected in a clinical context, can be explained from the random nature of tumor cell killing by radiation and the need to kill every cell, as a single cell may give rise to tumor regrowth (22). Furthermore, RBE values, measured or predicted by computer models, are used in clinical treatment planning approaches, which are continually being updated [e.g., Ref. (40, 41)].

It has been argued recently that further studies measuring RBE values may be of limited usefulness because they will have little impact on reducing the uncertainties in ion beam therapy (4, 6). However, determinations of RBEs can help guide understanding of mechanistic underpinnings to the increased effectiveness of higher LET radiations and, thus, may lead to better identification, based on genetic profiles or biomarker evaluation, of patients' tumors that may benefit most from charged particle therapy.

Shifting the Paradigm of a Generic RBE for Clinical Proton Beam Therapy

Clinical proton beam therapy has been based on the use of a generic RBE of ~1.1 at the center of the spread-out Bragg peak (SOBP) for cancer as well as for normal tissues (8). This RBE value represents an average of a wide range of experimental data *in vitro* and *in vivo* and has been intended to be a conservative estimate (8, 42). However, there is now a growing appreciation that the use of a generic value ignores RBE variations that may result, for example, from the heterogeneity of human cancers, LET variations along the SOBP, or the particular clinical endpoint under consideration (42–46). In this section, we will focus primarily on recent data that indicate a dependence of RBE on certain DNA repair defects, with the implication being that proton therapy may

have a biological advantage in human tumors that harbor such defects.

There exists very little experimental data on RBE variations in human cancers. In a 2002 review by Paganetti and colleagues (8), the average RBE at the mid-SOBP was estimated as ~1.2 *in vitro* and ~1.1 *in vivo*. However, most of the 20 cell lines considered in that analysis were of rodent origin resulting in a somewhat higher *in vitro* RBE. Only seven human cancer cell lines were included. There is growing evidence for considerable genomic heterogeneity across cancers even of the same type and histology, and it is increasingly appreciated that much of the variations in treatment sensitivity observed clinically are due to genomic heterogeneity, which may include alterations of DNA repair pathways (47–49). Therefore, it is highly doubtful that small numbers of non-representative cell lines are adequate pre-clinical models for assessing clinically relevant variations in RBE values in human cancers. In a recent screen of 17 lung cancer cell lines, RBE estimates at the mid-SOBP of a clinical beam relative to Co60 photons [Co60 equivalent (Eq)] ranged from 0.93 to 1.77 and 1.09 to 1.48 for clonogenic survival fractions of 0.5 and 0.1, respectively (44). In five cell lines (29%), the RBE increase was statistically different from 1.1. Furthermore, in at least three of these cell lines, the RBE increase correlated with defects in the so-called FA/BRCA pathway of DNA repair, and this observation was confirmed in several isogenic cell line models. The FA/BRCA pathway is critical for the maintenance and repair of DNA replication forks [reviewed in Ref. (34, 50)]. Inactivation of any of the FA/BRCA genes has been known to result in hypersensitivity to a variety of anti-cancer agents. However, apart from an involvement of the RAD51 recombinase (FANCR) in the cellular response to proton radiation (43, 51), the importance of the FA/BRCA genes for the repair of proton damage to DNA had been unknown. These observations are clinically significant because genetic or epigenetic defects in the FA/BRCA pathway have been found in large subsets of human cancers (34).

What are the mechanisms through which the FA/BRCA pathway acts on proton damage? For low-LET radiation, which includes X-rays and protons, it has been estimated that 20–40% of the initial damage is clustered, and the majority of clustered damage is present as non-DSB damage (52, 53). Proton radiation causes slightly more complex clustered DNA damages than photons, which is a reflection of the different LET values, i.e., ~2.5 keV/μm for protons at mid-SOBP versus ~0.3–2.0 keV/μm for different photon radiations. DNA repair-proficient tumor cells and normal cells remove these damages almost equally well, consistent with a proton RBE of 1.1 (Co60Eq). Because the FA genes are specifically involved in replication fork maintenance and repair, it can be inferred that the RBE increase that is seen with defects in this pathway results from impaired repair of forks that collide with clustered proton damages. The requirement for the FA/BRCA pathway is greater for proton damage compared to damage caused by, for example, X-rays, even though the RBE (Co60Eq) and LET of these two radiation modalities are almost identical [RBE(Co60) ~1.1 and LET = 2.0–2.5 keV/μm]. This is illustrated in **Figure 1A**. Proton-irradiated FA/BRCA-defective cells will accumulate greater numbers of DNA DSB in S-phase and subsequently G2-phase than X-irradiated cells, as has been shown experimentally (44) (Willers et al., unpublished). Interestingly, an increase in the size of DSB-associated foci persisting after proton irradiation has been observed (44), likely signifying unrepaired clustered damages (**Figure 1A**). It has been proposed that these DSB foci could serve as predictive biomarkers to identify cancers that may be more susceptible to proton beam therapy (44). Alternatively, genetic or epigenetic defects in the FA/BRCA pathway could be detected through genomics techniques in order to identify patients for proton therapy. This approach will require a more detailed knowledge of the genes involved in the cellular response to clustered proton damages. The available data indicate that functional loss of any of several key genes in the FA/BRCA pathway will increase the RBE, with the best current estimate being an average RBE of 1.33 (95% confidence limits, 1.25–1.41) at mid-SOBP as shown in **Figure 1B**. This is a conservative estimate derived at a surviving fraction of 0.1. For 0.5 survival fraction, which is more applicable to fraction sizes of 2 Gy as used in the clinic and which overlaps with the shoulder of the survival curves, the RBE values of the most proton-sensitive cell lines tended to be even higher than for 0.1 survival fraction. For example, the five most sensitive lung cancer cell lines in the report by Liu et al. (44) had an average RBE of 1.30 (range, 1.22–1.48) and 1.46 (range, 1.31–1.77) at survival fractions of 0.1 and 0.5, respectively.

In conclusion, these recent pre-clinical data strongly suggest inter-tumoral heterogeneity of proton RBE that may yield opportunities to identify proton susceptible tumors in the clinic within the next few years. This "New Biology" of protons in cancer coupled with the increasing knowledge of RBE variations as a function of physical proton beam parameters in both cancers and normal tissues is expected to shift the paradigm of a generic proton RBE to a variable RBE.

RBE Determinations with Heavy Charged Particles

The proton studies just described provide a possible DNA repair capacity-based explanation for some of the variation seen in proton RBE values at a given LET. Could a similar finding apply to human tumors exposed to high-LET charged particles? Unfortunately, no single study with a substantial number of cell lines has yet been done for any heavy ion, although many small studies with a few cell lines each have been performed. Some large compilations of cell survival RBE values for many cell types, endpoints and radiation qualities have been published recently (7, 54, 55), and the composite data clearly show that RBEs depend on LET, endpoint, ion, etc. In this section, we focus on analysis of RBE values for human tumor cells exposed to ions heavier than protons. Published papers that describe the cell survival RBE of human tumor cells have been searched by using PubMed; many of these papers are included in the compilations mentioned. A total of 430 RBE values were collected from 36 published papers (56–91). When authors provided RBE values along with dose–response data, those values were used. In cases where authors showed dose–response curves but did not cite any RBE value, an isoeffect line was drawn in the dose–response curves to read corresponding doses of ions and reference photons. As reference beam, 30 papers used X-rays and 6 papers used gamma-rays.

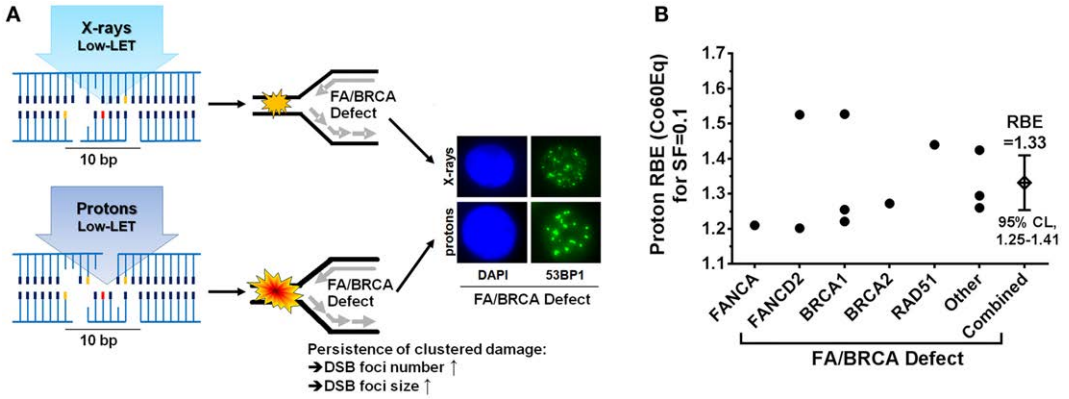

FIGURE 1 | **A "New Biology" of proton beam therapy**. **(A)** Illustration of how FA/BRCA defects may sensitize cells to proton irradiation. Left, clustered DNA damages after equal physical doses of X-rays and mid-SOBP protons are slightly different despite similar LET (2–2.5 keV/μm) and identical RBE in repair-proficient cells (~1.1). In the presence of a FA/BRCA defect that affects the repair of replication forks encountering clustered damages, there will be greater unrepaired damage after proton-irradiation, as marked by an increased number and relative size of repair-related protein accumulations of DNA double-strand break markers. Representative immunofluorescence microscopy images showing nucleus (DAPI) and 53BP1 foci (green) in FANCD2-mutant cells are shown on the right. **(B)** Summary of RBE estimates relative to Co60 photons as a function of defects in the FA/BRCA pathway (44, 45). Other, taken from unpublished data (Willers et al.); CoEq, Co60 equivalent; SF, surviving fraction; CL, confidence limits.

For the analyses here, the biological differences in effect between X-rays and gamma-rays were not considered.

Endpoint

Endpoint is one of the major factors, which affects the values of RBE (7, 54, 55, 92). The RBE data as a function of LET sorted by endpoint are shown in **Figures 2** and **3**. All papers included in **Figure 2** presented RBE values for colony formation after exposure to a range of single doses. Within a total of 363 RBE values, 295 values in 31 papers were calculated using an isoeffect dose of 10% survival (D10). The other values that were calculated included D0, D30, D50, D75, ratio of alpha parameters, or isodose effectiveness. The RBE values for D10 ranged from 1.03 to 4.99, showing the "classic" increase in RBE with LET followed by a decrease at higher LET (22) although the range in RBE values at any given LET is substantial in many cases. The RBE values based on D0, D30, D50, and D75 also showed considerable variation at any given LET, but, as expected, there was a trend for higher RBE values at higher levels of survival (22). Some of the highest RBE values were derived using the alpha ratio; this, too, is consistent with higher RBEs at higher survival, since alpha ratios would tend to be derived based on high survival data.

The other endpoint that tends to show high RBE values is apoptosis (**Figure 3B**). This is consistent with the observations that most solid tumor cell lines are resistant to X-ray-induced apoptosis (93) and that apoptosis may be characterized by the alpha-component of the cell survival curve [reviewed, e.g., in Ref. (94)]. In a recent review on proton radiobiology, Tommasino and Durante (95) pointed out that there is a general tendency for an increased apoptotic response with increasing LET and that tumor cells resistant to photon-induced apoptosis may have apoptosis triggered by an alternative pathway by protons, a suggestion that could likely extend to heavier charged particles. However, it should also be pointed out that several groups, including Brown and colleagues (96), have demonstrated that apoptosis induction can be markedly affected by tumor cell genetics and the overall level of cell killing as determined in a clonogenic assay *in vitro* may not correlate well with apoptosis induction [also reviewed in Ref. (94)].

Two papers reported RBE values calculated for residual unrepaired chromatin breaks using premature chromosome condensation (PCC) (**Figure 3A**), with the paper by Suzuki et al. using primary cells obtained by biopsy from patients (67, 72). Authors of both studies noted the good correlation between their data on residual chromatin breaks as measured using the PCC technique and colony formation, and concluded that the PCC technique was a potential predictive assay of tumor response to ion therapy. Information on correlation of chromatin breaks using PCC with DNA repair protein foci formation and/or FA/BRCA pathway status, as discussed above for potential use with proton therapy patients, would be helpful for assessment of possible predictive assays.

Ion

The data on RBE values calculated using D10 and sorted by ions are shown in **Figure 4**. A total of 29 papers reported 247 RBE values for carbon-ion beam, whereas there were 21 RBE values for helium ions in 3 papers, 24 values for neon ion in 2 papers, 6 values for boron ions in 1 paper, 6 values for silicon beam in 2 papers, 5 values for iron beam in 3 papers, 2 values for nitrogen beam in one paper, and 3 values for argon beam in 2 papers. The RBE values showed substantial variation at any given LET, independent of ion species used, but in all cases the RBE increased with LET to a maximum then decreased at high-LET levels. It is well known that the RBE values of carbon ions peak around an LET of 100 keV/μm (7, 54, 55, 92). The other ion beams had peaks between LETs of 100 and 200 keV/μm, with a trend toward a maximum at higher LET with heavier ions.

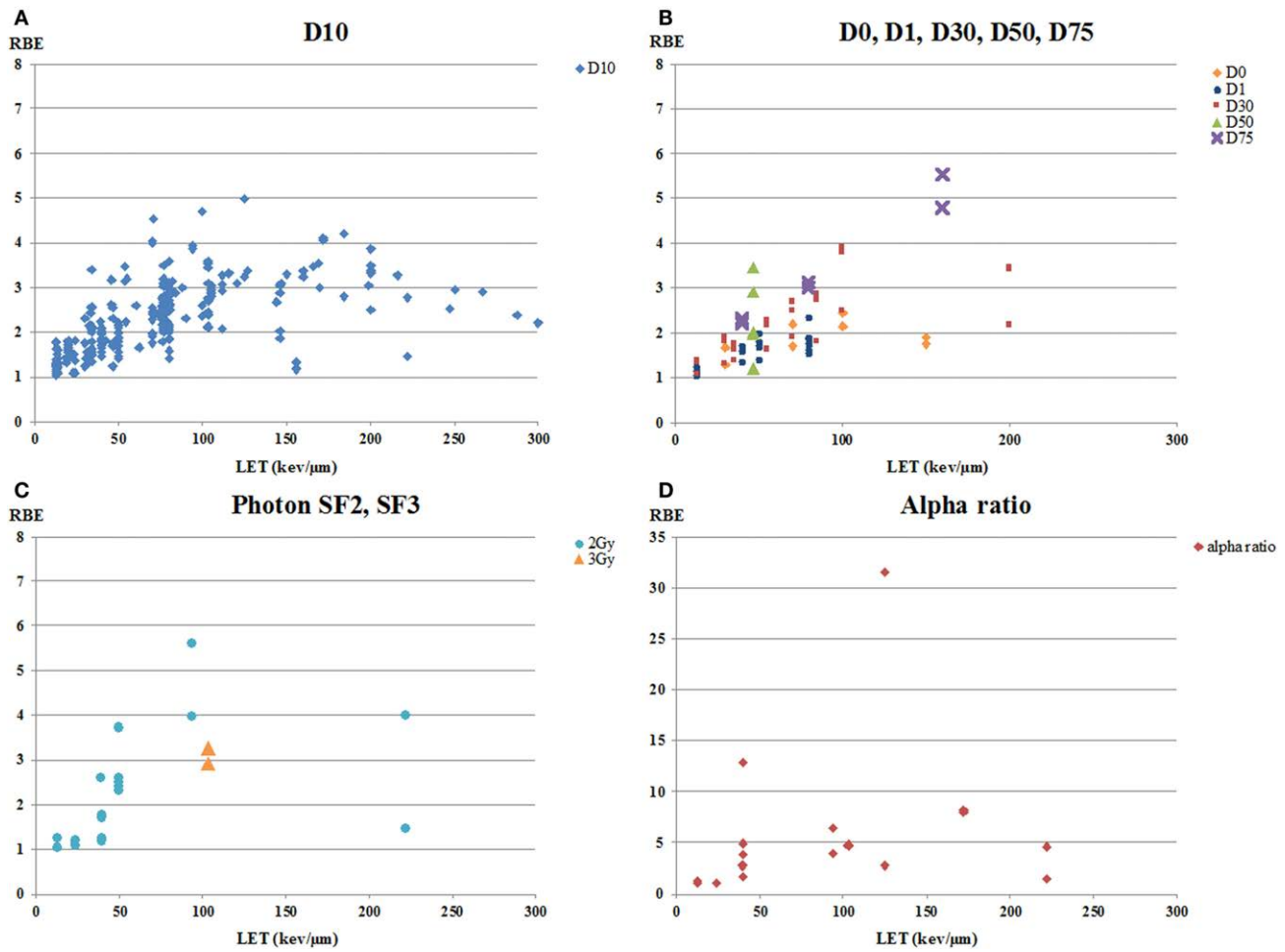

FIGURE 2 | RBE versus LET for human tumor cell lines for various endpoints. RBE values are all based on colony formation assays. **(A)** RBE values calculated as the ratio of isoeffect doses at 10% survival (D10). **(B)** RBE values calculated as ratios of doses for D0, D30, D50, and D75. D0 was calculated by fitting the survival curve to the single-hit multi-target (SHMT) model: $S/S0 = 1 - (1 - e^{-D/D0})^n$. **(C)** RBE values calculated as the ratio of doses at the level of photon doses of 2 Gy (SF2) or 3 Gy (SF3). **(D)** RBE values calculated as the ratios of the alpha parameters of survival curves.

Furusawa et al. (59) exposed human salivary gland tumor cells to carbon, neon, and helium ion beams and calculated the RBE values of each beam. They showed that the RBE values for helium ions were higher than those for the other ions, which seems unexpected. This finding deserves more investigation as there is some interest in development of helium ion beams for cancer therapy since they have less lateral dose than protons (i.e., a better dose distribution) (97), which might make their use particularly relevant in children. Furthermore, in their report, Furusawa et al. show that the peaks of the RBE values shifted to higher LET values with increasing atomic number, an observation that had been made earlier on the basis of work by a number of authors [e.g., Ref. (11, 98, 99)] as reviewed by Skarsgard (2). Such findings deserve emphasis as they highlight the fact that LET is not adequate as the sole descriptor of energy deposition in cells and tissues, but that ion track structure, the nanometer scale distribution of energy, must be considered when evaluating biological effects. In this context, it is interesting to note that NASA's model for calculating risk of radiation-induced cancer from space radiation takes into account track structure of heavy ions rather than simply LET (100). In a clinical context in heavy ion therapy, the LEM, which is used for RBE prediction, also provides particle species and LET-specific RBE values that are then propagated, using a treatment planning system, to a representative RBE value at each position in the irradiated field (9, 101), a process needed because ion fragmentation produces a mixed radiation field.

With regard to ions, it is worth pointing out that we did not include data with oxygen ions in **Figure 4** because we found only one study using oxygen ions, and that work used only a single LET (87). That work reported that for four human hepatocellular carcinoma cell lines irradiated in the SOPB of oxygen ions with a mean energy of 154 MeV/u (LET of 146 keV/µm), the clonogenic RBE_{10} values ranged from 1.9 to 3.1, with the values not being significantly different from those obtained in the same study using 130 MeV/u carbon ions (LET of 112 keV/µm). However, this study is noteworthy because of the current interest in using

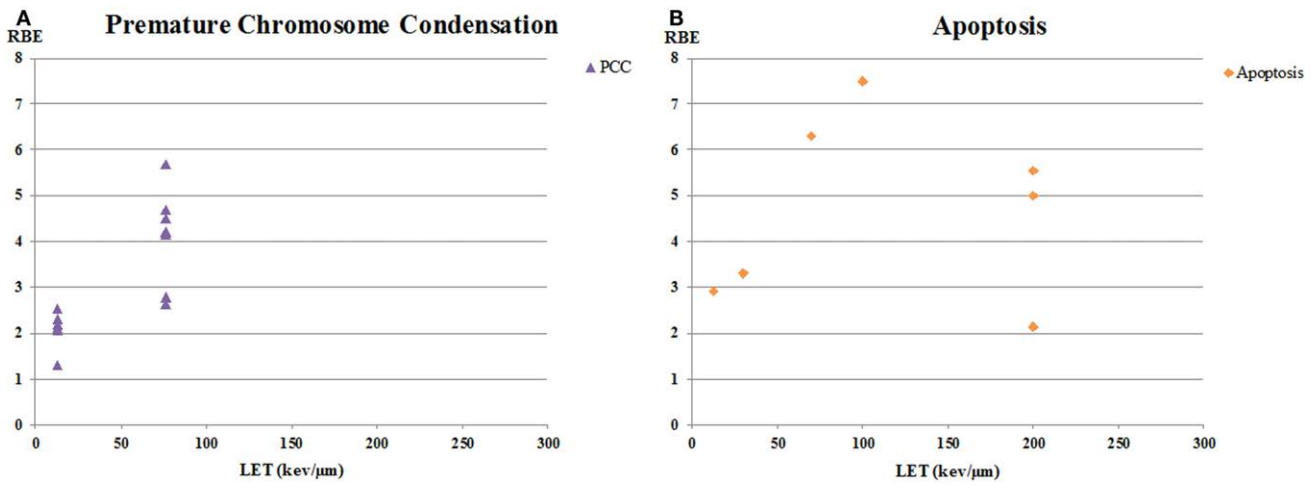

FIGURE 3 | **RBE versus LET for human tumor cell lines for chromatin breaks and apoptosis**. **(A)** is from data on unrejoined chromatin breaks in cells after premature chromosome condensation (PCC). Residual unrejoined chromatin breaks were detected using Giemsa staining in cells after chromatin condensation. **(B)** is RBE values for apoptosis.

oxygen ions, with their lower OER, in treating tumors with large hypoxic fractions (102).

Type of Tumor Cells

The data on RBE values as a function of LET for carbon-ion beam only, calculated using D10 and sorted by tumor type, are shown in **Figure 5**. **Figure 6** shows a subset of the data separated out by adenocarcinoma and squamous cell carcinoma. The graphs show data only for LET < 100 keV/μm. The number of data points, or cell lines, varies greatly with tumor type. Generally, the brain tumors (composite slope of 0.018) and adenocarcinomas (composite slope of 0.018) appear to have lower slopes for the RBE versus LET curves than do squamous cell carcinomas (composite slope of 0.024 or higher). It should be noted, however, that data from Suzuki et al. (71) for cervical cancer included in the squamous cell carcinoma graph were derived from primary cultured cells from biopsies from patients, the only data from primary cultures included in this analysis. These primary culture data appear to have lower slopes than the other squamous cell data, although it should also be noted that the steeper slopes for the established squamous carcinoma cell lines are determined by only four data points at high-LET values. Thus, it is not possible to determine whether there is a systematic difference between primary squamous cell cultures compared to established tumor cell lines or between squamous cell carcinomas and adenocarcinomas. It is not clear from clinical data with carbon ions whether a difference exists between sensitivity of squamous tumors and adenocarcinomas, suggesting an area for further *in vitro*, *in vivo*, and/or clinical study. For comparison, it can be pointed out that in a similar analysis approach, Ando (54) found that the RBE versus LET plot for cultured human fibroblasts had a slope of 0.027, which the author noted was steeper than the composite slope for the human tumor data he analyzed.

The RBE values for the pancreas cancer cells are the lowest in all the data (64). The slope of the graph of pancreas is 0.0084, which is gentler than the others. This might suggest that pancreatic cancer would not be a good candidate for carbon-ion therapy, yet clinical trials of carbon ions for pancreas cancer in Japan have shown promising results (4, 103). The clinical results may reflect properties of the human tumors *in situ,* such as high hypoxia, radioresistance (high cancer stem cell component?), and anatomic location, that might not be evident in studies of isolated tumor cells.

It is noteworthy that there are few tumor cell data on RBE values with charged particles for prostate cancer or bone and soft tissue cancers, which are the two cancer types with the most patients treated to-date with carbon ions at NIRS in Japan (103). Furthermore, we found no experimental RBE data for human cell lines of mucosal malignant melanoma, adenoid cystic carcinoma, or rectal carcinoma, which are all being treated with carbon ions at NIRS with favorable outcomes (103).

D10 has been used as the parameter for calculating RBE values in this analysis by tumor type (**Figures 5** and **6**) because that is the parameter most frequently reported in the literature. However, the use of D10 may have minimized the ability to see differences between tumor cell types, resulting in the relatively similar values of the slopes of the RBE versus LET curves for the various tumor cells. Generally, inherent photon radiosensitivity differences between cell types become most evident at high and low cell survival levels, and it has long been recognized that RBE values are larger at high survival levels than at low ones because of the "shoulder" on photon survival curves (22). For example, this is consistent with the data shown in **Figure 2** where RBEs based on alpha ratio (generally reflecting high survival, low dose results) tend to be higher than those based on D10. Since it has been shown that photon dose–response curves for different tumor cell types have significant differences [e.g., Ref. (104, 105)], one might expect that the RBE

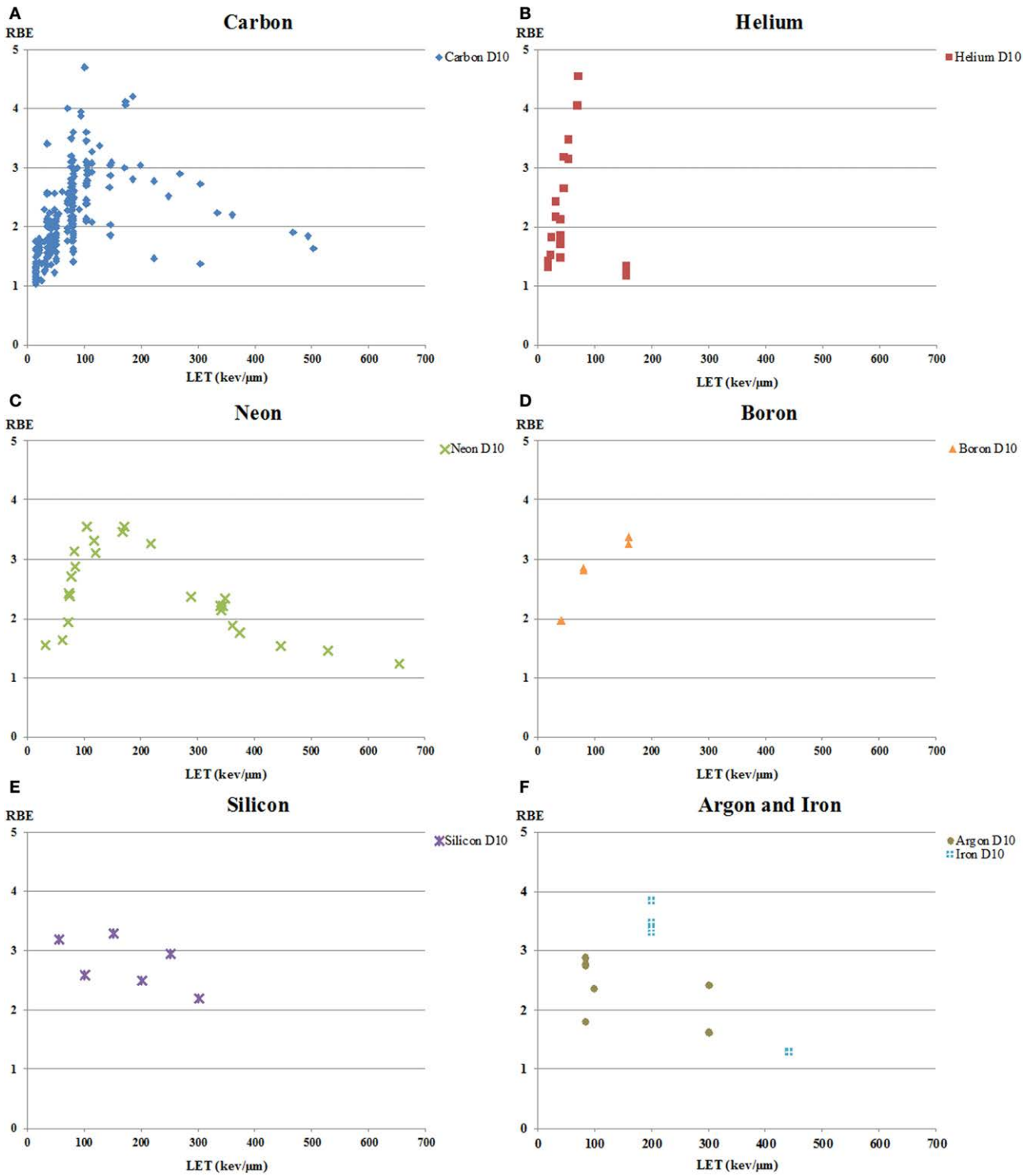

FIGURE 4 | RBE at 10% survival (D10) versus LET for human tumor cell lines exposed to various charged particles heavier than protons. RBE values derived at 10% survival from clonogenic survival curves from all available literature are shown as a function of LET for human tumor cells exposed to **(A)** carbon ions; **(B)** helium ions; **(C)** neon ions; **(D)** boron ions; **(E)** silicon ions; and **(F)** argon and iron ions. The RBE values showed substantial variation at any given LET, independent of ion species, but in all cases the RBE increased with LET to a maximum, then decreased at high-LET levels.

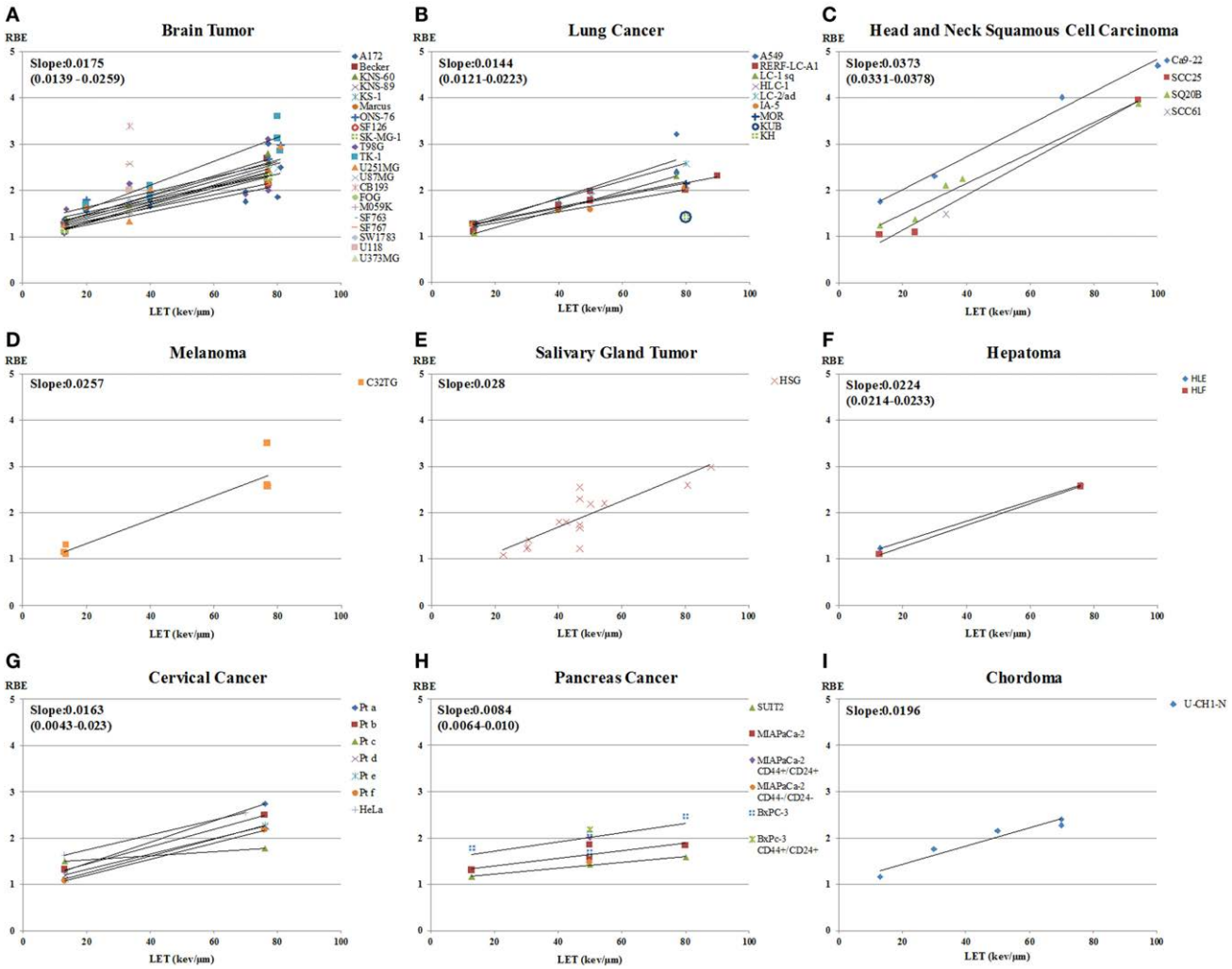

FIGURE 5 | RBE at 10% survival versus LET for cells from various types of human tumors exposed to carbon ions. RBE values as a function of LET for carbon-ion beam only, calculated using D10 and sorted by tumor type, are shown. Tumor types included are: **(A)** brain tumor; **(B)** lung cancer; **(C)** head and neck squamous cell carcinoma; **(D)** melanoma; **(E)** salivary gland tumor; **(F)** hepatoma; **(G)** cervical cancer; **(H)** pancreatic cancer and **(I)** chordoma. The graphs include data only for LET < 100 keV/µm. The number of data points, or cell lines, varies greatly with tumor type. The slopes of the RBE versus LET curves are calculated for each cell line and tumor type.

versus LET curves would also differ in a manner consistent with the photon sensitivity. The finding here (**Figures 5** and **6**) that the differences seem small may reflect the use of the less discriminating parameter, D10. If sufficient data existed to do this analysis with a parameter more weighted toward lower or, especially, higher survival levels, e.g., alpha ratio, greater differences in dependence of RBE on LET for various cell types might be seen.

Role of Genetic Background of Tumor Cells in Response to Charged Particles

In light of the proton data, discussed above, indicating a correlation between cell lines with higher proton RBE values and defects in DNA repair, specifically in HR repair, we wondered whether the same finding would extend to heavier ions, notably carbon ions. Although the literature data on RBEs for human tumor cell lines shows substantial variations at any given LET, even just for carbon ions (**Figures 2–6**), we could not find any information in the literature on possible DNA repair deficiencies, particularly in HR repair, for the cell lines with the highest RBEs after carbon-ion irradiation, e.g., TK-1 brain tumor, Ca9–22 gingival squamous cell carcinoma, SQ20B head-and-neck cancer. Therefore, experiments to ascertain carbon RBE values for human tumor cell lines known to be defective in the FA/BRCA DNA repair pathway are warranted. Furthermore, both the proton data of Liu et al. (44) and the carbon-ion data of Suzuki et al. (70) on residual unrepaired DNA damage (assays of 53BP1 foci and DNA damage revealed by PCC, respectively) suggest that such assays may be useful biodosimeters to select patients for charged particle therapy.

What would be the clinical application of increased tumor RBE values in subsets of patients? Identifying patients with proton- and/or heavy ion-sensitive tumors may allow us to: (a) de-escalate the physical dose of charged particles if normal tissue

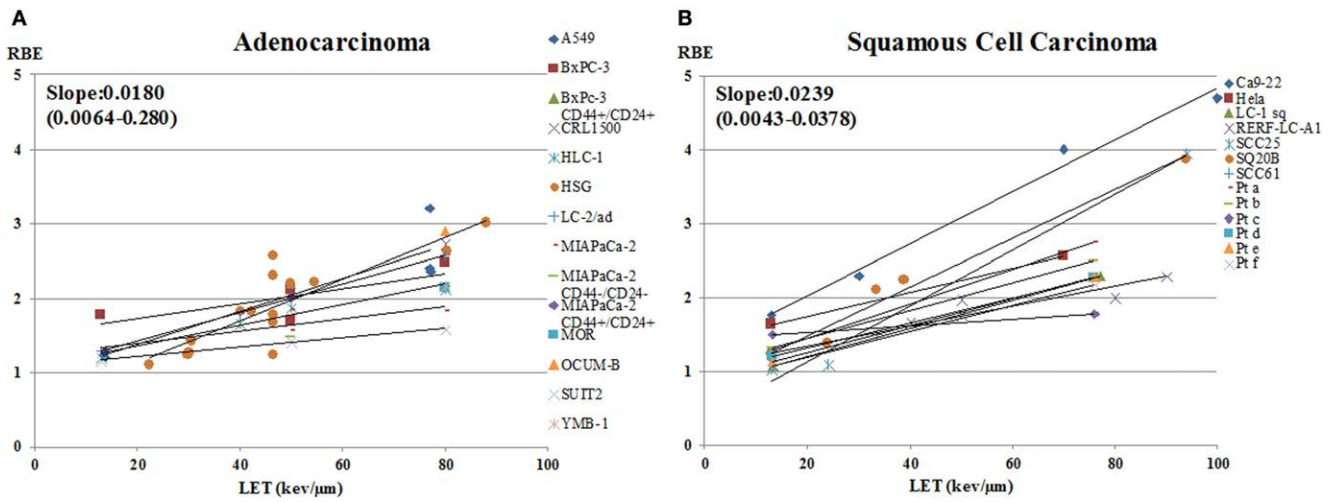

FIGURE 6 | RBE at 10% survival versus LET for cells from human adenocarcinomas and squamous cell carcinomas exposed to carbon ions. RBE values as a function of LET for carbon ion beam only, calculated using D10 for **(A)** adenocarcinomas and **(B)** squamous cell carcinomas. The graphs show data only for LET < 100 keV/µm. The slopes of the curves are shown for each cell line.

damage is a particular concern; (b) select patients for proton or heavy ion treatment slots who would have not otherwise had the opportunity to be treated with such radiations, thereby increasing the odds of local tumor control; or (c) biologically optimize tumor-directed therapy, for example, by employing intensity-modulated ion therapy algorithms to superimpose an LET increase on the already pre-existing RBE advantage, thereby further improving local tumor control. Because RBE values tend to increase with increasing fractionation sensitivity of tumors (i.e., decreasing alpha/beta values) (42), there exists additional opportunity to improve the outcome of ion beam therapy in tumors with low alpha/beta values, such as prostate or breast cancer. However, this approach will require better knowledge of the inter-tumoral variation of alpha/beta values and the development of predictive biomarkers to identify appropriate tumors.

SENSITIVITY OF CANCER STEM-LIKE CELLS TO CHARGED PARTICLES

In recent years, considerable interest has developed in the possibility that cancer stem-like cells (CSCs) in human tumors could be major contributors to resistance of tumors to conventional photon radiotherapy (RT) (106–108). However, intriguing data also suggest that the presence of CSCs might be overcome by carbon-ion therapy (89, 109). In this section, we discuss such a potential from a radiobiological perspective.

Cancer stem-like cells, also called cancer-initiating cells (CICs), are tumorigenic and have the potential to give rise to all cell types identified in hematological cancers and in several types of solid tumors (110). CSCs are regarded as "roots of cancer," analogous to normal stem cells in hierarchical tissues, although the origin of CSCs is still not clear and various theories have been proposed to explain their origin (111). It is believed that tumor growth is driven by a discrete subpopulation of CSCs that are defined by their capacity for self-renewal and their ability to generate heterogeneous lineages of cancer cells (110). The CSCs can survive and usually persist in tumors for a substantial length of time as a distinct population and can eventually cause cancer recurrence after treatment and tumor metastasis. It seems reasonable to suggest that cancer cure can be achieved only if this population is eliminated.

There is growing evidence that CSCs are inherently resistant to conventional fractionated RT. This radioresistant phenomenon of CSCs has been described within the framework of the four Rs of radiobiology: (i) repair, (ii) redistribution, (iii) reoxygenation, and (iv) repopulation (112).

(i) Regarding DNA repair, CSCs exhibit fewer DNA DSBs after exposure to ionizing radiation than non-tumorigenic cancer cells, which has been correlated with efficient DNA repair machinery due to constitutive hyperphosphorylation of the DNA checkpoint kinases Chk1 and Chk2 (106).

(ii) Regarding redistribution, quiescent or slowly cycling cells, normal or cancer stem cells, generally are radioresistant, although dose fractionation can cause redistribution of radioresistant S-phase cells into a more sensitive phase of the cell cycle. If this happens only in tumor cells, it could result in a therapeutic benefit for slowly cycling normal cells, sparing late responding normal tissues during fractionation. However, if tumors also have a significant proportion of CSCs that are slowly cycling, any benefit from redistribution may not apply (112).

(iii) Regarding reoxygenation, if the niche in which CSCs reside is hypoxic, during radiation fractionation the quiescent CSCs may be exposed to increasing oxygen levels causing increasing radiosensitivity due to transition of cells into an activated, proliferative state. It appears that in some cases,

the CSC niche may be in perivascular regions (113, 114) where they may be exposed to rapidly changing cycles of hypoxia-reoxygenation (112). During reoxygenation, the cells would become more radiosensitive, and reoxygenation triggers metabolic processes that generate damaging reactive oxygen species (ROS). However, CSCs manifest enhanced protection against ROS (107, 108). It was reported that expression of the CSC marker CD44, in particular that of a variant isoform (CD44v), contributes to ROS defense by promoting the synthesis of glutathione (GSH), a primary intracellular antioxidant radical scavenger (115). Hence, the roles of hypoxia, reoxygenation, and ROS defenses in CSCs appear quite complex, and more research is required to elucidate their roles in radiation response.

(iv) Regarding repopulation, it was reported that developmental signaling pathways, such as TGF-β, Notch, Wnt/B-catenin, and Sonic hedgehog pathways greatly contribute to maintenance of CSCs, as they do with normal tissue stem cells (112). Intrinsic inter-conversion and dynamic equilibrium between CSCs and non-stem cancer cells (NSCCs) exist under normal and irradiation conditions, and TGF-β might have important roles in the equilibrium (116).

In addition to the four Rs of radiobiology, it has been shown that CSCs can acquire radioresistance through activation of anti-apoptotic Bcl-2 (117) and serine/threonine protein kinase B (PKB, also known as AKT) survival signaling (118, 119). Hence, there is substantial reason to believe that CSCs are a radiation-resistant cell population in at least some tumors exposed to photon irradiation.

On the other hand, intriguing studies have reported that CSCs may be more effectively killed by carbon ions compared to photons in colon and pancreas cancers both *in vitro* and *in vivo* (89, 109, 120), and CSCs from colon and breast cancers may be more efficiently eliminated by proton irradiation than photon treatment, at least *in vitro* (121, 122). One or more of several processes may explain the observations that ion beams have biological advantages for killing CSCs compared to photons. These include the diminished capacity for NHEJ repair, which may play an important role in the quiescent G0 cell cycle phase, after heavy ion exposure (39); a decreased OER with heavy ions (59, 123), and an efficacy in dealing with radioresistant tumor cells (*TP53*-mutated and BCL2-overexpressing cells) (124) compared with results produced by photon beams. We demonstrated that heavy ion beams depress AKT-related survival signaling (125). Therefore, we speculate that heavy ion beams may target CSCs *via* depression of AKT survival signaling. Indeed, we demonstrated that the population of CSCs is only slightly increased or unchanged after carbon-ion irradiation because carbon ions may simultaneously kill CSCs and non-CSCs, while X-rays have less effect on CSCs than on the bulk cancer cells (126). These results suggest that carbon ions may enhance apoptosis and autophagy through activation of death signaling and may target CSCs *via* the depression of AKT survival signaling (**Figure 7**). However, it should be noted that the observations of CSCs being preferentially more sensitive to charged particles is not universal as it has been reported that head-and-neck cancer CSCs are resistant

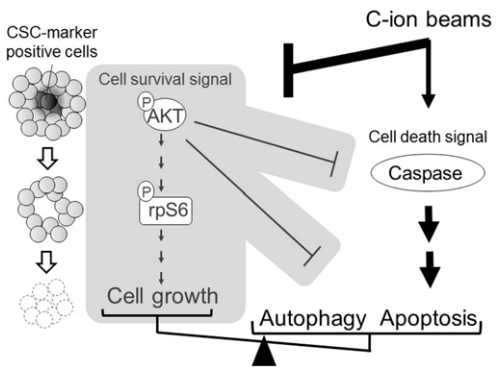

FIGURE 7 | A model for carbon ion-induced apoptosis and autophagy through the enhancement of death signals and the depression of survival signals. The model is based on AKT survival signaling as shown in our work (126). An arrow "→" indicates enhancement; a sidewise "⊣" indicates depression.

to both photon and carbon-ion irradiation (127). Clearly, more detailed studies are necessary, for example, using tumor samples from carbon- and photon-irradiated patients, to understand the potential significant therapeutic benefit of heavier charged particles on CSCs. It is also worth investigating whether, or how, the enhanced DNA repair advantages in CSCs might relate to the potential for development of biomarkers based on residual DNA damage for identifying patients whose cancers might be treated more efficaciously using charged particles, as discussed in the section above.

SENSITIVITY OF HYPOXIC TUMOR CELLS TO CHARGED PARTICLES

A long-recognized property of tumors is their development of hypoxic regions. It has also been documented, for many years, that hypoxic cells are resistant to photons, but that resistance is reduced when hypoxic cells are irradiated with higher LET particles (22). Suit et al. (3) postulated that the potential gain from high-LET radiations in the clinic may be due principally to the lower OER (ratio of doses for a given endpoint in hypoxic to well-aerated cells). This section discusses the reduced hypoxic protection with carbon-ion therapy and how that might be exploited in cancer therapy.

Cellular sensitivity to low-LET radiations (photons, clinical energy protons) depends on the degree of hypoxia at the time of irradiation, increasing in a sigmoid fashion from an OER = 1.0 (no difference between anoxic and well-aerated cells) at very low oxygen levels to a maximum (OER ~ 3.0) usually obtained by about 2–3% oxygen (22, 128). Sensitivity also depends on the duration of exposure to the hypoxic conditions. There are two distinct mechanisms that promote oxygen deficiency in tumor cells; each exposes cells to different periods of hypoxia. Acute or perfusion-limited hypoxia is caused by poorly formed or dysfunctional vasculature that can cause transient closing of blood vessels that deprives the surrounding cells of an appropriate oxygen

supply (129). On the other hand, in chronic or diffusion-limited hypoxia, the imbalance of oxygen supply and consumption in actively proliferating tumor cells causes cells far from blood vessels to experience a deficiency in oxygenation for long periods of time (130). Historically, most studies of hypoxic radioresistance have dealt with chronic hypoxia, but experiments investigating the influence of acute and chronic oxygenation conditions on cell response have shown increased radioresistance for the acute case (131–133). Ma and colleagues demonstrated that for both X-ray and carbon-ion irradiation, cells under acute anoxia were more radioresistant than those under chronic anoxia, whereas cells subjected to acute and chronic hypoxia (0.5% O_2) exhibited no significant difference in sensitivity (131, 132). They argued that prolonged exposure to anoxia induced a breakdown in cellular energy metabolism, which led to delays in cell cycle progression. They found that cells were arrested in the G1 phase of the cell cycle with a significant decrease in the number of active S-phase cells after 24 h of hypoxia. However, abrupt changes in the oxygenation status did not result in changes in the cell cycle distribution. The energy deficiency of cells also has been associated with the reduction of DNA damage repair (133). Therefore, chronically hypoxic cells were found to be more vulnerable to radiation damage.

The poor performance of photons in curing hypoxic tumor cells has prompted researchers to turn to high-LET radiation, such as ion beams that have lower OERs [reviewed, e.g., in Ref. (22, 128, 134, 135)]. Radiation damage from low-LET beams is mostly mediated by free radicals (indirect effects), i.e., secondary electrons generated from the ionizations interact with molecules, such as water, to produce free radicals which in turn damage the DNA. In contrast to their low-LET counterparts, the contribution of radiation damage by direct ionizations in DNA is higher for high-LET beams. Here, the secondary electrons directly interact with the critical target, thus producing, at least in part, different damage. Hence, the oxygen effect can be explained, at least in part, by differences in induction and repair of DNA damage. Hirayama et al. reported that the rejoining kinetics of DNA DSBs incurred from carbon-ion irradiation were the same for cells in oxic and hypoxic conditions (136). This led them to postulate that DNA DSBs produced by carbon ions are the same for the two oxygenation conditions. However, their results for X-ray irradiation showed a dependence of the repair dynamics on the oxygen level, with DSBs generated under oxic conditions rejoined more efficiently than those produced under hypoxia. They postulated that this resulted from different mechanisms for DNA damage depending on oxygenation, namely, that in the presence of oxygen, oxygen-reacting radicals could cause additional DNA DSBs but in hypoxia more damage is produced by direct ionizations or by radicals irrelevant to oxygen. Furthermore, the repair times were longer after carbon-ion irradiation and more unrepaired DNA DSBs remained after 5 h while for X-rays almost all DSBs were efficiently rejoined. This can be explained by the high ionization density generated along the track of heavy charged particles that produces complex DNA damages, making repair more difficult. Therefore, the OER decreases with increasing LET values, with the OER of carbon ions about half that with X-rays. Typical survival curves obtained using carbon-ion and X-ray irradiation under oxic and hypoxic conditions are illustrated in **Figure 8**. The difference with oxygenation status is diminished with the high-LET carbon ions and the survival curves tend to converge. By contrast, the larger variation in the cell response seen for X-ray irradiation is reflected by the higher OER value. A consequence of the enhanced radioresistance observed in X-ray survival curves under hypoxia is that $RBE_{hypoxic}$ generally exceeds RBE_{oxic}. *In vitro* studies have also shown that OER approaches unity at dose-averaged LETs of ~300 keV/μm (59, 134). Oxygen ions, with their high-LET values within therapeutic fields, might be advantageous for tumors with significant hypoxic fractions. Scifoni et al. (135) compared computed OER values in a tumor irradiated with oxygen or carbon ions, and showed that, assuming the same dose in the entrance region, there was a dramatic decrease in OER for the oxygen ions.

The advantage of high-LET carbon ions over photons in treating tumor hypoxia has been confirmed in the clinical setting by Nakano et al. (137). They measured the intratumor oxygen partial pressure of uterine cervical cancer patients prior to and at the fifth day of treatment with either photons or carbon ions using a polarographic electrode. The 4-year local control rates were found to be independent of the oxygenation condition for carbon-ion treatment, whereas the control rate for photon therapy of patients with high pO_2 status was more than twice that with low pO_2.

It has been suggested that further improvements in treatment outcome with carbon therapy can be achieved by considering the time course of reoxygenation of hypoxic areas in the tumor. According to Antonovic et al. (138), the number of fractions and the dose per fraction for carbon therapy can be optimized by taking into account the effect of local oxygenation changes on tumor control probability. In the future, more detailed studies are necessary to take into account the OER and rates of reoxygenation in treatment planning for carbon-ion RT, as are underway (134, 135).

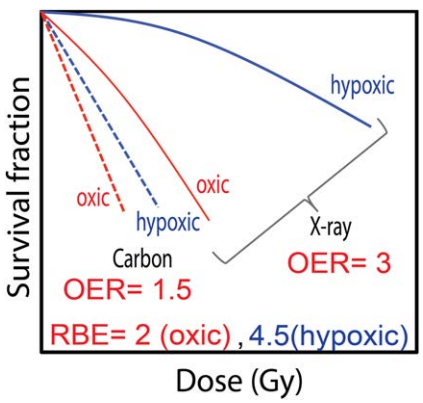

FIGURE 8 | The dependence of survival curves on oxygen concentration typically observed after exposure to X-rays and carbon ions. The importance of the oxygen effect is reduced with high-LET carbon-ion irradiation as is apparent in the small separation of the survival curves compared to that seen with X-rays. The large difference between the cell response in air and hypoxia for X-rays results in a $RBE_{hypoxic}$ that is greater than RBE_{oxic}.

DOSE FRACTIONATION WITH CHARGED PARTICLES

Fractionated irradiation is a valuable tool in conventional RT to reduce early and late effects in normal tissue by allowing repair of sublethal damage or increase tumor response due to reoxygenation of a hypoxic tumor. The linear quadratic (LQ) model describes cell killing using single-hit and double-hit components (22). The shape of the curve is determined by:

$$SF(D) = e^{-(\alpha D + \beta D^2)}. \quad (1)$$

The α parameter describes the linear component of the curve, while the β component describes the quadratic portion of the curve. The α/β ratio, the point at which linear cell killing is equivalent to quadratic cell killing, is an important parameter used to model cell killing by radiation. Presently, this ratio is used as a staple for predicting the clinical effects in response to RT despite various limitations. A high α/β ratio, seen in many human tumors, suggests a predominance of the α component, implying a decreased response to fractionation and, therefore, clinical benefit from hypofractionation (decreased number of fractions of larger dose per fraction). A lower α/β ratio is usually associated with late responding normal tissue and is the basis for the therapeutic gain achieved using hyperfractionation (increased number of fractions of small dose per fraction), which allows for greater repair/recovery of normal tissues (139). However, some human tumors, e.g., prostate cancer, melanoma, and some sarcomas, may have α/β values similar to late responding tissues (140–142).

In image-guided RT, intensity-modulated RT, and X-ray stereotactic body RT (SBRT), there are tendencies to reduce the number of fractions and increase the dose per fraction (i.e., hypofractionation) (143, 144). With carbon-ion RT, superiority of the physical dose distribution can lead to a reduction in the number of fractions (145), allowing hypofractionation. There are few relevant experimental data using human tumor cells on hypofractionation effects with high-LET charged particles. Experiments involving high-LET fast neutron beams demonstrated that increasing the dose per fraction tended to decrease the RBE for both tumor and normal tissues (146). However, the dose-dependent decrease in the RBE for the tumor was less pronounced than that for normal tissues, such as skin and lung (147). These experiments led to the assumption that the therapeutic gain of carbon-ion RT would increase when the dose per fraction increased. This assumption was confirmed in animal experiments that compared RBE for carbon ions between tumor and skin (148). In additional studies with high-LET radiation, RBE depends on dose and dose per fraction: dose-dependent decrease of RBE was reported after fast neutrons to normal skin, intestine, growing cartilage, and hematopoietic tissues (149), and after Ne-ions to the skin of mice and hamsters (150). The change in dose dependence is caused by the higher α/β ratio of target cells after high-LET radiation than after photons (151).

The value of the α term increases with increasing LET in both tumor and normal tissue, while the issue of whether the value of the β term changes with LET remains controversial (148, 152). In our study (153) by evaluating the therapeutic gain of carbon-ion fractionation using intestinal crypt survival and tumor growth delay (TGD) assays, the values of the α and β terms for the mouse fibrosarcoma (NFSa) tumor are close to those reported by Ando et al. (148), while those for normal tissues are different (**Figure 9**). In addition, the LET-dependent increase (e.g., slope of the regression line) of the α term for NFSa is similar to that for human salivary gland tumor cells (148, 154). LET-dependent increase of α terms for crypt is greater than that for the early skin reaction after daily fractionated doses to leg skin (148), whereas it is similar to that for the late skin reaction after 4-h interval fractionations to foot skin (154). These results indicate that therapeutic gain for carbon-ion RT depends on the normal tissue and fractionation schedule. Further studies with mouse skin and rat spinal cord where the normal tissues were exposed to varying numbers of fractions and doses per fraction of γ-rays and carbon ions have shown that the magnitude of damage repair depends on both the number of fractions and the size of dose per fraction for high-LET radiation (155, 156). It was concluded that repair of radiation injury is much reduced with dose per fraction, especially with 125 keV/μm carbon ions. Unfortunately, few studies of fractionation effects with carbon ions have been performed with tumors, especially human tumors.

As discussed above, hypoxia is one of the main factors reducing local control in some solid tumors, and fractionation in RT may have an advantage because of reoxygenation of the hypoxic areas. It has been reported that reoxygenation in several tumors irradiated with carbon ions occurs earlier than that in those irradiated with photons (157, 158). Reoxygenation in the NFSa fibrosarcoma was observed at 4 days, 1 day, and within 0.5 days after irradiation with photons, low-LET carbon ions (14 and 18 keV/μm) and high-LET carbon ions (43, 58, and 74 keV/μm), respectively (157). Thus, short-term fractionated irradiation with carbon ions may be effective in the treatment of tumors, at least in part, because of altered reoxygenation.

The clinical RBE is replaced by an LET-dependent RBE for *in vitro* cell killing data determined in single-dose experiments and is employed to design the SOBP and in the Japanese treatment planning system for carbon-ion RT (159, 160). A question remains as to whether the biological effects with fractionated doses are also uniform within the SOBP. Uzawa et al. evaluated uniformity of a new ridge filter that was designed based on α and β values for various LETs to cause mouse foot skin reaction by carbon-ion fractionated irradiation (154). The physical dose distribution of the new ridge filter was almost identical to the ridge filter designed based on *in vitro* cell kill. While the LQ model is useful for conversion between relatively low radiation doses as used in conventional RT, it has been suggested that it is not applicable to higher fractional doses or smaller fraction numbers (6, 161). It has been questioned whether the LQ model is applicable to hypofractionated carbon-ion RT. For establishment of the optimal fractionation strategy in carbon-ion RT, applicability of the LQ model should be investigated in future studies.

With photon RT, the rapidly expanding use of hypofractionation even to the extreme of single fractions as used in stereotactic radiosurgery (SRS) and SBRT has lead to recent discussion about whether "new" biology should be advanced to explain the greater than expected anti-tumor efficacy of some hypofractionation

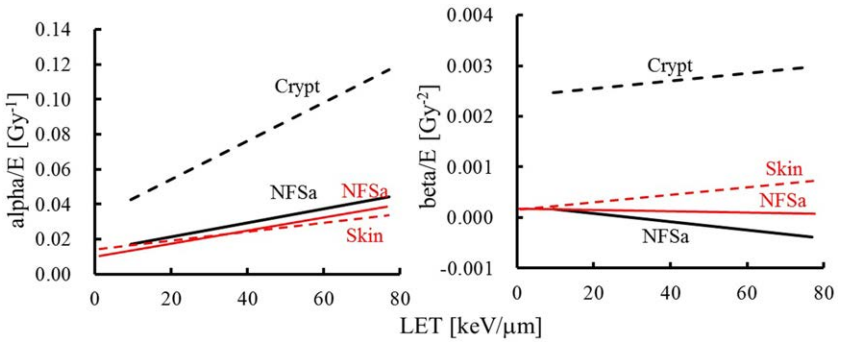

FIGURE 9 | α and β terms for mouse normal tissues and tumors plotted against LET. The comparison of survival parameters of Ando et al. (red) (148) and our study (153) using crypt survival and tumor growth delay assays (black). The solid lines show NFSa tumor and broken lines show the normal tissues (crypt or skin).

regimens. Some have proposed that consideration of only the clonogenic survival of only the tumor cells is not sufficient to account for the observed responses [e.g., Ref. (162, 163)], although not all agree [e.g., Ref. (164–166)]. Brown et al. reviewed the clinical data for early-stage NSCLC and suggested that radiobiological modeling with the LQ model is adequate to explain the efficacy of SRS and SBRT (166). Fowler showed the potential advantages of hypofractionation for prostate cancer by using the LQ model and concluded that use of the LQ model can yield consistent results, for example, the remarkable agreement for tumor effects of some of the best schedules in regular use (167). It is likely that the same considerations apply to carbon-ion therapy, although few data exist, especially for human tumors in experimental situations. Here, we briefly review some aspects that may pertain.

In some situations, vascular damage may be a dominant pathway for tumor suppression. Irradiation of human tumor xenografts or rodent tumors with 5–10 Gy in a single dose causes relatively mild vascular damages. On the other hand, numerous studies with experimental tumors indicate that irradiation with doses higher than 10 Gy in a single fraction or 20–60 Gy in limited numbers of fractions causes severe vascular damage, including endothelial cell apoptosis, leading to the deterioration of the intratumor microenvironment and indirect death of tumor cells (163, 168, 169). Little is known about the vascular changes in human tumors treated with high-dose hypofractionation, particularly with heavy ions, but experimentation is indicated to address whether radiation-induced vascular damage and the resulting indirect death of tumor cells may play important roles in the response of tumors to high-dose hypofractionation with charged particles.

In addition to potential vascular effects, it has been suggested that high-dose irradiation evokes immune reactions and thereby eradicates tumor cells that escaped radiation-induced death (170, 171). In support of such notion, a recent report showed that ablative RT dramatically increased T-cell priming in lymphoid tissues, leading to reduction/eradication of the primary tumor or distant metastasis in a $CD8^+$ T-cell dependent fashion (170). Several studies have shown that carbon ions induce anti-tumor immunity (172–176), although the effects of high-LET radiation on immune function have not been studied in detail. Hence, enhanced immune reactions might be involved in the response of tumors to high-dose hypofractionation, especially with charged particles (177).

It is also noteworthy that, unlike photon irradiation, particle irradiation may suppress the metastatic potential of cancer cells (172, 178), and a recent paper has shown that there is a decrease in metastasis with decreasing fraction number of carbon ions (179). Clearly, further studies are warranted to gain better insights into the effects of high-dose hypofractionation with heavy ions on tumor vasculature, immune system, and metastasis, and how such biology might impact human tumor RBE values and therapeutic gain.

CONCLUSION

In a recent review of charged particle therapy, Loeffler and Durante (4) stated that "Considering the current uncertainties in clinical results [with charged particles] and the difficulties in performing clinical trials, research in physics and radiobiology should reduce the cost/benefit ratio." In this review, we have focused on discussion of selected aspects of radiobiological data with human tumors exposed to protons and heavier charged particles, raising specific instances where further laboratory research may contribute to improving particle therapy. With increasing understanding of the genetic heterogeneity in human tumors, particularly with regard to alterations in DNA repair pathways, a fruitful research area appears to be elucidation of DNA repair pathways selectively involved in repair of the unique clustered DNA damages caused by charged particles. With increases in such knowledge, the differences can be exploited to identify patients who may be better treated with particles because of characteristics of their tumors and to develop novel pharmacologic approaches that capitalize on the differences in DNA damage and repair. Another area ripe for charged particle biology study with implications to clinical advances is in cancer stem cells. The intriguing observations that cancer stem cells from human tumors may be more effectively killed by carbon ions than by photons begs for further study on mechanisms involved – altered DNA repair? location in a hypoxic niche? – and consideration of how to exploit such a difference

to the advantage of ion therapy. Finally, the biology underlying the notable clinical effectiveness of high dose, hypofractionated charged particles, which may be explained by radiosensitivity of tumor cells themselves at high doses or may involve vasculature and/or immune system responses, requires further elucidation.

This article has focused on data from *in vitro* studies of human tumor cells, for reasons described in the Section "Introduction" and recognizing that there are limitations when applying *in vitro* findings to the *in vivo* and clinical situations. However, it is also clear that because of the stochastic natures of radiation-induced cell killing and tumor cure and the, albeit simplistic, relationship of the two endpoints *via* $TCP = e^{-(SF \times M)}$ (where TCP is tumor control probability, SF is surviving fraction, and M is number of clonogens), understanding effects of radiations of varying qualities on the tumor cells themselves can be informative. The questions and issues raised herein require follow-up *in vivo* studies leading to transfer of knowledge to the clinic, but guidance from the *in vitro* work, e.g., on use of DNA damage assays and exploiting DNA repair as biomarkers for patient selection or using *in vitro* survival α/β information to help guide design of hypofractionation protocols *in vivo* and in the clinic, is critical.

AUTHOR CONTRIBUTIONS

KH, HK, TK, AP, YY, QL, HW, and AT contributed to the conception, drafting, and revising of the review article.

ACKNOWLEDGMENTS

This work was supported by the National Cancer Institute of the National Institutes of Health under Award Number R21CA182259 (KH), the Gunma University Initiative for Advanced Research (KH), Federal Share of program income earned by Massachusetts General Hospital on C06 CA059267, Proton Therapy Research and Treatment Center (HW and KH), Ministry of Education, Culture, Sports, Science and Technology of Japan (MEXT) Number 15H05945 (AT), Gunma University Program for Cultivating Global Leaders in Heavy Ion Therapeutics and Engineering of the MEXT (AP), Research Project with heavy ions at the Gunma University Heavy Ion Medical Center (HK, TK, AP, YY, and AT). The content is solely the responsibility of the authors and does not necessarily represent the official views of the National Institutes of Health.

REFERENCES

1. Wilson RR. Radiological use of fast protons. *Radiology* (1946) **47**:487–91. doi:10.1148/47.5.487
2. Skarsgard LD. Radiobiology with heavy charged particles: a historical review. *Phys Med* (1998) **14**(Suppl. 1):1–19.
3. Suit H, DeLaney T, Goldberg S, Paganetti H, Clasie B, Gerweck L, et al. Proton vs carbon ion beams in the definitive radiation treatment of cancer patients. *Radiother Oncol* (2010) **95**:3–22. doi:10.1016/j.radonc.2010.01.015
4. Loeffler JS, Durante M. Charged particle therapy – optimization, challenges and future directions. *Nat Rev Clin Oncol* (2013) **10**:411–24. doi:10.1038/nrclinonc.2013.79
5. Durante M, Loeffler JS. Charged particles in radiation oncology. *Nat Rev Clin Oncol* (2010) **7**:37–43. doi:10.1038/nrclinonc.2009.183
6. Durante M. New challenges in high-energy particle radiobiology. *Br J Radiol* (2014) **87**(1035):20130626. doi:10.1259/bjr.20130626
7. Friedrich T, Scholz U, Elsasser T, Durante M, Scholz M. Systematic analysis of RBE and related quantities using a database of cell survival experiments with ion beam irradiation. *J Radiat Res* (2013) **54**(4):494–514. doi:10.1093/jrr/rrs114
8. Paganetti H, Niemierko A, Ancukiewicz M, Gerweck LE, Goitein M, Loeffler JS, et al. Relative biological effectiveness (RBE) values for proton beam therapy. *Int J Radiat Oncol Biol Phys* (2002) **53**:407–21. doi:10.1016/S0360-3016(02)02754-2
9. Friedrich T, Grun R, Scholz U, Elsasser T, Durante M, Scholz M. Sensitivity analysis of the relative biological effectiveness predicted by the local effect model. *Phys Med Biol* (2013) **58**(19):6827–49. doi:10.1088/0031-9155/58/19/6827
10. Barendsen GW. Responses of cultured cells, tumors, and normal tissues to radiation of different linear energy transfer. *Curr Top Radiat Res Q* (1968) **4**:293–356.
11. Blakely EA, Ngo FQH, Curtis SB, Tobias CA. Heavy-ion radiobiology: cellular studies. *Adv Radiat Biol* (1984) **11**:295–389. doi:10.1016/B978-0-12-035411-5.50013-7
12. Sorensen BS, Overgaard J, Bassler N. In vitro RBE-LET dependence for multiple particle types. *Acta Oncol* (2011) **50**:757–62. doi:10.3109/0284186X.2011.582518
13. Kraft G, Kramer M, Scholz M. LET, track structure and models. A review. *Radiat Environ Biophys* (1992) **31**:161–80. doi:10.1007/BF01214825
14. Goodhead DT. Initial events in the cellular effects of ionizing radiations: clustered damage in DNA. *Int J Radiat Biol* (1994) **65**:7–17. doi:10.1080/09553009414550021
15. Ward JF. The complexity of DNA damage: relevance to biological consequences. *Int J Radiat Biol* (1994) **66**:427–32. doi:10.1080/09553009414551401
16. Hada M, Sutherland BM. Spectrum of complex DNA damages depends on the incident radiation. *Radiat Res* (2006) **165**:223–30. doi:10.1667/RR3498.1
17. Goodhead DT. Mechanisms for the biological effectiveness of high-LET radiations. *J Radiat Res* (1999) **40**(Suppl):1–13. doi:10.1269/jrr.40.S1
18. Goodhead DT. Fifth Warren K. Sinclair keynote address: issues in quantifying the effects of low-level radiation. *Health Phys* (2009) **97**(5):394–406. doi:10.1097/HP.0b013e3181ae8acf
19. Nikjoo H, O'Neill P, Wilson WE, Goodhead DT. Computational approach for determining the spectrum of DNA damage induced by ionizing radiation. *Radiat Res* (2001) **156**:577–83. doi:10.1667/0033-7587(2001)156[0577:CAFDTS]2.0.CO;2
20. Georgakilas AG, O'Neill P, Stewart RD. Induction and repair of clustered DNA lesions: what do we know so far? *Radiat Res* (2013) **180**(1):100–9. doi:10.1667/RR3041.1
21. Sridharan DM, Asaithamby A, Bailey SM, Costes SV, Doetsch PW, Dynan WS, et al. Understanding cancer development processes after HZE-particle exposure: roles of ROS, DNA damage repair and inflammation. *Radiat Res* (2015) **183**(1):1–26. doi:10.1667/RR13804.1
22. Hall EJ, Giaccia A. *Radiobiology for the Radiologist*. Philadelphia, PA: Lippincott Williams & Wilkins Publishers (2012).
23. Morgan WF, Sowa MB. Non-targeted effects induced by ionizing radiation: mechanisms and potential impact on radiation induced health effects. *Cancer Lett* (2015) **356**(1):17–21. doi:10.1016/j.canlet.2013.09.009
24. Kadhim MA, Hill MA. Non-targeted effects of radiation exposure: recent advances and implications. *Radiat Prot Dosimetry* (2015) **166**(1–4):118–24. doi:10.1093/rpd/ncv167
25. Sowa MB, Goetz W, Baulch JE, Pyles DN, Dziegielewski J, Yovino S, et al. Lack of evidence for low-LET radiation induced bystander response in normal human fibroblasts and colon carcinoma cells. *Int J Radiat Biol* (2010) **86**(2):102–13. doi:10.3109/09553000903419957
26. Yang H, Asaad N, Held KD. Medium-mediated intercellular communication is involved in bystander responses of X-irradiated normal human fibroblasts. *Oncogene* (2005) **24**:2096–103. doi:10.1038/sj.onc.1208439
27. de Toledo SM, Buonanno M, Li M, Asaad N, Qin Y, Gonon G, et al. The impact of adaptive and non-targeted effects in the biological responses to low dose/low fluence ionizing radiation: the modulating effect of linear energy transfer. *Health Phys* (2011) **100**(3):290–2. doi:10.1097/HP.0b013e31820832d8
28. McMahon SJ, McGarry CK, Butterworth KT, Jain S, O'Sullivan JM, Hounsell AR, et al. Cellular signalling effects in high precision radiotherapy. *Phys Med Biol* (2015) **60**(11):4551–64. doi:10.1088/0031-9155/60/11/4551

29. Asur R, Butterworth KT, Penagaricano JA, Prise KM, Griffin RJ. High dose bystander effects in spatially fractionated radiation therapy. *Cancer Lett* (2015) **356**(1):52–7. doi:10.1016/j.canlet.2013.10.032
30. Willers H, Dahm-Daphi J, Powell SN. Repair of radiation damage to DNA. *Br J Cancer* (2004) **90**:1297–301. doi:10.1038/sj.bjc.6601729
31. Hiom K. Coping with DNA double strand breaks. *DNA Repair (Amst)* (2010) **9**(12):1256–63. doi:10.1016/j.dnarep.2010.09.018
32. Lieber MR. The mechanism of double-strand DNA break repair by the nonhomologous DNA end-joining pathway. *Annu Rev Biochem* (2010) **79**:181–211. doi:10.1146/annurev.biochem.052308.093131
33. Jeggo PA, Geuting V, Lobrich M. The role of homologous recombination in radiation-induced double-strand break repair. *Radiother Oncol* (2011) **101**(1):7–12. doi:10.1016/j.radonc.2011.06.019
34. Willers H, Pfaffle HN, Zou L. Targeting homologous recombination repair in cancer. In: Kelley MR, editor. *DNA Repair in Cancer Therapy: Molecular Targets and Clinical Applications*. Waltham, MA: Academic Press (2012). p. 119–60.
35. Klein Douwel D, Boonen RA, Long DT, Szypowska AA, Raschle M, Walter JC, et al. XPF-ERCC1 acts in unhooking DNA interstrand crosslinks in cooperation with FANCD2 and FANCP/SLX4. *Mol Cell* (2014) **54**(3):460–71. doi:10.1016/j.molcel.2014.03.015
36. Frankenberg-Schwager M, Gebauer A, Koppe C, Wolf H, Pralle E, Frankenberg D. Single-strand annealing, conservative homologous recombination, nonhomologous DNA end joining, and the cell cycle-dependent repair of DNA double-strand breaks induced by sparsely or densely ionizing radiation. *Radiat Res* (2009) **171**(3):265–73. doi:10.1667/RR0784.1
37. Zafar F, Seidler SB, Kronenberg A, Schild D, Wiese C. Homologous recombination contributes to the repair of DNA double-strand breaks induced by high-energy iron ions. *Radiat Res* (2010) **173**(1):27–39. doi:10.1667/RR1910.1
38. Yajima H, Fujisawa H, Nakajima NI, Hirakawa H, Jeggo PA, Okayasu R, et al. The complexity of DNA double strand breaks is a critical factor enhancing end-resection. *DNA Repair (Amst)* (2013) **12**(11):936–46. doi:10.1016/j.dnarep.2013.08.009
39. Takahashi A, Kubo M, Ma H, Nakagawa A, Yoshida Y, Isono M, et al. Nonhomologous end-joining repair plays a more important role than homologous recombination repair in defining radiosensitivity after exposure to high-LET radiation. *Radiat Res* (2014) **182**(3):338–44. doi:10.1667/RR13782.1
40. Steinstrater O, Scholz U, Friedrich T, Kramer M, Grun R, Durante M, et al. Integration of a model-independent interface for RBE predictions in a treatment planning system for active particle beam scanning. *Phys Med Biol* (2015) **60**(17):6811–31. doi:10.1088/0031-9155/60/17/6811
41. Inaniwa T, Kanematsu N, Matsufuji N, Kanai T, Shirai T, Noda K, et al. Reformulation of a clinical-dose system for carbon-ion radiotherapy treatment planning at the National Institute of Radiological Sciences, Japan. *Phys Med Biol* (2015) **60**(8):3271–86. doi:10.1088/0031-9155/60/8/3271
42. Paganetti H. Relative biological effectiveness (RBE) values for proton beam therapy. Variations as a function of biological endpoint, dose, and linear energy transfer. *Phys Med Biol* (2014) **59**(22):R419–72. doi:10.1088/0031-9155/59/22/R419
43. Grosse N, Fontana A, Hug EB, Lomax A, Coray A, Augsburger M, et al. Deficiency in homologous recombination renders mammalian cells more sensitive to proton versus photon irradiation. *Int J Radiat Oncol Biol Phys* (2014) **88**(1):175–81. doi:10.1016/j.ijrobp.2013.09.041
44. Liu Q, Ghosh P, Magpayo N, Testa M, Tang S, Gheorghiu L, et al. Lung cancer cell line screen links Fanconi anemia/BRCA pathway defects to increased relative biological effectiveness of proton radiation. *Int J Radiat Oncol Biol Phys* (2015) **91**(5):1081–9. doi:10.1016/j.ijrobp.2014.12.046
45. Fontana AO, Augsburger MA, Grosse N, Guckenberger M, Lomax AJ, Sartori AA, et al. Differential DNA repair pathway choice in cancer cells after proton- and photon-irradiation. *Radiother Oncol* (2015) **116**(3):374–80. doi:10.1016/j.radonc.2015.08.014
46. Guan F, Bronk L, Titt U, Lin SH, Mirkovic D, Kerr MD, et al. Spatial mapping of the biologic effectiveness of scanned particle beams: towards biologically optimized particle therapy. *Sci Rep* (2015) **5**:9850. doi:10.1038/srep09850
47. Garnett MJ, Edelman EJ, Heidorn SJ, Greenman CD, Dastur A, Lau KW, et al. Systematic identification of genomic markers of drug sensitivity in cancer cells. *Nature* (2012) **483**(7391):570–5. doi:10.1038/nature11005
48. Imielinski M, Berger AH, Hammerman PS, Hernandez B, Pugh TJ, Hodis E, et al. Mapping the hallmarks of lung adenocarcinoma with massively parallel sequencing. *Cell* (2012) **150**(6):1107–20. doi:10.1016/j.cell.2012.08.029
49. Network CGAR. Comprehensive genomic characterization of squamous cell lung cancers. *Nature* (2012) **489**(7417):519–25. doi:10.1038/nature11404
50. Wang AT, Smogorzewska A. SnapShot: Fanconi anemia and associated proteins. *Cell* (2015) **160**(1–2):354–e1. doi:10.1016/j.cell.2014.12.031
51. Rostek C, Turner EL, Robbins M, Rightnar S, Xiao W, Obenaus A, et al. Involvement of homologous recombination repair after proton-induced DNA damage. *Mutagenesis* (2008) **23**(2):119–29. doi:10.1093/mutage/gem055
52. Gulston M, Fulford J, Jenner T, de Lara C, O'Neill P. Clustered DNA damage induced by gamma radiation in human fibroblasts (HF19), hamster (V79-4) cells and plasmid DNA is revealed as Fpg and Nth sensitive sites. *Nucleic Acids Res* (2002) **30**(15):3464–72. doi:10.1093/nar/gkf467
53. Sutherland BM, Bennett PV, Sutherland JC, Laval J. Clustered DNA damages induced by X-rays in human cells. *Radiat Res* (2002) **157**:611–6. doi:10.1667/0033-7587(2002)157[0611:CDDIBX]2.0.CO;2
54. Ando K. Review of RBE data on ion beams from Chiba: influence of LET and biological system. *Dose Reporting in Ion Beam Therapy*. Vienna: International Atomic Energy Agency (2007). p. 89–98.
55. Ando K, Kase Y. Biological characteristics of carbon-ion therapy. *Int J Radiat Biol* (2009) **85**(9):715–28. doi:10.1080/09553000903072470
56. Ando S, Nojima K, Ishihara H, Suzuki M, Ando M, Majima H, et al. Induction by carbon-ion irradiation of the expression of vascular endothelial growth factor in lung carcinoma cells. *Int J Radiat Biol* (2000) **76**(8):1121–7. doi:10.1080/09553000050111596
57. Belli M, Bettega D, Calzolari P, Cherubini R, Cuttone G, Durante M, et al. Effectiveness of monoenergetic and spread-out Bragg peak carbon-ions for inactivation of various normal and tumour human cell lines. *J Radiat Res* (2008) **49**(6):597–607. doi:10.1269/jrr.08052
58. Combs SE, Bohl J, Elsasser T, Weber KJ, Schulz-Ertner D, Debus J, et al. Radiobiological evaluation and correlation with the local effect model (LEM) of carbon ion radiation therapy and temozolomide in glioblastoma cell lines. *Int J Radiat Biol* (2009) **85**(2):126–37. doi:10.1080/09553000802641151
59. Furusawa Y, Fukutsu K, Aoki M, Itsukaichi H, Eguchi-Kasai K, Ohara H, et al. Inactivation of aerobic and hypoxic cells from three different cell lines by accelerated (3)He-, (12)C- and (20)Ne-ion beams. *Radiat Res* (2000) **154**(5):485–96. doi:10.1667/0033-7587(2000)154[0485:IOAAHC]2.0.CO;2
60. Ito A, Nakano H, Kusano Y, Hirayama R, Furusawa Y, Murayama C, et al. Contribution of indirect action to radiation-induced mammalian cell inactivation: dependence on photon energy and heavy-ion LET. *Radiat Res* (2006) **165**(6):703–12. doi:10.1667/RR3557.1
61. Iwadate Y, Mizoe J, Osaka Y, Yamaura A, Tsujii H. High linear energy transfer carbon radiation effectively kills cultured glioma cells with either mutant or wild-type p53. *Int J Radiat Oncol Biol Phys* (2001) **50**(3):803–8. doi:10.1016/S0360-3016(01)01514-0
62. Kagawa K, Murakami M, Hishikawa Y, Abe M, Akagi T, Yanou T, et al. Preclinical biological assessment of proton and carbon ion beams at Hyogo Ion Beam Medical Center. *Int J Radiat Oncol Biol Phys* (2002) **54**(3):928–38. doi:10.1016/S0360-3016(02)02949-8
63. Kamlah F, Hanze J, Arenz A, Seay U, Hasan D, Juricko J, et al. Comparison of the effects of carbon ion and photon irradiation on the angiogenic response in human lung adenocarcinoma cells. *Int J Radiat Oncol Biol Phys* (2011) **80**(5):1541–9. doi:10.1016/j.ijrobp.2011.03.033
64. Matsui Y, Asano T, Kenmochi T, Iwakawa M, Imai T, Ochiai T. Effects of carbon-ion beams on human pancreatic cancer cell lines that differ in genetic status. *Am J Clin Oncol* (2004) **27**(1):24–8. doi:10.1097/01.coc.0000046037.75545.AD
65. Matsumoto Y, Iwakawa M, Furusawa Y, Ishikawa K, Aoki M, Imadome K, et al. Gene expression analysis in human malignant melanoma cell lines exposed to carbon ions. *Int J Radiat Biol* (2008) **84**:299–314. doi:10.1080/09553000801953334
66. Matsuzaki H, Miyamoto T, Miyazawa Y, Okazumi S, Koide Y, Isono K. Biological effects of heavy ion beam on human breast cancers. *Breast Cancer* (1998) **5**(3):261–8. doi:10.1007/BF02966706

67. Ofuchi T, Suzuki M, Kase Y, Ando K, Isono K, Ochiai T. Chromosome breakage and cell lethality in human hepatoma cells irradiated with X rays and carbon-ion beams. *J Radiat Res* (1999) **40**(2):125–33. doi:10.1269/jrr.40.125
68. Persson LM, Edgren MR, Stenerlow B, Lind BK, Hedlof I, Jernberg AR, et al. Relative biological effectiveness of boron ions on human melanoma cells. *Int J Radiat Biol* (2002) **78**(8):743–8. doi:10.1080/09553000210140091
69. Stenerlow B, Pettersson OA, Essand M, Blomquist E, Carlsson J. Irregular variations in radiation sensitivity when the linear energy transfer is increased. *Radiother Oncol* (1995) **36**(2):133–42. doi:10.1016/0167-8140(95)01591-4
70. Suzuki M, Kase Y, Yamaguchi H, Kanai T, Ando K. Relative biological effectiveness for cell-killing effect on various human cell lines irradiated with heavy-ion medical accelerator in Chiba (HIMAC) carbon-ion beams. *Int J Radiat Oncol Biol Phys* (2000) **48**(1):241–50. doi:10.1016/S0360-3016(00)00568-X
71. Suzuki M, Kase Y, Nakano T, Kanai T, Ando K. Residual chromatin breaks as biodosimetry for cell killing by carbon ions. *Adv Space Res* (1998) **22**(12):1663–71. doi:10.1016/S0273-1177(99)00031-9
72. Suzuki M, Kase Y, Kanai T, Ando K. Correlation between cell killing and residual chromatin breaks measured by PCC in six human cell lines irradiated with different radiation types. *Int J Radiat Biol* (2000) **76**(9):1189–96. doi:10.1080/09553000050134429
73. Suzuki M, Kase Y, Kanai T, Ando K. Change in radiosensitivity with fractionated-dose irradiation of carbon-ion beams in five different human cell lines. *Int J Radiat Oncol Biol Phys* (2000) **48**(1):251–8. doi:10.1016/S0360-3016(00)00606-4
74. Takahashi A, Ohnishi K, Tsuji K, Matsumoto H, Aoki H, Wang X, et al. WAF1 accumulation by carbon-ion beam and alpha-particle irradiation in human glioblastoma cultured cells. *Int J Radiat Biol* (2000) **76**(3):335–41. doi:10.1080/095530000138673
75. Takahashi A, Ohnishi K, Ota I, Asakawa I, Tamamoto T, Furusawa Y, et al. p53-dependent thermal enhancement of cellular sensitivity in human squamous cell carcinomas in relation to LET. *Int J Radiat Biol* (2001) **77**(10):1043–51. doi:10.1080/09553000110066095
76. Takahashi A, Matsumoto H, Yuki K, Yasumoto J, Kajiwara A, Aoki M, et al. High-LET radiation enhanced apoptosis but not necrosis regardless of p53 status. *Int J Radiat Oncol Biol Phys* (2004) **60**(2):591–7. doi:10.1016/j.ijrobp.2004.05.062
77. Takahashi A, Matsumoto H, Furusawa Y, Ohnishi K, Ishioka N, Ohnishi T. Apoptosis induced by high-LET radiations is not affected by cellular p53 gene status. *Int J Radiat Biol* (2005) **81**:581–6. doi:10.1080/09553000500280484
78. Tsuboi K, Tsuchida Y, Nose T, Ando K. Cytotoxic effect of accelerated carbon beams on glioblastoma cell lines with p53 mutation: clonogenic survival and cell-cycle analysis. *Int J Radiat Biol* (1998) **74**(1):71–9. doi:10.1080/095530098141744
79. Tsuboi K, Moritake T, Tsuchida Y, Tokuuye K, Matsumura A, Ando K. Cell cycle checkpoint and apoptosis induction in glioblastoma cells and fibroblasts irradiated with carbon beam. *J Radiat Res* (2007) **48**(4):317–25. doi:10.1269/jrr.06081
80. Tsuchida Y, Tsuboi K, Ohyama H, Ohno T, Nose T, Ando K. Cell death induced by high-linear-energy transfer carbon beams in human glioblastoma cell lines. *Brain Tumor Pathol* (1998) **15**(2):71–6. doi:10.1007/BF02478886
81. Yamakawa N, Takahashi A, Mori E, Imai Y, Furusawa Y, Ohnishi K, et al. High LET radiation enhances apoptosis in mutated p53 cancer cells through caspase-9 activation. *Cancer Sci* (2008) **99**(7):1455–60. doi:10.1111/j.1349-7006.2008.00818.x
82. Ferrandon S, Magne N, Battiston-Montagne P, Hau-Desbat NH, Diaz O, Beuve M, et al. Cellular and molecular portrait of eleven human glioblastoma cell lines under photon and carbon ion irradiation. *Cancer Lett* (2015) **360**(1):10–6. doi:10.1016/j.canlet.2015.01.025
83. Schlaich F, Brons S, Haberer T, Debus J, Combs SE, Weber KJ. Comparison of the effects of photon versus carbon ion irradiation when combined with chemotherapy in vitro. *Radiat Oncol* (2013) **8**:260. doi:10.1186/1748-717X-8-260
84. Beuve M, Alphonse G, Maalouf M, Colliaux A, Battiston-Montagne P, Jalade P, et al. Radiobiologic parameters and local effect model predictions for head-and-neck squamous cell carcinomas exposed to high linear energy transfer ions. *Int J Radiat Oncol Biol Phys* (2008) **71**(2):635–42. doi:10.1016/j.ijrobp.2007.10.050
85. Kato TA, Tsuda A, Uesaka M, Fujimori A, Kamada T, Tsujii H, et al. In vitro characterization of cells derived from chordoma cell line U-CH1 following treatment with X-rays, heavy ions and chemotherapeutic drugs. *Radiat Oncol* (2011) **6**:116. doi:10.1186/1748-717X-6-116
86. Takiguchi Y, Miyamoto T, Nagao K, Kuriyama T. Assessment of the homogeneous efficacy of carbon ions in the spread-out Bragg peak for human lung cancer cell lines. *Radiat Med* (2007) **25**(6):272–7. doi:10.1007/s11604-007-0134-6
87. Habermehl D, Ilicic K, Dehne S, Rieken S, Orschiedt L, Brons S, et al. The relative biological effectiveness for carbon and oxygen ion beams using the raster-scanning technique in hepatocellular carcinoma cell lines. *PLoS One* (2014) **9**(12):e113591. doi:10.1371/journal.pone.0113591
88. Fujisawa H, Genik PC, Kitamura H, Fujimori A, Uesaka M, Kato TA. Comparison of human chordoma cell-kill for 290 MeV/n carbon ions versus 70 MeV protons in vitro. *Radiat Oncol* (2013) **8**:91. doi:10.1186/1748-717X-8-91
89. Oonishi K, Cui X, Hirakawa H, Fujimori A, Kamijo T, Yamada S, et al. Different effects of carbon ion beams and X-rays on clonogenic survival and DNA repair in human pancreatic cancer stem-like cells. *Radiother Oncol* (2012) **105**(2):258–65. doi:10.1016/j.radonc.2012.08.009
90. El Shafie RA, Habermehl D, Rieken S, Mairani A, Orschiedt L, Brons S, et al. In vitro evaluation of photon and raster-scanned carbon ion radiotherapy in combination with gemcitabine in pancreatic cancer cell lines. *J Radiat Res* (2013) **54**(Suppl 1):i113–9. doi:10.1093/jrr/rrt052
91. Combs SE, Zipp L, Rieken S, Habermehl D, Brons S, Winter M, et al. In vitro evaluation of photon and carbon ion radiotherapy in combination with chemotherapy in glioblastoma cells. *Radiat Oncol* (2012) **7**:9. doi:10.1186/1748-717X-7-9
92. Ando K, Kase Y, Matsufuji N. Light ion radiation biology. In: Brahme A, editor. *Comprehensive Biomedical Physics*. Amsterdam: Elsevier (2014). p. 195–210.
93. Brown JM, Attardi LD. The role of apoptosis in cancer development and treatment response. *Nat Rev Cancer* (2005) **5**(3):231–7. doi:10.1038/nrc1560
94. Held KD. Radiation-induced apoptosis and its relationship to loss of clonogenic survival. *Apoptosis* (1997) **2**:265–82. doi:10.1023/A:1026485003280
95. Tommasino F, Durante M. Proton radiobiology. *Cancers* (2015) **7**(1):353–81. doi:10.3390/cancers7010353
96. Brown JM, Wouters BG. Apoptosis, p53, and tumor cell sensitivity to anticancer agents. *Cancer Res* (1999) **59**:1391–9.
97. Grun R, Friedrich T, Kramer M, Zink K, Durante M, Engenhart-Cabillic R, et al. Assessment of potential advantages of relevant ions for particle therapy: a model based study. *Med Phys* (2015) **42**(2):1037–47. doi:10.1118/1.4905374
98. Wulf H, Kraft-Weyrather W, Miltenburger HG, Blakely EA, Tobias CA, Kraft G. Heavy-ion effects on mammalian cells: inactivation measurements with different cell lines. *Radiat Res Suppl* (1985) **8**:S122–34. doi:10.2307/3576639
99. Belli M, Cera F, Cherubini R, Haque AMI, Ianzini F, Moschini G, et al. The RBE of protons for cell inactivation: the experience with V79 cells. In: Amaldi U, Larsson B, editors. *Hadrontherapy in Oncology*. Amsterdam: Elsevier Science (1994). p. 702–5.
100. Cucinotta FA, Kim MH, Chappell LJ. *Space Radiation Cancer Risk Projections and Uncertainties – 2012. NASA/TP-2013-217375* (2013). Available from: http://ston.jsc.nasa.gov/collections/TRS
101. Friedrich T, Scholz U, Elsasser T, Durante M, Scholz M. Calculation of the biological effects of ion beams based on the microscopic spatial damage distribution pattern. *Int J Radiat Biol* (2012) **88**(1–2):103–7. doi:10.3109/09553002.2011.611213
102. Bassler N, Toftegaard J, Luhr A, Sorensen BS, Scifoni E, Kramer M, et al. LET-painting increases tumour control probability in hypoxic tumours. *Acta Oncol* (2014) **53**(1):25–32. doi:10.3109/0284186X.2013.832835
103. Kamada T, Tsujii H, Blakely EA, Debus J, De Neve W, Durante M, et al. Carbon ion radiotherapy in Japan: an assessment of 20 years of clinical experience. *Lancet Oncol* (2015) **16**(2):e93–100. doi:10.1016/S1470-2045(14)70412-7
104. Steel GG, McMillan TJ, Peacock JH. The radiobiology of human cells and tissues. In vitro radiosensitivity. The picture has changed in the 1980s. *Int J Radiat Biol* (1989) **56**(5):525–37. doi:10.1080/09553008914551691
105. Steel GG, Peacock JH. Why are some human tumours more radiosensitive than others? *Radiother Oncol* (1989) **15**(1):63–72. doi:10.1016/0167-8140(89)90119-9

106. Bao S, Wu Q, McLendon RE, Hao Y, Shi Q, Hjelmeland AB, et al. Glioma stem cells promote radioresistance by preferential activation of the DNA damage response. *Nature* (2006) **444**:756–60. doi:10.1038/nature05236
107. Phillips TM, McBride WH, Pajonk F. The response of CD24(-/low)/CD44+ breast cancer-initiating cells to radiation. *J Natl Cancer Inst* (2006) **98**:1777–85. doi:10.1093/jnci/djj495
108. Diehn M, Cho RW, Lobo NA, Kalisky T, Dorie MJ, Kulp AN, et al. Association of reactive oxygen species levels and radioresistance in cancer stem cells. *Nature* (2009) **458**(7239):780–3. doi:10.1038/nature07733
109. Cui X, Oonishi K, Tsujii H, Yasuda T, Matsumoto Y, Furusawa Y, et al. Effects of carbon ion beam on putative colon cancer stem cells and its comparison with X-rays. *Cancer Res* (2011) **71**(10):3676–87. doi:10.1158/0008-5472.CAN-10-2926
110. Pardal R, Clarke MF, Morrison SJ. Applying the principles of stem-cell biology to cancer. *Nat Rev Cancer* (2003) **3**:895–902. doi:10.1038/nrc1232
111. Khan IN, Al-Karim S, Bora RS, Chaudhary AG, Saini KS. Cancer stem cells: a challenging paradigm for designing targeted drug therapies. *Drug Discov Today* (2015) **20**(10):1205–16. doi:10.1016/j.drudis.2015.06.013
112. Pajonk F, Vlashi E, McBride WH. Radiation resistance of cancer stem cells: the 4 R's of radiobiology revisited. *Stem Cells* (2010) **28**:639–48. doi:10.1002/stem.318
113. Vlashi E, Kim K, Lagadec C, Donna LD, McDonald JT, Eghbali M, et al. In vivo imaging, tracking, and targeting of cancer stem cells. *J Natl Cancer Inst* (2009) **101**(5):350–9. doi:10.1093/jnci/djn509
114. Calabrese C, Poppleton H, Kocak M, Hogg TL, Fuller C, Hamner B, et al. A perivascular niche for brain tumor stem cells. *Cancer Cell* (2007) **11**(1):69–82. doi:10.1016/j.ccr.2006.11.020
115. Ishimoto T, Nagano O, Yae T, Tamada M, Motohara T, Oshima H, et al. CD44 variant regulates redox status in cancer cells by stabilizing the xCT subunit of system xc(-) and thereby promotes tumor growth. *Cancer Cell* (2011) **19**(3):387–400. doi:10.1016/j.ccr.2011.01.038
116. Yang G, Quan Y, Wang W, Fu Q, Wu J, Mei T, et al. Dynamic equilibrium between cancer stem cells and non-stem cancer cells in human SW620 and MCF-7 cancer cell populations. *Br J Cancer* (2012) **106**(9):1512–9. doi:10.1038/bjc.2012.126
117. Piao LS, Hur W, Kim TK, Hong SW, Kim SW, Choi JE, et al. CD133+ liver cancer stem cells modulate radioresistance in human hepatocellular carcinoma. *Cancer Lett* (2012) **315**(2):129–37. doi:10.1016/j.canlet.2011.10.012
118. Shimura T, Noma N, Oikawa T, Ochiai Y, Kakuda S, Kuwahara Y, et al. Activation of the AKT/cyclin D1/Cdk4 survival signaling pathway in radioresistant cancer stem cells. *Oncogenesis* (2012) **1**:e12. doi:10.1038/oncsis.2012.12
119. Xia P, Xu XY. PI3K/Akt/mTOR signaling pathway in cancer stem cells: from basic research to clinical application. *Am J Cancer Res* (2015) **5**(5):1602–9.
120. Sai S, Wakai T, Vares G, Yamada S, Kamijo T, Kamada T, et al. Combination of carbon ion beam and gemcitabine causes irreparable DNA damage and death of radioresistant pancreatic cancer stem-like cells in vitro and in vivo. *Oncotarget* (2015) **6**(8):5517–35. doi:10.18632/oncotarget.3584
121. Quan Y, Wang W, Fu Q, Mei T, Wu J, Li J, et al. Accumulation efficiency of cancer stem-like cells post γ-ray and proton irradiation. *Nucl Instr Meth Phys Res B* (2012) **286**:341–5. doi:10.1016/j.nimb.2011.11.019
122. Fu Q, Quan Y, Wang W, Mei T, Wu J, Li J, et al. Response of cancer stem-like cells and non-stem cancer cells to proton and γ-ray irradiation. *Nucl Instr Meth Phys Res B* (2012) **286**:346–50. doi:10.1016/j.nimb.2012.01.032
123. Blakely EA, Tobias CA, Yang TCH, Smith KC, Lyman JT. Inactivation of human kidney cells by high-energy monoenergetic heavy-ion beams. *Radiat Res* (1979) **80**:122–60. doi:10.2307/3575121
124. Nakagawa Y, Takahashi A, Kajihara A, Yamakawa N, Imai Y, Ota I, et al. Depression of p53-independent Akt survival signals in human oral cancer cells bearing mutated p53 gene after exposure to high-LET radiation. *Biochem Biophys Res Commun* (2012) **423**(4):654–60. doi:10.1016/j.bbrc.2012.06.004
125. Hamada N, Imaoka T, Masunaga S, Ogata T, Okayasu R, Takahashi A, et al. Recent advances in the biology of heavy-ion cancer therapy. *J Radiat Res* (2010) **51**(4):365–83. doi:10.1269/jrr.09137
126. Takahashi A, Ma H, Nakagawa A, Yoshida Y, Kanai T, Ohno T, et al. Carbon-ion beams efficiently induce cell killing in X-ray resistant human squamous tongue cancer cells. *Int J Med Phys Clin Eng Radiat Oncol* (2014) **3**:133–42. doi:10.4236/ijmpcero.2014.33019
127. Bertrand G, Maalouf M, Boivin A, Battiston-Montagne P, Beuve M, Levy A, et al. Targeting head and neck cancer stem cells to overcome resistance to photon and carbon ion radiation. *Stem Cell Rev* (2014) **10**(1):114–26. doi:10.1007/s12015-013-9467-y
128. Joiner MC, Van der Kogel AJ. *Basic Clinical Radiobiology*. London: Hodder Arnold (2009).
129. Fleming IN, Manavaki R, Blower PJ, West C, Williams KJ, Harris AL, et al. Imaging tumour hypoxia with positron emission tomography. *Br J Cancer* (2015) **112**(2):238–50. doi:10.1038/bjc.2014.610
130. Vaupel P, Harrison L. Tumor hypoxia: causative factors, compensatory mechanisms, and cellular response. *Oncologist* (2004) **9**(Suppl 5):4–9. doi:10.1634/theoncologist.9-90005-4
131. Tinganelli W, Ma NY, Von Neubeck C, Maier A, Schicker C, Kraft-Weyrather W, et al. Influence of acute hypoxia and radiation quality on cell survival. *J Radiat Res* (2013) **54**(Suppl 1):i23–30. doi:10.1093/jrr/rrt065
132. Ma NY, Tinganelli W, Maier A, Durante M, Kraft-Weyrather W. Influence of chronic hypoxia and radiation quality on cell survival. *J Radiat Res* (2013) **54**(Suppl 1):i13–22. doi:10.1093/jrr/rrs135
133. Zolzer F, Streffer C. Increased radiosensitivity with chronic hypoxia in four human tumor cell lines. *Int J Radiat Oncol Biol Phys* (2002) **54**(3):910–20. doi:10.1016/S0360-3016(02)02963-2
134. Wenzl T, Wilkens JJ. Modelling of the oxygen enhancement ratio for ion beam radiation therapy. *Phys Med Biol* (2011) **56**(11):3251–68. doi:10.1088/0031-9155/56/11/006
135. Scifoni E, Tinganelli W, Weyrather WK, Durante M, Maier A, Kramer M. Including oxygen enhancement ratio in ion beam treatment planning: model implementation and experimental verification. *Phys Med Biol* (2013) **58**(11):3871–95. doi:10.1088/0031-9155/58/11/3871
136. Hirayama R, Furusawa Y, Fukawa T, Ando K. Repair kinetics of DNA-DSB induced by X-rays or carbon ions under oxic and hypoxic conditions. *J Radiat Res* (2005) **46**(3):325–32. doi:10.1269/jrr.46.325
137. Nakano T, Suzuki Y, Ohno T, Kato S, Suzuki M, Morita S, et al. Carbon beam therapy overcomes the radiation resistance of uterine cervical cancer originating from hypoxia. *Clin Cancer Res* (2006) **12**(7 Pt 1):2185–90. doi:10.1158/1078-0432.CCR-05-1907
138. Antonovic L, Lindblom E, Dasu A, Bassler N, Furusawa Y, Toma-Dasu I. Clinical oxygen enhancement ratio of tumors in carbon ion radiotherapy: the influence of local oxygenation changes. *J Radiat Res* (2014) **55**(5):902–11. doi:10.1093/jrr/rru020
139. Schlaff CD, Krauze A, Belard A, O'Connell JJ, Camphausen KA. Bringing the heavy: carbon ion therapy in the radiobiological and clinical context. *Radiat Oncol* (2014) **9**(1):88. doi:10.1186/1748-717X-9-88
140. Bentzen SM, Ritter MA. The alpha/beta ratio for prostate cancer: what is it, really? *Radiother Oncol* (2005) **76**(1):1–3. doi:10.1016/j.radonc.2005.06.009
141. Bentzen SM, Overgaard J, Thames HD, Overgaard M, Vejby Hansen P, von der Maase H, et al. Clinical radiobiology of malignant melanoma. *Radiother Oncol* (1989) **16**(3):169–82.
142. Williams MV, Denekamp J, Fowler JF. A review of alpha/beta ratios for experimental tumors: implications for clinical studies of altered fractionation. *Int J Radiat Oncol Biol Phys* (1985) **11**(1):87–96. doi:10.1016/0360-3016(85)90366-9
143. Lo SS, Fakiris AJ, Chang EL, Mayr NA, Wang JZ, Papiez L, et al. Stereotactic body radiation therapy: a novel treatment modality. *Nat Rev Clin Oncol* (2010) **7**(1):44–54. doi:10.1038/nrclinonc.2009.188
144. Kupelian PA, Thakkar VV, Khuntia D, Reddy CA, Klein EA, Mahadevan A. Hypofractionated intensity-modulated radiotherapy (70 gy at 2.5 Gy per fraction) for localized prostate cancer: long-term outcomes. *Int J Radiat Oncol Biol Phys* (2005) **63**(5):1463–8. doi:10.1016/j.ijrobp.2005.05.054
145. Schulz-Ertner D, Nikoghosyan A, Hof H, Didinger B, Combs SE, Jakel O, et al. Carbon ion radiotherapy of skull base chondrosarcomas. *Int J Radiat Oncol Biol Phys* (2007) **67**(1):171–7. doi:10.1016/j.ijrobp.2006.08.027
146. Denekamp J, Waites T, Fowler JF. Predicting realistic RBE values for clinically relevant radiotherapy schedules. *Int J Radiat Biol* (1997) **71**(6):681–94. doi:10.1080/095530097143699
147. Denekamp J, Harris SR, Morris C, Field SB. The response of a transplantable tumor to fractionated irradiation. II. Fast neutrons. *Radiat Res* (1976) **68**(1):93–103. doi:10.2307/3574537

148. Ando K, Koike S, Uzawa A, Takai N, Fukawa T, Furusawa Y, et al. Biological gain of carbon-ion radiotherapy for the early response of tumor growth delay and against early response of skin reaction in mice. *J Radiat Res* (2005) **46**(1):51–7. doi:10.1269/jrr.46.51
149. Field SB, Hornsey S. RBE values for cyclotron neutrons for effects on normal tissues and tumours as a function of dose and dose fractionation. *Eur J Cancer* (1971) **7**(2):161–9. doi:10.1016/0014-2964(71)90011-9
150. Leith JT, Woodruff KH, Lyman JT. Early effects of single doses of 375 MeV/nucleon 20Neon ions on the skin of mice and hamsters. *Radiat Res* (1976) **65**(3):440–50. doi:10.2307/3574375
151. Joiner MC. Linear energy transfer and relative biological effectiveness. 4th ed. In: Joiner MC, van der Kogel AJ, editors. *Basic Clinical Radiobiology*. London: Hodder Arnold (2009). p. 68–77.
152. Jones B. The apparent increase in the {beta}-parameter of the linear quadratic model with increased linear energy transfer during fast neutron irradiation. *Br J Radiol* (2010) **83**(989):433–6. doi:10.1259/bjr/68792966
153. Yoshida Y, Ando K, Ando K, Murata K, Yoshimoto Y, Musha A, et al. Evaluation of therapeutic gain for fractionated carbon-ion radiotherapy using the tumor growth delay and crypt survival assays. *Radiother Oncol* (2015) **117**(2):351–7. doi:10.1016/j.radonc.2015.09.027
154. Uzawa A, Ando K, Kase Y, Hirayama R, Matsumoto Y, Matsufuji N, et al. Designing a ridge filter based on a mouse foot skin reaction to spread out Bragg-peaks for carbon-ion radiotherapy. *Radiother Oncol* (2015) **115**(2):279–83. doi:10.1016/j.radonc.2015.04.007
155. Ando K, Koike S, Uzawa A, Takai N, Fukawa T, Furusawa Y, et al. Repair of skin damage during fractionated irradiation with gamma rays and low-LET carbon ions. *J Radiat Res* (2006) **47**(2):167–74. doi:10.1269/jrr.47.167
156. Karger CP, Peschke P, Sanchez-Brandelik R, Scholz M, Debus J. Radiation tolerance of the rat spinal cord after 6 and 18 fractions of photons and carbon ions: experimental results and clinical implications. *Int J Radiat Oncol Biol Phys* (2006) **66**(5):1488–97. doi:10.1016/j.ijrobp.2006.08.045
157. Ando K, Koike S, Ohira C, Chen YJ, Nojima K, Ando S, et al. Accelerated reoxygenation of a murine fibrosarcoma after carbon-ion radiation. *Int J Radiat Biol* (1999) **75**(4):505–12. doi:10.1080/095530099140438
158. Oya N, Sasai K, Shibata T, Takagi T, Shibuya K, Koike S, et al. Time course of reoxygenation in experimental murine tumors after carbon-beam and X-ray irradiation. *J Radiat Res* (2001) **42**(2):131–41. doi:10.1269/jrr.42.131
159. Kanai T, Matsufuji N, Miyamoto T, Mizoe J, Kamada T, Tsuji H, et al. Examination of GyE system for HIMAC carbon therapy. *Int J Radiat Oncol Biol Phys* (2006) **64**(2):650–6. doi:10.1016/j.ijrobp.2005.09.043
160. Kanai T, Furusawa Y, Fukutsu K, Itsukaichi H, Eguchi-Kasai K, Ohara H. Irradiation of mixed beam and design of spread-out Bragg peak for heavy-ion radiotherapy. *Radiat Res* (1997) **147**(1):78–85. doi:10.2307/3579446
161. Shibamoto Y, Otsuka S, Iwata H, Sugie C, Ogino H, Tomita N. Radiobiological evaluation of the radiation dose as used in high-precision radiotherapy: effect of prolonged delivery time and applicability of the linear-quadratic model. *J Radiat Res* (2012) **53**(1):1–9. doi:10.1269/jrr.11095
162. Song CW, Kim MS, Cho LC, Dusenbery K, Sperduto PW. Radiobiological basis of SBRT and SRS. *Int J Clin Oncol* (2014) **19**(4):570–8. doi:10.1007/s10147-014-0717-z
163. Park HJ, Griffin RJ, Hui S, Levitt SH, Song CW. Radiation-induced vascular damage in tumors: implications of vascular damage in ablative hypofractionated radiotherapy (SBRT and SRS). *Radiat Res* (2012) **177**(3):311–27. doi:10.1667/RR2773.1
164. Williams JP, Brown SL, Georges GE, Hauer-Jensen M, Hill RP, Huser AK, et al. Animal models for medical countermeasures to radiation exposure. *Radiat Res* (2010) **173**:557–78. doi:10.1667/RR1880.1
165. Brown JM, Carlson DJ, Brenner DJ. Dose escalation, not "new biology," can account for the efficacy of stereotactic body radiation therapy with non-small cell lung cancer. In reply to Rao et al. *Int J Radiat Oncol Biol Phys* (2014) **89**(3):693–4. doi:10.1016/j.ijrobp.2014.03.014
166. Brown JM, Carlson DJ, Brenner DJ. The tumor radiobiology of SRS and SBRT: are more than the 5 Rs involved? *Int J Radiat Oncol Biol Phys* (2014) **88**(2):254–62. doi:10.1016/j.ijrobp.2013.07.022
167. Fowler JF. The radiobiology of prostate cancer including new aspects of fractionated radiotherapy. *Acta Oncol* (2005) **44**(3):265–76. doi:10.1080/02841860410002824
168. Garcia-Barros M, Paris F, Cordon-Cardo C, Lyden D, Rafii S, Haimovitz-Friedman A, et al. Tumor response to radiotherapy regulated by endothelial cell apoptosis. *Science* (2003) **300**(5622):1155–9. doi:10.1126/science.1082504
169. Fuks Z, Kolesnick R. Engaging the vascular component of the tumor response. *Cancer Cell* (2005) **8**(2):89–91. doi:10.1016/j.ccr.2005.07.014
170. Lee Y, Auh SL, Wang Y, Burnette B, Meng Y, Beckett M, et al. Therapeutic effects of ablative radiation on local tumor require CD8+ T cells: changing strategies for cancer treatment. *Blood* (2009) **114**(3):589–95. doi:10.1182/blood-2009-02-206870
171. Matsumura S, Wang B, Kawashima N, Braunstein S, Badura M, Cameron TO, et al. Radiation-induced CXCL16 release by breast cancer cells attracts effector T cells. *J Immunol* (2008) **181**(5):3099–107. doi:10.4049/jimmunol.181.5.3099
172. Ogata T, Teshima T, Kagawa K, Hishikawa Y, Takahashi Y, Kawaguchi A, et al. Particle irradiation suppresses metastatic potential of cancer cells. *Cancer Res* (2005) **65**(1):113–20.
173. Tamaki T, Iwakawa M, Ohno T, Imadome K, Nakawatari M, Sakai M, et al. Application of carbon-ion beams or gamma-rays on primary tumors does not change the expression profiles of metastatic tumors in an in vivo murine model. *Int J Radiat Oncol Biol Phys* (2009) **74**(1):210–8. doi:10.1016/j.ijrobp.2008.12.078
174. Matsunaga A, Ueda Y, Yamada S, Harada Y, Shimada H, Hasegawa M, et al. Carbon-ion beam treatment induces systemic antitumor immunity against murine squamous cell carcinoma. *Cancer* (2010) **116**(15):3740–8. doi:10.1002/cncr.25134
175. Ohkubo Y, Iwakawa M, Seino K, Nakawatari M, Wada H, Kamijuku H, et al. Combining carbon ion radiotherapy and local injection of alpha-galactosylceramide-pulsed dendritic cells inhibits lung metastases in an in vivo murine model. *Int J Radiat Oncol Biol Phys* (2010) **78**(5):1524–31. doi:10.1016/j.ijrobp.2010.06.048
176. Yoshimoto Y, Oike T, Okonogi N, Suzuki Y, Ando K, Sato H, et al. Carbon-ion beams induce production of an immune mediator protein, high mobility group box 1, at levels comparable with X-ray irradiation. *J Radiat Res* (2015) **56**(3):509–14. doi:10.1093/jrr/rrv007
177. Durante M, Reppingen N, Held KD. Immunologically augmented cancer treatment using modern radiotherapy. *Trends Mol Med* (2013) **19**(9):565–82. doi:10.1016/j.molmed.2013.05.007
178. Ogata T, Teshima T, Inaoka M, Minami K, Tsuchiya T, Isono M, et al. Carbon ion irradiation suppresses metastatic potential of human non-small cell lung cancer A549 cells through the phosphatidylinositol-3-kinase/Akt signaling pathway. *J Radiat Res* (2011) **52**(3):374–9. doi:10.1269/jrr.10102
179. Karger CP, Scholz M, Huber PE, Debus J, Peschke P. Photon and carbon ion irradiation of a rat prostate carcinoma: does a higher fraction number increase the metastatic rate? *Radiat Res* (2014) **181**(6):623–8. doi:10.1667/RR13611.1

Conflict of Interest Statement: The authors declare that preparation of this article was conducted in the absence of any commercial or financial relationships that could be construed as a potential conflict of interest.

Copyright © 2016 Held, Kawamura, Kaminuma, Paz, Yoshida, Liu, Willers and Takahashi. This is an open-access article distributed under the terms of the Creative Commons Attribution License (CC BY). The use, distribution or reproduction in other forums is permitted, provided the original author(s) or licensor are credited and that the original publication in this journal is cited, in accordance with accepted academic practice. No use, distribution or reproduction is permitted which does not comply with these terms.

frontiers in Oncology

ORIGINAL RESEARCH
published: 08 January 2016
doi: 10.3389/fonc.2015.00294

Exposure to Carbon Ions Triggers Proinflammatory Signals and Changes in Homeostasis and Epidermal Tissue Organization to a Similar Extent as Photons

*Palma Simoniello[1†], Julia Wiedemann[1,2†], Joana Zink[1], Eva Thoennes[1], Maike Stange[1], Paul G. Layer[2], Maximilian Kovacs[3], Maurizio Podda[3], Marco Durante[1,2] and Claudia Fournier[1,4]**

[1] Department of Biophysics, GSI Helmholtzzentrum für Schwerionenforschung, Darmstadt, Germany, [2] Department of Biology, Technische Universität Darmstadt, Darmstadt, Germany, [3] Department of Dermatology, Darmstadt Hospital, Darmstadt, Germany, [4] Hochschule Darmstadt, Darmstadt, Germany

OPEN ACCESS

Edited by:
Joel S. Greenberger, University of Pittsburgh Medical Center-Shadyside, USA

Reviewed by:
Michael Wayne Epperly, University of Pittsburgh Cancer Institute, USA
Christopher James Bakkenist, University of Pittsburgh School of Medicine, USA

***Correspondence:**
Claudia Fournier
c.fournier@gsi.de

[†]Palma Simoniello and Julia Wiedemann have contributed equally to this work.

Specialty section:
This article was submitted to Radiation Oncology, a section of the journal Frontiers in Oncology

Received: 24 August 2015
Accepted: 10 December 2015
Published: 08 January 2016

Citation:
Simoniello P, Wiedemann J, Zink J, Thoennes E, Stange M, Layer PG, Kovacs M, Podda M, Durante M and Fournier C (2016) Exposure to Carbon Ions Triggers Proinflammatory Signals and Changes in Homeostasis and Epidermal Tissue Organization to a Similar Extent as Photons. Front. Oncol. 5:294. doi: 10.3389/fonc.2015.00294

The increasing application of charged particles in radiotherapy requires a deeper understanding of early and late side effects occurring in skin, which is exposed in all radiation treatments. We measured cellular and molecular changes related to the early inflammatory response of human skin irradiated with carbon ions, in particular cell death induction and changes in differentiation and proliferation of epidermal cells during the first days after exposure. Model systems for human skin from healthy donors of different complexity, i.e., keratinocytes, coculture of skin cells, 3D skin equivalents, and skin explants, were used to investigate the alterations induced by carbon ions (spread-out Bragg peak, dose-averaged LET 100 keV/μm) in comparison to X-ray and UV-B exposure. After exposure to ionizing radiation, in none of the model systems, apoptosis/necrosis was observed. Carbon ions triggered inflammatory signaling and accelerated differentiation of keratinocytes to a similar extent as X-rays at the same doses. High doses of carbon ions were more effective than X-rays in reducing proliferation and inducing abnormal differentiation. In contrast, changes identified following low-dose exposure (≤0.5 Gy) were induced more effectively after X-ray exposure, i.e., enhanced proliferation and change in the polarity of basal cells.

Keywords: human skin equivalent, keratinocytes, differentiation, apoptosis, inflammation, proliferation, ionizing irradiation, carbon ions

Abbreviations: cl, cleaved; D, dermis; fl, full length; HSE, human skin equivalent; M, marker; PC, positive control; SB, stratum basale; SC, stratum corneum; SG, stratum granulosum; SS, stratum spinosum.

INTRODUCTION

The increasing application of charged particles in radiotherapy motivates our assessment of inflammatory reactions and homeostasis of tissue exposed to carbon ions and to compare the response to X-rays. In the current study, we focus on the analysis of cell death, proliferation, differentiation, and reorganization of different layers of the epidermis.

Charged particles display particular physical characteristics, such as high mass and electrical charge, resulting in an inverted depth dose profile compared to photons with a high relative dose deposition at the end of their trajectory. This enables a volume conform treatment of deep-seated tumors (1) as well as sparing of critical organs. In addition, when using ions heavier than protons, the exposure of cells or tissue in the "Bragg Peak" region at the end of the trajectory leads to a higher local intensity of ionizing events, and thereby clusters of DNA damage (2). As a consequence, an enhanced biological efficiency compared to photons is observed (3, 4).

New treatment approaches with carbon ions make use of these advantages by increasing the dose to the tumor to enhance the tumor control probability (1, 2). However, this also implies the delivery of a higher dose to the surrounding normal tissue, including skin (5). Skin reactions associated with carbon ion therapy for deep-seated tumors are reported to be moderate and comparable to classical photon exposure (6). However, dose escalation trials in particle therapy applying a higher dose via only 1–2 entrance channels may cause skin toxicity (5). A typical case is breast cancer proton therapy, where the target (lumpectomy cavity) is shallow, and therefore skin toxicity is the limiting factor for beam arrangement and prescription doses (7, 8).

Skin is of interest because a considerable part of the side effects occurring after radiotherapy are observed in this organ due to its sensitivity (9) and its involvement in all radiation exposures (10). Radiation effects observed in the epidermis of the skin are erythema, desquamation and, for very high doses, late necrosis. In the dermis late effects occur, i.e., persisting vascular damage and fibrosis (11–13). In addition, anti-inflammatory effects induced by low-dose radiation (14) exposure can be anticipated as they are already shown for UV exposure (15, 16).

In the work presented here, we aimed to investigate the cellular and molecular changes related to the early inflammatory response of irradiated skin, in particular the occurrence of cell death and changes in differentiation and proliferation of the epidermal cells. In this context, a comparison between X-rays and carbon ions was intended. The first experiments were performed in monolayer- and cocultures of skin cells (keratinocytes, cocultured with fibroblasts); the respective results are reported in the supplement.

Based on these results obtained in cell cultures, we used a 3D human skin equivalent (HSE) and human skin explants to approach the physiological conditions in tissue and tested the following working hypotheses:

(1) Cell death of keratinocytes does not play a major role in the inflammatory response to ionizing radiation within the first days postexposure.
(2) An early release of inflammatory cytokines in irradiated skin tissue may be elicited by other typical changes (proliferation, differentiation, and tissue organization) than cell death.
(3) Taking into account previous knowledge about irradiation-induced changes in tissue, we hypothesize that activation of proliferation, differentiation, and tissue organization may be affected.
(4) Carbon ions, delivered to normal skin under therapy conditions, induce similar effects related to inflammation, proliferation, differentiation, and tissue organization compared to the same physical doses of photons.

Throughout the assessment of cell death, cytokine release, homeostasis, and tissue organization, the effects of carbon ions, using an extended Bragg Peak as a therapy-like configuration, were compared to X-rays. As the efficiency of carbon ions in inducing the respective effects has not been reported for skin cells and tissue before, we have chosen the same low and moderate doses to compare the radiation qualities and, in addition, a high X-ray dose to take into account a potential higher but not yet determined efficiency of carbon ions. A considerable number of data sets on non-ionizing UV-B exposure are available, and therefore UV-B irradiation served as a reference, and the respective results for all model systems used are reported in the supplement.

MATERIALS AND METHODS

Tissue Culture

Human full-thickness skin equivalent constructs (EpiDermFT™), referred to as HSE herein, were purchased from MatTek Corporation (Ashland, MA, USA) and cultured according to the manufacturer's protocol. The HSE consists of an epidermal layer composed of normal human epidermal keratinocytes, which is not submerged in culture medium and a dermal layer built up of fibroblasts and extracellular matrix (collagen1). All HSE constructs were equilibrated for at least 16 h before the experiments were started. During irradiation, the samples were maintained in PBS (Biochrom; Berlin, Germany) and fresh medium was added after irradiation. Media exchange was repeated on a daily basis until the experiment was terminated.

Human skin tissue explants were obtained from surgical discard (Dermatology Clinic, Darmstadt, Germany). The study was approved by the Local Ethics Committee (FF136/2014). The skin was washed in PBS, cut into small pieces (5 mm × 5 mm) and explanted in cell culture inserts (BD Falcon, Heidelberg Germany). The membrane of the inserts was in contact with medium (RPMI 1640, with 10% FCS and 2% Pen/Strep; all Biochrom, Berlin, Germany). The skin explants were cultured under standard conditions.

Irradiation

X-ray irradiation (X-RAD 320 R X, 250 kV, 16 mA) of HSE was performed with a dose rate of 1 Gy/min (0.5–10 Gy).

Carbon ion irradiation (0.5–2 Gy) was performed using a pencil beam in a spread-out Bragg peak (SOBP) with 20.0 mm width equivalent to a depth of 5 cm in water (110–145 MeV/μm;

LET 100 keV/μm), at the heavy-ion synchrotron (SIS) at GSI Helmholtzzentrum für Schwerionenforschung (Darmstadt, Germany). A subset of carbon ion irradiations has been performed with the same parameters of exposure at the heavy-ion synchrotron of the Heidelberg Ion-Beam Therapy Center HIT (Heidelberg, Germany).

For carbon ion irradiation, the HSE were positioned vertically. In order to protect the samples from drying out, a sterile gaze soaked with prewarmed PBS was put in the wells under the membrane, and the wells were closed with Parafilm during exposure, which typically took 10 min.

Histochemistry, Immunohistochemistry, Imaging, and Quantitative Analysis

For histological analyses, HSE was fixed in a 4% PFA-solution, processed for paraffin embedding, and cut into 5 μm sections using a microtome (RM2235; Leica Microsystems, Wetzlar, Germany). For hematoxylin and eosin (H&E) staining, slides were deparaffinized, rehydrated, and stained according to commonly used procedures (17).

For immunostaining, the sections were deparaffinized, rehydrated, treated with 10 mM citrate acid buffer (pH 6.0), and heated in a microwave to unmask the antigens. After rinsing in deionized water, the slides were incubated in 0.3% H_2O_2 for 30 min to block the endogenous peroxidase activity. After washing in PBS (three times), non-specific binding sites were blocked by incubating the sections with blocking solution (1.5% normal goat serum in PBS with 0.1% (v/v) Triton X-100). Finally, the slides were incubated with the primary antibody at 4°C overnight. Used antibodies and dilutions were: rabbit anti-active caspase-3 (Ab-2; Calbiochem, San Diego, CA, USA; 1:100), rabbit anti-Ki67 (SP6, ab16667; Abcam, Cambridge, UK; 1:100), and rabbit anti-E-Cadherin (EP700Y; ab40772; Abcam, Cambrigde, UK; 1:500). The detection of the binding of the primary antibody was performed with the Ultra-Sensitive ABC Peroxidase rabbit IgG staining kit (Thermo Scientific, Waltham, MA, USA) and the ImmPACT VIP-Peroxidase substrate kit (Vector, Burlingame, CA, USA) or SigmaFast-DAB-Tablets (Sigma, St. Louis, MO, USA) according to the manufacturer's protocol. The nuclei were counterstained with hematoxylin and the slides were dehydrated, cleared in xylene, and mounted. HSE, submerged entirely with medium, was used as positive control for apoptosis.

Tissue sections were imaged using an Olympus BX61 microscope with an E-330 camera (Olympus, Hamburg, Germany). For the quantitative or semiquantitative analysis, 20 pictures per sample were taken with a 40-fold magnification. Pyknotic cells in the stratum corneum (parakeratosis) and in the viable epidermis were counted by eye and the mean per field of view was calculated. Ki67-positive cells (proliferation) were also counted by eye and normalized on the total number of basal cells. The thickness of the stratum corneum and the viable epidermis were measured using the software Image J. The thickness of the stratum corneum was normalized on the thickness of the viable epidermis. For the semiquantitative analysis of the structure of the basal layer, for each picture, it was evaluated if the cells in the basal layer were palisadic, in part or completely cobblestoned; the fraction of pictures displaying the respective characteristic is given. Each analysis was performed from two independent experiments, in total for four samples ($n = 4$, $N = 2$); values are given as SEM.

Western Blot

The HSE epidermis was separated mechanically from dermis and lysed separately in RIPA buffer as previously described (18). In addition, tissue was homogenized with a pestle and with ultrasound treatment. Proteins were loaded (10 μg) and separated on 12% SDS-polyacrylamide gels, and then transferred to polyvinylidenfluoride membranes (Immobilon-P; Merck Millipore, Billerica, MA, USA). After blotting, the membranes were washed and incubated overnight at 4°C in 5% dry milk (Carl Roth GmbH, Karlsruhe, Germany) in Tris-buffered saline to reduce non-specific binding. Membranes were incubated with the primary antibodies for 2 h at room temperature.

Primary antibodies used were rabbit anti-caspase-3 (Cell Signaling, Danvers, MA, USA; 1:1000) and rabbit anti-PARP (46D11; Cell Signaling, Danvers, MA, USA; 1:1000). GAPDH (rabbit anti-GAPDH, Cell Signaling, Danvers, MA, USA; 1:1000) and α-Tubulin (mouse anti-α-Tubulin; Sigma, Steinheim, Germany; 1:4000) were used as a loading control. HaCaT cells, irradiated with 10 Gy X-rays and lysed 5 days after exposure, were used as a positive control. After washing, the membrane was incubated with a horseradish peroxidase-conjugated secondary antibody for 1 h at room temperature (anti-mouse IgG or anti-rabbit IgG HRP linked antibody; GE Healthcare, München, Germany; 1:10,000). Protein expression was visualized using enhanced chemiluminescence (Pierce ECL Plus Western; Thermo Scientific, Waltham, MA, USA) according to the manufacturer's instructions and detected on a X-ray film.

Enzyme-Linked Immunosorbent Assay

To quantify the levels of released cytokines in the medium of HSE, ELISA kits for the detection of TNF-α, IL-2, IL-6, IL-8, IL-10, TGF-β (all ELISA Ready-SET-go!; eBioscience, San Diego, CA, USA), and IL-1α (Platinum ELISA, eBioscience, San Diego, CA, USA) were used according to the manufacturer's protocol. The measured values for each sample were normalized on the controls. In the first step, we checked the cytokine release from each sample before irradiation separately, but as the values were very similar to each other, this additional normalization step according to Varnum et al. (19) was not pursued. The concentration of HMGB1 in the medium of HSE was measured using an ELISA kit (human HMGB1; Cloud-Clone-Corp., Houston, TX, USA), according to the manufacturer's instructions and normalized on the controls.

Statistical Analysis

Unless stated otherwise, the error bars represent the mean ± SEM. Statistical significance was tested using a Student's *t*-test. The number of independent irradiation experiments (N) and the total number of samples (n) are mentioned in the figure legends. At least two irradiation experiments and four samples were analyzed.

RESULTS

The results obtained in keratinocytes (normal human epidermal keratinocytes; NHEK), either in monolayers or cocultured with fibroblasts (normal human epidermal fibroblasts; NHDF), are presented in the supplement. The results obtained in a 3D HSE and in human skin explants are presented in the following paragraphs for X-ray and carbon irradiation, for UVB exposure in the supplement.

Induction of Apoptosis

We first assessed clonogenic cell survival after radiation exposure (Figure S1 in Supplementary Material). As expected, the dose–response curve shows a typical shoulder for X-ray, whereas the curve is linear for carbon ions, indicating a higher efficiency of carbon ions compared to X-ray in terms of cell inactivation. Please note that for cell inactivation, monoenergetic carbon ions (170 keV/μm) were used, whereas all the following experiments have been performed with SOBP carbon ions (100 keV/μm), which corresponds to the conditions used in radiotherapy.

Then, we investigated if this cell inactivation is due to the induction of cell death during 144 h after exposure to ionizing radiation (X-rays and SOBP carbon ions) in a monolayer culture of keratinocytes. In addition, we repeated this experiment in cocultures of keratinocytes and fibroblasts. The results are shown in Figures S1, S2, and S4 in Supplementary Material. In spite of clearly detectable cytogenetic damage in terms of micronuclei formation for both radiation qualities, the results did not indicate an occurrence of apoptosis (no detection of annexin V positive cells, pyknotic nuclei, apoptotic bodies, activated caspase-3, and cleaved PARP), not even at high doses, and showed only low levels of necrosis (release of HMGB, High Mobility Group Box 1 protein, an established marker for necrosis (20, 21), Figure S5 in Supplementary Material).

From these results, we hypothesized that cell death of keratinocytes does not play a major role in the inflammatory response to ionizing radiation, at least not within the first days after exposure. To test this in tissue, we moved on using a model system of higher complexity, i.e., a commercially available, three-dimensional HSE, and for selected experiments also human skin explants. We used the same physical doses of photons and carbon ions (0.5 and 2 Gy), and in addition a higher dose (10 Gy) of photon irradiation.

The occurrence of apoptosis was assessed in irradiated HSE and human skin up to 72 h after exposure. **Figure 1A** shows representative pictures of the immunodetection of active caspase-3 in HSE tissue sections, 24 h after exposure to moderate/high doses. In the positive control, apoptotic cells were identified in the basal layer by positive caspase-3 staining and condensed pyknotic nuclei. In contrast, no pyknotic nuclei or cells positive for active caspase-3 could be detected after irradiation, regardless of radiation quality and dose. This also applies for 72 h after irradiation (Figure S6A in Supplementary Material). Consistently, no cleaved caspase-3 and PARP (only assessed for X-ray exposure) were detected in lysates of irradiated HSE (western blot analysis for 24 h after exposure, **Figure 1B**, additional time points shown in Figure S6B in Supplementary Material). For X-ray exposure, these observations were confirmed in sections of *ex vivo* irradiated human skin explants where no active caspase-3 and no pyknotic nuclei were observed (**Figure 1C**). The use of TUNEL assay turned out to be inappropriate to detect apoptotic cells because differentiating keratinocytes showed intensive staining, irrespective of radiation exposure, and can therefore not be distinguished from apoptotic cells (not shown), which is in line with independent observations (22).

In addition, signs of necrosis were not observed morphologically and release of HMGB1 was not detectable after irradiation neither in the medium of HSE nor in the medium of human skin explants (not shown).

All in all, our results indicate no major role for early apoptosis and necrosis neither for photon nor for carbon ion exposure within 72 h after irradiation. This we conclude from the absence of caspase-3-dependent apoptosis, HMGB1 release, and typical morphological alterations, observed in a 3D HSE, and confirmed in human skin explants, irradiated *ex vivo*.

Release of Cytokines Related to Inflammation

By analyzing cytokine release after irradiation of NHEK, an upregulation of proinflammatory cytokines on the level of gene and protein expression has been shown (12). In good agreement with published data, our own results have shown an enhanced release of IL-1α, IL-2, and TGF-β (Figure S7A in Supplementary Material, only assessed for X-rays). For IL-6 and IL-8, the measured cytokine concentration in the supernatant of the controls was below the detection limit. Thus, the relative radiation-induced increase could not be calculated reliably. The induction of IL-6 was induced by moderate doses of X-ray and UV-B irradiation, whereas IL-8 was only inducible by a high UV-B intensity (40 mJ/cm^2, not shown).

Of note, when the keratinocytes have been cocultured with normal dermal fibroblasts, a significant influence on the pattern of release, i.e. an inhibitory feedback loop between release of IL-1α and TGF-β, has been observed in the non-irradiated cells, which is in agreement with published data (Figure S7B in Supplementary Material) (23–26). Despite this modulating effect, a radiation-induced moderate increase in the release of IL-1α, and a clear increment of IL-6 and IL-8 release, has been detected 24 h after photon irradiation, whereas no significant change of TGF-β has been measured (Figure S7C in Supplementary Material, only assessed for X-ray).

Based on these findings, we assessed the cytokine release for relevant candidates after exposure to X-rays and carbon ions in the HSE. The results are summarized in **Figure 2**. As the kinetics of cytokine release turned out to be different for low versus high doses and for X-ray versus carbon ion exposure, the intended comparison of the respective impact of both radiation qualities was difficult. Furthermore, the release of TNF-α und IL-2 was very low, below the detection limit in all HSE experiments, except in positive controls of human skin, which were generated by submerging the skin explant with liquid. When these human skin explants were irradiated additionally, an increase of TNF-α could be measured (not shown).

For X-ray exposure (**Figure 2A**), we observed a trend for an enhancement of IL-1α release 24 h after 2 and 10 Gy, whereas after

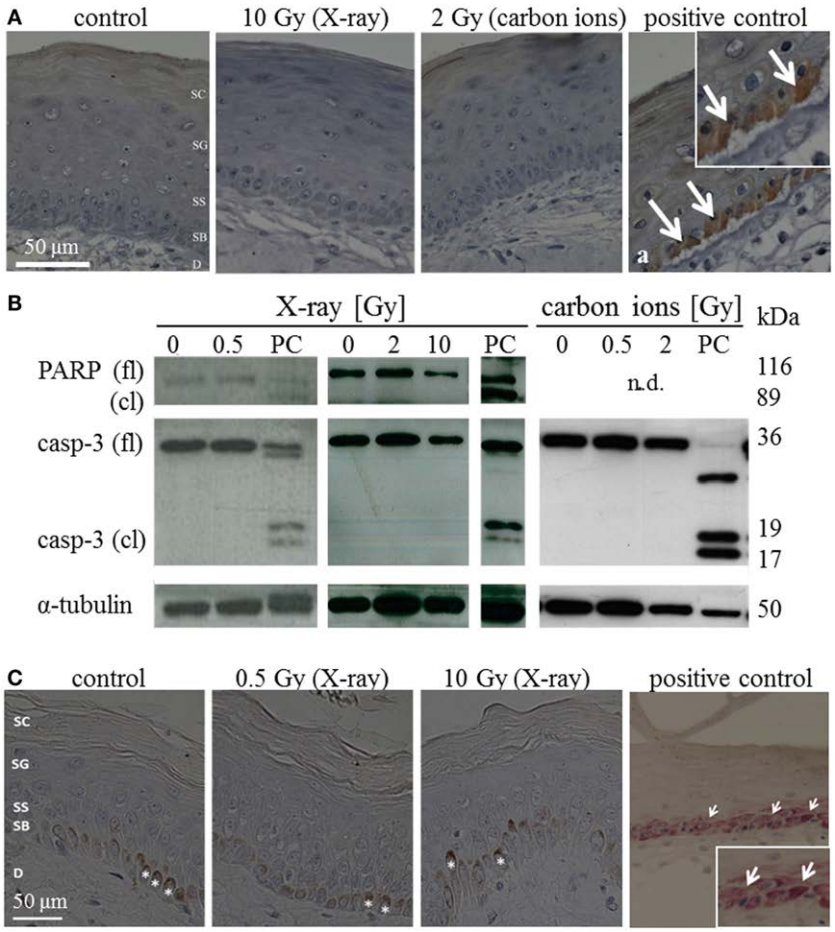

FIGURE 1 | Detection of apoptosis *in situ* and in western blot in HSE and human skin explants 24 h after irradiation with high doses of X-ray and carbon ions. **(A)** Immunodetection of active caspase-3 (brown) in HSE; cleaved caspase-3 was not detected in the epidermis after irradiation, but in the PCs (arrows in a); $N = 3$, $n = 5$. **(B)** Western blot analysis of caspase-3 and PARP in HSE; apoptosis is detected by the presence of caspase-3 and PARP cleavage fragments (17 and 19 kDa; 89 kDa) in PCs; active/cleaved caspase-3 and cleaved PARP were not detected in the epidermis of HSE after irradiation; $N = 2$, $n = 4$. **(C)** Immunodetection of cleaved caspase-3 (pink) in human skin explants; cleaved caspase-3 was not found after low or high doses of X-rays; *: melanocytes in the basal layer (brown); $N = 3$, $n = 5$.

48 h, the increment was around threefold compared to the level of controls, although not significant. For the highest X-ray dose (10 Gy), the increase was the same as for 2 Gy, and for 0.5 Gy, the release was unchanged at both time points. However, this was the only change observed after exposure to 10 Gy X-rays. The release of IL-6 after X-ray irradiation was only slightly, albeit significantly enhanced for 2 Gy at both time points (1.5-fold).

The level of the chemoattractant IL-8 protein showed a more than twofold enhancement after exposure to 0.5 Gy as early as 24 h after irradiation, and the increment for 2 Gy was significant at 24 h and also at 48 h postirradiation. As in the case of IL-6, no change in IL-8 release was observed for 10 Gy at none of the time points assessed.

Notably, for carbon ions (**Figure 2B**), after 24 h, no increment in the release of any of the measured cytokines was observed. At 48 h after exposure, there was a trend for an enhancement of IL-1α, but not for IL-6 release. The release of IL-8 was significantly increased about a factor of two.

The cytokines that are considered to have an anti-inflammatory effect at early times after irradiation, TGF-β and IL-10 (12, 27, 28), were not enhanced up to 48 h after exposure, regardless of the radiation quality. Although for IL-10, a significant enhancement was measured 48 h after carbon ion exposure (**Figure 2B**), the increment was around 1.5-fold compared to controls, raising the question about the biological significance of this modification.

Taken together, for the inflammatory cytokines IL-6 and IL-8, an enhancement within 48 h was detected after X-ray irradiation (**Figure 2A**). However, the observed changes were not strictly dose-dependent, and after carbon ion exposure (**Figure 2B**), only small changes were measured compared to the same physical doses of X-rays (0.5 and 2 Gy).

Abnormal and Accelerated Differentiation

Epidermal homeostasis is maintained by a balance between proliferating and differentiating keratinocytes. For epithelial and other tissues (29, 30), early radiation-induced changes in

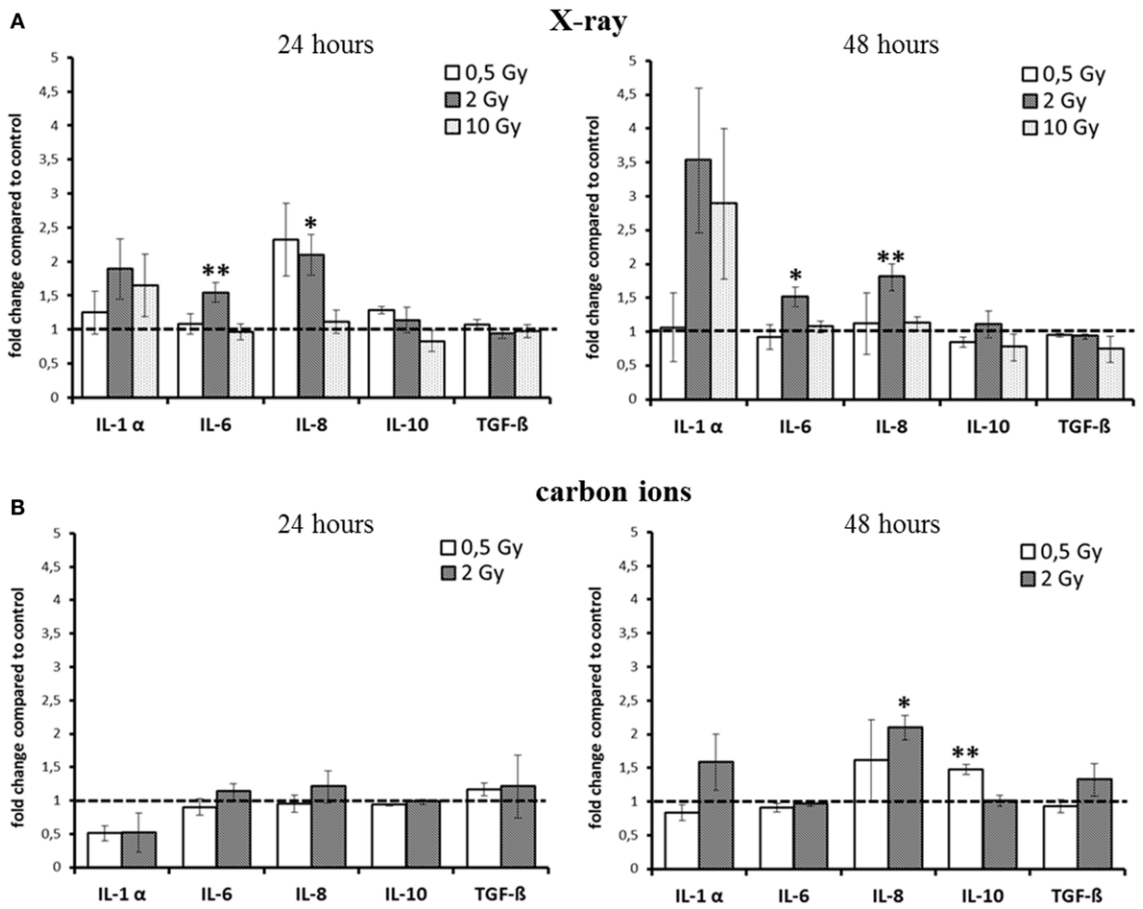

FIGURE 2 | Detection of cytokine release from HSE after irradiation with X-ray and carbon ions. **(A)** Enhancement of IL-6 and IL-8 release 24 and 48 h after exposure to moderate doses of X-rays. **(B)** No changes 24 h after carbon ion irradiation, enhanced release of IL-10 and IL-8 was detected 48 h after irradiation with carbon ions; SEM; $^{*}p \leq 0.05$, $^{**}p \leq 0.01$; $N = 2$–3, $n = 3$–10; IL-2 and TNF-α were not detectable.

proliferation, differentiation of keratinocytes, and reorganization of the epidermal layer are discussed to play a crucial role in early inflammation of the skin (31). Keratinocytes are organized in stratified layers. The basal layer (stratum basale) contains proliferating keratinocytes, which migrate into the upper layers (stratum spinosum and stratum granulosum) during their differentiation process by disconnecting from the basal membrane. During this process, morphology and protein expression profiles change. When keratinocytes finally reach the outer layer of the epidermis (stratum corneum), they have lost their nuclei and are terminally differentiated to cornified cells, which constitute the mechanical barrier of the skin, protecting the organisms against any type of external stress (10).

An abnormal pattern of morphology and differentiation is the occurrence of keratinocytes with pyknotic nuclei. If they are observed in the stratum corneum, which in healthy tissue consists of denucleated keratinocytes, this phenomenon is called parakeratosis and is associated with skin diseases (32, 33). These cells are also found in the viable part of the epidermis and in this case they are termed "sunburn cells", as they were first described after UV exposure (34, 35).

We assessed parakeratosis and "sunburn cells" in irradiated HSE at 24 and 72 h after exposure (**Figure 3**). In **Figure 3A**, a representative picture of parakeratosis is shown. Quantification was achieved by counting the number of pyknotic cells in the stratum corneum per field of view. As can be seen in **Figure 3B**, we observed parakeratosis at a low level in non-irradiated HSE (0.1–0.6 pyknotic nuclei in the stratum corneum per field of view) and an indication for an increase, albeit not statistically significant in HSE after carbon ion exposure. In **Figure 3C**, so-called "sunburn cells" are shown, which are not only characterized by pyknotic nuclei but also by an eosinophilic cytoplasm and the occurrence in the viable epidermis (34, 35). Quantification (**Figure 3D**) of these cells in the viable epidermis revealed a comparable increase 24 h after exposure to a moderate dose of X-ray and carbon ions (2 Gy), which was still persisting 72 h after irradiation. Notably, the increment was not observed for a low (0.5 Gy) and a high X-ray dose (10 Gy).

In some studies, sunburn cells are reported to be apoptotic, because the morphological alteration overlaps for part of the cells with positive staining for activated, cleaved caspase-3 (36). This was clearly not the case for the HSE in our study; in none of the

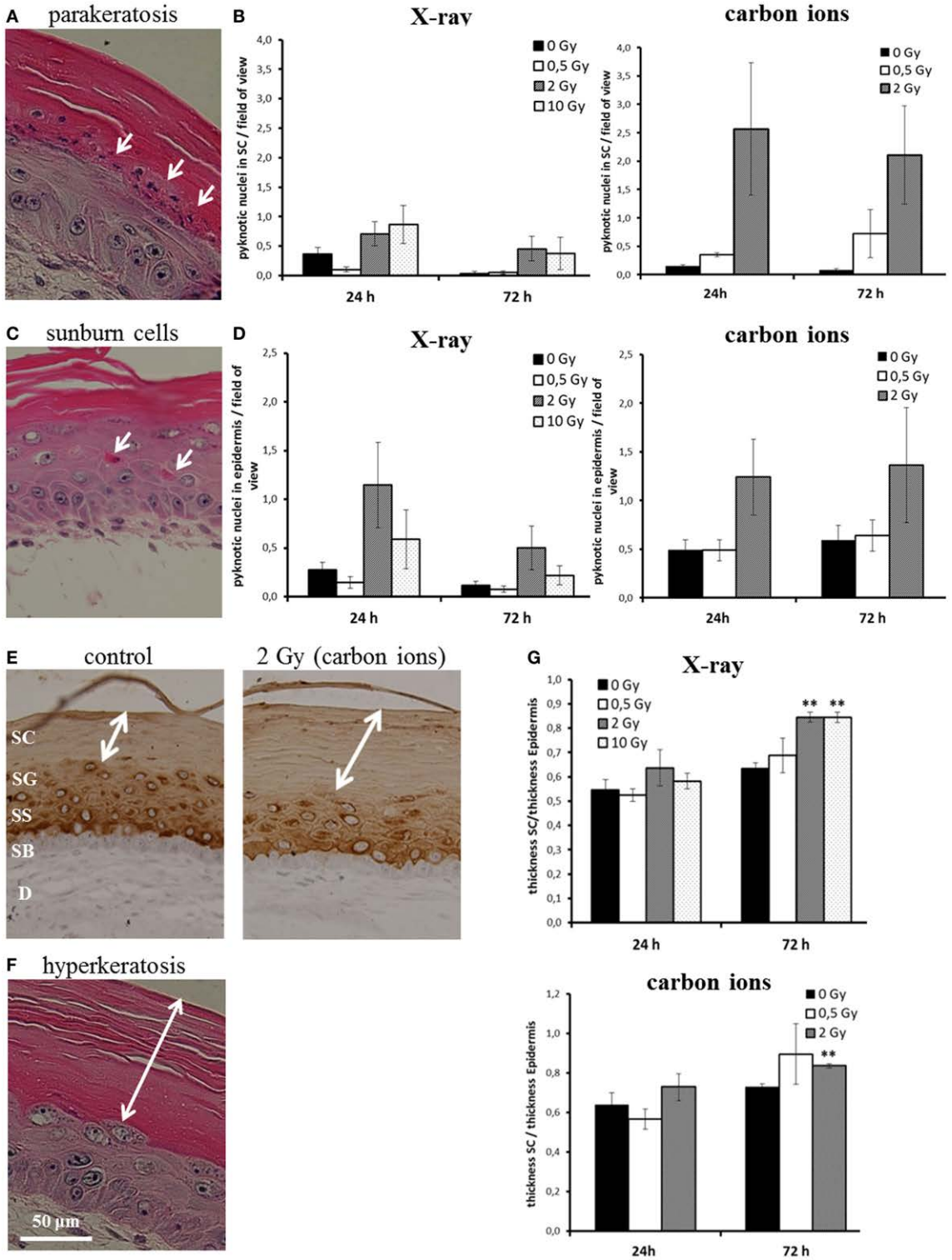

FIGURE 3 | Abnormal and accelerated differentiation in HSE after irradiation with X-ray and carbon ions. **(A)** Pyknotic keratinocytes are observed in the stratum corneum (parakeratosis). **(B)** Quantification of parakeratosis shows a slight increase after X-ray and a more pronounced increase after carbon ion exposure. **(C)** Morphology of typical "sunburn cells" characterized by pyknotic nuclei and an eosinophilic cytoplasm. **(D)** Quantification of "sunburn cells" shows a clear increase after 2 Gy of X-ray and carbon ions exposure. **(E)** Cytokeratin 10 expression (only in differentiating layers) in HSE 72 h after irradiation with carbon ions shows an enhanced thickness of the stratum corneum, where Cytokeratin 10 is not expressed. **(F)** Thickening of the stratum corneum (hyperkeratosis). **(G)** Quantification of hyperkeratosis shows an increase of the thickness of the stratum corneum 72 h after X-ray and carbon ion irradiation; SEM; $^{*}p \leq 0.05$, $^{**}p \leq 0.01$; $N = 2$, $n = 4$.

experimental conditions, a colocalization of sunburn cells and caspase-3 positive staining was detected (see **Figure 1**; Figure S6 in Supplementary Material).

Another physiological change reported after UV-B exposure (37) is the thickening of the stratum corneum. The stratum corneum is the epidermal layer where the differentiation is terminal and Cytokeratin 10 is not expressed (38) (example shown in **Figure 3E**). The thickening of the stratum corneum corresponds to an accelerated differentiation leading to an accumulation of cornified cells and is considered as a protective mechanism (39). In **Figure 3F**, a thickened stratum corneum (so-called "hyperkeratosis") of an irradiated HSE is depicted. For quantification, we measured the thickness of the stratum corneum and normalized this value to the thickness of the viable epidermis. As shown in **Figure 3G**, an increase of the stratum corneum was observed 72 h after exposure. The enhancement was significant for 2 and 10 Gy X-rays and 2 Gy carbon ions, whereas irradiation with a low dose (0.5 Gy) did not yield an effect.

The results show that abnormal differentiation patterns occur for moderate doses and were more pronounced for carbon ion than for X-ray exposure, whereas accelerated differentiation is significantly enhanced for X-ray exposure, also for a high dose, and for carbon ions, only a trend is observed. Both abnormal and accelerated differentiation is not detectable for low doses.

Proliferation

Enhanced proliferation due to a chronically activated state of keratinocytes has been reported for human skin, where skin biopsies have been taken from patients who had undergone radiotherapy and investigated months later (31). As we have observed accelerated differentiation for moderate and high doses, we set out to investigate a potential association with enhanced proliferation at early times after irradiation.

Proliferation activity was measured by Ki67 staining 72 h after irradiation of HSE. **Figure 4A** shows Ki67-positive cells in the basal layer. In controls, around 5% of the basal cells were positive for Ki67. Quantification of the fraction of Ki67-positive cells is depicted in **Figure 4B**, normalized on the level of non-irradiated HSE. An enhanced proliferation activity was observed after irradiation with a low X-ray dose (0.5 Gy), though not significant due to interexperimental variation. For higher X-ray doses and a low dose of carbon ions (0.5 Gy), no changes were observed, whereas following exposure to 2 Gy carbon ions a reduced fraction of proliferating cells was detected.

An increase in proliferation activity of the basal cells for 0.5 Gy and an unchanged activity for 10 Gy was confirmed in first experiments using explants of human skin (**Figure 4C**), which were *ex vivo* exposed to X-ray irradiation (24 and 48 h).

These results show an enhanced proliferation occurring only after exposure to a low dose of X-rays, but not for carbon ions, pointing to a specific effect, which is inversely correlated to increasing dose and ionizing density. According to this, at higher doses, no changes or even a reduced proliferation activity have been detected, the latter indicating an inhibition of cell cycle progression. This is consistent with the results obtained in NHEK (Figure S8 in Supplementary Material).

Changed Polarity of the Basal Cells

The polarity of the basal keratinocytes is a prerequisite for a balanced homeostasis of the epidermal layer (40). The typical palisade-like morphology of the basal cells allows for an attachment to the basal membrane and for a regular alignment, determining the polarity of the basal cells. When the basal cells are not attached to the basal membrane, the order and structure of the basal layer is disturbed, potentially leading to uncontrolled proliferation and migration (41).

After irradiation, we observed a transition from the typical palisade-like morphology to a cobblestoned morphology of the basal cells, as shown in a representative picture in **Figure 5A**. As quantification is difficult, we performed a semiquantitative scoring by determining if in the field of view all basal cells display a palisade-like morphology or if the cells have undergone a partial or a complete transition to a cobblestoned morphology. The semiquantitative evaluation in **Figure 5B** shows a shift to a cobblestoned morphology for X-ray exposure compared to controls. A transition to more areas with cobblestoned morphology was observed 24 and 72 h after irradiation, and in some fields of view, all basal cells displayed a cobblestoned morphology. Interestingly, the effect was inversely correlated with increasing dose and most pronounced after 0.5 Gy. Similar changes were found after carbon ion irradiation (**Figure 5B**) but less pronounced comparing the low dose (0.5 Gy) for both radiation qualities. In addition, we observed an alteration, which may be related to the described changes in morphology and polarity of basal keratinocytes, i.e., a delocalization of E-Cadherin from the cytoplasmic membrane to the cytoplasm (**Figure 5C**).

In summary, the transition of basal cells from a palisade-like to a cobblestoned morphology, indicating a change in polarity and disorganization of the basal layer, occurs for low and high doses, and for all radiation qualities. However, the effect is clearly more pronounced for low compared to high doses and for X-rays compared to carbon ions comparing the same physical doses.

DISCUSSION

The early and late skin response to ionizing radiation in classical photon therapy is clinically well known (31, 42) and constitutes a dose-limiting factor (43, 44). However, for reactions occurring within the first days in the epidermal layer of the skin, the cellular and molecular basis is explored much more intensive for UV exposure than for ionizing irradiation. For carbon ion exposure, the early radiation response of skin tissue has been investigated for the first time on a cellular level in our current study.

Cell Death Does Not Play a Major Role in the Early Radiation Response of Skin

The onset of an inflammatory reaction is one of the first events after irradiation of skin (45), and cell death can trigger this response (14, 46). Given the well-known enhanced efficiency for cell inactivation and higher relative biological effectiveness (RBE) of two to five of carbon ions (depending on the energy) compared to photons in mammalian cell types (47–49), a careful investigation of cell death induction in epidermal cells within the first days after exposure was conducted. As expected, clonogenic survival

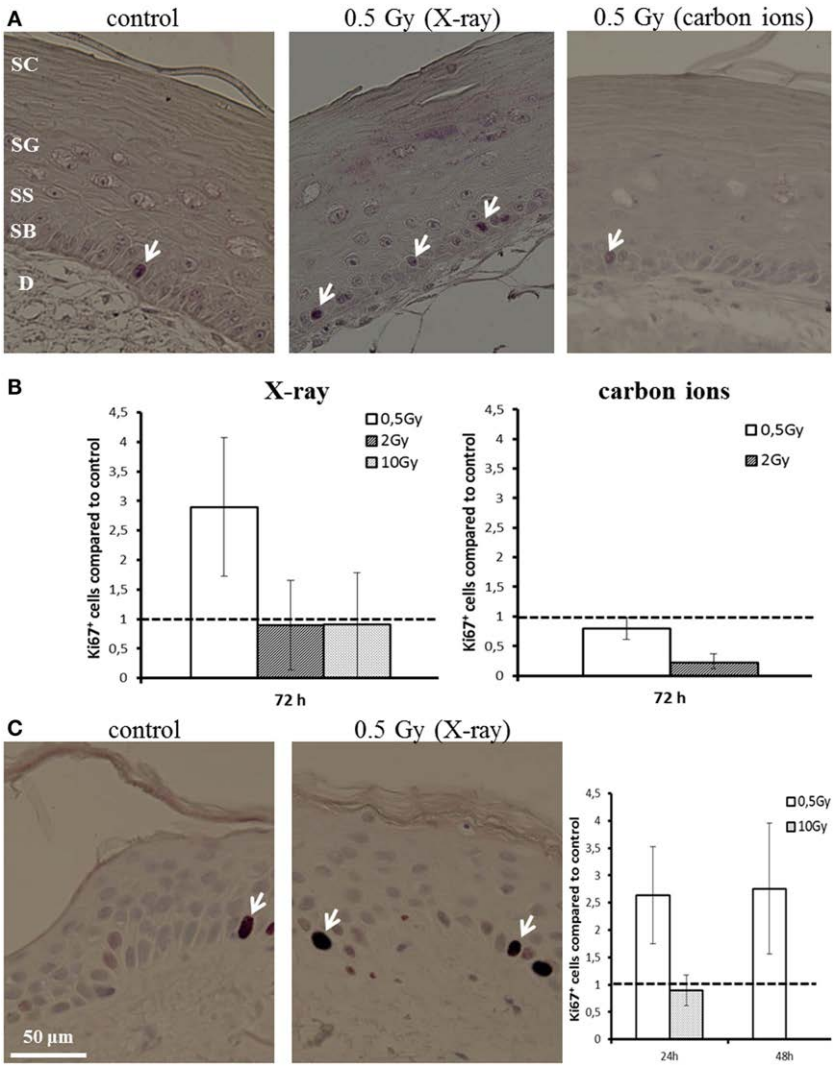

FIGURE 4 | Proliferation activity measured by Ki67 staining in HSE and human skin explants after irradiation with X-ray and carbon ions. **(A)** Ki67-positive cells (arrows) in the basal layer of HSE. **(B)** Number of Ki67-positive cells in the HSE, normalized on the total number of cells in the basal layer and shown relative to the controls, shows enhanced proliferation after 0.5 Gy X-ray irradiation. **(C)** Ki67-positive cells in human skin explants (arrows); quantification shows an increase of proliferation after low dose of X-rays; $N = 2$, $n = 4$.

of NHEK was reduced after X-ray exposure and even more pronounced after high LET carbon ion irradiation (170 keV/µm, Figure S1A in Supplementary Material). However, cell death was not detectable in mono and coculture of NHEK (Figures S1 and S4 in Supplementary Material, assessed for X-rays), which is consistent with reported results, where no or only a minor early increment in apoptotic cells was observed in primary keratinocytes exposed to moderate and high doses of γ-rays (50, 51). This indicates different mechanisms of clonogenic inactivation, such as accelerated differentiation, as shown for other primary cells (49, 52).

Using the more complex skin models, HSE and human skin explants, we confirmed that caspase-3-dependent apoptosis and necrosis do not play a role within the first days after radiation exposure to both X-rays and carbon ions in the assessed dose range (**Figure 1**). A low level of apoptosis, remaining unchanged after irradiation of the same HSE as used in our experiments, was also mentioned in an independent study (53). In biopsies of radiotherapy patients, the low basic level of apoptosis was increased only after more than 6 weeks (42), and in animal experiments, caspase-3-dependent apoptosis (22) and epidermal cell loss (54) were shown for very high doses. We conclude that apoptosis occurs only for very high doses and/or later than a few days. Early after exposure to low and moderate doses, apoptosis and necrosis do not contribute to inflammatory reactions.

Carbon Ions and X-Rays Trigger an Early Release of ProInflammatory Signals in Irradiated HSE with Similar Efficiency

For X-ray exposure, an early upregulation of inflammatory pathways on the transcriptional level in the irradiated epidermis is well established and has been investigated in skin biopsies of

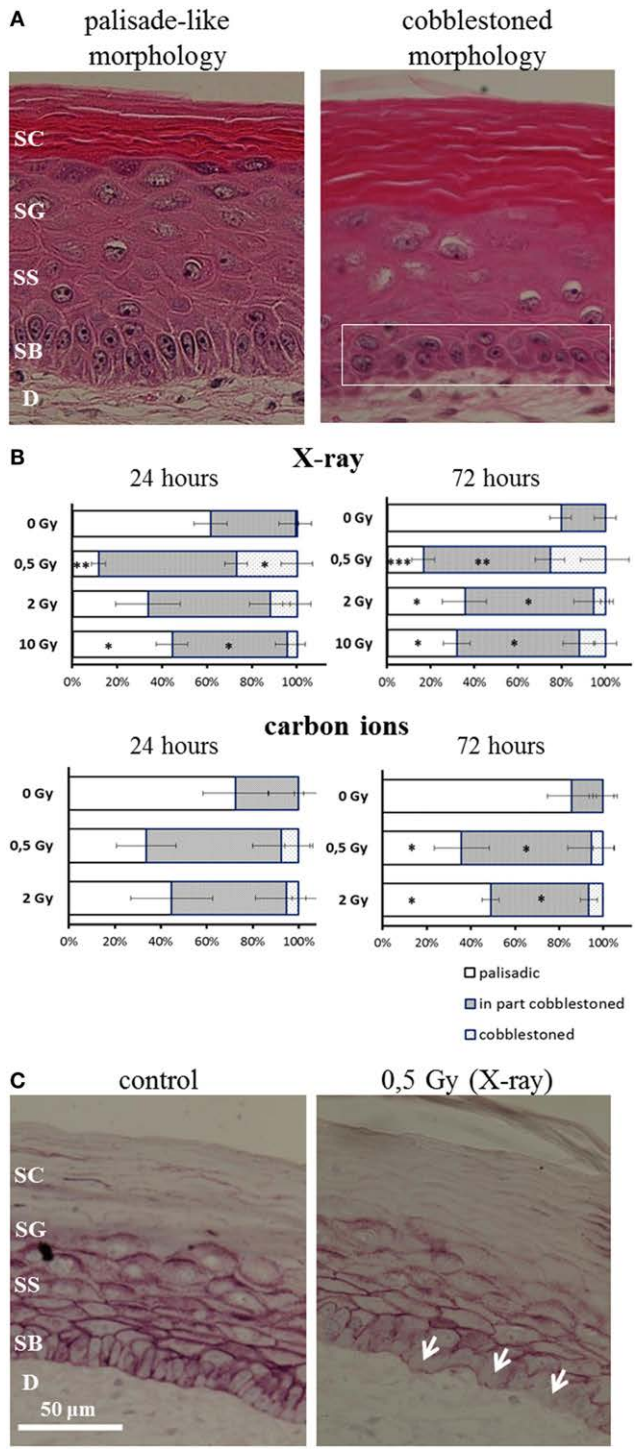

FIGURE 5 | Changed polarity of basal cells in HSE after irradiation with X-ray and carbon ions. **(A)** Transition of palisade-like morphology of basal cells to a cobblestoned morphology indicating a change in polarity and disorganization of the basal layer. **(B)** Quantification of palisade-like morphology and cobblestoned (partial or total) morphology shows a transition for all doses of X-ray and carbon ions; most pronounced and highly significant for 0.5 Gy. **(C)** E-Cadherin staining shows a delocalization of the protein in the cells from the basal layer (arrows) 72 h after irradiation with 0.5 Gy X-rays; SEM; $^{*}p \leq 0.05$, $^{**}p \leq 0.01$; $^{***}p \leq 0.001$; $N = 2$, $n = 4$.

radiotherapy patients, in HSE (12, 53, 55, 56), and in keratinocytes in animal and cell culture studies (50, 57). We could show in a HSE that both photon and carbon ion irradiation induce an early, significantly increased release of cytokines, which are known to trigger inflammation, such as IL-6 and IL-8, and a trend in increase of IL-1α. Anti-inflammatory cytokines (TGF-β and IL-10) were not elevated after exposure, except for a small enhancement of IL-10 at 48 h following carbon ion irradiation. This argues against an anti-inflammatory response at low doses elicited in the model systems investigated here. However, TGF-β mRNA was reported to be upregulated for high γ-ray doses (58), probably related to its key role in the late fibrotic response of skin.

In our study, comparing the same physical doses, the response to carbon ion irradiation compared to X-ray exposure was weak, detectable only after 48 h and significant only for IL-8 release (**Figure 2**). This indicates a similar enhancement in the release of proinflammatory cytokines after X-ray and carbon ion exposure. However, this is more a relative statement concerning the efficiency of carbon ions compared to X-rays than a result which fully represents the inflammatory response in a skin model such as a HSE, because a partially, but not fully overlapping pattern of X-ray induced cytokine release was detected in a study conducted by an independent group in the same HSE (19).

The Differentiation of Epidermal Cells After Irradiation is in Part Abnormal and Accelerated

Typical features that might contribute to the onset of an inflammatory reaction in skin are changes in proliferation and differentiation of keratinocytes, as reported for radiotherapy patients and irradiated animals (31, 59, 60). The normal differentiation and migration process implies nuclear disintegration of the keratinocytes that have reached the stratum corneum (10). When nucleated cells are found in the stratum corneum, the differentiation process is abnormal and called "parakeratosis". We observed parakeratosis after exposure to carbon ions (2 Gy), whereas only a weak induction was detected after irradiation with moderate and high X-ray doses (**Figure 3B**). In line with a change occurring at higher ionizing densities, parakeratosis was reported also for proton irradiation in an epidermis equivalent (61).

Another indicator of abnormal development is the occurrence of cells with pyknotic nuclei and eosinophilic cytoplasm, which are located in the viable epidermis. We found an increased number of those cells, albeit at a low level, after exposure to moderate doses of X-rays and, longer persisting, for carbon ions (2 Gy; **Figure 3D**). However, unlike "sunburn cells", which have been observed after UV exposure (34, 35), these cells did not show positive staining for activated caspase-3 and were not found in the basal layer. This result indicates that cells with a sunburn-like morphology detected after X-ray and carbon ion irradiation can be ascribed to abnormal differentiation and that this process is not necessarily associated with classical caspase-3-dependent apoptosis. Based on the morphological similarity, the occurrence of these cells might be a prestep for parakeratosis.

In contrast to the aberrant features (parakeratosis, "sunburn cells"), which occur to a higher extent after carbon ion exposure,

we found indications for non-aberrant, but accelerated differentiation after exposure to moderate and high but not for a low X-ray dose. Quantitative analysis revealed a significant enhancement of thickness of the stratum corneum (hyperkeratosis) for X-rays and for carbon ions. Similar observations in an epidermal skin equivalent are reported for proton exposure (61) and less pronounced for higher LET ions (62). All in all, our own and published data indicate for X-ray and charged particles of the lower LET range that the induced imbalance of the differentiation process manifests as accelerated and not really aberrant as observed for higher LET radiation qualities.

The Proliferation Activity of Basal Cells is Enhanced for a Low Dose of X-Rays

Differentiation and cell proliferation are directly associated; therefore, we also studied the proliferation activity of the basal cells in the HSE, which we found to be enhanced for a low X-ray dose (**Figure 4**). Notably, in human *ex vivo* irradiated skin, we could confirm the enhanced proliferation activity of epidermal cells induced by low X-ray doses (**Figure 4C**). For higher X-ray doses and for carbon ions, the proliferation activity was unchanged or even inhibited, which is in line with results from animal photon studies (22, 54, 60, 63) and consistent with the cell cycle arrest that we observed in NHEK (**Figures 4A,B**; Figure S8 in Supplementary Material).

Our results suggest that increased proliferation is a low-dose effect, which is induced within a few days after exposure. Furthermore, the effect seems to be related to ionizing density, which is endorsed by the observation of an increased proliferation after exposure to charged particles with a relatively low LET [protons (61) and oxygen (62)], which was not detected for heavy ions with a higher LET in the HSE construct used in our study (62). These findings and our results indicate a low-dose effect, which is induced by low or moderate LET radiation, and may correspond to an early onset of tissue regeneration but does not occur at high doses and high LET, where cell cycle arrest and terminal differentiation are dominating.

Obvious Changes in the Organization of the Basal Layer Occur After Exposure to Low Doses of X-Rays

In addition to changed differentiation and proliferation, we observed a radiation-induced transition from the typical palisade-like to a cobblestoned morphology of the basal cells for X-rays and carbon ions (**Figure 5A**). This is independent of the anchorage to the basal membrane, indicating a changed polarity of the basal cells. Semiquantitative analysis revealed a more pronounced effect for low compared to higher doses and comparing the same physical doses, a more pronounced effect for X-rays than for carbon ions (see **Figure 5B**) and comparing the same physical doses, a more pronounced effect for X-rays than for carbon ions.

A changed polarity has been characterized as a cellular change concomitant to the onset of proliferation and/or to migration (64), in particular in carcinogenic development. Anchorage-independent growth of epidermal cells can be evoked by irradiation as established in a murine epidermal cell line. Interestingly, we detected a delocalization of E-Cadherin from the cytoplasma membrane in HSE after X-ray and carbon ion exposure (**Figure 5C**). E-Cadherin is involved in cell–cell contacts of keratinocytes, and the transition to a cobblestoned morphology of the basal keratinocytes implies a dissociation of the intercellular contacts in the basal layer. The translocalization of E-Cadherin could be involved in the molecular mechanisms of radiation-induced anchorage independence, which was observed in our study. According to the results obtained so far, changed epidermal tissue organization plays a role for both X-ray and carbon ion exposure.

CONCLUSION

Our results show that ionizing irradiation has an effect on the differentiation and organization of the epidermal layers in the skin equivalent. Densely ionizing charged particle are more effective than X-rays per unit dose in the induction of several biological endpoints, including DNA damage, chromosome aberrations, mutations, and cell killing. Our results suggest that exposure to carbon ions under therapy-like conditions triggers proinflammatory signals and changes in homeostasis and epidermal tissue organization to a similar extent as photons, independent of cell death. On the other hand, heavy ions and X-rays modify epidermal tissue organization at low doses and differentiation at high doses. How these tissue-specific effects can be related to the initial DNA damage, whose quality is different after low and high LET radiation, is unclear yet. Recently, Kang et al. (65) have shown that DNA damage response activates the GATA4 pathway, thus inducing inflammatory responses and reducing proliferation. The establishment of a direct link between DNA repair and late changes in homeostasis is important to explain why some effects can be differently revealed at low/high doses or low/high LET.

ACKNOWLEDGMENTS

We want to acknowledge the dedicated help of G. Alphonse and C. Rodriguez-Lafrasse (University Lyon, France) in establishing methods for the assessment of apoptosis in cells. We would like to thank K. Petschick, C. Caliendo, A. Bentzer, and L. Madl for their excellent help with the experiments. We thank M. Scholz, T. Friedrich, W. Becher (GSI); S. Brons, K. Weber, T. Haberer (HIT); and the respective dosimetry teams from GSI and HIT for the dedicated support during the experimental runs. We acknowledge the hospital team of the dermatology clinic (Darmstadt, Germany) for providing skin tissue samples.

FUNDING

This work was supported by DFG (GRK1657), BMBF (GREWIS; 02NUK017A), PARTNER Project, HGS-hire, and Verein zur Förderung der Tumortherapie mit schweren Ionen e.V.

SUPPLEMENTARY MATERIAL

The Supplementary Material for this article can be found online at http://journal.frontiersin.org/article/10.3389/fonc.2015.00294

REFERENCES

1. Durante M, Loeffler JS. Charged particles in radiation oncology. *Nat Rev Clin Oncol* (2010) **7**:37–43. doi:10.1038/nrclinonc.2009.183
2. Loeffler JS, Durante M. Charged particle therapy – optimization, challenges and future directions. *Nat Rev Clin Oncol* (2013) **10**:411–24. doi:10.1038/nrclinonc.2013.79
3. Scholz M. Effects of ion radiation on cells and tissues. In: Kausch H, editor. *Radiation Effects on Polymers for Biological Use*. Berlin Heidelberg: Springer-Verlag (2003). p. 95–155. doi:10.1007/3-540-45668-6
4. Kraft G. Radiobiological effects of very heavy ions: inactivation, induction of chromosome aberrations and strand breaks. *Nucl Sci Appl* (1987) **3**:1–28.
5. Yanagi T, Kamada T, Tsuji H, Imai R, Serizawa I, Tsujii H. Dose-volume histogram and dose-surface histogram analysis for skin reactions to carbon ion radiotherapy for bone and soft tissue sarcoma. *Radiother Oncol* (2010) **95**:60–5. doi:10.1016/j.radonc.2009.08.041
6. Rieber JG, Kessel KA, Witt O, Behnisch W, Kulozik AE, Debus J, et al. Treatment tolerance of particle therapy in pediatric patients. *Acta Oncol* (2015) **54**:1049–55. doi:10.3109/0284186X.2014.998273
7. Whaley JT, Kirk M, Cengel K, McDonough J, Bekelman J, Christodouleas JP. Protective effect of transparent film dressing on proton therapy induced skin reactions. *Radiat Oncol* (2013) **8**:19. doi:10.1186/1748-717X-8-19
8. Galland-Girodet S, Pashtan I, MacDonald SM, Ancukiewicz M, Hirsch AE, Kachnic LA, et al. Long-term cosmetic outcomes and toxicities of proton beam therapy compared with photon-based 3-dimensional conformal accelerated partial-breast irradiation: a phase 1 trial. *Int J Radiat Oncol Biol Phys* (2014) **90**:493–500. doi:10.1016/j.ijrobp.2014.04.008
9. Shore RE. Radiation-induced skin cancer in humans. *Med Pediatr Oncol* (2001) **36**:549–54. doi:10.1002/mpo.1128
10. Kolarsick PAJ, Kolarsick MA, Goodwin C. Anatomy and physiology of the skin. *J Dermatol Nurs Assoc* (2011) **3**:203–13. doi:10.1097/JDN.0b013e3182274a98
11. Peter R. The cutaneous radiation syndrome. In: MacVittie TJ, Weiss JF, Browne D, editors. *Advances in the Treatment of Radiation Injuries*. Oxford: Elsevier (1996). p. 237–41.
12. Müller K, Meineke V. Radiation-induced alterations in cytokine production by skin cells. *Exp Hematol* (2007) **35**:96–104. doi:10.1016/j.exphem.2007.01.017
13. Berkey FJ. Managing the adverse effects of radiation therapy. *Am Fam Physician* (2010) **82**(381–8):394.
14. Rödel F, Frey B, Manda K, Hildebrandt G, Hehlgans S, Keilholz L, et al. Immunomodulatory properties and molecular effects in inflammatory diseases of low-dose x-irradiation. *Front Oncol* (2012) **2**:120. doi:10.3389/fonc.2012.00120
15. Aubin F. Mechanisms involved in ultraviolet light-induced immunosuppression. *Eur J Dermatol* (2003) **13**:515–23.
16. Schwarz T. Mechanisms of UV-induced immunosuppression. *Keio J Med* (2005) **54**:165–71. doi:10.2302/kjm.54.165
17. Suvarna KS, Layton C, Bancroft JD. *Bancroft's Theory and Practice of Histological Techniques*. 7th ed. Elsevier Health Sciences (2012). Available from: https://books.google.com/books?id=wPPU4NyGm3gC&pgis=1
18. Fournier C, Wiese C, Taucher-Scholz G. Accumulation of the cell cycle regulators TP53 and CDKN1A (p21) in human fibroblasts after exposure to low- and high-LET radiation. *Radiat Res* (2004) **161**:675–84. doi:10.1667/RR3182
19. Varnum SM, Springer DL, Chaffee ME, Lien KA, Webb-Robertson B-JM, Waters KM, et al. The effects of low-dose irradiation on inflammatory response proteins in a 3D reconstituted human skin tissue model. *Radiat Res* (2012) **178**:591–9. doi:10.1667/RR2976.1
20. Bell CW, Jiang W, Reich CF, Pisetsky DS. The extracellular release of HMGB1 during apoptotic cell death. *Am J Physiol Cell Physiol* (2006) **291**:C1318–25. doi:10.1152/ajpcell.00616.2005
21. Raucci A, Palumbo R, Bianchi ME. HMGB1: a signal of necrosis. *Autoimmunity* (2007) **40**:285–9. doi:10.1080/08916930701356978
22. Ahmed EA, Agay D, Schrock G, Drouet M, Meineke V, Scherthan H. Persistent DNA damage after high dose in vivo gamma exposure of minipig skin. *PLoS One* (2012) **7**:e39521. doi:10.1371/journal.pone.0039521
23. Le Poole IC, Boyce ST. Keratinocytes suppress transforming growth factor-beta1 expression by fibroblasts in cultured skin substitutes. *Br J Dermatol* (1999) **140**:409–16. doi:10.1046/j.1365-2133.1999.02700.x
24. Maas-Szabowski N, Stark HJ, Fusenig NE. Keratinocyte growth regulation in defined organotypic cultures through IL-1-induced keratinocyte growth factor expression in resting fibroblasts. *J Invest Dermatol* (2000) **114**:1075–84. doi:10.1046/j.1523-1747.2000.00987.x
25. Matsumura T, Hayashi H, Takii T, Thorn CF, Whitehead AS, Inoue J-I, et al. TGF-beta down-regulates IL-1alpha-induced TLR2 expression in murine hepatocytes. *J Leukoc Biol* (2004) **75**:1056–61. doi:10.1189/jlb.0104108
26. Lian X, Yang L, Gao Q, Yang T. IL-1alpha is a potent stimulator of keratinocyte tissue plasminogen activator expression and regulated by TGF-beta1. *Arch Dermatol Res* (2008) **300**:185–93. doi:10.1007/s00403-007-0828-8
27. Martin M, Lefaix J, Delanian S. TGF-beta1 and radiation fibrosis: a master switch and a specific therapeutic target? *Int J Radiat Oncol Biol Phys* (2000) **47**:277–90. doi:10.1016/S0360-3016(00)00435-1
28. King A, Balaji S, Le LD, Crombleholme TM, Keswani SG. Regenerative wound healing: the role of interleukin-10. *Adv Wound Care* (2014) **3**:315–23. doi:10.1089/wound.2013.0461
29. Grivennikov SI, Greten FR, Karin M. Immunity, inflammation, and cancer. *Cell* (2010) **140**:883–99. doi:10.1016/j.cell.2010.01.025
30. Barcellos-Hoff MH, Nguyen DH. Radiation carcinogenesis in context: how do irradiated tissues become tumors? *Health Phys* (2009) **97**:446–57. doi:10.1097/HP.0b013e3181b08a10
31. Sivan V, Vozenin-Brotons M-C, Tricaud Y, Lefaix J-L, Cosset J-M, Dubray B, et al. Altered proliferation and differentiation of human epidermis in cases of skin fibrosis after radiotherapy. *Int J Radiat Oncol Biol Phys* (2002) **53**:385–93. doi:10.1016/S0360-3016(01)02732-8
32. Lowes MA, Bowcock AM, Krueger JG. Pathogenesis and therapy of psoriasis. *Nature* (2007) **445**:866–73. doi:10.1038/nature05663
33. Johnson-Huang LM, Lowes MA, Krueger JG. Putting together the psoriasis puzzle: an update on developing targeted therapies. *Dis Model Mech* (2012) **5**:423–33. doi:10.1242/dmm.009092
34. Lippens S, Hoste E, Vandenabeele P, Agostinis P, Declercq W. Cell death in the skin. *Apoptosis* (2009) **14**:549–69. doi:10.1007/s10495-009-0324-z
35. Van Laethem A, Claerhout S, Garmyn M, Agostinis P. The sunburn cell: regulation of death and survival of the keratinocyte. *Int J Biochem Cell Biol* (2005) **37**:1547–53. doi:10.1016/j.biocel.2005.02.015
36. Qin J-Z, Chaturvedi V, Denning MF, Bacon P, Panella J, Choubey D, et al. Regulation of apoptosis by p53 in UV-irradiated human epidermis, psoriatic plaques and senescent keratinocytes. *Oncogene* (2002) **21**:2991–3002. doi:10.1038/sj.onc.1205404
37. Elias PM. Stratum corneum defensive functions: an integrated view. *J Invest Dermatol* (2005) **125**:183–200. doi:10.1111/j.0022-202X.2005.23668.x
38. Maverakis E, Miyamura Y, Bowen MP, Correa G, Ono Y, Goodarzi H. Light, including ultraviolet. *J Autoimmun* (2010) **34**:J247–57. doi:10.1016/j.jaut.2009.11.011
39. Elias PM, Gruber R, Crumrine D, Menon G, Williams ML, Wakefield JS, et al. Formation and functions of the corneocyte lipid envelope (CLE). *Biochim Biophys Acta* (2014) **1841**:314–8. doi:10.1016/j.bbalip.2013.09.011
40. Muroyama A, Lechler T. Polarity and stratification of the epidermis. *Semin Cell Dev Biol* (2012) **23**:890–6. doi:10.1016/j.semcdb.2012.08.008
41. Jamal S, Schneider RJ. UV-induction of keratinocyte endothelin-1 downregulates E-cadherin in melanocytes and melanoma cells. *J Clin Invest* (2002) **110**:443–52. doi:10.1172/JCI13729
42. Turesson I, Nyman J, Qvarnström F, Simonsson M, Book M, Hermansson I, et al. A low-dose hypersensitive keratinocyte loss in response to fractionated radiotherapy is associated with growth arrest and apoptosis. *Radiother Oncol* (2010) **94**:90–101. doi:10.1016/j.radonc.2009.10.007
43. Hopewell JW. Mechanisms of the action of radiation on skin and underlying tissues. *Br J Radiol Suppl* (1986) **19**:39–47.
44. Bentzen SM, Saunders MI, Dische S, Bond SJ. Radiotherapy-related early morbidity in head and neck cancer: quantitative clinical radiobiology as deduced from the CHART trial. *Radiother Oncol* (2001) **60**:123–35. doi:10.1016/S0167-8140(01)00358-9
45. Gottlöber P, Steinert M, Weiss M, Bebeshko V, Belyi D, Nadejina N, et al. The outcome of local radiation injuries: 14 years of follow-up after the Chernobyl accident. *Radiat Res* (2001) **155**:409–16. doi:10.1667/0033-7587(2001)155[0409:TOOLRI]2.0.CO;2
46. Fink SL, Cookson BT. Apoptosis, pyroptosis, and necrosis: mechanistic description of dead and dying eukaryotic cells. *Infect Immun* (2005) **73**:1907–16. doi:10.1128/IAI.73.4.1907-1916.2005

47. Weyrather WK, Ritter S, Scholz M, Kraft G. RBE for carbon track-segment irradiation in cell lines of differing repair capacity. *Int J Radiat Biol* (1999) **75**:1357–64. doi:10.1080/095530099139232
48. Suzuki M, Kase Y, Yamaguchi H, Kanai T, Ando K. Relative biological effectiveness for cell-killing effect on various human cell lines irradiated with heavy-ion medical accelerator in Chiba (HIMAC) carbon-ion beams. *Int J Radiat Oncol Biol Phys* (2000) **48**:241–50. doi:10.1016/S0360-3016(00)00568-X
49. Fournier C, Scholz M, Weyrather WK, Rodemann HP, Kraft G. Changes of fibrosis-related parameters after high- and low-LET irradiation of fibroblasts. *Int J Radiat Biol* (2001) **77**:713–22. doi:10.1080/095530000110045025
50. Petit-Frere C, Capulas E, Lyon DA, Norbury CJ, Lowe JE, Clingen PH, et al. Apoptosis and cytokine release induced by ionizing or ultraviolet B radiation in primary and immortalized human keratinocytes. *Carcinogenesis* (2000) **21**:1087–95. doi:10.1093/carcin/21.6.1087
51. Rachidi W, Harfourche G, Lemaitre G, Amiot F, Vaigot P, Martin MT. Sensing radiosensitivity of human epidermal stem cells. *Radiother Oncol* (2007) **83**:267–76. doi:10.1016/j.radonc.2007.05.007
52. Fournier C, Winter M, Zahnreich S, Nasonova E, Melnikova L, Ritter S. Interrelation amongst differentiation, senescence and genetic instability in long-term cultures of fibroblasts exposed to different radiation qualities. *Radiother Oncol* (2007) **83**:277–82. doi:10.1016/j.radonc.2007.04.022
53. Von Neubeck C, Shankaran H, Karin NJ, Kauer PM, Chrisler WB, Wang X, et al. Cell type-dependent gene transcription profile in a three-dimensional human skin tissue model exposed to low doses of ionizing radiation: implications for medical exposures. *Environ Mol Mutagen* (2012) **53**:247–59. doi:10.1002/em.21682
54. Morris GM, Hopewell JW. Changes in the cell kinetics of pig epidermis after single doses of X rays. *Br J Radiol* (1988) **61**:205–11. doi:10.1259/0007-1285-61-723-205
55. Berglund SR, Rocke DM, Dai J, Schwietert CW, Santana A, Stern RL, et al. Transient genome-wide transcriptional response to low-dose ionizing radiation in vivo in humans. *Int J Radiat Oncol Biol Phys* (2008) **70**:229–34. doi:10.1016/j.ijrobp.2007.09.026
56. Goldberg Z, Rocke DM, Schwietert C, Berglund SR, Santana A, Jones A, et al. Human in vivo dose-response to controlled, low-dose low linear energy transfer ionizing radiation exposure. *Clin Cancer Res* (2006) **12**:3723–9. doi:10.1158/1078-0432.CCR-05-2625
57. Liu W, Ding I, Chen K, Olschowka J, Xu J, Hu D, et al. Interleukin 1beta (IL1B) signaling is a critical component of radiation-induced skin fibrosis. *Radiat Res* (2006) **165**:181–91. doi:10.1667/RR3478.1
58. Martin M, Lefaix JL, Pinton P, Crechet F, Daburon F. Temporal modulation of TGF-beta 1 and beta-actin gene expression in pig skin and muscular fibrosis after ionizing radiation. *Radiat Res* (1993) **134**:63–70. doi:10.2307/3578502
59. Dörr W. Modulation of repopulation processes in oral mucosa: experimental results. *Int J Radiat Biol* (2003) **79**:531–7. doi:10.1080/09553002310001600925
60. Liu K, Kasper M, Trott KR. Changes in keratinocyte differentiation during accelerated repopulation of the irradiated mouse epidermis. *Int J Radiat Biol* (1996) **69**:763–9. doi:10.1080/095530096145508
61. Mezentsev A, Amundson SA. Global gene expression responses to low- or high-dose radiation in a human three-dimensional tissue model. *Radiat Res* (2011) **175**:677–88. doi:10.1667/RR2483.1
62. Von Neubeck C, Geniza MJ, Kauer PM, Robinson RJ, Chrisler WB, Sowa MB. The effect of low dose ionizing radiation on homeostasis and functional integrity in an organotypic human skin model. *Mutat Res* (2015) **775**:10–8. doi:10.1016/j.mrfmmm.2015.03.003
63. Dörr W, Emmendörfer H, Weber-Frisch M. Tissue kinetics in mouse tongue mucosa during daily fractionated radiotherapy. *Cell Prolif* (1996) **29**:495–504. doi:10.1111/j.1365-2184.1996.tb00992.x
64. Steude J, Kulke R, Christophers E. Interleukin-1-stimulated secretion of interleukin-8 and growth-related oncogene-alpha demonstrates greatly enhanced keratinocyte growth in human raft cultured epidermis. *J Invest Dermatol* (2002) **119**:1254–60. doi:10.1046/j.1523-1747.2002.19616.x
65. Kang C, Xu Q, Martin TD, Li MZ, Demaria M, Aron L, et al. The DNA damage response induces inflammation and senescence by inhibiting autophagy of GATA4. *Science* (2015) **349**:aaa5612. doi:10.1126/science.aaa5612

Conflict of Interest Statement: The authors declare that the research was conducted in the absence of any commercial or financial relationships that could be construed as a potential conflict of interest.

The reviewers, Michael Wayne Epperly and Christopher James Bakkenist, and handling Editor Joel S. Greenberger declared their shared affiliation, and the handling Editor states that the process nevertheless met the standards of a fair and objective review.

Copyright © 2016 Simoniello, Wiedemann, Zink, Thoennes, Stange, Layer, Kovacs, Podda, Durante and Fournier. This is an open-access article distributed under the terms of the Creative Commons Attribution License (CC BY). The use, distribution or reproduction in other forums is permitted, provided the original author(s) or licensor are credited and that the original publication in this journal is cited, in accordance with accepted academic practice. No use, distribution or reproduction is permitted which does not comply with these terms.

frontiers in Oncology

ORIGINAL RESEARCH
published: 29 March 2016
doi: 10.3389/fonc.2016.00064

The Effect of X-Ray and Heavy Ions Radiations on Chemotherapy Refractory Tumor Cells

Zhan Yu[1,2], Carola Hartel[1], Diana Pignalosa[1], Wilma Kraft-Weyrather[1], Guo-Liang Jiang[2,3], David Diaz-Carballo[4] and Marco Durante[1,5]*

[1] Department of Biophysics, GSI Helmholtzzentrum für Schwerionenforschung, Darmstadt, Germany, [2] Department of Radiation Oncology, Shanghai Proton and Heavy Ion Center, Shanghai, China, [3] Department of Oncology, Shanghai Medical College, Fudan University, Shanghai, China, [4] Institute of Molecular Oncology and Experimental Therapeutics, Marienhospital Herne, Ruhr University of Bochum Medical School, Herne, Germany, [5] Institute of Condense Matter Physics, Darmstadt University of Technology, Darmstadt, Germany

Purpose: The purpose of this study is to link both numeric and structural chromosomal aberrations to the effectiveness of radiotherapy in chemotherapy refractory tumor cells.

Materials and methods: Neuroblastoma (LAN-1) and 79HF6 glioblastoma cells derived from patients and their chemoresistant sublines were artificially cultured as neurospheres and irradiated by X-rays and heavy ions sources. All the cell lines were irradiated by Carbon-SIS with LET of 100 keV/μm. However, 79HF6 cells and LAN-1 cells were also irradiated by Carbon-UNILAC with LET of 168 keV/μm and Nickel ions with LET of 174 keV/μm, respectively. The effect of radiation on the survival and proliferation of cells was addressed by standard clonogenic assays. In order to analyze cell karyotype standard Giemsa staining, multicolor fluorescence *in situ* hybridization (mFISH) and multicolor banding (mBAND) techniques were applied.

Results: Relative biological effectiveness values of heavy ion beams relative to X-rays at the D_{10} values were found between 2.3 and 2.6 with Carbon-SIS and Nickel for LAN-1 and between 2.5 and 3.4 with Carbon-SIS and Carbon-UNILAC for 79HF6 cells. Chemorefractory LAN-1^{RETO} cells were found more radioresistant than untreated LAN-1^{WT} cells. 79HF6^{RETO} glioblastoma cells were found more radiosensitive than cytostatic sensitive cells 79HF6^{WT}. Sphere formation assay showed that LAN-1^{RETO} cells were able to form spheres in serum-free culture, whereas 79HF6 cells could not. Most of 79HF6^{WT} cells revealed a number of 71–90 chromosomes, whereas 79HF6^{RETO} revealed a number of 52–83 chromosomes. The majority of LAN-1^{WT} cells revealed a number of 40–44 chromosomes. mFISH analysis showed some stable aberrations, especially on chromosome 10 as judged by the impossibility to label this region with specific probes. This was corroborated using mBAND analysis.

Conclusion: Heavy ion irradiation was more effective than X-ray in both cytostatic naive cancer and chemoresistant cell lines. LAN-1^{RETO} chemoresistant neuroblastoma cells were found to be more radioresistant than the cytostatic naive cells (LAN-1^{WT}), whereas this effect was not found in 79HF6 cells.

Keywords: chemoresistance, X-ray and heavy ion irradiation, relative biological effectiveness, neuroblastoma, glioblastoma

OPEN ACCESS

Edited by:
John Varlotto, University of Massachusetts Medical Center, USA

Reviewed by:
Wenyin Shi, Thomas Jefferson University, USA
Evagelia C. Laiakis, Georgetown University, USA
John Eley, University of Maryland School of Medicine, USA

****Correspondence:***
Zhan Yu
zhan.yu@sphic.org.cn

Specialty section:
This article was submitted to Radiation Oncology, a section of the journal Frontiers in Oncology

Received: *30 September 2015*
Accepted: *07 March 2016*
Published: *29 March 2016*

Citation:
Yu Z, Hartel C, Pignalosa D, Kraft-Weyrather W, Jiang G-L, Diaz-Carballo D and Durante M (2016) The Effect of X-Ray and Heavy Ions Radiations on Chemotherapy Refractory Tumor Cells. Front. Oncol. 6:64. doi: 10.3389/fonc.2016.00064

INTRODUCTION

There is convincing evidence that many solid and hematological malignancies are organized hierarchically and contain a small population of cancer stem cells (CSCs) that possess the capacity to self-renew and to cause the heterogeneous lineages of cells that form the tumor (1). Consequently, cell heterogeneity of tumors may play an important role in tumor persistence and metastasis formation. Additionally, there is growing evidence that CSCs are inherently resistant to radiation and perhaps other conventional anticancer treatments, i.e., chemotherapy (2–4). These intrinsic mechanisms of resistance are responsible for a significant number of tumor recurrences (2, 3). Consequently, an effective anticancer treatment can only be achieved if this population is eliminated.

Chemotherapy has the advantage over radiotherapy in fighting the disseminated metastatic situation but at higher costs for the organism as a whole. Contrary to that, radiotherapy is a more localized treatment, but it is less applicable once the cancer has spread to several regions. Contemporaneous studies have consistently shown that CSC phenotypes are triggered after chemotherapy courses with an accompanied radioresistance of cancer cells both *in vitro* and *in vivo* probably by preferential activation of the DNA damage response (5). This indicates the urgent necessity for reevaluation of conventional therapies and searching for new ones that focus on CSCs to enhance the efficacy of cancer treatments.

Neuroblastoma is one of the most common extracranial pediatric tumors with a wide spectrum of clinical forms. The long-term survival of children with a high-risk clinical phenotype is <40% (especially those with MYCN amplification) (6). Glioblastoma is the most aggressive brain tumor in adults. In spite of multimodal therapy, the median survival is only around 14 months with early recurrences (and infiltrative events) in the brain (7). The existence (and local spread) of CSCs may be an important reason for the treatment failure due to its resistance to conventional therapy, which leads to a poor prognosis.

Culturing cancer cells in the presence of a low dose of chemotherapeutic agents is one of the approaches to enrich subpopulations with CSC-like phenotypes and related physiology. Etoposide is a topoisomerase inhibitor and causes DNA breaks enforcing apoptosis in dividing cancer cells. It is used as a standard chemotherapy in many tumors, such as neuroblastoma. However, etoposide is also known as an inducing agent of multidrug-resistant cancer phenotypes. In this study, low dose of etoposide was used to enrich CSCs fraction in glioblastoma and neuroblastoma cell lines.

Particle radiotherapy is becoming more widely used because proton and heavy ions have a favorable depth–dose distribution and a higher relative biological effectiveness (RBE) compared with photon. Once cancer cells are exposed to this therapy, they suffer a complex and clustered DNA damage, which is unable to be repaired by cellular mechanisms independent of the reactive oxygen species formed after exposing cells to charged particles. Consequently, malignant cells are less radioresistance because the mechanisms responsible for DNA reparation work less effective (8).

Our works aimed at studying the survival of chemoresistant cells compared with their wild-type parentals after being exposed to X-rays and heavy ions. We also addressed the question if the karyotype and chromosomal number deviations are related to the survival.

MATERIALS AND METHODS

Cell Lines and Culture Conditions

Two parental and their subtypes highly chemotherapy refractory cell lines LAN-1^{WT}, LAN-1^{RETO} neuroblastoma and 79HF6^{WT}, 79HF6^{RETO} glioblastoma multiforme derived from human tumors were used in this investigation. The LAN-1 cells were isolated from a bone marrow metastasis of a 2-year-old boy with neuroblastoma (clinical Stage IV), and the 79HF6 cells were isolated from a female adult patient. The etoposide-resistant sublines usyed in this work exhibit CSC features among a set of CSC markers, broad spectrum of cross-resistance to several cytostatics, and radioresistance. The phenotype characteristics and the CSC features were published previously (5). Cells were cultured in Dulbecco's modified Eagle medium (DMEM), supplemented with 10% fetal calf serum (FCS) and 1% penicillin/streptomycin (all purchased from Biochrom AG, Berlin, Germany), and kept in a humidified atmosphere of 5% CO_2 at 37°C. Resistant to ETOposide (RETO) cells were constantly cultured in the medium containing 4 μg/ml etoposide (Teva, Germany). The cell doubling time (t_D) was determined in the exponential phase of the growth with the GSI in house program gd (©M. Krämer, 2003).

Clonogenic Assay

Clonogenic assay was performed to determine both clonogenic behavior and cell survival rates after irradiation. Cells were seeded in T25 flask containing around 100 viable colonies after irradiation. LAN-1^{WT} and LAN-1^{RETO} cells were incubated for 9 days. 79HF6^{WT} cells were incubated for 11 days, whereas 79HF6^{RETO} cells were incubated for 25 days. Colonies were fixed and stained with methylene blue. Colonies containing more than 50 cells were defined as survivors.

Sphere Formation Assay

Cells were cultured in serum-free neurobasal A medium (Gibco, Life Technologies, Germany) supplemented with B27 (Gibco, Life Technologies, Germany), 10 ng/ml human fibroblast growth factor-basic (Biochrom, Germany), 20 ng/ml human epidermal growth factor (Biochrom, Germany), and 0.1% bovine serum albumin fraction V (Roche Diagnostics, Germany) to observe the formation of neurospheres (9).

Karyotyping

For chromosome preparations, cells were seeded 48 h in T75 culture flasks with 10 ml medium before the experiment in order to allow stabile attachment. One hundred microliters of colcemid (Roche Deutschland Holding GmbH, Germany) with the concentration of 10 μg/ml were added to the cultures. After 3.5 h of incubation for LAN-1 and 79HF6^{WT} and 4 h for 79HF6^{RETO}, cells were trypsinized and harvested. Cell suspension was

pelleted and carefully treated with prewarmed (37°C) 0.075M potassium chloride solution for 8 min and then fixed with 3:1 ratio of MeOH:glacial acetic acid for 30 min at room temperature. After washing, cells were resuspended in proper volume of the mentioned fixative and dropped on wet slides. The slides were then air-dried for 24 h. The slides were stained with 5% Giemsa (Merck, Germany) solution for 10 min, washed with distilled water, and dried overnight.

Multicolor Fluorescence *In Situ* Hybridization Technique and Multicolor Banding Technique

For multicolor fluorescence *in situ* hybridization (mFISH) analysis, the slides were hybridized using the 24XCyte mFISH kit (Metasystems, Altlussheim, Germany) according to the protocol recommended by the manufacturer. In brief, the slides were first subjected to a denaturation followed by dehydration. An appropriate volume of DNA denatured probe was incubated in a humidified chamber at 37°C in the dark for 2 days. Afterward, the remaining hybridization probe was washed off. Finally, all DNA material was counterstained using DAPI/antifade (250 ng/ml), and the slide was covered. The chromosomal dispersal was analyzed using fluorescence microscopy Imager Z1 (Zeiss, Germany). Probes labeled with FITC, Orange, Texas Red®, Aqua, Cy™5 (Cy5), and 4′,6-diamidino-2-phenylindol (DAPI) fluorochromes were used to visualize chromosomal segments. Karyotypes were (re)constructed using the Isis/mFISH software (Metasystems). The procedure of multicolor banding (mBAND) is similar to that of mFISH, performed with the mBAND kit (Metasystems, Altlussheim, Germany), as previously described.

Ionizing Irradiation

All the irradiations were performed in GSI. The X-ray irradiation was carried out using an Isovolt DS1 X-ray machine (Seifert, Ahrensberg, Germany), exposing cells to 250 kVp and 16 mA.

Ion irradiation was performed in a synchrotron machine of the GSI. For irradiation at Carbon-SIS facility, cells were cultured in T12.5 culture flasks and were completely filled with culture medium before irradiation. The cells were irradiated with 10 mm spread out Bragg peak (SOBP) with LET of 100 keV/μm. All the cell lines were irradiated by Carbon-SIS. For experiments using a Carbon-UNILAC, 79HF6 cells were cultured in 3 cm Petri dishes and placed into compatible Petri dish magazines for irradiation. The carbon ions had a primary energy of 11.4 MeV/u and the energy decreased to 9.9 MeV/u when stopping on target with the corresponding LET of 168 keV/μm (10). After irradiation, the inner border of Petri dish was cleaned using sterile cotton to remove unirradiated medium accumulated at the bottom of the inner border, because dishes were irradiated in a vertical position. As survival of cells is related to the LET of the beam, we use those two carbon beams with different LETs. LAN-1 cells were also irradiated by Nickel ions with energy of 1 GeV/u and LET of 174 keV/μm, because the beam time is limited in GSI and we got the chance of irradiated by Nickel ions with similar LET to Carbon-UNILAC, which is a higher LET beam compared with Carbon-SIS.

Samples in triplicate were subjected to irradiation sections for each dose with X-ray, heavy ions, and repeated at least three times. The irradiation doses for LAN-1^{WT} were fixed from 0 to 7 Gy for X-ray, from 0 to 2 Gy for Carbon, and from 0 to 2 Gy for Nickel. However, the doses for LAN-1^{RETO} were from 0 to 9 Gy for X-ray, 0 to 3.2 Gy for Carbon, and 0 to 2 Gy for Nickel. The doses for 79HF6^{WT} and 79HF6^{RETO} were applied from 0 to 10 Gy for X-ray, 0 to 5 Gy for Carbon-SIS, and 0 to 2.72 Gy for Carbon-Unilac.

Cell survival curves of X-ray were fitted with the linear-quadratic model (Eq. 1):

$$S = e^{\left(-\alpha D - \beta D^2\right)} \quad (1)$$

Cell survival curves of heavy ions were fitted with a pure exponential equation (Eq. 2):

$$S = e^{(-\alpha D)} \quad (2)$$

RBE_{10} values were calculated at 10% of survival level according to Eq. 3:

$$RBE_{10} = D_{10}\ \text{X-ray} / D_{10}\ \text{ions} \quad (3)$$

All of the fitting was performed with the GSI in house program gd (©M. Krämer, 2003).

Statistical Analysis

Experiments were performed at least in triplicate, and the survival fraction of cells was given as mean ± SD. Karyotype and mBAND figures were descriptive and therefore not statistically analyzed.

RESULTS

Differential Growth Patterns of LAN-1 Neuroblastoma and Glioblastoma 79HF6 Cell Lines

All four cell lines, both wild type and resistant, grew adherently. The growth kinetic for all cells shows differential pattern as jugged by their doubling times. In this regard, the replication of LAN-1^{WT}, LAN-1^{RETO}, 79HF6^{WT}, and 79HF6^{RETO} was observed at 21.7 ± 0.7, 16.9 ± 0.8, 21.6 ± 0.3, and 56.7 ± 5.2 h, respectively. LAN-1^{WT} could form spheres when cultured in serum-free neurobasal A medium, whereas the other tumor cells lines were not able to form neurospheres once cultured under this condition (**Figure 1**). LAN-1^{RETO} and 79HF6^{RETO} chemotherapy refractory cells are able to stably grow in the medium containing low concentrations of etoposide. The growth kinetic of LAN-1^{RETO} cells showed a faster cell replication than the wild-type parentals. Contrary to that, 79HF6^{RETO} cells grew slower than 79HF6^{WT}. These dissimilar growth patterns are in part a consequence of the development of chemoresistance of both tumor entities, which are biochemically dissimilar.

Effectiveness of Heavy Ion Irradiation in Comparison to X-Ray

As previously published by our group and others, resistance to etoposide induces radioresistance in both LAN-1 neuroblastoma

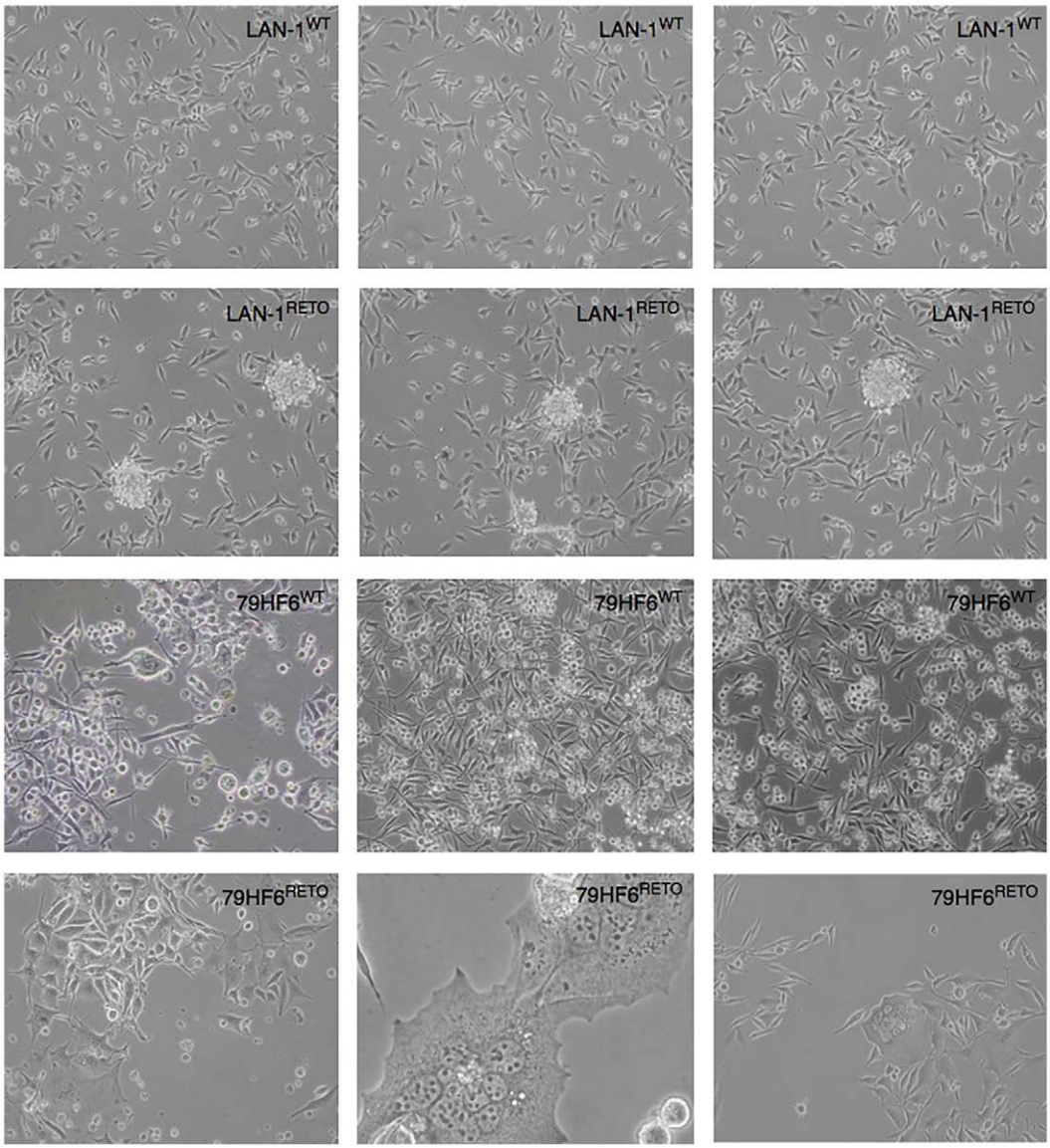

FIGURE 1 | **Neurosphere-forming cells**. LAN-1$^{WT/RETO}$ neuroblastoma cells and 79HF6$^{WT/RETO}$ glioblastoma cells have shown different morphology in serum-free neurobasal A medium. Resistant LAN-1 subline showed the capacity to form neurospheres, whereas their wild-type parental cells are not able to form spheres. 79HF6$^{WT/RETO}$ cells did not alter their growth pattern once incubated in this defined condition. Magnification: LAN-1, 10×; 79HF6^{WT}, 10×; 79HF6^{RETO}, 10×; central picture, 20×. Pictures are representative for different experiments.

and glioblastoma 79HF6 cell lines (5). To explore how heavy ion irradiation has advantages over the conventional X-ray exposures, we monitored the cell survival of these cells exposure to Carbon and Nickel ion irradiation.

The survival curves showed that heavy ion irradiation was more effective than X-ray in all four cell lines (**Figures 2** and **3**). The RBE values of heavy ions beam relative to X-rays at the D_{10} values were from 2.3 to 2.6 for LAN-1 cells and 2.5 to 3.4 for 79HF6 cells (**Table 1**). For LAN-1 cells, the etoposide-resistant subtypes (cultured in the presence of etoposide) were found to be more radioresistant than WT cells (cultured without etoposide) after X-ray and heavy ion irradiation (**Figure 2**), but for 79HF6 cells, RETO cells are more sensitive than WT cells after X-ray and heavy ion irradiation (**Figure 3**).

Chromosomal Aberrations Found in LAN-1 Neuroblastoma and Glioblastoma 79HF6 Cell Lines

In order to search for the cause of radioresistance, we analyzed the karyotype of all cells used in our study. Most of LAN^{-} cells had 40–44 chromosomes, and mFISH showed some stable

aberrations, especially on chromosome 10 with an unstained region (**Figure 4**), and mBAND showed the unstained region located on 10p (**Figure 5**).

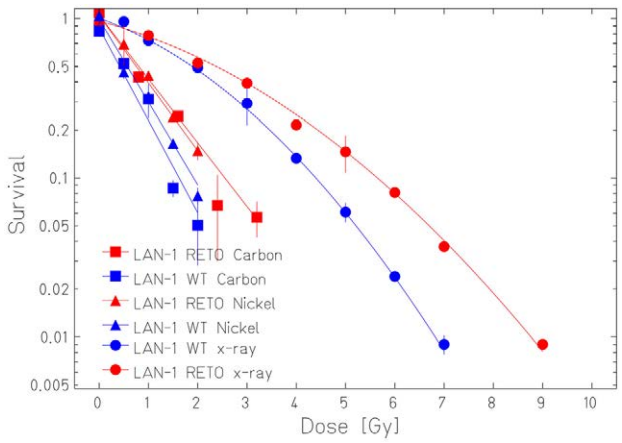

FIGURE 2 | Survival of LAN-1 neuroblastoma cells after ionizing irradiation. LAN-1$^{WT/RETO}$ cells were irradiated with X-ray, Nickel (174 keV/μm), and Carbon-SIS (100 keV/μm). Graphic depicts the results of three independent experiments. Points, the mean survival fractions; bars, SD.

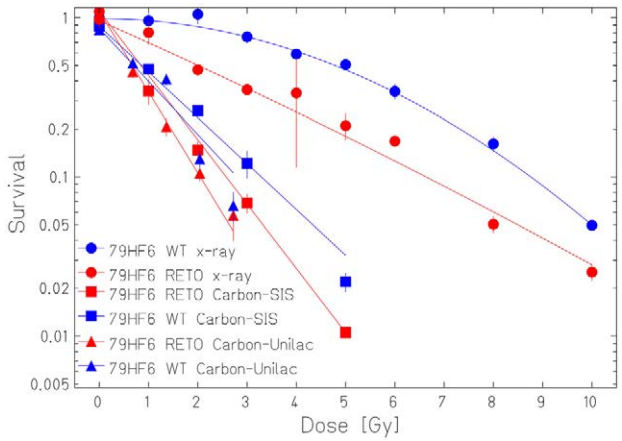

FIGURE 3 | Survival of 79HF6 glioblastoma cells after ionizing irradiation. 79HF6$^{WT/RETO}$ cells were irradiated with X-ray, Carbon-SIS (100 keV/μm), and Carbon-Unilac (168 keV/μm). Graphic depicts the results of three independent experiments. Points, the mean survival fractions; bars, SD.

The chromosomal number in 79HF6 glioblastoma cells enormously differed in the resistant subline. Most of the 79HF6^{WT} cells revealed a number of 71–90 chromosomes, whereas 79HF6^{WT} cells reflected 52–83 chromosomes. The chromosomal number of 79HF6^{RETO} revealed two peaks (**Figure 6**). It indicated that when cells were exposed to etoposide, the chromosome had the tendency to decrease to its relative normal ploidy. This phenomenon could be explained as the effort of tumor cells on maintaining gene stability. Diploid chromosomal distribution is more stable compared with polyploidy numbers, especially when tumor cells suffer the injury of chemical agents or other stressors. Tumors cells carrying a polyploidy derived a subgroup with a more stable karyotype in order to maintain the gene stability.

DISCUSSION

Cancer stem cells show continuous self-renewal, extensive parenchymal migration/infiltration, and potential for full or partial differentiation in all cell types, which constitute a tumor. To explore how LAN-1 neuroblastoma and glioblastoma 79HF6 cell lines growth, we cultured these cells under optimal conditions for propagation in serum-free neurobasal A medium. It is known that under these conditions, cells displayed profound biological differences in growth patterns and were enforced to grow as non-adherent, multicellular spheres, inducing CSC-like populations (9).

Every cell type obviously showed different morphologies, as they were cultured in serum-free medium or serum-contained medium. Sphere formation assay (11, 12) performed to select CSC phenotypes from both cell types revealed that LAN-1^{RETO} cells were able to form neurospheres after culturing them in serum-free medium, instead LAN-1^{WT}, 79HF6^{WT}, and 79HF6^{RETO} cells were not capable to form neurospheres under the same conditions. CSCs may have the competence of durable self-renew, the capacity to develop and maintain tumor-related cell heterogeneity, differentiation, as well as the ability of both radioresistance and chemoresistance. To confirm the existence of CSC features, cells were transplanted to hosts and expected to induce tumor and maintain the features of parental tumor cells (13, 14). Studies in the past (5) have shown that both cell lines have CSC-like features, including chemoresistance and radioresistance to X-ray.

Our studies revealed that heavy ions had higher cell killing efficiency in both neuroblastoma and glioblastoma cell lines, despite its chemoresistance and chromosomal normality status. 79HF6^{WT} cells were very resistant to X-ray. The survival rates of these cells were nearly not affected with 1 or 2 Gy of exposure to X-ray and were still around 5% with 10 Gy. This could explain why

TABLE 1 | Relative biological effectiveness values of heavy ions in LAN-1 neuroblastoma and 79HF6 glioblastoma cells.

Cell line	Carbon	Carbon-SIS	Carbon-Unilac	Nickel
LAN-1^{WT}	2.60 ± 0.20	–	–	2.30 ± 0.20
LAN-1^{RETO}	2.28 ± 0.09	–	–	2.42 ± 0.04
79HF6^{WT}	–	2.50 ± 0.10	2.90 ± 0.20	–
79HF6^{RETO}	–	2.70 ± 0.50	3.40 ± 0.20	–

The relative biological effectiveness (RBE) values of heavy ions beam relative to X-rays at the D_{10} values were found between 2.3 and 2.6 for LAN-1 and 2.5 and 3.4 for 79HF6 cells, respectively.

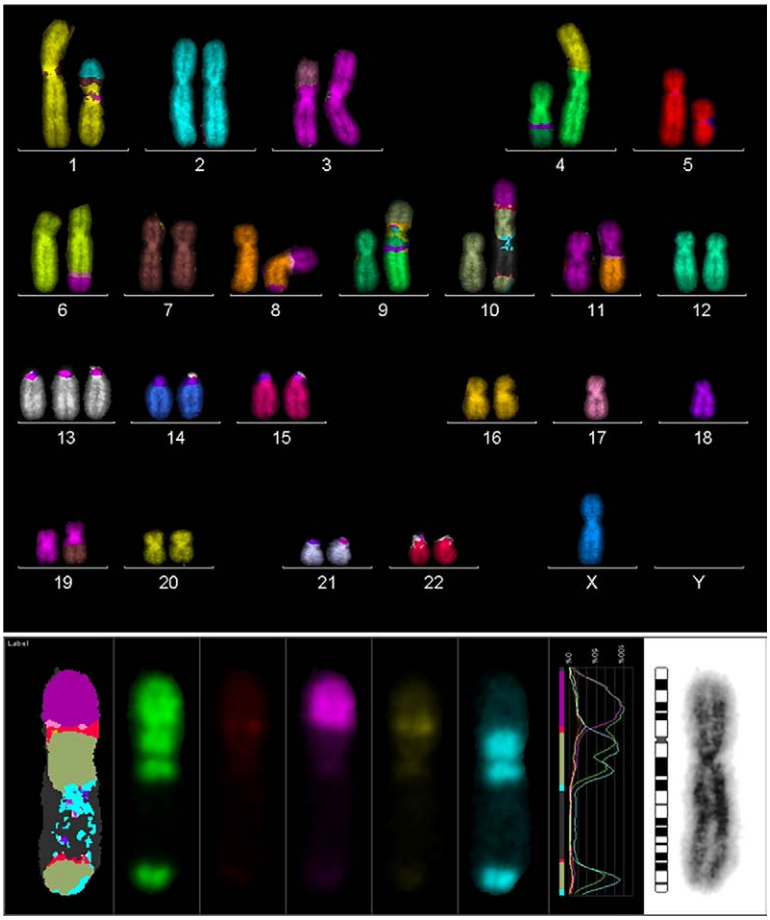

FIGURE 4 | Karyotype of LAN-1 neuroblastoma cells analyzed by mFISH. LAN-1 cells revealed a range of 40–44 chromosomes per cell. Besides the segmental exchange between chromosomes, the most prominent observation in this cell line was an unstained region in chromosome 10. Structurally, chromosome 10 appeared to be intact (lower picture) once stained with Giemsa, but lower arms were not able to hybridize with the corresponding probes. Picture is representative for several cells analyzed under the same conditions. Magnification 100×.

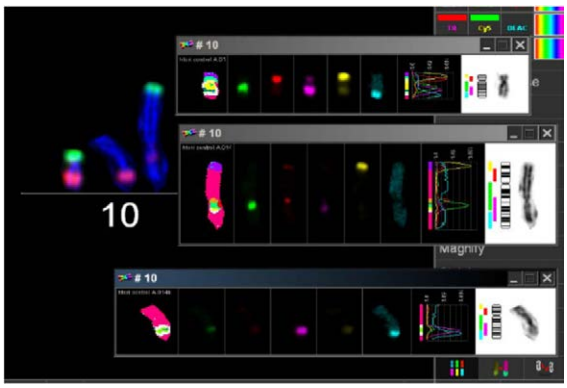

FIGURE 5 | mBAND analysis of chromosome 10 of LAN-1 neuroblastoma cells. As detected in the karyotype, LAN-1 cells showed an unstained region that was localized on 10p. This arm was not able to hybridize with the corresponding probes directed toward this region. Picture is representative for several cells analyzed under the same conditions. Magnification 100×.

glioblastoma is so hard to be treated in clinic with conventional X-ray. However, RBE_{10} was 2.5–2.9, which indicates that heavy ions had notable advantages in killing radioresistant tumors as glioblastoma.

Our studies also revealed that LAN-1^{RETO} cells were found more radioresistant to X-ray than LAN-1^{WT}. Contrary to that, 79HF6^{RETO} glioblastoma cells were less radioresistant than its wild-type parentals. The probable reason for this difference could be the different growth rates or the chromosomal number (15, 16). 79HF6^{RETO} revealed a high variation in number of chromosomes in comparison to the wild-type cells that are more homogeneous. Thus, cells with a chromosomal abnormality in number are more sensible to ion irradiation. Although LAN-1^{RETO} cells were made more resistant to radiation and were able to form neurospheres after exposure to etoposide, the opposite was true for 79HF6^{RETO}. This may imply the higher level point that general CSC features are enhanced by etoposide in LAN-1 and CSC features may be reduced by etoposide in 79HF6. This difference could be caused by the inherent biological difference of neuroblastoma and glioblastoma. It may also be related to the

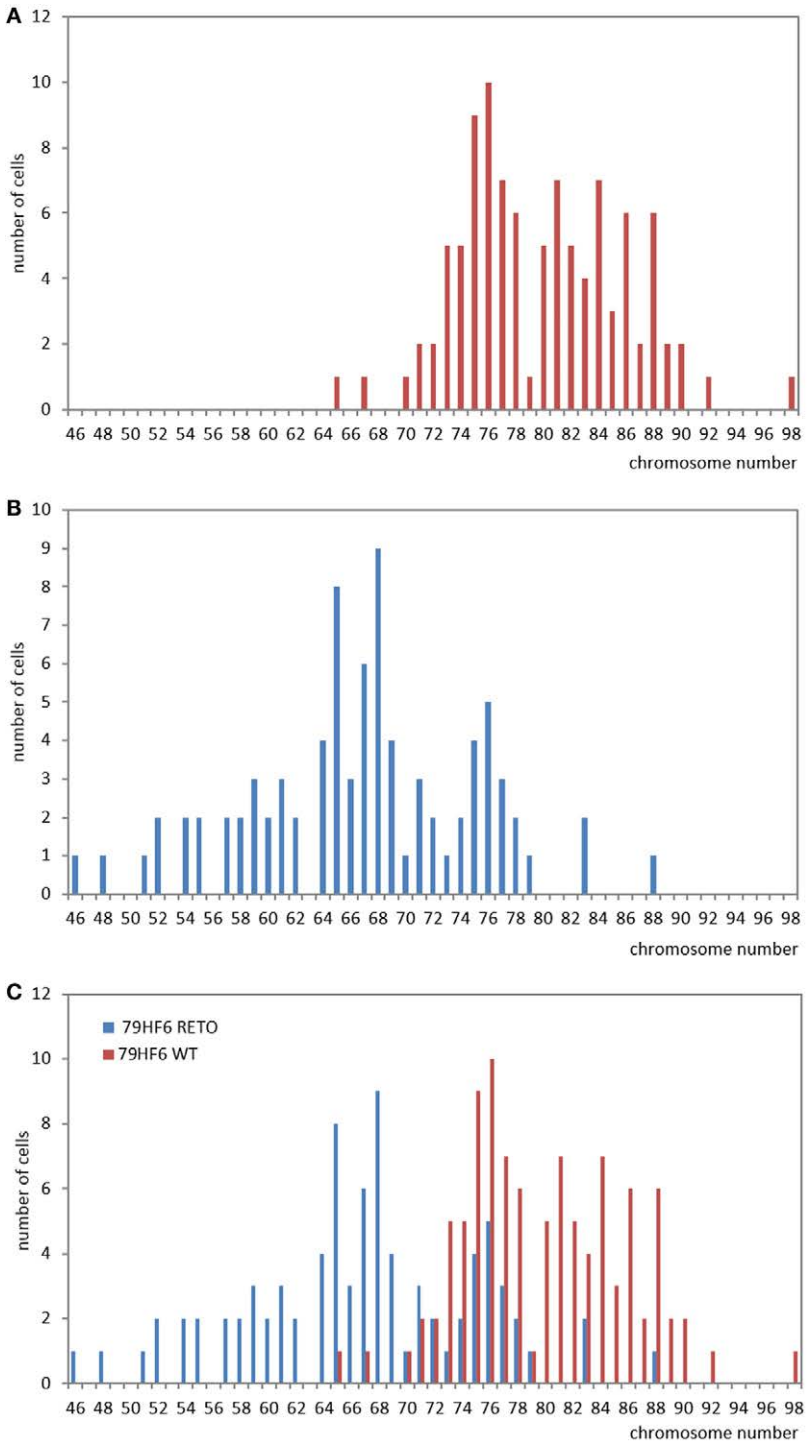

FIGURE 6 | Studies on chromosome number in 79HF6 glioblastoma cells. 79HF6$^{WT/RETO}$ glioblastoma cells revealed strong differences in their chromosome number. Wild-type cells showed polyploidy **(A)**. On the contrary, the resistant subline 79HF6^{RETO} showed less numerical aberrations **(B)**. Both diagrams were merged to provide an overall look of the chromosomal dispersion in both cells types **(C)**. These differences were found to be highly significant once applied a descriptive statistic. Graphics are representative for several experiments with the same experimental conditions.

concentration of etoposide. When the concentration is different, the results could change. Clearly, more work is needed to find the reason.

The biological hallmark of neuroblastomas is the complexity of the genetic abnormalities developed by the tumor cells, which are powerful prognostic markers. The most

consistent abnormalities found in this tumor entity include ploidy changes, deletions of chromosome arms, amplification of the MYCN oncogene, and most frequently gains of chromosome arm 17q (6). There was a region in LAN-1 cells, which could not be stained by any fluorescence after mFISH procedure on chromosome no. 10. The analysis of mBAND corroborated that the unstained region was located on chromosome arm 10p. Homogeneously staining regions (HSRs) were localized on chromosome arm 10p and 10q of neuroblastoma cells with G-banding technique (17). HSR was cytogenetic evidence of a probable gene amplification. The unstained region of mFISH and mBAND of LAN-1^{WT} cells was probably caused by repeated gene amplification or very short gene sequences. When gene segments are shorter than the probes of mFISH and mBAND, the fluorescently labeled probes could not properly anneal with the complementary sequences. Because of this, chromosome arm 10p showed an unlabeled region.

Recurrent loss of genetic material is normally found on chromosome arms 3p, 10p, 10q, 16q, and 20q in the hereditary neuroblastomas, in addition to regions usually deleted in sporadic neuroblastomas (1p36 and 11q) (18). These chromosomal sites may harbor tumor suppressor genes. Furthermore, loss of heterozygosis (LOH) at chromosome 10 is found exclusively at 10p11.23–p15.1 and consequently associated with MYCN-amplified Stage IV tumors in neuroblastoma tumors (19). LOH could induce different changes in one pair of alleles on certain gene and loss of part or even whole gene sequence of the allele. Usually, LOH is commonly related to the deficiency of tumor suppressor genes, i.e., p53. In the case where two alleles exist, the tumor suppressor gene will suppress the generation of tumors. In normal cells, when one allele is abnormal or lost, this defective suppression drive cells to immortalization. Thus, chromosome 10p probably encloses certain tumor suppressor genes. In our study, chromosome 17 reflects a deletion. Considering that p53 gene is located on this chromosome, the lack of p53 gene due to LOH induces a defeat of tumor suppressor functions in these cells. Previous studies showed that tumor suppressor genes, i.e., p53 and so on, could regulate cell survival and death (20, 21). Chromosomal aberrations in these cells subsequently affecting tumor suppressor gene expressing could influence the survival of cells.

In summary, heavy ion irradiation is more effective than X-ray for both untreated and chemoresistant tumor cell lines. For LAN-1 cells, the chemoresistant subpopulation LAN-1^{RETO} is definitely more radioresistant than untreated cells (WT), while this effect was not found in 79HF6 cells.

AUTHOR CONTRIBUTIONS

ZY: substantial contributions to the conception of the work, performing the experiments, analysis, and interpretation of data for the work and drafting the work. CH: substantial contributions to the conception of the work, performing the experiments, analysis. DP: substantial contributions to performing the experiments, analysis. WK-W: substantial contributions to the conception of the work, revising it critically for important intellectual content. G-LJ: substantial contributions to the conception of the work, revising it critically for important intellectual content. DD-C: substantial contributions to the conception of the work, revising it critically for important intellectual content. MD: substantial contributions to the conception of the work, revising it critically for important intellectual content.

REFERENCES

1. Vermeulen L, de Sousa e Melo F, Richel DJ, Medema JP. The developing cancer stem-cell model: clinical challenges and opportunities. *Lancet Oncol* (2012) **13**(2):e83–9. doi:10.1016/S1470-2045(11)70257-1
2. Singh A, Settleman J. EMT, cancer stem cells and drug resistance: an emerging axis of evil in the war on cancer. *Oncogene* (2010) **29**(34):4741–51. doi:10.1038/onc.2010.215
3. Creighton CJ, Li X, Landis M, Dixon JM, Neumeister VM, Sjolund A, et al. Residual breast cancers after conventional therapy display mesenchymal as well as tumor-initiating features. *Proc Natl Acad Sci U S A* (2009) **106**(33):13820–5. doi:10.1073/pnas.0905718106
4. Buck E, Eyzaguirre A, Barr S, Thompson S, Sennello R, Young D, et al. Loss of homotypic cell adhesion by epithelial-mesenchymal transition or mutation limits sensitivity to epidermal growth factor receptor inhibition. *Mol Cancer Ther* (2007) **6**(2):532–41. doi:10.1158/1535-7163.MCT-06-0462
5. Díaz-Carballo D, Gustmann S, Jastrow H, Acikelli AH, Dammann P, Klein J, et al. Atypical cell populations associated with acquired resistance to cytostatics and cancer stem cell features: the role of mitochondria in nuclear encapsulation. *DNA Cell Biol* (2014) **33**(11):749–74. doi:10.1089/dna.2014.2375
6. Maris JM, Hogarty MD, Bagatell R, Cohn SL. Neuroblastoma. *Lancet* (2007) **369**(9579):2106–20. doi:10.1016/S0140-6736(07)60983-0
7. Evers P, Lee PP, DeMarco J, Agazaryan N, Sayre JW, Selch M, et al. Irradiation of the potential cancer stem cell niches in the adult brain improves progression-free survival of patients with malignant glioma. *BMC Cancer* (2010) **10**:384. doi:10.1186/1471-2407-10-384
8. Pignalosa D, Durante M. Overcoming resistance of cancer stem cells. *Lancet Oncol* (2012) **13**(5):e187–8. doi:10.1016/S1470-2045(12)70196-1
9. Barrantes-Freer A, Kim E, Bielanska J, Giese A, Mortensen LS, Schulz-Schaeffer WJ, et al. Human glioma-initiating cells show a distinct immature phenotype resembling but not identical to NG2 glia. *J Neuropathol Exp Neurol* (2013) **72**(4):307–24. doi:10.1097/NEN.0b013e31828afdbd
10. Kraft G, Daues H, Fischer B, Kopf U, Liebold HP, Quis D, et al. Irradiation chamber and sample changes for biological samples. *Nucl Instrum Methods* (1980) **168**:175–9. doi:10.1016/0029-554X(80)91249-5
11. Reynolds BA, Tetzlaff W, Weiss S. A multipotent EGF-responsive striatal embryonic progenitor cell produces neurons and astrocytes. *J Neurosci* (1992) **12**(11):4565–74.
12. Reynolds BA, Weiss S. Generation of neurons and astrocytes from isolated cells of the adult mammalian central nervous system. *Science* (1992) **255**(5052):1707–10. doi:10.1126/science.1553558
13. Cho RW, Clarke MF. Recent advances in cancer stem cells. *Curr Opin Genet Dev* (2008) **18**:48–53. doi:10.1016/j.gde.2008.01.017
14. Lobo NA, Shimono Y, Qian D, Clarke MF. The biology of cancer stem cells. *Annu Rev Cell Dev Biol* (2007) **23**:675–99. doi:10.1146/annurev.cellbio.22.010305.104154
15. Yang X, Darling JL, McMillan TJ, Peacock JH, Steel GG. Heterogeneity of radiosensitivity in a human glioma cell line. *Int J Radiat Oncol Biol Phys* (1992) **22**(1):103–8. doi:10.1016/0360-3016(92)90988-T
16. Till JE. Radiosensitivity and chromosome numbers in strain L mouse cells in tissue culture. *Radiat Res* (1961) **15**:400–9. doi:10.2307/3571245
17. Sawyer JR, Miller JP, Roloson GJ. A novel reciprocal translocation (14;15)(q11;q24) in a congenital mesoblastic nephroma. *Cancer Genet Cytogenet* (1996) **88**(1):39–42. doi:10.1016/0165-4608(95)00302-9

18. Altura RA, Maris JM, Li H, Boyett JM, Brodeur GM, Look AT. Novel regions of chromosomal loss in familial neuroblastoma by comparative genomic hybridization. *Genes Chromosomes Cancer* (1997) **19**(3):176–84. doi:10.1002/(SICI)1098-2264(199707)19:3<176::AID-GCC7>3.0.CO;2-V
19. Mora J, Cheung NK, Oplanich S, Chen L, Gerald WL. Novel regions of allelic imbalance identified by genome-wide analysis of neuroblastoma. *Cancer Res* (2002) **62**(6):1761–7.
20. Wee KB, Aguda BD. Akt versus p53 in a network of oncogenes and tumor suppressor genes regulating cell survival and death. *Biophys J* (2006) **91**(3):857–65. doi:10.1529/biophysj.105.077693
21. Tarunina M, Alger L, Chu G, Munger K, Gudkov A, Jat PS. Functional genetic screen for genes involved in senescence: role of Tid1, a homologue of the *Drosophila* tumor suppressor l(2)tid, in senescence and cell survival. *Mol Cell Biol* (2004) **24**(24):10792–801. doi:10.1128/MCB.24.24.10792-10801.2004

Conflict of Interest Statement: The authors declare that the research was conducted in the absence of any commercial or financial relationships that could be construed as a potential conflict of interest.

Copyright © 2016 Yu, Hartel, Pignalosa, Kraft-Weyrather, Jiang, Diaz-Carballo and Durante. This is an open-access article distributed under the terms of the Creative Commons Attribution License (CC BY). The use, distribution or reproduction in other forums is permitted, provided the original author(s) or licensor are credited and that the original publication in this journal is cited, in accordance with accepted academic practice. No use, distribution or reproduction is permitted which does not comply with these terms.

frontiers in Oncology

ORIGINAL RESEARCH
published: 20 January 2016
doi: 10.3389/fonc.2016.00005

The Influence of C-Ions and X-rays on Human Umbilical Vein Endothelial Cells

Alexander Helm[1], Ryonfa Lee[1†], Marco Durante[1,2] and Sylvia Ritter[1]*

[1] Department of Biophysics, GSI Helmholtz Centre for Heavy Ion Research, Darmstadt, Germany, [2] Department of Condensed Matter Physics, Technical University of Darmstadt, Darmstadt, Germany

OPEN ACCESS

Edited by:
John Varlotto,
University of Massachusetts Medical Center, USA

Reviewed by:
Michael Wayne Epperly,
University of Pittsburgh Cancer Institute, USA
Clemens Grassberger,
Harvard Medical School, USA
Eric Chi-Ching Ko,
UC Davis Comprehensive Cancer Center, USA

***Correspondence:**
Alexander Helm
a.helm@gsi.de

†Present address:
Ryonfa Lee,
Nuffield Department of Population Health, University of Oxford, Oxford, UK

Specialty section:
This article was submitted to Radiation Oncology, a section of the journal Frontiers in Oncology

Received: 23 September 2015
Accepted: 04 January 2016
Published: 20 January 2016

Citation:
Helm A, Lee R, Durante M and Ritter S (2016) The Influence of C-Ions and X-rays on Human Umbilical Vein Endothelial Cells. Front. Oncol. 6:5. doi: 10.3389/fonc.2016.00005

Damage to the endothelium of blood vessels, which may occur during radiotherapy, is discussed as a potential precursor to the development of cardiovascular disease. We thus chose human umbilical vein endothelial cells as a model system to examine the effect of low- and high-linear energy transfer (LET) radiation. Cells were exposed to 250 kV X-rays or carbon ions (C-ions) with the energies of either 9.8 MeV/u (LET = 170 keV/μm) or 91 MeV/u (LET = 28 keV/μm). Subculture of cells was performed regularly up to 46 days (~22 population doublings) post-irradiation. Immediately after exposure, cells were seeded for the colony forming assay. Additionally, at regular intervals, mitochondrial membrane potential (MMP) (JC-1 staining) and cellular senescence (senescence-associated β-galactosidase staining) were assessed. Cytogenetic damage was investigated by the micronucleus assay and the high-resolution multiplex fluorescence *in situ* hybridization (mFISH) technique. Analysis of radiation-induced damage shortly after exposure showed that C-ions are more effective than X-rays with respect to cell inactivation or the induction of cytogenetic damage (micronucleus assay) as observed in other cell systems. For 9.8 and 91 MeV/u C-ions, relative biological effectiveness values of 2.4 and 1.5 were obtained for cell inactivation. At the subsequent time points, the number of micronucleated cells decreased to the control level. Analysis of chromosomal damage by mFISH technique revealed aberrations frequently involving chromosome 13 irrespective of dose or radiation quality. Disruption of the MMP was seen only a few days after exposure to X-rays or C-ions. Cellular senescence was not altered by radiation at any time point investigated. Altogether, our data indicate that shortly after exposure C-ions were more effective in damaging endothelial cells than X-rays. However, late damage to endothelial cells was not found for the applied conditions and endpoints.

Keywords: cardiovascular disease, endothelial cells, high-LET radiation, carbon ions, carbon ion therapy, chromosome 13, micronucleus formation, senescence-associated β-galactosidase

Abbreviations: CPD, cumulative population doublings; HUVEC, human umbilical vein endothelial cells; JC-1, 5,5′,6,6′-tetrachloro-1,1′,3,3′-tetraethylbenzimidazolyl-carbocyanine iodide; LET, linear energy transfer; mFISH, multiplex fluorescence *in situ* hybridization; MMP, mitochondrial membrane potential; RBE, relative biological effectiveness; SA-β-gal, senescence-associated β-galactosidase.

INTRODUCTION

An increased risk of cardiovascular disease (CVD), i.e., any disease involving the heart or blood vessels, such as ischemic heart disease, myocardial infarction, or hypertension, is a known consequence of radiotherapy for the treatment of certain types of cancer, such as breast cancer or Hodgkin lymphoma, where the heart is typically part of the radiation field and thus may be exposed to relatively high doses of ionizing radiation (IR) (1, 2). Although modern radiotherapy techniques aim to spare organs at risk such as the heart, coronary arteries may still be affected and thus a risk for cardiovascular damage remains (3, 4). Furthermore, there is growing evidence of an increased risk of CVD at low and moderate doses of IR stemming mainly from atomic bomb survivors and occupationally exposed groups, typically developing with a long latency (5–7). Generally, radiation-induced cell killing of endothelial cells and a subsequent induction of a pro-inflammatory response are considered as the mechanism triggering arteriosclerosis and ischemic heart disease (6, 8, 9). The mechanisms by which low and moderate doses of IR provoke CVD are still poorly understood. However, direct damage to endothelial cells followed by an inflammatory response seems to play also a role at low doses (6, 10).

Radiation-induced damage to the endothelium may simply be a consequence of cell loss due to cell killing, as discussed by Little et al. (6). Yet, also radiation-induced genomic instability, oxidative stress disrupting mitochondrial function, and accelerated cellular senescence have been implicated in the pathogenesis of arteriosclerosis (8, 11–14). So far, most data are available on the effects of low-linear energy transfer (LET) radiation, while only few data on the impact of high-LET radiation exist, yet suggesting a higher risk (10). With an increasing use of high-LET particles such as carbon ions (C-ions) in cancer therapy or radiosurgery (15–17), an assessment of their possible cardiovascular effects is important.

To gain a deeper insight into the effects of high-LET radiation on endothelial cells, we chose human umbilical vein endothelial cells (HUVEC) as a model system. HUVEC have been already used to study the radiation response to both low- and high-LET radiation investigating, e.g., cell survival, apoptosis, gene expression, or angiogenesis [e.g., Ref. (18–20)]. We exposed cells to C-ions with two different energies relevant for cancer therapy, i.e., 9.8 and 91 MeV/u corresponding to LET values of 170 and 28 keV/μm. For comparison, X-ray experiments were performed. The focus was set on doses ≤1.5 Gy. We investigated clonogenic cell survival, apoptosis, and cytogenetic damage expressed as micronuclei formation or chromosomal aberrations, premature senescence, and the integrity of the mitochondrial membrane potential (MMP). Measurements were performed up to 46 days post-irradiation.

MATERIALS AND METHODS

Cell Culture

Human umbilical vein endothelial cells were purchased from PromoCell (Heidelberg, Germany) and cultured according to the manufacturer's protocol in medium optimized for the cultivation of primary endothelial cells from large blood vessels. Briefly, cells were maintained in basal Endothelial Cell Growth Medium supplemented with Endothelial Cell Growth Kit components. The final supplement concentrations in the medium were 2% fetal calf serum, 0.1 ng/ml epidermal growth factor, 1 μg/ml hydrocortisone, 1 ng/ml basic fibroblast growth factor, and 0.4% endothelial cell growth supplement. Cells were passaged every 4–5 days upon reaching ~80% confluency. For cell detachment, a mixture of 0.05% trypsin and 0.02% EDTA was used and neutralized with trypsin neutralizing solution containing 0.05% trypsin inhibitor in 0.1% BSA and plated at a density of 6.6×10^3 cells/cm^2 unless otherwise stated. Medium was changed for every 2–3 days, and the cumulative population doubling (CPD) was determined. All cell culture products were purchased from PromoCell.

Irradiation

Sub-confluent cultures with a CPD level of about 6 (culture age: about 11 days) were exposed to X-rays or C-ions with an initial energy of either 11.4 or 100 MeV/u at GSI Helmholtz Centre for Heavy Ion Research (Darmstadt, Germany). For the exposure to X-rays or high energy C-ions, cells were seeded into 25 cm^2 culture flasks, whereas for the exposure to low energy C-ions, cells were plated into 35 mm Petri dishes.

X-ray irradiation was performed at a Seifert (Germany) X-ray machine operated at 250 kV and 16 mA with a 1 mm Al + 1 mm Cu filtering. The dose rate was about 1.5 Gy/min. Exposure to 11.4 MeV/u C-ions was done at the linear accelerator UNILAC, as described in detail elsewhere (21, 22). At sample position, the energy was 9.8 MeV/u corresponding to an LET of 170 keV/μm. Irradiation with 100 MeV/u C-ions was performed at the heavy ion synchrotron SIS with the raster scanning technique (23). The resulting energy on target was 91 MeV/u with an LET of 28 keV/μm. For C-ions, the irradiation time was in the range of 0.5–2 min depending on dose and accelerator conditions. All exposures were done at room temperature, and control samples were sham irradiated.

For longer follow-up studies (up to 46 days post-irradiation corresponding to 22 population doublings), we limited the analyses to doses at an isosurvival level of about 50 and 20%, respectively. Cell survival of 50% was expected for 0.75 Gy X-rays, 0.35 Gy 91 MeV/u C-ions, and 0.25 Gy 9.8 MeV/u C-ions, while a survival rate of 20% was estimated for 1.5, 0.75, and 0.5 Gy, respectively. Further details on particle fluences and the number of particle traversals per nucleus are given in Table S1 in Supplementary Material.

Clonogenic Cell Survival

Cell survival was measured using the standard colony forming assay (24). In brief, directly after exposure cells were trypsinized, counted, and plated in triplicate into 25 or 75 cm^2 tissue culture flasks. The number of cells seeded was estimated to result in a statistically significant formation of at least 100 colonies. After 12 days of incubation, cells were fixed and stained. Cell clusters consisting of at least 50 cells were counted as a colony.

Micronuclei

To assess the cytogenetic damage 24 h after radiation exposure, the micronucleus assay was applied as described in Fenech (25) with minor modifications. Briefly, cells were incubated for 4 h following irradiation and subsequently treated with 0.75 μg/ml cytochalasin-B for 20 h. Cells were then washed in PBS, fixed in 8% formaldehyde for 5 min, and stained with DAPI (0.2 μg/ml) for 15 min at room temperature. At least 1000 cells were scored, and the number of binucleated cells containing micronuclei was determined. For follow-up studies, i.e., >24 h, cells were regularly subcultured and at selected time points the spontaneously occurring frequency of cells carrying micronuclei was analyzed by scoring 1000 cells per dose and time point.

Apoptosis

For analysis at the early time point, cells were fixed in 8% formaldehyde and stained with DAPI as described for the micronuclei samples. Additionally, cells were subcultered and at consecutive time points 5×10^4 cells were seeded in 35 mm tissue culture dishes and incubated for 2 more days until fixation and staining. At least 1000 cells were scored per dose and time point. Apoptotic cells were identified under a fluorescence microscope (400× magnification) by the typical morphological changes of the cell nucleus, such as chromatin condensation or fragmentation (26, 27).

Senescence-Associated β-Galactosidase

Analysis of cellular senescence-associated β-galactosidase activity (SA-β-gal) was performed using the Senescence Cell Staining kit (Sigma-Aldrich, Germany) according to the manufacturer's protocol. At several time points after radiation exposure (2 up to 44 days), cells were seeded at a density of 5×10^4 in 35 mm tissue culture dishes. Two days later, cells were fixed and staining. At least 2000 cells were scored by light microscopy (400× magnification), and the fraction of cells exhibiting a blue stain, i.e., SA-β-gal activity, was determined.

Mitochondrial Membrane Potential

To assess the influence of radiation exposure on the MMP (also referred to as $\Delta\Psi_M$), the cationic, lipophilic dye 5,5′,6,6′-tetrachloro-1,1′,3,3′-tetraethylbenzimidazolyl-carbocyanine iodide (JC-1) was applied. The dye shifts its fluorescence signal from 525 nm (green) to 595 nm (red) due to a dimerization in the presence of protons thus indicating a functional MMP. For MMP analyses, samples were collected 12, 24, and 48 h after exposure. Measurements at later time points were performed using ~80% confluent cultures. Analysis of the MMP was performed as described previously (28) with modifications. Briefly, cells were harvested and incubated for 10 min in medium containing JC-1 (5 μg/ml) at 37°C. Thereafter, cells were washed twice with PBS analyzed by flow cytometry using a Pas III Particle Analysing System and the software FloMax (both from Partec, Germany). The fraction of predominantly red cells, i.e., cells mainly containing mitochondria with an intact MMP, was determined in at least 1×10^4 cells of each sample. As a positive control, cells were treated with 2 mM 2,4-dinitrophenol 10 min before JC-1 staining, resulting in ~5% of cells with a red fluorescent signal.

Chromosome Analysis

Chromosome aberrations were analyzed in control cultures at CPD 13 ± 2 and in the progeny of irradiated cells at CPD 22 ± 2. For cytogenetic analyses, cells were seeded into 75 cm^2 flasks and cultured for 2 days. Then, colcemid (0.1 μg/ml) was added for 3 h to accumulate metaphase cells. Chromosome spreads were prepared according to the standard procedures, e.g., cells were trypsinized, treated with hypotonic solution, fixed, and dropped on wet slides. Slides were stained using multiplex fluorescence *in situ* hybridization (mFISH). For mFISH analysis, slides were hybridized with the 24XCyte mFISH probe kit from MetaSystems (Altlussheim, Germany) following the instructions of the manufacturer. Chromosome spreads were examined using an Olympus BX61 microscope (Olympus, Tokyo, Japan) equipped with six filter sets specific for the applied fluorochromes. Images of the metaphases were captured (100× objective) with a charged coupled device camera, and karyotyping was performed using the ISIS/mFISH software. Both, structural and numerical aberrations were recorded in at least 100 metaphases per dose and time point. Structural aberrations were classified following the mPAINT system, as described in detail elsewhere (29). In the present study, breaks and simple exchanges were detected. Breaks were referred to as terminal deletions, when the centric and acentric part of the same chromosome were present within the cell. Terminal deletions involved either both chromatids at the same location (chromosome-type breaks, csb) or only one chromatid (chromatid-type break, ctb). Additionally, lone truncated chromosomes (T) were found, i.e., the acentric part of chromosome was not visible. Simple exchanges include translocations (complete, incomplete, and one-way forma) and dicentrics.

Statistics

When applicable, data were expressed as the mean value ± SEM or SD as indicated. For data stemming from one experiment only, Poisson statistics were applied to calculate the error bars as indicated, and statistical analysis was performed using a Fisher's exact test as indicated. Survival data have been normalized by evaluating the plating efficiency not considering control data (0 Gy) only, but rather by performing a fit of the form ($\alpha \times d + o$) to the experimental data, where o is an offset term, which reflects the plating efficiency, determined from all data points. This procedure is more precise, as all measured data are subject to the same plating efficiency and consequently all data points can be exploited to derive this quantity. Deviations for 0 Gy to full survival arises, as also control measurements are affected by uncertainty. Based on the α-values derived from the linear fitting, a Student's t-test was used for statistical analysis. Curve fitting of the micronuclei formation 24 h after exposure was performed according to

$$Y = p_1 D \times e^{-p_2 D} \quad (1)$$

where Y is the yield of micronuclei, D the dose, and p_1 and p_2 fitting parameters. Statistical analysis was performed based

on the parameters derived from the fitting using a Student's *t*-test. Generally, differences were considered significant if the *p*-value ≤0.01.

RESULTS

Radiation Affects Clonogenic Cell Survival and Micronuclei Formation in a Dose- and LET-Dependent Manner 24 h after Exposure

To examine the putative radiation effect directly after exposure, a clonogenic cell survival assay was performed (**Figure 1**). For the three radiation types investigated cell survival decreased with dose and showed a clear LET dependence, i.e., 9.8 MeV/u C-ions with LET = 170 keV/μm were most effective, followed by 91 MeV/u C-ions with LET = 28 keV/μm and X-rays with 2 keV/μm. As all survival curves are linear, the relative biological effectiveness (RBE) does not depend on survival level, resulting in values of 2.4 and 1.5 for 9.8 and 91 MeV/u C-ions, respectively. Next, we measured cytogenetic damage in cells undergoing first division after exposure (24 h after exposure, cytochalasin-B treatment). The analysis showed an LET-dependent formation of micronuclei in binucleated cells (**Figure 2**). Within the limited dose range examined a saturation in the yield of cells carrying micronuclei was observed for >0.5 Gy 9.8 MeV/u C-ions (**Figure 2**) and >2 Gy X-rays. Thus, the damage induced by IR in first division cells clearly depends on the radiation quality and dose. Apoptosis was assessed 48 h after radiation exposure by investigation of morphological criteria of the cell nuclei. A slightly yet insignificantly increased fraction of apoptotic cells was observed in the irradiated samples independent of dose or radiation quality (**Figure 3**).

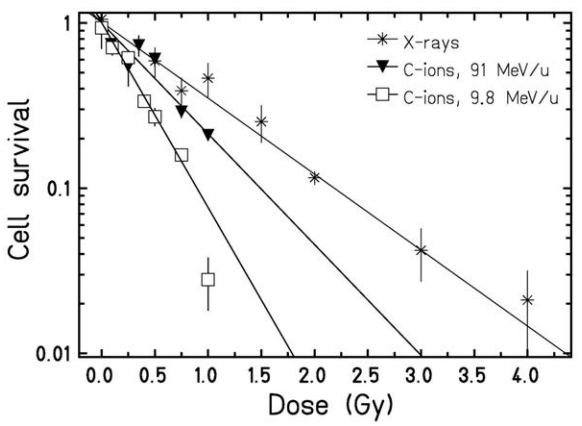

FIGURE 1 | Clonogenic cell survival of HUVEC. Cells were plated immediately after exposure to X-rays or C-ions. Data points represent the mean X ± SD from replicates stemming from one (C-ions) or three (X-rays) experiments. Curves were fitted by a linear function. Based on the α-values, clonogenic cell survival was found significantly ($p < 0.01$, Student's *t*-test) different for the three radiation types.

Radiation-Induced Damage Is Transient Rather Than Persistent in Cells Cultured up to 46 Days Following Exposure

For investigation of putative late effects of IR, we cultured both exposed cells and sham-irradiated cells up to 46 days corresponding to 22 population doublings post-irradiation (Figure S1 in Supplementary Material). Generally, radiation exposure did not severely alter the population growth compared to the control. Only in one case, i.e., after exposure to 1.5 Gy X-rays, a slightly lower CPD was found toward the end of the culture time.

Next, we determined the amount of cells harboring micronuclei after an extended culture time (**Figure 4**). To allow for a better comparison, we plotted the mean value (±SD) of all controls over time instead of single data points. As shown in **Figure 4**, in all irradiated samples, the fraction of HUVEC containing micronuclei was significantly increased 2 days after exposure. For C-ions, the increase was dose dependent. Generally, at the following time points, only small differences between irradiated and sham-irradiated control cultures were found. Yet, exposure to the high doses (0.5 and 0.75 Gy) low and high energy C-ions resulted in an increased fraction of cells containing micronuclei when comparing to the respective controls (not displayed) 21 and 20 days post-irradiation, respectively. These increases are above the range of the mean value of pooled controls from all experiments and its upper SD, as indicated in the graph (**Figure 4**). Subsequent investigation time points did not reveal significant dose effects compared to the controls. Thus, analysis of the formation of micronuclei provided no evidence for a radiation-induced chromosomal damage in the progeny of irradiated cells.

Furthermore, we investigated radiation-induced apoptosis in the descendants of irradiated cells. The morphological analysis of

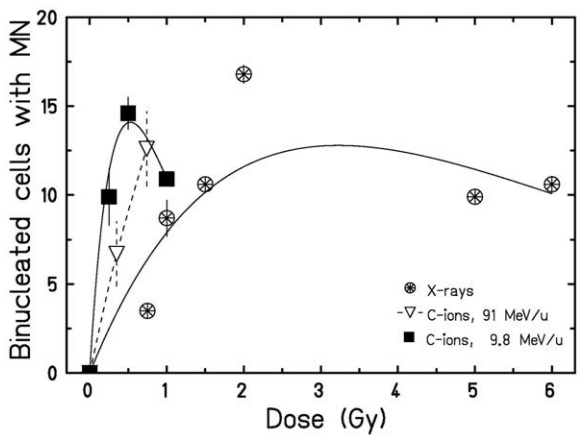

FIGURE 2 | Micronuclei formation 24 h after exposure. Following irradiation, cells were incubated with cytochalasin-B, and the amount of binucleated cells containing micronuclei was determined. Data points represent the mean X ± SEM (for data points with $n = 2$) or error was calculated according to Poisson statistics for data points stemming from one experiment. Curves for X-rays and 9.8 MeV/u C-ions were fitted as described. For 91 MeV/u C-ions, lines are drawn to guide the eye. Statistical analysis using a Student's *t*-test revealed significant differences for 9.8 MeV/u C-ions when compared to X-rays ($p < 0.01$).

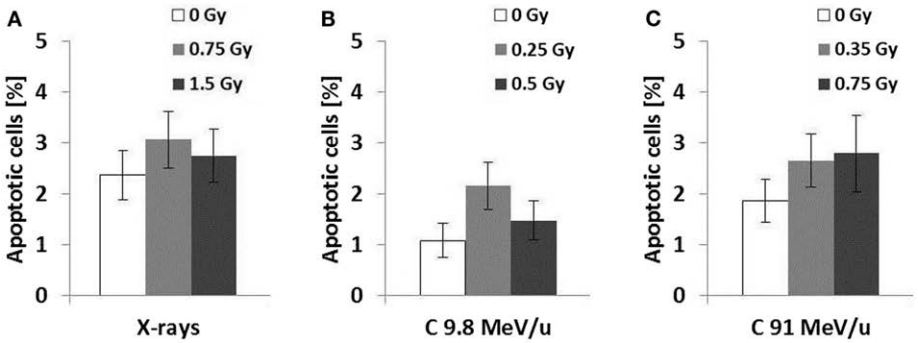

FIGURE 3 | Apoptosis 48 h after exposure. Cells were fixed 48 h following radiation exposure to X-rays **(A)**, 9.8 MeV/u C-ions **(B)**, and 91 MeV/u C-ions **(C)**. The fraction of apoptotic cells was determined according to morphological criteria of the nucleus. Error was calculated according to Poisson statistics. Fisher's exact test revealed no significant differences between all samples ($n = 1$, $p > 0.01$).

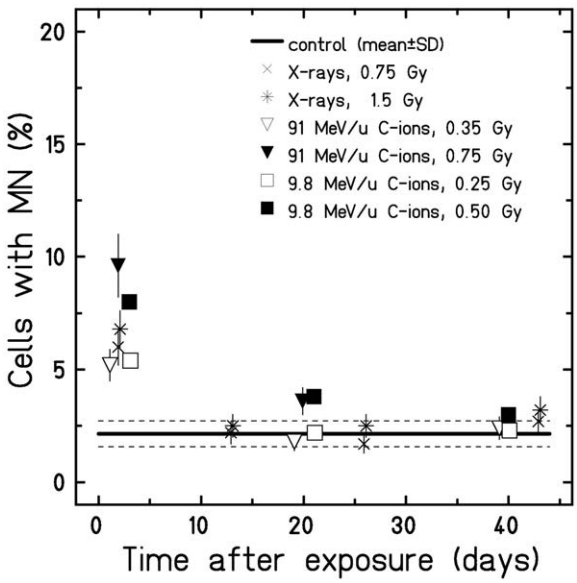

FIGURE 4 | Micronuclei formation in cells after extended culture time. Cells were fixed at several time points after exposure (w/o cytochalasin-B), and all cells harboring micronuclei were scored. The error was calculated according to Poisson statistics, and a Fisher's exact test was performed ($n = 1$). Only 2 days after exposure, micronuclei formation was found significantly higher compared to the control (mean ± SD). Note that for better visualization, the samples 2 days after exposure to the different radiation types were plotted separated from each other despite stemming from the same time point.

the cell nuclei showed no differences in the fraction of apoptotic cells in irradiated samples compared to the respective controls (data not shown).

Additionally, the putative damage on the MMP was studied by applying the proton-sensitive dye JC-1. In control cultures ($n = 4$), the proportion of cells with an intact MMP (mainly red-fluorescing cells) amounted to 79 ± 8.4% (mean ± SD) over the whole time interval investigated (data not shown). After exposure to X-rays or C-ions, we found a slight decrease in cells with an intact MMP between 3 and 8 days post-irradiation, partly falling below the value of the lower SD (i.e., about 71%) down to 61% (for 1.5 Gy X-rays and 0.35 Gy C-ions 91 MeV/u, data not shown). To elucidate whether higher doses are required to profoundly impair mitochondrial function in HUVEC cultures within this period of time, we exposed cells to 1.5, 4, and 10 Gy X-rays and analyzed the MMP daily until 10 days after exposure (Figure S2 in Supplementary Material). We found that 2 days after exposure for all three doses applied, the amount of cells exhibiting mainly red fluorescence was lower compared to the respective control and the lower SD of all controls. Three days after irradiation with 1.5 Gy X-rays, the fraction of cells containing mitochondria with mostly intact MMP rose and reached the control level by day 5. For cells exposed to 4 Gy X-rays, recovery started at day 6 and the control value was reached by day 7, whereas the exposure to 10 Gy resulted in a persistently decreased level of cells with an intact MMP over the period investigated. Hence, the dose dependence was expressed rather in the recovery time than in the fraction of cells with intact MMP.

Furthermore, the expression of SA-β-gal was investigated in the progeny of irradiated and non-irradiated HUVEC to assess whether the radiation exposure induced premature senescence. Generally, the fraction of SA-β-gal positive cells raised with an increasing CPD. The proportion was comparable in irradiated samples and the respective controls. Only in one sample, i.e., 6 days after exposure to 0.5 Gy C-ions 9.8 MeV/u, an increased fraction of SA-β-gal positive cells was found and thus may be considered false positive (Figure S3 in Supplementary Material). Altogether, these data indicate that within the dose range investigated neither X-ray nor C-ion exposure induces a premature cellular senescence of HUVEC cultures.

Analysis of Chromosomal Aberrations by the mFISH Technique Revealed Specific Alterations in the Progeny of Non-Irradiated and Irradiated HUVEC Cultures

To verify the observation that the progeny of non-irradiated and irradiated cells do not express an elevated level of cytogenetic

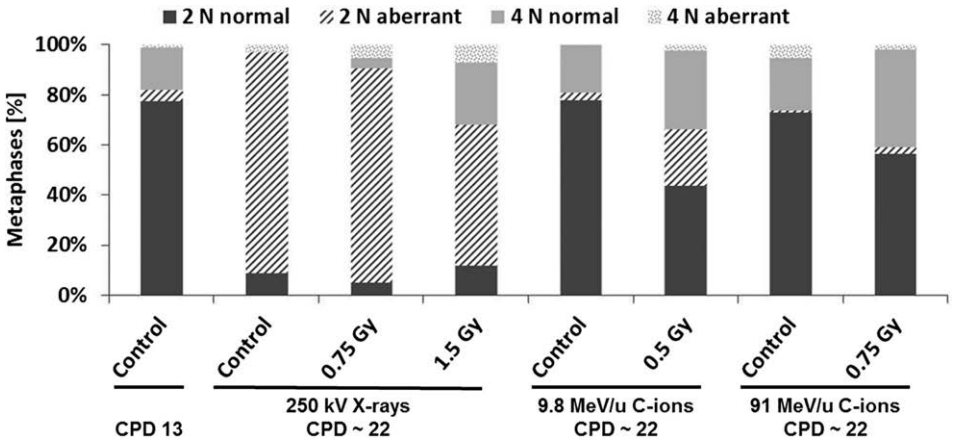

FIGURE 5 | Analysis of structural chromosome aberrations in HUVEC cultures (non-irradiated and irradiated) by means of the mFISH technique. The fractions of normal and aberrant diploid/hypodiploid cells (referred to as ~2N) and tetraploid/hypotetraploid cells (referred to as ~4N) are given ($n = 1$). The terms hypodiploidy or tetradiploidy indicate the loss of one or two chromosomes. Cells were analyzed in controls at a CPD level of 13 ± 2 and about 9 population doublings after exposure (CPD ~22).

damage (**Figure 4**), we measured chromosome aberrations in all cultures about 9 doublings post-irradiation corresponding to a CPD level of ~22. Additionally, the baseline level of aberrations was determined (CPD level ~13). The analyses were performed by means of the high-resolution mFISH technique. As shown in **Figure 5**, in non-irradiated HUVEC cultures at CPD ~13 most cells had a normal (2N) karyotype, occasionally the loss of one chromosome was observed. Overall, about 80% of the cells were diploid or hypodiploid. Notably, also tetraploid cells (4N) and a few cells with a hypotetraploid karyotype were registered (in total 20% of the population). Structural aberrations (mainly breaks and translocations) were detected in ~5% of cells analyzed. With increasing CPD, only small changes occurred in two control cultures (C-ion studies), but chromosome 13 appeared to be non-randomly involved. Either it was truncated or one copy was lost. In one control culture (X-ray study), the proportion of cells with a ~2N karyotype was much higher at CPD ~22, i.e., amounted to 97%. Notably, also the number of cells with structural aberrations was highly elevated, i.e., 88/97 ~2N cells and 3/3 ~4N cells were aberrant. In all affected cells, the same aberration, a large truncation of the q-arm of chromosome 13, was observed indicating a clonal origin.

Chromosome analysis in cells at CPD ~22 (**Figure 5**) consistently showed that the fraction of ~4N cells was generally higher in the progeny of irradiated cells than in the respective controls culture. Structural aberrations were found in all cultures and were generally translocations (sporadic or clonal) or truncated chromosomes. As observed in the control cultures chromosome 13 was non-randomly involved in aberrations. Likewise, the loss of one or two chromosomes was registered. Again, chromosome 13 was over-represented (**Figure 6**). A summary of the data is shown in Table S2 in Supplementary Material.

Altogether, these data show that in HUVEC chromosome 13 is inherently unstable. Frequently, cells with a lost or truncated chromosome were observed. Based on the number of

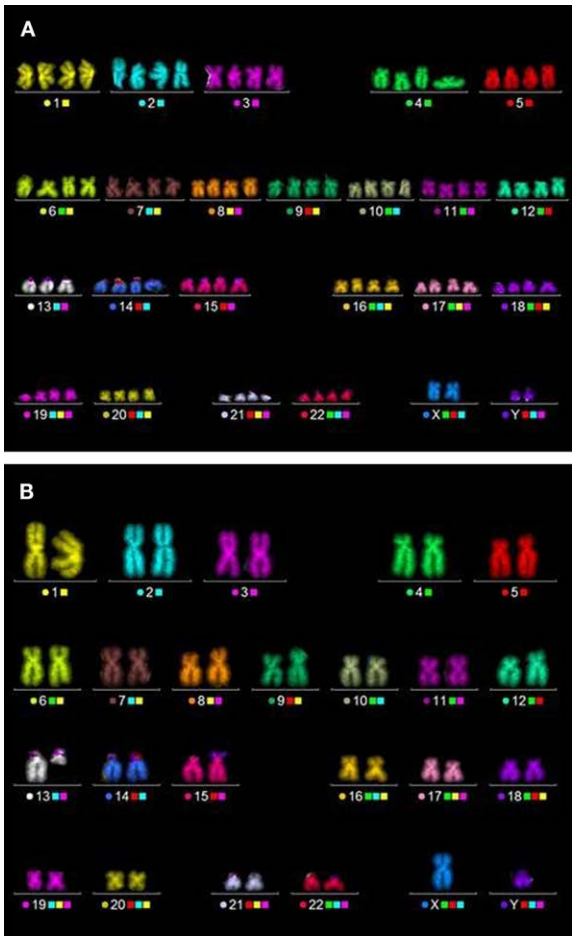

FIGURE 6 | Typical aberrations detected in HUVEC by means of the mFISH technique. (A) Hypotetraploid cell, one copy of chromosome 13 is lost. **(B)** Diploid cell, one chromosome is truncated (here: non-irradiated cells, CPD ~22).

cells affected (i.e., the clone sizes), the loss or the deletion of a large part of the q-arm of chromosome 13 results in a survival advantage. As these changes are clonal they remain undetected by micronucleus analysis.

DISCUSSION

Epidemiological data demonstrate an increased risk of CVD when the heart and its adjacent blood vessels are exposed to relatively high doses of low-LET radiation as a consequence of radiotherapy, e.g., breast cancer or Hodgkin lymphoma (1, 2, 30). An increased risk of CVD at low or moderate doses of IR is indicated by epidemiological data stemming mainly from atomic bomb survivors or occupationally exposed groups (7, 31). However, the mechanisms leading to CVD after exposure to IR remain to be elucidated. The available data point at damage to the endothelial cells as the initial event in pathogenesis (31). Hence, we chose HUVEC as a model system. This system bears two advantages. First, the umbilical cord provides a cost-effective source of endothelial cells. Second, in several studies, the effect of low LET on HUVEC has already been examined [e.g., Ref. (32, 33)]. Since data on high-LET C-ions are scarce but of great interest owing to the increased use of C-ions in modern radiotherapy (15–17), we analyzed the response of HUVEC after exposure to C-ions with energies relevant for radiotherapy (see Table S1 in Supplementary Material).

Radiation Induces a Dose- and LET-Dependent Damage in HUVEC 24 h Following Exposure

In HUVEC, radiation-induced damage in terms of clonogenic survival was found to depend on both dose and LET (**Figure 1**). For 91 MeV/u C-ions, an RBE value of 1.5 was obtained, whereas 9.8 MeV/u C-ions resulted in an RBE of 2.4. This is in line with the data reported for other cell lines [e.g., Ref. (34, 35)]. Cell survival of HUVEC after exposure to low-LET radiation was already measured by others (36, 37), but the radiosensitivity of cells used in the present study was much higher. For example, in the present study, a surviving fraction of 10% was reached after exposure to 2 Gy X-rays (**Figure 1**), whereas 4 and 5 Gy were needed for the same effect in the studies of Manti et al. and Hei et al., respectively. Furthermore, the survival data published by both authors show a shoulder, typically observed after exposure to low-LET photons. By contrast, our X-ray data display no shoulder. Lack of a shoulder points to a higher radiosensitivity and might be caused, for example, by a reduced DNA repair capacity as reported for Ku80-deficient cell lines [e.g., Ref. (34)]. Since HUVEC originate from apparently healthy donors, it is unlikely that the observed difference in the shape of the survival curves is attributable to compromised DNA repair. Yet, one possible explanation is a difference in the cell culture condition. In the present study, a specialized medium for primary endothelial cells was used with 2% serum, while Hei et al. cultured HUVEC in medium with 20% serum. Manti et al. studied also the response of HUVEC after exposure to C-ions with different LET values (13 and 100 keV/μm) and reported a clear dose and LET dependence as found in our study, too. For C-ions with a high LET (100 keV/μm), Manti et al. did not find a shoulder either.

As observed for cell survival, C-ions were more effective than X-rays with respect to the formation of micronuclei in binucleated cells (**Figure 2**). Analogously, 9.8 MeV/u C-ions were more effective than 91 MeV/u C-ions due to the higher LET. The fraction generally increased with dose, however, after X-ray irradiation, a saturation was found for doses >2 Gy (data not shown). The available data indicate that for 9.8 MeV/u C-ions, the saturation occurred at a much lower dose (>0.5 Gy). Yet, for firm conclusions, measurements have to be performed over a wider range of doses. A dose-dependent increase in the rate of micronuclei in various rat, bovine, or human endothelial cell cultures (38, 39), and a saturation effect for doses around 2 Gy X-rays (38) has been reported by others and is in line with our findings (**Figure 2**). Since we screened for micronuclei in binucleated cells, the saturation may be correlated with a hampered cell division capacity for higher doses. Furthermore, cytochalasin-B is cytotoxic, thus an increased rate of apoptosis may compete with the formation of binucleated cells, additionally leading to an underestimation of the damage induced by IR.

In contrast to the damage induced as reduced clonogenic survival or micronuclei formation, apoptosis was found to be only slightly higher after exposure, independent from dose or applied radiation quality (**Figure 3**). A small increase in the fraction of apoptotic cells for HUVEC after exposure to low doses of X-rays is in line with literature (20).

Taken together, radiation does induce damage up to 24 h following exposure that depends both on dose and the LET value. Such damage to endothelial cells may be considered the initial event in the pathogenesis of CVD (31). However, CVD has a long latency period. Therefore, we investigated whether genetic damage persists in cultures and whether other cellular processes implicated in the pathogenesis of CVD were affected up to 46 days after exposure corresponding to 22 population doublings.

Radiation-Induced Damage Does Not Persist

Genomic instability, disrupted mitochondrial function, and accelerated replicative cellular senescence are implicated in pathogenesis of arteriosclerosis (8, 11–14). To address this topic, we assessed micronuclei formation, occurrence of chromosomal aberrations, apoptosis, and changes in the MMP as well as the expression of SA-β-gal in HUVEC cultured up to 22 population doublings after exposure (Figure S1 in Supplementary Material). For follow-up investigations, we focused on low doses up to 0.75 and 1.5 Gy for C-ions and X-rays, respectively, comparable to each other by isosurvival levels.

A dose-dependent effect on the number of cells with micronuclei was still visible at 48 h following exposure (**Figure 4**). At the later time points, the fraction of cells with micronuclei was similar in irradiated and control cultures indicating that the genomic stability of the cells was not affected by IR. Genomic instability expressed as micronuclei formation is a known consequence of exposure to IR (40). Yet, to the best

of our knowledge, no other data sets for endothelial cells cultured for a prolonged time post-irradiation are available for comparison.

Premature senescence is considered as a key cellular stress response resulting, e.g., from DNA damage (41–43). Likewise, data indicate that premature senescence may contribute to the pathogenesis of arteriosclerosis (44, 45). Along this line, we examined the activation of SA-β-gal, a marker of cellular senescence (46) in the progeny of irradiated HUVEC.

Generally, no radiation-induced alterations were found over the time course investigated when compared to controls (Figure S3 in Supplementary Material). Only in one sample (0.5 Gy of 9.8 MeV/u C-ions), an elevated number of SA-β-gal positive cells was found 6 days after exposure that did not persist. Published data for endothelial cells are in contrast to our results. For example, Grossi et al. (47) registered a higher number of SA-β-gal expressing HUVEC several passages after exposure to 1.75 Gy X-rays or 0.5 Gy C-ions (13 keV/μm), i.e., doses comparable to the one in the current study. An increased number of endothelial cells, including HUVEC expressing SA-β-gal, was also observed after exposure to higher doses (2–10 Gy) of X-rays (48–50). Reasons for this different response are still unknown. Yet, studies over an extended culture time consistently showed an increase in the number of SA-β-gal positive endothelial cells with cell age (47, 51, 52). Our data support this finding.

There is evidence that radiation-induced oxidative stress and hampered mitochondrial function (53) play a role in endothelial dysfunction and CVDs (31, 54, 55). For example, in heart tissue, an impairment of mitochondrial proteins related to oxidative phosphorylation (e.g., complex I and III) was demonstrated following exposure to ≤2 Gy X-rays (56). Therefore, we examined the MMP, a key parameter of mitochondrial function. The dye JC-1, whose red fluorescence is directly correlated with the integrity of the MMP (57), was applied (data not shown). We found a slight decrease in the amount of cells containing mainly mitochondria with an intact MMP shortly after exposure (i.e., up to 8 days) independent of the radiation type and dose. Yet, by applying higher doses of X-rays (1.5, 4, and 10 Gy), we recorded an impairment of mitochondrial function in HUVEC that increased with dose (Figure S2 in Supplementary Material). Likewise, a decrease of the MMP following staining with JC-1 or other fluorescent dyes after high doses of X-rays (≤10 Gy) was reported for other cell lines (58–60).

A stress-triggered decrease of the MMP may be related to the onset of apoptosis via cytochrome *c* release and subsequent signaling pathways (61). In this context, our findings collectively provide no evidence for a delayed radiation-induced apoptosis in HUVEC.

Interestingly, the number of structural and numerical chromosomal aberrations increased with culture time in the progeny of unirradiated and irradiated cells. Consistently, chromosome 13 was involved. While, to the best of our knowledge, truncation of chromosome 13 in HUVEC has not yet been described, its loss has already been reported by others (51, 62, 63) and was accompanied by a growth advantage, i.e., leading to clonal expansion. Our data show that not only the complete deletion of chromosome 13 but also a deletion of a large part of the q-arm of chromosome 13 confers a growth advantage to the affected cells. Noteworthy, the q-arm of chromosome 13 harbors the *Rb* gene, encoding for the Rb protein, a well-known tumor suppressor and regulator of the cell cycle (64) that may account for an enhanced replication. As the number of cells with cytogenetic changes increased with time in irradiated cultures and the respective controls in a similar way, it is reasonable to assume that these cytogenetic changes are a feature of aging HUVEC that is barely affected by IR within the dose range examined (0.5–1.5 Gy). Moreover, our data revealed considerable inter-experimental differences in the number and types of aberrations in HUVEC cultures at CPD level 22 (see **Figure 4**; Table S2 in Supplementary Material). Pronounced inter-experimental differences in the aberration yield were also reported for other cell types, e.g., human foreskin fibroblasts and skin fibroblasts, subcultured up to CPD level 50 (41). Reasons underlying this phenomenon remain to be elucidated.

Taken together, our data point to a radiosensitivity for HUVEC directly after exposure to radiation, i.e., mainly by cell killing and even low or moderate doses as used in this study result in a reduced cellular survival. This is important if endothelial cell damage is taken into account as the initial step in the pathogenesis of arteriosclerosis (31). It was hypothesized that endothelial cell damage may trigger pro-inflammatory signals, which finally results in the enhanced formation of arteriosclerotic lesions [e.g., Ref. (6, 31)]. Yet, the link between radiation-induced damage and pro-inflammatory signaling remains poorly understood and requires further investigation. Since we found C-ions LET dependently more effective (RBE of 1.5 and 2.4 for 91 and 9.8 MeV/u C-ions, respectively) than X-rays, our results demonstrate the need of further studies in order to better estimate a putative risk of high-LET radiation.

AUTHOR CONTRIBUTIONS

AH, RL, MD, and SR have substantially contributed to the conception and design of the work, as well as the acquisition, analysis, and interpretation of the data.

ACKNOWLEDGMENTS

The authors acknowledge P. Hessel and D. Szypkowski for skillful assistance as well as M. Scholz, T. Friedrich, W. Becher, and G. Lenz for planning and realizing the particle exposure of cells.

SUPPLEMENTARY MATERIAL

The Supplementary Material for this article can be found online at http://journal.frontiersin.org/article/10.3389/fonc.2016.00005

REFERENCES

1. Darby SC, Ewertz M, McGale P, Bennet AM, Blom-Goldman U, Brønnum D, et al. Risk of ischemic heart disease in women after radiotherapy for breast cancer. *N Engl J Med* (2013) **368**:987–98. doi:10.1056/NEJMoa1209825
2. Aleman BMP, Moser EC, Nuver J, Suter TM, Maraldo MV, Specht L, et al. Cardiovascular disease after cancer therapy. *EJC Suppl* (2014) **12**:18–28. doi:10.1016/j.ejcsup.2014.03.002
3. Hodgson DC. Late effects in the era of modern therapy for Hodgkin lymphoma. *Hematology Am Soc Hematol Educ Program* (2011) **2011**:323–9. doi:10.1182/asheducation-2011.1.323
4. Lemanski C, Thariat J, Ampil FL, Bose S, Vock J, Davis R, et al. Image-guided radiotherapy for cardiac sparing in patients with left-sided breast cancer. *Front Oncol* (2014) **4**:257. doi:10.3389/fonc.2014.00257
5. Howe GR, Zablotska LB, Fix JJ, Egel J, Buchanan J. Analysis of the mortality experience amongst U. S. Nuclear Power Industry Workers after chronic low-dose exposure to ionizing radiation. *Radiat Res* (2004) **162**:517–26. doi:10.1667/RR3258
6. Little MP, Tawn EJ, Tzoulaki I, Wakeford R, Hildebrandt G, Paris F, et al. Review and meta-analysis of epidemiological associations between low/moderate doses of ionizing radiation and circulatory disease risks, and their possible mechanisms. *Radiat Environ Biophys* (2009) **49**:139–53. doi:10.1007/s00411-009-0250-z
7. Little MP. A review of non-cancer effects, especially circulatory and ocular diseases. *Radiat Environ Biophys* (2013) **52**:435–49. doi:10.1007/s00411-013-0484-7.A
8. Schultz-Hector S, Trott K-R. Radiation-induced cardiovascular diseases: is the epidemiologic evidence compatible with the radiobiologic data? *Int J Radiat Oncol Biol Phys* (2007) **67**:10–8. doi:10.1016/j.ijrobp.2006.08.071
9. Rader DJ, Daugherty A. Translating molecular discoveries into new therapies for atherosclerosis. *Nature* (2008) **451**:904–13. doi:10.1038/nature06796
10. Hoel DG. Ionizing radiation and cardiovascular disease. *Ann N Y Acad Sci* (2006) **1076**:309–17. doi:10.1196/annals.1371.001
11. Andreassi MG, Botto N. DNA damage as a new emerging risk factor in atherosclerosis. *Trends Cardiovasc Med* (2003) **13**:270–5. doi:10.1016/S1050-1738(03)00109-9
12. Di Lisa F, Kaludercic N, Carpi A, Menab R, Giorgio M. Mitochondria and vascular pathology. *Pharmacol Rep* (2009) **61**:123–30. doi:10.1016/S1734-1140(09)70014-3
13. Finsterer J. Is atherosclerosis a mitochondrial disorder? *Vasa* (2007) **36**:229–40. doi:10.1024/0301-1526.36.4.229
14. Ito TK, Yokoyama M, Yoshida Y, Nojima A, Kassai H, Oishi K, et al. A crucial role for CDC42 in senescence-associated inflammation and atherosclerosis. *PLoS One* (2014) **9**:e102186. doi:10.1371/journal.pone.0102186
15. Bert C, Engenhart-Cabillic R, Durante M. Particle therapy for noncancer diseases. *Med Phys* (2012) **39**:1716–27. doi:10.1118/1.3691903
16. Tsujii H, Kamada T. A review of update clinical results of carbon ion radiotherapy. *Jpn J Clin Oncol* (2012) **42**:670–85. doi:10.1093/jjco/hys104
17. Loeffler JS, Durante M. Charged particle therapy – optimization, challenges and future directions. *Nat Rev Clin Oncol* (2013) **10**:411–24. doi:10.1038/nrclinonc.2013.79
18. Takahashi Y, Teshima T, Kawaguchi N, Hamada Y, Mori S, Madachi A, et al. Heavy ion irradiation inhibits in vitro angiogenesis even at sublethal dose. *Cancer Res* (2003) **63**:4253–7.
19. Lanza V, Pretazzoli V, Olivieri G, Pascarella G, Panconesi A, Negri R. Transcriptional response of human umbilical vein endothelial cells to low doses of ionizing radiation. *J Radiat Res* (2005) **46**:265–76. doi:10.1269/jrr.46.265
20. Rombouts C, Aerts A, Beck M, De Vos WH, Van Oostveldt P, Benotmane MA, et al. Differential response to acute low dose radiation in primary and immortalized endothelial cells. *Int J Radiat Biol* (2013) **89**:841–50. doi:10.3109/09553002.2013.806831
21. Kraft G, Daues HW, Fischer B, Kopf U, Leibold H, Quis D, et al. Irradiation chamber and sample changes for biological samples. *Nucl Instrum Methods* (1980) **168**:175–9. doi:10.1016/0029-554X(80)91249-5
22. Kraft-Weyrather W, Kraft G, Ritter S, Scholz M, Stanton J. The preparation of biological targets for heavy-ion experiments up to 20 MeV/u. *Nucl Instrum Methods Phys Res A* (1989) **282**:22–7. doi:10.1016/0168-9002(89)90104-6
23. Haberer T, Becher W, Schardt D, Kraft G. Magnetic scanning system for heavy ion therapy. *Nucl Instrum Methods Phys Res A* (1993) **330**:296–305. doi:10.1016/0168-9002(93)91335-K
24. Franken NAP, Rodermond HM, Stap J, Haveman J, van Bree C. Clonogenic assay of cells in vitro. *Nat Protoc* (2006) **1**:2315–9. doi:10.1038/nprot.2006.339
25. Fenech M. The in vitro micronucleus technique. *Mutat Res* (2000) **455**:81–95. doi:10.1016/S0027-5107(00)00065-8
26. Meijer AE, Kronqvist U-SE, Lewensohn R, Harms-Ringdahl M. RBE for the induction of apoptosis in human peripheral lymphocytes exposed in vitro to high-LET radiation generated by accelerated nitrogen ions. *Int J Radiat Biol* (1998) **73**:169–77. doi:10.1080/095530098142554
27. Johnson VL, Ko SCW, Holmstrom TH, Eriksson JE, Chow SC. Effector caspases are dispensable for the early nuclear morphological changes during chemical-induced apoptosis. *J Cell Sci* (2000) **113**:2941–53.
28. Cosarizza A, Baccarani-Contri M, Kalashnikova G, Franceschi C. A new method for the cytofluorimetric analysis of mitochondrial membrane potential using the J-aggregate forming lipophilic cation 5,5',6,6'-tetrachloro-1,1',3,3'-tetraethylbenzimidazolcarbocyanine iodide (JC-1). *Biochem Biophys Res Commun* (1993) **197**:40–5. doi:10.1006/bbrc.1993.2438
29. Cornforth M. Analyzing radiation-induced complex chromosome rearrangements by combinatorial painting. *Radiat Prot Dosimetry* (2001) **155**:643–59.
30. Hooning MJ, Botma A, Aleman BMP, Baaijens MHA, Bartelink H, Klijn JGM, et al. Long-term risk of cardiovascular disease in 10-year survivors of breast cancer. *J Natl Cancer Inst* (2007) **99**:365–75. doi:10.1093/jnci/djk064
31. Hendry JH, Akahoshi M, Wang LS, Lipshultz SE, Stewart FA, Trott KR. Radiation-induced cardiovascular injury. *Radiat Environ Biophys* (2008) **47**:189–93. doi:10.1007/s00411-007-0155-7
32. Chen Y-H, Pan S-L, Wang J-C, Kuo S-H, Cheng JC-H, Teng C-M. Radiation-induced VEGF-C expression and endothelial cell proliferation in lung cancer. *Strahlenther Onkol* (2014) **190**:1154–62. doi:10.1007/s00066-014-0708-z
33. Ebrahimian T, Le Gallic C, Stefani J, Dublineau I, Yentrapalli R, Harms-Ringdahl S, et al. Chronic gamma-irradiation induces a dose-rate-dependent pro-inflammatory response and associated loss of function in human umbilical vein endothelial cells. *Radiat Res* (2015) **183**:447–54. doi:10.1667/RR13732.1
34. Weyrather WK, Ritter S, Scholz M, Kraft G. RBE for carbon track-segment irradiation in cell lines of differing repair capacity. *Int J Radiat Biol* (1999) **75**:1357–64. doi:10.1080/095530099139232
35. Habermehl D, Ilicic K, Dehne S, Rieken S, Orschiedt L, Brons S, et al. The relative biological effectiveness for carbon and oxygen ion beams using the raster-scanning technique in hepatocellular carcinoma cell lines. *PLoS One* (2014) **9**:e113591. doi:10.1371/journal.pone.0113591
36. Hei TK, Marchese MJ, Hall EJ. Radiosensitivity and sublethal damage repair in human umbilical cord vein endothelial cells. *Int J Radiat Oncol Biol Phys* (1987) **13**:879–84. doi:10.1016/0360-3016(87)90103-9
37. Manti L, Durante M, Elsaesser T, Gialanella G, Pugliese M, Ritter S, et al. Premature senescence in human endothelial cells exposed to carbon ions. *GSI Sci Rep* (2007) **1**:350.
38. Raicu M, Vral A, Thierens H, De Ridder L. Radiation damage to endothelial cells in vitro, as judged by the micronucleus assay. *Mutagenesis* (1993) **8**:335–9. doi:10.1093/mutage/8.4.335
39. Laurent C, Voisin P, Pouget J-P. DNA damage in cultured skin microvascular endothelial cells exposed to gamma rays and treated by the combination pentoxifylline and alpha-tocopherol. *Int J Radiat Biol* (2006) **82**:309–21. doi:10.1080/09553000600733150
40. Morgan WF. Is there a common mechanism underlying genomic instability, bystander effects and other nontargeted effects of exposure to ionizing radiation? *Oncogene* (2003) **22**:7094–9. doi:10.1038/sj.onc.1206992
41. Zahnreich S, Melnikova L, Winter M, Nasonova E, Durante M, Ritter S, et al. Radiation-induced premature senescence is associated with specific cytogenetic changes. *Mutat Res* (2010) **701**:60–6. doi:10.1016/j.mrgentox.2010.03.010
42. Vavrova J, Rezacova M. The importance of senescence in ionizing radiation-induced tumour suppression. *Folia Biol (Praha)* (2011) **57**:41–6.
43. Shah DJ, Sachs RK, Wilson DJ. Radiation-induced cancer: a modern view. *Br J Radiol* (2012) **85**:1166–73. doi:10.1259/bjr/25026140
44. Yentrapalli R, Azimzadeh O, Sriharshan A, Malinowsky K, Merl J, Wojcik A, et al. The PI3K/Akt/mTOR pathway is implicated in the premature senescence of primary human endothelial cells exposed to chronic radiation. *PLoS One* (2013) **8**:e70024. doi:10.1371/journal.pone.0070024

45. Favero G, Paganelli C, Buffoli B, Rodella LF, Rezzani R. Endothelium and its alterations in cardiovascular diseases?: life style intervention. *Biomed Res Int* (2014) **2014**:801896. doi:10.1155/2014/801896
46. Dimri GP, Leet X, Basile G, Acosta M, Scorrt G, Roskelley C, et al. A biomarker that identifies senescent human cells in culture and in aging skin in vivo. *Proc Natl Acad Sci U S A* (1995) **92**:9363–7. doi:10.1073/pnas.92.20.9363
47. Grossi G, Bettega D, Calzolari P, Durante M, Elsässer T, Gialanella G, et al. Late cellular effects of 12 C ions. *Nuovo Cim* (2008) **31**:39–47. doi:10.1393/ncc/i2008-10278-4
48. Oh C, Bump EA, Kim J-S, Janigro D, Mayberg MR. Induction of a senescence-like phenotype in bovine aortic endothelial cells by ionizing radiation. *Radiat Res* (2001) **156**:232–40. doi:10.1667/0033-7587(2001)156[0232:IOASLP]2.0.CO;2
49. Igarashi K, Sakimoto I, Kataoka K, Ohta K, Miura M. Radiation-induced senescence-like phenotype in proliferating and plateau-phase vascular endothelial cells. *Exp Cell Res* (2007) **313**:3326–36. doi:10.1016/j.yexcr.2007.06.001
50. Kim KS, Kim JE, Choi KJ, Bae S, Kim DH. Characterization of DNA damage-induced cellular senescence by ionizing radiation in endothelial cells. *Int J Radiat Biol* (2014) **90**:71–80. doi:10.3109/09553002.2014.859763
51. Zhang L, Aviv H, Gardner JP, Okuda K, Patel S, Kimura M, et al. Loss of chromosome 13 in cultured human vascular endothelial cells. *Exp Cell Res* (2000) **260**:357–64. doi:10.1006/excr.2000.4997
52. Wagner M, Hampel B, Bernhard D, Hala M, Zwerschke W, Jansen-Dürr P. Replicative senescence of human endothelial cells in vitro involves G1 arrest, polyploidization and senescence-associated apoptosis. *Exp Gerontol* (2001) **36**:1327–47. doi:10.1016/S0531-5565(01)00105-X
53. Kim JH, Jenrow KA, Brown SL. Mechanisms of radiation-induced normal tissue toxicity and implications for future clinical trials. *Radiat Oncol J* (2014) **32**:103–15. doi:10.3857/roj.2014.32.3.103
54. Davidson SM, Duchen MR. Endothelial mitochondria: contributing to vascular function and disease. *Circ Res* (2007) **100**:1128–41. doi:10.1161/01.RES.0000261970.18328.1d
55. Donato AJ, Eskurza I, Silver AE, Levy AS, Pierce GL, Gates PE, et al. Direct evidence of endothelial oxidative stress with aging in humans: relation to impaired endothelium-dependent dilation and upregulation of nuclear factor-kappaB. *Circ Res* (2007) **100**:1659–66. doi:10.1161/01.RES.0000269183.13937.e8
56. Barjaktarovic Z, Schmaltz D, Shyla A, Azimzadeh O, Schulz S, Haagen J, et al. Radiation-induced signaling results in mitochondrial impairment in mouse heart at 4 weeks after exposure to X-rays. *PLoS One* (2011) **6**:e27811. doi:10.1371/journal.pone.0027811
57. Smiley ST, Reers M, Mottola-Hartshorn C, Lin M, Chen A, Smith TW, et al. Intracellular heterogeneity in mitochondrial membrane potentials revealed by a J-aggregate-forming lipophilic cation JC-1. *Proc Natl Acad Sci U S A* (1991) **88**:3671–5. doi:10.1073/pnas.88.9.3671
58. Lyng FM, Seymour CB, Mothersill C. Production of a signal by irradiated cells which leads to a response in unirradiated cells characteristic of initiation of apoptosis. *Br J Cancer* (2000) **83**:1223–30. doi:10.1054/bjoc.2000.1433
59. Wang W, Yang S, Su Y, Xiao Z, Wang C, Li X, et al. Enhanced antitumor effect of combined triptolide and ionizing radiation. *Clin Cancer Res* (2007) **13**:4891–9. doi:10.1158/1078-0432.CCR-07-0416
60. Nair S, Nair RRK, Srinivas P, Srinivas G, Pillai MR. Radiosensitizing effects of plumbagin in cervical cancer cells is through modulation of apoptotic pathway. *Mol Carcinog* (2008) **47**:22–33. doi:10.1002/mc
61. Samraj AK, Sohn D, Schulze-Osthoff K, Schmitz I. Loss of caspase-9 reveals its essential role for caspase-2 activation and mitochondrial membrane depolarization. *Mol Biol Cell* (2007) **18**:84–93. doi:10.1091/mbc.E06
62. Kimura M, Cao X, Patel S, Aviv A. Survival advantage of cultured human vascular endothelial cells that lost chromosome 13. *Chromosoma* (2004) **112**:317–22. doi:10.1007/s00412-004-0276-6
63. Anno K, Hayashi A, Takahashi T, Mitsui Y, Ide T, Tahara H. Telomerase activation induces elongation of the telomeric single-stranded overhang, but does not prevent chromosome aberrations in human vascular endothelial cells. *Biochem Biophys Res Commun* (2007) **353**:926–32. doi:10.1016/j.bbrc.2006.12.112
64. Giacinti C, Giordano A. RB and cell cycle progression. *Oncogene* (2006) **25**:5220–7. doi:10.1038/sj.onc.1209615

Conflict of Interest Statement: The authors declare that the research was conducted in the absence of any commercial or financial relationships that could be construed as a potential conflict of interest.

Copyright © 2016 Helm, Lee, Durante and Ritter. This is an open-access article distributed under the terms of the Creative Commons Attribution License (CC BY). The use, distribution or reproduction in other forums is permitted, provided the original author(s) or licensor are credited and that the original publication in this journal is cited, in accordance with accepted academic practice. No use, distribution or reproduction is permitted which does not comply with these terms.

frontiers in Oncology

REVIEW
published: 21 March 2016
doi: 10.3389/fonc.2016.00061

Transcription Factors in the Cellular Response to Charged Particle Exposure

Christine E. Hellweg, Luis F. Spitta, Bernd Henschenmacher, Sebastian Diegeler and Christa Baumstark-Khan*

Cellular Biodiagnostics, Department of Radiation Biology, Institute of Aerospace Medicine, German Aerospace Centre (DLR), Cologne, Germany

Charged particles, such as carbon ions, bear the promise of a more effective cancer therapy. In human spaceflight, exposure to charged particles represents an important risk factor for chronic and late effects such as cancer. Biological effects elicited by charged particle exposure depend on their characteristics, e.g., on linear energy transfer (LET). For diverse outcomes (cell death, mutation, transformation, and cell-cycle arrest), an LET dependency of the effect size was observed. These outcomes result from activation of a complex network of signaling pathways in the DNA damage response, which result in cell-protective (DNA repair and cell-cycle arrest) or cell-destructive (cell death) reactions. Triggering of these pathways converges among others in the activation of transcription factors, such as p53, nuclear factor κB (NF-κB), activated protein 1 (AP-1), nuclear erythroid-derived 2-related factor 2 (Nrf2), and cAMP responsive element binding protein (CREB). Depending on dose, radiation quality, and tissue, p53 induces apoptosis or cell-cycle arrest. In low LET radiation therapy, p53 mutations are often associated with therapy resistance, while the outcome of carbon ion therapy seems to be independent of the tumor's p53 status. NF-κB is a central transcription factor in the immune system and exhibits pro-survival effects. Both p53 and NF-κB are activated after ionizing radiation exposure in an ataxia telangiectasia mutated (ATM)-dependent manner. The NF-κB activation was shown to strongly depend on charged particles' LET, with a maximal activation in the LET range of 90–300 keV/μm. AP-1 controls proliferation, senescence, differentiation, and apoptosis. Nrf2 can induce cellular antioxidant defense systems, CREB might also be involved in survival responses. The extent of activation of these transcription factors by charged particles and their interaction in the cellular radiation response greatly influences the destiny of the irradiated and also neighboring cells in the bystander effect.

Keywords: charged particles, p53, Nrf2, NF-κB, AP-1, Sp1, CREB, EGR-1

OPEN ACCESS

Edited by:
Marco Durante, GSI Helmholtz Centre for Heavy Ion Research, Germany

Reviewed by:
Drexell Hunter Boggs, University of Alabama Birmingham, USA
Akihisa Takahashi, Gunma University, Japan

****Correspondence:***
Christine E. Hellweg
christine.hellweg@dlr.de

Specialty section:
This article was submitted to Radiation Oncology, a section of the journal Frontiers in Oncology

Received: *30 September 2015*
Accepted: *03 March 2016*
Published: *21 March 2016*

Citation:
Hellweg CE, Spitta LF, Henschenmacher B, Diegeler S and Baumstark-Khan C (2016) Transcription Factors in the Cellular Response to Charged Particle Exposure. Front. Oncol. 6:61. doi: 10.3389/fonc.2016.00061

INTRODUCTION

Understanding the cellular radiation response is an essential prerequisite for improving cancer radiotherapy, including carbon ion therapy. The same holds true for the risk assessment of astronauts' and for effective countermeasure development.

Radiotherapy of cancer with protons and carbon ions profits from a more precise dose deposition with charged particle beams in the tumor and in the case of carbon ions, also a higher biological

effectiveness in cell killing compared to conventional radiotherapy. There are hints that with carbon ions, cell killing is less dependent on factors such as oxygen concentration and alterations in cellular signaling pathways such as the p53 pathway.

Astronauts on exploration missions are subjected to not only greater amounts of natural radiation in space than they receive on Earth but also to a differing radiation quality, which can result in immediate and long-term risks. Besides protons and α-particles, heavier nuclei are part of the radiation field encountered in space. Heavy ions represent an important part of galactic cosmic rays because of their high biological effectiveness (1).

The radiation quality of energetic ions, including protons, α-particles, and heavy ions, is usually characterized by the linear energy transfer (LET) in matter which is a measure of the average energy transferred when an ionizing particle passes through matter and loses energy (2). Indirectly, it gives information about the ionization density along the particle track.

In the cellular response to radiation, several sensors detect the induced DNA damage and trigger signal transduction pathways, resulting in cell death or survival with or without mutations (3, 4). The activation of several signal transduction pathways by ionizing radiation (IR) results in altered expression of series of target genes. The promoters or enhancers of these genes may contain binding sites for one or more transcription factors, and a specific transcription factor can influence the transcription of multiple genes. A meta-analysis revealed that two p53-dependent genes, GADD45 (especially GADD45α) and CDKN1A, and genes associated with the NER pathway (e.g., XPC) are consistently upregulated by IR exposure (5). Importantly, the transcribed subset of target genes is critical for the decision between resuming normal function after cell-cycle arrest and DNA repair, entering senescence, or proceeding through apoptosis in cases of severe DNA damage (5) and thereby for the cellular destiny and for the outcome of cancer radiotherapy. The changes in gene expression induced by IR *via* transcription factors depend on dose, dose rate, time after irradiation, radiation quality, cell type, inherited or accumulated mutations in signaling pathways, cell-cycle phase, and possibly on other factors (**Table 1**). Twelve years ago, the transcription factors to be activated after exposure to clinically relevant doses of IR were summarized, resulting in the short list of p53, nuclear factor κB (NF-κB), and the specificity protein 1 (SP1)-related retinoblastoma control proteins (RCPs) (6). In this review, the role of transcription factors in the cellular response to IR is summarized with a special focus on charged particles as far as data are available.

p53

The transcription factor *TP53* (*p53*) was first described in 1979 (7), and many names have been attributed to the factor that belongs to the class of tumor suppressor genes. The transcription factor was called "an acrobat in tumorigenesis" (8), the "good and bad cop" (9), a "death star" (10), and even the "guardian of the genome" (11). p53 is involved in the regulation of cellular survival, immune responses, and inflammation, resulting in eminent importance in cancerogenesis and inflammation. Nowadays, it is known that defects in p53 are directly or indirectly involved in the majority (>50%) of human cancers as described by the International Cancer Genome Consortium (ICGC).

The human p53 gene is located on the short arm of chromosome 17 (17p13) and the protein size is 393 amino acids (~43 kDa). It is composed of several domains: the N-terminus contains a transactivation domain for downstream gene activation (1–43). A proline rich domain follows that mediates the response to DNA damage through apoptosis (58–101). The DNA-binding region or domain (DBD) is next (102–292) followed by an oligomerization domain (320–355) that interacts with other p53 monomers (p53 is capable of tetramerize). The C-terminus (356–393) is leucine rich and contains three putative nuclear localization signals (NLS) and so-called nuclear export signals (NES). It is postulated that when oligomerization occurs, NES are masked and p53 is retained in the nucleus. The DBD is the core domain, and it is composed of a variety of structural motifs. Single mutations within this domain can cause a major conformational change. There are in total 12 isoforms of p53 in humans discovered until now (12).

p53 has been recognized as an important checkpoint protein in the DNA damage response (DDR), which transcriptionally controls target genes involved in multiple response pathways that are as diverse as cell-cycle arrest and survival or death by apoptosis (13). It is thereby important for explaining the diversity of cellular responses to IR exposure. p53 has a short half-life and is stabilized in response to a variety of cellular stresses after phosphorylation by ataxia telangiectasia mutated (ATM) (13). After exposure to IR, phosphorylation of the serine residues 15 and 20 on p53 by checkpoint kinase 2 (CHK2) reduces its binding to MDM2, which in its bound state targets p53 for degradation by the proteasome pathway (**Figure 1**). Thus, dissociation of p53 from MDM2 prolongs the half-life of p53 (14). Other proteins, such as Pin 1, Parc, and p300, and p300/CBP-associated factor (PCAF) histone acetyltransferases regulate the transactivation activity of p53 (13). For efficient repair, especially in non-dividing cells, cellular levels of deoxyribonucleotides are increased during the DDR by p53-dependent transcriptional induction of the ribonucleotide reductase RRM2B (p53R2) (15).

It is accepted that the severity of DNA damage is the critical factor in directing the signaling cascade toward reversible cell-cycle arrest or apoptosis (13, 15). As part of the signaling cascade, the abundance of p53 protein, specific posttranslational modifications, and its interaction with downstream effectors, such as GADD45α or p21, may be responsible for directing the cellular response at this decision point (14).

Recently, Gudkov and Komarova (16) proposed that after total body irradiation (TBI) of mice severe damage occurs in tissues prone to p53-dependent apoptosis [the apoptosis response of p53 after X-irradiation was already shown in murine experiments 1996 by Norimura et al. (17)], such as the hematopoietic system, hair follicles, and oligodendroblasts in the spinal cord. Other tissues, such as the vascular endothelial cells (ECs) of the small intestine react to p53 activation by cell-cycle arrest and activation of DNA repair (16). Connective tissues and epithelial cells usually respond with growth arrest to p53 activation (16). The authors conclude from animal models that p53 is the key component of the toxicity of IR or radiomimetic (DNA damaging) drugs. It

TABLE 1 | Transcription factor activation by ionizing radiation.

Experimental model	Radiation quality	Dose	Method	Effect	Reference
p53					
H1299 (originally p53 null)	X-rays	2–5 Gy	Colony-forming ability (CFA) assay, acridine orange/ethidium bromide staining, Western blot, quantitative real time RT-PCR (RT-qPCR)	Wildtype p53 cells: higher sensitivity compared to p53 null or mutated p53 cells	(172)
	^{12}C 290 MeV/u	2–5 Gy		Low LET radiation ⇒ p53-dependent apoptosis High LET ⇒ p53-independent apoptosis	
A549, AGS, and MCF-7	X-rays	0–12 Gy	RT-qPCR, Western blot, flow cytometry, luciferase reporter assay, CFA assay	miR-375 overexpression ⇒ p53 expressions ⇓	(173)
	Etoposide	0–100 μM		Radiosensitivity ⇓	
HCT116 (colorectal cells) p53 wt and ko cells	X-rays	0–8 Gy	Viability assay (transwell co-culture), micronuclei and apoptosis evaluation, beta-galactosidase staining, RT-qPCR	Low doses: no difference between cell lines Higher doses: significant differences, e.g., micronuclei ⇑ and apoptotic cells ⇑ in p53$^{-/-}$ cells, p53$^{+/+}$: high levels of senescence	(174)
Lung epithelial cells	α-particles (^{238}Pu) X-rays	0–1.2 Gy 0–2.5 Gy	Flow cytometry	p53 expression levels ⇑	(175)
HCT116	^{12}C 290 MeV/u	0–3 Gy	CFA assay, flow cytometry, iimmunofluorescence	X-rays ⇒ higher sensitivity and apoptosis ⇑ in p53$^{+/+}$ cells	(176)
	X-rays	0–8 Gy		C-ions ⇒ no difference of sensitivity (mitotic catastrophe ⇑ in p53$^{-/-}$ cells, apoptosis ⇑ in p53$^{+/+}$ cells)	
NF-κB					
Human, mouse, rat, hamster normal, transformed and tumor cell lines and primary cells, animal models (rat, mouse)	X-rays, γ-radiation, protons, α-particles, Fe ions, C ions, Ar ions	0.05–100 Gy	EMSA, Western blot, immunofluorescence, reporter assays, oligonucleotide enzyme-linked immunosorbent assay (ELISA)	Dose, cell line/cell type, and radiation quality-dependent activation	(70)
Nrf2					
NIH-3T3 MCF7-AREc32 Embryonic fibroblasts from wt and Nrf2 ko mice	γ-radiation ^{137}Cs source	2–8 Gy, 10 Gy	Luciferase assay, RT-qPCR, Western blot, CFA assay, ROS measurement (H_2DCFH-DA)	No short-term activation of Nrf2 activation Late activation of Nrf2 Nrf2 activation after fractionated irradiation	(88)
PC3 and DU145 prostate cancer cell lines	γ-radiation ^{60}Co source	1–10 Gy	Electrophoretic mobility shift assay (EMSA), RT-qPCR	Differences in basal Nrf2 expression determine resistance to irradiation	(99)
		4 and 8 Gy	Knockdown (kd) of Nrf2 and heme oxygenase-1 (HO-1) expression using short hairpin RNA (shRNA)	High basal Nrf2 activity ⇒ Nrf2 activity ⇑, target gene expression ⇑ (DU145 cells) ⇒ higher radioresistance than PC3 cells Knockdown of Nrf2 ⇒ cell death ⇑	
Murine T-cell lymphoma cell line EL-4	γ-radiation ^{60}Co source	4 Gy	shRNA-kd, RT-qPCR, EMSA	ERK and Nrf2 interact in radioresistance of EL-4 cells	(102)
Dermal fibroblasts from wt mice and Nrf2 and Keap1-KO mice	UV-A-UV-B radiation	10.000 mJ/cm^2	Western blot, immunofluorescence, flow cytometry	UV-A, but not UV-B, induces Nrf2 activity, cellular survival depends on Nrf2	(103)

(Continued)

TABLE 1 | Continued

Experimental model	Radiation quality	Dose	Method	Effect	Reference
C57BL/6, CD-1, and SJL/C57BL/6 CD45.1 mice	γ-radiation	6.9, 7.0, 7.1, 7.25, 7.3, 10 Gy TBI	RT-qPCR	Interplay between Nrf2 and Notch signaling, Nrf2 mediates Notch signaling and increases hematopoietic stem cell function	(106)
Mx-Cre-Keap1$^{flox/flox}$	^{137}Cs source				
CMVCre-Keap1$^{flox/flox}$	$^{12}C^{6+}$ ions	2 Gy	RT-qPCR of Nrf2 downstream genes NAD(P)H quinine oxidoreductase 1 (NQO1), HO-1, gamma-glutamyl cysteine synthetase (γ-GCS), immunofluorescence, Western blot	NQO1, HO-1, γ-GCS ⇑ in curcumin-pretreated mice	(108)
Keap1$^{flox/flox}$ mice					
HCEC CT7s cells (immortalized colon epithelic cells)	γ-radiation ^{137}Cs source (cells)	4–5 Gy	Immunohistochemistry, Western blot, subcellular fractionation, immunofluorescence, assay for chromosomal aberrations at metaphase, shRNA against Nrf2, DNA fiber assay, ChIP qPCR	Nrf2 enhances DDR and reduces number of DNA DSB	(109)
C57BL/6 wt mice	X-rays (mice)	7.5–10 Gy TBI		Nrf2 ⇒ 53BP1 expression ⇑	
EA.hy926 and HMVEC cells	Photons from linear accelerator	0, 0.3, 0.5, 0.7, 1 Gy	RT-qPCR, flow cytometry, Western blot, enzyme activity of glutathione peroxidase, EMSA	Non-linear activation of Nrf2 and target genes	(107)
				Nrf2 activation prior to irradiation ⇒ cell adhesion ⇑	
				Nrf2 expression and binding to DNA lowest at 0.5 Gy	
CREB					
Human U1-Mel cell line	^{60}Co γ-rays	4.5 Gy	EMSA with nuclear extracts	CREB DNA binding ⇑	(123)
Jurkat leukemic T cell line	10 MV X-rays	1.5 and 6 Gy	Western blot	CREB phosphorylation ⇑	(115)
K562 erythroleukemia cells	10 MV X-rays	1.5 and 15 Gy	Western blot	CREB phosphorylation ⇑	(119)
Chinese Hamster V79 cells	$^{12}C^{5+}$ ions	0.1 and 1 Gy	Western blot	p44/42 MAPK ⇑	(125)
AG1522 human diploid skin fibroblasts	α-particles (^{238}Pu source)	0.01, 0.05, and 0.10 Gy	Western blot	p38 MAPK and ERK 1/2 ⇑	(126)
AP-1					
AG1522 human diploid skin fibroblast	α-particles (^{238}Pu source)	0.003 and 0.006 Gy	EMSA	AP-1 DNA-binding activity ⇑	(126)
MRC5CV1 normal human fibroblasts	^{137}Cs γ-rays	20 Gy	Western blot EMSA	c-jun phosphorylation ⇑ AP-1 DNA-binding activity ⇑	(131)
ROS 17/2.8 osteoblasts	X-rays	5 Gy	EMSA with supershift	AP-1 DNA-binding activity ⇑	(132)
Spontaneously immortalized human breast epithelial cell line MCF-10F	α-particles, LET 150 keV/μm	6 and 1.2 Gy	Northern blot and immunochemical protein staining	c-jun, c-fos, FRA1 RNA, and protein expression ⇑	(135)
C57BL/6J mice	^{56}Fe ions, 1000 MeV/n, LET 148 keV/μm	1.6 Gy	SOD 1/2 and catalase activity, NADPH oxidase activity assay and immunohistochemistry of p-H3	SOD 1/2, catalase, NADPH oxidase and mitogenic activity ⇑	(98)
Sp1					
Normal human diploid fibroblasts	6 MV X-rays	0.5, 2.5, 5, 10, 20, 40 Gy	Western blot	Sp1 expression and phosphorylation ⇑	(141)
U1-Mel cells	^{137}Cs γ-rays	3 and 4.5 Gy	EMSA and Western blot	Sp1 DNA binding and phosphorylation ⇑	(142)

(Continued)

TABLE 1 | Continued

Experimental model	Radiation quality	Dose	Method	Effect	Reference
H1299	α-particles, LET 123 keV/μm	1 Gy	IPA upstream regulator analysis	Sp1 network involvement	(145)
Normal human fibroblasts (HFL 3)	C ions, 290 MeV/n, LET 70 keV/μm Fe ions, 500 MeV/n, LET 200 keV/μm	2 Gy	PCC assay and immunofluorescence	DNA-PKc autophosphorylation ⇑	(146)
EGR-1					
Isolated lymphocytes	Na ^{211}At α-particles	0.05–1.6 Gy	RT-qPCR	EGR-1 gene expression ⇑	(134)
Prostate cancer cells PC-3	100 kV X-rays	5 Gy	Western blot	Protein induction ⇑	(147)
Human HL 525 myeloid leukemia cells	^{137}Cs γ-rays	20 Gy	Western blot	Protein expression ⇑	(148)

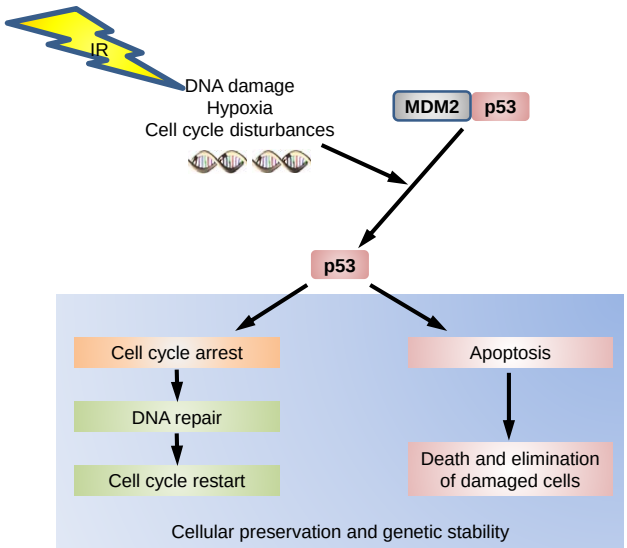

FIGURE 1 | The p53 pathway. p53 is under normal conditions inactivated by murine double minute 2 (MDM2). When, e.g., DNA damage occurs, p53 dissociates from its regulatory MDM2 complex by various pathways. In this active state, phosphorylated p53 will induce a cell-cycle arrest to permit either repair and therefore survival of the cell or induce apoptosis to eliminate a damaged cell.

thereby contributes to the hematopoietic component of the acute radiation syndrome and leads to severe adverse effects of cancer treatment (16).

p53-dependent GADD45α upregulation may play a role in apoptosis by activating the c-Jun N-terminal kinase (JNK) and/or p38 mitogen-activated protein kinase (MAPK) signaling pathways (18). Besides GADD45α, p53 regulates the expression of other proteins involved in apoptosis, including membrane-bound proteins, such as Fas/CD95, TP53 apoptosis effector related to PMP22 (PERP), and KILLER/DR5, cytoplasm-localized proteins, such as p53-inducible death domain-containing protein (PIDD) and PIGs, and mitochondrial proteins, such as BAX, NOXA, PUMA, p53Aip1, and BID (13, 14). The induction of these pro-apoptotic genes seems to be tissue specific (13). p53 also directly interacts with BAX, BCL-XL, and BCL-2 at the mitochondrial membrane (14).

So far, p53 plays a crucial role in the cellular radiation response. In future, the treatment of patients suffering from cancer will be personalized; this means that the combination of cytostatic agents and radiotherapy has to be individualized also depending on the tissue affected. For colorectal carcinoma cell lines, many tests are being performed with distinct agents where, e.g., gemcitabine, paclitaxel, or irinotecan are used in order to optimize the treatment results in combination with carbon ions. It has been already shown that after C-12 ion irradiation in cells lacking p53, paclitaxel and gemcitabine were very effective as well as irinotecan on p53 wild-type (wt) cells (19). Nevertheless, a problem with targeting the p53 pathway as a helping tool in cancer therapy by activation and thereby unleashing the protective attitudes of this pathway is that in hematological malignancies

there is a low incidence of p53 mutations. Here, maybe MDM2 proteins can be addressed.

The bystander effect is a field that still needs to be understood and where experiments and the effects of a possible p53 response are barely recognized. First observations though, show that in mammalian cells lacking p53 in comparison to wt p53, the cells respond upon heavy ion exposure in the already known ways when directly irradiated (20). This fact is also to be taken into consideration when irradiation of patients is to be performed even though it does not play a major role, since the main goal is still targeting and eliminating the malignant tumors in an efficient manner.

The *tyrosine kinase c-abl* is a functional analogous to p53 in regulation of programmed cell death and DNA repair (21) interacting with p53 indirectly through modification of upstream regulators [homeodomain-interacting protein kinase 2 (HIPK2)] (22). C-abl is the ubiquitously expressed product of the cellular homolog of the transforming gene of Abelson murine leukemia virus (v-abl) shuttling between cytoplasm and nucleus of the cell (21, 23). Cytoplasmic c-abl is assumed to function in association with the F-actin cytoskeleton while nuclear c-abl participates in cell-cycle regulation, DDR, and apoptosis (23). Sparsely ionizing leads to an activation of c-abl (21, 24, 25) *via* phosphorylation by ATM at Ser-465 (26) and by DNA-dependent protein kinase (DNA-PK) (21, 23). It can function as a negative regulator of DNA repair progression, inhibiting DSB re-joining and downregulating γH2AX, decreasing the recruitment of DNA repair factors to the damage site (21), or c-abl can phosphorylate DNA PK and Rad51 to abolish their binding to DNA, thereby impeding their function (21, 25). It can also promote apoptosis with a direct influence on the p73-dependent DDR by phosphorylating the YES-associated protein (YAP). Upon phosphorylation, YAP acts together with p73 on pro-apoptotic gene targets (**Figure 2**) (21, 22).

In response to densely IR, c-abl has been surmised to partake in a p53-independent induction of apoptosis. In the model described, c-abl activates caspase 9 *via* phosphorylation at Tyr 153, initiating the cleavage of caspase 3 as a point of no return in apoptosis induction (27).

In summary, a potential role in the cellular radiation response can be attributed to c-abl as mediator of apoptosis and coordinator of DNA repair. Albeit greater focus on densely IR, such as carbon therapy, has to be introduced to fully conclude its role for this radiation quality.

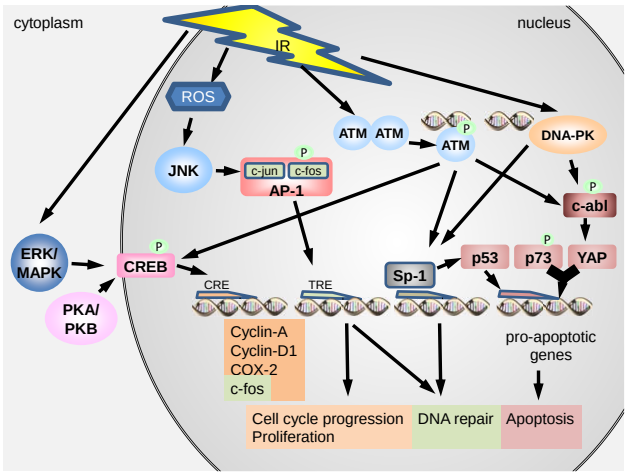

FIGURE 2 | Activation of the transcription factors CREB, AP-1, SP1, p73, and YAP upon irradiation ionizing radiation (IR) can activate protein kinase A (PKA) and B (PKB) as well as ERK/MAPK in the cytoplasm. Exposure to IR can produce reactive oxygen species (ROS) in the cytoplasm and nucleus and DNA double-strand breaks (DNA DSB) in the nucleus. PKA/PKB, ERK/MAPK, and ATM can phosphorylate CREB, which then translocates into the nucleus to bind CRE elements in order to express pro-survival proteins. ATM and DNA-PK can phosphorylate c-abl, which in turn phosphorylates YAP. Phosphorylated YAP acts together with p73 to stimulate expression of pro-apoptotic genes. ATM and DNA-PK can further induce Sp1, which can act pro-apoptotic by inducing p53 or pro-survival by regulating the DNA damage response and inducing DNA repair. IR-induced ROS can activate JNK to phosphorylate the AP-1 complex, thereby initiating DNA binding to TRE genes. Expression of TRE genes leads to induction of DNA repair and promotion of cell-cycle progression.

NUCLEAR FACTOR κB

Although several genes induced by IR are p53-regulated, the majority are p53-independent (28–31), with the transcription factor NF-κB playing a contributing role (29, 31).

NF-κB/Rel proteins comprise a family of structurally related eukaryotic transcription factors that are involved in the control of a large number of cellular and organismal processes, such as immune system development and performance, inflammation, developmental processes, cellular growth, and apoptosis (32–35). Homo- or heterodimers of NF-κB1 (p50/p105), NF-κB2 (p52/p100), RelA (p65), RelB, or c-Rel (**Figure 3**) can be activated in response to hundreds of agents (36–38) and thereby modulate environment-induced gene expression. Besides immune modulating agents and pathogen-derived agents (lipopolysaccharides), a variety of other cellular stress factors are able to induce this pathway, such as cytokines, phorbol esters, viruses, ultraviolet (UV) radiation, reactive oxygen species (ROS), necrotic cell products, growth factor depletion, hypoxia, heat shock, and IR (38–41).

In the inactive state, NF-κB is retained in the cytoplasm by the inhibitory *IκB proteins* (**Figure 4**), which controls nuclear translocation of NF-κB by masking its NLS (42, 43). *IκB proteins* bind through their ankyrin repeat domain (ARD) to NF-κB. In their free state, IκB proteins are unstable and rapidly degraded, while binding to NF-κB strongly increases their stability (43). The three (NFκBIA, NFκBIB, and NFκBIE) genes code for the canonical IκB proteins, IκBα, IκBβ, and IκBє (**Figure 4**) (43). The p50:p65 heterodimer is mainly bound by IκBα. p105 and p100 proteins, which are involved in the alternative NF-κB pathway, contain the inhibitory part already in their C-terminal region in addition to the NF-κB part in the N-terminal half. Two novel IκBs (IκBζ and BCL-3) were described. BCL-3 is a non-inhibiting IκB family member that acts as transcriptional co-activator for p50:p50 and p52:p52 homodimers (44). Further novel atypical IκB proteins were recently reviewed by Arnemann et al. (45).

Upon activation, IκBα can be degraded by several proteases (46) and the released NF-κB translocates to the nucleus and

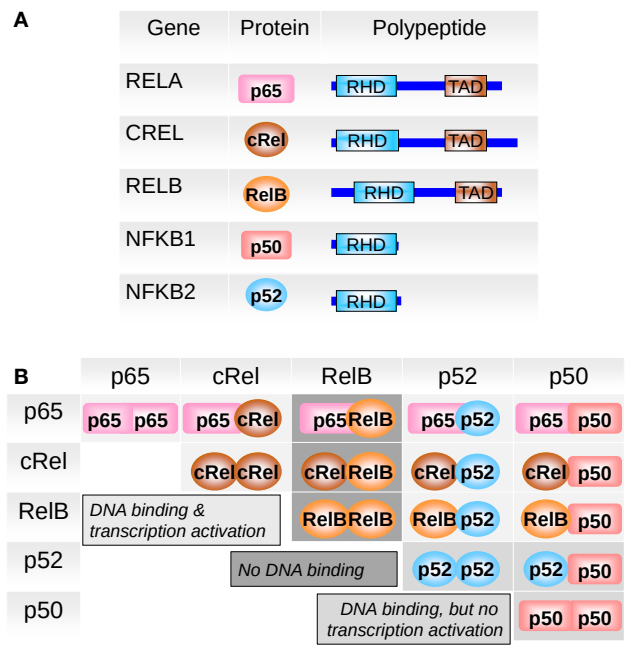

FIGURE 3 | The members of the NF-κB family. **(A)** NF-κB subunits each contain a Rel homology domain (RHD) for dimerization and DNA binding. p65 (RelA), c-Rel, and RelB bear transcriptional activation domains (TAD). **(B)** The 5 NF-κB monomers can associate to 15 potential dimers. Of these, nine can bind DNA and activate gene transcription (light gray), three (the p50 or p52 only containing dimers) bind DNA but do not activate transcription (medium gray), and three do not bind DNA (dark gray). Adapted from O'Dea and Hoffmann (43).

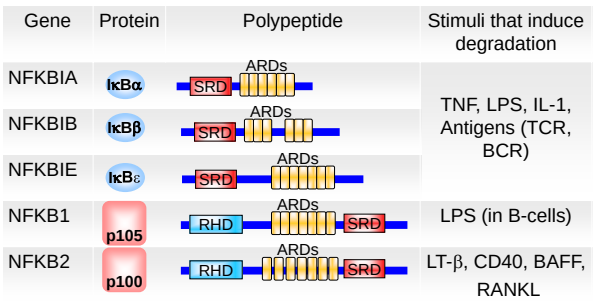

FIGURE 4 | The members of the inhibitor of NF-κB (IκB) family. IκB proteins contain ankyrin repeat domains (ARDs) and signal response domains (SRDs) and are degraded in response to different signals (BCR, B-cell receptor; TCR, T-cell receptor; LPS, lipopolysaccharide; LT-β, lymphotoxin-β; BAFF, B-cell-activating factor; RANKL, receptor activator of NF-κB ligand). The ARDs on p105 and p100 (which are proteolytically processed to p50 and p52 NF-κB monomers, respectively) can act to self-inhibit p50 and p52. p100 can also form a multimeric complex in which it can inhibit other latent NF-κB dimers. Adapted from O'Dea and Hoffmann (43).

binds to κB or κB-like DNA motifs [NF-κB response elements, NREs with the consensus sequence GGGRNNN(N)YCC][1] initiating gene transcription. NREs have been identified in the promoter or enhancer regions of more than 200 genes, including a number of IκBs, growth factors, proinflammatory cytokines (TNF-α, IL-1, IL-6) and enzymes (cyclooxygenase-2, COX-2), chemokines (IL-8/CXCL8; monocyte chemotactic cytokine 1, MCP-1/CCL2), angiogenic factors (vascular endothelial growth factor, VEGF), degradative enzymes (matrix metalloproteinases, MMPs), and adhesion molecules (intercellular adhesion molecule-1, ICAM-1; vascular cell adhesion molecule-1, VCAM-1; E-selectin). These target genes are involved in inflammation, innate immune responses, angiogenesis, tumor progression, and metastasis in various cancers and fibrosis (39, 44, 47, 48). NF-κB regulated expression of cytokines and extracellular matrix proteases after heavy ion exposure might contribute to extracellular matrix remodeling (49). Activation of NF-κB by high radiation doses (1–10 Gy) could contribute to the inflammatory response observed, e.g., in the developing brain after radiation exposure (50).

In addition, NF-κB also regulates the expression of many genes whose products are involved in the control of cell proliferation and cell death (51). In a cell culture model, it has been found that ATM plays a role in sustained activation of NF-κB in response to DNA DSB (52, 53), probably by its PI-3-kinase-like activity (54). Activation of the NF-κB pathway does not only protect cells from apoptosis after treatment with various genotoxic agents *via* expression of anti-apoptotic proteins, such as Bcl-2, GADD45β, TRAF-1, TRAF-2, cIAP-1, and cIAP-2 (55), but also gives transformed cells a growth and survival advantage and further renders tumor cells therapy resistant (56). NF-κB acts also as a transcriptional enhancer for the protective enzyme manganese superoxide dismutase (Mn-SOD) and might thereby contribute to therapy resistance. NF-κB also enhances the expression of degradative enzymes supporting the idea that it makes a major contribution to tumor progression and metastasis in various cancers (48). Therefore, NF-κB was identified quite early as potential target of innovative cancer therapies (57). Due to this anti-apoptotic effects NF-κB activation, it is an important stress response that may modulate the outcome of chemotherapy- and radiotherapy-induced toxicity.

For cells of the immune system, a misdirection of the NF-κB correlated process that normally creates immunoglobulin diversity might result in increased survivability of cells with oncogenic chromosomal translocations that prevent apoptosis and promote proliferation of pre-malignant cells. Constitutive activity of NF-κB or its over-expression has been reported for many human cancer cells (including breast cancer, colon cancer, prostate cancer, and lymphoid cancers) and can cause malignant changes in lymphoid cells in tissue culture.

NF-κB–Rel complexes can be activated and be functional in three different subpathways in different cells and tissues: the canonical or classical pathway, the alternative or non-canonical pathway, and the genotoxic stress-induced pathway (58–60).

In the *canonical or classical pathway*, the signals for activation of NF-κB are generated by cytokines, e.g., TNF-α or IL-1, by growth factors, by ligands of toll-like receptors (TLRs) or by antigens, which bind to the T-cell receptor (TCR) or the B-cell receptor (BCR). The NF-κB is mostly composed of p50:p65 and p50:c-Rel dimers.

[1]N, any nucleotide, R, purine, and Y, pyrimidine.

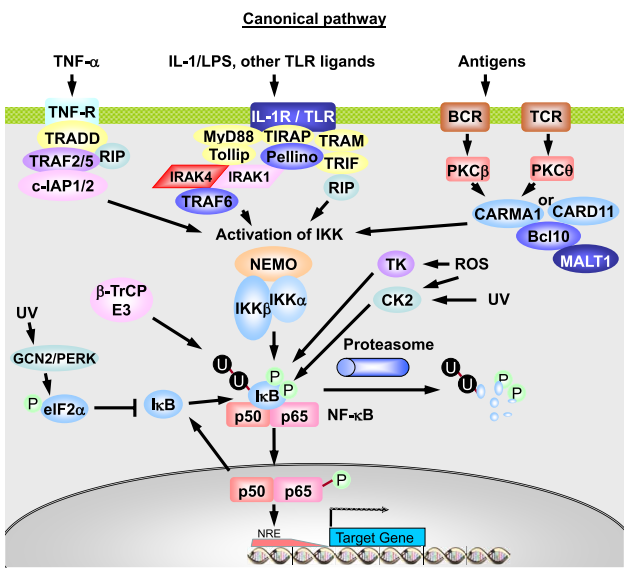

FIGURE 5 | The canonical or classical NF-κB pathway. The binding of TNF-α to TNF-R leads to a rapid recruitment of TRADD, RIP1, TRAF2, TRAF5, c-IAP1, and c-IAP2. Formation of this complex triggers TRAF2/5 and c-IAP1/2 to catalyze polyubiquitination of RIP1 and autoubiquitination of TRAF2 and/or c-IAP1 (not shown). Modified RIP1 then recruits the TAK1/TAB1/TAB2 (only TAK1 shown) and IKKα/IKKβ/NEMO complexes, leading to TAK1 activation and TAK1-mediated activation of IKKβ. Upon IL-1 stimulation of IL-1R, proteins, such as MyD88, Tollip, IRAK-1, and IRAK-4, are recruited, leading to IRAK1/4-dependent binding of TRAF6 and Pellino. TRAF6 then undergoes autoubiquitination, whereas Pellino catalyzes IRAK1 ubiquitination. Ubiquitinated TRAF6 in turn serves as a platform to recruit the TAK1/TAB1/TAB2 complex, resulting in TAK1 activation and finally IKKβ activation. TLR signaling can be MyD88 dependent or independent through TRAM, TRIF, and RIP. Activated IKK then phosphorylates IκBα, resulting in its ubiquitination and degradation. This IκBα degradation allows p50:p65 dimer to translocate to the nucleus and activate the expression of genes involved in inflammation, innate immunity, and cell survival. Ultraviolet (UV) irradiation reduces IκB levels *via* activation of GCN2 or PERK, which phosphorylate the initiation factor eIF2α, and *via* casein kinase 2 (CK2) and thymidine kinase (TK). Phosphorylated eIF2α blocks IκB synthesis. The BCR and TCR are expressed by B- and T-lymphocytes and do not act one the same cell. Adapted from O'Dea and Hoffmann (43) and Habelhah (44).

A central event in the pattern of NF-κB complex activation (**Figure 5**) is the activation of IκB kinase (IKK). This is achieved *via* a complex pathway involving several adaptor proteins, ubiquitin ligases, binding proteins, and kinases, such as receptor-interacting protein 1 (RIP1) and TNF-R-associated factor 2, 5, or 6 (TRAF2/5/6) (43, 44, 58–60), resulting in activation of IKK kinases (*IKK-K*). These kinases are responsible for phosphorylation of IKK and might be TGF-β-activated protein kinase 1 (TAK1) or MAPK kinase kinase 3 (MEKK3) after stimulation with TNF-α (44). The exact contribution of different kinases to IKK activation is not completely known, and redundancy in function may occur.

The *IKK* complex is composed of the two catalytic subunits, IKKα and IKKβ,[2] and the regulatory subunit, IKKγ/NF-κB essential modulator (NEMO) (43). The activated IKK phosphorylates IκB at the serine residues 32 and 36 in the signal responsive domain and thereby targets IκB for ubiquitination (61). Phosphorylated IκB is polyubiquitinylated by the E3 ubiquitin ligase containing β-TrCP and subsequently degraded by the 26S proteasome (43, 58, 59). Alternatively, IκB can be phosphorylated at tyrosine 42, which has the potential to connect NF-κB directly to membrane receptor-associated tyrosine kinases (62).

Receptor signaling as described above in the canonical pathway is often dependent on the synthesis of autocrine factors, such as cytokines (64).

In response to TNF-α, IκBα is rapidly degraded, followed by NF-κB-dependent resynthesis. Persisting stimulation by binding of TNF-α to its receptor (TNF-R) results in cycles of IκBα degradation and resynthesis (43). After TNF-α stimulation, the deubiquitinases A20 (or TNF-α-induced protein 3, TNFAIP3) or CYLD (gene mutated in familial Cylindromatosis)[3] limit NF-κB activation (44, 65).

Activation of NF-κB after antigen binding to the TCR or BCR is mediated *via* activation of a phospholipase, which produces diacylglycerol, the activator of protein kinases C (PKC). PKC phosphorylates caspase recruitment domain 11 (CARD11), which then recruits other adaptor proteins – BCL-10 and MALT1 forming the CBM complex[4] with CARD11 in B-cells – leading finally to phosphorylation of IKKβ and ubiquitination of NEMO (**Figure 5**). The activated IKK complex phosphorylates IκB, leading to its degradation, as described above (65).

The *alternative or non-canonical pathway* is involved in non-inflammatory signaling, e.g., in lymph node development and osteoclastogenesis (43). It starts at membrane receptors of the TNF-R superfamily with binding of B-cell activation factor (BAFF), lymphotoxin β (LTβ), CD40 ligand (CD40L), or receptor activator of NF-κB ligand (RANKL) (**Figure 6**). BAFF is critical for B-cell survival. LTβ is involved in lymph node development. CD40L has functions in the adaptive immune response, such as B-cell proliferation and differentiation, and immunoglobulin isotype switching. RANKL is essential for osteoclast differentiation from monocytes. Receptor–ligand binding results in activation of the IKKα-containing kinase complex by NF-κB-inducing kinase (*NIK*) and sometimes of the canonical IKKβ-containing complex (43, 44). TRAF2, c-IAP1, and c-IAP2 negatively regulate NIK *via* ubiquitination- and proteasome-dependent degradation (43). In unstimulated cells, NIK is marked for degradation by the TRAF2/c-IAP1/2 complex. After receptor binding, NIK is stabilized and forms trimers that activate the IKKα complex.

In the alternative pathway, inactive NF-κB consists of a p100:RelB heterodimer. p100 in the p100:RelB complex

[2] "The commonly used anti-inflammatory drugs aspirin and sodium salicylate exert their effects in part by acting as competitive inhibitors of the ATP-binding site of IKKβ" (63).

[3] Mutations in the CYLD gene are very rare, affected patients develop benign tumors on the skin due to increased cell growth mediated by overactive NF-κB (66).

[4] Abnormal BCR signaling *via* CD79 and the CBM complex was observed in B-cell lymphomas (44, 65). Elevated MALT1 expression was also observed in lymphomas of mucosal-associated lymphoid tissue and might be explained in early stages by constant antigenic stimulation, and later by chromosomal translocations that position the MALT1 gene under the control of heterologous promoters (38).

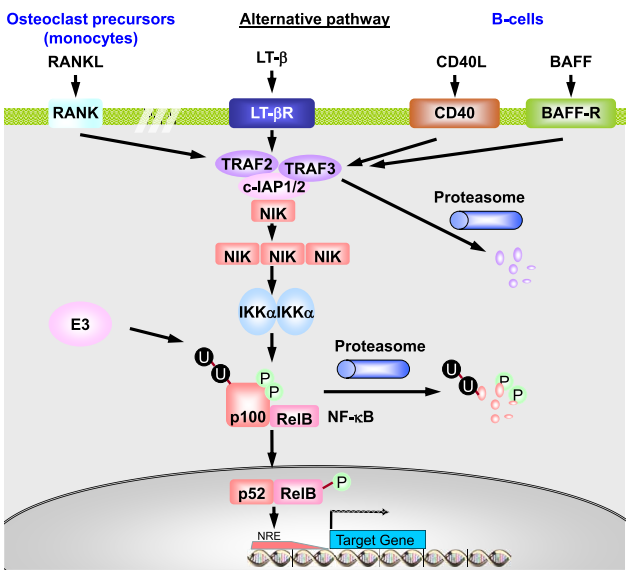

FIGURE 6 | The non-canonical or alternative NF-κB pathway. In unstimulated cells, TRAF3 constitutively recruits NIK to the TRAF2–c-IAP1/2 complex, promoting c-IAP1/2-mediated K48-ubiquitination and degradation of NIK. Ligation of CD40 by CD40L leads to recruitment of the TRAF3–TRAF2–c-IAP1/2 complex to the receptor, where TRAF2 catalyzes polyubiquitination of c-IAP1/2. It thereby promotes ubiquitin E3 ligase activity of c-IAP1/2 toward TRAF3, leading to proteasomal degradation of the latter. As a result, NIK can no longer be recruited to the TRAF2–c-IAP1/2 complex. This leads to stabilization and accumulation of newly synthesized NIK and its activation presumably *via* autophosphorylation, resulting in activation of the IKKα homodimer. Activated IKKα then phosphorylates p100, leading to proteasome-mediated processing of p100 to p52. The p52:RelB heterodimer then translocates to the nucleus and regulates transcription of target genes. CD40L promotes antibody isotype switching in mature B-cells, RANKL initiates osteoclastogenesis from precursor cells, BAFF induces immune cell survival and proliferation of B-cells, and LT-β regulates lymph node development. The receptors represented here on one cell are therefore restricted to distinct cell types and usually do not act in parallel. Adapted from O'Dea and Hoffmann (43) and Habelhah (44).

is phosphorylated by the activated IKKα, which results in polyubiquitination of p100 and proteolytic degradation of the NF-κB-inhibiting C-terminal region of p100, releasing p52 (43). The resulting p52:RelB dimer translocates to the nucleus where it initiates transcription of genes involved in lymphoid organogenesis, immune cell survival, proliferation and maturation, and osteoclastogenesis (44). It results in low level nuclear translocation of NF-κB for hours or days (43).

Several cross-talk mechanisms of inflammatory and developmental NF-κB signaling *via* the canonical and the alternative pathway were described (43). For example, developmental signals can also activate canonical p50:p65 dimers bound to a dimer of p100 (called IκBδ) (43). The activated NIK as part of the alternative pathway may amplify canonical IKK activation (43). CD40L can activate the canonical and the alternative NF-κB pathway (65).

Recently, a role for RelB was suggested in the therapy resistance of prostate cancer, which was explained by RelB-dependent induction of MnSOD (67).

DNA DSB in the cell nucleus can activate the *genotoxin-induced pathway* (68). Early studies supposed DNA-PK (69), PI3K, and MAPK (64) as mediators of radiation-induced NF-κB activation. In a cell culture model, it has been found that *ATM* plays a role in sustained activation of NF-κB in response to DNA DSB (52, 53), probably by its PI-3-kinase-like activity (54). Activation of NF-κB *via* this pathway after exposure to IR was described in detail in a recent review (70). Briefly, DNA damage initiates the SUMOylation of *NEMO* by the sumo ligase PIASy in a complex with PIDD and RIP1, fostering NEMO's localization in the nucleus (43). This nuclear SUMOylated NEMO associates with ATM with the result of monoubiquitination of NEMO, which is the signal for its cytoplasmic export (43). SUMOylated NEMO in complex with ATM therefore represents the long searched nuclear to cytoplasmic shuttle of the NF-κB activating signal (68). The protein ELKS binds to the cytoplasmic ATM–NEMO complex, enabling ATM-dependent activation of the canonical IKK complex (43). As described for the canonical pathway, IKK activation leads to IκBα degradation and NF-κB activation. The canonical p50:p65 heterodimer initiates gene transcription in the nucleus.

The role of the NF-κB pathway in cellular radiosensitivity was addressed by several studies (6). In a human ovarian cancer cell line, a human breast cancer cell line, and a murine melanoma cell line, radiation-activated NF-κB protected the cells from radiation-induced apoptosis (71). Inhibition of NF-κB activity can be achieved by overexpression of dominant-negative, phosphorylation-defective IκB. This has been reported to enhance the radiosensitivity of human fibrosarcoma cells (72), xenografted fibrosarcomas in mice (73) and human brain tumor cells (61, 74, 75), and to influence X-ray-induced mutations and apoptosis in human malignant glioma cells (76). For low LET radiation, NF-κB inhibition increased radiosensitivity of many cancer cells (6).

As activation of the NF-κB pathway is supposed to play a role in the negative regulation of both death receptor- and stress-induced apoptosis (44), survival of cells with residual DNA damage might thus be favored. Also, NF-κB's role in the deregulation of inflammatory responses contributes to its tumor-promoting and progression-favoring characteristics (44).

Constitutive NF-κB activation is often found in human cancers, e.g., breast, thyroid, bladder, and colon cancer (56, 77–80). It is thought to be important for maintaining survival of the cancer cells and for angiogenesis or chemoresistance (43, 81). The mechanisms that lead to constitutively activated NF-κB (82) and its critical role in tumor progression are currently only partly understood for some tumors. Mutations of the NFKBIA gene, which encodes IκBα or alterations of its expression level, might be an explanation for the increased NF-κB activity in tumors. In a recent study analyzing 790 human glioblastomas, deletion or low expression of NFKBIA was associated with unfavorable outcomes (83), possibly resulting from uncontrolled NF-κB activity. In 37.5% of patients with Hodgkin lymphoma, mutations in the NFKBIA gene in the tumor cells were detected (84). Lake et al. (85) found NFKBIA mutations in 3 of 20 Hodgkin lymphoma patients (15%). In addition, a NFKBIA polymorphism (A to G variation, rs696

in the 3′ UTR)[5] was associated with colorectal cancer risk and poor treatment prognosis (86). In human adult T-cell leukemia or lymphoma associated with human T-cell leukemia virus type I, activation of the NF-κB pathway by the virus protein Tax *via* the canonical and the alternative pathway seems to be involved in the transformation process (47). Another mechanism of constitutive NF-κB activation was described in malignant melanoma cells: an elevated endogenous ROS production resulted in constitutive NF-κB translocation to the nucleus (87).

NUCLEAR ERYTHROID-DERIVED 2-RELATED FACTOR 2

Nuclear erythroid-derived 2 (NF-E2)-related factor 2 (Nrf2) that binds the antioxidant DNA response element (ARE) to induce cellular antioxidant defense systems was shown to be activated 5 days after irradiation (88). Nrf2 was identified in studies investigating the activation of detoxifying enzymes in the presence of electrophilic chemicals, such as ROS. It belongs to the cap "n" collar (CNC) family of basic leucine zipper (bZIP) transcription factors. In vertebrates, they include the p45–NF-E2 factors and the NF-E2-related factors Nrf1, Nrf2, and Nrf3. In fact, Nrf2 was first identified as a homolog of NF-E2 and was found to interact with NF-E2-binding sites (89). The natural repressor protein of Nrf2 is Kelch-like associated ECH-associated protein 1 (Keap1), also called inhibitor of Nrf2 (INrf2).

Whereas NF-E2 was found in erythroid cells, Nrf1 and Nrf2 expression was observed in many tissues (90). In humans, the Nrf2 gene is located on chromosome 2q31 and in mice on chromosome 2. Target genes of Nrf2 contain a specific binding region, the ARE or electrophilic response element (EpRE). The ARE consensus sequence is TGA(G/C)NNNGC (89). Target genes of Nrf2 include detoxifying enzymes and antioxidative enzymes, such as glutathione-*S*-transferase, superoxide dismutase (SOD), or NADPH reductase.

The Nrf2 gene consists of five exons and four introns and its promoter region contains two ARE sequences, indicating that Nrf2 controls to some extent its own expression. ARE regions are also found in the promoter regions of Keap1 and the small Maf protein MafG (91–93). The presence of an ARE sequence in the Keap1 gene suggests an auto-regulatory feedback loop between Nrf2 and Keap1 (93).

The Nrf2 protein consists of 605 amino acids in humans and 597 amino acids in mice (90, 94), and is subdivided into six domains, which are evolutionary highly conserved and are termed Nrf2–ECH homology domains, abbreviated Neh1–6. They play important roles in binding to DNA, activation and inactivation of Nrf2. Protein structure, genetics regulation, and history of discovery of Nrf2 are summarized in the in-depth reviews of Baird and Dinova-Kostova (94), Ramkissoon et al. (90), and Morita and Motohashi (89). Baird and Dinova-Kostova discuss

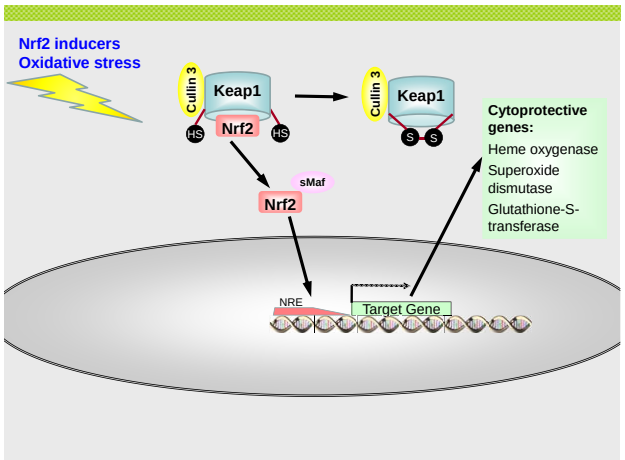

FIGURE 7 | **The Nrf2–ARE pathway**. Nrf2 is sequestered in the cytoplasm by Keap1 and targeted for ubiquitination by Cullin 3 and proteasomal degradation. Under conditions of oxidative stress or by chemical activators the thiol groups of cysteine residues of Keap1 are oxidized. This leads to the formation of disulfide bridges, which changes the conformation of Keap1 which is unable to bind Nrf2 now. Nrf2 is no released from Keap1 and translocates to the nucleus by forming heterodimers with sMaf proteins. In the nucleus, the Nrf2–sMaf complex binds to antioxidant responsive element (ARE) sequence in the promoter region of Nrf2 target genes, leading to the expression of antioxidative enzymes, such as heme oxygenase, superoxide dismutase, and glutathione-*S*-transferase.

several possible activation and regulation mechanisms of Nrf2, i.e., the sequester and release model, which was used in **Figure 7**, the "dissociation of Keap1 and Cullin 3 model," the "hinge and latch model," the "Keap1 nucleocytoplasmic shuttling model," and the "ubiquitination of Keap1 model," as well as some evidence suggesting that Nrf2 directly senses stressors (94). In this review, the "sequester and release model" will be featured (**Figure 7**), but it should be mentioned that it is a significant simplification of the actual mechanism underlying Nrf2 regulation within cells. What is most important from a radiation biological point of view about Nrf2 and its repressor Keap1, it is the fact that the Nrf2–ARE pathway is redox sensitive. IR induces the formation of free radicals, mainly due to radiolysis of water molecules within cells.

Reactive oxygen species form adducts with DNA, proteins, carbohydrates, and lipids. Cells are naturally exposed to ROS due to metabolic processes and by other environmental cues. Cells possess different defense mechanisms to maintain their redox equilibrium by increasing the expression of antioxidative enzymes. The activity of Nrf2 depends on the ROS level within a cell.

Nuclear erythroid-derived 2-related factor 2 is repressed by the protein Keap1 under physiological conditions. Keap1 consists of 624 amino acids and is rich in cysteine residues (25 in mice and 27 in humans) (94). Keap1 binds to Nrf2 and sequesters it in the cytoplasm and acts as a scaffold for the Cullin 3–Rbx1-E3 ubiquitin ligase, thereby promoting the proteasomal degradation of Nrf2. Under basal conditions, the half-life period of Nrf2 is thus only 10–30 min (90). As mentioned above, Keap1 possesses many cysteine residues, whose thiol groups are oxidized by ROS, leading to the formation of disulfide bridges. This changes

[5]UTR, untranslated region at the 3′ end of the mRNA. The reference single nucleotide polymorphism (SNP) Cluster Report rs696 is available in the National Center for Biotechnology Information (NCBI) SNP database (http://www.ncbi.nlm.nih.gov).

the conformation of Keap1, releasing Nrf2 from its binding to Keap1. Nrf2 then translocates to the nucleus together with co-transcriptional factors, such as small Mafs (also belonging to the class of bZip transcription factors). Nrf2 forms heterodimers with the small Mafs, which then bind to ARE regions.

Nuclear erythroid-derived 2-related factor 2 has many interaction partners: apart from the small Maf proteins (MafG, MafF, and MafK), another cotranscription factor is the CREB-binding protein (CBP). Nrf2 activity is downregulated by nuclear import of Keap1 where it binds Nrf2 and exports it back to the cytoplasm. Furthermore, the kinase Fyn phosphorylates the tyrosine residue 568 of Nrf2, which is a signal for the nuclear export of Nrf2 (90). Of importance is also the interaction of Nrf2 and NF-κB. NF-κB competes for CBP binding and inhibits Maf kinases (95). Keap1 was shown to contribute to the degradation of the NF-κB subunit p65 (96). ERK1/2-dependent pathways were suggested to mediate Nrf2 activation by low-dose γ-irradiation (97).

McDonald et al. (88) investigated the impact of γ-irradiation on Nrf2 activity in mouse embryonic fibroblasts derived from Nrf2 wt and knockout (ko) mice. They analyzed the expression of Nrf2 target genes by quantitative real time RT-PCR (RT-qPCR) and Nrf2 activity by a luciferase reporter system. The reporter system consisted of a plasmid where a firefly luciferase gene was fused with a promoter containing the ARE. No significant increase of either target gene expression or Nrf2 activity could be observed in this cell line 24 h after single exposure to even a high dose of up to 10 Gy of γ-radiation. Yet, 5 days after irradiation, Nrf2 activity markedly increased and this response persisted up to 8 and 15 days after irradiation. By shifting to a fractional irradiation over a time period of 5 days, a significant increase in Nrf2 target gene expression and increased reporter gene expression was observed 3 h after the end of fractionated irradiation. Additionally, they observed no effect on cellular survival of inducing Nrf2 prior to irradiation in murine fibroblasts, lymphocytes, and dendritic cells by using different chemical activators that activate Nrf2 in a brief time period of a few hours. However, immortalized fibroblasts derived from Nrf2-ko mice were more susceptible to irradiation than immortalized fibroblasts derived from Nrf2 wt mice. The increase of ROS inside cells was delayed as well with a response after 5 days. The level of ROS as measured by the fluorescence dye 2′,7′-dichlorofluorescin diacetate (DCF-DA) only increased 5 days after irradiation and was higher in Nrf2-ko fibroblasts, which moreover showed a higher basal ROS level. McDonald et al. (88) concluded from these results that Nrf2 is important for regulating long-term radiation effects and functions as a buffer system for maintaining the redox equilibrium in cells; a function than cannot be altered by exogenous chemical factors, but it is important for long-term cellular survival after radiation exposure. They speculated that long-term radiation effects may be related to an altered mitochondrial function, which results an increased production of ROS. Datta et al. (98) confirmed this for cells of the small intestine by exposing mice to γ-irradiation and accelerated iron (Fe-56, 1000 MeV/n; LET 148 keV/μm) ions. They observed a more potent induction of oxidative stress, DNA damage, and apoptosis in the small intestine of mice, which were exposed to energetic iron ions compared to mice that were γ-irradiated. Interestingly, they also observed long-term changes in the metabolism and gene expression in the intestinal tissue of mice up to 1 year after irradiation: mitochondrial function was altered and the level of ROS produced by mitochondrial metabolism increased as well as expression of NADPH oxidase, resulting in persistent elevated ROS level in the small intestine. Datta et al. (98) suspect that the induction of long-term effects after irradiation is important for the evaluation of chronic or late radiation effects.

Jayakumar et al. (99) found a connection between differences in Nrf2 expression and radiation resistance in the two different prostate cancer cell lines PC3 and DU145. Both cell lines were exposed to γ-radiation and Nrf2 content was measured prior to and after irradiation. Both cell lines differed in Nrf2 expression under basal conditions. It was found that cellular survival was higher after irradiation in the cell line DU145, which showed a higher basal Nrf2 activity. Furthermore, the level of basal and induced ROS after irradiation was higher in PC3 cells, which in contrast to DU145 exhibited a lower basal activity of Nrf2. In both cell lines, Nrf2 protein content increased after irradiation, whereas the protein level of Keap1 was reduced. Also, the expression of antioxidant enzymes increased after irradiation in both cell lines, but this response was significantly stronger in the DU145 cell line. Cellular survival was reduced in both cell lines and especially in the cell line with low basal Nrf2 expression PC3, after exposure to the chemical Nrf2 inhibitor retinoic acid. This outcome was enhanced when Nrf2 was knocked down on transcript level by transfecting both cell lines with small interfering RNA (siRNA) against Nrf2. These findings indicate that Nrf2 is important for cellular survival after exposure to IR and that radiation resistance of different cell lines, especially cancer cell lines depends upon differences in basal Nrf2 activity and upregulation of Nrf2. Examining the expression of Nrf2 in tumor tissue may therefore be important for the planning and predicting the outcome of therapeutic irradiation. Furthermore, as predominantly antioxidant enzymes were upregulated, there seems to be an association between oxidative stress and cellular survival after irradiation. Independently from radiation biological considerations, Wang et al. (100) showed that Nrf2 is antagonized by retinoic acid receptor α (RARα) in the small intestine of mice after treatment with retinoic acid, this opens the possibility to modulate Nrf2 activity chemically. Mathew et al. (101) showed that the Nrf2 activator sulforaphane (which also shows anti-cancerous effects) protects fibroblasts against IR.

In a similar setting, Patwardhan et al. (102) showed that T cell lymphoma EL-4 cells exhibit a high basal Nrf2 activity, show lower ROS levels than non-tumorigenic cells and that enhanced radiation resistance is linked to higher Nrf2 activity. siRNA against Nrf2 or treatment with all-*trans* retinoic acid (ATRA also called Tretinoin as a pharmaceutical) enhanced radiosensitivity of EL-4 cells.

Apart from IR, such as X-rays and γ-radiation, Nrf2 was also shown to be activated by UV radiation (103). Dermal fibroblasts showed an increased accumulation of Nrf2 in the nucleus after exposure to UV-A irradiation, but not after UV-B irradiation. Moreover, fibroblasts derived from Nrf2-ko mice exhibited a 1.7-fold increase in apoptosis after UV-A exposure compared to fibroblasts derived from wt mouse. The opposite effect was observed in Keap1-ko fibroblasts; here, the apoptosis rate was half of the rate observed in fibroblasts isolated from wt mice.

Nuclear erythroid-derived 2-related factor 2 also seems to be important for the function adult stem cells. Hochmuth et al. (104) showed that inactivation of the Nrf2 analog CncC in *Drosophila* was required for the maturation of intestinal stem cells. CncC is constitutively active in intestinal stem cells and its inactivation by Keap1 is a signal for intestinal stem cell proliferation. They observed that increased ROS levels lead to increased proliferation of intestinal stem cells, a similar effect could be observed by knocking down CncC with siRNA. This work indicates that the activation pattern of CncC is reversed in stem cells compared with differentiated cells. Whereas in differentiated cells ROS activate CncC or Nrf2, in intestinal stem cells CncC is inactivated by ROS to allow for an increased proliferation of intestinal stem cells to renew the intestinal tissue. This seems to imply an activation mode of Nrf2 that depends on cell type and developmental stage. How oxidative stress inactivates Nrf2 in intestinal stem cells remains to be investigated. Tsai et al. (105) could confirm the role of Nrf2 in controlling stem cell proliferation. They confirmed the findings of Hochmuth et al. (104) in hematopoietic stem cells. Reduced Nrf2 activity or lack of Nrf2 led to hyperproliferation of stem cells and progenitor cells. This was accompanied by a reduced self-renewal of hematopoietic stem cells and reduction of quiescence. Nrf2 proved to be a crucial factor in the regulation and function of hematopoietic stem cells. Whereas both studies did not involve radiation, Kim et al. (106) showed that Nrf2 contributes strongly to the survival of hematopoietic stem cells in a mouse model of total body γ-irradiation. Nrf2-ko mice had a lower survival and a higher impairment of hematopoietic function compared to Nrf2 wt mice. Furthermore, activation of Nrf2 prior to irradiation increased overall survival of mice after TBI. Additionally, hematopoiesis was increased in mice, which were treated with the Nrf2 activator 2-trifluoromethyl-2-methoxychalone (TMC).

Recently, Large et al. (107) investigated the role of Nrf2 in the low-dose response of ECs. Surprisingly, they found a decreased expression of Nrf2 after low-dose X-irradiation (0.5 Gy) in EA.hy926 ECs and primary human dermal microvascular ECs (HMVEC), additionally the DNA binding of Nrf2 was lowered. The expression of Nrf2 target genes and the activity of Nrf2 itself followed a non-linear pattern of expression, meaning that the observed level of mRNA increased and decreased interchangeably with increasing doses (0, 0.3, 0.5, 0.7, and 1 Gy). In all cases, the expression of glutathione peroxidase (GPx) and SOD as well as the Nrf2 binding activity were lowest after 0.5 Gy X-irradiation. This finding is interesting, as it indicates that at least in these cell lines low-dose irradiation may induce an unusual pattern of Nrf2 expression and activity and that certain doses may decrease Nrf2 activity. As they treated cells prior to irradiation with TNF-α to simulate inflammation, there might be an involvement of NF-κB, as TNF-α activates it, in the expression and activity pattern of Nrf2.

Relatively little is known about the role of Nrf2 in the cellular radiation response to heavy ion irradiation. Quite recently, Xie et al. (108) showed that curcumin (an Nrf2 activator) reduces cognitive impairment in mice after exposure carbon ions (4 Gy). They observed an upregulation of Nrf2 and Nrf2 downstream genes, NAD(P)H quinine oxidoreductase 1 (NQO1), heme oxygenase-1 (HO-1), and γ-glutamyl cysteine synthetase (γ-GCS) in the brain tissue of mice that were treated with curcumin. Kim et al. (109) found increased survival of colonic epithelial cells after exposure to iron ions (Fe-56) when Nrf2 was activated prior to radiation exposure. They focused on the interaction of Nrf2 and p53 binding protein 1 (p53BP1), as p53BP1 contains three ARE sequences. Activation of Nrf2 in colon epithelial cells prior to irradiation reduced the frequency of G1 and S/G2 chromosome aberrations. In general, the DDR was enhanced by Nrf2 activation.

The response of Nrf2 to radiation may be an important factor in tumor therapy. Mutations in Nrf2 and Keap1 are known to occur in various cancer cell lines and to confer protection to cancer cell lines toward chemo- or radiotherapy. Some cancer cell lines possess a high basal activity of Nrf2, which increases their resistance against radiation (110). In general, Nrf2 is accumulated in tumors and high levels of Nrf2 expression lead to a poor prognosis for cancer patients (111). In a lung cancer study, samples were taken from 178 lung squamous cell carcinomas (SqCCs) (112, 113) and, apart from 53BP1, most mutations were found in three genes associated with the Nrf2–ARE pathway, NFE2L2 (the gene name of Nrf2), Keap1, and Cul3 (the gene name of Cullin 3). Increased resistance to radiation therapy was linked to a high level of Nrf2.

Further studies of the function and activity of Nrf2 after exposure of cells to heavy ions, especially carbon ions, may give hints how to improve radiation therapy and will be of significance for the planning of long-term human space missions.

ROLE OF OTHER TRANSCRIPTION FACTORS IN THE CELLULAR RADIATION RESPONSE

In addition to the two key transcription factors in the cellular damage response, p53 and NF-κB, and the oxidative stress-induced Nrf2, several other transcription factors are activated in response to IR exposure (**Figure 2**). ATM-mediated phosphorylation of c-Abl appears to increase the transcription of stress response genes *via* activation of Jun kinase (15). Also, other MAPK pathways are activated, resulting, e.g., in formation of the transcription factor activated protein 1 (AP-1), which controls proliferation, senescence, differentiation, and apoptosis *via* growth factors (114). Cataldi et al. (115) propose a role for the transcription factor cyclic adenosine monophosphate (cAMP)-responsive element-binding protein (CREB) in survival responses of Jurkat T-cells after exposure to IR. The transcription factor Sp1, which is involved in cell differentiation, cell growth, apoptosis, immune responses, response to DNA damage, and chromatin remodeling, is rapidly phosphorylated in response to DNA damage, but this phosphorylation did not affect its transcriptional activity (116). The colocalization of phosphorylated Sp1 with activated ATM kinase in nuclear foci was interpreted as a sign for a role of Sp1 in DNA repair (116). A colocalization in nuclear foci was also observed for the forkhead box-O 3 (FOXO-3) transcription factor that is involved in cell-cycle control (117).

cAMP-Responsive Element-Binding Protein

cAMP-responsive element-binding protein (CREB) is a 43-kDa bZIP nuclear transcription factor involved in cAMP signaling (115). Its activation *via* phosphorylation leads to binding of the transcription factor to the cAMP-responsive element (CRE), a highly conserved sequence, inducing transcription of target genes for several cellular functions, including regulation of apoptosis and proliferation (118, 119). CREB phosphorylation is cell type and stimulus dependent. It is therefore possible for a wide range of molecules to activate the transcription factor. PKA, PKB, and ERK/MAPK phosphorylate CREB at Serine 133 (119, 120), whereas ATR and ATM phosphorylate the factor at Serine 111 and 121, respectively, in response to IR and oxidative stress (121, 122).

Sparsely IR is able to increase the binding of CREB to its consensus sequence (123). Furthermore, γ-irradiation has been shown to induce phosphorylation of CREB, thereby activating it (115, 119). Radiation-induced activation of CREB is connected with survival, as its target genes promote cellular proliferation, such as cyclin A, cyclin D1, proliferating cell nuclear antigen (PCNA), c-fos, and COX-2. In CREB knockdown studies, survival decreased (124). Co-incidental with CREB activation is low caspase-3 activity and a lack of Bax and Bcl2 level difference, further supporting an anti-apoptotic role (119).

Although an increase of ERK/MAPK expression after irradiation with carbon ions (125) and α-particles (126) was shown, no connection to CREB activation has been made. Therapeutic high LET studies lost their focus on CREB as survival factor, but it can be said that with the upcoming trend of therapeutic irradiation using heavy ions, CREB should be considered as means to increase radiosensitivity in tumor cells.

Activated Protein 1

Activated protein 1 (AP-1) is a transcription factor formed by homo- or heterodimerization of proteins of the Jun family (c-Jun, JunB, and JunD) or the Fos family (c-Fos, FosB, Fra-1, and Fra-2). Such dimers (AP-1 complexes) are able to recognize AP-1 binding sites containing the 12-*O*-tetradecanoylphorbol-13-acetate (TPA) response element (TRE), its DNA target sequence (127). C-jun regulates the expression of cyclin D1, a promoter of cell-cycle progression into G1-phase (128, 129). In addition to genes regulating cell-cycle progression, AP-1 controls its own expression, having a TRE in the promoter region of the c-jun gene (130).

The transcriptional activity of c-Jun can be enhanced by phosphorylation of Serine 63 and 73 by JNK. It has been shown that c-Jun is phosphorylated by JNK in the nucleus after γ-irradiation (**Figure 2**). Furthermore, the same study showed increased DNA-binding activity of AP-1 in response to sparsely IR with AP-1 complexes containing c-Jun as well as JunD and JunB (131). X-radiation has also been shown to increase DNA-binding activity of AP-1 (132). Exposure to an 18 MeV electron beam (4 Gy) activated AP-1 in HepG2 cells (133).

Elevated gene expression of c-jun and protein expression of AP-1-associated factors (c-jun, c-fos, Fra1, and JNK2) was observed in response to α-particles exposure (134, 135). Binding activity of AP-1 increased after irradiation with very low doses of α-particles (6 mGy). This binding was inhibited by SOD indicating a response of AP-1 to oxidative stress (126). Iron ion (Fe-56, 1000 MeV/n, LET 148 keV/μm) irradiation has been associated with proliferation of intestinal epithelium cells, connecting irradiation-induced oxidative stress with activation AP-1 (98).

Reactive oxygen species and other radiation-released free radicals can stimulate JNK and AP-1 activity (23), therefore promoting cell-cycle progression, although influence in apoptosis induction has also been reported (136). Additionally, the radiation-induced activation of AP-1 was also correlated to increased levels of glutamylcysteine synthetase, which is directly associated with synthesis of glutathione, a cellular radical scavenger (133). Therefore, AP-1 might be relevant in high LET radiation therapy by enhancing the cellular defense against ROS and regulation the cellular apoptotic response to radiation.

Specificity Protein 1

The Sp1 belongs to the specificity protein/Krüppel-like factor (Sp/XKLF) family of transcription factors that contain 3 conserved Cys2His2 zinc fingers for DNA binding (137). Loss of these zinc fingers abolishes not only DNA-binding capacity but also nuclear translocation (138). Sp1 is ubiquitously expressed in all mammalian cells and regulates cellular functions, such as apoptosis, cell-cycle progression, growth/proliferation, and metabolism (137, 139). The fate of Sp1 differs greatly depending on its posttranslational modification. Many different proteins modify Sp1 through all stages of the cell cycle *via* SUMOylation, glycosylation, ubiquitination, acetylation, or phosphorylation. Overexpression of Sp1 regulates apoptosis in a p53-dependent manner after suppression of cell growth (137).

ATM can activate Sp1 *via* phosphorylation in response to X-rays and H_2O_2 (140), which is recruited to DNA DSB and can promote repair in a non-transcriptional manner (141). Sp1 acts also in a transcriptional manner upon IR, as it is associated with coordination of cellular response after treatment with γ-rays, activated by DNA-PK through phosphorylation (142). Furthermore, an increased nuclear expression of Sp1 has been observed for irradiation with 20 Gy X-rays (143) as well as increased binding activity upon γ-irradiation (123, 144).

Microarray gene expression experiments assume activation of Sp1 in cells irradiated with α-particles (LET 123 keV/μm), and its involvement in subsequent cellular responses of directly and indirectly exposed (bystander) cells (145). The Sp1-dependent gene expression profile included up- and downregulation of 16 and 6 genes, respectively, in cells directly hit by α-particles, while upregulation of a smaller subset (10 genes) dominated in bystander cells (145). As with sparsely IR, Sp1 could act in a more administrative manner upon high LET radiation, as DNA-PK is strongly activated after carbon and iron ion exposure (146).

Sp1 has various roles in the DDR, ranging from orchestrating the response, to actively regulating apoptosis or repair. For cancer treatment with carbon ions, Sp1 is well worth investigating, as there are not many distinct approaches to study this versatile transcription factor in context of high LET particle irradiation.

Early Growth Response 1

The transcription factor early growth response 1 (EGR-1) is a member of the EGR family and is suggested to act as anti-proliferative signal for tumor cells, as well as an apoptotic enhancer (147). It has been shown to be activated by X- (147) and γ-rays (148). Radiation-induced activation of EGR-1 is associated with ROS (148). Upon irradiation, EGR-1 can act p53-independently as mediator for TNF-α-induced apoptosis (147). Gene expression of EGR-1 has been found to be increased also in response to irradiation with α-particles (134). The role of EGR-1 in the cellular radiation response is pro-apoptotic and in light of heavy ion radiation therapy, it would be instructive to know the extent of its pro-apoptotic capabilities upon high LET irradiation.

INFLUENCE OF LINEAR ENERGY TRANSFER ON TRANSCRIPTION FACTOR ACTIVATION

The cellular response to high LET radiation shows quantitative and in some aspects qualitative differences compared to the low LET radiation response. For different radiation types, the biological effects, observed at the same absorbed dose, depend on their quality (sparsely or densely IR). Comparison of the biological effects of different radiation qualities is usually being performed in terms of relative biological effectiveness (RBE).[6] In radiotherapy, the RBE is not only of highest interest for cell killing but also for late effects such as cancerogenesis (149). For the various biological endpoints, the RBE can depend on many factors, such as LET, dose rate, dose fractionation, radiation dose, and type of the irradiated cells or tissues.

One of the earliest systematic studies of the dependence of RBE on LET showed that the RBE reached a maximum at an LET of 100–200 keV/μm for survival of human kidney T1 cells after irradiation with deuterium ($^{2}_{1}H$) and α-particles (151–153). Thereafter, an LET–RBE function was determined for many biological endpoints and reached a maximum at with an LET from 90 to 200 keV/μm (154–157). In these studies, the RBE for mutation induction was higher compared to inactivation for all examined LETs (154). In HEK cells, the maximal RBE for reproductive cell death was 2.5 (158). For LETs above 900 keV/μm, RBE values for reproductive cell death dropped to 1 or below 1. Stoll et al. (159) also found an RBE for inactivation by high LET lead ions (>10,000 keV/μm) far below 1 and for nickel ions (>1000 keV/μm) around 1. In a human neuronal progenitor cell line (Ntera2), the RBE_{max} for apoptosis 48 h after iron ion exposure (1 GeV/n) was at least 3.4 (160). The RBE for induction of double-strand breaks was determined to be 1.8 for iron ions compared to X-rays, as detected by immunostaining of γ-H2AX 0.5 h after radiation exposure (161), or by pulsed-field gel electrophoresis (162) or other methods such as alkaline elution (163). For α-particles (LET 27–124 keV/μm), it ranged between 1.2 and 1.4 (164).

For improvement of cancer therapy, studies with several cancer cells and with various heavy ions, especially carbon ions, had been performed. In a microarray analysis of oral SqCC cells, 84 genes were identified that were modulated by carbon and neon ion (LET ~75 keV/μm) irradiation at all doses (1, 4, and 7 Gy) (165). Among these genes, three genes (TGFBR2, SMURF2, and BMP7) were found to be involved in the transforming growth factor β signaling pathway and two genes (CCND1 and E2F3) in the cell-cycle G1/S checkpoint regulation pathway. The relevance of these results for normal tissues cells or non-cancer cell lines has to be determined. In normal skin tissue, low doses (0.01 and 1 Gy) of IR resulted in transient alterations in the expression of genes involved in DNA and tissue remodeling, cell-cycle transition, and inflammation (TNF, interleukins) (166), suggesting an involvement of the NF-κB pathway, the main inflammatory pathway, in the cellular response to IR. As exposure to accelerated argon ions (95 MeV/n Ar, LET 271 keV/μm) resulted in strong activation of NF-κB in human cells (167), the RBE for NF-κB activation by heavy ions of different LET was determined (158). NF-κB-dependent gene induction after exposure to heavy ions was detected in stably transfected human 293 reporter cells. For comparison, cells were exposed to 150 kV X-rays. The maximal biologic effect ranged between 70 and 300 keV/μm. Argon ions (271 keV/μm) had the maximal potency (RBE ~9) to activate NF-κB-dependent gene expression in HEK cells. The effect of carbon ions was less pronounced and comparable the activation observed after X-ray exposure (168). Inhibition of ATM resulted in complete abolishment of NF-κB activation by X-rays and heavy ions. Therefore, NF-κB activation in response to heavy ions is ATM dependent and seems to be mediated by a nuclear signal from the damaged DNA as described for the genotoxin-induced NF-κB subpathway.

Assuming that NF-κB activation promotes survival, it can be hypothesized that the extreme capacity of energetic heavy ions in the LET range of 70–300 keV/μm to activate NF-κB's transcriptional effects might be responsible for the lower relative effectiveness in cell killing observed in this range. Above 300 keV/μm, the overkill effect (meaning that with further increase of the deposited energy in a small volume of the cell no more biologically relevant damages can be caused) possibly results in a decrease of the RBE.

Other groups report NF-κB translocation after exposure of normal human monocytes (MM6 cells) to 0.7 Gy of ^{56}Fe ions using a DNA-binding assay (169). This clearly indicates that high LET iron ion exposure induces rapid and persistent NF-κB activation. This activation of NF-κB was shown to be mediated through phosphorylation of IκBα and the subsequent proteasome-dependent degradation pathway. The iron study only revealed binding of NF-κB to its consensus sequence of 5′-GGGGACTTTCC-3′, and not transcriptional activation.

Scarce LET dependence data exist for p53 expression in human neuronal progenitor cells (160). Screening of gene expression in the nematode *Caenorhabditis elegans* suggests an LET

[6] The absorbed dose of a test radiation necessary to induce a defined biological endpoint and a defined severity of this endpoint (survival, cell cycle arrest, mutagenesis, chromosome aberrations, tumor induction in laboratory animals, and others) is compared to the dose of a reference radiation needed for induction of the same biological effect (150). Sparsely ionizing radiation such as γ-rays or X-rays is often used as reference radiation. In some cases, protons are applied as reference. The RBE is calculated according to the following formula:

$$RBE = \frac{\text{Absorbed dose of reference radiation inducing biologic effect (Gy)}}{\text{Absorbed dose of test radiation inducing biologic effect (Gy)}}$$

dependence or track structure dependence of the gene expression changes (170). In human lens epithelial cells, transcription and translation of CDKN1A [$p21^{CIP1/WAF1}$] are both temporally regulated after exposure to 4 Gy of high-energy accelerated iron-ion beams (~150 keV/μm) as well as to protons (~1 keV/μm) and X-rays, whereby the magnitude and kinetics of the expression enhancement seem to depend on the LET of the radiation (171).

CONCLUSION

Increased understanding of signaling pathways leading to transcription factor activation or inhibition in response to high LET radiation exposure will help to identify and make use of new targets for radiosensitization of tumor tissue and/or increasing radioresistance of surrounding normal tissue. The question which transcription factor offers a suitable target for charged particle cancer therapy is still open, as very few studies on transcription factor activation by carbon ions in tumor cells were performed. Also, not in all studies clinically relevant doses were applied, and extrapolation of the effects from high to lower doses is not constructive when the dose–response curves are unknown.

Although the role of p53 seems to be quite clear in low LET radiation therapy with increased radiosensitivity in case of functionality, this is not yet the case for charged particle therapy. Some studies suggest p53-independent cell killing by high LET which is a large advantage for treatment of tumors with p53 mutations. More studies with different cancer cell types are required. Concerning surrounding tissues, p53 inhibition might prevent precipitous apoptosis in apoptosis prone tissues. In tissues where p53-induced cell-cycle arrest dominates, p53 inhibition might impede this protective pathway and have detrimental effects.

The anti-apoptotic effects of NF-κB could support tumor cell survival during chemo- or radiotherapy; therefore, NF-κB is an interesting target for combined cancer therapies including carbon ion therapy. In several tumor cell types, inhibition of NF-κB resulted in radiosensitization. Activation of NF-κB in the normal tissue might not only limit detrimental effects by cell killing but also promote inflammation.

The activity of Nrf2 after irradiation seems to follow a complicated pattern, i.e., different time scales seem to be involved, and most striking is the occurrence of long-term effects in fibroblasts and intestinal epithelial cells. In the case of intestinal epithelial cells, the occurrence of long-term oxidative stress points to an inefficient activation of Nrf2 or a reduced oxidative stress response. It would be interesting to investigate this further. Of particular interest would be to compare differentiated cells with tissue-specific stem cells after irradiation; as in the case of intestinal stem cells, some studies suggest that oxidative stress inhibits the action of Nrf2 and that here might be differences between fully differentiated cells and stem cells in the regulation of Nrf2. Another open question is how to modulate the Nrf2 response in healthy tissue for radiation protection to reduce the side effects of radiation therapy and to mitigate radiation effects in spaces in case of manned missions. Modulating the elevated level of Nrf2 activity in cancer cells may be beneficial for cancer therapy. As described above, Nrf2 is upregulated in many cancer tissues and a high level of Nrf2 expression corresponds to a poor prognosis for patients. In this sense, Nrf2 can serve as an indicator for the outcomes of cancer radio- and chemotherapy. So far, relatively little is known about chemicals that may inhibit Nrf2 directly (apart from retinoic acid) or upregulate Keap1, research in this direction may lead to the discovery of novel drug candidates supplementing radiation therapy. Using siRNA for therapeutic means may also be an option for those cancers that show a high expression and activity of Nrf2.

CREB, AP-1, Sp1, and EGR-1 (or up- or downstream events in these pathways) were activated by low doses of high LET α-particles and the first three were also shown to be involved in the cellular response to carbon and/or iron ions. For low LET radiation, many studies suggest a subordinate importance of these factors in cellular radiation responses compared to p53, NF-κB, and Nrf2. Nevertheless, we discuss how modification of these transcription factors may influence therapy results.

CREB itself is a factor inducing cellular survival, activated by phosphorylation due to (among others) ATM. Amorino et al. (124) detected a decreased survival of CREB-ko cells after IR exposure compared to wt cells. As also high LET irradiation stimulates ATM kinase activity, which in turn can activate CREB, a potential therapy approach is to inhibit phosphorylation of CREB or its binding to DNA in the vicinity of cancerous tissue. This can be accomplished through siRNA or other CREB-inhibiting substances, which are then applied directly to target tissue (in case of superficial tumors) or transported to the tumor *via* homing probes (in case of hard-to-reach tumors). After reducing the survivability of the tumor in such a way, radiation-induced apoptosis *via* p53-dependent and -independent mechanisms can fight the tumor more effectively.

This approach bears the problem that, with drug-induced inhibition of CREB in tumor vicinity, also non-transformed tissue may be affected and therefore more susceptible for radiation-induced cell death. In this case, the high fidelity of dose deposition in heavy ion therapy may prove advantageous.

AP-1 is a sensory factor for oxidative stress and is activated by ROS and other free radicals besides IR (low LET like X- and γ-rays as well as high LET α particles). This activation can lead to apoptosis; therefore, a supplementary approach in heavy ion therapy would be to enrich AP-1 in tumor tissue, delivered as mentioned above, so that more AP-1 is activated by high LET radiation and apoptosis is induced more effectively in tumor cells. C-abl is a negative regulator of γH2AX and can induce apoptosis in a p53-independent manner. Therefore, a supplementary strategy for heavy ion therapy is again enrichment of the protein to increase apoptotic induction and weaken repair of damaged DNA in tumor cells.

Sp1 is, besides other functions, a regulator for apoptosis and the orchestration of the DDR and can initiate repair of DNA damages. An obvious strategy to reinforce high LET radiation effects would be inhibition of Sp1. However, the transcription factor assumes many various roles within the cell, so that manipulation of Sp1 might result in unwanted side effects. Genes regulated by Sp1 might be better targets for combating tumors and their expression in tumor cells in response to heavy ion irradiation should be analyzed.

Upon activation, the transcription factor EGR-1 has various pro-apoptotic and anti-proliferative effects in tumors. Its activation has been demonstrated so far for low LET irradiation and high LET α-particles. Before considering it as target in charged particle therapy, its response to carbon ion exposure should be determined. If high LET radiation induces pro-apoptotic effects in tumors cells *via* EGR-1 as well, an artificial enrichment of the factor could be beneficial.

These various strategies are attuned to particular effects of each respective transcription factor and could be amplified *via* combination. However, cross connectivity of these factors with other signaling pathways may exert considerable influence on the therapeutic result. Furthermore, radiation-induced bystander effects, inter- and intracellular modifications in response to various signaling factors, are strongly to be considered for both tumor and healthy tissue. It is undoubtedly certain that the more we know about pathway connections among themselves, especially in respect to heavy ion therapy, the better are chances to develop more effective strategies to fight tumors.

In summary, above mentioned transcription factors and associated proteins are involved in a wide spectrum of cellular functions upon treatment with IR, ranging from regulation of cell cycle, DNA repair, cell proliferation, differentiation, adhesion, migration, and apoptosis to immune responses including inflammation. All factors show increased activity and/or expression for low and (as far as tested) high LET irradiation and are involved in the cellular radiation response.

AUTHOR CONTRIBUTIONS

CH had the idea for this review, designed it and contributed the introduction, the NF-κB chapter, the NF-κB **Figures 3–6**, and the conclusion, redesigned **Figures 1**, **2**, **7**, inserted the references, corrected and edited all other parts, especially the conclusion, and did the revision according to the reviewers' comments. LS wrote the p53 chapter, contributed the p53 input for **Table 1**, and designed **Figure 1**. BH wrote the Nrf2 chapter, contributed the Nrf2 input for **Table 1**, and designed **Figure 7**. SD wrote the chapter "other transcription factors," contributed to **Table 1**, and invented **Figure 2**. CB-K contributed to the idea and design of the review and critically reviewed and corrected the manuscript.

ACKNOWLEDGMENTS

SD and BH were supported by a scholarship of the Helmholtz Space Life Sciences Research School (SpaceLife Grant No. VH-KO-300) funded by the Helmholtz Association and the German Aerospace Center (DLR). **Figures 3–6** were designed by CH for her habilitation thesis (Freie Universität Berlin, Faculty of Veterinary Medicine), which is not publicly available.

REFERENCES

1. Durante M. Space radiation protection: destination mars. *Life Sci Space Res* (2014) **1**:2–9. doi:10.1016/j.lssr.2014.01.002
2. ICRP. Glossary. In: Valentin J, editor. *The 2007 Recommendations of the International Commission on Radiological Protection. ICRP Publication 103 [Annals of the ICRP 37 (2–3)]*. Amsterdam: Elsevier (2007). p. 26.
3. Ohnishi T, Takahashi A, Ohnishi K. Studies about space radiation promote new fields in radiation biology. *J Radiat Res (Tokyo)* (2002) **43**(Suppl):S7–12. doi:10.1269/jrr.43.S7
4. National Aeronautics and Space Administration (NASA). *The Vision for Space Exploration [NP-2004-01-334-HQ]*. Washington, DC: NASA Headquarters (2004).
5. Snyder AR, Morgan WF. Gene expression profiling after irradiation: clues to understanding acute and persistent responses? *Cancer Metastasis Rev* (2004) **23**:259–68. doi:10.1023/B:CANC.0000031765.17886.fa
6. Criswell T, Leskov K, Miyamoto S, Luo G, Boothman DA. Transcription factors activated in mammalian cells after clinically relevant doses of ionizing radiation. *Oncogene* (2003) **22**:5813–27. doi:10.1038/sj.onc.1206680
7. Crawford LV, Pim DC, Gurney EG, Goodfellow P, Taylor-Papadimitriou J. Detection of a common feature in several human tumor cell lines – a 53,000-dalton protein. *Proc Natl Acad Sci U S A* (1981) **78**:41–5. doi:10.1073/pnas.78.1.41
8. Moll UM, Schramm LM. p53 – an acrobat in tumorigenesis. *Crit Rev Oral Biol Med* (1998) **9**:23–37. doi:10.1177/10454411980090010101
9. Sharpless NE, DePinho RA. p53: good cop/bad cop. *Cell* (2002) **110**:9–12. doi:10.1016/S0092-8674(02)00818-8
10. Vousden KH. p53: death star. *Cell* (2000) **103**:691–4. doi:10.1016/S0092-8674(00)00171-9
11. Lane DP. Cancer. p53, guardian of the genome. *Nature* (1992) **358**:15–6. doi:10.1038/358015a0
12. Bourdon JC, Fernandes K, Murray-Zmijewski F, Liu G, Diot A, Xirodimas DP, et al. p53 isoforms can regulate p53 transcriptional activity. *Genes Dev* (2005) **19**:2122–37. doi:10.1101/gad.1339905
13. Fei P, El-Deiry WS. p53 and radiation responses. *Oncogene* (2003) **22**:5774–83. doi:10.1038/sj.onc.1206677
14. Pawlik TM, Keyomarsi K. Role of cell cycle in mediating sensitivity to radiotherapy. *Int J Radiat Oncol Biol Phys* (2004) **59**:928–42. doi:10.1016/j.ijrobp.2004.03.005
15. Karagiannis TC, El-Osta A. Double-strand breaks: signaling pathways and repair mechanisms. *Cell Mol Life Sci* (2004) **61**:2137–47. doi:10.1007/s00018-004-4174-0
16. Gudkov AV, Komarova EA. Pathologies associated with the p53 response. *Cold Spring Harb Perspect Biol* (2010) **2**:a001180. doi:10.1101/cshperspect.a001180
17. Norimura T, Nomoto S, Katsuki M, Gondo Y, Kondo S. p53-dependent apoptosis suppresses radiation-induced teratogenesis. *Nat Med* (1996) **2**:577–80. doi:10.1038/nm0596-577
18. Harkin DP, Bean JM, Miklos D, Song YH, Truong VB, Englert C, et al. Induction of GADD45 and JNK/SAPK-dependent apoptosis following inducible expression of BRCA1. *Cell* (1999) **97**:575–86. doi:10.1016/S0092-8674(00)80769-2
19. Adeberg S, Baris D, Habermehl D, Rieken S, Brons S, Weber KJ, et al. Evaluation of chemoradiotherapy with carbon ions and the influence of p53 mutational status in the colorectal carcinoma cell line HCT 116. *Tumori* (2014) **100**:675–84. doi:10.1700/1778.19278
20. Suzuki M. [Significance of radiation-induced bystander effects in radiation therapy]. *Igaku Butsuri* (2014) **34**:70–8.
21. Meltser V, Ben-Yehoyada M, Reuven N, Shaul Y. c-Abl downregulates the slow phase of double-strand break repair. *Cell Death Dis* (2010) **1**:e20. doi:10.1038/cddis.2009.21
22. Reuven N, Adler J, Porat Z, Polonio-Vallon T, Hofmann TG, Shaul Y. The tyrosine kinase c-Abl promotes -interacting protein kinase 2 (HIPK2) accumulation and activation in response to DNA damage. *J Biol Chem* (2015) **290**:16478–88. doi:10.1074/jbc.M114.628982
23. Van Etten RA. Cycling, stressed-out and nervous: cellular functions of c-Abl. *Trends Cell Biol* (1999) **9**:179–86. doi:10.1016/S0962-8924(99)01549-4
24. Choi SY, Kim MJ, Kang CM, Bae S, Cho CK, Soh JW, et al. Activation of Bak and Bax through c-abl-protein kinase Cdelta-p38 MAPK signaling in

response to ionizing radiation in human non-small cell lung cancer cells. *J Biol Chem* (2006) **281**:7049–59. doi:10.1074/jbc.M512000200
25. Kharbanda S, Pandey P, Jin S, Inoue S, Bharti A, Yuan ZM, et al. Functional interaction between DNA-PK and c-Abl in response to DNA damage. *Nature* (1997) **386**:732–5. doi:10.1038/386732a0
26. Baskaran R, Wood LD, Whitaker LL, Canman CE, Morgan SE, Xu Y, et al. Ataxia telangiectasia mutant protein activates c-Abl tyrosine kinase in response to ionizing radiation. *Nature* (1997) **387**:516–9. doi:10.1038/387516a0
27. Mori E, Takahashi A, Yamakawa N, Kirita T, Ohnishi T. High LET heavy ion radiation induces p53-independent apoptosis. *J Radiat Res* (2009) **50**:37–42. doi:10.1269/jrr.08075
28. Amundson SA, Bittner M, Chen Y, Trent J, Meltzer P, Fornace AJ Jr. Fluorescent cDNA microarray hybridization reveals complexity and heterogeneity of cellular genotoxic stress responses. *Oncogene* (1999) **18**:3666–72. doi:10.1038/sj.onc.1202676
29. Park WY, Hwang CI, Im CN, Kang MJ, Woo JH, Kim JH, et al. Identification of radiation-specific responses from gene expression profile. *Oncogene* (2002) **21**:8521–8. doi:10.1038/sj.onc.1205977
30. Chaudhry MA, Chodosh LA, McKenna WG, Muschel RJ. Gene expression profile of human cells irradiated in G1 and G2 phases of cell cycle. *Cancer Lett* (2003) **195**:221–33. doi:10.1016/S0304-3835(03)00154-X
31. Chen X, Shen B, Xia L, Khaletzkiy A, Chu D, Wong JY, et al. Activation of nuclear factor kappaB in radioresistance of TP53-inactive human keratinocytes. *Cancer Res* (2002) **62**:1213–21.
32. Barnes PJ, Karin M. Nuclear factor-kappaB: a pivotal transcription factor in chronic inflammatory diseases. *N Engl J Med* (1997) **336**:1066–71. doi:10.1056/NEJM199704103361506
33. Schreck R, Rieber P, Baeuerle PA. Reactive oxygen intermediates as apparently widely used messengers in the activation of the NF-kappa B transcription factor and HIV-1. *EMBO J* (1991) **10**:2247–58.
34. Sonenshein GE. Rel/NF-kappa B transcription factors and the control of apoptosis. *Semin Cancer Biol* (1997) **8**:113–9. doi:10.1006/scbi.1997.0062
35. Wu M, Lee H, Bellas RE, Schauer SL, Arsura M, Katz D, et al. Inhibition of NF-kappaB/Rel induces apoptosis of murine B cells. *EMBO J* (1996) **15**:4682–90.
36. Pahl HL. Activators and target genes of Rel/NF-kappaB transcription factors. *Oncogene* (1999) **18**:6853–66. doi:10.1038/sj.onc.1203239
37. Bonizzi G, Karin M. The two NF-kappaB activation pathways and their role in innate and adaptive immunity. *Trends Immunol* (2004) **25**:280–8. doi:10.1016/j.it.2004.03.008
38. Karin M. Nuclear factor-kappaB in cancer development and progression. *Nature* (2006) **441**:431–6. doi:10.1038/nature04870
39. Ghosh S, May MJ, Kopp EB. NF-kappa B and Rel proteins: evolutionarily conserved mediators of immune responses. *Annu Rev Immunol* (1998) **16**:225–60. doi:10.1146/annurev.immunol.16.1.225
40. Li N, Karin M. Is NF-kappaB the sensor of oxidative stress? *FASEB J* (1999) **13**:1137–43.
41. Aggarwal BB, Sethi G, Nair A, Ichikawa H. Nuclear factor-kappa B: a holy grail in cancer prevention and therapy. *Curr Signal Transduct Ther* (2006) **1**:25–52. doi:10.2174/157436206775269235
42. Zabel U, Henkel T, Silva MS, Baeuerle PA. Nuclear uptake control of NF-kappa B by MAD-3, an I kappa B protein present in the nucleus. *EMBO J* (1993) **12**:201–11.
43. O'Dea E, Hoffmann A. NF-kappaB signaling. *Wiley Interdiscip Rev Syst Biol Med* (2009) **1**:107–15. doi:10.1002/wsbm.30
44. Habelhah H. Emerging complexity of protein ubiquitination in the NF-kappaB pathway. *Genes Cancer* (2010) **1**:735–47. doi:10.1177/1947601910382900
45. Annemann M, Plaza-Sirventa C, Schustera M, Katsoulis-Dimitrioua K, Kliche S, Schravena B, et al. Atypical IκB proteins in immune cell differentiation and function. *Immunol Lett* (2016) **171**:26–35. doi:10.1016/j.imlet.2016.01.006
46. Alkalay I, Yaron A, Hatzubai A, Orian A, Ciechanover A, Ben-Neriah Y. Stimulation-dependent IκBα phosphorylation marks the NF-κB inhibitor for degradation via the ubiquitin-proteasome pathway. *Proc Natl Acad Sci U S A* (1995) **92**:10599–603. doi:10.1073/pnas.92.23.10599
47. Shen HM, Tergaonkar V. NFkappaB signaling in carcinogenesis and as a potential molecular target for cancer therapy. *Apoptosis* (2009) **14**:348–63. doi:10.1007/s10495-009-0315-0
48. Duffey DC, Chen Z, Dong G, Ondrey FG, Wolf JS, Brown K, et al. Expression of a dominant-negative mutant inhibitor-kappaBalpha of nuclear factor-kappaB in human head and neck squamous cell carcinoma inhibits survival, proinflammatory cytokine expression, and tumor growth in vivo. *Cancer Res* (1999) **59**:3468–74.
49. NCRP. *Report No. 153: Information Needed to Make Radiation Protection Recommendations for Space Missions Beyond Low-Earth Orbit* (Vol. **153**). Bethesda, MD: National Council on Radiation Protection and Measurements (NCRP) (2006). p. 1–427.
50. Monje ML, Toda H, Palmer TD. Inflammatory blockade restores adult hippocampal neurogenesis. *Science* (2003) **302**:1760–5. doi:10.1126/science.1088417
51. Baichwal VR, Baeuerle PA. Activate NF-kappa B or die? *Curr Biol* (1997) **7**:R94–6. doi:10.1016/S0960-9822(06)00046-7
52. Li N, Banin S, Ouyang H, Li GC, Courtois G, Shiloh Y, et al. ATM is required for IkappaB kinase (IKKk) activation in response to DNA double strand breaks. *J Biol Chem* (2001) **276**:8898–903. doi:10.1074/jbc.M009809200
53. Piret B, Schoonbroodt S, Piette J. The ATM protein is required for sustained activation of NF-kappaB following DNA damage. *Oncogene* (1999) **18**:2261–71. doi:10.1038/sj.onc.1202541
54. Durocher D, Jackson SP. DNA-PK, ATM and ATR as sensors of DNA damage: variations on a theme? *Curr Opin Cell Biol* (2001) **13**:225–31. doi:10.1016/S0955-0674(00)00201-5
55. Wang CY, Mayo MW, Korneluk RG, Goeddel DV, Baldwin AS Jr. NF-kappaB antiapoptosis: induction of TRAF1 and TRAF2 and c-IAP1 and c-IAP2 to suppress caspase-8 activation. *Science* (1998) **281**:1680–3. doi:10.1126/science.281.5383.1680
56. Baldwin AS. Control of oncogenesis and cancer therapy resistance by the transcription factor NF-kappaB. *J Clin Invest* (2001) **107**:241–6. doi:10.1172/JCI11991
57. Waddick KG, Uckun FM. Innovative treatment programs against cancer: II. Nuclear factor-kappaB (NF-kappaB) as a molecular target. *Biochem Pharmacol* (1999) **57**:9–17. doi:10.1016/S0006-2952(98)00224-X
58. Hayden MS, Ghosh S. Signaling to NF-kappaB. *Genes Dev* (2004) **18**:2195–224. doi:10.1101/gad.1228704
59. Kulms D, Poppelmann B, Schwarz T. Ultraviolet radiation-induced interleukin 6 release in HeLa cells is mediated via membrane events in a DNA damage-independent way. *J Biol Chem* (2000) **275**:15060–6. doi:10.1074/jbc.M910113199
60. Li H, Lin X. Positive and negative signaling components involved in TNFalpha-induced NF-kappaB activation. *Cytokine* (2008) **41**:1–8. doi:10.1016/j.cyto.2007.09.016
61. Miyakoshi J, Yagi K. Inhibition of I kappaB-alpha phosphorylation at serine and tyrosine acts independently on sensitization to DNA damaging agents in human glioma cells. *Br J Cancer* (2000) **82**:28–33.
62. Imbert V, Rupec RA, Livolsi A, Pahl HL, Traenckner EB, Mueller-Dieckmann C, et al. Tyrosine phosphorylation of I kappa B-alpha activates NF-kappa B without proteolytic degradation of I kappa B-alpha. *Cell* (1996) **86**:787–98. doi:10.1016/S0092-8674(00)80153-1
63. Wong ET, Tergaonkar V. Roles of NF-kappaB in health and disease: mechanisms and therapeutic potential. *Clin Sci (Lond)* (2009) **116**:451–65. doi:10.1042/CS20080502
64. Dent P, Yacoub A, Contessa J, Caron R, Amorino G, Valerie K, et al. Stress and radiation-induced activation of multiple intracellular signaling pathways. *Radiat Res* (2003) **159**:283–300. doi:10.1667/0033-7587(2003)159[0283:SARIAO]2.0.CO;2
65. Staudt LM. Oncogenic activation of NF-kappaB. *Cold Spring Harb Perspect Biol* (2010) **2**:a000109. doi:10.1101/cshperspect.a000109
66. Netherlands Organization for Scientific Research. *Function of Cancer Genes Discovered*. ScienceDaily (2005). Available from: http://www.sciencedaily.com/releases/2005/05/050513224031.htm
67. Holley AK, Xu Y, St Clair DK, St Clair WH. RelB regulates manganese superoxide dismutase gene and resistance to ionizing radiation of prostate cancer cells. *Ann N Y Acad Sci* (2010) **1201**:129–36. doi:10.1111/j.1749-6632.2010.05613.x
68. Habraken Y, Piette J. NF-kappaB activation by double-strand breaks. *Biochem Pharmacol* (2006) **72**:1132–41. doi:10.1016/j.bcp.2006.07.015
69. Basu S, Rosenzweig KR, Youmell M, Price BD. The DNA-dependent protein kinase participates in the activation of NF kappa B following DNA damage. *Biochem Biophys Res Commun* (1998) **247**:79–83. doi:10.1006/bbrc.1998.8741

70. Hellweg CE. The nuclear factor kappaB pathway: a link to the immune system in the radiation response. *Cancer Lett* (2015) **368**:275–89. doi:10.1016/j.canlet.2015.02.019
71. Shao R, Karunagaran D, Zhou BP, Li K, Lo SS, Deng J, et al. Inhibition of nuclear factor-kappaB activity is involved in E1A-mediated sensitization of radiation-induced apoptosis. *J Biol Chem* (1997) **272**:32739–42. doi:10.1074/jbc.272.52.32739
72. Wang CY, Mayo MW, Baldwin AS Jr. TNF- and cancer therapy-induced apoptosis: potentiation by inhibition of NF-kappaB. *Science* (1996) **274**:784–7. doi:10.1126/science.274.5288.784
73. Wang CY, Cusack JC Jr, Liu R, Baldwin AS Jr. Control of inducible chemoresistance: enhanced anti-tumor therapy through increased apoptosis by inhibition of NF-kappaB. *Nat Med* (1999) **5**:412–7. doi:10.1038/10577
74. Yamagishi N, Miyakoshi J, Takebe H. Enhanced radiosensitivity by inhibition of nuclear factor kappa B activation in human malignant glioma cells. *Int J Radiat Biol* (1997) **72**:157–62. doi:10.1080/095530097143374
75. Ding GR, Honda N, Nakahara T, Tian F, Yoshida M, Hirose H, et al. Radiosensitization by inhibition of IkappaB-alpha phosphorylation in human glioma cells. *Radiat Res* (2003) **160**:232–7. doi:10.1667/RR3018
76. Ding GR, Yaguchi H, Yoshida M, Miyakoshi J. Increase in X-ray-induced mutations by exposure to magnetic field (60 Hz, 5 mT) in NF-kappaB-inhibited cells. *Biochem Biophys Res Commun* (2000) **276**:238–43. doi:10.1006/bbrc.2000.3455
77. Lee CH, Jeon YT, Kim SH, Song YS. NF-kappaB as a potential molecular target for cancer therapy. *Biofactors* (2007) **29**:19–35. doi:10.1002/biof.5520290103
78. Van Waes C. Nuclear factor-kappaB in development, prevention, and therapy of cancer. *Clin Cancer Res* (2007) **13**:1076–82. doi:10.1158/1078-0432.CCR-06-2221
79. Kim HJ, Hawke N, Baldwin AS. NF-kappaB and IKK as therapeutic targets in cancer. *Cell Death Differ* (2006) **13**:738–47. doi:10.1038/sj.cdd.4401877
80. Nakanishi C, Toi M. Nuclear factor-kappaB inhibitors as sensitizers to anticancer drugs. *Nat Rev Cancer* (2005) **5**:297–309. doi:10.1038/nrc1588
81. Dolcet X, Llobet D, Pallares J, Matias-Guiu X. NF-kB in development and progression of human cancer. *Virchows Arch* (2005) **446**:475–82. doi:10.1007/s00428-005-1264-9
82. Barkett M, Gilmore TD. Control of apoptosis by Rel/NF-kappaB transcription factors. *Oncogene* (1999) **18**:6910–24. doi:10.1038/sj.onc.1203238
83. Bredel M, Scholtens DM, Yadav AK, Alvarez AA, Renfrow JJ, Chandler JP, et al. NFKBIA deletion in glioblastomas. *N Engl J Med* (2011) **364**:627–37. doi:10.1056/NEJMoa1006312
84. Liu X, Yu H, Yang W, Zhou X, Lu H, Shi D. Mutations of NFKBIA in biopsy specimens from Hodgkin lymphoma. *Cancer Genet Cytogenet* (2010) **197**:152–7. doi:10.1016/j.cancergencyto.2009.11.005
85. Lake A, Shield LA, Cordano P, Chui DT, Osborne J, Crae S, et al. Mutations of NFKBIA, encoding IkappaB alpha, are a recurrent finding in classical Hodgkin lymphoma but are not a unifying feature of non-EBV-associated cases. *Int J Cancer* (2009) **125**:1334–42. doi:10.1002/ijc.24502
86. Gao J, Pfeifer D, He LJ, Qiao F, Zhang Z, Arbman G, et al. Association of NFKBIA polymorphism with colorectal cancer risk and prognosis in Swedish and Chinese populations. *Scand J Gastroenterol* (2007) **42**:345–50. doi:10.1080/00365520600880856
87. Brar SS, Kennedy TP, Whorton AR, Sturrock AB, Huecksteadt TP, Ghio AJ, et al. Reactive oxygen species from NAD(P)H:quinone oxidoreductase constitutively activate NF-kappaB in malignant melanoma cells. *Am J Physiol Cell Physiol* (2001) **280**:C659–76.
88. McDonald JT, Kim K, Norris AJ, Vlashi E, Phillips TM, Lagadec C, et al. Ionizing radiation activates the Nrf2 antioxidant response. *Cancer Res* (2010) **70**:8886–95. doi:10.1158/0008-5472.CAN-10-0171
89. Morita M, Motohashi M. Survival strategy and disease pathogenesis according to the Nrf2-small Maf heterodimer. In: Farooqui T, Farooqui AA, editors. *Oxidative Stress in Vertebrates and Invertebrates: Molecular Aspects of Cell Signaling*. Brisbane: Wiley (2012). p. 63–83.
90. Ramkissoon A, Shapiro AM, Loniewska MM, Wells PG. Neurodegeneration from drugs and aging-derived free radicals. In: Villamean FR, editor. *Molecular Basis of Oxidative Stress: Chemistry, Mechanisms, and Disease Pathogenesis*. Brisbane: Wiley (2013). p. 237–311.
91. Kwak MK, Itoh K, Yamamoto M, Kensler TW. Enhanced expression of the transcription factor Nrf2 by cancer chemopreventive agents: role of antioxidant response element-like sequences in the nrf2 promoter. *Mol Cell Biol* (2002) **22**:2883–92. doi:10.1128/MCB.22.9.2883-2892.2002
92. Katsuoka F, Motohashi H, Engel JD, Yamamoto M. Nrf2 transcriptionally activates the mafG gene through an antioxidant response element. *J Biol Chem* (2005) **280**:4483–90. doi:10.1074/jbc.M411451200
93. Lee OH, Jain AK, Papusha V, Jaiswal AK. An auto-regulatory loop between stress sensors INrf2 and Nrf2 controls their cellular abundance. *J Biol Chem* (2007) **282**:36412–20. doi:10.1074/jbc.M706517200
94. Baird L, Dinkova-Kostova AT. The cytoprotective role of the Keap1-Nrf2 pathway. *Arch Toxicol* (2011) **85**:241–72. doi:10.1007/s00204-011-0674-5
95. Liu GH, Qu J, Shen X. NF-kappaB/p65 antagonizes Nrf2-ARE pathway by depriving CBP from Nrf2 and facilitating recruitment of HDAC3 to MafK. *Biochim Biophys Acta* (2008) **1783**:713–27. doi:10.1016/j.bbamcr.2008.01.002
96. Yu M, Li H, Liu Q, Liu F, Tang L, Li C, et al. Nuclear factor p65 interacts with Keap1 to repress the Nrf2-ARE pathway. *Cell Signal* (2011) **23**:883–92. doi:10.1016/j.cellsig.2011.01.014
97. Tsukimoto M, Tamaishi N, Homma T, Kojima S. Low-dose gamma-ray irradiation induces translocation of Nrf2 into nuclear in mouse macrophage RAW264.7 cells. *J Radiat Res* (2010) **51**:349–53. doi:10.1269/jrr.10002
98. Datta K, Suman S, Kallakury BV, Fornace AJ Jr. Exposure to heavy ion radiation induces persistent oxidative stress in mouse intestine. *PLoS One* (2012) **7**:e42224. doi:10.1371/journal.pone.0042224
99. Jayakumar S, Kunwar A, Sandur SK, Pandey BN, Chaubey RC. Differential response of DU145 and PC3 prostate cancer cells to ionizing radiation: role of reactive oxygen species, GSH and Nrf2 in radiosensitivity. *Biochim Biophys Acta* (2014) **1840**:485–94. doi:10.1016/j.bbagen.2013.10.006
100. Wang XJ, Hayes JD, Henderson CJ, Wolf CR. Identification of retinoic acid as an inhibitor of transcription factor Nrf2 through activation of retinoic acid receptor alpha. *Proc Natl Acad Sci U S A* (2007) **104**:19589–94. doi:10.1073/pnas.0709483104
101. Mathew ST, Bergstrom P, Hammarsten O. Repeated Nrf2 stimulation using sulforaphane protects fibroblasts from ionizing radiation. *Toxicol Appl Pharmacol* (2014) **276**:188–94. doi:10.1016/j.taap.2014.02.013
102. Patwardhan RS, Checker R, Sharma D, Sandur SK, Sainis KB. Involvement of ERK-Nrf-2 signaling in ionizing radiation induced cell death in normal and tumor cells. *PLoS One* (2013) **8**:e65929. doi:10.1371/journal.pone.0065929
103. Hirota A, Kawachi Y, Itoh K, Nakamura Y, Xu X, Banno T, et al. Ultraviolet A irradiation induces NF-E2-related factor 2 activation in dermal fibroblasts: protective role in UVA-induced apoptosis. *J Invest Dermatol* (2005) **124**:825–32. doi:10.1111/j.0022-202X.2005.23670.x
104. Hochmuth CE, Biteau B, Bohmann D, Jasper H. Redox regulation by Keap1 and Nrf2 controls intestinal stem cell proliferation in *Drosophila*. *Cell Stem Cell* (2011) **8**:188–99. doi:10.1016/j.stem.2010.12.006
105. Tsai JJ, Dudakov JA, Takahashi K, Shieh JH, Velardi E, Holland AM, et al. Nrf2 regulates haematopoietic stem cell function. *Nat Cell Biol* (2013) **15**:309–16. doi:10.1038/ncb2699
106. Kim JH, Thimmulappa RK, Kumar V, Cui W, Kumar S, Kombairaju P, et al. Nrf2-mediated Notch pathway activation enhances hematopoietic reconstitution following myelosuppressive radiation. *J Clin Invest* (2014) **124**:730–41. doi:10.1172/JCI70812
107. Large M, Hehlgans S, Reichert S, Gaipl US, Fournier C, Rodel C, et al. Study of the anti-inflammatory effects of low-dose radiation: the contribution of biphasic regulation of the antioxidative system in endothelial cells. *Strahlenther Onkol* (2015) **191**:742–9. doi:10.1007/s00066-015-0848-9
108. Xie Y, Zhao QY, Li HY, Zhou X, Liu Y, Zhang H. Curcumin ameliorates cognitive deficits heavy ion irradiation-induced learning and memory deficits through enhancing of Nrf2 antioxidant signaling pathways. *Pharmacol Biochem Behav* (2014) **126**:181–6. doi:10.1016/j.pbb.2014.08.005
109. Kim SB, Pandita RK, Eskiocak U, Ly P, Kaisani A, Kumar R, et al. Targeting of Nrf2 induces DNA damage signaling and protects colonic epithelial cells from ionizing radiation. *Proc Natl Acad Sci U S A* (2012) **109**:E2949–55. doi:10.1073/pnas.1207718109
110. Shibata T, Kokubu A, Saito S, Narisawa-Saito M, Sasaki H, Aoyagi K, et al. Nrf2 mutation confers malignant potential and resistance to chemoradiation therapy in advanced esophageal squamous cancer. *Neoplasia* (2011) **13**:864–73. doi:10.1593/neo.11750
111. Jaramillo MC, Zhang DD. The emerging role of the Nrf2-Keap1 signaling pathway in cancer. *Genes Dev* (2013) **27**:2179–91. doi:10.1101/gad.225680.113

112. Abazeed M, Hammerman P, Creighton C, Adams D, Giacomelli A, Meyerson M. Nrf2 pathway activation regulates radiation resistance in lung squamous cell carcinoma. *Int J Radiat Oncol* (2012) **84**:S179–80. doi:10.1016/j.ijrobp.2012.07.465
113. Abazeed ME, Adams DJ, Hurov KE, Tamayo P, Creighton CJ, Sonkin D, et al. Integrative radiogenomic profiling of squamous cell lung cancer. *Cancer Res* (2013) **73**:6289–98. doi:10.1158/0008-5472.CAN-13-1616
114. Dent P, Yacoub A, Fisher PB, Hagan MP, Grant S. MAPK pathways in radiation responses. *Oncogene* (2003) **22**:5885–96. doi:10.1038/sj.onc.1206701
115. Cataldi A, Di Giacomo V, Rapino M, Zara S, Rana RA. Ionizing radiation induces apoptotic signal through protein kinase Cdelta (δ) and survival signal through Akt and cyclic-nucleotide response element-binding protein (CREB) in Jurkat T cells. *Biol Bull* (2009) **217**:202–12.
116. Iwahori S, Yasui Y, Kudoh A, Sato Y, Nakayama S, Murata T, et al. Identification of phosphorylation sites on transcription factor Sp1 in response to DNA damage and its accumulation at damaged sites. *Cell Signal* (2008) **20**:1795–803. doi:10.1016/j.cellsig.2008.06.007
117. Tsai WB, Chung YM, Takahashi Y, Xu Z, Hu MC. Functional interaction between FOXO3a and ATM regulates DNA damage response. *Nat Cell Biol* (2008) **10**:460–7. doi:10.1038/ncb1709
118. Choi YJ, Kim SY, Oh JM, Juhnn YS. Stimulatory heterotrimeric G protein augments gamma ray-induced apoptosis by up-regulation of Bak expression via CREB and AP-1 in H1299 human lung cancer cells. *Exp Mol Med* (2009) **41**:592–600. doi:10.3858/emm.2009.41.8.065
119. Cataldi A, di Giacomo V, Rapino M, Genovesi D, Rana RA. Cyclic nucleotide response element binding protein (CREB) activation promotes survival signal in human K562 erythroleukemia cells exposed to ionising radiation/etoposide combined treatment. *J Radiat Res* (2006) **47**:113–20. doi:10.1269/jrr.47.113
120. Zhang J, Wang Q, Zhu N, Yu M, Shen B, Xiang J, et al. Cyclic AMP inhibits JNK activation by CREB-mediated induction of c-FLIP(L) and MKP-1, thereby antagonizing UV-induced apoptosis. *Cell Death Differ* (2008) **15**:1654–62. doi:10.1038/cdd.2008.87
121. Dodson GE, Tibbetts RS. DNA replication stress-induced phosphorylation of cyclic AMP response element-binding protein mediated by ATM. *J Biol Chem* (2006) **281**:1692–7. doi:10.1074/jbc.M509577200
122. Shi Y, Venkataraman SL, Dodson GE, Mabb AM, LeBlanc S, Tibbetts RS. Direct regulation of CREB transcriptional activity by ATM in response to genotoxic stress. *Proc Natl Acad Sci U S A* (2004) **101**:5898–903. doi:10.1073/pnas.0307718101
123. Sahijdak WM, Yang CR, Zuckerman JS, Meyers M, Boothman DA. Alterations in transcription factor binding in radioresistant human melanoma cells after ionizing radiation. *Radiat Res* (1994) **138**:S47–51. doi:10.2307/3578760
124. Amorino GP, Hamilton VM, Valerie K, Dent P, Lammering G, Schmidt-Ullrich RK. Epidermal growth factor receptor dependence of radiation-induced transcription factor activation in human breast carcinoma cells. *Mol Biol Cell* (2002) **13**:2233–44. doi:10.1091/mbc.01-12-0572
125. Mitra AK, Bhat N, Sarma A, Krishna M. Alteration in the expression of signaling parameters following carbon ion irradiation. *Mol Cell Biochem* (2005) **276**:169–73. doi:10.1007/s11010-005-3903-5
126. Azzam EI, de Toledo SM, Spitz DR, Little JB. Oxidative metabolism modulates signal transduction and micronucleus formation in bystander cells from α-particle-irradiated normal human fibroblast cultures. *Cancer Res* (2002) **62**:5436–42.
127. Tanos T, Marinissen MJ, Leskow FC, Hochbaum D, Martinetto H, Gutkind JS, et al. Phosphorylation of c-Fos by members of the p38 MAPK family. Role in the AP-1 response to UV light. *J Biol Chem* (2005) **280**:18842–52. doi:10.1074/jbc.M500620200
128. Jochum W, Passegue E, Wagner EF. AP-1 in mouse development and tumorigenesis. *Oncogene* (2001) **20**:2401–12. doi:10.1038/sj.onc.1204389
129. Vermeulen K, Van Bockstaele DR, Berneman ZN. The cell cycle: a review of regulation, deregulation and therapeutic targets in cancer. *Cell Prolif* (2003) **36**:131–49. doi:10.1046/j.1365-2184.2003.00266.x
130. Marinissen MJ, Chiariello M, Gutkind JS. Regulation of gene expression by the small GTPase Rho through the ERK6 (p38 gamma) MAP kinase pathway. *Genes Dev* (2001) **15**:535–53. doi:10.1101/gad.855801
131. Lee SA, Dritschilo A, Jung M. Impaired ionizing radiation-induced activation of a nuclear signal essential for phosphorylation of c-Jun by dually phosphorylated c-Jun amino-terminal kinases in ataxia telangiectasia fibroblasts. *J Biol Chem* (1998) **273**:32889–94. doi:10.1074/jbc.273.49.32889
132. Chae HJ, Chae SW, Kang JS, Bang BG, Han JI, Moon SR, et al. Effect of ionizing radiation on the differentiation of ROS 17/2.8 osteoblasts through free radicals. *J Radiat Res* (1999) **40**:323–35. doi:10.1269/jrr.40.323
133. Morales A, Miranda M, Sanchez-Reyes A, Colell A, Biete A, Fernandez-Checa JC. Transcriptional regulation of the heavy subunit chain of gamma-glutamylcysteine synthetase by ionizing radiation. *FEBS Lett* (1998) **427**:15–20. doi:10.1016/S0014-5793(98)00381-0
134. Turtoi A, Schneeweiss FH. Effect of (211)At alpha-particle irradiation on expression of selected radiation responsive genes in human lymphocytes. *Int J Radiat Biol* (2009) **85**:403–12. doi:10.1080/09553000902838541
135. Calaf GM, Roy D, Hei TK. Immunochemical analysis of protein expression in breast epithelial cells transformed by estrogens and high linear energy transfer (LET) radiation. *Histochem Cell Biol* (2005) **124**:261–74. doi:10.1007/s00418-005-0033-9
136. Moreno-Manzano V, Ishikawa Y, Lucio-Cazana J, Kitamura M. Suppression of apoptosis by all-trans-retinoic acid. Dual intervention in the c-Jun N-terminal kinase-AP-1 pathway. *J Biol Chem* (1999) **274**:20251–8. doi:10.1074/jbc.274.29.20251
137. Chuang JY, Wu CH, Lai MD, Chang WC, Hung JJ. Overexpression of Sp1 leads to p53-dependent apoptosis in cancer cells. *Int J Cancer* (2009) **125**:2066–76. doi:10.1002/ijc.24563
138. Beishline K, Azizkhan-Clifford J. Sp1 and the 'hallmarks of cancer'. *FEBS J* (2015) **282**:224–58. doi:10.1111/febs.13148
139. Zhang JP, Zhang H, Wang HB, Li YX, Liu GH, Xing S, et al. Down-regulation of Sp1 suppresses cell proliferation, clonogenicity and the expressions of stem cell markers in nasopharyngeal carcinoma. *J Transl Med* (2014) **12**:222. doi:10.1186/s12967-014-0222-1
140. Olofsson BA, Kelly CM, Kim J, Hornsby SM, Azizkhan-Clifford J. Phosphorylation of Sp1 in response to DNA damage by ataxia telangiectasia-mutated kinase. *Mol Cancer Res* (2007) **5**:1319–30. doi:10.1158/1541-7786.MCR-07-0374
141. Beishline K, Kelly CM, Olofsson BA, Koduri S, Emrich J, Greenberg RA, et al. Sp1 facilitates DNA double-strand break repair through a nontranscriptional mechanism. *Mol Cell Biol* (2012) **32**:3790–9. doi:10.1128/MCB.00049-12
142. Yang CR, Wilson-Van PC, Planchon SM, Wuerzberger-Davis SM, Davis TW, Cuthill S, et al. Coordinate modulation of Sp1, NF-kappa B, and p53 in confluent human malignant melanoma cells after ionizing radiation. *FASEB J* (2000) **14**:379–90.
143. Nenoi M, Ichimura S, Mita K, Yukawa O, Cartwright IL. Regulation of the catalase gene promoter by Sp1, CCAAT-recognizing factors, and a WT1/Egr-related factor in hydrogen peroxide-resistant HP100 cells. *Cancer Res* (2001) **61**:5885–94.
144. Meighan-Mantha RL, Riegel AT, Suy S, Harris V, Wang FH, Lozano C, et al. Ionizing radiation stimulates octamer factor DNA binding activity in human carcinoma cells. *Mol Cell Biochem* (1999) **199**:209–15. doi:10.1023/A:1006958217143
145. Ghandhi SA, Ponnaiya B, Panigrahi SK, Hopkins KM, Cui Q, Hei TK, et al. RAD9 deficiency enhances radiation induced bystander DNA damage and transcriptomal response. *Radiat Oncol* (2014) **9**:206. doi:10.1186/1748-717X-9-206
146. Okayasu R, Okada M, Okabe A, Noguchi M, Takakura K, Takahashi S. Repair of DNA damage induced by accelerated heavy ions in mammalian cells proficient and deficient in the non-homologous end-joining pathway. *Radiat Res* (2006) **165**:59–67. doi:10.1667/RR3489.1
147. Ahmed MM, Sells SF, Venkatasubbarao K, Fruitwala SM, Muthukkumar S, Harp C, et al. Ionizing radiation-inducible apoptosis in the absence of p53 linked to transcription factor EGR-1. *J Biol Chem* (1997) **272**:33056–61. doi:10.1074/jbc.272.52.33056
148. Datta R, Taneja N, Sukhatme VP, Qureshi SA, Weichselbaum R, Kufe DW. Reactive oxygen intermediates target CC(A/T)6GG sequences to mediate activation of the early growth response 1 transcription factor gene by ionizing radiation. *Proc Natl Acad Sci U S A* (1993) **90**:2419–22. doi:10.1073/pnas.90.6.2419
149. Jäkel O. The relative biological effectiveness of proton and ion beams. *Z Med Phys* (2008) **18**:276–85. doi:10.1016/j.zemedi.2008.06.012
150. ICRP. *RBE for Deterministic Effects. ICRP Publication 58. Annals of the ICRP 20* (*4*). Oxford: Pergamon Press (1989).

151. Barendsen GW, Beusker TL, Vergroesen AJ, Budke L. Effects of different radiations on human cells in tissue culture. II. Biological experiments. *Radiat Res* (1960) **13**:841–9. doi:10.2307/3570859
152. Barendsen GW, Walter HM, Fowler JF, Bewley DK. Effects of different ionizing radiations on human cells in tissue culture. III. Experiments with cyclotron-accelerated alpha-particles and deuterons. *Radiat Res* (1963) **18**:106–19. doi:10.2307/3571430
153. Skarsgard LD. Radiobiology with heavy charged particles: a historical review. *Phys Med* (1998) **14**(Suppl 1):1–19.
154. Yatagai F. Mutations induced by heavy charged particles. *Biol Sci Space* (2004) **18**:224–34. doi:10.2187/bss.18.224
155. Thacker J, Stretch A, Stephens MA. Mutation and inactivation of cultured mammalian cells exposed to beams of accelerated heavy ions. II. Chinese hamster V79 cells. *Int J Radiat Biol Relat Stud Phys Chem Med* (1979) **36**:137–48. doi:10.1080/09553007914550891
156. Ainsworth EJ, Kelly LS, Mahlmann LJ, Schooley JC, Thomas RH, Howard J, et al. Response of colony-forming units-spleen to heavy charged particles. *Radiat Res* (1983) **96**:180–97. doi:10.2307/3576177
157. Kraft G, Kraft-Weyrather W, Ritter S, Scholz M, Stanton J. Cellular and subcellular effect of heavy ions: a comparison of the induction of strand breaks and chromosomal aberration with the incidence of inactivation and mutation. *Adv Space Res* (1989) **9**:59–72. doi:10.1016/0273-1177(89)90423-7
158. Hellweg CE, Baumstark-Khan C, Schmitz C, Lau P, Meier MM, Testard I, et al. Activation of the nuclear factor kappaB pathway by heavy ion beams of different linear energy transfer. *Int J Radiat Biol* (2011) **87**:954–63. doi:10.3109/09553002.2011.584942
159. Stoll U, Barth B, Scheerer N, Schneider E, Kiefer J. HPRT mutations in V79 Chinese hamster cells induced by accelerated Ni, Au and Pb ions. *Int J Radiat Biol* (1996) **70**:15–22. doi:10.1080/095530096145283
160. Guida P, Vazquez ME, Otto S. Cytotoxic effects of low- and high-LET radiation on human neuronal progenitor cells: induction of apoptosis and TP53 gene expression. *Radiat Res* (2005) **164**:545–51. doi:10.1667/RR3367.1
161. Whalen MK, Gurai SK, Zahed-Kargaran H, Pluth JM. Specific ATM-mediated phosphorylation dependent on radiation quality. *Radiat Res* (2008) **170**:353–64. doi:10.1667/RR1354.1
162. Löbrich M, Cooper PK, Rydberg B. Non-random distribution of DNA double-strand breaks induced by particle irradiation. *Int J Radiat Biol* (1996) **70**:493–503. doi:10.1080/095530096144680
163. Prise KM, Ahnstrom G, Belli M, Carlsson J, Frankenberg D, Kiefer J, et al. A review of dsb induction data for varying quality radiations. *Int J Radiat Biol* (1998) **74**:173–84. doi:10.1080/095530098141564
164. Frankenberg D, Brede HJ, Schrewe UJ, Steinmetz C, Frankenberg-Schwager M, Kasten G, et al. Induction of DNA double-strand breaks by 1H and 4He lons in primary human skin fibroblasts in the LET range of 8 to 124 keV/μm. *Radiat Res* (1999) **151**:540–9. doi:10.2307/3580030
165. Fushimi K, Uzawa K, Ishigami T, Yamamoto N, Kawata T, Shibahara T, et al. Susceptible genes and molecular pathways related to heavy ion irradiation in oral squamous cell carcinoma cells. *Radiother Oncol* (2008) **89**:237–44. doi:10.1016/j.radonc.2008.04.015
166. Berglund SR, Rocke DM, Dai J, Schwietert CW, Santana A, Stern RL, et al. Transient genome-wide transcriptional response to low-dose ionizing radiation in vivo in humans. *Int J Radiat Oncol Biol Phys* (2008) **70**:229–34. doi:10.1016/j.ijrobp.2007.09.026
167. Baumstark-Khan C, Hellweg CE, Arenz A, Meier MM. Cellular monitoring of the nuclear factor kappaB pathway for assessment of space environmental radiation. *Radiat Res* (2005) **164**:527–30. doi:10.1667/RR3397.1
168. Hellweg CE, Baumstark-Khan C, Schmitz C, Lau P, Meier MM, Testard I, et al. Carbon-ion-induced activation of the NF-kappaB pathway. *Radiat Res* (2011) **175**:424–31. doi:10.1667/RR2423.1
169. Natarajan M, Aravindan N, Meltz ML, Herman TS. Post-translational modification of I-kappa B alpha activates NF-kappa B in human monocytes exposed to ^{56}Fe ions. *Radiat Environ Biophys* (2002) **41**:139–44. doi:10.1007/s00411-002-0143-x
170. Nelson GA, Jones TA, Chesnut A, Smith AL. Radiation-induced gene expression in the nematode *Caenorhabditis elegans*. *J Radiat Res* (2002) **43**(Suppl):S199–203. doi:10.1269/jrr.43.S199
171. Chang PY, Bjornstad KA, Rosen CJ, McNamara MP, Mancini R, Goldstein LE, et al. Effects of iron ions, protons and X rays on human lens cell differentiation. *Radiat Res* (2005) **164**:531–9. doi:10.1667/RR3368.1
172. Takahashi A, Matsumoto H, Yuki K, Yasumoto J, Kajiwara A, Aoki M, et al. High-LET radiation enhanced apoptosis but not necrosis regardless of p53 status. *Int J Radiat Oncol Biol Phys* (2004) **60**:591–7. doi:10.1016/j.ijrobp.2004.05.062
173. Liu Y, Xing R, Zhang X, Dong W, Zhang J, Yan Z, et al. miR-375 targets the p53 gene to regulate cellular response to ionizing radiation and etoposide in gastric cancer cells. *DNA Repair (Amst)* (2013) **12**:741–50. doi:10.1016/j.dnarep.2013.06.002
174. Widel M, Lalik A, Krzywon A, Poleszczuk J, Fujarewicz K, Rzeszowska-Wolny J. The different radiation response and radiation-induced bystander effects in colorectal carcinoma cells differing in p53 status. *Mutat Res* (2015) **778**:61–70. doi:10.1016/j.mrfmmm.2015.06.003
175. Hickman AW, Jaramillo RJ, Lechner JF, Johnson NF. Alpha-particle-induced p53 protein expression in a rat lung epithelial cell strain. *Cancer Res* (1994) **54**:5797–800.
176. Amornwichet N, Oike T, Shibata A, Ogiwara H, Tsuchiya N, Yamauchi M, et al. Carbon-ion beam irradiation kills X-ray-resistant p53-null cancer cells by inducing mitotic catastrophe. *PLoS One* (2014) **9**:e115121. doi:10.1371/journal.pone.0115121

Conflict of Interest Statement: The authors declare that the research was conducted in the absence of any commercial or financial relationships that could be construed as a potential conflict of interest.

Copyright © 2016 Hellweg, Spitta, Henschenmacher, Diegeler and Baumstark-Khan. This is an open-access article distributed under the terms of the Creative Commons Attribution License (CC BY). The use, distribution or reproduction in other forums is permitted, provided the original author(s) or licensor are credited and that the original publication in this journal is cited, in accordance with accepted academic practice. No use, distribution or reproduction is permitted which does not comply with these terms.

frontiers in Oncology

REVIEW
published: 09 June 2016
doi: 10.3389/fonc.2016.00139

Translational Research to Improve the Efficacy of Carbon Ion Radiotherapy: Experience of Gunma University

*Takahiro Oike[1], Hiro Sato[1], Shin-ei Noda[1] and Takashi Nakano[1,2]**

[1] Department of Radiation Oncology, Gunma University Graduate School of Medicine, Gunma, Japan, [2] Gunma University Heavy Ion Medical Center, Gunma, Japan

Carbon ion radiotherapy holds great promise for cancer therapy. Clinical data show that carbon ion radiotherapy is an effective treatment for tumors that are resistant to X-ray radiotherapy. Since 1994 in Japan, the National Institute of Radiological Sciences has been heading the development of carbon ion radiotherapy using the Heavy Ion Medical Accelerator in Chiba. The Gunma University Heavy Ion Medical Center (GHMC) was established in the year 2006 as a proof-of-principle institute for carbon ion radiotherapy with a view to facilitating the worldwide spread of compact accelerator systems. Along with the management of more than 1900 cancer patients to date, GHMC engages in translational research to improve the treatment efficacy of carbon ion radiotherapy. Research aimed at guiding patient selection is of utmost importance for making the most of carbon ion radiotherapy, which is an extremely limited medical resource. Intratumoral oxygen levels, radiation-induced cellular apoptosis, the capacity to repair DNA double-strand breaks, and the mutational status of tumor protein p53 and epidermal growth factor receptor genes are all associated with X-ray sensitivity. Assays for these factors are useful in the identification of X-ray-resistant tumors for which carbon ion radiotherapy would be beneficial. Research aimed at optimizing treatments based on carbon ion radiotherapy is also important. This includes assessment of dose fractionation, normal tissue toxicity, tumor cell motility, and bystander effects. Furthermore, the efficacy of carbon ion radiotherapy will likely be enhanced by research into combined treatment with other modalities such as chemotherapy. Several clinically available chemotherapeutic drugs (carboplatin, paclitaxel, and etoposide) and drugs at the developmental stage (Wee-1 and heat shock protein 90 inhibitors) show a sensitizing effect on tumor cells treated with carbon ions. Additionally, the efficacy of carbon ion radiotherapy can be improved by combining it with cancer immunotherapy. Clinical validation of preclinical findings is necessary to further improve the treatment efficacy of carbon ion radiotherapy.

Keywords: carbon ion radiotherapy, patient selection, combination therapy, translational research, treatment planning

OPEN ACCESS

Edited by:
Marco Durante,
GSI Helmholtzzentrum für Schwerionenforschung, Germany

Reviewed by:
Jac Nickoloff,
Colorado State University, USA
Thomas Friedrich,
GSI Helmholtzzentrum für Schwerionenforschung, Germany

***Correspondence:**
Takashi Nakano
tnakano@gunma-u.ac.jp

Specialty section:
This article was submitted to Radiation Oncology, a section of the journal Frontiers in Oncology

Received: *27 January 2016*
Accepted: *23 May 2016*
Published: *09 June 2016*

Citation:
Oike T, Sato H, Noda SE and Nakano T (2016) Translational Research to Improve the Efficacy of Carbon Ion Radiotherapy: Experience of Gunma University. Front. Oncol. 6:139. doi: 10.3389/fonc.2016.00139

INTRODUCTION

Carbon ion radiotherapy holds great promise for cancer therapy. Carbon ions have two advantages over X-rays such as a sharp dose distribution and a strong cell-killing capacity (1). Clinical trials show that carbon ion radiotherapy has excellent antitumor effects (2, 3). Moreover, it is suggested that carbon ion radiotherapy is an effective treatment for tumors that are resistant to conventional X-ray radiotherapy (4–6).

The National Institute of Radiological Sciences (NIRS) initiated carbon ion radiotherapy in Japan in the year 1994 using the Heavy Ion Medical Accelerator in Chiba (HIMAC). Up until January 2016, more than 8000 patients with different types of cancer were treated at the NIRS. The excellent clinical outcomes encouraged widespread use of carbon ion radiotherapy (2). However, the high cost of constructing the accelerator system limits its practical application. New accelerator systems were designed to overcome this limitation; as a result, the cost of the accelerator systems was reduced to approximately $100,000,000 that accounts for one-third of the corresponding HIMAC parameters. Gunma University Heavy Ion Medical Center (GHMC) was launched in the year 2006 as a proof-of-principle institute for carbon ion radiotherapy based on the newly introduced compact accelerator systems. GHMC commenced operation of the accelerator systems in 2009 and performed the first carbon ion radiotherapy for cancer in 2010. All carbon ion radiotherapy carried out at GHMC has been performed as prospective clinical trial (**Table 1**). As of January 2016, GHMC has treated more than 1900 cancer patients with carbon ion radiotherapy, without any major incidents.

Along with carbon ion radiotherapy, GHMC engages in translational research to improve the efficacy of this treatment modality with financial support from the Japan Society for the Promotion of Science through its two umbrella programs: the Twenty-First Century Centers of Excellence Program (2004–2008) and the Strategic Young Researcher Overseas Visits Program for Accelerating Brain Circulation (2013–2016). Translational research at GHMC was further accelerated by establishment of the Gunma University Initiative for Advanced Research in 2015, in which the Department of Radiation Oncology of the Massachusetts General Hospital/Harvard Medical School launched a Japanese branch to stimulate interdisciplinary collaboration in the field of heavy ion radiation biology. In addition, GHMC contributes to the education and development of global leaders in the field of heavy ion radiation therapy through the Program for Cultivating Global Leaders in Heavy Ion Therapeutics and Engineering, supported by the Japanese Ministry of Education, Culture, Sports, Science, and

TABLE 1 | Clinical trails on carbon ion radiotherapy at GHMC.

Trial ID	Patient enrollment	Cancer type	Major indication criteria	Total dose/fr.	Combined therapy
Gunma0905	2012-	Cranial base tumor	No CNS invasion	60.8 GyRBE/16 fr.	–
Gunma0901	2010–2013	H&N cancer (except Sq, melanoma, sarcoma)	N0/1M0	57.6 or 64 GyRBE/16 fr.	–
Gunma0902	2012-	H&N musculoskeletal tumor	N0/1M0	70 GyRBE/16 fr.	–
Gunma0903	2012-	H&N melanoma	N0M0	57.6 or 64 GyRBE/16 fr.	Concurrent DTIC, ACNU, and VCR
Gunma0701	2010–2015	NSCLC	Stage I, peripheral, inoperable	60 GyRBE/4 fr.	–
Gunma1201	2013–2015	NSCLC	Stage III, inoperable	40 GyRBE/10 fr. (ENI) + 20 or 24 GyRBE/6 fr. (IFI)	–
Gunma0703	2010–2013	Hepatcellular carcinoma	Tumor diameter ≤10 cm	52.8 GyRBE/4 fr.	–
Gunma1203	2013	Hepatcellular carcinoma	Tumor diameter 3–10 cm	60 GyRBE/4 fr.	–
Gunma1303	2013–2015	Hepatcellular carcinoma	Adjacent to digestive tract	60 or 64.8 GyRBE/12 fr.	–
Gunma1301	2013–2015	Pancreatic cancer	T4N0/1, inoperable	52.8 or 55.2 GyRBE/12 fr.	Concurrent gemcitabine
Gunma1501	2015-	Pancreatic cancer	T4N0/1M0	55.2 GyRBE/12 fr.	Concurrent S-1
Gunma0801	2010-	Rectal cancer	Postoperative local recurrence	73.6 GyRBE/16 fr.	–
Gunma0702	2010–2013	Prostate cancer	≤T3	57.6 GyRBE/16 fr.	± Hormone therapy
Gunma1302	2013-	Prostate cancer	≤T3	57.6 GyRBE/16 fr.	± Hormone therapy
Gunma1103	2013-	Prostate cancer	Castration resistant cancer	57.6 GyRBE/16 fr.	± Hormone therapy
Gunma1202	2013–2014	Uterine cervical cancer	Locally advanced	36 GyRBE/12 fr. (WPI) + 19.2 GyRBE/4 fr. (IFI)	Concurrent CDDP followed by ICBT
Gunma1401	2014-	Uterine cervical cancer	Locally advanced	36 GyRBE/12 fr. (WPI) + 19.2 GyRBE/4 fr. (IFI)	Concurrent CDDP followed by ICBT
Gunma0904	2010–2013	Musculoskeletal tumors	N0M0	64, 67.2, or 70.4 GyRBE/16 fr.	–
Gunma1102	2011–2013	Musculoskeletal tumors (pediatric)	Age 6–16, inoperable	60.8, 64, 67.2, or 70.4 GyRBE/16 fr.	–
Gunma1101	2011-	Lymph node metastatic tumor	1–3 nodes in 1 irradiation field	48 or 52.8 GyRBE/12 fr.	–
Gunma1304	2013-	In-field recurrent tumor	previously treated by radiotherapy	Various according to disease site	–
Gunma1204	2013-	Tumor resistant to standard Tx	known to be resistant to standard Tx	Various according to disease site	–

fr., fractions; CNS, central nervous system; H&N, head and neck; Sq, squamous cell carcinoma; NSCLC, non-small cell lung carcinoma; DTIC, dacarbazine; ACNU, nimustine; VCR, vincristine; ENI, elective nodal irradiation; IFI, involved field irradiation; WPI, whole pelvic irradiation; CDDP, cisplatin; ICBT, intracavitary brachytherapy; Tx, therapy.

Technology (2012–2018). Here, we summarize achievements in translational research on carbon ion radiotherapy performed at GHMC through these scientific endeavors.

RESEARCH TO GUIDE THE SELECTION OF PATIENTS SUITABLE FOR CARBON ION RADIOTHERAPY

The number of newly diagnosed cancer patients worldwide is ~14 million/year (7). By contrast, the maximum number of patients that can be treated by carbon ion radiotherapy worldwide is estimated to be ~2100/year (**Table 2**) (8). Thus, carbon ion radiotherapy has the capacity to treat only 0.015% of the total patient population with a newly diagnosed cancer. Moreover, even in Japan, which has the highest density of facilities for carbon ion radiotherapy in the world, carbon ion radiotherapy has the capacity to treat only 0.20% of newly diagnosed cancer cases. These facts highlight the extremely limited availability of this medical resource. Although 11 facilities for carbon ion radiotherapy are currently under construction or are planned for construction (1), the critical shortage of facilities will not be resolved in any practical way for a few decades. Therefore, selecting patients who can derive the greatest benefit from carbon ion radiotherapy is of great importance. Early clinical experience shows that carbon ion radiotherapy is an effective treatment for tumors that are resistant to conventional X-ray radiotherapy (4–6); therefore, carbon ion radiotherapy will be the most beneficial for patients with these types of tumor. From this point of view, assays that predict the X-ray sensitivity of a tumor are urgently required to facilitate appropriate selection of patients for carbon ion radiotherapy.

Histopathological typing of tumors is performed to predict treatment responses in the clinical setting of X-ray radiotherapy. Nevertheless, the response varies widely according to tumor type, and even among those with the same histological type. Thus, additional indices that support prediction of X-ray sensitivity according to histopathological type are required. For many types of cancer, the SF2 value, i.e., the surviving fraction of X-irradiated tumor cells (irradiated *ex vivo* with a dose of 2 Gy) measured in a clonogenic survival assay, correlates with clinical outcome of X-ray radiotherapy (9). However, the SF2 value has shortcomings, i.e., primary culture of the tumor cells required for the clonogenic assay is difficult, and necessitates 2 weeks to obtain final results. Therefore, the SF2 value is not widely used in the clinic. Previously, we identified several cellular mechanisms that contribute to the resistance of cancer cells to X-rays, including intratumoral hypoxia, resistance to radiation-induced apoptosis, a high capacity for the repair of DNA double-strand breaks (DSBs), and mutations in certain oncogene and tumor suppressor genes. By focusing on these factors, we propose the following predictive assays for determining the X-ray sensitivity of cancer cells.

Intratumoral hypoxia is a major contributor to the X-ray resistance of cancer cells (10–12). Nakano et al. used a needle-type polarographic oxygen electrode to measure intratumoral oxygen partial pressure (pO_2) in patients with locally advanced uterine cervical cancer treated using X-ray radiotherapy (13) (**Figure 1**). The authors found that low pretreatment intratumoral pO_2 values correlated with poor outcomes after X-ray radiotherapy. On the other hand, carbon ion radiotherapy showed good antitumor effects in patients with locally advanced uterine cervical cancer, irrespective of pretreatment intratumoral pO_2 levels. These data indicate that assays to determine pretreatment intratumoral pO_2 values will be useful for identification of X-ray-resistant tumors profiting from carbon ion radiotherapy. Importantly, recent studies indicate that as many as 50% of tumors have hypoxic regions, which could underpin X-ray treatment failure and expand the indications for carbon ion radiotherapy (14). Cancer cell resistance to radiation-induced apoptosis is another major factor that contributes to X-ray resistance. Preclinical studies suggest that carbon ions effectively kill cancer cells that are resistant to apoptosis induced by X-ray irradiation (15, 16). Another mode

TABLE 2 | Number of cancer patients treated by carbon ion radiotherapy worldwide per year.

S. No.	Country	City	Facility	Case/year	Year
1	Japan	Chiba	NIRS	888	2013
2	Japan	Gunma	GHMC	448	2013
3	Japan	Hyogo	HIBMC	270	2013
4	Japan	Saga	HIMAT	132	2013
5	China	Lanzhou	HIRFL	27	2006–2013 in average
6	Germany	Heidelberg	HIT	274	2009–2013 in average
7	Italy	Pavia	CNAO	53	2012–2013 in average

NIRS, National Institute of Radiological Sciences; GHMC, Gunma University Heavy Ion Medical Center; HIBMC, Hyogo Ion-Beam Medical Center; HIMAT, Heavy Ion Medical Accelerator in Tosu; HIRFL, Heavy Ion Research Facility in Lanzhou; HIT, Heidelberg Ion-Beam Therapy Center; CNAO, Centro Nazionale Adroterapia Oncologica.
Data on facility #1–4 are based on the website of Association for Nuclear Technology in Medicine (written in Japanese): http://www.antm.or.jp/05_treatment/01.html. Data on facility #5–7 are based on Ref. (8).

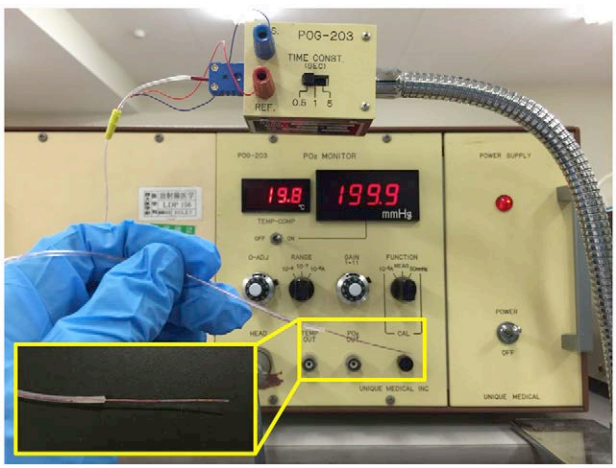

FIGURE 1 | Tools for intratumoral pO_2 measurement. A needle-type polarographic oxygen electrode is used by direct insertion into a tumor.

of clonogenic cell death, called mitotic catastrophe and necrosis, is involved in efficient killing of apoptosis-resistant cancer cells by carbon ions (15, 16). Apoptosis following irradiation is readily assessed by morphological observation of nuclei stained with 4′,6-diamidino-2-phenylindole dihydrochloride (DAPI) (**Figure 2**). Amornwichet et al. demonstrated that apoptosis in HCT116 colon cancer cells peaked at 72 h post-X-ray irradiation, as assessed by DAPI staining (16). This is consistent with the observation that radiation-induced apoptosis in solid tumors mainly corresponds to the so-called late apoptosis, which occurs a few days post-irradiation (17). Furthermore, the DAPI-based assay is easier and faster to perform than the clonogenic survival assay used to calculate the SF2 value. Therefore, DAPI staining of *ex vivo*-irradiated tumor specimens at 72 h post-irradiation is useful for identifying tumors that are resistant to X-ray-induced apoptosis and would therefore benefit from carbon ion radiotherapy.

Double-strand breaks are major cytotoxic lesions that cause cancer cell death after exposure to ionizing radiation (17). Preclinical studies indicate that the high capacity of cancer cells for DSB repair contributes to X-ray resistance (18, 19). Meanwhile, the cell-killing actions of carbon ions are less affected by intrinsic DSB repair capacity (18, 19). Most likely, complex carbon ion-induced DSBs are more difficult to repair than X-ray-induced DSBs; these persistent unrepaired DSBs then lead to mitotic catastrophe (16). These data indicate that tumors with a high capacity for DSB repair are suitable for carbon ion radiotherapy. DSB repair capacity can be evaluated by immunofluorescence staining for Ser139-phosphorylated histone H2AX (γH2AX) or p53-binding protein 1 (53BP1) because DSBs are detected as foci of γH2AX or 53BP1 (**Figure 3**) (20–22). The number of foci at 30 min post-irradiation can be used as an index for radiation-induced DSBs. On the other hand, the number of foci in irradiated cells decreases by more than 90% within 24 h post-irradiation, indicating that a major proportion of radiation-induced DSBs is repaired by that time point (20). Thus, the ratio of the foci number at 24 h post-irradiation to that at 30 min post-irradiation can be used as an index for DSB repair capacity.

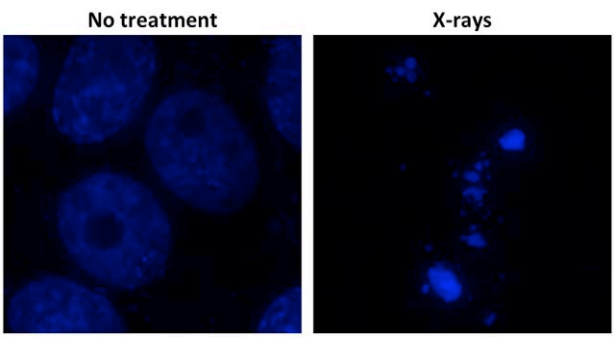

FIGURE 2 | Radiation-induced apoptosis, as assessed by DAPI staining. Cultured Ma-24 lung cancer cells were stained with DAPI at 72 h after irradiation using X-rays at a dose of 4 Gy. Apoptotic cells are identified by the appearance of apoptotic bodies, characterized by condensed and fragmented nuclei, under a fluorescence microscope.

Importantly, the high DSB repair capacity (as indicated by low number of foci at 24 h post-irradiation) is associated with a high rate of clonogenic survival (19). Hence, assay of γH2AX or 53BP1 foci in *ex vivo*-irradiated tumor specimens can be performed to identify tumors with a high capacity for DSB repair and suitable for carbon ion radiotherapy.

Cancer cells harbor modifications in a number of molecular pathways that affect intrinsic radiosensitivity. Mutations in oncogenes and tumor suppressor genes are common, and these mutations result in alterations in signaling pathways. We previously showed that inactivating mutations in the gene encoding tumor suppressor protein 53 (*TP53*) confer X-ray resistance on cancer cells (15, 16, 23). We also showed that epidermal growth factor receptor gene (*EGFR*) mutation-negative non-small cell lung cancer (NSCLC) cells are more resistant to X-rays than *EGFR* mutation-positive NSCLC cells (19). These findings were validated by clinical studies (24–27). Interestingly, investigations using isogenic cancer cell lines demonstrated that carbon ions can kill cancer cells irrespective of the mutational status of *TP53* and *EGFR* (15, 16, 19, 23). Taken together, these data indicate that the mutational status of *TP53*/*EGFR* is useful for selecting patients who are suited for carbon ion radiotherapy. Nevertheless, a recent genome-wide analysis revealed the presence of hundreds of gene mutations in a single tumor (28). Because the overall radiosensitivity of a tumor should be the result of this highly complex genetic context, the mutational

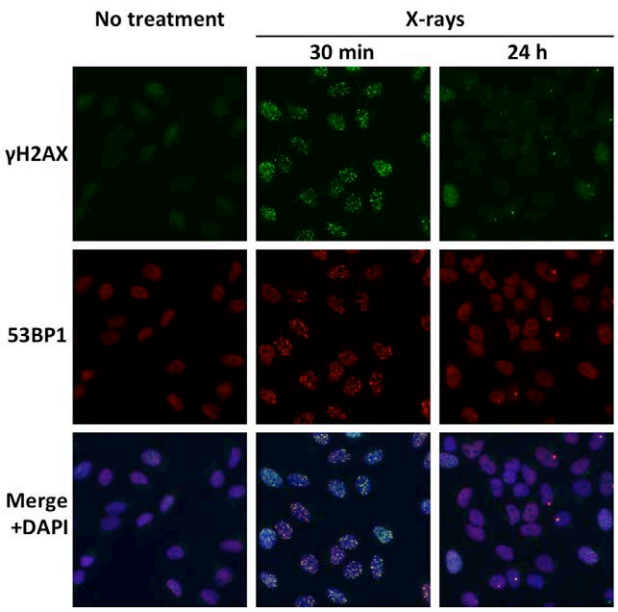

FIGURE 3 | Radiation-induced DSBs visualized by immunofluorescence staining of γH2AX and 53BP1. Cultured A549 lung cancer cells were immunostained for γH2AX and 53BP1 at 30 min or 24 h post-irradiation using X-rays at a dose of 1 Gy. DSBs are identified as foci of γH2AX and 53BP1. Merged images show high consistency between γH2AX foci and 53BP1 foci. A markedly smaller number of γH2AX and 53BP1 foci at 24 h compared with 30 min indicate the high capacity of the X-ray-resistant cell line for DSB repair.

status of only a small subset of well-known cancer-related genes (e.g., *TP53* and *EGFR*) may not be the best predictor of radiosensitivity. Thus, studies aimed at elucidating detailed gene mutation profiles to facilitate better prediction of tumor radiosensitivity are warranted.

RESEARCH AIMED AT OPTIMIZING CARBON ION RADIOTHERAPY

Optimization of carbon ion radiotherapy can be addressed using two approaches such as radiation physics and radiation biology. Both physics and biology play intertwining roles in treatment planning; therefore, advances in one field benefit the other. For example, increased irradiation accuracy results in less normal tissue toxicity. By contrast, accurate information about the biological characteristics of tumors and normal tissues aids optimal treatment planning. Biological factors that affect the treatment procedure, including biological responses to dose fractionation, normal tissue toxicity, tumor cell motility, and the bystander effect, are discussed below.

In X-ray radiotherapy, the rationale for dose fractionation is provided by the re-oxygenation and cell cycle redistribution of tumor cells, as well as a higher capacity for the repair of sublethal damage in normal tissues versus tumors (17). The cell-killing effect of carbon ions versus X-rays is less dependent on these factors (13, 17); therefore, the responses of tumors and normal tissues to carbon ions may be different from those to X-rays, even when the same dose fractionation schedule is utilized. To address this issue, Ando et al. used a mouse model to explore the effects of carbon ion dose fractionation on tumor and normal tissues (29). The investigators treated fibrosarcoma xenografts and host mouse skin with γ rays or carbon ion beams with three different linear energy transfer (LET) values (20, 42, and 77 keV/μm) and with different fractionation schedules (i.e., one to seven fractions). Interestingly, the relative biological effectiveness (RBE) values for tumor growth delay were higher than those for early skin reaction when 42- and 77-keV/μm carbon ion beams, but not γ rays or 20-keV/μm carbon ion beams, were employed in intermediate fractionation schedules (i.e., two to six fractions). The therapeutic gain (calculated as the ratio of the RBE value for tumor growth delay to that for early skin reaction) was maximized for the 42 keV/μm beams delivered in four fractions. Yoshida et al. examined the impact of carbon ion dose fractionation on the small intestine by assessing crypt survival in the mouse model employed above (30). In contrast to the results for early skin reaction, no therapeutic gain was observed for the intermediate fractionation schedules. This might be because intestinal crypt cells have a low capacity to repair sublethal damage induced by carbon ions. These two studies indicate that different strategies are required to optimize the dose fractionation schedules used for carbon ion radiotherapy in the skin versus the small intestine. With respect to the skin, the therapeutic window for carbon ion irradiation can be expanded by employing an intermediate hypofractionation strategy. Therefore, the actual fractionation schedule that corresponds to "intermediate" hypofractionation in the mouse model should be further explored in the clinic. On the other hand, the therapeutic window for carbon ions and X-rays in the small intestine may be comparable, and the benefit of dose fractionation may be lower for carbon ions than for X-rays. This indicates that, in abdominal irradiation to treat tumors such as uterine cervical cancer, the maximum tolerable carbon ion dose can be delivered in a smaller number of fractions, resulting in a shorter treatment period. In addition, hypofractionated carbon ion radiotherapy that results in the shorter treatment period compared with X-ray radiotherapy utilizing conventional 2 Gy/day fractionation can contribute to reduce tumor repopulation effect. Assessment of the effect of carbon ion dose fractionation in different tumors and normal tissues in the same mouse model should be further investigated, together with concomitant evaluation of factors that can affect the results of fractionated irradiation (i.e., oxygen levels, cell cycle profiles, and DSB repair capacity).

Carbon ion radiotherapy shows a steep dose fall-off; therefore, the treatment plans are more susceptible to target motion than the plan for three-dimensional conformal radiotherapy (3D-CRT) with X-rays. A larger target volume setting increases the robustness of the dose delivered to the tumor; however, it also increases toxicity to adjacent normal tissues. Therefore, it is necessary to determine the sensitivity of normal tissues to obtain the optimal target volume setting. The nervous system is critically at risk of radiotherapy toxicity, because it is a serial organ with low redundancy and low capacity for regeneration. The sensitivity of the central nervous system to carbon ions has been examined in multiple experimental models. Isono et al. evaluated the sensitivity of human neural stem cells to carbon ions and found that the RBE value, as assessed by cell proliferation, was 2.0 (31). Yoshida et al. examined the effects of carbon ion irradiation in normal rat brain (32). The authors used an organotypic slice culture of cerebellum excised from 10-day-old rats and assessed morphological changes and cellular apoptosis, defined as disorganization of the external granule cell layer and positive staining for TdT-mediated dUTP-biotin nick-end labeling (TUNEL), respectively. They found that the RBE value for rat cerebellum was 1.4–1.5. Kaminuma et al. also explored carbon ion-provoked apoptosis in the rat brain by performing a TUNEL assay in a primary culture of fetal hippocampal neurons (33). The RBE value was strikingly high at 10.2. Similarly, Al-Jahdari and colleagues investigated the sensitivity of the peripheral nervous system to carbon ions by employing dorsal root ganglia and sympathetic ganglion chains prepared from the chick embryo at days 8 and 16, representing the immature and mature peripheral nervous system (34). Growth cone collapse was assessed as an index of malfunction in the neuronal network, yielding an RBE value of 3.1–3.2 in day 8 neurons and 1.5–2.1 in day 16 neurons. Meanwhile, the RBE value assessed by TUNEL staining was 2.5–2.9 in day 8 neurons and 1.4–1.8 in day 16 neurons. Although it is difficult to draw a firm conclusion from the above studies employing different experimental models, nervous systems (central and peripheral) and endpoints, the data collectively indicate that the RBE value of the adult nervous system is ~1.4–2.1 when morphological changes and cellular apoptosis are utilized as endpoints. Given the fact that the RBE value for carbon ions in cancer cells is generally ~2–3, these findings suggest that carbon

ion radiotherapy has a wider therapeutic window than X-rays when used to treat tumors adjacent to the components of the central and peripheral nervous systems. Notably, these data also indicate that immature neurons are more sensitive to carbon ion irradiation than mature neurons. Thus, careful attention should be paid to neural toxicity when carbon ion radiotherapy is used to treat pediatric tumors.

The lung is another critical organ at risk in radiotherapy. Radiation-induced lung injury can be lethal in some patients and is a major dose-limiting factor for thoracic irradiation (35). Okano et al. used a crystal violet staining assay to examine the effect of carbon ions on the proliferation of immortalized human small airway epithelial cells (iSAECs) and normal human lung fibroblasts (36). The resultant RBE value was 3.2 for iSAECs and 2.2 for normal lung fibroblasts. On the other hand, ionizing radiation can indirectly damage normal lung tissue by triggering inflammatory reactions. Upregulation of intercellular adhesion molecule-1 (ICAM-1) expression on the surface of pulmonary endothelial cells participates in this inflammation-related process by increasing macrophage infiltration into the lung (37, 38). Kiyohara et al. compared ICAM-1 expression on the surface of human umbilical vein endothelial cells after irradiation with carbon ions and X-rays. The data showed that post-irradiation ICAM-1 expression levels were 2.56- and 2.47-fold higher after carbon ion irradiation than after X-ray irradiation at 1 and 2 Gy, respectively (39). These data signify that the estimated RBE values in normal lung tissue and lung cancer cells are comparable (~2–3) (19).

Several studies demonstrate that X-ray irradiation increases the motility of cancer cells (40, 41). The migration of irradiated cancer cells may influence the setting of target volumes, i.e., the margin from the gross tumor volume (GTV) to the clinical target volume (CTV). Murata et al. used a wound healing assay and F-actin staining to examine the effect of carbon ions on the motility of A549 lung cancer cells (42). Carbon ion irradiation promoted the healing of scratch wounds in cell monolayers and increased the formation of F-actin protrusions, both indicators of increased cancer cell motility. Interestingly, the RBE value based on cell motility was consistent with that based on cell survival (i.e., ~4 versus 3.9). This finding provides important insight into treatment planning, i.e., the GTV–CTV margin can be set in a comparable manner for X-rays and carbon ions.

The bystander effect is a phenomenon whereby non-irradiated cells adjacent to irradiated cells are killed (43). Previous research shows that the bystander effect is universal among most types of normal cells and tumor cells (43). However, the significance of the bystander effect among different types of cells after carbon ion irradiation is not fully understood. Harada et al. investigated the bystander effect in carbon ion-irradiated A549 cells by using carbon ion microbeams (diameter = 20 μm) to irradiate only 0.0001–0.002% of the cells in a culture plate (44). The entire cell population was then subjected to a clonogenic survival assay, resulting in an 8–14% reduction in cell survival. Thus, the bystander effect plays a highly significant role in carbon ion-induced killing of A549 lung cancer cells. By contrast, Wakatsuki et al. found that the bystander effect played no role in the killing of a HTB-94 chondrosarcoma cell line (45). These data highlight the fact that different cell types show different susceptibilities to the bystander effect induced by carbon ion irradiation by up to ~10%. Further research into the carbon ion radiotherapy-induced bystander effects in different tumor cells and normal cells is necessary to optimize treatment planning.

RESEARCH INTO COMBINATION THERAPY TO ENHANCE THE EFFICACY OF CARBON ION RADIOTHERAPY

Theoretically, a sufficiently high dose of ionizing radiation can sterilize any type of tumor (46). However, clinically applicable doses are delivered within a range that is tolerable by normal tissues (47). Dose escalation trials are underway to identify the maximum tolerable dose for carbon ion radiotherapy according to disease site (2). To date, clinical experience indicates that carbon ion radiotherapy can be delivered to many disease sites at higher biologically equivalent doses than 3D-CRT using X-rays. Carbon ion radiotherapy can also achieve nearly 100% tumor control probability in tumors that are uncontrollable by other radiation therapy modalities using X-rays and protons, such as spinal chordomas (1). Nonetheless, local recurrence occurs within the GTV, indicating the presence of a subset of carbon ion-resistant tumors.

To eradicate carbon ion-resistant tumors, it is important to establish an optimal form of combination treatment that increases the efficacy of carbon ion radiotherapy. To this end, several clinically available chemotherapeutic drugs have been tested in a preclinical setting. Kubo et al. examined the ability of carboplatin and paclitaxel to sensitize H460 lung cancer cells to carbon ion beams (48). Both sensitized cancer cells to carbon ion irradiation, with sensitizing ratios of 1.21 and 1.22, respectively (NB, a sensitizing ratio of >1 indicates that the radiation and the drug have a synergistic effect). These sensitizing ratios were comparable with those of X-rays. Similarly, Takahashi et al. demonstrated that etoposide sensitized X-ray-resistant rat yolk sac tumor cells to carbon ions, reporting a sensitizing ratio of ~1.2 (23). Carboplatin, paclitaxel, and etoposide are all currently used in combination with X-rays for clinical tumor treatment; carboplatin and paclitaxel are used to treat NSCLC, uterine cervical cancer, and esophageal cancer, and etoposide is used to treat small cell lung cancer. The combination of these drugs with carbon ions should likewise be tested in the clinic.

Several drugs currently under development have been tested for their ability to sensitize cells to carbon ion irradiation. Ma and colleagues examined the sensitizing effects of the Wee-1 inhibitor, MK-1775, using H1299 lung cancer cells (49). Wee-1 is a nuclear kinase protein involved in activating the G2 cell cycle checkpoint. Pretreatment for lung cancer cells with MK-1775 abrogated the induction of G2/M arrest after carbon ion irradiation, leading to an increase in mitotic catastrophe-mediated cell death. The sensitizing ratio of MK-1775 was 1.21 at 200 nM, a concentration at which MK-1775 alone reduces the surviving cell fraction by 50%. Musha et al. evaluated the sensitizing effect of the heat shock

protein 90 (Hsp90) inhibitor, 17-AAG, in LMF4 oral squamous cell carcinoma cells (50). Hsp90 forms a chaperone complex with client proteins, thereby stabilizing them. Because various Hsp90 client proteins [e.g., Akt, ErbB2, and hypoxia-inducible factor-1α (HIF-1α)] are associated with malignant cancer phenotypes, Hsp90 is regarded as a potent molecular target (51–53). 17-AAG sensitized tumor cells to carbon ions with a sensitizing ratio of 1.14 at 100 nM, a concentration at which 17-AAG alone reduces the surviving cell fraction by 30–40%, although the underlying mechanism is unclear. These data indicate that Wee-1 or Hsp90 inhibition is a viable strategy for sensitization of carbon ions, but the sensitizing effect requires further testing in animal models. As a monomodality treatment for cancer, MK-1775 is currently under investigation in phase I and phase II clinical trials (54). Meanwhile, a phase II clinical trial for 17-AAG was terminated due to the lack of adequate tumor response and the presence of normal tissue toxicity (55). Nevertheless, a number of next-generation Hsp90 inhibitors are now being tested in multiple clinical trials (55).

Cancer immunotherapy has recently provoked a great deal of interest. Novel molecular targeting therapies (including those targeting programed cell death 1, programed cell death-ligand 1, and cytotoxic T-lymphocyte-associated protein 4) all demonstrate marked antitumor effects (56–58). Evidence suggests that the antitumor immune response plays an important role in the antitumor efficacy of X-ray radiotherapy. Nakano et al. showed that pretreatment levels of intratumoral infiltration by Langerhans cells and T cells, the key players in antitumor immune responses, correlates with a favorable outcome in patients with uterine cervical cancer treated using X-ray radiotherapy (59). They also showed that concomitant use of X-rays and intratumoral injection of sizofiran, an immune-response modifying drug, increases intratumoral infiltration of Langerhans cells and T-cells in patients with uterine cervical cancer (60). Recently, Suzuki et al. demonstrated that an antigen-specific T cell response is activated in esophageal cancer patients receiving combined X-ray radiotherapy and chemotherapy (61). These data suggest that the efficacy of X-ray radiotherapy can be improved upon combination with assorted cancer immunotherapies.

To investigate whether the antitumor immune response contributes to the antitumor efficacy of carbon ion radiotherapy, Yoshimoto et al. examined the impact of carbon ion irradiation on the release of high-mobility group box 1 protein (HMGB1) after irradiation in various cancer cell lines (62). HMGB1 is released from tumor cells damaged by radiotherapy and/or chemotherapy. Elevated serum HMGB1 levels are associated with activation of the antigen-specific T cell responses after chemoradiotherapy (61). The investigators found that HMGB1 levels in conditioned culture media were significantly higher after carbon ion irradiation. The RBE values based on HMGB1 release were similar to those based on clonogenic survival. These data suggest that the antitumor immune response contributes to an antitumor effect not only in X-ray radiotherapy but also in carbon ion radiotherapy. Additional preclinical research investigating the effects of combinations of carbon ion radiotherapy and cancer immunotherapy is currently underway.

PERSPECTIVES

Carbon ion radiotherapy is a promising therapy for cancer. Appropriate patient selection based on individual tumor radiosensitivity is key to making the most of this medical resource with extremely limited availability. Recent advances in molecular biology research emphasize the need for functional predictive assays using tumor biopsy specimens for the practice of precision medicine (63). The utility of predictive assays for determining intratumoral oxygen levels, radiation-induced cellular apoptosis, DSB repair capacity, and gene mutational status should be tested in the clinic. Of note, recent studies demonstrate that a combination of distinct tumor features can work synergistically to predict prognosis in a subset of tumors, indicating the benefit of combined usage of these predictive assays (64). In addition, progress in the field of metabolomics indicates that non-invasive predictive assays based on biofluids, such as blood or urine, will be established in the near future (65, 66).

Researchers have accumulated extensive data concerning radiobiological properties of cancers and normal tissues. However, translation of biological data to the clinic remains far from satisfactory. This may be partially due the huge diversity in experimental systems used in radiation biology studies, making it difficult to draw solid conclusions for clinical applications. A meta-analytic approach to integrate the existing data is suggested. Moreover, specification of carbon ion beams including LET values employed in the studies must be carefully considered during the data translation process. Most *in vitro* studies used mono-energetic high-LET (i.e., ~100 keV/μm) carbon ion beams. However, several facilities, including NIRS and GHMC, now utilize spread-out Bragg peak (SOBP) carbon ion beams, which comprise a mixture of different LET beams, in the clinic. The biological effect of SOBP carbon ion beams likely differs from that of mono-energetic high-LET beams. Studies during the early era of carbon ion radiobiology provide plenty of data on the biological effect of SOBP carbon ion beams. Nevertheless, these data are difficult to interpret in the context of modern molecular biology and in a clinical setting because the biological effects were analyzed using biophysics models to deconvolute the mixed LET spectrum. Therefore, future studies should investigate the effects of SOBP carbon ion beams using current molecular biological techniques, particularly with respect to tumor hypoxia, radiation-induced apoptosis, and DSB repair.

Emerging molecular biology techniques are expected to contribute to further advancement of translational research in carbon ion radiobiology. First, next-generation sequencing technologies will almost certainly identify specific genomic and epigenomic profiles that affect radiosensitivity (28, 67) and can be combined with existing data concerning expression profiles related to radiosensitivity (68, 69). Second, advanced high-resolution microscopy techniques will clarify the molecular processes that occur following carbon ion irradiation. For example, Britton et al. visualized recruitment of a single Ku molecule at DSB sites, which is essential for the repair of DSBs induced by ionizing irradiation (70). Thus, advanced high-resolution microscopy will promote our understanding of the repair kinetics of complex DSBs induced by carbon ions. Third, emerging imaging technologies

will enable detailed visualization of intratumoral oxygen levels and metabolomic states (71). We anticipate that integration and translation of data in radiation biology will greatly improve the efficacy of carbon ion radiotherapy.

AUTHOR CONTRIBUTIONS

TO, HS and S-eN summarized data and drafted the manuscript. TN supervised the manuscript. All authors read and approved the final manuscript.

ACKNOWLEDGMENTS

We sincerely thank Dr. Atsushi Shibata and Dr. Atsuko Niimi (Gunma University) for their generous support in obtaining the data used in the figures. We thank Ms. Yuka Kimura and Ms. Yuka Hirota (Gunma University) for technical assistance.

FUNDING

This work was supported by Grants-in-Aid from the Ministry of Education, Culture, Sports, Science, and Technology of Japan for programs for Leading Graduate Schools, Cultivating Global Leaders in Heavy Ion Therapeutics and Engineering, and for Strategic Young Researcher Overseas Visits Program for Accelerating Brain Circulation. This work was also supported by Grants-in-Aid from the Japan Society for the Promotion of Science for Scientific Research (B) KAKENHI (24390288) and for the Twenty-First Century Centers of Excellence Program (K05).

SUPPLEMENTARY MATERIAL

The Supplementary Material for this article can be found online at http://journal.frontiersin.org/article/10.3389/fonc.2016.00139

REFERENCES

1. Loeffler JS, Durante M. Charged particle therapy-optimization, challenges and future directions. *Nat Rev Clin Oncol* (2013) 10:411–24. doi:10.1038/nrclinonc.2013.79
2. Kamada T, Tsujii H, Blakely EA, Debus J, De Neve W, Durante M, et al. Carbon ion radiotherapy in Japan: an assessment of 20 years of clinical experience. *Lancet Oncol* (2015) 16:e93–100. doi:10.1016/S1470-2045(14)70412-7
3. Combs SE, Debus J. Treatment with heavy charged particles: systematic review of clinical data and current clinical (comparative) trials. *Acta Oncol* (2013) 52:1272–86. doi:10.3109/0284186X.2013.818254
4. Shinoto M, Yamada S, Yasuda S, Imada H, Shioyama Y, Honda H, et al. Phase 1 trial of preoperative, short-course carbon-ion radiotherapy for patients with resectable pancreatic cancer. *Cancer* (2013) 119:45–51. doi:10.1002/cncr.27723
5. Jingu K, Tsujii H, Mizoe JE, Hasegawa A, Bessho H, Takagi R, et al. Carbon ion radiation therapy improves the prognosis of unresectable adult bone and soft-tissue sarcoma of the head and neck. *Int J Radiat Oncol Biol Phys* (2012) 82:2125–31. doi:10.1016/j.ijrobp.2010.08.043
6. Mizoe JE, Hasegawa A, Jingu K, Takagi R, Bessyo H, Morikawa T, et al. Results of carbon ion radiotherapy for head and neck cancer. *Radiother Oncol* (2012) 103:32–7. doi:10.1016/j.radonc.2011.12.013
7. Website: Cancer Research UK (2016). Available from: http://www.cancerresearchuk.org/health-professional/cancer-statistics/worldwide-cancer
8. Jermann M. Particle therapy statistics in 2013. *Int J Part Ther* (2014) 1:40–3. doi:10.14338/IJPT.14-editorial-2.1
9. Torres-Roca JF. A molecular assay of tumor radiosensitivity: a roadmap towards biology-based personalized radiation therapy. *Per Med* (2012) 9:547–57. doi:10.2217/pme.12.55
10. Kallman RF. The phenomenon of reoxygenation and its implications for fractionated radiotherapy. *Radiology* (1972) 105:135–42. doi:10.1148/105.1.135
11. Gatenby RA, Kessler HB, Rosenblum JS, Coia LR, Moldofsky PJ, Hartz WH, et al. Oxygen distribution in squamous cell carcinoma metastases and its relationship to outcome of radiation therapy. *Int J Radiat Oncol Biol Phys* (1988) 14:831–8. doi:10.1016/0360-3016(88)90002-8
12. Nordsmark M, Overgaard M, Overgaard J. Pretreatment oxygenation predicts radiation response in advanced squamous cell carcinoma of the head and neck. *Radiother Oncol* (1996) 41:31–9. doi:10.1016/S0167-8140(96)91811-3
13. Nakano T, Suzuki Y, Ohno T, Kato S, Suzuki M, Morita S, et al. Carbon beam therapy overcomes the radiation resistance of uterine cervical cancer originating from hypoxia. *Clin Cancer Res* (2006) 12:2185–90. doi:10.1158/1078-0432.CCR-05-1907
14. Hill RP, Bristow RG, Fyles A, Koritzinsky M, Milosevic M, Wouters BG. Hypoxia and predicting radiation response. *Semin Radiat Oncol* (2015) 25:260–72. doi:10.1016/j.semradonc.2015.05.004
15. Takahashi A, Matsumoto H, Yuki K, Yasumoto J, Kajiwara A, Aoki M, et al. High-LET radiation enhanced apoptosis but not necrosis regardless of p53 status. *Int J Radiat Oncol Biol Phys* (2004) 60:591–7. doi:10.1016/j.ijrobp.2004.05.062
16. Amornwichet N, Oike T, Shibata A, Ogiwara H, Tsuchiya N, Yamauchi M, et al. Carbon-ion beam irradiation kills X-ray-resistant p53-null cancer cells by inducing mitotic catastrophe. *PLoS One* (2014) 9:e115121. doi:10.1371/journal.pone.0115121
17. Joiner MC, van der Kogel A. *Basic Clinical Radiobiology*. Florida: CRC Press (2009).
18. Takahashi A, Kubo M, Ma H, Nakagawa A, Yoshida Y, Isono M, et al. Nonhomologous end-joining repair plays a more important role than homologous recombination repair in defining radiosensitivity after exposure to high-LET radiation. *Radiat Res* (2014) 182:338–44. doi:10.1667/RR13782.1
19. Amornwichet N, Oike T, Shibata A, Nirodi CS, Ogiwara H, Makino H, et al. The EGFR mutation status affects the relative biological effectiveness of carbon-ion beams in non-small cell lung carcinoma cells. *Sci Rep* (2015) 5:11305. doi:10.1038/srep11305
20. Löbrich M, Shibata A, Beucher A, Fisher A, Ensminger M, Goodarzi AA, et al. gammaH2AX foci analysis for monitoring DNA double-strand break repair: strengths, limitations and optimization. *Cell Cycle* (2010) 9:662–9. doi:10.1158/0008-5472.CAN-03-3207
21. Stiff T, O'Driscoll M, Rief N, Iwabuchi K, Löbrich M, Jeggo PA. ATM and DNA-PK function redundantly to phosphorylate H2AX after exposure to ionizing radiation. *Cancer Res* (2004) 64:2390–6. doi:10.1158/0008-5472.CAN-03-3207
22. Markova E, Vasilyev S, Belyaev I. 53BP1 foci as a marker of tumor cell radiosensitivity. *Neoplasma* (2015) 62:770–6. doi:10.4149/neo_2015_092
23. Takahashi T, Fukawa T, Hirayama R, Yoshida Y, Musha A, Furusawa Y, et al. In vitro interaction of high-LET heavy-ion irradiation and chemotherapeutic agents in two cell lines with different radiosensitivities and different p53 status. *Anticancer Res* (2010) 30:1961–7.
24. Ishikawa H, Mitsuhashi N, Sakurai H, Maebayashi K, Niibe H. The effects of p53 status and human papillomavirus infection on the clinical outcome of patients with stage IIIB cervical carcinoma treated with radiation therapy alone. *Cancer* (2001) 91:80–9. doi:10.1002/1097-0142(20010101)91:1<80:AID-CNCR11>3.0.CO;2-E
25. Huerta S, Hrom J, Gao X, Saha D, Anthony T, Reinhart H, et al. Tissue microarray constructs to predict a response to chemoradiation in rectal cancer. *Dig Liver Dis* (2010) 42:679–84. doi:10.1016/j.dld.2010.02.003
26. Nakano T, Oka K, Taniguchi N. Manganese superoxide dismutase expression correlates with p53 status and local recurrence of cervical carcinoma treated with radiation therapy. *Cancer Res* (1996) 56:2771–5.
27. Yagishita S, Horinouchi H, Katsui Taniyama T, Nakamichi S, Kitazono S, Mizugaki H, et al. Epidermal growth factor receptor mutation is associated with longer local control after definitive chemoradiotherapy in patients with

stage III nonsquamous non-small-cell lung cancer. *Int J Radiat Oncol Biol Phys* (2015) 91:140–8. doi:10.1016/j.ijrobp.2014.08.344
28. Alexandrov LB, Nik-Zainal S, Wedge DC, Aparicio SA, Behjati S, Biankin AV, et al. Signatures of mutational processes in human cancer. *Nature* (2013) 500:415–21. doi:10.1038/nature12477
29. Ando K, Koike S, Uzawa A, Takai N, Fukawa T, Furusawa Y, et al. Biological gain of carbon-ion radiotherapy for the early response of tumor growth delay and against early response of skin reaction in mice. *J Radiat Res* (2005) 46:51–7. doi:10.1269/jrr.46.51
30. Yoshida Y, Ando K, Ando K, Murata K, Yoshimoto Y, Musha A, et al. Evaluation of therapeutic gain for fractionated carbon-ion radiotherapy using the tumor growth delay and crypt survival assays. *Radiother Oncol* (2015) 117:351–7. doi:10.1016/j.radonc.2015.09.027
31. Isono M, Yoshida Y, Takahashi A, Oike T, Shibata A, Kubota Y, et al. Carbon-ion beams effectively induce growth inhibition and apoptosis in human neural stem cells compared with glioblastoma A172 cells. *J Radiat Res* (2015) 56:856–61. doi:10.1093/jrr/rrv033
32. Yoshida Y, Suzuki Y, Al-Jahdari WS, Hamada N, Funayama T, Shirai K, et al. Evaluation of the relative biological effectiveness of carbon ion beams in the cerebellum using the rat organotypic slice culture system. *J Radiat Res* (2012) 53:87–92. doi:10.1269/jrr.11139A
33. Kaminuma T, Suzuki Y, Shirai K, Mizui T, Noda SE, Yoshida Y, et al. Effectiveness of carbon-ion beams for apoptosis induction in rat primary immature hippocampal neurons. *J Radiat Res* (2010) 51:627–31. doi:10.1269/jrr.10050
34. Al-Jahdari WS, Suzuki Y, Yoshida Y, Hamada N, Shirai K, Noda SE, et al. The radiobiological effectiveness of carbon-ion beams on growing neurons. *Int J Radiat Biol* (2009) 85:700–9. doi:10.1080/09553000903020032
35. Yamashita H, Nakagawa K, Nakamura N, Koyanagi H, Tago M, Igaki H, et al. Exceptionally high incidence of symptomatic grade 2-5 radiation pneumonitis after stereotactic radiation therapy for lung tumors. *Radiat Oncol* (2007) 2:21. doi:10.1186/1748-717X-2-21
36. Okano N, Oike T, Saitoh J, Shirai K, Kiyono T, Enari M, et al. In vitro determination of the relative biological effectiveness of carbon ion beam irradiation in cells derived from human normal lung tissues. *Int J Radiat Oncol Biol Phys* (2014) 90:S787. doi:10.1016/j.ijrobp.2014.05.2275
37. Quarmby S, Kumar P, Kumar S. Radiation-induced normal tissue injury: role of adhesion molecules in leukocyte-endothelial cell interactions. *Int J Cancer* (1999) 82:385–95. doi:10.1002/(SICI)1097-0215(19990730)82:3<385:AID-IJC12>3.0.CO;2-5
38. Mollà M, Gironella M, Miquel R, Tovar V, Engel P, Biete A, et al. Relative roles of ICAM-1 and VCAM-1 in the pathogenesis of experimental radiation-induced intestinal inflammation. *Int J Radiat Oncol Biol Phys* (2003) 57:264–73. doi:10.1016/S0360-3016(03)00523-6
39. Kiyohara H, Ishizaki Y, Suzuki Y, Katoh H, Hamada N, Ohno T, et al. Radiation-induced ICAM-1 expression via TGF-β1 pathway on human umbilical vein endothelial cells; comparison between X-ray and carbon-ion beam irradiation. *J Radiat Res* (2011) 52:287–92. doi:10.1269/jrr.10061
40. Fujita M, Otsuka Y, Yamada S, Iwakawa M, Imai T. X-ray irradiation and Rho-kinase inhibitor additively induce invasiveness of the cells of the pancreatic cancer line, MIAPaCa-2, which exhibits mesenchymal and amoeboid motility. *Cancer Sci* (2011) 102:792–8. doi:10.1111/j.1349-7006.2011.01852.x
41. Zhai GG, Malhotra R, Delaney M, Latham D, Nestler U, Zhang M, et al. Radiation enhances the invasive potential of primary glioblastoma cells via activation of the Rho signaling pathway. *J Neurooncol* (2006) 76:227–37. doi:10.1007/s11060-005-6499-4
42. Murata K, Noda SE, Oike T, Takahashi A, Yoshida Y, Suzuki Y, et al. Increase in cell motility by carbon ion irradiation via the Rho signaling pathway and its inhibition by the ROCK inhibitor Y-27632 in lung adenocarcinoma A549 cells. *J Radiat Res* (2014) 55:658–64. doi:10.1093/jrr/rru002
43. Prise KM, O'Sullivan JM. Radiation-induced bystander signalling in cancer therapy. *Nat Rev Cancer* (2009) 9:351–60. doi:10.1038/nrc2603
44. Harada K, Nonaka T, Hamada N, Sakurai H, Hasegawa M, Funayama T, et al. Heavy-ion-induced bystander killing of human lung cancer cells: role of gap junctional intercellular communication. *Cancer Sci* (2009) 100:684–8. doi:10.1111/j.1349-7006.2009.01093.x
45. Wakatsuki M, Magpayo N, Kawamura H, Held KD. Differential bystander signaling between radioresistant chondrosarcoma cells and fibroblasts after x-ray, proton, iron ion and carbon ion exposures. *Int J Radiat Oncol Biol Phys* (2012) 84:e103–8. doi:10.1016/j.ijrobp.2012.02.052
46. Thariat J, Hannoun-Levi JM, Sun Myint A, Vuong T, Gérard JP. Past, present, and future of radiotherapy for the benefit of patients. *Nat Rev Clin Oncol* (2013) 10:52–60. doi:10.1038/nrclinonc.2012.203
47. Nakano T, Suzuki M, Abe A, Suzuki Y, Morita S, Mizoe J, et al. The phase I&II clinical study of carbon ion therapy for cancer of the uterine cervix. *Cancer J Sci Am* (1999) 5:362–9.
48. Kubo N, Noda SE, Takahashi A, Yoshida Y, Oike T, Murata K, et al. Radiosensitizing effect of carboplatin and paclitaxel to carbon-ion beam irradiation in the non-small-cell lung cancer cell line H460. *J Radiat Res* (2015) 56:229–38. doi:10.1093/jrr/rru085
49. Ma H, Takahashi A, Sejimo Y, Adachi A, Kubo N, Isono M, et al. Targeting of carbon ion-induced G(2) checkpoint activation in lung cancer cells using Wee-1 inhibitor MK-1775. *Radiat Res* (2015) 184:660–9. doi:10.1667/RR14171.1
50. Musha A, Yoshida Y, Takahashi T, Ando K, Funayama T, Kobayashi Y, et al. Synergistic effect of heat shock protein 90 inhibitor, 17-allylamino-17-demethoxygeldanamycin and X-rays, but not carbon-ion beams, on lethality in human oral squamous cell carcinoma cells. *J Radiat Res* (2012) 53:545–50. doi:10.1093/jrr/rrs012
51. Schulte TW, Blagosklonny MV, Ingui C, Neckers L. Disruption of the Raf-1-Hsp90 molecular complex results in destabilization of Raf-1 and loss of Raf-1-Ras association. *J Biol Chem* (1995) 270:24585–8. doi:10.1074/jbc.270.41.24585
52. Sato S, Fujita N, Tsuruo T. Modulation of Akt kinase activity by binding to Hsp90. *Proc Natl Acad Sci U S A* (2000) 97:10832–7. doi:10.1073/pnas.170276797
53. Peng X, Guo X, Borkan SC, Bharti A, Kuramochi Y, Calderwood S, et al. Heat shock protein 90 stabilization of ErbB2 expression is disrupted by ATP depletion in myocytes. *J Biol Chem* (2005) 280:13148–52. doi:10.1074/jbc.M410838200
54. De Witt Hamer PC, Mir SE, Noske D, Van Noorden CJ, Wurdinger T. WEE1 kinase targeting combined with DNA-damaging cancer therapy catalyzes mitotic catastrophe. *Clin Cancer Res* (2011) 17:4200–7. doi:10.1158/1078-0432.CCR-10-2537
55. Tatokoro M, Koga F, Yoshida S, Kihara K. Heat shock protein 90 targeting therapy: state of the art and future perspective. *EXCLI J* (2015) 14:48–58. doi:10.17179/excli2015-586
56. Robert C, Long GV, Brady B, Dutriaux C, Maio M, Mortier L, et al. Nivolumab in previously untreated melanoma without BRAF mutation. *N Engl J Med* (2015) 372:320–30. doi:10.1056/NEJMoa1412082
57. Powles T, Eder JP, Fine GD, Braiteh FS, Loriot Y, Cruz C, et al. MPDL3280A (anti-PD-L1) treatment leads to clinical activity in metastatic bladder cancer. *Nature* (2014) 515:558–62. doi:10.1038/nature13904
58. Hodi FS, O'Day SJ, McDermott DF, Weber RW, Sosman JA, Haanen JB, et al. Improved survival with ipilimumab in patients with metastatic melanoma. *N Engl J Med* (2010) 363:711–23. doi:10.1056/NEJMoa1003466
59. Nakano T, Oka K, Takahashi K, Morita S, Arai T. Roles of Langerhans cells and T-lymphocytes infiltrating cancer tissues in patients treated by radiation therapy for cervical cancer. *Cancer* (1992) 70:2839–44. doi:10.1002/1097-0142(19921215)70:12<2839:AID-CNCR2820701220>3.0.CO;2-7
60. Nakano T, Oka K, Hanba K, Morita S. Intratumoral administration of sizofiran activates Langerhans cell and T-cell infiltration in cervical cancer. *Clin Immunol Immunopathol* (1996) 79:79–86. doi:10.1006/clin.1996.0053
61. Suzuki Y, Mimura K, Yoshimoto Y, Watanabe M, Ohkubo Y, Izawa S, et al. Immunogenic tumor cell death induced by chemoradiotherapy in patients with esophageal squamous cell carcinoma. *Cancer Res* (2012) 72:3967–76. doi:10.1158/0008-5472.CAN-12-0851
62. Yoshimoto Y, Oike T, Okonogi N, Suzuki Y, Ando K, Sato H, et al. Carbon-ion beams induce production of an immune mediator protein, high mobility group box 1, at levels comparable with X-ray irradiation. *J Radiat Res* (2015) 56:509–14. doi:10.1093/jrr/rrv007
63. Friedman AA, Letai A, Fisher DE, Flaherty KT. Precision medicine for cancer with next-generation functional diagnostics. *Nat Rev Cancer* (2015) 15:747–56. doi:10.1038/nrc4015
64. Okayama H, Schetter AJ, Ishigame T, Robles AI, Kohno T, Yokota J, et al. The expression of four genes as a prognostic classifier for stage I lung

adenocarcinoma in 12 independent cohorts. *Cancer Epidemiol Biomarkers Prev* (2014) 23:2884–94. doi:10.1158/1055-9965.EPI-14-0182
65. Wikoff WR, Hanash S, DeFelice B, Miyamoto S, Barnett M, Zhao Y, et al. Diacetylspermine is a novel prediagnostic serum biomarker for non-small-cell lung cancer and has additive performance with pro-surfactant protein B. *J Clin Oncol* (2015) 33:3880–6. doi:10.1200/JCO.2015.61.7779
66. Mathé EA, Patterson AD, Haznadar M, Manna SK, Krausz KW, Bowman, et al. Noninvasive urinary metabolomic profiling identifies diagnostic and prognostic markers in lung cancer. *Cancer Res* (2014) 74:3259–70. doi:10.1158/0008-5472.CAN-14-0109
67. Roadmap Epigenomics Consortium, Kundaje A, Meuleman W, Ernst J, Bilenky M, Yen A, et al. Integrative analysis of 111 reference human epigenomes. *Nature* (2015) 518:317–30. doi:10.1038/nature14248
68. Tamaki T, Iwakawa M, Ohno T, Imadome K, Nakawatari M, Sakai M, et al. Application of carbon-ion beams or gamma-rays on primary tumors does not change the expression profiles of metastatic tumors in an in vivo murine model. *Int J Radiat Oncol Biol Phys* (2009) 74:210–8. doi:10.1016/j.ijrobp.2008.12.078
69. Nakano T, Oka K. Differential values of Ki-67 index and mitotic index of proliferating cell population: an assessment of cell cycle and prognosis in radiation therapy for cervical cancer. *Cancer* (1993) 72:2401–8. doi:10.1002/1097-0142(19931015)72:8<2401:AID-CNCR2820720818>3.0.CO;2-D
70. Britton S, Coates J, Jackson SP. A new method for high-resolution imaging of Ku foci to decipher mechanisms of DNA double-strand break repair. *J Cell Biol* (2013) 202:579–95. doi:10.1083/jcb.201303073
71. Matsuo M, Matsumoto S, Mitchell JB, Krishna MC, Camphausen K. Magnetic resonance imaging of the tumor microenvironment in radiotherapy: perfusion, hypoxia, and metabolism. *Semin Radiat Oncol* (2014) 24:210–7. doi:10.1016/j.semradonc.2014.02.002

Conflict of Interest Statement: The authors declare that the research was conducted in the absence of any commercial or financial relationships that could be construed as a potential conflict of interest.

Copyright © 2016 Oike, Sato, Noda and Nakano. This is an open-access article distributed under the terms of the Creative Commons Attribution License (CC BY). The use, distribution or reproduction in other forums is permitted, provided the original author(s) or licensor are credited and that the original publication in this journal is cited, in accordance with accepted academic practice. No use, distribution or reproduction is permitted which does not comply with these terms.

frontiers in Oncology

ORIGINAL RESEARCH
published: 13 June 2016
doi: 10.3389/fonc.2016.00137

Comparison of Individual Radiosensitivity to γ-Rays and Carbon Ions

*Grace Shim[1], Marie Delna Normil[1], Isabelle Testard[2], William M. Hempel[1], Michelle Ricoul[1] and Laure Sabatier[1]**

[1] Commissariat à l'Energie Atomique (CEA), DRF/PROCyTOX, Fontenay-aux-Roses, France, [2] CEA Grenoble, Laboratoire de Chimie et Biologie des Métaux, BIG, DRF, Grenoble, France

Carbon ions are an up-and-coming ion species, currently being used in charged particle radiotherapy. As it is well established that there are considerable interindividual differences in radiosensitivity in the general population that can significantly influence clinical outcomes of radiotherapy, we evaluate the degree of these differences in the context of carbon ion therapy compared with conventional radiotherapy. In this study, we evaluate individual radiosensitivity following exposure to carbon-13 ions or γ-rays in peripheral blood lymphocytes of healthy individuals based on the frequency of ionizing radiation (IR)-induced DNA double strand breaks (DSBs) that was either misrepaired or left unrepaired to form chromosomal aberrations (CAs) (simply referred to here as DSBs for brevity). Levels of DSBs were estimated from the scoring of CAs visualized with telomere/centromere-fluorescence *in situ* hybridization (TC-FISH). We examine radiosensitivity at the dose of 2 Gy, a routinely administered dose during fractionated radiotherapy, and we determined that a wide range of DSBs were induced by the given dose among healthy individuals, with highly radiosensitive individuals harboring more IR-induced breaks in the genome than radioresistant individuals following exposure to the same dose. Furthermore, we determined the relative effectiveness of carbon irradiation in comparison to γ-irradiation in the induction of DSBs at each studied dose (isodose effect), a quality we term "relative dose effect" (RDE). This ratio is advantageous, as it allows for simple comparison of dose–response curves. At 2 Gy, carbon irradiation was three times more effective in inducing DSBs compared with γ-irradiation (RDE of 3); these results were confirmed using a second cytogenetic technique, multicolor-FISH. We also analyze radiosensitivity at other doses (0.2–15 Gy), to represent hypo- and hyperfractionation doses and determined that RDE is dose dependent: high ratios at low doses, and approaching 1 at high doses. These results could have clinical implications as IR-induced DNA damage and the ensuing CAs and genomic instability can have significant cellular consequences that could potentially have profound implications for long-term human health after IR exposure, such as the emergence of secondary cancers and other pathobiological conditions after radiotherapy.

Keywords: individual radiosensitivity, carbon ions, radiotherapy, relative biological effect, linear energy transfer, isodose effect

OPEN ACCESS

Edited by:
Marco Durante, GSI, Germany

Reviewed by:
Kevin Prise, Queen's University Belfast, UK
Susan M. Bailey, Colorado State University, USA
Michael Cornforth, University of Texas Medical Branch, USA

****Correspondence:***
Laure Sabatier
laure.sabatier@cea.fr

Specialty section:
This article was submitted to Radiation Oncology, a section of the journal Frontiers in Oncology

Received: *02 February 2016*
Accepted: *23 May 2016*
Published: *13 June 2016*

Citation:
Shim G, Normil MD, Testard I, Hempel WM, Ricoul M and Sabatier L (2016) Comparison of Individual Radiosensitivity to γ-Rays and Carbon Ions. Front. Oncol. 6:137. doi: 10.3389/fonc.2016.00137

INTRODUCTION

Current radiotherapy regimens use photons or protons for the treatment of a plethora of malignancies. However, as ionizing radiation (IR) of high linear energy transfer (LET) may potentially offer radiobiological advantages over low LET IR due to their inherent physical dose distribution characteristics, cancer radiotherapy is now shifting to the use of high-LET heavier ion species (1). Low LET IR (e.g., X- and γ-rays) deposits exponentially decreasing amounts of energy, as a function of penetration depth in the target material, in a uniform pattern of distribution. High LET IR, such as heavy ions, on the other hand, are characterized by a relatively low entrance dose in the target material, followed by a pronounced sharp maximum dose near the end of their range called the Bragg peak, and energy close to 0 beyond the Bragg peak. This characteristic of high LET IR is useful especially for the treatment of deep-seated tumors in the human body, as it allows a great amount of energy to be precisely localized at the tumor site when it is placed at the Bragg peak, while minimally exposing the surrounding normal tissues (2).

Among various types of heavy ion species considered for radiotherapy, carbon ions are considered to have the most balanced and optimal properties in terms of physical dose distribution and relative biological effectiveness (RBE) along its Bragg peak curve (3). However, carbon ion radiotherapy is not yet widely used, with only a few centers worldwide (six in Asia and two in Europe) that have treated ~13,000 patients (as of December 2013), compared with ~50 active proton therapy centers worldwide that have treated over 105,000 patients (4). Though preliminary clinical data from the existing carbon ion therapy centers suggest favorable results for many of the malignancies that do poorly with conventional radiotherapy (3), further clinical research and development of more carbon ion (and other charged particles heavier than protons) therapy centers in the US and worldwide are hindered by the lack of sufficient clinical evidence of the benefit of carbon ion therapy over conventional radiotherapy that would cost-effectively justify the establishment of such expensive facilities (1). Further investigation is necessary to characterize and understand how carbon ion therapy works in comparison to conventional radiotherapy.

Clinical outcomes of radiotherapy can be significantly influenced by interindividual variations in sensitivity to IR, which is well established to exist in the general population. Highly radiosensitive patients, for instance, may develop early and/or late side effects due to radiation toxicity, while radioresistant patients may receive an insufficient dose of radiation due to dose limitations in current general radiotherapy protocols. However, current radiotherapy and radiation protection protocols do not take into account the individual variations in radiosensitivity, but rather rely on population averages of radiation responses. Refining these protocols to consider individual radiosensitivity, especially the more radiosensitive and cancer-prone, may help to alleviate the detrimental delayed effects of IR (5–7).

In this study, we evaluate individual radiosensitivity following exposure to carbon-13 ions or γ-rays in peripheral blood lymphocytes (PBL) of healthy blood donors using the telomere/centromere-fluorescence *in situ* hybridization (TC-FISH) technique. TC-FISH, which simultaneously stains telomeres and centromeres using peptide nucleic acid (PNA) probes (8), was shown in a recent study in our laboratory (9) to be a cost-effective method that significantly simplifies and improves the "gold standard" dicentric chromosome (DC) assay, which relies on the manual scoring of DCs following Giemsa staining by trained specialists. The radiosensitivity of each analyzed individual in this analysis was ranked based on the estimation of the frequency of IR-induced DNA double strand breaks (DSBs) that either was misrepaired or left unrepaired to form chromosomal aberrations (CAs). For brevity, we refer to these misrepaired or unrepaired DSBs that generate CAs simply as "DSBs" henceforth. Levels of DSBs were estimated from the scoring of CAs visualized with TC-FISH, including dicentrics, centric and acentric rings, and acentric fragments (with 0, 2, or 4 telomeres). We demonstrated in our previous article (9) that this modified scoring technique provides improved sensitivity compared with the classical DC analyses. Additionally, as presented in this same paper, we developed a novel automated system (TCScore) that can perform these TC-FISH analyses with the same efficacy as manual scoring, but in a fraction of time; this improved, automated approach will open up new horizons for the assessment of genotoxic risk and for biological dosimetry, particularly for low doses.

We examine radiosensitivity at the dose of 2 Gy, a routinely administered dose during fractionated radiotherapy (10, 11), and at other doses (0.2–15 Gy), to represent hypo- and hyperfractionation doses. As we are particularly interested in comparing the levels of biological effect (misrepaired or unrepaired DNA DSBs generating CAs in this case) at a particular dose of carbon irradiation compared with the same dose of γ-irradiation (isodose effect), we also define a quality we term "relative dose effect" (RDE). This ratio is advantageous as it allows for simple comparison of dose–response curves.

RESULTS

Individual Radiosensitivity Following Exposure to 2 Gy of γ-Rays

Individuals in this cohort of 18 healthy blood donors were first ranked in the order of increasing radiosensitivity based on the mean number of IR-induced DSBs (i.e., misrepaired or unrepaired DSBs that generated CAs) per cell following *in vitro* exposure of isolated PBL to 2 Gy of low LET γ-rays. The mean number of DSBs per cell was calculated based on the scoring of CAs following TC-FISH staining, as described in **Figures 1A,B**, in cells undergoing first mitosis at 60 h postirradiation. As shown in **Figure 2A**, individuals were designated as Donors A through R in this order of "radioresistant" to "radiosensitive" donors. We use this ranking throughout the study as the definition of each of these donors' radiosensitivity.

Following exposure to a dose of 2 Gy of γ-irradiation, there was a range of ~1.5–2.8 DSBs per cell (1.8-fold difference), and a mean of 2.17 DSBs per cell in the PBL samples. Comparison of data obtained from samples irradiated on different dates and analyzed by different individuals showed no significant differences in the measurement of the mean number of DSBs per donor ($p > 0.05$).

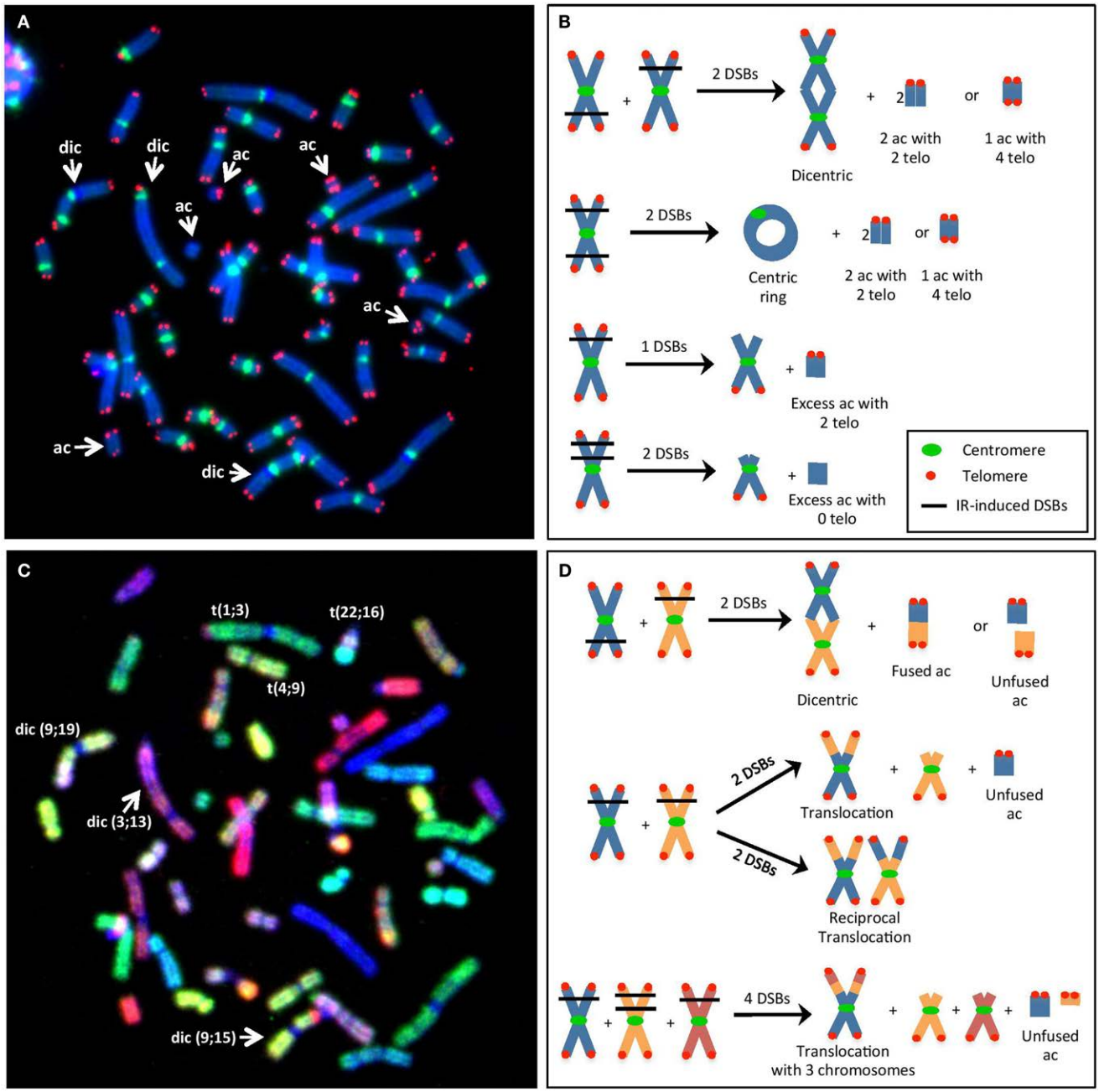

FIGURE 1 | **(A)** Visualization of IR-induced dicentric chromosomes (dic) and other chromosomal aberrations (CAs), such as acentric fragments (ac), using telomere/centromere-fluorescence *in situ* hybridization (TC-FISH). This image shows 3 dic and 5 ac [3 with 4 telomeres (telo), 1 with 2 telo, 1 with 0 telo]. **(B)** Examples of the method used to estimate the number of IR-induced DSBs per cell (i.e., misrepaired or unrepaired DSBs that generated CAs) using TC-FISH. A dic or a centric ring with an ac containing four telo was considered as two DSBs. Excess ac with two telomeres was considered as resulting from one DSB that failed to rejoin (terminal deletion). Excess ac with 0 telomeres were considered as resulting from 2 DSBs (interstitial deletion). Note that these sample images of chromosomes are not an analysis of **(A)**, and lines denoting DSBs from IR interactions are not necessary from traversal with the same IR track. **(C)** Visualization of IR-induced translocations using M-FISH. This image shows the same metaphase as in **(A)**. Each chromosome involved in the dic and ac can be identified. Furthermore, three additional translocations can be observed that was not able to be visualized using the TC-FISH technique. **(D)** Examples of the method used to estimate the number of IR-induced DSBs (i.e., misrepaired or unrepaired DSBs that generated CAs) using M-FISH. Dic or translocations involving two chromosomes often involve two DSBs, whereas more complex rearrangements with three chromosomes may involve four DSBs. Note that these sample images of chromosomes are not an analysis of **(C)**, and lines denoting DSBs from IR interactions are not necessary from traversal with the same IR track.

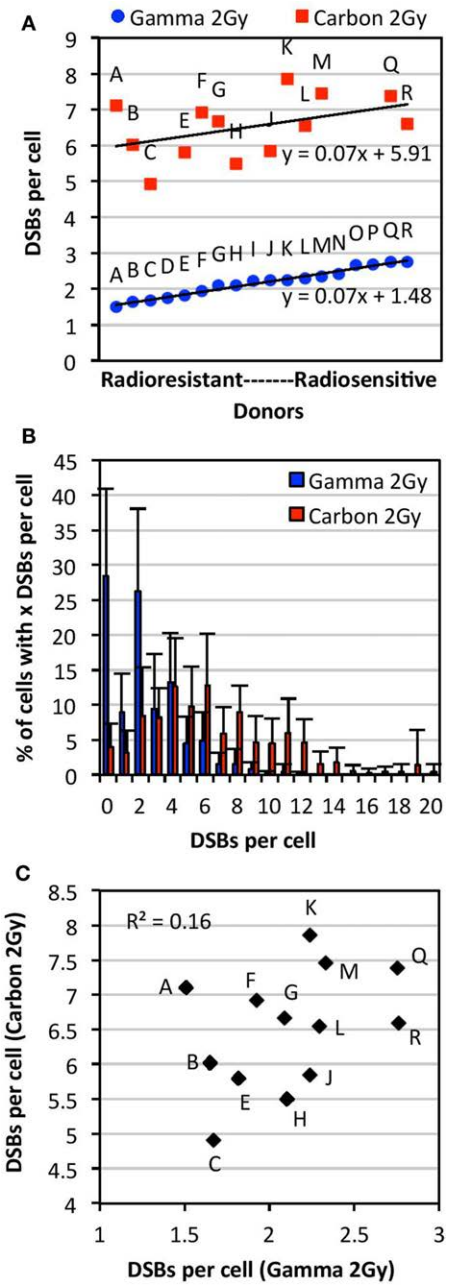

FIGURE 2 | Comparison of individual radiosensitivity following exposure to 2 Gy of either carbon-13 ions (75 MeV/u; LET ~36.5 keV/μm at the plateau region of the Bragg peak curve) or γ-rays. Individual radiosensitivity was evaluated in peripheral blood lymphocytes (PBL) of healthy blood donors in cells undergoing first mitosis at 60 h postirradiation; radiosensitivity of each individual was ranked using the TC-FISH technique based on the estimation of the frequency of IR-induced DNA DSBs (i.e., misrepaired or unrepaired DSBs that generated CAs), estimated as shown in **Figure 1B**. **(A)** Ranking of individual radiosensitivity to 2 Gy of carbon ions and γ-rays. Individuals were designated as Donors A ("radioresistant") through R ("radiosensitive") based on the order of increasing radiosensitivity following γ-irradiation. **(B)** Distribution of the number of DSBs per cell for each type of IR for all donors analyzed. **(C)** No correlations between individual radiosensitivity following *in vitro* exposure to 2 Gy of carbon ions and γ-rays (R^2 = 0.16).

Donors classified as more radiosensitive harbored more DSBs per cell, with a wider range of distribution of DSBs per cell, compared with the more radioresistant donors (Figure S1 in Supplementary Material). For example, the mean of the range of DSBs per cell in radioresistant donors (Donors A through F) was found to be 9.0 compared with 12.5 in radiosensitive donors (Donors M through R). This indicates the presence of more IR-induced damage in radiosensitive donors compared with radioresistant donors following exposure to a dose of 2 Gy of γ-rays.

No correlations were observed between this radiosensitivity and levels of spontaneous or IR-induced apoptosis (0–6 Gy; data not shown). Furthermore, no correlations were found (R^2 = 0.045; data not shown) between radiosensitivity to 2 Gy of γ-irradiation and the susceptibility to IR-induced apoptosis in the T4-EM subpopulation (measured as the slope of IR-induced apoptosis in T4-EM lymphocytes between the doses of 0 and 6 Gy of γ-irradiation), as previously described (12). Radiosensitivity may be moderately correlated with interindividual variability in the induction of global γH2AX fluorescence at 30 min postirradiation (R^2 = 0.595), but not at later time points postirradiation (3–24 h); global γH2AX fluorescence data of this cohort of PBL were previously published (13).

Individual Radiosensitivity Following Exposure to 2 Gy of Carbon Ions

Individual radiosensitivity following *in vitro* exposure to 2 Gy of high LET carbon-13 ions (75 MeV/u; LET ~36.5 keV/μm at the plateau region of the Bragg peak curve) was measured in PBL of 13 of the healthy blood donors analyzed for γ-irradiation above in cells undergoing first mitosis at 60 h postirradiation.

As shown in **Figure 2A**, interindividual differences in radiosensitivity was also observed following carbon irradiation, a range of ~5–8 DSB per cell was measured (1.6-fold difference), and a mean of 6.45 DSBs per cell in the PBL samples. As with γ-irradiation, radiosensitivity was not correlated with apoptosis and global γH2AX fluorescence (data not shown). Based on the ranking of increasing radiosensitivity following carbon irradiation, we find that the more radiosensitive donors to carbon irradiation harbored more DSBs per cell compared with the more radioresistant donors (Figure S2 in Supplementary Material); for example, the mean of the range of DSBs per cell in radioresistant donors (Donors C, H, E, and J) was found to be 14.8 compared with 19.8 in radiosensitive donors (Donors F, A, Q, M, and K).

No Correlations between Radiosensitivity to 2 Gy of γ-Rays and Carbon Ions

Comparison of radiosensitivity to carbon irradiation and γ-irradiation at the dose of 2 Gy showed a different order of increasing radiosensitivity within this cohort, as illustrated in **Figure 2A**. Indeed, the order of low to high radiosensitivity as classified according to 2 Gy of γ-irradiation did not hold for carbon irradiation following exposure to the same dose (**Figure 2A**). This indicates that donors are not equally sensitive to different types of IR. Interestingly, though the ranking of radiosensitivity to carbon ions and γ-rays was different within this cohort, the trend lines for radiosensitivity to each type of IR (plotted in the

order of increasing radiosensitivity to γ-rays) were parallel, both with a slope of 0.07. Notably, a high intracellular variability of IR-induced DSB among cells of the same donor was observed (data not shown). Intracellular variations following carbon irradiation were generally found to be larger than those following γ-irradiation. This may be expected due to the non-uniform spatial distribution of IR-induced DNA damage following heavy ion irradiation. A modest correlation was found between the dispersion of DSBs per donor (95% confidence interval) following γ- and carbon irradiation ($R^2 = 0.51$). As expected, carbon irradiation causes more dispersion in the number of DSBs induced per cell compared with γ-irradiation, with carbon ranging to up to 20 DSBs per cell and γ-rays ranging up to 12 DSBs (**Figure 2B**). This indicates that carbon irradiation causes a larger range of DSBs per cell and more IR damage that is less repaired compared with γ-rays. As shown in **Figure 2C**, we find that there are no correlations between radiosensitivity to carbon ions and γ-rays at the dose of 2 Gy ($R^2 = 0.16$).

RDE Factor of 3 after 2 Gy Irradiation Using Both TC-FISH and M-FISH Techniques

In this study, as we are particularly interested in the differences in the effectiveness of induction of DSBs (i.e., misrepaired or unrepaired DSBs that generated CAs) by carbon irradiation compared with γ-irradiation at a given dose (isodose effect), we define a new ratio, termed RDE, calculated simply by dividing the mean DSBs per cell determined using TC-FISH following exposure to carbon ions by that following exposure to the same dose of γ-rays. This ratio differs from the usual metric RBE (defined as the ratio of doses that produce an iso-effect) and is advantageous, as it allows for simple comparison of dose–response curves.

At the dose of 2 Gy, the mean number of DSBs per cell was found to be 2.17 DSB per cell after γ-irradiation (18 donors, as described in Section "Individual Radiosensitivity Following Exposure to 2 Gy of γ-Rays") and 6.45 DSB after carbon irradiation (13 donors, as described in Section "Individual Radiosensitivity Following Exposure to 2 Gy of Carbon Ions"). Therefore, the RDE of carbon ions was determined to be ~3 times that of γ-rays at the dose of 2 Gy using TC-FISH. The RBE at 2 Gy was found to be 2.6.

Relative dose effect results were confirmed using M-FISH analysis of chromosomal rearrangements, visualized as illustrated in **Figure 1C**. The number of DSBs per cell using M-FISH analysis was calculated, as illustrated in **Figure 1D**. At the dose of 2 Gy, M-FISH analyses in four donors (Donors A, C, L, and R) indicated 3.26 DSBs per cell after γ-irradiation and 9.81 DSBs per cell following carbon irradiation. As M-FISH is a more detailed analysis of chromosomal damage compared with TC-FISH (since M-FISH allows analysis of translocations, which are not visible with TC-FISH), it is expected that more DSBs per cell be calculated using M-FISH than using TC-FISH. However, as both techniques give an RDE factor of 3 at the dose of 2 Gy, the determination of RDE factor of carbon compared with γ-rays is independent of the method of scoring chromosomal damage. Thus, TC-FISH and M-FISH can be considered to be two alternative approaches for scoring chromosomal damage.

Based on these results, we propose that the TC-FISH technique is more practical for rapid assessment of genotoxic risk and for radiation dosimetry, as M-FISH is both expensive and time consuming in terms of hybridization technique and analysis compared with TC-FISH.

RDE at Other Doses: High RDE at Low Doses

To determine RDE at other doses, we compare mean DSBs per cell determined using TC-FISH following exposure to a range of doses (0.2–15 Gy) of carbon ions and γ-rays in a subset of the PBL of the healthy blood donors analyzed above. For γ-irradiation at all doses except for 2 Gy (which is the average of 18 donors; data in **Figure 2A**), the mean DSBs per cell represent the average of six donors (Donors C, F, H, J, K, and O). For carbon irradiation at all doses except for 2 Gy (which is the average of 13 donors; data in **Figure 2A**), the mean DSBs per cell represent the average of four donors (Donors G, H, K, and M).

Figure 3A shows a plot of the dose (0–5 Gy) of γ- or carbon irradiation and the mean number of DSBs per cell averaged for all donors analyzed. This plot indicated second order polynomial trends between the doses of 0 and 5 Gy for both IR types. This plot was expanded to doses of up to 15 Gy in **Figure 3B**, which shows data for the frequency of DSBs per cell (averaged for all donors analyzed) at each dose with the exact mean indicated above each bar. Error bars in **Figures 3A,B** represent the SD of the frequencies of DSBs per cell among the averaged donors, illustrating interindividual variations in radiosensitivity at various doses. RDE factors shown in **Figure 3C** were calculated by dividing the mean DSBs per cell following a dose of carbon irradiation by the mean DSBs per cell following the same dose of γ-irradiation (values shown in **Figure 3B**). The RDE factor is dose dependent, with high RDE factors at low doses (0.2 and 0.5 Gy), and an RDE factor approaching 1 at high doses (10 and 15 Gy).

DISCUSSION

In this study, we demonstrate that following *in vitro* irradiation with carbon ions or γ-rays at the dose of 2 Gy, a routinely administered dose during fractionated radiotherapy (10, 11), interindividual differences in radiosensitivity (measured in terms of misrepaired or unrepaired IR-induced DNA DSBs that led to the formation of CAs) exist in healthy individuals. In other words, a given dose of IR can induce a wide range of DNA damage among healthy individuals, with highly radiosensitive individuals harboring more IR-induced damage in the genome than radioresistant individuals following exposure to the same IR dose. These results could have important clinical implications as IR-induced DNA damage and the ensuing CAs and genomic instability can have significant cellular consequences that could potentially have profound implications for long-term human health after IR exposure, such as the emergence of secondary cancers and other pathobiological conditions after radiotherapy (14–16). A fast and reliable clinical method to measure radiosensitivity of cancer patients and/or predict radiotherapy toxicity (especially to identify hyper-radiosensitive individuals) would permit personalized

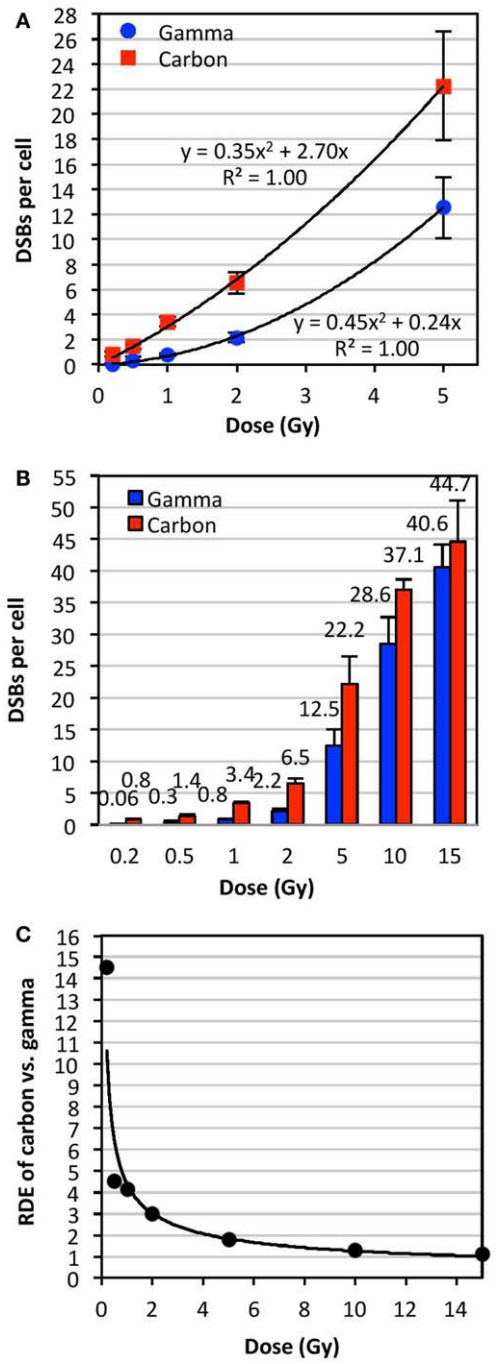

FIGURE 3 | **Relative dose effect (RDE) of carbon-13 ions (75 MeV/u; LET ~36.5 keV/μm at the plateau region of the Bragg peak curve) versus γ-rays at various doses**. We define RDE to be the ratio of biological effect at a given dose (isodose effect). The mean number of DSBs per cell was determined using TC-FISH as illustrated in **Figure 1B**, and dose–response curves were plotted for doses of up to **(A)** 5 Gy and **(B)** 15 Gy. The mean DSBs per cell for all donors analyzed are indicated above each bar in **(B)**. Error bars represent the SD of the frequencies of DSBs per cell among the donors. **(C)** RDE of carbon ion versus γ-rays as a function of dose.

radiotherapy treatment; however, such a method still remains to be established (17–20).

It is well established that radiosensitivity is closely linked to intrinsic, genetically determined differences in cellular responses to IR-induced damage, particularly the repair of DNA DSBs (7). In our previously published paper (13), we have demonstrated, in this same cohort of PBL from healthy individuals, a high level of interindividual variability in the induction and kinetics of γH2AX, an important DNA damage response (DDR) protein that facilitates the efficient repair of DSBs, following γ-irradiation; this variability, measured using global immunofluorescence microscopy and confirmed with flow cytometry, was found to increase with dose and diminish with repair time, in accordance with previously published observations (21–24). This finding supports the notion that these individuals vary in their DDR capacities. However, in this study, we show a moderate correlation between radiosensitivity and global γH2AX fluorescence at 30 min postirradiation ($R^2 = 0.595$), but no correlations at later time points postirradiation (3–24 h). These moderate to lack of correlations between radiosensitivity and γH2AX levels could be due to the rapid time-dependent changes in γH2AX levels postirradiation. Furthermore, the lack of correlation that we have observed between sensitivity to carbon and γ-irradiation may indicate that individuals may not be equally capable of repairing the different types of DNA damage induced by low LET and high LET IR. Indeed, high LET IR causes more *clustered* DNA DSBs and higher frequencies of complex chromosomal aberrations (CCAs) that may be less likely to be repaired correctly compared with equivalent doses of low LET IR (25–29).

Our results demonstrate that the yield of IR-induced DSBs fits a polynomial curve very close to linearity, in agreement with previous reports of upward curvature, especially following high LET IR (29, 30). We showed that RDE is dose dependent, with high RDE at low doses (0.2 and 0.5 Gy), and approaching 1 at high doses (10 and 15 Gy). This may indicate that the biological effectiveness of carbon at low doses, such as in surrounding tissue of the primary site of irradiation, may be significantly underestimated: IR exposure may be more harmful than expected. On the other hand, at very high doses per fraction, such as in hypofractionated radiotherapy schemes, biological effectiveness may be significantly overestimated. These results may be important to consider for carbon radiotherapy.

In this study, we have found that TC-FISH and M-FISH are two complementary methods for the scoring of DSBs and RDE determination at the dose of 2 Gy, as carbon ions caused three times more DSBs per cell compared with γ-irradiation with both techniques with this dose. We have recently further improved the speed of the TC-FISH technique and analysis in our laboratory with the development of a semi-automated software (TCScore) that is able to detect IR-induced CAs (dicentrics, rings, acentrics with 4, 2, 0 telomeres) with the same efficacy as manual scoring in a fraction of time (9). This software provides automated analysis of three-channel (RGB) images (red, green, and blue channels containing telomere, centromere, and

DAPI DNA staining information, respectively) split into their individual channels by any image processing software (e.g., Image J) and generates an intuitive and interactive report of CA classes that can be reviewed and corrected in batches by an investigator. This improved, automated approach will open up new horizons for the assessment of genotoxic risk for clinical uses (e.g., radiosensitivity assessment before radiotherapy) and for biological dosimetry following accidental exposure, particularly for low doses (9, 31). However, in order for these techniques to be used in the clinics for determining intrinsic individual radiosensitivity, analyses of a larger cohort of healthy individuals are needed to well establish the degree of variations within the whole human population.

Meanwhile, the M-FISH technique has been shown to be a powerful tool for detailed analyses of translocations and CCAs in the whole genome at very low to high doses of IR exposure, as it allows all chromosomal homolog pairs to be differentiated (32, 33). It was shown to be sensitive enough to detect translocations and other CAs at doses as low as 0.1 Gy of low LET IR (34). Though the long-term stability of translocations and the usefulness of this technique was recently validated (35), M-FISH analysis is laborious, time consuming (~5 days to obtain results), and expensive; standardization and automation will be key to improving the practical significance of FISH-based translocation assays. Furthermore, the frequencies of translocations at baseline and their persistence postirradiation at various doses, as well as potential interindividual variability in their levels, need to be further characterized, especially in the low dose range (36). Such data would be valuable for studying the long-term health risk of IR exposure and may generally contribute to understanding the link between CAs and human diseases and cancer (37).

In conclusion, it is evident that individual radiosensitivity exists among healthy individuals following irradiation with carbon ions and γ-rays, and individuals may not be equally sensitive to different types of IR. Furthermore, the RDE of carbon compared with γ-rays could be dose dependent, illustrating the complexity of the biological responses to IR. We propose that the calculation of IR-induced DSBs (i.e., misrepaired or unrepaired DSBs that generated CAs) using TC-FISH may be a sensitive and reliable approach to measuring individual radiosensitivity. The ability to rank and predict individual radiosensitivity has a wide range of real-world applications, as it directly impacts the formulation of cancer treatment strategies and the establishment of radiation protection guidelines. Refining radiotherapy and radiation protection protocols to consider individual radiosensitivity, especially the more radiosensitive and cancer-prone, may help to alleviate the detrimental delayed effects of IR.

MATERIALS AND METHODS

Cell Culture

Peripheral blood lymphocytes used in this study were isolated from the whole blood of 18 healthy blood donors (with negative viral status) from the Center of Blood Transfusions using the standard Ficoll isolation technique. Individuals included in this cohort were selected from a larger cohort of 63 individuals along the range of radiosensitivity measured previously based on the induction of IR-induced apoptosis (38); all analyses, however, were performed blindly. After isolation, lymphocytes were frozen in liquid nitrogen (−196°C) until use. Lymphocytes were unfrozen 24 h before irradiation and incubated at 37°C in an atmosphere of 5% CO_2 in RPMI 1640 medium (Gibco) supplemented with 20% fetal bovine serum (FBS; Eurobio) and antibiotics (penicillin/streptomycin; Gibco).

Irradiation

Peripheral blood lymphocytes were irradiated at various doses at room temperature (RT) with γ-rays from a Cesium-137 source at the CEA Fontenay-aux-Roses, France (dose-rate of 2 Gy/min).

Carbon-13 ($^{13}C^{6+}$) irradiations were performed on the Grand Accélérateur National d'Ions Lours GANIL (Caen, France) D1 high energy line (IRRABAT beam line) with energy of 75 MeV/u; details of dosimetry and other specifications were previously published (39). Lymphocytes were irradiated in small tubes with a glass wall of 2 mm thickness. Samples were irradiated at the plateau region of the Bragg peak curve; the mean LET at the sample was estimated to be ~36.5 keV/μm. The dosimetry was realized with the assistance of CIMAP–CIRIL physicists using a Faraday cup and an X-ray detector (5 μm stainless steel foil and photomultiplier). The photons emitted after traversal of the foil by the accelerated ions were counted, and a correlation at low fluences/doses was established with the real ion tracks measured on CR39 tracks detectors $(C_{12}H_{18}O_7)_n$. After exposure to the beam, the ion tracks in the CR39 were chemically etched for 8–12 min in 12 N KOH at 80°C. Several microscope fields were photographed using an Olympus Vanox-S, ×100, equipped with a Cohn Pieper FK-7512-Q video camera. The tracks were then counted using a homemade image analysis application from the Aphelion® software. X-ray detector doses were also subsequently correlated with the doses measured with an ionizing chamber (Unidos 23332 or 23344, PTW Freiburg, Germany, depending on the ion atomic number and its track length) for further verification of the dose/fluence ratio. The ionizing chamber was not used as reference dosimeter for the sample irradiations, since it was designed for measuring photon fluxes (utilized in radiotherapy).

Chromosome Preparation, Staining, and Image Acquisition

Peripheral blood lymphocytes were cultured for 60 h postirradiation, and metaphase preparations were performed using standard procedures (40). Slides with metaphase spreads were stored in −20°C until use, and were unfrozen and left at RT overnight before use.

For TC-FISH analysis, telomeres and centromeres were stained, as previously described (9) using telomere-specific Cyanine3-labeled PNA probes and centromere-specific FITC-labeled PNA probes (both from Panagene, Daejon, South Korea).

For M-FISH analysis, slides were hybridized with a 24XCyte mFISH kit (MetaSystems Altlussheim, Germany) according to the protocol recommended by the manufacturer.

After counterstaining of the DNA with 4′,6-diamidino-2-phenylindole (DAPI), slides were mounted with coverslips with PPD (1 mg/mL *p*-phenylenediamine-90% glycerol-10% PBS) and stored in a dark box at −4°C until automated image acquisition using the MetaSystems AutoCapt software. Images of metaphase cells were acquired with a charge-coupled device camera (Zeiss, Thornwood, NY, USA) coupled with a Zeiss Axioplan microscope. CAs were scored manually using the MetaSystems ISIS software.

Analysis of Chromosomal Aberrations

In this study, radiosensitivity was measured based on the mean number of IR-induced DSBs per cell (i.e., misrepaired or unrepaired DSBs that generated CAs) following TC-FISH staining (**Figure 1A**) in cells undergoing first mitosis at 60 h postirradiation. DSBs were calculated based on the manual scoring of CAs, as described in Ref. (9) and in **Figure 1B**. Based on the frequencies of dicentrics, centric and acentric rings, and acentric fragments (with 0, 2, or 4 telomeres), a precise estimate of the number of IR-induced DSBs that gave rise to the CA can be calculated at the studied doses, as illustrated in **Figure 1B**. Generally, a dicentric or a centric ring with an acentric fragment containing four telomeres are considered as two DSBs; excess acentric fragments with two telomeres are considered as resulting from one DSB (terminal deletion); and excess acentric fragments with 0 telomeres are considered as resulting from two DSBs (interstitial deletion).

Following M-FISH staining (**Figure 1C**), the number of DSBs per cell can be calculated based on the visualization of chromosomal rearrangements (that are not visible with TC-FISH). Examples are illustrated in **Figure 1D**; in general, dicentrics and translocations involving two chromosomes often involve two DSBs, whereas more complex rearrangements with three chromosomes may involve four DSBs.

AUTHOR CONTRIBUTIONS

GS analyzed and interpreted the data and drafted the manuscript. MN, IT, and MR worked to design, acquire, and analyze the data. WH aided in the interpretation of the data and edited the manuscript. LS directed the course of this study. All authors provided critiques for the content of the manuscript, approved of the final version of the manuscript, and attest to the accuracy and integrity of this work.

ACKNOWLEDGMENTS

The authors gratefully thank Andrea Ottolenghi for his valuable discussions.

FUNDING

This work was supported by grants from the European Community's Seventh Framework Program (EURATOM) contract Fission-2011-249689 (DOREMI) and from the CEA-NRBC.

SUPPLEMENTARY MATERIAL

The Supplementary Material for this article can be found online at http://journal.frontiersin.org/article/10.3389/fonc.2016.00137

REFERENCES

1. Schlaff CD, Krauze A, Belard A, O'Connell JJ, Camphausen KA. Bringing the heavy: carbon ion therapy in the radiobiological and clinical context. *Radiat Oncol* (2014) 9(1):88. doi:10.1186/1748-717X-9-88
2. Hall EJ. *Radiobiology for the Radiologist*. Philadelphia: Lippincott Williams & Wilkins (2006).
3. Kamada T, Tsujii H, Blakely EA, Debus J, De Neve W, Durante M, et al. Carbon ion radiotherapy in Japan: an assessment of 20 years of clinical experience. *Lancet Oncol* (2015) 16(2):e93–100. doi:10.1016/S1470-2045(14)70412-7
4. Jermann M. Particle therapy statistics in 2013. *Int J Part Ther* (2014) 1(1):40–3. doi:10.14338/IJPT.14-editorial-2.1
5. Granzotto A, Joubert A, Viau M, Devic C, Maalouf M, Thomas C, et al. [Individual response to ionising radiation: what predictive assay(s) to choose?]. *C R Biol* (2011) 334(2):140–57. doi:10.1016/j.crvi.2010.12.018
6. Joubert A, Vogin G, Devic C, Granzotto A, Viau M, Maalouf M, et al. [Radiation biology: major advances and perspectives for radiotherapy]. *Cancer Radiother* (2011) 15(5):348–54. doi:10.1016/j.canrad.2011.05.001
7. Advisory Group on Ionising Radiation. Human radiosensitivity. *Report of the Independent Advisory Group on Ionising Radiation*. Chilton: Health Protection Agency (2013).
8. Shi L, Fujioka K, Sun J, Kinomura A, Inaba T, Ikura T, et al. A modified system for analyzing ionizing radiation-induced chromosome abnormalities. *Radiat Res* (2012) 177(5):533–8. doi:10.1667/RR2849.1
9. M'Kacher R, Maalouf EE, Ricoul M, Heidingsfelder L, Laplagne E, Cuceu C, et al. New tool for biological dosimetry: reevaluation and automation of the gold standard method following telomere and centromere staining. *Mutat Res* (2014) 770(0):45–53. doi:10.1016/j.mrfmmm.2014.09.007
10. Denekamp J, Waites T, Fowler JF. Predicting realistic RBE values for clinically relevant radiotherapy schedules. *Int J Radiat Biol* (1997) 71(6):681–94. doi:10.1080/095530097143699
11. Hartel C, Nikoghosyan A, Durante M, Sommer S, Nasonova E, Fournier C, et al. Chromosomal aberrations in peripheral blood lymphocytes of prostate cancer patients treated with IMRT and carbon ions. *Radiother Oncol* (2010) 95(1):73–8. doi:10.1016/j.radonc.2009.08.031
12. Schmitz A, Bayer J, Dechamps N, Goldin L, Thomas G. Heritability of susceptibility to ionizing radiation-induced apoptosis of human lymphocyte subpopulations. *Int J Radiat Oncol Biol Phys* (2007) 68(4):1169–77. doi:10.1016/j.ijrobp.2007.03.050
13. Viau M, Testard I, Shim G, Morat L, Normil MD, Hempel WM, et al. Global quantification of gammaH2AX as a triage tool for the rapid estimation of received dose in the event of accidental radiation exposure. *Mutat Res Genet Toxicol Environ Mutagen* (2015) 793:123–31. doi:10.1016/j.mrgentox.2015.05.009
14. Sabatier L, Lebeau J, Dutrillaux B. Radiation-induced carcinogenesis: individual sensitivity and genomic instability. *Radiat Environ Biophys* (1995) 34(4):229–32. doi:10.1007/BF01209747
15. Raynaud CM, Sabatier L, Philipot O, Olaussen KA, Soria JC. Telomere length, telomeric proteins and genomic instability during the multistep carcinogenic process. *Crit Rev Oncol Hematol* (2008) 66(2):99–117. doi:10.1016/j.critrevonc.2007.11.006
16. Shim G, Ricoul M, Hempel WM, Azzam EI, Sabatier L. Crosstalk between telomere maintenance and radiation effects: a key player in the process of radiation-induced carcinogenesis. *Mutat Res Rev Mutat Res* (2014) 760:1–7. doi:10.1016/j.mrrev.2014.01.001
17. Fernet M, Hall J. Genetic biomarkers of therapeutic radiation sensitivity. *DNA Repair (Amst)* (2004) 3(8–9):1237–43. doi:10.1016/j.dnarep.2004.03.019

18. Andreassen CN, Dikomey E, Parliament M, West CM. Will SNPs be useful predictors of normal tissue radiosensitivity in the future? *Radiother Oncol* (2012) 105(3):283–8. doi:10.1016/j.radonc.2012.11.003
19. Il'yasova D, Kinev A, Melton CD, Davis FG. Donor-specific cell-based assays in studying sensitivity to low-dose radiation: a population-based perspective. *Front Public Health* (2014) 2:244. doi:10.3389/fpubh.2014.00244
20. Mirjolet C, Boidot R, Saliques S, Ghiringhelli F, Maingon P, Crehange G. The role of telomeres in predicting individual radiosensitivity of patients with cancer in the era of personalized radiotherapy. *Cancer Treat Rev* (2015) 41(4):354–60. doi:10.1016/j.ctrv.2015.02.005
21. Hamasaki K, Imai K, Nakachi K, Takahashi N, Kodama Y, Kusunoki Y. Short-term culture and gammaH2AX flow cytometry determine differences in individual radiosensitivity in human peripheral T lymphocytes. *Environ Mol Mutagen* (2007) 48(1):38–47. doi:10.1002/em.20273
22. Ismail IH, Wadhra TI, Hammarsten O. An optimized method for detecting gamma-H2AX in blood cells reveals a significant interindividual variation in the gamma-H2AX response among humans. *Nucleic Acids Res* (2007) 35(5):e36. doi:10.1093/nar/gkl1169
23. Andrievski A, Wilkins RC. The response of gamma-H2AX in human lymphocytes and lymphocytes subsets measured in whole blood cultures. *Int J Radiat Biol* (2009) 85(4):369–76. doi:10.1080/09553000902781147
24. Horn S, Barnard S, Rothkamm K. Gamma-H2AX-based dose estimation for whole and partial body radiation exposure. *PLoS One* (2011) 6(9):e25113. doi:10.1371/journal.pone.0025113
25. Sabatier L, Al Achkar W, Hoffschir F, Luccioni C, Dutrillaux B. Qualitative study of chromosomal lesions induced by neutrons and neon ions in human lymphocytes at G0 phase. *Mutat Res* (1987) 178(1):91–7. doi:10.1016/0027-5107(87)90090-X
26. Testard I, Dutrillaux B, Sabatier L. Chromosomal aberrations induced in human lymphocytes by high-LET irradiation. *Int J Radiat Biol* (1997) 72(4):423–33. doi:10.1080/095530097143194
27. Anderson RM, Marsden SJ, Wright EG, Kadhim MA, Goodhead DT, Griffin CS. Complex chromosome aberrations in peripheral blood lymphocytes as a potential biomarker of exposure to high-LET alpha-particles. *Int J Radiat Biol* (2000) 76(1):31–42. doi:10.1080/095530000138989
28. Testard I, Sabatier L. Assessment of DNA damage induced by high-LET ions in human lymphocytes using the comet assay. *Mutat Res* (2000) 448(1):105–15. doi:10.1016/S0027-5107(00)00006-3
29. Loucas BD, Durante M, Bailey SM, Cornforth MN. Chromosome damage in human cells by gamma rays, alpha particles and heavy ions: track interactions in basic dose-response relationships. *Radiat Res* (2013) 179(1):9–20. doi:10.1667/RR3089.1
30. Loucas BD, Eberle R, Bailey SM, Cornforth MN. Influence of dose rate on the induction of simple and complex chromosome exchanges by gamma rays. *Radiat Res* (2004) 162(4):339–49. doi:10.1667/RR3245
31. M'Kacher R, El Maalouf E, Terzoudi G, Ricoul M, Heidingsfelder L, Karachristou I, et al. Detection and automated scoring of dicentric chromosomes in nonstimulated lymphocyte prematurely condensed chromosomes after telomere and centromere staining. *Int J Radiat Oncol Biol Phys* (2015) 91(3):640–9. doi:10.1016/j.ijrobp.2014.10.048
32. Speicher MR, Gwyn Ballard S, Ward DC. Karyotyping human chromosomes by combinatorial multi-fluor FISH. *Nat Genet* (1996) 12(4):368–75. doi:10.1038/ng0496-368
33. Loucas BD, Cornforth MN. Complex chromosome exchanges induced by gamma rays in human lymphocytes: an mFISH study. *Radiat Res* (2001) 155(5):660–71. doi:10.1667/0033-7587(2001)155[0660:CCEIBG]2.0.CO;2
34. Nieri D, Berardinelli F, Antoccia A, Tanzarella C, Sgura A. Comparison between two FISH techniques in the *in vitro* study of cytogenetic markers for low-dose X-ray exposure in human primary fibroblasts. *Front Genet* (2013) 4:141. doi:10.3389/fgene.2013.00141
35. Cho MS, Lee JK, Bae KS, Han EA, Jang SJ, Ha WH, et al. Retrospective biodosimetry using translocation frequency in a stable cell of occupationally exposed to ionizing radiation. *J Radiat Res* (2015) 56(4):709–16. doi:10.1093/jrr/rrv028
36. Tucker JD. Low-dose ionizing radiation and chromosome translocations: a review of the major considerations for human biological dosimetry. *Mutat Res* (2008) 659(3):211–20. doi:10.1016/j.mrrev.2008.04.001
37. Beinke C, Meineke V. High potential for methodical improvements of FISH-based translocation analysis for retrospective radiation biodosimetry. *Health Phys* (2012) 103(2):127–32. doi:10.1097/HP.0b013e31824645fb
38. Schmitz A, Bayer J, Dechamps N, Thomas G. Intrinsic susceptibility to radiation-induced apoptosis of human lymphocyte subpopulations. *Int J Radiat Oncol Biol Phys* (2003) 57(3):769–78. doi:10.1016/S0360-3016(03)00637-0
39. Durantel F, Balanzat E, Cassimi A, Chevalier F, Ngono-Ravache Y, Madi T, et al. Dosimetry for radiobiology experiments at GANIL. *Nucl Instrum Methods Phys Res A* (2016) 816:70–7. doi:10.1016/j.nima.2016.01.052
40. International Atomic Energy Agency (IAEA). Cytogenetic dosimetry: applications in preparedness for and response to radiation emergencies. *Emergency Preparedness and Response Series*. Vienna: IAEA (2011). Available from: http://www-pub.iaea.org/books/IAEABooks/8735/Cytogenetic-Dosimetry-Applications-in-Preparedness-for-and-Response-to-Radiation-Emergencies

Conflict of Interest Statement: The authors declare that the research was conducted in the absence of any commercial or financial relationships that could be construed as a potential conflict of interest.

Copyright © 2016 Shim, Normil, Testard, Hempel, Ricoul and Sabatier. This is an open-access article distributed under the terms of the Creative Commons Attribution License (CC BY). The use, distribution or reproduction in other forums is permitted, provided the original author(s) or licensor are credited and that the original publication in this journal is cited, in accordance with accepted academic practice. No use, distribution or reproduction is permitted which does not comply with these terms.

frontiers in Oncology

ORIGINAL RESEARCH
published: 08 October 2015
doi: 10.3389/fonc.2015.00218

Decreased RXRα is associated with increased β-catenin/TCF4 in ^{56}Fe-induced intestinal tumors

*Shubhankar Suman[1], Santosh Kumar[1], Albert J. Fornace Jr.[1,2] and Kamal Datta[1]**

[1] Department of Biochemistry and Molecular and Cellular Biology, Lombardi Comprehensive Cancer Center, Georgetown University, Washington, DC, USA, [2] Center of Excellence in Genomic Medicine Research (CEGMR), King Abdulaziz University, Jeddah, Saudi Arabia

Although it is known that accumulation of oncogenic β-catenin is critical for intestinal tumorigenesis, the underlying mechanisms have not yet been fully explored. Post-translational β-catenin level is regulated via the adenomatous polyposis coli (APC)-dependent as well as the APC-independent ubiquitin–proteasome pathway (UPP). Employing an APC-mutant mouse model (APC$^{Min/+}$) the present study aimed to investigate the status of RXRα, an APC-independent factor involved in targeting β-catenin to UPP for degradation, in tumor-bearing and tumor-free areas of intestine after exposure to energetic ^{56}Fe ions. APC$^{Min/+}$ mice were exposed to energetic ^{56}Fe ions (4 or 1.6 Gy) and intestinal tumor samples and tumor-free normal intestinal samples were collected 100–110 days after exposure. The status of TCF4, β-catenin, cyclin D1, and RXRα was examined using immunohistochemistry and immunoblots. We observed increased accumulation of the transcription factor TCF4 and its co-activator β-catenin as well as their downstream oncogenic target protein cyclin-D1 in ^{56}Fe ion-induced intestinal tumors. Further, decreased expression of RXRα in tumors as well as in adjacent normal epithelium was indicative of perturbations in β-catenin proteasomal-targeting machinery. This indicates that decreased UPP targeting of β-catenin due to downregulation of RXRα can contribute to further accumulation of β-catenin and to ^{56}Fe-induced tumorigenesis.

Keywords: APC$^{Min/+}$, intestinal tumor, space radiation, heavy ion radiation, tumorigenesis, proteasome, β-catenin

OPEN ACCESS

Edited by:
Marco Durante, GSI, Germany

Reviewed by:
Kevin Prise, Queen's University Belfast, UK
Eric Chi-ching Ko, UC Davis Comprehensive Cancer Center, USA

***Correspondence:**
Kamal Datta, Department of Biochemistry and Molecular and Cellular Biology, Georgetown University, Research Building, Room E518, 3970 Reservoir Road, NW, Washington, DC 20057, USA
kd257@georgetown.edu

Specialty section:
This article was submitted to Radiation Oncology, a section of the journal Frontiers in Oncology

Received: *22 July 2015*
Accepted: *23 September 2015*
Published: *08 October 2015*

Citation:
Suman S, Kumar S, Fornace AJ Jr. and Datta K (2015) Decreased RXRα is associated with increased β-catenin/TCF4 in ^{56}Fe-induced intestinal tumors. Front. Oncol. 5:218. doi: 10.3389/fonc.2015.00218

Introduction

Heavy ion charged particle (HZE) radiation, such as ^{56}Fe ions, is prevalent in deep space, and is a major concern for astronauts' health (1). Recently, using APC$^{Min/+}$ mice, a well-accepted mouse model for human colorectal cancer (CRC), we found increased risk of CRC development accompanied by increased nuclear accumulation of oncogenic β-catenin and activation of its downstream signaling after exposure to ^{56}Fe ions (2–5). However, the mechanisms behind the accumulation of oncogenic β-catenin are not yet fully understood.

Cellular levels of free β-catenin are tightly regulated via the ubiquitin–proteasome pathway (UPP). Targeting of β-catenin to the proteasome and its subsequent degradation involves two adenomatous polyposis coli (APC)-dependent (i.e., APC/GSK3β/AXIN and APC/Siah1) and one APC-independent (RXRα-mediated) mechanisms (6). In gastrointestinal (GI) tumors, genes involved in APC-dependent (APC, Siah1, and Axin) targeting of β-catenin are often mutated (7–11), and similarly in APC$^{Min/+}$ mice, tumor formation is mostly driven through inactivation of the wild type

APC allele (12). Thus, APC-dependent proteasomal targeting of β-catenin is eventually disabled in these tumors. In the absence of proteasomal targeting, β-catenin accumulates and interacts with T-cell factor transcription factors (TCF4) in the nucleus leading to activation of oncogenic signaling pathways (13). In view of the known perturbations in APC-dependent proteasomal targeting of β-catenin early in the GI tumorigenesis process, only the APC-independent (RXRα-dependent) pathway would remain to control its accumulation. However, the status of the APC-independent proteasomal targeting of the β-catenin in heavy ion radiation-induced intestinal tumors has not been explored. In this study, using the $APC^{Min/+}$ intestinal tumor mouse model (14), we demonstrated downregulation of RXRα expression, which may complement the disabled APC-dependent proteasomal degradation pathway to increase β-catenin accumulation in ^{56}Fe-induced tumors. Downregulation of RXRα observed in this study could potentially play a crucial role in heavy ion radiation-induced increased risk of intestinal tumorigenesis and would warrant further investigation.

Materials and Methods

Mice and Genotyping

Male $APC^{Min/+}$ mice (The Jackson Laboratory, Bar Harbor, ME, USA) were bred with female C57BL/6J mice at the Georgetown University (GU)'s animal facility. Genotyping using tail DNA samples were done using reverse-transcription polymerase chain reaction (RT-PCR) to identify heterozygous offspring as per the Jackson Laboratory protocol. The mouse colony was maintained on standard certified rodent diet and filtered water in a humidity and temperature-controlled room with 12 h dark/light cycle. All experimental procedures were performed in compliance with the protocols approved by the Institutional Animal Care and Use Committee (IACUC) at GU and Brookhaven National Laboratory (BNL). Both the facilities are Association for Assessment and Accreditation of Laboratory and Animal Care International (AAALACI) accredited facilities and we followed The Guide for the Care and Use of Laboratory Animals.

Irradiation and Sample Collection

$APC^{Min/+}$ female mice (6–8-weeks old) were placed in well-ventilated transparent plastic boxes (1 mouse/box) allowing easy movement and irradiated with 4 or 1.6 Gy whole body ^{56}Fe radiation (energy: 1000 MeV/n; LET: 148 keV/μm; dose rate: 1 Gy/min) at the NASA Space Radiation Laboratory (NSRL) at BNL. These two doses were used in our previously published tumorigenesis experiments and samples collected during that study were used for molecular analysis in this study. For ^{56}Fe exposure, both control and treatment groups were shipped to BNL for irradiation and brought back to GU after irradiation in a temperature-controlled vehicle for a same day delivery to minimize stress to the animals. Age-matched ^{56}Fe-irradiated and control mice were euthanized by CO_2 asphyxiation between 100 and 110 days after radiation exposure. The small intestinal tract was surgically removed, washed with phosphate-buffered saline (PBS), and cut open longitudinally at room temperature. A dissecting scope (Leica MZ6, Buffalo Grove, IL, USA) was used to visualize and dissect tumors, which were then flash frozen in liquid nitrogen and stored at −80°C for further use. Also, intestinal samples (~3 cm) with tumor-bearing and surrounding tumor-free area were fixed overnight in 10% buffered formalin, embedded in paraffin, and 4 μm-thick sections were obtained for immunohistochemistry staining.

Immunohistochemistry

Intestinal sections ($n = 5$ mice per group) were used for immunohistochemistry with a protocol described earlier (3). Briefly, immunostaining for active-β-catenin (Cat#05-665, Millipore, Billerica, MA, USA; dilution: 1:100), TCF4 (Cat#05-511, Millipore; dilution: 1:100), RXRα (Cat#sc-553, Santa Cruz Biotechnology, Dallas, TX, USA; dilution: 1:40), and cyclin D1 (Cat#04-1151; Millipore; dilution: 1:150) were performed by soaking slides in antigen retrieval citrate buffer (pH 6.0; Dako, Carpinteria, CA, USA) and heating at 100°C for 15 min in a microwave oven. Further, endogenous peroxidase activity was quenched using 3% hydrogen peroxide in methanol followed by incubation in blocking buffer (5% bovine serum albumin in PBS) for 30 min. After blocking sections were incubated overnight at 4°C with the respective primary antibody. Signal detection and color development was done using SuperPicture 3rd Gen IHC detection kit (Cat#87-9673; Invitrogen, Carlsbad, CA, USA). Sections were counterstained using hematoxylin and images were acquired using bright field microscopy at a magnification of 20×. At least 10 randomly chosen images from the tumor-bearing as well as from the tumor-free areas were acquired from each mouse and a representative image from each group is shown in the results. Images were analyzed using color deconvolution and image-based tool for counting nuclei (ITCN) plug-ins of ImageJ v1.45 software (National Institutes of Health, Bethesda, MD, USA). Quantification data were statistically analyzed using two-tailed paired Student's *t*-test and difference between control and irradiated group was considered significant when *p*-value was <0.05. Error bars represent mean ± SEM.

Immunoblots

Frozen intestinal tumor samples ($n = 5$ mice per group) were pooled and used for immunoblot analysis of RXRα level with a protocol described previously (3). Briefly, samples were homogenized in ice-cold lysis buffer, centrifuged, and supernatant collected. Protein was estimated in supernatant and equal amount of protein was used for sodium dodecyl sulfate-polyacrylamide gel electrophoresis (SDS-PAGE). Protein was transferred to PVDF membrane, incubated with RXRα antibody, and protein detected using horseradish peroxidase (HRP) conjugated secondary antibody and enhanced chemiluminescence (ECL) detection system (Cat# 34080, Thermo Fisher Scientific, Rockford, IL, USA) and representative images shown in the results.

Results

Increased β-Catenin and TCF4 Levels in ^{56}Fe-Induced Intestinal Tumor

Intestinal tumors stained for β-catenin showed increased level in 4 Gy ^{56}Fe-irradiated samples relative to control tumors from

sham-irradiated mice (**Figures 1A,B**) and this is consistent with our previous results after 1.6 Gy ^{56}Fe irradiation (3). Higher levels were also observed for TCF4 in ^{56}Fe-irradiated intestinal tumors relative to controls (**Figures 1C,D**). Transcription factor TCF4 along with the transcriptional co-activator β-catenin are involved in transcribing pro-proliferative factors, such as cyclin D1, and increased cyclin D1 was observed in the current study (**Figures 1E,F**) as well.

Reduced Expression of RXRα in Tumor-Bearing and Tumor-Free Areas of APC$^{Min/+}$ Mice After Exposure to ^{56}Fe Radiation

Immunohistochemistry in tumor samples demonstrated that expression of RXRα was reduced after 4 Gy (**Figure 2A**). Quantification and statistical analysis of stained sections from five mice showed that RXRα was significantly lowered in ^{56}Fe-irradiated tumors relative to sham-irradiated tumors (**Figure 2B**). Intestinal tumors from 1.6 Gy ^{56}Fe-irradiated mice also showed decreased RXRα staining (**Figure 2C**) and quantification and statistical analysis showed that the staining in irradiated samples were significantly lower compared to controls (**Figure 2D**). However, quantification did not show significant difference in RXRα staining between two radiation doses. Immunoblots of 4 Gy (**Figure 2E**) and 1.6 Gy (**Figure 2F**) intestinal tumor samples also showed decreased RXRα. We also performed immunohistochemistry for RXRα on tumor-free intestinal sections from APC$^{Min/+}$ mice exposed to either 1.6 or 4 Gy ^{56}Fe ions. Staining of tumor-free intestinal section showed lower expression of RXRα after 4 Gy ^{56}Fe relative to corresponding controls (**Figure 3A**). Decreased RXRα after 4 Gy ^{56}Fe was statistically significant compared to sham-irradiated controls (**Figure 3B**). Conversely, we also observed downregulation of RXRα in 1.6 Gy irradiated samples

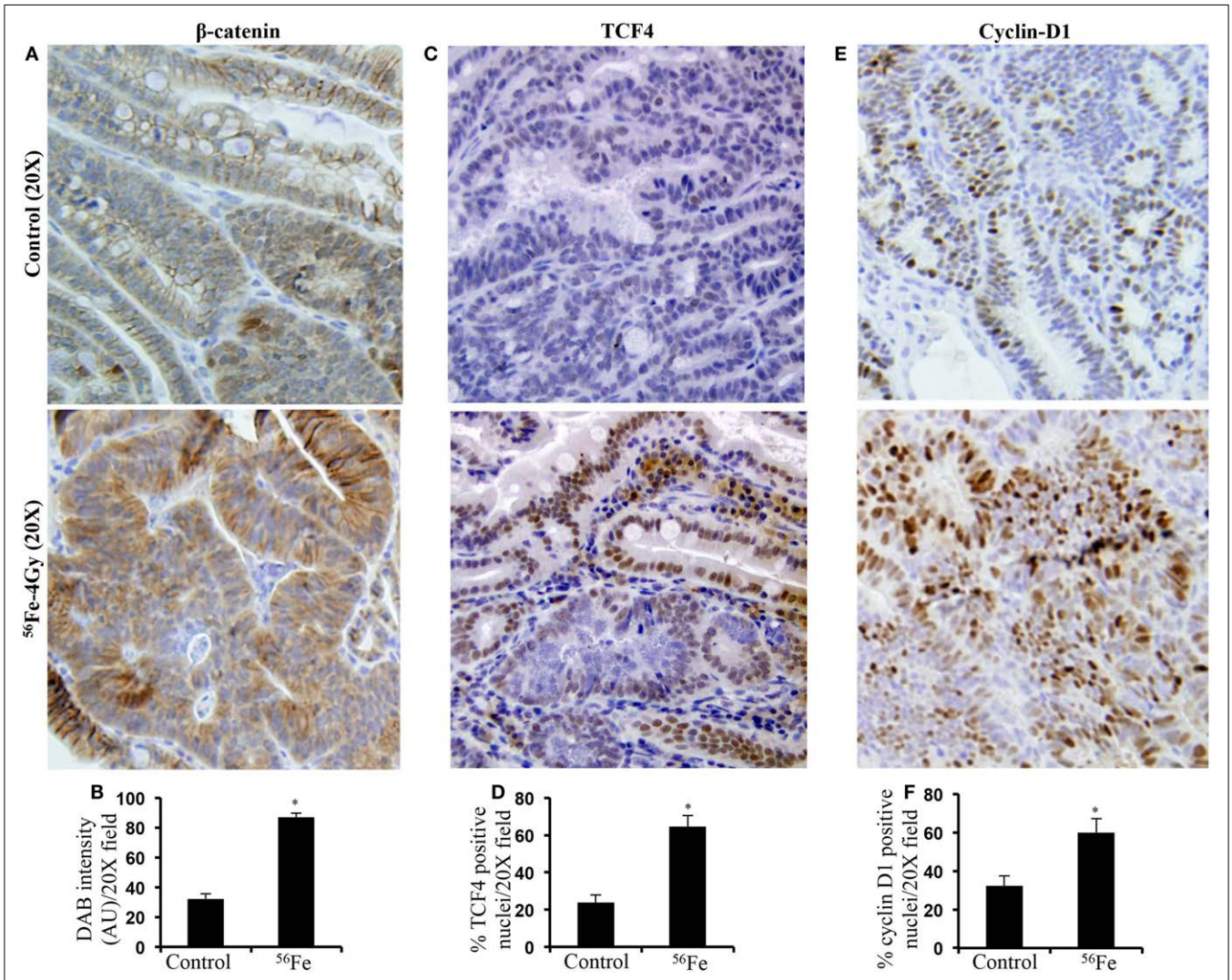

FIGURE 1 | Accumulation and activation of oncogenic β-catenin signaling in ^{56}Fe-induced intestinal tumors compared to spontaneous tumors from sham-irradiated mice (control). **(A)** Immunohistochemical detection of active-β-catenin in ^{56}Fe-induced intestinal tumors. **(B)** Quantification of β-catenin expression in intestinal tumors. **(C)** Immunohistochemical detection of β-catenin transcriptional regulator TCF4 in ^{56}Fe-induced intestinal tumors. **(D)** Quantification of TCF4 positive nuclei in intestinal tumors. **(E)** Immunohistochemical detection of β-catenin/TCF4 oncogenic target cyclin-D1 in ^{56}Fe-induced intestinal tumors. **(F)** Quantification of cyclin-D1 positive nuclei in intestinal tumors. Error bars represent mean ± SEM and $p < 0.05$ was considered significant. AU – Arbitrary Unit.

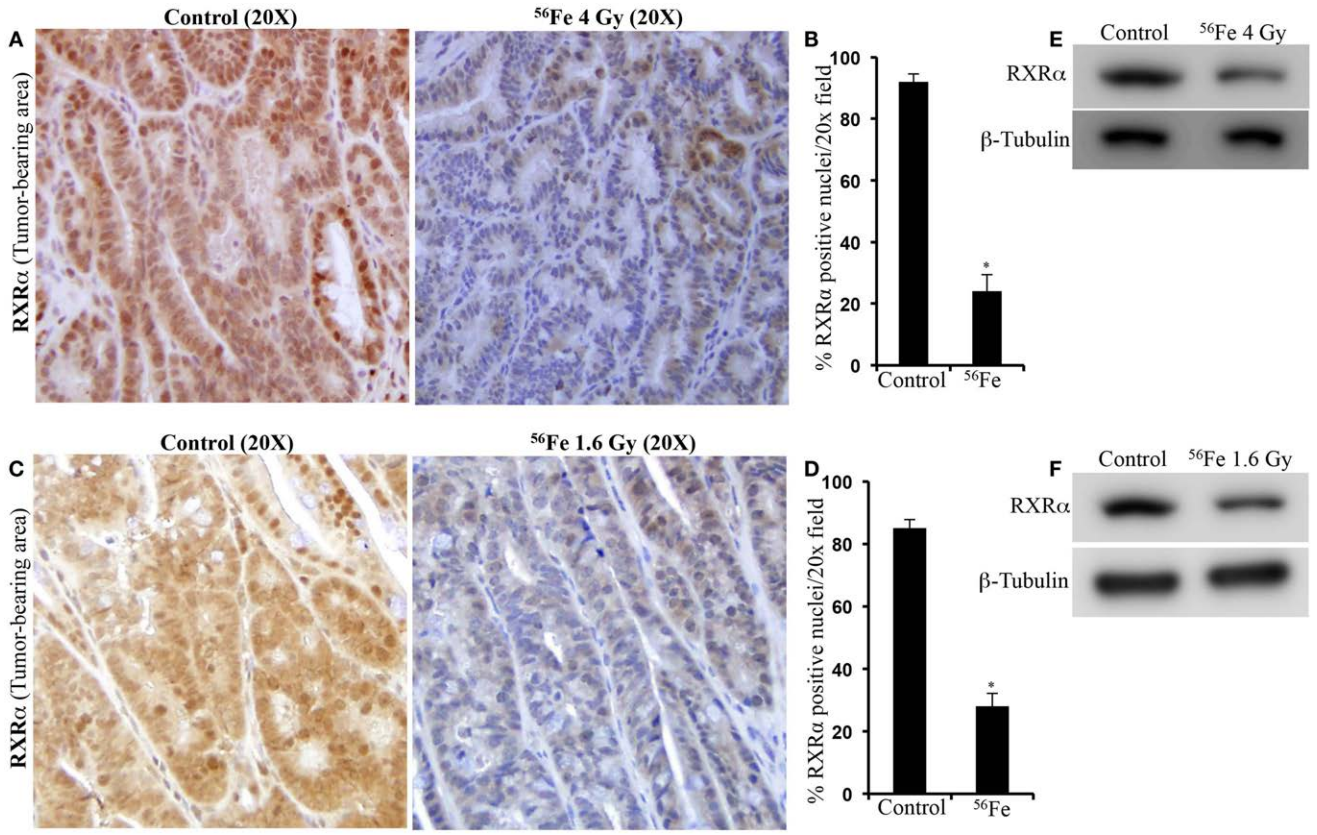

FIGURE 2 | Lower RXRα expression in ^{56}Fe-induced intestinal tumors. **(A)** Representative immunohistochemistry images showing expression of RXRα in spontaneous and 4 Gy ^{56}Fe-induced intestinal tumors. **(B)** Quantification of RXRα in spontaneous and 4 Gy ^{56}Fe-induced intestinal tumors. **(C)** Expression of RXRα in spontaneous and 1.6 Gy ^{56}Fe-induced intestinal tumors. **(D)** Quantification of RXRα in spontaneous and 1.6 Gy ^{56}Fe-induced intestinal tumors. **(E)** Immunoblots of RXRα in spontaneous and 4 Gy ^{56}Fe-induced intestinal tumors. **(F)** Immunoblots of RXRα in spontaneous and 1.6 Gy ^{56}Fe-induced intestinal tumors. Error bars represent mean ± SEM and $p < 0.05$ was considered significant.

compared to controls (**Figure 3C**) and quantification showed statistically significant difference between irradiated and sham-irradiated samples (**Figure 3D**).

Discussion

The carcinogenic potential of ionizing radiation is well known and using animal models it has been established that high-LET heavy ion radiation has higher carcinogenic potential compared to low-LET radiation (15). Increased frequencies of site-specific cancer following heavy ion exposure have been reported in various rodent models with upregulation of oncogenic signaling mediated through genetic, epigenetic, and/or physiological changes (3, 15–17). Earlier studies conducted in APC$^{Min/+}$ mice revealed increased tumor induction and a higher number of adenocarcinomas, which was associated with greater upregulation of β-catenin signaling after ^{56}Fe exposure relative to γ radiation; this is indicative of perturbations in the molecular events upstream of β-catenin (3). The purpose of the current study was to develop mechanistic insight into greater tumorigenesis observed in our previous work in APC$^{Min/+}$ mice after two doses of ^{56}Fe radiation relative to γ radiation. While pathways can be investigated in the wild-type mice, they are resistant to intestinal tumorigenesis. Therefore, we used APC-mutant mice not only to quantitatively assess tumor frequency but also to understand molecular pathway alterations, which may have contributed to tumor development after radiation exposure. While we reported previously that two doses of ^{56}Fe caused higher tumor frequency, we are yet to fully understand molecular characteristics of the tumors and tumor-adjacent normal tissues after ^{56}Fe irradiation. To this end, the results presented in the current study explain in part potential underlying mechanisms contributing to increased tumor frequency after ^{56}Fe irradiation. We have focused on the APC-independent mechanism of β-catenin degradation via UPP. In APC-deficient adenoma, accumulation of β-catenin complexed with nuclear TCF4 results in the increased expression of its oncogenic target genes, such as cyclin-D1 that promotes intestinal cell proliferation and polyp formation (18). In agreement with our published reports in APC$^{Min/+}$ mice exposed to 1.6 Gy of ^{56}Fe ion, the current study also observed similar activation of β-catenin at 4 Gy of ^{56}Fe ion along with increased TCF4 and cyclin-D1. Significant loss of RXRα was evident in tumors as well as in tumor-free areas of intestine after ^{56}Fe radiation and this could contribute to decreased proteasomal targeting of β-catenin, therefore enhancing cell survival and proliferation through β-catenin/TCF4 signaling. Notably, RXRα was downregulated in

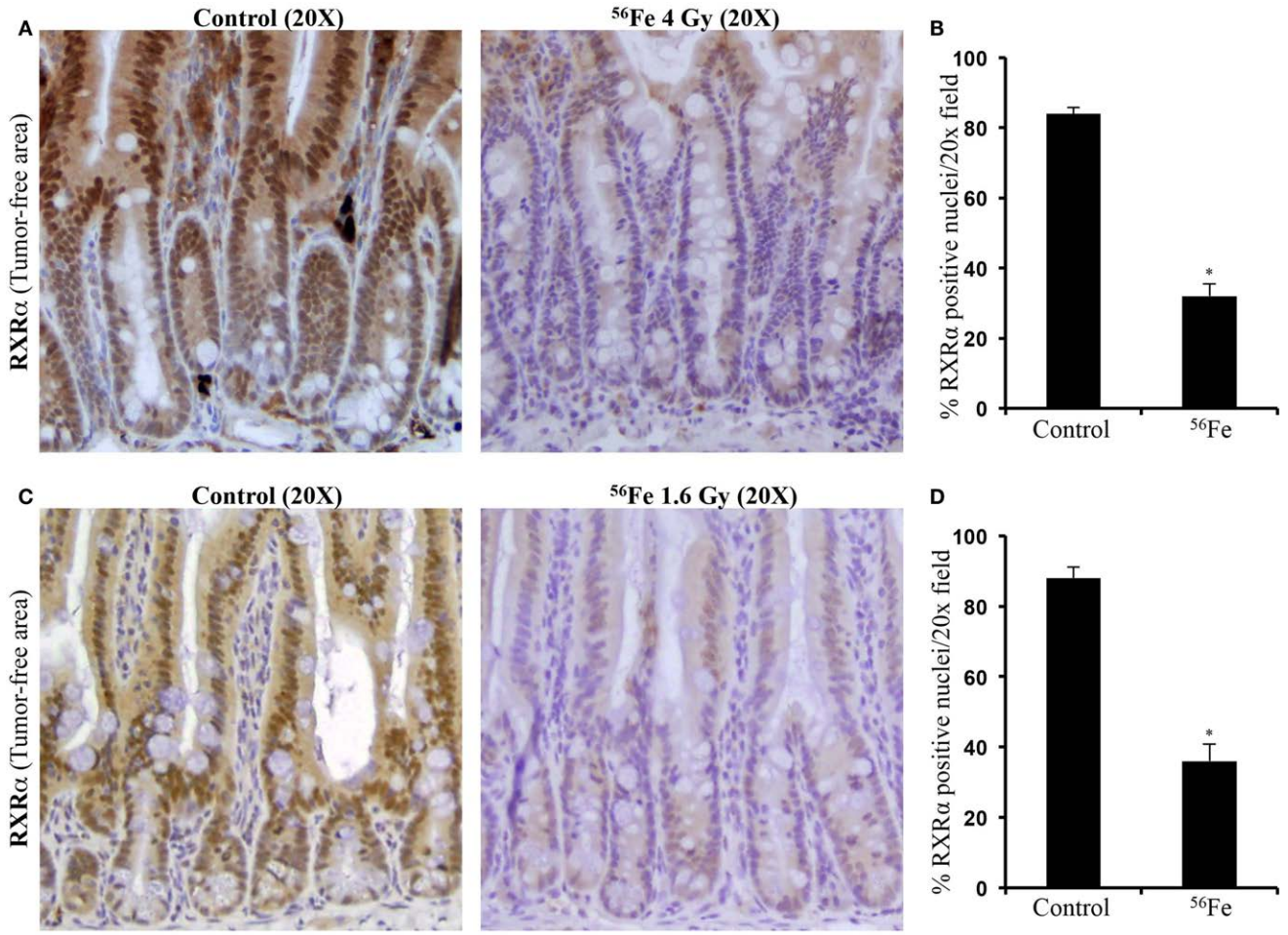

FIGURE 3 | Downregulation of RXRα was observed in tumor-free areas of intestinal samples from APC$^{Min/+}$ mice. **(A)** Decreased RXRα expression after 4 Gy ^{56}Fe radiation. **(B)** Quantification of immunohistochemistry images showed significant decrease in RXRα after 4 Gy ^{56}Fe. **(C)** Decreased RXRα expression after 1.6 Gy ^{56}Fe radiation. **(D)** Quantification of immunohistochemistry images showed significant decrease in RXRα after 1.6 Gy ^{56}Fe. Error bars represent mean ± SEM and $p < 0.05$ was considered significant.

both the radiation doses tested suggesting that the effect is independent of radiation dose and that the lower dose may have a proportionately greater effect relative to the higher dose. We recognize that the mean absorbed doses of energetic ^{56}Fe ions used in the current study are higher than the doses astronauts are expected to receive during prolonged space missions. These high doses of energetic ^{56}Fe ions were used as a proof of principle in our initial studies for establishing the differential effects, quantitatively and qualitatively, of space compared to γ radiation.

Loss of the remaining wild type APC allele has often been implicated as the primary mechanism for increased β-catenin signaling leading to tumor development in APC$^{Min/+}$ mice (12, 19, 20). In addition to APC, the β-catenin cellular level is also regulated through a direct proteasomal targeting mediated by RXRα (21) and downregulation of RXRα in human and rodent colonic tumors has been reported previously (22). Considering that protein turnover is critical for cellular homeostasis, availability of multiple independent pathways for protein degradation ensures that the potentially pro-carcinogenic β-catenin level remains within physiologic limits to limit cancer initiation and progression. Downregulation of RXRα in our model system may have played a role in ^{56}Fe radiation-induced more aggressive tumorigenesis reported earlier (3). Apart from driving proteasomal degradation of β-catenin, RXRα also functions to suppress β-catenin-mediated upregulation of oncogenes through direct protein–protein interaction (23) in colon cancer cells. Thus, loss of RXRα expression could further stabilize β-catenin signaling in tumor cells, leading to greater cell proliferation and higher number of invasive cancers associated with ^{56}Fe relative to γ radiation.

Nuclear receptor RXRα is known to heterodimerize with a host of other nuclear receptors, such as the vitamin D receptor (VDR) and retinoid acid receptor (RAR), and is involved through transactivation of target genes, such as p21, in regulating normal growth and development (23, 24). Consequently, loss of RXRα is expected to cause disordered cellular proliferation, and indeed, downregulation of RXRα has been widely reported in a number of cancers including CRC (21–26). Our result demonstrates for the first time that RXRα is downregulated in tumor-free areas

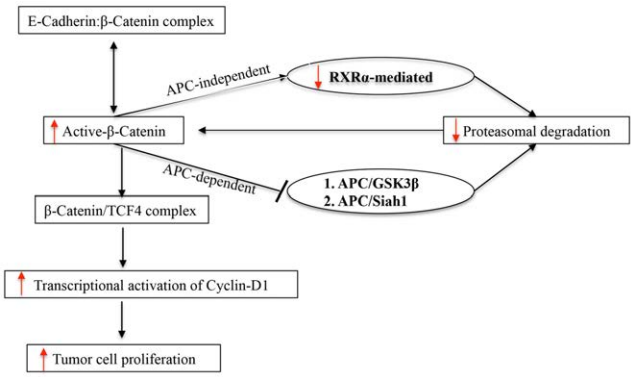

FIGURE 4 | Schematic representation of APC-dependent and APC-independent pathways of UPP involved in β-catenin degradation in APC$^{Min/+}$ mice.

of APC$^{Min/+}$ intestine ~100 days after radiation exposure. Considering that a significant number of intestinal adenomas has also been reported to arise without the loss of heterozygosity of the APC gene and these adenomas are often polyclonal (8, 20, 27), our results supports an APC-independent mechanism of β-catenin stabilization during ^{56}Fe-irradiated tumorigenesis. We believe that decreased RXRα expression in tumor-free areas of the intestine may be a reflection of the RXRα status in other areas of the GI tract and that this molecular event may be preceding intestinal tumorigenesis in APC$^{Min/+}$ mice. Furthermore, RXRα signaling is also linked to cellular redox regulation and it has been demonstrated that RXRα activation protects cell from oxidative stress and inhibition promotes ROS production (28, 29). Downregulation of RXRα observed ~100 days post-exposure in the current study aligns with our previous studies demonstrating chronic oxidative stress even 1 year after exposure to energetic ^{56}Fe ions (30). Although we observed persistent oxidative stress after γ radiation, it was less pronounced relative to equitoxic doses of ^{56}Fe radiation. Additionally, intestinal tumor frequency and grade was also higher after ^{56}Fe relative to equitoxic doses of γ radiation. Considering that γ radiation responses were consistently lower relative to ^{56}Fe, in the current study, we have analyzed and presented ^{56}Fe-induced alterations of an alternate pathway involved in β-catenin regulation via RXRα. Our data, previous and current, demonstrate that effects of radiation on redox balance, carcinogenesis, and related molecular pathways are dependent on radiation quality and energy deposition characteristics. However, further in depth studies will be required to dissect the link between heavy ion radiation exposure and long-term molecular alterations, such as oxidative stress and RXRα downregulation. In summary, our results show that energetic heavy ion radiation is capable of lowering RXRα in tumor as well as non-tumor intestinal epithelial cells. Due to its roles in multiple cellular processes, continuous downregulation of RXRα, we believe, will have major ramifications for intestinal cellular homeostasis with implications for carcinogenesis including colorectal carcinogenesis (**Figure 4**).

Author Contributions

Conceived and designed the experiments: SS and KD. Performed the experiments: SS and SK. Analyzed the data: SS, SK, and KD. Contributed reagents/materials/analysis tools: AF and KD. Wrote the paper: SS, AF, and KD. All authors read and approved this manuscript.

Acknowledgments

This study is supported in part by NASA grants NNX13AD58G and NNX09AU95G. We are very much thankful to the members of the NASA Space Radiation Laboratory (NSRL), especially to Drs. Peter Guida and Adam Rusek from Brookhaven National Laboratory for their excellent support in conducting heavy ion radiation exposures. We are also thankful to Steve Strawn and Pelagie Ake for administrative and animal facility supports. We acknowledge the Histopathology and Tissue Shared Resources at the Georgetown University supported by Award Number P30CA051008 from the National Cancer Institute.

References

1. Cucinotta FA, Kim MH, Chappell LJ, Huff JL. How safe is safe enough? Radiation risk for a human mission to Mars. *PLoS One* (2013) **8**:e74988. doi:10.1371/journal.pone.0074988
2. Trani D, Datta K, Doiron K, Kallakury B, Fornace AJJ. Enhanced intestinal tumor multiplicity and grade in vivo after HZE exposure: mouse models for space radiation risk estimates. *Radiat Environ Biophys* (2010) **49**:389–96. doi:10.1007/s00411-010-0292-2
3. Datta K, Suman S, Kallakury BV, Fornace AJJ. Heavy ion radiation exposure triggered higher intestinal tumor frequency and greater beta-catenin activation than gamma radiation in APC(Min/+) mice. *PLoS One* (2013) **8**:e59295. doi:10.1371/journal.pone.0059295
4. Cucinotta FA. Space radiation risks for astronauts on multiple International Space Station missions. *PLoS One* (2014) **9**:e96099. doi:10.1371/journal.pone.0096099
5. Trani D, Nelson SA, Moon BH, Swedlow JJ, Williams EM, Strawn SJ, et al. High-energy particle-induced tumorigenesis throughout the gastrointestinal tract. *Radiat Res* (2014) **181**:162–71. doi:10.1667/RR13502.1
6. Xiao JH, Ghosn C, Hinchman C, Forbes C, Wang J, Snider N, et al. Adenomatous polyposis coli (APC)-independent regulation of beta-catenin degradation via a retinoid X receptor-mediated pathway. *J Biol Chem* (2003) **278**:29954–62. doi:10.1074/jbc.M304761200
7. Kim CJ, Cho YG, Park CH, Jeong SW, Nam SW, Kim SY, et al. Inactivating mutations of the Siah-1 gene in gastric cancer. *Oncogene* (2004) **23**:8591–6. doi:10.1038/sj.onc.1208113
8. Segditsas S, Tomlinson I. Colorectal cancer and genetic alterations in the Wnt pathway. *Oncogene* (2006) **25**:7531–7. doi:10.1038/sj.onc.1210059
9. Russo A, Bazan V, Iacopetta B, Kerr D, Soussi T, Gebbia N. The TP53 colorectal cancer international collaborative study on the prognostic and predictive significance of p53 mutation: influence of tumor site, type of mutation, and adjuvant treatment. *J Clin Oncol* (2005) **23**:7518–28. doi:10.1200/JCO.2005.00.471
10. Hegde MR, Roa BB. Detecting mutations in the APC gene in familial adenomatous polyposis (FAP). *Curr Protoc Hum Genet* (2006) **Chapter 10**:Unit10.8. doi:10.1002/0471142905.hg1008s50
11. Satoh S, Daigo Y, Furukawa Y, Kato T, Miwa N, Nishiwaki T, et al. AXIN1 mutations in hepatocellular carcinomas, and growth suppression in cancer cells by virus-mediated transfer of AXIN1. *Nat Genet* (2000) **24**:245–50. doi:10.1038/73448
12. Levy DB, Smith KJ, Beazer-Barclay Y, Hamilton SR, Vogelstein B, Kinzler KW. Inactivation of both APC alleles in human and mouse tumors. *Cancer Res* (1994) **54**:5953–8.

13. Wei W, Chua MS, Grepper S, So S. Small molecule antagonists of Tcf4/beta-catenin complex inhibit the growth of HCC cells in vitro and in vivo. *Int J Cancer* (2010) **126**:2426–36. doi:10.1002/ijc.24810
14. Suman S, Fornace AJJ, Datta K. Animal models of colorectal cancer in chemoprevention and therapeutics development. In: Ettarh R, editor. *Colorectal Cancer – From Prevention to Patient Care*. Rijeka: InTech (2012). p. 277–300. doi:10.5772/28497
15. Bielefeldt-Ohmann H, Genik PC, Fallgren CM, Ullrich RL, Weil MM. Animal studies of charged particle-induced carcinogenesis. *Health Phys* (2012) **103**:568–76. doi:10.1097/HP.0b013e318265a257
16. Peng Y, Brown N, Finnon R, Warner CL, Liu X, Genik PC, et al. Radiation leukemogenesis in mice: loss of PU.1 on chromosome 2 in CBA and C57BL/6 mice after irradiation with 1 GeV/nucleon 56Fe ions, X rays or gamma rays. Part I. Experimental observations. *Radiat Res* (2009) **171**:474–83. doi:10.1667/RR1547.1
17. Weil MM, Bedford JS, Bielefeldt-Ohmann H, Ray FA, Genik PC, Ehrhart EJ, et al. Incidence of acute myeloid leukemia and hepatocellular carcinoma in mice irradiated with 1 GeV/nucleon (56)Fe ions. *Radiat Res* (2009) **172**:213–9. doi:10.1667/RR1648.1
18. Barker N, Morin PJ, Clevers H. The Yin-Yang of TCF/beta-catenin signaling. *Adv Cancer Res* (2000) **77**:1–24. doi:10.1016/S0065-230X(08)60783-6
19. Luongo C, Dove WF. Somatic genetic events linked to the Apc locus in intestinal adenomas of the Min mouse. *Genes Chromosomes Cancer* (1996) **17**: 194–8. doi:10.1002/1098-2264(199611)17:3<194::AID-GCC2870170302>3.0.CO;2-E
20. Bienz M, Clevers H. Linking colorectal cancer to Wnt signaling. *Cell* (2000) **103**:311–20. doi:10.1016/S0092-8674(00)00122-7
21. Dillard AC, Lane MA. Retinol increases beta-catenin-RXRalpha binding leading to the increased proteasomal degradation of beta-catenin and RXRalpha. *Nutr Cancer* (2008) **60**:97–108. doi:10.1080/01635580701586754
22. Janakiram NB, Mohammed A, Qian L, Choi CI, Steele VE, Rao CV. Chemopreventive effects of RXR-selective rexinoid bexarotene on intestinal neoplasia of Apc(Min/+) mice. *Neoplasia* (2012) **14**:159–68. doi:10.1593/neo.111440
23. Han A, Tong C, Hu D, Bi X, Yang W. A direct protein-protein interaction is involved in the suppression of beta-catenin transcription by retinoid X receptor alpha in colorectal cancer cells. *Cancer Biol Ther* (2008) **7**:454–9. doi:10.4161/cbt.7.3.5455
24. Shimizu M, Shirakami Y, Imai K, Takai K, Moriwaki H. Acyclic retinoid in chemoprevention of hepatocellular carcinoma: targeting phosphorylated retinoid X receptor-α for prevention of liver carcinogenesis. *J Carcinog* (2012) **11**:11. doi:10.4103/1477-3163.100398
25. Yamazaki K, Shimizu M, Okuno M, Matsushima-Nishiwaki R, Kanemura N, Araki H, et al. Synergistic effects of RXR alpha and PPAR gamma ligands to inhibit growth in human colon cancer cells – phosphorylated RXR alpha is a critical target for colon cancer management. *Gut* (2007) **56**:1557–63. doi:10.1136/gut.2007.129858
26. Zhang F, Meng F, Li H, Dong Y, Yang W, Han A. Suppression of retinoid X receptor alpha and aberrant β-catenin expression significantly associates with progression of colorectal carcinoma. *Eur J Cancer* (2011) **47**:2060–7. doi:10.1016/j.ejca.2011.04.010
27. Merritt AJ, Gould KA, Dove WF. Polyclonal structure of intestinal adenomas in ApcMin/+ mice with concomitant loss of Apc+ from all tumor lineages. *Proc Natl Acad Sci U S A* (1997) **94**:13927–31. doi:10.1073/pnas.94.25.13927
28. Shan P, Pu J, Yuan A, Shen L, Shen L, Chai D, et al. RXR agonists inhibit oxidative stress-induced apoptosis in H9c2 rat ventricular cells. *Biochem Biophys Res Commun* (2008) **375**:628–33. doi:10.1016/j.bbrc.2008.08.074
29. Ning RB, Zhu J, Chai DJ, Xu CS, Xie H, Lin XY, et al. RXR agonists inhibit high glucose-induced upregulation of inflammation by suppressing activation of the NADPH oxidase-nuclear factor-κB pathway in human endothelial cells. *Genet Mol Res* (2013) **12**:6692–707. doi:10.4238/2013.December.13.3
30. Datta K, Suman S, Kallakury BV, Fornace AJJ. Exposure to heavy ion radiation induces persistent oxidative stress in mouse intestine. *PLoS One* (2012) **7**:e42224. doi:10.1371/journal.pone.0042224

Conflict of Interest Statement: The authors declare that the research was conducted in the absence of any commercial or financial relationships that could be construed as a potential conflict of interest.

Copyright © 2015 Suman, Kumar, Fornace and Datta. This is an open-access article distributed under the terms of the Creative Commons Attribution License (CC BY). The use, distribution or reproduction in other forums is permitted, provided the original author(s) or licensor are credited and that the original publication in this journal is cited, in accordance with accepted academic practice. No use, distribution or reproduction is permitted which does not comply with these terms.

frontiers in Oncology

HYPOTHESIS AND THEORY
published: 11 March 2016
doi: 10.3389/fonc.2016.00057

HZE Radiation Non-Targeted Effects on the Microenvironment That Mediate Mammary Carcinogenesis

Mary Helen Barcellos-Hoff[1] and Jian-Hua Mao[2]*

[1] Department of Radiation Oncology, University of California San Francisco, San Francisco, CA, USA, [2] Lawrence Berkeley National Laboratory, Berkeley, CA, USA

Clear mechanistic understanding of the biological processes elicited by radiation that increase cancer risk can be used to inform prediction of health consequences of medical uses, such as radiotherapy, or occupational exposures, such as those of astronauts during deep space travel. Here, we review the current concepts of carcinogenesis as a multicellular process during which transformed cells escape normal tissue controls, including the immune system, and establish a tumor microenvironment. We discuss the contribution of two broad classes of radiation effects that may increase cancer: radiation targeted effects that occur as a result of direct energy deposition, e.g., DNA damage, and non-targeted effects (NTE) that result from changes in cell signaling, e.g., genomic instability. It is unknown whether the potentially greater carcinogenic effect of high *Z* and energy (HZE) particle radiation is a function of the relative contribution or extent of NTE or due to unique NTE. We addressed this problem using a radiation/genetic mammary chimera mouse model of breast cancer. Our experiments suggest that NTE promote more aggressive cancers, as evidenced by increased growth rate, transcriptomic signatures, and metastasis, and that HZE particle NTE are more effective than reference γ-radiation. Emerging evidence suggest that HZE irradiation dampens antitumor immunity. These studies raise concern that HZE radiation exposure not only increases the likelihood of developing cancer but also could promote progression to more aggressive cancer with a greater risk of mortality.

Keywords: cosmic radiation, cancer risk models, ionizing radiation exposure, carcinogenesis process

OPEN ACCESS

Edited by:
Marco Durante, GSI Helmholtzzentrum für Schwerionenforschung, Germany

Reviewed by:
M. Christine Hollander, National Institutes of Health, USA
Albert J. Fornace, Georgetown University Medical Center, USA

****Correspondence:***
Mary Helen Barcellos-Hoff
mary.barcellos-hoff@ucsf.edu

Specialty section:
This article was submitted to Radiation Oncology, a section of the journal Frontiers in Oncology

Received: *13 January 2016*
Accepted: *28 February 2016*
Published: *11 March 2016*

Citation:
Barcellos-Hoff MH and Mao J-H (2016) HZE Radiation Non-Targeted Effects on the Microenvironment That Mediate Mammary Carcinogenesis. Front. Oncol. 6:57. doi: 10.3389/fonc.2016.00057

Epidemiological data on radiation therapy, occupational exposures, and accidental or terrorist radiological events have established the carcinogenic potential of sparsely ionizing radiation that includes γ-rays and X-rays. Less is known about the carcinogenic potential of densely ionizing radiation from accelerated particles recently implemented in the clinic and that are of a concern for space flight. The galactic cosmic radiation environment consists of high atomic number (*Z*) and energy (HZE) charged particles that are characterized by high linear energy transfer (LET) along the particle track, i.e., densely ionizing, in contrast to most terrestrial low LET radiations that are sparsely ionizing. The unique pattern of energy deposition incurred by HZE particle traversal is of often the primary focus in evaluating the biological effects of the galactic cosmic radiation on astronauts (1, 2). During a 3-year flight in extra-magnetospheric space, 3% of the cells of the human body would be traversed on

Abbreviations: HZE, high *Z* and energy; LET, linear energy transfer; NTE, non-targeted effects; RBE, relative biological effect; RTE, radiation targeted effects; TGFβ, transforming growth factor β.

average by one Fe ion (3). Cancer risk from exposure to the deep space radiation environment could constrain mission parameters for astronauts. The cancer incidence following radiotherapy is low but significant late tissue effect and, though the favorable dose distribution that reduces dose to normal tissue is thought to provide protection, that of HZE particle radiotherapy is yet unknown.

High *Z* and energy particle radiation is of particular concern for cancer because the limited experimental data to date indicate that the relative biological effect (RBE) for densely ionizing HZE particles is several-to-many fold greater than sparsely ionizing radiation. HZE particles have a high RBE for many biological end points (4); however, some HZE biological effects are not observed following sparsely ionizing radiation (5) and some radiation effects, such as genomic instability, do not show classic dose dependence (6). As a consequence, measurements of individual biological events and their dose dependence do not describe how an organism will respond to radiation damage. HZE particles traversing a cell nucleus cause difficult to repair clustered DNA damage that is classified as a radiation targeted effects (RTE), i.e., due to the deposition of energy in the cell. Radiation exposure also elicits complex changes in signaling and phenotype, which are called non-targeted effects (NTE) because they are often observed in the neighbors or daughters of irradiated cells.

Radiation is classified as a complete carcinogen in the etiology of human tumors, including breast cancer, lung cancer, lymphoma, liver carcinoma, sarcoma, and glioma (7). Radiation-induced DNA damage elicits a rapid and efficient repair network, but the occasional misrepair of these lesions results in mutations, translocations, deletions, and amplifications, which are also hallmarks of cancer cells. Many risk models use the frequency of these RTE as the basis for estimating cancer risk. Such models assume that the probability of cancer is proportional to DNA damage and, hence, exposure, which is consistent with epidemiological association of cancer risk and polymorphisms in certain genes in the DNA repair pathway (8).

The risk paradigm broadly based on RTE, that is direct DNA damage, has been challenged by at least two classes of NTE: first, the demonstration that descendants of irradiated cells exhibit non-clonal damage (i.e., radiation-induced genomic instability) or altered phenotype; second, the designation of so-called "bystander" radiation effects, in which non-irradiated cells respond to signaling by irradiated cells (6). NTE can be functionally defined by particular experimental strategies (e.g., bystander experiments and media transfer) and occur by various mechanisms that involve gap junctions, soluble factors, and phenotypic transition that differ between cell types and between *in vitro* and *in vivo* models.

The crucial question is to determine under what conditions and to what extent NTE contribute to human health risks. Recent experimental studies of radiation carcinogenesis following low- and high LET radiation exposures are concerned with how complex organismal responses to radiation interact across levels of organization and time scales to impede or promote malignant processes (9). Mechanistic understanding of cancer has become much more detailed over the last two decades. There is growing recognition that cancer as a disease results from a systemic failure, in which many cells other than those with oncogenic genomes determine the frequency of clinical cancer (10). The challenge to predicting health effects in irradiated humans is to understand how complex radiation responses culminate in pathology.

CARCINOGENESIS IN CONTEXT

The understanding of cancer as a result of systemic failure, in which many cells other than those with oncogenic mutations/alterations determine the frequency and characteristics of clinical cancer, underscores tissue dysfunction, in which cancer cells are highly intertwined with the microenvironment (11, 12). Both tissue and organismal biology are subverted during malignant progression (13). More than a quarter of a century ago, studies by Mintz and Pierce demonstrated that malignancy could be suppressed by contact with normal tissues (14, 15). Many have even argued that disruption of the cell interactions and tissue architecture can be the primary drivers of carcinogenesis (16–20). Recent experiments with engineered models have focused on identifying the type and means by which normal cells mediate the development of cancer (21–24), but it is clear that host cells, e.g., stromal cells and bone marrow-derived cells (BMDC), sculpt carcinogenesis in a complex process that can either eliminate or accelerate malignancy.

Recent studies demonstrate that host biology is altered even before cancer is evident. A systems biology approach by Hanash and colleagues characterized the plasma proteome response in the inducible HER2/neu mouse model of breast cancer during tumor induction, progression, and regression. Mass spectrometry data derived from approximately 1.6 million spectra identified protein networks associated with tumor development. Some networks were derived from the tumor microenvironment and some from tumor cell secreted or shed proteins. The observed alterations developed prior to cancer detection, increased progressively with tumor growth, and reverted toward baseline with tumor regression. Importantly, these findings were mirrored with findings resulting from in-depth profiling of circulating proteins using prediagnostic plasma samples from women who participated in the Women's Health Initiative study and who subsequently developed breast cancer (25–27).

Although the prevailing radiation health paradigm focuses on radiation-induced DNA damage leading to mutations, numerous studies over the last 50 years have provided evidence that radiation carcinogenesis is more complex than generally appreciated [reviewed in Ref. (28)]. Terzaghi-Howe demonstrated that the expression of dysplasia *in vivo* and neoplastic transformation in culture of irradiated tracheal epithelial cells is inversely correlated to the number of cells seeded (29–32) and identified TGFβ as a key mediator (33). Our lab used a *Trp53* mutant mammary cell line to show that irradiating only the host increased the development of frank tumors fivefold (34). Saran and colleagues showed that partial body irradiation at a young age promotes *Ptch* mutant medulloblastoma (35).

Many studies using oncogenic mouse models indicate that the stroma is highly involved in early malignancy (36), which supports the idea of reciprocal evolution of the malignant cell and the tumor microenvironment (10). Although it is clear

that stroma composition and signaling is altered in human breast cancer (37), less is known about how and when stroma contributes to carcinogenesis and how carcinogens, such as radiation, might alter these processes. We postulate that the tumor microenvironment is built through rate-limiting steps of construction, expansion, and maturation that parallel initiation, promotion, and progression during multistage carcinogenesis (10). Construction of a "pre-cancer niche" is the necessary first step to generate a tumor microenvironment that is essential for initiated cells to survive and evolve into clinically evident cancers (**Figure 1**). The evolution of the tumor microenvironment *via* stromal cells and BMDC during subsequent niche expansion during promotion is mediated by cytokines secreted by either the initiated epithelial cells or those host cells recruited to the niche. Maturation of the tumor microenvironment, as evidenced by angiogenesis escape from immune suppression and generation of a stroma permissive for growth and often invasion, occurs during progression. Importantly, signaling is not just local but can also be mediated by cells, cytokines, and exosomes transported by the vasculature between the nascent cancer and distant sites include the bone marrow, which may reciprocate by expansion of cells, such as immature myeloid cells (IMC) that support tumor growth. Indeed, the pre-metastatic niche, first described by Lyden and colleagues, pre-dates and facilitates metastatic disease (38).

This model postulates that cancer survival and proliferation is as much a function of the successful niche construction as it is of specific cancer cell mutations. Indeed selective pressure for neoplastic mutations may be imposed by the composition of the niche, as well as by immune editing (39). Consequently, cancer represents an emergent property that requires a comprehensive analysis of the cell–cell interactions in the entire niche. Moreover, in contrast to initiation, which is a stochastic process by nature, niche construction represents a robust target for native immunosuppression and a potent target for cancer prevention. If microenvironments induced by radiation can promote neoplastic progression in unirradiated epithelial cells, events outside of the (targeted) box may significantly increase cancer risk. Understanding such non-targeted mechanisms readily lead

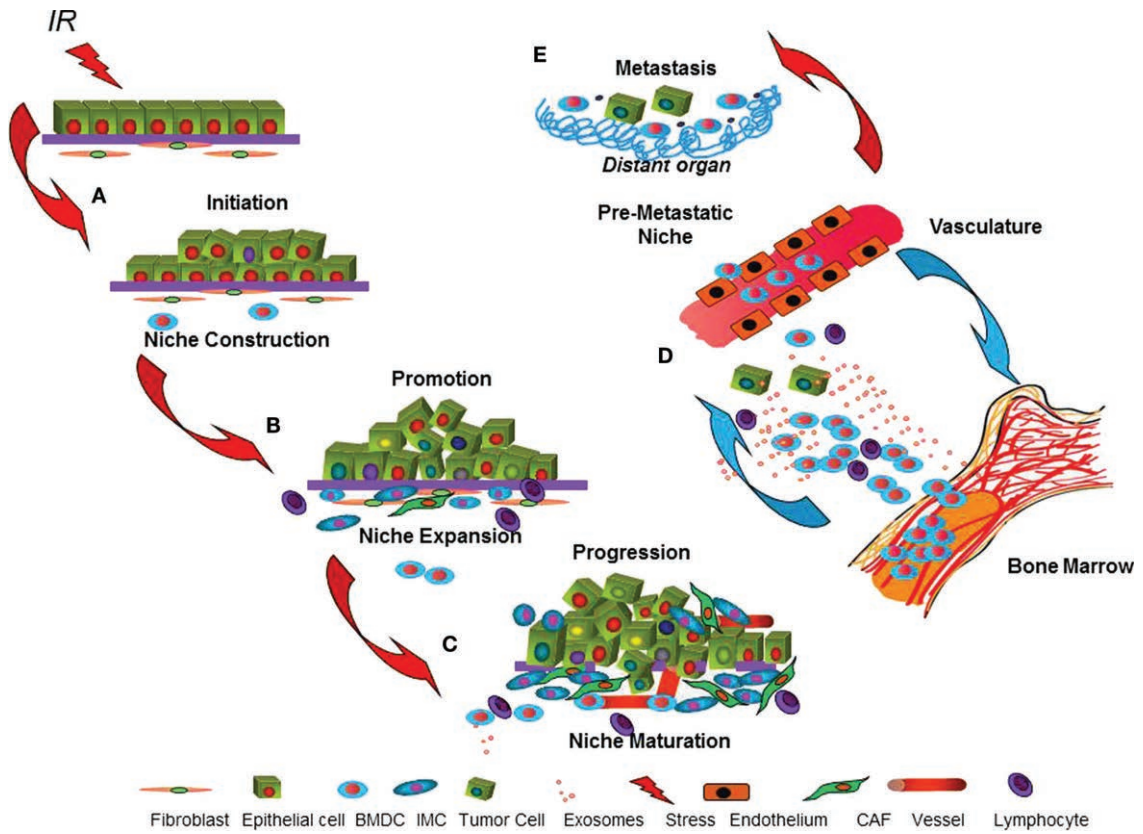

FIGURE 1 | **The dynamic cancer niche**. The cartoon depicts parallel processes postulated to occur in the target epithelium and microenvironment during multistage epithelial carcinogenesis. **(A)** Misrepaired DNA damage caused by radiation can malignantly *initiate* epithelial cells. Radiation effects on cell signaling and phenotype may promote concomitant niche *construction* by local or systemically recruited cells that improve initiated cell survival. **(B)** Within the epithelium, *promotion* is considered to be acquisition of additional genetic aberrations or epigenetic traits that enable malignancy. In parallel, niche *expansion*, due to signals produced by either the initiated epithelium or by the niche cells that support them, conscripts stromal cells and bone marrow-derived cells (BMDC). **(C)** *Maturation* of the tumor microenvironment that enables angiogenesis, immune suppression, and invasion is necessary for tumor *progression*. **(D)** Systemic influences, including signaling to and from *vasculature* and *bone marrow*, contribute throughout multistage carcinogenesis *via* participation of BMDC, lymphocytes, and immature myeloid cells (IMC) and their secreted cytokines and exosomes. **(E)** Some cancers are able to initiate new microenvironments, the *pre-metastatic niche*, in distant organs that facilitate *metastasis*.

to potential mechanisms for clinical interventions for health risks in future populations.

MODELING RADIATION CARCINOGENESIS

Most models of cancer risk and mitigation are focused on "targets," i.e., the cells that will undergo neoplastic transformation or the genetic alterations that initiate and promote this event. This is classically modeled in which carcinogenesis is thought to occur in four interdependent stages. The first stage is *initiation* and is typically caused by chemical, physical, or biological agents, which irreversibly and heritably alter the cell genome resulting in an enhanced growth potential. This potential is only realized, however, if the cell later undergoes *promotion*, the second stage of carcinogenesis. *Promotion* is often thought to be the rate-limiting step in carcinogenesis since it has been shown that initiation alone is not sufficient to induce cancer (40). In order to account for the observed power of age dependence in radiation-induced carcinomas, a multistage theory of carcinogenesis was introduced very early (41, 42). However, this model suggested five to seven rate-limiting stages, in contradiction with biological data. Some approaches addressed this contradiction by introducing the two-stage clonal expansion model, where a cell leads to a tumor by two separate mutations and clonal expansion (43–45). Integration of specific genetic mutations in tumor suppressor genes was originally introduced by Knudson (46). The current paradigm of carcinogenic risk remains heavily focused on predicting mutations of the genome leading to silencing of tumor suppressor genes or activation of oncogenes. However, such models neglect the influence of intercellular and extracellular interactions in the tumor growth and predict a final tumor that is unrealistic in that its cells are clonally identical.

Systems radiation biology seeks to integrate information about changes across time and scale that are determined by experimentation and to interrogate this to identify the critical events. By modeling the irradiated tissue/organ/organism as a system rather than a collection of non-interacting or minimally interacting cells, cancer can result as an emergent phenomenon of a perturbed system (47). A biological model in which radiation risk is the sum of dynamic and interacting processes could provide the impetus to reassess assumptions about radiation health effects in a healthy population and spur new approaches to prevent detrimental processes that lead to pathology.

Our studies have addressed this problem by separating RTE from NTE by using the mammary gland as a model system. The mouse mammary gland provides an experimentally malleable framework for separating the contribution of NTE on the host from the target epithelium. Mammary gland develops during the postnatal period such that the epithelium can be surgically removed and replaced, creating a tissue chimera. Transplanted syngeneic epithelium can have a specific germ line manipulation, such as a transgene or knockout, or can have received a specific type of exposure, such as radiation. We transplant *unirradiated Trp53 null* mouse mammary tissue into *irradiated* syngeneic wild-type hosts to study whether radiation NTE acting *via* the host affects the process of epithelial carcinogenesis. The *p53 null* mammary model originally described by Medina and colleagues has important features in common with human breast cancer (48). Although about a quarter of human breast cancers have p53 mutations, the utility of this model is that *Trp53 null* mouse mammary tissue develops normally until about 8 months of age, when both ductal carcinoma *in situ* and aneuploidy are evident, thus reproducing the long latency and early instability observed in most human breast cancers. Importantly, the *p53 null* tissue gives rise to histologically heterogeneous tumors that can be estrogen receptor negative or positive and genomically diverse, as are human breast cancers. Thus, the model of an oncogenically primed epithelium lacking p53 condenses the time necessary for spontaneous mutagenic events to accumulate.

The radiation-genetic chimera is used to determine whether and how radiation NTE contribute to mammary carcinogenesis (49). These data from provide strong support that NTE do contribute to radiation carcinogenesis and offer new insight into radiation quality effects that promote aggressive tumors, particularly upon exposure in middle age. Our studies summarized here have identified NTE-mediated mechanisms that include stem cell regulation, inflammation, and immune suppression that are important in determining the rate at which cancers develop and the type of cancer depends on radiation quality and genetic background.

The radiation chimera shows that NTE act *via* the microenvironment to accelerate tumorigenesis and affect critical characteristics (49). A notable observation was that the frequency of ER-negative tumors significantly doubled in irradiated hosts, which was replicated with HZE particle irradiation (50). Importantly, early radiation exposure increased ER-negative tumors in women treated with radiation for childhood cancer fourfold compared to a consecutive series of breast cancers not preceded by radiation (51). A new study by Horst and colleagues confirmed that radiation-preceded breast cancer in survivors of childhood cancer is significantly more likely to the aggressive, the so-called triple negative (negative for ER, progesterone receptor, and amplification of HER2) breast cancer (52). Interestingly, there is little evidence that the frequency of contralateral ER-negative breast cancer is increased in women treated with radiation for breast cancer (53), suggesting a physiological basis for the shift to ER-negative tumors, which are clinically less responsive and more likely to metastasize soon after detection.

To further explore how tumors arising in irradiated hosts are distinct from those that occur in non-irradiated hosts, we profiled total RNA from mammary cancers that arose in non-irradiated mice and irradiated mice (49). Permutation analysis was used to identify 156 genes that segregated tumors from irradiated or non-irradiated hosts. Significant enrichment of genes-involving leukocyte chemo-attraction and binding, monocyte maturation, and proliferation of tumor cell lines underscores the parallels between tumors forming in irradiated host and expression programs activated shortly after radiation exposure, even though the exposure occurred months before and the tumors arose from *unirradiated* epithelium.

We then used this strategy to generate a list of 323 genes and an irradiated host metaprofile (54). Bioinformatics analysis of

the human orthologs of the host irradiation metaprofile was used to conduct unsupervised hierarchical clustering of radiation-associated human cancer (54). The irradiated host metaprofile segregated sporadic cancers from radiation-preceded sarcomas (55) and radiation-preceded papillary thyroid carcinomas (56). These analyses support our hypothesis that the microenvironment mediates the development of radiation-preceded human cancers.

Four gene networks representing two cell types, stem cells and macrophages, and two processes, motility and autophagy, were identified in the irradiated host tumor signature. Tissue-specific stem cells or early progenitor cells are considered to be the critical cellular target in carcinogenesis (57–63), based, in part, on the idea that stem cell transformation can lead to unlimited progeny. A mammary stem cell (MaSC) signature, defined by Visvader and colleagues (64), is enriched in the mammary gland up to 1 month after mice are exposed to 10-cGy γ-radiation. We showed this signature is functional as indicated by a doubling of mammary repopulation capacity as well as the pool of cells defined by cell surface markers as associated with mammary repopulation (49). Additional experiments in conjunction with computational modeling led us to conclude that radiation elicits a durable but transient stem cell expansion in a TGFβ and Notch-dependent fashion in juveniles, but not adults (50). In model systems, we found that TGFβ increases self-renewal is blocked by γ-secretase inhibition, indicative of concomitant Notch signaling, which is also induced by low-dose irradiation. This temporary increase in self-renewal is similar to our earlier studies showing that both high- and low LET radiation exposure primes non-malignant human epithelial cells to undergo TGFβ-dependent epithelial–mesenchymal transition (65–67). These studies underscore that even a single radiation exposure can cause phenotypic re-programing.

CANCER AND INFLAMMATION

The concept that inflammatory responses are necessary components of cancer development has recently been formalized by Mantovani et al. (68) in a two-pathway model: the intrinsic versus extrinsic. In the intrinsic pathway, genetic mutations lead to release by the transformed cells of proinflammatory factors recruiting innate immune cells. For example, oncogenic *Ras* activates the transcription of the inflammatory cytokine interleukin-8 (IL-8). Other oncogenes, such as *Bcl2*, inhibit apoptosis leading to necrotic tumor cell death and release of damage-associated molecular pattern molecules that activate innate immune cells *via* toll-like receptors (68, 69). In both circumstances, the resulting host response is a smoldering inflammation that promotes tumor growth and invasion (68, 70). In the extrinsic pathway, the chronic inflammation results from inability of the immune system to resolve an infection (e.g., hepatitis B) or from a dysregulated immune response as in autoimmune diseases (e.g., inflammatory bowel disease). The persistent inflammation cooperates with pre-existing oncogenic mutations by providing the microenvironment that promotes cancer progression, but it may also induce DNA damage resulting in the acquisition of new mutations (71, 72).

The innate immune system functions as an "interpreter" of tissue damage that not only provides a first line of defense but also translates the information to wound repair and defense systems in the body by stimulating angiogenesis and activating adaptive immunity. Therefore, it is not surprising that various types of innate immune cells have been found as part of the tumor inflammatory infiltrate. Macrophages play a central role in most solid malignancies, and most studies have found that macrophage abundance, increased microvessel density, and reduced patient survival are highly correlated (73). In fact, macrophages present within tumors are defined as tumor-associated macrophages to denote a specific phenotype that is associated with the production of several proangiogenic factors and cytokines that suppress antitumor immune responses and promote tumor growth by maintaining protumorigenic inflammation.

The application of systems biology by Balmain and colleagues uncovered a differential hub for inflammation in skin cancer (74). While a positive association exists between chronic inflammation and cancer, the innate immune system is itself a network that can be disrupted by both positive and negative stimuli. Anti-inflammatory drugs can have contradictory effects on skin tumor development (75, 76), and over-expression of proinflammatory cytokines, such as IL-1, can prevent skin tumor formation in mouse models of chemically induced skin cancer (77). In contrast, germline deletion of TNF-α, another potent proinflammatory cytokine, also confers resistance to skin tumor formation (78). The role of inflammation in cancer is, therefore, very complex, with different consequences associated with acute or chronic inflammatory conditions.

How the interplay between inflammatory cells and genetically mutated neoplastic cells promotes cancer development and progression remains a subject of intense investigation. Several important pathways have been identified. Among them, IL-6 signaling pathways play a major role (79). Macrophages are the main source of IL-6 during acute inflammation and T cells during chronic inflammation. Importantly, IL-6 orchestrates the transition from acute inflammation, dominated by granulocytes, to chronic inflammation, dominated by monocytes/macrophages and regulates, together with TGFβ, the differentiation of naïve T cells to Th17 proinflammatory phenotype, thus influencing the type of adaptive immune response (80).

Seminal studies by Wright and colleagues identified non-clonal radiation-induced genomic instability in hematopoietic stem cells [reviewed in Ref. (6)], which they now explain as a result of altered cell interactions. Macrophages from irradiated mice could induce chromosomal instability in non-irradiated hematopoietic cells *via* production of TNFα and reactive oxygen and nitrogen species (81). Further studies showed that this effect was a function of mouse genotype, which affects the steady state M1 or M2 macrophage phenotype, which radiation exposure further amplifies (82). HZE particle NTE on inflammatory processes is supported by studies from Burns and colleagues who showed that chronic dietary exposure to vitamin A acetate can prevent almost all malignant and benign tumors that occur in rat skin exposed to electron radiation and most of those following ^{56}Fe ion irradiation (83). Gene expression analysis suggested that vitamin A reduced or blocked ^{56}Fe ion radiation-induced inflammation-related genes that were represented in the categories of "immune

response," "response to stress," "signal transduction," and "response to biotic stress" (84).

To investigate systemic effects of HZE, the *Trp53* null mammary radiation-chimera model was irradiated with low fluences (equivalent to average dose of 11, 30, and 81 cGy) of 350 MeV/amu ^{26}Si particles and compared to contemporaneous γ-irradiated (100 cGy) and sham-irradiated mice (85). The median time to tumor detection in mice irradiated with the lowest ^{26}Si fluence or γ-radiation was similar to that in sham-irradiated mice but decreased for transplants in mice exposed to higher fluences of ^{26}Si particles. As previously reported, the growth rate of tumors arising in irradiated mice was increased compared to those arising in sham-irradiated mice but was significantly faster than high fluence Si-irradiated mice compared to γ-irradiated mice. Since the initial growth rate of tumors arising in hosts irradiated with 11-cGy ^{26}Si particles was comparable to that of tumors arising in mice irradiated with 100 cGy sparsely ionizing γ-rays, we concluded that there is an RBE of about 10 for this endpoint.

The carcinoma spectrum arising in mice exposed to ^{26}Si particles is enriched for a subclass that is ER-negative and keratin 18-positive. These tumors in Si-irradiated mice developed metastases twice as often as non-irradiated mice. As ^{26}Si irradiation of hosts primarily promotes specific ER-negative subtypes, genomic analysis of these tumors compared to a comparable group from sham-irradiated mice. Consistent with these differences, an expression profile that distinguished K18 tumors arising in ^{26}Si-irradiated compared sham-irradiated mice was enriched in MaSC, stroma, and Notch signaling genes. These data suggest that the carcinogenic effects of NTE from densely ionizing radiation compared to sparsely ionizing radiation elicit more aggressive tumors. In humans, the type, the density, and the location of immune cells within the tumor are strongly associated with prognosis (86). Together, these data support the hypothesis that radiogenic cancer risk is augmented by alterations in a network of cellular interactions, at the center of which is the innate immune system.

IMMUNE SURVEILLANCE AND SUPPRESSION

A fundamental role of the immune system is enforcing tissue homeostasis, a task accomplished by mounting inflammatory reactions that involve the coordinated activation of innate and adaptive immune cells. Radiation perturbs tissue homeostasis by activating inflammatory reactions that often do not resolve, leading to a vicious cycle of subclinical tissue damage and smoldering inflammation (87, 88). Whereas one body of work has clearly established the capacity of chronic inflammation to initiate and promote cancer (88), other studies have revealed that an intact immune system can prevent/control and shape cancer by a process best conceptualized in the "cancer immunoediting" theory (89). During initial clonal expansion, recognition of the stressed transformed cells by innate immune cells results in production of interferon-γ, a cytokine shown to play a key role in immunosurveillance against tumors (90, 91). Killing of the preneoplastic cells by natural killer cells or macrophages activated by IFN-γ to produce cytocidal reactive oxygen and nitrogen species eventually leads to cross-presentation by dendritic cells of antigens from the dying tumor cells to T cells and activation of the adaptive immune system. The tumor-specific T cells may be able to destroy completely the incipient tumor, thus functioning as an extrinsic tumor suppressor mechanism that reduces the incidence of spontaneous and carcinogen-induced tumors, something for which there is unequivocal evidence in experimental models and supportive evidence in humans [reviewed in Ref. (39, 92)].

However, if complete elimination of transformed cells is not achieved, the immunological pressure results in selection of clones of cells that have acquired mutations or epigenetic changes conferring resistance to immune rejection, i.e., are "edited" by the immune system to select for those that are poorly immunogenic. This transition from elimination to escape can occur directly or even after a very long period of equilibrium, during which the immune response actively limits progression. The concept of equilibrium, which was initially formulated to explain clinical observations of occult tumors and tumor dormancy (93, 94), has been confirmed in experimental models showing that depletion of T cells leads to growth of occult tumors (95). Importantly, protumorigenic inflammation and antitumor immunity can co-exist in the same tumor, and interventions that can alter the balance in favor of one or the other may either accelerate or hinder tumor growth (88).

We found that lymphocyte infiltrate of *Trp53* null tumors arising in the irradiated mammary chimera correlates to tumor growth rate, i.e., faster growing tumors have less lymphocytic infiltrate, and that particle irradiation elicits the most rapidly growing tumors. This observation suggests that HZE particles have a systemic impact on the immune surveillance that leads to the development of more aggressive tumors.

GENETIC MEDIATORS OF CANCER

Epidemiological and genetic studies show that there is a strong genetic component that contributes to the differences between individuals in their response to DNA damage and cancer susceptibility (96, 97). High penetrance mutations in genes, such as BRCA1/2, are responsible for a proportion of cancers that show familial aggregation (98). However, the genetic basis of susceptibility to the majority of cancers that have no obvious familial aggregation is almost completely unknown (96, 99). Most studies to identify susceptibility loci for radiation-associated cancer are limited to candidate genes involved in response to DNA damage, but there is strong evidence that other processes are important; systems genetics seeks to uncover those components that result from complex interactions between pathways and cells.

Systems genetics, unlike traditional approaches to the analysis of disease that focus on single genes or proteins in isolation, attempts to integrate the complex interaction of many kinds of genetic and biological information – genomic DNA sequence, mRNA, and protein expression, and link these to disease phenotypes. Human studies have demonstrated strong associations between polymorphic variation and regulation of gene expression (100–102). Parallel studies in mice offer many advantages for the study of the genetic basis of complex traits. The ability to control genetic background and to carry out crosses between

mouse strains differing in their propensity to develop these diseases offers unprecedented opportunities to identify and investigate the primary genetic loci that control susceptibility. In addition, studies with mice allow precise exposures, standardized husbandry to control other environmental components of risk, and comprehensive analysis of phenotypes.

Applying these approaches to mouse strains with differing susceptibility to diseases identifies signaling hubs that may be important targets for therapy or prevention (103). A systems genetics approach consists of a network view of the genetic and gene expression architecture of normal host tissues that are compared after perturbation by radiation or tumor development (104, 105). An example of this strategy used gene expression profiles of skin from a population of *mus spretus* backcrossed to *mus musculus* mice to reveal the normal skin gene expression motifs associated with sensitivity to carcinogen-induced skin tumor development in contrast to those that were resistant. This analysis revealed both cell-autonomous (cell cycle and stem cell lineage) and non-cell-autonomous (inflammation and innate immunity) components that were differentially expressed in the susceptible animals. Interestingly, the highly susceptible mice exhibited increased levels of anti-inflammatory genes within the inflammation associated network, leading to the conclusion that chronic and acute inflammation are, respectively, tumor-promoting versus suppressive (106).

Multiple tumor types in mice, including thymomas, soft tissue sarcomas, and osteosarcomas, can be induced by exposure to low LET radiation, but induction is typically infrequent and tumors have long latency (i.e., survival time post-radiation). Engineered loss or misregulation of p53 increases the detection sensitivity. Radiation induces the same spectrum of tumors in p53-deficient mice that lack one or both p53 alleles; however, the survival time is dramatically reduced after a single exposure to ionizing radiation (107). Likewise, the *Trp53* null BALB/c inbred mouse strain is sensitive to mammary carcinogenesis, and radiation exposure enhances this susceptibility (108–110). The utility of this model is that tumors are diverse by all criteria, markers, histology, metastatic capacity, and genomic profiling, in a fashion that is remarkably aligned with human breast cancer (48, 111).

Recent experiments focus on the genetic contribution to NTE using the mammary chimera (112). Radioresistant SPRET/EiJ was mated to radiosensitive (BALB/c) mice, and then the progeny were backcrossed to BALB/c to generate F1 backcrossed mice (F1Bx). Our prior experiments using inbred BALB/c mice showed that host irradiation decreased *Trp53* null tumor latency, increased frequency of tumor formation at a year post-transplantation, and that tumors arising in irradiated hosts grew more rapidly (49). Consistent with our previous observations, the growth rate of *Trp53* null mammary carcinomas was greater in irradiated F1Bx host mice, a feature associated with aggressive tumors, compared to unirradiated mice. However, *Trp53* null tumor latency increased in irradiated hosts and tumor frequency was reduced by 9.6% ($p = 0.04$) at 18 months posttransplantation compared to sham-irradiated F1Bx hosts. The revelation that NTE delay rather than accelerate mammary cancers in genetically diverse hosts underscores the outcome of radiation exposure in terms of carcinogenesis depends of genetic background.

Introgression was used to determine the genetic loci that affected *Trp53* null mammary tumor latency of the radioresistant SPRET/EiJ genome using genome-wide genotyping. Only two loci were associated with tumor latency in sham-irradiated mice. Tumors in mice homozygous for the BALB/c allele at loci on chromosomes 2 and 14 appeared with a significantly shorter latency than those mice, in which one allele was from BALB/c and the other from SPRET/EiJ at these loci. Interestingly, neither of the loci affected latency in irradiated hosts. In contrast, 15 genetic loci were associated with tumor latency in irradiated mice, 11 alleles confer resistance to tumor development, and 4 alleles conferred susceptibility.

Together, the use of systems genetics with the radiation-chimera model provides new insight into the processes that mediate carcinogenic susceptibility to radiation. To further explore stromal genetic associations with cancer risk after exposure to low LET radiation, we used ingenuity pathway analysis (IPA) to identify 696 candidate genes located within the identified loci. Of these, 185 genes were within 4 loci on chromosomes 2, 11, 14, and 16 where homozygous BALB/C alleles associate with increased latency for cancer arising in irradiated mice. These genes were enriched in four pathways, γ-glutamyl cycle, leukotriene biosynthesis, alanine biosynthesis III, and glutathione biosynthesis. In contrast, 511 genes enriched for 24 pathways were within 11 regions where heterozygous SPRET/EiJ alleles associate with increased latency. Importantly, these 11 loci were enriched for genes involved in regulating the immune response including signaling pathways of natural killer cells and cytokines. Radiation-induced activation of pathways that control release of inflammatory cytokines varies among mouse strains (113, 114) and is postulated to contribute to genetic susceptibility to radiation-induced leukemia (113). Analysis of the upstream regulators of these candidate genes indicated that the TGFβ and p53 pathways might also be involved in mammary tumor susceptibility.

The observation that many more genetic loci are linked with tumor latency in the radiation-treated cohort than in the sham-irradiated cohort suggests the interesting idea that genetic contribution is actually specific to NTE, in contrast to the widely held belief that radiation exaggerates inherent susceptibility. This is exemplified by the work of Onel and colleagues who identified PRDM1 (Blimp-1), a transcriptional regulator of cell specification, with the risk of second malignancies only in those treated with radiation for childhood malignancy (115). In individuals with the homozygous protective allele, the incidence of second cancers is 3:100 by 30 years after exposure, whereas in those who were homozygous for the allele, risk is 1:3. Thus, the risk allele conferred risk comparable to BRCA1 mutation, but only in the context of radiation.

SUMMARY

Identifying mechanisms of NTE is essential to understand the biology of irradiated tissues. Two fundamental aspects of NTE in carcinogenesis warrant careful consideration for further understanding of cancer risk in irradiated populations. First is

that radiation NTE may alter the shape of the dose response. Recent modeling by Cucinotta and colleagues suggest that NTE may be particularly important in the low-dose region of concern for occupational exposures. Second, NTE are targetable; the biology that ensues after exposure is persistent and may be "reset" after the fact to limit carcinogenic potential. This offers the possibility of protecting those at greatest risk, for example, children who are treated with charged particles for childhood malignancy, in which the clear benefit of dose distribution may come at the price of long-term cancer risk. Moreover, NTE will likely provide insight into the use of particles for cancer therapy as there are common microenvironment components, such as the immunoregulatory axis and the vasculature, that are likely critical to treatment outcome.

AUTHOR CONTRIBUTIONS

Dr. MHB-H outlined and wrote the manuscript. Dr. J-HM edited and contributed to this manuscript.

FUNDING

NNX13AF06G, Barcellos-Hoff, Mary Helen: 10/01/2012–01/30/2016. National Aeronautics and Space Agency: HZE radiation effects on malignant progression in human epithelial cells. Little is known about the mechanisms that underlie the greater biological effectiveness of high LET irradiation to promote solid cancer in experimental models. We hypothesize that both genetic and phenotypic changes contribute to radiation carcinogenesis. Role: P.I.

REFERENCES

1. Fry RJM, Nachtwey DS. Radiation protection guidelines for space missions. *Health Phys* (1988) **55**:159–64. doi:10.1097/00004032-198808000-00006
2. Todd P. Unique biological aspects of radiation hazards – an overview. *Adv Space Res* (1983) **3**:187–94. doi:10.1016/0273-1177(83)90189-8
3. Curtis SB, Letaw JR. Galactic cosmic rays and cell-hit frequencies outside the magnetosphere. *Adv Space Res* (1989) **9**:292–8. doi:10.1016/0273-1177(89)90452-3
4. Blakely EA, Kronenberg A. Heavy-ion radiobiology: new approaches to delineate mechanisms underlying enhanced biological effectiveness. *Radiat Res* (1998) **150**:S126–45. doi:10.2307/3579815
5. Costes S, Streuli CH, Barcellos-Hoff MH. Quantitative image analysis of laminin immunoreactivity in skin basement membrane irradiated with 1 GeV/nucleon iron particles. *Radiat Res* (2000) **154**:389–97. doi:10.1667/0033-7587(2000)154[0389:QIAOLI]2.0.CO;2
6. Lorimore SA, Coates PJ, Wright EG. Radiation-induced genomic instability and bystander effects: inter-related nontargeted effects of exposure to ionizing radiation. *Oncogene* (2003) **22**:7058–69. doi:10.1038/sj.onc.1207044
7. Preston DL, Ron E, Tokuoka S, Funamoto S, Nishi N, Soda M, et al. Solid cancer incidence in atomic bomb survivors: 1958-1998. *Radiat Res* (2007) **168**:1–64. doi:10.1667/RR0763.1
8. Smith TR, Levine EA, Perrier ND, Miller MS, Freimanis RI, Lohman K, et al. DNA-repair genetic polymorphisms and breast cancer risk. *Cancer Epidemiol Biomarkers Prev* (2003) **12**:1200–4.
9. Barcellos-Hoff MH, Adams C, Balmain A, Costes SV, Demaria S, Illa-Bochaca I, et al. Systems biology perspectives on the carcinogenic potential of radiation. *J Radiat Res* (2014) **55**:i145–54. doi:10.1093/jrr/rrt211
10. Barcellos-Hoff MH, Lyden D, Wang TC. The evolution of the cancer niche during multistage carcinogenesis. *Nat Rev Cancer* (2013) **13**:511–8. doi:10.1038/nrc3536
11. Bissell MJ, Radisky D, Rizki A, Weaver VM, Petersen OW. The organizing principle: microenvironmental influences in the normal and malignant breast. *Differentiation* (2002) **70**:537–46. doi:10.1046/j.1432-0436.2002.700907.x
12. Barcellos-Hoff MH, Medina D. New highlights on stroma-epithelial interactions in breast cancer. *Breast Cancer Res* (2005) **7**:33–6. doi:10.1186/bcr972
13. Coussens LM, Werb Z. Inflammatory cells and cancer: think different! *J Exp Med* (2001) **193**:23F–6F. doi:10.1084/jem.193.6.F23
14. Mintz B, Illmensee K. Normal genetically mosaic mice produced from malignant teratocarcinoma cells. *Proc Natl Acad Sci U S A* (1975) **72**:3585–9. doi:10.1073/pnas.72.9.3585
15. Pierce GB, Shikes R, Fink LM. *Cancer: A Problem of Developmental Biology*. Englewood Cliffs: Prentice-Hall, Inc. (1978).
16. Rubin H. Cancer as a dynamic developmental disorder. *Cancer Res* (1985) **45**:2935–42.
17. Barcellos-Hoff MH. The potential influence of radiation-induced microenvironments in neoplastic progression. *J Mammary Gland Biol Neoplasia* (1998) **3**:165–75. doi:10.1023/A:1018794806635
18. Sonnenschein C, Soto AM. Somatic mutation theory of carcinogenesis: why it should be dropped and replaced. *Mol Carcinog* (2000) **29**:205–11. doi:10.1002/1098-2744(200012)29:4<205::AID-MC1002>3.0.CO;2-W
19. Bissell MJ, Radisky D. Putting tumours in context. *Nat Rev Cancer* (2001) **1**:1–11. doi:10.1038/35094059
20. Wiseman BS, Werb Z. Stromal effects on mammary gland development and breast cancer. *Science* (2002) **296**:1046–9. doi:10.1126/science.1067431
21. Kuperwasser C, Chavarria T, Wu M, Magrane G, Gray JW, Carey L, et al. From the cover: reconstruction of functionally normal and malignant human breast tissues in mice. *Proc Natl Acad Sci U S A* (2004) **101**:4966–71. doi:10.1073/pnas.0401064101
22. Bhowmick NA, Ghiassi M, Bakin A, Aakre M, Lundquist CA, Engel ME, et al. Transforming growth factor-b1 mediates epithelial to mesenchymal transdifferentiation through a Rho-A-dependent mechanism. *Mol Biol Cell* (2001) **12**:27–36. doi:10.1091/mbc.12.1.27
23. Maffini MV, Soto AM, Calabro JM, Ucci AA, Sonnenschein C. The stroma as a crucial target in rat mammary gland carcinogenesis. *J Cell Sci* (2004) **117**:1495–502. doi:10.1242/jcs.01000
24. de Visser KE, Eichten A, Coussens LM. Paradoxical roles of the immune system during cancer development. *Nat Rev Cancer* (2006) **6**:24–37.
25. Pitteri SJ, Faca VM, Kelly-Spratt KS, Kasarda AE, Wang H, Zhang Q, et al. Plasma proteome profiling of a mouse model of breast cancer identifies a set of up-regulated proteins in common with human breast cancer cells. *J Proteome Res* (2008) **7**:1481–9. doi:10.1021/pr7007994
26. Amon LM, Pitteri SJ, Li CI, McIntosh M, Ladd JJ, Disis M, et al. Concordant release of glycolysis proteins into the plasma preceding a diagnosis of ER+ breast cancer. *Cancer Res* (2012) **72**:1935–42. doi:10.1158/0008-5472.CAN-11-3266
27. Pitteri SJ, Kelly-Spratt KS, Gurley KE, Kennedy J, Buson TB, Chin A, et al. Tumor microenvironment-derived proteins dominate the plasma proteome response during breast cancer induction and progression. *Cancer Res* (2011) **71**:5090–100. doi:10.1158/0008-5472.CAN-11-0568
28. Barcellos-Hoff MH. Integrative radiation carcinogenesis: interactions between cell and tissue responses to DNA damage. *Semin Cancer Biol* (2005) **15**:138–48. doi:10.1016/j.semcancer.2004.08.010
29. Terzaghi M, Little JB. X-radiation-induced transformation in C3H mouse embryo-derived cell line. *Cancer Res* (1976) **36**:1367–74.
30. Terzaghi M, Nettesheim P. Dynamics of neoplastic development in carcinogen-exposed tracheal mucosa. *Cancer Res* (1979) **39**:3004–10.
31. Terzaghi-Howe M. Inhibition of carcinogen-altered rat tracheal epithelial cell proliferation by normal epithelial cells in vivo. *Carcinogenesis* (1986) **8**:145–50. doi:10.1093/carcin/8.1.145
32. Terzaghi-Howe M. Changes in response to, and production of, transforming growth factor type b during neoplastic progression in cultured rat tracheal epithelial cells. *Carcinogenesis* (1989) **10**:973–80. doi:10.1093/carcin/10.6.973
33. Terzaghi-Howe M. Interactions between cell populations influence expression of the transformed phenotype in irradiated rat tracheal epithelial cells. *Radiat Res* (1990) **121**:242–7. doi:10.2307/3577772

34. Barcellos-Hoff MH, Ravani SA. Irradiated mammary gland stroma promotes the expression of tumorigenic potential by unirradiated epithelial cells. *Cancer Res* (2000) **60**:1254–60.
35. Mancuso M, Pasquali E, Leonardi S, Tanori M, Rebessi S, Di Majo V, et al. Oncogenic bystander radiation effects in patched heterozygous mouse cerebellum. *Proc Natl Acad Sci U S A* (2008) **105**:12445–50.
36. Mueller MM, Fusenig NE. Friends or foes – bipolar effects of the tumor stroma in cancer. *Nat Rev Cancer* (2004) **4**:839–49. doi:10.1038/nrc1477
37. Finak G, Bertos N, Pepin F, Sadekova S, Souleimanova M, Zhao H, et al. Stromal gene expression predicts clinical outcome in breast cancer. *Nat Med* (2008) **14**:518–27. doi:10.1038/nm1764
38. Kaplan RN, Riba RD, Zacharoulis S, Bramley AH, Vincent L, Costa C, et al. VEGFR1-positive haematopoietic bone marrow progenitors initiate the pre-metastatic niche. *Nature* (2005) **438**:820–7. doi:10.1038/nature04186
39. Dunn GP, Old LJ, Schreiber RD. The three Es of cancer immunoediting. *Annu Rev Immunol* (2004) **22**:329–60. doi:10.1146/annurev.immunol.22.012703.104803
40. Berenblum I, Shubik P. The persistence of latent tumour cells induced in the mouse's skin by a single application of 9:10-dimethyl-1:2-benzanthracene. *Br J Cancer* (1949) **3**:384–6. doi:10.1038/bjc.1949.42
41. Armitage P, Doll R. The age distribution of cancer and a multi-stage theory of carcinogenesis. *Br J Cancer* (1954) **8**:1–12. doi:10.1038/bjc.1954.1
42. Armitage P, Doll R. A two-stage theory of carcinogenesis in relation to the age distribution of human cancer. *Br J Cancer* (1957) **11**:161–9. doi:10.1038/bjc.1957.22
43. Moolgavkar SH, Dewanji A, Venzon DJ. A stochastic two-stage model for cancer risk assessment. I. The hazard function and the probability of tumor. *Risk Anal* (1988) **8**:383–92. doi:10.1111/j.1539-6924.1988.tb00502.x
44. Moolgavkar SH, Knudson AG Jr. Mutation and cancer: a model for human carcinogenesis. *J Natl Cancer Inst* (1981) **66**:1037–52.
45. Moolgavkar SH, Luebeck G. Two-event model for carcinogenesis: biological, mathematical, and statistical considerations. *Risk Anal* (1990) **10**:323–41. doi:10.1111/j.1539-6924.1990.tb01053.x
46. Knudson AG Jr. Mutation and cancer: statistical study of retinoblastoma. *Proc Natl Acad Sci U S A* (1971) **68**:820–3. doi:10.1073/pnas.68.4.820
47. Barcellos-Hoff MH. Cancer as an emergent phenomenon in systems radiation biology. *Radiat Env Biophys* (2007) **47**:33–8. doi:10.1007/s00411-007-0141-0
48. Medina D, Kittrell FS, Shepard A, Stephens LC, Jiang C, Lu J, et al. Biological and genetic properties of the p53 null preneoplastic mammary epithelium. *FASEB J* (2002) **16**:881–3.
49. Nguyen DH, Oketch-Rabah HA, Illa-Bochaca I, Geyer FC, Reis-Filho JS, Mao JH, et al. Radiation acts on the microenvironment to affect breast carcinogenesis by distinct mechanisms that decrease cancer latency and affect tumor type. *Cancer Cell* (2011) **19**:640–51. doi:10.1016/j.ccr.2011.03.011
50. Tang J, Fernandez-Garcia I, Vijayakumar S, Martinez-Ruiz H, Illa-Bochaca I, Nguyen DH, et al. Irradiation of juvenile, but not adult, mammary gland increases stem cell self-renewal and estrogen receptor negative tumors. *Stem Cells* (2013) **32**:649–61. doi:10.1002/stem.1533
51. Castiglioni F, Terenziani M, Carcangiu ML, Miliano R, Aiello P, Bertola L, et al. Radiation effects on development of HER2-positive breast carcinomas. *Clin Cancer Res* (2007) **13**:46–51. doi:10.1158/1078-0432.CCR-06-1490
52. Horst KC, Hancock SL, Ognibene G, Chen C, Advani RH, Rosenberg SA, et al. Histologic subtypes of breast cancer following radiotherapy for Hodgkin lymphoma. *Ann Oncol* (2014) **25**:848–51. doi:10.1093/annonc/mdu017
53. Stovall M, Smith SA, Langholz BM, Boice JD Jr, Shore RE, Andersson M, et al. Dose to the contralateral breast from radiotherapy and risk of second primary breast cancer in the WECARE study. *Int J Rad Oncol Biol Phys* (2008) **72**:1021–30. doi:10.1016/j.ijrobp.2008.02.040
54. Nguyen DH, Fredlund E, Zhao W, Perou CM, Balmain A, Mao J-H, et al. Murine microenvironment metaprofiles associate with human cancer etiology and intrinsic subtypes. *Clin Cancer Res* (2013) **19**:1353–62. doi:10.1158/1078-0432.CCR-12-3554
55. Hadj-Hamou NS, Ugolin N, Ory C, Britzen-Laurent N, Sastre-Garau X, Chevillard S, et al. A transcriptome signature distinguished sporadic from post-radiotherapy radiation-induced sarcomas. *Carcinogenesis* (2011) **32**:929–34. doi:10.1093/carcin/bgr064
56. Delys L, Detours V, Franc B, Thomas G, Bogdanova T, Tronko M, et al. Gene expression and the biological phenotype of papillary thyroid carcinomas. *Oncogene* (2007) **26**:7894–903. doi:10.1038/sj.onc.1210588
57. Clifton KH, Tanner MA, Gould MN. Assessment of radiogenic cancer initiation frequency per clonogenic rat mammary cell in vivo. *Cancer Res* (1986) **46**:2390–5.
58. Potten CS, Loeffler M. Stem cells: attributes, cycles, spirals, pitfalls and uncertainties. Lessons for and from the crypt. *Development* (1990) **110**:1001–20.
59. Smith GH, Chepko G. Mammary epithelial stem cells. *Microsc Res Tech* (2001) **52**:190–203. doi:10.1002/1097-0029(20010115)52:2<190::AID-JEMT1005>3.0.CO;2-O
60. Reya T, Morrison SJ, Clarke MF, Weissman IL. Stem cells, cancer, and cancer stem cells. *Nature* (2001) **414**:105–11. doi:10.1038/35102167
61. Preston DL, Mattsson A, Holmberg E, Shore R, Hildreth NG, Boice JD Jr. Radiation effects on breast cancer risk: a pooled analysis of eight cohorts. *Radiat Res* (2002) **158**:220–35. doi:10.1667/0033-7587(2002)158[0220:REOBCR]2.0.CO;2
62. Welm BE, Tepera SB, Venezia T, Graubert TA, Rosen JM, Goodell MA. Sca-1(pos) cells in the mouse mammary gland represent an enriched progenitor cell population. *Dev Biol* (2002) **245**:42–56. doi:10.1006/dbio.2002.0625
63. Visvader JE, Lindeman GJ. Mammary stem cells and mammopoiesis. *Cancer Res* (2006) **66**:9798–801. doi:10.1158/0008-5472.CAN-06-2254
64. Lim E, Wu D, Pal B, Bouras T, Asselin-Labat ML, Vaillant F, et al. Transcriptome analyses of mouse and human mammary cell subpopulations reveal multiple conserved genes and pathways. *Breast Cancer Res* (2010) **12**:R21. doi:10.1186/bcr2560
65. Andarawewa KL, Costes SV, Fernandez-Garcia I, Chou WS, Ravani SA, Park H, et al. Radiation dose and quality dependence of epithelial to mesenchymal transition (EMT) mediated by transforming growth factor β. *Int J Rad Oncol Biol Phys* (2011) **79**:1523–31. doi:10.1016/j.ijrobp.2010.11.058
66. Andarawewa KL, Erickson AC, Chou WS, Costes SV, Gascard P, Mott JD, et al. Ionizing radiation predisposes nonmalignant human mammary epithelial cells to undergo transforming growth factor beta induced epithelial to mesenchymal transition. *Cancer Res* (2007) **67**:8662–70. doi:10.1158/0008-5472.CAN-07-1294
67. Park CC, Henshall-Powell RL, Erickson AC, Talhouk R, Parvin B, Bissell MJ, et al. Ionizing radiation induces heritable disruption of epithelial cell interactions. *Proc Natl Acad Sci U S A* (2003) **100**:10728–33. doi:10.1073/pnas.1832185100
68. Mantovani A, Allavena P, Sica A, Balkwill F. Cancer-related inflammation. *Nature* (2008) **454**:436–44. doi:10.1038/nature07205
69. Sparmann A, Bar-Sagi D. Ras-induced interleukin-8 expression plays a critical role in tumor growth and angiogenesis. *Cancer Cell* (2004) **6**:447–58. doi:10.1016/j.ccr.2004.09.028
70. Zeh HJ, Lotze MT. Addicted to death: invasive cancer and the immune response to unscheduled cell death. *J Immunother* (2005) **28**:1–9. doi:10.1097/00002371-200501000-00001
71. Guerra C, Schuhmacher AJ, Cañamero M, Grippo PJ, Verdaguer L, Pérez-Gallego L, et al. Chronic pancreatitis is essential for induction of pancreatic ductal adenocarcinoma by K-Ras oncogenes in adult mice. *Cancer Cell* (2007) **11**:291–302. doi:10.1016/j.ccr.2007.01.012
72. Farber JL, Kyle ME, Coleman JB. Mechanisms of cell injury by activated oxygen species. *Lab Invest* (1990) **62**:670–9.
73. Lewis CE, Pollard JW. Distinct role of macrophages in different tumor microenvironments. *Cancer Res* (2006) **66**:605–12. doi:10.1158/0008-5472.CAN-05-4005
74. Quigley D, To M, Kim IJ, Lin K, Albertson D, Sjolund J, et al. Network analysis of skin tumor progression identifies a rewired genetic architecture affecting inflammation and tumor susceptibility. *Genome Biol* (2011) **12**:R5. doi:10.1186/gb-2011-12-1-r5
75. Viaje A, Slaga TJ, Wigler M, Weinstein IB. Effects of antiinflammatory agents on mouse skin tumor promotion, epidermal DNA synthesis, phorbol ester-induced cellular proliferation, and production of plasminogen activator. *Cancer Res* (1977) **37**:1530–6.
76. Fischer SM, Gleason GL, Mills GD, Slaga TJ. Indomethacin enhancement of TPA tumor promotion in mice. *Cancer Lett* (1980) **10**:343–50. doi:10.1016/0304-3835(80)90052-X
77. Murphy J-E, Morales RE, Scott J, Kupper TS. IL-1{alpha}, innate immunity, and skin carcinogenesis: the effect of constitutive expression of IL-1{alpha} in epidermis on chemical carcinogenesis. *J Immunol* (2003) **170**:5697–703. doi:10.4049/jimmunol.170.11.5697

78. Moore RJ, Owens DM, Stamp G, Arnott C, Burke F, East N, et al. Mice deficient in tumor necrosis factor-[alpha] are resistant to skin carcinogenesis. *Nat Med* (1999) **5**:828–31. doi:10.1038/10462
79. Naugler WE, Karin M. The wolf in sheep's clothing: the role of interleukin-6 in immunity, inflammation and cancer. *Trends Mol Med* (2008) **14**:109–19. doi:10.1016/j.molmed.2007.12.007
80. Bettelli E, Carrier Y, Gao W, Korn T, Strom TB, Oukka M, et al. Reciprocal developmental pathways for the generation of pathogenic effector TH17 and regulatory T cells. *Nature* (2006) **441**:235–8. doi:10.1038/nature04753
81. Lorimore SA, Chrystal JA, Robinson JI, Coates PJ, Wright EG. Chromosomal instability in unirradiated hemaopoietic cells induced by macrophages exposed in vivo to ionizing radiation. *Cancer Res* (2008) **68**:8122–6. doi:10.1158/0008-5472.CAN-08-0698
82. Coates PJ, Rundle JK, Lorimore SA, Wright EG. Indirect macrophage responses to ionizing radiation: implications for genotype-dependent bystander signaling. *Cancer Res* (2008) **68**:450–6. doi:10.1158/0008-5472.CAN-07-3050
83. Burns FJ, Tang MS, Frenkel K, Nádas A, Wu F, Uddin A, et al. Induction and prevention of carcinogenesis in rat skin exposed to space radiation. *Radiat Environ Biophys* (2007) **46**:195–9. doi:10.1007/s00411-007-0106-3
84. Zhang R, Burns FJ, Chen H, Chen S, Wu F. Alterations in gene expression in rat skin exposed to 56Fe ions and dietary vitamin A acetate. *Radiat Res* (2006) **165**:570–81. doi:10.1667/RR3556.1
85. Illa-Bochaca I, Ouyang H, Tang J, Sebastiano C, Mao J-H, Costes SV, et al. Densely ionizing radiation acts via the microenvironment to promote aggressive Trp53 null mammary carcinomas. *Cancer Res* (2014) **74**:7137–48. doi:10.1158/0008-5472.CAN-14-1212
86. Bindea G, Mlecnik B, Angell HK, Galon J. The immune landscape of human tumors: implications for cancer immunotherapy. *Oncoimmunology* (2014) **3**:e27456. doi:10.4161/onci.27456
87. Medzhitov R. Inflammation 2010: new adventures of an old flame. *Cell* (2010) **140**:771–6. doi:10.1016/j.cell.2010.03.006
88. Grivennikov SI, Greten FR, Karin M. Immunity, inflammation, and cancer. *Cell* (2010) **140**:883–99. doi:10.1016/j.cell.2010.01.025
89. Mittal D, Gubin MM, Schreiber RD, Smyth MJ. New insights into cancer immunoediting and its three component phases-elimination, equilibrium and escape. *Curr Opin Immunol* (2014) **27C**:16–25. doi:10.1016/j.coi.2014.01.004
90. Street SE, Cretney E, Smyth MJ. Perforin and interferon-gamma activities independently control tumor initiation, growth, and metastasis. *Blood* (2001) **97**:192–7. doi:10.1182/blood.V97.1.192
91. Dunn GP, Koebel CM, Schreiber RD. Interferons, immunity and cancer immunoediting. *Nat Rev Immunol* (2006) **6**:836–48. doi:10.1038/nri1961
92. Vesely MD, Kershaw MH, Schreiber RD, Smyth MJ. Natural innate and adaptive immunity to cancer. *Annu Rev Immunol* (2011) **29**:235–71. doi:10.1146/annurev-immunol-031210-101324
93. Myron Kauffman H, McBride MA, Cherikh WS, Spain PC, Marks WH, Roza AM. Transplant tumor registry: donor related malignancies. *Transplantation* (2002) **74**:358–62. doi:10.1097/00007890-200208150-00011
94. MacKie RM, Reid R, Junor B. Fatal melanoma transferred in a donated kidney 16 years after melanoma surgery. *N Engl J Med* (2003) **348**:567–8. doi:10.1056/NEJM200302063480620
95. Koebel CM, Vermi W, Swann JB, Zerafa N, Rodig SJ, Old LJ, et al. Adaptive immunity maintains occult cancer in an equilibrium state. *Nature* (2007) **450**:903–7. doi:10.1038/nature06309
96. Ponder BAJ. Cancer genetics. *Nature* (2001) **411**:336–41. doi:10.1038/35077207
97. Balmain A, Gray J, Ponder B. The genetics and genomics of cancer. *Nat Genet* (2003) **33**:238–44. doi:10.1038/ng1107
98. Welcsh PL, King M-C. BRCA1 and BRCA2 and the genetics of breast and ovarian cancer. *Hum Mol Genet* (2001) **10**:705–13. doi:10.1093/hmg/10.7.705
99. Peto J. Cancer epidemiology in the last century and the next decade. *Nature* (2001) **411**:390–5. doi:10.1038/35077256
100. Myers AJ, Gibbs JR, Webster JA, Rohrer K, Zhao A, Marlowe L, et al. A survey of genetic human cortical gene expression. *Nat Genet* (2007) **39**:1494–9. doi:10.1038/ng.2007.16
101. Emilsson V, Thorleifsson G, Zhang B, Leonardson AS, Zink F, Zhu J, et al. Genetics of gene expression and its effect on disease. *Nature* (2008) **452**:423–8. doi:10.1038/nature06758
102. Morley M, Molony CM, Weber TM, Devlin JL, Ewens KG, Spielman RS, et al. Genetic analysis of genome-wide variation in human gene expression. *Nature* (2004) **430**:743–7. doi:10.1038/nature02797
103. Chen Y, Zhu J, Lum PY, Yang X, Pinto S, MacNeil DJ, et al. Variations in DNA elucidate molecular networks that cause disease. *Nature* (2008) **452**:429–35. doi:10.1038/nature06757
104. Mao J-H, Balmain A. Genomic approaches to identification of tumour-susceptibility genes using mouse models. *Curr Opin Genet Dev* (2003) **13**:14–9. doi:10.1016/S0959-437X(03)00005-4
105. Balmain A. Cancer as a complex genetic trait: tumor susceptibility in humans and mouse models. *Cell* (2002) **108**:145–52. doi:10.1016/S0092-8674(02)00622-0
106. Quigley DA, To MD, Pérez-Losada J, Pelorosso FG, Mao J-H, Nagase H, et al. Genetic architecture of murine skin inflammation and tumor susceptibility. *Nature* (2009) **458**:505–8. doi:10.1038/nature07683
107. Mao J-H, Perez-losada J, Wu D, DelRosario R, Tsunematsu R, Nakayama KI, et al. Fbxw7/Cdc4 is a p53-dependent, haploinsufficient tumour suppressor gene. *Nature* (2004) **432**:775–9. doi:10.1038/nature03155
108. Blackburn AC, Brown JS, Naber SP, Otis CN, Wood JT, Jerry DJ. BALB/c alleles for Prkdc and Cdkn2a interact to modify tumor susceptibility in Trp53+/- mice. *Cancer Res* (2003) **63**:2364–8.
109. Okayasu R, Suetomi K, Yu Y, Silver A, Bedford JS, Cox R, et al. A deficiency in DNA repair and DNA-PKcs expression in the radiosensitive BALB/c mouse. *Cancer Res* (2000) **60**:4342–5.
110. Yu Y, Okayasu R, Weil MM, Silver A, McCarthy M, Zabriskie R, et al. Elevated breast cancer risk in irradiated BALB/c mice associates with unique functional polymorphism of the Prkdc (DNA-dependent protein kinase catalytic subunit) gene. *Cancer Res* (2001) **61**:1820–4.
111. Jerry DJ, Kittrell FS, Kuperwasser C, Laucirica R, Dickinson ES, Bonilla PJ, et al. A mammary-specific model demonstrates the role of the p53 tumor suppressor gene in tumor development. *Oncogene* (2000) **19**:1052–8. doi:10.1038/sj.onc.1203270
112. Zhang P, Lo A, Huang Y, Huang G, Liang G, Mott J, et al. Identification of genetic loci that control mammary tumor susceptibility through the host microenvironment. *Sci Rep* (2015) **5**:8919. doi:10.1038/srep08919
113. Tartakovsky B, Goldstein O, Krautghamer R, Haran-Ghera N. Low doses of radiation induce systemic production of cytokines: possible contribution to leukemogenesis. *Int J Cancer* (1993) **55**:269–74. doi:10.1002/ijc.2910550217
114. Haran-Ghera N, Krautghamer R, Lapidot T, Peled A, Dominguez MG, Stanley ER. Increased circulating colony-stimulating factor-1 (CSF-1) in SJL/J mice with radiation-induced acute myeloid leukemia (AML) is associated with autocrine regulation of AML cells by CSF-1. *Blood* (1997) **89**:2537–45.
115. Best T, Li D, Skol AD, Kirchhoff T, Jackson SA, Yasui Y, et al. Variants at 6q21 implicate PRDM1 in the etiology of therapy-induced second malignancies after Hodgkin's lymphoma. *Nat Med* (2011) **17**:941–3. doi:10.1038/nm.2407

Conflict of Interest Statement: The authors declare that the research was conducted in the absence of any commercial or financial relationships that could be construed as a potential conflict of interest.

Copyright © 2016 Barcellos-Hoff and Mao. This is an open-access article distributed under the terms of the Creative Commons Attribution License (CC BY). The use, distribution or reproduction in other forums is permitted, provided the original author(s) or licensor are credited and that the original publication in this journal is cited, in accordance with accepted academic practice. No use, distribution or reproduction is permitted which does not comply with these terms.

frontiers in Oncology

REVIEW
published: 14 October 2015
doi: 10.3389/fonc.2015.00231

Ionizing particle radiation as a modulator of endogenous bone marrow cell reprogramming: implications for hematological cancers

*Sujatha Muralidharan[1], Sharath P. Sasi[2], Maria A. Zuriaga[1], Karen K. Hirschi[3], Christopher D. Porada[4], Matthew A. Coleman[5,6], Kenneth X. Walsh[1], Xinhua Yan[2,7] and David A. Goukassian[1,2,7]**

[1] Whitaker Cardiovascular Institute, Boston University School of Medicine, Boston, MA, USA, [2] Cardiovascular Research Center, GeneSys Research Institute, Boston, MA, USA, [3] Yale Cardiovascular Research Center, Yale School of Medicine, New Haven, CT, USA, [4] Wake Forest Institute for Regenerative Medicine, Wake Forest School of Medicine, Winston-Salem, NC, USA, [5] Radiation Oncology, School of Medicine, University of California Davis, Sacramento, CA, USA, [6] Lawrence Livermore National Laboratory, Livermore, CA, USA, [7] Tufts University School of Medicine, Boston, MA, USA

OPEN ACCESS

Edited by:
Marco Durante,
GSI Helmholtzzentrum für Schwerionenforschung, Germany

Reviewed by:
Joshua Silverman,
New York University Medical Center, USA
Kamal Datta,
Georgetown University, USA
Lin Su,
Johns Hopkins University, USA

***Correspondence:**
David A. Goukassian
david.goukassian@tufts.edu;
dgoukass@bu.edu

Specialty section:
This article was submitted to Radiation Oncology, a section of the journal Frontiers in Oncology

Received: 10 August 2015
Accepted: 01 October 2015
Published: 14 October 2015

Citation:
Muralidharan S, Sasi SP, Zuriaga MA, Hirschi KK, Porada CD, Coleman MA, Walsh KX, Yan X and Goukassian DA (2015) Ionizing particle radiation as a modulator of endogenous bone marrow cell reprogramming: implications for hematological cancers. Front. Oncol. 5:231. doi: 10.3389/fonc.2015.00231

Exposure of individuals to ionizing radiation (IR), as in the case of astronauts exploring space or radiotherapy cancer patients, increases their risk of developing secondary cancers and other health-related problems. Bone marrow (BM), the site in the body where hematopoietic stem cell (HSC) self-renewal and differentiation to mature blood cells occurs, is extremely sensitive to low-dose IR, including irradiation by high-charge and high-energy particles. Low-dose IR induces DNA damage and persistent oxidative stress in the BM hematopoietic cells. Inefficient DNA repair processes in HSC and early hematopoietic progenitors can lead to an accumulation of mutations whereas long-lasting oxidative stress can impair hematopoiesis itself, thereby causing long-term damage to hematopoietic cells in the BM niche. We report here that low-dose ^{1}H- and ^{56}Fe-IR significantly decreased the hematopoietic early and late multipotent progenitor (E- and L-MPP, respectively) cell numbers in mouse BM over a period of up to 10 months after exposure. Both ^{1}H- and ^{56}Fe-IR increased the expression of pluripotent stem cell markers *Sox2*, *Nanog*, and *Oct4* in L-MPPs and 10 months post-IR exposure. We postulate that low doses of ^{1}H- and ^{56}Fe-IR may induce endogenous cellular reprogramming of BM hematopoietic progenitor cells to assume a more primitive pluripotent phenotype and that IR-induced oxidative DNA damage may lead to mutations in these BM progenitors. This could then be propagated to successive cell lineages. Persistent impairment of BM progenitor cell populations can disrupt hematopoietic homeostasis and lead to hematologic disorders, and these findings warrant further mechanistic studies into the effects of low-dose IR on the functional capacity of BM-derived hematopoietic cells including their self-renewal and pluripotency.

Keywords: HSC, progenitors, radiation, endogenous reprogramming, hematological cancer

INTRODUCTION

Exposure to ionizing radiation (IR), specifically high-energy protons (^{1}H) and ions with high charge and high energy (HZE particles), is one of the major risks during spaceflight beyond low Earth orbit (LEO) (1, 2). For example, astronauts on future Mars missions are expected to encounter ~0.6 Sv of IR during 180 days transit to Mars (3). In this case, it is estimated that each cell in an astronaut's body will be traversed by a low-dose ^{1}H every 3–4 days, helium nuclei every few weeks, and HZE particles, such as iron (^{56}Fe), every few months. The radiation encountered by astronauts in LEO in proximity of the van Allen belt is mostly from ^{1}H particles from solar winds, trapped in the earth's magnetic field (4). This type of low linear energy transfer (LET) radiation, including γ rays and X-rays, deposit relatively little energy as they pass through matter. However, venturing beyond the van Allen belt and into deep space, astronauts will encounter a significant amount of galactic cosmic radiation which contains not only high-energy ^{1}H and alpha particles but also high-LET radiation from HZE particles, such as ^{56}Fe and ^{28}Si (4). These high-LET HZE ions have a greater propensity for ionization and they deposit large amounts of energy along their tracks; and thus have greater potential for causing damage to tissues. These types of low- and high-LET radiation are also encountered on earth. For example, low energy ^{1}H and HZE carbon ion IR are being used in cancer radiotherapy regimens for patients suffering from breast cancer, esophageal cancer, adenocarcinoma, and hepatocellular carcinoma (5–10). To date, the biological effects of low-dose ^{1}H and HZE ion IR have not been fully investigated.

Radiation dose is an important factor for consideration in the biological effects of low- and high-LET radiation. Although epidemiological studies based on atomic bomb survivors and cancer radiotherapy patients have provided insight into the biological effects of moderate to high doses of IR (11, 12), the effects of low-dose IR over long periods of time remain to be elucidated. A single high dose of radiation may induce significant tissue and cell damage; however, the biological effects of low-dose IR may be more relevant in disease processes, owing to IR-induced aberrations at the genetic or epigenetic levels. This "reprogramming" can be propagated in surviving cells and can have long-term implications in the health of the IR exposed individual.

This article focuses on the biological relevance of low-dose low-LET ^{1}H and high-LET HZE ^{56}Fe radiation. Charged ^{1}H particles are the most abundant radiation found in deep space and HZE particles (1% of galactic cosmic rays) contribute to more than 40% of the equivalent dose exposure for the astronauts (4, 13, 14). Notably, low-energy ^{1}H particles are also being used as a source of radiation for the treatment of cancers owing to their favorable radiation dose distribution in cancerous tissue (15, 16). Therefore, studying the biological consequences of these types of radiation is of significance for understanding the consequences of both space missions and cancer therapy regimens.

EFFECTS OF IONIZING RADIATION ON THE BONE MARROW

Radiation-Induced DNA Damage and Oxidative Stress in BM Cells

Ionizing radiation promotes the induction and accumulation of mutations as a result of DNA damage and inefficient DNA repair. IR deposits energy along specific "tracks" which lead to clustering of DNA lesions (17). The extent of clustering depends on the ionization density and type of radiation, with more clustered damage often observed after exposure to heavy-ion radiation, such as ^{56}Fe particles. Such clustered DNA damage caused by high-LET radiation can lead to double strand breaks (DSBs) in DNA and mutations in the absence of proper DNA repair processes (18). Such DSBs can be repaired by non-homologous end-joining (NHEJ) or homologous recombination (HR). The NHEJ pathway seems to play a significant role in DNA repair after exposure to either ^{1}H or heavy-ion radiation while HR appears to be more important after heavy-ion radiation (19). Error-prone DNA repair during NHEJ, due to lack of a suitable template, can be a source of mutations post-IR. It should be noted that cells within the bone marrow (BM) often exhibit low levels of expression of many DNA repair proteins, suggesting they may have an inherent inability to repair DNA damage induced by radiation, and therefore are at increased risk of mutations (20). In support of this contention are studies showing that BM cells from mice exposed to 0.5–3 Gy, 1 GeV/n radiation with ^{56}Fe particles showed significantly increased chromosomal damage using multi-color FISH techniques (21, 22). ^{1}H-IR of 1 Gy, 100 MeV also induced significant DNA damage in mouse BM cells, as assessed by phospho-H2AX foci and multi-color FISH analysis (23, 24).

Exposure of cells to IR can also increase oxidative stress in cells by inducing reactive oxygen or nitrogen species (ROS or RNS), which are the result of interactions between IR and water with other biomolecules in the cell (25). ^{1}H-IR of 1 Gy, 150 MeV caused increased oxidative stress as determined by ROS levels and concomitant increases in expression of Nox4 in BM cells (24). ROS and RNS thus generated can interact with DNA and cause more DNA lesions, in addition to those induced by direct DNA damage caused in the radiation tracks. Chronic exposure to oxidative stress can lead to accumulation of such DNA lesions and promote mutagenesis (26). Therefore, the DNA damage and oxidative stress induced in BM by IR, specifically ^{1}H- and ^{56}Fe-IR, could lead to accumulation of DNA lesions and result in mutations in the hematopoietic stem and progenitor cells.

Hematopoiesis in Adult Bone Marrow

The BM niche is the predominant site of hematopoiesis and the differentiation of blood cells. This unique microenvironmental niche is also extremely sensitive to low-dose IR exposure (27–29). Disruption of hematopoietic homeostasis can result in hematologic disorders and impact the function of vital organs; for example, abnormalities in hematopoietic cells in the BM can be propagated to the successive blood lineages and result in

leukemia. Therefore, it is important to understand the effects of exposure to ^{1}H- and ^{56}Fe-IR on BM.

Unlike the ablative effect of gamma radiation (γ-IR) on the BM, both short- and long-term effects of particle radiation on this site of hematopoiesis are less understood. Hematopoietic stem cells (HSCs) comprise <0.1% of the BM of adults, yet they produce all of the circulating blood cells that are responsible for constant maintenance and immune protection of the body (28). This exquisitely regulated process known as hematopoiesis occurs in the BM of adults and is responsible for both the maintenance of the primitive HSC and for inducing maturation of these cells to specific blood lineages as the need arises for those particular cell types. Discrete functions performed by the hematopoietic niche may require different growth factors and diverse interactions with different cells types within the site. These various interactions between HSCs and BM stromal cells ensure appropriate cell output to the circulation that change with specific stimuli and demands. Definitive hematopoiesis in the adult BM begins with the differentiation of self-renewing HSCs to hematopoietic multipotent progenitor cells (HPCs or MPPs) (28, 30). These progenitor cells can give rise to the different blood lineages but lack self-renewal capacity. The MPPs develop into committed common lymphoid (CLP) and myeloid (CMP) progenitor cells. The CLP population differentiates into the lymphocyte (NK, B, and T cells) lineages while the CMP gives rise to megakaryocytes, erythrocytes, monocytes, and granulocytes (neutrophils, basophils, and eosinophils). These mature blood cells then exit the BM and enter circulation where they perform important functions. Erythrocytes (red blood cells) are important for oxygen transport, megakaryocytes for blood clotting, and white blood cells (WBCs; namely lymphocytes, monocytes, and granulocytes), function in adaptive and innate immune defenses. Therefore, the process of hematopoiesis in the BM controls the development of all these blood lineages and is responsible for maintaining hematologic homeostasis.

Effects of ^{1}H Radiation on Circulating Blood Cells and Hematopoietic Precursors

Many studies have examined the effects of radiation on circulating blood cells. Irradiation of mice with up to 2 Gy of ^{1}H caused significant changes to the peripheral immune cell populations, with different populations exhibiting different sensitivities (31–33). Within the lymphocyte populations, B cells were found to be most sensitive to radiation, followed by T cells and then NK cells which were the most resistant (31). Decreases in WBC populations were dependent on ^{1}H-IR dose, but not on dose rate, energy, or fractionation (32, 33). The effects of simulated solar particle events, which are comprised of ^{1}H (up to 155 MeV), with a heterogeneous ^{1}H dose distribution, also revealed significant reduction (60–90% compared to baseline) in frequencies of circulating WBCs, lymphocytes, neutrophils, monocytes, and eosinophils in both murine and porcine models (34, 35). Murine splenic immune cell populations were impaired at 4 months post-IR with 2 Gy ^{1}H, indicating a long-term radiation effect on the precursor hematopoietic populations (36). This was confirmed in recent studies demonstrating that total body irradiation of mice with 1 Gy, 150 MeV of ^{1}H caused significant reduction in HSC (Lin^{-}c-kit^{+}Sca-1^{+}) numbers and pluripotency, even at time points as late as 22 weeks after radiation (24). These changes were attributed to the increased levels of oxidative stress in the HSCs, causing increased HSC cell cycling and reduced self-renewal capacity, and resulting in long-term HSC injury. Although ^{1}H-IR is a low-LET radiation, its effects on DNA are more damaging than X-rays, indicating the greater capacity to induce changes at the molecular level (37).

Effects of HZE ^{56}Fe Particle Radiation on Circulating Blood Cells and Hematopoietic Precursors

Exposure to HZE particles, such as ^{56}Fe, can have even more detrimental effects on BM hematopoietic precursors and mature blood cells. Rats exposed to 1–4 Gy (5 GeV/nucleon) of ^{56}Fe-IR had significantly lower counts of circulating leukocytes and monocytes compared to non-irradiated rats for as long as 9 months post-IR (38). Mice irradiated with 6–8 Gy (1 GeV/nucleon) of ^{56}Fe particles also showed significantly lower WBC counts 7 days post-IR and lower recovery at 4 weeks post-IR compared to γ-IR mice (39). Examination of the BM revealed extensive cell death, cell cycle arrest and significant selective reduction of myeloid precursor cells in mice exposed to 2–4 Gy of ^{56}Fe-IR. Cell cycle arrest of BM cells at the G_1 phase up to 66 h post-IR was also found in another study with mice irradiated with 1 Gy (1 GeV/nucleon) of ^{56}Fe ions (40). Cell cycle arrest corresponded to an increase in cells with ^{56}Fe radiation-induced chromosomal aberrations (41). At the molecular level, exposure to 600 MeV, 0.4 Gy ^{56}Fe radiation induced DNA hypermethylation in HPCs up to 22 weeks post-IR, suggesting epigenetic reprogramming (42).

Therefore, we *hypothesize* that particle radiation, such as ^{1}H and ^{56}Fe, which induce profound changes in BM hematopoietic cells, including at the molecular level, may play a significant role in the development of hematological cancers, and thus merits further studies.

EXPOSURE TO ^{1}H AND ^{56}FE RADIATION HAS LONG-TERM EFFECTS ON BONE MARROW HEMATOPOIETIC MULTIPOTENT PROGENITOR POPULATIONS

^{1}H and ^{56}Fe Radiation Induced Significant Decrease in Bone Marrow Multipotent Progenitor Cell Numbers

To extend our knowledge of the effects of particle radiation on BM hematopoietic populations, whole-body radiation was performed on mice with 0.5 Gy (1 GeV) ^{1}H and 0.15 Gy (1 GeV/n) ^{56}Fe particles. Fluorescence-activated cell sorting (FACS) was then used to isolate early and late multipotent progenitors (E- and L-MPPs) from BM cells over a time course of 40 weeks post-IR. E-MPPs were defined as Lin^{-}/c-kit^{+}/Sca1^{+}/CD34^{+}/AC133^{+} and L-MPPs were Lin-/c-kit^{+}/Sca1^{+}/CD34^{+}/AC133^{-} (43, 44). Compared to control mice, ^{1}H-IR caused an initial transient spike in E-MPP and L-MPP cell numbers followed by significant downregulation of these populations at 8 weeks post-IR (**Figures 1A,B**; **Table 1**).

In contrast, ^{56}Fe-IR caused significant loss of E-MPPs and L-MPPs immediately after IR, which was maintained up to 8 weeks post-IR (**Figures 1A,B**; **Table 1**). By 40 weeks, the E-MPP and L-MPP populations had recovered and were comparable to control levels for both ^{1}H and ^{56}Fe radiation (**Figures 1A,B**). These findings are consistent with the study that showed γ-IR, even at the low dose of 0.4 Gy, was observed to rapidly induce apoptosis in human embryonic stem (ES) cells (45).

^{1}H and ^{56}Fe Radiation Significantly Upregulated Expression of Pluripotency Markers in Bone Marrow L-MPPs

Human ES cells that survived γ-IR exposure exhibited features of pluripotency at 3 weeks post-IR exposure (45). To decipher the molecular events in our radiation study, the expression of pluripotency markers *Sox2*, *Nanog*, and *Oct4* was examined in

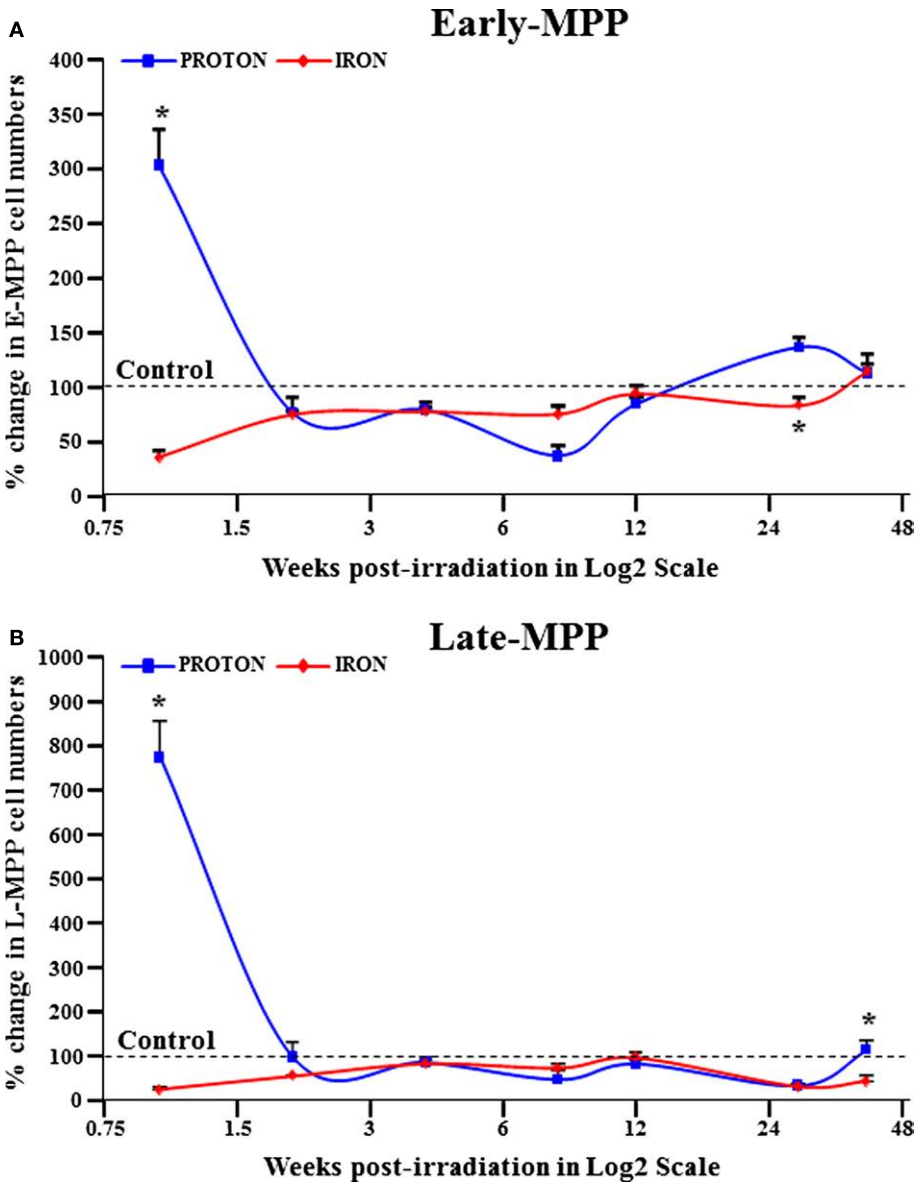

FIGURE 1 | E-MPP and L-MPP cell numbers are downregulated by ^{56}Fe- and ^{1}H-IR but recover to control levels by 40 weeks post-IR. Effect of full-body single dose of proton (^{1}H) at 0.5 Gy, 1 GeV and iron (^{56}Fe) at 0.15 Gy, 1 GeV/nucleon of ionizing radiation (IR) on survival of multipotent progenitor cell populations was examined. The survival of **(A)** E-MPPs and **(B)** L-MPPs in the BM after particle IR in C57BL/6NT mice were determined at 1, 2, 4, 8, 12, 28, and 40 weeks post-IR. Total BM-derived mononuclear cells were triple-stained with FITC-labeled RAM34 antibody (that consists of CD34, c-kit, and Sca1 antibodies), PE-Cy7-AC133, and PE-hematopoietic lineage cocktail (CD3e, Ly-6G/Ly-6C, CD11b, CD45R/B220, TER-119), then sorted by FASC for **(A)** E-MPPs (CD34^{+}/c-kit^{+}/Sca-1^{+}/AC133^{+}/Lin^{-}) and **(B)** L-MPPs (CD34^{+}/c-kit^{+}/Sca-1^{+}/AC133^{-}/Lin^{-}). Percentage changes in cell numbers were calculated relative to control sham irradiated mice, which was set to 100% for each time point. Solid lines represent mean ± SEM (n = 6/group) for ^{1}H-IR (solid blue lines) and ^{56}Fe-IR (solid red lines). "*" represents statistically significant differences compared to control with $p < 0.05$.

TABLE 1 | ^{56}Fe- and ^{1}H-IR resulted in decreased E-MPP and L-MPP cell numbers.

IR type	Weeks						
	1	2	4	8	12	28	40
(A) E-MPP							
^{1}H%	665↑*	3↓	13↓	52↓	17↓	66↓	15↑
^{56}Fe%	74↓	44↓	16↓	26↓	3↓	69↓	55↓**
(B) L-MPP							
^{1}H%	203↑*	23↓	21↓	63↓	16↓	36↑***	13↑
^{56}Fe%	65↓	25↓	23↓	25↓	6↓	17↓	15↑

Representation of % change difference in cell number for (A) E-MPPs (CD34^{+}/c-kit^{+}/Sca-1^{+}/AC133^{+}/Lin^{-}) and (B) L-MPPs (CD34^{+}/c-kit^{+}/Sca-1^{+}/AC133^{-}/Lin^{-}) from full-body ^{1}H-IR and ^{56}Fe-IR mice when compared to respective control cell numbers at each time point set at 100%. The arrows show the direction up or down for the population change.
$^{*}p < 0.001$.
$^{**}p < 0.01$.
$^{***}p < 0.03$.

the L-MPPs for a period of 40 weeks following irradiation with ^{1}H or ^{56}Fe particles. The qRT-PCR analysis revealed a significant increase in expression of these markers at 8 and 40 weeks after both ^{1}H and ^{56}Fe irradiation (**Figures 2A–C**). Of note, it has been shown that ES cells exposed to 3 Gy high-LET carbon ion radiation also maintain their pluripotent state and express Oct3/4 and Sox2; data which agree with our current observations (46). Based on these observations, one could hypothesize that the increase in expression of the pluripotency markers in L-MPPs at 8 weeks post-radiation with ^{1}H or ^{56}Fe in our study could be the result of preferential expansion of radio-resistant cells. Indeed, this contention is supported by cancer biology studies that have shown a correlation between expression of Oct4 and Sox2 protein and increased resistance of cancer cells to radiotherapy (47, 48). However, the reduced cell numbers we observed at the 8-week time point post-IR (**Figure 1B**; **Table 1**) argues against this explanation. An alternative hypothesis to explain our observations is that ^{1}H- or ^{56}Fe-IR-induced genetic "reprogramming" of the existing L-MPPs. Consistent with this notion, γ-IR was reported to induce reprogramming of cancer stem cells that express the pluripotency genes *Oct4*, *Sox2*, *Nanog*, and *Klf4* in a Notch-dependent manner for up to 5 days post-IR (47, 49). Furthermore, forced expression of *Nanog*, *Oct4*, *Sox2*, and *Lin28* were sufficient to reprogram human somatic cells into pluripotent stem cells (50). Constitutive overexpression of *Nanog* alone is sufficient to promote proliferation of human ES cells while maintaining pluripotency and *Oct4* expression (51, 52). Collectively, our data and previously published data strongly suggest that low doses of ^{1}H- or ^{56}Fe-IR may induce reprogramming of the L-MPPs to a state of pluripotency while promoting proliferation to replenish the progenitor populations.

Analysis of L-MPPs After Exposure to ^{1}H and ^{56}Fe Radiation Revealed Distinct Long-Term Genetic Programming

A significant increase in expression of these genes was also observed at 40 weeks post-irradiation with ^{1}H and ^{56}Fe particles (**Figures 2A–C**). In order to examine this more closely, a multitude of hematopoiesis-related genes were analyzed in the L-MPPs at the 40-week time point, employing a PCR array for a pilot study (**Table 2**). Overall, ^{1}H- and ^{56}Fe-IR induced distinct genetic programs in the L-MPPs, with observable similarities and differences. We found that exposure of L-MPPs to either ^{56}Fe- or ^{1}H-IR markedly downregulated the expression of several genes that play key functions in the process of hematopoiesis, including *CD164* (sialomucin), which increases adhesion of CD34 + cells to BM stroma and downregulates HPC proliferation (53, 54), and *Fut10*, which can fucosylate selectins for recruitment of progenitors to BM stroma (55, 56) (**Table 2**). It is possible that downregulation of adhesion molecules could be involved in mobilization of progenitor cells and increase their proliferation. Transcription factors that play an important role in hematopoiesis, such as *Cbfb* and *Ash2l*, were downregulated to a greater extent in L-MPPs exposed to ^{56}Fe-IR compared to ^{1}H-IR indicating a larger insult by ^{56}Fe radiation on BM cells (**Table 2**) (57, 58). This conclusion is also supported by the observed decrease in expression of immune receptors *TLR3* and *TLR4*, and the co-receptor *CD14* in ^{56}Fe-IR L-MPPs, indicating compromised immune responses and immune cell mobilization (**Table 2**) (59, 60). However, ^{1}H-IR L-MPPs showed an increase in expression of these genes, signifying activation of a different epigenetic program. Increased TLR3, TLR4, and CD14 expression on hematopoietic progenitor cells has been correlated with skewing toward myeloid cell differentiation as observed in aging (61, 62). It is possible that the ^{1}H- and ^{56}Fe-IR may promote the differentiation of these progenitors into the myeloid and lymphoid lineages, respectively. ^{1}H-IR exposed L-MPPs showed increased expression of *Notch1* and its downstream target, *Rbpj*. In contrast, L-MPP cells from mice exposed to ^{56}Fe-IR showed a discernable decrease in expression of these genes (**Table 2**). Since activation of Notch1 was shown to promote myeloid differentiation via Rbpj (63), these data may be indicative of myeloid and lymphoid skewing in MPPs induced by ^{1}H- and ^{56}Fe-IR, respectively. On the other hand, expression of other Notch signaling molecules (*Notch4*, *Jag1*, and *Jag2*) were increased in L-MPPs exposed to ^{1}H- and ^{56}Fe-IR (**Table 2**). Interestingly, increased Notch signaling could potentially promote endogenous reprogramming of the cells, as indicated by reports of increased differentiation of cancer stem cells in response to Notch inhibition (64, 65). Therefore, these preliminary gene expression data also supports the possibility of radiation-induced reprogramming of BM progenitors to maintain pluripotency.

Other studies illustrating radiation-induced endogenous reprogramming have been largely conducted in cancer models. For example, inhibition of Notch signaling partially prevented radiation-induced reprogramming of differentiated breast cancer cells (isolated from patients) into cancer stem cells, thereby preventing their re-acquisition of expression of pluripotency genes *Oct4*, *Nanog*, and *Klf4* (47). High doses of γ-IR was also shown to re-program hepatocellular cancer cell lines to acquire stemness phenotype (49). At the molecular level, radiation can induce epigenetic reprogramming in terms of DNA methylation which can also have important implications in BM progenitor populations (66). Mouse mesenchymal stem cells exposed to non-IR promoted an adipose phenotype (67). Collectively, these observations lend

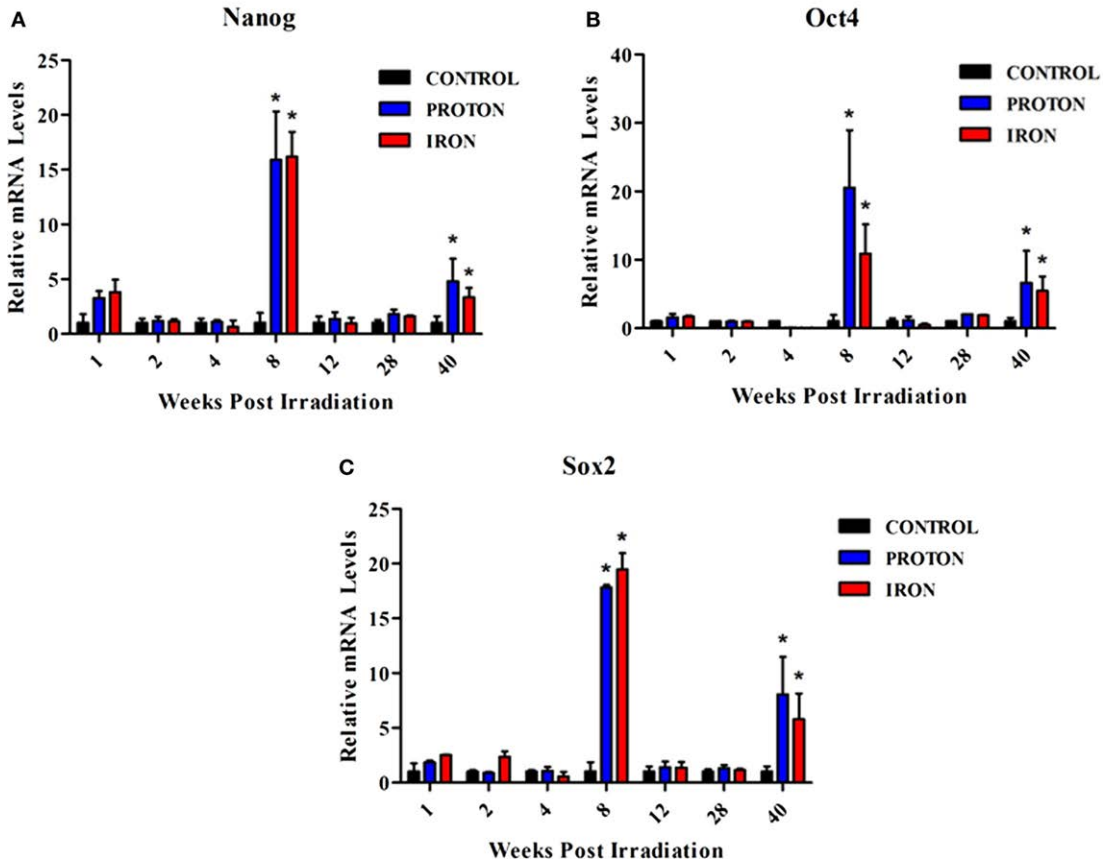

FIGURE 2 | Expression of pluripotency markers are upregulated in BM-derived L-MPPs post-irradiation with ^{1}H or ^{56}Fe particles. After whole-body irradiation with 0.5 Gy, 1 GeV ^{1}H and 0.15 Gy, 1 GeV/n ^{56}Fe particles, mononuclear cells from bone marrow of C57BL/6NT mice were sorted into L-MPPs (CD34^{+}/c-kit^{+}/Sca-1^{+}/AC133^{-}/Lin^{-}) by FACS at multiple time points over 40 weeks post-IR. Levels of **(A)** *Nanog*, **(B)** *Oct4*, and **(C)** *Sox2* were analyzed using Taqman probes by qRT-PCR. Relative mRNA levels were calculated with respect to control sham irradiated animals. Bars represent mean ± SEM (n = 6/group) for control (solid black bars), ^{1}H-IR (solid blue bars), and ^{56}Fe-IR (solid red bars). "*" represents statistically significant differences compared to control with $p < 0.05$.

TABLE 2 | Exposure to ^{1}H or ^{56}Fe particles caused notable changes in hematopoietic genes in L-MPPs at 40 weeks post-radiation.

Group	Gene	Relative mRNA levels in ^{1}H-IR L-MPPs	Relative mRNA levels in ^{56}Fe-IR L-MPPs
Transcription factors	Cbfb	0.75↓	0.30↓
	Ash21	0.98↓	0.45↓
Adhesion molecules	CD164	0.484↓	0.28↓
	FutlO	0.22↓	0.06↓
Immune receptors	TLR4	2.91↑	0.73↓
	TLR3	12.81↑	0.63↓
	CD14	1.32↑	0.03↓
Notch signaling	Notch1	1.83↑	0.60↓
	Notch4	5.24↑	2.29↑
	Jagl	7.22↑	2.72↑
	Jag2	2.152↑	1.75↑
	Rbpj	1.622↑	0.32↓

After whole-body irradiation with 0.5 Gy, 1 GeV ^{1}H and 0.15 Gy, 1 GeV/n ^{56}Fe particles, mononuclear cells from bone marrow of C57BL/6NT mice were sorted into L-MPPs (CD34^{+}/c-kit^{+}/Sca-1^{+}/AC133^{-}/Lin^{-}) by FACS at 40 weeks post-IR. These experiments were repeated at least twice. Expression of multiple hematopoietic gene transcripts was analyzed using a RT^{2} PCR array. Fold changes were calculated with respect to control sham irradiated animals. The arrows show the direction up or down for the fold change.

further credibility to our postulation of radiation-induced reprogramming of BM cells, at the molecular level.

IMPLICATIONS OF RADIATION-INDUCED CHANGES IN BONE MARROW HEMATOPOIETIC PROGENITOR CELLS

In our studies into the effects of low-dose low-LET ^{1}H and high-LET ^{56}Fe-IR on BM hematopoietic progenitor populations, the most striking results were the significant loss of cell numbers and the changes in pluripotent markers in the surviving cells. The long-lasting decrease in the E-MPP and L-MPP populations in the irradiated mice over the course of 40 weeks suggests disrupted hematopoietic homeostasis. Such perturbation of hematopoiesis has the potential to lead to hematological disorders including blood cancers. With regard to the observed genetic changes induced by IR in the surviving L-MPP cell fractions at the 8- and 40-week time point, and supported by the literature reviewed herein, we posit that low-dose IR, especially particle radiation, can induce mutations in the hematopoietic progenitor pools in

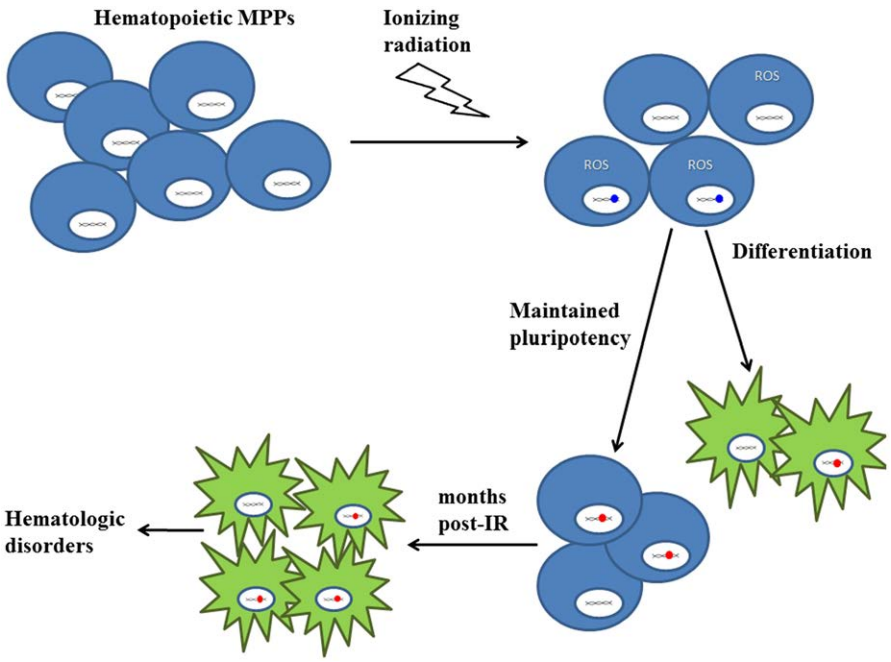

FIGURE 3 | Proposed model on the effects of low-LET ^{1}H and high-LET ^{56}Fe radiation on hematopoietic progenitor cells in the bone marrow niche. There is a significant decrease in MPP population numbers upon exposure to particle radiation. The majority of surviving cells experience DNA damage (depicted in blue) and oxidative stress (depicted by ROS), which could result in DNA mutations (depicted in red). While some MPPs continue to differentiate into blood cells, the remaining cells are "reprogrammed" to maintain pluripotency. As a result, even months post-IR, these "reprogrammed" MPPs [containing IR-induced mutations (depicted in red)] persist and give rise to differentiated blood cells, thereby propagating mutations to subsequent lineages, which may cause hematologic disorders, such as cancer. Blue cells represent multipotent progenitor cells and green cells represent differentiated blood cells.

the BM while concomitantly reprogramming them to a more primitive pluripotent state. While such reprogramming may be beneficial to replenish the progenitor cell pools within the radiation-depleted BM compartments, it may also have severe repercussions on the functions of the subsequent blood cell lineages (**Figure 3**). One can readily envision the radiation-induced reprogramming of BM progenitor cells, which may also contain radiation-induced mutations, will affect the phenotypes of multiple lymphoid and myeloid cell populations, thereby propagating the mutations to differentiated blood lineages. In particular, the propagation of mutations in oncogenes could promote risk for hematological cancers. It should be noted that high doses of IR are more likely to induce cell apoptosis, which may produce short-term effects, but low-dose radiation can cause significant long-term consequences by inducing mutations that will persist and differentiate into blood cells with altered function. Therefore, exposure to low-dose ^{56}Fe or ^{1}H particle radiation, as experienced by astronauts in spaceflight or cancer patients that undergo radiation therapy (specifically, the protracted full-body doses), can cause long-term effects in BM cells, thereby increasing their risks of developing (secondary) blood cancers.

AUTHOR CONTRIBUTIONS

SM – performed PCR, data analysis, wrote, and edited the manuscript; SS – performed and supervised all experimental studies, analyzed data, and edited the manuscript; MZ – performed PCR and data analysis; KH – reviewed and edited the manuscript; CP – reviewed and edited the manuscript; MC – reviewed and edited the manuscript; KW – reviewed and edited the manuscript; XY – reviewed and edited the manuscript; and DG – conceived the study, designed research, analyzed data, and wrote and edited the manuscript.

ACKNOWLEDGMENTS

We would like to thank members of Flow Cytometry Core at TUFTS University, School of Medicine – Allen Parmelee and Stephen Kwok. We would also like to thank members of NASA Space Radiation Laboratory (NSRL) and Biological Environmental and Climate Sciences Department at Brookhaven National Laboratory – Drs. Adam Rusek and Peter Guida and their teams for the help and support of our research studies.

FUNDING

This work was supported by the National Aeronautic and Space Administration (NASA) under Grant No. NNX11AD22G and American Heart Association (AHA) under Grant No. 14GRNT18860032 to DAG and NASA Grant No. NNX13AB67G to CDP.

REFERENCES

1. Czupalla M, Horneck G, Blome HJ. The conceptual design of a hybrid life support system based on the evaluation and comparison of terrestrial testbeds. *Adv Space Res* (2005) **35**:1609–20. doi:10.1016/j.asr.2005.06.010
2. Reitz G. Characteristic of the radiation field in low Earth orbit and in deep space. *Z Med Phys* (2008) **18**:233–43. doi:10.1016/j.zemedi.2008.06.015
3. Kerr RA. Planetary exploration. Radiation will make astronauts' trip to Mars even riskier. *Science* (2013) **340**:1031. doi:10.1126/science.340.6136.1031
4. Chancellor JC, Scott GB, Sutton JP. Space radiation: the number one risk to astronaut health beyond low earth orbit. *Life (Basel)* (2014) **4**:491–510. doi:10.3390/life4030491
5. Lomax AJ, Cella L, Weber D, Kurtz JM, Miralbell R. Potential role of intensity-modulated photons and protons in the treatment of the breast and regional nodes. *Int J Radiat Oncol Biol Phys* (2003) **55**:785–92. doi:10.1016/S0360-3016(02)04210-4
6. Sugahara S, Tokuuye K, Okumura T, Nakahara A, Saida Y, Kagei K, et al. Clinical results of proton beam therapy for cancer of the esophagus. *Int J Radiat Oncol Biol Phys* (2005) **61**:76–84. doi:10.1016/j.ijrobp.2004.04.003
7. Widesott L, Amichetti M, Schwarz M. Proton therapy in lung cancer: clinical outcomes and technical issues. A systematic review. *Radiother Oncol* (2008) **86**:154–64. doi:10.1016/j.radonc.2008.01.003
8. Newhauser WD, Fontenot JD, Mahajan A, Kornguth D, Stovall M, Zheng Y, et al. The risk of developing a second cancer after receiving craniospinal proton irradiation. *Phys Med Biol* (2009) **54**:2277–91. doi:10.1088/0031-9155/54/8/002
9. Hamada N, Imaoka T, Masunaga S, Ogata T, Okayasu R, Takahashi A, et al. Recent advances in the biology of heavy-ion cancer therapy. *J Radiat Res* (2010) **51**:365–83. doi:10.1269/jrr.09137
10. Okada T, Kamada T, Tsuji H, Mizoe JE, Baba M, Kato S, et al. Carbon ion radiotherapy: clinical experiences at National Institute of Radiological Science (NIRS). *J Radiat Res* (2010) **51**:355–64. doi:10.1269/jrr.10016
11. Hayashi T, Kusunoki Y, Hakoda M, Morishita Y, Kubo Y, Maki M, et al. Radiation dose-dependent increases in inflammatory response markers in A-bomb survivors. *Int J Radiat Biol* (2003) **79**:129–36. doi:10.1080/09553002021000038662
12. Darby SC, Mcgale P, Taylor CW, Peto R. Long-term mortality from heart disease and lung cancer after radiotherapy for early breast cancer: prospective cohort study of about 300,000 women in US SEER cancer registries. *Lancet Oncol* (2005) **6**:557–65. doi:10.1016/S1470-2045(05)70251-5
13. Simpson J. Elemental and isotopic composition of the galactic cosmic rays. *Annu Rev Nucl Part Sci* (1983) **33**:323–82. doi:10.1146/annurev.ns.33.120183.001543
14. Mewaldt RA. Galactic cosmic ray composition and energy spectra. *Adv Space Res* (1994) **14**:737–47. doi:10.1016/0273-1177(94)90536-3
15. Raju MR. Proton radiobiology, radiosurgery and radiotherapy. *Int J Radiat Biol* (1995) **67**:237–59. doi:10.1080/09553009514550301
16. Loeffler JS, Smith AR, Suit HD. The potential role of proton beams in radiation oncology. *Semin Oncol* (1997) **24**:686–95.
17. Burdak-Rothkamm S, Prise KM. New molecular targets in radiotherapy: DNA damage signalling and repair in targeted and non-targeted cells. *Eur J Pharmacol* (2009) **625**:151–5. doi:10.1016/j.ejphar.2009.09.068
18. Tokuyama Y, Furusawa Y, Ide H, Yasui A, Terato H. Role of isolated and clustered DNA damage and the post-irradiating repair process in the effects of heavy ion beam irradiation. *J Radiat Res* (2015) **56**:446–55. doi:10.1093/jrr/rru122
19. Gerelchuluun A, Manabe E, Ishikawa T, Sun L, Itoh K, Sakae T, et al. The major DNA repair pathway after both proton and carbon-ion radiation is NHEJ, but the HR pathway is more relevant in carbon ions. *Radiat Res* (2015) **183**:345–56. doi:10.1667/RR13904.1
20. So EY, Ouchi T. Decreased DNA repair activity in bone marrow due to low expression of DNA damage repair proteins. *Cancer Biol Ther* (2014) **15**:906–10. doi:10.4161/cbt.28883
21. Brooks A, Bao S, Rithidech K, Couch LA, Braby LA. Relative effectiveness of HZE iron-56 particles for the induction of cytogenetic damage in vivo. *Radiat Res* (2001) **155**:353–9. doi:10.1667/0033-7587(2001)155[0353:REOHIP]2.0.CO;2
22. Rithidech KN, Honikel L, Whorton EB. mFISH analysis of chromosomal damage in bone marrow cells collected from CBA/CaJ mice following whole body exposure to heavy ions (56Fe ions). *Radiat Environ Biophys* (2007) **46**:137–45. doi:10.1007/s00411-006-0092-x
23. Rithidech KN, Honikel LM, Reungpatthanaphong P, Tungjai M, Golightly M, Whorton EB. Effects of 100MeV protons delivered at 0.5 or 1cGy/min on the in vivo induction of early and delayed chromosomal damage. *Mutat Res* (2013) **756**:127–40. doi:10.1016/j.mrgentox.2013.06.001
24. Chang J, Feng W, Wang Y, Luo Y, Allen AR, Koturbash I, et al. Whole-body proton irradiation causes long-term damage to hematopoietic stem cells in mice. *Radiat Res* (2015) **183**:240–8. doi:10.1667/RR13887.1
25. Kryston TB, Georgiev AB, Pissis P, Georgakilas AG. Role of oxidative stress and DNA damage in human carcinogenesis. *Mutat Res* (2011) **711**:193–201. doi:10.1016/j.mrfmmm.2010.12.016
26. Cooke MS, Evans MD, Dizdaroglu M, Lunec J. Oxidative DNA damage: mechanisms, mutation, and disease. *FASEB J* (2003) **17**:1195–214. doi:10.1096/fj.02-0752rev
27. Rossi DJ, Bryder D, Seita J, Nussenzweig A, Hoeijmakers J, Weissman IL. Deficiencies in DNA damage repair limit the function of haematopoietic stem cells with age. *Nature* (2007) **447**:725–9. doi:10.1038/nature05862
28. Orkin SH, Zon LI. Hematopoiesis: an evolving paradigm for stem cell biology. *Cell* (2008) **132**:631–44. doi:10.1016/j.cell.2008.01.025
29. Mandal PK, Blanpain C, Rossi DJ. DNA damage response in adult stem cells: pathways and consequences. *Nat Rev Mol Cell Biol* (2011) **12**:198–202. doi:10.1038/nrm3060
30. Kondo M. Lymphoid and myeloid lineage commitment in multipotent hematopoietic progenitors. *Immunol Rev* (2010) **238**:37–46. doi:10.1111/j.1600-065X.2010.00963.x
31. Kajioka EH, Andres ML, Li J, Mao XW, Moyers MF, Nelson GA, et al. Acute effects of whole-body proton irradiation on the immune system of the mouse. *Radiat Res* (2000) **153**:587–94. doi:10.1667/0033-7587(2000)153[0587:AEOWBP]2.0.CO;2
32. Ware JH, Sanzari J, Avery S, Sayers C, Krigsfeld G, Nuth M, et al. Effects of proton radiation dose, dose rate and dose fractionation on hematopoietic cells in mice. *Radiat Res* (2010) **174**:325–30. doi:10.1667/RR1979.1
33. Maks CJ, Wan XS, Ware JH, Romero-Weaver AL, Sanzari JK, Wilson JM, et al. Analysis of white blood cell counts in mice after gamma- or proton-radiation exposure. *Radiat Res* (2011) **176**:170–6. doi:10.1667/RR2413.1
34. Sanzari JK, Cengel KA, Wan XS, Rusek A, Kennedy AR. Acute hematological effects in mice exposed to the expected doses, dose-rates, and energies of solar particle event-like proton radiation. *Life Sci Space Res (Amst)* (2014) **2**:86–91. doi:10.1016/j.lssr.2014.01.003
35. Sanzari JK, Wan SX, Diffenderfer ES, Cengel KA, Kennedy AR. Relative biological effectiveness of simulated solar particle event proton radiation to induce acute hematological change in the porcine model. *J Radiat Res* (2014) **55**:228–44. doi:10.1093/jrr/rrt108
36. Gridley DS, Pecaut MJ. Whole-body irradiation and long-term modification of bone marrow-derived cell populations by low- and high-LET radiation. *In vivo* (2006) **20**:781–9.
37. Hada M, Sutherland BM. Spectrum of complex DNA damages depends on the incident radiation. *Radiat Res* (2006) **165**:223–30. doi:10.1667/RR3498.1
38. Gridley DS, Obenaus A, Bateman TA, Pecaut MJ. Long-term changes in rat hematopoietic and other physiological systems after high-energy iron ion irradiation. *Int J Radiat Biol* (2008) **84**:549–59. doi:10.1080/09553000802203614
39. Datta K, Suman S, Trani D, Doiron K, Rotolo JA, Kallakury BV, et al. Accelerated hematopoietic toxicity by high energy (56)Fe radiation. *Int J Radiat Biol* (2012) **88**:213–22. doi:10.3109/09553002.2012.639434
40. Rithidech KN, Golightly M, Whorton E. Analysis of cell cycle in mouse bone marrow cells following acute in vivo exposure to 56Fe ions. *J Radiat Res* (2008) **49**:437–43. doi:10.1269/jrr.07109
41. Ritter S, Nasonova E, Furusawa Y, Ando K. Relationship between aberration yield and mitotic delay in human lymphocytes exposed to 200 MeV/u Fe-ions or X-rays. *J Radiat Res* (2002) **43**(Suppl):S175–9. doi:10.1269/jrr.43.S175
42. Miousse IR, Shao L, Chang J, Feng W, Wang Y, Allen AR, et al. Exposure to low-dose (56)Fe-ion radiation induces long-term epigenetic alterations in mouse bone marrow hematopoietic progenitor and stem cells. *Radiat Res* (2014) **182**:92–101. doi:10.1667/RR13580.1
43. Guo Y, Lubbert M, Engelhardt M. CD34- hematopoietic stem cells: current concepts and controversies. *Stem Cells* (2003) **21**:15–20. doi:10.1634/stemcells.21-1-15

44. Arndt K, Grinenko T, Mende N, Reichert D, Portz M, Ripich T, et al. CD133 is a modifier of hematopoietic progenitor frequencies but is dispensable for the maintenance of mouse hematopoietic stem cells. *Proc Natl Acad Sci U S A* (2013) **110**:5582–7. doi:10.1073/pnas.1215438110
45. Wilson KD, Sun N, Huang M, Zhang WY, Lee AS, Li Z, et al. Effects of ionizing radiation on self-renewal and pluripotency of human embryonic stem cells. *Cancer Res* (2010) **70**:5539–48. doi:10.1158/0008-5472.CAN-09-4238
46. Luft S, Pignalosa D, Nasonova E, Arrizabalaga O, Helm A, Durante M, et al. Fate of D3 mouse embryonic stem cells exposed to X-rays or carbon ions. *Mutat Res Genet Toxicol Environ Mutagen* (2014) **760**:56–63. doi:10.1016/j.mrgentox.2013.12.004
47. Lagadec C, Vlashi E, Della Donna L, Dekmezian C, Pajonk F. Radiation-induced reprogramming of breast cancer cells. *Stem Cells* (2012) **30**:833–44. doi:10.1002/stem.1058
48. Shen L, Huang X, Xie X, Su J, Yuan J, Chen X. High expression of SOX2 and OCT4 indicates radiation resistance and an independent negative prognosis in cervical squamous cell carcinoma. *J Histochem Cytochem* (2014) **62**:499–509. doi:10.1369/0022155414532654
49. Ghisolfi L, Keates AC, Hu X, Lee DK, Li CJ. Ionizing radiation induces stemness in cancer cells. *PLoS One* (2012) **7**:e43628. doi:10.1371/journal.pone.0043628
50. Yu J, Vodyanik MA, Smuga-Otto K, Antosiewicz-Bourget J, Frane JL, Tian S, et al. Induced pluripotent stem cell lines derived from human somatic cells. *Science* (2007) **318**:1917–20. doi:10.1126/science.1151526
51. Chambers I, Colby D, Robertson M, Nichols J, Lee S, Tweedie S, et al. Functional expression cloning of Nanog, a pluripotency sustaining factor in embryonic stem cells. *Cell* (2003) **113**:643–55. doi:10.1016/S0092-8674(03)00392-1
52. Zhang X, Neganova I, Przyborski S, Yang C, Cooke M, Atkinson SP, et al. A role for NANOG in G1 to S transition in human embryonic stem cells through direct binding of CDK6 and CDC25A. *J Cell Biol* (2009) **184**:67–82. doi:10.1083/jcb.200801009
53. Zannettino AC, Buhring HJ, Niutta S, Watt SM, Benton MA, Simmons PJ. The sialomucin CD164 (MGC-24v) is an adhesive glycoprotein expressed by human hematopoietic progenitors and bone marrow stromal cells that serves as a potent negative regulator of hematopoiesis. *Blood* (1998) **92**:2613–28.
54. Doyonnas R, Yi-Hsin Chan J, Butler LH, Rappold I, Lee-Prudhoe JE, Zannettino AC, et al. CD164 monoclonal antibodies that block hemopoietic progenitor cell adhesion and proliferation interact with the first mucin domain of the CD164 receptor. *J Immunol* (2000) **165**:840–51. doi:10.4049/jimmunol.165.2.840
55. Xia L, Mcdaniel JM, Yago T, Doeden A, Mcever RP. Surface fucosylation of human cord blood cells augments binding to P-selectin and E-selectin and enhances engraftment in bone marrow. *Blood* (2004) **104**:3091–6. doi:10.1182/blood-2004-02-0650
56. Wan X, Sato H, Miyaji H, Mcdaniel JM, Wang Y, Kaneko E, et al. Fucosyltransferase VII improves the function of selectin ligands on cord blood hematopoietic stem cells. *Glycobiology* (2013) **23**:1184–91. doi:10.1093/glycob/cwt055
57. Speck NA, Stacy T, Wang Q, North T, Gu TL, Miller J, et al. Core-binding factor: a central player in hematopoiesis and leukemia. *Cancer Res* (1999) **59**:1789s–93s.
58. Wang J, Zhou Y, Yin B, Du G, Huang X, Li G, et al. ASH2L: alternative splicing and downregulation during induced megakaryocytic differentiation of multipotential leukemia cell lines. *J Mol Med (Berl)* (2001) **79**:399–405. doi:10.1007/s001090100222
59. Wieland CW, Van Lieshout MH, Hoogendijk AJ, Van Der Poll T. Host defence during *Klebsiella* pneumonia relies on haematopoietic-expressed Toll-like receptors 4 and 2. *Eur Respir J* (2011) **37**:848–57. doi:10.1183/09031936.00076510
60. Burberry A, Zeng MY, Ding L, Wicks I, Inohara N, Morrison SJ, et al. Infection mobilizes hematopoietic stem cells through cooperative NOD-like receptor and Toll-like receptor signaling. *Cell Host Microbe* (2014) **15**:779–91. doi:10.1016/j.chom.2014.05.004
61. Nagai Y, Garrett KP, Ohta S, Bahrun U, Kouro T, Akira S, et al. Toll-like receptors on hematopoietic progenitor cells stimulate innate immune system replenishment. *Immunity* (2006) **24**:801–12. doi:10.1016/j.immuni.2006.04.008
62. Granick JL, Simon SI, Borjesson DL. Hematopoietic stem and progenitor cells as effectors in innate immunity. *Bone Marrow Res* (2012) **2012**:165107. doi:10.1155/2012/165107
63. Schroeder T, Just U. Notch signalling via RBP-J promotes myeloid differentiation. *EMBO J* (2000) **19**:2558–68. doi:10.1093/emboj/19.11.2558
64. Fan X, Khaki L, Zhu TS, Soules ME, Talsma CE, Gul N, et al. NOTCH pathway blockade depletes CD133-positive glioblastoma cells and inhibits growth of tumor neurospheres and xenografts. *Stem Cells* (2010) **28**:5–16. doi:10.1002/stem.254
65. Sikandar SS, Pate KT, Anderson S, Dizon D, Edwards RA, Waterman ML, et al. NOTCH signaling is required for formation and self-renewal of tumor-initiating cells and for repression of secretory cell differentiation in colon cancer. *Cancer Res* (2010) **70**:1469–78. doi:10.1158/0008-5472.CAN-09-2557
66. Zielske SP. Epigenetic DNA methylation in radiation biology: on the field or on the sidelines? *J Cell Biochem* (2015) **116**:212–7. doi:10.1002/jcb.24959
67. Bock J, Fukuyo Y, Kang S, Phipps ML, Alexandrov LB, Rasmussen KO, et al. Mammalian stem cells reprogramming in response to terahertz radiation. *PLoS One* (2010) **5**:e15806. doi:10.1371/journal.pone.0015806

Conflict of Interest Statement: The authors declare that the research was conducted in the absence of any commercial or financial relationships that could be construed as a potential conflict of interest.

Copyright © 2015 Muralidharan, Sasi, Zuriaga, Hirschi, Porada, Coleman, Walsh, Yan and Goukassian. This is an open-access article distributed under the terms of the Creative Commons Attribution License (CC BY). The use, distribution or reproduction in other forums is permitted, provided the original author(s) or licensor are credited and that the original publication in this journal is cited, in accordance with accepted academic practice. No use, distribution or reproduction is permitted which does not comply with these terms.

frontiers in Oncology

CORRECTION
published: 25 November 2015
doi: 10.3389/fonc.2015.00255

Corrigendum: Ionizing Particle Radiation as a Modulator of Endogenous Bone Marrow Cell Reprogramming: Implications for Hematological Cancers

*Sujatha Muralidharan[1], Sharath P. Sasi[2], Maria A. Zuriaga[1], Karen K. Hirschi[3], Christopher D. Porada[4], Matthew A. Coleman[5,6], Kenneth X. Walsh[1], Xinhua Yan[2,7] and David A. Goukassian[1,2,7]**

[1] Whitaker Cardiovascular Institute, Boston University School of Medicine, Boston, MA, USA, [2] Cardiovascular Research Center, GeneSys Research Institute, Boston, MA, USA, [3] Yale Cardiovascular Research Center, Yale School of Medicine, New Haven, CT, USA, [4] Wake Forest Institute for Regenerative Medicine, Wake Forest School of Medicine, Winston-Salem, NC, USA, [5] Radiation Oncology, School of Medicine, University of California Davis, Sacramento, CA, USA, [6] Lawrence Livermore National Laboratory, Livermore, CA, USA, [7] Tufts University School of Medicine, Boston, MA, USA

Keywords: progenitors, endogenous reprogramming, hematological cancer, radiation, HSC

A corrigendum on

Ionizing Particle Radiation as a Modulator of Endogenous Bone Marrow Cell Reprogramming: Implications for Hematological Cancers
by Muralidharan S, Sasi SP, Zuriaga MA, Hirschi KK, Porada CD, Coleman MA, et al. Front Oncol (2015) ***5****:231. doi: 10.3389/fonc.2015.00231*

OPEN ACCESS

Edited and Reviewed by:
Marco Durante, GSI Helmholtzzentrum für Schwerionenforschung, Germany

****Correspondence:***
David A. Goukassian
david.goukassian@tufts.edu, dgoukass@bu.edu

Specialty section:
This article was submitted to Radiation Oncology, a section of the journal Frontiers in Oncology

Received: *29 October 2015*
Accepted: *05 November 2015*
Published: *25 November 2015*

Citation:
Muralidharan S, Sasi SP, Zuriaga MA, Hirschi KK, Porada CD, Coleman MA, Walsh KX, Yan X and Goukassian DA (2015) Corrigendum: Ionizing Particle Radiation as a Modulator of Endogenous Bone Marrow Cell Reprogramming: Implications for Hematological Cancers. Front. Oncol. 5:255. doi: 10.3389/fonc.2015.00255

In the paper titled "Ionizing Particle Radiation as a Modulator of Endogenous Bone Marrow Cell Reprogramming: Implications for Hematological Cancers," there was secretarial error made at our end in "Figure 1," which should be corrected. At some point of the submission in Figure 1, A and B were disarranged in the slide. No other correction is needed as the text and figure legends are correct.

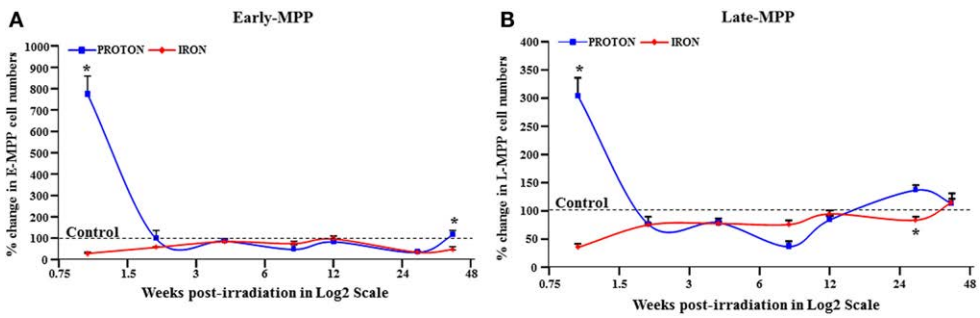

FIGURE 1 | E-MPP and L-MPP cell numbers are downregulated by ^{56}Fe- and ^{1}H-IR but recover to control levels by 40 weeks post-IR. Effect of full-body single dose of proton (^{1}H) at 0.5 Gy, 1 GeV and iron (^{56}Fe) at 0.15 Gy, 1 GeV/nucleon of ionizing radiation (IR) on survival of multipotent progenitor cell populations was examined. The survival of **(A)** E-MPPs and **(B)** L-MPPs in the BM after particle IR in C57BL/6NT mice were determined at 1, 2, 4, 8, 12, 28, and 40 weeks post-IR. Total BM-derived mononuclear cells were triple-stained with FITC-labeled RAM34 antibody (that consists of CD34, c-kit, and Sca1 antibodies), PE-Cy7-AC133, and PE-hematopoietic lineage cocktail (CD3e, Ly-6G/Ly-6C, CD11b, CD45R/B220, TER-119), then sorted by FASC for **(A)** E-MPPs (CD34^{+}/c-kit^{+}/Sca-1^{+}/AC133^{+}/Lin^{-}) and **(B)** L-MPPs (CD34^{+}/c-kit^{+}/Sca-1^{+}/AC133^{-}/Lin^{-}). Percentage changes in cell numbers were calculated relative to control sham irradiated mice, which was set to 100% for each time point. Solid lines represent mean ± SEM (n = 6/group) for ^{1}H-IR (solid blue lines) and ^{56}Fe-IR (solid red lines). "*" represents statistically significant differences compared to control with $p < 0.05$.

Conflict of Interest Statement: The authors declare that the research was conducted in the absence of any commercial or financial relationships that could be construed as a potential conflict of interest.

Copyright © 2015 Muralidharan, Sasi, Zuriaga, Hirschi, Porada, Coleman, Walsh, Yan and Goukassian. This is an open-access article distributed under the terms of the Creative Commons Attribution License (CC BY). The use, distribution or reproduction in other forums is permitted, provided the original author(s) or licensor are credited and that the original publication in this journal is cited, in accordance with accepted academic practice. No use, distribution or reproduction is permitted which does not comply with these terms.

frontiers in Oncology

ORIGINAL RESEARCH
published: 14 June 2016
doi: 10.3389/fonc.2016.00138

Radiation-Induced Reprogramming of Pre-Senescent Mammary Epithelial Cells Enriches Putative CD44^{+}/CD24$^{-/low}$ Stem Cell Phenotype

Xuefeng Gao[1,2,3,4], Brock J. Sishc[5,6]*, Christopher B. Nelson[5], Philip Hahnfeldt[4], Susan M. Bailey[5] and Lynn Hlatky[4]*

[1] Inserm UMR 1181, Biostatistics, Biomathematics, Pharmacoepidemiology and Infectious Diseases (B2PHI), Paris, France, [2] Institut Pasteur, UMR 1181, B2PHI, Paris, France, [3] Université de Versailles St Quentin, UMR 1181, B2PHI, Paris, France, [4] Center of Cancer Systems Biology, Tufts University, Boston, MA, USA, [5] Department of Environmental and Radiological Health Sciences, Colorado State University, Fort Collins, CO, USA, [6] Department of Radiation Oncology, University of Texas Southwestern Medical Center, Dallas, TX, USA

OPEN ACCESS

Edited by:
Marco Durante,
GSI, Germany

Reviewed by:
Kevin Prise,
Queen's University Belfast, UK
Eddy S. Yang,
University of Alabama-Birmingham
School of Medicine, USA

***Correspondence:**
Xuefeng Gao
xuefeng.gao@pasteur.fr;
Brock J. Sishc
brock.sishc@utsouthwestern.edu

Specialty section:
This article was submitted
to Radiation Oncology,
a section of the journal
Frontiers in Oncology

Received: 31 January 2016
Accepted: 23 May 2016
Published: 14 June 2016

Citation:
Gao X, Sishc BJ, Nelson CB, Hahnfeldt P, Bailey SM and Hlatky L (2016) Radiation-Induced Reprogramming of Pre-Senescent Mammary Epithelial Cells Enriches Putative CD44^{+}/CD24$^{-/low}$ Stem Cell Phenotype.
Front. Oncol. 6:138.
doi: 10.3389/fonc.2016.00138

The enrichment of putative CD44^{+}/CD24$^{-/low}$ breast stem cell populations following exposure to ionizing radiation (IR) has been ascribed to their inherent radioresistance and an elevated frequency of symmetric division during repopulation. However, recent studies demonstrating radiation-induced phenotypic reprogramming (the transition of non-CD44^{+}/CD24$^{-/low}$ cells into the CD44^{+}/CD24$^{-/low}$ phenotype) as a potential mechanism of CD44^{+}/CD24$^{-/low}$ cell enrichment have raised the question of whether a higher survival and increased self-renewal of existing CD44^{+}/CD24$^{-/low}$ cells or induced reprogramming is an additional mode of enrichment. To investigate this question, we combined a cellular automata model with *in vitro* experimental data using both MCF-10A non-tumorigenic human mammary epithelial cells and MCF-7 breast cancer cells, with the goal of identifying the mechanistic basis of CD44^{+}/CD24$^{-/low}$ stem cell enrichment in the context of radiation-induced cellular senescence. Quantitative modeling revealed that incomplete phenotypic reprogramming of pre-senescent non-stem cells (reprogramming whereby the CD44^{+}/CD24$^{-/low}$ phenotype is conveyed, along with the short-term proliferation capacity of the original cell) could be an additional mode of enriching the CD44^{+}/CD24$^{-/low}$ subpopulation. Furthermore, stem cell enrichment in MCF-7 cells occurs both at lower doses and earlier time points, and has longer persistence, than that observed in MCF-10A cells, suggesting that phenotypic plasticity appears to be less regulated in breast cancer cells. Taken together, these results suggest that reprogramming of pre-senescent non-stem cells may play a significant role in both cancer and non-tumorigenic mammary epithelial populations following exposure to IR, a finding with important implications for both radiation therapy and radiation carcinogenesis.

Keywords: radiation, breast cancer cells, cancer stem cells, reprogramming, senescence, cellular automata

INTRODUCTION

Current dogma states that the recurrence of cancer in patients treated with radiation therapy is driven by the survival of radiation-resistant clonogens repopulating and replacing reproductively dead cells. This therapeutic resistance has been attributed to cells existing in hypoxic tumor regions where the lack of oxygen decreases the efficacy of radiation-induced cell killing. However, the contention that tumor-initiating or cancer stem cells, an inherently radioresistant population with increased DNA repair capacity, elevated expression of endogenous anti-oxidant defenses, and a slower rate of cell division are the potential drivers of this phenomenon, has prompted a good deal of interest in targeting cancer stem cells (1). Cancer stem cells were originally identified in acute myeloid leukemia (2, 3) and since have been identified in solid tumors and cell lines, including breast (4), prostate (5), lung (6), glioblastoma (7), and squamous cell carcinoma of the head and neck (8).

Previous studies have demonstrated that putative stem cells in normal and malignant mammary tissues are characterized by a $CD44^+/CD24^-$ phenotype (4, 9). Normal breast epithelial cells exhibiting the $CD44^+/CD24^-$ phenotype express genes associated with stem cells and somatic cell reprogramming at higher levels, and can asymmetrically divide and differentiate giving rise to sub-phenotypes of basal and luminal cells (10). Some human mammary epithelial cell lines, most notably MCF-10A non-malignant cells have been demonstrated the propensity to recapitulate ductal morphogenesis in the humanized fat pads of mice (11), offering strong evidence for a stem-like/progenitor subpopulation. *In vitro,* MCF-10A cells spontaneously acquire the $CD44^+/CD24^-$ phenotype via epithelial–mesenchymal transition (EMT) (12). In human breast cancers, the rare $CD44^+/CD24^{-/low}$ subpopulation shares properties with normal stem cells, including increased reproductive capacity and the ability to give rise to diverse cell lineages (4). $CD44^+/CD24^-$ cells isolated from some human breast cancer cell lines (e.g., MCF-7) and patient tumors demonstrate many stem-cell like properties *in vitro* and *in vivo* (13). Importantly, the purified $CD44^+/CD24^-$ cells (mesenchymal-like cancer stem cell state) are able to generate heterogeneous populations that recreate the proportion of $CD44^+/CD24^-$ and aldehyde dehydrogenase (ALDH) expressing cells (epithelial-like cancer stem cell state) present in the original cell lines (including MCF-7) (14), indicating that cellular plasticity enables breast cancer stem cells to transit between different phenotypes.

Radiation therapy is a common component of multimodal treatment designed to improve loco-regional control and overall survival in patients after breast-conserving surgery (15). After a single IR exposure (2–20 Gy γ-rays) we found the effective dose range for significantly enhancing the size of the stem cell pool differs between MCF-7 breast cancer cells and MCF-10A non-tumorigenic cells. Consistent with a previous report (16), following an acute radiation exposure of 10 Gy, the proportion of cells that are $CD44^+/CD24^{-/low}$ in both cell lines is elevated and peaks around day 5 after IR. This enrichment has been attributed to a higher radioresistance of $CD44^+/CD24^{-/low}$ cells and/or a switch from an asymmetric to symmetric type of division of $CD44^+/CD24^{-/low}$ cells, which then produce two identical $CD44^+/CD24^{-/low}$ daughter cells leading to a relative and absolute increase in $CD44^+/CD24^{-/low}$ subpopulation (17). In addition, Lagadec et al. demonstrated that radiation might reprogram a fraction of surviving non-stem committed cells (CCs) into the $CD44^+/CD24^{-/low}$ phenotype in some breast cancer cells (16). Notably, in our *in vitro* experiments, the fraction of senescent cells [cells that permanently withdraw from the cell cycle in response to diverse stress (18) (e.g., radiation-induced DNA damage), and can be identified by β-galactosidase (19)] increases and gradually dominates the population (~70%) during the 10 days post 10 Gy IR in both cell lines. The enrichment of stem cells in the irradiated populations prompted us to investigate how the fate of irradiated cells, in particular those experiencing IR-induced senescence, may influence cellular repopulation following exposure.

To explore the mechanistic basis for the elevated fraction of $CD44^+/CD24^{-/low}$ phenotype observed in normal and breast cancer cell populations following irradiation, we combined *in vitro* experiments with a cellular automata (CA) model to test mechanistic alternatives. Comparing simulation results with *in vitro* data demonstrated that neither (i) endowing normal and cancer stem cells with a lower radiosensitivity (i.e., a higher survival rate after irradiation), (ii) increasing the frequency of symmetric self-renewal division of stem cells, and (iii) increasing the rate of phenotypic reprogramming of surviving intact CCs to a full stem cell state, nor any combination of i, ii, and iii, were able to elevate the calculated stem cell percentage to match the observed percentage of $CD44^+/CD24^{-/low}$ cells following an acute dose of 10 Gy.

Unsuccessful model fitting based on the aforementioned hypotheses turned our attention to the potential contribution of IR-induced pre-senescent CCs (non-stem cells with short-term proliferation capacity due to radiation damage) to the replenishment of the stem cell pool through reprogramming. To this end, we considered two additional mechanisms: (iv) that, in addition to (iii), pre-senescent CCs can also be reprogramed to a stem cell state (i.e., $CD44^+/CD24^{-/low}$), albeit limited in this case to the remaining proliferative capacity they had before reprogramming (i.e., becoming pre-senescent SCs); or (v) all surviving CCs, whether pre-senescent, can have a potential to acquire a stem cell state with unlimited proliferative capacity. By fitting the model parameters in order to reproduce both the temporal dynamics of $CD44^+/CD24^{-/low}$ cells and the proportion of senescent cells in the population during the first 10 days after irradiation, we found that allowing for pre-senescent CCs to have additional reprogramming capability as described in mechanisms (iv) can explain experimental results not reconcilable with mechanisms (i)– (iii) or (v). Furthermore, we observed that IR induced a high reprogramming rate that lasted longer in MCF-7 cells compared to MCF-10A cells.

In conclusion, our study suggests that IR-induced incomplete phenotypic reprogramming of pre-senescent non-stem cells in irradiated MCF-10A and MCF-7 cells might be a contributing factor to the enrichment of the $CD44^+/CD24^{-/low}$ phenotype. Incomplete phenotypic reprogramming of pre-senescent CCs also gives rise to a heterogeneous stem cell pool consisting of

a fraction of cells that express the stem cell marker, but have a short-term proliferative potential. Finally, we find MCF-7 breast cancer cells to be more sensitive to acute, high-dose IR than MCF-10A non-tumorigenic mammary epithelial cells in terms of phenotypic reprogramming.

MATERIALS AND METHODS

Cell Culture

The human mammary epithelial, non-tumorigenic cell line MCF-10A was purchased from ATCC and cultured in 1:1 Dulbecco's modified essential medium (DMEM)/Ham's F12 growth medium (Hyclone) supplemented with 5% fetal bovine serum (FBS), 10 μg/mL insulin (Sigma), 20 ng/mL epidermal growth factor (EGF;Sigma), 0.5 μg/mL hydrocortisone (Sigma), 0.1 μg/mL cholera toxin (Sigma), and 1% glutamax (Life Technologies). The human mammary carcinoma cell line MCF-7 (kind gift from L. Chubb, CSU Animal Cancer Center) was grown in DMEM supplemented with 10% FBS and 1% glutamax (Life Technologies). Cells were grown at 37°C in a humidified incubator at 5% CO_2 passaged 1–2 times per week.

Mammosphere Assay

Sphere-forming assay was utilized to confirm stem-like properties of MCF-7 cells. Briefly, monolayer cultures were grown in low adherence dishes (Corning) at a low density in Mammocult sphere-forming media (Stem Cell Technologies). Limiting dilution assays were performed in 96-well plates comparing sorted $CD44^+/CD24^{-/low}$ to bulk monolayer cell cultures. Spheres were allowed to form for 10 days, and spheres larger than 60 μm in diameter were scored (20).

Irradiations

For clonogenic cell survival assays, cells were seeded 48 h prior to irradiation at a density of 3×10^5 cells per T25 flask. Monolayer cultures were irradiated in a Mark I Irradiator (J.L. Shepherd) utilizing a Cs-137 source at acute doses of 1, 2, 4, 5, 8, and 10 Gy or sham irradiated as a control. Following irradiation, cells were allowed to repair for 6 h and plated in triplicate at low density in 100-mm cell culture plates (Greiner) containing 10 mL of culture medium. Cells were incubated for 12 days (MCF-7) or 16 days (MCF-10A), fixed in 100% ethanol, and stained with 0.05% crystal violet solution. Colonies were scored based on the presence of 50 or more cells and scored independently by two individuals.

Flow Cytometry Analysis

All flow cytometry analyses were performed at the Colorado State University Animal Cancer Center on a Beckman Coulter CyAN ADP 9 Color analyzer running Summit Version 3.0 flow cytometry analysis software. Mammary epithelial stem cells were identified based on expression of $CD44^+/CD24^{-/low}$ immunotype and stem-like properties were confirmed utilizing the ALDEfluro Assay (Stem Cell Technologies). Monolayer MCF-7 and MCF-10A mammary epithelial cell cultures were stained for CD44 and CD24 expression. Briefly, ~3×10^5 cells were dissociated from cell culture surface using 0.25% Trypsin-EDTA, pelleted, washed, and re-suspended in 30 μL of Flow Cytometry wash buffer (1X PBS, 1% FBS, and 1% Penicillin/Streptomyocin). Six microliters of direct FITC-conjugated mouse monoclonal anti-human CD44 antibody (BD Pharmingen #555478) and 6 μL of direct PE-conjugated mouse monoclonal anti-human CD24 antibody (BD Pharmingen #555428). Cells were then incubated for 30–60 min in the dark at 4°C. Following incubation, cells were pelleted and re-suspended in 500 μl of cold 1 × PBS and kept on ice until analysis. Analysis gates were established using cells from an unstained control and anti-mouse Ig,κ antibody capture beads (BD Pharmingen #552843).

Identification of Senescent Cell Fraction

The fraction of senescent cells was determined via β-galactosidase staining. Cells were stained using β-galactosidase staining kit (Cell Signaling Technologies) and imaged on a confocal microscope at a 20× magnification utilizing a color camera. Cells were scored as positive based on the presence of blue pigmentation in the nuclei of adherent cells.

Cellular Automata Model

A CA model is used to simulate the dynamics and interactions of single cells in the growth of cell population (21). In a CA model, a system is represented as a collection of autonomous decision-making agents (e.g., cells). Each agent is endowed some intrinsic state variables and behaves and interacts with each other and its external environment given a set of predefined rules. Stochastic interactions of single cells as well as with their external environment result in complex population dynamics. The CA framework can capture the interactive consequences of these dynamics while allowing for the examination of phenotypical and functional heterogeneity, such as stem cell biology.

The system is defined on a two-dimensional square lattice ($L \times L$ lattice points) with periodic boundary conditions. As *in silico* cells live on a square lattice with $(15\ \mu m)^2$ grid points, a single migration step to a neighboring location is calibrated as 15 or 21 μm in an 8-cell Moore neighborhood (21). Each lattice point can stay empty or be occupied by one cell. If a free lattice site is found within the Moore neighborhood of a cell, it can migrate with a probability p_m, or divide to produce a new cell provided the maturation has been reached. A proliferative cell turns quiescent when it is completely surrounded by other cells but can re-enter the cell cycle when a neighboring free space is available. As per the stem cell hypothesis, stem cells reside at the top of the hierarchy and produce progenitor cells, which in turn give rise to CCs. For present purposes, a CC will refer to a non-stem cell. A stem cell is capable of dividing into two stem cells (symmetric division) with probability p_S, or a stem cell and a CC with probability $1 - p_S$ (asymmetrical division). The duplication of a non-senescent CC results in two CCs. A CC ceases to divide after some number of divisions, a phenomenon known as replicative senescence, or the Hayflick limit. The parameter ρ will refer to the number of remaining divisions a cell is capable of undergoing before it becomes senescent (the value ρ for a stem cell is, thus, $\rho = \infty$).

It has been found that normal and neoplastic non-stem cells can spontaneously convert to a stem-like state (22). In our model, CCs are eligible for reprogramming with probability p_r. The rate of symmetric division (p_S) and reprogramming rate (p_r) were

estimated together in order to match the control frequency of $CD44^+/CD24^{-/low}$ in both cell lines (Figure S1 in Supplementary Material). We referred a stem cell study by Tang et al. (11) in order to guess the initial value of p_S.

To reproduce the population dynamics *in vitro*, we began with a fixed division cycling time in the CA model. However, the resultant growth curves were exponential, which could not explain the population dynamics *in vitro*, in which the cell proliferation rate decreases at later time points (Figure S2 in Supplementary Material). Indeed, cell population growth can be affected by the surrounding environment, such as (a) cell–cell contact inhibition (already implemented in the CA model), (b) nutrient availability, and (c) accumulation of toxic wastes. In our experiments, fresh culture medium was added to the cultures to ensure adequate cellular nutrition levels. However, no cell culture medium was removed following irradiation in order to prevent removal of potential reprogramming signals. Therefore, it is reasonable to presume that the decreasing proliferation rate of control growth (sham irradiated) is mostly a result of *c*. To depict this phenomenon simply, we introduced a cell cycle regulation mechanism implicitly as a function of cell population density:

$$\text{Cell cycle} = c_0 e^{k*(\text{population density})}$$

where c_0 is the initial cycling time and *k* is the inhibition coefficient. The values of c_0 and *k* were estimated by matching the population dynamics *in vitro* (Figure S3 in Supplementary Material). The estimated *k* value was smaller for MCF-7 cells than MCF-10A cells (**Table 1**) suggesting that breast cancer cells are more resistant to a stressful microenvironment than non-cancerous cells, which belongs to one hallmark of cancer (evading growth suppressors) (23).

After radiation exposure, cells exhibit mitotic delay while attempting to repair radiation-induced DNA damage (27). Several studies have demonstrated that a large fraction of normal fibroblasts irradiated in G1-phase and reseeded after irradiation, do not re-enter the cell cycle but remained permanently arrested (28–30). Accordingly, we assumed that a cell either undergoes a permanent cycle arrest with a probability p_a or experiences transient arrest for a randomly chosen time between 0 and 10 days following radiation exposure. Cell survival probability after irradiation was determined via clonogenic assay (Figure S4 in Supplementary Material). Some studies have demonstrated that MCF-7 cells undergo mostly IR-induced senescence instead of apoptosis (31–33). By day 10 of our experiment following a 10 Gy single-dose IR, the senescent phenotype (SA-β-gal positive cells) had increased not only in ratio but also in number relative to day 0 within the proliferating cell population for both cell lines (**Figures 2C,D**; Figure S3 in Supplementary Material), which indicates the existence of cells in a pre-senescent state (have short-term proliferations before undergoing a senescent state). Therefore, we assigned to the pre-senescent CCs and pre-senescent SCs a temporal range of short-term proliferation potential ρ_{psn}. The range of values for ρ_{psn} was estimated by matching the irradiated population dynamics (Figure S3 in Supplementary Material) and senescent cell fractions *in vitro* (**Figures 2C,D**). Cell cycle arrest has been found to prevent reprogramming (34, 35). Hence, a reprogramming rate $p_r = 0$ was applied to CCs in an arrested state and senescent cells.

A diagram of the simulation process and decisions at the cell level is shown in Figure S5 in Supplementary Material. The model parameters and their values are summarized in **Table 1**.

RESULTS

MCF-10A and MCF-7 Populations Show Different Dose Ranges Over Which There is Substantial $CD44^+/CD24^{-/low}$ Cell Fraction Modification

In MCF-10A cells, at day 5 after irradiation with a single dose of 5 Gy or lower, the fraction of $CD44^+/CD24^{-/low}$ cells showed no difference compared to control (**Figure 1A**); whereas a dose as low as 2 Gy induced an enrichment of the $CD44^+/CD24^{-/low}$ subpopulation among MCF-7 cells (**Figure 1B**) (20). When the IR dose increased to 20 Gy, a tremendously high enrichment of $CD44^+/CD24^{-/low}$ subpopulation appeared in MCF-10A cells (**Figure 1A**). By contrast, a 20 Gy single dose did not further increase the fraction of $CD44^+/CD24^{-/low}$ subpopulation in MCF-7 cells (**Figure 1B**). Presumably, the mechanisms for regulating the $CD44^+/CD24^{-/low}$ cells are not easily altered in the non-tumorigenic population vs. cancer cells, suggesting a potentially pivotal role for this enrichment in tumor re-growth following radiation therapy.

TABLE 1 | Model parameters and values.

Parameter	Meaning	Value		Reference
		MCF-10A	MCF-7	
R	MCF-10A or MCF-7 cell diameter	15 μm	15 μm	(24)
V	Cell migration speed	23.4 μm h^{-1}	23.4 μm h^{-1}	(25, 26)
c_0	Initial cell cycle	17 h	24 h	Fitting *in vitro* data
k	Cell cycle inhibition coefficient	18	2.97	Fitting *in vitro* data
p_d	Spontaneous cell death rate of CC	0.004 $CC^{-1}day^{-1}$	0.02 $CC^{-1}day^{-1}$	Fitting *in vitro* data
p_s	Symmetric self-renewing division rate	10% SC (C)	10% (C)	Fitting *in vitro* data
p_r	Phenotypic reprogramming rate	0.004 $CC^{-1}day^{-1}$ (C)	0.0017 $CC^{-1}day^{-1}$(C)	Fitting *in vitro* data
p_a	Probability of permanent arrest	0.63	0.76	Fitting *in vitro* data
SF	Overall survival rate following acute 10 Gy IR	0.0071	0.0031	Clonogenic assay
ρ_{psn}	Proliferation potential of pre-senescent cells	2–6 divisions	0–9 divisions	Fitting *in vitro* data

C, control/sham irradiated with 0 Gy.

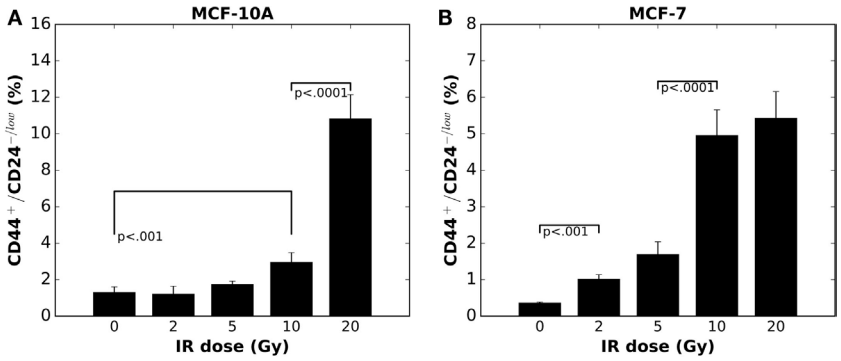

FIGURE 1 | Radiation-induced enrichment of CD44$^+$/CD24$^{-/low}$ putative stem cells in (A) MCF-10A cells and (B) MCF-7 cells *in vitro* is in a dose dependent manner (mean ± SD; *n* = 3).

Enrichment of CD44$^+$/CD24$^{-/low}$ Phenotype in MCF-10A and MCF-7 Cells May Not Derive Purely from Intact Surviving Cells

To evaluate the mechanistic basis of IR-induced enrichment of CD44$^+$/CD24$^{-/low}$ phenotype in MCF-10A and MCF-7 cells, we tested the following hypothesis: (i) low radiosensitivity of stem cells (maximum tested: 100% survival after radiation exposure), (ii) increased symmetric division frequency (maximum tested: 100% per stem cell division) of stem cells, and (iii) increased reprogramming frequency of undamaged cycling CCs (maximum tested: 100% per intact CC per day). The resulting fractions of senescent cells were similar to one another for the three mechanisms, which roughly reproduced the observed dynamics of state with a decreased reproductive capacity positive cell staining *in vitro* (**Figures 2C,D**). Surprisingly, however, neither of the three mechanisms alone were able to produce the observed high percentage of CD44$^+$/CD24$^{-/low}$ cells observed in either cell line (**Figures 2A,B**), nor were combinations of any two mechanisms able to generate the high fraction of stem cells especially at day 5 after exposure to 10 Gy (data not shown). Combining all three mechanisms (e.g., >50% survival rate of SCs, 100% symmetric division rate, and 100% reprogramming rate of non-arrested intact CCs) produced a comparable fraction of CD44$^+$/CD24$^{-/low}$ in MCF-10A cells (**Figure 2A**) but not in MCF-7 cells. However, the resulting ratio of senescent cells (~43% *in silico*) was smaller than that observed (67% *in vitro*; **Figure 2C**) at day 10 after irradiation, which makes it less likely that the possibility of the combination of above three mechanisms is a major force in enriching the stem cell pool.

Radiation-Induced Incomplete Phenotypic Reprogramming of Pre-Senescent Non-Stem Cells Appears More Likely To Be an Additional Mode of Enriching CD44$^+$/CD24$^{-/low}$ Cells

The above disparities led us to consider alternative explanations; specifically, phenotypic reprogramming of pre-senescent non-stem cells. In the latter case, it has been demonstrated that cellular senescence is not a limit to reprogramming and that age-related cellular physiology is reversible (36). Nevertheless, it is unknown to what extent reproductive potential can be regained by the reprogramming of senescent cells, e.g., 0–100%. Instead of testing the recovery of proliferative capacity in a quantitative manner, we simply assume that reprogramming of a pre-senescent CC can be either (iv) incomplete (i.e., pre-senescent CCs are reprogramed to pre-senescent SCs but inherit the remaining proliferative potential) or (v) complete (i.e., pre-senescent CCs are reprogramed to SCs and reacquire unlimited proliferative potential). Simulation results showed that both hypotheses (iv) and (v) could successfully reproduce a comparable ratio of CD44$^+$/CD24$^{-/low}$ cells observed 10 days after 10 Gy (**Figures 2E,F**). However, following hypothesis (v), at day 10 after 10 Gy, the fraction of senescent cells in simulations was lower than observed *in vitro* in both cell lines (**Figures 2G,H**). Considering these findings together, the enrichment of CD44$^+$/CD24$^{-/low}$ phenotype in MCF-10A and MCF-7 cells is more likely driven to a large extent by incomplete phenotypic reprogramming. As a consequence, the enriched stem cell pool would be mixed with a fraction of stem cells that have a short-term proliferative potential (**Figure 3**). Therefore, the signature of CD44$^+$/CD24$^{-/low}$ is no longer accurate for presenting the overall "stemness" of the irradiated cell population.

The IR-Induced Reprogramming Events Persist Longer in MCF-7 Breast Cancer Cells than in MCF-10A Non-Tumorigenic Mammary Epithelial Cells

During the process of parameter fitting in order to reproduce the dynamics of the CD44$^+$/CD24$^{-/low}$ subpopulation after a 10 Gy single-dose IR, we found differential changes in the kinetics of reprogramming between MCF-10A and MCF-7 cells. For MCF-10A cells, the fitted reprogramming rate only transiently increased to 0.09 per CC (intact or pre-senescent) per day for 38 h during days 3–5 after IR (**Figure 2E**). By contrast, the reprogramming rate of MCF-7 cells increased to 0.08 per CC (intact or pre-senescent) per day immediately following the radiation exposure and through day 4 (**Figure 2F**), then decreased to 0.0198 per CC

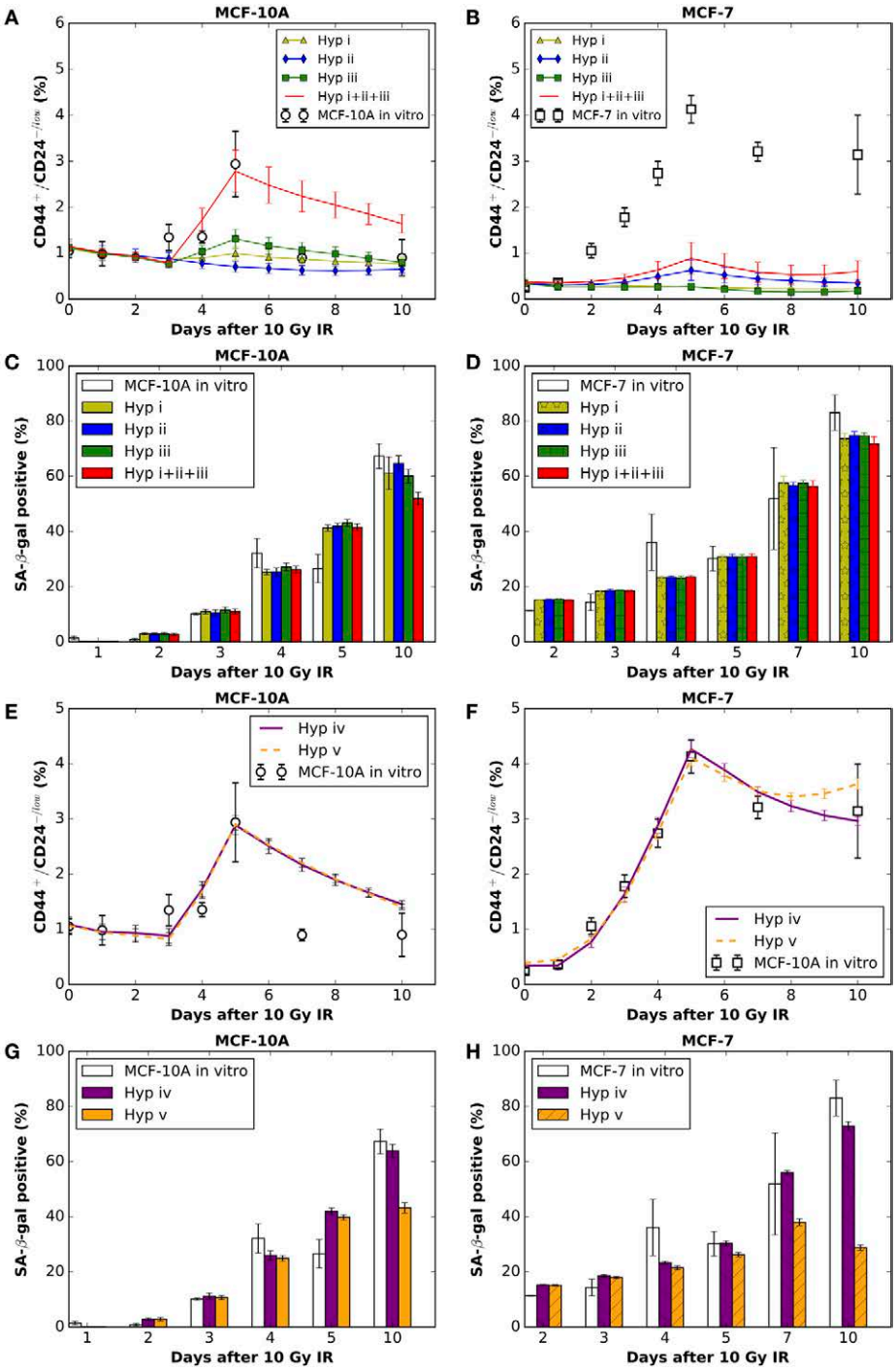

FIGURE 2 | The comparisons between model simulation results (mean ± SD; *n* = 10 simulations) of applying hypothesis (i), (ii), or (iii) (alone or in combinations) and *in vitro* data (mean ± SD; *n* = 3) on the (A) % of CD44⁺/CD24⁻ˡᵒʷ cells in MCF-10A cells and (B) MCF-7 cells; and the (C) % of SA-β-gal positive cells in MCF-10A cells and (D) MCF-7 cells. The comparisons between simulation results of applying hypothesis (iv) or (v) and *in vitro* data on the **(E)** % of CD44⁺/CD24⁻ˡᵒʷ cells in MCF-10A cells and **(F)** MCF-7 cells; and the **(G)** % of SA-β-gal positive cells in MCF-10A cells and **(H)** MCF-7 cells. Hyp stands for hypothesis in the figure legends. Best fitting for MCF-10A cells under Hyp (iv) [corresponding to **(E,G)**]: reprogramming rate (p_r) increases to 0.09 per CC (intact or pre-senescent) per day for 38 h during days 3–5 after irradiation. Best fitting for MCF-7 cells under Hyp (iv) [corresponding to **(F,H)**]: reprogramming rate (p_r) increases to 0.08 per CC (intact or pre-senescent) per day during first 4 days after irradiation, then decreases to 0.0198 for the following time points.

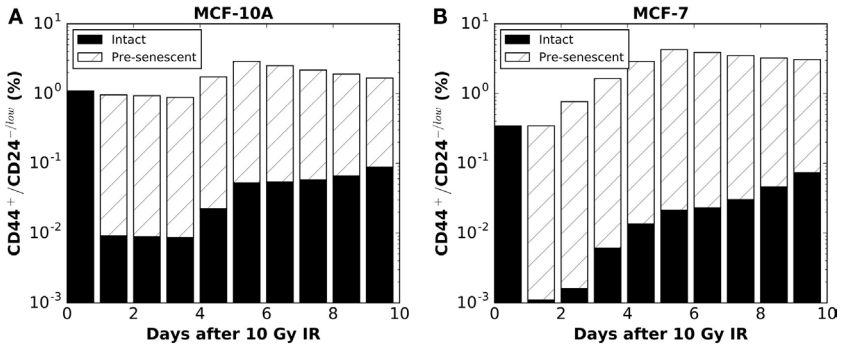

FIGURE 3 | Following the hypothesis of IR-induced incomplete phenotypic reprogramming, the model simulation predicted the proportions of intact (solid colors) vs. pre-senescent (striped colors) CD44⁺/CD24⁻/ˡᵒʷ sub-populations for (A) MCF-10A cells (corresponding to Hyp (iv) curve in Figure 2E) and (B) MCF-7 cells [corresponding to Hyp (iv) curve in Figure 2F]. Data points are plotted on a log scale.

(intact or pre-senescent) per day although it remained elevated relative to the control (0.0017 per CC per day; **Table 1**).

Taken together, these results demonstrate that the equilibrium of $CD44^+/CD24^{-/low}$ cells is more tightly regulated in non-tumorigenic than cancer cells in response to an acute 10 Gy dose of radiation; deregulation of this process may play a role in carcinogenesis by providing an advantage to cells that are more capable of being reprogramed to a stem-like state.

DISCUSSION AND CONCLUSION

Maintenance of the pool of putative stem cells requires a finely tuned balance between self-renewal, differentiation, and recruitment (dedifferentiation or reprogramming). Alterations in the equilibrium of maintaining adult stem cells can affect tissue homeostasis as well as cancer progression and carcinogenesis. Radiation-induced enrichment of stem cells has been attributed to advanced DNA-damage repair mechanisms (37, 38), enhanced survival and subsequent expansion of the (more resistant) quiescent fraction of stem cells as they return to a proliferative state (39), a switch from asymmetric to symmetric stem cell self-renewal division (40), and an increased frequency of reprogramming (16, 41). For this study of MCF-10A and MCF-7 cells, a CA model was used to test several hypotheses, including (i) lower radiosensitivity (or higher survival rate) of SCs, (ii) increased symmetric division frequency, (iii) increased phenotypic reprogramming frequency of intact non-arrested CCs, (iv) incomplete reprogramming of pre-senescent CCs to pre-senescent SCs with short-term proliferative capacity, and (v) complete reprogramming of pre-senescent CCs to SCs with unlimited proliferative capacity. Our simulation results showed that incomplete phenotypic reprogramming (hypothesis iv) could reproduce the dynamics of $CD44^+/CD24^{-/low}$ cells, as well as the fraction of SA-β-gal positive senescent cells *in vitro* for both cell lines (20). Following IR-induced incomplete phenotypic reprogramming, the resultant stem cell pool is expected to be heterogeneous, with the reprogramed cells expressing putative stem cell markers ($CD44^+/CD24^{-/low}$), but possessing only short-term proliferation potential. Therefore, such heterogeneity would suggest that a large stem cell pool may not necessarily implicate a strong population re-growth potential if a high proportion of stem cells have a short-term proliferation potential. To test this hypothesis, we plan to purify the IR-enriched stem cells, and then compare their colonization and mammosphere formation capacity with unirradiated stem cells. It has been previously demonstrated that in primary breast xenografts, $CD44^+/CD24^-$ and ALDH expressing cells identified overlapping, but non-identical cell populations, both of which were able to initiate tumors in NOD/SCID mice (42). Importantly, $ALDH^+$ and $CD44^+/CD24^{-/low}$ cells can transit between each other via EMT and mesenchymal–epithelial transition (MET) (14), highlighting the necessity of using both CD44/CD24 and ALDH for measuring changes in stem cell pool size after irradiation. Additionally, co-staining with β-gallactosidase will determine whether senescent cells express stem cell markers.

In our previous study (40), we showed that radiation-induced accelerated proliferation of glioma stem cells may contribute to their increased frequency in recurrent glioblastoma. To our knowledge, IR-induced proliferation of $CD44^+/CD24^{-/low}$ compartments *in vitro* lacks experimental support. Indeed, Wicha and colleagues (14) have shown that the $CD44^+/CD24^-$ signature is associated with a low proliferative capacity. However, if we assume expansion of $CD44^+/CD24^{-/low}$ cellular compartments via accelerated symmetric division after radiation exposure, some would be expected to localize adjacently, a prediction that could be confirmed by co-localization of $CD44^+/CD24^{-/low}$ cells after irradiation.

Phenotypic plasticity appears to be more tightly regulated in MCF-10A non-tumorigenic mammary epithelial cells in response to an acute radiation exposure of 10 Gy or lower. In contrast, relatively high plasticity can be induced in MCF-7 breast cancer cells by a lower dose if IR (i.e., ≤10 Gy). When dose is increased to 20 Gy, an elevated level of cellular reprogramming might be evoked in the normal breast epithelium cells, resulting in enrichment of stem cell pools. The reprogramming capacity of breast cancer cells seems to reach a plateau at 10 Gy, beyond which no significant increase in the percentage of $CD44^+/CD24^{-/low}$ cells is observed. Notably, the IR-induced high rate of phenotypic reprogramming lasted longer in MCF-7 cells than MCF-10A cells, where it appears only transiently.

Molecular mechanisms governing reprogramming in the context of radiation therapy remain elusive, although our recent study demonstrated that IR-induced stem cell enrichment is telomerase dependent (20). Genomic analysis of cell populations at the time points corresponding to the modeling done here may strengthen the case for IR-induced reprogramming. Specifically, the difference in reprogramming response with regard to non-cancer vs. cancer cells could reflect deregulation of anti-tumor molecular machinery such as occurs during the process of carcinogenesis, which may also tightly regulate the ability of cells to be reprogramed, providing fertile ground to explore new mechanisms driving this disease. Wicha and colleagues suggested HER2 as a potential driver of cancer stem cells in luminal breast cancers (43). They showed that knockdown of HER2 abrogates MCF-7 cells tumorsphere formation. According to a study by Chung et al. (44), HER2 can induce stem cell marker expression and SLUG upregulation that promote the EMT phenotype in MCF-7 cells. Indeed, HER2 is overexpressed in MCF-7 cells following IR (45). Quantitative measurement of HER2 expression levels and kinetics in senescent normal epithelial and breast cancer cells may provide invaluable information on the role of senescent cells in regulating cellular population dynamics after ionizing radiation exposure.

ETHICS STATEMENT

No animal or human subjects were utilized in this research. All other use of human materials (ie. cell lines) was conducted according to standard biosafety and ethics guidelines at Colorado State University.

AUTHOR CONTRIBUTIONS

Design of the work: XG, BS, SB, PH, and LH. Drafting the work: XG and BS. Data acquisition: BS and CN. Data analysis: XG and BS. Revising the work critically for important intellectual content: PH, LH, and SB. Final approval of the version to be published: PH, SB, and LH.

ACKNOWLEDGMENTS

Support for this research from NASA (NNX08AB65G and NNX14AS02G to SB, NNX13AJ01G to LH) and National Cancer Institute (U54 CA149233 to LH) are gratefully acknowledged. We also thank Han Li and Yan Li of the Pasteur Institute for their helpful discussions.

SUPPLEMENTARY MATERIAL

The Supplementary Material for this article can be found online at http://journal.frontiersin.org/article/10.3389/fonc.2016.00138

FIGURE S1 | Simulation reproducing the fraction of CD44^{+}/CD24$^{-/low}$ cells in the control 494 condition (sham irradiation) for (A) MCF-10A cells and (B) MCF-7 cells (mean ± SD; *n* = 10 simulations).

FIGURE S2 | Unsuccessful fitting of cell population dynamics by applying reported 496 average cell cycle time *in vitro* for both (A) MCF-10A cells (fitting curve: average cell cycle time 20 497 hours (46); mean ± SD; *n* = 10 simulations) and (B) MCF-7 cells (fitting curve: average cell cycle time 498 26.8 hours (47); mean ± SD; *n* = 10 simulations).

FIGURE S3 | Simulation reproducing population dynamics with sham irradiation or a 10 500 Gy single-dose IR for (A) MCF-10A cells and (B) MCF-7 cells (mean ± SD; *n* =10 simulations). Hyp 501 stands for hypothesis in the figure legends.

FIGURE S4 | Clonogenic survival fraction of (A) MCF-10A cells and (B) MCF-7 cells 503 and fitted curve with linear quadratic equation.

FIGURE S5 | Diagram of the simulation process and decisions on the cell level.

REFERENCES

1. Chen K, Huang Y-H, Chen J-L. Understanding and targeting cancer stem cells: therapeutic implications and challenges. *Acta Pharmacol Sin* (2013) 34:732–40. doi:10.1038/aps.2013.27
2. Bruce WR, van der Gaag H. A quantitative assay for the number of murine lymphoma cells capable of proliferation in vivo. *Nature* (1963) 199:79–80. doi:10.1038/199079a0
3. Bonnet D, Dick JE. Human acute myeloid leukemia is organized as a hierarchy that originates from a primitive hematopoietic cell. *Nat Med* (1997) 3:730–7. doi:10.1038/nm0797-730
4. Al-Hajj M, Wicha MS, Benito-Hernandez A, Morrison SJ, Clarke MF. Prospective identification of tumorigenic breast cancer cells. *Proc Natl Acad Sci USA* (2003) 100:3983–8. doi:10.1073/pnas.0530291100
5. Kerr CL, Hussain A. Regulators of prostate cancer stem cells. *Curr Opin Oncol* (2014) 26(3):328–33. doi:10.1097/CCO.0000000000000080
6. Gadepalli VS, Deb SP, Deb S, Rao RR. Lung cancer stem cells, p53 mutations and MDM2. *Subcell Biochem* (2014) 85:359–70. doi:10.1007/978-94-017-9211-0_19
7. Pointer KB, Clark PA, Zorniak M, Alrfaei BM, Kuo JS. Glioblastoma cancer stem cells: biomarker and therapeutic advances. *Neurochem Int* (2014) 71:1–7. doi:10.1016/j.neuint.2014.03.005
8. Murillo-Sauca O, Chung MK, Shin JH, Karamboulas C, Kwok S, Jung YH, et al. CD271 is a functional and targetable marker of tumor-initiating cells in head and neck squamous cell carcinoma. *Oncotarget* (2014) 5:6854–66. doi:10.18632/oncotarget.2269
9. Stingl J, Eaves CJ, Zandieh I, Emerman JT. Characterization of bipotent mammary epithelial progenitor cells in normal adult human breast tissue. *Breast Cancer Res Treat* (2001) 67:93–109. doi:10.1023/A:1010615124301
10. Mani SA, Guo W, Liao M-J, Eaton EN, Ayyanan A, Zhou AY, et al. The epithelial-mesenchymal transition generates cells with properties of stem cells. *Cell* (2008) 133:704–15. doi:10.1016/j.cell.2008.03.027
11. Tang J, Fernandez-Garcia I, Vijayakumar S, Martinez-Ruis H, Illa-Bochaca I, Nguyen DH, et al. Irradiation of juvenile, but not adult, mammary gland increases stem cell self-renewal and estrogen receptor negative tumors. *Stem Cells* (2014) 32:649–61. doi:10.1002/stem.1533
12. Bhat-Nakshatri P, Appaiah H, Ballas C, Pick-Franke P, Goulet R, Badve S, et al. SLUG/SNAI2 and tumor necrosis factor generate breast cells with CD44+/CD24- phenotype. *BMC Cancer* (2010) 10:411. doi:10.1186/1471-2407-10-411
13. Yan W, Chen Y, Yao Y, Zhang H, Wang T. Increased invasion and tumorigenicity capacity of CD44+/CD24- breast cancer MCF7 cells in vitro and in nude mice. *Cancer Cell Int* (2013) 13:62. doi:10.1186/1475-2867-13-62
14. Liu S, Cong Y, Wang D, Sun Y, Deng L, Liu Y, et al. Breast cancer stem cells transition between epithelial and mesenchymal states reflective of their normal counterparts. *Stem Cell Reports* (2014) 2:78–91. doi:10.1016/j.stemcr.2013.11.009
15. Overgaard M, Hansen PS, Overgaard J, Rose C, Andersson M, Bach F, et al. Postoperative radiotherapy in high-risk premenopausal women with breast cancer who receive adjuvant chemotherapy. *N Engl J Med* (1997) 337:949–55. doi:10.1056/NEJM199710023371401

16. Lagadec C, Vlashi E, Donna Della L, Dekmezian C, Pajonk F. Radiation-induced reprogramming of breast cancer cells. *Stem Cells* (2012) 30:833–44. doi:10.1002/stem.1058
17. Phillips TM, McBride WH, Pajonk F. The response of CD24-/low/CD44+ breast cancer-initiating cells to radiation. *J Natl Cancer Inst* (2006) 98:1777–85. doi:10.1093/jnci/djj495
18. Campisi J. Senescent cells, tumor suppression, and organismal aging: good citizens, bad neighbors. *Cell* (2005) 120:513–22. doi:10.1016/j.cell.2005.02.003
19. Dimri GP, Lee X, Basile G, Acosta M, Scott G, Roskelley C, et al. A biomarker that identifies senescent human cells in culture and in aging skin in vivo. *Proc Natl Acad Sci USA* (1995) 92:9363–7. doi:10.1073/pnas.92.20.9363
20. Sishc BJ, Nelson CB, McKenna MJ, Battaglia CLR, Herndon A, Idate R, et al. Telomeres and telomerase in the radiation response: implications for instability, reprograming, and carcinogenesis. *Front Oncol* (2015) 5:257. doi:10.3389/fonc.2015.00257
21. Gao X, McDonald JT, Hlatky L, Enderling H. Cell-cell interactions in solid tumors – the role of cancer stem cells. In: d'Onofrio A, Cerrai P, Gandolfi A, editors. *New Challenges for Cancer Systems Biomedicine*. Milan, Italy: Springer (2012). p. 191–204.
22. Chaffer CL, Brueckmann I, Scheel C, Kaestli AJ, Wiggins PA, Rodrigues LO, et al. Normal and neoplastic nonstem cells can spontaneously convert to a stem-like state. *Proc Natl Acad Sci U S A* (2011) 108:7950–5. doi:10.1073/pnas.1102454108
23. Hanahan D, Weinberg RA. Hallmarks of cancer: the next generation. *Cell* (2011) 144:646–74. doi:10.1016/j.cell.2011.02.013
24. An J, Lee J, Lee SH, Park J, Kim B. Separation of malignant human breast cancer epithelial cells from healthy epithelial cells using an advanced dielectrophoresis-activated cell sorter (DACS). *Anal Bioanal Chem* (2009) 394(3):801–9. doi:10.1007/s00216-009-2743-7
25. Gilles C, Polette M, Zahm JM, Tournier JM, Volders L, Foidart JM, et al. Vimentin contributes to human mammary epithelial cell migration. *J Cell Sci* (1999) 112(Pt 24):4615–25.
26. Baker EL, Srivastava J, Yu D, Bonnecaze RT, Zaman MH. Cancer cell migration: integrated roles of matrix mechanics and transforming potential. *PLoS One* (2011) 6:e20355. doi:10.1371/journal.pone.0020355
27. McCord AM, Jamal M, Williams ES, Camphausen K, Tofilon PJ. CD133+ glioblastoma stem-like cells are radiosensitive with a defective DNA damage response compared with established cell lines. *Clin Cancer Res* (2009) 15:5145–53. doi:10.1158/1078-0432.CCR-09-0263
28. Fournier C, Taucher-Scholz G. Radiation induced cell cycle arrest: an overview of specific effects following high-LET exposure. *Radiother Oncol* (2004) 73(Suppl 2):S119–22. doi:10.1016/S0167-8140(04)80031-8
29. Di Leonardo A, Linke SP, Clarkin K, Wahl GM. DNA damage triggers a prolonged p53-dependent G1 arrest and long-term induction of Cip1 in normal human fibroblasts. *Genes Dev* (1994) 8:2540–51. doi:10.1101/gad.8.21.2540
30. Linke SP, Clarkin KC, Wahl GM. p53 mediates permanent arrest over multiple cell cycles in response to γ-irradiation. *Cancer Res* (1997) 57:1171–9.
31. Bravatà V, Minafra L, Russo G, Forte GI, Cammarata FP, Ripamonti M, et al. High-dose ionizing radiation regulates gene expression changes in the MCF7 breast cancer cell line. *Anticancer Res* (2015) 35(5):2577–91.
32. Yu Y-C, Yang P-M, Chuah Q-Y, Huang Y-H, Peng C-W, Lee Y-J, et al. Radiation-induced senescence in securin-deficient cancer cells promotes cell invasion involving the IL-6/STAT3 and PDGF-BB/PDGFR pathways. *Sci Rep* (2013) 3:1675. doi:10.1038/srep01675
33. Essmann F, Engels IH, Totzke G, Schulze-Osthoff K, Jänicke RU. Apoptosis resistance of MCF-7 breast carcinoma cells to ionizing radiation is independent of p53 and cell cycle control but caused by the lack of caspase-3 and a caffeine-inhibitable event. *Cancer Res* (2004) 64:7065–72. doi:10.1158/0008-5472.CAN-04-1082
34. Ruiz S, Panopoulos AD, Herrerías A, Bissig KD, Lutz M, Berggren WT, et al. A high proliferation rate is required for cell reprogramming and maintenance of human embryonic stem cell identity. *Curr Biol* (2011) 21(1):45–52. doi:10.1016/j.cub.2010.11.049
35. Greve TS, Judson RL, Blelloch R. microRNA control of mouse and human pluripotent stem cell behavior. *Annu Rev Cell Dev Biol* (2013) 29:213–39. doi:10.1146/annurev-cellbio-101512-122343
36. Lapasset L, Milhavet O, Prieur A, Besnard E, Babled A, Aït-Hamou N, et al. Rejuvenating senescent and centenarian human cells by reprogramming through the pluripotent state. *Genes Dev* (2011) 25:2248–53. doi:10.1101/gad.173922.111
37. Bao S, Wu Q, McLendon RE, Hao Y, Shi Q, Hjelmeland AB, et al. Glioma stem cells promote radioresistance by preferential activation of the DNA damage response. *Nature* (2006) 444:756–60. doi:10.1038/nature05236
38. Karimi-Busheri F, Rasouli-Nia A, Mackey JR, Weinfeld M. Senescence evasion by MCF-7 human breast tumor-initiating cells. *Breast Cancer Res* (2010) 12:R31. doi:10.1186/bcr2583
39. Pajonk F, Vlashi E, McBride WH. Radiation resistance of cancer stem cells: the 4 R's of radiobiology revisited. *Stem Cells* (2010) 28:639–48. doi:10.1002/stem.318
40. Gao X, McDonald JT, Hlatky L, Enderling H. Acute and fractionated irradiation differentially modulate glioma stem cell division kinetics. *Cancer Res* (2013) 73:1481–90. doi:10.1158/0008-5472.CAN-12-3429
41. Gao X, McDonald JT, Naidu M, Hahnfeldt P, Hlatky L. A proposed quantitative index for assessing the potential contribution of reprogramming to cancer stem cell kinetics. *Stem Cells Int* (2014) 2014:249309. doi:10.1155/2014/249309
42. Ginestier C, Hur MH, Charafe-Jauffret E, Monville F, Dutcher J, Brown M, et al. ALDH1 is a marker of normal and malignant human mammary stem cells and a predictor of poor clinical outcome. *Cell Stem Cell* (2007) 1:555–67. doi:10.1016/j.stem.2007.08.014
43. Ithimakin S, Day KC, Malik F, Zen Q, Dawsey SJ, Bersano-Begey TF, et al. HER2 drives luminal breast cancer stem cells in the absence of HER2 amplification: implications for efficacy of adjuvant trastuzumab. *Cancer Res* (2013) 73:1635–46. doi:10.1158/0008-5472.CAN-12-3349
44. Chung SS, Giehl N, Wu Y, Vadgama JV. STAT3 activation in HER2-overexpressing breast cancer promotes epithelial-mesenchymal transition and cancer stem cell traits. *Int J Oncol* (2013) 44:403. doi:10.3892/ijo.2013.2195
45. Cao N, Li S, Wang Z, Ahmed KM, Degnan ME, Fan M, et al. NF-κB-mediated HER2 overexpression in radiation-adaptive resistance. *Radiat Res* (2009) 171(1):9–21. doi:10.1667/RR1472.1
46. Starcevic SL, Diotte NM, Zukowski KL, Cameron MJ, Novak RF. Oxidative DNA damage and repair in a cell lineage model of human proliferative breast disease (PBD). *Toxicol Sci* (2003) 75(1):74–81. doi:10.1093/toxsci/kfg154
47. Pasquier J, Magal P, Boulangé-Lecomte C, Webb G, Le Foll F. Consequences of cell-to-cell P-glycoprotein transfer on acquired multidrug resistance in breast cancer: a cell population dynamics model. *Biol Direct* (2011) 6:5. doi:10.1186/1745-6150-6-5

Conflict of Interest Statement: The authors declare that the research was conducted in the absence of any commercial or financial relationships that could be construed as a potential conflict of interest.

Copyright © 2016 Gao, Sishc, Nelson, Hahnfeldt, Bailey and Hlatky. This is an open-access article distributed under the terms of the Creative Commons Attribution License (CC BY). The use, distribution or reproduction in other forums is permitted, provided the original author(s) or licensor are credited and that the original publication in this journal is cited, in accordance with accepted academic practice. No use, distribution or reproduction is permitted which does not comply with these terms.

frontiers in Oncology

ORIGINAL RESEARCH
published: 24 November 2015
doi: 10.3389/fonc.2015.00257

Telomeres and Telomerase in the Radiation Response: Implications for Instability, Reprograming, and Carcinogenesis

Brock J. Sishc[1,2], Christopher B. Nelson[2], Miles J. McKenna[2], Christine L. R. Battaglia[2], Andrea Herndon[2], Rupa Idate[2], Howard L. Liber[2] and Susan M. Bailey[2]*

[1] Division of Molecular Radiation Oncology, Department of Radiation Oncology, University of Texas Southwestern Medical Center Dallas, Dallas, TX, USA, [2] Department of Environmental and Radiological Health Sciences, Colorado State University, Fort Collins, CO, USA

Telomeres are nucleoprotein complexes comprised of tandem arrays of repetitive DNA sequence that serve to protect chromosomal termini from inappropriate degradation, as well as to prevent these natural DNA ends from being recognized as broken DNA (double-strand breaks) and triggering of inappropriate DNA damage responses. Preservation of telomere length requires telomerase, the specialized reverse transcriptase capable of maintaining telomere length via template-mediated addition of telomeric repeats onto the ends of newly synthesized chromosomes. Loss of either end-capping function or telomere length maintenance has been associated with genomic instability or senescence in a variety of settings; therefore, telomeres and telomerase have well-established connections to cancer and aging. It has long been recognized that oxidative stress promotes shortening of telomeres, and that telomerase activity is a radiation-inducible function. However, the effects of ionizing radiation (IR) exposure on telomeres *per se* are much less well understood and appreciated. To gain a deeper understanding of the roles, telomeres and telomerase play in the response of human cells to IRs of different qualities, we tracked changes in telomeric end-capping function, telomere length, and telomerase activity in panels of mammary epithelial and hematopoietic cell lines exposed to low linear energy transfer (LET) gamma(γ)-rays or high LET, high charge, high energy (HZE) particles, delivered either acutely or at low dose rates. In addition to demonstrating that dysfunctional telomeres contribute to IR-induced mutation frequencies and genome instability, we reveal non-canonical roles for telomerase, in that telomerase activity was required for IR-induced enrichment of mammary epithelial putative stem/progenitor cell populations, a finding also suggestive of cellular reprograming. Taken together, the results reported here establish the critical importance of telomeres and telomerase in the radiation response and, as such, have compelling implications not only for accelerated tumor repopulation following radiation therapy but also for carcinogenic potential following low dose exposures as well, including those of relevance to spaceflight-associated galactic cosmic radiations.

Keywords: telomeres, telomerase, ionizing radiation, stem cells, cellular reprograming, instability, carcinogenesis, instability

OPEN ACCESS

Edited by:
Marco Durante, GSI, Germany

Reviewed by:
John P. Murnane, University of California San Francisco, USA
Caterina Tanzarella, Roma Tre University, Italy

****Correspondence:***
Brock J. Sishc
brock.sishc@utsouthwestern.edu

Specialty section:
This article was submitted to Radiation Oncology, a section of the journal Frontiers in Oncology

Received: *10 September 2015*
Accepted: *06 November 2015*
Published: *24 November 2015*

Citation:
Sishc BJ, Nelson CB, McKenna MJ, Battaglia CLR, Herndon A, Idate R, Liber HL and Bailey SM (2015) Telomeres and Telomerase in the Radiation Response: Implications for Instability, Reprograming, and Carcinogenesis. Front. Oncol. 5:257. doi: 10.3389/fonc.2015.00257

INTRODUCTION

Telomeres, protective features of chromosomal termini composed of tandem arrays of repetitive G/C-rich sequence (5′-TTAGGG-3′ in vertebrates), end in a 3′ single-stranded overhang and are associated with a host of proteins collectively termed "shelterin" (1, 2). Telomere-specific binding proteins include the telomere repeat factors 1 and 2 (TRF1 and TRF2; bind double-stranded telomeric DNA) and protection of telomeres 1 (POT1; binds single-stranded telomeric DNA) (3–5). These end-binding proteins are thought to facilitate invasion of the 3′ single-stranded overhang into the telomeric DNA duplex, forming a lariat-like structure termed a T-loop (6). The T-loop is proposed as an architectural answer to the "end-capping problem," in that it not only helps protect the end of the chromosome from nucleolytic degradation but also serves to prevent this naturally occurring DNA double-stranded end from being recognized as broken DNA (i.e., a double-strand break; DSB) and initiating inappropriate damage responses (e.g., non-homologous end joining; NHEJ). Due to the semiconservative nature of DNA replication and the requirement for an RNA primer in lagging-strand synthesis, conventional polymerases are unable to replicate to the very end of the chromosome. This so-called "end replication problem" (7, 8) results in progressive erosion of the telomere with each round of cellular division (~30–150 bp per cell division) and is the molecular mechanism underlying the finite replicative lifespan of human somatic cells known as the Hayflick limit (9). Once some stipulated number of telomeres reaches a critically shortened length, a persistent DNA damage response (DDR) is triggered that results in a state of permanent cell cycle arrest known as replicative senescence (10). Direct links between telomere dysfunction – in terms of either significant shortening or compromise of end-capping structure/function – instability and cancer, as well as senescence- and age-related degenerative pathologies (e.g., cardiovascular disease) have been demonstrated (11–13).

Clearly, during carcinogenesis, cells must devise a means of maintaining their telomeres in order to overcome the barrier of senescence and achieve replicative immortality. The overwhelming majority of human cancers (~90%) accomplish this task by the way of reactivation of telomerase (14); the remaining ~10% of cancers maintain telomere length in a telomerase-independent fashion, relying instead on the homologous recombination (HR)-associated alternative lengthening of telomeres (ALT) pathway (15). Telomerase is a specialized reverse transcriptase consisting of a catalytic subunit, telomerase reverse transcriptase (hTERT), which utilizes its telomerase RNA component (hTERC) to synthesize telomeric DNA *de novo* (16, 17). In humans, telomerase activity is transcriptionally repressed in the majority of somatic cells, being expressed at appreciable levels only in adult stem- and germ-line cells (18). It is becoming increasingly appreciated that telomere maintenance and telomerase activity are critical elements of intricate cellular networks that regulate cellular lifespan, genome stability, and carcinogenesis. Indeed, recent studies suggest that telomerase has novel molecular functions well beyond its canonical role in telomere length maintenance, including transcriptional regulation and cellular reprograming, which may well underlie *all* of the hallmarks of cancer (19).

Adult stem cells (SCs), rare subpopulations within tissues that possess extended replicative lifespans by virtue of possessing telomerase activity, are defined by the distinctive properties of self-renewal and the potential to differentiate along various lineages. Deregulation of SC compartments is generally deemed a contributing factor in the development of cancer stem cells (CSCs), which are also referred to as tumor-initiating cells (20). For example, a subpopulation of CSCs ($CD44^{+}/CD24^{low/-}$) has been identified in human breast tumors and established breast cancer cell lines that display enhanced tumor-forming capacity in mouse xenograft models (21). Also relevant in this regard, are reports that ionizing radiation (IR) alters the cellular dynamics of tissue and tumor repopulation following exposure and further, that such alteration may be dependent on radiation quality, i.e., linear energy transfer (LET). LET describes the amount of energy an ionizing particle transfers to the material traversed per unit distance and is the predominant factor underlying differences in relative biological effectiveness (RBE) of charged particle vs. photon radiations. For example, high dose per fraction low LET X-ray exposures have been associated with subsequent enrichment of putative CSC populations in a variety of tumor types including breast, colon, lung, prostate, squamous cell carcinoma of the head and neck, and melanoma (22–32). Tang et al. demonstrated that low dose γ-ray and charged particle exposures (Fe and Si ions) in combination with transforming growth factor beta (TGF-β) resulted in increased self-renewal of $CK14^{+}/CK18^{+}$SC populations in the humanized mammary fat pads of juvenile mice (33). Such IR-induced SC enrichment has been implicated in radiotherapy failure, accelerated repopulation, and evasion of tumors to CSC targeted therapies (34). Studies increasingly support SCs as critical considerations in the radiation response, whether associated with treatment of cancer (radiotherapy) or exposure of normal tissues (carcinogenesis) as occurs unavoidably in conjunction with radiotherapy and a variety of medical diagnostic procedures, as well as accidentally (e.g., nuclear power plant accidents) and during spaceflight.

It is widely viewed that IR-induced enrichment of CSCs results from mobilization and asymmetric division of existing CSCs, which have been shown to be more radioresistant than their more differentiated non-stem cancer cell (NSCC) counterparts, due not only to their residing in relatively hypoxic niches but also because they possess enhanced DNA repair kinetics, superior endogenous oxidative stress defenses, and slower cell turnover rates (35). Importantly, however, Lagadec et al. have shown that IR-induced enrichment of $CD44^{+}/CD24^{low/-}$ and aldehyde dehydrogenase (ALDH) activity high breast CSCs can also result from the reprograming or conversion of NSCCs back into CSCs by inducing expression of transcriptional factors utilized in the generation of induced pluripotent stem cells (iPSCs), e.g., Oct4, Sox2, and Nanog (29). Additional evidence of such "plasticity" was provided by Yang et al., who not only

confirmed IR-induced reprograming but also demonstrated that CSC populations maintain an equilibrium within established cell lines, and that the return to equilibrium is facilitated by radiation exposure and TGF-β (23). Therefore, enrichment of CSC populations following radiation exposure may arise either by way of mobilization (i.e., asymmetric division) of existing, radioresistant SC populations in response to injury, or via IR-induced reprograming (i.e., conversion) of NSCCs into CSCs, or perhaps more likely, some combination of the two processes. Implicit in these observations, is the reality that therapeutic strategies seeking to target CSC populations must address both mobilization and reprograming in order to be effective.

Interestingly, the reverse transcriptase component of telomerase (hTERT) has also been implicated as a promoter of "stemness" via interactions with the Wnt/β-catenin signaling and NF-κB inflammation response pathways (36–40), although such findings remain controversial (41, 42). Telomerase activity has also been shown to be radiation-inducible in a variety of tumors and cancer cell lines, including mammary carcinoma, acute myeloid leukemia (AML), colon carcinoma, squamous cell carcinoma of the oral cavity, lymphoma, and nasopharyngeal carcinoma (28, 43–50). Such observations led us to suspect unappreciated correlations between these processes. Furthermore, exposures to high LET, high charge, high energy (HZE) particles, such as those delivered during carbon ion radiotherapy or encountered in the deep space environment, have been shown to invoke very different biological responses than low LET radiations, which may well include IR-induced telomerase activity and subsequent SC enrichment. The effects of IR exposure, particularly radiations of different qualities, on telomere maintenance and/or function are poorly understood [reviewed in Ref. (51)], even though telomeres themselves have been regarded as "hallmarks of radiosensitivity" (52), and recently proposed as informative biomarkers of radiosenstivity for the purposes of personalized medicine (53). Indeed, short telomeres have been shown to enhance IR sensitivity in several settings (54–57), being associated with impaired and/or delayed DSB repair kinetics (54, 58), as well as with persistent chromosomal breaks and cytogenetic profiles characterized by complex aberrations and massive fragmentation (54). However, it is important to note that longer telomeres do not necessarily confer radioresistance. It is also debatable whether such a relationship holds true in telomerase positive cells, as there are reports of no correlation between telomere length and radiosensitivity (59). Other contrasting reports include longer telomeres in irradiated (4 Gy X-rays) vs. unirradiated cells 14 days after exposure (45), as well as significantly shortened telomeres, specifically in the shortest telomere fraction, in the peripheral blood of radiotherapy patients within a relatively short span of time (3 months or less) following treatment for a variety of cancer types (60). Interestingly, low LET X-rays and low energy (high LET) protons have been shown to induce very different telomeric responses, in that telomeres were shortened 96 h post-X-ray exposure and associated with anaphase bridges and dicentrics, while high LET protons evoked telomere lengthening at 24 and 96 h (56).

Considerable controversy and uncertainty surround such results and the processes responsible for them, but accumulating evidence, including much of our own [e.g., Ref. (61–67)], continue to support intimate relationships between functionally intact telomeres and the genomic, cellular, and organismal responses to radiation exposure. Here, we provide new insight into the roles of telomeres and telomerase in the radiation response. Specifically, we investigated the influence of dose, dose rate, and radiation quality on IR-induced changes in telomere function, length, and telomerase activity in panels of cancer and non-cancer mammary epithelial and hematopoietic cells. Depletion of the telomeric end-binding proteins TRF1, TRF2, or POT1 resulted in dysfunctional telomeres that were uncapped as opposed to critically shortened, which (1) increased spontaneous and IR-induced mutation frequencies in a radiation quality-dependent manner, with POT1 depletion being especially effective, and (2) contributed to instability in that they were susceptible to fusion with each other and to IR-induced DSBs, as well as to recombination (telomere sister chromatid exchange; T-SCE). Furthermore, we demonstrate that IR-induced SC enrichment is telomerase dependent, and separate modeling efforts support the necessity of contribution from cellular reprograming for such enrichment (manuscript in preparation, Gao et al.). Better understanding of these fundamental processes involving telomeres and telomerase following IR exposure, particularly of different radiation qualities, is vital, as they play potentially critical roles in accelerated tumor repopulation following radiotherapy, as well as IR-induced carcinogenesis following exposure, including those of relevance to astronauts.

MATERIALS AND METHODS

Cell Culture

The spontaneously immortalized non-tumorigenic human mammary epithelial cell line MCF-10A was purchased from ATCC and was cultured as described previously (68) in 1:1 Dulbecco's modified essential medium (D-MEM)/Ham's F12 growth medium (Hyclone) supplemented with 5% fetal bovine serum (FBS), 10 μg/mL insulin (Sigma), 20 ng/mL epidermal growth factor (EGF; Sigma), 0.5 μg/mL hydrocortisone (Sigma), 0.1 μg/mL cholera toxin (Sigma), and 1% GlutaMAX (Gibco, Life Technologies). The human mammary carcinoma cell line MCF-7 (kind gift from L. Chubb, CSU Flint Animal Cancer Center) was grown in D-MEM supplemented with 10% FBS and 1% GlutaMAX. The primary normal mammary epithelial cell line AG11137 (Coriell) was grown in MCDB 170 complete growth medium (US biological) supplemented with 5 μg/mL insulin, 10 ng/mL EGF, 0.5 μg/mL hydrocortisone, 56 μg/mL bovine pituitary extract (Life Technologies), and 1% GlutaMAX.

A human low passage lymphoblastoid cell line (LCL15044, kind gift from A. Sigurdsson, National Institute of Health) was grown in RPMI medium supplemented with 15% FBS and 1% GlutaMAX. The WTK1 human lymphoblastoid cell line was derived from the WI-L2 line (69), and used for mutation analysis,

as they are heterozygous at the thymidine kinase (TK) locus; they also have a single amino acid substitution in codon 237 at TP53. WTK1 cells were grown in RPMI medium supplemented with 10% horse serum and 1% GlutaMAX. The human, therapy-induced AML cell line KG1a (kind gift from Michelle LeBeau, University of Chicago) was grown in RPMI media supplemented 20% FBS and 1% GlutaMAX. Normal human peripheral blood mononuclear cells (PBMCs) were collected in accordance with approved IRB protocol [#13-4379H] in 10 mL spray-coated K2EDTA tubes and cultured in PB-MAX karyotyping medium containing the activating mitogen, phytohemagglutinin M (PHA-M) and supplemented with 1% antibiotic/antimycotic (Gibco, Life Technologies).

A variety of control cell lines were included for comparison. Primary BJ-1 normal human foreskin fibroblasts (kind gift from J. Shay, University of Texas Southwestern Medical Center) and hTERT-immortalized BJ-1 (BJ-1-hTERT; kind gift from J. Bedford, Colorado State University) were grown in a 4:1 mixture of D-MEM high glucose medium (Hyclone)/M-199 (Hyclone) supplemented with 10% FBS and 1% GlutaMAX. The human osteosarcoma ALT cell lines U2OS and SAOS2 (kind gift from D. Gustafson CSU Flint Animal Cancer Center) were grown in McCoy's 5A growth medium (Gibco, Life Technologies) supplemented with 10% FBS and 1% GlutaMAX. The highly telomerase-positive human immortal HeLa cell line was purchased from ATCC and cultured in D-MEM high glucose medium, supplemented with 10% FBS and 1% GlutaMAX. All cells were maintained in a humidified incubator at 37°C in 5% CO_2 and passaged 1–2 times/week.

Irradiations and Clonogenic Cell Survival

For γ-Ray Exposures

For γ-ray exposures, cells were exposed to various, acute doses of ^{137}Cs γ-rays in a Mark I irradiator (J. L. Shepherd) located at Colorado State University. Cells were exposed at a dose rate of 2.5 Gy/min with rotation. For LDR exposures, cells were incubated under a ^{137}Cs source to total doses of 1 or 4 Gy γ-rays at dose rates of 4.9 and 3.12 cGy/h. Unirradiated controls were kept in a separate incubator under identical conditions.

Exposures to 1 GeV/n ^{56}Fe Ions

Exposures to 1 GeV/n ^{56}Fe ions (HZE) were delivered at the NASA Space Radiation Laboratory (NSRL), located at Brookhaven National Laboratory (BNL), Upton, NY, USA. Flasks of cells were shipped from Colorado State University in insulated containers at room temperature and were exposed to acute doses of 1 or 2 Gy at a dose rate of ~1 Gy/min. Immediately following exposure, cells were shipped overnight back to Colorado State University for processing and analysis.

Clonogenic Cell Survival

MCF-7 and MCF-10A cells were seeded in triplicate 48 h prior to irradiation and allowed to incubate under standard culture conditions to ensure that all cultures were in log phase. Cells were irradiated with an acute dose of 1–10 Gy of ^{137}Cs γ-rays. Cells were then allowed to incubate for 16 h overnight to allow for repair to occur. Cells were then trypsinized, counted, and plated at the appropriate density in quadruplicate into 60 mm culture dishes. Cells were allowed to incubate for 10 (MCF-7) or 14 days (MCF-10A). Plates were then fixed in absolute ethanol, stained in crystal violet, and colonies with >50 cells counted. This process was repeated three times to generate the data presented here.

Telomeric siRNA Knockdowns

As per our previous reports (62–64, 68), small interfering RNA (siRNA)-mediated knockdown of the telomere-binding proteins TRF1, TRF2, and POT1 was performed in the WTK1 lymphoblastoid cell line prior to shipment to BNL for irradiation. Cells were cotransfected (RNAiMAX; Life Technologies) with a pool of four individual siRNAs directed against each target protein. Specific siRNA sequences are as follows: for TRF1: 5′CAAAUUCUCAUAUGCCUUU3′, CAGUAGUAGUCCUUUGAUA, AGAGUAACCUAUAAG CAUG, and UACCAGAGUUAAAGCAUAU; TRF2: GAACAAGCGCAUGACAAUA, GCAAGGCAGCUACGG AAUC, GACAGUACAACCAAUAUAA, and CCGA ACAGCUGUGAUGAUU; and POT1: GUAGA AGCCUUACGUGUUU, GAUAAAACAUCGUGGAU UC, GCAUAUCCGUGGUUGGAAU, and UAACUUGC CUGCUCUUUAG. Reduced protein levels were verified via Western blot 72 h post-transfection using monoclonal antibodies for TRF1 (Novus Biologicals 57-6), TRF2 (Novus Biologicals NB110-57130SS), and POT1 (Novus Biologicals NB500-176).

Depletion of hTERT and hTERC levels in MCF-7 and MCF-10A cells was achieved using prevalidated Silencer Select siRNAs purchased from Ambion (Life Technologies, hTERT: 4392420 and hTERC: 4390771). Non-target control (NTC) siRNA (Life Technologies, AM4611) was utilized as a negative control. The effectiveness of hTERT and hTERC depletion in reducing telomerase activity was verified using RT-qPCR TRAP.

Cytogenetic Analyses

Chromosome-Orientation Fluorescence *In situ* Hybridization

Chromosome-orientation fluorescence *in situ* hybridization (CO-FISH) was employed to evaluate IR-induced chromosomal instability and performed as previously described (62, 70) with some modification. Following irradiation, cell cultures were incubated for various times, trypsinized, and subcultured into medium containing 5-bromo-2-deoxyuridine (BrdU, 10 μM; Sigma-Aldrich) for one cell cycle. Slides were stained with Hoechst 33258 (0.50 ng/μL; Sigma-Aldrich) for 15 min and exposed to 365 nm UV light (Stratalinker 2400) for 25 min. Following UV exposure, BrdU incorporated strands were digested with Exonuclease III (3 U/μL in provided reaction buffer; Promega) at room temperature for 10 min. Slides were hybridized with a Cy-3 conjugated $(TTAGGG)_3$ PNA telomere probe (0.2 μg/mL; Applied Biosystems) at 37°C for 1.5 h, rinsed in 70% formamide at 32°C for 10 min, and dehydrated in another ethanol series before re-probing at 37°C for 2 h. Following the second

hybridization, slides were rinsed with 70% formamide at 32°C for 15 min followed by 5 min rinse in PN buffer. Chromosomes were counterstained with DAPI (4,6-diamidine-2-phenylindole dihydrochloride; Vectashield, Vector Laboratories). Preparations were examined and images captured and analyzed using a Zeiss Axioskop2 Plus microscope equipped with a Photometrics Coolsnap ES2 camera and running Metavue 7.1 software.

Scoring Criteria

Telomere sister chromatid exchange was scored as a CO-FISH telomere signal split between the two chromatids of a metaphase chromosome, which were often of unequal intensity due to unequal SCE (71). Telomere fusion necessitates that telomeres of adjoining chromosomes/chromatids fuse into a single CO-FISH signal and the DAPI signal remain continuous (61). Telomere–DSB (T-DSB) fusion appears as single-sided (i.e., on only one chromatid of a mitotic chromosome) interstitial blocks of CO-FISH telomere signal (66, 67). Statistical analyses by Chi-square or Fisher's exact test (Sigma Stat 3.5; Systat Software) was done to determine significance.

Mutation Frequency Analysis

Mutation Assay

WTK1 lymphoblasts were treated with CHAT (10–5M 2′-deoxycytidine, 2×10^{-4}M hypoxanthine, 2×10^{-7}M aminopterin, and 1.75×10^{-5}M thymidine; Sigma) for 2 days and CHT (CHAT without aminopterin) for 1 day to eliminate pre-existing TK^- mutants. Following CHAT treatment, cells were transfected with TRF1, TRF2, or POT1 siRNA and/or treated with the DNA-PKcs inhibitor Nu7026 (Sigma-Aldrich). Three days later, cells were irradiated with γ-rays or HZE particles. Two days after irradiation, when phenotypic expression of newly induced mutants was complete, the mutant fractions (MFs) were determined. For plating efficiency, 1 cell/well was seeded, or for scoring mutants, 2000 cells/well were seeded in the presence of 2 μg/mL trifluorothymidine (TFT; Sigma-Aldrich). Fresh TFT was added 11 days after plating, and plates were scored for positive or negative wells after 20 days. The MFs were calculated using the Poisson distribution, and statistical analyses were done by *t*-tests using Sigma Stat 3.5 (Systat Software).

Telomere Length Analysis

Interphase Telomere Fluorescence *In situ* Hybridization

Samples were prepared using standard cytogenetic techniques as described previously with slight modifications (68, 72, 73). Briefly, cultured cell pellets were resuspended in 8 mL of 75 mM potassium chloride (KCl; hypotonic) and incubated for 30 min at 37°C. Following incubation, 1 mL of fixative (3:1 methanol acetic acid) was added, cells were pelleted at 1000 rpm for 5 min, resuspended in 6 mL fixative, and stored at −20°C. Fixed cell pellets were then washed and dropped onto glass slides for telomere fluorescence *in situ* hybridization (FISH), which was performed as described previously with modifications (74). Briefly, slides were treated with 100 μg/mL RNASE A in 150 mM NaCl, 15 mM sodium citrate buffer for 30 min at 37°C, dehydrated through an ethanol series (75, 85, and 100%), and denatured in a 70% formamide/2× saline sodium citrate (SSC) solution at 70°C for 2 min. A telomere peptide nucleic acid (PNA) probe $(TTAGGG)_3$ labeled with Cy-3 was hybridized onto the slides at 37°C overnight. Slides were washed twice each in 50% formamide/2× SSC, 2× SSC, and 0.1% NP-40 in 2× SSC for 2.5 min each at 43°C. Finally, slides were mounted in Prolong Gold Antifade reagent (Invitrogen) containing 4′,6-diamidino-2-phenylindole, dihydrochloride (DAPI).

Image Z stacks were taken using a Zeiss Axio Imager.Z2 microscope, with a Coolsnap ES2 camera running Metamorph 7.7 (Molecular Devices). For each slide, 30–50 images were obtained, each consisting of 22, 0.2 μm stacks. Metamorph nearest neighbor deconvolution and stack compression functions were applied, followed by image thresholding (upper and lower threshold values were held consistent across experiment). Finally, a region of interest was created for each nucleus, and the intensities of individual telomeres obtained in metamorph. Fluorescence values in each batch of FISH were standardized to the fluorescence intensity of an LY-R mouse lymphoma cell pellet as an internal control. LY-R cells have long brightly staining telomeres and their use for standardization, which was adapted from Q-FISH (75), represents a means to accurately compare relative telomere lengths from run to run.

Senescence-Associated β-Galactosidase Assay

Irradiated and control cells were rinsed twice with PBS, fixed for 15 min in 4% paraformaldehyde at room temperature, rinsed with PBS and covered with freshly prepared β-galactosidase staining solution (Cell Signaling Cat #9806). Cells were incubated at 37°C in a dry incubator for 18 h, staining solution was aspirated and replaced with 70% glycerol, then imaged immediately on an EVOS digital microscope. Images were taken of each sample under phase contrast at 40×. Blinded subjective scoring of blue cells was used to quantify senescent cell fractions.

Telomerase Analysis

Telomerase Activity

Telomerase activity was evaluated using the telomere repeat amplification protocol (TRAP) assay originally described by Herbert et al. (76) and adapted for quantitative real-time PCR by Hou et al. (77). Briefly, whole cell lysates were prepared from cultured cell pellets and lysed in cold MPER mammalian protein extraction buffer (Thermo Fisher) containing a protease inhibitor cocktail (Roche) and RNasin ribonuclease inhibitor (Promega) at a ratio of 100 μL of buffer per 1,000,000 cells. Lysates were cleared by centrifugation at 14,000 rpm for 10 min at 4°C and stored at −80°C. Protein concentration was determined using the Bradford Assay (Biorad).

The SYBR green master mix (Promega) included all components for the RTQ-PCR. Each well contained between 0.1 and 0.25 μg protein lysate, 50% volume SYBR green master mix, 0.2 μg T4 gene32 protein (New England Biolabs, Ipswitch, MA, USA), 0.1 μg of each primer TS (5′-AATCCGTCGAGCAGAGTT-3′) and ACX (5′-GCGCGG$(CTTACC)^3$CTAACC-3′) (Integrated DNA Technologies), and RNase/DNase-free water to achieve a final well volume of 25 μL. The PCR and detection were performed on a CFX 96 (Biorad). In addition to the treatment samples, a series of controls were included on each plate: (1) no

template control with TS primer only, (2) no template control with ACX primer only, (3) no template control with TS and ACX primers (used in normalization of samples), (4) heat inactivated control with template (protein lysate) and TS and ACX primers, and (5) HeLa cell lysate with TS and ACX primers (a positive control).

The RTQ-PCR program included the following steps: step 1, one cycle 25°C 20 min (telomerase elongates the TS primer by adding TTAGGG repeat sequences); step 2, one cycle 95°C 3 min (heat activation of the enzyme in the SYBR master mix); step 3, 40 cycles of 95°C 20 s, 50°C 30 s, and 72°C 1 min 30 s (PCR amplification allows for detection by real-time instrument); and step 4, 80 cycles 0.10 s per cycle (melt curve to ensure no primer dimer formation). Each sample was run in triplicate on a 96-well plate format allowing for an average Ct to be obtained per sample. Utilizing the average Ct value, the relative percent telomerase activity in each sample is calculated using the Delta Delta Ct method ($2^{-\Delta\Delta Ct}$) (78). Briefly, to calculate the percent relative activity for each sample, first normalize the average sample Ct to the no template control with TS and ACX primers. This is referred to as the delta Ct value. The delta Ct value of each sample is subtracted from the delta Ct value of a chosen comparative sample, in this case a normal feline mucous membrane cell lysate, yielding a delta delta Ct value (ΔΔCt). Using the $2^{-\Delta\Delta Ct}$, a relative value is generated for each sample comparison and when multiplied by 100 is the relative percent of telomerase activity (RTA) of the sample compared to the control. The RTA can be compared between samples assayed across different plates. Results from two runs were averaged.

Telomerase Expression

Telomerase expression (hTERT and hTERC) was evaluated by quantitative reverse transcription PCR (qRT-PCR). Total RNA was harvested from irradiated and unirradiated samples using the Qiagen RNeasy kit (Qiagen). RNA was quantified using a Nanodrop 1000 spectrophotometer and reverse transcribed using the Verso cDNA kit (Thermo Scientific). Real-time PCR was performed using SYBR green master mix (Promega) according to the manufactures protocol and performed using a CFX 96 system (Biorad). The real-time cycle was as follows: cycle 1 at 95°C 15 min, cycle 2 (50×) step 1 at 95°C 15 s, step 2 at 58°C 30 s, and step 3 at 72°C 30 s. A melt curve was included to assess primer dimers and non-specific amplification as follows: cycle 3 at 95°C 30 s, cycle 4 at 55°C 30 s, and cycle 5 (80×) at 55°C 10 s. Primers were designed using the Primer3 program (79) using a published cDNA library for hTERT (80) and hTERC (80). hTERT primers were added (final concentration 300 nM) including a forward sequence: 5′CCATCAGAGCCAGCTTCACCT3′ and reverse sequence: 5′TCACCTGCAAATCCAGAAACA3′. hTERC primers were added (final concentration 300 nM) including a forward sequence: 5′AAGAGTTGGGCTCTGTCAGC3′ and reverse sequence: 5′TCCCACAGCTCAGGGAATC3′. Primers for transferrin receptor (TFRC) were included (final concentration 100 nM) as a housekeeping gene with the forward sequence: 5′CGCTGGTCAGTTCGTGATTA3′ and the reverse sequence: 5′GCATTCCCGAAATCTGTTGT3′. Relative hTERT and hTERC RNA expressions were analyzed using the $2^{-\Delta\Delta Ct}$ method.

Telomerase Activity Inhibition

Telomerase activity inhibition was accomplished using the small molecule inhibitor MST-312 (Sigma), also known as telomerase inhibitor 1× (81). Briefly, MST-312 was solubilized at concentrations recommended by the manufacturer in sterile DMSO and stored at −20°C for no more than 1 month prior to use. Dose response for inhibition of telomerase activity was established, and MST-312 (1–3 μM) was added to cultures 6 h prior to experimentation.

Thiazolyl Blue Tetrazolium Bromide (MTT) Assay

Thiazolyl blue tetrazolium bromide (MTT) assay was used to evaluate potential cytotoxic effects of the MST-312 telomerase inhibitor as described previously (82). Briefly, 2000 cells/well of a 96-well plate were seeded 24 h prior to addition of inhibitor. Media were removed and replaced with fresh media containing varying concentrations of MST-312 or an equivalent DMSO control. Cells were incubated in the presence of inhibitor for 48 or 72 h. At the time of analysis, media was once again removed from wells, and cells were resuspended in fresh media containing 0.5 mg/mL MTT reagent and incubated at 37°C for 3.5 h. Following incubation, media was removed and 150 μL MTT solvent (4 mM HCl, 0.1% NP-40, all in isopropanol) was added to each well and set to agitate on a shaker at room temperature for 15 min. After agitation, plates were read on a Modulus Microplate reader (Turner Biosystems) at 600 nm absorbance.

Stem Cell Analyses

Immunophenotyping

Putative human mammary epithelial CSCs were identified based on the expression of $CD44^{+}/CD24^{low/-}$ surface markers (83–85). Putative CSCs from human hematopoietic cell lines were identified based on the expression of $CD34^{+}/CD38^{low/-}$ or $CD34^{+}$ expression alone (86). All analyses were performed on a CyAn ADP Analyzer with nine-color capability (Beckman Coulter CY20130) located at the Colorado State University Veterinary Teaching Hospital. Monolayers MCF-7 and MCF-10A mammary epithelial cells or hematopoietic cells in suspension were dissociated and stained for marker expression. Briefly, ~300,000 cells were dissociated from cell culture surface using 0.25% trypsin-EDTA, pelleted, washed, and resuspended in 30 μL flow cytometry wash buffer (1× PBS, 1% FBS, and 1% penicillin/streptomycin), 6 μL of FITC-conjugated mouse monoclonal antihuman CD44 antibody (BD Pharmingen #555478), and 6 μL of Pe-conjugated mouse monoclonal antihuman CD24 antibody (BD Pharmingen #555428). Cells were incubated for 30–60 min in the dark at 4°C, then pelleted and resuspended in 500 μL cold 1× PBS and kept on ice until analysis. Analysis gates were established using cells from unstained controls and antimouse Ig,κ antibody capture beads (BD Pharmingen #552843). For lymphoblastoid suspension cultures, cells were stained as above with 6 μL of direct PE-conjugated mouse monoclonal antihuman CD34 antibody (BD Pharmingen #555822) and 6 μL of direct FITC-conjugated mouse monoclonal antihuman CD38 antibody (BD Pharmingen #560982).

Aldefluor Assay

Enhanced ALDH activity, an accepted marker of SCs, was detected using the ALDEFLUOR Kit (Stem Cell Technologies) as described previously (29). Briefly, ~300,000 MCF-7 or MCF-10A cells were trypsinized, resuspended in aldefluor buffer, and incubated with aldefluor reagent (both provided and as recommended by manufacturer). Samples from all treatment groups were also treated with the ALDH inhibitor DEAB (Stem Cell Technologies) and utilized as negative controls to establish gating. Cells were pelleted, aspirated, resuspended in buffer containing efflux inhibitor, and analyzed on a flow cytometer.

Mammosphere Assay

Evidence of SC character was also evaluated in MCF-7 and MCF-10A mammosphere cultures and their respective sorted populations, which were plated in low bind cell culture plates (Nunc) using Mammocult Media (Stem Cell Technologies). Cells were plated into 96-well plates at limiting dilutions, then allowed to form spheres for up to 10 days with fresh media supplementation every 3 days. Sphere formation was evaluated on day 10 using an inverted bright field microscope, and spheres with a size >100 μM in diameter were scored.

RESULTS

Depletion of Telomeric End-Capping Proteins Increases Radiation-Induced Mutation Frequencies and Chromosomal Instability

We have shown that TRF2 fails to colocalize with IR-induced DSBs and so is not an "early responder" to such DNA damage (87). However, siRNA depletion of any of the directly binding end-capping telomere proteins TRF1, TRF2, or POT1 resulted in elevated spontaneous and IR-induced mutation frequencies (MF) at the heterozygous TK locus in human lymphoblastoid cells (WTK1) following both γ-ray and 1 GeV/n ^{56}Fe ion exposures (**Figure 1**). Overall, IR-induced MFs upon telomere protein depletion were similar both quantitatively and qualitatively, although POT1 depletion resulted in the highest elevation of MF (significant at 2 Gy Fe). No statistically significant differences in MF between γ-rays and 1 GeV/n ^{56}Fe ions (HZE) were observed in these experiments. However, in this same lymphoblast mutation system, an RBE for Fe of ~3 was recently suggested; this resulted from utilizing a different, more immediate plating protocol that facilitated recovery of more mutants following HZE exposure (88). Therefore, we can now surmise that the MFs for Fe in the earlier experiments reported here are likely two to threefold higher than shown. This in turn would imply important differences for HZE exposures in the context of telomere deficiencies. Interestingly, telomere deficiencies consistently resulted in higher MF than inhibition of DNA-PKcs kinase activity, a well-characterized contributor to DNA repair, providing additional support for the significance of telomere proteins in the DDR. Furthermore, MF in the context of combined TRF2 knockdown and inhibition of DNA-PKcs kinase activity was not additive, suggesting that they act in the same pathway. These results are consistent with the proposition that TRF2 prevents C-NHEJ-mediated end fusion, while DNA-PK thwarts alternative-NHEJ at telomeres; thus, telomeres are protected by a "lock with two bolts" (89). Curvilinear dose responses for individual knockdowns were also suggested (**Figure 1**), indicating intertrack interaction of multiple lesions at higher doses, and likely reflecting additional interactions between dysfunctional telomeres and IR-induced DSBs (T-DSB fusions) (66); such a supposition is supported by increased frequencies of these events at 2 Gy (**Figure 2**).

The contribution of telomere end-capping function to IR-induced chromosomal instability was also evaluated, as per our previous works (61–63, 67). T-SCE is a recognized marker of unregulated telomeric recombination events (71), whereas telomere–DSB (T-DSB) fusion events result from inappropriate end joining (66). Quantification of T-SCE and T-DSB fusion frequencies associated with siRNA knockdown of TRF2 or POT1 in WTK1 cells, both spontaneously and following acute exposure to either 2 Gy γ-rays or 2 Gy 1 GeV/n ^{56}Fe ions is shown (**Figure 2**). Successful siRNA knockdown of TRF1, TRF2, and POT1 in WTK1 cells 72 h post-transfection was verified by Western blot (Figure S1 in Supplementary Material).

Depletion of either TRF2 or POT1 elevated T-SCE frequencies following both γ-ray and HZE 2 Gy exposure as compared to 0 Gy controls. No statistically significant difference between γ-rays and HZE was observed with TRF2 deficiency. However, HZE was much more effective than γ-rays at inducing T-SCE in the context of POT1 deficiency, consistent with the demonstrated role of POT1 during replication (90, 91). Depletion of either TRF2 or POT1 also elevated T-DSB fusion events following 2 Gy γ-ray or HZE exposure (as compared to 0 Gy controls). Again, no statistically significant difference between γ-rays and HZE was observed with TRF2 deficiency, a finding consistent with TRF2's role in suppressing ATM at telomeres (90). Interestingly, with POT1 deficiency, HZE was less effective at inducing T-DSB than γ-rays, supportive of these events not being replication dependent, but rather NHEJ mediated, as previously shown (67). Together, these results convincingly demonstrate that telomeric proteins influence the DDR/repair following IR exposure.

Ionizing Radiation Exposure Increases Telomerase Activity

Previous reports have demonstrated elevated telomerase activity following IR exposure; however, results are often conflicting in regard to dose, dose rate, radiation quality, method of telomerase activity measurement, and cell line examined. Therefore, we sought to more clearly characterize telomerase activity in response to a variety of IR exposures in both tumor and non-tumor cells. We selected panels of human mammary epithelial and hematopoietic cell lines representing a wide range of inherent/background levels of telomerase activity (high/low/very low) that included cancer (MCF-7 and KG1a), non-tumorigenic immortalized [spontaneously (MCF-10A) or via EBV (WTK1)], and normal primary mammary (AG11137) and low passage lymphoblastoid (LCL15044) cell lines. Telomerase activity was evaluated relative to the telomerase-positive HeLa cell line (**Figure 3**). The ALT cell lines U2OS and SAOS2 (telomerase-independent maintenance of

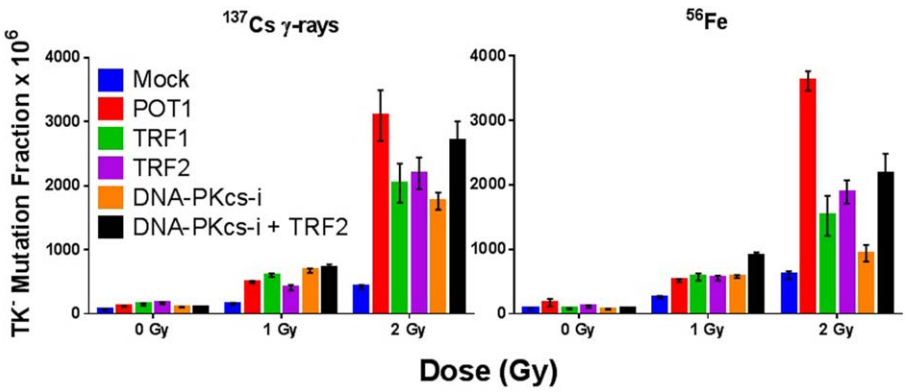

FIGURE 1 | Compromise of telomeric end-capping function elevates spontaneous and radiation-induced mutagenesis. TK⁻ mutation frequency (MF) in WTK1 lymphoblastoid cells exposed to 0, 1, or 2 Gy γ-rays or ^{56}Fe ions at 1 GeV/n following siRNA knockdown of telomere-binding proteins POT1, TRF1, and TRF2, and/or inhibition of DNA-PKcs kinase activity.

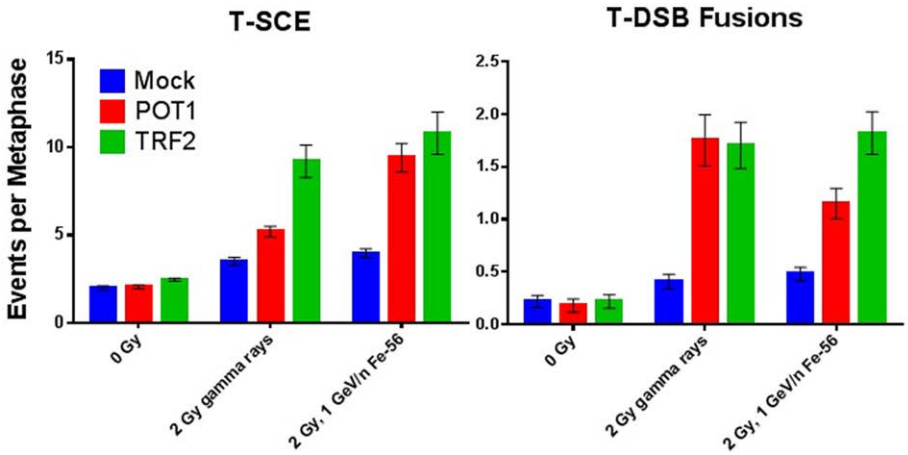

FIGURE 2 | Compromise of telomeric end-capping function increases radiation-induced T-SCE and telomere–DSB fusion events. T-SCE and telomere–DSB fusion frequencies in WTK1 lymphoblastoid cells exposed to 0 Gy, 2 Gy γ-rays, or 2 Gy 1 GeV/n ^{56}Fe ions following siRNA knockdown of telomere-binding proteins POT1 or TRF2.

telomeres) and BJ-1 primary foreskin fibroblasts (very low telomerase activity) were utilized as negative controls, and hTERT immortalized BJ-1 fibroblasts (BJ-1-hTERT) were also used as an internal control.

Acute exposure to γ-rays (10 Gy) prompted significantly elevated levels of telomerase activity within 24–48 h in the mammary MCF-7 cells (high inherent telomerase activity, 24 h; $p = 0.0140$, 48 h; $p = 0.0011$); a slight, but non-significant ($p = 0.2473$) elevation of telomerase activity was also observed in MCF-10A cells (lower inherent telomerase activity) at 48 h (**Figure 4A**). In contrast, a significant reduction of telomerase activity ($p = 0.0001$) was observed 48 h postexposure in the AG11137 primary mammary epithelial cells (very low inherent telomerase activity). Evaluation of telomerase RNA expression in MCF-7 and MCF-10A following acute 10 Gy γ-ray exposure, specifically mRNA levels of the catalytic subunit hTERT and expression levels of the RNA template hTERC, revealed that hTERT expression in MCF-7 cells was significantly increased in the same timeframe that telomerase activity was elevated (24–48 h, 24 h; $p = 0.0001$, 48 h; $p = 0.0001$); hTERC levels in MCF-7 remained significantly elevated for up to 5 days (24 h; $p = 0.0001$, 120 h; $p = 0.0011$). In MCF-10A, hTERT expression was significantly decreased 72–120 h postexposure (72 h; $p = 0.0326$, 120 h; $p = 0.0337$), and hTERC expression in MCF-10A was significantly decreased 72–120 h (72 h; $p = 0.0005$, 120 h; $p = 0.0001$; **Figure 4D**).

The highly telomerase-positive KG1a cell line displayed significantly increased levels of telomerase activity 24–48 h postexposure (1 Gy, 24 h; $p = 0.0024$, 48 h; $p = 0.0001$, 4 Gy, 24 h; $p = 0.0019$, 48 h; $p = 0.0001$; **Figure 4B**), which was dose dependent (1 and 4 Gy γ-rays). A significantly elevated level of

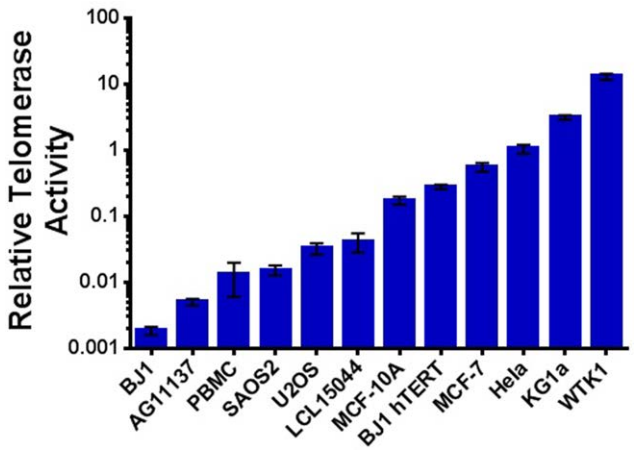

FIGURE 3 | Telomerase activity in cancer and non-cancer cell lines. Relative telomerase activity as determined using the qRT-PCR-based TRAP assay and arranged in order from least to greatest background level; normal human PBMCs are also included. Consistent with expectation, a natural break occurs between those with very low/low activity (LCL15044 and to the left; normal, ALT, and often considered negative) and those with higher levels of telomerase (MCF-10A and to the right; immortalized, transformed, and cancer). Data are represented on a log scale, and all values are reported as telomerase activity relative to HeLa cells.

telomerase activity was also observed in the WTK1 cell line (high inherent telomerase activity) at 24 h postexposure ($p = 0.0143$), but only at 4 Gy. The low passage transformed normal lymphoblastoid cell line LCL15044 (very low telomerase activity) showed elevated telomerase activity at 24 h post 1 and 4 Gy exposure, but neither rose to the level of significance. Interestingly, normal PBMCs (very low telomerase activity) showed elevated activity 48 h post 1 Gy acute γ-ray exposure, which was significant ($p = 0.0394$; **Figure 4C**).

Next, we sought to determine if telomerase activity was elevated in response to chronic low dose rate (LDR) γ-ray exposure. MCF-7, MCF-10A, KG1a, and WTK1 cells (relatively high telomerase activity) were incubated under chronic LDR conditions to total doses of 1 or 4 Gy, delivered at dose rates of 0, 1.17, 3.12, and 4.98 cGy/h. Telomerase activity was not significantly elevated at either 1 or 4 Gy total dose, at any dose rate, in any cell line examined (**Figure 5A**). These results imply that in contrast to acute exposures, elevation of telomerase activity is not triggered by low LET, LDR exposures. However, normal human PBMCs exposed to chronic LDR radiation did respond with elevated levels of telomerase activity relative to unirradiated controls (**Figure 5B**).

Telomere Length Is Shortened Despite Elevated Telomerase Activity Postexposure

To evaluate the effect of elevated telomerase activity post-IR exposure, we assessed telomere length in dividing MCF-7 and MCF-10A cell populations at 5 and 10 days after a single acute dose (10 Gy γ-rays). Unexpectedly, telomere length was significantly shortened at the population level 5 days postexposure in both MCF-7 ($p = 0.0001$) and MCF-10A ($p = 0.0003$) (as compared to 0 Gy controls), despite the observed elevation of telomerase activity 24–48 h after exposure (**Figure 6A**). There was no change in telomere length immediately following a 10 Gy dose of γ-rays, ruling out the possibility of IR-induced changes in telomere/probe-binding affinity (not shown). Furthermore, histogram analysis of individual telomere lengths demonstrated that IR exposure shortened all of the telomeres in the population (i.e., shifted the entire distribution; **Figure 6B**), suggesting that IR does not "target" the shortest telomeres, those presumed to be more radiation sensitive. The observed post-IR telomere shortening also corresponded with a significant increase in senescent cells (SA-Beta gal positive) at day 5, which remained significantly elevated until at least day 10 (**Figure 6C**). This finding is consistent with well-documented IR-induced senescence; our results suggest an underlying contribution of telomere shortening and/or the inability of telomeres to repair themselves postexposure (92–94). Furthermore, by day 10 postexposure, telomere length in the surviving cell population began to recover, despite reduced levels of telomerase activity during this same time period. These results support the notion that following IR exposure, telomerase is acting outside of its canonical role in elongating telomeres. Telomere length was also decreased in PBMCs following an acute exposure (1 Gy) of γ-rays at both 2 and 5 days (2 days; $p = 0.0328$, 5 days; $p = 0.0362$; **Figure 6D**). Interestingly, a similar decrease in telomere length was observed following a 1 Gy LDR exposure at 5 ($p = 0.0250$) (but not 2) days (**Figure 6E**).

Elevation of Telomerase Activity Precedes IR-Induced Enrichment of Putative Stem Cell Populations

As normal SC and CSC populations generally possess higher telomerase activity than their non-stem counterparts, and IR-induced enrichment of putative SC populations in mammary carcinoma cells has been reported by multiple groups (23, 28, 29, 31, 83), we hypothesized that observations of elevated telomerase activity following IR exposure may result from the enrichment of CSC populations. Therefore, we examined enrichment of putative $CD44^{+}/CD24^{low/-}$ SC populations with time in MCF-7 and MCF-10A following an acute 10 Gy γ-ray exposure. At the therapeutically relevant dose of 10 Gy, survival in both cell lines was determined to be <1%, even when using a delayed plating method (**Figure 7A**). However, despite this low number of survivors, a significant enrichment in the percentage of $CD44^{+}/CD24^{low/-}$ MCF-7 cells began to emerge approximately day 2 post exposure ($p = 0.0001$), peaked at day 5 ($p = 0.0001$), and remained elevated at day 7 ($p = 0.0001$; **Figure 7B**). Interestingly, IR-induced enrichment of $CD44^{+}/CD24^{low/-}$ cells in MCF-10A cells also occurred at day 5 postexposure ($p = 0.0001$); however, unlike MCF-7 cells, enrichment of putative SCs in MCF-10A was very abrupt. Furthermore, IR-induced enrichment of mammary $CD44^{+}/CD24^{low/-}$ cells at day 5 in MCF-7 displayed a dose response and appeared to have a threshold dose of >5 Gy in MCF-10A, meaning that it did

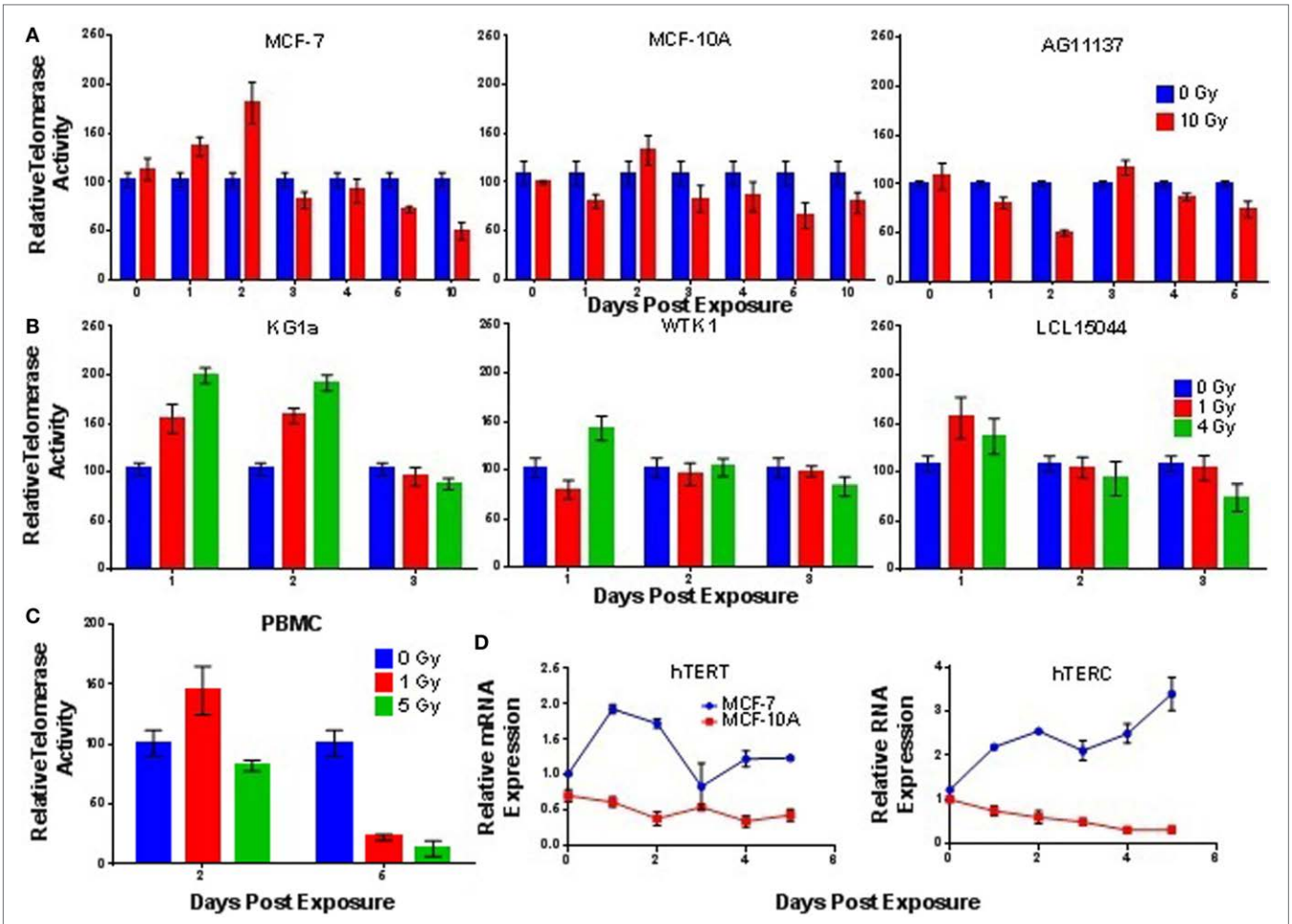

FIGURE 4 | Telomerase activity is elevated at early times following acute γ-ray exposure. Telomerase activity was assessed as a function of time in panels of **(A)** cultured mammary epithelial cell lines, **(B)** hematopoietic cell lines, and **(C)** stimulated peripheral blood mononuclear cells (PBMCs) following acute γ-ray exposures: 10 Gy (mammary epithelial), 1 and 4 Gy (hematopoietic), and 1 and 5 Gy (PBMCs). In general, cell lines with higher levels of background activity experienced higher, more significant elevation of activity 24–48 h postexposure, the notable exception being normal PBMCs (very low telomerase activity; significant IR-induced elevation). Telomerase activity in irradiated cells is reported relative to unirradiated control samples collected at the same time point. **(D)** Time course of hTERT mRNA and hTERC levels in MCF-7 and MCF-10A cells following acute 10 Gy exposure.

not significantly occur at doses lower than 5 Gy (**Figure 7C**). Stem-like character of radiation-enriched SC populations was further verified using the aldefluor assay, in which significant enrichment of $ALDH^{high}$ cells was observed 5 days post acute 10 Gy γ-ray exposure (MCF-7; $p = 0.004$, MCF-10A; $p = 0.001$; **Figure 7D**); mammospheres were also generated from sorted populations, providing additional confirmation of stemness in the $CD44^{+}/CD24^{low/-}$ populations (not shown). Counter to our initial hypothesis, IR-induced elevation of telomerase activity preceded the observed enrichment of SC compartments, indicating that they are not directly correlated (i.e., are not one in the same), once again suggesting that telomerase is acting in non-canonical ways, likely having to do with SCs, and in agreement with previous reports (19, 38). Representative scatter plots of MCF-7 and MCF-10A cells immunotyped using $CD44^{+}/CD24^{low/-}$ antibodies or the aldefluor assay are shown (Figure S2 in Supplementary Material).

To determine whether the IR-induced enrichment of putative SC populations observed in mammary epithelial cells is a more general phenomenon that might also occur at lower doses, we examined expression of the $CD34^{+}/CD38^{-}$ immunotype in the hematopoietic cell line KG1a and the $CD34^{+}$ immunotype in WTK1 and LCL15044 cell lines 1–3 days post 1 or 4 Gy γ-ray acute exposure (**Figure 8**). Interestingly, significant increases in $CD34^{+}$ populations were observed in both WTK1 and LCL15044 lymphoblastoid cell lines (>99.8% $CD34^{-}$ in unirradiated conditions) following either a 1 or 4 Gy exposure for up to 3 days. In contrast, KG1a cells, which possessed a much higher background compartment of $CD34^{+}/CD38^{-}$ cells (20–30%), demonstrated a dose-dependent decrease in $CD34^{+}/CD38^{-}$ levels with IR exposure (**Figure 8**). This result indicates that radiation does not induce enrichment of putative SC populations in all cell lines, cancer types, or tissues, which may, at least to some degree, be dependent on background levels.

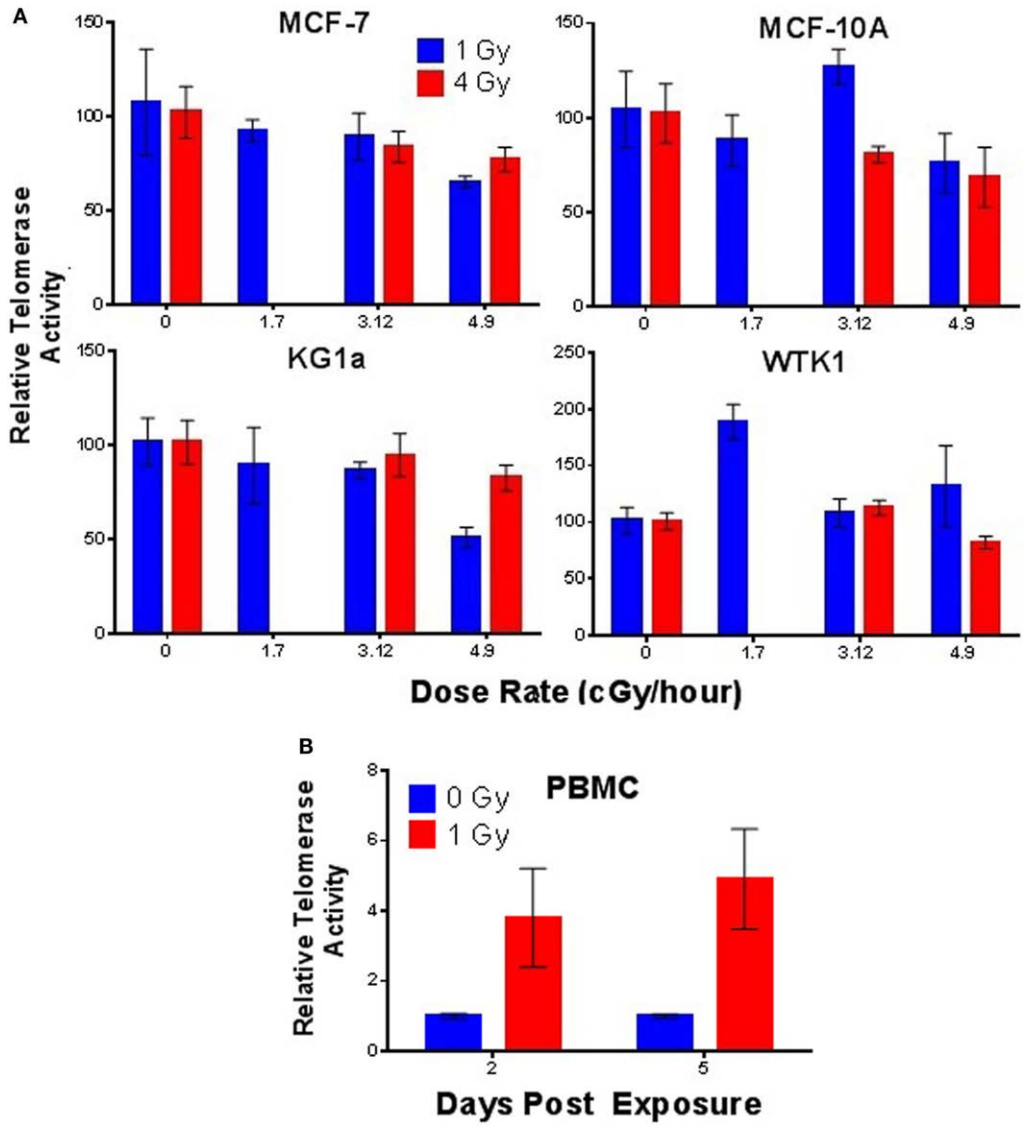

FIGURE 5 | Telomerase activity following low dose rate γ-ray exposures. **(A)** Telomerase activity was assessed in MCF-7, MCF-10A, KG1a, and WTK1 (relatively high levels of telomerase) chronically exposed to γ-rays at cumulative doses of 1 or 4 Gy at dose rates of 1.7, 3.12, or 4.9 cGy/h. In general, no elevation of telomerase activity was observed, with the exception of WTK1 at 1 Gy, 1.7 cGy/h. **(B)** In contrast, telomerase activity in stimulated PBMCs (very low telomerase activity) exposed to a total dose of 1 Gy delivered at low dose rate of 4.9 cGy/h, was significantly elevated (days 2 and 5). Data are expressed as telomerase activity relative to unirradiated controls within each group.

Telomerase Activity Is Required for IR-Induced Enrichment of Putative CSC Populations

To further investigate the role of telomerase in promoting IR-induced enrichment of putative SC populations, we employed both a small molecule inhibitor of telomerase activity (MST-312) and siRNA depletion of the catalytic subunit (hTERT) of telomerase. MCF-7 and MCF-10A cells were treated with MST-312 at non-cytotoxic concentrations as determined by MTT assay (**Figure 9A**), which resulted in significant and dose-dependent decreases in telomerase activity (**Figure 9B**). Subsequent exposure to an acute dose of 10 Gy γ-rays and incubation for 5 days demonstrated that inhibition of telomerase activity effectively blocked IR-induced putative SC enrichment in both MCF-7 and MCF-10A (**Figure 9C**). This finding was further substantiated utilizing siRNA directed against hTERT, which also significantly reduced the level of telomerase activity in both MCF-7 and MCF-10A (**Figure 9B**). Consistent with results using the inhibitor (MST-312), reduction of telomerase activity via depletion of hTERT also blocked IR-induced putative SC enrichment in both MCF-7 and MCF-10A (**Figure 9C**). As expected, siRNA depletion of the RNA subunit, hTERC, did not reduce telomerase activity, nor did it block SC enrichment

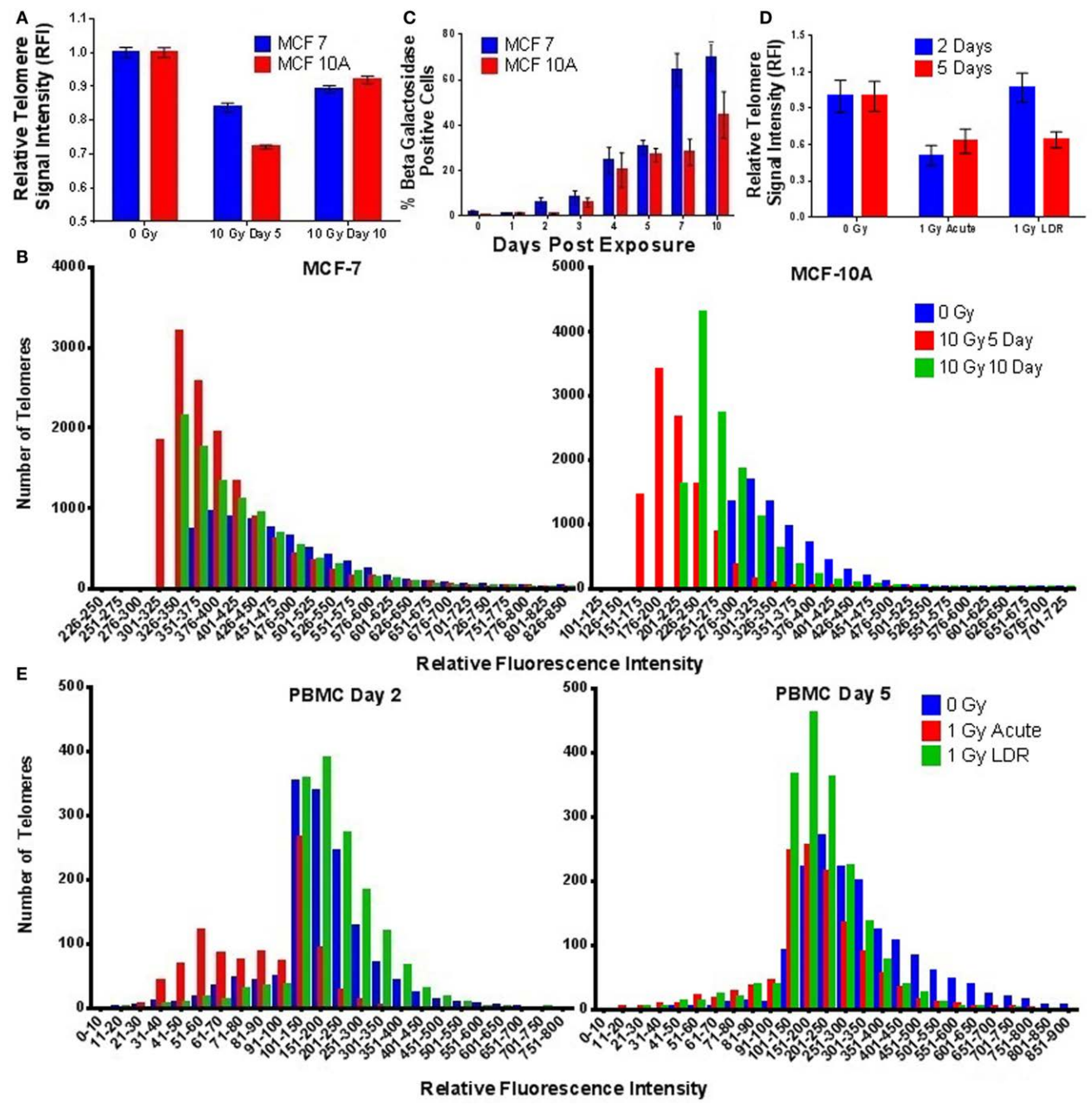

FIGURE 6 | Ionizing radiation-induced telomere shortening in mammary epithelial cells and stimulated PBMCs. **(A)** Telomere length was significantly shortened in MCF-7 and MCF-10A cells at the population level 5 days postacute γ-ray exposure (10 Gy). By 10 days, telomere length had increased but still remained significantly shortened compared to unirradiated controls. **(B)** Histograms of individual telomere lengths in MCF-7 and MCF-10A cells reveal significant shortening of all telomeres at days 5 and 10 postexposure. **(C)** Time course of senescence associated β-galactosidase staining in MCF-7 and MCF-10A cells following acute γ-ray exposure (10 Gy). **(D)** Telomere length was significantly shortened in stimulated PBMCs at 2 and 5 days postacute γ-ray exposure (1 Gy) and at 5 days post-LDR γ-ray exposure (1 Gy) delivered at a dose rate of 4.9 cGy/h (24 h). **(E)** Histograms of individual PBMC telomere lengths following acute and LDR exposures (1 Gy) at 2 and 5 days.

(not shown). Together, these data provide strong evidence in support of the necessity of telomerase activity for IR-induced enrichment of $CD44^{+}/CD24^{low/-}$ putative mammary CSC populations postexposure.

DISCUSSION

The results reported here provide valuable insight into the critical roles telomeres and telomerase play in the radiation response

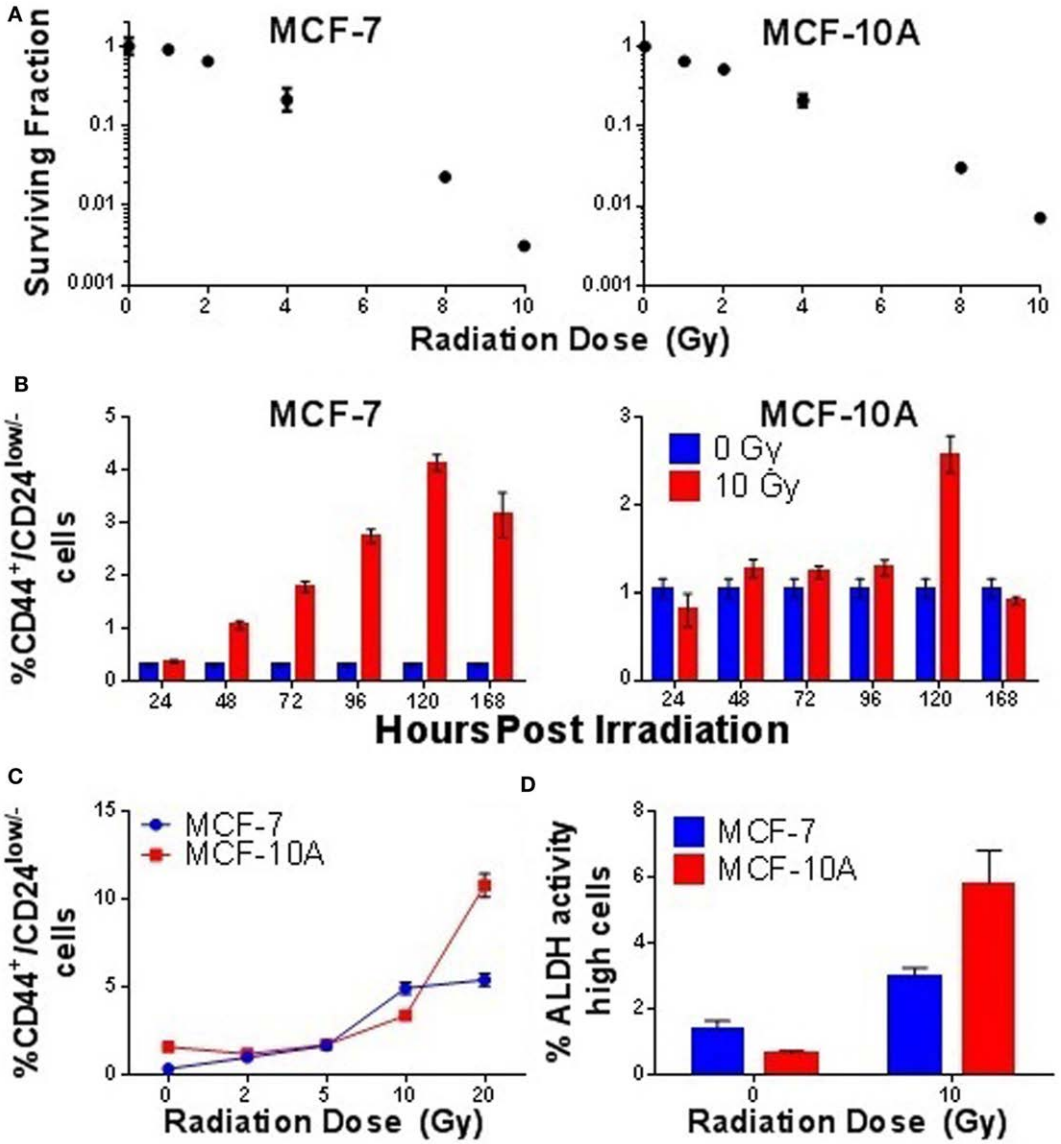

FIGURE 7 | Ionizing radiation-induced enrichment of putative mammary stem cell populations. Responses of MCF-7 and MCF-10A mammary epithelial cells to acute γ-ray exposure (10 Gy). **(A)** Clonogenic survival curves and IR dose response. **(B)** Time course evaluation of putative mammary stem cell compartments. **(C)** Radiation dose response of putative mammary stem cells 5 days postexposure. **(D)** Quantification of ALDH high cells 5 days postexposure, confirming stem cell nature of sorted $CD44^+/CD24^-$ populations.

and thereby support further exploration for their roles in the context of both radiotherapy and IR-induced carcinogenesis. Specifically, we have assessed the roles telomeres play in maintaining genomic stability following IR exposure, elaborated on the role telomerase plays in cell survival and repopulation postexposure, and identified a potentially targetable role of telomerase activity in cells exposed to therapeutically relevant doses of low LET radiation.

Disruption of telomeric end-capping via siRNA depletion of end-binding proteins TRF1, TRF2, or POT1 increased IR-induced mutation frequencies and chromosomal instability. Of relevance in this regard are reports of decreased expression of TRF2 associated with increased breast cancer malignancy (95), as well as the demonstration of telomere fusions in early human breast carcinoma (96). Furthermore, our finding of telomere uncapping with POT1 deficiency is consistent with POT1 mutations identified in a subset of patients with chronic lymphocytic leukemia (CLL), which were associated with increased levels of chromosomal fusions involving telomeres (97). A particularly relevant recent report specifically associated various POT1 variants with telomere length and radiosensitivity in colon and gastric adenocarcinoma (98). Our results provide additional support for the view that in addition to critical telomere shortening, telomeres rendered dysfunctional by virtue of deficiencies in

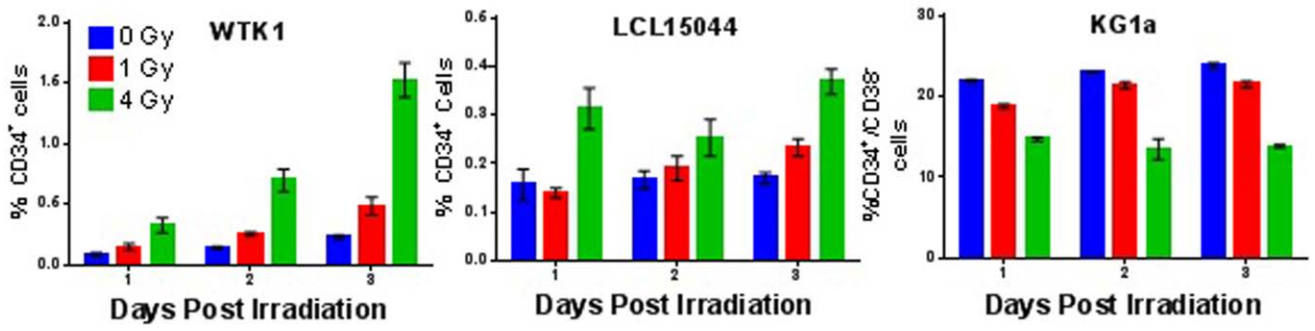

FIGURE 8 | Ionizing radiation-induced enrichment of putative hematopoietic stem cell populations. Time course analysis depicting percentages of CD34+ (WTK1 and LCL15044) and CD34+/CD38− (KG1a), 1, 2, and 3 days postacute γ-ray exposure (0, 1, or 4 Gy).

telomeric proteins and the end-capping failure that ensues, also contribute to the carcinogenic potential of radiation exposure.

It is also noteworthy that while deficiencies in TRF1 or TRF2 appeared similar to those associated with NHEJ deficiency in regard to telomere instability, which presumably occurred via ATM-mediated classic NHEJ (99), the response of cells to IR exposure in the setting of POT1 knockdown differed. Not only did POT1 depletion result in significantly higher mutation frequencies in response to γ-rays and ^{56}Fe ions (2 Gy; relative to TFR1 and TRF2 knockdown) but also a very different pattern of chromosomal instability was observed. Specifically, while TRF1 and TRF2 knockdown resulted in elevated frequencies of both T-SCE and T-DSB fusion events in response to both γ-rays and ^{56}Fe ions, POT1 knockdown displayed a higher level of T-SCE (HR mediated) events in response to ^{56}Fe ions relative to γ-rays, with the opposite being true for T-DSB (NHEJ mediated) events. These observations are consistent with the proposed roles for POT1 in suppressing ATR at telomeres (90) and facilitating a RPA-to-POT1 switch (91) during replication, and thereby suppressing telomeric recombination, here particularly in response to the complex damage induced by high LET radiation exposure. Taken together with the reported association of POT1 variants with radiosensitivity and colon and gastric adenocarcinoma (98), our results suggest that heavy ion radiation therapy may be particularly effective in treating these cancers.

Consistent with previous reports, we also demonstrate that telomerase activity is an IR-inducible function. We elaborate that *in vitro*, this phenomenon appears to be peculiar to cell lines with high background levels of telomerase activity (e.g., cancer and potentially SCs), and further that increased telomerase activity appears to be primarily an acute dose response, as LDR γ-ray exposures (at least at 1 and 4 Gy cumulative doses) did not elevate telomerase activity in the cell lines examined. Importantly, however, telomerase activity was elevated in PBMCs post-LDR exposure. Expression analysis of the hTERT mRNA and the hTERC RNA component of telomerase in MCF-7 cells coincided (temporally) with the elevations of telomerase activity, suggesting that this process may be transcriptionally regulated. Expression of telomerase subunits in MCF-10A cells was dramatically different in that both hTERT mRNA and hTERC steadily decreased from 1 to 5 days postexposure, a finding consistent with the absence of significant elevation of telomerase activity in this same timeframe. It is also important to appreciate, however, that although not significant, increases in telomerase activity were observed in the non-tumor MCF-10A and normal LCL15044 mammary epithelial cell lines following acute IR exposure, indicating that telomerase may indeed be induced, but the low background level of activity in these cell lines may yield such an increase relatively insignificant. Additionally, evaluation of telomerase activity in stimulated normal human PBMCs (low background level) revealed a significant increase following an acute dose (1 Gy), 2 days postexposure. Also in contrast to cultured cells, a significant increase in telomerase activity was observed in stimulated PBMCs 2 and 5 days post-LDR exposure (total 1 Gy delivered at a dose rate of 4.9 cGy/h). One potential explanation for this could be the more heterogeneous nature of cells in stimulated peripheral blood (including stem/progenitor cells) creating a disparate signaling environment relative to the more homogenous cells found in cultured lines. These findings suggest that IR-induced changes in telomerase activity are relevant to LDR environmental exposures *in vivo*, including those encountered during spaceflight. Current investigations in our laboratory are testing this hypothesis in astronauts to explore associated changes in telomerase activity and telomere length.

As the canonical role of telomerase is to elongate telomeres, and reports of changes in telomere length following IR exposure are contradictory, suggesting both lengthening and shortening at early times postexposure, we evaluated telomere length in dividing MCF-7 and MCF-10A cells at 5 and 10 days postexposure, time points more appropriate for the assessment of surviving rather than dying cells. Interestingly, at the cell population level, telomere length was significantly shortened 5 days postexposure in both MCF-7 and MCF-10A cells. While telomere length remained significantly shorter than unirradiated controls 10 days postexposure, significant lengthening of telomeres occurred as compared to 5 days post-IR, despite both cell lines displaying significantly decreased telomerase activity during this time period. Several studies have shown association between short telomeres and radiation sensitivity (52, 55); therefore, we sought to determine whether a specific subpopulation of cells, with

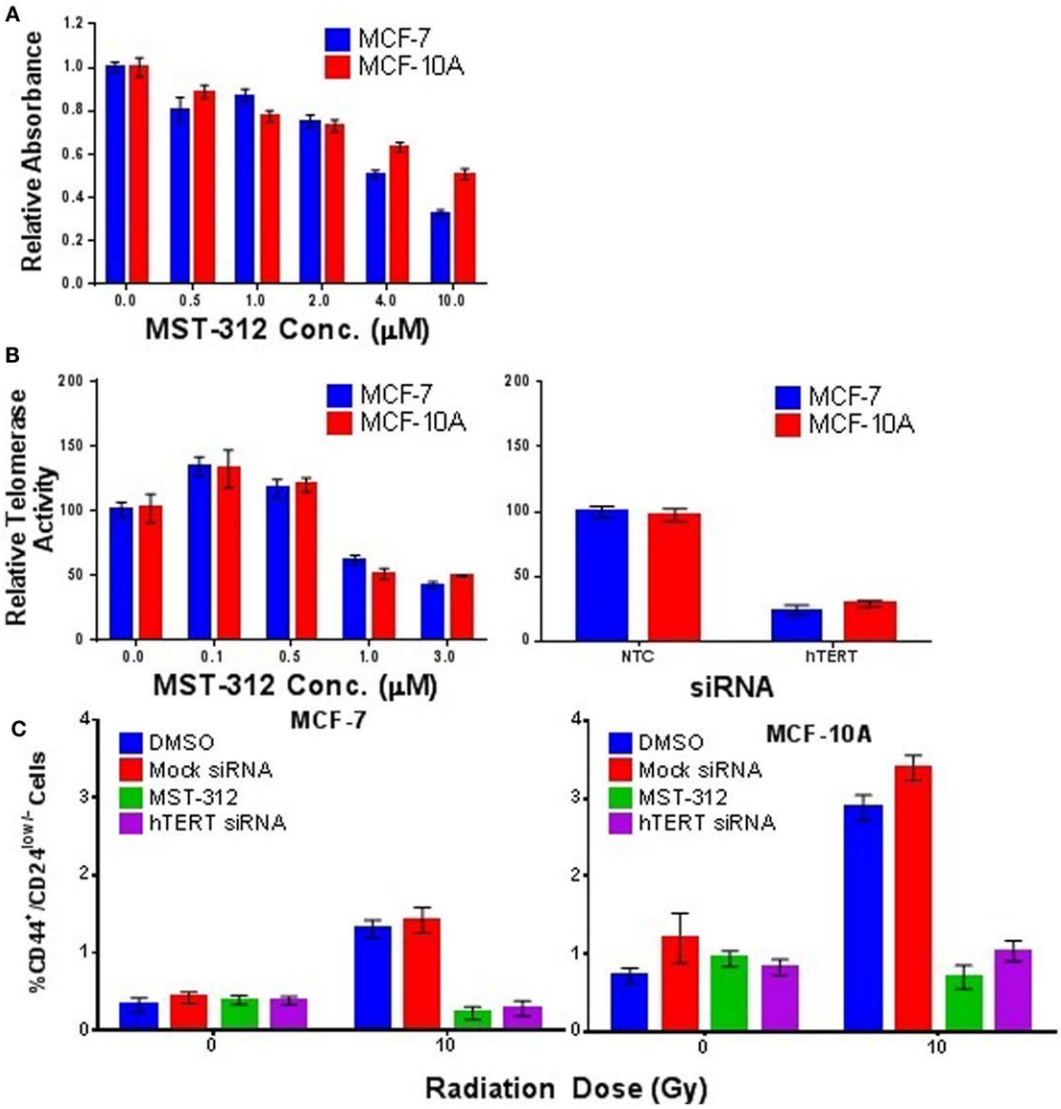

FIGURE 9 | Telomerase activity is required for IR-induced enrichment of putative, CD44^{+}/CD24$^{low/-}$ putative mammary stem cell populations. **(A)** MTT assay establishing relative toxicity of the telomerase inhibitor MST-312 in MCF-7 and MCF-10A cells. **(B)** MST-312 reduced telomerase activity in a dose-dependent fashion in both cell lines. Treatment with siRNA targeted to the catalytic subunit hTERT also significantly reduced telomerase activity; siRNA targeted to hTERC did not (not shown). **(C)** Reduction of telomerase activity via either telomerase inhibition (MST-312) or siRNA knockdown (hTERT) prevented IR-induced enrichment of CD44^{+}/CD24$^{low/-}$ cell populations 5 days postacute γ-ray exposure (10 Gy).

relatively short telomeres, was driving the response. Histogram analysis of individual telomere lengths demonstrated that all of the telomeres in the cell population were shortened and the entire distribution of telomere length was shifted monomodally to the left; thus, IR was not acting on a specific subset of radiation sensitive cells. Furthermore, the observed lengthening between days 5 and 10 also shifted the population monomodally indicating that in the cells surviving exposure, all telomeres are being lengthened, not simply preferential elongation of the critically short telomeres. These findings portend consequences for both carcinogenesis and repopulation of tumor cells following high dose radiation therapy in that short telomeres observed at 5 days could contribute to genomic instability and thus increase the propensity for carcinogenic events in surrounding normal tissue, as well as the propensity of further progression in of the tumor. Furthermore, telomere elongation in the surviving cells observed at 5–10 days postexposure strongly suggests a role in the survival/repopulation of irradiated cells and so supports blocking or manipulating this process as an effective means of preventing carcinogenesis and tumor recurrence following radiation therapy.

The suggestions that telomerase appeared to be functioning outside of its canonical role at telomeres led us to interrogate alternative possibilities for the increases in activity observed following exposure. Previous reports have suggested that

telomerase activity in NCSCs and CSCs greatly exceeds that of their more differentiated counterparts, particularly with regard to mammary carcinoma. An accumulating body of evidence has begun to amass suggesting that IR induces the enrichment of CSC compartments in culture and *in vivo*. In addition, this process may be governed by the reprograming of NSCC into CSC, rather than the selection of radioresistant CSC populations, and this phenomenon may be both kinetic and highly regulated. Therefore, we speculated that the elevation of telomerase activity observed following IR exposure was the result of enriched SC populations. A time course of $CD44^+/CD24^{low/-}$ putative CSC populations in MCF-7 cultures following an acute 10 Gy exposure revealed a steady enrichment of $CD44^+/CD24^{low/-}$ cells which peaked 5 days postexposure but remained significantly elevated for at least 7 days. However, no significant enrichment of $CD44^+/CD24^{low/-}$ cells was observed until after 72 h, which occurred after the peak of telomerase activity had subsided. Furthermore, in MCF-10A cells, a significant, albeit transient, enrichment of $CD44^+/CD24^{low/-}$ cells was observed 5 days postexposure, with only slight increase in telomerase activity at early times following exposure. Thus, telomerase activity was not elevated in response to $CD44^+/CD24^{low/-}$ cell enrichment, but rather preceded it. $CD44^+/CD24^{low/-}$ dose response, clonogenic survival, and growth kinetic analysis of MCF-7 and MCF-10A cells following an acute 10 Gy exposure was conducted to further characterize the IR-induced enrichment of SC populations. The level of CSC enrichment at the peak time point of 5 days postexposure was dose dependent in MCF-7 with a significant increase detected as low as 2 Gy. In contrast, there appeared to be a threshold dose for MCF-10A of between 5 and 10 Gy for significant enrichment.

These findings led to a collaborative effort using agent-based modeling (ABM) to determine mathematically if the observed enrichment in SC compartments following IR exposure resulted from the selection of radioresistant SC populations at the time of irradiation, or conversely, was a result of reprograming non-stem into SCs. Modeling indicated that a significant reprograming component must be in place to account for the relative percentage enrichment of SC populations (in the <1% of surviving cells) 5 days postexposure, which occurred in both MCF-7 and MCF-10A. Furthermore, both reprograming and symmetric division of surviving SC populations must be employed to account for the observed enrichment (manuscript in preparation, Gao et al.).

In order to confirm that IR-induced reprograming was not unique to mammary epithelial cells, we evaluated expression of the CD34/CD38 immunophenotype in the hematopoietic cell lines KG1a, WTK1, and LCL15044. As WTK1 and LCL15044 are terminally differentiated lymphoblastoid lines that express <0.01% $CD34^+$ cells at background levels, induction of reprograming was assessed using CD34 as the primary marker. In agreement with results using mammary epithelial cells, we observed a significant enrichment of $CD34^+$ cells in both WTK1 and LCL15044, which increased with dose and time, out to 3 days postexposure. SC enrichment was again preceded by a general trend toward elevated telomerase activity following acute IR exposure, although neither WTK1 nor LCL15044 experienced significantly increased levels of telomerase activity. Interestingly, the only cell line that did not display IR-induced enrichment of CSC was KG1a, a therapy-induced leukemia. In this instance, the background level of $CD34^+/CD38^-$ CSCs was significantly decreased in a time- and dose-dependent manner following IR exposure. As telomerase activity was significantly increased in KG1a cells during this same time frame, the results give further credence to our claim that the elevation of telomerase activity observed following IR exposure is not an artifact of enriched SC/CSC populations. This finding is important in that it illustrates IR exposure does not serve to increase SC compartments in all situations and may in fact act differentially on existing CSC populations, perhaps especially when those populations exist at high background levels.

Finally, as increased telomerase activity did not coincide temporally with putative SC enrichment in either MCF-7 or MCF-10A cells, we hypothesized that telomerase may be playing a role to promote IR-induced SC enrichment. To test this hypothesis, we employed a small molecule inhibitor (MST-312) as well as siRNA knockdown of the catalytic hTERT component of telomerase. Both MST-312 and hTERT siRNA significantly reduced telomerase activity in both MCF-7 and MCF-10A, and both very effectively blocked IR-induced enrichment of $CD44^+/CD24^{low/-}$ putative SC populations evaluated 5 days post-IR exposure (10 Gy; **Figure 9**). These results convincingly demonstrated that telomerase activity is essential for SC enrichment in response to IR exposure and so have important implications for radiotherapy, as telomerase inhibitors are currently entering Phase III randomized trials in humans. When taken together with the observation that although elevated post-IR exposure, telomerase activity is not acting to elongate telomeres, it becomes clear that telomerase is functioning outside its canonical role. Further investigation is needed to probe underlying mechanisms, but candidate pathways include Wnt/β-catenin signaling, in which hTERT has been shown (albeit controversially) to act as a transcriptional coactivator of β-catenin target genes important for stemness and dedifferentiation (37, 39, 41, 100). Additionally, TGF-β signaling has been proposed to regulate CSC kinetics in culture and *in vivo*, and hTERT has also been implied as a downstream cotranscriptional regulator (40).

The results presented here serve to highlight and more clearly define the critical roles telomeres and telomerase play in regulating the radiation response in both normal and cancer cells. Specifically, we demonstrated that loss of telomere end-capping function results in increased mutation burden and chromosomal events that fuel instability; furthermore, this mutation burden may be especially elevated in response to high LET radiation, particularly in the context of POT1 deficiency. We also establish that telomerase is activated by IR exposure, but the extent of such elevation is dose, dose rate, and cell type dependent, making assessment of risks posed by IR-induced increases in telomerase activity complex and requiring further exploration. Third, we confirmed and elaborated upon previous findings that acute low LET IR exposure enriches putative mammary CSCs in culture and expanded these studies to include lymphoblastoid lines, which are of great relevance to carcinogenesis and spaceflight risk. Lastly, we demonstrated the requirement of telomerase activity in promoting IR-induced putative SC enrichment in mammary epithelial cells of both cancer and non-cancer origin, a finding with important implications for radiation therapy. Taken together, these findings serve to strengthen the view that telomeres and

telomerase are far more than casual observers constrained to the ends of chromosomes. Rather, they occupy a central role in the cellular radiobiological response, governing everything from cellular lifespan (aging), cellular plasticity (SCs), and genomic integrity (instability), to survivability and carcinogenic potential following exposure.

AUTHOR CONTRIBUTIONS

BS made substantial contributions to the concept and design of the work, as well as the acquisition, analysis and interpretation of the data, drafting, and critically revising the work. CN, MM, CB, AH, and RI contributed to the acquisition and analysis of data for the work, and critically revising. HL and SB made substantial contributions to the concept and design of the work and to drafting and revising the work. All authors gave approval and agree to be accountable for all aspects of the work.

ACKNOWLEDGMENTS

The authors thank Dr. Ryan Dregalla for his efforts in acquiring some of the cytogenetic data shown, and Dr. Elizabeth Ryan for helpful discussions. Support for this research from NASA (NNX08AB656; NNX14AB02G; NNX14AH51G) is also gratefully acknowledged.

SUPPLEMENTARY MATERIAL

The Supplementary Material for this article can be found online at http://journal.frontiersin.org/article/10.3389/fonc.2015.00257

FIGURE S1 | Western blot validation of siRNA knockdown of telomeric binding proteins TRF1, TRF2, and POT1 in WTK1 cells.

FIGURE S2 | Representative scatter plots of MCF-7 and MCF-10A cells. (A) Immunotyped based on the expression of cell surface markers CD44 and CD24 and (B) validation of stem cell-like properties using aldefluor assay.

REFERENCES

1. Moyzis RK, Buckingham JM, Cram LS, Dani M, Deaven LL, Jones MD, et al. A highly conserved repetitive DNA-sequence; (Ttaggg)N; present at the telomeres of human-chromosomes. *Proc Natl Acad Sci U S A* (1988) **85**:6622–6. doi:10.1073/pnas.85.18.6622
2. de Lange T. Shelterin: the protein complex that shapes and safeguards human telomeres. *Genes Dev* (2005) **19**:2100–10. doi:10.1101/gad.1346005
3. Bianchi A, Smith S, Chong L, Elias P, de Lange T. TRF1 is a dimer and bends telomeric DNA. *EMBO J* (1997) **16**:1785–94. doi:10.1093/emboj/16.7.1785
4. Broccoli D, Smogorzewska A, Chong L, de Lange T. Human telomeres contain two distinct Myb-related proteins, TRF1 and TRF2. *Nat Genet* (1997) **17**:231–5. doi:10.1038/ng1097-231
5. Baumann P, Cech TR. Pot1, the putative telomere end-binding protein in fission yeast and humans. *Science* (2001) **292**:1171–5. doi:10.1126/science.1060036
6. Griffith JD, Comeau L, Rosenfield S, Stansel RM, Bianchi A, Moss H, et al. Mammalian telomeres end in a large duplex loop. *Cell* (1999) **97**:503–14. doi:10.1016/S0092-8674(00)80760-6
7. Olovnikov AM. Principle of marginotomy in template synthesis of polynucleotides. *Dokl Akad Nauk SSSR* (1971) **201**:1496–9.
8. Watson JD. Origin of concatameric T4 DNA. *Nature* (1972) **239**:197–201.
9. Hayflick CB. The limited *in vitro* lifetime of human diploid cell strains. *Exp Cell Res* (1965) **37**:614–36. doi:10.1016/0014-4827(65)90211-9
10. Harley CB, Futcher AB, Greider CW. Telomeres shorten during aging of human fibroblasts. *Nature* (1990) **345**:458–60. doi:10.1038/345458a0
11. DePinho RA. The age of cancer. *Nature* (2000) **408**:248–54. doi:10.1038/35041694
12. Murnane JP, Sabatier L. Chromosome rearrangements resulting from telomere dysfunction and their role in cancer. *Bioessays* (2004) **26**:1164–74. doi:10.1002/bies.20125
13. Haycock PC, Heydon EE, Kaptoge S, Butterworth AS, Thompson A, Willeit P. Leucocyte telomere length and risk of cardiovascular disease: systematic review and meta-analysis. *BMJ* (2014) **349**:g4227. doi:10.1136/bmj.g4227
14. Kim NW, Piatyszek MA, Prowse KR, Harley CB, West MD, Ho PLC, et al. Specific association of human telomerase activity with immortal cells and cancer. *Science* (1994) **266**:2011–5. doi:10.1126/science.7605428
15. Bryan TM, Englezou A, Dalla-Pozza L, Dunham MA, Reddel RR. Evidence for an alternative mechanism for maintaining telomere length in human tumors and tumor-derived cell lines. *Nat Med* (1997) **3**:1271–4. doi:10.1038/nm1197-1271
16. Greider CW, Blackburn EH. Identification of a specific telomere terminal transferase-activity in tetrahymena extracts. *Cell* (1985) **43**:405–13. doi:10.1016/0092-8674(85)90170-9
17. Greider CW, Blackburn EH. A telomeric sequence in the RNA of tetrahymena telomerase required for telomere repeat synthesis. *Nature* (1989) **337**:331–7. doi:10.1038/337331a0
18. Reya T, Morrison SJ, Clarke MF, Weissman IL. Stem cells, cancer, and cancer stem cells. *Nature* (2001) **414**:105–11. doi:10.1038/35102167
19. Low KC, Tergaonkar V. Telomerase: central regulator of all of the hallmarks of cancer. *Trends Biochem Sci* (2013) **38**:426–34. doi:10.1016/j.tibs.2013.07.001
20. Zhou BB, Zhang H, Damelin M, Geles KG, Grindley JC, Dirks PB. Tumour-initiating cells: challenges and opportunities for anticancer drug discovery. *Nat Rev Drug Discov* (2009) **8**:806–23. doi:10.1038/nrd2137
21. Al-Hajj M, Wicha MS, Benito-Hernandez A, Morrison SJ, Clarke MF. Prospective identification of tumorigenic breast cancer cells. *Proc Natl Acad Sci U S A* (2003) **100**:3983–8. doi:10.1073/pnas.0530291100
22. Joshua B, Kaplan MJ, Doweck I, Pai R, Weissman IL, Prince ME, et al. Frequency of cells expressing CD44, a head and neck cancer stem cell marker: correlation with tumor aggressiveness. *Head Neck* (2012) **34**:42–9. doi:10.1002/hed.21699
23. Yang G, Quan Y, Wang W, Fu Q, Wu J, Mei T, et al. Dynamic equilibrium between cancer stem cells and non-stem cancer cells in human SW620 and MCF-7 cancer cell populations. *Br J Cancer* (2012) **106**:1512–9. doi:10.1038/bjc.2012.126
24. O'Flaherty JD, Barr M, Fennell D, Richard D, Reynolds J, O'Leary J, et al. The cancer stem-cell hypothesis: its emerging role in lung cancer biology and its relevance for future therapy. *J Thorac Oncol* (2012) **7**:1880–90. doi:10.1097/JTO.0b013e31826bfbc6
25. Ailles LE, Weissman IL. Cancer stem cells in solid tumors. *Curr Opin Biotechnol* (2007) **18**:460–6. doi:10.1016/j.copbio.2007.10.007
26. Chan KS, Volkmer JP, Weissman I. Cancer stem cells in bladder cancer: a revisited and evolving concept. *Curr Opin Urol* (2010) **20**:393–7. doi:10.1097/MOU.0b013e32833cc9df
27. Du Z, Qin R, Wei C, Wang M, Shi C, Tian R, et al. Pancreatic cancer cells resistant to chemoradiotherapy rich in "stem-cell-like" tumor cells. *Dig Dis Sci* (2011) **56**:741–50. doi:10.1007/s10620-010-1340-0
28. Karimi-Busheri F, Rasouli-Nia A, Mackey JR, Weinfeld M. Senescence evasion by MCF-7 human breast tumor-initiating cells. *Breast Cancer Res* (2010) **12**:R31. doi:10.1186/bcr2583
29. Lagadec C, Vlashi E, Della Donna L, Dekmezian C, Pajonk F. Radiation-induced reprogramming of breast cancer cells. *Stem Cells* (2012) **30**:833–44. doi:10.1002/stem.1058
30. Murillo-Sauca O, Chung MK, Shin JH, Karamboulas C, Kwok S, Jung YH, et al. CD271 is a functional and targetable marker of tumor-initiating cells in head and neck squamous cell carcinoma. *Oncotarget* (2014) **5**:6854–66. doi:10.18632/oncotarget.2269
31. Lagadec C, Vlashi E, Della Donna L, Meng Y, Dekmezian C, Kim K, et al. Survival and self-renewing capacity of breast cancer initiating cells during fractionated radiation treatment. *Breast Cancer Res* (2010) **12**:R13. doi:10.1186/bcr2479
32. Silvestre DC, Pineda JR, Hoffschir F, Studler JM, Mouthon MA, Pflumio F, et al. Alternative lengthening of telomeres in human glioma stem cells. *Stem Cells* (2011) **29**:440–51. doi:10.1002/stem.600

33. Tang J, Fernandez-Garcia I, Vijayakumar S, Martinez-Ruiz H, Illa-Bochaca I, Nguyen DH, et al. Irradiation of juvenile, but not adult, mammary gland increases stem cell self-renewal and estrogen receptor negative tumors. *Stem Cells* (2013) **32**(3):649–61. doi:10.1002/stem.1533
34. Butof R, Dubrovska A, Baumann M. Clinical perspectives of cancer stem cell research in radiation oncology. *Radiother Oncol* (2013) **108**:388–96. doi:10.1016/j.radonc.2013.06.002
35. Ogawa K, Yoshioka Y, Isohashi F, Seo Y, Yoshida K, Yamazaki H. Radiotherapy targeting cancer stem cells: current views and future perspectives. *Anticancer Res* (2013) **33**(3):747–54.
36. Hoffmeyer K, Raggioli A, Rudloff S, Anton R, Hierholzer A, Del Valle I, et al. Wnt/beta-catenin signaling regulates telomerase in stem cells and cancer cells. *Science* (2012) **336**:1549–54. doi:10.1126/science.1218370
37. Greider CW. Molecular biology. Wnt regulates TERT – putting the horse before the cart. *Science* (2012) **336**:1519–20. doi:10.1126/science.1223785
38. Martinez P, Blasco MA. Telomeric and extra-telomeric roles for telomerase and the telomere-binding proteins. *Nat Rev Cancer* (2011) **11**:161–76. doi:10.1038/nrc3025
39. Park JI, Venteicher AS, Hong JY, Choi J, Jun S, Shkreli M, et al. Telomerase modulates Wnt signalling by association with target gene chromatin. *Nature* (2009) **460**:66–72. doi:10.1038/nature08137
40. Chung SS, Aroh C, Vadgama JV. Constitutive activation of STAT3 signaling regulates hTERT and promotes stem cell-like traits in human breast cancer cells. *PLoS One* (2013) **8**:e83971. doi:10.1371/journal.pone.0083971
41. Listerman I, Gazzaniga FS, Blackburn EH. An investigation of the effects of the core protein telomerase reverse transcriptase on wnt signaling in breast cancer cells. *Mol Cell Biol* (2014) **34**:280–9. doi:10.1128/MCB.00844-13
42. Strong MA, Vidal-Cardenas SL, Karim B, Yu H, Guo N, Greider CW. Phenotypes in mTERT(+)/(-) and mTERT(-)/(-) mice are due to short telomeres, not telomere-independent functions of telomerase reverse transcriptase. *Mol Cell Biol* (2011) **31**:2369–79. doi:10.1128/MCB.05312-11
43. Finnon P, Silver AR, Bouffler SD. Upregulation of telomerase activity by X-irradiation in mouse leukaemia cells is independent of Tert, Terc, Tnks and Myc transcription. *Carcinogenesis* (2000) **21**:573–8. doi:10.1093/carcin/21.4.573
44. Leteurtre F, Li X, Gluckman E, Carosella ED. Telomerase activity during the cell cycle and in gamma-irradiated hematopoietic cells. *Leukemia* (1997) **11**:1681–9. doi:10.1038/sj.leu.2400784
45. Neuhof D, Ruess A, Wenz F, Weber KJ. Induction of telomerase activity by irradiation in human lymphoblasts. *Radiat Res* (2001) **155**:693–7. doi:10.1667/0033-7587(2001)155[0693:IOTABI]2.0.CO;2
46. Ogawa Y, Nishioka A, Hamada N, Terashima M, Inomata T, Yoshida S, et al. Changes in telomerase activity of advanced cancers of oral cavity and oropharynx during radiation therapy: correlation with clinical outcome. *Int J Mol Med* (1998) **2**:301–7.
47. Sawant SG, Gregoire V, Dhar S, Umbricht CB, Cvilic S, Sukumar S, et al. Telomerase activity as a measure for monitoring radiocurability of tumor cells. *FASEB J* (1999) **13**:1047–54.
48. Terashima M, Ogawa Y, Toda K, Nishioka A, Inomata T, Kubonishi I, et al. Effects of irradiation on telomerase activity in human lymphoma and myeloma cell lines. *Int J Mol Med* (1998) **2**:567–71.
49. Wang X, Liu Y, Chow LS, Wong SC, Tsao GS, Kwong DL, et al. Regulation of telomerase activity by gamma-radiation in nasopharyngeal carcinoma cells. *Anticancer Res* (2000) **20**(1A):433–7.
50. Hyeon Joo O, Hande MP, Lansdorp PM, Natarajan AT. Induction of telomerase activity and chromosome aberrations in human tumour cell lines following X-irradiation. *Mutat Res* (1998) **401**:121–31. doi:10.1016/S0027-5107(97)00321-7
51. Sridharan DM, Asaithamby A, Bailey SM, Costes SV, Doetsch PW, Dynan WS, et al. Understanding cancer development processes after HZE-particle exposure: roles of ROS, DNA damage repair and inflammation. *Radiat Res* (2015) **183**:1–26. doi:10.1667/RR13804.1
52. Ayouaz A, Raynaud C, Heride C, Revaud D, Sabatier L. Telomeres: hallmarks of radiosensitivity. *Biochimie* (2008) **90**:60–72. doi:10.1016/j.biochi.2007.09.011
53. Mirjolet C, Boidot R, Saliques S, Ghiringhelli F, Maingon P, Crehange G. The role of telomeres in predicting individual radiosensitivity of patients with cancer in the era of personalized radiotherapy. *Cancer Treat Rev* (2015) **41**:354–60. doi:10.1016/j.ctrv.2015.02.005
54. Wong KK, Chang S, Weiler SR, Ganesan S, Chaudhuri J, Zhu CM, et al. Telomere dysfunction impairs DNA repair and enhances sensitivity to ionizing radiation. *Nat Genet* (2000) **26**(1):85–8.
55. Goytisolo FA, Samper E, Martin-Caballero J, Finnon P, Herrera E, Flores JM, et al. Short telomeres result in organismal hypersensitivity to ionizing radiation in mammals. *J Exp Med* (2000) **192**:1625–36. doi:10.1084/jem.192.11.1625
56. Berardinelli F, Antoccia A, Buonsante R, Gerardi S, Cherubini R, De Nadal V, et al. The role of telomere length modulation in delayed chromosome instability induced by ionizing radiation in human primary fibroblasts. *Environ Mol Mutagen* (2013) **54**:172–9. doi:10.1002/em.21761
57. Berardinelli F, Nieri D, Sgura A, Tanzarella C, Antoccia A. Telomere loss, not average telomere length, confers radiosensitivity to TK6-irradiated cells. *Mutat Res* (2012) **740**:13–20. doi:10.1016/j.mrfmmm.2012.11.004
58. Drissi R, Wu J, Hu Y, Bockhold C, Dome JS. Telomere shortening alters the kinetics of the DNA damage response after ionizing radiation in human cells. *Cancer Prev Res (Phila)* (2011) **4**:1973–81. doi:10.1158/1940-6207.CAPR-11-0069
59. Smirnova A, Gamba R, Khoriauli L, Vitelli V, Nergadze SG, Giulotto E. TERRA expression levels do not correlate with telomere length and radiation sensitivity in human cancer cell lines. *Front Oncol* (2013) **3**:115. doi:10.3389/fonc.2013.00115
60. Maeda T, Nakamura K, Atsumi K, Hirakawa M, Ueda Y, Makino N. Radiation-associated changes in the length of telomeres in peripheral leukocytes from inpatients with cancer. *Int J Radiat Biol* (2012) **89**(2):106–9. doi:10.3109/09553002.2013.734945
61. Bailey SM, Meyne J, Chen DJ, Kurimasa A, Li GC, Lehnert BE, et al. DNA double-strand break repair proteins are required to cap the ends of mammalian chromosomes. *Proc Natl Acad Sci U S A* (1999) **96**:14899–904. doi:10.1073/pnas.96.26.14899
62. Zhang Q, Williams ES, Askin KF, Peng Y, Bedford JS, Liber HL, et al. Suppression of DNA-PK by RNAi has different quantitative effects on telomere dysfunction and mutagenesis in human lymphoblasts treated with gamma rays or HZE particles. *Radiat Res* (2005) **164**:497–504. doi:10.1667/RR3366.1
63. Zhang Y, Lim CU, Williams ES, Zhou J, Zhang Q, Fox MH, et al. NBS1 knockdown by small interfering RNA increases ionizing radiation mutagenesis and telomere association in human cells. *Cancer Res* (2005) **65**:5544–53. doi:10.1158/0008-5472.CAN-04-4368
64. Zhang Y, Zhou J, Cao X, Zhang Q, Lim CU, Ullrich RL, et al. Partial deficiency of DNA-PKcs increases ionizing radiation-induced mutagenesis and telomere instability in human cells. *Cancer Lett* (2007) **250**:63–73. doi:10.1016/j.canlet.2006.09.021
65. Hagelstrom RT, Blagoev KB, Niedernhofer LJ, Goodwin EH, Bailey SM. Hyper telomere recombination accelerates replicative senescence and may promote premature aging. *Proc Natl Acad Sci U S A* (2010) **107**:15768–73. doi:10.1073/pnas.1006338107
66. Bailey SM, Cornforth MN, Ullrich RL, Goodwin EH. Dysfunctional mammalian telomeres join with DNA double-strand breaks. *DNA Repair* (2004) **3**:349–57. doi:10.1016/j.dnarep.2003.11.007
67. Williams ES, Klingler R, Ponnaiya B, Hardt T, Schrock E, Lees-Miller SP, et al. Telomere dysfunction and DNA-PKcs deficiency: characterization and consequence. *Cancer Res* (2009) **69**:2100–7. doi:10.1158/0008-5472.CAN-08-2854
68. Le PN, Maranon DG, Altina NH, Battaglia CL, Bailey SM. TERRA, hnRNP A1, and DNA-PKcs interactions at human telomeres. *Front Oncol* (2013) **3**:91. doi:10.3389/fonc.2013.00091
69. Levy JA, Virolainen M, Defendi V. Human lymphoblastoid lines from lymph node and spleen. *Cancer* (1968) **22**:517–24. doi:10.1002/1097-0142(196809)22:3<517::AID-CNCR2820220305>3.0.CO;2-A
70. Bailey SM, Goodwin EH, Cornforth MN. Strand-specific fluorescence in situ hybridization: the CO-FISH family. *Cytogenet Genome Res* (2004) **107**:14–7. doi:10.1159/000079565
71. Bailey SM, Brenneman MA, Goodwin EH. Frequent recombination in telomeric DNA may extend the proliferative life of telomerase-negative cells. *Nucleic Acids Res* (2004) **32**:3743–51. doi:10.1093/nar/gkh691

72. Poon SS, Lansdorp PM. Quantitative fluorescence in situ hybridization (Q-FISH). *Curr Protoc Cell Biol* (2001) **18**:14. doi:10.1002/0471143030.cb1804s12
73. Ourliac-Garnier I, Londono-Vallejo A. Telomere length analysis by quantitative fluorescent in situ hybridization (Q-FISH). *Methods Mol Biol* (2011) **735**:21–31. doi:10.1007/978-1-61779-092-8_3
74. Dregalla RC, Zhou J, Idate RR, Battaglia CL, Liber HL, Bailey SM. Regulatory roles of tankyrase 1 at telomeres and in DNA repair: suppression of T-SCE and stabilization of DNA-PKcs. *Aging* (2010) **2**(10):691–708.
75. Wong HP, Slijepcevic P. Telomere length measurement in mouse chromosomes by a modified Q-FISH method. *Cytogenet Genome Res* (2004) **105**:464–70. doi:10.1159/000078220
76. Herbert BS, Hochreiter AE, Wright WE, Shay JW. Nonradioactive detection of telomerase activity using the telomeric repeat amplification protocol. *Nat Protoc* (2006) **1**:1583–90. doi:10.1038/nprot.2006.239
77. Hou M, Xu D, Bjorkholm M, Gruber A. Real-time quantitative telomeric repeat amplification protocol assay for the detection of telomerase activity. *Clin Chem* (2001) **47**(3):519–24.
78. Livak KJ, Schmittgen TD. Analysis of relative gene expression data using real-time quantitative PCR and the 2(-delta delta C(T)) method. *Methods* (2001) **25**:402–8. doi:10.1006/meth.2001.1262
79. Untergrasser A, Cutcutache I, Koressaar T, Ye J, Faircloth BC, Remm M, et al. Primer3 – new capabilities and interfaces. *Nucleic Acids Res* (2012) **40**(15):e115. Available from: http://steverozen.net/; http://bioinfo.ut.ee/primer3/Untergasser_etal_NuclAcidsRes2012.pdf
80. National Center for Biotechnology Information (NCBI). *TERT Telomerase Reverse Transcriptase [Homo sapiens (human)]*. Available from: http://www.ncbi.nlm.nih.gov/gene/7015
81. Seimiya H, Oh-hara T, Suzuki T, Naasani I, Shimazaki T, Tsuchiya K, et al. Telomere shortening and growth inhibition of human cancer cells by novel synthetic telomerase inhibitors MST-312, MST-295, and MST-1991. *Mol Cancer Ther* (2002) **1**(9):657–65.
82. Bes S, Tatou E, Vandroux D, Tissier C, Rochette L, Athias P. Physiological and metabolic actions of mycophenolate mofetil on cultured newborn rat cardiomyocytes in normoxia and in simulated ischemia. *Fundam Clin Pharmacol* (2004) **18**:287–98. doi:10.1111/j.1472-8206.2004.00237.x
83. Phillips TM, McBride WH, Pajonk F. The response of CD24(-/low)/CD44+ breast cancer-initiating cells to radiation. *J Natl Cancer Inst* (2006) **98**:1777–85. doi:10.1093/jnci/djj495
84. Sun H, Jia J, Wang X, Ma B, Di L, Song G, et al. CD44(+)/CD24 (-) breast cancer cells isolated from MCF-7 cultures exhibit enhanced angiogenic properties. *Clin Trans Oncol* (2012) **15**(1):46–54. doi:10.1007/s12094-012-0891-2
85. Sheridan C, Kishimoto H, Fuchs RK, Mehrotra S, Bhat-Nakshatri P, Turner CH, et al. CD44+/CD24- breast cancer cells exhibit enhanced invasive properties: an early step necessary for metastasis. *Breast Cancer Res* (2006) **8**:R59. doi:10.1186/bcr1610
86. Bonnet D, Dick JE. Human acute myeloid leukemia is organized as a hierarchy that originates from a primitive hematopoietic cell. *Nat Med* (1997) **3**:730–7. doi:10.1038/nm0797-730
87. Williams ES, Stap J, Essers J, Ponnaiya B, Luijsterburg MS, Krawczyk PM, et al. DNA double-strand breaks are not sufficient to initiate recruitment of TRF2. *Nat Genet* (2007) **39**(6):696–8.
88. Liber HL, Idate R, Warner C, Bailey SM. Radiation quality and mutagenesis in human lymphoblastoid cells. *Radiat Res* (2014) **182**:390–5. doi:10.1667/RR13817.1
89. Bombarde O, Boby C, Gomez D, Frit P, Giraud-Panis MJ, Gilson E, et al. TRF2/RAP1 and DNA-PK mediate a double protection against joining at telomeric ends. *EMBO J* (2010) **29**(9):1573–84. doi:10.1038/emboj.2010.49
90. Denchi EL, de Lange T. Protection of telomeres through independent control of ATM and ATR by TRF2 and POT1. *Nature* (2007) **448**:1068–71. doi:10.1038/nature06065
91. Flynn RL, Centore RC, O'Sullivan RJ, Rai R, Tse A, Songyang Z, et al. TERRA and hnRNPA1 orchestrate an RPA-to-POT1 switch on telomeric single-stranded DNA. *Nature* (2011) **471**:532–6. doi:10.1038/nature09772
92. Hewitt G, Jurk D, Marques FD, Correia-Melo C, Hardy T, Gackowska A, et al. Telomeres are favoured targets of a persistent DNA damage response in ageing and stress-induced senescence. *Nat Commun* (2012) **3**:708. doi:10.1038/ncomms1708
93. Fumagalli M, Rossiello F, Clerici M, Barozzi S, Cittaro D, Kaplunov JM, et al. Telomeric DNA damage is irreparable and causes persistent DNA-damage-response activation. *Nat Cell Biol* (2012) **14**:555. doi:10.1038/ncb0512-555b
94. Muraki K, Nyhan K, Han L, Murnane JP. Mechanisms of telomere loss and their consequences for chromosome instability. *Front Oncol* (2012) **2**:135. doi:10.3389/fonc.2012.00135
95. Diehl MC, Idowu MO, Kimmelshue KN, York TP, Jackson-Cook CK, Turner KC, et al. Elevated TRF2 in advanced breast cancers with short telomeres. *Breast Cancer Res Treat* (2011) **127**:623–30. doi:10.1007/s10549-010-0988-7
96. Tanaka H, Abe S, Huda N, Tu L, Beam MJ, Grimes B, et al. Telomere fusions in early human breast carcinoma. *Proc Natl Acad Sci U S A* (2012) **109**:14098–103. doi:10.1073/pnas.1120062109
97. Ramsay AJ, Quesada V, Foronda M, Conde L, Martinez-Trillos A, Villamor N, et al. POT1 mutations cause telomere dysfunction in chronic lymphocytic leukemia. *Nat Genet* (2013) **45**(5):526–30. doi:10.1038/ng.2584
98. Lei H, Zhou FX, Xu H, Peng XH, Zhang ZG, Wang WB, et al. Expression of various protection of telomeres 1 variants is associated with telomere length and radiosensitivity in colon and gastric adenocarcinoma cells. *Biomed Rep* (2015) **3**(3):420–4.
99. Rai R, Zheng H, He H, Luo Y, Multani A, Carpenter PB, et al. The function of classical and alternative non-homologous end-joining pathways in the fusion of dysfunctional telomeres. *EMBO J* (2010) **29**:2598–610. doi:10.1038/emboj.2010.142
100. Choi J, Southworth LK, Sarin KY, Venteicher AS, Ma W, Chang W, et al. TERT promotes epithelial proliferation through transcriptional control of a Myc- and Wnt-related developmental program. *PLoS Genet* (2008) **4**:e10. doi:10.1371/journal.pgen.0040010

Conflict of Interest Statement: The authors declare that the research was conducted in the absence of any commercial or financial relationships that could be construed as a potential conflict of interest.

Copyright © 2015 Sishc, Nelson, McKenna, Battaglia, Herndon, Idate, Liber and Bailey. This is an open-access article distributed under the terms of the Creative Commons Attribution License (CC BY). The use, distribution or reproduction in other forums is permitted, provided the original author(s) or licensor are credited and that the original publication in this journal is cited, in accordance with accepted academic practice. No use, distribution or reproduction is permitted which does not comply with these terms.

frontiers in Oncology

REVIEW
published: 07 July 2015
doi: 10.3389/fonc.2015.00150

Range verification methods in particle therapy: underlying physics and Monte Carlo modeling

*Aafke Christine Kraan**

Department of Physics, National Institute for Nuclear Physics (INFN), University of Pisa, Pisa, Italy

Hadron therapy allows for highly conformal dose distributions and better sparing of organs-at-risk, thanks to the characteristic dose deposition as function of depth. However, the quality of hadron therapy treatments is closely connected with the ability to predict and achieve a given beam range in the patient. Currently, uncertainties in particle range lead to the employment of safety margins, at the expense of treatment quality. Much research in particle therapy is therefore aimed at developing methods to verify the particle range in patients. Non-invasive *in vivo* monitoring of the particle range can be performed by detecting secondary radiation, emitted from the patient as a result of nuclear interactions of charged hadrons with tissue, including β^+ emitters, prompt photons, and charged fragments. The correctness of the dose delivery can be verified by comparing measured and pre-calculated distributions of the secondary particles. The reliability of Monte Carlo (MC) predictions is a key issue. Correctly modeling the production of secondaries is a non-trivial task, because it involves nuclear physics interactions at energies, where no rigorous theories exist to describe them. The goal of this review is to provide a comprehensive overview of various aspects in modeling the physics processes for range verification with secondary particles produced in proton, carbon, and heavier ion irradiation. We discuss electromagnetic and nuclear interactions of charged hadrons in matter, which is followed by a summary of some widely used MC codes in hadron therapy. Then, we describe selected examples of how these codes have been validated and used in three range verification techniques: PET, prompt gamma, and charged particle detection. We include research studies and clinically applied methods. For each of the techniques, we point out advantages and disadvantages, as well as clinical challenges still to be addressed, focusing on MC simulation aspects.

Keywords: hadron interactions, Monte Carlo modeling, range verification, PET, prompt gamma

OPEN ACCESS

Edited by:
Marco Durante,
GSI Helmholtzzentrum für Schwerionenforschung, Germany

Reviewed by:
Lembit Sihver,
Technische Universität Wien, Austria
Francesco Cerutti,
CERN, Switzerland

***Correspondence:**
Aafke Christine Kraan,
Department of Physics, INFN,
University of Pisa, Largo B. Pontecorvo 3, Pisa 56127, Italy
aafke.kraan@pi.infn.it

Specialty section:
This article was submitted to Radiation Oncology, a section of the journal Frontiers in Oncology

Received: *24 February 2015*
Accepted: *17 June 2015*
Published: *07 July 2015*

Citation:
Kraan AC (2015) Range verification methods in particle therapy: underlying physics and Monte Carlo modeling. Front. Oncol. 5:150. doi: 10.3389/fonc.2015.00150

1. Introduction

The main challenge in radiotherapy for cancer treatment is how to deliver high dose to the tumor region, while minimizing the irradiation of healthy tissue. One of the most important new modalities being developed for cancer therapy is irradiation with charged ions. Thanks to the characteristic dose deposition profile (Bragg peak), charged particles offer the possibility to deposit dose much more locally than the photons, so dose in healthy tissue can be minimized (1, 2). However, treatments with charged particles are more sensitive to uncertainties than photon treatments, because of their steep dose profile. Error sources include anatomical changes (e.g., organ motion, tumor regression,

weight loss), patient setup errors and range errors from uncertainties in CT Hounsfield units (HU), conversion of HU into particle stopping power, and reconstruction artifacts (3). These can result in under-dosage to the tumor and unwanted dose to healthy tissue. Because of these uncertainties, in particle therapy clinics, generally large safety margins around the tumor are employed, and/or probabilistic or robustly optimized conservative treatment plans are used. This may not be optimal for the patient and may impair the beneficial effects of charged particle therapy. Much research in particle therapy is therefore aimed at developing new methods, which enable to verify the particle range in patients.

Various techniques for particle range verification have been developed over the last decades (4). Non-invasive *in vivo* treatment monitoring can be performed by detecting secondary particles produced as a result of nuclear interactions of the incident particle beam with the patient tissue, like β^+ emitters, prompt photons, and charged fragments. Monte Carlo (MC) simulations have played a crucial role in the development and clinical application of range verification techniques. They can accurately describe particle transport and interactions of radiation with matter in complex geometries, such as fully detailed CT descriptions of the patient anatomy. This makes them a suitable tool for feasibility and detector design studies. Furthermore, *in vivo* non-invasive range monitoring methods generally rely on direct comparisons between measured and MC predicted distributions of secondary particles. The accuracy of the MC codes is therefore a crucial issue. Unfortunately, modeling nuclear interactions and the resulting secondary particle production is a highly complex task, because it involves nuclear physics interactions, for which no rigorous models exist.

Although much literature is available on interactions of charged particles in matter, reviews dedicated to particle therapy are scarce and nuclear interactions are often only discussed superficially. For instance, a dedicated review about interactions of charged particles in radiation therapy is written by Lomax (5), but it only very briefly touches on nuclear interactions. Moreover, it does not include range verification methods and MC models. The same applies to valuable reviews about physics of heavy charged particles (6, 7). Also, Gottschalk has written an excellent summary about proton interactions, including some nuclear physics (8), but it does not include MC codes and *in vivo* range verification. Very recently, a valuable review written by Newhauser and Zhang (9) about proton physics was published, including Monte Carlo and analytical modeling of proton interactions; however, nuclear interactions are discussed shortly and range verification techniques were not reviewed. And vice versa, thorough reviews about range verification methods are available (4), but the physics interactions and MC codes modeling them are described only very shortly. Extensive reviews exist about the usage of MC techniques in particle therapy (10, 11), but these do not contain a systematic description of interactions of charged hadrons in matter. Furthermore, the number of particle treatment centers around the world is growing, and thereby the demand for *in vivo* non-invasive range verification methods increases. In view of the rapidly evolving technical developments in the last years, we believe that an up-to-date description of the different range verification strategies, the state-of-the-art MC codes, and their underlying physics principles is timely.

This review intends to give a comprehensive overview of various aspects in modeling the physics processes that are relevant in range verification methods based on secondary particle detection in proton, carbon, and heavier ion irradiation. We will cover the physics principles behind the various range verification methods, the MC codes to simulate them, and the validation of the codes, including both clinically implemented methods as well as research studies. Hereby, we highlight the difficulties, limitations, and challenges related to physics modeling for range monitoring. This review is organized in the following way:

Section 2 is devoted to a brief description of interactions of charged particles in matter for energy ranges relevant in radiotherapy. We discuss both electromagnetic and nuclear interactions, and point out some practical consequences regarding beam fluence and dose. Moreover, we discuss some general approaches in modeling nuclear interactions, adopted by most state-of-the-art MC codes used in hadron therapy, and show how nuclear interactions give rise to production of β^+ emitters, prompt γ's, and charged fragments.

Range verification methods rely heavily on the accuracy of the particle transport code for describing dose deposition and nuclear fragmentation. Section 3 presents a summary of the available MC codes that are most widely used in particle therapy, and in particular in research related to particle range verification. For each MC generator, we briefly discuss how the relevant physics processes are modeled, and we give some examples of how these models are validated for proton and heavy ion therapy.

In Section 4, we review the use of MC codes in non-invasive particle range verification, focusing on three techniques: PET, prompt γ, and charged particle imaging. For each strategy, we describe selected examples of the application of the codes to treatment monitoring, as well as the available detectors. We also highlight some remaining clinical challenges regarding physics modeling.

In Section 5, we compare the three techniques, pointing out their strength and drawbacks. We also briefly touch on the development of hybrid systems. Finally, we describe some common efforts, which could improve the accuracy of signal prediction in treatment monitoring techniques.

2. Interactions of Charged Particles in Matter

In this section, we review electromagnetic and nuclear interactions of charged ions in matter. We narrow our focus to particle types and energies currently used in particle therapy centers worldwide. This means that we consider interactions of protons up to about 250 MeV and carbon ions up to about 450 MeV/u, i.e., penetrating into the human body up to about 40 cm. Before going into detail, let's first quickly look at their typical velocities. For a particle of kinetic energy E_{kin}, total energy E_{tot}, mass m_0, and momentum p, the particle velocity β in units of the velocity of light c is given by:

$$\beta \equiv \frac{v}{c} = \frac{pc}{E_{\text{tot}}} = \frac{\sqrt{E_{\text{tot}}^2 - m_0^2 c^4}}{E_{\text{kin}} + m_0 c^2} = \frac{\sqrt{E_{\text{kin}}^2 + 2E_{\text{kin}} m_0 c^2}}{E_{\text{kin}} + m_0 c^2} \quad (1)$$

For a proton with kinetic energy $E_{\text{kin}} = 250$ MeV and given the proton mass = 938 MeV/c^2, we find $\beta \approx 0.6$, while a carbon ion with energy 450 MeV/u has $\beta \approx 0.7$. Thus, in radiotherapy, we generally deal with moderately relativistic particles.

2.1. Electromagnetic Interactions

2.1.1. Electromagnetic Energy Losses for Charged Particles

Moderately relativistic charged particles interact with material by electrical (Coulomb) forces with the atomic electrons and with the material nuclei. The particle looses energy primarily by inelastic collisions with the atomic electrons, resulting in ionization and atomic excitation. These are *continuous* energy losses. When the ejected electron is so energetic that it can cause ionization itself, we call it a delta-ray. The amount of energy lost due to Coulomb interactions with the material nuclei is very small (12).

For charged particles other than electrons with charge number Z_{p} moving in a target material of atomic number Z_{t} and density ρ with velocity β larger than the orbital electron velocity, the mean ionization energy loss (or electronic stopping power) can be described by the Bethe-Bloch equation (12–14):

$$\frac{dE}{dx} = K\rho\frac{Z_{\text{p}}^2}{\beta^2}\frac{Z_{\text{t}}}{A_{\text{t}}}\left[\frac{1}{2}ln\left(\frac{2m_{\text{e}}c^2\beta^2\gamma^2T_{\max}}{I_{\text{e}}^2}\right) - \beta^2 - \frac{\delta}{2} - \frac{C}{Z_{\text{t}}}\right] \tag{2}$$

with $K = 4\pi N_{\text{A}} r_{\text{e}}^2 m_{\text{e}} c^2$, N_{A} Avogadro's number, r_{e} and m_{e} are the radius and mass of the electron, A_{t} the molar mass of the material, $\gamma = \frac{1}{\sqrt{1-1/\beta^2}}$, I_{e} is the mean ionization potential of the material. Furthermore, δ is the density correction, relevant only for ultra-relativistic charged particles, and C is a shell correction term, which becomes important when the particle velocity becomes closer to the velocity of the atomic electrons. Heavy ions, which are fully stripped at high velocities, get partly neutralized by picking up electrons from the target material as they slow down. This decreases the particles' effective charge $(Z_{\text{p}})_{\mathit{eff}}$ that has to replace Z_{p} in Eq. 2. The latter represents only the main contributions to the stopping power. There exist several higher-order corrections in Z_{p}, which have been proposed to improve Eq. 2, like Barkas, Bloch, and Mott corrections. For a more extensive discussion, we refer to a comprehensive review by Ziegler (12). The ionization potential can be parameterized for instance in Ref. (15):

$$I_{\text{e}}(Z_{\text{t}}) = (12Z_{\text{t}} + 7) \quad \text{eV for } Z_{\text{t}} \leq 13 \tag{3}$$

$$I_{\text{e}}(Z_{\text{t}}) = (9.76Z_{\text{t}} + 58.8Z_{\text{t}}^{-0.19}) \quad \text{eV for } Z_{\text{t}} > 13 \tag{4}$$

Here, $T_{\max}$ is the maximum kinetic energy, which can be transferred to a free electron in a single collision and is given, for an incident particle of mass M, in Ref. (14):

$$T_{\max} = \frac{2m_{\text{e}}c^2\beta^2\gamma^2}{1 + 2\gamma m_{\text{e}}/M + (m_{\text{e}}/M)^2} \tag{5}$$

For very low energies, when β becomes comparable or less than the velocity of the orbital electrons, the so-called Lindhard region, Eq. 2, is no longer valid. Then, the energy loss becomes proportional to β (16) and is of the order of:

$$\frac{dE}{dx} \cong 8\pi\rho\frac{N_{\text{A}}}{A_{\text{t}}}\frac{\hbar^2}{m_{\text{e}}}\frac{Z_{\text{p}}^{7/6}Z_{\text{t}}}{Z}\frac{\beta}{\beta_{\text{o}}}, \tag{6}$$

where $Z^{\frac{2}{3}} = Z_{\text{p}}^{\frac{2}{3}} + Z_{\text{t}}^{\frac{2}{3}}$ and $\beta_o = \frac{e^2}{4\pi\varepsilon_0\hbar c}$ ($\approx$0.0073) are the electron velocity in the classical lowest Bohr orbit of the hydrogen atom. In between the Bethe-Bloch and the Lindhard region, energy losses can be described by the low energy model of Anderson and Ziegler (17); alternatively, a polynomial can be used to join up the regions. For compound materials, the stopping power is the weighted sum of all the single elements, corrected for ionization energy.

The electronic stopping power as function of the kinetic energy of protons impinging on a water target is shown in **Figure 1**, where the various regions mentioned above are indicated. Also indicated is the nuclear stopping power resulting from Coulomb interactions of the incident particles with the atomic nuclei, which is seen to contribute very little to the total stopping power. In **Figure 2**, the energy loss as function of depth is given for protons (left) and ^{12}C ions (right) for various energies. The growing energy loss with decreasing particle velocity described by the Bethe-Bloch formula causes the characteristic Bragg peak.

The range R of a particle beam is the depth in the medium, at which half of the particles undergoing electromagnetic interactions have stopped. In practice, a dose measurement is used, where the range is defined as the distal 80% point of the Bragg peak (8).

The Bragg-peak is never perfectly sharp. First of all, the ionization energy loss of a charged particle traversing a medium is a stochastic process, so that the actual range of each single particle deviates from the expected mean value. This longitudinal widening of the Bragg peak is known as *range straggling*. Second, the beam is never perfectly mono-energetic. Depending on the machine, the spread is of the order of 1% of the energy (5).

Continuous ionization energy losses of charge particles are typically modeled in Monte Carlo codes analytically down to about 2 MeV, based on a continuous-slow-down-approach (CSDA) building on the Bethe-Bloch equation, but including relevant

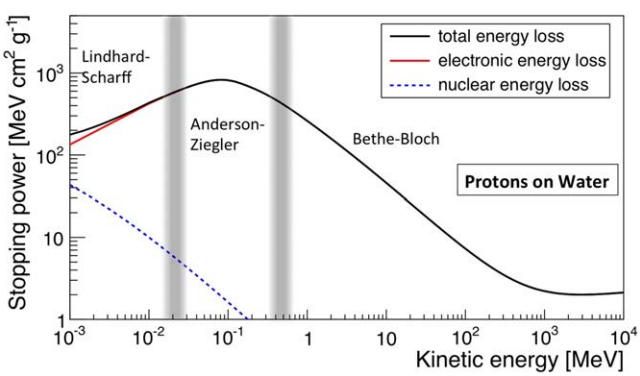

FIGURE 1 | Stopping power (d*E*/d*x*), in MeV cm^2 g^{-1}, for protons in water as function of kinetic energy. The total, electronic, and nuclear stopping power are shown, as well as the characteristic regions. Made using NIST data (18).

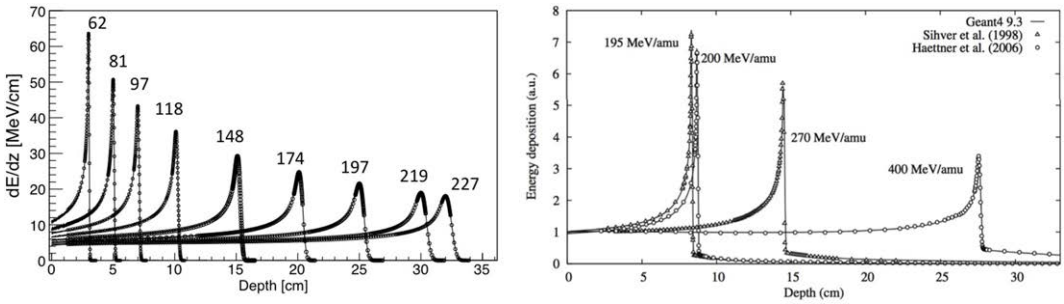

FIGURE 2 | Left: stopping power of protons with various energies in MeV, showing CNAO data and FLUKA simulations. Adapted from Ref. (19), with permission. **Right:** stopping power of carbon ions with various energies including data and Geant4 simulations. Reproduced from Ref. (20), with permission.

correction factors in Z_p. Below 2 MeV parameterizations are usually used. Energy straggling is partly taken into account by the emission of delta-rays, and it can be modeled using a statistical approach to include fluctuations, for instance, based on Gaussian fluctuations or the Landau or Vavilov theories (13).

2.1.2. Multiple Coulomb Scattering

Besides inelastic collisions with the atomic electrons, a charged particle also suffers numerous elastic Coulomb scatterings from the nuclei themselves. The energy loss as a result of multiple Coulomb scattering (MCS) is negligible, but it is nevertheless important for dosimetry, because it causes lateral broadening of the pencil beam. Theoretical calculations of the scattering angle are highly complex. One of the most complete derivations was performed by Molière (21), and various calculations in order to derive more practical formulas were performed afterwards, for instance by Lewis (22), Highland (23), and Gottschalk (24). Due to the Central Limit Theorem, the probability distribution of the net angle of deflection of a particle in a thick material is very nearly Gaussian, resulting from the sum of many small random deflections. An approximation for the probability distribution for the net angle of deflection by MCS in a material was derived by Highland (23), and can be approximated by a Gaussian distribution with a width given by:

$$\theta_0 = \frac{14.1\text{MeV}}{\beta cp} Z_p \sqrt{L/L_0}[1 + 0.038\ln(L/L_0)] \qquad (7)$$

where L the thickness of the scattering material and L_0 the radiation length. The gaussian description is not perfect, and the presence of large-angle tails, which are the result of single scatters in the target, are not quite negligible and are typically simulated in MC codes. Also, for heavy particles, nuclear form factors should be applied, as well as Fano corrections (13). **Figure 3** shows the lateral beam widening for proton and carbon projectiles.

Multiple Coulomb scattering is generally modeled in Monte Carlo codes through a combination of "condensed" MC simulations methods (most frequently based on Molière or Lewis theory, the latter also allowing to predict moments of lateral displacement) and the possibility for single large-angle scatterings. While in the former method, only the net displacement, energy loss, and change of direction at the end of the particle track are calculated, the latter allows simulating discrete single scatterings.

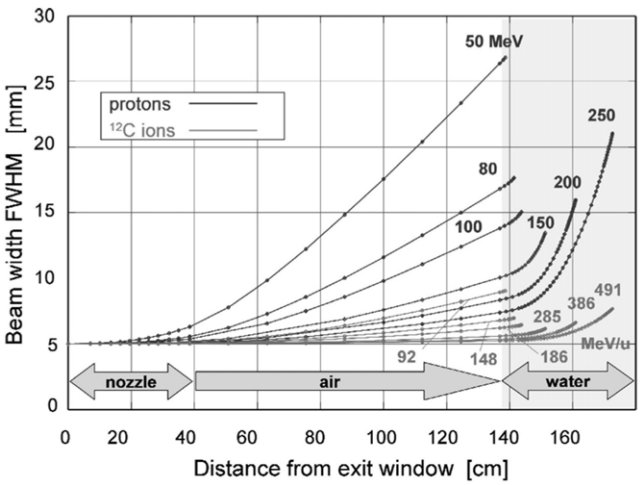

FIGURE 3 | Lateral scattering (FWHM – full width at half maximum) as function of distance from the beam exit window for various proton and carbon energies, calculated for a nozzle based on the GSI therapy facility. The beam enters the patient body at a distance of 1.40 m from the exit. Reproduced from Ref. (25), with permission.

2.2. Nuclear Interactions

Charged particles can also suffer nuclear interactions with the material nuclei. These interactions contribute significantly less to energy losses than electromagnetic processes. Still, they are highly relevant for range verification methods, as we will see below. Contrary to electromagnetic interactions, no rigorous models exist to describe them. In the following, we briefly describe the common approaches to model nuclear interactions, as adopted by most state-of-the-art MC codes.

2.2.1. General Aspects

In most MC codes, nuclear interactions are handled in two separate steps. First, the probability that a nuclear event happens is sampled, based on nuclear cross sections. Depending on the incident particle and energy, these can be calculated "on-the-fly," i.e., on an event-by-event basis using for instance parameterized formulas and/or physics models, or by "looking-up" a pre-evaluated cross section from a nuclear database. Examples of large nuclear databases are the Evaluated Nuclear Data File (ENDF) (26), the Japanese Evaluated Nuclear Data Libraries (JENDL) (27), and the

Exchange Format (EXFOR) database (28). These contain data of thousands of experiments stored in a given format, which can be accessed from all over the world.

Once an event happens, the outcome must be sampled. This can be done with appropriate nuclear interaction models, or by using information on spectra and angular distributions from evaluated nuclear databases. As we will see in Section 3, different transport codes use data libraries in different energy regions, and for reactions induced by different projectiles.

Nuclear interactions (collisions) can be divided into:

- Elastic collisions: here kinetic energy is conserved, and the nucleus stays intact. This is similar to multiple Coulomb scattering, but now due to strong rather than electromagnetic interactions. Such interactions are not occurring so frequently, but still they cause a certain amount of broadening of the beam, which is simulated with Monte Carlo codes.
- Inelastic collisions: here, a more violent reaction between projectile and target occurs, where total kinetic energy is not conserved. The projectile may knock out secondary particles (protons, neutrons, deuterons, α's, etc.) from the nucleus and break into fragments if it is an ion.

The probability $P(x)$ of *not* having undergone a given nuclear interaction after traveling distance x in a material is given by:

$$P(x) = \frac{N(x)}{N(0)} = e^{-\frac{x}{\lambda_{\text{int}}}}, \tag{8}$$

where $N(0)$ is the number of incident particles, $N(x)$ the number of incident particles after a distance x, λ_{int} the mean free path or interaction length. The latter is given by $\lambda_{\text{int}} = \frac{A_{\text{t}}}{N_{\text{A}}\sigma\rho}$, where σ is the total cross section. Since there are some important differences in modeling the nuclear interactions for proton and heavier ions, we discuss them separately.

2.2.2. Nuclear Interactions of Protons

It is usually assumed that a proton hitting the atomic nucleus initiates a series of nucleon-nucleon collisions, which leads to emission of protons, neutrons, light fragments, and to equilibration of the remnant nucleus. This process can be described as a sequence of three stages (29, 30), displayed schematically in **Figures 4** and **5** (top):

- (Generalized) Intra-nuclear cascade (INC)[1]: this model is commonly used to describe nuclear interactions of nucleons with energies above 50 MeV to hundreds of GeV. Originally proposed in the fourties by Serber and Heisenberg (31), and successfully implemented in the sixties by Bertini et al. (32), it forms the basis for nuclear interactions in most modern MC codes. The basic idea is that the incident particle interacts with quasi-free nucleons in the target nucleus through a series of two-body interactions. The target nucleus is modeled as a Fermi gas of cold, free, nucleons. The nucleons inside this intranuclear medium are accounted for by a nuclear density distribution, a nuclear potential, and the Pauli exclusion principle. This "free" nucleon approach is justified if the De Broglie wavelength λ_{h} of the incident particle is much smaller than the average distance $<d>$ between the nucleons in the material nucleus, and much smaller than the mean free path λ_{N} inside the nucleus:

$$\lambda_{\text{h}} = \frac{2\pi\hbar}{p} \ll \langle d \rangle = \left(\frac{3}{4\pi\rho_{\text{N}}}\right)^{1/3} \tag{9}$$

$$\lambda_{\text{h}} = \frac{2\pi\hbar}{p} \ll \lambda_{\text{N}} = \frac{1}{\sigma\rho_{\text{N}}} \tag{10}$$

where σ is the proton-nucleon cross section and ρ_{N} is the intranuclear density (typically 0.17 nucleons/fm^3 at the center of nuclei). Another requirement for this approach to be valid is that the time in which a collision happens is smaller than the time between the collisions, so that they take place independently. For radiotherapeutic energy ranges, it is not immediately obvious that this approach is valid. For instance, a proton of kinetic energy 250 MeV has $\lambda_{\text{h}} \sim 1$ fm, which is roughly the same as $<d>$, making the condition in Eq. 9 invalid. It turns out that the INC model works surprisingly well at much lower energies than one would expect, thanks to quantum effects that increase the effective mean free path of nucleons in the nuclear medium, like Pauli blocking, nucleon-nucleon correlations, etc.

Once a nuclear interaction happens, the code has to model the outcome. For therapeutic proton energies, only elastic scatterings occur because these energies below the pion production threshold of 290 MeV. The final state particles in the scattering process are called secondaries. The time in which they are produced corresponds to the time-scale of strong interactions: 10^{-22}–10^{-23} s. The secondaries have high energy and can scatter again in the same nucleus, or escape, etc. Not only protons and neutrons can be emitted, but also light nuclear fragments of high energy, through the *coalescence* mechanism, in which emitted nucleons, which are near in phase space, are grouped. All particles are tracked down until they are all below a given energy threshold, usually a few tens of MeV. This process is called an *intranuclear cascade*. The description of this process is highly complex, because all secondaries must be transported through the nuclear medium correctly, requiring accurate descriptions of the nuclear density, quantum effects, the nuclear potential, binding energy, Fermi-motion, and so on. A thorough description of the physics and useful references can be found in Ref. (29, 30).

- Pre-equilibrium: in this stage, the energy of the particles in the cascade has reached a lower limit, usually a few tens of MeV, but the nucleus is not yet in thermal equilibrium. It is commonly modeled in MC codes according to the exciton model (33, 34), a semiclassical model introduced to explain high-energy emitted particles in nuclear reactions. The evolution of the nuclear reaction is also pictured as successive nucleon-nucleon collisions, but within a particle-hole, or "exciton," formalism, where nucleons are excited from within the Fermi sea, leaving a hole. Protons, neutrons, and light fragments (through coalescence) are emitted and the residual nucleus is left in an equilibrium state, with a certain excitation energy shared among the remaining nucleons.

[1]The *intranuclear* cascade refers to the cascade inside the nucleus, as opposed to the *inter-nuclear* transport of a particle from one nucleus to another.

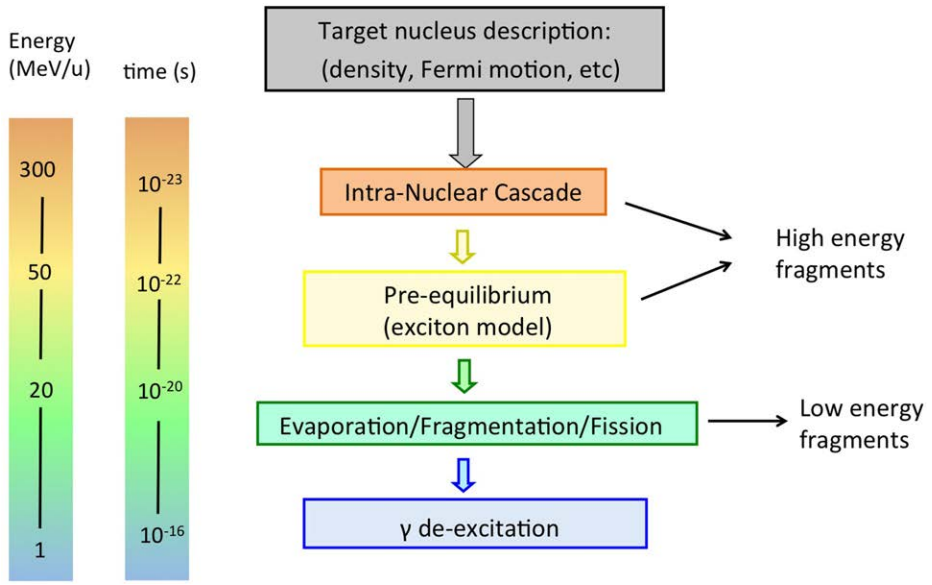

FIGURE 4 | Schematic display of stages in a nucleon-nucleus interaction relevant for radiotherapy, together with time scale and energy of interacting particle.

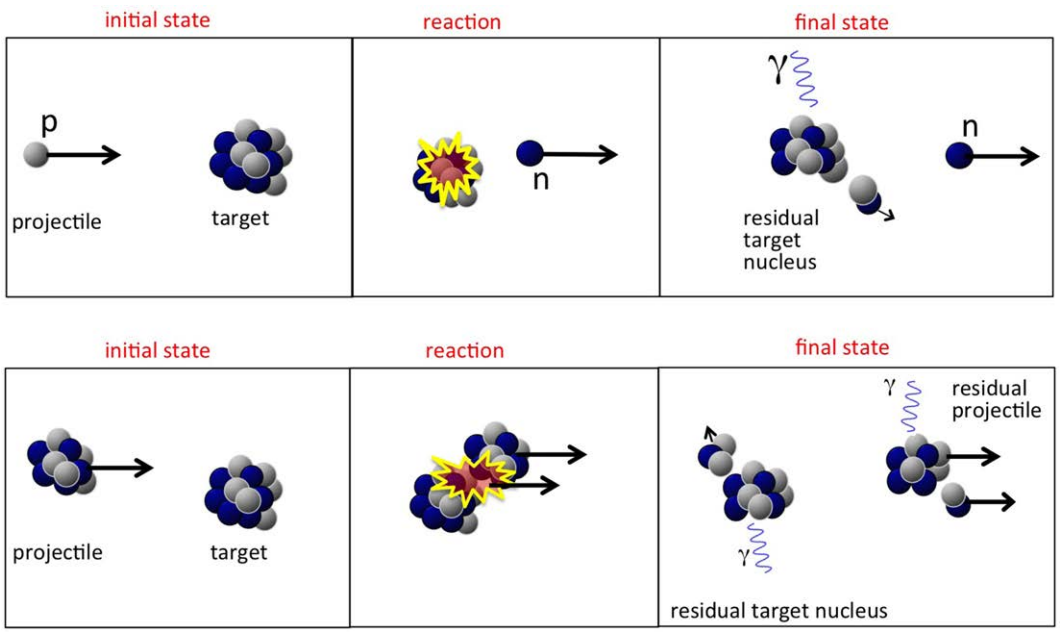

FIGURE 5 | Top: sketch of a possible nucleon-nucleus reaction in proton therapy, whereby a neutron is created. **Bottom:** sketch of nucleus-nucleus reaction in heavy ion therapy, with creation of light fragments.

- De-excitation step: depending on the mass of the target nucleus and on the energy left, the nucleus can dissipate its remaining energy in several ways.
  - Nuclear evaporation according to the Weisskopf-Ewing approach (35). Here, light fragments (α, d^3,H^3, He) with kinetic energies of a few MeV can be successively emitted from the excited nucleus, similar to evaporation from a hot system.
  - Fission: the excited nucleus breaks into two fragments: applies to high Z nuclei only, roughly $Z \gtrsim 65$. Apart from implants, high-Z nuclei are not found in the human body and this process is hardly relevant here.
  - Fermi-breakup (36): this mechanism applies to light nuclei (usually $A \lesssim 16$), where the excitation energy of the excited nucleus may be larger than the binding energy of some fragmentation channels. In this case, the excited

nucleus disassembles in one step into smaller fragments. Fermi-breakup is relevant for radiotherapy, because the human body is mainly composed of low-Z nuclei.
- Gamma emission: What's left after the previous stages is a residual nucleus, with may be still somewhat excited. The final excitation energy is given off through the emission of γ rays.

The first two steps are often referred to as "dynamic" stages of the process, with an overall time scale of about 10^{-22} s, while the last step is "slow," typically $10^{-18}-10^{-16}$ s. It must be noted that the emission of secondary particles in proton therapy is entirely due to the target nuclei, as was displayed in **Figure 5** (top).

2.2.3. Nuclear Interactions of Heavy Ions

The fundamental difference between nucleus-nucleus reactions and nucleon-nucleus reactions is that the incoming nucleons are not free. This has some important phenomenological implications. Most models for nucleus-nucleus interactions are variants of the "abrasion-ablation" model. During the fast stage (abrasion, time scale ~$10^{-22}-10^{-23}$ s), the projectile and target nuclei overlap, resulting in a kind of reaction zone. An excited quasi-projectile is formed with much of the initial velocity, a quasi-target fragment at rest, and several excited light fragments. During the slow step (ablasian, time scale ~$10^{-18}-10^{-16}$ s), the remaining projectile, target and light fragments de-excite by evaporating light nuclei or fragments. It must be noted that in this case *both* target and projectile-nuclei can fragment, as opposed to proton irradiation, where only the target-like nuclei can fragment. This is illustrated in **Figure 5**, showing a sketch of a nucleus-nucleus interaction. The projectile fragments travel further in the forward direction, loosing energy through ionization and undergoing further interactions. These fragments have approximately the same velocities and directions as their mothers, but larger ranges than the primary ions because range scales with A/Z^2. This leads to the characteristic tail beyond the Bragg peak (see **Figure 2**, right). The evaporation products from the projectile fragments are evaporated isotropically in the reference frame of the projectile fragment. The target fragments have short ranges and high stopping power, and their evaporation products are evaporated isotropically in the reference frame of the target fragments.

For describing the dynamic stage of the reaction, various models have been developed, differing mainly in the treatment of the nuclear field affecting the propagation of the particles inside the nucleus.

- Intra-nuclear cascade model, for high-energy nuclei, with energies above about 100 MeV/u. The description is similar to what was outlined above for protons. The highly excited nuclei loose energy through a series of two-body reactions and scattering off quasi-free nucleons. More than one nucleon-nucleus interaction can take place in one nucleus-nucleus collision.
- Quantum molecular dynamics (QMD), for energies from 50 to about 400 MeV/u. This model can be seen as sophisticated form of the INC model. Here, each nucleon is described by a gaussian wave packet, and all nucleons in the projectile and target nuclei are participants in the collision process. By minimizing the Hamiltonian that describes nucleon-nucleon-interactions in the overlapping projectile and target nuclei, it predicts the formation of heavy or light nuclei and secondary protons and neutrons. Because of their complexity, these models are generally much slower in MC codes than the normal INC model.
- Boltzmann-Master-Equation (BME): this is a sophisticated model to simulate the pre-equilibrium stage, describing the thermalization of composite nuclei for projectiles with energies below 100 MeV/u down to the evaporation/fission/breakup stage. Based on a set of time-dependent transport equations, BME describes how a statistical state far from equilibrium evolves to an equilibrium state, through a sequence of two-body interactions and emission of unbound particles (neutrons/protons) and clusters (heavy/light nuclei).

For the de-excitation phase in nucleus-nucleus interactions, the same models as those already described for nucleon-nucleus interactions are used: evaporation, fission, Fermi-breakup, and gamma emission.

2.2.4. Consequences of Nuclear Reactions

There are some important practical consequences of nuclear interactions in hadron therapy:

- Nuclear reactions cause a significant loss of beam fluence. The number of particles left at depth x depends on the inelastic nuclear cross section through the relation in Eq. 8. For instance, for 160 MeV protons hitting a water target, roughly 20% of the incident protons will be lost at the Bragg peak position at about 16 cm (8). For carbon ions, this number is much higher: for 290 MeV/u carbon ions impinging on water, in average 50% of the ions have undergone a nuclear reaction at the end of range at around 16 cm (37).
- The dose distributions are modified. In the buildup region of the Bragg curve, secondary particles contribute considerably to the total energy deposition. Moreover, the height of the Bragg peak is modified. In addition, in case of heavy ion irradiation, dose is also delivered beyond the Bragg peak. Finally, the low energetic secondary particles (including neutrons), which are typically emitted at larger angles, contribute to the "low dose envelope" around the beam. Even though the dose contribution of a single pencil beam is tiny, when combining thousands of them, the dosimetrical and biological effects cannot be neglected (38, 39), because the charged fragments can be particularly damaging (see Section 2.3).
- Various types of secondary particles are produced, which can be used for particle range verification. All three stages of the nuclear reactions contribute to the production of secondaries. The INC and pre-equilibrium stage mostly lead to production of high-energy secondary particles (with energies that may exceed even a hundred MeV), emitted mostly in the forward direction in the laboratory frame. The slow part of the nuclear interaction leads to lower energy secondaries, emitted more or less isotropically in the center-of-mass frame of the mother nucleus. In the case of ion projectile emissions, this implies mostly forward in the laboratory system due to the kinematic

boost. Three types of secondaries are used for range monitoring in hadron therapy:

- β^+ emitting isotopes: among the many fragments produced during irradiation are β^+ emitting fragments. **Table 1** shows the most frequently produced β^+ emitters in a human body treated with proton therapy together with their half-lives and the incident proton threshold energy. Other reactions are listed elsewhere (40). Depending on the value of their half-life, the β^+ emitters emit at a later time a positron, which after traveling a small distance (of order mm), annihilates with an electron in the medium into two coincidence gammas of 511 keV. These can be measured with a PET detector, enabling to extract information about the beam path. In Section 4.2, we come back to the PET method.
- Prompt gammas, which accompany the nuclear reactions along much of the proton path. Prompt photons are emitted with energies ranging from 0 to about 10 MeV. More details and energy spectra will be discussed in Section 4.3.
- Charged fragments are produced, which can possibly be measured and used for verifying particle range, will be discussed in Section 4.4. The secondary particles are usually characterized by energy spectra and double differential cross section measurements, i.e., particle fragment yields as a function of their energy, at different angles.

TABLE 1 | Most frequently occurring nuclear reaction channels for positron emitter production in proton therapy.

β^+-emitter	Half-life (min)	Reaction channel	Threshold energy (MeV)
^{15}O	2.037	^{16}O(p,pn)^{15}O	16.79
^{11}C	20.385	^{12}C(p,pn)^{11}C	20.61
		^{14}N(p,2p2n)^{11}C	3.22
		^{16}O(p,3p3n)^{11}C	59.64
		^{16}O(p,α d)^{11}C	27.50
^{13}N	9.965	^{16}O(p,2p2n)^{13}N	5.66
		^{14}N(p,pn)^{13}N	11.44
^{30}P	2.498	^{31}P(p,pn)^{30}P	19.7
^{38}K	7.636	^{40}Ca(p,2p2n)^{38}K	21.2

Adapted from Ref. (40, 41).

2.3. Dosimetry Considerations

The absorbed dose D in a patient is related to the stopping power by Gottschalk (8):

$$D(\text{Gy}) = 1.602 \times 10^{-10} \times F \frac{dE}{dx} \frac{1}{\rho} \tag{11}$$

where F is the particle fluence in cm^{-2}, ρ the target density in g/cm^3, and dE/dx the stopping power in MeV/cm. For clinical dose calculations in particle therapy, the mass stopping power ((dE/dx)/ρ) is obtained from stoichiometric calibrations curves, which link CT Houndsfield units in each voxel to mass stopping power values, such as proposed by Schneider et al. (42).

To estimate biological effects, considering the physical dose proves to be inadequate because biological damage caused by radiation depends, e.g., strongly on the particle type and energy. Although it is beyond the scope of this article to discuss biological effects, a few concepts are relevant. The linear energy transfer (LET) of a particle beam is the energy deposited locally per unit path length, on microscopic level. Particles with high-LET such as ^{12}C ions cause more lethal damage to the cancerous cells than proton or photon beams. Therefore, each ion type has a relative biological effectiveness (RBE) assigned, defined as the ratio of biological effectiveness of one type of ionizing radiation relative to X-rays, given the same amount of absorbed energy. The RBE in the Bragg peak region is close to 1 for protons (43) and between 3 and 4 for Carbon ions (44). For the latter, it must be included in treatment planning (45).

2.4. Modeling Uncertainties and Validation

Two major uncertainties in calculating the stopping power and particle range in MC codes are the material density and the ionization energy I_e in water. Stopping powers deduced from CT scans suffer additionally from uncertainties like the calibration of the CT scanner, conversion HU to stopping power. The dependence on I_e is only logarithmic, but variations in the evaluated value give range uncertainties of about 1–2% for mono-energetic proton beams (46), and even larger range uncertainties were found for in patient tissues (47). In addition, the accuracy of stopping power and range calculation depends also on other factors, like the accuracy of the knowledge on the particle energy of the machine, the precision and accuracy of the measurement device, the step sizes in the MC code, the accuracy of the beamline description, the treatment head, and so on.

Stopping power models in Monte Carlo codes used in medical physics are usually benchmarked with standard quality assurance (QA) in-house dosimetry measurements on homogeneous and heterogeneous targets, typically performed with ionization chambers, calorimeters, and Faraday cups. With the latter, it is possible to measure the longitudinal charge distribution of primary and secondary particles, and to separate the nuclear interaction component from the electromagnetic component. Lateral scattering models can be validated by measuring lateral dose profiles. The validation of MC codes at therapeutic energies is important, because many MC codes have originally been developed for high-energy physics, pertaining to different energy regions.

Uncertainties in modeling nuclear interactions come mostly from uncertainties in cross sections, whereby total cross sections and double differential (energy and angle) cross sections are most relevant. The size and impact of these uncertainties is strongly dependent on the purpose of the measurement: dosimetry, shielding, non-invasive range monitoring, and so on. Especially when parameterizations used in MC codes are based on a few measurements or when no data are available at all and models must be relied on, uncertainties can be substantial, as is the case for instance for production of β^+ emitters. Additional uncertainties apply when tissue composition is deduced from CT scans. We come back to this in Section 4, where non-invasive range verification techniques are discussed. Uncertainties on total cross section calculations are quantified by Sihver et al. (48), presenting comparisons of various nuclear interaction models with each other and with experimental data in an energy range relevant for radiotherapy.

Although dosimetry can certainly help to validate nuclear interaction models, it is often impossible to perform direct

experimental validation of the nuclear models in MC codes. A first validation of nuclear interaction models, which can be done in-house, is Faraday-cup measurements. Charged fragment production is generally validated with experimental data collected over the years of various thin and thick target measurements, including both integral and differential quantities. An example of a recent experiment contributing to the collection of relevant data is the Fragmentation of Ions Relevant for Space and Therapy (FIRST) experiment (49), aiming at cross section measurements for projectile-target combinations and energies relevant for ion beam therapy. Selected examples of the validation of MC codes relevant for non-invasive range monitoring will be given in Sections 3 and 4.

3. MC Codes

In this section, we summarize relevant features of the three most frequently used MC codes in hadron therapy studies: Geant4, FLUKA, and MCNP6/X. For each, we discuss transport and interactions, as well as the validation for hadron therapy simulations: depth-dose profiles, nucleon-nucleus interactions, and nucleus-nucleus interactions. While we describe in this section the general aspects like dose calculations and secondary particle production, in Section 4 we will narrow the focus to range monitoring. Extensive reviews about the general use of MC codes in radiotherapy can be found elsewhere (10, 11).

3.1. FLUKA

FLUKA (50, 51) (FLUktuierende KAskade) is a general purpose MC generator for the transport and interactions in matter of particles from a few keV to cosmic ray energies. Originally developed for high-energy physics, it is nowadays widely used for shielding applications, detector design, cosmic ray showers, and medical physics. The code is written in FORTRAN.

3.1.1. Particle Transport and Interactions

Charged particle transport is done through a Multiple Coulomb scattering algorithm (52) based on Moliere's theory, with Fano corrections, and supplemented by an optional single scattering method. Ionization energy losses are based on statistical approach reproducing ionization and fluctuations therein (53, 54), including δ ray emission and energy straggling.

Hadron-nucleus interactions are modeled in FLUKA with the PEANUT (Pre-Equilibrium Approach to NUclear Thermalization) model (30, 51), which is valid in a very broad energy range, from reaction threshold up to a few tens of TeV. This model simulates the first two stages of nuclear reactions described in Section 2.2.2. The intranuclear cascade (INC) stage includes many sophisticated features, including nuclear potential effects like curvature of the path, and quantum effects, like Pauli blocking, nucleon-nucleon correlations, etc. The pre-equilibrium stage is based on the exciton formalism from Blann (34). A coalescence algorithm is used for emission of composite projectiles. PEANUT ends when all particles are below a certain threshold, of the order of 10–20 MeV. The final relaxation step in FLUKA includes models for simulating nuclear evaporation, fission, Fermi-breakup ($A \leq 17$), and gamma emission. Recently, a direct deuteron formation mechanism has been added in FLUKA (55). Cross sections are based on parameterized fits and tabulated data, when available. Otherwise, they are calculated with appropriate models. For low energy neutron transport, FLUKA is linked with ENDF and JENDL.

Nucleus-nucleus interactions are handled in FLUKA through interfaces to event generators, which simulate the dynamic part of the nucleus-nucleus interaction. Between 100 MeV/u and 5 GeV/u, a relativistic quantum molecular dynamics (rQMD) model is used (56). Below 100 MeV per nucleon, nucleus-nucleus collisions are treated following the BME theory (57). These models are all coupled to the internal FLUKA models for the slow phase of the interaction through evaporation/fission/breakup and gamma emission. For patient simulations, 3-D voxel geometries like CT scans or other 3-D descriptions of human body can be read by FLUKA. FLUKA Advanced InteRface (FLAIR) is a modern user-friendly interface to FLUKA, which facilitates editing input files, execution of the code, and visualization of the results.

3.1.2. Validation

Depth-dose profiles are important to check the validity of both the electromagnetic and hadronic physics. FLUKA simulations have been thoroughly validated with experimental depth-dose data for protons and heavy ions (19, 51, 58). An example for protons is given in **Figure 2** (left), showing the comparison of measured depth dose profile and the FLUKA simulation for various energies.

Hadronic interactions in FLUKA have been extensively benchmarked against a variety of experimental data (51, 55, 59, 60). An example relevant for proton irradiation is shown in **Figure 6** (left), showing the simulated and measured secondary neutron double differential energy spectra, resulting from 160 MeV protons impinging on a Zr target. Still for proton irradiation, **Figure 6** (right) shows the validation of the production of the β^+ emitter ^{11}C from proton irradiation of a ^{12}C target. Also, longitudinal charge distributions of proton beams measured with Faraday cups have been compared with FLUKA simulations to test the nuclear models (54).

For ^{12}C irradiation, **Figure 7** nicely demonstrates the reliability of the nucleus-nucleus interaction models. In this study by Mairani et al. (60), simulations were compared with measurements (63) of secondary particles behind a 15.9 cm water target, irradiated with 400 MeV/u ^{12}C-ions. The transmitted primary beam and the angular distribution of the secondary fragments were measured. This plot demonstrates that the MCS model together with the nuclear interaction models describes absolute yield and angular distribution of the ^{12}C beam and the produced fragments.

The performance of FLUKA to simulate the specific reaction products like β^+ emitters and prompt γ's will be shown in Section 4.

3.2. Geant4

Geant4 (64) is an open-source modern MC toolkit for simulating the passage of particles in matter, written in C++. Originally designed for the LHC experiments, its use has been extended to medical physics, space science, nuclear physics, accelerator physics, and so on. A set of standard physics settings for proton therapy was proposed by Jarlskog and Paganetti (65), but this

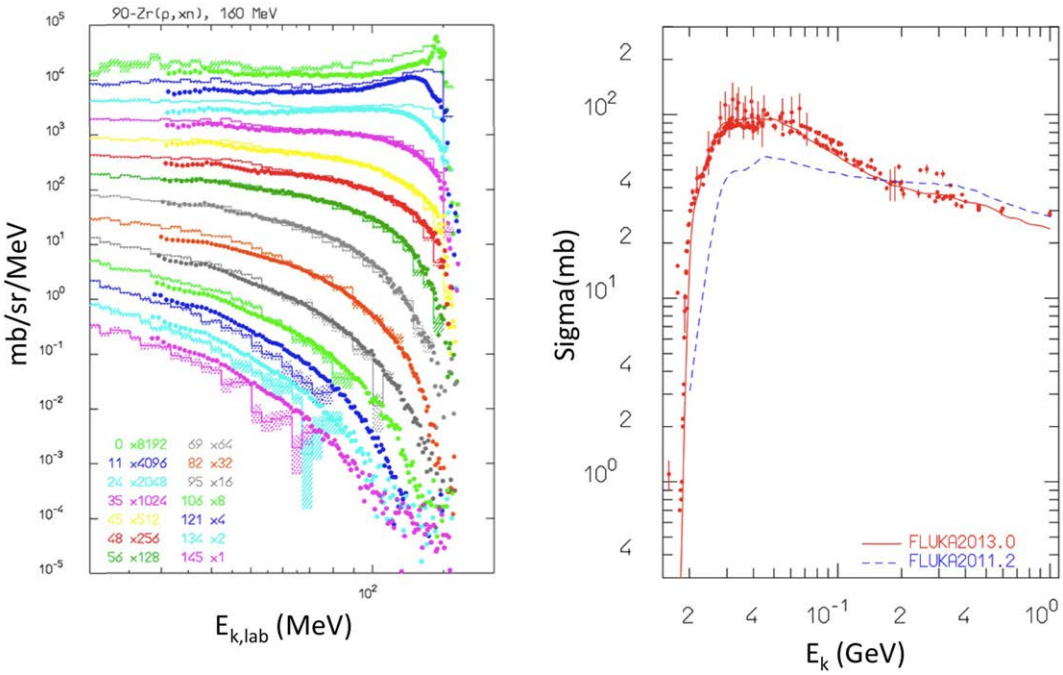

FIGURE 6 | Left: double differential energy spectra of emitted neutrons at different angles, from 160 MeV protons impinging on a Zr target. Histograms are FLUKA results, points are experimental data from Ref. (61, 62). Reproduced from Ref. (51), with permission. **Right:** cross section for $^{nat12}C(px)^{11}C$ production from protons irradiation as computed with fluka2013.0 (red, upper curve), and fluka2011.2 (blue, lower curve) compared with data retrieved from the EXFOR library (28). Reproduced from Ref. (55), with permission.

prescription has been modified. Below we discuss the most relevant Geant4 physics models that are commonly used for hadron therapy simulations. Details and references can be found in the Geant4 manual (64) and in dedicated lectures (37).

3.2.1. Particle Transport and Interactions

Electromagnetic energy losses for hadron therapy studies are usually based on the so-called "electromagnetic standard package option 3" list. Protons with energy above 2 MeV are in Geant4, simulated according to the Bethe-Bloch formula, while below 2 MeV stopping power parameterizations are used. The multiple scattering model is based on Lewis theory (22). For range straggling, appropriate fluctuation models are provided.

Concerning hadronic interactions, Geant4 offers various models. Starting with protons, the dynamic part of inelastic nuclear interactions can be simulated with the Binary Cascade Model (BIC). This model simulates the INC stage described in Section 2.2.2 and includes relevant nuclear potential effects and quantum effects, similar to FLUKA. This can be followed by a pre-equilibrium stage ("precompound" model), which is based on the exciton formalism from Griffin (33). Geant4 also offers alternative models to BIC: the intra-nuclear cascade Liège (INCL) model from Boudard et al. (66), and the Bertini-model (32), differing in many aspects, including the treatment of the nuclear potential, nuclear density, and coalescence. For simulating the de-excitation step, Geant4 includes several possibilities: standard evaporation model based on the Weisskopf-Ewing approach (for emissions of nucleons and light fragments, up to ^{4}He), generalized evaporation model (GEM, including also emissions of heavier fragments), fission, multi-fragmentation (for nuclei with excitation energy above 3 MeV/u), Fermi-breakup ($A < 17$ and $Z < 9$), and gamma emission. To evaluate nuclear cross sections, Geant4 is linked to various nuclear databases, including ENDF, and when no data are available calculations are used.

For heavier projectiles like ^{12}C, Geant4 provides various possibilities. The dynamic stage of the nucleus-nucleus interactions can be simulated with the G4BinaryLightIonReaction (BLI) model, a semi-classical INC model, but extended to take into account that more than one nucleon participates in the reaction. Geant4 also offers the sophisticated G4QMDReaction model, a newly implemented nucleus-nucleus interaction model based on QMD. Alternatively, the INCL++ (Intra-Nuclear-Cascade Liège) model can be used. All of them must be coupled to the aforementioned de-excitation models.

3.2.2. Validation

Starting with protons, good agreements between measured and simulated depth-dose profile were reported in Ref. (67, 68). Geant4 was also shown to satisfactorily describe lateral beam widening (68), although others reported disagreements (67). Hadronic interactions were also validated against measured Faraday cup data (65). For carbon ion therapy, various groups reported good agreements of dose-depth profiles, including the fragmentation tail (20, 69–71), an example of which is shown in **Figure 2**.

Several authors investigated the validity of nuclear fragmentation models for particle therapy. Much work has been reported

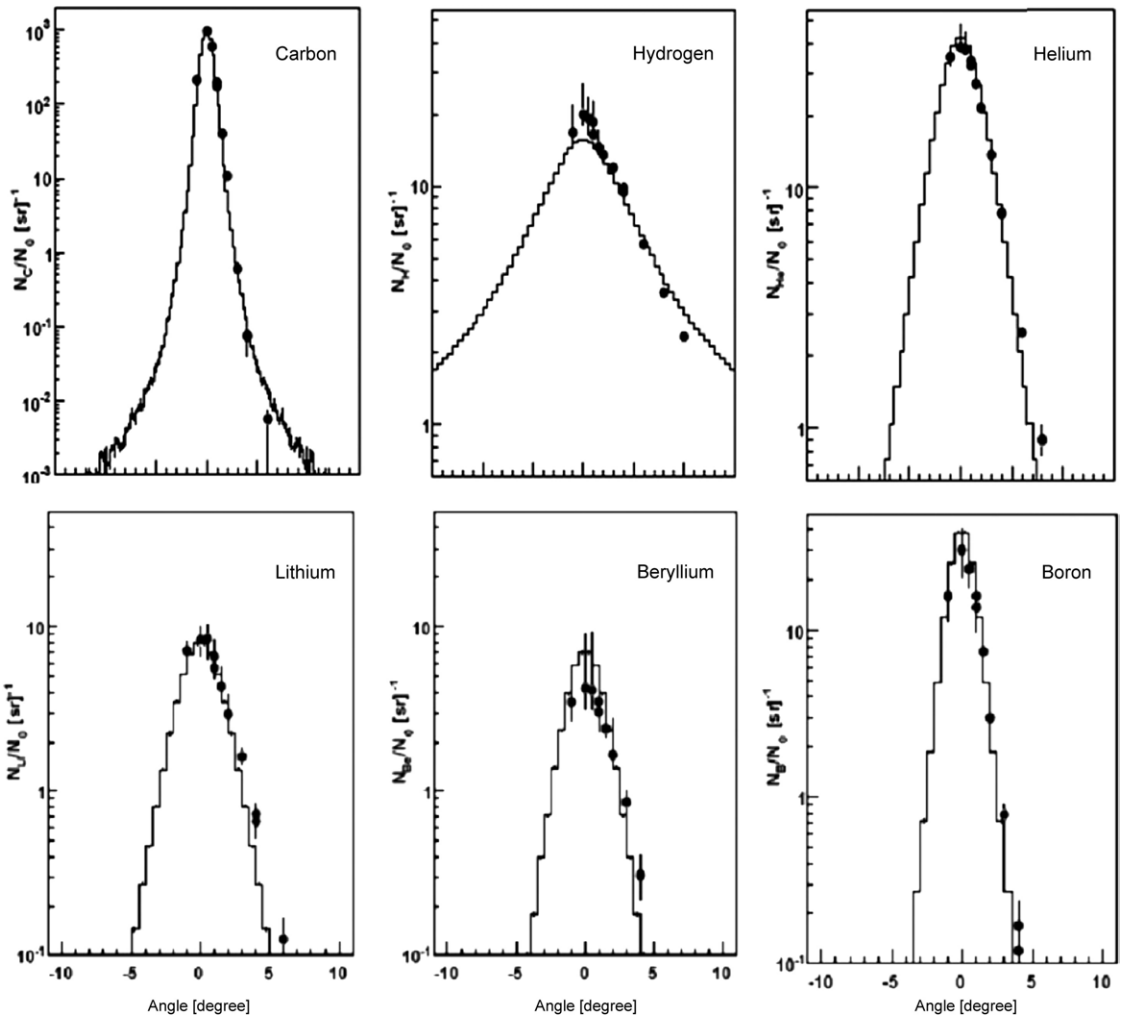

FIGURE 7 | Measurements (63) (circles) and FLUKA simulations (histograms) of angular distributions of a carbon beam (left top) and secondary fragments (others) measured behind a 15.9 cm water target, irradiated with a 400 MeV/u ^{12}C ions. Reproduced from Ref. (60), with permission.

by Pshenichnov et al. (69, 72, 73), making use of a dedicated framework MC model for Heavy-Ion Therapy (MCHIT). Comparisons between simulated and measured depth-dose curves, nuclear fragmentation build-up curves, angular distributions, and yields of secondary particles (including β^+ emitters) were performed for protons and heavier ion beams impinging on homogeneous targets, leading to improvements in the nuclear modeling in Geant4. MCHIT is also currently being used for validating microdosimetric models (74).

More recently, validations of the newly implemented Geant4 models relevant for nucleus-nucleus interactions have been performed. Böhlen et al. (59) reported a good agreement of the QMD model with data in describing nuclear fragmentation in carbon irradiations. Also, Robert et al. (75) studied depth-dose profiles and secondary particle production in proton and carbon therapy for Geant4 and FLUKA. Comparing depth-dose profiles and energy spectra at various angles of charged particles and prompt gammas, they identified the main differences between the codes. Absolute yields were found to differ by roughly 20 and 100% for β^+ emitters and prompt photons. Also, De Napoli et al. (76) and Dudouet et al. (77) presented comparisons between measured and simulated double differential energy spectra, including the BIC, QMD, and INCL++ models, for mono-energetic carbon beams impinging on various thin targets. None of the models could satisfactorily describe yields, angular and double differential energy distributions.

Geant4 validation studies for β^+ and prompt gamma emissions will be discussed in Section 4.

3.2.3. Geant4-Based Applications

Because the high level of experience required to use Geant4 has proven to be a barrier for clinical usage, several user-friendly tools making use of the Geant4 physics have been developed.

Geant4 Application for Emission Tomography (GATE) (78) is an open-source MC framework making use of the Geant4 libraries. Originally dedicated to PET and SPECT systems, GATE also offers the possibility for hadron therapy simulations, including *in vivo* range monitoring using PET (79). GATE allows

simulating very complex geometries like commercial PET or SPECT scanners, time dependent quantities phenomena, and it also offers image reconstruction tools.

Another example is Tool for Particle Simulation (TOPAS) (80), a simulation tool dedicated to proton therapy simulations. Recently, an extensive validation of TOPAS has been performed for proton therapy treatments with the passive scattering technique at MGH (81), based on routinely performed quality assurance (QA) measurements (lateral and longitudinal dose measurements, and so on). TOPAS has been used for range verification studies with prompt gamma imaging, as will be described in Section 4.3.2.

Particle therapy simulation framework (PTSIM) (82) is a Geant4 software tool which can be used to model a complete hadron therapy treatment, including beam delivery system, a treatment head, and patient data obtained from CT images. It has been used for carbon therapy simulations with the facilities in Japan.

Finally, Geant4-based architecture for medicine-oriented simulations (GAMOS) (83) is another Geant4-based simulation framework aimed at nuclear medicine simulations, including hadron therapy applications.

3.3. MCNPX/6

3.3.1. Particle Transport and Interactions

Monte Carlo N-Particle version 6 (MCNP6) (84) is a general purpose MC generator for simulating radiation transport and interactions in matter. MCNP6 is the result of merging and extending the older MCNP5 (85) and Monte Carlo N-Particle eXtended (MCNPX) (86) codes, written in FORTRAN.

Continuous ionization energy losses are modeled analytically according to the Bethe-Bloch formula, using ionization potentials recommended by the ICRU data. Energy straggling is based on the Vavilov straggling model (87), and multiple scattering is based on Rossi's theory (88).

At present, MCNP6 has 5 different models for simulating nuclear interactions for medical physics (84): CEM03.03, Bertini, INCL+ ABLA, LAQGSM03.03, and ISABEL. For proton therapy simulations, the Cascade-Exciton Model (CEM) is currently recommended and is the default option. This model, originally proposed over 30 years ago in Dubna (89) and refined over the years, incorporates all three stages of nuclear reactions described in Section 2.2.2. The INC description includes many important aspects such as quantum effects, nuclear binding energies, coalescence, and so on. The pre-equilibrium stage is modeled with the exciton formalism, and evaporation/Fermi-breakup/fission can be used for the final relaxation step. The second model, Bertini (32), was successfully used in the past for proton therapy simulations (90–92), but performs worse in describing angular distributions of secondary particles, and is currently not maintained anymore. The third model, Intra nuclear-cascade Liége (INCL) model (66), can alternatively be used in combination with the ABLA evaporation model, but is slower.

To simulate nucleus-nucleus interactions in heavy ion therapy simulations like ^{12}C, the fourth model, Los Alamos version of the Quark Gluon String Model (LAQGSM) (29) is suggested. As the CEM model, LAQGSM describes all three stages of nuclear interactions, and is valid over a large energy range even up to 1 TeV. However, the description of INC stage is entirely different from that in the CEM model, taking into account the time of interactions, the so-called "trawling effect," etc. (see more details and further references in (29)). LAQGSM models the interactions of fast cascade particles (called "participants") with nucleon spectators of both the target and projectile nuclei and includes also interactions between two participants. The modeling of the pre-equilibrium stage and final relaxation stage is similar to the CEM model. Finally, the fifth nuclear interaction model, ISABEL, was used in the past for simulating nucleus-nucleus interactions, but is no longer updated.

Below 150 MeV, MCNP6 uses nuclear data libraries (26, 93) evaluated from measured cross section data and calculations with appropriate nuclear models. At higher incident energies, nuclear reaction models mentioned above are used.

Concerning the usage of 3-D patient descriptions, MCNP6 includes the possibility to import 3-D voxel geometries like CT scans.

3.3.2. Validation

Longitudinal and lateral dose distributions in MCNPX and MCNP5 have been validated for proton therapy by various research groups (90–92). The modeling of nuclear interactions with MCNP6 with the CEM and the LAQGSM models has been recently extensively validated by Mashnik et al. (94–96). Fragmentation measurements from a vast set of recent and older experiments were compared to MCNP6 simulations, as documented in comprehensive Validation and Verification (V&V) Los Alamos reports (94, 95). Comparisons included total cross sections and double differential energy spectra for neutrons, protons, and light fragments (up to ^{4}He) produced during irradiation of protons, light and heavy ions impinging on many different homogeneous targets. **Figure 8** demonstrates an example of the validation, showing a measured double differential neutron spectrum for a thin ^{12}C target bombarded with a 290 MeV/u ^{12}C beam, together with MCNP6 predictions with the LAQGDM model. A very good agreement was obtained.

Relevant for proton therapy simulations is a recent validation of the CEM model in proton-induced fragmentation reactions on low-Z targets (96), focusing on intermediate proton energies (10 MeV $<$ 1 GeV). For various fragment types produced during nuclear reactions in different targets, measurements of total inelastic cross sections, yields, excitation functions, and double differential spectra of products were compared with simulations. Overall, very satisfying agreements between data and MCNP6 were obtained.

3.4. Other MC Codes

Here, we will only briefly report on other MC codes that are used for particle therapy.

Particle and Heavy Ion Transport code System (PHITS) (99) is a general purpose MC particle and heavy ion transport code written in FORTRAN, which can be used for simulating proton and heavy ion treatments. Ionization processes are simulated with the continuous slow down approximation. For low energy neutron

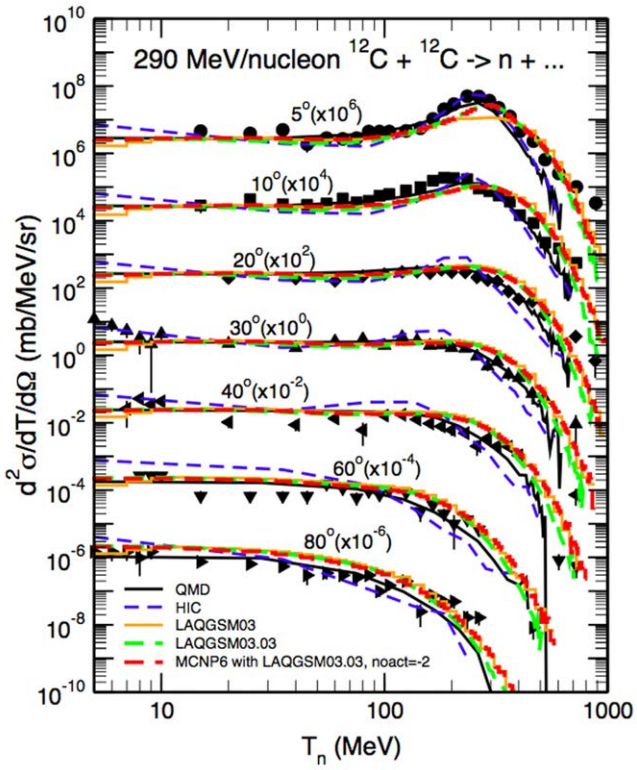

FIGURE 8 | Experimental neutron spectra (97) at different angles from a thin 12C target bombarded with a 290 MeV/u 12C beam compared with Japanese QMD calculations (98), the Bertini INC model (32) coupled to an evaporation model (HIC), the Los Alamos version of the Quark-Gluon String Model used as a stand alone code LAQGSM03.03 [see Ref. (29)], and with MCNP6 using the LAQGSM03.03 event-generator [see Ref. (94)]. Reproduced from Ref. (94).

induced reactions, PHITS employs the cross sections from the JENDL nuclear data library. For nuclear reactions of higher energy neutrons and other particles, various sophisticated models are available, including the Microscopic Transport Model (JAM), the JAERI Quantum Molecular Dynamics Model (JQMD), the INCL model, and the INCL-ELF model. For details and references about these models and their validation, see Ref. (99). PHITS can also determine profiles of all secondary particles, including prompt γ's, and perform microdosimetric calculations.

HIBRAC is a one-dimensional simulation tool developed by Sihver and Mancusi (100) in FORTRAN, used in various clinics worldwide in treatment planning for ion beam therapy. The code is based on semi-empirical total and fragmentation reaction cross section formulas for proton-nucleus and nucleus-nucleus reactions, and models are used for calculating stopping power and energy straggling. The code can accurately predict fluence, dose, dose-average LET, track-average LET, and energy distributions as a function of the penetration depth of light ion beams in any solid or fluid target material. Predictions of the code have been validated with experimental data (depth-dose profiles, fluence) from the GSI and Chiba facilities. HIBRAC can also be used for predicting PET profiles (101), albeit only in 1-D.

SHIELD-HIT (102) is another MC code dedicated to ion therapy. It is a FORTRAN written code that is derived from the SHIELD code, originally developed at the Joint Institute for Nuclear Research in Dubna, Russia. It is possible to transport nuclei, nucleons, anti-nucleons, pions, and kaons up to 1 TeV/u and down to 1 MeV/u. It includes all processes relevant for electromagnetic interactions (straggling, MCS, ionization losses) and nuclear interactions. Nuclear fragmentation is handled by the many stage dynamical model (MSDM), simulating all three stages in nuclear reactions. The SHIELD-HIT code is primarily used in particle therapy for calculation of stopping power ratios, fluence correction factors, and anti-proton calculations.

Another MC code developed for treatment planning is the Voxel Monte Carlo for proton therapy (VMCpro) code (103), a fast MC framework, also written in FORTRAN. VMCpro simulates proton transport in human tissue based on a condensed history technique. The code is based on various approaches and parameterizations, for instance a simplified multiple coulomb scattering algorithm and density scaling functions instead of actual material compositions. Nuclear interactions are treated as corrections to electromagnetic processes. Valid results for depth-dose predictions were obtained with VMCpro, and being order of magnitude faster than for instance FLUKA and Geant, the code is a valuable tool for treatment planning.

PENELOPE is a MC code written in FORTRAN that was originally limited to the transport and interactions of photons, electrons, and positrons. It has recently been extended to protons (104) (PENH). The main motivation for the extension is to provide the medical physics community with a fast and reliable MC code for instance to perform dose calculations from treatment plans. Dose distributions obtained with PENH have been benchmarked with Geant4 (GATE) and FLUKA predictions (104).

4. MC Signal Modeling for *In vivo* Range Verification

4.1. Introduction

In this section, we discuss the three most widely researched modalities for *in vivo* non-invasive hadron therapy verification, which exploit secondary particles produced in nuclear reactions: PET (Section 4.2), prompt gamma (Section 4.3), and charged particle imaging (Section 4.4). For each of them, we introduce the technique and briefly discuss different detector types. The latter is relevant here, because it can affect the way the MC predictions are made. Furthermore, we describe examples of the MC predictions and validation procedures adopted by various research groups, and touch briefly on clinical challenges related to MC simulations. Because the focus of our review is on the physics and MC modeling, we do not discuss logistical, technical, and economical issues related to clinical integration, image reconstruction, signal analysis, clinical interpretation of detected range deviations, nor do we discuss the expected sensitivity of the techniques. These are discussed in other works (4, 10, 11). A brief comparison of the three techniques will be presented in Section 5.

Finally, other imaging methods that are currently investigated for treatment verification include proton radiography (105), proton tomography (106), and ionoacoustic imaging (107); however,

we do not consider them here. The same applies for positron emitting probing beams, such as for instance investigated at the Chiba facility (108).

4.2. PET-Based Treatment Verification

4.2.1. Treatment Monitoring Strategies

In Section 2, we have seen how nuclear reactions of incident protons and nuclei give rise to the production of β^+ emitting fragments. By detecting the two 511 keV photons by positron annihilation, spatial distributions of the β^+ decay points can be obtained. Often one-dimensional profiles along the beam-axis are chosen to display the activity along the beam path. In **Figure 9**, such profiles are displayed for various incident beam types impinging on a PMMA target. Normalization is arbitrary here. Two things can be noticed. First, the shape of the β^+ activity profiles of light beams is remarkably different from those of heavier nuclei. While for the p, ^{3}He, ^{7}Li ion beams, the induced activity is only due to positron-emitting *target residuals* produced all along the beam path; for the ^{12}C and ^{16}O beams, there is an additional contribution in the activity from β^+ emitting *projectile residuals* when they stop, near the end of range, explaining the activity peak. Second, we see that no direct correlation exists between β^+-activity and the dose, which is not surprising, being based on different physics processes. Nevertheless, by comparing the measured PET data with reference distributions, it is possible to estimate whether the dose was delivered successfully. Large discrepancies between expected and measured PET data indicate problems in dose delivery. Such reference distributions are generally made with MC simulations on the basis of the treatment plan, time-course of irradiation, the patient CT, detector geometry, and imaging procedure (109). The application of PET to hadron therapy dose monitoring has been studied for about 20 years and is currently a well-established, although not widely used, method. Recent reviews can be found for instance in Ref. (4, 41).

PET data acquisition strategies are usually categorized as follows:

- In-beam data acquisition, where the PET system is integrated in the beam delivery system and data are acquired during or immediately after irradiation inside the treatment room (109–117). Data-taking during irradiation is attractive, because this allows detecting activity from ^{15}O and other short-lived isotopes, and avoids having to deal with biological signal washout in the human body. Moreover, no repositioning of the patient is necessary. On the other hand, disadvantages include the high costs for integration into the treatment site, geometrical limitations on the detector, and the associated image artifacts. A special challenge is acquisition during beam extraction, where background from random coincidences tends to paralyze the PET detectors (118). The most commonly chosen solution in synchrotron facilities is to take data during spill-pauses, although at cyclotrons data-taking during beam extraction was shown to be feasible (115, 119).
- In-room data acquisition, where data are acquired quickly after irradiation with a full-ring PET detector installed in the treatment room. This methodology was explored at MGH (120, 121). The advantage is that signal washout is reduced, and problems related to patient transport and repositioning are minimized. Disadvantages include a longer treatment room occupation time and difficulties in co-registration of the PET image with the planning CT.
- Offline data acquisition, where data are acquired with a full-ring PET after patient irradiation outside the treatment room (122–125). The advantages are the low costs and the complete angular coverage. However, the delay between particle delivery and monitoring greatly limits the offline method. Signal decay and biological washout processes rapidly cause signal degradation, which is difficult to model accurately (124, 126).

4.2.2. PET Systems for Treatment Verification

Depending on the data acquisition strategy, different detectors can be used for PET-based treatment monitoring.

- Planar PET systems, for in-beam monitoring. A planar configuration was used at GSI for in-beam PET monitoring of patients treated with ^{12}C ions (109, 111), using data acquired during spill-pauses and after treatment. Planar configurations have also been developed in Japan at Chiba (128) and have been used to monitor patient treatments with ^{12}C at the Kaswhiwa facility (113). Moreover, a compact planar PET system enabling data acquisition during and after treatment has been developed at INFN and was tested on phantoms at CATANA (115, 119) and CNAO (116). Adding TOF information could help in reducing background to signal noise (129).
- Full-ring commercial PET scanners, which can be used only for monitoring after treatment. Such scanners have been used for in-room (120, 121) and offline data acquisition (122–125).
- Alternative geometries: ring-shaped PET systems are being investigated in Japan for in-beam data acquisition, including a dual-ring (130) and a full-ring (114) PET system, cut at a slant angle. The latter geometry is promising, because it would represent the first in-beam system with complete angular acceptance. Also, C-shaped and partial ring PET systems were studied with GATE for in-beam PET (131).

4.2.3. Prediction of β^+ Activity

Many different approaches have been used in research and clinical studies for predicting the PET activity signal. We describe them for proton, carbon, and heavier ion therapy.

Starting with protons, pioneering studies performed by Parodi et al. (122, 132) for offline PET monitoring of proton treatments at MGH were based on FLUKA simulations. Rather than relying on the internal FLUKA nuclear cross sections, the activity was calculated by folding the proton track length with external experimental cross section data (132). For activity predictions in patients, correction factors for biological washout were applied *a posteriori* on the basis of the CT scan, where regions with low, intermediate, and high perfusion were identified. The reliability of the MC predictions turned out to depend on treatment site, mostly because of problems in modeling biological washout (124).

More recent studies focusing on in-room proton therapy at MGH used Geant4 for predicting PET activity distributions (120, 121, 133). First, they compared PET measurements on homogeneous targets with MC activity predictions using different cross section data libraries. The cross section values that best described

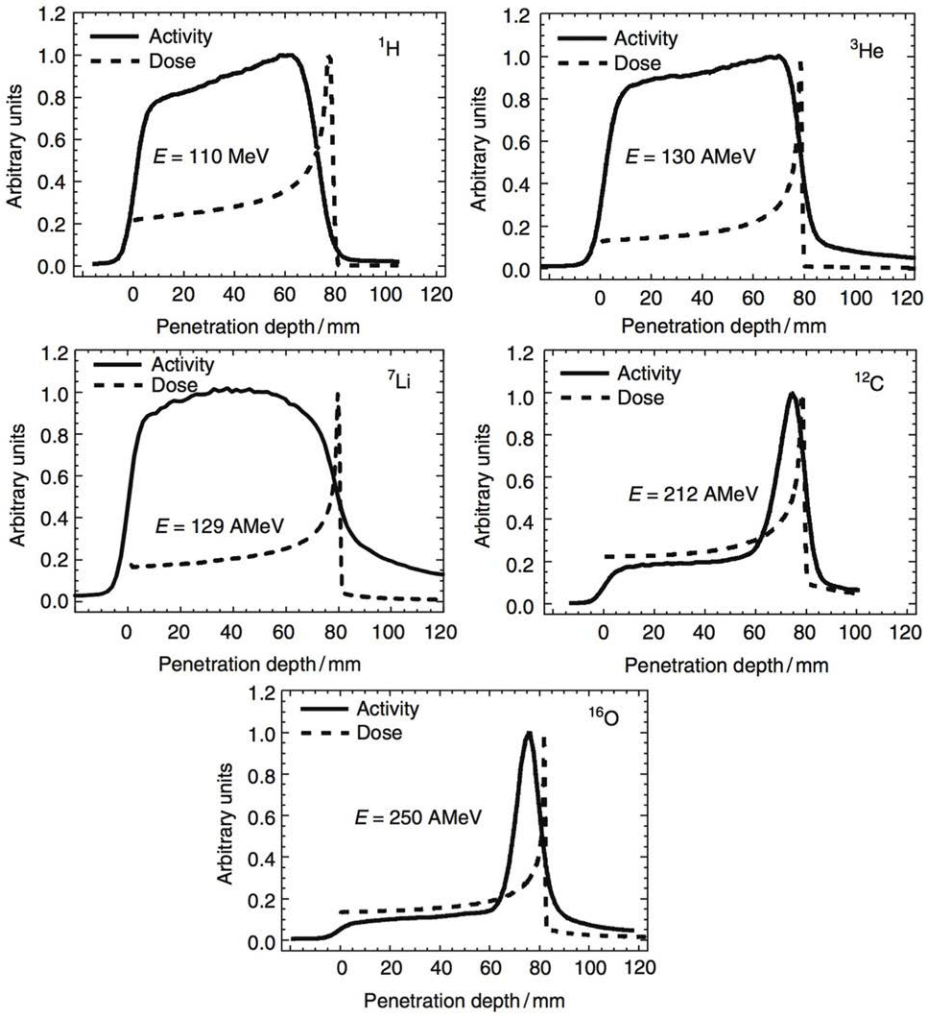

FIGURE 9 | Measured positron emission activity together with the dose distribution for irradiation of a PMMA target with different projectiles: protons, ^{3}He, ^{7}Li, ^{12}C, and ^{16}O. Reproduced from Ref. (127), with permission.

the measurements were chosen for the patient MC simulations (133). Including this tuning, the Geant4 predictions were successfully used for patient monitoring (120, 121).

A similar procedure was studied by Bauer et al. (134) for offline PET data acquisition in proton therapy at HIT. FLUKA was used to investigate the effect of directly including in-house activity measurements for homogeneous materials into the simulation. Fine-tuned cross sections turned out to reduce uncertainties, improving the modeling of proton-induced positron-emitter production.

Kraan et al. used FLUKA to predict the PET activity measured in homogeneous targets during and after proton irradiation with an in-beam PET system at the CATANA cyclotron (119) and at the CNAO treatment facility (116). **Figure 10** shows an example of measurements performed at CNAO for irradiation of a PMMA phantom with a homogeneous proton beam (top figures) and a SOBP (bottom figures), together with the FLUKA simulation, for various acquisition time intervals. A good agreement between data and MC simulations was found.

In carbon irradiation, the signal modeling is somewhat different, and other approaches have been applied. For the early PET studies on patients treated with carbon ions at the GSI facility (109, 111), a dedicated MC simulation tool (POSGEN) was developed by Pönisch et al. (135) for calculating the activity. A simplified and fast simulation approach was applied, based on the assumption that the dominant contribution to the β^+ activity profile comes from projectile residuals. The calculation was split in two steps: a one-time step to calculate the activity from target residuals assuming a homogeneous medium, and a patient and fraction specific step to calculate the projectile contribution. The code used relied on cross section models developed by Sihver et al. (100) to handle nuclear interaction processes. It was validated and applied clinically for the in-beam monitoring project at GSI (110, 111, 136), and also used for modeling the PET activity for moving targets (137).

Following the improvements of the internal nuclear models in FLUKA, Sommerer et al. (138) assessed the performance of FLUKA by comparing measured and simulated activity profiles

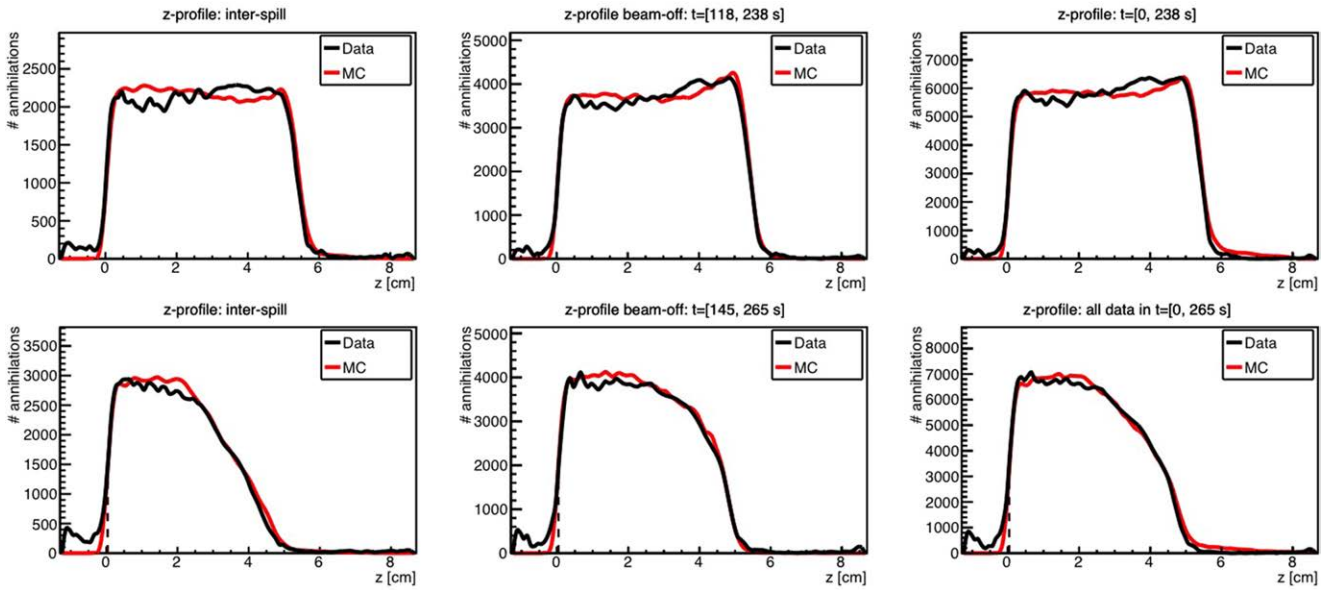

FIGURE 10 | Top: 1-D profile along the *z*-axis of the measured (black) and MC simulated activity (red) induced by a 95 MeV proton beam impinging on a PMMA target during 118 s. **Bottom:** the same but for the 2 Gy treatment plan, delivered in 145 s. Inter-spill (left), beam-off (center), and all together (right) are displayed separately. Adapted from Ref. (116).

in homogeneous target irradiated with carbon and oxygen beams. The code was extensively benchmarked with data and has been used for offline-treatment verification after carbon ion therapy of patients at HIT (125, 139). **Figure 11** shows an example of a measured and MC predicted activity profile along the beam-axis for a glioblastoma patient treated at HIT.

Still regarding carbon treatments, Pshenichnov (70, 72, 73) has assessed the performance of the Geant4 MC code to describe PET activity measurements at GSI, using the dedicated MCHIT tool described in Section 3.2.2. However, these studies dealt mainly with homogeneous targets, and were not extended to patients.

Various groups have compared β^+ activity predictions from different MC codes (101, 140, 141) with each other and with measurements, including FLUKA, Geant4/GATE, MCNPX, SHIELD-HIT, PHITS, HIBRAC, and POSGEN. These studies report large differences up to 50% in yield between the codes and the measurements, but mostly because simulations were based on different cross section models, confirming the need to use experimental cross sections in MC codes, when possible.

For other ions than protons and carbon, only few MC studies for PET-based treatment monitoring were performed. Pshenichnov et al. (73) used Geant4/MCHIT to calculate the activity induced in ^{3}He treatments, and compared these predictions with data from Fiedler et al. (142), but significant discrepancies were found. PET measurements for mono-energetic ^{16}O beams were presented by Sommerer et al. (138), and compared with FLUKA simulations, finding a good agreement. Finally, PET measurements with ^{3}Li were performed (143) but no MC calculations were included.

Besides predictions based on full MC, various attempts to predict the PET activity analytically were done, allowing for much faster predictions. Parodi and Bortfeld (144) developed an analytical method to calculate activity by a convolution product of dose and a number of filter functions. This approach was extended by Attanasi et al. (145), but never clinically applied. Solving the inverse problem, i.e., finding the dose from activity measurements, was also studied (146, 147) with deconvolution methods, but the complexity of the problem makes it challenging to apply to real patients. Recently, Miyatake and Nishio (148) developed a promising analytical activity pencil beam algorithm.

Finally, there are treatment centers which do not use MC simulations for treatment verification. At the Kashiwa facility, treatment verification has been based on comparing the PET distributions measured during the various fractions with first day measurements (113). At the Hyogo facility, PET activity is directly compared visually with the prescribed dose to verify the beam path (149). A similar procedure but with markers was applied at the Florida Proton Therapy Institute (123).

To summarize, different approaches exist for obtaining the PET reference activity distributions. It is generally agreed on that MC predictions provide the best reference distributions. So far, the FLUKA and Geant4 generators have been used for providing reference distributions in clinical studies, yielding good agreements for PET measurements in carbon and proton irradiation.

4.2.4. Challenges in Clinical Implementation

Many of the above studies have shown how PET treatment verification provides relevant clinical information. At the same time, these studies have highlighted some important limitations in the MC simulations, which should be resolved if PET is to become a widespread treatment verification technique in hadron therapy. Several issues remain to be addressed:

- Insufficient knowledge on cross section values, leading to uncertainties in β^+ yield and in absolute particle range, as

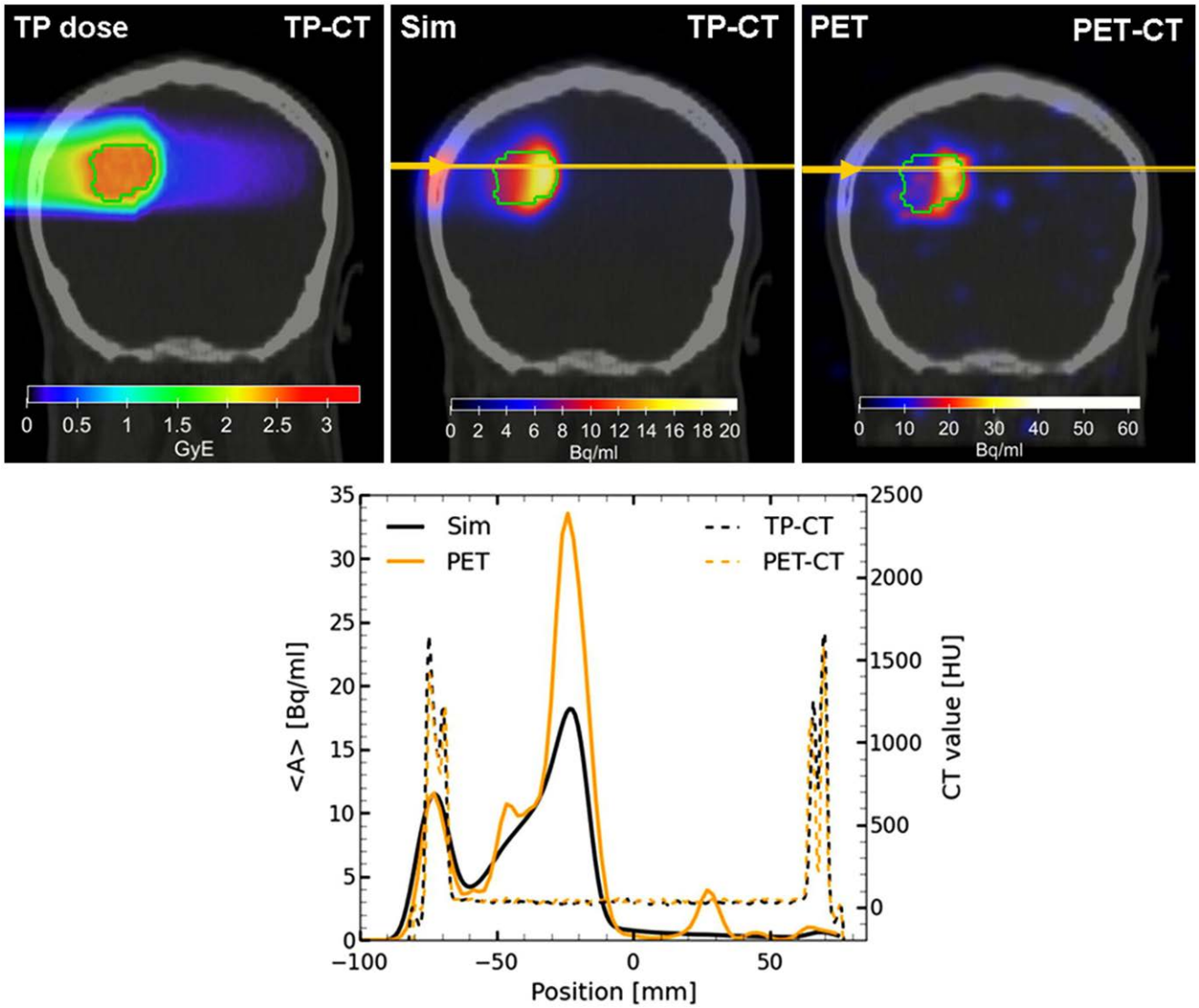

FIGURE 11 | Top left: colourwash overlays of the planning CT image (TP-CT) in the coronal view with the RBE-weighted dose distributions as obtained from the TP system (TP dose). **Top center:** the simulated activity pattern overlaid on the PET-CT image (Sim). **Top right:** the measured PET image (PET) overlaid on the PET-CT image. The solid green line marks the planning target volume. **Bottom:** the profile plot of the simulated and the measured activity (solid) as well as the corresponding CT image values (dashed) along the yellow line in panels Sim and PET in beam direction. Reproduced from Bauer et al. (125), with permission.

was shown by various studies. España et al. (133) reported that cross section uncertainties on activity fall-off position lead to a 1 and 5 mm uncertainty on the activity fall-off position, for 5 and 30 min in-room data-taking, respectively. To illustrate the problem, let's consider **Figure 6** (right), which showed the production cross section of the β^+ emitter ^{11}C. Although this plot shows large errors and conflicting data, it is an example of an accurately known cross section. In fact, for other β^+ emitters (^{12}N, ^{14}O, ^{8}B, etc), the situation is much worse, having to rely on only very few, sometimes very old, measurements including large errors to benchmark the codes. Obviously, new cross section measurements for production of various β^+ emitters would be helpful. In particular, these should include systematic, high quality, double differential energy spectra, with different types of projectiles, energies, and targets.

- Inaccuracies in MC predictions from the unknown elemental composition. While for dose calculations, the CT based stoichiometric calibration is typically sufficient, this is not the case for predicting quantities heavily relying on specific nuclear reaction channels (150). The impact of CT calibrations is especially significant for proton therapy, where the β^+ activity comes entirely from target residuals. The uncertainty on distal fall-off position of the PET signal was estimated to be about 1 mm for proton therapy (150). For carbon ions, the dependence is less pronounced (135). Additional information about the tissue may be extracted from the characteristic time decay curve of the PET signal (151) or from MRI.

- Inaccuracies in modeling biological washout, most relevant for off-line imaging. Our goal was to describe the physics aspects, and hence it is beyond the scope of this work to describe biological aspects. However, it has been repeatedly reported in offline PET studies that simulating biological washout correctly is highly complex and is a major limitation of the offline PET method.
- Speed and complexity of the MC simulations. The current frameworks like FLUKA and Geant4 are too slow, require a too steep learning curve, and too specialized knowledge to be applied widely in clinical practice.
- Extension of PET as monitoring tool for treatments of moving target, as for instance studied at Oncoray (137). The patient studies discussed above mostly concern static tumors. PET could be a valuable tool to monitor the accuracy of treatments of moving targets, but modeling the expected signal with MC is still largely uncovered.
- Automatic assessment of the predicted and measured activity maps, as investigated by various groups (see for instance Ref. (152, 153)).
- Translation of PET activity maps to dose. Despite the complicated and mathematically ill-defined problem, new research on this subject would be very valuable, because dose is an easily interpretable quantity for physicians. The current PET treatment monitoring is based on interpretation of activity maps, which require special knowledge about the activity signal, and is therefore much less appreciated by clinical personnel.

4.3. Treatment Verification with Prompt Gammas

As discussed in Sections 2.2.2–2.2.4, prompt gammas are emitted as a result of nuclear reactions during particle delivery along much of the particle path, with energies varying from 0 to about 10 MeV (for typical spectra see **Figure 12**, to be discussed below). We first briefly discuss the detectors, then describe MC validation studies with prompt gammas, and finally some clinical challenges.

4.3.1. Prompt Gamma Detection Devices

The energies of prompt gammas from nuclear reactions are too high for standard single gamma detection devices like SPECT to be efficient, and dedicated detector designs are needed. There are different prompt gamma imaging systems under investigation, of which some are design studies based on MC simulations, and others real prototypes. Let's briefly discuss some of them.

- Collimated gamma cameras. By placing the camera at 90° with respect to the beam-axis and moving the device parallel to the beam-axis, a 1-D prompt gamma profile can be measured. This was the design used in the first studies where the correlation between the Bragg peak position and the prompt gamma emission profile was demonstrated, for proton (156) and carbon (157) irradiation. This design has since then been recycled by various research groups for proton therapy (158–163) and carbon treatment verification (164, 165). To increase the detection efficiency and to be able to measure the 1-D profile without having to move the detector, an array-type multi-slit camera has been designed using MCNPX simulations (166). Knife-edge-shaped slit cameras have also been investigated (154, 167, 168). Here, instead of a parallel collimator a slit-collimator is employed. Promising measurements with a collimator slit-camera prototype tested with clinical proton beams have recently been presented by Perali et al. (168), estimating a precision (σ) on single spot range determination of 2 mm. Recently, Pinto et al. published a review of absolute prompt gamma yields measured with proton- and carbon-ion beams with single-slit experiments (169). At phantom entrance, the average number of detected prompt gammas was found to be of order 10^{-4} per incident carbon ion and 10^{-5} per incident proton.
- Compton cameras. Here, a multi-stage detector can measure the initial energy and direction of the photons undergoing Compton scattering in the detector. Various Compton camera prototypes have been realized (170–174) and various detector design studies have been performed with Geant4 MC simulations (175–179). The advantage of the Compton camera is that it has the potential to provide 3-D images.
- Other devices. Prompt-gamma timing camera (180). This is a promising new method, where instead of the spatial position the characteristic time-of-flight of the photons is used to extract information about the particle range. The underlying idea is that the transit time from phantom entrance to detector increases with the particle range, which causes measurable effects in timing spectra. Furthermore, energy-and-time resolved prompt gamma detection has also been proposed (160, 163), and will be discussed below.

4.3.2. Prompt Gamma Monte Carlo Validation Studies

A large amount of simulation and validation studies have been performed for prompt gamma imaging in proton and carbon therapy. Below we discuss some selected examples, first for proton and then for carbon therapy.

Starting with protons, Polf et al. (159) compared Geant4 simulations (version 9.1) to estimate the prompt gamma ray emission produced in water, Lucite, and bone-equivalent plastic during proton irradiation. Using a collimated gamma camera, they compared the acquired prompt gamma energy spectra with simulations, finding an overall satisfying agreement.

The MCNPX code was tested by Smeets et al. (154), who compared energy spectra measured with a knife-edge-shaped slit camera with MCNPX predictions (154). When applying a data-driven neutron background subtraction method, a satisfying agreement was obtained between data and MC simulations for the prompt gamma energy spectrum and yield. Without background subtraction, when the prompt gamma spectrum was contaminated heavily by neutron contributions, the description was unsatisfying.

Verburg et al. (181) performed an extensive validation of the nuclear cross sections of specific gamma-emission channels, identified by lines in the measured energy spectra, of the Geant4 (9.5) and MCNP6 codes, as well as for two pre-equilibrium reaction codes (TALYS and EMPIRE), for protons up to 200 MeV. Cross section predictions as a function of incident proton energy of the MC codes were compared to evaluated data from the ENDF/B-VII database. Using the BIC model for Geant4 and

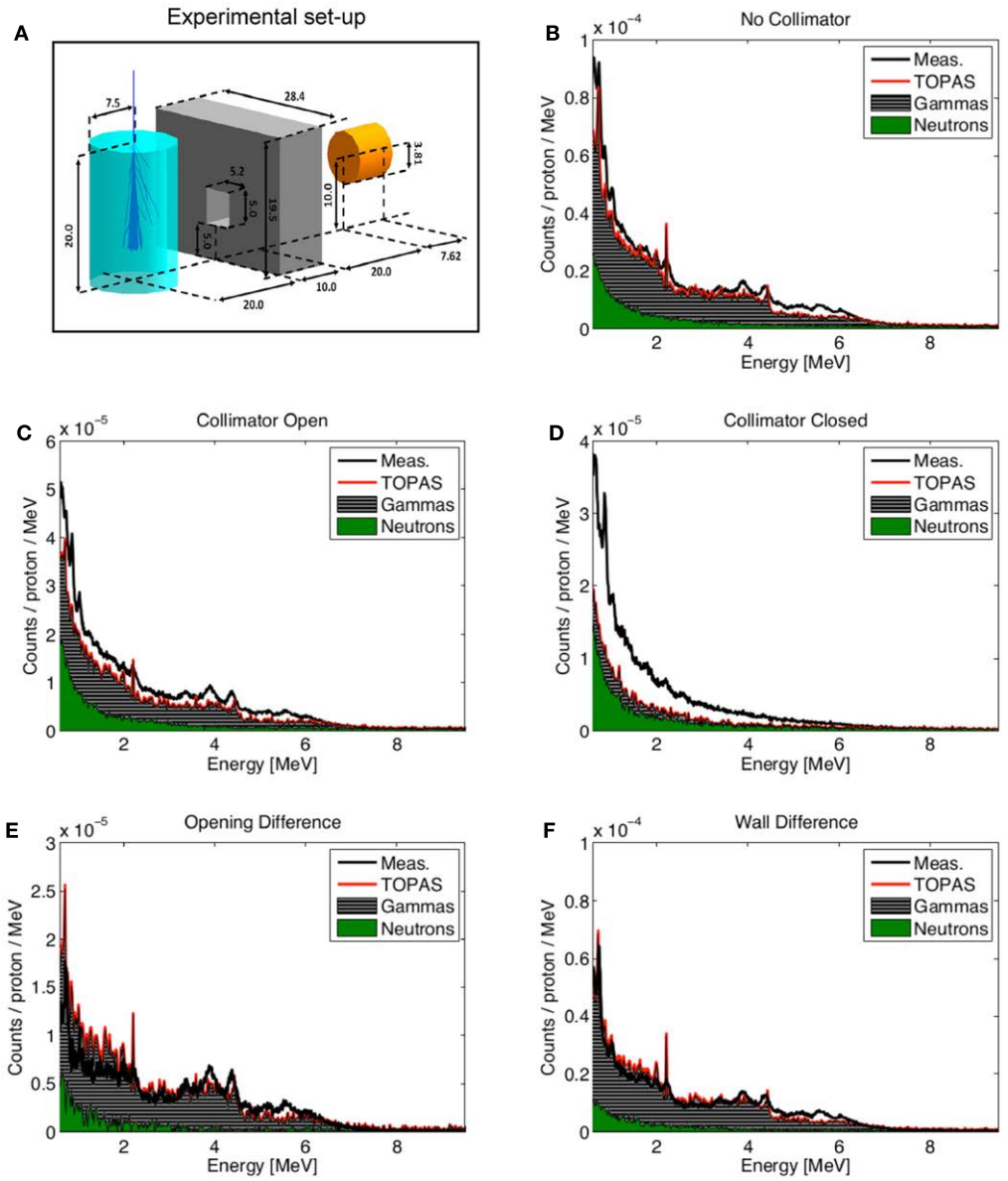

FIGURE 12 | Measured and simulated (TOPAS) energy spectra at the end of range of a monoenergetic 160 MeV proton pencil beam impinging along the central axis of a cylindrical PMMA target. Experimental setup **(A)** together with measured and simulated energy spectra for different collimator configurations **(B–F)**. "Opening difference" is Collimator Open minus Collimator Closed, and "Wall-difference" means No Collimator minus Collimator closed, i.e., a configuration in which neutron background is subtracted. Measurements from Smeets et al. (154). Figure reproduced from Ref. (154, 155), with permission.

the Bertini model in MCNP6, significant differences were found between measurements and predictions of the most important reaction channels, mostly in the low energy region (<20 MeV) where the codes tend to underestimate the cross sections by a factor two. The TALYS and EMPIRE values were somewhat better.

Still focusing on protons, a recent study by Dedes et al. (182) investigated the accuracy of Geant4 code (version 9.4) using the BIC model for nucleon-nucleus interactions. Different measurements of prompt gamma energy spectra with a collimated camera placed at different angles (mostly 90° w.r.t. the beam axis) were performed, and compared to Geant4 predictions. Additionally, the measurements from Smeets et al. (154) were used for comparison. The prompt gamma yield was generally overestimated using the Geant4 BIC model, evidencing the need for further improvements in the nuclear models.

A similar study was recently performed with TOPAS (155), where the same measured energy spectra from Smeets et al. (154) were compared with TOPAS simulations, also using the Geant4 BIC model. In contrast to Dedes et al. (182), an overall good agreement in yield and prompt gamma spectra between TOPAS predictions and measurements were obtained, when subtracting the neutron background. The results are shown in **Figure 12**. Moreover, the accuracy of prompt gamma imaging was estimated

for a clinical scenario. A 4 mm accuracy was estimated for a prostate tumor treatment with a dose of only 15 cGy delivered with passively scattered protons, a promising result.

Closely related to range monitoring, research has been performed to evaluate the sensitivity of the prompt gamma energy spectra in proton therapy to tissue composition (160, 163, 183). At the end of range, when the projectile energy has decreased and only a few relaxation channels are possible, discrete lines in the gamma spectrum are visible (see **Figure 12**). These have been shown to be sensitive to the elemental composition of the sample (160, 183). In particular, the measured spectra can be used directly as input in the MC predictions to increase their accuracy (163).

For carbon beams, the Geant4 performance for prompt gamma predictions was tested in several studies using the older nuclear INC models (184) and newly implemented QMD model (182). At low energies (95 MeV/u), the QMD model describes well energy spectra and yields when tuning the free parameters in the model. At higher energies, the observed remaining overestimation by Geant4 comes from the secondary proton and neutron contributions, which are not correctly described by the BIC model, as was seen also in the previously mentioned study by Dedes et al. (182).

Recently, the performance of FLUKA was investigated for prompt gamma production in ^{12}C irradiation of a PMMA target (55). An example of a predicted spatial prompt gamma profile along the beam path measured at 90°(from Ref. (184)) is given in **Figure 13**, showing a good agreement.

Finally, there are studies exploiting a completely different type of prompt gammas, coming from Cherenkov radiation from secondary electrons produced during particle irradiation (185). In this context, a study by Yamaguchi et al. (186) measured low energy prompt photons (around 65 keV) to verify the ^{12}C range, which could provide a complementary approach to other methods for range verification for shallow target treatments.

To summarize, for proton beams, a reasonable description of the prompt gamma yield could be obtained, although disagreements were reported as well, especially to describe neutron contributions. Concerning carbon beams, QMD models are generally still in a development status, but current implementations are promising.

4.3.3. Challenges for Clinical Implementation

The clinical implementation of the prompt gamma technique is still facing several challenges, which are discussed elsewhere (4). Concerning MC modeling, we have seen that the accuracy of the MC simulations has been much improved recently, but many issues still remain to be improved. Eventually, the prompt gamma imaging method will depend on comparisons between data and expectations calculated from 3-D patient descriptions like CT's, just like the PET imaging method. Whichever measurements will be performed (1-D, 2-D, 3-D spatial distribution, timing profiles, energy spectra), the MC codes will provide the reference. Current challenges in signal modeling to be addressed include:

- Nuclear models in most MC generators are not fully satisfying. Predicted cross sections are not always in agreement with data, and the neutron background is poorly understood. New cross section measurements at various angles for protons and carbon beams on thin targets covering the whole range of therapeutic energies would be useful (160, 163).
- Increasing the speed of the calculations is also important. Research on how to perform faster and more efficient calculations of prompt gamma yields was presented in recent articles (104, 187). Separating the MC physics generation step and the detector simulation step as done in Ref. (166) can additionally help.

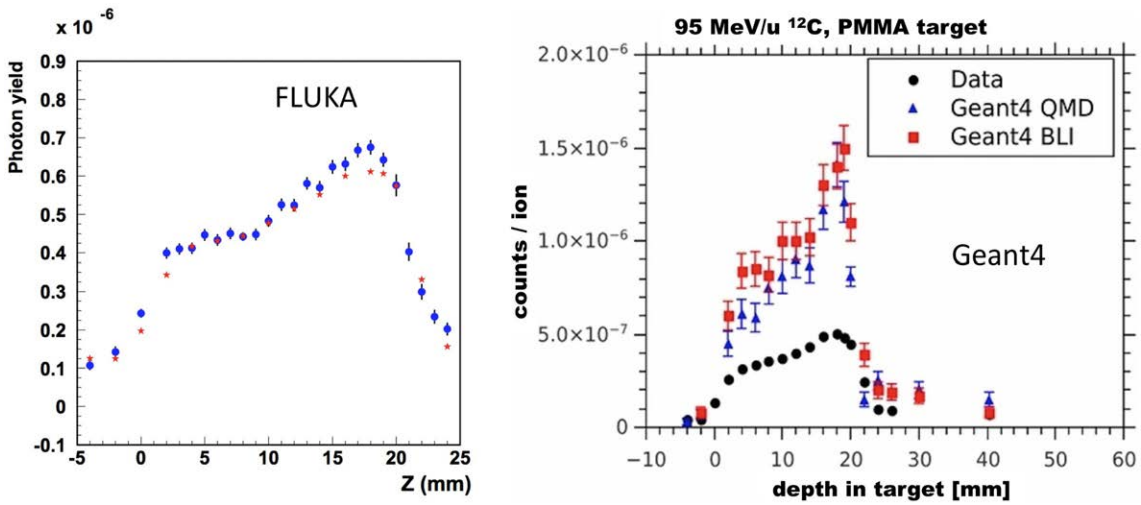

FIGURE 13 | Left: prompt photon yield at 90° as a function of depth for a 95 MeV/n ^{12}C beam impinging on a PMMA target. The Bragg peak position is at about 20 mm. Data (red stars) are from Ref. (184), re-evaluated as described in Ref. (169), and FLUKA simulations (blue circles) are shown. Reproduced from Ref. (55), with permission. **Right:** the same data, compared with simulations of Geant4 using the QMD model with different values of a free parameter. Reproduced from Ref. (182), with permission.

- In-house validation of the applied MC codes. Each research center has to validate its own MC framework using their own beamline and detection system, as was shown to work best also for PET monitoring. MC validation tests with the help of the standard QA measurements as proposed in Ref. (155) should be a starting point for validating the code.
- Performing data-MC comparisons for heterogeneous targets, including patients. Although studies on heterogeneous phantoms have been initiated (188), much more research is needed to verify the reliability of the MC codes when the phantom is heterogeneous and when the elemental composition must be obtained from a CT scan.
- Performing uncertainty analysis, for instance quantifying the influence of CT calibrations, ionization potential, or nuclear cross sections on the MC predictions, as has been studied for PET imaging too.

4.4. Charged Particle Imaging

Another method which offers the possibility to determine the particle range is the analysis of the charged particles that are created during nuclear fragmentation in the patient (Section 2.2), and which exit the patient (189, 190). This method has so far been limited to carbon irradiation, where the amount of high-energy secondary charged particles is larger than in proton therapy.

In the interaction vertex imaging (IVI) method, the trajectories of the charged particles exiting from a target are reconstructed and extrapolated back to their production point. Henriquet et al. (191) presented a feasibility study for this technique in carbon therapy, using Geant4 (9.2) simulations. An angle of 30° with respect to the beam-axis was chosen to detect charged particles. For homogeneous phantoms, milimetric precision was expected when monitoring with single pencil beams of 2×10^5 carbon ions. The approach was experimentally tested by Gwosch et al. (192), measuring charged particles exciting from homogeneous targets irradiated with carbon ions at HIT. The tracking device was placed at an angle of 30° from the beam-axis. The accuracy for monitoring the beam-range was found to be 1–3 mm, but based on pencil beams with much higher statistics than what is used clinically.

Detection of secondary charged particles for range monitoring was also investigated by others. Agodi et al. (193) and Piersanti et al. (194) irradiated a PMMA target with mono-energetic carbon ions with various energies. Trajectories of charged particles with kinetic energies up to several tens of MeV were measured with a tracking device, placed at 60° and 90° angle with respect to the beam axis. A clear correlation between the measured 1-D profile of the charged particle yield and the dose was found, and a reasonable agreement with FLUKA predictions (see **Figure 14**). These measurements at large angle are very valuable for the validation of nuclear models in MC codes.

A large-area proton range telescope is being developed by the TERA collaboration (195), with expected acceptance of 30 cm× 30 cm perpendicular to the beam.

Current challenges in signal modeling being faced for this range monitoring technique are very similar to those already mentioned in PET and prompt gamma monitoring. However, a very accurate MC prediction of the angular distributions of the fragments is even more crucial in this case, relying on prediction at large angles. Double differential energy spectra are especially useful for the validation of MC codes, such as recent measurements by De Napoli et al. (76) and Dudouet et al. (77). Concerning the detector, the acceptance and efficiency should still be increased.

5. Discussion and Future Outlook

The enormous amount of literature written about range monitoring demonstrates the worldwide interest in the subject. With the number of particle facilities growing, and in view of the increasingly considered hypofractionation schemes for dose delivery, non-invasive particle range verification methods will become even

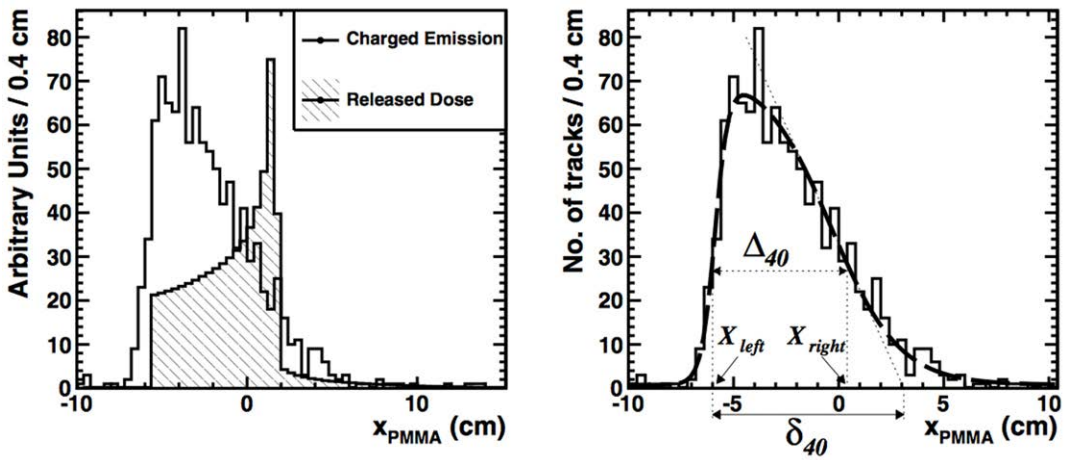

FIGURE 14 | Left: FLUKA simulation of the depth-dose profile (hatched histogram) superimposed on the longitudinal profile of charged secondary particles (solid line) as a function of x_{PMMA}, the primary beam direction. **Right:** the corresponding data (histogram) and data analysis (smooth line). Reproduced from Ref. (194), with permission.

more needed in the future. MC simulations are of prime importance in the development and application of range monitoring. In this review, we intended to describe the physics modeling and MC codes that are applied in the currently most widely researched range monitoring techniques, and to highlight therein the difficulties and challenges.

We have seen that the main inaccuracies in physics modeling have turned out to be very similar for the three techniques, because they rely all on an accurate description of electromagnetic and nuclear interactions of hadrons in matter. Summarizing, the common inaccuracies include:

- Uncertainties in describing nuclear interactions, including cross sections and interaction models. For PET, we saw in Section 4.2.4 that cross section uncertainties can lead to uncertainties in activity distal fall-off position of several millimeters. New double differential thin and thick target cross section measurements for specific reaction products in the entire energy range of therapeutic protons and heavy ions are the best way to improve the accuracy.
- Uncertainties in densities and elemental composition of the target. For PET, such uncertainties were of the order of a millimeter for proton therapy, as mentioned in Section 4.2.4. MRI could possibly improve the knowledge on elemental composition, as well as evaluating the elemental composition during range monitoring. For PET-based methods, the latter can be done by measuring time-decay curves of the PET signal, as was remarked in Section 4.2.4, while for prompt γ monitoring the discrete spectral lines could be used, as referenced in Section 4.3.2.
- Uncertainties on the position of the Bragg peak, coming from uncertainties in the ionization potential I and in the ionization model. As was discussed in Section 2.4, variations in the measured value of I in water lead to an uncertainty of several percent in Bragg peak position. In-house Bragg peak measurements could help to validate the MC code, thereby reducing this uncertainty.

For PET treatment verification, these uncertainties can add up to several millimeters, with nuclear interaction modeling as main source of uncertainty. For prompt gammas and charged particle imaging, the uncertainties have not been quantified, but are probably of similar size. A clinically valuable system should ideally provide a 1–2 mm estimation on range, preferably using single or few spots in the treatment plan, i.e., 10^8 and 10^6 particles for proton and carbon therapy. Thus, reducing the MC uncertainties to below 1–2 mm is crucial. However, it could be a shared effort for the PET, prompt gamma, and charged particle imaging communities.

Keeping in mind the underlying physics and the achieved results of the three monitoring techniques, let's briefly summarize their advantages and disadvantages. Starting with PET, this is a well-established method proven to provide clinically useful post-treatment information on the dose delivery. Unfortunately, the response-time is intrinsically limited by the decay time of the β^+ emitters. However, with online PET systems that acquire data during irradiation, a relatively quick response is expected, making such systems particularly valuable. Geometrical problems in planar configurations can be decreased when TOF information is used or with innovative geometrical designs. So far, post-treatment verification has been performed based on entire treatment plans, so that enough statistics is collected. Pre-treatment range measurements with one or a few single pencil-beams are difficult, but using larger online detectors it may be feasible in the future.

Prompt gamma detection has an important advantage with respect to PET, because prompt gammas are produced immediately when irradiating a target. This technique can thus provide real-time information, and issues with biological washout or movement are absent. Moreover the number of prompt gamma events produced is much larger than the number of annihilation photons used in PET treatment verification. However, much research in detector development is still needed to bring this technique to the clinic. Single pencil-beam monitoring seems feasible, although additional research is needed to confirm this. The accuracy of MC simulations has been much improved recently, but some crucial issues still remain to be studied, including neutron backgrounds, as well as dedicated studies with heterogeneous phantoms and patients.

Charged particle measurements can additionally provide a way to monitor the range. Predictions of MC codes for secondary particle production at large angles are generally not yet fully satisfactory. Although the expected sensitivity is smaller than with PET and prompt gammas, charged particles could for instance provide useful additional information in combination with other techniques, i.e., as part of a "hybrid" system. An example of such a system is being built in the framework of the INSIDE project (196), where a planar TOF PET system is combined with a tracking system to provide range monitoring measurements at the CNAO treatment facility in Pavia, Italy. More MC studies to assess the value of this kind of hybrid systems would be very useful, for instance it would be highly interesting to study triple system, combining PET, prompt gamma, and charged particle measurements.

Direct comparison studies with MC simulations are a good way to compare the techniques. However, such studies are scarce. Moteabbed et al. (197) performed a patient simulation study with Geant4 comparing the PET and prompt gamma techniques in proton treatments. They found that prompt gamma imaging was potentially advantageous for certain tumor types; however, the study was based on in-room PET and moreover the Geant4 code has significantly changed. New comparison studies between the various techniques would therefore be timely. Since the accuracy of each technique undoubtedly depends on treatment site, tumor type, depth, volume, treatment plan, particle beam, and so on, it is important that such comparison studies include large patient groups, and present their results as quantitative as possible.

Finally, the diversity of the literature studied here, encompassing nuclear physics, MC codes, detectors, and clinical challenges, highlights how much knowledge from different fields has been combined in the developments of range monitoring strategies.

In particular, the literature studied to describe the modeling of nuclear interactions in the human body covers a time span of more than 70 years. Having even omitted biological issues, it is clear that modeling the underlying physics in MC codes and developing the ultimate range verification technique requires expertise which goes far beyond the field of medical physics alone.

6. Conclusion

This review was aimed at providing a description of the most relevant aspects of the underlying physics and modeling in MC codes used in treatment monitoring techniques based on secondary particle detection. The complexity and variety of the underlying physics makes an accurate description of the production of secondary particles a highly challenging and non-trivial task. We have shown how various research groups validate and apply different MC codes to obtain their reference distributions, needed for a comparison with data.

Acknowledgments

Many thanks to Alberto Del Guerra, Stepan Mashnik, Denis Dauvergne, Paola Sala, Etienne Testa, Vincenzo Patera, and Valeria Rosso for useful comments about the manuscript. This research was financially supported by the Galileo Galilei School, the University of Pisa, and INFN Pisa.

References

1. Wilson RR. Radiological use of the fast protons. *Radiology* (1946) **47**:487–91. doi:10.1148/47.5.487
2. Loeffler JS, Durante M. Charged particle therapy – optimization, challenges and future directions. *Nat Rev Clin Oncol* (2013) **10**:411–24. doi:10.1038/nrclinonc.2013.79
3. Paganetti H. Range uncertainties in proton therapy and the role of Monte Carlo simulations. *Phys Med Biol* (2012) **57**:R99–117. doi:10.1088/0031-9155/57/11/R99
4. Knopf AC, Lomax A. In vivo proton range verification: a review. *Phys Med Biol* (2013) **58**(15):R131–60. doi:10.1088/0031-9155/58/15/R131
5. Lomax A. Charged particle therapy: the physics of interaction. *Cancer J* (2009) **15**(4):285–91. doi:10.1097/PPO.0b013e3181af5cc7
6. Kraft G. Tumor therapy with heavy charged particles. *Nucl Phys B* (2000) **45**(Suppl2):S473–544. doi:10.1016/S0146-6410(00)00112-5
7. Schardt D, Elsässer T, Schultz-Ertner D. Heavy-ion tumor therapy: physical and biological benefits. *Rev Mod Phys* (2010) **82**:383. doi:10.1103/RevModPhys.82.383
8. Gottschalk B. Physics of proton interactions in matter. In: Paganetti H, editor. *Proton Therapy Physics*. Boca Raton, FL: Taylor and Francis Group (2012). p. 19–60.
9. Newhauser WD, Zhang R. The physics of proton therapy. *Phys Med Biol* (2015) **60**:R155–209. doi:10.1088/0031-9155/60/8/R155
10. Paganetti H. Monte Carlo simulations. In: Paganetti H, editor. *Proton Therapy Physics*. Boca Raton, FL: Taylor and Francis Group (2012). p. 265–304.
11. Seco J, Verhaegen F. *Monte Carlo Techniques in Radiation Therapy*. Boca Raton, FL: Taylor and Francis Group (2013).
12. Ziegler JF. The stopping of energetic light ions in elemental matter. *J Appl Phys* (1999) **85**:1249–72. doi:10.1063/1.369844
13. Leo WR. *Techniques for Nuclear and Particle Physics Experiments*. Second ed. New York, NY: Springer Verlag (1994).
14. Olive KA (Particle Data Group), et al. Review of Particle Physics. *Chin Phys C* (2014) **38**:090001. doi:10.1088/1674-1137/38/9/090001 (2006) J Phys G 33:1,
15. Benton EV, Henke RP. Heavy particle range energy relations for dielectric nuclear track detectors. *Nucl Intrum Meth* (1969) **67**:87–92. doi:10.1016/0029-554X(69)90545-X
16. Lindhard J, Nielsen V, Scharff M, Thomsen P. Integral equations governing radiation effects. *Mat Fys Medd Dan Vid Selks* (1963) **33**(10):1.
17. Ziegler JF, Biersack JP, Littmark U, Anderson HH. *The Stopping and Ranges of Ions in Matter*. New York: Pergamon Press (1977).
18. NIST database. Available from: www.nist.gov/pml/data/asd.cfm
19. Molinelli S, Mairani A, Mirandola A, Vilches Freixas G, Tessonnier T, Giordanengo S, et al. Dosimetric accuracy assessment of a treatment plan verification system for scanned proton beam radiotherapy: one-year experimental results and Monte Carlo analysis of the involved uncertainties. *Phys Med Biol* (2013) **58**:3837–47. doi:10.1088/0031-9155/58/11/3837
20. Lechner A, Ivanchenko VN, Knobloch J. Validation of recent Geant4 physics models for application in carbon ion therapy. *Nucl Instrum Methods Phys Res B* (2010) **268**:2343–54. doi:10.1016/j.nimb.2010.04.008
21. Molière G. Theorie der streuung schneller geladenen teilchen II mehrfach- und vielfachstreuung. *Z Naturforschg* (1948) **3a**:78–97.
22. Lewis HW. Multiple scattering in an infinite medium. *Phys Rev* (1950) **78**(5):526–9. doi:10.1103/PhysRev.78.526
23. Highland VL. Some practical remarks on multiple scattering. *Nucl Instrum Methods* (1975) **129**:497–9. doi:10.1016/0029-554X(75)90743-0
24. Gottschalk B. On the scattering power of radiotherapy protons. *Med Phys* (2010) **37**(1):352–67. doi:10.1118/1.3264177
25. Weber U, Kraft G. Comparison of carbon ions versus protons. *Cancer J* (2009) **15**(4):325–32. doi:10.1097/PPO.0b013e3181b01935
26. Chadwick MB, Herman M, Oblozinsky P, Dunn ME, Danon Y, Kahler AC, et al. ENDF/B-VII.1 nuclear data for science and technology: cross sections, covariances, fission product yields and decay data. *Nucl Data* (2011) **112**(12):2887–996. doi:10.1016/j.nds.2011.11.002
27. JENDL. Available from: http://wwwndc.jaea.go.jp/jendl/jendl.html
28. EXFOR. Available from: www-nds.iaea.org/exfor/exfor.htm
29. Mashnik SG, Gudima KK, Prael RE, Sierk AJ, Baznat MI, Mokhov NV. CEM03.03 and LAQGSM03.03: event generators for the MCNP6, MCNPX and MARS15 transport codes. *Invited Lectures at Joint ICTP-IAEA Advanced Workshop on Model Codes for Spallation Reactions*. Trieste: ICTP (2008). LANL Report LA-UR-08-2931, Los Alamos. arXiv:0805.0751.
30. Ferrari A, Sala PR. The physics of high energy reactions. *Proceed. Workshop on Nucl. Reaction Data and Nuclear Reactor Physics, Design and Safety*. (Vol. 2). Trieste: ICTP (1998). p. 424–532.
31. Serber R. Nuclear reactions at high energies. *Phys Rev* (1947) **72**:1114–5. doi:10.1103/PhysRev.72.1114
32. Bertini HW, Gabriel TA, Santoro RT, Hermann OW, Larson NM, Hunt JM. *HIC-1: A First Approach to the Calculation of Heavy-Ion Reactions at Energies 50 MeV/Nucleon*. Oak Ridge: *ORNL-TM-4134* (1974).
33. Griffin JJ. Statistical model of intermediate structure. *Phys Rev Lett* (1966) **17**(29):478–80. doi:10.1103/PhysRevLett.17.478
34. Blann M. Precompound analyses of spectra and yields following nuclear capture of stopped pi-. *Phys Rev C* (1983) **28**:1648. doi:10.1103/PhysRevC.28.1648
35. Weisskopf VF. Statistics and nuclear reactions. *Phys Rev* (1937) **52**:295–303. doi:10.1103/PhysRev.52.295
36. Fermi E. High energy nuclear events. *Progr Theor Phys* (1950) **5**:570–83. doi:10.1143/ptp/5.4.570
37. Cussol D. *Nuclear Physics and Hadron Therapy*. La Colle sur Loup: Lectures at Ecole Joliot Curie (2011).
38. Pedroni E, Scheib S, Böhringer T, Coray A, Grossmann M, Lin S, et al. Experimental characterization and physical modelling of the dose distribution of scanned proton pencil beams. *Phys Med Biol* (2005) **50**(3):541–61. doi:10.1088/0031-9155/50/3/011
39. Sawakuchi GO, Titt U, Mirkovic D, Ciangaru G, Zhu XR, Sahoo N, et al. Monte Carlo investigation of the low-dose envelope from scanned proton pencil beams. *Phys Med Biol* (2010) **55**(3):711–h21. doi:10.1088/0031-9155/55/3/011
40. Beebe-Wang J, Vaska P, Dilmanian FA, Peggs SG, Schlyer DJ. Simulation of proton therapy treatment verification via PET imaging of induced positron-emitters. *IEEE Proc Nuc Sci Symp Conf Rec*. (Vol. 4) Portland (2003). p. 2496–500.

41. Zhu X, El Fahkri G. Proton therapy verification with PET imaging. *Theranostics* (2013) **3**(10):731–40. doi:10.7150/thno.5162
42. Schneider W, Bortfeld T, Schlegel W. Correlation between CT numbers and tissue parameters needed for Monte Carlo simulations of clinical dose distributions. *Phys Med Biol* (2000) **45**(2):459–78. doi:10.1088/0031-9155/45/2/314
43. Paganetti H. Relative biological effectiveness (RBE) values for proton beam therapy. Variations as a function of biological endpoints, dose and linear energy transfer. *Phys Med Biol* (2014) **59**(22):R419–72. doi:10.1088/0031-9155/59/22/R419
44. Wilkens JJ, Oelfke U. Direct comparison of biologically optimized spread-out bragg peaks for protons and carbon ions. *Int J Radiat Oncol Biol Phys* (2008) **70**(1):262–6. doi:10.1016/j.ijrobp.2007.08.029
45. Krämer M, Durante M. Ion beam transport calculations and treatment plans in particle therapy. *Eur Phys J D* (2010) **60**:195–202. doi:10.1088/0031-9155/58/8/2471
46. Andreo P. On the clinical spatial resolution achievable with proton and heavier charged particle radiotherapy beams. *Med Phys Biol* (2009) **54**(11):N205–15. doi:10.1088/0031-9155/54/11/N01
47. Besemer A, Paganetti H, Bednarz B. The clinical impact of uncertainties in the mean excitation energy of human tissues during proton therapy. *Phys Med Biol* (2013) **58**(4):887–902. doi:10.1088/0031-9155/58/4/887
48. Sihver L, Lantz M, Takechi M, Kohama A, Ferrari A, Cerutti F, et al. A comparison of total reaction cross section models used in particle and heavy ion transport codes. *Adv Space Res* (2012) **49**:812–9. doi:10.1016/j.asr.2011.11.029
49. Agodi C, Abou-Haidar Z, Alvarez MAG, Aumann T, Balestra F, Battistoni G, et al. FIRST experiment: fragmentation of ions relevant for space and therapy. *J Phys* (2013) **420**:012061. doi:10.1088/1742-6596/420/1/012061
50. Ferrari A, Sala PR, Fassö A, Ranft J. FLUKA: a multi-particle transport code. *CERN Yellow Report CERN 2005-10, INFN/TC 05/11, SLAC-R-773*. (2012). Available from: www.fluka.org
51. Battistoni G, Muraro S, Sala PR, et al. The FLUKA code: description and benchmarking. *AIP Proceedings Had**ronic** Shower Simulation Workshop 2006*. (Vol. 896), Tsukuba: Fermilab (2007). p. 31–49.
52. Ferrari A, Sala R, Guaraldi R, Padoani F. An improved multiple scattering model for charged particle transport. *Nucl Instrum Methods Phys Res B* (1992) **71**:412–26. doi:10.1016/0168-583X(92)95359-Y
53. Fassö A, Ferrari A, Ranft J, et al. New developments in FLUKA modelling of hadronic and EM interactions. *KEK Proceedings 3rd Workshop on Simulating Accelerator Radiation Environments (SARE 3)*. (Vol. 97) Tsukuba (1997). 32 p.
54. Rinaldi I, Ferrari A, Mairani A, Paganetti H, Parodi K, Sala PR. An integral test of FLUKA nuclear models with 160 MeV proton beams in multi-layer Faraday cups. *Phys Med Biol* (2011) **56**(13):4001–11. doi:10.1088/0031-9155/56/13/016
55. Böhlen TT, Cerutti F, Chin MPW, Fassò A, Ferrari A, Ortega PG, et al. The FLUKA code: developments and challenges for high energy and medical applications. *Nucl Data* (2014) **120**:211–4. doi:10.1016/j.nds.2014.07.049
56. Andersen V, Ballarini F, Battistoni G, Campanella M, Carboni M, Cerutti F, et al. The FLUKA code for space applications: recent developments. *Adv Space Res* (2004) **34**(6):1302–10. doi:10.1016/j.asr.2003.03.045
57. Cerutti F, Battistoni G, Capezzalli G, Colleoni P, Ferrari E, Gadioli E, et al. Low Energy nucleus-nucleus reactions: the BME approach and its interface with FLUKA. *Proceed. 11th Int Conf on Nuclear Reaction Mechanisms*. Varenna (2006). p. 507–11.
58. Sommerer F, Parodi K, Ferrari A, Poljanc K, Enghardt W, Aiginger H. Investigating the accuracy of the FLUKA code for transport of therapeutic ion beams in matter. *Phys Med Biol* (2006) **51**:4385–98. doi:10.1088/0031-9155/51/17/017
59. Böhlen TT, Cerutti F, Dosanjh M, Ferrari A, Gudowska I, Mairani A, et al. Benchmarking nuclear models of FLUKA and GEANT4 for hadron therapy. *Phys Med Biol* (2010) **55**(19):5833–47. doi:10.1088/0031-9155/55/19/014
60. Mairani A, Brons S, Cerutti F, Fassö A, Ferrari A, Krämer M, et al. The FLUKA Monte Carlo code coupled with the local effect model for biological calculations in carbon ion therapy. *Phys Med Biol* (2010) **55**(17):4273–89. doi:10.1088/0031-9155/55/15/006
61. Scobel W, Trabandt M, Blann M, Pohl BA, Remington BA, Byrd RC, et al. Preequilibrium (p,n) reaction as a probe for the effective nucleon-nucleon interaction in multistep direct processes. *Phys Rev C* (1990) **41**(5):2010–20. doi:10.1103/PhysRevC.41.2010
62. Nakamoto T, Ishibashi K, Matsufuji N, Shigyo N, Maehata K, Meigo S, et al. Spallation neutron measurement by time-of-flight method with a short flight path. *Nucl Sci Technol* (1995) **32**(9):827–33. doi:10.1080/18811248.1995.9731784
63. Haettner E, Iwase H, Schardt D. Experimental fragmentation studies with 12C therapy beams. *Radiat Prot Dosimetry* (2006) **122**(1–4):485–7. doi:10.1093/rpd/ncl402
64. Agostinelli S, Allison J, Amako K, Apostolakis J, Araujo H, Arce P, et al. Geant4: a simulation toolkit. *Nucl Instrum Methods* (2003) **506**(6):250–303. doi:10.1016/S0168-9002(03)01368-8
65. Jarlskog CZ, Paganetti H. Physics settings for using the Geant4 toolkit in proton therapy. *IEEE Trans Nucl Sci* (2008) **55**(3):1018–25. doi:10.1109/TNS.2008.922816
66. Boudard A, Cugnon J, Leray S, Volant C. Intranuclear cascade model for a comprehensive description of spallation reaction data. *Phys Rev C* (2002) **66**:044615. doi:10.1103/PhysRevC.66.044615
67. Grevillot L, Frisson T, Zahra N, Bertrand D, Stichelbaut F, Freud N, et al. Optimization of Geant4 settings for proton pencil beam scanning simulations using GATE. *Nucl Instrum Methods Phys Res B* (2010) **268**(20):3295–305. doi:10.1088/0031-9155/56/16/008
68. Peterson SW, Polf J, Bues M, Ciangaru G, Archambault L, Beddar S, et al. Experimental validation of a Monte Carlo proton therapy nozzle model incorporating magnetically steered protons. *Phys Med Biol* (2009) **54**(10):3217–29. doi:10.1088/0031-9155/54/10/017
69. Mishustin I, Pshenichnov I, Greiner W. Modelling heavy ion energy deposition in extended media. *Eur Phys J D* (2010) **60**(1):109–14. doi:10.1140/epjd/e2010-00187-3
70. Pshenichnov I, Botvina A, Mishustin I, Greiner W. Nuclear fragmentation reactions in extended media studied with the GEANT4 toolkit. *Nucl Instrum Methods Phys Res B* (2010) **268**(15):604–15. doi:10.1016/j.nimb.2009.12.023
71. Toshito T, Bagulya A, Lechner A, Ivanchenko A, Maire M, Akagi T, et al. Validation of new Geant4 electromagnetic physics models for ion therapy applications. *Progr Nucl Sci Technol* (2011) **2**:918–22.
72. Pshenichnov I, Mishustin I, Greiner W. Distributions of positron-emitting nuclei in proton and carbon-ion therapy studied with GEANT4. *Phys Med Biol* (2006) **51**(23):6099–112. doi:10.1088/0031-9155/51/23/011
73. Pshenichnov I, Larionov A, Mishustin I, Greiner W. PET monitoring of cancer therapy with 3He and 12C beams: a study with the GEANT4 toolkit. *Phys Med Biol* (2007) **52**(24):7295–312. doi:10.1088/0031-9155/52/24/007
74. Burigo L, Pshenichnov I, Mishustin I, Bleicher M. Microdosimetry spectra and RBE of 1H, 4He, 7Li, 12C nuclei in water studied in Geant4. *Nucl Instrum Methods Phys Res B* (2014) **320**:89–99. doi:10.1016/j.nimb.2013.10.018
75. Robert C, Dedes G, Battistoni G, Böhlen TT, Buvat I, Cerutti F, et al. Distributions of secondary particles in proton and carbon-ion therapy: a comparison between GATE/Geant4 and FLUKA Monte Carlo codes. *Phys Med Biol* (2013) **58**(9):2879–99. doi:10.1088/0031-9155/58/9/2879
76. De Napoli M, Agodi C, Battistoni G, Blancato AA, Cirrone GAP, Cuttone G, et al. Carbon fragmentation measurements and validation of the Geant4 nuclear reaction models for hadron therapy. *Phys Med Biol* (2012) **57**(22):7651. doi:10.1088/0031-9155/57/22/7651
77. Dudouet J, Cussol D, Durand D, Labalme M. Benchmarking Geant4 nuclear models for hadron therapy with 95 MeV/nucleon carbon ions. *Phys Rev C* (2014) **89**(5):54616–7. doi:10.1103/PhysRevC.89.054616
78. Jan S, Benoit D, Becheva E, Carlier T, Cassol F, Descourt P, et al. GATE V6: a major enhancement of the GATE simulation platform enabling modelling of CT and radiotherapy. *Phys Med Biol* (2011) **56**(4):881–901. doi:10.1088/0031-9155/56/4/001
79. Sébastien J, Frisson T, Sarrut D. GATE simulation of 12C hadrontherapy treatment combined with a PET imaging system for dose monitoring: a feasibility study. *IEEE Trans Nucl Sci* (2013) **60**:423–9. doi:10.1109/TNS.2012.2233496
80. Perl J, Schümann J, Shin J, Faddegon B, Paganetti H. TOPAS: an innovative proton Monte Carlo platform for research and clinical applications. *Med Phys* (2012) **39**(11):6818–37. doi:10.1118/1.4758060
81. Testa M, Schümann J, Lu H-M, Shin J, Faddegon B, Perl J, et al. Experimental validation of the TOPAS Monte Carlo system for passive scattering proton therapy. *Med Phys* (2013) **40**(12):121719. doi:10.1118/1.4828781
82. Aso T, Maeda Y, Iwai G, Takase W, Sasaki T, Watase Y, et al. Extension of the particle therapy simulation framework to hospital information systems and

multigrid environments. *Proceed IEEE 15th Int Conf on Computational Science and Engineering*. Phapos (2012). p. 229–34.
83. Arce P, Lagares JI, Harkness L, Desorgher L, de Lorenzo G, Abreu Y, et al. GAMOS: an easy and flexible way to use GEANT4. *IEEE Proc Nuc Sci Symp Conf Rec*. Valencia (2011). p. 2230–7.
84. Goorley T, James M, Booth T, Brown F, Bull J, Cox LJ, et al. Initial MCNP6 release overview. MCNP6 version 0.1. *Nucl Technol* (2012) **180**(3):298–315. doi:10.13182/NT11-135
85. X-5 Monte Carlo Team. *MCNP – A General Monte Carlo N-Particle Transport Code, Version 5" – Volume I: Overview and Theory*. Los Alamos National Laboratory (2003). Available from: https://mcnp.lanl.gov/mcnp5.shtml.
86. LANL MCNPX 2.60 Users's Guide (2008). Available from: https://mcnpx.lanl.gov
87. Vavilov PV. Ionization losses of high energy heavy particles. *Soviet Phys JEPT* (1957) **5**:749–51.
88. Rossi B, Griesen K. Cosmic-ray theory. *Rev Mod Phys* (1941) **13**:240–309. doi:10.1103/RevModPhys.13.240
89. Gudima KK, Mashnik SG, Toneev VD. Cascade-exciton model of nuclear reactions, JINR Communications (1980) P2- 80-774 and P2-80-777, Dubna (1980). *Nucl Phys A* (1983) **401**:329. doi:10.1016/0375-9474(83)90532-8
90. Reed AL. Medical physics calculations with MCNP: a primer. *LANL Report LA-UR-07-4133*. Los Alamos (2007).
91. Newhauser W, Fontenot J, Zheng Y, Polf J, Titt U, Koch N, et al. Monte-Carlo simulations for configuring and testing an analytical proton dose-calculation algorithm. *Phys Med Biol* (2007) **52**(15):4569–84. doi:10.1088/0031-9155/52/15/014
92. Koch N, Newhauser WD, Titt U, Gombos D, Coombes K, Starkschall G. Monte Carlo calculations and measurements of absorbed dose per monitor unit for the treatment of uveal melanoma with proton therapy. *Phys Med Biol* (2008) **53**(6):1581–94. doi:10.1088/0031-9155/53/6/005
93. Chadwick MB, Hughes HG, Little RC, Pitcher EJ, Young PG. Nuclear data for accelerator-driven systems. *Progr Nucl Energy* (2001) **38**(**I–2**):179–219. doi:10.1016/S0149-1970(00)00102-5
94. Mashnik SG. Validation and verification of MCNP6 against high-energy experimental data and calculations by other codes. II. The LAQGSM testing primer. *LANL Report LA-UR-11-05627*. Los Alamos (2011). Available from: https://mcnp.lanl.gov/.
95. Mashnik SG. Validation and verification of MCNP6 against high- energy experimental data and calculations by other codes. III. The MPI testing primer. *LANL Report LA-UR-13-26944*. Los Alamos (2013). Available from: https://mcnp.lanl.gov/.
96. Mashnik SG, Kerby LM. MCNP6 fragmentation of light nuclei at intermediate energies. *Nucl Instrum Methods Phys Res A* (2014) **764**:59–81. doi:10.1016/j.nima.2014.07.016
97. Iwata Y, Murakami T, Sato H, Iwase H, Nakamura T, Kurosawa T, et al. Double-differential cross sections for the neutron production from heavy-ion reactions at energies E/A 290–600 MeV. *Phys Rev C* (2001) **64**:054609. doi:10.1103/PhysRevC.64.054609
98. Niita K, Chiba S, Maruyama S, Maruyama T, Takada H, Fukahori T, et al. Analysis of the (N,xN) reactions by quantum molecular dynamics plus statistical decay model. *Phys Rev C* (1995) **52**:2620.
99. Sato T, Niita K, Matsuda N, Hashimoto S, Iwamoto Y, Noda S, et al. Particle and heavy ion transport code system PHITS, version 2.52. *Nucl Sci Technol* (2013) **50**(9):913–23. doi:10.1080/00223131.2013.814553
100. Sihver L, Mancusi D. Present status and validation of HIBRAC. *Radiat Meas* (2009) **44**(1):38–46. doi:10.1016/j.radmeas.2008.11.004
101. Rohling H, Sihver L, Priegnitz M, Enghardt W, Fiedler F. Comparison of PHITS, GEANT4, and HIBRAC simulations of depth-dependent yields of beta+-emitting nuclei during therapeutic particle irradiation to measured data. *Phys Med Biol* (2013) **58**(18):6355–68. doi:10.1088/0031-9155/58/18/6355
102. Hansen DC, Lu hr A, Sobolevsky N, Bassler N. Optimizing SHIELD-HIT for carbon ion treatment. *Phys Med Biol* (2012) **57**:2393–409. doi:10.1088/0031-9155/57/8/2393
103. Fippel M, Soukup M. A Monte Carlo dose calculation algorithm for proton therapy. *Med Phys* (2004) **31**(8):2263–73. doi:10.1118/1.1769631
104. Sterpin E, Sorriaux J, Vynckier S. Extension of PENELOPE to protons: simulation of nuclear reactions and benchmark with Geant4. *Med Phys* (2013) **40**:111705. doi:10.1118/1.4823469
105. Steward VW, Koehler AM. Proton beam radiography in tumor detection. *Science* (1973) **179**(4076):913–4. doi:10.1126/science.179.4076.913
106. Schulte RW, Bashkirov V, Klock MC, Li T, Wroe AJ, Evseev I, et al. Density resolution of proton computed tomography. *Med Phys* (2005) **32**(4):1035–46. doi:10.1118/1.1884906
107. Assmann W, Kellnberger S, Reinhardt S, Lehrack S, Edlich A, Thiroff PG, et al. Ionoacoustic characterization of the proton Bragg peak with submillimeter accuracy. *Med Phys* (2015) **42**(2):567. doi:10.1118/1.4905047
108. Iseki Y, Kanai T, Kanazawa M, Kitagawa A, Mizuno H, Tomitani T, et al. Range verification system using positron emitting beams for heavy-ion radiotherapy. *Phys Med Biol* (2004) **49**(14):3179–95. doi:10.1088/0031-9155/49/14/012
109. Enghardt W, Parodi K, Crespo P, Fiedler F, Pawelke J, Pönisch F, et al. Dose quantification from in-beam positron emission tomography. *Radiother Oncol* (2004) **73**(Suppl 2):S96–8. doi:10.1016/S0167-8140(04)80024-0
110. Parodi K. *On the Feasibility of Dose Quantification with In-Beam PET Data in Radiotherapy with 12C and Proton Beams*. PhD thesis, Dresden University of Technology, in Forschungszentrum Rossendorf Wiss-Techn-Ber FZR-415, Dresden (2004).
111. Enghardt W, Crespo P, Fiedler F, Hinz R, Parodi K, Pawelke J, et al. Charged hadron tumour therapy monitoring by means of PET. *Nucl Instrum Methods Phys Res A* (2004) **525**:284–8. doi:10.1016/j.nima.2004.03.128
112. Crespo P, Shakirin G, Enghardt W. On the detector arrangement for in-beam PET for hadron therapy monitoring. *Phys Med Biol* (2006) **51**(9):2143–63. doi:10.1088/0031-9155/51/9/002
113. Nishio T, Miyatake A, Ogino T, Nakagawa K, Saijo N, Esumi H. The development and clinical use of a beam ON-LINE PET system mounted on a rotating gantry port in proton therapy. *Int J Radiat Oncol Biol Phys* (2010) **76**(1):277–86. doi:10.1016/j.ijrobp.2009.05.065
114. Tashima H, Yamaya T, Yoshida E, Kinouchi S, Watanabe M, Tanaka E. A single-ring OpenPET enabling PET imaging during radiotherapy. *Phys Med Biol* (2012) **57**(14):4705–18. doi:10.1088/0031-9155/57/14/4705
115. Sportelli G, Belcari N, Camarlinghi N, Cirrone GA, Cuttone G, Feretti S, et al. First full-beam PET acquisitions in proton therapy with a modular dual-head dedicated system. *Phys Med Biol* (2014) **59**(1):43–60. doi:10.1088/0031-9155/59/1/43
116. Kraan AC, Battistoni G, Belcari N, Camarlinghi N, Cappucci F, Ciocca M, et al. First tests for an online treatment monitoring system with in-beam PET for proton therapy. *J Instrum* (2015) **10**:C01010. doi:10.1088/1748-0221/10/01/C01010
117. Shao Y, Sun X, Lou K, Zhu XR, Mirkovich D, Pönisch F, et al. In-beam PET imaging for on-line adaptive proton therapy: an initial phantom study. *Phys Med Biol* (2014) **59**(14):3373–88. doi:10.1088/0031-9155/59/13/3373
118. Crespo P, Barthel T, Frais-Kölbl H, Griesmayer E, Heidel K, Parodi K, et al. Suppression of random coincidences during in-beam PET measurements at ion beam radiotherapy facilities. *IEEE Trans Nucl Sci* (2005) **52**(4):980–7. doi:10.1109/TNS.2005.852637
119. Kraan AC, Battistoni G, Belcari N, Camarlinghi N, Cirrone GA, Cuttone G, et al. Proton range monitoring with in-beam PET: Monte Carlo activity predictions and comparison with cyclotron data. *Eur J Med Phys* (2014) **30**(5):559–69. doi:10.1016/j.ejmp.2014.04.003
120. Zhu X, España S, Daartz J, Liebsch N, Ouyang J, Paganetti H, et al. Monitoring proton radiation therapy with in-room PET imaging. *Phys Med Biol* (2011) **56**(13):4041–57. doi:10.1088/0031-9155/56/13/019
121. Min CH, Zhu X, Winey BA, Grogg K, Testa M, El Fakiri G, et al. Clinical application of in-room positron emission tomography for in vivo treatment monitoring in proton radiation therapy. *Int J Radiat Oncol Biol Phys* (2013) **86**(1):183–9. doi:10.1016/j.ijrobp.2012.12.010
122. Parodi K, Paganetti H, Shi HA, Michaud S, Loeffler JS, DeLaney TF, et al. Patient study of in-vivo verification of beam delivery and range, using positron emission tomography and computed tomography imaging after proton therapy. *Int J Radiat Oncol Biol Phys* (2007) **68**(3):920–34. doi:10.1016/j.ijrobp.2007.01.063
123. Hsi WC, Indelicato DJ, Vargas C, Duvvuri S, Li Z, Palta J. In-vivo verification of the beam-path by using post-treatment PET/CT imaging. *Med Phys* (2009) **36**(9):4136–46. doi:10.1118/1.3181422
124. Knopf AC, Parodi K, Paganetti H, Bortfeld T, Daartz J, Engelsman J, et al. Accuracy of proton beam range verification using post-treatment positron emission tomography/computed tomography as function of treatment site.

Int J Radiat Oncol Biol Phys (2011) **79**(1):297–304. doi:10.1016/j.ijrobp.2010.02.017
125. Bauer J, Unholtz D, Sommerer F, Kurz F, Haberer T, Herfarth K, et al. Implementation and initial clinical experience of offline PET/CT-based verification of scanned carbon ion treatment. *Radiother Oncol* (2013) **107**(2):218–26. doi:10.1016/j.radonc.2013.02.018
126. Parodi K. Monte Carlo calculations for PET-based treatment verification of ion beam therapy. In: Seco J, Verhaegen F, editors. *Monte Carlo Techniques in Radiation Therapy*. Boca Raton, FL: Taylor and Francis Group (2013). p. 251–62.
127. Fiedler F, Kunath D, Priegnitz M, Enghardt W. Online irradiation control by means of PET. In: Linz U, editor. *Ion Beam Therapy Fundamentals, Technology, Clinical Applications*. Berlin: Springer-Verlag (2012). p. 527–43. doi:10.1007/978-3-642-21414-1_31
128. Iseki Y, Mizuno H, Futami Y, Tomitani T, Kanai T, Kanazawa M, et al. Positron camera for range verification of heavy ion radiotherapy. *Nucl Instrum Methods Phys Res A* (2003) **515**(3):840–9. doi:10.1016/j.nima.2003.07.005
129. Crespo P, Shakirin G, Fiedler F, Enghardt W, Wagner A. Direct time-of-flight for quantitative, real-time in-beam PET: a concept and feasibility study. *Phys Med Biol* (2007) **52**(23):6795–811. doi:10.1088/0031-9155/52/23/002
130. Yamaya T, Yoshida E, Inaniwa T, Sato S, Nakajima Y, Wakizata H, et al. Development of a small prototype for a proof-of-concept of OpenPET imaging. *Phys Med Biol* (2011) **56**(4):1123–37. doi:10.1088/0031-9155/56/4/015
131. An SJ, Beak Ch H, Lee K, Chung YH. A simulation study of a C-shaped in-beam PET system for dose verification in carbon beam therapy. *Nucl Instrum Methods Phys Res B* (2013) **698**:37–43. doi:10.1016/j.nima.2012.09.050
132. Parodi K, Ferrari A, Sommerer F, Paganetti H. Clinical CT-based calculations of dose and positron emitter distributions in proton therapy using the FLUKA Monte Carlo code. *Phys Med Biol* (2007) **52**(12):3369–87. doi:10.1088/0031-9155/52/12/004
133. España S, Zhu X, Daartz J, El Fakhri H, Bortfeld T, Paganetti H. The reliability of proton-nuclear interaction cross-section data to predict proton-induced PET images in proton therapy. *Phys Med Biol* (2011) **56**(9):2687–98. doi:10.1088/0031-9155/56/9/003
134. Bauer J, Unholtz D, Kurz C, Parodi K. An experimental approach to improve the Monte Carlo modelling of offline PET/CT imaging of positron emitters induced by scanned proton beams. *Phys Med Biol* (2013) **58**(15):5193–213. doi:10.1088/0031-9155/58/15/5193
135. Pönisch F, Parodi K, Hasch BG, Enghardt W. The modelling of positron emitter production and PET imaging during carbon ion therapy. *Phys Med Biol* (2004) **49**(23):5217–32. doi:10.1088/0031-9155/49/23/002
136. Fiedler F, Shakirin G, Skowron J, Braess H, Crespo P, Kunath D, et al. On the effectiveness of ion range determination from in-beam PET data. *Phys Med Biol* (2010) **55**(7):1989–98. doi:10.1088/0031-9155/55/7/013
137. Laube K, Menkel S, Bert C, Enghardt W, Helmbrecht S, Saito N, et al. 4D particle therapy PER simulations for moving targets irradiated with scanned ion beams. *Phys Med Biol* (2013) **58**(3):513–33. doi:10.1088/0031-9155/58/3/513
138. Sommerer F, Cerutti F, Parodi K, Ferrari A, Enghardt W, Aiginger H. In-beam PET monitoring of mono-energetic 16O and 12C beams: experiments and FLUKA simulations for homogeneous targets. *Phys Med Biol* (2009) **54**(13):3979–96. doi:10.1088/0031-9155/54/13/003
139. Parodi K, Bauer J, Kurz C, Mairani A, Sommerer F, Unholtz D, et al. Monte Carlo modelling and in-vivo imaging at the Heidelberg Ion Beam Therapy Center. *Proceed Nucl Science Symposium and Med Imaging Conf (NSS/MIC) IEEE*. (2011). Available from: http://ieeexplore.ieee.org/xpl/mostRecentIssue.jsp?punumber=6144196
140. Lühr A, Priegnitz M, Fiedler F, Sobolevsky N, Bassler N. Dependence of simulated positron emitter yields in ion beam cancer therapy on modelling nuclear fragmentation. *Appl Radiat Isot* (2014) **83**:165–70. doi:10.1016/j.apradiso.2012.12.018
141. Seravalli E, Robert C, Bauer J, Stichelbaut F, Kurz C, Smeets J, et al. Monte Carlo calculations of positron emitter yields in proton radiotherapy. *Phys Med Biol* (2012) **57**(6):1659–73. doi:10.1088/0031-9155/57/6/1659
142. Fiedler F, Crespo P, Parodi K, Sellesk M, Enghardt W. The feasibility of in-beam PET for therapeutic beams of 3He. *IEEE Trans Nucl Sci* (2005) **53**(4):2757–60. doi:10.1109/TNS.2006.877854
143. Priegnitz M, Möckel D, Parodi K, Sommerer F, Fiedler F, Enghardt W. In-beam PET measurements of 7Li3+ irradiation induced beta+ activity. *Phys Med Biol* (2008) **53**(16):4443–53. doi:10.1088/0031-9155/53/16/015
144. Parodi K, Bortfeld T. A filtering approach based on Gaussian-powerlaw convolutions for local PET verification of proton radiotherapy. *Phys Med Biol* (2006) **51**:1991–2009. doi:10.1088/0031-9155/51/8/003
145. Attanasi F, Knopf A, Parodi K, Paganetti H, Bortfeld T, Rosso V, et al. Extension and validation of an analytical model for in vivo PET verification of proton therapy a phantom and clinical study. *Phys Med Biol* (2911) **56**:5079–98. doi:10.1088/0031-9155/56/16/001
146. Remmele S, Hesser J, Paganetti H, Bortfeld T. A deconvolution approach for PET-based dose reconstruction in proton therapy. *Phys Med Biol* (2011) **56**(23):7601–19. doi:10.1088/0031-9155/56/23/017
147. Fourkal E, Fan J, Veltchev I. Absolute dose reconstruction in proton therapy using PET imaging modality: feasibilty study. *Phys Med Biol* (2009) **54**(11):N217–28. doi:10.1088/0031-9155/54/11/N02
148. Miyatake A, Nishio T. Application of activity pencil beam algorithm using measured distribution data of positron emitter nuclei for therapeutic SOBP proton beam. *Med Phys* (2013) **40**(9):091709. doi:10.1118/1.4818057
149. Abe M. Charged particle radiotherapy at the Hyogo Ion Beam Medical Center: characteristics, technology and clinical results. *Proc Jpn Acad Ser B Phys Biol Sci* (2007) **83**(6):151–63. doi:10.2183/pjab.83.151
150. España S, Paganetti H. The impact of uncertainties in the CT conversion algorithms when predicting proton beam ranges in patients from dose and PET activity distributions. *Phys Med Biol* (2010) **55**(24):7557–71. doi:10.1088/0031-9155/55/24/011
151. Cho J, Ibbott G, Gillin M, Gonzalez-Lepera C, Min CH, Zhu X, et al. Determination of elemental tissue composition following proton treatment using positron emission tomography. *Phys Med Biol* (2013) **58**(11):3815–35. doi:10.1088/0031-9155/58/11/3815
152. Frey K, Unholtz D, Bauer J, Debus J, Min CH, Bortfeld T, et al. Automation and uncertainty analysis of a method for in-vivo range verification in particle therapy. *Phys Med Biol* (2014) **59**(19):5903–19. doi:10.1088/0031-9155/59/19/5903
153. Kuess P, Birkfellner W, Enghardt W, Helmbrecht S, Fiedler F, Georg D. Using statistical measures for automated comparison of in-beam PET data. *Med Phys* (2012) **39**(10):5874–81. doi:10.1118/1.4749962
154. Smeets J, Roellinghoff F, Prieels D, Stichelbaut F, Benilov A, Busca P, et al. Prompt gamma imaging with a slit camera for real time range control in proton therapy. *Phys Med Biol* (2012) **57**(11):3371–405. doi:10.1088/0031-9155/57/11/3371
155. Testa M, Min CH, Verburg JM, Schümann J, Lu HM, Paganetti H. Range verification of passively scattered proton beams based on prompt gamma time patterns. *Phys Med Biol* (2014) **59**(15):4181–95. doi:10.1088/0031-9155/59/15/4181
156. Min CH, Kim CH, Youn MY, Kim JW. Prompt gamma measurements for locating the dose falloff region in the proton therapy. *Appl Phys Lett* (2006) **89**(18):183517. doi:10.1063/1.2378561
157. Testa E, Bajard M, Chevallier M, Dauvergne D, LeFoulher F, Poizat J-C, et al. Monitoring the Bragg peak location of 73 MeV/u carbon ion beams by means of prompt gamma-ray measurements. *Appl Phys Lett* (2008) **93**(9):093506. doi:10.1063/1.2975841
158. Kim D, Yim H, Kim JW. Pinhole camera measurements of prompt gamma-rays for detection of beam range variation in proton therapy. *J Korean Phys Soc* (2009) **55**(4):1673–6. doi:10.3938/jkps.55.1673
159. Polf JC, Peterson S, McCleskey M, Roeder BT, Spiridon A, Beddar S, et al. Measurement and calculation of characteristic prompt gamma ray spectra emitted during proton irradiation. *Phys Med Biol* (2009) **54**:N519–27. doi:10.1088/0031-9155/54/22/N02
160. Verburg MJ, Riley K, Bortfeld T, Seco J. Energy and time resolved detection of prompt gamma rays for proton range verification. *Phys Med Biol* (2013) **58**(20):L37–49. doi:10.1088/0031-9155/58/20/L37
161. Roellinghoff F, Benilov A, Dauvergne D, Dedes G, Freud N, Janssens G, et al. Real-time proton beam range monitoring by means of prompt-gamma detection with a collimated camera. *Phys Med Biol* (2014) **59**(5):1327–38. doi:10.1088/0031-9155/59/5/1327
162. Pinto M, Dauvergne D, Freud N, Krimmer J, Letang J, Ray C, et al. Design optimisation of a TOF-based collimated camera prototype for online hadron-therapy monitoring. *Phys Med Biol* (2014) **59**(24):7653–74. doi:10.1088/0031-9155/59/24/7653
163. Verburg JM, Seco J. Proton range verification through prompt gamma-ray spectroscopy. *Phys Med Biol* (2014) **59**(23):7089–106. doi:10.1088/0031-9155/59/23/7089

164. Testa E, Bajard M, Chevallier M, Dauvergne D, Le Foulher F, Freud N, et al. Dose profile monitoring with carbon ions by means of prompt-gamma measurements. *Nucl Instrum Methods Phys Res B* (2009) **267**(6):993–6. doi:10.1016/j.nimb.2009.02.031
165. Testa M, Bajard M, Chevallier M, Dauvergne D, Freud N, Henriquet P, et al. Real-time monitoring of the Bragg peak position in ion therapy by means of single photon detection. *Radiat Environ Biophys* (2010) **49**(3):337–43. doi:10.1007/s00411-010-0276-2
166. Min CH, Lee HR, Kim CH, Lee SB. Development of array-type prompt gamma measurement system for in vivo range verification in proton therapy. *Med Phys* (2012) **39**(4):2100–7. doi:10.1118/1.3694098
167. Bom V, Joulaeizadeh L, Beekman F. Real-time prompt gamma monitoring in spot-scanning proton therapy using imaging through a knife-edge-shaped slit. *Phys Med Biol* (2012) **57**(2):297–308. doi:10.1088/0031-9155/57/2/297
168. Perali I, Celani A, Bombelli L, Fiorini C, Camera F, Clementel E, et al. Prompt gamma imaging of proton pencil beams at clinical dose rates. *Phys Med Biol* (2014) **59**(19):5849–71. doi:10.1088/0031-9155/59/19/5849
169. Pinto M, Bajard M, Brons S, Chevallier M, Dauvergne D, Dedes G, et al. Absolute prompt-gamma yield measurements for ion beam therapy monitoring. *Phys Med Biol* (2015) **60**(2):565–94. doi:10.1088/0031-9155/60/2/565
170. Seo H, Park JH, Kim CH, Lee JH, Lee CS, Sung Lee J. Compton-edge-based energy calibration of double-sided silicon strip detectors in Compton camera. *Nucl Instrum Methods Phys Res A* (2011) **633**:S108–10. doi:10.1016/j.nima.2010.06.138
171. Kurosawa S, Kubo H, Ueno K, Kabuki SH, Iwaki S, Takahashi M, et al. Prompt gamma detection for range verification in proton therapy. *Curr Appl Phys* (2012) **12**(2):364–8. doi:10.1016/j.cap.2011.07.027
172. Llosá G, Cabello J, Callier S, Gillam JE, Lacasta C, Rafecas M, et al. First Compton telescope prototype based on continuous LaBr3-SiPM detectors. *Nucl Instrum Methods Phys Res A* (2013) **718**:130–3. doi:10.1016/j.nima.2012.08.074
173. Hueso-Gonzalez F, Golnik C, Berthel M, Dreyer A, Enghardt W, Fiedler F, et al. Test of Compton camera components for prompt gamma imaging at the ELBE bremsstrahlung beam. *J Instrum* (2014) **9**:05002. doi:10.1088/1748-0221/9/05/P05002
174. Krimmer J, Ley J-L, Abellan C, Cachemiche J-P, Caponetto L, Chen X, et al. Development of a Compton camera for medical applications based on silicon strip and scintillation detectors. *Nucl Instrum Methods Phys Res A* (2014) **787**:98–101. doi:10.1016/j.nima.2014.11.042
175. Peterson SW, Robertson D, Polf J. Optimizing a three-stage compton camera for measuring prompt gamma rays emitted during proton radiotherapy. *Phys Med Biol* (2010) **55**(22):6841–56. doi:10.1088/0031-9155/55/22/015
176. Roellinghoff F, Richard M-H, Chevallier M, Constano J, Dauvergne D, Fred N, et al. Design of a compton camera for 3-D prompt gamma imaging during ion beam therapy. *Nucl Instrum Methods Phys Res A* (2011) **648**:S20–3. doi:10.1016/j.nima.2011.01.069
177. Kormoll T, Fiedler F, Schöne S, Wüstemann J, Zuber K, Enghardt W. A Compton imager for in-vivo dosimetry of proton beams. *Nucl Instrum Methods Phys Res A* (2011) **626-627**:114–9. doi:10.1016/j.nima.2010.10.031
178. Robertson D, Polf JC, Peterson SW, Gillin MT, Beddar S. Material efficiency studies for a Compton camera designed to measure characteristic prompt gamma rays emitted during proton beam radiotherapy. *Phys Med Biol* (2011) **56**(10):3047. doi:10.1088/0031-9155/56/10/010
179. Richard MH, Chevallier M, Dauvergne D, Freud N, Henriquet P, LeFouher F, et al. Design guidelines for a double scattering compton camera for prompt-Î^3 imaging during ion beam therapy: a Monte Carlo simulation study. *IEEE Trans Nucl Sci* (2011) **58**(1):87–94. doi:10.1109/TNS.2010.2076303
180. Golnik C, Hueso-González F, Müller A, Dendooven P, Enghardt W, Fiedler F, et al. Range assessment in particle therapy based on prompt gamma-ray timing measurements. *Phys Med Biol* (2014) **59**(18):5399–422. doi:10.1088/0031-9155/59/18/5399
181. Verburg JM, Shih HA, Seco J. Simulation of prompt gamma ray emission during proton radiotherapy. *Phys Med Biol* (2012) **57**(17):5459–72. doi:10.1088/0031-9155/57/17/5459
182. Dedes G, Pinto M, Dauvergne D, Freud N, Krimmer J, Létang JM, et al. Assessment and improvements of Geant4 hadronic models in the context of prompt-gamma hadrontherapy monitoring. *Phys Med Biol* (2014) **59**(7):1747–72. doi:10.1088/0031-9155/59/7/1747
183. Polf JC, Panthi R, Mackin DS, McCleskey M, Saastamoinen A, Roeder BT, et al. Measurement of characteristic prompt gamma rays emitted from oxygen and carbon in tissue- equivalent samples during proton beam irradiation. *Phys Med Biol* (2013) **58**(17):5821–31. doi:10.1088/0031-9155/58/17/5821
184. Le Foulher F, Bajard M, Chevallier M, Dauvergne D, Freud N, Henriquet P, et al. Monte Carlo simulations of prompt gamma emission during carbon ion irradiation. *IEEE Trans Nucl Sci* (2010) **57**:2768–72. doi:10.1109/TNS.2010.2048042
185. Helo Y, Kacperek A, Rosenberg I, Royle G, Gibson AP. The physics of Cerenkov light production during proton therapy. *Phys Med Biol* (2014) **59**(23):7107–23. doi:10.1088/0031-9155/59/23/7107
186. Yamaguchi A, Torikai K, Kawachi N, Shimada H, Satoh T, Nagao Y, et al. Beam range estimation by measuring brehmsstrahlung. *Phys Med Biol* (2012) **57**(10):2843–56. doi:10.1088/0031-9155/57/10/2843
187. Polf JC, Mackin D, Lee E, Avery S, Beddar S. Detecting prompt gamma emission during proton therapy: the effects of detector size and distance from the patient. *Phys Med Biol* (2014) **59**(9):2325–40. doi:10.1088/0031-9155/59/9/2325
188. Pinto M, De Rydt M, Dauvergne D, Dedes G, Freud N, Krimmer, J. et al. Technical Note: Experimental carbon ion range verification in inhomogeneous phantoms using prompt gammas. *Med Phys* (2015) **42**(5):2342. doi:10.1118/1.4917225
189. Dauvergne D, Battaglia M, Montarou G, Testa E. New methods of real-time control imaging for ion therapy. *NIRS-ETOILE Joint Symposium on Carbon Ion Therapy*. Lyon (2009). Available from: http://hal.in2p3.fr/in2p3-00363382
190. Amaldi U, Hajdas W, Iliescu S, Malakhov N, Samaratti J, Sauli F, et al. Advanced quality assurance for CNAO. *Nucl Instrum Methods Phys Res A* (2010) **617**:248–9. doi:10.1016/j.ejmp.2014.07.341
191. Henriquet P, Testa E, Chevallier M, Dauvergne D, Dedes G, Freud N, et al. Interaction vertex imaging (IVI) for carbon ion therapy monitoring: a feasibility study. *Phys Med Biol* (2012) **57**(14):4655–69. doi:10.1088/0031-9155/57/14/4655
192. Gowsch K, Hartmann B, Jakubek J, Granja C, Soukup P, Jäkel O, et al. Non-invasive monotoring of therapeutic carbon ion beams in a homogeneous phantom by tracking pf secondary ions. *Phys Med Biol* (2013) **58**(11):3755–73. doi:10.1088/0031-9155/58/11/3755
193. Agodi C, Battistoni G, Bellini F, Cirrone GAP, Collamati F, Cuttone G, et al. Charged particles flux measurement from PMMA irradiated by 80 MeV/u carbon ion beam. *Phys Med Biol* (2012) **57**(18):5667. doi:10.1088/0031-9155/57/18/5667
194. Piersanti L, Bellini F, Bini F, Collamati F, DeLucia E, Durante M, et al. Measurement of charged particle yields from PMMA irradiated by a 220 MeV/u 12C beam. *Phys Med Biol* (2014) **59**(7):1857–72. doi:10.1088/0031-9155/59/7/1857
195. Bucciantonio M, Amaldi U, Kieffler R, Malakhov N, Sauli F, Watts D. Fast readout of GEM detectors for medical imaging. *Nucl Instrum Methods Phys Res A* (2013) **718**:160–3. doi:10.1016/j.nima.2012.10.046
196. Marafini M, et al. Innovative solutions for in-beam dosimetry in hadrontherapy. *Submitted to ACTA Physics Polonica Proceedings of II Symposium on Positron Emission Tomography*. Krakov: Jagiellonian University of Krakov (2014).
197. Moteabbed M, España A, Paganetti H. Monte Carlo patient study on the comparison of prompt gammas and PET imaging for range verification in proton therapy. *Phys Med Biol* (2011) **56**(4):1063–82. doi:10.1088/0031-9155/56/4/012

Conflict of Interest Statement: The author declares that the research was conducted in the absence of any commercial or financial relationships that could be construed as a potential conflict of interest.

Copyright © 2015 Kraan. This is an open-access article distributed under the terms of the Creative Commons Attribution License (CC BY). The use, distribution or reproduction in other forums is permitted, provided the original author(s) or licensor are credited and that the original publication in this journal is cited, in accordance with accepted academic practice. No use, distribution or reproduction is permitted which does not comply with these terms.

frontiers in Oncology

ORIGINAL RESEARCH
published: 27 June 2016
doi: 10.3389/fonc.2016.00156

Experimental Comparison of Knife-Edge and Multi-Parallel Slit Collimators for Prompt Gamma Imaging of Proton Pencil Beams

Julien Smeets[1], Frauke Roellinghoff[1,2,3], Guillaume Janssens[1], Irene Perali[4,5], Andrea Celani[6], Carlo Fiorini[4,5], Nicolas Freud[3], Etienne Testa[2] and Damien Prieels[1]*

[1] Ion Beam Applications SA, Louvain-la-Neuve, Belgium, [2]IPNL, Université Lyon 1 and CNRS/IN2P3, Lyon, France, [3]Université Lyon, INSA – Lyon, Université Lyon 1, UJM-Saint Etienne, CNRS, Inserm, Centre Léon Bérard, CREATIS UMR 5220 U1206, Lyon, France, [4] Politecnico di Milano, Dipartimento di Elettronica, Informazione e Bioingegneria, Milano, Italy, [5] Istituto Nazionale di Fisica Nucleare, Sezione di Milano, Milano, Italy, [6] XGLab SRL, Milano, Italy

More and more camera concepts are being investigated to try and seize the opportunity of instantaneous range verification of proton therapy treatments offered by prompt gammas emitted along the proton tracks. Focusing on one-dimensional imaging with a passive collimator, the present study experimentally compared in combination with the first, clinically compatible, dedicated camera device the performances of instances of the two main options: a knife-edge slit (KES) and a multi-parallel slit (MPS) design. These two options were experimentally assessed in this specific context as they were previously demonstrated through analytical and numerical studies to allow similar performances in terms of Bragg peak retrieval precision and spatial resolution in a general context. Both collimators were prototyped according to the conclusions of Monte Carlo optimization studies under constraints of equal weight (40 mm tungsten alloy equivalent thickness) and of the specificities of the camera device under consideration (in particular 4 mm segmentation along beam axis and no time-of-flight discrimination, both of which less favorable to the MPS performance than to the KES one). Acquisitions of proton pencil beams of 100, 160, and 230 MeV in a PMMA target revealed that, in order to reach a given level of statistical precision on Bragg peak depth retrieval, the KES collimator requires only half the dose the present MPS collimator needs, making the KES collimator a preferred option for a compact camera device aimed at imaging only the Bragg peak position. On the other hand, the present MPS collimator proves more effective at retrieving the entrance of the beam in the target in the context of an extended camera device aimed at imaging the whole proton track within the patient.

Keywords: proton therapy, range verification, prompt gamma imaging

OPEN ACCESS

Edited by:
Marco Durante, GSI Helmholtzzentrum für Schwerionenforschung, Germany

Reviewed by:
Sunyoung Jang, Princeton Radiation Oncology, USA
John Eley, University of Maryland School of Medicine, USA

****Correspondence:***
Julien Smeets
julien.smeets@iba-group.com

Specialty section:
This article was submitted to Radiation Oncology, a section of the journal Frontiers in Oncology

Received: *31 January 2016*
Accepted: *10 June 2016*
Published: *27 June 2016*

Citation:
Smeets J, Roellinghoff F, Janssens G, Perali I, Celani A, Fiorini C, Freud N, Testa E and Prieels D (2016) Experimental Comparison of Knife-Edge and Multi-Parallel Slit Collimators for Prompt Gamma Imaging of Proton Pencil Beams. Front. Oncol. 6:156. doi: 10.3389/fonc.2016.00156

INTRODUCTION

Proton therapy materializes the medical physicist's goal to specifically target tumor volumes while sparing surrounding healthy – and potentially critical – organs. But this improved precision demands improved accuracy in order to prevent any under- or overshoot. Safety margins are applied, and research efforts are invested in order to reduce range uncertainties before treatment

delivery, monitor range during treatment, and verify range after treatment. Luckily, proton therapy offers several distinctive opportunities for treatment quality control, for example through activated nuclei along the proton beam path that can be imaged by a PET scan device (1), through proton-induced acoustic waves that could be measured by an ultra-sound probe (2), or through physiological impacts that can later be observed on MRI acquisitions (3).

In this regard, Jongen and Stichelbaut (4) suggested to image the prompt gammas emitted by proton-excited nuclei in order to take advantage of the straightforward correlation of their spatial emission distribution with the proton range. First experimental evidences reported by Min et al. (5) triggered interest for the Prompt Gamma Imaging (PGI) approach and its promises of instantaneous feedback on an individual spot basis with non-invasive equipment. Recent efforts culminated in the alternative ideas of taking benefit from the time emission distribution of prompt gammas through the Prompt Gamma Timing (PGT) method by Golnik et al. (6), or from their energy emission distribution through the Prompt Gamma Spectroscopy (PGS) method by Verburg and Seco (7).

The PGI, PGT, and PGS approaches have their own specificities, advantages, and disadvantages in terms of sensitivity, generated information, cost, footprint, supported beam conditions, and robustness to different sources of uncertainties. The preferred approach is thereby dependent on the favored features. In the near future, the ongoing development of prototype systems will hopefully allow experimental comparisons in order to assess what approach is offering the preferred tradeoff depending on the clinical context under consideration (clinical case, treatment mode, treatment workflow).

The PGI field has been very dynamic over the last years, with a large number of camera concepts being investigated, optimized, and prototyped. These are not only relying on passive collimators but also on sophisticated electronic collimation techniques through different designs of Compton cameras (8) that offer the advantage of discarding the negative impact of a passive collimator in terms of weight and signal attenuation, at the cost of reduced scoring efficiency in the detection stages and increased complexity in electronics and data treatment.

The present study is focused on PGI, more specifically with passive collimators, in order to leverage on the promises of this option as the one most suited to diagnosing the largest number of spots of a pencil beam scanning (PBS) treatment delivery and the one most accommodating the various beam time structures of the different types of accelerators used in clinical facilities (synchrotron, cyclotron, and synchrocyclotron), the maximum instantaneous clinical beam currents of which can differ over several orders of magnitude.

The information on which feedback is presently missing during treatment delivery is the beam penetration depth within the patient, so that 1D imaging was most often privileged so far, with two main options in the form of multi-parallel slit (MPS) (9) and knife-edge slit (KES) (10) collimators meant at producing the best possible projection of the prompt gamma emission fall-off ~3 mm before the proton mean maximum penetration depth. The concrete, practical objective of the present study is the experimental comparison of the performance of these two types of collimators in combination with the first prompt gamma camera prototype built by Perali et al. (11) in order to identify the most advantageous design for the clinical evaluation of the camera prototype. In addition to the Bragg peak position, the performance of both collimators in retrieving the entrance point of the beam in the target is also compared. In case of absence of complementary imaging modalities, the measurement of the entrance point could help diagnose the cause of any mismatch of the Bragg peak position with respect to treatment plan expectations.

MATERIALS AND METHODS

Camera Design

Individual spots of a PBS treatment plan typically range between 10^6 and 10^8 protons for a typical 2 Gy fraction. Nuclear collisions cause ~1 prompt gamma to escape the patient every 10 protons (12), resulting in a large number of prompt gammas per spot. But these are challenging to detect as they are emitted instantaneously, with multi-MeV energy and spread over 4π steradians. The use of a thick collimator as well as fast and dense crystals is therefore required, which in turn limits the solid angle that can be covered by a camera device of reasonable weight and cost. As a consequence, the spatial resolution of the collimator needs to be compromised in order to favor the counting statistics and achieve a clinically viable efficiency of the order of 1 prompt gamma detected every 10^5 protons (13). The subsequent, poor spatial resolution as well as the significant statistical fluctuations of the signal of a single spot is then compensated for by the use of *a priori* information when comparing the actually measured profile to a reference computed one reflecting the treatment plan hypotheses (14).

The present study relies on the first unit prompt gamma camera built by Perali et al. (11) that demonstrated, in combination with a KES collimator, sufficient detection speed and efficiency for compatibility with clinical irradiation scenarios. The camera is a dedicated, very-fast, 1-dimensional, high-energy gamma imaging device built upon two rows of 20 LYSO crystal slabs, directly coupled to arrays of SiPMs (Silicon Photomultipliers) and read out by 40 independent acquisition channels that can be operated in two different modes. During a proton irradiation, each channel is operated in fast mode and scores the number of events that are detected above a first, lower-threshold comparator and below a second, upper-threshold comparator. The levels of these two comparators correspond to the energy selection window of the camera. They are set as a result of the camera energy calibration, based on spectra of known energy lines acquired in slow mode. Each of the 40 LYSO slabs is 4 mm wide along beam axis, 100 mm high, and 31.5 mm deep, for a total crystal volume of 504 cm^3 producing a 1D image of 8 cm width.

Collimator Designs

Two collimators made of tungsten alloy (17.0 g/cm^3) were prototyped for experimental comparison. The first one is a KES collimator design reproducing dimensions from Smeets et al. (12) that

were selected by eye inspection of the detection profiles resulting from extensive parameter variation tests with Monte Carlo code MCNPX version 2.5.0 (15). The second one is a MPS collimator design implementing the conclusions of Roellinghoff (16) for an optimal prompt gamma profile falloff retrieval precision from extensive parameter variation tests with simulation platform GATE version 6 (17) built upon Monte Carlo code Geant4 version 9.4p01, under the first constraint of the 4 mm segmentation of the present camera system and the second constraint of a weight equal to that of the walls of the 40 mm thick KES collimator for direct comparability.

Both collimators are schemed in **Figure 1**. The KES collimator has a single 6 mm and 53.1° [=2*acot(2)] aperture. The MPS collimator has parallel apertures of 2.4 mm gap separated by tungsten alloy sheets that are 1.6 mm thick and 100 mm deep, matching the 4 mm segmentation of the camera and resulting in a fill factor of 40% which, combined with the 100 mm depth, equals the 40 mm thickness of the KES collimator in terms of attenuation efficiency. In line with their optimizations, the KES collimator is used in a 5:4 magnification ratio corresponding to 10 cm Field-Of-View (FOV) along beam axis, while the MPS collimator positioned right against the camera in a 1:1 magnification ratio corresponding to 8 cm FOV.

Roellinghoff (16) showed that a comparison of KES and MPS collimators, in the ideal conditions of a MPS collimator with infinitely thin septa and a KES collimator of which the solid angle variation along the FOV would be neglected, can result in fully identical Bragg peak retrieval precisions and spatial resolutions upon relevant scaling of the dimensions. Simulations with GATE then brought confirmation that this result can reasonably hold when considering realistic designs. Similar performances can be targeted in a general context. In the present, practical context, we deviated in at least two notable ways from conditions of equal performance. First, a MPS collimator to be compared to the present KES one would preferably involve a larger pitch than the present 4 mm one (actually a 12 mm one) to compromise spatial resolution at the benefit of detection efficiency, which would have required an alternative manufacturing of the present camera system. Second, we did not impose coherent scaling of the distances between beam axis, collimator and crystals for both collimators. We instead decided to only impose an identical distance between beam axis and the collimator entrance face (actually 200 mm) in order to reflect a practical constraint of positioning the camera as close as possible to beam axis while avoiding collision with the patient. Beyond this collimator entrance face constraint, crystals were independently positioned at optimal distances, which results in a closer distance to beam axis (and subsequently in a favored detection efficiency) for the MPS setup over the KES one. The overall balance of these two deviations from conditions of equal performance is a better detection efficiency for the KES collimator and a better spatial resolution for the MPS one.

Proton Beam Tests

Measurements were performed in October 2013 at the West German Proton Therapy Centre Essen (WPE) with a proton beam delivered by an IBA C230 isochronous cyclotron in a

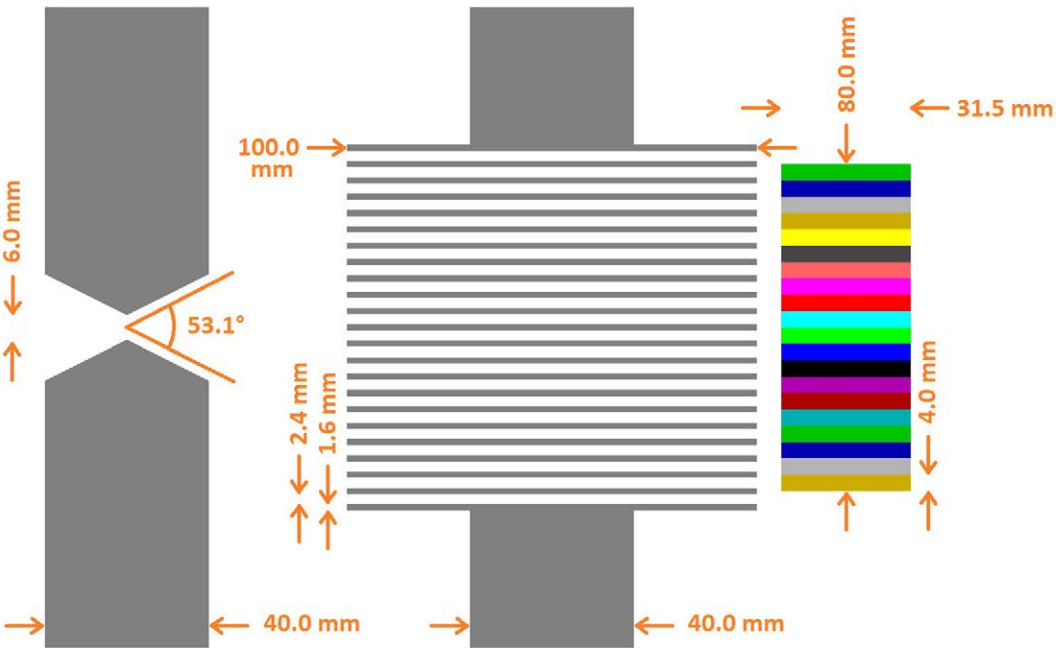

FIGURE 1 | **Superimposed collimator geometries**. The KES collimator (left) is superimposed with the MPS collimator (center) and the crystals (right). All distances with respect to the crystals are conserved. In the real prototype version (cf. **Figure 2**) used for beam tests, the parallel apertures of the MPS collimator are 0.1 mm wider (2.5 instead of 2.4 mm) in order to preserve alignment in presence of the 0.1 mm absorber sheets inserted in between the crystal slabs of the real camera device.

treatment room equipped with a PBS-dedicated nozzle. All acquisitions were performed for 10 s from a single spot at isocenter delivered along the axis of a PMMA target that is 7.5 cm in radius. Delivered proton charge was integrated by an electrometer connected to an ionization chamber intercepting the whole section of the pencil beam inside the nozzle. With the beam already on, the 10 s charge integration was synchronized manually with each camera acquisition. This was observed to result in a maximum error of 3% in charge collection over six repetitions of a same acquisition. Accurate absolute calibration was not required for our comparative evaluation and the ionization chamber was therefore not calibrated for the temperature and pressure of the day, so that the absolute calibration cannot be assumed to be at the 1% level. The energy calibration of the camera was performed by combining the characteristic gamma rays identified from a spectrum acquisition of the prompt gammas emitted by a water target during proton irradiation and a spectrum acquisition of the gammas resulting from the decays of Na-24 produced by the previous proton irradiation of an aluminum target.

Both collimator setups are pictured in **Figure 2**. For direct comparability, the two collimators were positioned with their entrance face at 200 mm from beam axis. As a result, the center of the KES aperture was 220 mm from beam axis and the center of the crystals was 176 mm from the center of the KES aperture, while the center of the MPS collimator was 250 mm from beam axis and the crystals were right behind.

Acquisitions were recorded with each setup at 100, 160, and 230 MeV to cover the clinical range, first with the center of the FOV aligned with the expected range in PMMA (6.7 cm at 100 MeV, 15.2 cm at 160 MeV, and 28.4 cm at 230 MeV) and second with the center of the FOV aligned with the entrance point of the beam inside the target. The cylindrical PMMA target was 20 cm along beam axis at 100 and 160 MeV and 40 cm at 230 MeV. Acquisitions were recorded with different energy windows and only the ones with the window 3–6 MeV are presented here as they were assessed to result in the preferred compromise between count rate, robust calibration and, most importantly, falloff retrieval precision over the different beam energies. All acquisitions were recorded at beam current values within the clinical range: ~1 nA at 100 MeV, 2 nA at 160 MeV, and 4 nA at 230 MeV.

Performance Evaluation

The performance of either collimator setup in each acquisition was rated by applying the approach of Roellinghoff et al. (18) as described in Perali et al. (11). Starting from the very high statistic detection profile of the 10 s acquisition, corresponding to the order of 10^{11} protons, 1000 profiles were sampled for three different numbers of protons (1E8, 3E8, and 1E9 protons) and were then matched with the original very high statistic profile (as if it were the result of the expected signal computation model once perfectly calibrated) in order to estimate the intrinsic falloff retrieval precision. The lateral shift between each low-statistic sample profile and its high-statistic original profile is determined as the one minimizing the root-squared difference between the two profiles from all tested shifts between −20 mm and +20 mm by steps of 0.25 mm. This lateral shift should here equal 0 in case of exact retrieval and the average error over the 1000 sample profiles delivers a reliable indication of the intrinsic quality of the detection profile generated by either collimator. The larger the amplitude of the prompt gamma signal detected thanks to a good detection efficiency and/or the sharper the edges of the detected falloff thanks a good spatial resolution, the better the falloff retrieval precision. Roellinghoff et al. (18) showed that the falloff retrieval precision is inversely proportional to the square root of the number of protons, so that they exhibit a linear relation in a log–log plot. For each acquisition of either collimator setup, this linear relation was interpolated so as to determine the number of protons corresponding to a 2 sigma precision of 4 mm, which, in line with Perali et al. (11), was arbitrarily chosen as reference for our study.

In order to improve the falloff retrieval precision, all profiles where applied a Gaussian smoothing with a Full Width At Half Maximum (FWHM) equal to that of the impulse response of the collimator as determined from simulations with Monte Carlo code MCNPX version 2.5.0. This smoothing advantageously attenuates the spatial frequencies that are too high to result from the collimator projection and that essentially correspond to slab-to-slab variations in the number of counts due to statistical fluctuations and, to a lesser extent, to the lack of uniformity resulting from uncertainties on the individual energy calibration of each slab and, in case of the MPS collimator, from the uncertainty (±0.1 mm) on the thickness of the tungsten alloy

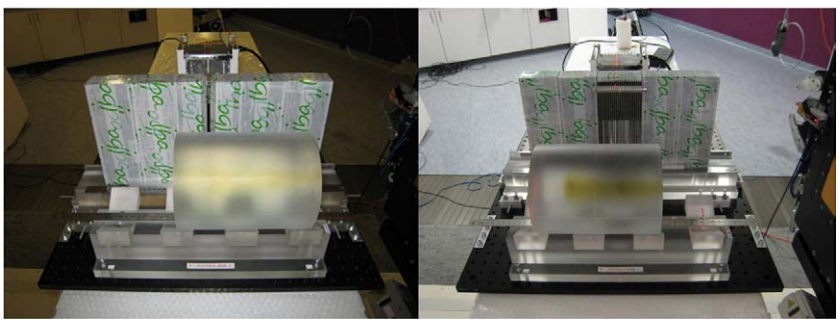

FIGURE 2 | **Experimental prompt gamma camera setups**. The KES collimator setup is pictured on the left and the MPS collimator on the right.

sheets causing some of the parallel apertures to be slightly wider or narrower.

RESULTS

The simulated impulse response of both collimator setups is compared in **Figure 3**. A 4.44 MeV gamma point source was considered for this evaluation as it is the most intense characteristic prompt gamma ray resulting from the irradiation of carbon and oxygen at the center of our 3–6 MeV window. The MPS collimator exhibits a thrice better spatial resolution with 7 mm FWHM versus 22 mm for the KES one. The KES collimator is scoring more signal with poorer spatial resolution and records a slightly lower background of uncorrelated signal. In the KES configuration, the crystals are further both from the collimator and the beam axis, which reduces the detection efficiency of gammas that, with or without scattering, succeed in emerging from the 40 mm tungsten thickness.

The detection profiles recorded by both collimators at 100, 160, and 230 MeV, when imaging the Bragg peak as well as when imaging the entrance of the beam in the target, are compared in **Figure 4**. The KES and MPS acquisitions were applied a 22 and 7 mm FWHM Gaussian smoothing, respectively.

The performance of each acquisition in **Figure 3** is rated in **Table 1** in terms of computed number of protons (in units of 1E8 protons) necessary to reach a 2 sigma precision of 4 mm on range estimation. Each value is the average over three computations with different seed numbers to the random number generator that is used to generate the sample profiles from the measured one according to a Poisson process. The relative SD of the three computations ranged from 2 to 6%.

For all acquisitions in **Table 1**, the number of protons to reach a 2 sigma precision of 4 mm on Bragg peak (or entrance) falloff retrieval is in the order of 10^8 protons, showing that statistically meaningful feedback is possible on a single spot basis for the few highest weighted spots of the order of 10^8 protons close to the target distal edge. On the other hand, neighbor spot aggregation will be necessary for the majority of spots of the order of 10^7 protons, and no statistically meaningful information can result from the proximal lowest weighted spots of the order of 10^6 protons.

A first remark on these results is that the performance criterion of a 2 sigma precision of 4 mm was considered here because it applies identically to the retrieval of both the Bragg peak and the entrance point of each pencil beam for direct comparison and is independent of the choice of any distal margin recipe. As a consequence, this criterion fails to reflect the fact that achieving a 2 sigma precision of 4 mm at 230 MeV is clinically much more valuable than achieving it at 100 MeV in terms of margin reduction. If we arbitrarily assume a distal margin recipe of 3.5% + 2 mm based on 1.5 sigma (19), the distal margin in our PMMA target would be 4 mm at 100 MeV and 12 mm at 230 MeV at the 1.5 sigma level.

A second remark is that the performance criterion of a 2 sigma precision of 4 mm is an arbitrary choice applied to the context of this collimator comparison and is not a lower bound on the precision achievable by either collimator in any context. Increasing the number of protons considered, positioning the collimator closer to beam axis, reducing beam energy, and increasing the oxygen to carbon composition ratio in the target are all factors that, alone or combined, would cause a better precision in other contexts.

A third remark is that, at the date of these measurements, only one of the two rows of 20 LYSO slabs was mounted on camera, so that the detection efficiency reported in **Figures 3** and **4** is exactly half that of the full camera. For a more meaningful rating of the performance of the camera, we assumed the double detection efficiency of the full camera in the performance values further reported in **Table 1**.

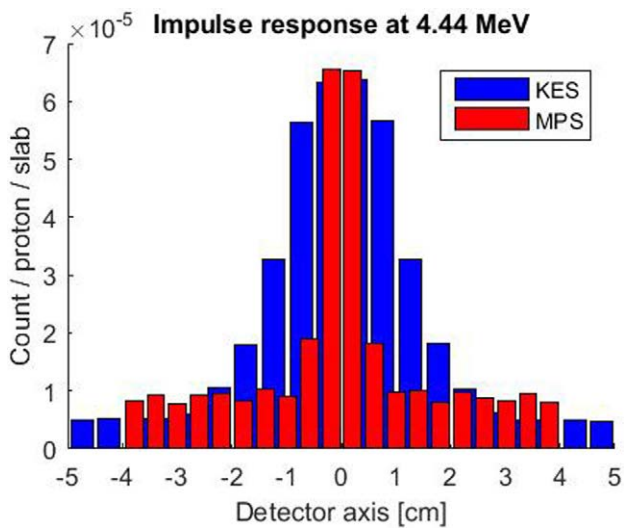

FIGURE 3 | Simulated impulse response of both collimator setups for a 4.44 MeV point source along beam axis at the center of the FOV. The KES collimator response is plotted in blue and the MPS one in red.

DISCUSSION

Performance values in **Table 1** reveal two trends. First, whatever the collimator, increasing beam energy reduces the performance. This was fully expected both from simulations and past measurements by Min et al. (5) for the MPS collimator and Smeets et al. (12) for the KES one. Second, the Bragg Peak retrieval performance of the KES collimator is better than the MPS one in combination with the camera device under consideration. Roughly twice less protons are needed by the KES to reach a given precision. This result was the very focus of the present study, and the KES design was therefore selected to equip the present prompt gamma camera device for further assessment of its performance during clinical treatment delivery as illustrated in **Figure 5**. The very first prompt gamma acquisition of a patient treatment was recently performed with it by Richter et al. (20) at the Universitäts Protonen Therapie Dresden at OncoRay.

Beyond these first observations, performances values in **Table 1** highlight another interesting finding. For the KES collimator, the performance in retrieving the entrance position also degrades when increasing beam energy and, whatever the

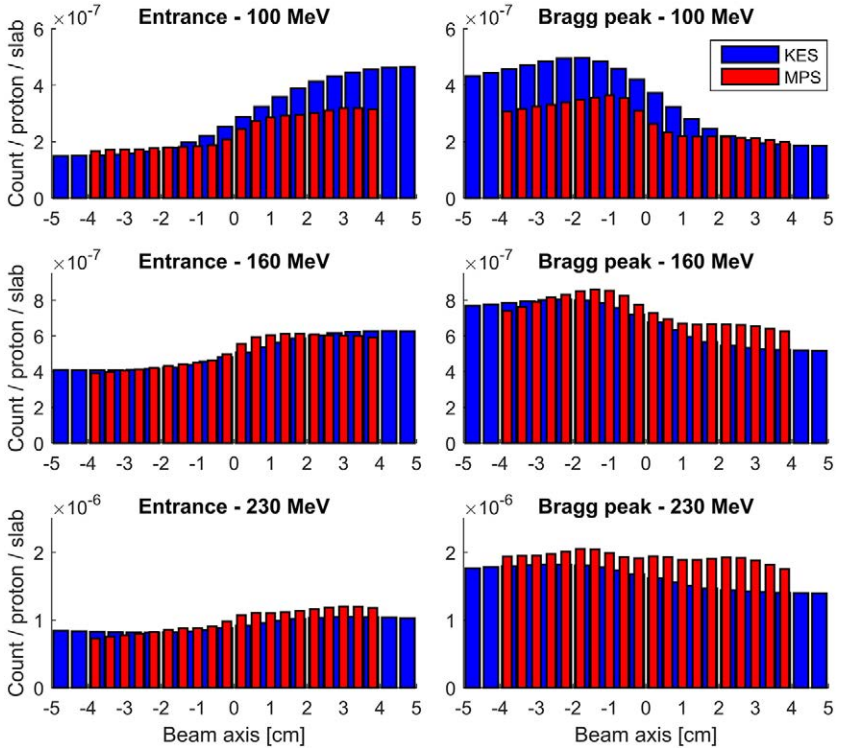

FIGURE 4 | **Measured prompt gamma profiles with a 3–6 MeV energy window**. All acquisitions were performed for 10 s at clinical beam currents between 1.1 and 4.7 nA, corresponding to numbers of protons incident on the target between 7E10 and 3E11. The KES collimator response is plotted in red and the MPS one in blue.

TABLE 1 | Computed number of protons (in units of 1E8 protons) necessary to reach a 2 sigma precision of 4 mm on range estimation for the detection efficiency of the full camera.

	Entrance		Bragg peak	
	KES	MPS	KES	MPS
100 MeV	0.82	1.42	0.35	0.65
160 MeV	2.92	1.87	1.19	1.71
230 MeV	3.15	1.62	2.01	4.44

Each value is the mean value of three computations with different seeds to the random number generator. The relative SD of the three computations ranged from 2 to 6%.

energy, the performance in retrieving the entrance position, is always poorer than the performance in retrieving the Bragg peak position. This was already demonstrated in Perali et al. (11). In contrast, the MPS collimator succeeds in maintaining a valuable and stable performance at all beam energies for the entrance point. As a result, at 160 and 230 MeV, the MPS collimator not only exhibits better performance for the entrance than for the Bragg peak but also achieves better performance for the entrance than the KES collimator.

The origin of these different behaviors at entrance and Bragg peak lies in the anisotropy of proton-induced neutron emissions that generate most of the measured background signal at high beam energies. When either collimator is aligned at the entrance face of the target, the measured neutron background is not uniform but sloped because proton-induced neutron emissions are forward-peaked and, in contrast to the Bragg peak depth, there are at the entrance depth no neutrons generated downstream to compensate the anisotropy of those emitted beyond the entrance depth. Both collimators are inefficient at collimating those neutrons. In the case of the KES collimator, the neutron background at target entrance has an opposite slope to that of the reversed 1D projection of the correlated prompt gamma, whereas both components add up slopes of equal sign in case of the MPS collimator. As a consequence, when beam energy increases, the slope of the neutron signal gradually cancels that of the prompt gamma signal projected by the KES collimator, whereas it adds a positive contribution to that of the prompt gamma signal projected by MPS collimator and roughly compensates for the reduced prompt gamma emission at entrance by higher energy protons so as to maintain a rather stable performance whatever the beam energy.

The conclusion of the present study is that KES collimator proved better for Bragg peak depth retrieval, whereas the MPS collimator proved better for entrance depth retrieval. On the one hand, it is unfortunate as it would have been more convenient to benefit from the best performance for both extremities of the proton range with one single design. On the other hand, it is fortunate that the MPS collimator is the one achieving the best performance for the entrance position as it is also the one the FOV of which can most straightforwardly be increased in order to image the whole proton track without compromising the uniformity. The compact prototype in **Figure 5** was built with a KES collimator for clinical

FIGURE 5 | **Prompt gamma camera prototype trolley positioning system**. The complete trolley is drawn on the left and the real KES collimator is pictured on the right.

evaluation as it is meant for the measurement of the Bragg peak depth with its 10 cm FOV. Measuring the entrance point by PGI implies a significant increase in cost, weight and footprint of the camera in order to cover proton ranges up to 32 cm in patients that need be evaluated in terms of clinical value. Further investigations will assess the combination of the Bragg peak image by the camera with other imaging modalities (X-ray shots, CBCT, and/or optical tracking) that have the potential to advantageously substitute the PGI acquisition of the entrance depth.

Finally, two limitations to the generality of the results of the present study should be underlined. First, the 4 mm segmentation of the camera system (resulting from an optimization of the tradeoff between the detection efficiency, the count rate and the number of channels and photodetectors) is not optimal for an MPS collimator that tends to favor larger pitches (16, 21) whereas the KES collimator performance is less sensitive to any variation of the crystal segmentation (12). Second, the MPS collimator was here suffering from a higher level of background when imaging the Bragg peak at high beam energies and it might therefore be anticipated that the addition of any background reduction method (at the cost of an increase in the complexity of the camera design), for example by means of a TOF discrimination technique (22), would benefit more to the MPS than to the KES collimator. A comparison of the performance of KES and MPS collimators in the context of a camera with a different segmentation and/or featuring any additional background discrimination technique (and thereby relying on a different tradeoff between cost, performance, and complexity) may lead to different conclusions.

AUTHOR CONTRIBUTIONS

Collimator design simulations and manufacturing: FR, JS, NF, ET, and DP. Camera design, manufacturing and calibration: IP, AC, and CF. Experiment preparation: FR, JS, GJ, IP, AC, CF, and DP. Experiment conduct: JS, FR, GJ, IP, AC, and DP. Data analysis methodology: FR, GJ, JS, NF, and ET. Data analysis software: GJ. Data analysis conduct and result redaction: JS. Result discussion and manuscript review: FR, GJ, IP, AC, CF, NF, ET, and DP.

ACKNOWLEDGMENTS

This work received funding from the European Union Seventh Framework Program (FP7/2007–2013) under grant agreement nos 241851 (ENVISION) and 264552 (ENTERVISION). We would like to gratefully thank Denis Dauvergne from IPNL, Jean Michel Létang from CREATIS and Sébastien Henrotin, Ben Reynders, Eric Demoitié and Riccardo Saitta from IBA and for their precious contributions to the preparation and realization of the measurements.

REFERENCES

1. Parodi K, Paganetti H, Shih HA, Michaud S, Loeffler JS, DeLaney TF, et al. Patient study of in vivo verification of beam delivery and range, using positron emission tomography and computed tomography imaging after proton therapy. *Int J Radiat Oncol Biol Phys* (2007) 68:920–34. doi:10.1016/j.ijrobp.2007.01.063
2. Jones KC, Witztum A, Sehgal CM, Avery S. Proton beam characterization by proton-induced acoustic emission: simulation studies. *Phys Med Biol* (2014) 59:6549–63. doi:10.1088/0031-9155/59/21/6549
3. Krejcarek SC, Grant PE, Henson JW, Tarbell NJ, Yock TI. Physiologic and radiographic evidence of the distal edge of the proton beam in craniospinal irradiation. *Int J Radiat Oncol Biol Phys* (2007) 68:646–9. doi:10.1016/j.ijrobp.2007.02.021
4. Jongen Y, Stichelbaut F. Verification of the proton beam position in the patient by the detection of prompt gamma-rays emission. *39th Meeting of the Particle Therapy Co-Operative Group*. San Francisco, CA (2003).
5. Min CH, Kim CH, Youn MY, Kim JW. Prompt gamma measurements for locating the dose falloff region in the proton therapy. *Appl Phys Lett* (2006) 89:183517. doi:10.1063/1.2378561
6. Golnik C, Hueso-González F, Müller A, Dendooven P, Enghardt W, Fiedler F, et al. Range assessment in particle therapy based on prompt γ-ray timing measurements. *Phys Med Biol* (2014) 59:5399–422. doi:10.1088/0031-9155/59/18/5399
7. Verburg J, Seco J. Proton range verification through prompt γ-ray spectroscopy. *Phys Med Biol* (2014) 59:7089–106. doi:10.1088/0031-9155/59/23/7089
8. Kabuki S, Kazuki U, Kurosawa S, Iwaki S, Kubo H, Miuchi K, et al. Study on the use of electron-tracking Compton gamma-ray camera to monitor the therapeutic proton dose distribution in real time. *2009 IEEE Nuclear Science Symposium Conference Record (NSS/MIC)*. Orlando, FL: IEEE (2009). p. 2437–40.
9. Min CH, Park JG, Kim CH. Development of an array-type prompt gamma detection system for the online measurement of the range of the proton beam in a patient: a Monte Carlo feasibility study. *J Korean Phys Soc* (2008) 52:888–91. doi:10.3938/jkps.52.888
10. Bom V, Joulaeizadeh L, Beekman F. Real-time prompt gamma monitoring in spot-scanning proton therapy using imaging through a knife-edge-shaped slit. *Phys Med Biol* (2012) 57:297–308. doi:10.1088/0031-9155/57/2/297
11. Perali I, Celani A, Bombelli L, Fiorini C, Camera F, Clementel E, et al. Prompt gamma imaging of proton pencil beams at clinical dose rate. *Phys Med Biol* (2014) 59:5849–71. doi:10.1088/0031-9155/59/19/5849
12. Smeets J, Roellinghoff F, Prieels D, Stichelbaut F, Benilov A, Busca P, et al. Prompt gamma imaging with a slit camera for real-time range control in proton therapy. *Phys Med Biol* (2012) 57:3371–405. doi:10.1088/0031-9155/57/11/3371
13. Priegnitz M, Helmbrecht S, Janssens G, Perali I, Smeets J, Vander Stappen F, et al. Measurement of prompt gamma profiles in inhomogeneous targets

with a knife-edge slit camera during proton irradiation. *Phys Med Biol* (2015) 60:4849–71. doi:10.1088/0031-9155/60/12/4849

14. Sterpin E, Janssens G, Smeets J, Vander Stappen F, Prieels D, Priegnitz M, et al. Analytical computation of prompt gamma ray emission and detection for proton range verification. *Phys Med Biol* (2015) 60:4915–46. doi:10.1088/0031-9155/60/12/4915
15. Pelowitz D, editor. *MCNPX User's Manual Version 2.5.0. Los Alamos National Laboratory Report LA-CP-05-0369*. Los Alamos (2005).
16. Roellinghoff F. *Design and Implementation of a Prompt-Gamma Camera for Real-Time Monitoring of Ion Beam Therapy [PhD Thesis]*. France: Institut National des Sciences Appliquées de Lyon (2015).
17. Jan S, Benoit D, Becheva E, Carlier T, Cassol F, Descourt P, et al. GATE V6: a major enhancement of the GATE simulation platform enabling modelling of CT and radiotherapy. *Phys Med Biol* (2011) 56:881–901. doi:10.1088/0031-9155/56/4/001
18. Roellinghoff F, Benilov A, Dauvergne D, Dedes G, Freud N, Janssens G, et al. Real-time proton beam range monitoring by means of prompt-gamma detection with a collimated camera. *Phys Med Biol* (2014) 59:1327–38. doi:10.1088/0031-9155/59/5/1327
19. Paganetti H. Range uncertainties in proton therapy and the role of Monte Carlo simulations. *Phys Med Biol* (2012) 57:R99–117. doi:10.1088/0031-9155/57/11/R99
20. Richter C, Pausch G, Barczyk S, Priegnitz M, Keitz I, Thiele J, et al. First clinical application of a prompt gamma based in vivo proton range verification system. *Radiother Oncol* (2016) 118(2):232–7. doi:10.1016/j.radonc.2016.01.004
21. Pinto M, Dauvergne D, Freud N, Krimmer J, Létang J-M, Ray C, et al. Design optimisation of a TOF-based collimated camera prototype for online hadrontherapy monitoring. *Phys Med Biol* (2014) 59:7653–74. doi:10.1088/0031-9155/59/24/7653
22. Biegun AK, Seravalli E, Lopes PC, Rinaldi I, Pinto M, Oxley DC, et al. Time-of-flight neutron rejection to improve prompt gamma imaging for proton range verification: a simulation study. *Phys Med Biol* (2012) 57:6429–44. doi:10.1088/0031-9155/57/20/6429

Conflict of Interest Statement: Part of the authors and their institutions have filed patent applications relevant to this work.

The authors declare that the research was conducted in the absence of any commercial or financial relationships that could be construed as a potential conflict of interest.

Copyright © 2016 Smeets, Roellinghoff, Janssens, Perali, Celani, Fiorini, Freud, Testa and Prieels. This is an open-access article distributed under the terms of the Creative Commons Attribution License (CC BY). The use, distribution or reproduction in other forums is permitted, provided the original author(s) or licensor are credited and that the original publication in this journal is cited, in accordance with accepted academic practice. No use, distribution or reproduction is permitted which does not comply with these terms.

frontiers in Oncology

REVIEW
published: 12 April 2016
doi: 10.3389/fonc.2016.00080

Compton Camera and Prompt Gamma Ray Timing: Two Methods for *In Vivo* Range Assessment in Proton Therapy

Fernando Hueso-González[1,2], Fine Fiedler[3], Christian Golnik[2], Thomas Kormoll[2], Guntram Pausch[2], Johannes Petzoldt[2], Katja E. Römer[3] and Wolfgang Enghardt[1,2,4]*

[1] Institute of Radiooncology, Helmholtz-Zentrum Dresden – Rossendorf, Dresden, Germany, [2] OncoRay – National Center for Radiation Research in Oncology, Faculty of Medicine and University Hospital Carl Gustav Carus, Technische Universität Dresden, Dresden, Germany, [3] Institute of Radiation Physics, Helmholtz-Zentrum Dresden – Rossendorf, Dresden, Germany, [4] German Cancer Consortium (DKTK), German Cancer Research Center (DKFZ), Heidelberg, Germany

Proton beams are promising means for treating tumors. Such charged particles stop at a defined depth, where the ionization density is maximum. As the dose deposit beyond this distal edge is very low, proton therapy minimizes the damage to normal tissue compared to photon therapy. Nevertheless, inherent range uncertainties cast doubts on the irradiation of tumors close to organs at risk and lead to the application of conservative safety margins. This constrains significantly the potential benefits of protons over photons. In this context, several research groups are developing experimental tools for range verification based on the detection of prompt gammas, a nuclear by-product of the proton irradiation. At OncoRay and Helmholtz-Zentrum Dresden-Rossendorf, detector components have been characterized in realistic radiation environments as a step toward a clinical Compton camera. On the one hand, corresponding experimental methods and results obtained during the ENTERVISION training network are reviewed. On the other hand, a novel method based on timing spectroscopy has been proposed as an alternative to collimated imaging systems. The first tests of the timing method at a clinical proton accelerator are summarized, its applicability in a clinical environment for challenging the current safety margins is assessed, and the factors limiting its precision are discussed.

Keywords: proton therapy, range verification, *in vivo* dosimetry, Compton imaging, block detector, scintillation, prompt gamma ray timing

OPEN ACCESS

Edited by:
Marco Durante, GSI Helmholtz Centre for Heavy Ion Research, Germany

Reviewed by:
Nitin Ohri, Albert Einstein College of Medicine, USA
Paulo A. V. Crespo, University of Coimbra, Portugal

****Correspondence:***
Fernando Hueso-González
fernando.hueso@oncoray.de

Specialty section:
This article was submitted to Radiation Oncology, a section of the journal Frontiers in Oncology

Received: *29 September 2015*
Accepted: *21 March 2016*
Published: *12 April 2016*

Citation:
Hueso-González F, Fiedler F, Golnik C, Kormoll T, Pausch G, Petzoldt J, Römer KE and Enghardt W (2016) Compton Camera and Prompt Gamma Ray Timing: Two Methods for In Vivo Range Assessment in Proton Therapy. Front. Oncol. 6:80. doi: 10.3389/fonc.2016.00080

1. INTRODUCTION

In the first decades of the 20th century, during the rise of particle accelerators, physicists studied the interaction of fast charged particles with matter. The energy loss of *heavy* ions (as opposed to *light* electrons) within a target medium was described by Bethe's stopping power formula (1). The ionization, namely, the Coulomb collisions where the accelerated ions strip out electrons of the atoms of the target, is the predominant loss mechanism for non-relativistic ion beams (2).

The engineering race toward high-energy accelerators endowed heavy charged particles a penetration depth in tissue comparable to the body dimensions. This opened up the possibility of using protons for medical applications, as neutrons, electrons, gamma, or X-rays had been applied before

in the field of radiotherapy, which emerged after Röntgen's X-ray discovery in 1895 (3).

In 1946, Wilson predicted the physical, in particular dosimetric, properties of a proton beam (4) for a therapeutic scenario and founded the field of proton therapy. The straight beam trajectory, the finite particle range, as well as the increase of the ionization density close to the stopping point, aroused the interest of the medical community. In the context of cancer treatment, this ionizing radiation was expected to damage the cells of the target tumor and eventually cause their death, while sparing most efficiently surrounding normal tissue.

The first experimental treatments were performed during the 1950s at Berkeley Radiation Laboratory, USA, and in Uppsala, Sweden (2, 5). However, it was not until 1990 that the first hospital-based proton facility in Loma Linda University (USA) was created. Since then, the number of therapy centers has increased steadily, and carbon or other ions have been also introduced. Nowadays, more than 15,000 patients are treated per year in around 50 facilities worldwide (5).

Several distinguishing features of accelerated protons are listed below:

- *The particle range*: the protons stop at a defined penetration depth, which depends on their initial velocity.
- *The Bragg peak*: the ionization cross section increases for low proton velocities, so that the dose deposition density is maximum close to the particle range (2). Conversely, the dose at the entrance point is minimum.
- *The distal penumbra*: beyond the particle range, the dose deposition falls steeply to zero.
- *The lateral penumbra*: the beam trajectory is straight and the spread in the transversal dimension due to multiple Coulomb scattering is small but increases steadily with depth [(6), p. 15].
- *Tissue composition*: the dose deposition curve and proton range are strongly dependent on the stopping power of the traversed tissue (on its density and composition).
- *Secondary products*: neutrons, annihilation photons, and prompt gammas are produced throughout the proton track. These secondary by-products release a small dose compared to the incident protons (2), and they can exit the patient. Neutron emission is focused in forward direction (7).

In theory, proton therapy has several advantages over conventional photon therapy:

- *The distal edge*: the steep dose gradient at the distal edge is promising for sparing critical organs close to the irradiated tumor. In contrast, the slowly falling depth dose curve of photons impedes that strategy.
- *The integral dose*: thanks to the Bragg peak, the dose can be focused on the tumor volume, and the damage on normal tissue before and beyond is minimized. For photons, the dose in healthy tissue can only be distributed on a larger volume by irradiating from several directions, but its integral is higher than for protons.

The main drawbacks compared to photons are:

- The capital expenditure on the facility construction and the higher clinical operating costs (8, 9).
- The lack of large clinical trials and evidence about the superiority of proton beam therapy for the majority of tumor entities (10). Whether or not the lower integral dose translates to better clinical outcome (11), e.g., less normal-tissue toxicity, is yet to be proven.
- Range uncertainties (12) of the proton beam due to intrinsic factors, such as patient or organ motion, as well as restricted knowledge about the tissue composition, are prone to yield severe differences with respect to the planned dose, specially at the distal edge, whereas photon plans are much less sensitive in this regard (13). To circumvent the risk, safety margins are applied and robust treatment plans are designed, at the price of an increase of the dose in the normal tissue compared to the dose-optimum (but more risky) plan.

These disadvantages question the cost-effectiveness of ion beam therapy and fuel the controversy about their clinical superiority [(14), chapters 2.11–2.13] over photon therapy. There is an urgent need for techniques that tackle one of the major weaknesses of proton therapy: the intrinsic range uncertainties, which limit the ultimate precision with which ion beams can be safely delivered. The most common sources of range errors are:

- Stopping power ambiguity due to degeneracy of Hounsfield values depending on tissue composition (15).
- Patient alignment errors.
- Anatomy changes between or during treatment fractions, as cavity filling, change of weight, tissue swelling, or tumor shrinkage.
- Organ motion in the thoracic and abdominal region.
- Biological factors (16).

The proton range is strongly dependent on the composition of the traversed tissue. Photons are less dependent on these factors, and the absence of a sharp edge constrains the maximum dose deviations due to target shifts or path composition variations. The absence of tools in clinical routine for measuring *in vivo* and in real time, the actual distal fall-off edge, together with the high sensitivity of the proton range to tissue composition, force medical physicists to add safety margins and apply field patching techniques in order to obtain a robust treatment plan (17). Notwithstanding the theoretically superior dose profile of ions, broad safety margins (**Figure 1**) waste substantially the outstanding traits of ion over photon beam therapy.

It should be emphasized that most cancers are treated successfully with surgery, electron or photon therapy, chemotherapy, brachytherapy, whereas proton therapy covers just a residual percentage (18). Still, the improvement in the accelerator technology, delivery systems, and the trend toward personalized medicine make proton beams an attractive alternative for certain patient ages and types of tumors. It is estimated that ~10% of cancer patients, especially children, would benefit from proton therapy (reduction of late side effects) compared to conventional techniques (18). Hence, proton therapy is still in the headlines, the number of facilities is increasing from year to year, and questions concerning the improvement of the technique and quality assurance are of great interest.

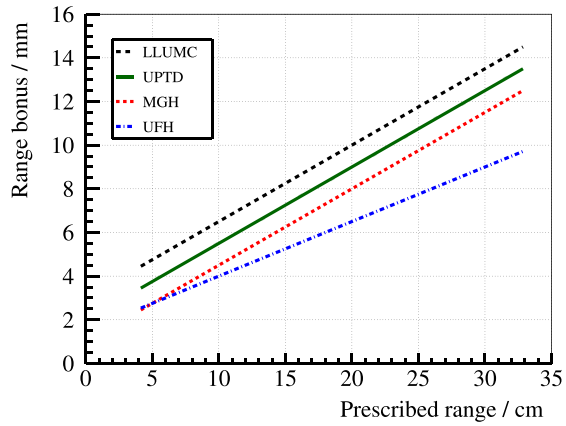

FIGURE 1 | Safety margins applied at different clinical proton therapy facilities: (3.5% + 3-mm) at Loma Linda University Medical Center (LLUMC) (3.5% + 2-mm) at Universitäts Protonen Therapie Dresden (UPTD) (3.5% + 1-mm) at Massachusetts General Hospital (MGH) and (2.5% + 1.5-mm) at University of Florida Health Proton Therapy Institute (UFH). *Range bonus* refers to the margin added to the prescribed range to ensure full tumor coverage even in the case of an undershoot. These centers may apply bigger margins in specific treatment scenarios (62).

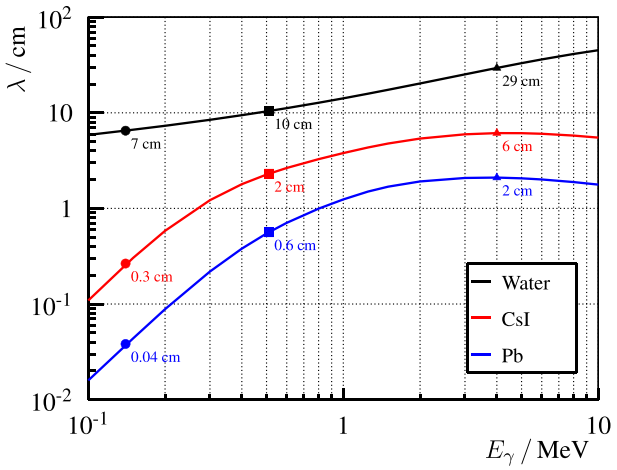

FIGURE 3 | Mean free path λ of photons of energy E_γ in different representative materials: water (body), CsI (detector), and Pb (collimator). λ is calculated as the inverse of the total attenuation factor μ that is extracted from (63). Explicit points at typical energies are drawn: 140-keV for ^{99}Tc (nuclear medicine), 511-keV for PET, and 4-MeV for PGI.

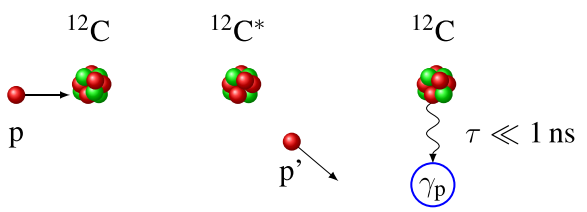

FIGURE 2 | Schematic of a typical prompt gamma ray production process ^{12}C(p,p')^{12}C*. Left: nuclear collision of a proton (p) with a ^{12}C nucleus of the target. Center: the proton is scattered (p′) and the nucleus is left in an excited state ^{12}C*. Right: the relaxation to the ground state ^{12}C is accompanied by a 4.4-MeV prompt gamma emission γ_p.

In this context, several groups across the world aim at an experimental device that measures the particle range and even the dose profile, preferably in real time (13). Numerous techniques have been proposed in the last two decades and are reviewed in Ref. (13, 19, 20). This paper fits into this context and summarizes two different methods for monitoring the dose delivery of proton beams in real time based on Prompt Gamma Imaging (PGI).

Prompt gamma rays, a by-product emitted in nuclear reactions along the proton track, cf. **Figure 2**, cover a broad energy spectrum with several prominent characteristic lines, cf. Ref. (21). The high gamma ray energy ensures that they can be detected outside the patient without severe attenuation. The spatial emission distribution correlates to the dose deposition map of the incident protons (21, 22) and provides an indirect measurement of the particle range. Such correlation is dependent on prompt gamma ray energy and tissue composition (23–26) and stems from the maximum of the nuclear cross section at low (~10-MeV) proton energies (27).

These gamma rays are *prompt*, i.e., they are emitted almost instantaneously after the collision, which is interesting for real-time range verification. The gamma ray production over 1-MeV is considerable, around 0.16 per proton (on average) at 160-MeV beam energy (28). The gamma ray emission rate depends on the beam current, duty cycle, and micro-time structure of the considered accelerator. Taking as an example the Cyclone® 230 (C230) isochronous cyclotron of IBA (Louvain-la-Neuve, Belgium) and a realistic treatment plan with pencil beam scanning, the peak beam current is ≈2-nA, there are about 10^9 gamma ray emissions per second, and 10^6-s^{-1} events are registered in a ø2″ × 2″ $LaBr_3$ scintillator at 30-cm distance (29). This large gamma ray rate, as well as the inherent neutron background, poses a serious challenge on the detector and electronics design. Note that the so-called neutron background is mostly indirect, due to the detection of gamma rays following neutron interactions or neutron captures in surrounding materials, rather than from the interactions of neutrons in the detector itself.

In the field of nuclear medicine, commercial gamma cameras are used in clinical routine to obtain images of gamma ray distributions. Hence, one may think that the imaging of prompt gamma rays is not an issue, as the technology is already established. However, together with the detection rate and background, the high gamma ray energies and polychromatic energy spectrum prevent the direct use of the gamma camera as PGI device. In comparison, the gamma ray energies in nuclear medicine range between 80 and 511-keV. This significant difference is outlined in **Figure 3**: larger collimators and detectors are needed to absorb high-energy prompt gamma rays, normally after multiple interaction processes. For example, a 2-mm layer of lead has a 99% attenuation power for 140-keV photons, but only 9% for 4.4-MeV gammas; a 1-cm thick CsI crystal has a detection efficiency of 98% for the first and just 15% for the latter.

Thick collimators reduce the system efficiency and deteriorate the image quality, whereas large detectors increase critically the system price and enlarge the footprint. Hence, alternative concepts are needed.

Dedicated PGI detector systems have been designed and tested in the last decade based on active or passive collimation. A pin-hole camera (30) is the pioneer approach to scan the prompt gamma emission distribution in a right angle to the beam track. Many research groups have performed experiments based on slit cameras at proton or carbon beams (31–37). The knife-edge-shaped camera has demonstrated the feasibility of millimeter range verification at clinical current intensities (38) in real time on a spot basis with realistic treatment plans and heterogeneous phantoms (39).

Among actively collimated systems, most efforts are concentrated on the Compton camera (40). It comprises multiple position sensitive gamma ray detectors, which are arranged in one scatterer and one absorber, or in several scatter planes. The prompt gamma rays reach the detectors, and the energy deposit as well as the point of interaction in each plane are measured, cf. **Figure 4** for the two-plane camera. The Compton equation (41) relates the scattering angle θ to the initial (E_γ) and final (E_γ') photon energies:

$$\begin{aligned} E_\gamma &= L_s + L_a \\ E_\gamma' &= L_a \\ \cos\theta &= 1 - m_e c^2 \left(1/E_\gamma' - 1/E_\gamma \right) \end{aligned} \quad (1)$$

where L_s and L_a are the energies released in scatterer and absorber, respectively, and $m_e c^2 = 511$-keV is the electron rest energy. In contrast to a slit camera, no collimation is needed in order to reconstruct the angle of incidence of the gamma ray, and two-dimensional (2D) or even three-dimensional (3D) images instead of one-dimensional (1D) profiles may be obtained. More single gamma rays and directions can be detected, but the condition of simultaneous interaction in the different camera stages limits the overall efficiency. Furthermore, the instrumentation requirements in terms of spatial, time, and energy resolution for the detectors of a Compton camera are especially high, and the reconstruction algorithm is complex and computationally intensive, as the incident direction cannot be recovered univocally for each event. Nowadays, a PGI Compton camera prototype demonstrating range verification in a clinical scenario is still a challenge several institutes aim at (42–47), and the only published experimental results at a proton beam are constrained to <2-MeV gammas (48, 49) or to beam currents far below the clinical case (50). Technical complexity, electronics expense, low coincident efficiency, high detector load, radiation background, and the elevated percentage of random coincidences are intrinsic hurdles that cast doubts on the applicability of this concept (19).

In the recent years, one can identify a trend toward less complicated PGI systems, at least concerning hardware. These may have a faster translation into clinical practice due to their lower price (35, 37, 51). The Prompt Gamma Ray Timing (PGT) method (28) is one of these novel approaches, which relies on a single monolithic detector with excellent timing resolution and no collimation. As a consequence of the measurable transit time of ions through matter, the detection times of prompt gamma rays encode essential information about their spatial emission point. **Figure 5** illustrates this physical effect: the deeper the proton interaction (prompt gamma emission) point, the larger the proton transit time and time of flight of the gammas to the detector. Applying the Continuous Slowing Down Approximation (CSDA), the transit time can be derived mathematically (28) if the

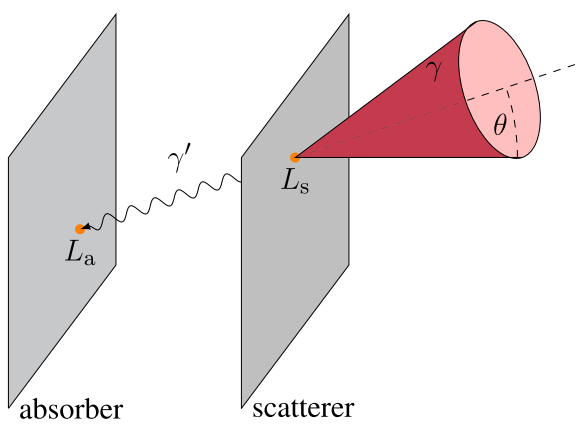

FIGURE 4 | Incoherent scattering event in a two-plane Compton camera. The cone surface contains the possible incidence directions (any generatrix) of the initial photon (γ). It interacts with the scatterer plane and deposits an energy L_s. The scattered photon (γ') releases the rest of the energy L_a in the absorber. The line connecting both interaction points (in orange) is the propagation direction of γ'. This defines the axis (directrix) of the aforementioned cone, with half-opening (scattering) angle θ and vertex at the scatter point.

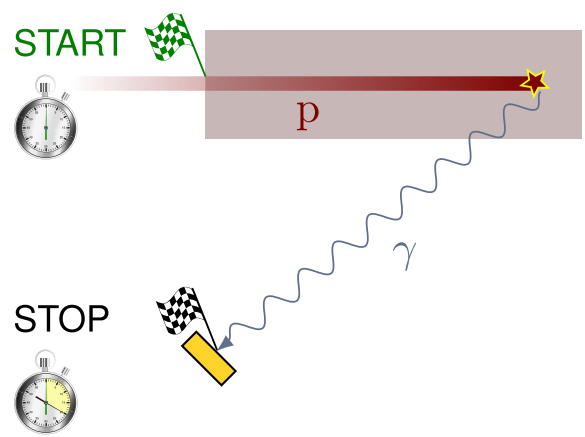

FIGURE 5 | Illustrative sketch of the PGT method. The therapeutic proton p (the projectile) slows down as it penetrates the target and interacts with a nucleus, which emits a prompt gamma ray. The time between the entrance of the proton to the target (the start flag) and the arrival of the gamma ray to the detector (the stop flag at the yellow rectangle) encodes the proton transit time and gamma time of flight, which can be correlated to the depth of interaction of the proton (gamma emission point).

initial beam energy E_0 and target composition are known. First, the proton energy variation per unit length yields

$$\frac{dE}{dz} = -\rho(z)S(E) \tag{2}$$

where E is the kinetic energy, $\rho(z)$ the mass density of the target at a depth z, and $S(E)$ the stopping power, that depends on target material and thus indirectly on the depth z. The kinetic energy E of the proton at any depth $z > z_0$ is

$$E(z) = E_0 - \int_{z_0}^{z} \rho(z')S(E(z'))dz' \tag{3}$$

The relativistic velocity v of the particle is a function of the kinetic energy E:

$$v(E) = c\sqrt{1-(1+E/m_p c^2)^{-2}} \tag{4}$$

where m_p is the proton rest mass. Finally, the equation of the proton transit time yields

$$t_p(z) = \int_{z_0}^{z} \frac{1}{v(E)}dz' = \int_{E(z)}^{E_0} \frac{1}{v(E)\rho(z'(E))S(E)}dE \tag{5}$$

where dz' has been exchanged with dE using equation (2).

The low cost and small footprint of PGT makes this concept very tempting. A major limitation is that the time spectra are not only blurred by the resolution of the detector but also by the time width of the accelerated bunches. This implies that the PGT method is not applicable at all clinical accelerators: only to those with a specific micro-time structure. For the widespread accelerator C230 (5), the micro bunch time spread can reach up to 2-ns for clinical beam energies (29). Here, range shifts can be identified based on distribution momenta. It is under exploration whether PGT is only applicable for pencil beams or also for passively scattered ones. In order to know if other types of clinical accelerators are compatible with the PGT approach, the specific micro pulse structure has to be measured.

Rather than an in-depth review of the literature, this manuscript provides a summary of two separate topics developed within the collaborative framework of ENTERVISION (52): the characterization of detector components for the absorber plane of a clinical Compton camera and the first test of the PGT method with heterogeneous phantoms at a clinical proton center, corresponding to the publications (53) and (29), respectively.

2. COMPARISON OF BGO AND LSO SCINTILLATION DETECTORS

$Bi_4Ge_3O_{12}$ (BGO) and Lu_2SiO_5:Ce (LSO) scintillators are straightforward candidates to absorber detectors of a Compton camera aiming at PGI. These are used traditionally in Positron Emission Tomography (PET) scanners. Despite its higher price and 30% lower photoabsorption efficiency, LSO has gained importance due to its higher light yield and fast decay time. It is questionable if this conclusion can be transcribed to the PGI scenario. In order to assess the choice between the two options, benchmark experiments are conducted at different accelerators for comparing BGO and LSO detectors in terms of energy, spatial, and time resolution. Other factors, such as intrinsic radiation, absorption efficiency, and cost-effectiveness ratio, are also discussed.

2.1. Materials

The basic detection unit in commercial PET scanners is the block detector. It consists of a square matrix of segmented or pixellated scintillating crystals coupled to four light-sharing Photomultiplier Tubes (PMT), as depicted in **Figure 6**. The pixel where the gamma

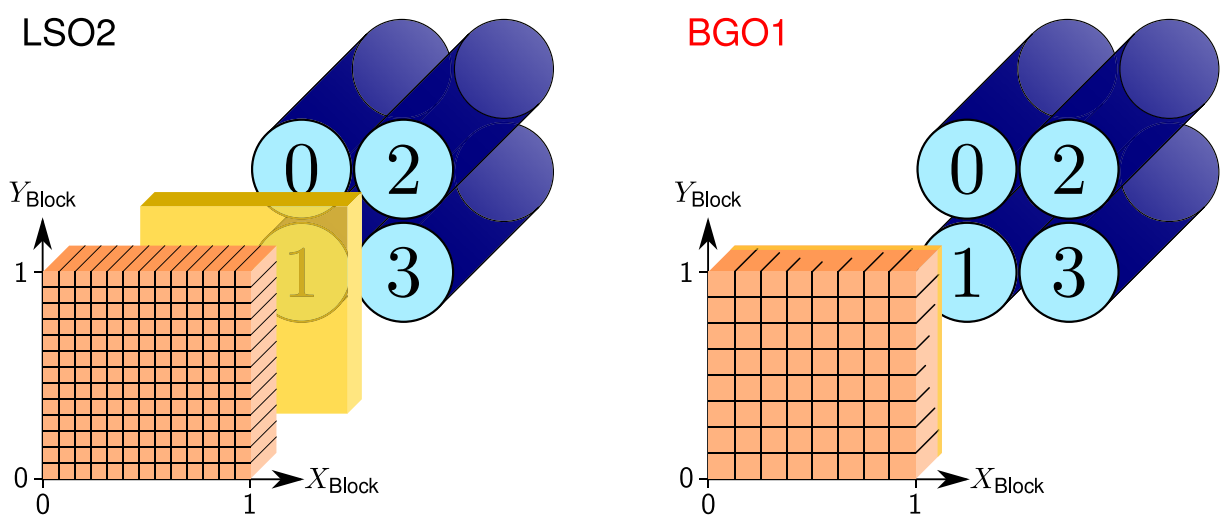

FIGURE 6 | Sketch of the LSO2 (left) and BGO1 (right) block detectors with the PMT numbering convention and crystal coordinate system, namely, the X_{Block} and Y_{Block} axis (relative position between 0 and 1). Crystals are depicted in orange, PMTs in blue, and the light guide in yellow. Reproduced with permission from Ref. (53).

ray interacts can be calculated based on the ratio of light collected by each PMT. The block detectors used in this comparative study and their properties are listed in **Table 1**. They are named as LSO2 and BGO1 when referring to the concrete detector results, in contrast to LSO and BGO when speaking about general features of the scintillation materials.

2.2. Results

In **Figure 7**, the relative energy resolution R_E as Full Width at Half Maximum (FWHM) of the LSO2 and BGO1 detectors is compared. The energy resolution of LSO2 is better across the whole energy range. At 511-keV, $R_{E,LSO2} \approx 11\%$ and $R_{E,BGO1} \approx 18\%$. Nonetheless, the differences are less pronounced for high-energy photopeaks (53, 54). At 4.4-MeV, $R_{E,LSO2} \approx 7\%$ versus $R_{E,BGO1} \approx 8\%$. In other words, LSO2 excels at the PET scenario (below 1-MeV), whereas for the PGI scenario (above 2-MeV), the difference in performance is less significant, and the higher price of LSO does not imply a much better detector quality.

The reason for the comparable energy resolution at high energies is the following. The relative energy resolution R_E depends on two independent contributions: the statistical and the intrinsic one. The first one depends on the light yield and is proportional to the inverse square root of number of (collected) scintillation photons. The latter is due to non-linearity effects (55) and is dependent on the crystal structure. At low photon energies, i.e., the range of usual radioactive sources or in case of PET, the statistical contribution dominates over the intrinsic one. As LSO has a four times higher light yield than BGO, its energy resolution is significantly better. At high photon energies, i.e., the PGI energy range, the number of scintillation photons is larger, so that the statistical contribution is smaller and the intrinsic contribution starts to dominate. This intrinsic factor is comparable for BGO and LSO (54, 56, 57), which explains their similar performance concerning energy resolution at the PGI energy range.

With respect to the spatial resolution, one can conclude that the discrimination power between pixels of the flood map increases with the energy range for both block detectors, cf. **Figure 8**. This effect is also due to the lower statistical relative uncertainty of events with high-energy deposit. The spots in the flood map of BGO1 are broader than those of LSO2 in any case, but become very sharp in the PGI range. This points out that one could segment the BGO1 block detector in, e.g., 13 × 13 instead of 8 × 8 and achieve the spatial resolution of LSO2 without jeopardizing the pixel discrimination in the flood map of the PGI range.

Regarding the time resolution, cf. **Figure 9**, the LSO2 detector beats BGO1 over the whole energy range thanks to the larger light yield and shorter decay time. A good time resolution is mandatory for a PGI Compton camera in order to suppress delayed radiation background (58). In order to analyze if the timing resolution of BGO1 is sufficient for this goal, we calculate the figure of merit FoM_{BSR} (59):

$$FoM_{BSR} = 1 - \frac{\sqrt{\Sigma_{t,det}^2 + \Sigma_{t,bunch}^2}}{T_{bunch}} \tag{6}$$

where $\Sigma_{t,det}$ is the detector time resolution as FWHM, $\Sigma_{t,bunch}$ the bunch time spread (FWHM), and $T_{bunch} = f_{bunch}^{-1}$ the bunch period (the inverse of the radio frequency). This ratio measures the amount of background that can be suppressed thanks to timing measurements in a pulsed accelerator. In the case of the C230 machine, where $T_{bunch} = 9.4$-ns and $\Sigma_{t,bunch} \approx 2$-ns (for 100-MeV protons) (29), the background suppression ratios for 4-MeV prompt gammas are $FoM_{BSR,LSO2} = 84\%$ and $FoM_{BSR,BGO1} = 64\%$. LSO2 has undoubtedly better performance, but BGO1 could be also acceptable.

Other material features, such as the decay time and the intrinsic radioactivity, are worth to discuss. The decay time of BGO (7.5 times longer than LSO) implies a limit of around 300-kcps detector load. Taking into account the high rates expected in the PGI scenario, about 1-Mcps, one might be forced to reduce the area of the BGO block detectors or increase the distance to the beam axis. These rates are also quite challenging for the electronics and data processing. On the other hand, it is well known that LSO has a high intrinsic radioactivity below 1-MeV

TABLE 1 | Comparison of the properties of the different block detectors from Siemens Medical Solutions USA, Inc. Molecular Imaging Division, whose sketch is depicted in Figure 6.

Detector name	LSO2	BGO1
Active volume (mm³)	52.7 × 52.7 × 20.0	52.7 × 52.7 × 20.0
Granularity	Independent pixels	Segmented crystal
Pixel matrix	13 × 13	8 × 8
Pixel dimensions (mm³)	4.0 × 4.0 × 20.0	6.4 × 6.4 × 20.0
Light guide	Coupled to block	Cut into block
Operating voltage	+900 V	+1350 V
Commercial scanner	Biograph PET/CT	ECAT EXACT 47 PET

Spatial dimensions are given as height × width × depth. Reproduced with permission from Ref. (53).

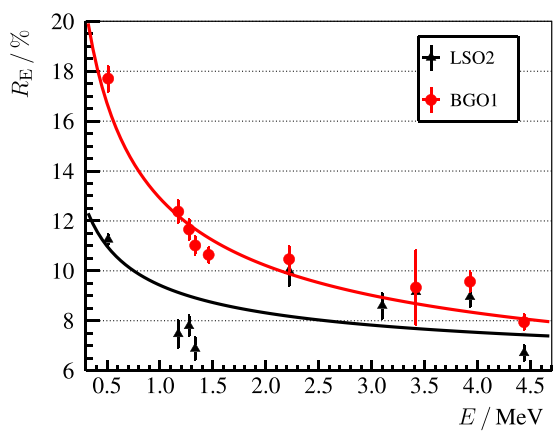

FIGURE 7 | Relative energy resolution $R_E = \Sigma_E/E$ of the LSO2 (black line) and BGO1 (red line) block detectors as a function of energy deposit E. Σ_E refers to the FWHM of the photopeak. The empirical fit to the experimental points is $R_E = (3.8 \pm 0.3)\% / \sqrt{E / \text{MeV}} + (5.6 \pm 0.3)\%$ for LSO2 and $R_E = (9.2 \pm 0.5)\% / \sqrt{E / \text{MeV}} + (3.7 \pm 0.4)\%$ for BGO1. Reproduced with permission from Ref. (53).

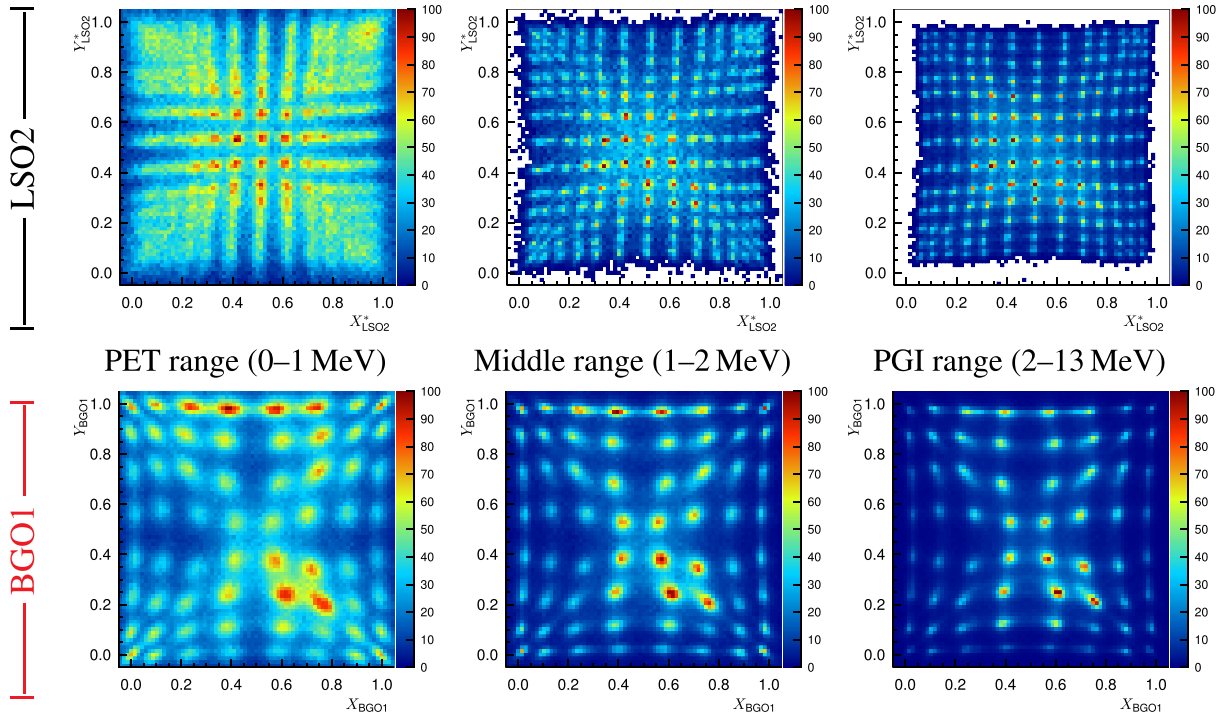

FIGURE 8 | Block detector flood map (top figure: LSO2 and bottom figure: BGO1) for different energy ranges at the ELBE accelerator (distortion correction applied for LSO2). Non-uniformities are due to the fact that the focused bremsstrahlung beam spot is smaller than the detector size as well as the different extension (number of bins) of each pixel spot in the map. Reproduced with permission from Ref. (53).

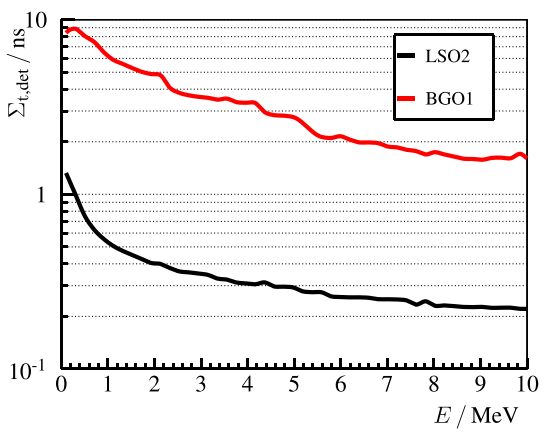

FIGURE 9 | Time resolution $\Sigma_{t,det}$ (FWHM) of the LSO2 (black line) and BGO1 (red line) block detectors measured at the ELBE accelerator as a function of the released energy. The experimental points are approximately reproduced by the curves $\Sigma_{t,det} = (460 \pm 10)\,\text{ps} / \sqrt{E / \text{MeV}} + (80 \pm 5)\,\text{ps}$ for LSO2 and $\Sigma_{t,det} = (4900 \pm 500)\,\text{ps} / \sqrt{E / \text{MeV}} + (10 \pm 10)\,\text{ps}$ for BGO1. Reproduced with permission from Ref. (53).

due to ^{176}Lu, namely, through β^- decay and subsequent gamma ray cascade. The simultaneous detection of the electron (stopped in the LSO crystal) and the gamma ray (in the scatterer plane) could produce a significant fraction of false coincidences in a Compton camera.

3. PROMPT GAMMA RAY TIMING WITH HETEROGENEOUS TARGETS

The PGT method is a promising and novel method for range verification proposed by Golnik et al. (28) based on experiments with homogeneous phantoms at a research accelerator. To further explore its potential and the limitations that may appear when translating the concept to a realistic irradiation scenario, specific experiments at a clinical proton center with heterogeneous targets are conducted. The concrete goals are to test the robustness of the PGT method, its precision, and limitations, as well as the capability of detecting range shifts due to heterogeneities. Furthermore, the next steps toward a clinical PGT prototype are identified.

3.1. Materials

The experiment is carried out at the Westdeutsches Protonentherapiezentrum Essen (WPE), Germany. This clinical proton center comprises a C230 cyclotron, with a radio frequency close to 106-MHz. A horizontal pencil beam (no scanning) in the gantry treatment room irradiates a cylindrical target, see **Figure 10** (bottom). The inner shell contains slices of custom thickness and composition, so that different heterogeneous targets can be configured. Available materials are polymethyl methacrylate (PMMA), air (hollow slice), and cortical bone. The detectors listed in **Table 2** are set up at an angle α and distance d, as described in **Figure 10** (top). Whenever a target is thick

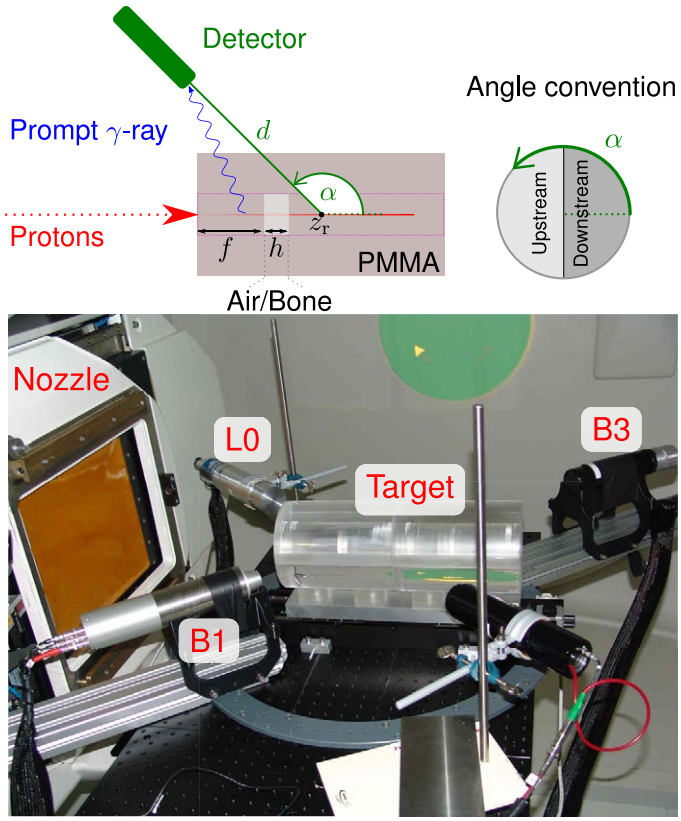

FIGURE 10 | Top: sketch of the experimental setup at the WPE proton therapy facility and of the longitudinal cross section of the target. The accelerated protons bunched with 106 MHz collide with the PMMA cylindrical target. It contains a cavity or bone insert of thickness *h* located at a distance *f* from the beam entrance point. Bottom: photograph of the experimental setup with three detectors at different ring angles α. The linear stage on the center of the ring holds the two hollow joined half cylinders, in which PMMA, cavity, or bone slices can be inserted. The beam incidence is horizontal from the left, where the snout of the nozzle is seen. Reproduced with permission from Ref. (29).

TABLE 2 | Monolithic scintillation detectors available in the experiment.

Alias	Material	ø × Length	Rationale
B1	BaF_2	[25:38] mm × 30 mm	Time resolution
B3	BaF_2	48 mm × 31 mm	Time resolution
L0	$LaBr_3$:Ce	2″ × 2″	Energy resolution

B3 and L0 are cylindrical, whereas B1 is a tapered cone (for optimum time resolution). Reproduced with permission from Ref. (29).

enough to completely stop the impinging protons, we label it as *full* (for a given proton energy).

3.2. Results

The bunch time spread is an important limiting factor for the PGT method. In **Figure 11** (left), the bunch width is characterized as a function of the proton energy, ranging from 350-ps at 230-MeV to 2-ns at 100-MeV. The time spread can be reduced up to a factor of two by adjusting the momentum spread limiting slits, cf. **Figure 11** (right), the main component of the energy selection system of the C230 cyclotron (60).

For the acquisition of PGT spectra, the detection time of the gamma rays with respect to the arrival of the protons to the target has to be measured. As usual in research accelerators, the radio frequency can be used as reference time for the bunch arrival (except for an offset). However, **Figure 12** shows that this offset is not constant on a large time scale (29). These phase drifts of the proton bunch with respect to the RF signal may be caused due to temperature changes or main coil current instabilities, among other factors.

With regard to homogeneous targets, the stacked target experiment is accomplished as follows: homogeneous PMMA targets of various thicknesses are irradiated with 230-MeV protons. The increase of the target thickness correlates to an increase of the area of the PGT distribution and a shift to the right in its mean value, due to the enlarged region of prompt gamma emission, as observed in **Figure 13** (left). As the bunch time spread is significantly lower than the proton transit time, one can resolve the prompt gamma emission density as a function of the (timewise) depth with much less blurring than for 160 or 100-MeV proton energies. In **Figure 13** (right), we calculate the PGT distributions according to the analytical simple Box (simBox) model (28). The shape is qualitatively similar to the experimental spectra, but the model is too simple to reproduce, e.g., the fall-off edge corresponding to the Bragg peak or the background radiation.

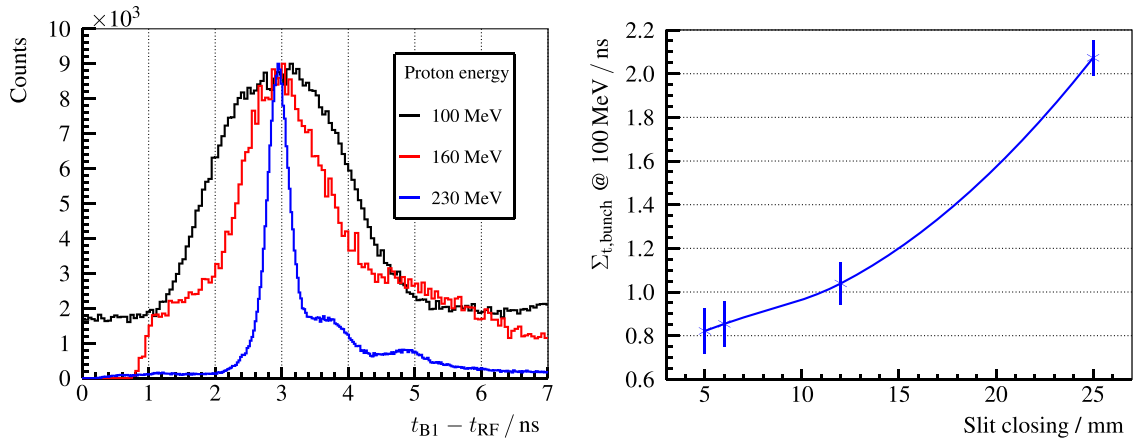

FIGURE 11 | Left: PGT spectra of the B1 detector with a thin PMMA target for three different proton energies and the usual slit closing (25-mm) at the WPE gantry. Right: bunch time spread $\Sigma_{t,bunch}$ at 100-MeV proton energy and a full PMMA target for the B3 detector. Reproduced with permission from Ref. (29).

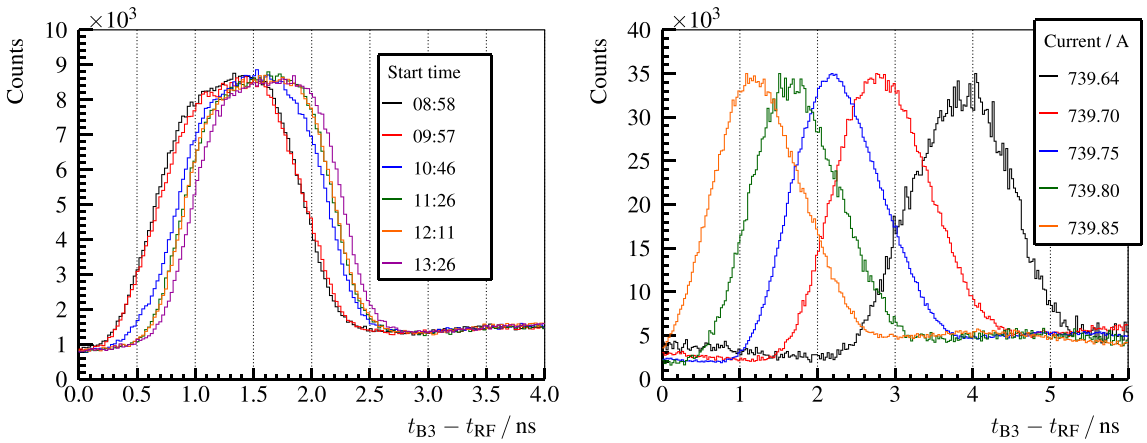

FIGURE 12 | Left: PGT spectra of the B3 detector, a homogeneous PMMA target and a proton energy of 230-MeV. Independent redundant measurements of about 5-min with a separation of around 1-h are overlaid. Right: PGT spectra of the B3 detector, a full homogeneous PMMA target, and a proton energy of 160-MeV for different values of the main coil current of the cyclotron (detailed in the legend). Reproduced with permission from Ref. (29).

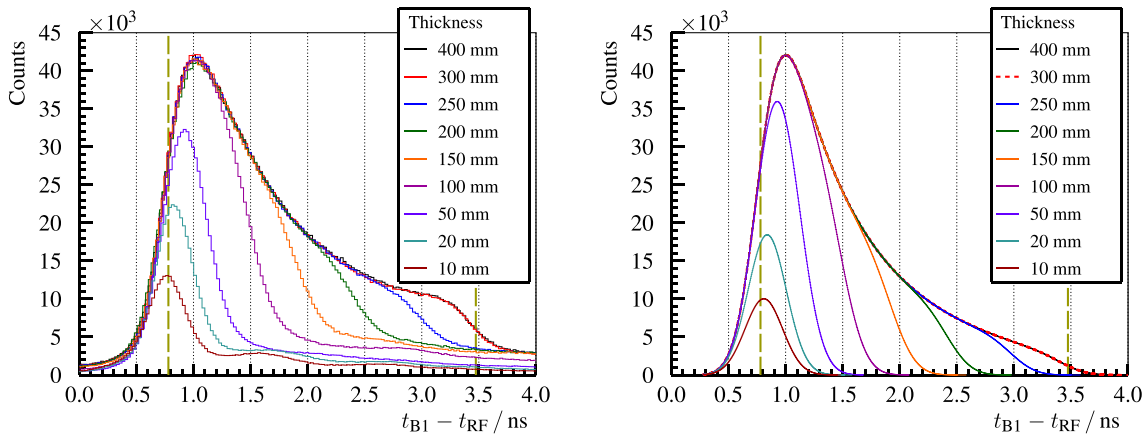

FIGURE 13 | Left: experimental PGT spectra of the B1 detector for 230-MeV protons and different PMMA target thicknesses. Right: spectra calculated with the analytical simBox model (28). Both: the two vertical dashed lines refer to the expected front face and proton range positions. Reproduced with permission from Ref. (29).

Concerning heterogeneous targets, air cavities of different thicknesses are placed at different depths inside a full PMMA target. The experimental results are shown in **Figure 14**. The deficit in the gamma ray production inside the air cavity can be identified as a dip in the PGT spectra at a time position and with a magnitude correlated to its location and thickness, respectively. The falling edge of the spectrum shifts steadily to the right according to the cavity thickness (beam overshoot).

An analogous experiment with a bone insert (20-mm thick) at different positions is carried out (29). The resulting PGT spectra are depicted in **Figure 15** (left). An increase of the gamma ray production due to the higher density of bone is visible in the PGT spectrum at a time correlated to the insert position. A shift to the left in the falling edge of the distribution can be identified (undershoot) with respect to the homogeneous case. In **Figure 15** (right), the PGT spectra are converted to depth profiles by using the transit time equation, cf. equation (5), and applying detector solid angle and gamma time-of-flight corrections.

In **Figure 16**, for 230-MeV protons, the effect of a beam overshoot (air cavity) and undershoot (bone insert) on PGT spectra is compared with respect to a reference measurement (homogeneous PMMA target). Moreover, the detectability of the range shift based on the location of the trailing edge is analyzed as a function of the number of irradiated protons. For clinical treatment plans, the strongest spot in pencil beam scanning, which is usually at the distal edge, yields close to 10^8 protons. This hints that a single detector is able to recover 5-mm range errors of the distal spot based on the PGT method with realistic beam currents at the C230 accelerator.

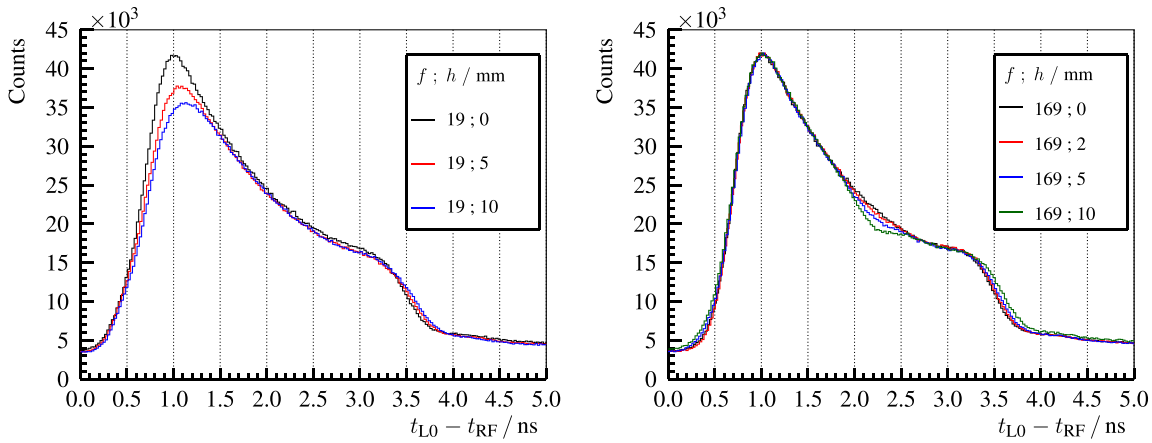

FIGURE 14 | Experimental PGT spectra of the L0 detector for 230-MeV protons and different air cavities inside the full (400-mm) PMMA target at *f* and *h* (front face position and thickness as described in Figure 10). Reproduced with permission from Ref. (29).

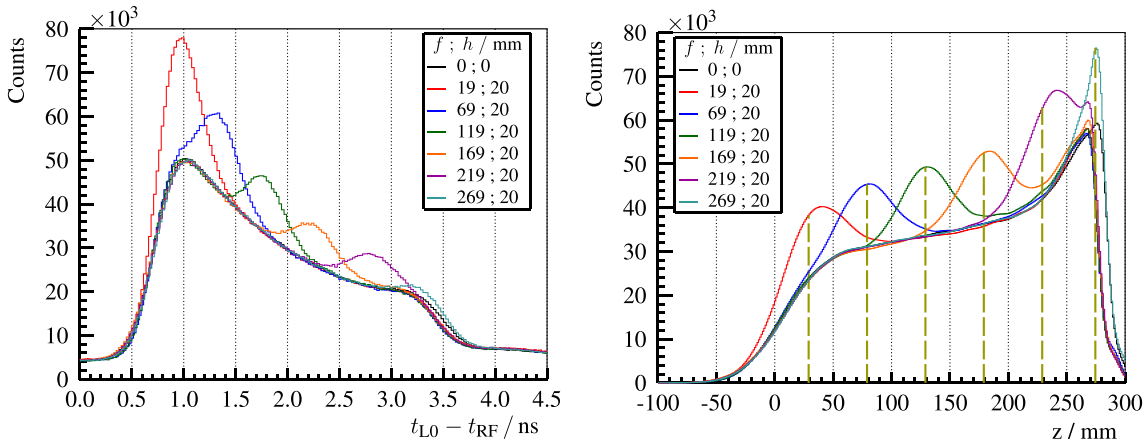

FIGURE 15 | Left: experimental PGT spectra of the L0 detector for 230-MeV protons and a bone insert inside the full (400-mm) PMMA target at *f* and *h* (front face position and thickness as described in Figure 10). Right: time to distance axis conversion from the left PGT spectra after application of stopping power, sensitivity, and gamma time-of-flight corrections as well as background subtraction. *z* refers to the depth with respect to the target's front face (beam entrance point). Vertical dashed lines mark the centroid of the bump according to the simBox model. Reproduced with permission from Ref. (29).

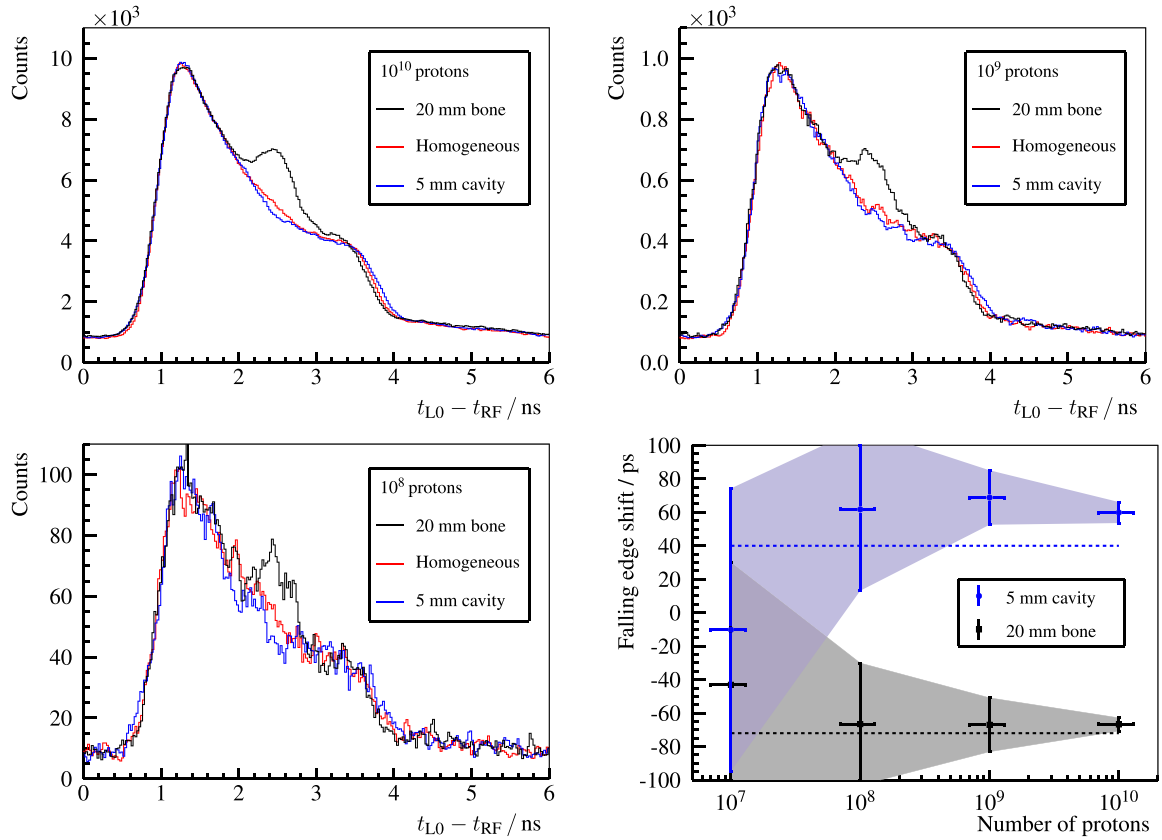

FIGURE 16 | Top row and bottom left plot: PGT spectra of the L0 detector for 230-MeV protons. The homogeneous case (red curve) corresponds to a full PMMA target (400-mm). A heterogeneous slice is placed inside the full PMMA target at f = 169-mm and h = 5-mm (air cavity – blue curve) or f = 169-mm and h = 20-mm (bone insert – black curve), where f and h are the front face position and thickness, as described in **Figure 10**. The legend header contains the number of protons associated with each spectrum. Bottom right: shift of the falling edge with respect to the homogeneous case depending on the number of protons. The dashed lines depict the expected shift of the trailing edge according to the simBox model. Reproduced with permission from Ref. (29).

4. DISCUSSION

Prompt gamma rays, produced in nuclear reactions of accelerated protons with tissue, are valid signatures for retrieving the range of therapeutic protons. Several imaging systems are under development in the scientific community. Among others, the Compton camera and the Prompt Gamma Ray Timing (PGT) method have been studied intensively during the last years in collaboration with the ENTERVISION project (52).

A Compton camera requires position-sensitive detectors with high resolution and efficiency. The characterization of different candidate detectors in the PGI energy range is mandatory for assessing the material choice based on measurements that complement previous simulations and textbook knowledge. BGO and LSO block detectors from commercial PET scanners are compared in terms of energy, spatial, and time resolution, as well as price, absorption efficiency, and intrinsic background. As expected, the overall performance of LSO is better, but BGO closes the gap in the PGI range. The reason is that the high gamma ray energies (compared to the PET scenario) and thus number of scintillation photons balances the lower light yield. In addition, BGO has a higher photoabsorption efficiency, no intrinsic radioactivity, and low cost. Hence, BGO is a competitive alternative for the absorber of a Compton camera, thanks to the superior cost-effectiveness ratio in the PGI field (53).

PGT is an innovative method for range assessment based on a low footprint detector setup at minimum expense. First tests at a clinical accelerator and with heterogeneous phantoms reveal the capability of measuring 5-mm range shifts (due to heterogeneities) for beam spots with 10^8 protons (29). The bunch time spread is a crucial factor that affects the resolution of the PGT method. It depends on the delivered proton energy and the settings of the energy selection system. Furthermore, bunch phase drifts are found throughout the experiment, which pose a challenge on the robustness of the PGT method on a large time scale. Hence, it is advisable to introduce a proton bunch monitor (60, 61) that measures the bunch time structure as well as the potential phase drifts. A larger detector load and acquisition throughput are mandatory to improve the number of gamma rays detected per proton, so that statistically significant conclusions on range errors can be drawn for more spots of the treatment plan. Quantification of the range shifts based on more sophisticated models or simulations are also necessary. Experiments with upgraded detectors and electronics, realistic treatment plans, and anthropomorphic

phantoms are ongoing. These are the next steps toward clinical translation and development of a first robust prototype.

AUTHOR CONTRIBUTIONS

All authors were involved in the conceptual design, management, support, and accomplishment of the experiments reviewed in this paper as well as in the critical revision of the data analysis and obtained results.

ACKNOWLEDGMENTS

The authors like to thank S. Akhmadaliev[3], D. Bemmerer[3], M. Berthel[2], A. K. Biegun, J. v. Borany[3], P. Dendooven, A. Dreyer[2], A. Hartmann[3], K. Heidel[3], S. Helmbrecht[3], G. Janssens, A. Junghans[3], U. Just[2], M. Kempe[3], A. Laso-García[3], D. Prieels, M. Priegnitz[3], H. Rohling[3], K. Schmidt[3], S. Schöne[3], R. Schwengner[3], J. Smeets, M. Sobiella[3], F. Vander Stappen, A. Wagner[3], L. Wagner[3], and D. Weinberger[3] for the excellent assistance as well as the crews of the different accelerators for stable operations. (Superscipts refer to affiliation numbers).

FUNDING

The summarized work was supported by the German Federal Ministry of Education and Research (BMBF-03Z1NN12) and the European Commission (FP7 Grant Agreement No. 241851 and No. 264552, and IA-ENSAR FP7 Contract No. RII3-CT-2010-262010).

REFERENCES

1. Bethe H. Zur Theorie des Durchgangs schneller Korpuskularstrahlen durch Materie. *Ann Phys* (1930) **397**(3):325–400. doi:10.1002/andp.19303970303
2. Newhauser WD, Zhang R. The physics of proton therapy. *Phys Med Biol* (2015) **60**(8):R155. doi:10.1088/0031-9155/60/8/R155
3. Röntgen WC. On a new kind of rays. *Science* (1896) **3**(59):227–31. doi:10.1126/science.3.59.227
4. Wilson RR. Radiological use of fast protons. *Radiology* (1946) **47**(5):487. doi:10.1148/47.5.487
5. Particle Therapy Co-Operative Group. *Patient Statistics*. Villigen: Particle Therapy Co-Operative Group (2014). Available from: http://www.ptcog.ch/archive/patient_statistics/Patientstatistics-updateMar2014.pdf
6. Fiedler F. *Anwendung des in-Beam PET Therapiemonitorings auf Präisionsbestrahlungen mit Helium-Ionen*. Ph.D. thesis, Technische Universität Dresden, Dresden (2008). Available from: http://nbn-resolving.de/urn:nbn:de:bsz:14-ds-1206441845447-47490
7. Robert C, Dedes G, Battistoni G, Böhlen TT, Buvat I, Cerutti F, et al. Distributions of secondary particles in proton and carbon-ion therapy: a comparison between GATE/Geant4 and FLUKA Monte Carlo codes. *Phys Med Biol* (2013) **58**(9):2879. doi:10.1088/0031-9155/58/9/2879
8. Goitein M, Jermann M. The relative costs of proton and X-ray radiation therapy. *Clin Oncol* (2003) **15**(1):S37–50. doi:10.1053/clon.2002.0174
9. Peeters A, Grutters JP, Pijls-Johannesma M, Reimoser S, Ruysscher DD, Severens JL, et al. How costly is particle therapy? Cost analysis of external beam radiotherapy with carbon-ions, protons and photons. *Radiother Oncol* (2010) **95**(1):45–53. doi:10.1016/j.radonc.2009.12.002
10. Freeman T. *Proton Therapy: Randomized Trials or Model-Based Selection?* Bristol: Medical Physics Web (2015). Available from: http://medicalphysicsweb.org/cws/article/opinion/61592
11. Freeman T. *Will Protons Gradually Replace Photons?* Bristol: Medical Physics Web (2012). Available from: http://medicalphysicsweb.org/cws/article/research/50584
12. Deasy J. ICRU report 49, stopping powers and ranges for protons and alpha particles. *Med Phys* (1994) **21**(5):709–10. doi:10.1118/1.597176
13. Knopf A-C, Lomax A. In vivo proton range verification: a review. *Phys Med Biol* (2013) **58**(15):R131. doi:10.1088/0031-9155/58/15/R131
14. Orton CG, Hendee WR. *Controversies in Medical Physics: A Compendium of Point/Counterpoint Debates*. College Park, MD: American Association of Physicists in Medicine (2008). p. 110–23. Available from: https://www.aapm.org/pubs/books/PointCounterpointCompendium.pdf
15. Andreo P. On the clinical spatial resolution achievable with protons and heavier charged particle radiotherapy beams. *Phys Med Biol* (2009) **54**(11):N205. doi:10.1088/0031-9155/54/11/N01
16. Grün R, Friedrich T, Krämer M, Zink K, Durante M, Engenhart-Cabillic R, et al. Physical and biological factors determining the effective proton range. *Med Phys* (2013) **40**(11):111716. doi:10.1118/1.4824321
17. Albertini F, Hug EB, Lomax AJ. Is it necessary to plan with safety margins for actively scanned proton therapy? *Phys Med Biol* (2011) **56**(14):4399. doi:10.1088/0031-9155/56/14/011
18. Amaldi U, Kraft G. Radiotherapy with beams of carbon ions. *Rep Prog Phys* (2005) **68**(8):1861. doi:10.1088/0034-4885/68/8/R04
19. Smeets J. *Prompt Gamma Imaging with a Slit Camera for Real Time Range Control in Particle Therapy*. Ph.D. thesis, Université Claude Bernard Lyon 1, Lyon (2012). Available from: http://theses.ulb.ac.be/ETD-db/collection/available/ULBetd-10182012-123741/unrestricted/Thesis.pdf
20. Kraan AC. Range verification methods in particle therapy: underlying physics and Monte Carlo modelling. *Front Oncol* (2015) **5**:150. doi:10.3389/fonc.2015.00150
21. Verburg JM, Riley K, Bortfeld T, Seco J. Energy- and time-resolved detection of prompt gamma-rays for proton range verification. *Phys Med Biol* (2013) **58**(20):L37. doi:10.1088/0031-9155/58/20/L37
22. Min C-H, Kim CH, Youn M-Y, Kim J-W. Prompt gamma measurements for locating the dose falloff region in the proton therapy. *Appl Phys Lett* (2006) **89**(18):183517. doi:10.1063/1.2378561
23. Moteabbed M, España S, Paganetti H. Monte Carlo patient study on the comparison of prompt gamma and PET imaging for range verification in proton therapy. *Phys Med Biol* (2011) **56**(4):1063. doi:10.1088/0031-9155/56/4/012
24. Polf JC, Panthi R, Mackin DS, McCleskey M, Saastamoinen A, Roeder BT, et al. Measurement of characteristic prompt gamma rays emitted from oxygen and carbon in tissue-equivalent samples during proton beam irradiation. *Phys Med Biol* (2013) **58**(17):5821. doi:10.1088/0031-9155/58/17/5821
25. Gueth P, Dauvergne D, Freud N, Létang JM, Ray C, Testa E, et al. Machine learning-based patient specific prompt-gamma dose monitoring in proton therapy. *Phys Med Biol* (2013) **58**(13):4563. doi:10.1088/0031-9155/58/13/4563
26. Janssen F, Landry G, Lopes PC, Dedes G, Smeets J, Schaart DR, et al. Factors influencing the accuracy of beam range estimation in proton therapy using prompt gamma emission. *Phys Med Biol* (2014) **59**(15):4427. doi:10.1088/0031-9155/59/15/4427
27. Kozlovsky B, Murphy RJ, Ramaty R. Nuclear deexcitation gamma-ray lines from accelerated particle interactions. *Astrophys J Suppl Ser* (2002) **141**(2):523. doi:10.1086/340545
28. Golnik C, Hueso-González F, Müller A, Dendooven P, Enghardt W, Fiedler F, et al. Range assessment in particle therapy based on prompt γ-ray timing measurements. *Phys Med Biol* (2014) **59**(18):5399. doi:10.1088/0031-9155/59/18/5399
29. Hueso-González F, Enghardt W, Fiedler F, Golnik C, Janssens G, Petzoldt J, et al. First test of the prompt gamma ray timing method with heterogeneous targets at a clinical proton therapy facility. *Phys Med Biol* (2015) **60**(16):6247. doi:10.1088/0031-9155/60/16/6247
30. Seo KS, Kim CH, Kim JW. Comparison of titanium hydride (TiH_2) and paraffin as neutron moderator material in a prompt gamma scanning system. *J Korean Phys Soc* (2006) **48**(4):855. doi:10.3938/jkps.48.855. Available from: http://www.kps.or.kr/jkps/abstract_view.asp?articleuid=CB6536D4-BA6B-4C17-A954-7B0A6A2566B7&globalmenu=3&localmenu=10

31. Testa E, Bajard M, Chevallier M, Dauvergne D, Le Foulher F, Freud N, et al. Monitoring the Bragg peak location of 73MeV/u carbon ions by means of prompt γ-ray measurements. *Appl Phys Lett* (2008) **93**(9):093506. doi:10.1063/1.2975841
32. Lee HR, Park JH, Kim CH, Min CH. Design optimization of a 2D prompt-gamma measurement system for proton dose verification. *J Korean Phys Soc* (2012) **61**(2):239–42. doi:10.3938/jkps.61.239
33. Pinto M, Dauvergne D, Freud N, Krimmer J, Letang JM, Ray C, et al. Design optimisation of a TOF-based collimated camera prototype for online hadrontherapy monitoring. *Phys Med Biol* (2014) **59**(24):7653. doi:10.1088/0031-9155/59/24/7653
34. Cambraia Lopes P, Pinto M, Simoes H, Biegun A, Dendooven P, Oxley D, et al. Optimization of collimator designs for real-time proton range verification by measuring prompt gamma rays. *Nuclear Science Symposium and Medical Imaging Conference (NSS/MIC)*. Anaheim, CA: IEEE (2012). p. 3864–70. doi:10.1109/NSSMIC.2012.6551886
35. Verburg JM, Seco J. Proton range verification through prompt gamma-ray spectroscopy. *Phys Med Biol* (2014) **59**(23):7089. doi:10.1088/0031-9155/59/23/7089
36. Verburg JM, Testa M, Seco J. Range verification of passively scattered proton beams using prompt gamma-ray detection. *Phys Med Biol* (2015) **60**(3):1019. doi:10.1088/0031-9155/60/3/1019
37. Testa M, Min CH, Verburg JM, Schümann J, Lu HM, Paganetti H. Range verification of passively scattered proton beams based on prompt gamma time patterns. *Phys Med Biol* (2014) **59**(15):4181. doi:10.1088/0031-9155/59/15/4181
38. Perali I, Celani A, Bombelli L, Fiorini C, Camera F, Clementel E, et al. Prompt gamma imaging of proton pencil beams at clinical dose rate. *Phys Med Biol* (2014) **59**(19):5849. doi:10.1088/0031-9155/59/19/5849
39. Priegnitz M, Helmbrecht S, Janssens G, Perali I, Smeets J, Stappen FV, et al. Measurement of prompt gamma profiles in inhomogeneous targets with a knife-edge slit camera during proton irradiation. *Phys Med Biol* (2015) **60**(12):4849. doi:10.1088/0031-9155/60/12/4849
40. Everett D, Fleming J, Todd R, Nightingale J. Gamma-radiation imaging system based on the Compton effect. *Proc Inst Electr Eng* (1977) **124**(11):995. doi:10.1049/piee.1977.0203
41. Compton AH. A quantum theory of the scattering of X-rays by light elements. *Phys Rev* (1923) **21**(5):483–502. doi:10.1103/PhysRev.21.483
42. Seo H, Park JH, Ushakov A, Kim CH, Kim JK, Lee JH, et al. Experimental performance of double-scattering Compton camera with anthropomorphic phantom. *J Instrum* (2011) **6**(01):C01024. doi:10.1088/1748-0221/6/01/C01024
43. Krimmer J, Ley J-L, Abellan C, Cachemiche J-P, Caponetto L, Chen X, et al. Development of a Compton camera for medical applications based on silicon strip and scintillation detectors. *Nucl Instrum Methods Phys Res A* (2014) **787**:98–101. doi:10.1016/j.nima.2014.11.042
44. Llosá G, Cabello J, Callier S, Gillam J, Lacasta C, Rafecas M, et al. First Compton telescope prototype based on continuous LaBr3-SiPM detectors. *Nucl Instrum Methods Phys Res A* (2013) **718**(0):130–3. doi:10.1016/j.nima.2012.08.074
45. Thirolf P, Lang C, Aldawood S, Van der Kolff H, Maier L, Schaart D, et al. Development of a Compton camera for online range monitoring of laser-accelerated proton beams via prompt-gamma detection. *EPJ Web of Conferences*. (Vol. **66**), Florence: EDP Sciences (2014). 11036 p. doi:10.1051/epjconf/20146611036
46. Kormoll T, Fiedler F, Schöne S, Wüstemann J, Zuber K, Enghardt W. A Compton imager for in-vivo dosimetry of proton beams – a design study. *Nucl Instrum Methods Phys Res A* (2011) **626-627**:114–9. doi:10.1016/j.nima.2010.10.031
47. McCleskey M, Kaye W, Mackin D, Beddar S, He Z, Polf J. Evaluation of a multistage CdZnTe Compton camera for prompt γ imaging for proton therapy. *Nucl Instrum Methods Phys Res A* (2015) **785**(0):163–9. doi:10.1016/j.nima.2015.02.030
48. Kabuki S, Ueno K, Kurosawa S, Iwaki S, Kubo H, Miuchi K, et al. Study on the use of electron-tracking Compton gamma-ray camera to monitor the therapeutic proton dose distribution in real time. *Nuclear Science Symposium Conference Record (NSS/MIC)*. (Vol. **J05-13**), Orlando, FL: IEEE (2009). p. 2437–40. doi:10.1109/NSSMIC.2009.5402130
49. Kurosawa S, Kubo H, Ueno K, Kabuki S, Iwaki S, Takahashi M, et al. Prompt gamma detection for range verification in proton therapy. *Curr Appl Phys* (2012) **12**(2):364–8. doi:10.1016/j.cap.2011.07.027
50. Polf JC, Avery S, Mackin DS, Beddar S. Imaging of prompt gamma rays emitted during delivery of clinical proton beams with a Compton camera: feasibility studies for range verification. *Phys Med Biol* (2015) **60**(18):7085. doi:10.1088/0031-9155/60/18/7085
51. Assmann W, Kellnberger S, Reinhardt S, Lehrack S, Edlich A, Thirolf PG, et al. Ionoacoustic characterization of the proton Bragg peak with submillimeter accuracy. *Med Phys* (2015) **42**(2):567–74. doi:10.1118/1.4905047
52. ENTERVISION. *Research Training in 3D Digital Imaging for Cancer Radiation Therapy*. Geneva: CERN – European Laboratory for Particle Physics (2015). Available from: http://entervision.web.cern.ch/entervision/
53. Hueso-González F, Biegun AK, Dendooven P, Enghardt W, Fiedler F, Golnik C, et al. Comparison of LSO and BGO block detectors for prompt gamma imaging in ion beam therapy. *J Instrum* (2015) **10**(9):09015. doi:10.1088/1748-0221/10/09/P09015
54. Roemer K, Pausch G, Bemmerer D, Berthel M, Dreyer A, Golnik C, et al. Characterization of scintillator crystals for usage as prompt gamma monitors in particle therapy. *J Instrum* (2015) **10**(10):10033. doi:10.1088/1748-0221/10/10/P10033
55. Dorenbos P, de Haas J, van Eijk C. Non-proportionality in the scintillation response and the energy resolution obtainable with scintillation crystals. *IEEE Trans Nucl Sci* (1995) **42**(6):2190–202. doi:10.1109/23.489415
56. Balcerzyk M, Moszynski M, Kapusta M, Wolski D, Pawelke J, Melcher C. YSO, LSO, GSO and LGSO. a study of energy resolution and nonproportionality. *IEEE Trans Nucl Sci* (2000) **47**(4):1319–23. doi:10.1109/23.872971
57. Moszynski M, Balcerzyk M, Czarnacki W, Kapusta M, Klamra W, Syntfeld A, et al. Intrinsic energy resolution and light yield nonproportionality of BGO. *IEEE Trans Nucl Sci* (2004) **51**(3):1074–9. doi:10.1109/TNS.2004.829491
58. Biegun AK, Seravalli E, Lopes PC, Rinaldi I, Pinto M, Oxley DC, et al. Time-of-flight neutron rejection to improve prompt gamma imaging for proton range verification: a simulation study. *Phys Med Biol* (2012) **57**(20):6429. doi:10.1088/0031-9155/57/20/6429
59. Hueso-González F, Golnik C, Berthel M, Dreyer A, Enghardt W, Fiedler F, et al. Test of Compton camera components for prompt gamma imaging at the ELBE bremsstrahlung beam. *J Instrum* (2014) **9**(05):05002. doi:10.1088/1748-0221/9/05/P05002
60. Petzoldt J, Roemer KE, Enghardt W, Fiedler F, Golnik C, Hueso-González F, et al. Characterization of the microbunch time structure of proton pencil beams at a clinical treatment facility. *Phys Med Biol* (2016) **61**(6):2432. doi:10.1088/0031-9155/61/6/2432
61. Werner T, Dreyer A, Golnik C, Hueso-Gonzalez F, Enghardt W, Straessner A, et al. Studies of a proton phase beam monitor for range verification in proton therapy. *ANIMMA Conference Record 2015*. Lisbon (2015).
62. Paganetti H. Range uncertainties in proton therapy and the role of Monte Carlo simulations. *Phys Med Biol* (2012) **57**(11):R99. doi:10.1088/0031-9155/57/11/R99
63. Hubbell JH, Seltzer SM. *Tables of X-Ray Mass Attenuation Coefficients and Mass Energy-Absorption Coefficients from 1 keV to 20 MeV for Elements Z = 1 to 92 and 48 Additional Substances of Dosimetric Interest*. Gaithersburg, MD: NIST (2004). Available from: http://www.nist.gov/pml/data/xraycoef/

Conflict of Interest Statement: The authors declare that the research was conducted in the absence of any commercial or financial relationships that could be construed as a potential conflict of interest.

Copyright © 2016 Hueso-González, Fiedler, Golnik, Kormoll, Pausch, Petzoldt, Römer and Enghardt. This is an open-access article distributed under the terms of the Creative Commons Attribution License (CC BY). The use, distribution or reproduction in other forums is permitted, provided the original author(s) or licensor are credited and that the original publication in this journal is cited, in accordance with accepted academic practice. No use, distribution or reproduction is permitted which does not comply with these terms.

frontiers in Oncology

TECHNOLOGY REPORT
published: 02 February 2016
doi: 10.3389/fonc.2016.00014

First Images of a Three-Layer Compton Telescope Prototype for Treatment Monitoring in Hadron Therapy

Gabriela Llosá, Marco Trovato, John Barrio, Ane Etxebeste, Enrique Muñoz, Carlos Lacasta, Josep F. Oliver, Magdalena Rafecas, Carles Solaz and Paola Solevi*

Instituto de Física Corpuscular (IFIC-CSIC/UVEG), Valencia, Spain

A Compton telescope for dose monitoring in hadron therapy is under development at IFIC. The system consists of three layers of $LaBr_3$ crystals coupled to silicon photomultiplier arrays. ^{22}Na sources have been successfully imaged reconstructing the data with an ML-EM code. Calibration and temperature stabilization are necessary for the prototype operation at low coincidence rates. A spatial resolution of 7.8 mm FWHM has been obtained in the first imaging tests.

Keywords: Compton camera, Compton telescope, hadron therapy, treatment monitoring, $LaBr_3$

OPEN ACCESS

Edited by:
Marco Durante, GSI, Germany

Reviewed by:
Denis Dauvergne, CNRS, France
Vincenzo Patera, Sapienza University of Rome, Italy

****Correspondence:***
Gabriela Llosá
gabriela.llosa@ific.uv.es

Specialty section:
This article was submitted to Radiation Oncology, a section of the journal Frontiers in Oncology

Received: *16 October 2015*
Accepted: *13 January 2016*
Published: *02 February 2016*

Citation:
Llosá G, Trovato M, Barrio J, Etxebeste A, Muñoz E, Lacasta C, Oliver JF, Rafecas M, Solaz C and Solevi P (2016) First Images of a Three-Layer Compton Telescope Prototype for Treatment Monitoring in Hadron Therapy. Front. Oncol. 6:14. doi: 10.3389/fonc.2016.00014

1. INTRODUCTION

Hadron therapy allows a more precise delivery of charged particles in the tumor region as compared to photons. In order to fully exploit the benefits of this technique and reduce the safety margins applied, the dose administration requires accurate verification of the treatment delivery in real time. PET techniques currently employed suffer from some limitations such as low efficiency or the fact that the metabolic processes carry away the activity (biological washout). Also, positron production does not follow irradiation immediately and the difficulties of integrating the monitoring device with the treatment delivery make it hard to combine simultaneous treatment and monitoring. Different ways of achieving real-time monitoring are under investigation, employing other types of secondary particles emitted by the tissue after irradiation, such as prompt gamma-rays, which are emitted by the excited tissue nuclei within nanoseconds after irradiation (1). The ENVISION[1] European project has addressed this problem by improving PET systems and developing novel devices for the detection of prompt gammas.

Collimated systems (2, 3) and Compton cameras (4–7) are possible alternatives to image such gamma-rays, with energies mainly in the range of 0.5 to about 10 MeV. Prompt gamma timing techniques are also being investigated (8). Such systems have proven their ability to distinguish range shifts in beam tests. Compton cameras can offer higher efficiency than collimated cameras, as well as 3D imaging. For the construction of Compton cameras, different detector materials and geometries are being investigated, including silicon detectors, CZT, gas chambers, or scintillator detectors. Two approaches are followed: two-layer Compton cameras, with the traditional approach of a scatter detector followed by an absorber detector, and multiple-layer Compton cameras, requiring at least three interactions in three detectors. Two-layer Compton cameras have higher efficiency, but they rely on the knowledge of the incoming gamma-ray energy or on full absorption on the second detector for the determination of its energy. In this application, full absorption is difficult due to the high energies of the gamma-rays and the energy spectrum is broad and continuous up to high energies. The detection of three interactions on three

[1] http://envision.web.cern.ch/ENVISION/

detector layers fully determines the energy of the incoming gamma-ray, improving detector resolution but decreasing efficiency by an order of magnitude with respect to the two-layer option.

A Compton telescope (multilayer Compton camera) based on several planes of continuous $LaBr_3$ crystals coupled to silicon photomultiplier (SiPM) arrays is under development at IFIC, Valencia (9). We aim to combine both two- and three-layer modalities in one system to maximize resolution and efficiency. In addition, we have developed a method to estimate the energy from two-layer events. The choice of $LaBr_3$ as scintillator detector makes it possible to achieve excellent energy and timing resolution. $LaBr_3$ has been employed in Compton telescopes for gamma-ray astronomy in the megaelectronvolt range (10). SiPMs are fast and their reduced thickness minimizes the probability of gamma-rays interacting in the photodetector. This facilitates gamma-rays to escape one detector and reach the next one. The whole system is light, portable, scalable, and easy to operate. We have assembled a three-layer version of the system. In this article, we present the first images obtained with the three-layer prototype, assessing the imaging capabilities of the device.

2. MATERIALS AND METHODS

2.1. Prototype Description

The prototype consists of three detector layers, each one attached to a readout electronics board (**Figure 1**) (11). The first layer is made of a 27.2 mm × 26.8 mm × 5 mm $LaBr_3$ crystal coupled to four Hamamatsu MPPC S11830-3340MF monolithic arrays, with 4 × 4 pixels each. The arrays are biased individually. The second and third layers are composed of crystals of size 32 mm × 36 mm and thickness of 5 and 10 mm, respectively, coupled to four S11064-050P(X1)arrays with a common bias for all of them.

The readout of each plane is done with a custom-made data acquisition (DAQ) system that drives the 64-channel ASIC VATA64HDR16 (12). The DAQ board is equipped with an FPGA that controls the acquisition process, an 8-bit ADC (analog-to-digital converter) to digitize the data, and it is connected to a PC through Ethernet connection. The ASIC allows individual adjustment of the bias voltage of the 64 SiPM elements in the array through input DACs (digital-to-analog converters) in each channel.

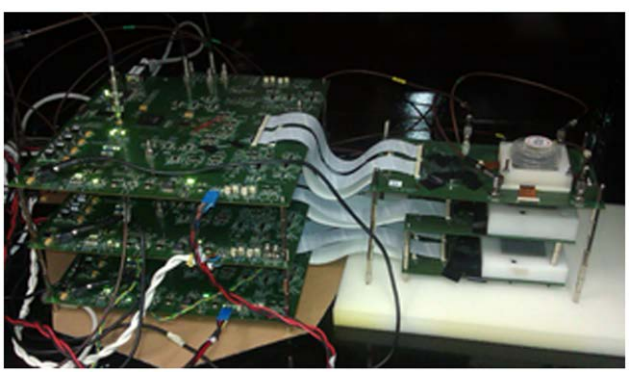

FIGURE 1 | Three-layer Compton telescope prototype and readout electronics.

2.2. Detector Characterization

The three detector layers have been characterized independently by taking data with radioactive sources of different energies (^{22}Na, ^{137}Cs, and ^{60}Co). The light generated in the crystal by the gamma-rays is detected by the 64-pixel elements of the SiPM array. For each event, the signals produced in each of the pixels are digitized and stored for data analysis.

The uniformity of the detector response has also been evaluated. The ^{22}Na source is placed 15 cm away from the detector in order to ensure a uniform illumination. The signals in each channel are histogrammed for all the events acquired, and the average signal per channel is assumed to be constant for a high number of events (>10,000) (13). This way, the differences in response among channels can be appreciated. In order to equalize the response, the bias voltage per channel is adjusted through the ASIC input DACs.

In order to obtain the energy spectra, for each event the 64 ADC values of the SiPM signals are summed up and histogrammed. A calibration curve is obtained by taking data with sources of different energies, fitting a Gaussian function to the photopeaks in the spectra in order to determine the peak position in ADC counts, and plotting the peak position versus the source energy.

The determination of the interaction position in the crystal is carried out with the method described in Ref. (14), which is based on a model of the light distribution in the photodetector, taking into account both the photons that reach it directly and those that are first reflected on the crystal sides. In order to determine the intrinsic spatial resolution, data are taken with a ^{22}Na source placed at different positions of the detector surface. The source is electronically collimated by operating the detector in time coincidence with a small detector, restricting the position at which the photons interact.

The current–voltage characteristics of the SiPM depend on the operating temperature. This is mainly due to the change in the breakdown voltage of the SiPM, which results in a different overvoltage for a given bias voltage applied to the detector. The variations of the photopeak position of the energy spectra with temperature have been studied. ^{22}Na energy spectra are taken with the detectors in a climatic chamber, at different temperatures. A figure representative of the detector gain is calculated from the two photopeak positions of ^{22}Na in each case.

2.3. Prototype Operation

The three detector layers have been assembled in order to work in time coincidence. The trigger signal generated by each detector is sent to a NIM coincidences unit. The coincidence is given by the overlap of the trigger signals of the three detectors, which is 25 ns wide. The threshold applied to the detectors is around 50 keV. The output coincidence signal is sent back to each of the DAQ boards in order to start the data acquisition.

The distance from the source to the first layer is 35 mm. The distances from the first to the second layer and from the second to the third are 60 and 65 mm, respectively. Coincidence data with the three layers have been taken placing the system inside a climatic chamber in order to maintain the temperature constant (the measurement was done at 25.5°C) and avoid temperature variations during data acquisition.

Data are taken with a ^{22}Na source of 0.25 mm active diameter and 700 kBq activity. The data recorded in the three detectors are calibrated and summed up for each event. The energies and interaction positions in the three layers are the input of the image reconstruction code.

2.4. Image Reconstruction

For image reconstruction in Compton cameras, conventional two-interaction events require to know the energy of the incoming photon or full absorption in the second detector in order to obtain the cone surface defined by all the possible photon trajectories. In hadron therapy monitoring, this is not possible due to the wide emission spectrum and the high photon energies. To overcome this limitation, the incoming photon energy can be estimated during the image reconstruction process, *spectral reconstruction* (15). However, havin g three layers allows us to access to three-interaction events, which convey enough information to directly determine this energy and, therefore, the associated cone surface.

An image reconstruction software based on the statistical iterative algorithm maximum likelihood-expectation maximization (ML-EM) has been developed. These data are acquired in coincidence list-mode and the interaction positions and energies are directly used (not histogrammed) for avoiding resolution loss. The reconstruction code (16) implements the above-mentioned strategy to reconstruct the three-interaction events data.

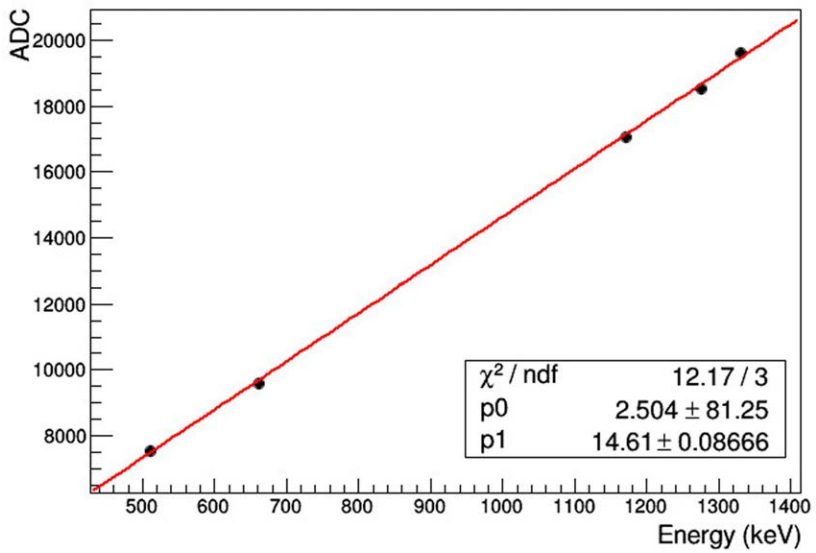

FIGURE 2 | Photopeak position vs. source energy for detector calibration.

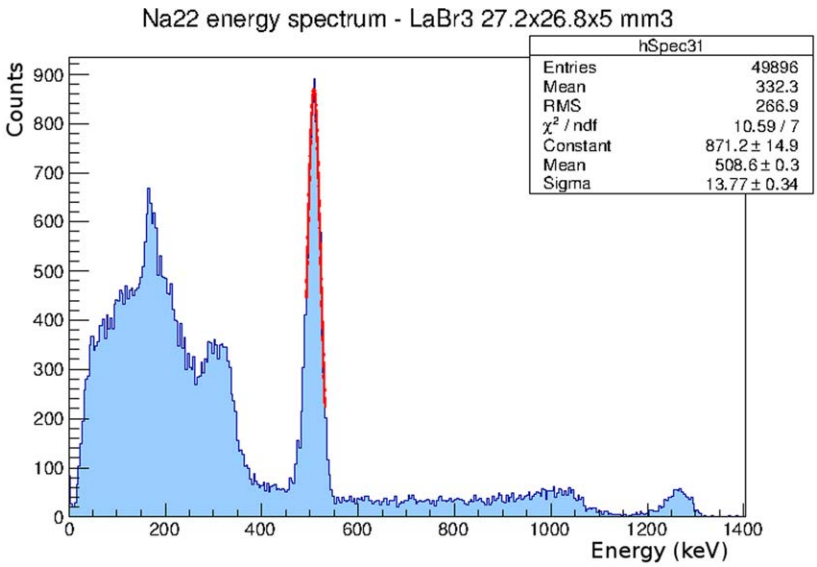

FIGURE 3 | ^{22}Na energy spectrum obtained with the first detector. The energy resolution is 6.4% FWHM at 511 keV.

3. RESULTS

3.1. Detector Characterization

The detectors employed in the prototype have been characterized in terms of energy and spatial resolution.

The results of the first detector calibration are shown in **Figure 2**, where it can be seen that the response is linear up to 1.33 MeV. Similar results are obtained with the other two detectors. **Figure 3** shows a ^{22}Na energy spectrum obtained also with the first detector. A Gaussian fit to the 511 keV photopeak results in an energy resolution of 6.4% FWHM. An energy resolution of 7.4% FWHM and 7.2% FWHM at 511 keV has been obtained with the second and third layers, respectively.

The intrinsic spatial resolution achieved with the three detectors is of the order of 1 mm FWHM (17). The uniformity of the pixel response achieved applying the DAC corrections is around 5% in the first detector, and around 10% in the second and third detectors. The difference is due to the fact that the first detector employs monolithic arrays that have a more uniform response within each array, and the four of them can be biased individually, adjusting better the four bias reference voltages.

The effects of temperature variations are shown in **Figure 4**, which shows ^{22}Na energy spectra taken at different temperatures. The difference in gain can be clearly appreciated.

In **Figure 5**, the gain values obtained from the energy spectra are plotted versus temperature. The gain decrease with temperature is about 5%/°C.

3.2. Prototype Results

The ^{22}Na energy spectrum corresponding to the sum of the energies recorded in the three detector layers in coincidence in each event is shown in **Figure 6**. The two ^{22}Na photopeaks (511 and 1275 keV)

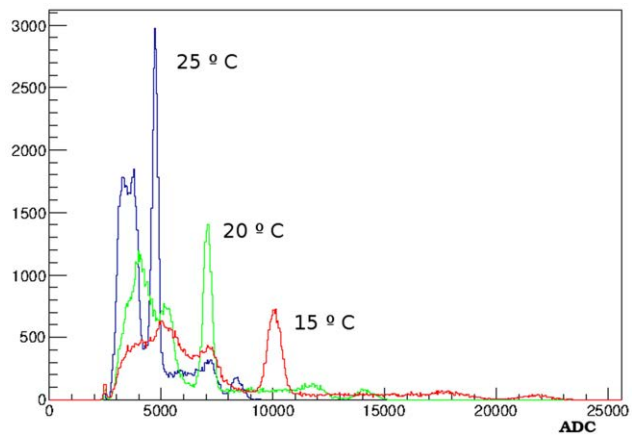

FIGURE 4 | ^{22}Na spectra obtained at different temperatures where one can see the gain variation.

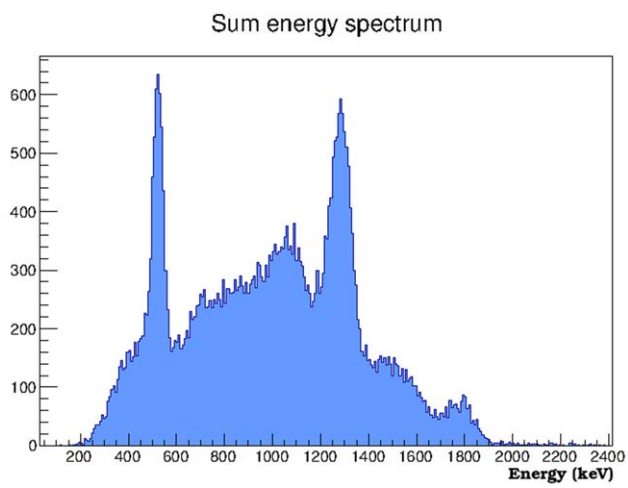

FIGURE 6 | Calibrated energy spectrum obtained by summing the energies recorded in the three detectors in coincidence for each event.

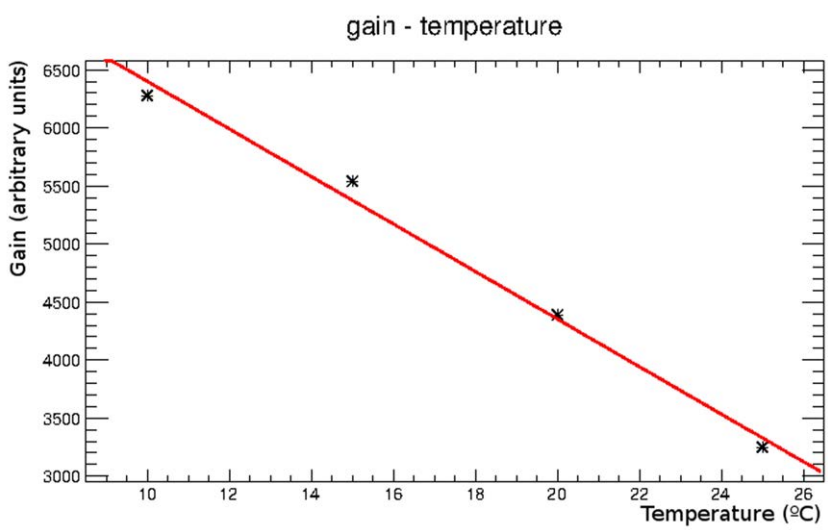

FIGURE 5 | Gain obtained from the calibration curves at different temperatures, plotted as a function of temperature.

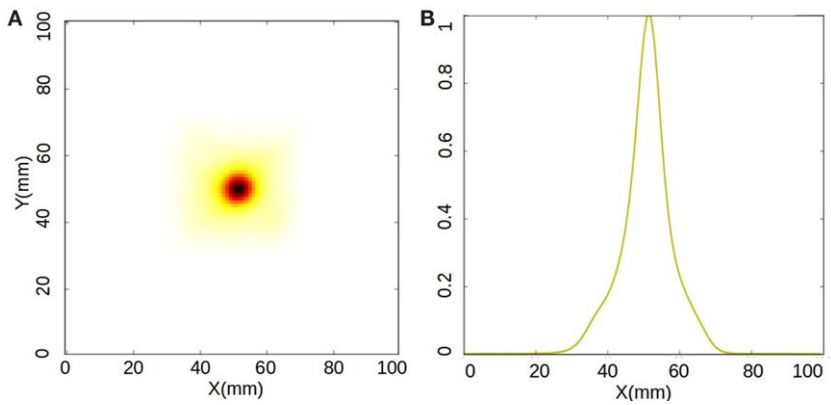

FIGURE 7 | (A) 2D view of the reconstructed image of the ^{22}Na source at the source plane. **(B)** Profile through the peak of the plot. The resolution is 7.8 mm FWHM.

can be observed. A sum peak of the previous two due to accidental coincidences can also be seen. The count rate with the tested geometry is 0.3 events/s and the calculated efficiency is about 7×10^{-6}.

The processed data are employed for image reconstruction. **Figure 7A** shows a 2D view of a reconstructed image with a total energy cut between 800 and 1400 keV in the sum spectrum, after 30 iterations. **Figure 7B** shows a profile along the x axis through the maximum of the reconstructed image. A Gaussian fit to the profile results in a spatial resolution of 7.8 mm FWHM for the geometry employed and the cuts applied. In the tests reported here, it was not possible to obtain an image employing the data corresponding to the 511 keV photopeak.

4. DISCUSSION AND FUTURE WORK

A Compton telescope composed of three layers of $LaBr_3$ crystals coupled to SiPM arrays has been successfully constructed and operated. The energy resolution obtained with the newest detector (first detector) 6.4% FWHM at 511 keV is closer to the one specified by the crystal manufacturer and measured by us with a PMT, 3.5% FWHM (17) and compatible with other measurements with SiPMs (18). Further improvements of the SiPM array pixel uniformity and photon detection efficiency in the $LaBr_3$ peak emission wavelength (380 nm), together with an improved detector coupling should make it possible to achieve the excellent energy resolution expected with this kind of scintillator crystal. The intrinsic spatial resolution of the detectors, close to 1 mm FWHM, is appropriate for the application. The timing resolution must also be characterized and brought close to 1 ns FWHM in order to reject the neutron background (19). The response of the detectors to temperature variations has been studied, and the temperature calibration can be applied to compensate for temperature changes when temperature control is not possible.

Even with this non-optimized setup, it has been possible to obtain an image of a ^{22}Na source in the laboratory. An image reconstruction code has been developed, and it is ready for its use. The resolution of the reconstructed image in this first attempt is 7.8 mm FWHM at 35 mm distance from the first detector.

The spatial resolution achieved should still be improved in order to determine the position of the distal falloff with few millimeter accuracy, as it is required for hadron therapy monitoring (20).

As expected, the experimental results obtained in this first test are behind similar systems in a more advanced development status. Comparison of the results with other approaches is not possible at this point due to the different sizes, configurations, and geometries. Work is being carried out to optimize the system results and estimate its potential capabilities.

A Monte Carlo simulation code has also been developed to optimize the detector configuration and determine the necessary improvements for its application to hadron therapy monitoring.

AUTHOR CONTRIBUTIONS

GL has supervised the work, helped to carry it out, and wrote the article. MT has set up the device and done the measurements described. All other authors have contributed to some parts of the work: CS, electronics; EM and AE, analysis software; CL, acquisition software; JB, measurements; PS and JO, image reconstruction; MR, supervision and guidance for the image reconstruction part of the work.

ACKNOWLEDGMENTS

This work was supported in part by the European Commissions 7th Framework Programme through the ENVISION (G. A. num 241851) project and the Marie Curie ITN ENTERVISION (G. A. num 264552), by the Spanish Ministerio de Economia y Competitividad (FPA2010-14891, FIS2011-14585-E, and FPA2014-53599-R), the UVEG (UV-INV-PRECOMP12-80755), and the Generalitat Valenciana (GV/2013/133 and GVISIC/2012/020). Group members are supported by Ramón y Cajal, UVEG Atraccio de Talent, and Generalitat Valenciana contracts.

REFERENCES

1. Min C, Kim C, Youn M, Kim J. Prompt gamma measurements for locating dose falloff region in proton therapy. *Appl Phys Lett* (2006) **89**:183511–3. doi:10.1063/1.2378561
2. Kim D, Yim H, Kim J-W. Pinhole camera measurements of prompt gamma-rays for detection of beam range variation in proton therapy. *J Korean Phys Soc* (2009) **55**:1673–6. doi:10.3938/jkps.55.1673
3. Roellinghoff F, Benilov A, Dauvergne D, Dedes G, Freud N, Janssens G, et al. Real-time proton beam range monitoring by means of prompt-gamma detection with a collimated camera. *Phys Med Biol* (2014) **59**:1327–38. doi:10.1088/0031-9155/59/5/1327
4. Richard M-H, Chevallier M, Dauvergne D, Freud N, Henriquet P, Foulher FL, et al. Design guidelines for a double scattering Compton camera for prompt-gamma imaging during ion beam therapy: a Monte Carlo simulation study. *IEEE Trans Nucl Sci* (2011) **58**:87–94. doi:10.1109/TNS.2010.2076303
5. Kormoll T, Fiedler F, Schone S, Wustemann J, Zuber K, Enghardt W. A Compton imager for in-vivo dosimetry of proton beams – a design study. *Nucl Instrum Methods Phys Res A* (2011) **626**:114–9. doi:10.1016/j.nima.2012.01.072
6. Kurosawa S, Kubo H, Ueno K, Kabuki S, Iwaki S, Takahashi M, et al. Prompt gamma detection for range verification in proton therapy. *Curr Appl Phys* (2012) **12**:364–8. doi:10.1016/j.cap.2011.07.027
7. Polf JC, Avery S, Mackin DS, Beddar S. Imaging of prompt gamma rays emitted during delivery of clinical proton beams with a Compton camera: feasibility studies for range verification. *Phys Med Biol* (2015) **60**:7085–99. doi:10.1088/0031-9155/60/18/7085
8. Golnik C, Hueso-González F, Mueller A, Dendooven P, Enghardt W, Fiedler F, et al. Range assessment in particle therapy based on prompt-ray timing measurements. *Phys Med Biol* (2014) **59**:5399–422. doi:10.1088/0031-9155/59/18/5399
9. Llosá G, Cabello J, Callier S, Gillam JE, Lacasta C, Rafecas M, et al. First Compton telescope prototype based on continuous LaBr3-SiPM detectors. *Nucl Instrum Methods Phys Res A* (2013) **718**:130–3. doi:10.1016/j.nima.2012.08.074
10. Bloser PF, Ryan JM, Legere JS, Julien M, Bancroft CM, McConnell ML, et al. A new low-background Compton telescope using LaBr3 scintillator. In: *Proc. SPIE 7435, UV, X-Ray, and Gamma-Ray Space Instrumentation for Astronomy XVI* (2009). doi:10.1117/12.826191
11. Trovato M, Solevi P, Torres-Espallardo I, Gillam J, Lacasta C, Rafecas M, et al. A three layer Compton telescope for dose monitoring in hadron therapy. *IEEE NSS MIC* Seattle, WA: IEEE (2014).
12. Stankova V, Barrio J, Gillam JE, Lacasta C, Rafecas M, Solaz C, et al. Multichannel DAQ system for SiPM matrices. *Nuclear Science Symposium and Medical Imaging Conference (NSS/MIC)*. Anaheim, CA: IEEE (2012). p. 1069–71. doi:10.1109/NSSMIC.2012.6551270
13. Barrio J, Etxebeste A, Lacasta C, Muñoz E, Oliver J, Solaz C, et al. Performance of vata64hdr16 ASIC for medical physics applications based on continuous crystals and SiPMS. *J Instrum* (2015) **10**:12001. doi:10.1088/1748-0221/10/12/P12001
14. Li Z, Wedrowski M, Bruyndonckx P, Vandersteen G. Nonlinear least-squares modelling of 3d interaction position in a monolithic scintillator block. *Phys Med Biol* (2010) **55**:6515–32. doi:10.1088/0031-9155/55/21/012
15. Xu D, He Z. Gamma-ray energy-imaging integrated spectral deconvolution. *Nucl Instrum Methods Phys Res A* (2007) **574**:98–109. doi:10.1016/j.nima.2007.01.171
16. Gillam JE, Oliver JF, Torres-Espallardo I, Lacasta C, Llosá G, Trovato M, et al. Simulated one pass listmode for fully 3d image reconstruction of a Compton camera data. *IEEE NSS MIC Conference Record* (2012). p. 3298–305. doi:10.1109/NSSMIC.2012.6551752
17. Llosá G, Cabello J, Gillam JE, Lacasta C, Oliver JF, Rafecas M, et al. Second LaBr3 Compton telescope prototype. *ANIMMA 2013 Conference Record* Marseille: IEEE (2013). p. 1–4.
18. Seifert S, van Dam HT, Huizenga J, Vinke R, Dendooven P, Lohner H, et al. Monolithic LaBr3:Ce crystals on silicon photomultiplier arrays for time-of-flight positron emission tomography. *Phys Med Biol* (2012) **57**:2219–33. doi:10.1088/0031-9155/57/8/2219
19. Biegun AK, Seravalli E, Lopes PC, Rinaldi I, Pinto M, Oxley DC, et al. Time-of-flight neutron rejection to improve prompt gamma imaging for proton range verification: a simulation study. *Phys Med Biol* (2012) **57**:6429–44. doi:10.1088/0031-9155/57/20/6429
20. Moteabbed M, España S, Paganetti H. Monte Carlo patient study on the comparison of prompt gamma and pet imaging for range verification in proton therapy. *Phys Med Biol* (2011) **56**:1063–82. doi:10.1088/0031-9155/56/4/012

Conflict of Interest Statement: The authors declare that the research was conducted in the absence of any commercial or financial relationships that could be construed as a potential conflict of interest.

Copyright © 2016 Llosá, Trovato, Barrio, Etxebeste, Muñoz, Lacasta, Oliver, Rafecas, Solaz and Solevi. This is an open-access article distributed under the terms of the Creative Commons Attribution License (CC BY). The use, distribution or reproduction in other forums is permitted, provided the original author(s) or licensor are credited and that the original publication in this journal is cited, in accordance with accepted academic practice. No use, distribution or reproduction is permitted which does not comply with these terms.

frontiers in Oncology

ORIGINAL RESEARCH
published: 28 January 2016
doi: 10.3389/fonc.2016.00010

Assessment of Geant4 Prompt-Gamma Emission Yields in the Context of Proton Therapy Monitoring

Marco Pinto[1†], Denis Dauvergne[1], Nicolas Freud[2], Jochen Krimmer[1], Jean M. Létang[2] and Etienne Testa[1]*

[1] CNRS/IN2P3 UMR 5822, IPNL, Université de Lyon, Université Lyon 1, Villeurbanne, France, [2] CREATIS, CNRS UMR 5220, INSERM U1044, INSA-Lyon, Centre Léon Bérard, Université de Lyon, Université Lyon 1, Lyon, France

Monte Carlo tools have been long used to assist the research and development of solutions for proton therapy monitoring. The present work focuses on the prompt-gamma emission yields by comparing experimental data with the outcomes of the current version of Geant4 using all applicable proton inelastic models. For the case in study and using the binary cascade model, it was found that Geant4 overestimates the prompt-gamma emission yields by $40.2 \pm 0.3\%$, even though it predicts the prompt-gamma profile length of the experimental profile accurately. In addition, the default implementations of all proton inelastic models show an overestimation in the number of prompt gammas emitted. Finally, a set of built-in options and physically sound Geant4 source code changes have been tested in order to try to improve the discrepancy observed. A satisfactory agreement was found when using the QMD model with a wave packet width equal to $1.3\,\text{fm}^2$.

Keywords: proton therapy, hadrontherapy, prompt gammas, Geant4, online monitoring, in-beam monitoring, collimated camera, nuclear fragmentation models

OPEN ACCESS

Edited by:
Francis A. Cucinotta, University of Nevada Las Vegas, USA

Reviewed by:
Joshua Silverman, New York University Medical Center, USA
Yu Kuang, University of Nevada Las Vegas, USA

****Correspondence:***
Etienne Testa
e.testa@ipnl.in2p3.fr

†Present address:
Marco Pinto, Ludwig Maximilians University, Munich, Germany

Specialty section:
This article was submitted to Radiation Oncology, a section of the journal Frontiers in Oncology

Received: *30 September 2015*
Accepted: *11 January 2016*
Published: *28 January 2016*

Citation:
Pinto M, Dauvergne D, Freud N, Krimmer J, Létang JM and Testa E (2016) Assessment of Geant4 Prompt-Gamma Emission Yields in the Context of Proton Therapy Monitoring. Front. Oncol. 6:10. doi: 10.3389/fonc.2016.00010

1. INTRODUCTION

Particle therapy, namely proton and carbon-ion therapy, has been the subject of growing interest, primarily due to the favorable ballistic properties of ion–matter interactions, which allow for a high degree of dose conformality in the tumor while minimizing the dose in the healthy tissue. However, such properties pose some challenges in terms of quality assurance of the treatment when compared, for example, to photon radiation therapy since ions are more sensitive to both planning and treatment uncertainties (1, 2). Several verification protocols and monitoring approaches have been proposed to address this issue, among which the detection of prompt gammas (PG) for ion range monitoring. Prompt gammas are the result of nuclear interactions between the incident ion and the tissue nuclei. Their emission can be considered as instantaneous after the interaction, thus providing a strong correlation with the ion range (3, 4). Moreover, when compared with the positron emission tomography monitoring, already in clinical use for the same purpose, prompt-gamma monitoring does not suffer from signal washout and time dependency. In addition, the energy threshold for the nuclear reactions producing positron emitters is higher than the one for the emission of PG, hence a better correlation with the ion range is observed for the latter (5). However, the need for dedicated devices with high acquisition rate capabilities, the broad energy range of the emitted prompt gammas, and the extensive background render it a particularly demanding technique.

The inherent complexity of the nuclear processes leading to the emission of prompt gammas makes Monte Carlo tools one of the main resources employed in the study of this form of particle therapy monitoring, namely in terms of camera optimization [e.g., Ref. (6–10)]. In this regard, Geant4 (11) has been one of the chosen tools due to ease of use and open-source distribution. However, as already described in the literature (8, 12–15), the hadronic inelastic models implemented in Geant4 tend to overestimate prompt-gamma emission. There is no evidence so far that the spatial prediction is also affected; hence, it is still possible to use the spatial prompt-gamma distributions to find correlations with ion range. Nevertheless, relying on an overestimated signal raises a concern for the optimization of devices to exploit the information provided by the prompt-gamma emission since the precision to detect ion range shifts is inversely proportional to the collected signal (16).

The present study addresses the issue of discrepancies in prompt-gamma emission yields after proton irradiation using Geant4 by comparing all applicable proton inelastic models with experimental data. In addition, we propose and test several approaches within the existing models to try to improve the accuracy of Geant4 for prompt-gamma emission yields.

2. MATERIALS AND METHODS

2.1. Experimental Data

The experimental data were collected during an experimental campaign at the Westdeutsches Protonentherapiezentrum Essen (WPE, Essen, Germany) (17). The setups comprised a single-slit collimator, a detector, and a target aligned with the beam axis. The single-slit collimator was positioned orthogonally with respect to the beam axis and the alignment and positioning of the different setup elements were accomplished by means of lasers and rulers, respectively. The cylindrical polymethyl methacrylate (PMMA) target with a 75-mm radius and 200-mm length was positioned on top of a moving table, thus allowing to perform measurements along the target. The step size of the different longitudinal positions was not fixed, and it was dependent on factors like ion range and need for a better description of some prompt-gamma profile features (e.g., at the target entrance or close to the end of the ion path). The collimator was made of a tungsten alloy with a 4-mm slit opening and, when applicable, the shielding consisted of lead blocks. Two setups were considered. The data of the first setup (setup 1) were collected by means of a LYSO detector, while in the second one (setup 2), the LYSO and $LaBr_3$ detectors were used.

A schema of setups 1 and 2 can be observed in **Figures 1** and **2**, respectively.

In order to select the prompt gammas from the extensive background, the time-of-flight (TOF) technique was used in conjunction with a VME-based acquisition system with NIM modules and discrete logic and analogic electronics. The TOF windows applied during the analysis were always sufficiently large to include all the visible prompt-gamma events. The TOF stop signal was given by the high-frequency (HF) signal of the cyclotron running in pulsed mode. The stop signal was actually provided by a discriminator converting the HF signal into a digital logic one whose frequency was divided by a factor of ~5 with respect to the HF frequency to cope with the time-to-amplitude (TAC) module limitations. The TOF spectra measured in these conditions correspond therefore to ~5 periods of the HF signal. The circular beam spot was around 5 mm sigma at isocenter, considering a Gaussian spatial beam distribution (18). Energy thresholds were also applied to the data in order to reduce the background component. The energies considered were obtained after calibration with gamma sources. Therefore, it is an absorbed gamma-equivalent energy but, for the sake of simplicity, it will be simply referred to as energy. The lower-energy threshold for the detectors in the post-processing steps was 1 MeV, while the upper one was 7 and 12 MeV for the LYSO and $LaBr_3$ detectors, respectively. The difference between the two upper-energy thresholds is due to the distinct usable energy range of each detector. In addition, scalers were also used to account for the dead time of the acquisition system.

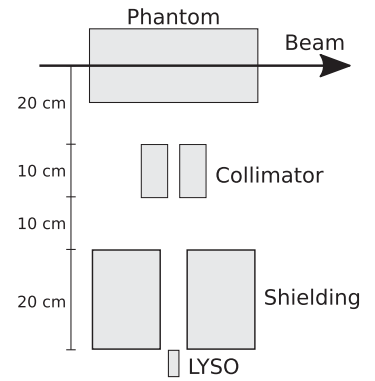

FIGURE 1 | Schematic illustration of setup 1 (not to scale).

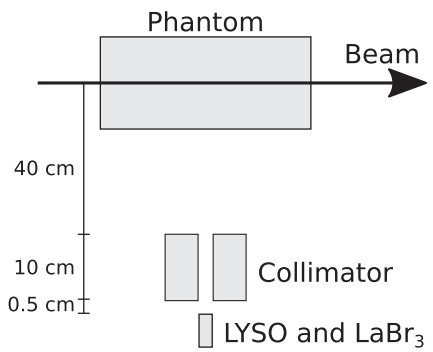

FIGURE 2 | Schematic illustration of setup 2 (not to scale).

This experiment was conducted using a single proton energy (160 MeV) and with a suitable beam intensity to avoid pile-up and excessive dead time. The number of incoming protons was given by the ionization chamber (IC) placed inside the beam nozzle, thus allowing for the normalization of the data. The IC was calibrated against a Bragg peak chamber positioned at the target entrance.

In order to make a better comparison between experimental and simulated data, both data sets are subjected to a background subtraction procedure. It was decided to follow the procedure followed by Pinto et al. (17), where the `TSpectrum` routine of ROOT (19) is used.

Additional details about these experimental data can be found elsewhere (17), namely, in terms of TOF analysis and absolute yields.

2.2. Geant4 Data

The Geant4 version 10.01.p02 was used as it was the last stable release at the time of the present study. In this version, there are five proton hadronic inelastic models for the energy range considered herein: binary cascade (BIC), Bertini cascade (BERT), precompound (PRECO), Liège intranuclear cascade (INCL), and quantum molecular dynamics (QMD). It should be noted that the QMD model is usually never considered for proton interactions, but its implementation in Geant4 is fully prepared for using it in such a case. QMD is the most comprehensive hadronic inelastic model in Geant4 and its complexity is often regarded as needless to describe proton interactions since there are other models able to perform the same task with similar accuracy but requiring much less computing time (usually around one order of magnitude less).

The description of these models is outside the scope of the present paper, but additional information can be found in the Geant4 web page (https://cern.ch/geant4) and the references therein.

The simulation of the experimental setups requires a high amount of computing resources due to its small solid angle; hence, a method to consider all possible models was selected. First, a proton inelastic model was selected to be used for the simulation of the experimental setups and subsequent comparison with the experimental data. Since the developers of Geant4 recommend the use of the BIC model for the present case, it was decided to choose it to be the reference model. In a second stage, the physical models were used to retrieve a longitudinal distribution of prompt gammas escaping the target with an angular acceptance of $\pm 1.5°$[similar to the procedure followed by Biegun et al. (20)]. Finally, the comparison between the experimental data and those from the simulation of the full setups with the reference model provides an estimate of the corresponding experimental yields for the case where PG escapes from the target. This makes possible and a meaningful comparison between all the physical models while optimizing the use of computing resources. Nevertheless, such an approach discards the potential influence of the neutron-induced gammas created in the collimator and/or shielding. In any case, those events should not overlap with the PG peak and after background subtraction and TOF selection they are assumed not to have an impact on the results (17).

The implementation of the experimental setups in Geant4 included target, collimator, shielding blocks, detectors, and nozzle components. In order to account for the extensive background due to the pile-up of events from previous proton bunches, an off-line procedure was applied to the simulated data to mimic the beam frequency (106 MHz). Additionally, as mentioned previously, the simulated data were analyzed with the same software as the experimental ones, thus reducing possible discrepancies that could have been introduced by the use of different analysis routines. It should be noted that the same experimental absorbed energy thresholds were used for the simulated data (i.e., 1–7 MeV for the LYSO detector and 1–12 MeV for the $LaBr_3$ one).

Table 1 shows the most relevant physical models other than the proton hadronic inelastic ones used in the simulations.

2.3. Comparison between Experimental and Simulated Data

The Geant4 benchmarking included two endpoints, arguably the two most relevant ones: yields and information correlated with the ion range. The former has an impact on, for example, camera optimization, while the latter plays a major role in a monitoring scenario. The yields were assessed using the reference model and comparing its outcomes with the experimental data. The discrepancy was then evaluated by computing the average relative difference between selected simulated and experimental data points. The rationale for such a selection was the need to avoid high-gradient signal regions since they could have a significant and misleading impact on the calculation of the relative difference due to spatial uncertainties. Therefore, the points considered were between 20 mm (to avoid the entrance of the target positioned at 0 mm – see, e.g., **Figure 3**) and 140 mm (to avoid the PG profile falloff). The projected proton range for the experimental data was 154.72 mm (21) (not including nozzle elements).

Concerning the information provided by the prompt-gamma profile correlated with the proton range, Pinto et al. (22) proposed

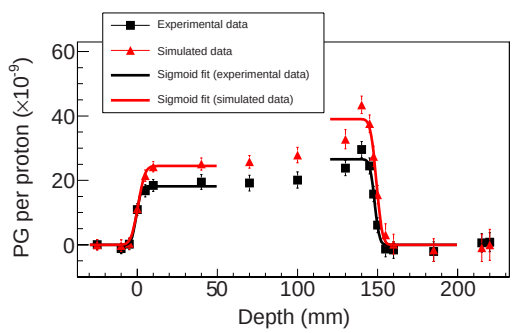

FIGURE 3 | Experimental and simulated data for setup 1 using the LYSO detector and considering an energy selection of $1 \leq$ energy ≤ 7 MeV. The fits using sigmoid functions in order to retrieve the PGPL are also shown (the range plotted is the same of the fit procedure). The simulated data were obtained with the BIC model for proton inelastic interactions.

TABLE 1 | The most relevant physical models used for the simulations (not including the proton inelastic ones).

Hadronic inelastic neutrons		Hadronic inelastic ions (heavier than H^+)	Others
$<$20 MeV	$\geq$20 MeV		
G4NeutronHPInelastic	G4BinaryCascade	G4IonBinaryCascadePhysics	G4HadronElasticPhysicsHP

the use of the quantity designated as prompt-gamma profile length (PGPL) to measure the distance between the rise in the prompt-gamma profile at the entrance of a target or patient and the falloff close to the end of the ion path. They showed that this quantity is correlated with the ion range for the case of carbon-ion irradiation. Herein, the same approach will be used, and it comprises the fit of sigmoid functions to both the prompt-gamma profile entrance and falloff. The PGPL is obtained through the subtraction between the two inflection points retrieved after the fit to both positions. This function has been initially proposed by Henriquet et al. (23) to study the interaction vertex imaging approach for carbon-ion monitoring. However, the application of the PGPL concept was only possible for the data from the setup 1 because the data from setup 2 were too scarce for a meaningful fitting procedure.

2.4. Geant4 Improvement

After the comparison between the outcome of the aforementioned models and the experimental data, a systematic study of the possibilities for improvement using each model was carried out. Such a study distinguishes between two cases, one in which built-in options of each model are changed, and the other where changes to the source code are made. It is emphasized that any change in the models is always driven by some physical meaning. If the purpose was otherwise, one could probably apply correction factors to the simulated data. However, this approach may pose additional problems since it may be very difficult to assess the factors for all biologically relevant materials and proton energies. In fact, tuning the free and physically bounded parameters of the Geant4 source code is logical since historically Geant4 was developed for high-energy physics, for which both the projectile energies and targets are significantly different from the ones of medical physics. Therefore, it is expected that hadronic inelastic models and their parameters are optimized mainly for high-energy physics scenarios and that they may be adjusted to yield better accuracy for the application in the study herein. As an example, Dedes et al. (12) found that one of the hard-coded free parameters of the QMD model was optimized for interactions similar to Au + Au. When optimizing that parameter for targets relevant to medical physics, the authors were able to obtain an agreement between experimental and simulated data for prompt-gamma emission yields when considering carbon-ion irradiation.

3. RESULTS

3.1. Experimental vs. Simulated Data

Figures 3–5 show the experimental and simulated data for both setups and detectors. It can be observed that the simulated data are consistently overestimated with respect to the experimental results. The relative differences are presented in **Table 2**. Additionally, the fits to retrieve the PGPL are also depicted in **Figure 3**. The estimated PGPL for the experimental data is 148.3 ± 0.9 mm, while for the simulated case is 148.2 ± 0.8 mm.

It should be noted that the error bars were estimated with the same procedure followed by Pinto et al. (17), in which the statistical uncertainties (1 SD) for each data point and the uncertainties imparted by the background subtraction method are taken into consideration. Due to the nature of the latter, it is not unreasonable to consider that the error bars may be under-/overestimated since it is not possible with the current set of data to estimate accurately the background superimposed with the prompt-gamma signal.

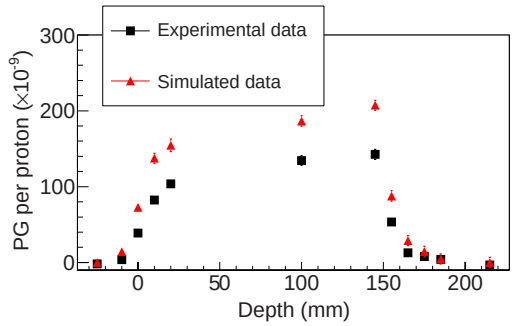

FIGURE 4 | Experimental and simulated data for setup 2 using the LYSO detector and considering an energy selection of $1 \leq$ energy ≤ 7 MeV. The simulated data were obtained with the BIC model for proton inelastic interactions.

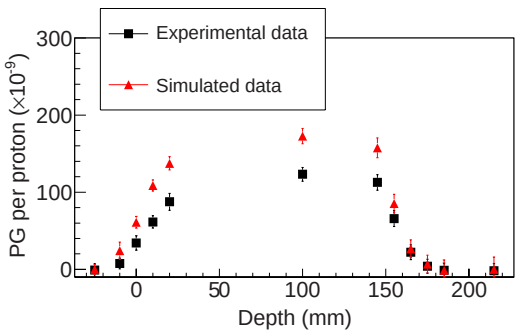

FIGURE 5 | Experimental and simulated data for setup 2 using the $LaBr_3$ detector and considering an energy selection of $1 \leq$ energy ≤ 12 MeV. The simulated data were obtained with the BIC model for proton inelastic interactions.

TABLE 2 | Average relative difference between experimental and simulated data computed using the data points between 20 and 140 mm.

	Average relative difference (%)
Setup 1 LYSO	39.9 ± 0.7
Setup 2 LYSO	39.9 ± 0.3
Setup 2 $LaBr_3$	41.5 ± 0.6
Average	40.2 ± 0.3

The average considering the values of the three cases was calculated with the standard weighted least-squares formula (24).

3.2. Default Proton Hadronic Inelastic Models

Figure 6 shows the longitudinal profiles obtained with the default implementation of all applicable Geant4 proton inelastic models along with the reference model scaled down to account for the estimated overestimation. Since the different upper-energy thresholds did not have an impact on the overestimation, the

simulated data depicted in **Figures 6** and **7** consider events with $1 \leq \text{energy} \leq 12$ MeV.

3.3. Improved Proton Hadronic Inelastic Models

Figure 7 depicts the longitudinal profiles obtained after using a given built-in option of Geant4 or making a given change in the source code. The naming used and the different changes are summarized in **Table 3**.

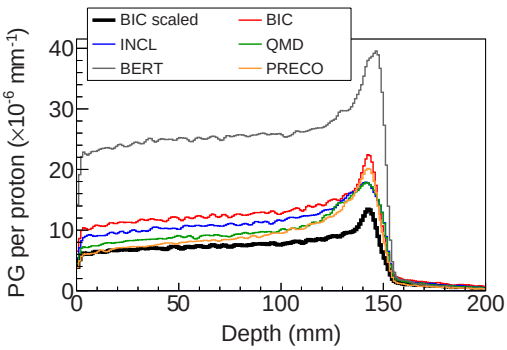

FIGURE 6 | Longitudinal profiles of the photons escaping the PMMA target having an angular acceptance of ±1.5°. These profiles were obtained with the default models of Geant4 and the "BIC scaled," which corresponds to the BIC case scaled down to compensate the estimated overestimation of 40.2% (see **Table 2**).

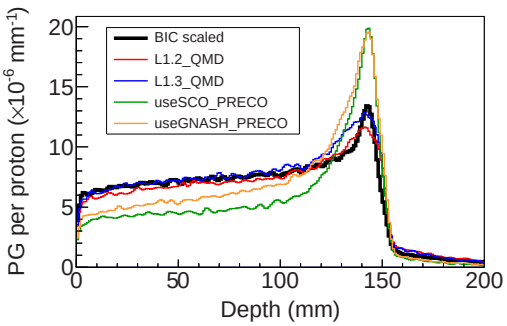

FIGURE 7 | Longitudinal profiles of the photons escaping the PMMA target having an angular acceptance of ±1.5° using a given built-in option in Geant4 or a change in the source code. The "BIC scaled" profile refers to the BIC case scaled down to compensate the estimated overestimation of 40.2% (see **Table 2**). The naming conventions are presented in **Table 3**.

4. DISCUSSION

The results herein show that Geant4 consistently overestimates the prompt-gamma emission yields for the present case, which is in agreement with the conclusions of previous studies. However, the main difference of this study is the use of all applicable proton inelastic models for the energy regime in medical physics. As already suggested elsewhere (8), Bertini cascade model is the one yielding the worst agreement. This was partially corrected when using the precompound model as the model for the pre-equilibrium stage instead of its own implementation. This profile was not shown because, even after this change, the yields are at the same level as the default binary cascade model. The emission predicted by the default precompound model for shallow depths is accurate but then it increasingly diverges from the expected yields along the depth.

In addition, the PGPL is in excellent agreement between experimental and simulated data for the single case investigated. However, the assessment of the accuracy of simulations in estimating it in clinical conditions can only be performed when a shift of proton range is considered and the subsequent correlation with proton range is determined. Therefore, further studies with increasingly complex phantoms are required to assert such an agreement [for example, studies similar to Priegnitz et al. (25)]. Nonetheless, it indicates that even if Geant4 overestimates the prompt-gamma yields, it still can predict accurately the PGPL for the present case.

Concerning the improvement of Geant4, it is possible to observe that the QMD model using the wave packet width equal to 1.3 fm^2 yielded the best agreement with the BIC scaled case. This value contrasts with the one proposed by Dedes et al. (12) for carbon-ion irradiation, which was 0.8 fm^2, but that work dealt with a different projectile and systems with substantial higher energy. The default value for the wave packet width in the QMD model is 2 fm^2. This indicates that further studies are required to fully assess the most adequate value for this parameter, namely, with other clinically relevant targets and energies. The cases presented with the precompound model show a clear underestimation of the PG yield for most of the proton path. However, it increases distally to values that are similar to the ones obtained without the use of the built-in options (compare the PG profile using the default precompound model in **Figure 6** and the ones in **Figure 7**). Even though no testing was performed to find the reason for this behavior, one can assume that it may be related to the modeling stage after the precompound, i.e., the deexcitation. The lower the proton energy the more likely it is to send the fragments to the deexcitation earlier in the modeling process, as the fragments will have gradually less excitation

TABLE 3 | Built-in options (type 1) and source code changes (type 2) tested allowing for a reduction in the prompt-gamma emission yields compatible with the expected experimental data.

Option	Naming	Model	Type	Geant4 class
Wave packet width equal to 1.2 fm^2	L1.2_QMD	QMD	2	G4QMDParameters
Wave packet width equal to 1.3 fm^2	L1.3_QMD	QMD	2	G4QMDParameters
Use of soft cutoff for deexcitation	useSCO_PRECO	PRECO	1	Not applicable
Use of GNASH transitions	useGNASH_PRECO	PRECO	1	Not applicable

The column "Geant4 class" refers to the class where some source code change was done if applicable.

energy. Although only four changes have been shown, many others were attempted but they yielded either a non-significant or an excessive reduction in the PG emission yields. Usually, the discussion about improving simulations is linked to the improvement of cross sections [e.g., Ref. (15) for the discrete emission]. However, even though the cross section data available should indeed be improved, the type of approach followed herein provides Geant4 users with additional possibilities as they can also improve their outcomes through scientifically sound changes to the default implementation of Geant4, both in terms of the default options chosen by the developers and the free and physically bounded parameters.

It should be noted that accurate cross sections are, in general, important for a better modeling of the prompt-gamma emission. However, most of the applicable models in Geant4 are model-driven and not data-driven; hence, the simulation outcomes are based on sound physical models benchmarked with available experimental data. In the prompt-gamma emission context, this is not true for the discrete emission that relies on tabulated data for the possible nuclear transitions. Therefore, for most cases, only the total inelastic hadronic cross sections are used to then sample an inelastic hadronic interaction. Since the present work addresses the total prompt-gamma emission (continuous and discrete), and it is known that the total inelastic hadronic cross sections in Geant4 are relatively accurate for the present application [e.g., see Ref. (15)], the authors did not consider an in-depth study of the implemented cross section data in Geant4 and their influence in the total prompt-gamma emission.

Regardless of the model and the parameter to optimize for a practical application of Geant4 in the clinical routine of proton therapy and prompt-gamma monitoring, the approach toward the improvement of Geant4 will ultimately depend on the experimental data gathered with different materials and proton energies and the outcomes of Geant4 after those conditions. If a single parameter value yields a good agreement with such data while in accordance with the nuclear physics theory, then it would be straightforward to have it implemented within the models by simply replacing the default value. However, if it is not the case (i.e., dependency with the target nuclei and/or energy), one needs to find the corresponding values strengthened by theoretical developments and, for example, implement a look-up table of parameter values for several material-energy pairs to be used with the models.

AUTHOR CONTRIBUTIONS

The contributors listed in the author list meet at least one of the four authorship criteria following International Committee of Medical Journal Editors (ICMJE) recommendations.

ACKNOWLEDGMENTS

The present work was performed in the framework of FP7-ENTERVISION network (Grant Agreement number 264552), FP7-ENVISION programme (Grant Agreement number 241851), LabEx PRIMES ANR-11-LABX-0063/ANR-11-IDEX-0007, ETOILE's research programme (PRRH) at Université Claude Bernard Lyon 1 (UCBL), and France Hadron (ANR-11-INBS-0007). We would also like to acknowledge IBA for providing the nozzle details of the system installed at the clinical facility WPE, Essen and for hosting the experiment there. Finally, we gratefully acknowledge IN2P3 Computing Center (CNRS) for providing a significant amount of the computing resources and services needed for this work.

REFERENCES

1. Knopf AC, Lomax A. In vivo proton range verification: a review. *Phys Med Biol* (2013) **58**(15):R131. doi:10.1088/0031-9155/58/15/R131
2. Paganetti H. Range uncertainties in proton therapy and the role of Monte Carlo simulations. *Phys Med Biol* (2012) **57**(11):R99. doi:10.1088/0031-9155/57/11/R99
3. Min C-H, Kim CH, Youn M-Y, Kim J-W. Prompt gamma measurements for locating the dose falloff region in the proton therapy. *Appl Phys Lett* (2006) **89**(18):183517. doi:10.1063/1.2378561
4. Testa E, Bajard M, Chevallier M, Dauvergne D, Foulher FL, Freud N, et al. Monitoring the Bragg peak location of 73 MeV/u carbon ions by means of prompt gamma-ray measurements. *Appl Phys Lett* (2008) **93**(9):093506. doi:10.1063/1.2975841
5. Moteabbed M, España S, Paganetti H. Monte Carlo patient study on the comparison of prompt gamma and PET imaging for range verification in proton therapy. *Phys Med Biol* (2011) **56**(4):1063. doi:10.1088/0031-9155/56/4/012
6. Min CH, Lee HR, Kim CH, Lee SB. Development of array-type prompt gamma measurement system for in vivo range verification in proton therapy. *Med Phys* (2012) **39**(4):2100–7. doi:10.1118/1.3694098
7. Park JH, Seo H, Kim YS, Kim CH, Lee JH, Lee CS, et al. Monte Carlo simulations on performance of double-scattering Compton camera. *J Instrum* (2012) **7**(01):C01009. doi:10.1088/1748-0221/7/01/C01009
8. Pinto M, Dauvergne D, Freud N, Krimmer J, Letang JM, Ray C, et al. Design optimisation of a TOF-based collimated camera prototype for online hadrontherapy monitoring. *Phys Med Biol* (2014) **59**(24):7653. doi:10.1088/0031-9155/59/24/7653
9. Richard M-H, Chevallier M, Dauvergne D, Freud N, Henriquet P, Le Foulher F, et al. Design guidelines for a double scattering compton camera for prompt-γ imaging during ion beam therapy: a Monte Carlo simulation study. *IEEE Trans Nucl Sci* (2011) **58**(1):87–94. doi:10.1109/TNS.2010.2076303
10. Smeets J, Roellinghoff F, Prieels D, Stichelbaut F, Benilov A, Busca P, et al. Prompt gamma imaging with a slit camera for real-time range control in proton therapy. *Phys Med Biol* (2012) **57**(11):3371. doi:10.1088/0031-9155/57/11/3371
11. Agostinelli S, Allison J, Amako K, Apostolakis J, Araujo H, Arce P, et al. Geant4 – a simulation toolkit. *Nucl Instrum Methods Phys Res A* (2003) **506**(3):250–303. doi:10.1016/S0168-9002(03)01368-8
12. Dedes G, Pinto M, Dauvergne D, Freud N, Krimmer J, Létang JM, et al. Assessment and improvements of Geant4 hadronic models in the context of prompt-gamma hadrontherapy monitoring. *Phys Med Biol* (2014) **59**(7):1747–72. doi:10.1088/0031-9155/59/7/1747
13. Le Foulher F, Bajard M, Chevallier M, Dauvergne D, Freud N, Henriquet P, et al. Monte Carlo simulations of prompt-gamma emission during carbon ion irradiation. *IEEE Trans Nucl Sci* (2010) **57**(5):2768–72. doi:10.1109/TNS.2010.2048042
14. Polf JC, Mackin D, Lee E, Avery S, Beddar S. Detecting prompt gamma emission during proton therapy: the effects of detector size and distance from the patient. *Phys Med Biol* (2014) **59**(9):2325. doi:10.1088/0031-9155/59/9/2325
15. Verburg JM, Shih HA, Seco J. Simulation of prompt gamma-ray emission during proton radiotherapy. *Phys Med Biol* (2012) **57**(17):5459. doi:10.1088/0031-9155/57/17/5459
16. Roellinghoff F, Benilov A, Dauvergne D, Dedes G, Freud N, Janssens G, et al. Real-time proton beam range monitoring by means of prompt-gamma detection with a collimated camera. *Phys Med Biol* (2014) **59**(5):1327. doi:10.1088/0031-9155/59/5/1327

17. Pinto M, Bajard M, Brons S, Chevallier M, Dauvergne D, Dedes G, et al. Absolute prompt-gamma yield measurements for ion beam therapy monitoring. *Phys Med Biol* (2015) **60**(2):565–94. doi:10.1088/0031-9155/60/2/565
18. Grevillot L, Bertrand D, Dessy F, Freud N, Sarrut D. A Monte Carlo pencil beam scanning model for proton treatment plan simulation using GATE/GEANT4. *Phys Med Biol* (2011) **56**(16):5203. doi:10.1088/0031-9155/56/16/008
19. Brun R, Rademakers F. ROOT – an object oriented data analysis framework. *Nucl Instrum Methods Phys Res A* (1997) **389**(1–2):81–6. doi:10.1016/S0168-9002(97)00048-X
20. Biegun AK, Seravalli E, Lopes PC, Rinaldi I, Pinto M, Oxley DC, et al. Time-of-flight neutron rejection to improve prompt gamma imaging for proton range verification: a simulation study. *Phys Med Biol* (2012) **57**(20):6429–44. doi:10.1088/0031-9155/57/20/6429
21. Ziegler J, Biersack J, Ziegler M. *SRIM, the Stopping and Range of Ions in Matter*. Morrisville, NC: Lulu Press Co. (2008).
22. Pinto M, Rydt MD, Dauvergne D, Dedes G, Freud N, Krimmer J, et al. Technical note: experimental carbon ion range verification in inhomogeneous phantoms using prompt gammas. *Med Phys* (2015) **42**(5):2342–6. doi:10.1118/1.4917225
23. Henriquet P, Testa E, Chevallier M, Dauvergne D, Dedes G, Freud N, et al. Interaction vertex imaging (IVI) for carbon ion therapy monitoring: a feasibility study. *Phys Med Biol* (2012) **57**(14):4655. doi:10.1088/0031-9155/57/14/4655
24. Beringer J, Arguin J-F, Barnett RM, Copic K, Dahl O, Groom DE, et al. Review of particle physics. *Phys Rev D* (2012) **86**:010001. doi:10.1103/PhysRevD.86.010001
25. Priegnitz M, Helmbrecht S, Janssens G, Perali I, Smeets J, Vander Stappen F, et al. Measurement of prompt gamma profiles in inhomogeneous targets with a knife-edge slit camera during proton irradiation. *Phys Med Biol* (2015) **60**(12):4849–71. doi:10.1088/0031-9155/60/12/4849

Conflict of Interest Statement: The authors declare that the research was conducted in the absence of any commercial or financial relationships that could be construed as a potential conflict of interest.

Copyright © 2016 Pinto, Dauvergne, Freud, Krimmer, Létang and Testa. This is an open-access article distributed under the terms of the Creative Commons Attribution License (CC BY). The use, distribution or reproduction in other forums is permitted, provided the original author(s) or licensor are credited and that the original publication in this journal is cited, in accordance with accepted academic practice. No use, distribution or reproduction is permitted which does not comply with these terms.

frontiers in Oncology

ORIGINAL RESEARCH
published: 11 May 2016
doi: 10.3389/fonc.2016.00116

The FLUKA Code: An Accurate Simulation Tool for Particle Therapy

Giuseppe Battistoni[1], Julia Bauer[2], Till T. Boehlen[3], Francesco Cerutti[4], Mary P. W. Chin[4], Ricardo Dos Santos Augusto[4,5], Alfredo Ferrari[4], Pablo G. Ortega[4], Wioletta Kozłowska[4,6], Giuseppe Magro[7], Andrea Mairani[7,8], Katia Parodi[5,8], Paola R. Sala[1,4], Philippe Schoofs[4], Thomas Tessonnier[2] and Vasilis Vlachoudis[4]*

[1] INFN Sezione di Milano, Milan, Italy, [2] Uniklinikum Heidelberg, Heidelberg, Germany, [3] EBG MedAustron GmbH, Wiener Neustadt, Austria, [4] CERN, Geneva, Switzerland, [5] Ludwig Maximilian University of Munich, Munich, Germany, [6] Medical University of Vienna, Vienna, Austria, [7] Centro Nazionale di Adroterapia Oncologica, Pavia, Italy, [8] Heidelberger Ionenstrahl-Therapiezentrum (HIT), Heidelberg, Germany

Monte Carlo (MC) codes are increasingly spreading in the hadrontherapy community due to their detailed description of radiation transport and interaction with matter. The suitability of a MC code for application to hadrontherapy demands accurate and reliable physical models capable of handling all components of the expected radiation field. This becomes extremely important for correctly performing not only physical but also biologically based dose calculations, especially in cases where ions heavier than protons are involved. In addition, accurate prediction of emerging secondary radiation is of utmost importance in innovative areas of research aiming at *in vivo* treatment verification. This contribution will address the recent developments of the FLUKA MC code and its practical applications in this field. Refinements of the FLUKA nuclear models in the therapeutic energy interval lead to an improved description of the mixed radiation field as shown in the presented benchmarks against experimental data with both ^{4}He and ^{12}C ion beams. Accurate description of ionization energy losses and of particle scattering and interactions lead to the excellent agreement of calculated depth–dose profiles with those measured at leading European hadron therapy centers, both with proton and ion beams. In order to support the application of FLUKA in hospital-based environments, Flair, the FLUKA graphical interface, has been enhanced with the capability of translating CT DICOM images into voxel-based computational phantoms in a fast and well-structured way. The interface is capable of importing also radiotherapy treatment data described in DICOM RT standard. In addition, the interface is equipped with an intuitive PET scanner geometry generator and automatic recording of coincidence events. Clinically, similar cases will be presented both in terms of absorbed dose and biological dose calculations describing the various available features.

Keywords: Monte Carlo, simulation, hadrontherapy

OPEN ACCESS

Edited by:
Francis A. Cucinotta, University of Nevada Las Vegas, USA

Reviewed by:
Yidong Yang, University of Miami Miller School of Medicine, USA
Francesca Ballarini, University of Pavia and INFN, Italy

****Correspondence:***
Paola R. Sala
paola.sala@cern.ch

Specialty section:
This article was submitted to Radiation Oncology, a section of the journal Frontiers in Oncology

Received: *30 November 2015*
Accepted: *25 April 2016*
Published: *11 May 2016*

Citation:
Battistoni G, Bauer J, Boehlen TT, Cerutti F, Chin MPW, Dos Santos Augusto R, Ferrari A, Ortega PG, Kozłowska W, Magro G, Mairani A, Parodi K, Sala PR, Schoofs P, Tessonnier T and Vlachoudis V (2016) The FLUKA Code: An Accurate Simulation Tool for Particle Therapy. Front. Oncol. 6:116. doi: 10.3389/fonc.2016.00116

1. INTRODUCTION

Popularity of Monte Carlo (MC) techniques in the field of medical physics is increasing rapidly in recent years. This is specifically the case for hadron therapy. MC simulations are an essential tool for the design and commissioning of novel clinical facilities, allowing a detailed description of the beam line and the delivery system. They are also widely used for bunker design, shielding,

and radiation protection. MC calculations are a valuable tool for the commissioning of Treatment Planning Systems (TPSs). Furthermore, MC codes can represent a unique instrument for validation, and possibly the improvement, of analytical TPS's. In situations where experimental validation is unavailable and/or analytical methods are inadequate, MC simulation allows patient-specific dose calculation. Aspects where MC techniques can be more effective compared to traditional, analytical methods may be summarized as follows:

- MC methods take into account more realistically the composition of the human body (1–3), with a possible advantage over the water-equivalent approach typically used in analytical TPS's.
- MC methods naturally include mixed field description and three-dimensional spread of the particle fluence, reliably describing the transport, and the interaction of the primary beam and of the secondaries (4, 5).
- In-beam monitoring of the irradiation through positron emission tomography or the detection of prompt photons from nuclear de-excitation can be performed using MC simulations, taking into full account the complexity of the mixed radiation field and tissue stoichiometry (3, 6–8).

The FLUKA code (8, 9) is a general purpose Monte Carlo code simulating the interaction and transport of hadrons, heavy ions, and electromagnetic particles. It is jointly developed by the European Organization for Nuclear Research (CERN) and the Italian Institute for Nuclear Physics (INFN). It is built and maintained with the best possible physical models in terms of completeness and accuracy. This approach, usually defined as microscopic, allows sound physical bases to be given to each step. Performance is optimized comparing with particle production data at the single interaction level. No tuning whatsoever on integral data, like calorimeter resolutions, thick target yields, etc., is performed. Therefore, final predictions are obtained with a minimal set of free parameters, fixed for all energies and target/projectile combinations. Results in complex cases as well as scaling laws and properties emerge naturally from the underlying physical models and the basic conservation laws are fulfilled *a priori*. Moreover, the microscopic approach preserves correlations within interactions and among the shower components, and it provides predictions where no experimental data are directly available. When needed, powerful biasing techniques are available to reduce computing time. Descriptions of FLUKA models and extensive benchmarking can be found in the literature (a collection of references can be obtained through the website, www.fluka.org).

Physics models of superior quality have extended the use of FLUKA to medical applications. Apart from physics, FLUKA is one of the first general-purpose MC codes, which translates DICOM files into voxel geometry as part of the combinatorial geometry package of FLUKA (10, 11). Recent developments in the user interface [Flair (12, 13)] further expanded the user-base of FLUKA. Features well received by users include the high-level management of the entire simulation process, including geometry generation (supported by interactive editing and versatile display) and material assignment (supported by built-in libraries, which include ICRU and ICRP tissue compositions). Additional functionalities include semi-automated generation of PET scanners and semi-automated recording of coincident events.

In Section 2, we shall review the status of ionization/multiple scattering models in FLUKA, together with the tools for biological dose simulations. The status of proton and ion nuclear interaction models, including fragmentation, will be reviewed, supported by examples of particle production with benchmarks. Section 3 will be dedicated to the application of FLUKA to the techniques for *in vivo* monitoring of hadron therapy. A detailed presentation of the Flair interface in the context of radiation therapy can be found in Section 4. Finally, a review of the current application of FLUKA in two centers for hadrontherapy (CNAO and HIT) will be presented in Section 5.

2. DOSE AND BIOLOGICAL DOSE

2.1. Charged Particle Interactions in Matter

The most important atomic processes undergone by charged particles when traversing media consist of Coulomb scattering with both atomic electrons and nuclei. The effect of this same basic process is very different for electrons and nuclei because of their difference in mass. Inelastic interactions with atomic electrons are by far the dominant source of charged particle energy losses (also referred to as electronic stopping power), while they give a contribution proportional to the atomic number Z to angular deflections. Elastic collisions with atomic nuclei result in negligible energy losses – usually referred to as nuclear stopping power – but the angular deflection is proportional to Z^2. As a consequence, angular deflections are associated mostly with scattering on atomic nuclei, but for the lightest elements where the two contributions become comparable.

Energy losses of charged particles are commonly expressed as an average energy loss per unit path length. The slowing down of energetic protons and ions in matter is governed by collisions with the atomic electrons and leads to the characteristic shape of the depth–dose profile of heavy charged particles with a peaking energy deposition, the so-called Bragg peak.

The nuclear stopping power contribution to the total energy loss of protons and ions in the energy range of relevance for therapy is negligible and will not be discussed further.

The implementation of the electromagnetic physics models in FLUKA, which describe continuous energy losses of heavy charged particles, energy loss straggling, delta-ray production, and multiple Coulomb scattering, is briefly described in the following.

2.2. Electronic Stopping Power

Electronic stopping powers are computed by FLUKA starting from the Bethe–Bloch (14–16) formalism. Several corrections to the standard formulation have been implemented in FLUKA in the recent years, allowing to obtain the high precision requested for the transport of therapeutic beams. The implementation follows, with modifications, extensions and refinements, the

functional forms presented in Ref. (17), complemented by Ziegler (18–20) at the lowest energies.

The formula for the average energy loss of particles much heavier than electrons and with charge z can be expressed by:

$$\left(\frac{dE}{dx}\right)_0 = \frac{2\pi n_e r_e^2 m_e c^2 z_{\text{eff}}^2}{\beta^2} \left[\ln\left(\frac{2m_e c^2 \beta^2 T_{\max}}{I^2\left(1-\beta^2\right)}\right) - 2\beta^2 + 2zL_1(\beta) + 2z^2 L_2(\beta) + K_M(z,\beta) - 2\frac{C(\beta)}{Z} - \delta(\beta)\right] \quad (1)$$

for spin 0 particles and similarly for spin 1/2 particles. β is the projectile velocity relative to the speed of light, n_e is the target material electron density ($n_e = \frac{\rho N_{Av} Z}{A}$ for an element), I its mean excitation energy, M is the projectile mass, and $\gamma = \frac{1}{\sqrt{1-\beta^2}}$ and T_{max} is the maximum energy transfer to a stationary electron, which is dictated by kinematics and given by:

$$T_{\max} = \frac{2m_e c^2 \beta^2 \gamma^2}{1 + 2\gamma \frac{m_e}{M} + \left(\frac{m_e}{M}\right)^2} \quad (2)$$

Contrary to common approximations, all terms in equation (2) are kept in the FLUKA formulation. The "mean exitation energy" I is a sort of logarithmic average over all ionization and excitation levels of the target material. FLUKA uses for I the values recommended in Ref. (17); however, the user can override them if new experimental data so suggest, as it is the case for water.

The terms δ, C/Z, L_1, L_2, and K_M are all corrections to the Bethe–Bloch formalism. δ is the so called "density correction," extensively discussed in the literature, and connected with medium polarization which, in FLUKA, is computed according to (21). C is the shell correction, which takes into account the effect of atomic bonds. This correction becomes important at low energies and, in FLUKA, it is extracted from the proton stopping power values reported in Ref. (17, 22) once all other corrections are undone. z_{eff} is the projectile "effective charge," which takes into account the partial neutralization of the projectile charge when its velocity is not much larger than those of the atomic electrons. For sufficiently large velocities, or for very light ions (e.g., protons and alphas) $z_{eff} = z$, otherwise FLUKA makes use of the effective charge parametrizations proposed in Ref. (23); however, with different parameters in order to disentangle the effect of the L_1, L_2, and K_M corrections, which were not considered in the original paper.

The code takes into account the z^3, Barkas (24), and z^4, Bloch (25), corrections (indicated by L_1 and L_2) to the first Born approximation according to the formalisms presented in Ref. (17, 26, 27). A further correction K_M, which is not commonly included in stopping power calculations but which turns out to be important for medium-heavy projectiles, is associated with the electron-ion Mott cross section (28). The Bethe–Bloch equation is based on the electron-ion scattering cross sections computed in first Born approximation; however, when the $z\alpha << 1$ (α is the fine structure constant) condition does no longer hold higher order corrections must be applied. The Mott cross section includes those corrections; however, it is mathematically and computationally very complex. In FLUKA, the Mott cross section parameterization proposed in Ref. (29) as further modified in Ref. (30) are used to compute the correction to the average stopping power, as well as the associated corrections to the secondary electron production cross section and to the energy loss fluctuations.

For protons and alphas, the resulting unrestricted electronic stopping power values are fully consistent by construction to those available at Ref. (22, 31) as long as I is left unchanged. The FLUKA formalism has been demonstrated to be able to reproduce with high accuracy, and with a unique value of I for a given target, experimental data at energies up to several hundreds of MeV/n for ions ranging from protons to uranium, as shown in Section 2.6.

2.3. Secondary Electrons and Energy Loss Fluctuations

Fluctuations associated with charged particle energy losses are an important topic since they determine the shape and position of the Bragg peak. Indeed, its location does not correspond to the nominal particle energy but is situated slightly in front. The classical approaches to this problem, the Landau (32) and Vavilov (33) distributions, suffer from several limitations and are of difficult application in Monte Carlo codes (see Ref. (34) for a discussion).

An alternative approach (34) has been devised for FLUKA, which exploits the properties of the cumulants (35) of distributions. The approach can account for an arbitrary threshold for the explicit production of secondary electrons ("δ" rays), for arbitrary step-lengths, and for the contribution of distant collisions to energy loss fluctuations, while assuring the exact match of the average restricted stopping power. It also includes the effect of the Mott correction on energy loss fluctuations.

The explicit production and transport of secondary electrons can be described in FLUKA with a user defined threshold as low as 1 keV.

2.4. Multiple Coulomb Scattering

An extended model for charged particle transport through the multiple scattering formalism based on the Molière Theory (36–38) has been specially developed for FLUKA (39, 40).

It can be applied from very small to relatively large steps with a remarkable insensitivity of the resulting distributions. It is complemented by the possibility of switching to single Coulomb scatterings, a possibility which was first proposed and implemented in FLUKA.

Examples of the performances of this model when applied to therapy beams and energies can be found in Ref. (41).

2.5. Nuclear Interaction Models

As a consequence of nuclear reactions, the intensity of therapeutic hadron beams is attenuated all along the propagation in tissue. It follows that the dose delivered by primary ions is reduced with increasing depth. While nuclear recoils result typically in negligible spatial modifications of the delivered dose, secondary nucleons, particles, and fragments produced in nuclear reactions

can considerably affect the spatial pattern of energy deposition and must be carefully taken into account. For proton beams, only target fragmentation is possible. For heavier ions, projectile fragmentation is the most important process leading to the build-up of secondary particles along the penetration depth. Because of the reaction kinematics, projectile fragments travel nearly in forward direction at almost the same velocity as the incident particle. The secondary lower-charge fragments have typically a longer range than the primary beam and give rise to an undesirable dose deposition beyond the Bragg peak. Furthermore, the fragments angular emission can contribute to an additional lateral spread of the beam particularly evident at the distal side of the Bragg peak, where the primary projectiles are stopped and the dose deposition is due to nuclear fragments only. Hence, in the case of heavy ions, nuclear fragmentation reactions are responsible for the deterioration of the physical selectivity in the longitudinal and transversal dimension especially around the Bragg peak region. The amount of fragments produced generally increases with the mass and charge of the primary particle.

The FLUKA nuclear interaction model, called PEANUT (42–45), provides the nuclear environment for hadron, photon, muon, and neutrino interactions from a few MeV up to the energies, for instance, of the CERN Large Hadron Collider. At energies of interest for therapy, PEANUT models the interactions along the steps of a generalized intranuclear cascade (GINC), followed by an exciton based preequilibrium particle emission and by an equilibrium phase. Detailed descriptions of the "fast" reaction stages, as well as comparisons with particle emission data, can be found in the literature (42–46). A combined benchmark on nuclear interactions and electromagnetic interactions is described in Ref. (47). Produced nuclei form a thermally equilibrated system, characterized by its excitation energy. This system can "evaporate" nucleons, or fragments, or γ rays, or even fission, to dissipate the residual excitation. Evaporation and fission in FLUKA are based on statistical approaches (42, 48).

For light residual nuclei ($A < 16$), where the excitation energy may overwhelm the total binding energy, a statistical fragmentation (Fermi Break-up) model is implemented (49–51). The excitation energy still remaining after evaporation is dissipated via emission of γ-rays, as will be described in Section 3. Recently, competition of gamma ray emission with particle evaporation has also been implemented. As will be described in the following sections, the low excitation stages of nuclear interactions are presently under strong development.

Reactions initiated by ions are dealt with by different event generators, depending on the projectile energy. The one related to the highest energies (10, 52, 53) is not of interest for therapy applications and will not be described here.

For ions in the few GeV/n energy range and down to ≈0.1 GeV/n, FLUKA uses an interface to a modified version of RQMD-2.4 (54, 55). RQMD is a relativistic quantum molecular dynamics model that can also be run in intranuclear cascade mode. Examples of FLUKA results compared with experimental data when running with the modified RQMD-2.4 model can be found in Ref. (10, 56). Since RQMD provides only the fast stage of the reaction, excited fragments from RQMD are further processed by PEANUT. This allowed also to profit from all the improvements that are ongoing in PEANUT. In **Figure 1**, the neutrons emitted at en energy close to the projectile one are mainly caused by evaporation. The latest development in the RQMD interface is the inclusion of the preequilibrium stage in the treatment of residual fragments. This stage improves the distribution of high energy ejectiles, in particular for projectile energies in the sub-GeV/n region. An example of the latest performances of FLUKA + RQMD is shown in **Figure 1**. The agreement is remarkable, especially because RQMD is used at an energy that is at its very limit of application.

The Boltzmann Master Equation [BME (58)] model has been implemented into FLUKA to deal with the lowest energies, below about 150 MeV/n (FLUKA switches gradually between RQMD and BME at threshold). The BME event generator (59) in FLUKA simulates thermalization of a composite nucleus, created in the complete or incomplete fusion of two ions, by sampling from the results of the numerical integration of the BMEs. While complete fusion covers the lowest impact parameter interval, for more peripheral collisions a three body picture of the reaction is implemented. At even higher impact parameters, single nucleon mode break-up/transfer is modeled. Recently, the BME event generator has been interfaced with the PEANUT pre-equilibrium module in order to treat the first de-excitation stage of all nuclei for which

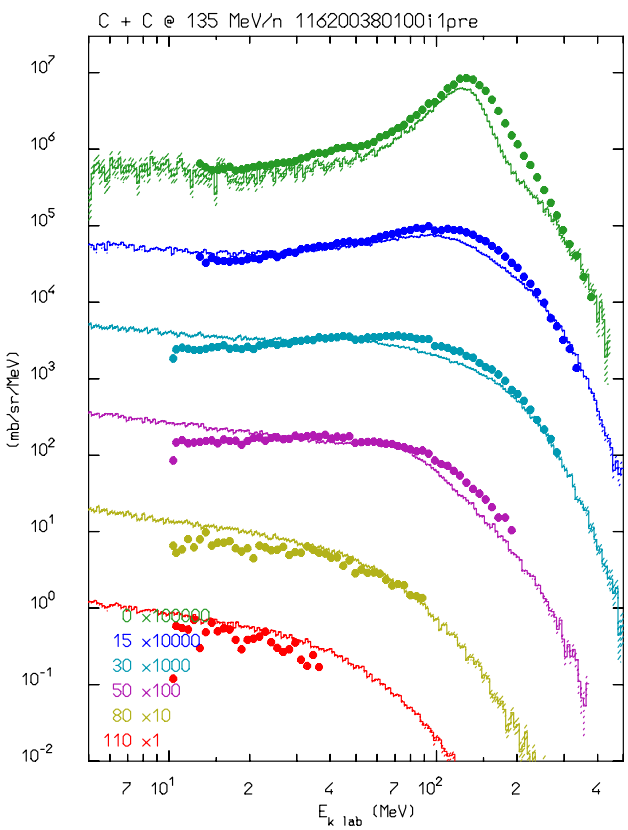

FIGURE 1 | Double differential neutron production for 135 MeV/n ^{12}C interactions in a thin carbon target. FLUKA–RQMD predictions as a function of neutron energy at several detection angles are shown as histrograms and compared with experimental data (dots) from Ref. (57).

BME information is not (yet) available. This development is particularly important, for instance, for reactions induced by alpha particles, as shown in **Figure 2**, where double differential neutron production by a 100 MeV/n ^{4}He beam impinging on a thick carbon target is compared to measurements. As for RQMD, the final de-excitation of the remaining equilibrated nucleus is handled by the FLUKA evaporation/fission/fragmentation module.

2.6. Comparisons with Depth–Dose Curves and Lateral-Dose Profiles

FLUKA has been intensively benchmarked against depth–dose data and lateral-dose profiles from various accelerators used for research and clinical ion-beam therapy (IBT), which have been typically acquired with different water columns with parallel-plate ionization chambers [depth–dose (61, 62)] and small volume ionization chambers in water [lateral-dose profiles (63)]. As a consequence of its performances, it is used at IBT centers for independent dose verification in phantom and patient geometries (see Section 5) as well as to generate basic physics input data for clinical treatment planning systems tailored to proton and carbon ion delivery with modern beam scanning (64). These latter TPS basic data include MC-calculated laterally integrated depth–dose distributions, depth–dependent parameters of lateral Gaussian distributions fitted on the MC lateral-dose profiles, and MC-generated carbon ion fragment spectra for biological calculations (41, 61, 62, 65, 66). Recently, FLUKA has also been chosen by a commercial vendor as a validation tool and to provide physics input data for their newly developed carbon ion module (67).

Figure 3 shows exemplary depth–dose profiles simulated by FLUKA for proton and carbon ions in the therapeutic energy range, compared to measurements taken at the Heidelberg ion therapy center (HIT) with the PeakFinder water column (PTW Freiburg) (61). The nominal energies before the beamline for the presented ions are 54.19, 142.66, and 221.05 MeV/u for protons, and 200.28, 299.94, and 430.10 MeV/u for carbon ions. Since nuclear processes determine notably the shape of the depth–dose profiles, especially for carbon ion and high energy proton beams, these comparisons are not only a sensitive benchmark for the electromagnetic physics models but represent, at the same time, an integral benchmark for the nuclear models in their capabilities of predicting non-elastic nuclear interactions. For different high-accuracy data sets, FLUKA is able to reproduce the position of the Bragg peaks of proton and carbon ion beams with a single ionization potential on average within the experimental uncertainties of about 100 μm. The average dose-weighted dose-difference $(\overline{\Delta D / D})$ is below 1% for protons and below 1.5% for carbon ions.

An extensive experimental characterization of the other ions available at HIT in comparison to FLUKA simulations is also being performed. A first in-depth characterization of depth–dose profiles of oxygen ion beams has been presented in Ref. (68), and several investigations with helium ion beams are ongoing for both mono-energetic and spread-out Bragg peaks. **Figure 4** shows the comparisons between depth–dose profiles acquired with the above mentioned PeakFinder and FLUKA simulations for the different ions available at HIT and different initial beam energies spanning the whole therapeutic range. The nominal energies before the beamline for the displayed ions are 54.19, 79.78, 200.28, and 300.13 MeV/u, for protons, helium, carbon, and oxygen ions, respectively. Quantitative assessment of the level of agreement between measured and simulated depth–dose distributions of these ions has been determined by calculating the weighted chi-square difference for irradiation of an energy yielding the same range (ca. 15 cm in water) without ripple filter, as proposed in Ref. (68). The smaller the weighted chi-square difference is, the higher the similarity is between measurements and simulations. The results indicate for the clinically used protons and carbon ions a level of chi-square agreement of 5.8×10^{-5} and 1.1×10^{-4}, respectively. Compared to this reference level, the helium ions exhibit promising weighted chi-square differences of

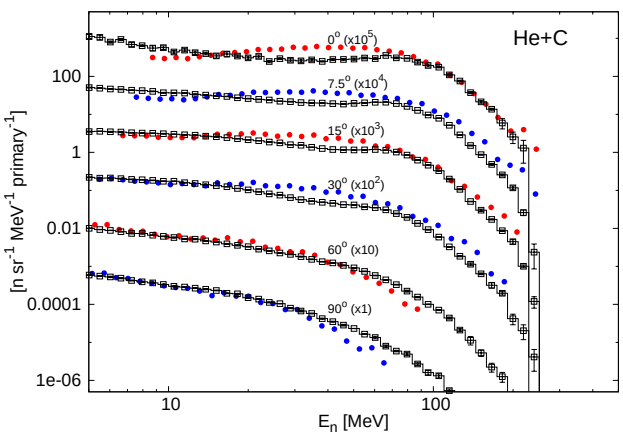

FIGURE 2 | Double differential spectra of neutrons from 100 MeV/n alphas on a thick carbon target, scaled as indicated at the different angles with respect to the beam direction. Full circles are experimental data (60), histograms with empty symbols are FLUKA predictions.

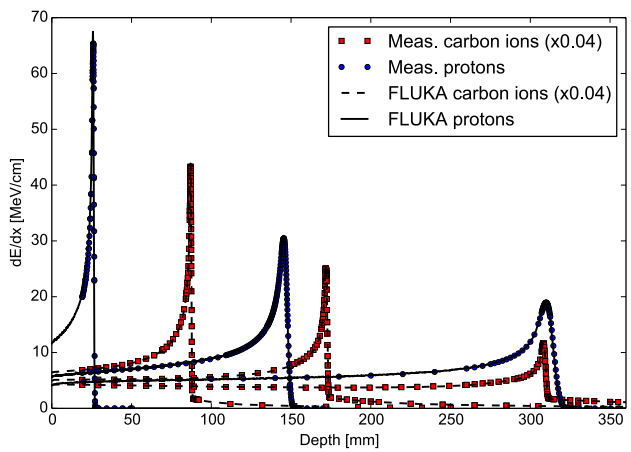

FIGURE 3 | FLUKA simulations of depth–dose profiles of protons and carbon ions with therapeutic ranges in comparison with measured data at HIT (61). The nominal energies before the beamline are 54.19, 142.66, and 221.05 MeV/u forprotons, and 200.28, 299.94, and 430.10 MeV/u for carbon ions.

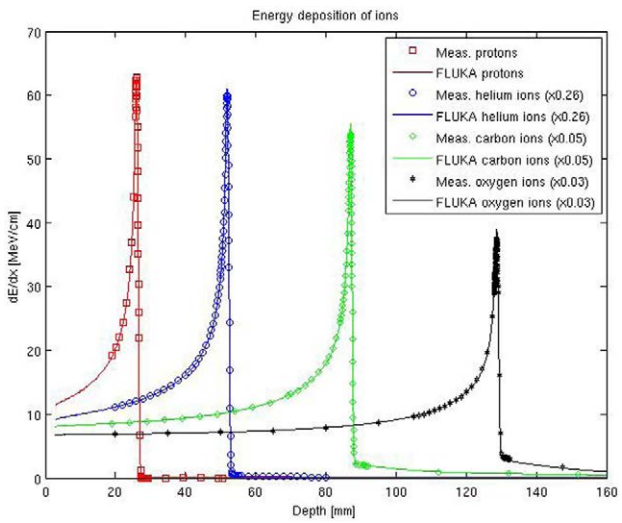

FIGURE 4 | FLUKA simulations of depth–dose profiles of protons, helium, carbon, and oxygen ions with therapeutic ranges in comparison with measured data at HIT. The nominal energies before the beamline are 54.19, 79.78, 200.28, and 300.13 MeV/u, for protons, helium, carbon, and oxygen ions, respectively.

2.1×10^{-4} and oxygen ions 5.6×10^{-5}. Additionally, the average dose-weighted dose-difference was evaluated, again for the same energies chosen to provide the same range, and found to be 0.6% for protons, 1.6% for helium ions, 0.8% for carbon ions, and 1.3% for oxygen ions. Again, range agreement within 110 μm could be obtained for both He and O ions over the entire therapeutic energy range with a single ionization potential value in water. Compared to the extensively validated and already clinically used protons and carbon ions, the overall agreement observed for helium and oxygen ions is encouraging, but room for Monte Carlo model improvements is still possible, especially if more experimental data will become available in the therapeutic energy range and for materials of clinical relevance.

In terms of lateral-dose profiles, **Figure 5** shows an example of agreement between FLUKA simulations, including the detailed modeling of the HIT beamline according to Ref. (41), and measurements for protons (nominal energy of 157.43 MeV/u before the beamline) and carbon ions (nominal energy of 299.94 MeV/u before the beamline), sampled at two different depths in water in the entrance region, at approximately 16 mm, and shortly before the Bragg peak, at approximately 152 mm. Taking into account unavoidable uncertainties of the measured data in the low-dose region, as well as averaging volume effects of the small cylindrical ionization chambers of 1.5 mm radius in comparison to the dose gradient (63), the agreement is quite satisfactory. A more extensive quantitative comparison of FLUKA simulations and experimental lateral dose-data collected at different energies and depths can be found in Ref. (69).

2.7. Biological Calculations

A major rationale for the application of ion beams in tumor therapy is their increased relative biological effectiveness (RBE) in the Bragg peak region, especially for carbon and heavier ions. For dose prescription in carbon ion therapy, the increased effectiveness has to be taken into account in treatment planning while, in proton therapy, a constant RBE of 1.1 is typically applied as recommended by ICRU (70).

In order to describe the biological effect with FLUKA, an external radiobiological database has to be integrated. The database can be obtained from experimental data or starting from event-by-event track structure simulations. This approach was adopted in the past to characterize therapeutic proton beams from a physical and biophysical point of view (71, 72). Afterward, the approach has been used in the study of chromosome aberration induction in human cells by neutrons (73). The theory of dual radiation action [TDRA (74)] has been included to describe the non-linear response due to mixed fields, and it has been the basis of more recent calculations interfacing FLUKA with the biophysical model LEM [Local Effect Model (75)], which allows prediction of RBE and RBE-weighted dose (D_{RBE}) distributions in carbon ion beam therapy (4, 66). Starting from these promising works, we decided to develop a general interface within the linear-quadratic formalism (76) available in FLUKA. The users should provide their own biological database in terms of α and β of different components of the mixed radiation field as a function of energy per nucleon. In order to compute the biological effect, FLUKA applies an approach based on the dose-weighted averages $\overline{\alpha}_j$ and $\overline{\beta}_j$:

$$\overline{\alpha}_j = \frac{\sum_i \Delta d_{i,j} \cdot \alpha_{i,j}}{\sum_i \Delta d_{i,j}} \quad \text{and} \quad \sqrt{\overline{\beta}_j} = \frac{\sum_i \Delta d_{i,j} \cdot \sqrt{\beta_{i,j}}}{\sum_i \Delta d_{i,j}}, \qquad (3)$$

where $\Delta d_{i,j}$ is the dose from the i-th charged particle (composing the mixed radiation field) with associated $\alpha_{i,j}$ and $\beta_{i,j}$ in voxel j, and i runs over all particles depositing dose in voxel j. RBE and RBE-weighted dose values can be determined for each voxel of the patient knowing the absorbed dose and the dose weighted ave ages $\overline{\alpha}_j$ and $\overline{\beta}_j$ [e.g., see Ref. (4)]. As an example in **Figure 6**, the $\overline{\alpha}$ and $\overline{\beta}$ (left panel) and the absorbed dose and D_{RBE} (right panel) for a carbon ions biologically optimized Spread-Out Bragg peak as available at CNAO are reported. A single-field irradiation plan has been optimized with the CNAO TPS (SIEMENS *syngo*® PT Treatment) to achieve a homogeneous dose distribution of 3 Gy (RBE) in a cubic shaped target (side = 6 cm) centered at 9 cm depth in water. The FLUKA recalculations have been performed for a representative cell line characterized by $(\alpha/\beta)_{ph}$ = 2 Gy (α_{ph} = 0.1 Gy^{-1} and β_{ph} = 0.05 Gy^{-2}) using the same biological database as implemented in the TPS (75). This database is calculated using the radio-biological model LEM I (75), which has been *in vitro* and *in vivo* validated. LEM I is the standard biological model employed at the carbon ion therapy facilities in Europe and has has been developed and benchmarked by the GSI biophysics group.

3. *IN VIVO* VERIFICATION

3.1. Introduction

The inverse depth–dose deposition profiles of high energetic proton and ion beams can be used to obtain highly conformal dose

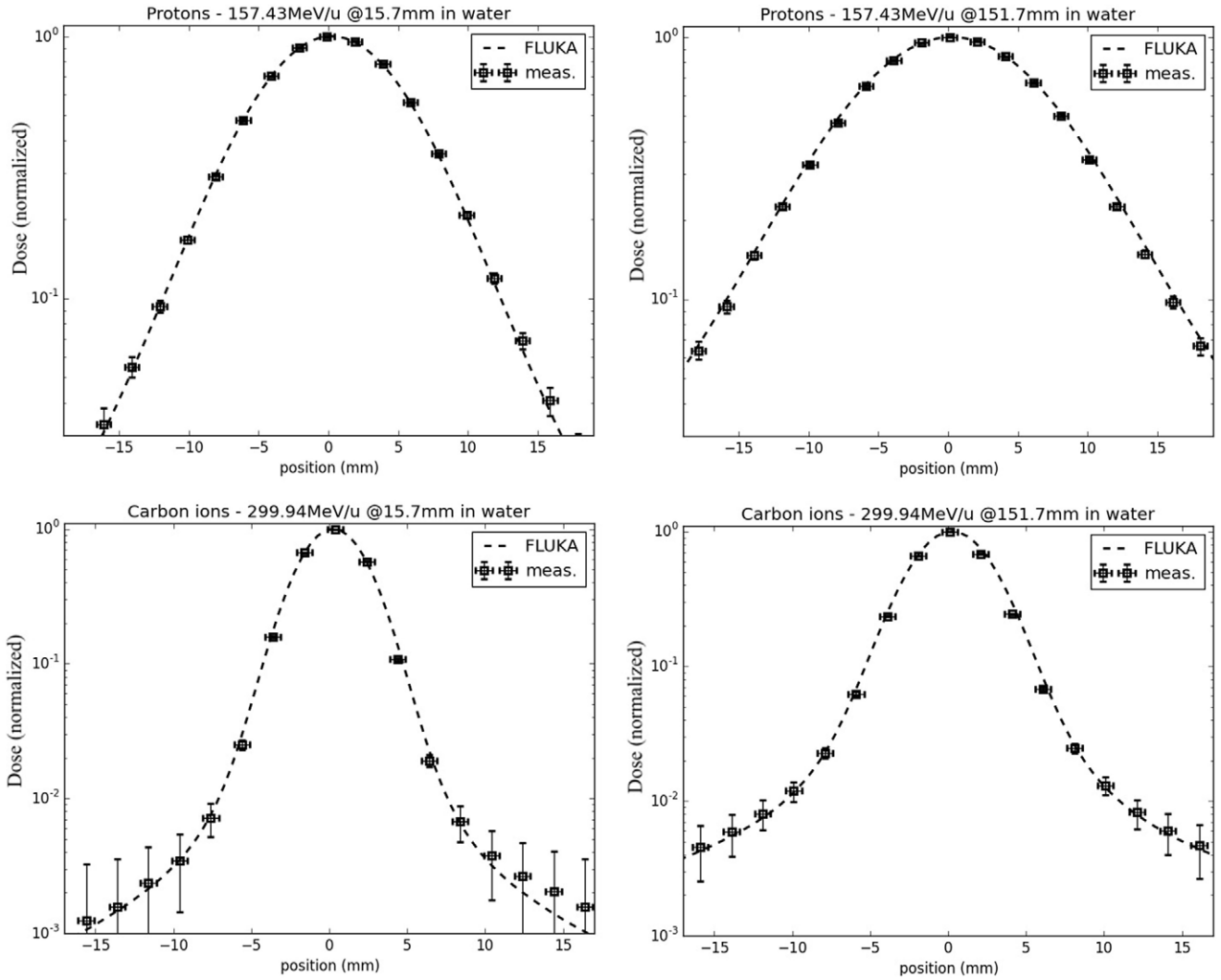

FIGURE 5 | FLUKA simulations of lateral-dose profiles of protons (top) and carbon ions (bottom) in water, with a nominal initial energy before the beamline of 157.43 and 299.94 MeV/u, respectively, sampled in the entrance region (left) and shortly before the Bragg peak (right), in comparison to experimental measurements taken at HIT.

distributions for therapeutic purposes. However advantageous, it is then crucial to ensure treatments are delivered with high precision, according to the planner's prescription. Techniques, which aim to verify the patient geometry as well as the correct treatment delivery before, during, or directly after treatment, have therefore been increasingly investigated in recent years in literature. *In vivo* range monitoring *via* β^+-emitter distributions by PET is currently the most advanced monitoring technique routinely used in clinical environments. Simulation studies indicated the feasibility to detect range misses in the order of 6 mm and larger (77), and even better results were reported for favorable anatomical indications in multiple clinical pilot studies with different PET implementations (3, 78–81).

While results achieved with this technique are promising, widespread clinical use of PET monitoring is presently still hampered by several issues. The coincidence measurements of 511 keV annihilation photons allow reconstruction of β^+-emitter maps, which have a complex correlation with the delivered dose. Hence, only a limited correlation between signal on the one hand, and dose and beam range on the other hand, can be achieved. Besides, an extended acquisition time (of the minute-scale) is needed because of the low β^+ activity and relatively small signal-to-noise ratio (SNR) (6). Furthermore, an additional signal attenuation is due to the long delay before starting acquisition after patient irradiation. This delay, of the order of a few minutes, appears in the commonly used in-room or off-line PET monitoring method. Finally, metabolic washout, PET and CT co-registration, and possible patient movements lead to a further decrease of the resolution (79).

The use of prompt-γ's for monitoring was proposed to overcome some of the inherent limitations of the PET technique. Besides a possibly larger signal strength compared to PET

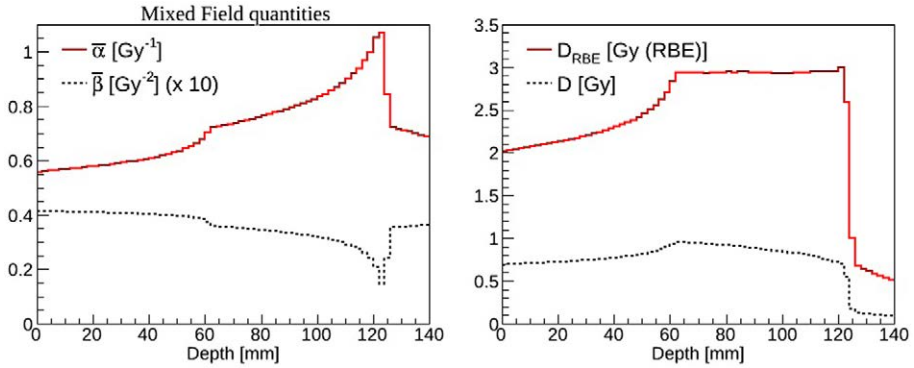

FIGURE 6 | Left panel: $\bar{\alpha}$ (solid line) and $\bar{\beta}$ (dashed line) mixed radiation field values calculated as a function of depth in water. The $\bar{\beta}$ results have been rescaled by a factor of ten for display purposes. Right panel: absorbed dose (dashed line) and D_{RBE} (solid line) values calculated as a function of depth in water.

resulting in a larger SNR, this method allows in a straightforward way for real-time monitoring and might provide a better correlation of the prompt-γ signal with dose and beam particle ranges (82). These potential advantages have yet to be demonstrated in a clinical setting. For such purposes, large efforts have been spent in the design and optimization of detection devices and setups suitable for use in clinics (83–91). Research in this field is still ongoing, as well as feasibility and sensitivity studies aiming at revealing the expected performance and limitations of prompt-γ range and dose monitoring (82, 92–95). Monte Carlo (MC) particle transport codes, such as FLUKA (9, 50) are essential tools for such studies.

Using these simulation tools for the above-mentioned applications, implicitly relies on their predictive power, i.e., the accurate description of a range of physics processes relevant to the problem. Dose distribution predictions with MC codes were shown to largely satisfy clinical needs in proton and carbon ion treatment planning a given geometry (61, 96). On the other hand, the development and validation of MC codes for prompt-γ production is significantly less advanced. This is partly due to the large complexity of non-elastic nuclear reactions.

Some recent studies have been aimed at elucidating and comparing the predictive capability for prompt-γ production of proton and ion beams of some MC and nuclear reaction codes (95, 97–99). Independently from the general agreement about the scarcity of available experimental data, various modeling approaches and measurements have been reported to differ by a factor of 2 to 12 in prompt-γ emissions. In particular, differences in the predictions of the distal fall-off positions up to a few millimeters as well as remarkable discrepancies in the relative shapes of the prompt-γ profiles are noted. These findings clearly highlight the need for further development and validation of physics models in order to predict prompt-γ yields of high energy ion beams, based on a solid measurement database.

This section presents a set of physics models describing prompt-γ-emission and β-emitter production as a result of non-elastic nuclear collisions of proton and ion beams. Newly developed and refined models are described, which account for discrete and continuous components of γ emission spectra including Doppler effect.

The performance of the models for applications to imaging is evaluated using cross section and thick target data.

3.2. FLUKA Model Developments for *In Vivo* Verification

The accuracy of physics models included in particle transport codes is of great relevance, especially as their importance in particle therapy has steadily increased over the last years (5). Both β^+ emitters and prompt γ production occur in the very last stage of nuclear interactions, therefore they are sensitive to the details of all the reaction "history."

The relative production probabilities of different residual nuclei are influenced by the exact amount of excitation energy left in the system, by the exact balance of binding energy, but also, and this is more difficult to simulate, by the level structure of the excited and residual nuclei. Not only the level energies but also spin and parity have an influence on isotope production and photon emission. This is particularly true in the Bragg peak region, where the available projectile energy is barely sufficient to initiate the reaction. Low energy nuclear models in FLUKA have undergone a steady development with a particular attention to processes of interest for hadron therapy.

The most important reactions for PET monitoring of proton therapy are ^{16}O(p,x)^{15}O and ^{12}C(p,x)^{11}C (98). They can proceed through emission of either independent nucleons or deuterons. The emission of composite ejectiles, like d, t, ^{3}He, and α, is described in FLUKA by the coalescence algorithm in the first stages of the reaction, and by evaporation of fragments in the equilibrium stages. Coalescence is a postemission process, meaning that all combinations of unbound nucleons are checked and the possible formation of light fragments (up to mass 10) is decided based on phase space closeness at the nucleus periphery. This approach works reasonably well at medium/high energies. However, at energies below a few tens of MeV, where binding energies play a crucial role, coalescence is increasingly ineffective in reproducing the data. Recently, a direct deuteron formation mechanism, where the deuteron is formed before being emitted, has been

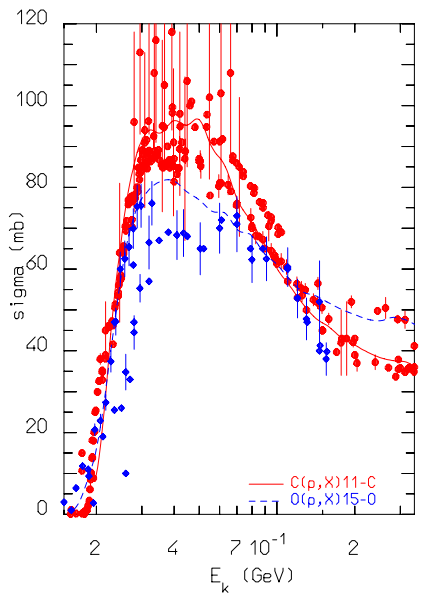

FIGURE 7 | FLUKA predictions for the reactions $^{nat,12}C(p,x)^{11}C$ and $^{nat,16}O(p,x)\ ^{15}O$ cross sections as a function of projectile energy, compared against data retrieved from the EXFOR library (101).

TABLE 1 | Isotope production cross sections (in millibar) for the fragmentation of 86 MeV/n ^{12}C ion projectiles on a carbon target.

Isotope	Exp.	FLUKA (%)
^{11}C	43	54 ± 1
^{10}C	4	2 ± 7
^{11}B	42	54 ± 1
^{10}B	28	25 ± 2
^{8}B	2.4	3 ± 6

Data (104, 105) are compared to FLUKA predictions, integrated over the measured angular range from 2° to 22°. The experimental uncertainty is on the order of 10% (106).

implemented in FLUKA. This mechanism greatly improved the predictive power for reactions, such as (p,d). An example outlining the effectiveness of the new approach and directly relevant for proton therapy monitoring with PET is given in **Figure 7**. The level of accuracy reached allows to overcome the previously stated need (100) to convolute simulated fluxes with cross section data.

An interesting verification of FLUKA predictions against experimental data taken with a prototype PET system can be found in Ref. (102). For what concerns ion beams, the availability of experimental data on β^+ emitter is scarce, more would be needed to perform a careful evaluation of model predictions. However, the results presented in **Table 1** on carbon–carbon interactions at low energy show a reasonable agreement, within 25%, for the production of ^{11}C. Indeed, the early work described in Ref. (103) already showed a satisfactory agreement between data and simulations on a full phantom and PET setup.

Finally, it has to be reminded that electromagnetic models can also play a role in the reproduction of PET reality. A correct reproduction of positron slowing down before annihilation is of course mandatory, but FLUKA goes further in precision and includes an accurate reproduction of the effects of electron binding energy and orbital motion on the emitted photon pair. The resulting acollinearity of the photon pair has been favorably compared with experimental data in Ref. (107).

At the end of the nuclear evaporation stage, the PEANUT model dissipates the residual excitation energy through emission of cascades of γ rays. Whenever possible, photon energies and branching ratios are sampled according to a database of known levels and transitions, derived from the most recent release of the RIPL (108) data provided by IAEA. The evaporation stage is also constrained to proceed through known levels when they are available. A first attempt to account for the angular distribution of emitted photons has been implemented, following the formalism in Ref. (109).

Whenever the level compilation is non-existent or incomplete, photon energies are sampled according to a statistical/rotational model that has been validated in the past (110).

The most stringent requirement for a model of prompt photon production is the capability to reproduce excitation functions of single γ lines. Those depend on the capability to reproduce both the branchings in the various reaction channels, and the γ de-excitation flow. Examples of such excitation functions for proton-induced reactions in carbon are shown in **Figure 8**, where FLUKA results compare favorably with experimental data (111).

3.3. Model Comparison with Integral Measurements

Complementary to single interaction data, which can give a direct evaluation of the model performances, the study of integrated data for therapeutically relevant scenarios allows an estimation of the model performance for specific applications, such as conceptual and detector design studies.

3.3.1. FLUKA Configuration and Modeling of the Setups

Several prompt-γ measurements using ion beams have been conducted in recent years with the purpose to characterize and quantify γ production for therapeutic scenarios. **Table 2** lists prompt-γ measurements selected for comparison. They span differing experimental setups for proton and carbon ion beams at various therapeutic energies and include polymethyl methacrylate (PMMA) and water targets. In all considered experiments, the beam hits a homogeneous tissue-like target with the detectors positioned in a direction perpendicular to the beam axis.

Measured data include γ emission profiles with depth as well as photon energy spectra. For each experiment, the relevant measurement configurations and main setup elements were modeled to scale for FLUKA simulations as specified by the experimentalists, including notably: beams, targets, collimators, and detectors (see **Figure 9**).

Neutrons were the major source of contamination in detectable counts. For noise rejection purposes, S_{II} and S_{III} were both time gated and energy windowed, applying a 2 MeV low-energy threshold. These settings were reproduced for the simulations. Lead collimators were placed between the target

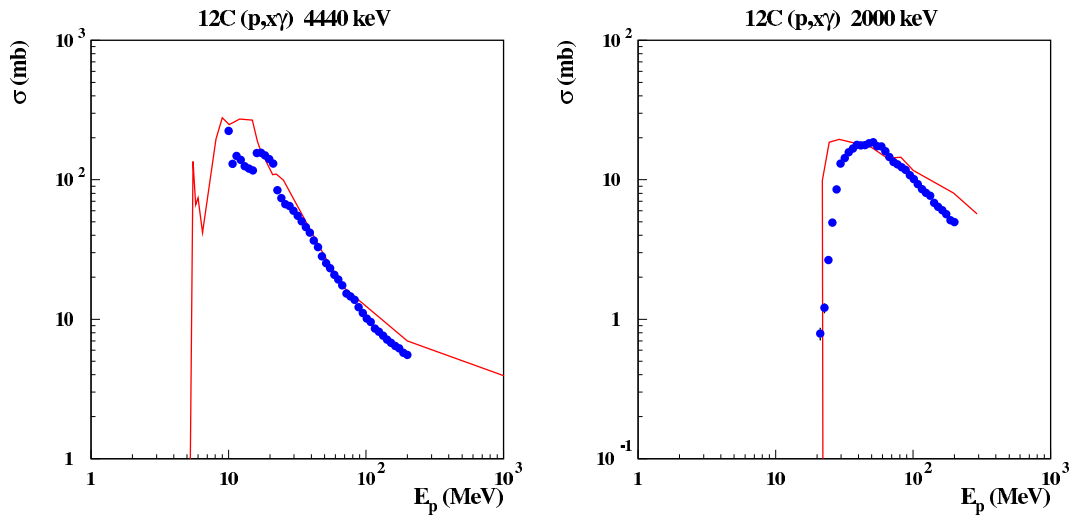

FIGURE 8 | Excitation function for the emission of discrete γ lines from proton-induced reactions on carbon. Left: the 4.440 MeV line, corresponding to the de-excitation of the 1st excited level in ^{12}C, the 2nd excited level in ^{11}B, the 2nd excited level in ^{11}C. Right: the 2.0 MeV line, from the 1st excited levels of ^{11}C and ^{11}B. Curves are FLUKA predictions, dots are evaluated data from Ref. (111).

TABLE 2 | Prompt-γ experiments selected for comparison with simulations.

Setup	Beam	Target	Detector	Facility	Exp. reference
S_I	160 MeV proton	PMMA	NaI	WPE, Essen	(112)
S_{II}	95 MeV/u ^{12}C	PMMA	BaF_2	GANIL, Caen	(95)
S_{III}	310 MeV/u ^{12}C	Water	BaF_2	GSI, Darmstadt	(95)

and the detector, as shown in **Figure 9**. The reader is referred to the original references for further experimental details (see **Table 2**).

The measurement setup S_I was repeated in three different configurations: (1) with no collimation device, (2) with a lead block, instead of the collimator, in front of the detector, and (3) with the collimator, as depicted in **Figure 9**. The dataset is presented as a background-subtracted photon spectrum in two manners. These difference spectra aim to obtain a larger gamma-to-neutron signal ratio in the experimental data. The first one, termed "opening difference" in the following, is the difference of the spectra for the opened (3) and the closed (2) collimator configuration. The second one, termed "wall difference," is the difference of the spectra acquired for the no-collimator (1) and the closed-collimator (2) configuration. The geometry shown in **Figure 9** (left) is for a target-to-detector distance of 50 cm. A separate dataset for target-to-detector distance 100 cm was also acquired (112). The detector, a NaI crystal, was determined to have a resolution of 7% full width at half maximum (FWHM) at 662 keV (112). The simulated energy spectra were therefore convoluted with the Gaussian distribution reflecting the measured detector resolution.

Certain experimental details, which are not accounted for by the simulations, may have an effect on the experimental data, causing artifacts. These potentially include ghosting from preceding beam pulses as well as geometry, setup, and reconstruction details, which are not reproduced by the simulations.

3.3.2. Prompt-Gamma Energy Spectra

Simulations of photon spectra resulting from proton beams are presented in **Figure 10** in comparison with measurements for setup S_I with and without accounting for the intrinsic detector resolution. Data are presented as background-subtracted photon spectra for the configurations "opening difference" and "wall difference." Measured and simulated spectra are normalized to the number of primary protons and the energy bin, originally 9.83 keV.

Overall, the agreement between simulated spectra and experimental data is excellent. In particular, an agreement within about 10% is found for the "opening difference"-spectra. For the "wall difference"-spectra (difference between closed-collimator and no-collimator configurations), the accuracy of the simulation is also favorable, achieving an agreement within 10% for energies beyond 2 MeV. The result is remarkable, considering that the "wall difference" configuration is more sensitive to measurement artifacts not accounted for by the simulation, such as activation produced by previous beam pulses, pile-up of low energy particles, and scatter-radiation from the nozzle, which is partly screened by the collimator.

3.3.3. Integral Prompt-Gamma Yields as a Function of Depth

The validation of the code in depth profile experiments is essential for prompt-γ studies. **Figure 11** shows simulations and measurements of photon-depth profiles resulting from carbon beams for setup S_{II} and S_{III}. Note that the measured data, previously

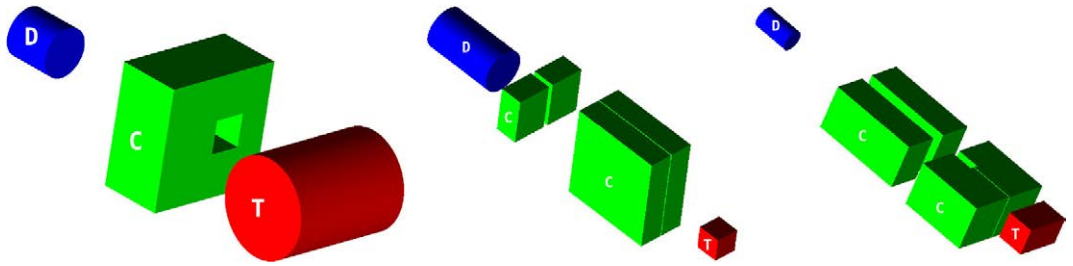

FIGURE 9 | Simulated configurations of targets (T), collimators (C), and detectors (D) for S_I (left), S_{II} (middle), and S_{III} (right), each drawn to scale. The beam impinges perpendicularly on the center of the target face marked with a 'T'.

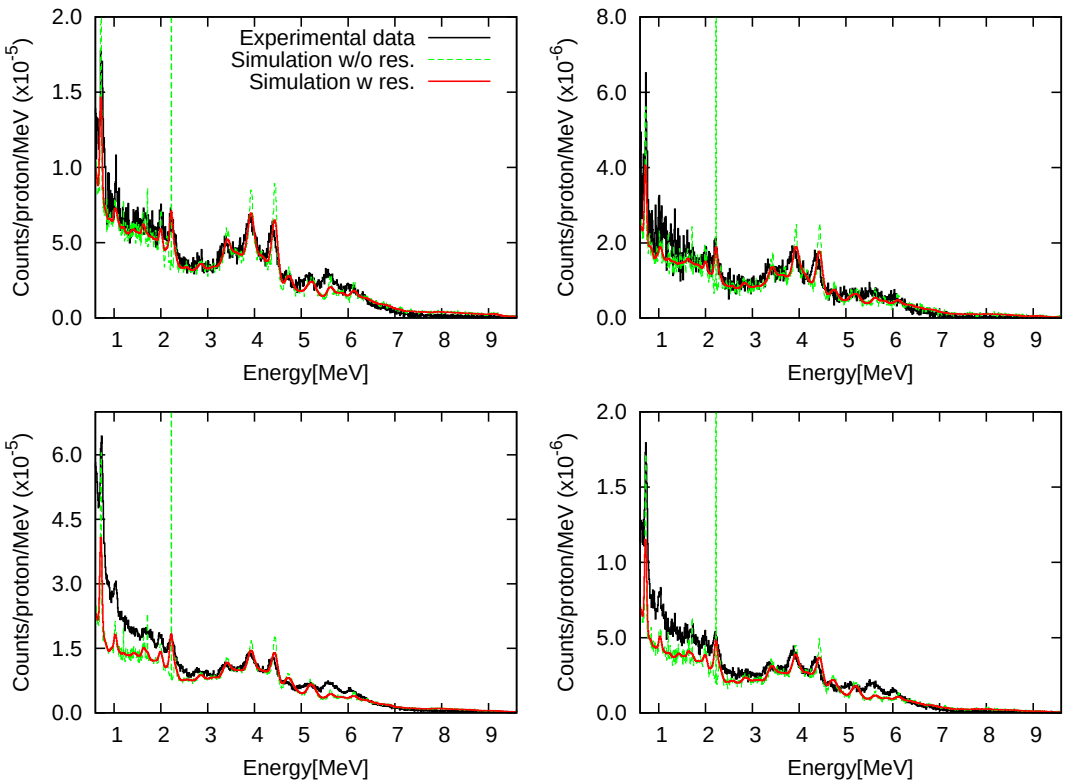

FIGURE 10 | Background-subtracted photon energy spectra for setup S_I with target-detector distances of 50 cm (left) and 100 cm (right) are shown for the "opening difference" (top) and the "wall difference" (bottom). Simulated spectra with and without intrinsic detector resolution are presented in comparison with measured data (112).

reported in Ref. (95), have recently been revised by the authors, providing a new absolute normalization (113, 114) and revision of the systematic uncertainties. Hence, updated experimental data are presented in **Figure 11**. The initial experimental data points, measured at −2 and −4 cm for setup S_{II} and −1.5 cm for setup S_{III}, are taken at depths before the start of the phantoms. Only a very small photon yield in air is expected for these positions. The measured signals for these depths can therefore be assumed to represent mostly measurement background. Hence, a background subtraction using the revised data of 6.3×10^{-7} (S_{II}) and 4.0×10^{-7} (S_{III}) counts/primary ion has been additionally performed, in order to obtain measured photon yields close to zero for measured data points before the start of the phantoms. A smearing due to detector resolution has been applied to simulated data. For the measured data points, vertical bars indicate the systematic uncertainties as reported in the original papers. For the simulated data points, vertical bars indicate the statistical uncertainty.

By introducing the corrections discussed above, the comparisons show not only a satisfactory agreement in the relative shapes of the profiles but also a good absolute agreement for setups. These findings are consistent with the expected agreement from

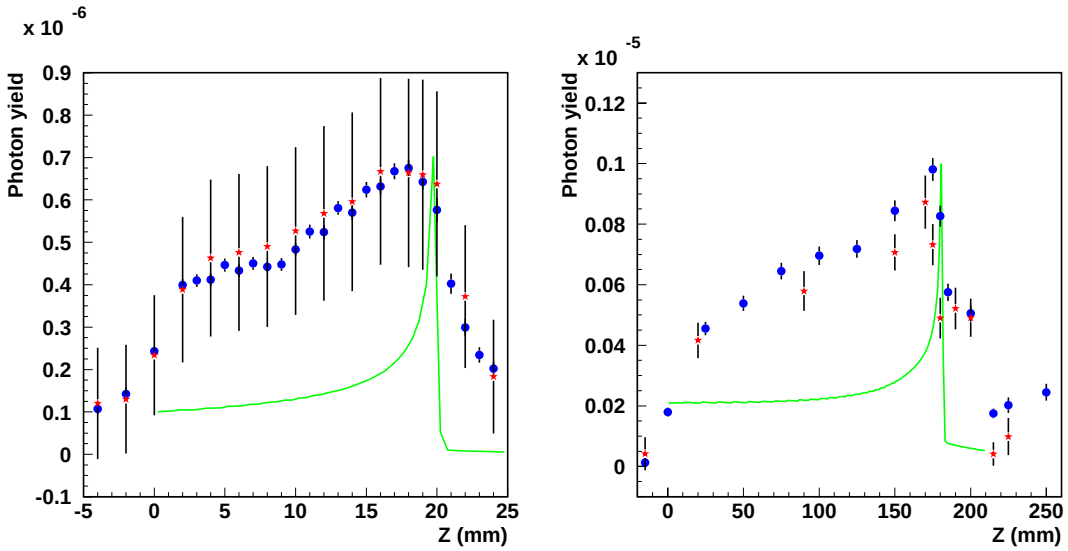

FIGURE 11 | **Integral photon yield as a function of depth**. Simulated (blue circles) and measured [red asterisks (95, 114)] data are shown for carbon ion beams for setup S_{II} (left, 95 MeV/n on PMMA, the original experimental data have been re-evaluated in 2012) and S_{III} (right, 310 MeV/n on water). Simulated depth–dose distributions are also shown as green lines with arbitrary normalization.

the comparisons of the prompt-γ energy spectra in the previous section.

4. FLAIR AND ITS APPLICATIONS TO RADIATION THERAPY

4.1. Introduction

Flair (12, 13) (**Figure 12**) is a user-friendly graphical interface for the FLUKA (8, 9, 50) Monte Carlo transport code. It provides an Integrated Development Environment (IDE) for all stages of FLUKA simulations, from building an error free input file, to debugging, creation of user written routines, execution, status monitoring, data processing, and plot generation. The program employs a custom 2D/3D fully functional graphical editor (13) and debugger for building geometries.

The graphics editor provides very fast graphics with real-time 3D ray-traced rendering of complex geometries as well a dynamic layer mechanism allowing the user to fully customize and create sophisticated views overlaid on the geometry. The use of the program greatly enhances the productivity of the users and provides much steeper learning curve for the beginners. Thanks to the modular design of Flair, recently it was enhanced with the possibility to import, display, process, and convert DICOM files to FLUKA compatible input, as well as with an automatic PET geometry generator. The geometry generator eases the construction of a PET detector with general parameters. The user can also benefit from multiple templates of commercial PET scanners provided within the interface. This section describes the current state of implementation of the medical tools already functional inside Flair as well the future plans. The program and the source code can be freely downloaded from Ref. (115).

4.1.1. DICOM Description

Digital Imaging and Communications in Medicine (DICOM) (116) is a standard for handling, storing, printing, and transmitting information in medical imaging. DICOM supports a wide range of medical images across the fields of radiology, cardiology, pathology, and dentistry. The format is quite versatile and can host practically any kind of information.

Depending on the modality type of each file, a different class has been implemented in Flair to cope with it. Presently, Flair is able to handle the following modalities:

- *CT* – Computed tomography, represented with multiple files each containing a 2D sliced Z image.
- *MR* – Magnetic resonance imaging, with all the necessary information in a single (or multiple files) containing a 3D representation.
- *RTDOSE* – Radiotherapy dose distribution.
- *RTPLAN* – Radiotherapy treatment plan.
- *RTSTRUCT* – Radiotherapy structure set, describing structures/objects.

4.2. DICOM *Processing* in Flair

Flair is using pydicom (117), an open source package for reading and writing DICOM files using the python programing language, and the numerical python – NumPy (118) libraries for processing the DICOM files. Pydicom can read and write all standard DICOM files, including nested sequences such as found in DICOM RT files or in structured reports.

The user is able to inspect selected DICOM files either graphically from the Flair DICOM slice viewer or from the enhanced tree structure text browser (**Figure 13**). The slice viewer is capable of displaying the 2D slices from the DICOM for the CT, MR, RTDOSE, and RTSTRUCT modalities and allows the user to

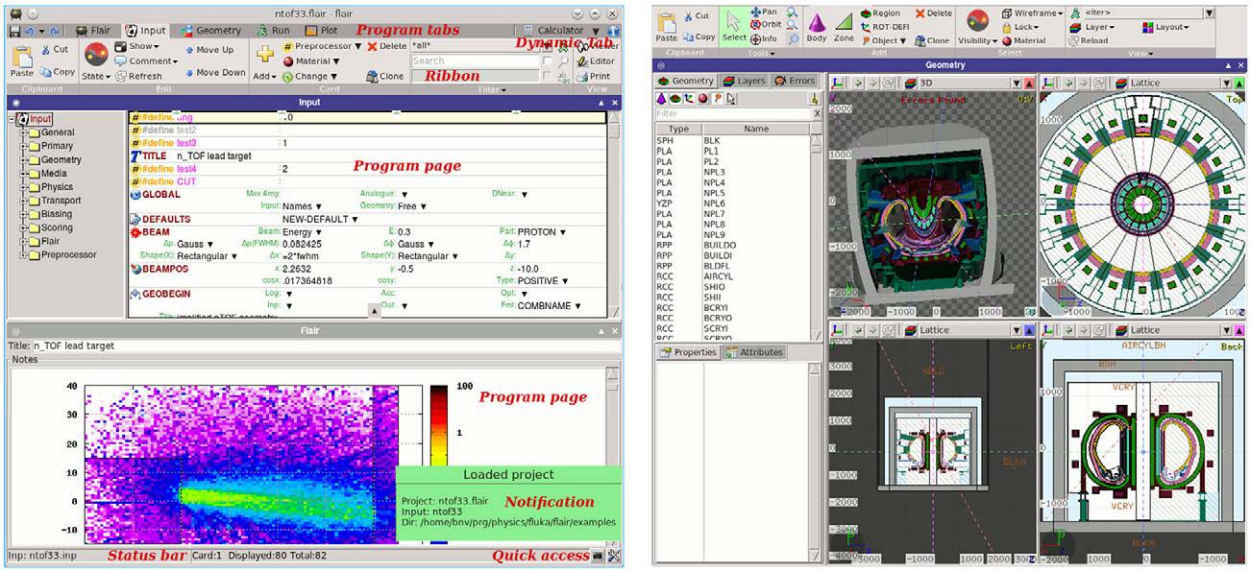

FIGURE 12 | **Flair graphical interface (left), graphical geometry editor (right)**.

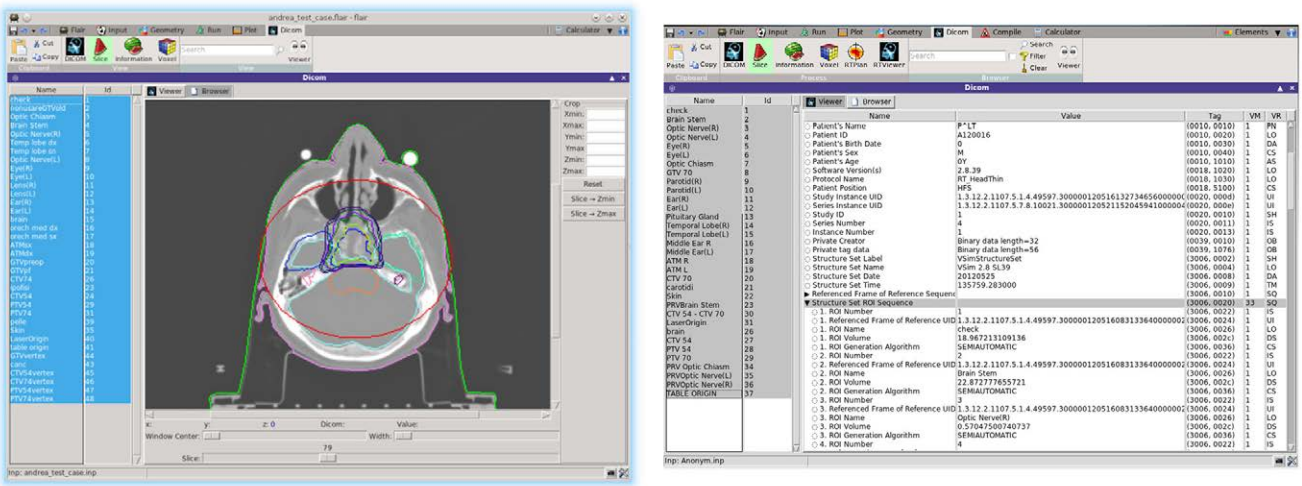

FIGURE 13 | **Flair dicom viewer, with RTSTRUCT superimposed (left); DICOM tree browser (right)**.

perform simple operations on the slices (like cropping, rescaling, etc.). For RTSTRUCT files, the structures are overlaid on the corresponding display of the CT/MRI slices.

Recent development effort was put on providing a better visualization and comparison between TPS and FLUKA re-calculated dose values. The new RTViewer (**Figure 14**) is able to present 2D cross-sectional CT images for axial, coronal, and sagittal planes combined with the RTDOSE and FLUKA calculations results. It also supports the user with visualization of the differences between MC calculated dose values and TPS prescription. Current development is focused on displaying MR scans, merging three planes with the overlaying ROIs defined in RTSTRUCT, and providing the user with referenced DVH plots.

4.2.1. DICOM to Voxel Conversion

The CT scans contain integer values (so-called *Hounsfield Units*) reflecting the X-ray attenuation coefficient μ_x as a linear transformation of the original attenuation coefficient relative to the one from distilled water at standard temperature and pressure (STP) conditions:

$$HU_x = 1000(\mu_x - \mu_{H20}) / (\mu_{H20} - \mu_{air}) \quad (4)$$

typically in the range of $-1000 \leq \text{HU} \leq 3500$.

Air has typically a HU of −1000, which is the lowest HU value in the file. In FLUKA, we loosely use the word *organ* to indicate a group of voxels (or even more than one group) made of the

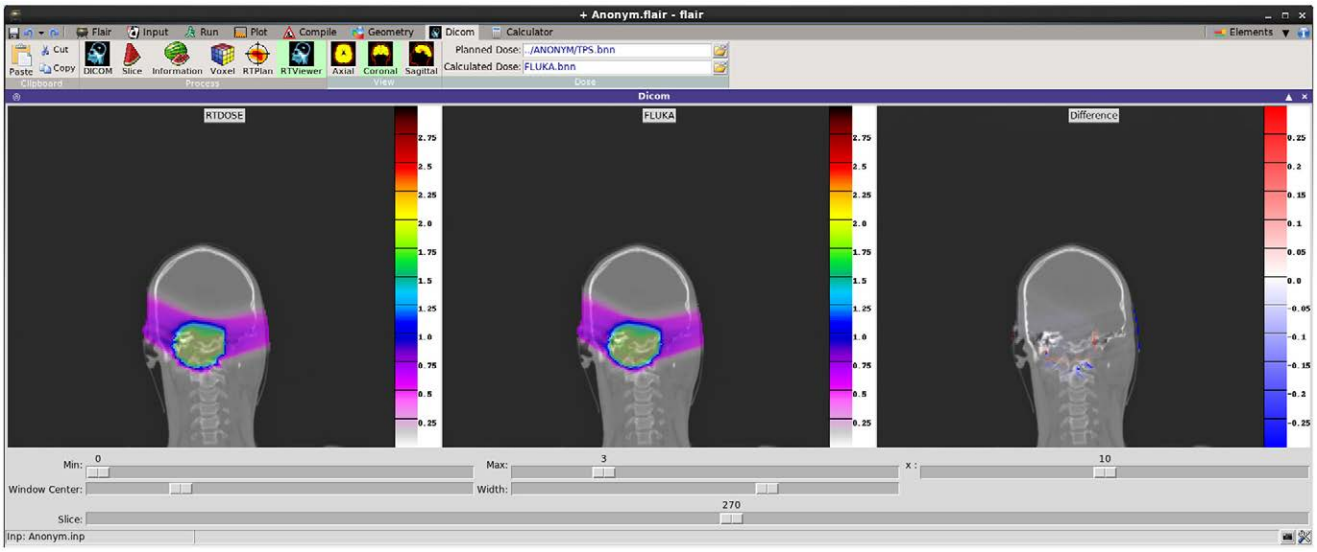

FIGURE 14 | **New DICOM Viewer interface**. Coronal CT plane with mapped physical dose [Gy] from RTDOSE and FLUKA calculation. On the right differences between obtained values [Gy].

same *tissue* material (same HU value or in a given HU interval). Internally, FLUKA will handle each organ as a constructive solid geometry region, possibly in addition to other conventional *non-voxel* regions defined by the user.

Assigning a separate material to each of the ~3000–5000 HU values, typically present in a CT, is neither memory- nor CPU-efficient for simulations. Therefore, ranges of HU are grouped into organs while providing a mechanism to allow a continuous HU-dependent scaling of interaction properties of the materials. Flair includes the Schneider (1) parametrization, which segments the CT into 24 materials of defined elemental composition based on the analysis of 71 human CT scans, and assigns to each material a *nominal mean density*, e.g., using the density at the center of each HU interval (1, 119, 120).

Real density (and related physical quantities) varies continuously with HU value, therefore in FLUKA, we split the 24 material description in smaller intervals (41 intervals in total), and we apply a scaling correction. Specific ranges of HU values share the same material and during transport an additional scaling factor is applied on the density for the nuclear and for the electronic processes, based on the real HU value. To accommodate for this change, the FLUKA voxel format was enhanced to include the possibility to embed FLUKA input cards that contain all the information on the materials, assignments, and correction factors.

4.2.2. Radiotherapy Treatment Information

As already mentioned, Flair is now capable of importing also the radiotherapy treatment data described in the dedicated DICOM RT (RTSTRUCT, RTDOSE, RTPLAN) standard.

4.2.2.1. RTSTRUCT

The radiotherapy structure set object of the DICOM standard is used for the transfer of patient structures and related data, between the devices found within and outside the radiotherapy department. It contains mainly the information for regions of interest (ROIs) and points of interest (e.g., dose reference points). The ROIs can be used during the simulation for calculating Dose Volume Histograms (DVH) or perform special scoring on an organ basis. The ROIs are represented as the points belonging to a closed polygon using 2D coordinates (not rounded to the pixel size of the corresponding CT image).

When selecting an RTSTRUCT file to be embedded into the VOXEL file, Flair will identify for each voxel to which ROIs it belongs. The case of voxels belonging to more than one ROI is also taken into account. A matrix containing the voxel to ROI correspondence is included in the VOXEL file read by FLUKA. This additional matrix is used by Flair for plotting purposes and/or by FLUKA for scoring and DVH calculations (**Figure 13**).

Flair provides some checks on the structures like calculating volumes using the true polygonal information or the discretization to voxels. Typical differences up to a few percent can be noticed induced by the quantization process.

4.2.2.2. RTDOSE

The RTDOSE can be converted to a FLUKA USRBIN, a 3D mesh tally. This is possible for all modalities having a PixelData tag like CT, MR, and RTDOSE. Once converted, it can be further used for plotting and comparing the results, e.g., from the output of a treatment planning system with a FLUKA simulation. In the RTViewer (**Figure 14**), the user can import the chosen sequence dose data or compare the entire treatment fraction and visualize it mapped on the CT scans. USRBIN can be also used as a primary source particles generator, e.g., the PET/CT dose description followed after an FDG (**Figure 15**).

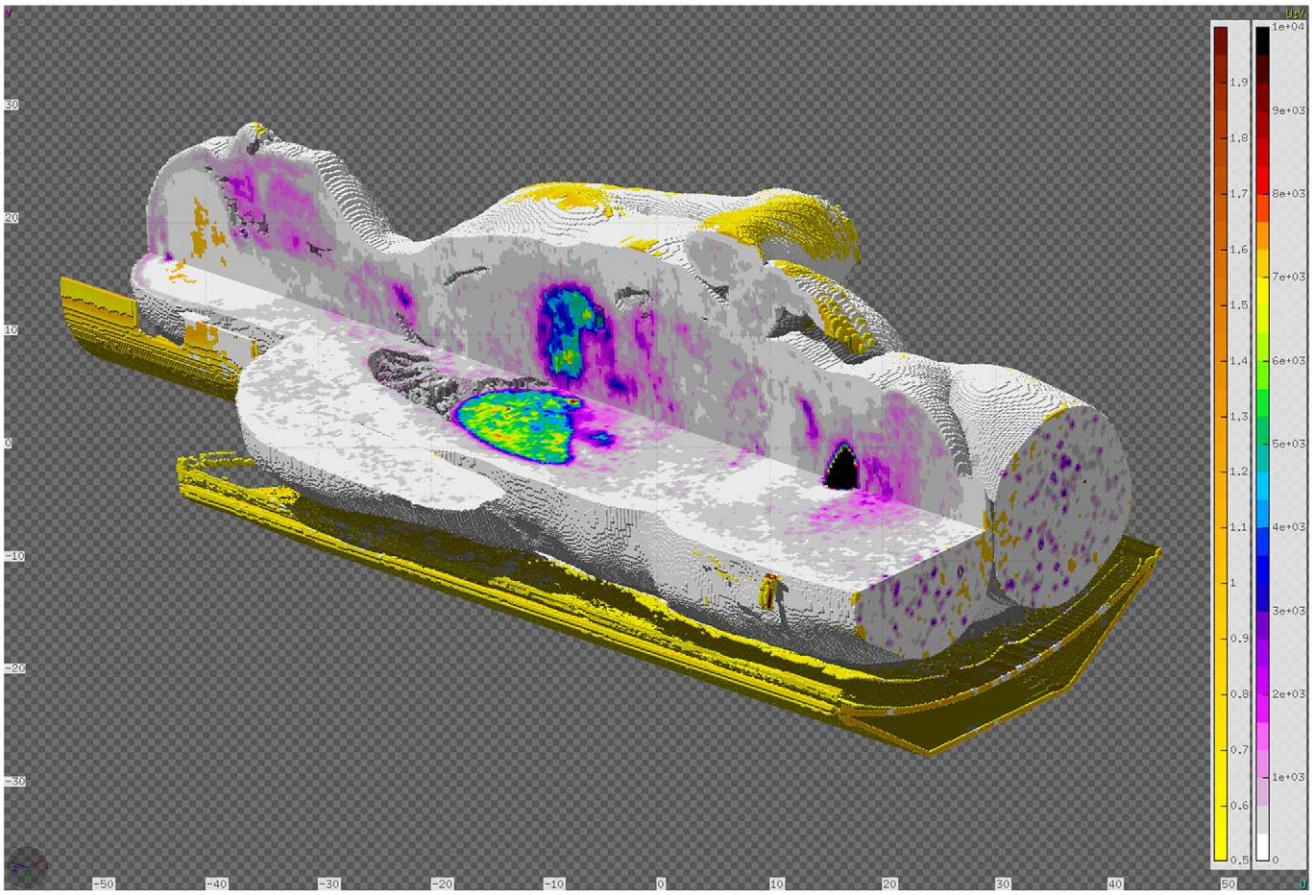

FIGURE 15 | DICOM to VOXEL import of CT data together with the RTDOSE superimposed. Displayed using the Flair geometry editor.

4.2.2.3. RTPLAN

The RTPLAN contains the information on the treatment plans generated usually by a Treatment Planning System (TPS). Typically such plans provide the information about the treatment fractions, describing the external beams of hadron therapy application. Parameters defined for every single beam spot in the plan are grouped into the beam sequence, where they are enumerated using the control points. Control points checklist includes several information, i.e., particles energy, scan spot position, and number of monitor units. In addition, for each beam sequence, the information for particle type, position of the isocenter according to the DICOM file and gantry, patient and table angles are defined. Flair is currently able to export the most frequently used beam sequence parameters into an external file, from which the special RTPLAN source routine reads and determines the entry source for the FLUKA simulations. While exporting data, Flair performs validation checks on the DICOM file using available control variables.

When defining the beam spot position, RTPLAN refers to its own coordinate system – *Gantry Coordinate* system and *Isocenter Position*. Flair is able to apply correct rotations and translations to the VOXEL structure, and as a result updates the FLUKA input file in order to prepare the fully functional ready-to-run simulation for each single beam field. Further, postprocessing enables to combine simulation beam sequences outputs to one fractional dose file and to visualize it in RTViewer. Current work is focusing on importing less frequently used RTPLAN parameters and simplifying the entire process of treatment plan re-simulation.

4.3. PET Scanner Simulation Tools for FLUKA

PET is a commonly used imaging technique, based on detecting in coincidence the pair of annihilation photons created from the decay of a β^+ emitter. Such positron-emitter nuclei are traditionally inoculated to the patient by means of a radio-pharmaceutical drug, in order to analyze the metabolic activity of the body tissue and in the hope of detecting hints of unusual behavior from tumor cells. As an example, Fludeoxyglucose or 18F-FDG is a glucose-analog radio-pharmaceutical, where a normal hydroxyl group is substituted by the ^{18}F radioactive isotope. This substance is used to study the glucose consumption of the cells.

Apart from its traditional use in nuclear medicine, PET is nowadays the only clinically available method for a non-invasive monitoring of the dose delivery for hadron therapy.

However, as mentioned in Section 3.1, there are still important concerns when using commercially available PET scanners for proton or ion beam treatment monitoring, usually compelling to drastically redesign them. Monte Carlo codes are thus crucial to evaluate the performance of new PET prototypes and are an essential tool to infer the dose map from the positron-emitter distribution. To ease the simulation of full PET scanner simulations with FLUKA, taking advantage of the latest developments on the models for beta-emitter production presented in Section 3, Flair incorporates a dedicated PET scanner tool, which covers all the steps from the creation of the geometry of the PET ring to the reconstruction of the image from the coincidence events.

4.3.1. Building the PET Geometry

With the aim of covering most of the collinear pairs of annihilation photons, the geometry of PET scanners is generally composed of an array of detector scintillators, describing a complete or partially opened cylindrical structure.

Consequently, PET detectors can be built by replication of simple rectangular parallelepiped sub-units. The PET geometry tool exploits the replication capabilities of the FLUKA code (through its LATTICE cards) to generate a PET detector based on few simple geometrical parameters. The interface of the tool is intuitive, with illustrations that give a visual explanation of the meaning of each parameter (see **Figure 16**).

The natural cylindrical coordinate system of PET scanners is exploited by associating the (R, θ, Z) coordinates with the *(radial/depth, azimuthal, and axial)* coordinates. The interface divides the required parameters in three levels:

- *Block level,* defined as the array of basic scintillators. The parameters that define the block are the number of scintillators in each direction, the elemental detector dimensions, and the separation among contiguous scintillators.
- *Module level,* taken as the array of blocks. The parameters for the module are the number of blocks in each direction coordinate and the separation among neighboring blocks.
- *Ring level,* which defines the global properties of the PET. The parameters are, then, the number of modules along the ring, the radius of the ring, the vector defining the axis of the scanner, the center coordinates of the scanner, the material of the scintillator, the surrounding region where the scanner will be located and the opening angle, in case a partial ring is required.

The replication of the modules along the ring can be structured in partial or full rings, controlled by the opening angle θ_{open}, which ranges from 0° to 180° (complete ring). The incorporation of partial rings is interesting for "in-beam" PET, where the scanner has to be integrated with other elements at the irradiation room (121). Based on the azimuthal dimensions of the module and θ_{open}, the interface is capable of estimating the maximum number of modules that could fit in the available space.

From the previous parameters, the tool generates the input and geometry files (see **Figure 17**) providing the basic cards for a FLUKA simulation. Apart from the basic structure, any

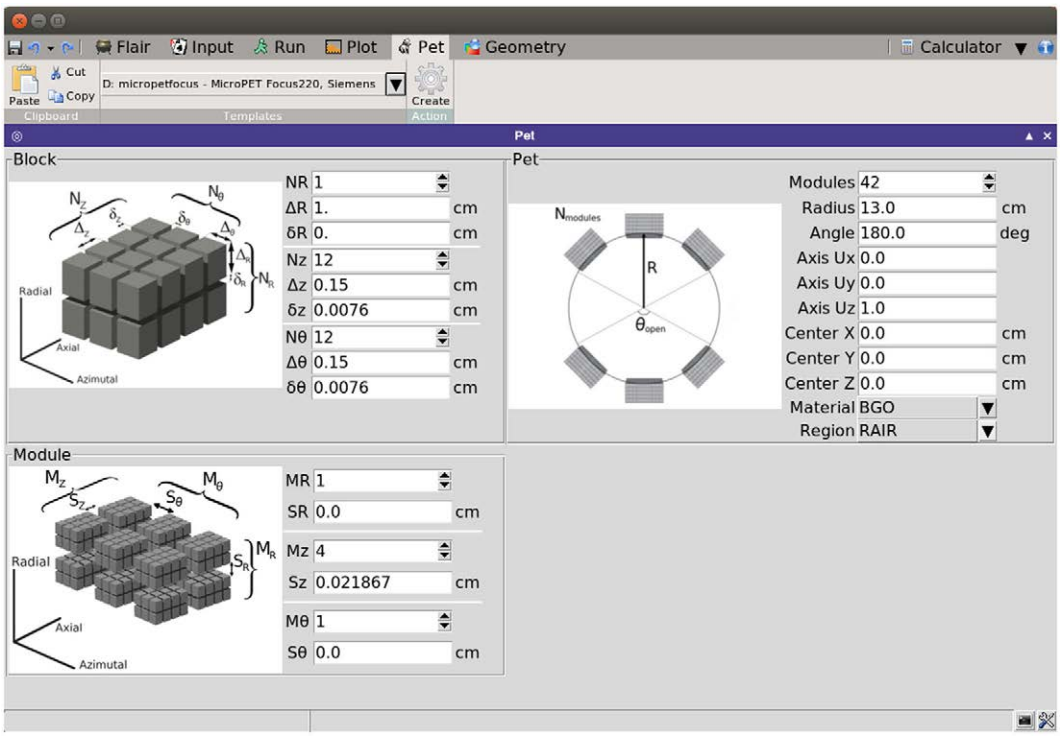

FIGURE 16 | **Flair interface of the PET geometry tool**.

additional elements of the detector should be included manually if necessary. This may include the septa for 2D acquisition mode, shielding elements, etc. The construction of the phantom target, the distribution of radioisotopes, or the beam structure should be further modeled by the user, depending on the specific requirements of the problem under study.

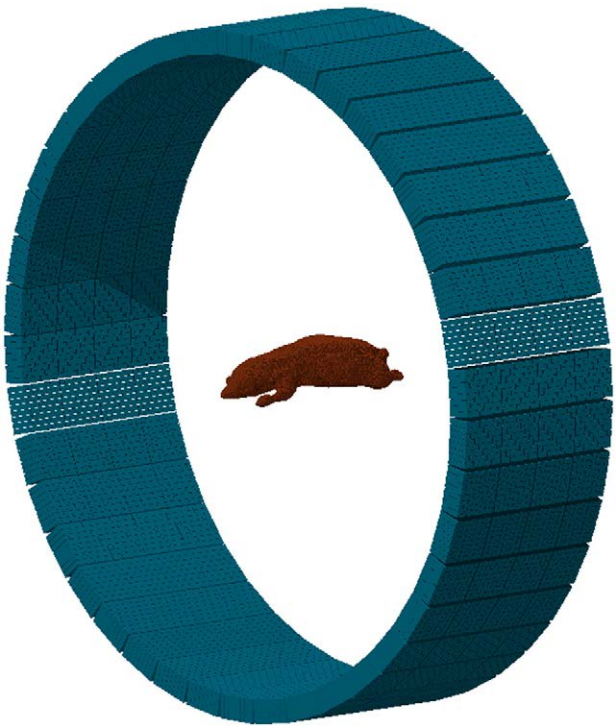

FIGURE 17 | Example of a MicroPET P4 scanner built with the PET geometry tool. The phantom is a high-quality, segmented mouse phantom (122, 123), imported to FLUKA voxels with the DICOM tool.

With the purpose of providing the user with a starting ground and facilitating the efficient implementation of a PET scanner, the interface presents several templates of commercial PET detectors, such as Ecat EXACT HR+ (CPS) (124), Ecat HRRT (Siemens) (125), Hi-Rez (Siemens) (126), Allegro (Philips) (127), GE Advance (GEMS) (128), MicroPET P4 (Concorde) (129), MicroPET Focus 220 (Siemens) (130), and Mosaic (Philips) (131). The parameters for such scanners can be further modified before building the geometry, thus serving as a base for detector design and optimizations.

4.3.2. Scoring of Coincident Events

In PET, the reconstruction problem consists of obtaining a tomographic slice image from a set of projections. The projections are built by delineating a set of parallel line of responses (LOR), the imaginary line that unites two coincidence events, through the 2D phantom, assigning the integral of all the events registered along each LOR to a single pixel in the projection. Once several projections have been acquired, each of them corresponding to a different angle of the LOR with respect to the phantom, the PET reconstruction of the object can be performed. The set of projections at different angles is called a *sinogram*, which is a linearization of the original image (see **Figure 18**).

In FLUKA, a collection of scoring routines, complementary to the PET geometry tool, have been implemented, with the goal of acquiring the energy deposition events of the PET scintillators and the subsequent organization of such individual events in coincidence events. The scoring routines are divided in two steps. In a first step, FLUKA simulates the nuclear interactions and tracks the decaying particles through the phantom up to the PET scanner. The portion of energy of such particles deposited in the scintillators is then stored as an individual event, and all

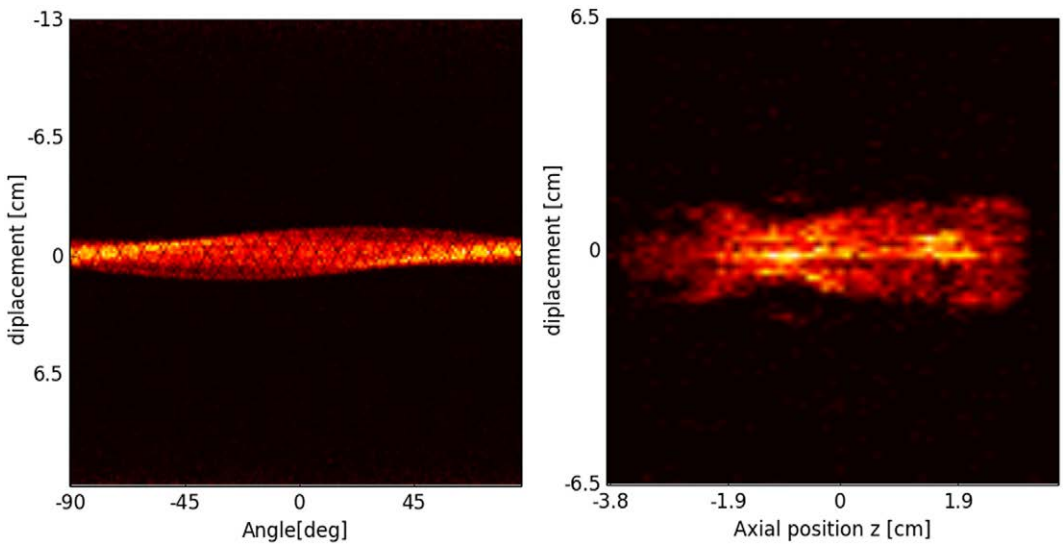

FIGURE 18 | Sinogram (left) and projection image (right) of the segmented mouse phantom of Figure 17, using a MicroPET P4 scanner.

the information regarding the event is dumped in a list mode output file. The scoring of individual events can be optimized with several editable parameters:

- the *energy window*, so only particles with a certain amount of deposited energy are scored;
- the *minimum scoring time*, that discards particles arriving at the PET before a time threshold;
- the *time resolution of the detector*;
- the *dead-time of the detector*, which is the time needed for the scintillator to process an event.

Accordingly, one output file with a list of individual events is generated per FLUKA run. In a second step, the set of list mode files is processed, and the coincidence events are produced. The coincidence events output file is organized in *sinograms*, in a *Interfile 3.3* file, a standardized binary intermediate file format for nuclear medicine image data files (132).

The goal is to merge and organize the information produced by the PET data acquisition in a standardized way the user is already familiarized with, and which could be employed with external visualization or reconstruction software. For the sinogram output format, different parameters are available to customize the scoring options: *Arc Correction*, *Maximum Ring Difference (MRD)*, *Number of Segments*, *Span* and *Mashing Factor*. These parameters determine the 2D/3D acquisition mode and its characteristics (see Ref. (133) for further details). The values of these parameters can be conveniently modified by the user.

In addition, simple reconstruction algorithms are planned to be implemented in Flair, so the user can have an image of the object within the same interface. Two algorithms are under development: *2D Filtered Back-Projection* (FBP) and *Maximum-Likelihood Expectation-Maximization* (MLEM). On the one hand, FBP is a simple but fast algorithm, based on the Fourier Transform of the projection and interpolation in Fourier space. The 2D FT transform of the object obtained is then inverted to form the final image. MLEM, on the other hand, is an iterative method that best estimates the reconstruction image by maximizing the likelihood function. It finds the mean number of radioactive decays that better fits the sinogram with the highest likelihood. The output reconstructed image is then stored in USRBIN file, so the result can be further analyzed in Flair.

5. APPLICATION OF THE FLUKA CODE FOR CLINICAL CALCULATIONS AT HIT AND CNAO

The FLUKA code has already been used to support clinical applications prior to the comprehensive extension of the Flair functionality to handle RT objects as described in Section 4.

Dedicated frameworks were implemented in the past at the Heidelberg Ion Beam Therapy Center (HIT, Germany) and the National Center of Oncological Hadrontherapy (CNAO, Italy) providing automated FLUKA MC simulations of clinical treatment plans delivered by actively scanned proton and carbon ion beams (66, 134). Results obtained with these early frameworks have intensively been validated against clinical data and therefore provided a valuable reference for the benchmarking of several RT functionalities during the extension of Flair. The frameworks provide all functionality required for pre-processing of the DICOM RT input data as well as the postprocessing of the FLUKA output. Graphical user interfaces allow to access the fully automated data handling and are realized at HIT within the MeVisLab environment [www.mevislab.de (135)] and at CNAO with MATLAB®. Physical and RBE-weighted dose distributions are calculated for individual treatment fields and the entire fraction using a global RBE of 1.1 for proton beams and a dedicated implementation of the LEM I framework, which is also used by the treatment planning system (TPS) (4, 75, 136) for carbon ion beams. During the physical and biological calculations dose-to-medium is always converted on-the-fly into dose-to-water, thus providing dose distributions in both formalisms, and dose-averaged LET can optionally be generated for proton beams. In order to assure consistency with the TPS, the FLUKA physics settings are the same as used for the generation of the TPS basic data in water (41, 61, 65). For CT-based calculations, the MC patient model relies on the stoichiometric calibration of Ref. (1, 3) with proper facility and CT-number dependent adjustments of the electromagnetic and nuclear processes as in Ref. (2) for consistency with the CT-range calibration curves used by the TPS for all available CT protocols.

The RaySearch RayStation® TPS has been recently (2015) installed at CNAO, and the proton beam line is currently under commissioning. Being specifically thought to provide fast visualization environments and dose statistics tools, a TPS should represent the gold-standard interface to help physicists and physicians to also include MC simulations within the clinical routine. Therefore, in addition to the in-house MATLAB® tools, an interface has been developed for converting FLUKA outputs in RTDOSE DICOM files. As an example, **Figure 19** reports the physical dose distribution for the study of a 3-fields carbon ions plan (upper panels) for the irradiation of a retro-orbital metastasis. Depth–dose distributions (lower-left panels) and DVHs (lower-right panels) are also displayed. Good agreement has been found between MC and TPS calculated distributions for this challenging case both in terms of profiles and DVHs.

Figure 20 reports the RBE-weighted dose distribution (D_{RBE}) of a clinical-like carbon ion therapy plan, delivered to the upper spine region in a single right-lateral field, calculated with the TPS (SIEMENS *syngo*® PT Treatment) and the HIT in-house MC framework (66) described above. Shown are the two-dimensional overlays of D_{RBE} on top of the treatment planning CT image (**Figure 20** upper panels), D_{RBE} profiles along a representative line in beams eye view (**Figure 20** lower-left panel) and the DVH for the PTV and the relevant organ at risk (spinal cord, **Figure 20** lower-right panel). We observe a good agreement between the TPS and the MC calculations, with the MC yielding a slightly higher D_{RBE} level in the target region leading to an increase of D_{50} in the PTV of ≈2%, and of V_{10} in the spinal cord of ≈3%. The slight overestimation of RBE-weighted dose compared to the TPS calculation is attributed to differences in the mixed radiation field description of TPS and MC as discussed in more detail in Ref. (66).

Recently, Flair has been successfully applied at CNAO for performing dose forward calculations with proton beams.

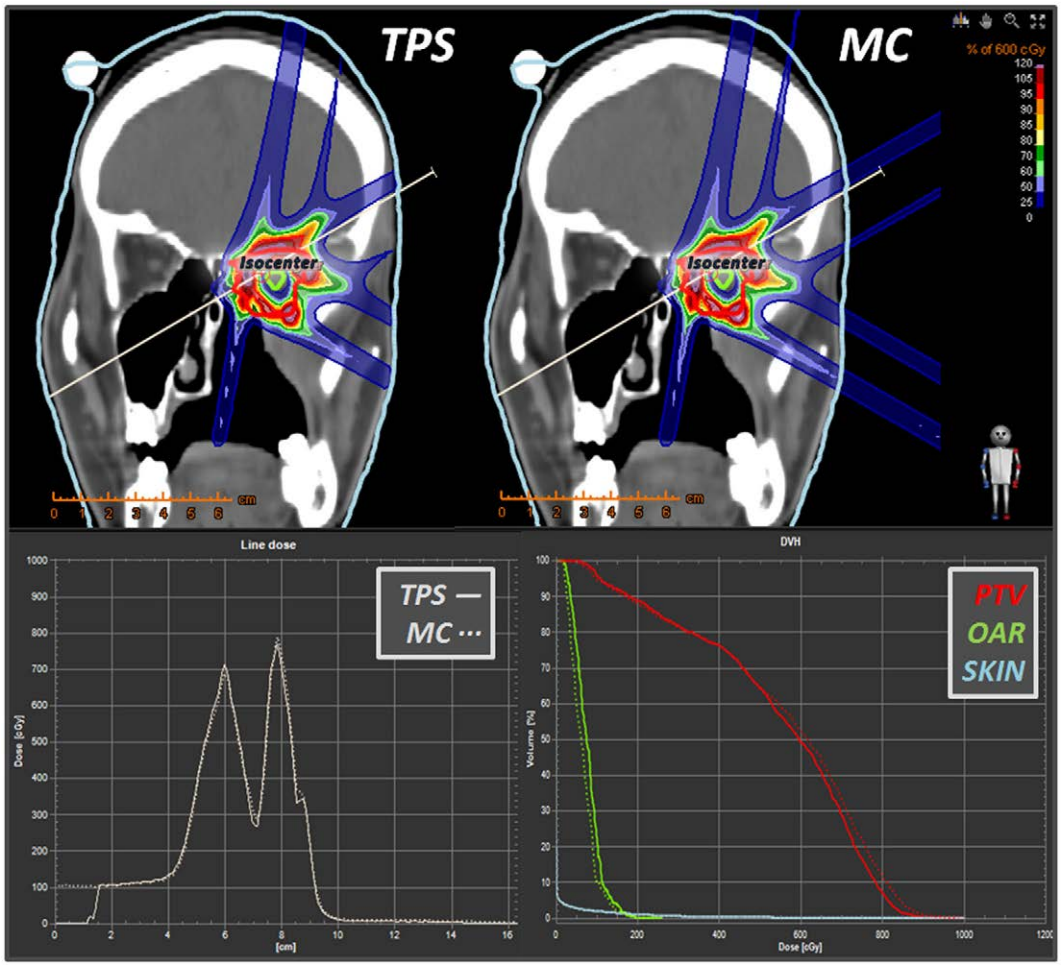

FIGURE 19 | Some snapshots taken from RayStation® showing a comparison (in coronal view) between a *syngo*® 3-fields carbon ions plan vs. its MC dose forward recalculation. Lower panels display the line dose and the DVH calculator tools. Differently from the TPS, which displays dose only within the "external-type" structure, the MC dose-to-water scoring is extended to the whole field of view of the CT scan.

In **Figure 14**, an example of TPS- and MC-calculated dose distributions for a patient-like two fields treatment of a skull-base chondrosarcoma is shown. The satisfactory agreement, as proven by the plotted dose differences (right panel in **Figure 14**), supports the future usage of Flair as standard re-calculation tool at CNAO.

6. CONCLUSION

The electromagnetic and nuclear models of FLUKA enable to reasonably well reproduce measured depth- and lateral-dose profiles in water for all the spectrum of ions of therapeutic interest, making it the code of choice for generation of TPS input data at leading European centers in Germany and Italy, as well as a valuable tool to support analytical TPS developments of some commercial vendors. In the last years, special efforts have been devoted to improvements of the FLUKA nuclear interaction models, which provide benchmarked and reliable results for interaction cross sections and particle production by proton and ion beams at therapeutic energies. In particular, they allow to treat in a consistent way the transport and interaction of primary particles and all produced fragments, including transport of electromagnetic particles. All reaction generators share the same equilibrium particle emission, thus profiting together of the past and latest developments of the evaporation, fragmentation, and deexcitation models. Low energy nuclear models are of utmost importance for applications to *in vivo* verification techniques. FLUKA is presently able to reproduce within experimental errors the production of β^+ emitters by protons at energies of interest for therapy, and at 25% or better accuracy in the case of carbon projectiles. The newly developed and refined FLUKA models for prompt γ production were shown to reproduce reasonably discrete line cross sections as well as integral energy spectra and yield-vs.-depth data for proton and carbon ion beams. The general trends of the experimental cross-sectional data are consistently reproduced by the models. This includes cross-sectional data of discrete lines for different targets, notably data for carbon, nitrogen, and oxygen nuclei.

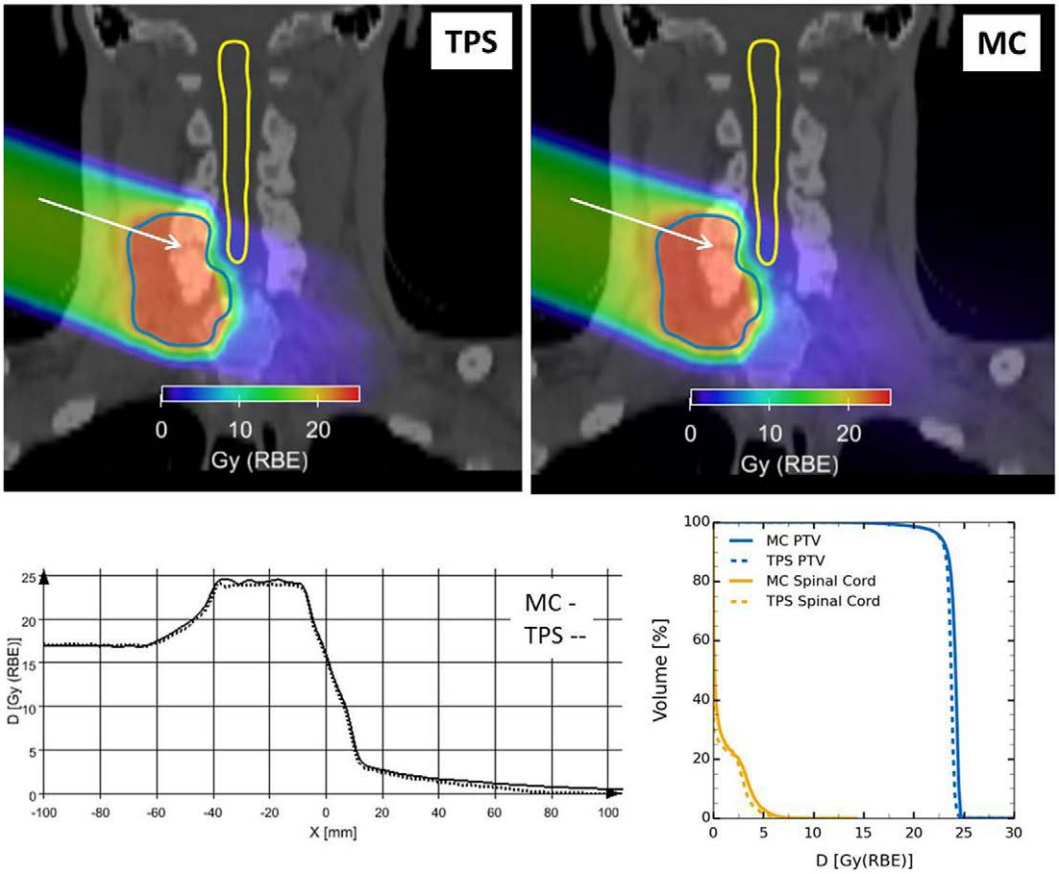

FIGURE 20 | **Clinical-like carbon ion therapy plan delivered to the upper spine region in a single right-lateral field**. Top: overlay views of RBE-weighted dose distributions obtained from the TPS (left) and the FLUKA framework (right) on the treatment planning CT image. Outlined are the PTV and the spinal cord. Bottom: comparison of TPS and MC RBE-weighted dose profiles along the white arrow drawn in the overlay views (left); dose volume histograms for PTV and spinal cord for both TPS and MC RBE-weighted dose distributions (right).

The relative shape of photon profiles as a function of depth as well as the absolute photon yield per primary proton and carbon ion (**Figure 11**) are well reproduced after the last revision of the experimental data (114). The comparisons with the experimental yield-depth data presented here suggest an accuracy of about 15–20% for the prediction of absolute yields. The comparisons of simulated and measured energy spectra for proton beams (**Figure 10**) showed a very good agreement (mostly within 10%) for photon energies higher than 2 MeV. This is an energy range of interest for prompt-γ monitoring and spectroscopy. Progresses on nuclear interaction models are still ongoing, in particular for what concerns low mass ion beams, and a better treatment of spin/parity effects all along the reaction chain.

FLUKA's physics model reliability is coupled with the versatile features of its Flair graphical interface, creating the necessary input directly from the computed tomography and radiotherapy files. This provides a powerful and user-friendly way to carry out Monte Carlo simulations for medical applications. Flair currently employs a fully functional DICOM CT/MT converter to VOXEL geometry, processing of the RTSTRUCT and RTDOSE modalities, and an automatic PET geometry generator. Work is ongoing on using the RTPLAN and toward the development of a Monte Carlo Treatment Planning System optimizer.

MC dose forward calculation has proven to be a valuable asset to support the development of commercial TP systems in the past. The reported implementations of the FLUKA code in automated workflow environments at HIT and CNAO are intensively used to study the impact of known shortcomings of the analytical approach in particle therapy treatment planning. They provide flexible and robust tools to address daily demands required for high quality patient treatment.

AUTHOR CONTRIBUTIONS

GB: promoting the use and development of FLUKA in therapy applications, verifications of physical models, and production of text for the introduction. JB: verification and application of the code in clinical environment, production of text and figures for Section 5. TB: comparison of FLUKA models with dose profiles data, data analysis, and production of text and figures

for Section 2. FC: development of FLUKA models for ion interactions in matter and production of text and figures for Sections 2 and 3. MC: development of methods for fluka simulations, analysis of results in prompt photon and PET applications, and critical revision of the manuscript. RA: development of FLUKA models and their application to hadron therapy, and production of text for Section 3. AF: main FLUKA developer, applications to hadronthetrapy and production of text and figures for Sections 2 and 3. PO: comparisons of FLUKA results with data on prompt photons, development of the PET modeler, and production of text and figures for Sections 3 and 4. WK: development of the flair interface for medical applications and production of text and figures for Section 4. GM: applications of FLUKA in clinical environment and production of text and figures for Section 5. AM: development of FLUKA models for ion interactions in matter, implementation of biological effectiveness in FLUKA, clinical applications, and production of text and figures for Sections 2 and 5. KP: pioneering and continuing FLUKA applications to hadrontherapy, data taking and analysis, and production of text and figures for Section 2. PRS: main FLUKA developer, coordination of the manuscript preparation, and production of text and figures for Sections 2 and 3. PS: developments of nuclear properties database for FLUKA, comparisons of FLUKA results with data, and general editing of the manuscript. TT: data taking, analysis and comparisons with MonteCarlo of dose-depth distributions, and production of text and figures for Section 2. VV: main author of Flair, applications to hadrontherapy, and production of text for Section 4.

ACKNOWLEDGMENTS

JB acknowledges the financial support by BMBF (German Ministry for Research and Education), project SPARTA (grant agreement number 01IB13001G). PO acknowledges the financial support from the European Unions Marie Curie COFUND grant (PCOFUND-GA-2011-291783). TT acknowledges funding from the German Research Foundation (DFG Klinische Forschergruppe Schwerionentherapie 214).

REFERENCES

1. Schneider W, Bortfeld T, Schlegel W. Correlation between CT numbers and tissue parameters needed for Monte Carlo simulations of clinical dose distributions. *Phys Med Biol* (2000) **45**(2):459. doi:10.1088/0031-9155/45/2/314
2. Jiang H, Paganetti H. Adaption of GEANT4 to Monte Carlo dose calculations based on CT data. *Med Phys* (2004) **31**:28118. doi:10.1118/1.1796952
3. Parodi K, Paganetti H, Shih HA, Michaud S, Loeffler JS, DeLaney TF, et al. Patient study of in vivo verification of beam delivery and range, using positron emission tomography and computed tomography imaging after proton therapy. *Int J Radiat Oncol Biol Phys* (2007) **68**(3):920–34. doi:10.1016/j.ijrobp.2007.01.063
4. Mairani A, Brons S, Cerutti F, Fasso A, Ferrari A, Kramer M, et al. The FLUKA Monte Carlo code coupled with the local effect model for biological calculations in carbon ion therapy. *Phys Med Biol* (2010) **55**:4273–89. doi:10.1088/0031-9155/55/15/006
5. Böhlen TT, Cerutti F, Dosanjh M, Ferrari A, Gudowska I, Mairani A, et al. Benchmarking nuclear models of FLUKA and GEANT4 for carbon ion therapy. *Phys Med Biol* (2010) **55**(19):5833. doi:10.1088/0031-9155/55/19/014
6. Enghardt W, Parodi K, Crespo P, Fiedler F, Pawelke J, Pönisch F. Dose quantification from in-beam positron emission tomography. *Radiother Oncol* (2004) **73**(Suppl 2):S96–8. doi:10.1016/S0167-8140(04)80024-0
7. Sommerer F, Cerutti F, Parodi K, Ferrari A, Enghardt W, Aiginger H. In-beam PET monitoring of mono-energetic (16)O and (12)C beams: experiments and FLUKA simulations for homogeneous targets. *Phys Med Biol* (2009) **54**(13):3979. doi:10.1088/0031-9155/54/13/003
8. Battistoni G, Böhlen TT, Cerutti F, Chin PW, Esposito LS, Fassò A, et al. Overview of the FLUKA code. *Ann Nucl Energy* (2015) **82**:10. doi:10.1016/j.anucene.2014.11.007
9. Ferrari A, Sala PR, Fassò A, Ranft J. *FLUKA: A Multi-Particle Transport Code*. Technical report CERN-2005-10, INFN/TC_05/11, SLAC-R-773, CERN, INFN, SLAC. Geneva: CERN (2005).
10. Andersen V, Ballarini F, Battistoni G, Campanella M, Carboni M, Cerutti F, et al. The FLUKA code for space applications: recent developments. *Adv Space Res* (2004) **34**(6):1302–10. doi:10.1016/j.asr.2003.03.045 Space Life Sciences: Radiation Risk Assessment and Radiation Measurements in Low Earth Orbit
11. Ballarini F, Biaggi M, Biaggi LD, Ferrari A, Ottolenghi A, Panzarasa A, et al. Role of shielding in modulating the effects of solar particle events: Monte Carlo calculation of absorbed dose and {DNA} complex lesions in different organs. *Adv Space Res* (2004) **34**(6):1338–46. doi:10.1016/j.asr.2003.08.055 Space Life Sciences: Radiation Risk Assessment and Radiation Measurements in Low Earth Orbit
12. Vlachoudis V. FLAIR: a powerful but user friendly graphical interface for FLUKA. *Proceedings International Conference on Mathematics, Computational Methods & Reactor Physics*. La Grange Park, IL: American Nuclear Society (2009). p. 1–11.
13. Vlachoudis V, Sinuela-Pastor D. Numerically robust geometry engine for compound solid geometries. *Proc Int Joint International Conference on Supercomputing in Nuclear Applications and Monte-Carlo 2013 (SNA+MC 2013)*. Les Ulis: EDP Sciences – Web of Conferences (2014). p. 1–6.
14. Uehling EA. Penetration of heavy charged particles in matter. *Annu Rev Nucl Sci* (1954) **4**(1):315–50. doi:10.1146/annurev.ns.04.120154.001531
15. Bethe H, Ashkin J, Segré E. Chapter passage of radiations through matter. In: Segrè E, editor. *Experimental Nuclear Physics, Volume 1*. New York: Wiley (1959). p. 166–357.
16. Committee on Nuclear Science, Subcommittee on Penetration of Charged Particles, National Academy of Sciences. *Studies in Penetration of Charged Particles in Matter (Nuclear Science)*. NAS: Washington, DC (1964).
17. ICRU 49. *Stopping Power and Ranges for Protons and Alpha Particles*. Technical report. Bethesda, MD: ICRU (1993). ICRU Report No 49.
18. Ziegler JF. *The Stopping and Ranges of Ions in Matter: Helium: Stopping Powers and Ranges in All Elemental Matter*. Elmsford, NY: Pergamon Press (1977). 4 p.
19. Ziegler JF, Biersack JP, Littmark U. *The Stopping and Ranges of Ions in Matter*. New York: Pergamon Press (1985). p. 1–5.
20. Ziegler JF. Stopping of energetic light ions in elemental matter. *J Appl Phys* (1999) **85**(3):1249–72. doi:10.1063/1.369844
21. Sternheimer R, Berger M, Seltzer S. Density effect for the ionization loss of charged particles in various substances. *At Data Nucl Data Tables* (1984) **30**(2):261–71. doi:10.1016/0092-640X(84)90002-0
22. NIST. *PSTAR*. (2015). Available from: http://physics.nist.gov/PhysRefData/Star/Text/PSTAR.html
23. Hubert F, Bimbot R, Gauvin H. Semi-empirical formulae for heavy ion stopping powers in solids in the intermediate energy range. *Nucl Instrum Methods Phys Res B* (1989) **36**(4):357–63. doi:10.1016/0168-583X(89)90339-X
24. Barkas WH, Dyer NJ, Heckmann HH. Resolution of the σ^--mass anomaly. *Phys Rev Lett* (1963) **11**(1):26–8. doi:10.1103/PhysRevLett.11.138
25. Bloch F. Zur bremsung rasch bewegter teilchen beim durchgang durch die materie. *Ann Phys* (1933) **16**:285. doi:10.1002/andp.19334080303
26. Ashley JC, Ritchie RH, Brandt W. Effect in the stopping power of matter for charged particles. *Phys Rev B* (1972) **5**(7):2393–7. doi:10.1103/PhysRevB.5.2393
27. Ashley JC, Ritchie RH, Brandt W. Z 1 3-dependent stopping power and range contributions. *Phys Rev A* (1973) **8**(5):2402–8. doi:10.1103/PhysRevA.8.2402

28. Mott NF. The scattering of fast electrons by atomic nuclei. *Proc R Soc A* (1929) **124**:425–42. doi:10.1098/rspa.1929.0127
29. Lijian T, Qing H, Zhengming L. Analytic fitting to the mott cross section of electrons. *Radiat Phys Chem* (1995) **45**(2):235–45. doi:10.1016/0969-806X(94)00063-8
30. Jun I, Kim W, Evans R. Electron nonionizing energy loss for device applications. *IEEE Trans Nucl Sci* (2009) **56**(6):3229–35. doi:10.1109/TNS.2009.2033692
31. NIST. *ASTAR*. (2015). Available from: http://physics.nist.gov/PhysRefData/Star/Text/ASTAR.html
32. Landau L. On the energy loss of fast particles by ionization. *J Phys USSR* (1944) **8**:201.
33. Vavilov PV. Ionization losses of high-energy heavy particles. *Sov Phys JETP* (1957) **5**:749.
34. Ferrari A, Sala P, Fassò A, Ranft J. *New Developments in FLUKA Modelling Hadronic and EM Interactions*. Tsukuba: KEK (1997). p. 32–43.
35. Stuart A, Ord KJ. *Kendall's Advanced Theory of Statistics*. 5th ed. New York: Oxford University Press (1987).
36. Molière G. Theorie der streuung schneller geladener teilchen ii mehrfach-und vielfachstreuung. *Z Naturforsch A* (1948) **3**(2):78–97.
37. Molière G. Theorie der streuung schneller geladener teilchen. iii. die vielfachstreuung von bahn-spuren unter berücksichtigung der statistischen kopplung. *Z Naturforsch A* (1955) **10**:177.
38. Bethe HA. Molière's theory of multiple scattering. *Phys Rev* (1953) **89**:1256 66. doi:10.1103/PhysRev.89.1256
39. Ferrari A, Sala PR, Guaraldi R, Padoani F. An improved multiple scattering model for charged particle transport. *Nucl Instrum Methods Phys Res B* (1992) **71**(4):412–26. doi:10.1016/0168-583X(92)95359-Y
40. Fassò A, Ferrari A, Sala P. Electron-photon transport in FLUKA: status. In: Kling A, Barão F, Nakagawa M, Távora L, Vaz P, editors. *Proc. MonteCarlo 2000 Conference, Lisbon*. Berlin: Springer-Verlag (2001). p. 159–64.
41. Parodi K, Mairani A, Sommerer F. Monte Carlo-based parametrization of the lateral dose spread for clinical treatment planning of scanned proton and carbon ion beams. *J Radiat Res* (2013) **54**(Suppl 1):i91–6. doi:10.1093/jrr/rrt051
42. Fassò A, Ferrari A, Ranft J, Sala P. FLUKA: status and prospective for hadronic applications. In: Kling A, Barão F, Nakagawa M, Távora L, Vaz P, editors. *Proc. MonteCarlo 2000 Conference, Lisbon*. Berlin: Springer-Verlag (2001). p. 159–64.
43. Fassò A, Ferrari A, Ranft J, Sala PR. FLUKA: performances and applications in the intermediate energy range. In: Dragovitsch P, Linn S, Burbank M, editors. *Proc. 1st AEN/NEA Specialists' Meeting on Shielding Aspects of Accelerators, Targets and Irradiation Facilities (SATIF 1)*. Paris: OECD (1995). p. 287–304.
44. Ferrari A, Sala PR. The physics of high energy reactions. In: Gandini A, Reffo G, editors. *Proc Workshop on Nuclear Reaction Data and Nuclear Reactors Physics, Design and Safety*. Miramare-Trieste, Italy: World Scientific (1998). 424 p. Available from: http://www.fluka.org/content/publications/1996_trieste.pdf
45. Battistoni G, Cerutti F, Engel R, Fassò A, Ferrari A, Gadioli E, et al. Recent developments in the FLUKA nuclear reaction models. In: Gadioli E, editor. *Proc. 11th Int. Conf. Nucl. React. Mech*. Milano: Università degli studi di Milano (2006). p. 483–95.
46. Battistoni G, Boehlen T, Cerutti F, Chin PW, Esposito LS, Fassò A, et al. Overview of the FLUKA code. *Ann Nucl Energy* (2015) **82**:10–8. doi:10.1016/j.anucene.2014.11.007 Joint International Conference on Supercomputing in Nuclear Applications and Monte Carlo 2013, SNA + MC 2013. Pluri- and Trans-disciplinarity, Towards New Modeling and Numerical Simulation Paradigms
47. Rinaldi I, Ferrari A, Mairani A, Paganetti H, Parodi K, Sala P. An integral test of FLUKA nuclear models with 160 Mev proton beams in multi-layer Faraday cups. *Phys Med Biol* (2011) **56**(13):4001. doi:10.1088/0031-9155/56/13/016
48. Weisskopf V. Statistics and nuclear reactions. *Phys Rev* (1937) **52**:295. doi:10.1103/PhysRev.52.295
49. Ferrari A, Ranft J, Roesler S, Sala P. Cascade particles, nuclear evaporation, and residual nuclei in high energy hadron-nucleus interactions. *Eur Phys J C Part Fields* (1996) **70**(3):413–26. doi:10.1007/s002880050119
50. Böhlen T, Cerutti F, Chin M, Fassò A, Ferrari A, Ortega P, et al. The FLUKA code: developments and challenges for high energy and medical applications. *Nucl Data Sheets* (2014) **120**:211–4. doi:10.1016/j.nds.2014.07.049
51. Cerutti F, Sala P, Mairani A, Ferrari A. New developments in FLUKA. *Proc. 13th Int. Conf. Nucl. Reac. Mechan*. Varenna, Italy (2012).
52. Roesler S, Engel R, Ranft J. The Monte Carlo event generator DPMJET-III. In: Kling A, Barão F, Nakagawa M, Távora L, Vaz P, editors. *Proc. Monte Carlo 2000 Conference, Lisbon, 2000*. Berlin: Springer-Verlag (2001). p. 1033–8.
53. Ballarini F, Battistoni G, Brugger M, Campanella M, Carboni M, Cerutti F, et al. The physics of the FLUKA code: recent developments. *Adv Space Res* (2007) **40**(9):1339–49. doi:10.1016/j.asr.2007.05.031
54. Sorge H, Stocker H, Greiner W. Relativistic quantum molecular dynamics approach to nuclear collisions at ultrarelativistic energies. *Nucl Phys A* (1989) **498**(3):567–76. doi:10.1016/0375-9474(89)90641-6
55. Sorge H. Flavor production in Pb(160 *A* Gev) on Pb collisions: effect of color ropes and hadronic rescattering. *Phys Rev C* (1995) **52**:3291–314. doi:10.1103/PhysRevC.52.3291
56. Aiginger H, Andersen V, Ballarini F, Battistoni G, Campanella M, Carboni M, et al. The FLUKA code: new developments and application to 1 Gev/n iron beams. *Adv Space Res* (2005) **35**(2):214–22. doi:10.1016/j.asr.2005.01.090 Space Life Sciences: Ground-Based Iron-Ion Biology and Physics, Including Shielding
57. Sato H, Kurosawa T, Iwase H, Nakamura T, Uwamino Y, Nakao N. Measurements of double differential neutron production cross sections by 135 Mev/nucleon He, C, Ne and 95 Mev/nucleon Ar ions. *Phys Rev C* (2001) **64**:034607. doi:10.1103/PhysRevC.64.034607
58. Cavinato M, Fabrici E, Gadioli E, Erba EG, Risi E. Boltzmann master equation theory of angular distributions in heavy-ion reactions. *Nucl Phys A* (1998) **643**(1):15–29. doi:10.1016/S0375-9474(98)00545-4
59. Cerutti F, Battistoni G, Capezzali G, Colleoni P, Ferrari A, Gadioli E, et al. Low energy nucleus-nucleus reactions: the BME approach and its interface with FLUKA. *Proc. 11th Int. Conf. Nuclear Reaction Mechanisms*. Varenna, Italy (2006).
60. Kurosawa T, Nakao N, Nakamura T, Uwamino Y, Shibata T, Nakanishi N, et al. Measurements of secondary neutrons produced from thick targets bombarded by high-energy helium and carbon ions. *Nucl Sci Eng* (1999) **132**:30–57.
61. Parodi K, Mairani A, Brons S, Hasch BG, Sommerer F, Naumann J, et al. Monte Carlo simulations to support start-up and treatment planning of scanned proton and carbon ion therapy at a synchrotron-based facility. *Phys Med Biol* (2012) **57**(12):3759. doi:10.1088/0031-9155/57/12/3759
62. Mirandola A, Molinelli S, Freixas GV, Mairani A, Gallio E, Panizza D, et al. Dosimetric commissioning and quality assurance of scanned ion beams at the Italian National Center for Oncological Hadrontherapy. *Med Phys* (2015) **42**(9):5287. doi:10.1118/1.4928397
63. Schwaab J, Brons S, Fieres J, Parodi K. Experimental characterization of lateral profiles of scanned proton and carbon ion pencil beams for improved beam models in ion therapy treatment planning. *Phys Med Biol* (2011) **56**(24):7813. doi:10.1088/0031-9155/56/24/009
64. Haberer T, Becher W, Schardt D, Kraft G. Magnetic scanning system for heavy ion therapy. *Nucl Instrum Methods Phys Res A* (1993) **330**:296–305. doi:10.1016/0168-9002(93)91335-K
65. Molinelli S, Mairani A, Mirandola A, Freixas GV, Tessonnier T, Giordanengo S, et al. Dosimetric accuracy assessment of a treatment plan verification system for scanned proton beam radiotherapy: one-year experimental results and Monte Carlo analysis of the involved uncertainties. *Phys Med Biol* (2013) **58**(11):3837. doi:10.1088/0031-9155/58/11/3837
66. Bauer J, Sommerer F, Mairani A, Unholtz D, Farook R, Handrack J, et al. Integration and evaluation of automated Monte Carlo simulations in the clinical practice of scanned proton and carbon ion beam therapy. *Phys Med Biol* (2014) **59**(16):4635. doi:10.1088/0031-9155/59/16/4635
67. RaySearch Laboratories. *Raystation Carbon Ion Planning*. (2015). Available from: http://www.raysearchlabs.com
68. Kurz C, Mairani A, Parodi K. First experimental-based characterization of oxygen ion beam depth dose distributions at the Heidelberg Ion-Beam Therapy Center. *Phys Med Biol* (2012) **57**(15):5017. doi:10.1088/0031-9155/57/15/5017

69. Tessonnier T, Marcelos T, Mairani A, Brons S, Parodi K. Phase space generation for proton and carbon ion beams for external users' applications at the Heidelberg Ion Therapy Center. *Front Oncol* (2016) **5**:297. doi:10.3389/fonc.2015.00297
70. ICRU. ICRU Report 78. Prescribing, recording, and reporting proton-beam therapy. *J ICRU* (2007) **7**(2). doi:10.1093/jicru/ndm021
71. Biaggi M, Ballarini F, Burkard W, Egger E, Ferrari A, Ottolenghi A. Physical and biophysical characteristics of a fully modulated 72 MeV therapeutic proton beam: model predictions and experimental data. *Nucl Instrum Methods Phys Res B* (1999) **159**(1):89–100. doi:10.1016/S0168-583X(99)00551-0
72. Biaggi M, Ballarini F, Ferrari A, Ottolenghi A, Pelliccioni M. A Monte-Carlo code for a direct estimation of radiation risk. *Phys Med* (2001) **17**(Suppl 1):103–5.
73. Ballarini F, Biaggi M, Edwards A, Ferrari A, Ottolenghi A, Pelliccioni M, et al. Estimating mixed field effects: an application supporting the lack of a non-linear component for chromosome aberration induction by neutrons. *Radiat Prot Dosimetry* (2003) **103**(1):19–27. doi:10.1093/oxfordjournals.rpd.a006109
74. Zaider M, Rossi HH. The synergistic effects of different radiations. *Radiat Res* (1980) **83**:732–9. doi:10.2307/3575352
75. Scholz M, Kellerer AM, Kraft-Weyrather W, Kraft G. Computation of cell survival in heavy ion beams for therapy – the model and its approximation. *Radiat Environ Biophys* (1997) **36**:59–66. doi:10.1007/s004110050055
76. Joiner MC, van der Kogel A. *Basic Clinical Radiobiology Fourth Edition*. Boca Raton, FL: CRC Press (2009).
77. Fiedler F, Shakirin G, Skowron J, Braess H, Crespo P, Kunath D, et al. On the effectiveness of ion range determination from in-beam PET data. *Phys Med Biol* (2010) **55**(7):1989–98. doi:10.1088/0031-9155/55/7/013
78. Bauer J, Unholtz D, Sommerer F, Kurz C, Haberer T, Herfarth K, et al. Implementation and initial clinical experience of offline PET/CT-based verification of scanned carbon ion treatment. *Radiother Oncol* (2013) **107**(2):218–26. doi:10.1016/j.radonc.2013.02.018
79. Knopf A-C, Parodi K, Paganetti H, Bortfeld T, Daartz J, Engelsman M, et al. Accuracy of proton beam range verification using post-treatment positron emission tomography/computed tomography as function of treatment site. *Int J Radiat Oncol Biol Phys* (2011) **79**(1):297–304. doi:10.1016/j.ijrobp.2010.02.017
80. Zhu X, España S, Daartz J, Liebsch N, Ouyang J, Paganetti H, et al. Monitoring proton radiation therapy with in-room PET imaging. *Phys Med Biol* (2011) **56**(13):4041. doi:10.1088/0031-9155/56/13/019
81. Nischwitz SP, Bauer J, Welzel T, Rief H, Jäkel O, Haberer T, et al. Clinical implementation and range evaluation of in vivo PET dosimetry for particle irradiation in patients with primary glioma. *Radiother Oncol* (2015) **115**(2):179–85. doi:10.1016/j.radonc.2015.03.022
82. Moteabbed M, España S, Paganetti H. Monte Carlo patient study on the comparison of prompt gamma and PET imaging for range verification in proton therapy. *Phys Med Biol* (2011) **56**(4):1063–82. doi:10.1088/0031-9155/56/4/012
83. Richard MH, Chevallier M, Dauvergne D, Freud N, Henriquet P, Le Foulher F, et al. Design guidelines for a double scattering Compton camera for prompt-gamma imaging during ion beam therapy: a Monte Carlo simulation study. *IEEE Trans Nucl Sci* (2011) **58**(1):87–94. doi:10.1109/TNS.2010.2076303
84. Seo H, Park JH, Ushakov A, Kim CH, Kim JK, Lee JH, et al. Experimental performance of double-scattering Compton camera with anthropomorphic phantom. *J Instrum* (2011) **6**:C01024. doi:10.1088/1748-0221/6/01/C01024
85. Peterson SW, Robertson D, Polf J. Optimizing a three-stage Compton camera for measuring prompt gamma rays emitted during proton radiotherapy. *Phys Med Biol* (2010) **55**(22):6841–56. doi:10.1088/0031-9155/55/22/015
86. Kim D, Yim H, Kim JW. Pinhole camera measurements of prompt gamma-rays for detection of beam range variation in proton therapy. *J Korean Phys Soc* (2009) **55**(4):1673–6. doi:10.3938/jkps.55.1673
87. Min CH, Park JG, Kim CH. Preliminary study for determination of distal dose edge by measuring 90-deg prompt gammas with an array-type prompt gamma detection system. *Nucl Technol* (2009) **168**(1):89–92.
88. Min CH, Park JG, An SH, Kim CH. Determination of optimal energy window for measurement of prompt gammas from proton beam by Monte Carlo simulations. *J Nucl Sci Technol* (2008) **45**(Suppl 5):28–31. doi:10.1080/00223131.2008.10875777
89. Kang BH, Kim JW. Simulation study on a prompt gamma detection system for use in proton therapy. *J Korean Phys Soc* (2008) **52**(3, Pt 1, SI):810–3. doi:10.3938/jkps.52.810
90. Kang B-H, Kim J-W. Monte Carlo design study of a gamma detector system to locate distal dose falloff in proton therapy. *IEEE Trans Nucl Sci* (2009) **56**(1):46–50. doi:10.1109/TNS.2008.2005189
91. Biegun AK, Seravalli E, Lopes PC, Rinaldi I, Pinto M, Oxley DC, et al. Time-of-flight neutron rejection to improve prompt gamma imaging for proton range verification: a simulation study. *Phys Med Biol* (2012) **57**(20):6429. doi:10.1088/0031-9155/57/20/6429
92. Min CH, Lee HR, Yeom YS, Cho S, Kim CH. Determination of the distal dose edge in a human phantom by measuring the prompt gamma distribution: a Monte Carlo study. *J Korean Phys Soc* (2010) **56**(6, Pt 1, SI):2059–62. doi:10.3938/jkps.56.2059
93. Min CH, Lee HR, Kim CH. Two-dimensional prompt gamma measurement simulation for in vivo dose verification in proton therapy: a Monte Carlo study. *Nucl Technol* (2011) **175**(1, SI):11–5.
94. Kim JW, Kim D. Development of dosimetry tools for proton therapy research. *Radiat Meas* (2010) **45**(10, SI):1417–21. doi:10.1016/j.radmeas.2010.05.031
95. Le Foulher F, Bajard M, Chevallier M, Dauvergne D, Freud N, Henriquet P, et al. Monte Carlo simulations of prompt-gamma emission during carbon ion irradiation. *IEEE Trans Nucl Sci* (2010) **57**(5, Pt 2):2768–72. doi:10.1109/TNS.2010.2048042
96. Paganetti H, Jiang H, Parodi K, Slopsema R, Engelsman M. Clinical implementation of full Monte Carlo dose calculation in proton beam therapy. *Phys Med Biol* (2008) **53**:4825–53. doi:10.1088/0031-9155/53/17/023
97. Verburg JM, Shih HA, Seco J. Simulation of prompt gamma-ray emission during proton radiotherapy. *Phys Med Biol* (2012) **57**(17):5459. doi:10.1088/0031-9155/57/17/5459
98. Robert C, Dedes G, Battistoni G, Böhlen TT, Buvat I, Cerutti F, et al. Distributions of secondary particles in proton and carbon-ion therapy: a comparison between GATE/Geant4 and FLUKA Monte Carlo codes. *Phys Med Biol* (2013) **58**:2879. doi:10.1088/0031-9155/58/9/2879
99. *European Novel Imaging Systems for Ion Therapy (Funded under 7th FWP) (Seventh Framework Programme)*. (2010). Available from: http://envision.web.cern.ch/envision/
100. Seravalli E, Robert C, Bauer J, Stichelbaut F, Kurz C, Smeets J, et al. Monte Carlo calculations of positron emitter yields in proton radiotherapy. *Phys Med Biol* (2012) **57**(6):1659. doi:10.1088/0031-9155/57/6/1659
101. IAEA. *Exfor Library*. (2014). Available from: https://www-nds.iaea.org/exfor/exfor.htm
102. Rosso V, Battistoni G, Belcari N, Camarlinghi N, Ferrari A, Ferretti S, et al. A new PET prototype for proton therapy: comparison of data and Monte Carlo simulations. *J Instrum* (2013) **8**(03):C03021. doi:10.1088/1748-0221/8/03/C03021
103. Sommerer F. *Experiments and FLUKA Simulations of C12 and O16 Beams for Therapy Monitoring by Means of In-Beam Positron Emission Tomography*. Ph.D. thesis, Vienna University of Technology, Vienna (2007).
104. Mougey J. Experiments with 1.03 GeV ^{12}C ions. *Nucl Phys A* (1982) **387**(1):109–27. doi:10.1016/0375-9474(82)90195-6
105. Ryde H, Collaboration B-C-C-G-L-S. The physics of heavy ion collisions at 100 MeV per nucleon. *Phys Scr* (1983) **1983**(T5):114.
106. Mougey J, Ost R, Buenerd M, Cole A, Guet C, Lebrun D, et al. Projectile fragments from 86 MeV/nucleon ^{12}C induced reactions. *Phys Lett B* (1981) **105**(1):25–9. doi:10.1016/0370-2693(81)90032-0
107. Böhlen TT, Ferrari A, Patera V, Sala PR. Describing Compton scattering and two-quanta positron annihilation based on Compton profiles: two models suited for the Monte Carlo method. *J Instrum* (2012) **7**(07):07018. doi:10.1088/1748-0221/7/07/P07018
108. Capote R, Herman M, Obložinský P, Young P, Goriely S, Belgya T, et al. RIPL reference input parameter library for calculation of nuclear reactions and nuclear data evaluations. *Nucl Data Sheets* (2009) **110**(12):3107–214. doi:10.1016/j.nds.2009.10.004 Special Issue on Nuclear Reaction Data
109. Tolhoek H, Cox J. Angular distribution and polarization of gamma radiation emitted by oriented nuclei. *Physica* (1953) **19**:101–19. doi:10.1016/S0031-8914(53)80010-8

110. Ferrari A, Ranft J, Roesler S, Sala PR. The production of residual nuclei in peripheral high energy nucleus-nucleus interactions. *Z Phys C* (1996) **71**:75.
111. Kozlovsky B, Murphy RJ, Ramaty R. Nuclear deexcitation gamma-ray lines from accelerated particle interactions. *Astrophys J Suppl Ser* (2002) **141**(2):523. doi:10.1086/340545
112. Smeets J, Roellinghoff F, Prieels D, Stichelbaut F, Benilov A, Busca P, et al. Prompt gamma imaging with a slit camera for real-time range control in proton therapy. *Phys Med Biol* (2012) **57**(11):3371. doi:10.1088/0031-9155/57/11/3371
113. ENVISION. *WP3: Compilation of γ-ray Yield Data, Estimation of Radiation Background Influencing Prompt Photon Imaging*. WP3 Report n.1. Technical report, Geneva: The ENVISION Consortium, CERN (2012).
114. Testa E. Personal Communication, Data Shared on the ENVISION Internal Website. (2012).
115. Vasilis Vlachoudis. *Flair*. (2014). Available from: http://www.fluka.org/flair
116. NEMA Organization. *Digital Imaging and Communications in Medicine (DICOM) Standard*. (2014). Available from: http://dicom.nema.org
117. Mason D. SU-E-T-33: pydicom: an open source DICOM library. *Med Phys* (2011) **38**(6):3493–3493. doi:10.1118/1.3611983
118. van der Walt S, Colbert S, Varoquaux G. The NumPy array: a structure for efficient numerical computation. *Comput Sci Eng* (2011) **13**(2):22–30. doi:10.1109/MCSE.2011.37
119. Parodi K, Ferrari A, Sommerer F, Paganetti H. Clinical ct-based calculations of dose and positron emitter distributions in proton therapy using the fluka Monte Carlo code. *Phys Med Biol* (2007) **52**(12):3369. doi:10.1088/0031-9155/52/12/004
120. Parodi K, Paganetti H, Cascio E, Flanz JB, Bonab AA, Alpert NM, et al. PET CT imaging for treatment verification after proton therapy: a study with plastic phantoms and metallic implants. *Med Phys* (2007) **34**(2):419–35. doi:10.1118/1.2401042
121. Shakirin G, Braess H, Fiedler F, Kunath D, Laube K, Parodi K, et al. Implementation and workflow for pet monitoring of therapeutic ion irradiation: a comparison of in-beam, in-room, and off-line techniques. *Phys Med Biol* (2011) **56**(5):1281. doi:10.1088/0031-9155/56/5/004
122. Stout D, Chow P, Silverman R, Leahy RM, Lewis X, Gambhir S, et al. Creating a whole body digital mouse atlas with PET, CT and cryosection images. *Mol Imaging Biol* (2002) **4**(4):S27.
123. Dogdas B, Stout D, Chatziioannou AF, Leahy RM. Digimouse: a 3D whole body mouse atlas from CT and cryosection data. *Phys Med Biol* (2007) **52**(3):577. doi:10.1088/0031-9155/52/3/003
124. Brix G, Zaers J, Adam LE, Bellemann ME, Ostertag H, Trojan H, et al. Performance evaluation of a whole-body PET scanner using the nema protocol. *J Nucl Med* (1997) **38**(10):1614–23.
125. Wienhard K, Schmand M, Casey M, Baker K, Bao J, Eriksson L, et al. The ECAT HRRT: performance and first clinical application of the new high resolution research tomograph. *IEEE Trans Nucl Sci* (2002) **49**(1):104–10. doi:10.1109/TNS.2002.998689
126. Brambilla M, Secco C, Dominietto M, Matheoud R, Sacchetti G, Inglese E. Performance characteristics obtained for a new 3–dimensional lutetium oxyorthosilicatebased whole-body PET/CT scanner with the National Electrical Manufacturers Association NU 2–2001 standard. *J Nucl Med* (2005) **46**(12):2083–91.
127. Talguen V, Turzo A, Bizais Y, Visvikis D. Evaluation of attenuation correction methodology in the allegro PET system. *IEEE Trans Nucl Sci* (2004) **51**(5):2688–92. doi:10.1109/TNS.2004.835741
128. Lewellen T, Kohlmyer S, Miyaoka R, Schubert S, Stearns C. Investigation of the count rate performance of the general electric advance positron emission tomograph. *Nuclear Science Symposium and Medical Imaging Conference, 1994., 1994 IEEE Conference Record*. (Vol. **3**) Piscataway, NJ: IEEE (1994). p. 1169–73.
129. Tai YC, Chatziioannou A, Siegel S, Young J, Newport D, Goble RN, et al. Performance evaluation of the microPET P4: a PET system dedicated to animal imaging. *Phys Med Biol* (2001) **46**:1845–62. doi:10.1088/0031-9155/46/7/308
130. Lehnert W, Meikle S, Newport D. Count rate performance of the MicroPET focus 220 animal scanner in singles transmission scanning mode. *IEEE Trans Nucl Sci* (2008) **55**(5):2493–500. doi:10.1109/TNS.2008.2000888
131. Huisman MC, Reder S, Weber AW, Ziegler SI, Schwaiger M. Performance evaluation of the Philips MOSAIC small animal PET scanner. *Eur J Nucl Med Mol Imaging* (2007) **34**(4):532–40. doi:10.1007/s00259-006-0271-7
132. Todd-Pokropek A, Cradduck TD, Deconinck FD. A file format for the exchange of nuclear medicine image data: a specification of interfile version 3.3. *Nucl Med Commun* (1992) **13**(9):673–99. doi:10.1097/00006231-199209000-00007
133. Fahey FH. Data acquisition in pet imaging. *J Nucl Med Technol* (2002) **30**(2):39–49.
134. Tessonnier T, Mairani A, Cappucci F, Mirandola A, Vilches Freixas G, Molinelli S, et al. Development and application of tools for Monte Carlo based simulations in a particle beam radiotherapy facility. *Appl Radiat Isot* (2012) **83**:155–8. doi:10.1016/j.apradiso.2012.12.019
135. Unholtz D, Sommerer F, Bauer J, van Straaten D, Haberer T, Debus J, et al. Post-therapeutical β^+-activity measurements in comparison to simulations towards in-vivo verification of ion beam therapy. *Conference Record of the IEEE Nuclear Science Symposium and Medical Imaging Conference in Valencia*. Spain (2011).
136. Kramer M, Scholz M. Rapid calculation of biological effects in ion radiotherapy. *Phys Med Biol* (2006) **51**:1959–70. doi:10.1088/0031-9155/51/8/001

Conflict of Interest Statement: The authors declare that the research was conducted in the absence of any commercial or financial relationships that could be construed as a potential conflict of interest.

The reviewer FB declared a shared affiliation, though no other collaboration, with the authors GB and PS to the handling Editor, who ensured that the process nevertheless met the standards of a fair and objective review.

Copyright © 2016 Battistoni, Bauer, Boehlen, Cerutti, Chin, Dos Santos Augusto, Ferrari, Ortega, Kozłowska, Magro, Mairani, Parodi, Sala, Schoofs, Tessonnier and Vlachoudis. This is an open-access article distributed under the terms of the Creative Commons Attribution License (CC BY). The use, distribution or reproduction in other forums is permitted, provided the original author(s) or licensor are credited and that the original publication in this journal is cited, in accordance with accepted academic practice. No use, distribution or reproduction is permitted which does not comply with these terms.

frontiers in Oncology

ORIGINAL RESEARCH
published: 07 December 2015
doi: 10.3389/fonc.2015.00270

Comparative Characterization Study of a $LaBr_3$(Ce) Scintillation Crystal in Two Surface Wrapping Scenarios: Absorptive and Reflective

Saad Aldawood[1,2], Ines Castelhano[1,3], Roman Gernhäuser[4], Hugh Van Der Kolff[1,5], Christian Lang[1], Silvia Liprandi[1], Rudolf Lutter[1], Ludwig Maier[4], Tim Marinšek[1], Dennis R. Schaart[5], Katia Parodi[1] and Peter G. Thirolf[1]*

[1] Faculty of Physics, Ludwig-Maximilians-University Munich, Munich, Germany, [2] Department of Physics and Astronomy, King Saud University, Riyadh, Saudi Arabia, [3] Faculty of Science, University of Lisbon, Lisbon, Portugal, [4] Physik Department E12, Technical University Munich, Garching, Germany, [5] Faculty of Applied Science, Radiation Science and Technology, Delft University of Technology, Delft, Netherlands

OPEN ACCESS

Edited by:
Marco Durante,
GSI, Germany

Reviewed by:
Yidong Yang,
University of Miami Miller School of Medicine, USA
Bilgin Kadri Aribas,
A. Y. Ankara Oncology Education and Research Hospital, Turkey

***Correspondence:**
Saad Aldawood
s.aldawood@physik.uni-muenchen.de

Specialty section:
This article was submitted to Radiation Oncology, a section of the journal Frontiers in Oncology

Received: 22 September 2015
Accepted: 19 November 2015
Published: 07 December 2015

Citation:
Aldawood S, Castelhano I, Gernhäuser R, Van Der Kolff H, Lang C, Liprandi S, Lutter R, Maier L, Marinšek T, Schaart DR, Parodi K and Thirolf PG (2015) Comparative Characterization Study of a $LaBr_3$(Ce) Scintillation Crystal in Two Surface Wrapping Scenarios: Absorptive and Reflective. Front. Oncol. 5:270. doi: 10.3389/fonc.2015.00270

The properties of a 50 mm × 50 mm × 30 mm monolithic $LaBr_3$:Ce scintillator crystal coupled to a position-sensitive multi-anode photomultiplier (PMT, Hamamatsu H9500), representing the absorbing detector of a Compton camera under study for online ion (proton) beam range verification in hadron therapy, was evaluated in combination with either absorptive or reflective crystal surface coating. This study covered an assessment of the energy and position-dependent energy resolution, exhibiting a factor of 2.5–3.5 improvement for the reflectively wrapped crystal at 662 keV. The spatial dependency was investigated using a collimated ^{137}Cs source, showing a steep degradation of the energy resolution at the edges and corners of the absorptively wrapped crystal. Furthermore, the time resolution was determined to be 273 ps (FWHM) and 536 ps (FWHM) with reflective and absorptive coating, respectively, using a ^{60}Co source. In contrast, the light spread function (LSF) of the light amplitude distribution on the PMT segments improved for the absorptively wrapped detector. Both wrapping modalities showed almost no differences in the energy-dependent photopeak detection efficiency.

Keywords: $LaBr_3$:Ce scintillator, γ spectroscopy, medical imaging, crystal surface coating, Compton camera

1. INTRODUCTION

Particle therapy has opened a new horizon particularly for the treatment of tumors in the vicinity of critical organs at risk, due to the sharp dose localization in the Bragg peak. However, in order to fully exploit the beneficial properties of the well localized dose deposition in the tumor volume, a precise monitoring of the ion beam range is mandatory. For this purpose, an online monitoring system based on a Compton camera designed to detect prompt (multi-MeV) γ rays, induced by nuclear reactions between the ion beam and biological tissue, is being developed at LMU Munich (7, 19). This camera is composed of six customized double-sided Si-strip detectors (DSSSD), with an active area of a 50 mm × 50 mm, a thickness of 500 μm and segmentation of 128 strips on each side, acting as scatterer (tracker), while the absorber detector is formed by 50 mm × 50 mm× 30 mm monolithic $LaBr_3$:Ce scintillator. Besides the ability of detecting the scattered photon, this camera is also able to track the Compton electron (from multi-MeV prompt photons), due to the layered structure of the

scatterer detectors. This feature does not only contribute to increase the reconstruction efficiency of the camera (enabling the reconstruction of incompletely absorbed photon events), but it also enhances the sensitivity to the source position of an incident photon from a Compton cone to an arc segment (5, 19).

The favorable properties of the $LaBr_3$:Ce scintillator material make it the preferable detector in particular for our application in medical imaging. It has a very high light yield [61000 photons/MeV (21)] with a minor non-linearity of 6% between 60 and 1275 keV (4, 17). The material density [5.06 g/cm^3 (4)] and effective atomic number [$Z_{eff} = 46.9$ (10)], result in a high stopping efficiency. Moreover, this detector provides an excellent energy resolution from low photon energies [~3% at 662 keV (21)] up to high energies, thus keeping the ability to resolve the full energy peak from escape peaks over a wide energy range up to about 25 MeV (3). The superior timing properties of $LaBr_3$:Ce, due to the fast decay time of 16 ns (1) are reflected in typical time resolutions of a few hundred picoseconds (depending on the crystal dimensions). This facilitates the use of the time-of-flight (TOF) technique, e.g., to suppress neutron background or to improve the image quality as it has been reported in positron emission tomography (PET) (6, 16).

This work aims to characterize a 50 mm × 50 mm × 30 mm monolithic $LaBr_3$:5%Ce (15) scintillator crystal, wrapped with either absorptive or (after modification by the manufacturer) reflective layer, in order to determine the optimum performance of a detector configuration to be used as an absorbing detector in a Compton camera which is presently under development for proton (ion) beam range monitoring.

2. MATERIALS AND METHODS

The monolithic $LaBr_3$:Ce scintillator (50 mm × 50 mm × 30 mm) is read out by a position-sensitive (16 × 16) multi-anode photomultiplier (PMT, Hamamatsu H9500), with 256 segments of 3 mm × 3 mm each and a coupling window of 1.5 mm thickness. The crystal was encapsulated together with the PMT in an aluminum housing, which has an entrance window of 0.5 mm thickness. The light guide (specification details are unpublished) is optically coupled between the crystal and the PMT by the manufacturer. The operational voltage of this PMT was set to be −1100 V. In order to reduce the complexity of the signal processing electronics, 4 neighboring segments with an area of 6 mm × 6 mm were combined to form 64 output channels. The detector properties, such as energy resolution, photopeak detection efficiency, time resolution, and light spread function (LSF), were evaluated.

The energy resolution was studied as a function of the γ ray energy using ^{152}Eu (110 kBq), ^{60}Co (32 kBq), and ^{137}Cs (163 kBq) calibration sources, placed in an axial distance of 25 cm of the detector surface. The data was fitted using a two-parameter function expressed as

$$\frac{\Delta E}{E} = 100 \times \frac{\sqrt{A + B \times E}}{E} \tag{1}$$

where A and B are free parameters (14). In addition, the position-dependent energy resolution was investigated by scanning the detector with a 1 mm collimated ^{137}Cs source of 86 MBq activity and a 2 dimensional step size of 6 mm, forming 8 × 8 irradiation positions with the pencil γ ray beam pointing to the center of the respect PMT pixel group and 5 min measurement time at each position. At each irradiation position, the relative energy resolution $\frac{\triangle E}{E}$ was determined, thus generating an energy resolution map for the detector crystal with reflective and absorptive side coating, respectively. In both measurements, the evaluation of the energy resolution was based on the sum dynode signal of the PMT (Hamamatsu H9500). This signal was fed to an amplifier and Constant Fraction Discriminator (CFD) module (Mesytec, MCFD-16) and then to a VME-based Charge-to-Digital Convertor (Mesytec, MQDC-32) to enable digitized list-mode data acquisition and subsequent spectra analysis.

The photopeak detection efficiency of the $LaBr_3$:Ce detector was evaluated using the known activities of the calibration sources. This required measuring the ratio of photons detected in the photopeak to the number of initially emitted γ rays for the specific transitions. In this case, a ^{152}Eu source of 110 kBq activity was used in order to cover a wide range of photon energies between 121 and 1408 keV. The energy spectrum was derived from the sum dynode of the PMT. The data was corrected by background subtraction. Dead time and solid angle corrections were applied.

The timing performance of the $LaBr_3$:Ce scintillator was investigated relative to a fast reference plastic detector (BC-418) using a coincidence method. First, the time resolution of the reference detector was determined by measuring the coincidence time between two simultaneously emitted γ rays from a ^{60}Co source, using two identical plastic detectors (BC-418) coupled to fast PMTs (photonis XP2020/Q). The two signals of these detectors were fed to an amplifier plus CFD module (Mesytec, MCFD-16) and subsequently to a Time-to-Digital Converter (TDC, C.A.E.N. Mod. V775). Then, the time resolution of one reference detector $\Delta T_{plast.1}$ was extracted according to

$$\Delta T_{plast.1} = \sqrt{\frac{(\triangle t_{plast.1+2})^2}{2}} \tag{2}$$

where the $\Delta T_{plast.1+2}$ is the total time resolution measured by the two identical reference detectors.

Subsequently, one of the reference detectors was replaced by the $LaBr_3$:Ce detector in order to measure the coincidence time resolution of this system. Knowing the time resolution of the reference detector and the combined time resolution (ΔT_{tot}) of plastic and $LaBr_3$:Ce scintillator, the time resolution of the $LaBr_3$:Ce detector can be obtained as

$$\Delta T_{LaBr_3} = \sqrt{(\Delta T_{tot})^2 - (\Delta T_{plast.1})^2} \tag{3}$$

Finally, the spatial resolution properties of the $LaBr_3$:Ce scintillator was evaluated by the Light Spread Function (LSF), defined as the FWHM of the radial projection of the light distribution of the multi-anode PMT pixels. In order to extract the relevant light

amplitude distributions correlated to the incident γ rays, some correction steps have to be applied consecutively:

- Gain matching: Since each channel of the 64 PMT output signals was processed by individual spectroscopic electronics, potential gain variations between channels have to be corrected. Therefore, two pulser signals with different amplitudes (50 and 100 mV) were injected to each amplifier channel in order to match the relative amplification gains of all channels.
- QDC pedestal: The charge-to-digital converter (QDC) continuously produces low-amplitude signals originating from the dark current. The intensity and energetic position of this signal varies from channel to channel. Thus, digitized data was acquired without input signal to the QDC in order to define (after applying a Gaussian fit to the pedestal peaks) a fixed pedestal subtraction threshold that was determined as 3 σ above the pedestal peak centroid.
- PMT uniformity: In order to allow for a correction of the gain variations between the 256 pixels of the multi-anode PMT (H9500), a gain non-uniformity matrix is provided by the PMT manufacturer (Hamamatsu). Since each 4 neighboring pixels of the PMT were electronically summed in this study, the corresponding gain values of the non-uniformity matrix were averaged to derive new correction factors for the 64 output channels. These relative correction factors range from 1.0 to 1.8.
- Crystal light distribution uniformity: Scattering or reflections of the scintillation light mainly in the corner or edge regions of the crystal could lead to an inhomogeneous spatial response of the crystal to impinging radiation. This can be corrected by registering the light amplitude distribution, resulting from a homogeneous flood source covering the crystal front surface, allowing to derive a correction map. Fortunately, the $LaBr_3$:Ce crystal offers an elegant alternative. Since the internal radioactivity of the $LaBr_3$:Ce detector (here 140 Bq, exhibiting besides distinct transitions from ^{138}La and ^{227}Ac (11, 18) a continuum ranging up to about 2.6 MeV) can be assumed to be homogeneously distributed inside the crystal with isotropic emission of the corresponding γ rays. The photon energy region of this background radiation equivalent to the impinging γ rays (in this case 662 keV from a ^{137}Cs source) was used to determine the position-dependent correction matrix. This takes into account the energy dependence of the scatter/reflection processes near corners and edges of the crystal, affecting the light collection behavior.

After applying the above corrections, an 8×8 grid scan of the $LaBr_3$:Ce detector using a 1-mm collimated ^{137}Cs (86 MBq) source was performed to visualize the correlated movement of the source position. Then, one of the four central irradiation position measurements from this grid scan was selected to derive the LSF by performing a radial projection of the light amplitude distribution of the PMT pixels.

3. RESULTS AND DISCUSSION

3.1. Energy Resolution

Figure 1 displays the energy resolution for photon energies from 121 to 1332 keV, as determined for the reflectively and absorptively coated $LaBr_3$:Ce crystal, respectively. The dotted curves parameterize the energy dependence of the relative energy resolution according to the two-parameter function indicated in Equation (1). The relative energy resolution $\frac{\Delta E}{E}$ was found to be 12.5 and 3.5% at 662 keV for the absorptively and reflectively wrapped crystal, respectively. Throughout the energy range, the reflectively wrapped crystal exhibited a significantly improved energy resolution. In general, the energy resolution $\Delta E/E$ of a scintillation detector read out by a photomultiplier can be expressed as

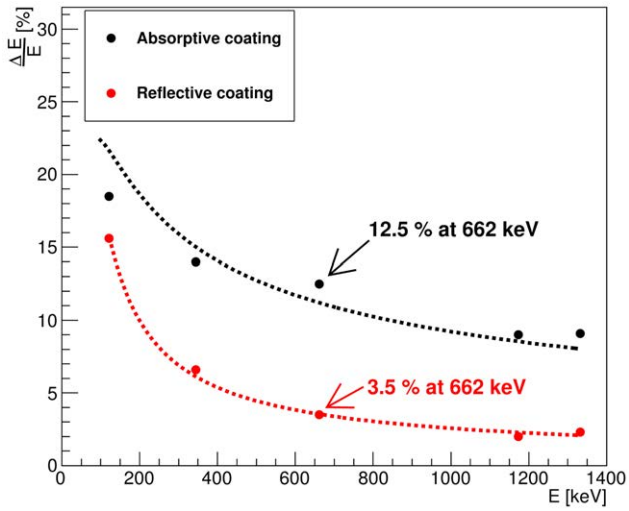

FIGURE 1 | Energy resolution as a function of the photon energy values measured by a $LaBr_3$:Ce detector with reflective (red) and absorptive (black) side surface coating obtained with ^{152}Eu, ^{137}Cs, and ^{60}Co calibration sources. The dotted lines represent a two-parameter function fit as indicated in Equation (1).

$$\left(\frac{\Delta E}{E}\right)^2 = \delta_{intr}^2 + \delta_{tran}^2 + \delta_{st}^2 \quad (4)$$

where δ_{intr} is the intrinsic detector resolution affected, e.g., by crystal inhomogeneities, δ_{tran} is the transfer resolution that is correlated to the optical coupling properties of the crystal to the PMT readout, including the photocathode quantum efficiency as well as the focusing of photoelectrons to the first dynode, and δ_{st} is the statistical contribution of the PMT (12). The last two factors will determine the statistical uncertainty of the PMT, as it is directly affected by the number of photoelectrons generated at the photocathode and the photoelectron collection efficiency at the first dynode (13).

Since the same crystal and optical coupling were used with reflective and absorptive crystal wrapping, the intrinsic term can safely be expected to give the same contributions to the overall energy resolution in both scenarios. As the generated scintillation light is partially absorbed by the absorbing wrapping material and consequently the number of the photoelectrons that reach the PMT is drastically reduced, the statistical term δ_{st} should contribute to the degradation of the energy resolution in the absorptively coated crystal, since δ_{st} is inversely proportional to

the square root of the number of photoelectrons.

$$\delta_{st} = 2.35\sqrt{\frac{1+\nu_M}{N_{phe}}} \quad (5)$$

where ν_M is the variance of the PMT gain, typically between 0.1 and 0.2, and N_{phe} is the number of photoelectrons (12). The transfer term δ_{tran} is also expected to contribute to the energy resolution deterioration in the absorptively wrapped crystal, since in this crystal the collection of the scintillation light at the photocathode strongly depends on the interaction position at which the scintillation light is generated. This can be noticed throughout the study of the spatial dependence of the energy resolution using the 1 mm collimated ^{137}Cs source. Moreover, even for a given position of interaction, the probability for a scintillation photon to arrive at the photocathode will depend much more strongly on the initial angle of emission than in the reflectively wrapped crystal. **Figure 2** shows the resulting 2D energy resolution map of the absorptively wrapped $LaBr_3$:Ce crystal at 662 keV. The energy resolution is gradually degrading from 8% in the central region to about 10 and 16% at the detector's edges and corners, respectively. This can be attributed to the reduction of scintillation light reaching the PMT (thus reducing the number of photoelectrons) due to the absorption of scattered and reflected photons hitting the absorptively coated side surfaces of the scintillation crystal. This effect is much stronger for scintillation photons generated in the edge or corner regions compared to the central region of the crystal. In contrast, this effect disappears with the reflective coating of the $LaBr_3$:Ce crystal as indicated in **Figure 3**. The corresponding 2D energy resolution is only slightly varying with the irradiation position, as can be seen from the respective x and y projections (averaged over the complementary dimension). An averaged relative energy resolution $\frac{\Delta E}{E} = 3.8 \pm 0.04\%$ is achieved in this scenario. The drastic improvement by about a factor of 2.5–3.5 compared to the absorptive coating clearly emphasizes the need to preserve the full amount of scintillation light (and thus photoelectrons N_{phe}) via the reflective wrapping of the crystal, thus, reducing the statistical fluctuations in of N_{phe} at each irradiation position.

3.2. Photopeak Efficiency

The $LaBr_3$:Ce photopeak detection efficiency ε_{ph} was determined with reflective and absorptive crystal coating over an energy range between 121 and 1408 keV, as displayed in **Figure 4**. With both types of crystal surface coating, the full energy detection efficiency, corrected for solid angle and data aquisition dead time, starts from high values of $\varepsilon_{ph} \approx 80\%$ at low energies (121 keV) due to the crystal thickness of 30 mm, the high effective atomic number Z_{eff} and the density of the detector material, rendering the probability of the photoelectric interaction to be dominant in this energy region. However, the observed drop of ε_{ph} with increasing photon energy correlates with the emerging dominance

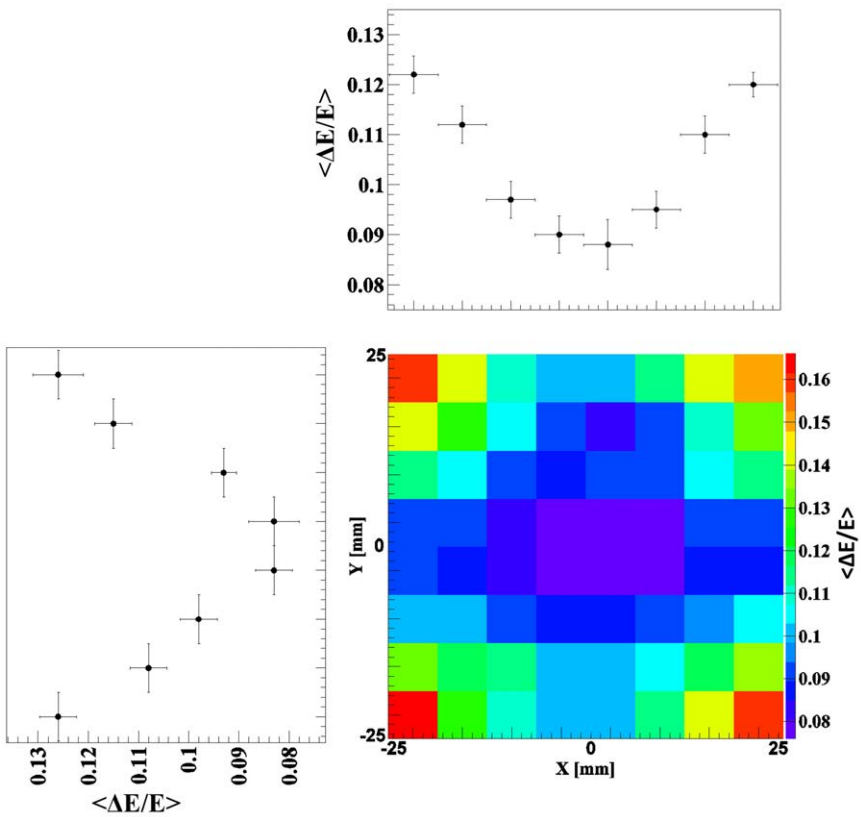

FIGURE 2 | 2D energy resolution map together with its X and Y projection obtained by scanning the absorptively wrapped $LaBr_3$:Ce crystal with a 1-mm collimated ^{137}Cs source and step a size of 6 mm in x and y direction.

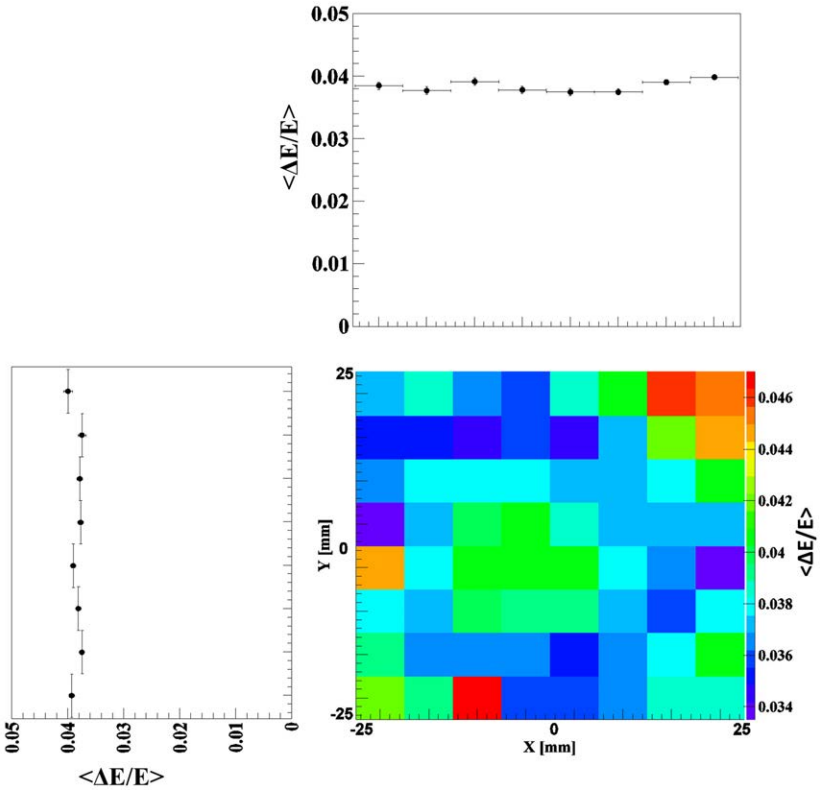

FIGURE 3 | 2D energy resolution map measured by scanning the reflectively coated $LaBr_3$:Ce crystal with a 1-mm collimated ^{137}Cs source and step a size of 6 mm in x and y direction. The x and y projections (averaged over the complementary direction) show an almost position independent energy resolution of 3.8% on average.

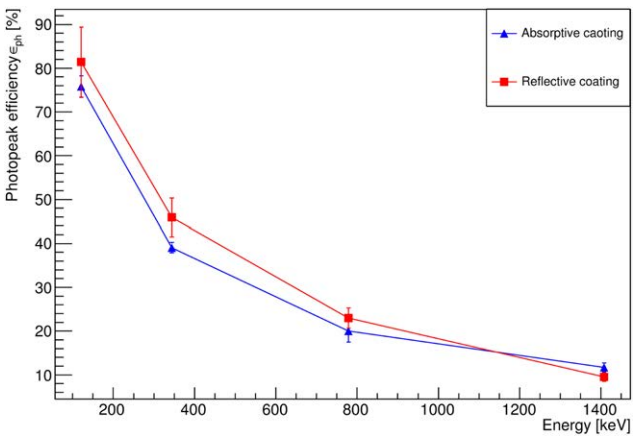

FIGURE 4 | Photopeak detection efficiency of the absorptively (blue) and reflectively (red) wrapped $LaBr_3$:Ce crystal using a ^{152}Eu calibration source. Background, solid angle, and DAQ dead time corrections were applied to these data. The solid lines are to guide the eye.

of multiple interactions, such as Compton scattering for high energy photons contributing to reduce the photopeak efficiency. **Figure 4** also shows that the photopeak detection efficiency within experimental uncertainties is almost independent of the different surface coatings as expected.

3.3. Time Resolution

The timing properties of the $LaBr_3$:Ce detector were investigated for the alternative crystal coatings relative to a fast reference plastic scintillator. **Figure 5A** shows the coincidence time peak of two simultaneously emitted photons from ^{60}Co, measured by two identical plastic detectors (BC-418), exhibiting a FWHM of 365 ± 8 ps. From Equation (2), the time resolution of a single reference detector was found to be 258 ± 5 ps (FWHM). A similar result was obtained for a BC-418 scintillation detector coupled to the same PMT type (photonis XP2020/Q) by (6) to be 235 ps (FWHM). **Figures 5B,C** indicate 376 ± 8 ps (FWHM) and 595 ± 8 ps (FWHM) as the coincidence time measured for the reflectively and absorptively wrapped $LaBr_3$:Ce detector, respectively, in coincidence with the reference plastic detector. Using the measured time resolution of the reference detector, the time resolution of the $LaBr_3$:Ce detector was extracted using Equation (3) to be 536 ± 6 ps (FWHM) with absorptive and 273 ± 6 ps (FWHM) with reflective wrapping. Since the same crystal, PMT, electronics and time pick-off method were used in both side surface wrapping scenarios, the improvement in the time resolution of the $LaBr_3$:Ce detector by more than a factor of 2 can clearly be attributed to the maximized light collection in the reflectively wrapped crystal. Consequently, the number of collected photoelectrons per event is correspondingly maximized, thus reducing the statistical fluctuations that affect the time resolution, which scales inversely proportional to the square root of the number of photoelectrons (2, 8).

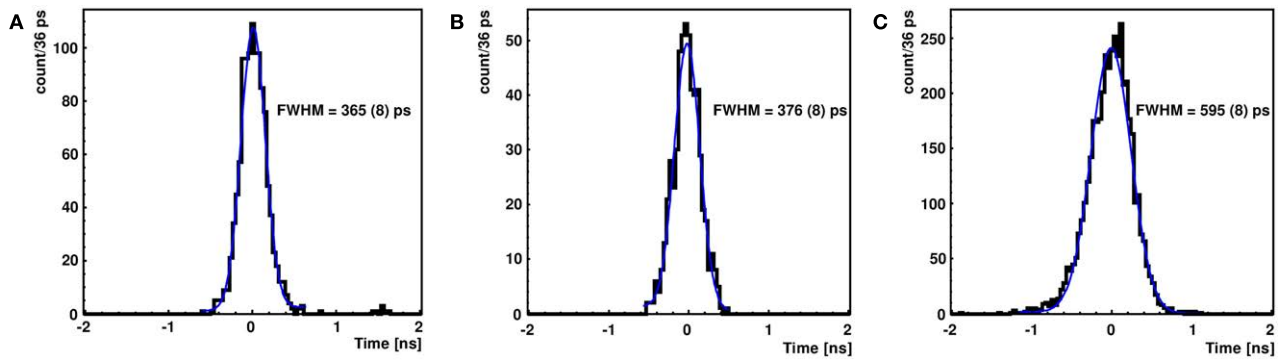

FIGURE 5 | Time coincidence peak of two simultaneously emitted photons from ^{60}Co measured by two identical plastic detectors (BC418) (A) and by a reflectively (B) as well as an absorptively (C) wrapped $LaBr_3$:Ce detector measured against the reference plastic detector. The blue curve represents a Gaussian fit used to derive the indicated FWHM values.

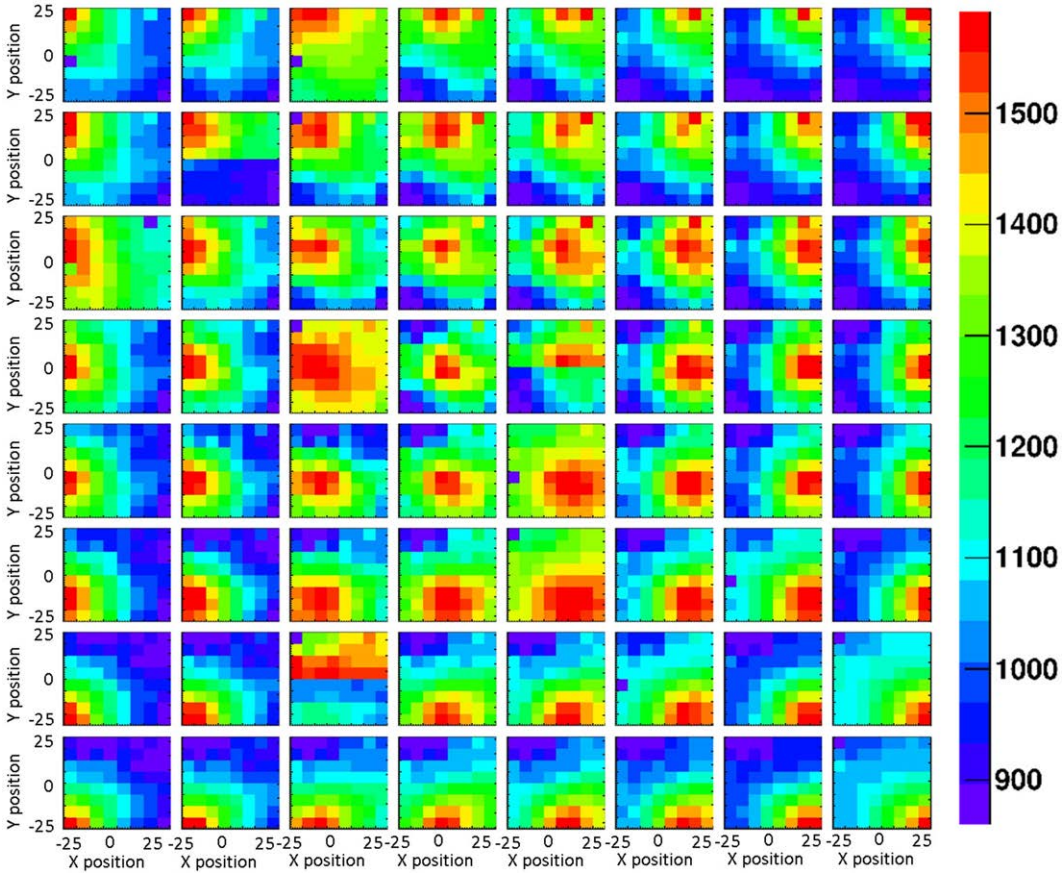

FIGURE 6 | 2D light amplitude distribution obtained from an 8 × 8 grid scan of the absorptively wrapped $LaBr_3$:Ce detector, using a 1 mm collimated ^{137}Cs source with a step size of 6 mm in x and y direction. Each subpicture represents light amplitude distribution of an irradiation position. The corresponding correlation of the resulting light amplitude distributions (after the analysis steps described in Sect. 2) with the shift of the irradiation position is clearly visible.

3.4. Light Spread Function

The impact of the crystal surface coating on the position sensitivity of the $LaBr_3$:Ce detector was studied using the 1 mm collimated ^{137}Cs source. **Figures 6** and **7** show 2D light amplitude distributions for each irradiation position on a 8 × 8 grid with 6 mm step size in x and y direction. The irradiation position is clearly correlated with the shape of the measured light distribution both with absorptive and reflective surface wrapping after applying the correction steps discussed in section 2.

The LSF, which corresponds to a radial projection of the 2D light amplitude distribution, is used to evaluate the impact of the crystal wrapping type on the detector's spatial resolution.

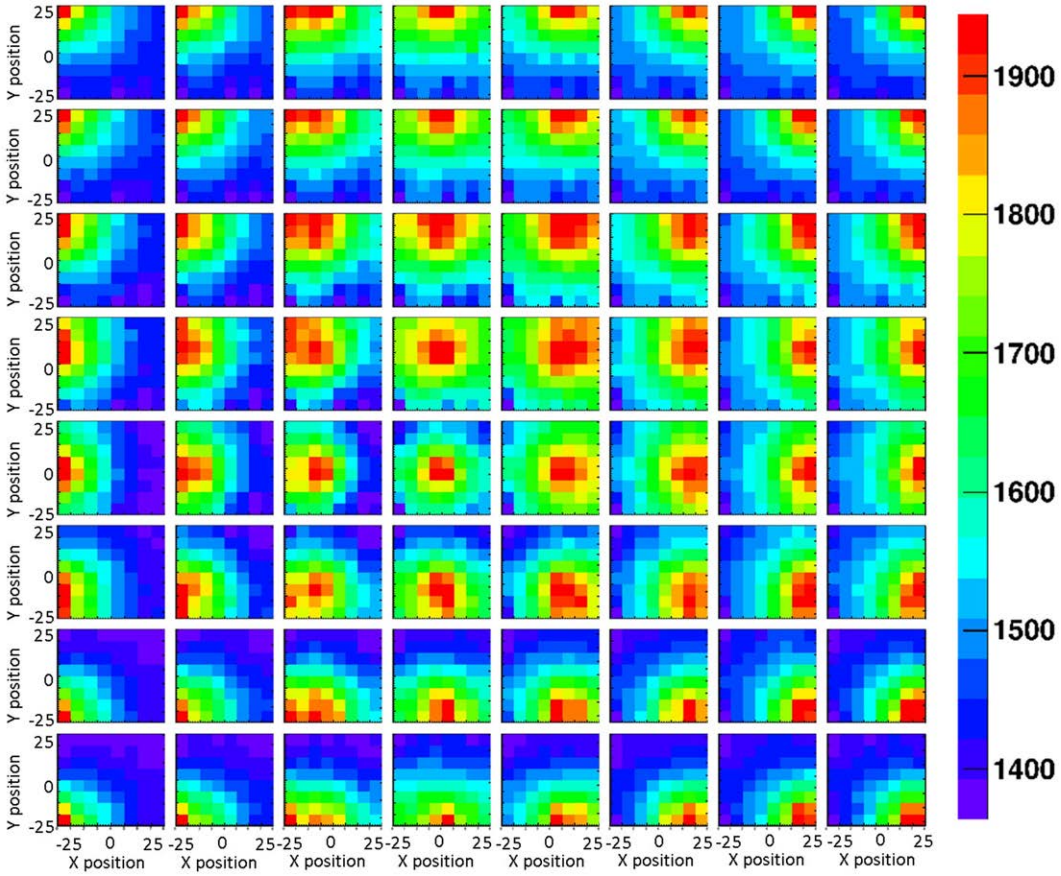

FIGURE 7 | A grid scan of 8 × 8 irradiation positions of the reflectively coated $LaBr_3$:Ce detector, using a 1-mm collimated ^{137}Cs source. The source irradiation position can be clearly tracked by the intensity of the detector 2D light distribution.

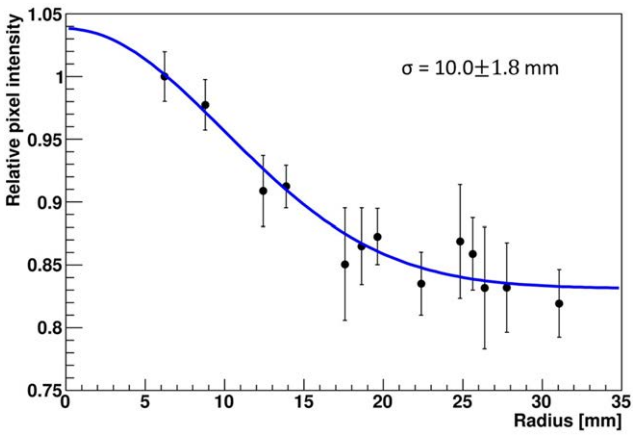

FIGURE 8 | Radial projection of the 2D light amplitude distribution obtained from a central irradiation position of the absorptively wrapped $LaBr_3$:Ce detector. In this study, 4 neighboring segments of the 16 × 16 multi-anode PMT were combined. The blue curve represents a Gaussian fit to the data, the resulting width σ is indicated.

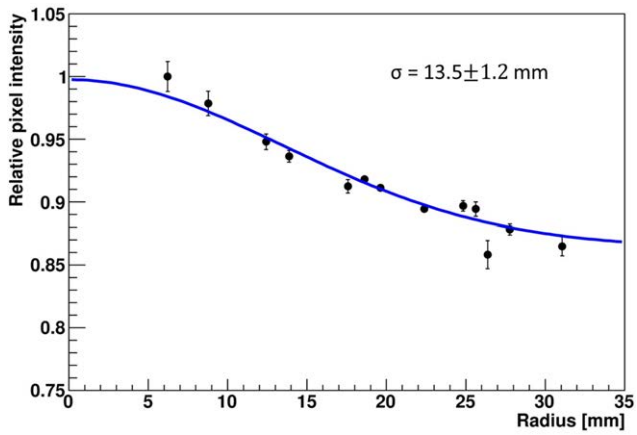

FIGURE 9 | Radial projection of the 2D light amplitude distribution derived from a central irradiation position of the reflectively wrapped $LaBr_3$:Ce detector. The blue curve represents a Gaussian fit to the data, the resulting width σ is indicated.

The absorptively wrapped $LaBr_3$:Ce detector exhibits a LSF of 23.5 ± 4 mm FWHM ($\sigma = 10.0 \pm 1.8$ mm) derived from the radial projection fit of the 2D light distribution as indicated in **Figure 8**. In contrast and derived from **Figure 9**, it was measured to be 31.7 ± 3 mm FWHM ($\sigma = 13.5 \pm 1.2$ mm) for the reflectively $LaBr_3$:Ce detector. As expected, the reflective coating degrades

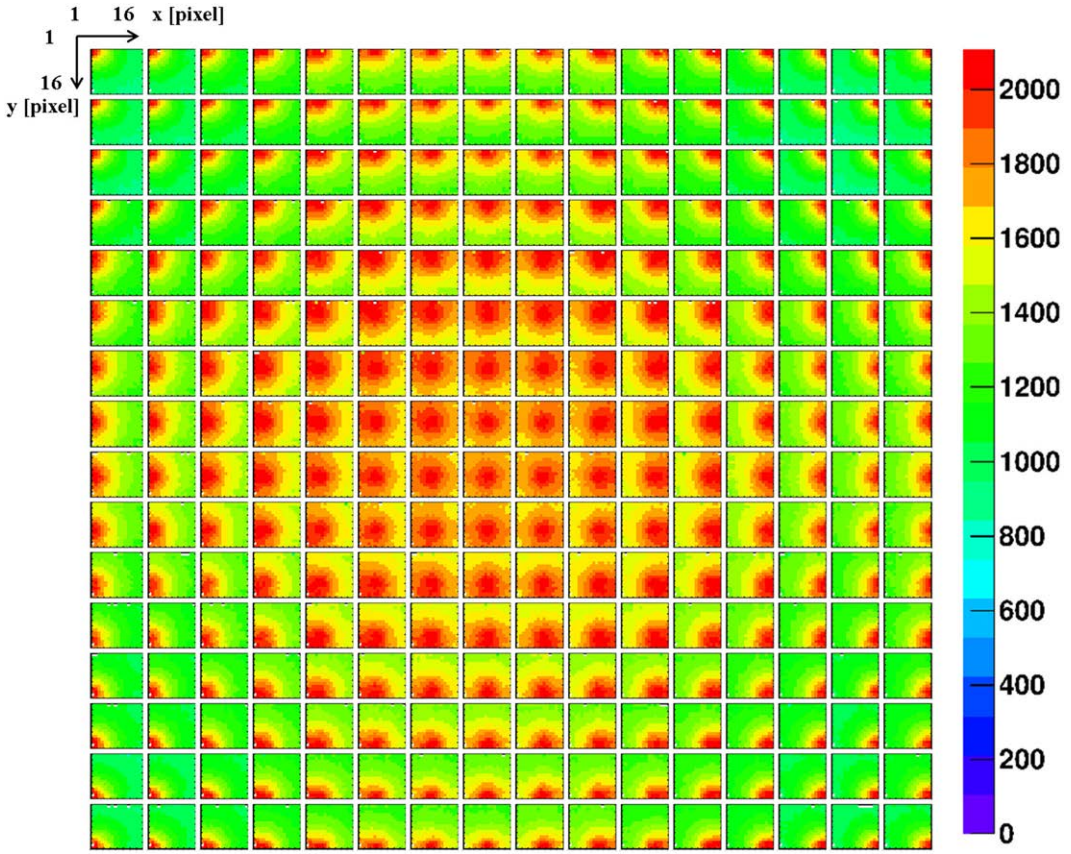

FIGURE 10 | A grid scan of 16 × 16 irradiation positions of the reflectively coated monolithic $LaBr_3$:Ce detector, using a 1 mm collimated ^{137}Cs source and a grid step size of 3 mm in x and y direction. All 256 segments of the multi-anode PMT are individually read out. The resulting 2D light amplitude distribution of each irradiation position clearly indicates a systematically different pattern for the 256 different source positions.

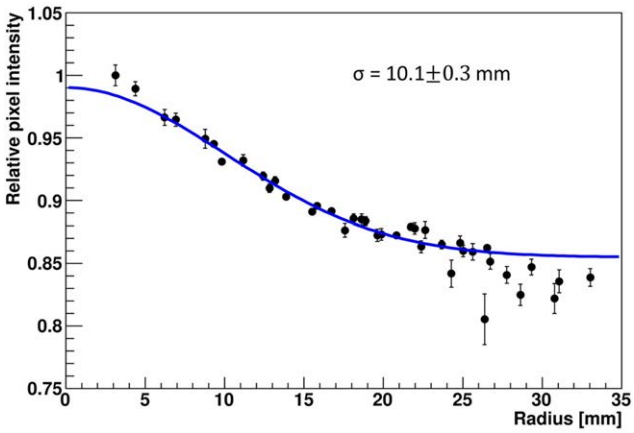

FIGURE 11 | Radial projection of the 2D light amplitude distribution derived from a central irradiation position of the reflectively wrapped $LaBr_3$:Ce detector coupled to a 16 × 16 multi-anode PMT. The blue curve represents a Gaussian fit to the data, the resulting width σ is indicated.

the position sensitivity of the detector due to the scintillation light scattering at the edges and corners of the crystal. However, this degradation does not prevent the detector from resolving the photon source-position correlation as shown in **Figure 7**. While so far, measurement and analysis of the $LaBr_3$:Ce has been performed using an initial version of the signal processing electronics with 64 signal readout channels, in the further progress of the R&D project the readout electronics was upgraded to the full capacity of 256 channels needed for an individual readout of the 16 × 16 multi-anode PMT segments. Consequently, the position-dependent collimated irradiation was repeated with a finer grid step of 3 mm in x and y direction, resulting in the light amplitude correlation map shown in **Figure 10**, where 16 × 16 2D maps are displayed, each with 16 pixel in x and y, respectively (compared to 8 × 8 pixel in **Figures 6** and **7**). The higher granularity of the segmented readout and the scan stepsize enables as well a refined analysis of the LSF for the reflectively coated crystal (note that the electronics upgrade was performed after the crystal modification from absorptive to reflective coating). The resulting LSF is shown in **Figure 11** exhibiting a width of 23.7 ± 0.7 mm FWHM ($\sigma = 10.1 \pm 0.3$ mm), comparable to the findings for the less segmented, absorptively wrapped crystal. Based on these findings, the position information for the impinging primary photon is planned to be derived from the monolithic $LaBr_3$:Ce scintillator using the "k-nearest neighbor" (k-NN) method developed at TU Delft (20), which requires an even finer 2D grid scan of the detector (0.5 mm collimation, 0.5 mm stepsize) (9).

4. CONCLUSION

A monolithic $LaBr_3$:Ce detector (50 mm × 50 mm × 30 mm) coupled to a position-sensitive multi-anode PMT was characterized with reflective and absorptive crystal surface coating for the purpose of optimizing the absorbing detector of a Compton camera, intended to be used as a monitoring system for ion (proton) beam range monitoring in hadron therapy. The photopeak efficiency of the detector is negligibly affected by the type of crystal coating. The reflective coating contributes to improving the energy and time resolution of the detector, because it enhances the light collection that reduces statistical fluctuations in both cases. However, this type of coating degrades the detector position sensitivity due to the increase in light scattering at the edges and corners of the crystal. While at the first glance, it appears counterproductive to use reflective side surface wrapping (plus polished crystal surface treatment) in a scenario where position resolution is targeted via a multi-anode PMT readout, in our case it is nevertheless mandatory, since an optimized energy resolution is of equal importance when operating the crystal in the context of a Compton camera. From the results obtained in this study, the reflectively wrapped $LaBr_3$:Ce scintillator qualifies to be the optimum choice for the Compton camera absorbing detector. This is further emphasized by the presented measurements with the upgraded, highly granular electronic readout for all of the 256 PMT segments.

AUTHOR CONTRIBUTIONS

SA: main author, acquisition, data collection, analysis, interpretation; IC, HK, CL, SL, TM: participate in experimental work and design; RG: experimental design, revising, and final approval to be published; RL: data acquisition; LM: experimental design; DS, KP, PT: interpretation, revising, and final approval to be published.

ACKNOWLEDGMENTS

This work was supported by the DFG Cluster of Excellence MAP (Munich-Centre for Advanced Photonics) and by King Saud University, Riyadh, Saudi Arabia.

REFERENCES

1. Bizarri G, de Haas J, Dorenbos P, van Eijk C. Scintillation properties of ø1x;1 inch 3 $LaBr_3$:% 5 percent Ce^{3+} crystal. *IEEE Trans Nucl Sci* (2006) **53**(2):615–9. doi:10.1109/TNS.2006.870090
2. Choong W-S. Timing resolution of scintillation-detector systems: a Monte Carlo analysis. *Phys Med Biol* (2009) **54**(21):6495. doi:10.1088/0031-9155/54/21/004
3. Giaz A, Pellegri L, Riboldi S, Camera F, Blasi N, Boiano C, et al. Characterization of large volume 3.5 inch * 8 inch $LaBr_3$:Ce detectors. *Nucl Instr Meth A* (2013) **729**:910–21. doi:10.1016/j.nima.2013.07.084
4. Higgins W, Churilov A, van Loef E, Glodo J, Squillante M, Shah K. Crystal growth of large diameter $LaBr_3$:Ce and $CeBr_3$. *J Cryst Growth* (2008) **310**:2085–9. doi:10.1016/j.jcrysgro.2007.12.041
5. Kanbach G, Andritschke R, Zoglauer A, Ajello M, McConnell M, Macri J, et al. Development and calibration of the tracking Compton/Pair telescope MEGA. *Nucl Instr Meth A* (2005) **541**:310–22. doi:10.1016/j.nima.2005.01.071
6. Kuhn A, Surti S, Karp J, Raby P, Shah K, Perkins A, et al. Design of a lanthanum bromide detector for time-of-flight PET. *IEEE Trans Nucl Sci* (2004) **51**:2550–7. doi:10.1109/TNS.2004.835777
7. Lang C, Habs D, Parodi K, Thirolf PG. Sub-millimeter nuclear medical imaging with high sensitivity in positron emission tomography using beta+gamma coincidences. *J Instrum* (2014) **9**:P01008. doi:10.1088/1748-0221/9/01/P01008
8. Lecoq P, Auffray E, Brunner S, Hillemanns H, Jarron P, Knapitsch A, et al. Factors influencing time resolution of scintillators and ways to improve them. *IEEE Trans Nucl Sci* (2010) **57**:2411–6. doi:10.1109/TNS.2010.2049860
9. Marinšek T. (2015). *Deriving Spatial Information from a Monolithic $LaBr_3$ Scintillator*. M.Sc. thesis, Munich: LMU.
10. Mazumdar I, Gothe D, Kumar GA, Yadav N, Chavan P, Patel S. Studying the properties and response of a large volume (946 cm^3) $LaBr_3$:Ce detector with up to 22.5 MeV. *Nucl Instr Meth A* (2013) **705**:85–92. doi:10.1016/j.nima.2012.12.093
11. Milbrath B, Choate B, Fast J, Hensley W, Kouzes R, Schweppe J. Comparison of $LaBr_3$:Ce and NaI(Tl) scintillators for radio-isotope identification devices. *Nucl Instr Meth A* (2007) **572**:774–84. doi:10.1016/j.nima.2006.12.003
12. Moszynski M, Zalipska J, Balcerzyk M, Kapusta M, Mengesha W, Valentine J. Intrinsic energy resolution of NaI(Tl)1. *Nucl Instr Meth A* (2002) **484**:259–69. doi:10.1016/S0168-9002(01)01964-7
13. Pani R, Cinti M, Scaf R, Pellegrini R, Vittorini F, Bennati P, et al. Energy resolution measurements of $LaBr_3$:Ce scintillating crystals with an ultra-high quantum efficiency photomultiplier tube. *Nucl Instr Meth A* (2009) **610**:41–4. doi:10.1016/j.nima.2009.05.058
14. Reeder, P. L. and Stromswold, D. C. (2004). Pacific Northwest National Laboratory report ppnl-14735. *Performance of Large NaI(Tl) Gamma-Ray Detectors Over Temperature -50°C to +60°C*, Available from: http://www.pnl.gov/main/publications/external/technical_reports/pnnl-14735.pdf
15. Saint-Gobain (2009). *Brilliance Scintillators Performance Summary*. Scintillation Products Technical Note. Available from: http://www.crystals.saint-gobain.com/uploadedFiles/SG-Crystals/Documents/Technical/SGC%20BrilLanCe%20Scintillators%20Performance%20Summary.pdf
16. Schaart DR, Seifert S, Vinke R, van Dam HT, Dendooven P, Löhner H, et al. $LaBr_3$:Ce and SiPMs for time-of-flight PET: achieving 100 ps coincidence resolving time. *Phys Med Biol* (2010) **55**:N179. doi:10.1088/0031-9155/55/7/N02
17. Shah K, Glodo J, Klugerman M, Moses W, Derenzo S, Weber M. $LaBr_3$:Ce scintillators for gamma-ray spectroscopy. *IEEE Trans Nucl Sci* (2003) **50**:2410–3. doi:10.1109/TNS.2003.820614
18. Sonzogni A. Nuclear data sheets for A = 138. *Nucl Data Sheets* (2003) **98**(3):515–664. doi:10.1006/ndsh.2003.0004
19. Thirolf PG, Lang C, Aldawood S, Kolff HGVD, Maier L, Schaart D, et al. Development of a Compton camera for online range monitoring of laser-accelerated proton beams via prompt-gamma detection. *EPJ Web Conf* (2014) **66**:11036. doi:10.1051/epjconf/20146611036
20. van Dam H, Seifert S, Vinke R, Dendooven P, Lohner H, Beekman F, et al. Improved nearest neighbor methods for gamma photon interaction position determination in monolithic scintillator PET detectors. *IEEE Trans Nucl Sci* (2011) **58**:2139–47. doi:10.1109/TNS.2011.2150762
21. van Loef E, Dorenbos P, van Eijk C, Krämer K, Güdel H. Scintillation properties of LaBr3:Ce_{3+} crystals: fast, efficient and high-energy-resolution scintillators. *Nucl Instr Meth A* (2002) **486**:254–8. doi:10.1016/S0168-9002(02)00712-X

Conflict of Interest Statement: The authors declare that the research was conducted in the absence of any commercial or financial relationships that could be construed as a potential conflict of interest.

Copyright © 2015 Aldawood, Castelhano, Gernhäuser, Van Der Kolff, Lang, Liprandi, Lutter, Maier, Marinšek, Schaart, Parodi and Thirolf. This is an open-access article distributed under the terms of the Creative Commons Attribution License (CC BY). The use, distribution or reproduction in other forums is permitted, provided the original author(s) or licensor are credited and that the original publication in this journal is cited, in accordance with accepted academic practice. No use, distribution or reproduction is permitted which does not comply with these terms.

frontiers in Oncology

ORIGINAL RESEARCH
published: 18 December 2015
doi: 10.3389/fonc.2015.00281

Fast Pencil Beam Dose Calculation for Proton Therapy Using a Double-Gaussian Beam Model

Joakim da Silva[1,2], Richard Ansorge[1] and Rajesh Jena[2]*

[1] Cavendish Laboratory, Department of Physics, University of Cambridge, Cambridge, UK, [2] Department of Oncology, University of Cambridge, Cambridge, UK

The highly conformal dose distributions produced by scanned proton pencil beams (PBs) are more sensitive to motion and anatomical changes than those produced by conventional radiotherapy. The ability to calculate the dose in real-time as it is being delivered would enable, for example, online dose monitoring, and is therefore highly desirable. We have previously described an implementation of a PB algorithm running on graphics processing units (GPUs) intended specifically for online dose calculation. Here, we present an extension to the dose calculation engine employing a double-Gaussian beam model to better account for the low-dose halo. To the best of our knowledge, it is the first such PB algorithm for proton therapy running on a GPU. We employ two different parameterizations for the halo dose, one describing the distribution of secondary particles from nuclear interactions found in the literature and one relying on directly fitting the model to Monte Carlo simulations of PBs in water. Despite the large width of the halo contribution, we show how in either case the second Gaussian can be included while prolonging the calculation of the investigated plans by no more than 16%, or the calculation of the most time-consuming energy layers by about 25%. Furthermore, the calculation time is relatively unaffected by the parameterization used, which suggests that these results should hold also for different systems. Finally, since the implementation is based on an algorithm employed by a commercial treatment planning system, it is expected that with adequate tuning, it should be able to reproduce the halo dose from a general beam line with sufficient accuracy.

Keywords: pencil beam, proton therapy, dose calculation, double Gaussian, graphics processing unit, adaptive radiotherapy

OPEN ACCESS

Edited by:
Marco Durante, GSI, Germany

Reviewed by:
Dalong Pang, Georgetown University Hospital, USA
Andrea Fontana, Istituto Nazionale di Fisica Nucleare, Italy

****Correspondence:***
Joakim da Silva
jd491@cam.ac.uk

Specialty section:
This article was submitted to Radiation Oncology, a section of the journal Frontiers in Oncology

Received: *29 September 2015*
Accepted: *30 November 2015*
Published: *18 December 2015*

Citation:
da Silva J, Ansorge R and Jena R (2015) Fast Pencil Beam Dose Calculation for Proton Therapy Using a Double-Gaussian Beam Model. Front. Oncol. 5:281. doi: 10.3389/fonc.2015.00281

INTRODUCTION

Fast dose calculation finds use in a variety of radiotherapy applications and is an active area of research (1). Due to the high level of dose conformity, the small number of treatment fields, and the sensitivity to material changes in the beam path, adaptive treatment techniques relying on fast, repeated dose calculation are of particular interest in proton therapy. A considerable amount of work has therefore gone into using graphics processing units (GPUs) to speed up proton therapy Monte Carlo (MC) dose calculation in order to allow daily dose recalculation (2–6). However, more advanced adaptive techniques, such as real-time dose monitoring, would involve calculating the dose online as it is being delivered. For a treatment employing pencil beam (PB) scanning, this

would require the calculation time of individual energy layers to be short in comparison with the time between energy layers or the length of a typical motion phase. For such applications, GPU MC dose calculation on a single workstation remains too slow by at best one, and generally two or more, orders of magnitude. In a previous paper, we therefore presented a GPU implementation of the widely used PB algorithm, especially developed for use in online calculation (7). The presented dose calculation engine was capable of calculating a two-field, base-of-skull test case in 0.22 s, with individual energy layers of the same case taking 6.4 ms or less to calculate. The short calculation times were largely attributed to the efficient GPU implementation of the computationally expensive kernel superposition (KS) step of the algorithm (8). Although the accuracy of the calculation in the high- and medium-dose regions was seen to be high, with γ-index passing rates matching those of a PB algorithm in clinical use, the implementation used a single-Gaussian kernel to describe the lateral dose profiles of PBs. It is well-known that such a beam model cannot accurately predict the low-dose halo made up of particles traveling at large angles with the beam direction, originating from nuclear interactions, inhomogeneous scattering in the nozzle, or large-angle Rutherford scattering. Despite the low halo dose, their large widths mean that the halos from a number of PBs may overlap to produce a noticeable impact on the overall dose distribution. Modeling of the halo dose is therefore necessary to predict the field-size dependence of the central dose in energy layers. In addition, the halos are responsible for the low-dose region further away from the target, which might be of interest when trying to predict the risk of developing side effects or secondary tumors.

Although PB algorithms for proton therapy have traditionally employed the single-Gaussian beam model, the above reasons have led to modern treatment planning systems (TPSs) almost exclusively making use of more complex models. Generally, these add one or more additional terms for modeling the halo dose to the Gaussian kernel describing the contribution from primary particles. A common method is to use a second, wider Gaussian to describe the halo, an approach first suggested for dose calculation in electron therapy (9). The potential to use the same approach in proton therapy was later pointed out in a paper describing the implementation of a commercial TPS (10). Pedroni et al. presented the first implementation of a double-Gaussian beam model for scanned PBs, using a parameterization based on measurements of the increase in central dose in square fields of increasing side length (11). Later the same year, Soukup et al. presented a different implementation, where the parameterization was instead based on MC simulations of nuclear interactions in water, which was adopted in the commercial TPS XiO Proton (Elekta AB, Stockholm, Sweden) (12). Since then a range of parameterizations, based on measurements, MC simulations, and analytical calculations, have been presented (13–17). Furthermore, several extensions to the double-Gaussian model have been suggested, including using a double-Gaussian model also for the PB shape in air, adding a third Gaussian to the beam model, and adding different non-Gaussian functions to the kernel (18–24).

From the above discussion, it is clear that to be fully comparable to a modern TPS, a calculation engine for online dose monitoring must include a model for the halo dose. Starting with an existing implementation, a double-Gaussian beam model could easily be implemented by simply rerunning the calculation a second time for the halo contribution. The difficulty in a fast implementation, however, stems from the width of the halo: for a double-Gaussian beam model, the width of the halo contribution is expected to be about two to three times larger than that of the primary contribution. The most time-consuming step of the PB algorithm is the KS, where the computational PBs (CPBs) – the computational elements of the PB algorithm obtained from the sub-PB splitting of physical PBs (7) – are widened perpendicular to the beam direction through a superposition of the kernels describing their lateral shape. The number of voxels reached by the kernel at a given depth, and thereby the calculation time of the KS step, is proportional to the square of the CPB width and inversely proportional to the square of the CPB spacing. Therefore, the calculation of a two to three times wider halo dose is expected to take four to nine times longer than that of the primary contribution, threatening to make the calculation time prohibitively long for real-time applications. Here, we describe the integration of a double-Gaussian beam model, based on the algorithm by Soukup et al. (12), into our previously presented GPU dose calculation engine, which aims to reduce the calculation time of the halo dose. It does so in part by employing the method described in Ref. (12), where, in the calculation of the halo dose, a single "nuclear" PB, henceforth referred to as halo PB (HPB), is assigned to each physical PB. Assuming 3 mm PB spacing and 1 mm CPB spacing for the primary contribution, this lack of sub-PB splitting reduces the number of HPBs, and thus their computational load, by a factor of nine. In addition, we employ a separate beam's-eye-view (BEV) coordinate system for the halo dose. This is defined in the same way as the CPB coordinate system described in our previous implementation (7) but is based on the HPB grid spacing. Using the same assumption as above, this effectively reduces the resolution of the halo calculation by a factor of three, and thereby the computational load of the KS by another factor of nine. Thus, using this approach, the time required by the KS step for the HPBs is expected to be not more than 11% of that for the primary CPBs. Although the main focus of the work was the implementation of the double-Gaussian beam model and its performance, it also includes a comparison of two parameterization approaches for the double-Gaussian beam model, so that their effect on the calculation time could be investigated.

MATERIALS AND METHODS

Algorithm

The PB implementation presented in this paper assumes that the dose D to a point (x, y, z) can be described by a double-Gaussian beam model according to

$$\begin{aligned} \mathrm{D}(x,y,z) = &\sum_{\mathrm{i}\in\mathrm{CPB}} \left(1-u(E_{\mathrm{i}}, z_{\mathrm{WE,i}})\right)\times N_{\mathrm{i}}\times I_{\mathrm{IDD}}(E_{\mathrm{i}},z_{\mathrm{WE,i}}) \\ &\times G(x-x_{\mathrm{i}},y-y_{\mathrm{i}},\sigma_{\mathrm{CPB,i}}) + \sum_{\mathrm{j}\in\mathrm{HPB}} u(E_{\mathrm{j}},z_{\mathrm{WE,j}}) \\ &\times N_{\mathrm{j}}\times I_{\mathrm{IDD}}(E_{\mathrm{j}},z_{\mathrm{WE,j}})\times G(x-x_{\mathrm{j}},y-y_{\mathrm{j}},\sigma_{\mathrm{HPB,j}}) \end{aligned} \quad (1)$$

The first sum on the right-hand side of Eq. 1 represents the dose from primary particles, which is calculated according to the original implementation using the single-Gaussian beam model presented elsewhere (7). Consequently, the index of summation, i, runs over the CPBs resulting from the sub-PB splitting of the physical PBs, and each factor inside the summation (except for the first one) is further identical to what was previously presented. Specifically, N_i is the CPB weight, E_i is the initial beam energy, $z_{WE,i}$ is the water-equivalent path length (WEPL), I_{IDD} is the integral depth dose (IDD), G is the Gaussian function, and $\sigma_{CPB,i}$ is the SD of the primary Gaussian, henceforth referred to as the CPB width. In Eq. 1, $u(E_i, z_{WE,i}) \in [0,1]$ is the halo fraction, defined as the share of the integral dose that is deposited by the halo, which is given by the halo dose parameterization. Consequently, the factor $[1 - u(E_i, z_{WE,i})]$ gives the fraction of the integral dose at a given WEPL that is deposited by primary particles. It should be noted that, although the CPB widths are calculated as described in the original publication, the values of the parameters E_S and δ, which enter the width calculation as free parameters in the implementation, have to be adjusted in the double-Gaussian beam model. This is because the values (14.1 MeV and 0.21 mm, respectively) obtained for the single-Gaussian beam model were based on how well the shape of the calculated PBs reproduced the total dose distributions, including contributions from the low-dose halo, from individual PBs as obtained by MC simulations. When employing the double-Gaussian model, these should instead be determined by a fit to the primary contribution alone. Therefore, the contribution from the halo should be subtracted from the total dose before finding the best values of E_S and δ, and these must therefore be determined separately for each halo dose parameterization.

The dose contribution from the low-dose halo is given by the second sum on the right-hand side of Eq. 1. In this case, the sum is taken over HPBs, which, since no sub-PB splitting is applied, coincide in number and position with the physical PBs. Therefore, the weight, N_j, of HPB j is equal to that of the corresponding physical PB. The width of HPB j, $\sigma_{HPB,j}$, is defined in accordance with Ref. (12) as

$$\sigma_{HPB}(E,z) = \sqrt{\sigma_{PB}^2(E,z) + \sigma_{LA}^2(E,z_{WE})} \tag{2}$$

where σ_{PB} is the total width of the contribution from primary protons before the sub-PB splitting, and σ_{LA} is the large-angle component given by the halo dose parameterization. Similar to u, and contrary to σ_{CPB} (and thus σ_{PB}), σ_{LA} depends only on the initial beam energy and the WEPL.

Beam Model Parameterizations

Two different parameterizations for the halo fraction, u, and the large-angle component, σ_{LA}, were investigated. The first parameterization, which will be referred to as the Soukup model, makes use of the unmodified analytical fits to MC data of nuclear interaction products given in Ref. (12), given by

$$\begin{aligned} u(E,z_{WE}) = {} & 0.052\log\left(1.13 + \frac{z_{WE}}{11.2 - 0.023R_0(E)}\right) \\ & + 0.35\frac{0.0017R_0^2(E) - R_0(E)}{\left(R_0(E)+3\right)^2 - z_{WE}^2} - 1.61\times10^{-9} \\ & \times z_{WE} \times \left(R_0(E)+3\right)^2 \end{aligned} \tag{3}$$

where, if the right-hand side becomes negative, $u(E, z_{WE})$ is set to 0, and

$$\begin{aligned} \sigma_{LA}(E,z_{WE}) = {} & 2.85 + 0.0014R_0(E)\times\log(z_{WE}+3) \\ & + 0.06z_{WE} - 7.4\times10^{-5}\times z_{WE}^2 - 0.22\frac{R_0(E)}{\left(z_{WE} - R_0(E) - 5\right)^2} \end{aligned} \tag{4}$$

In the above equations, $R_0(E)$ is the Bragg peak (BP) depth in water for a PB of initial energy E. Past the BP, both u and σ_{LA} are assumed to take the same value as at the BP depth (although this is only stated explicitly for u in the original publication). In order to calculate the new values for E_S and δ for the primary contribution, the radial halo distributions of individual PBs in water were calculated using the expression inside the second sum on the right-hand side of Eq. 1 together with Eqs 3 and 4. The results were then subtracted from the corresponding radial dose distributions obtained from MC simulations to obtain the expected radial dose distribution of the primary particles. For each depth and energy, these were then fitted with a Gaussian function to extract the values for σ_{PB} in water. Since σ_{HPB} in Eq. 1 itself depends on σ_{PB}, this process was done iteratively, using σ_{PB} from the single-Gaussian implementation as the starting point. However, due to σ_{LA} generally being at least a factor of two larger than σ_{PB}, the exact value of the latter was seen to play a limited role, resulting in the calculation converging after a single iteration. The resulting values of σ_{PB} were finally used to obtain the new values for the parameters E_S and δ in the same way as for the single-Gaussian beam model (7).

The second parameterization, which will be referred to as the direct model, relied on fitting sums of two Gaussians directly to the total radial dose distributions obtained from MC simulations, similar to Parodi et al. (17). This was done through a non-linear least squares fit using the trust-region algorithm provided with the Optimization Toolbox of Matlab (Mathworks, Natick, MA, USA). Despite the fact that the radial dose distributions quickly become very small for large radii, the contributions at large radii are important for two reasons. First, the radial distributions do not reflect the larger volumes receiving the contributions from larger radii, which is part of the reason why the low-dose halo is of interest in the first place. Second, since the dose fraction of the halo is expected to be smaller, but the width of its Gaussian larger than for the primary particles, its dose contribution will be dwarfed close to the central axis, and its parameters must thus be determined mainly from the dose at large radii. Therefore, in order for the optimization not to ignore the

small contributions at large radii, the contribution to each radial bin was weighted according to the total area of a ring of the same width, i.e., with $\pi\left(r_{i+1}^2 - r_i^2\right)$ for the bin between radius r_i and r_{i+1}. The fit allowed the three parameters σ_{PB}, σ_{HPB}, and u to be obtained simultaneously for each PB energy and depth in water. Values of σ_{LA} for different depths were then obtained from σ_{PB} and σ_{HPB} by rearranging Eq. 2. In order to reduce the noise present in the calculated depth curves for u and σ_{LA} (c.f. **Figure 2**), these were fitted with cubic splines to obtain the final parameterizations. Past the BP, where few charged particles remain in the beam, the basis for using separate Gaussians for charged primaries and secondaries starts to break down. This was characterized by a sharp drop in u (likely due to the charged secondaries stopping earlier than primaries), followed by u tending toward unity, while σ_{LA} grows very large, consistent with the figures shown in Ref. (17). The behavior is likely explained by the limited number of charged particles past the BP causing the second Gaussian to be fitted to the "aura" of uncharged secondaries (24), which is more appropriately described by a non-Gaussian function (20, 21, 23, 24). Although a double-Gaussian fit still provides some improvement in this region (c.f. bottom row of **Figure 1**), the aura was ignored, consistent with our approach at shallower depths. Thus, past 102% of the BP depth, the same solution of keeping the values of u and σ_{LA} constant as for the Soukup model was employed. The values of E_S and δ were finally obtained from σ_{PB} in the same way as before.

Implementation

Incorporating the double-Gaussian beam model in Eq. 1 into the existing PB dose calculation engine could in theory be achieved by carrying out the same calculation procedure twice: once for the primary and once for the halo contributions. However, there are two strong arguments against this solution. First, several parts of the implementation rely on assigning one thread per lateral voxel position. While this works well for the large number of CPBs used to calculate the primary contribution, the number of HPBs is expected to be about nine times lower since no sub-PB splitting is applied. Therefore, small- and medium-sized treatment fields would likely not contain enough HPBs to saturate a modern GPU. Second, several of the intermediates and results obtained in the calculation of the primary contribution, importantly the WEPL and σ_{CPB} (from which σ_{PB} is obtained), are also needed to calculate the halo contribution. Therefore, repeating the whole calculation would either require recalculating the necessary intermediates or keeping large amounts of data in global memory between the two rounds of calculations. Instead, it was deemed more efficient to maintain the structure presented in the original publication [c.f. **Figure 2** in Ref. (7)] for the calculation of the primary contribution and to interleave it with the halo dose calculation. While the calculation of primary dose thus remains identical to what was previously presented, the following paragraph describes the changes made to the dose calculation engine in order to accommodate the halo dose calculation.

The only part of the implementation that was significantly modified compared to the original was the one calculating and storing the integral dose and kernel parameter for the CPBs, which was extended to perform the same operations for the HPBs as well. Due to the smaller number of HPBs than CPBs, the additional operations were carried out only by the threads corresponding to CPBs whose positions coincide with that of a HPB. Although it led to the majority of threads being idle during the additional operations, this method was deemed preferable compared to using a separate calculation step for the HPBs, which would in any case not have enough parallelism to saturate the GPU. For each step along the z-axis, the widths of the HPBs were calculated according to Eq. 2. The required value of σ_{LA}^2 was found by linear interpolation into a 2D texture containing the selected parameterization, and σ_{PB}^2 was calculated by adding in quadrature the PB width at the patient surface, σ_{air} (E, z_0), to the value of σ_{CPB} already calculated for the primary contribution. Furthermore, the integral dose for the halo contribution was obtained by multiplying the local IDD contribution, the full PB weight, and u, where u was again obtained by interpolating into a 2D texture. (A multiplication with $(1 - u)$ was similarly introduced in the calculation of the integral dose for the primary contribution.) To be compatible with the efficient KS implementation presented in a previous paper, the obtained values for the integral voxel dose and kernel parameter were then converted to dimensionless voxel units (8). These values were stored in two additional global memory arrays alongside those of the primary contribution. The KS step of the halo dose was identical to that of the primary contribution, and the two KS steps were carried out sequentially for each energy layer. However, due to the different resolutions of the CPB and HPB BEV systems, the BEV halo dose was kept in a separate BEV dose array. For the same reason, the transformation of the BEV halo dose to the global dose grid after completing the calculation for all energy layers also had to be done separately from the BEV primary dose.

Validation and Benchmarking

The double-Gaussian beam model was validated and benchmarked in the same way as the original dose calculation engine (7). In brief, all the reference dose distributions were obtained using the Fluka MC code, employing the beam line parameters and nozzle geometry of the Centro Nazionale di Adroterapia Oncologica (CNAO) treatment center in Pavia, Italy (25, 26). For the single PB validation, the radial dose distribution from a PB of BP depth 220 mm in water was calculated using 1 mm CPB spacing and a global dose grid resolution of 1 mm × 1 mm × 1 mm and was compared with the corresponding reference PB. For patient case validation, a base-of-skull plan for a 55.6 cm^3 planning tumor volume target consisting of two oblique fields of 38 and 45 energy layers was used. The PB spacing (and thus HPB spacing) was 3 mm, the CPB spacing was again set to 1 mm, and, in order to match the resolution of the provided reference MC simulation, a global dose resolution of 2 mm × 2 mm × 2 mm was used. The same patient case was also used in the benchmarking. In addition, benchmarking was carried out on a plan for a cubic target of side length 100 mm extending 100–200 mm below the surface of a water tank and

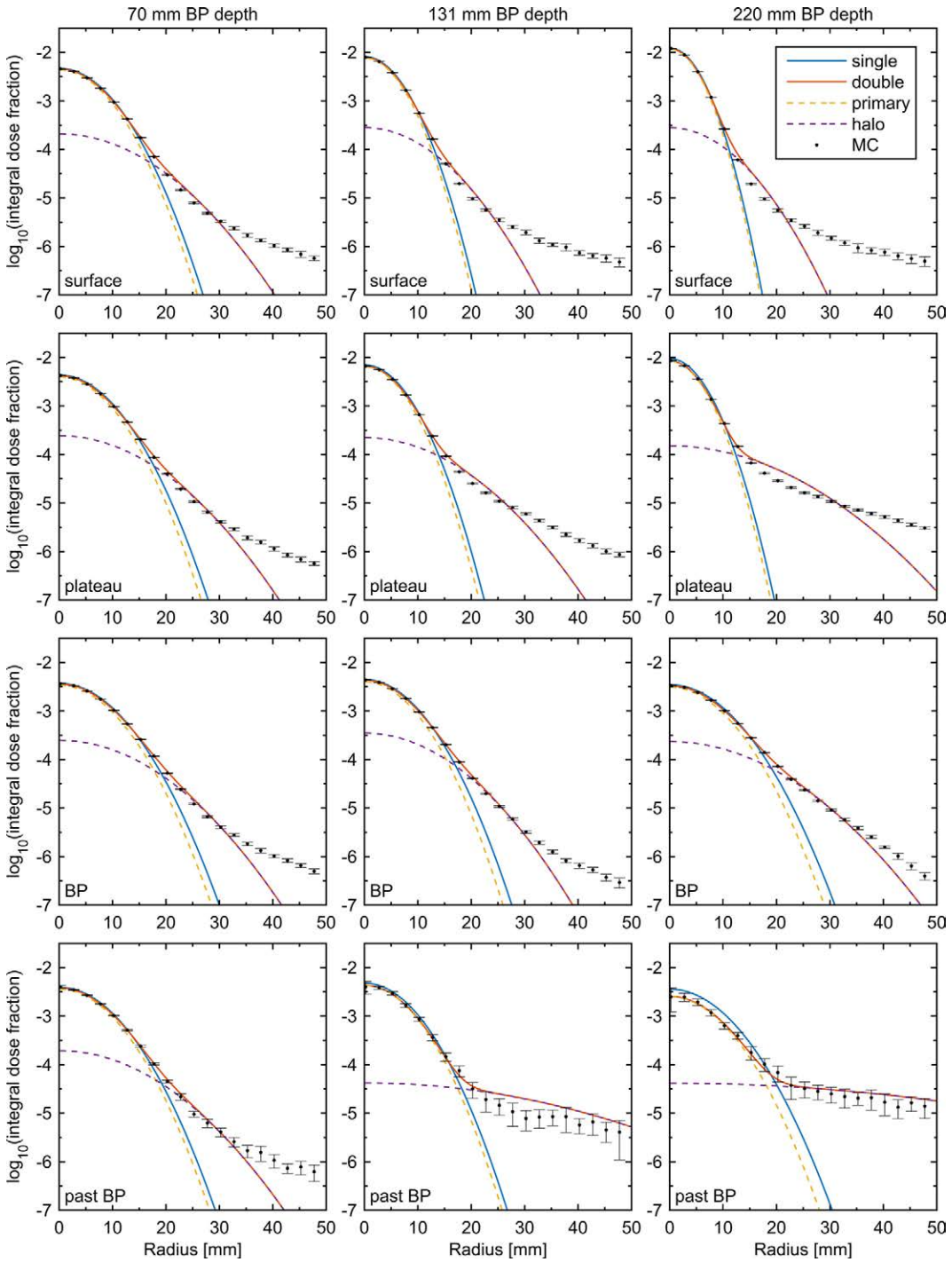

FIGURE 1 | Radial dose profiles as simulated by MC (black dots with error bars) fitted using single- and double-Gaussian models (solid lines). Dashed lines show the components of the double-Gaussian model. The error bars correspond to three times the estimated SD from the MC simulation, and to avoid crowding only every fifth MC data point is shown. Columns, from left to right, correspond to PBs with BP depths 70, 131, and 220 mm. Rows, from top to bottom, correspond to the profiles at the surface, at 40% of the BP depth, at the BP depth, and at 104% of the BP depth. The legend of the top left panel applies to all panels.

consisting on 20 energy layers. For this plan, the PB spacing was 3 mm, the CPB spacing was set to 1 mm, and a global dose resolution of 1 mm × 1 mm × 1 mm was used. The calculations were carried out on a Tesla K40 GPU from Nvidia (Santa Clara, CA, USA) with 2880 cores running at a clock frequency of 875 MHz.

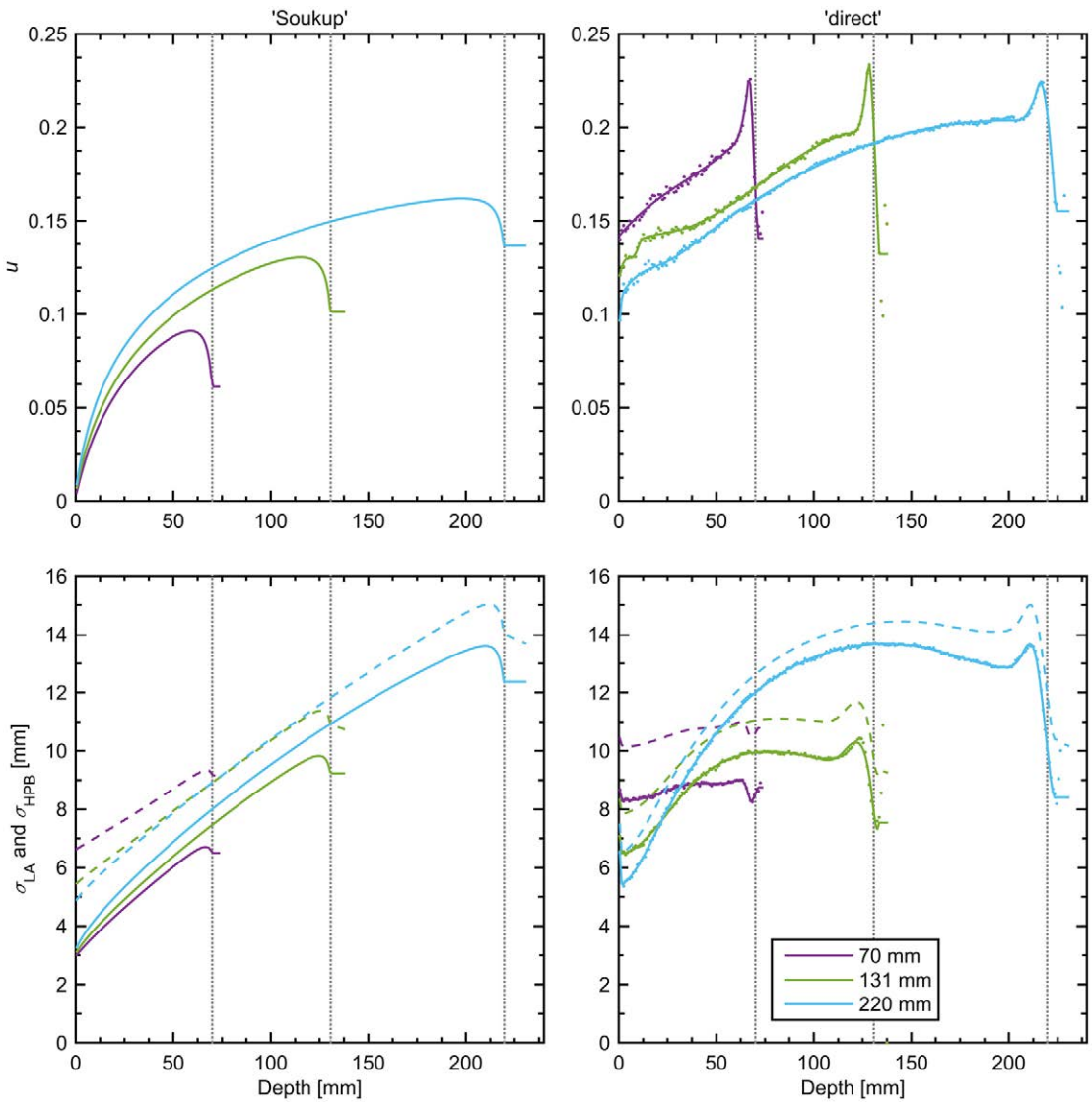

FIGURE 2 | Halo fraction, *u*, of the total dose (top row), σ_{LA} (bottom row, solid lines), and σ_{HPB} in water (bottom row, dashed lines) for the two parametrizations at three different beam energies. The individual data points used to fit the splines of the direct model are shown as dots (frequently coinciding with the corresponding line) in the right-hand panels, making visible the oscillating behavior in the model past 102% of the BP depth (with some dots falling outside the panels). Data for each parameterization are shown until 105% of the BP depth, the largest WEPL considered in the calculation. The BP depth for each line color is given by the legend in the bottom right panel and is also indicated by vertical dotted lines.

RESULTS

Beam Model Parameterizations

The results of directly fitting a sum of two Gaussians to the radial profiles of PBs of three different energies in water are shown in **Figure 1**. Each PB is shown at four depths, corresponding to the surface, 40% of the BP depth, the full BP depth, and 104% of the BP depth, and for comparison direct fits using a single-Gaussian are shown. A clear deviation from a single Gaussian is seen for all beam energies and at all depths, including the surface, indicating that nuclear interactions may not be the only factor contributing to the low-dose halo in the beam line modeled. For larger radii, it is clear that even an ideal double-Gaussian model breaks down far away from the central axis. However, for all depths up until just after the BP, this happens at a dose level, which is at least one order of magnitude smaller than for the single-Gaussian model.

Figure 2 shows curves of *u* and σ_{LA} according to the two parameterizations considered and for three beam energies with BPs at 70, 131, and 220 mm depth in water. A striking feature of this figure is the large difference in the shapes and magnitudes of both *u* and σ_{LA} between the models, especially at low beam energies. This shows that the assumptions made in the parameterization do indeed impact the resulting beam model. Although it was hard to perform a quantitative comparison with the data shown by Parodi et al. (17), the shapes and magnitudes of their curves for the CNAO treatment center seem to agree with those of the direct model presented here,

as expected from the similar method used. The direct model also shows the closest agreement with the measurement-based parameterization by Pedroni et al. in terms of the shapes of the curves for u and σ_{HPB}, although their values of u were seen to be almost half the size, and their values of σ_{HPB} a few millimeters larger (11). In addition to the differences in u and σ_{LA}, a difference was also seen in the new values of E_S, which were 13.8 MeV for the Soukup model and 13.0 MeV for the direct model. The new values of the empirical correction δ were, in the same order, 0.00 and 0.06 mm. The low values are expected since any major deviations from the multiple-scattering model should now be incorporated in the halo contribution. For the Soukup model, the halo fraction is close to 0 at the surface, which means that the width of the primary contribution at the surface should be given by the total PB width in air, as was the case for the single-Gaussian beam model. However, as can be seen from **Figure 2**, the halo fraction at the surface is non-zero for the direct model. The calculated PB width in air at the surface thus corresponds to the effective width of the primary and halo contributions taken together, and subsequently the width of the primary contribution must be smaller than this. It was seen that, in order to obtain the correct total beam width at the entrance point, the width of the primary contribution had to be set 2–4% smaller than the calculated PB width in air across the different energies. Therefore, when using the direct model, the entry width used in the calculation of the weights for the primary CPBs was set to 97% of the width calculated in air.

Validation

Figure 3 shows the difference in calculated dose for a PB of 220 mm BP depth when comparing the presented dose calculation engine using different halo dose parameterizations with the reference MC simulation. The result obtained for the previously presented single-Gaussian beam model is included for reference, showing that both parameterizations considerably reduce the average error in comparison. Unsurprisingly, the smallest average error was achieved for the direct model, with the Soukup model performing surprisingly well despite the lack of beam line-specific tuning. The error ranges in **Figure 3** were −0.8 to 2.1 and −1.8 to 2.0%, respectively, for the Soukup and direct models, compared to −1.1 to 5.3% for the single-Gaussian model. The small value of the lower boundary of the direct model was caused by the large underestimation seen along the central axis close to the surface in **Figure 3**.

Figure 4 shows γ-index maps according to the 2%/2 mm criterion for the reference patient case. Although the γ-index is a poor measure of the agreement in the low-dose region, better modeling of the halo dose is expected to be somewhat reflected in the γ-index due to the contribution of overlapping halos from multiple PBs to the high- and medium-dose regions. The γ-index passing rates for voxels receiving at least 10% of the prescription dose according to the 2%/2 mm criterion were 97.9% for the Soukup model and 97.4% for the direct model, compared to 96.7% for the single-Gaussian model. For the less strict 3%/3 mm criterion, the passing rates for the Soukup and direct models were 99.4 and 99.2%, respectively, similar to the 99.2% obtained for the single-Gaussian model.

Benchmarking

Despite the differences seen in **Figure 2**, the performance of the two parameterizations of the double-Gaussian beam model was very similar. The calculation times for the patient case were 241 and 244 ms, respectively, for the Soukup and direct models. This constitutes increases in the calculation time of 8 and 9% compared to the 224 ms required by the single-Gaussian model. The increase in calculation time for individual energy layer was seen to be larger and shifted toward smaller energy layers: the shortest calculation time (excluding memory transfers and deallocations)

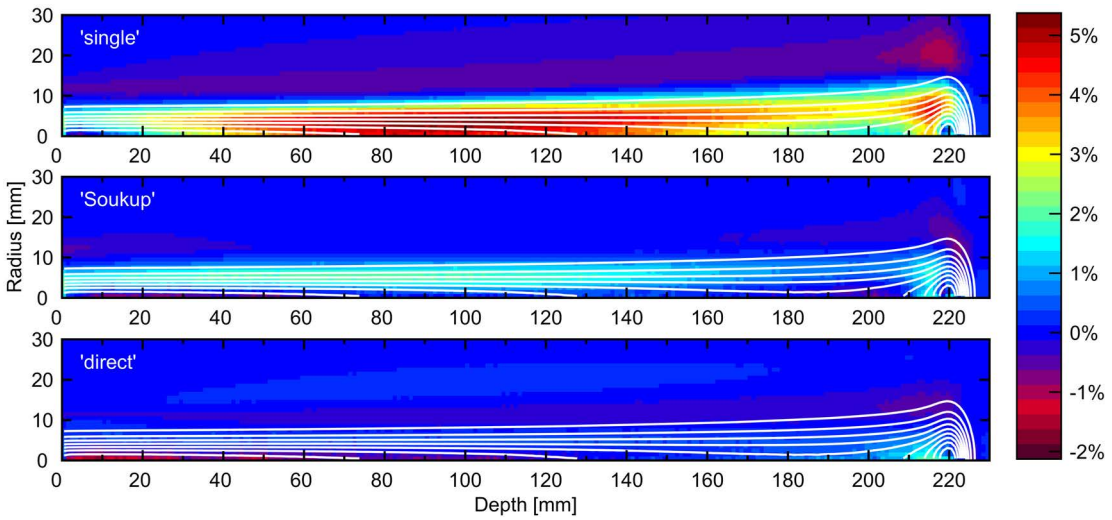

FIGURE 3 | Errors in radial distributions as a percentage of maximum dose for a PB of 220 mm BP depth when comparing the presented implementation to a MC simulation. The panels show the previously presented single-Gaussian implementation (top), the Soukup model (middle), and the direct model (bottom). The contours show the MC isodose curves, with each line corresponding to a multiple of 10% of the max dose.

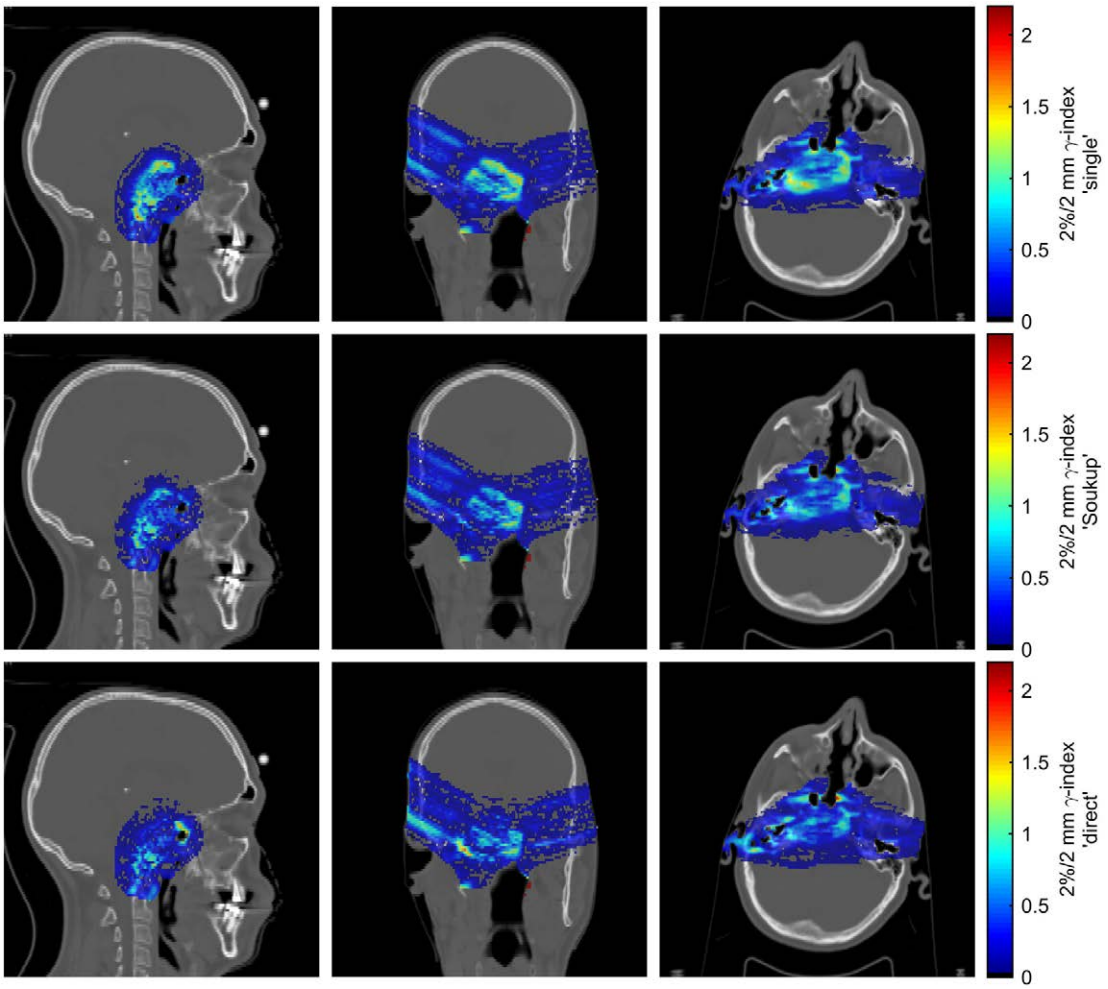

FIGURE 4 | Maps of the 2%/2 mm γ-index for the patient case for different beam model parametrizations. The rows correspond, from top to bottom, to the single-Gaussian, Soukup, and direct models. Columns, from left to right, show sagittal, coronal, and axial slices roughly through the center of the target.

for an energy layer was 3.2 and 3.3 ms for the two models, or about 50% longer than for the single-Gaussian model, whereas the longest calculation time was 8.1 and 8.4 ms, or around 25% longer than for the single-Gaussian beam model. The overall increase in calculation time was slightly larger for the deeper test case consisting of a cubic target in water, which required 153 ms using the Soukup model and 157 ms using the direct model, which is 13 and 16% longer than the 135 ms required by the single-Gaussian model. The calculation times for the shallowest energy layer were 7.4 and 7.6 ms, and for the deepest energy layer 16.5 and 16.8 ms. Compared to the 6.0 and 13.3 ms required by the single-Gaussian beam model for the shallowest and deepest energy layer, this corresponds to an increase of roughly 25% in both cases.

DISCUSSION

Validity of Approach

The reason for including two parameterizations of the double-Gaussian beam model was primarily to investigate their effect on the calculation time. Consequently, the tuning of the beam models implemented was kept as simple as possible, without much of the time-consuming and detailed analysis that is associated with the commissioning of a clinical dose calculation engine. Therefore, the result obtained using the presented models may not be representative of the selected algorithm or the parameterization methods themselves, other than to serve as a lower bound for their accuracy. On the contrary, smaller errors can be expected for both models if, for example, model-specific tuning or energy-dependent tuning were used, as discussed in the following subsection. The two models are, however, expected to capture the essence of the two main types of parameterizations, namely, those aimed specifically at modeling the contributions from nuclear interactions and those based on direct fitting of lateral profiles (which thus also include other contributions to the halo). Therefore, the presented parameterizations should be indicative of how sensitive the performance of the implementation is to the model used.

It should be pointed out that in the original implementation (12), the dose from CPBs and HPBs was calculated directly in the global dose grid. Therefore, the lack of sub-PB splitting for the halo dose served only to limit the number of HPBs but did not reduce the resolution used in the KS step. However, using a single HPB per PB already limits the effective resolution of the halo calculation. Therefore, when the KS is carried out in BEV coordinates as here, using the same reduced resolution also in the KS step should not affect the accuracy of the calculation, provided that the kernel varies slowly across the BEV voxels. Since, compared to the CPBs, the HPB kernel widths are increased by a similar amount to the voxel spacing, this should hold also for the HPBs. Thus, the effect of the lower resolution in the KS step is not expected to affect the accuracy of the calculation noticeably.

Beam Model Parameterizations

Since the Soukup model was implemented directly from the analytical expressions given in Eqs 3 and 4, little room was left for adjustments of the parameterization itself. Despite this, it resulted in a clear improvement over the single-Gaussian model both in the dose for a single PB in **Figure 3** and in the 2%/2 mm γ-index passing rates in the patient case. The overall improvement in the γ-indices compared to the single-Gaussian beam model can also be seen in **Figure 4**. Still, the model assumes that there is no halo dose at the surface (c.f. **Figure 2**), whereas the MC results shown in **Figure 1** clearly suggest the presence of such a contribution across the therapeutic range of energies for the beam line considered in this work. Therefore, using a more accurate description of the beam profile in air, such as a sum of two Gaussians, would likely further reduce the errors in the plateau region. A simple version of such an improvement would affect only how the weights are distributed between CPBs, and thus would have a negligible effect on the calculation time.

Although the direct parameterization method showed the best overall agreement for the single PB in water in **Figure 3**, the agreement was slightly worse than for the ideal fits of a sum of two Gaussians seen in **Figure 1**. The main reason for this is thought to be that, in order to more accurately model the multiple scattering in beams passing through different materials, the CPB widths of the primary contribution were calculated, as previously described (7), rather than obtained directly from the fit in water. Therefore, the width of the primary contribution at any given depth is constrained by the parameters E_S and δ, and, contrary to the halo contribution, cannot vary arbitrarily. More interestingly, the better average agreement did not translate to the γ-index passing rates, where the Soukup model showed better results. Looking at **Figure 4**, the γ-indices for these two models display similar behavior except for in limited regions where the indices for the direct model are considerably higher (c.f. the lower part of the left field in the coronal view of **Figure 4**). The reasons for this are not entirely clear. One explanation could be the relatively large underestimation of the PB central axis dose to a small number of voxels close to the surface seen in **Figure 3**. Another could be the larger halo fraction, which excludes more than just the nuclear interaction products from the more accurate physical modeling of the primary contribution. A third might be the rather arbitrary reduction of the width of the PB entrance profile that was employed to make the direct parameterization compatible with the existing beam model in air. In an improvement of the direct parameterization, constraints set on the primary contribution by E_S and δ could thus be included already in the fitting of the sum of two Gaussians. Furthermore, since the fit was seen to be relatively flexible, a preference to limit the size of the halo fraction could be included in order not to remove too much of the weight from the primary contribution. Finally, the empirical shrinking of the entrance dose applied here could be more accurately incorporated in the description of the beam profile in air.

Calculation Times

The benchmarking showed that, using one HPB per physical PB, the incorporation of a double-Gaussian beam model into the presented dose calculation engine lead to an increase in the total calculation time of no more than 16% for the two treatment plans tested. The increase in calculation time was larger for individual energy layers, ranging from about 50% for a small, shallow energy layer to around 25% for energy layers large enough to saturate the GPU. Both in the case of complete treatment plans and single energy layers, the increase in calculation time varied by only a few percentage points between the two parameterization models tested. These findings have two major consequences. The first is that employing either of the investigated parameterizations of the double-Gaussian beam model does not impact upon the suitability of the presented dose calculation engine for use in online dose calculation applications; calculation times of 16.5–16.8 ms for the deepest energy layer of the presented plans are still considerably shorter than the time between energy layers or the duration of a typical motion phase. The second is that as long as the presented implementation of the double-Gaussian beam model is used, the calculation time is unlikely to change significantly for other, beam line-specific or more sophisticated, parameterizations of the halo dose. Together, these indicate that, using a single GPU, it is possible to achieve fast enough calculation times for online dose calculation while maintaining the same accuracy as a widely adopted clinical algorithm, independent of the specific beam line.

The larger increase in calculation time for single energy layers than for complete treatment plans can be explained by the varying fractions of the total calculation time spent on different steps of the calculation. The calculation of complete treatment plans was dominated by the KS step, which, using the single-Gaussian beam model, was responsible for 76% of the calculation time for the patient plan and 88% of the calculation time for the cubic test case (excluding the time spent on memory transfers in both cases). Using the double-Gaussian parameterizations, the increase in calculation time for the KS step was 3–5% for the patient case and 14–18% for the cubic test case, which therefore resulted in increases of a similar order in the total calculation time for entire plans. For the individual energy layers, on the other hand, where the KS step is carried out only once, the calculation times of the steps that are carried out once per beam direction become comparable to the KS time. The calculation times for these steps generally increased more than that for the KS step when going from the single-Gaussian to the double-Gaussian beam model. In particular, the time required to set up the calculation and allocate

memory for BEV intermediates and the time to copy the dose distribution to texture memory both increased by between 20 and 40%. Furthermore, due to the larger number of voxels reached by the halo, the time required to transform the dose from the BEV coordinate system to the global dose grid roughly doubled. In the light of this, the overall increases in calculation time of 50% for a small energy layer or 25% for large energy layers are not surprising.

CONCLUSION

We have described how a double-Gaussian beam model was incorporated into an existing implementation of the PB algorithm running on a GPU while avoiding the prohibitive increase in calculation time expected from the large halo width. The increase in calculation time was not larger than 16% for entire treatment plans, and about 25% for large energy layers, which are the most time-consuming to calculate. Therefore, the addition of a double-Gaussian beam model does not alter the suitability of the presented implementation for use in online dose calculation. The calculation time was further shown to be relatively unaffected by the specific parameterization used to describe the halo dose contribution. Despite the calculation of the halo contribution being simplified compared to that of the primary, it was based on the same algorithm as a widely used commercial TPS. Therefore, it is expected that with adequate tuning, it will be able to reproduce with sufficient accuracy the halo dose of a general beam line. Based on these observations, we conclude that, using a single GPU, dose distributions from individual energy layers can be calculated with comparable accuracy to a modern clinical TPS well within the time of a typical motion phase or change of beam energy.

AUTHOR CONTRIBUTIONS

JS, RA, and RJ contributed to the conception and design of the study, and JS was responsible for the acquisition and analysis of the data. JS drafted the work that was critically revised for important intellectual content by RA and RJ. All authors approve of the submitted version and agree to be accountable for all aspects of the work.

ACKNOWLEDGMENTS

We would like to thank Mario Ciocca, Giuseppe Magro, Andrea Mairani, and Silvia Molinelli at CNAO (Pavia, Italy) for sharing data and models of the CNAO beam line, and for providing the patient case and corresponding dose distribution calculated with Fluka. We would further like to thank Till Böhlen at MedAustron (Wiener Neustadt, Austria) for help with MC simulations of individual PBs. This research was funded by the European Commission Seventh Framework People Programme through the ENTERVISION project, grant agreement 264552. RJ is funded in part by Cancer Research UK, grant number 13716. The Tesla K40 GPU used for benchmarking was donated by the Nvidia Corporation through their Hardware Grant Program.

REFERENCES

1. Jia X, Ziegenhein P, Jiang SB. GPU-based high-performance computing for radiation therapy. *Phys Med Biol* (2014) **59**:R151–82. doi:10.1088/0031-9155/59/4/R151
2. Yepes PP, Mirkovic D, Taddei PJ. A GPU implementation of a track-repeating algorithm for proton radiotherapy dose calculations. *Phys Med Biol* (2010) **55**:7107–20. doi:10.1088/0031-9155/55/23/S11
3. Kohno R, Hotta K, Nishioka S, Matsubara K, Tansho R, Suzuki T. Clinical implementation of a GPU-based simplified Monte Carlo method for a treatment planning system of proton beam therapy. *Phys Med Biol* (2011) **56**:287–94. doi:10.1088/0031-9155/56/22/N03
4. Jia X, Schümann J, Paganetti H, Jiang SB. GPU-based fast Monte Carlo dose calculation for proton therapy. *Phys Med Biol* (2012) **57**:7783–97. doi:10.1088/0031-9155/57/23/7783
5. Giantsoudi D, Schuemann J, Jia X, Dowdell S, Jiang S, Paganetti H. Validation of a GPU-based Monte Carlo code (gPMC) for proton radiation therapy: clinical cases study. *Phys Med Biol* (2015) **60**:2257. doi:10.1088/0031-9155/60/6/2257
6. Tseung HWC, Ma J, Beltran C. A fast GPU-based Monte Carlo simulation of proton transport with detailed modeling of nonelastic interactions. *Med Phys* (2015) **42**:2967–78. doi:10.1118/1.4921046
7. Da Silva J, Ansorge R, Jena R. Sub-second pencil beam dose calculation on GPU for adaptive proton therapy. *Phys Med Biol* (2015) **60**:4777–95. doi:10.1088/0031-9155/60/12/4777
8. Da Silva J, Ansorge R, Jena R. Efficient scatter-based kernel superposition on GPU. *J Parallel Distrib Comput* (2015) **84**:15–23. doi:10.1016/j.jpdc.2015.07.003
9. Lax I, Brahme A. Electron beam dose planning using Gaussian beams energy and spatial scaling with inhomogeneities. *Acta Oncol* (1985) **24**:75–85. doi:10.3109/02841868509134369
10. Russell KR, Isacsson U, Saxner M, Ahnesjö A, Montelius A, Grusell E, et al. Implementation of pencil kernel and depth penetration algorithms for treatment planning of proton beams. *Phys Med Biol* (2000) **45**:9–27. doi:10.1088/0031-9155/45/1/302
11. Pedroni E, Scheib S, Böhringer T, Coray A, Grossmann M, Lin S, et al. Experimental characterization and physical modelling of the dose distribution of scanned proton pencil beams. *Phys Med Biol* (2005) **50**:541–61. doi:10.1088/0031-9155/50/3/011
12. Soukup M, Fippel M, Alber M. A pencil beam algorithm for intensity modulated proton therapy derived from Monte Carlo simulations. *Phys Med Biol* (2005) **50**:5089–104. doi:10.1088/0031-9155/50/21/010
13. Sawakuchi GO, Titt U, Mirkovic D, Ciangaru G, Zhu XR, Sahoo N, et al. Monte Carlo investigation of the low-dose envelope from scanned proton pencil beams. *Phys Med Biol* (2010) **55**:711–21. doi:10.1088/0031-9155/55/3/011
14. Schwaab J, Brons S, Fieres J, Parodi K. Experimental characterization of lateral profiles of scanned proton and carbon ion pencil beams for improved beam models in ion therapy treatment planning. *Phys Med Biol* (2011) **56**:7813–27. doi:10.1088/0031-9155/56/24/009
15. Ulmer W, Schaffner B. Foundation of an analytical proton beamlet model for inclusion in a general proton dose calculation system. *Radiat Phys Chem* (2011) **80**:378–89. doi:10.1016/j.radphyschem.2010.10.006
16. Clasie B, Depauw N, Fransen M, Gomà C, Panahandeh HR, Seco J, et al. Golden beam data for proton pencil-beam scanning. *Phys Med Biol* (2012) **57**:1147–58. doi:10.1088/0031-9155/57/5/1147
17. Parodi K, Mairani A, Sommerer F. Monte Carlo-based parametrization of the lateral dose spread for clinical treatment planning of scanned proton and carbon ion beams. *J Radiat Res* (2013) **54**:i91–6. doi:10.1093/jrr/rrt051
18. Ciangaru G, Sahoo N, Zhu XR, Sawakuchi GO, Gillin MT. Computation of doses for large-angle Coulomb scattering of proton pencil beams. *Phys Med Biol* (2009) **54**:7285–300. doi:10.1088/0031-9155/54/24/003
19. Sawakuchi GO, Zhu XR, Poenisch F, Suzuki K, Ciangaru G, Titt U, et al. Experimental characterization of the low-dose envelope of spot scanning proton beams. *Phys Med Biol* (2010) **55**:3467–78. doi:10.1088/0031-9155/55/12/013

20. Fuchs H, Ströbele J, Schreiner T, Hirtl A, Georg D. A pencil beam algorithm for helium ion beam therapy. *Med Phys* (2012) **39**:6726–37. doi:10.1118/1.4757578
21. Li Y, Zhu RX, Sahoo N, Anand A, Zhang X. Beyond Gaussians: a study of single-spot modeling for scanning proton dose calculation. *Phys Med Biol* (2012) **57**:983–97. doi:10.1088/0031-9155/57/4/983
22. Zhu X, Poenisch F, Lii M, Sawakuchi G, Titt U, Bues M, et al. Commissioning dose computation models for spot scanning proton beams in water for a commercially available treatment planning system. *Med Phys* (2013) **40**:041723. doi:10.1118/1.4798229
23. Bellinzona V, Ciocca M, Embriaco A, Fontana A, Mairani A, Mori M, et al. On the parametrization of lateral dose profiles in proton radiation therapy. *Phys Med* (2015) **31**:484–92. doi:10.1016/j.ejmp.2015.05.004
24. Gottschalk B, Cascio EW, Daartz J, Wagner MS. On the nuclear halo of a proton pencil beam stopping in water. *Phys Med Biol* (2015) **60**:5627–54. doi:10.1088/0031-9155/60/14/5627
25. Ferrari A, Sala PR, Fasso A, Ranft J. *FLUKA: A Multi-Particle Transport Code*. Menlo Park, CA: Stanford Linear Accelerator Center (SLAC) (2005).
26. Böhlen TT, Cerutti F, Chin MPW, Fassò A, Ferrari A, Ortega PG, et al. The FLUKA code: developments and challenges for high energy and medical applications. *Nucl Data Sheets* (2014) **120**:211–4. doi:10.1016/j.nds.2014.07.049

Conflict of Interest Statement: The authors declare that the research was conducted in the absence of any commercial or financial relationships that could be construed as a potential conflict of interest.

Copyright © 2015 da Silva, Ansorge and Jena. This is an open-access article distributed under the terms of the Creative Commons Attribution License (CC BY). The use, distribution or reproduction in other forums is permitted, provided the original author(s) or licensor are credited and that the original publication in this journal is cited, in accordance with accepted academic practice. No use, distribution or reproduction is permitted which does not comply with these terms.

frontiers in Oncology

ORIGINAL RESEARCH
published: 30 November 2015
doi: 10.3389/fonc.2015.00258

First Steps Toward Ultrasound-Based Motion Compensation for Imaging and Therapy: Calibration with an Optical System and 4D PET Imaging

Julia Schwaab[1], Christopher Kurz[2], Cristina Sarti[1], André Bongers[1], Frédéric Schoenahl[3], Christoph Bert[4,5], Jürgen Debus[2], Katia Parodi[2,6] and Jürgen Walter Jenne[1,7]*

[1] Mediri GmbH, Heidelberg, Germany, [2] Department of Radiation Oncology, Heidelberg Ion-Beam Therapy Center (HIT), Heidelberg University Hospital, Heidelberg, Germany, [3] Siemens Healthcare AG, Zurich, Switzerland, [4] GSI Helmholtzzentrum für Schwerionenforschung, Darmstadt, Germany, [5] Strahlenklinik, Erlangen University Hospital, Erlangen, Germany, [6] Department of Experimental Physics – Medical Physics, Ludwig-Maximilian-University, Munich, Germany, [7] Fraunhofer MEVIS, Bremen, Germany

OPEN ACCESS

Edited by:
Jay Steven Loeffler,
Massachusetts General Hospital,
USA

Reviewed by:
Dalong Pang,
Georgetown University Hospital, USA
Sunyoung Jang,
Princeton Radiation Oncology, USA

***Correspondence:**
Julia Schwaab
j.schwaab@mediri.com

Specialty section:
This article was submitted to
Radiation Oncology,
a section of the journal
Frontiers in Oncology

Received: 13 July 2015
Accepted: 06 November 2015
Published: 30 November 2015

Citation:
Schwaab J, Kurz C, Sarti C, Bongers A, Schoenahl F, Bert C, Debus J, Parodi K and Jenne JW (2015) First Steps Toward Ultrasound-Based Motion Compensation for Imaging and Therapy: Calibration with an Optical System and 4D PET Imaging. Front. Oncol. 5:258. doi: 10.3389/fonc.2015.00258

Target motion, particularly in the abdomen, due to respiration or patient movement is still a challenge in many diagnostic and therapeutic processes. Hence, methods to detect and compensate this motion are required. Diagnostic ultrasound (US) represents a non-invasive and dose-free alternative to fluoroscopy, providing more information about internal target motion than respiration belt or optical tracking. The goal of this project is to develop an US-based motion tracking for real-time motion correction in radiation therapy and diagnostic imaging, notably in 4D positron emission tomography (PET). In this work, a workflow is established to enable the transformation of US tracking data to the coordinates of the treatment delivery or imaging system – even if the US probe is moving due to respiration. It is shown that the US tracking signal is equally adequate for 4D PET image reconstruction as the clinically used respiration belt and provides additional opportunities in this concern. Furthermore, it is demonstrated that the US probe being within the PET field of view generally has no relevant influence on the image quality. The accuracy and precision of all the steps in the calibration workflow for US tracking-based 4D PET imaging are found to be in an acceptable range for clinical implementation. Eventually, we show *in vitro* that an US-based motion tracking in absolute room coordinates with a moving US transducer is feasible.

Keywords: ultrasound imaging, ultrasound-based motion compensation, 4D PET imaging, ultrasound calibration, ultrasound in PET/CT

INTRODUCTION

Permanent target motion, particularly in the abdomen, due to respiration or patient movement is still a challenge in many diagnostic and therapeutic procedures (1) and demands methods to detect and compensate this motion.

Especially in external beam radiation therapy, but also in diagnostic imaging, several approaches to avoid distorted images or substantial dose errors were proposed: mechanical motion mitigation via active breath hold or gating relative to the respiratory cycles are common ideas, which, however,

extend treatment time and rely on the physical condition of the patient, as well as on a precise monitoring of the patient movement (2, 3). Several groups investigated motion detection by breathing belts or optical systems (4–6). These methods can detect irregularities like coughing or heavy breath takes but they only describe external motion and cannot observe the actual positions of inner organs. An example used in clinical practice is the breathing belt of the Respiratory Gating System AZ-733V (ANZAI Medical Co., Ltd., Tokyo, Japan), which only yields 1D tracking information of the outer abdominal movement.

Especially for tumor therapy with actively scanned ion beams, adaptive motion tracking (7, 8) promises to be fast and accurate at the same time, but this requires elaborate patient models that combine the external motion information to internal organ motion. Fluoroscopy offers the possibility to visualize inner structures, but it should not be used continuously during treatment because of the radiation burden (9). The *Calypso System* (Calypso Medical Technology, Seattle, WA, USA) used in prostate RT utilizes implanted RF-transponders for continuous motion tracking of the tumor (10). However, in this case, small beacons have to be implanted accurately near the tumor as fiducials.

An absolute, non-invasive, real-time capable method to monitor inner organs and register organ motion without any exposure to ionizing radiation would be the use of diagnostic ultrasound (US) imaging (sonography). It could be used continuously to detect the motion of a tumor either directly or by observing surrogate surrounding organs, for example, vessels (11) or the diaphragm (12). First experiments have shown that diagnostic US can be implemented successfully to radiosurgery using the CyberKnife (Accuray Inc., Sunnyvale, CA, USA) (13, 14). However, these two approaches rely on the tracking of fiducial markers, which might need to be implanted to the patient. The *Clarity* system (Elekta AB, Stockholm, Sweden), e.g., uses sonography to support inter-fractional positioning and recently to detect intra-fractional displacements of the prostate with a fixed US probe and at a rather low frame rate (2 Hz). In contrast to this quasi-static approach, our goal is to develop an US-based motion tracking method for real-time motion correction in 4D positron emission tomography (PET) imaging as used, e.g., for radiation therapy planning and verification. In addition, we want to consider a moving US tracking probe, e.g., attached to the patient skin and moved due to respiration, which requires a previous calibration of the tracking system – as also performed by Bruder et al. (15) for the CyberKnife.

The aim of this work was to integrate US-based motion monitoring to 4D PET imaging. This work is split into four parts: first, optical and US tracking systems were calibrated in order to provide absolute coordinate information independently of a moving US probe. Second, the US tracking was applied to 4D PET imaging and compared to the commercial ANZAI system, which is used in clinical practice. Third, artifact effects of the US probe in the PET/computed tomography (CT) field of view were investigated. Finally, US tracking in absolute coordinates was performed during 4D PET imaging in order to test the feasibility of the proposed workflow and the reliability of this new experimental setup.

METHODS

Calibration of US Tracking System

The optical US motion tracking setup comprises an US tracking system with a probe that is coupled to an optical marker as well as an optical tracking system, which detects the probe motion (see **Figure 1**).

When organ motion is detected by an optical US tracking system, there are four coordinate systems involved (see **Figure 1**): the one of the ultrasound images, the one of the optical marker tool T that is mounted statically on the US probe, the one of the optical sensor S, and the world coordinate system W, e.g., the treatment room. A point p_{US} is transformed to world coordinates as follows:

$$p_W = T_{S\ to\ W} \cdot T_{T\ to\ S} \cdot T_{US\ to\ T} \cdot p_{US} \quad (1)$$

A coordinate transformation from system A to system B is described by the affine 4×4 transformation matrix $T_{A\ to\ B}$. In order to perform a real-time coordinate transformation from US to W, we designed and implemented an all-in-one software application, which was used for both the calibration procedures as well as for the tracking.

For free-hand US calibration, a precisely manufactured phantom in a water bath (see **Figure 2**) is imaged several times with the US probe that is simultaneously tracked by an optical measurement system. To make sure that the acquired measurements yield a distinct (bijective) solution, all six degrees of freedom in the probe motion had to be taken into account and, thus, it was necessary to include multiple US images taken from different probe positions and orientations in the calibration process. The size of the water bath and the construction of the phantom allowed a broad polar and azimuthal imaging angle of the US probe.

The points p_{US} on the US images, representing the phantom structure, are correlated to their position p_W in the world coordinate system as described in Eq. (1). Using the known transformation $T_{T\ to\ S}$, which reports the corresponding position and orientation of the probe, the transformations $T_{US\ to\ T}$ and $T_{S\ to\ W}$ can be determined by optimization calculation. The ratio of distances in real world to pixel in the US image (mm/pix) is included in $T_{US\ to\ T}$. Due to the US image sector angle of 60°, it is the same in the *x*- and *y*-direction of the image.

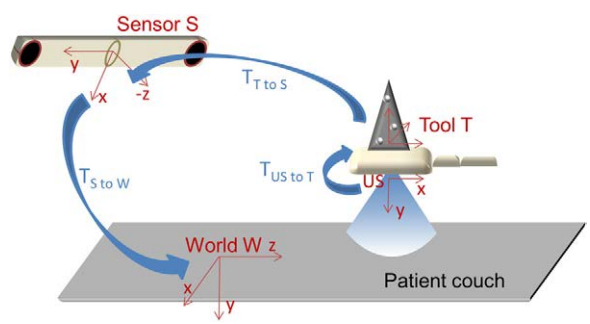

FIGURE 1 | The four involved coordinate systems in ultrasound motion tracking: ultrasound image plane US ($z_{US} = 0$), optical marker tool T, optical sensor S as well as treatment room ("world") W, and the transformations between them.

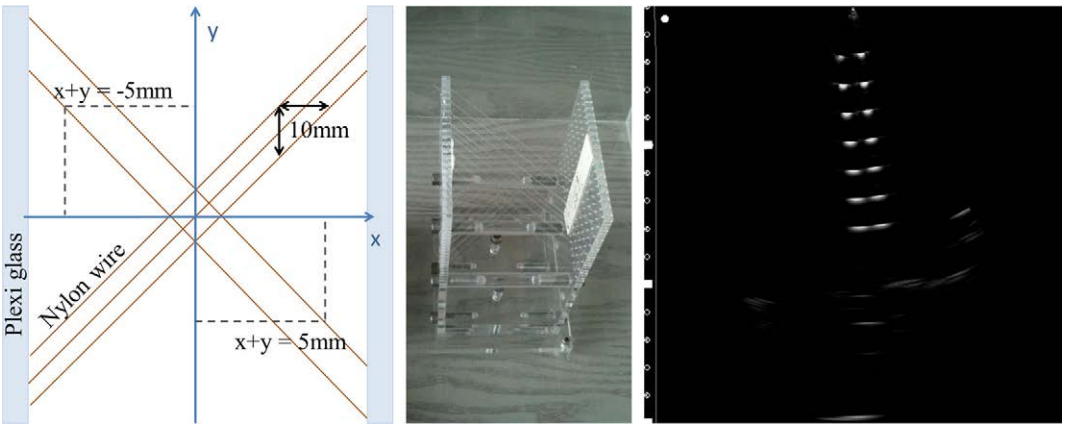

FIGURE 2 | The multi-cross wire water phantom. Schematic view from the top (left) and photograph (middle) as well as a typical ultrasound scan of the wire construction imaged from the top (right).

The US images and the corresponding position of the US probe were recorded and evaluated automatically. In total, 10 equivalent calibration measurements (to check the reproducibility), each consisting of 64 US images were performed. In previous experiments, the number of 64 images was found to be a good compromise between precision and feasibility of the calibration. The results were checked for their reconstruction accuracy and calibration reproducibility (precision) similarly to the methods described in (16). It is our understanding that the accuracy of a measurement describes the degree of closeness of the measurement result to its true value. Whereas the precision stands for the degree to which repeated measurements under unchanged conditions show the same results. The accuracy of the calibration result for $T_{\mathrm{US\ to\ T}}$ was determined in additional measurements using a point phantom in the water bath. To compute the precision, random points were projected from US to T using all 10 calibration results, respectively. Then, the variance in their positions was determined.

In this work, the world coordinate system was identical to the treatment room coordinates of a commercial PET/CT scanner (PET combined with CT). The transformation $T_{\mathrm{S\ to\ W}}$ between the 3D coordinates of the optical sensor and the world coordinate system was determined by placing an optical marker tool at defined positions on the patient table and recording the corresponding position of the tool (at rest) in the optical sensor system. Thus, every position of the tool could be determined in both the two relevant coordinate systems and yielded three equations for the optimization of $T_{\mathrm{S\ to\ W}}$.

The patient table of the PET/CT could be moved automatically with a precision of 0.1 mm in two directions (up and down, in and out of the bore). Motions in the third direction (x_W-axis of the PET/CT) were performed by hand with the aid of a ruler, which was mounted statically on the patient table. The precision of this supported free hand movement was 0.5 mm. To calibrate the optical sensor, in total, seven different runs, each with 10 different points in space, were conducted. To calculate the point reconstruction accuracy, each one of the seven measurement data sets served as cross-validation test data for the remaining six optimized transformation matrices. The calibration reproducibility (precision) was calculated by transforming three arbitrary but fixed points from the sensor coordinate system to the world coordinates using the seven optimized transformation matrices, respectively. The averaged deviations of the transformed points from their mean were used as estimation for the precision.

Integration of US Tracking to 4D PET Image Reconstruction

In this part of the study, motion compensation in 4D PET imaging based on the presented US tracking system was compared to the performance of a commercial breathing belt. The experimental setup is shown in **Figure 3** (*left*). A point source was moved along the PET/CT scanner axis by a respiratory motion phantom. A rubber ball was rigidly attached to the point source and put into a water-filled tank, which the US probe was coupled to through a Mylar foil window. Motion was simultaneously detected by the breathing belt, directly at the motion phantom as a standard reference, and by the US system, tracking the contour of the rubber ball. The whole setup was placed in the bore of the PET/CT scanner. A regular cosine^4-shaped motion pattern with a peak-to-peak amplitude of 3 cm and a period of 4 s as well as a real patient motion trajectory with a maximum peak-to-peak amplitude of 3 cm were investigated. The latter one was recorded once during a real 30-min 4D patient PET/CT scan using the breathing belt and could be reproduced by the motion phantom. All trajectories were one dimensional along the scanner axis and inside the bore.

The US tracking algorithm (12) uses active contours (17) and conditional density propagation (18). Active contours, also called snakes, are deformable splines, which are often applied to noisy 2D images for delineation of object outlines. Conditional density propagation ("Condensation") is then employed to track this contour. Based on the brightness values of an initially segmented target contour on the current US image, the algorithm yields five coordinates describing the position (translation in *x*-/*y*-direction), orientation (rotation within *x*–*y* plane) and scaling (scaling in *x*-/*y*-direction) of the target structure in real-time.

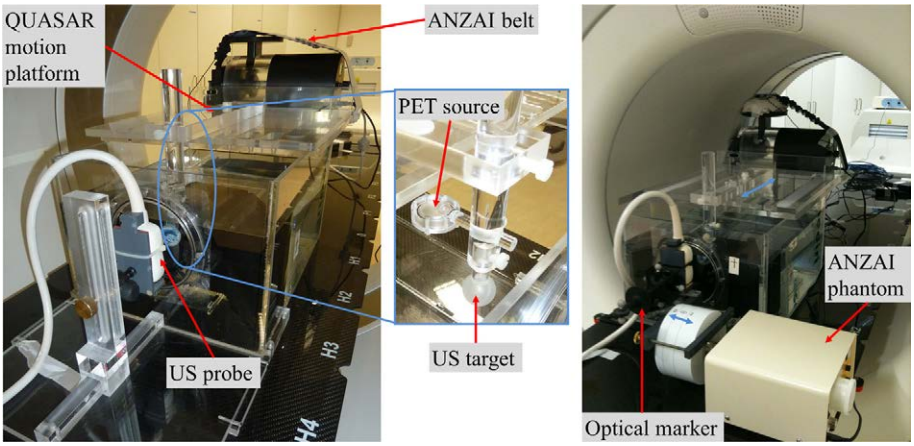

FIGURE 3 | Experimental setup for ultrasound-based motion tracking with static US probe (left) and with the US probe being moved by the ANZAI respiratory phantom (right) (from the optical sensor's point of view). The setup was positioned on the patient table of the PET/CT scanner. The US target (rubber ball) and the rigidly attached PET ^{22}Na point source were moved by the QUASAR motion platform. Motion was detected by the ANZAI breathing belt and the US probe in parallel.

Positron emission tomography data were acquired every single millisecond in list-mode (LM) format with time tags. To enable a 4D image reconstruction, the positions in time of the inhale peaks, usually provided by the ANZAI respiratory gating system, were written into the acquired LM data stream as the so-called gate-tags. In the performed gated 4D PET image reconstruction (which is presently the only available time-resolved reconstruction opportunity on the scanner used), the LM data are subdivided into a user-defined number of phases between each two gate-tags on the basis of phase sorting: this means that the data between two inhale peaks are split into equal time bins. Each phase is reconstructed separately, resulting in a significant reduction of the point-source motion in each phase, but also in a decrease of the number of counts and herewith a decrease of the signal-to-noise ratio. In this study, 4D PET LM data have been subdivided into eight phases, as typically done in 4D patient examinations, and reconstructed by a filtered back-projection. Image reconstruction included attenuation correction based on a CT scan that was acquired prior to the measurement. The CT scan was a so-called free-breathing CT taking into account the complete experimental setup that was in the bore. The separately reconstructed PET images of the eight motion phases have then been manually registered to a common reference phase, chosen as the first phase after the maximum inhale peak, summed up, and divided by the number of phases. In contrast to the standard ANZAI motion surrogate, the US tracking device cannot be coupled directly to the PET/CT scanner. Instead, the US motion signal was acquired in parallel on a separate computer system and merged into the acquired LM data retrospectively. For this, the inhale peaks in the US tracking signal, considering only the displacement parameter along the scanner (z_W-) axis, have been determined, corrected for the time offset between the two computer systems and were used to replace the ANZAI gate-tags within the acquired LM data. The temporal offset was computed by averaging the temporal shifts between corresponding inhale peaks of both motion monitoring systems. The inhale peaks were determined by means of Gaussian fitting. The manipulated LM stream, now containing US-based gate-tags, was then fed back in the PET/CT scanner, and reconstructed in the same way as the original LM data with ANZAI gate-tags. This enables a direct comparison of 4D-gated PET based once on the new US tracking device and once on the reference ANZAI system. The quantity of interest in this comparison was chosen to be the width of the point source in the direction of motion (along the scanner z-axis) in the reconstructed image, determined by a Gaussian fit at the x/y position of maximum activity.

Investigations of Artifact Effects of the US Probe in the PET/CT Field of View

In order to investigate the artifact effects of the US probe being within the lines of response of the PET detector ring, PET images of three radioactive point sources were acquired while the US probe was positioned close by the sources within the PET field of view. As shown in **Figure 4**, the three point sources were positioned in a horizontal diagonal line within a fixed small acrylic glass table construction, which was aligned with the laser cross hairs of the PET scanner. Five measurements were performed: one reference measurement without the US transducer and four measurements with the US transducer being fixated at different positions relative to the point sources. The four US probe positions were (a) next to the acrylic glass table in a central position at its edge, (b) next to the acrylic glass table close to a corner, (c) under the acrylic glass table, thus, approximately 6 cm under the central point source, and (d) lying on the table directly over the central point source. For each setup, an attenuation correction CT was acquired so that the US probe was taken into account during PET image reconstruction. The measured activities as well as the relative positions of the three point sources in the reconstructed image were compared, respectively.

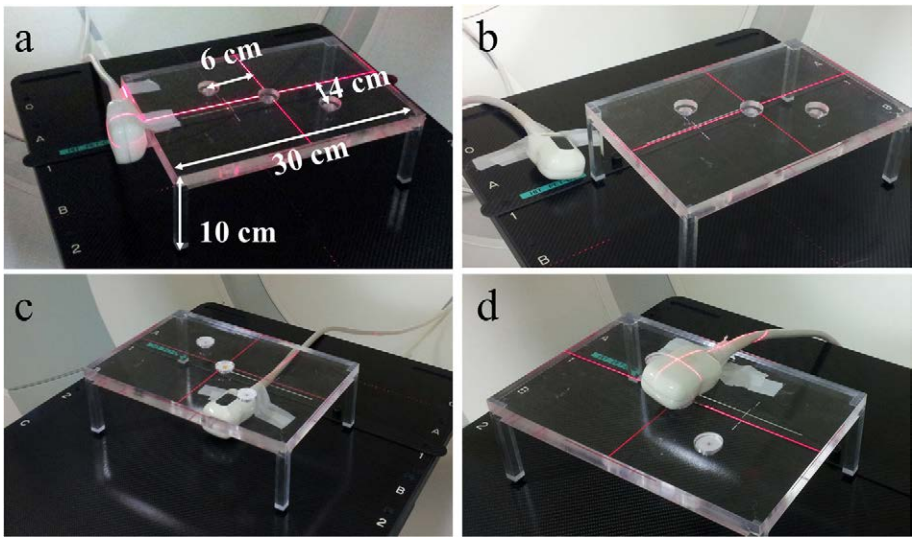

FIGURE 4 | Experimental setup for investigation of the US transducer's influence on PET image reconstruction. The three radioactive point sources were aligned in a horizontal diagonal line within the acrylic glass table. The measurement was repeated with the transducer in four different positions: **(A)** next to table (edge), **(B)** next to table (corner), **(C)** under table, and **(D)** on table.

Ultrasound-Based Motion Tracking with a Moving Probe *In Vitro*

The last part of this work was performed to test the feasibility of the whole calibration procedure as well as the US tracking in absolute coordinates using the optical tracking system. Therefore, a similar setup as described in section 2.2 was used. However, as shown in **Figure 3** (*right*), the US probe in front of the water tank was mounted on an additional motion phantom. It moved the probe sinusoidally ($A = 20$ mm peak-to-peak, $T = 4$ s) along the (horizontal) x_W- axis of the treatment room coordinate system and, thus, orthogonally to the target motion. The setup was positioned on the patient table. The optical sensor was mounted statically on a tripod in front of the PET/CT scanner. The PET and US data were acquired simultaneously during 12 min, which means that 240 periods of the target motion ($A = 40$ mm peak-to-peak along z_W, $T = 3$ s) were included.

As the radioactive point source was coupled rigidly to the moving US target, the transformed US tracking data could be compared to the position data of the reconstructed 4D PET images considering two constant offsets: the shift between rubber ball and radioactive point source was determined from the CT image of the setup and the distance between the PET coordinates and the world coordinates was defined by the manufacturer.

EXPERIMENTAL SETUP

The US tracking system used in this study is called Sonoplan II. It is developed by mediri GmbH, Heidelberg, Germany, and based on DiPhAS (digital phased array system, Fraunhofer IBMT, St. Ingbert, Germany). The US probe includes two 5.5 MHz phased array transducers (each with 64 elements), which are aligned perpendicular to each other (in one probe), allowing simultaneous imaging of two image planes. For optical tracking of the US probe motion, the Passive Polaris Spectra measurement system (Northern Digital Inc., Waterloo, ON, Canada) was used.

The calibration of the US tracking system was performed using a precisely manufactured water phantom. As shown in **Figure 2**, this multi-cross wire phantom consists of 29 nylon wires clamped between two acrylic glass plates with a distance of 80 mm. **Figure 2** (*right*) shows a typical US image of the wire phantom. Every bright point in the US image representing a phantom wire yielded two equations, which could be fed into the Levenberg–Marquardt optimization algorithm (19, 20) implemented in our software.

The combined PET/CT scanner that was used during this study is a Biograph mCT, manufactured by Siemens Molecular Imaging, Knoxville, TN, USA.

Two respiratory motion phantoms have been used during this study. To move the radioactive point source (PET marker) and the rubber ball (US marker), the commercial QUASAR respiratory motion platform (Modus Medical Devices Inc., London, ON, Canada) was employed. For the last part of this study, the US probe itself was moved by the motion phantom of the Respiratory Gating System AZ-733V (ANZAI Medical Co., Ltd., Tokyo, Japan). The breathing belt was also part of the ANZAI Respiratory Gating System.

The radioactive point sources employed in this study were ^{22}NA point sources or different activities.

RESULTS

Calibration of the Ultrasound Tracking System

The precision of the US calibration was 1.0 ± 0.5 mm and the accuracy was 4.7 ± 2.0 mm. The calibration of the optical tracking

system in the treatment room yielded an accuracy of 0.8 ± 0.2 mm and a precision of 0.5 ± 0.3 mm. The calibration results showed to be independent of the specifically chosen 10 measurement positions, as long as these were spread widely over the accessibly measurement volume. Thus, the overall accuracy of the tracking system was 4.8 ± 2 mm and its precision was 1.1 ± 0.6 mm.

Integration of Ultrasound Tracking to 4D PET Image Reconstruction

The acquired tracking data of the US system and the ANZAI surrogate are compared to each other in **Figure 5**. Of the 10 available tracking parameters determined by the US device for both imaging planes, only the displacement in the direction of motion (*z*-axis of the PET scanner), used in the retrospective LM data manipulation, is depicted. The other parameters were found to be constant in time for the selected one-dimensional motion aligned to the perpendicular US planes. As shown for both investigated motion patterns, a good agreement between the two tracking systems was found. Minor deviations were typically seen in the exhale part of the trajectory. In the performed 4D-gated PET image reconstruction, however, only the positions of the inhale peaks were of importance. Here, a typical deviation in time of less than 100 ms was found for all the investigated breathing patterns.

As shown in **Figure 6** for the cosine[4] motion, movement of the point source led to a considerable smearing of the point-like activity in the direction of motion and to a remarkably larger integral activity in the 3D reconstructed image due to the reduced partial volume effect. If, on the other hand, a 4D-gated image reconstruction was performed, motion-induced blurring was significantly reduced and the original Gaussian shape of the point source as well as the correct integral activity was recovered. This is shown in **Figure 6** (*right*) for both considered motion monitoring systems, the breathing belt and the US tracking. Still, compared to the static reference, the full width at half maximum (FWHM) increased from 5.2 ± 0.2 (1σ) to 8.2 ± 0.2 (1σ) mm due to the residual motion within each of the eight considered motion phases.

An overview of the FWHMs obtained by the 1D Gaussian fit along the direction of motion in the 4D-reconstructed PET images, based once on the ANZAI and once on the US tracking signal, is presented in **Table 1**, together with the SDs of the above-mentioned time differences between ANZAI and US

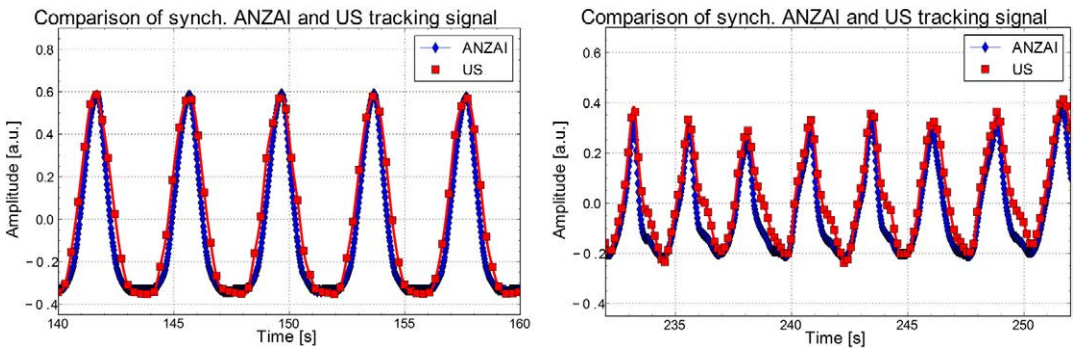

FIGURE 5 | Comparison of US- (squares) and ANZAI-detected (rhombi) motion trajectory. As the US system provides a considerably lower frame rate, the data have been interpolated. A generally good agreement between the two data sets was found. Particularly the positions in time of the inhale peaks agree precisely, typically within 100 ms.

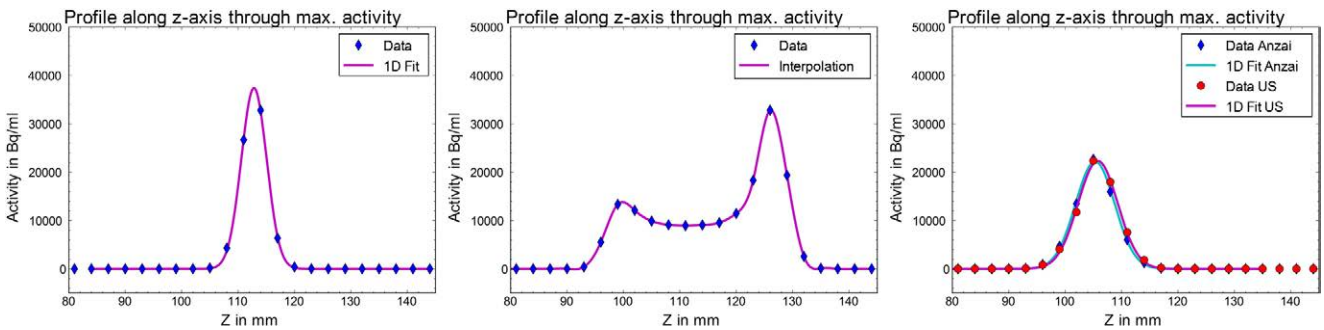

FIGURE 6 | Activity profiles of static (*left*) and moving (cosine[4]) point source in PET images. Middle: the activity of the source is smeared over the whole motion amplitude (here 3 cm) if not corrected for. Right: using the 4D gated reconstruction based on the breathing belt (blue rhombi) as well as the ultrasound (red dots) signal, the Gaussian shape and integral activity can be recovered.

TABLE 1 | Overview of the determined point-source FWHMs and the standard deviations of the inhale peak time differences.

Motion shape	Sinusoidal	Cosine^4	Cosine^4	Cosine^4	Patient-like
	$T = 4$ s	$T = 4$ s	$T = 4$ s	$T = 2.5$ s	$A_{max} = 3$ cm
	$A = 4$ cm	$A = 3$ cm	$A = 2$ cm	$A = 3$ cm	
$FWHM_Z$ (millimeter) ANZAI	9.6	8.2	7.2	8.3	7.3
$FWHM_Z$ (millimeter) US	9.6	8.3	7.4	8.3	7.5
STD (Δt) (millisecond)	50.0	32.3	41.4	33.6	81.1

The combined error of the manual registration and the Gaussian fit in the FWHMs was determined to be 0.2 mm. Within this error, the results retrieved with breathing belt and US tracking agree for all investigated cases.

inhale peaks. The depicted FWHM values have an uncertainty of 0.2 mm originating from the manual registration of the reconstructed phases to the chosen reference phase, in addition to the uncertainty of the performed fit. An error of 0.2 mm in the manual registration process was estimated by multiple registrations of the same data set and comparison of the determined FWHMs. The error in the 1D Gaussian fitting was typically below 0.1 mm. Taking these uncertainties into account, a very good qualitative agreement between the clinically used ANZAI gating system and the US tracking system was found. As expected, a higher motion amplitude generally resulted in a larger FWHM due to an enhanced residual motion in the single breathing phases. Concerning the patient-like data set, it has to be considered that the average breathing amplitude was about 2 cm, i.e., smaller than maximum peak-to-peak amplitude of 3 cm. The breathing period, on the other hand, did not affect the results because of the used phase-based sorting of the LM data.

Investigations of Artifact Effects of the Ultrasound Probe in the PET/CT Field of View

The applicability of US tracking for 4D PET reconstruction under the aspect of the US probe being in the detector field of view was tested. The measured activities of the three point sources were compared for the diverse transducer positions (**Table 2**). The values for each point source varied only slightly, up to 3.5%. There is one exception case for the central point source when the US probe was put directly on top of it. Here, an overcorrection in the reconstruction causes a deviation relative to the reference activity of 20.7%. Furthermore, the geometric distortions of the reconstruction were analyzed. Therefore, the top left point source was chosen as fixed point and always registered to its reference position. The deviations of the other two point sources from their reference position served as quantification of the image distortion. As can be seen in **Table 3**, the maximum deviation was 2.2 mm, which, however, is still below the PET voxel size.

TABLE 2 | Measured activities of the three point sources (top left, middle, bottom right) for the four different US transducer positions compared to the reference without transducer.

	Top left (10^8 Bq)	Middle (10^7 Bq)	Bottom right (10^8 Bq)
Reference	2.95	8.25	2.93
Next to table (edge)	3.01 (+2.0%)	8.17 (−1.0%)	2.83 (−3.4%)
Next to table (corner)	2.89 (−2.0%)	8.23 (−0.2%)	2.91 (−0.7%)
Under table	2.99 (+1.4%)	8.23 (−0.2%)	2.88 (−1.7%)
Over table	2.86 (−3.1%)	9.96 (+20.7%)	2.93 (+0.0%)

TABLE 3 | Geometric distortion caused by the US transducer being within the lines of response of the PET scanner.

	Middle (Δx, Δy, Δz) (millimeter)	Bottom right (Δx, Δy, Δz) (millimeter)
Next to table (edge)	0.0, 0.8, 0.3	−0.2, 2.2, 0.5
Next to table (corner)	0.3, 0.0, 0.3	0.6, 0.0, 0.8
Under table	0.4, 0.0, 0.4	0.6, 0.0, 0.8
Over table	0.1, 0.0, 0.3	0.6, 0.0, 0.8

The top left source was always registered to its reference position. The numbers represent the deviations of both the other sources from their reference position for all four transducer positions.

Ultrasound-Based Motion Tracking with a Moving Probe *In Vitro*

The setup could be installed at the PET scanner without problems, and both, the optical and the US tracking systems, performed as expected. The overall frame rate for the transformed tracking data was approximately 10 Hz due to the frame rate of the optical tracking, which we did not succeed to raise during this study. In **Figure 7**, the transformed US tracking data are plotted together with the PET reconstruction data along the x_W- and z_W-axes of the treatment room (world) coordinate. The US tracking data (gray dots) has a variance of 0.7 and 2.2 mm in x_W- and z_W-direction, respectively. These values range within the accuracy of the US calibration, which was found to be below 4.8 mm. The average positions of the point source for each of the 12 considered phases are plotted as black rhombi.

As shown in **Figure 7** (top), there is a discrepancy in the PET and US data of 4.8 ± 1.0 mm along the x-axis of the treatment room coordinates. This ranges within the accuracy of the US tracking system. Although the target was not moving along the x_W-axis, the US tracking data show a residual motion in the x_W-direction of ±2 mm with 3-s period. However, this is 80% less than the actual motion of the probe in x_W-direction of ±10 mm. In **Figure 7** (bottom), the measured target motion has the expected amplitude of 40 mm. The US and PET data coincide very well.

DISCUSSION

Calibration of the Ultrasound Tracking System

The calibration of the US system was performed with a multi-cross wire water phantom inspired by other multi wire and point

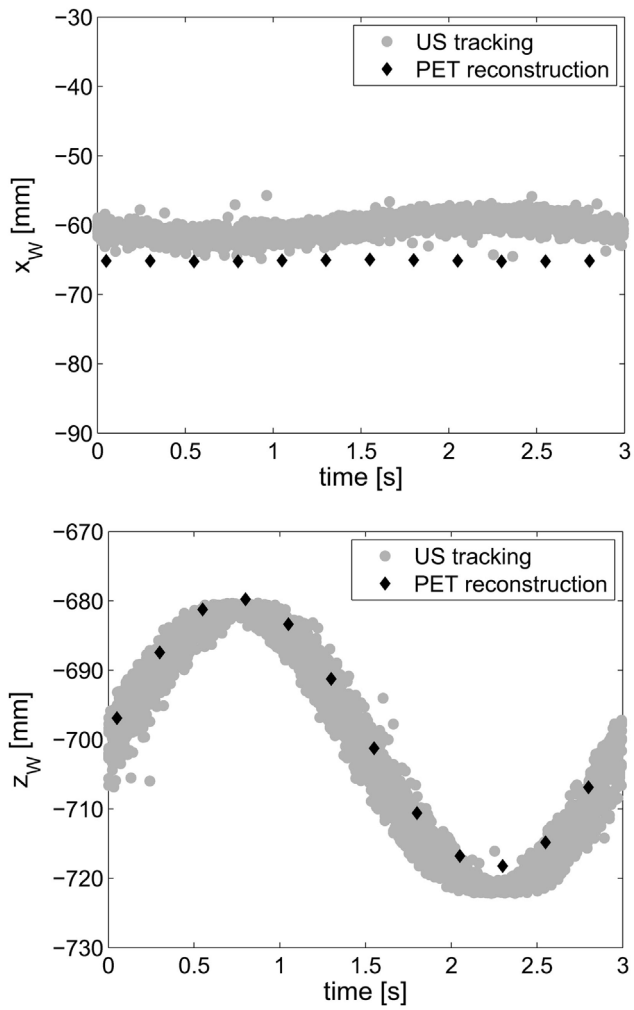

FIGURE 7 | Ultrasound tracking data transformed to world coordinates (gray dots) and PET reconstruction data along the x_W- and z_W-axes. The PET data have been corrected for the constant offsets both between rubber ball and radioactive point source as well as between the PET coordinates and the world coordinates.

phantoms (21–25). It combines the simplicity of a single-point phantom with the possibility of semi-automated segmentation.

The US calibration was performed at a penetration depth of 140 mm, which would be reasonable for abdominal applications. The accuracy was 4.8 mm and 4.9 mm for image planes 1 and 2, respectively. Considering the probe architecture with 64 elements in each of the two arrays and the large penetration depth, which yields a relatively poor resolution in the images, this is a reasonable value. The precision of the presented calibration method was determined to 1.0 and 1.5 mm for image planes 1 and 2, respectively. Hsu et al. (26) used another multi-wire phantom to perform a free-hand US calibration and achieved an accuracy of 3.0 mm and a precision of 1.2 mm for a curvilinear probe with a penetration depth of 150 mm. In the literature, various values that seem to describe a better performance with higher accuracy and precision can be found (16, 27). However, in most cases, they are obtained at a penetration depth of only about 30 mm and in addition to a higher frequency, which may be a reason for a higher resolution and better results.

For future works, a new phantom that can be scanned from even more diverse positions and orientations could help enhance the quality of the calibration. An alternative approach would be to integrate the optical marker in the construction plan of the US probe and manufacture it with adequate precision. Employing another transducer with a higher number of elements or using higher harmonics could also enhance the US image accuracy and, thus, the accuracy of the whole calibration.

The optical tracking system was calibrated such that it could yield the position and orientation of any optical marker tool within the measurement volume of the sensor not only in the sensor coordinate system but also in target space, i.e., treatment room coordinates. The accuracy of the presented calibration method is 0.8 ± 0.2 mm and the precision is 0.5 ± 0.3 mm. This is slightly below the volumetric accuracy that is reported by the manufacturer of the optical sensor. They determined the measuring accuracy to 0.30 mm (28). The accuracy and precision of the overall calibration procedure were determined to be 4.8 ± 2 mm and 1.1 ± 0.6 mm, respectively. This is fully acceptable for PET image reconstruction considering that it refers to absolute treatment room coordinates and yields *in situ* tracking information. In light of radiotherapy, it might be necessary to further improve the accuracy based on the amendments mentioned above.

Integration of Ultrasound Tracking to 4D PET Image Reconstruction

In a first experimental study with moving ^{22}Na point sources, a good agreement of the motion trajectories, simultaneously detected by the standard ANZAI pressure surrogate and the prototype US tracking system, was found. The method of retrospectively replacing the ANZAI gate-tags in the acquired LM PET data by the determined US gate-tags proved to work reliably. Concerning the motion mitigation in time-resolved PET imaging of moving point sources, an equivalent performance of both systems could be demonstrated (**Figure 6**). If no motion correction was applied, the activity distribution in the reconstructed 4D PET image showed the expected smearing and a higher integral activity, which was due to the reduced partial volume effect of the moving point source. If, however, motion correction was applied, the original Gaussian shape of the activity distribution could be recovered. As the first phase after the inhale peak was chosen as reference phase, the position of the activity distribution was slightly shifted toward "exhale" in the motion-corrected cases (**Figure 6** *right*).

A previous synchronization of each independent data set was found to be necessary in order to correct for the observed, non-constant time offset between the two different operating systems, which the tracking routines were run on. Consequently, the time offsets had to be determined at the beginning of each single PET acquisition. This problem can likely be solved by running the US tracking directly on the ANZAI computer, which was not

feasible in this study as the ANZAI computer is in clinical use and additional software installation not allowed. As reported in (29), part of the found time offsets might also be attributed to delays in the US tracking software. It was, however, shown that these delays can be overcome by an artificial neural network motion prediction.

In the presented results, a superiority of the US tracking system could not be shown due to the chosen setup and the used gated 4D PET image reconstruction, only relying on the position of the gate-tags, i.e., the inhale peaks, and not on the actual source position. In order to demonstrate the promised advantages of US tracking, a more detailed investigation with a more complex, 3D point-source motion, and a more sophisticated way of sorting the acquired LM data into the different motion phases, making use of all 10 provided US tracking parameters, would be of need and will be tackled in forthcoming studies.

Investigations of Artifact Effects of the Ultrasound Probe in the PET/CT Field of View

The influence of the US transducer being within the detector ring of the PET scanner showed to play a minor role in the image reconstruction. The induced changes in the measured activity of three point sources were all below 3.5%, which is only marginal. There was only one exception when the probe was lying directly on the central source. Here, the activity was overestimated in the reconstruction by 20.7%. However, this was caused by an overcorrection of the actually measured activities due to artifact effects of the US probe in the attenuation correction CT. These artifact effects will decrease when the CT is acquired with additional tissue (e.g., a patient) in the scanner. Furthermore, the geometric distortion in the reconstructed images due to the US probe was found to be smaller than 2.2 mm, which is negligible compared to the voxel size of the PET scanner.

Ultrasound-Based Motion Tracking with a Moving Probe *In Vitro*

In this experiment, the validity of the calibration and the practicality of the overall workflow were assessed. The setup showed that the proposed method allows real-time tracking in absolute coordinates even if the US probe was moved, e.g., by using an adhesive probe attached to the patient's skin.

The presented data prove that the main motion of the target is reproduced in the correct direction with the expected amplitude regardless of the probe moving or standing still. The probe motion could be mitigated by 80% (from 20 to 4 mm) due to the optical tracking. Taking into account that the chosen motion amplitudes represented the maximum values observed in respiratory motion, this result is quite promising. The frame rate should indeed be enhanced, however, 10 Hz are already sufficient for respiratory motion, which is in the scale of some seconds. Although the overall accuracy of the tracking system is only slightly below 5 mm, it is still acceptable taking into account that the tracking information is 2D and is acquired *in situ*. Clinically established non-ionizing portable systems mostly track surrogates or the patient surface and yield 1D information. For phase-based gated PET imaging as it is performed at the moment, this information might be sufficient. However, as soon as 4D-PET/CT systems are able to exploit tracking information from the complete amplitude, potentially in two dimensions, a comprehensive US-based tracking system will be beneficial. Abdominal structures as the liver vessels or the diaphragm allow for good 2D tracking not only of breathing motion but also of extraordinary patient movement, which then could be accounted for by advanced reconstruction algorithms of the imaging modality.

In the future, the presented optical US tracking system may be integrated into any time-resolved imaging process, such as 4D treatment planning or *in vivo* PET validation (30). Also, the presented method may find application in gated radiotherapy (31) or in conjunction with actively scanned ion-beams (29). To further exploit the opportunities and advantages of US tracking, it would be interesting to use both image planes of the T-probe or even a 3D transducer but this is beyond the scope of this report. Moreover, a registration process that fits a previously determined 3D model of the target to the actual US slice would enhance the procedure. Furthermore, an MRI compatible version of DiPhAS is being developed by mediri GmbH and Fraunhofer IBMT (32). The system is shielded with copper and development versions of the US probe can be attached to the patient's skin as a sticker.

CONCLUSION

In this work, a combined optical US tracking system for motion compensation in diagnostic and therapeutic systems with a moving probe was calibrated, implemented to 4D PET imaging, and evaluated. The accuracy and precision of all necessary calibration steps were found to be promising for clinical use. The functionality of all hardware and software components was tested in a proof of principle *in vitro* experiment to examine the overall reliability and feasibility of the proposed calibration workflow. Our initial study showed that 4D PET imaging based on US motion tracking is feasible. In a first experimental campaign, we could show that results equivalent to the clinically used ANZAI respiratory gating system could be achieved in 4D-gated PET. Further studies with more complex motion patterns, particularly with uncorrelated motions in more than one dimension, should aim to show the anticipated benefits from US motion tracking.

ACKNOWLEDGMENTS

Parts of this work were supported by the EU FP7 Project ENVISION (European NoVel Imaging Systems for ION therapy) under grant agreement no. 241851, and by the "Bundesministerium für Bildung und Forschung" (BMBF) BIO-DISC 5 Project no. 0315726A. The authors would like to thank Johannes Heitz and Dörte van Straaten, mediri GmbH, for their help in preparing the manuscript.

REFERENCES

1. Bert C, Durante M. Motion in radiotherapy: particle therapy. *Phys Med Biol* (2011) **56**:R113. doi:10.1088/0031-9155/56/16/R01
2. Stromberg JS, Sharpe MB, Kim LH, Kini VR, Jaffray DA, Martinez AA, et al. Active breathing control (ABC) for Hodgkin's disease: reduction in normal tissue irradiation with deep inspiration and implications for treatment. *Int J Radiat Oncol Biol Phys* (2000) **48**:797. doi:10.1016/S0360-3016(00)00681-7
3. Giraud P, Morvan E, Claude L, Mornex F, Le Pechoux C, Bachaud JM, et al. Respiratory gating techniques for optimization of lung cancer radiotherapy. *J Thorac Oncol* (2011) **6**:2058. doi:10.1097/JTO.0b013e3182307ec2
4. Baroni G, Garibaldi C, Riboldi M, Spadea MF, Catalano G, Tagaste B, et al. A. 3D optoelectronic analysis of interfractional patient setup variability in frameless extracranial stereotactic radiotherapy. *Int J Radiat Oncol Biol Phys* (2006) **64**:635. doi:10.1016/j.ijrobp.2005.07.964
5. Chang Z, Liu T, Cai J, Chen Q, Wang Z, Yin FF. Evaluation of integrated respiratory gating systems on a Novalis Tx system. *J Appl Clin Med Phys* (2011) **12**:3495.
6. Schaerer J, Fassi A, Riboldi M, Ceveri P, Baroni G, Sarrut D. Multi-dimensional respiratory motion tracking from markerless optical surface imaging based on deformable mesh registration. *Phys Med Biol* (2012) **57**:357. doi:10.1088/0031-9155/57/2/357
7. Bert C, Saito N, Schmidt A, Chaudhri N, Schardt D, Rietzel E. Target motion tracking with a scanned particle beam. *Med Phys* (2007) **34**:4768. doi:10.1118/1.2815934
8. Saito N, Bert C, Chaudhri N, Gemmel A, Schardt D, Durante M, et al. Speed and accuracy of a beam tracking system for treatment of moving targets with scanned ion beams. *Phys Med Biol* (2009) **54**:4849. doi:10.1088/0031-9155/54/16/001
9. Berbeco RI, Jiang SB, Sharp GC, Chen GT, Mostafavi H, Shirato H. Integrated radiotherapy imaging system (IRIS): design considerations of tumour tracking with linac gantry-mounted diagnostic x-ray systems with flat-panel detectors. *Phys Med Biol* (2004) **49**:243. doi:10.1088/0031-9155/49/2/005
10. Kupelian P, Willoughby T, Mahadevan A, Djemil T, Weinstein G, Jani S, et al. Multi-institutional clinical experience with the Calypso system in localization and continuous, real-time monitoring of the prostate gland during external radiotherapy. *Int J Radiat Oncol Biol Phys* (2007) **67**:1088–98. doi:10.1016/j.ijrobp.2006.10.026
11. De Luca V, Tschannen M, Székely G, Tanner C. A learning-based approach for fast and robust vessel tracking in long ultrasound sequences. *Med Image Comput Comput Assist Interv* (2013) **16**(Pt 1):518–25.
12. Zhang X, Günther M, Bongers A. Real-time organ motion tracking in ultrasound imaging using active contours and conditional density propagation. *Med Imaging Augment Reality* (2010) **6326**:286. doi:10.1007/978-3-642-15699-1_30
13. Blanck O, Jauer P, Ernst F, Bruder R, Schweikard A. Pilot-Phantomstudie zur ultraschallgeführten, robotergestützten Radiochirurgie (German article). *44. Jahrestagung der DGMP*; 2013 Sep 18-21. Cologne: DGMP (2013). p. 122–3.
14. Schlosser J, Salisbury K, Xing L, Hritov D. Hybrid X-ray/ultrasound imaging approach for aatient positioning and real-time tracking in IGRT. *Med Phys* (2011) **38**:3389. doi:10.1118/1.3611549
15. Bruder R, Ipsen S, Jauer P, Ernst F, Blanck O, Schweikard A. MO-D-144-02: ultasound transducer localization using the CyberKnife's X-ray system. *Med Phys* (2013) **40**:405. doi:10.1118/1.4815272
16. Hsu PW, Prager RW, Gee AH, Treece GM. Rapid, easy and reliable calibration for freehand 3D ultrasound. *Ultrasound Med Biol* (2006) **32**:823. doi:10.1016/j.ultrasmedbio.2006.02.1427
17. Kass M, Witkin A, Terzopoulos D. Snakes: active contour models. *Int J Comput Vis* (1988) **1**(4):321. doi:10.1007/BF00133570
18. Isard M, Blake A. CONDENSATION – conditional density propagation of visual tracking. *Int J Comput Vis* (1998) **29**(1):5. doi:10.1023/A:1008078328650
19. Levenberg K. A method for the solution of certain non-linear problems in least squares. *Q Appl Math* (1944) **2**:164.
20. Marquardt DW. An algorithm for least-squares estimation of nonlinear parameters. *J Soc Ind Appl Math* (1963) **11**:431. doi:10.1137/0111030
21. Detmer PR, Bashein G, Hodges T, Beach KW, Filer EP, Burns DH, et al. 3d ultrasonic image feature localization based on magnetic scanhead tracking: in vitro calibration and validation. *Ultrasound Med Biol* (1994) **20**:923. doi:10.1016/0301-5629(94)90052-3
22. Leotta DF. An efficient calibration method for freehand 3-D ultrasound imaging systems. *Ultrasound Med Biol* (2004) **30**:999. doi:10.1016/j.ultrasmedbio.2004.05.007
23. Rousseau F, Hellier P, Barillot C. Confhusius: a robust and fully automatic calibration method for 3D freehand ultrasound. *Med Image Anal* (2005) **9**:25. doi:10.1016/j.media.2004.06.021
24. Prager RW, Rohling RN, Gee AH, Berman L. Rapid calibration for 3-D freehand ultrasound. *Ultrasound Med Biol* (1998) **24**:855. doi:10.1016/S0301-5629(98)00044-1
25. Boctor EM, Jain A, Choti MA, Taylor RH, Fichtinger G. Rapid calibration method for registration and 3D tracking of ultrasound images using spatial localizer. In: Walker WF, Insana MF, editors. *Proc. SPIE 5035, Medical Imaging 2003: Ultrasonic Imaging and Signal Processing*. San Diego, CA (2003). 521 p. doi:10.1117/12.479953
26. Hsu PW, Prager RW, Gee AH, Treece GM. Real-time freehand 3D ultrasound calibration. *Ultrasound Med Biol* (2008) **34**:239. doi:10.1016/j.ultrasmedbio.2007.07.020
27. Rousseau F, Hellier P, Letteboer M, Niessen W, Barillot C. Quantitative evaluation of three calibration methods for 3-D freehand ultrasound. *IEEE Trans Med Imaging* (2006) **25**:1492. doi:10.1109/TMI.2006.877097
28. Wiles AD, Thompson DG, Frantz DD. Accuracy assessment and interpretation for optical tracking systems. In: *Proc. SPIE 5367, Medical Imaging 2004: Visualization, Image-Guided Procedures, and Display*. (2004). 421 p. doi:10.1117/12.536128
29. Prall M, Kaderka R, Saito N, Schwaab J, Sarti C, Parodi K, et al. Ion beam tracking using ultrasound motion detection. *Med Phys* (2014) **41**(4):041708. doi:10.1118/1.4868459
30. Kurz C, Bauer J, Bert C, Bongers A, Jenne J, Richter D, et al. First steps towards 4D offline PET-based treatment verification at the Heidelberg Ion Beam Therapy Center. *Radiother Oncol* (2012) **102**:S55. doi:10.1016/S0167-8140(12)70101-9
31. Boda-Heggemann J, Guckenberger M, Ganswindt U, Belka C, Wertz H, Blessing M, et al. Image guided radiotherapy (German article). *Radiologe* (2012) **52**:213. doi:10.1007/s00117-011-2192-0
32. Jenne J, Tretbar S, Hewener H, Speicher D, Schwaab J, Sarti C, et al. An MR-compatible ultrasound platform for therapy control and guidance. *44. Jahrestagung der DGMP*. Cologne: Harald Treuer (2013). p. 623–4.

Conflict of Interest Statement: The authors declare that the research was conducted in the absence of any commercial or financial relationships that could be construed as a potential conflict of interest.

Copyright © 2015 Schwaab, Kurz, Sarti, Bongers, Schoenahl, Bert, Debus, Parodi and Jenne. This is an open-access article distributed under the terms of the Creative Commons Attribution License (CC BY). The use, distribution or reproduction in other forums is permitted, provided the original author(s) or licensor are credited and that the original publication in this journal is cited, in accordance with accepted academic practice. No use, distribution or reproduction is permitted which does not comply with these terms.

frontiers in Oncology

REVIEW
published: 03 August 2016
doi: 10.3389/fonc.2016.00177

Monitoring of Hadrontherapy Treatments by Means of Charged Particle Detection

Silvia Muraro[1], Giuseppe Battistoni[1], Francesco Collamati[2], Erika De Lucia[2], Riccardo Faccini[3,4], Fernando Ferroni[3,4], Salvatore Fiore[4,5], Paola Frallicciardi[6,7], Michela Marafini[4,8], Ilaria Mattei[1], Silvio Morganti[3,4], Riccardo Paramatti[4], Luca Piersanti[2], Davide Pinci[4], Antoni Rucinski[4,6], Andrea Russomando[3,4], Alessio Sarti[4,6,8], Adalberto Sciubba[4,6,8], Elena Solfaroli-Camillocci[3,4], Marco Toppi[2], Giacomo Traini[3,4], Cecilia Voena[4] and Vincenzo Patera[4,6,8]*

[1] INFN Sezione di Milano, Milano, Italy, [2] Laboratori Nazionali di Frascati dell'INFN, Frascati, Italy, [3] Dipartimento di Fisica, Sapienza Università di Roma, Roma, Italy, [4] INFN Sezione di Roma, Roma, Italy, [5] UTTMAT, ENEA, Roma, Italy, [6] Dipartimento di Scienze di Base e Applicate per Ingegneria, Sapienza Università di Roma, Roma, Italy, [7] Istituto di Ricerche Cliniche Ecomedia, Empoli, Italy, [8] Museo Storico della Fisica e Centro Studi e Ricerche "E. Fermi", Roma, Italy

OPEN ACCESS

Edited by:
Francis A. Cucinotta,
University of Nevada – Las Vegas, USA

Reviewed by:
Dalong Pang,
Georgetown University, USA
Vivek Verma,
University of Nebraska Medical Center, USA

***Correspondence:**
Giuseppe Battistoni
giuseppe.battistoni@mi.infn.it

Specialty section:
This article was submitted to Radiation Oncology, a section of the journal Frontiers in Oncology

Received: 27 April 2016
Accepted: 15 July 2016
Published: 03 August 2016

Citation:
Muraro S, Battistoni G, Collamati F, De Lucia E, Faccini R, Ferroni F, Fiore S, Frallicciardi P, Marafini M, Mattei I, Morganti S, Paramatti R, Piersanti L, Pinci D, Rucinski A, Russomando A, Sarti A, Sciubba A, Solfaroli-Camillocci E, Toppi M, Traini G, Voena C and Patera V (2016) Monitoring of Hadrontherapy Treatments by Means of Charged Particle Detection. Front. Oncol. 6:177. doi: 10.3389/fonc.2016.00177

The interaction of the incoming beam radiation with the patient body in hadrontherapy treatments produces secondary charged and neutral particles, whose detection can be used for monitoring purposes and to perform an on-line check of beam particle range. In the context of ion-therapy with active scanning, charged particles are potentially attractive since they can be easily tracked with a high efficiency, in presence of a relatively low background contamination. In order to verify the possibility of exploiting this approach for in-beam monitoring in ion-therapy, and to guide the design of specific detectors, both simulations and experimental tests are being performed with ion beams impinging on simple homogeneous tissue-like targets (PMMA). From these studies, a resolution of the order of few millimeters on the single track has been proven to be sufficient to exploit charged particle tracking for monitoring purposes, preserving the precision achievable on longitudinal shape. The results obtained so far show that the measurement of charged particles can be successfully implemented in a technology capable of monitoring both the dose profile and the position of the Bragg peak inside the target and finally lead to the design of a novel profile detector. Crucial aspects to be considered are the detector positioning, to be optimized in order to maximize the available statistics, and the capability of accounting for the multiple scattering interactions undergone by the charged fragments along their exit path from the patient body. The experimental results collected up to now are also valuable for the validation of Monte Carlo simulation software tools and their implementation in Treatment Planning Software packages.

Keywords: hadrontherapy, real time monitoring, particle detection

1. INTRODUCTION

The use of particle therapy (PT) is becoming more and more effective for the treatment of solid cancer. The most common beams used nowadays in PT are protons, while the use of carbon ions, available worldwide only in a limited number of treatment centers, is now becoming more and more attractive.

The implementation of PT treatments that use ^{4}He beams, considered so far for the treatment of uveal melanoma (1, 2) and of patients with meningioma of the skull base or spine (3) is now being considered also for pencil beam treatments (4). The use of ^{16}O beams (5), another option, is also envisaged in the near future (6).

Light ion beams have a peculiar profile of released dose in tissues: this makes these beams very effective in the selective treatment of tumors, sparing the adjacent healthy tissues, compared with the standard X-ray-based treatment (7). A consequence of this higher spatial selectivity of PT is also stringent requirements on the accuracy that has to be achieved in the delivered dose monitoring.

Several factors affect the uncertainty on the position of the dose release in PT treatments. The calibration of the computed tomography (CT) images, or morphologic changes that can occur between the CT and the several irradiation sessions of a PT treatment, operated in different days, are among these possible sources of uncertainty. The correct dose release can also be affected by patient mis-positioning and organ motion during the treatment. All these contributions can sum up to a total uncertainty of the order of few millimeters on the actual voxel under treatment (8).

The treatment planning system (TPS) carefully manages the region around the tumor and the organs at risk, using a safety factor on the deliverable dose accounting for the uncertainty on its distribution. In order to protect the patient from the risks due to possible dose release misplacement, the number and the geometry of the treatment beam fields are properly designed.

A real-time monitoring procedure can, therefore, increase the quality assurance and the efficacy of a PT treatment (9). The main goal of on-line, "in-treatment," monitoring devices is the measurement of the dose release longitudinal shape, and in particular the determination of the actual Bragg peak (BP) position for each beam energy and target voxel. The physical processes of ion beam interaction with the tissues drive the energy release to proceed through electromagnetic interactions with the patient, while the emission of radiation escaping the patient, allowing for an imaging of its source, is due to strong interactions. These processes are the basis of the development of new approaches for the determination of the BP position.

There are three nuclear processes well suited for monitoring applications: production of β^{+} emitters nuclei, excitation of nuclei, and charged particle production in inelastic interactions. Nuclear β^{+} decays produce positrons that annihilate with the electrons surrounding the emission position and yield almost back-to-back 511 keV photon pairs. Photon detection can be exploited to measure the β^{+} production position, and correlate it with the Bragg peak position (10–14). Since the organic tissue is mostly constituted of carbon, hydrogen, and oxygen, the β^{+} emitting isotopes that are most likely to be produced are ^{10}C, ^{11}C, ^{15}O, and ^{13}N.

The beam interaction with the patient body, along the path toward the target voxel, can also excite nuclei and produce de-excitations photons emitted in a very short (<1 ns) decay time interval (prompt photons). The energy range of these photons extends up to about 10 MeV (15–18).

The target nucleus fragmentation, to which the projectile fragmentation has to be added in the case of PT performed with ions heavier than protons, can result in the production of charged fragments of smaller mass that could be exploited for monitoring purposes. Such fragmentation is a high cross-section strong process that it is not trivial to describe and quantify in the energy regime of interest, where the interaction projectiles have an energy ranging between 20 and 200 MeV/u and nuclear interactions are particularly difficult to model.

The velocity of fragmentation products is close to, or even larger than that of primary ions, while the latter experience a higher stopping power. For this reason, the fragments range is longer with respect to that of beam particles: this reflects into a characteristic dose tail behind the BP. This effect is particularly relevant for the treatments; therefore, it has been studied with dedicated nuclear cross-section experiments (19, 20) and with measurements of carbon ion collisions with water targets (21–24). By these experiments, fragmentation products proven to be peaked in the forward region and mostly contained within a cone of few degrees with respect to the beam axis. Protons, which represent the largest contribution, showed instead tails at large emission angles.

Several measurements have been performed during the last decade, to evaluate the dose contribution for healthy tissues, due to the production of beam fragments. More recent studies have been focused on the possibility of exploiting the secondary particle production (and in particular the highly penetrating proton component) for monitoring purposes, as it can be used to estimate the position of the dose profile distal edge.

A first proposal was advanced in Ref. (25) that introduced the method of "interaction vertex imaging" (IVI); this method aims at reconstructing the nuclear emission vertices distribution and correlates it with the BP position, by the detection of secondary protons. In measurements performed at small angle (26, 27), using solid state tracking devices at 30° with respect to the beam direction, the distal edge of the beam has been estimated with an accuracy of 1.3 mm. In addition, variations of the beam width (transverse dimension) have been measured with a precision of 0.9 mm.

On the basis of simple geometrical considerations, the production at large angles with respect to the incoming beam direction appears to be the most interesting for monitoring applications. The quality of the single charged particle trajectory reconstruction at large angles compensates for the expected reduced statistics.

It is naturally expected that the charged particle yield at large angle remains relevant in the case of beams of particles heavier than protons. Therefore, the use of charged particle detection for the on-line monitoring of PT treatments can be especially appealing in carbon therapy. The effective implementation of this technique requires the investigation of several different aspects. The spatial distribution of charged particles emitted at large angle by a tissue-equivalent target irradiated by a therapeutic beam has to be measured accurately in order to exploit the correlation with the longitudinal dose profile and, finally, with the BP position. These measurements have to be performed as a function of different projectile types and energies, characterizing

the yield of the different produced fragments and their angular distribution. Furthermore, in order to make an effective use of this approach in clinical practice, it is necessary to correlate each detected track with the position and direction of the primary beam. This also allows to take into account energy loss and scattering in the patient's materials. Therefore, this methodology for on-line monitoring can be effectively applied to ion therapy with active beam scanning (28).

The design and implementation of a tracking device suitable for clinical applications will also require an accurate study and optimization of the detector size and positioning in order to maximize the achievable track yield and detection resolution and match the clinical requirements on the dose release monitoring.

In section 2, we will review the main available experimental results regarding the yield of charged particles produced by therapeutic beams interaction with different targets. In section 3, the methods to correlate the spatial distribution of measured secondary particles with the BP position will be presented, introducing also some general considerations about the actual feasibility of charged particle monitoring in ion beam therapy.

2. CHARGED PARTICLES PRODUCTION BY THERAPEUTIC BEAMS

The research and development process of novel techniques for on-line monitoring applications to PT treatments relies heavily on a detailed experimental knowledge of the secondary radiations emitted by beam interaction with the patient body.

Improving the accuracy on the measurement of the flux of secondary particles and their angular and kinetic energy spectra has been the main goal of several experiments recently performed in the research centers of Laboratori Nazionali del Sud (LNS, Catania), Helmholtzzentrum Gesellschaft für Schwerionenforschung (GSI, Darmstadt), Heidelberg Ion-Beam Therapy center (HIT, Heidelberg), and Grand Accélérateur National d'Ions Lourds (GANIL, Caen) with ion beams of different types and energies.

Helium, carbon, and oxygen ion beam interactions with water or polymethyl methacrylate (PMMA) targets of different shapes were studied, in the beam energy range relevant for hadrontherapy monitoring applications, by means of high efficiency charged particle tracking detectors.

Charged fragments, subject of this review, have been studied in two different angular ranges: particles detected at an angle θ with respect to the beam incoming direction between 0° and 45° (26, 27) and particles detected at large θ (60°, 90°, and 120°) angles (29, 30).

The θ spectrum of produced particles is of key importance when designing on-line monitoring devices to be integrated in hadrontherapy treatment rooms. The quest for the highest statistics data sample is hardened by the mechanical restrictions imposed by the patient positioning and related safety devices, and has also to account for beam induced background and backtracking issues for configurations at angles close to the beam incoming direction.

Although the secondary production at large angle was thought for a long time to be negligible, the experimental results have actually unveiled that the light charged fragments production, mainly protons and hydrogen isotopes, occurs even at very large θ angles with an integrated yield compatible with the requirements set by on-line monitoring applications.

The measurements performed with a small PMMA target (4 cm thickness) at LNS using a carbon beam with 80 MeV/u energy, also confirmed that a significant production of charged fragments occurs in BP proximity (29). This experimental result suggests that monitoring by means of charged fragments detection could be exploited also superficial tumor treatments.

Hereafter, we present the experimental setup used for the different measurements and the yield of charged particles produced at different angles.

2.1. Small Angle Production

A first set of measurements was performed at HIT (26), using carbon ions, of kinetic energies relevant for PT applications, impinging on a cylindrical PMMA phantom with size comparable to the human head (diameter: 160 mm, height: 90 mm). Aim of the test was to characterize the beams available in the HIT facility, looking at the secondary charged fragments produced in the interaction with the PMMA target.

The beams available in HIT have full width at half maximum (FWHM) values that are energy-dependent and range typically from 4 to 20 mm. The available energies, in the range of 48–221 MeV for protons and 89–430 MeV/u for carbon ions, correspond to beam ranges in water between 2 and 30 cm.

The directions of secondary charged particles emitted from the PMMA phantom were measured using two parallel 300-μm thick silicon pixel layers at a distance of 3.6 mm (Timepix detector). The Timepix (31) detector was placed at $\theta = 30°$ at a 10-cm distance from the PMMA center. The choice of the θ angle was driven by the needed robustness of the back-projection method for the data analysis on the one hand, and by the secondary ion yield, i.e., the multiplicity of secondary ions per primary ion, which decreases with increasing angle from the beam axis, on the other.

Different energy, width, and position configurations of the carbon beam were studied. The nominal beam intensity was set to 2×10^7 ions/s and for each investigated beam parameter setting and about 2×10^9 primary carbon ions were irradiated on the phantom when collecting the various data samples. The obtained secondary charged particle directions were analyzed using the back-projection method from Ref. (32).

In all the tested configurations, a non-negligible production of charged particles was observed with a production spectrum that was correlated to the dose release in the phantom, as shown in **Figure 1** for a carbon ion beam of 250.08 MeV/u kinetic energy and FWHM of 4.3 mm.

As the principal aim of the test was to characterize the beam parameters with the tracking detector, no measurement of the charged fragments flux was performed. However, taking into account that the size of the sensitive area of the used detector (~2 cm^2) allows to cover only a small fraction (~0.15%) of the

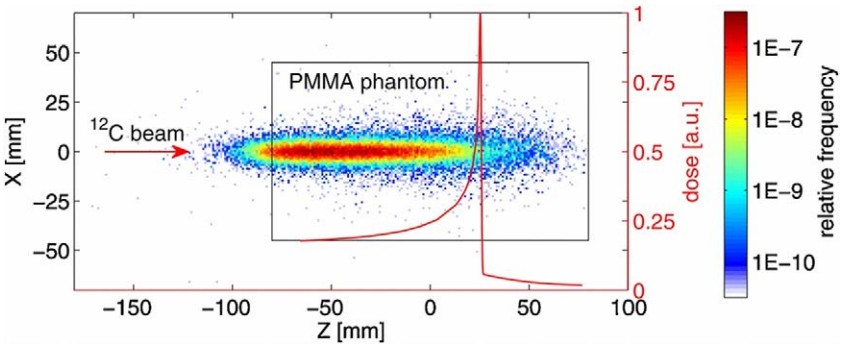

FIGURE 1 | Distribution of the track back-projections for 5 × 10⁴ measured secondary charged particles produced by the interaction of a carbon beam with a PMMA phantom at the HIT facility (26). The dimensions of the cylindrical PMMA phantom are illustrated by the black rectangle (view from the side). The origin of the coordinate system is aligned with the center of the phantom that was placed in the isocentre. The carbon ion beam was directed along the *Z*-axis. The depth dose distribution measured in water and scaled to the phantom water equivalent path length (WEPL) is shown by the red curve. Due to experimental limitations, the depth-dose distribution could be measured only for water depths greater than 20 mm. Initial carbon ion beam parameters: E = 250.08 MeV/u, FWHM = 4.3 mm. © Institute of Physics and Engineering in Medicine. Reproduced by permission of IOP Publishing. All rights reserved.

forward hemisphere around a patient, and that by decreasing the detector dead time and using a ring of detectors around the patient will greatly enhance the particles statistics, the authors concluded, on the basis of the measured yields, that the monitoring of single beam spots at the distal edge of typical brain tumor treatments with charged particles is a realistic opportunity.

Other tests were performed at small angles using PMMA and water targets: a 95 MeV/u ^{12}C beam was used at GANIL (21) to study the fragments production from PMMA targets of various thicknesses at small angles; a 200 MeV/u ^{12}C beam was used at GSI (22) to study the production of light fragments from the beam interaction with a 128-mm-thick water target at $\theta < 30°$; a 310 MeV/u ^{12}C ion beam irradiating a 21-cm-thick water target was used to study the light fragments production at 30° and 45° (27).

While the GANIL studies implemented ΔE-E telescopes at different angles, using thin silicon layers and a final stage with CsI and BGO ~7.5-cm-long scintillators placed ~20 cm away from the target, the GSI experiment used ΔE-E telescope built with a NE102 scintillator paddle followed by a BaF_2 crystal placed 3 m away from the target. In the GANIL setup, the charged fragment identification was performed using the ΔE vs. E distributions, while in the GSI experiment performed using the 200 MeV/u carbon ion beam the additional information coming from the fragments time of flight computed using the BaF_2 detector signals was used.

In the study performed with the 310 MeV/u energy carbon ion beam, a single telescope was alternatively placed at 30° and 45° with respect to the beam and in the forward direction, at a distance of 2.2 m from the target center. This telescope was composed by a thin plastic scintillator followed by a NaI(Tl) scintillator cylinder 5 cm in diameter and 5 cm in length. Thin scintillators were set upstream from the target to allow Time of Flight (ToF) measurements, triggered by incident ions, as it was done for the study performed at 200 MeV/u. The ToF of the detected particle, together with the energy deposited in the telescope detector, allowed to identify protons, deuterons, and tritons. **Figure 2** shows the results obtained for the 310 MeV/u beam data sample (right) compared to Monte Carlo simulation (left) performed with the Geant v.4 9.2 toolkit (33).

High-energy particles, with ToF lower than a given threshold, escape the scintillator depositing only a fraction of their energy in it. This determines the triangular shape of the distributions for each particle type. The maximum equivalent energy deposited by protons in the 5 cm long NaI scintillator (upper point of the triangular shape distribution), on the vertical axis, was set to the corresponding energy deposition calculated by SRIM (34).

Figure 3 shows the measured and simulated values of the detected proton yields as a function of the detection angle for the three beam energies (95, 200, and 310 MeV/u). The observed yield decrease is consistent between data and MC, as a function of the θ angle. The yield discrepancies between open symbols (exp. data) and filled symbols (sim.) are at most at the 40% level. The observed yields in all the angular configurations are compatible with the requirements of on-line monitoring applications, as discussed in Section 3.

2.2. Large Angle Production

The production of charged secondary particles from the irradiation of a PMMA target has been studied at large θ angles (≥60°) for fully stripped carbon ion beams at the LNS, GSI, and HIT facilities with energies ranging from 80 to 220 MeV/u. The experimental setup, which had only small variations in the different laboratories where the data acquisition was performed, is presented in a schematic view in **Figure 4** for the experiment performed in GSI using a carbon beam of 220 MeV/u energy impinging on a PMMA target.

The tracking detectors and the details of the analysis performed on the reconstructed track sample are common to all the experiments.

An array of 4 LYSO crystals, each measuring 1.5 cm × 1.5 cm × 12 cm, was placed at 60°, 90°, and 120° with respect to the beam line, at ~70 cm from the PMMA center. The scintillation light of the crystals was detected with a PMT triggered in

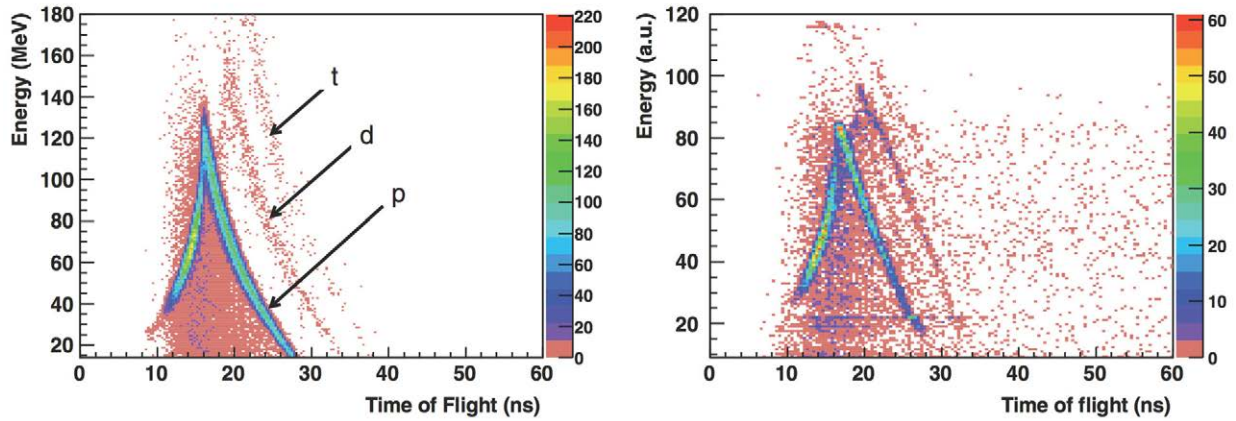

FIGURE 2 | From Ref. (27): energy vs. time of flight (expressed in nanoseconds) distributions obtained for 310 MeV/u carbon ions incident on a 21-cm-thick water target with the telescope located at 30° with respect to the beam direction at 2.2 m from the target center. Left: simulation with Geant v.4 9.2 toolkit, right: measurements (GSI experiment). p, d, and t refer to protons, deuterons, and tritons in the simulated distributions (the background events are mainly due to fragmentation reactions in the scintillator). © Institute of Physics and Engineering in Medicine. Reproduced by permission of IOP Publishing. All rights reserved.

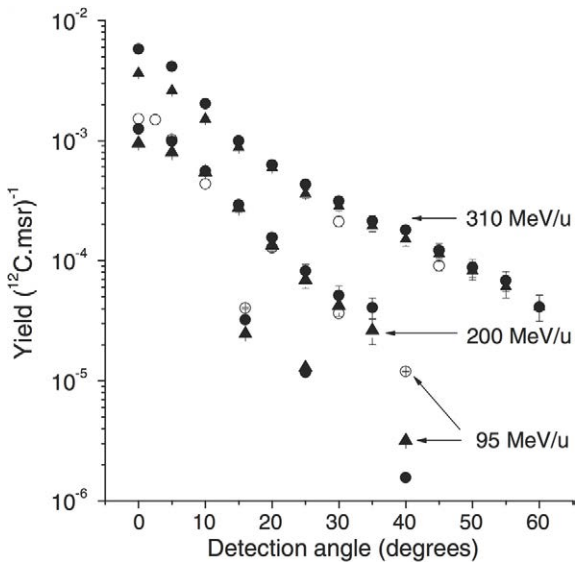

FIGURE 3 | From Ref. (27): experimental (open symbols) and simulated (filled symbols) proton emission yields as a function of emission angle and carbon ion energy (and target thickness): 310 MeV/u ^{12}C, 210 mm water target (GSI experiment), 200 MeV/u ^{12}C, 128 mm water target (22), and 95 MeV/u ^{12}C, 25 mm PMMA target (21). Simulations performed with the QMD (circles) and BC (triangles) models are shown. © Institute of Physics and Engineering in Medicine. Reproduced by permission of IOP Publishing. All rights reserved.

coincidence, within 80 ns, with the Start Counter system sketched in **Figure 4**. Details on the energy and time calibration of the LYSO crystals can be found in Ref. (35).

A 21-cm-long drift chamber (20) was placed at ~50 cm from the PMMA center, along the line of flight connecting the PMMA to the LYSO crystals. The drift chamber provided a 2-dimensional track reconstruction by alternated horizontal (*x-z* plane V-view) and vertical (*y-z* plane U-view) layers of wires. Twelve layers, six on each view, provided high tracking efficiency, tracking redundancy, and excellent spatial resolution, which turned out to be ≤200 μm with a single cell efficiency of ≃ 96%.

The experimental setup has been simulated by means of the FLUKA Monte Carlo software (36, 37) taking into account the trigger logic, the experimental energy thresholds and the quenching effect in the scintillator (38). MC results have been used to evaluate the setup efficiencies, geometrical acceptances, and to guide the development and tuning of the Particle IDentification.

The main difference with respect to what reported in **Figure 4** for the 80 MeV/u nucleon energy measurement performed at LNS is the absence of Start Counter 2, since only one start counter was used, and the absence of the Veto detector. Furthermore, the LNS experiment was performed only detecting charged fragments at 90° with respect to the beam incoming direction.

The HIT experimental setup, used to study helium, carbon, and oxygen beams was using only one start counter, as well, but implemented a different Veto detector: a Long Thin Scintillator (LTS) was used and placed just along the PMMA, between the target and the DCH detector, in order to compute the Time of Flight of the charged fragments. The angular production configurations that were tested were, respectively, $\theta = 60°$ and 90°.

In the LNS experiment, the interactions of an 80 MeV/u fully stripped ^{12}C ion beam with a 4 cm × 4 cm × 4 cm PMMA target were studied (29). At GSI a thicker, 20 cm × 5 cm × 5 cm, PMMA target was irradiated with a 220 MeV/u fully stripped ^{12}C beam (30). During the GSI data taking the PMMA phantom was positioned on a movable table, connected to a micrometric screw, capable of shifting the phantom position along the beam (*x*) axis of about few millimeters.

The beam rate in all cases, ranged from hundreds of kilo Hertz to few Mega Hertz and was monitored with a 1.1-mm-thick

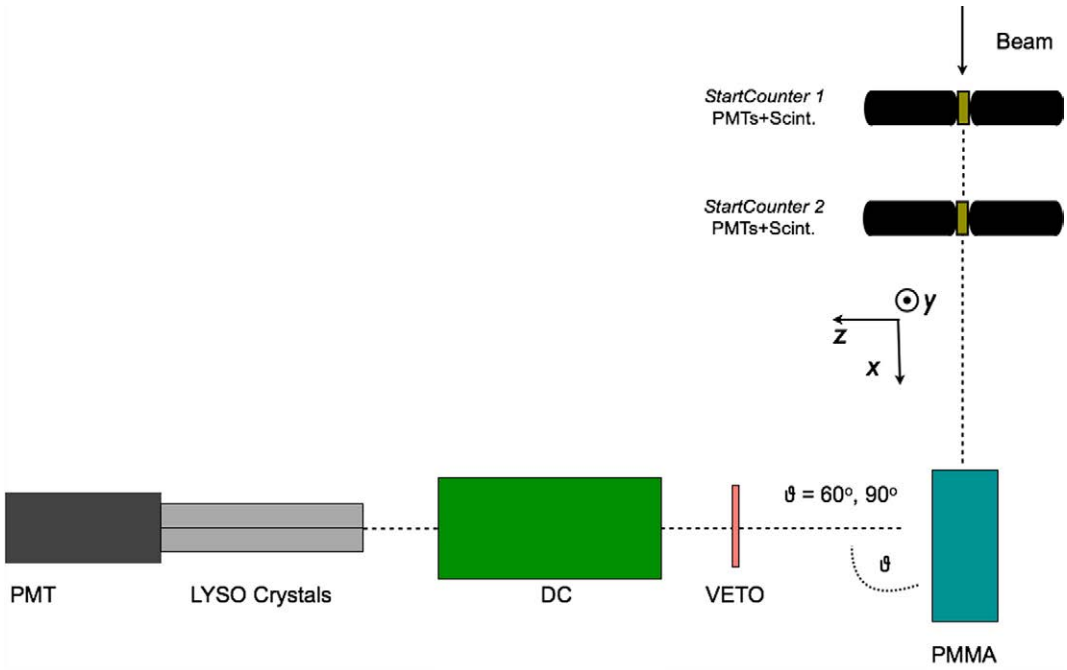

FIGURE 4 | From Ref. (30): top schematic view of the experimental setup for the 90° configuration used for the data acquisition performed in the GSI laboratory using a fully stripped carbon ion beam of 220 MeV/u. The small differences presented in the LNS and GSI setup are described in detail in the text.
© Institute of Physics and Engineering in Medicine. Reproduced by permission of IOP Publishing. All rights reserved.

scintillator (Start Counter) placed on the beam line between the beam exit window and the PMMA entrance side.

Charged particles were identified starting from the tracks reconstructed in the DC using at least eight fired cells (hits), since tracks traversing the full detector are expected to have twelve hits associated. To identify the tracks, the distribution of the deposited energy in the LYSO detector (ELYSO) as a function of Time of Flight (ToF) was exploited. As an example, **Figure 5** shows the measured distribution for the data collected at LNS. In the data sample (left panel) for ToF values around zero, the area delimited by the first dashed line is populated by a fast low-energy component, due to electrons produced, in the PMMA material, by Compton scattering of the de-excitation photons induced by beam interactions.

The central most populated band, delimited by the two dashed lines, is constituted by protons whose detected energy spans within a very wide range. These protons also caused the saturation of the LYSO crystals QDC for $E_{\mathrm{LYSO}} > 24$ MeV, clearly visible. Similar populations in the (ToF, E_{LYSO}) plane with an additional component of deuterons, above the second dashed line, are shown by the FLUKA simulation (right panel). This component is not clearly visible in data.

The data signature, with the bands relative to the different hydrogen isotopes, is common to all the experiments performed in the LNS, GSI, and HIT facilities, with a relative population of the different bands that depends on the beam type, beam energy, and settings (RMS), the PMMA thickness traversed by the fragments toward the exit window, as well as the possible different response of the LYSO crystals. The saturation that can be seen in the data distribution at energies E_{LYSO} larger than 23 MeV is due to the limited range of the QDC used during the data acquisition.

The only band visible in the (ToF, E_{LYSO}) plane for the data collected at LNS (shown in **Figure 5**) has been defined using the data and MC distributions in order to identify and select protons in the data sample and measure their yield.

Similar distributions in the (ToF, E_{LYSO}) plane have been observed for the GSI 220 MeV/u data both at 90° and 60°. The velocity (β) spectrum of secondary charged particles represents an important information for monitoring purposes, since, in order to emerge from the patient's body and to be detected, they have to cross several centimeters of tissue. The β values distributions were obtained in two different ways in the LNS and GSI, HIT data analyses. While for the HIT test, the measurement of the ToF of the charged fragments was performed directly using the signal from a scintillator close to the exit path of the fragment inside the PMMA target; in the LNS and GSI setup, no dedicated detector was available and a dedicated unfolding had to be performed to take into account the travel time of the incoming ion inside the PMMA and the occurrence of secondary fragment production.

Figure 6 shows the distributions of $\beta = \frac{v}{c}$ and the corresponding detected kinetic energy E_{kin} for the identified protons, obtained using the ToF measurement together with the distance between LYSO crystals and PMMA for the data collected at LNS. This detected kinetic energy can be related to the proton kinetic energy at emission time, $E_{\mathrm{kin}}^{\mathrm{Prod}}$, considering the energy loss in the PMMA and the quenching effect of the scintillating light for low energy protons.

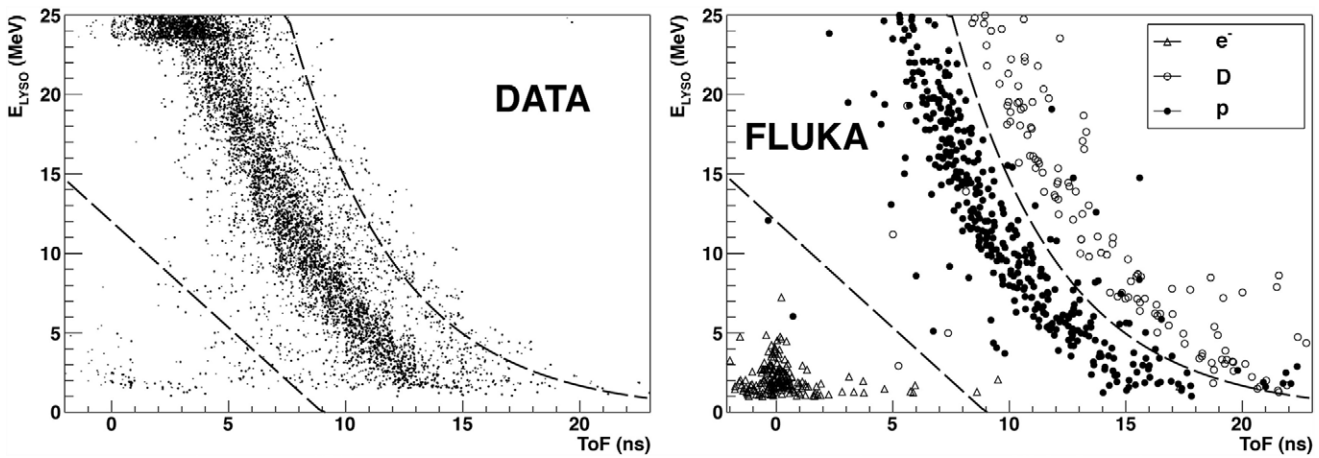

FIGURE 5 | From Ref. (29): distribution of the detected energy in the LYSO crystals as a function of the Time of Flight for the data sample collected at the LNS facility using a carbon ion beam at 80 MeV/u. The distribution observed in the data (left) and FLUKA Simulation (right) samples are shown. © Institute of Physics and Engineering in Medicine. Reproduced by permission of IOP Publishing. All rights reserved.

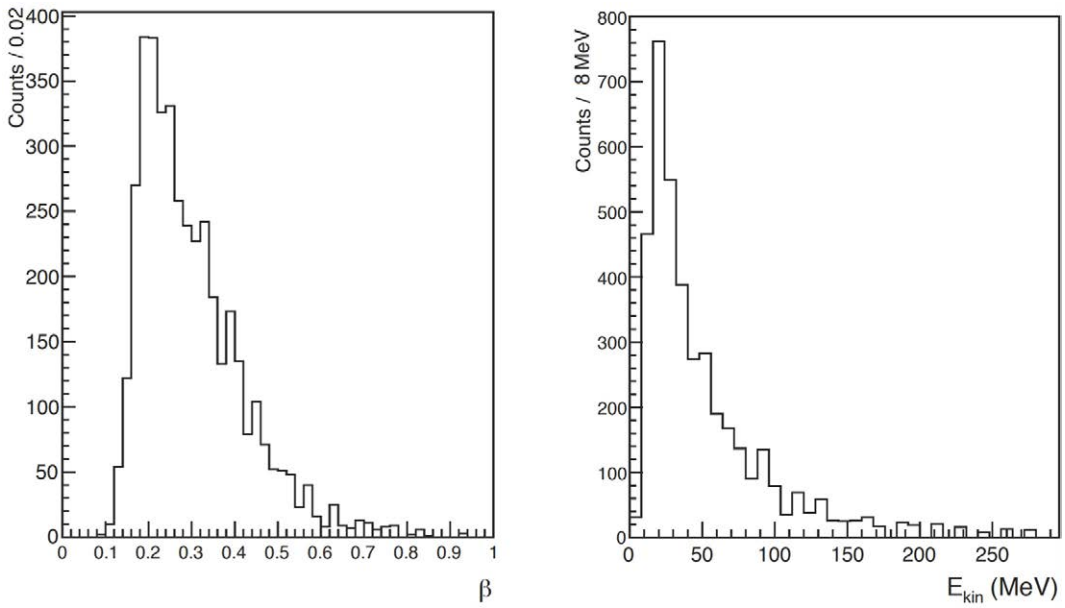

FIGURE 6 | From Ref. (29): distribution of $\beta = \frac{v}{c}$ (left) and kinetic energy (right) of charged secondary particles identified as protons in the LNS data sample. © Institute of Physics and Engineering in Medicine. Reproduced by permission of IOP Publishing. All rights reserved.

In the analysis of the particle ToF for the GSI data, the finite size of the beam spot, multiple scattering of charged particles traversing the PMMA target, different energy losses, and slowing down of the various isotopes that passed through the target were taken into account. The sample is dominated by the proton contribution both in 90° and 60° samples.

The β distributions (β_{rec}) of the dominant protons contribution are shown in **Figure 7** for the setup configuration at 90° (squares) and 60° (circles), respectively. For each angular configuration, all spectra were normalized to the relative number of isotope species detected by the LYSO crystal. In order to use the secondary protons for monitoring purposes, the effect of crossing some centimeters of patient's tissue has to be taken into account. Therefore, protons with detected kinetic energies greater than 50–60 MeV are the most interesting for the above-mentioned application.

Using the data collected at LNS, the flux of the secondary protons emitted from the beam interaction with the PMMA has been measured at 90° with respect to the beam direction and in the geometrical acceptance of the triggering LYSO crystals, since this configuration maximizes the sensitivity to the Bragg peak position. To determine the rate of emitted charged secondary particles that reached the LYSO crystals, the number of carbon

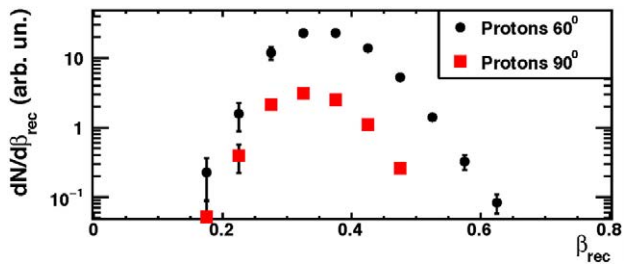

FIGURE 7 | From Ref. (30): measured emission velocity (β_{rec}) distributions for protons in the data sample collected at the GSI facility using a 220 MeV/u carbon ion beam. The error bars show the total (statistical plus systematic) uncertainty. © Institute of Physics and Engineering in Medicine. Reproduced by permission of IOP Publishing. All rights reserved.

ions impinging on the PMMA target has been calculated by counting the number of signals in the Start Counter taking into account the Start Counter efficiency, the discrimination time and the acquisition dead time.

The minimum required energy to detect a proton in the LYSO crystals was evaluated using the FLUKA simulation to be $E_{\text{kin}}^{\text{Prod}} = 7.0 \pm 0.5$ MeV. FLUKA has also been used to compute the emission energy ($E_{\text{kin}}^{\text{Prod}} = 83 \pm 5$ MeV) of a proton with an average detected kinetic energy $E_{\text{kin}} = 60$ MeV. The uncertainty that affects the result is mainly due to the finite size of both the beam spot $\mathcal{O}$ (1 cm) and profile.

The production fluxes of light charged fragments at 90° with the 80 MeV/u LNS carbon beam, obtained requiring a kinetic energy at production greater than 7 or 83 MeV are, hence, respectively $(7.1 \pm 0.14_{\text{stat}} \pm 0.32_{\text{sys}}) \times 10^{-5} sr^{-1}$ and $(2.14 \pm 0.06_{\text{stat}} \pm 0.10_{\text{sys}}) \times 10^{-5} sr^{-1}$ with the systematic contribution mainly due to identification of protons and to the uncertainty on the production kinetic energy related to the beam's transversal profile uncertainty. A very good stability of the result is observed with respect to the rate of the carbon ions impinging on the PMMA.

In a similar way, the results for the $Z = 1$ overall charged particles *fluxes* have been measured at GSI. The results obtained using a 220 MeV/u carbon ion beam, for the 60° and 90° experimental configurations are the following:

$$\frac{dN}{dN_C d\Omega}(\theta = 60^\circ) = (12.59 \pm 0.08_{\text{stat}} \pm 0.76_{\text{sys}}) \times 10^{-3} sr^{-1}$$

$$\frac{dN}{dN_C d\Omega}(\theta = 90^\circ) = (2.74 \pm 0.02_{\text{stat}} \pm 0.16_{\text{sys}}) \times 10^{-3} sr^{-1}$$

where the leading contributions to the systematic uncertainty is the evaluation of the dead time in data acquisition. The results are compatible with the extrapolations made from the yields measured at smaller angles and measured with different ion beam energies and target media.

The data taken with ^{12}C beam at HIT confirmed the GSI measurements and non-negligible production of protons at large angles was also observed for other ion species. **Figure 8** shows the longitudinal emission profiles of protons detected at $\theta = 90°$,

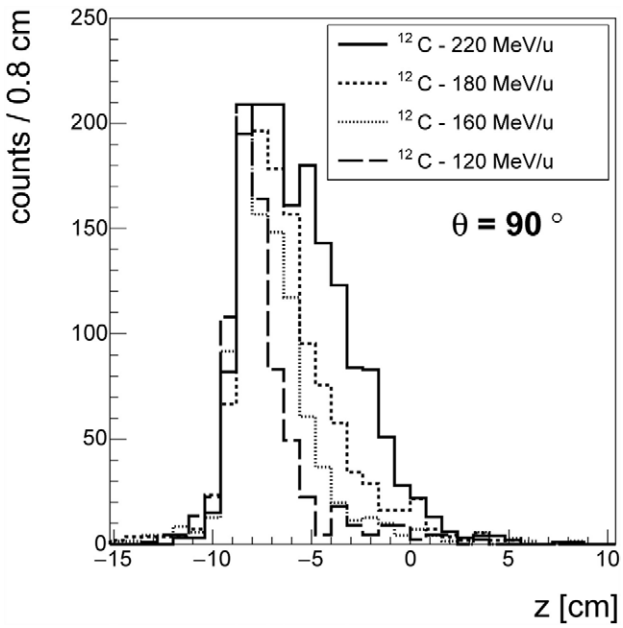

FIGURE 8 | Emission profile of the charged fragments in the case of the ^{12}C beam at different energies at $\theta = 90°$ with respect to the primary beam direction.

for carbon beams at four different energies (120, 160, 180, and 220 MeV/u). As in Ref. (30), the emission shape could be correlated to the beam entrance window and the BP position. While the fluxes calculation is still being finalized, the production of charged secondary fragments at large angle is found to be consistent with what already measured in different experimental setups and centers.

The HIT experimental setup was also used to measure the secondary particles production that occurs in the PMMA targets by the interactions of ^{4}He and ^{16}O beams at therapeutical energies. When studying these ion beam particles, the thickness of the PMMA target was changed as a function of the ion type and energy, in order to keep the BP at about 1 cm before the end of the target. This configuration was used in order to reduce to a minimum the systematic uncertainty related to the forward interaction of the heavy fragments with the PMMA target after the BP, for the forward production studies performed with BGO detectors.

The analysis of the data collected with ^{4}He and ^{16}O beams is being finalized in order to produce a measurement of the absolute production fluxes: the observed raw yields are, however, encouraging for what concerns on-line monitoring applications.

3. THE EXPLOITATION OF CHARGED PARTICLE DETECTION FOR RANGE MONITORING

3.1. The Charged Particles Emission Distribution

The measurement of the emission shape distribution of the charged particles produced by the beam interactions with the

patient tissue was recently presented in Ref. (25, 27) in the context of discussing the possible strategies for the development of an on-line tool for PT treatments monitoring. Two possible approaches were investigated with the help of Monte Carlo simulations calibrated on the measurement reported in Ref. (21, 22): single proton interaction vertex imaging (IVI) and double proton IVI, whose principle is sketched in **Figure 9**.

More sophisticated algorithms based on the determination of most likely trajectory [MLEM, for instance, Ref. (39)] could be also envisaged, but the simple imaging approach sketched in **Figure 9** is already showing the monitoring approach fundamental principles.

Although Double Proton imaging would lead, in principle, to a safer determination of the primary path in the target by requiring the simultaneous emission and detection of a pair of protons, it reduces too much the statistic of the available signal sample.

A Single Proton imaging approach turns out then to be the only possible solution. However, in this case, the knowledge in real time of the beam position in the transverse plane during the monitoring procedure would be needed. As this information can be easily obtained from the beam delivery system, the emission point of the detected secondary particle can be obtained as the point of closest approach between the known beam line and the measured secondary particle direction.

The discussion about the optimal angle at which a monitoring detector exploiting the secondary charged radiation should be placed with respect to the primary beam direction (see **Figure 9**) was addressed, for the first time, in the framework of the IVI approach. Still, the choice of such geometrical parameter has a strong dependence on the angular distribution of the emitted charged secondary fragments and on the final accuracy that is achievable on the BP position. This turns out to be fundamental in any dose profile monitoring application.

At small detection angles, the emission flux increases and the charged particles energy spectrum is shifted toward higher kinetic energies. This configuration maximizes the charged fragments statistics that can escape the patient body, and be detected, while minimizing the Multiple Scattering (MS) inside the patient.

On the other hand, the accuracy on the charged emission point is maximal, for geometrical reasons, for orthogonal detection with respect to the beam line. As shown in **Figure 10**, if the projection (shadow) of the beam spot on the beam line is taken into account, the spatial resolution on the emission shape worsens as $(\sin\theta)^{-1}$. This effect is described by a term $\simeq \sigma_{beam} \times \cot(\theta)$ that becomes dominant for small detection angles. The above considerations lead the authors of Ref. (30) to focus on the measurements at large angle with respect to the primary beam directions, as already discussed in Section 2. When designing an operational setup to be used in actual treatments, the accuracy gain that could be achieved, from a geometrical point of view, at large θ has to be taken into account in combination with the already mentioned larger statistic and the higher average kinetic energy of the emitted particle at smaller angles, in order to obtain the necessary optimum trade off.

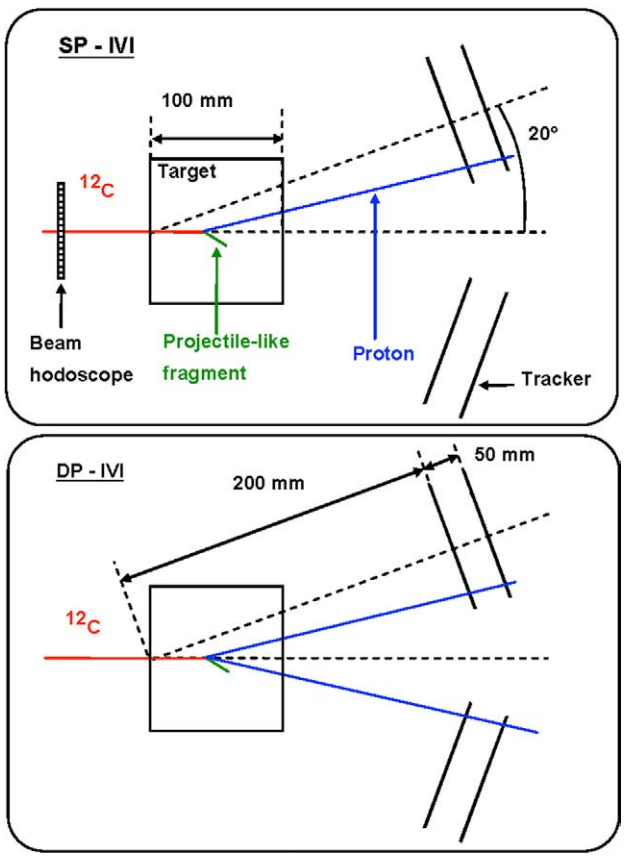

FIGURE 9 | Principle of single proton interaction vertex imaging (SP-IVI) and double proton IVI (DP-IVI) as analyzed in Ref. (27). © Institute of Physics and Engineering in Medicine. Reproduced by permission of IOP Publishing. All rights reserved.

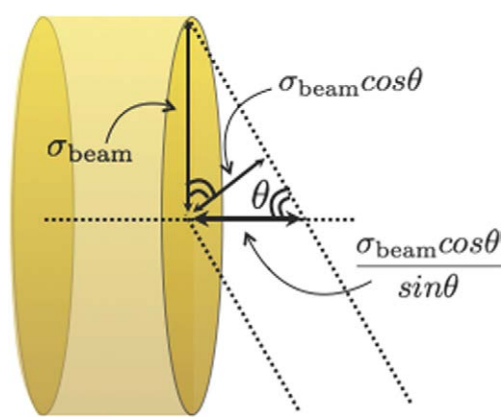

FIGURE 10 | From Ref. (30): schematic view of the beam spot size contribution to the uncertainty on the reconstruction of the fragments emission region in the case of an experimental setup placed at an angle θ with respect to the primary beam direction. © Institute of Physics and Engineering in Medicine. Reproduced by permission of IOP Publishing. All rights reserved.

A key point in the range monitoring with charged particles is the correlation of the charged secondary emission profile with the beam dose release, and in particular with the BP position. A typical approach is to correlate the fall-off of the emission profile with the BP position, as shown in **Figure 11** from Ref. (27), where the fall-off of the simulated SP-IVI reconstructed vertex distributions for a 95 MeV/u ^{12}C beam is shown in case of different thicknesses of material (PMMA) crossed from the emission point to the detector. The smooth lines correspond to fits of equation (1) where the complementary error function (erfc) is being used.

$$f(x) = a + b \times erfc[c(x-d)] \quad (1)$$

The d parameter, which corresponds to the inflection point position, is assumed to provide information that can be correlated to the primary ion range.

The authors of Ref. (27) pointed out that the target thickness slightly affects the vertex distribution shape, since the secondary protons absorption affects the low-energy protons produced upstream less than those emitted at the end of the ion path. They also concluded that, probably, the proposed fit function is not appropriate in high attenuation conditions.

In Ref. (30), a different function is proposed to fit the longitudinal emission distribution of charged particles detected at large angles (equation (2)).

$$f(x) = p_0 \frac{1}{1+exp\left(\frac{x-p_1}{p_2}\right)} \frac{1}{1+exp\left(-\frac{x-p_3}{p_4}\right)} + p_5. \quad (2)$$

Figure 12 (left) shows the measured longitudinal emission distribution of charged particles emitted at 90° (solid line) by a 220 MeV/u ^{12}C beam in a PMMA phantom, with a superimposed depth-dose profile as calculated with the FLUKA Monte Carlo code (36, 37) (hatched-area distribution). A clear correlation is observed between the beam entrance position in the target and the rising edge of the x_{PMMA} distribution.

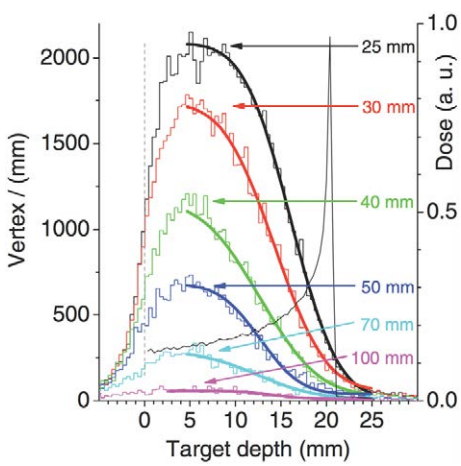

FIGURE 11 | Simulation of SP-IVI reconstructed vertex distributions for a low beam energy 12C of 95 MeV/u in PMMA for different targets thickness, as calculated in Ref. (27). © Institute of Physics and Engineering in Medicine. Reproduced by permission of IOP Publishing. All rights reserved.

The right panel of **Figure 12** shows that the x_{PMMA} distribution is well described by equation (2): parameters p_3 and p_1 are, respectively, related to the rising and falling edge of the distribution, while the rising and falling slopes of the function are described by p_4 and p_2. A flat background contribution is accounted for through parameter p_5. The beam finite size can be explicitly added at different detection angles with respect to the beam direction as a convolution term of a Gaussian function with $\sigma \simeq \sigma_{beam} \times \cot(\theta)$. equation (2) accurately described all the measured emission profiles for different isotopes and data samples taken with different geometrical conditions (beam entrances) and angle configurations (60° and 90°).

Using this functional form, two quantities have been derived that are directly related to the beam range: Δ_{40} and δ_{40}, as shown in the right panel of **Figure 12**. Δ_{40} represents the width of the $f(x)$ distribution at 40% of its maximum, X_{left} and X_{right} being, respectively, the corresponding x-values at the rising and falling edges. δ_{40} represents the distance between X_{left} and the x-intercept of the tangent to $f(x)$ at $x = X_{right}$.

Several elements influenced the accuracy of the proposed methods in monitoring the Bragg peak position: the multiple scattering undergone by the fragments inside the body, the collected sample statistics, and the intrinsic fluctuation of the emission process related to the nuclear interactions. This last contribution has been studied using a fixed number (10^3) of detected fragments. Samples of 10^3 tracked charged fragments were created out of the datasets acquired at each angular configuration, for a total of 13 samples at 90° and 100 samples at 60°. When comparing the measurements of Δ_{40} and δ_{40} performed at different angles, the finite spot size of the beam σ_{beam} (**Figure 10**) was taken into account.

The accuracy on the measurement of the Δ_{40}, δ_{40}, and X_{left} together with the average values of Δ_{40} and δ_{40} are shown in **Table 1**. The accuracy achieved for the statistic of the reference sample (1k tracks) is of the order of 3 mm. The measured absolute values of Δ_{40} and δ_{40} should be compared with the path $\Delta_{beam} = 8.90 \pm 0.03$ cm, traveled by the primary beam from its entrance position in the target to the Bragg peak position, which was determined from the MC simulation used for the beam setup and calibration.

The reference sample (10^3 particles) used in Ref. (30) to validate the performances of the monitoring technique proposed, due to the reduced detector solid angle $\Delta\Omega \simeq 10^{-4}$ sr, was produced by a number of carbon ions equal to $\simeq 2.3 \times 10^8$ at 90° and to $\simeq 4.7 \times 10^7$ at 60°. Those numbers can be reduced significantly (by even a factor 100) by increasing the solid angle of the tracker detector that, for clinical applications, can have a larger active area and be positioned closer to the patient.

To make a comparison with a standard carbon treatment, the number of carbon ions that are needed to give a 1 Gy dose to the distal part of the tumor (whose monitor accuracy is particularly important) has been computed: assuming that a slice of 1 cm × 1 cm with 2-mm thickness is irradiated, about 10^7 carbon ions will be needed, distributed in a number of single spot pencil

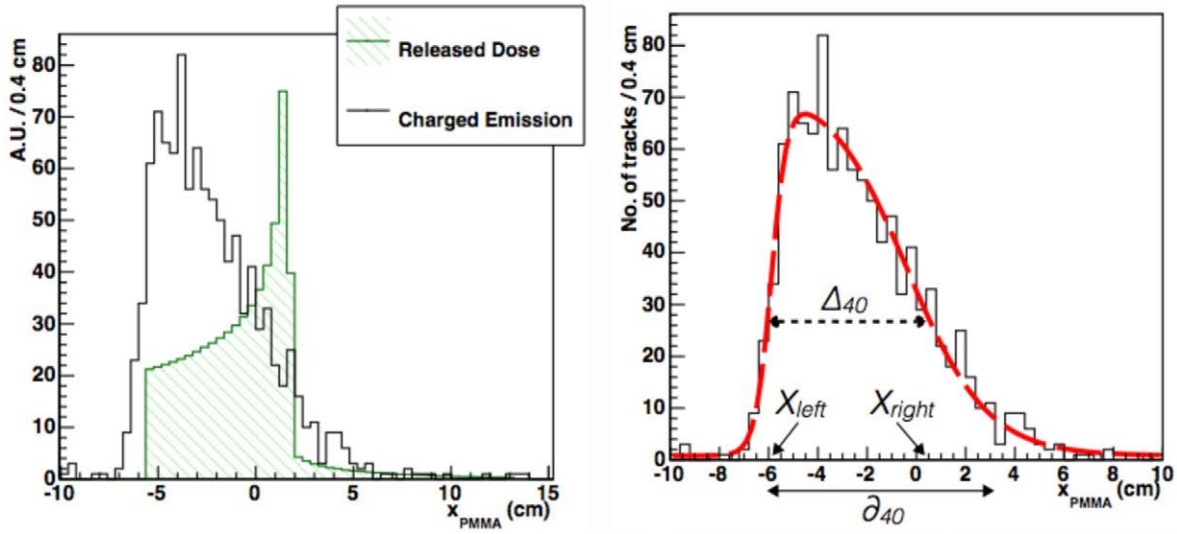

FIGURE 12 | From Ref. (30): left, longitudinal profile (solid line) of secondary charged particles as a function of the penetration in a PMMA phantom at 90° detection angle (beam entrance −6.15 cm). Superimposed (hatched), it is shown the beam depth-dose distribution as from MC simulations. Right, longitudinal profile (solid line) as above but with the PDF from equation (2) superimposed. The dotted and solid arrows show the graphical representation of Δ_{40} and δ_{40}, respectively. The variables X_{left} and X_{right} are also shown. © Institute of Physics and Engineering in Medicine. Reproduced by permission of IOP Publishing. All rights reserved.

TABLE 1 | Dispersion and mean values of the parameters used to describe the charged fragments emission distribution for each angle configuration tested in Ref. (30).

Angle (deg)	σ_Δ (cm)	σ_δ (cm)	$\sigma_{X_{left}}$ (cm)	$\overline{\Delta_{40}}$ (cm)	$\overline{\delta_{40}}$ (cm)
90	0.34	0.37	0.08	6.60	9.40
60	0.31	0.28	0.09	6.83	9.44

The parameters are correlated to the beam entrance position in the PMMA and to the BP as described in Ref. (30). The resolutions are evaluated as the RMS of the measurements performed in the different beam entrance configurations and data samples.

beam each one made of about 2×10^5 primaries. The numbers of produced charged fragments that will be detected by a given $\Delta\Omega$ detector at 90° and 60°can be easily deduced from the results quoted above.

Beside the number of primary ions that are used, another important parameter that has to be considered when discussing real case scenarios is the amount of patient tissue crossed by the secondary particles in their exit path, before their detection. As the absorption increases with the traversed matter, a reduction of the flux up to a factor 10 has to be considered in case of tumors that are located very deeply in the patient body, as can be inferred from **Figure 11**.

The accuracy achievable is, therefore, function of the signal tracks statistics, and hence on the dose administered in a given fraction, and of the absorption due to the depth of the tumor. In order to enhance the signal statistics, a possible strategy is to envisage the monitor of a group of pencil beams in the same treatment slice. At the same time, the maximization of the geometrical acceptance of the monitor device is also crucial, getting as close as possible to the patient, to enhance the collected tracks sample statistics and, hence, the accuracy attainable with a small number of pencil beams.

3.2. An Application to the Clinical Environment: The Dose Profiler

As discussed in the previous section, in order to exploit the detection of charged particles for range monitoring in PT a large acceptance is needed. Other requirements to be taken into account in the detector design are compactness, reliability, and high tracking efficiency. We will consider, as practical example to discuss the application to a clinical environment, the Dose Profiler (DP) device (40) developed in the framework of the INSIDE (INnovative Solutions for In-beam Dosimetry in hadronthErapy) project (41). The tracker implemented within INSIDE is built out of six double planes of scintillating fibers oriented in two orthogonal views to provide bi-dimensional readout, with a sensitive area of about 20 cm × 20 cm. The fiber transverse section (500 μm × 500 μm) provides the necessary spatial resolution for an accurate reconstruction of the charged tracks, considering that the resolution on the fragment emission point is dominated by the Coulomb and nuclear scattering undergone in the patient tissues in the exit path.

Some of the practical features related to the application of a charged particle-based monitoring technique to PT treatments were addressed using Monte Carlo simulations. A real case scenario was studied in detail by performing an accurate FLUKA MC simulation of the treatment with ^{12}C ions undergone by a patient at the Italian hadrontherapy center CNAO (42). The treatment was a two-port irradiation of a chordoma (volume of about 45 cm^3) placed almost at the center of the head.

The simulation reproduced all the details of the beam delivery and the actual geometry of the patient, importing the CT image (see **Figure 13**). The output from the Treatment Planning System (Syngo by Siemens) was coupled to the simulation input and a single fraction of the treatment was considered for one of the two beam ports. The energy of the ^{12}C primary ions for such a treatment was in the range of 137.28–243.42 MeV/u. The total number of primaries used for the simulation of a given treatment fraction was 2.7×10^8.

Prompt photons and secondary protons emerging from the patient with an energy greater than 1 and 20 MeV, respectively, were studied. The INSIDE tracking detector was placed at a distance of 40 cm from the tumor at about 60° with respect to the beam direction. The total number of photons and protons entering in the detector acceptance are 2.7×10^6 and 6.4×10^5, respectively.

In **Figure 14**, the expected numbers of photons and protons for each carbon ion entering the detector active area, placed at 60° with respect to the primary beam incoming direction, are shown as a function of the beam energy. The Monte Carlo evaluation of the proton flux at 220 MeV/u is compatible with the results reported in Section 2.

The application of these techniques to the "online" (in-treatment) monitoring of the beam range requires a calibration of the

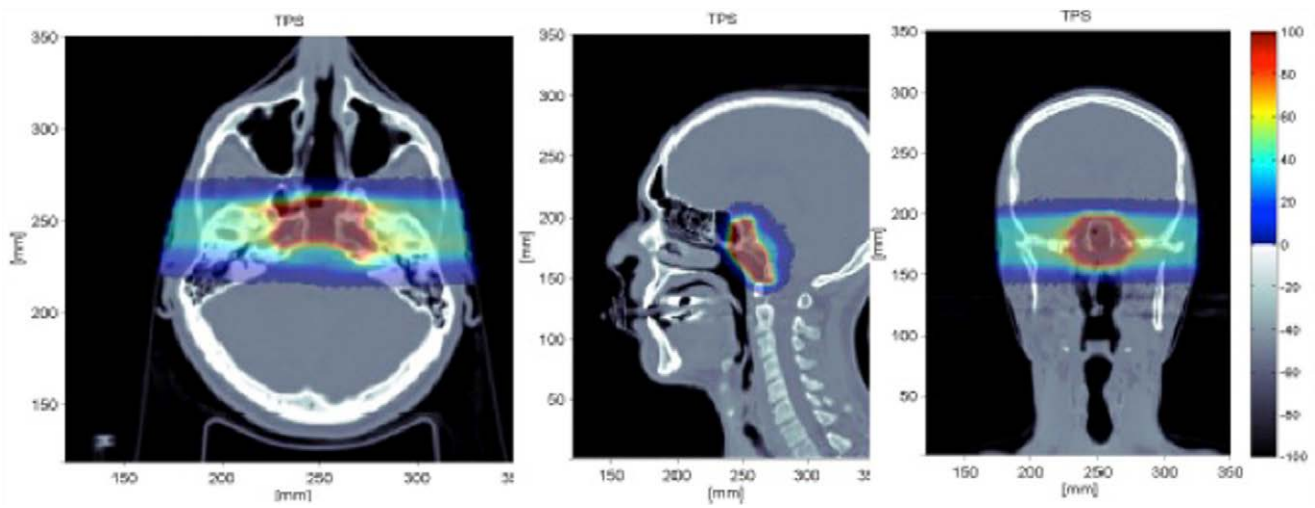

FIGURE 13 | Simulated treatment plan of a chordoma as displayed by the Treatment Planning System (Syngo TPS by Siemens) for a patient treated with ^{12}C ions at the Italian hadrontherapy center CNAO (42): transaxial (left), sagittal (center), coronal (right) views. Courtesy of CNAO.

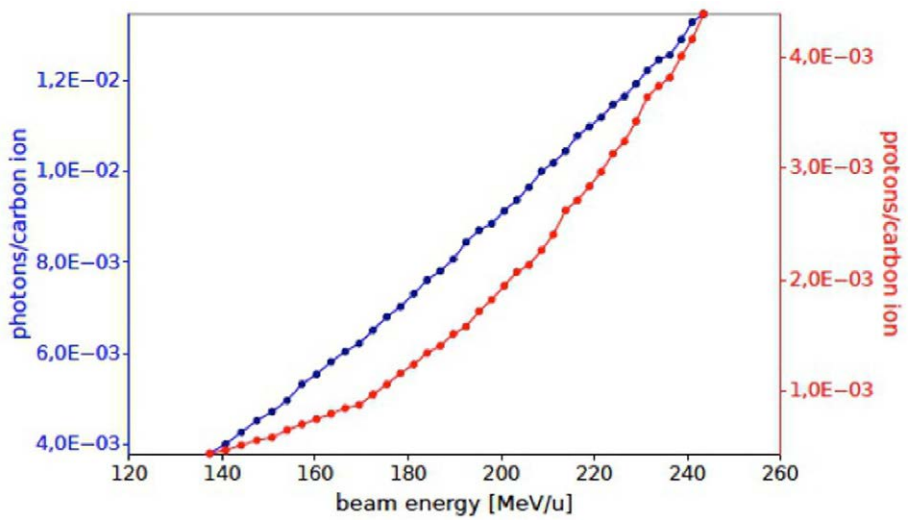

FIGURE 14 | Number of prompt photons (blue) and protons (red) per carbon ion in the acceptance of the INSIDE Dose Profiler detector as obtained by the simulated treatment planning at an angle of ~60° with respect to the primary beam, for a single fraction of the treatment of Figure 13.

measured parameters used to describe the longitudinal emission distribution (the Δ_{40}, δ_{40} parameters introduced in the previous paragraph). The dependence of Δ_{40} and δ_{40} against the actual BP position for the energy of interest or, correspondingly for the carbon beam range of interest in PT, has to be performed by means of an extended campaign of experimental measurements.

In order to implement the monitoring technique here proposed in actual clinical cases, a possible strategy is described in the following. Any complex geometry, like the case of a patient, having different materials, densities, and thicknesses will produce a longitudinal emission profile that will be quite different from the reference case presented so far. However, since all the relevant information is in principle contained in the patient's CT, it is possible to develop a method that allows to take into account all the deformations of the secondary charged emission shape due to the absorption of charged fragments in the patient tissue, as indicated in **Figure 11**.

The reference emission shape, whose correlation with the BP position is known, can be obtained from the measured emission shape by unfolding the expected absorption as a function of thickness (obtainable from the CT) along the reconstructed track direction. A function describing particle absorption in different materials can be reliably obtained by Monte Carlo simulation. In order to give a proof of principle of the proposed method, we have developed a Monte Carlo simulation calibrated with the data reported in Section 2. Using the same beam and detector conditions employed in the real case scenario simulation shown in **Figure 13** (primary ^{12}C beam of 220 MeV/u, DP detector), the attenuation of protons emitted at 90° with respect to the beam incoming direction has been obtained for PMMA as a function of the thickness of material crossed by the fragments. Results are shown in **Figure 15**.

In real case scenarios, look-up tables will be used for different beam energies and "water equivalent material" thicknesses. The emission shapes predicted for different thicknesses of **Figure 15** have been fitted using the function of equation (2). In order to parameterize the functional shape for an arbitrary value x of thickness, the variation of the six p_i parameters that enter the function definition has been studied as a function of x by means of simple polynomial fits, as shown in **Figure 16**, in the 2.5–10 cm range.

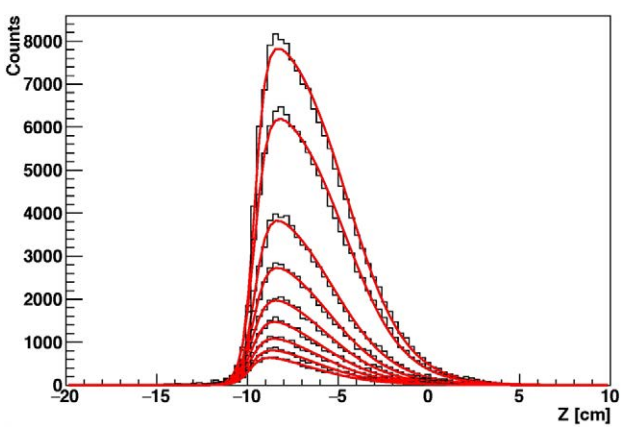

FIGURE 15 | Simulation of the reconstructed longitudinal profile of the emission points of secondary protons as detected at 90° with respect to the beam direction, for ^{12}C beam of 220 MeV/u irradiating a cylindrical PMMA target, for different targets radii.

Once the "look-up tables" are available, to take into account the variation of the p_i parameters as a function of the material thickness, the emission function of equation (2) can be generalized as a two variables function of z, the emission point along the beam path, and of the crossed material thickness x traversed in the escape path from the phantom, using the $p_i(x)$ functions:

$$f(z,x) = p_0(x)\frac{1}{1+exp\left(\frac{z-p_1(x)}{p_2(x)}\right)}\frac{1}{1+exp\left(-\frac{z-p_3(x)}{p_4(x)}\right)} + p_5(x). \quad (3)$$

A weighting function can be defined for each charged secondary track with emission point reconstructed at position z and with crossed material x before escaping the patient:

$$w(z,x) = \frac{f(z,x_0)}{f(z,x)} \quad (4)$$

Here, the reference x_0 correspond to the minimum 2.5 cm thickness of the PMMA used to collect the data (30) on which the simulation has been trained. In order to take into account the absorption effect, any detected track will contribute to the emission shape with a weight $w(z, x)$ evaluated using the measured z and the x obtained from CT.

In order to demonstrate the feasibility of the proposed approach, we have simulated a simple system, shown in **Figure 17**, where a ^{12}C beam propagates in a PMMA sphere of 10-cm radius (density $\rho = 1.2$ g/cm^3), that contains a smaller sphere of density $\rho_o = 0.6$ g/cm^3 and radius = 3 cm. The detector used for the MC simulations is the INSIDE Dose Profiler, placed at a 40 cm distance from the center of the larger sphere. In this case, the thickness x of crossed material can be calculated analytically.

Figure 18 shows the result of the unfolding procedure. The left panel shows the MC profile of the emitted charged secondary particles as produced by the beam, while the emission profile reconstructed by the detector is shown in the central panel. The distortion in the reconstructed shape due to the different material thickness is evident as well as the heavy implications for the correct evaluation of the BP position when using the biased reconstructed distribution without any correction. By weighting each reconstructed track with the inverse of the weight $w(z, x)$ defined in equation (4), the result shown in the right panel is produced, where the re-weighted profile is superimposed to the generated one. The nice agreement obtained proves the feasibility of a measurement of the true charged secondaries emission profile, once the detailed map of the material crossed by the detected protons is known. In a real case scenario, a software system capable of exploiting on-line all the useful information from the CT has to be implemented.

The proposed technique, beside the monitoring of the BP position, could also be used to provide additional information about the patient positioning. By the correlation of the beam entrance position in the patient to X_{left} (for the definition and the expected

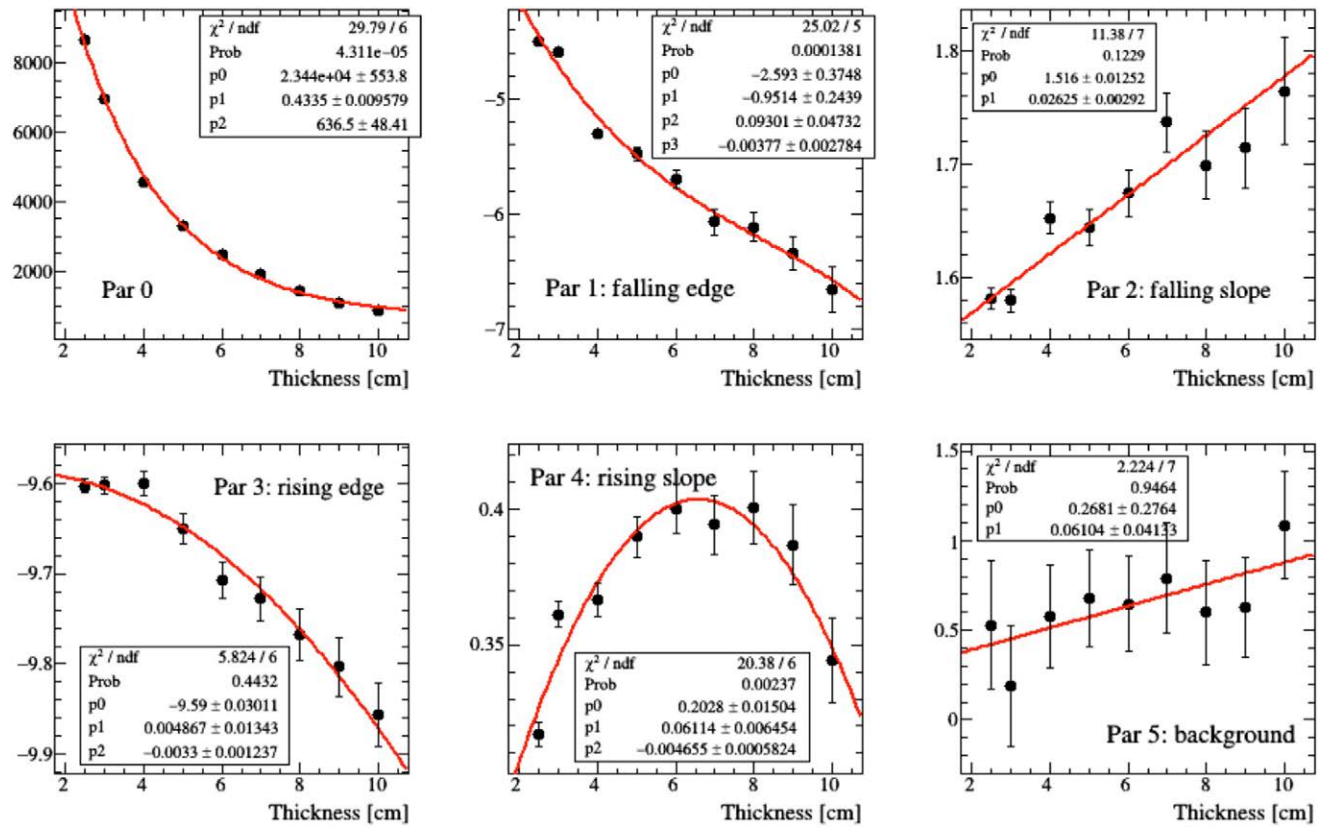

FIGURE 16 | **Polynomial fit modeling the evolution of the parameters of equation (2) resulting for different thicknesses of material crossed by the charged secondary particle as shown in Figure 15**.

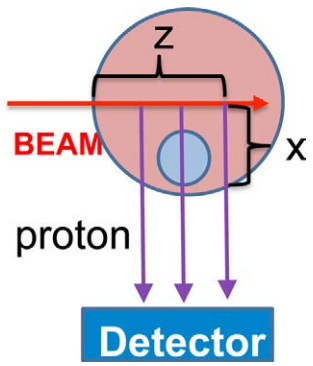

FIGURE 17 | **Simulation setup for a proof of concept of the material absorption deconvolution**.

resolution refer to **Table 1** and **Figure 12**) a fast and precise feedback on possible patient mis-positioning could be provided during the treatment.

4. CONCLUDING REMARKS

Nowadays, the baseline approach for PT range monitoring is through PET imaging, typically undergone by the patient immediately after the treatment. In order to improve the treatment reliability and ensure an accurate control on the dose deposition, different research groups are developing and optimizing a dedicated monitoring device capable of being operated during the treatment.

Techniques based on the detection of secondary prompt photons are recently starting clinical experimentation: first prototypes are being developed and tested "in room" with an optimization focused mainly on applications to proton therapy (43). At the same time, a monitoring technique based on the detection of charged particles is being developed. The preliminary studies and experimental results presented in this review showed that promising performances are expected for such technique when applied to the monitoring of ion treatments, as proton projectiles would produce an insufficient yield of charged secondaries.

An advantageous strategy that can be pursued to achieve the desired monitoring space resolution implies the detection of fragments emitted at large angles with respect to the beam incoming direction, even at the price of having a lower yield of particles as they are emitted preferentially in the forward direction. In this case, the reduction of the MS undergone inside the patient body and the reduction of the beam shadow effect will help significantly in matching the monitoring requirements posed by the clinical application.

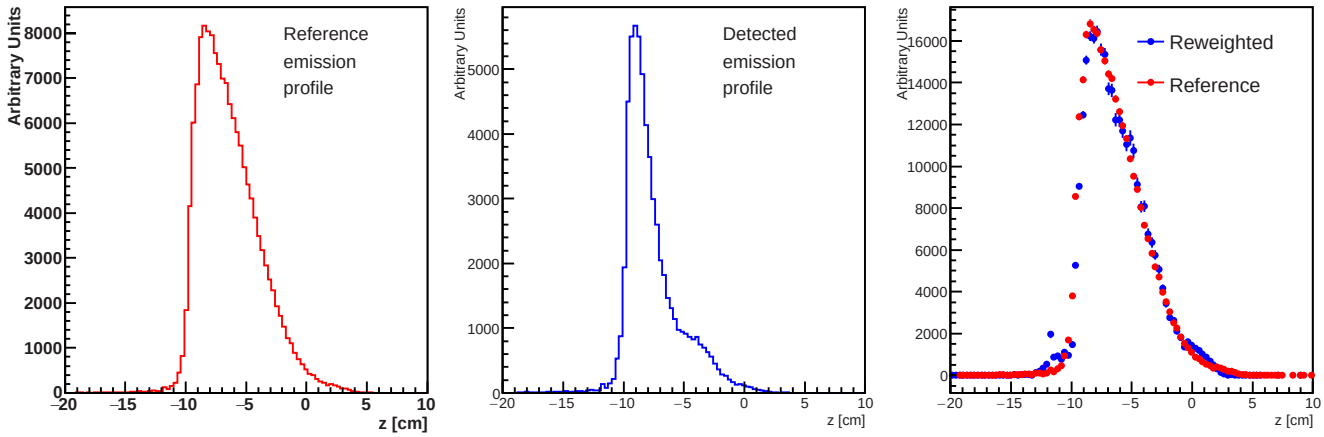

FIGURE 18 | True (left panel) and detected (middle panel) secondary charged particles emission profiles obtained from the MC simulation setup of Figure 17. The right panel shows the effect of the re-weighting procedure described in the text, needed to account for the different material traversed by the secondary fragments.

The application of a charged particle-based monitoring could be problematic in case of deep seated tumors, because of the re-absorption of charged secondaries inside the patient itself. However the technique feasibility is fully recovered in the context of hypo-fractionated treatments. For those treatments, the need for *on-line* range check is even more compelling as very large doses are delivered in one or few shots, and the total dose for the single irradiation session, and the related secondary yields, can be almost one order of magnitude larger than the standard treatments.

The three leading techniques that are nowadays being considered for in-beam range monitoring (PET, prompt gammas and charged particles) offer in principle different advantages and pose different problems. The performance comparison of the three approaches is not trivial. One reason is that many of the proposed detectors and approaches still do not have firmly established performances, since they are in a research and development phase. Another reason resides in the limited reliability of the nuclear interactions description in Monte Carlo codes in the energy range of few hundreds MeV/u. In this respect, the process of secondary charged particles emission at large angles is one of the most difficult to benchmark for the existing models.

The increasing amount of data coming from dedicated experimental campaigns, and the impressive modeling activity performed by the code developers, is allowing the MC simulation research field to evolve quickly. An example of recently achieved results is in Ref. (44) and in Ref. (13) specifically for the PET technique.

Finally, the relative performances of the three techniques strongly depend on the tumor size and position and on the absolute dose release foreseen for a given treatment. Combined approaches in which two or more secondary signals are simultaneously exploited are, thus, promising.

A first example of such integrated approach is being developed within the INSIDE (41) project: here, two planar PET heads made of pixellated LYSO crystals are operated in combination with the Dose Profiler, a large area charged particles tracker made of orthogonal layers of scintillating fibers. The PET subsystem has ToF and DAQ capabilities that allow for in-beam operation, while the tracker is focused on the detection of charged secondaries emitted at large angle (60°–90°) with respect to the beam direction. The test of the integrated device is foreseen in 2016, in the CNAO therapy center.

AUTHOR CONTRIBUTIONS

SM: Monte Carlo simulation and the reconstruction work reported in Section 3.2. GB: data taking, data analysis, and Monte Carlo simulation. FC: data taking and Monte Carlo simulation. EL: data taking and data analysis. RF: experiment management and data analysis. FF: data analysis. SF: experiment preparation. PF: data taking and data analysis. MM: experiment preparation, data taking, and data analysis. IM: experiment preparation, data taking, and data analysis. S. Morganti: data taking. RP: data analysis. LP: experiment preparation and data taking. VP: project coordinator, data analysis, and Monte Carlo simulation. DP: experiment preparation and data taking. A. Rucinski: data analysis. A. Russomando: data taking. A. Sarti: experiment preparation, data taking, and data analysis. A. Sciubba: experiment preparation and data taking. ES-C: laboratory activity and data taking. MT: experiment preparation, data taking, and data analysis. GT: data analysis and laboratory activity. CV: data analysis.

ACKNOWLEDGMENTS

The authors are indebted to the medical physicists of CNAO, the colleagues of RDH experiment in INFN and of the INSIDE project for their contributions and support. This work has been financially supported by INFN and by the italian national research program PRIN MIUR 2010-2011 2010P98A75 (INSIDE).

REFERENCES

1. Char DH, Quivey JM, Castro JR, Kroll S, Phillips T. Helium ions versus iodine 125 brachytherapy in the management of uveal melanoma: a prospective, randomized, dynamically balanced trial. *Ophthalmology* (1993) 100:1547–54. doi:10.1016/S0161-6420(93)31446-6
2. Castro JR, Char DH, Petti PL, Daftari IK, Quivey JM, Singh RP, et al. 15 years experience with helium ion radiotherapy for uveal melanoma. *Int J Radiat Oncol Biol Phys* (1997) 39:989–96. doi:10.1016/S0360-3016(97)00494-X
3. Kaplan ID, Castro JR, Phillips TL. Helium charged particle radiotherapy for meningioma: experience at UCLBL. University of California Lawrence Berkeley Laboratory. *Int J Radiat Oncol Biol Phys* (1994) 28:257–61. doi:10.1016/0360-3016(94)90165-1
4. Fuchs H, Strobele J, Schreiner T, Hirtl A, Georg D. A pencil beam algorithm for helium ion beam therapy. *Med Phys* (2012) 39:6726–37. doi:10.1118/1.4757578
5. Kurz C, Mairani A, Parodi K. First experimental-based characterization of oxygen ion beam depth dose distributions at the heidelberg ion-beam therapy center. *Phys Med Biol* (2012) 57(15):5017. doi:10.1088/0031-9155/57/15/5017
6. Tommasino F, Scifoni E, Durante M. New ions for therapy. *Int J Part Ther* (2015) 2:428. doi:10.14338/IJPT-15-00027.1
7. Loeffer JS, Durante M. Charged particle therapy optimization, challenges and future directions. *Nat Rev Clin Oncol* (2013) 10:411. doi:10.1038/nrclinonc.2013.79
8. Knopf A, Lomax A. In vivo proton range verification. *Phys Med Biol* (2013) 58:131. doi:10.1088/0031-9155/58/15/R131
9. Kraan AC. Range verification methods in particle therapy: underlying physics and Monte Carlo modeling. *Front Oncol* (2015) 5:150. doi:10.3389/fonc.2015.00150
10. Bauer J, Unholtz D, Sommerer F, Kurz C, Haberer T, Herfarth K, et al. Implementation and initial clinical experience of offline PET/CT-based verification of scanned carbon ion treatment. *Radiother Oncol* (2013) 107:218. doi:10.1016/j.radonc.2013.02.018
11. Bennett GW, Archambeau JO, Archambeau BE, Meltzer JI, Wingate CL. Visualization and transport of positron emission from proton activation in vivo. *Science* (1978) 200:1151. doi:10.1126/science.200.4346.1151
12. Pshenichnov I, Mishustin I, Greiner W. Distributions of positron-emitting nuclei in proton and carbon-ion therapy studied with GEANT4. *Phys Med Biol* (2006) 51(23):6099. doi:10.1088/0031-9155/51/23/011
13. Kraan AC, Battistoni G, Belcari N, Camarlinghi N, Cirrone GA, Cuttone G, et al. Proton range monitoring with in-beam pet: Monte Carlo activity predictions and comparison with cyclotron data. *Phys Med* (2014) 30:559. doi:10.1016/j.ejmp.2014.04.003
14. Priegnitz M, Möckel D, Parodi K, Sommerer F, Fiedler F, Enghardt W. In-beam pet measurement of 7li3+ irradiation induced beta+-activity. *Phys Med Biol* (2008) 53(16):443. doi:10.1088/0031-9155/53/16/015
15. Agodi C, Bellini F, Cirrone GAP, Collamati F, Cuttone G, De Lucia E, et al. Precise measurement of prompt photon emission from 80 MeV/u carbon ion beam irradiation. *J Instrum* (2012) 7:03001. doi:10.1088/1748-0221/7/03/P03001
16. Agodi C, Bellini F, Cirrone GAP, Collamati F, Cuttone G, De Lucia E, et al. Erratum: precise measurement of prompt photon emission from 80 MeV/u carbon ion beam irradiation. *J Instrum* (2013) 8(11):E11002. doi:10.1088/1748-0221/8/11/E11002
17. Mattei I, Battistonil G, Binii F, Collamati F, De Lucia E, Durante M, et al. Prompt-γ production of 220 MeV/u 12-C ions interacting with a PMMA target. *J Instrum* (2015) 10(10):10034. doi:10.1088/1748-0221/10/10/P10034
18. Polf JC, Panthi R, Mackin DS, McCleskey M, Saastamoinen A, Roeder BT, et al. Measurement of characteristic prompt gamma rays emitted from oxygen and carbon in tissue-equivalent samples during proton beam irradiation. *Phys Med Biol* (2013) 58:5821. doi:10.1088/0031-9155/58/17/5821
19. Agodi C, Abou-Haidar Z, Alvarez MAG, Aumann T, Balestra F, Battistoni G, et al. FIRST experiment: fragmentation of ions relevant for space and therapy. *J Phy Conf Series* (2013) 420:012061. doi:10.1088/1742-6596/420/1/012061
20. Pleskac R, Abou-Haidar Z, Agodi C, Alvarez MAG, Aumann T, Battistoni G, et al. The FIRST experiment at GSI. *Nucl Instrum Meth A* (2012) 678:130. doi:10.1016/j.nima.2012.02.020
21. Braunn B, Labalme M, Ban G, Chevallier M, Colin J, Cussol D, et al. Nuclear reaction measurements of 95 MeV/u 12-C interactions on PMMA for hadrontherapy. *Nucl Instrum Meth B* (2011) 269:2676. doi:10.1016/j.nimb.2011.08.010
22. Gunzert-Marx K, Iwase H, Schardt D, Simon RS. Secondary beam fragments produced by 200 MeV/u 12-C ions in water and their dose contributions in carbon ion radiotherapy. *New J Phys* (2008) 10:075003. doi:10.1088/1367-2630/10/7/075003
23. Haettner E, Iwase H, Schardt D. Experimental fragmentation studies with 12-C therapy beams. *Radiat Prot Dosimetry* (2006) 122:485. doi:10.1093/rpd/ncl402
24. Matsufuji N, Komori M, Sasaki H, Akiu K, Ogawa M, Fukumura A, et al. Spatial fragment distribution from a therapeutic pencil-like carbon beam in water. *Phys Med Biol* (2005) 50:3393. doi:10.1088/0031-9155/50/14/014
25. Amaldi U, Hajdas W, Iliescu S, Malakhov N, Samarati J, Sauli F, et al. Advanced quality assurance for CNAO. *Nucl Instrum Meth A* (2010) 617:248. doi:10.1016/j.nima.2009.06.087
26. Gwosch K, Hartmann B, Jakubek J, Granja C, Soukup P, Jäkel O, et al. Non-invasive monitoring of therapeutic carbon ion beams in a homogeneous phantom by tracking of secondary ions. *Phys Med Biol* (2013) 58:3755. doi:10.1088/0031-9155/58/11/3755
27. Henriquet P, Testa E, Chevallier M, Dauvergne D, Dedes G, Freud N, et al. Interaction vertex imaging (IVI) for carbon ion therapy monitoring: a feasibility study. *Phys Med Biol* (2012) 57:4655. doi:10.1088/0031-9155/57/14/4655
28. Shiomi M, Mori S, Shinoto M, Nakayama Y, Kamada T, Yamada S. Comparison of carbon-ion passive and scanning irradiation for pancreatic cancer. *Radiother Oncol* (2016) 119:326. doi:10.1016/j.radonc.2016.04.026
29. Agodi C, Battistoni G, Bellini F, Cirrone GA, Collamati F, Cuttone G, et al. Charged particle's flux measurement from PMMA irradiated by 80 MeV/u carbon ion beam. *Phys Med Biol* (2012) 57:5667. doi:10.1088/0031-9155/57/18/5667
30. Piersanti L, Bellini F, Bini F, Collamati F, De Lucia E, Durante M, et al. Measurement of charged particle yields from PMMA irradiated by a 220 MeV/u 12-C beam. *Phys Med Biol* (2014) 59:1857. doi:10.1088/0031-9155/59/7/1857
31. Llopart X, Ballabriga R, Campbell M, Tlustos L, Wong W. Timepix, a 65k programmable pixel readout chip for arrival time, energy and/or photon counting measurements. *Nucl Instrum Meth A* (2007) 581:485–94. doi:10.1016/j.nima.2007.08.079
32. Jakubek J, Granja C, Hartmann B, Jaekel O, Martisikova M, Opalka L, et al. Imaging with secondary radiation in hadron therapy beams with the 3D sensitive voxel detector. In Townsend D, editor. *Nuclear Science Symposium and Medical Imaging Conference (NSS/MIC), 2011 IEEE*. Piscataway (2011). p. 2281–4. doi:10.1109/NSSMIC.2011.6153862
33. Apostolakis J, Asai M, Bogdanov A, Burkhardt H, Cosmo G, Elles S, et al. Geometry and physics of the GEANT4 toolkit for high and medium energy applications. *Radiat Phys Chem* (2009) 78(10):859–73. doi:10.1016/j.radphyschem.2009.04.026
34. Ziegler JF, Ziegler M, Biersack J. SRIM the stopping and range of ions in matter. *Nucl Instrum Meth B* (2010) 268:1818–23. doi:10.1016/j.nimb.2010.02.091
35. Agodi C, Bellini F, Cirrone GAP, Collamati F, Cuttone G, De Lucia E, et al. Study of the time and space distribution of beta+ emitters from 80 MeV/u carbon ion beam irradiation on PMMA. *Nucl Instrum Meth B* (2012):283:1. doi:10.1016/j.nimb.2012.04.021
36. Boehlen T, Cerutti F, Chin M, Fassó A, Ferrari A, Ortega P, et al. The FLUKA code: developments and challenges for high energy and medical applications. *Nucl Data Sheets* (2014) 120:211–4. doi:10.1016/j.nds.2014.07.049
37. Ferrari A, Sala P, Fassò A, Ranft J. *FLUKA: A Multi-Particle Transport Code*. (2005). Technical Report No.: CERN-2005-10, INFN/TC_05/11, SLAC-R-773, CERN, INFN, SLAC.
38. Koba Y, Iwamota H, Kiyohara K, Nagasaki T, Wayabeyashi G, Uozumi Y, et al. Scintillation efficiency of inorganic scintillators for intermediate–energy charged particles. *Prog Nucl Sci Technol* (2011) 1:218. doi:10.15669/pnst.1.218
39. Shepp L, Vardi Y. Maximum likelihood reconstruction for emission tomography (maximum likelihood expectation maximization). *IEEE Trans Med Imaging* (1982) 1:113. doi:10.1109/TMI.1982.4307558

40. Battistoni G, Collamati F, De Lucia E, Faccini R, MArafini M, Mattei I, et al. Design of a tracking device for on-line dose monitoring in hadrontherapy. *Nucl Instrum Meth A* (2016). doi:10.1016/j.nima.2016.05.095
41. Marafini M, Attili A, Battistoni G, Belcari N, Bisogni MG, Camarlinghi N, et al. The INSIDE project: innovative solutions for in-beam hadronteraphy. *Acta Phys Pol A* (2015) 127:1465. doi:10.12693/APhysPolA.127.1465
42. Rossi S. The national centre for oncological hadrontherapy (CNAO): status and perspectives. *Phys Med* (2015) 31:333. doi:10.1016/j.ejmp.2015.03.001
43. Richter C, Pausch G, Barczyk S, Priegnitz M, Keitz I, Thiele J, et al. First clinical application of a prompt gamma based in vivo proton range verification system. *Radiother Oncol* (2016) 118:232. doi:10.1016/j.radonc.2016.01.004
44. Robert C, Dedes G, Battistoni G, Böhlen T, Buvat I, Cerutti F, et al. Distributions of secondary particles in proton and carbon-ion therapy: a comparison between GATE/GEANT4 and FLUKA monte carlo codes. *Phys Med Biol* (2013) 58:2879. doi:10.1088/0031-9155/58/9/2879

Conflict of Interest Statement: The authors declare that the research was conducted in the absence of any commercial or financial relationships that could be construed as a potential conflict of interest.

Copyright © 2016 Muraro, Battistoni, Collamati, De Lucia, Faccini, Ferroni, Fiore, Fralliciardi, Marafini, Mattei, Morganti, Paramatti, Piersanti, Pinci, Rucinski, Russomando, Sarti, Sciubba, Solfaroli-Camillocci, Toppi, Traini, Voena and Patera. This is an open-access article distributed under the terms of the Creative Commons Attribution License (CC BY). The use, distribution or reproduction in other forums is permitted, provided the original author(s) or licensor are credited and that the original publication in this journal is cited, in accordance with accepted academic practice. No use, distribution or reproduction is permitted which does not comply with these terms.

frontiers in Oncology

ORIGINAL RESEARCH
published: 18 March 2016
doi: 10.3389/fonc.2016.00062

Monte Carlo Calculations Supporting Patient Plan Verification in Proton Therapy

Thiago V. M. Lima[1,2,3], Manjit Dosanjh[1], Alfredo Ferrari[1], Silvia Molineli[4], Mario Ciocca[4] and Andrea Mairani[4]*

[1] European Organization for Nuclear Research (CERN), Geneva, Switzerland, [2] Division of Surgery and Interventional Science, University College London, London, UK, [3] Fachstelle Strahlenschutz, Kantonsspital Aarau AG, Aarau, Switzerland, [4] Department of Medical Physics, Fondazione CNAO, Pavia, Italy

Patient's treatment plan verification covers substantial amount of the quality assurance (QA) resources; this is especially true for Intensity-Modulated Proton Therapy (IMPT). The use of Monte Carlo (MC) simulations in supporting QA has been widely discussed, and several methods have been proposed. In this paper, we studied an alternative approach from the one being currently applied clinically at Centro Nazionale di Adroterapia Oncologica (CNAO). We reanalyzed the previously published data (Molinelli et al. (1)), where 9 patient plans were investigated in which the warning QA threshold of 3% mean dose deviation was crossed. The possibility that these differences between measurement and calculated dose were related to dose modeling (Treatment Planning Systems (TPS) vs. MC), limitations on dose delivery system, or detectors mispositioning was originally explored, but other factors, such as the geometric description of the detectors, were not ruled out. For the purpose of this work, we compared ionization chambers' measurements with different MC simulation results. It was also studied that some physical effects were introduced by this new approach, for example, inter-detector interference and the delta ray thresholds. The simulations accounting for a detailed geometry typically are superior (statistical difference – p-value around 0.01) to most of the MC simulations used at CNAO (only inferior to the shift approach used). No real improvement was observed in reducing the current delta ray threshold used (100 keV), and no significant interference between ion chambers in the phantom were detected (p-value 0.81). In conclusion, it was observed that the detailed geometrical description improves the agreement between measurement and MC calculations in some cases. But in other cases, position uncertainty represents the dominant uncertainty. The inter-chamber disturbance was not detected for the therapeutic protons energies, and the results from the current delta threshold are acceptable for MC simulations in IMPT.

Keywords: Monte Carlo calculations, treatment plan verification, proton therapy, delta ray effect, dose disturbance

OPEN ACCESS

Edited by:
Francis A. Cucinotta, University of Nevada Las Vegas, USA

Reviewed by:
Dalong Pang, Georgetown University Hospital, USA
John Eley, University of Maryland School of Medicine, USA

****Correspondence:***
Thiago V. M. Lima
thiago.vmlima@ksa.ch

Specialty section:
This article was submitted to Radiation Oncology, a section of the journal Frontiers in Oncology

Received: *29 September 2015*
Accepted: *04 March 2016*
Published: *18 March 2016*

Citation:
Lima TVM, Dosanjh M, Ferrari A, Molineli S, Ciocca M and Mairani A (2016) Monte Carlo Calculations Supporting Patient Plan Verification in Proton Therapy. Front. Oncol. 6:62. doi: 10.3389/fonc.2016.00062

1. INTRODUCTION

Delivering an appropriate radiation therapy dose starts by preparing the most suitable treatment plan for each patient. This is done by conforming the delivered dose to the clinical target volume and avoiding critical organs (2) in order to limit the observed side effects on the surrounding tissue in the patient. Proton beams, with their defined range, can play an important part in increasing

this conformity (3). Monte Carlo (MC) simulations are one of the proposed three different dose calculation algorithms, alongside ray trace and pencil beam. Although MC has been considered the gold standard between these approaches in respect to its accuracy, pencil beam model is mostly used in the treatment plan system (TPS) due to its compromise between accuracy and computational time.

After finding the best solution for how to deliver the dose, a verification process is needed in order to check if the equipment is able to deliver the planned treatment fields. Several methods have been proposed, such as the ones by PSI (4) and MD Anderson (5), but at Italian National Center for Oncological Hadron Therapy (CNAO), the method developed by GSI and used at HIT (1, 6), is adopted. CNAO is a hospital-based hadrontherapy facility equipped with a custom synchrotron and Dose Delivery System (DDS) to provide actively scanned proton beams with energies of 62–227 MeV/u and carbon with 115–400 MeV/u, corresponding to ranges in water of 3–32 and 3–27 cm for protons and carbon ions, respectively (7).

Individual treatment plan verifications in the experimental environment can be very time and manpower intensive, and it is prone to dose delivery uncertainties and setup errors. Molinelli et al. (1) presented CNAO's quality assurance results for all the patients treatment plans verification that have been performed in CNAO with proton beams concerning 1 year (September 2011–August 2012). Nine cases have been found where the quality assurance warning threshold was exceeded, which is fixed at 3% mean absolute deviation between measurements and TPS. Originally, the possibility explored was that these differences between measurement and calculated dose were related to dose modeling (TPS vs. MC), limitations on DDS, or detectors mispositioned (shift), but other factors were not ruled out, such as oversimplification of the dose modeling.

FLUKA (8, 9) was the MC code chosen for this work due to its demonstrated capabilities (10, 11) and available powerful graphical interface (12).

In this work, we have evaluated if improvements could be applied to the MC simulations in order to get better agreement with the measured data on these previously described cases (**Figure 1**). More specifically, we studied the use of more detailed representation of the detectors (13, 14) and the effect of physical processes that these could introduce in the MC simulation results, for example, the required threshold settings for specific scenarios (15).

2. MATERIALS AND METHODS

2.1. TPS Patient Plan Verification

The TPS used in CNAO is the CE-marked *syngo*® RT Planning by Siemens AG Healthcare (Erlangen, Germany) version VB10, which is based on TRiP98 (16, 17).

The current CNAO quality assurance procedure (1, 18) specifies that for each patient, plan verification will be performed (6). For this, a water tank with a 3D detector block controlled by a motorized arm (PTW) is used. This enables to measure the deposited dose at different known depths and positions. This detector block provides a support holder for the ionization chambers (IC), in such way that an individual IC do not mask the direct path of the beam to other the IC (PTW pin point IC – **Figure 2**). IC

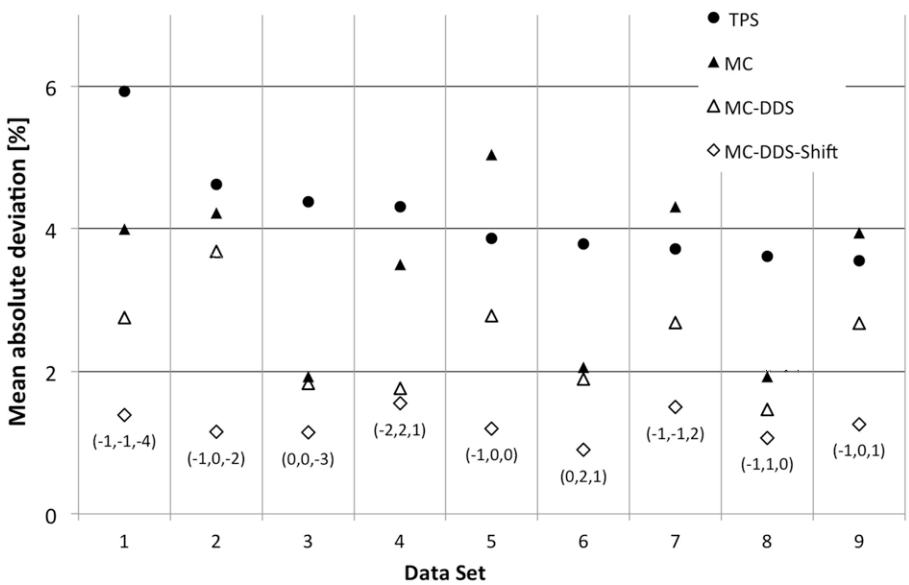

FIGURE 1 | **CNAO patient plan verification results for the nine cases above the warning threshold (6)**. For each data set exceeding the warning level, the mean absolute deviation is plotted. Measurements are compared to four different scenarios of calculated values: ● – TPS calculated dose, ▲ – MC simulated dose based on treatment plan data, Δ – MC simulated dose based on DDS log files, and ◊ – MC simulated dose based on DDS log files and corrected for the optimal 3D holder shift. For the last case, the applied translation vector, expressed in millimeters, is also reported between brackets.

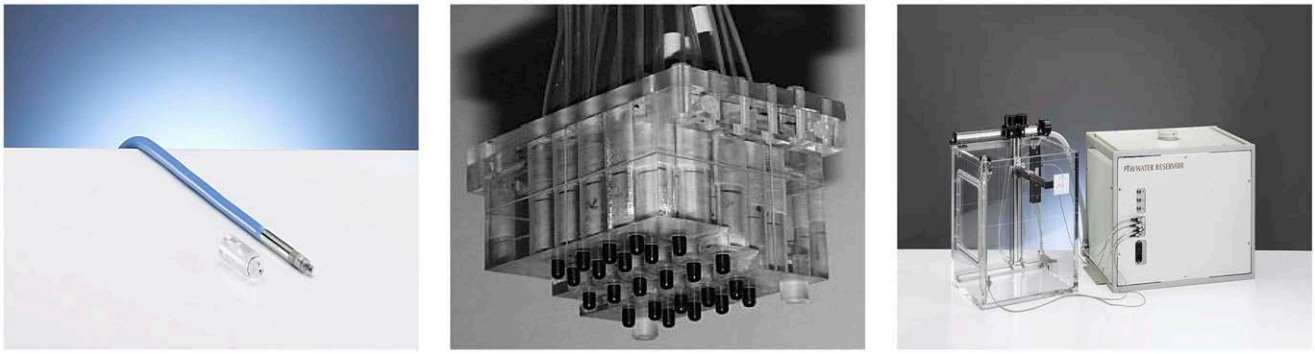

FIGURE 2 | **Different tools used in the treatment plan verification**. The pin point ionization chamber (left), the 3D detector block (center), and the water tank with motorized arm (right) by PTW.

measurement values are then compared with the ones calculated by the TPS (equation (1)). For data set analysis, the mean deviation is calculated as the difference between measured ($dmeas_i$) and calculated dose ($dcalc_i$), normalized to the maximum beam dose ($dmax$) and averaged over N IC positions i:

$$\sum_{i}^{N} \frac{1}{N} \frac{\left| dmeas_i - dcalc_i \right|}{dmax} \% \tag{1}$$

The number of points, N, included in the calculation can be equal or lower than 12, depending on the data set. The TPS provides a 3D-averaged dose gradient for each IC position. Points with a calculated gradient higher than 0.04 Gy mm^{-1} are excluded from the analysis, since they could not be measured sufficiently accurately due to the finite size of the detector sensitive volume and experimental setup uncertainties. For QA measurements in reference conditions, the applied acceptance threshold is 5% for both mean deviation and SD over a data set.

2.2. Monte Carlo Simulations

FLUKA is a multipurpose MC transport code originally designed for high-energy physics but with extensive use in medical applications (10, 11). For the purpose of this paper, the HADROTHErapy suite of physical settings (known as Defaults) was selected. All geometry updates and modifications were completed with the aid of FLAIR (a graphics user interface of FLUKA).

2.2.1. Current MC-Based Plan Verification

A complete detailed description of CNAO facility, including accelerator design and rooms layout, can be found in the literature (1, 7). For the simulation purposes, the geometry description accounted for the different structures, mainly from the monitors of the DDS, present in the beam path. The validation of this DDS description with FLUKA has been described previously (1). In **Figure 3**, the photo of the end of the nozzle in one of the treatment rooms is shown together with its description in a 3-dimensional model and its description within the FLUKA simulation.

Current MC patient plan verifications, as per TPS, use a simpler approach to geometrically represent the IC when calculating the dose deposition. All detectors' structures and holders are not included, and the detector dose is sampled from the dose distribution in a water tank. By doing that, the structure and materials of the IC are not taken into consideration for the simulation. MC obtains the deposited dose in the chambers by calculating the average dose to water over several voxels, corresponding to the active volume of the detector, situated in the positions where the chambers is located.

2.2.2. New Detailed Geometry

The previously described approach, with its geometric approximations and simplifications, obtained deviations below 3% for the majority of studied cases. But for these nine cases where the agreement between the TPS calculations and measurements was above this threshold, we decided to investigate the impact of using a detailed geometry in order to account for the dose disturbances, mainly from scattered particles produced in the wall of the IC and detector holder. In the new detailed geometry, all geometry described above is kept with the inclusion of the PTW3D block and IC description (respecting all structures, dimensions, and material compositions). Detailed technical drawings were obtained from the manufactures (PTW Freiburg). Flair geometry editor was instrumental and extremely helpful in dealing with drawing and 3D visualization (**Figure 4**). As for the original MC approach, the absolute mean dose deviation is calculated applying equation (1).

2.2.3. Delta Rays

Delta rays are defined as electrons that acquire sufficiently high kinetic energies through collisions so as to enable them to carry this energy a significant distance away from the track of the primary particle and produce their own ionization of absorber atoms (19). The FLUKA "HADROTHErapy" option uses per default delta ray production and transport cuts of 100 keV. We have chosen to vary the threshold limits in order to evaluate if the observed variation between measurements and FLUKA simulations was influenced by the delta rays threshold value.

The dose to water was calculated by averaging the dose deposited in the sensitive volume of the IC. And in order to study the

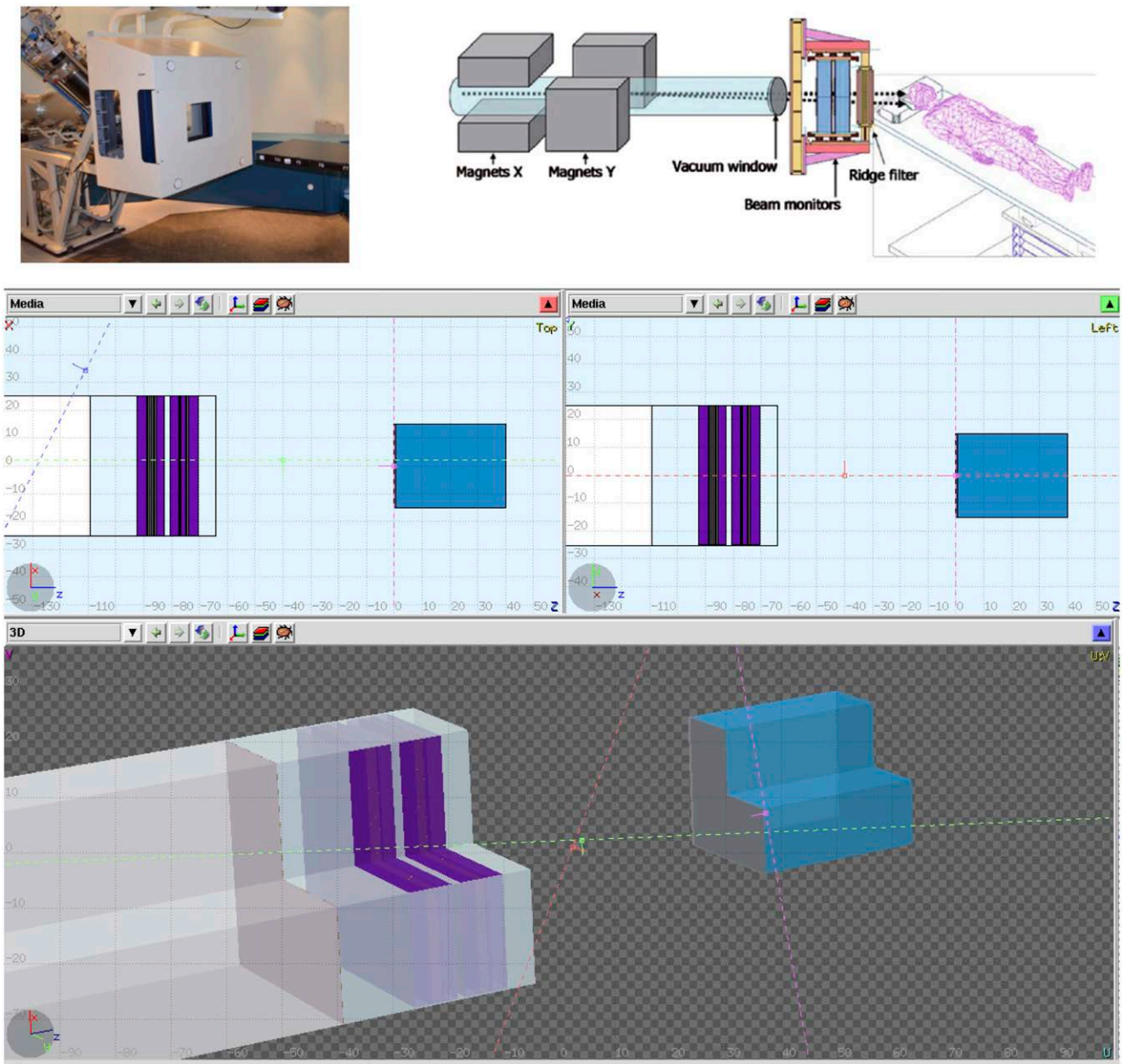

FIGURE 3 | **CNAO dose delivering system can be seen in these figures**. A photo of the system, a model with its components description, and the final model used in the Monte Carlo simulations.

effect of the delta rays threshold, all regions surrounding the sensitive volume had their threshold changed. In this work, we studied the effect of using 10 and 1000 keV in comparison to the default of 100 keV.

2.2.4. Organization of This Work

In total, nine fields from different patients' plans were analyzed, including MC simulations (for both described geometries) and dose deposition matrices from TPS and IC results (from plan verification quality assurance). The analysis of the data and this section are divided as follows:

- *Geometry effect – Section 3.1*: compared data obtained from the MC with and without the complete geometry, with experimental data and TPS calculated dose values.
- *Influence of the δ-rays thresholds – Section 3.2*: compared data obtained from MC simulations of two different fields for different thresholds (10, 100, and 1000 keV). For that, all regions in, or in direct contact with, the active volume had its threshold modified for the purpose of these simulations (**Figure 5**).
- *Chamber–chamber effect – Section 3.3*: at CNAO, the measurements are made with half of the proposed number of the detectors (24); so data from MC simulations were compared

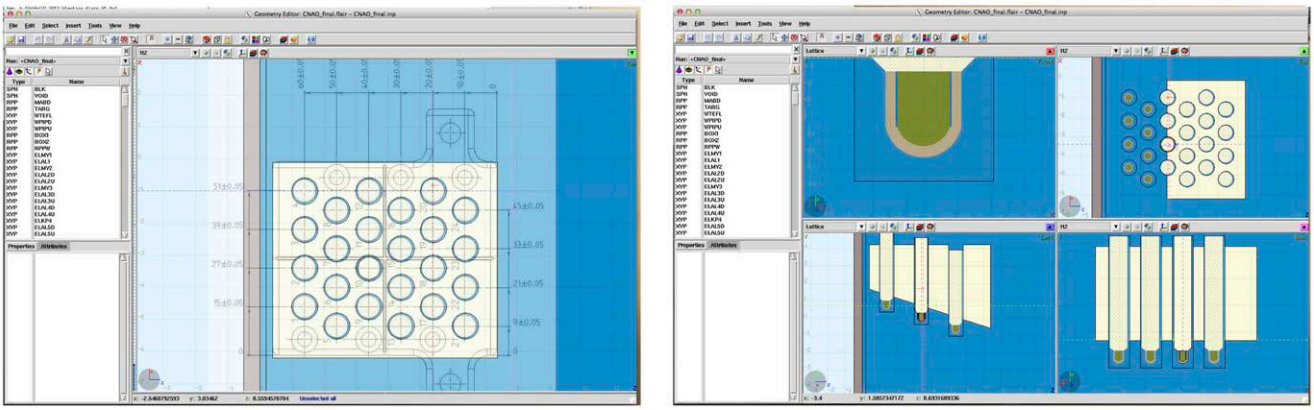

FIGURE 4 | **Demonstration of the powerful tools available in FLAIR**. On the left, the technical drawing superimposed on the generated geometry is shown, and on the right, the final geometry of the phantom in 4 different views is reported.

with two different setups, one with all 24 IC versus the same setup with 12 IC.

3. RESULTS

3.1. The Influence of a Detailed Geometry Implementation

In **Figure 6**, it was compared for each data set results obtained implementing detailed geometry, Section 2.2.4, in relation to the ones obtained by Molinelli et al. (1).

An advantage was noticed when using a more detailed geometry (MC-NGeo-DDS), as it can be seen by the 6 cases where better results were obtained in comparison to the previous MC-DDS (MC simulations based on DDS log files). In order to understand if the difference between these MC simulations and if the measurements are significant, the relative difference between MC and measurements was calculated and analyzed.

A p-value of 0.003 was obtained between MC-DDS (current MC geometry description) and MC-NGeo-DDS (more detailed geometry description) by using a 2-tailed *t-test*, which describes that the obtained results by the more detailed geometry approach are significantly better in relation to the current MC Geometry description.

3.2. The Influence of Delta Rays Threshold

The effect in the absorbed dose and computational time was analyzed for two patients' data sets with different δ-ray thresholds. As described previously, in Section 2.2, with FLUKA MC code, the user is able to set different thresholds for both production and transport of different particles. Initially as expected, some differences were noted between the individual measurements for each threshold and comparison to the current default threshold, set at 100 keV (**Figure 7**). When compared to the measurements individually and as data set (**Figure 7**), no comparable advantage was noticed by using different thresholds.

When comparing the computational time when the δ-ray threshold is changed, it was observed that by increasing the threshold (from 100 to 1000 keV), the average time to simulate all primaries reduced by 11.45 ± 3.39%, and when the threshold was reduced (from 100 to 10 keV), the average time to simulate all primaries increased by 43.49 ± 22.02%.

3.3. Chamber–Chamber Effect

Another aspect analyzed was the fact that instead of using the full 24 positions available in the ionization chambers holder (see **Figure 4**), only 12 positions were used, allowing for investigating the influence of chamber–chamber effect. A 2-tailed *t-test* was performed, as in Section 3.1, and no statistical significant difference (p-value 0.996) was found between both simulations with 12 or 24 chambers. **Figure 8** shows the calculated deviations for the different data sets for both MC and TPS.

4. DISCUSSION

4.1. The Influence of a Detailed Geometry

In this work, we evaluated the effect of the IC geometry description in MC simulation for patient plan verification. We compared our geometrical description with the current approach used. **Figure 6** showed that by improving the details of the detectors geometry description, on average, we obtained a mean deviation of 1.90% with 0.63% 1 SD for the 9 cases in comparison to the current method (1), which obtained a mean deviation of 2.36% (0.75%).

Another source of uncertainty is the positioning of the phantom. In order to evaluate if the deviations found were introduced not only by the MC simulations but also by the position of these detectors during measurements, we simulate the effect of introducing this uncertainty.

We simulated different detector positions within ±1 mm in all direction for one of the data set (Data Set 2) around the original position, in total, 27 positions miming uncertainties in the detector positioning. A new minimum of 1.94% was found at (1, −1, 1) as dx, dy, and dz, respectively, in comparison to 2.40% as reported by Molinelli et al. (1).

The obtained mean deviation in respect to the applied offset can be seen in **Figure 9**. It can be seen that the obtained deviation varies with the positioning of the detector block in a systematic manner,

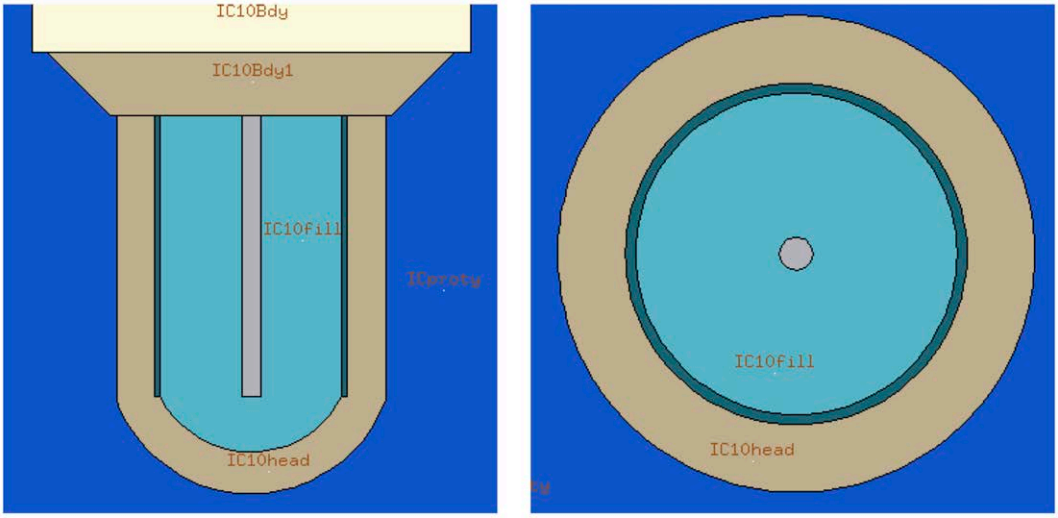

FIGURE 5 | **Flair representation of internal structures of the ionization chamber**. The detector active volume is labeled as "IC10fil" for the IC number 10. All regions in, or in direct contact with, the active volume had its threshold modified for the purpose of these simulations.

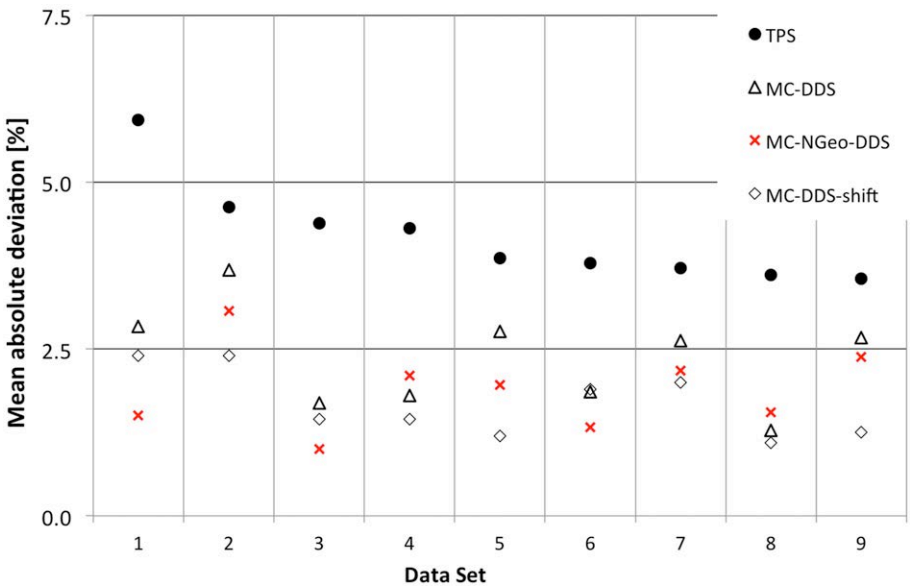

FIGURE 6 | **Results for the effects of different approaches when performing patient plan verification in relation to geometry description**.

where a minimum and a maximum deviation can be obtained by optimizing the detector position. This also shows that for this data set, the importance of a proper positioning of the water phantom.

4.2. Chamber–Chamber Effect

In addition to the benefits of using a more detailed geometry description, additional points needed to be evaluated as possible contribution to errors and uncertainties. The first one was the interference seen by a detector from the interaction of beam to previously positioned detectors. Although this effect had been evaluated for carbon ions (20) in the case of protons which are more susceptible to the broadening, it had not been evaluated. In our study, no significant difference was seen between the measurements with and without the extra detectors.

4.3. The Influence of Delta Rays Threshold

Another possible factor which will influence the MC simulation results with more detailed detector geometry is the choice of delta rays threshold. For this reason, we evaluated threshold in our detailed geometry. We found that current thresholds used by

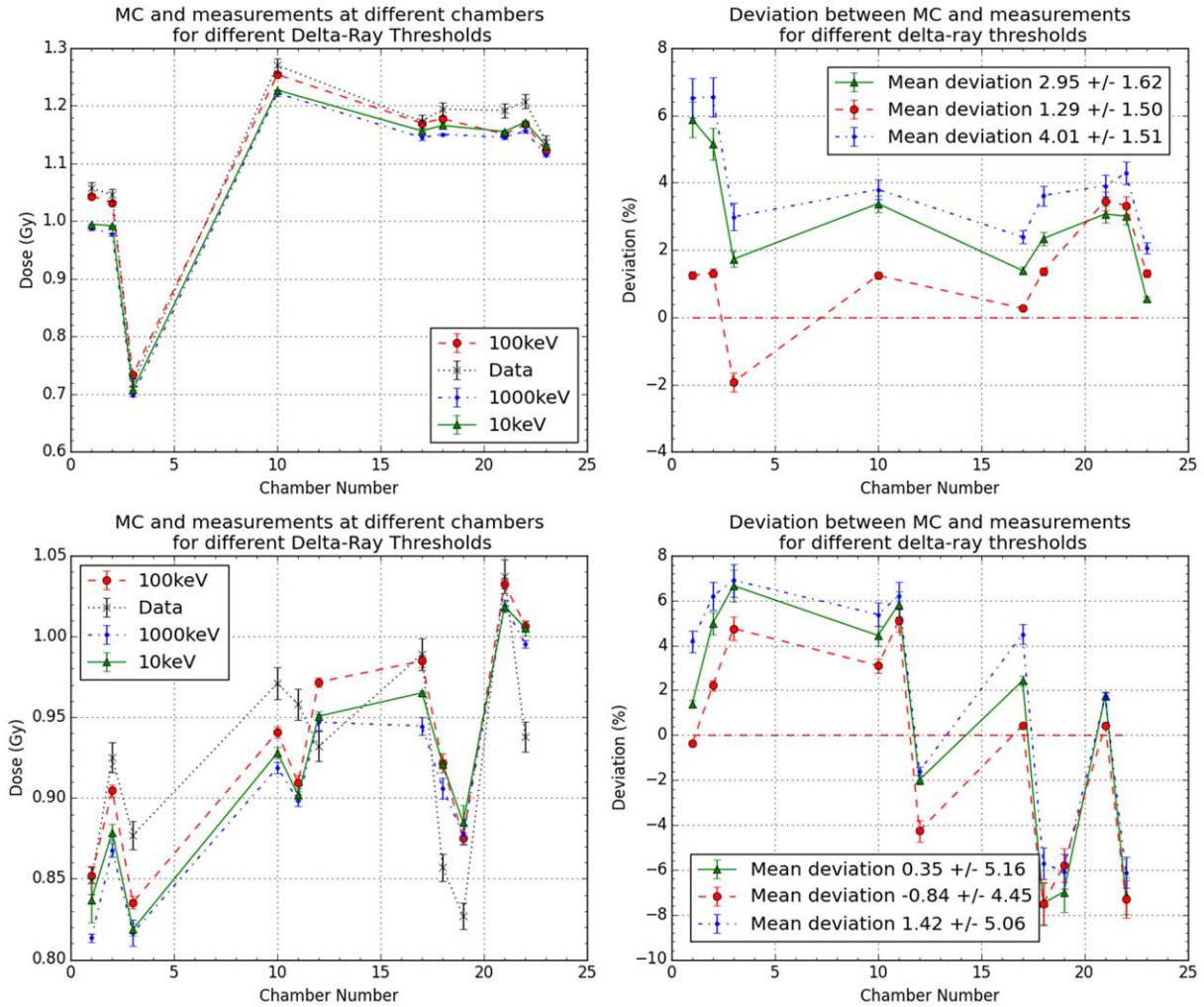

FIGURE 7 | **Results for the effects of different delta rays thresholds in the more detailed geometry MC simulations for data sets 1 and 2**. It is plotted as the comparison between measurements and MC with different thresholds for the two cases (left) and their obtained deviations in respect to measurements (right).

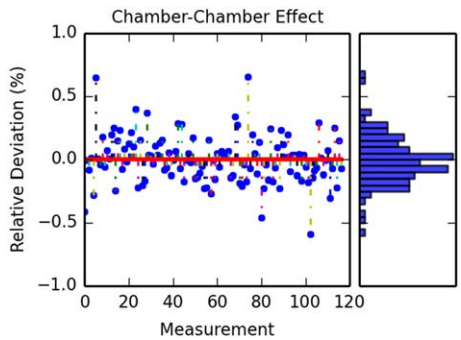

FIGURE 8 | **Calculated differences between simulation with 12 and 24 ionization chambers**. The figure on the left shows the different deviation for each IC measurement for all the data sets. The figure on the right shows the obtained histogram of these deviations.

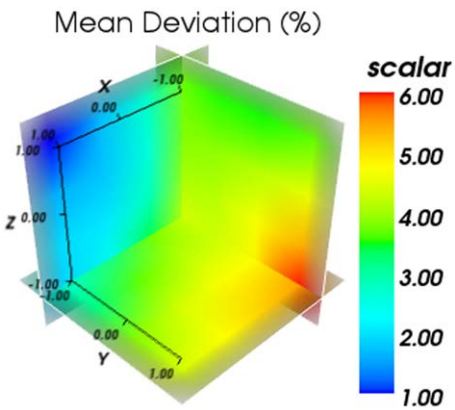

FIGURE 9 | **Results for the obtained mean deviation in respect to the applied offset**. The color bar represents the mean average deviation obtained in %.

the default, which have been previously analyzed (11), are still sufficient for this detailed geometry, and no improvement was observed by the reduction of these.

5. CONCLUSION

The use of MC simulations in aiding patient plan verification has been evaluated. In this work, we studied the effect of improving the detectors geometry description in the MC simulations. We showed that even in the most challenging scenarios of very non-uniform fields, a more detailed geometric description of the detectors results in better agreement with the measurements, although at the cost of more computational time (18.8% in average). If taken into considerations that only 9 patient in an entire year period crossed the threshold, this increase of time should not limit the use of a more detailed geometry description. Additionally, we saw that for few cases where the uncertainty of mispositioning was more relevant than the modeling uncertainties, the use of detailed geometry description in the MC simulation was not able to improve agreement with measurements. For these cases, it was only possible to obtain a better agreement after the detector position was shifted.

AUTHOR CONTRIBUTIONS

All the authors participated in the different stages of the work, from conception, analysis, and writing.

ACKNOWLEDGMENTS

We would like to thank the help and input from Mr. A. Fedynich, Mr. L. Morejon, and Dr. P. Velten. In addition, this work would not be made possible without the valuable help from Dr. Vlachoudis at CERN and the Medical Physics group at CNAO.

FUNDING

This research project has been supported by a Marie Curie Early Initial Training Network Fellowship of the European Community's Seventh Programme under contract number PITN-GA-2010-264552-ENTERVISION. In addition, TVML was also supported by UCL and the Wellcome Trust ISSF Award (097815/Z/11/B).

REFERENCES

1. Molinelli S, Mairani A, Mirandola A, Vilches Freixas G, Tessonnier T, Giordanengo S, et al. Dosimetric accuracy assessment of a treatment plan verification system for scanned proton beam radiotherapy: one-year experimental results and Monte Carlo analysis of the involved uncertainties. *Phys Med Biol* (2013) **58**(11):3837–47. doi:10.1088/0031-9155/58/11/3837
2. ICRU. Report 78: prescribing, recording, and reporting proton-beam therapy. *J ICRU* (2007) **7**(2):135–139.
3. Kraft G. Tumor therapy with heavy charged particles. *Prog Part Nucl Phys* (2000) **45**:S473–544. doi:10.1016/S0146-6410(00)00112-5
4. Lomax A, Böhringer T, Bolsi A, Coray D, Emert F, Goitein G, et al. Treatment planning and verification of proton therapy using spot scanning: initial experiences. *Med Phys* (2004) **31**(11):3150. doi:10.1118/1.1779371
5. Arjomandy B, Sahoo N, Ciangaru G, Zhu R, Song X, Gillin M. Verification of patient-specific dose distributions in proton therapy using a commercial two-dimensional ion chamber array. *Med Phys* (2010) **37**(11):5831. doi:10.1118/1.3505011
6. Karger CP, Jäkel O, Hartmann GH. A system for three-dimensional dosimetric verification of treatment plans in intensity-modulated radiotherapy with heavy ions. *Med Phys* (1999) **26**(10):2125–32. doi:10.1118/1.598728
7. Rossi S. The status of CNAO. *Eur Phys J Plus* (2011) **126**(8):78. doi:10.1140/epjp/i2011-11078-8
8. Ferrari A, Sala PR, Fassò A, Ranft J. *FLUKA: A Multi-Particle Transport Code (Program Version 2005)*. Geneva: CERN (2005).
9. Böhlen TT, Cerutti F, Chin MPW, Fassò A, Ferrari A, Ortega PG, et al. The FLUKA code: developments and challenges for high energy and medical applications. *Nucl Data Sheets* (2014) **120**(C):211–4. doi:10.1016/j.nds.2014.07.049
10. Mairani A, Böhlen TT, Schiavi A, Tessonnier T, Molinelli S, Brons S, et al. A Monte Carlo-based treatment planning tool for proton therapy. *Phys Med Biol* (2013) **58**(8):2471–90. doi:10.1088/0031-9155/58/8/2471
11. Parodi K, Mairani A, Brons S, Hasch BG, Sommerer F, Naumann J, et al. Monte Carlo simulations to support start-up and treatment planning of scanned proton and carbon ion therapy at a synchrotron-based facility. *Phys Med Biol* (2012) **57**(12):3759–84. doi:10.1088/0031-9155/57/12/3759
12. Vlachoudis V. FLAIR: a powerful but user friendly graphical interface for FLUKA. *International Conference on Mathematics, Computational Methods & Reactor Physics, Saratoga Springs, New York, May 3–7, 2009*. LaGrange Park, IL: American Nuclear Society, (2009).
13. Goitein M. A technique for calculating the influence of thin inhomogeneities on charged particle beams. *Med Phys* (1978) **5**(4):258–64. doi:10.1118/1.594509
14. Urie MM, Sisterson JM, Koehler AM, Goitein M, Zoesman J. Proton beam penumbra: effects of separation between patient and beam modifying devices. *Med Phys* (1986) **13**(5):734–41. doi:10.1118/1.595974
15. Böhlen TT, Dosanjh M, Ferrari A, Gudowska I, Mairani A. FLUKA simulations of the response of tissue-equivalent proportional counters to ion beams for applications in hadron therapy and space. *Phys Med Biol* (2011) **56**(20):6545–61. doi:10.1088/0031-9155/56/20/002
16. Krämer M, Scholz M. Treatment planning for heavy-ion radiotherapy: calculation and optimization of biologically effective dose. *Phys Med Biol* (2000) **45**(11):3319–30. doi:10.1088/0031-9155/45/11/313
17. Krämer M, Jäkel O, Haberer T, Kraft G, Schardt D, Weber U. Treatment planning for heavy-ion radiotherapy: physical beam model and dose optimization. *Phys Med Biol* (2000) **45**(11):3299–317. doi:10.1088/0031-9155/45/11/313
18. Ciocca M, Mairani A, Mirandola A, Molinelli S, Freixas GV, Donetti M, et al. OC-0057 commissioning and quality assurance of scanned proton beams produced by a synchrotron for particle radiotherapy. *Radiother Oncol* (2012) **103**:S22–3. doi:10.1016/S0167-8140(12)70396-1
19. IAEA. *Radiation Oncology Physics: A Handbook for Teachers and Students*. 882 Technical report. Vienna, Austria: IAEA (2005).
20. Parcerisa DS. *Experimental and Computational Investigation of Water-to-Air Stopping Power Ratio for Ion Chamber Dosimetry in Carbon Ion Radiotherapy*. PhD thesis. Germany: University of Heidelberg (2012).

Conflict of Interest Statement: The authors declare that the research was conducted in the absence of any commercial or financial relationships that could be construed as a potential conflict of interest.

Copyright © 2016 Lima, Dosanjh, Ferrari, Molineli, Ciocca and Mairani. This is an open-access article distributed under the terms of the Creative Commons Attribution License (CC BY). The use, distribution or reproduction in other forums is permitted, provided the original author(s) or licensor are credited and that the original publication in this journal is cited, in accordance with accepted academic practice. No use, distribution or reproduction is permitted which does not comply with these terms.

frontiers in Oncology

ORIGINAL RESEARCH
published: 11 January 2016
doi: 10.3389/fonc.2015.00297

Phase Space Generation for Proton and Carbon Ion Beams for External Users' Applications at the Heidelberg Ion Therapy Center

Thomas Tessonnier[1,2], Tiago Marcelos[2], Andrea Mairani[3,4], Stephan Brons[3] and Katia Parodi[2,3]*

[1] Department of Radiation Oncology, Heidelberg University Clinic, Heidelberg, Germany, [2] Department of Medical Physics, Ludwig Maximilians University, Munich, Germany, [3] Heidelberg Ion Beam Therapy Center, Heidelberg, Germany, [4] Centro Nazionale di Adroterapia Oncologica, Pavia, Italy

In the field of radiation therapy, accurate and robust dose calculation is required. For this purpose, precise modeling of the irradiation system and reliable computational platforms are needed. At the Heidelberg Ion Therapy Center (HIT), the beamline has been already modeled in the FLUKA Monte Carlo (MC) code. However, this model was kept confidential for disclosure reasons and was not available for any external team. The main goal of this study was to create efficiently phase space (PS) files for proton and carbon ion beams, for all energies and foci available at HIT. PSs are representing the characteristics of each particle recorded (charge, mass, energy, coordinates, direction cosines, generation) at a certain position along the beam path. In order to achieve this goal, keeping a reasonable data size but maintaining the requested accuracy for the calculation, we developed a new approach of beam PS generation with the MC code FLUKA. The generated PSs were obtained using an infinitely narrow beam and recording the desired quantities after the last element of the beamline, with a discrimination of primaries or secondaries. In this way, a unique PS can be used for each energy to accommodate the different foci by combining the narrow-beam scenario with a random sampling of its theoretical Gaussian beam in vacuum. PS can also reproduce the different patterns from the delivery system, when properly combined with the beam scanning information. MC simulations using PS have been compared to simulations, including the full beamline geometry and have been found in very good agreement for several cases (depth dose distributions, lateral dose profiles), with relative dose differences below 0.5%. This approach has also been compared with measured data of ion beams with different energies and foci, resulting in a very satisfactory agreement. Hence, the proposed approach was able to fulfill the different requirements and has demonstrated its capability for application to clinical treatment fields. It also offers a powerful tool to perform investigations on the contribution of primary and secondary particles produced in the beamline. These PSs are already made available to external teams upon request, to support interpretation of their measurements.

Keywords: phase space, particle therapy, Monte-Carlo, FLUKA, patient dose calculation, experimental measurements

OPEN ACCESS

Edited by:
Marco Durante, GSI, Germany

Reviewed by:
Jiankui Yuan, University Hospitals Case Medical Center, USA
Samuel Chao, Cleveland Clinic, USA

****Correspondence:***
Thomas Tessonnier
thomas.tessonnier@med.uni-heidelberg.de

Specialty section:
This article was submitted to Radiation Oncology, a section of the journal Frontiers in Oncology

Received: *30 September 2015*
Accepted: *14 December 2015*
Published: *11 January 2016*

Citation:
Tessonnier T, Marcelos T, Mairani A, Brons S and Parodi K (2016) Phase Space Generation for Proton and Carbon Ion Beams for External Users' Applications at the Heidelberg Ion Therapy Center. Front. Oncol. 5:297. doi: 10.3389/fonc.2015.00297

INTRODUCTION

In the particle therapy field, Monte-Carlo (MC) codes provide a powerful tool to perform accurate calculations, with a precise description of the transport and interactions of the beam with the traversed materials, compared to the current treatment planning systems (TPS) as the one used at Heidelberg Ion Therapy Center (HIT; Syngo RT Planning TPS, Siemens AG Healthcare), which is based on analytical algorithms using fast pencil-beam dose calculation (1). At HIT, the FLUKA MC code (2, 3) was chosen to support the creation of the TPS basic input data (4). The beamline has been modeled in great details, particularly the vacuum window and the Beam and Application Monitoring System (BAMS), composed of two multiwire proportional chambers and three ionization chambers that are monitoring the beam, providing accurate data for the parameterization of the lateral dose spread for additional input to the analytical clinical TPS (5). A MC framework, without using the beamline model but a beamline approximation closely resembling the TPS approach, has been also developed and is used to perform both dose forward calculation and range verification (6–8), providing a powerful computational tool to complement the clinical TPS.

The use of modeled beamlines in MC applications has been described in many works for beam delivery with active energy selection (5, 9–11), for passive energy selection with pencil-beam scanning (12, 13), or for passive scattering (14, 15). In our case, due to confidential issues with the beamline geometry, the model is not available for external users in need of precise simulation, neither for data analysis comparisons after irradiation at HIT nor for simulation-related researches.

This paper proposes a solution to this problem with the creation of phase space (PS) files containing the characteristics (charge, mass, energy, coordinates and direction cosines, generation) of every particles (primary protons and carbon ions as well as secondaries) at the end of the beamline, for each of the 255 available initial beam energies. Furthermore, the adaptation to the delivery pattern from the raster scanning system (16) has to be possible with these PSs, as well as the accommodation of the four different foci used clinically at HIT, i.e., the full-width half maximum (FWHM) of the lateral beam sizes in air at isocenter according to the accelerator database (the so-called library of ion beam characteristics or LIBC). PS files created from beamline geometries, in the particle therapy field, have already been investigated for proton beam applications with passive beam delivery or scanned beams of fixed lateral size (13, 15, 17–19). Our approach proposes a novel narrow-beam approximation to generate PS that can be accurately adapted to reproduce all the foci available at HIT and scanning pattern of irradiation plans for both protons and carbon ions. Several validations steps against simulation with the full beamline geometry will be presented. Simulations using the PS approach will be compared to measurements in a water phantom. An application of the proposed approach to a small target patient plan will be shown and compared to the results of the simplified MC framework. For this plan, the two approaches will be evaluated against measurements in a water phantom.

MATERIALS AND METHODS

Phase Space Generation

Monte-Carlo Code and Modeling Approaches of the HIT Beamline

Different approaches have been used concerning the modeling of the beamline for MC simulation at HIT. The detailed geometrical model (5) allows simulating more precisely transport and interactions occurring in the beamline, particularly inside the BAMS, for accurate prediction of lateral beam scattering (**Figure 1**). The different foci are representative of the spread of an initially small (few millimeters) beam in vacuum into the beamline and air. In the simplified MC framework, the beamline is approximated by an energy reduction before the propagation of the particles in vacuum, according to the water equivalent thickness of the beamline and air distance to the isocenter. The focus is then adapted geometrically to its nominal one at the isocenter (8), similar to the TPS approach. With this simplified approach, forward recalculation of planned treatments could well reproduce corresponding dosimetric measurements in most of the cases, with differences below 3% (8). However, the approximations made in such MC framework [the so-called TPS-like approach (8)] could have limitation for extreme cases of small fields, due to an underestimation of large angle lateral scattering in the elements before the target. Furthermore, with the explicit modeling of the beamline geometry, information on the primary and secondary particles exiting the BAMS could be tracked, as well as their impacts. Hence, in order to give the possibility to external users to perform precise simulations using the detailed geometrical modeling of the beamline, without disclosing its confidential components, we developed an original PS approach (see Section "Phase Space Narrow-Beam Approach").

The FLUKA version used for this study is the 2011.2c. In order to reproduce HIT reference Bragg curves, several optimizations have been made on the initial beam momentum spread for every energy as well as the ionization potential in water, similar to previous studies using older FLUKA versions (4, 20). The "HADROTHErapy" settings with the "EVAPORation" physics model were used for both PS generation and dosimetric verification. For time-efficient generation of PS files as well as data space saving, photons and electrons were not transported, thus depositing their energy at the production point.

Phase Space Requirements

The PS files characterize the beam on a plane perpendicular to its propagation at a defined position along the beam path, by describing the properties of every crossing particle (charge, mass, energy, coordinates and direction cosines, generation).

Several goals were defined prior to the generation of the PS. For every initial beam energy of protons and carbon ions, a unique PS should be generated and adapted to all the possible foci available at HIT. The FWHM in air at isocenter obtained with the PS should not be different from the reference foci values of the TPS basic data or LIBC (i.e., FWHM in air at isocenter) within the tolerances defined internally at HIT to account for possible daily variations of the beam shape [(−15, 25%) of the reference]. The same tolerances are

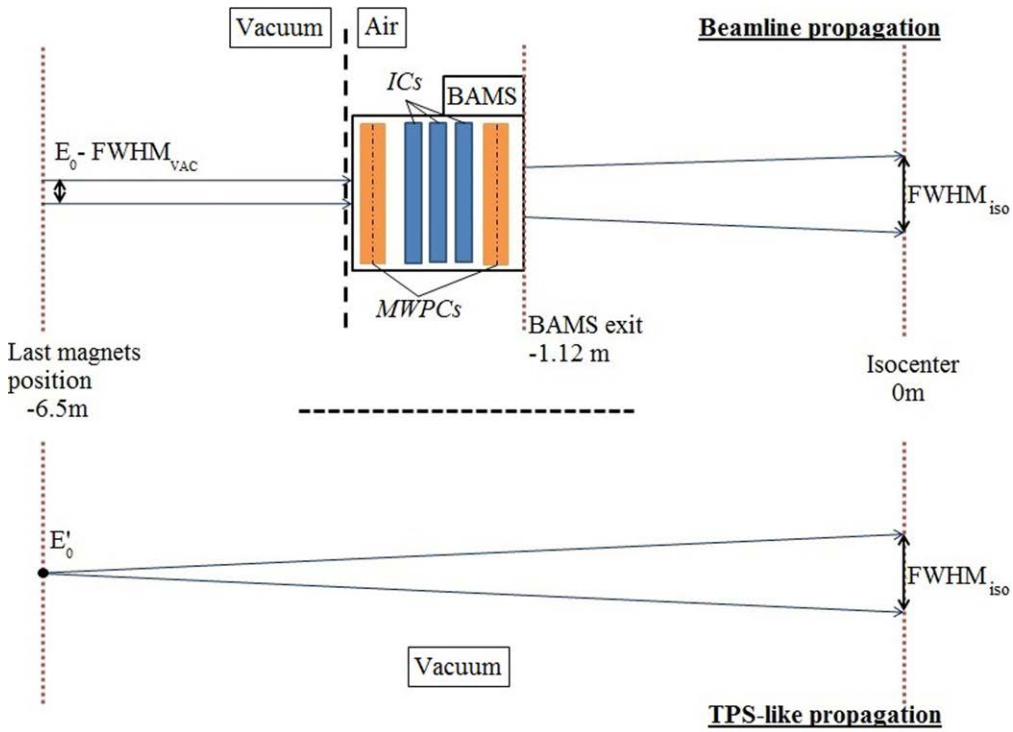

FIGURE 1 | Schematic of different MC approaches for simulation transport: on the upper panel, the detailed beamline allowing precise description of the particle interactions, from a beam with an initial energy E_0 and an initial focus $FWHM_{vac}$; on the bottom panel the simplified TPS-like approach propagating the particle in vacuum to the isocenter, with an initial energy E'_0 taking into account the energy reduction of E_0 due to the BAMS water equivalent thickness and adapted geometrically to the same $FWHM_{iso}$ used by the TPS at isocenter.

defined for comparing the simulations using the new PS approach to measurements of FWHM in water at different depths. For the comparisons between the full beamline geometry (BL approach) and the PS approach, we decided that the differences in FHWM at isocenter in air should be inferior to 3%. Additional requirements include a consistent propagation of the primary and secondary particles, meaning that particles generated from the same primary history have to be transported together. Also, the PS approach should lend itself to beam propagation according to the raster scanning pattern of the treatment plan. A reasonable compromise between the size of the PS files and the number of simulated particles has to be found, in order to have enough available statistics per energy and also saving all the needed information.

Phase Space Narrow-Beam Approach

In order to respect the requirements on the adaptability of a unique PS to different foci, we develop an original narrow-beam approach for PS files generation. It can be explained by analogy with a homogeneous analytical system, whose response R_δ to a Dirac signal δ is its impulse response *S*. In addition, the response R_G of this system to a Gaussian signal *G* will be the convolution between the signal *G* and the impulse response *S*.

$$R_\delta = S * \delta = S$$

$$R_G = S * G$$

In this way, when using an infinitely narrow ("zero-width") beam propagated in the beamline (by analogy δ), the PS scored at the end of the BAMS of the beamline (by analogy the system), specifically the information on the particles position, represents the impulse response *S* of this system.

Therefore, an adaptation to every focus is possible by convoluting the PS with the information on the particle position, using a Gaussian distribution *G* to represent the beam in vacuum before entering the beamline. It is known that the result of the convolution between two Gaussian functions is still a Gaussian, with a width (standard deviation, SD) σ(G1*G2) corresponds to the quadratic addition of the widths of the two Gaussians G1 and G2, σ(G1) and σ(G2). Assuming that the fluence distribution of this PS is Gaussian-like, this approach is consistent with the quadratic addition as in Parodi et al. (5), with σ the beam focus at isocenter, σ_0 the beam broadening at isocenter due to a "zero-width" beam and σ_{ini} the estimated initial beam in vacuum:

$$\sigma(G1 * G2)^2 = \sigma(G1)^2 + \sigma(G2)^2$$

$$\sigma^2 = \sigma_0^2 + \sigma_{ini}^2$$

For every focus, a different value of the beam initial size in vacuum is needed and has to be estimated. The theoretical Gaussian FWHM of the beam in vacuum (before the beamline) is investigated as a function of the energy using this narrow-beam

approach. By scoring the position of the primary particles at the isocenter, for several energies in the therapeutic range, and evaluating the FWHM of their distributions at the center of the beam spot along the horizontal axis, the FWHM of the vacuum Gaussian beam $FWHM_{Vacuum}(focus)$ can be retrieved using the following equation for every focus:

$$FWHM_{Vacuum}(focus)^2 = FWHM_{Isocenter}(focus)^2 - FWHM_{Isocenter}(\delta)^2$$

where $FWHM_{Isocenter}(focus)$ is the FWHM size at isocenter in air for one focus extracted from the HIT LIBC database, $FWHM_{Isocenter}(\delta)$ is the FWHM size in air at isocenter after the propagation of an infinitely narrow beam. The energies investigated are {48.12, 54.19, 80.90, 106.82, 132.30, 157.43, 182.66, 221.05} MeV/u for protons and {88.83, 100.07, 150.42, 200.28, 250.08, 299.94, 350.84, 430.10} MeV/u for carbon ions.

The calculated values of $FWHM_{Vacuum}(focus)$ are compared to the expected ones from previous work (4) and are used for the final validation of the PS approach as well as for the rest of the study. A total of 10 million primary histories are simulated for each run.

With the beam records of the irradiation, where the information about the size of the focus at the isocenter are recorded, a new estimated focus size in vacuum could be calculated by replacing the nominal $FWHM_{Isocenter}(focus)$ with the one extrapolated from the upstream measurement of the BAMS.

Phase Space Scoring

Phase space files are generated for protons and carbon ions, for every energy of the HIT accelerator library with the optimized beam momentum spread in the simulation, transporting 10 million primary particles in total, which results in files with a total size of about 500 Mb each. The lateral size of the beam is set to a zero-width distribution (see Section "Phase Space Narrow Beam Approach"). The scoring is done on a 4 m^2 plane perpendicular to the beam direction at the end of the BAMS, just after the last element of the beamline, i.e., the second multiwire proportional chamber, at about 112 cm before the isocenter.

Two files are created. The first file corresponds to the scoring of the primary beam with the information about the energy, the position in the plane (X,Y position), and the direction cosines (X and Y cosines). The second file contains the information about the secondary particles (except photons and electrons) in terms of energy, position, direction cosines, charge, and mass information of every particle. Last information to be saved in both files is the generation number of the primary, which allows linking primary to secondary particles during the propagation process.

To ensure that the PS is representative of the different interactions occurring in the beamline, the starting positions of the narrow beam are randomly selected in a 5 mm*5 mm square around the central axis. Information on these starting positions is kept during the beam propagation in the beamline to the scoring position, and then subtracted to the scored position of every particle in the PS files.

Phase Space Propagation for Scanned Beam Delivery

While performing a treatment plan simulation using the PS, the so-called PS approach, the propagation process is divided in five steps:

- Reading the plan used for irradiation and segmenting the requested number of primary histories for the simulation run among the different energy slices according to the weight of the number of particles per slice compared to the total number of particles of the plan. This is the only step of the process that is not random in order to read the PS files only one by one, not to overload the computer memory.
- Reading the PS file of the current energy slice and linking primary and secondary particles.
- Selecting randomly a generation number among the 10 million possible, to be handled as the next primary history. Then loading all the particles related to this primary history into the stack of particles to be propagated. Every possibility can be handled (a primary with no secondaries, only secondaries, primary and secondaries, no particles scored in the PS).
- The convolution process at the single particle level is performed by adding the position information (X_{PS}, Y_{PS}) of each particle of the stack (loaded from the PS) to, respectively, two distinct random positions (X_{Vac}, Y_{Vac}) selected from a Gaussian distribution with a FWHM size corresponding to the expected Gaussian size of the beam in vacuum for the selected focus (see **Figure 2** and Section "Phase Space Narrow Beam Approach"). This initial Gaussian distribution in vacuum is assumed to have the same FWHM in X and Y. The final position of the particle to be transported is then $X_{PS} + X_{Vac}$, $Y_{PS} + Y_{Vac}$.
- Selecting randomly one of the planned positions at isocenter (X'_{iso}, Y'_{iso}) in the current energy slice, with probability weighted by the number of particles to be delivered to this spot compared to the total one of the energy slice. In order to reach this position, the PSs have to be rotated from the original position (X_{iso}, Y_{iso}, corresponding to the position of the central beam axis at isocenter) to the selected coordinate (X'_{iso}, Y'_{iso}). This means finding a new position on the PS plane (X'_{Bams}, Y'_{Bams}) with respect to the original one along the central axis (X_{Bams}, Y_{Bams}) and adapting the new direction cosines (d') from the original one of the selected particles (d) in order to target the selected isocenter position after propagation (**Figure 2**).

This method holds the advantage that even with only 10 million particles in the PS, the convolution with random positions of the beam Gaussian shape in vacuum increases the number of combinations of position and energy, thus, decreasing the probability to have the same event repeated twice.

Validation and Comparisons

Validations of the PS Approach

Validations of the PS approach are performed against the BL approach, i.e., propagation with the beamline geometry, for different cases. The first pencil-beam validation step is focused on the differences between the two approaches in terms of

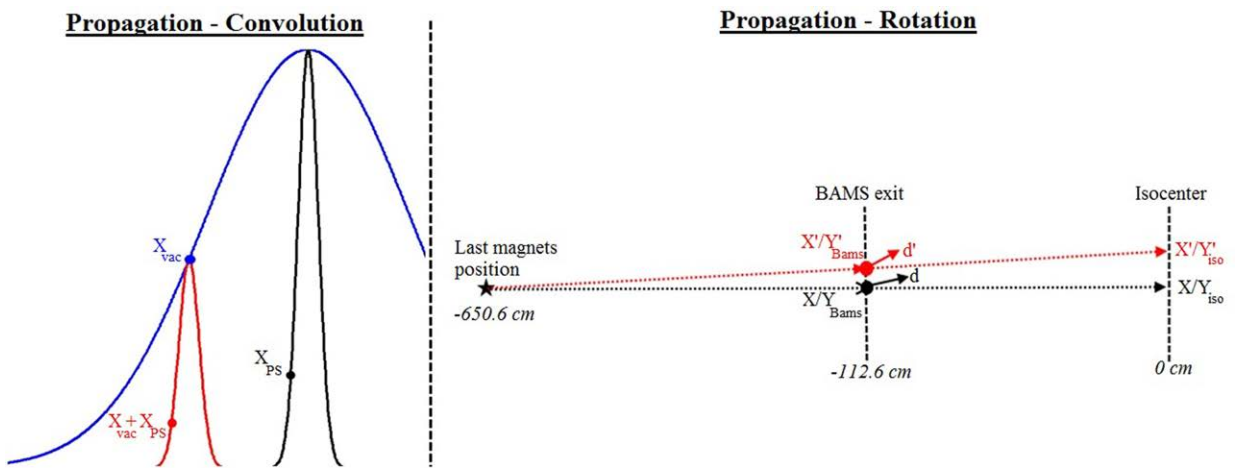

FIGURE 2 | Propagation process: on the left panel, convolution results (red) between the PS from the narrow beam (black) and the Gaussian in vacuum (blue): new position ($X_{vac} + X_{PS}$) obtained from the original position on the phase space (X_{PS}) and the selected position on the Gaussian in vacuum (X_{vac}); on the right panel, rotation of the beam to the expected position: transformation from the *X/Y* position at the BAMS with a direction cosine d to the new X'_{Bams}/Y'_{Bams} position at the BAMS with the direction cosines d' in order to reach the X'_{iso}/Y'_{iso} position at isocenter.

fluence distributions and particle spectra for a central beam delivery without scanning. For the additional validation steps with scanned beam delivery featuring line scans and spread out Bragg-peak (SOBP) distributions, the comparisons are made on the dose results.

Pencil-Beam Validation

For both protons and carbon ions, two energies have been investigated, namely the lowest (respectively, 48.12 and 88.83 MeV/u) and the highest (respectively, 221.06 and 430.10 MeV/u), for the smallest and largest foci (i.e., focus indexes 1 and 4) used in clinical routine. Different PS files were generated at different positions along the beam path in order to investigate the beam propagation in air for a fixed central pencil beam: PS_{BAMS} is recorded on a 4 m^2 plane at the BAMS exit at the same position as the one generated with the narrow-beam approach, while PS_{iso} is recorded on a 4 m^2 plane at the isocenter. Three scenarios are compared for the different energies:

- Simulations with BL approach with different focus sizes: $PS_{BAMS,BL}$(focus) and $PS_{iso,BL}$(focus), starting from a beam in vacuum with the estimated beam size in vacuum before the beamline.
- Simulations with BL approach for the narrow-beam propagation: $PS_{BAMS,BL}(\delta)$ and $PS_{iso,BL}(\delta)$, starting from an infinitely narrow beam in vacuum before the beamline, as in the PS generation process.
- Simulations with the PS approach for different focus sizes: $PS_{iso,PS}$(focus), starting from the PS in air at the BAMS exit position (where the PS have been generated).

The fluence and energy distributions are investigated for both primary and secondary particles.

On the planes perpendicular to the beam propagation, at the BAMS exit position and the isocenter, the FWHM of the fluence distributions at the center of the pencil-beam spot along the horizontal axis are reported, as well as the FWHM of the vertically integrated profiles.

For the vertically integrated profiles at the isocenter, the absolute global differences are also analyzed. It corresponds to

$$Difference_{global}(x) = 100 \times \frac{|Fluence_{PS}(x) - Fluence_{BL}(x)|}{\max(Fluence_{BL})}$$

with *Fluence(x)* the fluence on the profile at the position *x* (for both approaches), and $max(Fluence_{BL})$ the maximum fluence along the profile. The mean of these differences and its SD σ, as well as the maximal deviation, are reported. These values are calculated in a region of the profiles where the fluence is superior to 0.1% of the maximal fluence. The bin size of the profile is 0.2 mm.

For the energy spectrum, the same analysis is performed on the different PS files acquired at the isocenter, however, the *x* variable corresponds to an energy bin in the energy distribution. The bin size is 0.04 MeV/u. The energy spectrum of the secondaries is qualitatively analyzed as their proportion compared to the primaries is low (maximum probability for an energy bin around 0.05% per primaries), hence, only the trend and similarities of the spectrum are compared.

For the BL and the PS approaches, scenario 10 and 5 million primary histories are simulated, respectively. For quantitative purposes, only 5 million primary histories are used for the analysis, for both approaches, in order to have a fair comparison.

Line Scan Validation

For both protons and carbon ions, we designed plans corresponding to a vertical line scan, extending from −5 cm to +5 cm with a

1 mm step and centered horizontally (i.e., at 0 cm). Three initial beam energies within the therapeutic range are investigated, a low energy (80.90 and 150.42 MeV/u for protons and carbon ions, respectively), a middle energy (157.43 and 299.94 MeV/u, respectively), and the highest energy (221.06 and 430. MeV/u), in combination with each of the four foci used in clinical routine; thus, resulting in a total of 24 line scans. The geometry of the simulated target represents the water phantom used for plan verification measurements, positioned at the treatment isocenter, with a 5 mm PMMA entrance window. The bin size of the dose scoring grid is set to 0.5 mm × 0.5 mm × 0.5 mm. To ensure enough statistics, 100 million primary histories were simulated for both approaches in 100 statistically independent runs. Both laterally integrated depth dose profiles, scored along the beam penetration in water, and lateral dose profiles, sampled at the entrance of the target, are compared between the BL and PS approach. For every dose profile, we investigate both the absolute local dose relative difference:

$$Difference_{local}(x) = 100 \times \frac{|Dose_{PS}(x) - Dose_{BL}(x)|}{Dose_{BL}(x)}$$

and the absolute global dose relative difference:

$$Difference_{global}(x) = 100 \times \frac{|Dose_{PS}(x) - Dose_{BL}(x)|}{\max(Dose_{BL})}$$

with *Dose(x)* being the dose of the profile at the position *x* (for both approaches), and $max(Dose_{BL})$ being the maximum dose along the profile.

SOBP Validation

Spread out Bragg-peak plans have been simulated with both the PS and the BL approaches for protons and carbon ions, in the latter case using the ripple filter geometry (21), used to broaden the narrow Bragg peaks of carbon ions, as done in clinical practice. SOBP plans are designed to deliver 1 Gy to a 5 cm × 5 cm × 3 cm target, centered at 10 cm depth in water. The same MC geometry with the water phantom is used, as described in Section "Line Scan Validation." The dose scoring grid is set to a bin size of 1 mm × 1 mm × 1 mm. 100 million primary histories are used to simulate these plans. In this more clinical-like scenario, only the absolute global differences of the doses between the BL and PS approaches are investigated along the central depth dose profile and for the lateral dose profiles sampled at the entrance of the target and in the middle of the SOBP.

Comparisons of the PS Approach with Measurements

The line scan plans, presented in Section "Line Scan Validation," have also been irradiated at the experimental room of HIT. The measurements were performed in a water phantom coupled with 24 motorized Pinpoint ionization chambers (PTW, 0.03 cm^3). The chambers are positioned in a block composed of six horizontal lines with four chambers (separated of 12 mm one to each other within the same line) at six depths along the beam path, separated by 10 mm. In the vertical direction, the lines are grouped by two, and these three groups of two lines are separated from each other by 7 mm. Within a same group of two lines, these two lines are shifted by 6 mm horizontally to avoid interferences from one line to the other one. This allows acquiring four positions at the same depth, i.e., for the same horizontal profile, for six depths in each measurement. Then for the same block position in depth, six measurements were performed with a 2 mm horizontal shift perpendicular to the beam direction to complete the lateral profiles. The lateral extension of each profile is 46 mm. The block was put at three positions along the beam path in order to sample lateral profiles at the entrance of the phantom, in the plateau of the Bragg peak and near the Bragg peak. The measurements were acquired for every combination of particle type/energy/focus presented previously.

For this comparison, the MC simulations using the PS approach are the same as the one presented previously. However, in order to have a fair comparison between the PS approach and the measurements, the sensitive volume of the ionization chamber has been taken into account in the MC dose results, by averaging the dose value of the voxel of interest with the surrounding ones to obtain a resulting integration volume close to the one of the ionization chamber.

The lateral profiles are analyzed quantitatively at three different depths, for each energy and focus, and the FWHM values of both measurements and simulation are compared. For the lowest energy, with a range of around 53 mm, the depths analyzed are 15.7, 30.7, and 45.7 mm. For the middle energy, with a range around 172 mm, the depths analyzed are 15.7, 85.7, and 151.7 mm. For the highest energy, with a range around 308 mm, the depths analyzed are 15.7, 195.7, and 267.7 mm. The mean and the SD of the absolute differences are reported for protons and carbon ions.

Application to a Small Target Clinical Case

A challenging clinical entity has been selected for testing the PS application: an arterio-venous malformation (AVM) that is a small target inferior to 20 ml in most of the cases and below 3 ml in our study, treated at HIT with protons in one fraction of 18 Gy RBE at the isodose 80%. Magro et al. (11) found for small targets at shallow depth discrepancies between TPS and measurements in water up to ~19%.

Among the four beams of the plan, we selected the one delivering the highest dose. Dosimetric measurements for this beam were performed in the same water phantom described in the Section "Comparisons of the PS Approach with Measurements," and compared to the dose calculations resulting from the PS approach and the simplified MC framework using the TPS-like approach. Several lateral profiles in the horizontal direction, with a 1 mm lateral step, are acquired at different depths of 19.7, 29.7, 39.7, and 49.7 mm.

Furthermore, using the information from the irradiation beam records registered by the BAMS, it was found that all foci were on average 1 mm larger than the ones of the TPS database, used in both the PS (in terms of the beam vacuum size added to the narrow-beam approach) and TPS-like simulations. Hence, new expected Gaussian sizes of the beam in vacuum were generated and an additional simulation was performed for the PS approach

with these new parameters for comparison to the measurements and the previous simulations.

The geometry for the MC simulations is using the same water phantom target as for the SOBP simulations. The dose scoring grid is with a bin size of 1 mm × 1 mm × 1 mm and the number of primary histories is set to 5% of the beam total number of particles, which is five times higher than the recommended statistics according to Bauer et al. (8).

In a second step, forward dose calculations of the whole plan in the patient CT geometry have been performed for both the TPS-like approach and the PS one, using the reference LIBC foci value at isocenter. The results are compared in terms of dose profiles sampled within the target region [planning target volume (PTV)] region and PTV dose volume histograms.

RESULTS

Validation of the PS Approach

Gaussian Shape in Vacuum

For carbon ions, the calculated FWHM values of the Gaussian lateral beam distribution in vacuum are within 0.2 mm to the ones expected: 2.5, 5, 7.5, and 9.5 mm for the foci from 1 to 4. For focus 1, the mean calculated FWHM (μ) is 2.46 mm with a SD σ of 0.15 mm, μ = 5.02 ± 0.09 mm, μ = 7.47 ± 0.07 mm, and μ = 9.49 ± 0.06 mm for foci 2, 3, and 4, respectively. As the focus increases, the σ decreases due to an easiest FWHM evaluation in regard to the bin size. Considering the bin size of 0.2 mm and the small difference to the expected value, the nominal values are kept for the whole work.

Differently, for protons the calculated FWHM values are far different from the initial values of {2.5, 6, 8, and 10} mm assumed in a previous work, which was only using a simplified beamline modeling for guiding the LIBC generation (4). It should also be reminded that for foci higher than focus 1, the FWHM foci values for the low energy region (<100 MeV/u) are not corresponding to the cited values, due to an asymptotical convergence to avoid too large beam at isocenter (4). From the simulated eight energies in the therapeutic range, an interpolation is done (**Figure 3**). For focus 1, we found μ = 6.46 ± 2.05 mm on the whole energy range. For energies above 100 MeV/u, for focus 2 we obtained μ = 7.69 ± 0.37 mm, for focus 3 μ = 9.40 ± 0.30 mm, and for focus 4 μ = 11.16 ± 0.26 mm. These new values are used for the whole study in order to reach with the PS simulation a good agreement to the LIBC foci values at isocenter, which are also used by the TPS.

Pencil-Beam Validation

Fluence Distributions

For the two extreme foci analyzed, the lateral profiles obtained at isocenter with the PS and BL approaches are similar, regardless of the considered energy and ion species (**Figure 4**). The absolute global differences between the two approaches are under 2.5% for protons and under 1.3% for carbon ions (**Table 1**). The FWHM values of the lateral profiles, for the profiles in the center of the pencil beam spot and for the vertically integrated profiles at the BAMS exit positions and at isocenter, are reported in **Table 2**. For protons (for both energies and foci), the maximal difference is equal to 0.1 mm for the vertically integrated profiles and 0.2 mm for the horizontal profile along the spot center. For carbon ions (both energies and foci) the maximal difference is equal to 0.1 mm for the vertically integrated profile and 0.2 mm for the profile sampled along the spot center. For both particles type, the difference to the nominal expected values at the isocenter from the database is under 3.5% and 0.5 mm with the FWHM values in vacuum obtained from the Section "Gaussian Shape in Vacuum."

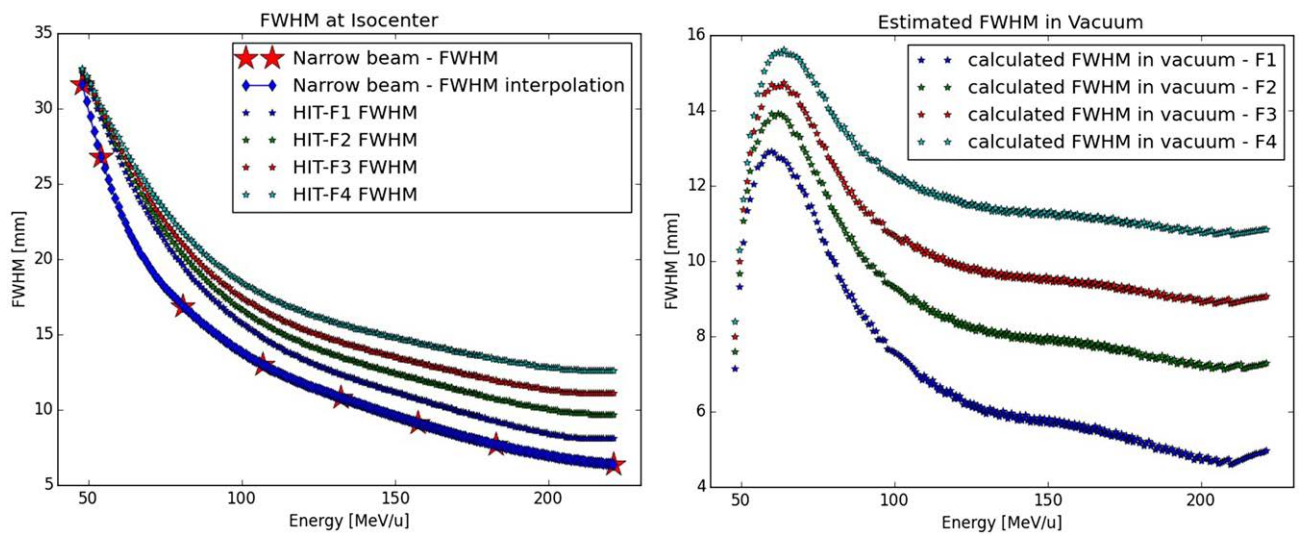

FIGURE 3 | Calculation of the protons Gaussian FWHM in vacuum: on the left panel, the different FWHM size of the proton foci at isocenter from the LIBC are displayed as a function of the energy, as well as the calculated FWHM size for the narrow-beam approach (star) and its interpolation; on the right panel, the results of the quadratic subtraction between the two previous quantities yielding the initial beam size in vacuum for the different foci as function of the energy.

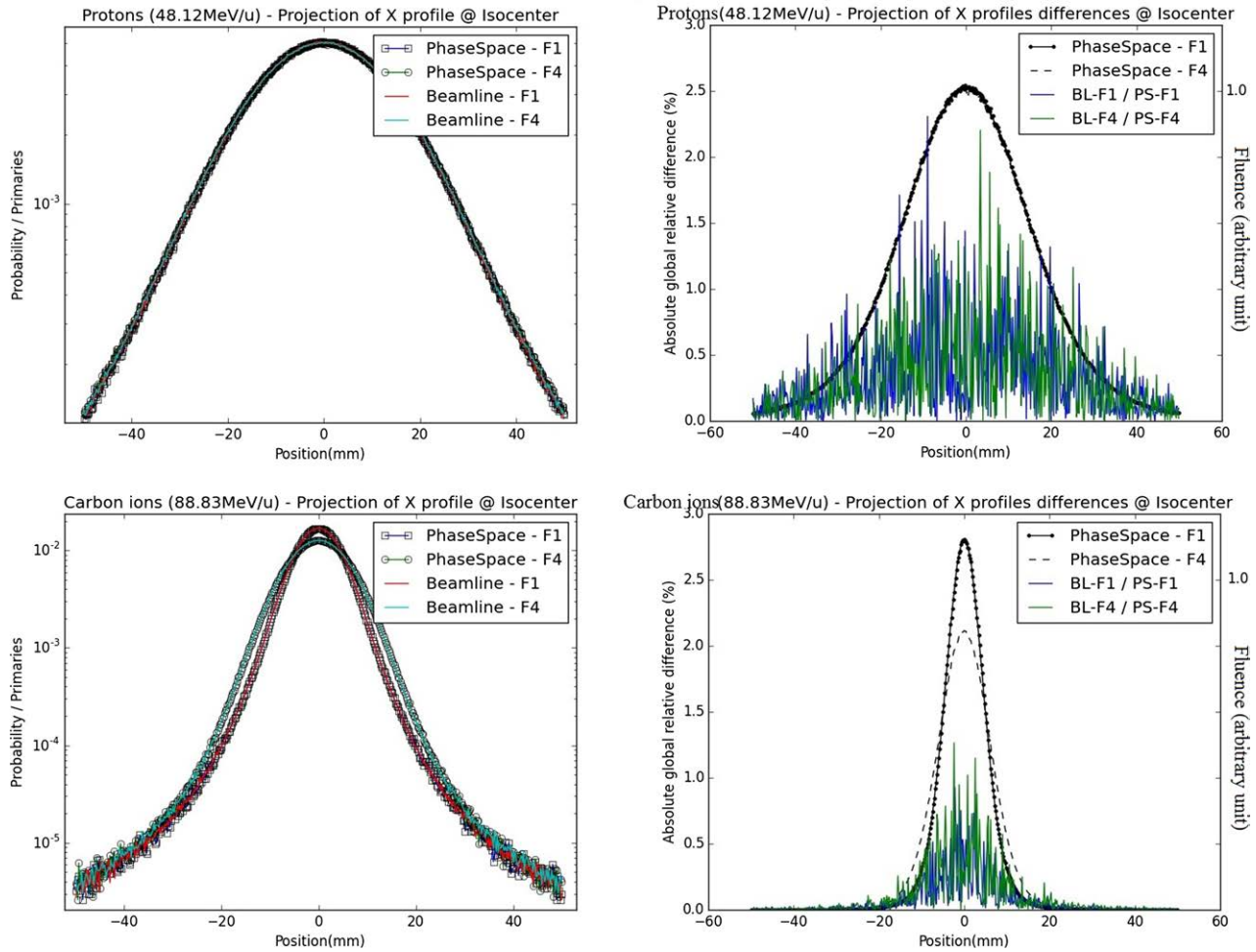

FIGURE 4 | Energy spectra difference for protons and carbon ions at the isocenter in air: on the left panels, absolute differences in primary spectra obtained with the PS and BL approaches are displayed for foci 1 and 4 (blue and red) together with the primary spectra shape (in black, similar for foci 1 and 4 and both approaches); on the right panel, secondary spectra at isocenter are displayed for the beamline approach (narrow beam and focus 1) and the PS approach; the upper panels correspond to protons, energy 48.12 MeV/u, and the bottom panels correspond to carbon ions, energy 88.83 MeV/u.

TABLE 1 | Primary particle fluence differences at the isocenter (absolute global differences with mean μ, SD σ, and maximum value) between the PS and the BL approaches for both foci 1 and 4 for the vertically integrated lateral profile distributions, in percentages compared to the maximum fluence and in a zone of interest with an fluence >0.01% of the maximum one.

	Protons						Carbon ions					
	48.12 MeV/u			221.06 MeV/u			88.83 MeV/u			430.10 MeV/u		
	μ (%)	σ (%)	Max (%)	μ (%)	σ (%)	Max (%)	μ (%)	σ (%)	Max (%)	μ (%)	σ (%)	Max (%)
F1	0.33	0.32	2.30	0.06	0.13	0.91	0.07	0.13	0.93	0.02	0.06	0.83
F4	0.35	0.34	2.20	0.08	0.17	1.30	0.10	0.18	1.26	0.05	0.12	0.85

Energy Spectrum

From visual analysis, for the primary particles of both carbon ions and protons, the different energy spectra at the isocenter are similar for the different foci simulated with the BL (foci 1, 4, and narrow beam) or while using the PS approach for the foci 1 and 4. Quantitatively, the energy spectra at the isocenter of the BL and the PS approaches are highly similar regarding their differences (**Figure 5**). The absolute global differences between the BL and the PS approaches are reported in the **Table 3**. The maximal deviation for protons is 0.46% and for carbon ions 0.68%.

For the less abundant secondary particles, the different approaches show profiles with the same trend for both protons and carbon ions (**Figure 5**).

TABLE 2 | FWHM, in millimeter, of the different fluence distributions for protons and carbon ions, with respect to the reference one from the LIBC: FWHM values for profiles sampled at the center of the beam spot and for vertically integrated profiles (Int. profiles), for two positions in depth in air (exit of the BAMS and isocenter) for both foci 1 and 4.

		Position	Profiles (mm)	Int. profiles (mm)	Profiles (mm)	Int. profiles (mm)
			48.12 MeV/u		221.06 MeV/u	
Protons	DB-F1	Isocenter	32.4	/	8.7	/
	DB-F4	Isocenter	32.6	/	12.6	/
	BL-Narrow	BAMS	4.1	4.2	0.9	0.9
		Isocenter	32.0	34.1	6.8	6.8
	BL-F1	BAMS	8.6	8.6	5.0	5.0
		Isocenter	32.4 (0%)	34.5	8.9 (2.3%)	9.1
	BL-F4	BAMS	9.4	10.6	10.8	10.8
		Isocenter	32.5 (−0.3%)	35.0	13.0 (3.2%)	13.5
	PS-F1	Isocenter	32.3 (−0.3%)	34.6	9.0 (3.4%)	9.2
	PS-F4	Isocenter	32.6 (−0.6%)	35.0	12.8 (1.6%)	13.5
			88.83 MeV/u		430.10 MeV/u	
Carbon ions	DB-F1	Isocenter	9.8	/	3.4	/
	DB-F4	Isocenter	13.4	/	9.8	/
	BL-Narrow	BAMS	1.3	1.3	0.4	0.4
		Isocenter	9.6	9.6	2.5	2.5
	BL-F1	BAMS	2.9	2.9	2.7	2.7
		Isocenter	10.0 (2%)	10.4	3.5 (3%)	3.6
	BL-F4	BAMS	9.7	10.3	9.6	9.6
		Isocenter	13.7 (2.2%)	14.2	9.9 (1%)	9.9
	PS-F1	Isocenter	9.8 (0%)	10.4	3.5 (3%)	3.5
	PS-F4	Isocenter	13.6 (1.5%)	14.2	9.8 (0%)	9.9

For the different foci at isocenter, the variations in percentage to the LIBC foci value are shown in bracket. DB stands for the LIBC database values, BL for the BL approach values, and PS for the PS approach.

Line Scan Validation

The line scan validation step exhibits similar results for the simulations performed with the BL and the PS approaches, both in terms of depth as well as lateral dose profiles (**Figure 6**).

For both types of particles and all explored combinations of energy and focus values, the absolute global dose relative difference between the PS and the BL approaches is below 0.5% for the laterally integrated depth dose profiles, and the local dose relative difference is below 0.8%. For the lateral profiles, the maximal absolute global dose relative differences are less than 0.5%, while the absolute local dose relative differences reach higher values in low dose regions, but still well below the MC percentage errors (**Figure 6**), as calculated over the 100 statistically independent runs.

SOBP Validation

In terms of extended SOBP fields, both the simulated approaches yield depth and lateral dose profiles in excellent agreement with each other (**Figure 7**), with absolute global dose relative differences below under 0.5% regardless of the considered ion species.

Comparison of PS-Based Simulations with Dosimetric Measurements

The different water phantom dosimetric measurements show good agreements with the PS approach simulations (**Figure 8**). In terms of lateral profiles sampled at three different depths in water, the differences (in mm and percentage) of the fitted FWHM values are displayed in **Table 4** for both particles types, and all investigated combinations of energies/foci. The maximal relative FWHM differences found for protons are about 6.5 and 5.8% corresponding, respectively, to FWHM differences of 0.8 and 1.1 mm. The mean absolute difference of the absolute value is 0.5 mm with a SD of 0.3 mm. The maximal absolute difference found for carbon ions is of −0.9 mm (relative difference of −7.5%), the mean absolute difference is 0.2 mm with a SD of 0.2 mm.

Application to a Small Target Clinical Case

The comparison of the measurements acquired at different depths in water exhibits absolute global differences below 6% with the conventional PS approach (i.e., utilizing the beam width in vacuum discussed in the Section "Gaussian Shape in Vacuum"), while under 2% with the optimized PS approach which takes into account the actual deviation of +1 mm for the delivered foci with respect to the nominal TPS (LIBC) values. In such extreme scenario, the TPS-like approach implemented in the MC framework, using the nominal TPS FWHM values, yields deviations up to 25% (**Figure 9**).

The results of the dose calculations, using the nominal FWHM values at isocenter, for the full plan projected on the CT patient geometry show the same tendency in terms of the lateral profiles and dose volume histogram (**Figure 9**). Specifically, the main findings can be summarized as follows:

- 95% of the volume receives 16.9 Gy for PS approach against 19.44 Gy for the TPS-like one.
- 5% of the volume receives 22.5 Gy for PS approach against 26.1 Gy for TPS-like one.

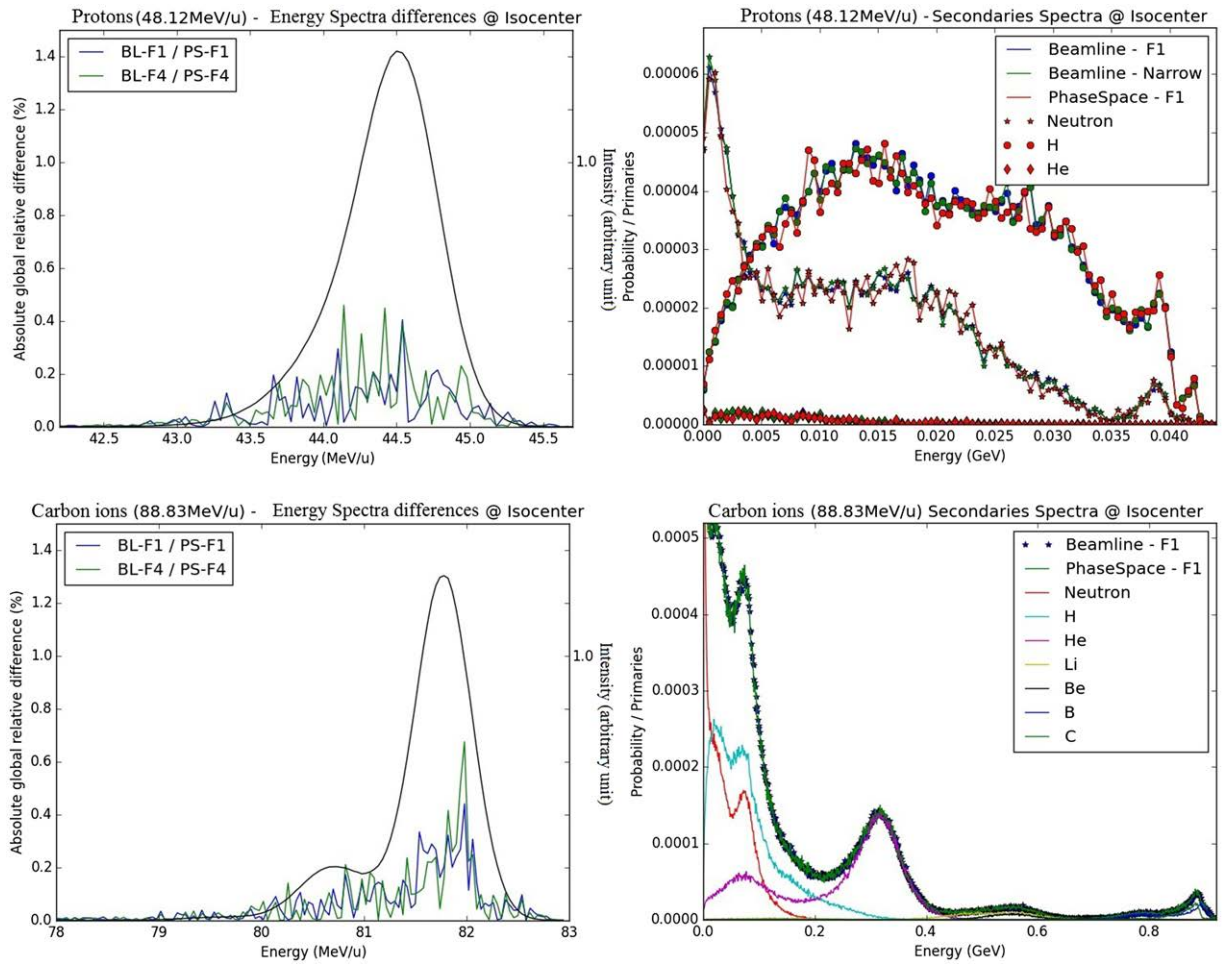

FIGURE 5 | Fluence distributions for protons and carbon ions at the isocenter in air – vertically integrated profiles: on the left panels, vertically integrated profiles (projections of X profiles) from BL and PS approaches are displayed for foci 1 and 4 in semi-logarithmic scale; on the right panels, absolute relative differences between lateral distributions from PS and BL approaches are displayed for foci 1 and 4 of the smallest energy (blue/red) together with their respective shapes (black); the upper panel corresponds to protons (48.12 MeV/u), the bottom panel corresponds to carbon ions (88.83 MeV/u).

TABLE 3 | Primary particles energy spectra differences at the isocenter (absolute global differences with mean μ, SD σ, and maximum value) between the PS and the BL simulation approaches for both foci 1 and 4, in percentages compared to the maximum fluence and in a zone of interest with an fluence >0.01% of the maximum one.

	Protons						Carbon ions					
	48.12 MeV/u			221.06 MeV/u			88.83 MeV/u			430.10 MeV/u		
	μ (%)	σ (%)	Max (%)	μ (%)	σ (%)	Max (%)	μ (%)	σ (%)	Max (%)	μ (%)	σ (%)	Max (%)
F1	0.05	0.07	0.41	0.04	0.06	0.31	0.06	0.08	0.44	0.07	0.08	0.35
F4	0.06	0.10	0.46	0.05	0.07	0.30	0.06	0.10	0.68	0.08	0.10	0.42

DISCUSSIONS

Validation of the PS

Monte Carlo simulations using the proposed PS approach show an overall very good (typically within 0.5% for the absolute global dose difference) agreement to the approach implementing the explicit modeling of the beamline.

The initial sampling of the infinitely narrow beam randomly spread within a 5 mm × 5 mm area before the beamline allows to include into the PS the information on different interactions that can occur in the beamline, particularly in the multiwire proportional chambers where the wires are separated by a 1 mm distance. Without this sampling, the spectra of the particles would have been different between the PS and the BL approaches, since

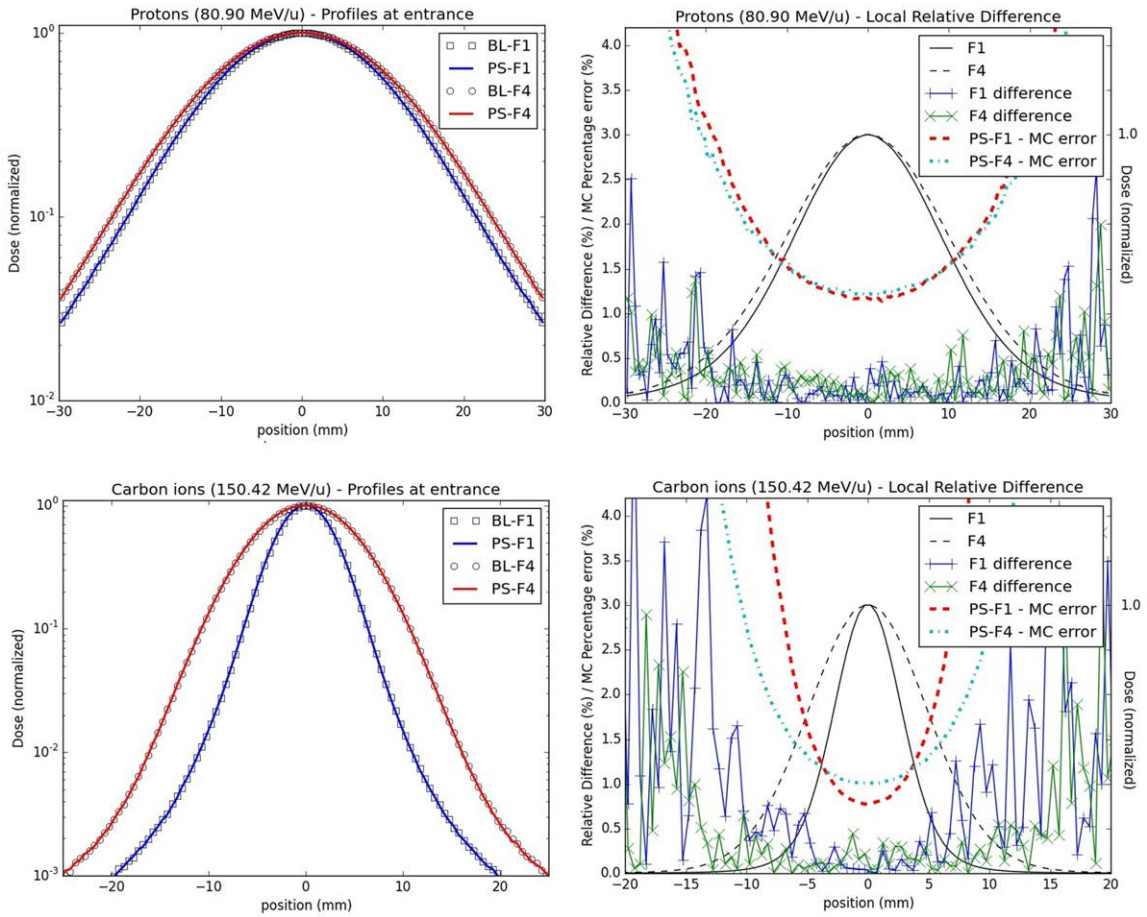

FIGURE 6 | Lateral dose profiles for line scan validations: lateral dose profiles for the lowest energy studied for both protons (upper panels, 80.90 MeV/u) and carbon ions (bottom panels, 150.42 MeV/u) at the isocenter in water; the left panels display the profiles from foci 1 and 4 for the PS (full line) and the BL approaches (stripes) in a semi-logarithmic scale; on the right panels, the profiles (black lines) together with their local relative difference (cross) and MC percentage errors (dashed lines) for foci 1 and 4 are shown.

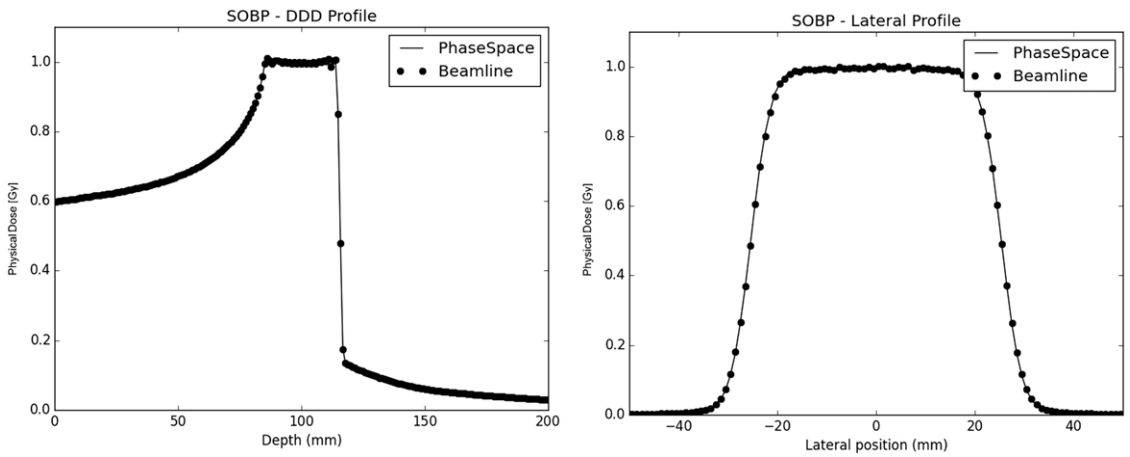

FIGURE 7 | SOBP Profiles in water: on the left panel, the depth dose profiles of both the PS (full line) and the beamline (dot line) approaches are plotted together; on the right panel the lateral dose profiles at the center of the SOBP for both the PS (full line) and the BL (dot line) approaches are shown.

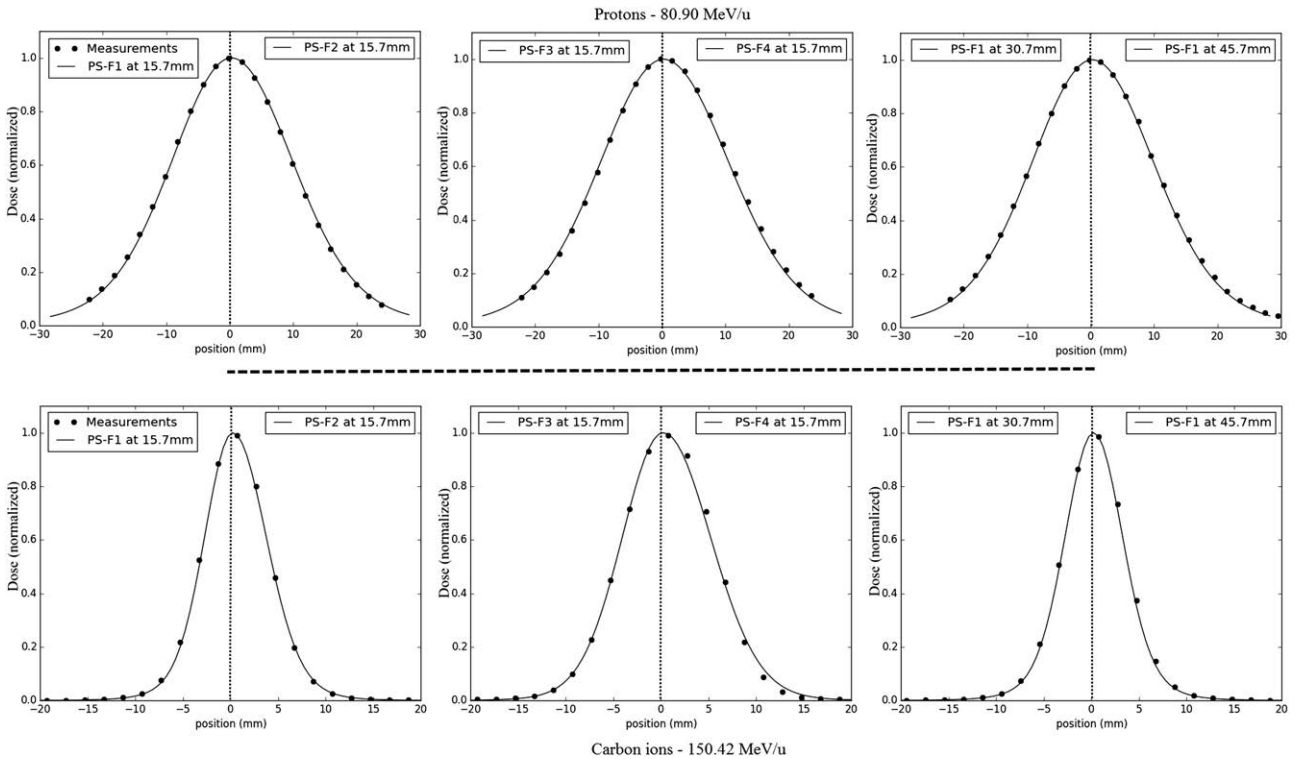

FIGURE 8 | Dose calculations and measurements for lateral dose profile comparisons from line scans: half-profiles of the different foci are plotted for the same low energy, from left to right for focus 1 to focus 4 at 15.7 mm in water, and for two other depths for focus 1 (30.7 and 40.7 mm); the upper panels correspond to protons comparisons (energy 80.90 MeV/u), the bottom panels to carbon ions comparisons (energy 150.42 MeV/u); results are normalized to the maximum.

TABLE 4 | FWHM differences, in millimeter and percentages, between the PS simulation approach and dosimetric measurements, at different depths in water, for all investigated combinations of particles/energies/foci.

		Protons				Carbon ions			
	Depth (mm)	**F1**	**F2**	**F3**	**F4**	**F1**	**F2**	**F3**	**F4**
Low energy	15.7	−0.2 mm, −1.0%	0.5 mm, 2.2%	0.4 mm, 1.8%	−0.9 mm, −3.7%	−0.4 mm, −5.7%	−0.2 mm, −1.8%	−0.2 mm, −1.5%	−0.3 mm, −2.1%
	30.7	−0.3 mm, −1.3%	0.4 mm, −1.5%	−0.3 mm, −1.1%	−0.8 mm, −3.1%	−0.3 mm, −3.5%	0.0 mm, 0.0%	0.0 mm, 0.0%	−0.1 mm, −0.1%
	45.7	−0.5 mm, −2.2%	0.0 mm, 0.0%	0.2 mm, 0.8%	−0.7 mm, −2.8%	−0.2 mm, −3.2%	0.1 mm, 0.9%	−0.1 mm, −0.5%	−0.2 mm, −1.4%
Middle energy	15.7	−0.1 mm, −0.7%	0.2 mm, 1.2%	0.4 mm, 3.1%	−0.5 mm, −2.8%	−0.1 mm, −2.8%	0.1 mm, 2.0%	−0.2 mm, −1.7%	**−0.9 mm, −7.5%**
	85.7	0.3 mm, 2.1%	0.4 mm, 2.7%	0.6 mm, 3.5%	0.2 mm, 1.0%	0.3 mm, 6.6%	0.4 mm, 5.44%	0.0 mm, 0.0%	−0.7 mm, −5.7%
	151.7	0.3 mm, 2.0%	0.8 mm, 5.0%	0.8 mm, 4.4%	0.5 mm, 2.6%	0.2 mm, 2.7%	0.4 mm, 6.1%	0.3 mm, 3.6%	−0.1 mm, −1.3%
High energy	15.7	0.3 mm, 2.9%	0.4 mm, 4.1%	**0.8 mm, 6.5%**	0.2 mm, 1.3%	0.2 mm, 3.7%	0.1 mm, 2.0%	0.0 mm, 0.0%	−0.1 mm, −1.1%
	195.7	0.3 mm, 2.4%	0.7 mm, 4.6%	0.1 mm, 0.3%	0.9 mm, 5.2%	−0.1 mm, −1.5%	0.1 mm, 1.6%	0.1 mm, 1.0%	−0.3 mm, 2.7%
	267.7	0.3 mm, 1.8%	0.7 mm, 3.8%	**1.1 mm, 5.8%**	0.9 mm, 4.5%	−0.1 mm, −1.1%	0.3 mm, 4.0%	0.4 mm, 4.4%	0.1 mm, 1.0%

Measurements are the reference FWHM. "Low energy" corresponds, respectively, for protons and carbon ions, to 80.90 and 150.42MeV/u, "middle energy" to 157.43 and 299.94 MeV/u, and "high energy" to 221.06 and 430.10 MeV/u.
The numbers in bold correspond to the most extreme variation observed for protons and carbon ions.

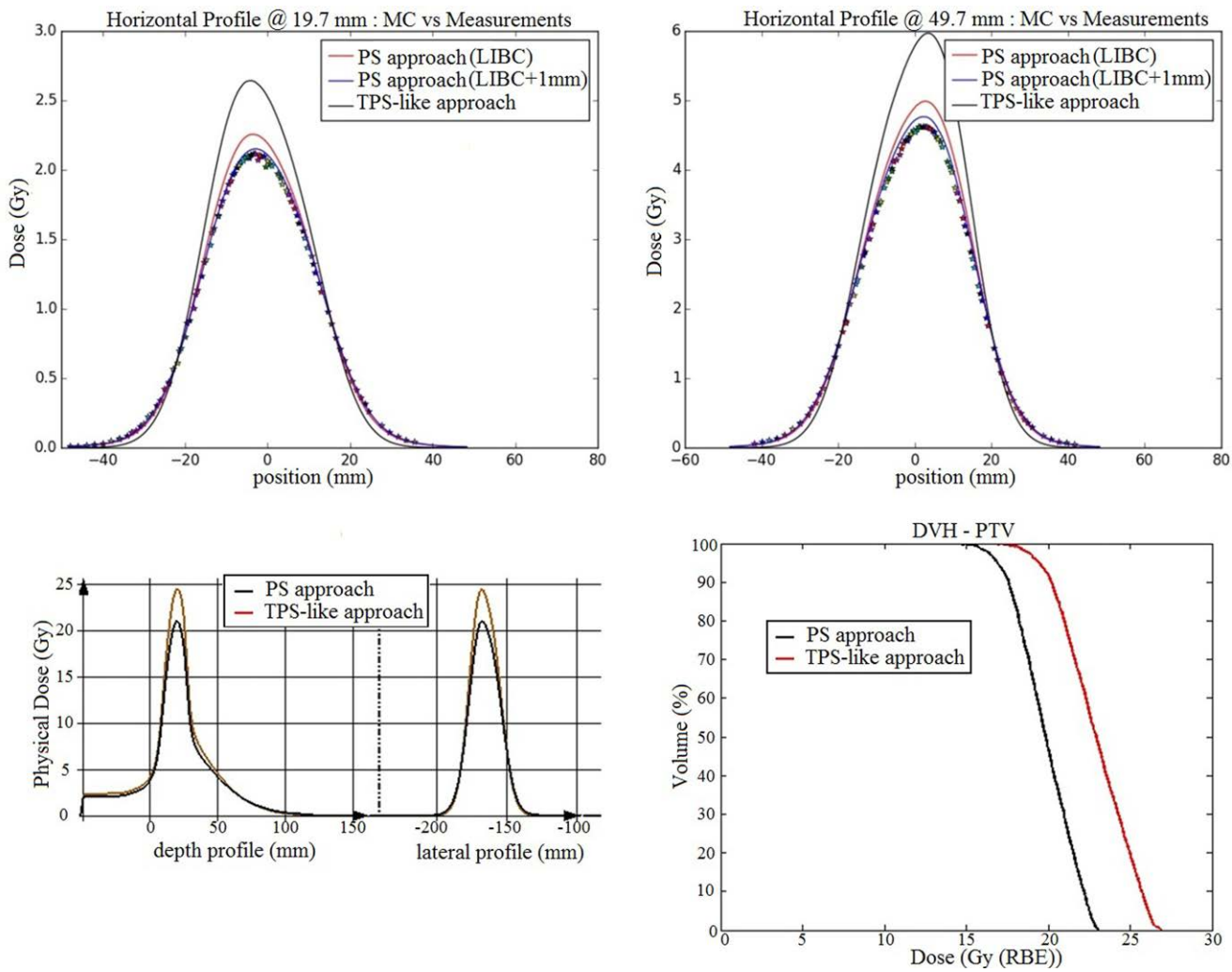

FIGURE 9 | PS approach against TPS-like approach for a small target clinical case: on the upper panels, dose verification measurements (stars) are displayed against simulations with the TPS-like approach using the database foci values (black), the normal PS approach (red) with the foci in vacuum estimated from the database foci values, and the modified PS approach (blue) using the foci values in vacuum calculated from the beam records, at two different depths in water (19.7 and 49.7 mm); on the bottom left panel, the dose profile at the PTV level in the CT patient geometry is plotted in red for the TPS-like approach and black for the PS approach, using the reference LIBC foci, for one beam; the bottom right panel displays dose volume histograms of the dose calculated with the two studied approaches.

some particles of the narrow-beam approach would not interact as expected with the beamline. This would also lead to deviations in terms of fluence distribution and dose deposition due to wrong direction cosines, reducing the FWHM for the fluence distributions of the PS approach, and thus resulting in a higher dose deposition in the center of the beam spot. The energy spectra of the particles obtained with the BL approach were found very similar for both foci 1 and 4, regardless of the sampling position at the end of the BAMS or at the isocenter. This means that either with a small or a large FWHM Gaussian size in vacuum, there is no major impact on the energy spectra, thus, confirming that the used initial sampling area 25 mm^2 is adequate. Furthermore, while investigating in more details the impact of the sampling area, new PSs were generated for a 100 mm^2 area. The fluence distribution comparison between the original and new PS did not show any relevant differences. No major differences were found for the director cosines distribution or the energy spectra either for the PS generated with the different foci and PS generated with the different sampling area, since in all these cases the initial beam is large enough to cover the multiwire proportional chambers pattern, where the wires are separated by 1 mm in the horizontal and vertical directions.

The absolute differences for the vertically integrated fluence distributions, obtained for the pencil-beam validation, are mainly due to the bin size and the resulting lower statistics per bin, since when changing the bin size from a 0.2–0.6 mm, the maximal differences drop from 2.5–0.6% for protons and from 1.3 to 0.5% for carbon ions.

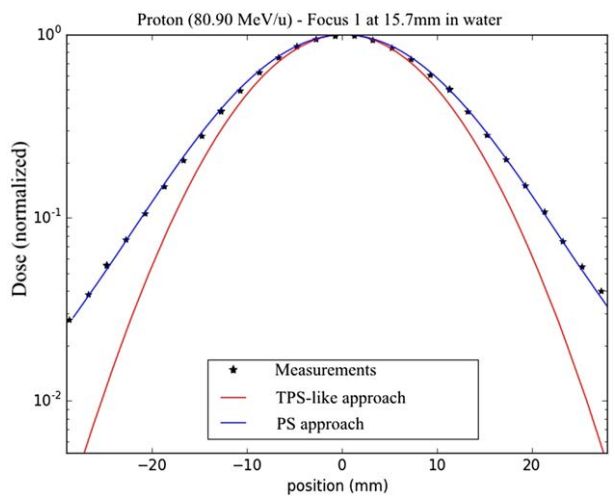

FIGURE 10 | Dose results and measurements at 15.7 mm in water, for lateral dose profiles from line scans for the lowest energy protons and focus 1 with a semi-logarithmic scale; the TPS-like approach is displayed in red, the PS approach in blue and the measurements with the star dots.

The dose differences between the PS and the BL simulation approaches for the line scans and the SOBP validation are within the statistical uncertainties.

These results show that we could fulfill the initial requirements on the adaptation of a unique PS to the different foci and the consistency of the propagation starting from the PS sampling plane, including the handling of the raster scanning process.

Comparisons of the PS-Based Simulations to Dosimetric Measurements

The overall agreement of the PS approach simulations to the lateral profile measurements in water is good, with a maximal FWHM deviation of −7.5% or 1.1 mm for the extreme cases and a mean deviation below 0.5 mm, which is corresponding to the bin size. These results are deemed as highly acceptable, taking into account the even larger tolerance of experimental foci deviations at HIT, which is from +25% to −15%.

For larger foci, particularly for carbon ions, the measured profiles exhibit asymmetric shapes in the horizontal directions, which are not modeled in our simulation. This shape is the resulting effect of the knock-out extraction process of the beam in the synchrotron, occurring in the horizontal plane, which is of trapezoidal shape (22). However, its effects are smeared out due to the scattering in the beamline, air, and water, particularly for small foci and lower energies.

Application to a Small Target Clinical Case

The PS approach shows good results compared to dosimetric measurements in the water phantom, with an acceptable maximal deviation of 5.8%, taking into account uncertainties in the dose gradient for such an extreme case of a small target volume. Moreover, our findings also prove the power of the PS approach to adapt easily to the "real" conditions of irradiation as monitored by the BAMS, improving significantly the results. In particular, we show that MC simulations with the PS approach can use the record of the irradiation to refine from the measured foci the estimate of the actual beam size in vacuum for each energy slice. Combined with the approach used in Tessonnier et al. (23), using the measured positions of every single raster scanning spot and its associated number of particles, it could provide a powerful tool for forward calculation closer to the "real" irradiation conditions.

On the other hand, the simplified TPS-like approach of the MC framework exhibits a large overestimation of the dose with a smaller size of the irradiated volume. This is because it underestimates the large angle spread of the beam due to the BAMS and the air between the end of the beamline and the target position, resulting in higher dose values in the center of every spot. This is shown in the comparison for the lowest beam energy and focus for protons used in the line scan comparisons between the new PS approach, the TPS-like one and measurements (**Figure 10**). These results show that beyond the accurate transport of particles in the target, the initial conditions of the beam are also fundamental. This observation is consistent with the results of Magro et al. (11) between the same TPS and MC simulations for small targets at shallow depths. Beamline approximations used for MC simulations are giving, in general, good results, as shown in Bauer et al. (8) for the MC framework, where the differences between simulations and measurements are in average below 3%, or in Grassberger et al. (12) where their model compared to a full beamline propagation show differences inferior to 1% in the middle of a SOBP. However, a precise model is fundamental for extreme cases of small targets sensitive to the exact modeling of the few individual pencil beams.

CONCLUSION

A novel PS approach has been successfully introduced and validated against simulations with the full beamline geometry. It provides an accurate description of the beam to be propagated to a target (phantom/patient) as it includes the information of the interaction in the beamline in a generic way (the so-called narrow-beam approximation), allowing adaptation to different beam foci with the same data. The PS approach could bring significant improvement to the dose calculation compared to the simplified approach implemented in the current MC framework for consistency to the TPS approach, especially for the here investigated extreme situation of a small target at shallow depths.

The generated PSs can be made available for external teams upon request.

The implementation of the PS approach in the MC framework and generation of PS files for the other particles (helium and oxygen ions) available at HIT are underway.

AUTHOR CONTRIBUTIONS

TT conducted the work, developed the phase space approach, participated in the generation and propagation of the phase spaces with the FLUKA Monte-Carlo code as well as the

different simulation, and participated in the experimental measurements. TM participated in the phase space propagation development. AM participated in every Monte-Carlo FLUKA-related tasks (phase space generations and simulations). SB participated in experimental measurements. KP supervised the whole work.

ACKNOWLEDGMENTS

TT and TM acknowledge funding from the German research foundation (DFG, KFO214) and EU (ERASMUS exchange program), respectively. We would like to thank the accelerator team and the medical physics team for the fruitful discussions.

REFERENCES

1. Krämer M, Jakel O, Haberer T, Kraft G, Schardt D, Weber U. Treatment planning for heavy-ion radiotherapy: physical beam model and dose optimization. *Phys Med Biol* (2000) **45**:3299–317. doi:10.1088/0031-9155/45/11/313
2. Böhlen TT, Cerutti F, Chin MPW, Fassò A, Ferrari A, Ortega PG, et al. The fluka code: developments and challenges for high energy and medical applications. *Nucl Data Sheets* (2014) **120**:211–4. doi:10.1016/j.nds.2014.07.049
3. Ferrari A, Sala PR, Fassò A, Ranft J. *"FLUKA: A Multi-Particle Transport Code". INFN-TC-05–11, SLAC-R-773, CERN-2005-10, 2005*. (2005). Available from: http://www.fluka.org/fluka.php?id=license&mm2=3
4. Parodi K, Mairani A, Brons S, Hasch BG, Sommerer F, Naumann J, et al. Monte Carlo simulations to support start-up and treatment planning of scanned proton and carbon ion therapy at a synchrotron-based facility. *Phys Med Biol* (2012) **57**:3759. doi:10.1088/0031-9155/57/12/3759
5. Parodi K, Mairani A, Sommerer F. Monte Carlo-based parameterization of the lateral dose spread for clinical treatment planning of scanned proton and carbon ion beams. *J Radiat Res* (2013) **54**:i91–6. doi:10.1093/jrr/rrt051
6. Bauer J, Unholtz D, Kurz C, Parodi K. An experimental approach to improve the Monte Carlo modelling of offline PET/CT-imaging of positron emitters induced by scanned proton beams. *Phys Med Biol* (2013) **58**:5193–213. doi:10.1088/0031-9155/58/15/5193
7. Bauer J, Unholtz D, Sommerer F, Kurz C, Haberer T, Herfarth K, et al. Implementation and first clinical experience of offline PET/CT-based verification of scanned carbon ion treatment at the Heidelberg Ion-Beam Therapy Centre. *Radiother Oncol* (2013) **107**:218–26. doi:10.1016/j.radonc.2013.02.018
8. Bauer J, Sommerer F, Mairani A, Unholtz D, Farook R, Handrack J, et al. Integration and evaluation of automated Monte Carlo simulations in the clinical practice of scanned proton and carbon ion beam therapy. *Phys Med Biol* (2014) **59**:4635. doi:10.1088/0031-9155/59/16/4635
9. Molinelli S, Mairani A, Mirandola A, Freixas GV, Tessonnier T, Giordanengo S, et al. Dosimetric accuracy assessment of a treatment plan verification system for scanned proton beam radiotherapy: one-year experimental results and Monte Carlo analysis of the involved uncertainties. *Phys Med Biol* (2013) **58**:3837. doi:10.1088/0031-9155/58/11/3837
10. Mairani A, Bohlen TT, Schiavi A, Tessonnier T, Molinelli S, Brons S, et al. A Monte Carlo-based treatment planning tool for proton therapy. *Phys Med Biol* (2013) **58**:2471. doi:10.1088/0031-9155/58/8/2471
11. Magro G, Molinelli S, Mairani A, Mirandola A, Panizza D, Russo S, et al. Dosimetric accuracy of a treatment planning system for actively scanned proton beams and small target volumes: Monte Carlo and experimental validation. *Phys Med Biol* (2015) **60**:6865–80. doi:10.1088/0031-9155/60/17/6865
12. Grassberger C, Lomax A, Paganetti H. Characterizing a proton beam scanning system for Monte Carlo dose calculation in patients. *Phys Med Biol* (2015) **60**:633–45. doi:10.1088/0031-9155/60/2/633
13. Paganetti H, Jiang H, Parodi K, Slopsema R, Engelsman M. Clinical implementation of full Monte Carlo dose calculation in proton beam therapy. *Phys Med Biol* (2008) **53**:4825. doi:10.1088/0031-9155/53/17/023
14. Paganetti H, Jiang H, Lee SY, Kooy H. Accurate Monte Carlo for nozzle design, commissioning, and quality assurance in proton therapy. *Med Phys* (2004) **31**:2107–18. doi:10.1118/1.1762792
15. Stankovskiy A, Kerhoas-Cavata S, Ferrand R, Nauraye C, Demarzi L. Monte Carlo modelling of the treatment line of the Proton Therapy Center in Orsay. *Phys Med Biol* (2009) **54**:2377–94. doi:10.1088/0031-9155/54/8/008
16. Haberer T, Becher W, Schardt D, Kraft G. Magnetic scanning system for heavy ion therapy. *Nucl Instrum Methods Phys Res A* (1993) **330**:296–305. doi:10.1016/0168-9002(93)91335-K
17. Ramos-Méndez JR, Perl J, Schümann J, Shin J, Paganetti H, Faddegon B. Improved efficiency in Monte Carlo simulation for passive-scattering proton therapy. *Phys Med Biol* (2015) **60**:5019–35. doi:10.1088/0031-9155/60/13/5019
18. Schümann J, Paganetti H, Shin J, Faddegon B, Perl J. Efficient voxel navigation for proton therapy dose calculation in TOPAS and Geant4. *Phys Med Biol* (2012) **57**:3281–93. doi:10.1088/0031-9155/57/11/3281
19. Parodi K, Ferrari A, Sommerer F, Paganetti H. Clinical CT-based calculations of dose and positron emitter distributions in proton therapy using the FLUKA Monte Carlo code. *Phys Med Biol* (2007) **52**:3369–87. doi:10.1088/0031-9155/52/12/004
20. Kurz C, Mairani A, Parodi K. First experimental-based characterization of oxygen ion beam depth dose distributions at the Heidelberg Ion-Beam Therapy Center. *Phys Med Biol* (2012) **57**:5017–34. doi:10.1088/0031-9155/57/15/5017
21. Weber U, Kraft G. Design and construction of a ripple filter for a smoothed depth dose distribution in conformal particle therapy. *Phys Med Biol* (1999) **44**:2765–75. doi:10.1088/0031-9155/44/11/306
22. Ondreka D, Weinrich U. The Heidelberg ion therapy (HIT) accelerator coming into operation. *Proceeding of EPAC08*. Genoa: (2008).
23. Tessonnier T, Mairani A, Cappucci F, Mirandola A, Vilches Freixas G, Molinelli S, et al. Development and application of tools for Monte Carlo based simulations in a particle beam radiotherapy facility. *Appl Radiat Isot* (2014) **83**:155–8. doi:10.1016/j.apradiso.2012.12.019

Conflict of Interest Statement: The authors declare that the research was conducted in the absence of any commercial or financial relationships that could be construed as a potential conflict of interest.

Copyright © 2016 Tessonnier, Marcelos, Mairani, Brons and Parodi. This is an open-access article distributed under the terms of the Creative Commons Attribution License (CC BY). The use, distribution or reproduction in other forums is permitted, provided the original author(s) or licensor are credited and that the original publication in this journal is cited, in accordance with accepted academic practice. No use, distribution or reproduction is permitted which does not comply with these terms.

frontiers in Oncology

ORIGINAL RESEARCH
published: 24 December 2015
doi: 10.3389/fonc.2015.00291

Treatment Parameters Optimization to Compensate for Interfractional Anatomy Variability and Intrafractional Tumor Motion

Romain Brevet[1], Daniel Richter[2], Christian Graeff[1], Marco Durante[1] and Christoph Bert[1,2]*

[1] GSI Helmholtzzentrum für Schwerionenforschung, Darmstadt, Germany, [2] FAU Erlangen-Nürnberg and Universitätsklinikum Erlangen, Erlangen, Germany

Scanned ion beam therapy of lung tumors is severely limited in its clinical applicability by intrafractional organ motion, interference effects between beam and tumor motion (interplay), as well as interfractional anatomic changes. To compensate for dose deterioration caused by intrafractional motion, motion mitigation techniques, such as gating, have been developed. However, optimization of the treatment parameters is needed to further improve target dose coverage and normal tissue sparing. The aim of this study was to determine treatment-planning parameters that permit to recover good target coverage for each fraction of lung tumor treatments. For 9 lung tumor patients from MD Anderson Cancer Center (Houston, Texas), a total of 70 weekly time-resolved computed tomography (4DCT) datasets, which depict the evolution of the patient anatomy over the several fractions of the treatment, were available. Using the GSI in-house treatment planning system TRiP4D, 4D simulations were performed on each weekly 4DCT for each patient using gating and optimization of a single treatment plan based on a planning CT acquired prior to treatment. The impact on target dose coverage ($V_{95\%,\mathrm{CTV}}$) of variations in focus size and length of the gating window, as well as different additional margins and the number of fields was analyzed. It appeared that interfractional variability could potentially have a larger impact on $V_{95\%,\mathrm{CTV}}$ than intrafractional motion. However, among the investigated parameters, the use of a large beam spot size, a short gating window, additional margins, and multiple fields permitted to obtain an average $V_{95\%,\mathrm{CTV}}$ of 96.5%. In the presented study, it was shown that optimized treatment parameters have an important impact on target dose coverage in the treatment of moving tumors. Indeed, intrafractional motion occurring during the treatment of lung tumors and interfractional variability were best mitigated using a large focus, a short gating window, additional margins, and three fields.

Keywords: medical physics, radiotherapy, particle therapy, ions, treatment planning, moving targets, moving organs

OPEN ACCESS

Edited by:
John Varlotto, University of Massachusetts Medical Center, USA

Reviewed by:
Dalong Pang, Georgetown University Hospital, USA
Clemens Grassberger, Harvard Medical School, USA

****Correspondence:***
Christian Graeff
c.graeff@gsi.de

Specialty section:
This article was submitted to Radiation Oncology, a section of the journal Frontiers in Oncology

Received: *24 September 2015*
Accepted: *07 December 2015*
Published: *24 December 2015*

Citation:
Brevet R, Richter D, Graeff C, Durante M and Bert C (2015) Treatment Parameters Optimization to Compensate for Interfractional Anatomy Variability and Intrafractional Tumor Motion. Front. Oncol. 5:291. doi: 10.3389/fonc.2015.00291

1. INTRODUCTION

Treating moving targets, such as non-small cell lung cancer (NSCLC) tumors, using photon radiation therapy has been investigated (1) and is being clinically used nowadays combined to real-time tracking (2, 3). However, using heavy-ion scanned beam therapy has shown many advantages compared to conventional radiotherapy (4, 5) by reducing the number of fields, which have to be used as well as the dose delivered to the organs at risk (OARs) in the vicinity of the tumor. It also demands high precision and accuracy when applied to moving tumors because of the possible dose delivery errors induced by range shifts themselves due to intrafractional motion, interfractional anatomic changes, and patient misalignments (6, 7). This is why several motion mitigation techniques, such as gating, rescanning, or tracking have been developed and are still under development (8). Gating (9, 10) is a technique which consists in turning the beam on when the moving tumor reaches a precise motion state, in general, at the end of exhalation while the tumor is the most stable. It has shown great potential and has thus been successfully used in Japan in ion beam therapy with passive absorbers for beam shaping (11–13). Active scanned beam delivery introduces interplay effects (14) and even though tumor motion mitigation techniques are used, these effects can lead to non-conformal dose delivery. In order to address specifically this problem, 4D treatment planning systems (4DTPS) have been implemented (15, 16) and permit to simulate the treatment of moving targets using gating while also taking interplay effects into account. Nonetheless, treatment parameters still have to be optimized to maximize motion mitigation obtained using gating. Several studies have been performed to determine the influence of different parameters on the dose delivery: Bert et al. (17) proposed to increase pencil beam overlap to mitigate interplay effects as well as Steidl (18) and Richter (19) whose studies displayed the effects of different lateral grid spacing, isoenergy slice distance, focus size, and Bragg peak width. In a combination gating and rescanning, Furukawa et al. (20) proposed a method called phase-controlled rescanning, aiming at compensating further the residual tumor motion within the gating window. Rescanning was used as mitigation technique by Knopf et al. (21), and the impact of the entry channel was also investigated through different field scenarios. Target definition including tumor motion, size, and position (22), as well as range-adapted margins, were discussed (15, 23–25) and implemented (26). However, those studies concentrated on intrafractional motion compensation, meaning that the possible anatomic variability between the time of the treatment planning CT and treatment or also between fractions was not taken into account. Simulations were, in general, restricted to a single 4DCT taken for treatment planning. The purpose of this study was to investigate which parameters could be isolated and optimized in order to compensate correctly for both intrafractional tumor motion and interfractional anatomic changes and/or patient misalignments. To this end, in a cohort of patients with a time series of 4DCTs and for different combinations of treatment and/or beam parameters, one gating plan was optimized using the first weekly 4DCT of each patient and was forward calculated on the successive 4DCTs of the weeks following treatment planning. Results were then compared to determine the best configuration.

2. MATERIALS AND METHODS

2.1. Patient Cohort

Data from 9 NSCLC lung tumor patients from the MD Anderson Cancer Center (MDACC) (27) were used to perform this study, reaching a total of 70 weekly 4DCT datasets. Each 4DCT was composed of 10 3DCTs representing 10 different phase-based tumor motion phases over the breathing cycle. End-exhale, referred to as phase n° 5, was set as the reference state. Number of weeks, motion amplitude, angles for single field and multiple fields calculations, and clinical target volumes (CTVs) with and without additional margins are listed in **Table 1**. The number of weekly 4DCTs per patient varied between 6 and 10; each 4DCT was treated as a single fraction, with the first 4DCT as the planning CT. Most of the patients have an average tumor motion below 5 mm and only one patient shows a tumor motion above 20 mm (Patient 9).

2.2. Treatment Planning

2.2.1. Image Registration

Rigid registration of reference phases of each subsequent CT was performed to mimic patient setup and alignment. Then non-rigid registration was used between each 4DCT motion phase using Plastimatch (28). For each patient, clinical target volumes (CTVs) as well as OAR contours (esophagus, heart, and spinal cord) were

TABLE 1 | Description of the 9 NSCLC patients from MDACC (see Figure 1 for field angles illustration): patient number, number of weeks available, mean motion amplitude and range, field angle for single field calculations (SFUD), field angles for multiple fields calculations (SFUD1, 2, and 3), volume of the CTV, and volumes of the extended target: 3 mm isotropic (I3), 3 mm + 3% range (R3), and combination of both (I3 + R3).

Patient	Weeks	Motion (mm)	Angles (°)				Volumes (cc)			
			SFUD	SFUD1	SFUD2	SFUD3	CTV	I3	R3	I3 + R3
1	8	3.4	240	180	225	270	236	322	406	518
2	6	8.6	0	0	315	270	574	718	891	1057
3	9	10.1	0	270	315	0	161	213	335	409
4	8	3.3	225	180	225	270	676	819	925	1089
5	10	4.1	0	0	315	270	372	472	648	791
6	8	1.8	0	0	315	270	705	828	935	1072
7	7	1.6	180	180	225	270	124	172	253	322
8	8	4	180	180	225	270	45	65	102	133
9	6	23.5	180	180	225	270	125	164	203	250

provided by physicians of MDACC for the first weekly 4DCT. Lung contours were extracted from the weekly 4DCTs using an in-house algorithm. Files containing vector fields (between the first week and the following ones) obtained using deformable registration (29) were then used to propagate the previously mentioned contours from the reference phase of the first weekly CT to the reference phases of the following ones (16). Finally, vector field files yielded by deformable registration applied on the 10 states of each weekly 4DCT permitted to propagate the contours from the reference state to the 9 other motion states.

2.2.2. Optimization and 4D Calculations

In this study, the technique used to mitigate motion was gating. All gating plans were simulated using ^{12}C ions and the GSI treatment planning system TRiP4D (16), based on TRiP98 and modified to allow 4D-dose calculations. For each patient, plans were initially optimized to the internal target volume (ITV) of the first week's CT using one unique planned dose of 8.1 Gy(RBE). Motion-related geometrical and range changes were considered according to Graeff et al. (26). The generated raster scanning plan was then used for all 4D calculations of the first week itself and the following ones as well. It means that only one plan was used per patient and that there was no replanning before simulations of the fractions following the first optimized one. In each case, the ITV was built using a combination of five CTVs (26) from five different motion phases representing 25% of the amplitude. The motion surrogate was defined according to Lujan et al. (30), i.e., a sine to the power of 4 with a unique period of 3.6 s. Only one starting phase (0°) was studied because, due to gating, beam delivery for different starting phases is quickly synchronized after the first few spills of the synchrotron accelerator, thus calculations yield very similar results for different starting phases. As other fixed treatment parameters, the distance between each raster position was set to 2 mm on each isoenergy slice (IES), and the distance between two IESs was set to 3 mm water equivalent using a ripple filter of 3 mm (31).

2.2.3. Investigated Parameters

The impact of different treatment plan parameters on the dose delivery was investigated using the field angles listed in **Table 1**. First, using one single field (see column "SFUD" of **Table 1** and **Figure 1**) and ITV margins only, variations in focus size and length of the gating window (GW) were performed. Three GWs: 11.9, 30, and 50% of the amplitude and three beam foci: 6, 10, and 15 mm (FWHM) were chosen as varying parameters. Two configurations in particular were compared:

- *LFSG*: large focus (15 mm) and short GW (11.9%),
- *SFLG*: small focus (6 mm) and long GW (50%).

As a second part, using the same single field angles, different planning target volumes (PTV) created by adding additional margins to the originally optimized plans were also investigated as another solution to recover good target coverage. Three different cases were studied: 3 mm isotropic margins (geometrical, referred to as I3), 3 mm + 3% range margins (water equivalent, referred to as R3), and combination of both (referred to as I3 + R3, see **Figure 2**). Resulting dose deliveries were compared to the results obtained using ITV margins only. Combinations of GWs and foci (same 3 foci and 3 GWs than in the previous paragraph) were again investigated in each case to observe the impact of additional margins on the range. Finally, still using the 9 possible GW/focus combinations, the number of fields was varied from 1 to 3 (see **Table 1** for field angle values, columns "SFUD1" to "SFUD3" and **Figure 1**) using only ITV margins first and then using the additional PTV margins which had been determined to yield the best results in the second section of this chapter, resulting in the following cases:

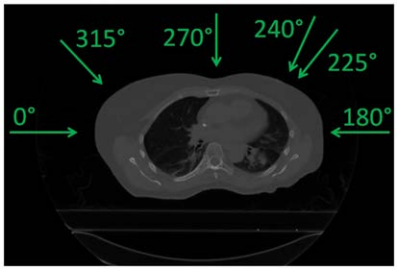

FIGURE 1 | Field angles used (see Table 1).

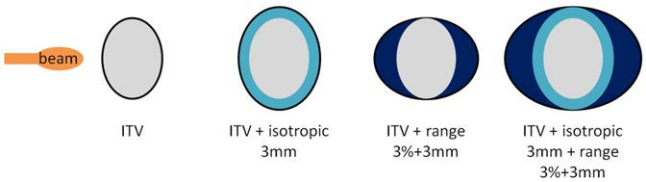

FIGURE 2 | Different margins cases used in the second part of the study. From the left to the right, configurations displayed are referred to as ITV, I3, R3, and I3 + R3.

- *SFITV*: single field to ITV only,
- *SFPTV*: single field to the isotropic/range margins (same as I3 + R3),
- *2FITV*: ITV only but with 2 fields,
- *2FPTV*: same margins as SFPTV but with 2 fields,
- *3FITV*: ITV only but with 3 fields,
- *3FPTV*: same margins as SFPTV but with 3 fields.

2.3. Data Analysis

In each case, the dose distribution of each week was obtained by accumulating the dose delivered to each motion state on the reference phase of the 4DCTs using state-to-state non-rigid vector fields. To estimate the impact of each previously described parameter and configuration on the dose delivery, the following two indexes were used:

- *Target coverage*, V_{95}: volume of the target to which 95% of the planned dose is delivered, representing the quality of target dose coverage, unit is percentage of volume,

- *Conformity number (CN)* (32): allowing a quantification of the high-dose regions inside and outside the tumor (the higher, the better) and defined by:

$$CN = \frac{V_{95\%,\mathrm{CTV}}}{V_{\mathrm{CTV}}} \times \frac{V_{95\%,\mathrm{CTV}}}{V_{95\%}} \quad (1)$$

where $V_{95\%,\mathrm{CTV}}$ is the V_{95} value defined above, V_{CTV} the volume of the CTV, and $V_{95\%}$ the total volume which receives at least 95% of the dose.

The main focus of this study is the impact of treatment plan parameters on dose delivery. All dose calculations were computed for weekly simulations but not for the cumulated total treatment regime. Therefore, OAR limit dose values from the literature were not taken into account but are used only a general indicator of plan quality. This study aims at determining clearly the effect of the investigated parameters on the decreased quality of the dose delivery due to both interfractional anatomy changes and intrafractional tumor motion. In each case, a Wilcoxon signed-rank test was performed using a level of significance of 0.05 to estimate the difference between two sets of datapoints. In the case of samples containing more than 10 values, the p-value (p) was computed using the obtained z-score (z).

3. RESULTS

All simulations were performed on the weekly 4DCTs with a planned dose of 8.1 Gy(RBE), which corresponds to a single field dose as reported by NIRS (5) according to LEM IV (33). In all the following figures, the average value (marker), the median value (horizontal bar in the box), the 25th and 75th percentile, and the total range of all values are given. In some cases, different types of simulations were studied and referred to as

- *3D0 simulations:* planned, static dose simulations using the first weekly CT (week 0 in reference phase),
- *4D0 simulations:* 4D dose simulations using the first weekly 4DCT (week 0) and the same plan than 3D0 simulations, which contains the effects of intrafractional motion only,
- *4DN simulations:* 4D dose simulations using all the following weekly 4DCTs (weeks 1 to 5–9) and the same plan than 3D0 simulations, which contains the effects of both intrafractional motion and interfractional patient anatomic changes.

3.1. Beam Focus and Gating Window

Figure 3 and **Table 2** show V_{95} and CN for different GW/focus combinations, for all patients. 3D simulations show good results for all focus sizes, with slightly better target coverage and slightly worse conformity for the largest focus ($p < 0.05$). The 4D0 simulations show the effect of intrafractional tumor motion on target dose coverage: V_{95} decreases with a large variability for the smaller focus sizes. A large focus and gating window of 30% restores target coverage to the static values. CN, however, shows no significant ($p < 0.05$) change with GW or focus but decreases slightly compared to static calculations. 4DN results of the following weeks permit to investigate the effect of both interfractional changes but also intrafractional motion. Comparison to 4D0 shows a similar trend for GW and focus size, but the interfractional changes result in approximately 10 worse target coverage and CN. Without margins, adequate target coverage cannot be reached for any simulation with a small focus/large GW and less for than half with a large focus/small GW. Dose cuts for these combinations are displayed for the 7th weekly CT of patient 3 in **Figures 4A–F**, respectively.

3.2. Margins

Not surprisingly, margins are necessary to achieve target coverage including interfractional changes. **Figure 5** and **Table 3** show the impact on V_{95} and CN for ITV only (ITV), ITV + 3 mm isotropic margins (I3), ITV + 3% + 3 mm range margins (R3), and a combination of both margins (I3 + R3), respectively. 3D0 simulations reveal that range margins have a larger impact on CN than

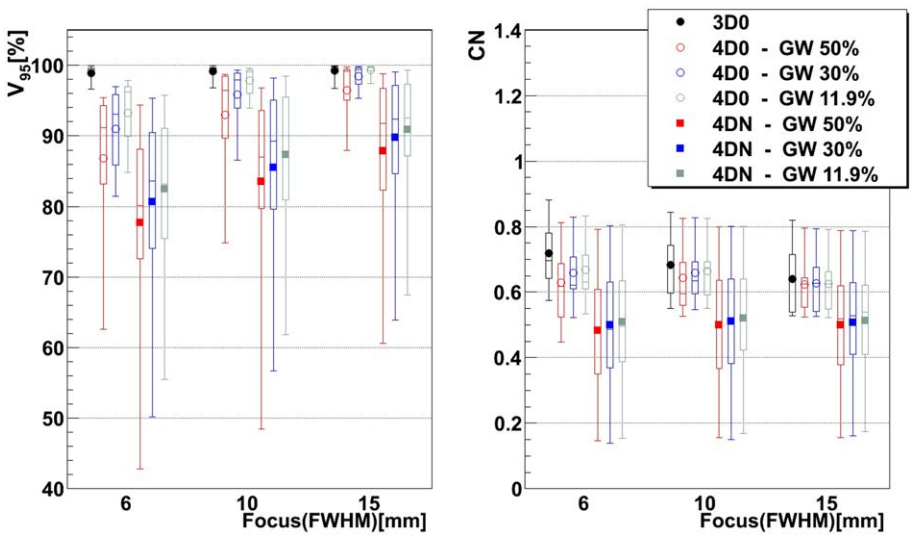

FIGURE 3 | Impact of the focus and the GW on V_{95} and CN. Each 3D0 and 4D0 bar is composed of 9 points and each 4DN bar of 61 points.

TABLE 2 | Results of the influence of the focus and gating window on V_{95} and CN.

Simulations	Focus (mm)	Gating window (%)	V_{95} (%)			CN			$V_{95} > 95\%$ (%)
			Min.	Mean	Max.	Min.	Mean	Max.	
3D0	6	–	96.6	98.9	99.9	0.57	0.72	0.88	100
	10	–	96.8	99.1	99.9	0.55	0.68	0.84	100
	15	–	96.7	99.2	99.9	0.53	0.64	0.82	100
4D0	6	50	62.6	86.8	95.4	0.45	0.63	0.81	11.1
		30	81.4	91.0	97.0	0.52	0.66	0.83	33.3
		11.9	84.9	93.2	97.9	0.53	0.67	0.83	55.6
	10	50	74.8	93.0	98.7	0.53	0.64	0.83	66.7
		30	86.5	95.9	99.3	0.55	0.66	0.83	66.7
		11.9	94.0	97.9	99.6	0.55	0.66	0.83	88.9
	15	50	88.0	96.5	99.8	0.52	0.62	0.80	77.8
		30	95.4	98.5	99.8	0.53	0.63	0.79	100
		11.9	97.4	99.3	99.9	0.52	0.63	0.79	100
4DN	6	50	42.8	77.7	94.3	0.15	0.48	0.79	0
		30	50.2	80.6	95.4	0.14	0.50	0.80	1.6
		11.9	55.4	82.5	95.8	0.15	0.51	0.81	4.9
	10	50	48.4	83.5	96.8	0.16	0.50	0.80	11.5
		30	56.7	85.5	98.2	0.15	0.51	0.80	27.9
		11.9	61.8	87.4	98.5	0.17	0.52	0.80	29.5
	15	50	60.6	87.9	98.8	0.16	0.50	0.79	37.7
		30	63.9	89.8	99.1	0.16	0.51	0.79	41
		11.9	67.5	90.9	99.3	0.17	0.51	0.79	42.6

isotropic ones ($p < 0.05$), as shown in **Table 3**. Calculations on the planning CT (4D0) show a minor but significant impact from increased margins. CN is degraded through increasing margins ($p < 0.05$). Interestingly, the isotropic margins show a comparable effect to range margins in the 4D calculations, as opposed to 3D. As a consequence, also the combined margins further decrease CN. The margin size shows a considerable impact on interfractional changes, decreasing the target coverage gap between 4D0 and 4DN from 10 to 2% with the I3 + R3 combination. Range margins are more effective than isotropic margins ($p < 0.05$). The same trend can be observed for CN, which decreases with margin size ($p < 0.05$), but reaches nearly the level of 4D0 for I3 + R3. The percentage of successful fractions ($V_{95} > 95\%$) reaches 68.7% on average for I3 + R3, but 90.2% for the I3 + R3 for the large focus/small GW. Exemplary dose distributions (using the 1st and again the 7th weekly CTs of patient 3) using the largest focus and the shortest GW combined to ITV margins (ITV), and to ITV plus I3, R3, and I3 + R3 are displayed in **Figures 4D–O**, respectively.

3.3. Number of Fields

Figure 6 and **Table 4** show the impact of the number of fields for the ITV only and for ITV with I3 + R3, subsequently called PTV. Again, 3D0 simulations yield excellent target coverage, but multiple fields slightly improve CN for the ITV only, while they degrade CN for PTV margins ($p < 0.05$, see **Table 4**). Using more than one field helps to mitigate intrafractional motion, with increasing V_{95} for both ITV and PTV margins ($p < 0.05$). PTV margins improve target coverage but considerably decrease CN (both $p < 0.05$). The same effect can be observed for 4DN, where more than one field and PTV margins significantly increase V_{95}. The conformity can essentially be restored to the static or 4D0 value using PTV margins and three fields. For this combination, more than 80% of simulations lead to adequate target coverage, and 93.4% for the small focus/large GW, see also **Figure 6**. A dose distribution example using week 6 of patient 3 from single field ITV simulations (SFITV) and single field, 2 fields, and 3 fields PTV simulations (SFPTV, 2FPTV, and 3FPTV) are shown in **Figures 4D–F** and **7A–F**, respectively.

3.4. Tumor Motion and Size Dependence

The influence of the motion magnitude on V_{95} is displayed in **Figure 8A**. In case of the green combination (small focus, long GW, ITV, and one field), patients with a small motion (<6 mm) show an average V_{95} of 85%, as opposed to 65% for patients with a large motion. This difference of 20% is reduced to 3% if a large focus, a small GW, PTV margins, and 3 fields are used, which also yields mean $V_{95} > 95\%$ for both groups. Dependence of CN to the size is shown in **Figure 8B**. Patients with a smaller tumor (<200 cc) show mean CN of 25 and 16% lower than large tumors (>200 cc).

4. DISCUSSION

In this study, a time series of 4DCTs of lung cancer patients was investigated for inter- and intrafractional effects of motion, anatomic changes, and setup errors. Most studies of particle therapy for moving targets focus on 4DCTs at a single time point, assuming nearly perfect treatment conditions. In this respect, the findings of this study offer highly important, previously unstudied information for a more clinically realistic scenario.

4.1. Beam Focus and Gating Window

Results show that the larger the focus and the shorter the GW, the better V_{95}, meaning that intrafractional motion mitigation is more effective using a large focus and a short GW, as illustrated in **Figure 4**. Only the volume of the target (see **Table 1** and **Figure 8**)

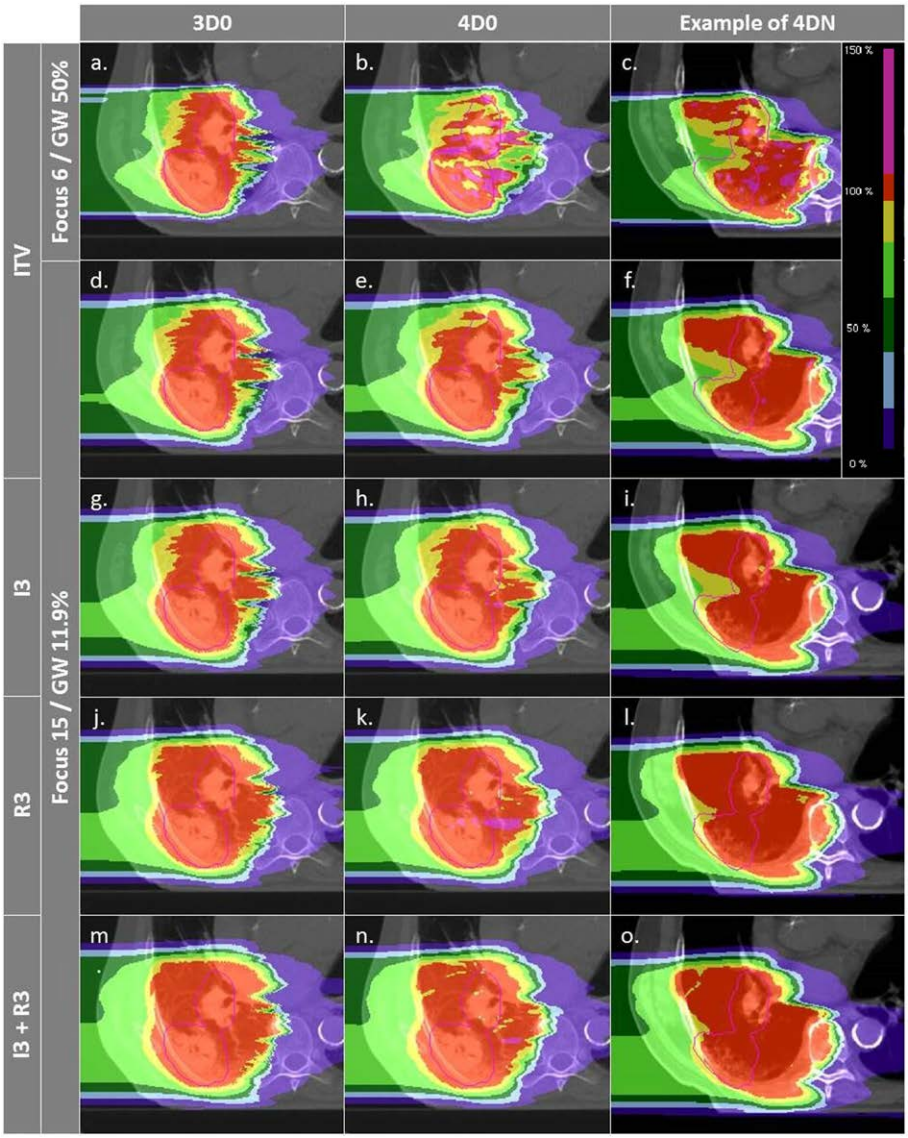

FIGURE 4 | Dose distributions of patient 3 using different weekly CTs. Pink contours represent the CTV (week 6). Cases **(A–C)** and **(D–F)** are obtained using the SFLG and the LFSG configurations, respectively, simulations (week 6). Cases **(A–F)** are obtained using the SFLG and the LFSG configurations, respectively, with ITV margins only. Examples **(G–P)** are obtained using the LFSG configuration and 3 mm isotropic margins, 3 mm + 3% range margins, and the combination of both previous margins, respectively.

seems to have a direct impact on CN: CN values yielded for simulations done with larger targets (patients 1, 2, 4, 5, and 6) are higher than values obtained for simulations done with smaller ones (patients 3, 7, 8, and 9); that can be observed in **Figure 8** (and especially for the presented cases with ITV margins only). Thus, GW and focus do not show a significant influence on CN, which does not have a particular behavior regarding those parameters and is more patient specific: only patient 9 showed large weekly CN variability (range = 0.3) over the different GW/focus configurations compared to all other patients with a range < 0.1 [more details in Brevet (34)]. Thus, although V_{95} increases using a large focus and a short GW, the total volume to which 95% of the planned dose is delivered increases as well, i.e., OARs in the vicinity of the tumor are irradiated. In both studies by Steidl (18) and Richter (19), a larger focus permits to obtain better results in terms of target coverage, which is in agreement with what has been observed here. However, while a decreasing CN is obtained with increasing focus size in the study by Steidl (18), this behavior is not present in the study by Richter (19) and here. This can be explained by the fact that Steidl (18) used a different CN, which integrates the dose values obtained in all the voxels of the CTV and thus ignores the high interplay dependency of V_{95}, the latter being itself the main component of the here used CN. Richter (19) shows that CN is decreasing with larger foci only for static cases (a behavior which can be also observed for static cases in **Figure 3**), while it is more patient specific for cases with motion and tends to converge on values obtained with static cases. The same behavior was observed in the study by Brevet (34): weekly

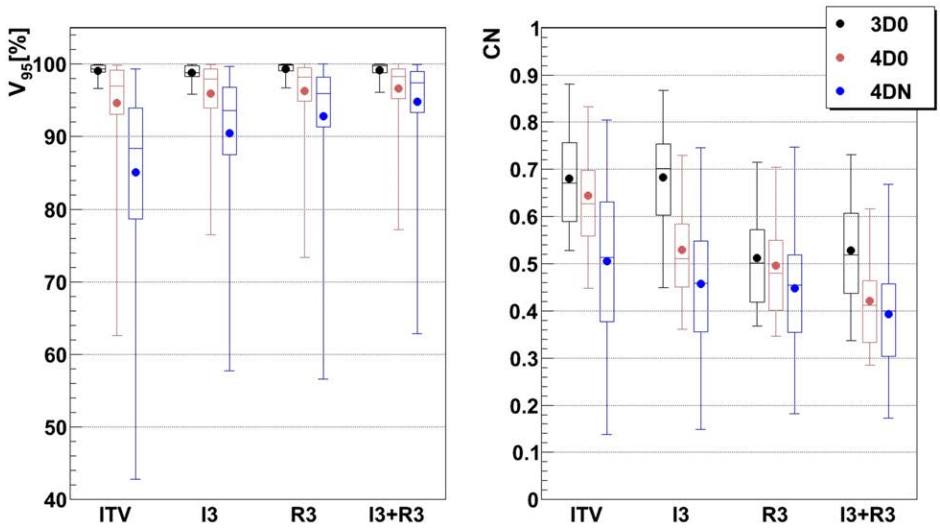

FIGURE 5 | Impact of additional margins on V_{95} and CN: ITV (ITV margins only), I3 (3 mm isotropic margins), R3 (3 mm + 3% range margins), and I3 + R3 (3 mm isotropic + 3 mm + 3% range margins). Each 3D0 bar is composed of results obtained using all 9 patients and 3 foci, representing 27 points, and each 4D0 and 4DN bar are composed of results obtained using all 9 patients, 3 foci, and 3 GWs, representing 81 and 549 points, respectively.

TABLE 3 | Results of the influence of ITV margins (ITV), 3 mm isotropic margins (I3), 3 mm + 3% range margins (R3), and a combination of the two last ones (I3 + R3) on V_{95} and CN.

Simulations	Margins	V_{95} (%)			CN			V_{95} > 95% (%)
		Min.	Mean	Max.	Min.	Mean	Max.	
3D0	ITV	96.6	99.1	99.9	0.53	0.68	0.88	100
	I3	95.9	98.8	100	0.45	0.68	0.87	100
	R3	96.7	99.4	100	0.37	0.51	0.72	100
	I3 + R3	96.2	99.1	100	0.34	0.53	0.73	100
4D0	ITV	62.6	94.7	99.9	0.45	0.64	0.83	66.7
	I3	76.5	95.9	100	0.36	0.53	0.73	70.4
	R3	73.4	96.3	100	0.35	0.50	0.70	74.1
	I3 + R3	77.2	96.6	100	0.29	0.42	0.62	75.3
4DN	ITV	42.8	85.1	99.3	0.14	0.50	0.81	21.9
	I3	57.8	90.5	99.7	0.15	0.46	0.75	40.4
	R3	56.6	92.8	100	0.18	0.45	0.75	56.3
	I3 + R3	62.8	94.8	100	0.17	0.39	0.67	68.7

Each margins case of the 3D0 calculations was done using the 3 foci described previously. In the case of 4D0 and 4DN values, the 9 possible focus/GW combinations presented previously were used.

results of each patient show that CN is patient and week specific and that no discernable trend for focus or GW can be found. As a global result, CN is slightly higher for larger foci, but when studied separately for each patient and each week, CN values do not show a systematic behavior. It can also be noticed that the focus size has a much more significant influence on the results compared to gating window. This is due to the size of the largest focus (15 mm), which is larger than the tumor motion for patients 1–8 or similar to the tumor motion for patient 9 (see **Table 1**). Hence, it is much easier to cover the moving tumor using this large focus. As using a small GW can increase treatment time considerably, this setting should be adjusted patient specifically.

Interfractional changes tend to dominate intrafractional ones, which can be reliably mitigated with gating and a large focus. The case shown in **Figure 4** illustrates this (cf. **Figures 4B,E**), but also the dominant cause for interfractional dose errors: considerable change in range to the target. Though this depends on the chosen entry channel, **Figures 4C,F** show an extreme overshoot compared to the planned treatment dose. This is an extreme case, though, with considerable dose to OARs. On average, the impact is less severe, as can be seen by CN being restored nearly to the planned static value for multiple fields and large margins. An analysis of individual OARs and dose constraints would be necessary for more specific conclusions.

4.2. Margins

For intrafractional motion, Knopf et al. (25) and Albertini et al. (35), using different sorts of margins, confirmed that margins permit indeed to compensate efficiently for tumor motion. Here, additional margins to a range ITV were studied

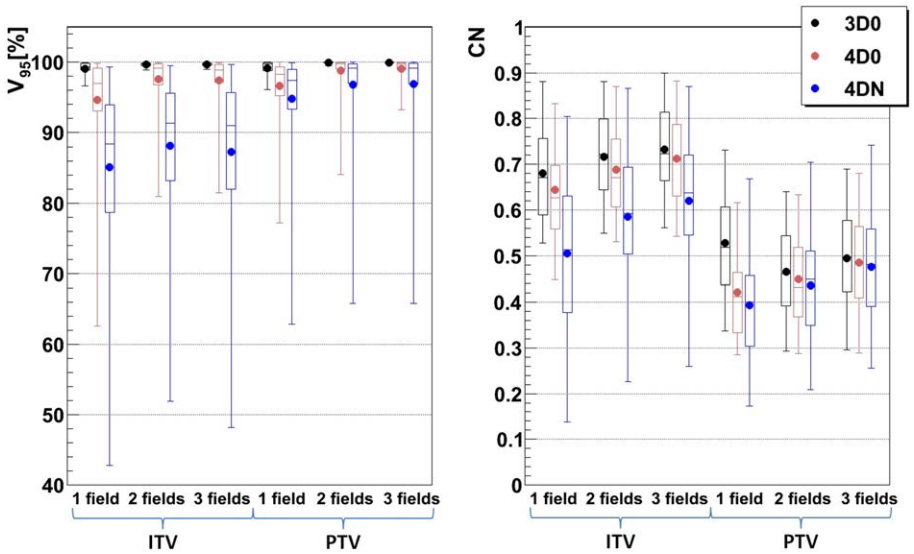

FIGURE 6 | Impact of different numbers of fields on V_{95} and CN: 1, 2, and 3 fields with ITV (ITV margins only) and PTV (3 mm isotropic + 3 mm + 3% range margins). Each 3D0 bar is composed of results obtained using all 9 patients and 3 foci, representing 27 points, and each 4D0 and 4DN bar are composed of results obtained using all 9 patients, 3 foci, and 3 GWs, representing 81 and 549 points, respectively.

TABLE 4 | Results of the influence of ITV and PTV margins and of different numbers of fields on V_{95} and CN.

Simulations	Margins	Fields	V_{95} (%)			CN			V_{95} > 95% (%)
			Min.	Mean	Max.	Min.	Mean	Max.	
3D0	ITV	1	96.6	99.1	99.9	0.53	0.68	0.88	100
		2	98.9	99.7	100	0.55	0.72	0.88	100
		3	99.0	99.7	100	0.56	0.73	0.90	100
	PTV	1	96.2	99.1	100	0.34	0.53	0.73	100
		2	99.5	99.9	100	0.29	0.47	0.64	100
		3	99.9	100	100	0.30	0.49	0.69	100
4D0	ITV	1	62.6	94.7	99.9	0.45	0.64	0.83	66.7
		2	80.9	97.6	100	0.53	0.69	0.87	82.7
		3	81.4	97.5	99.9	0.54	0.71	0.88	84
	PTV	1	77.2	96.6	100	0.29	0.42	0.62	75.3
		2	84.0	98.8	100	0.29	0.45	0.63	92.6
		3	93.3	99.0	100	0.29	0.48	0.68	93.8
4DN	ITV	1	42.8	85.1	99.3	0.14	0.50	0.81	21.9
		2	51.9	88.1	99.5	0.23	0.59	0.87	29.1
		3	48.2	87.3	99.7	0.26	0.62	0.87	30.1
	PTV	1	62.8	94.8	100	0.17	0.39	0.67	68.7
		2	65.8	96.8	100	0.21	0.44	0.70	81.2
		3	65.8	96.9	100	0.26	0.48	0.74	82.5

Each margins case of the 3D0 calculations was done using the 3 foci described previously. In the case of 4D0 and 4DN values, the 9 possible focus/GW combinations presented previously were used.

to recover misdosage from the interfractional changes. **Figure 5** shows improving results when the irradiated volume is extended. Sorted by increasing order, isotropic, range, and combined isotropic/range margins yield better target coverage, for both 4D0 and 4DN simulations: V_{95} and CN are sensitive to additional ITV-PTV margins. V_{95} improves indeed significantly in terms of distribution range and mean value. And even though the effects of interfractional changes can still be observed for 4DN simulations (low minimal V_{95} value), using a combination of additional isotropic and range margins permits to increase the fraction of successful fractions from 21 to nearly 70%. It means that combining those two margins to extend the irradiated region improves coverage of the possible anatomic changes from fraction to fraction. CN, however, reduces due to some additional dose delivered in the vicinity of the target volume. This can be observed in **Figures 4D–O**: V_{95} is improved but the irradiated volume outside the tumor clearly increases gradually as more additional margins are used.

Figures 4D–F,M–O show how margins can allow dose recovery in the tumor for a patient with severe intra- and interfractional

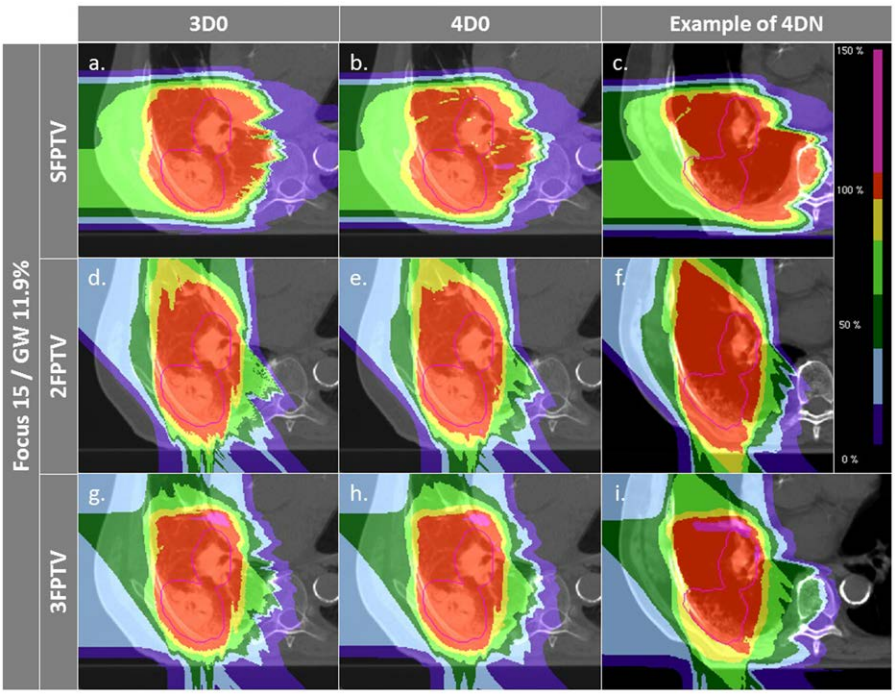

FIGURE 7 | Dose distributions of patient 3 using different weekly CTs. Pink contours represent the CTV. First column displays 3D0 simulations, second column 4D0 simulations, and the third one 4DN simulations using week 6. Cases **(A–I)** are obtained using the LFSG configuration combined to isotropic and range margins and one, two, and three fields, respectively.

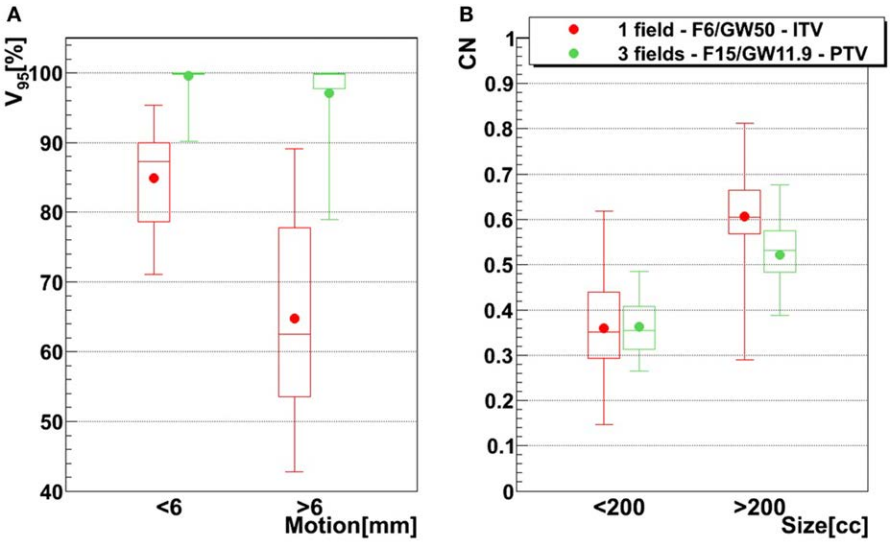

FIGURE 8 | Influence of motion magnitude on V_{95} tumor size on CN, using two different treatment configurations. The red configuration represents simulations done using one field, a focus of 6 mm, a 50% GW, and ITV margins only, and the green configuration represents three fields, a focus of 15 mm, a 11.9% GW, and PTV margins (3 mm isotropic + 3 mm + 3% range margins). For the left graph **(A)**, bars representing tumors whose motion is lower than 6 mm are composed of 21 points (three patients, 21 weeks), while bars representing tumors whose motion is larger than 6 mm are composed of 49 points (six patients, 49 weeks). In the case of the right graph **(B)**, small tumor (<200 cc) bars are composed of 30 points (four patients, 30 weeks) and big tumor (>200 cc) bars are composed of 40 points (five patients, 40 weeks). See **Table 1** for more details about patients.

motion. In this case, the combination of range and isotropic margins permits to reach a mean V_{95} value 20% higher compared to the use of ITV margins only. Thus, the conclusions of Knopf et al. (25) and Albertini et al. (35), stating that intrafractional motion can be mitigated by the use of margins, can be extended by the fact that margins also allow to compensate

efficiently for dose delivery deterioration caused by interfractional changes. However, it is also clearly visible that OARs, such as the spinal cord and the ipsilateral lung, are irradiated with a higher dose.

4.3. Number of Fields

To dilute the dose to OARs, multiple fields are typically employed and have also been shown to help mitigate intrafractional motion Knopf et al. (21) through an enhanced rescanning effect. Combined with ITV margins only, multiple fields significantly improve V_{95} and CN. Using two or three field did not result in an improvement in target coverage. This can be explained by the lack of an automatic optimization method for field directions. Using a generic, geometric approach to choose field directions, it became more likely with three fields to pass through tissue heavily affected by interfractional changes. Thus, a field affected, e.g., by a range shift would deteriorate target coverage instead of further improving it. This effect was minor and not significant, though. On the other hand, conformity could be further improved by distributing dose to more entry channels, which decreases V_{95} outside of the target and thus improves CN. This shows that choosing field directions carefully to avoid regions that are likely affected by interfractional changes would result both in good target coverage and good CN. Added PTV margins as expected improve the results further. V_{95} average values for 4DN simulations tend to converge to the values obtained for 4D0 simulations, showing that interfractional changes are almost completely mitigated. Outliers remain with an inadequate target coverage, but more than 90% of successful fractions become possible. CN is however drastically reduced due to the extended irradiated volume, which is now partly composed of normal tissue from the surrounding OARs. With the remaining difference of V95 between 4D0 and 4DN of 1.2% (range 0–21%), interfractional changes appear to be sufficiently compensated. Dose distributions in **Figures 7A–I** illustrate the great advantage of using three fields combined with additional margins. It allows obtaining a conformal dose distribution, with a target which is completely and homogeneously covered, and reduced high-dose regions outside the tumor. Again, field directions can be chosen differently to avoid or decrease further the irradiated volume of lung visible in **Figures 7G–I**.

This study has some limitations. The focus was set on identifying relevant planning parameters. To identify these, most plans would not be clinically valid or deliverable, but are helpful in showing the effect of isolated technical parameters. A further issue is the (unavoidable) use of deformable image registration to both propagate contours across the different CTs and phases and also to accumulate dose in the reference phase of each CT. Careful quality insurance was performed, using checker-board and false-color images as well as inspection of the resulting vector fields, with resulting errors to be expected in the order of 2 mm (36). To mimic patient setup, CTs were rigidly registered against each other, which might be more accurate than positioning with orthogonal X-rays, so that additional margins would be required. Finally, though serial 4DCT data was available, each 4DCT represented only a single breathing cycle. Variable breathing cycles could be studied using synthesized MR/CT data (37).

5. CONCLUSION

The aim of this study was to identify optimized treatment planning parameters in order to compensate for dose delivery deterioration caused by intrafractional tumor motion and interfractional variability. It was found that the use of a large focus (15 mm, FWHM), a short gating window (11.9% of the motion amplitude), ITV-PTV margins (3 mm isotropic + 3% + 3 mm range margins), and 3 fields yielded the best results in terms of target dose coverage. Less than 6% of fractions remained below 95%. In conclusion, in this first study combining state-of-the-art 4D dose calculation with serial 4DCT data, a combination of these parameters together with careful choice of field directions permits safe fractionated target dose coverage for NSCLC patients treated with ^{12}C ions.

AUTHOR CONTRIBUTIONS

RB performed the simulations, evaluated the data, and wrote the manuscript. DR contributed to the study design, advised on 4D-dose calculation, and revised the manuscript. CG contributed to the study design and data evaluation and revised the manuscript. CB designed the study and revised the manuscript. MD supervised the study and extensively revised the manuscript.

FUNDING

Funded as an ESR within the EU-FP-7 ENTERVISION framework, Grant Agreement no. 264552. Further funds were received by DFG KFO 214./2.

REFERENCES

1. Korreman SS. Motion in radiotherapy: photon therapy. *Phys Med Biol* (2012) **57**(23):R161–91. doi:10.1088/0031-9155/57/23/R161
2. Brown WT, Wu X, Fayad F, Fowler JF, Amendola BE, Garcia S, et al. Cyberknife radiosurgery for stage I lung cancer: results at 36 months. *Clin Lung Cancer* (2007) **8**(8):488–92. doi:10.3816/CLC.2007.n.033
3. Kilby W, Dooley JR, Kuduvalli G, Sayeh S, Maurer CR Jr. The cyberknife robotic radiosurgery system in 2010. *Technol Cancer Res Treat* (2010) **9**(5):433–52. doi:10.1177/153303461000900502
4. Amaldi H, Kraft G. Recent applications of synchrotrons in cancer therapy with carbon ions. *Europhys News* (2005) **36**(4):114–8. doi:10.1051/epn:2005402
5. Tsujii H, Kamada T, Baba M, Tsuji H, Kato H, Kato S, et al. Clinical advantages of carbon-ion radiotherapy. *New J Phys* (2008) **10**(7):075009. doi:10.1088/1367-2630/10/7/075009
6. Mori S, Wolfgang J, Lu HM, Schneider R, Choi NC, Chen GTY. Quantative assessment of range fluctuations in charged particle lung irradiation. *Int J Radiat Oncol Biol Phys* (2008) **70**(1):253–61. doi:10.1016/j.ijrobp.2007.08.049
7. Bert C, Durante M. Motion in radiotherapy: particle therapy. *Phys Med Biol* (2011) **56**(16):R113–44. doi:10.1088/0031-9155/56/16/R01
8. Knopf A, Hug E, Lomax A. Scanned proton radiotherapy for mobile targets – which plan characteristics require rescanning, which maybe not? *Proc. 16th Int. Conf. on the Use of Computers in Radiation Therapy*. Amsterdam. (2010).
9. Ohara K, Okumura T, Akisada M, Inada T, Mori T, Yokota H, et al. Irradiation synchronized with the respiration gate. *Int J Radiat Oncol Biol Phys* (1989) **17**:853–7. doi:10.1016/0360-3016(89)90078-3
10. Minohara S, Kanai T, Endo M, Noda K, Kanazawa M. Respiratory gated irradiation system for heavy-ion radiotherapy. *Int J Radiat Oncol Biol Phys* (2000) **47**(4):1097–103. doi:10.1016/S0360-3016(00)00524-1

11. Tsujii H, Mizoe J, Kamada T, Baba M, Kato S, Kato H, et al. Overview of clinical experiences on carbon ion radiotherapy at NIRS. *Radiother Oncol* (2004) **73**(S2):41. doi:10.1016/S0167-8140(04)80012-4
12. Iwata H, Murakami M, Demizu Y, Miyawaki D, Terashima K, Niwa Y, et al. High-dose proton therapy and carbon-ion therapy for stage I nonsmall cell lung cancer. *Cancer* (2010) **116**(10):2476–85. doi:10.1002/cncr.24998
13. Tsujii H, Kamada T. A review of update clinical results of carbon ion radiotherapy. *Jpn J Clin Oncol* (2012) **42**(8):670–85. doi:10.1093/jjco/hys104
14. Bert C, Grözinger SO, Rietzel E. Quantification of interplay effects of scanned particle beams and moving targets. *Phys Med Biol* (2008) **34**(9):2253–65. doi:10.1088/0031-9155/53/9/003
15. Bert C, Rietzel E. 4D treatment planning for scanned ion beams. *Radiat Oncol* (2007) **2**:24. doi:10.1186/1748-717X-2-24
16. Richter D, Schwarzkopf A, Trautmann J, Krämer M, Durante M, Jäkel O, et al. Upgrade and benchmarking of a 4D treatment planning system for scanned ion beam therapy. *Med Phys* (2013) **40**(5):051722. doi:10.1118/1.4800802
17. Bert C, Gemmel A, Saito N, Rietzel E. Gated irradiation with scanned particle beams. *Int J Radiat Oncol Biol Phys* (2009) **73**(4):1270–5. doi:10.1016/j.ijrobp.2008.11.014
18. Steidl P. *Gating for Scanned Ion Beam Therapy*. (2011). Ph.D. thesis, TU Darmstadt.
19. Richter D. *Treatment Planning for Tumors with Residual Motion in Scanned Ion Beam Therapy*. (2012). Ph.D. thesis, TU Darmstadt.
20. Furukawa T, Inaniwa T, Sato S, Tomitani T, Minohara S, Noda K, et al. Design study of a raster scanning system for moving target irradiation in heavy-ion radiotherapy. *Med Phys* (2007) **34**(3):1085–97. doi:10.1118/1.2558213
21. Knopf AC, Hong TS, Lomax A. Scanned proton radiotherapy for mobile targets – the effectiveness of re-scanning in the context of different treatment planning approaches and for different motion characteristics. *Phys Med Biol* (2011) **56**(22):7257–71. doi:10.1088/0031-9155/56/22/016
22. ICRU. ICRU report 62: prescribing, recording and reporting proton-beam therapy (supplement to ICRU report 50). *J ICRU* (1999).
23. Koto M, Miyamoto T, Yamamoto N, Nishimura H, Yamada S, Tsujii H. Local control and recurrence of stage I non-small cell lung cancer after carbon ion radiotherapy. *Radiother Oncol* (2004) **71**(2):147–56. doi:10.1016/j.radonc.2004.02.007
24. Engelsman M, Rietzel E, Kooy HM. Four-dimensional proton treatment planning for lung tumors. *Int J Radiat Oncol Biol Phys* (2006) **64**(5):1589–95. doi:10.1016/j.ijrobp.2005.12.026
25. Knopf AC, Boye D, Lomax A, Mori S. Adequate margin definition for scanned particle therapy in the incidence of intrafractional motion. *Phys Med Biol* (2013) **58**(17):6079–94. doi:10.1088/0031-9155/58/17/6079
26. Graeff C, Durante M, Bert C. Motion mitigation in intensity modulated particle therapy by internal target volumes covering range changes. *Med Phys* (2012) **39**(10):6004–13. doi:10.1118/1.4749964
27. Britton KR, Starkschall G, Tucker SL, Pan T, Nelson C, Chang JY, et al. Assessment of gross tumor volume regression and motion changes during radiotherapy for non-small-cell lung cancer as measured by four-dimensional computed tomography. *Int J Radiat Oncol Biol Phys* (2007) **68**(4):1036–46. doi:10.1016/j.ijrobp.2007.01.021
28. Shackleford JA, Kandasamy N, Sharp GC. On developing b-spline registration algorithms for multi-core processors. *Phys Med Biol* (2010) **55**(21):6329–51. doi:10.1088/0031-9155/55/21/001
29. Saito N, Durante M, Bert C. *Image Registration for Moving Tumour Treatment with Ion Beam*. GSI Scientific Report 2011. (2012). p. 544.
30. Lujan AE, Larsen EW, Balter JM, Haken RKT. A method for incorporating organ motion due to breathing into 3D dose calculations. *Med Phys* (1999) **26**(5):715–20. doi:10.1118/1.598577
31. Weber U, Kraft G. Design and construction of a ripple filter for a smoothed depth dose distribution in conformal particle therapy. *Phys Med Biol* (1999) **44**(11):2765–75. doi:10.1088/0031-9155/44/11/306
32. van't Riet A, Mak CA, Moerland MA, Elders LH, van der See W. A conformation number to quantify the degree of conformity in brachytherapy and external beam irradiation: application to the prostate. *Int J Radiat Oncol Biol Phys* (1997) **37**(3):731–6. doi:10.1016/S0360-3016(96)00601-3
33. Elsässer T, Weyrather WK, Friedrich T, Durante M, Iancu G, Krmer M, et al. Quantification of the relative biological effectiveness for ion beam radiotherapy: direct experimental comparison of proton and carbon ion beams and a novel approach for treatment planning. *Int J Radiat Oncol Biol Phys* (2010) **78**(4):1177–83. doi:10.1016/j.ijrobp.2010.05.014
34. Brevet R. *Optimized Treatment Parameters to Account for Interfractional Variability in Scanned Ion Beam Therapy of Lung Cancer*. (2015). Ph.D. thesis, TU Darmstadt.
35. Albertini F, Hug EB, Lomax AJ. Is it necessazy to plan with safety margins for actively scanned proton therapy? *Phys Med Biol* (2011) **56**(14):4399–416. doi:10.1088/0031-9155/56/14/011
36. Brock KK, Consortium DRA. Results of a multi-institution deformable registration accuracy study (MIDRAS). *Int J Radiat Oncol Biol Phys* (2010) **76**(2):583–96. doi:10.1016/j.ijrobp.2009.06.031
37. Boye D, Lomax T, Knopf A. Mapping motion from 4D-MRI to 3D-CT for use in 4D dose calculations: a technical feasibility study. *Med Phys* (2013) **40**(6):061702. doi:10.1118/1.4801914

Conflict of Interest Statement: The authors declare that the research was conducted in the absence of any commercial or financial relationships that could be construed as a potential conflict of interest.

Copyright © 2015 Brevet, Richter, Graeff, Durante and Bert. This is an open-access article distributed under the terms of the Creative Commons Attribution License (CC BY). The use, distribution or reproduction in other forums is permitted, provided the original author(s) or licensor are credited and that the original publication in this journal is cited, in accordance with accepted academic practice. No use, distribution or reproduction is permitted which does not comply with these terms.

frontiers in Oncology

REVIEW
published: 03 December 2015
doi: 10.3389/fonc.2015.00265

Introduction to the EC's Marie Curie Initial Training Network Project: The European Training Network in Digital Medical Imaging for Radiotherapy (ENTERVISION)

Manjit Dosanjh, Manuela Cirilli and Sparsh Navin*

CERN, Geneva, Switzerland

Between 2011 and 2015, the ENTERVISION Marie Curie Initial Training Network has been training 15 young researchers from a variety of backgrounds on topics ranging from in-beam Positron Emission Tomography or Single Particle Tomography techniques, to adaptive treatment planning, optical imaging, Monte Carlo simulations and biological phantom design. This article covers the main research activities, as well as the training scheme implemented by the participating institutes, which included academia, research, and industry.

Keywords: imaging, training, real time, hadron therapy, proton therapy, radiotherapy

OPEN ACCESS

Edited by:
Marco Durante,
GSI Helmholtzzentrum für Schwerionenforschung, Germany

Reviewed by:
Kevin Prise,
Queen's University Belfast, UK
Mario A. Bernal,
State University of Campinas, Brazil

****Correspondence:***
Manjit Dosanjh
manjit.dosanjh@cern.ch

Specialty section:
This article was submitted to Radiation Oncology, a section of the journal Frontiers in Oncology

Received: *30 September 2015*
Accepted: *12 November 2015*
Published: *03 December 2015*

Citation:
Dosanjh M, Cirilli M and Navin S (2015) Introduction to the EC's Marie Curie Initial Training Network Project: The European Training Network in Digital Medical Imaging for Radiotherapy (ENTERVISION). Front. Oncol. 5:265. doi: 10.3389/fonc.2015.00265

INTRODUCTION

Cancer is a major societal issue, and by 2030 its global incidence is expected to increase by more than 75% in developed countries and by more than 90% in developing countries (1). A major challenge for cancer therapy is the complex and multifaceted nature of the disease, which calls for personalized treatments and an ever-expanding set of approaches in the oncologists' toolbox. Radiotherapy (RT) has been used to treat tumors for more than a century, and still plays a major role in oncology: today, 50% of cancer patients receive RT, half of them with curative intent and is second only to surgery as a primary cure. At present, the mainstay of RT is photon therapy: this has become highly sophisticated, with methods like image-guided RT, intensity-modulated RT, stereotactic radiosurgery.

Despite the technological advances in RT approaches, the underlying dose deposition mechanism will always be the same: for photons, the deposited energy falls off exponentially as the photon beam traverses the body (except in the case of broad beams since scattering produces a departure of the attenuation from the exponential behavior). This makes it difficult to protect neighboring healthy tissues during treatment, which is an issue for deep lying tumors, tumors in/near critical organs, and pediatric tumors.

This is why RT with protons and other ions, known as Hadron Therapy (HT), has been proposed: in this case, most of the energy of the therapeutic beam is deposited at the end of its range in a characteristically peaked distribution (the Bragg peak), sparing the healthy tissue on the way to and beyond the tumor target.

The use of highly conformal dose distributions to improve the clinical outcomes of RT can be a double-edged sword. First, the target volume definition must be extremely accurate: if this is not the case, some tumor regions will not only receive a lower dose, as it also happens in RT with photons, but might not be irradiated at all, due to the steep dose gradients with protons

and other ions. Temporal anatomic variations and organ motion have a more significant adverse influence on dose distributions in HT compared to RT with photons, making advanced imaging techniques a prerequisite for successful HT.

Independent studies carried out in Austria, France, Germany, Italy, and Sweden under the umbrella of the European Network for Light Ion Hadron Therapy (ENLIGHT) (2) provided evidence that 10–20% of RT cases may benefit from HT (3): these were conservative estimates, and therefore the actual numbers could be even higher.

While it is clear that photons will remain the backbone of RT, it is timely that the superior dose profiles of protons and carbon ions are fully exploited in clinical practice. Besides the need for clinical trials, the scientific community has strongly advocated for technology developments that would bring the current HT technology to the high standards of modern photon therapy.

Medical imaging is a key area to ensure the full exploitation of the potential of HT, in particular through quality assurance during treatment. Moreover, as new treatment centers are opening throughout Europe, there is an increasing demand for qualified experts in the multidisciplinary domains connected to HT. These issues were addressed by the ENTERVISION training project, a Marie Curie Initial Training Network aimed at educating young researchers in online 3D digital imaging for HT.

THE EUROPEAN TRAINING NETWORK IN DIGITAL MEDICAL IMAGING FOR RADIOTHERAPY (ENTERVISION)

The ENTERVISION Marie Curie Initial Training Network was funded by the European Commission (EC) and launched in 2011, with the aim of educating young researchers in advanced medical imaging techniques for quality assurance of HT. Ten academic institutes and research centers of excellence, and a leading European company in HT (see **Table 1**), recruited 15 researchers from a variety of academic backgrounds over the course of 4 years (see **Figure 1**).

The ENTERVISION researchers were assigned individual research projects on topics ranging from in-beam Positron Emission Tomography (PET) or Single Particle Tomography techniques to adaptive treatment planning, optical imaging, Monte Carlo (MC) simulations, and biological phantom design. The majority of the researchers were also enrolled in a PhD program at a partner University, and a personalized career development plan was established by their supervisors for each researcher. In addition, the researchers took part in the network-wide training organized several times a year, offering a diversified portfolio of scientific courses, complemented by specific courses aimed at developing soft skills such as leadership and CV writing.

A unique feature of the ENTERVISION project was its connection with the EC-funded R&D project ENVISION, aimed at developing solutions for quantitative real-time non-invasive monitoring of HT for stationary and moving organs, accurate determination of delivered dose, and fast feedback to the Treatment Planning System (TPS) for optimal adaptation strategies. In fact, ENVISION acted as a "hands-on" training platform for the Marie Curie researchers, who had the opportunity to interact directly with senior scientists working at the forefront of research in quality assurance for HT.

TABLE 1 | ENTERVISION partners: this table lists the Institutes, Universities, and companies participating to ENTERVISION.

Acronym	Full name	Country
CERN	European Organization for Nuclear Research	Switzerland
CNRS	Centre National pour la Recherche Scientifique	France
GSI	GSI Helmholtzzen-trum für Schwer-ionenforschung GmbH	Germany
CSIC	Agencia Estatal Consejo Superior de Investigaciones Científicas	Spain
INFN	Istituto Nazionale di Fisica Nucleare	Italy
UCAM	University of Cambridge	UK
TUD	Technische Universität Dresden	Germany
TERA	TERA Foundation	Italy
IBA	Ion Beam Applications	Belgium
UCBL	Université Claude Bernard Lyon 1	France
UKL-HD	Universitätsklinikum Heidelberg	Germany

The ENTERVISION researchers also benefited from the involvement in the ENLIGHT network. Throughout the project, the trainees have been encouraged to build a multidisciplinary network: this will not only help them with their future careers, but will ultimately improve the transfer of knowledge and collaboration between the various disciplines of cancer treatment.

Detailed Research Program of ENTERVISION

The superior dose distribution of protons and other ions with respect to photons can be a double-edged sword if a series of factors (target volume definition, anatomical variations, organ motion) are not accurately determined and taken into account. A three-dimensional non-invasive imaging technique for real-time monitoring of the delivered dose is highly desirable, and several efforts toward this goal have been pursued within ENTERVISION.

At present, the most advanced method for HT quality assurance is PET. The use of heavy scintillating crystals coupled to silicon photomultipliers (SiPM) is one of the most promising solutions for future PET scanners. Developments in the field of particle detectors are focused on the use of time of flight (TOF) information that aims to improve the sensitivity by improving the signal to noise ratio.

ENTERVISION tackled the development of a characterization chain to measure the rising time profiles of signals in scintillating crystals used both for PET and high-energy physics (4). A rise-time measurement bench has been set up, where crystals are irradiated with a 511 keV gamma source, and the light produced is detected by a photomultiplier. In order to investigate the effect of thermalization inside the lattice, excitations at two lower energies are also foreseen. A pulsed X-ray machine excites the crystal with 20 keV photon pulses, and scintillation photons are collected with a streak camera system. The crystals are also exposed to 20 eV excitation energies at a vacuum ultraviolet (VUV) laser

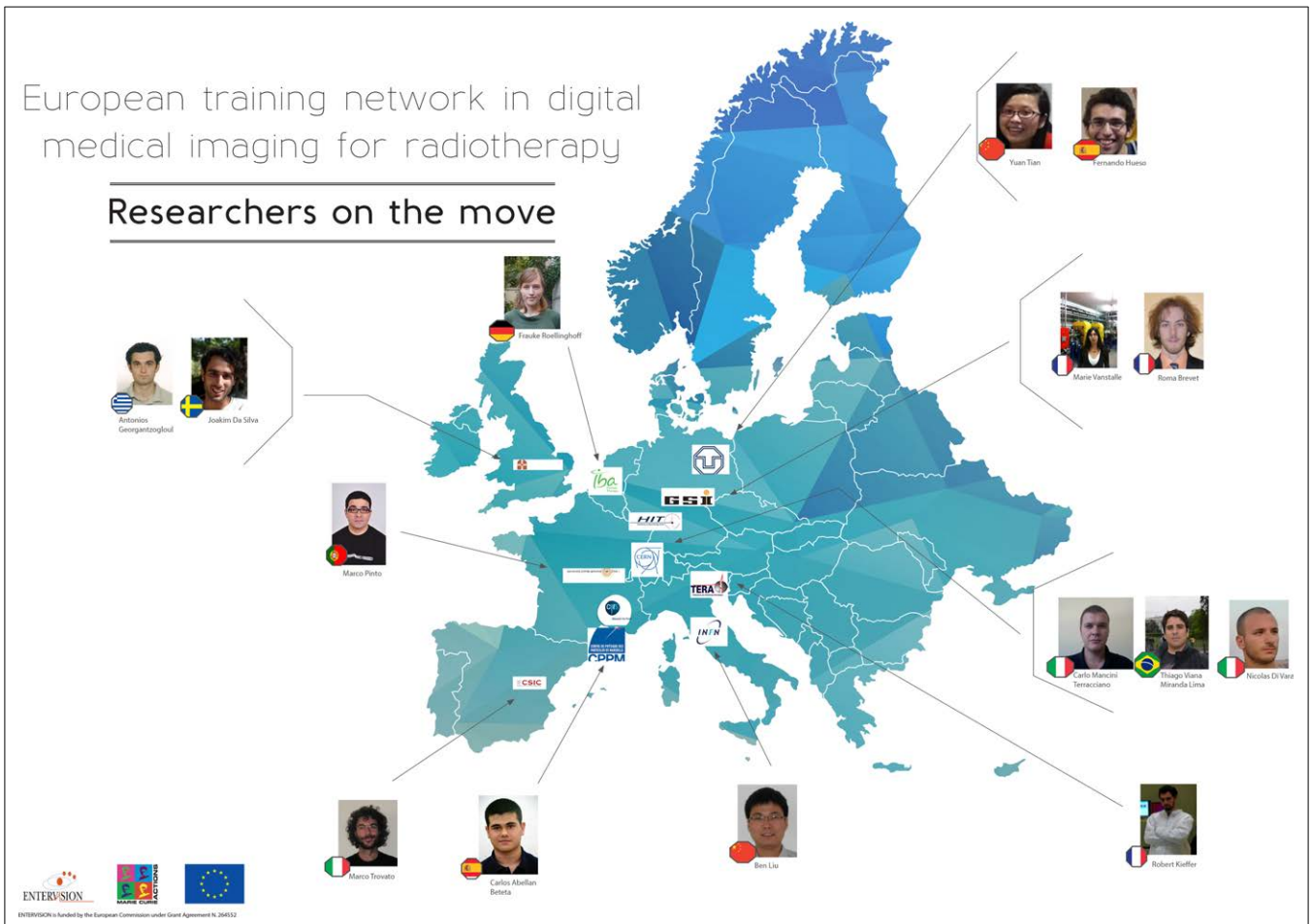

FIGURE 1 | Distribution of ENTERVISION researchers per nationality and recruiting institute.

driven facility. This measurement chain allows complete access to thermalization lengths. Simulations in Geant4 (5) drive the choice of interesting crystal samples and set-up geometries.

Alternative detector choices have also been explored. One of the ENTERVISION researchers built a TOF–PET demonstrator with Multigap Resistive Plate Chambers (MRPCs) (6), achieving a preliminary time resolution of 240 ps sigma, and worked on a proton range telescope, developing an FPGA firmware to allow high rate acquisition (one million event per second) (7). They collaborated with another ENTERVISION researcher in order to prove the feasibility of distributing clocks over a MicroTCA-based optical fiber network, in order to synchronize electronic front-end boards at the pico-second scale. This would allow to perform TOF over a large-scale system dedicated to in-beam PET.

One of the challenges in using PET for HT monitoring, is to evaluate the motion-influenced artifacts. Within the framework of ENTERVISION, the influence of various motion parameters (peakiness, the ratio of inspiration and expiration, frequency, amplitude, drift, and parameter combination) was investigated through 40 experiments with radioactive sources performed at the GSI in-beam PET installation. 4D PET images were reconstructed, compared, and evaluated. The lateral field position and the particle deposition depth were studied with irradiated phantom experiments. PET artifacts caused by special respiratory motion cases (e.g., larger peak to peak amplitude) were also investigated. A potential artifact-compensation method was proposed, and a preliminary trial was conducted (8).

Single-particle imaging, i.e., detection of prompt photons, protons, or neutrons also resulting from nuclear interactions in the tissues, is emerging as a promising modality for dose monitoring during HT. ENTERVISION focused on improving prompt photon detection in the clinical scenario, through the development and test of gamma cameras, with both passive and active collimation systems.

One of the research projects carried out detailed comparisons between a multi-parallel-slit and a knife-edge slit collimator configuration (9). Detailed MC simulations allowed the setting of guidelines for choosing the optimal configuration of both camera types for various trade-offs between efficiency and spatial resolution. Measurements with a dedicated detector concept demonstrated, for the first time the capability of acquiring images at full clinical beam current, and further validated the results of simulation. Prototypes for both collimator types have been built and tested.

Active collimation systems (Compton cameras) have been also explored in depth. The ENTERVISION researchers assembled

and tested a variety of detector geometries, materials, and read-out schemes. One of these is a three-layer Compton telescope based on continuous LaBr3 crystals and SiPM. The third layer has been completed recently, and included a new type of SiPM to increase the active area. The larger active area and a specific bias operating voltage for a single SiPM array brought an improvement of the energy resolution (10).

In parallel, a Compton camera has been developed and extensively tested in various beam conditions. Lutetium oxyorthosilicate (LSO) and bismuth germinate (BGO) commercial PET block detectors have been intensively tested and analyzed at different accelerators, in order to compare their performance and choose the absorber material. A considerable effort was made to improve the robustness and speed of the multi-threaded custom data acquisition system (DAQ) and to develop a platform for fast analysis. A prompt gamma-ray timing method for *in vivo* range verification has been proposed and tested at a clinical proton therapy facility, showing the great potential of this timing technique, with low footprint and cost and fast range retrieval (11).

In this variegated detector landscape, one ENTERVISION project aimed at developing a multi-purpose DAQ suitable for different medical imaging set-ups. The mezzanine boards work flawlessly, and the firmware is finished, tested and working. This firmware is intended to serve as a framework for detector developers, providing all the necessary tools to implement a full-featured DAQ without dealing with the board's complexity, but by just writing the specific application VHDL and C code needed. Compatibility at a physics level has been verified with different read-out boards, while firmware-level compatibility is undergoing. In its current state, the DAQ system can be used in many different scenarios, from simple demonstrators to full featured imaging systems (12).

Highly realistic calculation models and fast simulation codes are required for most of these quality assurance tools. The high sensitivity of HT to motion and changes in patient anatomy calls for adaptive treatment delivery, where the delivered dose is actively monitored. Fast dose calculation, specifically recalculation of an existing treatment plan in modified anatomies, constitutes a crucial component in such a system. Also, the interaction of the incoming therapeutic beam with human tissues leads to the production of nuclear fragments and secondary light particles; hence, an accurate estimate of the dose deposited in the cancerous and healthy tissues requires sophisticated simulation tools based on nuclear reaction models. The validity of such models has to be assessed through extensive comparisons with as many sets of experimental data as possible.

One of the ENTERVISION research projects (13) focused on improving the nuclear models for carbon ion break-up. In particular, the researcher had the opportunity to work in collaboration with iThemba LABS where an experiment (14) with 33 MeV/n 12C ions on C, Au, Nb, and Polyethylene targets has been carried out. This experiment is the only one that took data studying in correlation all the fragments produced by the quasi elastic breakup of 12C in 8Be and 4He. Studying exclusively such a process is of particular interest because many experiments showed a broad peak in the 4He production with an energy per nucleon close to the beam energy. Moreover, as the 8Be decay almost immediately in two 4He, this is the only way to disentangle the He4 produced directly from 12C and from Be8 as intermediate state. Additionally, such a unique study sets a robust benchmark for future models and MC simulations. Unusual features in the energy distributions of the fragments suggest an H contamination of the targets, a hypothesis confirmed by a second experiment with a polyethylene target. The contribution of H contaminants to carbon break-up experiments has been studied, modeled, and included in the FLUKA (15) simulation code, and will be available for future studies. It will be useful especially in the simulation for the proton therapy, as it will more accurately simulate the production of high linear energy transfer (LET) particles.

ENTERVISION also contributed to the simulation for INSIDE (16), a multimodal monitoring system for the assessment of HT accuracy. One of the researchers developed and benchmarked various FLUKA-based simulations for different scopes. The experimental set-up for a beam test, where prototype detectors and electronics were evaluated, was simulated. The MC prediction was found in good agreement with data, and the code could then be used for the simulation of the full-size detector. Another important aspect was the evaluation, through the simulation of realistic treatment conditions, of the radiation damage induced on the detector by the neutrons produced during patient irradiation. The lifetime of the INSIDE detectors was thus estimated to be at least 5 years. Finally, the specific treatment plan of a patient irradiated at CNAO was simulated using FLUKA, and the results were compared with the commercial TPS used at the facility. The isodose distributions were found in good agreement, and the simulation could then be used to evaluate the Relative Biological Effectiveness (RBE) during treatment.

As prompt gamma monitoring is emerging as a promising imaging modality to monitor the range of the particles used to treat tumors, it is of the utmost importance to have an accurate description of the physical models used in MC tools for modeling the emission of prompt gammas. ENTERVISION performed an extensive and comprehensive analysis of several experiments, in order to create a large set of data to benchmark simulations: these included nine experiments with homogeneous targets such as water and polymethylmethacrylate (PMMA) and three experiments with inhomogeneous targets such as PMMA with a Teflon piece or a lung-equivalent material, performed at several experimental and clinical facilities around Europe and involving different targets, detectors, and set-ups. A real-size prototype for prompt gamma monitoring was developed and optimized, focusing on obtaining the best possible precision in the retrieval of the ion range inside the patient and, at the same time, on providing additional data for comparison with simulations (17).

One of the ENTERVISION researchers participated to an experiment performed in collaboration with University La Sapienza (Rome) where PMMA phantom was irradiated by 220 MeV/u carbon-ions (18). The primary ions outgoing from the exit window were monitored with a plastic scintillator, and two arms were placed at 90° on each side of the phantom. The energy spectra of the prompt-γ produced by interaction of the 12C ions with PMMA target have been measured, and the prompt-γ rates per incident 12C values for the two measured angles were compared and found in agreement. The data were compared

with MC simulations performed with Geant4, using two different models: the Quantum Molecular Dynamics (QMD) model of ion-ion collisions and the Binary Cascade light ion model (BIC). An acceptable agreement, both qualitative and quantitative, was obtained between energy spectra (experimental and simulated) and prompt-γ rates, especially for QMD model. Therefore, this study allowed confirming that the QMD model is more accurate than BIC model to reproduce both γ-yields values and γ-spectra as it is the case for charged particles. This originates from the fact that BIC does not take into account properly inelastic scattering processes between ions like (12C + 12C) and (12C + 16O), and also neutron scattering.

ENTERVISION also investigated how graphics processing units (GPUs) can be used to speed up analytical dose calculation for HT (19). Initially, a prototype for a simple dose calculation engine was implemented in Matlab together with a graphical user interface (GUI) and the necessary facilities to open Computed Tomography (CT) images in the Digital Imaging and Communications in Medicine (DICOM) format. The simple dose calculation engine was subsequently implemented to run on GPU and an interface between the GPU code and the GUI was created to allow data to be loaded, stored and analyzed in Matlab, but the calculation to be carried out on a GPU. Following this proof-of-principle study, the work began to create an efficient parallel GPU implementation of the widely used pencil beam algorithm. The implementation was tuned and validated through comparisons between data and MC simulations. The results produced by the GPU implementation showed the same level of accuracy as the dose distribution calculated by the analytical algorithm provided with the commercial TPS used for the treatment. The sub-second calculation times also compared very favorably with those found in the literature, and were short enough to allow for on-line dose calculation applications. Finally, initial work was done to investigate a novel method for analytical dose calculation for proton therapy that would be suitable for parallel implementation.

On the clinical side, weekly 4D CT datasets (9 Non-Small Cell Lung Cancer (NSCLC) patients representing 70 weekly 4D CT datasets) from the University of Texas MD Anderson Cancer Center were used to investigate the impact of several parameters on dose delivery, target coverage and homogeneity, to eventually allow recovery for dose delivery errors caused by intra- and inter-fraction motion. Gating plans (including 4D calculations) were simulated with the GSI treatment planning software TRiP4D (20). Optimization was performed with the first week of each patient using a range-corrected internal target volume (ITV) on states of the moving tumor. The resulting plans were then used for all following weeks. In-depth studies showed that the combination of ITV, isotropic margins, and range margins yielded the best results in terms of target coverage, even though this led to the irradiation of a higher portion of normal tissue. Finally, simulations using one, two, or three fields were performed; for each case, results obtained using ITV only and ITV with additional isotropic and range margins were compared. The best results were obtained using three fields combined to additional isotropic and range margins in terms of target coverage. Using several fields also permitted the reduction of high dose delivery regions in normal tissue. Rescanning will be investigated as a next step to also explicitly address intra-fraction motion. Lung contours extraction is also currently in progress to investigate more precisely the dose delivered to the tissue surrounding the tumor (21).

Finally, ENTERVISION also tackled issues related to biological and physical doses. Development of clinical treatment protocols for any type of cancer RT is dependent on the availability of high quality information on the biological efficacy of radiation doses using a range of beam qualities. This is true especially in HT. In order to gain robust data for use in clinical protocols, multiple cell irradiation experiments must be performed at different dose points, using a range of generic and patient specific tumor cell lines. It is important to be able to verify quickly the biological effects of complex dose distributions in homeomorphic phantoms, alongside measurements of physical dose. A dedicated phantom was designed, tested, and optimized to correctly correlate the biological and physical dose distributions (22).

In this context, specific software for individual cell recognition for microbeam targeting and tracking post-irradiation was developed (23). Bright-field illumination microscopy was chosen as an imaging method in order to avoid potential toxicity from fluorescence excitation. However, the obtained images of cells are characterized by a high degree of complexity since the specialized cell dishes used for microbeam irradiation exhibit highly inhomogeneous optical properties. A cell recognition pipeline has been established using digital image processing techniques and principles from statistics and cluster analysis. This pipeline is able to recognize cellular structures avoiding the majority of the substrate features. It has been tested on both polypropylene and plastic substrates, and in various cell lines including V79 Chinese hamster cells, T98G and U251 human glioblastoma cells.

Additionally, initial time-lapse data have been obtained so as to follow the cells' life post-irradiation. The biological end-point is the maintenance of cells' clonogenic ability when irradiated with high-LET radiation using charged particle microbeams. Cell tracking has been applied based on the topological correlation of cells and cell divisions can be effectively detected when cells are separated. Location feedback from frame to frame has been integrated in order to correct false cell detection or linking. The process can be used as a near real-time application in electrostatic cell irradiation. Currently, the software can effectively recognize and irradiate roughly 1,200 cells when real-time tracking is needed, while this number can be increased to more than 2,500 when GPU is used. If real-time tracking is not necessary, then the number of cells capable of irradiation and tracking is only limited by the mechanical properties of the end-station microscope.

Training Program of ENTERVISION

Network-wide events and training courses were organized throughout the duration of the project. They served the dual purpose of educating the researchers and of creating occasions for them to meet, connect with each other, and establish an extensive professional network with the leading experts in the field.

Courses were aimed at building the researchers' scientific knowledge, as well as at enhancing their communication and leadership skills (see **Table 2**). The ENTERVISION technical training portfolio included detectors for medical imaging, electronics, Treatment Delivery Systems, and dosimetry.

TABLE 2 | ENTERVISION network-wide training courses.

Course title	Trainers and organizers
Basic training ENTERVISION training course: beam production and delivery, hands-on accelerator, treatment planning, dosimetry, radiobiology basics, particle therapy physics	GSI UKL-HD
ENTERVISION Summer School in Lyon: from physics to medical imaging	UCBL CNRS
ENTERVISION Leadership Development Course	UCAM University of Surrey Evolve Leadteam Ltd
Hands-on detectors and electronics course	CSIC IFIC Valencia
Industrial processes	IBA
CV writing	CERN Viva Consult
Intellectual Property	CERN Knowledge Transfer Group

As health applications need industrial support to be deployed successfully in hospitals and clinics, a course on industrial processes was also run. A course on Intellectual Property management made the young researchers aware of the valorization chain for their scientific results. The ENTERVISION researchers also had the opportunity to join the courses on the impact of gantries and imaging on HT techniques run by a previous Marie Curie Actions Initial Training Network, PARTNER.

Soft-skills courses tackled leadership, curriculum writing, and communication. The project has been widely disseminated, and the researchers have been encouraged and motivated to take part in outreach activities, at their home institute or elsewhere, including video interviews (24). In September 2013, several ENTERVISION researchers came to CERN to actively participate in the activities for the European Researchers' night and the laboratory's Open Days. ENTERVISION also co-sponsored a panel at the EuroScience Open Forum (ESOF) 2014 in Copenhagen chaired by the project coordinator on "Everything you wanted to know about cancer but were afraid to ask."

The researchers have also been attending the annual meetings of the ENLIGHT network and of the other EC-funded projects run under the ENLIGHT umbrella (in particular of ENVISION). In these occasions, they have presented their work and listened to and interacted with the experts in the HT field, leading to unique learning and networking opportunities.

CONCLUSION

ENTERVISION has trained 15 researchers in fields connected to advanced medical imaging techniques for quality assurance during cancer treatment with HT. The researchers have formed a close-knit network, which they are exploiting to their advantage now and for the future. A number of them have already used the contacts they established during ENTERVISION to secure new positions as soon as they finished their Marie Curie projects.

In 2013, ENTERVISION has been chosen as "a success story illustrating the good use of European funds for research" and "as a flagship project for Marie Curie Actions for the promotion of the H2020 program, as a so-called 'gold project.'" The EC Directorate-General for Research and Innovation chose 37 projects in total from the previous funding scheme (FP7), with ENTERVISION being the only project representing the Marie Curie Actions. In the same year, ENTERVISION was featured in a press release from the EC to mark the visit to CERN of the EU Commissioner for Education, Culture, Multilingualism and youth.

A number of highly valuable and interesting results have been obtained within the framework of ENTERVISION, as proved by the papers published in this special issue. In addition, 30 posters, 20 oral presentations, and 35 publications featured in international conferences and journals. ENTERVISION researchers took part in the European Researcher's Night programme and CERN Open days in 2013, and contributed to the publication of Accastampato (25).

AUTHOR CONTRIBUTIONS

MD – Project proposer and coordinator of the ENTERVISION and ENVISION projects. MC – ENVISION technical coordinator and overall Communication and Dissemination officer. SN – ENTERVISION dissemination and technical coordinator.

ACKNOWLEDGMENTS

The authors wish to thank all the ENTERVISION researchers, their supporting Institutes, and their supervisors for four intense years of scientific activity and networking.

FUNDING

ENTERVISION was funded by the European Commission under Grant Agreement n. 264552.

REFERENCES

1. Bray F, Jemal A, Grey N, Ferlay J, Forman D. Global cancer transitions according to the human development index (2008–2030): a population-based study. *Lancet Oncol* (2012) **13**(8):790–801. doi:10.1016/S1470-2045(12)70211-5
2. Dosanjh M, Cirilli M, Greco V, Meijer AE. The European network for light ion hadron therapy. *J Health Phys* (2012) **103**(5):674–80. doi:10.1097/HP.0b013e3182606520
3. Glimelius B, Ask A, Bjelkengren G, Björk-Eriksson T, Blomquist E, Johansson B, et al. Number of patients potentially eligible for proton therapy. *Acta Oncol.* (2005) **44**(8):836–49. doi:10.1080/02841860500361049
4. Di Vara N. *Study of Time Profiles of Heavy Scintillating Crystals*. Ph.D. thesis, Univeristy of Milano Bicocca, Milan (2014).
5. Agostinelli S, Allison J, Amako K, Apostolakis J, Araujo H, Arce P. Geant4 – a simulation toolkit. *Nucl Instrum Methods Phys Res A* (2003) **506**(3):250–303. doi:10.1016/S0168-9002(03)01368-8
6. Amaldi U, Borghi G, Bucciantonio M, Kieffer R, Samarati J, Sauli F, et al. Development of TOF-PET detectors based on the multi-gap resistive plate chambers. *Nucl Instr Methods A* (2015) **778**:85–91. doi:10.1016/j.nima.2015.01.018
7. Bucciantonio M, Amaldi U, Kieffer R, Sauli F, Watts D. Development of a fast proton range radiography system for quality assurance in hadrontherapy. *Nucl Instrum Methods Phys Res A* (2013) **732**:564–7. doi:10.1016/j.nima.2013.05.110

8. Tian Y, Stützer K, Enghardt W, Priegnitz M, Helmbrecht S, Bert C, et al. Technical note: experimental investigation of irregular motion impact on 4D PET based particle therapy monitoring. *Phys Med Biol*.
9. Smeets J, Roellinghoff F, Prieels D, Stichelbaut F, Benilov A, Busca P, et al. Prompt gamma imaging with a slit camera for real-time range control in proton therapy. *Phys Med Biol* (2012) **57**(11):3371–405. doi:10.1088/0031-9155/57/11/3371
10. Llosá G, Cabello J, Callier S, Gillam JJ, Lacasta C, Rafecas M, et al. First Compton telescope prototype based on continuous LaBr3-SiPM detectors. *Nucl Inst Meth Phys Res Sec A* (2013) **718**:130–3. doi:10.1016/j.nima.2012.08.074
11. Golnik C, Hueso-González F, Müller A, Dendooven P, Enghardt W, Fiedler F, et al. Range assessment in particle therapy based on prompt γ-ray timing measurements. *Phys Med Biol* (2014) **59**(18):5399–422. doi:10.1088/0031-9155/59/18/5399
12. Abellan C, Cachemiche J-P, Rethore F, Morel C. A data acquisition system for medical imaging. *Advancements in Nuclear Instrumentation Measurement Methods and their Applications (ANIMMA)*. (2013). p. 1–7.
13. Mancini C. *Analysis and Interpretation of Carbon Ion Fragmentation in the Bragg Peak Energy Range*. Ph.D. thesis, University of Roma Tre, Rome (2015)
14. Förtsch SV, Mira J, Smit FD, Steyn GF, Bassini R, Cowley AA, et al. Binary projectile fragmentation of 12C at an incident energy of 33.3 MeV/nucleon. *12th International Conference on Nuclear Reaction Mechanisms*, June 15–19, 2009. Varenna: Villa Monastero (2009). p. 545–52
15. Ferrari A, Sala PR, Fasso A, Ranft J. *FLUKA: A Multi-Particle Transport Code, CERN-2005-10 (2005), INFN/TC_05/11, SLAC-R-773*. (2005).
16. Marafini M, Attili A, Battistoni G, Belcari N, Bisogni MG, Camarlinghi N, et al. The INSIDE Project: innovative solutions for in-beam dosimetry in hadrontherapy, Acta Physica Polonica. *Proceedings of II Symposium on Positron Emission Tomography*. (Vol. 127). Poland: Jagiellonian University of Krakov (2015).
17. Pinto M, Dauvergne D, Freud N, Krimmer J, Letang JM, Ray C, et al. Design optimisation of a TOF-based collimated camera prototype for online hadrontherapy monitoring. *Phys Med Biol* (2014) **59**(24):7653–74. doi:10.1088/0031-9155/59/24/7653
18. Vanstalle M, La Tessa C, Schuy C, Sarti A, Piersanti L, Patera V et al. *Detection of Secondary Particles from 12C Fragmentation in an Anthropomorphic Phantom for SOBP Position Monitoring*. GSI Scientific Report (2011)
19. da Silva J, Ansorge R, Jena R. Efficient scatter-based kernel superposition on GPU. *J Parallel Distrib Comput* (2015) **84**:15–23. doi:10.1016/j.jpdc.2015.07.003
20. Richter D, Trautmann J, Schwarzkopf A, Kraemer M, Gemmel A, Jaekel O, et al. *4D Treatment Planning Implementations for TRiP98*. GSI Scientific Report (2010)
21. Brevet R. *Optimized Treatment Parameters to Account for Interfractional Variability in Scanned Ion Beam Therapy of Lung Cancer*. Ph.D. thesis, University of Darmstadt, Darmstadt (2015)
22. Lima TVM, Ciocca M, Ferrari A, Mairani A, Molinelli S, Dosanjh M. Monte Carlo calculations supporting patient plan verification in proton therapy. *Front Oncol*.
23. Georgantzoglou A, Merchant MJ, Jeynes JC, Wéra AC, Kirkby KJ, Kirkby NF, et al. Automatic cell detection in bright-field microscopy for microbeam irradiation studies. *Phys Med Biol* (2015) **60**(16):6289–303. doi:10.1088/0031-9155/60/16/6289
24. Outreach Material. Available from: http://cern.ch/ENTERVISION/news.html
25. Available from: http://www.accastampato.it/en/home/copertina-11/

Conflict of Interest Statement: The authors declare that the research was conducted in the absence of any commercial or financial relationships that could be construed as a potential conflict of interest.

Copyright © 2015 Dosanjh, Cirilli and Navin. This is an open-access article distributed under the terms of the Creative Commons Attribution License (CC BY). The use, distribution or reproduction in other forums is permitted, provided the original author(s) or licensor are credited and that the original publication in this journal is cited, in accordance with accepted academic practice. No use, distribution or reproduction is permitted which does not comply with these terms.

frontiers in Oncology

REVIEW
published: 25 January 2016
doi: 10.3389/fonc.2016.00009

Medical Applications at CERN and the ENLIGHT Network

Manjit Dosanjh, Manuela Cirilli, Steve Myers and Sparsh Navin*

CERN, Geneva, Switzerland

State-of-the-art techniques derived from particle accelerators, detectors, and physics computing are routinely used in clinical practice and medical research centers: from imaging technologies to dedicated accelerators for cancer therapy and nuclear medicine, simulations, and data analytics. Principles of particle physics themselves are the foundation of a cutting edge radiotherapy technique for cancer treatment: hadron therapy. This article is an overview of the involvement of CERN, the European Organization for Nuclear Research, in medical applications, with specific focus on hadron therapy. It also presents the history, achievements, and future scientific goals of the European Network for Light Ion Hadron Therapy, whose co-ordination office is at CERN.

Keywords: particle physics, imaging, radiotherapy, detectors, accelerators, hadron therapy

OPEN ACCESS

Edited by:
Francis A. Cucinotta, University of Nevada Las Vegas, USA

Reviewed by:
Volodymyr Nahirnyak, Bukovina State Medical University, Ukraine
Derek Irving Lowenstein, Brookhaven National Laboratory (Retired), USA

****Correspondence:***
Manjit Dosanjh
manjit.dosanjh@cern.ch

Specialty section:
This article was submitted to Radiation Oncology, a section of the journal Frontiers in Oncology

Received: *30 September 2015*
Accepted: *11 January 2016*
Published: *25 January 2016*

Citation:
Dosanjh M, Cirilli M, Myers S and Navin S (2016) Medical Applications at CERN and the ENLIGHT Network. Front. Oncol. 6:9. doi: 10.3389/fonc.2016.00009

INTRODUCTION

Physics underpins many techniques and technologies that are used for both diagnosis and treatment of a variety of diseases: discoveries from basic physics research have been closely linked to medicine for centuries, and numerous tools developed by physicists to pursue their scientific goals have found their way into hospitals around the world.

In particular, innovative ideas and technologies originating from particle physics have been playing an increasingly important role in medicine over the last 100 years since the advent of radiation-based medical diagnosis and treatment. Nowadays, state-of-the-art techniques derived from particle accelerators, detectors, and physics computing are routinely used in clinical practice and medical research centers: from technology for Positron Emission Tomography (PET) scanners, to dedicated accelerators for cancer therapy, simulations, and data analytics.

Hadron therapy, also known as particle therapy, epitomizes the connection between basic physics (the property of particles traversing matter) and medicine (cancer treatment). Using protons and other ions to treat cancer demands large accelerators; this links radiation therapy to the development of increasingly powerful accelerators for particle physics research. At the same time, hadron therapy is a truly multidisciplinary venture that requires input from oncologists, radiation biologists, medical physicists, particle physicists, and computing scientists.

CERN, the European Organization for Nuclear Research (**Figure 1**) is the world's largest particle physics laboratory. Its contribution to particle physics research and related technologies has been outstanding since its establishment in 1954. CERN's primary mission is basic research in particle physics; yet, the laboratory seeks possibilities to transfer its know-how and technology to other fields, including health, in order to maximize the societal impact of its research.

In this context, the European Network for Light Ion Hadron Therapy (ENLIGHT) was launched at CERN in 2002, to connect research centers, institutions, and scientists, involved in the research, promotion, and realization of hadron therapy in Europe.

This article briefly recaps the history of medical applications at CERN and then provides an overview of the present situation, with particular emphasis on research and development connected to hadron therapy. The role of ENLIGHT and its research program are also covered.

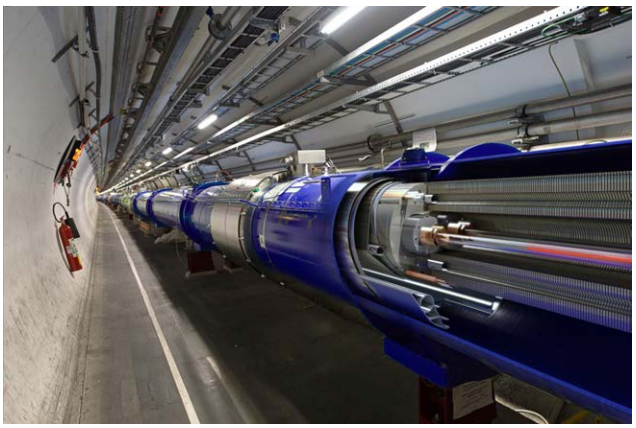

FIGURE 1 | The Large Hadron Collider (LHC). CERN's flagship project, the LHC is a 27-km circular accelerator where protons collide at a center-of-mass energy of 13 TeV. The initial 3-year LHC run, which began with a collision energy of 7 TeV, rising to 8 TeV, led to the discovery of the Higgs boson in 2012.

FROM PARTICLE PHYSICS TO HEALTH

Fundamental research in particle physics not only pushes back the boundaries of our knowledge of the Universe but also catalyzes innovative technology developments: frontier instruments like the Large Hadron Collider (LHC) and its detectors require technologies and performance that exceed the available industrial know-how.

The three technology pillars of particle physics – accelerators, detectors, and computing tools – have all found their way into the medical field. Accelerators have been used for radiation therapy of cancer for decades. Medical applications of particle detectors are epitomized by PET, which is a direct application of light-sensing techniques. Data handling and simulation tools developed by physicists have found use in the biomedical field, for example, in establishing personalized treatment plans.

A host of highly specialized technologies is associated with each of the three pillars. To transfer this wealth of know-how to medicine, it is essential not only to identify which technologies are potentially interesting for medical applications but also what is their relevance for the medical community. In order to maximize the societal benefit from particle physics, the physicists' and medical doctors' research activities should be harmonized. This can only be achieved through multidisciplinary networks and collaborations, where scientists of different specialties all make their contributions to establish a common roadmap. Physicists, engineers, and computer scientists would share their knowledge and technologies, thus giving first-hand information to the medical community on the latest technical progress; conversely, doctors and biologists would present their needs and vision for the medical tools of the future, thus triggering breakthrough ideas and technical developments in specific areas.

Experience gained in particle and accelerator physics may serve more than just a technology, which shapes up the medicine of the future. Scientific collaborations in particle physics have been bringing together thousands of scientists from every corner of the world to work on the largest and most complex experiments ever conducted by mankind. Collaboration has become second nature of particle physicists, who have learned to work collectively on a common goal and who rely on mutual consensus to make decisions. The collaborative model of particle physics, represented in literature (1) has been translated into a flexible yet effective management structure for the experiments. This new paradigm for teamwork has proven its worth, and could serve as a model to follow for the emerging multidisciplinary ventures in medical applications.

CERN and Medical Applications: A Brief History

Over the past 60 years, CERN has developed a world-renowned expertise in the three core technology domains of particle physics – accelerators, detectors, and large-scale computing – as well as in many ancillary technologies. The transfer of technology and know-how has always been one of the missions of the Laboratory, even before the formal establishment of a technology transfer unit in the late 80s. Early medical applications activities date back to the 1970s and have been initiated mostly by individual interests.

The multi-wire proportional chamber conceived in 1968 by the CERN physicist Georges Charpak not only opened a new era for particle physics and earned its inventor the 1992 Nobel Prize in Physics but also found important applications in biology, radiology, and nuclear medicine (2, 3).

In 1975, the CERN physicist David Townsend in collaboration with the University of Geneva and the Geneva Cantonal Hospital made important contributions to the reconstruction of PET images and to the development of 3D PET (4–6).

After these individual efforts, CERN witnessed the first collaborative endeavors in medical applications in the 90s. A partnership was established with TERA Foundation (Italy), MedAustron (Austria), and Onkologie 2000 (Czech Republic) to initiate the Proton Ion Medical Machine Study (PIMMS). The PIMMS study is tightly connected to the birth of the ENLIGHT network for hadron therapy in 2002.

In the same years, both the Medipix (7) and Crystal Clear (8) collaborations began exploring possible medical applications of technologies developed for the LHC detectors (hybrid silicon pixel detectors and scintillating crystals, respectively). The Crystal Clear Collaboration developed various PET scanners with variable geometry suitable for both small and large animals. One of them became commercially available to customers worldwide.

Emerging interest in theranostics, i.e., the possibility to perform both imaging and treatment at the same time, has brought radioisotopes for medical use under the spotlight. For the past 50 years, CERN has been hosting ISOLDE, a facility dedicated to the production of a large variety of radioactive ion beams for different experiments in the fields of nuclear and atomic physics, solid-state physics, materials science, and life sciences. Over 1,200 radioisotope beams of more than 70 chemical elements have been made available for fundamental and applied research, including in the medical field. A particular achievement was the demonstration of the efficiency of ^{149}Terbium, one of the lightest alpha emitters, for treatment at the level of single cancer cells (9).

The CERN Medical Applications Office

For several decades, there have been highly successful individual "pockets" of medical technology developments going on at CERN, as well as in the physics communities that have strong formal collaborations with the laboratory. These efforts had considerable success, and the CERN researchers have also been playing key roles in various international multidisciplinary collaborations and networks in specific fields (such as medical imaging, hadron therapy, radioisotopes, data analytics and handling, medical simulations). But a profound shift in the global approach of the laboratory to the whole issue of knowledge transfer to healthcare was needed.

The laboratory shifted a gear in January 2014 by establishing the CERN Medical Applications (CMA) office (10) with the following main goals:

- identify, make available, and foster the applicability of the CERN's core technologies in accelerators, detectors, simulation, large-scale computing, and data handling that are pertinent to medical applications;
- co-ordinate and structure related activities within the organization;
- catalyze collaborations with external partners, including industry, in a concerted manner.

For the first time in the history of the laboratory, a small amount of "seed" funding and manpower resources for medical applications activities was assigned in the Medium Term (5 year) Plan.

The challenge and aim for the CMA Office is to ensure that state-of-the-art technologies and know-how developed at CERN are used or modified to provide clinical applications that are valuable for the medical community. In order to achieve this goal, the laboratory must prioritize its R&D program for medical applications according to the main concerns and needs of doctors. At the same time, resources for this program should be allocated without compromising particle physics research, which is the core mission of CERN. This process requires the input and guidance of external experts from various disciplines. In keeping with the tried and tested CERN practice, an advisory committee composed of external experts was formed. The committee, called the International Strategy Committee (ISC), comprises specialists from a wide range of medical fields as well as from medical physics. Internally, the Head of the CMA Office is assisted by the CERN Medical Applications Steering Group (CMASG), comprised CERN scientists leading CERN's projects in the field, as well as of experts from the CERN Knowledge Transfer group and the CERN EU office.

As a first step, the CMA Office identified the key medical physics activities that were already ongoing or were just starting. They included a variety of topics: tools for data handling and data analytics, detectors for medical imaging, radiation dosimetry instruments and techniques, novel accelerators for optimized cancer treatment, facilities for researching new radioisotopes or for biomedical studies, and the vast realm of non-cancer applications.

The ultimate scientific goal of the CMA program is to provide more reliable, more efficient, and more cost-effective treatment options, as well as to ensure early diagnosis of serious illnesses.

PARTICLE THERAPY

The idea of using accelerated beams of protons for cancer treatment was proposed by a visionary physicist and founder of Fermilab, Robert Wilson in 1946 (11). Protons and light ions have unique physical properties. They penetrate a patient with minimal lateral diffusion, depositing most of their energy at the end of their range (in the so-called Bragg peak), effectively sparing healthy tissue on their way to the tumor. In addition, they can be focused into narrow pencil beams allowing a precise radiation dose profile and tumor conformed treatment.

This idea was first tested at the Lawrence Berkeley National Laboratory (LBNL) (12). At the time, the accelerators available were not powerful enough to treat deep-seated tumors. Advancement in accelerator technology coupled with improved medical imaging and computing made proton therapy a viable option for routine medical applications in the 1970s. However, it is only since the 1990s that patients started being treated in clinical settings. The first hospital-based facility to treat patients was at Loma Linda, USA. Since protons are hadrons, proton therapy is also referred to as hadron therapy.

The use of ions increases target conformity on the basis of physics principles, i.e., the dose distribution. In this respect, carbon ions have a smaller lateral penumbra than protons, which may allow a better protection of normal tissue. Also, carbon ions have a higher linear energy transfer (LET) compared to protons and photons, which directly correlates with a higher relative biological effectiveness (RBE). LET of carbon ion beams increases steadily as they pass through the body, reaching a maximum in the Bragg peak region: this property is an obvious therapeutic advantage when treating deep-seated tumors. Carbon ions are also more efficient in hypoxic tumors, which are resistant to both photon and proton radiation. The lower acute or late toxicity of carbon ions compared to protons leads to an enhanced quality of life both during and after cancer treatment (13).

The first dedicated carbon ion facility became operational in 1994 at the Heavy-Ion Medical Accelerator Centre (HIMAC) in Japan (14, 15). In Europe, the first patient was treated with carbon ions at the Gesellschaft für Schwerionenforschung (GSI) laboratory in Darmstadt, Germany, in 1997 (16).

With the growing interest in particle therapy, the first dual ion (protons and carbon ions) clinical facility in Europe, established in Heidelberg, Germany, started treating patients at the end of 2009. This was followed by CNAO in Pavia, Italy, which started treating patients in 2011. The third dual ion center in Europe at MedAustron in Wiener Neustadt, Austria, is expected to start treating patients in 2016.

CERN AND PARTICLE THERAPY

CERN has been playing an active role in hadron therapy with the design of a dedicated synchrotron for protons and carbon ions (PIMMS) and the involvement in ENLIGHT. At present, efforts in hadron therapy are focused on establishing a facility to provide ion beams for research.

The Proton Ion Medical Machine Study

The PIMMS group was formed following an agreement between the MedAustron (Austria) and the TERA Foundation (Italy) to combine their efforts in the design of a cancer therapy synchrotron. The study group was later joined by Onkologie 2000 (Czech Republic). CERN agreed to host this study in its PS Division; the PIMMS team started their work in January 1996, and continued working for a period of 3 years.

Proton Ion Medical Machine Study aimed at producing a synchrotron design optimized for treating cancer patients with protons and carbon ions. The proposed design was detailed in two reports issued in 2000 (17). The PIMMS concept was further enhanced by TERA, and implemented at CNAO and MedAustron. Except the initial design study, CERN has also contributed to the realization of the CNAO and MedAustron treatment centers, in particular with expertise in accelerators and magnets, and with training of personnel. Both projects have been accomplished through networks of national and international collaborations.

OPEN-Access MEDical Facility

The need for an open-access facility for R&D with ion beams in the context of medical applications was first raised at the ENLIGHT meeting in 2005 in Oropa, Italy. This was reiterated by a wide multidisciplinary scientific community at the 2010 Physics for Health workshop, where CERN was asked to take a lead on this initiative. In order to establish OPENMED (OPEN-Access MEDical Facility), the possibility of modifying the existing CERN low energy ion ring (LEIR) accelerator was evaluated in the open brainstorming session in 2012. Again, the broad positive feedback from the medical and radiobiological communities was received (18).

OPEN-Access MEDical Facility intends to provide suitable ion beams for a multitude of interdisciplinary studies, including radiation biology, nuclear physics models for medicine, detectors and instrumentation for dosimetry, diagnostics, and imaging. OPENMED will complement a few existing or planned beam lines for this kind of multidisciplinary research, providing ample beam time without the constraints of a clinical setting. Ideally, all centers hosting research beam lines should form a pan-European collaborative network that will allocate beam time to researchers in an effective and concerted way.

The cost of establishing such a facility entirely dedicated to the R&D with ion beams for the medical community will be significantly less at CERN than in a place that lacks the accelerator chain, the expertise to maintain it, and the general infrastructure needed to host the research purposes (see **Figure 2**). The project entails

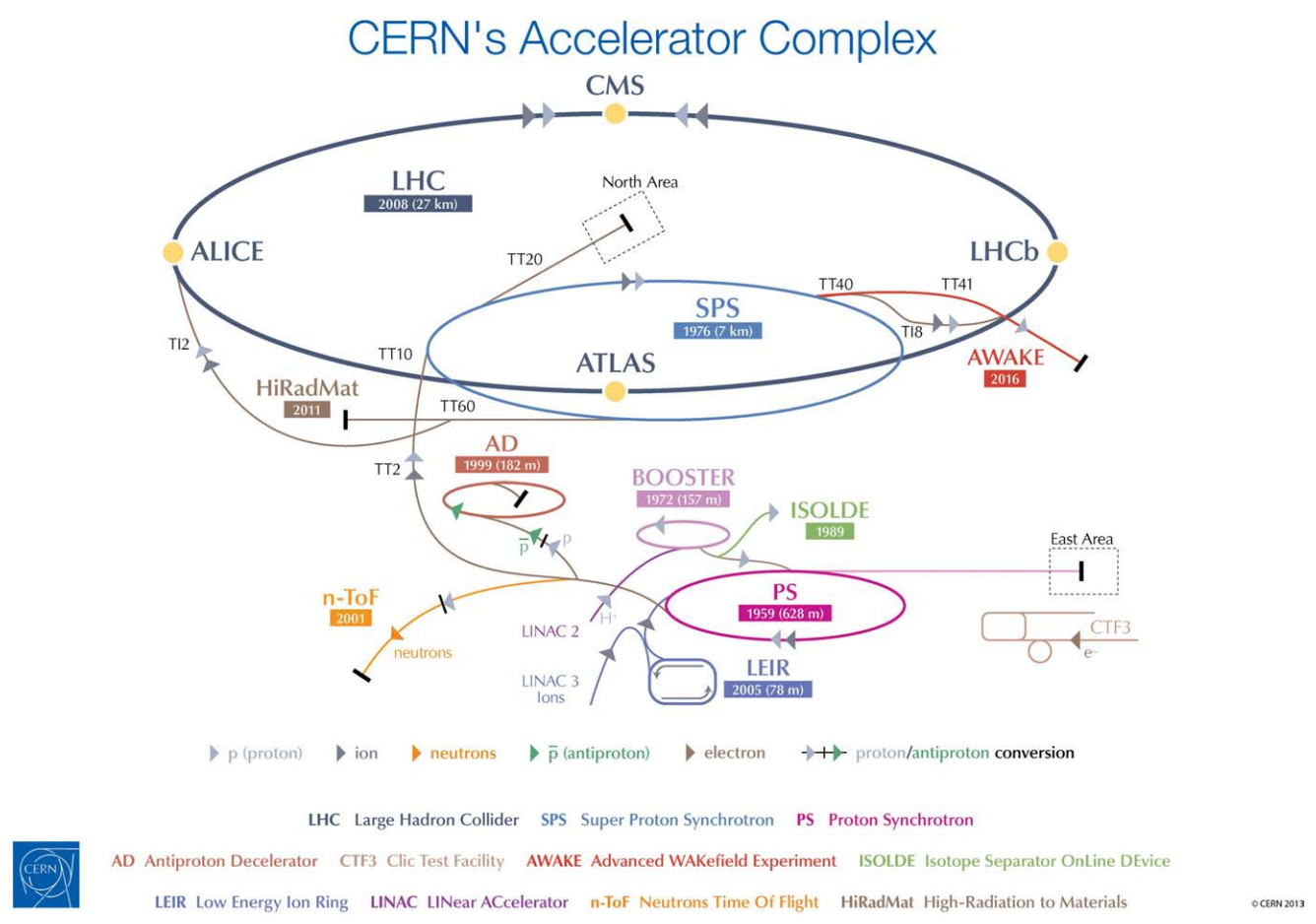

FIGURE 2 | CERN's accelerator chain. The proposed OPENMED facility would use beams from the existing LEIR machine.

modifications of the existing LEIR accelerator, which is currently being used for 1 month a year to inject heavy ions into the LHC. The beam energy and size, and its capability of providing up to 9 months of beam time per year, make LEIR an ideal candidate for conversion into OPENMED, which will run without perturbing the scheduled LHC operation (19).

Research at OPENMED will make a significant contribution to the progress of medical physics, biomedical research, medical simulations, and the development of innovative detectors and beam instrumentation.

Studies at OPENMED will ultimately lead to a more safe, optimal, and cost-effective treatment of cancer with radiation. Medical and radiobiological collaborators will be able to investigate the biological impact of different ion beams at various energies on tumor cells and biological materials, and then to optimize radiation therapy for different types of cancer. The research will be carried out on cell cultures and tissues, and it is not foreseen to conduct live animal or human experiments.

In fact, the impressive ion beam radiobiology experiments have been performed over the past 50 years. They were fragmented in time and were performed with different beam qualities and cell systems. All of them need to be systematically reexplored in one single setting, under standardized dosimetry and laboratory conditions, in larger panels of biologically well-characterized human cancer and normal tissue cell systems. The ultimate gain would be a comprehensive model that can individualize therapy, incorporating clinical, biological and physics inputs. Also, it is imperative to develop state-of-the-art instrumentation and methods to bring the performance of hadron therapy to the level of the most advanced photon therapy techniques.

OPEN-Access MEDical Facility will offer ample opportunities for testing novel radiation detectors, medical instrumentation, optimized delivery of the therapeutic beam to patients, diagnostics, and dosimetry. The experimental verification and improvement of biological simulation models will also be possible, along with the studies of complex processes such as nuclear fragmentation.

Experiments at OPENMED will be selected by a panel of experts and carried out within the international collaborations, capitalizing on CERN's culture of scientific openness, and attracting experts from a variety of fields. OPENMED will become a hub for interdisciplinary exchange, offering R&D opportunities for research in medical radiation biology as well as for the development of a wide portfolio of particle physics techniques, which may be translated into medical applications: detectors, simulation, accelerators, simulation, data handling, and data analytics. These activities would complement other work elsewhere, and contribute to boost the impact of particle physics research on healthcare (20).

ENLIGHT – THE EUROPEAN NETWORK FOR LIGHT ION HADRON THERAPY

Hadron therapy is the epitome of a multidisciplinary and transnational venture: its full development requires the competences of physicists, physicians, radiobiologists, engineers, and IT experts, as well as collaboration between research and industrial partners. ENLIGHT was established to co-ordinate European efforts in using ion beams for radiation therapy and to catalyze collaboration and co-operation among the different disciplines involved (21). ENLIGHT had its inaugural meeting in February 2002 at CERN and was funded by the European Commission (EC) for its first 3 years (2002–2005).

Despite the end of EC funding in 2005, the following year the network members decided to maintain ENLIGHT alive, with the primary mandate to develop strategies to obtain the necessary funding for hadron therapy research, and to establish and implement common standards and protocols for treating patients. Since then, the co-ordination office has been run at CERN. The current membership exceeds 400 participants from more than 20 countries across Europe.

While the network itself flourishes without the dedicated funding, the R&D activities have been funded primarily through EC projects.

Between 2008 and 2015, four EC projects have been started under the umbrella of ENLIGHT, for a total funding of 24 million Euro: PARTNER, ULICE, ENVISION and ENTERVISION. All these projects are directed toward different aspects of developing, establishing, and optimizing hadron therapy (22).

The Particle Training Network for European Radiotherapy (PARTNER) was a 4-year Marie Curie Training project aimed at educating young biologists, engineers, radio-oncologists, and physicists in the various aspects of hadron therapy. PARTNER provided research and training opportunities for 29 young scientists from a variety of backgrounds and countries between 2008 and 2012, allowing them to actively develop modern techniques for treating cancer in close collaboration with the leading European institutions.

The Union of Light Ion Centres in Europe (ULICE) was an infrastructure project which started in 2009 in response to a need for greater access to hadron therapy facilities for clinical and technological research (see **Figure 3**). The project was built

FIGURE 3 | The ENLIGHT network. Group picture of the participants to the 2011 ENLIGHT meeting at the Marburg facility, which will start treating patients soon.

around three pillars: development of instruments and protocols; increasing co-operation between facilities and research communities within the research infrastructure; and transnational access to treatment centers.

A key challenge in particle therapy today is quality assurance during treatment, which needs advanced medical imaging techniques. This issue has been tackled by the ENVISION project, which started in 2010 and covered developments in time-of-flight in-beam PET, in-beam single particle tomography, organ motion monitoring techniques, simulation, and treatment planning. Additionally, ENVISION served as the training platform for ENTERVISION, a Marie-Curie Initial Training Network aimed at educating young researchers in online 3D digital imaging.

Future Priorities and Challenges

Since the annual meeting in summer 2014, the ENLIGHT community has started discussing the future of the network, in terms of both structure and scientific priorities. It is clear that the focus of R&D for hadron therapy has shifted since the birth of ENLIGHT. It is because the number of clinical centers (and especially centers with proton therapy) has dramatically increased (see **Figures 4** and **5**). Also, while technology developments are still needed in order to ensure increasing accuracy and more cost efficient treatment, further development of proton therapy is now solidly in the hands of industry. The advent of single-room facilities will bring proton therapy, albeit with some restrictions, to smaller hospitals and clinical centers.

From the clinical standpoint, a large number of facilities worldwide would allow the medical community to perform randomized trials to optimize hadron therapy. However, it should be noted that there is a certain reluctance within the hadron therapy community to begin clinical trials from scratch, since a large number of patients has been now treated with both protons and carbon ions, with quite positive results for the main indications. In addition, most of the patients who contact a hadron therapy center are well informed about the treatment, and they expect to be treated with particles.

From the clinical standpoint, the major challenges for ENLIGHT in the coming years will be, on the clinical side, to catalyze collaborative efforts in defining a roadmap for randomized trials (23) and in studying the issue of RBE in details. The efforts concerning technology developments will be continued on quality assurance through imaging and on the design of compact accelerators and gantries for ions heavier than protons. Information technologies will take a central stage, since medical data sharing, data analytics, and decision support systems for patient and treatment selection are key topics.

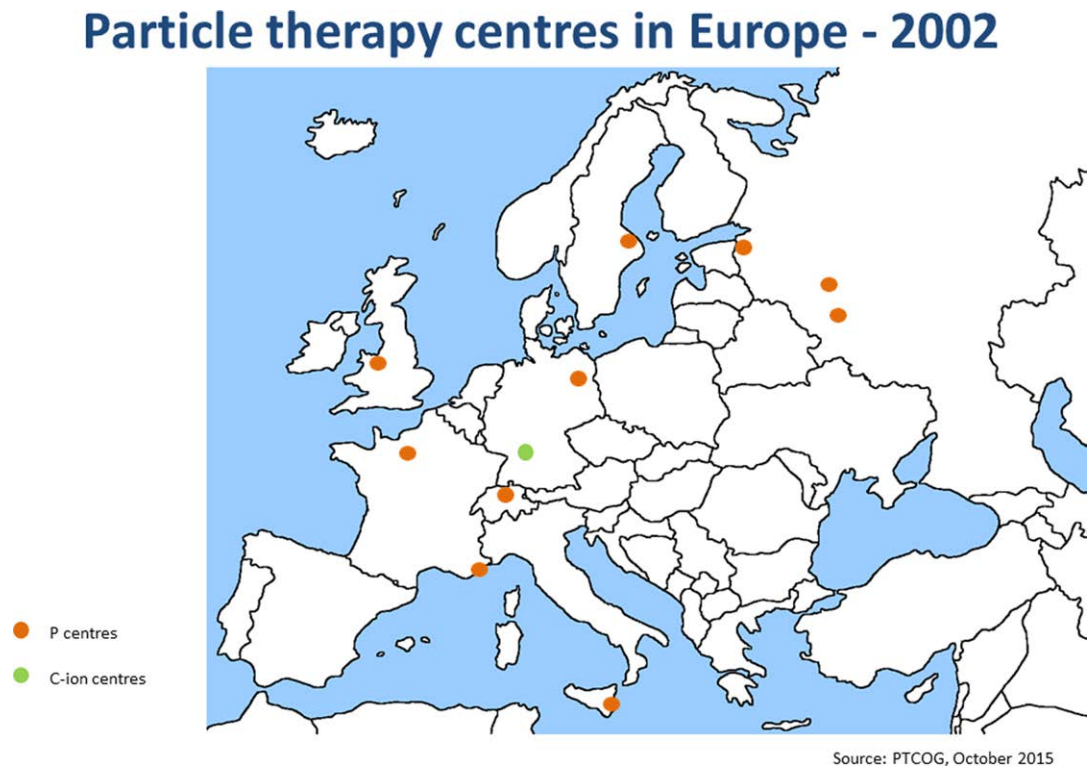

FIGURE 4 | Hadron therapy centers in Europe in 2002. This picture shows the distribution and number of hadron therapy centers when ENLIGHT was started.

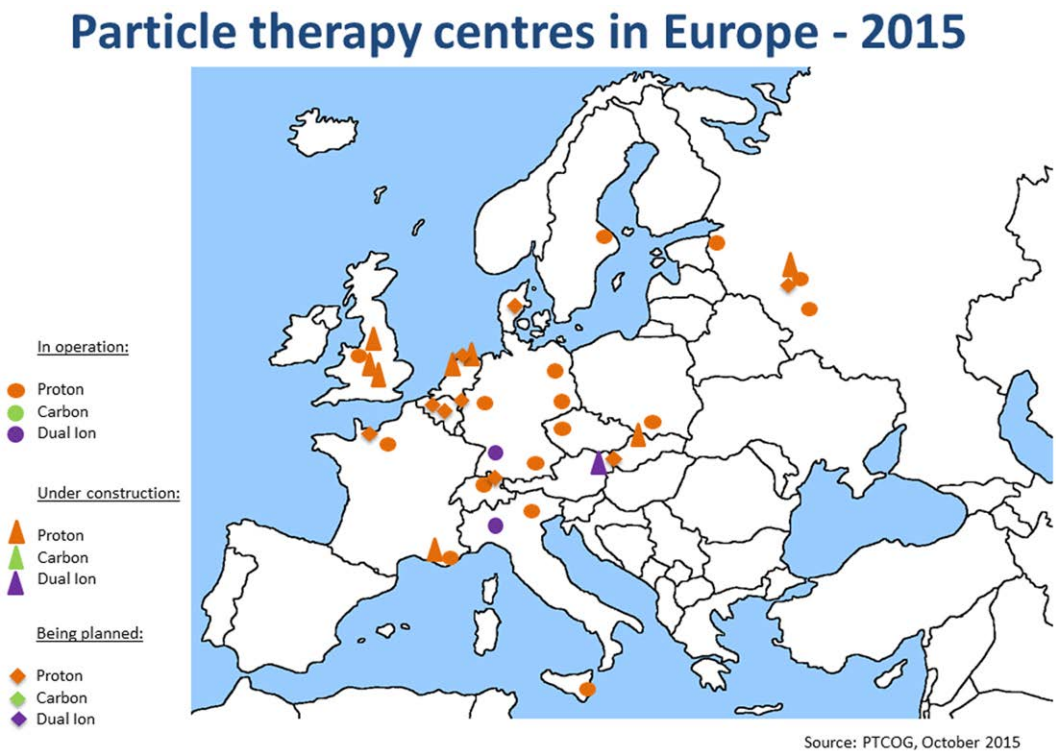

FIGURE 5 | Hadron therapy centers in Europe in September 2015. This picture shows the present distribution and number of hadron therapy centers.

Providing training will be a major focus in the coming years, as the growing number of facilities requires more and more trained personnel: the aim will be to train professionals who are highly skilled in their specialty but at the same time are familiar with the multidisciplinary aspects of hadron therapy.

CONCLUSION

Cross-fertilization between particle physics and medicine continues to be important for improved healthcare. This process needs to be fueled through multidisciplinary exchanges, and geared toward the needs of the medical community. Since 2014, CERN has begun structuring its medical applications activities and has established an international panel of medical and technical experts to assist the laboratory in setting priorities and choosing the future R&D directions.

This paper focuses on the activities related to hadron therapy. CERN has a tight bond with ENLIGHT, since the launch of the network in 2002. ENLIGHT has been very successful in gathering funds for hadron therapy research across Europe and has catalyzed a number of successful projects and collaborations. At present, the ENLIGHT community is establishing a roadmap for the future, taking into account the changes that occurred in the hadron therapy landscape in the past few years.

AUTHOR CONTRIBUTIONS

MD – ENLIGHT co-ordinator and CERN Medical Applications deputy, MC – Communication and dissemination officer for CERN Medical Applications, SM – Head of CERN Medical Applications, and SN – Technical contributions to CERN Medical Applications and ENLIGHT activities.

ACKNOWLEDGMENTS

The authors wish to thank the members of the CERN CMASG and ISC, and the ENLIGHT community.

FUNDING

ULICE was funded under European Commission Grant Agreement Number 228436. PARTNER was funded under Grant Agreement Number 215840. ENVISION was funded under Grant Agreement Number 241851. ENTERVISION was funded under Grant Agreement Number 264552.

REFERENCES

1. Boisot M, Nordberg M, Yami S, Nicquevert B. *Collisions and Collaborations: The Organization of Learning in the ATLAS Experiment at the LHC*. Oxford: Oxford University Press (2011). 315 p.
2. Boussard JM, Oppenheim C, Charpak Y, Kalifa G. Professor Charpak's numerical radiology apparatus: principles and functioning. *J Radiol (Paris)* (1995) **76**(10):931;43.
3. Kalifa G, Charpak Y, Maccia C, Fery-Lemonnier E, Bloch J, Boussard JM, et al. Evaluation of a new low-dose digital X-ray device: first dosimetric and clinical results in children. *Pediatr Radiol* (1998) **28**(7):557–61. doi:10.1007/s002470050413
4. Schorr B, Townsend D, Clack R. A general method for three-dimensional filter computation (positron emission tomography application). *Phys Med Biol* (1983) **28**(9):1009–19. doi:10.1088/0031-9155/28/9/001
5. Schorr B, Townsend D. Filters for three-dimensional limited-angle tomography. *Phys Med Biol* (1981) **26**(2):305–12. doi:10.1088/0031-9155/26/2/009
6. Townsend D, Frey P, Donath A, Clack R, Schorr B, Jeavons A. Volume measurement in vivo using positron tomography. *Nucl Instrum Methods Phys Res* (1984) **221**(1):105–12. doi:10.1016/0167-5087(84)90188-1
7. The Medipix Collaboration. Available from: http://cern.ch/medipix
8. The Crystal Clear collaboration. Available from: http://cern.ch/crystalclear
9. Müller C, Reber J, Haller S, Dorrer H, KösTer U, Johnston K, et al. Folate receptor targeted alpha-therapy using terbium-149. *Pharmaceuticals* (2014) **7**(3):353–65. doi:10.3390/ph7030353
10. *CERN Technologies for Medical Applications: Status Report, 17th Session of CERN Council.* (2015). Report No. CERN/3206. Available from https://cds.cern.ch/record/2054105?ln=en
11. Wilson RR. Radiological use of fast protons. *Radiology* (1946) **47**(5):487–91. doi:10.1148/47.5.487
12. Lawrence JH, Tobias CA, Born JL, McCombs RK, Roberts JE, Anger HO, et al. Pituitary irradiation with high-energy proton beams: a preliminary report. *Cancer Res* (1958) **18**(2):121–34.
13. Schlaff CD, Krauze A, Belard A, O'Connell JJ, Camphausen KA. Bringing the heavy: carbon ion therapy in the radiobiological and clinical context. *Radiat Oncol* (2014) **9**:88. doi:10.1186/1748-717X-9-88
14. Hirao Y, Ogawaa H, Yamadaa S, Satoa Y, Yamadaa T, Satoa K, et al. Heavy ion synchrotron for medical use – HIMAC project at NIRS-Japan. *Nucl Phys A* (1992) **538**:541–50. doi:10.1016/0375-9474(92)90803-R
15. Yamada S. *Proceedings of PAC95*. Dallas (1995). Available from: http://epaper.kek.jp/p95/ARTICLES/MAD/MAD03.PDF
16. Kraft G, Badura E, Becher W, Böhne D, Brand H, Brusasco H et al. First patient treatment at GSI with heavy ions. In: *Proceedings of Joint Accelerator Conferences* (1998). Available from: http://accelconf.web.cern.ch/AccelConf/e98/PAPERS/FRX02A.PDF
17. Badano L, Benedikt M, Bryant PJ, Crescenti M, Holy P, Maier AT et al. *Proton-Ion Medical Machine Study (PIMMS) Report*. Accelerator Complex Study Group supported by the Med-AUSTRON, Onkologie-2000 and the TERA Foundation and Hosted by CERN. Available from: https://cds.cern.ch/record/385378?ln=en; https://cds.cern.ch/record/449577/
18. Dosanjh M, Jones B, Myers S. A possible biomedical facility at the European Organization for Nuclear Research (CERN). *Br J Radiol* (2013) **86**:20120660. doi:10.1259/bjr.20120660
19. Abler D, Garonna A, Carli C, Dosanjh M, Peach K. Feasibility study for a biomedical experimental facility based on LEIR at CERN. *J Radiat Res* (2013) **54**:i162–116. doi:10.1093/jrr/rrt056
20. Holzscheiter MH, Bassler N, Dosanjh M, Singers Sørensen B, Overgaard J. A community call for a dedicated radiobiological research facility to support particle beam cancer therapy. *Radiother Oncol* (2012) **105**:1–3. doi:10.1016/j.radonc.2012.08.005
21. Dosanjh M, Cirilli M, Greco V, Meijer AE. The European network for light ion hadron therapy. *J Health Phys* (2012) **103**(5):674–80. doi:10.1097/HP.0b013e3182606520
22. Dosanjh M, Jones B, Mayer R. ENLIGHT and other EU-funded projects in hadron therapy. *Br J Radiol* (2010) **83**:811–3. doi:10.1259/bjr/49490647
23. Combs SE, Dosanjh M, Pötter R, Orecchia R, Haberer T, Durante M, et al. Towards clinical evidence in particle therapy: ENLIGHT, PARTNER, ULICE and beyond. *J Radiat Res* (2013) **54**:i6–12. doi:10.1093/jrr/rrt039

Conflict of Interest Statement: The authors declare that the research was conducted in the absence of any commercial or financial relationships that could be construed as a potential conflict of interest.

Copyright © 2016 Dosanjh, Cirilli, Myers and Navin. This is an open-access article distributed under the terms of the Creative Commons Attribution License (CC BY). The use, distribution or reproduction in other forums is permitted, provided the original author(s) or licensor are credited and that the original publication in this journal is cited, in accordance with accepted academic practice. No use, distribution or reproduction is permitted which does not comply with these terms.

frontiers in Oncology

ORIGINAL RESEARCH
published: 11 August 2015
doi: 10.3389/fonc.2015.00184

A simpler energy transfer efficiency model to predict relative biological effect for protons and heavier ions

*Bleddyn Jones**

Gray Laboratory, CRUK/MRC Oxford Insitute for Radiation Oncology, University of Oxford, Oxford, UK

The aim of this work is to predict relative biological effectiveness (RBE) for protons and clinically relevant heavier ions, by using a simplified semi-empirical process based on rational expectations and published experimental results using different ion species. The model input parameters are: Z (effective nuclear charge) and radiosensitivity parameters α_L and β_L of the control low linear energy transfer (LET) radiation. Sequential saturation processes are assumed for: (a) the position of the turnover point (LET_U) for the LET–RBE relationship with Z, and (b) the ultimate value of α at this point (α_U) being non-linearly related to α_L. Using the same procedure for β, on the logical assumption that the changes in β with LET, although smaller than α, are symmetrical with those of α, since there is symmetry of the fall off of LET–RBE curves with increasing dose, which suggests that LET_U must be identical for α and β. Then, using iso-effective linear quadratic model equations, the estimated RBE is scaled between α_U and α_L and between β_U and β_L from for any input value of Z, α_L, β_L, and dose. The model described is fitted to the data of Barendsen (alpha particles), Weyrather et al. (carbon ions), and Todd for nine different ions (deuterons to Argon), which include variations in cell surviving fraction and dose. In principle, this new system can be used to complement the more complex methods to predict RBE with LET such as the local effect and MKM models which already have been incorporated into treatment planning systems in various countries. It would be useful to have a secondary check to such systems, especially to alert clinicians of potential risks by relatively easy estimation of relevant RBEs. In clinical practice, LET values smaller than LET_U are mostly encountered, but the model extends to higher values beyond LET_U for other purposes such as radiation, protection, and astrobiology. Considerable further research is required, perhaps in a dedicated international laboratory, using a basket of different models to determine what the best system or combination of systems will be to make proton and ion beam radiotherapy as safe as possible and to produce the best possible clinical results.

Keywords: RBE, protons, ions, radiotherapy, radiobiology

OPEN ACCESS

Edited by:
Brian Timothy Collins,
Georgetown University Hospital, USA

Reviewed by:
Dalong Pang,
Georgetown University Hospital, USA
Kevin Prise,
Queen's University Belfast, UK

***Correspondence:**
Bleddyn Jones,
Gray Laboratory, CRUK/MRC Oxford Insitute for Radiation Oncology,
University of Oxford,
Oxford OX3 7DQ, UK
bleddyn.jones@oncology.ox.ac.uk

Specialty section:
This article was submitted to Radiation Oncology, a section of the journal Frontiers in Oncology

Received: *13 May 2015*
Accepted: *27 July 2015*
Published: *11 August 2015*

Citation:
Jones B (2015) A simpler energy transfer efficiency model to predict relative biological effect for protons and heavier ions. Front. Oncol. 5:184. doi: 10.3389/fonc.2015.00184

Introduction

Positively charged particle therapy is increasing worldwide. Its numerous potential advantages in cancer therapy depend on the Bragg peak effect (1–4), but the increase in linear energy transfer (LET) causes enhanced biological effects which change normal tissue tolerances, as well as tumor control probabilities. LET, typically reported as kiloelectron volt per micrometer, refers to the ratio

of energy released from a radiation beam per unit micrometer track length and is used as a measure of radiation quality. It can be expressed in two different ways, either as the mean or the dose averaged LET. Relative biological effect (RBE) is defined as the ratio of dose of a low LET radiation divided by the control high LET dose required for the same biological effect. RBE, although measured quite simply in this way, depends on the complexities of how radiation of different qualities interact with different biological systems due to:

(1) The energy, depth, and mixture of Bragg peak or non-Bragg peak regions over a volume of interest.
(2) The increased local complexity, or clustering, of DNA damage with increasing LET (5).
(3) The increasing difficulty in repairing the more clustered damage, resulting in increased radiosensitivity and reduced fractionation sensitivity.

Some authors have developed relatively simple LET–RBE models for protons (6–8). For ion beams, there are several complex formulations that tentatively describe the relationship between LET and RBE (9–14), each with varying degrees of success, and have been used for clinical applications. These ion beam models are based on the fundamental interactions of particle physics with matter and contain multiple assumptions and input requirements, such as knowledge of particle trajectories relative to cells, cross sectional probabilities, the relative proportion of cell nucleus to cell volume for each cell, critical biological sub-volumes, repair capacities, and extrapolations with dose, etc. They all utilize long mathematical constructs which can be daunting to less mathematically gifted individuals. Whereas it is satisfying to build exploratory theoretical models in such a way, it is impossible to know these exact conditions within a real cancer and surrounding normal tissues. These various approaches have been used to predict ion beam RBE values for variable LET values for the irradiation of specific cell types (usually the V-79 cell derived from Chinese Hamsters), but with mixed results, although they are used routinely in clinical practice for carbon ion treatment planning. Only some authors have attempted an approach for normalizing the RBE differences between different ions, as in the work of Katz (9), who used the parameter Z^2/β^2 to calculate the radial distribution of dose (where Z is nuclear charge and β is the relativistic velocity).

What do we know with certainty about LET and RBE? Measured relationships between LET and RBE generally show increases with LET until a maximum value is achieved, followed by a decrease to RBE values just above unity. Also, there are important basic findings, shown by multiple authors (15–18), which are essential to incorporate into any model that adequately describes the change of RBE changing with LET. They are:

- The initial slope of RBE with LET is linear when plotted on linear scales (19).
- The LET value (LET_U) which confers the maximum cell killing efficiency (at the turnover point) increases non-linearly with the nuclear charge of a particle (the Z number), which denotes the electrostatic positive charge of the particle nucleus. LET_U values increase with Z, but smaller increments in LET_U occur with increasing Z, which suggests a saturation effect. Ions with the smallest Z values are consequently more efficient in increasing RBE per unit increase in LET, possibly because the energy released is more locally absorbed than is the case for higher Z ions with larger event sizes and more energetic gamma emissions.
- The magnitude of the RBE is not only dependent on the particle type (or Z), but also depends on LET, dose (and so the surviving fraction of cells), and the cell type (and its ability to repair radiation damage).
- The magnitude of the RBE depends on cell type (seemingly regardless of the ion used), with cells that are intrinsically more radiosensitive (to very low LET radiations) having lower RBEs than their more radio-resistant counterparts.
- The RBE increases when the cell-surviving fraction is reduced (for lower doses), but the LET–RBE turnover point position remains constant. Thus, the overall symmetry is preserved.
- In terms of the linear quadratic model (LQ) of radiation effect, the α value increases with LET to a far greater extent than β (20–22). The relative increase in α with LET is greatest for cells/tissues which have the lowest, most radio-resistant, low LET α_L values, with smaller increases in α for systems which have the most radiosensitive, highest intrinsic α_L values, as will be shown later.
- These experimental findings apply to well-oxygenated cells, but are modified in radiologically hypoxic conditions (16), probably since the α parameter-related cell kill is not so influenced by oxygen as is the β parameter-related cell kill.

This article considers how a much "simpler LET efficiency model" can estimate the LET–RBE relationships described above and their modification with dose, Z, and the two low LET intrinsic radiosensitivities α_L and β_L. These models require fewer input parameters and assumptions than do the far more complex models already referred to above. Such a model could be used to complement the other systems: in this sense, two predictions may carry more reliability if they are in close agreement.

Materials and Methods

The Experimental Data

There are relatively few published experiments that provide a reasonable estimate of LET turnover positions (LET_U) for clinically used particles. These include the data sets of Belli et al. (18), Barendsen et al. (15), Furusawa et al. (16), and Weyrather et al. (17). These experiments were not designed to accurately determine LET_U, but to show overall phenomena and to determine the range of RBE values. Inevitably, overall accuracy is further undermined by biological variation, use of different cellular assays in various laboratories, use of different LET interpretations and measurements over wide ranges with consequent use of a logarithmic scaled abscissa, which masks the uniform initial linear slope of the relationship. To obtain the best available estimate of LET_U, only the most unequivocal examples of maximum radiosensitivities, or RBE, over a small range of LET near to LET_U, were used. Data where LET_U could not be determined to reasonable accuracy, as in some of the HRG cellular data of Furusawa et al. (16) and in

some carbon ion experiments, were excluded. The LET_U values (keV/μm) so obtained were 30.5 (protons), 103.4 (helium), 208 (carbon), and 233 (neon). Although data exist for heavier ions such as silicon and argon, these do not provide a sufficiently accurate estimate (23).

For model fitting, the experimental studies of Todd (24), using a wide range of ions (deuterons, helium, lithium, boron, carbon, oxygen, nitrogen, neon, and argon), of Barendsen (deuterons and helium) (15), and of Weyrather et al. (carbon) (17) were used to test data against the modeled predictions.

The highest α radiosensitivity obtained (α_U), in the region of LET_U, for each ion species, was plotted against the low LET (control) α_L value from the same data. These values are shown in later graphical plots, and include variation due to the LET_U position uncertainty. The accuracy of the β radiosensitivity parameter is less easy to determine for high LET radiations (compared with low LET radiations), for reasons discussed elsewhere (8, 22). It is known that β increases to a lesser extent than α with LET. In order to maintain the observed constant position of LET_U with increasing dose (and reduced surviving fraction), and the overall symmetry of the LET–RBE relationship, both α and β must follow similar functions which rise to a maximum at LET_U. Otherwise, the overall symmetry of the LET–RBE curves with increasing dose would be broken: for example, if LET_U would be different for α and β, the LET_U would be observed to change with dose, which is not the case.

Detailed Description of Model

The turnover of RBE with LET, is a well-reported phenomenon often attributed to "overkill" or wasted local dose. This process can be interpreted as increasing efficiency of cell kill in the upward phase, followed by later inefficiency. In physics terms, the number of particle trajectories crossing a cell reduces by a reciprocal function of increasing LET after the turnover point. This is necessary in order to maintain the same overall dose to a wider volume with increasing LET. At the same time, increasing LET produces greater clustering of dose deposition, but over-clustering will not necessarily lead to enhanced biological effects. In bio-physical terms, increasing LET must, initially, enhance the intrinsic radiosensitivity parameters, the increment in α far exceeding that in β (25). This is because a greater proportion of more clustered damage is non-repairable by the non-homologous end joining process, although the repair of sub-lethal damage (within the more sparsely clustered damage regions) continues, although probably with lower fidelity, and even the recombination repair mechanism may also be overwhelmed by increasingly complex lesions affecting the same sites on sister chromatids.

Ionizing radiation damage in biological systems causes a hierarchy of effects: the most commonly occurring DNA base change and single strand breaks are followed by less frequent double strand breaks, nearly all of which are repaired in the case of low LET radiation. An excess of a mixture of these forms of damage in a locality of a chromosome can lead to a chromosome break, certain types of which inevitably confers lethality. Thus, the essential lesion is the "lethal" form of chromosome break (LCB) for most forms of radiation cell death at clinical doses. The local deposition of energy that results in the maximum probability of a single LCB must represent the maximum efficiency of the system, since further energy deposition and greater DNA and chromosomal structural change in the same locality will result in no extra effect; in fact any dose deposited in excess of that required to achieve a LCB will be "wasted dose," representing inefficiency, and is often referred to as the overkill effect.

On a local basis, with LET defined as being the energy deposited over a 1 μm section of track, this distance is appropriate for chromosomal radiation effects since it is roughly the width of a single chromosome.

Relationship between Z and LET_U

The position of the turnover point can be estimated for different Z values. It is apparent from publications quoted above (15–18) that LET_U increases with Z, but the effect appears to saturate (i.e., further increase in LET have diminishing returns as far as the LET_U value is concerned). The Betha–Bloch equation for estimating the rate of energy loss with distance (x) traversed (dE/dx), which represents LET, contains a Z^2 term in the numerator usually reflecting the charge of a fully electron stripped ion or proton. Larger Z values will also be associated with larger mass numbers and greater momentum with larger event volumes due to more complex nuclear collisions and energetic γ-ray emissions. Beyond the necessary critical dimension (be this radial or linear as a surrogate), biological killing efficiency will not increase if the event size becomes too large and physically beyond the individual chromosome. So, a saturation effect is to be expected. The smallest values of $Z = 1$ for a proton effectively reduces dE/dx, but the proton LET_U is only 30.5 keV/μm, suggesting that lighter charged particles exert more localized effects (caused by short range low energy secondary electrons). In this respect, the proton is more efficient at causing an increment in RBE with LET [but proton LET values are quite small, e.g., a LET of only 1–8 keV/μm in typical clinical exposures (26, 27) when using scanned proton beams may cause RBEs as high as 1.8 or more (8)].

The application of a simple differential equation can represent this process. Let us assume that Z is a continuous variable and if the initial rate of change in LET_U with Z is S and that this value then decreases in proportion to LET_U itself, representing a saturation effect controlled by the constant k, so that

$$\frac{d\mathrm{LET_U}}{dZ} = S - k \cdot \mathrm{LET_U} \tag{1}$$

which by integration of both sides and rearrangement leads to

$$\mathrm{LET_U} = S/k(1 - \mathrm{Exp}\,[\,-k(Z)\,], \tag{2}$$

where S/k represents the maximum possible value of LET_U.

Equation 2 can be normalized to the proton ($Z = 1$) LET_U of 30.5 keV/μm found by Belli et al. (16), so that for any Z a term $Z - 1$ is used such that:

$$\mathrm{LET_U} = 30.5 + S/k(1 - \mathrm{Exp}[-k(Z-1)]) \tag{3}$$

This equation is used for data fitting purposes.

Changes in Radiosensitivities with LET

By increasing LET gradually, from the control low LET value of say clinical 4–6 MV photons (X-rays), we obtain small increases in the probability of additional LCBs; the energy deposition becomes maximally efficient (let this be represented by 100% efficiency for normalization purposes), and at higher LET values beyond LET_U, the efficiency is reduced below 100% because of excess local energy deposition.

The separate relationship between α_L (the low LET control α value) and α_U (the value of α at the turnover point where $LET = LET_U$) also exhibits saturation effects. In other words, the increment in α with LET show diminishing returns, since the lowermost α_L values have the highest gain in α. This effect is found with fast neutrons and with charged particle data, as shown in the Section "Results" below.

For an initial slope of A and a rate constant j, the rate of change of α_U with α_L will fall in proportion to α_U, so that

$$\frac{d\alpha_U}{d\alpha_L} = A - j \cdot \alpha_U, \tag{4}$$

which leads after integration to:

$$\alpha_U = A/j(1 - \mathrm{Exp}\,[-j\alpha_L])\,. \tag{5}$$

The β parameter can either be modeled in a similar way but with smaller overall changes, or to simplify matters for tentative modeling purposes, it could be assumed to be invariant at low doses where β-related cell kill is small. The data of Weyrather et al. (17) show that β values rises from a control value of 0.026 Gy^{-2} to a maximum of 0.044 Gy^{-2} in V-79 cells, and likewise from 0.02 to 0.42 Gy^{-2} for the CHO cells (α/β value of 0.192 Gy^{-2} in one instance must be artifactual due to the fitting program), i.e., by up to a factor of around two, which is small compared to the maximum increments in α with LET of around 10. There is more abundant data for 64 MV fast neutrons where β undoubtedly increases (22). Although such neutron experiments will probably underestimate the maximum possible rise in α and β, since the neutron LET spectrum (and its average value) may not necessarily be close to the LET_U for an ionic beam. Nevertheless, further analysis of these data, which compare neutrons with megavoltage X-rays show fits of $\beta_{neu} = 1.54\ \beta_{x-ray}$ or β_{neu} 0.097 $[1 - \mathrm{Exp}\,(23.6\ \beta_{x-ray})$, as will be shown below]. The experimental variation in such data is considerable and the two fitted equations were obtained after elimination of: repair deficient cells (where $\alpha > 0.6\,Gy^{-1}$), or where neutron β values close to zero, or if the increment in β exceeded that in α (suggesting experimental artifact). It should be noted that α_U and β_U values will be higher than the maximum values obtained for fast (64 MV) neutrons, and so the neutron data cannot be used directly to determine RBE changes for ion beam data.

A similar "saturation" function, is used to link β_L with β_U, as given elsewhere (8):

$$\beta_U = (R/u) \cdot (1 - \mathrm{Exp}[-u\beta_L]). \tag{6}$$

Where $R = 2.5$ and $u = 25$, which provides a modest increase in b, and is compatible with the limited data discussed already, and with a maximum ceiling value of 0.1 Gy^{-2} for β_U.

Obtaining α_H and β_H values

In simple mathematical terms, a discontinuous or biphasic (efficiency followed by inefficiency) model can be used, where for LET values up to that of LET_U, increasing efficiency is represented as a linear simple proportional relationship, as used by Wilkens and Oelfke for protons (6), and where the α value at any LET higher than the control and lower than the turnover value will be

$$\alpha_H = \alpha_L + \frac{LET_x - LET_C}{LET_U - LET_C} \cdot (\alpha_U - \alpha_L) \tag{7}$$

where α_H is the α value at any particular LET value (LET_x) between the control and ultimate value of LET_x [which represents any LET value between the control value of LET_C (where α is α_L)] and LET_U, where the maximum α of α_U occurs.

For the initial linear portion of the relationship, there will be a uniform gradient of

$$\frac{\alpha_U - \alpha_L}{LET_U - LET_C} \tag{8}$$

between the value of LET_C and LET_U, which fulfills the requirement for linearity in this range of LET. It follows that, for example, if LET_C and LET_U are 1.2 and 120 KeV/μm respectively, with α_L and α_U of say 0.3 and 1.3 Gy^{-1}, then for a LET_x value of 60, the process is only (1.3–0.3)/(120–1.2) × (60–1.2), which is close to being 50% efficient, and for a LET_x of 90, the efficiency will be (1.3–0.3)/(120–1.2) × (90–1.2), which is close to 75% efficiency.

In this way, the efficiency of cell kill per unit dose will increase linearly with LET, leading up to maximum efficiency (defined as 100%) at LET_U.

For values of LET beyond the turnover point (where $LET > LET_U$), the additional energy transferred does not contribute to extra lethality, but is wasted. That is, the excess energy ($LET_x - LET_U$) beyond the optimal released energy is wasted. Consequently, inefficiency, expressed in energy terms by $(LET_x - LET_U)/LET_U$ increases. To express this in terms of efficiency, the relationship of: % efficiency = 100 − % inefficiency is used, and the α_H value is then scaled between α_U and α_C.

Accordingly, the equation for α_H for $LET > LET_U$ then changes to be:

$$\alpha_H = \alpha_L + \left(1 - \frac{LET_x - LET_U}{LET_U}\right) \cdot (\alpha_U - \alpha_L) \tag{9}$$

which effectively expresses the reduction in α with increasing LET. In this way, if LET_x is 180 and LET_U is 120, the value of α_U at the turnover point of 100% efficiency will fall to 1 − (180 − 120)/180, which provides around 67% efficiency. For a LET_x of 240, we obtain 1 − (240 − 120)/240, which is 50% efficient. These efficiencies are of course relative to a normalized value of 100% at the turnover point.

Similar equations are used to provide β_H, by proportionate scaling between β_L and β_U. These are obtained by simply replacement of α_L, α_H, and α_U by β_L, β_H, and β_U respectively in Eqs (7) and (9).

Reduction of RBE with Dose

The reduction in RBE with reduced surviving fraction and increasing dose is obtained by the solution of the following isoeffect equation for high and low LET radiations at a dose d_L and d_H, for low and high LET respectively:

$$\alpha_L d_L + \beta_L {d_L}^2 = \alpha_H d_H + \beta_H {d_H}^2 \tag{10}$$

The solution for d_L is then divided d_H to provide the RBE, as shown in other publications (8, 24, 25).

For clinical iso-effect calculations, the solution of the following biological effective dose (BED) equations are used for the low and high LET:

$$n\,d_L\left(1+\frac{d_L}{\left(\frac{\alpha}{\beta}\right)_L}\right)=m\,d_H\left(\mathrm{RBE}_{\mathrm{Max}}+\frac{\mathrm{RBE}^2_{\mathrm{Min}}\cdot d_H}{\left(\frac{\alpha}{\beta}\right)_L}\right),\quad(11)$$

where n and m are the respective numbers of fractions for the low and high LET.

The RBE parameters are replaced by LET (and the new parameters given in the sequence of equations described above) and then solved for d_H. Total doses to provide the same BED can then be calculated for different numbers of fractions.

Computer programs using Mathematica (Champagne, IL, USA) software were constructed using the above equations.

Results

The relationship between Z and $\mathrm{LET_U}$ shown in **Figure 1**, using pooled data for proton, helium, carbon, and neon ions (13–16), were fitted by Eq. (3).

The Clatterbridge fast neutron data (21), show the relationship between α_L (for values up to 0.8 Gy^{-1}) and α_H, and between β_L and β_H, are shown in **Figures 2A,B**, respectively. In each case, the linear and non-linear fits are not significantly different ($p > 0.05$), although the residuals are smallest for the non-linear equations, which also have the advantage of not extrapolating to infinitely high radiosensitivity values.

The relationship between α_L and α_U for various ions are shown in **Figure 3**, fitted to data from the literature [with data where negative β values obtained excluded]. The fitted equation is shown in the figure, but also with a least squares fit for a linear no-intercept relationship of $\alpha_U = 6.47\ \alpha_L$ ($p < 0.001$, $R^2 = 0.899$) for α_L values less than 0.35 Gy^{-1}, the more radio-resistant part of the radiosensitivity spectrum.

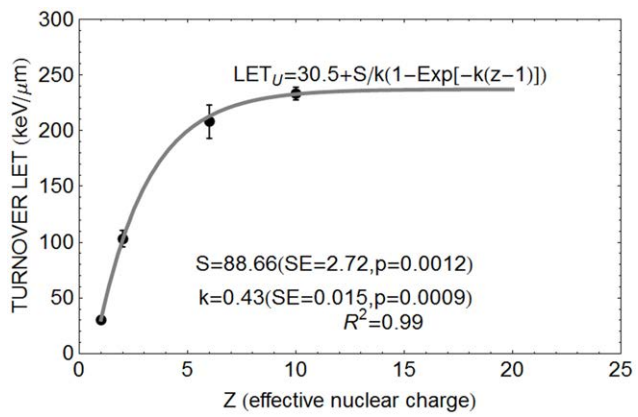

FIGURE 1 | Data points for relationship between *Z* and turnover point LET value $\mathrm{LET_U}$ with fitted parameter values based on Eq. (3).

Fits to Experimental RBE Data Sets

The model is superimposed to the experimental data sets, using different cell lines, of Barendsen (**Figure 4**) and Weyrather et al. (**Figures 5A,B**) and Todd (**Figures 6** and **7**).

The data of Barendsen used mono-energetic deuterium or helium (alpha) particles in one human cell type, with highly symmetrical curves which turnover at around 110 keV/μm. In this case (see **Figure 4**), the model fits the data reasonably well at all levels of surviving fraction. However, since this data set exists as plotted graphical surviving fraction results without access to the original data, there is inevitable uncertainty in assessing the low

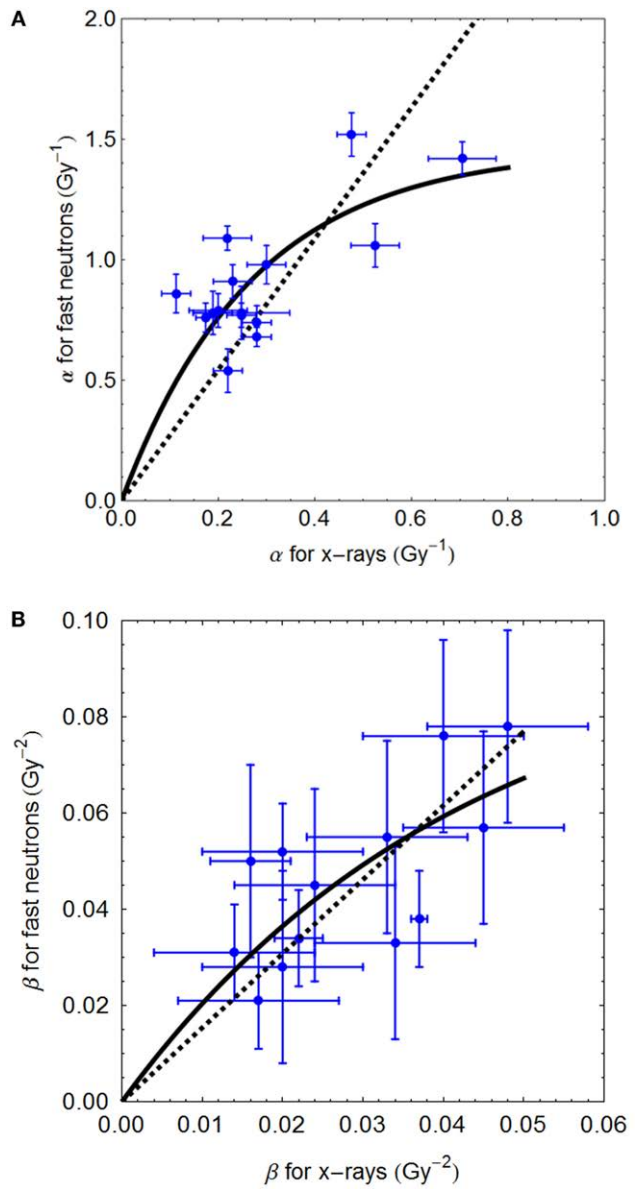

FIGURE 2 | (A,B) Sixty-four megavolt fast neutron relationships between low and high LET radiosensitivity parameters. Linear no-intercept and non-linear least squares fits are respectively: **(A)** $\alpha_H = 2.72\alpha_L$ and $\alpha_H = 5.37/3.68\,(1 - e^{-3.68\alpha_L})$; **(B)** $\beta_H = 1.57\cdot\beta_L$ and $2.29/23.57(1 - e^{-23.57\,\beta_L})$ using Mathematica software.

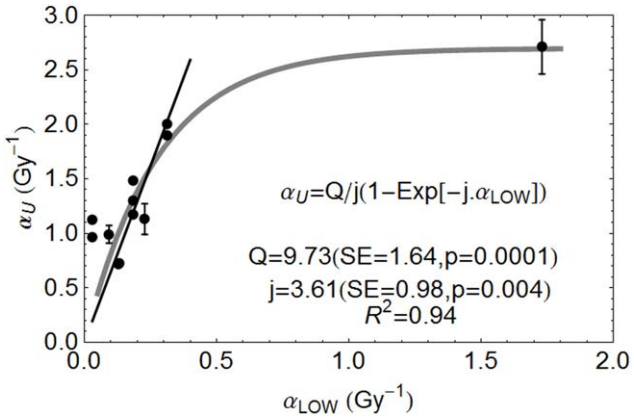

FIGURE 3 | Ion beam relationships between radiosensitivity parameters at low and high LET at the turnover point (α_H is here α_U) and fitted by the parameters shown, using Mathematica software. Error bars are not available for all data used. Reproduced with permission from Ref. (8).

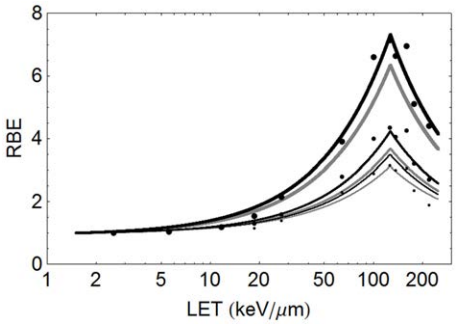

FIGURE 4 | Mono-energetic alpha particle data of Barendsen (with large points indicating 50% survival, medium sized points 10% survival, and the smallest points 5% survival, using the proposed model to provide fit lines, with black indicating use of parameters $\alpha_L = 0.16\,Gy^{-1}$, $\alpha_U = 1.31\,Gy^{-1}$, $\beta_L = 0.046\,Gy^{-2}$, $\beta_U = 0.15\,Gy^{-2}$ and gray using parameters $\alpha_L = 0.15\,Gy^{-1}$, $\alpha_U = 1.35\,Gy^{-1}$, $\beta_L = 0.03\,Gy^{-2}$, $\beta_U = 0.08\,Gy^{-2}$. The thickest lines are for 50% survival, medium lines for 10% survival, and thinnest lines for 5% survival.

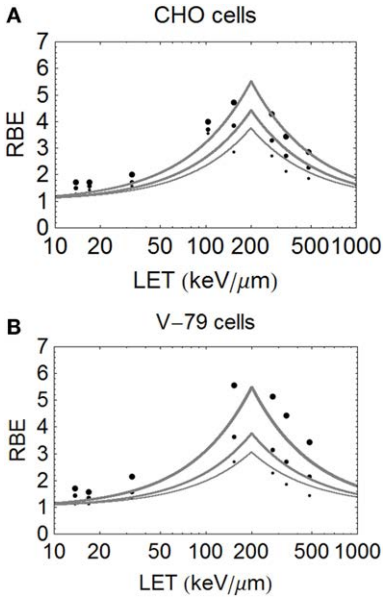

FIGURE 5 | (A,B) Model fitted data of Weyrether et al. for C ions for three different cell lines and doses, coded in the same way as for **Figure 4** with respect to line thickness and surviving fraction **(A)** for CHO cells and **(B)** for V-79 cells.

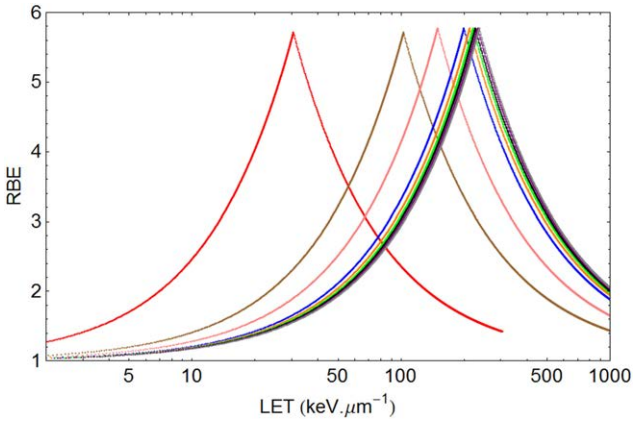

FIGURE 6 | Graphical displays of RBE and LET with unique turnover point positions for multi-ion data of Todd, assuming $\alpha = 0.14\,Gy^{-1}$ and $\beta = 0.05\,Gy^{-2}$ for a dose of 1.5 Gy. From left to right the ionic elements are shown as follows, with color code and LET_U (rounded to nearest integer for values over 100) in parentheses: Deuterium (red, 30.5), Helium (brown, 103), Lithium (pink, 150), Boron (blue, 200), Carbon (orange, 213), Nitrogen (green, 221), Oxygen (Black, 227), Neon (purple, 232), and Argon (gray, 237).

and high LET α and β values, which make the RBE determination even more difficult. The plot was obtained by assessment using $\alpha_L = 0.16$, $\alpha_U = 1.31$, $\beta_L = 0.046$, $\beta_U = 0.15$ obtained by crude measurements of survival curves and RBE plots, each on a logarithmic and linear scales, drawn by artists and which contain displacements of many data points for convenience of display, but the data set is better fitted by $\alpha_L = 0.15$, $\alpha_U = 1.35$, $\beta_L = 0.03$, $\beta_U = 0.08$, as shown in **Figure 4**. The Barendsen data set suffers from retrospective inaccuracies in estimating parameters from diagrams in publications rather than use of the raw data, but the graphic shows the sensitivity of the model to the input parameters.

The critical dependency of each RBE limit on the ratio of α and β at low and high LET respectively, demonstrates the importance of obtaining the most accurate possible data, rather than depending on published material which does not contain precise surviving fraction outcomes. The Barendsen data set also suggests a higher value of LET_U for alpha particles than obtained above using the formula based on *Z* in pooled data, at around 127 instead of 103 keV/μm; also the α_U is predicted to be 1.18 Gy^{-1} by Eq. (3). This illustrates the uniqueness of each data set and the distorting effect of pooling of data from different laboratories using different cell systems etc.

The important carbon ion data of Weyrather et al. (17), from GSI, which covers a broader range of LET values, shows an apparently constant turnover point for different cell types and surviving fractions (**Figures 5A,B**). The data are published with the LQ

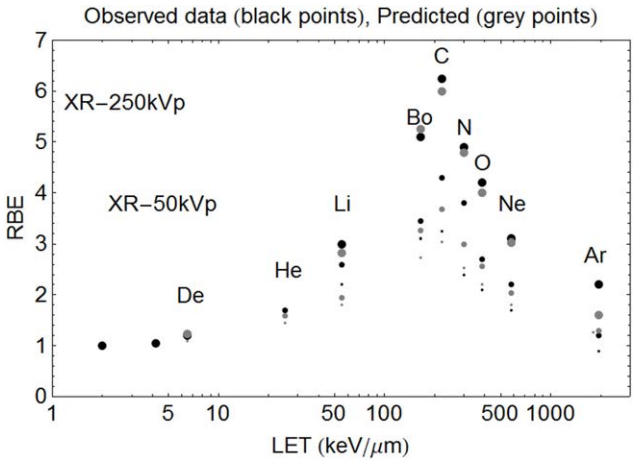

FIGURE 7 | Model predictions shown with data of Todd using the new *Z*-based model to determine LET_U and α_U, β_U respectively, with LQ model correction for dose. The largest sized points are for SF = 50%, the intermediate sized points are for SF = 10%, and the smallest sized points are for SF = 1%. The ions used and their LET (keV/μm) values are given respectively in parentheses. Deuterium (6.5), Helium (25), Lithium (55), Boron (165), Carbon (220), Nitrogen (300), Oxygen (385), Neon (580), and Argon (1940). Observed RBE data are printed as black points, with estimated RBE values as gray points. Starting on the left hand side the first two black points are for 250 and 50 kV X-rays respectively, followed by deuterons etc.

radiosensitivities, although the ions have a small variation in their LET spectrum (with a maximum spread of less than 5% for the highest LET values which reduces further with decreasing LET). So, it is unlikely that energy and LET spread contribute to the deviations from the modeled curves seen at lower LET values. The RBE values found at low LET values seem higher than expected, possibly due to biological sample variation, especially since irradiations were performed using two different accelerator systems (for LET values above and below 100 keV/μm) in different laboratories and presumably at different times. These data, although very informative, inevitably contain greater heterogeneity than the data of Barendsen, and the data are less well fitted. Another more stochastic approach is to use a Poisson function, which will be presented in a further publication.

In the case of Todd's multi-ion data (24), a range of different mono-energetic ions were used (protons, deuterium, helium, lithium, boron, carbon, nitrogen, oxygen, neon, and argon), which implies that there will be at least nine different curves, one for each *Z* value, and each with unique turnover points. Such heterogeneous data were fitted surprisingly well by allocating a unique turnover point for each ion species, before estimation of the RBE, as shown in **Figure 6**, followed by the RBE estimations for each ionic species in **Figure 7**.

Clinical Radiobiology

It is possible to tentatively assess changes in total dose required for different fractionation schedules using protons, helium, and carbon ions, as shown in **Figures 8A–C**. The variations in LET are representative of the wide expected clinical ranges for non-Bragg peak regions and spread out Bragg peaks of different sizes and for scanned beams. It should be noted that the changes in total

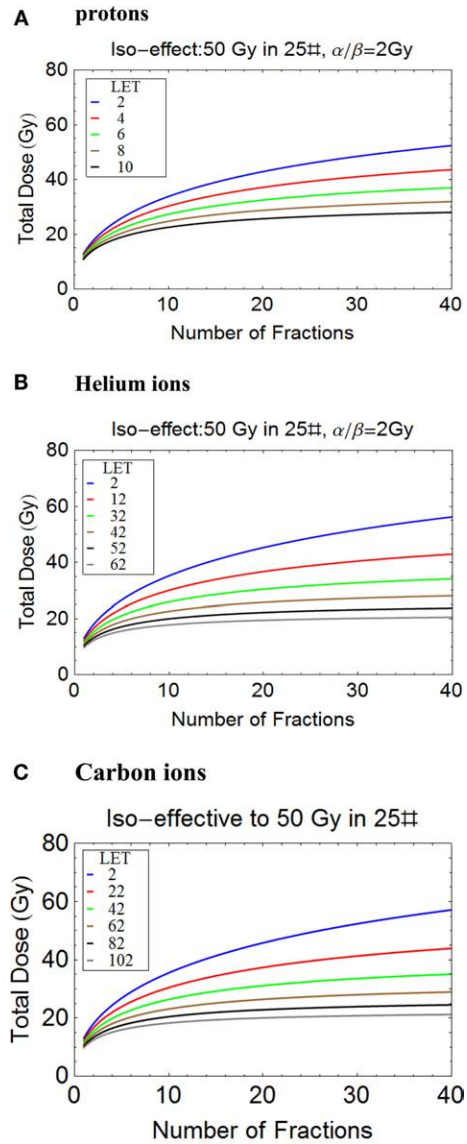

FIGURE 8 | (A-C) Plots of total iso-effective dose versus number of fractions for the given iso-effect and α/β ratio. **(A)** Protons, **(B)** Helium ions, **(C)** Carbon ions.

dose required with number of fractions (and consequently dose per fraction) are remarkably similar for the respective LET ranges used. This indicates the importance of LET mapping as well as dose mapping in the clinic, since RBEs and consequently changes in total dose with fractionation can be the same for a wide range of ions, as determined by their *Z* value and LET.

Discussion

Simple differential equations which model saturation effects are commonly used in the physical sciences and in biology, with notable examples in pharmacokinetics. Saturation in the radiation context applies to the relationship between the effective event size and the bio-target. Maximum efficiency represents the maximum

cell killing effect caused by locally absorbed energy, which differs from the energy released, some of which may be wasted by causing more local damage than is necessary to cause lethality, or is dissipated over a wider than necessary critical volume.

The new model offers a relatively simpler semi-empirical mathematical method for assessing changes in RBE with LET than has previously been available and provides a second order approximation. It can be more easily understood and used by clinicians, biologists, and others, without recourse to more complex mathematics. Also, the two saturation-based assumptions made, in comparison, are fewer than the assumptions required in other RBE models. For highly controlled and relatively homogenous data sets, this deterministic approach provides reasonable estimates of RBE. For protons, a variant of this approach has been published recently (8). The model depends on the assumptions of the LQ model where α and β are high level parameters, being ultimate coefficients of radiation induced cell death, rather than basic components of radiation effect such as DNA strand breaks etc.

The model is not intended to supplant existing models of RBE, but to be complementary. It would be highly advantageous in clinical practice if more than one model could be used, with clinical decisions allowed to proceed if at least two are in reasonable agreement. Thus, the LEM, MKM, and variants of the Katz models should continue to be used, and compared with the new model.

Improved input data would undoubtedly further improve the accuracy of the model. Rather than attempt to fit historical data, which are limited in terms of accurate determination of "maximum efficiency" turnover points, it would be better to conduct rigorous experiments to test hypotheses connected with the above models, such as the relationship of the initial slope to more precise estimates of the turnover point position (LET_U) in different ions. This also requires a further stochastic interpretation necessary to match a range of LET values as would be encountered in many clinical beams. There is ample scope for research in this respect.

Some authors have emphasized the inverse association between low LET α/β and the final RBE (7, 13). This follows since α/β reflects repair capacity and intrinsic radiosensitivities, and is valid more at low doses. From the definitions of RBE_{max} and RBE_{min}, it is easy to show that the former will be inversely related to related to $(\alpha/\beta)_L$, but the latter directly proportional to the square root of $(\alpha/\beta)_L$ (21, 28). The former assumption can be used for low dose per fraction treatments, where RBE_{max} dominates the RBE. The need to include changes in β with LET is necessary for estimations of RBE at higher doses, and where α/β is small as in human late tissue effects. The new model also preserves the overall symmetry of the curves at increasing dose. Accurate estimation of β from cell survival curves, especially when α values are large, are notoriously difficult to achieve. Our knowledge of how β changes with increasing LET is less well documented than for the larger and easier to measure changes in α with increasing LET. Only by meticulously conducted large scaled experiments, with greater than usual numbers of cell survival experiments, can these parameters be estimated to greater and sufficient accuracy.

Since neutrons are uncharged, they do not fall easily into this model, although the main products of neutron interactions such as recoil protons and other ions do, such that a spectrum of LET values will result, which in principle could be translated into RBE using the modeling described in this report. Again this would require further specific study.

There is considerable scope for the application of simpler RBE predictive models. Ideally prospective experiments should be performed with specific attention to LET–RBE turnover point position for different ions, the initial slope of the increment in RBE and the maximum value of α and β relative to their low LET values. These need to be determined for extensive *in vitro* libraries of human cell lines and, if confirmed, extended to more complex *in vivo* experiments. A single international center would be ideal for this purpose, as has already been proposed at CERN (29, 30). There, it might be possible to create a new extensive data base for LET–RBE relationships, and to re-confirm or refute the basic RBE principles listed on p. 3. Of special concern are the slopes of the relationship, and improved accuracy for key LET_U parameter, using multiple ion species in an appropriate panel of human cell lines, and to a much higher degree of accuracy than previously obtained. In this way, the data shown in **Figures 1** and **3** could be enhanced by experiments on multiple ion species. Also, the results of all available models should be compared in such a single laboratory.

Such a project must be regarded as "essential science" for informing clinical practice, so that the best outcomes from particle therapy may in the future be fully, rather than partially, realized. Many practical enigmas remain within particle therapy (8, 31).

It is noteworthy for medical scientists to realize that in the first 6 weeks of the experiments that lead to the discovery of the theoretically predicted Higgs Boson, the entire laws of particle physics were not only re-confirmed, but to a much higher level of accuracy than previously achieved. Similar goals must be attempted in radiobiology, although over a longer time frame. This would provide the tools for greater predictive accuracy to particle radiotherapy, to improve its efficacy, as well as provide enhanced knowledge for human radiation protection, including astrobiology.

Acknowledgments

To colleagues who have inspired me over many years to seek solutions to high LET problems, especially Roger Dale, Gillies McKenna, John Hopewell, Oliver Scott, Jack Fowler, Mark Hill, Herman Suit, Peter O'Neil, and Dudley Goodhead. I am grateful to CERN, Geneva for a Visiting Scientist award during 2014, and to the Director General for the award of Guest Professor 2015–2016. Also, to the generosity of the Principal and Fellows of Brasenose College, Oxford. BJ has been an investigator on several UK Research Council and EU FP-7 funded grants concerned with particle therapy, including ENVISION (241851), ENTERVISION (264552), and ULICE (228436).

References

1. Durante M, Loeffler JS. Charged particles in radiation oncology. *Nat Rev Clin Oncol* (2010) **7**:37–43. doi:10.1038/nrclinonc.2009.183
2. Jones B. The potential advantages of charged particle radiotherapy using protons or light ions. *Clin Oncol* (2008) **20**:555–63. doi:10.1016/j.clon.2008.02.012
3. Kamada T, Tsujii H, Blakely EA, Debus J, De Neve W, Durante M, et al. Carbon ion radiotherapy in Japan: an assessment of 20 years of clinical experience. *Lancet Oncol* (2015) **16**(2):e93–100. doi:10.1016/S1470-2045(14)70412-7
4. Combs SE, Debus J. Treatment with heavy charged particles: systematic review of clinical data and current clinical (comparative) trials. *Acta Oncol* (2013) **52**(7):1272–86. doi:10.3109/0284186X.2013.818254
5. Anderson RM, Stevens DL, Sumption ND, Townsend KM, Goodhead DT, Hill MA. Effect of linear energy transfer (LET) on the complexity of alpha-particle-induced chromosome aberrations in human CD34+ cells. *Radiat Res* (2007) **167**(5):541–50. doi:10.1667/RR0813.1
6. Wilkens JJ, Oelfke U. A phenomenological model for the relative biological effectiveness in therapeutic proton beams. *Phys Med Biol* (2004) **49**(13):2811–25. doi:10.1088/0031-9155/49/13/004
7. Carabe A, Moteabbed M, Depauw N, Schuemann J, Paganetti H. Range uncertainty in proton therapy due to variable biological effectiveness. *Phys Med Biol* (2012) **57**:1159–72. doi:10.1088/0031-9155/57/5/1159
8. Jones B. Towards achieving the full clinical potential of proton therapy by inclusion of LET and RBE models. *Cancers (Basel)* (2015) **7**(1):460–80. doi:10.3390/cancers7010460
9. Katz R, Ackerson B, Homoyooufar M, Sharma SC. Inactivation of cells by heavy ion bombardment. *Radiat Res* (1971) **47**:402–25. doi:10.2307/3573247
10. Elsässer T, Krämer M, Scholz M. Accuracy of the local effect model for the prediction of biologic effects of carbon ion beams in vitro and in vivo. *Int J Radiat Oncol Biol Phys* (2008) **71**(3):866–72. doi:10.1016/j.ijrobp.2008.02.037
11. Kase Y, Kanai T, Matsufuji N, Furusawa Y, Elsässer T, Scholz M. Biophysical calculation of cell survival probabilities using amorphous track structure models for heavy-ion irradiation. *Phys Med Biol* (2008) **53**(1):37–59. doi:10.1088/0031-9155/53/1/003
12. Grün R, Friedrich T, Krämer M, Zink K, Durante M, Engenhart-Cabillic R, et al. Assessment of potential advantages of relevant ions for particle therapy: a model based study. *Med Phys* (2015) **42**(2):1037–47. doi:10.1118/1.4905374
13. Hawkins RB. A microdosimetric-kinetic model for the effect of non-Poisson distribution of lethal lesions on the variation of RBE with LET. *Radiat Res* (2003) **160**(1):61. doi:10.1667/RR3010
14. Inaniwa T, Suzuki M, Furukawa T, Kase Y, Kanematsu N, Shirai T, et al. Effects of dose-delivery time structure on biological effectiveness for therapeutic carbon-ion beams evaluated with microdosimetric kinetic model. *Radiat Res* (2013) **180**(1):44–59. doi:10.1667/RR3178.1
15. Barendsen GW. Responses of cultured cells, tumours and normal tissues to radiations of different linear energy transfer. *Curr Topics Radiat Res Q* (1968) **4**:293–356.
16. Furusawa Y, Fukutsu K, Aoki M, Itsukaichi H, Eguchi-Kasai K, Ohara H, et al. Inactivation of aerobic and hypoxic cells from three different cell lines by accelerated (3)He-, (12)C- and (20)Ne-ion beams. *Radiat Res* (2000) **154**(5):485–96. doi:10.1667/0033-7587(2000)154[0485:IOAAHC]2.0.CO;2 Erratum in: Radiat Res. 2012 177(1):129-131.
17. Weyrather WK, Ritter S, Scholz M, Kraft G. RBE for carbon track-segment irradiation in cell lines of differing repair capacity. *Int J Radiat Biol* (1999) **75**(11):1357–64. doi:10.1080/095530099139232
18. Belli M, Bettega D, Calzolari P, Cera F, Cherubini R, Dalla Vecchia M, et al. Inactivation of human normal and tumour cells irradiated with low energy protons. *Int J Radiat Biol* (2000) **76**(6):831–9. doi:10.1080/09553000050028995
19. Sørensen BS, Overgaard J, Bassler N. In vitro RBE-LET dependence for multiple particle types. *Acta Oncol* (2011) **50**(6):757–62. doi:10.3109/0284186X.2011.582518
20. Hawkins RB. The relationship between the sensitivity of cells to high-energy photons and the RBE of particle radiation used in radiotherapy. *Radiat Res* (2009) **172**(6):761–76. doi:10.1667/RR1655.1
21. Jones B, Underwood TC, Carabe-Fernandez A, Dale RG. Further analysis of fast neutron relative biological effects and implications for charged particle therapy. *Br J Radiol* (2011) **84**:S11–8. doi:10.1259/bjr/67509851
22. Jones B. The apparent increase in the β-parameter of the linear quadratic model with increased linear energy transfer during particle irradiation. *Br J Radiol* (2010) **83**(989):433–6. doi:10.1259/bjr/68792966
23. Friedrich T, Scholz U, Elsässer T, Durante M, Scholz M. Systematic analysis of RBE and related quantities using a database of cell survival experiments with ion beam irradiation. *J Radiat Res* (2013) **54**(3):414–514. doi:10.1093/jrr/rrs114
24. Todd P. Heavy-ion irradiation of cultured human cells. *Radiat Res* (1967) **7**:196–207. doi:10.2307/3583713
25. Goodhead DT. Inactivation and mutation of cultured mammalian cells by aluminium characteristic ultrasoft X-rays. III. Implications for theory of dual radiation action. *Int J Radiat Biol Relat Stud Phys Chem Med* (1977) **32**:43–70. doi:10.1080/09553007714550751
26. Grassberger C, Trofimov A, Lomax A, Paganetti H. Variations in linear energy transfer within clinical proton therapy fields and the potential for biological treatment planning. *Int J Radiat Oncol Biol Phys* (2011) **80**(5):1559–66. doi:10.1016/j.ijrobp.2010.10.027
27. Paganetti H. Relative biological effectiveness (RBE) values for proton beam therapy. Variations as a function of biological endpoint, dose, and linear energy transfer. *Phys Med Biol* (2014) **59**(22):R419–72. doi:10.1088/0031-9155/59/22/R419
28. Jones B, Wilson P, Nagano A, Fenwick J, McKenna G. Dilemmas concerning dose distribution and the influence of relative biological effect (RBE) in proton beam therapy of medulloblastoma. *Br J Radiol* (2012) **85**:912–8. doi:10.1259/bjr/24498486
29. Holzscheiter MH, Bassler N, Dosanjh M, Sørensen BS, Overgaard J. A community call for a dedicated radiobiological research facility to support particle beam cancer therapy. *Radiother Oncol* (2012) **105**(1):1–3. doi:10.1016/j.radonc.2012.08.005
30. Dosanjh M, Jones B, Myers S. A possible biomedical facility at CERN. *Br J Radiol* (2013) **86**(1025):20120660. doi:10.1259/bjr.20120660
31. Suit H, DeLaney T, Goldberg S, Paganetti H, Clasie B, Gerweck L, et al. Proton vs carbon ion beams in the definitive radiation treatment of cancer patients. *Radiother Oncol* (2010) **95**:3–22. doi:10.1016/j.radonc.2010.01.015

Conflict of Interest Statement: The author declares that the research was conducted in the absence of any commercial or financial relationships that could be construed as a potential conflict of interest.

Copyright © 2015 Jones. This is an open-access article distributed under the terms of the Creative Commons Attribution License (CC BY). The use, distribution or reproduction in other forums is permitted, provided the original author(s) or licensor are credited and that the original publication in this journal is cited, in accordance with accepted academic practice. No use, distribution or reproduction is permitted which does not comply with these terms.

frontiers in Oncology

CORRECTION
published: 18 February 2016
doi: 10.3389/fonc.2016.00032

Corrigendum: A Simpler Energy Transfer Efficiency Model to Predict Relative Biological Effect for Protons and Heavier Ions

*Bleddyn Jones**

Department of Oncology, Gray Institute for Radiation Oncology and Biology, Oxford, UK

Keywords: RBE, protons, ions, radiotherapy, radiobiology

A corrigendum on

A Simpler Energy Transfer Efficiency Model to Predict Relative Biological Effect for Protons and Heavier Ions

by Jones B. Front Oncol (2015) ***5****:184. doi: 10.3389/fonc.2015.00184*

OPEN ACCESS

Edited and Reviewed by:
Francis A. Cucinotta,
University of Nevada Las Vegas, USA

Correspondence:
Bleddyn Jones
bleddyn.jones@oncology.ox.ac.uk

Specialty section:
This article was submitted to Radiation Oncology, a section of the journal Frontiers in Oncology

Received: *14 December 2015*
Accepted: *31 January 2016*
Published: *18 February 2016*

Citation:
Jones B (2016) Corrigendum: A Simpler Energy Transfer Efficiency Model to Predict Relative Biological Effect for Protons and Heavier Ions. Front. Oncol. 6:32. doi: 10.3389/fonc.2016.00032

An error was caused by inaccurate transcription of one equation from the computer programmes in the above paper (1). On page 4 of the above article, in the paragraph before Eq. 9, the biological 'inefficiency' should be expressed by $(LET_x - LET_U)/(LET_x - LET_C)$, that is the local energy deposition (LET_x) in excess of the maximum efficiency energy deposition (LET_U), divided by the local energy deposition that exceeds that imparted by the control radiation (LET_C).

This means that Eq. 9 should be modified to be:

$$\alpha_H = \alpha_L + \left(1 - \frac{LET_x - LET_U}{LET_x - LET_C}\right) \cdot (\alpha_U - \alpha_L)$$

The author apologises for this error, although is pleased to state that the graphical displays were all achieved using the correct equation as given above.

REFERENCE

1. Jones BA. Simpler energy transfer efficiency model to predict relative biological effect for protons and heavier ions. *Front Oncol* (2015) **5**:184. doi:10.3389/fonc.2015.00184

Conflict of Interest Statement: The author declares that the research was conducted in the absence of any commercial or financial relationships that could be construed as a potential conflict of interest.

Copyright © 2016 Jones. This is an open-access article distributed under the terms of the Creative Commons Attribution License (CC BY). The use, distribution or reproduction in other forums is permitted, provided the original author(s) or licensor are credited and that the original publication in this journal is cited, in accordance with accepted academic practice. No use, distribution or reproduction is permitted which does not comply with these terms.

frontiers in Oncology

ORIGINAL RESEARCH
published: 06 April 2016
doi: 10.3389/fonc.2016.00076

Calculating Variations in Biological Effectiveness for a 62 MeV Proton Beam

Mario Pietro Carante[1,2] *and Francesca Ballarini*[1,2]*

[1] Physics Department, University of Pavia, Pavia, Italy, [2] Istituto Nazionale di Fisica Nucleare – Sezione di Pavia, Pavia, Italy

A biophysical model of radiation-induced cell death and chromosome aberrations [called BIophysical ANalysis of Cell death and chromosome Aberrations (BIANCA)] was further developed and applied to therapeutic protons. The model assumes a pivotal role of DNA cluster damage, which can lead to clonogenic cell death following three main steps: (i) a DNA "cluster lesion" (CL) produces two independent chromosome fragments; (ii) fragment mis-rejoining within a threshold distance *d* gives rise to chromosome aberrations; (iii) certain aberration types (dicentrics, rings, and large deletions) lead to clonogenic inactivation. The yield of CLs and the probability, *f*, that a chromosome fragment remains un-rejoined even if other fragment(s) are present within *d*, were adjustable parameters. The model, implemented as a MC code providing simulated dose–responses directly comparable with experimental data, was applied to pristine and modulated Bragg peaks of the proton beam used to treat eye melanoma at INFN-LNS in Catania, Italy. Experimental survival curves for AG01522 cells exposed to the Catania beam were reproduced, supporting the model assumptions. Furthermore, cell death and chromosome aberrations at different depths along a spread-out Bragg peak (SOBP) dose profile were predicted. Both endpoints showed an increase along the plateau, and high levels of damage were found also beyond the distal dose fall-off, due to low-energy protons. Cell death and chromosome aberrations were also predicted for V79 cells, in the same irradiation scenario as that used for AG01522 cells. In line with other studies, this work indicated that assuming a constant relative biological effectiveness (RBE) along a proton SOBP may be sub-optimal. Furthermore, it provided qualitative and quantitative evaluations of the dependence of the beam effectiveness on the considered endpoint and dose. More generally, this work represents an example of therapeutic beam characterization avoiding the use of experimental RBE values, which can be source of uncertainties.

Keywords: cell death, chromosome aberrations, protons, hadron therapy, biophysical models, Monte Carlo simulations, relative biological effectiveness

OPEN ACCESS

Edited by:
Marco Durante, GSI, Germany

Reviewed by:
Kevin Prise, Queen's University Belfast, UK
Giuseppe Pablo Cirrone, Istituto Nazionale di Fisica Nucleare, Italy

***Correspondence:**
Francesca Ballarini
francesca.ballarini@unipv.it

Specialty section:
This article was submitted to Radiation Oncology, a section of the journal Frontiers in Oncology

Received: *01 October 2015*
Accepted: *21 March 2016*
Published: *06 April 2016*

Citation:
Carante MP and Ballarini F (2016) Calculating Variations in Biological Effectiveness for a 62 MeV Proton Beam. Front. Oncol. 6:76. doi: 10.3389/fonc.2016.00076

INTRODUCTION

According to the Particle Therapy Co-operative Group[1], 49 proton therapy centers were operating and 32 were under construction in June 2015. The rationale of using protons instead of conventional radiotherapy relies on the ability of these particles to reduce the dose to normal tissues, thanks to the dose localization in the (spread-out) Bragg peak (SOBP) (1). In addition to different types of tumors,

[1] http://www.ptcog.ch/

protons can also be used to treat non-cancer diseases, such as arteriovenous malformations (2).

Protons are usually considered low-LET radiation, and a constant relative biological effectiveness (RBE) of 1.1, mainly derived from animal experiments, is generally applied in the clinical practice. However, both *in vitro* and *in vivo* studies indicate that proton effectiveness increases with decreasing energy, which is increasing LET. This implies an increase of effectiveness with depth along the SOBP, as well as an extension of the biologically effective range. *In vivo*, the average RBE at mid-SOBP is ~1.1, ranging from 0.7 to 1.6 (3); *in vitro* data on clonogenic cell survival indicate an average value at mid-SOBP of ~1.2, ranging from 0.9 to 2.1 (3). Furthermore, the RBE depends not only on the particle energy but also on many other factors, including dose, dose-rate, cell type, and biological endpoint. For instance, both *in vitro* and *in vivo* data show a significant RBE increase for lower fractional doses [e.g., Ref. (4, 5)], especially for cells and tissues with low α/β ratio (6). This may be one of the reasons why *in vivo* experiments, most of which have been performed at higher doses, suggest lower RBE values with respect to *in vitro* studies. It should also be considered that, although the main endpoint of interest for tumor cells is cell death, other endpoints (e.g., mutations, non-lethal chromosome aberrations, etc.) might be relevant for normal tissues.

Although clinical results do not indicate that the use of a constant RBE is incorrect, no trials specifically targeted RBE variations; moreover, tighter treatment margins may increase the importance of taking into account such variations (7). Applying a constant RBE of 1.1 may lead to an underestimation of the damage to normal tissues, especially for treatments involving organs at risk just beyond the tumor, such as the retina for eye tumors and the heart for (left) breast tumors, which are becoming a major application of protontherapy [e.g., Ref. (8)]. On the other side, the currently available RBE data might be insufficient to support a change in clinical practice (7). Incorporating variations in biological effectiveness without directly considering the RBE may be an alternative strategy. For instance, it has been suggested that LET distributions in the patient can be used to guide treatment plan optimization (9).

In this framework, a biophysical model of radiation-induced cell death and chromosome aberrations called BIophysical ANalysis of Cell death and chromosome Aberrations (BIANCA) (10–13) was developed at the University of Pavia and INFN-Pavia, Italy. The model, which in the last few years has been tested against *in vitro* cell survival data and has been applied in the framework of Boron Neutron Capture Therapy (14), assumes that DNA cluster damage can lead to chromosome aberrations and that some aberration types lead to clonogenic cell death. This approach allows calculating cell survival without relying on the concept of RBE. Furthermore, the capability of the model to calculate the induction of different chromosome aberration types, in addition to cell death, makes it suitable for applications in the framework of normal tissue damage evaluation, since some chromosome aberrations are known to be related to the risk to normal tissues (15). In the present work, after comparing simulated dose–response curves for chromosome aberrations with experimental data taken from the literature, the model was applied to the 62-MeV proton beam used to treat ocular melanoma at the CATANA facility of INFN-LNS in Catania, Italy (16). Experimental survival curves taken from the literature (17) for AG01522 cells exposed to pristine and SOBPs from the CATANA beam were reproduced, and cell death and chromosome aberrations were calculated for different depth positions along a SOBP. Finally, cell death and chromosome aberrations were predicted for another cell line (V79) exposed to the same dose profile used for AG01522 cells.

MATERIALS AND METHODS

Model Assumptions

The BIANCA model is based on the following assumptions: (1) radiation induces DNA "cluster lesions" (CLs), and each CL gives rise to two independent chromosome fragments; (2) two chromosome fragments can undergo rejoining only if their *initial* distance is smaller than a threshold distance d, leading to chromosome aberrations in case of mis-rejoining (accidental unrejoining is allowed); and (3) dicentrics, rings, and large deletions lead to clonogenic cell death.

A characterization of the "critical" DNA damage(s), which is damage type(s) that can lead to important endpoints such as chromosome aberrations and cell death, is still an open question in radiobiology. Therefore, we chose not to provide a definition for the quantity "CL," leaving the mean number of CLs per unit radiation dose and per unit DNA mass (that is, the mean number of CLs per Gy and per Dalton, which can be easily converted into CLs per Gy and per cell) as an adjustable parameter. In a previous work (13), CL yields for different radiation qualities showed good agreement with yields of kilo-base-pair (kbp) DNA fragments, suggesting that DSB clusters at the kbp scale, possibly in addition to other levels of clustering, may play a relevant role.

Assumption (2) reflects the fact that fragment rejoining is thought to be distance dependent. The adoption of a step function, rather than a continuously decreasing function, implicitly takes into account the existence in the cell nucleus of repair centers, where DSBs should migrate for repair. For instance, 1–2 μm DSB migration distances have been estimated for MCF10A epithelial cells (18). In previous works [e.g., Ref. (13)], where the threshold distance d was considered as an adjustable parameter, a d value of 5 μm led to good agreement with experimental survival curves for AG1522 human fibroblasts and V79 hamster fibroblasts exposed to different radiation qualities. However, this value seems to be larger than most estimations available in the literature. In the present work, a different approach was adopted, setting the value of d equal to the mean distance between two adjacent chromosome territories (which resulted to be 3.0 μm for AG cells and 3.6 μm for V79 cells), basing on the idea that repair mainly takes place in small channels separating adjacent chromosome domains (19). The expression "chromosome territories" refers to distinct regions of the cell nucleus, with negligible reciprocal overlapping, where the various chromosomes are localized during interphase, that is most of the cell cycle. According to this approach, d is no more an adjustable parameter, but is fixed *a priori* basing on the specific features of the considered cell nucleus (i.e., nucleus shape and dimensions and number of chromosomes).

In previous works, a chromosome fragment having at least one potential partner for rejoining (that is, at least another fragment within the threshold distance *d*) was assumed to undergo rejoining with 100% probability. On the contrary in the present work, we considered a more realistic scenario where a fragment, even if one or more potential "partners" are available within *d*, has a given probability *f* of remaining un-rejoined. This assumption is consistent with studies indicating that a certain fraction of exchange-type chromosome aberrations are "incomplete," i.e., not all the involved chromosome fragments are finally rejoined [e.g., Ref. (20–22)]. The observed probability of unrejoining tends to be cell-line-dependent, since in general radiosensitive cells show higher frequencies of deletions with respect to normal or radioresistant cells. For instance, in ataxia-telangiectasia (A-T) cells exposed to X-rays, the fraction of un-rejoined breaks was five to six times higher than that for normal fibroblasts (23). Concerning a possible dependence on radiation quality, contradicting results can be found in the literature. While some works report an increase of incomplete exchanges with LET [e.g., Ref. (21)], others do not indicate a LET-dependence [e.g., Ref. (20, 22)]. For the sake of simplicity, in the present work we assumed that, for a given cell line, the value of *f* was cell line dependent but LET independent.

Assumption (3) derives from the relationship between chromosome aberrations and cell death shown by many works available in the literature. In particular, for AG1522 fibroblasts exposed to X-rays, Cornforth and Bedford (24) found a one-to-one relationship between the mean number per cell of "Lethal Aberrations" (defined as dicentrics plus rings plus deletions visible in Giemsa) and –lnS, where S is the fraction of surviving cells. According to another work, an analogous relationship may hold for V79 cells as well (25).

Dose–Response Simulations

Like in previous works, AG1522 cell nuclei were modeled as cylinders with elliptical base (height: 4 μm; major axis: 20 μm; minor axis: 10 μm), and V79 cell nuclei were modeled as cylinders with circular base (height and radius: 6 μm). A discussion on these choices can be found in Carante et al. (13). Each interphase chromosome territory was represented as the union of adjacent cubic voxels of 0.2 μm side to obtain chromosome territories with volume proportional to their DNA content. The various territories were simultaneously constructed step-by-step, with the first step consisting of random selection of a "starting voxel" for each chromosome territory. In each of the subsequent steps, a new voxel was assigned to each territory; the new voxel was randomly selected among the six closest neighbors of the voxel that was assigned to that territory in the preceding step. After constructing the various chromosome territories, each of the voxels assigned to a given territory was associated with one of the two chromosome arms, applying a probability proportional to the arm DNA content.

To simulate the exposure to a given dose of X-rays, a CL yield (mean number of CLs per Gy and per cell) was multiplied by that dose to obtain the mean number of CLs per cell. For each cell, which is for each run of the code, an "actual" number of CLs was then extracted from a Poisson distribution, and those CLs were distributed within the nucleus volume uniformly, since X-rays are sparsely ionizing radiation. For protons, the simulation for a given dose started calculating the mean number of (primary) particles traversing the cell nucleus, with direction parallel to the axis of the cylinder representing the nucleus. Such mean number was calculated by $n = S \times D/(0.16 \times L)$, where S is the nucleus cross-sectional area in square micrometer, D is the absorbed dose in Gy, L is the radiation LET in keV/μm, and 0.16 is a factor coming from the conversion between eVs and Joules. For each cell, an "actual" number of nucleus traversals was then extracted from a Poisson distribution having mean value n, and for each traversal an entrance point in the nucleus was randomly selected. The mean number of CLs per nucleus traversal was then calculated multiplying the nucleus traversal length (in micrometer) by the mean number of CLs per micrometer. The latter was obtained by $CL/\mu m = 0.16 \times (CL\ Gy^{-1}\cdot cell^{-1}) \times L/V$, where V is the cell nucleus volume in cubic micrometer, L is the radiation LET in keV/μm, and 0.16 is the conversion factor mentioned above. For each nucleus traversal, an "actual" number of CLs was extracted from a Poisson distribution, and these CLs were uniformly distributed along the segment representing that traversal.

The subsequent simulation steps consisted of the following: identification of the chromosome and the chromosome-arm that was hit by each CL; rejoining of chromosome fragments within the threshold distance *d*; scoring of lethal aberrations (dicentrics, rings and deletions visible in Giemsa); and calculation of the corresponding surviving fraction. Chromosome fragments having a DNA content smaller than 3 Mega-base-pairs (Mbp) were assumed as not visible in metaphase, as reported by Cornforth and Bedford (24). A discussion on the role of this value can be found in Carante et al. (13). For each dose, the code was run 10,000 times, allowing to obtain a relative error smaller than 2%. The repetition for different doses provided simulated dose–response curves for chromosome aberrations or cell survival, directly comparable with experimental data.

RESULTS AND DISCUSSION

Chromosome Aberrations

According to the approach adopted in the current version of the model, (clonogenic) cell death depends on chromosome aberrations, in particular the so-called "lethal aberrations" (dicentrics, rings, and deletions). Comparisons between calculated and experimental yields of different chromosome aberration types have been published in previous works [e.g., Ref. (12, 26–29)]. However, new comparisons were performed following the introduction of some modifications: in the present work, as mentioned above, the threshold distance for chromosome fragment rejoining, *d*, was fixed as the mean distance between two adjacent chromosome territories, and a chromosome fragment was allowed to remain un-rejoined (with probability *f*) also when possible "partners" were present within *d*.

A detailed and systematic discussion on this issue is beyond the scope of the present work, and will be object of a separate paper. As an example, **Figure 1** shows dose–response curves for dicentrics, rings, and deletions (both separately and summed up to give total aberrations) induced in AG1522 cells exposed

to X-rays. The lines are simulation outcomes, the points are experimental data taken from the literature (24). The error bars associated with the experimental points, which represent 95% confidence about means as reported in Ref. (24), were calculated from the aberration yields and the number of analyzed cells reported in table 2 of the experimental paper. Both for dicentrics and rings, the calculated aberration yields were within the experimental errors, with the only exception of dicentrics at 6 Gy. Incidentally, the capability of reproducing separately the yields of dicentrics and rings supports the assumption adopted for *d*, since higher *d* values overestimated the ratio of dicentrics to rings (the so-called "*F*-ratio"), whereas lower *d* values underestimated the *F*-ratio (results not shown). Concerning deletions, the question seems more qualitative than quantitative: while the simulated response is basically linear, the experimental response shows a non-negligible quadratic component. This can be explained considering that in the simulations most deletions were "terminal deletions," which being due to a single chromosome break involve a single-particle mechanism proportional to dose, whereas most experimental deletions were of the "interstitial" type, which requiring two chromosome breaks (also) involves a two-particle mechanism proportional to the square of dose. The observation of so many interstitial deletions following exposure to X-rays, which are sparsely ionizing radiation, is not easy to explain. One possible reason might be related to the particular experimental protocol, according to which the cells were sub-cultured for 24 h after irradiation.

The curves reported in **Figure 1** were obtained with a *f* value of ~0.2, and a CL yield of ~1.3 CL $Gy^{-1}\cdot cell^{-1}$. This value is lower than the value used to reproduce total aberration yields in previous works [e.g., Ref. (12)] where parameter *f* was not introduced, which means $f = 0$. This can be explained considering that in the present work, where a chromosome fragment is allowed to remain un-rejoined also in presence of potential partners within the threshold distance, the yield of deletions – and thus of total aberrations – increased, implying that a lower CL yield was sufficient to get the same yield of total aberrations. Although it was possible to reproduce the yields of total aberrations also assuming that $f = 0$ (12), at most doses the yields of deletions were underestimated by a factor ~2, and the yields of dicentrics were overestimated, again by a factor ~2. On the contrary, as shown in **Figure 1**, the introduction of a *f* value higher than 0 allowed obtaining a good agreement not only with total aberrations as a whole (upper curve) but also with dicentrics, rings, and deletions considered separately (three lower curves). A determination of the "best" *f* value was beyond the scope of the present work. However, it is worth reporting that attempting to reproduce the (experimental) yields of total aberrations with lower *f* values (and higher CL yields) led to an underestimation of deletions associated with an overestimation of dicentrics, whereas higher *f* values (with lower CL yields) led to an overestimation of deletions associated with an underestimation of dicentrics (results not shown).

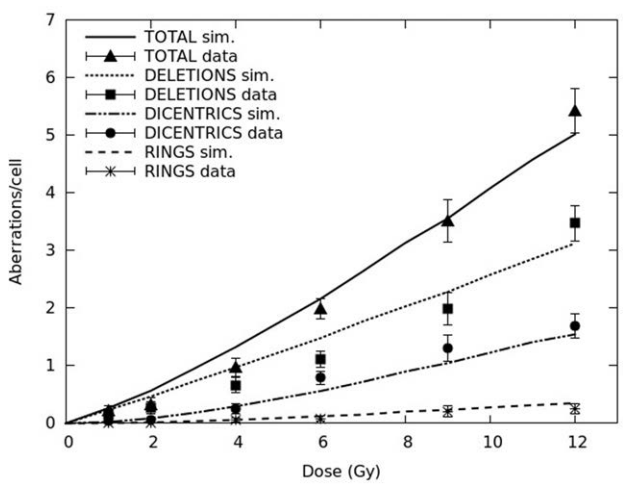

FIGURE 1 | Yields (mean number per cell) of different aberration types (dicentrics, rings, and deletions, as well as total lethal aberrations) in AG1522 primary normal human fibroblasts exposed to different doses of X-rays. The lines are simulation outcomes, the points are experimental data taken from Cornforth and Bedford (24).

Survival Curves

The model was then applied to cell survival, focusing on protons due to their wide use in hadron therapy. The first step of the work consisted of reproducing experimental survival curves obtained with the 62-MeV proton beam available at the CATANA ocular melanoma facility of INFN-LNS in Catania, Italy (16, 17). In that experiment (17), AG01522 primary normal human fibroblasts were exposed to six pristine Bragg peaks (with minimum and maximum water-equivalent depth of 1.7 and 30.7 mm, respectively) and at six depth positions along a SOBP (with minimum and maximum water-equivalent depth of 1.5 and 31.2 mm, respectively). After irradiation, the cells were immediately trypsinized, counted, seeded, and incubated to allow for macroscopic colony formation; colonies consisting of at least 50 cells were scored as viable. Further details can be found in the original paper (17).

Figure 2 reports simulated survival curves for the six pristine peaks (corresponding to the following LET values: 1.1, 4.0, 7.0, 11.9, 18.0, and 22.6 keV/μm), together with the experimental data for comparison and their error bars, which represent one SD. Raw numbers were obtained from the authors of the experimental work. All simulations were performed adopting the same value of *f* used to calculate chromosome aberrations in AG human fibroblasts, which is 0.2. On the contrary, the yield of CLs, which depends on radiation quality, was adjusted separately for each curve. The curves reported in **Figure 2** were obtained using CL yields in the range ~4.1–8.0 CL $Gy^{-1}\cdot cell^{-1}$, increasing with the radiation LET. The increase with LET is consistent with the clustering nature of CLs [e.g., Ref. (28, 30)]. Analogous to chromosome aberrations, the CL yields used to obtain the curves shown in **Figure 2** were (slightly) lower with respect to those used in previous works. Again, this is related to the introduction of parameter *f*, which implying higher yields of lethal aberrations, also implies lower survival levels; as a consequence, a lower CL yield was sufficient to get the same survival curve for a given radiation quality. In general, the simulation outcomes showed satisfactory agreement with the experimental data. In some

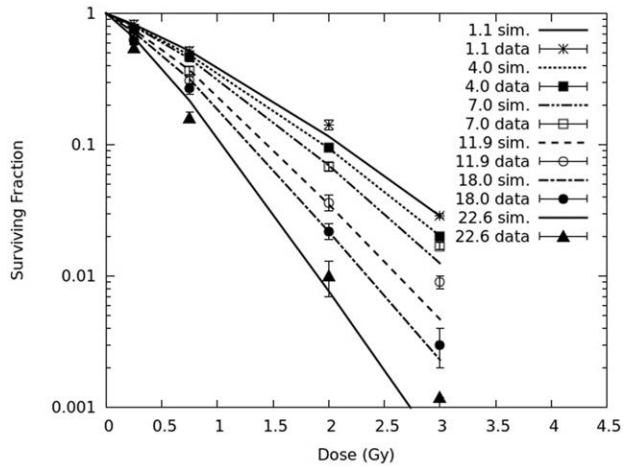

FIGURE 2 | Cell survival curves for AG01522 primary normal human fibroblasts exposed to six pristine proton Bragg peaks (corresponding to the following LET values: 1.1, 4.0, 7.0, 11.9, 18.0, and 22.6 keV/μm). The lines are simulation outcomes, the points are experimental data taken from Chaudhary et al. (17).

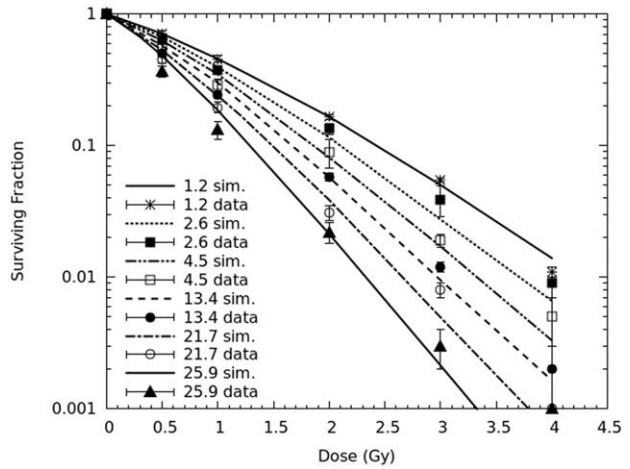

FIGURE 3 | Cell survival curves for AG01522 primary normal human fibroblasts irradiated at six depth positions along a proton SOBP (corresponding to the following dose-averaged LET values: 1.2, 2.6, 4.5, 13.4, 21.7, and 25.9 keV/μm). The lines are simulation outcomes, the points are experimental data taken from Chaudhary et al. (17).

cases, typically for curves corresponding to higher LET values, there was a tendency to underestimate the experimental survival at the highest considered dose, which was 3 Gy. This issue is under investigation. More specifically, for 1.1 and 4.0 keV/μm the value of the reduced chi-square was around 1. Higher values were found for the other four curves, mainly due to the point at 3 Gy; however, at least in two cases (7.0 and 22.6 keV/μm), the simulations were close to the fit performed by the authors, since the relative difference between calculated and fitted survival was smaller than 20%.

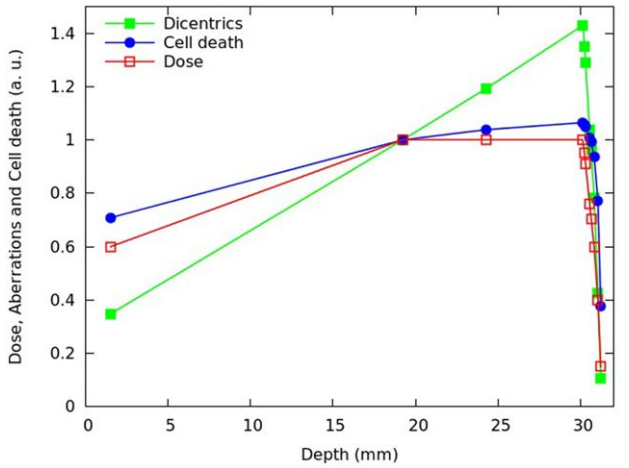

FIGURE 4 | Calculated fraction of inactivated cells (blue symbols) and calculated mean number of dicentrics per cell (green symbols) at different depths of the SOBP dose profile reported in Chaudhary et al. (17), which is also shown in the figure (red symbols). Each quantity was normalized with respect to the proximal position. The lines are simply guides for the eye.

In **Figure 3**, simulated survival curves are compared with the experimental data obtained by Chaudhary et al. at the six depth positions along the SOBP, corresponding to the following dose-averaged LET values: 1.2, 2.6, 4.5, 13.4, 21.7, and 25.9 keV/μm. Again, all simulations were performed without changing the value of *f*, whereas the CL yield was adjusted separately for each radiation quality, that is for each curve. Despite a tendency to underestimate the experimental survival at high doses, already mentioned for the pristine peaks, CL yields in the range ~3.7–6.4 CL $Gy^{-1}\cdot cell^{-1}$, increasing with LET, led to a satisfactory agreement with the experimental curves. Analogous to the results for the pristine peaks, also for the spread-out peak the agreement between simulations and experiments was particularly good for the lower LET curves, since a reduced chi-square around 1 was obtained for 1.2, 2.6, and 4.5 keV/μm. Higher (reduced) chi-square values were found for 13.4, 21.7, and 25.9 keV/μm, mainly due to the points at the highest doses (3 and 4 Gy). However, with the only exception of the point at 3 Gy for the 21.7 keV/μm curve, the relative difference between calculated and fitted survival was not larger than 20%. It is also worth mentioning that, since the higher LET values refer to the descending part of the SOBP, where the doses are lower, the underestimation of the experimental survival at high doses of higher LET did not lead to important consequences on the predictions of cell killing and chromosome aberrations along the SOBP dose profile that will be shown in **Figures 4–9**.

Interestingly, the CL yields used for the curves reported in **Figure 3** were lower than the CL yields used for the pristine peaks (**Figure 2**). This is consistent with the higher RBE observed in the experimental work for the pristine peaks with respect to the SOBP (17), and may be related to the fact that a SOBP consists of a mixed radiation field that can only be associated with an average

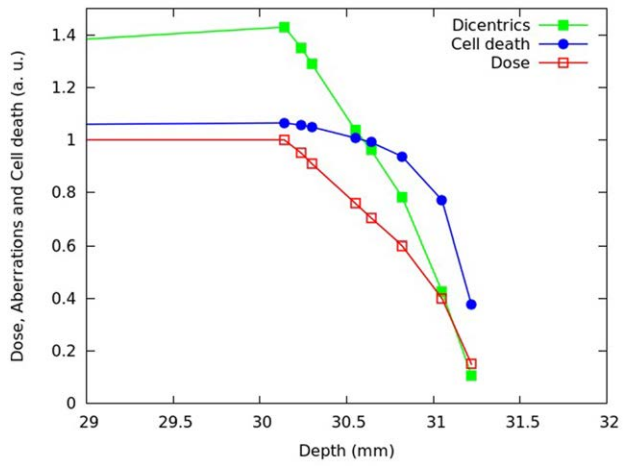

FIGURE 5 | Distal and fall-off region of the SOBP shown in Figure 4.

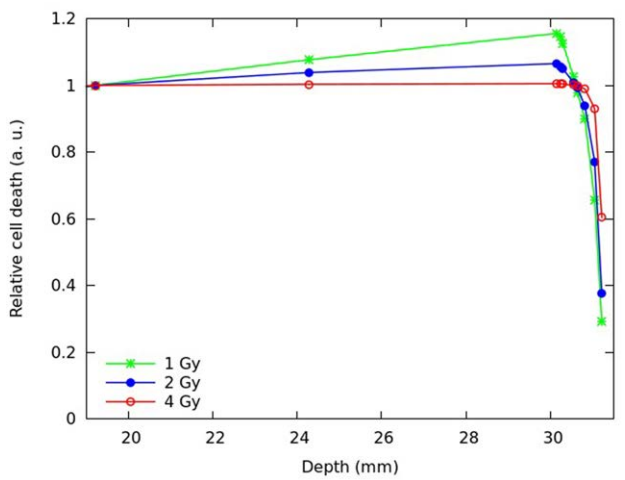

FIGURE 6 | Predicted fraction of inactivated cells at different depths along the SOBP, assuming a plateau dose of 1 Gy (green symbols), 2 Gy (blue symbols), or 4 Gy (red symbols). Each quantity was normalized with respect to the proximal position. The lines are simply guides for the eye.

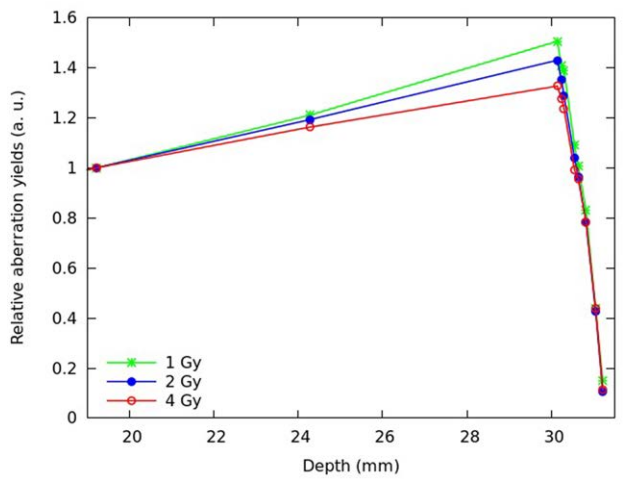

FIGURE 7 | Predicted mean number of dicentrics per cell at different depths along the SOBP, assuming a plateau dose of 1 Gy (green symbols), 2 Gy (blue symbols), or 4 Gy (red symbols). Each quantity was normalized with respect to the proximal position; the lines are simply guides for the eye.

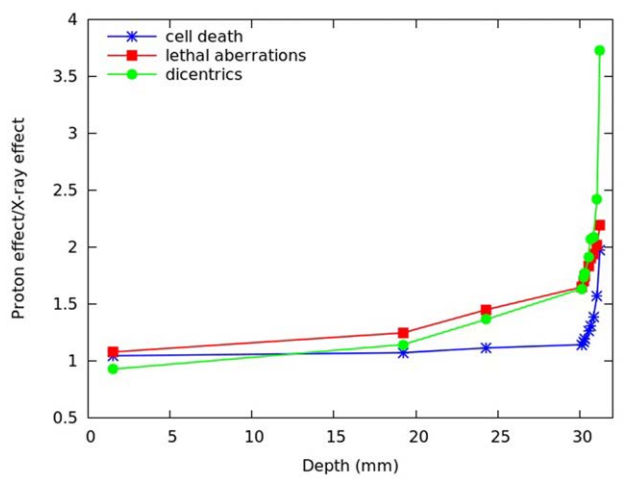

FIGURE 8 | R_I (ratio between proton-induced and X-ray-induced cell inactivation after the same dose, blue symbols), R_{LA} (ratio between proton-induced and X-ray-induced lethal aberrations after the same dose, red symbols), and R_{DIC} (ratio between proton-induced and X-ray-induced dicentrics after the same dose, green symbols) calculated at different depths of the SOBP dose profile used in Chaudhary et al. (17), assuming a plateau dose of 2 Gy. The lines are simply guides for the eye.

LET, rather than a single LET value. This issue has been discussed for carbon beams by Belli et al. (31), who suggested that these differences between SOBP and monoenergetic beams may also depend on the specific cell line, in addition to the ion type. More specifically, according to these authors, a systematic deviation may be related to the averaging procedures in the presence of a LET distribution along the SOBP. Moreover, if this distribution is large enough to include high-LET values falling close to or beyond the RBE maximum, the so-called "overkilling effect" might result in a further decrease in biological effectiveness (31).

Applications for Protontherapy

After reproducing the survival curves reported in Chaudhary et al. (17) for the pristine peaks and the various SOBP positions, the model was applied to investigate the depth- and dose dependence of the beam effectiveness along the SOBP, in terms of both cell death and chromosome aberrations. For different depths in water of the SOBP dose profile reported in Chaudhary et al. (17), **Figures 4** and **5** report the relative fraction of inactivated cells and the relative yield of dicentrics, assuming a dose of 2 Gy in the plateau region. The term "relative" means that each quantity

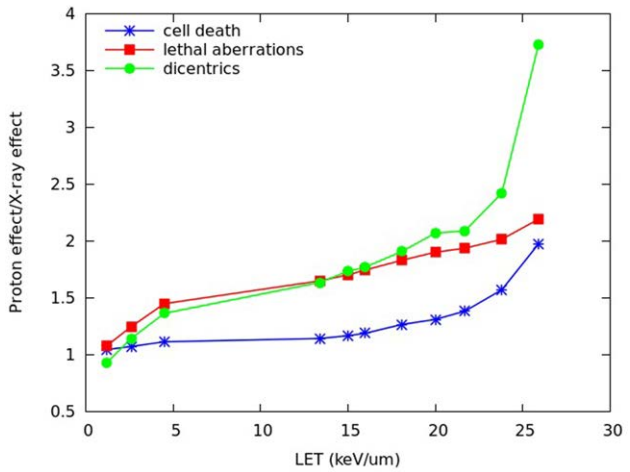

FIGURE 9 | R_I (ratio between proton-induced and X-ray-induced cell inactivation after the same dose, blue symbols), R_{LA} (ratio between proton-induced and X-ray-induced lethal aberrations after the same dose, red symbols), and R_{DIC} (ratio between proton-induced and X-ray-induced dicentrics after the same dose, green symbols) for the (dose-averaged) LET values corresponding to the depth positions considered in Figure 8. The lines are simply guides for the eye.

was normalized with respect to the proximal point. For the six depth positions considered in the experimental work (i.e., 1.52, 19.22, 24.28, 30.14, 30.82, and 31.22 mm), the cell killing calculations did not add substantial information with respect to the experimental work. However, the model allowed predicting the fraction of surviving cells also for other positions, with focus on the dose fall-off region that can be critical for normal tissue damage (see **Figure 5**). Moreover, the model provided predictions of chromosome aberrations, which were not investigated in Chaudhary et al. (17). This information may be useful in the framework of normal tissue damage evaluation, since certain types of chromosome aberrations (typically, reciprocal translocations) are known to be related to cell conversion to malignancy (15). For this reason, dicentric yields were shown in **Figures 4** and **5**: dicentric yields are thought to be not significantly different than the yields of reciprocal translocations, which are the symmetrical counterpart of dicentrics among inter-chromosomal simple exchanges.

Consistent with the experimental data reported in Chaudhary et al. (17) and with other works available in the literature [e.g., Ref. (4, 32, 33)], the beam effectiveness – both for cell death and for chromosome aberrations – was found to increase with depth along the plateau, and high levels of biological damage were also found beyond the distal fall-off. For instance at ~31 mm in water, where the physical dose was about 40% of the proximal dose, the fraction of inactivated cells was almost 80% of the fraction of inactivated cell at the proximal position. This can be explained taking into account that, as protons slow down, their LET increases leading to a higher biological effectiveness. Furthermore, the (relative) increase in chromosome aberrations with increasing depth along the plateau was more pronounced with respect to cell killing: while cell killing increased by a factor ~1.1, the yield of dicentrics (and, thus, reciprocal translocations) in the distal position was more than 1.4 times higher with respect to the proximal position. This is an example of dependence of biological effectiveness on the considered endpoint.

Predictions of cell death and chromosome aberrations were also performed assuming different plateau doses. **Figures 6** and **7** report predictions for the fraction of inactivated cells (**Figure 6**) and the mean number of dicentrics per cell (**Figure 7**) at different depths of the SOBP, assuming a plateau dose of 1 or 4 Gy. For comparison, the figure also reports the results for 2 Gy. Again, the results were normalized with respect to the proximal position.

Increasing the physical dose (from 2 to 4 Gy) reduced the increase in biological effectiveness along the plateau, whereas decreasing the dose (from 2 to 1 Gy) led to an even more pronounced increase in effectiveness. This is consistent with the well-known dose-dependence of RBE, which tends to be higher at lower doses and vice versa. However, while for cell death, the highest considered dose (4 Gy) led to an almost flat biological effectiveness along the plateau; for chromosome aberrations, even that dose implied an increase in effectiveness.

To compare the effectiveness of protons with that of X-rays, the ratio between the level of effect (cell death or chromosome aberrations) induced by a given dose of protons and the level of effect induced by the same dose of X-rays was also investigated for different positions along the SOBP dose profile. Although this quantity has not the same meaning as the RBE, which is defined as the iso-effect ratio between the X-ray dose and the proton dose, both these ratios reflect variations in biological effectiveness. **Figure 8** reports, for different depths along the SOBP dose profile assuming a plateau dose of 2 Gy, the calculated ratio between proton-induced cell death (i.e., fraction of inactivated cells) and cell death induced by the same dose of X-rays. This ratio will be called R_I, where "I" means "inactivation." The figure also reports the ratio between the yield of lethal aberrations (i.e., mean number of lethal aberrations per cell) induced by protons and the yield of lethal aberrations induced by the same dose of X-rays, which will be called R_{LA}, as well as the ratio between the yield of dicentrics induced by protons and the yield of dicentrics induced by the same dose of X-rays, which will be called R_{DIC}.

As expected, all these ratios increased with depth due to the increase in proton LET. However, their depth dependence showed different features. In particular, R_{DIC} (ratio between proton- and X-ray dicentrics) increased up to more than 3.5, whereas R_{LA} (ratio between proton- and X-ray lethal aberrations) and R_I (ratio between proton- and X-ray cell inactivation) increased up to about 2. Again, this is an example of different effectiveness when different endpoints – even different types of chromosome aberrations – are considered. The fact that dicentrics, considered as representative of reciprocal translocations, showed a more pronounced increase with respect to lethal aberrations and cell death may have implications in the evaluation of the risk to normal tissues.

In **Figure 9,** the same quantities reported in **Figure 8**, that is R_I, R_{LA}, and R_{DIC}, are plotted as a function of the (dose-averaged) LET, rather than as a function of depth. With the exception of the two points at the lowest LET, this revealed a basically linear increase

of R_{LA} with LET. Therefore, at least for LET values in the range ~5–25 keV/μm, additional R_{LA} values (where "additional" means in correspondence of additional LET values and, thus, additional depth positions, with respect to those considered in **Figures 8** and **9**) may be derived by linear interpolation. If the yield of lethal aberrations induced by the same dose of X-rays is known (for instance, from experiments), R_{LA} would then provide the yield of lethal aberrations induced by protons (LA_p). According to our model, LA_p would then allow calculating proton cell survival for these additional depth positions.

After considering AG human fibroblasts, the model was applied to V79 hamster fibroblasts, which are rather radio-resistant and are widely used in the characterization of hadron therapy beams. The final goal consisted of predicting cell death and chromosome aberrations for V79 cells along the SOBP dose profile used in Chaudhary et al. (17) to irradiate AG01522 cells. As a preliminary step, to adjust the model parameters before performing such predictions, experimental survival curves taken from the literature for V79 cells exposed to different monoenergetic proton beams, as well as X-rays as a reference (32, 34), were reproduced. **Figure 10** reports calculated survival curves for X-rays and four monoenergetic proton beams (with LET values in the range 7.7–27.6 keV/μm), together with experimental data taken from Ref. (32, 34). All the curves reported in **Figure 10** were obtained with $f \approx 0.1$. The difference with respect to the value used for AG cells, which was ~0.2, may be related to the different repair features of these two cell lines. More specifically, AG cells are likely to possess a less efficient repair machinery, implying higher levels of un-rejoined chromosome fragments and, thus, higher f values.

Like for AG01522 cells, also for V79 cells the yield of CLs was adjusted separately for each radiation quality, that is for each curve. The X-ray curve reported in **Figure 10** was obtained using a CL yield of 1.5 CL $Gy^{-1}\cdot cell^{-1}$, whereas the four proton curves were obtained with CL yields in the range ~2.0–3.2 $CL\cdot Gy^{-1}\cdot cell^{-1}$, increasing with LET. With these values, the general agreement between the simulation outcomes and the experimental data reported in Ref. (32, 34) was satisfactory. More specifically, for the curve at the lowest LET (7.7 keV/μm), the value of the reduced chi-square was 1.8. Higher (reduced) chi-square values were found for the other curves, for which the maximum relative difference between simulated and measured survival was 47%. However, the maximum relative difference with respect to the data fits provided in (32, 34) was 35%.

Similarly to AG01522 cells, the CL yields used in the present work were lower with respect to previous works in which parameter f was not introduced in the model. Furthermore, the CL yields for V79 cells were lower than the CL yields for AG01522 cells exposed to similar radiation qualities, as a consequence of the lower radiosensitivity of V79 cells. In fact, as discussed in detail in previous works [e.g., Ref. (13)], although the CL yield mainly depends on radiation quality, it is also modulated by the specific target cell response. This is consistent with the biophysical meaning of this parameter, which represents a type of DNA damage that is severe and difficult to be repaired.

Figures 11 and **12** report predictions of cell death (i.e., fraction of inactivated cells) and chromosome aberrations (i.e., mean number of dicentrics per cell) for V79 cells along the proton SOBP used in Chaudhary et al. (17), as well as the dose profile reported in Chaudhary et al. (17). The results, which were obtained assuming a plateau dose of 2 Gy, were normalized with respect to the proximal position. Among the considered LET values and, thus, the corresponding depth positions, four are those reported in **Figure 10**, whereas the others [i.e., 3.0, 10.1, and 20.0 keV/μm, for which the survival data for comparison were taken from Ref.

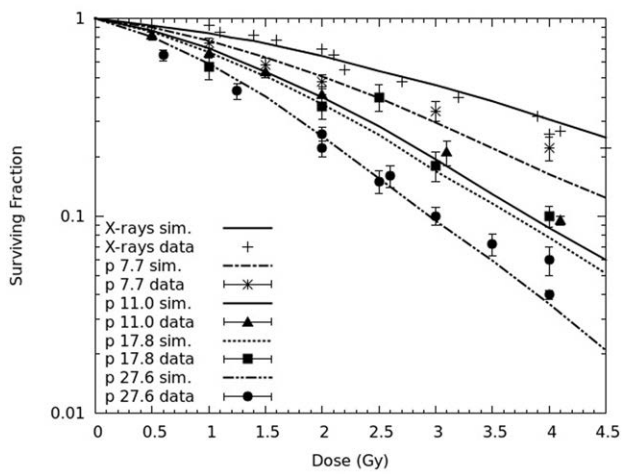

FIGURE 10 | Survival curves for V79 cells exposed to four monoenergetic proton beams (LET: 7.7, 11.0, 17.8, and 27.6 keV/μm), as well as X-rays as a reference. The lines are simulation outcomes, the points are experimental data taken from the literature: (32) for X-rays, 7.7 keV/μm protons and 11.0 keV/μm protons; (34) for X-rays, 17.8 keV/μm protons, and 27.6 keV/μm protons.

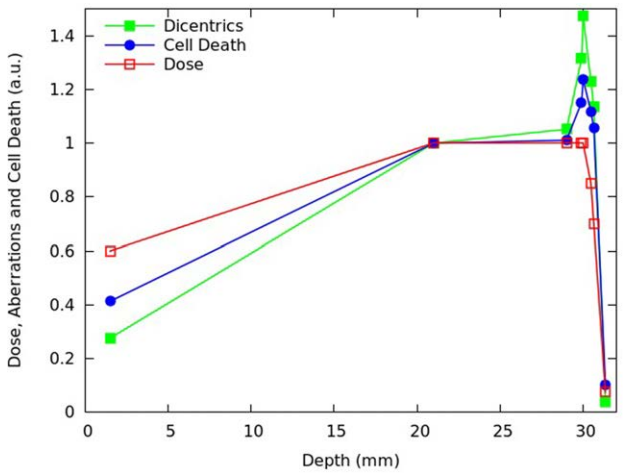

FIGURE 11 | Predicted fraction of inactivated cells (blue symbols) and mean number of dicentrics per cell (green symbols) for V79 cells at different depths of the SOBP dose profile reported in Chaudhary et al. (17), which is also shown in the figure (red symbols). Each quantity was normalized to the proximal point. The lines are simply guides for the eye.

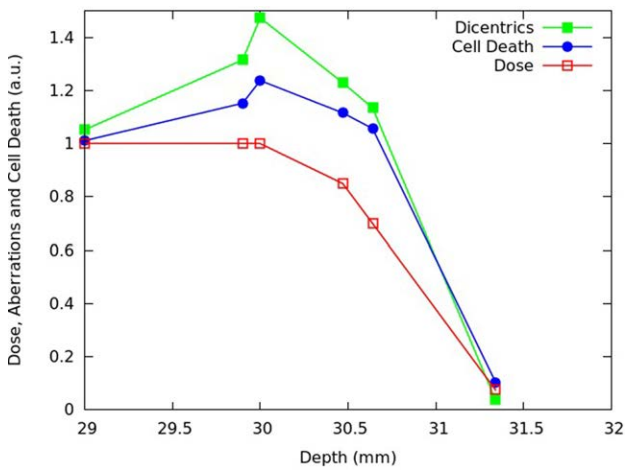

FIGURE 12 | Distal and fall-off region of the SOBP shown in Figure 11.

(4, 32, 34), respectively] were not reported in **Figure 10** to avoid making the figure too crowded.

Like for AG01522 cells, the beam effectiveness was found to increase along the plateau, and high levels of biological damage were also found beyond the distal dose fall-off. Moreover, the increase in chromosome aberrations along the plateau was more pronounced than the increase in cell killing, reflecting the radiation effectiveness dependence on the specific endpoint. Interestingly, the increase in biological effectiveness was more pronounced for V79 cells than for AG01522 cells: for instance, for V79 cells the fraction of inactivated cells increased along the plateau by a factor that was more than 1.2, whereas for AG01522 cells this factor was <1.1. This is consistent with the higher RBE generally shown by cells exhibiting smaller α/β ratios (7), as is the case of V79 cells.

CONCLUSION

A biophysical model of radiation-induced cell death and chromosome aberrations, which assumes a pivotal role of DNA cluster damage and lethal aberrations, was further developed and applied to therapeutic protons. After testing an improved version against experimental data, the model was applied to pristine and modulated Bragg peaks of the proton beam used to treat eye melanoma at INFN-LNS in Catania, Italy. Experimental survival curves for AG01522 cells exposed to the Catania beam were reproduced. Cell death and chromosome aberrations were then predicted at different depth positions along a SOBP dose profile, both for AG01522 cells and for V79 cells. In line with other studies, this work indicated that assuming a constant RBE along a proton SOBP may be sub-optimal. Furthermore, the simulations helped quantifying the dependence of the beam effectiveness on the considered endpoint and dose, as well as the cell radiosensitivity.

More generally, this work provides an example of therapeutic beam characterization that is not based on RBE, which can be a source of uncertainties. This approach represents a starting point in view of possible future works in which treatment plan optimization may be directly based on the calculated level of biological effect (typically, fraction of inactivated cells and yields of chromosome aberrations). Of course, to be of practical use, the model should be "coupled" to a TPS and/or a radiation transport code. Moreover, the model should be further refined, e.g., by extending it to other cell lines and correcting the tendency to overestimate the effectiveness at the lower survival levels, if this tendency will be confirmed.

AUTHOR CONTRIBUTIONS

MC performed the simulations, interpreted the results, and revised the manuscript. FB designed the work, interpreted the results, and drafted the work. Both authors approved the final version of the manuscript.

ACKNOWLEDGMENTS

The authors are grateful to M. Cornforth, K. Prise, and G. Schettino for data sharing and useful discussions. We also thank the Reviewers for their valuable comments.

FUNDING

This work was partially supported by the Italian Institute of Nuclear Physics (INFN), under the project "ETHICS."

REFERENCES

1. Durante M, Loeffler JS. Charged particles in radiation oncology. *Nat Rev Clin Oncol* (2010) **7**:37–43. doi:10.1038/nrclinonc.2009.183
2. Bert C, Engenhart-Cabillic R, Durante M. Particle therapy for noncancer diseases. *Med Phys* (2012) **39**:1716–27. doi:10.1118/1.3691903
3. Paganetti H, Niemierko A, Ancukiewicz M, Gerweck LE, Goitein M, Loeffler JS, et al. Relative biological effectiveness (RBE) values for proton beam therapy. *Int J Radiat Oncol Biol Phys* (2002) **53**:407–21. doi:10.1016/S0360-3016(02)02754-2
4. Wouters BG, Lam GK, Oelfke U, Gardey K, Durand RE, Skarsgard LD. Measurements of relative biological effectiveness of the 70 MeV proton beam at TRIUMF using V79 cells and the high precision cell sorter assay. *Radiat Res* (1996) **146**:159–70. doi:10.2307/3579588
5. Bettega D, Calzolari P, Chauvel P, Courdi A, Herault J, Iborra N, et al. Radiobiological studies on the 65 MeV therapeutic proton beam at Nice using human tumour cells. *Int J Radiat Biol* (2000) **76**:1297–303. doi:10.1080/09553000050151565
6. Gerweck LE, Kozin SV. Relative biological effectiveness of proton beams in clinical therapy. *Radiother Oncol* (1999) **50**:135–42. doi:10.1016/S0167-8140(98)00092-9
7. Paganetti H, van Luijk P. Biological considerations when comparing proton therapy with photon therapy. *Semin Radiat Oncol* (2013) **23**:77–87. doi:10.1016/j.semradonc.2012.11.002
8. Chang JH, Lee NK, Kim JY, Kim YJ, Moon SH, Kim TH, et al. Phase II trial of proton beam accelerated partial breast irradiation in breast cancer. *Radiother Oncol* (2013) **108**:209–14. doi:10.1016/j.radonc.2013.06.008
9. Grassberger C, Paganetti H. Elevated LET components in clinical proton beams. *Phys Med Biol* (2011) **56**:6677–91. doi:10.1088/0031-9155/56/20/011
10. Ballarini F. From DNA radiation damage to cell death: theoretical approaches. *J Nucl Acids* (2010) **2010**:350608. doi:10.4061/2010/350608

11. Ballarini F, Altieri S, Bortolussi S, Giroletti E, Protti N. A model of radiation-induced cell killing: insights into mechanisms and applications for hadrontherapy. *Radiat Res* (2013) **180**:307–15. doi:10.1667/RR3285.1
12. Ballarini F, Altieri S, Bortolussi S, Carante M, Giroletti E, Protti N. The BIANCA model/code of radiation-induced cell death: application to human cells exposed to different radiation types. *Radiat Environ Biophys* (2014) **53**:525–33. doi:10.1007/s00411-014-0537-6
13. Carante MP, Altieri S, Bortolussi S, Postuma I, Protti N, Ballarini F. Modelling radiation-induced cell death: role of different levels of DNA damage clustering. *Radiat Environ Biophys* (2015) **54**:305–16. doi:10.1007/s00411-015-0601-x
14. Ferrari C, Bakeine J, Ballarini F, Boninella A, Bortolussi S, Bruschi P, et al. In vitro and in vivo studies of boron neutron capture therapy: boron uptake/washout and cell death. *Radiat Res* (2011) **175**:452–62. doi:10.1667/RR2156.1
15. Rabbits T. Chromosomal translocations in human cancer. *Nature* (1994) **372**:143. doi:10.1038/372143a0
16. Cuttone G, Cirrone GAP, Di Franco G, La Monaca V, Lo Nigro S, Ott J, et al. CATANA protontherapy facility: the state of art of clinical and dosimetric experience. *Eur Phys J Plus* (2011) **126**:65. doi:10.1140/epjp/i2011-11065-1
17. Chaudhary P, Marshall T, Perozziello FM, Manti L, Currell FJ, Hanton F, et al. Relative biological effectiveness variation along monoenergetic and modulated bragg peaks of a 62-MeV therapeutic proton beam: preclinical assessment. *Int J Radiat Oncol Biol Phys* (2014) **90**:27–35. doi:10.1016/j.ijrobp.2014.05.010
18. Neumaier T, Swenson J, Pham C, Polyzos A, Lo AT, Yang P-A, et al. Evidence for formation of DNA repair centers and dose-response nonlinearity in human cells. *Proc Natl Acad Sci U S A* (2012) **109**:443–8. doi:10.1073/pnas.1117849108
19. Bridger JM, Herrmann H, Muenkel C, Lichter P. Identification of an interchromosomal compartment by polymerisation of nuclear-targeted vimentin. *J Cell Sci* (1998) **111**:1241–53.
20. Wu H, George K, Yang TC. Estimate of the frequency of true incomplete exchanges in human lymphocytes exposed to 1 GeV/u Fe ions in vitro. *Int J Radiat Biol* (1999) **75**:593–9. doi:10.1080/095530099140230
21. Wu H, Furusawa Y, George K, Kawata T, Cucinotta FA. Analysis of unrejoined chromosomal breakage in human fibroblast cells exposed to low- and high-LET radiation. *J Radiat Res* (2002) **43**:S181–5. doi:10.1269/jrr.43.S181
22. Boei JJ, Vermeulen S, Mullenders LH, Natarajan AT. Impact of radiation quality on the spectrum of induced chromosome exchange aberrations. *Int J Radiat Biol* (2001) **77**:847–57. doi:10.1080/09553000110054610
23. Cornforth MN, Bedford JS. On the nature of a defect in cells from individuals with ataxia-telangiectasia. *Science* (1985) **227**:1589–91. doi:10.1126/science.3975628
24. Cornforth M, Bedford J. A quantitative comparison of potentially lethal damage repair and the rejoining of interphase chromosome breaks in low passage normal human fibroblasts. *Radiat Res* (1987) **111**:385–405. doi:10.2307/3576926
25. Carrano AV. Chromosome aberrations and radiation-induced cell death. I. Transmission and survival parameters of aberrations. *Mutat Res* (1973) **17**:341–53. doi:10.1016/0027-5107(73)90007-9
26. Ottolenghi A, Ballarini F, Biaggi M. Modelling chromosomal aberration induction by ionising radiation: the influence of interphase chromosome architecture. *Adv Space Res* (2001) **27**:369–82. doi:10.1016/S0273-1177(01)00004-7
27. Ballarini F, Ottolenghi A. A model of chromosome aberration induction and CML incidence at low doses. *Radiat Environ Biophys* (2004) **43**:165–71. doi:10.1007/s00411-004-0246-7
28. Ballarini F, Ottolenghi A. A model of chromosome aberration induction: applications to space research. *Radiat Res* (2005) **164**:567–70. doi:10.1667/RR3365.1
29. Ballarini F, Alloni D, Facoetti A, Ottolenghi A. Heavy-ion effects: from track structure to DNA and chromosome damage. *New J Phys* (2008) **10**:075008. doi:10.1088/1367-2630/10/7/075008
30. Goodhead DT. Energy deposition stochastics and track structure: what about the target? *Radiat Prot Dosimetry* (2006) **122**:3–15. doi:10.1093/rpd/ncl498
31. Belli M, Bettega D, Calzolari P, Cherubini R, Cuttone G, Durante M, et al. Effectiveness of monoenergetic and Spread-Out Bragg Peak Carbon ions for inactivation of various normal and tumour cell lines. *J Radiat Res* (2008) **49**:597–607. doi:10.1269/jrr.08052
32. Belli M, Cera F, Cherubini R, Dalla Vecchia M, Haque AMI, Ianzini F, et al. RBE-LET relationship for cell inactivation and mutation induced by low energy protons in V79 cells: further results at the LNL facility. *Int J Radiat Biol* (1998) **74**:501–9. doi:10.1080/095530098141375
33. Biaggi M, Ballarini F, Burkard W, Egger E, Ferrari A, Ottolenghi A. Physical and biophysical characteristics of a fully modulated 72 MeV therapeutic proton beam: model predictions and experimental data. *Nucl Instrum Methods Phys Res B* (1999) **159**:89–100. doi:10.1016/S0168-583X(99)00551-0
34. Folkard M, Prise KM, Vojnovic B, Newman HC, Roper MJ, Michael BD. Inactivation of V79 cells by low-energy protons, deuterons and helium-3 ions. *Int J Radiat Biol* (1996) **69**:729–38. doi:10.1080/095530096145472

Conflict of Interest Statement: The authors declare that the research was conducted in the absence of any commercial or financial relationships that could be construed as a potential conflict of interest.

Copyright © 2016 Carante and Ballarini. This is an open-access article distributed under the terms of the Creative Commons Attribution License (CC BY). The use, distribution or reproduction in other forums is permitted, provided the original author(s) or licensor are credited and that the original publication in this journal is cited, in accordance with accepted academic practice. No use, distribution or reproduction is permitted which does not comply with these terms.

frontiers in Oncology

ORIGINAL RESEARCH
published: 06 July 2015
doi: 10.3389/fonc.2015.00145

Modeling combined chemotherapy and particle therapy for locally advanced pancreatic cancer

Marco Durante[1,2]*, *Francesco Tommasino*[1,2] *and Shigeru Yamada*[3]

[1] Department of Biophysics, GSI Helmholtzzentrum für Schwerionenforschung, Darmstadt, Germany [2] Department of Physics, Trento Institute for Fundamental Physics and Applications (TIFPA), National Institute for Nuclear Physics (INFN), University of Trento, Trento, Italy, [3] Research Center Hospital for Charged Particle Therapy, National Institute of Radiological Sciences (NIRS), Chiba, Japan

Pancreatic ductal adenocarcinoma is the only cancer for which deaths are predicted to increase in 2014 and beyond. Combined radiochemotherapy protocols using gemcitabine and hypofractionated X-rays are ongoing in several clinical trials. Recent results indicate that charged particle therapy substantially increases local control of resectable and unresectable pancreas cancer, as predicted from previous radiobiology studies considering the high tumor hypoxia. Combination with chemotherapy improves the overall survival (OS). We compared published data on X-ray and charged particle clinical results with or without adjuvant chemotherapy calculating the biological effective dose. We show that chemoradiotherapy with protons or carbon ions results in 1 year OS significantly higher than those obtained with other treatment schedules. Further hypofractionation using charged particles may result in improved local control and survival. A comparative clinical trial using the standard X-ray scheme vs. the best current standard with carbon ions is crucial and may open new opportunities for this deadly disease.

Keywords: pancreatic cancer, protontherapy, heavy ion therapy, chemoradiotherapy, gemcitabine

OPEN ACCESS

Edited by:
Chris Schultz,
Medical College of Wisconsin, USA

Reviewed by:
Kevin Camphausen,
National Cancer Institute, USA
Nitin Ohri,
Albert Einstein College of Medicine, USA

Correspondence:
Marco Durante,
Department of Biophysics, GSI Helmholtzzentrum für Schwerionenforschung,
Planckstraße 1, Darmstadt 64291, Germany
m.durante@gsi.de

Specialty section:
This article was submitted to Radiation Oncology, a section of the journal Frontiers in Oncology

Received: *03 April 2015*
Accepted: *15 June 2015*
Published: *06 July 2015*

Citation:
Durante M, Tommasino F and Yamada S (2015) Modeling combined chemotherapy and particle therapy for locally advanced pancreatic cancer. Front. Oncol. 5:145. doi: 10.3389/fonc.2015.00145

Introduction

Pancreatic cancer (PC), usually ductal adenocarcinoma, is the fourth cause of cancer-related death in USA (1) and the only cancer for which deaths are predicted to increase in Europe for both men and women in 2015 (2). Even after surgery, the mortality from PC is very high. Radiotherapy is used for radical treatment in locally advanced unresectable tumors (LAUPC), generally in combination with chemotherapy, or prior to surgery for potentially resectable malignancies. However, prognosis remains very poor, with <5% of patients surviving for 5 years after diagnosis (3). This makes PC a priority for finding better ways to control it and better treatments. Early tumors usually do not cause symptoms, so that the disease is typically not diagnosed until it has spread beyond the pancreas itself, either with distal metastasis or with infiltration in the neuroplexus. This is one of the reasons for the poor survival rate. Moreover, PC is very hypoxic (4), which makes it radioresistant and promotes epithelial–mesenchymal transition; is resistant to apoptosis; and presents a dense tumor stroma, which acts as a barrier against immune cells, preventing immune suppression (5).

Radiobiology studies suggest that charged particle therapy (CPT) using protons or carbon ions is more effective for treatment of PC than X-rays. In fact, accelerated ions have a reduced oxygen enhancement ratio (OER), and are therefore exquisitely effective against hypoxic tumors (6). Moreover, high doses of densely ionizing radiation elicit a strong immune response, which

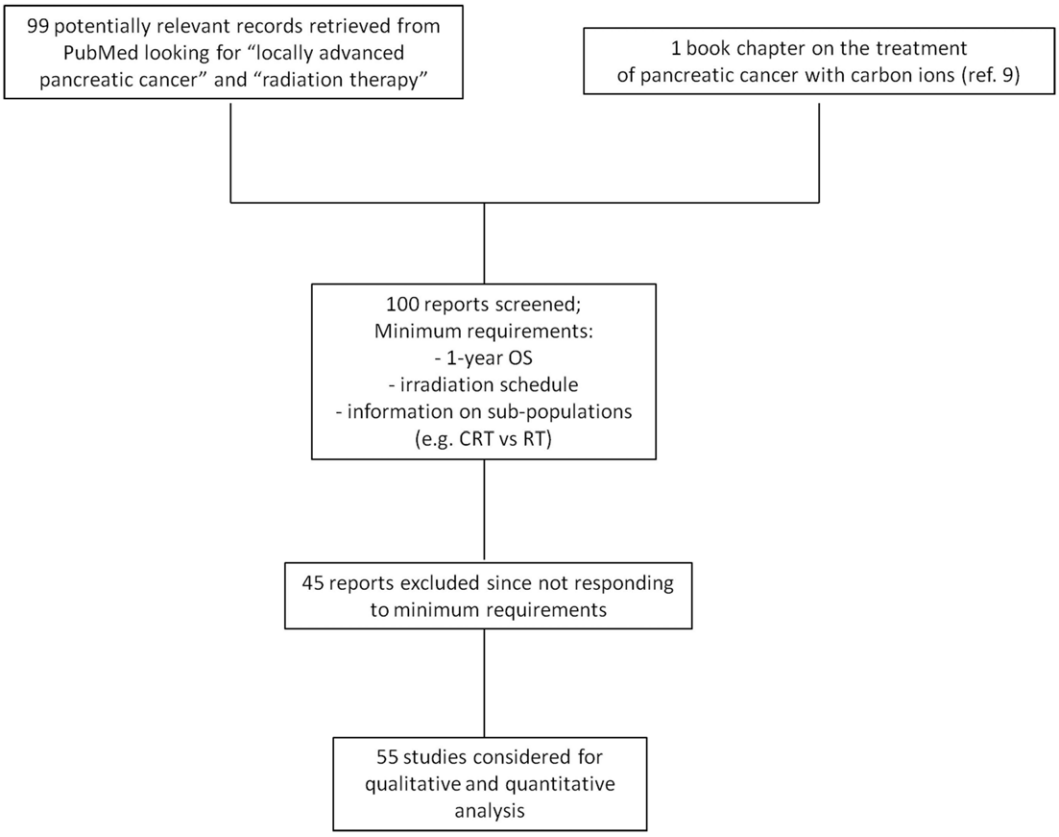

FIGURE 1 | Diagram summarizing the selection criteria of the studies included in the analysis.

can be exploited to destroy not only the primary tumor but also distal metastasis (7). Carbon ion radiotherapy (CIRT) is currently performed in only two centers in Europe (HIT in Germany and CNAO in Italy) and none in USA (where many centers use protons only for CPT), but much more experience has been accumulated in Asia, especially at the National Institute for Radiological Sciences (NIRS) in Chiba, Japan. A recent external review of 20 years of CIRT at NIRS highlighted treatment of PC as the most promising application of CIRT, with results clearly superior to any other treatment modalities, especially for LAUPC (8).

Based on these very promising preliminary Japanese results, the US National Cancer Institute (NCI), in his efforts to promote CIRT in USA, issued a solicitation for a prospective randomized phase-III trial comparing CIRT to X-ray therapy for LAUPC in combination with chemotherapy, having survival as main endpoint[1]. This trial may provide the first evidence of a superiority of CIRT in a common and deadly cancer. Planning of the trial is complicated by the many different variables – not only radiation quality but also chemotherapy regime, fractionation, and treatment plan. Here, we review all the current results in treatment of LAUPC and use a mathematical model to describe the dependence on survival on the biological effective dose (BED) with X-rays and CPT in combination with chemotherapy.

[1]Solicitation number BAA-N01CM51007-51 (April 17, 2015) available online through FedBizOpps at http://www.fbo.gov

Materials and Methods

Data Collection

We searched the literature for all data available on radiotherapy, chemotherapy, and combined treatments. The research criteria and outcomes are summarized in the diagram shown in **Figure 1**. The patient populations generally consist of adults with adenocarcinoma histology, locally advanced tumor presentation, and generally tumors not in direct contact to duodenum and stomach. Radiotherapy included conformal radiotherapy (3DCRT), intensity-modulated radiation therapy (IMRT), stereotactic body radiotherapy (SBRT), protontherapy, and CIRT. Data from CIRT are limited to the NIRS experience and include data as yet only published in the institute annual report and in a recent book (9). Adjuvant, neo-adjuvant, or concomitant chemotherapies were all included in the search, using different drugs. Our data collection was compared with a recent meta-analysis of radiochemotherapy in LAUPC (10), and has been updated on April 2015.

Modeling

To compare the largely variable fractionation and chemotherapy schedules reported in the literature, we used the common quantity of BED (11), which has been extended to chemotherapy to quantify the effect of the drug in terms of radiation-equivalent dose (12). Because many published papers have short follow-up, and not all endpoints are reported, we concentrated on the 1-year

overall survival (OS). We assumed that the overall 1-year survival probability OS is a combination of the survival probability following the radiation (RS) and chemotherapy (CS) treatment, i.e.,

$$\mathrm{OS} = \mathrm{CS} + \mathrm{RS}\,(1 - \mathrm{CS}) \tag{1}$$

Equation 1 implies a purely additive effect of chemotherapy and radiotherapy in the treatment of LAUPC. The dose–response for the OS probability can be expressed with the same functions used for the tumor control probability: Poisson, logistic, or probit models (13). We elected to use the logistic function, which is based on the linear-quadratic model, following the recent model of chemoradiation treatment in bladder cancer (14). Thus, we wrote:

$$\mathrm{RS} = \frac{1}{1 + exp\left[4\gamma_{50}\left(1 - \frac{\mathrm{BED}}{D_{50}}\right)\right]} \tag{2}$$

where γ_{50} is the normalized dose-response gradient and D_{50} the BED corresponding to a survival in a radiotherapy only treatment of 50% at 1 year.

Combining Eqs 1 and 2, we finally obtain

$$\mathrm{OS} = \frac{1 + \mathrm{CS} \cdot exp\left[4\gamma_{50}\left(1 - \frac{\mathrm{BED}}{D_{50}}\right)\right]}{1 + exp\left[4\gamma_{50}\left(1 - \frac{\mathrm{BED}}{D_{50}}\right)\right]} \tag{3}$$

In a recent analysis of chemoradiation therapy in LAUPC, Moraru et al. (15) used a radiosensitization factor in the BED formula and fitted the LAUPC 1 year OS data with a modified linear-quadratic formula. In general, it is very hard to distinguish additive from synergistic model in chemoradiation data (16). *In vitro* experiments can provide some information, but do not necessarily reflect the complex *in vivo* microenvironment. Some chemotherapy drugs used for LAUPC treatment apparently sensitize cell cultures to X-rays (17, 18), but simple additive effects are observed when the drugs are given *in vitro* concomitantly to charged particles (19, 20). Moreover, in many clinical protocols, chemotherapy is given as adjuvant or neo-adjuvant, and even when concomitant is often continued after the radiotherapy cycle. We therefore assumed, in our analysis, that the simple additive model of Eqs 1 and 3.

The BED was calculated using the Fowler formula (11):

$$\mathrm{BED} = nd\left(1 + \frac{d}{\alpha/\beta}\right) - \frac{\ln(2)}{\alpha} \cdot \frac{T}{T_d} \tag{4}$$

with:

- n: number of fractions
- d: dose/fraction
- T: overall treatment time
- $\alpha = 0.393\ \mathrm{Gy}^{-1}$, $\beta = 0.058\ \mathrm{Gy}^{-2}$, $\alpha/\beta = 6.77$ Gy (21)
- T_d: tumor doubling time, fixed to 42 days (15).

The dose/fraction d was given in Gy for X-ray data, and Gy(RBE) (or GyE) for CPT. For protontherapy, 1 Gy(RBE) = 1.1 Gy (22). In CIRT, Gy(RBE) was calculated according to the NIRS model (23), whose results can be different, depending on the dose and target size, from those that would be obtained using the LEM model (24), implemented in the European CIRT facilities.

Fitting

Clinical data extracted from the published papers were weighted with a vertical error bar, given by the SD of the OS using Poisson statistics:

$$\mathrm{OS}_{1-\mathrm{Year}} = \frac{n_\mathrm{s}}{n_\mathrm{tot}} \pm \frac{\sqrt{n_\mathrm{s}}}{n_\mathrm{tot}} \tag{5}$$

where n_s and n_tot indicate the number of surviving patients at 1 year and the total number of patients included in the study, respectively. When possible, a horizontal error bar was also included, corresponding to the range of the doses used. A first weighed fit of the radiotherapy-alone data was performed using Eq. 2 to estimate the two parameters γ_{50} and D_{50}. The chemoradiation data were then fitted using Eq. 3 having CS as only fitting parameter: γ_{50} and D_{50} were indeed taken from the radiotherapy fit. Many different chemotherapy drugs were used in old and new studies. Gemcitabine is one of the most successful and currently adopted, also in the CIRT trials. We have therefore divided the data into gemcitabine only, other drugs, and gemcitabine plus other drugs. Overall, no statistically significant differences were noted among the three groups. We have therefore fitted the data together, even if we plotted the points in different colors. Finally, for fitting the CPT data, we expressed the BED in Gy(RBE) as described above, and used Eq. 3 with a fixed CS and γ_{50} taken from the fit of the chemoradiation data with X-rays. In fact, we assume that CPT has an impact on the D_{50} due to the putative improved dose distribution in the target and to the radiobiological properties beyond the calculated RBE used in the Gy(RBE).

Results

Single Treatment Data

Chemoradiation is generally considered the best standard of cure for LAUPC. For this reason, only a few studies are available with radiotherapy alone, and some of them are old (**Table 1**). Some recent studies using SBRT have been excluded. An initial trial in

TABLE 1 | Clinical data for treatment of LAUPC using X-ray radiotherapy alone.

Reference	Year	Total dose (Gy)	Fractions	Sample size	1 year OS	2 years OS	Median OS
Moertel et al. (38)	1969	35–40	20	28	7%	N/A	N/A
Moertel et al. (39)	1981	60	30	25	10%	N/A	5.3 months
Ceha et al. (40)	2000	70–72	35–36	44	39%	N/A	10 months
Cohen et al. (41)	2005	59.4	33	49	20%	N/A	7.1 months
Wang et al. (42)	2015	46	23	14	35%	14%	7.4 months

Stanford using high-dose (25 Gy) single-fraction reports a 100% survival at 1 year, but this was limited to six patients (25). Later results from Stanford using SBRT are included in **Table 2**. On the other hand, a Danish study using 45 Gy in three fractions gave very low OS and high toxicity (26). This study was also excluded in our analysis, because these poor outcomes were likely a result of inaccurate positioning, lack of effective motion management techniques, and lack of dose constraints for OARs (27).

The data are plotted in **Figure 2**, along with the fit using Eq. 2. Fitting parameters are reported in **Table 2**. The $D_{50} = 107$ Gy clearly shows how impractical is the treatment of LAUPC with X-rays alone. For comparison, Dale et al. (16) estimated a BED at 50% complete response for bladder cancer of 54.4 Gy. From the analysis of the trials using chemotherapy alone (10), an average 1-year survival below 20% can be estimated.

Chemoradiation

Meta-analysis of the clinical data has already shown an advantage in chemoradiation compared to radiotherapy or chemotherapy alone (10). Most clinical trials for LAUPC resort to chemoradiation protocols. Gemcitabine (**Table 3**) is often regarded as the standard treatment. Several other drugs, such as capecitabine, fluorouracil (5-FU), cisplatin, docetaxel, cetuximab, and fluoropyrimidine prodrug S-1, have been used in the past or in new trials (**Table 4**), and often combination of gemcitabine and any of the other drugs (**Table 5**) are applied. The standard

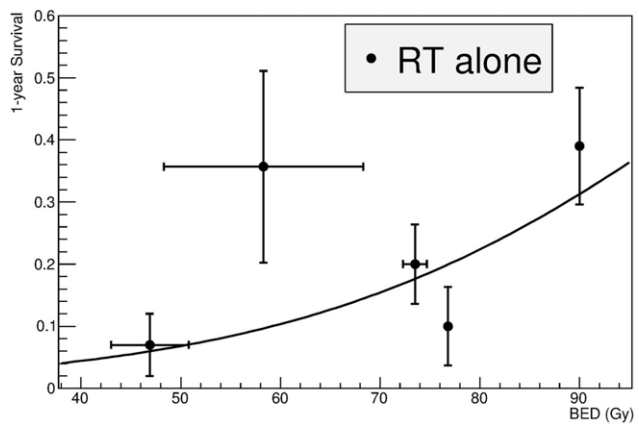

FIGURE 2 | Fit of the clinical data for treatment of LAUPC with X-ray radiotherapy alone. Studies are listed in **Table 1**. BED is calculated by Eq. 4. Fitting was performed by Eq. 2 and fitting parameters are in **Table 3**.

TABLE 2 | Clinical data for treatment of LAUPC using X-ray therapy plus gemcitabine.

Reference	Year	Total dose (Gy)	Fractions	Chemotherapy	Sample size	1 year OS	2 years OS	Median OS (months)
Wolff et al. (43)	2001	30	10	Gem, 350–500 mg/m^2/week for 7 weeks	18	66%	N/A	6
Epelbaum et al. (44)	2002	50.4	28	Gem, 1000 mg/m^2 weekly before and after RT, Gem 400 mg/m^2 weekly during RT	20	30%	N/A	N/A
Joensuu et al. (45)	2004	50.4	28	Gem, 20/50/100 mg/m^2 twice weekly before RT	28	55%	N/A	25
Okusaka et al. (46)	2004	50.4	28	Gem, 250 mg/m^2 weekly + maintenance 1000 mg/m^2 weekly for 3 weeks every 4 weeks	38	28%	23%	9.5
Murphy et al. (47)	2007	36	15	Gem, 1000 mg/m^2 on days 1, 8, and 15	74	46%	13%	11.2
Small et al. (48)	2008	36	15	Gem, 1000 mg/m^2 2–3 times/week before, during, and after RT treatment	14	47%	N/A	N/A
Igarashi et al. (49)	2008	40–50.4	20–28	Gem, 40 mg/m^2 twice/week + maintenance 1000 mg/m^2 for 3 weeks	15	60%	N/A	15
Schnellenberg et al. (50)	2008	25	1	Gem, 1000 mg/m^2 weekly for 3 weeks before RT + maintenance weekly	16	50%	N/A	11.4
Polistina et al. (51)	2010	30	3	Gem, 1000 mg/m^2 weekly for 6 weeks before RT + maintenance weekly	23	39.1%	0%	10.6
Loehrer et al. (52)	2011	50.4	28	Gem, 600 mg/m^2 weekly before and during RT	34	50%	12%	11.1
Schnellenberg et al. (53)	2011	25	1	Gem, 1000 mg/m^2 weekly before and after RT	20	50%	20%	11.8
Cardenes et al. (54)	2011	50.4	28	Gem, 600 mg/m^2 weekly before and during RT + maintenance 1000 mg/m^2 weekly	28	30%	11%	10.3
Shibuya et al. (55)	2011	54	30	Gem, 250 mg/m^2 weekly during RT + maintenance 1000 mg/m^2 every 4 weeks (discretional)	21	74%	N/A	16.6
Mahadevan et al. (56)	2011	24–36	3	Gem, 1000 mg/m^2 weekly before, during, and after RT (at least 6 cycles)	39	72%	33%	20
Huang et al. (57)	2011	50.4–63	28–35	Gem, 1000 mg/m^2 weekly during RT + induction/adjuvant (discretional)	55	51%	N/A	12.5
Mukherjee et al. (58)	2013	50.4	28	Gem, induction 300 mg/m^2 + concurrent 1000 mg/m^2	38	64.2%	N/A	13.4
Gurka et al. (59)	2013	25	5	Gem, 1000 mg/m^2 weekly before and after RT	10	50%	N/A	12.2
Herman et al. (60)	2014	33	5	Gem, 1000 mg/m^2 weekly before and after RT	49	59%	18%	13.9

TABLE 3 | Fitting parameters calculated using the Eqs 2 or 3.

Dataset	Table	γ_{50}	D_{50} [Gy or Gy(RBE)]	Chemotherapy survival rate (CS)	Figure
Radiotherapy (X-rays) alone	1	1.2 ± 0.5	107 ± 16	N/A	2
Radiotherapy (X-rays) + gemcitabine	2	1.2 (fixed)	107 (fixed)	0.39 ± 0.03	3
Radiotherapy (X-rays) + chemotherapy other than gemcitabine	4	1.2 (fixed)	107 (fixed)	0.32 ± 0.02	3
Radiotherapy (X-rays) + chemotherapy (all protocols combined)	3–5	1.2 (fixed)	107 (fixed)	0.36 ± 0.01	4
CPT + chemotherapy	6	1.2 (fixed)	75 ± 9	0.36 (fixed)	5

X-ray course is 50.4 Gy in 1.8 Gy/fraction, giving a BED of 63 Gy. We did not find significant differences in the groups treated with different drugs, considering the very high scatter of the data also due to the completely different protocols adopted. **Figure 3** shows, for example, a comparison of the data in **Tables 3** and **4**, pointing only to a slight trend for better results in protocols using gemcitabine compared to other drugs. **Figure 4** shows the fit of all the data compared to X-rays alone. Having fixed the γ_{50} and D_{50} parameters, we estimated the only parameter $CS = 0.36 \pm 0.01$ (**Table 2**). The radiation dose corresponding to this survival probability RS = CS can be estimated by Eq. 2 as

$$\text{BED (chemo – equivalent)} = D_{50}\left(1 - \frac{\ln \frac{1-RS}{RS}}{4\gamma_{50}}\right) \quad (6)$$

leading to a chemo-equivalent dose of 94 Gy. This high value underlines the large improvement that chemotherapy gives on the survival of LAUPC patients. Dale and co-workers (16) estimated 43.6 Gy for the BED chemo-equivalent in bladder cancer. They also demonstrated that the chemo-equivalent dose is not a constant and will be of course much lower if we calculate it for a higher survival level.

Charged Particle Therapy

Although only a few studies are available with CPT, the data in **Table 6** show that they are the best current options for LAUPC. A 2-year survival rate around 50% was reached with protons (28) or C-ions (9) in combination with gemcitabine, a value far exceeding any other chemoradiation trial using X-rays and any cocktail of drugs. The data with CIRT alone (no chemotherapy) are clearly superior to those with X-rays alone and comparable to the results with chemoradiation at the same X-rays BED. The best 1-year OSs for combined chemotherapy (gemcitabine) and CPT are those from Hyogo (28) using protons up to 70.2 Gy(RBE) in 26 fractions, but they came at a cost of grade 3–5 toxicity in 10% of the patients, especially gastric ulcer and hemorrhage. CIRT toxicity was much more mild, with 17% of the patients experiencing grade 3 GI toxicity, in the form of appetite loss. Low toxicity was observed for the duodenum, both for protons and ^{12}C-ions. The fit of the chemoradiation with CPT, using the same CS and γ_{50} parameters calculated for X-rays + chemotherapy, is shown in **Figure 5**. This fit assumes that CPT does not change the effect of the chemotherapy compared to X-rays, but results in a lower D_{50} due to biological and/or physical improvements compared to X-rays. Should these improvements be already included in the RBE model used to calculate the equivalent dose in Gy(RBE), we should see the same effect at the same BED [see Ref. (23) for CIRT in Japan; RBE = 1.1 for protons]. Instead, the best fit is reduced to $D_{50} = 75 \pm 9$ Gy(RBE) for CPT (**Table 2**). This 50% improvement is caused either by a better physics, enabling treatment of infiltrations in the neuroplexus, or to a better biology, especially to a reduced OER (6) or to a stronger immune response (7) using CPT compared to X-rays.

Discussion

The large interest for the use of CPT in LAUPC comes from the exceptional clinical results (8), supported by our clinical data analysis in **Figure 5**. These results reflect the biological rationale of reduced OER for high-LET radiation and possible dose escalation with limited side effects exploiting the Bragg peak. The high GI toxicity observed in the Hyogo trial (28) seems to set a threshold at a BED around 100 Gy(RBE). The question is whether the same threshold applies to CIRT, where the sharper dose edges of the treatment plan may reduce the exposure of the critical organs compared to protons, whose lateral scattering is much higher than for heavy ions (6). An example of a treatment plan of a pancreatic head cancer with carbon ions is shown in **Figure 6**. It is possible to give a high-dose against tumor and neuroplexus with acceptable doses to stomach or duodenum. The dose distribution can further improve using raster scanning instead of passive modulation, as shown in **Figure 7**. The new NIRS facility is now equipped with raster scanning, and so are the HIT and CNAO facilities now treating the first LAUPC patients with C-ions. Under these optimal conditions, it appears feasible to exceed a BED of 100 Gy(RBE) with acceptable toxicities.

Modeling chemotherapy in terms of equivalent radiation dose is an effective method to predict outcomes of dose-escalation trials (12, 16). The large scatter in the chemoradiation data leads, however, to a poor goodness-of-fit in **Figures 3** and **4**. This is due in part to the many different protocols used in chemotherapy for LAUPC, and to inclusion of data published in over 30 years using very different methods both for drug and radiation delivery. In this paper, we have decided to analyze all the data available in the literature, without including the treatment year as a function in the model. We have also assumed no synergistic interaction between chemicals and radiation. Finally, Eq. 4 should be modified for protons or carbon ions, where α/β is higher than for X-rays leading to a lower dependence on fractionation. Due to the lack of sufficient information leading to an educated guess for other parameters and models, we decided to stick to the conventional logistic function, replacing Gy with Gy(RBE) in **Table 6**. The basic assumption remains that a higher BED will result in a higher OS in LAUPC patients, an assumption clearly supported by the analysis of the several trials included in our data mining. Our analysis supports the concept that a dose escalation will improve OS, and toxicity is the limiting factor. In **Table 7**, we have calculated with the

TABLE 4 | Clinical data for treatment of LAUPC using X-ray therapy plus chemotherapy, excluding the trials with gemcitabine.

Reference	Year	Total dose (Gy)	Fractions	Chemotherapy	Sample size	1 year OS	2 years OS	Median OS (months)
Moertel et al. (39)	1981	40 60	20 30	5-FU 500 mg/m^2 3 days/week during RT, maintenance 5-FU 500 mg/m^2 weekly	83 85	46% 35%	N/A N/A	11.4 8.4
Wagener et al. (61)	1996	40	20	Epirubicin + Cisplatin + 5-FU	53	49%	N/A	10.8
Ishii et al. (62)	1997	50.4	28	5-FU 500 mg/m^2 3 days/week during RT	20	41.8%	N/A	10.3
Fisher et al. (63)	1999	45	25	5-FU 150–250 mg/m^2 continuous infusion 24 h/day during RT	25	32%	N/A	9
Andre et al. (64)	2000	45	25	5-FU 375 mg/m^2 + Cisplatin 15 mg/m^2 daily during RT (first and last week) + maintenance after RT	32	31%	12.5%	9
Boz et al. (65)	2001	59.4	33	5-FU 150–300 mg/m^2 continuous infusion 24 h/day during RT	42	30%	N/A	9.1
Safran et al. (66)	2001	50.4	28	Paclitaxel 50 mg/m^2 weekly during RT	44	30%	N/A	8
Li et al. (67)	2003	50.4–61.2	28–34	5-FU 500 mg/m^2 for 3 days every 2 weeks during RT, Gem 1000 mg/m^2 after RT	16	31%	0%	6.7
Morganti et al. (68)	2004	39.6–59.4	22–33	5-FU 1000 mg/m^2 during RT at days 1–4 and 21–24	50	31.3%	N/A	N/A
Cohen et al. (41)	2005	59.4	33	5-FU 1000 mg/m^2 at days 1–4 and 21–24 + Mitomycin 10 mg/m^2 at day 2 during RT	55	31%	N/A	8.4
Park et al. (69)	2006	20	10	5-FU 500 mg/m^2 for 3 days twice during RT with 2 weeks break	56	37%	14.6%	10.4
Chauffert et al. (70)	2008	60	30	5-FU 300 mg/m^2 5 days/week for 6 weeks + Cisplatin 20 mg/m^2 5 days/week on weeks 1 and 5, maintenance Gem 1000 mg/m^2 weekly	59	32%	N/A	8.6
Crane et al. (71)	2009	50.4	28	Capecitabine 825 mg/m^2 twice daily + Bevacizumab 5 mg/kg on days 1, 15, and 29; maintenance Gem 1000 mg/m^2 weekly + Bevacizumab 5 mg/kg every 2 weeks	82	47%	N/A	11.9
Sudo et al. (72)	2011	50.4	28	S-1 80 mg/m^2 daily during and after RT	34	70.6%	N/A	16.8
Oberic et al. (73)	2011	54	30	Docetaxel 20 mg/m^2 weekly + 5-FU 200 mg/m^2 daily during RT	20	40%	N/A	10
Brunner et al. (74)	2011	55.8	33	5-FU 1000 mg/m^2 on days 1–5 and 29–33 + Mitomycin 10 mg/m^2 on days 1–29 during RT	35	40%	N/A	9.7
Huang et al. (57)	2011	50.4–63	28–35	5-FU 200–300 mg/m^2 5 days/week or 5-FU 500 mg/m^2 on days 1–3 and 29–31 or capecitabine 1300–1600 mg/m^2 daily during RT	38	24%	N/A	10.2
Malik et al. (75)	2012	50.4	28	5-FU based during RT*	84	52.6%	N/A	10.9
Ikeda et al. (76)	2012	50.4	28	S-1 80 mg/m^2 twice daily during RT, maintenance S-1 80 mg/m^2 daily after RT	60	72%	N/A	16.2
Schinchi et al. (77)	2012	50	40	S-1 80 mg/m^2 twice daily during and after RT	50	62%	27%	14.3
Mukherjee et al. (58)	2013	50.4	28	Capecitabine 830 mg/m^2 5 days/week induction and concurrent to RT	36	79.2%	N/A	13.4
Herman et al. (78)	2013	50.4	28	5-FU 200 mg/m^2 daily during RT, maintenance Gem 1000 mg/m^2 weekly 5-FU 200 mg/m^2 daily + TNFerade weekly during RT, maintenance Gem 1000 mg/m^2 weekly	90 187	36.7% 41%	10.3% 11.3%	10 10
Ducreaux et al. (79)	2014	54	30	Docetaxel 20 mg/m^2 + Cisplatin 20 mg/m^2 weekly during RT	51	41%	31%	9.6
Rembielak et al. (80)	2014	50.4	28	Cetuximab loading dose 400 mg/m^2 + 250 mg/m^2 weekly during RT	21	33%	11%	7.5
Kwak et al. (81)	2014	50.4	28	5-FU 600–1000 mg/m^2 during RT, maintenance Gem 200 mg/m^2 weekly	34	40%	10%	9

**Limited information about chemotherapy.*

TABLE 5 | Clinical data for treatment of LAUPC using X-ray therapy plus a chemotherapy cocktail including gemcitabine.

Reference	Year	Total dose (Gy)	Fractions	Chemotherapy	Sample size	1 year OS	2 years OS	Median OS
Chung et al. (82)	2004	45	25	Gem 1000 mg/m^2 weekly + Doxifluoridine 600 mg/m^2 daily during and after RT	22	50%	N/A	12
Haddock et al. (83)	2007	45	25	Gem 30 mg/m^2 + Cisplatin 10 mg/m^2 twice weekly during first 3 weeks of RT, Gem 1000 mg/m^2 weekly after RT	48	40%	N/A	10.2
Hong et al. (84)	2008	45	25	Gem 1000 mg/m^2 weekly + Cisplatin 70 mg/m^2 two times during RT, maintenance Gem 1000 mg/m^2 weekly + Cisplatin 70 mg/m^2 every 4 weeks	38	63.3%	27.9%	16.7
Mamon et al. (85)	2011	50.4	28	Gem 200 mg/m^2 weekly + 5-FU 200 mg/m^2 5 days/week during RT, maintenance Gem 1000 mg/m^2 weekly	78	51%	N/A	12.2
Crane et al. (86)	2011	50.4	28	Gem 1000 mg/m^2 + Oxaliplatin 100 mg/m^2 before RT + Capecitabine 825 mg/m^2 twice daily on RT days, cetuximab 500 mg/m^2 every 2 weeks before and during RT	69	66%	25%	19.2
Brunner et al. (74)	2011	55.8	31	Gem 300 mg/m^2 + Cisplatin 30 mg/m^2 weekly during RT	58	53%	N/A	12.7
Ch'Ang et al. (87)	2011	50.4	28	Gem 800 mg/m^2 + Oxaliplatin 85 mg/m^2 + 5-FU/Leucovorin 3000/150 mg/m^2 twice/week before RT, Gem 400 mg/m^2 weekly during RT	50	68%	20.6%	14.5
Tozzi et al. (88)	2013	45	6	Gem-based before RT	30	47%	N/A	11
Ke et al. (89)	2014	50.4	28	Gem 1000 mg/m^2 weekly + S-1 40 mg/m^2 twice daily before RT, S-1 80 mg/m^2 twice daily during RT, S-1 80 mg/m^2 twice daily 1 month after RT	32	75%	34.4%	15.2
Wang et al. (42)	2015	46	23	Gem-based (sub-groups)	16	71.1%	40.6%	19.5

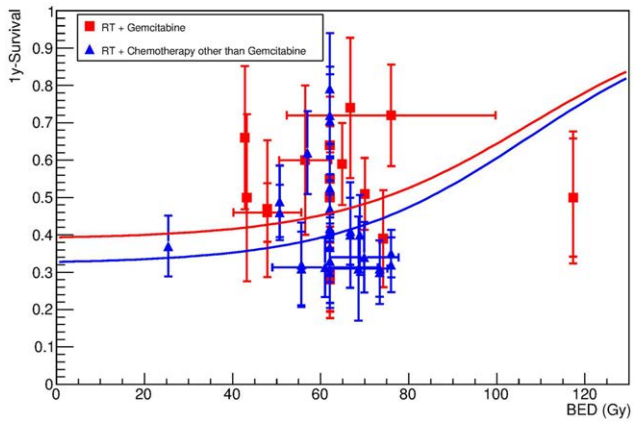

FIGURE 3 | One-year survival as a function of the BED for patients undergoing X-ray radiotherapy plus gemcitabine (red symbols), or other chemotherapy drugs (blue symbols). Data are reported in **Tables 2** and **4**. The lines show the result of the fit (Eq. 3), which was performed assuming that γ_{50} and D_{50} are obtained by fitting the data in treatments using radiotherapy only (**Figure 1**). The only free fitting parameter is the chemotherapy survival CS (see **Table 3**). The results suggest that the final outcome does not strongly depend on the specific chemotherapy treatment, although some advantage seems to be associated to the use of gemcitabine.

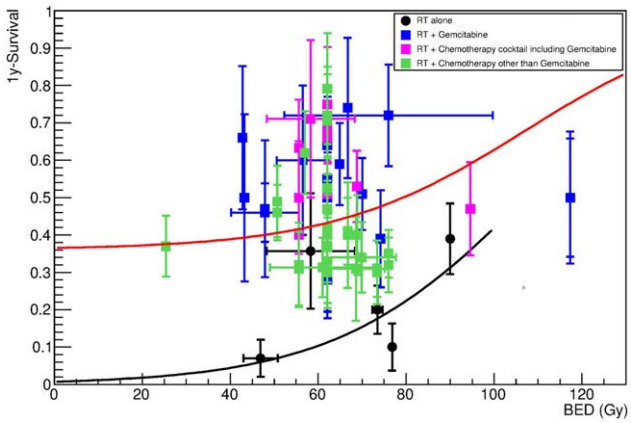

FIGURE 4 | One-year survival as a function of the BED for patients undergoing X-ray radiotherapy alone (black symbols), or in combination with any chemotherapy treatments. Details about chemotherapy regimen are reported in **Tables 4–6**. The lines show the result of the fit (black for radiotherapy-alone data, red for all chemotherapy data pooled together), which was performed assuming that γ_{50} and D_{50} are obtained by fitting RT-alone data. Fitting parameters with Eq. 3 are in **Table 3**.

logistic model (Eq. 3) the expected survival in hypofractionated dose-escalation trials and compared with the standard chemoradiation treatment and other schedules proposed for SBRT using X-rays (15, 27). The standard at NIRS is 12 fractions in 3 weeks, and with the current maximum dose/fraction the OS at 1 year is expected to improve from 40 to 70% compared to the standard X-ray regime (50.4 Gy in 28 fractions). Reaching 18 fractions with the same dose/fraction, it could be possible to double the survival. Further hypofractionation, down to a single dose of 25 Gy(RBE) is very attractive in terms of expected survival, but raises concerns for the GI toxicity. C-ions delivered by raster scanning should provide the optimal dose distributions (**Figure 7**) compared to CIRT with passive scattering and protons, where the lateral scattering unavoidably leads to a dose penumbra around the PTV. However, for beam scanning, the issue of motion mitigation must be tackled very carefully, because of the known problem of the interplay. Currently, NIRS is using respiratory gating to compensate especially the movements of stomach and duodenum in the PTV

(**Figure 8**). A treatment with high number of fractions compensates the interplay between beam scanning and organ motion, but this compensation is lost in radiosurgery (29). In the treatment of hepatocellular carcinoma with ^{12}C-ions at the HIT facility in Heidelberg, it has been shown that the simple increase from 1 to 4 fractions substantially improved the dose target coverage and reduced overdosage (V107 from 32 to 4%) (30), this means that keeping the hypofractionation schemes above 4 fractions, major inhomogeneities should be avoided. Nevertheless, the range uncertainties due to bowel movement, stomach peristalsis, and breathing, have to be solved to reduce toxicity to the many critical organs surrounding the pancreas. Motion mitigation strategy include respiratory gating or layer stacking boost irradiation, such as used at NIRS for treating PC (31), and 4D optimization of the plan based on 4DCT (32). Patients with tumors in a favorable location, preferably >1 cm from the closest luminal organ, should be selected for the dose escalation.

The solution of this problem is an important step to push toward higher doses and fewer fractions thus leading to a substantial improvement in survival can be expected using chemoradiation protocols with CPT rather than X-rays. The first

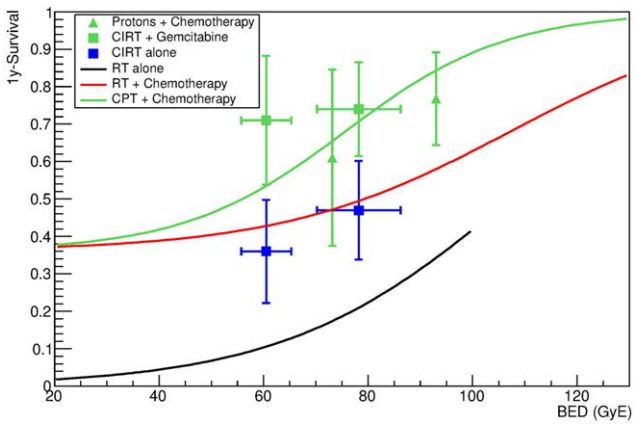

FIGURE 5 | One-year survival as a function of the BED for patients undergoing CPT with or without additional chemotherapy. Blue symbols refer to patients receiving radiotherapy with C-ions without additional chemotherapy. Green symbols refer to data obtained with proton (triangles) and carbon ions (full squares) in combination with chemotherapy. Data are given in **Table 6**. The green line shows the result of the fit of data for chemotherapy combined with proton or carbon ions. The fit was performed using γ_{50} and CS from X-ray + chemotherapy data. The only free parameter is therefore D_{50}. The black and red lines show the results of the fit for X-rays alone and X-rays plus chemotherapy, and are reported for comparison. Fitting parameters are in **Table 3**.

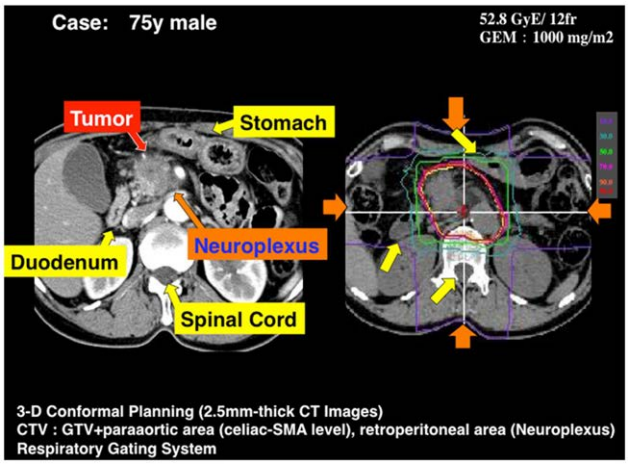

FIGURE 6 | A typical treatment plan used at NIRS for a locally advanced pancreatic head cancer. The beam is shaped with passive modulation and four opposite fields are applied with respiratory gating. GTV includes the primary tumor and lymph nodes involved.
CTV = PTV + neuroplexus infiltration (periarterial area) + proximal lymph nodes. PTV = CTV + 5 mm, excluding GI tract.

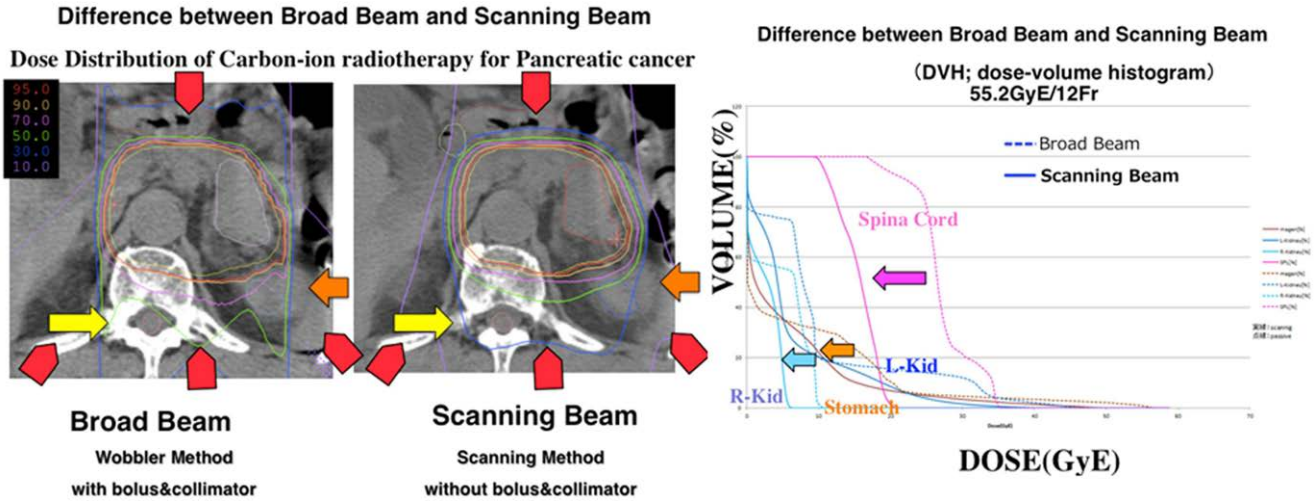

FIGURE 7 | Comparison of the current passive beam modulation treatment plan with a spot scanning treatment plan for LAUPC. In the right panel, the dose–volume histogram for different organs is shown for passive modulation (dotted line) and raster scanning (solid line). Dose to the spinal cord and kidney are highly reduced. Potential reduction is also clear for stomach and duodenum, whose movements are, however, critical.

TABLE 6 | Clinical data for treatment of LAUPC using CPT.

Reference	Year	Radiation quality	Total dose in Gy (RBE)	Fractions	Chemotherapy	Sample size	1 year OS	2 years OS	Median OS
Terashima et al. (28)	2012	Protons	67.5	25	Gem, 800 mg/m^2/week for 3 weeks	50	76.8%	50%	N/A
Sachsman et al. (90)	2014	Protons	59.4	33	Capecitabine, 1000 mg twice/day; 5 days/week on radiation treatment days only	11	61%	31%	18.4
Yamada et al. (9)	2014	Carbon ions	38.4–43.2	12	–	19	36%	5%	N/A
					Gem 1000 mg/m^2/week for 3 weeks	24	71%	21%	N/A
			45.6–52.8	12	–	27	47%	16%	N/A
					Gem 1000 mg/m^2/week for 3 weeks	47	74%	54%	N/A

TABLE 7 | Expected improvement in survival according to our model in chemoradiation trials using CPT.

Dose/fraction in Gy or Gy(RBE)	Radiation quality	Fractions	Total dose in Gy or Gy(RBE)	BED in Gy or Gy(RBE)	Expected 1 year survival rate	Comments
1.8	X-rays	28	50.4	62.9	42%	Current standard fractionation scheme
2.25	X-rays	33	74.3	97.8	61%	Proposed dose-escalation trial at Medical College of Winsconsin (15)
6.6	X-rays	5	33	65.2	45%	Standard for SBRT in adjuvant settings (27)
2.7	Protons	26	70.2	97.4	75%	Maximum dose reached at Hyogo
4.6	C-ions	12	55.2	92.5	71%	Maximum dose reached at NIRS
5.85	C-ions or protons	12	70.2	130.6	82%	Maximum total dose reached with protons in Hyogo using the number of fraction from NIRS
25	C-ions or protons	1	25	117.5	76%	Maximum dose used in single-fraction X-ray radiosurgery for LAUPC (27)
4.6	C-ions or protons	18	82.8	138.6	84%	Expected doubling of the OS with conventional X-ray fractionation scheme, using the dose/fraction from NIRS

*BED is calculated by Eq. 4. Expected 1 year survival is calculated using Eq. 3 and the parameters in **Table 3**.*

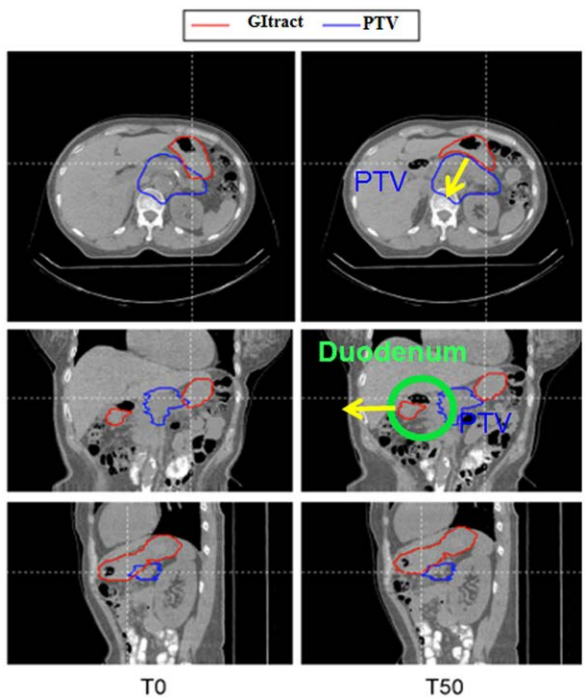

FIGURE 8 | 4DCT analysis of the movement of the critical organs during treatment of LAUPC at NIRS with C-ions. T0 is the peak inhalation and T50 the peak exhalation phases. Stomach and duodenum move in and out the PTV in the two phases.

clinical CIRT vs. IMRT trial for LAUPC should compare the standard chemoradiation treatment (**Table 7**, row 1), with the NIRS most advanced protocol (**Table 7**, row 5). The additional advantage of using the standard protocols is that at the dose/fraction of 4.6 Gy(RBE) reached in the escalation trial at NIRS, there is practically no difference between the biological dose calculated at NIRS and those predicted by LEM (24) and implemented in European CIRT facilities. However, in a multi-centric trial, it will be unavoidable to have different systems for dose delivery, motion management, patient selection, etc. For instance, NIRS is using passive modulation, CNAO raster scanning, and HIT can use the gantry. Nevertheless, a comparative trial for LAUPC is absolutely necessary to support the use of CIRT and to confirm the very promising data in the phase I–II trials at NIRS (8). The lack of comparative, phase-III clinical trials is generally considered as a major hindrance to a more widespread use of CPT in the clinics (33). A trial on LAUPC may definitely clarify the clinical advantage of CPT in such a lethal tumor.

Apart from the international comparative trial, further developments of phase-II trials with CPT should point to two directions. First, several molecular markers, such as mutations in *SMAD4/DPC4*, have been validated as prognostic factors in PCs (34). Whole-genome sequencing and copy number variation analysis suggest that PCs can be divided into four genetic subtypes, with potential clinical utility (35). Trials with CPT combined with molecular analysis of these genes are highly needed, because CPT may elicit different molecular pathways than conventional X-rays (36). Combined CIRT + gemcitabine may be especially

effective against pancreatic stem-like cells, as suggested by a recent *in vitro* study (37), and hence, study of stem cells markers and genetic pathways will be highly desirable. In addition, further hypofractionation is desirable if the problems of the organ movements are tackled as described above. For instance, the use of 12 fractions (such as done at NIRS) with the total dose used for protons in Hyogo is expected to push the 1-year survival over 80% (**Table 7**, row 6). A careful motion mitigation strategy should be rapidly implemented to allow this further escalation.

Acknowledgments

The work was partly supported by the Portfolio Technologie und Medizin, Helmholtz Gemeinschaft and INFN-TIFPA (Trento).

References

1. Siegel RL, Miller KD, Jemal A. Cancer statistics, 2015. *CA Cancer J Clin* (2015) **65**:5–29. doi:10.3322/caac.21254
2. Malvezzi M, Bertuccio P, Rosso T, Rota M, Levi F, La Vecchia C, et al. European cancer mortality predictions for the year 2015: does lung cancer have the highest death rate in EU women? *Ann Oncol* (2015) **26**:779–86. doi:10.1093/annonc/mdv001
3. Wolfgang CL, Herman JM, Laheru DA, Klein AP, Erdek MA, Fishman EK, et al. Recent progress in pancreatic cancer. *CA Cancer J Clin* (2013) **63**:318–48. doi:10.3322/caac.21190
4. Koong AC, Mehta VK, Le QT, Fisher GA, Terris DJ, Brown JM, et al. Pancreatic tumors show high levels of hypoxia. *Int J Radiat Oncol Biol Phys* (2000) **48**:919–22. doi:10.1016/S0360-3016(00)00803-8
5. Olive KP, Jacobetz MA, Davidson CJ, Gopinathan A, McIntyre D, Honess D, et al. Inhibition of Hedgehog signaling enhances delivery of chemotherapy in a mouse model of pancreatic cancer. *Science* (2009) **324**:1457–61. doi:10.1126/science.1171362
6. Loeffler JS, Durante M. Charged particle therapy – optimization, challenges and future directions. *Nat Rev Clin Oncol* (2013) **10**:411–24. doi:10.1038/nrclinonc.2013.79
7. Durante M, Reppingen N, Held KD. Immunologically augmented cancer treatment using modern radiotherapy. *Trends Mol Med* (2013) **19**:565–82. doi:10.1016/j.molmed.2013.05.007
8. Kamada T, Tsujii H, Blakely EA, Debus J, De Neve W, Durante M, et al. Carbon ion radiotherapy in Japan: an assessment of 20 years of clinical experience. *Lancet Oncol* (2015) **16**:e93–100. doi:10.1016/S1470-2045(14)70412-7
9. Yamada S, Terashima K, Shinoto M, Yasuda S, Shiomi M, Isozaki T. Pancreatic cancer. In: Tsujii H, Kamada T, Shirai K, Noda K, Tsuji H, Karasawa K, editors. *Carbon Ion Radiotherapy*. Berlin: Springer-Verlag (2014). p. 221–8.
10. Chen Y, Sun X-J, Jiang T-H, Mao A-W. Combined radiochemotherapy in patients with locally advanced pancreatic cancer: a meta-analysis. *World J Gastroenterol* (2013) **19**:7461–71. doi:10.3748/wjg.v19.i42.7461
11. Fowler JF. 21 years of biologically effective dose. *Br J Radiol* (2010) **83**:554–68. doi:10.1259/bjr/31372149
12. Jones B, Dale RG. The potential for mathematical modelling in the assessment of the radiation dose equivalent of cytotoxic chemotherapy given concomitantly with radiotherapy. *Br J Radiol* (2005) **78**:939–43. doi:10.1259/bjr/40226390
13. Bentzen SM, Tucker SL. Quantifying the position and steepness of radiation dose-response curves. *Int J Radiat Biol* (1997) **71**:531–42. doi:10.1080/095530097143860
14. Plataniotis G, Dale RG. Radio-chemotherapy for bladder cancer: contribution of chemotherapy on local control. *World J Radiol* (2013) **5**:267–74. doi:10.4329/wjr.v5.i8.267
15. Moraru IC, Tai A, Erickson B, Li XA. Radiation dose responses for chemoradiation therapy of pancreatic cancer: an analysis of compiled clinical data using biophysical models. *Pract Radiat Oncol* (2014) **4**:13–9. doi:10.1016/j.prro.2013.01.005
16. Plataniotis G, Dale RG. Assessment of the radiation-equivalent of chemotherapy contributions in 1-phase radio-chemotherapy treatment of muscle-invasive bladder cancer. *Int J Radiat Oncol Biol Phys* (2014) **88**:927–32. doi:10.1016/j.ijrobp.2013.11.242
17. Pauwels B, Vermorken JB, Wouters A, Ides J, Van Laere S, Lambrechts HAJ, et al. The role of apoptotic cell death in the radiosensitising effect of gemcitabine. *Br J Cancer* (2009) **101**:628–36. doi:10.1038/sj.bjc.6605145
18. Wouters A, Pauwels B, Burrows N, Baay M, Deschoolmeester V, Vu TN, et al. The radiosensitising effect of gemcitabine and its main metabolite dFdU under low oxygen conditions is in vitro not dependent on functional HIF-1 protein. *BMC Cancer* (2014) **14**:594. doi:10.1186/1471-2407-14-594
19. El Shafie RA, Habermehl D, Rieken S, Mairani A, Orschiedt L, Brons S, et al. In vitro evaluation of photon and raster-scanned carbon ion radiotherapy in combination with gemcitabine in pancreatic cancer cell lines. *J Radiat Res* (2013) **54**:i113–9. doi:10.1093/jrr/rrt052
20. Schlaich F, Brons S, Haberer T, Debus J, Combs SE, Weber K-J. Comparison of the effects of photon versus carbon ion irradiation when combined with chemotherapy in vitro. *Radiat Oncol* (2013) **8**:260. doi:10.1186/1748-717X-8-260
21. Chapman JD. Can the two mechanisms of tumor cell killing by radiation be exploited for therapeutic gain? *J Radiat Res* (2014) **55**:2–9. doi:10.1093/jrr/rrt111
22. Tommasino F, Durante M. Proton radiobiology. *Cancers (Basel)* (2015) **7**:353–81. doi:10.3390/cancers7010353
23. Kanai T, Matsufuji N, Miyamoto T, Mizoe J, Kamada T, Tsuji H, et al. Examination of GyE system for HIMAC carbon therapy. *Int J Radiat Oncol Biol Phys* (2006) **64**:650–6. doi:10.1016/j.ijrobp.2005.09.043
24. Steinsträter O, Grün R, Scholz U, Friedrich T, Durante M, Scholz M. Mapping of RBE-weighted doses between HIMAC- and LEM-based treatment planning systems for carbon ion therapy. *Int J Radiat Oncol Biol Phys* (2012) **84**:854–60. doi:10.1016/j.ijrobp.2012.01.038
25. Koong AC, Le QT, Ho A, Fong B, Fisher G, Cho C, et al. Phase I study of stereotactic radiosurgery in patients with locally advanced pancreatic cancer. *Int J Radiat Oncol Biol Phys* (2004) **58**:1017–21. doi:10.1016/j.ijrobp.2003.11.004
26. Hoyer M, Roed H, Sengelov L, Traberg A, Ohlhuis L, Pedersen J, et al. Phase-II study on stereotactic radiotherapy of locally advanced pancreatic carcinoma. *Radiother Oncol* (2005) **76**:48–53. doi:10.1016/j.radonc.2004.12.022
27. Moningi S, Marciscano AE, Rosati LM, Ng SK, Teboh Forbang R, Jackson J, et al. Stereotactic body radiation therapy in pancreatic cancer: the new frontier. *Expert Rev Anticancer Ther* (2014) **14**:1461–75. doi:10.1586/14737140.2014.952286
28. Terashima K, Demizu Y, Hashimoto N, Jin D, Mima M, Fujii O, et al. A phase I/II study of gemcitabine-concurrent proton radiotherapy for locally advanced pancreatic cancer without distant metastasis. *Radiother Oncol* (2012) **103**:25–31. doi:10.1016/j.radonc.2011.12.029
29. Bert C, Durante M. Particle radiosurgery: a new frontier of physics in medicine. *Phys Med* (2014) **30**:535–8. doi:10.1016/j.ejmp.2014.04.011
30. Richter D, Saito N, Chaudhri N, Härtig M, Ellerbrock M, Jäkel O, et al. Four-dimensional patient dose reconstruction for scanned ion beam therapy of moving liver tumors. *Int J Radiat Oncol Biol Phys* (2014) **89**:175–81. doi:10.1016/j.ijrobp.2014.01.043
31. Mori S, Shinoto M, Yamada S. Four-dimensional treatment planning in layer-stacking boost irradiation for carbon-ion pancreatic therapy. *Radiother Oncol* (2014) **111**:258–63. doi:10.1016/j.radonc.2014.02.014
32. Graeff C. Motion mitigation in scanned ion beam therapy through 4D-optimization. *Phys Med* (2014) **30**:570–7. doi:10.1016/j.ejmp.2014.03.011
33. Mitin T, Zietman AL. Promise and pitfalls of heavy-particle therapy. *J Clin Oncol* (2014) **32**:2855–63. doi:10.1200/JCO.2014.55.1945
34. Vincent A, Herman J, Schulick R, Hruban RH, Goggins M. Pancreatic cancer. *Lancet* (2011) **378**:607–20. doi:10.1016/S0140-6736(10)62307-0
35. Waddell N, Pajic M, Patch AM, Chang DK, Kassahn KS, Bailey P, et al. Whole genomes redefine the mutational landscape of pancreatic cancer. *Nature* (2015) **518**:495–501. doi:10.1038/nature14169
36. Durante M. New challenges in high-energy particle radiobiology. *Br J Radiol* (2014) **87**:20130626. doi:10.1259/bjr.20130626
37. Sai S, Wakai T, Vares G, Yamada S, Kamijo K, Kamada T, et al. Combination of carbon ion beam and gemcitabine causes irreparable DNA damage and death of

radioresistant pancreatic cancer stem-like cells *in vitro* and *in vivo*. *Oncotarget* (2015) **6**:5517–35.
38. Moertel CG, Childs DS, Reitemeier RJ, Colby MY, Holbrook MA. Combined 5-fluorouracil and supervoltage radiation therapy of locally unresectable gastrointestinal cancer. *Lancet* (1969) **2**(7626):865–7. doi:10.1016/S0140-6736(69)92326-5
39. Moertel CG, Frytak S, Hahn RG, O'Connell MJ, Reitemeier RJ, Rubin J, et al. Therapy of locally unresectable pancreatic carcinoma: a randomized comparison of high dose (6000 rads) radiation alone, moderate dose radiation (4000 rads + 5-fluorouracil), and high dose radiation + 5-fluorouracil. The Gastrointestinal Tumor Study Group. *Cancer* (1981) **48**:1705–10. doi:10.1002/1097-0142(19811015)48:8<1705::AID-CNCR2820480803>3.0.CO;2-4
40. Ceha HM, van Tienhoven G, Gouma DJ, Veenhof CH, Schneider CJ, Rauws EA, et al. Feasibility and efficacy of high dose conformal radiotherapy for patients with locally advanced pancreatic carcinoma. *Cancer* (2000) **89**:2222–9. doi:10.1002/1097-0142(20001201)89:11<2222::AID-CNCR10>3.0.CO;2-V
41. Cohen SJ, Dobelbower R, Lipsitz S, Catalano PJ, Sischy B, Smith TJ, et al. A randomized phase III study of radiotherapy alone or with 5-fluorouracil and mitomycin-C in patients with locally advanced adenocarcinoma of the pancreas: Eastern Cooperative Oncology Group Study E8282. *Int J Radiat Oncol Biol Phys* (2005) **62**:1345–50. doi:10.1016/j.ijrobp.2004.12.074
42. Wang Z, Ren Z-G, Ma N-Y, Zhao J-D, Zhang Z, Ma X-J, et al. Intensity modulated radiotherapy for locally advanced and metastatic pancreatic cancer: a mono-institutional retrospective analysis. *Radiat Oncol* (2015) **10**:4–11. doi:10.1186/s13014-014-0312-5
43. Wolff RA, Evans DB, Gravel DM, Lenzi R, Pisters PW, Lee JE, et al. Phase I trial of gemcitabine combined with radiation for the treatment of locally advanced pancreatic adenocarcinoma. *Clin Cancer Res* (2001) **7**:2246–53.
44. Epelbaum R, Rosenblatt E, Nasrallah S, Faraggi D, Gaitini D, Mizrahi S, et al. Phase II study of gemcitabine combined with radiation therapy in patients with localized, unresectable pancreatic cancer. *J Surg Oncol* (2002) **81**:138–43. doi:10.1002/jso.10159
45. Joensuu TK, Kiviluoto T, Kärkkäinen P, Vento P, Kivisaari L, Tenhunen M, et al. Phase I-II trial of twice-weekly gemcitabine and concomitant irradiation in patients undergoing pancreaticoduodenectomy with extended lymphadenectomy for locally advanced pancreatic cancer. *Int J Radiat Oncol Biol Phys* (2004) **60**:444–52. doi:10.1016/j.ijrobp.2004.03.026
46. Okusaka T, Ito Y, Ueno H, Ikeda M, Takezako Y, Morizane C, et al. Phase II study of radiotherapy combined with gemcitabine for locally advanced pancreatic cancer. *Br J Cancer* (2004) **91**:673–7. doi:10.1038/sj.bjc.6602001
47. Murphy JD, Adusumilli S, Griffith KA, Ray ME, Zalupski MM, Lawrence TS, et al. Full-dose gemcitabine and concurrent radiotherapy for unresectable pancreatic cancer. *Int J Radiat Oncol Biol Phys* (2007) **68**:801–8. doi:10.1016/j.ijrobp.2006.12.053
48. Small W, Berlin J, Freedman GM, Lawrence T, Talamonti MS, Mulcahy MF, et al. Full-dose gemcitabine with concurrent radiation therapy in patients with nonmetastatic pancreatic cancer: a multicenter phase II trial. *J Clin Oncol* (2008) **26**:942–7. doi:10.1200/JCO.2007.13.9014
49. Igarashi H, Ito T, Kawabe K, Hisano T, Arita Y, Kaku T, et al. Chemoradiotherapy with twice-weekly administration of low-dose gemcitabine for locally advanced pancreatic cancer. *World J Gastroenterol* (2008) **14**:5311–5. doi:10.3748/wjg.14.5311
50. Schellenberg D, Goodman KA, Lee F, Chang S, Kuo T, Ford JM, et al. Gemcitabine chemotherapy and single-fraction stereotactic body radiotherapy for locally advanced pancreatic cancer. *Int J Radiat Oncol Biol Phys* (2008) **72**:678–86. doi:10.1016/j.ijrobp.2008.01.051
51. Polistina F, Costantin G, Casamassima F, Francescon P, Guglielmi R, Panizzoni G, et al. Unresectable locally advanced pancreatic cancer: a multimodal treatment using neoadjuvant chemoradiotherapy (gemcitabine plus stereotactic radiosurgery) and subsequent surgical exploration. *Ann Surg Oncol* (2010) **17**:2092–101. doi:10.1245/s10434-010-1019-y
52. Loehrer PJ, Feng Y, Cardenes H, Wagner L, Brell JM, Cella D, et al. Gemcitabine alone versus gemcitabine plus radiotherapy in patients with locally advanced pancreatic cancer: an Eastern Cooperative Oncology Group trial. *J Clin Oncol* (2011) **29**:4105–12. doi:10.1200/JCO.2011.34.8904
53. Schellenberg D, Kim J, Christman-Skieller C, Chun CL, Columbo LA, Ford JM, et al. Single-fraction stereotactic body radiation therapy and sequential gemcitabine for the treatment of locally advanced pancreatic cancer. *Int J Radiat Oncol Biol Phys* (2011) **81**:181–8. doi:10.1016/j.ijrobp.2010.05.006
54. Cardenes HR, Moore AM, Johnson CS, Yu M, Helft P, Chiorean EG, et al. A Phase II Study of Gemcitabine in combination with radiation therapy in patients with localized, unresectable, pancreatic cancer. *Am J Clin Oncol* (2011) **34**:460–5. doi:10.1097/COC.0b013e3181e9c103
55. Shibuya K, Oya N, Fujii T, Doi R, Nakamura A, Matsuo Y, et al. Phase II study of radiation therapy combined with weekly low-dose gemcitabine for locally advanced, unresectable pancreatic cancer. *Am J Clin Oncol* (2011) **34**:115–9. doi:10.1097/COC.0b013e3181c4c7a8
56. Mahadevan A, Miksad R, Goldstein M, Sullivan R, Bullock A, Buchbinder E, et al. Induction gemcitabine and stereotactic body radiotherapy for locally advanced nonmetastatic pancreas cancer. *Int J Radiat Oncol Biol Phys* (2011) **81**:615–22. doi:10.1016/j.ijrobp.2011.04.045
57. Huang J, Robertson JM, Margolis J, Balaraman S, Gustafson G, Khilanani P, et al. Long-term results of full-dose gemcitabine with radiation therapy compared to 5-fluorouracil with radiation therapy for locally advanced pancreas cancer. *Radiother Oncol* (2011) **99**:114–9. doi:10.1016/j.radonc.2011.05.038
58. Mukherjee S, Hurt CN, Bridgewater J, Falk S, Cummins S, Wasan H, et al. Gemcitabine-based or capecitabine-based chemoradiotherapy for locally advanced pancreatic cancer (SCALOP): a multicentre, randomised, phase 2 trial. *Lancet Oncol* (2013) **14**:317–26. doi:10.1016/S1470-2045(13)70021-4
59. Gurka MK, Collins SP, Slack R, Tse G, Charabaty A, Ley L, et al. Stereotactic body radiation therapy with concurrent full-dose gemcitabine for locally advanced pancreatic cancer: a pilot trial demonstrating safety. *Radiat Oncol* (2013) **8**:44. doi:10.1186/1748-717X-8-44
60. Herman JM, Chang DT, Goodman KA, Dholakia AS, Raman SP, Hacker-Prietz A, et al. Phase 2 multi-institutional trial evaluating gemcitabine and stereotactic body radiotherapy for patients with locally advanced unresectable pancreatic adenocarcinoma. *Cancer* (2015) **121**:1128–37. doi:10.1002/cncr.29161
61. Wagener DJT, Hoogenraad WJ, Rougier P, Lusinchi A, Taal BG, Veenhof CHN, et al. Results of a phase II trial of epirubicin and cisplatin (EP) before and after irradiation and 5-fluorouracil in locally advanced pancreatic cancer: an EORTC GITCCG study. *Eur J Cancer* (1996) **32**:1310–3. doi:10.1016/0959-8049(96)00070-6
62. Ishii H, Okada S, Tokuuye K, Nose H, Okusaka T, Yoshimori M, et al. Protracted 5-fluorouracil infusion with concurrent radiotherapy as a treatment for locally advanced pancreatic carcinoma. *Cancer* (1997) **79**:1516–20. doi:10.1002/(SICI)1097-0142(19970415)79:8<1516::AID-CNCR11>3.3.CO;2-5
63. Fisher BJ, Perera FE, Kocha W, Tomiak A, Taylor M, Vincent M, et al. Analysis of the clinical benefit of 5-fluorouracil and radiation treatment in locally advanced pancreatic cancer. *Int J Radiat Oncol Biol Phys* (1999) **45**:291–5. doi:10.1016/S0360-3016(99)00197-2
64. André T, Balosso J, Louvet C, Hannoun L, Houry S, Huguier M, et al. Combined radiotherapy and chemotherapy (cisplatin and 5-fluorouracil) as palliative treatment for localized unresectable or adjuvant treatment for resected pancreatic adenocarcinoma: results of a feasibility study. *Int J Radiat Oncol Biol Phys* (2000) **46**:903–11. doi:10.1016/S0360-3016(99)00478-2
65. Boz G, De Paoli A, Innocente R, Rossi C, Tosolini G, Pederzoli P, et al. Proceedings of the 25th National Congress of the Italian Association of Pancreatology Study (AISP). Cernobbio, Como (Italy). September 20-22, 2001. *JOP* (2001) **2**(5 Suppl):330–54.
66. Safran H, Moore T, Iannitti D, Dipetrillo T, Akerman P, Cioffi W, et al. Paclitaxel and concurrent radiation for locally advanced pancreatic cancer. *Int J Radiat Oncol Biol Phys* (2001) **49**:1275–9. doi:10.1016/S0360-3016(00)01527-3
67. Li C-P, Chao Y, Chi K-H, Chan W-K, Teng H-C, Lee R-C, et al. Concurrent chemoradiotherapy treatment of locally advanced pancreatic cancer: gemcitabine versus 5-fluorouracil, a randomized controlled study. *Int J Radiat Oncol Biol Phys* (2003) **57**:98–104. doi:10.1016/S0360-3016(03)00435-8
68. Morganti AG, Valentini V, Macchia G, Mattiucci GC, Costamagna G, Deodato F, et al. 5-fluorouracil-based chemoradiation in unresectable pancreatic carcinoma: phase I-II dose-escalation study. *Int J Radiat Oncol Biol Phys* (2004) **59**:1454–60. doi:10.1016/j.ijrobp.2004.01.035
69. Park JK, Ryu JK, Lee JK, Yoon WJ, Lee SH, Kim YT, et al. Gemcitabine chemotherapy versus 5-fluorouracil-based concurrent chemoradiotherapy in locally advanced unresectable pancreatic cancer. *Pancreas* (2006) **33**:397–402. doi:10.1097/01.mpa.0000236725.26672.be

70. Chauffert B, Mornex F, Bonnetain F, Rougier P, Mariette C, Bouché O, et al. Phase III trial comparing intensive induction chemoradiotherapy (60 Gy, infusional 5-FU and intermittent cisplatin) followed by maintenance gemcitabine with gemcitabine alone for locally advanced unresectable pancreatic cancer. Definitive results of the 2. *Ann Oncol* (2008) **19**:1592–9. doi:10.1093/annonc/mdn281
71. Crane CH, Winter K, Regine WF, Safran H, Rich TA, Curran W, et al. Phase II study of bevacizumab with concurrent capecitabine and radiation followed by maintenance gemcitabine and bevacizumab for locally advanced pancreatic cancer: Radiation Therapy Oncology Group RTOG 0411. *J Clin Oncol* (2009) **27**:4096–102. doi:10.1200/JCO.2009.21.8529
72. Sudo K, Yamaguchi T, Ishihara T, Nakamura K, Hara T, Denda T, et al. Phase II study of oral S-1 and concurrent radiotherapy in patients with unresectable locally advanced pancreatic cancer. *Int J Radiat Oncol Biol Phys* (2011) **80**:119–25. doi:10.1016/j.ijrobp.2010.01.027
73. Oberic L, Viret F, Baey C, Ychou M, Bennouna J, Adenis A, et al. Docetaxel- and 5-FU-concurrent radiotherapy in patients presenting unresectable locally advanced pancreatic cancer: a FNCLCC-ACCORD/0201 randomized phase II trial's pre-planned analysis and case report of a 5.5-year disease-free survival. *Radiat Oncol* (2011) **6**:124. doi:10.1186/1748-717X-6-124
74. Brunner TB, Sauer R, Fietkau R. Gemcitabine/cisplatin versus 5-fluorouracil/mitomycin C chemoradiotherapy in locally advanced pancreatic cancer: a retrospective analysis of 93 patients. *Radiat Oncol* (2011) **6**:88. doi:10.1186/1748-717X-6-88
75. Malik NK, May KS, Chandrasekhar R, Ma WW, Flaherty L, Iyer R, et al. Treatment of locally advanced unresectable pancreatic cancer: a 10-year experience. *J Gastrointest Oncol* (2012) **3**:326–34. doi:10.3978/j.issn.2078-6891.2012.029
76. Ikeda M, Ioka T, Ito Y, Yonemoto N, Nagase M, Yamao K, et al. A multicenter phase II trial of S-1 with concurrent radiation therapy for locally advanced pancreatic cancer. *Int J Radiat Oncol Biol Phys* (2013) **85**:163–9. doi:10.1016/j.ijrobp.2012.03.059
77. Shinchi H, Maemura K, Mataki Y, Kurahara H, Sakoda M, Ueno S, et al. A phase II study of oral S-1 with concurrent radiotherapy followed by chemotherapy with S-1 alone for locally advanced pancreatic cancer. *J Hepatobiliary Pancreat Sci* (2012) **19**:152–8. doi:10.1007/s00534-011-0400-y
78. Herman JM, Wild AT, Wang H, Tran PT, Chang KJ, Taylor GE, et al. Randomized phase iii multi-institutional study of tnferade biologic with fluorouracil and radiotherapy for locally advanced pancreatic cancer: final results. *J Clin Oncol* (2013) **31**:886–94. doi:10.1200/JCO.2012.44.7516
79. Ducreux M, Giovannini M, Baey C, Llacer C, Bennouna J, Adenis A, et al. Radiation plus docetaxel and cisplatin in locally advanced pancreatic carcinoma: a non-comparative randomized phase II trial. *Dig Liver Dis* (2014) **46**:950–5. doi:10.1016/j.dld.2014.06.006
80. Rembielak AI, Jain P, Jackson AS, Green MM, Santorelli GR, Whitfield GA, et al. Phase II trial of cetuximab and conformal radiotherapy only in locally advanced pancreatic cancer with Concurrent Tissue Sampling Feasibility Study. *Transl Oncol* (2014) **7**:55–64. doi:10.1593/tlo.13724
81. Kwak Y, Lee JH, Lee M, Chun H, Kim D, You YK, et al. Definitive concurrent chemoradiotherapy in locally advanced pancreatic cancer. *Radiat Oncol J* (2014) **32**:49–56. doi:10.3857/roj.2014.32.2.49
82. Chung HW, Bang SM, Park SW, Chung JB, Kang JK, Kim JW, et al. A prospective randomized study of gemcitabine with doxifluridine versus paclitaxel with doxifluridine in concurrent chemoradiotherapy for locally advanced pancreatic cancer. *Int J Radiat Oncol Biol Phys* (2004) **60**:1494–501. doi:10.1016/j.ijrobp.2004.05.061
83. Haddock MG, Swaminathan R, Foster NR, Hauge MD, Martenson JA, Camoriano JK, et al. Gemcitabine, cisplatin, and radiotherapy for patients with locally advanced pancreatic adenocarcinoma: results of the North Central Cancer Treatment Group Phase II Study N9942. *J Clin Oncol* (2007) **25**:2567–72. doi:10.1200/JCO.2006.10.2111
84. Hong SP, Park JY, Jeon TJ, Bang S, Park SW, Chung JB, et al. Weekly full-dose gemcitabine and single-dose cisplatin with concurrent radiotherapy in patients with locally advanced pancreatic cancer. *Br J Cancer* (2008) **98**:881–7. doi:10.1038/sj.bjc.6604247
85. Mamon HJ, Niedzwiecki D, Hollis D, Tan BR, Mayer RJ, Tepper JE, et al. A phase 2 trial of gemcitabine, 5-fluorouracil, and radiation therapy in locally advanced nonmetastatic pancreatic adenocarcinoma: cancer and Leukemia Group B (CALGB) 80003. *Cancer* (2011) **117**:2620–8. doi:10.1002/cncr.25742
86. Crane CH, Varadhachary GR, Yordy JS, Staerkel GA, Javle MM, Safran H, et al. Phase II trial of cetuximab, gemcitabine, and oxaliplatin followed by chemoradiation with cetuximab for locally advanced (T4) pancreatic adenocarcinoma: correlation of Smad4(Dpc4) immunostaining with pattern of disease progression. *J Clin Oncol* (2011) **29**:3037–43. doi:10.1200/JCO.2010.33.8038
87. Ch'Ang HJ, Lin YL, Wang HP, Chiu YF, Chang MC, Hsu CH, et al. Induction chemotherapy with gemcitabine, oxaliplatin, and 5-fluorouracil/leucovorin followed by concomitant chemoradiotherapy in patients with locally advanced pancreatic cancer: a Taiwan cooperative oncology group phase II study. *Int J Radiat Oncol Biol Phys* (2011) **81**:e749–57. doi:10.1016/j.ijrobp.2010.10.034
88. Tozzi A, Comito T, Alongi F, Navarria P, Iftode C, Mancosu P, et al. SBRT in unresectable advanced pancreatic cancer: preliminary results of a mono-institutional experience. *Radiat Oncol* (2013) **8**:148. doi:10.1186/1748-717X-8-148
89. Ke Q. S-1 plus gemcitabine chemotherapy followed by concurrent radiotherapy and maintenance therapy with S-1 for unresectable pancreatic cancer. *World J Gastroenterol* (2014) **20**:13987. doi:10.3748/wjg.v20.i38.13987
90. Sachsman S, Nichols RC, Morris CG, Zaiden R, Johnson EA, Awad Z, et al. Proton therapy and concomitant capecitabine for non-metastatic unresectable pancreatic adenocarcinoma. *Int J Part Ther* (2014) **1**:692–701. doi:10.14338/IJPT.14-00006.1

Conflict of Interest Statement: The authors declare that the research was conducted in the absence of any commercial or financial relationships that could be construed as a potential conflict of interest.

Copyright © 2015 Durante, Tommasino and Yamada. This is an open-access article distributed under the terms of the Creative Commons Attribution License (CC BY). The use, distribution or reproduction in other forums is permitted, provided the original author(s) or licensor are credited and that the original publication in this journal is cited, in accordance with accepted academic practice. No use, distribution or reproduction is permitted which does not comply with these terms.

frontiers in Oncology

ORIGINAL RESEARCH
published: 27 November 2015
doi: 10.3389/fonc.2015.00262

Paving the Road for Modern Particle Therapy – What Can We Learn from the Experience Gained with Fast Neutron Therapy in Munich?

Hanno M. Specht[1], Teresa Neff[1], Waltraud Reuschel[1], Franz M. Wagner[2], Severin Kampfer[1], Jan J. Wilkens[1,3], Winfried Petry[2] and Stephanie E. Combs[1,3]*

[1] Department of Radiation Oncology, Klinikum rechts der Isar, Technische Universität München, Munich, Germany,
[2] Forschungs-Neutronenquelle Heinz Maier-Leibnitz II (FRM II), Technische Universität München, Garching, Germany,
[3] Institute of Innovative Radiotherapy (iRT), Department of Radiation Science, Helmholtz Zentrum München, Oberschleißheim, Germany

While neutron therapy was a highly topical subject in the 70s and 80s, today there are only a few remaining facilities offering fast neutron therapy (FNT). Nevertheless, up to today more than 30,000 patients were treated with neutron therapy. For some indications like salivary gland tumors and malignant melanoma, there is clinical evidence that the addition of FNT leads to superior local control compared to photon treatment alone. FNT was available in Munich from 1985 until 2000 at the Reactor Neutron Therapy (RENT) facility. Patient treatment continued at the new research reactor FRM II in 2007 under improved treatment conditions, and today it can still be offered to selected patients as an individual treatment option. As there is a growing interest in high-linear energy transfer (LET) therapy with new hadron therapy centers emerging around the globe, the clinical data generated by neutron therapy might help to develop biologically driven treatment planning algorithms. Also FNT might experience its resurgence as a combinational partner of modern immunotherapies.

Keywords: fast neutron therapy, fast neutrons, reactor neutrons, RBE, adenoidcystic carcinoma, high-LET radiation

OPEN ACCESS

Edited by:
Marco Durante, GSI, Germany

Reviewed by:
Bleddyn Jones, Univeristy of Oxford, UK
Piero Fossati, Università di Milano, Italy

****Correspondence:***
Hanno M. Specht
hanno.specht@tum.de

Specialty section:
This article was submitted to Radiation Oncology, a section of the journal Frontiers in Oncology

Received: *09 September 2015*
Accepted: *11 November 2015*
Published: *27 November 2015*

Citation:
Specht HM, Neff T, Reuschel W, Wagner FM, Kampfer S, Wilkens JJ, Petry W and Combs SE (2015) Paving the Road for Modern Particle Therapy – What Can We Learn from the Experience Gained with Fast Neutron Therapy in Munich? Front. Oncol. 5:262. doi: 10.3389/fonc.2015.00262

INTRODUCTION

Radiation therapy is one of the three essential pillars of cancer treatment. Today photon treatment delivered by linear accelerators is the most commonly used treatment modality. There is, however, a strong physical and biological rationale for the use of particle therapy in radiation oncology. Due to the high relative biological effectiveness (RBE), neutron beam therapy might offer an advantage compared to photon beam therapy, especially in the treatment of malignancies known to be radioresistant (1, 2). This is a result of the high linear energy transfer (LET), which is in the range of about 200 keV/μm for 2 MeV neutron beams, about 200-fold higher than with conventional photon beams (3). The RBE for a 2 MeV neutron beam is estimated to be somewhere between 2 and 7 (4). This means that 1 Gy delivered by fast neutron therapy (FNT) should be as effective in killing cancer cells as 2–7 Gy of photon treatment. The numbers stated here implicate large uncertainties with the RBE varying between different tumor entities and even within the entities depending on the tumor

grading (5). Especially for brain tumors and late reacting tissues, the RBE is estimated to be in the upper part of the range (6).

Neutron therapy might be able to overcome the negative effect of tumor hypoxia, since the oxygen enhancement ratio of neutrons is only about 1.3 compared to up to 3 in photons (7). Furthermore, there is only a weak dependency on the cell cycle, meaning that non-proliferating cells can also be effectively targeted with neutron therapy (8).

International clinical trials were enthusiastically embraced from the mid 1970s through the mid 1980s, only to be abandoned in the late 1980s as clinicians observed unacceptable side effects. Although the number of patients treated with FNT up to today might be as high as 30,000, so far, large randomized studies comparing neutron therapy to standard photon radiation are not available and they will probably not be carried out in the future. For certain indications studies in the past clearly indicated a favorable outcome in terms of local control (LC) for neutron treatment compared to conventional photon treatment alone. This was shown for salivary gland tumors (9, 10), adenoidcystic carcinoma (ACC) of the trachea (11), prostate cancer (12, 13), pleural mesothelioma (14), or malignant melanomas (15, 16). Although most of these studies only recruited small patient numbers, for certain indications such as incompletely excised or unresectable salivary gland tumors, neutron therapy not only achieved superior LC (17) but also improved overall survival (OS) (18). To further increase the efficacy of neutron therapy and to reduce unwanted side effects, efforts were made to improve treatment conformality by introducing 3-D treatment planning systems (19–21). The Karmanos Cancer Center FNT facility in Detroit, MI, USA even had a delivery system for intensity modulated radiotherapy (IMRT) commissioned, but it was shut down in 2011. Up to today, four FNT facilities continue to operate worldwide as depicted in **Table 1** (22).

Besides FNT, where mean neutron energies range between one and a few tens of MeV, neutron therapy can also be delivered as boron neutron capture therapy (BNCT). For this second branch of neutron therapy, low energy neutrons [thermal (<0.5 eV) or epithermal neutrons (0.5–10 keV)] but high neutron fluxes are needed (as they can be delivered by research reactors) and boron compounds are injected in order to selectively damage tumor cells. However, because patient treatment with BNCT was never carried out at the research reactor in Munich, results observed with BNCT will not be covered here and the difficulties regarding the compound biological effect (23), and the physical dose calculation will not be further discussed in this article.

This article aims to describe the experience gained with FNT in Munich within almost 30 years of clinical use and to outline how this experience might be of clinical relevance in modern particle therapy.

MATERIALS AND METHODS

Neutron Therapy in Munich Between 1985 and 2000 (FRM I)

Neutron treatment in Munich started at the first research reactor in the so called Reactor Neutron Therapy (RENT)-facility. From 1985 until the shutdown of the reactor in 2000, 715 patients were treated with FNT. Treatment indications and patient numbers are depicted in **Figure 1**. The main treatment indications were curative treatment of salivary gland tumors, curative and palliative treatment of head-and-neck cancers and palliative treatment of breast cancer recurrences. Over the years the indication spectrum changed; while earlier patients were treated in curative intent for salivary gland tumors or other lesions, recently, treatment has shifted to palliative indications, predominantly skin metastases mainly from breast cancer or malignant melanoma. Most of the patients were treated in combination with conventional photon or electron beams, where FNT was applied as a local boost. Most commonly, 3–5 fractions at a single dose of 2 Gy (physical dose, RBE approximately 3) were applied to the center of the tumor (24).

Of these 715 patients, 48 patients with ACC of the salivary glands were evaluated for LC and OS as well as for treatment related toxicities. Patients were at a median age of 55 years, and most patients had received surgery prior to FNT. After conventional photon irradiation with 2 Gy single dose up to a median total dose of 50 Gy (range 50–56 Gy) a median neutron dose of 6 Gy (range 4.5–7.5 Gy) at a median single dose of 1.5 Gy (range 1.5 Gy–2 Gy) was applied. Patient characteristics in detail are shown in **Table 2**.

Moreover, 46 breast cancer patients with local recurrences on the thoracic wall were evaluated for initial treatment tumor response within the macroscopic tumor and for LC. Median time to ipsilateral chest wall recurrence after initial cancer treatment was 22 months (range 4–65 months). If the time interval between conventional photon RT within primary treatment and chest wall

TABLE 1 | Current status of operating neutron facilities worldwide [status as stated at the IAEA Technical Meeting 2013 (F1-TM-44771)].

Location	Source	Mean energy (MeV)	50% depth (cm)	Beam direction	Collimator type	First patient treated	Patients treated (*n*)
University of Washington Medical Center, Seattle, USA	Cyclotron p(50.5) + Be	20	14	Isocentric	Multi leaf	1984	2960
iThemba Laboratory for Accelerator Based Science (LABS), Cape Town, South Africa	Cyclotron p(66) + Be	25	16	Isocentric	Multi blade trimmer	1988	1788
Tomsk Polytechnic University, Tomsk, Russian Federation	Cyclotron d(13.6) + Be	6.3	6	Horizontal	Inserts	1983	1500
FRM II, Technische Universität München, Garching, Germany	Uranium converter	1.9	5	Horizontal	Multi leaf	2007	124

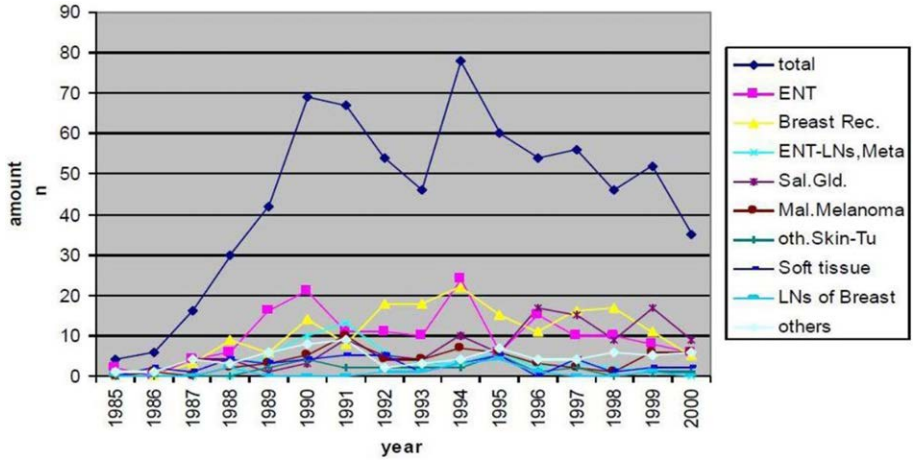

FIGURE 1 | Patient numbers and treatment indications of FNT at FRM I (RENT facility) between 1985 and 2000.

TABLE 2 | Characteristics of patients with adenoidcystic carcinomas of the salivary glands treated with FNT.

	n
Age (years)	55 (17–80)
Prior therapy	
Surgery	45 (94%)
Biopsy	3 (6%)
Resection-status after surgery	
R0	12 (25%)
R1/2	33 (69%)
Pathological Tumor Stage after surgery	
pT1/2	24 (44%)
pT3/4	18 (38%)
Lymphatic spread	10 (21%)

recurrence was shorter than 12 months, patients were treated with FNT only at a total dose of 10 Gy and a single dose of 2 Gy (1–2 times a week). If the time interval between initial treatment and cancer recurrence was more than 12 months, first re-irradiation with conventional, normo-fractionated photon radiotherapy was applied to the area of recurrence up to a total dose of 30 Gy (2 Gy daily). Afterwards macroscopic tumor lesions received a neutron boost with a single dose of 2 Gy up to a total dose of 6 Gy (1–2 times a week).

New Research Reactor – Improved Treatment Conditions at FRM II

Treatment at the new research reactor Forschungs-Neutronenquelle Heinz Maier-Leibnitz (FRM II) started in 2007 under improved conditions. The most noticeable change is the installation of a multi leaf collimator (MLC) with a maximum field size of 30 $cm^2 \times 20$ cm^2. Like RENT, the beam is characterized by a neutron–photon mix and applied at a dose rate of 0.52 Gy/min neutron dose and 0.20 Gy/min photon dose in a depth of 2 cm (25). Fast neutrons are generated by a nuclear fission reactor and

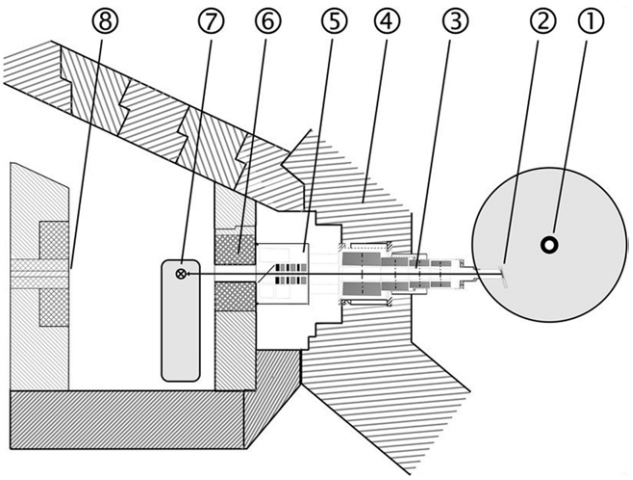

FIGURE 2 | Layout of the FNT facility at the new research reactor (FRM II): 1 Reactor core, 2 Neutron converter, 3 Neutron beam line, 4 Reactor pool wall, 5 Filter unit, 6 Multi leaf collimator, 7 Treatment table, 8 Beam stopper.

a uranium converter plate. The patients can be positioned in front of the horizontal beam line by a 3-D motorized couch (**Figure 2**).

Between 2007 and 2013, 124 patients were treated, until the reactor was shut down due to major revisions. FNT continues since July 2015. Again, for most patients FNT was used as a local boost following external photon therapy. Patients treated at FRM II were between 19 and 94 years old (median 64) and the main primaries were breast cancer (40%), malignant melanoma (18%), and head-and-neck cancers (squamous 10%, ACC 15%, **Figure 3**). Most of the treatment indications were superficial skin lesions (69%) followed by salivary gland tumors (15%) and lymph node metastases (10%, **Figure 4**). A median total dose of 6 Gy (max 12 Gy, min 1.4 Gy) at a median single dose of 2 Gy was applied.

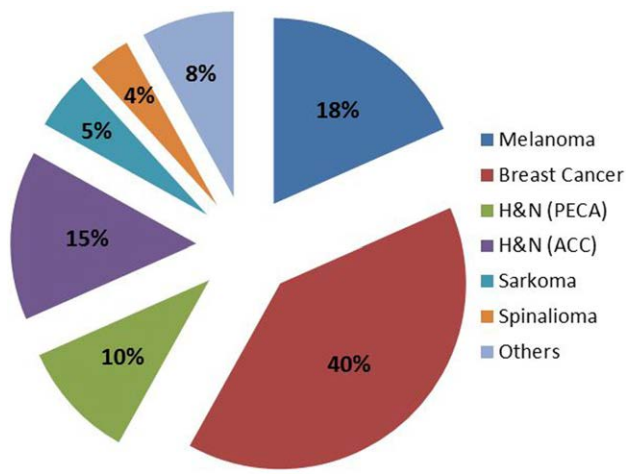

FIGURE 3 | Primary tumors of patients treated with FNT between 2007 and 2013 at FRM II.

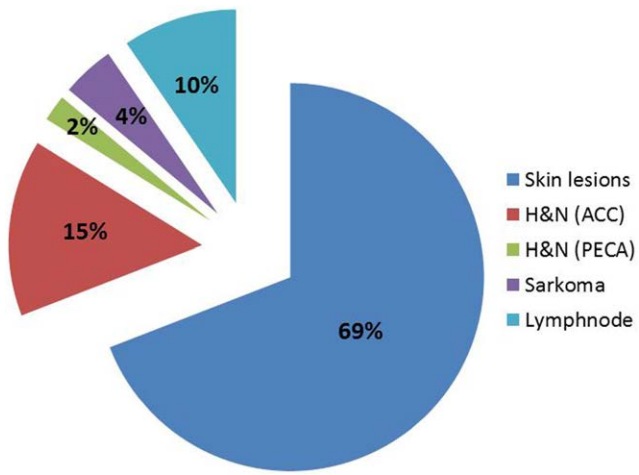

FIGURE 4 | Treatment indications for FNT at FRM II between 2007 and 2013.

For head-and-neck cancer patients thermoplastic mask systems were used and Computer tomography (CT) imaging acquired in treatment position was used to define the target volume and optimal beam positioning. For superficial skin lesion, the target volumes were determined clinically and light fields were used to define the optimal treatment position and MLC shape.

Thirty seven patients with superficial skin lesions were evaluated for tumor response and the effect of FNT on their quality of life (QoL) was also evaluated. A median total dose of 6 Gy (range 2–12 Gy) was applied at a median single dose of 2 Gy. Mean treatment field size was 12.6 (±6.6 cm) × 10.2 cm (±4.2 cm), and FNT was applied with a mean treatment time of 162 s (±23.5 s) per session.

Ethics Statement

All patients were treated in accordance with the principles of the Declaration of Helsinki. The scientific use of retrospective data has been explicitly allowed by Bavarian federal law (BayKrG Art 27(4)). Additionally, all patients gave their written informed consent and agreed that their scientific data could be used.

RESULTS

Due to the manifold treatment indications that were treated with FNT between 1985 and 2013, we focused on subgroup of patients for data presentation in the present manuscript in order to deliver data comparable to with other treatment possibilities. Therefore groups of patients were pooled according to the entity treated and the technique used and analyzed separately with special focus on LC, OS, and toxicity. Because of the relatively low numbers of patients treated with FNT compared to conventional photon therapy and due to the individual character of FNT treatments, a thorough patient follow up was enforced. Patients were regularly seen in a dedicated outpatient department and if patients did not show up for their appointment, their general practitioners were contacted for follow up and toxicity information.

Primary Treatment for Adenoidcystic Carcinomas of the Salivary Gland at RENT

Patient data was analyzed at a median follow up time of 8 years (range 2–17 years). In terms of LC, only 15% of the patients showed local tumor progression within the initial site during follow-up. This resulted in LC rates at 5, 10, and 15 years of 90, 85, and 85%. Eighty percent of the patients were still alive after 5 years. This dropped to 60% after 10 years due to the development of distant metastases, as they are common in this tumor entity. Five patients (10%) showed severe late side effects in terms of skin toxicity with ulceration of the skin and seven patients (15%) developed osteonecrosis within the mandible.

Palliative Treatment for Thoracic Wall Recurrences at RENT

Patient data were analyzed at a median follow up time of 23 months (range 4–65 months). More than 2/3 of the patients (68%) showed complete remission of macroscopic chest wall metastases within the radiation field during follow up. Another 29% of the patients at least showed partial remission leaving only one patient without tumor response after FNT. Median time to tumor progression (in- and outside of the treatment field) was 9 month and LC after 3 years was 55%. After FNT (with or without photon treatment) patients showed acute side effects with radiodermatitis up to grade II (CTCAE V4.0). During follow-up, five patients (10%) showed a grade II fibrosis within the treatment field, no grade III or IV side effects were observed.

Palliative Treatment for Metastatic Skin Lesions at FRM II

In terms of tumor response macroscopic skin lesions showed a good response after FNT with 25% achieving complete remission, 56% partial remission and 19% had stable disease within the treated region at first follow up 6 weeks after completion of FNT. Nearly all patients (97%) stated that their personal situation was improved by the FNT.

DISCUSSION

Although FNT has been around since the 1970s, the number of publications on this topic is limited and unlike in most fields of oncology, the number of publications per year has not increased, but even decreased over the last decades (see **Figure 5**). This is explained by the clinical difficulties that developed during the application of FNT: In spite of benefits based on the biological properties of neutrons, the rates of treatment-induced side effects limited the widespread use of neutron therapy, and thus almost removed neutron centers from clinical radiation oncology (9, 26, 27). For certain indications, however, few centers are still in operation, including also approaches with BNCT (28–30).

Due to the distinct physical features of neutrons, radiation protection remains challenging and high precision modern radiotherapy, as it can be delivered by a modern linear accelerator with photons, requires tremendous efforts in terms of costs and infrastructure to realize. Horrible side effects, which were caused in the early days of FNT when the new technique was enthusiastically embraced and the knowledge on dosing and treatment planning was not yet existent, sank deep into the collective memory (31–35). Also the clinical use of a fixed neutron RBE was bound to cause problems, despite good radiobiological data which showed its variability. There are several papers describing the theoretical difficulties associated with neutron RBE's and how difficult it would be to improve the therapeutic ratio by using biological effective dose comparisons and modeling the relation between RBE and dose per fraction (36, 37). Therefore it seems like the radiation community is about to draw the veil of oblivion over FNT.

Even if the knowledge on FNT is still limited and the studies that were carried out so far will not hold up to today's standard of randomized, well controlled studies and even if there are some authors who question an advantage of High-LET radiation in terms of tumor control at all (38) it can be stated that there is conclusive evidence on the capability of FNT to offer improved LC compared to photon treatment (9, 29, 39, 40). And this is also true for tumor entities that are known to be resistant to conventional radiation treatment. However, even if LC can be achieved, this often does not lead to a favorable OS, since survival is often limited by early distant metastases, as it was just recently shown by Liao et al. (16) and as it is also supported by our data on ACC patients.

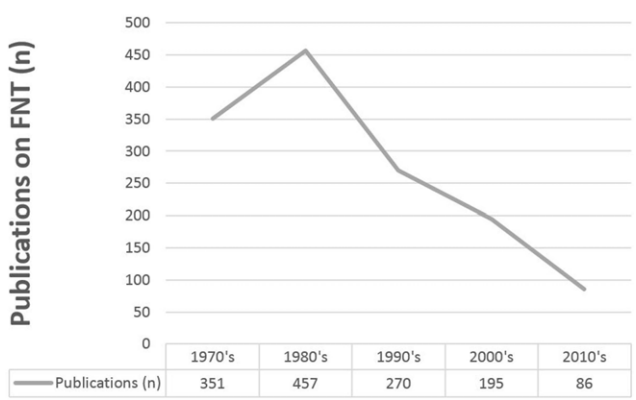

FIGURE 5 | Manuscripts on FNT (PubMed search: Fast neutron therapy, results pooled by decades).

Therefore in most treatment indications, FNT is considered useful today, and OS might not be the appropriate tool to measure the treatment success. We saw some tremendous improvement in QoL for individual patients due to tumor regression and reduced effort in wound care. Most of the patients treated with FNT stated that they had profited from this treatment and that their personal situation was improved after FNT. The main reason for this is, as stated above, in our opinion the good tumor response. Since most lesions treated were superficial, the treatment success was also easily comprehensible to the patient. So it can be stated that for superficial metastases, FNT offers a well-tolerated and effective treatment option. The high RBE also leads to short treatment times and few treatment sessions, which adds to the attractiveness in terms of a palliative treatment option.

The experience made with FNT should be evaluated carefully since it might be useful not only to learn more about FNT itself, but also about high-LET particle therapy in general. Since neutron therapy has been around since the 1970s, there are long-term survivors that can help to identify risk and chances associated with heavy-particle therapy. It has to be mentioned in this regard that there is a potentially increased risk of secondary malignancies caused by neutron irradiation, especially to healthy tissues outside of the treatment field. Large concerted efforts such as the Euratom Allegro project are currently carried out to further evaluate this topic (41). In the treatment of patients with ACC of the salivary gland, we saw some patients with osteonecrosis of the mandibular bone. Of course the relative numbers of those complications are considerably high compared to the numbers we are accepting in the photon community. But it also has to be considered that some of these patients had large tumors that were already infiltrating the bone, so the reason for the osteonecrosis is not necessarily the treatment but the tumor itself. This fact is reflected by the high rate of incomplete resections (more than 2/3 of the evaluated patients), and it can certainly be seen as a selection bias against FNT. But still, this is also a warning that high LET-radiation and comparatively high single doses might not be appropriate in sensitive areas, especially when the tools to determine the anatomical dose application are limited.

Another point, why it might be too early to forget about FNT, is the recent developments in cancer immunotherapy. In 2013, immunotherapy was elected as the breakthrough of the year (42). Now, even in some patients with metastasized melanoma, long-term survivors can be found (43). The combination of radiotherapy and immunotherapy seems to be a fruitful collaboration. Since immunotherapy is able to offer improved OS but often fails to achieve LC in progressive tumor lesions, local radiotherapy might prove to be an ideal combination. Not only can radiotherapy lead to LC within the treatment field, it can even cause tumor regression outside of the treatment field, the so called abscopal effects (44). So far neither the optimal time point to combine the modalities nor the optimal dosing schedule is known. But there is reason to believe if the radiotherapy would cause a greater immune-stimulatory effect, than the collaboration between the two treatment partners would be even more effective. FNT might be able to achieve this immune-stimulatory effect due

to its high LET. Since FNT is usually applied only once or twice per week, lymphocyte depletion within the treatment field, as it is caused by daily routine radiotherapy, might be less pronounced. Thus, especially in patients were immunotherapy is appropriate, such as malignant melanoma, combination with FNT for skin lesions could be a promising alternative.

CONCLUSION

Fast neutron therapy using reactor generated fission neutrons is limited due to the relatively low penetration depth of the beam. Therefore, in most cases, therapy is limited to superficial lesions as they often occur in recurrent breast cancer at the thoracic wall or in recurrent malignant melanoma (skin lesions). To measure the treatment success in these palliative concepts, determination of the OS or progression free survival might not be an appropriate tool. Some clinically meaningful improvements in terms of local tumor regression with relatively low side effects were observed, leading to improved QoL and a reduced effort for wound management for the individual patients. Patients treated with FNT should be treated within clinical study protocols and the remaining neutron facilities should share their experiences, as it is done for other hadron therapies as well (45). As there is a growing interest in high-LET therapy with a growing number of hadron therapy centers around the globe, the clinical data generated by neutron therapy might help to develop biologically driven treatment planning algorithms. Also recent advances in immunotherapy call to reevaluate the benefit of neutron therapy, where good local tumor control can be achieved within short treatment times and immune-modulatory effects might be more pronounced compared to conventional irradiation.

AUTHOR CONTRIBUTIONS

Study design: HS, JW, WP, SC. Acquisition of data: HS, TN, WR. Analysis and interpretation of data: HS, SK, SC. Drafting of manuscript: HS. Initial critical revision: WR, FW, SK, JW, SC. Revision of manuscript: HS, JW, FW.

REFERENCES

1. Theron T, Slabbert J, Serafin A, Böhm L. The merits of cell kinetic parameters for the assessment of intrinsic cellular radiosensitivity to photon and high linear energy transfer neutron irradiation. *Int J Radiat Oncol Biol Phys* (1997) **37**(2):423–8. doi:10.1016/S0360-3016(96)00533-0
2. Wambersie A, Hendry J, Gueulette J, Gahbauer R, Pötter R, Grégoire V. Radiobiological rationale and patient selection for high-LET radiation in cancer therapy. *Radiother Oncol* (2004) **73**(Suppl 2):S1–14. doi:10.1016/S0167-8140(04)80004-5
3. Goodhead DT. Mechanisms for the biological effectiveness of high-LET radiations. *J Radiat Res* (1999) **40**(Suppl):1–13. doi:10.1269/jrr.40.S1
4. Schmid E, Schlegel D, Guldbakke S, Kapsch RP, Regulla D. RBE of nearly monoenergetic neutrons at energies of 36 keV-14.6 MeV for induction of dicentrics in human lymphocytes. *Radiat Environ Biophys* (2003) **42**(2):87–94. doi:10.1007/s00411-003-0200-0
5. Broerse JJ, Battermann JJ. Fast neutron radiotherapy: for equal or for better? *Med Phys* (1981) **8**(6):751–60. doi:10.1118/1.594851
6. Battermann JJ. Fast neutron therapy for advanced brain tumors. *Int J Radiat Oncol Biol Phys* (1980) **6**(3):333–5. doi:10.1016/0360-3016(80)90142-X
7. Vaupel P, Harrison L. Tumor hypoxia: causative factors, compensatory mechanisms, and cellular response. *Oncologist* (2004) **9**(Suppl 5):4–9. doi:10.1634/theoncologist.9-90005-4
8. Gragg RL, Humphrey RM, Thames HD Jr, Meyn RE. The response of Chinese hamster ovary cells to fast neutron radiotherapy beams. III. Variation in biological effectiveness with position in the cell cycle. *Radiat Res* (1978) **76**(2):283–91. doi:10.2307/3574779
9. Laramore GE, Krall JM, Griffin TW, Duncan W, Richter MP, Saroja KR, et al. Neutron versus photon irradiation for unresectable salivary gland tumors: final report of an RTOG-MRC randomized clinical trial. radiation therapy oncology group. Medical research council. *Int J Radiat Oncol Biol Phys* (1993) **27**(2):235–40. doi:10.1016/0360-3016(93)90233-L
10. Brackrock S, Krüll A, Röser K, Schwarz R, Riethdorf L, Alberti W. Neutron therapy, prognostic factors and dedifferentiation of adenoid cystic carcinomas (ACC) of salivary glands. *Anticancer Res* (2005) **25**(2B):1321–6.
11. Bittner N, Koh WJ, Laramore GE, Patel S, Mulligan MS, Douglas JG. Treatment of locally advanced adenoid cystic carcinoma of the trachea with neutron radiotherapy. *Int J Radiat Oncol Biol Phys* (2008) **72**(2):410–4. doi:10.1016/j.ijrobp.2008.01.016
12. Laramore GE, Krall JM, Thomas FJ, Russell KJ, Maor MH, Hendrickson FR, et al. Fast neutron radiotherapy for locally advanced prostate cancer. Final report of radiation therapy oncology group randomized clinical trial. *Am J Clin Oncol* (1993) **16**(2):164–7. doi:10.1097/00000421-199304000-00018
13. Lindsley KL, Cho P, Stelzer KJ, Koh WJ, Austin-Seymour M, Russell KJ, et al. Fast neutrons in prostatic adenocarcinomas: worldwide clinical experience. *Recent Results Cancer Res* (1998) **150**:125–36. doi:10.1007/978-3-642-78774-4_7
14. Patel SA, Kusano AS, Truong A, Stelzer KJ, Laramore GE. Fast neutron radiotherapy in the treatment of malignant pleural mesothelioma. *Am J Clin Oncol* (2015) **38**(1):47–50. doi:10.1097/COC.0b013e3182880b7a
15. Bremer M, Neuhofer C, Auberger T, Zimmermann FB, Kneschaurek P, Reuschel W, et al. Palliative radiotherapy of malignant melanoma with reactor fission neutron therapy (RENT): a prospective study. *Radiat Oncol Investig* (1999) **7**(2):118–24. doi:10.1002/(SICI)1520-6823(1999)7:2<118::AID-ROI8>3.0.CO;2-6
16. Liao JJ, Parvathaneni U, Laramore GE, Thompson JA, Bhatia S, Futran ND, et al. Fast neutron radiotherapy for primary mucosal melanomas of the head and neck. *Head Neck* (2014) **36**(8):1162–7. doi:10.1002/hed.23428
17. Krüll A, Schwarz R, Engenhart R, Huber P, Lessel A, Koppe H, et al. European results in neutron therapy of malignant salivary gland tumors. *Bull Cancer Radiother* (1996) **83**:125s–9s. doi:10.1016/0924-4212(96)84897-3
18. Stannard C, Vernimmen F, Carrara H, Jones D, Fredericks S, Hille J, et al. Malignant salivary gland tumours: can fast neutron therapy results point the way to carbon ion therapy? *Radiother Oncol* (2013) **109**(2):262–8. doi:10.1016/j.radonc.2013.08.013
19. Garny S, Rühm W, Zankl M, Wagner FM, Paretzke HG. First steps towards a fast-neutron therapy planning program. *Radiat Oncol* (2011) **6**:163. doi:10.1186/1748-717X-6-163
20. Popescu A. Changes in prescribed doses for the Seattle neutron therapy system. *Phys Med Biol* (2008) **53**(11):2985–90. doi:10.1088/0031-9155/53/11/015
21. Soderberg J, Alm Carlsson G, Ahnesjo A. Monte Carlo evaluation of a photon pencil kernel algorithm applied to fast neutron therapy treatment planning. *Phys Med Biol* (2003) **48**(20):3327–44. doi:10.1088/0031-9155/48/20/005
22. IAEA. Research reactor users' network (RRUNs): advances in neutron therapy. *IAEA Technical Meeting (F1-TM-44771)*. Mainz (2013).
23. Coderre JA, Morris GM, Micca PL, Hopewell JW, Verhagen I, Kleiboer BJ, et al. Late effects of radiation on the central nervous system: role of vascular endothelial damage and glial stem cell survival. *Radiat Res* (2006) **166**(3):495–503. doi:10.1667/RR3597.1
24. Clasen B, et al. [Priniciples of fission neutron therapy for malignant head and neck cancer at the research reactor (RENT) of the Technische Universitaet Muenchen]. *Otorhinolaryngol Nova* (1991) **1**:102–8. doi:10.1055/s-2007-998223
25. Wagner FM, Kneschaurek P, Kastenmüller A, Loeper-Kabasakal B, Kampfer S, Breitkreutz H, et al. The Munich fission neutron therapy facility MEDAPP at the research reactor FRM II. *Strahlenther Onkol* (2008) **184**(12):643–6. doi:10.1007/s00066-008-1878-3
26. Spratt DE, Salgado LR, Riaz N, Doran MG, Tam M, Wolden S, et al. Results of photon radiotherapy for unresectable salivary gland tumors: is neutron

radiotherapy's local control superior? *Radiol Oncol* (2014) **48**(1):56–61. doi:10.2478/raon-2013-0046
27. Griffin TW. Fast neutron therapy: its promise and its past. *Int J Radiat Oncol Biol Phys* (1980) **6**(3):387–8. doi:10.1016/0360-3016(80)90157-1
28. Wang LW, Chen YW, Ho CY, Hsueh Liu YW, Chou FI, Liu YH, et al. Fractionated BNCT for locally recurrent head and neck cancer: experience from a phase I/II clinical trial at Tsing Hua open-pool reactor. *Appl Radiat Isot* (2014) **88**:23–7. doi:10.1016/j.apradiso.2013.11.134
29. Kageji T, Nagahiro S, Mizobuchi Y, Matsuzaki K, Nakagawa Y, Kumada H. Boron neutron capture therapy (BNCT) for new*ly-diagnosed* glioblastoma: comparison of clinical results obtained with BNCT and conventional treatment. *J Med Invest* (2014) **61**(3–4):254–63. doi:10.2152/jmi.61.254
30. Zonta A, Pinelli T, Prati U, Roveda L, Ferrari C, Clerici AM, et al. Extracorporeal liver BNCT for the treatment of diffuse metastases: what was learned and what is still to be learned. *Appl Radiat Isot* (2009) **67**(7–8 Suppl):S67–75. doi:10.1016/j.apradiso.2009.03.087
31. Errington RD, Ashby D, Gore SM, Abrams KR, Myint S, Bonnett DE, et al. High energy neutron treatment for pelvic cancers: study stopped because of increased mortality. *BMJ* (1991) **302**(6784):1045–51. doi:10.1136/bmj.302.6784.1045
32. MacDougall RH, Orr JA, Kerr GR, Duncan W. Fast neutron treatment for squamous cell carcinoma of the head and neck: final report of Edinburgh randomised trial. *BMJ* (1990) **301**(6763):1241–2. doi:10.1136/bmj.301.6763.1241
33. Schmitt G, Schnabel K, Sauerwein W, Scherer E. Neutron and neutron-boost irradiation of soft tissue sarcomas: a 4.5 year analysis of 139 patients. *Radiother Oncol* (1983) **1**(1):23–9. doi:10.1016/S0167-8140(83)80004-8
34. Steingraber M, Lessel A, Jahn U. Fast neutron therapy in treatment of soft tissue sarcoma – the Berlin-Buch study. *Bull Cancer Radiother* (1996) **83 Suppl**:122s–4s. doi:10.1016/0924-4212(96)84896-1
35. Maor MH, Errington RD, Caplan RJ, Griffin TW, laramore GE, Parker RG, et al. Fast-neutron therapy in advanced head and neck cancer: a collaborative international randomized trial. *Int J Radiat Oncol Biol Phys* (1995) **32**(3):599–604. doi:10.1016/0360-3016(94)00595-C
36. Dale RG, Jones B. The assessment of RBE effects using the concept of biologically effective dose. *Int J Radiat Oncol Biol Phys* (1999) **43**(3):639–45. doi:10.1016/S0360-3016(98)00364-2
37. Jones B, Underwood TS, Carabe-Fernandez A, Timlin C, Dale RG. Fast neutron relative biological effects and implications for charged particle therapy. *Br J Radiol* (2011) **84**(Spec No 1):S11–8. doi:10.1259/bjr/67509851
38. Suit H, DeLaney T, Goldberg S, Paganetti H, Clasie B, Gerweck L, et al. Proton vs carbon ion beams in the definitive radiation treatment of cancer patients. *Radiother Oncol* (2010) **95**(1):3–22. doi:10.1016/j.radonc.2010.01.015
39. Huber PE, Debus J, Latz D, Zierhut D, Bischof M, Wannenmacher M, et al. Radiotherapy for advanced adenoid cystic carcinoma: neutrons, photons or mixed beam? *Radiother Oncol* (2001) **59**(2):161–7. doi:10.1016/S0167-8140(00)00273-5
40. Wambersie A. Fast neutron therapy at the end of 1988 – a survey of the clinical data. *Strahlenther Onkol* (1990) **166**(1):52–60.
41. Ottolenghi A, Smyth V, Trott KR. The risks to healthy tissues from the use of existing and emerging techniques for radiation therapy. *Radiat Prot Dosimetry* (2011) **143**(2–4):533–5. doi:10.1093/rpd/ncq524
42. Couzin-Frankel J. Breakthrough of the year 2013. Cancer immunotherapy. *Science* (2013) **342**(6165):1432–3. doi:10.1126/science.342.6165.1432
43. Di Giacomo AM, Calabrò L, Danielli R, Fonsatti E, Bertocci E, Pesce I, et al. Long-term survival and immunological parameters in metastatic melanoma patients who responded to ipilimumab 10 mg/kg within an expanded access programme. *Cancer Immunol Immunother* (2013) **62**(6):1021–8. doi:10.1007/s00262-013-1418-6
44. Barker CA, Postow MA. Combinations of radiation therapy and immunotherapy for melanoma: a review of clinical outcomes. *Int J Radiat Oncol Biol Phys* (2014) **88**(5):986–97. doi:10.1016/j.ijrobp.2013.08.035
45. Combs SE, Djosanjh M, Pötter R, Orrechia R, Haberer T, Durante M, et al. Towards clinical evidence in particle therapy: ENLIGHT, PARTNER, ULICE and beyond. *J Radiat Res* (2013) **54**(Suppl 1):i6–12. doi:10.1093/jrr/rrt039

Conflict of Interest Statement: The authors declare that the research was conducted in the absence of any commercial or financial relationships that could be construed as a potential conflict of interest.

Copyright © 2015 Specht, Neff, Reuschel, Wagner, Kampfer, Wilkens, Petry and Combs. This is an open-access article distributed under the terms of the Creative Commons Attribution License (CC BY). The use, distribution or reproduction in other forums is permitted, provided the original author(s) or licensor are credited and that the original publication in this journal is cited, in accordance with accepted academic practice. No use, distribution or reproduction is permitted which does not comply with these terms.

frontiers in Oncology

ORIGINAL RESEARCH
published: 20 November 2015
doi: 10.3389/fonc.2015.00256

Increase in Tumor Control and Normal Tissue Complication Probabilities in Advanced Head-and-Neck Cancer for Dose-Escalated Intensity-Modulated Photon and Proton Therapy

Annika Jakobi[1†], Armin Lühr[1,2,3*†], Kristin Stützer[1], Anna Bandurska-Luque[1,4], Steffen Löck[1], Mechthild Krause[1,2,3,4,5], Michael Baumann[1,2,3,4,5], Rosalind Perrin[1‡] and Christian Richter[1,2,3,4,5]*

[1] OncoRay – National Center for Radiation Research in Oncology, Faculty of Medicine, University Hospital Carl Gustav Carus, Technische Universität Dresden, Helmholtz-Zentrum Dresden – Rossendorf, Dresden, Germany, [2] German Cancer Consortium (DKTK), Partner Site Dresden, Dresden, Germany, [3] German Cancer Research Center (DKFZ), Heidelberg, Germany, [4] Department of Radiation Oncology, Faculty of Medicine, University Hospital Carl Gustav Carus, Technische Universität Dresden, Dresden, Germany, [5] Institute of Radiooncology, Helmholtz-Zentrum Dresden – Rossendorf, Dresden, Germany

Introduction: Presently used radiochemotherapy regimens result in moderate local control rates for patients with advanced head-and-neck squamous cell carcinoma (HNSCC). Dose escalation (DE) may be an option to improve patient outcome, but may also increase the risk of toxicities in healthy tissue. The presented treatment planning study evaluated the feasibility of two DE levels for advanced HNSCC patients, planned with either intensity-modulated photon therapy (IMXT) or proton therapy (IMPT).

Materials and methods: For 45 HNSCC patients, IMXT and IMPT treatment plans were created including DE via a simultaneous integrated boost (SIB) in the high-risk volume, while maintaining standard fractionation with 2 Gy per fraction in the remaining target volume. Two DE levels for the SIB were compared: 2.3 and 2.6 Gy. Treatment plan evaluation included assessment of tumor control probabilities (TCP) and normal tissue complication probabilities (NTCP).

Results: An increase of approximately 10% in TCP was estimated between the DE levels. A pronounced high-dose rim surrounding the SIB volume was identified in IMXT treatment. Compared to IMPT, this extra dose slightly increased the TCP values and to a larger extent the NTCP values. For both modalities, the higher DE level led only to a small increase in NTCP values (mean differences <2%) in all models, except for the risk of aspiration, which increased on average by 8 and 6% with IMXT and IMPT, respectively, but showed a considerable patient dependence.

Conclusion: Both DE levels appear applicable to patients with IMXT and IMPT since all calculated NTCP values, except for one, increased only little for the higher DE level. The estimated TCP increase is of relevant magnitude. The higher DE schedule needs to be investigated carefully in the setting of a prospective clinical trial, especially regarding toxicities caused by high local doses that lack a sound dose–response description, e.g., ulcers.

Keywords: photon radiotherapy, proton radiotherapy, tumor control probability, normal tissue complication probability, head-and-neck cancer

OPEN ACCESS

Edited by:
Marco Durante, GSI Helmholtzzentrum für Schwerionenforschung, Germany

Reviewed by:
Wenyin Shi, Thomas Jefferson University, USA
Laura Cella, National Research Council, Italy

***Correspondence:**
Annika Jakobi
annika.jakobi@oncoray.de;
Armin Lühr
armin.luehr@oncoray.de

†Annika Jakobi and Armin Lühr have contributed equally to this work.

***‡Present address:**
Rosalind Perrin, Paul Scherrer Institute, Villigen, Switzerland

Specialty section:
This article was submitted to Radiation Oncology, a section of the journal Frontiers in Oncology

Received: *28 August 2015*
Accepted: *06 November 2015*
Published: *20 November 2015*

Citation:
Jakobi A, Lühr A, Stützer K, Bandurska-Luque A, Löck S, Krause M, Baumann M, Perrin R and Richter C (2015) Increase in Tumor Control and Normal Tissue Complication Probabilities in Advanced Head-and-Neck Cancer for Dose-Escalated Intensity-Modulated Photon and Proton Therapy. Front. Oncol. 5:256. doi: 10.3389/fonc.2015.00256

INTRODUCTION

Standard of care for inoperable advanced head-and-neck squamous cell carcinoma (HNSCC) patients is concurrent radiochemotherapy, which today is still associated with a substantial recurrence rate (1, 2). Thus, an improvement of treatment outcome is desirable. Radiotherapy intensification to the primary tumor volume may improve patient outcome, since most recurring HNSCC after radiotherapy develop at the site of the initial primary tumor volume (3–5). Treatment intensification with radiation dose escalation (DE) is possible by applying non-uniform dose distributions. The simultaneous integrated boost (SIB) technique exploits the advantage of maintaining the treatment time – a critical factor in HNSCC radiotherapy (6–10). Radioresistant tumors may increasingly be identified by molecular profiling (11, 12), and radioresistant sub-regions within individual tumor volumes may be identified with functional imaging such as positron emission tomography (PET) (13, 14). Several groups have proposed dose painting of sub-volumes using hypoxia imaging with fluoromisonidazole (FMISO) PET (15–18). Since the capability of the dose painting approach to increase local tumor control is controversial, another approach is DE on the whole tumor volume (19, 20). However, treatment intensification may lead to an increase in side effects. Accordingly, higher dose conformity with proton therapy (PT) compared to advanced photon therapy (XT) may be beneficial. To estimate the overall benefit of treatment intensification, the probable gain in tumor control needs to be balanced against a potential increase in toxicity risk. This can be done in the treatment planning stage by comparing the resulting differences in tumor control probability (TCP) with those in normal tissue complication probability (NTCP).

Inhomogeneous dose prescriptions [e.g., different doses to gross tumor volume (GTV) and elective tumor volume] are driven by the clinical experience of a spatially heterogeneous dose–response in the target volume. Therefore, realistic modeling of TCP has to allow for dosimetric as well as radiobiological heterogeneity within the target. A recently presented TCP approach (21) provides dose–response relations for each of the considered target sub-volumes that base on clinical outcome data on the recurrence distribution in the tumor volume [e.g., Ref. (22)]. In contrast, if a homogeneous dose–response in the entire target volume was assumed, TCP estimates would suggest a low probability of treatment failures in the high-risk tumor sub-volume and most failures in the low-dose elective sub-volume (21), contradicting clinically observed data on failure patterns.

Regarding NTCP, in a previous work, we identified locally advanced HNSCC patients with substantial benefit from PT by comparing intensity-modulated XT (IMXT) with intensity-modulated PT (IMPT), focusing on patient sub-groups with similar primary tumor location (23). Therein, IMPT compared to IMXT showed the general capability to reduce NTCP. Moreover, we estimated the benefit of a mixed modality treatment (IMXT followed by IMPT for sequential boost treatment) by considering the NTCP reduction compared to IMXT alone revealing a minor effect in most of the patient cases (24). Following these studies, a prospective multi-centric clinical study is currently planned in our institution aiming at the evaluation of the effect of a 2.3 Gy DE in the treatment of advanced HNSCC.

In the present *in silico* study, we assessed the feasibility of a fractionation schedule for further treatment intensification via the SIB technique with a DE level of 2.6 Gy in comparison to the 2.3 Gy DE level applied in the previous work. We estimated TCP for these two DE levels and set the expected gain in relation to a potential increase in NTCP values.

MATERIALS AND METHODS

Patient Data, Treatment Schedule, Volume Definition, Treatment Planning

Computed tomography (CT) and fluorodeoxyglucose (FDG) PET datasets of 45 patients treated between 2006 and 2013 at the University Hospital Dresden, Germany were available for the present analysis. Datasets consisted of a pre-treatment FDG PET/CT and a sequential FDG PET/CT recorded after approximately 20 fractions. All patients gave written consent for the use of their data. The study was approved by the institutional Ethics committee. A treatment schedule was defined that consists of two main treatment series planned on two different CT datasets: series I, a treatment series of 25 fractions for the elective clinical target volume (CTV_{elec}), was planned on a baseline CT with 2 Gy per fraction plus a SIB starting at the eleventh fraction allowing for a hypoxia PET stratification based on a scan during treatment. This SIB volume ($GTV_{SIB\text{-}I}$) was either defined as the GTV or, in the case of N3 status, as GTV and the N3 lymph nodes. A $CTV_{gross\text{-}I}$ was generated by isotropic extension of 5–10 mm of the $GTV_{SIB\text{-}I}$ and corrected for air cavities and bones if not infiltrated. Series II, a sequential boost of 11 fractions, was planned on a sequential PET/CT dataset taken after 20 treatment fractions. A dose of 2 Gy per fraction was prescribed to the CTV consisting of a geometrical expansion of the GTV and suspect lymph nodes ($CTV_{gross\text{-}II}$). Additionally, the sequential boost contained a SIB to FDG-avid volumes inside the GTV identified on the FDG–PET scan after 20 treatment fractions ($GTV_{SIB\text{-}II}$). Planning target volumes (PTV) were created for the CTV expanding 5 mm in cranio-caudal direction and 4 mm in plane, retaining a 3 mm distance to the external patient contour. Prescribed dose levels were 50 Gy to the CTV_{elec}, 72 Gy to the CTV_{gross} and 79.8 Gy (DE1) or 87.6 Gy (DE2) to the SIB volume, depending on the DE level. The equivalent dose in 2 Gy fractions (EQD2) in the SIB volume was 81.3 Gy and 91.0 Gy, respectively, assuming an α/β ratio of 10 Gy. A constant correction factor of 1.1 was used for the higher relative biological effectiveness (RBE) of protons compared to photons, such that all values given in Gy actually mean Gy(RBE) for IMPT. Delineated organs at risk (OAR) were spinal cord, brain stem, ipsi- and contralateral parotid gland, ipsi- and contralateral brachial plexus, mucosa, swallowing muscles, larynx, esophagus, mandible, ipsi- and contralateral temporomandibular joints, ipsi- and contralateral submandibular and sublingual glands.

Intensity-modulated photon therapy treatment plans were based on seven equidistant 6 MV photon beams. A field reduction to five beams was considered for Series II for one-sided sequential boost volumes. IMPT treatment plans were based on a three field

beam arrangement with beam angles of −40°, 40°, and 180°, but changes of these angles were possible for one-sided sequential boost volumes in Series II. Optimization goals for target structures were to irradiate at least 95% of the target volumes (PTV_{elec}, PTV_{gross}, GTV_{SIB}) above 95% of the prescribed dose ($V_{95} > 95\%$). Furthermore, volumes above 107% (V_{107}) of the prescribed dose should be minimized. Such high-dose volume was accepted in the PTV if these were required to ensure the V_{95} in the GTV_{SIB}. OAR constraints with priority over target goals were defined for spinal cord ($D_{max} < 45$ Gy), brain stem ($D_{max} < 54$ Gy), and brachial plexus ($D_{max} < 72$ Gy). To ensure that these constraints are met despite possible positioning uncertainties, the optimization was performed for these OARs with an additional margin of 3 mm considering the same dose constraint (brain stem and brachial plexus) or a slightly increased dose constraint ($D_{max} < 48$ Gy for spinal cord). For other OARs, doses were to be minimized without compromising target coverage. A more detailed description of the patient characteristics, treatment schedule, target definition, and treatment planning is presented in Jakobi et al. (23).

Physical Dose Evaluation, TCP and NTCP Modeling

Dose parameters in the PTV and GTV_{SIB} were evaluated separately for both treatment series. For dose gradient evaluation, a relative dose distribution was created by normalizing each voxel to its prescribed target dose, as schematically shown in **Figure 1A** for the low DE level of 2.3 Gy. The dose was cumulated from both treatment series with a deformable image registration (DIR) on the pre-treatment CT and used to estimate TCP and NTCP. The DIR was validated in a previous study (25). In the target volume, the fractionation effect was considered by voxel-wise calculation of EQD2 ($\alpha/\beta = 10$ Gy). For evaluation of NTCP, fractionation effect corrections were performed depending on model requirements.

Tumor control probabilities modeling with local control as endpoint was based on an approach described by Lühr et al. [abstract in Ref. (21)]. This approach considers that the target volume consists of disjoint sub-volumes (schematically depicted in **Figure 2**), which differ in dose–response. The target structures CTV_{elec}, CTV_{gross}, and GTV_{SIB} were considered as target sub-volumes. To ensure that all sub-volumes were disjoint, inner sub-volumes were excluded from outer sub-volumes (e.g., GTV_{SIB} from CTV_{gross}). According to clinically observed spatial failure patterns and the dose–response of a comparable patient cohort, the model approach assigns different dose–response curves to each sub-volume (cf. **Figure 2**) – each curve specified by its values for D_{50}, the dose that yields a TCP of 50%, and γ_{50}, the steepness of the TCP curve at the dose D_{50}. In this study, the overall dose–response for homogeneous irradiation was approximated by $D_{50} = 70$ Gy and $\gamma_{50} = 1.5$ – assuming patients with advanced HNSCC – and by the relative proportions of local failures $f = 0.80$, 0.18, and 0.02 in GTV_{SIB}, CTV_{gross}, and CTV_{elec}, respectively (22, 26). The D_{50} and γ_{50} parameters resulting from the sub-volume TCP approach (assuming the Poisson TCP model) for the three considered sub-volumes are listed in **Table 1**. TCP calculations were performed within the modeling framework of the recently developed ReCompare (REmote COMparison of PARticlE and photon plans) tool (27, 28).

Normal tissue complication probabilities values were calculated using recently published models for the following toxicities

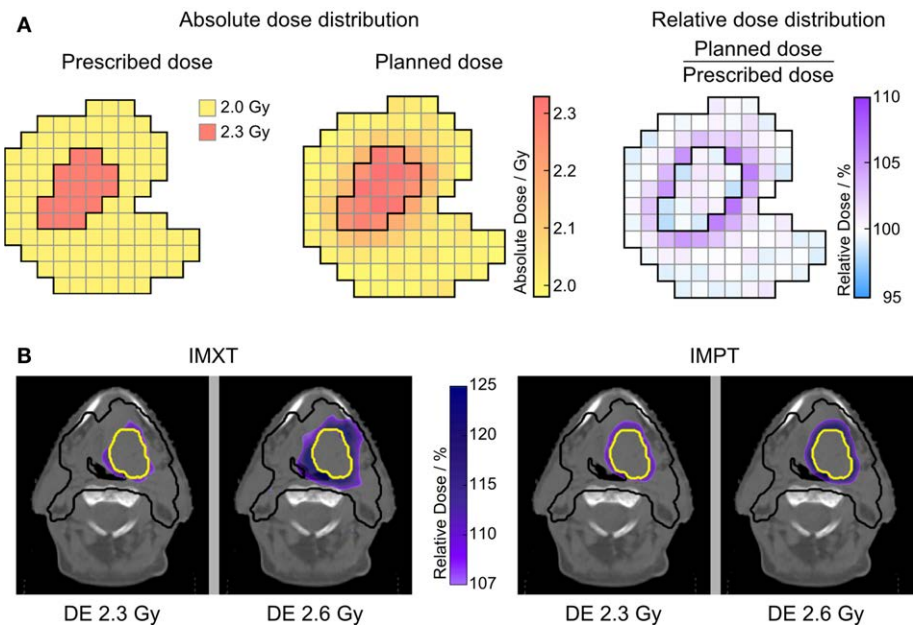

FIGURE 1 | Relative dose distributions. **(A)** Illustration of calculating the voxel-wise relative dose distribution, exemplarily for DE level of 2.3 Gy. For the high DE level, the SIB volume is normalized to 2.6 Gy in the same way. **(B)** Relative dose distribution in the elective target only showing high-dose areas outside ICRU constraints (>107%). All four SIB treatment plans for one patient are shown for series I treatment, illustrating the larger high-dose rim around the SIB volume for the high DE level of 2.6 Gy. PTV_{elec} is outlined in black, GTV_{SIB-I} in yellow.

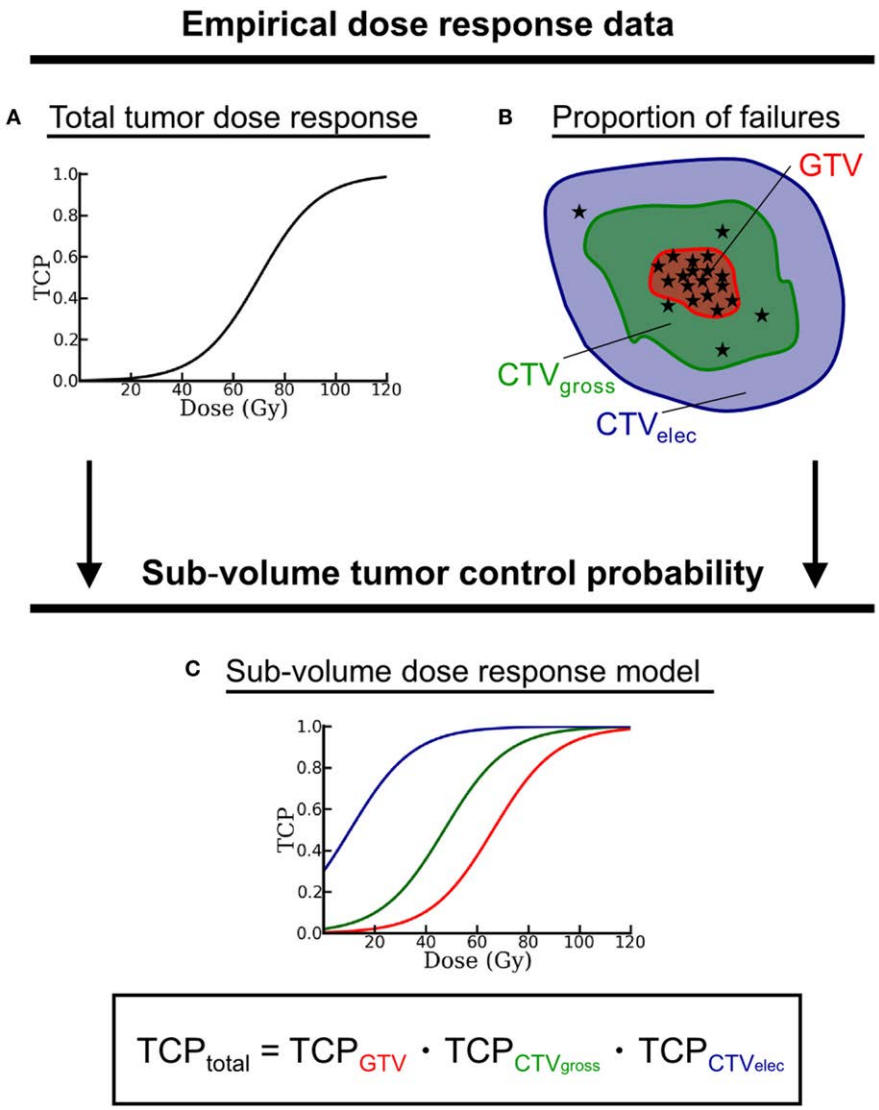

FIGURE 2 | Schematic drawing of the sub-volume TCP model approach. Empirical dose–response data from comparable patient cohorts – given as **(A)** dose–response curve and **(B)** spatial distribution of local failures (represented by the asterisks) – serve as input to generate **(C)** one dose–response curve for each target sub-volume. The total TCP results from the product of all sub-volume TCP. Note, all target sub-volumes have to be disjoint. Therefore, inner sub-volumes are excluded from outer encompassing structures.

TABLE 1 | TCP model parameters determining the dose–response in the target sub-volumes.

Sub-volume	D_{50}/Gy	γ_{50}/%/%	f
Total	70.00[a]	1.50[a]	1.00
GTV_{SIB}	66.79	1.43	0.80[a]
CTV_{gross}	40.36	0.86	0.18[a]
CTV_{elec}	6.73	0.14	0.02[a]

They base on empirical total TCP parameters (D_{50}, γ_{50}) and on observed failure proportions f and were determined according to the sub-volume TCP approach.
[a]Values served as input data for the sub-volume model parameters D_{50} and γ_{50}.

and endpoints: incidence of acute oral mucositis (grade ≥3); aspiration assessed by videofluoroscopy; xerostomia in terms of salivary flow reduction 12 months after therapy; subjective and objective swallowing dysfunctions; incidence risk of late larynx edema (grade ≥2); and trismus (jaw-opening <35 mm). Details on the model parameters can be found in Ref. (29–34) and as an overview in Jakobi et al. (23). Modeling the risk of a specific toxicity in a patient was skipped when a substantial portion of the NTCP-relevant organ was infiltrated by the tumor (physician's decision).

To estimate the relative effect of the treatment intensification on tumor control and toxicity, individual patient matched-pair analyses of TCP and NTCP values were performed between the two different DE levels: $\Delta TCP = TCP_{DE2} - TCP_{DE1}$ and $\Delta NTCP = NTCP_{DE2} - NTCP_{DE1}$. The evaluation was carried out separately for IMXT and IMPT. Statistically significant differences between the DE levels were tested by two-sided paired *t*-tests with

a significance level of 0.05. We analyzed the sensitivity of the TCP results by quantifying the dependence of ΔTCP on the input parameters D_{50} and γ_{50} for a homogeneous dose–response. One of the two input parameters was kept at its nominal value (70 Gy and 1.5, respectively) while the other parameter was varied within a certain range: 60 Gy $\leq D_{50} \leq$ 80 Gy and $0.5 \leq \gamma_{50} \leq 3.0$.

RESULTS

Target Dose Evaluation

Dose coverage of the respective PTV (PTV_{elec}, $PTV_{sequential\ boost}$) and GTV_{SIB} structures ($GTV_{SIB\text{-}I}$, $GTV_{SIB\text{-}II}$) evaluated with V_{95} was similar for both DE schedules, independent of the treatment modality. The pursued minimum criterion ($V_{95} > 95\%$) was fulfilled in all cases (IMXT and IMPT) except for V_{95} of $GTV_{SIB\text{-}II}$ in both DE levels for one patient with a tumor close to a prioritized organ (brachial plexus).

High-dose volumes, evaluated by V_{107} in a structure composed of the respective PTV excluding the respective GTV_{SIB}, the latter expanded by 5 mm, showed a significant increase between the two DE levels. For IMXT treatment, the mean patient-wise difference (±SD) $V_{107,DE2} - V_{107,DE1} = 4.4$ (±3.9)% ($p < 0.001$) is much larger than for IMPT with $V_{107,DE2} - V_{107,DE1} = 0.1$ (±1.6)% ($p = 0.004$). This is illustrated in **Figure 1B** by the relative dose distribution showing a large increase in dose above 107% surrounding the $GTV_{SIB\text{-}I}$ for IMXT, while the increase for IMPT is small. V_{107} of the GTV_{SIB} was 0% in 44 of 45 patients.

Evaluation of TCP

Mean TCP values for all 45 HNSCC patients are given in the upper part of **Table 2** for both DE levels. Significant differences between the two DE levels exist for all evaluated target structures for both modalities ($p < 0.001$). TCP values decreased from CTV_{elec} to $CTV_{gross\text{-}I}$ to $GTV_{SIB\text{-}I}$, i.e., from the outer to the inner target sub-volumes. The higher DE level led to a relevant increase in TCP values for the $GTV_{SIB\text{-}I}$ (9.6% for both modalities) and the total TCP (9.6% with IMXT, 9.3% with IMPT), while the differences for $CTV_{gross\text{-}I}$ and CTV_{elec} were small with mean differences of 1 and 0%, respectively, independent of the treatment modality (**Figure 3A**). This was expected since the DE with the SIB technique focused on the GTV, while the dose to CTV_{elec} and $CTV_{gross\text{-}I}$ was targeted to remain stable between both DE levels. The small differences in TCP values for the $CTV_{gross\text{-}I}$ between the DE levels resulted from the increase in dose that spilled out of the GTV into the surrounding $CTV_{gross\text{-}I}$. TCP values for IMXT were in general slightly larger than for IMPT. This resulted from increased dose in the target regions around the $GTV_{SIB\text{-}I}$ for IMXT, caused by its less conformal dose distribution of the integrated boost.

The estimated absolute TCP values depended on the employed model parameters. The mean increase in TCP from DE1 to DE2 was rather robust against the variation of the model parameters D_{50} and γ_{50} in intervals clinically reasonable for advanced HNSCC (**Figure 4**). For example, halving and doubling the slope parameter γ_{50} from a nominal value of 1.5–0.75 and 3 reduced the mean ΔTCP by about 0.03 and by 0.002, respectively. In comparison, the dependence of ΔTCP on D_{50} was stronger and the estimated gain in TCP between the DE levels increased monotonously for more radioresistant tumors (higher D_{50}). The ΔTCP variation was very similar for IMXT and IMPT.

TABLE 2 | Mean (±1 SD) total and tumor sub-volume TCP values (upper rows) and NTCP values of the evaluated models (lower rows) for the two DE levels and both treatment modalities.

	IMXT		IMPT	
	TCP_{DE1}/%	TCP_{DE2}/%	TCP_{DE1}/%	TCP_{DE2}/%
Total	66.3 ± 0.9	75.9 ± 1.3	65.5 ± 0.8	74.8 ± 1.3
GTV_{SIB}	73.7 ± 0.8	83.2 ± 1.2	73.5 ± 0.9	83.1 ± 1.2
CTV_{gross}	92.2 ± 0.6	93.3 ± 1.0	91.7 ± 0.5	92.7 ± 1.0
CTV_{elec}	97.7 ± 0.4	97.7 ± 0.4	97.1 ± 0.5	97.1 ± 0.5
	$NTCP_{DE1}$/%	$NTCP_{DE2}$/%	$NTCP_{DE1}$/%	$NTCP_{DE2}$/%
Oral mucositis	45.8 ± 9.0	46.2 ± 9.2	40.0 ± 12.4	40.2 ± 12.5
Xerostomia	20.5 ± 10.9	20.6 ± 11.2	6.7 ± 4.6	6.7 ± 4.6
Aspiration	57.5 ± 23.2	65.8 ± 23.4	37.5 ± 25.1	43.8 ± 26.8
Dysphagia[a]	47.5 ± 11.4	49.5 ± 11.9	36.7 ± 13.1	37.7 ± 13.5
Swall. Solids[b]	34.4 ± 9.7	36.6 ± 10.5	25.7 ± 10.9	26.6 ± 11.4
Swall. Liquids[b]	10.3 ± 4.4	11.4 ± 5.2	9.0 ± 4.7	9.5 ± 5.1
Larynx edema	77.8 ± 25.0	79.0 ± 24.9	64.6 ± 36.9	65.4 ± 37.0
Trismus	30.9 ± 5.7	31.0 ± 5.8	26.0 ± 3.7	26.0 ± 3.8

[a]*Physician-rated swallowing dysfunction.*
[b]*Patient-rated swallowing problems of different severity.*

Evaluation of NTCP

Mean NTCP values for all 45 HNSCC patients are given in the lower part of **Table 2** for both DE levels. Absolute NTCP values were patient dependent and toxicity dependent. The integral dose in the patient external contour outside the target volume did not increase with the DE level. Similarly, dose to the OARs were in most cases only slightly increased. As a consequence, the influence of the DE level on NTCP values was almost negligible in most of the evaluated NTCP models with mean ΔNTCP values of approximately 1%. Only the risk of aspiration, modeled with the dose to the pharyngeal constrictor muscle (PCM), was substantially increased from DE1 to DE2 by on average (±SD) 8 (±4)% ($p < 0.001$) for all patients with IMXT and 6 (±4)% ($p < 0.001$) with IMPT (**Figure 3B**).

Additionally, the analysis revealed that all NTCP values for IMXT were larger than for IMPT ($p < 0.001$ for all evaluated models), especially for the risk of xerostomia and aspiration. This reflects the ability of IMPT to create more conformal dose distributions compared to IMXT. As a result, the ΔNTCP were also smaller in most cases for IMPT.

DISCUSSION

We conducted an analysis of the effect of DE for 45 HNSCC patients by comparing TCP and NTCP values of two different dose levels for IMXT as well as IMPT treatment in an *in silico* study. DE applied by the SIB technique allows for a confined treatment intensification focusing on the region of highest risk for recurrence with both, IMXT and IMPT. This is reflected by the estimated TCP values, which clearly increased for the GTV

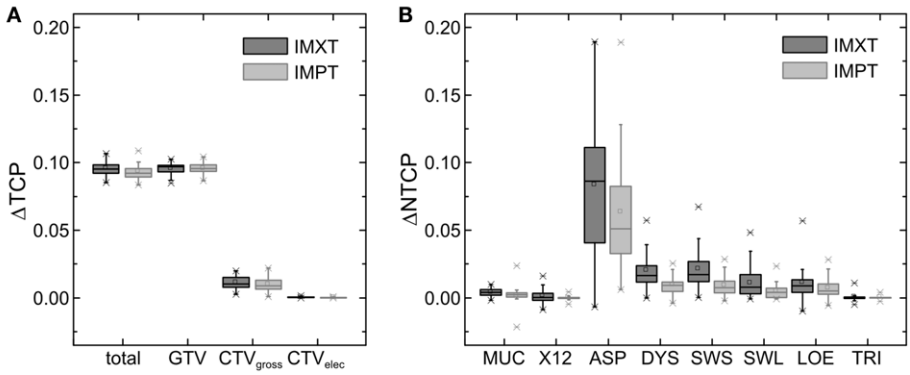

FIGURE 3 | Estimated differences between the two dose escalation levels for IMXT and IMPT: (A) ΔTCP and (B) ΔNTCP. MUC, oral mucositis; X12, xerostomia after 12 months; ASP, aspiration; DYS, physician-rated swallowing dysfunction; SWS, patient-rated problems with swallowing solids; SWL, patient-rated problems with swallowing liquids; LOE, laryngeal edema; TRI, trismus.

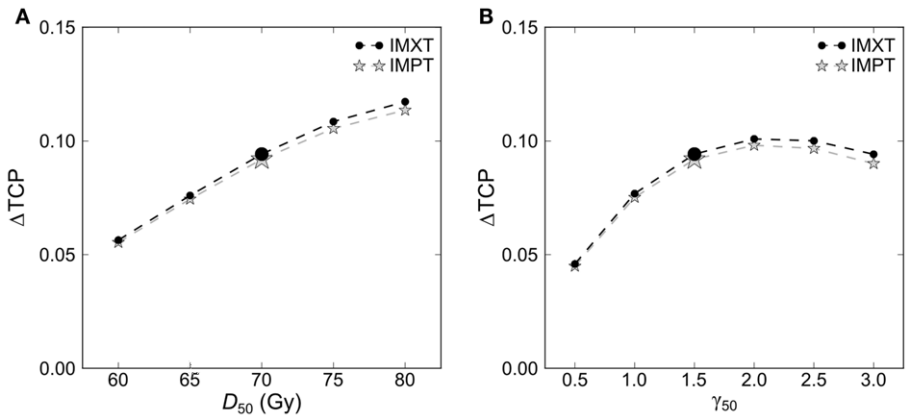

FIGURE 4 | Dependence of the difference in total tumor control probability ΔTCP between the two dose escalation levels on the model input parameters (A) D_{50} and (B) γ_{50}. Results are shown for IMXT and IMPT plans. The enlarged symbols mark the parameter values used in this study.

(the targeted region for treatment intensification) while the values remained almost unchanged for the surrounding target volumes, CTV$_{gross}$ and CTV$_{elec}$. Similarly, the dose to surrounding healthy tissues was only marginally increased for the higher DE level and the difference in NTCP values was practically negligible for all considered toxicities except for aspiration. The increase of estimated NTCP for aspiration resulted primarily from higher maximum doses in the PCM, since the model for aspiration uses a generalized equivalent uniform dose (gEUD) as input that is close to the maximum dose. Thus, an increase of high doses even in a small localized region of the PCM has a large impact on the NTCP value estimated by the employed aspiration model. Accordingly, setting a specific dose constraint for this organ in the treatment plan optimization may be appropriate in a DE study. All other employed NTCP models are based on mean organ dose as gEUD (or close to that) and their NTCP values were less sensitive to changes in local dose, leading to the observed small ΔNTCP values.

Treatment plans for PT possessed steeper dose gradients leading to a reduced high-dose spill into the tissue surrounding the SIB volume (high-dose rim) compared to IMXT plans. As a result, the ΔNTCP values were larger for IMXT than for IMPT. Also ΔTCP was slightly enhanced with IMXT for the two CTV sub-volumes. This difference in dose conformity together with the already lower NTCP level for IMPT let IMPT appear as a potential option for DE treatment in selected cases where IMXT leads to an unacceptable increase of NTCP values. However, for the lower DE level, DE1, with 2.3 Gy per fraction in the SIB volume (i.e., close to 2 Gy), the spill-over dose that increased the V_{107} in the CTV was still comparable between IMXT and IMPT. Thus, for such a low DE level the spill-over dose similarly affects the increase in toxicity risk for both treatment modalities. The small extent of spill-over for DE1 can be explained by the allowed dose variation in the two target volumes from 95% up to 107% of the prescribed dose, which is considered acceptable according to constraints of the International Commission on

Radiation Units and Measurements (ICRU) (35). For example, a dose level of 2.3 Gy in the SIB volume requires (V_{95}) a minimum of 2.19 Gy, while 2 Gy in the surrounding CTV permits (V_{107}) a maximum of 2.14 Gy. Thus for DE1, both allowed dose limits are close together.

Based on the evaluated increase in toxicity risk via NTCP, a DE with a SIB of 2.6 Gy seems as feasible as a 2.3 Gy SIB for both modalities. Only for one toxicity endpoint (aspiration), an increase in risk was predicted by the NTCP models. At the same time, the expected benefit of the higher DE was a gain of about 10% in TCP which may be even higher for more radioresistant tumors (higher D_{50}). The NTCP increase in aspiration of about the same magnitude is of clinical concern, as aspiration pneumonia may be the consequence and thus might be unacceptable in this relation, calling for a well-chosen dose limit for the PCM. The overall small increase in toxicity risk for most models for the evaluated DE level is in accordance with other published studies. Isotoxic DE from 70 Gy to comparable dose levels was rated feasible with a SIB in a small treatment planning study by Thorwarth et al. (36), where a DE of 50% (DE2 in the present study would corresponds to about 25%) was assessed as upper limit by evaluation of dosimetric data for a smaller number of OARs. Leclerc et al. (37) demonstrated the clinical applicability of a SIB with 2.5 Gy per fraction in a multi-centric phase I–II study, however, with a reduced total dose of 75 Gy (EQD2 = 78.1 Gy) and less advanced tumor stages.

This is the first study that employs the sub-volume TCP model to analyze the potential gain of different DE levels limited to a high-risk target sub-volume. The approach builds on established empirical knowledge on dose–response for homogeneous dose irradiation and corresponding spatially heterogeneous patterns of treatment failures. Recently, Vogelius et al. used a conceptually similar approach to analyze the potential of a data-driven dose-painting strategy for HNSCC (38). Assuming D_{50} to be close to 60.5 Gy, they found a substantial increase in local control with an estimated TCP of 89% for spatially optimized dose prescriptions. Considering the same D_{50} parameter, this TCP value is in good agreement with a TCP of about 87% estimated with the approach of the current study for the high DE level DE2. An ongoing Danish clinical trial that tests the data-driven dose-painting approach is supposed to provide clinical evidence that further supports the used TCP model.

Normal tissue complication probability evaluation was restricted to published toxicity models. The only toxicity, for which an increased risk of NTCP was found, differed from the others in modeling by being sensitive to local high-dose levels. This may also occur for other dose limiting toxicities, e.g., for ulceration of tissue, which was shown to be sensitive to high local doses within small volumes (39). Treatment planning studies evaluating the feasibility of DE in the view of potential side effects are limited to known dose–response effects and are a first step allowing for an ethically justifiable clinical trial. Thus, the theoretical feasibility of the DE schedule, demonstrated with the presented treatment planning study, needs to be carefully validated in a clinical setting.

A limitation of the presented analysis is the use of nominal dose distributions. As Müller et al. (40) and Góra et al. (41) showed, IMPT treatment plans are more prone to dose distortions originating from anatomical changes of the patients. Such changes can decrease the dose conformity to the target volume and thus deteriorate the TCP. Furthermore, they can result in increased dose to nearby healthy tissues, increasing the NTCP. The presented treatment planning study design included a one-step adaptation strategy to reduce the effects of patient anatomy changes on the dose distribution. Changes in anatomy would impose in a similar way on the dose distributions of the two compared DE levels, reducing their effect on the differences evaluated in the present study. However, the adaptation approach introduces an additional uncertainty by using a DIR for dose accumulation. Again, this uncertainty affects both DE levels in a similar way, reducing its influence on the difference values. In a clinical setting, close consideration is required to limit the effect of anatomical changes, e.g., by implementing plan adaptation protocols.

Another limitation originates from uncertainties connected to the modeling of the TCP and NTCP values. As a consequence, the results need to be interpreted carefully, especially, when absolute TCP and NTCP values are considered. However, this study focused on differences between model values for the two DE levels. Such relative results tend to be more robust, as some uncertainties may affect the absolute NTCP and TCP values in a similar way, having a minor effect on the differences. For example, the D_{50} parameter sensitivity analysis, which covered a broad D_{50} interval – i.e., a large range of patient characteristics – led to a variation of the absolute TCP on the order of 35% (e.g., DE1 of IMXT: from 83 to 47%). Evaluating for the same data the impact on ΔTCP resulted in a variation of only 7% (cf. **Figure 4**). For NTCP values a comprehensive parameter sensitivity analysis was beyond the scope of this study. A case study for the physician-rated dysphagia model showed that for IMXT a doubling or halving of the input parameters led to a relative change of mean ΔNTCP of approximately 50%, i.e., from 2 to 3% and to 1%, respectively. However, absolute NTCP values were similar to values found in other publications using these models, and thus the model parameters seem to be reliable for the presented patient cohort (31, 42). Consequently, even for less favorable model parameters (low D_{50} or γ_{50}), a substantial ΔTCP increase of 5% between the DE levels was estimated, while ΔNTCP remained at a smaller level in the case study. Assuming for the other models an effect of similar magnitude, and considering the small NTCP values for most patients, model parameter changes would lead to only little changes regarding the presented statements.

CONCLUSION

The presented *in silico* study evaluated two treatment intensification strategies differing in the SIB dose level to the high-risk tumor sub-volume for advanced HNSCC patients. The increase of the DE level from 2.3 to 2.6 Gy per fraction was feasible with IMXT and IMPT retaining integral dose and NTCP values of all but one endpoint. For aspiration, an increase in estimated toxicity risk was identified. The relevant increase in TCP between the DE levels originated from a higher TCP in the SIB volume, which is of the same order of magnitude as the estimated

increase in aspiration toxicity and much higher than the increase of the other evaluated toxicities. Weighing the large TCP gain against the little NTCP increase of all evaluated models, the use of the higher DE level may be beneficial from a clinical point of view, except for those situations, where aspiration is of clinical concern. Since the analysis was restricted to available toxicity models, these findings need to be further investigated in prospective clinical studies.

AUTHOR CONTRIBUTIONS

AJ participated in the design of the treatment planning study, chose the NTCP models, performed the treatment planning, physical dose and NTCP analysis and interpretation of the data, and drafted the manuscript. AL created the TCP model, performed the TCP calculations, analyzed the TCP data, and drafted the manuscript. KS performed parts of the treatment planning, the processing (dose summation, DIR, NTCP calculations) and interpretation of the data for the physical dose, and NTCP analysis. AB-L participated in the design of the treatment planning study, performed the delineation of volumes for treatment planning, and advised in the NTCP model choice. SL processed the data for the TCP calculation (dose summation, TCP calculation) and calculated the relative dose distributions. MK, MB, RP, and CR participated in the design of the treatment planning study and provided general supervision. MK and CR contributed to the data interpretation. All authors revised and approved the manuscript.

ACKNOWLEDGMENTS

The authors thank Milos Kovacevic for his support in data preparation.

FUNDING

AJ, KS, AB-L, RP, and CR were funded by the Bundesministerium für Bildung und Forschung (BMBF-03Z1N51).

REFERENCES

1. Grégoire V, Lefebvre J-L, Licitra L, Felip E. Squamous cell carcinoma of the head and neck: EHNS-ESMO-ESTRO Clinical Practice Guidelines for diagnosis, treatment and follow-up. *Ann Oncol* (2010) **21**:184–6. doi:10.1093/annonc/mdq185
2. Pignon J-P, le Maître A, Maillard E, Bourhis J. Meta-analysis of chemotherapy in head and neck cancer (MACH-NC): an update on 93 randomised trials and 17,346 patients. *Radiother Oncol* (2009) **92**:4–14. doi:10.1016/j.radonc.2009.04.014
3. Marks JE, Bedwinek JM, Lee F, Purdy JA, Perez CA, Purdy A. Dose-response analysis for nasopharyngeal carcinoma: an historical perspective. *Cancer* (1982) **50**:1042–50. doi:10.1002/1097-0142(19820915)50:6
4. Daly ME, Lieskovsky Y, Pawlicki T, Yau J, Pinto H, Kaplan M, et al. Evaluation of patterns of failure and subjective salivary function in patients treated with intensity modulated radiotherapy for head and neck squamous cell carcinoma. *Head Neck* (2007) **29**:211–20. doi:10.1002/hed.20505
5. Dawson LA, Anzai Y, Marsh L, Martel MK, Paulino A, Ship JA, et al. Patterns of local-regional recurrence following parotid-sparing conformal and segmental intensity-modulated radiotherapy for head and neck cancer. *Int J Radiat Oncol Biol Phys* (2000) **46**:1117–26. doi:10.1016/S0360-3016(99)00550-7
6. Hansen O, Overgaard J, Hansen HS, Overgaard M, Morten H, Karsten EJ, et al. Importance of overall treatment time for the outcome of radiotherapy of advanced head and neck carcinoma: dependency on tumor differentiation. *Radiother Oncol* (1997) **43**:47–51. doi:10.1016/S0167-8140(97)01904-X
7. Lauve A, Morris M, Schmidt-Ullrich R, Wu Q, Mohan R, Abayomi O, et al. Simultaneous integrated boost intensity-modulated radiotherapy for locally advanced head-and-neck squamous cell carcinomas: II – clinical results. *Int J Radiat Oncol Biol Phys* (2004) **60**:374–87. doi:10.1016/j.ijrobp.2004.03.010
8. Vosmik M, Odrázka K, Dolezel M, Vaculíková M, Kordac P, Zouhar M, et al. IMRT with the use of simultaneous integrated boost in treatment of head and neck cancer: acute toxicity evaluation. *Acta Medica (Hradec Kralove)* (2006) **49**:167–73.
9. Butler EB, Teh BS, Grant WH, Uhl BM, Kuppersmith RB, Chiu JK, et al. SMART (simultaneous modulated accelerated radiation therapy) boost: a new accelerated fractionation schedule for the treatment of head and neck cancer with intensity modulated radiotherapy. *Int J Radiat Oncol Biol Phys* (1999) **45**:21–32. doi:10.1016/S0360-3016(99)00101-7
10. Bütof R, Baumann M. Time in radiation oncology – keep it short! *Radiother Oncol* (2013) **106**:271–5. doi:10.1016/j.radonc.2013.03.007
11. Lohaus F, Linge A, Tinhofer I, Budach V, Gkika E, Stuschke M, et al. HPV16 DNA status is a strong prognosticator of loco-regional control after postoperative radiochemotherapy of locally advanced oropharyngeal carcinoma: results from a multicentre explorative study of the German Cancer Consortium Radiation Oncology Group (DKTK-ROG). *Radiother Oncol* (2014) **113**:317–23. doi:10.1016/j.radonc.2014.11.011
12. Lassen P, Overgaard J, Eriksen JG. Expression of EGFR and HPV-associated p16 in oropharyngeal carcinoma: correlation and influence on prognosis after radiotherapy in the randomized DAHANCA 5 and 7 trials. *Radiother Oncol* (2013) **108**:489–94. doi:10.1016/j.radonc.2013.08.036
13. Zips D, Zöphel K, Abolmaali N, Perrin R, Abramyuk A, Haase R, et al. Exploratory prospective trial of hypoxia-specific PET imaging during radiochemotherapy in patients with locally advanced head-and-neck cancer. *Radiother Oncol* (2012) **105**:21–8. doi:10.1016/j.radonc.2012.08.019
14. Hentschel M, Appold S, Schreiber A, Abolmaali N, Abramyuk A, Dörr W, et al. Early FDG PET at 10 or 20 Gy under chemoradiotherapy is prognostic for locoregional control and overall survival in patients with head and neck cancer. *Eur J Nucl Med Mol Imaging* (2011) **38**:1203–11. doi:10.1007/s00259-011-1759-3
15. Flynn RT, Bowen SR, Bentzen SM, Rockwell Mackie T, Jeraj R. Intensity-modulated x-ray (IMXT) versus proton (IMPT) therapy for theragnostic hypoxia-based dose painting. *Phys Med Biol* (2008) **53**:4153–67. doi:10.1088/0031-9155/53/15/010
16. Thorwarth D, Eschmann S-M, Paulsen F, Alber M. Hypoxia dose painting by numbers: a planning study. *Int J Radiat Oncol Biol Phys* (2007) **68**:291–300. doi:10.1016/j.ijrobp.2006.11.061
17. Lee NY, Mechalakos JG, Nehmeh S, Lin Z, Squire OD, Cai S, et al. Fluorine-18-labeled fluoromisonidazole positron emission and computed tomography-guided intensity-modulated radiotherapy for head and neck cancer: a feasibility study. *Int J Radiat Oncol Biol Phys* (2008) **70**:2–13. doi:10.1016/j.ijrobp.2007.06.039
18. Schütze C, Bergmann R, Brüchner K, Mosch B, Yaromina A, Zips D, et al. Effect of [(18)F]FMISO stratified dose-escalation on local control in FaDu hSCC in nude mice. *Radiother Oncol* (2014) **111**(1):81–7. doi:10.1016/j.radonc.2014.02.005
19. Horsman MR, Mortensen LS, Petersen JB, Busk M, Overgaard J. Imaging hypoxia to improve radiotherapy outcome. *Nat Rev Clin Oncol* (2012) **9**:674–87. doi:10.1038/nrclinonc.2012.171
20. Zschaeck S, Haase R, Abolmaali N, Perrin R, Stützer K, Appold S, et al. Spatial distribution of FMISO in head and neck squamous cell carcinomas during radio-chemotherapy and its correlation to pattern of failure. *Acta Oncol* (2015) **54**(9):1355–63. doi:10.3109/0284186X.2015.1074720
21. Lühr A, Löck S, Jakobi A, Stützer K, Richter C, Baumann M, et al. PO-0911: method to estimate tumour response in boost scenarios based on clinical data. *Radiother Oncol* (2015) **115**(Suppl):S471–2. doi:10.1016/S0167-8140(15)40903-X

22. Due AK, Vogelius IR, Aznar MC, Bentzen SM, Berthelsen AK, Korreman SS, et al. Recurrences after intensity modulated radiotherapy for head and neck squamous cell carcinoma more likely to originate from regions with high baseline [18F]-FDG uptake. *Radiother Oncol* (2014) **111**:360–5. doi:10.1016/j.radonc.2014.06.001
23. Jakobi A, Bandurska-Luque A, Stützer K, Haase R, Löck S, Wack L-J, et al. Identification of patient benefit from proton therapy for advanced head and neck cancer patients based on individual and subgroup NTCP analysis. *Int J Radiat Oncol Biol Phys* (2015) **92**:1165–74. doi:10.1016/j.ijrobp.2015.04.031
24. Jakobi A, Stützer K, Bandurska-Luque A, Löck S, Haase R, Wack L-J, et al. NTCP reduction for advanced head and neck cancer patients using proton therapy for complete or sequential boost treatment versus photon therapy. *Acta Oncol* (2015) **54**(9):1658–64. doi:10.3109/0284186X.2015.1071920
25. Stützer K, Jakobi A, Haase R, Bandurska-Luque A, Löck S, Krause M, et al. Characterization of deformation vector fields for the registration of dose distributions in adaptive treatment planning and sequential boost protocols. In: Klöck S, editor. *Abstr. – Jt. Conf. SSRMP, DGMP, ÖGMP*. Zürich: Dreiländertagung der Medizinischen Phys (2014). p. 140–2.
26. Okunieff P, Morgan D, Niemierko A, Suit HD. Radiation dose-response of human tumors. *Int J Radiat Oncol Biol Phys* (1995) **32**:1227–37. doi:10.1016/0360-3016(94)00475-Z
27. Lühr A, Löck S, Roth K, Helmbrecht S, Jakobi A, Petersen JB, et al. Concept for individualized patient allocation: ReCompare – remote comparison of particle and photon treatment plans. *Radiat Oncol* (2014) **9**:59. doi:10.1186/1748-717X-9-59
28. Löck S, Roth K, Skripcak T, Worbs M, Helmbrecht S, Jakobi A, et al. Implementation of a software for REmote COMparison of PARticlE and photon treatment plans: ReCompare. *Z Med Phys* (2015) **25**:287–94. doi:10.1016/j.zemedi.2015.02.001
29. Bhide S, Gulliford S, Schick U, Miah A, Zaidi S, Newbold K, et al. Dose-response analysis of acute oral mucositis and pharyngeal dysphagia in patients receiving induction chemotherapy followed by concomitant chemo-IMRT for head and neck cancer. *Radiother Oncol* (2012) **103**:88–91. doi:10.1016/j.radonc.2011.12.027
30. Eisbruch A, Kim HM, Feng FY, Lyden TH, Haxer MJ, Feng M, et al. Chemo-IMRT of oropharyngeal cancer aiming to reduce dysphagia: swallowing organs late complication probabilities and dosimetric correlates. *Int J Radiat Oncol Biol Phys* (2011) **81**:e93–9. doi:10.1016/j.ijrobp.2010.12.067
31. Houweling AC, Philippens MEP, Dijkema T, Roesink JM, Terhaard CHJ, Schilstra C, et al. A comparison of dose-response models for the parotid gland in a large group of head-and-neck cancer patients. *Int J Radiat Oncol Biol Phys* (2010) **76**:1259–65. doi:10.1016/j.ijrobp.2009.07.1685
32. Rancati T, Fiorino C, Sanguineti G. NTCP modeling of subacute/late laryngeal edema scored by fiberoptic examination. *Int J Radiat Oncol Biol Phys* (2009) **75**:915–23. doi:10.1016/j.ijrobp.2009.04.087
33. Lindblom U, Gärskog O, Kjellén E, Laurell G, Levring Jäghagen E, Wahlberg P, et al. Radiation-induced trismus in the ARTSCAN head and neck trial. *Acta Oncol* (2014) **53**:620–7. doi:10.3109/0284186X.2014.892209
34. Christianen MEMC, Schilstra C, Beetz I, Muijs CT, Chouvalova O, Burlage FR, et al. Predictive modelling for swallowing dysfunction after primary (chemo) radiation: results of a prospective observational study. *Radiother Oncol* (2012) **105**:107–14. doi:10.1016/j.radonc.2011.08.009
35. ICRU. *ICRU Report 50 – Prescribing, Recording and Reporting Photon Beam Therapy*. Bethesda, MD: (1993).
36. Thorwarth D, Soukup M, Alber M. Dose painting with IMPT, helical tomotherapy and IMXT: a dosimetric comparison. *Radiother Oncol* (2008) **86**:30–4. doi:10.1016/j.radonc.2007.11.003
37. Leclerc M, Maingon P, Hamoir M, Dalban C, Calais G, Nuyts S, et al. A dose escalation study with intensity modulated radiation therapy (IMRT) in T2N0, T2N1, T3N0 squamous cell carcinomas (SCC) of the oropharynx, larynx and hypopharynx using a simultaneous integrated boost (SIB) approach. *Radiother Oncol* (2013) **106**:333–40. doi:10.1016/j.radonc.2013.03.002
38. Vogelius IR, Håkansson K, Due AK, Aznar MC, Berthelsen AK, Kristensen CA, et al. Failure-probability driven dose painting. *Med Phys* (2013) **40**:081717. doi:10.1118/1.4816308
39. Madani I, Duprez F, Boterberg T, Van De Wiele C, Bonte K, Deron P, et al. Maximum tolerated dose in a phase I trial on adaptive dose painting by numbers for head and neck cancer. *Radiother Oncol* (2011) **101**:351–5. doi:10.1016/j.radonc.2011.06.020
40. Müller BS, Duma MN, Kampfer S, Nill S, Oelfke U, Geinitz H, et al. Impact of interfractional changes in head and neck cancer patients on the delivered dose in intensity modulated radiotherapy with protons and photons. *Phys Med* (2015) **31**:266–72. doi:10.1016/j.ejmp.2015.02.007
41. Góra J, Kuess P, Stock M, Andrzejewski P, Knäusl B, Paskeviciute B, et al. ART for head and neck patients: on the difference between VMAT and IMPT. *Acta Oncol* (2015) **54**(8):1166–74. doi:10.3109/0284186X.2015.1028590
42. Van der Laan HP, van de Water TA, van Herpt HE, Christianen MEMC, Bijl HP, Korevaar EW, et al. The potential of intensity-modulated proton radiotherapy to reduce swallowing dysfunction in the treatment of head and neck cancer: a planning comparative study. *Acta Oncol* (2013) **52**:561–9. doi:10.3109/0284186X.2012.692885

Conflict of Interest Statement: The authors declare that the research was conducted in the absence of any commercial or financial relationships that could be construed as a potential conflict of interest.

Copyright © 2015 Jakobi, Lühr, Stützer, Bandurska-Luque, Löck, Krause, Baumann, Perrin and Richter. This is an open-access article distributed under the terms of the Creative Commons Attribution License (CC BY). The use, distribution or reproduction in other forums is permitted, provided the original author(s) or licensor are credited and that the original publication in this journal is cited, in accordance with accepted academic practice. No use, distribution or reproduction is permitted which does not comply with these terms.

frontiers in Oncology

REVIEW
published: 28 January 2016
doi: 10.3389/fonc.2016.00008

Protons, Photons, and the Prostate – Is There Emerging Evidence in the Ongoing Discussion on Particle Therapy for the Treatment of Prostate Cancer?

Kilian C. Schiller[1], Gregor Habl[1] and Stephanie E. Combs[1,2,3,]*

[1] Department of Radiation Oncology, Klinikum rechts der Isar, Technische Universität München (TUM), München, Germany, [2] Institute of Innovative Radiotherapy (iRT), Department of Radiation Sciences (DRS), Helmholtz Zentrum München, Oberschleißheim, Germany, [3] Deutsches Konsortium für Translationale Krebsforschung (dktk), Partner Site München, München, Germany

Proton therapy is actively and repeatedly discussed within the framework of particle therapy for the treatment of prostate cancer (PC). The argument in favor of treating the prostate with protons is partly financial: given that small volumes are treated, treatment times are low, resulting in a hypothetical high patient throughput. However, such considerations should not form the basis of medical decision-making. There are also physical and biological arguments which further support the use of particle therapy for PC. The only relevant randomized data currently available is the study by Zietman and colleagues, comparing a high to a low proton boost, resulting in a significant increase in PSA-free survival in the experimental (high dose) arm (1). With modern photon treatments and image-guided radiotherapy (IGRT), equally high doses can be applied with photons and, thus, a randomized trial comparing high-end photons to protons is warranted. For high-linear energy transfer (LET) particles, such as carbon ions, the increase in relative biological effectiveness could potentially convert into an improvement in outcome. Additionally, through the physical differences of protons and carbon ions, the steeper dose gradient with carbon ions and the lack of beam broadening in the carbon beam lead to a superior dose distribution supporting the idea of hypofractionation. Biological and clinical data are emerging, however, has practice-changing evidence already arrived?

Keywords: protons, prostate cancer, carbon ions, clinical trials, IMRT

OPEN ACCESS

Edited by:
Marco Durante, GSI, Germany

Reviewed by:
Sunyoung Jang, Princeton Radiation Oncology, USA
Michael Chuong, University of Maryland, USA

****Correspondence:***
Stephanie E. Combs
stephanie.combs@tum.de

Specialty section:
This article was submitted to Radiation Oncology, a section of the journal Frontiers in Oncology

Received: *24 July 2015*
Accepted: *11 January 2016*
Published: *28 January 2016*

Citation:
Schiller KC, Habl G and Combs SE (2016) Protons, Photons, and the Prostate – Is There Emerging Evidence in the Ongoing Discussion on Particle Therapy for the Treatment of Prostate Cancer? Front. Oncol. 6:8. doi: 10.3389/fonc.2016.00008

INTRODUCTION

Proton beam therapy (PBT) among particle therapy for prostate cancer (PC) remains a highly topical subject in the uro-oncological community. It is fueled by discussions concerning questionable superiority to photon treatment with regard to survival or local control, higher costs and cost-effectiveness, better tolerance for patients due to fewer side effects, and, last but not least, continuous patient inquiries regarding the therapy (2). This is represented by numerous ongoing trials and publications; the search for "proton therapy AND PC" on clinicaltrials.gov generates 36

hits alone (3). As biological and clinical data are emerging, the question remains: has practice-changing evidence already been uncovered?

PHOTONS

The goal in radiotherapy (RT) of localized PC is a lethal dose to tumor cells, while ensuring that the smallest possible dose is applied to surrounding tissues, such as rectum and bladder, and thereby avoiding side effects and toxicities for patients.

Nowadays photons are the most commonly used treatment in RT for PC. Photons have no mass and no charge and, therefore, travel easily through target materials. There is an initial increase of energy as they interact with the target material electrons (e.g., the body), which enhances the radiation effect. As a result of this, their peak dose is reached within a few centimeters from the entrance surface – the so-called "dose accumulation effect." In the deeper trajectory through the body subsequently, the radiation dose decreases until it exits the body. 3D plans initially had a significant dose deposition in the entry and exit fields. With multiple field plans, rapid arc or helical techniques, these doses tend to be significantly smaller, but often a dose bath with low-to-moderate doses over surrounding organs cannot be avoided in order to deliver a deathly dose to cancer cells (4). The possible side effects include gastrointestinal (GI) and genitourinary (GU) problems and a potentially slightly higher risk for secondary malignancies (5). Therefore, photon radiation therapy does not seem appropriate in terms of its physical characteristics to treat those organs located at a great depth within the body. Despite modern improvements in technologies, such as multi-leaf collimators, intensity-modulated radiotherapy (IMRT), or image-guided radiotherapy (IGRT), photon-beam therapy will always include a certain level of entrance and exit doses, resulting in healthy tissue receiving low-to-moderate radiation doses. While these doses are most likely not associated with a prominent side effect risk, such issues necessitate a serious consideration of alternative treatment options, including particle therapy.

PARTICLE THERAPY

As of 2013, more than 123,000 patients had received therapy with heavy particles worldwide, PBT accounting for the majority of this, with over 106,000 patients treated (6). While protons can be termed particles, they are not considered "heavy," and from their effect they can be categorized as low-linear energy transfer (LET) radiation, comparable to photons. Heavy particles include carbon ions, oxygen as well as neutrons, and others. Particles may be charged (protons, carbon ions) or neutral (neutrons). The term "heavy particle therapy" is generally used to distinguish it from conventional X-Ray RT, which uses massless photons. As most research undertaken so far has investigated protons, we shall mainly focus on them in the following article. Experience with other heavy particles is limited to a mere seven operating carbon ion facilities worldwide, treatment with carbon ions can be considered experimental and, therefore, reliable evidence is only just emerging and no conclusions can yet be drawn with regard to their effectiveness or toxicity.

PROTONS

Due to their physical characteristics, protons potentially offer a treatment method in which smaller areas receive radiation doses and, thus, bring about fewer side effects. Proton beams are created by a cyclotron or synchrotron, whereby the proton is separated from hydrogen molecules. Protons travel fast through tissue, with minimal room for interaction; in depth the velocity is reduced, interactions occur, and the energy is deposited: they, therefore, stop very abruptly in tissues reaching a very specific depth: the so-called "Bragg peak" (7), see **Figure 1**. Here, the majority of energy is being deposited. Heavy particles, compared to photons, have a greater radiobiological effect (1.1 times for protons and 2–3 for carbon ions) and, therefore, greater potential to damage cancer cells by interacting more densely with tissue, causing higher levels of ionization per unit length (8, 9). The dose then rapidly decreases to 0 as heavy particles (opposed to photons) stop within the body. Thus, the integral dose with protons is approximately 60% lower than that of any external beam photon technique (10, 11).

In theory, this is ideal for treating tumors near to sensitive structures, such as the brain and spinal cord, as well as for childhood cancers in order to reduce the dose to healthy surrounding organs. PBT can potentially show a clinical superiority compared to photons and is, to a certain extent, established in some populations such as pediatric indications or uveal melanoma, at least in some regions worldwide (12–14).

It is important in all populations to note that RT comes with the risk of developing secondary malignancies years to decades later. Although this risk is low with modern techniques, it is in focus for radiation oncologists, and patients alike. With the sharp dose deposition of particles, there are presumably a smaller number of secondary malignancies due to the lower dose to surrounding healthy structures. Nevertheless PBT, as opposed to photon therapy, generates neutrons as a by-product, which can

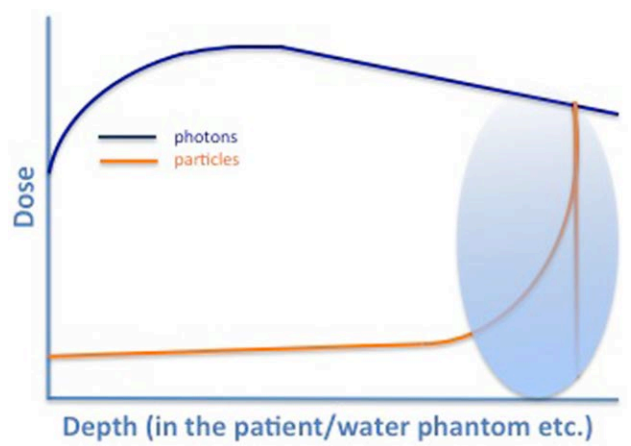

FIGURE 1 | Characteristic dose profile for photons (green), protons (yellow), and carbon ions (black). Typical Bragg Peak (red) for particles that can be directed into defined regions depending on the energy used [adapted from Combs et al. (7)].

be scattered into adjacent normal tissues, especially with passive beam techniques. These neutrons have a strong biological effect and, thus, could theoretically increase the risk of secondary malignancies (15). Despite such theoretical concerns, a large retrospective study did not find statistically significant differences in secondary malignancies between patients treated with protons and those treated with photons – 5.2% of all PBT-treated patients had secondary malignancies versus 7.5% in the photon treatment group (16).

The width of the Bragg peak is within the millimeter range and usually not wide enough to cover a whole treatment volume. Several of those peaks must be superimposed to treat effectively a tumor of a certain length and volume – the so-called "spread-out Bragg peak" (SOBP). There can be some uncertainty about the exact location of the Bragg peak due to tissue inhomogeneities. Here, PBT skeptics argue that there is no widely used method for confirming the proton range, or that the SOBP encompasses the prostate *in vivo*, making sufficient margins essential for a successful therapy and thereby diminishing the possible advantage of smaller radiation volumes.

Another technical challenge is that, because of the steep dose gradient (Bragg peak), the plan parameters and patient positioning must be highly precise in order to obtain a high dose within the tumor region while maximizing the protection of organs at risk (OAR). This makes the uncertainty regarding the range of motion in human tissue one of the major hurdles of RT with protons, meaning that particle therapy is more vulnerable to target motion than photon irradiation (17).

Yoon et al. also describe an increased sensitivity to target motion of PBT because of deep dose depletion beyond the SOBP (18).

In RT of PC, the range of motion can be divided into inter- and intrafractional movements. Interfractional movements occur between two radiation appointments, e.g., due to filling of the bladder and rectum. Intrafractional movements happen within one radiation session, e.g., due to breathing, bowel gas, or small patient movements. Because of this, measurements in PBT should be made even during dose delivery and can be accomplished via positron emitters (PET camera) or induced gamma radiation (Compton camera) (19, 20). Motion mitigation strategies are essentially important to exploit the full potential of particle therapy; this includes scanning approaches, such as rescanning, gating, or implementation of motion-surrogates, such as markers (21–23).

CARBON IONS

As opposed to protons, which can be considered to have radiobiological features similar to photons [relative biological effectiveness (RBE) = 1.1 for protons], other heavy particles have higher LET characteristics, leading to substantial differences in radiobiological interactions. Due to their mass, carbon ions have a higher biological effectiveness compared to protons with a comparable depth-dose profile. The RBE of the carbon ion beams has been estimated as 2.0–3.0 (9). This means that they are twice to three times more effective in killing cancer cells than proton or photon beams as they are more likely to cause deathly DNA double-strand breaks. Thus, carbon ions have radiobiological advantages, including more effective killing of intrinsic radio-resistant tumors, hypoxic tumor cells, and tumor cells in the G0 or S phase (24).

Furthermore, they possess an even sharper dose distribution than protons, but the dose in the region beyond the distal end of the peak is higher in carbon ion beams than proton beams, because carbon ions undergo nuclear interactions producing a fragmentation tail beyond the dose peak (25, 26).

In terms of its medical application, carbon ion therapy has been described as being advantageous *inter alia* for PC. Regarding the anti-tumor effect of carbon ion RT for PC, Ishikawa et al. reported survival data and biochemical relapse-free rates for almost 1000 patients with 20 or 16 fractions at the ion beam center in Chiba, Japan. The 5-year overall survival and cause-specific survival rates for all patients were 95.3 and 98.8%, respectively; the 5-year relapse-free and local control rates were 90.6 and 98.3%, respectively. Especially noteworthy is that the outcomes for biochemical relapse-free survival also included the high-risk group and that hypo-fractionated carbon ion RT seems to have had radiobiological benefit for PC (24, 27). In a more recent Phase I/II study from 2014, Nomiya et al. described a shortened course with only 12 fractions as another feasible option, however, the long-term outcome of such an approach is still pending (28).

Certainly, there are advantages of carbon ion RT, as an option with high biological effectiveness over low-LET radiations, such as photon therapy or PBT, and carbon ion therapy may prove to make a substantial difference in certain patient populations. However, precise definition of clinical study protocols and critical evaluation of patient data together with intake of molecular characteristics of tumors and normal tissue can help to optimally stratify patients for different radiation modalities leading to individualized radiotherapy (*i*RT). (**Figure 2**).

TECHNOLOGICAL ASPECTS

Common passive scattering systems will be replaced by spot scanning systems in charged particle beam therapy in medium

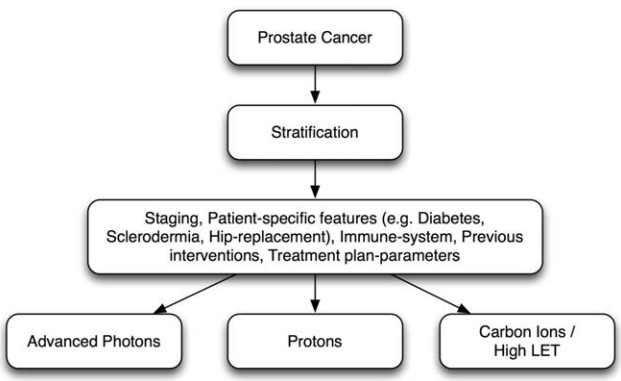

FIGURE 2 | Individualized radiotherapy (iRT): prostate cancer patient stratification for different radiation modalities.

term. It is in routine clinical use at the Paul Scherrer Institute (PSI) in Darmstadt. Advantages are the precise dose distribution and planning options for using intensity-modulated proton beam therapy (IMPT). The application is safe but several aspects for uncertainties, such as the robustness to movements of the target and to IMPT plans, must be taken into account when working with spot scanning techniques. Zhu et al. reported on the single-field integrated boost (SFIB) technique for spot scanning proton therapy based on single-field optimization (SFO) treatment planning techniques (29).

Regarding beam delivery, most experience has mainly been acquired with horizontal beam lines. The success of radiotherapy treatment is strongly increased through the possibility of applying the beam to the target using different angles, such as in IMRT. Hence, the worldwide first gantry for charged particle was brought online in October 2012 at the Heidelberg Ion Therapy Center (HIT), Heidelberg.

DISCUSSION

The success of irradiation in patients with localized PC correlates with the administered dose, meaning that a higher dose to the prostatic gland leads to better cancer control (1).

Several randomized trials have shown a benefit of dose escalation to 78–79 Gy for men treated with external radiation for localized PC. Previous data suggested a benefit with even higher doses. In a trial by Coen et al., the safety and efficacy of 82 Gy (a 2 Gy equivalent) delivered with conformal PBT was tested. The estimated rate of ≥Grade 3 late toxicity at 18 months was 6%, indicating that this may be the maximal dose that can be delivered safely with this technique and fractionation (30).

On the other hand, with new techniques such as IMRT (± rapid arc) or IGRT, photon radiation encumbers OAR with low-to-moderate doses. Such doses normally do not cause noticeable side effects for patients, and photon therapy has reached a high level of patient comfort and acceptance. In a similar way, IMRT is described to have excellent efficacy and low toxicity in the treatment of PC, even with elevated final doses (31, 32).

It has, thus, become the standard procedure for RT of PC in many institutes due to the significantly reduced toxicities compared with what has been observed with conventional 3D-approaches.

The feasibility of high-dose IMRT (up to 81 Gy) has been demonstrated in studies with large numbers of patients and has been proven to have comparably low side effects (33–35).

This was stated earlier by Mock et al.: they described IMRT as more effectively enabling dose reductions to OAR in the medium dosage range compared to 3D conformal radiotherapy. Furthermore, they indicated possible benefits of the two-field PBT technique, which reduces doses to surrounding tissues compared to photon-beam RT (36). The physical properties of protons may, thus, decrease common GI and GU side effects even further.

As early as 1983, Duttenhaver et al. discussed proton versus a conventional megavoltage X-Ray (photon) boost, finding no difference in local tumor control (LC), disease-free survival (DFS), or overall survival (OS), yet fewer side effects with an elevated proton boost. Photon RT has evolved since then, as described above, with numerous technical advances, while PBT has yet to prove itself through better LC, OS, or significantly fewer side effects (37).

In dosimetric studies of a small patient group Vargas et al. were able to show a reduced mean rectal (59%) and bladder (35%) dose for PBT compared to IMRT (38). Early outcomes from single arm, prospective trials confirmed these assumptions. Nihei et al. described the incidence of late ≥grade 2 rectal and bladder toxicity at 2 years to be 2.0 and 4.1%, respectively (39).

Similarly, Mendenhall et al. found good early outcomes with image-guided proton therapy, suggesting high efficacy and minimal toxicity with 1.9% grade 3 GU symptoms and <0.5% grade 3 GI toxicities (39, 40). Generally, the dose to healthy tissues in the range <50% of the target prescription was substantially lower with proton therapy (41).

A retrospective analysis of the Medicare database compared early toxicity in 421 men using PBT with 842 matched controls treated with IMRT. A statistically significant decrease in GU toxicity at 6 months for PBT was seen, but this difference had disappeared at one year. There were no other significant differences in toxicity between the two techniques at either 6 or 12 months post-treatment. Yu et al. concluded that although PBT is substantially more cost-intensive than IMRT, no difference in toxicity in a comprehensive cohort of Medicare beneficiaries with PC at 12 months post-treatment was found (42).

Keeping in mind that the amount of bladder exposed to low doses of radiation predicts early toxicity the difference in toxicity seen by Yu et al. is plausible, since in previous studies it has been shown that one improvement in radiation dose distribution for PBT compared to IMRT led to a reduction in the amount of bladder exposed to low and intermediate levels of radiation (36, 41, 43). This dose reduction was most likely responsible for the transient improvement in the Yu study.

However, other studies have found IMRT to be favorable over PBT with regard to toxicity. An analysis from the Medicare Surveillance, Epidemiology, and End Results (SEER) database in the USA identified 684 men treated with PBT between 2002 and 2007 and compared these with a cohort treated with IMRT.

Intensity-modulated radiotherapy was associated with significantly less GI morbidity. However, there were no statistically significant differences in other toxicities, nor a significant difference in the frequency with which patients required additional cancer therapy (44).

There are still no completed randomized trials comparing PBT with photon-beam therapy in men with clinically localized PC (45).

With regard to the OS data, a few major studies have been conducted. One of the major dose-escalation studies was carried out at The Proton Center in Boston. Zietman et al. randomized 393 patients with a PSA <5 ng/ml to a low-dose arm (50.4 Gy photon therapy + 19.8 GyE proton boost) and a high-dose arm (50.4 Gy photon + 28.8 GyE proton boost). The analysis revealed a significant difference in biochemical recurrence-free survival

in favor of the high-dose arm. Subgroup analysis of low and high-risk patients (depending on the Gleason score) showed a significant advantage for the high-dose group in both cases. An impact on the OS rate was not observed. Both acute and late toxicities were not increased in either arm compared to the incidence of comparable photon studies (1, 46). However, modern photon treatments allow comparable high-dose application with utmost precision and safety; thus, the latter trial might be termed mainly not as a trial comparing photons and protons, but high-dose to low-dose treatments.

Finally, the American Society for Radiation Oncology (ASTRO) released a list recommending the use of PBT after an evidence-based review for certain tumors, including central nervous system and pediatric malignancies. For others, among them PC, it recommends treatment only within the setting of clinical trials, as there was evidence for the efficacy of PBT but no suggestion that it is superior to photon-based approaches (47, 48).

COST ASPECT

Concerning costs, several aspects must be highlighted: the construction costs of proton facilities, maintenance costs and outcome, also concerning throughput compared to photon radiation.

First, Keener et al. estimated the building cost for a new PBT center to be between 100 and 250 million US-Dollars. This is the equivalent of about 40 times the price of setting up a state-of-the-art photon radiation center (49).

As for maintenance and cost-effectiveness, Johnstone et al. calculated that a high number (single gantry 85%) of "simple" cases with a faster throughput are necessary for proton facilities to work cost effectively (50).

Proton beam therapy for PC is often described as simple, compared to pediatric or central nervous system indications, where longer setup and/or treatment times are required. A modern proton center requires treating a caseload and emphasizing simple patients with high throughput even before operating costs or any profit are achieved (50). In theory, this means that a PBT facility treating only patients with PC would run cost effectively and profitably.

With regard to compensation, Yu et al. found median Medicare reimbursement in the USA to be over 32,000 US-Dollars for proton RT and over 18,000 for IMRT. In a retrospective study of over 27,000 patients, they found no toxicity difference at 12 months post-treatment, despite the cost being almost double (42).

Furthermore, in a cost utility analysis per quality-adjusted life year (QALY) from a literature search between 2003 and 2013, PBT was not found to be cost-effective in any of the analysis (51).

A very interesting open phase 3 study (NCT01230866) is underway and could make a significant difference to PBT cost-effectiveness, as well as to the life quality of patients. The study compares standard dose of RT (44 treatments) with a hypofractionation concept (five treatments) (52).

This study could dramatically decrease the treatment costs of PBT if the hypofraction arm performs similar or better than normofractionated treatment. It could also improve the life quality of patients as a result of the decreased number of treatment appointments. However, only recently the biological rationale of hypofractionation was revisited questioning the current α/β concepts – newer data assume that prostate α/β are, after all, more closely comparable to those of rectal or other normal tissue than initially believed, thus, questioning the real rationale of hypofractionation (53).

In summary, technology for PC RT has made important advances. However, its associated costs have escalated, thus, making cost-effectiveness analysis critical to assess. So far, all aspects of PBT remain far more expensive than photon radiation therapy, meaning that cost consciousness should outweigh standard PBT for PC as long as there is no clear evidence from controlled randomized trials supporting the superiority of PBT, so that the surplus of money spent can be well-invested. However, data are available that proton therapy can be applied, and especially in the pediatric population referral to a high-end particle therapy center should be evaluated. For carbon ions, patients should be treated within clinical trials until the full potential and the biological rationale can be shown in patient treatments.

In conclusion, proton therapy is worth being discussed in modern oncology with assets leading to potentially advantageous treatments; however, this should not lead to unreflected discussions and recommendations that proton therapy is the necessary independently of indication patient age, comorbidities, and other factors. For PC, it will be interesting to follow the ongoing research to see which technique "will be the road less traveled."

CONCLUSION

A high publication rate confirms continued high interest in PBT and its characteristics. Reading through such publications, one gets the impression that the authors often take a similar stance to ASTRO, who finished the abstract of their evidence-based review with the words: "More robust prospective clinical trials are needed to determine the appropriate clinical setting for PBT" (47).

There is much discussion and disagreement concerning toxicities, cost–effectiveness, and the potential for better outcomes (2). However, PBT is certainly cost-intensive and yet has great potential with regard to basic physics and biological principles. Nevertheless, the advantages so far seem to remain theoretical and are brought about by a better dose distribution.

Several trials are underway, among them a multi-institutional randomized phase III Nacional Cancer Institute study (A Phase III Randomized Clinical Trial of Proton Therapy Versus IMRT for low or intermediate risk PC; clinicaltrials.gov ID NCT01617161) comparing PBT to IMRT (54). It is now in its third year and, together with others, will hopefully shed some more light onto the discussion of PC and RT with photons and particles, which in the end will lead to individualized radiotherapy (*i*RT) concepts.

REFERENCES

1. Zietman AL, Bae K, Slater JD, Shipley WU, Efstathiou JA, Coen JJ, et al. Randomized trial comparing conventional-dose with high-dose conformal radiation therapy in early-stage adenocarcinoma of the prostate: long-term results from proton radiation oncology group/american college of radiology 95-09. *J Clin Oncol* (2010) **28**:1106–11. doi:10.1200/JCO.2009.25.8475
2. Habl G, Debus J. There is evidence for the superiority of protons and heavy ions, pro radiotherapy in prostate cancer. *Med Radiol* (2014) **2015**:277–89. doi:10.1007/174_2014_972
3. U.S. National Institutes of Health (2015). ClinicalTrials.gov
4. Kosaki K, Ecker S, Habermehl D, Rieken S, Jakel O, Herfarth K, et al. Comparison of intensity modulated radiotherapy (IMRT) with intensity modulated particle therapy (IMPT) using fixed beams or an ion gantry for the treatment of patients with skull base meningiomas. *Radiat Oncol* (2012) **7**:44. doi:10.1186/1748-717X-7-44
5. Paganetti H. Assessment of the risk for developing a second malignancy from scattered and secondary radiation in radiation therapy. *Health Phys* (2012) **103**:652–61. doi:10.1097/HP.0b013e318261113d
6. Jermann M. Particle therapy statistics in 2013. *Int J Particle Ther* (2014) **1**:40–3. doi:10.14338/IJPT.14-editorial-2.1
7. Combs SE, Schulz-Ertner D, Herfarth KK, Krempien R, Debus J. [Advances in radio-oncology. From precision radiotherapy with photons to ion therapy with protons and carbon ions]. *Chirurg* (2006) **77**:1126–32. doi:10.1007/s00104-006-1268-2
8. Niederhuber JE, Armitage JO, Doroshow JH, Kastan MB, Tepper JE. *Abeloff's Clinical Oncology*. Philadelphia: Elsevier (2014).
9. Kanai T, Matsufuji N, Miyamoto T, Mizoe J, Kamada T, Tsuji H, et al. Examination of GyE system for HIMAC carbon therapy. *Int J Radiat Oncol Biol Phys* (2006) **64**:650–6. doi:10.1016/j.ijrobp.2005.09.043
10. DeLaney TF. Proton therapy in the clinic. *Front Radiat Ther Oncol* (2011) **43**:465–85. doi:10.1159/000322511
11. Delaney TF, Kooy HM. *Protons and Charge Particle Radiotherapy*. Philadelphia: Lippincott Williams & Wilkins (2008).
12. Egger E, Zografos L, Schalenbourg A, Beati D, Bohringer T, Chamot L, et al. Eye retention after proton beam radiotherapy for uveal melanoma. *Int J Radiat Oncol Biol Phys* (2003) **55**:867–80. doi:10.1016/S0360-3016(02)04200-1
13. Miralbell R, Lomax A, Cella L, Schneider U. Potential reduction of the incidence of radiation-induced second cancers by using proton beams in the treatment of pediatric tumors. *Int J Radiat Oncol Biol Phys* (2002) **54**:824–9. doi:10.1016/S0360-3016(02)02982-6
14. Munzenrider JE. Proton therapy for uveal melanomas and other eye lesions. *Strahlenther Onkol* (1999) **175**(Suppl 2):68–73. doi:10.1007/BF03038893
15. Brenner DJ, Hall EJ. Secondary neutrons in clinical proton radiotherapy: a charged issue. *Radiother Oncol* (2008) **86**:165–70. doi:10.1016/j.radonc.2007.12.003
16. Chung CS, Yock TI, Nelson K, Xu Y, Keating NL, Tarbell NJ. Incidence of second malignancies among patients treated with proton versus photon radiation. *Int J Radiat Oncol Biol Phys* (2013) **87**:46–52. doi:10.1016/j.ijrobp.2013.04.030
17. Paganetti H. Range uncertainties in proton therapy and the role of Monte Carlo simulations. *Phys Med Biol* (2012) **57**:R99–117. doi:10.1088/0031-9155/57/11/R99
18. Yoon M, Shin D, Kwak J, Park S, Lim YK, Kim D, et al. Characteristics of movement-induced dose reduction in target volume: a comparison between photon and proton beam treatment. *Med Dosim* (2009) **34**:191–201. doi:10.1016/j.meddos.2008.08.004
19. Frey K, Unholtz D, Bauer J, Debus J, Min CH, Bortfeld T, et al. Automation and uncertainty analysis of a method for in-vivo range verification in particle therapy. *Phys Med Biol* (2014) **59**:5903–19. doi:10.1088/0031-9155/59/19/5903
20. Mackin D, Peterson S, Beddar S, Polf J. Evaluation of a stochastic reconstruction algorithm for use in Compton camera imaging and beam range verification from secondary gamma emission during proton therapy. *Phys Med Biol* (2012) **57**:3537–53. doi:10.1088/0031-9155/57/11/3537
21. Habermehl D, Henkner K, Ecker S, Jakel O, Debus J, Combs SE. Evaluation of different fiducial markers for image-guided radiotherapy and particle therapy. *J Radiat Res* (2013) **54**(Suppl 1):i61–8. doi:10.1093/jrr/rrt071
22. Habermehl D, Naumann P, Bendl R, Oelfke U, Nill S, Debus J, et al. Evaluation of inter- and intrafractional motion of liver tumors using interstitial markers and implantable electromagnetic radiotransmitters in the context of image-guided radiotherapy (IGRT) – the ESMERALDA trial. *Radiat Oncol* (2015) **10**:143. doi:10.1186/s13014-015-0456-y
23. Richter D, Graeff C, Jakel O, Combs SE, Durante M, Bert C. Residual motion mitigation in scanned carbon ion beam therapy of liver tumors using enlarged pencil beam overlap. *Radiother Oncol* (2014) **113**:290–5. doi:10.1016/j.radonc.2014.11.020
24. Shioyama Y, Tsuji H, Suefuji H, Sinoto M, Matsunobu A, Toyama S, et al. Particle radiotherapy for prostate cancer. *Int J Urol* (2015) **22**:33–9. doi:10.1111/iju.12640
25. Tsujii H, Kamada T. A review of update clinical results of carbon ion radiotherapy. *Jpn J Clin Oncol* (2012) **42**:670–85. doi:10.1093/jjco/hys104
26. Chen GT, Castro JR, Quivey JM. Heavy charged particle radiotherapy. *Annu Rev Biophys Bioeng* (1981) **10**:499–529. doi:10.1146/annurev.bb.10.060181.002435
27. Ishikawa H, Tsuji H, Kamada T, Akakura K, Suzuki H, Shimazaki J, et al. Carbon-ion radiation therapy for prostate cancer. *Int J Urol* (2012) **19**:296–305. doi:10.1111/j.1442-2042.2012.02961.x
28. Nomiya T, Tsuji H, Maruyama K, Toyama S, Suzuki H, Akakura K, et al. Phase I/II trial of definitive carbon ion radiotherapy for prostate cancer: evaluation of shortening of treatment period to 3 weeks. *Br J Cancer* (2014) **110**:2389–95. doi:10.1038/bjc.2014.191
29. Zhu XR, Poenisch F, Li H, Zhang X, Sahoo N, Wu RY, et al. A single-field integrated boost treatment planning technique for spot scanning proton therapy. *Radiat Oncol* (2014) **9**:202. doi:10.1186/1748-717X-9-202
30. Coen JJ, Bae K, Zietman AL, Patel B, Shipley WU, Slater JD, et al. Acute and late toxicity after dose escalation to 82 GyE using conformal proton radiation for localized prostate cancer: initial report of American College of Radiology Phase II study 03-12. *Int J Radiat Oncol Biol Phys* (2011) **81**:1005–9. doi:10.1016/j.ijrobp.2010.06.047
31. Cahlon O, Hunt M, Zelefsky MJ. Intensity-modulated radiation therapy: supportive data for prostate cancer. *Semin Radiat Oncol* (2008) **18**:48–57. doi:10.1016/j.semradonc.2007.09.007
32. Cahlon O, Zelefsky MJ, Shippy A, Chan H, Fuks Z, Yamada Y, et al. Ultra-high dose (86.4 Gy) IMRT for localized prostate cancer: toxicity and biochemical outcomes. *Int J Radiat Oncol Biol Phys* (2008) **71**:330–7. doi:10.1016/j.ijrobp.2007.10.004
33. Zelefsky MJ, Chan H, Hunt M, Yamada Y, Shippy AM, Amols H. Long-term outcome of high dose intensity modulated radiation therapy for patients with clinically localized prostate cancer. *J Urol* (2006) **176**:1415–9. doi:10.1016/j.juro.2006.06.002
34. Zelefsky MJ, Fuks Z, Hunt M, Lee HJ, Lombardi D, Ling CC, et al. High dose radiation delivered by intensity modulated conformal radiotherapy improves the outcome of localized prostate cancer. *J Urol* (2001) **166**:876–81. doi:10.1097/00005392-200109000-00017
35. Zelefsky MJ, Fuks Z, Hunt M, Yamada Y, Marion C, Ling CC, et al. High-dose intensity modulated radiation therapy for prostate cancer: early toxicity and biochemical outcome in 772 patients. *Int J Radiat Oncol Biol Phys* (2002) **53**:1111–6. doi:10.1016/S0360-3016(02)02857-2
36. Mock U, Bogner J, Georg D, Auberger T, Potter R. Comparative treatment planning on localized prostate carcinoma conformal photon- versus proton-based radiotherapy. *Strahlenther Onkol* (2005) **181**:448–55. doi:10.1007/s00066-005-1317-7
37. Duttenhaver JR, Shipley WU, Perrone T, Verhey LJ, Goitein M, Munzenrider JE, et al. Protons or megavoltage X-rays as boost therapy for patients irradiated for localized prostatic carcinoma. An early phase I/II comparison. *Cancer* (1983) **51**:1599–604. doi:10.1002/1097-0142(19830501)51:9<1599::AID-CNCR2820510908>3.0.CO;2-O
38. Vargas C, Fryer A, Mahajan C, Indelicato D, Horne D, Chellini A, et al. Dose-volume comparison of proton therapy and intensity-modulated radiotherapy for prostate cancer. *Int J Radiat Oncol Biol Phys* (2008) **70**:744–51. doi:10.1016/j.ijrobp.2007.07.2335
39. Nihei K, Ogino T, Onozawa M, Murayama S, Fuji H, Murakami M, et al. Multi-institutional Phase II study of proton beam therapy for organ-confined prostate cancer focusing on the incidence of late rectal toxicities. *Int J Radiat Oncol Biol Phys* (2011) **81**:390–6. doi:10.1016/j.ijrobp.2010.05.027
40. Mendenhall NP, Li Z, Hoppe BS, Marcus RB Jr, Mendenhall WM, Nichols RC, et al. Early outcomes from three prospective trials of image-guided proton

therapy for prostate cancer. *Int J Radiat Oncol Biol Phys* (2012) **82**:213–21. doi:10.1016/j.ijrobp.2010.09.024
41. Trofimov A, Nguyen PL, Coen JJ, Doppke KP, Schneider RJ, Adams JA, et al. Radiotherapy treatment of early-stage prostate cancer with IMRT and protons: a treatment planning comparison. *Int J Radiat Oncol Biol Phys* (2007) **69**:444–53. doi:10.1016/j.ijrobp.2007.03.018
42. Yu JB, Soulos PR, Herrin J, Cramer LD, Potosky AL, Roberts KB, et al. Proton versus intensity-modulated radiotherapy for prostate cancer: patterns of care and early toxicity. *J Natl Cancer Inst* (2013) **105**:25–32. doi:10.1093/jnci/djs463
43. Karlsdottir A, Johannessen DC, Muren LP, Wentzel-Larsen T, Dahl O. Acute morbidity related to treatment volume during 3D-conformal radiation therapy for prostate cancer. *Radiother Oncol* (2004) **71**:43–53. doi:10.1016/j.radonc.2004.01.014
44. Sheets NC, Goldin GH, Meyer AM, Wu Y, Chang Y, Sturmer T, et al. Intensity-modulated radiation therapy, proton therapy, or conformal radiation therapy and morbidity and disease control in localized prostate cancer. *JAMA* (2012) **307**:1611–20. doi:10.1001/jama.2012.460
45. DiBiase SJ. *External Beam Radiation Therapy for Localized Prostate Cancer* (2015). Available from: http://www.uptodate.com
46. Zietman AL, DeSilvio ML, Slater JD, Rossi CJ Jr, Miller DW, Adams JA, et al. Comparison of conventional-dose vs high-dose conformal radiation therapy in clinically localized adenocarcinoma of the prostate: a randomized controlled trial. *JAMA* (2005) **294**:1233–9. doi:10.1001/jama.294.10.1233
47. Allen AM, Pawlicki T, Dong L, Fourkal E, Buyyounouski M, Cengel K, et al. An evidence based review of proton beam therapy: the report of ASTRO's emerging technology committee. *Radiother Oncol* (2012) **103**:8–11. doi:10.1016/j.radonc.2012.02.001
48. Nguyen PL, Trofimov A, Zietman AL. Proton-beam vs intensity-modulated radiation therapy. Which is best for treating prostate cancer? *Oncology* (2008) **22**:748–54; discussion 754, 757.
49. Keener AB. Arrests reveal debate about costs and benefits of proton therapy. *Nat Med* (2014) **20**:1081. doi:10.1038/nm1014-1081
50. Johnstone PA, Kerstiens J, Richard H. Proton facility economics: the importance of "simple" treatments. *J Am Coll Radiol* (2012) **9**:560–3. doi:10.1016/j.jacr.2012.03.014
51. Amin NP, Sher DJ, Konski AA. Systematic review of the cost effectiveness of radiation therapy for prostate cancer from 2003 to 2013. *Appl Health Econ Health Policy* (2014) **12**:391–408. doi:10.1007/s40258-014-0106-9
52. *Study of Hypo-Fractionated Proton Radiation for Low Risk Prostate Cancer*. ClinicalTrials.gov, NCT01230866. Proton Collaborative Group (2015).
53. Baumann M, Holscher T, Denham J. Fractionation in prostate cancer – is it time after all? *Radiother Oncol* (2010) **96**:1–5. doi:10.1016/j.radonc.2010.06.001
54. *Proton Therapy vs. IMRT for Low or Intermediate Risk Prostate Cancer (PARTIQoL)*. ClinicalTrials.gov, NCT01617161.

Conflict of Interest Statement: The authors declare that the research was conducted in the absence of any commercial or financial relationships that could be construed as a potential conflict of interest.

Copyright © 2016 Schiller, Habl and Combs. This is an open-access article distributed under the terms of the Creative Commons Attribution License (CC BY). The use, distribution or reproduction in other forums is permitted, provided the original author(s) or licensor are credited and that the original publication in this journal is cited, in accordance with accepted academic practice. No use, distribution or reproduction is permitted which does not comply with these terms.

frontiers in Oncology

PERSPECTIVE
published: 07 June 2016
doi: 10.3389/fonc.2016.00140

The Emerging Role of Carbon-Ion Radiotherapy

*Daniel K. Ebner and Tadashi Kamada**

Research Center for Charged Particle Therapy, National Institute of Radiological Sciences, Chiba, Japan

Carbon-ion radiotherapy (CIRT) has progressed rapidly in technological delivery, indications, and efficacy. Owing to a focused dose distribution in addition to high linear energy transfer and subsequently high relative biological effect, CIRT is uniquely able to target otherwise untreatable hypoxic and radioresistant disease while opening the door for substantially hypofractionated treatment of normal and radiosensitive disease. CIRT has increasingly garnered international attention and is nearing the tipping point for international adoption.

Keywords: particle beam therapy, carbon-ion radiotherapy, adaptation, performance, radioresistance

OPEN ACCESS

Edited by:
Marco Durante,
GSI, Germany

Reviewed by:
William F. Hartsell,
Northwestern Medicine Chicago Proton Center, USA
Takashi Nakano,
Gunma University, Japan

***Correspondence:**
Tadashi Kamada
kamada.tadashi@qst.go.jp

Specialty section:
This article was submitted to Radiation Oncology, a section of the journal Frontiers in Oncology

Received: *25 January 2016*
Accepted: *23 May 2016*
Published: *07 June 2016*

Citation:
Ebner DK and Kamada T (2016) The Emerging Role of Carbon-Ion Radiotherapy. Front. Oncol. 6:140. doi: 10.3389/fonc.2016.00140

INTRODUCTION

In 1952, the first human patients were treated by John Lawrence and Cornelius Tobias with helium and deuteron particle beams (1). Subsequently, interest in particle beams expanded, with proton facilities emerging throughout the world. However, as the biological impact of protons mirrored that of X-ray therapy, attention turned to heavier ions due to a higher biological impact owing to higher linear energy transfer (LET) (2). In 1975, with the installation of the BEVALAC to the Lawrence Berkeley Laboratory (LBL), extensive research into the clinical potential of heavy-ion beams more formally began (3).

In response to the initial successes at LBL, in 1984, the Japanese government began construction on the world's first heavy-ion facility designated for medical use at the National Institute of Radiological Sciences (NIRS), staffing it with scientists returning from the BEVALAC and LBL. The Heavy Ion Medical Accelerator in Chiba (HIMAC) was completed in 1993, with clinical trials in carbon-ion radiotherapy (CIRT) beginning in June 1994.

Similar to the BEVALAC, the HIMAC provided for passive-beam irradiation. NIRS was alone in offering CIRT until 1997, when the GSI Carbon-Ion Radiotherapy Facility in Germany came into operation, pioneering raster scanning heavy-ion beams in clinical practice. GSI treated 440 patients with good results before its closure in 2008 (4). NIRS completed development of a pencil-beam raster scanning (PBS) treatment facility in 2012, and initial clinical trials are promising.

Developments in diagnostic technologies have enabled new therapeutic applications, such as markerless respiration-gated PBS irradiation. The enhanced radiobiological effect of the carbon-ion, concentrated and converged into a highly conformal dose distribution coinciding with target-respiratory movement, has allowed for medical care of radioresistant, previously untreatable disease (5–7). Further, these advantages have provided for hypofractionated radiotherapy of more common diseases, as well as improved adverse effect profiles, in comparison to conventional therapy. Altogether, this has lead to excellent treatment results in numerous diseases.

To date, nearly 70 protocols have been conducted at NIRS to delineate CIRT efficacy, safety, optimal treatment indications, and dose fractionation (8). Protocols begin with phase I dose-escalation studies focused on minimizing adverse effects. This is followed by phase II evaluation of treatment efficaciousness with longitudinal follow-up. If feasible, protocols exploring hypofractionation

follow. Initial protocols began with low doses and an average of 18 fractions, but after critical review of technical and clinical data, today cases average 11–12 fractions. One or two total fractions are possible for indicated lung and liver disease, respectively. As such, the Hospital of the NIRS has reached a treatment capacity of between 900 and 1000 patients per year.

Carbon-ion radiotherapy facilities and faculty continue to grow in number and experience, with 8+ operational centers and over 15,000 patients treated to date (9). In Japan, in addition to the four heavy-ion radiotherapy facilities in operation prior to 2015, the Kanagawa Cancer Center's carbon-ion facility began treatment in December 2015, and plans exist to construct facilities in Osaka City as well as Yamagata and Okinawa Prefectures. In light of the concentration of CIRT facilities in Japan, the Japan Carbon-ion Radiation Oncology Study Group (J-CROS) was organized to coordinate multi-institutional studies moving forward. Internationally, Austria will open a CIRT center in 2017, with centers in South Korea, Taiwan, China, and the United States in various states of development. Further, the clinical successor to the GSI Carbon-Ion Radiotherapy Facility, the Heidelberg Ion Therapy Center (HIT), has begun a number of randomized trials, testing carbon(-boost) versus other irradiation modalities (10–14).

In this paper, we aim to update on the expanding role of CIRT in cancer treatment as of 2016.

FEATURES OF CIRT

In comparison with conventional radiotherapy, particle beams possess different physical and biological characteristics that must be weighed when considering treatment. While conventional radiation generally passes continually through a biological target, with dose delivered roughly equivalently throughout the beam path, particle beams release energy at the inverse of their velocity (**Figure 1**). Particle beams thus deliver a lower entry dose, depositing the majority of their energy at the flight path terminus, yielding an asymptotic dose peak (the "Bragg Peak") (15). This allows for a dose concentration distribution impossible with conventional irradiation methods.

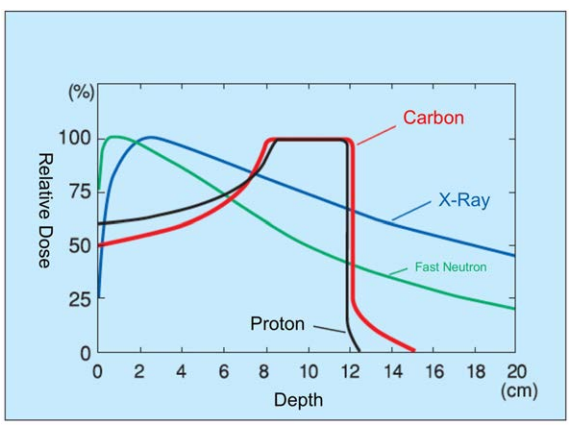

FIGURE 1 | **Dose distribution of heavy-particle beams**.

Today, proton dominates particle therapy. However, the larger mass of carbon results in decreased beam scattering, yielding a sharper dose distribution border with minimal penumbra (16). Radiobiologically, carbon-ion beams result in two to three times the relative biological effect (RBE; the biological effectiveness of one type of ionized radiation relative to another, given the same amount of absorbed energy) of proton and conventional irradiation methods (17). In comparison with photon therapy, CIRT does not show an oxygen effect, sublethal damage repair, and has less cell-cycle-related radiosensitivity.

These unique characteristics formed the rationale in initially applying carbon to radioresistant and/or hypoxic disease. Further indications then arose: the sharp dose distribution allows therapeutic dose delivery to disease juxtaposed with vital, radiosensitive organs (18–20). With radionormal or radiosensitive disease, short-term hypofractionated treatment becomes possible, owing to diminished dose delivered to healthy tissue.

CARBON-ION RADIOTHERAPY TREATMENT

To date, over 9000 patients have undergone CIRT at NIRS, with 12,000 across all facilities in Japan and over 15,000 worldwide. In 2003, upon review of the first 9 years of NIRS' clinical trials, the Japanese government allowed CIRT availability to the general public. CIRT has demonstrated efficacy against prostate, head and neck, lung, and liver cancers, bone and soft tissue sarcomas, locally recurrent rectal cancer, and pancreatic cancer, including locally advanced disease (8, 19, 21). Below, we provide a brief summary of the current most common indications and the data supporting their treatment.

At NIRS, over 2000 prostate cancer patients have been treated with CIRT, comprising approximately a fourth of CIRT-treated cases. Half of these cases are considered high risk at the time of treatment (determined by high PSA, T3 status, or high Gleason score). Initially, dose escalation in 20 fractions was performed, followed by investigation of hypofractionation. From 2007 to 2013, 781 patients were treated with 57.6 Gy (RBE) delivered in 16 fractions, with 5-year overall survival (OS) and biochemical relapse-free rates of 96.9 and 92.8%, respectively. No grade 3 or higher toxicity was seen. In 2014, treatment shifted to 12 fractions [51.2 Gy (RBE)] delivered over 3 weeks, yielding 100% cause-specific survival at a median follow-up of 32.3 months. At this dose-fractionation, no grade 3 or greater acute or late toxicities were observed, comparing favorably to conventional radiotherapy. Long-term data are pending, and further hypofractionation is being considered (22–24). Internationally, two randomized trials comparing proton and carbon are under recruitment at HIT (10).

Highly radioresistant non-squamous-cell carcinomas accounted for the majority of head and neck disease treated at NIRS, consisting of 11% of CIRT cases there. In a review of 240 patients (243 lesions), over a 9-year period, excellent results have been reported. 91% of patients received 57.6 Gy (RBE) with the remainder receiving 64.0 Gy (RBE), both delivered in 16 fractions. Approximately half of the high-dose group consisted of bone and soft tissue sarcomas of the head and neck. The 5-year

local control (LC) rate was 68% across all head and neck cancers, with OS of 47% (LC/OS histological breakdown: 75/35% mucosal malignant melanoma, 73/68% adenoid cystic carcinoma (ACC), 73/56% adenocarcinoma, 24/36% sarcomas, 61/31% papillary adenocarcinoma, and 61/17% squamous cell carcinoma). Acute grade 3 skin and mucosal reactions were seen in 15 (6%) and 24 (10%) of patients, respectively, with no acute grade 4 or higher toxicity seen. No late skin grade 3 or greater toxicities were noted. Late mucosal side effects included no grade 3, but four cases of grade 4 ipsilateral blindness (25, 26). In 109 head-and-neck-based malignant mucoscal melanoma patients treated concomitantly with dacarbazine, nimustine, and vincristine (DAV), a 5-year LC rate of 82% with OS of 52% was achieved versus 33% OS with carbon alone (27). At HIT, carbon ions were used as boost in ACC, achieving 78% LC at 4 years, with rates of severe late toxicity <5% (28).

A majority of bone and soft tissue tumors are radioresistant and form a prototypical disease for CIRT treatment. Thus, despite being comparatively rare, these make up 11% of CIRT cases at NIRS. In particular, in both the skull base and trunk, chordoma, osteosarcoma, spinal tumors, and retroperitoneal tumors treated with CIRT have demonstrated satisfactory results (27, 29–33). Skull base and paracervical disease treated with 48.0–60.8 Gy (RBE) in 16 fractions yielded an overall LC and OS rate of 86 and 85%, respectively (LC/OS: 87/90% chordomas, 81/76% chondrosarcomas, 89/73% olfactory neuroblastomas, and 83/86% meningiomas). 24.5% of patients experienced grade 2 or greater radiation-induced brain injury (RIBI) (7.0% symptomatic), with a single case of grade 4 RIBI (27, 34, 35). This reinforced similar results from GSI, where LC of 70% at 5 years in chordoma and 87% at 4 years in chondrosarcomas, with limited toxicity, were achieved (36, 37). Randomized trials at HIT for these diseases are underway. In unresectable primary spinal sarcoma, following a dose of 52.8–70.4 Gy (RBE) in 16 fractions, 5-year LC and OS were 79 and 52%, respectively, with smaller disease (<100 cm^3) demonstrating 100% LC. Three patients (6%) experienced a grade 3 or greater adverse effect, and seven experienced vertebral body compression (32). In unresectable retroperitoneal sarcoma, following dosing of 52.8–73.6 Gy (RBE) in 16 fractions, 5-year LC and OS was 69 and 50%, respectively. No grade 3 or greater toxicity was noted (33). In unresectable truncal osteosarcoma, following a median 70.4 Gy (RBE) applied in 16 fractions, LC of 62% and OS of 33% was seen, with no grade 3 or greater toxicity noted. Worse outcomes were seen in patients with a clinical target volume >500 cm^3 (31). At HIT, locally unresectable osteosarcomas are treated with carbon and chemotherapy in an ongoing trial that includes the only cohort of CIRT-treated pediatric patients. Results are forthcoming (11, 12).

With lung and liver cancers, the improved dose distribution and strong RBE of CIRT led to prospective trials in hypofractionation, yielding excellent results (20, 38–40). Lung cancers encompass 11% of cases at NIRS, and currently, single-fraction delivery of 50 Gy (RBE) is indicated for Stage I, T1 and T2 non-small-cell disease. This has demonstrated a 5-year LC rate of 80.4% for patients receiving doses of 36.0 Gy (RBE) or more (T1: 86.0% and T2: 71.7%), with 5-year OS of 56.3%. For patients receiving 48 or 50 Gy (RBE), 2-year LC and OS were both 95% (39). The first non-Japanese lung cancer CIRT trial, at HIT, will be a prospective clinical trial on patients with chest wall infiltration (10). Hepatocellular carcinoma, making up 10% of CIRT indications, leads to notably poor survival rates due to inherent radiosensitivity of the liver combined with poor resectability (41). Current hypofractionation efforts led to a two-fraction regime consisting of 45.0 Gy (RBE). This has yielded OS and LC rates of 71 and 83% at 3 years, respectively. No grade 3+ reactions were noted in a 45 Gy (RBE) or higher dose treatment group (42). Of note, four-fraction, 52.8-Gy (RBE) treatment of tumors lying near to the porta hepatis has yielded good control: 5-year LC of 87.8% with OS of 22.2% without similar side-effect profiles to non-porta hepatis cases (20). The PROMETHEUS-1 trial at HIT reported initial results in 2013: at 11 months, LC of 100% was achieved with no severe adverse events reported (43).

Locally recurrent rectal cancer (5% of cases), pancreatic cancer (4% of cases), and cervical adenocarcinoma and related cancers (gynecological tumors encompass 3% of cases) all demonstrate degrees of radioresistance, but CIRT has demonstrated excellent performance in treating these diseases. A phase I/II dose-escalation study of 170 recurrent rectal cancer patients was performed at NIRS, with escalating dose between 67.2 and 73.6 Gy (RBE) delivered over 16 fractions in 4 weeks. LC at 3 years was 92% for 73.6 Gy (RBE), with OS of 59% at 73.6 Gy (RBE) at 5 years. No acute grade 3 or greater adverse events were seen, with two grade 3 late skin and one grade 3 late gastrointestinal reaction noted (44, 45). The forthcoming PANDORA-01 trial at HIT will further evaluate use of carbon in the setting of recurrent rectal cancer (13). The results for locally advanced pancreatic cancer have drawn international attention with combined CIRT-gemcitabine therapy, yielding a 1- and 2-year freedom from local progression rate (FFLP), evaluated by ^{18}FDG uptake, of 63 and 30%, with OS at 1 and 2 years of 73 and 35%, respectively. When limited to Stage III disease, 2-year FFLP and OS improved to 40 and 48%, respectively. 53% of patients experienced grade 3–4 hematological toxicity, and 7% experienced grade 3 anorexia. One case (1%) of grade 3 intratumoral infection was noted. None of these reactions were life-threatening (21). The forthcoming PHOENIX-01 trial at HIT will evaluate advanced pancreatic cancer treatment with scanning carbon-ion beam irradiation in combination with gemcitabine (14). With regard to cervical cancer, 58 locally advanced adenocarcinoma cases were treated in a dose-escalation study [62.4–74.4 Gy (RBE) in 20 fractions] between 1998 and 2010, with 5-year LC of 54.5% and OS of 38.1%. One patient experienced a grade 4 rectal complication, with no other grade 3 or higher toxicities reported (46).

Radiotherapeutic treatment of brain malignancies remains a substantial challenge. Combs and colleagues conducted a pooled analysis of HIT and Japanese data regarding the usage of carbon-ion boost (CIB) in the treatment of anaplastic astrocytoma (AA) and glioblastoma (GBM) (47–49). Postoperatively, 50-Gy photon with nimustine hydrochloride was administered, with 16.8–24.8 Gy (RBE) CIRT provided as boost. In GBM and AA, median OS was 18 and 35 months with CIRT versus 14 and 39 months with standard postoperative radiochemotherapy (RCT) with

temozolomide. Progression-free survival of GBM and AA were 6 and 6 months (RCT) and 8 and 34 months (CIRT), respectively. The potential benefit of CIRT noted is under further evaluation in the CLEOPATRA trial at HIT (47).

Overall, CIRT has demonstrated good adaptability for difficult-to-treat, radioresistant disease, while allowing accelerated, hypofractionated treatment of other disease. Distant metastasis remains a challenge, but initial evaluations of CIRT concurrent with chemotherapy has demonstrated satisfactory performance (21, 27).

FUTURE DIRECTIONS

The future of charged particle therapy as of 2016 appears bright, with implementation of respiration-gated fast PBS (50), markerless tracking (51), a range-shifter-free multiple-energy modulation system, and completion of the second carbon-ion rotating gantry in the world at NIRS, following the first at Heidelberg. Nine plus new CIRT centers are opening worldwide. However, the high cost associated with the construction, maintenance, and operation of CIRT facilities, as well as the corresponding costs in staff development and support, presents a challenge for extension of the technology outside of the developed world.

As such, a great deal of work remains. Development in cost-saving and improved miniaturization of existing technology is necessary. To date, these efforts have produced CIRT accelerator and synchrotrons at one-third the cost and size of the original HIMAC, which are in operation at the Saga-HIMAT, Gunma University, and Kanagawa Cancer Center i-ROCK facilities. Superconduction technology allowed for the recently completed rotating gantry at NIRS to be built with a length and diameter of 13 and 5.5 m, respectively, versus the existing gantry at HIT, which is 25 m × 13 m (52). Ongoing development aims to further employ superconducting technology in the accelerator and overall device, producing a total CIRT setup dubbed the "Super MINIMAC" that will fit within 20 m^2. Meanwhile, limited research has been published on the cost-efficacy of CIRT (53–55), which would appear to improve with each new technological development; focused evaluation may be necessary to facilitate international development.

In Japan, CIRT is available as a private treatment to the general public. Discussion to extend national insurance coverage to CIRT is ongoing. However, despite the current cost burden for patients (3.2 million yen/~28,000 USD for a treatment course, regardless of fractionation; in Germany, treatment costs ~1000 Euro per fraction), the number of patients from both within and outside Japan continues to increase.

Clinically, as the majority of cases treated with CIRT in the world were treated at NIRS, the majority of available clinical data is focused at a single institution spread over 20 years (19). As center numbers increase, multi-institutional trials and randomized, internationally coordinated trials may begin.

An international ecosystem supporting and interweaving CIRT clinical, physical, and biological development is also necessary. It is known that the LET of particle beams are non-homogenous throughout the irradiated region, yielding variations in RBE (56). As carbon is a high LET beam, these variations are more appreciable than with low LET proton irradiation. Due to a risk of consequent under- or over-treatment and toxicity, complex dosing models are required in the use of heavy ions. Of particular note, the RBE model varies between international institutions. Within Japan, the MKM2010 model, a revision of the Microdosimetric Kinetic Model, has been developed and implemented (57). In Europe, versions of the local effect model (LEM) are dominant. Efforts to improve international standardization are progressing, with work by Fossati and colleagues providing for MKM2010 dose translation to the LEM model and vice versa (58). Improved model accuracy and careful manipulation of the high LET/RBE regions may enable LET painting of tumors (59). This "intensity modulated carbon therapy" may further improve dose distribution, and research to this end is underway.

CONCLUSION

Since 1970, heavy-ion radiotherapy has progressed rapidly in technological delivery and, consequently, in indications and efficacy. The ability for the carbon-ion beam to offer short-term, minimally invasive, function-, tissue-, and form-sparing treatment has garnered international attention, with the technology nearing the tipping point for international adoption. Technically, enhanced international collaboration is needed to produce an intercenter translatable dosing model consensus and to enhance results at the common borders between radiobiology and particle physics. Societally, cost and access to treatment remains a challenge, particularly in developing countries. However, evidence continues to mount for the superiority of carbon in the treatment of radioresistant, hypoxic disease. Coupled with the opportunity for substantially abbreviated treatment of common disease, carbon-ion radiotherapy looks increasingly appealing as a treatment modality deserving worldwide availability.

AUTHOR CONTRIBUTIONS

DKE and TK wrote and edited the manuscript.

REFERENCES

1. Tobias CA, Anger HO, Lawrence JH. Radiological use of high energy deuterons and alpha particles. *Am J Roentgenol Radium Ther Nucl Med* (1952) 67:1–27.
2. Curtis SB. Plans for the high-energy, heavy-ion facility (BEVALAC) at Berkeley. *Eur J Cancer* (1974) 10:388.
3. Castro JR, Quivey JM, Lyman JT, Chen G, Phillips TL, Tobias CA. Radiotherapy with heavy charged-particles at Lawrence Berkeley Laboratory. *J Can Assoc Radiol* (1980) 31:30–4.
4. Kraft G. *History of the Heavy Ion Therapy at GSI*. (2013). p. 1–17. Available from: https://three.jsc.nasa.gov/articles/Krafts_GSI.pdf
5. Kanai T, Endo M, Minohara S, Miyahara N, Koyama-ito H, Tomura H, et al. Biophysical characteristics of HIMAC clinical irradiation system for heavy-ion radiation therapy. *Radiat Oncol Biol* (1999) 44:201–10. doi:10.1016/S0360-3016(98)00544-6
6. Minohara S, Kanai T, Endo M, Noda K, Kanazawa M. Respiratory gated irradiation system for heavy-ion radiotherapy. *Radiat Oncol Biol* (2000) 47:1097–103. doi:10.1016/S0360-3016(00)00524-1

7. Mizota M, Kanai T, Yusa K, Akagi T, Shimbo M, Yamashita H, et al. Reconstruction of biologically equivalent dose distribution on CT-image from measured physical dose distribution of therapeutic beam in water phantom. *Phys Med Biol* (2002) 47:935–45. doi:10.1088/0031-9155/47/6/306
8. Tsujii H, Kamada T, Shirai T, Noda K, Tsuji H, Karasawa K. In: Tsujii H, Kamada T, Shirai T, Noda K, Tsuji H, Karasawa K, editors. *Carbon-Ion Radiotherapy*. Tokyo: Springer Science & Business Media (2013). p. 127–309.
9. Jermann M. Particle therapy statistics in 2014. *Int J Part Ther* (2015) 2:50–4. doi:10.14338/IJPT-15-00013
10. Combs SE, Debus J. Treatment with heavy charged particles: systematic review of clinical data and current clinical (comparative) trials. *Acta Oncol* (2013) 52:1272–86. doi:10.3109/0284186X.2013.818254
11. Blattmann C, Oertel S, Schulz-Ertner D, Rieken S, Haufe S, Ewerbeck V, et al. Non-randomized therapy trial to determine the safety and efficacy of heavy ion radiotherapy in patients with non-resectable osteosarcoma. *BMC Cancer* (2010) 10:96. doi:10.1186/1471-2407-10-96
12. Combs SE, Kessel KA, Herfarth K, Jensen A, Oertel S, Blattmann C, et al. Treatment of pediatric patients and young adults with particle therapy at the Heidelberg Ion Therapy Center (HIT): establishment of workflow and initial clinical data. *Radiat Oncol* (2012) 7:170. doi:10.1186/1748-717X-7-170
13. Combs SE, Kieser M, Habermehl D, Weitz J, Jäger D, Fossati P, et al. Phase I/II trial evaluating carbon ion radiotherapy for the treatment of recurrent rectal cancer: the PANDORA-01 trial. *BMC Cancer* (2012) 12:137. doi:10.1186/1471-2407-12-137
14. Combs SE, Habermehl D, Kieser M, Dreher C, Werner J, Haselmann R, et al. Phase I study evaluating the treatment of patients with locally advanced pancreatic cancer with carbon ion radiotherapy: the PHOENIX-01 trial. *BMC Cancer* (2013) 13:419. doi:10.1186/1471-2407-13-419
15. Brown A, Suit H. The centenary of the discovery of the Bragg peak. *Raiother Oncol* (2004) 73(3):265–8. doi:10.1016/j.radonc.2004.09.008
16. Durante M, Loeffler JS. Charged particles in radiation oncology. *Nature Reviews Clinical Oncology* (2010) 7:37–43. doi:10.1038/nrclinonc.2009.183
17. Raju MR, Carpenter SG. A heavy particle comparative study. Part IV: acute and late reactions. *Br J Radiol* (1978) 51:720–7. doi:10.1259/0007-1285-51-609-720
18. Tsujii H, Kamada T. A review of update clinical results of carbon ion radiotherapy. *Jpn J Clin Oncol* (2012) 42:670–85. doi:10.1093/jjco/hys104
19. Kamada T, Tsujii H, Blakely EA, Debus J, De Neve W, Durante M, et al. Carbon ion radiotherapy in Japan: an assessment of 20 years of clinical experience. *Lancet Oncol* (2015) 16:e93–100. doi:10.1016/S1470-2045(14)70412-7
20. Imada H, Kato H, Yasuda S, Yamada S, Yanagi T, Kishimoto R, et al. Comparison of efficacy and toxicity of short-course carbon ion radiotherapy for hepatocellular carcinoma depending on their proximity to the porta hepatis. *Radiother Oncol* (2010) 96:231–5. doi:10.1016/j.radonc.2010.05.019
21. Shinoto M, Yamada S, Terashima K, Yasuda S. Carbon-ion radiotherapy with concurrent gemcitabine for patients with locally advanced pancreatic cancer. *Int J Radiat Oncol* (2015) 95:498–504. doi:10.1016/j.ijrobp.2015.12.362
22. Okada T, Tsuji H, Kamada T, Akakura K, Suzuki H, Shimazaki J, et al. Carbon ion radiotherapy in advanced hypofractionated regimens for prostate cancer: from 20 to 16 fractions. *Int J Radiat Oncol Biol Phys* (2012) 84:968–72. doi:10.1016/j.ijrobp.2012.01.072
23. Nomiya T, Tsuji H, Maruyama K, Toyama S, Suzuki H, Akakura K, et al. Phase I/II trial of definitive carbon ion radiotherapy for prostate cancer: evaluation of shortening of treatment period to 3 weeks. *Br J Cancer* (2014) 110:2389–95. doi:10.1038/bjc.2014.191
24. Ishikawa H, Tsuji H, Kamada T, Akakura K, Suzuki H, Shimazaki J, et al. Carbon-ion radiation therapy for prostate cancer. *Int J Urol* (2012) 19:296–305. doi:10.1111/j.1442-2042.2012.02961.x
25. Mizoe J-E, Hasegawa A, Jingu K, Takagi R, Bessyo H, Morikawa T, et al. Results of carbon ion radiotherapy for head and neck cancer. *Radiother Oncol* (2012) 103:32–7. doi:10.1016/j.radonc.2011.12.013
26. Jingu K, Tsujii H, Mizoe J-E, Hasegawa A, Bessho H, Takagi R, et al. Carbon ion radiation therapy improves the prognosis of unresectable adult bone and soft-tissue sarcoma of the head and neck. *Int J Radiat Oncol Biol Phys* (2012) 82:2125–31. doi:10.1016/j.ijrobp.2010.08.043
27. Hasegawa A, Koto M, Takagi R. Carbon-ion radiotherapy for malignant head and neck cancer. *NIRS & MedAustron Joint Symposium on Carbon Ion Radiotherapy, 2013*. (2014). p. 6–13. Available from: http://www.nirs.go.jp/publication/proceedings/NIRS_MedAustron/proceedings.pdf
28. Schulz-Ertner D, Nikoghosyan A, Didinger B, Münter M, Jäkel O, Karger CP, et al. Therapy strategies for locally advanced adenoid cystic carcinomas using modern radiation therapy techniques. *Cancer* (2005) 104:338–44. doi:10.1002/cncr.21158
29. Kamada T, Tsujii H, Tsuji H, Yanagi T, Mizoe J, Miyamoto T, et al. Efficacy and safety of carbon ion radiotherapy in bone and soft tissue sarcomas. *J Clin Oncol* (2002) 20:4466–71. doi:10.1200/JCO.2002.10.050
30. Imai R, Kamada T, Sugahara S, Tsuji H, Tsujii H. Carbon ion radiotherapy for sacral chordoma. *Br J Radiol* (2011) 84:S48–53. doi:10.1259/bjr/13783281
31. Matsunobu A, Imai R, Kamada T, Imaizumi T, Tsuji H, Tsujii H, et al. Impact of carbon ion radiotherapy for unresectable osteosarcoma of the trunk. *Cancer* (2012) 118:4555–63. doi:10.1002/cncr.27451
32. Matsumoto K, Imai R, Kamada T, Maruyama K, Tsuji H, Tsujii H, et al. Impact of carbon ion radiotherapy for primary spinal sarcoma. *Cancer* (2013) 119:3496–503. doi:10.1002/cncr.28177
33. Serizawa I, Kagei K, Kamada T, Imai R, Sugahara S, Okada T, et al. Carbon ion radiotherapy for unresectable retroperitoneal sarcomas. *Radiat Oncol Biol* (2009) 75:1105–10. doi:10.1016/j.ijrobp.2008.12.019
34. Mizoe J-E, Hasegawa A, Takagi R, Bessho H, Onda T, Tsujii H. Carbon ion radiotherapy for skull base chordoma. *Skull Base* (2009) 19:219–24. doi:10.1055/s-0028-1114295
35. Koto M, Hasegawa A, Takagi R, Fujikawa A, Morikawa T, Kishimoto R, et al. Risk factors for brain injury after carbon ion radiotherapy for skull base tumors. *Radiother Oncol* (2014) 111:25–9. doi:10.1016/j.radonc.2013.11.005
36. Schulz-Ertner D, Karger CP, Feuerhake A, Nikoghosyan A, Combs SE, Jäkel O, et al. Effectiveness of carbon ion radiotherapy in the treatment of skull-base chordomas. *Radiat Oncol Biol* (2007) 68:449–57. doi:10.1016/j.ijrobp.2006.12.059
37. Schulz-Ertner D, Nikoghosyan A, Hof H, Didinger B, Combs SE, Jäkel O, et al. Carbon ion radiotherapy of skull base chondrosarcomas. *Radiat Oncol Biol* (2007) 67:171–7. doi:10.1016/j.ijrobp.2006.08.027
38. Miyamoto T, Baba M, Sugane T, Nakajima M, Yashiro T, Kagei K, et al. Carbon ion radiotherapy for stage I non-small cell lung cancer using a regimen of four fractions during 1 week. *J Thorac Oncol* (2007) 2:916–26. doi:10.1097/JTO.0b013e3181560a68
39. Yamamoto N. Carbon ion radiotherapy for lung cancer. *HIMAC International Symposium*. (2015). Available from: http://www.nirs.go.jp/ENG/publication/proceedings/pdf/HIMAC_International_Symposium2015.pdf
40. Yasuda S, Isozaki Y, Yamada S. Carbon ion radiotherapy for hepatocellular carcinoma. *HIMAC International Symposium*. (2015). Available from: http://www.nirs.go.jp/ENG/publication/proceedings/pdf/HIMAC_International_Symposium2015.pdf
41. Hennequin C, Quero L, Rivera S. Radiosensitivity of hepatocellular carcinoma. *Cancer Radiother* (2011) 15:39–42. doi:10.1016/j.canrad.2010.11.004
42. Yasuda S, Harada M, Yamada S, Shiomi M, Isozaki T, Kamada T. Carbon-ion radiotherapy for hepatocellular carcinoma. *Conference Proceedings of NIRS-MedAustron Joint Conference on Carbon-Ion Radiotherapy*. (2013).
43. Habermehl D, Debus J, Ganten T, Ganten M-K, Bauer J, Brecht IC, et al. Hypofractionated carbon ion therapy delivered with scanned ion beams for patients with hepatocellular carcinoma – feasibility and clinical response. *Radiat Oncol* (2013) 8:59. doi:10.1186/1748-717X-8-59
44. Yamada S, Anzai M, Okada N. Carbon ion radiotherapy for patients with pelvic recurrence of rectal cancer. *HIMAC International Symposium*. (2015). Available from: http://www.nirs.go.jp/ENG/publication/proceedings/pdf/HIMAC_International_Symposium2015.pdf
45. Yamada S, Kamada T, Ebner DK, Shinoto M, Maier A, Terashima K, et al. Carbon-ion radiotherapy for pelvic recurrence of rectal cancer. *Int J Radiat Oncol* (2016). doi:10.1016/j.ijrobp.2016.04.022
46. Wakatsuki M, Kato S, Ohno T, Karasawa K, Kiyohara H, Tamaki T, et al. Clinical outcomes of carbon ion radiotherapy for locally advanced adenocarcinoma of the uterine cervix in phase 1/2 clinical trial (protocol 9704). *Cancer* (2014) 120:1663–9. doi:10.1002/cncr.28621
47. Combs SE, Bruckner T, Mizoe J-E, Kamada T, Tsujii H, Kieser M, et al. Comparison of carbon ion radiotherapy to photon radiation alone or in

combination with temozolomide in patients with high-grade gliomas: explorative hypothesis-generating retrospective analysis. *Radiother Oncol* (2013) 108:132–5. doi:10.1016/j.radonc.2013.06.026
48. Mizoe J-E, Tsujii H, Hasegawa A, Yanagi T, Takagi R, Kamada T, et al. Phase I/II clinical trial of carbon ion radiotherapy for malignant gliomas: combined X-ray radiotherapy, chemotherapy, and carbon ion radiotherapy. *Radiat Oncol Biol* (2007) 69:390–6. doi:10.1016/j.ijrobp.2007.03.003
49. Hasegawa A, Mizoe J-E, Tsujii H, Kamada T, Jingu K, Iwadate Y, et al. Experience with carbon ion radiotherapy for WHO Grade 2 diffuse astrocytomas. *Int J Radiat Oncol Biol Phys* (2012) 83:100–6. doi:10.1016/j.ijrobp.2011.06.1952
50. Mori S, Zenklusen S, Inaniwa T, Furukawa T, Imada H, Shirai T, et al. Conformity and robustness of gated rescanned carbon ion pencil beam scanning of liver tumors at NIRS. *Radiother Oncol* (2014) 111:431–6. doi:10.1016/j.radonc.2014.03.009
51. Mori S. Real-time image-processing algorithm for markerless tumour tracking using X-ray fluoroscopic imaging. *Br J Radiol* (2014) 87:20140001. doi:10.1259/bjr.20140001
52. Shirai T. Hardware development and medical physics. *2nd International Symposium on Heavy-Ion Radiotherapy and Advanced Technology*; 2016 Jan 9; Tokyo (2016). p. 10–14. Available from: http://www.nirs.qst.go.jp/rd/reports/proceedings/pdf/2nd_International_Symposium_2016.pdf
53. Mobaraki A, Ohno T, Yamada S, Sakurai H, Nakano T. Cost-effectiveness of carbon ion radiation therapy for locally recurrent rectal cancer. *Cancer Sci* (2010) 101:1834–9. doi:10.1111/j.1349-7006.2010.01604.x
54. Ohno T. Particle radiotherapy with carbon ion beams. *EPMA J* (2013) 4:9. doi:10.1186/1878-5085-4-9
55. Jäkel O, Land B, Combs SE, Schulz-Ertner D, Debus J. On the cost-effectiveness of carbon ion radiation therapy for skull base chordoma. *Radiother Oncol* (2007) 83:133–8. doi:10.1016/j.radonc.2007.03.010
56. Tommasino F, Scifoni E, Durante M. New ions for therapy. *Int J Part Ther* (2015) 2:428–38. doi:10.14338/IJPT-15-00027.1
57. Inaniwa T, Kanematsu N, Matsufuji N, Kanai T, Shirai T, Noda K, et al. Reformulation of a clinical-dose system for carbon-ion radiotherapy treatment planning at the National Institute of Radiological Sciences, Japan. *Phys Med Biol* (2015) 60:3271–86. doi:10.1088/0031-9155/60/8/3271
58. Fossati P, Molinelli S, Matsufuji N, Ciocca M, Mirandola A, Mairani A, et al. Dose prescription in carbon ion radiotherapy: a planning study to compare NIRS and LEM approaches with a clinically-oriented strategy. *Phys Med Biol* (2012) 57:7543–54. doi:10.1088/0031-9155/57/22/7543
59. Tinganelli W, Durante M, Hirayama R, Krämer M, Maier A, Kraft-Weyrather W, et al. Kill-painting of hypoxic tumours in charged particle therapy. *Sci Rep* (2015) 5:17016. doi:10.1038/srep17016

Conflict of Interest Statement: The authors declare that the research was conducted in the absence of any commercial or financial relationships that could be construed as a potential conflict of interest.

Copyright © 2016 Ebner and Kamada. This is an open-access article distributed under the terms of the Creative Commons Attribution License (CC BY). The use, distribution or reproduction in other forums is permitted, provided the original author(s) or licensor are credited and that the original publication in this journal is cited, in accordance with accepted academic practice. No use, distribution or reproduction is permitted which does not comply with these terms.

frontiers in Oncology

REVIEW
published: 11 January 2016
doi: 10.3389/fonc.2015.00302

The Role of Hypofractionated Radiation Therapy with Photons, Protons, and Heavy Ions for Treating Extracranial Lesions

*Aaron Michael Laine, Arnold Pompos, Robert Timmerman, Steve Jiang, Michael D. Story, David Pistenmaa and Hak Choy**

Department of Radiation Oncology, University of Texas Southwestern Medical Center, Dallas, TX, USA

Traditionally, the ability to deliver large doses of ionizing radiation to a tumor has been limited by radiation-induced toxicity to normal surrounding tissues. This was the initial impetus for the development of conventionally fractionated radiation therapy, where large volumes of healthy tissue received radiation and were allowed the time to repair the radiation damage. However, advances in radiation delivery techniques and image guidance have allowed for more ablative doses of radiation to be delivered in a very accurate, conformal, and safe manner with shortened fractionation schemes. Hypofractionated regimens with photons have already transformed how certain tumor types are treated with radiation therapy. Additionally, hypofractionation is able to deliver a complete course of ablative radiation therapy over a shorter period of time compared to conventional fractionation regimens making treatment more convenient to the patient and potentially more cost-effective. Recently, there has been an increased interest in proton therapy because of the potential further improvement in dose distributions achievable due to their unique physical characteristics. Furthermore, with heavier ions the dose conformality is increased and, in addition, there is potentially a higher biological effectiveness compared to protons and photons. Due to the properties mentioned above, charged particle therapy has already become an attractive modality to further investigate the role of hypofractionation in the treatment of various tumors. This review will discuss the rationale and evolution of hypofractionated radiation therapy, the reported clinical success with initially photon and then charged particle modalities, and further potential implementation into treatment regimens going forward.

Keywords: hypofractionation, photon therapy, ion beam therapy, SBRT, SABR

OPEN ACCESS

Edited by:
Marco Durante,
GSI Helmholtzzentrum für Schwerionenforschung, Germany

Reviewed by:
Maurizio Amichetti,
APSS srl, Italy
Carlo Greco,
Champalimaud Foundation, Portugal

***Correspondence:**
Hak Choy
hak.choy@utsouthwestern.edu

Specialty section:
This article was submitted to Radiation Oncology, a section of the journal Frontiers in Oncology

Received: *31 August 2015*
Accepted: *14 December 2015*
Published: *11 January 2016*

Citation:
Laine AM, Pompos A, Timmerman R, Jiang S, Story MD, Pistenmaa D and Choy H (2016) The Role of Hypofractionated Radiation Therapy with Photons, Protons, and Heavy Ions for Treating Extracranial Lesions. Front. Oncol. 5:302. doi: 10.3389/fonc.2015.00302

INTRODUCTION

After the discovery of X-rays in 1895 and radioactivity in 1896, initial radiation cancer treatments were mostly hypofractionated. Treatments were limited in giving higher doses to the skin and superficial structures than to a deeper tumor target. Quality assurance measures were lacking to ensure accurate dose deposition. These approaches lead to tumor responses, however, with significant late tissue effects. Despite these shortcomings, hypofractionation remained the primary treatment

schedule due to patient convenience and technical considerations with treatment delivery.

Early radiotherapy pioneers, including Friedrich Dessauer, sought to address the limitations with the state of technology for delivering hypofractionated treatments. In 1905, Dessauer proposed that clinical outcomes could be improved with the application of homogeneous dose to the tissue and eventually leading to the formulation of ideas of multibeam or multisource irradiation (1).

At the same time, Claudius Regaud was performing his seminal experiments relating to the irradiation of the testis. He observed that cells undergoing mitosis were more sensitive to radiation, whereas the more differentiated cells were less sensitive (2). This work lead to the "Law of Bergonie and Tribondeau" stating that the effects of irradiation on cells are more intense, the greater their reproductive activity, the longer their mitotic phases, and the less differentiated, forming the biological basis for fractionation (3).

By the 1920s, despite the advocacy of Regaud, Antoine Béclère, and Henri Coutard, multiple fractionated treatments were still less popular than hypofractionated treatments. The approach promoted by Ludwig Seitz and Hermann Wintz, favoring intensive short courses of radiotherapy for treatment of cervical cancer, was widely adopted (4).

In 1932, Henri Coutard presented his landmark findings at the American Congress of Roentgenology, demonstrating that protracted-fractionated external beam therapy had cured deep tumors with significantly less toxicity previously seen (5). From this point forward, radiation oncologists across the world mostly abandoned hypofractionated as a method for curative treatment. Interestingly, Coutard believed in both approaches stating that choice of fractionation should depend on the initial volume of the target (small targets warrant hypofractionation, whereas large should be more protracted) (6).

It took until the 1950s, when Lars Leksell, a neurosurgeon, broke from the perceived wisdom of conventionally fractionated radiotherapy (CFRT) by using large-dose single sessions of radiation delivery in the central nervous system (7). In conjunction with a radiation physicist, Borge Larsson, they created the first Gamma Knife (Elekta AB, Stockholm, Sweden). Although a single large-dose radiation treatment was historically intolerable, Leksell's approach defied conventional wisdom by its technology and conduct. Unlike CFRT, which often irradiates much larger volumes of normal tissue to the prescription dose than the tumor itself if a limited number of beams are utilized, Leksell's stereotactic radiosurgery surgery (SRS) went to great lengths to avoid delivering high dose to non-targeted tissues. Whatever normal tissue was included, either by being adjacent to the target or by inferior dosimetry, was likely damaged. However, if this damaged tissue was small in volume or non-eloquent, the patient did not suffer clinically apparent toxicity, even as a late event.

Building upon these results, investigators in Sweden at the Karolinska Institute in Sweden by Lax and Blomgren, departed from the established traditions of CFRT and began to explore the use of alternative hypofractionated radiation treatment regimens for the lung, liver, and selected other malignant extracranial tumors. Furthermore, technical advancements in linear accelerators allowing for the delivery of increased beam energies made deep-seeded tumors more accessible with less toxicity. They constructed a stereotactic body frame that would simultaneously enable comfortable and reliable immobilization and dampening of respiratory motion, treating patients with extracranial, localized tumors with ablative doses of radiation that ranged from 7.7 to 45 Gy in 1–4 fractions (8). At the same time in Japan, Uematsu and colleagues developed technologies to deliver stereotactic radiation to lung tumors (9). Initially, the treatments were called extracranial stereotactic radioablation, and later stereotactic body radiation therapy (SBRT) (10, 11). More recently, the descriptive term stereotactic ablative radiotherapy (SABR) has been used (12).

Radiobiologic Modeling of High Dose per Fraction with Photons

Classical understanding of the mechanisms of radiation induced tumor cell killing centers on the hypothesis that DNA is the main target of ionizing radiation, leading to single- and double-strand breaks. Different mathematical models have been developed to compare tumor control and normal tissue toxicity profiles for various radiation schedules and fraction sizes. The most commonly used is the linear quadratic (LQ) model, which describes cell killing as a single hit versus double hit hypothesis, where the linear cell kill is expressed by the α component, while the quadratic cell kill is expressed by the β component (13). The α/β ratio is obtained from isoeffect curves using the survival fractions of a cell line at different doses per fraction (14). This ratio is primarily utilized to predict the clinical effects in response to changes in fraction size. With regard to tumors, a high α/β ratio predicts higher sensitivity to CFRT, while a lower α/β ratio predicts lower sensitivity to CFRT. Most tumors typically possess a high α/β ratio (~8–10) relative to most normal tissues, which demonstrate lower α/β ratios (~1–4).

Not all hypofractionated radiotherapy is ablative. In general, ablation occurs at dose levels that correspond to the exponential (linear region on a logarithmic scale) portion of the cell-survival curve, which would generally involve daily dose levels of >8 Gy. Below this dose range, cells have more capacity to repair. The logarithm of cell survival as a function of dose in the lower-dose region exhibits a curviness called the shoulder. More conventional and non-ablative hypofractionated radiotherapy is delivered on the shoulder. The range of 2.25–8 Gy per fraction, still considered hypofractionated, has mostly been used for palliation of metastatic disease. More recently, though, investigators treating common diseases, such as breast and prostate cancer, have used non-ablative hypofractionation in patients with curable tumors. This was partly for the cost savings associated with fewer overall fractions, but in some cases such hypofractionation has a biological rationale for improving the therapeutic ratio. A summary of the degrees of hypofractionated radiotherapy is shown in **Table 1**.

Biological effective dose (BED) quantifies the true biological dose delivered by a particular combination of dose per fraction and total dose to a certain tissue characterized by a specified α/β ratio. Based on experimental and clinical data, the LQ model seems to predict BED accurately for fraction sizes <3.25 Gy (15). Due to the fact that typical doses for SBRT/SABR fall outside of

TABLE 1 | Various daily fractionation options.

Fractionation regimen	Typical dose per fraction (Gy)
Conventionally fractionated radiotherapy	1.5–2.0
Hypofractionated radiotherapy	>2.0–8.0
Ablative radiotherapy	>8.0

this range, the LQ model breaks down as it does not accurately predict the BED for abbreviated hypofractionated regimens (15–18). Development of more accurate models to predict the responses of tumors to hypofractionated radiotherapy have been attempted. The universal survival curve, modified linear quadratic model (LQL), and the generalized LQ model all have shown better radiobiological modeling of high dose per fraction than the LQ model, with moderate success at maintaining accuracy within the conventionally fractionated range (15, 17, 19). These models primarily predict the tumor control to hypofractionated radiotherapy; however, better estimation of normal tissue toxicity with larger doses per fraction is required.

Limitations to predict clinically relevant endpoints exist in simple radiobiological modeling due to the presence of additional factors, including dose rate, period of time over which treatment is delivered, tissue type irradiated, and competing cell death mechanisms besides DNA damage. These may include immunological activation mediated by the release of antigens, damage to cell membranes and organelles, and additional mechanisms related to ablative therapy (20).

Several groups have described tissues and their radiation response according to the organization of the smallest functional subunit (21, 22). Structurally defined tissues can only repair radiation damage by recruiting their own stem cells and have a lower radiation tolerance per functional subunit. Generally, organs comprised such structurally defined subunits, also called parallel functioning tissues, and are large organs, such as the peripheral lung and liver. Parallel organs display significant redundancy in the number of subunits performing the same function to overcome the poor tolerance to damage. By contrast, tissues made up of predominately of structurally undefined subunits are much more tolerant of radiation damage per subunit because of their ability to recruit clonogenic cells from neighboring tissues for repair. Organs made up of structurally undefined subunits, such as the esophagus, major ducts and airways, and spinal cord, are referred as serially functioning tissues and perform critical functions acting as a conduit. Despite possessing a higher radiation tolerance, if a section of a serially functioning tissue is damaged anywhere along its length, all downstream function may be affected (23). The potential to elicit such tissue injury when utilizing ablative doses is a major consideration needed to be taken into account when developing treatment plans.

Technical and Safety Considerations of Ablative Therapy with Photons

Abbreviated hypofractionated treatments require highly conformal dose distributions that fall off very rapidly in all directions, which require the use of multiple shaped beams (24, 25). Most modern SBRT/SABR treatments utilize 10–12 highly collimated beams or multiple conformal arcs. Effort should be made to create truly isotropically decreasing dose gradients around targets, within the limitations due to potential collisions between the patient or couch and the accelerator head.

The gross tumor volume should be derived by incorporating advanced imaging techniques to assist in the differentiation between tumor and adjacent normal tissue. The planning treatment volume comprises the final target for high-dose conformal coverage and includes an accounting for organ motion. Limitation of the high- and intermediate-dose spillage should be attempted with careful determination of the volume they incorporate. Such spillage should be prioritized to avoid potential adjacent serially functioning tissues to reduce potential injury and downstream effects.

In summary, the defining characteristics of SBRT/SABR include the following (23): (1) secure immobilization avoiding patient movement for the typical long treatment sessions; (2) accurate repositioning from simulation to treatment; (3) minimization of normal tissue exposure attained by using multiple (e.g., 10 or more) or large-angle arcing small aperture fields; (4) rigorous accounting of organ motion; (5) stereotactic registration (i.e., via fiducial markers or surrogates) of tumor targets and normal tissue avoidance structures to the treatment delivery machine; and (6) ablative dose fractionation delivered to the patient with subcentimeter accuracy.

CLINICAL RESULTS OF HYPOFRACTIONATION WITH PHOTONS

Non-Small Cell Lung Cancer

For patients with medically inoperable non-small cell lung cancer (NSCLC), dose escalation using conventional fractionation was initially explored to improve the probability of local control. Radiation Therapy Oncology Group (RTOG) Protocol 7301 investigated multiple dosing regimens for patients with T1-3 N0-2 disease, including 40 Gy delivered in a split regimen of two courses of 20 Gy delivered in 5 fractions (40 Gy total in 10 fractions) with a 2-week break between courses, and continuous regiments escalating the dose from 40 to 60 Gy. The failure rate within the irradiated volume was 48% in the 40 Gy continuous regimen, 38% for the 40 Gy split course and 50 Gy regimen, and 27% in the 60 Gy continuous regimen (26). RTOG Protocol 9311 then escalated doses from 65 to 90.3 Gy using 3D conformal radiation therapy in inoperable patients, and found that treatment could safely be delivered in daily fraction sizes of 2.15 Gy to a total dose of 77.4 Gy, or 83.8 Gy provided that the volume of lung receiving 20 Gy could be constrained to less than 25% of the total lung volume. The study attained locoregional control rates at 2 years of 55–78% at the maximum tolerated dose (MTD) (27).

In order to continue to improve LC and OS in this patient population, protocols have sought to improve the therapeutic ratio with the addition of chemotherapy or by changing the dose per fraction. Researchers at Indiana University reported a Phase 1 study in which patients with T1–T2 N0 NSCLC were treated with escalating doses of SBRT/SABR, starting at 24 Gy in three fractions and increasing to 60 Gy (for T1 lesions) or 72 Gy (for T2

lesions) in three fractions to determine the MTD. The MTD was not reached for T1 lesions at 60 Gy, and for T2 lesions an MTD of 66 Gy was established based on bronchitis, pericardial effusion, hypoxia, and pneumonitis. Crude rates of local failure were 21% in both the T1 and T2 cohorts, and a dose–response was noted with only one local failure observed with fraction sizes of >16 Gy per fraction (10, 28). These doses were calculated without correction for tissue inhomogeneity; subsequent doses used inhomogeneity correction and, as a result, appear slightly lower.

A subsequent Phase 2 multicenter trial (RTOG 0236) further evaluated the toxicity and efficacy of SBRT in a high-risk population of patients with T1-2aN0 (lesions <5 cm in size) early stage, medically inoperable NSCLC. Doses of 54 Gy in three fractions were delivered, and an estimated 3-year local control rate of 97.6% was observed, with an overall survival rate of 55.8% at 3 years (29). Based on this study, SBRT/SABR is now the standard of care for medically inoperable early-stage NSCLC or those patients who refuse surgery. Further work is being done to optimize dose delivery for early stage NSCLC; the RTOG conducted RTOG Protocol 0915, a randomized Phase II study that compared two different SBRT/SABR treatment schedules for medically inoperable patients with Stage I peripheral NSCLC, in which patients were randomized to receive 34 Gy in a single fraction or 48 Gy in four daily consecutive fractions of 12 Gy per fraction. This protocol is now closed to accrual, and final results are pending; preliminary data suggest that 34 Gy may be more efficacious with respect to local control and equivalent in toxicity profile, and a comparison of 34 Gy in one fraction to 54 Gy in three fractions is planned.

Primary Liver Cancer

In a phase I feasibility trial at Indiana University, patients with hepatocellular carcinoma (HCC) were treated with dose escalation from 36 Gy in three fractions to a total dose of 48 Gy in three fractions if dose-limiting toxicities were not suffered (30). Patients were eligible for this trial if they had Child–Pugh score A or B, a solitary tumor <6 cm in size or three lesions with total diameter <6 cm and adequate liver function. Key normal tissue constraints were that one-third of the uninvolved liver received ≤10 Gy for Child–Pugh class A patients and that one-third of the uninvolved liver received ≤15 Gy for Child–Pugh class B patients. In this study, the dose was successfully escalated to patients with Child–Pugh class A to 48 Gy in three fractions without reaching dose-limiting toxicity. However, in patients with Child–Pugh class B cirrhosis, the maximum tolerated dose was 40 Gy in five fractions due to two patients suffering Grade 3 liver toxicity. With long-term follow-up, the Indiana experience found positive rates of 2-year local control of 90% among the treated population. There were no long-term grade 3 or higher non-hematologic toxicities and 20% of patients were found to experience progression in the Child–Pugh score at 3 months (31).

A second key phase I/II trial was performed by Princess Margaret University and the University of Toronto (32). In this trial, patients with Child–Pugh score A with no more than five liver tumors with a maximal dimension of 15 cm were enrolled. Patients in this trial were treated to a dose of 30 to 54 Gy in six fractions, with the maximum effective irradiated liver volume of 60%. No patients in this trial suffered classic radiation-induced liver disease (RILD) or dose-limiting toxicity, with a decline in Child–Pugh score at 3 months occurring in 29% of the cohort. Like the Indiana experience, the local tumor control was excellent at 87% at 1 year. These two trials provide data for the efficacy for SBRT/SABR in the setting of well-controlled and designed clinical trials.

While these studies were limited to patients with preserved to mildly elevated liver function, there is evidence for the treatment of patients with Child–Pugh B7 or B8 with SBRT/SABR as well. The Princess Margaret group performed a prospective study with patients having Child–Pugh B7 or 8 with less than 10 cm of HCC tumor (33). Patients received a median dose of 30 Gy in five fractions; however, as expected with their more fragile liver function, 63% of the cohort had a decline in their Child–Pugh score at 3 months. Sorafenib is a tyrosine kinase inhibitor that was used in patients with advanced HCC, showing an improvement in overall survival compared to placebo. Currently, an RTOG trial 1112 is enrolling patients with advanced stage HCC to daily sorafenib versus SBRT/SABR alone followed by daily sorafenib. The primary endpoint of the trial is overall survival with secondary endpoints, evaluating the safety profile of SBRT/SABR plus sorafenib. This trial will potentially further expand the utilization of SBRT/SABR patients with advanced HCC.

Prostate Cancer

Recent analysis and review of clinical outcomes, primarily after treatment with brachytherapy, argue for a low α/β for prostate cancer of ~1.5 (34–38). Several recent clinical trials were designed with the explicit assumption of this low α/β ratio by utilizing more hypofractionated regimens in comparison with conventional schedules (39–44). Altogether, these trials show that the treatment can be delivered much more quickly and conveniently using equivalent effective doses with hypofractionation without compromising PSA control or significant toxicity so long as careful technique and normal tissue dose tolerance is respected. Building upon this premise, even more abbreviated hypofractionated approaches (6.5–10 Gy per fraction) have been investigated.

The Virginia Mason Medical Center published one of the first experiences with prostate SBRT/SABR, describing their results from a phase I/II trial delivering 33.5 Gy in five fractions (45). Median follow-up was 41 months. There was one acute grade 3 urinary toxicity (urinary retention requiring catheterization) and no acute grades 4–5 toxicities. Late grade 2 GU and GI toxicity rates were 20 and 7.5%, respectively, with no grade 3 or higher toxicities. Four-year actuarial freedom from biochemical recurrence (FFBR) was 90%.

The feasibility of increasing SBRT/SABR dose was investigated at Stanford University in a phase II trial (46). 36.25 Gy in five fractions of 7.25 Gy was delivered to the prostate plus a 3–5 mm margin. In 67 patients with low to intermediate-risk features (Gleason score 3 + 3 or 3 + 4, PSA ≤10 ng/mL, and clinical stage ≤T2b), there were no grade 4 or higher toxicities. Late grades 2 and 3 GU toxicity rates were 5 and 3.5%, respectively. Late grade 2 GI toxicity was 2% with no grade 3 or higher toxicities seen. Patients who received QOD treatments were less likely to experience grades

1–2 GI and GU toxicities than those who received QD treatments. Four-year PSA relapse-free survival was 94%.

The largest prospective study of prostate SBRT/SABR is from the Winthrop University Hospital (47). A total of 304 patients (69% low-risk, 27% intermediate-risk, 4% high-risk) were treated. The first 50 patients received 35 Gy in five fractions of 7 Gy with the subsequent 254 patients receiving 36.25 Gy in five fractions of 7.25 Gy. Lower-dose patients had a median follow-up of 30 months and the higher-dose patients had a median follow-up of 17 months. There were no grades 3–4 acute complications. Late grade 2 GU and GI toxicity was 14 and 7%, respectively. Five patients had late grade 3 GU toxicity with no late grades 4–5 toxicities. For patients who were potent prior to treatment, 75% stated that they remained sexually potent. Actuarial 5-year biochemical recurrence-free survival was 97% for low-risk, 90.7% for intermediate-risk, and 74.1% for high-risk patients.

A recent pooled analysis of 1100 patients from prospective phase II trials using SBRT/SABR for the treatment of prostate cancer in which a median dose of 36.25 Gy was delivered in four to five fractions demonstrated a 93% 5-year biochemical relapse-free survival rate for all patients (95% for low-risk, 84% for intermediate-risk, and 81% for high-risk) with favorable long-term patient reported outcomes with respect to urinary and bowel functions (48, 49).

Compared to the prior studies using similar dose fractionation regimens, a multicenter phase I/II trial investigation using significantly higher doses was performed (50). In the phase I portion, 45 patients, in 3 cohorts of 15, were treated with 45, 47.5, and 50 Gy in five equal fractions, respectively. No dose-limiting toxicities (grades 3–5) occurred within the first 90 days post-treatment. GI grade ≥2 and grade ≥3 toxicity occurred in 18 and 2%, respectively, and GU grade ≥2 and grade ≥3 toxicity occurred in 31 and 4%, respectively. Initial PSA control was 100%. These encouraging results led to the further enrollment on the phase II trial at the 50 Gy dose level studying late toxicity. An additional 46 patients were enrolled for a total of 91 (64% intermediate-risk and 36% low-risk). With a median follow-up of 42 months, PSA control remained at 99% (51). Ultimately, dose escalation to treat prostate cancer is limited by toxicity to the bladder or rectum. As reported in an update by Kim et al., the toxicity profile was favorable in the initial phase I results; however, in the phase II portion, the profile changed and five patients (10.6%) developed high-grade rectal toxicity (52).

HYPOFRACTIONATION WITH PROTON AND HEAVIER ION THERAPY

Background

Protons and other heavier charged particles offer some theoretical advantages over photons that can be utilized in hypofractionated dose delivery regimes.

As charged particles move in tissue, they deposit energy (dose) and cause ionization of tissue and create highly reactive free radicals. This has two important consequences. One is that after traversing tissue for a certain depth, they impart all of their initial kinetic energy and they stop moving. In other words, charged particles have a finite range in tissue, unlike a photon beam, that can only be exponentially attenuated but not stopped. The second consequence is that these free radicals cause biological damage. As more dose is deposited, more ionization occurs generating more free radicals, leading to a higher biological damage. The amount of absorbed dose per unit track length [called the linear energy transfer (LET) to tissue] increases as they lose speed along their paths. At first, very gradually in the tissue entrance region where particles are moving with speed close to the speed of light, but then very rapidly toward the end of their range where they substantially slow down so that a peak of deposited dose occurs at a depth proportional to the initial kinetic energy of the charged particle. Beyond this peak, no further significant dose is deposited. This scientific phenomenon was described and experimentally discovered by William Bragg at that time (53). As mentioned above, the range in tissue is proportional to initial kinetic energy of the particles. Hence, particle accelerators are needed to get the initial speed high enough so they reach even deep seeded tumors. In 1930, the American physicist Ernest O. Lawrence and his associates were the first to invent a cyclotron to accelerate protons. Since then, the technology has substantially improved and many proton cyclotrons and particle synchrotrons have been built to reach energies high enough for cancer treatment applications.

The idea to use proton and charged particle beams for cancer treatment came in 1946, when Wilson wrote his seminal paper (54). He realized that the fundamental difference in dose as a function of depth (depth–dose curve) of proton and heavy-charged particles, in comparison with photons, can be used to spare healthy tissue at the tissue entrance region where smaller amount of energy is released, but to achieve high tumor control at the peak, where much larger amount of the beam energy is being released. Also healthy tissue can be spared beyond where no protons are present since they already stopped at the peak region. The first proton patient was treated in 1954 at Lawrence Berkeley National Laboratory (LBNL) nuclear research facility and the first clinical center to use proton-based therapy was based at Loma-Linda and initially used to treat pituitary hormone suppression in metastatic breast carcinoma.

Ions heavier than a proton were first used for cancer therapy in the 1970s after Cornelius Tobias hypothesized that they could provide additional clinical advantages (55). Heavier ions have reduced lateral scattering compared with protons. This translates into faster lateral dose fall off (called sharper lateral penumbra) leading to a better ability to conform dose to the target region; hence, higher therapeutic doses can be prescribed to tumors located in near proximity to radiosensitive organs at risk. Another huge advantage of heavier ions is that they interact with tissue they create a small amount of radioactive positron emitting isotopes that can be imaged in PET/CT scanners providing direct *in vivo* information about the spatial distribution of delivered dose. The higher ionization density created by heavier ions leads to their increased radiobiological effects on tissues. Initial radiobiology research and clinical treatment used beams of nuclei of helium, carbon, neon, silicon, and argon atoms; however, most of the clinical experiences with ions heavier than protons involves carbon, because this particle has approximately the same biological

potency as photons or protons in the tissue entrance region and three to four times larger potency in the Bragg peak region even if the same dose was absorbed (56).

Radiobiological Modeling of Hypofractionation with Protons and Heavier Ions

A generalized statement is that the higher the electric charge of the charged particle, the higher the energy loss per unit track length (quadratically higher) while penetrating tissue. Therefore, the LET is 36 times higher for carbon ions compared with protons when they move with the same speed (57). The increased LET has a consequence of increased biological potency expressed by relative biological effectiveness (RBE) that is defined as a quotient describing how many times more dose is needed to be delivered by photons than by charged particles to achieve the same biological endpoint. Clinical proton beams are of low LET with a RBE very close to that of high-energy photons. Recently, the International Commission on Radiation Units and Measurement (ICRU) proposed a RBE of 1.10 regardless of depth in tissue for proton therapy (58). The RBE of heavier ions to be clinically used is still under investigation (59–61).

As mentioned above, another difference between protons and carbon is that the RBE for carbon ions varies, with an increase in the Bragg peak region. This increase in RBE needs to be accounted for in treatment planning in order to have an appropriate prescribed dose (59, 62, 63). Calculation of the RBE is complex in that it depends on multiple factors, including the particle species, ion beam energy, dose, tissue type being irradiated, and biological endpoint. An accurate description of RBE dependence on dose is even more critical in the setting of hypofractionation (64–66). Recently, an excellent review of how variation of the RBE of ion beams in the setting of hypofractionated radiotherapy was presented by Friedrich et al. (60). In general, increasing the dose per fraction leads to lower RBE of the tumor and normal tissue (67). Data suggest that the RBE of the tumor decreases more slowly than the RBE of the normal tissue (68, 69). Therefore, hypofractionated heavy-ion treatment can be used to spare the organs at risk while escalating dose to the tumor.

Technical Considerations of Hypofractionation with Protons and Heavier Ions

Very tight prescription dose conformity to the target and very sharp dose fall off between tumor tissue and healthy tissue are essential for hypofractionation approach to succeed. As described in Section "Background," the physics of heavy-charged particle interactions with tissue theoretically offers superior solutions to achieve both of these goals with respect to photons. It is the beam delivery techniques that differ between photons and charged particles. Heavy-charged particle therapy physics and engineering has yet to develop the most advanced therapy, namely the equivalent of the volumetric photon arc therapy that would fully utilize the physics advantages of heavier charged particles.

Most particles centers are currently using scattering techniques with energy modulators, patient-specific collimators, and compensators to spread out protons and carbon ions both in longitudinal and lateral directions for treatment. Scattering beam delivery is easier for planning and quite robust in the treatment of a moving target. There are two major downsides of this technique. It requires the usage of patient and beam direction-specific collimators and compensators, which limits the number of irradiation directions that could practically be feasible. Another downside of this approach is that the dose to the preceding normal tissue in the entrance path is very difficult to modulate and conform to the target. It is, therefore, higher compared with modern beam scanning techniques, leading potentially to an increased risk in the development of secondary malignancies and other healthy tissue toxicities. Recently, more active beam delivery techniques, spot scanning or raster scanning, have been developed. Spot scanning is superior to passive beam delivery in terms of the improved dose profile and the reduced amount of material in the beam line, which decreases the leakage or radiations and neutrons (56). However, the capability to treat moving targets with scanning beams remains a challenge since longitudinal (in the direction of energy) beam modulation is still relatively slow. Approaches, such as target motion tracking, have been proposed (70) with systems capable of fast energy change of individual spots. Real-time detection of tumor and surrounding organ motion is vital for such a technique to succeed and remains a problem.

Another important consideration is how to deliver multidirectional particle beams. As mentioned above, highly conformal rapid dose fall off that is achieved with SABR photon therapy relies on the utilization of multiple beam angles. If the same is used with heavy-charged particles, both high-dose and intermediate-dose volume regions outside of the targeted area can substantially be reduced. Furthermore, with photons, the size of tumor targets (radius, r) to which high dose hypofractionation can be applied is limited to 2–3 centimeters in diameter. This is due to the fact that even for relatively small (Δr) region of high dose over spillage, the volume receiving the high dose grows quadratically with r and linearly with Δr. Doubling the target size "r" would require to reduce the high dose over spillage Δr by factor of 4 to keep the same volume of high dose over spillage. This is impossible to achieve with photons, but heavier charged particles have the Δr intrinsically much lower than photons both in front, beyond, and lateral to tumors.

Currently, many heavy-ion centers used fixed angle beams from different directions and tilt the patient's couch to provide different entrance angles, but multiple CT scans and treatment plans are necessary and the magnitude of patient tilt is limited. The use of a rotating gantry would allow for a beam delivery from any angle. Currently, the first heavy-ion rotating gantry is in use at the Heidelberg Ion Therapy Center (HIT) in Germany and another is currently under construction at the National Institute of Radiological Sciences (NIRS) in Japan. Further results from these centers should help to shed light on if the clinical advantages live up to the theoretical dosimetric advantages listed above.

Clinical Results of Hypofractionation with Protons and Heavier Ions

The higher conformal beam delivery with particles, compared to photons, allows for dose escalation to the tumor without exposing the adjacent organs at risk to higher doses (56, 71). Compared with

photon therapy, it is assumed that using particles results in a lower integral dose to normal tissues and a lower whole-body neutron exposure (72). To date, more hypofractionated approaches have been utilized in carbon-ion therapy compared to proton therapy, where more conventional fractionation regimens are employed (57). Additionally, most of the clinical data on proton and carbon therapy were collected from patients treated with passively scattered beams. More recently, active scanned proton and carbon-ion beams have been developed and used for clinical treatment.

Non-Small Cell Lung Cancer

For early stage I peripheral NSCLC tumors, local control rates are high for hypofractionated photons. The use of protons and carbon ions for the treatment of early stage tumors have been studied to avoid lung toxicity by sparing normal lung tissue while facilitating escalated dose to the tumor.

At Loma Linda University, medically inoperable patients with clinical T1–T2, N0, M0 NSCLC were treated with hypofractionated proton therapy (73). The dose delivered was escalated from 51 to 60 GyE, then to 70 GyE in 10 fractions over 2 weeks. Four-year local control for T1 tumors treated with either 60 or 70 GyE were 86 and 91%, respectively. Decreased control rates were seen for T2 tumors, 45 and 74%, respectively. Good outcomes were seen for patients with peripheral T1 tumors, with 4-year local control of 96%, disease-specific survival of 88%, and overall survival of 60%. No treatment-related adverse events of grade 2 or higher were observed.

Nihei et al. treated 37 inoperable patients with Stage I NSCLC (74). A total dose of 70 to 94 GyE was delivered in 20 fractions in 4–5 weeks. Two-year local control rates for Stages 1A and 1B tumors were 100 and 90%, respectively. Three patients (8%) experienced grade 3 pulmonary toxicity.

Hata et al. treated 21 patients (11 with Stage 1A and 10 with Stage 1B) NSCLC were treated with 50 GyE (three patients) or 60 GyE (18 patients) in 10 fractions over 15 days (75). Two-year local control rates were 100% for Stage 1A and 90% for Stage 1B, respectively. The overall and cause-specific survival rates in all patients were 74 and 86% at 2 years, respectively. No grade 3 or higher toxicities were observed.

The initial dose-escalation experience with treating Stage I NSCLC tumors with carbon ions was reported by Miyamoto et al. (76). The first stage phase I/II trial using 18 fractions over 6 weeks for 47 patients and the second one using nine fractions over 3 weeks for 34 patients were conducted by the dose-escalation method from 59.4 to 95.4 GyE in incremental steps of 10% and from 68.4 to 79.2 GyE, respectively. The local control rates in the first and second trials were 64 and 84%, respectively. The doses greater than 86.4 GyE at 18 fractions and 72 GyE at nine fractions achieved a local control of 90 and 95%, respectively. Grade 3 radiation pneumonitis occurred in three of 81 patients, but they fully recovered.

Building upon this experience, Miyamoto et al. further treated 29 Stage 1A and 21 Stage 1B patients who were treated with 72 GyE in nine fractions over 3 weeks (77). There was 1 in-field (Stage 1A) and 1 margin (Stage 1B) failure. Two- and 5-year actuarial local control rates were 98 and 95%, respectively. There was one grade 3 late skin reaction. A further phase II study using a regimen of a fixed dose of 52.8 GyE for T1 tumors and 60 GyE for T2 tumors in four fractions over 1 week was performed (78). The local control rate at 5 years for all patients was 90% (T1: 98%, T2: 80%). No grade 3 or higher toxicities were seen. Currently, a dose-escalation study for single-fraction treatment is underway at the NIRS, where initial results have shown higher local control and survival rates with minimal toxicity (79). A comparison of the outcomes of treating NSCLC with different modalities is shown in **Table 2**.

A recent meta-analysis compared particle beam therapies and SBRT/SABR versus CFRT (81). Five studies with proton therapy and three studies with carbon-ion therapy were included. Due to the limited number of patients available for analysis, no significant results were able to be obtained for locally advanced NSCLC; however, statistical comparisons were able to be made for stage I tumors. They summarized that CFRT had worse overall survival and disease-free survival compared to SBRT/SABR and particle beam therapies. The corrected pooled estimates for 5-year overall survival and DFS rates were 19 and 43% for CFRT, 42 and 63% for SBRT/SABR, 40 and 52% for protons, and 42 and 64%for carbon ions, respectively. Lastly, adverse events appeared to be reduced by using particle therapies compared to photon therapies.

These results document that high 2- to 5-year local control rates of Stage I NSCLC are being achieved by several methods. The carbon-ion therapy 5-year local control results are >95% with minimal toxicity. The 2-year proton local control rates are similar to those by SBRT/SABR but evidently with lesser risk of complications. Longer follow-up is required to assess the clinical efficacy of these three modalities.

Liver Cancer

Fukumitsu et al. treated 51 HCC patients with protons to a total dose of 66 GyE in 10 fractions (82). Patients were Child–Pugh class A or B and whose tumors were ≤10 cm (88% ≤5 cm), 39% of patients had multiple tumors and were ≥2 cm from porta hepatitis and GI tract. The 3- and 5-year local control rates were 95 and 88%, respectively. Alpha fetal protein levels dropped from 97 ng/mL before treatment to 16 ng/mL afterwards ($p < 0.0001$). Patients experienced only minor acute reactions of Grade 1 or less, and three patients experienced late sequelae of Grade 2 or higher.

Chiba et al. reported on their results using proton beam therapy to treat 162 patients with HCC with a total of 192 lesions (83). The median total dose delivered was 72 GyE in 16 fractions over 29 days. Eighty-three percentage of the lesions were <5 cm in size. The 5-year local control rate was 87%. Thirteen tumors locally recurred between 7 and 43 months (median, 21 months) after the completion of the irradiation. Maximal diameter of tumors that had recurred was median 4.7 cm ranging from 2.0 to 7.0 cm before irradiation. Five patients had late sequelae of grade 2 or higher.

Bush et al. performed a phase II trial in which 76 patients received 63 GyE in 15 fractions over 3 weeks (84). The mean tumor size was 5.5 cm. Fifteen patients (20%) experienced local treatment failure. Only three patients developed solitary local failure, the majority (36%) developed new lesions within the liver. No patients developed RILD.

TABLE 2 | Non-small cell lung cancer.

Reference	Radiation	Dose GyE	Dose/Fx GyE	Stage	*n*	Local control (%)	Late toxicity ≥grade 3
Timmerman et al. (10)	X	60 66	20 23	T1 T2	70	89 at 3 years	10% peripheral 27% central
Timmerman et al. (29)	X	54	18	T1–2a	59	98 at 3 years	15%
Baba et al. (80)	X	44–52	11–13	T1–2	124	80 at 3 years	3%
Bush et al. (73)	P	51–60	5.1–60	T1 T2	68	86 at 4 years 45 at 4 years	None
Nihei et al. (74)	P	70–94	3.5–4.9	T1a T1b	37	100 at 2 years 90 at 2 years	None 15%
Hata et al. (75)	P	50–60	5–6	T1a T1b	21	100 at 2 years 90 at 2 years	None
Miyamoto et al. (76)	C	59.4–95.4 68.4–79.2	3.3–5.3 7.6–8.8	T1–2	81	76 at 5 years	None
Miyamoto et al. (77)	C	72	8	T1a–b	50	95 at 5 years	2%
Miyamoto et al. (78)	C	52.8 60	13.2 15	T1 T2	79	98 at 5 years 80 at 5 years	None

X, photon therapy; P, proton therapy; C, carbon-ion therapy; Fx, fraction; GyE, gray or gray equivalent; n, patient number.

Komatsu et al. published a retrospective analysis of 343 patients treated with either protons (242 patients) or carbon ions (101 patients) (85). Eight protocols for proton therapy (52.8–84 GyE in 4–38 fractions) and four protocols for carbon-ion therapy (52.8–76 GyE in 4–20 fractions) were used during the study period. The 5-year local control rate was 90% for proton and 93% for carbon ions. Univariate analysis identified tumor size as an independent risk factor for local recurrence. Grade ≥3 late toxicities were observed in eight patients on proton therapy and in four patients on carbon-ion therapy, and 4 of 12 patients were diagnosed with RILD. No patients died of treatment-related toxicity.

Kato et al. presented results of 24 patients treated on a dose-escalation trial (49.5–79.5 GyE in dose increments of 10% in a fixed 15 fraction setting within 5 weeks) (86). The overall local control rate was 92, 81, and 81% at 1, 3, and 5 years, respectively. No local failures were seen at a dose level of 72 GyE or higher. Except for one early skin reaction, no Grade 3 or worse adverse effects occurred at any dose level from 49.5 to 79.5 GyE. More recently, a four-fraction regimen has been investigated at NIRS. Sixty-nine patients have been treated using this regimen with a reported 5-year local control rate of 81% (79). An accelerated schedule of two fractions in 2 days is being studied further. Another dose-escalation trial is currently underway by Combs et al. at the HIT (87). The Prometheus trial escalates the dose from 40 to 56 GyE in four fractions (87).

A comparison of the outcomes of treating HCC with different modalities is shown in **Table 3**. At present, the clinical results of protons appear to be equivalent to those of carbon therapy. It will be important to determine the long-term functional status of the liver following dose escalation.

Prostate Cancer

Proton ± photon therapy was used to treat 1255 patients at Loma Linda University (88). The patients were stage I–IIIA who had no prior surgery or hormone therapy. Radiation dose was 74 GyE in 37 fractions for patients receiving protons only. The 5- and 10-year biochemical no evidence of disease (bNED) was 75 and 73%, respectively. The rate of grades 3–4 rectal and bladder complications was 1%.

The first phase III clinical trial of photons versus protons was conducted by Shipley et al. (89). A total of 189 patients with stages T3–T4 were initially treated with 50.4 Gy by photons to the prostate and pelvic nodes followed by either a photon boost to 67.2 Gy or a proton boost to 75.6 GyE. Patients did not receive any concomitant or adjuvant hormone therapy. The local control at 5 and 8 years for the photon arm were 80 and 60%, respectively, and for the proton arm were 92 and 77%, respectively. Complications in the photon and proton arms at 8 years were as follows: persistent rectal bleeding 2 versus 9%; urethral stricture 2 versus 4%, and hematuria 2 versus 2%.

A phase III trial was performed at MGH and Loma Linda University, which randomly assigned patients with T1b–T2b and PSA≤15 ng/mL to treatment by proton beams to the prostate to 19.8 or 28.8 GyE followed by 50.4 Gy with photons to the pelvis (90). Dose fractionation was 1.8 Gy/fraction for the entire regimen. A total of 393 men were randomized. The 10-year ASTRO biochemical failure rates were 32% for conventional dose and 17% for high-dose radiation therapy. Dose escalation also was shown to benefit patients with low-risk disease. Two percentage of patients in both arms experienced late grade ≥3 genitourinary toxicity, and 1% of patients in the high-dose arm experienced late grade ≥3 gastrointestinal toxicity.

Recently, prospective proton-only trials have been performed at the University of Florida (91). A total of 211 patients were enrolled and received 78 GyE in 39 fractions for low-risk disease ($N = 89$), dose escalation from 78 to 82 GyE for intermediate-risk disease ($N = 82$), and 78 GyE with concomitant docetaxel followed by androgen deprivation for high-risk disease ($N = 40$). With early follow-up of 2 years, progression-free survival was 99% for the entire population (100% for low-risk, 99% for

TABLE 3 | Hepatocellular carcinoma.

Reference	Radiation	Dose GyE	Dose/Fx GyE	Stage	Size (Ave)	*n*	Local control (%)	Late toxicity ≥grade 3
Andolino et al. (31)	X	36–48 40	13–16 8	CPC-A CPC-B	3.2 cm	36 24	90 at 2 years	35% heme/liver
Bujold et al. (32)	X	24–54	4–9	CPC-A	7.2 cm	102	87 at 1 year	30% (7 G5)
Culleton et al. (33)	X	30	5	CPC-B CPC-C	5.1 cm	28 1	55 at 1 year	63% ↑CP ≥2
Fukumitsu et al. (82)	P	66	6.6	CPC-A CPC-B	2.8 cm	51	88 at 5 years	1 Lung
Chiba et al. (83)	P	72	4.5	CPC-A–C	3.8 cm	162	87 at 5 years	3% ≥G2
Bush et al. (84)	P	63	4.2	CPC-A–C	5.5 cm	76	80 (2–60 m)	None
Komatsu et al. (85)	P C	52.8–84 52.8–76	2–13.2 3.8–13.2	CPC-A–C	<5 cm 74%	242 101	90 at 5 years 93 at 5 years	3% 4%
Kato et al. (86)	C	49.5–79.5	3.3–5.3	CPC-A–B	5 cm	24	81 at 5 years	25% ↑CP ≥2

X, photon therapy; P, proton therapy; C, carbon-ion therapy; Fx, fraction; GyE, gray or gray equivalent; n, patient number; CPC, Child–Pugh Class.

intermediate-risk and 94% for high-risk). Only 1.9% Grade 3 GU symptoms and <0.5% Grade 3 GI toxicities were observed.

Several carbon-ion dose-escalation studies have been performed at the NIRS since 1995. These early trials were summarized by Tsuji et al. (92). The two previous Phase I/II studies performed dose escalation from the initial dose of 54.0 GyE in 20 fractions to 72.0 GyE in 20 fractions in 10% increments followed by fixed radiation dose of 66.0 GyE in 20 fractions. A total of 201 patients were analyzed at the 66.0 GyE dose level with a median follow-up of 30 months. The bNED for the low-risk patients was 100% and for the high-risk patients was 81% at 5 years. In the first Phase I/II study, 6 out of 14 patients treated with a high target dose (72.0 GyE) developed Grade 3 morbidities of the rectum or genitourinary system. At the 66.0-GyE dose level, no Grade 3 or higher toxicities were observed in either the rectum or genitourinary system, and the incidences of Grade 2 rectum or genitourinary morbidity were only 1.0 and 6.0%, respectively.

More recently, a total dose of 57.6 GyE in 16 fractions has been explored (93). A total of 664 patients (250 patients at 66.0 GyE in 20 fractions; 216 63.0 GyE in 20 fractions; 198 in 57.6 GyE in 16 fractions) with at least 1-year follow-up were analyzed in regard to late radiation toxicity. The 5-year biochemical relapse-free survival was 90% for the entire group. The 5-year BRF of patients treated with 16 fractions was 89% compared with 90% for patients treated with 20 fractions. Per risk group, the 5-year BRF was 90, 97, and 88% for low-, intermediate, and high-risk patients (94). No grade 3 or higher GI toxicity was seen in any of the groups and only one grade 3 GU toxicity was seen in the 20 fraction regimen and no grade 3 or higher GU adverse effects were seen in the 16 fraction regimen. Lately, patients have been treated with the scanning beam in the new NIRS facility with 12 fractions in 3 weeks (79). Also the HIT has conducted a randomized phase II trial using protons or carbon ions treating with a 66 GyE in 20 fractions and the results are still pending (95).

A comparison of the outcomes of treating prostate cancer with different modalities is shown in **Table 4**.

Cost-Effectiveness of Hypofractionated Therapy

Due to the aging of the population in industrialized countries, the number of patients who develop malignancies is expected to increase. With more patients receiving cancer-directed therapies, this is predicted to become a major burden for health care systems (96). There has been increasing pressure within the medical community to identify and promote more cost-effective treatment modalities. A significant percentage of the cost of cancer therapy is due to drug therapies (97). This highlights the growing need for a value-based system that considers cost-effectiveness in determining cancer drug prices. There is a lack of correlation between drug efficacy and cost, with prices remaining high despite the entrance of competitive agents to the market (98).

The incremental cost-effectiveness ratio (ICER) is a statistic used in cost-effectiveness analysis to summarize the cost-effectiveness of a health care intervention. It is defined by the difference in cost between two possible interventions, divided by the difference in their effect. It represents the average incremental cost associated with one additional unit of the measure of effect.

Using an ICER approach, actually, radiation therapy is an extremely cost-effective cancer therapeutic option in comparison to systemic modalities. For example, in using improvement in 2-year overall survival as the heath outcome effect, the ICER is ~$3,800 for bevacizumab for the treatment of NSCLC (99), ~$4,800 for pemetrexed for the treatment of NSCLC (100), ~$3,700 for imatinib for the treatment of chronic myeloid leukemia (101), compared to a significantly reduced cost for carbon-ion therapy for recurrent colorectal adenocarcinoma (102).

Cost-effective analysis of various hypofractionated regimens for different disease sites has been performed. For patients with stage I NSCLC, Shah et al. analyzed the cost-effectiveness of SBRT/SABR versus surgical resection (103). The mean costs and quality-adjusted life expectancies for SBRT/SABR, wedge resection, and lobectomy were calculated. For patients determined to be marginally operable, SBRT/SABR was determined to be the most cost-effective strategy. Mitera et al. compared conventional versus SBRT/SABR for medically inoperable stage I NSCLC (104). Overall survival

TABLE 4 | Prostate cancer.

Reference	Radiation	Dose GyE	Dose/Fx GyE	Stage	*n*	Local control or bNED%	Late toxicity ≥grade 3
Madsen et al. (45)	X	33.5	6.7	≤T2a PSA≤10 GS≤6	40	bNED 90% at 4 years	G2 GU 20% G2 GI 7.5%
King et al. (46)	X	36.25	7.25	≤T2b PSA≤10 GS≤7 (3 + 4)	67	bNED 94% at 4 years	GU 3.5% GI 0%
Katz et al. (47)	X	35–36.25	7–7.25	69% low 27% intermediate 4% high	304	bNED 97% at 5 years bNED 91% at 5 years bNED 74% at 5 years	GU 2.5% G2 GI 7%
Boike et al. (50) and Kim et al. (52)	X	45–50 50	9–10 10	≤T2b PSA ≤20 GS ≤7	45 46	bNED 99% at 3.5 years	GU 5.5% GI 6.6%
Slater et al. (88)	P ± X	74	2	Low, intermediate, high	1225	bNED 75% at 5 years	GU, GI 1%
Shipley et al. (89)	X + P X	67.2 75.6	1.9	T3-4, N0-N2, M0	96 93	LC 81% at 5 years LC 92% at 5 years	GU, GI 2% GU 4%; GI 9%
Zietman et al. (90)	X + P	70.2 79.2	1.8 1.8	≤T2b PSA ≤15 GS any	197 196	bNED 61% at 5 years bNED 80% at 5 years	GU 2%; GI 1% GU 1%; GI 1%
Mendenhall et al. (91)	P	78 78–82 78	2 2 2	Low Intermediate High	89 82 40	bNED 100% at 2 years bNED 99% at 2 years bNED 94% at 2 years	GU 1.9% GI < 0.5%
Tsuji et al. (92)	C	54–72 66	2.7–3.6 3.3	≤T3 PSA any GS any	94 201	bNED 92% at 5 years	Six points at 72 GyE None at 66 GyE
Okata et al. (93)	C	63 57.6	3.15 3.6	≤T3 PSA any GS any	216 198	bNED 90% at 5 years bNED 89% at 5 years	1 pt GU at 63 GyE

X, photon therapy; P, proton therapy; C, carbon-ion therapy; Fx, fraction; GyE, gray or gray equivalent; n, patient number; PSA, prostate-specific antigen; bNED, biochemical no evidence of disease; LC, local control; GU, genitourinary; GI, gastrointestinal.

was the primary effectiveness end point used in their calculations. ICER per life-year gained for SBRT/SABR versus CFRT was $1,120, favoring SBRT/SABR as a cost-effective treatment.

For the treatment of localized prostate cancer, comparisons of the costs associated with IMRT versus SBRT/SABR were determined. Delivery of SBRT/SABR is technically more labor-intensive then IMRT; however, treatment is completed in only five fractions compared to 39–48 fractions required for IMRT. A Markov decision analysis model showed that the mean cost of SBRT/SABR is $22,152 versus $35,431 for IMRT (105). A separate analysis by Sher et al. confirmed an ICER favoring SBRT/SABR compared to IMRT (106). Treatment efficacy, rectal toxicity and impotence, and the potential for unseen late effects due to SBRT/SABR were the critical parameters affecting the outcome of the model, highlighting the importance of longer term follow-up to better determine these variables.

Recent criticisms in regard to the use of particle therapy for the treatment of certain malignancies have been raised (107, 108). The investment costs are considerably higher than those for conventional photon therapy (109). Specifically, comparative evidence is lacking on the safety and efficacy of particle therapy versus alternative therapies.

Grutters et al. utilized Markov models to compare treatment with carbon ions, protons, CFRT, and SBRT/SABR for the treatment of patients with inoperable stage I NSCLC (110). Carbon-ion therapy yielded the most quality-adjusted life years per patient of 2.67. Carbon-ion therapy had the highest probability of being cost-effective at 52%, followed by SBRT/SABR at 47%, proton therapy at 2%, and CFRT at 0%.

Comparison of the cost-effectiveness of IMRT, SBRT/SABR, and protons for the treatment of localized prostate cancer were reported by Parthan et al. (111). They found that assuming that each treatment modality results in equivalent long-term efficacy, SBRT/SABR is more cost-effective in improving quality-adjusted survival compared to IMRT or proton therapy. With longer-term follow-up data, it will be interesting to see how carbon ions would compare in the above analysis. The early efficacy and toxicity suggest that it would compare favorably to SBRT/SABR for treating prostate cancer.

The role of cost-effectiveness for particle therapy was excellently reviewed by Pijls-Johannesma et al. (112). In summary, adequate reimbursement is necessary to support such innovative yet costly treatments. Further incorporation of hypofractionated regimens for particle therapy would allow for a higher capacity of patients treated. Currently, the billing model within the United States reimburses per fraction delivered, therefore, motivating more prolonged treatment regimens to be employed. Protons currently share this same model, thereby limiting its utilization.

By potentially promoting reimbursement by treatment course for heavy-ion therapy, promotion of higher capacity by treating more patients with fewer fractions could be adopted.

DISCUSSION AND FUTURE CONSIDERATIONS

As shown in this review, using more hypofractionated regimens for photon therapy have resulted in high control rates with minimal normal tissue toxicity. Stereotactic ablative approaches with X-rays have already become the standard of care for patients with inoperative stage I NSCLC. Promising early clinical results highlight the trend to utilize more hypofractionated treatments for other disease sites.

The potential for the further improvement in treatment outcomes by using particle therapy is also generating excitement. Carbon ions, in particular, are attractive due to their superior physical dose distribution, higher RBE, and increased effectiveness in hypoxic tumors, which is expected to generate clinical gains. A systematic approach has been carried out at NIRS and GSI/HIT to determine the optimal dose fractionation regimens for various disease sites, resulting in the majority of tumors being treated with hypofractionated schemes.

Comparing data for different particle treatments is challenging due to different dose regimens, fractionated regimens, and different RBE calculation for carbon ions in different centers. It has been proposed that in the future more prospective clinical trials are necessary to confirm the theoretical benefit of carbon ions. The studies should focus on treatment-related toxicity in addition to local tumor control and survival. However, there is ongoing debate on the necessity to conduct randomized trials before implementing new technologies (57, 112–114). Some argue that based on the principles of equipoise between photons and particle therapy, randomization of patients between the two arms could be unethical (67). Further discussion on these issues should be addressed in future international working groups. In addition, more research into the costs and the optimal way in which to define reimbursement levels for carbon-ion therapy are critical for more widespread implementation.

CONCLUSION

With advances in imaging and treatment delivery techniques, the use of more hypofractionated regimens has become more widely employed. Hypofractionated treatment approaches are highly efficacious and safe for the treatment of certain tumors, more cost-effective compared to conventional fractionated approaches, are more efficient use of clinical resources, and also are more convenient for the patient by greatly reducing their treatment course. By utilizing hypofractionated regimens, the potential clinical advantage of particle therapy could be achieved.

ACKNOWLEDGMENTS

We would like to thank Zabi Wardak and Michael Folkert for their assistance in data collection.

FUNDING

This work was supported by funding from the National Institutes of Health (1P20 CA183639-01A1).

REFERENCES

1. Dessauer F. Beiträge zur Bestrahlung tiefliegender Prozesse. *Med Klin* (1905) **1**:526–9.
2. Regaud C, Blanc J. Actions des rayons X sur les diverses generations de la lignée spermatique: extrème sensibilié des spermatogonies à ces rayons. *Compt Rend Soc Biol* (1906) **61**:163–5.
3. Bergonie J, Tribondeau L. Interpretation de quelques resultats de la radiotherapie et essai de fixaation d'une technique rationelle. *Compt Rend Acad Sci Paris* (1906) **143**:983–5.
4. Seitz L, Wintz H. *Unsere Methode der Rontgen-Tiefentheapie und ihre Erfolge*. Berlin: Urban und Schwarzenberg (1920).
5. Coutard H. Roentgen therapy of epitheliomas of the tonsillar region, hypopharynx and larynx from 1920 to 1926*. *AJR Am J Roentgenol* (1932) **28**:313–31.
6. Coutard H. Note preliminaire sur la radiographic du larynx normal et du larynx cancereux. *J Belge Radiol* (1924) **13**:487–90.
7. Leksell L. The stereotaxic method and radiosurgery of the brain. *Acta Chir Scand* (1951) **102**(4):316–9.
8. Blomgren H, Lax I, Naslund I, Svanstrom R. Stereotactic high dose fraction radiation therapy of extracranial tumors using an accelerator. Clinical experience of the first thirty-one patients. *Acta Oncol* (1995) **34**(6):861–70. doi:10.3109/02841869509127197
9. Uematsu M, Shioda A, Tahara K, Fukui T, Yamamoto F, Tsumatori G, et al. Focal, high dose, and fractionated modified stereotactic radiation therapy for lung carcinoma patients: a preliminary experience. *Cancer* (1998) **82**(6):1062–70. doi:10.1002/(SICI)1097-0142(19980315)82:6<1062::AID-CNCR8>3.0.CO;2-G
10. Timmerman R, Papiez L, McGarry R, Likes L, DesRosiers C, Frost S, et al. Extracranial stereotactic radioablation: results of a phase I study in medically inoperable stage I non-small cell lung cancer. *Chest* (2003) **124**(5):1946–55. doi:10.1378/chest.124.5.1946
11. Potters L, Steinberg M, Rose C, Timmerman R, Ryu S, Hevezi JM, et al. American Society for Therapeutic Radiology and Oncology and American College of Radiology practice guideline for the performance of stereotactic body radiation therapy. *Int J Radiat Oncol Biol Phys* (2004) **60**(4):1026–32. doi:10.1016/j.ijrobp.2004.07.701
12. Loo BW Jr, Chang JY, Dawson LA, Kavanagh BD, Koong AC, Senan S, et al. Stereotactic ablative radiotherapy: what's in a name? *Pract Radiat Oncol* (2011) **1**(1):38–9. doi:10.1016/j.prro.2010.07.001
13. Joiner M, Kogel A. *Basic Clinical Radiobiology*. London: Hodder Arnold (2009).
14. Lee SP, Leu MY, Smathers JB, McBride WH, Parker RG, Withers HR. Biologically effective dose distribution based on the linear quadratic model and its clinical relevance. *Int J Radiat Oncol Biol Phys* (1995) **33**(2):375–89. doi:10.1016/0360-3016(95)00162-R
15. Wang JZ, Huang Z, Lo SS, Yuh WT, Mayr NA. A generalized linear-quadratic model for radiosurgery, stereotactic body radiation therapy, and high-dose rate brachytherapy. *Sci Transl Med* (2010) **2**(39):39ra48. doi:10.1126/scitranslmed.3000864
16. Astrahan M. Some implications of linear-quadratic-linear radiation dose-response with regard to hypofractionation. *Med Phys* (2008) **35**(9):4161–72. doi:10.1118/1.2962611
17. Guerrero M, Li XA. Extending the linear-quadratic model for large fraction doses pertinent to stereotactic radiotherapy. *Phys Med Biol* (2004) **49**(20):4825–35. doi:10.1088/0031-9155/49/20/012
18. Kirkpatrick JP, Meyer JJ, Marks LB. The linear-quadratic model is inappropriate to model high dose per fraction effects in radiosurgery. *Semin Radiat Oncol* (2008) **18**(4):240–3. doi:10.1016/j.semradonc.2008.04.005

19. Park C, Papiez L, Zhang S, Story M, Timmerman RD. Universal survival curve and single fraction equivalent dose: useful tools in understanding potency of ablative radiotherapy. *Int J Radiat Oncol Biol Phys* (2008) **70**(3):847–52. doi:10.1016/j.ijrobp.2007.10.059
20. Story M, Kodym R, Saha D. Exploring the possibility of unique molecular, biological, and tissue effects with hypofractionated radiotherapy. *Semin Radiat Oncol* (2008) **18**(4):244–8. doi:10.1016/j.semradonc.2008.04.006
21. Wolbarst AB, Chin LM, Svensson GK. Optimization of radiation therapy: integral-response of a model biological system. *Int J Radiat Oncol Biol Phys* (1982) **8**(10):1761–9. doi:10.1016/0360-3016(82)90299-1
22. Yaes RJ, Kalend A. Local stem cell depletion model for radiation myelitis. *Int J Radiat Oncol Biol Phys* (1988) **14**(6):1247–59. doi:10.1016/0360-3016(88)90404-X
23. Timmerman RD, Kavanagh BD, Cho LC, Papiez L, Xing L. Stereotactic body radiation therapy in multiple organ sites. *J Clin Oncol* (2007) **25**(8):947–52. doi:10.1200/JCO.2006.09.7469
24. Cardinale RM, Wu Q, Benedict SH, Kavanagh BD, Bump E, Mohan R. Determining the optimal block margin on the planning target volume for extracranial stereotactic radiotherapy. *Int J Radiat Oncol Biol Phys* (1999) **45**(2):515–20. doi:10.1016/S0360-3016(99)00203-5
25. Papiez L, Timmerman R, DesRosiers C, Randall M. Extracranial stereotactic radioablation: physical principles. *Acta Oncol* (2003) **42**(8):882–94. doi:10.1080/02841860310013490
26. Perez CA, Pajak TF, Rubin P, Simpson JR, Mohiuddin M, Brady LW, et al. Long-term observations of the patterns of failure in patients with unresectable non-oat cell carcinoma of the lung treated with definitive radiotherapy. Report by the Radiation Therapy Oncology Group. *Cancer* (1987) **59**(11):1874–81. doi:10.1002/1097-0142(19870601)59:11<1874::AID-CNCR2820591106>3.0.CO;2-Z
27. Bradley J, Graham MV, Winter K, Purdy JA, Komaki R, Roa WH, et al. Toxicity and outcome results of RTOG 9311: a phase I-II dose-escalation study using three-dimensional conformal radiotherapy in patients with inoperable non-small-cell lung carcinoma. *Int J Radiat Oncol Biol Phys* (2005) **61**(2):318–28. doi:10.1016/j.ijrobp.2004.06.260
28. McGarry RC, Papiez L, Williams M, Whitford T, Timmerman RD. Stereotactic body radiation therapy of early-stage non-small-cell lung carcinoma: phase I study. *Int J Radiat Oncol Biol Phys* (2005) **63**(4):1010–5. doi:10.1016/j.ijrobp.2005.03.073
29. Timmerman R, Paulus R, Galvin J, Michalski J, Straube W, Bradley J, et al. Stereotactic body radiation therapy for inoperable early stage lung cancer. *JAMA* (2010) **303**(11):1070–6. doi:10.1001/jama.2010.261
30. Cardenes HR, Price TR, Perkins SM, Maluccio M, Kwo P, Breen TE, et al. Phase I feasibility trial of stereotactic body radiation therapy for primary hepatocellular carcinoma. *Clin Transl Oncol* (2010) **12**(3):218–25. doi:10.1007/s12094-010-0492-x
31. Andolino DL, Johnson CS, Maluccio M, Kwo P, Tector AJ, Zook J, et al. Stereotactic body radiotherapy for primary hepatocellular carcinoma. *Int J Radiat Oncol Biol Phys* (2011) **81**(4):e447–53. doi:10.1016/j.ijrobp.2011.04.011
32. Bujold A, Massey CA, Kim JJ, Brierley J, Cho C, Wong RK, et al. Sequential phase I and II trials of stereotactic body radiotherapy for locally advanced hepatocellular carcinoma. *J Clin Oncol* (2013) **31**(13):1631–9. doi:10.1200/JCO.2012.44.1659
33. Culleton S, Jiang H, Haddad CR, Kim J, Brierley J, Brade A, et al. Outcomes following definitive stereotactic body radiotherapy for patients with Child-Pugh B or C hepatocellular carcinoma. *Radiother Oncol* (2014) **111**(3):412–7. doi:10.1016/j.radonc.2014.05.002
34. Brenner DJ, Hall EJ. Fractionation and protraction for radiotherapy of prostate carcinoma. *Int J Radiat Oncol Biol Phys* (1999) **43**(5):1095–101. doi:10.1016/S0360-3016(98)00438-6
35. Brenner DJ, Martinez AA, Edmundson GK, Mitchell C, Thames HD, Armour EP. Direct evidence that prostate tumors show high sensitivity to fractionation (low alpha/beta ratio), similar to late-responding normal tissue. *Int J Radiat Oncol Biol Phys* (2002) **52**(1):6–13. doi:10.1016/S0360-3016(01)02664-5
36. Duchesne GM, Peters LJ. What is the alpha/beta ratio for prostate cancer? Rationale for hypofractionated high-dose-rate brachytherapy. *Int J Radiat Oncol Biol Phys* (1999) **44**(4):747–8.
37. Fowler J, Chappell R, Ritter M. Is alpha/beta for prostate tumors really low? *Int J Radiat Oncol Biol Phys* (2001) **50**(4):1021–31. doi:10.1016/S0360-3016(01)01607-8
38. Williams SG, Taylor JM, Liu N, Tra Y, Duchesne GM, Kestin LL, et al. Use of individual fraction size data from 3756 patients to directly determine the alpha/beta ratio of prostate cancer. *Int J Radiat Oncol Biol Phys* (2007) **68**(1):24–33. doi:10.1016/j.ijrobp.2006.12.036
39. Arcangeli G, Saracino B, Gomellini S, Petrongari MG, Arcangeli S, Sentinelli S, et al. A prospective phase III randomized trial of hypofractionation versus conventional fractionation in patients with high-risk prostate cancer. *Int J Radiat Oncol Biol Phys* (2010) **78**(1):11–8. doi:10.1016/j.ijrobp.2009.07.1691
40. Kuban DA, Nogueras-Gonzalez GM, Hamblin L, Lee AK, Choi S, Frank SJ, et al. Preliminary report of a randomized dose escalation trial for prostate cancer using hypofractionation. *Int J Radiat Oncol Biol Phys* (2010) **78**(3):S58–9. doi:10.1016/j.ijrobp.2010.07.170
41. Pollack A, Walker G, Horwitz EM, Price R, Feigenberg S, Konski AA, et al. Randomized trial of hypofractionated external-beam radiotherapy for prostate cancer. *J Clin Oncol* (2013) **31**(31):3860–8. doi:10.1200/JCO.2013.51.1972
42. Kupelian PA, Willoughby TR, Reddy CA, Klein EA, Mahadevan A. Hypofractionated intensity-modulated radiotherapy (70 Gy at 2.5 Gy per fraction) for localized prostate cancer: Cleveland clinic experience. *Int J Radiat Oncol Biol Phys* (2007) **68**(5):1424–30. doi:10.1016/j.ijrobp.2007.01.067
43. Lukka H, Hayter C, Julian JA, Warde P, Morris WJ, Gospodarowicz M, et al. Randomized trial comparing two fractionation schedules for patients with localized prostate cancer. *J Clin Oncol* (2005) **23**(25):6132–8. doi:10.1200/JCO.2005.06.153
44. Yeoh EE, Holloway RH, Fraser RJ, Botten RJ, Di Matteo AC, Butters J, et al. Hypofractionated versus conventionally fractionated radiation therapy for prostate carcinoma: updated results of a phase III randomized trial. *Int J Radiat Oncol Biol Phys* (2006) **66**(4):1072–83. doi:10.1016/j.ijrobp.2006.06.005
45. Madsen BL, Hsi RA, Pham HT, Fowler JF, Esagui L, Corman J. Stereotactic hypofractionated accurate radiotherapy of the prostate (SHARP), 33.5 Gy in five fractions for localized disease: first clinical trial results. *Int J Radiat Oncol Biol Phys* (2007) **67**(4):1099–105. doi:10.1016/j.ijrobp.2006.10.050
46. King CR, Brooks JD, Gill H, Presti JC Jr. Long-term outcomes from a prospective trial of stereotactic body radiotherapy for low-risk prostate cancer. *Int J Radiat Oncol Biol Phys* (2012) **82**(2):877–82. doi:10.1016/j.ijrobp.2010.11.054
47. Katz AJ, Santoro M, Diblasio F, Ashley R. Stereotactic body radiotherapy for localized prostate cancer: disease control and quality of life at 6 years. *Radiat Oncol* (2013) **8**:118. doi:10.1186/1748-717X-8-118
48. King CR, Collins S, Fuller D, Wang PC, Kupelian P, Steinberg M, et al. Health-related quality of life after stereotactic body radiation therapy for localized prostate cancer: results from a multi-institutional consortium of prospective trials. *Int J Radiat Oncol Biol Phys* (2013) **87**(5):939–45. doi:10.1016/j.ijrobp.2013.08.019
49. King CR, Freeman D, Kaplan I, Fuller D, Bolzicco G, Collins S, et al. Stereotactic body radiotherapy for localized prostate cancer: pooled analysis from a multi-institutional consortium of prospective phase II trials. *Radiother Oncol* (2013) **109**(2):217–21. doi:10.1016/j.radonc.2013.08.030
50. Boike TP, Lotan Y, Cho LC, Brindle J, DeRose P, Xie XJ, et al. Phase I dose-escalation study of stereotactic body radiation therapy for low- and intermediate-risk prostate cancer. *J Clin Oncol* (2011) **29**(15):2020–6. doi:10.1200/JCO.2010.31.4377
51. Kim DW, Straka C, Cho LC, Timmerman RD. Stereotactic body radiation therapy for prostate cancer: review of experience of a multicenter phase I/II dose-escalation study. *Front Oncol* (2014) **4**:319. doi:10.3389/fonc.2014.00319
52. Kim DW, Cho LC, Straka C, Christie A, Lotan Y, Pistenmaa D, et al. Predictors of rectal tolerance observed in a dose-escalated phase 1-2 trial of stereotactic body radiation therapy for prostate cancer. *Int J Radiat Oncol Biol Phys* (2014) **89**(3):509–17. doi:10.1016/j.ijrobp.2014.03.012
53. Brown A, Suit H. The centenary of the discovery of the Bragg peak. *Radiother Oncol* (2004) **73**(3):265–8. doi:10.1016/j.radonc.2004.09.008
54. Wilson RR. Radiological use of fast protons. *Radiology* (1946) **47**(5):487–91. doi:10.1148/47.5.487
55. Tobias CA, Lyman JT, Chatterjee A, Howard J, Maccabee HD, Raju MR, et al. Radiological physics characteristics of the extracted heavy ion beams of the Bevatron. *Science* (1971) **174**(4014):1131–4. doi:10.1126/science.174.4014.1131
56. Durante M, Loeffler JS. Charged particles in radiation oncology. *Nat Rev Clin Oncol* (2010) **7**(1):37–43. doi:10.1038/nrclinonc.2009.183

57. Suit H, DeLaney T, Goldberg S, Paganetti H, Clasie B, Gerweck L, et al. Proton vs carbon ion beams in the definitive radiation treatment of cancer patients. *Radiother Oncol* (2010) **95**(1):3–22. doi:10.1016/j.radonc.2010.01.015
58. Prescribing, recording, and reporting proton-beam therapy: contents. *J ICRU* (2007) **7**(2):210. doi:10.1093/jicru/ndm021
59. Elsasser T, Weyrather WK, Friedrich T, Durante M, Iancu G, Kramer M, et al. Quantification of the relative biological effectiveness for ion beam radiotherapy: direct experimental comparison of proton and carbon ion beams and a novel approach for treatment planning. *Int J Radiat Oncol Biol Phys* (2010) **78**(4):1177–83. doi:10.1016/j.ijrobp.2010.05.014
60. Friedrich T, Scholz U, Durante M, Scholz M. RBE of ion beams in hypofractionated radiotherapy (SBRT). *Phys Med* (2014) **30**(5):588–91. doi:10.1016/j.ejmp.2014.04.009
61. Grun R, Friedrich T, Kramer M, Zink K, Durante M, Engenhart-Cabillic R, et al. Assessment of potential advantages of relevant ions for particle therapy: a model based study. *Med Phys* (2015) **42**(2):1037–47. doi:10.1118/1.4905374
62. Inaniwa T, Furukawa T, Kase Y, Matsufuji N, Toshito T, Matsumoto Y, et al. Treatment planning for a scanned carbon beam with a modified microdosimetric kinetic model. *Phys Med Biol* (2010) **55**(22):6721–37. doi:10.1088/0031-9155/55/22/008
63. Kramer M, Scholz M. Treatment planning for heavy-ion radiotherapy: calculation and optimization of biologically effective dose. *Phys Med Biol* (2000) **45**(11):3319–30. doi:10.1088/0031-9155/45/11/313
64. Carabe-Fernandez A, Dale RG, Hopewell JW, Jones B, Paganetti H. Fractionation effects in particle radiotherapy: implications for hypo-fractionation regimes. *Phys Med Biol* (2010) **55**(19):5685–700. doi:10.1088/0031-9155/55/19/005
65. Carabe-Fernandez A, Dale RG, Jones B. The incorporation of the concept of minimum RBE (RbEmin) into the linear-quadratic model and the potential for improved radiobiological analysis of high-LET treatments. *Int J Radiat Biol* (2007) **83**(1):27–39. doi:10.1080/09553000601087176
66. Jones B, Underwood TS, Carabe-Fernandez A, Timlin C, Dale RG. Fast neutron relative biological effects and implications for charged particle therapy. *Br J Radiol* (2011) **84**(Spec No 1):S11–8. doi:10.1259/bjr/67509851
67. Schlaff CD, Krauze A, Belard A, O'Connell JJ, Camphausen KA. Bringing the heavy: carbon ion therapy in the radiobiological and clinical context. *Radiat Oncol* (2014) **9**(1):88. doi:10.1186/1748-717X-9-88
68. Ando K, Koike S, Uzawa A, Takai N, Fukawa T, Furusawa Y, et al. Biological gain of carbon-ion radiotherapy for the early response of tumor growth delay and against early response of skin reaction in mice. *J Radiat Res* (2005) **46**(1):51–7. doi:10.1269/jrr.46.51
69. Denekamp J, Waites T, Fowler JF. Predicting realistic RBE values for clinically relevant radiotherapy schedules. *Int J Radiat Biol* (1997) **71**(6):681–94. doi:10.1080/095530097143699
70. Schulz-Ertner D, Karger CP, Feuerhake A, Nikoghosyan A, Combs SE, Jakel O, et al. Effectiveness of carbon ion radiotherapy in the treatment of skull-base chordomas. *Int J Radiat Oncol Biol Phys* (2007) **68**(2):449–57. doi:10.1016/j.ijrobp.2006.12.059
71. Schulz-Ertner D, Tsujii H. Particle radiation therapy using proton and heavier ion beams. *J Clin Oncol* (2007) **25**(8):953–64. doi:10.1200/JCO.2006.09.7816
72. Uhl M, Herfarth K, Debus J. Comparing the use of protons and carbon ions for treatment. *Cancer J* (2014) **20**(6):433–9. doi:10.1097/PPO.0000000000000078
73. Bush DA, Cheek G, Zaheer S, Wallen J, Mirshahidi H, Katerelos A, et al. High-dose hypofractionated proton beam radiation therapy is safe and effective for central and peripheral early-stage non-small cell lung cancer: results of a 12-year experience at Loma Linda University Medical Center. *Int J Radiat Oncol Biol Phys* (2013) **86**(5):964–8. doi:10.1016/j.ijrobp.2013.05.002
74. Nihei K, Ogino T, Ishikura S, Nishimura H. High-dose proton beam therapy for stage I non-small-cell lung cancer. *Int J Radiat Oncol Biol Phys* (2006) **65**(1):107–11. doi:10.1016/j.ijrobp.2005.10.031
75. Hata M, Tokuuye K, Kagei K, Sugahara S, Nakayama H, Fukumitsu N, et al. Hypofractionated high-dose proton beam therapy for stage I non-small-cell lung cancer: preliminary results of a phase I/II clinical study. *Int J Radiat Oncol Biol Phys* (2007) **68**(3):786–93. doi:10.1016/j.ijrobp.2006.12.063
76. Miyamoto T, Yamamoto N, Nishimura H, Koto M, Tsujii H, Mizoe JE, et al. Carbon ion radiotherapy for stage I non-small cell lung cancer. *Radiother Oncol* (2003) **66**(2):127–40. doi:10.1016/S0167-8140(02)00367-5
77. Miyamoto T, Baba M, Yamamoto N, Koto M, Sugawara T, Yashiro T, et al. Curative treatment of stage I non-small-cell lung cancer with carbon ion beams using a hypofractionated regimen. *Int J Radiat Oncol Biol Phys* (2007) **67**(3):750–8. doi:10.1016/j.ijrobp.2006.10.006
78. Miyamoto T, Baba M, Sugane T, Nakajima M, Yashiro T, Kagei K, et al. Carbon ion radiotherapy for stage I non-small cell lung cancer using a regimen of four fractions during 1 week. *J Thorac Oncol* (2007) **2**(10):916–26. doi:10.1097/JTO.0b013e3181560a68
79. Kamada T, Tsujii H, Blakely EA, Debus J, De Neve W, Durante M, et al. Carbon ion radiotherapy in Japan: an assessment of 20 years of clinical experience. *Lancet Oncol* (2015) **16**(2):e93–100. doi:10.1016/S1470-2045(14)70412-7
80. Baba F, Shibamoto Y, Ogino H, Murata R, Sugie C, Iwata H, et al. Clinical outcomes of stereotactic body radiotherapy for stage I non-small cell lung cancer using different doses depending on tumor size. *Radiat Oncol* (2010) **5**:81. doi:10.1186/1748-717X-5-81
81. Grutters JP, Kessels AG, Pijls-Johannesma M, De Ruysscher D, Joore MA, Lambin P. Comparison of the effectiveness of radiotherapy with photons, protons and carbon-ions for non-small cell lung cancer: a meta-analysis. *Radiother Oncol* (2010) **95**(1):32–40. doi:10.1016/j.radonc.2009.08.003
82. Fukumitsu N, Sugahara S, Nakayama H, Fukuda K, Mizumoto M, Abei M, et al. A prospective study of hypofractionated proton beam therapy for patients with hepatocellular carcinoma. *Int J Radiat Oncol Biol Phys* (2009) **74**(3):831–6. doi:10.1016/j.ijrobp.2008.10.073
83. Chiba T, Tokuuye K, Matsuzaki Y, Sugahara S, Chuganji Y, Kagei K, et al. Proton beam therapy for hepatocellular carcinoma: a retrospective review of 162 patients. *Clin Cancer Res* (2005) **11**(10):3799–805. doi:10.1158/1078-0432.CCR-04-1350
84. Bush DA, Kayali Z, Grove R, Slater JD. The safety and efficacy of high-dose proton beam radiotherapy for hepatocellular carcinoma: a phase 2 prospective trial. *Cancer* (2011) **117**(13):3053–9. doi:10.1002/cncr.25809
85. Komatsu S, Fukumoto T, Demizu Y, Miyawaki D, Terashima K, Sasaki R, et al. Clinical results and risk factors of proton and carbon ion therapy for hepatocellular carcinoma. *Cancer* (2011) **117**(21):4890–904. doi:10.1002/cncr.26134
86. Kato H, Tsujii H, Miyamoto T, Mizoe JE, Kamada T, Tsuji H, et al. Results of the first prospective study of carbon ion radiotherapy for hepatocellular carcinoma with liver cirrhosis. *Int J Radiat Oncol Biol Phys* (2004) **59**(5):1468–76. doi:10.1016/j.ijrobp.2004.01.032
87. Combs SE, Habermehl D, Ganten T, Schmidt J, Edler L, Burkholder I, et al. Phase i study evaluating the treatment of patients with hepatocellular carcinoma (HCC) with carbon ion radiotherapy: the PROMETHEUS-01 trial. *BMC Cancer* (2011) **11**:67. doi:10.1186/1471-2407-11-67
88. Slater JD, Rossi CJ Jr, Yonemoto LT, Bush DA, Jabola BR, Levy RP, et al. Proton therapy for prostate cancer: the initial Loma Linda University experience. *Int J Radiat Oncol Biol Phys* (2004) **59**(2):348–52. doi:10.1016/j.ijrobp.2003.10.011
89. Shipley WU, Verhey LJ, Munzenrider JE, Suit HD, Urie MM, McManus PL, et al. Advanced prostate cancer: the results of a randomized comparative trial of high dose irradiation boosting with conformal protons compared with conventional dose irradiation using photons alone. *Int J Radiat Oncol Biol Phys* (1995) **32**(1):3–12. doi:10.1016/0360-3016(95)00063-5
90. Zietman AL, Bae K, Slater JD, Shipley WU, Efstathiou JA, Coen JJ, et al. Randomized trial comparing conventional-dose with high-dose conformal radiation therapy in early-stage adenocarcinoma of the prostate: long-term results from proton radiation oncology group/american college of radiology 95-09. *J Clin Oncol* (2010) **28**(7):1106–11. doi:10.1200/JCO.2009.25.8475
91. Mendenhall NP, Li Z, Hoppe BS, Marcus RB Jr, Mendenhall WM, Nichols RC, et al. Early outcomes from three prospective trials of image-guided proton therapy for prostate cancer. *Int J Radiat Oncol Biol Phys* (2012) **82**(1):213–21. doi:10.1016/j.ijrobp.2010.09.024
92. Tsuji H, Yanagi T, Ishikawa H, Kamada T, Mizoe JE, Kanai T, et al. Hypofractionated radiotherapy with carbon ion beams for prostate cancer. *Int J Radiat Oncol Biol Phys* (2005) **63**(4):1153–60. doi:10.1016/j.ijrobp.2005.04.022
93. Okada T, Tsuji H, Kamada T, Akakura K, Suzuki H, Shimazaki J, et al. Carbon ion radiotherapy in advanced hypofractionated regimens for prostate cancer: from 20 to 16 fractions. *Int J Radiat Oncol Biol Phys* (2012) **84**(4):968–72. doi:10.1016/j.ijrobp.2012.01.072
94. Ishikawa H, Tsuji H, Kamada T, Akakura K, Suzuki H, Shimazaki J, et al. Carbon-ion radiation therapy for prostate cancer. *Int J Urol* (2012) **19**(4):296–305. doi:10.1111/j.1442-2042.2012.02961.x

95. Habl G, Hatiboglu G, Edler L, Uhl M, Krause S, Roethke M, et al. Ion prostate irradiation (IPI) – a pilot study to establish the safety and feasibility of primary hypofractionated irradiation of the prostate with protons and carbon ions in a raster scan technique. *BMC Cancer* (2014) **14**:202. doi:10.1186/1471-2407-14-202
96. Meropol NJ, Schrag D, Smith TJ, Mulvey TM, Langdon RM Jr, Blum D, et al. American society of clinical oncology guidance statement: the cost of cancer care. *J Clin Oncol* (2009) **27**(23):3868–74. doi:10.1200/JCO.2009.23.1183
97. Kantarjian HM, Fojo T, Mathisen M, Zwelling LA. Cancer drugs in the United States: Justum Pretium – the just price. *J Clin Oncol* (2013) **31**(28):3600–4. doi:10.1200/JCO.2013.49.1845
98. Pfister DG. The just price of cancer drugs and the growing cost of cancer care: oncologists need to be part of the solution. *J Clin Oncol* (2013) **31**(28):3487–9. doi:10.1200/JCO.2013.50.3466
99. Sandler A, Gray R, Perry MC, Brahmer J, Schiller JH, Dowlati A, et al. Paclitaxel-carboplatin alone or with bevacizumab for non-small-cell lung cancer. *N Engl J Med* (2006) **355**(24):2542–50. doi:10.1056/NEJMoa061884
100. Ciuleanu T, Brodowicz T, Zielinski C, Kim JH, Krzakowski M, Laack E, et al. Maintenance pemetrexed plus best supportive care versus placebo plus best supportive care for non-small-cell lung cancer: a randomised, double-blind, phase 3 study. *Lancet* (2009) **374**(9699):1432–40. doi:10.1016/S0140-6736(09)61497-5
101. O'Brien SG, Guilhot F, Larson RA, Gathmann I, Baccarani M, Cervantes F, et al. Imatinib compared with interferon and low-dose cytarabine for newly diagnosed chronic-phase chronic myeloid leukemia. *N Engl J Med* (2003) **348**(11):994–1004. doi:10.1056/NEJMoa022457
102. Mobaraki A, Ohno T, Yamada S, Sakurai H, Nakano T. Cost-effectiveness of carbon ion radiation therapy for locally recurrent rectal cancer. *Cancer Sci* (2010) **101**(8):1834–9. doi:10.1111/j.1349-7006.2010.01604.x
103. Shah A, Hahn SM, Stetson RL, Friedberg JS, Pechet TT, Sher DJ. Cost-effectiveness of stereotactic body radiation therapy versus surgical resection for stage I non-small cell lung cancer. *Cancer* (2013) **119**(17):3123–32. doi:10.1002/cncr.28131
104. Mitera G, Swaminath A, Rudoler D, Seereeram C, Giuliani M, Leighl N, et al. Cost-effectiveness analysis comparing conventional versus stereotactic body radiotherapy for surgically ineligible stage I non-small-cell lung cancer. *J Oncol Pract* (2014) **10**(3):e130–6. doi:10.1200/JOP.2013.001206
105. Hodges JC, Lotan Y, Boike TP, Benton R, Barrier A, Timmerman RD. Cost-effectiveness analysis of stereotactic body radiation therapy versus intensity-modulated radiation therapy: an emerging initial radiation treatment option for organ-confined prostate cancer. *J Oncol Pract* (2012) **8**(3 Suppl):31s–7s. doi:10.1200/JOP.2012.000548
106. Sher DJ, Parikh RB, Mays-Jackson S, Punglia RS. Cost-effectiveness analysis of SBRT versus IMRT for low-risk prostate cancer. *Am J Clin Oncol* (2014) **37**(3):215–21. doi:10.1097/COC.0b013e31827a7d2a
107. Halperin EC. Overpriced technology in radiation oncology. *Int J Radiat Oncol Biol Phys* (2000) **48**(4):917–8. doi:10.1016/S0360-3016(00)00756-2
108. Zietman AL. The Titanic and the Iceberg: prostate proton therapy and health care economics. *J Clin Oncol* (2007) **25**(24):3565–6. doi:10.1200/JCO.2007.11.9768
109. Goitein M, Jermann M. The relative costs of proton and X-ray radiation therapy. *Clin Oncol (R Coll Radiol)* (2003) **15**(1):S37–50. doi:10.1053/clon.2002.0174
110. Grutters JP, Pijls-Johannesma M, Ruysscher DD, Peeters A, Reimoser S, Severens JL, et al. The cost-effectiveness of particle therapy in non-small cell lung cancer: exploring decision uncertainty and areas for future research. *Cancer Treat Rev* (2010) **36**(6):468–76. doi:10.1016/j.ctrv.2010.02.018
111. Parthan A, Pruttivarasin N, Davies D, Taylor DC, Pawar V, Bijlani A, et al. Comparative cost-effectiveness of stereotactic body radiation therapy versus intensity-modulated and proton radiation therapy for localized prostate cancer. *Front Oncol* (2012) **2**:81. doi:10.3389/fonc.2012.00081
112. Pijls-Johannesma M, Pommier P, Lievens Y. Cost-effectiveness of particle therapy: current evidence and future needs. *Radiother Oncol* (2008) **89**(2):127–34. doi:10.1016/j.radonc.2008.07.015
113. Bentzen SM. Randomized controlled trials in health technology assessment: overkill or overdue? *Radiother Oncol* (2008) **86**(2):142–7. doi:10.1016/j.radonc.2008.01.012
114. Goitein M, Cox JD. Should randomized clinical trials be required for proton radiotherapy? *J Clin Oncol* (2008) **26**(2):175–6. doi:10.1200/JCO.2007.14.4329

Conflict of Interest Statement: The authors declare that the research was conducted in the absence of any commercial or financial relationships that could be construed as a potential conflict of interest.

Copyright © 2016 Laine, Pompos, Timmerman, Jiang, Story, Pistenmaa and Choy. This is an open-access article distributed under the terms of the Creative Commons Attribution License (CC BY). The use, distribution or reproduction in other forums is permitted, provided the original author(s) or licensor are credited and that the original publication in this journal is cited, in accordance with accepted academic practice. No use, distribution or reproduction is permitted which does not comply with these terms.

frontiers in Oncology

REVIEW
published: 10 February 2016
doi: 10.3389/fonc.2016.00013

A Review of Radiotherapy-Induced Late Effects Research after Advanced Technology Treatments

Wayne D. Newhauser[1,2], Amy Berrington de Gonzalez[3], Reinhard Schulte[4] and Choonsik Lee[3]*

[1] Department of Physics and Astronomy, Louisiana State University, Baton Rouge, LA, USA, [2] Department of Physics, Mary Bird Perkins Cancer Center, Baton Rouge, LA, USA, [3] Radiation Epidemiology Branch, National Institutes of Health, Rockville, MD, USA, [4] Department of Basic Sciences, Loma Linda University Medical Center, Loma Linda, CA, USA

The number of incident cancers and long-term cancer survivors is expected to increase substantially for at least a decade. Advanced technology radiotherapies, e.g., using beams of protons and photons, offer dosimetric advantages that theoretically yield better outcomes. In general, evidence from controlled clinical trials and epidemiology studies are lacking. To conduct these studies, new research methods and infrastructure will be needed. In the paper, we review several key research methods of relevance to late effects after advanced technology proton-beam and photon-beam radiotherapies. In particular, we focus on the determination of exposures to therapeutic and stray radiation and related uncertainties, with discussion of recent advances in exposure calculation methods, uncertainties, *in silico* studies, computing infrastructure, electronic medical records, and risk visualization. We identify six key areas of methodology and infrastructure that will be needed to conduct future outcome studies of radiation late effects.

Keywords: late effects, dose, risk, measurement, calculation, proton, photon

OPEN ACCESS

Edited by:
Marco Durante, GSI Helmholtz Centre for Heavy Ion Research, Germany

Reviewed by:
Valdir Carlos Colussi, University Hospitals Seidman Cancer Center, USA
Oleg V. Belyakov, International Atomic Energy Agency, Austria

****Correspondence:***
Wayne D. Newhauser
newhauser@lsu.edu

Specialty section:
This article was submitted to Radiation Oncology, a section of the journal Frontiers in Oncology

Received: *31 October 2015*
Accepted: *12 January 2016*
Published: *10 February 2016*

Citation:
Newhauser WD, de Gonzalez AB, Schulte R and Lee C (2016) A Review of Radiotherapy-Induced Late Effects Research after Advanced Technology Treatments. Front. Oncol. 6:13. doi: 10.3389/fonc.2016.00013

INTRODUCTION

About one in two men and women born today will be diagnosed with some form of cancer in their lifetime (1). Worldwide cancer incidence in 2012 was estimated at 14.1 million new cases and 8.2 million deaths (2). In the United States, cancer incidence rates are projected to generally stabilize over the next decade, but the incidence will increase by more than 20% due to changes in demographics (3). Almost two-thirds of all cancer patients receive some form of radiation therapy during the course of treatment (4), predominantly with external-beam *photon therapy*. Treatments with beams of charged particles have become popular, especially *proton therapy* (5), and a few heavier charged particle facilities have been built in Europe and Asia for research and patient care. The main rationale for using charged particle beams is that they sterilize the tumor, like X-ray therapies, while delivering less radiation dose to healthy tissues (6, 7).

Advances in radiation therapy have contributed to improvements in long-term outcomes for cancer patients. For example, 5-year survival of cancer in the United States has increased to approximately 68% in adults and 83% in children (8). By 2020, there will be almost 20 million cancer survivors in the United States (9). Long-term survivors are at increased risk to develop treatment-induced side effects, such as radiogenic second cancer, complications of the cardiovascular (10, 11) and central nervous (12, 13) systems, fertility problems (14), and myriad other toxicities (15). These

problems can be caused by disease (e.g., damage caused by a primary cancer) or by medical care, such as surgery, chemotherapy, and radiation therapy. For many patients, these will play out long after the primary cancer is cured. For example, in survivors of childhood cancer, the risks of morbidity and mortality remain elevated beyond the fourth decade of life (16).

The link between radiation therapy and several serious late effects has been well documented in the literature. Radiation epidemiology studies revealed increased risk for subsequent cancers after radiotherapy (17). One of the most striking examples being the cumulative risk of subsequent breast cancer after radiotherapy for Hodgkin's lymphoma of 30% by age 55 (18). The clinical oncology literature reports that radiation is implicated in many subsequent cancers (19) and that mortality of primary cancers is decreasing, with increases in rates of mortality attributable to subsequent neoplasms, cardiac death, and pulmonary death largely due to treatment-related causes (20). Although radiotherapy significantly reduces breast cancer mortality and recurrence, the heart dose from older radiation treatments was found to materially impact total long-term survival (21). For some types of cancers, and in some pediatric cancers, second cancers can cause more deaths than the primary cancers (22). Second cancers account for 17–19% of all cancers, and, as a group, are one of the most common cancers in the USA (23). In adults, the proportion of second cancers related to radiotherapy was estimated at approximately 8% on average, with proportions varying from 4 to 24% for the specific sites considered (24). Corresponding estimates for children are not currently known but are likely to be considerably higher, given the increased radiosensitivity of children to some cancers and generally longer survival. For these and other reasons, the assessment of risks of late effects after radiotherapy has received increasing attention in the literature, including the impact of advanced technologies on outcomes (25, 26).

Advances in technology seek to improve cancer outcomes in two major ways, namely, by irradiating cancerous tissues in ways that lead to improved control of tumors and by reducing doses to healthy tissues to reduce treatment complications. Many advanced technologies have been implemented to further these goals, including treatment systems that use modulated beams of photons and protons. Unlike most new medical devices and drugs, advanced RTs are being widely deployed based on predicted improvements in outcome rather than superiority observed in prospective randomized clinical trials. The necessity of such trials is controversial (27). Furthermore, large economic forces are at play; proton and heavy-ion treatment units are the most expensive medical devices on the market and are perceived as a potentially disruptive technology in oncology. Clearly, additional new scientific approaches and knowledge would help to inform decision making in the future (28).

Currently, major gaps in scientific knowledge include (1) the long-term health problems of long-term cancer survivors, especially a decade or more after exposure; (2) the impact of radiation modality, dose, quality, and fractionation on the risk of late effects; (3) the applicability of risk models derived from healthy populations exposed to lower dose radiation to high-dose fractionated exposures in populations of cancer survivors; (4) the applicability of population-based risk models to individual patients, whose sensitivity to radiogenic late effects may vary with genetic profile and other factors; and (5) the impact of late effects after *advanced technology radiotherapies*, including incidence, severity, and economic considerations. Filling these gaps will require new research strategies, methods, and infrastructure.

The objective of this manuscript is to provide a review of selected research methodologies for radiogenic late effects after advanced technology radiation therapies. More specifically, we review aspects of relevance to proton-beam and photon-beam radiotherapies. We focus on craniospinal irradiation (CSI) as an illustrative example treatment to highlight current research capabilities and their limitations as this is one of the treatments for which proton therapy could be very beneficial. In particular, we review the determination of exposures to therapeutic and stray radiation and related uncertainties in the context of radiation late effects.

RECENT ADVANCES IN RESEARCH METHODS

A few introductory remarks are necessary to provide a context for the thrust of our review. In the last decade, considerable progress has been made toward research methods of relevance to the risk of late effects after advanced technology radiation therapies. However, long-term clinical and epidemiological outcome studies of charged particle therapies are scarce (29). These studies are difficult to perform for many reasons, including a lack of dose and risk assessment tools that are suitable for prospective outcome studies. Currently, most photon therapy outcome studies are performed retrospectively, with the doses being reconstructed by specialists using proprietary research tools (30). Similar tools for charged particle are nascent.

To review progress and explore limitations of current tools, we shall consider the illustrative case of CSI for medulloblastoma. This is a particularly interesting case because it is common among pediatric brain tumors; approximately 80% of patients survive 5 years or more (31); the therapeutic radiation fields are large, variable in size, shape, and anatomic location (32); the therapeutic and stray radiation impacts many healthy tissues and organs (33); patients vary in age at diagnosis (34) and anatomic stature; it is commonly delivered with photon or proton beams; there are large differences in predicted doses and risks between photon and proton beams (35); genomics strongly influence outcomes (36); dose and risk assessments are technically challenging (26); and there is sufficient recent literature to form a coherent picture. The methodological literature includes dose measurements; dose calculations using clinical treatment planning systems (TPSs), *Monte Carlo simulations*, and *analytical models*; radiation quality; risk models; and other aspects.

Craniospinal irradiation attempts to limit the administration of tumor-sterilizing doses to several target volumes, including the spinal axis, the cranium, and a surgical resection volume near the posterior fossa. However, even the most advanced radiotherapies deliver low levels of stray radiation to the patient's whole body. Observational data for various treatment sites revealed that nearly nine of every 10 subsequent tumors develop outside PTV (37). Thus, to fully understand late effects after external beam radiotherapy,

one must, at a minimum, determine exposures from therapeutic and stray radiation to all of the organs and tissues of the body.

Assessment of Radiation Exposure

Today, there are four major methods to determine radiation exposure from external beam radiotherapy, including measurements, analytical calculations (dose algorithms embedded in TPSs and nascent stand-alone algorithms), and Monte Carlo simulations.

Traditionally, measurements are used to develop, configure, and test dose calculation methods of various kinds, including pencil beam algorithms in clinical TPSs, research Monte Carlo codes, and other dose models. Methodologies for the measurement of therapeutic doses are generally well established and straightforward. Measurements of stray radiation are challenging and less well established. In particular, stray neutron radiation is experimentally difficult and subject to large uncertainties. High-energy photon beams produce neutrons via photoneutron interactions, and high-energy protons liberate neutrons via nuclear reactions.

Analytical dose algorithms are typically used in TPSs. They generally provide excellent dosimetric accuracy inside the therapeutic field and fast computation speeds. However, they severely underestimate stray radiation exposures, especially leakage radiation emanating from the treatment unit (38). Consequently, they are not suitable for research on the effects of radiation in that region (**Figure 1**). Recently, analytical models have been developed to calculate both therapeutic and stray radiotherapy exposures (**Figure 2**). Analytical models for whole-body exposure assessments are the least well developed of the four methods.

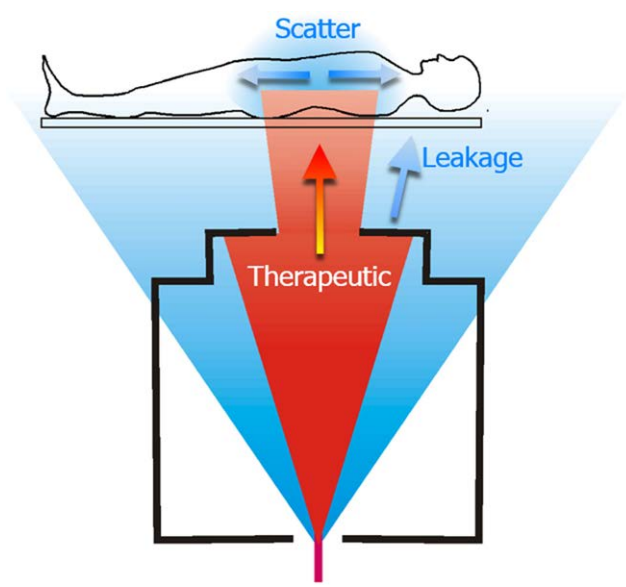

FIGURE 1 | Schematic diagram of a proton therapy treatment of the spinal axis. The therapeutic dose is shown in red and unwanted stray radiation is shown in blue. The stray radiation comprises leakage radiation emanating from the treatment machine, and scatter radiation that is produced as the therapeutic radiation interacts with the patient. Figure from Ref. (26).

Monte Carlo simulations are generally well suited for research studies that require calculations of radiation exposures both inside and outside the treatment field. Of the four methods discussed here, the Monte Carlo method has advanced the most in recent years. For example, whole-body dose assessments that were computationally intractable in 2000 are now feasible in a research setting. This progress is attributable to refinements in general-purpose Monte Carlo codes, their adaptation to radiotherapy applications, and advances in parallel computing and low-cost electronic memory. Most Monte Carlo systems for radiotherapy simulations are built on general-purpose, full-featured codes, such as MCNP/X (39) and FLUKA (40, 41) with additional radiotherapy pre- and post-processing codes (42, 43), or with toolkits, such as GEANT4 (44) with radiotherapy packages (45). Important features include good interaction data and models, advanced source modeling and tallying features, parallel computing capability, variance reduction options, and statistical tests for convergence. Despite stunning breakthroughs in capabilities, today the Monte Carlo simulation method is seldom used for clinical treatment planning. One of the main reasons is that the method requires *high-performance computing* resources.

The selection of a dose assessment method involves consideration of the requirements of a particular study and the performance characteristics of available methods. Currently, no single method meets all the commonly encountered requirements on speed, accuracy, cost, and convenience. Consequently, most research studies require two or more methods to determine radiation doses. Traditionally, late-effect studies have utilized TPS calculations of therapeutic radiation dose and analytical calculations of stray radiation, where both methods were validated against measurements. In recent years, Monte Carlo simulations have played an increasing role. In the remainder of this manuscript, we focus on aspects of these methods that are of greatest relevance to researching the late effects from advanced technology radiotherapies, i.e., photon and proton beams. In the last part of this section, we mention the key advances in other disciplines that have had an enabling effect on the research methodologies presented here.

Proton Therapy

Interest in the late effects after proton radiation therapy has increased dramatically since the turn of the century, perhaps in part because of early publications on stray neutron exposures and because of the late toxicities observed after neutron beam therapy in previous decades. The latter experience tells a cautionary tale of the latent dangers of any new form of radiation treatment. In retrospect, it is remarkable that clinical proton therapy was practiced more than four decades before the first publications on stray neutron exposures appeared. Neutrons are of particular concern given their higher, but very uncertain, relative biological effectiveness (RBE) in humans. Neutron RBE values ware derived primarily from experimental data because, to date, there have not been any epidemiological studies that have been able to compare the risks with those of photon irradiation directly in a sufficient sample size. Binns and Hough (46) reported the first measurements of neutron exposures in developmental proton therapy beamline, which were alarmingly high. However, that beamline was never used for patient treatments because of the excessive

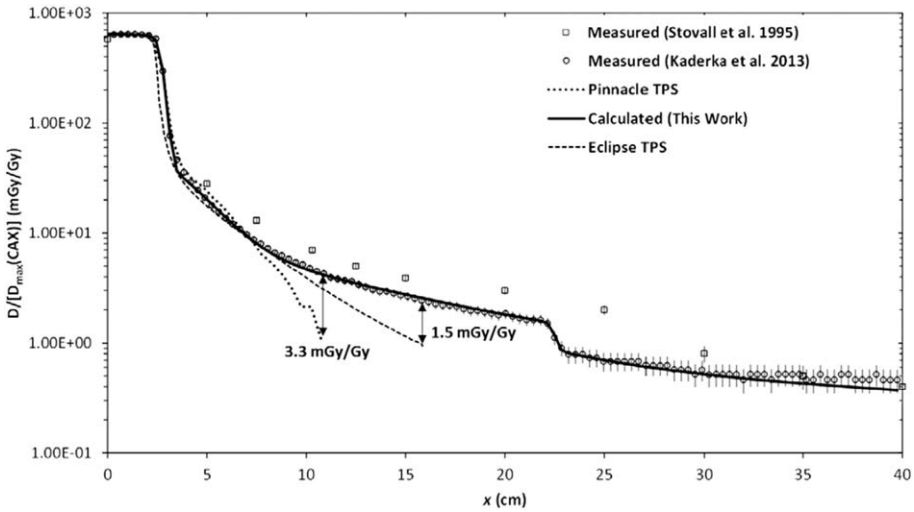

FIGURE 2 | Absorbed dose *D* as a function of lateral distance *x* from the photon therapy beam. The calculated and measured absorbed dose values are normalized to the maximum therapeutic dose at the central axis D_{max}(CAX). The radiation fields were produced by electron linear accelerator. Figure from Ref. (38).

neutron exposures. In 1998, Agosteo et al. published a seminal paper that reported on Monte Carlo simulations of stray photon and neutron exposures from proton therapy beamlines (47). Yan et al. (48) reported the first clinically relevant measurements of neutron spectra and exposures. They characterized each of the three heavily used clinical beamlines at the Harvard Cyclotron Laboratory (HCL) using multiple measurement techniques. The results of these three studies suggested that neutron exposures were not negligible and that careful attention should be paid to characterizing and minimizing neutron exposures for clinically used proton beamlines.

Indeed, a few years on, Hall (49) rescaled published neutron exposure data from the Harvard Cyclotron Laboratory (HCL) with simplistic risk calculations. He opined that passively scattered proton therapy may not be indicated for some patients, especially children, because of the second cancer risks from the whole-body neutron exposures. Although the key assumptions in his paper would be ultimately proven incorrect, the underlying concerns were justified. Specifically, a large international expansion of proton therapy had begun without due diligence regarding neutron exposures and their consequences.

By the time of Hall's paper, systematic investigations of neutron exposures from proton therapy were already underway. Beginning in 2005, a series of reports was published that studies the systematics of therapeutic proton and stray neutron exposures, such as their dependence on proton-beam energy, field size, range modulation width, depth in phantom, collimator thickness, and other treatment factors (43, 50–60). The systematics were mostly investigated using general-purpose Monte Carlo simulations, a bellwether of the increasingly important role that Monte Carlo holds in radiotherapy research. Subsequent confirmatory measurements have been comparatively sparse but important; benchmark measurements confirmed the high-energy neutron physics models in Monte Carlo codes (61); end-to-end benchmarking confirmed Monte Carlo models of diverse clinically used proton beamlines (50, 62); and code intercomparisons further increased confidence in Monte Carlo simulations for clinically relevant beamlines, such as that in Ref. (63).

Recently, increased attention has been paid to developing reference data on neutron exposures (64), on methodology to experimentally benchmark predictive models (65), and to estimate mean radiation weighting factors and RBE values for neutrons (66–68).

By 2009, research methodologies had advanced sufficiently to allow for the first dose and theoretical risk assessment study, which was reported for CSI that included both therapeutic and stray neutron radiation (33). The modeling included a refined and more complete analysis of a case study reported in the seminal paper by Miralbell et al. (69), now including dose and risk from stray neutron exposures from passively scattered and scanned proton beams. The results confirmed the qualitative finding of Miralbell et al., namely, that proton therapy conferred lower risk than photon therapy. The modeling study contradicted Hall's speculation that scanned proton beams provide substantially lower risk compared with scattered proton beams. It also increased knowledge of the mean radiation weighting factor for neutrons, allowing meaningful comparisons of proton and photon CSIs, in spite of the large uncertainty in the neutron RBE for carcinogenesis. Limitations of the study included the use of linear non-threshold risk models for radiation protection (70), the use of a stylized adult phantom, and simplified treatment planning. In rapid succession, these limitations were overcome in a series of papers on CSI that included newer risk models for radiogenic cancers (71), relaxed assumptions about linear non-threshold (LNT) risk behavior (72), personalized voxel phantoms (73), and highly realistic treatment planning methods (32). Another study reported ways to reduce stray radiation from passively scattered CSI to levels approaching those from scanned beams (74). Conversely, adding final collimators to scanned beams may sharpen the lateral penumbra, thereby reducing dose just outside

the target (75, 76), which increases the neutron leakage exposure. Findings common to these studies are that many small details matter and that it is difficult to know *a priori* which details will have a profound effect on risk after CSI. An example of a treatment factor of importance is the superior–inferior location of the junction of the abutting cranial and upper spinal fields, which can have a profound effect on thyroid risk. Another is the selection of margin size on the spinal fields, which has a strong impact on the risk to lung and other organs. Details of the research methodology also matter, such as the exclusion of the contents of the bladder and colon when delineating the organs and tissues at risk (77) and blood in the heart (35).

In the last 5 years, much progress has been made toward practical analytical models of neutron leakage exposures. A simple analytical model was proposed in 2010 (78) for 250 MeV beams, improved and extended to cover the 100–250-MeV proton-beam energy interval (67, 79), and validated for low-energy proton beams for ocular treatments (79, 80). The analytical model was extended to include range modulation and implemented in a research TPS (81).

Analytical models of exposures from neutrons generated inside the patient were investigated by Schneider et al. (82), who reported a simple parameterization for a spherical water phantom. Currently, analytical algorithms are lacking for predicting internal neutrons.

Photon Therapy

In the early 2000s, intensity modulated photon radiation therapy (IMRT) was widely deployed. Hall and Wuu pointed out that the fluence modulation increases the monitor units by a factor of 2–3, thereby proportionately increasing the whole-body exposures from leakage radiation (83). They estimated this could lead to a doubling of the second cancer incidence at 10 years. Hence, the improved sparing of normal tissue immediately surrounding the tumor comes at the cost of increased exposure of the whole body to leakage radiation.

Generally speaking, commercial TPSs use deterministic dose algorithms that provide adequate accuracy in-field and near-field. However, approximately 10 cm distance or more outside the treatment field, the accuracy is typically worse than 40% and deteriorates dramatically with increasing distance. Because of the high incidence of late effects that are observed outside the treatment field, it will be essential to solve this problem, i.e., to achieve a dosimetric accuracy of 20% or better in all tissues.

Specialized Monte Carlo models were developed in 1980s for external beam radiotherapy research. One widely used code is based on the Electron Gamma Shower (EGS) code (84) with an add-on module (BEAM) (85) to compute photon and electron fluences emanating from an electron linac. Another add-on module named DOSExyz (86) facilitates dose computation in matrices of voxels, e.g., from CT image sets. Several fast Monte Carlo codes have been developed for radiotherapy dosimetry applications, including Voxel Monte Carlo (VMC) (87), dose planning method (DPM) (88), and MCDOSE (89). Most of the fast Monte Carlo calculation codes are designed for in-field or near-field dose calculations. General purpose codes, such as MCNP (39) and GEANT4 (44), include physics models for the production and transport of photoneutrons and have been used in many types of radiotherapy sources and clinical accelerators. At least one commercial TPS offers an electron Monte Carlo algorithm (90, 91). There has been effort to combine the commercial TPS and calibrated fast Monte Carlo codes to provide organ dose calculations in both in-field and out-of-field regions for epidemiological studies (92). The Monte Carlo method has been an invaluable research tool for studying therapeutic and stray radiation exposures.

Analytical models have been used to predict stray radiation exposures for several decades for conventional radiotherapy (30). However, the literature on models for *contemporary* treatment units and *advanced* treatment techniques has been extremely limited, as recently reviewed in Ref. (38). An empirical model was developed for photon CSI (93, 94) to model out-of-field radiation exposures. That model parameterized measured data in an approach conceptually similar to that of Stovall et al. (95). Recently, a fast and simple physics-based analytical model was reported for a widely used type of medical linear accelerator (38). This approach is currently being further validated for use with 12 different types of linacs and treatment techniques, including advanced technology treatments and techniques, such as IMRT, volumetric modulated arc therapy (VMAT), IMRT with flattening-filter-free (FFF) beams, tomotherapy, and robotic-arm linac therapy. The advantages of a physics-based approach include reduced requirements for measured data, increased predictive capabilities, broader applicability, fast computation time, and simplicity compared to Monte Carlo models. Analytical models for advanced technology radiotherapies are progressing rapidly but not yet sufficiently developed for routine use in clinical treatment planning. Major challenges lie in balancing the competing requirements of simplicity, dosimetric accuracy, and applicability. With the increasing diversity of advanced radiotherapies, it is not yet clear if this approach will be able to simultaneously meet all requirements.

Measurements have long been considered the most reliable source of information on stray radiation exposures and are needed to validate predictive models. For advanced technology photon radiotherapies, numerous measurements have been reported in air, water-box phantoms, or anthropomorphic phantoms, such as those in Ref. (38, 64, 96, 97). Most advanced technology photon therapies are administered at photon energies below the threshold for photoneutron production. For this reason and for brevity, exposures from photoneutrons are not discussed further.

In Silico Clinical Trials

In many situations, it is difficult or impossible to carry out observational studies, including randomized clinical trials and radiation epidemiology studies. We briefly review reasons for this that are relevant to the advanced technology radiotherapies.

There is an inherent challenge to understanding the late effects from "advanced technology" treatments. Specifically, by the time the late effects manifest, the treatment under investigation becomes standard or obsolete. The latency time for solid tumors typically is longer than 5 years and may be several decades. This problem is exacerbated by the decreasing technology lifetimes because of accelerating technological progress. Other potentially challenging factors to conducting clinical and other observational trials

include requirements on equipoise, accrual of sufficient patients to achieve statistical power and significance, and high costs.

However, good decision making in the clinical and policy arenas is informed by the best available evidence. If observational evidence is not available, evidence can be generated using the alternative strategy of computer simulated or *in silico* trials. *In silico* trials utilize representative cohorts (including detailed volumetric images of patient anatomy), clinically detailed and realistic treatment planning methods, physically complete dose assessments (therapeutic and stray radiation exposures), dose–response functions (risk models) from previous observational studies, and rigorous uncertainty analyses. Comparative *in silico* studies use paired data (both the standard and the experimental treatments are simulated for each patient). *In silico* studies are faster and less expensive than traditional observational trials, although their ultimate role will be complimentary rather than competitive.

A lack of equipoise is perhaps the greatest barrier to conducting a randomized clinical trial comparing photon versus proton-beam CSI. By the mid 2010s, the remarkable advances in research methodologies made it possible to perform *in silico* clinical trials that compared predicted risks after proton and photon CSI. The dose reconstructions included whole-body calculations of therapeutic and stray radiation, all the major tissues and organs of the bodies, clinical realism, and the largest cohort studied ($n = 17$) with complete dose reconstructions. The quantities reported included organ doses (98), radiogenic cancer risk (35), and cardiac toxicity (35, 99).

The *in silico* approach enabled systematic exploration of the influence of host factors on predicted risk, including age at exposure, attained age (72), anatomic stature, and sex on predicted risk (35, 100). Studies were performed to explore the risks of various cancer endpoints, including incidence, mortality, excess relative risk, excess absolute risk, lifetime attributable risk, and ratios of various risk quantities as well as non-cancer endpoints, such as cardiac toxicity (35), fertility complications (68), and radiation-induced necrosis (101).

Some progress has been made in understanding the uncertainties in comparative risk predictions in the radiotherapy setting, but many important questions remain open. Uncertainties in risks of radiogenic cancers were reviewed in Ref. (102, 103). The role of sensitivity tests to assess the impact of poorly known uncertainties in biologic aspects of risk comparisons after CSI was demonstrated by Newhauser et al. (33). Specifically, they showed that significant results can be obtained despite the large uncertainties in the RBE of neutrons for carcinogenesis. Also for CSI, Zhang et al. (72) reported on the influence of the risk model selected, including deviations from LNT behavior due to effects, such as cell sterilization at therapeutic doses. Uncertainties of *in silico* trials comparing predicted risks of late effects were investigated using a rigorous propagation of errors by Fontenot et al. (104) and subsequently extended by Rechner et al. (77), Zhang et al. (99), and Nguyen et al. (105). These studies all depend to some extent on the assumption that the extrapolation of risks from low-dose acute exposures to high-dose fractionated exposure is the same for all cancer sites. This might vary from one organ or tissue to the next (106), e.g., due to differences in stem cell repopulation in different organs. Additional progress is needed to quantify the uncertainties in risk models used in comparative studies, such as possible organ-specific variations in the transportation of risk models from Japanese survivors of nuclear detonations to other populations.

Given the many uncertainties in the risk modeling, it is essential to take on the challenge of developing epidemiological and clinical studies to assess the late effects of proton therapy directly, particularly in children who are known to be more radiosensitive to some cancers. The first randomized trial to compare the late effects of proton with photon therapy for breast cancer treatment was recently funded by PCORI and includes 22 US proton centers with an aim of randomizing approximately 2000 women.[1] This study, which was not yet recruiting patients at the time of this writing, will test the hypothesis that proton therapy reduces cardiovascular disease risks compared to photon therapy. The Pediatric Proton Consortium Registry is currently open to enroll children treated with proton radiation in the United States with the goal to characterize the population receiving proton therapy, regardless of technology used, to evaluate its benefits over other radiation therapies (107). Smaller trials are underway to compare effectiveness in prostate, lung, and head and neck cancer. As far as we are aware, no large-scale randomized trials or epidemiological studies of proton therapy in children are currently underway. As noted previously, they are the patients who are at greatest risks for radiation-related second cancers. The American Society for Therapeutic Radiation Oncology advises against using proton therapy in common cancers, such as prostate cancer, outside well-designed clinical trials.[2] As the number of proton therapy centers continues to expand in the US, Europe, and Asia, concerted efforts should be made to directly study the late effects of this treatment, especially the development of infrastructure to assess whole-body exposures.

Related Technologies

Several related technologies have had an enabling effect of methodological research. First and foremost is the remarkable advancement in the capabilities and accuracy of general-purpose Monte Carlo codes, a workhorse of research on medical dosimetry. In fact, the field of radiation oncology owes a debt of gratitude to the nuclear physics community for providing general-purpose Monte Carlo simulation codes and outstanding support, all at little or no cost to the medical community. Whole-body simulations, which have appeared in the literature recently (100), were considered computationally intractable at the turn of the century because of limitations of the Monte Carlo codes' capabilities, as well as computational expense.

Advances in high-performance computing have had a profoundly enabling effect on computational dosimetry. The most important developments have been the proliferation of low-cost, high-reliability, and parallel computing methods. Several approaches have been used, including clusters of CPUs (108), grid technologies (109), and graphics processing units (110).

The second most important enabling technology is the electronic medical record, which allows a high degree of automation and dependability. This includes standardization of file formats, communications protocols, and interoperability. This has been helpful to researchers, for example, in performing post-processing

[1] http://www.pcori.org

[2] http://www.choosingwisely.org

tasks, such as anonymization of electronic radiotherapy medical records (111), and will become vitally important for outcome studies in the future.

The visualization of radiation risk and detriment will likely become important in the future. In particular, it appears interesting to visualize risks superposed on images of patient anatomy, much like radiation exposure is visualized in contemporary treatment planning (**Figure 3**). However, for a given dose distribution, the distribution of risk may be radically different due to variations in the radiation sensitivity of individual organs and tissues (26). From a technical standpoint, meaningful visualization of risk presents many challenges, some of which may be overcome (26, 112). Risk visualization methods are nascent and are currently unavailable in contemporary TPSs.

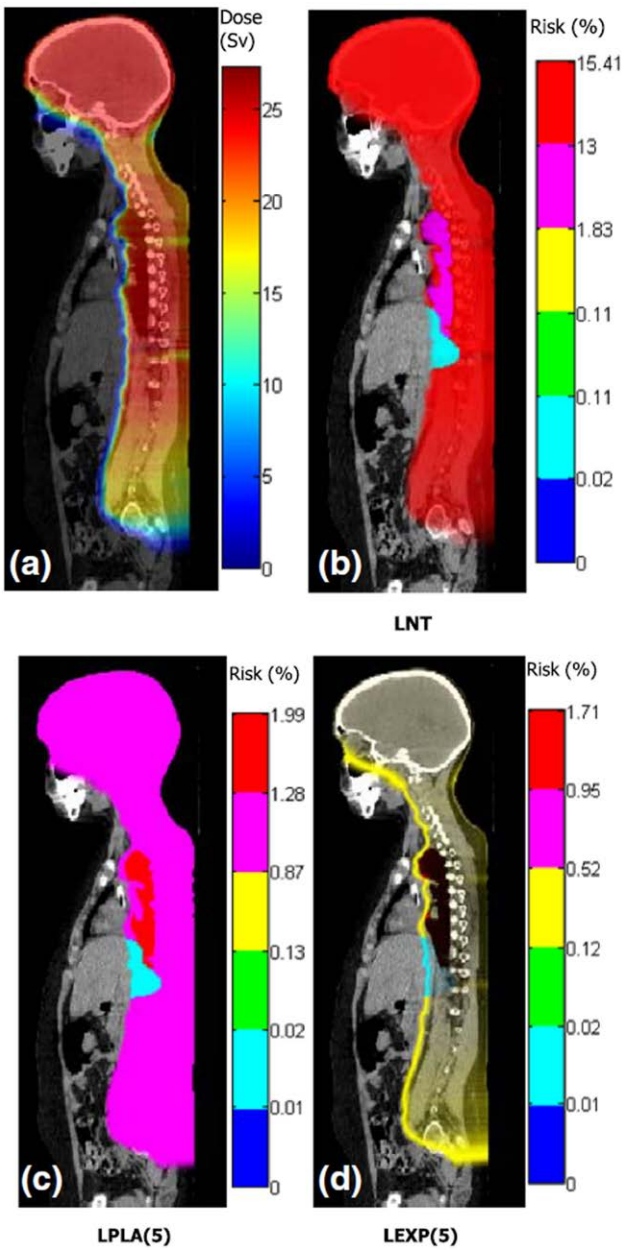

FIGURE 3 | Distributions of dose and risk superposed on sagittal images of anatomy for craniospinal irradiation. (A) shows equivalent dose and **(B–D)** show lifetime risks of second cancer incidence based on different dose–risk relationships [LNT: linear non-threshold model, LPLA (5): linear plateau model with bending point at 5 Sv, and LEXP (5): linear exponential model with bending point at 5 Sv]. Figure from Ref. (112).

Given the progress in capabilities to predict radiation exposures and risks, it has become technically possible to develop methods to algorithmically minimize predicted risk (113). Such methods could become an automatic step in routine radiotherapy treatment planning. Algorithmic minimization of risk of late effects is nascent and is currently unavailable in TPSs. Substantial additional research, development, and validation will be required before this can be used for human use, e.g., in prospective clinical decision making regarding the care individual patients receive.

DISCUSSION

Worldwide, the number of incident cancer cases is expected to increase over the next decade. Cancer survival rates are expected to increase further with improved diagnosis, treatment, and survivorship care. For these and other reasons, additional attention must be paid to reduce the incidence of treatment-related morbidity, such as fatal radiogenic second cancers.

Achieving this goal will require new research strategies and methods to supplement and enhance the traditional ones. In general, each new generation of advanced technology enables the delivery of superior (and more complex) therapeutic and stray dose distributions in the body. The exposures vary with a wide variety of treatment factors and host factors. To prospectively assess the full potential of advanced technology treatments to improve outcomes, new methods and capabilities are urgently needed to assess radiation exposures. Promising recent studies, including several examples mentioned in this review article, suggest that it might become feasible to routinely predict radiation exposures to all the tissues and organs of the body in the near future.

At the present time, clinical TPSs provide acceptable dosimetric accuracy for exposures to therapeutic radiation. However, outside the treatment field, the accuracy is generally poor and at distant locations, the exposures are typically not calculated at all. Additional research and development will be needed to develop dose prediction algorithms that provide an acceptable compromise of dosimetric accuracy, computational speed, and ease of use.

To accomplish that, we will need to know much more about the processes governing radiation exposures and risks. In recent years, our understanding of the magnitude and systematics of stray radiation exposures has increased dramatically for advanced proton and photon therapies and further progress is anticipated. However, many key uncertainties remain regarding the magnitude of risks from high-dose fractionated exposures, critical substructures of organs (such as the heart), applicability of risk models based on data from the Japanese atomic bomb survivors to non-Japanese populations, and the RBE of neutrons. From the literature, a coherent picture is emerging in which stray exposures are generally numerically small but the corresponding risks may be large, e.g., 30% or larger lifetime risk of second cancer for some patients. Risks

of radiation late effects are of particular concern for patients of young age and with good prognoses for long-term survival.

Advances in research methodologies and capabilities will be necessary. Some key needs for research and clinical settings include

(1) Algorithms to calculate exposures to tissues outside the treatment field.
(2) Primary and secondary reference fields of high-energy neutrons to allow for calibration of instruments to measure exposure.
(3) Improved methods to reproducibly and consistently determine radiation quality.
(4) Methods to accumulate exposures from therapeutic and imaging procedures.
(5) Tools for risk visualization, analysis, communication, and documentation.
(6) Algorithmic methods to support decision making in avoiding non-essential radiation risks.

Ideally, these will be implemented in ways that support the critical need for efficient, large-scale studies of the radiation late effects of proton therapy. When implemented, this will facilitate multidisciplinary research that integrates key aspects of radiation oncology (114), epidemiology (115, 116), physics (117), and survivorship (118, 119). In addition, this may be relevant to some radiobiologic research, such as abscopal (120) and other non-targeted effects (e.g., radiation-induced bystander effect, genomic instability, and the radiation response of stem cells) (121) and modulation of radiation response (e.g., radiosensitizers and radioprotectors) and novel combination therapies (122). The American Association of Physicists in Medicine pointed out potential dangers of using biological models for clinical radiotherapy and provided guidelines and methodology for quality assurance (123).

CONCLUSION

In past decades, studies of medical exposures have increased knowledge of radiation risks. However, dose–response functions have large uncertainties because many studies lacked the large sample sizes and high-quality radiation exposure data needed to more accurately estimate risk. Now, for the first time, it appears within reach, scientifically and technically, to prospectively calculate complete, whole-body exposures to virtually all major advanced technology radiotherapy patients. This will be possible because of widespread adoption of the electronic medical record, improved understanding of the physics of stray radiation exposures, advances in high-performance computing, and advances in algorithms to predict radiation exposures. When realized, the availability of exposure data for large populations will open new frontiers of research in radiation epidemiology, clinical oncology, and cancer survivorship.

AUTHOR CONTRIBUTIONS

WN drafted the manuscript. AG, CL, and RS edited and expanded the text of the manuscript. All authors reviewed and approved the manuscript.

ACKNOWLEDGMENTS

We thank Dr. Robert Carver for helpful discussions and Mr. William Donahue, Mr. Chris Schneider, and Ms. Lydia Jagetic for assistance in the preparation of this manuscript.

FUNDING

This work was supported in part by the Bella Bowman Foundation.

REFERENCES

1. Howlader N, Noone A, Krapcho M. *SEER Cancer Statistics Review, 1975-2009 (Vintage 2009 Populations)*. Bethesda, MD: National Cancer Institute (2012). Available from: http://seer.cancer.gov/archive/csr/1975_2009_pops09/
2. Ferlay J, Soerjomataram I, Dikshit R, Eser S, Mathers C, Rebelo M, et al. Cancer incidence and mortality worldwide: sources, methods and major patterns in GLOBOCAN 2012. *Int J Cancer* (2015) **136**(5):E359–86. doi:10.1002/ijc.29210
3. Weir HK, Thompson TD, Soman A, Møller B, Leadbetter S. The past, present, and future of cancer incidence in the United States: 1975 through 2020. *Cancer* (2015) **121**(11):1827–37. doi:10.1002/cncr.29258
4. Delaney G, Jacob S, Featherstone C, Barton M. The role of radiotherapy in cancer treatment. *Cancer* (2005) **104**(6):1129–37. doi:10.1002/cncr.21324
5. Loeffler JS, Durante M. Charged particle therapy-optimization, challenges and future directions. *Nat Rev Clin Oncol* (2013) **10**(7):411–24. doi:10.1038/nrclinonc.2013.79
6. Wilson RR. Radiological use of fast protons. *Radiology* (1946) **47**(5):487–91. doi:10.1148/47.5.487
7. Durante M, Loeffler JS. Charged particles in radiation oncology. *Nat Rev Clin Oncol* (2010) **7**(1):37–43. doi:10.1038/nrclinonc.2009.183
8. Siegel RL, Miller KD, Jemal A. Cancer statistics, 2015. *CA Cancer J Clin* (2015) **65**(1):5–29. doi:10.3322/caac.21314
9. de Moor JS, Mariotto AB, Parry C, Alfano CM, Padgett L, Kent EE, et al. Cancer survivors in the United States: prevalence across the survivorship trajectory and implications for care. *Cancer Epidemiol Biomarkers Prev* (2013) **22**(4):561–70. doi:10.1158/1055-9965.EPI-12-1356
10. Darby SC, Ewertz M, McGale P, Bennet AM, Blom-Goldman U, Brønnum D, et al. Risk of ischemic heart disease in women after radiotherapy for breast cancer. *N Engl J Med* (2013) **368**(11):987–98. doi:10.1056/NEJMoa1209825
11. Mulrooney DA, Yeazel MW, Kawashima T, Mertens AC, Mitby P, Stovall M, et al. Cardiac outcomes in a cohort of adult survivors of childhood and adolescent cancer: retrospective analysis of the Childhood Cancer Survivor Study cohort. *BMJ* (2009) **339**:b4606. doi:10.1136/bmj.b4606
12. Krull KR, Sabin ND, Reddick WE, Zhu L, Armstrong GT, Green DM, et al. Neurocognitive function and CNS integrity in adult survivors of childhood Hodgkin lymphoma. *J Clin Oncol* (2012) **30**(29):3618–24. doi:10.1200/JCO.2012.42.6841
13. Krull KR, Minoshima S, Edelmann M, Morris B, Sabin ND, Brinkman TM, et al. Regional brain glucose metabolism and neurocognitive function in adult survivors of childhood cancer treated with cranial radiation. *J Nucl Med* (2014) **55**(11):1805–10. doi:10.2967/jnumed.114.142950
14. Antal Z, Sklar CA. Gonadal function and fertility among survivors of childhood cancer. *Endocrinol Metab Clin North Am* (2015) **44**(4):739–49. doi:10.1016/j.ecl.2015.08.002
15. Oeffinger KC, Mertens AC, Sklar CA, Kawashima T, Hudson MM, Meadows AT, et al. Chronic health conditions in adult survivors of childhood cancer. *N Engl J Med* (2006) **355**(15):1572–82. doi:10.1056/NEJMsa060185
16. Armstrong GT, Kawashima T, Leisenring W, Stratton K, Stovall M, Hudson MM, et al. Aging and risk of severe, disabling, life-threatening, and fatal events

in the childhood cancer survivor study. *J Clin Oncol* (2014) **32**:1218–27. doi:10.1200/JCO.2013.51.1055
17. de Gonzalez AB, Gilbert E, Curtis R, Inskip P, Kleinerman R, Morton L, et al. Second solid cancers after radiation therapy: a systematic review of the epidemiologic studies of the radiation dose-response relationship. *Int J Radiat Oncol Biol Phys* (2013) **86**(2):224–33. doi:10.1016/j.ijrobp.2012.09.001
18. Travis LB, Hill D, Dores GM, Gospodarowicz M, Van Leeuwen FE, Holowaty E, et al. Cumulative absolute breast cancer risk for young women treated for Hodgkin lymphoma. *J Natl Cancer Inst* (2005) **97**(19):1428–37. doi:10.1093/jnci/dji290
19. Applebaum MA, Cohn SL. Surveillance of childhood cancer survivors: a lifelong affair. *J Clin Oncol* (2015) **33**:3531–2. doi:10.1200/JCO.2015.62.7703
20. Armstrong GT, Liu Q, Yasui Y, Neglia JP, Leisenring W, Robison LL, et al. Late mortality among 5-year survivors of childhood cancer: a summary from the childhood cancer survivor study. *J Clin Oncol* (2009) **27**(14):2328–38. doi:10.1200/JCO.2008.21.1425
21. Clarke M, Collins R, Darby S, Davies C, Elphinstone P, Evans V, et al. Effects of radiotherapy and of differences in the extent of surgery for early breast cancer on local recurrence and 15-year survival: an overview of the randomised trials. *Lancet* (2005) **366**:2087–106. doi:10.1016/S0140-6736(05)67887-7
22. Tubiana M. Can we reduce the incidence of second primary malignancies occurring after radiotherapy? A critical review. *Radiother Oncol* (2009) **91**(1):4–15. doi:10.1016/j.radonc.2008.12.016
23. Morton LM, Swerdlow AJ, Schaapveld M, Ramadan S, Hodgson DC, Radford J, et al. Current knowledge and future research directions in treatment-related second primary malignancies. *Eur J Cancer Suppl* (2014) **12**(1):5–17. doi:10.1016/j.ejcsup.2014.05.001
24. de Gonzalez AB, Curtis RE, Kry SF, Gilbert E, Lamart S, Berg CD, et al. Proportion of second cancers attributable to radiotherapy treatment in adults: a cohort study in the US SEER cancer registries. *Lancet Oncol* (2011) **12**(4):353–60. doi:10.1016/S1470-2045(11)70061-4
25. Harrison R. Introduction to dosimetry and risk estimation of second cancer induction following radiotherapy. *Radiat Meas* (2013) **57**:1–8. doi:10.1016/j.radmeas.2013.01.018
26. Newhauser WD, Durante M. Assessing the risk of second malignancies after modern radiotherapy. *Nat Rev Cancer* (2011) **11**(6):438–48. doi:10.1038/nrc3069
27. Suit H, Kooy H, Trofimov A, Farr J, Munzenrider J, DeLaney T, et al. Should positive phase III clinical trial data be required before proton beam therapy is more widely adopted? No. *Radiother Oncol* (2008) **86**(2):148–53. doi:10.1016/j.radonc.2007.12.024
28. Pignol J-P, Janus C. The evaluation of innovation in radiation oncology – what can we do and what should we do? *Acta Oncol* (2015) **54**: 1251–3. doi:10.3109/0284186X.2015.1067719
29. Terasawa T, Dvorak T, Ip S, Raman G, Lau J, Trikalinos TA. Systematic review: charged-particle radiation therapy for cancer. *Ann Intern Med* (2009) **151**(8):556–65. doi:10.7326/0003-4819-151-8-200910200-00145
30. Stovall M, Weathers R, Kasper C, Smith SA, Travis L, Ron E, et al. Dose reconstruction for therapeutic and diagnostic radiation exposures: use in epidemiological studies. *Radiat Res* (2006) **166**(1 Pt 2):141–57. doi:10.1667/RR3525.1
31. Smith MA, Seibel NL, Altekruse SF, Ries LA, Melbert DL, O'Leary M, et al. Outcomes for children and adolescents with cancer: challenges for the twenty-first century. *J Clin Oncol* (2010) **28**(15):2625–34. doi:10.1200/JCO.2009.27.0421
32. Giebeler A, Newhauser WD, Amos RA, Mahajan A, Homann K, Howell RM. Standardized treatment planning methodology for passively scattered proton craniospinal irradiation. *Radiat Oncol* (2013) **8**(1):32. doi:10.1186/1748-717X-8-32
33. Newhauser WD, Fontenot JD, Mahajan A, Kornguth D, Stovall M, Zheng Y, et al. The risk of developing a second cancer after receiving craniospinal proton irradiation. *Phys Med Biol* (2009) **54**(8):2277–91. doi:10.1088/0031-9155/54/8/002
34. Smoll NR, Drummond KJ. The incidence of medulloblastomas and primitive neurectodermal tumours in adults and children. *J Clin Neurosci* (2012) **19**(11):1541–4. doi:10.1016/j.jocn.2012.04.009
35. Zhang R, Howell RM, Taddei PJ, Giebeler A, Mahajan A, Newhauser WD. A comparative study on the risks of radiogenic second cancers and cardiac mortality in a set of pediatric medulloblastoma patients treated with photon or proton craniospinal irradiation. *Radiother Oncol* (2014) **113**(1):84–8. doi:10.1016/j.radonc.2014.07.003
36. Ramaswamy V, Remke M, Adamski J, Bartels U, Tabori U, Wang X, et al. Medulloblastoma subgroup-specific outcomes in irradiated children: who are the true high-risk patients? *Neuro Oncol* (2016) **18**:291–7. doi:10.1093/neuonc/nou357
37. Diallo I, Haddy N, Adjadj E, Samand A, Quiniou E, Chavaudra J, et al. Frequency distribution of second solid cancer locations in relation to the irradiated volume among 115 patients treated for childhood cancer. *Int J Radiat Oncol Biol Phys* (2009) **74**(3):876–83. doi:10.1016/j.ijrobp.2009.01.040
38. Jagetic LJ, Newhauser WD. A simple and fast physics-based analytical method to calculate therapeutic and stray doses from external beam, megavoltage X-ray therapy. *Phys Med Biol* (2015) **60**(12):4753–75. doi:10.1088/0031-9155/60/12/4753
39. Hendricks JS, McKinney GW, Wilcox TA, James MR. *MCNPX 2.7.A Extensions*. LA-UR-12-00135. Los Alamos National Laboratory (2012).
40. Ferrari A, Sala PR, Fassò A, Ranft J. *FLUKA: A Multi-Particle Transport Code*. CERN-2005-010 (2005).
41. Böhlen T, Cerutti F, Chin M, Fasso A, Ferrari A, Ortega P, et al. The FLUKA code: developments and challenges for high energy and medical applications. *Nucl Data Sheets* (2014) **120**:211–4. doi:10.1016/j.nds.2014.07.049
42. Jabbari I, Monadi S. Development and validation of MCNPX-based Monte Carlo treatment plan verification system. *J Med Phys* (2015) **40**(2):80. doi:10.4103/0971-6203.158678
43. Newhauser W, Fontenot J, Zheng Y, Polf J, Titt U, Koch N, et al. Monte Carlo simulations for configuring and testing an analytical proton dose-calculation algorithm. *Phys Med Biol* (2007) **52**(15):4569–84. doi:10.1088/0031-9155/52/15/014
44. Agostinelli S, Allison J, Amako K, Apostolakis J, Araujo H, Arce P, et al. GEANT4-a simulation toolkit. *Nucl Instr Methods Phys Res A* (2003) **506**(3):250–303. doi:10.1016/s0168-9002(03)01368-8
45. Perl J, Shin J, Schümann J, Faddegon B, Paganetti H. An innovative proton Monte Carlo platform for research and clinical applications. *Med Phys* (2012) **39**(11):6818–37. doi:10.1118/1.4758060
46. Binns PJ, Hough JH. Secondary dose exposures during 200 MeV proton therapy. *Radiat Prot Dosimetry* (1997) **70**(1–4):441–4. doi:10.1093/oxfordjournals.rpd.a031993
47. Agosteo S, Birattari C, Caravaggio M, Silari M, Tosi G. Secondary neutron and photon dose in proton therapy. *Radiother Oncol* (1998) **48**(3):293–305. doi:10.1016/S0167-8140(98)00049-8
48. Yan X, Titt U, Koehler AM, Newhauser WD. Measurement of neutron dose equivalent to proton therapy patients outside of the proton radiation field. *Nucl Instrum Methods Phys Res A* (2002) **476**(1–2):429–34. doi:10.1016/S0168-9002(01)01483-8
49. Hall EJ. Intensity-modulated radiation therapy, protons, and the risk of second cancers. *Int J Radiat Oncol Biol Phys* (2006) **65**(1):1–7. doi:10.1016/j.ijrobp.2006.01.027
50. Polf JC, Newhauser WD. Calculations of neutron dose equivalent exposures from range-modulated proton therapy beams. *Phys Med Biol* (2005) **50**(16):3859–73. doi:10.1088/0031-9155/50/16/014
51. Polf JC, Newhauser WD, Titt U. Patient neutron dose equivalent exposures outside of the proton therapy treatment field. *Radiat Prot Dosimetry* (2005) **115**(1–4):154–8. doi:10.1093/rpd/nci264
52. Titt U, Zheng Y, Vassiliev ON, Newhauser WD. Monte Carlo investigation of collimator scatter of proton-therapy beams produced using the passive scattering method. *Phys Med Biol* (2008) **53**(2):487–504. doi:10.1088/0031-9155/53/2/014
53. Zheng Y, Fontenot J, Taddei P, Mirkovic D, Newhauser W. Monte Carlo simulations of neutron spectral fluence, radiation weighting factor and ambient dose equivalent for a passively scattered proton therapy unit. *Phys Med Biol* (2008) **53**(1):187–201. doi:10.1088/0031-9155/53/1/013
54. Zheng Y, Newhauser W, Fontenot J, Taddei P, Mohan R. Monte Carlo study of neutron dose equivalent during passive scattering proton therapy. *Phys Med Biol* (2007) **52**(15):4481–96. doi:10.1088/0031-9155/52/15/008
55. Mesoloras G, Sandison GA, Stewart RD, Farr JB, Hsi WC. Neutron scattered dose equivalent to a fetus from proton radiotherapy of the mother. *Med Phys* (2006) **33**(7):2479–90. doi:10.1118/1.2241868

56. Jarlskog CZ, Lee C, Bolch WE, Xu XG, Paganetti H. Assessment of organ-specific neutron equivalent doses in proton therapy using computational whole-body age-dependent voxel phantoms. *Phys Med Biol* (2008) **53**(3):693. doi:10.1088/0031-9155/53/3/012
57. Moyers M, Benton E, Ghebremedhin A, Coutrakon G. Leakage and scatter radiation from a double scattering based proton beamline. *Med Phys* (2008) **35**(1):128–44. doi:10.1118/1.2805086
58. Koch N, Newhauser W. Virtual commissioning of a treatment planning system for proton therapy of ocular cancers. *Radiat Prot Dosimetry* (2005) **115**(1–4):159–63. doi:10.1093/rpd/nci224
59. Wroe A, Clasie B, Kooy H, Flanz J, Schulte R, Rosenfeld A. Out-of-field dose equivalents delivered by passively scattered therapeutic proton beams for clinically relevant field configurations. *Int J Radiat Oncol Biol Phys* (2009) **73**(1):306–13. doi:10.1016/j.ijrobp.2008.09.030
60. Clasie B, Wroe A, Kooy H, Depauw N, Flanz J, Paganetti H, et al. Assessment of out-of-field absorbed dose and equivalent dose in proton fields. *Med Phys* (2010) **37**(1):311–21. doi:10.1118/1.3271390
61. Tayama R, Fujita Y, Tadokoro M, Fujimaki H, Sakae T, Terunuma T. Measurement of neutron dose distribution for a passive scattering nozzle at the proton medical research center (PMRC). *Nucl Instrum Methods Phys Res A* (2006) **564**(1):532–6. doi:10.1016/j.nima.2006.04.028
62. Fontenot JD, Newhauser WD, Titt U. Design tools for proton therapy nozzles based on the double-scattering foil technique. *Radiat Prot Dosimetry* (2005) **116**(1–4 Pt 2):211–5. doi:10.1093/rpd/nci229
63. Randeniya SD, Taddei PJ, Newhauser WD, Yepes P. Intercomparison of Monte Carlo radiation transport codes MCNPX, GEANT4, and FLUKA for simulating proton radiotherapy of the eye. *Nucl Technol* (2009) **168**(3):810–4.
64. La Tessa C, Berger T, Kaderka R, Schardt D, Burmeister S, Labrenz J, et al. Characterization of the secondary neutron field produced during treatment of an anthropomorphic phantom with X-rays, protons and carbon ions. *Phys Med Biol* (2014) **59**(8):2111. doi:10.1088/0031-9155/59/8/2111
65. Farah J, Martinetti F, Sayah R, Lacoste V, Donadille L, Trompier F, et al. Monte Carlo modeling of proton therapy installations: a global experimental method to validate secondary neutron dose calculations. *Phys Med Biol* (2014) **59**(11):2747. doi:10.1088/0031-9155/59/11/2747
66. Yonai S, Kase Y, Matsufuji N, Kanai T, Nishio T, Namba M, et al. Measurement of absorbed dose, quality factor, and dose equivalent in water phantom outside of the irradiation field in passive carbon-ion and proton radiotherapies. *Med Phys* (2010) **37**(8):4046–55. doi:10.1118/1.3458721
67. Perez-Andujar A, Zhang R, Newhauser W. Monte Carlo and analytical model predictions of leakage neutron exposures from passively scattered proton therapy. *Med Phys* (2013) **40**(12):121714. doi:10.1118/1.4829512
68. Perez-Andujar A, Newhauser WD, Taddei PJ, Mahajan A, Howell RM. The predicted relative risk of premature ovarian failure for three radiotherapy modalities in a girl receiving craniospinal irradiation. *Phys Med Biol* (2013) **58**(10):3107–23. doi:10.1088/0031-9155/58/10/3107
69. Miralbell R, Lomax A, Cella L, Schneider U. Potential reduction of the incidence of radiation-induced second cancers by using proton beams in the treatment of pediatric tumors. *Int J Radiat Oncol Biol Phys* (2002) **54**(3):824–9. doi:10.1016/S0360-3016(02)02982-6
70. ICRP. *ICRP Publication 60: 1990 Recommendations of the International Commission on Radiological Protection*. Ann ICRP (1991).
71. BEIR VII. *Health Risks from Exposure to Low Levels of Ionizing Radiation: BEIR VII – Phase 2*. Washington DC: The National Academies Press (2006).
72. Zhang R, Howell RM, Giebeler A, Taddei PJ, Mahajan A, Newhauser WD. Comparison of risk of radiogenic second cancer following photon and proton craniospinal irradiation for a pediatric medulloblastoma patient. *Phys Med Biol* (2013) **58**(4):807–23. doi:10.1088/0031-9155/58/4/807
73. Zhang R, Fontenot JD, Mirkovic D, Hendricks JS, Newhauser WD. Advantages of MCNPX-based lattice tally over mesh tally in high-speed Monte Carlo dose reconstruction for proton radiotherapy. *Nucl Technol* (2013) **183**(1):101–6.
74. Taddei PJ, Mirkovic D, Fontenot JD, Giebeler A, Zheng Y, Titt U, et al. Reducing stray radiation dose for a pediatric patient receiving proton craniospinal irradiation. *Nucl Technol* (2009) **168**(1):108–12.
75. Dowdell SJ, Clasie B, Depauw N, Metcalfe P, Rosenfeld AB, Kooy HM, et al. Monte Carlo study of the potential reduction in out-of-field dose using a patient-specific aperture in pencil beam scanning proton therapy. *Phys Med Biol* (2012) **57**(10):2829. doi:10.1088/0031-9155/57/10/2829
76. Hyer DE, Hill PM, Wang D, Smith BR, Flynn RT. A dynamic collimation system for penumbra reduction in spot-scanning proton therapy: proof of concept. *Med Phys* (2014) **41**(9):091701. doi:10.1118/1.4837155
77. Rechner LA, Howell RM, Zhang R, Etzel C, Lee AK, Newhauser WD. Risk of radiogenic second cancers following volumetric modulated arc therapy and proton arc therapy for prostate cancer. *Phys Med Biol* (2012) **57**(21):7117–32. doi:10.1088/0031-9155/57/21/7117
78. Zhang R, Perez-Andujar A, Fontenot JD, Taddei PJ, Newhauser WD. An analytic model of neutron ambient dose equivalent and equivalent dose for proton radiotherapy. *Phys Med Biol* (2010) **55**(23):6975–85. doi:10.1088/0031-9155/55/23/S01
79. Schneider C, Newhauser W, Farah J. An analytical model of leakage neutron equivalent dose for passively-scattered proton radiotherapy and validation with measurements. *Cancers (Basel)* (2015) **7**(2):795–810. doi:10.3390/cancers7020795
80. Farah J, Bonfrate A, De Marzi L, De Oliveira A, Delacroix S, Martinetti F, et al. Configuration and validation of an analytical model predicting secondary neutron radiation in proton therapy using Monte Carlo simulations and experimental measurements. *Phys Med* (2015) **31**(3):248–56. doi:10.1016/j.ejmp.2015.01.017
81. Eley J, Newhauser W, Homann K, Howell R, Schneider C, Durante M, et al. Implementation of an analytical model for leakage neutron equivalent dose in a proton radiotherapy planning system. *Cancers (Basel)* (2015) **7**(1):427–38. doi:10.3390/cancers7010427
82. Schneider U, Agosteo S, Pedroni E, Besserer J. Secondary neutron dose during proton therapy using spot scanning. *Int J Radiat Oncol Biol Phys* (2002) **53**(1):244–51. doi:10.1016/S0360-3016(01)02826-7
83. Hall EJ, Wuu C-S. Radiation-induced second cancers: the impact of 3D-CRT and IMRT. *Int J Radiat Oncol Biol Phys* (2003) **56**(1):83–8. doi:10.1016/S0360-3016(03)00073-7
84. Nelson WR, Hirayama H, Rogers DW. *EGS4 Code System*. Menlo Park, CA: Stanford Linear Accelerator Center (1985).
85. Rogers D, Faddegon B, Ding G, Ma CM, We J, Mackie T. BEAM: a Monte Carlo code to simulate radiotherapy treatment units. *Med Phys* (1995) **22**(5):503–24. doi:10.1118/1.597552
86. Walters B, Kawrakow I, Rogers DWO. *DOSXYZnrc Users Manual*. NRCC Report PIRS-794revB (2016).
87. Kawrakow I, Fippel M, Friedrich K. 3D electron dose calculation using a voxel based Monte Carlo algorithm (VMC). *Med Phys* (1996) **23**(4):445–57. doi:10.1118/1.597673
88. Sempau J, Wilderman SJ, Bielajew AF. DPM, a fast, accurate Monte Carlo code optimized for photon and electron radiotherapy treatment planning dose calculations. *Phys Med Biol* (2000) **45**(8):2263. doi:10.1088/0031-9155/45/8/315
89. Ma C-M, Li J, Pawlicki T, Jiang S, Deng J. MCDOSE – a Monte Carlo dose calculation tool for radiation therapy treatment planning. In: Wolfgang S, Bortfeld T, editors. *The Use of Computers in Radiation Therapy*. Heidelberg: Springer (2000). p. 123–5.
90. Pemler P, Besserer J, Schneider U, Neuenschwander H. Evaluation of a commercial electron treatment planning system based on Monte Carlo techniques (eMC). *Z Med Phys* (2006) **16**(4):313–29. doi:10.1078/0939-3889-00330
91. Chetty IJ, Curran B, Cygler JE, DeMarco JJ, Ezzell G, Faddegon BA, et al. Report of the AAPM task group no. 105: issues associated with clinical implementation of Monte Carlo-based photon and electron external beam treatment planning. *Med Phys* (2007) **34**(12):4818–53. doi:10.1118/1.2795842
92. Lee C, Jung JW, Pelletier C, Pyakuryal A, Lamart S, Kim JO, et al. Reconstruction of organ dose for external radiotherapy patients in retrospective epidemiologic studies. *Phys Med Biol* (2015) **60**(6):2309. doi:10.1088/0031-9155/60/6/2309
93. Taddei PJ, Jalbout W, Howell RM, Khater N, Geara F, Homann K, et al. Analytical model for out-of-field dose in photon craniospinal irradiation. *Phys Med Biol* (2013) **58**(21):7463–79. doi:10.1088/0031-9155/58/21/7463
94. Taddei PJ, Khater N, Zhang R, Geara FB, Mahajan A, Jalbout W, et al. Inter-institutional comparison of personalized risk assessments for second malignant neoplasms for a 13-year-old girl receiving proton versus photon craniospinal irradiation. *Cancers (Basel)* (2015) **7**(1):407–26. doi:10.3390/cancers7010407

95. Stovall M, Blackwell CR, Cundiff J, Novack DH, Palta JR, Wagner LK, et al. Fetal dose from radiotherapy with photon beams: report of AAPM radiation therapy committee task group no. 36. *Med Phys* (1995) **22**(1):63–82. doi:10.1118/1.597557
96. Kry SF, Howell RM, Titt U, Salehpour M, Mohan R, Vassiliev ON. Energy spectra, sources, and shielding considerations for neutrons generated by a flattening filter-free clinac. *Med Phys* (2008) **35**(5):1906–11. doi:10.1118/1.2905029
97. Kragl G, Baier F, Lutz S, Albrich D, Dalaryd M, Kroupa B, et al. Flattening filter free beams in SBRT and IMRT: dosimetric assessment of peripheral doses. *Z Med Phys* (2011) **21**(2):91–101. doi:10.1016/j.zemedi.2010.07.003
98. Howell RM, Giebeler A, Koontz-Raisig W, Mahajan A, Etzel CJ, D'Amelio AM Jr, et al. Comparison of therapeutic dosimetric data from passively scattered proton and photon craniospinal irradiations for medulloblastoma. *Radiat Oncol* (2012) **7**:116. doi:10.1186/1748-717X-7-116
99. Zhang R, Howell RM, Homann K, Giebeler A, Taddei PJ, Mahajan A, et al. Predicted risks of radiogenic cardiac toxicity in two pediatric patients undergoing photon or proton radiotherapy. *Radiat Oncol* (2013) **8**(1):184. doi:10.1186/1748-717X-8-184
100. Taddei PJ, Mahajan A, Mirkovic D, Zhang R, Giebeler A, Kornguth D, et al. Predicted risks of second malignant neoplasm incidence and mortality due to secondary neutrons in a girl and boy receiving proton craniospinal irradiation. *Phys Med Biol* (2010) **55**(23):7067–80. doi:10.1088/0031-9155/55/23/S08
101. Freund D, Zhang R, Sanders M, Newhauser W. Predictive risk of radiation induced cerebral necrosis in pediatric brain cancer patients after VMAT versus proton therapy. *Cancers (Basel)* (2015) **7**(2):617–30. doi:10.3390/cancers7020617
102. NCRP. *Uncertainties in the Estimation of Radiation Risks and Probability of Disease Causation (Report No. 171)*. Bethesda, MD: Nation Council on Radiation Protection (2012).
103. Preston RJ, John DB Jr, Brill AB, Ranajit C, Rory C, Hoffman FO, et al. Uncertainties in estimating health risks associated with exposure to ionising radiation. *J Radiol Protect* (2013) **33**(3):573. doi:10.1088/0952-4746/33/3/573
104. Fontenot JD, Bloch C, Followill D, Titt U, Newhauser WD. Estimate of the uncertainties in the relative risk of secondary malignant neoplasms following proton therapy and intensity-modulated photon therapy. *Phys Med Biol* (2010) **55**(23):6987–98. doi:10.1088/0031-9155/55/23/S02
105. Nguyen J, Moteabbed M, Paganetti H. Assessment of uncertainties in radiation-induced cancer risk predictions at clinically relevant doses. *Med Phys* (2015) **42**(1):81–9. doi:10.1118/1.4903272
106. Berrington de Gonzalez A, Wong J, Kleinerman R, Kim C, Morton L, Bekelman JE. Clinical investigation: risk of second cancers according to radiation therapy technique and modality in prostate cancer survivors. *Int J Radiat Oncol Biol Phys* (2015) **91**:295–302. doi:10.1016/j.ijrobp.2014.10.040
107. Kasper HB, Raeke L, Indelicato DJ, Symecko H, Hartsell W, Mahajan A, et al. The pediatric proton consortium registry: a multi-institutional collaboration in US proton centers. *Int J Part Ther* (2014) **1**(2):323–33. doi:10.14338/IJPT.13-00006.1
108. Gropp W, Lusk E, Doss N, Skjellum A. A high-performance, portable implementation of the MPI message passing interface standard. *Parallel Comput* (1996) **22**(6):789–828. doi:10.1016/0167-8191(96)00024-5
109. Vadapalli R, Yepes P, Newhauser W, Lichti R. Grid-enabled treatment planning for proton therapy using Monte Carlo simulations. *Nucl Technol* (2011) **175**(1):16–21.
110. Yepes PP, Mirkovic D, Taddei PJ. A GPU implementation of a track-repeating algorithm for proton radiotherapy dose calculations. *Phys Med Biol* (2010) **55**(23):7107. doi:10.1088/0031-9155/55/23/S11
111. Newhauser W, Jones T, Swerdloff S, Cilia M, Carver R, Halloran A, et al. Anonymization of DICOM electronic medical records for radiation therapy. *Comput Biol Med* (2014) **53**:134–40. doi:10.1016/j.compbiomed.2014.07.010
112. Zhang R, Mirkovic D, Newhauser WD. Visualization of risk of radiogenic second cancer in the organs and tissues of the human body. *Radiat Oncol* (2015) **10**(1):107. doi:10.1186/s13014-015-0404-x
113. Rechner LA, Eley JG, Howell RM, Zhang R, Mirkovic D, Newhauser WD. Risk-optimized proton therapy to minimize radiogenic second cancers. *Phys Med Biol* (2015) **60**(10):3999–4013. doi:10.1088/0031-9155/60/10/3999
114. Hudson MM, Meyer WH, Pui C-H. Progress born from a legacy of collaboration. *J Clin Oncol* (2015) **33**:2935–7. doi:10.1200/JCO.2015.63.4535
115. Boice JD Jr, Lauriston S. Taylor lecture: radiation epidemiology-the golden age and future challenges. *Health Phys* (2011) **100**(1):59–76. doi:10.1097/HP.0b013e3181f9797d
116. Ron E, Jacob P. Late health effects of ionizing radiation: bridging the experimental and epidemiologic divide. *Radiat Res* (2010) **174**(6b):789–92. doi:10.1667/RRXX24.1
117. Newhauser W. Complexity of advanced radiation therapy necessitates multidisciplinary inquiry into dose reconstruction and risk assessment. *Phys Med Biol* (2010) **55**(23). doi:10.1088/0031-9155/55/23/E01
118. de González AB, Morton LM. Converting epidemiologic studies of cancer etiology to survivorship studies: approaches and challenges. *Cancer Epidemiol Biomarkers Prev* (2012) **21**(6):875–80. doi:10.1158/1055-9965.EPI-12-0131
119. Bhatia S, Armenian SH, Armstrong GT, van Dulmen-den Broeder E, Hawkins MM, Kremer LC, et al. Collaborative research in childhood cancer survivorship: the current landscape. *J Clin Oncol* (2015) **33**:3055–64. doi:10.1200/JCO.2014.59.8052
120. Siva S, MacManus MP, Martin RF, Martin OA. Abscopal effects of radiation therapy: a clinical review for the radiobiologist. *Cancer Lett* (2015) **356**(1):82–90. doi:10.1016/j.canlet.2013.09.018
121. Kavanagh J, Waring E, Prise K. Radiation responses of stem cells: targeted and non-targeted effects. *Radiat Prot Dosimetry* (2015) **166**:110–7. doi:10.1093/rpd/ncv161
122. Le Q-T, Shirato H, Giaccia AJ, Koong AC. Emerging treatment paradigms in radiation oncology. *Clin Cancer Res* (2015) **21**:3393–401. doi:10.1158/1078-0432.CCR-14-1191
123. Allen Li X, Alber M, Deasy JO, Jackson A, Ken Jee K-W, Marks LB, et al. The use and QA of biologically related models for treatment planning: short report of the TG-166 of the therapy physics committee of the AAPM. *Med Phys* (2012) **39**(3):1386–409. doi:10.1118/1.3685447

Conflict of Interest Statement: The authors declare that the research was conducted in the absence of any commercial or financial relationships that could be construed as a potential conflict of interest.

Copyright © 2016 Newhauser, de Gonzalez, Schulte and Lee. This is an open-access article distributed under the terms of the Creative Commons Attribution License (CC BY). The use, distribution or reproduction in other forums is permitted, provided the original author(s) or licensor are credited and that the original publication in this journal is cited, in accordance with accepted academic practice. No use, distribution or reproduction is permitted which does not comply with these terms.

frontiers in Oncology

MINI REVIEW
published: 26 November 2015
doi: 10.3389/fonc.2015.00261

Secondary Malignancy Risk Following Proton Radiation Therapy

Bree R. Eaton†, Shannon M. MacDonald, Torunn I. Yock and Nancy J. Tarbell*

Department of Radiation Oncology, Massachusetts General Hospital, Harvard Medical School, Boston, MA, USA

Radiation-induced secondary malignancies are a significant, yet uncommon cause of morbidity and mortality among cancer survivors. Secondary malignancy risk is dependent upon multiple factors including patient age, the biological and genetic predisposition of the individual, the volume and location of tissue irradiated, and the dose of radiation received. Proton therapy (PRT) is an advanced particle therapy with unique dosimetric properties resulting in reduced entrance dose and minimal to no exit dose when compared with standard photon radiation therapy. Multiple dosimetric studies in varying cancer subtypes have demonstrated that PRT enables the delivery of adequate target volume coverage with reduced integral dose delivered to surrounding tissues, and modeling studies taking into account dosimetry and radiation cell biology have estimated a significantly reduced risk of radiation-induced secondary malignancy with PRT. Clinical data are emerging supporting the lower incidence of secondary malignancies after PRT compared with historical photon data, though longer follow-up in proton treated cohorts is awaited. This article reviews the current dosimetric and clinical literature evaluating the incidence of and risk factors associated with radiation-induced secondary malignancy following PRT.

Keywords: proton, radiotherapy, radiation, second malignancy

OPEN ACCESS

Edited by:
Marco Durante, GSI, Germany

Reviewed by:
Dalong Pang, Georgetown University Hospital, USA
Uwe Schneider, University of Zurich and Radiotherapy Hirslanden, Switzerland
Wayne D. Newhauser, Louisiana State University, USA

****Correspondence:***
Bree R. Eaton
brupper@emory.edu

†Present address:
Bree R. Eaton, Winship Cancer Institute of Emory University, Atlanta, GA, USA

Specialty section:
This article was submitted to Radiation Oncology, a section of the journal Frontiers in Oncology

Received: *14 September 2015*
Accepted: *09 November 2015*
Published: *26 November 2015*

Citation:
Eaton BR, MacDonald SM, Yock TI and Tarbell NJ (2015) Secondary Malignancy Risk Following Proton Radiation Therapy. Front. Oncol. 5:261. doi: 10.3389/fonc.2015.00261

INTRODUCTION

Radiation-induced secondary malignancies are a rare, yet significant late effect of radiation treatment among cancer survivors. The second malignancy risk is dependent upon the patient's age, the radiation dose received and volume of normal tissue irradiated, as well as the patients' family history of cancer and unique biological risk for malignancy (1, 2). As the risk is life-long and cumulative, children and young adults expected to survive many decades following definitive cancer therapy are at greatest risk for developing a radiation-induced malignancy. Long-term follow-up of the Childhood Cancer Survivor Study has demonstrated that there has been an increase in mortality attributed to second malignancies over time and the death rate due to a subsequent malignancy exceeds that due to all other causes at 25 years after first cancer diagnosis (3, 4). Retrospective series of large cohorts of pediatric patients treated with older photon radiotherapy techniques have reported a cumulative incidence of second malignancies ranging from 9.3 to 19% at 30 years (1, 5, 6), which can have profound effects on patient quality of life and mortality (4–6).

Proton therapy (PRT) is an advanced radiation technique now used with the hope of reducing late effects of radiotherapy. A proton beam has a unique dose-deposition pattern characterized by reduced entrance dose and minimal to no exit dose compared with conventional photon irradiation (7). Treating with protons gives the radiation oncologist the ability to maintain target volume coverage

required for efficacious therapy, while minimizing dose delivered to nearby normal tissues (8). A primary expected benefit of this decrease in dose to normal tissues is reduced risk of secondary malignancies (9) as well as other radiation-induced acute and late effects. In this article, we will review selected dosimetric and clinic data addressing the impact of PRT treatment on secondary malignancy risk.

DOSIMETRIC COMPARISONS

In a treatment planning comparison study evaluating PRT in comparison to standard photon techniques and intensity-modulated radiation therapy (IMRT) for a variety of malignancies, the use of protons has been demonstrated to substantially reduce the volume of normal tissues receiving medium to low doses (below about 70% of the target dose) when compared with both standard and IMRT photon plans (8). Over all cases, the use of protons lead to a reduction of the total integral dose by a factor of three compared to standard photon techniques and at least a factor of two compared to intensity-modulated photon plans (8). Many similar dosimetric comparison studies have been performed for a variety of specific tumor types among children and adults and have clearly demonstrated the superior ability of PRT to spare normal tissues from unwanted radiation (9–12). With the use of craniospinal irradiation for medulloblastoma, the dosimetric benefit of protons is particularly striking as organs anterior to the vertebrae are spared from receiving unwanted radiation with PRT (12) (**Figure 1**). In effort to quantify the effect of the reduced total integral dose delivered with PRT on secondary malignancy risk, studies have further utilized modeling systems based on dosimetric comparisons, organ equivalent dose, and radiation protection models to approximate the benefit of protons with regard to second malignancies.

In an analysis of pediatric rhabdomyosarcoma and medulloblastoma cases, Miralbell et al. (13) analyzed the dosimetry of conventional photons, IMRT, and scattered and scanned proton plans and estimated secondary cancer risk according to the International Commission on Radiologic Protection (ICRP). Results revealed that proton plans reduced the expected incidence of radiation-induced secondary cancers for the rhabdomyosarcoma case by a factor ≥2 and for the medulloblastoma case by a factor of 8–15 when compared with either IMRT or conventional X-ray plans (13). Furthermore, cost-effectiveness analysis which has included the risk of secondary malignancies for patients with medulloblastoma has shown that proton treatment is associated with higher quality adjusted life years

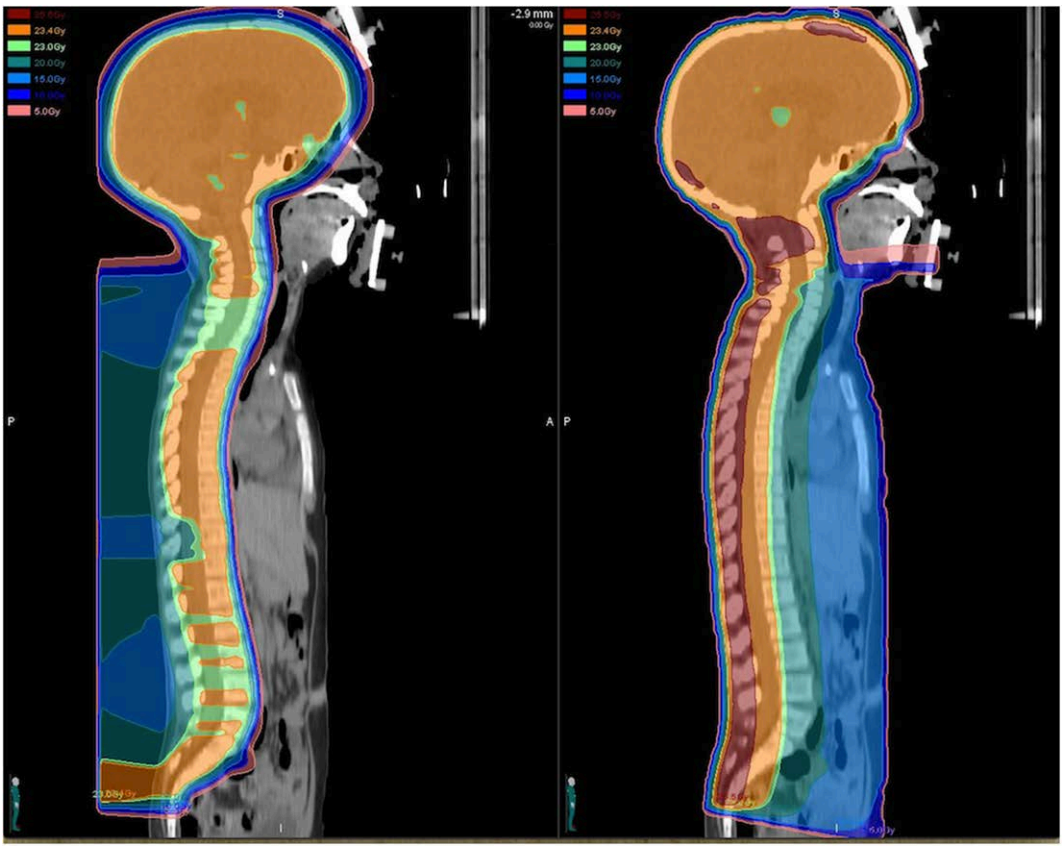

FIGURE 1 | Dose distributions for a proton (left) and photon (right) craniospinal plan prescribed to 23.4 Gy (relative biological equivalents) are illustrated for comparison. The proton craniospinal plan provides considerable sparing of normal tissues anterior to the spinal canal and delivers a significantly reduced total integral dose to the patient.

and reduced cost, in part due to the estimations of reduced incidence of secondary malignancies (14, 15). In a similar study from Moteabbed et al. (16), dose distributions from passive scattered protons, pencil bean scanning protons, and IMRT and volumetric-modulated arc therapy (VMAT) photon plans for six pediatric patients with brain and head-and-neck tumors were used to calculate the excess absolute risk (EAR) and lifetime attributable risk (LAR) for developing a second tumor in the soft tissue and skull. The LAR for IMRT/VMAT relative to proton plans ranged from 1.3 to 4.6 for soft tissue and from 3.5 to 9.5 for the skull. Larger absolute LAR was observed for younger patients and when using linear risk models (16). Paganetti et al. (17) used phantom data and a sophisticated risk model based on cell kill, mutation, repopulation, and inhomogeneous organ doses to estimate the LAR of second malignancy within the RT field for representative cases of optic glioma and vertebral body Ewing's sarcoma on a 4- and 14-year-old fully contoured phantom. This study found that protons may reduce the risk of second malignancy by a factor ranging from 2 to 10 and also demonstrated that LAR was affected by different methods of proton RT planning (17).

Multiple other dosimetric and secondary risk modeling studies have been performed for adult malignancies with similar results. In a dosimetric comparison between PRT and IMRT among 11 patients with low-grade glioma prescribed 54 Gy (RBE), the equivalent uniform dose delivered to adjacent normal tissues was found to be 10–20 Gy lower with protons (18). Using biological modeling of radiation induced toxicities, the mean ratio for excess risk of radiation induced second tumors with IMRT as compared to protons was found to be 2.2 (range 1.6–6.5). The mean excess risk of a PRT induced second tumor in the brain per 10,000 cases per year was 47 (range 11–83), while the mean risk for IMRT was 106 (range 70–134) (18). In an analysis of conventional parallel opposed and intensity-modulated photon and proton treatment plans for a patient with Hodgkin's disease, spot scanning PRT was found to decrease the secondary malignancy risk by a factor of 2 based on the ICRP calculation scheme and normal tissue dose distribution (19).

Yoon et al. (20) used ion chambers and CR-39 detectors to measure the secondary dose delivered to tissues outside of the target volume (measured at 20–60 cm from the isocenter) during irradiation with IMRT and PRT for patients with prostate and head-and-neck cancer and estimated organ-specific radiation-induced cancer risk by applying organ equivalent dose estimations to dose distributions. The average secondary doses for prostate patients ranged between 3 and 1 mSv/Gy with IMRT, which was approximately one order of magnitude higher than for PRT. Although the average secondary doses of IMRT were higher than those of PRT for head-and-neck cancers, these differences were not significant. Organ equivalent dose calculations showed that, for prostate cancer patients, the risk of secondary cancers in out-of-field organs, such as the stomach, lungs, and thyroid, was at least five times higher for IMRT than for PRT (20). A second dosimetric comparison among prostate cancer patients evaluating protons and 6 MV IMRT photon plans was performed by Fontenot et al. (21), and the secondary malignancy risk was estimated by taking into account both primary and secondary contributions to total dose delivered on an organ-specific basis and using risk models from the Committee on the Biological Effects of Ionizing Radiation. It was found that PRT reduced the risk of a secondary malignancy by 26–39% compared with IMRT, which was attributed to the substantial sparing of the rectum and bladder by the PRT plans in this study (21).

NEUTRON SCATTER

Secondary dose from neutron scatter produced during radiotherapy contributes to the total effective dose delivered to the patient and the secondary malignancy risk but is not accounted for in most dosimetric comparisons. The neutron scatter with PRT results from protons losing energy as they interact with the range modulator and apertures (22). In some circumstances, neutron dose delivered outside of target tissues with passively scattered protons has been estimated to be much greater than with either scanned PRT, intensity modulated, or conventional photon treatment (23). This has sparked controversy about the effect of PRT on secondary malignancy risk and the relative benefit of pencil beam scanning vs. passive scattering proton treatment (22–26).

The neutron dose equivalent with pencil beam scanning for a medium size target volume can reach approximately 1% of the treatment dose in the region of the Bragg peak (27). In non-target tissues of the patient, the neutron dose contributes approximately 0.004 and 0.002 Sv/treatment Gy, for large and medium target volumes, respectively, a factor which is about two times that of photon therapy (26). However, because this dose delivered to the non-target area from neutron scatter is far less than that resulting from primary dose fall-off, multiple authors have concluded that primary dosimetric comparisons are sufficient for estimation of secondary malignancy risk. Thus, the total integral dose delivered to the patient remains much less with either passive scattered or pencil bean scanning protons in comparison with photon treatment (24, 26).

Dosimetric comparisons taking into account the contribution of neutron scatter have concluded that PRT still delivers a reduced total integral dose when compared with photon irradiation (24). In an analysis of 30 patients with prostate cancer from Schneider et al. (27), the impact of X-ray scatter, neutron radiation, and the primary dose distribution on secondary cancer incidence were analyzed for convention and intensity-modulated photon plans as well as spot scanning PRT. After considering both primary dose and scatter dose contributions, it was estimated that the use of spot-scanned protons reduced the secondary cancer incidence by as much as 50% when compared with photon therapy (27). Pencil beam scanning PRT may provide the greatest opportunity to reduce the impact of neutron scatter on secondary malignancy risk as the out-of-field neutron dose produced by a scattered proton beam has been estimated to be more than 100 times that off a scanned proton beam (28). However, secondary malignancy risk due to scatter radiation from passively scattered proton beam treatment remains low. A study evaluating the total lifetime risk of a second cancer from stray radiation alone to be 1.5% for passively scatter craniospinal proton treatment and 0.8% for scanned craniospinal proton treatment (29). And when taking

into account the therapeutic radiation as well as scatter radiation dose, passively scattered and scanned proton beam treatment similarly reduced the secondary cancer risk in comparison with IMRT photon treatment (29).

CLINICAL DATA

Clinical data comparing the secondary malignancy incidence in long-term survivors following proton and photon therapy are limited given the significant follow-up time necessary to effectively evaluate radiation induced malignancy. However, a reduced incidence of radiation induced second cancer with PRT as compared to photon therapy has been reported in multiple series with early follow-up. Chung et al. (30) performed a large case matched comparison of 588 patients treated with PRT at the Harvard cyclotron from 1973 to 2001 and 588 patients treated with photon therapy from the Surveillance, Epidemiology, and End Results Program. Patients were matched with respect to age at radiation treatment, sex, year of treatment, cancer histology, and treatment site, and the median follow-up time was 6.7 years for proton patients and 6.0 years for photon patients. The majority of patients were adults with tumors of the prostate, central nervous system or head-and-neck region. The crude rate of second malignancies was 5.2% among the proton cohort (29 patients) vs. 7.5% in photon cohort (42 patients). On multivariable analysis, PRT was associated with a decreased risk of second malignancy [adjusted hazard ratio, 0.52 (95% confidence interval, 0.32–0.85), $p = 0.009$] when compared with photon therapy (30).

Multiple clinical series of pediatric patients have reported excellent outcomes with very low rates of second malignancies after PRT (**Table 1**). Among a prospective phase II study of PRT for 59 children with medulloblastoma and a median follow-up of 7 years (range 3.9–10.3), no patients have suffered from a second malignancies (31). The results from the 45 standard risk patients from this phase II study were then compared to a case matched series of 43 patients treated with photons over a similar time period (32). Three patients from the photon cohort experienced a second malignancy, including an astrocytoma, intracranial desmoid tumor, and thyroid cancer occurring 12.9, 3.7, and 12.7 years after treatment, respectively, while none of the proton patients developed a second tumor (32). Sethi et al. (33) retrospectively analyzed the incidence of secondary malignancy among patients treated with either proton or photon therapy for retinoblastoma. After a median follow-up of 6.9 years (range, 1.0–24.4 years) for the 55 patients in the proton cohort and 13.1 years (range, 1.4–23.9 years) for the 31 patients in the photon cohort, the 10-year cumulative incidence of RT-induced or in-field second malignancies was significantly less among the proton cohort (0 vs. 14%, $p = 0.015$) (33). One proton patient with bilateral retinoblastoma did develop an out-of-field osteosarcoma of the femur (33). Other proton series among children with ependymoma (34), low-grade glioma (35), Ewing's sarcoma (36), and rhabdomyosarcoma (37) have also reported no cases of PRT associated solid tumors (**Table 1**) after limited follow-up. Though longer follow-up is required for effective secondary malignancy risk comparison between proton and photon radiotherapy, these early clinical reports suggest a reduced incidence of radiation induced secondary cancers with PRT.

TABLE 1 | Secondary malignancy outcome data in pediatric patients treated with proton radiotherapy.

Reference	Diagnosis	*N*	Follow-up median (range)	Secondary solid tumor incidence (%)
Yock et al. (31)	Medulloblastoma	59	7 years (3.9–10.3)	0
Greenberger et al. (35)	Low-grade glioma	32	7.6 years (3.2–18.2)	0
Sethi et al. (33)	Retinoblastoma	55	6.9 years (1.0–24.4)	5[a]
MacDonald et al. (34)	Ependymoma	70	3.8 years (1–11.7)	0
Ladra et al. (37)	Rhabdomyosarcoma	57	3.9 years (1.2–8.5)	0
Rombi et al. (36)	Ewings sarcoma	30	3.2 years (1.5–7.4)	0[b]

[a]*One patient with bilateral retinoblastoma developed a non-metastatic osteosarcoma of the femur.*
[b]*Four patients developed secondary hematologic malignancies.*

CONCLUSION

Multiple dosimetric studies have demonstrated the ability of PRT to deliver efficacious target volume coverage while reducing the total integral dose delivered to normal tissues when compared with photon therapy. Modeling systems taking into account these dosimetric comparisons, organ equivalent dose and radiation protection models have predicted a significantly reduced risk of secondary malignancy with PRT among multiple pediatric and adult malignancies. Though neutron scatter may be higher in tissues outside of the target volume with proton treatment, the secondary dose contribution is small and thus the total integral dose remains less with protons than with photon therapy. Pencil beam scanning systems provide the greatest opportunity to reduced secondary dose from neutron scatter and further reduced the secondary malignancy risk from proton treatment. Though clinical data are limited, early reports of prospective and retrospective series suggest a reduced incidence of secondary malignancy in patients treated with protons, and further analyses with longer follow-up are awaited. The data support the continued use of PRT in effort to reduce the incidence of secondary malignancies among children and adults expected to survive their disease.

AUTHOR CONTRIBUTIONS

All authors contributed to the interpretation of the original research reviewed here, drafting the work or revising it critically for important intellectual content, and gave final approval of the version to be published. All authors agree to be accountable for all aspects of the work in ensuring that questions related to the accuracy or integrity of any part of the work are appropriately investigated and resolved.

REFERENCES

1. Meadows AT, Friedman DL, Neglia JP, Mertens AC, Donaldson SS, Stovall M, et al. Second neoplasms in survivors of childhood cancer: findings from the childhood cancer survivor study cohort. *J Clin Oncol* (2009) **27**(14):2356–62. doi:10.1200/JCO.2008.21.1920
2. Ng J, Shuryak I. Minimizing second cancer risk following radiotherapy: current perspectives. *Cancer Manag Res* (2015) **7**:1–11. doi:10.2147/CMAR.S47220
3. Armstrong GT, Liu Q, Yasui Y, Neglia JP, Leisenring W, Robison LL, et al. Late mortality among 5-year survivors of childhood cancer: a summary from the childhood cancer survivor study. *J Clin Oncol* (2009) **27**(14):2328–38. doi:10.1200/JCO.2008.21.1425
4. Mertens AC, Liu Q, Neglia JP, Wasilewski K, Leisenring W, Armstrong GT, et al. Cause-specific late mortality among 5-year survivors of childhood cancer: the childhood cancer survivor study. *J Natl Cancer Inst* (2008) **100**(19):1368–79. doi:10.1093/jnci/djn310
5. Gold DG, Neglia JP, Dusenbery KE. Second neoplasms after megavoltage radiation for pediatric tumors. *Cancer* (2003) **97**(10):2588–96. doi:10.1002/cncr.11356
6. Jenkin D. Long-term survival of children with brain tumors. *Oncology (Williston Park)* (1996) **10**(5):715–9.
7. Hoffman KE, Yock TI. Radiation therapy for pediatric central nervous system tumors. *J Child Neurol* (2009) **24**(11):1387–96. doi:10.1177/0883073809342275
8. Lomax AJ, Bortfeld T, Goitein G, Debus J, Dykstra C, Tercier PA, et al. A treatment planning inter-comparison of proton and intensity modulated photon radiotherapy. *Radiother Oncol* (1999) **51**(3):257–71. doi:10.1016/S0167-8140(99)00036-5
9. Yock TI, Caruso PA. Risk of second cancers after photon and proton radiotherapy: a review of the data. *Health Phys* (2012) **103**(5):577–85. doi:10.1097/HP.0b013e3182609ba4
10. Ladra MM, Edgington SK, Mahajan A, Grosshans D, Szymonifka J, Khan F, et al. A dosimetric comparison of proton and intensity modulated radiation therapy in pediatric rhabdomyosarcoma patients enrolled on a prospective phase II proton study. *Radiother Oncol* (2014) **113**(1):77–83. doi:10.1016/j.radonc.2014.08.033
11. MacDonald SM, Safai S, Trofimov A, Wolfgang J, Fullerton B, Yeap BY, et al. Proton radiotherapy for childhood ependymoma: initial clinical outcomes and dose comparisons. *Int J Radiat Oncol Biol Phys* (2008) **71**(4):979–86. doi:10.1016/j.ijrobp.2007.11.065
12. St Clair WH, Adams JA, Bues M, Fullerton BC, La Shell S, Kooy HM, et al. Advantage of protons compared to conventional X-ray or IMRT in the treatment of a pediatric patient with medulloblastoma. *Int J Radiat Oncol Biol Phys* (2004) **58**(3):727–34. doi:10.1016/S0360-3016(03)01574-8
13. Miralbell R, Lomax A, Cella L, Schneider U. Potential reduction of the incidence of radiation-induced second cancers by using proton beams in the treatment of pediatric tumors. *Int J Radiat Oncol Biol Phys* (2002) **54**(3):824–9. doi:10.1016/S0360-3016(02)02982-6
14. Lundkvist J, Ekman M, Ericsson SR, Jonsson B, Glimelius B. Cost-effectiveness of proton radiation in the treatment of childhood medulloblastoma. *Cancer* (2005) **103**(4):793–801. doi:10.1002/cncr.20844
15. Mailhot Vega RB, Kim J, Bussière M, Hattangadi J, Hollander A, Michalski J, et al. Cost effectiveness of proton therapy compared with photon therapy in the management of pediatric medulloblastoma. *Cancer* (2013) **119**(24):4299–307. doi:10.1002/cncr.28322
16. Moteabbed M, Yock TI, Paganetti H. The risk of radiation-induced second cancers in the high to medium dose region: a comparison between passive and scanned proton therapy, IMRT and VMAT for pediatric patients with brain tumors. *Phys Med Biol* (2014) **59**(12):2883–99. doi:10.1088/0031-9155/59/12/2883
17. Paganetti H, Athar BS, Moteabbed M, A Adams J, Schneider U, Yock TI. Assessment of radiation-induced second cancer risks in proton therapy and IMRT for organs inside the primary radiation field. *Phys Med Biol* (2012) **57**(19):6047–61. doi:10.1088/0031-9155/57/19/6047
18. Dennis ER, Bussiere MR, Niemierko A, Lu MW, Fullerton BC, Loeffler JS, et al. A comparison of critical structure dose and toxicity risks in patients with low grade gliomas treated with IMRT versus proton radiation therapy. *Technol Cancer Res Treat* (2013) **12**(1):1–9. doi:10.7785/tcrt.2012.500276
19. Schneider U, Lomax A, Lombriser N. Comparative risk assessment of secondary cancer incidence after treatment of Hodgkin's disease with photon and proton radiation. *Radiat Res* (2000) **154**(4):382–8. doi:10.1667/0033-7587(2000)154[0382:CRAOSC]2.0.CO;2
20. Yoon M, Ahn SH, Kim J, Shin DH, Park SY, Lee SB, et al. Radiation-induced cancers from modern radiotherapy techniques: intensity-modulated radiotherapy versus proton therapy. *Int J Radiat Oncol Biol Phys* (2010) **77**(5):1477–85. doi:10.1016/j.ijrobp.2009.07.011
21. Fontenot JD, Lee AK, Newhauser WD. Risk of secondary malignant neoplasms from proton therapy and intensity-modulated x-ray therapy for early-stage prostate cancer. *Int J Radiat Oncol Biol Phys* (2009) **74**(2):616–22. doi:10.1016/j.ijrobp.2009.01.001
22. Gottschalk B. Neutron dose in scattered and scanned proton beams: in regard to Eric J. Hall (Int J Radiat Oncol Biol Phys 2006;65:1-7). *Int J Radiat Oncol Biol Phys* (2006) **66**(5):1594. doi:10.1016/j.ijrobp.2006.08.014
23. Hall EJ. Intensity-modulated radiation therapy, protons, and the risk of second cancers. *Int J Radiat Oncol Biol Phys* (2006) **65**(1):1–7. doi:10.1016/j.ijrobp.2006.01.027
24. Paganetti H, Bortfeld T, Delaney TF. Neutron dose in proton radiation therapy: in regard to Eric J. Hall (Int J Radiat Oncol Biol Phys 2006;65:1-7). *Int J Radiat Oncol Biol Phys* (2006) **66**(5):1594–5. doi:10.1016/j.ijrobp.2006.08.014
25. Hall EJ. The impact of protons on the incidence of second malignancies in radiotherapy. *Technol Cancer Res Treat* (2007) **6**(4 Suppl):31–4. doi:10.1177/15330346070060S405
26. Schneider U, Agosteo S, Pedroni E, Besserer J. Secondary neutron dose during proton therapy using spot scanning. *Int J Radiat Oncol Biol Phys* (2002) **53**(1):244–51. doi:10.1016/S0360-3016(01)02826-7
27. Schneider U, Lomax A, Pemler P, Besserer J, Ross D, Lombriser N, et al. The impact of IMRT and proton radiotherapy on secondary cancer incidence. *Strahlenther Onkol* (2006) **182**(11):647–52. doi:10.1007/s00066-006-1534-8
28. Jiang H, Wang B, Xu XG, Suit HD, Paganetti H. Simulation of organ-specific patient effective dose due to secondary neutrons in proton radiation treatment. *Phys Med Biol* (2005) **50**(18):4337–53. doi:10.1088/0031-9155/50/18/007
29. Newhauser WD, Fontenot JD, Mahajan A, Kornguth D, Stovall M, Zheng Y, et al. The risk of developing a second cancer after receiving craniospinal proton irradiation. *Phys Med Biol* (2009) **54**(8):2277–91. doi:10.1088/0031-9155/54/8/002
30. Chung CS, Yock TI, Nelson K, Xu Y, Keating NL, Tarbell NJ. Incidence of second malignancies among patients treated with proton versus photon radiation. *Int J Radiat Oncol Biol Phys* (2013) **87**(1):46–52. doi:10.1016/j.ijrobp.2013.04.030
31. Yock T, Yeap BY, Ebb D, et al. Pediatric medulloblastoma: clinical outcomes from a prospective phase II study of proton radiotherapy. *Lancet Oncol* (2015). doi:10.1016/S1470-2045(15)00167-9
32. Eaton BR, Esiashvili N, Kim S, et al. Clinical outcomes among children with standard risk medulloblastoma treated with proton and photon radiotherapy: a comparison of disease control and overall survival. *Int J Radiat Oncol Biol Phys* (2015). doi:10.1016/j.ijrobp.2015.09.014
33. Sethi RV, Shih HA, Yeap BY, Mouw KW, Petersen R, Kim DY, et al. Second nonocular tumors among survivors of retinoblastoma treated with contemporary photon and proton radiotherapy. *Cancer* (2014) **120**(1):126–33. doi:10.1002/cncr.28387
34. Macdonald SM, Sethi R, Lavally B, Yeap BY, Marcus KJ, Caruso P, et al. Proton radiotherapy for pediatric central nervous system ependymoma: clinical outcomes for 70 patients. *Neuro Oncol* (2013) **15**(11):1552–9. doi:10.1093/neuonc/not121
35. Greenberger BA, Pulsifer MB, Ebb DH, MacDonald SM, Jones RM, Butler WE, et al. Clinical outcomes and late endocrine, neurocognitive, and visual profiles of proton radiation for pediatric low-grade gliomas. *Int J Radiat Oncol Biol Phys* (2014) **89**(5):1060–8. doi:10.1016/j.ijrobp.2014.04.053
36. Rombi B, DeLaney TF, MacDonald SM, Huang MS, Ebb DH, Liebsch NJ, et al. Proton radiotherapy for pediatric Ewing's sarcoma: initial clinical outcomes. *Int J Radiat Oncol Biol Phys* (2012) **82**(3):1142–8. doi:10.1016/j.ijrobp.2011.03.038
37. Ladra MM, Szymonifka JD, Mahajan A, Friedmann AM, Yong Yeap B, Goebel CP, et al. Preliminary results of a phase II trial of proton radiotherapy

for pediatric rhabdomyosarcoma. *J Clin Oncol* (2014) **32**(33):3762–70. doi:10.1200/JCO.2014.56.1548

Conflict of Interest Statement: The authors declare that the research was conducted in the absence of any commercial or financial relationships that could be construed as a potential conflict of interest.

Copyright © 2015 Eaton, MacDonald, Yock and Tarbell. This is an open-access article distributed under the terms of the Creative Commons Attribution License (CC BY). The use, distribution or reproduction in other forums is permitted, provided the original author(s) or licensor are credited and that the original publication in this journal is cited, in accordance with accepted academic practice. No use, distribution or reproduction is permitted which does not comply with these terms.

frontiers in Oncology

PERSPECTIVE
published: 21 October 2015
doi: 10.3389/fonc.2015.00235

The impact of neutrons in clinical proton therapy

Uwe Schneider[1,2]* *and Roger Hälg*[1,2]

[1] *Institute of Physics, Science Faculty, University of Zürich, Zürich, Switzerland,* [2] *Radiotherapy Hirslanden, Zürich, Switzerland*

In proton therapy, high-energy proton beams cause the production of secondary neutrons. This leads to an unwanted dose contribution, which can be considerable for tissues outside of the target volume regarding the long-term health of cancer patients. Due to the high biological effectiveness of neutrons with regard to cancer induction, small neutron doses can be important. Published comparisons of neutron dose measurements and the corresponding estimates of cancer risk between different treatment modalities differ over orders of magnitude. In this report, the controversy about the impact of the neutron dose in proton therapy is critically discussed and viewed in the light of new epidemiological studies. In summary, the impact of neutron dose on cancer risk can be determined correctly only if the dose distributions are carefully measured or computed. It is important to include not only the neutron component into comparisons but also the complete deposition of energy as precisely as possible. Cancer risk comparisons between different radiation qualities, treatment machines, and techniques have to be performed under similar conditions. It seems that in the past, the uncertainty in the models which lead from dose to risk were overestimated when compared with erroneous dose comparisons. Current risk models used with carefully obtained dose distributions predict a second cancer risk reduction for active protons vs. photons and a more or less constant risk of passive protons vs. photons. Those findings are in general agreement with newly obtained epidemiologically results.

Keywords: proton therapy, neutrons, second cancer

OPEN ACCESS

Edited by:
Marco Durante,
GSI Helmholtzzentrum für Schwerionenforschung, Germany

Reviewed by:
Andrea Ottolenghi,
University of Pavia, Italy
Wayne D. Newhauser,
Louisiana State University, USA

***Correspondence:**
Uwe Schneider
uwe.schneider@uzh.ch

Specialty section:
This article was submitted to Radiation Oncology, a section of the journal Frontiers in Oncology

Received: *14 August 2015*
Accepted: *06 October 2015*
Published: *21 October 2015*

Citation:
Schneider U and Hälg R (2015) The impact of neutrons in clinical proton therapy. Front. Oncol. 5:235. doi: 10.3389/fonc.2015.00235

INTRODUCTION

During proton therapy, neutrons are produced. This is known since protons are used for applications in radiation therapy. It is also known that the neutron absorbed dose is small. However, neutrons are highly biological effective and thus even a small absorbed dose might cause side effects in the patient, the most severe of which is the induction of a second primary cancer. For this reason, since the 1990s, the following main approaches to quantify the neutron absorbed and equivalent dose in radiotherapy patients include:

(i) Neutron, proton, and photonuclear cross-sections and neutron kerma coefficients for radiation therapy were determined based on experimental data and nuclear model calculations. Such data permit calculations of absorbed dose in the body from therapy beams, and through use of kerma coefficients allow absorbed dose to be estimated for a given neutron energy distribution. Most work in the beginning was done by Chadwick (1) and was extended afterward by many other authors.

(ii) Monte Carlo simulations of the neutron dose and neutron energy spectra were performed for typical proton therapy facilities. First work was published by Agosteo et al. (2) and Siebers (3) and further work was published since then, including very detailed simulations of proton therapy beam lines including realistic patient geometries.
(iii) Measurements and calculations of the quality factor of neutrons with the endpoint of cancer induction (and/or chromosomal aberrations, clonogenic survival, neoplastic transformations, etc.) were performed. Many studies were conducted starting in the 1970s. Much work was motivated by space radiation research and the A-bomb survivor analysis [e.g., Ref. (4–6)]. Later, also nanodosimetric measurements were used to characterize the quality factor of neutrons produced by proton beams (7).
(iv) Measurements of neutron absorbed dose and neutron dose equivalent at proton therapy beam lines were executed. First, measurements on passive beam lines were undertaken by Binns and Hough (8) and Yan et al. (9) and for active beam lines by Schneider et al. (10). Since then, a large number of neutron dose measurements were reported including several beam lines, in patient measurements, as well as measurements in treatment rooms, including a variety of dosimeters and set-ups including neutron energy spectra measurements. In addition, analytical methods were developed to determine neutron dose equivalent (11).

The resulting measured or simulated neutron dose distributions were used to estimate the risk for radiotherapy patients to develop secondary malignancies. Two strategies were usually applied. Either the neutron dose distribution was viewed as an additional dose burden to the patient, independently of the delivered dose to treat the tumor. As the neutron doses are usually low, radiation protection models were used to convert dose to risk. Another possibility is to combine the neutron dose with the dose distribution delivered by the therapy protons. The resulting dose levels are then much larger than the scope of radiation protection models and thus newly developed RT-risk-models were used to study the impact of the additional neutron dose. The latter models include, therefore, also the impact of integral dose changes on cancer risk. In the year 2006, two reports (12, 13), using these concepts, were published. The two strategies which were used to estimate second cancer risk came to completely contrary conclusions. Hall (12) estimated the risk of second malignancies by analyzing the stray and neutron doses alone and concluded that passive proton therapy would result in up to 20 times more second cancers than conventional photon radiotherapy. On the other hand, Schneider et al. (13, 14) determined cancer risk by analyzing the complete dose distribution including the energy deposited by primary protons and neutrons. They found for active proton therapy a decrease in second cancer risk. For passive proton therapy, by scaling the neutron dose, the risk was more or less the same when compared to conventional photons. This resulted in a heavily discussed controversy about the future of proton therapy.

In this report, we highlight the controversy about the impact of the neutron dose in proton therapy, which is critically discussed and viewed in the light of new epidemiological studies. The aim of this work is not to provide a review summarizing the current knowledge of neutron dose measurements, calculations or simulations, and the resulting cancer risk estimates.

MEASURED AND SIMULATED NEUTRON DOSE

It is of importance that dose and risk comparisons with regard to radiation quality and treatment technique are performed using the same phantom or patient, the same experimental equipment and is based on the same clinical indication. Treatment planning should be performed using the same dose constraints for target and normal tissues. If measurements of different experimental set-ups are compared very easily, apples and oranges are compared. **Figure 1A** shows a dose comparison from Ref. (12), where measurements obtained by different researchers were compared.

On the basis of **Figure 1A**, Hall (12) has drawn the conclusion that IMRT with photons would double the incidence of solid cancers in long-term survivors and passive proton therapy would result in up to 20 times more second malignancies. The dose scaling of the different experimental results, which led to **Figure 1A**, were highly questioned and resulted in the exchange of several letters to the editor.

A fair comparison of stray doses is shown in **Figure 1B**, which was obtained using for the investigated treatment modalities and techniques the same phantom and the same treatment indication (15). For the measurements at the passive proton therapy, beam line compensators were used which were produced specifically for this case. As a result, the distribution of the neutron dose of scattered protons is completely different when compared to the published data of Hall (12) reaching two orders of magnitude at 40 cm distance from the field edge. Clearly, the conclusion drawn by Hall was wrong, as he used erroneous stray dose estimates. Using the dose results of **Figure 1B**, one would expect for passive proton therapy approximately the same amount of neutron dose than photon stray dose produced by conventional 3D conformal radiotherapy. However, it should be noted here that the neutron measurements are related to large errors and that the quality factor for cancer induction is not well known. In addition, the effect of prompt gamma radiation in proton therapy was not considered.

MODELS OF SECOND CANCER INDUCTION

Estimates Based on Dose Comparison

Using simple dose comparisons for risk estimates by applying data, as shown in **Figure 1**, can be unsafe for two reasons. The decrease of dose as a function from field edge is exponential or sometimes even more than exponential. Since risk is both a function of dose and irradiated volume, it is very important to analyze carefully the shape of the dose curves close to the target volume. For example, when using IMRT techniques with photons, the dose far away from the field edge might by larger when compared to 3DCRT. However, the dose close to the field edge is lower for IMRT techniques. The reason for this is that IMRT produces less phantom scatter, which is the major stray dose component close to

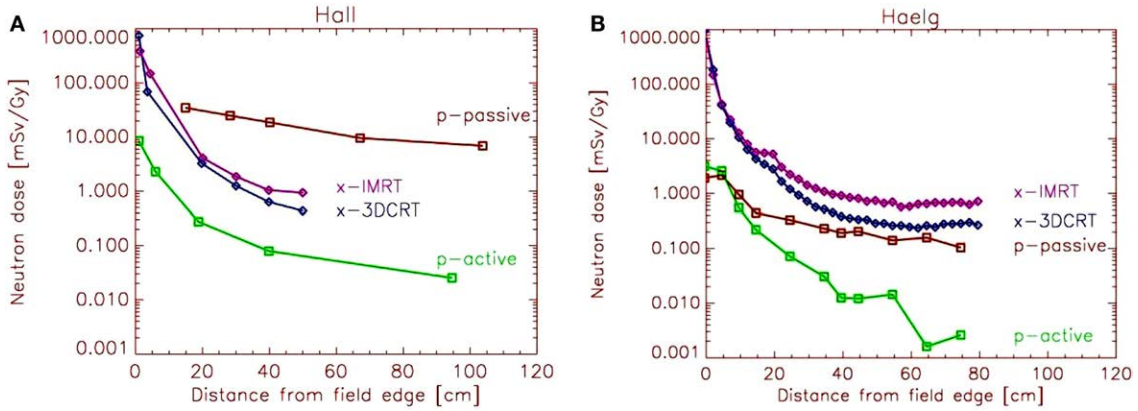

FIGURE 1 | (A) Eric Hall's comparison (12) of neutron dose equivalent per treatment Gray as a function from the distance of the field edge. Measurements of several researchers were combined by scaling the neutron dose. **(B)** Comparison of neutron dose equivalent by Hälg et al. (13). The measurements were performed under the same conditions for each treatment modality.

the target. Although the affected volume might be small, the dose at around 10 cm from the field edge can be more than a magnitude larger than far away from the treatment field.

The second reason is that we do not get an idea about the full 3D-dose distribution by analyzing only certain components of the dose, e.g., the neutron dose. Generally the dose distribution can be separated into two parts. The in-field dose is created by particles impinging on the patient through the opening of the beam aperture. This includes in-field scattering mainly produced by Compton scattering (photons) and multiple Coulomb scattering or inelastic nuclear interactions (protons and ions). The out-of-field dose is generated by phantom scatter and radiation scattered by the treatment head, leakage radiation through the collimators and neutrons, and prompt gammas produced either in the machine or the patient.

For a reliable risk estimate of the patient, it is required to study the deposited energy of all components. In doing so, the characteristics of dose deposition of the different radiation qualities are taken into account. If, for example, photons are compared to protons, the integral dose in the highly irradiated volumes is always a factor of 2–3 lower for protons, independently of the treatment technique (16). That must have an impact on cancer induction and cannot be neglected.

In summary, relative risk estimates using comparisons of dose distributions are possible. However, it is essential that the correct dose distributions are compared, including all relevant stray dose components. The comparisons must be obtained by selecting carefully the same conditions for all treatment types in questions if dose measurements or simulations are performed. Currently, measurements as well as analytical or Monte Carlo simulations can predict stray doses with a precision of around 20–50%.

Estimates Based on Risk Models

Simple models to predict risk of radiation-induced cancer for radiotherapy dose levels are based on conventional concepts from radiation protection, i.e., ICRP (17) or BEIR (18). These models are based on the linear approximation of the risks of the Atomic-bomb survivors and use effective dose (the tissue-weighted sum of the equivalent doses in all specified tissues) for risk estimation. Basic risk factors are usually modified by a dose and dose-rate effectiveness factor (DDREF) for the application to low dose-rates. The linear model is only valid for doses up to around 1–2 Gy and as such, is in general, not applicable to complete radiotherapy dose distribution.

Radiation protection models can be safely applied exclusively to the dose originating from scatter radiation. In principle, the linear model is applied to very low doses with a threshold of around 100 mSv. The threshold represents the maximum applied scatter dose during a typical radiotherapy treatment (**Figure 1B**, if scaled to a typical RT dose). As for such estimates, only the out-of-field-dose is considered, but the in-field dose distribution completely neglected, cancer risk is not a function of the integral dose, but proportional to the amount of scatter dose. As a consequence, such studies result in an estimated increase of cancer risk of modern radiotherapy techniques (12). The reason for this is the larger amount of scatter, leakage, and neutron dose of those treatment modalities compared to conventional treatment techniques. While in such situations the application of radiation protection concepts may be appropriate, since exclusively the low doses are investigated, the main disadvantage of such an approach is that the in-field dose distribution (>100 mSv) is completely neglected. Thus, risk estimates based on scatter dose would only include second cancer induction far away from the treated side. It is reported, however, that only around 20% of all radiation-induced malignancies are found far away from the treated volume (19).

In summary, radiation protection models should be used only with extreme care for risk estimates in radiotherapy since they are developed exclusively for low dose. When applied to scatter radiation, such models can predict only a fraction of observed second malignancies.

It is also possible to take for cancer risk estimates the complete 3D-dose distribution (in- and out-of-field) into account by using semi-empirical models of cancer induction. Such models include the effect of dose fractionation and represent the dose–response relationships more accurately. The involved uncertainties are still huge for most of the organs and tissues. A major reason for this

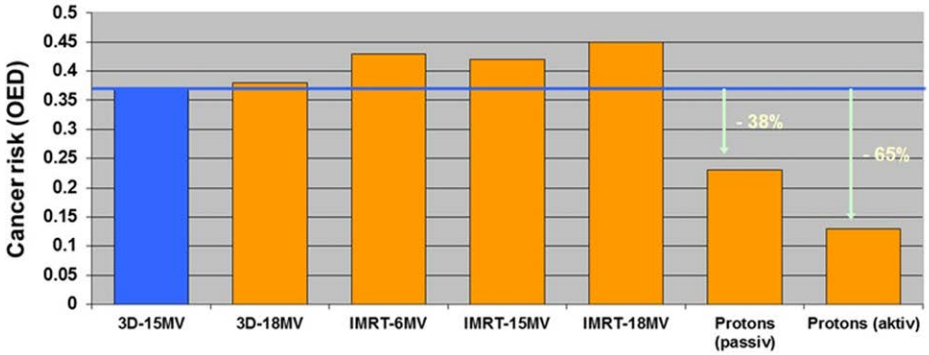

FIGURE 2 | Modeled second cancer risk after radiotherapy of the prostate relative to a historic radiation treatment (four-field-box in blue). The data were taken from Ref. (14) and updated with better dose measurements (15). Prostate cancer was chosen for comparison with the epidemiological study of Chung et al. (21) as their patient cohort consisted mainly of prostate patients.

is that the underlying processes of the induction of carcinoma and sarcoma are not well known. Most uncertainties are related to the time patterns of cancer induction, the population specific dependencies and to the organ-specific cancer induction rates. For radiotherapy treatment plan optimization, these factors are irrelevant as a treatment plan comparison is performed for a patient of specific age, sex, etc. If a treatment plan is compared relative to another, a precision of around 10% can be achieved (20). Such a model was used in Ref. (13) for cancer risk estimates after prostate radiotherapy by using the complete 3D-dose distribution including stray dose estimates. It was found that the additional dose of neutrons during proton radiotherapy is balanced by the integral dose advantage of proton beams. The predicted risk of passively scattered protons is, thus, slightly lower than of photon 3DCRT. Actively applied proton beams resulted in more than 50% reduced risk prediction relative to 3DCRT (**Figure 2**).

QUALITATIVE COMPARISON OF MODEL PREDICTIONS WITH EPIDEMIOLOGICAL FINDINGS

In 2006, when contradicting model results were published (12, 13), no epidemiological study regarding second cancers after proton therapy or IMRT was available. The users of proton therapy machines, and also the clinicians who were using photon IMRT, were confused about which models to believe. On the one hand, Eric Hall (12) predicted, by using stray dose comparisons, a 2- and 20-time larger second cancer risk for IMRT and passive proton therapy, respectively. On the other hand, risk models that were applied to the complete dose distribution of a patient predicted more or less the same risk for IMRT using 6 MV photons and passive proton therapy (13, 14).

In 2013, the first epidemiological study on a comparison of second cancer risk between a photon and proton-treated group was published by Chung et al. (21). They found that the use of proton radiation therapy using passively scattered protons was not associated with a significantly increased risk of secondary malignancies compared with photon therapy. Although they state, that longer follow-up of these patients is needed to determine if there is a significant decrease in second malignancies, they found an adjusted hazard ratio of 0.52 [95% confidence interval, 0.32–0.85] of protons vs. photons. These first epidemiological results strongly suggest that the exaggerated risk estimates of Ref. (12) which were based on a faulty stray dose comparison were wrong.

In a study published 2014, Sethi et al. (22) examined in-field and out-of-field cancer incidence in proton vs. photon-treated patients with retinoblastoma. In-field cancer was significantly higher in photon-treated patients. With an ~7-year median follow-up, the incidence of out-of-field cancer did not significantly differ in the proton- vs. photon-treated patients. These results are in accordance with the integral dose advantage of protons vs. photons and the comparable stray doses for scattered protons and 3DCRT, as shown in **Figure 1B**.

CONCLUSION

Most criticisms of cancer risk estimates are usually given to the uncertainties of risk models, which lead from dose to second cancer risk. We are concerned that there is too little thought being given to the very simple ideas on which cancer risk models are based upon and too little objections about accepting the implications of such models. However, even more important are the errors and uncertainties in the dose distributions, which are the basis of risk modeling. If the dose is wrongly quantified, like in **Figure 1A**, this leads inevitably to wrong risk estimates, regardless of the quality of the used risk models. It is also important to always take the full dose distribution into account and not only parts of it. This is of particular importance when photon therapy is compared to proton therapy, as the integral dose advantage of proton therapy in the highly irradiated volumes can be balanced by the neutron dose in the areas distant from the irradiation fields. Unfortunately, researchers are often using oversimplified dose estimates, by applying risk models e.g., to dose distributions obtained from radiotherapy treatment planning systems.

In summary, if carefully obtained dose distributions are used with appropriate risk models to predict second cancer for radiotherapy patients, a reduction for active and passive proton therapy is predicted when compared to photons. Those findings are in general agreement with newly obtained epidemiologically results.

The estimates performed by Hall (12) resulting in an order of magnitude enhanced risk of passive proton therapy are contradicted by the findings of the epidemiological studies and various risk estimates for radiotherapy patients.

In the future, it is important to gain more knowledge on the RBE of neutrons with regard to cancer induction. It is necessary to study RBE for tumor induction as a function of neutron dose, energy, dose-rate, tissue type, and size of the exposed patient. Currently, the EU project ANDANTE (23) is exploring the question of neutron RBE.

More research is also necessary to improve the precision of out-of-field neutron dose calculations including the energy spectra. This could make whole-body dose calculations available for risk estimates of individual radiotherapy patients.

REFERENCES

1. Chadwick MB. Neutron, proton, and photonuclear cross-sections for radiation therapy and radiation protection. *Radiat Environ Biophys* (1998) **37**(4):235–42. doi:10.1007/s004110050124
2. Agosteo S, Birattari C, Caravaggio M, Silari M, Tosi G. Secondary neutron and photon dose in proton therapy. *Radiother Oncol* (1998) **48**(3):293–305. doi:10.1016/S0167-8140(98)00049-8
3. Siebers JV. Application of Monte Carlo to proton beam radiation therapy. In: Kling A, editor. *Monte Carlo 2000 – Advanced Monte Carlo for Radiation Physics, Particle Transport Simulation and Applications*. (Lisbon, Portugal) (2000) p. 1051–6.
4. Clapp NK, Darden EB Jr, Jernigan MC. Relative effects of whole-body sublethal doses of 60-MeV protons and 300-kVp X-rays on disease incidences in RF mice. *Radiat Res* (1974) **57**(1):158–86. doi:10.2307/3573764
5. Lloyd DC, Edwards AA, Prosser JS, Bolton D, Sherwin AG. Chromosome aberrations induced in human lymphocytes by D-T neutrons. *Radiat Res* (1984) **98**(3):561–73. doi:10.2307/3576488
6. Sasaki MS, Endo S, Ejima Y, Saito I, Okamura K, Oka Y, et al. Effective dose of A-bomb radiation in Hiroshima and Nagasaki as assessed by chromosomal effectiveness of spectrum energy photons and neutrons. *Radiat Environ Biophys* (2006) **45**(2):79–91. doi:10.1007/s00411-006-0051-6
7. Wroe A, Rosenfeld A, Schulte R. Out-of-field dose equivalents delivered by proton therapy of prostate cancer. *Med Phys* (2007) **34**(9):3449–56. doi:10.1118/1.2759839 Erratum in: *Med Phys*. 2008 35(7):3398.
8. Binns PJ, Hough JH. Secondary dose exposures during 200 MeV proton therapy. *Radiat Prot Dosimetry* (1997) **70**(1–4):441–4. doi:10.1093/oxfordjournals.rpd.a031993
9. Yan X, Titt U, Koehler AM, Newhauser WD. Measurement of neutron dose equivalent to proton therapy patients outside of the proton radiation field. *Nucl Instrum Meth A* (2002) **476**:429–34. doi:10.1118/1.4816653
10. Schneider U, Agosteo S, Pedroni E, Besserer J. Secondary neutron dose during proton therapy using spot scanning. *Int J Radiat Oncol Biol Phys* (2002) **53**(1):244–51. doi:10.1016/S0360-3016(01)02826-7
11. Zhang R, Pérez-Andújar A, Fontenot JD, Taddei PJ, Newhauser WD. An analytic model of neutron ambient dose equivalent and equivalent dose for proton radiotherapy. *Phys Med Biol* (2010) **55**(23):6975–85. doi:10.1088/0031-9155/55/23/S01
12. Hall EJ. Intensity-modulated radiation therapy, protons, and the risk of second cancers. *Int J Radiat Oncol Biol Phys* (2006) **65**(1):1–7. doi:10.1016/j.ijrobp.2006.01.027
13. Schneider U, Lomax A, Pemler P, Besserer J, Ross D, Lombriser N, et al. The impact of IMRT and proton radiotherapy on secondary cancer incidence. *Strahlenther Onkol* (2006) **182**(11):647–52. doi:10.1007/s00066-006-1534-8
14. Schneider U, Lomax A, Lombriser N. Comparative risk assessment of secondary cancer incidence after treatment of Hodgkin's disease with photon and proton radiation. *Radiat Res* (2000) **154**(4):382–8. doi:10.1667/0033-7587(2000)154[0382:CRAOSC]2.0.CO;2
15. Hälg RA, Besserer J, Boschung M, Mayer S, Lomax AJ, Schneider U. Measurements of the neutron dose equivalent for various radiation qualities, treatment machines and delivery techniques in radiation therapy. *Phys Med Biol* (2014) **59**(10):2457–68. doi:10.1088/0031-9155/59/10/2457
16. Lomax AJ, Bortfeld T, Goitein G, Debus J, Dykstra C, Tercier P-A, et al. A treatment planning inter-comparison of proton and intensity modulated photon radiotherapy. *Radiother Oncol* (1999) **51**:257–71. doi:10.1016/S0167-8140(99)00036-5
17. ICRP. The 2007 Recommendations of the International Commission on Radiological Protection. ICRP Publication 103. *Ann ICRP* (2007) **37**:1–332.
18. Biological Effects of Ionizing Radiation Committee. *BEIR VII: Health Risks from Exposure to Low Level of Ionizing Radiation*. Washington, DC: National Research Council, The National Academies (2006).
19. Travis LB, Hill DA, Dores GM, Gospodarowicz M, van Leeuwen FE, Holowaty E, et al. Breast cancer following radiotherapy and chemotherapy among young women with Hodgkin disease. *JAMA* (2003) **290**:465–75. doi:10.1001/jama.290.4.465
20. Nguyen J, Moteabbed M, Paganetti H. Assessment of uncertainties in radiation-induced cancer risk predictions at clinically relevant doses. *Med Phys* (2015) **42**(1):81–9. doi:10.1118/1.4903272
21. Chung CS, Yock TI, Nelson K, Xu Y, Keating NL, Tarbell NJ. Incidence of second malignancies among patients treated with proton versus photon radiation. *Int J Radiat Oncol Biol Phys* (2013) **87**(1):46–52. doi:10.1016/j.ijrobp.2013.04.030
22. Sethi RV, Shih HA, Yeap BY, Mouw KW, Petersen R, Kim DY, et al. Second nonocular tumors among survivors of retinoblastoma treated with contemporary photon and proton radiotherapy. *Cancer* (2014) **120**(1):126–33. doi:10.1002/cncr.28387
23. Ottolenghi A, Baiocco G, Smyth V, Trott K; ANDANTE Consortium. The ANDANTE project: a multidisciplinary approach to neutron RBE. *Radiat Prot Dosimetry* (2015) **166**:311–5. doi:10.1093/rpd/ncv158

Conflict of Interest Statement: The authors declare that the research was conducted in the absence of any commercial or financial relationships that could be construed as a potential conflict of interest.

Copyright © 2015 Schneider and Hälg. This is an open-access article distributed under the terms of the Creative Commons Attribution License (CC BY). The use, distribution or reproduction in other forums is permitted, provided the original author(s) or licensor are credited and that the original publication in this journal is cited, in accordance with accepted academic practice. No use, distribution or reproduction is permitted which does not comply with these terms.

frontiers in Oncology

METHODS
published: 25 January 2016
doi: 10.3389/fonc.2015.00305

Applications of High-Throughput Clonogenic Survival Assays in High-LET Particle Microbeams

Antonios Georgantzoglou[1], Michael J. Merchant[2], Jonathan C. G. Jeynes[3], Natalie Mayhead[4], Natasha Punia[5], Rachel E. Butler[5] and Rajesh Jena[1]*

[1] Department of Oncology, Addenbrooke's Hospital, University of Cambridge, Cambridge, UK, [2] Manchester Academic Health Science Centre, Institute of Cancer Sciences, University of Manchester, The Christie NHS Foundations Trust, Manchester, UK, [3] Centre for Biomedical Modelling and Analysis, University of Exeter, Exeter, UK, [4] Ion Beam Centre, University of Surrey, Guildford, UK, [5] Department of Microbial and Cellular Sciences, University of Surrey, Guildford, UK

OPEN ACCESS

Edited by:
Francis A. Cucinotta,
University of Nevada Las Vegas, USA

Reviewed by:
Joshua Silverman,
New York University Medical Center, USA
John C. Roeske,
Loyola University Medical Center, USA

***Correspondence:**
Antonios Georgantzoglou
ag718@cam.ac.uk

Specialty section:
This article was submitted to Radiation Oncology, a section of the journal Frontiers in Oncology

Received: 30 September 2015
Accepted: 18 December 2015
Published: 25 January 2016

Citation:
Georgantzoglou A, Merchant MJ, Jeynes JCG, Mayhead N, Punia N, Butler RE and Jena R (2016) Applications of High-Throughput Clonogenic Survival Assays in High-LET Particle Microbeams. Front. Oncol. 5:305. doi: 10.3389/fonc.2015.00305

Charged particle therapy is increasingly becoming a valuable tool in cancer treatment, mainly due to the favorable interaction of particle radiation with matter. Its application is still limited due, in part, to lack of data regarding the radiosensitivity of certain cell lines to this radiation type, especially to high-linear energy transfer (LET) particles. From the earliest days of radiation biology, the clonogenic survival assay has been used to provide radiation response data. This method produces reliable data but it is not optimized for high-throughput microbeam studies with high-LET radiation where high levels of cell killing lead to a very low probability of maintaining cells' clonogenic potential. A new method, therefore, is proposed in this paper, which could potentially allow these experiments to be conducted in a high-throughput fashion. Cells are seeded in special polypropylene dishes and bright-field illumination provides cell visualization. Digital images are obtained and cell detection is applied based on corner detection, generating individual cell targets as *x*–*y* points. These points in the dish are then irradiated individually by a micron field size high-LET microbeam. Post-irradiation, time-lapse imaging follows cells' response. All irradiated cells are tracked by linking trajectories in all time-frames, based on finding their nearest position. Cell divisions are detected based on cell appearance and individual cell temporary corner density. The number of divisions anticipated is low due to the high probability of cell killing from high-LET irradiation. Survival curves are produced based on cell's capacity to divide at least four to five times. The process is repeated for a range of doses of radiation. Validation shows the efficiency of the proposed cell detection and tracking method in finding cell divisions.

Keywords: clonogenic survival assay, high-LET radiation, microbeam, bright-field imaging, cell tracking

Abbreviations: FOV, field of view; LQ, Linear-Quadratic; LET, linear energy transfer; PE, plating efficiency; SF, survival fraction; U251, U-251 MG pleomorphic human glioblastoma (cells); WSVM, Wolfson Surrey vertical microbeam.

INTRODUCTION

Charged particle therapy is increasingly becoming a valuable tool in cancer treatment, mainly due to the favorable interaction of particle radiation with matter: it maximizes the dose attributed to a specific depth of tissue by adjusting the beam energy and intensity, creating a peak of dose called Bragg peak (1). Although thousands of patients have been already treated with particle therapy during the last 60 years, uncertainties still limit the application of this treatment method. One of the limiting factors is the lack of correlation between the delivered dose of radiation and the biological output (2). Clinical trials boost the knowledge and experience in handling particle therapy situations but data are limited. However, working with high-throughput *in vitro* biological cell assays can provide valuable information regarding the interaction of single cells with charged particle radiation (3).

CLONOGENIC SURVIVAL ASSAY

Basic Principles

Cell radiosensitivity can be examined by performing a clonogenic survival assay *in vitro*. The clonogenic integrity post-irradiation is examined by the ability to divide and form colonies of at least 50 cells (4). The outcome is the correlation between deposited radiation dose and biological end-point investigated. The basic principles of this tool are well-manifested in the literature (4, 5); therefore, only a short overview will follow. Biological cells are seeded in a number of dishes and each dish is irradiated with a known type of radiation with different dose for every dish. One or more dishes are not irradiated (control dishes) and these are used to calculate the plating efficiency (PE). The ultimate goal of a clonogenic survival assay is the production of a graph in which the logarithmic survival fraction (SF) is correlated with the dose.

Radiobiological Models

Although different models have been proposed to describe the relation between cell SF and dose, the linear-quadratic (LQ) model is widely recognized although questioned over its universal fit. According to this model, the cell survival curve exhibits a linear decrease with dose for lower doses while it has a steeper fall-off for higher doses (i.e., quadratic), expressing a higher impact from high-dose radiation to cells. Eq. 1 provides the formula that correlates the dose with the SF:

$$\mathrm{SF} = e^{(-\alpha D - \beta D^2)} \tag{1}$$

where α (Gy^{-1}) and β (Gy^{-2}) are the cell radiosensitivity parameters (6), specific for a particular experiment and cell type. The ratio α/β gives the dose (Gy) where both components, linear and quadratic, have equal contribution to cell survival.

Nevertheless, at low doses, data are not reliable due to low cell killing probability and survival rates are generated through extrapolation toward zero-dose (7). However, mammalian cells' increased radiosensitivity in very low doses (<10 cGy) result in enhanced cell killing (8, 9) and, hence, an Induced-Repair term has been suggested to correct for the adverse cell response in low doses; Eq. 1 becomes Eq. 2:

$$\mathrm{SF} = e^{\left(-\alpha D\left(1+\left(\frac{\alpha s}{\alpha}-1\right)e^{-D/D_c}\right)-\beta D^2\right)} \tag{2}$$

where α_s is the slope of the low-dose curve of the corrected model, while D_c is the dose at which cells start to become radioresistant (10). Besides low doses, the LQ model may overestimate the irradiation effect at doses >5–6 Gy (7).

Apart from the LQ model, the local-effect model has been introduced. This model is based on the notion that cell inactivation is caused almost entirely by ion traversals in the local area of cell nucleus and it depends only on the number and proximity of those traversals (11, 12). The effect is independent to radiation type with equal doses causing equal effects; therefore, the radiobiological effect from charged particle radiation can be derived from the respective effect from photon radiation (13). According to this model, the SF is described by Eq. 3:

$$-\ln \mathrm{SF} = \begin{cases} \alpha_X D + \beta_X D^2, D \le D_t \\ \alpha_X D + \beta_X D^2 + s_{\max}(D - D_t), D > D_t \end{cases} \tag{3}$$

$$s_{\max} = \alpha_X + 2\beta_X D_t \tag{4}$$

where s_{max} is the maximum slope, α_X and β_X are the slopes for the photon LQ model and D_t is the threshold dose above which the SF decreases exponentially (11).

Cell Survival Studies with High-LET Radiation

Cell survival depends strongly on the linear energy transfer (LET) of the beam that is the radiation energy deposited in matter per unit of distance. Research so far has indicated that high-LET radiation (generally LET >10 keV/μm) is more effective in cell killing with the survival curve being much steeper than in low-LET radiation. Since the beginning of 1960s, it was shown that high-LET α-particles produce an exponential kidney T_1 cell survival curve that becomes linear and steep for higher doses (14). Low-energy high-LET protons produced lower SF in V79 Chinese hamster cells (15), while high-LET α-particles produced clustered DNA damage (16). High-LET carbon ions resulted in as low as 5% survival of AG1522D cells in experiments at GSI (17) when five particles hit each cell. This evidence is strongly supported by experiments in NIRS which showed that high-LET carbon ions are more effective in killing human colon cancer stem-like cells (18), pancreatic cancer stem-like cells (19), or A549 lung cancer cells and human embryonic kidney cell than low-LET X-rays (20). Moreover, high-LET α-particles induced a lower than 10% survival of A549 lung cancer cells for a dose of 2 Gy compared to the respective rate of higher than 50% for X-ray irradiation (6, 21).

Drawbacks of Existing Method

Although clonogenic survival assays are used widely to quantify radiation effects, there are some practical complications. First, in some laboratories, cells are seeded into special chambers that fit into the charged particle facilities. Following irradiation, cells have to be detached and re-seeded to normal dishes for follow-up (9), which may lead to additional cell death. Moreover, the

standard protocol involves invasive cell staining methods for macroscopic colony counting, which ultimately leads to cell killing. The staining process is also characterized by difficulty in transfection for some cell lines while stains fade with time due to cellular physiological processes or even divisions. Colonies are counted after 5–6 cell divisions; depending on the specific cell cycle time, this process can be slow providing results even after 2 weeks. Additionally, when cells are irradiated with an average of one particle per cell, particle distribution follows the Poisson statistics: 37% of the cells receive the prescribed number of particles, 26% receive more than this dose while the rest 37% of the cells do not receive any dose (22).

CLONOGENIC SURVIVAL ASSAY USING HIGH-LET MICROBEAM IRRADIATION

In this paper, we present the theoretical base and the methodology for a new type of clonogenic survival assay for high-throughput cell irradiation, designed for high-LET targeted irradiation experiments, providing examples for its application. The proposed method focuses on the detection of mitotic catastrophe (cell death after unsuccessful attempt to divide) as a result of cell response to radiation; it does not assess the traditional colony formation potential but operates as a complementary technique. This method involves the precise irradiation of numerous single cells *in vitro* using a charged particle microbeam, with subsequent follow-up of cell response through label-free bright-field time-lapse imaging.

Microbeams in Radiobiology

Although modern microbeams were originally designed for non-radiobiological experiments, they can be used to irradiate cells *in vitro*. They produce radiation beams with high spatial accuracy since their field size can be smaller than 1 μm (23, 24), enough to selectively target a cell compartment, such as the nucleus which has a typical diameter of 5–10 μm (25). They also overcome the problem of particle Poisson hit distribution of broad-beam facilities by irradiating all cells with a precise dose of a number of N particles, leading to uniform dose distribution.

Dosimetry in microbeam irradiation is highly important in subcellular level. The attributed dose depends on the LET, particle fluence, and cell density (9). The latter is not always stable. Although a cell is considered to have similar density to water, it is not known whether this approximation remains constant over time (26). Moreover, the change in cell thickness may well affect the delivered dose as thicker cells increase the radiation interaction and, thus, the energy deposition.

Rationale of High-LET Clonogenic Survival

When using high-LET radiation to perform a clonogenic survival assay, the objectives are subtly distinct. High-LET radiation is densely ionizing radiation and it is responsible for complex lesions that may include several DNA bases, single-strand or double-strand breaks (25). When a molecule of DNA is traversed by a high-LET charged particle, multiple such lesions are produced (27). In many cases, the cell is unable to repair those multiple lesions while false damage identification and misrepair can also happen (28). Therefore, in high-LET irradiation, if four to five divisions occur and originate from the same cell, then there is a high probability that this cell has maintained its reproductive integrity (29). Therefore, the assessment of mitotic catastrophe can provide reliable and complementary data to colony formation assay regarding the cell response. Moreover, the investigation of clonogenic potential of the progeny could provide evidence for late-appearing effects.

Surrey Vertical Microbeam and Secondary Microscope

The Wolfson Surrey vertical microbeam (WSVM) was used in this research as a facility that provides highly focused high-LET radiation. A complete description of this microbeam can be found in Merchant et al. (30) and Jeynes et al. (31). Therefore, only a short overview will follow. The WSVM was specifically designed for radiobiological experiments and, hence, its vertical configuration achieves minimum cell stress. It has an estimated maximum irradiation capacity of 20,000 cells per hour. The smallest achieved radiation spot size is 1 μm, which makes the beam suitable for irradiating individual cells. It provides a range of particles, from protons to calcium ions, with energies from 0.5 to 12 MeV.

On top of the beam exit, there is an integrated up-right microscopy facility that serves in cell imaging and microbeam targeting. The microscopy facility provides full environmental control to ensure optimum living conditions for the cells: temperature of 37°C, humidity of 95%, and CO_2 flow of 5%. A three-axis motorized stage provides dish movement across all directions x–y–z for cell targeting. An objective water-dipping lens is mounted above the dish, while a digital camera system provides cell imaging.

However, due to difficulties in maintaining suitable environmental conditions for the cells at the microbeam microscopy facility, a secondary microscope was used to perform long time-lapse validation experiments. In those experiments, U-251 MG pleomorphic human glioblastoma (U251) cells were used. A Nikon Eclipse Ti-E confocal microscope was used in bright-field illumination mode with a Nikon CFI S Plan Fluor 40× objective.

Principles of Suggested Method

Dish Preparation

The design of the cell dish that is used in most microbeams is crucial to the irradiation outcome. At the WSVM, the radiation beam has to penetrate the dish bottom in order to reach and irradiate the cells. Nevertheless, due to the low output energy, the radiation beam will strongly interact with the dish material if the latter has certain thickness. Common plastic or glass substrates with thickness in the region of 150 μm are not suitable for these experiments. Therefore, thin polypropylene foils, with thickness of 4 μm, are used as substrate material in order to avoid strong interaction between the radiation beam and the substrate (32, 33). The polypropylene foil is kept between two metallic parts and a rubber o-ring, creating a water-tight environment for the cells and the culture medium.

The seeding process was carried out as previously described (33). However, the density of cells in the dish is a factor that needs special consideration. Research has indicated that density has to be low in order to allow cells to evolve and divide, exploiting their clonogenic colony formation ability. More specifically, either very low densities of 2–8 (34), 5 (35), and 6.4 cells/mm^2 (36) or higher densities of 120 cells/mm^2 (37) have been accounted in the literature. Although the proposed method does not exploit cells' clonogenic potential but rather their proliferative capacity, it was decided to follow the established protocol in cell seeding.

Cell Imaging

Fluorescence microscopy is the most common imaging method in microbeam community as it is used in many microbeam facilities (23, 24). However, enhanced photo-toxicity to the cells due to excess stain excitation in time-lapse imaging may lead to additional cell damage and, hence, overestimation of irradiation effect. Therefore, it has been suggested that alternative to fluorescence imaging methods should be used in clonogenic survival experiments (38, 39).

Phase contrast is an excellent alternative that offers good image quality. It has been previously used in α-particle collimated irradiation devices (40–42) or even microbeams (43) but it is difficult to implement in the WSVM vertical configuration due to conflicts with the path of the beam. Therefore, label-free bright-field illumination microscopy is used to provide cell imaging for reasons that have been justified in the literature (33, 39). Cell imaging is performed in two separate sessions. First, prior to cell irradiation, the dish is inspected under the microscope and an area containing cells is chosen. The size of this area depends on the number of cells to be irradiated. A wider area provides more targets for irradiation. The chosen area is virtually divided into field of views (FOV), depending on the FOV of the objective (**Figure 1**). An electrostatic scanning is then performed: the system stage-dish moves at the position of the first FOV under the objective, an image is acquired, image analysis is performed for cell target definition (i.e., *x*–*y* points of cell centroid) and the targets are sent to the microbeam for irradiation. After irradiating the cells of the first FOV, the dish moves to the next FOV. The process is repeated until all cells in the selected dish area are irradiated.

As soon as the irradiation process finishes, the beam stops. The follow-up of irradiated cells is achieved through time-lapse bright-field imaging and cell tracking. Depending on the cell cycle duration, cells should be ideally followed for at least four cell cycles in order to detect division abnormalities in the progeny of the irradiated cells. Time-lapse imaging of the previously irradiated area is performed every 10 min.

Cell Detection in Bright-Field Microscopy

Although cell detection techniques have been described in the literature, these are dedicated to phase contrast (42, 44) or fluorescence imaging for microbeam irradiation. Phase-contrast image processing is based on the notion that cells are bright and the background is dark. Therefore, general image processing tools, such as thresholding, morphological processing and shape detection can synthesize a reliable pipeline through which cell detection is achieved (42). However, bright-field cell images suffer from certain drawbacks. They usually exhibit very low cell visibility and they include not only cells but also debris. Also, the use of polypropylene as substrate generates characteristic "loop" artifacts that severely interfere in both cell visibility and cell detection. Therefore, a special cell detection method was developed.

The cell detection method for microbeam targeting in bright-field imaging has been already analyzed (33) but a brief description is given in this paper. Images are acquired in a weakly defocusing mode (i.e., ±2–4 μm from the perfectly focused plane) in order to enhance cell visibility, which is a standard contrast-enhancement technique in bright-field illumination mode (45). MATLAB® (The MathWorks, Natick, MA, USA) is used as software platform to design the cell detection module. Apparent cellular features originating either from the nucleus or the cytoplasm are detected using the Harris corner detector (46). This feature detection technique presents high selectivity in cellular features, while it limits substantially the detection of artifacts and background features.

The increased cell feature selectivity leads to using clustering techniques for grouping corners and forming cellular representations. Agglomerative hierarchical clustering is used to eliminate outlier corners, while a density-based technique groups the remaining corners capitalizing on their high density in cellular areas. Weighted centroids are calculated as *x*–*y* coordinates that

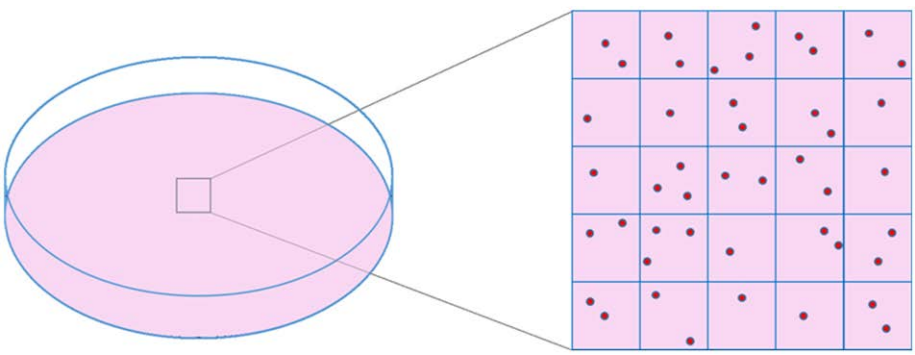

FIGURE 1 | Schematic representation of cell dish area selection and virtual division of this area into frames, based on objective's FOV size.

are used as targets for irradiation or as cell markers for ensuring cell existence post-irradiation.

Cell Tracking and Division Detection in Bright-Field Microscopy

Cell tracking was achieved by using a detection-based technique called two-point microrheology (47). Cells are sequentially detected in all time-lapse images as described in Section "Cell Detection in Bright-Field Microscopy." Each detected point x–y corresponds to one cell. Through cell tracking, each cell position is propagated in all time-frames by searching for its spatially nearest point in the following frames. Moreover, each cell is examined concurrently with its spatially nearest cell in order to avoid errors due to trajectory mixing during position linking. The linking depends on one input parameter that is the maximum predicted distance (in pixels) traveled by cells between two successive time-frames.

The cell tracking module has been adjusted in order to provide either off-line tracking after the completion of time-lapse imaging or on-line tracking in between successive time-lapse acquisitions. Using the latter, individual cell revisiting is possible in order to inspect the cell response to radiation in real time or even re-irradiate specific cells.

A critical requirement of this method is the ability to detect cell divisions in bright-field time-lapse images since these events determine the clonogenic potential. Detection of cell division is achieved through integrating a hybrid method. First, the number of cells is counted between two consecutive time-lapse acquisitions. The site in the dish where a candidate new cell appears is recorded as a possible site of division. Then, for each cell, the α-shape (48) or concave hull is calculated in order to provide a rough estimation of the cell outline. This calculation is based on connecting the outside corners that belong to a single cell. From the cell outline, the cellular area is calculated. Using the estimated cellular area from the α-shape and the number of corners attributed to this cell, a new parameter is defined as the corner density d per 100 pixels, for each cell, described by Eq. 5:

$$d = \frac{\text{number of corners}}{\text{area in pixels}} \times 100. \quad (5)$$

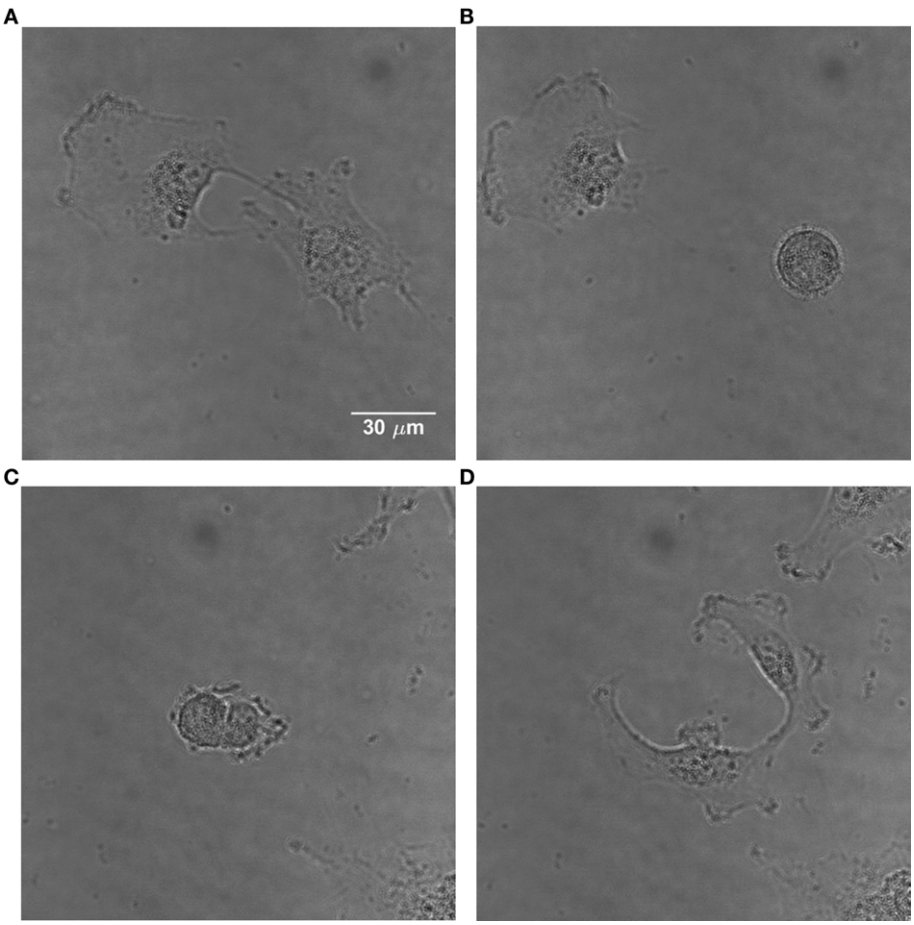

FIGURE 2 | Time-lapse images of U251 cells showing the change in morphology of a dividing cell. **(A)** Non-dividing adherent U251 cells. **(B)** One of them divides, obtaining a characteristic round shape. **(C)** The dividing cell starts the separation process. **(D)** The cell has divided and the daughter cells become adherent.

Apart from the corner density, the eccentricity is calculated for each cell; this parameter describes the cell shape (49). It is well-known that mammalian cells obtain a characteristic elliptical or even round shape with highly condensed material when they intend to divide (**Figure 2**). Therefore, the eccentricity e is calculated according to Eq. 6, characterizing a cell as dividing or non-dividing:

$$e = 2\frac{\sqrt{\left(\frac{M}{2}\right)^2 - \left(\frac{m}{2}\right)^2}}{M} \tag{6}$$

where M is the major and m is the minor axis of the potential ellipsis. A similar measurement of compactness has been also used by other researchers (42).

Evaluation of Clonogenic Potential

Following the cell detection prior and post-irradiation as well as the calculation of corner density and eccentricity, the next step is the calculation of the clonogenic parameters. The control dish is examined after 3–4 days, depending on the cell cycle, and the PE is calculated based on Eq. 7. Concerning the SF, this is calculated based on the number of cells that divided twice post-irradiation and not on the colony formation. Therefore, the SF is defined by Eq. 8:

$$\text{PE} = \frac{\text{Number of cells that formed colonies}}{\text{Number of cells seeded}} \tag{7}$$

$$\text{SF} = \frac{\text{Number of cells divided } N \text{ times after irradiation}}{\text{Number of cells seeded} \times \text{PE}} \tag{8}$$

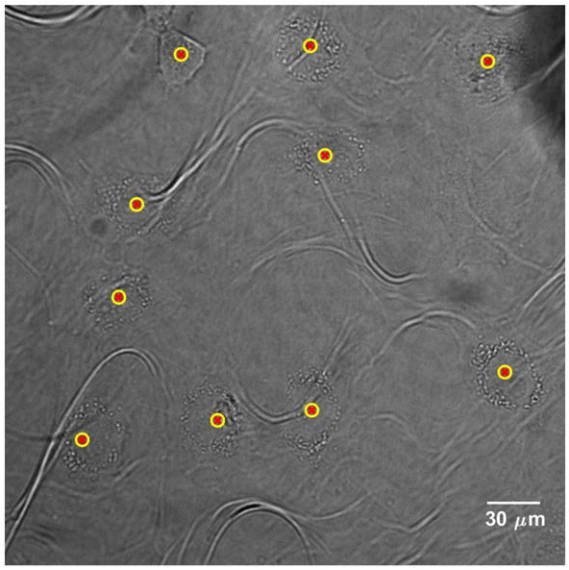

FIGURE 3 | Cell detection application on bright-field image of HeLa human cervix cells, acquired with a 40× objective. Yellow-red markers define the *x–y* positions that characterize the cell presence. The "loop" artifacts originate from the polypropylene substrate since it becomes transparent in bright-field microscopy.

In this case, the SF resembles another measurement, the mitotic index, which is the ratio of successfully divided cells to the total irradiated cells (50).

VALIDATION OF PROPOSED METHOD

Cell Detection

Cells are detected for each FOV and their positions are recorded in a list. The latter is updated every time a new cell is detected. **Figure 3** shows the application of the cell detection module on an image of semi-adherent HeLa human cervix cells, obtained with a 40× objective. The density of cells in this area is higher than the optimum one.

Cell Tracking and Cell Division Detection

The proposed method for cell tracking and cell division detection was tested on images of V79 Chinese hamster cells on polypropylene substrate. No errors were detected but the sets of images did not contain any divisions. Therefore, the module was tested on images of U251 cells on a glass-bottomed dish. **Figure 4** shows the detection of two daughter cells (right, with red–yellow markers), originating from a single parent cell (left). **Figure 5** shows the tracking diagram of the cell(s) of **Figure 4**, where the motion pattern can be identified while **Figure 6** shows their lineage tree. The latter provides all the data needed to successfully identify a division: the two daughter cells are associated with a specific parent cell while the system records the time and frame at which the two cells were detected as separate entities.

Figure 7 shows the progression of corner density in the parent cell of **Figure 4** and the corner density of one of the daughter cells. Corner density takes value in the range of 3.0–3.5 per 100 pixels for adherent cells while it reaches values higher than 5.5 in the actual cytokinesis process. At this stage, post-division, corner density decreases again for the daughter cells as soon as they become adherent again.

DISCUSSION

The use of bright-field illumination instead of the more commonly used fluorescence excitation prevents the induction of excess photo-toxicity and it avoids photo-bleaching effects. Therefore, the observation of cell reaction post-irradiation includes only radiation effects without effects originating from the toxic action of fluorescence stains. Although bright-field images are highly complex and cells become invisible in many cases, the cell detection method is successful at detecting at least 88% of the cells (33).

It has been well-understood from the early days of research with high-LET radiation that the latter generates linear survival curves with steep slope as a result of the high probability of cell killing, especially in the high-dose areas (14), while current evidence continuously confirms this notion (17, 19). However, very few cell types die soon after irradiation, through a programed death path. Research has shown that although mitotic index reached a minimum value at 4 h post-irradiation, cells may start to divide after this period of time (51). Most cells die when they

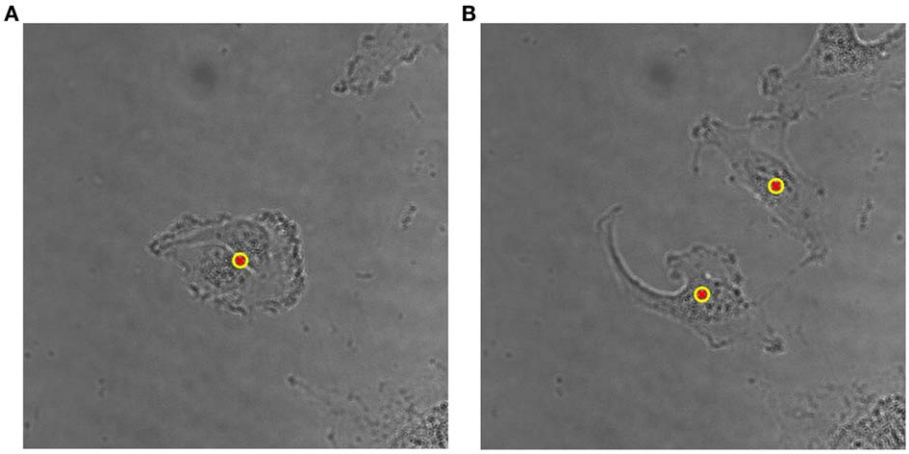

FIGURE 4 | (A) Detailed view of original bright-field image of U251 cells on glass substrate, taken with 40× objective, with a single (parent) cell detected, indicated by an overlaid yellow–red marker. **(B)** Detection of two daughter cells post-division. The time difference between the two frames is 50 min.

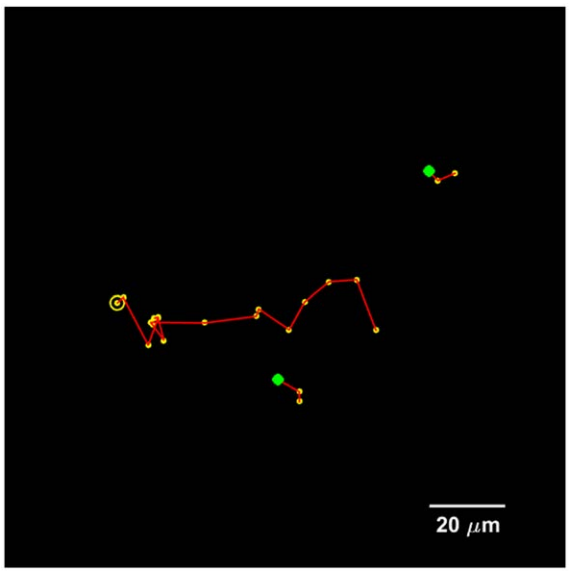

FIGURE 5 | Tracking diagram of the U251 cell(s) that are present in Figure 4 for a total duration of 20 frames, which corresponds to 3.5 h. The yellow circle indicates the initial parent position, each yellow marker indicates subsequent positions, and the green markers indicate the initial positions of the daughter cells.

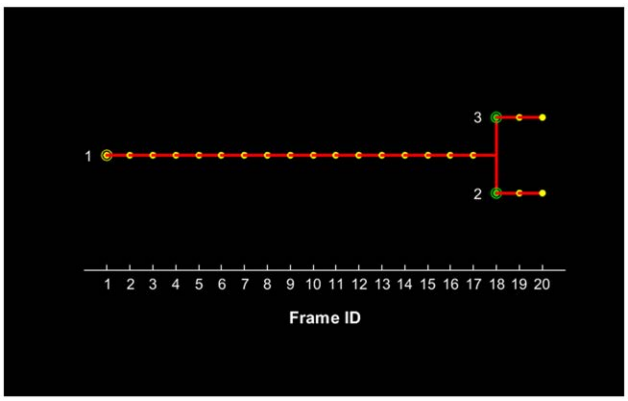

FIGURE 6 | Lineage tree of the U251 cell(s) presented in Figure 4 for a total duration of 20 frames, which corresponds to 3.5 h. The initial parent cell (#1) position is denoted with a yellow circle and its presence is recorded for each subsequent position up to frame #17. After this frame, the parent cell is not recorded and the two daughter cells appear with their first record denoted with green circles.

attempt to divide since they cannot complete this process. Some cells may even divide successfully but they may bequeath hereditary effects that may cause death to the progeny. Therefore, it is essential to develop and/or integrate a cell tracking module that can track cells through time and detect divisions for more than one cell cycle. The assessment of mitotic catastrophe can enhance the knowledge of cell response to radiation and complement the colony formation assay.

The cell tracking module is effective on connecting cell trajectories. It is independent to the cell detection module since it connects only points and not entire cell structures. Therefore, it can be used to link trajectories for any cell detection method. The dependence of this module on only one input parameter makes the tracking application less complicated. The individual on-line cell tracking gives the opportunity for automated revisiting of cells at any time-point during the time-lapse imaging process in order to inspect or even re-irradiate one or more cells.

The cell division detection module bases its application on the cell appearance during the crucial division process. Cells obtain a more distinct appearance that makes their detection easier even in complex bright-field images. Their condensed material provides a highly textured view that produces a high number of more closely located corners than that of the adherent cells prior to cytokinesis. This texture gives a sharp increase in corner density,

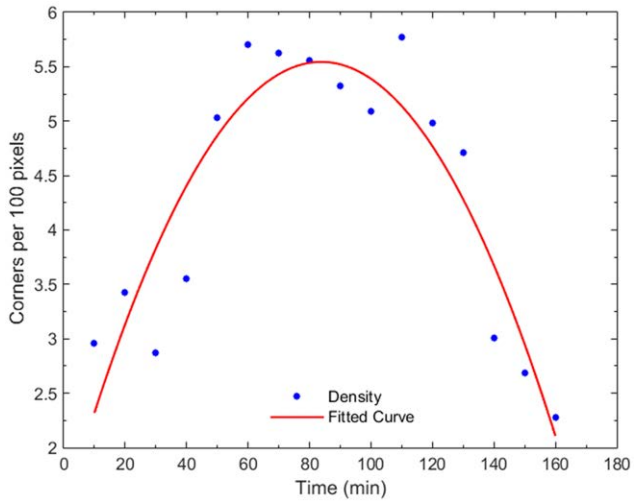

FIGURE 7 | Plot of corner density with time, for a dividing cell and one of its daughter cells. In early mitosis, the corner density increases substantially (t = 50–80 min) since the cell becomes round with high-frequency internal details. At the cytokinesis stage, the density drops while, post-mitosis (t = 140 min), the density drops to non-dividing value because the cell expands.

indicating a possible site of division. The division is confirmed by the sharp decrease of the eccentricity value: cell shape approximates an ellipsis or even circle and eccentricity approaches a value close to 0.

CONCLUSION

A new method for clonogenic survival assay using high-LET microbeam radiation was proposed. The low probability of cell survival post-irradiation with high-LET particles shifted the clonogenic potential from colony formation to successful division of the progeny of irradiated cells and assessment of mitotic catastrophe. Cell tracking in bright-field illumination time-lapse images may provide a mechanism for high-throughput assessment of radiation response using stable cell-culture of patient-derived material.

AUTHOR CONTRIBUTIONS

All authors contributed to the revision and the approval, and agreed with this work. AG contributed to the conception and initiated this work, MM contributed to the conception of this work and performed image acquisitions, JJ performed cell dish preparation and imaging, NM performed cell dish preparation, NP and RB assisted in image acquisition while RJ had the overall overview of this work.

ACKNOWLEDGMENTS

The authors would like to acknowledge the financial support of the EC Marie Curie ITN ENTERVISION Grant Agreement No 264552 (AG). The authors would also like to thank the Bioimaging and Flow Cytometry Core Facility, University of Surrey, for giving them the opportunity to perform crucial experiments for this research.

REFERENCES

1. Durante M, Loeffler JS. Charged particles in radiation oncology. *Nat Rev Clin Oncol* (2010) **7**(1):37–43. doi:10.1038/nrclinonc.2009.183
2. Carabe A, Moteabbed M, Depauw N, Schuemann J, Paganetti H. Range uncertainty in proton therapy due to variable biological effectiveness. *Phys Med Biol* (2012) **57**(5):1159–72. doi:10.1088/0031-9155/57/5/1159
3. Guan F, Bronk L, Titt U, Lin SH, Mirkovic D, Kerr MD, et al. Spatial mapping of the biologic effectiveness of scanned particle beams: towards biologically optimized particle therapy. *Sci Rep* (2015) **5**:9850. doi:10.1038/srep09850
4. Franken NAP, Rodermond HM, Stap J, Haveman J, van Bree C. Clonogenic assay of cells in vitro. *Nat Protoc* (2006) **1**(5):2315–9. doi:10.1038/nprot.2006.339
5. Munshi A, Hobbs M, Meyn RE. Clonogenic cell survival assay. In: Blumenthal RD, editor. *Chemosensitivity: Volume 1 In vitro Assays*. Totowa, NJ: Humana Press (2005). p. 21–8.
6. Riquier H, Wera AC, Heuskin AC, Feron F, Lucas S. Comparison of X-ray and alpha particle effects on a human cancer and endothelial cells: survival curves and gene expression profiles. *Radiother Oncol* (2013) **106**(3):397–403. doi:10.1016/j.radonc.2013.02.017
7. Joiner MC. Quantifying cell kill and cell survival. In: Joiner MC, van der Kogel A, editors. *Basic Clinical Radiobiology*. 4th ed. Boca Raton, FL: CRC Press (2009). p. 41–55.
8. Joiner MC, Marples B, Lambin P, Short SC, Turesson I. Low-dose hypersensitivity: current status and possible mechanisms. *Int J Radiat Oncol* (2001) **49**(2):379–89. doi:10.1016/S0360-3016(00)01471-1
9. Wéra AC, Heuskin AC, Riquier H, Michiels C, Lucas S. Low-LET proton irradiation of A549 non-small cell lung adenocarcinoma cells: dose response and RBE determination. *Radiat Res* (2013) **179**(3):273–81. doi:10.1667/RR3008.1
10. Short SC, Joiner MC. Cellular response to low-dose irradiation. *Clin Oncol* (1998) **10**(2):73–7. doi:10.1016/S0936-6555(05)80480-7
11. Scholz M, Kellerer AM, Kraft-Weyrathe W, Kraft G. Computation of cell survival in heavy ion beams for therapy. The model and its approximation. *Radiat Environ Biophys* (1997) **36**(1):59–66. doi:10.1007/s004110050055
12. Scholz M, Elsässer T. Biophysical models in ion beam radiotherapy. *Adv Space Res* (2007) **40**(9):1381–91. doi:10.1016/j.asr.2007.02.066
13. Elsässer T, Weyrather WK, Friedrich T, Durante M, Iancu G, Krämer M, et al. Quantification of the relative biological effectiveness for ion beam radiotherapy: direct experimental comparison of proton and carbon ion beams and a novel approach for treatment planning. *Int J Radiat Oncol Biol Phys* (2010) **78**(4):1177–83. doi:10.1016/j.ijrobp.2010.05.014
14. Barendsen GW, Walter HMD, Fowler JF, Bewley DK. Effects of different ionizing radiations on human cells in tissue culture: III. Experiments with cyclotron-accelerated alpha-particles and deuterons. *Radiat Res* (1963) **18**(1):106–19. doi:10.2307/3571430
15. Folkard M, Prise KM, Vojnovic B, Davies S, Roper MJ, Michael BD. The irradiation of V79 mammalian cells by protons with energies below 2 MeV. Part I: experimental arrangement and measurements of cell survival. *Int J Radiat Biol* (1989) **56**(3):221–37. doi:10.1080/09553008914551401
16. Milligan JR, Aguilera JA, Paglinawan RA, Ward JF, Limoli CL. DNA strand break yields after post-high LET irradiation incubation with endonuclease-III and evidence for hydroxyl radical clustering. *Int J Radiat Biol* (2001) **77**(2):155–64. doi:10.1080/09553000010013445
17. Fournier C, Zahnreich S, Kraft D, Friedrich T, Voss KO, Durante M, et al. The fate of a normal human cell traversed by a single charged particle. *Sci Rep* (2012) **2**:643. doi:10.1038/srep00643
18. Cui X, Oonishi K, Tsujii H, Yasuda T, Matsumoto Y, Furusawa Y, et al. Effects of carbon ion beam on putative colon cancer stem cells and its comparison with X-rays. *Cancer Res* (2011) **71**(10):3676–87. doi:10.1158/0008-5472.CAN-10-2926
19. Oonishi K, Cui X, Hirakawa H, Fujimori A, Kamijo T, Yamada S, et al. Different effects of carbon ion beams and X-rays on clonogenic survival and

DNA repair in human pancreatic cancer stem-like cells. *Radiother Oncol* (2012) **105**(2):258–65. doi:10.1016/j.radonc.2012.08.009
20. Niemantsverdriet M, van Goethem MJ, Bron R, Hogewerf W, Brandenburg S, Langendijk JA, et al. High and low LET radiation differentially induce normal tissue damage signals. *Int J Radiat Oncol* (2011) **83**(4):1291–7. doi:10.1016/j.ijrobp.2011.09.057
21. Wéra AC, Riquier H, Heuskin AC, Michiels C, Lucas S. In vitro irradiation station for broad beam radiobiological experiments. *Nucl Instrum Meth B* (2011) **269**(24):3120–4. doi:10.1016/j.nimb.2011.04.104
22. Prise KM, Schettino G. Microbeams in radiation biology: review and critical comparison. *Radiat Prot Dosimetry* (2011) **143**(2–4):335–9. doi:10.1093/rpd/ncq388
23. Heiss M, Fischer BE, Jakob B, Fournier C, Becker G, Taucher-Scholz G. Targeted irradiation of mammalian cells using a heavy-ion microprobe. *Radiat Res* (2006) **165**(2):231–9. doi:10.1667/RR3495.1
24. Hable V, Greubel C, Bergmaier A, Reichart P, Hauptner A, Krucken R, et al. The live cell irradiation and observation setup at SNAKE. *Nucl Instrum Meth B* (2009) **267**(12–13):2090–7. doi:10.1016/j.nimb.2009.03.071
25. Prise KM, Schettino G, Folkard M, Held KD. New insights on cell death from radiation exposure. *Lancet Oncol* (2005) **6**(7):520–8. doi:10.1016/S1470-2045(05)70246-1
26. Barberet P, Vianna F, Karamitros M, Brun T, Gordillo N, Moretto P, et al. Monte-Carlo dosimetry on a realistic cell monolayer geometry exposed to alpha particles. *Phys Med Biol* (2012) **57**(8):2189–207. doi:10.1088/0031-9155/57/8/2189
27. Lomax ME, Folkes LK, O'Neill P. Biological consequences of radiation-induced DNA damage: relevance to radiotherapy. *Clin Oncol* (2013) **25**(10):578–85. doi:10.1016/j.clon.2013.06.007
28. Gulston M, de Lara C, Jenner T, Davis E, O'Neill P. Processing of clustered DNA damage generates additional double-strand breaks in mammalian cells post-irradiation. *Nucleic Acids Res* (2004) **32**(4):1602–9. doi:10.1093/nar/gkh306
29. Puck TT, Marcus PI. Action of X-rays on mammalian cells. *J Exp Med* (1956) **103**:653–66. doi:10.1084/jem.103.5.653
30. Merchant MJ, Jeynes JCG, Grime GW, Palitsin V, Tullis IDC, Barber P, et al. A focused scanning vertical beam for charged particle irradiation of living cells with single counted particles. *Radiat Res* (2012) **178**(3):182–90. doi:10.1667/RR2847.1
31. Jeynes JCG, Merchant MJ, Barazzuol L, Barry M, Guest D, Palitsin VV, et al. "Broadbeam" irradiation of mammalian cells using a vertical microbeam facility. *Radiat Environ Biophys* (2013) **52**(4):13–21. doi:10.1007/s00411-013-0487-4
32. Flaccavento G, Folkard M, Noble JA, Prise KM, Vojnovic B. Substrate evaluation for a microbeam endstation using unstained cell imaging. *Appl Radiat Isot* (2009) **67**(3):460–3. doi:10.1016/j.apradiso.2008.06.017
33. Georgantzoglou A, Merchant MJ, Jeynes JCG, Wéra AC, Kirkby KJ, Kirkby NF, et al. Automatic cell detection in bright-field microscopy for microbeam irradiation studies. *Phys Med Biol* (2015) **60**(15):6289–304. doi:10.1088/0031-9155/60/16/6289
34. Folkard M, Vojnovic B, Prise KM, Bowey AG, Locke RJ, Schettino G, et al. A charged-particle microbeam: I. Development of an experimental system for targeting cells individually with counted particles. *Int J Radiat Biol* (1997) **72**(4):375–85. doi:10.1080/095530097143158
35. Maeda M, Usami N, Kobayashi K. Low-dose hypersensitivity in nucleus-irradiated V79 cells studied with synchrotron X-ray microbeam. *J Radiat Res* (2008) **49**(2):171–80. doi:10.1269/jrr.07093
36. Schettino G, Folkard M, Prise KM, Vojnovic B, Bowey AG, Michael BD. Low-dose hypersensitivity in Chinese hamster V79 cells targeted with counted protons using a charged-particle microbeam. *Radiat Res* (2001) **156**(5):526–34. doi:10.1667/0033-7587(2001)156%5B0526:LDHICH%5D2.0.CO;2
37. Konishi T, Oikawa M, Suya N, Ishikawa T, Maeda T, Kobayashi A, et al. SPICE-NIRS microbeam: a focused vertical system for proton irradiation of a single cell for radiobiological research. *J Radiat Res* (2013) **54**(4):736–47. doi:10.1093/jrr/rrs132
38. Bigelow AW, Ross GJ, Randers-Pehrson G, Brenner DJ. The Columbia University microbeam II endstation for cell imaging and irradiation. *Nucl Instrum Meth B* (2005) **231**(1–4):202–6. doi:10.1016/j.nimb.2005.01.057
39. Gault N, Rigaud O, Poncy JL, Lefaix JL. Biochemical alterations in human cells irradiation with α particles delivered by macro- or microbeams. *Radiat Res* (2007) **167**(5):551–62. doi:10.1667/RR0684.1
40. Søyland C, Hassfjellb SP, Steen HB. A new alpha-particle irradiator with absolute dosimetric determination. *Radiat Res* (2000) **153**(1):9–15. doi:10.1667/0033-7587(2000)153%5B0009:ANAPIW%5D2.0.CO;2
41. Søyland C, Hassfjell SP. A novel 210Po-based a-particle irradiator for radiobiological experiments with retrospective a-particle hit per cell determination. *Radiat Environ Biophys* (2000) **39**(2):125–30. doi:10.1007/s004110000050
42. Altman MB, Wang SJ, Whitlock JL, Roeske JC. Cell detection in phase-contrast images used for alpha-particle track-etch dosimetry: a semi-automated approach. *Phys Med Biol* (2005) **50**(2):305–18. doi:10.1088/0031-9155/50/2/009
43. Veselov O, Polak W, Ugenskiene R, Lebed K, Lekki J, Stachura Z, et al. Development of the IFJ single ion hit facility for cell irradiation. *Radiat Prot Dosimetry* (2006) **122**(1–4):316–19. doi:10.1093/rpd/ncl437
44. Roeske JC, Søyland C, Wang SJ, Stinchcomb TG, Hassfjell SP, Whitlock JL, et al. Image processing tools for alpha-particle track-etch dosimetry. *Cancer Biother Radiopharm* (2003) **18**(3):425–30. doi:10.1089/108497803322285170
45. Agero U, Monken CH, Ropert C, Gazzinelli RT, Mesquita ON. Cell surface fluctuations studied with defocusing microscopy. *Phys Rev E Stat Nonlin Soft Matter Phys* (2003) **67**(5). doi:10.1103/PhysRevE.67.051904
46. Harris C, Stephens M. A combined corner and edge detector. Proceedings of the 4th Alvey Vision Conference. Manchester: The British Machine Vision Association (1988). p. 147–51.
47. Crocker JC, Hoffman BD. Multiple-particle tracking and two-point microrheology in cells. In: Wang YL, Discher DE, editors. *Cell Mechanics*. 1st ed. Amsterdam: Elsevier/Academic Press (2007). p. 141–78.
48. Edelsbrunner H, Kirkpatrick DG, Seidel R. On the shape of a set of points in the plane. *IEEE Trans Inf Theory* (1983) **29**(4):551–9. doi:10.1109/TIT.1983.1056714
49. Plissiti ME, Nikou C, Charchanti A. Combining shape, texture and intensity features for cell nuclei extraction in Pap smear images. *Pattern Recognit Lett* (2011) **32**(6):838–53. doi:10.1016/j.patrec.2011.01.008
50. Demuth T, Hopf NJ, Kempski O, Sauner D, Herr M, Giese A, et al. Migratory activity of human glioma cell lines in vitro assessed by continuous single cell observation. *Clin Exp Metastasis* (2000) **18**(7):589–97. doi:10.1023/A:1011927004307
51. Geard CG. Initial changes in cell cycle progression of Chinese hamster V-79 cells induced by high-LET charged particles. *Radiat Res* (1980) **83**(3):696–709. doi:10.2307/3575349

Conflict of Interest Statement: The authors declare that the research was conducted in the absence of any commercial or financial relationships that could be construed as a potential conflict of interest.

Copyright © 2016 Georgantzoglou, Merchant, Jeynes, Mayhead, Punia, Butler and Jena. This is an open-access article distributed under the terms of the Creative Commons Attribution License (CC BY). The use, distribution or reproduction in other forums is permitted, provided the original author(s) or licensor are credited and that the original publication in this journal is cited, in accordance with accepted academic practice. No use, distribution or reproduction is permitted which does not comply with these terms.

frontiers in Oncology

ORIGINAL RESEARCH
published: 01 December 2015
doi: 10.3389/fonc.2015.00269

Charged Particle Therapy with Mini-Segmented Beams

F. Avraham Dilmanian[1,2,3], John G. Eley[4], Adam Rusek[5,6] and Sunil Krishnan[7]*

[1] Department of Radiation Oncology, Health Sciences Center, Stony Brook University, Stony Brook, NY, USA, [2] Department of Neurology, Health Sciences Center, Stony Brook University, Stony Brook, NY, USA, [3] Department of Radiology, Health Sciences Center, Stony Brook University, Stony Brook, NY, USA, [4] Department of Radiation Oncology, School of Medicine, University of Maryland, Baltimore, MD, USA, [5] Brookhaven National Laboratory, Upton, NY, USA, [6] NASA Space Radiation Laboratory, Upton, NY, USA, [7] Department of Radiation Oncology, MD Anderson Cancer Center, Houston, TX, USA

One of the fundamental attributes of proton therapy and carbon ion therapy is the ability of these charged particles to spare tissue distal to the targeted tumor. This significantly reduces normal tissue toxicity and has the potential to translate to a wider therapeutic index. Although, in general, particle therapy also reduces dose to the proximal tissues, particularly in the vicinity of the target, dose to the skin and to other very superficial tissues tends to be higher than that of megavoltage x-rays. The methods presented here, namely, "interleaved carbon minibeams" and "radiosurgery with arrays of proton and light ion minibeams," both utilize beams segmented into arrays of parallel "minibeams" of about 0.3 mm incident-beam size. These minibeam arrays spare tissues, as demonstrated by synchrotron x-ray experiments. An additional feature of particle minibeams is their gradual broadening due to multiple Coulomb scattering as they penetrate tissues. In the case of interleaved carbon minibeams, which do not broaden much, two arrays of planar carbon minibeams that remain parallel at target depth, are aimed at the target from 90° angles and made to "interleave" at the target to produce a solid radiation field within the target. As a result, the surrounding tissues are exposed only to individual carbon minibeam arrays and are therefore spared. The method was used in four-directional geometry at the NASA Space Radiation Laboratory to ablate a 6.5-mm target in a rabbit brain at a single exposure with 40 Gy physical absorbed dose. Contrast-enhanced magnetic resonance imaging and histology 6-month later showed very focal target necrosis with nearly no damage to the surrounding brain. As for minibeams of protons and light ions, for which the minibeam broadening is substantial, measurements at MD Anderson Cancer Center in Houston, TX, USA; and Monte Carlo simulations showed that the broadening minibeams will merge with their neighbors at a certain tissue depth to produce a solid beam to treat the target. The resulting sparing of proximal normal tissue allows radiosurgical ablative treatments with smaller impact on the skin and shallow tissues. This report describes these two methods and discusses their potential clinical applications.

Keywords: proton therapy, light-ion therapy, carbon therapy, proton minibeams, light-ion minibeams, carbon minibeams, tissue-sparing effect, interleaved carbon minibeams

OPEN ACCESS

Edited by:
Marco Durante, GSI, Germany

Reviewed by:
John E. Mignano, Tufts Medical Center, USA
Kevin Du, NYU Langone Medical Center, USA

****Correspondence:***
F. Avraham Dilmanian
avraham.dilmanian@stonybrook.edu

Specialty section:
This article was submitted to Radiation Oncology, a section of the journal Frontiers in Oncology

Received: *02 October 2015*
Accepted: *16 November 2015*
Published: *01 December 2015*

Citation:
Dilmanian FA, Eley JG, Rusek A and Krishnan S (2015) Charged Particle Therapy with Mini-Segmented Beams. Front. Oncol. 5:269. doi: 10.3389/fonc.2015.00269

INTRODUCTION

The first utilization of segmented beams to increase superficial normal tissue tolerance to radiation was in grid therapy (1). The method was used in conjunction with 250-kVp orthovoltage x-rays in the early twentieth century to ameliorate the skin damage produced during radiation therapy of deeply seated tumors because of the low-dose penetration of the low-energy x-rays. The method involved positioning metal grids with openings as large as 2 cm on the patient's skin. The resulting skin-sparing effect was solely due to the "dose–volume effect" according to which the tissue's tolerance to radiation increases as its volume decreases (2, 3). Dose–volume is also the basis for all techniques of stereotactic radiosurgery [see, for example, Ref. (4)] in which high doses can be given to small targets, sometimes in a single-dose fraction.

Although the introduction of the megavoltage (MV) x-ray machines into radiation therapy, which occurred in the middle of the twentieth century, solved the problem of damage to the skin and other proximal tissues from low-energy orthovoltage x-rays the challenge to find better beams for radiation therapy did not go away. This is because the dose distribution produced in tissues from MV x-rays is far from ideal. As seen in **Figure 1**, they give unnecessary dose to the normal tissues surrounding the target both proximal and distal to the target. Furthermore, their lateral dose penumbra is very large. Although proton and carbon ion beams clearly produce a better dose confinement at the target because of their Bragg-Peak feature, they both lack the shallow-tissue-sparing effect of high-energy x-rays, which is considered a significant shortcoming.

Two major developments that occurred since the time of grid therapy in experimental radiation therapy indicate a great potential for segmented beams at much smaller beam sizes than those used in grid therapy to improve radiation therapy. First, Zeman et al. (5–7), studying the tolerance of the mouse cerebellum to pencil beams of 25-μm to 1-mm diameter in the 1950s, showed that the mouse cerebellum tolerates the smaller beams considerably better than 1-mm beams. Specifically, microscopic beams of 25 and 75 μm did not cause tissue necrosis (i.e., loss of the tissue's blood perfusion) at doses up to 10,000 Gy, although they lead to neuronal cell death in their direct beam path, while 1-mm beams of 120–300 Gy literally ablate brain tissues at certain time points within the 24–120 days post-irradiation; these results include 300 Gy (5) and 140 Gy (7) ablations at 24 days and 280 Gy ablation at 120 days (6). Second, it was shown in the 1990s that the rat cerebellum tolerates arrays of parallel, very thin planes of synchrotron x-rays at very high doses. Specifically, Slatkin et al. showed at the National Synchrotron Light Source (NSLS), Brookhaven National Laboratory (BNL) that arrays of parallel, 37-μm synchrotron x-rays, spaced 75 μm on-center (microbeams) of ~50 keV median energy were tolerated by the rat cerebellum at up to 250 Gy in-beam in-depth without producing any visible effect on the H&E-stained brain tissue 3 months later (8). The excitement produced by the observed tissue-sparing effect led to the start of a new line of research at both the NSLS and the European Synchrotron Radiation Facility (ESRF) in Grenoble, France, called microbeam radiation therapy (MRT) (9–16). The early experiments in both these labs included measuring the tolerance of the central nervous system (CNS) in very young animals to very high doses of x-ray microbeams; these included brains of duck embryos irradiated to 120 Gy (9) and cerebella of suckling rats and weanling piglets irradiated to 300 Gy (13). We note that it has become a convention in the field of MRT to call beams with 0.3-mm size and larger "minibeams."

The effects observed in the above studies were categorically different from grid therapy in two ways. First, it showed that tissues much deeper that skin can tolerate huge doses, and second, as shown in the presentation of mechanistic bases for this larger tissue tolerance later in this report, the effect goes far beyond the dose–volume effect and involves what is called "prompt microscopic biological repair effect" including capillary blood vessel repair (10–12, 14, 16).

The next major development in the field occurred some 10 years later when it was shown at the NSLS that arrays of synchrotron X-ray microbeams as thick as 0.68 mm (minibeams) still retain much of their tissue-sparing effect in the rat spinal cord and brain (17). Furthermore, it showed that two such arrays aimed at the target from 90° angles, with gaps between the beams equal to the minibeams' thickness, can be "interleaved" (or "interlaced") to produce a solid radiation field at the target (17) (**Figure 2A**). The method was used with 0.68 mm beams to ablate a 3-mm target in a rat brain at 120 Gy with a solid interlaced beam at the target; very little damage was observed in the H&E-stained tissue outside the target (17).

The above finding about the sizable tissue-sparing effect of minibeams as thick as 0.7-mm opened the way for charged particle minibeams to be evaluated in similar preclinical studies. The first such evaluation was with carbon ion minibeams at the NASA Space Radiation Laboratory (NSRL) at BNL. They were used in

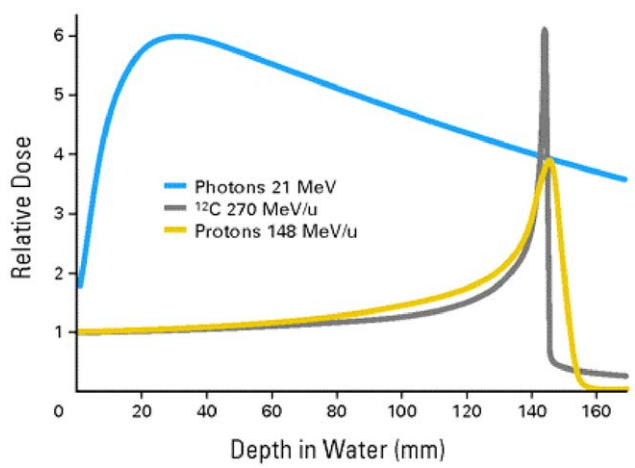

FIGURE 1 | Depth-dose distributions from 10 MV x-rays, proton beams, and carbon ion beams superimposed with each other for comparison.

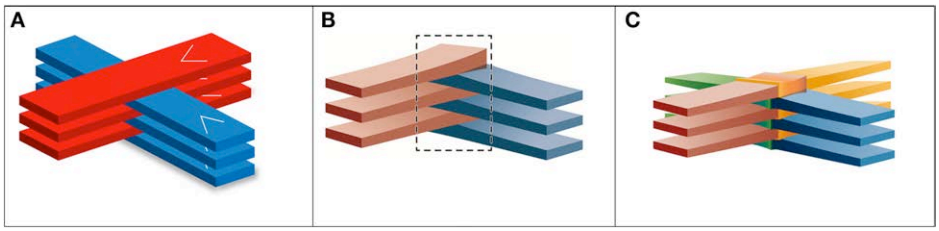

FIGURE 2 | Schematic views of interleaved x-ray minibeams and two- and four-directional interleaved carbon minibeams.

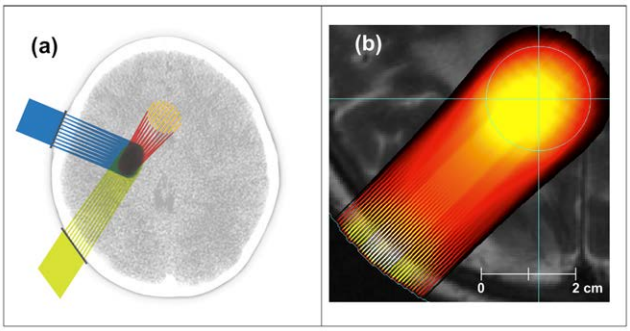

FIGURE 3 | Treating a target in the brain with proton minibeams: (A) schematic view of exposures from three orthogonal directions, (B) Monte Carlo simulation of a single exposure on the background of a brain MRI.

the "interlaced" (or "interleaved") geometry (**Figures 2B,C**) to ablate a small target in the rabbit brain (18). The rabbits evaluated in 6 months with contrast-enhanced magnetic resonance imaging (MRI) and histology showed virtually no damage to the surrounding tissues. The method, however, could not be implemented with protons and light ions because of their excessive broadening with tissue depth. However, it was shown through dosimetric measurements with proton minibeams and Monte Carlo simulations with proton and light-ion minibeams that minibeams in such arrays can be designed to merge with their neighbors at a certain depth in the subject to produce a solid beam for treating targets while sparing the skin and other shallow tissues (19) (**Figure 3**).

MATERIALS AND METHODS

Although the minibeams' decline of tissue sparing with increasing beam size is gradual; nevertheless, any treatment planning with minibeams will require defining an upper size limit for the minibeams' usage. For the following reasons, we suggest that this limit will be set at 0.7 mm. First, studies with 0.68 mm planar synchrotron x-ray minibeams with 0.68 mm gaps between them showed that irradiation of nearly the entire rat brain with these beam arrays at 170 Gy beams were greatly tolerated for the 7-month period of observation (17). Specifically, not only did the rats not demonstrate any neurological or histological deficits but they also gained weight normally (17). On the other hand, studies by Zeman et al. with 1 mm diameter 25-MeV deuteron pencil beams demonstrated complete tissue ablation of the mouse cerebellum at doses as little as 140 Gy within 280 days. These results indicate that the minibeams' tissue-sparing effect declines quite sharply at beam dimensions beyond 0.68 mm. Although 0.7-mm might be considered a conservative upper limit, its choice is justified because possible clinical use of charged particle minibeams will require very high incident doses to produce adequate target doses.

The incident minibeam width of 0.3-mm used in all experimental and simulation studies presented below was chosen in the context of the above consideration for the upper limit of the allowable minibeam size. It provides us with some dynamic maneuvering range of the beam thickness before reaching the upper limit. We also point out that choosing incident beams smaller than 0.3 mm is technically difficult, and at the same time it does not add much to that maneuvering range. As for the choice of the array's minibeam spacing, an on-center value of 0.7-mm seems to ideal for most cases because it makes the minibeams merge with each other immediately after they reach their maximum allowable size.

Interleaved Carbon Minibeams

The rabbit study described below was carried out in accordance with the recommendations of the Institutional Animal Care and Use Committee (IACUC) of BNL. BNL is accredited by the American Association for Accreditation of Laboratory Animal Care, Inc. (AAALAC). The protocol was approved by the BNL's IACUC.

Figure 4 shows the schematic view of the four-directional interleaved carbon ion minibeams used to ablate a 6.5-mm target in a rabbit brain (18). The details were the following. The minibeams' incident-beam thickness was 0.3 mm, and their beam spacing on-center was 1.05 mm on-center; this spacing was much larger than twice the incident-beam thickness to accommodate the gradual minibeam broadening in tissues. **Figure 5** shows a "to-scale" presentation of two of the four carbon minibeam arrays used in the study. The study used 124–135 MeV/nucleon carbon energies to create the spread-out-Bragg-peak (SOBP). The total dose produced at the target from all four directions in the SOBP was 40 Gy physical absorbed dose, which corresponds

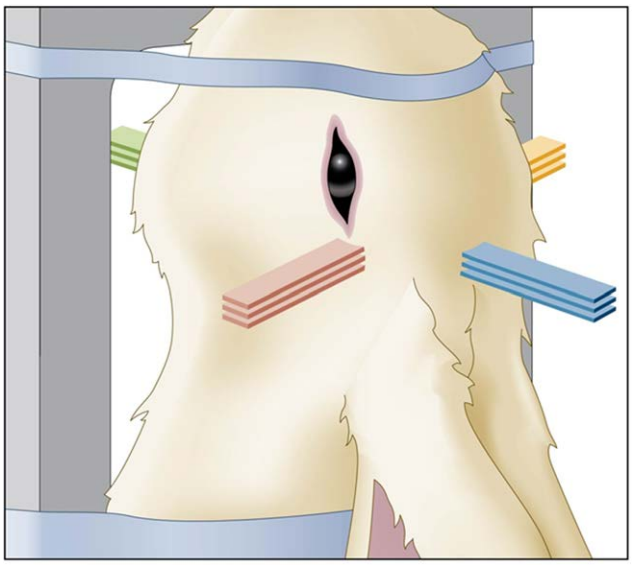

FIGURE 4 | Schematic view of the rabbit head irradiated with four-directional interleaved carbon minibeams.

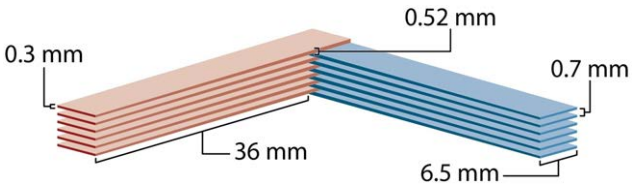

FIGURE 5 | Two-directional interleaved carbon minibeams drawn to scale for the rabbit experiment.

to 120 photon-equivalent Gy (GyE) using an average relative biological effectiveness value of 3.0 at the target. The following dosimetry account shows that this dose was produced by minibeams of 14 Gy in-beam incident physical dose in each of the four interleaving arrays. First, it was shown (18) that the particular geometry involving 14 Gy "pedestal" incident dose leads to 20 Gy physical dose at the SOBP. Therefore, the target dose would have been 20 Gy (and not 40 Gy) if we had only two interleaving arrays (see **Figure 2B** for geometry). The 40-Gy physical target dose was produced by virtue of having a four-directional incident-beam geometry (**Figure 2C**).

Proton and Light-Ion Minibeams

Figure 3A is a schematic representation of treating a brain tumor with three minibeams arrays aimed at the target from mutually orthogonal angles, whereas **Figure 3B** presents the results of Monte Carlo simulations of minibeams' merging in one such array and overlaid on a clinical MRI scan of the brain. The method's physical feasibility was established by measurements at MD Anderson Cancer Center and by Monte Carlo simulations (19).

The measurements at the MD Anderson Proton Therapy Center included the broadening rate on chromographic film of a 109-MeV proton pencil beams with 0.3-mm incident-beam diameter. The beams were produced by a pinhole collimator made of a 1-cm thick tungsten–copper alloy and the measurements were carried out using a stack of radiochromic films interspersed with 2-mm plastic sheets positioned downstream of the collimator. The film stack was irradiated to 10 Gy peak dose to measure the minibeam's broadening (19). In another measurement, a pattern of 100 MeV planar proton minibeams of 0.3-mm thickness, spaced 1-mm on-center was captured on a chromographic film (19); the minibeam array was produced using a 5-cm thick tungsten multislit collimator.

RESULTS

Interleaved Carbon Minibeams

The carbon minibeams' rate of beam broadening with tissue depth is quite suitable for interleaved carbon minibeams of target sizes such as that of the brain but not for larger sizes. In this regard, the criterion is that the minibeams' width at the proximal side of the target should not substantially exceed 0.7 mm where their tissue-sparing effect starts to gradually diminish. For example, in the above study, a minibeam width of 0.525 mm was produced at the target's proximal side, which was 36-mm deep (tissue equivalent) (18). This broadening is in agreement with the criterion that in the method's future clinical application the maximum allowable depth of the proximal side of the target is 6.5 cm; heavier ion beams such as oxygen might be used for treating deeper tumors (18).

The rabbit, observed for 6 months, did not show any behavioral deficits. Contrast-enhanced MRI showed extensive gadolinium contrast leakage only from the target tissue but not the surrounding tissues. Furthermore, H&E tissue staining showed a necrotic target tissue with no sign of damage and a slide only 5.5 mm away from the center of the target showed no damage along the four interleaving beam arrays (18).

Proton and Light-Ion Minibeams

Figure 6 shows the measured minibeam broadening rate for 109-MeV proton pencil beams superimposed with the Monte Carlo simulations of the same minibeam width in water. The experimental minibeam width was defined as the full width at half-maximum of the beam's image on the digitized film. The figure shows that the measured and the simulated 0.7-mm beam width for this beam energy are reached at 22 and 23.5 mm, respectively (19).

Figure 7 shows a schematic view of a three-dimensional minibeam converging in an array of proton pencil minibeams with 0.3-mm incident-beam thickness and 0.7-mm beam spacing on-center. It demonstrates the physical feature of the event, emphasizing the effect of the acceleration of the broadening rate as the beam approaches the merging point. This acceleration can

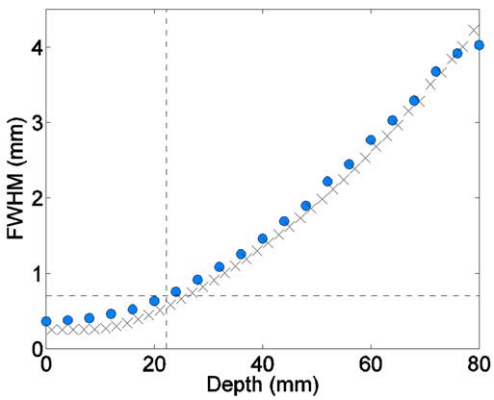

FIGURE 6 | Proton pencil minibeams' broadening for 109 MeV beam energy (circles: film measurements; x marks: the simulations in water).

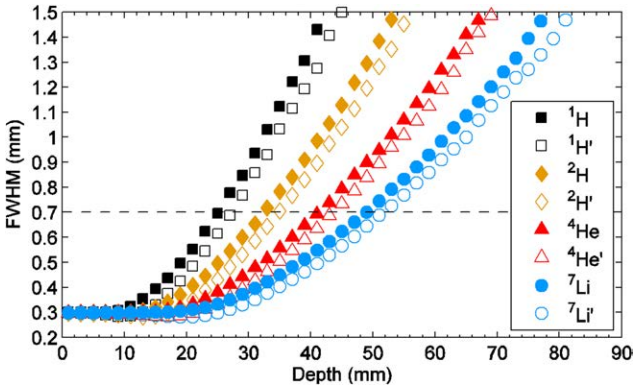

FIGURE 8 | Monte Carlo simulation of the broadening rates in water of 0.3-mm pencil-shaped (solid marks) and planar (hollow marks) minibeams of protons, deuterons, and He-4 and Li-7 ions, all at the incident-beam energy, leading to 10-cm depth in water.

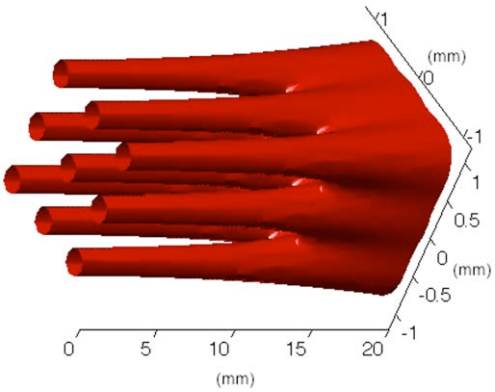

FIGURE 7 | Monte Carlo simulations of a three-dimensional pattern of proton pencil minibeams converging at a target.

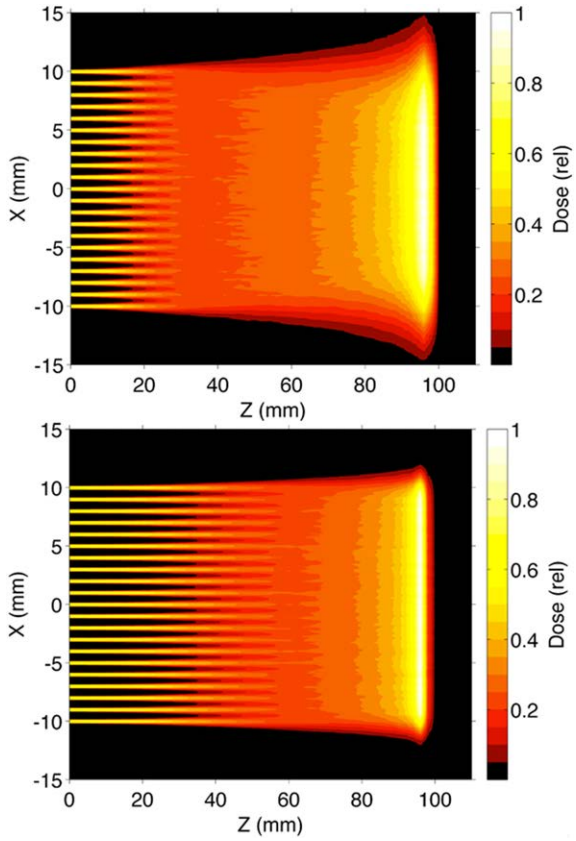

FIGURE 9 | Monte Carlo simulation of the dose distribution with depth in water of the 0.3-mm proton and Li-7 planar minibeam arrays of Figure 8, spaced 1.0-mm on-center.

be clearly seen also in **Figure 8** that shows the Monte Carlo simulation results of the broadening rates of 0.3-mm pencil-shaped and planar minibeams of protons, deuterons, and helium 4 and lithium 7 ions penetrating water at incident energies leading to 10 cm water depth. The acceleration effect of the beam broadening is clearly manifested by the curving-up feature of the curves.

Finally, **Figure 9** shows the two-dimensional pattern of the minibeam broadening for the planar minibeams of protons and lithium 7 of **Figure 8**, with 1.0 mm minibeam spacing on-center. The simulations indicate that water depths at which the minibeams in these two arrays fully merge with their neighbors are 29 and 56 mm, respectively (19).

DISCUSSION

The data and perspectives presented in this section are mostly discussions related to the clinical potential of interleaved carbon minibeams and gradually broadening arrays of proton and light-ion minibeams that converge at the tumor. In the course of this discussion, comparison is made with the radiation therapy methods currently in clinical use, including MV x-rays, protons,

and carbon ions. In this context, an important subject is the incident dose in the individual minibeams, which are clearly much higher than those used in the incident conventional beams to make up for the non-irradiated tissue slices residing between the incident minibeams.

Comparing interleaved carbon minibeams with conventional carbon therapy the advantage is smaller radiation impact on the non-targeted tissues, particularly the proximal tissues. This can allow reducing the number of dose fractions and/or increasing the target dose, which can be important in treating radioresistant tumors.

Comparing proton minibeams with conventional proton therapy, the advantage is mostly saving the skin and the proximal tissues. The method's application can include the facilitation of dose hypofractionation. But, most importantly, the method can reduce the damage to certain eloquent and/or radiosensitive organs in the brain such as the cerebral cortex that is involved in gliogenesis, especially in children (20), and therefore its sparing may reduce cognitive deficits. The method can also reduce the integral biological brain dose, another important factor in reducing cognitive deficits when targets in the brain are treated (21–23).

Comparing both methods with conventional MV x-ray methods such as intensity-modulated radiation therapy (IMRT), radiosurgery, and stereotactic body radiotherapy (SBRT), the advantages include all advantages of the corresponding conventional charged-particle methods together with the above advantage of the minibeam-implemented charged-particle methods. For both methods that include the Bragg-peak feature of the particle methods, while for carbon therapy, it also includes larger target RBE and smaller lateral dose falloff.

Mechanisms Underlying the Tissue-Sparing Effect of the X-Ray Microbeams and Minibeams

The microbeams' tissue-sparing effect is thought to be based on two phenomena, namely, the "dose–volume effect" (2, 3) and the "prompt, microscopic, biological repair effect" (10–12, 14, 16). As indicated above, dose–volume effect means that the tissue's tolerance to radiation increases as the volume of the irradiated tissue decreases (2, 3). The effect, valid for any target size, has been the basis for grid therapy (1) and stereotactic radiosurgery (4). On the other hand, the prompt, microscopic, biological repair is specific to microbeams and minibeams at beam sizes below about 0.7 mm. It is primarily related to the fast (within hours and days) repair of the capillary blood vessels via the regeneration of angiogenic cells surviving between the microbeams and minibeams (10, 12).

Quantitative Estimation of the Magnitude of the Minibeams' Tissue-Sparing Effect

One can quantitatively compare the maximum tolerance of the rat brain to minibeams and solid beams using Ref. (17, 24), respectively. While in the former, the entire brain tolerated, both behaviorally and histologically, 0.68 mm planar minibeams with 0.68-mm gaps between them at 170 Gy for the 7-month observation period (17), the latter's local 22.5-Gy solid beam irradiation led to "histological evidence for the development of necrosis in the white matter after a latent period of >26 weeks" (24). This puts the dose-tolerance advantage of minibeams to that of solid beams over 7.5-fold.

Magnitude of the Incident-Beam Doses in Clinical Interleaved Carbon Minibeams

Comparing the incident dose in 0.3-mm carbon minibeams spaced 0.7-mm on-center to carbon solid beams, both delivering the same target dose from two 90° incident directions, the minibeams' incident dose should be 4- to 4.7-times larger. This is because (a) doses from 90°-pairs of interleaving arrays do not add up and (b) minibeams' dose is diluted by 2- to 2.33-fold (0.7/0.3 ratio for 0.3 minibeams broadening to 0.7 mm just before the target) on the way to the target because of their beam broadening. This high dose of 0.3-mm carbon minibeams should be well tolerated by the skin and the other proximal tissues because as discussed above the tolerance advantage of 0.68-mm minibeams with 0.68-mm gaps between them over solid beams in about 7.5:1.0, and therefore that of 0.3 minibeam with 0.4-mm gaps between them should be even higher, probably over 10-fold. Therefore, a 4.7-fold higher dose in the incident minibeams compared to a solid beam should be tolerable.

Magnitude of the Incident-Beam Doses of Protons and Light-Ion Minibeams

Comparing the incident dose in 0.3-mm proton or light-ion minibeams spaced 0.7-mm on-center to that of proton or light-ion solid beams, both delivering the same target dose, the incident minibeam dose should be 2.3-fold higher when using planar minibeams and 6.9-fold higher when using pencil-shaped minibeams. This is because of the much smaller yield of the collimator producing pencil-shaped beams. Although using the above argument for the much higher tissue tolerance of the tissues to minibeams than solid beams the proton minibeams should still be tolerated, the clinical utilization of the pencil-shaped beams seems less attractive. This problem, however, is solved with the use of light-ion minibeams such as He-4 or Li-7 because the smaller rate of minibeams broadening allows the use of smaller than 0.7-mm beam spacing on-center to still spare several centimeters of proximal tissues. In that regards, the collimator yield for 0.3-mm beams spaced 0.5-mm on-center is 28.3% compared to 14.4% for 0.7-mm pencil-beam spacing, and the minibeams dose will be only be 3.5-fold higher than that from incident solid beams.

Comparing the Dose–Depth Distributions in a Brain Tumor Phantom Produced by MV X-Rays, Solid Proton Beams, and Proton Minibeams

Although the "biological dose" from incident proton minibeams cannot be calculated without detailed experiments, a rough estimate of the dose can be made through our knowledge of the magnitude of minibeam's tissue-sparing effect. Here, we compare the dose–depth distributions in a 15-cm deep water phantom of

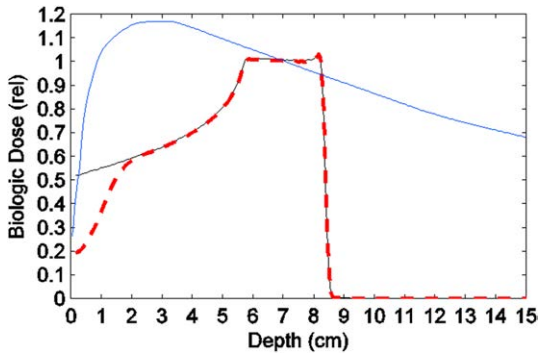

FIGURE 10 | Comparing the depth-dose distributions in a phantom of (a) a 10-MV x-ray beam, (b) an incident solid proton beam with its spread-out Bragg-peak, and (c) estimated biological dose from an incident proton minibeam array undergoing the same pattern of Bragg-peak spreading as above.

(a) a 10-MV x-ray beam, (b) an incident solid proton beam with its SOBP over a 2.5-cm target starting at 5.5-cm depth from the surface, and (c) estimated biological dose from an incident array of proton minibeams merging into a solid beam at 2.5-cm depth, which has undergone the same pattern of Bragg-peak spreading as the solid proton beam (**Figure 10**). As seen in this figure, the entrance biological dose of the proton minibeams is set to 1/3 of the physical dose of the solid proton beams. This estimate is the product of two factors. First, the incident dose in each minibeams should be 2.3 times (for 0.3-mm minibeams spaced 0.7-mm on-center) that of the solid beam to make up for the un-irradiated slices of tissue between the minibeams. Second, the magnitude of the tissue-sparing effect for 0.3-mm minibeams is estimated to be sevenfold from the earlier discussion in this section. This makes the biological dose compared to the solid beam of protons $2.3/7.0 = 0.33$. In other words, despite the 2.3-fold larger in-beam physical dose needed, still the biological dose is only 33% of the physical dose of the incident solid proton beam. The figure pictorially demonstrates the tissue-sparing effect of the proton minibeams in shallow tissues and their contribution to reduce the integral brain dose.

Potential Clinical Challenges

The use of interleaved carbon minibeams requires the immobilization of both the proximal tissues and the target tissues. This limits the method's clinical applications to benign and malignant tumors of the brain and spinal cord, neurological targets, head-and-neck tumors, breast cancer (with the breast immobilized), and tumors of the spinal column and the extremities. The neurological targets may include those that give rise to epilepsy, trigeminal neuralgia, tremor, and obsessive compulsive disorder. As a remote possibility, the method might be applicable to treat tumors of the chest and abdomen such as those of the liver and pancreas when administered under anesthesia as a single fraction.

However, the requirements for proton and light-ion minibeams are much more relaxed. There, the immobilization requirements apply only to the proximal tissues that have to be spared, and not to any deeper normal tissues or the target. Since the tissue-sparing range of proton minibeams is only 2–3 cm tissue depth, abdominal target can be treated by immobilizing the shallow tissues by physical means using the multislit collimator or a frame positioned in front of it. Of course, all possible applications indicated above for carbon minibeams can also be treated with proton and light-ion minibeams.

A legitimate concern regarding proton and light-ion minibeams pertains to the dose to the patient from the neutrons produced in the multislit collimator. Best estimates of this dose are that they are a very small fraction of the incident dose, even when accounting for biological effectiveness of neutrons. In addition, they can be further reduced by introducing an air gap between the collimator and the subject's skin. This issue was further discussed more recently with the journal following a Letter to the Editor (25). The conclusion was that for protons and for a 5-cm gap between the collimator and the skin the dose will be about 1% of the peak target dose. Because the gap can be made larger that 5-cm we do not expect this issue to be a major factor in charged particle minibeam therapy.

Ease of Clinical Implementation

Both methods can be readily integrated into current clinical practice of carbon therapy, proton therapy, or light-ion therapy by positioning a multislit collimator in the path of the broad incident beam. They are entirely compatible with passively scattered beam or spot-scanned beams. Interleaved carbon minibeams require two of four 90° irradiations, while the treatment with protons and light-ion minibeams could also ideally be done at 90° angles to avoid production of tissue irradiations with shallow-angle minibeam exposures producing incomplete tissue-sparing in these areas, called minibeam star artifacts. Also, two fixed horizontal beam-lines aiming at the target from 90° could be used for simultaneous administration of two arrays. Finally, both methods can be administered in the raster scanning mode, thus further reducing the dose to the proximal tissues.

AUTHOR CONTRIBUTIONS

FD participated in all studies and in writing the manuscript. JE participated in the proton minibeam studies and in writing the manuscript. AR participated in the interleaved carbon minibeam studies. SK participated in the proton minibeam studies an in writing the manuscript.

ACKNOWLEDGMENTS

The studies presented in this report were supported by grants from the Musella Brain Tumor Foundation, Voices against Brain Cancer, Concerned Women of the Grove, and the Stony Brook's Targeted Research Opportunities Program. Supports were also provided by the Radiation Oncology Departments of Stony Brook University and MD Anderson Cancer Center. One of us (FD) thanks Stony Brook Cancer Center, Radiation Oncology, and Radiology for support, and one of us (SK) acknowledges the John E. and Dorothy J. Harris Endowment Professorship. We also thank Tiffany Bowman and Katherine Gebhart for assistance with graphic arts.

REFERENCES

1. Harris W. Recent clinical experience with the grid in the x-ray treatment of advanced cancer; preliminary report. *Radiology* (1952) **58**(3):343–50. doi:10.1148/58.3.343
2. Withers HR, Taylor JMG, Maciejewski B. Treatment volume and tissue tolerance. *Int J Radiat Oncol Biol Phys* (1998) **14**:751–9. doi:10.1016/0360-3016(88)90098-3
3. Lawrence YR, Li XA, el Naqa I, Hahn CA, Marks LB, Merchant TE, et al. Radiation dose-volume effects in the brain. *Int J Radiat Oncol Biol Phys* (2010) **76**(3 Suppl):S20–7. doi:10.1016/j.ijrobp.2009.02.091
4. Kondziolka D, Shin SM, Brunswick A, Kim I, Silverman JS. The biology of radiosurgery and its clinical applications for brain tumors. *Neuro Oncol* (2015) **17**(1):29–44. doi:10.1093/neuonc/nou284
5. Zeman W, Curtis HJ, Gebhard EL, Haymaker W. Tolerance of mouse-brain tissue to high-energy deuterons. *Science* (1959) **130**(3391):1760–1. doi:10.1126/science.130.3391.1760-a
6. Zeman W, Curtis HJ, Baker CP. Histopathologic effect of high-energy-particle microbeams on the visual cortex of the mouse brain. *Radiat Res* (1961) **15**:496–514. doi:10.2307/3571293
7. Curtis HJ. The use of deuteron microbeam for simulating the biological effects of heavy cosmic-ray particles. *Radiat Res Suppl* (1967) **7**:250–7. doi:10.2307/3583718
8. Slatkin DN, Spanne PO, Dilmanian FA, Gebbers J-O, Laissue JA. Subacute neuropathological effects on rats of micro-planar beams of x-rays from a synchrotron wiggler. *Proc Natl Acad Sci U S A* (1995) **92**:8783–7. doi:10.1073/pnas.92.19.8783
9. Dilmanian FA, Morris GM, Le Duc G, Huang X, Ren B, Bacarian T, et al. Response of avian embryonic brain to spatially segmented X-ray microbeams. *Cell Mol Biol* (2001) **47**:485–93.
10. Dilmanian FA, Qu Y, Liu S, Cool CD, Gilbert J, Hainfeld JF, et al. X-ray microbeams: tumor therapy and central nervous system research. *Nucl Instrum Methods Phys Res A* (2005) **548**:30–7. doi:10.1016/j.nima.2005.03.062
11. Serduc R, Vérant P, Vial JC, Farion R, Rocas L, Rémy C, et al. In vivo two-photon microscopy study of short-term effects of microbeam irradiation on normal mouse brain microvasculature. *Int J Radiat Oncol Biol Phys* (2006) **64**:1519–27. doi:10.1016/j.ijrobp.2005.11.047
12. Dilmanian FA, Qu Y, Feinendegen LE, Peña LA, Bacarian T, Henn FA, et al. Tissue-sparing effect of X-ray microplanar beams particularly in the CNS: is a bystander effect involved? *Exp Hematol* (2007) **35**(4 Suppl 1):69–77. doi:10.1016/j.exphem.2007.01.014
13. Laissue JA, Blattmann H, Wagner HP, Grotzer MA, Slatkin DN. Prospects for microbeam radiation therapy of brain tumours in children to reduce neurological sequelae. *Dev Med Child Neurol* (2007) **49**(8):577–81. doi:10.1111/j.1469-8749.2007.00577.x
14. Dilmanian FA, Jenkins AL, Olschowka J, Zhong Z, Park JY, Desnoyers NR, et al. X-ray microbeam irradiation of the contusion-injured rat spinal cord temporarily improves hind-limb function. *Radiat Res* (2013) **179**:76–88. doi:10.1667/RR2921.1
15. Laissue JA, Bartzsch S, Blattmann H, Bräuer-Krisch E, Bravin A, Dalléry D, et al. Response of the rat spinal cord to X-ray microbeams. *Radiother Oncol* (2013) **106**(1):106–11. doi:10.1016/j.radonc.2012.12.007
16. Bouchet A, Lemasson B, Christen T, Potez M, Rome C, Coquery N, et al. Synchrotron microbeam radiation therapy induces hypoxia in intracerebral gliosarcoma but not in the normal brain. *Radiother Oncol* (2013) **108**(1):143–8. doi:10.1016/j.radonc.2013.05.013
17. Dilmanian FA, Zhong Z, Bacarian T, Benveniste H, Romanelli P, Wang R, et al. Interlaced X-ray microplanar beams: a radiosurgery approach with clinical potential. *Proc Natl Acad Sci U S A* (2006) **103**(25):9709–14. doi:10.1073/pnas.0603567103
18. Dilmanian FA, Rusek A, Fois GR, Olschowka J, Desnoyers NR, Park JY, et al. Interleaved carbon minibeams: an experimental radiosurgery method with clinical potential. *Int J Radiat Oncol Biol Phys* (2012) **84**(2):514–9. doi:10.1016/j.ijrobp.2011.12.025
19. Dilmanian FA, Eley JG, Krishnan S. Minibeam therapy with protons and light ions: physical feasibility and the potential to reduce radiation side effects and to facilitate hypofractionation. *Int J Radiat Oncol Biol Phys* (2015) **92**(2):469–74. doi:10.1016/j.ijrobp.2015.01.018
20. Rodgers SP, Trevino M, Zawaski JA, Gaber MW, Leasure JL. Neurogenesis, exercise, and cognitive late effects of pediatric radiotherapy. *Neural Plast* (2013) **2013**:698528. doi:10.1155/2013/698528
21. McAllister B, Archambeau JO, Nguyen MC, Slater JD, Loredo L, Schulte R, et al. Proton therapy for pediatric cranial tumors: preliminary report on treatment and disease-related morbidities. *Int J Radiat Oncol Biol Phys* (1997) **39**(2):455–60. doi:10.1016/S0360-3016(97)00079-5
22. Allen AM, Pawlicki T, Dong L, Fourkal E, Buyyounouski M, Cengel K, et al. An evidence based review of proton beam therapy: the report of ASTRO's emerging technology committee. *Radiother Oncol* (2012) **103**(1):8–11. doi:10.1016/j.radonc.2012.02.001
23. Armoogum KS, Thorp N. Dosimetric comparison and potential for improved clinical outcomes of paediatric CNS patients treated with protons or IMRT. *Cancers (Basel)* (2015) **7**(2):706–22. doi:10.3390/cancers7020706
24. Calvo W, Hopewell JW, Reinhold HS, Yeung TK. Time- and dose-related changes in the white matter of the rat brain after single doses of x rays. *Br J Radiol* (1998) **61**:1043–52. doi:10.1259/0007-1285-61-731-1043
25. Dilmanian FA, Eley JG, Krishnan S. In Reply to Sahadevan. *Int J Radiat Oncol Biol Phys* (2015) 92(5):1164–65. doi:10.1016/j.ijrobp.2015.08.051

Conflict of Interest Statement: F. Avraham Dilmanian has a patent on interleaved carbon minibeams. F. Avraham Dilmanian, John G. Eley, and Sunil Krishnan have a pending patent on minibeams of protons and light ions. Adam Rusek declares that the research was conducted in the absence of any commercial or financial relationships that could be construed as a potential conflict of interest.

Copyright © 2015 Dilmanian, Eley, Rusek and Krishnan. This is an open-access article distributed under the terms of the Creative Commons Attribution License (CC BY). The use, distribution or reproduction in other forums is permitted, provided the original author(s) or licensor are credited and that the original publication in this journal is cited, in accordance with accepted academic practice. No use, distribution or reproduction is permitted which does not comply with these terms.

frontiers in Oncology

TECHNOLOGY REPORT
published: 19 September 2017
doi: 10.3389/fonc.2017.00223

Clinical and Research Activities at the CATANA Facility of INFN-LNS: From the Conventional Hadrontherapy to the Laser-Driven Approach

Giuseppe A. P. Cirrone[1], Giacomo Cuttone[1], Luigi Raffaele[1,2], Vincenzo Salamone[1,2], Teresio Avitabile[2], Giuseppe Privitera[2], Corrado Spatola[2], Antonio G. Amico[1], Giuseppina Larosa[1], Renata Leanza[1], Daniele Margarone[3], Giuliana Milluzzo[1], Valeria Patti[1,4], Giada Petringa[1], Francesco Romano[1,5], Andrea Russo[2], Antonio Russo[1], Maria G. Sabini[1,4], Francesco Schillaci[1], Valentina Scuderi[1,3] and Lucia M. Valastro[1,4]*

[1] Laboratori Nazionali del Sud, Istituto Nazionale di Fisica Nucleare (INFN-LNS), Catania, Italy, [2] Azienda Ospedaliero Universitaria Policlinico Vittorio Emanuele, Presidio Gaspare Rodolico, Catania, Italy, [3] ELI-Beamlines Project, Institute of Physics ASCR, v.v.i. (FZU), Prague, Czechia, [4] Medical Physics Section, Cannizzaro Hospital, Catania, Italy, [5] National Physical Laboratory, Acoustic and Ionizing Radiation Division, Middlesex, United Kingdom

OPEN ACCESS

Edited by:
Marco Durante, Trento Institute for Fundamentals Physics Applications (TIFPA - INFN), Italy

Reviewed by:
Joshua Silverman, New York University, United States
Francesco Tommasino, University of Trento, Italy

***Correspondence:**
Giuseppe A. P. Cirrone
pablo.cirrone@lns.infn.it

Specialty section:
This article was submitted to Radiation Oncology, a section of the journal Frontiers in Oncology

Received: *11 April 2016*
Accepted: *01 September 2017*
Published: *19 September 2017*

Citation:
Cirrone GAP, Cuttone G, Raffaele L, Salamone V, Avitabile T, Privitera G, Spatola C, Amico AG, Larosa G, Leanza R, Margarone D, Milluzzo G, Patti V, Petringa G, Romano F, Russo A, Russo A, Sabini MG, Schillaci F, Scuderi V and Valastro LM (2017) Clinical and Research Activities at the CATANA Facility of INFN-LNS: From the Conventional Hadrontherapy to the Laser-Driven Approach. Front. Oncol. 7:223. doi: 10.3389/fonc.2017.00223

The CATANA proton therapy center was the first Italian clinical facility making use of energetic (62 MeV) proton beams for the radioactive treatment of solid tumors. Since the date of the first patient treatment in 2002, 294 patients have been successful treated whose majority was affected by choroidal and iris melanomas. In this paper, we report on the current clinical and physical status of the CATANA facility describing the last dosimetric studies and reporting on the last patient follow-up results. The last part of the paper is dedicated to the description of the INFN-LNS ongoing activities on the realization of a beamline for the transport of laser-accelerated ion beams for future applications. The ELIMED (ELI-Beamlines MEDical and multidisciplinary applications) project is introduced and the main scientific aspects will be described.

Keywords: proton therapy, dosimetry, clinical follow-up, Monte Carlo, laser-driven, ELIMED

1. INTRODUCTION

In developed countries, radiotherapy together with surgery is the most used approach for cancer therapy. The conventional and also most common form of radiotherapy make use of photons and electrons beams accelerated by linear accelerators. On the other hand, radiotherapy with hadron (protons and/or ions), in the last 10 years, is gaining more and more popularity thanks to its better physical and biological properties.

The use of energetic protons (energy sufficient to reach a tumor located in the human body) in medical applications was first suggested by Robert Wilson in 1946 (1) and in 1954 (2) the first patient was finally treated. Nowadays, according to the Particle Therapy Cooperative Group statistics (2), there are 58 active centers and 32 are under construction. Since first treatment, in 2015 about 154,000 patients have been treated with hadrontherapy. In Italy, the first hadrontherapy facility (see Section 2 for more details) started its operations in 2002. Since that time, two additional facilities have been developed and started their operation in Italy on the last decade: the CNAO foundation (3) where proton and carbon beams of 250 MeV and 450 AMeV, respectively, are available; and the proton therapy facility in Trento (web site: https://www.apss.tn.it/protonterapia).

Even if hadrontherapy, from many different reasons and aspects, is still a pioneering technique, nevertheless, its relevance in the clinical world and superiority with respect to the conventional radiation is evident for many clinical cases. It represents the election therapy in most of the choroidal and iris melanomas occurrences. In the case of the pediatric medulloblastoma, where the whole brain and spinal chord is irradiated, proton therapy greatly reduces the dose in the healthy tissue and sensibly reduces the associated risks of secondary tumor occurrence. In the breast cancer treatment, finally, is becoming more and more evident that, the use of protons, produces evident advantages like the reduction of the occurrence of lung secondary tumors and coronary diseases. The reader is suggested to read the excellent following list of publications reporting the current status of hadrontherapy and its principal advantages and drawbacks (4–13): and references therein.

Despite the evident advantage over conventional radiotherapy, the spread is limited by the high costs and complexity of the facilities. In this framework, the authors in Ref. (4, 12) clearly state that further in the future we will probably see the "*the first proton single room facility based on the illumination of a thin target with powerful (10^{18}–10^{20} Wcm^{-2}) and short (30 fs to 50 fs) laser pulse*." At moment, the major challenges in laser-driven based radiotherapy is the development of a well-controlled, reliable, energetic ion beams of very high quality able to meet the medical requirements adopted in the clinical routine (see Section 5.3).

2. CATANA, THE ITALIAN EYE PROTON THERAPY FACILITY

The *CATANA* (Centro di AdroTerapia Applicazioni Nucleari Avanzate) facility, built thanks to the collaboration between INFN-LNS and Public Health Policlinic named AOU-Vittorio Emanuele of Catania (I), is operational since 2002 and successfully treated more than 300 patients. The facility is dedicated to the radiation treatment of ocular melanomas with the 62 MeV proton beams accelerated by the INFN-LNS superconducting cyclotron. The most frequent neoplasia treated with proton beams is the uveal melanoma, followed by other eye diseases like choroidal metastases, conjunctival tumors, and eyelid tumors (14, 15). The CATANA facility is based on a passive transport system of a 62-MeV proton beam. The proton maximal range, at the irradiation point, is about 30 mm, ideal for the treatment of eye tumors. The necessary maximum range and energy modulation are achieved by means of a set of Perspex absorbers, variable in thickness, and modulator wheels.

2.1. Main Characteristics of the Beamline

The CATANA beamline has been developed at INFN-LNS of Catania (**Figure 1**). Accelerated protons exit in air through 50 μm Kapton window. Upstream the exit window, a first thin (15 μm) tantalum scattering foil is placed in vacuum: it performs a first broadening of the beam. After the Kapton window, in air, a second thicker (25 μm) tantalum foil, equipped with a brass stopper of 4 mm in diameter, is used to perform the second beam scattering. This double foil scattering system is designed to obtain an optimal homogeneity of the final proton beam, in terms of lateral dose distribution contemporary minimizing the energy losses. A typical experimental transversal dose distribution for the 62-MeV clinical proton beam is shown in **Figure 2**. Reported data are acquired in water with a Hi-pSi diode (0.6 mm detector diameter) at 12 mm water-equivalent in depth, corresponding to the middle of a Spread Out Bragg Peak (SOBP). Range shifter and range modulator are positioned

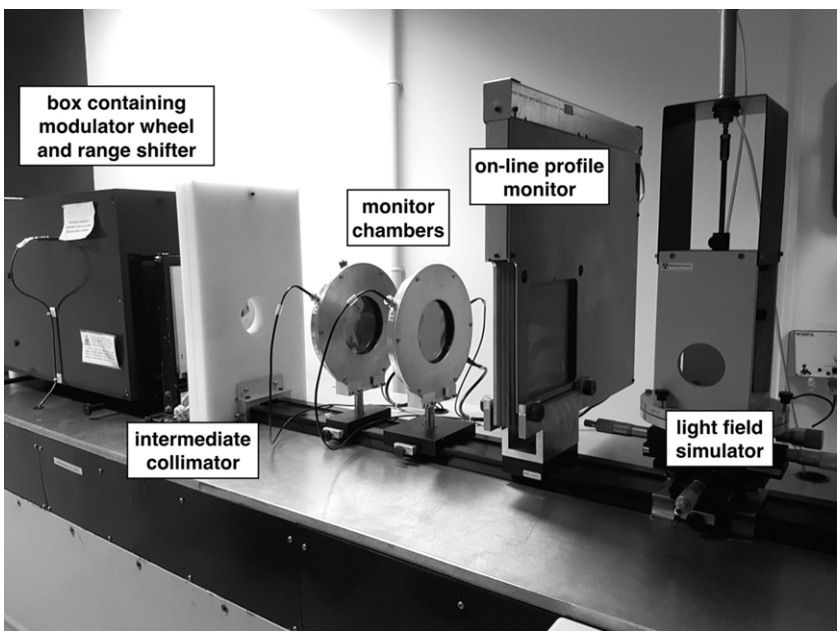

FIGURE 1 | Central section of the CATANA proton therapy beamline with some transport (collimators, modulators, and range shifters) and diagnostic (monitor chambers, on-line profile monitoring, and field simulator).

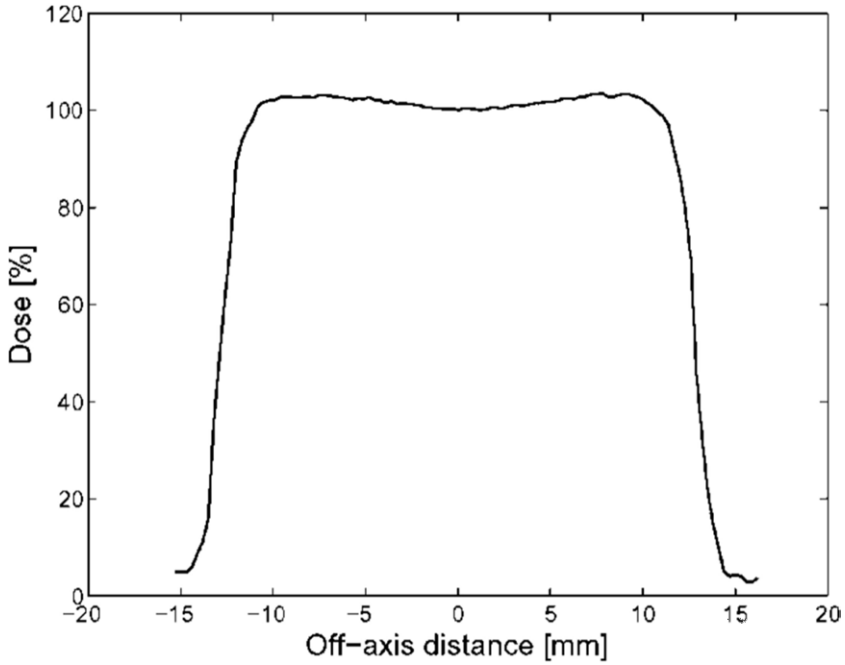

FIGURE 2 | Experimental lateral dose distribution acquired with a silicon diode. This picture reproduced with the permission of the authors.

downstream the scattering system. The radiation field is simulated using a diffused light field. Two transmission monitor ionization chambers, providing the on-line control of the dose delivered to the patient represent the key elements of the patient dosimetry system (16–18).

3. BEAM DOSIMETRY AND MONITORING

The procedures and methods to perform the absolute and relative estimation of the released dose constitute a key point in the life of an hadrontherapy facility. Because of steep dose distal and lateral gradients, detectors with high spatial resolution, energy, and dose rate independent have to be used.

In the case of monoenergetic and modulated proton beams, only plane-parallel chambers are recommended for measuring depth–dose distributions; ion chambers must fully satisfy IAEA requirements (19) as for electrode separation ($h < 2$ mm), guard ring width ($\geq 1.5\ h$), cavity diameter to cavity height (≥ 5), and bias voltage. The PTW TM34045 *Advanced Markus*, parallel-plate ion chamber ($V = 0.02$ cm^3) was adopted as reference for depth–dose measurements at CATANA proton therapy facility. Dose measurements are carried out in a water phantom where the chamber is moved with a scanning resolution of the order of 0.1 mm.

For modulated proton beams, a set of physical parameters have to be measured, strictly connected to the needed clinical requirements (**Figure 3**):

1. The beam range, referred as the 90% distal point of the peak;
2. The extension of the SOBP, defined as the distance of 95% dose points, proximal, and distal;
3. The reference depth (z_{ref});
4. The beam quality (Q), measured as the value of the residual range, defined as $R_{res} = R_p - z_{ref}$, where R_p is the depth at which the absorbed dose beyond the SOBP falls to 10%.
5. The longitudinal homogeneity, defined as $\left(\frac{D_{max}}{D_{min}}\right) \times 100\%$ within the SOBP.

At the CATANA proton therapy facility, different detectors (Diamonds, p-type silicon diodes) were tested to be used for the characterization on modulated proton beams as an alternative to the Advanced Markus chamber. The PTW Dosimetry Diode PR Type 60020 is a p-type silicon diode detector with physical dimensions of 7 mm diameter, 45.5 mm length, and an extremely small sensitive volume of 0.02 mm^3 (20).

All measurements with the PTW diode were performed with the detector axis parallel to the beam axis (axial orientation), as recommended by the manufacturer for application in clinical proton beams. No polarization field is used for the silicon diode and a PTW Unidos Type E electrometer is adopted for the current measure. **Figure 4** reports the depth–dose distribution of a modulated proton beam acquired by the PTW diode PR 60020 and the Advanced Markus Chamber; as recommended, data were normalized to the middle of SOBP, i.e., at reference depth (z_{ref}).

The dose distribution physical parameters of the clinical beam are reported in **Table 1** where the results obtained from the PTW diode are compared with the reference ones obtained with the Advanced Markus chamber. Negligible differences, all within the experimental uncertainties related to detector positioning and determination of effective point of measurements, are observed.

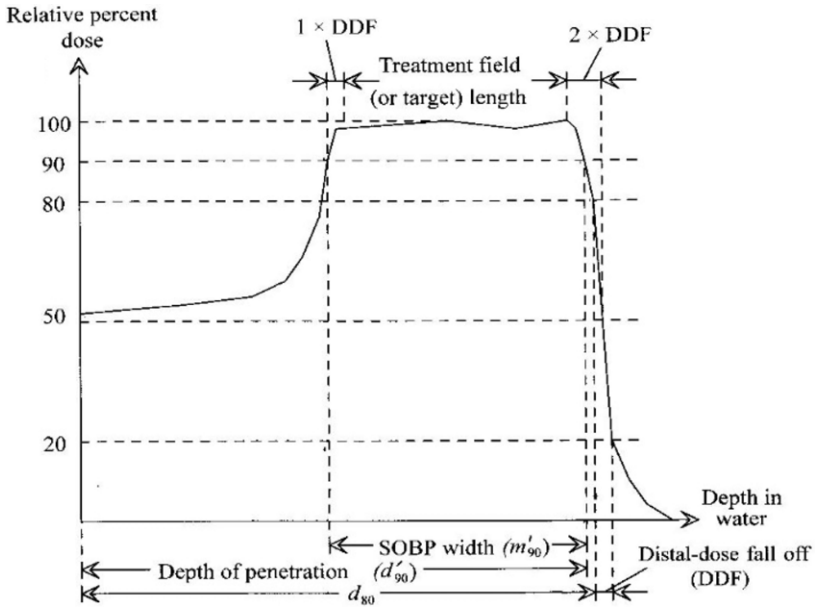

FIGURE 3 | Parameters to evaluate modulated proton beam.

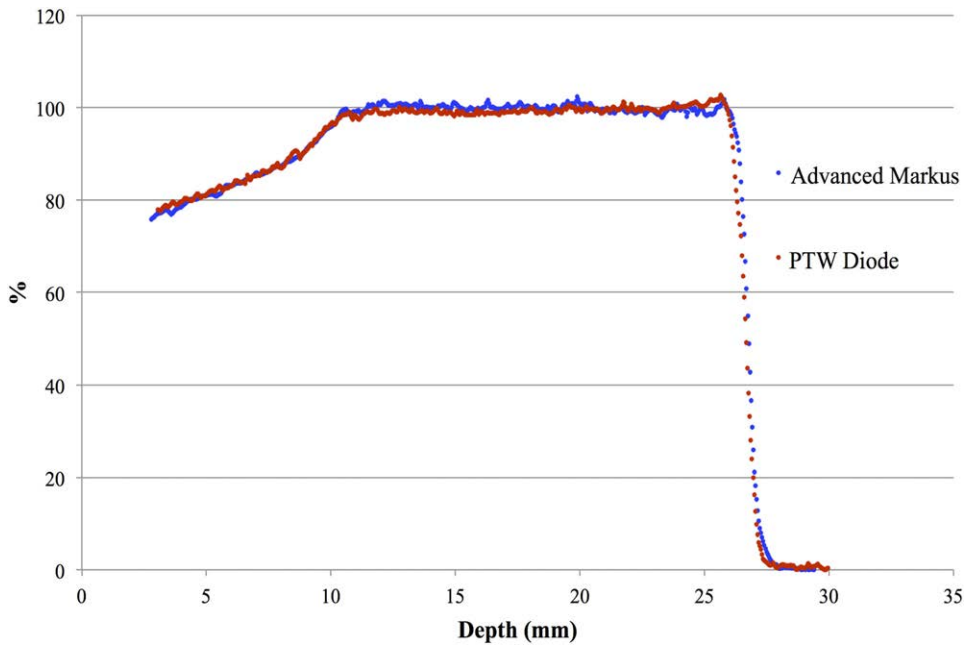

FIGURE 4 | Central axis depth–dose distribution of a modulated clinical proton beam measured by the PTW diode PR 60020 and the Advanced Markus Chamber. This picture reproduced with the permission of the authors.

The lateral dose profiles of a passively scattered beam are characterized in terms of:

1. Field size (dimension of the transversal dose distribution profile at the level of *W*50%).
2. Lateral penumbra (LP, *d*80–20%).
3. Flatness and symmetry.

GafChromic EBT3 film is the reference detector for measurement of lateral dose profiles, because of a nearly water-equivalent effective atomic number (Z_{eff}(EBT) = 6.98 compared to $Z_{eff}(water)$ = 7.3) and sub-mm spatial resolution (up to 100 μm), when read out by conventional flatbed scanners. Irradiated films are digitized in transmission mode 24 h after irradiation. Scanning is performed using the flatbed scanner

TABLE 1 | Comparison of the parameters measured by the PTW diode PR 60020 and the Advanced Markus Chamber.

	Advanced Markus [mm]	PTW diode [mm]	Difference [mm]
95% Prossimal	9.772	9.706	0.066
95% Distal	26.203	26.098	0.105
Range (90%)	26.380	26.188	0.193
Penumbra (80–20%)	0.488	0.629	0.140
SOBP width (95–95%)	16.431	16.391	0.039
Penumbra (90–10%)	0.799	0.898	0.099

TABLE 2 | Field parameters measured with the EBT3 film along the X- and Y-axis.

	Field size [mm]	$W_{95\%}$ [mm]	Penumbra [mm]	Homogeneity [%]	Symmetry [%]
Axis Y	20.82	16.64	1.6	2.8	104.3
Axis Z	13.25	9.89	1.5	0.9	101.5

EPSON Expression 10000XL, and the red channel of 48 bit RGB images is extracted and saved. EBT3 calibration (21) is carried out on the horizontal beamline of the CATANA facility. Several strips 3 cm × 3 cm are irradiated in a Solid Water phantom at 1 mm depth in the entrance plateau of the Bragg curve, corresponding to a *residual range* of about 30 mm; the reference 25 mm diameter circular collimator is used for calibration. Films are irradiated to a proton dose in the range of 0.25–4 Gy at a dose rate of 15 Gy/min, corresponding to the eye clinical dose rate. Calibration curves for 62 MeV protons is well fitted by a third order polynomial and is in agreement with the curve for 6 MV photon beams, indicating a nearly water equivalence of the EBT3 film.

The response in dose of EBT3 film was found to be energy independent (≤2%) in the energy range of eye proton therapy. This range corresponds to residual ranges beyond the irradiation depth that stays in the interval between 6 mm (25 MeV) and 29 mm (58 MeV). For these reasons, the EBT3 films can be used for dosimetric verification (1D, 2D distributions) of standard circular collimators as well as of irregularly shaped patient collimators with very small lateral extension (**Table 2**).

Both cylindrical and plane-parallel chambers, calibrated in terms of absorbed dose to water at the reference quality Q_0 (N_{D,w,Q_0}), are recommended for use as reference instruments for the Users proton beam calibration. For low proton energies, as for eye proton therapy, with SOBP smaller than 2 cm, plane-parallel ion chambers must be used. In modulated clinical proton beams, the monitor chambers are calibrated (in terms of cGy/U.M.) by a dose measurement in the middle of SOBP according with the recommendations of TRS-398 (19). The absolute value of the absorbed dose in water, at the calibration depth in a proton beam of quality Q, is calculated according to the following expression:

$$D_{w,Q} = M_Q \times N_{D,w,Q_0} \times k_{Q,Q_0} \quad (1)$$

where M_Q is the reading of the dosimeter at the reference position; N_{D,w,Q_0} is the calibration factor in terms of absorbed dose to water for the dosimeter at the reference quality Q_0; The factor k_{Q,Q_0} is a chamber-specific factor that accounts for the difference between the reference quality (Q_0) and the user proton beam quality; the reference beam (Q_0) is generally the ^{60}Co. The Classic PTW TM23343 parallel-plate Markus chamber (V = 0.055 cm^3) has been adopted at CATANA proton therapy facility as reference dosimeter (22). Beam calibration is provided for the reference circular collimator 25 mm in diameter. As for all passive systems, a single calibration has to be performed for each individual treatment field, because of the strong dependence of the beam calibration on range shifter thickness and SOBP width (see **Figure 5**) (22, 23). The variation in the Output Factor $\left(OF = \frac{cGy}{Monitor\,Units}\right)$ with decreasing beam area has been measured at the beamline commissioning, for the same monitor unit setting, by radiochromic films; the experimental results were normalized to the reference collimator output. We found that the beam output factor decreases by less than 3% over a range of field area from 490 mm^2 (reference collimator) to the smallest clinical used (about 50 mm^2).

4. MONTE CARLO SIMULATIONS

Use of the Monte Carlo simulation is of extreme importance in Hadrontherapy. Monte Carlo is, in fact, the most precise approach for the calculation of dose deposition in human tissues being able to exactly reproduce the anatomical structures and the complex particle beams involved in an hadrontherapy treatment.

4.1. Monte Carlo Simulation of the CATANA Beamline

The CATANA beamline has been simulated in details using the Monte Carlo code Geant4 (24, 25). It is a toolkit for the simulation of particle tracking in the matter, written in C++, and developed by an international collaboration composed of more than 100 of Researchers coming from the most important Institutes worldwide. Initially developed for the simulation for high-energy physics experiments, it is now widely used in several fields, as space and medical applications (26). More than 10 years ago, we developed a free and open source application that simulates the CATANA transport beamline, named Hadrontherapy (**Figure 6** (left)), currently available inside the public release of the Geant4 code (27). In the last years, the application has been sensibly improved, introducing several modules dedicated to the study of different aspects. It is now configured as a general-purposes example that aims to study issues related to hadrontherapy with protons and light ion beams. Hadrontherapy allows the simulation, *via* simple macro commands, of the whole transport beamline including all the necessary transport elements. The application has been extensively validated against experimental data; as an example, depth–dose distributions in water for 62 MeV proton beams obtained with the Geant4 Hadrontherapy example are compared in **Figure 6** (right) with the experimental ones. Once validated, the application has been used also in the clinical practice, to support the patient treatments especially for specific cases where complications due to the anatomical configuration may introduce uncertainties in the treatment plan. In

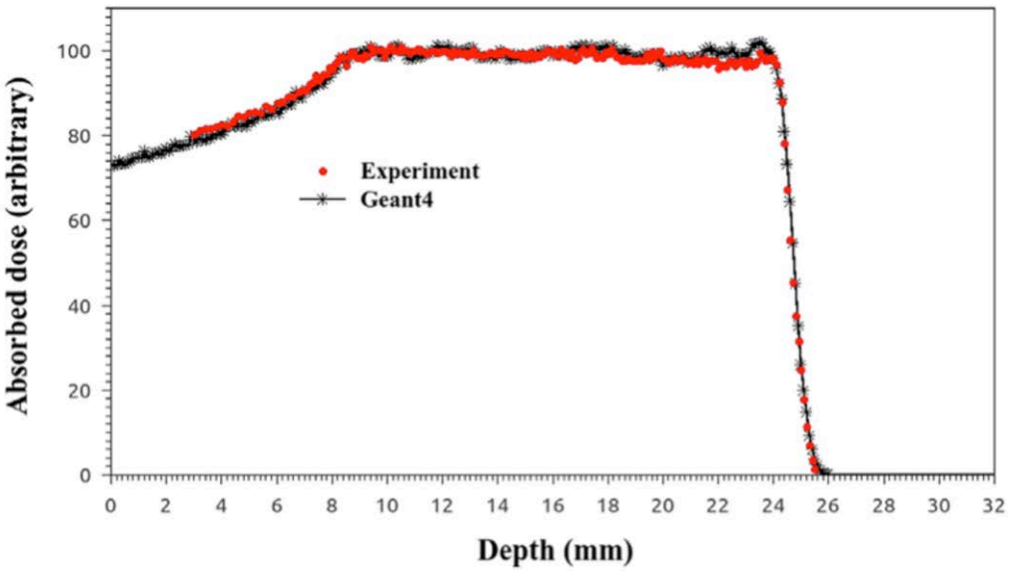

FIGURE 5 | Comparison between simulated and experimental depth–dose distributions with a modulator realized using the new approach.

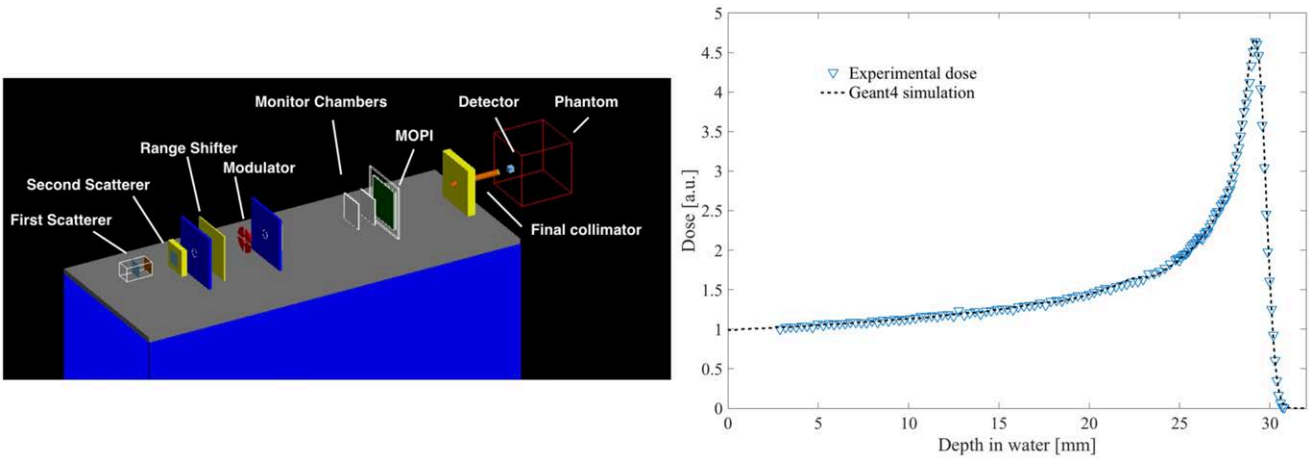

FIGURE 6 | Screenshot from the Hadrontherapy application with the complete simulation of the CATANA proton therapy beamline (left); comparison between and experimental and simulated pristine Bragg peaks (right).

this concern, depth–dose distributions for the clinical cases have to be considered (SOBPs) and they are obtained with a modulator wheel in PMMA. A dedicated module has been developed for the simulation of this element. Recently, it has been deeply revised to provide the Users' with an easier tool for changing the modulation region according to the different longitudinal target sizes. In the following subsection, more details are given, showing also some benchmarks with experimental data.

4.2. New Approach for the Simulation of a Modulator Wheel

With the developed new modulator class, very specific modulators can be realized. The data in the input file are the number of modulator steps (including air gap), the thickness of each step (zero for air gap), and the absolute or relative weight of each step. A debugging activity has been carried out to fix some issues related to the obtained depth–dose distributions and to predict in a realistic way the experimental data. As a final result, in **Figure 5**, it is shown, as example, a comparison of the experimental SOBP and the one obtained with the Geant4 simulation using the new approach for the modulator design, where the good agreement between the two distributions is clearly visible.

4.3. Average LET Distributions

As already mentioned, a huge research activity has been carried out in these years in parallel to the clinical activity related to

the proton therapy treatments. In particular, thanks to the collaborations with other INFN Sections in Italy and also different Institutions in Europe, several radiobiology experiments have been performed to study the biological effects induced on tumor and healthy cells respect to different irradiation conditions. One of the most studied parameters on this concern is the dependence of the biological damage on the radiation quality, typically quantified by means of the average Linear Energy Transfer (LET). In particular, the dose-averaged LET is of great interest in radiobiology because, according to its definition, it takes into account also the different energy contribution of the primary beam, correctly weighting for the deposited dose at a specific depth. We developed a dedicated module inside the Hadrontherapy application to study the LET-dose distributions in configurations that are of interest for radiobiology experiments (28). In particular, we proposed and tested a tool allowing to compute the dose-averaged LET considering in the computation also the contribution due to secondary particles produced for nuclear interactions. We found that a non-negligible difference there is in the average LET in the entrance channel, if the secondary contribution is also taken into account. Indeed, an LET three time higher has been obtained in this case, respect to the one retrieved when only primary incident protons at 62 MeV are considered, which is about 1 keV/μm (**Figure 7**). Similar results have been obtained also for carbon ion beams, even though the effects of secondary particle contribution is quite different, and the same computations can be done for each kind of incident ion. Recently, we have developed a new algorithm that makes the LET calculation completely independent from simulation transport parameters. It is based on the using of a specific function implemented inside the Geant4 kernel, belonging to the class G4EMCalculator, which converts the energy of charged particles to unrestricted LET directly. This module is now included in the public version of the Hadrontherapy advanced example, since the last release of the Geant4 code, so that all the interested Users' can download and use it.

5. CLINICAL ACTIVITY: TREATMENT PROCEDURES AND RESULTS

5.1. Treatment Procedure and Patient Positioning

The knowledge of the tumor exact position is essential for eye proton therapy. To achieve this, radioopaque Tantalum clips, implanted around the lesion on the outer sclera, are used as reference points during the planning and irradiation phase. The surgeon also defined the tumor position and measurements as transverse and longitudinal base diameters, elevation or height, distance to the optic disk and to the macula. The final result of this procedure is a precise virtual reconstruction of the tumor and healthy tissue around it. Eye and tumor are reconstructed by the EYEPLAN treatment planning system that provides a correct proton dose distributions and eye position during the treatment.

Before the treatment starts, the patient is immobilized. First of all, a fixation device is made by means of a customized thermoplastic mask and bite block, with the patient in a seated

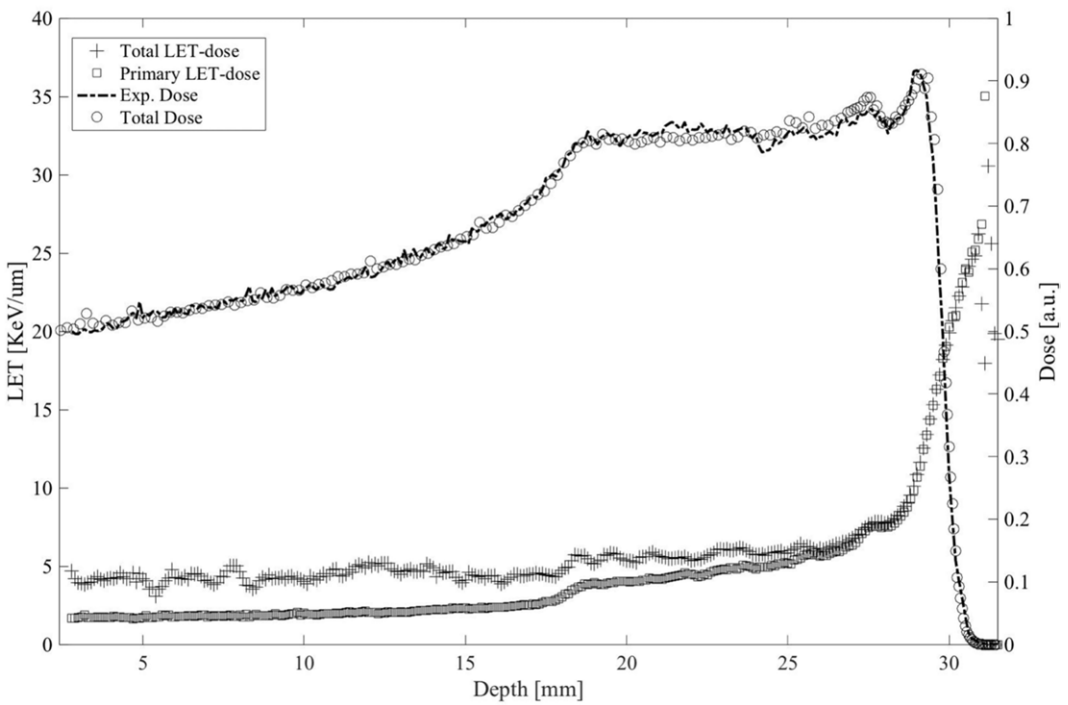

FIGURE 7 | Averaged LET-dose distributions calculated for only primary ion (square) and considering the contribute of the generated secondaries (cross) for a clinical spread-out Bragg proton peak calculated in water using the Hadrontherapy Geant4 simulation. Experimental and simulated SOBPs are also shown.

position. It is required the patient to gaze a light point and two orthogonal X-ray images (axial and lateral) are acquired. The radiographic system, based on two flat panels HAMAMATSU model C7921CA-02, is able to identify the eye position at the isocenter point through a comparison between the radiographic images and simulated reconstructions obtained by using EYEPLAN. The patient positioning chair is then moved to remove all misalignments. A measurement of the eyelid thickness and slope is also carried out to complete the planning procedures. The EYEPLAN software schematically displays a model of the patient eye (including the other anatomical parts such as lens, optic nerve, and fovea), and it provides a finally drawn of the tumor by means of the specified measurements and positions. The planned isodose levels for 90, 50, and 20% of the prescribed dose and the DVH of the tumor and the organ at risk are reported by the treatment planning system. Before the treatment is also verified the patient position because if eyelids cannot be retracted completely outside the irradiation field, they have to be included in the treatment plan, as well. A CCD camera is used to continuously verify the eye position during the irradiation. The treatment time is between 30 and 60 s.

5.2. Last Clinical Results

During the first 14 years of clinical activity, more than 300 patients have been treated at CATANA facility. Uveal melanoma has been the most frequent treated tumor, accounting for 252 treatments. Some other neoplasia has been treated by means of proton beams: conjunctival melanoma 5 patients, orbital rhabdomyosarcoma 3 patients, orbital non-Hodgkin lymphoma 4 patients, conjunctival papilloma 1 patient, eyelid and periorbital tissue carcinoma 18 patients, choroidal metastases, and other orbital tumors 11 patients (**Figure 8**).

Proton beam dose applied was the same for all melanoma patients: 60 Gy [RBE] are delivered in a hypofractionation regimen, with 4 fractions on 4 consecutive days. An RBE of 1.1 is applied for the whole physical dose distribution (SOBP). For other tumors, a lower total dose was given, ranged between 30 and 48 Gy [RBE], with the same hypofractionated regimen.

Proton beam radiation therapy (PBRT) is considered as a gold standard in the eye-conservative treatment of uveal melanoma, the most frequent ocular tumor in the adult, having demonstrated a tumor control rate and an overall survival rate comparable to those of enucleation trials (29–31). There are no available data from randomized trials for the application of proton beams to the treatment of other histologies, but only anecdotal data from case studies or single institution experiences. Then, inspired by the results of the proton beams in the treatment of uveal melanoma, so also for the other tumors of the orbital and periorbital region a conservative approach with proton therapy has been applied for 42 patients, for which there was no other therapeutic options.

Follow-up is available for all patients treated. It ranges from few months to 14 years, so the data can be considered mature for statistical considerations. Taking in account patients affected by uveal melanoma, according to the TNM-AJCC staging system (VII edition, 2010), they were classified as follow: T1 for 13 patients, T2 for 67 patients, and T3 for 172 patients (252 patients in total) (**Figure 9**).

The majority of uveal melanomas were located posteriorly to the eye equator (75%), in close vicinity to the vision OARs, optic disk, and macula. A tumor local control is the primary endpoint of ocular proton therapy: it is defined as a dimensional reduction or stabilization of the elevation of uveal tumor from the retinal surface. A surrogate of dimensional evaluation is the increasing tumor ultrasound reflectivity, especially in the case of thickness stabilization. According to these definitions, our patients have obtained a tumor control in 96% of cases (**Figures 10** and **11**). A secondary endpoint of ocular tumor proton therapy, as a conservative approach alternative to eye enucleation, is the maintenance of the eye (29). Independently from the tumor control and from the residual visual function,

Patients	
Sex	Male: 176
	Female: 118
Age	Range between: 12-88
	Median: 59
Diagnosis	Uveal melanoma: 252 pts
	Conjunctival melanoma: 5 pts
	Orbital rhabdomyosarcoma: 3 pts
	Orbital non-Hodgkin lymphoma: 4 pts
	Conjunctival papilloma: 1 pt
	Eyelid/periorbital carcinoma: 18 pts
	Other orbital tumors: 11 pt

FIGURE 8 | Characteristics of the treated patients.

Uveal melanoma patients	
TNM stage	T1: 13 pts
	T2: 67 pts
	T3: 172 pts
Location	Posterior to equator (choroid only): 69%
	Choroid + Ciliary body: 24%
	Iris: 6%

FIGURE 9 | Stage and location distribution (uveal melamona).

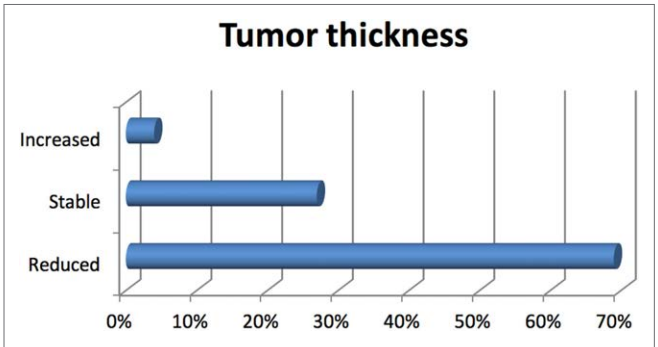

FIGURE 10 | Local control response by tumor thickness.

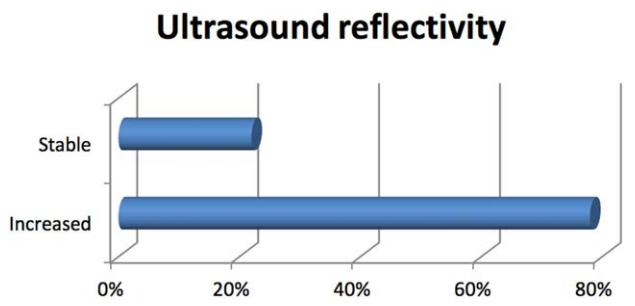

FIGURE 11 | Local control response by ultrasound reflectivity.

229 patients (90%) have maintained their eye. The major cause of secondary radiation-induced eye enucleation was neovascular glaucoma, in many cases occurring for big tumor volumes, conditioning an irradiation of large retinal surface. The time of enucleation ranged between 1.5, and 4 years from the completion of PBRT. In the group of patients with other histologies, a secondary enucleation was required. Another goal of ocular proton therapy is the maintenance of a functional eye, with an acceptable visual acuity. This is, of course, only possible in patients with a tumor located, at diagnosis, away from optic disk or macula, and with a visual function not yet compromised by other eye diseases. Taking into account these premises, in our series, a functional eye was maintained in about 40% of patients (18, 32, 33).

Ocular proton therapy is the treatment of choice in most ocular and orbital tumors, due to the high conformal treatment isodoses and the ability to spare the healthy surrounding tissues better than photon-beam treatment techniques. Despite this, due to the local extension and location of disease onset, the development of radiation-induced damages is often unavoidable. In our experience, radiation retinopathy of various degrees was seen in 22% of patients, radiation-induced cataract was detected in 35% of patients, and neovascular glaucoma developed in 18% of patients. Cause-specific survival was 92%, since 18 patients affected by uveal melanoma and 3 affected by other tumors died from metastatic disease. Ocular melanoma, both uveal and conjunctival, has a strong tendency to metastasize, especially in the liver, after many years from diagnosis, regardless of the local control of the primary tumor [H].

5.3. Potential Medical Applications of Laser-Driven Beams: The ELIMED Beamline at ELI-Beamlines

The acceleration of charged particle *via* ultra-intense and ultra-short laser pulses has gathered a strong interest in the scientific community in the past years, and it represents nowadays one of the most challenging topics in the relativistic laser–plasma interaction research. Indeed, it could represent a new path in particle acceleration and open new perspectives in multidisciplinary fields. Among many scenarios, one of the most interesting idea driving recent research activities consists in setting up high intensity laser–target interaction experiments to accelerate ions for medical applications, with main motivation of reducing cost and size of acceleration, currently associated with big and complex acceleration facilities (34, 35)..

Indeed, a development of more compact laser-based therapy centers could lead to a widespread availability of high-energy proton and carbon ion beams providing hadron therapy to a broader range of patients (34, 35).

However, to assume a realistic scenario where laser-accelerated particle beams are used for medical applications, several scientific and technological questions have to be answered and requirements to be fulfilled. Furthermore, the properties of laser-driven proton bunches significantly differ from those available at conventional accelerators, both in terms of pulse duration and peak dose rate. Thus, many scientific and technical challenges must be solved, first to demonstrate the feasibility of unique applications with laser-driven ion beams, and second to perform reliable and accurate physical and dosimetric characterization of such non-conventional beams, before starting any medical research and application. Different acceleration regimes have been experimentally investigated in the intensity range 10^{18}–10^{21} W/cm^2 in the so-called Target Normal Sheath Acceleration (TNSA) regime (36–38). Acceleration through this mechanism employs relatively thin foils (about 1 μm), which are irradiated by an intense laser pulse (of typical duration from 30 fs to 1 ps). At peak intensities of the order of 10^{18} W/cm^2 hot electrons are generated in the laser–target interaction whose energy spectrum is strictly related to the laser intensity itself. The average energy of the electrons is typically of MeV order, e.g., their collisional range is much larger than the foil thickness. Hence, they can propagate to the target rear and can generate very high space-charge fields able to accelerate the protons contained in the target. The induced electric fields, in fact, are of the order of several teravolts per meter and, therefore, they can ionize atoms and rapidly accelerate ions normal to the initially unperturbed surface. Typical TNSA ion distribution shows a broad energy spread, exceeding 100%, much larger compared to the 0.1–1% energy spread typical of ion beams delivered by conventional accelerators, a wide angular distribution with an half-angle approaching 30° which is very different from the typical parallel beam accelerated by the conventional machine and a very high intensities per pulse, i.e., up to 10^{10}–10^{12} particles per bunch, as well as a very short temporal profile (ps) compared to 10^7–10^{10} particles/s of conventional clinical proton beams. Moreover, the cutoff energy value can be likely considered as a spectrum feature still strongly dependent on the shot-to-shot reproducibility and stability and up to now, the maximum proton energy obtained with a solid target in the TNSA regime is about 85 MeV (39). In the last years, a significant amount of theoretical and experimental attention has been dedicated to explore other acceleration schemes that are expected to appear for intensity higher than 10^{21} W/cm^2 and ultra thin foils (40–44). The study on the optimization of the laser-driven source features has been coupled to the experimental investigations carried out on target nano-structures (45, 46) and recently also very innovative cryogenic technologies (47). Different types of structured target have been recently developed and tested aiming to improve the characteristics of the optical-accelerated beam at the source.

These results are particularly promising along the pathway for achieving laser-driven ion beams matching the parameters required for different multidisciplinary applications, including the medical ones. Moreover, such improvements in the laser-driven source features will allow reaching better conditions for potential collection and transport of such kind of beams. Indeed, coupled to the investigations recently carried out on different target types, the development of new strategies and advanced techniques for transport, diagnostics, and dosimetry of the optically accelerated particles represents a crucial step toward the clinical use of such non-conventional beams and to achieve well-controlled high-energy beams with suitable and reproducible bunch parameters for medical applications. In this context, a collaboration between the INFN-LNS (Nuclear Physics Laboratory, Catania, Italy) and the ASCR-FZU (Institute of Physics of the Czech Academy of Science) has been established in 2011. The main aim of the collaboration, named ELIMED (ELI-Beamlines MEDical applications), is to demonstrate that high-energy optically accelerated ion beams can be used for multidisciplinary applications, including the hadron therapy case, designing and assembling a complete transport beamline provided with diagnostics and dosimetric sections that will also enable the Users to apply laser-driven ion beams in multidisciplinary fields. In 2012, ELI-Beamlines started the realization of the laser facility, where one of the experimental hall, will be dedicated to ion and proton acceleration and will host the ELIMED beamline. In 2014, a 3-year contract has been signed between INFN-LNS and ELI-Beamlines to develop and realize the ELIMAIA beamline section dedicated to the collection, transport, diagnostics, and dosimetry of laser-driven ion beams. This section, named ELIMED as the collaboration, will be entirely developed by the LNS-INFN and will be delivered and assembled in the ELIMAIA experimental hall within the end of 2017. One of the purposes of the ELIMAIA beamline is to provide to the interested scientific community a user-oriented facility where accurate dosimetric measurements and radiobiology experiments can be performed (48). The technical solution proposed for the realization of the ELIMED beamline are described in Ref. (49). A schematic layout of the ELIMED section along the ELIMAIA beamline is shown in **Figure 12**.

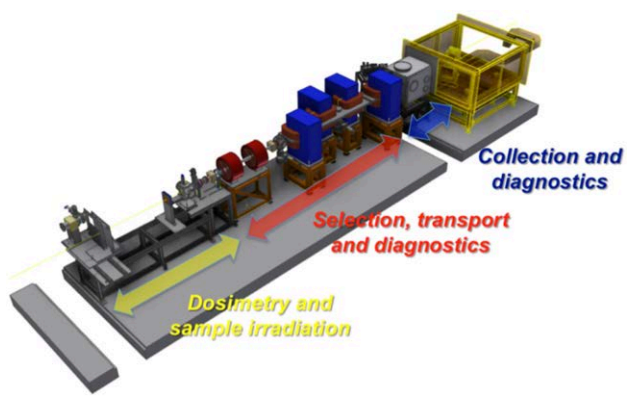

FIGURE 12 | Layout of the ELIMED beamline with the three different sections. This picture reproduced with the permission of the authors.

The beam transport line consists of an in vacuum section dedicated to the collection transport and selection of the optically accelerated particles. In particular, few cm downstream the target, a focusing system based on permanent magnet quadrupoles (PMQs) will be placed. A complete description of the designed system along with the study of the PMQs optics for different energies is given in Ref. (50). The focusing system will be coupled to a selector system (ESS) dedicated to the beam selection in terms of species and energy. The ESS consists of a series of 4 C-shape electromagnet dipoles. The magnetic chicane is based on a fixed reference trajectory with a path length of about 3 m. According to the feasibility study results, such a solution will allow to deliver ions up to 60 MeV/n with an energy bandwidth, depending on the slit aperture, varying from 5% up to 20% at the highest energies and for the different species selected ensuring a rather good transmission efficiency, 10^6–10^{11} ions/pulse. At the end of the in vacuum beamline, downstream the ESS, a set of conventional electromagnetic transport elements, two quadrupoles and two steering magnets, will allow refocusing of the selected beam and correcting for any possible misalignment. This last transport section will also allow providing a variable beam spot size between 0.1 and 10 mm.

A complete Monte Carlo simulation of the entire beamline and of the associated detectors (51) has been also performed using the Geant4 toolkit (24, 26). Moreover, when the system simulation will be ready, it will be used to study and optimize the particle transport at well-defined positions. The evaluation of dose, fluence, and particle distribution in the in-air section will be performed as well.

According to the beam transport simulation results, performed for the 60-MeV case with the beamline elements designed for ELIMAIA and considering a typical TNSA-like distribution with a cutoff energy of about 120 MeV and an angular divergence with a FWHM of 5 at 60 MeV, it is possible to deliver 60 MeV proton beam with a 20% energy spread with a rather uniform 10 mm × 10 mm spot size, beam divergence less than 0.5° and achieving a transmission efficiency of about 12%.

The simulation studies permitted us to estimate, in the worst conditions for the generated beams (biggest angular spread lowest expected particles number) the dose reaching the end of the beamline at each bunch. The value of 2 cGy per pulse for 60 MeV protons was found. This value, assuming a laser repetition rate of 1 Hz, would provide a pulsed proton beam with an average dose rate of about 1.2 Gy/min, which represents the minimal requirement for typical radiobiology experiments and is also promising considering the future possibility of running the PW laser available at ELI-Beamlines at a repetition rate of 10 Hz. Radiobiology experiments with laser-driven beams need on-line dosimetry measurements with a level of accuracy within 5%. Moreover, precise evaluations of the absolute dose released by the incoming radiation represent an extreme important requirement for many applications, as for instance the hadrontherapy one. However, the very high dose rate and the limited shot-to-shot reproducibility characterizing the laser-driven ion beams, do not allow to easily performing dose measurements, with the required accuracy, using conventional devices. Indeed, several effects have to be considered with high intensity, pulsed ion

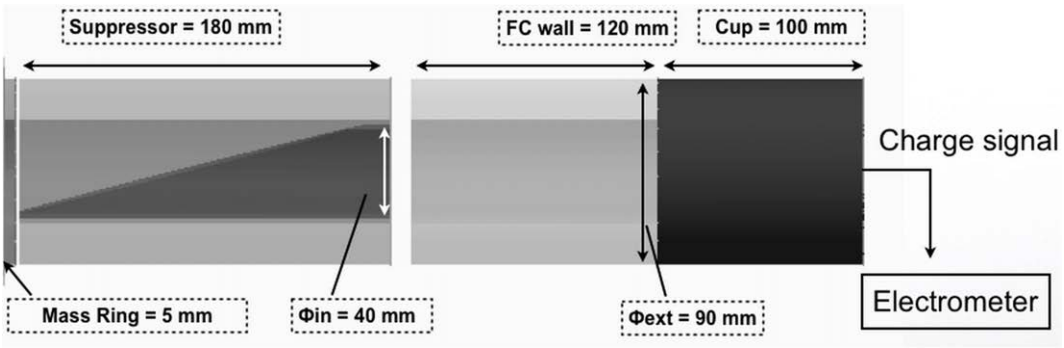

FIGURE 13 | Layout of the ELIMED Faraday Cup. Dimensions of the main components are indicated.

beams, as gas recombination, dose–rate dependence, and not-negligible electromagnetic pulse. Therefore, since no dosimetry protocol has been established, new technologies and innovative dosimeters must be developed to perform a correct, on-line dose measurement with laser-driven ion beams. The in-air section of the ELIMED beamline dedicated to dosimetry and irradiation will be composed of three main elements: a secondary emission monitor (SEM) and a multi-gap transmission ionization chamber (IC), will be used for relative dose measurements, whereas a Faraday Cup (FC), specifically designed to decrease the uncertainties in the collected charge has been realized (52) and will be placed at the irradiation point for absolute dose measurements. Moreover, a sample irradiation system (SIS) will be installed at the end of the in-air section, allowing the positioning of the cell samples with a sub-millimeter precision.

An accurate measurement of the absolute dose using a FC requires a precise measurement of the total charge carried by the beam, of the proton beam energy spectrum, and of the effective beam area; the latter needed to extract the fluence distribution (53). A typical Faraday Cup, used for ion beam dosimetry (53), consists of a thin entrance window, a suppressor electrode aimed to repel secondary electrons, and a collecting cup, able to stop the impinging primary beam and to collect the total charge as shown in **Figure 13**. In addition, our FC design, inspired by similar detectors already developed for ion beam dosimetry (54), contains a second beveled electrode, coaxial and internal to the standard one, aimed to optimize the charge collection efficiency and reduce the uncertainties, related to the charge collection, caused by the secondary electrons produced, as visible in **Figure 13**. The beam area and energy spectrum, needed for dose evaluation, will be measured using Gafchromic films (55). These dosimeters, although allow to obtain spatial dose distributions with high spatial resolution, are passive detectors, thus they need a post processing analysis. Further alternative solutions based optical fiber and spectrometer consisting of scintillator stacks to perform, respectively, on-line beam spot and energy spectrum measurements are currently under investigation. The detailed description of the Faraday Cup and the preliminary results obtained using conventional proton beams are discussed in Ref. (49). Other dosimetric systems are under consideration and evaluation. In particular, the use of TLD (Thermoluminescent detector) is under consideration as they are not sensible to the light with an acceptance dose range much extended as respect the CR39 detector. Preliminary tests and calibration procedures, using the TLD800 detectors model, have been already discussed and defined by the medical physicists of the Cannizzaro Hospital in Catania, where a long tradition and big expertise in these detectors is settled. TLD800, in fact, can detect doses in the range of the microgray that are the quantities expected in the first phases of the project.

6. CONCLUSION AND FUTURE PERSPECTIVES

CATANA is the first Italian proton therapy facility where 62 MeV protons have been used for the radiotherapy treatment of ocular melanomas. Since 2002, about 294 patients have been treated and follow-up results are consistent with the statistics so far produced (see PTCOG web site: http://www.ptcog.ch/). Many research studies have been triggered by the proton therapy activities. Among these, the development of new detectors and quality assurance methodology are of particular interest.

Moreover, the idea of new irradiation approaches, based on the use of laser-accelerated beams, has been developed. The latter was possible thanks to the collaboration with the ELI-Beamlines facility, where a new, users-open transport beamline for laser-accelerated beams will be realized and installed by INFN.

AUTHOR CONTRIBUTIONS

GC is the main proposer of the CATANA activity. GAPC and DM are the main proposers of the ELIMED activity and GAPC is responsible of the CATANA proton therapy room. GAPC, GPetringa, and FR contributed on the relative dosimetry and on the Monte Carlo simulations. FR and VScuderi contributed in the experimental and dosimetric part of the paper with particular regard to the laser-driven activities. FS and AntonioR are the main responsible of the ELIMED transport beamline. VSalamone

and LR contributions are on absolute dosimetry, dosimetry tests, and patients positioning. They are the medical physicists following the treatments. CS and GPrivitera are the oncologists and radiotherapist dedicated to the treatments. TA and AndreaR are the oculists who follow the patients after the treatment producing the follow-up results. VP, MS, and LV are the medical physicists involved in the use of TLD detectors in the laser-driven proton beams. GL, RL and AA contributed to the ELIMED dosimetry working on the Faraday Cup tests. GM contributed on the diagnostic and, partially, on the Monte Carlo activities of ELIMED.

REFERENCES

1. Wilson R. Radiological use of fast protons. *Radiology* (1946) 47:487–91. doi:10.1148/47.5.487
2. PTCOG2016. *Official Page of the Particle Therapy Cooperative Group* (2016). Available from: http://www.ptcog.ch/
3. Tuan J, Vischioni B, Fossati P, Srivastava A, Vitolo V, Iannalfi A, et al. Initial clinical experience with scanned proton beams at the Italian national center for hadrontherapy (cnao). *J Radiat Res* (2013) 54(1):i31–42. doi:10.1093/jrr/rrt036
4. Amaldi U, Bonomi R, Braccini S, Crescenti M, Degiovanni A, Garlasché M, et al. Accelerators for hadron therapy: from Lawrence cyclotrons to linacs. *Nucl Instrum Methods A* (2010) 620:563–77. doi:10.1016/j.nima.2010.03.130
5. Jones B. The case for particle therapy. *Br J Radiol* (2005) 78:1–8. doi:10.1259/bjr/81790390
6. Ma C, Maughan R. Within the next decade conventional cyclotrons for proton therapy will become obsolete and replaced by far less expensive machines using compact laser systems for the acceleration of the protons. *Med Phys* (2006) 33:571–3. doi:10.1118/1.2150220
7. Schulz-Ertner D, Jakel O, Schlegel W. Radiation therapy with charged particles. *Semin Radiat Oncol* (2006) 16:249–59. doi:10.1016/j.semradonc.2006.04.008
8. Scholz M. Heavy ion tumour therapy. *Nucl Instrum Methods B* (2000) 161:76–82. doi:10.1016/S0168-583X(99)00669-2
9. Kraft G. Tumortherapy with ion beams. *Nucl Instrum Methods A* (2000) 454:1–10. doi:10.1016/S0168-9002(00)00802-0
10. Schardt D. Tumour therapy with high energy carbon ion beams. *Nucl Phys* (2007) A787:633c–41c. doi:10.1016/j.nuclphysa.2006.12.097
11. Fokas E, Kraft G, An H, Engenhart-Cabillic R. Ion beam radiobiology and cancer: time to update ourselves. *Biochim Biophys Acta* (2009) 1796:216–29. doi:10.1016/j.bbcan.2009.07.005
12. Loeffler J, Durante M. Charged particle therapy-optimisation, challenges and future directions. *Nat Rev Clin Oncol* (2013) 10:411–24. doi:10.1038/nrclinonc.2013.79
13. De Ruysscher D, Mark Lodge M, Jones B, Brada M, Munro A, Jefferson T, et al. Charged particles in radiotherapy: a 5-year update of a systematic review. *Radiother Oncol* (2012) 103:5–7. doi:10.1016/j.radonc.2012.01.003
14. Miller DW. A review of proton beam radiation therapy. *Med Phys* (1995) 22(11):1943–54. doi:10.1118/1.597435
15. Fuss M, Loredo L, Blacharski PA, Grove RI, Slater JD. Proton radiation therapy for medium and large choroidal melanoma: preservation of the eye and its functionality. *Int J Radiat Oncol Biol Phys* (2001) 49:1053. doi:10.1016/S0360-3016(00)01430-9
16. Cuttone G, Cirrone GAP, Nigro SL, Raffaele L, Romeo N, Sabini MG, et al. News on the status of the CATANA project at INFN-LNS (ITALY). *Particle* (2002) 28:8–10.
17. Cirrone G, Cuttone G, Lojacono PA, Lo Nigro S, Mongelli V, Patti IV, et al. A 62-MeV proton beam for the treatment of ocular melanoma at Laboratori Nazionali del Sud-INFN. *IEEE Trans Nucl Sci* (2004) 51:860–5. doi:10.1109/TNS.2004.829535
18. Cuttone G, Cirrone GAP, Di Franco G, La Monaca V, Lo Nigro S, Ott J, et al. CATANA protontherapy facility: the state of art of clinical and dosimetric experience. *Eur Phys J Plus* (2011) 126:65. doi:10.1140/epjp/i2011-11065-1
19. The International Commission on Radiation Units and Measurements (ICRU), editor. *Absorbed dose Determination in External Beam Radiotherapy, An International Code of Practice for Dosimetry based on Standards of Absorbed Dose to Water* (Vol. Technical Report Series 398). Wien: International Atomic Energy Agency (2000).
20. McAuley GA, Teran AV, Slater JD, Slater JM, Wroe AJ. Evaluation of the dosimetric properties of a diode detector for small field proton radiosurgery. *J Appl Clin Med Phys* (2015) 16(6):51–64. doi:10.1120/jacmp.v16i6.5391
21. Martisikova M, Jake O. Dosimetric properties of Gafchromic (r) ebt films in monoenergetic medical ion beams. *Phys Med Biol* (2010) 55:3741–51. doi:10.1088/0031-9155/55/13/011
22. Daartz J, Engelsman M, Paganetti H, Bussière MR. Field size dependence of the output factor in passively scattered proton therapy: influence of range, modulation, air gap, and machine settings. *Med Phys* (2009) 36(7):3205–10. doi:10.1118/1.3152111
23. Karger C, Jäkel O, Palmans H, Kanai T. Dosimetry for ion beam radiotherapy. *Phys Med Biol* (2010) 55:R193–234. doi:10.1088/0031-9155/55/21/R01
24. Agostinelli S, Allison J, Amako K, Apostolakis J, Araujo H, Arce P, et al. Geant4 – a simulation toolkit. *Nucl Instrume Meth Phys Res A* (2003) 506:250–303. doi:10.1016/S0168-9002(03)01368-8
25. Allison J, Amako K, Apostolakis J, Arce P, Asai M, Aso T, et al. Recent developments in GEANT4. *Nucl Instrum Methods A* (2016) 835:186–225. doi:10.1016/j.nima.2016.06.125
26. Allison J, Amako K, Apostolakis J, Araujo H, Arce Dubois P, Asai M, et al. Geant4 developments and applications. *IEEE Trans Nucl Sci* (2006) 53(1):270–8. doi:10.1109/TNS.2006.869826
27. Cirrone GAP, Cuttone G, Di Rosa F, Raffaele L, Russo G, Guatelli S, et al. The geant4 toolkit capability in the hadron therapy field: simulation of a transport beam line. *Nucl Phys B* (2005) 150:54–7. doi:10.1016/j.nuclphysbps.2005.04.061
28. Romano F, Cirrone GAP, Cuttone G, Di Rosa F, Mazzaglia SE, Petrovic I, et al. A Monte Carlo study for the calculation of the average linear energy transfer (let) distributions for a clinical proton beam line and a radiobiological carbon ion beam line. *Phys Med Biol* (2011) 59:2863–82. doi:10.1088/0031-9155/59/12/2863
29. Damato B, Kackperek A, Chopra M, Sheen MA, Campbell IR, Errington RD. Proton beam radiotherapy of iris melanoma. *Int J Radiat Oncol Biol Phys* (2005) 63:109. doi:10.1016/j.ijrobp.2005.01.050
30. Levin D, Kooy H, Loeffler J, DeLaney TF. Proton beam therapy. *Br J Cancer* (2005) 93:849. doi:10.1038/sj.bjc.6602754
31. Egger E, Schalenbourg A, Zografos L, Beati D, Bohringer T, Chamot L, et al. Eye retention after proton beam radiotherapy for uveal melanoma. *Int J Radiat Oncol Biol Phys* (2003) 55:867. doi:10.1016/S0360-3016(02)04200-1
32. Spatola C, Privitera G, Raffaele L, Cuttone G, Cirrone GAP, Lo Nigro S, et al. Clinical application of proton beams in the treatments of uveal melanoma: the first therapies carried out in Italy and preliminary results. *Tumori* (2003) 89:502–9.
33. Spatola C, Privitera G, Raffaele L, Salamone V, Valastro LM, Cuttone G, et al. Protontherapy of ocular tumors: 5 years experience at Italian CATANA centre. *Riv Med* (2008) 14(1):97–101.
34. Bulanov S, Khoroshkov VS. Feasibility of using laser ion accelerators in proton therapy. *Plasma Phys Rep* (2002) 28(5):453–6. doi:10.1134/1.1478534
35. Bulanov SV, Wilkens JJ, Zh Esirkepov T, Korn G, Kraft G, Kraft SD, et al. Laser ion acceleration for hadron therapy. *Rev Top Probl* (2014) 57(12):1149–79. doi:10.3367/UFNe.0184.201412a.1265
36. Hatchett SP, Brown CG, Cowan TE, Henry EA, Johnson JS. Electron, photon and ion beams from the relativistic interaction of Petawatt laser pulses with solid targets. *Phys Plasmas* (2000) 7:2076. doi:10.1063/1.874030
37. Wilks S, Langdon AB, Cowan TE, Roth M, Singh M, Hatchett S, et al. Energetic proton generation in ultra-intense laser-solid interactions. *Phys Plasmas* (2001) 8:542–9. doi:10.1063/1.1333697
38. Macchi A, Sgattoni A, Sinigardi S, Borghesi M, Passoni M. Advanced strategies for ion acceleration using high-power lasers. *Plasma Phys Control Fusion* (2013) 55:124020. doi:10.1088/0741-3335/55/12/124020
39. Wagner F, Deppert O, Brabetz C, Fiala P, Kleinschmidt A, Poth P, et al. Maximum proton energy above 85 mev from the relativistic interaction of

laser pulses with micrometer thick ch2 targets. *Phys Rev Lett* (2016) 116(20): 205002. doi:10.1103/PhysRevLett.116.205002
40. Esirkepov T, Borghesi M, Bulanov SV, Mourou G, Tajima T. Highly efficient relativistic ion generation in the laser-piston regime. *Phys Rev Lett* (2004) 92:175003. doi:10.1103/PhysRevLett.92.175003
41. Esirkepov T, Yamagiwa M, Tajima T. Laser ion acceleration scaling laws in multiparametric particle-in-cell simulations. *Phys Rev Lett* (2006) 96:105001. doi:10.1103/PhysRevLett.96.105001
42. Henig A, Kiefer D, Markey K, Gautier DC, Flippo KA, Letzring S, et al. Enhanced laser driven ion acceleration in the relativistic transparency regime. *Phys Rev Lett* (2009) 103:045002. doi:10.1103/PhysRevLett.103.045002
43. Woods K, Boucher S, O'Shea FH, Hegelich BM. Beam conditioning system for laser driven hadron therapy. *Proceedings of the IPAC2013*. Shangay (2013).
44. Jung D, Yin L, Albright BJ, Gautier BC, Lezring S, Dromey B, et al. Efficient carbon ion beam generation from laser driven volume acceleration. *New J Phys* (2013) 15:023007. doi:10.1088/1367-2630/15/2/023007
45. Margarone D, Klimo O, Kim IJ, Prokůpek J, Limpouch J, Jeong TM, et al. Laser-driven proton acceleration enhancement by nanostructured foils. *Phys Rev Lett* (2012) 109:234801. doi:10.1103/PhysRevLett.109.234801
46. Margarone D, Kim IJ, Psikal J, Kaufman J, Mocek T, Choi IW, et al. Laser-driven high-energy proton beam with homogeneous spatial profile from a nanosphere target. *Phys Rev ST Accel Beams* (2015) 18:071304. doi:10.1103/PhysRevSTAB.18.071304
47. Garcia S, Chatain D, Perin J. Continuous production of a thin ribbon of solid hydrogen. *Laser Part Beams* (2014) 32(4):569–75. doi:10.1017/S0263034614000524
48. Cirrone GAP, et Margarone D. *Aip Conference Proceedings for 2nd ELIMED Workshop and Panel*. Catania (2013).
49. Cirrone GAP, Cuttone G, Romano F, Schillaci F, Scuderi V, Amato A, et al. Design and status of the ELIMED beam line for laser-driven ion beams. *Appl Sci* (2015) 5(3):427–45. doi:10.3390/app5030427
50. Schillaci F, Cirrone GAP, Cuttone G, Maggiore M, Andò L, Amato A, et al. Design of the ELIMAIA ion collection system. *J Instrum* (2015) 10:T12001. doi:10.1088/1748-0221/10/12/T12001
51. Proceedings AC, editor. *Monte Carlo Simulation for the ELIMED Transport Beamline* (Vol. 1546) (2013).
52. Cirrone GAP, Romano F, Scuderi V, Amato A, Candiano G, Cuttone G. Transport and dosimetric solutions for the ELIMED laser-driven beam line. *Nucl Instrum Methods Phys Res* (2015) 796:99–103. doi:10.1016/j.nima.2015.02.019
53. Cambria R, Hérault J, Brassart N, Silari M, Chauvel P. Proton beam dosimetry: a comparison between the faraday cup and an ionization chamber. *Phys Med Biol* (1997) 42:1185–1169. doi:10.1088/0031-9155/42/6/014
54. Thomas D, Hodges GS, Seely DG, Moroz NA, Kvale TJ. Performance enhancement study of an electrostatic faraday cup detector. *Nucl Instrum Methods Phys Res A* (2005) 536:11–21. doi:10.1016/j.nima.2004.07.211
55. Devic S, Seuntjens J, Sham E, Podgorsak EB, Schmidtlein CR, Kirov AS, et al. Precise radiochromic film dosimetry using a at-bed document scanner. *Med Phys* (2005) 32:2245–53. doi:10.1118/1.1929253

Conflict of Interest Statement: The authors declare that the research was conducted in the absence of any commercial or financial relationships that could be construed as a potential conflict of interest.

Copyright © 2017 Cirrone, Cuttone, Raffaele, Salamone, Avitabile, Privitera, Spatola, Amico, Larosa, Leanza, Margarone, Milluzzo, Patti, Petringa, Romano, Russo, Russo, Sabini, Schillaci, Scuderi and Valastro. This is an open-access article distributed under the terms of the Creative Commons Attribution License (CC BY). The use, distribution or reproduction in other forums is permitted, provided the original author(s) or licensor are credited and that the original publication in this journal is cited, in accordance with accepted academic practice. No use, distribution or reproduction is permitted which does not comply with these terms.

frontiers in Oncology

ORIGINAL RESEARCH
published: 08 June 2016
doi: 10.3389/fonc.2016.00097

Evaluation of Superconducting Magnet Shield Configurations for Long Duration Manned Space Missions

*Filippo Ambroglini[1], Roberto Battiston[2] and William J. Burger[3]**

[1]University of Perugia and INFN-Perugia, Perugia, Italy, [2]University of Trento and TIFPA, Trento, Italy, [3]FBK and TIFPA, Trento, Italy

A manned mission to Mars would present an important long-term health risk to the crew members due to the prolonged exposure to the ionizing radiation of galactic cosmic-rays. The radiation levels would largely exceed those encountered in the Apollo missions. An increase in the passive shielding provided by the spacecraft implies a significant increase of the mass. The advent of superconducting magnets in the early 1960s was considered an attractive alternative. The technology allows to generate magnetic fields capable to deflect the cosmic-rays in a manner analogous to the reduction of the particle fluxes in the upper atmosphere due to the Earth's dipole magnetic field. A series of the three studies have been conducted over the last 5 years, funded successively by European Space Agency (ESA), the NASA Innovative Advanced Concepts (NIAC) program, and the Union European's Seventh Framework Programme (FP7). The shielding configurations studied are based on high-temperature superconductors, which eliminate the need to operate with liquid helium. The mass estimates of the coils and supporting structure of the engineering designs are based on the current and expected near-future performance of the superconducting materials. In each case, the shield performance, in terms of dose reduction, is provided by a 3-dimensional Monte Carlo simulation, which treats in detail the electromagnetic and hadronic interactions of the galactic-cosmic rays, and the secondary particles they produce in the materials of the shield and spacecraft. A summary of the results of the studies, representing one of the most detailed and comprehensive efforts made in the field, is presented.

Keywords: long duration manned space missions, active magnetic shielding, radiation protection, Monte Carlo simulation

OPEN ACCESS

Edited by:
Marco Durante, GSI Helmholtzzentrum für Schwerionenforschung, Germany

Reviewed by:
Piero Spillantini, University of Florence, Italy
Eamonn Daly, European Space Agency, Netherlands

***Correspondence:**
William J. Burger
william.burger@cern.ch

Specialty section:
This article was submitted to Radiation Oncology, a section of the journal Frontiers in Oncology

Received: *30 September 2015*
Accepted: *04 April 2016*
Published: *08 June 2016*

Citation:
Ambroglini F, Battiston R and Burger WJ (2016) Evaluation of Superconducting Magnet Shield Configurations for Long Duration Manned Space Missions. Front. Oncol. 6:97. doi: 10.3389/fonc.2016.00097

1. INTRODUCTION

The exposure to the ionizing radiation of galactic cosmic-rays (GCR) and solar energetic particles (SEP) is an important concern for the health of the crew for long duration interplanetary missions. **Figure 1** shows the proton flux of a 10-day SEP event and the GCR fluxes for protons, carbon, and iron nuclei. The SEP events are characterized by the emission of high fluxes of lower energy particles, which may last on the order of hours or days. The GCR fluxes are modulated by the solar cycle characterized by alternating periods of maximum and minimum activity. Periods of maximum solar

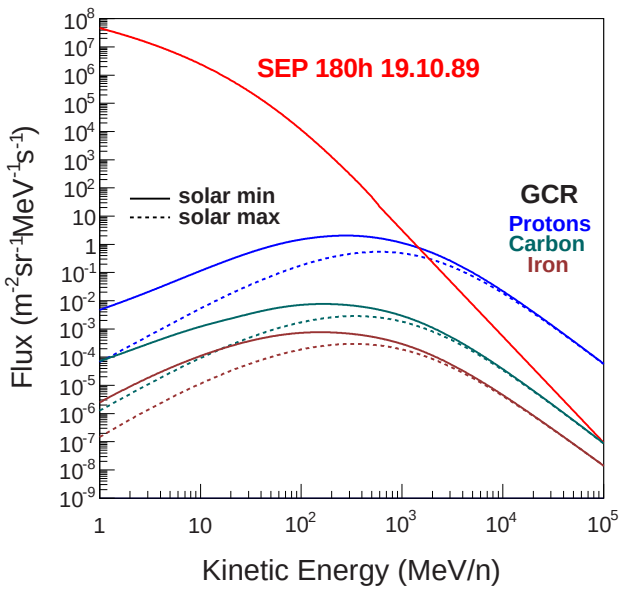

FIGURE 1 | The proton flux of a 10-day SEP event in October 1989, and the GCR proton, carbon, and iron nuclei fluxes for solar minimum and maximum periods (1).

activity result in the decrease of the low energy GCR flux due to their interaction with the higher particle flux emitted by the Sun.

The radiation risk arises from the damage caused by the energy lost by the charged particles in human tissue. The mean energy loss rate in a material due to ionization is given by the Bethe-Block equation,

$$\frac{dE}{dx} = 4\pi N_A r_e^2 m_e c^2 \frac{z^2}{\beta^2}\frac{Z}{A}\left[\frac{1}{2}\ln\frac{2m_e c^2\beta^2\gamma^2 T_m}{I^2} - \beta^2 - \frac{\delta}{2}\right] \quad (1)$$

where z and β are the particle's charge and velocity expressed in terms of the speed of light c. Z and A are the atomic number and mass of the material. The other terms in the equation are Avogadro's number N_A, the classical radius r_e and mass m_e of the election, the relativistic term $\gamma = \sqrt{1-\beta^2}$, the mean excitation energy I, the maximum kinetic energy energy lost in a collision with a free electron T_m, and a density correction term δ.

The ionization losses depend on the characteristics of the material traversed and the properties of the ionizing radiation. The materials may be classified as sensitive, for example, electronics and human tissue, and inert, i.e., insensitive to the ionizing radiation. Passive shielding refers to the slow down and absorption of the charged particles in inert materials. Particles with high ionization rates, i.e., with high charge z and low velocity β, are responsible for high doses in sensitive materials, whereas they are shielded efficiently by a passive absorber.

The ionization of the lower energy SEP protons represents a short-term risk due to the very high flux of the low velocity protons. The GCR fluxes represent a longer term risk exposing the crew members to lower life expectancy due to radiation induced cancers.

In addition to the ionization losses, the GCR protons and nuclei are subject to inelastic nuclear interactions in the material traversed, which produce lower energy secondary charged particles and neutrons. The ionization loss in the inert materials of the spacecraft provides passive shielding if sufficiently thick to contain the primary particles and their secondaries. In the case of SEP events, the required thickness of the shielding material would limit the protection to a small volume of the spacecraft, a shelter that would be occupied during the duration of the event.

The appearance of superconducting magnets in the early 1960s presented an alternative, an active magnetic shield (2). A particle with charge q and vector velocity $\mathbf{v}$ is deflected in the plane perpendicular to the magnetic field by the Lorentz force,

$$\mathbf{F} = q\mathbf{v}\times\mathbf{B}. \quad (2)$$

The particle moves in a circle in the deflection plane, with an angular deviation θ from the incident direction,

$$\theta \approx \frac{BL}{R} \quad (3)$$

where B is the magnetic flux density, L the length of the field region in the deflection plane, and R the magnetic rigidity, i.e., the particle's momentum divided by its electric charge.

The high field flux densities of superconducting magnets may be used to create an active magnetic shield, where particle deflection in the magnetic field replaces the energy ionization loss in the passive shield material. The alternative is particularly attractive for GCR protons, since the dose due to secondary particle production remains significant for realistic passive shielding configurations. In principle, the presence of large field volumes, free of material, would significantly reduce the secondary production, with a corresponding reduction in the shield mass with respect to a passive shield of equivalent performance.

Several groups have presented active shield designs based on superconducting magnet configurations. The more detailed studies concern shield configurations composed of toroid magnets. The performances are quoted in terms of the GCR flux reduction (3, 4) or dose reduction (5). Unconfined field configurations have been proposed without detailed estimations of the shielding performance (6, 7). The proposed unconfined fields require important modifications of the spacecraft architecture.

2. MAGNET SHIELD CONFIGURATIONS

Magnet shield configurations based on the high-temperature superconductors (HTSC) yttrium-barium-copper-oxide (YBCO) and magnesium diboride (MgB_2) were evaluated in the ESA (8), NIAC (9), and the Space Radiation Superconducting Shield (SR2S)[1] studies. The operating temperatures of the HTSC materials (~25 K) do not require the use of liquid helium, which represents a significant advantage in view of the technical difficulties

[1] Funded by grant agreement FP7-SPACE Ref. No. 313224 of the European Union's 7th Framework Programme (2007–2013).

encountered to guarantee the stability of the cryogenic system in space. A large volume magnetic shield operating with liquid helium was not considered technically feasible since it would require a significant extrapolation of current technologies.

The performance evaluations are based on the results obtained with 3-dimensional Monte Carlo simulations that propagate the charged particles in the magnet field, and generate interactions of the particles in the materials of the coils and support structures of the magnet shield. The material composition of the engineering shield designs, based on realistic extrapolations of existing technology, was used to describe the magnetic shields in the simulations. A brief description of the HTSC shields of the three studies follows.

2.1. ESA Study

YBCO superconductors are manufactured in the form of a 4-mm-wide tape with a thickness smaller than 0.2 mm. Multilayer cylindrical coils composed of YBCO tape may be used to form pure multipole fields by modulating the angle of the helical turns in successive tape layers (10). The magnesium diboride superconductors are produced in cable form; the individual MgB_2 wire elements are brittle and require a rigid support.

Two toroidal field configurations were considered in the ESA study. **Figure 2** illustrates the double-helix solenoid coil shield concept based on the YBCO superconductor. A dipole field is produced in each solenoid coil by reversing the current direction in the opposite-tilt-direction layers of the helical windings. The solenoid coils are oriented to produce a toroidal field around a 4-m-diameter cylindrical habitat in the simulation. The superposition of the fields of the 2-m-diameter coils results in a nearly homogeneous axial field with a BL ~4 Tm.

The second configuration of the ESA study was a racetrack coil toroid composed of MgB_2 superconducting cable. The field integral of the 12 racetrack coil toroid is 4.9 Tm. The racetrack geometry is commonly used in high energy physics. The dimensions of the low-temperature superconducting racetrack toroid of the Atlas experiment at the Large Hadron Collider (LHC-CERN) are comparable with the dimensions required for a radiation shield in the space application.

2.2. NIAC Study

A modified version of the YBCO coil shield was developed in the NIAC study. The dipole field, obtained with the multiple layer winding, was abandoned in favor of a simpler, single orientation winding used to produce a solenoid field. The coil

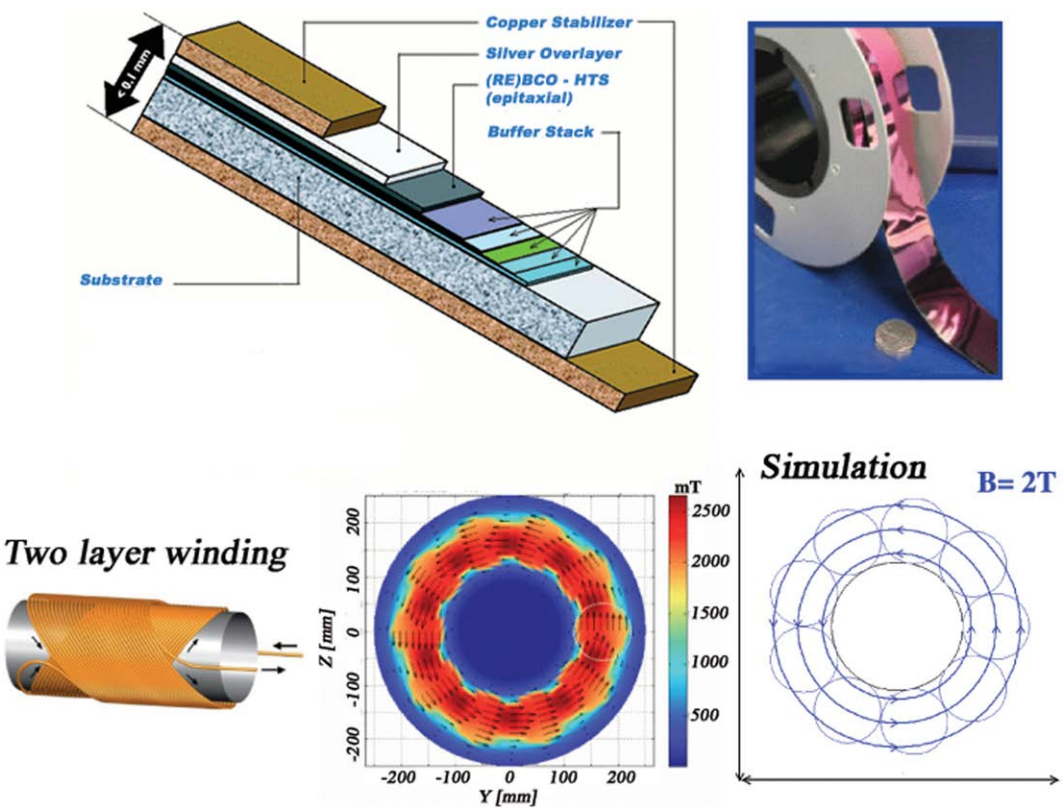

FIGURE 2 | The composition of the YBCO tape from SuperPower (top left) and a photograph of a 0.2-mm-thick tape produced by American Superconductor (top right). Two-layer winding used to produce the double-helix solenoid field (bottom left). The field map, from Advanced Magnet Lab (AML), of the toroidal field (8) around the habitat (bottom center) and the field used in the Monte Carlo simulation (bottom right).

diameter was increased to 8 m and the field flux density reduced to 1 T, yielding a maximum field integral of 8 Tm at the center of the coil, and an average value of 6.3 Tm, taking into account the path length variation across the diameter of the cylindrical coil.

The reduction of the number of YBCO tape layers increases the flexibility of the coils, and allows a compact storage for launch. After deployment in space, the coils expand to their full diameter when the current is applied, due to the effect of the Lorentz force acting on the current flowing in the flexible coils. The fringe fields of the 20-m-long solenoids are compensated by a central solenoid coil concentric with the cylindrical habitat, which reduces the field inside the habitat to an acceptable level. The 6 + 1 extendable solenoid coil shield is illustrated in **Figure 3**.

2.3. SR2S Study

The SR2S consortium has chosen to pursue the racetrack coil toroid configuration with the magnesium diboride cable. A continuous-coil toroid, consisting of 120 racetrack coils, with a field integral of 8 Tm, protects a 4.5-m-diameter, 6-m-long cylindrical habitat based on the design of the ESA Columbus scientific module of the International Space Station.

The habitat and the position of the coils around the habitat are shown in **Figure 4**. Each coil is surrounded by a 0.6-mm-thick KEVLAR support sheath. A 8.6-m-long support cylinder composed of a metal matrix composite material, aluminum-boron-carbide (Al-B4C), surrounds the habitat to support the Lorentz force acting on the coils in the direction of the habitat.

The multiplication of the number of coils in the continuous-coil design reduces the force acting on a single coil. The result is an overall reduction of the magnet shield mass and a greater mechanical tolerance for the toroid assembly.

3. MONTE CARLO SIMULATIONS

A Geant3 (11) simulation was used for the ESA and NIAC studies. The FORTRAN code, which is a modified version the AMS Monte Carlo simulation program, was used for the study of Ref. (5). Geant3 performs particle propagation in magnetic fields and

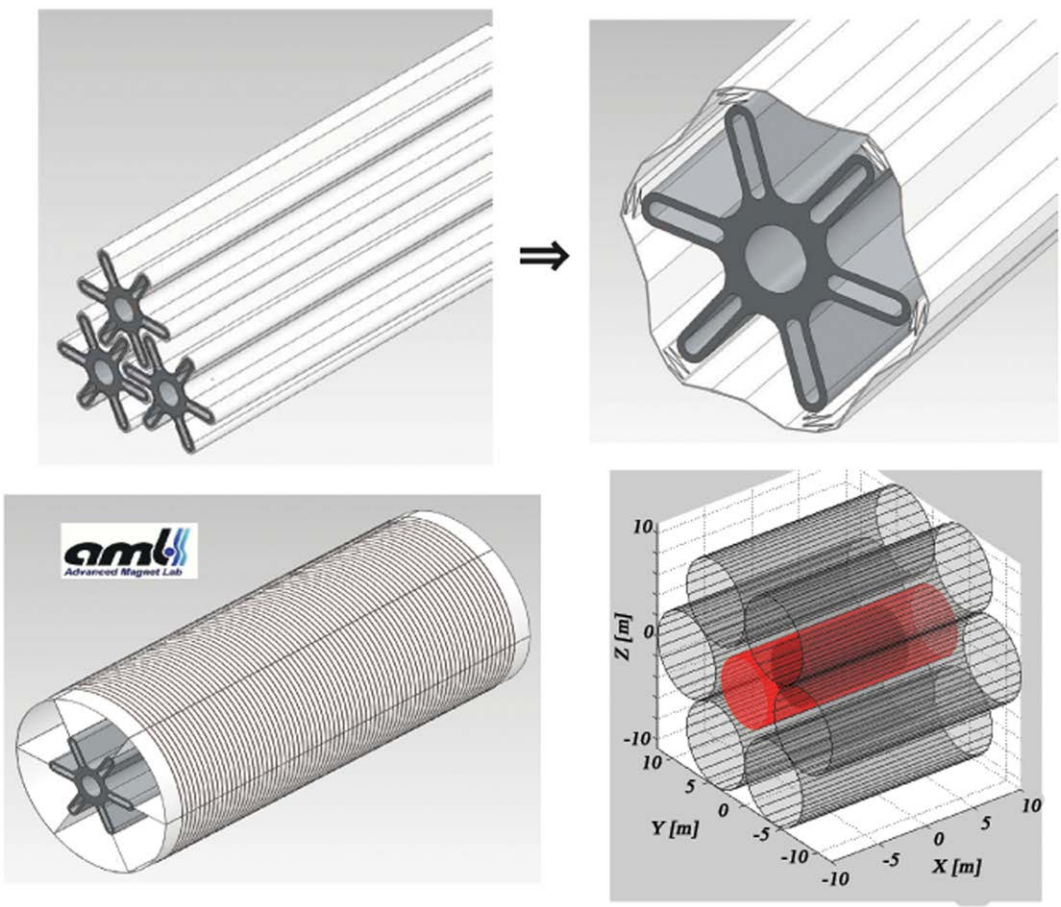

FIGURE 3 | The 6 + 1 extendable solenoid shield, developed by Advanced Magnet Lab (AML) in the NIAC study (9): coils packed for launch (top left), deployment in space (top right), the fully deployed 8-m-diameter solenoid coil (bottom left) and the final 6 + 1 configuration with the compensation solenoid (red) in the center (bottom right).

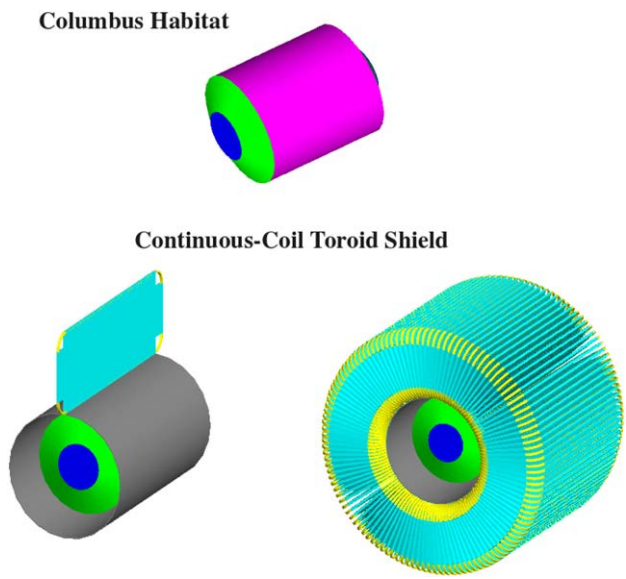

FIGURE 4 | The 4.5-m-diameter, 6 m long Columbus habitat (top), and the continuous-coil toroid shield of the S2RS study. A single racetrack coil (lower left) and the 120 coil toroid (lower right) are shown with the Al-B4C support cylinder (gray) that surrounds the Columbus habitat (blue-green). Each coil (yellow) is supported by a 0.6-mm-thick KEVLAR sheath (cyan).

materials with a detailed treatment of electromagnetic interactions. Additional models have been implemented for hadron interactions of proton and He nuclei (Geant-FLUKA (12)). Nuclear cross sections (13) and fragmentation models (14) have been implemented in the AMS Geant3 simulation.

Geant3 is no longer supported by CERN since the early 2000s and has been progressively replaced in the scientific community by the C++ program Geant4 (15). A Geant4 version of the Geant3 simulation used for the radiation studies has been developed during the 2-year NIAC study. The same methods for the dose determination and sampling are implemented in the two simulations. The Geant4 simulation was used for the SR2S study.

3.1. Dose Determination

The ionization energy losses (Equation (1)) recorded during the track propagation dE_i are converted to an dose equivalent ϵ_i (Sv) by multiplying the absorbed dose $\frac{dE_i}{m}$ (Gy), where m is the mass of the volume considered, by the quality factor $Q(L)$ defined by the unrestricted linear energy transfer in water L (keV/μm):

$$\epsilon_i = Q(L) \cdot \frac{dE_i}{m}, \tag{4}$$

with

$$L = \frac{dE_i}{dx} \tag{5}$$

and

$$Q(L) = \begin{cases} 1 & \text{for} \quad L \le 10 \\ 0.32 \cdot L - 3.2 & \text{for} \quad 10 < L < 100 \\ 300 / \sqrt{L} & \text{for} \quad L \ge 100 \end{cases}$$

The total dose equivalent $d_z(E_j)$ for an exposure time t due to GCR of charge Z and kinetic energy E_j is the sum of the dose equivalents recorded for N_j incident particles generated with the flux $f_z(E_j)$ ($cm^{-2}sr^{-1}s^{-1}MeV^{-1}$), in the energy interval ΔE_j (MeV), over the acceptance A (cm^2sr):

$$d_z(E_j) = \sum_i \epsilon_i \cdot \frac{A}{N_j} \cdot f_z(E_j) \cdot \Delta E_j \cdot t. \tag{6}$$

The total GCR dose D is obtained by extending the generation over suitable ranges in charge and kinetic energy. The contribution from charge Z is

$$d_z = \sum_j \left[\sum_i \epsilon_i \right]_j \cdot A \cdot \sum_j \frac{f_z(E_j) \cdot \Delta E_j}{N_j} \cdot t \tag{7}$$

and the total dose equivalent, including all charges up to Ni, $D = \sum_{z=1}^{z=28} d_z$.

Three terms contribute to the estimated dose level. The kinetic energy spectra $f_z(E_j)$ that are taken from the CREME 2009 GCR model (1) with an energy range from 1 to 10^5 MeV/n. A significant decrease of flux below 1 GeV/n is observed during the solar maximum (**Figure 1**). A solar cycle lasts 14 years divided roughly in equal length periods of solar maximum and minimum activity. The GCR spectra at solar minimum are used for the performance evaluation of the shield configurations. The second term t represents the mission length, or more precisely the duration of the exposure to the GCR flux in interplanetary space. Finally, the magnitude of the third term $\Sigma_i \epsilon_i$ depends on the effectiveness of the passive and active shielding elements.

3.2. Dose Sampling

The human body is represented in the simulations as a 24-cm-diameter, 180-cm-long water-filled cylinder. The cylinder is subdivided to define the regions used to compute the dose associated with the skin and blood-forming organs (BFO), respectively, the first 2 mm at the surface of the cylinder and a 2-mm-thick layer located a depth of 5 cm from the cylinder surface (**Figure 5**). The body dose refers to the ionization losses recorded in the full volume of the cylinder.

Figure 5 shows the positions of the six water cylinders used to record the dose levels in the cylindrical habitat. Three cylinders are present in each side ($\pm\hat{z}$) of the habitat. Cylinders 1 and 6 are aligned along the longitudinal axis; cylinders 2–5 are placed near the habitat cylindrical shell.

Secondary neutrons and gammas are generated and tracked. The non-ionizing, neutral particles do not contribute directly to the dose. The neutrons produce charged secondaries due to nuclear interactions in the water cylinder or surrounding

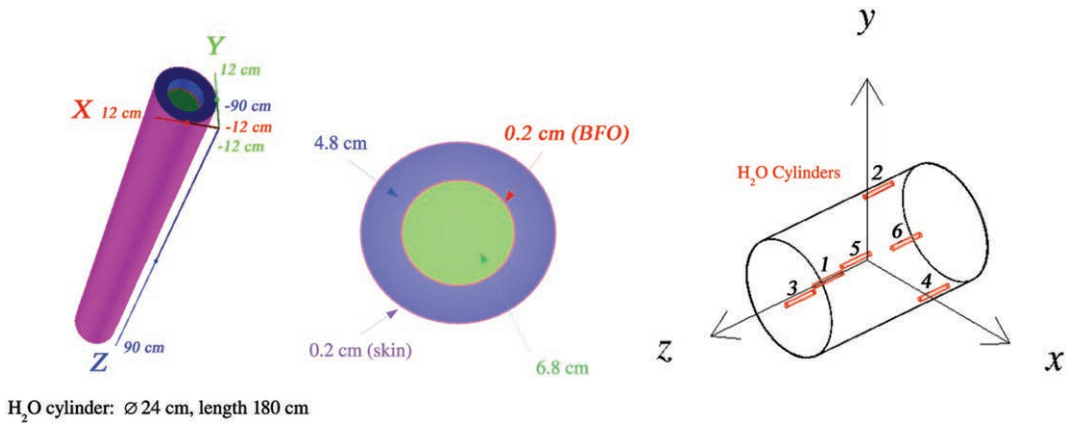

FIGURE 5 | At the left, the cylindrical water volume used to compute the dose of the skin and blood-forming organs (BFO). The body dose refers to the full volume of the 24-cm-diameter, 180-cm-long cylinder (81.4 kg). At the right, the positions of the six water cylinders in the cylindrical habitat.

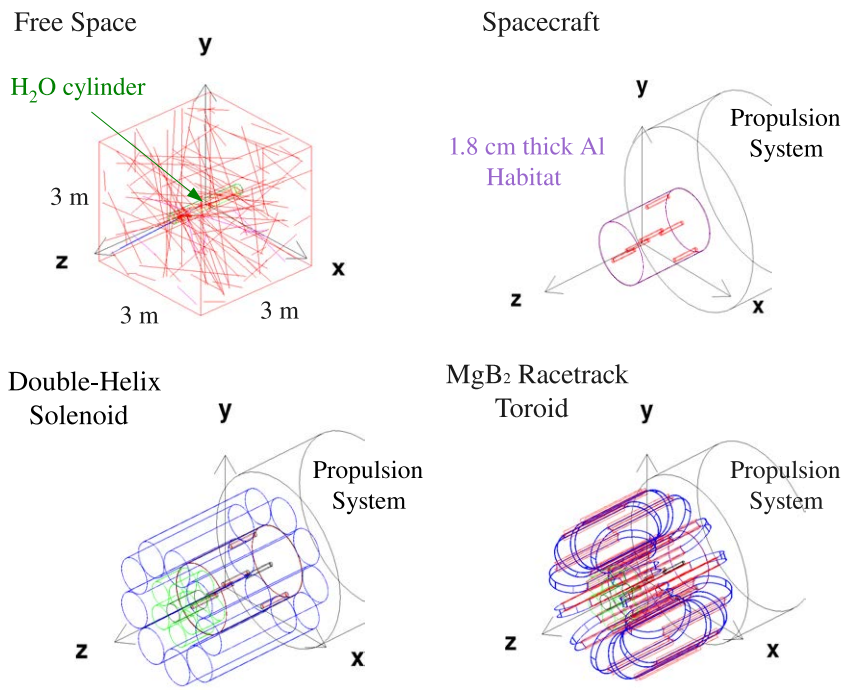

FIGURE 6 | The principal configurations evaluated in the ESA study (8): free space (upper left), spacecraft (upper right), the double-helix solenoid coil shield (lower left), and the racetrack coil toroid shield (lower right).

materials, which may contribute to the dose recorded in the water cylinders, e.g., energetic protons from elastic scattering on hydrogen nuclei. Gammas contribute via charged secondaries produced in electromagnetic interactions.

4. ESA STUDY RESULTS

The principal configurations evaluated in the Geant3 simulation in the ESA study were free space, the spacecraft, and the two toroidal field magnetic shields (**Figure 6**). The free space results were compared to previously published results. The dose levels of the active magnetic shield configurations were compared to the free space, habitat, and spacecraft doses.

4.1. Free Space

The free space doses were evaluated at solar minimum and maximum. A single water-filled cylinder is placed at the center of a

3 m × 3 m × 3 m vacuum-filled cube. The incident GCR nuclei are generated uniformly on the surface of the cube.

The annual dose equivalents for protons, He nuclei, and $Z > 2$ nuclei are reported in **Table 1**. The free space results were obtained with a sample of 10 M protons and He nuclei, and 50 M, $Z > 2$ nuclei, i.e., with respectively, 0.2 M/m^2 and 0.9 M/m^2 incident particles on the generation cube. The particle densities are factors 2 and 15–25 higher than those used for the shielding configuration results reported for the two charge groups. The effect of the generation statistics on the quoted free space doses is negligible (~1%).

The BFO annual dose equivalent of 62.4 cSV at solar minimum is compatible with values in the range between 58 and 70 cSv quoted in Ref. (16). The BFO annual dose at solar maximum, 35 cSv (16), is 10% lower than the 39.5 cSv reported in **Table 1**.

The ratio of the flux and dose reductions, between solar maximum and minimum, of the individual nuclei are shown in **Figure 7**. The local peak in the ratio at $Z = 9$ is explained by the absence of an anomalous GCR flux contribution for this element in the charge range $6 \leq Z \leq 10$ (1). The free space body dose equivalent is reduced by ~40% at solar maximum.

4.2. HTSC Toroidal Field Configurations

Two toroidal field configurations based on the YBCO and MgB_2 superconductors were studied. The axial field of the toroid shield configurations is adapted to the classical, cylindrical spacecraft geometry imposed by launch constraints. The confined field simplifies the design since a significant fringe field in the habitat would be unacceptable for the crew, and may affect vital operations of the spacecraft.

The YBCO double-helix solenoid and the MgB_2 racetrack coil toroid shield configurations are shown in **Figure 6**. The spacecraft structures are composed of a 4-m diameter, 5.5-m-long cylindrical habitat surrounded by 1.8-cm-thick aluminum, and the propulsion system. The propulsion system is represented in the simulation by a solid 1.16-m diameter, 6-m-long aluminum cylinder. Air is present in the interior of the habitat.

The orientation of the axial toroidal field in the *xy* plane deflects charged particles with a momentum $+p_z\hat{z}$ in the direction of the habitat. The diameter of the aluminum cylinder of the propulsion system exceeds the radial extension of the field volume in order to eliminate GCR entering the field volume from the $-\hat{z}$ direction.

The performance of the low-temperature superconducting (LTSC) toroid shield of Ref (5) was re-evaluated in the ESA study. The LTSC toroidal configuration is shown in **Figure 8**, with the particle tracks and recorded ionization losses in the water cylinder caused by an incident carbon nucleus.

The incident 2.85 GeV/n GCR carbon nucleus travels in the $(+\hat{x},+\hat{y},+\hat{z})$ direction, with $\frac{p_z}{p} = 0.83$, and is deflected toward the habitat where it interacts in a water cylinder creating secondary pions. One of muons from a pion decay is deflected across the habitat as it traverses the spacecraft. The event was selected among the millions generated by demanding that an ionization loss recorded in the water cylinders was produced by the recoil of an oxygen nucleus.

A second, smaller LTSC toroid (green) is present on the $+\hat{z}$ side of the spacecraft in **Figure 8**. A similar scheme for the double-helix solenoid coil toroid configuration was implemented in the simulation (**Figure 6**). However, no corresponding engineering study was made for the smaller toroid. Since the aim of the ESA study was to provide an assessment of the performance taking into account the contributions of the field and passive elements of realistic active magnetic shield designs, the performance evaluation was limited to the acceptance of the barrel region,

TABLE 1 | Annual free space dose equivalents (cSv/y).

	Solar minimum			Solar maximum		
Z	Skin	BFO	Body	Skin	BFO	Body
1	10.8	11.3	11.1	5.5	5.6	5.6
2	5.3	5.2	5.1	2.9	2.8	2.7
3–10	35.9	22.2	11.8	22.1	14.8	6.8
11–20	38.4	16.6	14.8	23.1	11.2	9.2
21–28	27.3	7.1	8.7	17.4	5.1	5.8
Total	117.7	62.4	51.5	71.0	39.5	30.1

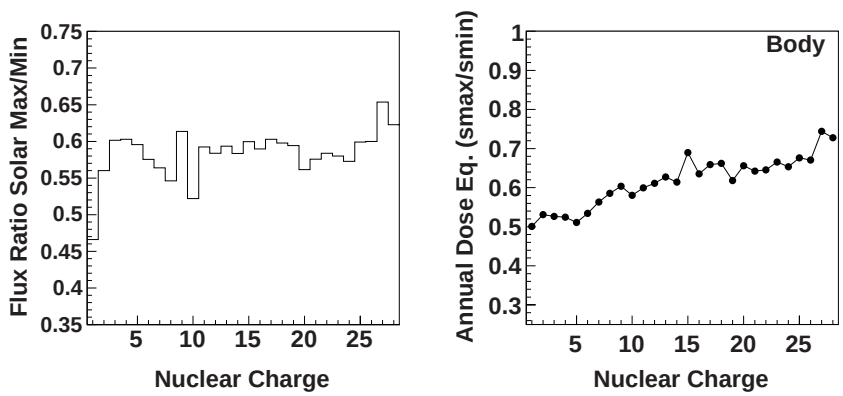

FIGURE 7 | The ratio of the energy-integrated cosmic-ray nuclei fluxes between solar maximum and minimum (1) (left) and the corresponding ratio of the free space body dose equivalent (right).

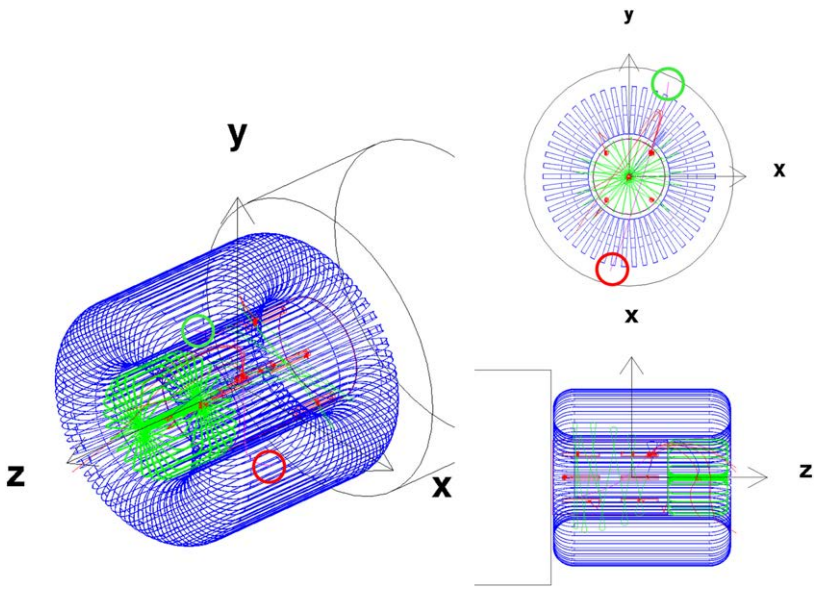

FIGURE 8 | A GCR carbon nucleus event with multiple ionization losses (red crosses) in the water cylinders. The carbon nucleus (magenta) interacts in a water cylinder producing secondary pions (blue), which decay into muons (green), and neutrinos (not displayed). The incident (exit) direction of the C nucleus (magenta) is indicated by the red (green) circle.

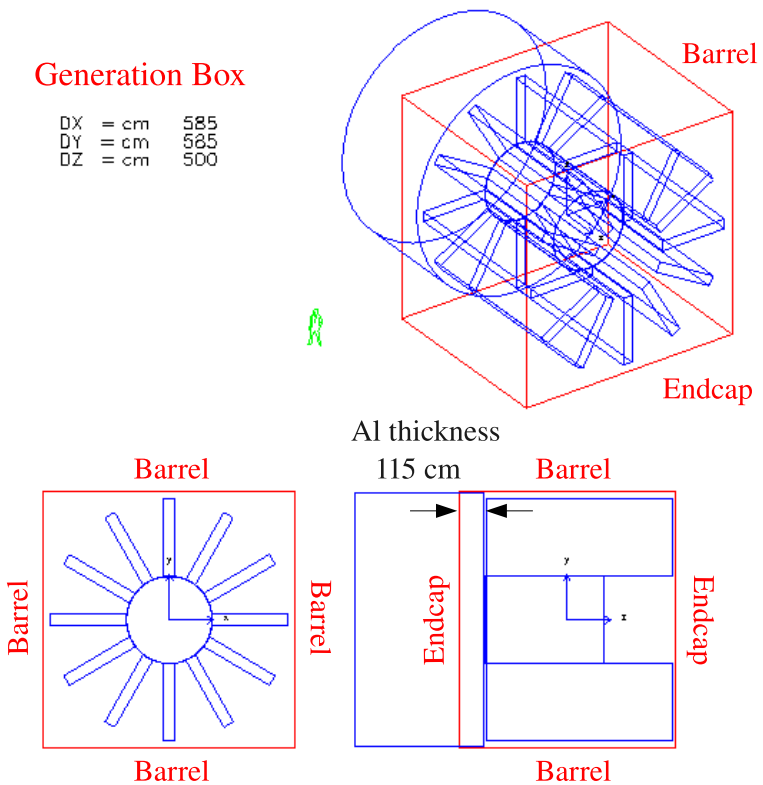

FIGURE 9 | The generation surface, a 11.7 m × 11.7 m × 10.0 m cube, used in the Geant3 simulation for the MgB_2 racetrack coil toroid of the ESA study. The effective thickness of the Al cylinder (propulsion system) is defined by the relative position of the spacecraft in the generation cube. The quoted performances for the three studies refer to dose levels produced by GCR generated on the four lateral sides of the cube (barrel region), which surround the active magnetic shields.

defined by the lateral sides of the generation box, illustrated in **Figure 9**.

The double-helix solenoid coils are represented in the simulation by eight layers of 90 μm copper, which has a charge density, and radiation length very close to the average values of the materials of the YBCO superconducting tape. The coil support is represented by 2-mm-thick carbon cylinder.

The MgB_2 superconducting coil is composed of copper, aluminum, Ti, and MgB_2 layers with thicknesses of 0.30, 1.65, 1.50, and 1.55 cm, respectively. A 5-mm-thick aluminum frame support surrounds the coils.

The results of the performance evaluation are presented in **Table 2**. For each magnet shield configuration, the field integral BL, the total mass in the Monte Carlo, the total estimated mass of the corresponding engineering design, and the annual BFO dose equivalent for the barrel region acceptance are reported. The annual BFO dose equivalent limit for low Earth orbit (LEO) is 50 cSv (16).

The two HTSC configurations have a comparable performance providing a ~25% reduction of habitat dose level. The smaller dose of HTSC racetrack coil may be attributed to the higher *B* and the larger shield mass in the simulation, i.e., a larger contribution from passive shielding.

The dose estimates of the HTSC double-helix solenoid coil toroid where obtained with 37 M protons and He nuclei, and 7 M, $Z > 2$ nuclei. The corresponding numbers for the HTSC racetrack coil toroid are 22.5 M protons and He nuclei, and 4 M, $Z > 2$ nuclei. The quoted uncertainties in **Table 2** represent the root-mean-square of the average dose recorded in the six cylinders, which reflects both the uniformity of the dose distribution in the habitat and statistical fluctuations.

The LTSC configuration BFO dose equivalent, obtained with a factor ~4.75 higher BL, is 40–50% lower than the values for the HTSC double-helix solenoid and racetrack coil shield configurations. The quoted shield mass of the LTSC configuration is the mass of the coils composed of aluminum.

The simulation and engineering masses are presented in **Table 2** to indicate the level of accuracy of the HTSC shield descriptions in the simulation. The results presented in **Table 2** are indicative. They represent the status attained at the end of the 1-year study. A definitive evaluation requires a complete description of the material of the active magnetic shield in order to take into account both passive and active shielding contributions to the dose reduction.

The results for the LTSC toroid over the full acceptance, 27.2 ± 1.5 cSv, including the shielding contributions of the second toroid and propulsion system, may be compared to the annual BFO dose equivalent of 18–33 cSv reported previously with the same simulation program (5). The range in the estimated dose reported in Ref. (5) reflects the estimated uncertainty in the GCR flux. The LTSC result of the ESA study was obtained with 37 M proton and He nuclei, and 15 M, $Z > 2$ nuclei.

TABLE 2 | A comparison of the ESA study active magnetic shields and habitat dose levels.

Configuration	BL (Tm)	M_{sim} (t)	M_{eng} (t)	BFO (cSv/y)
LTSC toroid	19	12.5	–	19.2 ± 1.1
HTSC double-helix solenoid coil toroid	4	11.2	47.2	29.3 ± 2.3
HTSC racetrack coil toroid	4.9	28.0	46.4	26.7 ± 1.1
Habitat	–	4.54	–	35.6 ± 1.8

*The first mass quoted refers to the shield mass present in the Monte Carlo simulation. The second is the mass estimate from the engineering designs. The annual BFO dose equivalents refer to the GCR flux at solar minimum (1) and the barrel region acceptance (**Figure 9**). The quoted uncertainties represent the root-mean-square deviation of the average dose recorded in the six water cylinders (**Figure 5**).*

4.3. Field and Coil Contributions

The explicit contribution of the coils to the dose reduction was made with a preliminary description of the double-helix solenoid coil, represented in the simulation by 1-cm-thick aluminum. The dose equivalents of the double-helix (DH) solenoid shield with BL = 2 Tm are compared in **Table 3** to the corresponding spacecraft doses, and a second DH solenoid shield dose estimate made without the coil material in the simulation.

The magnetic field and the material of the coils reduce the spacecraft BFO dose equivalent by 22%, with equal contributions to the reduction from the field and the passive shielding of the coils. The reduction of the spacecraft dose equivalents (~10%) due to the field alone is observed for all charge groups. The presence of the coils produces an additional reduction of the $Z > 2$ nuclei doses, and an increase of the proton and He nuclei doses due to the secondary particles produced in the coil material.

The results presented in **Table 3** were obtained with 25 M (spacecraft), 73 M (with coils), and 41 M (without coils) protons

TABLE 3 | Effect of the magnet material on the annual dose equivalents (cSv/y) at solar minimum.

	Spacecraft			DH with Al coils			DH without Al coils		
Z	Skin	BFO	Body	Skin	BFO	Body	Skin	BFO	Body
1	18.4	13.5	14.1	19.4	13.6	14.4	17.7	12.6	13.3
2	8.3	5.9	5.9	8.2	5.9	6.0	7.7	5.2	5.6
3–10	19.9	13.2	6.6	12.8	8.8	4.5	17.6	11.9	5.8
11–20	17.3	9.4	7.1	9.5	5.5	4.2	14.7	7.6	6.3
21–28	10.3	3.2	3.1	4.1	1.4	1.4	7.5	3.1	2.7
Total	74.2	45.2	36.8	54.0	35.2	30.5	65.2	40.4	33.7
Fraction of spacecraft dose				0.73	0.78	0.83	0.88	0.89	0.92

The double-helix solenoid shielding configuration doses correspond to the full acceptance, including the endcap regions.

and He nuclei. The corresponding numbers for $Z > 2$ nuclei are 3.7, 10.9, and 3.6 M, respectively. The uncertainties in the quoted total doses, based on the root-mean-square deviation of the average dose recorded in the six water cylinders, are 15% (spacecraft), 10% (with coils), and 15–20% (without coils).

5. NIAC STUDY RESULTS

The magnetic field, coil, and support structures of the 6 + 1 extendable solenoid shield configuration in the simulation are shown in **Figure 10**. Six, 8-m-diameter, 20-m-long solenoid shield coils surround a 6-m-diameter, 10-m-long, air-filled cylindrical habitat composed of 1.8-cm-thick aluminum. A 6.4-m-diameter, 20 m compensation solenoid coil surrounds the habitat to reduce the magnetic flux density to an acceptable level. In the simulation, a uniform 1 T field is present in the cylindrical volumes delimited by the solenoid shield coil dimensions, elsewhere the field is zero.

The YBCO solenoid shield coils are represented as 111-μm-thick copper cylinders. The support structures are composed of a 1-m-diameter, 1-cm-thick, 20-m-long graphite cylinder located in the center of the coil. The radial spokes are composed of six 2.5-mm-thick, 3.5-m-wide, 20-m-long graphite plates. The compensation solenoid consists of a 111-μm-thick copper cylinder and a 2.4-mm-thick graphite support cylinder. The composition and mass of the structural elements in the simulation, shield and habitat, are reported in Table S1 in Supplementary Material.

The annual BFO dose equivalent for the barrel region acceptance of the 6 + 1 extendable solenoid shield and the 1.8-cm-thick aluminum habitat (NIAC Phase I) are reported in **Table 4**. A total of 500 M protons and He nuclei, and 330 M, $Z > 2$ nuclei were generated on the surface of the 30 m × 30 m × 30 m cube positioned around the center of the habitat. The shielding performance of the habitat was obtained with 500 M protons and He nuclei, and 150 M, $Z > 2$ nuclei.

The 6 + 1 extendable solenoid shield configuration provides an additional ~20% reduction with respect to the habitat dose level. The dose reduction, normalized to the habitat dose, is comparable to the results for the two HTSC toroid configurations of the ESA study (**Table 2**).

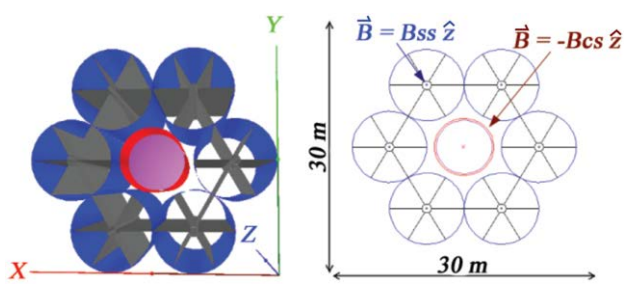

FIGURE 10 | The NIAC 6 + 1 extendable solenoid shield: shield solenoid coils (blue), carbon-fiber support structures (black), compensation solenoid coil (red), and habitat (magenta). The field regions are shown in the *xy* view on the right. The shield solenoid flux density is B_{ss} = 1T. The flux density of the compensation coil B_{CS} is chosen to minimize the net flux density in the habitat.

5.1. Dose Evaluation over the Full Acceptance

The 6 + 1 solenoid shield was employed in a preliminary spacecraft design for a mission to a near Earth asteroid (NEA). The additional spacecraft elements have been included in the simulation (**Figure 11**) to evaluate their influence on the full acceptance dose.

One side of the habitat is connected to a chemical propulsion system consisting of liquid hydrogen and oxygen tanks, and a combustion chamber. On the other side, an access tube connects the habitat to a re-entry vehicle containing liquid methane and oxygen tanks. The spherical and cylindrical fuel tanks, combustion chamber, access tube, re-entry vehicle, and hatches are composed

TABLE 4 | The dose levels of the 6 + 1 extendable solenoid shield and NIAC habitat.

Configuration	BL (Tm)	M_{sim} (t)	M_{eng} (t)	BFO (cSv/y)
HTSC 6 + 1 extendable solenoid shield	6.3	46.2	49.5	30.9 ± 0.9
NIAC Phase I habitat	–	10.1	–	36.7 ± 1.1

*The average value of the field integral across the 8-m-diameter cylindrical coil is quoted. The first mass quoted refers to the shield mass present in the Monte Carlo simulation. The second is the mass estimate from the engineering designs. The annual BFO dose equivalents refer to the GCR flux at solar minimum (1) and the barrel region acceptance (**Figure 9**). The quoted uncertainties represent the root-mean-square deviation of the average dose recorded in the six water cylinders (**Figure 5**).*

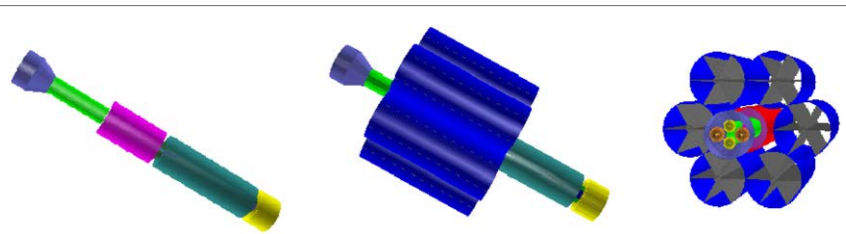

FIGURE 11 | The NEA chemical propulsion spacecraft in the simulation: re-entry vehicle (violet), access tube (light green), habitat (magenta), liquid hydrogen container (dark green), liquid oxygen container (yellow), YBCO shield solenoid coils (blue), YBCO compensation solenoid coil (red), and carbon fiber support structures of the solenoid coils (gray). The liquid methane (orange) and liquid oxygen (yellow) containers of the re-entry vehicle are visible in the view on the right.

of 1.8-cm-thick aluminum. The total spacecraft mass in the simulation, including the 6 + 1 extendable solenoid shield and habitat (Table S1 in Supplementary Material), is 88 t. A roughly equivalent mass, 19 and 22 t, has been added on each side of the habitat.

The composition and mass of the additional spacecraft structures are listed in Table S2 in Supplementary Material. The dose evaluation was made without the liquid propellants of the spacecraft propulsion system in order to reduce the computation time.

The annual GCR dose equivalents of the NEA spacecraft and 6 + 1 extendable solenoid shield configurations are compared in **Tables 5** and **6** for the barrel and endcap region acceptances, respectively. The dose received from the GCR of the barrel region increases due to the presence of the additional structures of the spacecraft. A decrease in the doses due to the GCR generated in the endcap regions is observed. The net effect of the additional passive shielding elements is negligible on the full acceptance dose.

The ratio of the full acceptance, NEA spacecraft skin, BFO, and body doses to the corresponding 6 + 1 shield doses are respectively 0.97 ± 0.22, 1.01 ± 0.19, and 1.01 ± 0.16. A 50 m × 50 m × 50 m generation cube was used for the NEA spacecraft dose estimation. The NEA spacecraft results are based on 700 M protons and He nuclei, and 365 M, $Z > 2$ nuclei.

The most significant dose increase in **Table 5** is observed for the GCR protons due to the increase of secondaries created in the extended spacecraft structures. The charged secondaries, produced by interaction of the GCR in the structures aligned along the cylindrical axis of the spacecraft, enter the field volume and are deflected toward the habitat. The effect is illustrated in Figure S1 in Supplementary Material. In order to be effective, the passive shielding elements of the spacecraft should be placed to obstruct the passage of particles arriving at both ends of the cylindrical volumes of the habitat and solenoid coils.

5.2. The 6 + 1 Extendable Solenoid Shield Performance

The effectiveness of the magnetic shield is defined by the comparison of the dose levels with and without the field, which indicates explicitly the contribution of the field to the overall dose reduction. The evaluation was performed for the 6 + 1 extendable solenoid shield of **Figure 10**, and the larger mass habitat of the NIAC Phase II study, which includes water and food volumes. The NIAC Phase II habitat is shown in Figure S2 in Supplementary Material. The dimensions of the aluminum habitat and water volume, and the composition and dimensions of the food volume are listed in Table S3 in Supplementary Material.

The annual GCR dose equivalents of the two habitats are compared in Table S4 in Supplementary Material. The increase in thickness of the aluminum wall from 1.8 to 4 cm reduces the dose levels by ~15% for the factor 3.5 increase in the habitat mass.

The dose levels of the 6 + 1 extendable solenoid shield, with and without the magnetic field, are presented in **Table 7**. The reduction due to the 6.3 Tm field represents ~5% of the total dose reduction. A total of 500 M protons and He nuclei, and

TABLE 5 | Annual GCR dose equivalents (cSv/y) at solar minimum, in the barrel region (Figure 9) for the 8 Tm extendable solenoid shield and the NEA chemical propulsion spacecraft configurations.

	6 + 1 Shield			6 + 1 Shield and Spacecraft		
Z	**Skin**	**BFO**	**Body**	**Skin**	**BFO**	**Body**
1	7.9 ± 0.3	7.6 ± 0.3	7.4 ± 0.2	9.5 ± 0.3	9.1 ± 0.5	8.8 ± 0.2
2	3.8 ± 0.2	3.4 ± 0.3	3.4 ± 0.1	4.4 ± 0.3	4.1 ± 0.7	3.8 ± 0.1
3–10	15.4 ± 0.7	10.8 ± 0.5	5.2 ± 0.3	15.6 ± 7.9	11.1 ± 5.5	5.4 ± 2.8
11–20	12.7 ± 0.8	6.9 ± 0.5	5.2 ± 0.4	12.9 ± 7.1	6.7 ± 3.8	5.5 ± 3.1
21–28	5.7 ± 0.8	2.2 ± 0.3	2.0 ± 0.3	5.9 ± 3.1	2.2 ± 1.1	2.1 ± 1.2
Total	45.5 ± 1.4	30.9 ± 0.9	23.2 ± 0.6	48.3 ± 11.1	33.2 ± 6.8	25.6 ± 4.4
Fraction of 6 + 1 Shield dose				1.06 ± 0.25	1.07 ± 0.22	1.10 ± 0.19

*The quoted uncertainties represent the root-mean-square deviation of the average dose recorded in the six water cylinders (**Figure 5**).*

TABLE 6 | Annual GCR dose equivalents (cSv/y) at solar minimum, in the endcap regions (Figure 9) for the 8 Tm extendable solenoid shield and the NEA chemical propulsion spacecraft configurations.

	6 + 1 Shield			6 + 1 Shield and Spacecraft		
Z	**Skin**	**BFO**	**Body**	**Skin**	**BFO**	**Body**
1	6.5 ± 0.4	6.1 ± 0.5	6.0 ± 0.2	5.9 ± 0.1	5.5 ± 0.2	5.4 ± 0.1
2	2.8 ± 0.3	2.3 ± 0.5	2.2 ± 0.1	2.3 ± 0.3	1.9 ± 0.2	1.9 ± 0.1
3–10	7.1 ± 1.3	3.5 ± 0.7	2.3 ± 0.4	5.4 ± 2.1	2.9 ± 1.2	1.8 ± 0.5
11–20	5.7 ± 1.2	1.9 ± 0.5	1.9 ± 0.4	4.1 ± 2.1	1.7 ± 0.9	1.4 ± 0.6
21–28	2.4 ± 0.8	0.4 ± 0.2	0.7 ± 0.2	1.8 ± 0.7	0.4 ± 0.2	0.5 ± 0.2
Total	24.5 ± 2.0	14.2 ± 1.1	13.1 ± 0.6	19.5 ± 3.1	12.4 ± 1.5	11.0 ± 0.8
Fraction of 6 + 1 Shield dose				0.80 ± 0.14	0.87 ± 0.12	0.84 ± 0.07

*The quoted uncertainties represent the root-mean-square deviation of the average dose recorded in the six water cylinders (**Figure 5**).*

TABLE 7 | The Geant3 annual GCR dose equivalents (cSv/y) at solar minimum for the 6 + 1 solenoid configuration, with and without the 6.3 Tm field for the acceptance corresponding to the barrel region (Figure 9).

	6 + 1 no field			6 + 1 field		
Z	**Skin**	**BFO**	**Body**	**Skin**	**BFO**	**Body**
1	10.4 ± 0.4	9.6 ± 0.4	9.4 ± 0.3	9.5 ± 0.6	8.5 ± 0.4	8.5 ± 0.3
2	4.9 ± 0.4	4.2 ± 0.2	4.0 ± 0.1	4.3 ± 0.2	3.8 ± 0.1	3.8 ± 0.1
3–10	11.5 ± 1.0	8.0 ± 0.9	4.1 ± 0.4	11.6 ± 1.1	8.2 ± 0.8	4.0 ± 0.4
11–20	7.9 ± 1.1	4.5 ± 0.7	3.4 ± 0.5	8.2 ± 1.2	4.5 ± 0.3	3.4 ± 0.4
21–28	2.8 ± 0.7	1.1 ± 0.3	1.0 ± 0.2	2.9 ± 0.7	1.1 ± 0.3	1.1 ± 0.3
Total	37.5 ± 1.7	27.6 ± 1.3	22.0 ± 0.7	36.5 ± 1.9	26.1 ± 1.0	20.8 ± 0.7
Fraction field on/off				0.97 ± 0.07	0.95 ± 0.06	0.95 ± 0.04

*The quoted uncertainties represent the root-mean-square deviation of the average dose recorded in the six water cylinders (**Figure 5**).*

TABLE 8 | Annual GCR dose equivalents (cSv/y) in free space at the solar minimum.

	Geant3			Geant4		
Z	**Skin**	**BFO**	**Body**	**Skin**	**BFO**	**Body**
1	10.8	11.3	11.1	12.2	12.9	12.8
2	5.3	5.2	5.1	5.8	4.6	4.8
3–10	35.9	22.2	11.8	13.6	6.1	7.4
11–20	38.4	16.6	14.8	19.9	9.2	11.4
21–28	27.3	7.1	8.7	24.7	11.1	14.3
Total	117.7	62.4	51.5	76.2	43.9	50.7

The effect of the generation statistics on the quoted free space doses is negligible (~1%).

205 M, $Z > 2$ nuclei were generated to produce the field off dose estimates, the corresponding numbers for the field on estimates are 500 and 330 M, respectively.

5.3. Geant3/Geant4 Comparison

The Geant3 simulation used for the radiation studies is compiled as a C++ program. The Geant3 user interface routines are prototyped in C++ with CFORTRAN (17). The routines are called from the C++ code to generate the GCR spectra, describe the materials and geometry of the spacecraft and magnetic shield configurations, and record the ionization losses in the water cylinders. The same C++ routines were used with Geant4. A comparison of the dose estimates of the two simulations, using the same methodology for the dose evaluation, indicates the influence of the different physics models implemented in the two simulations.

The Geant3 and Geant4 GCR free space dose equivalents at solar minimum are compared in **Table 8**. The total dose levels in the 2-mm-thick layers, skin and BFO, are 35 and 30% lower in Geant4, whereas the total dose recorded in the water cylinder (body) agree. The Geant4 proton dose equivalents are 10–15% higher. The Geant4 dose equivalents for the $Z \geq 2$ nuclei are lower, except for the BFO and body doses of the $Z > 20$ nuclei.

QGSP-BERT-HP and QBBC are Geant4 physics lists that group preselected models for hadron physics. QGSP-BERT-HP contains the quark-gluon string precompound model, coupled with the Bertini cascade model for proton and neutrons below 10 GeV (18). QBBC is a physics list containing a combination of various models created for space applications, radiation biology, and radiation protection (19). The Geant4 results were obtained with 50 M protons and He nuclei (QGSP-BERT-HP), 5 M, $Z > 2$ nuclei (QGSP-BERT-HP), and 5 M, $Z > 2$ (QBBC). No significant difference was observed in the Geant4 free space doses generated with the two different physics lists.

The Geant4 dose estimates for the 6 + 1 extendable solenoid shield are reported in **Table 9**. The contribution of the 6.3 Tm field to the total dose reduction is ~10%. The Geant4 field on and off results were obtained with 50 M protons and He nuclei, and 50 M, $Z > 2$ nuclei. The QGSP-BERT-HP was used for the hadron and nuclear interactions.

The relative performance of passive shielding in the two simulations may be compared using the Geant3 results for the NIAC Phase I habitat (Table S4 in Supplementary Material) and free space (**Table 8**). In the Geant3 simulation, the skin, BFO, and body dose equivalents of the NIAC Phase I habitat represent, respectively, 33.6 ± 1.8%, 22.3 ± 2.4%, and 24.7 ± 1.8% of the annual free space doses. The corresponding Geant4, NIAC Phase I habitat dose equivalents, 50.2 ± 2.8, 37.2 ± 2.3, and 39.5 ± 1.3 cSv/y, represent 34.2 ± 3.7%, 15.3 ± 5.2%, and 23.3 ± 2.6% of the corresponding free space doses in **Table 8**. The results for the two simulations indicate a comparable dose reduction for the 1.8-cm-thick aluminum habitat. The Geant4, NIAC Phase I habitat dose estimates were obtained with 25 M protons and He nuclei, and 23.5 M, $Z > 2$ nuclei.

In contrast to the Geant3 results in **Table 7**, a dose reduction in the presence of the field is observed in the Geant4 results for $Z > 2$ GCR nuclei, which results in a larger contribution of the field to the overall dose reduction. The difference is explained by the significantly thicker NIAC Phase II habitat used for the Geant3 performance evaluation, which enhances the performance of the passive shielding element for $Z > 2$ GCR nuclei (Table S4 in Supplementary Material).

The 1.8-cm-thick aluminum NIAC Phase I habitat was used for the Geant4 performance evaluation in order to compare the results with the continuous-coil toroid shield, and 1.5-cm-thick aluminum habitat, of the SR2S study.

5.4. Dose Equivalent and Absorbed Dose

The Geant3 and Geant4, free space absorbed doses are reported in **Table 10**. The Geant4 absorbed doses are systematically lower for the $Z \geq 2$ nuclei. The differences between the total skin, BFO, and body absorbed dose are 25, 12, and 5%, respectively.

TABLE 9 | The Geant4 annual GCR dose equivalents (cSv/y) at solar minimum for the 6 + 1 solenoid configuration (NIAC Phase I habitat), with and without the 6.3 Tm field for the acceptance corresponding to the barrel region (Figure 9).

	6 + 1 no field			6 + 1 field		
Z	**Skin**	**BFO**	**Body**	**Skin**	**BFO**	**Body**
1	10.2 ± 0.6	9.3 ± 0.8	9.8 ± 0.4	9.1 ± 0.8	8.4 ± 0.4	8.3 ± 0.3
2	3.7 ± 0.7	3.2 ± 0.3	3.2 ± 0.1	3.0 ± 0.2	2.6 ± 0.7	3.0 ± 0.2
3–10	5.1 ± 0.4	3.3 ± 0.4	3.7 ± 0.2	3.9 ± 0.2	2.9 ± 0.3	3.3 ± 0.2
11–20	8.0 ± 0.7	4.5 ± 0.6	5.4 ± 0.4	7.4 ± 0.9	4.1 ± 0.6	5.0 ± 0.4
21–28	9.4 ± 0.8	5.3 ± 0.6	6.7 ± 0.4	9.8 ± 1.1	5.6 ± 0.9	6.6 ± 0.5
Total	36.4 ± 1.5	25.6 ± 1.3	28.8 ± 0.7	33.2 ± 1.7	23.6 ± 1.4	26.2 ± 0.8
Fraction field on/off				0.91 ± 0.06	0.92 ± 0.07	0.91 ± 0.04

*The quoted uncertainties represent the root-mean-square deviation of the average dose recorded in the six water cylinders (**Figure 5**).*

TABLE 10 | Annual GCR absorbed doses (cGy/y) in free space at solar minimum.

	Geant3			Geant4		
Z	**Skin**	**BFO**	**Body**	**Skin**	**BFO**	**Body**
1	8.3	8.4	8.4	8.3	8.7	8.6
2	3.6	3.2	3.3	3.2	2.8	2.8
3–10	3.0	1.9	1.7	2.1	1.4	1.6
11–20	2.7	1.3	1.0	1.3	0.7	0.8
21–28	4.1	1.3	0.9	1.3	0.6	0.7
Total	21.7	16.1	15.3	16.2	14.2	14.5

The effect of the generation statistics on the quoted free space doses is negligible (~1%).

The free space absorbed doses are dominated by protons and He nuclei, the dominant components of GCR (~95%). The dose equivalent is obtained by multiplying the absorbed dose by the quality factor (equation (4)). Due to the strong dependence of the ionization loss on charge (Equation (1)), which affects the weighting of the quality factor, the GCR free space dose equivalents are dominated by the contribution of the $Z > 2$ nuclei (**Table 8**).

The estimated contribution of the field to the overall reduction of the absorbed dose for the 6 + 1 extendable solenoid shield is reported in **Tables 11** and **12**. The results are comparable to those obtained for the dose equivalents, i.e., ~5% with Geant3 (**Table 7**) and ~10% with Geant4 (**Table 9**).

The result of the comparative performance evaluation does not depend on the dose quoted. It would seem more appropriate to quote the dose equivalent, which better reflects the higher radiation risk associated with the larger energy losses of high charge nuclei (20).

6. SR2S RESULTS

The HTSC racetrack coils of the continuous-coil toroid shield (**Figure 4**) are described in the simulation by a cable core with a density of 3.0g/cm^3, composed of 57.4% aluminum, 8.6% MgB_2, 23% titanium, and 11% SiO_2. The cables are surrounded by 1.2-cm-thick aluminum.

A 0.6-mm-thick KEVLAR sheath (90 kg) surrounds each coil. The total mass of the 120 coil toroid is 79 t. The toroid is supported by a 5.5-m-diameter, 4.4-cm-thick, 8.6-m-long Al-B4C cylinder shell (60% boron), with a density of 2.6 g/cm^3, and a mass of 16.8 t. The total mass of the 8 Tm field configuration is 95.8 t. The individual contributions of the different elements to the total mass are shown in Figure S3 in Supplementary Material.

The shield performance with GCR protons and $Z \geq 2$ nuclei was evaluated with the field integral of 8 Tm. Higher field values were used to study the evolution of the proton and He nuclei doses with field strength and shield mass, and in particular the contributions of the charged secondaries and neutrons. The toroid fields used in the simulation are shown in **Figure 12**.

The 11.5 Tm shield configuration is obtained by increasing the coils dimensions. With the larger dimension coil, and an increase of the current density to the limiting value of the cable dimensions, the integral flux attains a value of 23 Tm. **Figure 12** shows the coil dimensions of the 8 Tm, and 11.5 (23) Tm configurations. The total shield mass in the simulation of the larger dimension coil configurations is 137 t.

The 4.5-m-diameter, 6-m-long Columbus habitat (**Figure 4**) is composed of a 1.5-cm-thick aluminum cylindrical shell and two 3.0-cm-thick aluminum endcaps. The mass of the habitat in the simulation is 4.36 t.

6.1. The Continuous-Coil Toroid Shield Performance

The annual GCR dose equivalents of the continuous-coil toroid shield, with and without the 8 Tm field, are compared in **Table 13**. The dose levels refer to the dose received in the barrel region of the 30 m × 30 m × 30 m cube, positioned around the center of the Columbus habitat. The Geant4 QBBC physics list was used for the hadron and nuclear interactions.

The magnetic field produces an additional 20–25% reduction of the dose levels provided by the passive shielding of the shield and habitat material. The corresponding annual skin, BFO, and body dose equivalents of the Columbus habitat are, respectively, 35.6 ± 0.9, 28.1 ± 1.3, and 30.2 ± 0.4 cSv/y. The magnetic shield reduces the habitat doses by 40–50%.

The evolution of the dose reduction with field strength and shield mass is illustrated in **Figure 13**. The reported annual body dose equivalents refer to GCR proton and He nuclei, which represent the dominant contribution (~85%) to the estimated total doses (**Table 13**). The 50 and 100 Tm fields, which require current

TABLE 11 | The Geant3 annual GCR absorbed dose (cGy/y) at solar minimum for the 6 + 1 solenoid configuration, with and without the 6.3 Tm field for the acceptance corresponding to the barrel region (Figure 9).

	6 + 1 no field			6 + 1 field		
Z	**Skin**	**BFO**	**Body**	**Skin**	**BFO**	**Body**
1	7.19 ± 0.25	6.74 ± 0.17	6.81 ± 0.18	6.53 ± 0.28	6.07 ± 0.18	6.15 ± 0.21
2	2.73 ± 0.06	2.42 ± 0.07	2.46 ± 0.04	2.67 ± 0.07	2.39 ± 0.03	2.47 ± 0.04
3–10	1.22 ± 0.05	0.93 ± 0.04	0.83 ± 0.03	1.26 ± 0.06	0.98 ± 0.04	0.86 ± 0.03
11–20	0.68 ± 0.06	0.43 ± 0.06	0.33 ± 0.02	0.72 ± 0.09	0.43 ± 0.02	0.35 ± 0.02
21–28	0.46 ± 0.09	0.21 ± 0.07	0.17 ± 0.02	0.48 ± 0.10	0.20 ± 0.05	0.19 ± 0.04
Total	12.28 ± 0.28	10.73 ± 0.21	10.60 ± 0.19	11.66 ± 0.32	10.07 ± 0.19	10.02 ± 0.22
Fraction field on/off				0.95 ± 0.03	0.94 ± 0.03	0.95 ± 0.03

*The quoted uncertainties represent the root-mean-square deviation of the average dose recorded in the six water cylinders (**Figure 5**).*

TABLE 12 | The Geant4 annual GCR absorbed dose (cGy/y) at solar minimum for the 6 + 1 solenoid configuration (NIAC Phase I habitat), with and without the 6.3 Tm field for the acceptance corresponding to the barrel region (Figure 9).

	6 + 1 no field			6 + 1 field		
Z	**Skin**	**BFO**	**Body**	**Skin**	**BFO**	**Body**
1	6.68 ± 0.20	6.39 ± 0.30	6.43 ± 0.21	5.70 ± 0.23	5.39 ± 0.13	5.42 ± 0.14
2	2.13 ± 0.17	1.89 ± 0.11	1.93 ± 0.07	1.92 ± 0.09	1.74 ± 0.16	1.82 ± 0.08
3–10	1.13 ± 0.03	0.86 ± 0.03	0.92 ± 0.02	1.04 ± 0.03	0.83 ± 0.03	0.89 ± 0.02
11–20	0.61 ± 0.03	0.40 ± 0.03	0.45 ± 0.02	0.59 ± 0.05	0.39 ± 0.03	0.45 ± 0.02
21–28	0.49 ± 0.05	0.30 ± 0.03	0.36 ± 0.02	0.52 ± 0.05	0.31 ± 0.04	0.36 ± 0.02
Total	11.04 ± 0.27	9.84 ± 0.32	10.09 ± 0.22	9.77 ± 0.26	8.66 ± 0.21	8.94 ± 0.16
Fraction field on/off				0.88 ± 0.03	0.88 ± 0.04	0.89 ± 0.03

*The quoted uncertainties represent the root-mean-square deviation of the average dose recorded in the six water cylinders (**Figure 5**).*

densities exceeding the performance of present-day HTSC, provide an indication of the dose reduction expected for significantly higher field flux densities.

The required increase in the screen mass, for the larger integral field values, results in a higher field off dose level due to an increase in the secondary dose. The increase is more than compensated by the magnetic field, which results in a steady decrease of the total dose with increasing field strength. The contribution of the field to the overall dose reduction is 45% at 23 Tm, the technological limit of the present-day HTSC. At 100 Tm, the field represents 70% of the observed dose reduction.

In general, an increase in material thickness is accompanied by an increase in the secondary dose for the GCR protons and He nuclei. For integral field values BL $\leq$ 8 Tm, the proton dose levels of the shielding configurations studied exceed the free space dose level. Above 11.5 Tm, the combination of mass and field of the continuous-coil toroid configurations result in proton dose levels below the free space value.

6.2. Secondary Particle Production

The effect of the magnetic field on the dose due to the secondary particles was studied in detail in the SR2S study. **Figure 14** shows the contributions of the primary GCR protons and He nuclei, and their secondaries, for the Columbus habitat alone, and the five field configurations.

The presence of the 8 Tm field does not compensate the dose due to the secondaries created in the shield material; consequently, the total dose due to protons and He nuclei exceed the level of the Columbus habitat. A decrease of both the primary and secondary doses is observed as the field integral BL increases.

The individual contributions of the primary and secondary particles are shown in **Figure 14**. The principal contributions to the secondary dose are due to protons and neutrons. The reported neutron dose levels refer to the ionization losses recorded in the water cylinders of the secondary particles created by neutron interactions in the material of the shield and habitat. The individual contributions of the secondaries denoted "others" include the mesons and baryons not explicitly quoted, and light nuclei.

The vertex distributions of the secondaries created by the primary GCR protons and He nuclei in the materials of the magnet shield and habitat, which contribute to the dose in the 8 and 23 Tm continuous-coil toroid shield configurations, are shown in top panel of **Figure 15**. The particles created in Al-B4C support cylinder surrounding the habitat are the principal source of the secondary dose.

The geometric acceptance limits the contribution of the particles created at a greater distance from the habitat. The contribution of the charged secondaries is further reduced by the presence of the magnetic field. The larger dimension coils and higher BL are responsible for the difference in the two vertex distributions.

The vertex distributions of the secondary neutrons and protons that contribute to the recorded dose levels are presented in the bottom panel of **Figure 15**. The effect of the field on the secondary

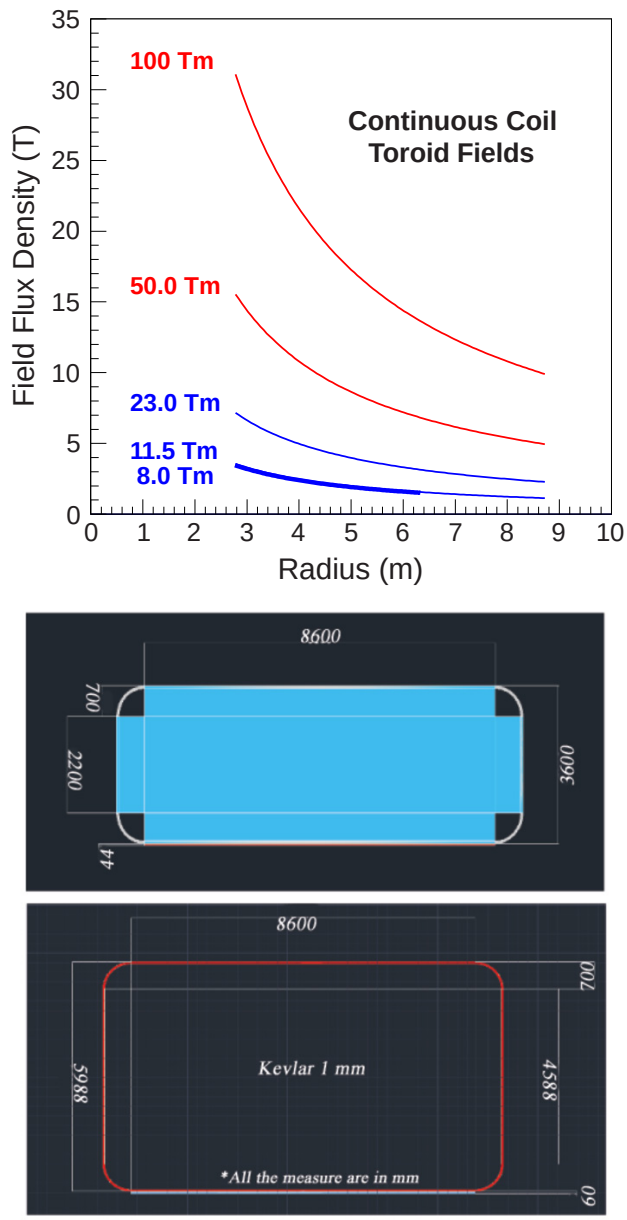

FIGURE 12 | **(Top Panel)** The toroid fields used for the performance evaluation. The field flux densities of 50 and 100 Tm require current densities that exceed the performance of present-day HTCS. **(Bottom Panel)** The dimensions (millimeter) of the racetrack coils of the 8 Tm (top) and 11.5 (23) Tm (bottom) continuous-coil toroid shield configurations.

protons results in a shorter radial extension of the volume, which contributes to the dose, compared to the region corresponding to the neutron contribution.

7. DISCUSSION

7.1. Physics Models and Dose Estimation

The Geant3 free space BFO dose equivalents of the ESA study (**Table 1**) were compared to previous estimates (16) to verify the dose calculation. The comparison of the Geant3 and Geant4 free space doses provides an estimate of the effect of the different physics models on the dose determination. A significant difference is observed in the dose levels due to GCR nuclei in the two simulations.

In Geant3, the interactions of the $Z > 2$ nuclei are dominated by ionization loss. In Geant4, the situation is modified by the presence of inelastic nuclear interactions that increases the level of secondary particle production. The difference is explained by the more extensive hadron interaction models available in Geant4.

The different weighting between ionization and the hadron interactions in the two simulations is illustrated by the systematically lower Geant4 free space doses for the $Z > 2$ nuclei in **Tables 8** and **10**. The lower rate of ionization of the primary GCR nuclei compared to secondary productions implies a relatively lower shielding efficiency of the material present in the shield structures and spacecraft, analogous to behavior observed for protons, due to the non-contained secondary particles.

The up-to-date hadron models in Geant4 result in ~30% lower estimate for the free space BFO dose equivalent (16). The change in the dose level due to the physics models is significant, on the order of the expected variations due to solar activity (40%) and the contributions of the magnetic field to the estimated dose reductions (10–50%). The Geant4 free space skin doses, 76.2 and 16.2 cGy/y, are in better agreement with the corresponding dose estimates based on the *in situ* measurements of the Mars Science Laboratory, respectively, 67.2 ± 12.0 and 17.6 ± 2.9 cGy/y (21).

The quoted free space dose values allow a comparison of the methodology and underlying physics used to determine the dose. However, they are not a realistic reference to define the efficiency of the shielding configuration, since the effect of the material that must be present (spacecraft) is ignored.

7.2. Active and Passive Shielding Elements

In the ESA study, the spacecraft consisted of a habitat and propulsion system. A characteristic of the axial field of the toroid shield is the asymmetric deflection for particles entering the field volume in the two directions parallel to the toroid axis (**Figure 8**). The material of the propulsion system is present to stop the particles that would be deflected in the direction of the habitat. The spacecraft was used as a reference for the comparison presented in **Table 3**, which indicates the relative contributions of the passive and active shielding elements to the dose reduction.

The magnet designs of the engineering studies were incorporated in the shield configuration description in the simulations used to provide the dose estimates. The emphasis was placed on the details of the shield design in terms of material composition and location, in order to accurately evaluate the shielding performance of the passive and active elements.

The magnetic shields were not integrated in an overall spacecraft design in the ESA and SR2S studies. The performance evaluations were made with respect to the dose levels of the habitat, limited to the acceptance shielded by the magnetic field volume, the barrel region defined in **Figure 9**.

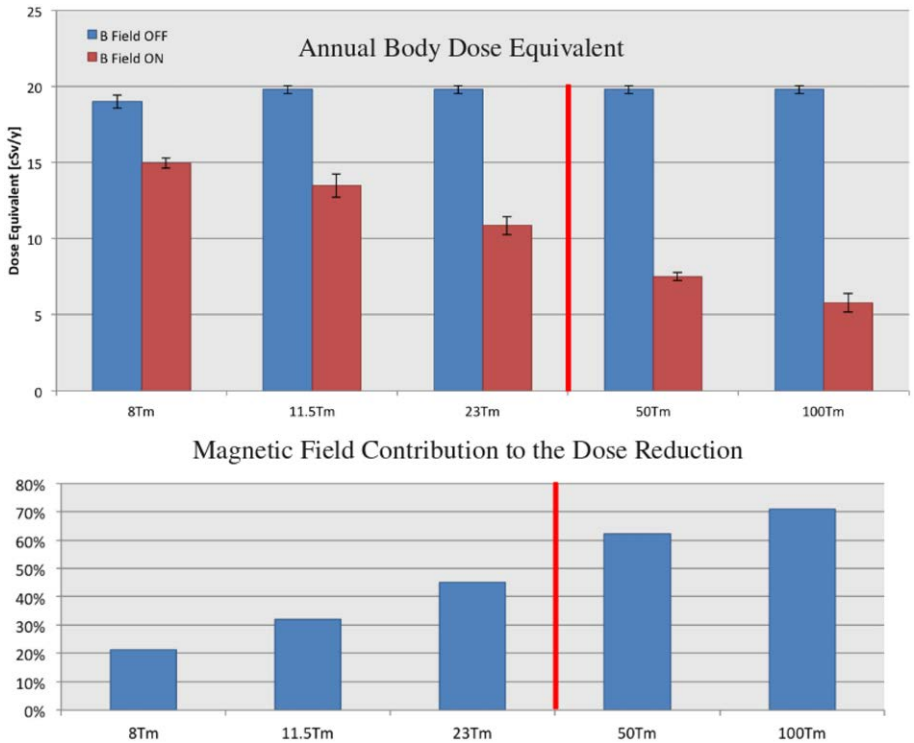

FIGURE 13 | The annual body dose equivalent doses due to GCR protons and He nuclei, with the field off and on, for the 8, 11.5, 23, 50, and 100 Tm continuous-coil toroids (top), and the corresponding contributions of the field to the dose reduction (bottom). The 50 and 100 Tm configurations require field flux densities that exceed the performance of present-day HTSC. The quoted doses refer to the barrel region acceptance (**Figure 9**). The displayed errors represent the root-mean-square deviation of the average dose recorded in the six water cylinders (**Figure 5**).

TABLE 13 | The Geant4 annual GCR dose equivalents (cSv/y) for the continuous-coil toroid (CCT) shield configuration, with and without the 8 Tm field, for the acceptance corresponding to the barrel region (Figure 9).

	CCT no field			CCT field		
Z	**Skin**	**BFO**	**Body**	**Skin**	**BFO**	**Body**
1	16.3 ± 0.5	15.2 ± 0.9	15.1 ± 0.3	12.3 ± 0.9	11.3 ± 0.4	11.6 ± 0.3
2	3.94 ± 0.13	3.84 ± 0.36	3.88 ± 0.08	3.56 ± 0.43	3.10 ± 0.27	3.40 ± 0.07
3–10	1.52 ± 0.08	1.32 ± 0.12	1.38 ± 0.08	1.17 ± 0.07	1.03 ± 0.04	1.06 ± 0.04
11–20	1.01 ± 0.10	0.80 ± 0.10	0.84 ± 0.09	0.75 ± 0.06	0.60 ± 0.04	0.65 ± 0.04
21–28	1.04 ± 0.13	0.74 ± 0.12	0.84 ± 0.14	0.90 ± 0.08	0.64 ± 0.11	0.72 ± 0.09
Total	23.8 ± 0.5	21.9 ± 1.0	22.1 ± 0.4	18.7 ± 1.0	16.7 ± 0.5	17.4 ± 0.3
Fraction field on/off				0.79 ± 0.06	0.76 ± 0.05	0.79 ± 0.02

*The quoted uncertainties represent the root-mean-square deviation of the average dose recorded in the six water cylinders (**Figure 5**).*

7.3. Spacecraft Design and Shield Optimization

The 6 + 1 extendable solenoid shield of the NIAC study was used in a preliminary spacecraft design (**Figure 11**) to extend the dose estimate over the full acceptance. The effect of the additional spacecraft structures was negligible. The dose reduction due to the material aligned along the axis of the cylindrical spacecraft was balanced by the dose increase due to charged secondaries created in structures placed on each side of the habitat (Figure S1 in Supplementary Material).

A further optimization of the overall performance requires a sufficient quantity of material to shield the magnetic field volume and limit the entry of particles that would be deflected in the direction of the habitat. The NIAC study demonstrates the need to integrate an active magnetic shield early in the spacecraft design.

The interplay between the magnetic field, and the passive shielding of the shield and spacecraft materials, requires a detailed knowledge of the geometry (**Figure 15**). The increase of the NIAC habitat thickness from 1.8 to 4.0 cm (Table S4 in Supplementary Material)

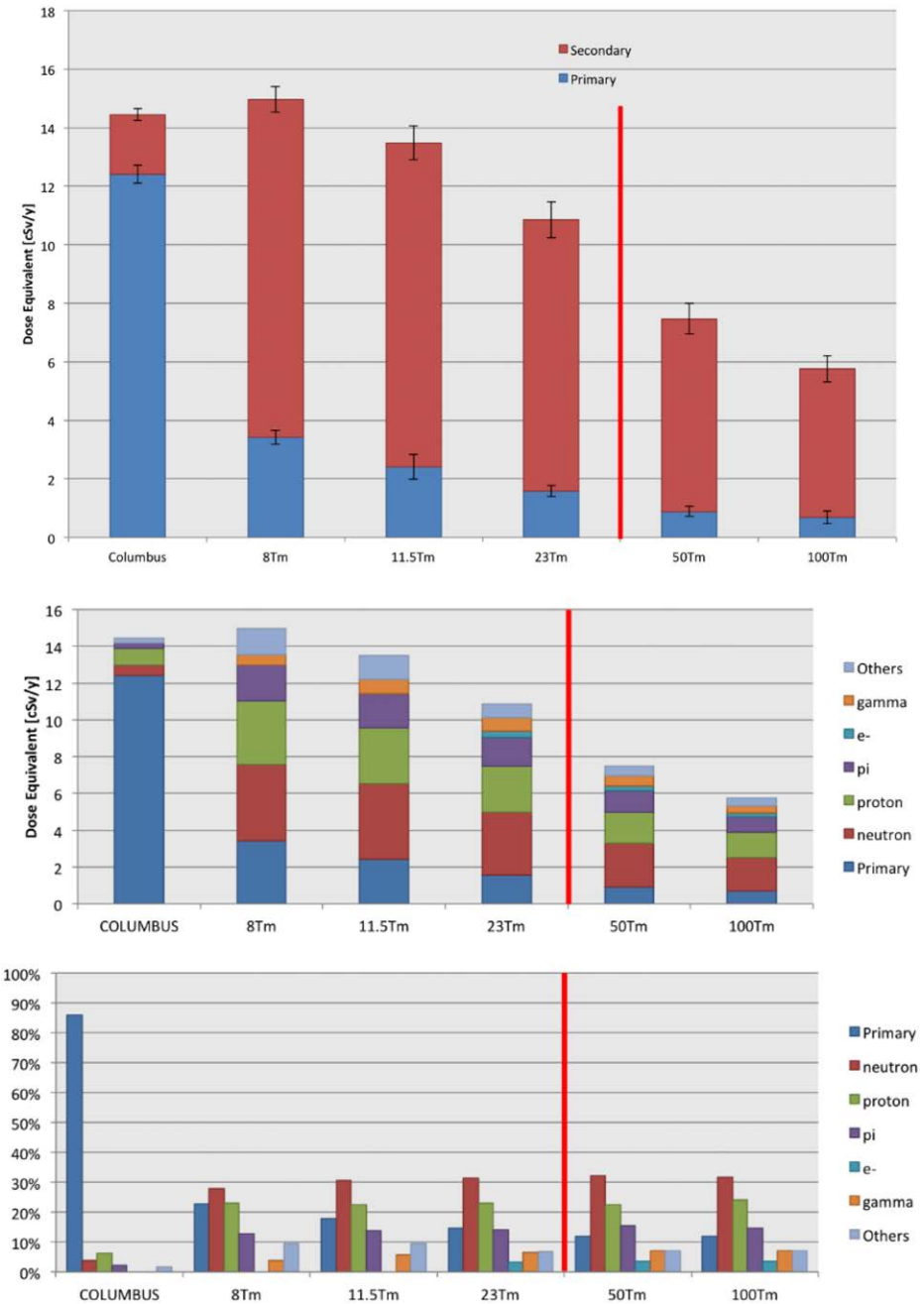

FIGURE 14 | (**Top panel)** The contributions of the primary GCR proton and He nuclei, and the secondaries produced in the material of the habitat and magnet shield to the annual body dose equivalent. The error bars represent the root-mean-square deviation of the average primary and secondary doses recorded in the six water cylinders (**Figure 5**). The quoted doses refer to the barrel region acceptance (**Figure 9**). The 50 and 100 Tm configurations require field flux densities that exceed the performance of present-day HTSC. **(Bottom panel)** The annual body dose equivalent of the primary GCR proton and He nuclei, and the secondary particles (top), and the contribution of each category to the total dose (bottom). The 50 and 100 Tm configurations require field flux densities that exceed the performance of present-day HTSC.

indicates the sensitivity of the magnetic shield performance to the mass distribution (**Tables 7** and **9**).

Mass reduction is a constant concern in each phase of a space project. A potential radiation shield is evaluated in terms of shielding performance and required mass. The original interest in active magnetic shielding was motivated by the possibility to reduce the mass required by a passive shield of equivalent performance. The theme motivated the decision of the NIAC study to abandon the toroidal field of the double-helix solenoid of the earlier ESA study, in favor of an extendable solenoid coil with a lower mass, flexible coil, which results in a larger field integral BL by maximizing *L*.

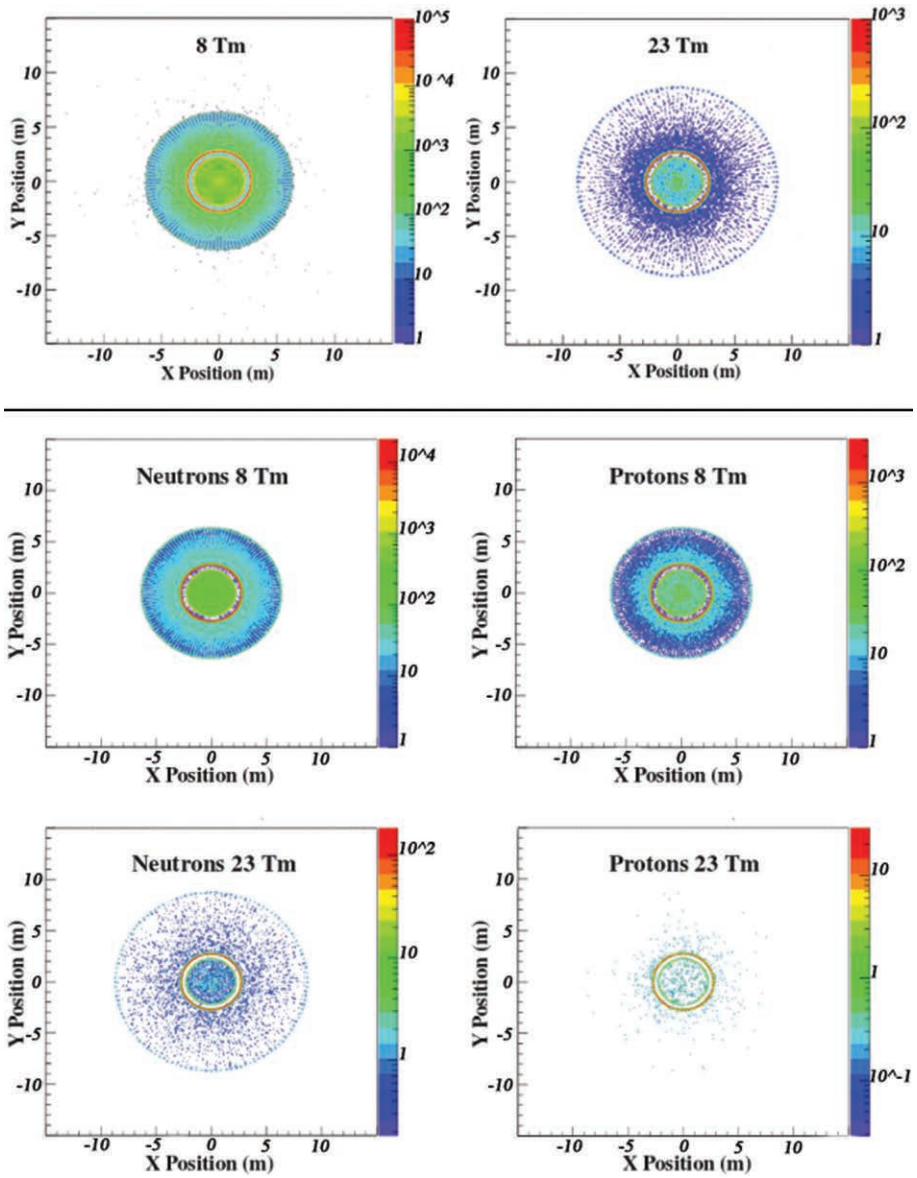

FIGURE 15 | (**Top panel)** The vertex distributions of the generated secondaries that contribute to the dose in the 8 and 23 Tm continuous-coil toroid shield configurations. The largest contribution to the secondary dose is due to interactions in the Al-B4C support cylinder surrounding the habitat, denoted by the red circular regions located inside the field volume in the *xy* projections. **(Middle and Bottom panels)** The vertex distributions of the generated secondary neutrons and protons that contribute to the dose in the 8 and 23 Tm continuous-coil toroid shield configurations.

7.4. Performance Comparison of the Advanced Designs

The performance of the NIAC 6 + 1 extendable solenoid and the SR2S continuous-coil toroid shields are presented in **Table 14**. The performance is expressed in terms of the contribution of the field to the overall dose reduction of the shield, including the passive shielding elements, and the combined shield plus habitat dose level with respect to the habitat dose level. The GCR annual BFO dose equivalent corresponding to the barrel acceptance is used for the comparison.

The 6 + 1 extendable solenoid shield results in a BFO dose equivalent of 23.6 cSv/y, the field is responsible for 8% of the total dose reduction. The dose level of the continuous-coil toroid configuration, 16.7 cSv/y, is 30% lower. The toroidal field contributes at the level of ~25% to the total dose reduction.

The difference observed between the reductions of the habitat dose levels is explained by the relative shielding efficiency for the $Z > 2$ nuclei, which contribute ~50% to the total dose of the solenoid shield (**Table 9**) and ~15% to the toroid shield dose (**Table 13**). The passive shielding of the larger mass continuous-coil toroid

TABLE 14 | The performance of the NIAC 6 + 1 extendable solenoid (ES) and the SR2S continuous-coil toroid (CCT) shields.

Shield	BL (Tm)	Mass (t)	BFO Dose Eq. (cSv/y)		% Field	% Habitat
			Field Off	Field On		
NIAC 6 + 1 ES	6.3	35	25.6 ± 1.3	23.6 ± 1.4	7.8 ± 0.6	12.3 ± 1.1
SR2S CCT	8	96	21.9 ± 1.0	16.7 ± 0.5	23.7 ± 1.3	59.4 ± 3.3

*The reported shield masses refer to the mass in the Geant4 simulation. The GCR annual BFO dose equivalents correspond to the barrel region acceptance (**Figure 9**). The quoted uncertainties represent the root-mean-square deviation of the average dose recorded in the six water cylinders (**Figure 5**). "% Field" is the dose reduction due to the field. "% Habitat" is the reduction of the habitat dose due to the magnetic shield.*

TABLE 15 | The GCR proton and He nuclei dose reductions for the 8, 11.5, and 23 Tm continuous-coil toroid (CCT) configurations.

Shield	BL (Tm)	Mass (t)	Body Dose Eq. (cSv/y)		% Field	% Habitat
			Field Off	Field On		
SR2S CCT	8	96	19.0 ± 1.0	14.4 ± 0.6	24 ± 2	1 ± 4
SR2S CCT	11.5	137	20.3 ± 2.1	12.8 ± 1.8	37 ± 9	12 ± 12
SR2S CCT	23	137	20.3 ± 2.1	10.5 ± 1.2	48 ± 6	28 ± 8

*The reported shield masses refer to the mass in the Geant4 simulation. The annual BFO dose equivalents correspond to the barrel region acceptance (**Figure 9**). The quoted uncertainties represent the root-mean-square deviation of the average dose recorded in the six water cylinders (**Figure 5**). "% Field" is the dose reduction due to the field. "% Habitat" is the reduction of the habitat dose due to the magnetic shield.*

effectively eliminates the dose contribution of the higher charge nuclei. In comparison, the difference in thickness of the two habitats has a negligible contribution. The ratio of the NIAC-to-Columbus BFO dose equivalents is 0.96 ± 0.08.

The body dose equivalent due to GCR protons and He nuclei exceed the value observed for the Columbus habitat for the 8 Tm continuous-coil toroid configuration (**Figure 14**). A further improvement in the performance is obtained by increasing the field integral BL. The effect on the proton and He nuclei annual BFO dose equivalents are presented in **Table 15**.

The 140 t, 23 Tm continuous-coil toroid shield configuration would result in a BFO dose equivalent of ~10 cSv/y. The contribution of the $Z > 2$ nuclei, 15% for the 8 Tm toroid shield (**Table 13**), may be considered negligible for the higher field, larger mass configuration. The presence of the magnetic field is responsible for 50% of the total reduction. The dose level, which corresponds to the part of the acceptance protected by the magnetic shield, ~75% of the total, is a factor ~5 smaller than the limit for LEO (16).

The performance for higher field integrals of the NIAC extendable solenoid coil shield concept is presented in Ref. (22). A comparable equivalent dose is quoted for a 19 Tm solenoid shield ($B = 4$ T, $L = 4.75$ m). The contribution of the field to the total dose reduction is not indicated.

8. CONCLUSION

The results obtained in the three studies conducted over the last 5 years[2] provide a realistic view of the current situation of a technology, which has been proposed for nearly 50 years as a solution for the radiation protection required for interplanetary manned space missions. The shielding performance of the engineering designs was evaluated with detailed 3-dimensional Monte Carlo simulations. The simulations are used extensively for the design of particle detectors for accelerator and astrophysics experiments. The same methodology has been used to design and evaluate the particle shields. In addition to the importance of the physics processes, a detailed description of the materials and the detector, or shield geometry is essential in each application.

The two HTSC candidates were identified and used in solenoid and race-track coil toroid magnet configurations in the initial ESA study. A wide survey of possible shielding configurations was made. The magnetic shield performance in terms of the contribution of the passive and active elements, a novelty, was presented.

The succeeding NIAC and SR2S studies concentrated on a single shield concept, which allowed to further develop the engineering design and improve the performance estimate. The results presented in **Table 14** represent the outcome of the efforts of the two complementary studies employing solenoid and toroid shield configurations. The best performance is obtained with the continuous-coil toroid shield based on the magnesium diboride HTSC: a 23 Tm configuration, with a mass of 140 t and a BFO dose equivalent of ~10 cSv/y (**Table 15**). The field accounts for 50% of the dose reduction.

The BFO dose equivalent, corresponding to 75% of the total acceptance, is a factor ~5 smaller than the current limits for LEO (16). The remaining acceptance should be protected by the passive shielding of the spacecraft. The presence of the active magnetic shield would render redundant a passive shielding shelter for SEP events.

A further improvement in performance requires field strengths exceeding the current densities of present-day HTSC. The situation may be improved by future developments in superconducting technology, or possibly by an innovative magnetic field configuration. An initial concept design, a minimal two-coil configuration was studied by SR2S. The unconfined field configuration, composed of two 18 MA-turn, 10 m × 20 m coils, results in a ~40% reduction of the habitat dose level (23).

[2] ESA (2011), NIAC (2012-2013), and SR2S (2013-2015).

More realistic configurations for a spacecraft shield, consisting of three or four, 3-coil toroids surrounding the habit are considered. The unconfined fields reach higher values of BL with magnetic flux densities compatible with the performance of the magnesium diboride HTSC. The reduction of the number of racetrack coils lowers the shield mass and reduces the dose due to secondary particles. The challenge is to obtain a superposition of the multiple toroidal fields, which results in an acceptable field intensity in the sensible regions of the spacecraft, and optimizes the shielding efficiency.

There are no established dose limits for interplanetary space travel. The long-term health risks due to a prolonged exposure to GCR are not well known. The two atomic bombings, irradiation during nuclear accidents, the lunar manned missions, and human activity in LEO do not represent exactly the conditions encountered during an interplanetary voyage.

A major effort has been made to develop a more precise assessment of the risk due to radiation exposure in space (24). Among the principal concerns are the biological effects caused by the high charge GCR nuclei. The observed biological effects require a reevaluation of quality factors and relative biological effectiveness (RBE) values used to compute dose levels, and establish future dose limits for interplanetary missions.

A priori, the increased biological risk due to the higher ionization energy loss may be compensated by the good efficiency of the passive shielding for the high charge nuclei. The performance of the SR2S continuous-coil toroid is limited by the contribution of secondaries created in the shield mass. If the reduction of the shield mass is not compensated by a sufficient increase of BL, for example, in the multi-toroid configuration, the dose contribution of the high charge GCR may become the limiting factor.

Risk assessment is affected often by the subjective perception of the danger, an aspect that will likely play a role in the planning of the first interplanetary mission, in particular for radiation protection against long-term health risks. A first manned mission to Mars will largely exceed the worldwide impact of the first landing on the Moon. The challenge is considerable in a world preoccupied by the reduction of costs and risks.

AUTHOR CONTRIBUTIONS

FA was co-responsable for the INFN Monte Carlo simulation performance evaluation of the SR2S study. RB was the project director of the ESA and SR2S studies. WB was responsable for the Monte Carlo performance evaluations of the ESA and NIAC studies, and co-responsable for the INFN performance evaluation of the SR2S study.

ACKNOWLEDGMENTS

The authors wish to recognize the invaluable support of Dr. Domenico D'Urso of INFN-Perugia, which made possible the high statistic Monte Carlo studies of the ESA, NIAC, and SR2S studies on the AMS computer farm at Perugia, and the indispensable contribution in matters of administration of dott.sa Marta Perucci of INFN-Perugia.

SUPPLEMENTARY MATERIAL

The Supplementary Material for this article can be found online at http://journal.frontiersin.org/article/10.3389/fonc.2016.00097

REFERENCES

1. *Cosmic Ray Effects on Micro Electonics*. Available from: https://creme.isde.vanderbilt.edu/CREME-MC
2. von Braun W. *Popular Science, January Issue*. (1969). p. 98–100.
3. Hoffman J, Fisher P, Batishchev O. *Use of Superconducting Magnet Technology for Astronauts Radiation Protection*. (2005). NIAC Phase 1 Final Report.
4. Spillantini P. Active shielding for long duration interplanetary manned missions. *Adv Space Res* (2010) **43**:900–16. doi:10.1016/j.asr.2010.01.025
5. Choutko V, Hofer H, Ting SCC. *The AMS Experiment and Magnet Faraday Cage for Human Space Exploration*. Ann Arbor, MI: NASA Active Radiation Shielding Workshop (2004).
6. Cocks FH. A deployable high temperature superconducting coil (DHTSC): a novel concept for producing magnetic shields against both solar flare and galactic radiation during manned interplanetary missions. *J Br Interplanet Soc* (1991) **44**:99–102.
7. Shepherd SG, Shepherd JPG. Toroidal magnetic spacecraft shield used to deflect energetic charged particles. *J Spacecr Rockets* (2009) **46**(1):177–84. doi:10.2514/1.37727
8. Battiston R, Burger WJ, Calvelli V, Musenich R, Choutko V, Datskov VI, et al. *Superconductive Magnet for Radiation Shielding of Human Spacecraft*. (2011). Final Report ESTEC Contract N. 4200023087/10/NL/AF. Noordwijk.
9. Westover SC, Meinke RB, Battiston R, Burger WJ, Van Sciver S, Washburn S, et al. *Magnet Architectures and Active Radiation Shield Study*. NASA Institute for Advanced Concepts (NIAC) (2012). Phase 1 Final Report.
10. Goodzeit CL, Ball MJ, Meinke RB. The double-helix dipole-a novel approach to accelerator magnet design. *IEEE Trans Appl Supercond* (2003) **13**(2):1365–8. doi:10.1109/TASC.2003.812672
11. Brun R, Bruyant F, Carminati F, Giani S, Maire M, McPherson A, et al. *Geant – Detector Description and Simulator Tool*. Geneva: CERN Program Library Long Write-up W5013, CERN (1994). p. 430.
12. Fassò A, Ferrari A, Ranft J, Sala PR. FLUKA: present status and future developments. *Proceedings of 4th International Conference on Calorimetry in High Energy Physics*; 1993 Sept 21–26; La Bidola, Italy. World Scientific. p. 493–502.
13. Tripathi RK, Cucinotta FA, Wilson JW. *Universal Parameterization of Absorption Cross Sections, Light Systems*. NASA/TP-1999-209726.
14. Sorge H. Flavor production in Pb (160A GeV) on Pb collisions: effect of color ropes and hadronic rescattering. *Phys Rev C* (1995) **52**(6):3291. doi:10.1103/PhysRevC.52.3291
15. Agostinelli S, Allison J, Amako K, Apostolakis J, Araujo H, Arce P, et al. Geant4 – a simulation toolkit. *Nucl Instrum Methods A* (2003) **506**:250. doi:10.1016/S0168-9002(03)01368-8
16. Rapp D. Radiation effects and shielding requirements in human missions to the moon and mars. *Mars* (2006) **2**:46–71. doi:10.1555/mars.2006.0004
17. Available from: https://sourceforge.net/projects/cfortran
18. *Physics Reference Manual, Version: Geant4.10.1* (2014). Available from: https://geant4.web.cern.ch/geant4/support/userdocuments.shtml
19. Ivantchenko AV, Ivanchenkobc VN, Quesada Molinad J-M, Incertia SL. Geant4 hadronic physics for space radiation environment. *Int J Radiat Biol* (2012) **88**(1–2):171–5. doi:10.3109/09553002.2011.610865
20. Durante M, Cucinotta F. Physical basis of radiation protection in space travel. *Rev Mod Phys* (2011) **83**:1245. doi:10.1103/RevModPhys.83.1245

21. Zeitlin C, Hassler DM, Cucinotta FA, Ehresmann B, Wimmer-Schweingruber RF, Brinza DE, et al. Measurements of energetic particle radiation in transit to Mars on the Mars Science Laboratory. *Science* (2013) **340**:1082. doi:10.1126/science.1235989
22. Washburn SA, Blattnig SR, Singleterry RC, Westover SC. Active magnetic radiation shielding system analysis and key technologies. *Life Sci Space Res* (2015) **4**:22. doi:10.1016/j.lssr.2014.12.004
23. Ambroglini F, Battiston R, Burger WJ, Calvelli V, Musenich R, Spillantini P, et al. *Proceedings of the 7th IAASS Conference, Space Safety Is No Accident*. Switzerland: Springer International Publishing (2015). doi:10.1007/978-3-319-15982-9
24. ICRP Publication 123. Assessment of radiation exposure of astronauts in space. *Ann ICRP* (2013) **42**(4):1–339.

Conflict of Interest Statement: The authors declare that the research was conducted in the absence of any commercial or financial relationships that could be construed as a potential conflict of interest.

Copyright © 2016 Ambroglini, Battiston and Burger. This is an open-access article distributed under the terms of the Creative Commons Attribution License (CC BY). The use, distribution or reproduction in other forums is permitted, provided the original author(s) or licensor are credited and that the original publication in this journal is cited, in accordance with accepted academic practice. No use, distribution or reproduction is permitted which does not comply with these terms.

frontiers in Oncology

ORIGINAL RESEARCH
published: 04 June 2015
doi: 10.3389/fonc.2015.00122

Issues for simulation of galactic cosmic ray exposures for radiobiological research at ground-based accelerators

*Myung-Hee Y. Kim[1], Adam Rusek[2] and Francis A. Cucinotta[3]**

[1] Wyle Science, Technology and Engineering Group, Houston, TX, USA, [2] Brookhaven National Laboratory, Upton, NY, USA and [3] Department of Health Physics and Diagnostic Sciences, University of Nevada Las Vegas, Las Vegas, NV, USA

For radiobiology research on the health risks of galactic cosmic rays (GCR) ground-based accelerators have been used with mono-energetic beams of single high charge, *Z* and energy, *E* (HZE) particles. In this paper, we consider the pros and cons of a GCR reference field at a particle accelerator. At the NASA Space Radiation Laboratory (NSRL), we have proposed a GCR simulator, which implements a new rapid switching mode and higher energy beam extraction to 1.5 GeV/u, in order to integrate multiple ions into a single simulation within hours or longer for chronic exposures. After considering the GCR environment and energy limitations of NSRL, we performed extensive simulation studies using the stochastic transport code, GERMcode (GCR Event Risk Model) to define a GCR reference field using 9 HZE particle beam–energy combinations each with a unique absorber thickness to provide fragmentation and 10 or more energies of proton and ^{4}He beams. The reference field is shown to well represent the charge dependence of GCR dose in several energy bins behind shielding compared to a simulated GCR environment. However, a more significant challenge for space radiobiology research is to consider chronic GCR exposure of up to 3 years in relation to simulations with animal models of human risks. We discuss issues in approaches to map important biological time scales in experimental models using ground-based simulation, with extended exposure of up to a few weeks using chronic or fractionation exposures. A kinetics model of HZE particle hit probabilities suggests that experimental simulations of several weeks will be needed to avoid high fluence rate artifacts, which places limitations on the experiments to be performed. Ultimately risk estimates are limited by theoretical understanding, and focus on improving knowledge of mechanisms and development of experimental models to improve this understanding should remain the highest priority for space radiobiology research.

Keywords: space radiobiology, galactic cosmic rays, cancer risk, central nervous system risk, radiation transport, shielding

OPEN ACCESS

Edited by:
William Small, Stritch School of Medicine Loyola University Chicago, USA

Reviewed by:
Dalong Pang, Georgetown University Hospital, USA
Joel S. Greenberger, University of Pittsburgh Medical Center-Shadyside, USA

***Correspondence:**
Francis A. Cucinotta, University of Nevada Las Vegas, Health Physics and Diagnostic Sciences, 4505 S. Maryland Parkway, Box 453037, Las Vegas, NV 89154-3037, USA
francis.cucinotta@unlv.edu

Specialty section:
This article was submitted to Radiation Oncology, a section of the journal Frontiers in Oncology

Received: *12 March 2015*
Accepted: *17 May 2015*
Published: *04 June 2015*

Citation:
Kim M-HY, Rusek A and Cucinotta FA (2015) Issues for simulation of galactic cosmic ray exposures for radiobiological research at ground-based accelerators. Front. Oncol. 5:122. doi: 10.3389/fonc.2015.00122

Introduction

A diverse range of health risks including cancer, central nervous system (CNS) effects, circulatory diseases, and cataracts are concerns for galactic cosmic rays (GCR) exposures during space travel (1–7). Many of these same risks are also concerns for normal tissue damage in Hadron therapy using

proton and carbon beams. In this paper, we discuss the simulation of GCR for space radiobiology research with the goal of providing a new tool for risk assessment and countermeasure research and development. However, the pros and cons of GCR simulation as a tool to augment studies with single particle species need also to be addressed. The GCR environment consists of protons and high charge Z and energy E (HZE) particles with charge number, Z from 1 to 28, with energies from <10 MeV/u to >50 GeV/u (8–10). Of note is that nuclear fragmentation occurs in a particle accelerator beam-line due to particle passage through air and beam monitoring devices, and in the tissue of animals or cell culture dishes, media, etc. used in experiments. Heavy ion fragmentation probabilities of more than 10% occur for most experimental conditions and thus pristine mono-energetic beams do not actually occur under any circumstances. We first consider the composition of the beams to be used for a GCR simulator using multiple beam and energies combined with absorbers to provide a reference field similar to the Z and E spectrum of the GCR occurring behind typical shielding amounts inside tissue in space. In addition, the temporal dependence of biological time scales in animal or cell models used in experiments relative to the most likely durations of a deep space mission to Mars of approximately 1000 days is considered.

In considering the problem of GCR simulation, we first note that there is no single GCR environment for space missions due to several variable factors including solar cycle modulation, differences due to spacecraft material types and amounts, the shielding of the Mars atmosphere and surface albedo radiation, and variability in self-shielding of different organs, due to the variability of astronaut size and weight. The GCR are modulated over the approximately 11-year solar cycle for energies below 5 GeV/u with more than two-times higher flux at solar minimum compared to solar maximum (8, 9). There is also a 22-year periodicity in solar cycles due to shifts in our sun's magnetic polarity (10) in successive 11-year cycles, which introduce a further GCR spectral variability. The primary energy spectra of each GCR particle species peaks at several hundred MeV/u, however, more than 50% of the GCR HZE flux is above 1500 MeV/u for typical shielding amounts (8–10). Within shielding or tissue, the energy spectra and fluence of each particle, $F(E, Z)$, changes due to the continuous slowing down of particles in interactions with atomic electrons, and nuclear interactions leading to fragmentation and the production of new particles, including neutrons, mesons, electrons, and gamma-rays from both the GCR and target atoms. The Earth's magnetic field shields exposures on International Space Station (ISS) missions (11) effectively blocking the primary GCR with energies below about 1 GeV/u. The surface of Mars exposures are modified by the Martian atmosphere and the albedo flux of particle produced in particle interaction with soils, while the soil composition is variable itself (12, 13). In addition, spacecraft passage through the Earth's radiation belts and solar particle event occurrence needs to be considered making an even more diverse range of exposures. Therefore an approach for a practical solution to GCR simulation is to consider a small number of reference fields that are representative of GCR, while allowing for reproducibility for radiobiological experimentation.

The NASA radiation quality factor (QF) uses particle track structure concepts leading to a radiation quality description based on two physical parameters, particle charge number, Z and kinetic energy per atomic mass unit, E, and has replaced the use of LET due to its inaccuracy as a unique descriptor of cancer risks (9, 11). For example, relative biological effectiveness factors (RBE's) for protons peak at LET values below 80 keV/μm while for Fe particles the RBE peak can be at an LET of 200 keV/μm or more (9, 11) as described in the NASA QF, while all particles have the same effectiveness as a function of LET in the older approaches. Importantly, biological effectiveness is predicted to decrease above 1 GeV/u for particles of approximately the same LET values due to the spreading of the particles track-width leading to larger contributions from δ-rays for relativistic particles compared to the more effective track core that is dominant for lower energy particle tracks (9, 11). For non-cancer risks, less is known about radiation quality dependence on particle type, and therefore investigations based on Z and E are also warranted.

Beyond defining reproducible reference fields, a second major consideration is the duration of chronic exposures necessary to elucidate risks in astronauts. The use of doses higher than the space condition can lead to misinformation about potential risks, especially for non-cancer effects where dose thresholds are likely and effect severity will increase with dose above a threshold. Considerations for the low GCR dose rates in space should be made in-light of the biological times scales of DNA damage processing, tissue regulation including cell turn-over in various tissues, molecular components of cognition in the CNS, and the evolution of pre-malignant cells in cancer development, etc. In this paper, we discuss how the low GCR dose rates in space lead to a straightforward approach to chronic exposures simulation. However, the length of exposures needed to avoid dose-rate artifacts will make a true simulation exceedingly costly.

The GCR simulator being developed at the NASA Space Radiation Laboratory (NSRL) located at Brookhaven National Laboratory (BNL) (14) was conceived by one of the present authors (Francis A. Cucinotta) in 2008 (15) during the development of the new BNL electron beam injector source (EBIS) for use at the NSRL and the BNL Relativistic Heavy Ion Collider (RHIC) (16). The upgrade includes a rapid beam switching mode of about 1-min intervals over multiple ion sources, and the addition of new power sources to allow higher beam energies up to 1.5 GeV/u for HZE particles and 4 GeV for protons compared to the current maximum (1.0 GeV/u for HZE particles and 2.5 GeV for protons). In this paper, we consider the design of GCR simulator at the NSRL and recommend a reference field defined by a GCR Z-spectrum in major energy bins that matches validated predictions of space radiation environments (12, 13, 17) for two specific shielding configurations. Pros and cons for space radiobiology research are then discussed and shown to limit the usefulness of a GCR simulator to a narrow range of research questions.

Materials and Methods

We focus on the development of a GCR simulator for the near solar minimum environment because of its higher concern for risk assessments. A second variable to consider is the amount and types of spacecraft shielding and a representative tissue self-shielding. Organ doses and dose equivalents show small variation from

GCR, and we therefore considered simulating the average tissue as represented by 5-cm tissue equivalent shielding often used to represent the blood forming organ (BFO) self-shielding distribution (8, 18). We note that experiments with small animals such as mice or rats along with holders, where animals are placed, lead to an additional 2–10 cm of tissue equivalent shielding, such that the use of 5-cm tissue equivalent shielding and these additions result in a simulation that accurately represents the average organ depth in humans. Target fragments produced from tissue atoms (19) will be simulated accurately at such depths of tissue because of the dominance of short-ranged proton and helium fragments produced locally from constituent atoms. We consider the typical spacecraft shielding thickness, which with internal equipment a thickness of about 20 g/cm^2 aluminum equivalent, while a minimum shielding of 5 g/cm^2 occurs. These two shielding configurations are denoted as the transfer vehicle and surface habitat. In the present paper, we did not consider simulation of exposures on the Mars surface, however this area will be considered in future work. For the Mars surface environment, the energy spectra of neutrons will be an important factor as described in our recent papers (12, 13).

Validated Space Environment Prediction

In order to estimate the space environment within spacecraft shielding, a large number of spaceflight measurements are considered and used to validate computer code predictions. The representation of the GCR particle distribution consists of the free space environment, radiation transport model, and shielding distribution. Extensive spectral measurements of particle type and energy distributons have been reported from satellite and baloon experiments in Antartica using large instruments (>10 kg) that are typically not used on human missions. These data have been used to formulate an accurate computer model of the free space GCR for particles from protons to nickel particles for energies from 0 to 50 GeV/u (10, 20). For the calculations in this report, we use the GCR environment model at 1977 solar minimum. As a model of the GCR environment behind shielding, we use the high-charge and energy (HZETRN) transport code (18, 21, 22), which solves for the spectrum of nuclear fragments from projectile and target nuclei in the continuous slowing down and straight-ahead approximation. The HZETRN code has been compared to extensive flight measurements for dose and dose equivalent on space shuttle, ISS, and Mars transit and Mars surface measurements and generally agree with these measurements to within ±15% (9, 12, 13, 17).

For the nuclear interactions of the primary GCR with the matter, the quantum multiple scattering theory of nuclear fragmentation (QMSFRG) model describes the production of light nuclei through the distinct mechanisms of nuclear abrasion and ablation, coalescence, and cluster knockout (22, 23). Helium interaction cross sections were described previously by Cucinotta et al. (24, 25) while the HZETRN code uses proton and neutron interaction cross sections from the Ranft and Bertini models of nuclear cascade and evaporation processes (18, 21).

Reference Fields at NSRL

In the design of GCR reference field, the changes in the beam composition or energy behind proposed absorbers due to energy loss and fragmentation and production of secondary radiation by the absorber are simulated using the GERMcode (26). For the design of a reproducable reference field, we consider a configuration with a small number of ion sources: p, ^{4}He, ^{16}O, ^{28}Si, and ^{56}Fe. Energy switching is then considered with possible absorbers to spread both the energy and fragment distribution to represent the GCR with some realistic measure in specific Z and E bins. Three energy changes each for ^{16}O, ^{28}Si, and ^{56}Fe are considered, and additional energy changes for p and ^{4}He beams, as described next. The use of a computer-controlled automated binary filter is assumed to allow for beam-specific variable absorber amounts to optimize the spreading and fragmentation of the beam for the purpose of obtaining the desired Z and E dependence of particles at the biological samples. The thickness of the absorber is chosen to reproduce the HZETRN code results for the Z-dependence of particle absorbed dose in the energy bins considered. Particles of lower energy (<50 MeV/u) are a minimal consideration for several reasons, including their stopping in absorbers or the entrance tissues of animals, the continuous slowing down of higher energy particles in the absorber will produce particles following a characteristic 1/LET(E) spectral shape (18) within tissues, and lower energy particles are produced locally in nuclear absorption events of high energy particles.

Light Ions

The NSRL can provide energies of protons and ^{4}He ranging from as low as 40 MeV/u to about 2.5 and 1 GeV/u currently and up to 4 and 1.5 GeV/u, respectively, with the proposed NSRL energy upgrade. In the design of broad energy range of protons and helium comprising the most abundant in GCR, the beam fluence of a specified energy bin is calculated from the dose and fluence relation,

$$D = \rho \Phi L \tag{1}$$

where, ρ is the density of material, Φ is the number of particles per unit area, fluence, and L is the rate of energy loss, LET. We consider a number of energy changes, 10 or more, for both proton and ^{4}He beams with the precise number considered in design tests of energy resolution relative to experimental simulation times. The QF or RBE for the $Z = 1$ and 2 particles above a few hundred MeV/u will be close to unity and largely independent of energy making the energy resolution a minor consideration for biological responses. Other H and He isotopes will be produced in the reference field due to projectile and target fragmentation of the various beam–target interactions that result from the overall simulation. The secondary mesons produced through multi-particle production processes at the highest energies (from 3 to 4 GeV) better represent the space situation compared to lower energy particles (<1 GeV/u) where pion production is dominated by one pion production cross-sections. However, these differences will not be significant for biological responses because high-energy pions and their decay products have low RBE, especially for shielding amounts below 100 g/cm^2.

HZE Particles

In order to accurately simulate the GCR charge and energy distribution of dose, three major HZE beams (^{16}O, ^{28}Si, and ^{56}Fe) are selected at three energies (500, 900, and 1500 MeV/u). By placing the absorber of polyethylene, the primary particles will interact

with the absorber losing energy and producing secondary nuclei through projectile fragmentation. The absorber thickness is chosen to match the Z-distribution predicted by the HZETRN code in three energy bins (0–500, 500–900, and >900 MeV/u). Here, an initial estimate of the absorber thickness of a specified primary ion at the energy bin is calculated from the absorption and extinction rate as,

$$\frac{D_j(E_{bin})}{D_{Z_group}(E_{bin})} = e^{(-\sigma_j(E)x_{pe})} \tag{2}$$

where, $D_j(E_{bin})$ is the dose of the primary j ion in the energy bin (j for ^{16}O, ^{28}Si, and ^{56}Fe; E_{bin} for $E < 500$ MeV/u, $E = 500$–900 MeV/u, or $E > 900$ MeV/u), $D_{Z_group}(E_{bin})$ is the total dose of the corresponding charge group in the energy bin for j (Z_group for $Z = 3$–8, $Z = 9$–14, or $Z = 15$–28), $\sigma_j(E)$ is the macroscopic absorption cross-section for the primary j with energy E, and x_{pe} is the depth of polyethylene absorber.

The dose without the absorber relative to those with the absorber is related to the primary beam and its fragments, respectively. Particle fluence is calculated using the GERMcode (26) for the primary ion without the absorber in Eq. 3a and for the beam fluence required to obtain the dose from fragmentation and energy loss by the absorber in Eq. 3b.

$$\Phi_j(E,x_0) = D_{(Z_{group})}(E_b in) \times B_{(abs,\,j)(E)} \times \Phi_j(E)\Phi_{(Gy\text{-}\mu m^2)} \tag{3a}$$

$$\Phi_j(E,x_{pe}) = D_{Z_group}\left(E_{bin}\right) \times (1. - B_{abs,\,j}(E)) \times \Phi_j(E)_{Gy\text{-}\mu m^2} \times \frac{D_j(E,x_0)}{D_j(E,x_{pe})} \tag{3b}$$

Here, D_{Z_group} (E_{bin}) are the dosimetric quantities predicted from the HZETRN code. $B_{abs,\,j}$ (E) is the beam absorption rate of the primary j ion at energy E as calculated in Eq. 2. The beam fluence of j ion at energy E to the area of 1 μm^2 for the exposure to 1 Gy, and the dose without absorber to that with the absorber, can be obtained from the GERMcode (26).

Duration and Order of Exposures

We next consider the proposed beam-energy combination described above and NSRL capability for inter-fraction time for mixed sources as short as 1 min, in order to recommend time profiles for GCR simulation. To obtain reasonable statistics 10 exposures each for our preliminary beam-energy combinations or ~350 fractions are considered as a first estimate resulting in a GCR simulation of about 6 h. When considering the total annual GCR dose of ~200 mGy/y, we note that a small number of particles per pulse has been used previously at NSRL with no technical issues (27). A more refined estimate considers the dose weighting required for different beams such that a higher number of proton and helium pulses compared to the O, Si, and Fe beams. In a shift from proton to proton, or proton to helium, exposures of different energies will occur frequently under these conditions, and therefore we estimate about 8–10 h-exposure duration would provide a reasonable simulation time based on beam delivery and dose weighting considerations alone. However, biological response time scales, including the kinetics of responses in experimental models compared to astronauts on space missions, lead to further considerations as described next.

We considered a kinetics formalism of the multi-hit model to estimate the number of cells hit by HZE particles during the evolution of a chronic exposure. The model assumes the particle hits are Poisson distributed. We consider the fluence rates for HZE particles alone or including protons and helium, and estimates of cell or tissue structure sensitive areas, A, with biological processes relaxation times, τ_{relax}, such as DNA repair or signal transduction. The mean hit-rate per day, H_r, is estimated using A and the fluence rate, F by

$$H_r = FA \tag{4}$$

The kinetics representation of the Poisson distribution of cells (or sensitive tissue areas) with 0, 1, 2, etc. hits denoted as n_i at any given time is given by the system of ordinary differential equations:

$$\frac{dn_o(t)}{dt} = -H_r n_0(t) + K_D \sum_{i=1} f_i \quad n_i(t) \tag{5a}$$

$$\frac{dn_i(t)}{dt} = H_r n_{i\text{-}1}(t) - (H_r + K_D + K(i)_{in}) n_i(t) \tag{5b}$$

Where K_D is the decay rate given by ln (2)/τ_{relax}, $K(i)_{in}$ is rate of cell death after the *ith*-hit, and f_i is the fraction of n_i cells that are not eliminated by the *ith*-hit. Using hit rates from the GERMcode simulations described in this report and several possible relaxation times, Eqs (5a) and (5b) are solved numerically to make predictions comparing these cell populations for chronic exposures of varying lengths.

The order of exposures in space is random as weighted by particle fluence for a given species and energy. Using random number generators, a random order of exposures can easily be obtained. For biological research replicate experiments are required, such that a computer model generated order should be used for each replicate experiment. Selecting a different order with proper weighting would not likely change the experimental results within expected uncertainties, however may require further considerations.

Results

Two spherical configurations of 20 and 5 g/cm^2-thick aluminum are used for an equivalent Mars transfer vehicle and the minimum amount for pressure vessel-wall in living quarter, respectively. The annual 5-cm tissue doses from exposure to GCR at 1977 solar minimum environment are simulated after passing through shielding configurations of a Mars transfer vehicle or a habitat. The Z-group dependence of the dose from the prediction of HZETRN code for the two shielding configurations are reported in **Tables 1 and 2** and **Figure 1**. These results show the expected dominance of protons and helium to tissue doses for typical shielding amounts. **Table 3** shows the HZETRN predictions of the energy spectra for hydrogen and helium particles for the two shielding configurations in different energy bins. The highest energy bin includes integral contributions from all particles above this energy. The light ion beam fluence per unit area at each energy is also shown in **Table 3**, which is calculated with regard to the corresponding dose fraction of light ions in each energy bin. Not shown are the

TABLE 1 | Contributions from different charge groups predicted by HZETRN code for two reference shielding designs.

Charge group, Z	Habitat + 5-cm tissue		Transfer vehicle + 5-cm tissue	
	Dose fraction	Dose, mGy/y	Dose fraction	Dose, mGy/y
$Z = 1$	0.60	120.8	0.70	145.0
$Z = 2$	0.21	42.5	0.19	38.5
$3 \leq Z \leq 8$	0.11	22.7	0.08	16.3
$9 \leq Z \leq 14$	0.04	8.5	0.02	4.0
$15 \leq Z \leq 28$	0.04	7.4	0.01	2.9
Sum	1.00	201.9	1.00	206.7

TABLE 2 | Comparison of doses of several charge (Z)-groups in three energy bins from the HZETRN code to the model GCR reference field (in parenthesis).

	Habitat + 5-cm tissue			Transfer vehicle + 5-cm tissue		
	Dose, mGy			Dose, mGy		
E, MeV/u	<500	500–900	>900	<500	500–900	>900
$Z = 3$–8	14.7 (14.2)	2.9 (3.0)	5.2 (5.6)	11.3 (10.9)	1.7 (1.8)	3.3 (3.6)
$Z = 9$–14	4.3 (4.6)	1.4 (1.4)	2.9 (2.7)	1.7 (1.8)	0.7 (0.7)	1.6 (1.5)
$Z = 15$–28	3.3 (3.3)	1.2 (1.2)	2.9 (2.9)	1.1 (1.1)	0.5 (0.5)	1.4 (1.3)

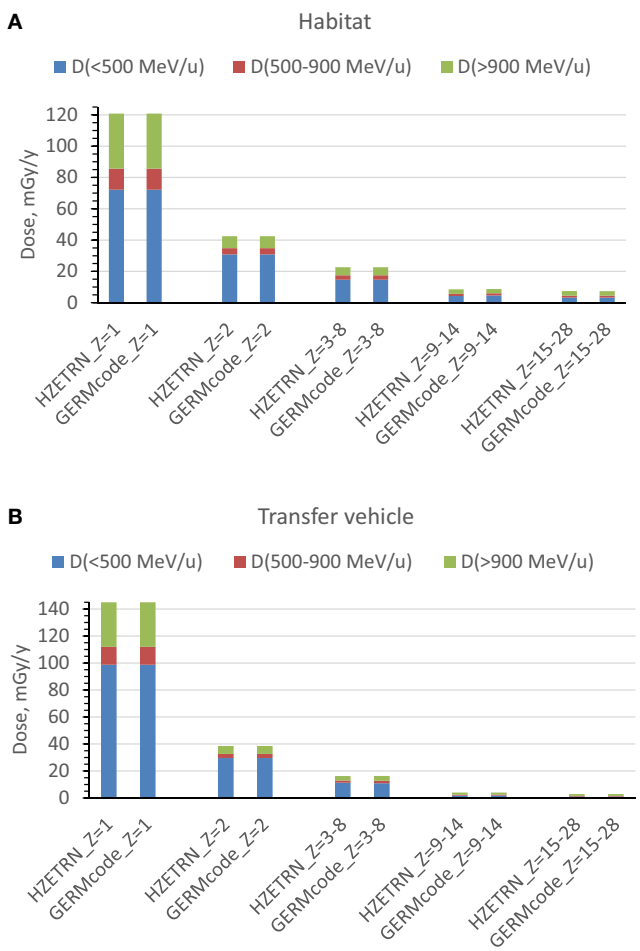

FIGURE 1 | Prediction of annual 5-cm tissue equivalent dose for energy and charge groups from exposure to annual GCR at 1977 solar minimum. (A) habitat, **(B)** transfer vehicle.

variation of the spectra at lower energies where hydrogen and helium particles reach high LET values (>10 keV/μm); however these particles follow a characteristic spectra of 1/LET(E) from atomic slowing down or are produced locally due to their small range (18). Thus they are adequately represented by the use of the 5-cm tissue equivalent shielding along with the additional materials of the tissue for the animal model considered.

Figure 2 shows comparisons on the GERMcode simulation to measurements at NSRL for Bragg curves in polyethylene for beams ^{28}Si at 0.4 and 0.98 GeV/u and ^{56}Fe at 0.3 and 0.97 GeV/u. The GERMcode accurately predicts the depth-dose distribution, and predicts the so-called tail distribution of fragments that go well beyond the range of the primary beam. As the kinetic energy and projectile beam mass increases, the Bragg peak is diminished and a nearly exponential depth-dose distribution will occur above a few GeV/u.

Table 4 shows the extinction fraction of the specified heavy ions of a GCR simulator needed to match the prediction of dose fraction of GCR ion from HZETRN code, and the prediction of the depth of polyethylene absorber according to Eq. (2) with the macroscopic absorption cross sections of the ions in polyethylene, σ_{abs}. In the design of a GCR simulator, the dose distribution from particles with charge numbers other than primary beam is through fragmentation of the selected heavy ion. **Tables 5** and **6** show the modified absorber depth to promote more fragments from high energy beams, by which the dose fraction of Z-group at each energy bin has been best matched to the prediction of HZETRN code. **Tables 5** and **6** also show the mean energy of the primary beam after penetrating the absorber distance. In the current design, the primary beam does not completely stop after the absorber depth (except 500 MeV/u ^{28}Si) due to the downgraded energy of the beam. A broad energy range behind the absorber depth results for the projectiles and fragments. The corresponding heavy ion beam fluence of the primary and the fragments at 5-cm tissue inside the habitat and the transfer vehicle are also shown in **Tables 5** and **6**, respectively.

The current GCR reference field using nine HZE beam-energy combinations with absorber is compared to simulated full GCR environments in terms of Z-group dose distribution in **Table 2**, where good agreement is found. The individual charge contributions to the dose distribution are shown in **Figures 3** and **4**. Improved matching of several GCR elements such as $Z = 6$, 10, and 12 will require the use of a larger number of primary beams. To minimize the error of overall Z-distribution of dose and to best match the Z-group dose as shown in **Table 2**, the required doses of the primary beams are listed in **Table 6**, $D_j(E)$. The resultant dose distribution in **Figures 3** and **4** shows that our minimal GCR reference field describes qualitatively very well the representative Z-distribution of dose for full simulated GCR environment, and can be easily improved by the use of a larger number of primary beams.

TABLE 3 | Beam energy and fluence for light ions (Z = 1 and 2).

Protons			^{4}He		
E_p, MeV	D_p, mGy	$\Phi_p/\mu m^2$	E_{He}, MeV/u	D_{He}, mGy	$\Phi_{He}/\mu m^2$
(A) INSIDE THE HABITAT (5 g/cm^2 ALUMINUM + 5-cm TISSUE)					
50	28.05	1.39×10^{-1}	50	14.54	1.80×10^{-2}
100	12.34	1.05×10^{-1}	100	4.42	9.36×10^{-3}
200	13.11	1.81×10^{-1}	200	4.86	1.68×10^{-2}
300	7.91	1.39×10^{-1}	300	3.07	1.35×10^{-2}
400	5.93	1.04×10^{-1}	400	2.23	1.14×10^{-2}
500	4.85	1.09×10^{-1}	500	1.69	9.52×10^{-3}
600	4.1	9.97×10^{-2}	600	1.32	7.98×10^{-3}
800	6.63	1.76×10^{-1}	800	1.95	1.30×10^{-2}
900	2.72	7.46×10^{-2}	900	0.75	5.14×10^{-3}
1000	2.42	6.79×10^{-2}	1000	0.63	4.43×10^{-3}
1200	4.09	1.18×10^{-1}	1200	7.01	5.08×10^{-2}
1400	3.31	9.79×10^{-2}			
1600	2.72	8.13×10^{-2}			
1800	2.27	6.85×10^{-2}			
2000	1.92	5.81×10^{-2}			
2500	18.46	5.59×10^{-1}			
Total	120.8		Total	42.47	
(b) INSIDE THE TRANSFER VEHICLE (20 g/cm^2 ALUMINUM + 5-cm TISSUE)					
50	40.28	2.00×10^{-1}	50	15.92	1.97×10^{-2}
100	18.58	1.58×10^{-1}	100	4.21	8.93×10^{-3}
200	18.61	2.57×10^{-1}	200	4.09	1.41×10^{-2}
300	9.71	1.71×10^{-1}	300	2.37	1.04×10^{-2}
400	6.53	1.15×10^{-1}	400	1.69	8.64×10^{-3}
500	5.02	1.14×10^{-1}	500	1.27	7.17×10^{-3}
600	4.12	1.00×10^{-1}	600	0.99	6.00×10^{-3}
800	6.5	1.73×10^{-1}	800	1.5	1.00×10^{-2}
900	2.63	7.20×10^{-2}	900	0.6	4.09×10^{-3}
1000	2.32	6.51×10^{-2}	1000	0.5	3.49×10^{-3}
1200	3.89	1.13×10^{-1}	1200	5.38	3.90×10^{-2}
1400	3.13	9.26×10^{-2}			
1600	2.56	7.67×10^{-2}			
1800	2.13	6.45×10^{-2}			
2000	1.8	5.46×10^{-2}			
2500	17.21	5.21×10^{-1}			
Total	145		Total	38.5	

The limitation of upper energy of the simulation compared to the GCR environment in space introduces some error because the dose above 1.5 GeV/u (4 GeV) for HZE particles (protons) is assumed to be represented by the upper energy bin as described above. The magnitude of this error will depend on which biological response is considered. Based on the central estimates of the NASA QF function for solid cancer risk (9), we estimated the error by using the HZETRN code, for which predictions with the QF held fixed at either 900 or 1500 MeV/u are compared to those using the actual energy dependence in the NASA QF values (**Figures 4** and **5** for 5 and 20 g/cm^2, respectively). The GCR simulator overestimates the dose equivalent because the NASA QF decreases above the cutoff energy. This is in contrast to the older QF models used by the International Commission on Radiological Protection (ICRP) for ground-based exposures where the LET dependence is such that QF increased with increasing energy above 1.5 GeV/u for most GCR heavy ions. The error using the NASA solid cancer QF basis is quite reasonable being <12 or 5% for a cutoff of 900 or 1500 MeV/u, respectively. It is important to emphasis the higher energies (>1 GeV/u) are needed at an accelerator to obtain particles of sufficient depth of penetration in a mixed-field as well as minimizing the error in dose equivalent simulations.

It is well known that for HZE particle fluence in space each cell nucleus would receive only 0 or 1 particle traversal with nearly 100% probability, such that there is a negligible probability for individual cells to receive two or more HZE particle hits on long-term space missions. Larger targets suggested by non-targeted effects or for damage to neuron cells including dendritic trees (4) lead to other considerations. At the other extreme, each cell will receive about 1 particle traversal per 2 days for proton fluence near solar minimum and about an equal number of δ-ray cell traversal (28). If a major consideration was about protons or δ-rays hitting the same target cell within the simulated time compared to the space condition of about one per day, then a minimal GCR simulation time of at least 2 days should be utilized.

Figure 6 shows the time-dependent probabilities for cells with 100 μm^2 area to receive 1 or >1 particle hit at a given time point during the actual GCR exposure over 1-year (**Figure 6A**) or NSRL simulations of 30 or 2 days (**Figures 6B,C**, respectively). Similar comparisons are shown in **Figure 7** for a larger area of 500 μm^2. Predictions for relaxation times of 1 or 7 days are shown assuming an average rate of cell inactivation of 10% per hit (29). For example for a 2 day, GCR simulation assuming a 100 μm^2 target size 5 or 10% of cells will receive two or more HZE hits for relaxation times of 1 or 7 days, respectively. Larger multi-hit percentages occur for the 500 μm^2 where the two or more HZE particle hit probability exceeds the one-hit probability for a 2 or 30 days simulation. This larger area would be more representative of areas suggested by non-targeted effects studies (30, 31) or neuronal cell structures (7). Cells with multiple hits will likely have a significantly higher response compared to cells with a single HZE traversal and thus could dominate responses, and short (<1 week) exposure times will likely lead to over-estimation of effect. Multiple-hit artifact contributions will increase for shorter simulation times. However, the beam-time costs and limitations in types of endpoints to be observed in experiments of this duration are large hurdles in using a GCR simulation for improving risks models and reducing their uncertainties.

Discussion

The transport code predictions discussed in this paper suggest that very detailed simulations of the Z and E dependence of HZE particle doses can be made with only a few beam type and energy changes using an automated absorber depth for each primary beam. Based on the current technologies at the NSRL GCR simulations within 8 h would be possible but would not be representative of the space situation because of the multiple-hits per cell or neuronal structure artifacts that would arise. GCR simulations based on particle charge and energy are needed due to the inaccuracy of LET as a descriptor for both cancer (9) and CNS effects (30). The error introduced by an HZE particle cut-off of 1500 MeV/u relative to the particle spectrum in space is small for the solid cancer dose equivalent, however the energy upgrade at NSRL is needed to obtain particles of significant range to represent spacecraft or planetary atmosphere shielding. Errors introduced for CNS or other risk estimates have not been evaluated and would

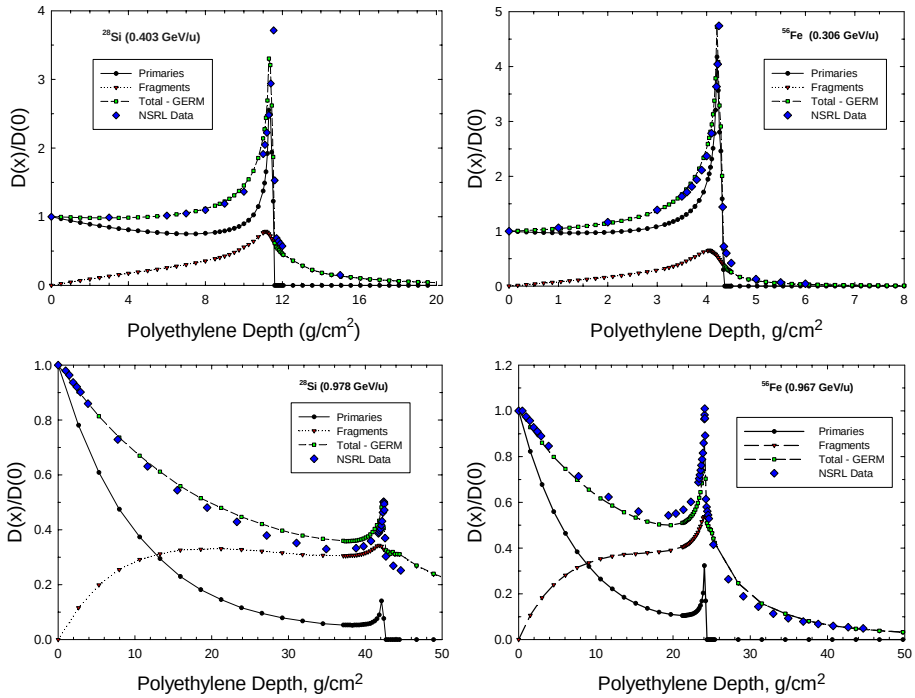

FIGURE 2 | Comparison of GERMcode and NSRL measurements for the depth-dose distribution in polyethylene shielding for ^{28}Si and ^{56}Fe beams.

TABLE 4 | Heavy ion beam extinction fraction for GCR simulator based on dose fraction of the beam predicted from the HZETRN code, absorber depth in polyethylene x_{pe}, for beam extinction fraction, and macroscopic absoprtion cross sections, σ_{abs}, of the beam in polyethylene.

HZE beam		GCR dose fraction of the ion	Habitat + 5 cm tissue		Transfer vehicle + 5-cm tissue		σ_{abs}, cm²/g
			Extinction	x_{pe}, g/cm²	Extinction	x_{pe}, g/cm²	
500 MeV/u	^{16}O	$D_{16O}/\Sigma(D_{3-8})$	0.305	17.8	0.169	26.6	0.0668
	^{28}Si	$D_{28Si}/\Sigma(D_{9-14})$	0.299	13.2	0.236	15.7	0.0916
	^{56}Fe	$D_{56Fe}/\Sigma(D_{15-28})$	0.410	6.8	0.309	9.0	0.1307
900 MeV/u	^{16}O	$D_{16O}/\Sigma(D_{3-8})$	0.447	18.0	0.382	20.5	0.0706
	^{28}Si	$D_{28Si}/\Sigma(D_{9-14})$	0.306	21.5	0.250	23.5	0.0966
	^{56}Fe	$D_{56Fe}/\Sigma(D_{15-28})$	0.430	8.2	0.327	12.9	0.1366
1500 MeV/u	^{16}O	$D_{16O}/\Sigma(D_{3-8})$	0.455	17.2	0.396	19.5	0.0722
	^{28}Si	$D_{28Si}/\Sigma(D_{9-14})$	0.290	21.5	0.240	24.0	0.0987
	^{56}Fe	$D_{56Fe}/\Sigma(D_{15-28})$	0.455	7.4	0.350	12.0	0.1392

be difficult to estimate based on the limitations in current CNS animal data (4).

High energy protons and helium particles are of low RBE and simulation of the details of their energy spectra above 100 MeV/u is not critical and can be considered in terms of their cumulative doses and target fragment production. However, a large number of energy changes for these beams should be possible based on previous exposures simulating solar particle events at NSRL. Neutrons are produced in the absorbers or tissue equivalent materials using our design through nuclear reactions. Additional neutrons are produced in tissues of mice or rats and holders to be employed in experiments. Low energy neutrons (<5 MeV) are known to have large RBEs for late effects and their dose contributions will be reproduced accurately if the high-energy charged particle composition and energy spectra are simulated accurately. Protons and helium particles create the most neutrons in space because of their much higher fluence amongst the GCR. Previous radiobiology studies with high energy proton beams using very thick absorbers (31) suggest that neutrons are ineffective in producing biological damage at high-energy (>100 MeV). This observation is readily predicted by the mean-free path of neutrons which is generally >10 cm for materials of interest. Because of the similarity of nuclear absorption cross sections, the secondary particles and target fragmentation spectrum produced by protons and neutrons of energies above a few hundred MeV are nearly identical. Thus high energy protons are biologically more effective compared to neutrons of the same energy per unit fluence because of their charge state. On the other hand, for very thick absorbers such

TABLE 5 | Heavy ion beam fluence in energy bin with polyethylene absorber for mixed-field spectrum inside the habitat (5 g/cm² aluminum + 5-cm tissue) to match the dose of *Z*-group at energy bin predicted from HZETRN code. The beam energy and average energy of the beam after the absorbor, E_{out}. are shown.

j	E, MeV/u	x_{pe}, g/cm²	E_{out}, Me V/u	$\frac{D_j(E,x_{pe})}{D_j(E,x_0)}$ [a]	Primary or fragments	$D_j(E)$, mGy[b]	$\Phi_j(E)$/μm²/Gy[a]	$\Phi_j(E)$/μm²
^{16}O	500	0		1	0.164	2.25	0.353	7.94×10^{-4}
		17.8	119	0.86	0.836	11.48		4.69×10^{-3}
	900	0		1	0.271	0.73	0.428	3.12×10^{-4}
		18	516	0.64	0.729	1.96		1.30×10^{-3}
	1500	0		1	0.282	1.36	0.465	6.34×10^{-4}
		17.2	1127	0.61	0.718	3.48		2.64×10^{-3}
^{28}Si	500	0		1	0.151	0.74	0.115	8.50×10^{-5}
		13.2	52	0.99	0.849	4.16		4.84×10^{-4}
	900	0		1	0.206	0.32	0.140	4.53×10^{-5}
		21.5	286	0.48	0.794	1.25		3.61×10^{-4}
	1500	0		1	0.207	0.68	0.152	1.03×10^{-4}
		21.5	886	0.4	0.793	2.61		9.91×10^{-4}
^{56}Fe	500	0		1	0.207	0.69	0.034	2.33×10^{-5}
		6.8	85	0.98	0.793	2.65		9.03×10^{-5}
	900	0		1	0.256	0.33	0.041	1.32×10^{-5}
		8.2	433	0.67	0.744	0.95		5.70×10^{-5}
	1500	0		1	0.276	0.83	0.044	3.66×10^{-5}
		7.4	1062	0.65	0.724	2.18		1.48×10^{-4}

[a] *The relative dose behind the absorber and the beam fluence to 1 μm²/Gy from GERMcode.*
[b] *Based on the Z-group of dose from the HZETRN prediction.*

TABLE 6 | Heavy ion beam fluence in energy bin with polyethylene absorber for mixed-field spectrum inside the transfer vehicle (20 g/cm² aluminum + 5-cm tissue) to match the dose of *Z*-group at energy bin predicted from HZETRN code. The beam energy and average energy of the beam after the absorbor, E_{out} are shown.

j	E, MeV/u	x_{pe}, g/cm²	E_{out}, MeV/u	$\frac{D_j(E,x_{pe})}{D_j(E,x_0)}$ [a]	Primary or fragments	$D_j(E)$, *m*Gy[b]	$\Phi_j(E)$/μm²/Gy[b]	$\Phi_j(E)$/μm²
^{16}O	500	0		1	0.076	0.82	0.353	2.89×10^{-4}
		26.6	10	1.22	0.924	9.9		2.86×10^{-3}
	900	0		1	0.237	0.38	0.428	1.61×10^{-4}
		20.5	484	0.61	0.763	1.21		8.48×10^{-4}
	1500	0		1	0.252	0.79	0.465	3.68×10^{-4}
		19.5	1097	0.57	0.748	2.35		1.90×10^{-3}
^{28}Si	500	0		1	0.096	0.19	0.115	2.24×10^{-5}
		15.7	0	1.4	0.904	1.82		1.50×10^{-4}
	900	0		1	0.17	0.13	0.140	1.84×10^{-5}
		23.5	249	0.46	0.83	0.64		1.94×10^{-4}
	1500	0		1	0.176	0.33	0.152	4.96×10^{-5}
		24	839	0.37	0.824	1.53		6.37×10^{-4}
^{56}Fe	500	0		1	0.136	0.15	0.034	4.98×10^{-6}
		9	4	1.3	0.864	0.94		2.43×10^{-5}
	900	0		1	0.208	0.1	0.041	4.11×10^{-6}
		12.9	273	0.57	0.792	0.39		2.76×10^{-5}
	1500	0		1	0.233	0.33	0.044	1.44×10^{-5}
		12	902	0.5	0.767	1.08		9.45×10^{-5}

[a] *Relative dose behind the absorber and beam fluence to 1 μm²/Gy from GERMcode.*
[b] *Based on the Z-group of dose from the HZETRN prediction.*

as on the Martian surface or within a solar particle event storm shelter, low energy neutrons and concurrent depletion of HZE particles by the Martian atmosphere suggest a distinct reference field could be considered to simulate neutron spectra following the results of Kim et al. (13).

There are many areas of space radiation research which should continue to focus on track segment irradiation, including mechanistic studies of radiation quality and the development of data bases for improving radiation quality function models or dose-rate effects for cancer and non-cancer risks using multiple single particle species (MSPS) approaches. Studies of end-points such as chromosomal aberrations have already been made in space where biophysical models are shown to well produce measurements from astronauts (32). Prediction of the frequency of

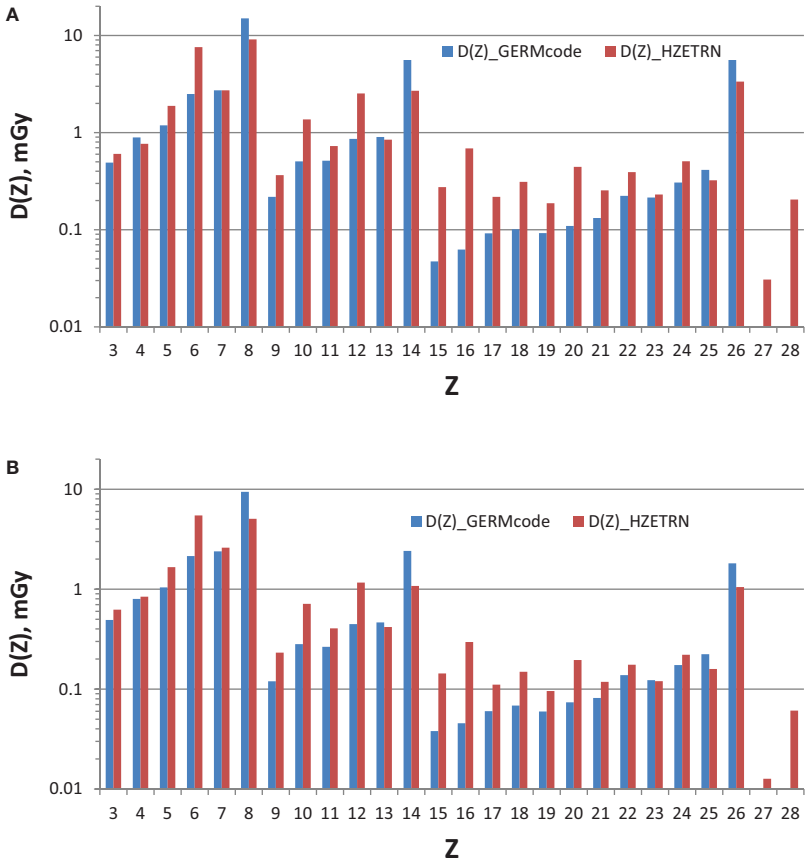

FIGURE 3 | *Z*-distribution of dose at 5-cm tissue by the GCR reference field using nine HZE beam-energy combinations compared to those by the simulated full GCR spectrum at 1977 solar minimum inside habitat wall (A) and transfer vehicle (B).

dicentric aberrations in lymphocytes (5.78×10^{-3}) were compared to data from a Mir-18 crew member ($6.4 + 2.0 \times 10^{-3}$) and demonstrated good agreement (33). To repeat DNA damage experiments at a GCR simulator or other similar cell culture experiments is not recommended by the present authors because it would add little to reducing the uncertainties in risk estimates. Experiments with animals to reduce risk estimate uncertainties present other considerations as discussed next.

We have shown that the duration of a chronic GCR-simulated exposure to accurately reproduce the space situation should be several weeks or longer. However, a precise estimate will require understanding underlying mechanism for risk for the biological model considered. DNA damage processing is complete within a few hours for low LET radiation and 1–2 days for high LET radiation (34–36). For example, high LET radiation has been shown to have a preference for homologous recombination repair (37) due to the generation of short fragments (36) due to clustered DNA damage. Tissue responses including the TGFβ-Smad signaling pathway have been shown to control the DNA damage response (38–40) and can remain activated for a week or longer *in vivo*. Long relaxation times may be important for fluence-rate and exposure time considerations as described above. Other considerations are the turn-over times of different tissue types and the distinct mechanisms for targeted and non-targeted effects in cancer risk. In addition, slowly and rapidly dividing tissues could present distinct optimal chronic exposure times, and abscopal effects should be considered.

Animal experiments over several weeks present some unique challenges to particle accelerator experiments. Older studies of cancer risks with fission neutrons and gamma-rays supported by the Atomic Energy Commission and the Department of Energy (DoE) in the United States (41–43) were performed for as long as 60-days using specially designed irradiation facilities to house animals and were often restricted to an 8 h/day exposure regime to both facilitate animal use feasibility and represent conditions of radiation workers at nuclear reactors. The current exposure room at NSRL was not designed for long-term animal exposure. Astronauts are exposed in space on a 24 h/day cycle and the restriction to an 8 h/day exposure could introduce differences in biological responses due to circadian rhythm effects or unrepresentative DNA damage processing, cell cycle, or signal transduction cycles. Long-term exposure studies of CNS effects and interest in simulation of microgravity effects on radiation responses using the hind-limb suspension model in mouse have not been made in the past and it

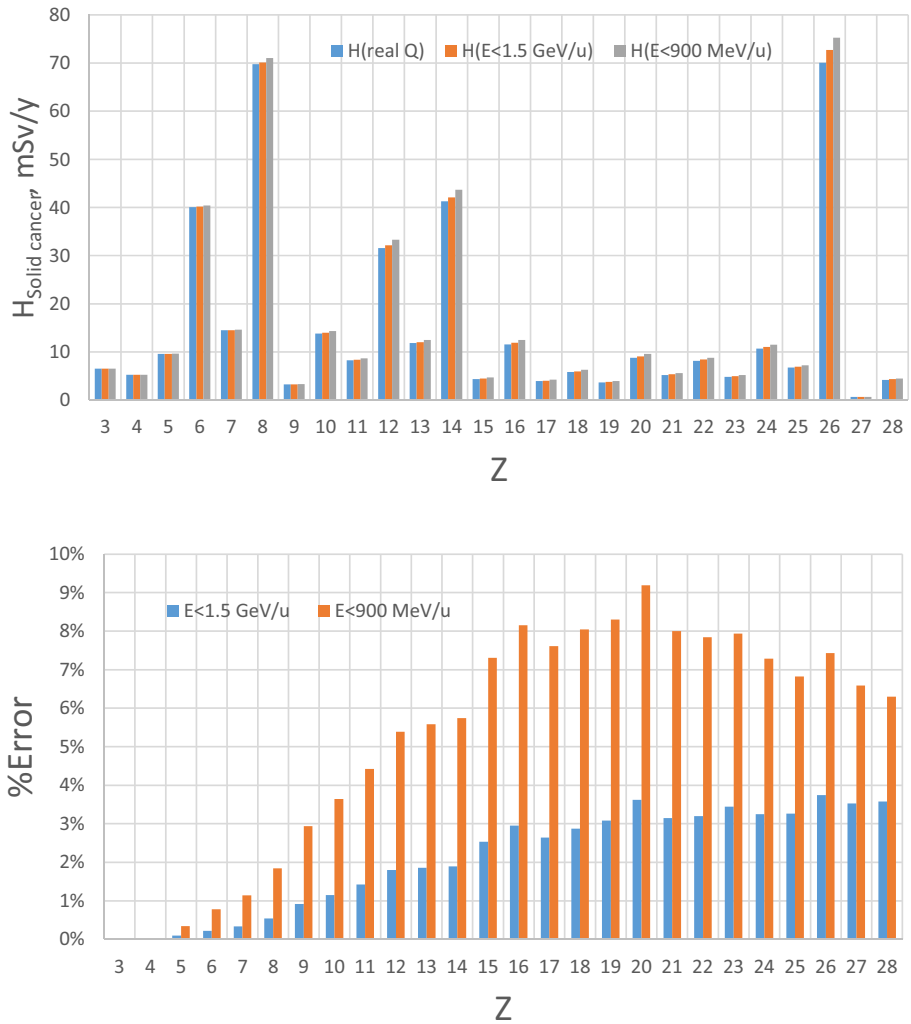

FIGURE 4 | Estimate of error of GCR simulator by accelerator energy cutoff of 1.5 GeV/u or 900 MeV/u for solid cancer risk at 5-cm tissue equivalent depth inside habitat wall from exposure to annual GCR at 1977 solar minimum.

is not clear what experimental validation is needed prior to such studies under chronic irradiation conditions.

In considering CNS risks changes to cognition including memory can be through multiple mechanisms leading to changes to synapse (7). Synapse formation, stabilization, and decay have a fast actin dependent component (less than one day) and a slow plasticity dependent component (days to years) (32, 44). The average lifetime of synapses will vary in different regions of the brain and in comparison of mice or rats and humans. A black-box approach could consider varying the duration of the exposure, from a few days to a few weeks, to observe how CNS responses are changing with exposure time. However such experiments would involve large beam-time costs at current rates of >$6000 (US) per beam-time hr, present new experimental challenges to CNS radiobiology with animal models, and limit the number of studies to be performed because of their duration and time constraints at NSRL. Therefore if absent of an important scientific hypothesis, such studies should not be pursued. Development of the knowledge to predict CNS risks is favored over such black-box approaches.

There are also practical limitations to long-term exposures of a large number of mice or other small animals. The number of studies that can be performed at duration of month or longer is likely restricted to few per year, and the large costs of beam time that would result from such studies is a major obstacle. Several hundred highly constrained mice can be irradiated in a 60×60 cm^2 beam configuration at NSRL for acute irradiation, however this approach is not practical for an exposure of several weeks including the requirement of replicate experiments for biological research. Risk model validation experiments are currently limited by the shortcomings in available biological models of human risks, and the larger number of risks of interest (1–7). In addition the statistical errors in animal model data for track segment irradiations would likely complicate the interpretation of the outcome of a validation experiment with a GCR simulator.

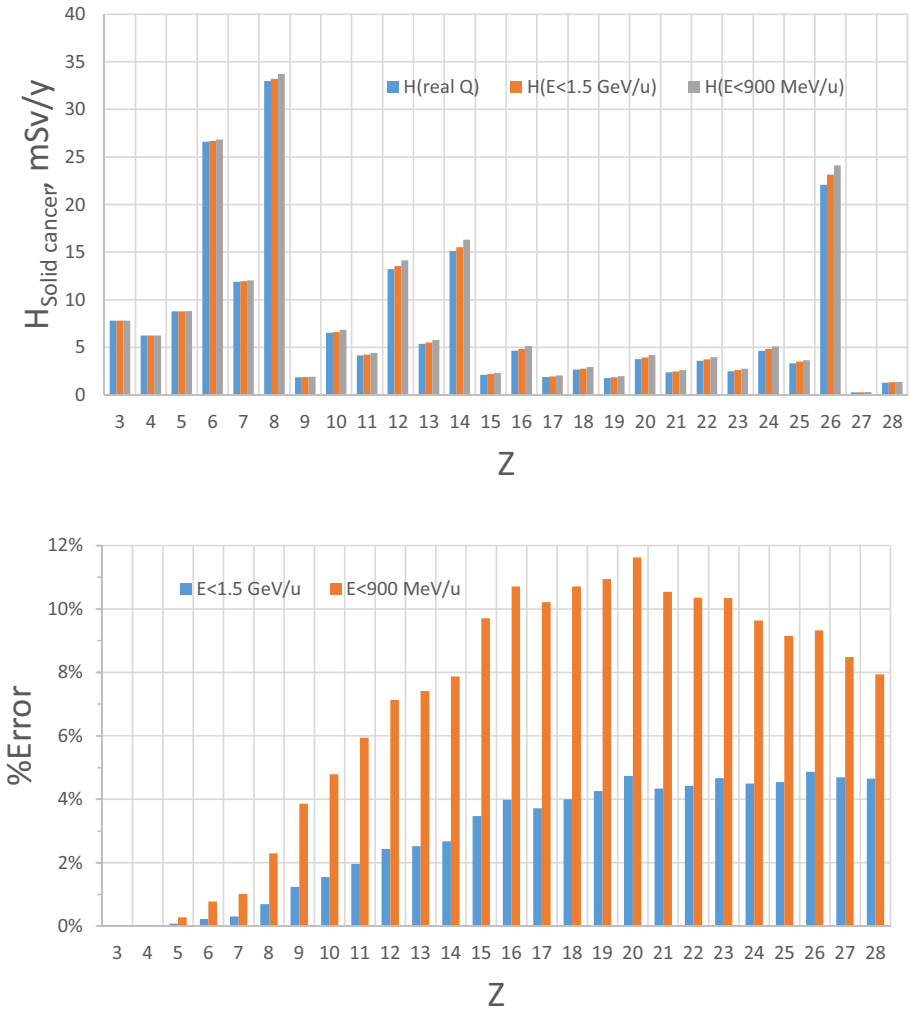

FIGURE 5 | Estimate of error of GCR simulator by accelerator energy cutoff of 1.5 GeV/u or 900 MeV/u for solid cancer risk at 5-cm tissue equivalent depth inside transfer vehicle from exposure to annual GCR at 1977 solar minimum.

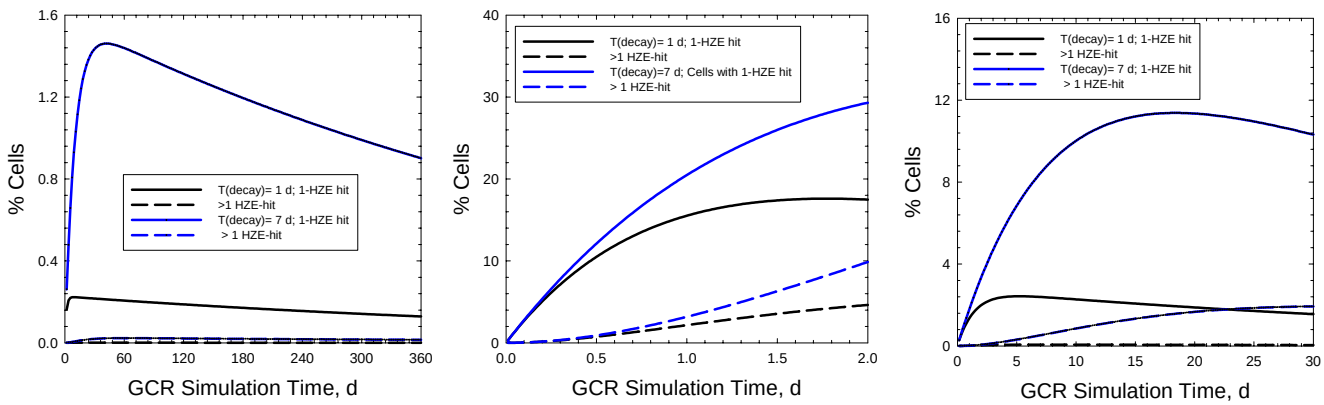

FIGURE 6 | Predictions of percentage of cells with 1 or >1 HZE particle hits as a function of exposure time in chronic irradiations with 20 g/cm^2 aluminum and 5-cm tissue shielding. Results for a 1-year mission **(A)** are compared to 30-days and 2-days ground-based simulations **(B,C)** for biological response relaxation times of 1- or 7-days assuming cell areas of 100 μm^2.

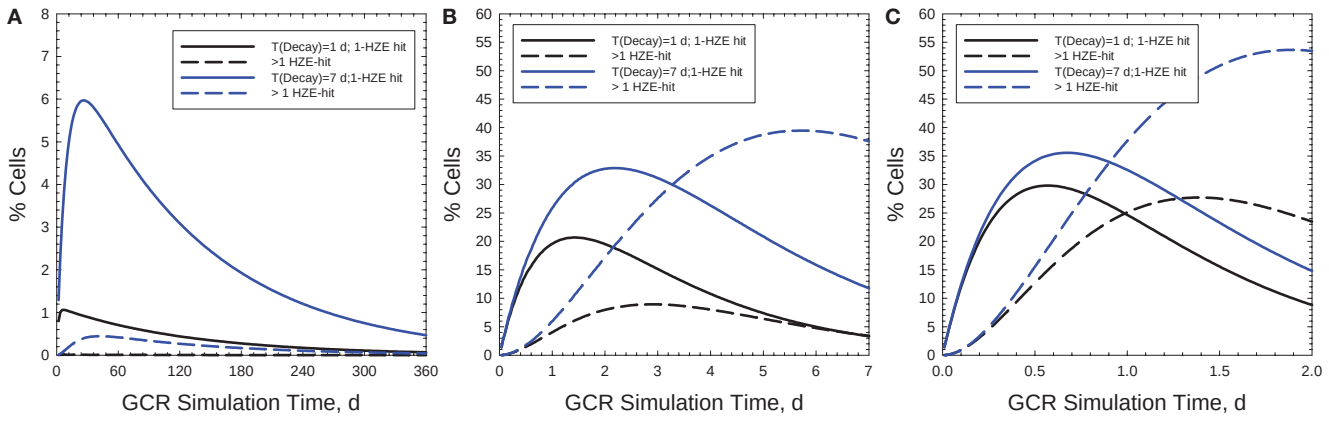

FIGURE 7 | Predictions of percentage of cells with 1 or >1 HZE particle hits as a function of exposure time in chronic irradiations with 20 g/cm^2 aluminum and 5-cm tissue shielding. Results for a 1-year mission **(A)** are compared to 30- and 2-days ground-based simulations **(B,C)** for biological response relaxation times of 1 or 7-day assuming cell areas of 500 μm^2.

It is of interest to explore new research areas that could be considered with a GCR simulation approach. One area of interest is a possible scientific hypothesis related to differences in biological responses for a mixed-field of particles of varying track structure due to synergistic interactions of particles of different radiation qualities. Very few low dose fractionation studies with protons and a single HZE particle species (45, 46) or fractionated HZE particles (47, 48) have been made and would be needed first to understand if synergistic effects are a valid concern. The few studies that have been made suggest that mixed radiation field synergistic effects, which violate the general principal of additivity used in radiation protection, will only occur if the mean inter-fraction times are <8 h (45–48). The validity of the additivity assumption used in radiation protection for the biological dose estimated for the endpoint of chromosomal aberrations was recently supported by a comparison of ISS crew-members participating in multiple ISS missions (49).

Another potential area of research with a GCR simulation is in the testing of biological countermeasures (BCM) with drug screening of panels of agents and different dosages for various space radiation risks. For BCM research, the matrix of risk types, radiation types and doses to be studied with different drug types and dosages in animals suggest the traditional approach to track segment irradiation may be at a very high cost for current space radiobiology efforts. On the other hand, the goals of BCM research are underdeveloped at this time. Acute risk BCM's may not be needed because SPE organ doses are readily mitigated with shielding and alert dosimetry. Acute risk BCM's may also be antagonistic to risks for late effects if they suppress apoptosis. Observations of low RBE's for leukemia induction by HZE particles (50) suggest BCMs for this risk may not be needed except for an unexpected SPE exposures during extra-vehicular activity. For the risks of CNS and non-cancer late effects even less is known, including if dose thresholds for these risks will be exceeded for specific exploratory space missions, or how to extrapolate from animal models to human. At this time, BCM's for solid cancer risks stand out as being a likely requirement for space missions. However, the mechanisms leading to the large RBE for HZE particle solid cancer and qualitative differences in tumor spectrum found in mice are poorly understood at this time (11). For mechanistic studies of GCR biological effects, the use of a GCR simulator would carry with it important concerns due to the complication of not knowing which spectral components produced an observed effect.

In summary, the development of our GCR simulation approach at NSRL is a promising long-term research goal especially for potential drug screening and BCM development approaches. However before such studies should be pursued, the mechanisms of space radiation risks and their underlying radiation quality and dose dependences need to be established. We find that the use of a GCR simulator to achieve uncertainty reduction in risk models suffers from several detrimental issues. Our analysis shows that for accelerator GCR simulations, a large percentage of cells will be hit with two or more particles in a simulated chronic exposure of a week or less and thus would not properly simulate the space condition. Therefore exposures of several weeks or longer will be needed to avoid such artifacts. This error will probably be higher for CNS risks compared to cancer risks because of the larger sizes of neuronal structures. GCR simulations for chronic times approaching 30 days are warranted to avoid any high dose-rate artifacts that will occur for shorter chronic exposures. There is no single "validation model" that can be suggested to measure risk and therefore is only through the totality of information from experimental and theoretical research that risk estimates are improved. Barring direct irradiation of humans at a GCR simulator, it is only through the development of more accurate biological models of space radiation risks and the underlying theoretical descriptions that these goals can be met, while the experimental complication of the use of mixed radiation fields would not likely facilitate this understanding. Near-term research focus should remain on these goals using track segment irradiations at low doses of HZE particles (<0.1 Gy) in support of the safety and well-being of astronauts participating in long-term space missions.

References

1. Cucinotta FA, Schimmerling W, Wilson JW, Peterson LE, Badhwar GD, Saganti PB, et al. Space radiation cancer risks and uncertainties for Mars missions. *Radiat Res* (2001) **156**:682–8. doi:10.1667/0033-7587(2001)156[0682:SRCRAU]2.0.CO;2
2. Cucinotta FA, Durante M. Cancer risk from exposure to galactic cosmic rays: implications for space exploration by human beings. *Lancet Oncol* (2006) **7**:431–5. doi:10.1016/S1470-2045(06)70695-7
3. Durante M, Cucinotta FA. The physical basis for radiation protection in space travel. *Rev Mod Phys* (2011) **83**:1245–81. doi:10.1103/RevModPhys.83.1245
4. Cucinotta FA, Alp M, Sulzman FM, Wang M. Space radiation risks to the central nervous system. *Life Sci Space Res* (2014) **2**:54–69. doi:10.1016/j.lssr.2014.06.003
5. Cucinotta FA, Manuel F, Jones J, Izsard G, Murray J, Djojonegoro B, et al. Space radiation and cataracts in astronauts. *Radiat Res* (2001) **156**:460–6. doi:10.1667/0033-7587(2001)156[0460:SRACIA]2.0.CO;2
6. Chylack LT Jr, Feiveson AH, Peterson LE, Tung WH, Wear ML, Marak LJ, et al. NASCA report 2: longitudinal study of relationship of exposure to space radiation and risk of lens opacity. *Radiat Res* (2012) **178**:25–32. doi:10.1667/RR2876.1
7. Cucinotta FA, Kim MY, Chappell LJ, Huff JL. How safe is safe enough: radiation risks for a human mission to Mars. *PLoS One* (2013) **8**(10):e74988. doi:10.1371/journal.pone.0074988
8. National Council on Radiation Protection and Measurements (NCRP). *Information Needed to Make Radiation Protection Recommendations for Space Missions Beyond Low-Earth Orbit*. Bethesda MD: The NCRP (2006). NCRP Report No. 153
9. Cucinotta FA, Kim MY, Chappell L. *Space Radiation Cancer Risk Projections and Uncertainties - 2012* Washington, DC: NASA (2013). NASA TP 2013-217375.
10. Badhwar GB, Cucinotta FA, O'Neill PM. An analysis of interplanetary space radiation exposure for various solar cycles. *Radiat Res* (1994) **138**:201–8. doi:10.2307/3578590
11. Cucinotta FA. Space radiation risks for astronauts on multiple international space station missions. *PLoS One* (2014) **9**(4):e96099. doi:10.1371/journal.pone.0096099
12. Hassler DM, Zeitlin C, Wimmer-Schweingruber RF, Ehresmann B, Rafkin S, Eigenbrode J, et al. The radiation environment on the surface of Mars measured on the Mars science laboratory's curiosity rover. *Science* (2014) **343**:6169–73. doi:10.1126/science.1244797
13. Kim MY, Cucinotta FA, Nounu H, Zeitlin C, Hassler DM, Rafkin SCR, et al. Comparison of Martian surface ionizing radiation measurements from MSL-RAD with Badhwar-O'Neill 2011/HZETRN model calculations. *J Geophys Res* (2014) **119**:1311–21. doi:10.1002/2013JE004549
14. Lowenstein DI, Rusek A. Technical developments at the NASA space radiation laboratory. *Radiat Environ Biophys* (2007) **46**:91–4. doi:10.1007/s00411-006-0084-x
15. NASA. *Report on the NSRL Mixed-Fields Radiation Capability Simulation Workshop. NASA Internal Report* Washington, DC: NASA (2008).
16. Allesi JG, Barton D, Beebe E, Bellavia S, Gould O, Kponou A, et al. The Brookhaven National Laboratory electron beam ion source for RHIC. *Rev Sci Instrum* (2010) **81**(2):02A509. doi:10.1063/1.3292937
17. Zeitlin C, Hassler DM, Cucinotta FA, Ehresmann B, Wimmer-Schweingruber RF, Brinza DE, et al. Measurements of energetic particle radiation in transit to Mars on the Mars science laboratory. *Science* (2013) **340**:1080–4. doi:10.1126/science.1235989
18. Wilson JW, Townsend LW, Chun SY, Buck WW, Khan F, Cucinotta FA. *BRYNTRN: A Baryon Transport Code*. Washington, DC: NASA. NASA TM-1988-4037.
19. Cucinotta FA, Wilson JW, Shinn JL, Badavi FF, Badhwar GD. Effects of target fragmentation on evaluation of LET spectra from space radiation: implications for space radiation protection studies. *Radiat Meas* (1996) **26**:923–34. doi:10.1016/S1350-4487(96)00070-4
20. Badhwar GD, O'Neill PM. An improved model of galactic cosmic radiation for space exploration missions. *Nucl Tracks Radiat Meas* (1992) **20**:403–10. doi:10.1016/1359-0189(92)90024-P
21. Wilson JW, Townsend LW, Shinn JL, Cucinotta FA, Costen RC, Badavi FF, et al. Galactic cosmic ray transport methods: past, present, and future. *Adv Space Res* (1994) **14**:841–52. doi:10.1016/0273-1177(94)90549-5
22. Cucinotta FA, Wilson JW, Townsend LW. Abrasion–ablation model for neutron production in heavy ion collisions. *Nucl Phys A* (1997) **619**:202–12. doi:10.1016/S0375-9474(97)00130-9
23. Cucinotta FA, Kim MY, Schneider I, Hassler DM. Description of light ion production cross sections and fluxes on the Mars surface using the QMSFRG model. *Radiat Environ Biophys* (2007) **46**:101–6. doi:10.1007/s00411-007-0099-y
24. Cucinotta FA, Townsend LW, Wilson JW. Production of ^{3}H at large momentum in α-^{12}C collisions at 2A GeV. *Phys Lett B* (1992) **282B**:1–6. doi:10.1016/0370-2693(92)90469-K
25. Cucinotta FA, Townsend LW, Wilson JW. *Description of Helium-Nucleus Interaction Cross Sections for Cosmic Ray Shielding Studies*. Washington, DC: NASA. NASA TP-1993-3285.
26. Cucinotta FA, Plante I, Ponomarev AL, Kim MY. Nuclear interactions in heavy ion transport and event-based risk models. *Radiat Prot Dosimetry* (2011) **143**:384–90. doi:10.1093/rpd/ncq512
27. Yang H, Magpayo N, Rusek A, Chiang I-H, Sivertz M, Held KD. Effects of very low fluences of high-energy protons or iron ions on irradiated and bystander cells. *Radiat Res* (2011) **176**:695–705. doi:10.1667/RR2674.1
28. Cucinotta FA, Nikjoo H, Goodhead DT. Comment on the effects of delta-rays on the number of particle-track transversals per cell in laboratory and space exposures. *Radiat Res* (1998) **150**:115–9. doi:10.2307/3579651
29. Cucinotta FA, Katz R, Wilson JW, Townsend LW, Nealy JE, Shinn JL. *Cellular Track Model of Biological Damage to Mammalian Cell Cultures from Galactic Cosmic Rays*. Washington, DC: NASA. NASA TP-1991-3055.
30. Rabin BM, Shukitt-Hale B, Joseph JA, Carrihill-Knoll KL, Carey AN, Cheng V. Relative effectiveness of different particles and energies in disrupting behavioral performance. *Radiat Environ Biophys* (2007) **46**:173–7. doi:10.1007/s00411-006-0071-2
31. Bertucci A, Durante M, Gialanella G, Grossi G, Manti L, Pugliese M, et al. Shielding of relativistic protons. *Radiat Environ Biophys* (2007) **46**:107–12. doi:10.1007/s00411-006-0088-6
32. Okabe S, Kim HD, Miwa A, Kuriu T, Okaso H. Continual remodeling of postsynaptic density and its regulation of synaptic activity. *Nat Neurosci* (1999) **2**:804–11. doi:10.1038/12175
33. Cucinotta FA, Wilson JW, Williams JR, Dicello JF. Analysis of Mir-18 results for physical and biological dosimetry: radiation shielding effectiveness in LEO. *Radiat Meas* (2000) **132**:181–91. doi:10.1016/S1350-4487(99)00273-5
34. Leatherbarrow EL, Harper J, Cucinotta FA, O'Neill P. Effect of track structure and LET on γ-H2AX foci formation as a beacon of DNA damage in mammalian cells. *Int J Radiat Biol* (2006) **82**:111–8. doi:10.1080/09553000600599783
35. Asaithamby A, Uematsu N, Chatterjee A, Story MD, Burma S, Chen DJ. Repair of HZE-particle-induced DNA double-strand breaks in normal human fibroblasts. *Radiat Res* (2008) **169**:437–46. doi:10.1667/RR1165.1
36. Li Y, Qian H, Wang Y, Cucinotta FA. A stochastic model of DNA fragment rejoining. *PLoS One* (2012) **7**(9):E44293. doi:10.1371/journal.pone.0044293
37. Wang H, Wang X, Zhang P, Wang Y. The Ku-dependent non-homologous end-joining but not other repair pathway is inhibited by high linear energy transfer ionizing radiation. *DNA Repair* (2008) **73**:725–33. doi:10.1016/j.dnarep.2008.01.010
38. Kirshner J, Jobling MF, Pajares MJ, Ravani SA, Glick A, Lavin M, et al. Inhibition of TGFβ1 signaling attenuates ATM activity in response to genotoxic stress. *Cancer Res* (2006) **66**:10861–8. doi:10.1158/0008-5472.CAN-06-2565
39. Wang M, Saha J, Hada M, Anderson JA, Pluth JM, O'Neill P, et al. Novel Smad proteins localize to IR-induced double-strand breaks: interplay between TGFβ and ATM pathways. *Nucleic Acids Res* (2013) **41**:933–42. doi:10.1093/nar/gks1038
40. Barcellos-Hoff MH, Cucinotta FA. New tricks for an old fox: impact of TGFβ on the DNA damage response and genomic stability. *Sci Signal* (2014) **7**:341–5. doi:10.1126/scisignal.2005474
41. Upton AC. Radiological effects of low doses. Implications for radiological protection. *Radiat Res* (1977) **71**:51–74. doi:10.2307/3574712
42. Ullrich RL, Storer JB. Influence of γ irradiation on the development of neoplastic disease in mice III. Dose-rate effects. *Radiat Res* (1979) **80**:325–42.

43. Grahn D, Lombard LS, Carnes BA. The comparative tumorigenic effects of fission neutrons and Cobalt-60 γ rays in $B6CF_1$ mouse. *Radiat Res* (1992) **129**:19–36. doi:10.2307/3577899
44. Matsuzaki M, Honkura N, Ellis-Davies GC, Kasai H. Structural basis of long-term potentiation in single dendritic spines. *Nature* (2004) **429**:761–6. doi:10.1038/nature02617
45. Bennett PV, Cutter NC, Sutherland BM. Split-dose exposures versus dual ion exposure in human cell neoplastic transformation. *Radiat Environ Biophys* (2007) **46**:119–24. doi:10.1007/s00411-006-0091-y
46. Hada M, Meador JA, Cucinotta FA, Gonda SR, Wu H. Chromosome aberrations induced by dual exposure of protons and iron ions. *Radiat Environ Biophys* (2007) **46**:125–30. doi:10.1007/s00411-006-0083-y
47. Alpen EL, Powers-Risius P, Curtis SB, DeGuzman R, Fry RJM. Fluence-based relative biological effectiveness for charged particle carcinogenesis in mouse harderian gland. *Adv Space Res* (1994) **14**:573–81. doi:10.1016/0273-1177(94)90512-6
48. Hada M, Chappell LJ, Wang M, George KA, Cucinotta FA. On the induction of chromosomal aberrations at fluence of less than one HZE particle per cell nucleus. *Radiat Res* (2014) **182**:368–79. doi:10.1667/RR13721.1
49. George KA, Rhone J, Beitman A, Cucinotta FA. Cytogenetic damage in the blood lymphocytes of astronauts: effects of repeat long-duration space missions. *Mutat Res* (2013) **756**:165–9. doi:10.1016/j.mrgentox.2013.04.007
50. Weil MM, Ray FA, Genik PC, Yu Y, McCarthy M, Fallgren CM, et al. Effects of ^{28}Si ions, ^{56}Fe ions, and protons on the induction of murine acute myeloid leukemia and hepatocellular carcinoma. *PLoS One* (2014) **9**(8):e104819. doi:10.1371/journal.pone.0104819

Conflict of Interest Statement: The authors declare that the research was conducted in the absence of any commercial or financial relationships that could be construed as a potential conflict of interest.

Copyright © 2015 Kim, Rusek and Cucinotta. This is an open-access article distributed under the terms of the Creative Commons Attribution License (CC BY). The use, distribution or reproduction in other forums is permitted, provided the original author(s) or licensor are credited and that the original publication in this journal is cited, in accordance with accepted academic practice. No use, distribution or reproduction is permitted which does not comply with these terms.

frontiers in Oncology

HYPOTHESIS AND THEORY
published: 22 February 2016
doi: 10.3389/fonc.2016.00038

Personalized Cancer Risk Assessments for Space Radiation Exposures

Paul A. Locke[1] *and Michael M. Weil*[2]*

[1] Department of Environmental Health Sciences, Johns Hopkins Bloomberg School of Public Health, Baltimore, MD, USA,
[2] Department of Environmental and Radiological Health Sciences, Colorado State University, Fort Collins, CO, USA

Individuals differ in their susceptibility to radiogenic cancers, and there is evidence that this inter-individual susceptibility extends to HZE ion-induced carcinogenesis. Three components of individual risk: sex, age at exposure, and prior tobacco use, are already incorporated into the NASA cancer risk model used to determine safe days in space for US astronauts. Here, we examine other risk factors that could potentially be included in risk calculations. These include personal and family medical history, the presence of pre-malignant cells that could undergo malignant transformation as a consequence of radiation exposure, the results from phenotypic assays of radiosensitivity, heritable genetic polymorphisms associated with radiosensitivity, and postflight monitoring. Inclusion of these additional risk or risk reduction factors has the potential to personalize risk estimates for individual astronauts and could influence the determination of safe days in space. We consider how this type of assessment could be used and explore how the provisions of the federal Genetic Information Non-discrimination Act could impact the collection, dissemination and use of this information by NASA.

Keywords: genetic susceptibility, radiation carcinogenesis, cancer risk, space radiation, cancer

OPEN ACCESS

Edited by:
Francis A. Cucinotta,
University of Nevada Las Vegas, USA

Reviewed by:
Yanwen Chen,
Case Western Reserve University, USA
David Gerhard Hoel,
Medical University of South Carolina, USA
Eliedonna Cacao,
University of Nevada Las Vegas, USA

***Correspondence:**
Michael M. Weil
michael.weil@colostate.edu

Specialty section:
This article was submitted to Radiation Oncology, a section of the journal Frontiers in Oncology

Received: *15 October 2015*
Accepted: *05 February 2016*
Published: *22 February 2016*

Citation:
Locke PA and Weil MM (2016) Personalized Cancer Risk Assessments for Space Radiation Exposures. Front. Oncol. 6:38. doi: 10.3389/fonc.2016.00038

INTRODUCTION

In spaceflight, astronauts are exposed to a radiation environment consisting of a uniform flux of background galactic cosmic radiation with intermittent pulses of high energy protons from solar particle events. As employers, NASA must comply with the federal Occupational Safety and Health Act, which (among other things) requires NASA to set radiation exposure limits to protect the health of astronauts on space missions (1). At the time of this writing, NASA's approach to setting permissible radiation exposure limits is unique among federal agencies. The risk of developing a fatal cancer from radiation exposure is calculated using a regularly updated model, currently NSCR 2012 (2) as recently revised (3). Career exposures are limited to doses that will not result in more than a 3% probability of fatal cancer (risk of exposure-induced death or REID) at the 95% upper confidence interval of the risk calculation. For an individual astronaut, the risk calculation takes into account the astronaut's age at exposure and sex, and assumes that he or she is a non-smoker. Because the risk for most radiation-induced cancers decreases with older ages at exposure and risks are greater in females than males, the effect is to allow less cumulative flight time for female and younger astronauts. Several reference missions, including a near Earth asteroid mission and Mars missions exceed the 3% REID for fatal cancer; so do multiple ISS missions exceeding a total duration of about 24 months for male astronauts and about 18 months for female astronauts during solar minimum (3, 4). This

article examines whether possible personalized risk approaches might be used to characterize these risks. It is important to point out that these excess risks also raise important ethical issues that are beyond the scope of this article (5).

The inclusions of age at exposure, sex, and smoking status in setting radiation dose limits can be viewed as steps toward personalizing risk assessments. There are additional approaches, either feasible or currently available, that could further personalize these assessments. Personalized risk calculations could potentially be used for pre-employment screening to select crew members for particular flights or could be provided to crew members and their flight surgeons for personal medical counseling with confidentiality safeguards. The legal issues raised by each of these uses are discussed below.

This article considers evidence that inter-individual differences contribute to cancer risk from radiation exposures, how these differences can be detected and how the information might be used. In addition, this article discusses how potential approaches for the detection of inter-individual differences in susceptibility to radiogenic cancer could impinge on the federal Genetic Information Non-discrimination Act of 2008 (GINA) and explores whether an employer (i.e., NASA) could lawfully use the information in employment or work assignment decisions.

Cancer risk is not generic. There are specific cancers that pose the greatest risks of exposure induced death. Using calculated REIDs from NSCR 2012 for 45-year-old male and female astronauts [Tables A3 and A7 in Ref. (2)], the greatest risks are for lung, stomach, colon, ovarian, breast, liver, and bladder cancers for females, and lung, colon stomach, bladder, liver, and prostate cancers for males. Leukemia is also a risk for both sexes. Each of these tumor types is likely unique in the extent to which susceptibility to them differs between individuals and in their amenability to preclinical detection.

APPROACHES

Personal and Family Medical History

Relative risk and absolute risk models and combinations of the two are used in risk calculations. Relative risk is calculated as a dose-dependent multiple of the background incidence of a cancer, whereas absolute risk is an added number of cases per unit dose that is independent of the background incidence. Which model best fits epidemiological data depends on the tumor type being modeled. The relative risk model assumes that radiation increases the incidence of spontaneous tumors and implicit in that assumption is that radiogenic cancers are the same or nearly the same as their spontaneous counterparts. There is evidence that the relative risk model reflects biological reality for at least some radiogenic cancers. The few radiogenic tumors that have been characterized carry the same cytogenetic and molecular aberrations as a subset of spontaneous tumors of the same histotype (6–11). For example, sporadic acute myeloid leukemias (AML) have a range of recurrent chromosomal aberrations, predominantly translocations. However, radiation-induced AML are generally associated with deletions on chromosome 5 and/or 7 (11), cytogenetic lesions that occur in only a few percent of sporadic AML (12). The most plausible explanation is that radiation can contribute a step or steps to some of the pathways leading to sporadic leukemias (e.g., those involving chromosome 5 or 7 deletions), but radiation is ineffective in complementing other leukemogenic pathways.

If the goal is to move from a population-based risk calculation to a personalized risk calculation for setting permissible space radiation doses for an individual astronaut, one possible approach would be to use the astronaut's background risk in place of the population background risk as the baseline for relative risk calculations. Individuals differ in their susceptibility to spontaneous cancers due to a number of factors related to lifestyle, genetic background, and poorly characterized environmental exposures. For example, a family history of some cancers (e.g., colorectal and breast cancer) confers greater risk. An individual with a first degree relative diagnosed with a colorectal cancer (CRC) is 2.4-fold more likely to develop CRC than someone without an affected relative (13). For that matter, the monozygotic (identical) twin of a man with colon cancer has about a 7-fold greater risk of developing colon cancer than a man with an unaffected twin, for woman with an affected monozygotic twin the risk is about 14-fold (14).

Risk calculators are readily available for some sporadic cancers. Several have been developed that assess individual breast cancer risk based on combinations of inputs on family history of breast and ovarian cancer, current age, race or ethnicity, breast biopsy history, age at menarche, breast tissue mammographic density, and reproductive history (15). Potentially, some of these inputs might be useful in personalizing radiogenic breast cancer risk calculations. Risk calculators are also available for CRC (16–18). The information input into these calculators includes family history, sex, current age, race and ethnicity, diet, body mass index, screening history, polyp history, use of aspirin, non-steroidal anti-inflammatory drugs, oral contraceptives and estrogen replacement, physical activity, smoking, and alcohol consumption.

Synopsis

Individual risk of radiation carcinogenesis might be more accurately calculated by including family history of cancer and/or personal medical history including a history of colon polyps or breast biopsies. An assumption in this approach is that breast or colon cancer risk from space radiation exposure can be predicted, at least partly, from background risk by a transfer model incorporating multiplicative risk. In the current risk model, this assumption is made for CRC through the use of a mixture model (0.7 multiplicative and 0.3 additive) [Ref. (2), p. 80]. An additive model is used for breast cancer because it better fits results of a meta-analysis, not because of a biological basis.

Detection of Preneoplastic Cells and Dormant Microtumors

Preneoplastic cells and dormant microtumors are frequently detectable in clinically normal individuals (19, 20), and it has been proposed that radiation exposure can lead to their promotion and/or progression. The best evidence for this comes from studies of leukemia. In 2005, Nori Nakamura advanced the

hypothesis some individuals harbor clones of hematopoietic cells with preleukemic mutations and consequently are susceptible to radiogenic leukemias (21). The putative mechanism is that radiation exposure induces additional leukemogenic mutations in the preleukemic cells leading to overt disease. Nakamura's hypothesis is based on epidemiological investigations of leukemia in atomic bomb survivors and the findings of Mori et al. (22) showing that leukemia relevant translocations can be detected in the blood of about 1% of newborns, the vast majority of whom will never develop leukemia.

The detection of preleukemic cells in peripheral blood samples from some clinically normal individuals has been extended to adults [e.g., Ref. (23–25)]. Data from large-scale whole exome sequencing studies using peripheral blood cells as a DNA source have been mined to identify individuals that carry clonal expanded somatic mutations in leukemia related genes. The frequency of people harboring these cells increases with age and is associated with an increased risk of hematopoietic cancer (26, 27). That increased risk suggests that at least some of the mutations detected in mature circulating blood cells occurred in stem or progenitor cells primitive enough to undergo leukemic transformation.

Perhaps the best evidence for the existence of preleukemic cells that can be driven to complete leukemic transformation by exposure to a genotoxic agent comes from recent observations by Wong and coworkers (28). Radiation-induced AML commonly carry *TP53* mutations. Wong found that two patients who developed AML following cytotoxic chemotherapy had identical *TP53* mutations in their leukemic cells and in blood samples collected prior to therapy. The likely explanation is that preleukemic cells (those with *TP53* mutations) progressed to frank leukemia as a consequence of cytotoxic chemotherapy, and the inference is that radiation exposure could have a similar effect.

Screening individuals for preleukemic cells using peripheral blood samples can be accomplished with existing technologies, either SNP arrays for genomic gains or losses or uniparental disomy, or next generation sequencing for defined mutations in clonal populations.

Some pre-invasive tumors can be detected *in situ*, with mammography for the detection of ductal carcinoma *in situ* and colonoscopy for the detection of adenomatous polyps being commonly used screens. Whether these neoplasias can be driven to malignancy by radiation exposure are unknown at this time and, consequently, the value of pre-exposure screening to lower radiogenic cancer risk is also unknown.

New early detection methods for a range of cancers are being clinically evaluated, and some examples that are relevant for tumor types of greatest interest for space flight are briefly mentioned here. Promising results have been reported for a CRC early detection test based on the identification of mutant *KRAS* sequences in DNA from tumor cells shed into stool. The assay is less intrusive than colonoscopy and therefore more likely to be used. Mammary epithelial cells are accessible for cytological screening for premalignant cells (29), and the test is offered to women at high risk for breast cancer. Its predictive value has not yet been established, but there are ongoing investigations on this approach including the incorporation of biomarker detection in the test. Low-dose computerized tomography (LDCT) lung cancer screening has been shown to decrease lung cancer mortality in heavy smokers or former smokers (30). LDCT frequently detects lesions in nonsmokers, but whether these lesions are dormant microtumors that can be promoted by radiation exposure is unknown.

Synopsis

Assays are currently available or in development for the detection of preneoplastic cells or dormant microtumors that could potentially undergo promotion or progress to frank cancer as a consequence of radiation exposure. Individuals with these incipient malignancies may be at higher risk for radiogenic cancer than those without. The various testing procedures involve simple imaging, the detection of overexpressed or aberrant proteins, or the detection of somatic mutations in DNA from cells collected using minimally invasive techniques. The potential of premalignant cells or dormant microtumors to progress as a consequence of radiation exposure is not known.

Phenotypic Assays of Sensitivity

The development of cell-based assays to identify radiation oncology patients sensitive to normal tissue injury has been an area of active research for many years. A logical extension of this research would be the development of assays for the identification of individuals susceptible to radiogenic cancers (or treatment-induced second malignant neoplasms in the context of radiation oncology). Cells collected from different individuals and irradiated *ex vivo* vary in their radiation responses as measured by endpoints putatively related to cancer such as clonogenic survival, DNA repair efficiency, transcriptional changes, number of cytogenetic aberrations, and proportion of cells undergoing apoptosis. Whether the inter-individual differences for any of these radiobiological endpoints predict inter-individual differences in susceptibility to radiogenic cancer is still speculative, but two assays are particularly interesting because they identify a sizable proportion of the population as being mildly radiation sensitive and are associated with sporadic cancer risk.

The G2 chromosomal radiosensitivity assay, which measures chromosome aberrations in cells irradiated in the G2 phase of the cell cycle, identifies about 5–10% of clinically normal individuals and about 40% of breast cancer patients as having enhanced chromosomal radiosensitivity (31, 32). The low dose rate (LDR) gamma-H2AX assay is based on quantifying residual DNA double strand breaks in cultured cells that have been irradiated at LDR. Fibroblasts from about 40% of clinically normal individuals fall in the mildly sensitive range, as do individuals heterozygous for *ATM* mutations, a group that has an elevated risk of breast cancer. Hereditary retinoblastoma patients who are at risk of second malignancies in the treatment field if they are treated with radiotherapy are also mildly sensitive in this assay (33, 34).

Human tumors and some human normal tissues can be propagated long term in immunosuppressed mice. Mice carrying human tumors from individual patients (patient derived xenografts) have been used to test the efficacies of alternative treatment regimens with the aim of tailoring treatment to specific tumors, thus personalizing cancer therapy. An obvious next step is the use of mice harboring normal human tissues to personalize radiogenic

cancer risk assessments. The advantage of irradiating human tissue samples maintained in mice as compared to irradiating tissue samples in culture is that the tissue samples in mice would be in a more physiological setting and could be assayed long after irradiation. For example, NASA is currently supporting research that involves irradiating mice with human hematopoietic systems (so-called "humanized" mice) and monitoring the human cells for leukemia related endpoints. While this research is designed to explore the effects of simulated space radiation on the human hematopoietic system, it raises the possibility of using the same system to assess individuals for susceptibility to radiation-induced leukemia. Mice can be humanized using hematopoietic stem cells mobilized into the peripheral blood of donors by treatment with GCSF. These mice could be exposed to radiation and their human hematopoietic cells monitored for preleukemic changes such as mutations or chromosomal aberrations associated with leukemia with the goal of identifying donors whose hematopoietic cells had higher or lower frequencies of such changes.

Synopsis

Assays are under development that would use cells collected from individuals and irradiated *ex vivo* to determine susceptibility to radiogenic cancer. The endpoints in these assays will not be cancer *per se*, but surrogates for cancer susceptibility such as persistent DNA repair foci, chromosomal aberrations, or tumor associated mutations.

Genotypic Assays of Sensitivity

It has been known at least since the mid-1950s that some murine inbred strains are more susceptible to specific radiogenic cancers than others (35). The most likely explanation for the strain differences in susceptibility is the genetic differences between the strains, an explanation that is strongly supported by the identification of some of the genetic polymorphisms responsible (36–38). There are multiple lines of evidence that the genetic susceptibility to radiation-induced cancers observed in mice extends to humans.

It is fairly straightforward to demonstrate that humans differ for radiation responses and the differences are, in part, heritable. Twin studies show a greater concordance for radiobiological endpoints between monozygotic twin pairs than between dizygotic twin pairs. The reasoning behind these studies is that monozygotic twin pairs share their entire genome whereas dizygotic twin pairs share only about half of their genomes, but both monozygotic and dizygotic twin pairs share the same environments. A greater concordance for a trait, such as the percentage of lymphocytes that undergo radiation-induced apoptosis, between monozygotic twin pairs than dizygotic twin pairs would be due to their greater genetic similarity. The endpoints that have been assayed and found to be under genetic control are chromatid breaks following irradiation of PHA-stimulated peripheral blood cells (39), radiation-induced apoptosis (40, 41), and radiation-induced cell cycle delay (41). These endpoints are potentially related to radiation carcinogenesis, but the findings are only suggestive that susceptibility to radiation-induced cancer is a heritable trait.

Perhaps the first epidemiological data suggesting there might be a heritable component to susceptibility to radiation-induced cancer was the finding of a high risk for breast cancer diagnosed before age 35 in A-bomb survivors suggesting interaction between radiation exposure and genetic susceptibility to early onset breast cancer (gene and radiation interaction) in a subgroup of women (42). More recently, a study of families in which multiple members had been irradiated for treatment of tinea capitis found familial aggregation of radiation-associated meningiomas (43) suggestive of genetic susceptibility.

Evidence for genetic susceptibility to radiogenic cancers also comes from clinical observations of patients with rare, heritable cancer syndromes. In these examples, increased risks of radiation-induced cancers are linked to mutations (albeit rare mutations) in known genes. Hereditary retinoblastoma patients have a high incidence of sarcomas, which is further elevated by radiotherapy (44–46), children with neurofibromatosis type I treated with radiation for optic pathway gliomas are at increased risk for second nervous system tumors (47), and Gorlin's syndrome patients treated with radiotherapy develop basal cell carcinomas in the treatment field (48). The early onset and high penetrance of retinoblastoma makes it highly unlikely anyone with the heritable form of the disease would be selected for the astronaut corps (though *de novo* mutations resulting in somatic mosaicism mean the possibility cannot be completely excluded). While the association of some rare heritable syndromes with increased risk for radiation-induced cancers is interesting, the real questions are whether susceptibility occurs in the absence of readily identifiable syndromic disease in clinically unremarkable individuals and whether susceptible individuals are extremely rare or common.

Some common genetic polymorphisms associated with increased or decreased risks of radiogenic cancers have been identified in genetic association studies (49–54). A limitation of this approach is that the polymorphisms detected are limited to those selected for the studies, which are in genes known to be mutated in cancer or related to response to ionizing radiation-induced DNA damage.

Genome-wide association studies (GWAS) avoid the bias toward genes considered likely to influence radiosensitivity by screening the entire genome. However, GWAS studies of spontaneous cancers typically yield modest risk estimates, an observation fueling skepticism about their use in studies of radiogenic cancers. There are two reasons why GWAS associations in radiation-induced cancers may prove to be stronger. The first is that associations become stronger as the tumor subtype is more rigorously defined. There is reason to believe that radiogenic tumors only arise along a subset of oncogenic pathways (see the example of radiation-induced AML above), so GWAS associations for radiogenic tumors may be stronger because these tumors are genetically less diverse. The second reason to expect stronger associations with radiogenic than spontaneous tumors is that association studies for adverse drug reactions often yield strong associations with relatively few cases. An explanation that has been advanced for this observation is that a single strong environmental input decreases the background of other

environmental causes that may operate in conjunction with other susceptibility loci (55). For example, in a study of Hodgkin's lymphoma patients treated with radiotherapy, Best et al. identified a haplotype on chromosome 6q21 that was strongly associated with second malignant neoplasias. *PRDM1* emerged from the study as a candidate gene (56).

Whether genotypic assays of radiosensitivity can improve the precision of risk assessment will depend on a number of factors. One is the extent to which heritable sequence variants determine cancer risk from high LET exposures. High LET radiation exposures result in more complex molecular lesions that are less amenability to repair [see Ref. (2) section 5.2]. Thus, it could be argued that sequence variants that result in subtle differences in DNA repair and damage response pathways would have a lessor impact on high LET radiation carcinogenesis. However, there are profound murine and rat strain (or stock) differences in susceptibility to specific tumor types induced by high LET radiation and at least one polymorphism controlling high LET carcinogenesis has been identified (37). These observations point to a role for sequence variants in determining high LET radiation risks.

Synopsis

Polymorphisms in the human genome have been associated with risks for radiogenic cancers in atomic bomb survivors, radiological technologists, radiotherapy patients and people with environmental radiation exposures. Whether genotyping for these susceptibility associated polymorphisms and others that are sure to be discovered in the future will identify individuals at higher risk for cancer from the types of radiation exposures experienced space flight is currently unknown.

PostFlight Monitoring

The NASA REID for radiation-induced cancer is not for all cancers, but rather for fatal cancers. Early detection reduces mortality for some tumor types [for the influence of tumor stage on mortality see Ref. (2), p. 51]. Regular postflight early detection cancer screening might therefore be expected to lower the risk of cancer death as a consequence of space radiation exposure assuming, of course, that radiogenic cancers are similar to their spontaneous counterparts. Early detection screens for breast, colorectal, and prostate cancer are already a routine part of medical care in the US. The relative benefits and risks of mammography screening for breast cancer, particularly before 50 years of age, and of prostate-specific antigen-based screening for prostate cancer are contentious. However, colonoscopy screening with polypectomy demonstrably reduces CRC incidence and mortality in patients with Lynch Syndrome, a heritable CRC syndrome (57–60), and also reduces sporadic CRC deaths (61). Progression from adenoma to carcinoma is accelerated in syndromic CRC, so patients with Lynch syndrome are screened at 1- or 2-year intervals. Whether standard screening intervals would be adequate to reduce CRC risk for an individual with a history of sizable exposures to space radiation is unknown.

Based on the National Lung Screening Trial (NLST), LDCT lung cancer screening decreases lung cancer mortality in current and former smokers (30). However, LDCT is not yet a routine test, it requires a high level of expertise to perform. Also, there are risks from overdiagnosis and false-positive results. These risks are important considerations because the benefits of LDCT were assessed in smokers and former smokers that varied widely in their risks for lung cancer (62) but were generally at much higher risk of lung cancer than that calculated for astronauts exposed to even maximum permissible radiation doses [Tables A1 and A5 in Ref. (2)]. An added consideration, which may be particularly relevant if LDCT were used to screen radiation exposed individuals, is additional radiation exposure from the scans themselves (63, 64).

Synopsis

Early detection can lower mortality for some tumor types. This reduced mortality can be incorporated in the current NASA risk model through adjustments to the incidence to mortality ratios for different tumor types. Doing so assumes that early detection of radiation-induced tumors leads to the same reduction in mortality as for sporadic tumors and that astronauts and former astronauts actually undergo early detection screenings.

APPLICABILITY OF GINA TO PERSONALIZED CANCER RISK APPROACHES

As a federal agency, NASA is required to furnish its employees with a workplace that is free from recognized hazards such as ionizing radiation that are causing, or likely to cause, death or serious physical harm (65). NASA is also required to establish and operate an occupational safety and health program to protect workers. Recognizing the unique needs of space exploration, the federal Occupational Safety and Health Administration (OSHA) granted NASA a waiver from ground based radiation standards while requiring it to establish supplemental standards appropriate for space missions (1, 66). NASA's Office of the Chief Medical and Health Officer is responsible for setting these standards, and issued a series of documents including NASA Procedural Requirements (NPR) 8900.1A (NASA Health and Medical Requirements for Human Space Exploration) and NPD 8900.5B (Health and Medical Policy for Human Space Exploration) in response (67, 68). In addition, NASA STD-3001, chapter 6, explicitly addresses ionizing protection in space environments (69).

Overview of GINA

The GINA, codified as 42 US §§2000ff, is a federal law that prohibits employment discrimination on the basis of genetic information (70). This statute has two major sections. Title I covers group health plans and insurers. Title II covers employers, such as NASA, and prohibits them from discriminating against employees and job applicants based on genetic information. It also prohibits employers from collecting genetic information, except under very limited circumstances. The US Equal Opportunity Employment Commission (EEOC), an independent commission charged with enforcing federal laws against job discrimination,

TABLE 1 | Summary of approaches to personalized cancer risk assessments.

Approach	Underlying concept	Examples of marker or data used
Personal/family medical history	For some tumor types radiogenic cancer risk is determined, in part, by background risk	Family or personal history of cancer, intestinal polyps, breast biopsies
Detection of preneoplastic cells, dormant microtumors	Preneoplastic cells and microtumors can be detected in clinically normal individuals; some of these can undergo promotion or progression due to radiation exposure	Blood or tissue aspirates assayed for cancer related mutations or biomarkers; *in situ* detection of pre-invasive tumors by imaging
Phenotypic assays of sensitivity	Radiogenic cancer susceptibility can be due to a number of genetic and non-genetic causes; *ex vivo* radiosensitivity assays of cells or tissues are agnostic in regard to the cause of susceptibility	LDR gamma-H2AX and G2 chromosomal radiosensitivity assays using peripheral blood cells or fibroblasts; cancer biomarker detection in cells or tissues irradiated in humanized mice
Genotypic assays of sensitivity	Individuals vary in their susceptibility to radiogenic cancer due to their genetic backgrounds	Genomic sequence polymorphisms

oversees GINA and has issued regulations to implement it (see 29 CFR §§1635.1 to 1635.12) (71). This article focuses on Title II of GINA and examines how its provisions could impact the implementation of the four approaches to personalized cancer risk assessments, summarized in **Table 1** and set out earlier in this article.

This statute and its implementing regulations are relatively new, and interpretation of its provisions is evolving [e.g., Ref. (72)]. The discussion of the applicability of GINA to NASA is based on the information available at the time of publication, and it is possible that subsequent events, especially litigation brought under GINA, could impact the way in which GINA is interpreted. The analyses are based on generalized circumstances and are not intended to provide legal advice.

One of the central provisions of GINA is that "it is an unlawful employment practice for an employer to request, require, or purchase genetic information with respect to an employee" [42 USC §2000ff-1(b)]. This provision turns on how the statute defines the term "genetic information." Under GINA, this term means information about an individual that includes "(i) such individual's genetic tests, (ii) the genetic tests of family members of such individual, and (iii) the manifestation of a disease or disorder in family members of such individual" [42 USC §2000ff(4)]. In addition, the term "genetic test" is "an analysis of human DNA, RNA, chromosomes, proteins, or metabolites, that detects genotypes, mutations, or chromosomal changes" [42 USC 2000ff(7)].

Collecting and Using Personalized Information for Space Radiation Risk Assessments

This article discusses four approaches to supplement personalized cancer risk assessments. The first approach would incorporate family and personal medical history, especially for breast cancer and CRC, into these assessments. The second approach would collect information about microtumors or preneoplastic cells that could undergo promotion and/or progression by radiation exposures to malignancies. The third and fourth approaches would rely on evaluations of radiosensitivity based on genotypic and phenotypic assays. Each of these approaches would seem to trigger the collection of genetic information under GINA and therefore would most likely be prohibited under the statute. The first approach falls squarely within GINA's prohibition of collecting personal and family medical information. The second approach would rely on the evaluation of cells and tissues based on their mutations, which also is a prohibited activity under GINA. The third and fourth approaches are keyed to radiosensitivity or genotype to phenotype associations, which again would require the collection of data that falls squarely within GINA's purview. In summary, based on GINA's intent and its statutory language, it appears that the data and methodologies set forth in this article that would be needed for personalization of cancer risk assessment would be prohibited by GINA. More specifically, under GINA it seems clear that NASA could not collect nor use to make employment decisions, information based on personalized cancer risk assessments that use the approaches set out in **Table 1**.

Two potential uses of more personalized cancer risk assessments are to screen NASA applicants and reduce employment risks to astronauts who are sent on space missions. GINA prohibits the use of genetic information and genetic tests for pre-employment screening. As this article points out, at present NASA's approach to setting permissible exposure limits relies on a cancer risk assessment model that takes into account the astronaut's age at exposure, sex, and smoking status. From a scientific perspective, this article suggests that among the steps to model improvement would be to utilize the increasingly powerful and more precise technologies that employ what, under GINA, would be classified as "genetic information" and "genetic tests." Construing the statute as currently interpreted, it would seem that collecting and using this information would contravene this law and its regulations.

PostFlight Monitoring and GINA

This article also suggests that postflight monitoring is potentially beneficial for astronauts. Such monitoring could result in reduced mortality for some tumor types, because early detection of tumors or pre-cancerous conditions could mean more effective, and timely, intervention. In this regard, GINA contains an exception to the collection of genetic information for employers who want to collect such information to assess the biological effects of toxic substances in the workplace. The employer can offer health and/or genetic services to employees in the form

of a confidential wellness and/or counseling program. GINA requires that such information can be collected and used if the employee provides voluntary written authorization before collection; only the employee and family members and the genetic counselor receive this information; and that the individual genetic information not be disclosed to employers [42 USC §2000ff-1(b)(5)]. Under this section of GINA, it might be possible to collect and use the type of genetic information that is contemplated by the approaches outlined in this article. Such information might be disclosable to NASA "only in aggregate terms that do not disclose the identity of specific employees" [42 USC §2000ff – 1(b)(5)(E)].

AUTHOR CONTRIBUTIONS

MW provided the discussion of various approaches available to personalize risk assessment for radiation carcinogenesis. PL evaluated the impact of the Genetic Information Nondiscrimination Act on the use of these approaches.

FUNDING

Research by MW is supported by grants NNX12AB54G and NNX15AK13G from the National Aeronautics and Space Administration.

REFERENCES

1. Sieffert AM. Astronaut health and safety regulations: ionizing radiation. *The SciTech Lawyer 10:4* (2014). Available from: http://www.americanbar.org/publications/scitech_lawyer/web_exclusives/sieffert_endnotes.html
2. Cucinotta FA, Kim MY, Chappell LJ. *Space Radiation Cancer Risk Projections and Uncertainties – 2012*. Hanover, MD: National Aeronautics and Space Administration (2013). NASA/TP-2013-217375.
3. Cucinotta FA, Alp M, Rowedder B, Kim MY. Safe days in space with acceptable uncertainty from space radiation exposure. *Life Sci Space Res (Amst)* (2015) **2**:54–69. doi:10.1016/j.lssr.2015.04.002
4. Cucinotta FA. Space radiation risks for astronauts on multiple International Space Station missions. *PLoS One* (2014) **9**:e96099. doi:10.1371/journal.pone.0096099
5. Institute of Medicine. *Health Standards for Long Duration and Exploration Spaceflight: Ethics Principles, Responsibilities, and Decision Framework*. Washington, DC: National Academies Press (2014).
6. Collins BJ, Schneider AB, Prinz RA, Xu X. Low frequency of BRAF mutations in adult patients with papillary thyroid cancers following childhood radiation exposure. *Thyroid* (2006) **16**:61–6. doi:10.1089/thy.2006.16.61
7. Donson AM, Erwin NS, Kleinschmidt-DeMasters BK, Madden JR, Addo-Yobo SO, Foreman NK. Unique molecular characteristics of radiation-induced glioblastoma. *J Neuropathol Exp Neurol* (2007) **66**:740–9. doi:10.1097/nen.0b013e3181257190
8. Lima J, Trovisco V, Soares P, Maximo V, Magalhaes J, Salvatore G, et al. BRAF mutations are not a major event in post-Chernobyl childhood thyroid carcinomas. *J Clin Endocrinol Metab* (2004) **89**:4267–71. doi:10.1210/jc.2003-032224
9. Nikiforov YE, Rowland JM, Bove KE, Monforte-Munoz H, Fagin JA. Distinct pattern of ret oncogene rearrangements in morphological variants of radiation-induced and sporadic thyroid papillary carcinomas in children. *Cancer Res* (1997) **57**:1690–4.
10. Rabes HM, Demidchik EP, Sidorow JD, Lengfelder E, Beimfohr C, Hoelzel D, et al. Pattern of radiation-induced RET and NTRK1 rearrangements in 191 post-Chernobyl papillary thyroid carcinomas: biological, phenotypic, and clinical implications. *Clin Cancer Res* (2000) **6**:1093–103.
11. Smith SM, Le Beau MM, Huo D, Karrison T, Sobecks RM, Anastasi J, et al. Clinical-cytogenetic associations in 306 patients with therapy-related myelodysplasia and myeloid leukemia: the University of Chicago series. *Blood* (2003) **102**:43–52. doi:10.1182/blood-2002-11-3343
12. Grimwade D, Hills RK, Moorman AV, Walker H, Chatters S, Goldstone AH, et al. Refinement of cytogenetic classification in acute myeloid leukemia: determination of prognostic significance of rare recurring chromosomal abnormalities among 5876 younger adult patients treated in the United Kingdom Medical Research Council trials. *Blood* (2010) **116**:354–65. doi:10.1182/blood-2009-11-254441
13. St John DJ, McDermott FT, Hopper JL, Debney EA, Johnson WR, Hughes ES. Cancer risk in relatives of patients with common colorectal cancer. *Ann Intern Med* (1993) **118**:785–90. doi:10.7326/0003-4819-118-10-199305150-00005
14. Lichtenstein P, Holm NV, Verkasalo PK, Iliadou A, Kaprio J, Koskenvuo M, et al. Environmental and heritable factors in the causation of cancer – analyses of cohorts of twins from Sweden, Denmark, and Finland. *N Engl J Med* (2000) **343**:78–85. doi:10.1056/NEJM200007133430201
15. Tyrer J, Duffy SW, Cuzick J. A breast cancer prediction model incorporating familial and personal risk factors. *Stat Med* (2004) **23**:1111–30. doi:10.1002/sim.1668
16. Colditz GA, Atwood KA, Emmons K, Monson RR, Willett WC, Trichopoulos D, et al. Harvard report on cancer prevention volume 4: Harvard Cancer Risk Index. Risk Index Working Group, Harvard Center for Cancer Prevention. *Cancer Causes Control* (2000) **11**:477–88. doi:10.1023/A:1008982121761
17. Freedman AN, Slattery ML, Ballard-Barbash R, Willis G, Cann BJ, Pee D, et al. Colorectal cancer risk prediction tool for white men and women without known susceptibility. *J Clin Oncol* (2009) **27**:686–93. doi:10.1200/JCO.2008.17.4797
18. Wells BJ, Kattan MW, Cooper GS, Jackson L, Koroukian S. Colorectal cancer predicted risk online (CRC-PRO) calculator using data from the multiethnic cohort study. *J Am Board Fam Med* (2014) **27**:42–55. doi:10.3122/jabfm.2014.01.130040
19. Folkman J, Kalluri R. Cancer without disease. *Nature* (2004) **427**:787. doi:10.1038/427787a
20. Welch HG, Black WC. Overdiagnosis in cancer. *J Natl Cancer Inst* (2010) **102**:605–13. doi:10.1093/jnci/djq099
21. Nakamura N. A hypothesis: radiation-related leukemia is mainly attributable to the small number of people who carry pre-existing clonally expanded pre-leukemic cells. *Radiat Res* (2005) **163**:258–65. doi:10.1667/RR3311
22. Mori H, Colman SM, Xiao Z, Ford AM, Healy LE, Donaldson C, et al. Chromosome translocations and covert leukemic clones are generated during normal fetal development. *Proc Natl Acad Sci U S A* (2002) **99**:8242–7. doi:10.1073/pnas.112218799
23. Boquett JA, Alves JR, de Oliveira CE. Analysis of BCR/ABL transcripts in healthy individuals. *Genet Mol Res* (2013) **12**:4967–71. doi:10.4238/2013.October.24.8
24. Brassesco MS, Montaldi AP, Gras DE, de Paula Queiroz RG, Martinez-Rossi NM, Tone LG, et al. MLL leukemia-associated rearrangements in peripheral blood lymphocytes from healthy individuals. *Genet Mol Biol* (2009) **32**:234–41. doi:10.1590/S1415-47572009000200005
25. Nambiar M, Raghavan SC. Chromosomal translocations among the healthy human population: implications in oncogenesis. *Cell Mol Life Sci* (2013) **70**:1381–92. doi:10.1007/s00018-012-1135-x
26. Genovese G, Kahler AK, Handsaker RE, Lindberg J, Rose SA, Bakhoum SF, et al. Clonal hematopoiesis and blood-cancer risk inferred from blood DNA sequence. *N Engl J Med* (2014) **371**:2477–87. doi:10.1056/NEJMoa1409405
27. Jaiswal S, Fontanillas P, Flannick J, Manning A, Grauman PV, Mar BG, et al. Age-related clonal hematopoiesis associated with adverse outcomes. *N Engl J Med* (2014) **371**:2488–98. doi:10.1056/NEJMoa1408617
28. Wong TN, Ramsingh G, Young AL, Miller CA, Touma W, Welch JS, et al. Role of TP53 mutations in the origin and evolution of therapy-related acute myeloid leukaemia. *Nature* (2015) **518**:552–5. doi:10.1038/nature13968
29. Khan SA. Management of other high-risk patients. In: Harris JR, Lippman ME, Morrow M, Osborne CK, editors. *Diseases of the Breast*. Philadelphia: Wolters Kluwer (2014). p. 268–81.
30. Aberle DR, Adams AM, Berg CD, Black WC, Clapp JD, Fagerstrom RM, et al. Reduced lung-cancer mortality with low-dose computed tomographic screening. *N Engl J Med* (2011) **365**:395–409. doi:10.1056/NEJMoa1102873

31. Roberts SA, Spreadborough AR, Bulman B, Barber JB, Evans DG, Scott D. Heritability of cellular radiosensitivity: a marker of low-penetrance predisposition genes in breast cancer? *Am J Hum Genet* (1999) **65**:784–94. doi:10.1086/302544
32. Scott D, Spreadborough A, Levine E, Roberts SA. Genetic predisposition in breast cancer. *Lancet* (1994) **344**:1444. doi:10.1016/S0140-6736(94)90616-5
33. Kato TA, Wilson PF, Nagasawa H, Fitzek MM, Weil MM, Little JB, et al. A defect in DNA double strand break processing in cells from unaffected parents of retinoblastoma patients and other apparently normal humans. *DNA Repair (Amst)* (2007) **6**:818–29. doi:10.1016/j.dnarep.2007.01.008
34. Kato TA, Nagasawa H, Weil MM, Little JB, Bedford JS. Levels of gamma-H2AX foci after low dose-rate irradiation distinguish human ATM heterozygotes and other mildly radiosensitive individuals. *Radiat Res* (2006) **166**:443–53. doi:10.1667/RR3604.1
35. Kaplan HS, Hirsch BB, Brown MB. Indirect induction of lymphomas in irradiated mice. IV. Genetic evidence of the origin of the tumor cells from the thymic grafts. *Cancer Res* (1956) **16**:434–6.
36. Mori N, Matsumoto Y, Okumoto M, Suzuki N, Yamate J. Variations in Prkdc encoding the catalytic subunit of DNA-dependent protein kinase (DNA-PKcs) and susceptibility to radiation-induced apoptosis and lymphomagenesis. *Oncogene* (2001) **20**:3609–19. doi:10.1038/sj.onc.1204497
37. Rosemann M, Gonzalez-Vasconcellos I, Domke T, Kuosaite V, Schneider R, Kremer M, et al. A Rb1 promoter variant with reduced activity contributes to osteosarcoma susceptibility in irradiated mice. *Mol Cancer* (2014) **13**:182–93. doi:10.1186/1476-4598-13-182
38. Yu Y, Okayasu R, Weil MM, Silver A, McCarthy M, Zabriskie R, et al. Elevated breast cancer risk in irradiated BALB/c mice associates with unique functional polymorphism of the Prkdc (DNA-dependent protein kinase catalytic subunit) gene. *Cancer Res* (2001) **61**:1820–4.
39. Wu X, Spitz MR, Amos CI, Lin J, Shao L, Gu J, et al. Mutagen sensitivity has high heritability: evidence from a twin study. *Cancer Res* (2006) **66**:5993–6. doi:10.1158/0008-5472.CAN-06-1007
40. Camplejohn RS, Hodgson S, Carter N, Kato BS, Spector TD. Heritability of DNA-damage-induced apoptosis and its relationship with age in lymphocytes from female twins. *Br J Cancer* (2006) **95**:520–4. doi:10.1038/sj.bjc.6603257
41. Finnon P, Robertson N, Dziwura S, Raffy C, Zhang W, Ainsbury L, et al. Evidence for significant heritability of apoptotic and cell cycle responses to ionising radiation. *Hum Genet* (2008) **123**:485–93. doi:10.1007/s00439-008-0500-1
42. Tokunaga M, Land CE, Tokuoka S, Nishimori I, Soda M, Akiba S. Incidence of female breast cancer among atomic bomb survivors, 1950-1985. *Radiat Res* (1994) **138**:209–23. doi:10.2307/3578591
43. Flint-Richter P, Sadetzki S. Genetic predisposition for the development of radiation-associated meningioma: an epidemiological study. *Lancet Oncol* (2007) **8**:403–10. doi:10.1016/S1470-2045(07)70107-9
44. Wong FL, Boice JD Jr, Abramson DH, Tarone RE, Kleinerman RA, Stovall M, et al. Cancer incidence after retinoblastoma. Radiation dose and sarcoma risk. *JAMA* (1997) **278**:1262–7. doi:10.1001/jama.278.15.1262
45. Kleinerman RA, Tucker MA, Tarone RE, Abramson DH, Seddon JM, Stovall M, et al. Risk of new cancers after radiotherapy in long-term survivors of retinoblastoma: an extended follow-up. *J Clin Oncol* (2005) **23**:2272–9. doi:10.1200/JCO.2005.05.054
46. Kleinerman RA, Tucker MA, Abramson DH, Seddon JM, Tarone RE, Fraumeni JF Jr. Risk of soft tissue sarcomas by individual subtype in survivors of hereditary retinoblastoma. *J Natl Cancer Inst* (2007) **99**:24–31. doi:10.1093/jnci/djk002
47. Sharif S, Ferner R, Birch JM, Gillespie JE, Gattamaneni HR, Baser ME, et al. Second primary tumors in neurofibromatosis 1 patients treated for optic glioma: substantial risks after radiotherapy. *J Clin Oncol* (2006) **24**:2570–5. doi:10.1200/JCO.2005.03.8349
48. Atahan IL, Yildiz F, Ozyar E, Uzal D, Zorlu F. Basal cell carcinomas developing in a case of medulloblastoma associated with Gorlin's syndrome. *Pediatr Hematol Oncol* (1998) **15**:187–91. doi:10.3109/08880019809167234
49. Bhatti P, Struewing JP, Alexander BH, Hauptmann M, Bowen L, Mateus-Pereira LH, et al. Polymorphisms in DNA repair genes, ionizing radiation exposure and risk of breast cancer in U.S. Radiologic technologists. *Int J Cancer* (2007) **122**:177–82. doi:10.1002/ijc.23066
50. Damiola F, Byrnes G, Moissonnier M, Pertesi M, Deltour I, Fillon A, et al. Contribution of ATM and FOXE1 (TTF2) to risk of papillary thyroid carcinoma in Belarusian children exposed to radiation. *Int J Cancer* (2014) **134**:1659–68. doi:10.1002/ijc.28483
51. Hayashi T, Ito R, Cologne J, Maki M, Morishita Y, Nagamura H, et al. Effects of IL-10 haplotype and atomic bomb radiation exposure on gastric cancer risk. *Radiat Res* (2013) **180**:60–9. doi:10.1667/RR3183.1
52. Sigurdson AJ, Bhatti P, Doody MM, Hauptmann M, Bowen L, Simon SL, et al. Polymorphisms in apoptosis- and proliferation-related genes, ionizing radiation exposure, and risk of breast cancer among U.S. Radiologic Technologists. *Cancer Epidemiol Biomarkers Prev* (2007) **16**:2000–7. doi:10.1158/1055-9965.EPI-07-0282
53. Sigurdson AJ, Land CE, Bhatti P, Pineda M, Brenner A, Carr Z, et al. Thyroid nodules, polymorphic variants in DNA repair and RET-related genes, and interaction with ionizing radiation exposure from nuclear tests in Kazakhstan. *Radiat Res* (2009) **171**:77–88. doi:10.1667/RR1327.1
54. Yoshida K, Nakachi K, Imai K, Cologne JB, Niwa Y, Kusunoki Y, et al. Lung cancer susceptibility among atomic bomb survivors in relation to CA repeat number polymorphism of epidermal growth factor receptor gene and radiation dose. *Carcinogenesis* (2009) **30**:2037–41. doi:10.1093/carcin/bgp247
55. Knight JA, Skol AD, Shinde A, Hastings D, Walgren RA, Shao J, et al. Genome-wide association study to identify novel loci associated with therapy-related myeloid leukemia susceptibility. *Blood* (2009) **113**:5575–82. doi:10.1182/blood-2008-10-183244
56. Best T, Li D, Skol AD, Kirchhoff T, Jackson SA, Yasui Y, et al. Variants at 6q21 implicate PRDM1 in the etiology of therapy-induced second malignancies after Hodgkin's lymphoma. *Nat Med* (2011) **17**:941–3. doi:10.1038/nm.2407
57. Dove-Edwin I, Sasieni P, Adams J, Thomas HJ. Prevention of colorectal cancer by colonoscopic surveillance in individuals with a family history of colorectal cancer: 16 year, prospective, follow-up study. *BMJ* (2005) **331**:1047. doi:10.1136/bmj.38606.794560.EB
58. Renkonen-Sinisalo L, Aarnio M, Mecklin JP, Jarvinen HJ. Surveillance improves survival of colorectal cancer in patients with hereditary nonpolyposis colorectal cancer. *Cancer Detect Prev* (2000) **24**:137–42.
59. Stupart DA, Goldberg PA, Algar U, Ramesar R. Surveillance colonoscopy improves survival in a cohort of subjects with a single mismatch repair gene mutation. *Colorectal Dis* (2009) **11**:126–30. doi:10.1111/j.1463-1318.2008.01702.x
60. Vasen HF, Taal BG, Nagengast FM, Griffioen G, Menko FH, Kleibeuker JH, et al. Hereditary nonpolyposis colorectal cancer: results of long-term surveillance in 50 families. *Eur J Cancer* (1995) **31A**:1145–8. doi:10.1016/0959-8049(95)00249-I
61. Zauber AG, Winawer SJ, O'Brien MJ, Lansdorp-Vogelaar I, van BM, Hankey BF, et al. Colonoscopic polypectomy and long-term prevention of colorectal-cancer deaths. *N Engl J Med* (2012) **366**:687–96. doi:10.1056/NEJMoa1100370
62. Bach PB, Kattan MW, Thornquist MD, Kris MG, Tate RC, Barnett MJ, et al. Variations in lung cancer risk among smokers. *J Natl Cancer Inst* (2003) **95**:470–8. doi:10.1093/jnci/95.6.470
63. Brenner DJ. Radiation risks potentially associated with low-dose CT screening of adult smokers for lung cancer. *Radiology* (2004) **231**:440–5. doi:10.1148/radiol.2312030880
64. Sarma A, Heilbrun ME, Conner KE, Stevens SM, Woller SC, Elliott CG. Radiation and chest CT scan examinations: what do we know? *Chest* (2012) **142**:750–60. doi:10.1378/chest.11-2863
65. Executive Order 12196, Occupational safety and health programs for Federal employees (26 February 1980).
66. 29 CFR §1960.18 – Supplementary standards.
67. NASA Procedural Requirements 8900.1A NASA Health and Medical Requirements for Human Space Exploration 2012.
68. NASA Policy Directive 8900.5B Health and Medical Policy for Human Space Exploration 2011.
69. *NASA STD-3001 NASA Space Flight Human System-Standard (Volumes 1 and 2)*. Washington, DC: National Aeronautics and Space Administration.

70. The Genetic Information Nondisclosure Act, 42 US Code §§2000ff-1 to 2000ff-11 (2015).
71. The Genetic Information Nondisclosure Act regulations, CFR §§1635.1 to 1635.12 (2015).
72. Lowe v. Atlas Logistics Group Retail Services (Atlanta), LLC, 102 F. Supp. 3d. 1360, 2015 WL 2058906 (ND Georgia 2015).

Conflict of Interest Statement: The authors declare that the research was conducted in the absence of any commercial or financial relationships that could be construed as a potential conflict of interest.

The reviewer, Eliedonna Cacao and handling Editor, Francis A. Cucinotta declared their shared affiliation, and the handling Editor states that the process nevertheless met the standards of a fair and objective review.

Copyright © 2016 Locke and Weil. This is an open-access article distributed under the terms of the Creative Commons Attribution License (CC BY). The use, distribution or reproduction in other forums is permitted, provided the original author(s) or licensor are credited and that the original publication in this journal is cited, in accordance with accepted academic practice. No use, distribution or reproduction is permitted which does not comply with these terms.

frontiers in Oncology

MINI REVIEW
published: 08 December 2015
doi: 10.3389/fonc.2015.00273

Radiation Measurements Performed with Active Detectors Relevant for Human Space Exploration

Livio Narici[1,2], Thomas Berger[2], Daniel Matthiä[2] and Günther Reitz[2]*

[1] Department of Physics University of Rome Tor Vergata and INFN-Roma2, Rome, Italy, [2] Institute of Aerospace Medicine, German Aerospace Center (DLR), Cologne, Germany

A reliable radiation risk assessment in space is a mandatory step for the development of countermeasures and long-duration mission planning in human spaceflight. Research in radiobiology provides information about possible risks linked to radiation. In addition, for a meaningful risk evaluation, the radiation exposure has to be assessed to a sufficient level of accuracy. Consequently, both the radiation models predicting the risks and the measurements used to validate such models must have an equivalent precision. Corresponding measurements can be performed both with passive and active devices. The former is easier to handle, cheaper, lighter, and smaller but they measure neither the time dependence of the radiation environment nor some of the details useful for a comprehensive radiation risk assessment. Active detectors provide most of these details and have been extensively used in the International Space Station. To easily access such an amount of data, a single point access is becoming essential. This review presents an ongoing work on the development of a tool that allows obtaining information about all relevant measurements performed with active detectors providing reliable inputs for radiation model validation.

Keywords: active radiation detectors, International Space Station, human space exploration, space radiation risk, database

OPEN ACCESS

Edited by:
Marco Durante, GSI, Germany

Reviewed by:
Evagelia C. Laiakis, Georgetown University, USA
Ulrich H. Straube, European Space Agency, Germany

****Correspondence:***
Livio Narici
narici@roma2.infn.it

Specialty section:
This article was submitted to Radiation Oncology, a section of the journal Frontiers in Oncology

Received: *30 September 2015*
Accepted: *23 November 2015*
Published: *08 December 2015*

Citation:
Narici L, Berger T, Matthiä D and Reitz G (2015) Radiation Measurements Performed with Active Detectors Relevant for Human Space Exploration. Front. Oncol. 5:273. doi: 10.3389/fonc.2015.00273

INTRODUCTION

Space radiation risks (on humans and instrumentation) are possibly the most severe challenge posed to human exploration of deep space (1). A reliable space radiation risk assessment requires further understanding in radiation biology and also more details about the characteristics of the radiation.

Future mission planning will be based on radiation models which will have to be able to describe to a sufficient level of accuracy the radiation environment the crew will be living in. Such models are under development and consist of a combination of source models, transport models, and computer-aided design (CAD) ability to describe the habitat (either a spacecraft or a space base). Each part as well as the entire final model will have to be properly validated by measurements, and consequently, these measurements will have to provide a similar degree of detail as the model. Passive detectors cannot provide information about, for example, temporal and spatial evolution, or the primary kinetic energy of the ions. Often not even active detectors permit to measure all these parameters.

The construction of future space vessels and space bases is expected to be of similar complexity compared to the International Space Station (ISS). This makes the ISS an important "validation habitat" for the mentioned radiation models. The radiation impinging on the ISS is, however,

modulated by the Earth magnetic field, and thus it has features that are not found in deep space. In particular, primary cosmic radiation at low latitude is heavily reduced comprising only high energy ions; charged particles with lower energies are deflected by the magnetic field. At high latitudes, this shielding effect of the magnetic field is much weaker and the radiation field is more similar to the one encountered in deep space.

Furthermore, in a region above Brazil (South Atlantic Anomaly, SAA), the tilt and shift of the magnetic dipole-axis compared to the rotation-axis of Earth result in a close approach of the radiation belt to the Earth's surface. In the radiation belt, a large amount of low charge ions (mostly protons) of relatively low energy is trapped.

Due to the latitude-dependent magnetic shielding and the presence of the SAA active detectors are advantageous for model validation for deep space; they can be used to select measurements from specific geographical regions and permit to construct a proper dataset for validation, i.e., from high latitudes.

Ideally, measurements and model developments should proceed in a process defining both the most suitable areas in the ISS to perform experiments and the required parameters that are to be measured. Although this approach is usually not realized, a high number of measurements have been and are being performed, which are useful for model validation.

Teams working on radiation models and looking for data for validation often encounter difficulties as literature searches are not always fruitful. Sometime this is due to the difficulty to extract numerical values from articles or it can be due to the delay in the publication procedure. Also, these searches are most often quite time consuming. Therefore, researchers heavily rely on personal communications from teams they have ongoing collaborations with.

It is obvious that a far better approach is having a single access point where all data can be found. In the future, this should lead to a worldwide accessible database. In order to foster the development of such a database and to provide to the scientific community a simple tool for the fast and successful identification of suitable data, a *search book* is being created in which all relevant information is to be collected.

This review provides a description of this *search book* that is a soon to be web-published compilation of basic information on active detector measurements of radiation environment for human exploration risk assessment, in particular, when, where (in the ISS or also in or on other relevant satellites/spacecraft), how (what kind of active detector, what kind of measurement), and who (a contributor for each dataset to whom any question about the corresponding data might be addressed).

The goal is to provide this information interactively available on the web. As this work is ongoing the list of active detectors in this article is not complete, and it will be a continuing task to update the data.

TIME FRAME AND MEASUREMENTS CONSIDERED

This review covers the ISS life span and includes also measurements performed during the same period at locations different than ISS, provided that they are of relevance for human space exploration. There are several reasons why the ISS is an ideal starting point:

(i) ISS is the best currently available test bed for radiation measurements aimed at model validation (see above);
(ii) detailed CAD simulations are being developed for ISS, and hopefully, these simulations will soon be able to track mass movements in the ISS; this would permit to compare radiation models and radiation measurements for different, well-defined shielding environments.
(iii) ISS is going to operate probably for another decade, providing the time frame needed for a coordinated approach of measurements and model development and validation (see above).

Concurrent measurements on Earth satellites as well as around Moon or Mars and in interplanetary space are also extremely important as they provide information about the radiation sources impinging on the ISS.

THE SUMMARY TABLES

Table 1 shows the measurement locations in the past 16 years, as well as the detector performing each measurement. A filled box indicates that measurements were taken during that year. Further details about the time and duration of each measurement as well as detector characteristics and relevant operational parameters will be provided on the web site.

We give a brief account of the latter in **Table 2** together with an email address as contact point for each of the considered instruments. For any further information and details, the reader is addressed to the references.

A BRIEF DESCRIPTION OF THE DETECTORS

The *R-16* detector (2–9) is a combination of two Argon filled ionization chamber with two different shielding. It has been also the first active detector in use in the ISS.

The DB-8 (2–9) detector is similar to the Liulin (see below). Four DB-8 units are a part of the ISS radiation monitoring system (RMS). All the DB-8 units are identical and two independent sensors with different shielding operate in each of the DB-8 units. The DB-8 units were located in different locations in the ZVEDA module to provide measurements in different shielding environments.

Liulin (10–42) labels a set of small detectors of very similar dimensions and operational principles but differing in read out, storing, and other characteristics that tailored each detector to the experiments it was built for. Details on these instruments can be found in the references, e.g., Ref. (40). All Liulin-type instruments use silicon detectors and measure the deposited energy and the number of charged particles hitting the device, which can be converted to dose rate and particle flux. The first Liulin was developed in the late 80s (43) for use in the MIR Station. The ISS instruments are Liulin-E094 (April to August 2001),

TABLE 1 | Overview of active detector measurements since the beginning of the ISS era.

Modulus	Detector	2000	2001	2002	2003	2004	2005	2006	2007	2008	2009	2010	2011	2012	2013	2014	2015
ISS, internal																	
USLab	Liulin-E094		■														
	IV-CPDS		■	■	■	■	■	■	■								
	ALTEA							■	■		■	■	■	■			
	Dosmap-Dostel		■														
Columbus	Dosis-Dostel-1										■	■		■	■	■	■
	Dosis-Dostel-2										■	■	■	■	■	■	■
	ALTEA													■			
	Tritel													■	■		
Zvezda	R-16	■	■	■	■	■	■	■	■	■	■	■	■	■	■	■	■
	DB-8		■	■	■	■	■	■	■	■	■	■	■	■	■	■	
	Alteino						■	■	■	■	■						
	MTR-Dostel									■							
	Tritel														■		
Zarya	Alteino										■						
Pirs	Alteino			■			■										
	Liulin-5								■	■	■	■					
Russ Segment	Liulin-ISS						■	■	■	■	■	■	■	■	■	■	■
MRM1	Liulin-5													■	■	■	■
ISS, external																	
External-USLab	EV1-CPDS			■	■												
	EV2-CPDS			■	■	■	■	■	■	■	■	■	■	■	■		
	EV3-CPDS			■	■	■	■	■	■	■	■	■	■	■	■	■	■
External-Columbus	R3DE									■	■						
	EuTEF-Dostel									■	■						
External-Zvezda	MTR-Dostel					■											
	R3DR										■	■				■	■
Satellite	**Detector**	**2000**	**2001**	**2002**	**2003**	**2004**	**2005**	**2006**	**2007**	**2008**	**2009**	**2010**	**2011**	**2012**	**2013**	**2014**	**2015**
Leo satellites																	
Foton-M2	R3D-B2						■										
Foton-M3	Liulin-Photo								■								
Foton-M3	R3D-B3								■								
Foton-M4	RD3-B3															■	
Bion-M1	RD3-B3														■		
Resurs-DK1	PAMELA							■	■	■	■	■	■	■	■	■	■
Moon satellites																	
Chandrayaan	RADOM									■	■						
LRO	CRaTER										■	■	■	■	■	■	■
Mars satellites																	
Odyssey	MARIE			■	■												
System	**Detector**	**2000**	**2001**	**2002**	**2003**	**2004**	**2005**	**2006**	**2007**	**2008**	**2009**	**2010**	**2011**	**2012**	**2013**	**2014**	**2015**
Mars cruise																	
Curiosity	MSL-RAD												■	■			
Mars surface																	
Curiosity	MSL-RAD													■	■	■	■

*Filled boxes indicate years in which measurements have been performed with the corresponding detector and on the corresponding location. To obtain more detailed information about the exact timing, the reader is suggested to read the relative references or contact the contact point (see **Table 2**). The table is still not complete (work in progress, see text).*

TABLE 2 | Details of the active radiation detectors that have been active on the ISS or that have performed measurements relevant to human exploration.

Detector	Sensor material	Year first use	No. of sensor	Typical sensor area and thickness		Telescope geometrical factor (single ended) (cm^2 sr)	LET (Si) acceptance (keV/μm)	Reference	Contact person
				Area (cm^2)	Thickness (mm)				
R-16	Argon (ion. Chamb.)	2000	1	[a]	[a]	–	–	(2–9)	Victor V. Benghin, v_benghin@mail.ru
DB-8	Silicon	2001	1	1	0.3	–	–	(2–9)	Victor V. Benghin, v_benghin@mail.ru
Liulin[b]	Silicon	2001	1	2	0.3	–	–	(10–42)[c]	Tsvetan P. Dachev, tdachev@bas.bg
CPDS[d]	Silicon	2001	12	5.8, 9, 26.8	0.3–1.0–5.0	3.2	0.3–30	(44, 45)	Kerry T. Lee, kerry.t.lee@nasa.gov
Alteino	Striped Silicon	2002	8	64	0.4	23.8	0.3–430	(46–52)	Marco Casolino, casolino@roma2.infn.it
ALTEA	Striped Silicon[e]	2006	6	128	0.4	115	3–700	(55–74)	Livio Narici, narici@roma2.infn.it
Liulin-5	Silicon	2007	3	2.3	0.4	1	1.2–170	(75–82)[f]	Jordanka Semkova, jsemkova@stil.bas.bg
Dostel[g]	Silicon	2001	2	6.9	0.4	8.2	0.5–400	(16, 83–89)	Thomas Berger, Thomas.Berger@dlr.de
Tritel	Silicon[h]	2012	2	2.2	0.3	2.5	0.2–290	(90–95)	Hirn Attila, hirn.attila@energia.mta.hu
PAMELA	Striped Silicon[i]	2006	6	37.3	0.3	21.6	0.03–97	(96–112)	Roberta Sparvoli, sparvoli@roma2.infn.it
MARIE	Silicon	2002	8	5.8, 9, 26.8	0.3–1.0–5.0	3.2	0.5–57	(113–118)	Cary Zeitlin, cary.j.zeitlin@nasa.gov
CRaTER	Silicon[j]	2009	6	9.6	0.15–1.0	0.6–24.6[k]	0.2–2200	(119–126)	Nathan Schwadron, nschwadron@guero.sr.unh.edu
MSL-RAD	Silicon segmented[l]	2011	3	13.9, 2.3, 1.9[m]	0.3	0.17–0.72[k]	0.1–1000	(127–135)	Donald M. Hassler, hassler@boulder.swri.edu

[a]Hemisphere connected with a cylinder, the internal radius of the hemisphere and the cylinder being 20 mm, the height of the cylinder being 20 mm.
[b]Several instruments in this family: Liulin-E094, Liulin-ISS, Liulin-Photo, RADOM, R3DE, R3DR, R3D-B2, R3D-B3.
[c]See also Liulin-5 references.
[d]Four CPDS: one intra-vehicular (IV-CPDS) and three extra-vehicular (EV-CPDS).
[e]Six identical telescopes deployed in different configurations: on an helmet-like holder, in a X, Y, and Z configuration, in a flat configurations.
[f]See also Liulin references.
[g]Several instruments in this family: DosMap-Dostel, MTR-Dostel, EuTEF-Dostel, Dosis-Dostel.
[h]Two sensors for each of the three cartesian directions (X, Y, Z) for a total of 6.
[i]PAMELA silicon tracker is part of a complex instrument featuring also a permanent magnet as well as a time of flight system (based on 6 fast plastic scintillators and a calorimeter. See references).
[j]Each pair of sensors (thin–thick) is sandwiched on tissue equivalent plastic.
[k]Depending on the coincidence choice.
[l]RAD includes also a CsI(Tl) scintillator, a plastic scintillator, and an anti-coincidence system, see references.
[m]The top sensor is segmented into two rings, others are like the inner part of A, see references.
Further details in the references.

Liulin-ISS (September 2005 to June 2014), Liulin-5 (May 2007 to present), R3DE (February 2008 to September 2009), and R3DR (March 2009 to August 2010), the latter two have been deployed outside the ISS. Several Liulins (R3D-B2, R3D-B3, Liulin-Photo) have also been used in Foton and Bion satellites flying in Low Earth Orbit (LEO) and in the Chandrayaan-1 satellite around the moon (RADOM). The Liulin-5 (75–82) is the first of a new Liulin type: it is a telescope using three silicon detectors providing both a coincidence (telescope) and a non-coincidence read out (for direct dose measurements).

The charged particle directional spectrometer (*CPDS*) (44, 45) is a detector used by NASA to monitor ISS radiation environment. It is a telescope with a 12 element silicon stack with different thickness (6 thick, 5 mm and 6 thinner, 0.3 and 1 mm) and a Cerenkov detector at the bottom. Thick detectors are for particle identification. The individual sensor cards are identical in design to those used on the MARIE instrument (see below). Three CPDS have been deployed externally (EV-CPDS). EV1-CPDS and EV3-CPDS were aligned with the $+X$ and $-X$ axis in the ISS coordinate system, while EV2-CPSDS with the $-Z$ axis. Another detector

(IV-CPDS) was deployed inside the USLab initially pointing to the $+X$ direction and since 8 August 2006 to the $+Z$ direction.

Alteino (46–52), often referred to as SilEye3, is an upgraded SilEye (53), which was successfully deployed in the MIR station. As all the ALTEA systems it originates from investigations of the radiation potentially causing the "Light Flash" anomalous perception to the astronauts [Ref. (54) and references therein]. Alteino features a stack of eight silicon striped sensors (each 80 mm × 80 mm × 0.38 mm) and two plastic scintillators: one in front of and one behind the silicon stack. Sensors are segmented in alternating directions (X and Y). The direction and the height in the stack of eight provide a set of three coordinates for each sensor traversal and for each particle, and permit to track its direction. Alteino is a pure telescope recording radiation only when both scintillators are hit. The detector has the size of a shoebox, and it is able to measure the LET in silicon and the flux and the trajectory of each ion, using the ability to know which of the sensor strip has been hit. Alteino was deployed in the Russian segment of the ISS, in the Russian space program and then in an ESA sponsored experiments under the ALTCRISS project. Alteino data were downloaded periodically via PCMCIA cards. Alteino provided detailed particle spectra in the Russian modules.

ALTEA (55–74) is a system of six identical silicon telescopes. Each telescope is similar to Alteino (also in size) but lacking the scintillators and featuring six striped silicon sensors with twice the area of the sensors used in Alteino (each 160 mm × 80 mm × 0.38 mm). The bi-directional geometrical factor is 230 cm^2 sr and the system is auto-triggered by traversing ions. The six telescopes are identical and in the periods of interest have been deployed either on a helmet shaped holder in different locations in the USLab, on a three axis (X, Y, and Z) holder in other locations in the USLab or in a flat configuration for measuring effectiveness of shielding materials in one location in Columbus. ALTEA data are downlinked via real time telemetry. A software package on ground provides flux, dose, dose equivalent, and spectra in real time. ALTEA ISS surveys allowed for the 3D characterization of the radiation environment in the USLab (relevant for model validation). Also of relevance is the study of the iron abundance (ISS – USLab), which is apparently lower than expected.

DosTel (16, 83–89) is a detector family based on two silicon detectors, each with an area of 6.94 cm^2 arranged in telescope geometry. With this setup, the DosTel applied for various experiments onboard space stations and shuttle missions can measure energy deposition of radiation hitting a detector ("dose mode") or coincidental hits in the two detectors ("telescope" or "LET" mode). From 2009 onward, two identical DosTel units have been deployed in Columbus looking in two directions (X and Y). The long duration of the DosTel measurements in Columbus permits to study the variation of the radiation during a long solar modulation period.

TRITEL (90–95) is a set of three small two elements silicon telescopes, mounted in a 3D configuration (X, Y, and Z). Each telescope is made of two sensors, 220 mm × 0.3 mm, and has a geometrical factor of 5.1 cm^2 sr. All sensors are identical, fully depleted, passivated implanted planar silicon (PIPS) detectors. TRITEL has been deployed in the ISS since 2012. TRITEL has been deployed in the Columbus modulus in the EPM rack (TRITEL-SURE, close to DosTel) and in the Zvezda modulus (TRITEL-RS).

PAMELA (96–112) was developed from an instrument that flew aboard the balloon missions MASS, TS93, and CAPRICE, with a design optimized for the study of antimatter in the cosmic radiation. For this type of investigation, it is necessary to have information about the particle charge, energy, and type of interaction from several redundant sub-detectors, in order to uniquely identify rare particles from background. It is composed of a Time-of-Flight (ToF) system, a magnetic spectrometer (MS), a sampling electromagnetic calorimeter (SeC), and a neutron detector (ND).

The ToF comprises six layers of fast plastic scintillators arranged in three double planes (S1, S2, and S3), with alternate layers placed orthogonal to each other. ToF information for charged particles is combined with track length information from the MS to determine particle velocities; particle charge (Z) can be determined up to $Z = 8$.

The MS consists of a permanent magnet and a silicon tracker (six equidistant 300 μm thick silicon detector planes inserted inside the magnetic cavity). Ionization loss measurements are also made in the silicon planes.

The SeC is made of 44 single-sided silicon sensor layers (380 μm thick) interleaved with 22 plates of tungsten absorber. The main task of the calorimeter is to select positrons and antiprotons from like-charged backgrounds, and it is therefore not of interest in our case; however, it also provides a measurement of the energy of the incident electrons independent from the MS, thus allowing a cross-calibration of the two energy determinations.

The ND is placed below the calorimeter with the aim to increase the electromagnetic and hadronic discrimination capability of the Pamela instrument.

PAMELA's most important scientific results are related to the anomalous positron abundance. Here, however, the highest interest is in the extraordinary spectrometric ability in the low energy regime (below few GeV/n) for small Z ($Z < 8$) ions.

MARIE (113–118) is a telescope with an eight element silicon stack with Cerenkov detector at the bottom with different thickness (4 thick, 5 mm and 4 thinner, 0.3 and 1 mm). Thick detectors are for particle identification. The individual sensor cards are identical in design to those used on the CPDS instrument (see above). MARIE has been mounted on Odyssey's equipment deck, pointing opposite to the spacecraft's velocity vector. Odyssey is in a circular 2-h polar orbit around Mars. Forward field of view (FOV) points into deep space, rear FOV is partially blocked by Mars. MARIE performed the first characterization of the Martian radiation environment aimed at the risk assessment for human exploration.

CRaTER (119–126) is a telescope with three silicon detector pairs sandwiching pieces of tissue-equivalent plastic. Each pair has one thin detector (150 mm) for measuring high-LET particles and one thick detector (1 mm) for low-LET particles. CRaTER is part of LRO in orbit around the Moon. In nominal orbit, one end of telescope points zenith, the other nadir (toward lunar surface) with the rear FOV entirely filled by the lunar disk. LRO was in a circular 2-h polar orbit above the Moon for the prime mission and is now in an elliptical orbit. The overall dimensions are 24 cm × 23 cm × 16 cm. Of important is the long period of

observations that permits to investigate the evolution of the deep space radiation environment during the solar cycle.

RAD (127–135) is a three-element silicon stack, a CsI(Tl) scintillator with p-i-n diode readout and a plastic scintillator at the bottom of the stack; an anti-coincidence system surrounds the CsI(Tl) scintillator and the plastic scintillator and enables their use as neutral particle detectors. It is mounted on the top deck of Curiosity rover pointing to the zenith. The rover is controlled so that tilt does not exceed 10°. During cruise phase, RAD was shielded from above by the Descent Vehicle and from below by the heat shield. On Mars, RAD was shielded by Martian atmosphere (~20 g cm^{-2} CO_2). The detector is small (mass 1.56 kg, total volume 240 cm^3) and has several coincidence and anti-coincidence capabilities. RAD allowed for the first detailed measurements of the Mars surface radiation environment.

ACTIVE DETECTORS IN SPACE: THE FUTURE

With the advances of the field, active detectors may partly replace passive detectors. Power requirements as well as required sensor dimensions are slowly entering the region of acceptability for a widespread use in space, both as area detectors (for which constraints on dimensions and power are not so strong and therefore requirements for detailed measurement of the radiation field can be fulfilled) and as personal detectors. In the latter case, the miniaturization would not allow for a complete characterization of the radiation field. Nevertheless, active personal dosimeters certainly would provide a more comprehensive picture than passive detectors, and they would permit real time monitoring and alarming capabilities [see, for example, Ref. (136)]. It would be desirable that the data of all future active devices flow into a network of databases in order to make it available in quasi real time for all interested teams.

CONCLUSION

The development of a *search book* comprising information about radiation measurements relevant for the validation of models for human exploration has been reported. While not yet complete the extent of measurements of active detectors is already impressive and constitutes a valuable tool for anyone developing or validating radiation models for deep space spacecraft or habitats.

Complementing information about other measurements and detectors will be added in the future, and a similar approach for passive detectors should be started. A final output on a web page is foreseen.

AUTHOR CONTRIBUTIONS

All authors (LN, TB, DM, and GR) have participated to the idea and to the writing of the Search Book and of this first mini review.

ACKNOWLEDGMENTS

The authors acknowledge the very important help given by all the researchers that collaborated in providing information about the devices they are or have been working with. Specifically, V. V. Benghin, M. Casolino, T. P. Dachev, A. Hirn, K. T. Lee, V. A. Shurshakov, J. V. Semkova, R. Sparvoli, and C. Zeitlin.

REFERENCES

1. Durante M, Cucinotta FA. Physical basis of radiation protection in space travel. *Rev Mod Phys* (2011) **83**:1245–81. doi:10.1103/RevModPhys.83.1245
2. Kuznetsov NV, Nymmik RA, Panasyuk MI, Sosnovets EN, Teltsov MV. Detection and prediction of absorbed radiation doses from solar proton fluxes onboard orbital stations. *Cosmic Res* (2004) **42**:203–9. doi:10.1023/B:COSM.0000033295.49916.83
3. Benghin VV, Petrov VM, Kireeva SA, Markov AV, Volkov AN, Aleksandrin AP, et al. Analysis of radiation dose increases caused by solar cosmic ray events observed by the radiation monitoring system on the Russian segment of the International Space Station. *Adv Space Res* (2005) **36**:1749–52. doi:10.1016/j.asr.2005.08.008
4. Petrov VM, Benghin VV, Shurshakov VA, Panasyuk MI, Kutuzov YV, Morozov OV, et al. Absorbed doses in October-November 2003 onboard the Russian segment of the International Space Station according to the data of radiation control system. *Cosmic Res* (2006) **44**:106–10. doi:10.1134/S0010952506020031
5. Benghin VV. On-board predicting algorithm of radiation exposure for the International Space Station radiation monitoring system. *J Atmos Sol Terr Phys* (2008) **70**:675–9. doi:10.1016/j.jastp.2007.08.045
6. Lishnevskii A, Panasyuk M, Benghin V, Petrov VM, Volkov AN, Nechayev OY. Variations of radiation environment onboard the ISS in the year 2008. *Cosmic Research* (2010) **48**:206–10. doi:10.1134/S0010952510030020
7. Lishnevskii A, Panasyuk M, Benghin V, Petrov VM, Volkov AN, Nechaev OY. Variations of radiation environment on the International Space Station in 2005-2009. *Cosmic Research* (2012) **50**:319–23. doi:10.1134/S0010952512040028
8. Lishnevskii A, Panasyuk M, Nechaev O, Benghin VV, Petrov VM, Volkov AN. Results of monitoring variations of absorbed dose rate onboard the International Space Station during the period 2005-2011. *Cosmic Research* (2012) **50**:391–6. doi:10.1134/S0010952512050036
9. Lishnevskii A, Benghin VV. A method for a short-term forecast of the absorbed dose accumulation dynamics on the International Space Station based on radiation monitoring system data. *Sol Syst Res* (2014) **48**:568–73. doi:10.1134/S0038094614070144
10. Dachev T, Tomov B, Matviichuk Y, Dimitrov P, Lemaire J, Gregoire G. Calibration results obtained with Liulin-4 type dosimeters. *Adv Space Res* (2002) **30**:917–25. doi:10.1016/S0273-1177(02)00411-8
11. Uchihori Y, Kitamura H, Fujitaka K, Dachev TP, Tomov BT, Dimitrov PG. Analysis of the calibration results obtained with Liulin-4J spectrometer-dosimeter on protons and heavy ions. *Radiat Meas* (2002) **35**:127–34. doi:10.1016/S1350-4487(01)00286-4
12. Dachev TP, Stassinopoulos EG, Tomov BT, Dimitrov PG, Matviichuk YN, Shurshakov VA. Analysis of the cyclotron facility calibration and aircraft results obtained by LIULIN-3M instrument. *Adv Space Res* (2003) **32**:67–71. doi:10.1016/S0273-1177(03)90372-3
13. Spurný F, Gschwind R, Dačev T. Response of a semiconductor spectrometer to photons-comparison between experimental data and MC-calculations. *Nucl Energy Saf* (2003) **11**:114–7.
14. Atwell W, Reddell B, Dachev T, Tomov B. International Space Station mobile dosimetry unit: a comparison of flight measurements with model calculations. *J Aerosp* (2004) **113**:350–8. doi:10.4271/2004-01-2277
15. Dachev TP, Spurny F, Reitz G, Tomov BT, Dimitrov PG, Matviichuk YN. Simultaneous investigation of galactic cosmic rays on aircrafts and on International Space Station. *Adv Space Res* (2005) **36**:1665–70. doi:10.1016/j.asr.2005.05.073
16. Reitz G, Beaujean R, Benton E, Burmeister S, Dachev T, Deme S, et al. Space radiation measurements on-board ISS – the DOSMAP experiment. *Radiat Prot Dosimetry* (2005) **116**:374–9. doi:10.1093/rpd/nci262

17. Dachev T, Atwell W, Semones E, Tomov B, Reddell B. ISS observations of SAA radiation distribution by Liulin-E094 instrument on ISS. *Adv Space Res* (2006) **37**:1672–7. doi:10.1016/j.asr.2006.01.001
18. Spurny F, Ploc O, Jadrnıckova I, Turek K, Dachev T, Gelev M. Monitoring of onboard aircraft exposure to cosmic radiation: May-December 2005. *Adv Space Res* (2007) **40**:1551–7. doi:10.1016/j.asr.2006.10.006
19. Spurný F, Ploc O, Dachev T. On the neutron contribution to the exposure level onboard space vehicles. *Radiat Prot Dosimetry* (2007) **126**:519–23. doi:10.1093/rpd/ncm104
20. Wilson JW, Nealy JE, Dachev TP, Tomov BT, Cucinotta FA, Badavi FF, et al. Time serial analysis of the induced LEO environment within the ISS 6A. *Adv Space Res* (2007) **40**:1562–70. doi:10.1016/j.asr.2006.12.030
21. Semkova J. Radiation detection and dosimetry for estimating the space weather radiation impact on crewmembers during long space missions. *C R Acad Bulg Sci* (2007) **60**:957–66.
22. Häder DP, Richter P, Schuster M, Dachev T, Tomov B, Georgiev P, et al. R3D-B2 – measurement of ionizing and solar radiation in open space in the BIOPAN 5 facility outside the FOTON M2 satellite. *Adv Space Res* (2009) **43**:1200–11. doi:10.1016/j.asr.2009.01.021
23. Damasso M, Dachev T, Falzetta G, Giardi MT, Rea G, Zanini A. The radiation environment observed by Liulin-photo and R3D-B3 spectrum-dosimeters inside and outside Foton-M3 spacecraft. *Radiat Meas* (2009) **44**:263–72. doi:10.1016/j.radmeas.2009.03.007
24. Dachev TP, Tomov BT, Matviichuk YN, Dimitrov PG, Spurny F. Monitoring lunar radiation environment: RADOM instrument on Chandrayaan-1. *Curr Sci* (2009) **96**:544–6.
25. Dachev TP, Tomov BT, Matviichuk YN, Dimitrov PG, Bankov NG. Relativistic electrons high doses at International Space Station and Foton M2/M3 satellites. *Adv Space Res* (2009) **44**:1433–40. doi:10.1016/j.asr.2009.09.023
26. Dachev TP. Characterization of near Earth radiation environment by Liulin type instruments. *Adv Space Res* (2009) **44**:1441–9. doi:10.1016/j.asr.2009.08.007
27. Slaba TC, Blattnig SR, Badavi FF, Stoffle NN, Rutledge RD, Lee KT, et al. Statistical validation of HZETRN as a function of vertical cutoff rigidity using ISS measurements. *Adv Space Res* (2011) **47**:600–10. doi:10.1016/j.asr.2010.10.021
28. Dachev TP, Tomov BT, Matviichuk YN, Dimitrov PG, Spurny F, Ploc O. Liulin type spectrometry-dosemetri instruments. *Radiat Prot Dosimetry* (2011) **144**:675–9. doi:10.1093/rpd/ncq506
29. Dachev TP, Spurny F, Ploc O. Characterization of radiation environment by Liulin type spectrometers. *Radiat Prot Dosimetry* (2011) **144**:680–3. doi:10.1093/rpd/ncq534
30. Vadawale SV, Goswami JN, Dachev TP, Tomov BN, Girish V. Monitoring of the earth and moon radiation environment with RADOM experiment onboard Chandrayaan-1. *Adv Geosci* (2011) **25**:121–33.
31. Dachev TP, Tomov BT, Matviichuk YN, Dimitrov PG, Vadawale SV, Goswami JN, et al. An overview of RADOM results for earth and moon radiation environment on Chandrayyan-1 satellite. *Adv Space Res* (2011) **48**:779–91. doi:10.1016/j.asr.2011.05.009
32. Dachev TP, Semkova J, Tomov B, Matviichuk Y, Dimitrov P, Koleva R, et al. Space Shuttle drops down the SAA doses on ISS. *Adv Space Res* (2011) **47**:2030–8. doi:10.1016/j.asr.2011.01.034
33. Dachev TP, Tomov BT, Matviichuk YN, Dimitrov PG, Bankov NG, Reitz G. Relativistic electron fluxes and dose rate variations during April-May 2010 geomagnetic disturbances in the R3DR data on ISS. *Adv Space Res* (2012) **50**:282–92. doi:10.1016/j.asr.2012.03.028
34. Schuster M, Dachev T, Richter P, Häder D-P, Lebert M. R3DE, radiation risk radiometer-dosimeter on the International Space Station (ISS) – radiation data recorded during 18 month of EXPOSE-E exposure to open space climate. *J Astrobiol* (2012) **12**:393–402. doi:10.1089/ast.2011.0743
35. Dachev T, Horneck G, Häder D-P, Lebert M, Richter P, Schuster M, et al. Time profile of cosmic radiation exposure during the EXPOSE-E mission: the R3D instrument. *J Astrobiol* (2012) **12**:403–11. doi:10.1089/ast.2011.0759
36. Semkova J, Dachev T, Koleva R, Maltchev S, Bankov N, Benghin V, et al. Radiation environment on the International Space Station during the solar particle events in March 2012. *Astrobiol Outreach* (2013) **1**:102. doi:10.4172/2332-2519.1000102
37. Dachev TP, Tomov BT, Matviichuk YN, Dimitrov PG, Bankov NG, Reitz G. Relativistic electron fluxes and dose rate variations observed on the International Space Station. *J Atmos Sol Terr Phys* (2013) **99**:150–6. doi:10.1016/j.jastp.2012.07.007
38. Dachev T. Analysis of the space radiation doses obtained simultaneously at 2 different locations outside ISS. *Adv Space Res* (2013) **52**:1902–10. doi:10.1016/j.asr.2013.08.011
39. Dachev TP. Profile of the ionizing radiation exposure between the earth surface and free space. *J Atmos Sol Terr Phys* (2013) **102**:148–56. doi:10.1016/j.jastp.2013.05.015
40. Dachev TP, Semkova JV, Tomov BT, Matviichuk YN, Maltchev PGS, Koleva R, et al. Overview of the Liulin type instruments for space radiation measurement and their scientific results. *Life Sci Space Res (Amst)* (2015) **4**:92–114. doi:10.1016/j.lssr.2015.01.005
41. Dachev T, Horneck G, Häder D-P, Schuster M, Lebert M. EXPOSE-R cosmic radiation time profile. *J Astrobiol* (2015) **14**:17–25. doi:10.1017/S1473550414000093
42. Dachev TP, Tomov BT, Matviichuk YN, Dimitrov PG, Bankov NG, Shurshakov VV, et al. "BION-M" No. 1 spacecraft radiation environment as observed by the RD3-B3 radiometer-dosimeter in April-May 2013. *J Atmos Sol Terr Phys* (2015) **123**:82–91. doi:10.1016/j.jastp.2014.12.011
43. Dachev TP, Matviichuk YN, Semkova JV, Koleva RT, Boichev B, Baynov P, et al. Space radiation dosimetry with active detections for the scientific program of the second Bulgarian cosmonaut on board the Mir space station. *Adv Space Res* (1989) **9**:247–51. doi:10.1016/0273-1177(89)90445-6
44. Badhwar GD. Radiation measurements on the International Space Station. *Phys Med* (2001) **17**:287–91.
45. Lee K, Flanders J, Semones E, Shelfer T, Riman F. Simultaneous observation of the radiation environment inside and outside the ISS. *Adv Space Res* (2007) **40**:1558–61. doi:10.1016/j.asr.2007.02.083
46. Bidoli V, Casolino M, De Pascale MP, Furano G, Minori M, Morselli A, et al. The Sileye-3/Alteino experiment for the study of light flashes, radiation environment and astronaut brain activity on board the International Space Station. *J Radiat Res* (2002) **43**:s47–52. doi:10.1269/jrr.43.S47
47. Casolino M, Bidoli V, Furano G, Minori M, Morselli A, Narici L, et al. The Sileye-3/Alteino experiment on board the International Space Station. *Nucl Phys B Proc Suppl* (2002) **113**:71–8.
48. Casolino M, Bidoli V, Minori M, Narici L, De Pascale MP, Picozza P, et al. Relative nuclear abundances inside ISS with Sileye-3/Alteino experiment. *Adv Space Res* (2006) **37**:1686–90. doi:10.1016/j.asr.2006.02.050
49. Casolino M, Bidoli V, Minori M, Narici L, De Pascale MP, Picozza P, et al. Detector response and calibration of the cosmic-ray detector of the Sileye-3/Alteino experiment. *Adv Space Res* (2006) **37**:1691–6. doi:10.1016/j.asr.2005.03.136
50. Scrimaglio R, Rantucci E, Segreto E, Nurzia G, Finetti N, Di Gaetano A, et al. Analysis of Sileye-3/Alteino data with a neural network technique: particle discrimination and energy reconstruction. *Adv Space Res* (2006) **37**:1697–703. doi:10.1016/j.asr.2005.12.004
51. Larsson O, Benghin VV, Casolino M, Chernikch IV, Di Fino L, Fuglesang C, et al. Relative nuclear abundances from C to Fe and integrated flux inside the Russian part of the ISS with the Sileye3/Alteino experiment. *J Phys G Nucl Part Phys* (2014) **41**:015202. doi:10.1088/0954-3899/41/1/015202
52. Larsson O, Benghin VV, Berger T, Casolino M, Di Fino L, Fuglesang C, et al. Measurements of heavy-ion anisotropy and dose rates in the Russian section of the International Space Station with the Sileye3/Alteino detector. *J Phys G Nucl Part Phys* (2015) **42**:025002. doi:10.1088/0954-3899/42/2/025002
53. Bidoli V, Casolino M, De Grandis E, De Pascale MP, Furano G, Morselli A, et al. In-flight performances of SilEye-2 experiment and cosmic ray abundances inside space station MIR. *J Phys G Nucl Part Phys* (2001) **27**:2051–64. doi:10.1088/0954-3899/27/10/307
54. Narici L. Heavy ions light flashes and brain functions: recent observations at accelerators and in spaceflight. *New J Phys* (2008) **10**:075010. doi:10.1088/1367-2630/10/7/075010
55. Casolino M, De Pascale MP, Morselli A, Narici L, Picozza P, Prigiobbe V, et al. Light flash observation in space: experiment ELFO. *Nuovo Cimento Soc Ital Fis D* (1997) **19**:1601–23.
56. Narici L, Bidoli V, Casolino M, De Pascale MP, Furano G, Modena I, et al. The ALTEA facility on the International Space Station. *Phys Med* (2001) **17s**:255–7.

57. Narici L, Bidoli V, Casolino M, De Pascale MP, Furano G, Morselli A, et al. ALTEA: anomalous long term effects in astronauts. A probe on the influence of cosmic radiation and microgravity on the central nervous system during long flights. *Adv Space Res* (2003) **31**:141–6. doi:10.1016/S0273-1177(02)00881-5
58. Narici L, Belli F, Bidoli V, Casolino M, De Pascale MP, Di Fino L, et al. The ALTEA/Alteino projects: studying functional effects of microgravity and cosmic radiation. *Adv Space Res* (2004) **33**:1352–7. doi:10.1016/j.asr.2003.09.052
59. Scrimaglio R, Nurzia G, Rantucci E, Segreto E, Finetti N, Di Gaetano A, et al. Simulation of the ALTEA experiment on the International Space Station with the Geant 3.21 program. *Adv Space Res* (2006) **37**:1770–6. doi:10.1016/j.asr.2004.11.029
60. Di Fino L, Belli F, Bidoli V, Casolino M, Narici L, Picozza P, et al. ALTEA data handling. *Adv Space Res* (2006) **37**:1710–5. doi:10.1016/j.asr.2005.01.105
61. Zaconte V, Belli F, Bidoli V, Casolino M, Di Fino L, Narici L, et al. ALTEA: flight model calibration at GSI. *Adv Space Res* (2006) **37**:1704–9. doi:10.1016/j.asr.2005.02.028
62. Zaconte V, Belli F, Bidoli V, Casolino M, Di Fino L, Narici L, et al. ALTEA: the instrument calibration. *Nucl Instrum Methods Phys Res B* (2008) **266**:2070–8. doi:10.1016/j.nimb.2008.02.072
63. La Tessa C, Di Fino L, Larosa M, Lee K, Mancusi D, Matthia D, et al. Simulation of ALTEA calibration data with PHITS, FLUKA and GEANT4. *Nucl Instrum Methods Phys Res B* (2009) **267**:3549–57. doi:10.1016/j.nimb.2009.06.086
64. La Tessa C, Di Fino L, Larosa M, Narici L, Picozza P, Zaconte V. Estimate of the space station thickness at a USLab site using ALTEA measurements and fragmentation cross sections. *Nucl Instrum Methods Phys Res B* (2009) **267**:3383–7. doi:10.1016/j.nimb.2009.06.107
65. Zaconte V, Casolino M, De Santis C, Di Fino L, La Tessa C, Larosa M, et al. The radiation environment in the ISS-USLab measured by ALTEA: spectra and relative nuclear abundances in the polar, equatorial and SAA regions. *Adv Space Res* (2010) **46**:797–9. doi:10.1016/j.asr.2010.02.032
66. Zaconte V, Casolino M, Di Fino L, La Tessa C, Larosa M, Narici L, et al. High energy radiation influences in the ISS-USLab: ion discrimination and particle abundances. *Radiat Meas* (2010) **45**:168–72. doi:10.1016/j.radmeas.2010.01.020
67. Di Fino L, Casolino M, De Santis C, Larosa M, La Tessa C, Narici L, et al. Heavy ions anisotropy measured by ALTEA in the International Space Station. *Radiat Res* (2011) **176**:397–406. doi:10.1667/RR2179.1
68. Larosa M, Agostini F, Casolino M, De Santis C, Di Fino L, La Tessa C, et al. Ion rates in the International Space Station during the December 2006 solar particle event. *J Phys G Nucl Part Phys* (2011) **38**:095102. doi:10.1088/0954-3899/38/9/095102
69. Narici L, Casolino M, Di Fino L, Larosa M, Larsson O, Picozza P, et al. Iron flux inside the International Space Station is measured to be lower than predicted. *Radiat Meas* (2012) **47**:1030–4. doi:10.1016/j.radmeas.2012.07.006
70. Di Fino L, Zaconte V, Ciccotelli A, Larosa M, Narici L. Fast probabilistic particle identification algorithm using silicon strip detectors. *Adv Space Res* (2012) **50**:408–14. doi:10.1016/j.asr.2012.04.015
71. Di Fino L, Zaconte V, Stangalini M, Sparvoli R, Picozza P, Piazzesi R, et al. Solar particle event detected by ALTEA on board the International Space Station. The March 7th, 2012 X5.4 flare. *J Space Weather Space Clim* (2014) **4**:A19. doi:10.1051/swsc/2014015
72. Berrilli F, Casolino M, Del Moro D, Di Fino L, Larosa M, Narici L, et al. The relativistic solar particle event of May 17th, 2012 observed on board the International Space Station. *J Space Weather Space Clim* (2014) **4**:A16. doi:10.1051/swsc/2014014
73. Di Fino L, Larosa M, Zaconte V, Casolino M, Picozza P, Narici L. Measurements on radiation shielding efficacy of polyethylene and Kevlar in the ISS (Columbus). *J Radiat Res* (2014) **55**:i64–5. doi:10.1093/jrr/rrt198
74. Narici L, Casolino M, Di Fino L, Larosa M, Picozza P, Zaconte V. Radiation survey in the International Space Station. *J Space Weather Space Clim* (2015). doi:10.1051/swsc/2015037
75. Semkova J, Koleva R, Shurshakov V, Benghin V, Maltchev St, Kanchev N, et al. Status and calibration results of Liulin-5 charged particle telescope designed for radiation measurements in a human phantom onboard the ISS. *Adv Space Res* (2007) **40**:1586–92. doi:10.1016/j.asr.2007.01.008
76. Semkova J, Koleva R, Maltchev S, Benghin V, Shurshakov V, Chernykh I, et al. Preliminary results of Liulin-5 experiment for investigation of the dynamics of radiation doses distribution in a human phantom aboard the International Space Station. *C R Acad Bulg Sci* (2008) **61**:787–94.
77. Semkova J, Koleva R, Maltchev St, Kanchev N, Benghin V, Chernykh I, et al. Radiation measurements inside a human phantom aboard the International Space Station using Liulin-5 charged particle telescope. *Adv Space Research* (2010) **45**:858–65. doi:10.1016/j.asr.2009.08.027
78. Semkova J, Koleva R. Overview on radiation quantities observed by Liulin-5 instrument in a human phantom on the International Space Station during the minimum of the 23rd solar cycle. *C R Acad Bulg Sci* (2010) **63**:1533–42.
79. Semkova J, Koleva R, Maltchev St, Bankov N, Benghin V, Chernykh I, et al. Depth dose measurements with the Liulin-5 experiment inside the spherical phantom of the Matroshka-R project onboard the International Space Station. *Adv Space Res* (2012) **49**:471–8. doi:10.1016/j.asr.2011.10.005
80. Semkova J, Koleva R, Bankov N, Malchev St, Petrov VM, Shurshakov VA, et al. Study of radiation conditions onboard the International Space Station by means of the Liulin-5 dosimeter. *Cosmic Res* (2013) **51**:124–32. doi:10.1134/S0010952512060068
81. Semkova J, Koleva R, Maltchev St, Bankov N, Benghin V, Chernykh I, et al. Radiation characteristics in the spherical tissue-equivalent phantom on the ISS during solar activity minimum according to the data from Liulin-5 experiment. *J Atmos Sol Terr Phys* (2013) **99**:157–63. doi:10.1016/j.jastp.2012.07.006
82. Semkova J, Dachev T, Koleva R, Bankov N, Maltchev S, Benghin V, et al. Observation of radiation environment in the International Space Station in 2012-March 2013 by Liulin-5 particle telescope. *J Space Weather Space Clim* (2014) **4**:A32. doi:10.1051/swsc/2014029
83. Reitz G, Beaujean R, Heilmann C, Kopp J, Leicher M, Strauch K. Results of dosimetric measurements in space missions. *Adv Space Res* (1998) **22**(4):495–500.
84. Beaujean R, Kopp J, Reitz G. Active dosimetry on recent space flights. *Radiat Prot Dosimetry* (1999) **85**:223–6.
85. Beaujean R, Reitz G, Kopp J. Recent European measurements inside Biorack. *Mutat Res* (1999) **430**:183–9.
86. Reitz G, Strauch K, Beaujean R, Kopp J, Luszik-Bhadra M, Heinrich W. Dosimetric mapping inside BIORACK on shuttle missions STS76, STS81 and STS1984. In: Brinckmann E, Varajão C, Perry M, editors. *SP1222 Biorack on Spacehab*. Noordwijk, Netherlands: ESA (1999). p. 161–9.
87. Beaujean R, Kopp J, Burmeister S, Petersen F, Reitz G. Dosimetry inside Mir station using a silicon detector telescope (DOSTEL). *Radiat Meas* (2002) **35**:433–8. doi:10.1016/S1350-4487(02)00074-4
88. Badhwar GD, Atwell W, Reitz G, Beaujean R, Heinrich W. Radiation measurements on the Mir orbital station. *Radiat Meas* (2002) **35**(5):393–422. doi:10.1016/S1350-4487(02)00072-0
89. Labrenz J, Burmeister S, Berger T, Heber B, Reitz G. Matroshka DOSTEL measurements onboard the International Space Station (ISS). *J Space Weather Space Clim* (2015). doi:10.1051/swsc/2015039
90. Pázmándi T, Deme S, Láng E. Space dosimetry with the application of a 3D silicon detector telescope: response function and inverse algorithm. *Radiat Prot Dosimetry* (2006) **120**:401–4. doi:10.1093/rpd/nci539
91. Hirn A, Apáthy I, Bodnár L, Csőke A, Deme S, Pázmándi T. Development of a complex instrument measuring dose in the Van Allen belts. *Acta Astronaut* (2008) **63**:878–85. doi:10.1016/j.actaastro.2008.04.001
92. Hirn A. Models of performances of dosimetric telescopes in the anisotropic radiation field in Low Earth Orbit. *Acta Astronaut* (2010) **66**:1368–72. doi:10.1016/j.actaastro.2009.11.016
93. Zábori B, Hirn A, Bencze P. The relationship between plasma effects and cosmic radiation studied with TriTel-LMP measurements during the ESEO mission. *Adv Space Res* (2011) **48**:240–53. doi:10.1016/j.asr.2011.03.020
94. Zábori B, Hirn A. TRITEL 3 dimensional space dosimetric telescope in the European student earth orbiter project of ESA. *Acta Astronaut* (2012) **71**:20–31. doi:10.1016/j.actaastro.2011.08.010
95. Kuwahara T, Hirn A, Apáthy I, Bodnár L, Csőke A, Deme S, et al. TRITEL-JMS: a three-dimensional silicon detector telescope dedicated for operation on board microsatellite RISESAT. *Trans Jpn Soc Aeronaut Space Sci* (2014) **12**:Tr_13–Tr_17. doi:10.2322/tastj.12.Tr_13
96. Adriani O, Barbarino GC, Bazilevskaya GA, Bellotti R, Boezio M, Bogomolov EA, et al. Pamela's measurements of magnetospheric

effects on high-energy solar particles. *Astrophys J Lett* (2015) **801**:L3. doi:10.1088/2041-8205/801/1/L3
97. Adriani O, Barbarino GC, Bazilevskaya GA, Bellotti R, Boezio M, Bogomolov EA, et al. TRAPPED proton fluxes at Low Earth Orbits measured by the Pamela experiment. *Astrophys J Lett* (2015) **799**:L4. doi:10.1088/2041-8205/799/1/L4
98. Adriani O, Barbarino GC, Bazilevskaya GA, Bellotti R, Boezio M, Bogomolov EA, et al. Measurement of boron and carbon fluxes in cosmic rays with the Pamela experiment. *Astrophys J* (2014) **791**:93. doi:10.1088/0004-637X/791/2/93
99. Adriani O, Barbarino GC, Bazilevskaya GA, Bellotti R, Boezio M, Bogomolov EA, et al. The PAMELA mission: heralding a new era in precision cosmic ray physics. *Phys Rep* (2014) **544**:323–70. doi:10.1016/j.physrep.2014.06.003
100. Adriani O, Barbarino GC, Bazilevskaya GA, Bellotti R, Bianco A, Boezio M, et al. Cosmic-ray positron energy spectrum measured by PAMELA. *Phys Rev Lett* (2013) **111**:081102. doi:10.1103/PhysRevLett.111.081102
101. Adriani O, Barbarino GC, Bazilevskaya GA, Bellotti R, Boezio M, Bogomolov EA, et al. Measurement of the isotopic composition of hydrogen and helium nuclei in cosmic rays with the PAMELA experiment. *Astrophys J* (2013) **770**:2. doi:10.1088/0004-637X/770/1/2
102. Adriani O, Barbarino GC, Bazilevskaya GA, Bellotti R, Boezio M, Bogomolov EA, et al. Time dependence of the proton flux measured by Pamela during the 2006 Ju*ly-2009* December solar minimum. *Astrophys J* (2013) **765**:91. doi:10.1088/0004-637X/765/2/91
103. Adriani O, Barbarino GC, Bazilevskaya GA, Bellotti R, Boezio M, Bogomolov EA, et al. Observations of the 2006 December 13 and 14 solar particle events in the 80MeVn-1-3 GeV n-1 range from space with the PAMELA detector. *Astrophys J* (2011) **742**:102. doi:10.1088/0004-637X/742/2/102
104. Adriani O, Barbarino GC, Bazilevskaya GA, Bellotti R, Boezio M, Bogomolov EA, et al. The discovery of geomagnetically trapped cosmic-ray antiprotons. *Astrophys J Lett* (2011) **737**:L29. doi:10.1088/2041-8205/737/2/L29
105. Adriani O, Barbarino GC, Bazilevskaya GA, Bellotti R, Boezio M, Bogomolov EA, et al. Cosmic-ray electron flux measured by the PAMELA experiment between 1 and 625 GeV. *Phys Rev Lett* (2011) **106**(20):201101. doi:10.1103/PhysRevLett.106.201101
106. Adriani O, Barbarino GC, Bazilevskaya GA, Bellotti R, Boezio M, Bogomolov EA, et al. PAMELA measurements of cosmic-ray proton and helium spectra. *Science* (2011) **332**:69–72. doi:10.1126/science.1199172
107. Adriani O, Barbarino GC, Bazilevskaya GA, Bellotti R, Boezio M, Bogomolov EA, et al. PAMELA results on the cosmic-ray antiproton flux from 60 MeV to 180 GeV in kinetic energy. *Phys Rev Lett* (2010) **105**:121101. doi:10.1103/PhysRevLett.105.121101
108. Adriani O, Barbarino GC, Bazilevskaya GA, Bellotti R, Boezio M, Bogomolov EA, et al. A statistical procedure for the identification of positrons in the PAMELA experiment. *Astropart Phys* (2010) **34**:1–11. doi:10.1016/j.astropartphys.2010.04.007
109. Adriani O, Barbarino GC, Bazilevskaya GA, Bellotti R, Boezio M, Bogomolov EA, et al. An anomalous positron abundance in cosmic rays with energies 1.5-100 GeV. *Nature* (2009) **458**:607–9. doi:10.1038/nature07942
110. Adriani O, Barbarino GC, Bazilevskaya GA, Bellotti R, Boezio M, Bogomolov EA, et al. New measurement of the antiproton-to-proton flux ratio up to 100 GeV in the cosmic radiation. *Phys Rev Lett* (2009) **102**:051101. doi:10.1103/PhysRevLett.102.051101
111. Adriani O, Barbarino G, Bazilevskaya GA, Bellotti R, Boezio M, Bogomolov EA, et al. Measurements of quasi-trapped electron and positron fluxes with PAMELA. *J Geophys Res Space Phys* (2009) **114**:A12218. doi:10.1029/2009JA014660
112. Picozza P, Galper AM, Castellini G, Adriani O, Altamura F, Ambriola M, et al. PAMELA – a payload for antimatter matter exploration and light-nuclei astrophysics. *Astropart Phys* (2007) **27**:296–315. doi:10.1016/j.astropartphys.2006.12.002
113. Badhwar GD. Martian radiation environment experiment (MARIE). *Space Sci Rev* (2004) **110**:131–42. doi:10.1023/B:SPAC.0000021009.68228.a8
114. Zeitlin C, Cleghorn T, Cucinotta F, Saganti P, Andersen V, Lee K, et al. Overview of the Martian radiation environment experiment. *Adv Space Res* (2004) **33**:2204–10. doi:10.1016/S0273-1177(03)00514-3
115. Atwell W, Saganti P, Cucinotta FA, Zeitlin CJ. A space radiation shielding model of the Martian radiation environment experiment (MARIE). *Adv Space Res* (2004) **33**:2219–21. doi:10.1016/S0273-1177(03)00527-1
116. Lee KT, Cleghorn T, Cucinotta F, Pinsky L, Zeitlin C. Heavy ion observations by MARIE in cruise phase and Mars orbit. *Adv Space Res* (2004) **33**:2211–4. doi:10.1016/S0273-1177(03)00519-2
117. Cleghorn TF, Saganti PB, Zeitlin CJ, Cucinotta FA. Solar particle events observed at Mars: dosimetry measurements and model calculations. *Adv Space Res* (2004) **33**:2215–8. doi:10.1016/S0273-1177(03)00518-0
118. Zeitlin C, Boynton WV, Mitrofanov I, Hassler D, Atwell W, Cleghorn TF, et al. Mars Odyssey measurements of galactic cosmic rays and solar particles in Mars orbit, 2002-2008. *Space Weather* (2010) **8**:11. doi:10.1029/2009SW000563
119. Spence HE, Case AW, Golightly MJ, Heine T, Larsen BA, Blake JB, et al. CRaTER: the cosmic ray telescope for the effects of radiation experiment on the lunar reconnaissance orbiter mission. *Space Sci Rev* (2010) **150**:243–84. doi:10.1007/s11214-009-9584-8
120. Schwadron NA, Baker T, Blake B, Case AW, Cooper JF, Golightly M, et al. Lunar radiation environment and space weathering from the cosmic ray telescope for the effects of radiation (CRaTER). *J Geophys Res Planets* (2012) **117**:E00H13. doi:10.1029/2011JE003978
121. Wilson JK, Spence H, Case AW, Blake JB, Golightly MJ, Kasper J, et al. The first cosmic ray albedo proton map of the moon. *J Geophys Res Planets* (2012) **117**:E00H23. doi:10.1029/2011JE003921
122. Case AW, Kasper JC, Spence H, Zeitlin C, Looper MD, Golightly MJ, et al. The deep space galactic cosmic ray lineal energy spectrum at solar minimum. *Space Weather* (2013) **11**:361–8. doi:10.1002/swe.20051
123. Zeitlin C, Case AW, Spence H, Schwadron NA, Golightly M, Wilson JK, et al. Measurements of galactic cosmic ray shielding with the CRaTER instrument. *Space Weather* (2013) **11**:284–96. doi:10.1002/swe.20043
124. Looper MD, Mazur JE, Blake JB, Spence HE, Golightly MJ, Case AW, et al. CRaTER observations and Geant4 simulations. *Space Weather* (2013) **11**:142–52. doi:10.1002/swe.20034
125. Joyce CJ, Schwadron NA, Wilson JK, Spence HE, Kasper J, Golightly M, et al. Validation of PREDICCS using CRaTER/LRO observations during three major solar events in 2012 using CRaTER and the EMMREM model. *Space Weather* (2013) **11**:1–11. doi:10.1002/swe.20059
126. Mazur JE, Zeitlin C, Schwadron N, Looper MD, Townsend LW, Blake JB, et al. Update on radiation dose from galactic and solar protons at the moon using the LRO/CRaTER microdosimeter. *Space Weather* (2015) **13**:363–4. doi:10.1002/2015SW001175
127. Hassler DM, Zeitlin C, Wimmer-Schweingruber RF, Böttcher S, Martin C, Andrews J, et al. The radiation assessment detector (RAD) investigation. *Space Sci Rev* (2012) **170**:503–58. doi:10.1007/s11214-012-9913-1
128. Zeitlin C, Hassler DM, Cucinotta FA, Ehresmann B, Wimmer-Schweingruber RF, Brinza DE, et al. Measurements of energetic particle radiation in transit to Mars on the Mars science laboratory. *Science* (2013) **340**:1080–4. doi:10.1126/science.1235989
129. Hassler DM, Zeitlin C, Wimmer-Schweingruber RF, Ehresmann B, Rafkin S, Eigenbrode JL, et al. Mars' surface radiation environment measured with the Mars science laboratory's curiosity rover. *Science* (2014) **343**:1244797. doi:10.1126/science.1244797
130. Köhler J, Ehresmann B, Martina C, Böhm E, Kharytonov A, Kortmann O, et al. Inversion of neutron/gamma spectra from scintillator measurements. *Nucl Instrum Methods Phys Res B* (2011) **269**:2641–8. doi:10.1016/j.nimb.2011.07.021
131. Köhler J, Zeitlin C, Ehresmann B, Wimmer-Schweingruber RF, Hassler D, Reitz G, et al. Measurements of the neutron spectrum on the Martian surface with MSL/RAD. *J Geophys Res Planets* (2014) **119**:594–603. doi:10.1002/2013JE004539
132. Ehresmann B, Zeitlin C, Hassler DM, Wimmer-Schweingruber RF, Böhm E, Böttcher S, et al. Charged particle spectra obtained with the Mars science laboratory radiation assessment detector (MSL/RAD) on the surface of Mars. *J Geophys Res Planets* (2014) **119**:468–79. doi:10.1002/2013JE004547
133. Rafkin SCR, Zeitlin C, Ehresmann B, Köhler J, Guo J, Kahanpää H, et al. Diurnal variations of energetic particle radiation at the surface of Mars as observed by the Mars science laboratory radiation assessment detector. *J Geophys Res Planets* (2014) **119**:1345–58. doi:10.1002/2013JE004525

134. Köhler J, Ehresmann B, Zeitlin C, Wimmer-Schweingruber RF, Hassler DM, Reitz G, et al. Measurements of the neutron spectrum in transit to Mars on the Mars science laboratory. *Life Sci Space Res (Amst)* (2015) **5**:6–12. doi:10.1016/j.lssr.2015.03.001
135. Guo J, Zeitlin C, Wimmer-Schweingruber RF, Hassler DM, Posner A, Heber B, et al. Variations of dose rate observed by MSL/RAD in transit to Mars. *Astron Astrophys* (2015) **577**:A58. doi:10.1051/0004-6361/201525680
136. Kroupa M, Bahadori A, Campbell-Rickets T, Empl A, Hoang SM, Idarraga-Munoz J, et al. A semiconductor radiation imaging pixel detector for space radiation dosimetry. *Life Sci Space Res (Amst)* (2015) **6**:69–78. doi:10.1016/j.lssr.2015.06.006

Conflict of Interest Statement: The authors declare that the research was conducted in the absence of any commercial or financial relationships that could be construed as a potential conflict of interest.

Copyright © 2015 Narici, Berger, Matthiä and Reitz. This is an open-access article distributed under the terms of the Creative Commons Attribution License (CC BY). The use, distribution or reproduction in other forums is permitted, provided the original author(s) or licensor are credited and that the original publication in this journal is cited, in accordance with accepted academic practice. No use, distribution or reproduction is permitted which does not comply with these terms.

frontiers in Oncology

REVIEW
published: 29 March 2016
doi: 10.3389/fonc.2016.00065

The Role of Nuclear Fragmentation in Particle Therapy and Space Radiation Protection

Cary Zeitlin[1] and Chiara La Tessa[2]*

[1] Lockheed Martin Information Services & Global Solutions, Houston, TX, USA, [2] Collider-Accelerator Department, Brookhaven National Laboratory, Upton, NY, USA

The transport of the so-called HZE particles (those having high charge, Z, and energy, E) through matter is crucially important both in space radiation protection and in the clinical setting where heavy ions are used for cancer treatment. HZE particles are usually considered those having $Z > 1$, though sometimes $Z > 2$ is meant. Transport physics is governed by two types of interactions, electromagnetic (ionization energy loss) and nuclear. Models of transport, such as those used in treatment planning and space mission planning must account for both effects in detail. The theory of electromagnetic interactions is well developed, but nucleus–nucleus collisions are so complex that no fundamental physical theory currently describes them. Instead, interaction models are generally anchored to experimental data, which in some areas are far from complete. The lack of fundamental physics knowledge introduces uncertainties in the calculations of exposures and their associated risks. These uncertainties are greatly compounded by the much larger uncertainties in biological response to HZE particles. In this article, we discuss the role of nucleus–nucleus interactions in heavy charged particle therapy and in deep space, where astronauts will receive a chronic low dose from galactic cosmic rays (GCRs) and potentially higher short-term doses from sporadic, unpredictable solar energetic particles (SEPs). GCRs include HZE particles; SEPs typically do not and we, therefore, exclude them from consideration in this article. Nucleus–nucleus collisions can result in the breakup of heavy ions into lighter ions. In space, this is generally beneficial because dose and dose equivalent are, on the whole, reduced in the process. The GCRs can be considered a radiation field with a significant high-LET component; when they pass through matter, the high-LET component is attenuated, at the cost of a slight increase in the low-LET component. Not only are the standard measures of risk reduced by fragmentation, but it can be argued that fragmentation also reduces the uncertainties in risk calculations by shifting the LET distribution toward one that is more concentrated at low LET, where biological effects are better understood. We review previous work in this area, including measurements made by the Radiation Assessment Detector during its journey to Mars and while on the surface of Mars aboard the Curiosity rover. Transport of HZE is also critically important in heavy-ion therapy, as it is necessary to know the details of the radiation field at the treatment site. This field is substantially modified compared to the incident pure (or nearly pure) ion beam by the same mechanisms of energy loss and nuclear fragmentation that pertain to the transport of space radiation.

Keywords: galactic cosmic rays, nuclear fragmentation models, nuclear interactions, Bragg curve, space radiation, space radiation shielding, heavy-ion therapy

OPEN ACCESS

Edited by:
Marco Durante,
GSI Helmholtz Centre for Heavy Ion Research, Germany

Reviewed by:
Vincenzo Patera,
Sapienza University of Rome, Italy
Lawrence Harvey Heilbronn,
University of Tennessee, USA

****Correspondence:***
Cary Zeitlin
cary.j.zeitlin@nasa.gov

Specialty section:
This article was submitted to Radiation Oncology, a section of the journal Frontiers in Oncology

Received: *01 December 2015*
Accepted: *07 March 2016*
Published: *29 March 2016*

Citation:
Zeitlin C and La Tessa C (2016) The Role of Nuclear Fragmentation in Particle Therapy and Space Radiation Protection. Front. Oncol. 6:65. doi: 10.3389/fonc.2016.00065

INTRODUCTION

The situation for cancer treatment with beams of heavy charged particles is quite different from that in space, but there is important overlap between the transport physics in the two settings. In the clinic, dose localization is of paramount importance, but nuclear fragmentation degrades localization. By contrast, the same process is beneficial in space, because high-LET particles are broken up into particles with lower LET and (in most cases) reduced biological effectiveness.

Fragmentation significantly complicates treatment planning, because the lower-LET particles produced in these reactions have greater ranges than the primary beam ions and, therefore, deposit energy beyond the distal edge of the Bragg peak. Low-LET particles may also be produced at significant angles with respect to the incoming beam, resulting in a lateral leakage of dose into healthy tissues. Target fragments, which consist of short-ranged, high-LET charged particles and neutrons, are emitted more or less isotropically from the struck nucleus, and may cause very large energy deposits anywhere along the path of the incident ion. Such reactions are particularly undesirable when they occur in the entrance region, since they tend to undermine one of the primary benefits of heavy ions for therapy, the large peak-to-plateau dose ratio. Target fragments are also produced by proton beams and complicate treatment planning in that modality (1).

These effects, particularly the irradiation of healthy tissues beyond the distal edge of the Bragg peak, effectively limit the maximum ion charge that can be used in treatment. For any given beam ion species, and any given depth of treatment volume, it is possible to find a beam energy that will yield a Bragg peak in the desired location. This might seem to suggest that the highest possible Z should be used, in order to maximize the peak-to-plateau ratio of biological dose. However, the distal edge problem worsens significantly with increasing beam charge. In the early days of heavy-ion therapy at the Lawrence Berkeley Laboratory's Bevalac, ions as heavy as neon ($Z = 10$) were used. Current practice in Japan and Europe has largely been focused on carbon ions ($Z = 6$) as representing a more optimal trade. Helium ions ($Z = 2$, mass number 4) are also of considerable interest, and our analysis of recently obtained cross-sectional data suggests that they may provide a localization advantage. This arises from the fact that the nucleons in helium nuclei are especially tightly bound, making them relatively less likely to fragment. When they do undergo fragmentation, the most copiously produced isotope is ^{1}H, which for a given kinetic energy per nucleon has almost exactly the same range as ^{4}He. This fact significantly reduces the distal edge problem, though deuterons (^{2}H) and neutrons produced in fragmentation reactions do deposit some energy in the distal edge.

In space, exposure to heavy ions increases cancer risk; in medicine, the same ions may be used to treat cancer. In the following, we will compare and contrast the effects of nuclear fragmentation in these two environments. An extensive literature on nuclear reactions relevant to spaceflight exists, and was recently reviewed by Norbury et al. (2) Since the beginning of human spaceflight, it has been recognized that energetic charged particles pose a health risk to explorers. When mission durations were short, on the order of hours or days and confined to low-Earth orbit (LEO), the main concerns were exposure to large solar-particle events (SPEs) and trapped radiation. SPEs, which typically produce protons with kinetic energies below 100 MeV, are a concern even on short missions for two reasons: first, because they can produce high dose rates, particularly in situations where shielding is minimal, and, second, because they are unpredictable and sometimes have sudden onsets (3). In LEO, there is geomagnetic shielding of galactic cosmic rays (GCRs) and also partial blocking of particle fluxes by the Earth (roughly a 35–40% effect, depending on altitude). Exposure to GCRs in LEO gives a small but steady dose rate, on the order of 100–300 μGy/day depending on the phase of the solar cycle; in such orbits, there is a roughly equal contribution from trapped radiation, so that in the absence of SPEs, total doses are well under 1 mGy/day. Considering that, in the ICRP 60 formulation (4), the average radiation quality factor in space is in the range from 6 to 7 (less behind shielding), this leads to exposures of <5 mSv/day in terms of dose equivalent. Although this is a far higher rate than encountered on Earth (about 4 mSv/year average in the United States), such exposures are not of concern for mission durations of a few days or weeks – they are far below threshold for acute effects, and small enough that they would not be expected to significantly increase lifetime fatal cancer risk.

The exposure scenario for long-duration missions into deep space is considerably different from those of short-duration missions to LEO or even to the Moon as in the Apollo era. Deep-space missions of the future are likely to be longer in duration than most if not all missions to date, with modestly shielded vehicles, and by definition will be outside the (partial) protection of LEO. In long-duration mission scenarios, the dominant radiation health risks are almost certain to be those from GCRs, including a significant component of heavy ions (5). Because GCRs tend to be highly energetic, most of them pass through the moderate shielding (probably on the order of 20 g cm^{-2}) that is to be expected on a vehicle built for crewed travel into deep space. Exposure to energetic heavy ions is unavoidable; however, shielding does attenuate the heavy ion flux due to nuclear interactions that cause the incident ions to fragment into lighter ions. Choosing shield materials to maximize nuclear fragmentation is at present the most viable strategy for reducing this exposure, though there is certainly a shielding depth at which the law of diminishing returns begins to pertain. Other approaches, including magnetic and electrostatic shielding, are not yet practical, nor is it feasible (from the cost perspective) to launch shields consisting of hundreds of gram per square centimeter of mass, or even many tens of gram per square centimeter.

In the following, we will review transport physics as it pertains to energetic charged particles encountered in space and used in radiation therapy, with particular emphasis on the unique roles played by nuclear fragmentation in these two very different settings. A brief overview of fragmentation models is also given. We will present both data and model calculations to support the conclusions outlined here, both for space radiation and for beams of interest in the clinic. It should be added that proton–nucleus collisions are also extremely important in both settings, but are not covered in detail here.

TRANSPORT OF ENERGETIC CHARGED PARTICLES

The transport of energetic particles through spacecraft walls, equipment racks, and human tissues determines the physical dose received by astronauts in space, and the same physical mechanisms affect the beams of charged particles that are used to irradiate tumors. When charged particles traverse matter, electromagnetic interactions cause ionization energy loss, which continuously slows the incident particles, increasing their LET. These interactions are between the electromagnetic field of the projectile and the electrons surrounding the atoms in the material being traversed. The projectiles considered here are bare nuclei, fully stripped of all electrons. These interactions produce a region of relatively dense ionization along the trajectory of the projectile and can also result in the production of long-ranged, high-energy "knock-on" electrons, also known as δ-rays, which can deposit dose at a considerable distance from the main track. Detailed models of track structure (6–8) describe these complexities, which include energy deposition at significant distances from the primary track in the plane transverse to the direction of the incident particle. Electromagnetic interactions also cause Coulomb multiple scattering, but for the particles and energies of interest here, we are for the most part not concerned with this process as it produces mostly very small angle deflections. The interested reader is referred to the literature (9).

The nuclear interactions of interest span a broad range of possibilities, from highly peripheral interactions in which only a small number of nucleons are removed from the projectile to central collisions in which the incoming projectile is fragmented into a high-multiplicity spray of light ions. Also of interest in nuclear interactions is the production of target fragments, including neutrons that are capable of penetrating large depths of matter before interacting.

Ionization Energy Loss

Ionization energy loss is a purely electromagnetic phenomenon in which a charged projectile interacts with the electrons in the atoms of the target medium. The energy lost by the projectile per unit path length is accurately described by the Bethe equation (9):

$$\frac{dE}{dx} = -k\rho\left(\frac{Z}{A}\right)_{mat}\left(\frac{Z}{\beta}\right)^2_{proj}\left[\log\left(\frac{2m_e\beta^2}{I\left(1-\beta^2\right)}\right)-\beta^2\right]$$

where k is a constant, Z refers to atomic number, A to mass number, β is the velocity of the moving particle relative to the speed of light, I is the ionization potential of the medium, and ρ its density. The subscript "mat" refers to the material being traversed (often referred to as the target, here as the shield), while "proj" refers to the projectile. The density effect, neglected in the equation above, is applicable at high energy, and additional corrections are needed at very low energies, where the curve turns over as particles approach their stopping points. The term in brackets is slowly varying with projectile energy, so that for moderate energies (β not too close to 1), dE/dx goes as (Z^2/β^2) of the projectile, and as (Z/A) of the target material. Integrating the dE/dx vs. energy curve yields the range–energy relation for any combination of projectile and target. To a very good approximation, the proton range for a given energy and material can be scaled to obtain the range of an ion with the same velocity (or energy per nucleon) having charge Z and mass number A according to (A/Z^2). Calculations of dE/dx have been shown to be highly accurate (typically to better than 1%) over a wide range of projectiles and targets; the main uncertainties are the ionization potentials. This part of the transport problem is well understood and can be modeled with high confidence. The dependence on Z^2 and energy can be seen in **Figure 1**, which shows straightforward dE/dx vs. energy calculations for ^{12}C ions and protons in water for kinetic energies of 10 MeV/nuc and above (the region of interest for space applications). The curves are approximately flat at high energies, but rise significantly at the lower energies that are especially relevant for hadron therapy.

Nuclear Interactions

The electromagnetic interactions described in the preceding section are well understood from both theoretical and experimental perspectives. Nuclear interactions are also a crucial aspect of transport, but are not nearly as well understood from the theoretical perspective. Interactions between a projectile and atoms of the target are ultimately described by quantum electrodynamics (QED), the most accurate physical theory yet devised; by contrast, nuclear interactions are many-body problems that defy present-day calculational methods at the most fundamental level. That is, the particles that participate in nuclear interactions are themselves composites (nuclei contain nucleons, and nucleons contain quarks and gluons), and the fundamental theory that describes these interactions is quantum chromodynamics (QCD), which is only tractable in the limit of interactions with large momentum transfers. QCD has not yet been successfully applied to nucleus–nucleus collisions at the energies of interest here. The lack of a fundamental theory has led to the development of many semi-empirical models to describe nucleus–nucleus interactions, and considerable effort continues to be put into development of these models and benchmarking them (10) against the limited set of pertinent data that are available (2).

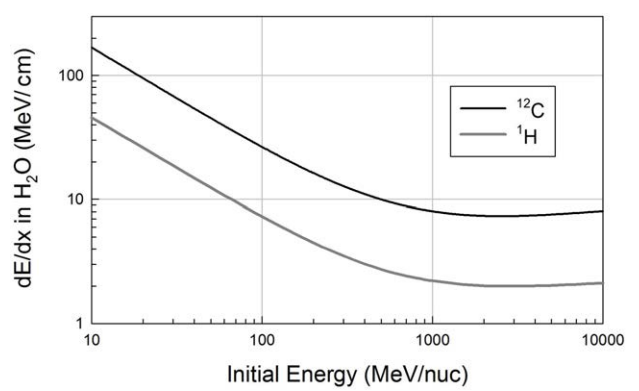

FIGURE 1 | Ionization energy loss curves for protons (^1H) and carbon ions in water, calculated from the Bethe equation.

Outgoing particles from a heavy-ion fragmentation reaction are typically described as either "projectile" fragments or "target" fragments. Projectile fragments approximately preserve the direction and velocity of the incident particle. Target fragments are produced when the nuclei in the medium being traversed participate in an interaction, and they or their remnants are left in an excited state. These states decay via emission of nucleons, including neutrons. Target fragments are emitted more or less isotropically in the laboratory frame, and have relatively low energies, on the order of tens of MeV or less. A nucleus–nucleus collision can, if it is central (i.e., head-on), produce a large multiplicity of projectile fragments, each of which has lower LET than did the incident ion, owing to the fact that dE/dx goes roughly as $(Z/\beta)^2$, and here β is roughly constant while Z decreases. The sum of the LETs of the projectile fragments is always less than the LET of the primary ion. Charged target fragments can have very high LETs, but have very short ranges. The typical target-fragment energy range is also the range in which the radiation weighting factor for neutrons is highest. Neutrons can also be produced as projectile fragments, stripped from the projectile.

Nuclear Cross Sections and Bragg Curves

Cross sections for nucleus–nucleus interactions that produce a charge change in the projectile are accurately described by a simple energy-independent model of overlapping spheres, as first postulated by Bradt and Peters (11). Wilson and Townsend (12) presented a slightly modified version for use in NASA space radiation transport codes:

$$\sigma_{cc} = \pi r_0^2 \left(A_{\text{proj}}^{1/3} + A_{\text{targ}}^{1/3} - 0.2 - 1/A_{\text{proj}} - 1/A_{\text{targ}} \right)^2$$

where σ_{cc} is the charge-changing cross section, the A values refer to the mass numbers of the projectile and target, and r_0 is the nucleon radius, which is known from other data to be roughly 1.2–1.5 fm. Several other variations on the basic Bradt–Peters model exist (13, 14), but all yield similar results. As will be discussed below, the Wilson–Townsend formula reproduces measured charge-changing cross sections over a wide range of projectile and target masses, for energies from a few hundred MeV/nuc to at least 1 GeV/nuc. We can use data to constrain r_0 and also to investigate the "nuclear transparency" term in the above formula, which is represented by a constant with value −0.2. This term corresponds to the probability that the spheres overlap without causing the projectile to lose charge; representing this probability by a simple constant may be an oversimplification.

Measured Bragg curves obtained with monoenergetic ion beams illustrate the competing effects of fragmentation and ionization energy loss. **Figure 2** shows depth-dose curves obtained for three different beams at the NASA Space Radiation Laboratory (NSRL) (15). The NSRL is a dedicated NASA facility at the Brookhaven National Laboratory. The Bragg curve data are publicly available on the NSRL web site. High-density polyethylene (CH_2, with density $\rho = 0.97$ g cm^{-3}) was used as a moderator and parallel-plate ionization chambers were used to record the relative ionization before and after the moderator; the ratio of the two (after to before) is plotted on the y-axis. The shortest-range beam of the three considered here is the 200 MeV/nuc ^{12}C, which penetrates to a depth of about 8.4 cm of the target material before stopping. The Bragg curve increases relatively quickly with increasing target depth due to the low energy of the primary beam ions; this case is dominated by energy loss. At 293 MeV/nuc, ions of the same species travel nearly twice as far compared to the 200 MeV/nuc ions, and the Bragg curve shows a slower rise and a smaller peak. This is because the initial dE/dx is lower at the higher energy, and also because fragmentation of the primary beam ions begins to exert a significant influence. Using published data (16), we estimate that ^{12}C ions in polyethylene of this density

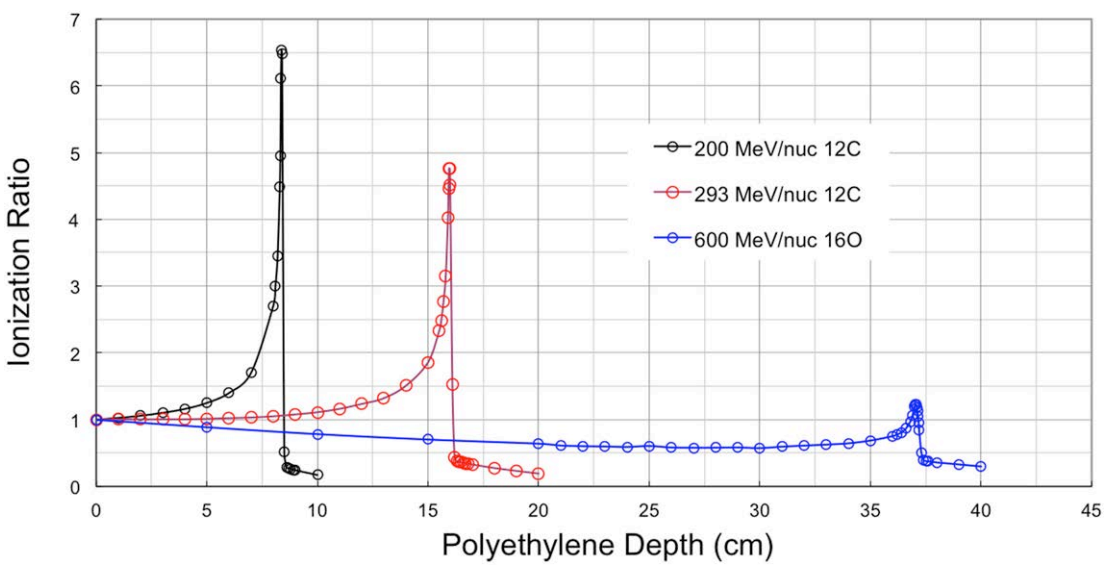

FIGURE 2 | **Bragg curve data from NSRL for three beams**.

have an interaction mean free path of about 23 cm. The fraction of surviving primaries at depth x is given by $e^{-x/\lambda}$ where λ is the interaction mean free path (mfp), so that over the first 12 cm of the target, some 40% of them undergo a charge-changing interaction, and at the Bragg peak (16 cm), roughly 50% of them have fragmented. About 20% of these interactions produce boron fragments ($Z = 5$), which have slightly longer ranges than the carbon primaries, and somewhat lower LET. These contribute to the distal edge just past the Bragg peak, while lighter fragmentation products – dominantly ^{4}He ions – give a non-negligible dose for several centimeter beyond the Bragg peak. The distal edge dose is also apparent for 200 MeV/nuc ^{12}C, but is not nearly as prominent because a smaller fraction of primary ions undergo fragmentation before reaching the Bragg peak.

The Bragg curve for 600 MeV/nuc ^{16}O is also shown in **Figure 2**, primarily to show a contrasting case in which fragmentation dominates over ionization energy loss. For this beam, dE/dx is initially relatively low and (compared to the lower-energy beams) in a relatively flat portion of the dE/dx curve. The Bragg peak, therefore, occurs deep in the target, at about 37 cm. Again using published data, the mfp for ^{16}O to undergo a charge-changing interaction in CH_2 of this density is found to be about 17 cm, so that the survival fraction of primaries at the ionization peak is only 11%. The remaining mix of particles has comparatively low LET, so that the peak ionization barely surpasses the initial value at the entrance. Over most of the target depth, the 600 MeV/nuc ^{16}O beam produces ionization ratios <1, that is, less than that of the initial, unfragmented beam. We will return to the subject of these Bragg curves in the discussion of fragmentation models below.

Projectile Fragments

Projectile fragments retain, to a large degree, the velocity and direction of the projectile, which makes intuitive sense considering that they are essentially intact pieces of the incident nucleus. However, velocities and directions are not exactly preserved, and the deviations are especially important in the clinical setting where these changes may contribute to dose outside the treatment volume. The changes of momentum of projectile fragments compared to the primary are mostly well-described by the statistical theory of Goldhaber (17). Projectile fragments in general have shifts in both transverse and longitudinal momentum; the change in each Cartesian coordinate is normally distributed, i.e., the probability distribution goes as $\exp(-p^2/2\sigma^2)$ where $\sigma^2 = \sigma_0^2 A_{\text{frag}}\left(A_{\text{proj}} - A_{\text{frag}}\right)/\left(A_{\text{proj}} - 1\right)$ and σ_0 is on the order of 90 MeV/c. Goldhaber's work elegantly derives these relationships in two independent ways: from considerations of the Fermi motion of the nucleons inside the projectile nucleus prior to the collision, and also from thermal equilibrium, with σ_0 directly related to the equilibrium temperature. The theory was developed to explain the momentum distributions measured in nuclear emulsion by Heckman et al. (18), and has been validated with more recent data (19–21) using an indirect method. In the latter work, σ_0 was tuned to match individual data sets, and the model was then used to make essential corrections for angular acceptance, enabling extraction of light-fragment production cross sections from measurements made at 0° with small-acceptance detectors. These cross sections probe central (i.e., head-on) collisions, whereas the more common peripheral interactions tend to produce fragments with a small charge change from the primary.

As previously mentioned, in the clinical setting, fragmentation reactions lead to undesirable results, because fragments do not necessarily deposit their energy in the treatment volume. A qualitative assessment can be made using the formulas above. Given a ^{12}C projectile and (as is commonly produced) a ^{4}He fragment, the width of the momentum distribution in one transverse dimension is about 38 MeV/c, and in the two transverse dimensions is 54 MeV/c. If an interaction occurs near the entrance, when the primary has a kinetic energy of, for example, 250 MeV/nuc, then the longitudinal momentum of the fragment is roughly 3 GeV/c, so that the distribution of the polar angle has a width of about 1°. Since the distribution is normal, 95% will be contained within a cone of 2° width, 99.7% within 3°, etc. If the distance between the interaction point and the nominal stopping point of the primary is 50 mm, then deflections of 2° or greater produce transverse offsets of 1.7 mm or greater. For particles starting in the center of the beam, fragments undergoing such small deflections may remain within the treatment volume, but some particles starting near the edge of the beam will produce fragments that deposit energy outside the desired volume. This behavior is readily modeled, as is Coulomb scattering, as described below. Fragmentation can be thought of as creating a halo of projectile fragments that will tend to smear out what would otherwise be a sharp lateral edge defined by the beam.

The fragmentation of ^{12}C into helium produces dose in the far distal edge of the Bragg curve. A reasonably accurate estimate of this effect can be deduced from elementary considerations (22). Closer to the Bragg peak, other fragment species contribute, but hydrogen and helium are the only ions that can penetrate far past the Bragg peak.

Target Fragments

Empirical understanding of the composition of GCRs and of nuclear fragmentation owes much to work done with nuclear emulsions flown to high altitudes in the late 1940s and 1950s (23). Using a visual detection medium allows for the observation of short-ranged, high-LET target fragments emerging from interaction vertices, sometimes referred to as "stars." An example of an interaction vertex is shown in **Figure 3**, in which a 130 MeV/nuc ^{28}Si beam ion (incident from the left) interacts with a heavy nucleus in the emulsion. These fragments are difficult to detect by other means, but they are important in that they produce very large, localized energy depositions in the vicinity of the interaction point. Both charged fragments and neutral particles (which, unlike the charged fragments, may penetrate long distances) can emerge from the remnants of the struck nucleus, which may in the immediate aftermath of the collision be in an excited state, from which it decays to a ground state via particle emission. Target fragments are emitted isotropically in the rest frame of the target, which to a good approximation is also the laboratory frame. In addition to the local energy depositions from charged fragments, the production of neutrons may be dosimetrically important, as their subsequent interactions can produce additional high-LET secondaries. In the context of radiation therapy, these may occur

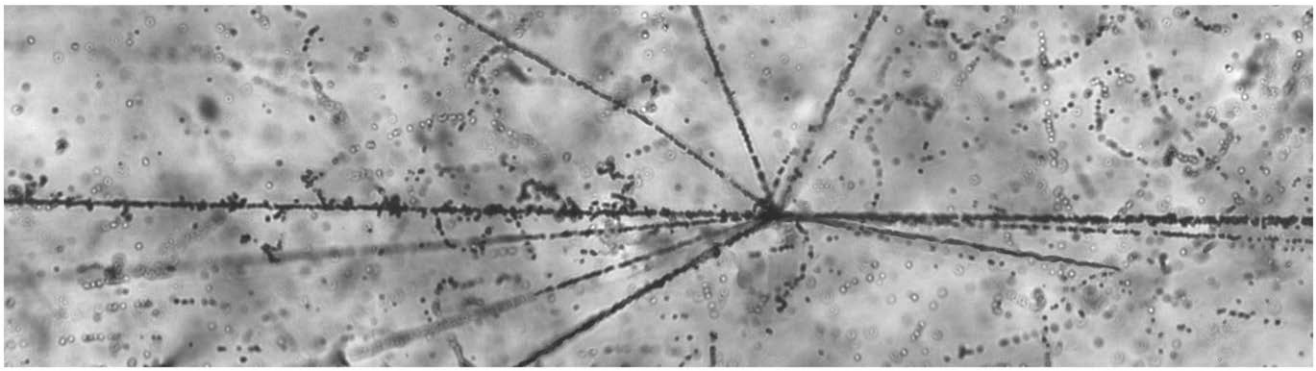

FIGURE 3 | A nuclear interaction "star" seen in photographic emulsion. The ^{28}Si beam ion is incident from the left. The backward-going tracks are target fragments.[1]

[1]The photomicrograph used in Figure 3 was made available by P. Zarubin et al. It, and many others, are available online at http://becquerel.jinr.ru/movies/movies.html

outside the tumor volume; in the context of space radiation, target-fragment neutrons produced in spacecraft walls can reach inhabited areas and contribute to crew exposures.

High Level Overview of Models

Monte Carlo codes, such as GEANT4 (24), MCNPX (25), FLUKA (26), and PHITS (27), have been developed by the high-energy and nuclear physics communities to model the transport of ions through matter. In the space radiation protection community, the same codes are used, along with an analytic transport model known as HZETRN that was developed within NASA by Wilson et al. (28) and subsequently extended (29). In the Monte Carlo codes, particles are followed in small steps through the medium, and the relevant physical processes (ionization energy loss, Coulomb scattering, and, for ions, nuclear interactions) are simulated in each step. The analytic approach, based on numerical solution of the Boltzmann equation, yields faster computation times in some cases, but many approximations are required, and these may compromise the accuracy of the results. For some purposes, such as spacecraft design, high accuracy is not needed in the initial stages and analytic calculations may suffice, but this approach is not applicable to treatment planning. Monte Carlo codes generally require considerable effort to define the geometry of the target (e.g., a large detector, a spacecraft, or a human in a therapy beam), and may require relatively long run times depending on the complexity of the geometry.

For either space radiation transport or treatment planning in a heavy ion beam, a nuclear physics model is needed, regardless of whether the analytic or Monte Carlo approach is used. The diversity of models likely accounts for the differences observed between codes (10, 30). In some of the Monte Carlo codes, there are also a variety of options available, i.e., the user selects a particular nuclear interaction model or models. Unlike HZETRN, the Monte Carlo codes do transport calculations in three dimensions, and are inherently capable of capturing important details of nuclear reactions that are lost in one-dimensional transport.

In the following sections, we use the PHITS Monte Carlo code to illustrate the important effects of shielding in modifying GCR fields (see Nuclear Interactions and Shielding in Space) and to compare calculated Bragg curves to the NSRL Bragg curve data (see Nuclear Interactions of Carbon Beams). These comparisons allow us to demonstrate some of the important capabilities of Monte Carlo codes vis-a-vis heavy ion transport, at least in relatively simple beamline geometry. This is not intended to constitute an endorsement of PHITS, but rather reflects our previous use of the code in similar geometries. Though the goal of reproducing Bragg curves may seem straightforward, it is in fact challenging to model the experimental results with high precision. And while not all aspects are perfectly reproduced, the relatively good agreement with the data gives us confidence that the model represents the mixtures of primaries and fragments that are present before, in, and beyond the Bragg peaks, providing insights that are not available from the data alone. It is highly likely that similar results would be obtained using the other Monte Carlo codes mentioned above.

NUCLEAR INTERACTIONS AND SHIELDING IN SPACE

In space, protons and high-charged nuclei undergo nuclear interactions as they traverse the hull of a spacecraft and the equipment inside. These are the same types of interactions that occur in the treatment setting as particle beams traverse healthy tissues on the way to the target volume. Nuclear interactions may produce a large number of secondary particles, particularly when incident energies are large. Shielding generally reduces the hazard from heavy ions due to the effects of nuclear fragmentation. Although heavy ions (those with charge $Z > 2$) represent only about 1% of the GCR flux, their contribution to dose in unshielded space can be 30 to 40% of the total. This disproportionate contribution can be understood by recalling that energy loss (which is directly related to dose imparted) is proportional to Z^2, that is, to the square of the projectile's charge. The dose-weighted average

charge of GCR heavy ions is about 10, so that the dose per particle is roughly 100 times greater than that of a proton having the same kinetic energy per nucleon. The contributions of GCR heavy ions to dose equivalent are even larger than their contributions to dose, owing to the large factors by which their fluxes are weighted. In free space, iron ions ($Z = 26$ and average LET about 155 keV/μm in water) make the largest contribution of any single ion species, despite being less abundant than protons by nearly four orders of magnitude.

Given that spacecraft to date have been constructed with aluminum hulls, and given our knowledge of the fragmentation cross sections of many ion species at typical GCR energies, we can estimate how much the fluxes of various primary ions are attenuated by fragmentation before passing through a hull. **Table 1** shows the results for several important species using cross sections calculated with the Townsend and Wilson energy-independent formula given above. Note that for the lighter ions, we expect there to be some replenishment by fragmentation of heavier ions (e.g., Fe + Al → Si + X, etc.); this is discussed further in Section "Measurements and Calculations for Space" below. There is also attenuation due to ionization energy loss, particularly at the larger depths, as will also be shown below. It is notable that 20 g cm^{-2} of aluminum is sufficient to break up the majority of incident iron ions and roughly half of magnesium and silicon ions.

The Role of Fragmentation in Space Radiation Protection

As the preceding has shown, fragmentation of primary GCR heavy ions as they traverse the hull of a spacecraft strongly influences the radiation environment inside. The flux of heavy ions is reduced behind shielding, which may result in a reduction in dose and certainly results in a reduction in dose equivalent. Because much of the uncertainty in the biological response to space radiation is due to uncertainty in response to heavy ions, the reduced flux of these ions behind shielding may also reduce some of the uncertainty in risk estimation.

It follows from the above considerations that an effective shield against GCRs is one that efficiently breaks up heavy incident ions into lighter ions. Put another way, we would expect materials with the largest cross sections per unit mass to be the best shields against GCRs. An important calculation verifying this was carried out by Wilson et al. (31), who found that a pure hydrogen shield would be extremely effective at reducing the dose equivalent from GCRs, and that the performance of other materials worsens with increasing atomic number. These calculations inspired subsequent experimental work (32, 33) that confirms the effectiveness of hydrogen in fragmenting heavy ions. It has subsequently been pointed out that the reductions of dose and dose equivalent at a point surrounded by hydrogenous shielding materials may be largely offset by the further transport of the components of the radiation field into a human body. That is, the fragmentation products of both proton–nucleus and nucleus–nucleus collisions, which include neutrons and low-energy protons, deposit doses of high-LET radiation inside the body that may be comparable to those from unattenuated GCR heavy ions, in terms of biological effect.

TABLE 1 | Calculated attenuation of high-energy ions by fragmentation in aluminum using geometric cross sections.

Ion	5 g cm^{-2} Al	10 g cm^{-2} Al	20 g cm^{-2} Al	40 g cm^{-2} Al
^{12}C	0.128	0.240	0.423	0.667
^{16}O	0.141	0.261	0.455	0.702
^{24}Mg	0.160	0.295	0.503	0.753
^{28}Si	0.169	0.309	0.522	0.772
^{56}Fe	0.213	0.381	0.617	0.853

Despite these complications, point measurements and calculations of dose and dose equivalent are still important for characterizing the radiation environment to which crew members are exposed. In particular the effects of fragmentation can be assessed in terms of the average radiation quality of the field at a particular point behind shielding. In the methodology prescribed by ICRP 60, the average quality factor is given by $< Q > = H/D$, where H is the dose equivalent and D the dose. The dose and dose equivalent are given by

$$D = \frac{1}{\rho}\int \frac{d\Phi}{dL} L dL \text{ and } H = \frac{1}{\rho}\int \frac{d\Phi}{dL} LQ(L) dL$$

where $d\Phi/dL$ is the differential fluence and the quality factor Q is solely a function of the LET, L, and ρ is the density of the target material in units of g cm^{-3}. NASA has revised the ICRP 60 quality factors (34) with separate factors for solid tumors and leukemia. The NASA quality factors depend on the effective charge and velocity of the ion according to (Z^{*2}/β^2), rather than LET, a change intended to represent track structure. However, for ease of calculations, and making use of our existing analysis tools, we use the more familiar ICRP 60 $Q(L)$ in the following. It is also notable that, subsequent to the publication of the revised NASA quality factors, analysis by Borak et al. (35) showed that the (Z^{*2}/β^2) dependences could be re-cast as LET dependences with only minor differences in the results for several space environment scenarios. The study was motivated by practical concerns about the difficulties of accurately measuring ion velocities at relativistic speeds using compact space-borne detectors.

As mentioned above, in free space, $< Q >$ takes on values between 6 and 7, depending on the phase of the solar cycle. Considering that roughly 99% of GCRs are hydrogen or helium nuclei with $Q = 1$, this relatively large average value is remarkable. However, as will be shown in the next section, $< Q >$ can be somewhat reduced by moderate depths of shielding.

Measurements and Calculations for Space

A large body of experimental data has been obtained in LEO, using detectors flown on the Mir Station, Space Shuttle, and the International Space Station (ISS). Historically, many of the measurements have been made using passive detectors, which integrate over all contributions. In the case of LEO, this means passive detectors record a $< Q >$ value that is the dose-averaged combination of the GCR and trapped radiation. This does not provide sufficient information to assess the effect of shielding on GCR $< Q >$ values. For that, we must use data from active detectors, such as DOSTEL (36, 37), that have time resolution

and which, therefore, allow for separate $< Q >$ measurements for GCR and trapped particles. Recent DOSTEL measurements from ISS indicate a GCR $< Q >$ in the vicinity of 3.1 in the Columbus module. This is quite comparable to results obtained by the Radiation Assessment Detector (RAD) detector (38), which measured a $< Q >$ of 3.82 ± 0.25 during the transit for Earth to Mars in 2011–2012 (39) inside the modestly shielded Mars Science Laboratory spacecraft, and a value of 3.05 ± 0.30 on the surface of Mars (40) under somewhat more shielded conditions. Because the dose rate is far less affected by shielding than is dose equivalent (owing mainly to the production of secondary radiation in the shield), the reduction in $< Q >$ is the main benefit of shielding.

Simple model calculations performed with PHITS give us some insight into the important characteristics of the GCR radiation field behind 20 g cm^{-2} of aluminum, which might be a typical shield for a human-crewed vehicle going into deep space. In this example, the GCR was treated as a pencil beam and shot at an aluminum target of the desired depth (7.4 cm). Particles crossing a cylindrical void downstream of the target were scored; the scoring region was 10 cm in diameter, large enough to contain the vast majority of particles emerging in the forward direction from the target. The void was separated from the downstream edge of the target by 1 mm of air, which stops extremely low-energy particles exiting the target. Although the simulated beam geometry, with a small parallel beam and a large detector, is not a realistic representation of the space environment, the scoring region used was large enough to capture the vast majority of particles exiting the target. This was tested with a simulated aluminum target 20 g cm^{-2} in depth; it was found that increasing the lateral dimensions of both the target and scoring regions by factors of two (a factor if 4 increase in areas) increased the number of scored charged particles by 3.3%. A total of 5×10^5 simulated events were run, sufficient to make statistical errors negligible in the analysis. For computing dosimetric quantities, only particles with at least 10 keV/nuc of kinetic energy were scored. (This cut excluded <0.1% of neutrons and about 0.05% of charged particles.)

Initial charge and energy distributions were based on the Badhwar–O'Neill GCR flux model (41), for a solar modulation potential corresponding roughly to average conditions in 2014 and 2015, the most recent (weak) solar maximum. The GCR energy spectrum is harder at solar maximum than at solar minimum, i.e., relatively fewer low-energy ions are present due to the shielding effect of the interplanetary magnetic field. We begin the discussion by re-examining an aspect mentioned above, the re-population of ion species by "feed-down" from fragmentation of heavier ions. **Table 2** shows, for the same ion species shown in **Table 1**, the expected losses due solely to fragmentation (based on energy-independent cross sections as per **Table 1**) and the predicted total attenuation of particle of that species, integrated over all incident energies using a more complete representation implemented in PHITS. The increased attenuation losses compared to those from fragmentation alone come about because some of the lower-energy GCR ions lose all their energy via ionization and come to rest in the shield. The picture of attenuation changes considerably when we consider only high-energy ions, as in the far-right column of **Table 2**. When incident ions with energies below 700 MeV/nuc are excluded (because many of them stop in 20 g cm^{-2} of aluminum), the number of carbon ions found after the target (counting ions of all energies) is actually greater than the number of incident by about 2%. This is due to feed-down from heavier species. There is a weaker, but not negligible, effect for the higher-Z GCRs, e.g., high-energy oxygen ions are only about one-third as depleted as would be expected simply based on fragmentation losses, etc. The results in **Table 2** also include the (presumably small) effects of energy dependence in the nuclear cross sections.

TABLE 2 | Calculated attenuation and re-population of GCR ion species using the PHITS model to simulate transport through aluminum.

Species	Charge-changing interaction probability in 20 g cm^{-2} Al	Attenuation in 20 g cm^{-2} Al (PHITS) including losses from ranging out	Attenuation in 20 g cm^{-2} Al (PHITS), $E_{incident}$ >700 MeV/nuc
C	0.42	0.43	−0.02
O	0.46	0.49	0.17
Mg	0.50	0.59	0.30
Si	0.52	0.61	0.36
Fe	0.62	0.69	0.51

Effects of Fragmentation on Dose and Dose Equivalent

Because a large proportion of GCRs have high energy, they are capable of producing large multiplicities of secondary particles as they traverse a spacecraft hull. These secondary particles are generally lower in LET than the primaries that created them. The net result tends to be (depending somewhat on the shield material and its depth) that dose is only slightly changed by the shield, but dose equivalent may be reduced significantly through the reduction in $< Q >$. **Table 3** shows some results from the simulation described above, with a narrow beam of 10^6 GCR-like ions incident on a 20 g cm^{-2} aluminum target.

The fractional change in dose from charged particles is simply the ratio of the $N \times <L>$ products, which works out to about a 12% decrease. There is an additional contribution to dose and dose equivalent from neutrons. In this example, we estimated the neutron contributions using conversion factors given in ICRP Publication 74 (42), in broad energy bins. The yield of neutrons is large, about 0.5 per incident GCR ion, making the statistical errors in the following quite small. Both dose and dose equivalent contributions of neutrons are on the order of 2% of the totals, so that the overall decrease in dose is roughly 10%. The dose equivalent from all particles behind the target is reduced from the incident dose equivalent by nearly 50%, driven mainly by the

TABLE 3 | Fluence and dose from PHITS simulation of GCRs on 20 g cm^{-2} Al.

	Number of charged particles (N)	Average LET$_\infty$ in water (keV/μm), $<L>$	$N \times <L>$	$< Q >$
Incident beam	10^6	0.700	7.0×10^5	6.55
After Al target	1.16×10^6	0.534	6.2×10^5	3.77

change in $< Q >$. Interestingly, the value of $< Q >$ found in this simulation is very close to the value of 3.8 found during the Mars transit measurement made by MSL-RAD, which was under highly inhomogeneous shielding that averaged roughly 20 g cm^{-2}. The shielding in that instance was a mix of materials, including tanks of hydrazine fuel that powered MSL's descent vehicle.

The PHITS results were checked against the HZETRN code as implemented in the NASA OLTARIS tool (43). HZETRN predicts about a 40% reduction for this depth of aluminum compared to the 50% reduction predicted by PHITS. Dose results showed a qualitatively similar trend, as OLTARIS predicts a 10% increase in dose behind the target. Lastly, OLTARIS predicts a $< Q >$ of 3.5 behind the shield, indicating that the bulk of the disagreement is likely to arise in the simulated multiplicities of low-LET particles, of which OLTARIS predicts a greater number. These drive up dose and to a lesser extent dose equivalent, while driving $< Q >$ to a lower value. The larger dose but smaller $< Q >$ result in nearly equal dose equivalent estimates from the two models.

These results are, in principle, dependent on the GCR flux model used. Even with a given model, results will vary as a function of the solar modulation specified for the calculation. An additional important caveat to the results above is that the simulations lacked a "back wall." That is, the target is followed by the scoring volume, with nothing additional downstream. If a second wall is added (a geometry significantly more like a spacecraft or surface habitat), the effects of neutrons and other particles backscattered from the back wall appear to be significant (44).

NUCLEAR INTERACTIONS OF CARBON BEAMS

The effects of nuclear fragmentation that were elucidated in the discussion of space radiation shielding are, of course, also at work in heavy-ion radiotherapy. Fragmentation of heavy ions reduces $< Q >$ at points behind modest depths of shielding in space, and this is generally desirable. It is, however, an undesirable effect in treatment, where one would like to have the highest possible biological effectiveness at the treatment site. Furthermore, as the above discussion highlighted, hydrogen is uniquely effective in terms of the fragmentation it causes per unit mass, and while this may eventually lead to the use and/or development of hydrogenous shields for space, it means that the high hydrogen content of healthy tissues in the entrance region efficiently fragments treatment beams.

Carbon Beam Bragg Curves

The Bragg curves shown above for 200 and 293 MeV/nuc ^{12}C were simulated, again using PHITS. In these simulations, the beamline geometry has a better correspondence to the treatment situation than does the simulation in which the GCR was treated as a pencil beam. It should be borne in mind that actual treatment planning makes use of spread-out Bragg peaks in order to treat finite tumor volumes. Furthermore, the simulations performed here did not represent the NSRL beamline in great detail. On the real beamline, the incident beam enters through a thin window, traverses an air gap, and enters the first ionization chamber. All ionization chambers have thin but finite entrance and exit windows, as well as foils that are not represented in the simulation, nor are the air gaps. Finally, the beam energy is not known precisely, and is actually inferred from the Bragg curve measurement. The fidelity of the simulation is, therefore, not perfect. Nonetheless, interesting trends are observed, as can be seen starting with **Figure 4**, which shows measured and simulated ionization ratios as a function of polyethylene target depth.

Agreement over the first 7 cm is excellent, but slight deviations begin to appear beyond that point, as the surviving carbon ions and heaviest fragments slow down and approach the ends of their ranges. The peak ratio in the simulation occurs slightly before that in the data (8.06 g cm^{-2} in the simulation, 8.13 g cm^{-2} in the

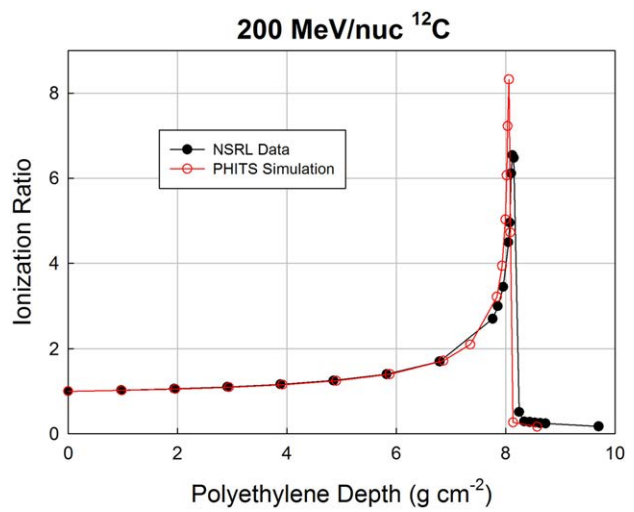

FIGURE 4 | Bragg curve data from NSRL and PHITS simulation for a 200 MeV/nuc ^{12}C beam.

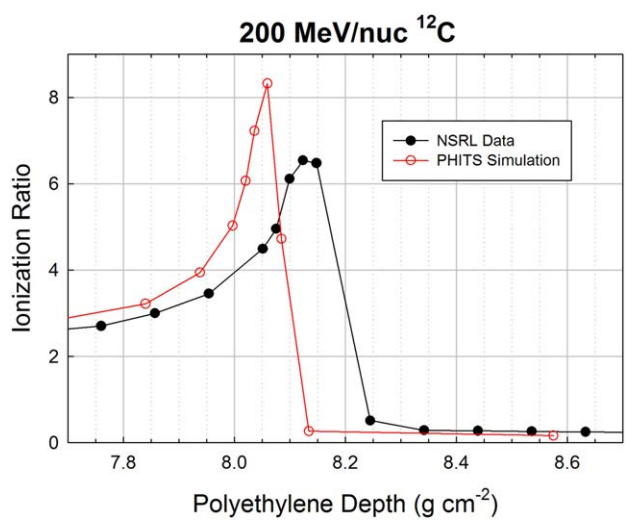

FIGURE 5 | Zoomed-in Bragg curve in the peak region of the 200 MeV/nuc ^{12}C beam.

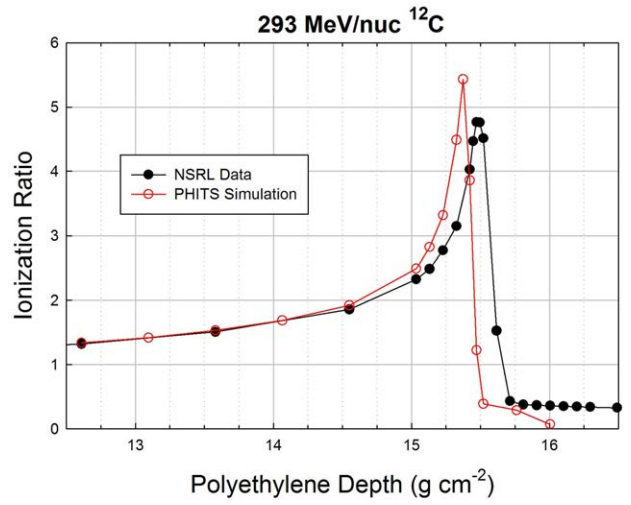

FIGURE 6 | Zoomed-in Bragg curve in the peak region of the 293 MeV/nuc ^{12}C beam.

data), and has a higher value (8.3 vs. 6.5). The discrepancies are more visible in **Figure 5**, which zooms in on the peak region. The distal edge appears to be less populated in the simulation than in the data, which is consistent with the simulation slightly underestimating the probability of fragmentation as the carbon ions traverse the target. If the model had a higher nuclear cross section, it would both reduce the peak value of the ionization ratio and increase the population of fragments in the distal edge.

The location of the simulated peak is slightly offset from the peak location in the data, by <1%. This could easily be an artifact of the inaccuracies of the simulated beamline, and/or a slight difference in beam energy between the nominal 200 MeV/nuc and the actual energy. If the difference between the measurement and simulation is attributable only (or dominantly) to the initial energy, the required extra range would be fully accounted for if the beam energy was 200.5 MeV/nuc, and in fact the NSRL team estimates the beam energy to have been 200.2 MeV/nuc (though 200.0 MeV/nuc was used in the simulation).

Finally, in **Figure 6**, we show data and simulations in a 4-cm region of the Bragg peak region for the 293 MeV/nuc ^{12}C beam. The differences between the data and simulation are qualitatively the same at this energy as at the lower energy: the peak is again slightly shifted to a smaller depth in the simulation (15.37 vs. 15.95 g cm^{-2}) and again has a higher peak value in the simulation (5.43 vs. 4.77). The higher peak values in the simulation vs. data for both ^{12}C energies are likely due to having simulated a perfectly monoenergetic incident beam, whereas the real beam has a finite momentum spread due to the optics of the beamline transport system.

The distal edge, which is populated mostly by hydrogen and helium ions (including a significant share of ^{2}H), falls off much more rapidly in the simulation than in the data. It is possible that the differences in the distal edge could be due to the limited radius of the cylindrical volume used in the simulation to score particles exiting the target, which was set to 10 cm, far wider than the pencil beam diameter (1 cm). Some of the simulated exiting particles were likely more than 10 cm from the beam axis and, hence, were not scored, whereas the actual ionization chambers that were used to obtain the data are much wider.

Our broader purpose here is not to diagnose possible shortcomings in the model or the beamline, but rather to show that even with a fairly crude simulation of the beamline, fragmentation and energy loss effects can be modeled with good fidelity for a therapy beam. The simulations also give insight into the composition of particles in the rising edge, Bragg peak, and distal edge of the beam. The simulations indicate that there are roughly equal numbers of H and He ions in the distal edge, of which the He ions contribute approximately 80% of the dose. In the peak region, about 45% of the charged ions are carbon ions that survive traversal through nearly 16 g cm^{-2}, well in line with the 50% estimate given above, especially since here the total count of particles includes fragments that are generally produced with multiplicities >1. The remaining particles consist of about one-third helium ions, 10% hydrogen ions, 7% boron, with the remainder divided more or less equally between lithium and beryllium. When higher-energy beams are used in treatment, the fraction of carbon ions in the Bragg peak region is even lower than this.

Geometric Cross Sections

A fairly large collection of nuclear cross section data was obtained in our previous experiments. Most but not all results have been published (16, 19–21). Projectiles included ^{4}He, ^{10}B, ^{12}C, ^{14}N, ^{16}O, ^{20}Ne, ^{24}Mg, ^{28}Si, ^{40}Ar, ^{48}Ti, and ^{56}Fe. Target data for H, C, Al, Cu, Sn, and Pb were obtained. Beam energies ranged from 230 to 1200 MeV/nuc, a range in which the approximation of energy-independent cross sections appears to be valid for targets other than H. Data were obtained for both total charge-changing cross sections and fragment production cross sections with no isotopic resolution. Here, we look at the measured charge-changing cross sections in comparison with the Wilson–Townsend formula given above, treating the nuclear radius (nominally 1.26 fm) and the transparency term (nominally 0.2) as adjustable parameters. A series of χ^2 values was calculated for agreement between the data and model, and is shown as a contour plot in **Figure 7** where the color indicates the level of agreement. Though the uncertainties on the charge-changing cross sections are typically on the order of ±3 to 5%, we have inflated them here to ±10% to obtain reasonable χ^2 values on the order of 1 per degree of freedom for the best fits. Clearly, the strong correlation between parameters yields relatively poor constraints. Equally good combinations occur in the range from 1.25 to 1.30 fm with transparency terms varying from 0.2 to 0.4 depending on the nuclear radius value.

For all parameter variations tried here, the majority of the χ^2 comes from data taken with the lighter targets (H, C, Al), while the agreement is substantially better with the heavier targets (Cu, Sn, Pb). If the search for minimum χ^2 is limited to just the light targets, the best-fit parameters are 1.235 fm for the nuclear radius and 0.16 for the transparency term.

A qualitatively similar analysis effort was undertaken by Heckman et al. (45) using nuclear emulsion data, with fits to the most basic form of the Bradt–Peters geometric cross section model. Across a range of projectile/target masses, a consistent

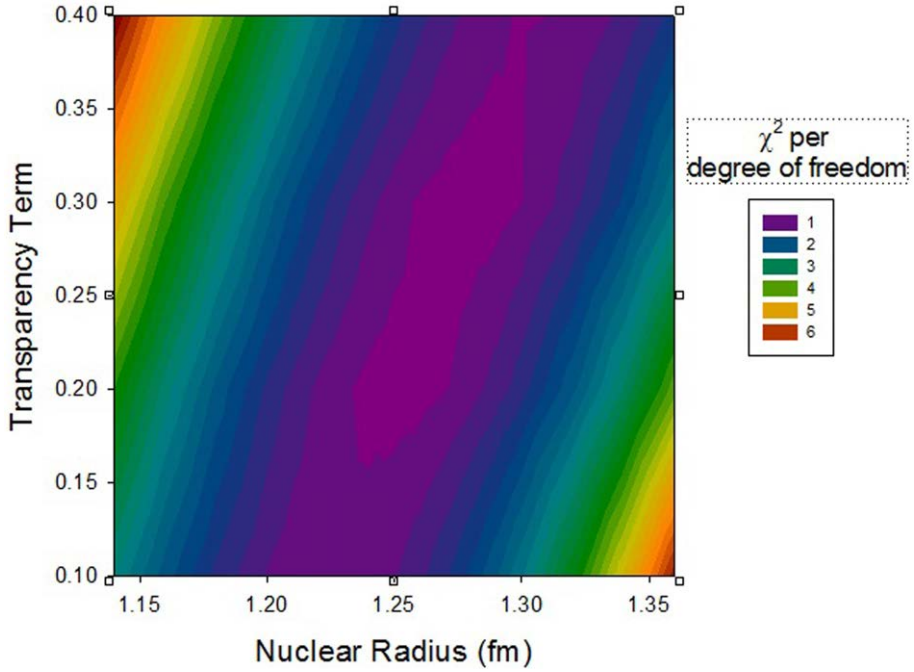

FIGURE 7 | **Contour plot of χ^2 for varying nuclear radius and transparency parameters in the geometric cross section formula**.

value of the nuclear radius, r_0, was found (1.36 ± 0.02 fm), but a highly variable value of b was needed to fit the data. Of particular interest, for ^{4}He projectiles, a very large b of 1.10 ± 0.04 was found, indicating fragmentation cross sections smaller than expected from the geometry of heavier ions. A likely explanation is the tight binding of the nucleons in ^{4}He, so that these ions are less likely than others to break up when undergoing peripheral collisions. In view of the deleterious effects of fragmentation in the treatment setting, this seems to suggest that ^{4}He might be a particularly good ion to use in therapy. The measured charge-changing cross sections on H and C show that the mfp of ^{4}He in polyethylene is 66 g cm^{-2}, so that at a penetration depth of 16 g cm^{-2} (the Bragg peak location of the 290 MeV/nuc ^{12}C beam), some 78% of the ^{4}He is still intact, compared to about 50% for ^{12}C. The corresponding energy for ^{4}He to stop at the same depth is about 155 MeV/nuc. Because of the difference in charge (2 vs. 6), the peak ionization ratio would be expected to be lower than the value of about 5 found for ^{12}C; a PHITS simulation suggests that the peak value would be between 4 and 5. This may be a worthwhile tradeoff given that the lateral and distal doses would be significantly less than they are with carbon beams.

CONCLUSION

Nuclear fragmentation is an important phenomenon both in space radiation protection, where it reduces exposure to heavy ions with high biological effectiveness, and in heavy-ion therapy where it dilutes the effectiveness of the primary beam ion and causes dose to be deposited outside the treatment volume. Previous code comparisons, along with the simulations and comparisons to beam and flight data shown here, give us confidence that current Monte Carlo codes are able to predict the combined effects of fragmentation and energy loss both in space and in carbon ion therapy with good fidelity. The small fragmentation cross section of ^{4}He suggests that it may be a particularly useful ion for therapy.

AUTHOR CONTRIBUTIONS

CZ did the majority of writing and the transport model calculations used in the paper. CT provided the NSRL experimental data and did a significant share of the writing, and proofread and corrected the parts written by CZ. The basic idea for the article grew out of discussions between the two authors about the pitfalls of carbon ion therapy and the quest to find the optimal treatment ion species for radiation therapy.

ACKNOWLEDGMENTS

We thank Drs. A. Rusek and M. Sivertz of Brookhaven National Laboratory for making the Bragg curve measurements at NSRL and for making the data publicly available. We thank Dr. P. Zarubin of the Joint Institute for Nuclear Research for the use of the emulsion photomicrograph used in **Figure 3**, and for valuable discussions. This work was supported at Lockheed Martin by the NASA Health and Human Performance Contract NNJ15HK11B, and at the Brookhaven National Laboratory under NASA contract NNJ07HE781 and the U.S. Department of Energy contract DE-AC-2-98CH10886.

REFERENCES

1. Tommasino F, Durante M. Proton radiobiology. *Cancers (Basel)* (2015) **7**:353–81. doi:10.3390/cancers7010353
2. Norbury JW, Miller J, Adamczyk AM, Heilbronn LH, Townsend LW, Blattnig SR, et al. Nuclear data for space radiation. *Radiat Meas* (2012) **47**:315–63. doi:10.1016/j.radmeas.2012.03.004
3. Mewaldt RA, et al. *Solar-Particle Energy Spectra During the Large Events of October-November 2003 and January 2005, International Cosmic Ray Conference* (Vol. **1**) (2005). p. 111–4.
4. International Commission on Radiological Protection. *ICRP Publication 60: 1990 Recommendations of the International Commission on Radiological Protection. No. 60*. Oxford: Elsevier Health Sciences (1991).
5. Durante M, Cucinotta FA. Physical basis of radiation protection in space travel. *Rev Mod Phys* (2011) **83**(4):1245. doi:10.1103/RevModPhys.83.1245
6. Katz R. RBE, LET and Z* 2/β 2. *Health Phys* (1970) **18**:175.
7. Chatterjee A, Schaefer HJ. Microdosimetric structure of heavy ion tracks in tissue. *Radiat Environ Biophys* (1976) **13**(3):215–27. doi:10.1007/BF01330766
8. Kiefer J, Straaten H. A model of ion track structure based on classical collision dynamics (radiobiology application). *Phys Med Biol* (1986) **31**(11):1201. doi:10.1088/0031-9155/31/11/002
9. Olive KA, Particle Data Group. Review of particle physics. *Chin Phys C* (2014) **38**(9):090001. doi:10.1088/1674-1137/38/9/090001
10. Sihver L, Mancusi D, Sato T, Niita K, Iwase H, Iwamoto Y, et al. Recent developments and benchmarking of the PHITS code. *Adv Space Res* (2007) **40**(9):1320–31. doi:10.1016/j.asr.2007.02.056
11. Bradt HL, Peters B. The heavy nuclei of the primary cosmic radiation. *Phys Rev* (1950) **77**(1):54. doi:10.1103/PhysRev.77.54
12. Townsend LW, Wilson JW. Energy-dependent parameterization of heavy-ion absorption cross sections. *Radiat Res* (1986) **106**:283–7. doi:10.2307/3576735
13. Sihver L, Tsao CH, Silberberg R, Kanai T, Barghouty AF. Total reaction and partial cross section calculations in proton-nucleus ($Z_t \leq 26$) and nucleus-nucleus reactions (Z_p and $Z_t \leq 26$). *Phys Rev C* (1993) **47**(3):1225. doi:10.1103/PhysRevC.47.1225
14. Tripathi RK, Cucinotta FA, Wilson JW. *Universal Parameterization of Absorption Cross Sections*. NASA Technical Paper 3621 Hampton: NASA (1997).
15. Lowenstein DI, Rusek A. Technical developments at the NASA space radiation laboratory. *Radiat Environ Biophys* (2007) **46**(2):91–4. doi:10.1007/s00411-006-0084-x
16. Zeitlin C, Guetersloh S, Heilbronn L, Miller J, Fukumura A, Iwata Y, et al. Fragmentation cross sections of 290 and 400 MeV/nucleon C 12 beams on elemental targets. *Phys Rev C* (2007) **76**(1):014911. doi:10.1103/PhysRevC.76.014911
17. Goldhaber AS. Statistical models of fragmentation processes. *Phys Lett* (1974) **53B**:306. doi:10.1016/0370-2693(74)90388-8
18. Heckman HH. *Proceedings of 5th International Conference on High-Energy Physics and Nuclear Structure, ed. G. Tibell*. Uppsala: Almqvist and Wiksell (1974).
19. Zeitlin C, Fukumura A, Heilbronn L, Iwata Y, Miller J, Murakami T. Fragmentation cross sections of 600 MeV/nucleon ^{20}Ne on elemental targets. *Phys Rev C* (2001) **64**(2):024902. doi:10.1103/PhysRevC.64.024902
20. Zeitlin C, Fukumura A, Guetersloh S, Heilbronn L, Iwata Y, Miller J, et al. Fragmentation cross sections of ^{28}Si at beam energies from to 290 A to 1200 A MeV. *Nucl Phys A* (2007) **784**(1):341–67. doi:10.1016/j.nuclphysa.2006.10.088
21. Zeitlin C, Guetersloh S, Heilbronn L, Miller J, Fukumura A, Iwata Y, et al. Fragmentation cross sections of medium-energy Cl-35, Ar-40, and Ti-48 beams on elemental targets. *Phys Rev C* (2008) **77**:034605. doi:10.1103/PhysRevC.77.034605
22. Zeitlin C. Physical interactions of charged particles for radiotherapy and space applications. *Health Phys* (2012) **103**:540–6. doi:10.1097/HP.0b013e3182611125
23. Bradt HL, Peters B. Investigation of the primary cosmic radiation with nuclear photographic emulsions. *Phys Rev* (1948) **74**(12):1828. doi:10.1103/PhysRev.74.1828
24. Agostinelli S, Allison J, Amako K, Apostolakis J, Araujo H, Arce P, et al. GEANT4 – a simulation toolkit. *Nucl Instrum Methods* (2003) **A506**:250–303. doi:10.1016/S0168-9002(03)01368-8
25. Pelowitz DB. *MCNPX User's Manual Version 2.5.0* (Vol. **76**). Los Alamos: Los Alamos National Laboratory (2005).
26. Fasso A, Ferrari A, Ranft J, Sala PR. *FLUKA: A Multi-Particle Transport Code, CERN-2005-10 (2005)*. INFN/TC_05/11, SLAC-R-773 (2005).
27. Niita K, Sato T, Iwase H, Nose H, Nakashima H, Sihver L. PHITS – a particle and heavy ion transport code system. *Radiat Meas* (2006) **41**(9):1080–90. doi:10.1016/j.radmeas.2006.07.013
28. Wilson JW, Badavi FF, Cucinotta FA, Shinn JL, Badhwar GD, Silberberg R, et al. *HZETRN: Description of a Free-Space Ion and Nucleon Transport and Shielding Computer Program*. Hampton: National Aeronautics and Space Administration, Langley Research Center (1995).
29. Wilson JW, Slaba TC, Badavi FF, Reddell BD, Bahadori AA. Advances in NASA radiation transport research: 3DHZETRN. *Life Sci Space Res* (2014) **2**:6–22. doi:10.1016/j.lssr.2014.05.003
30. Lin ZW, Adams JH, Barghouty AF, Randeniya SD, Tripathi RK, Watts JW, et al. Comparisons of several transport models in their predictions in typical space radiation environments. *Adv Space Res* (2012) **49**(4):797–806. doi:10.1016/j.asr.2011.11.025
31. Wilson JW, Kim M, Schimmerling W, Badavi FF, Thibeault SA, Cucinotta FA, et al. Issues in space radiation protection: galactic cosmic rays. *Health Phys* (1995) **68**(1):50–8. doi: doi:10.1097/00004032-199501000-00006
32. Zeitlin C, Guetersloh S, Heilbronn L, Miller J. Measurements of materials shielding properties with 1 GeV/nuc ^{56}Fe. *Nucl Instrum Methods Phys Res B* (2006) **252**(2):308–18. doi:10.1016/j.nimb.2006.08.011
33. Guetersloh S, Zeitlin C, Heilbronn L, Miller J, Komiyama T, Fukumura A, et al. Polyethylene as a radiation shielding standard in simulated cosmic-ray environments. *Nucl Instrum Methods Phys Res B* (2006) **252**(2):319–32. doi:10.1016/j.nimb.2006.08.019
34. Cucinotta FA, Kim MHY, Chappell L. *Space Radiation Cancer Risk Projections and Uncertainties – 2012*. NASA TP 2013-217375 (2012).
35. Borak TB, Heilbronn LH, Townsend LW, McBeth RA, de Wet W. Quality factors for space radiation: a new approach. *Life Sci Space Res* (2014) **1**:96–102. doi:10.1016/j.lssr.2014.02.005
36. Beaujean R, Kopp J, Burmeister S, Petersen F, Reitz G. Dosimetry inside MIR station using a silicon detector telescope (DOSTEL). *Radiat Meas* (2002) **35**(5):433–8. doi:10.1016/S1350-4487(02)00074-4
37. Berger T, Bilski P, Hajek M, Puchalska M, Reitz G. The MATROSHKA experiment: results and comparison from extravehicular activity (MTR-1) and intravehicular activity (MTR-2A/2B) exposure. *Radiat Res* (2013) **180**(6):622–37. doi:10.1667/RR13148.1
38. Hassler DM, Zeitlin C, Wimmer-Schweingruber RF, Böttcher S, Martin C, Andrews J, et al. The radiation assessment detector (RAD) investigation. *Space Sci Rev* (2012) **170**(1–4):503–58. doi:10.1007/s11214-012-9913-1
39. Zeitlin C, Hassler DM, Cucinotta FA, Ehresmann B, Wimmer-Schweingruber RF, Brinza DE, et al. Measurements of energetic particle radiation in transit to Mars on the Mars Science Laboratory. *Science* (2013) **340**(6136):1080–4. doi:10.1126/science.1235989
40. Hassler DM, Zeitlin C, Wimmer-Schweingruber RF, Ehresmann B, Rafkin SCR, Eigenbrode JL, et al. Mars' surface radiation environment measured with the Mars Science Laboratory's Curiosity rover. *Science* (2014) **343**(6169):1244797. doi:10.1126/science.1244797
41. O'Neill PM, Golge S, Slaba TC. *Badhwar – O'Neill 2014 Galactic Cosmic Ray Flux Model*. NASA/TP 218569 (2015)
42. ICRP. Conversion coefficients for use in radiological protection against external radiation. *Ann ICRP* (1996) **26**:3–4. ICRP Publication 74.
43. Singleterry RC, Blattnig SR, Clowdsley MS, Qualls GD, Sandridge CA, Simonsen LC, et al. OLTARIS: on-line tool for the assessment of radiation in space. *Acta Astronaut* (2011) **68**(7):1086–97. doi:10.1016/j.actaastro.2010.09.022
44. Slaba TC, Clowdsley MS. *Radiation Hazard for Deep Space Human Exploration* (2015). Available from: http://swrc.gsfc.nasa.gov/main/sites/swrc/presentations/2015_NASA_SWx_Workshop/Slaba1_radhazard_gsfc-swrc_sep2015_tcs.pdf

45. Heckman HH, Greiner DE, Lindstrom PJ, Shwe H. Fragmentation of 4He, 12C, 14N, and 16O nuclei in nuclear emulsion at 2.1 GeV/nucleon. *Phys Rev C* (1978) **17**:1735–47. doi:10.1103/PhysRevC.17.1735

Conflict of Interest Statement: The authors declare that the research was conducted in the absence of any commercial or financial relationships that could be construed as a potential conflict of interest.

Copyright © 2016 Zeitlin and La Tessa. This is an open-access article distributed under the terms of the Creative Commons Attribution License (CC BY). The use, distribution or reproduction in other forums is permitted, provided the original author(s) or licensor are credited and that the original publication in this journal is cited, in accordance with accepted academic practice. No use, distribution or reproduction is permitted which does not comply with these terms.

Advantages of publishing in Frontiers

OPEN ACCESS
Articles are free to read, for greatest visibility

COLLABORATIVE PEER-REVIEW
Designed to be rigorous – yet also collaborative, fair and constructive

FAST PUBLICATION
Average 85 days from submission to publication (across all journals)

COPYRIGHT TO AUTHORS
No limit to article distribution and re-use

TRANSPARENT
Editors and reviewers acknowledged by name on published articles

SUPPORT
By our Swiss-based editorial team

IMPACT METRICS
Advanced metrics track your article's impact

GLOBAL SPREAD
5'100'000+ monthly article views and downloads

LOOP RESEARCH NETWORK
Our network increases readership for your article

Frontiers
EPFL Innovation Park, Building I • 1015 Lausanne • Switzerland
Tel +41 21 510 17 00 • Fax +41 21 510 17 01 • info@frontiersin.org
www.frontiersin.org

Find us on